Available online at www.sciencedirect.com
ScienceDirect
Organic Electronics 8 (2007) 1–7
Organic Electronics
www.elsevier.com/locate/orgel

Resonant tunneling transport in highly organized oligoacene assemblies

A. Rochefort *, P. Boyer, B. Nacer [1]

Department of Engineering Physics, École Polytechnique de Montréal and Regroupement québécois sur les matériaux de pointe (RQMP), Montréal, Qué., Canada

Received 1 May 2006; accepted 7 September 2006
Available online 10 November 2006

Abstract

Electronic structure and transport properties of low dimensional organic systems have been theoretically investigated. On isolated molecules, a drastic decrease of the band gap by more than 4.5 eV is observed in acene molecules containing up to 15 members rings. The additional band gap decrease observed upon molecular assembling does not depend on the nature of the molecules but more on the separation between them. Oligoacene assemblies with intermolecular spacing $d_{mol} \leqslant 3.8$ Å are characterized by an improved π-electron coupling that facilitates the electrical transport through resonant tunneling mechanism. For such molecular arrangement, we have computed significant band dispersion (≈340 meV), high transmittance ($\overline{T}(E) \sim 1$), and relatively high mobility for holes and electrons (0.1–0.9 cm^2/V s) in both resonant π-valence and π^*-conduction bands.
© 2006 Elsevier B.V. All rights reserved.

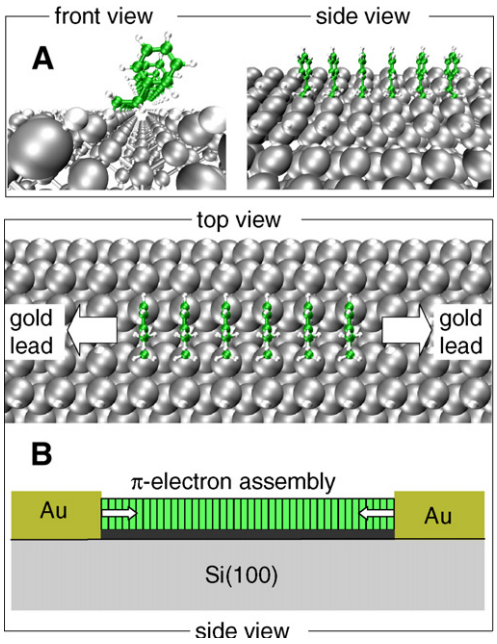
PACS: 31.15.Ct; 31.15.Ew; 73.20.At; 73.61.Ph; 73.63.-b

Keywords: Resonant tunneling; Electron transport; Organic assembly; Mobility; Band gap; Low dimensional systems

The formation of a highly organized molecular structure constitutes a cornerstone in the technological development of high mobility organic semiconductor devices [1]. Among the numerous methods that favor low dimensional molecular organization, there are techniques such as organic chemistry synthesis exploiting intermolecular hydrogen bonding [2] and approaches exploiting self-assembling on metallic or semiconducting surfaces [3]. Through a judicious choice of the surface, this last technique could lead to the creation of a dense and well-organized low dimensional nanostructure [3,4]. A surface such as the hydrogenated Si(1 0 0) is characterized by Si–Si distance of 3.8 Å along the row dimer direction on which organic molecules are self-directed assembled by a chain reaction growth mechanism [3,5]. An example of such organized arrangement is shown at Scheme 1A in which styrene molecules were covalently attached to the Si(1 0 0)[2 × 1] surface along the dimer row direction. Once the conjugated molecules are tightly packed into an organized conformation, we may expect a substantial dispersion of low-energy π-band, and a subsequent

* Corresponding author.
E-mail address: alain.rochefort@polymtl.ca (A. Rochefort).
[1] On leave from University Cadi Ayyad, Faculty of Science and Technology, Department of Physics, Marrakech, Morocco.

1566-1199/$ - see front matter © 2006 Elsevier B.V. All rights reserved.
doi:10.1016/j.orgel.2006.09.006

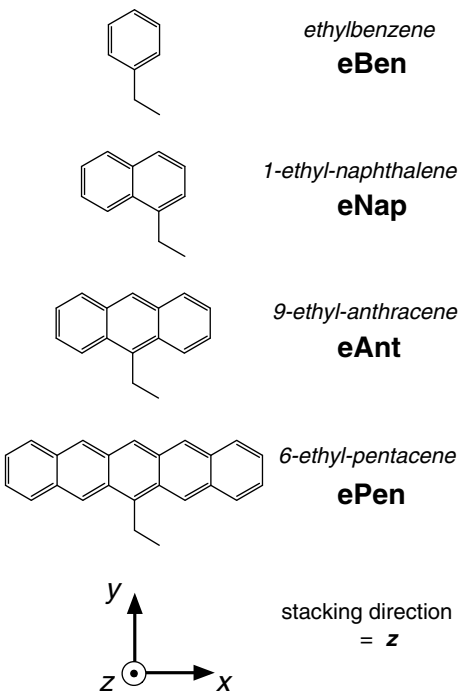


Scheme 1. Self-directed assembly of styrene on the reconstructed H–Si(100)[2 × 1] surface that lead to a well organized structure along the dimer row direction (A). The weak coupling between Si surface states and the low-energy π-electron states which are delocalized over the entire assembly allows the creation of a molecular size conduction channel (B).

improvement of intermolecular electron transport properties [6,7]. This suggests that π-electron transport can be modulated by placing gold electrodes at both ends of the assembly as proposed at Scheme 1B, and where the Si(100) surface is mainly used as a template to attach and organize molecular species.

The simplest and probably the richest existing molecular species to investigate fundamental aspects of π-stacking are small acenes such as naphthalene, anthracene, tetracene, and pentacene assemblies [9]. Most of the previous experimental and theoretical studies on oligoacenes addressed issues related to the electronic structure and transport properties of very good or even perfect crystalline phases in which most of the molecules adopt a herringbone-like structure [9]. Due to the relatively weak intermolecular π-electron coupling, these systems usually have a rather low mobility (10^{-6}–10^{-2} $cm^2/V\,s$) and demonstrate relatively poor switching abilities [10]. Recent interest for pentacene-based systems originates from the significant improvement in the production of good quality single crystals that give much higher mobility (0.1–10 $cm^2/V\,s$) than those of polycrystalline samples [10,11]. Although several excellent works have been performed on well-defined crystals, very few have investigated the electronic properties of stacked oligoacenes into low dimensional nanostructures to study strong π-electron delocalization [12]. In this paper, we present the results of tight-binding and DFT calculations on the electronic and electron transport properties of perfect π-stacked oligoacene wires that could possibly be synthesized on Si(100).

The individual acene molecules studied are shown in Scheme 2 as well as the stacking direction. The ethyl fragment represents the anchoring group that is usually bounded to the silicon surface when a self-directed reaction has been performed. We previously observed that the formation of a covalent Si–C bond between Si(100) and such acene molecule is characterized by a charge transfer that is limited to the first Si and C atoms [13]. In addition, we observed no significant mixing between Si surface states and those related to low-lying π-electron of the assembly. We may then confidently assume that the Si surface does not have a significant electronic effect on the remaining conjugated moiety of interest, and we omit the presence of Si in our calculations. Hence, we are focusing on the perfect oligoacene stacking in which the intermolecular distance is fixed for most cases to 3.8 Å which corresponds to the Si–Si distance between surface atoms in the dimer-row direction of the hydrogenated Si(100) surface.



Scheme 2. Acene molecules considered in the formation of an organized wire and their stacking direction.

Most of the electronic structure calculations were performed within the tight-binding extended Hückel theory (EHT) formalism. The band-like electrical transport properties of 1D structures were computed using Green's function approach [14] within the Landauer–Büttiker formalism. The Hamiltonian and overlap matrices used in this formalism were also obtained from the EHT model that explicitly evaluates overlap matrix elements [15]. The transport properties were evaluated in the stacking direction by placing a gold electrode composed of a plane of 29 Au atoms with (1 1 1) crystal arrangement, at both ends of the stack (d(Au-stack) = 2.0 Å). The metallic contacts consist of a sufficient number of Au atoms to create a large contact area relative to the junction ends, and the short d(Au-stack) distance was chosen to minimize contact resistance [7]. In contrast to bulk materials [16], the influence of the gold electrodes on the electronic structure of such molecular arrangement occurs within the very first connected molecules. For systems containing ten or more molecules, we can confidently place the Fermi energy at the mid-gap of the π-stacked assembly. The electronic structure calculations within the EHT formalism can reproduce, at least qualitatively, for similar molecular species, the results of more accurate computational techniques, such as density functional theory [7,8]. We also used a different approach to qualitatively evaluate mobility of holes and electrons for each oligoacene assembly at room-temperature (298 K). This hopping-mode technique formally used within the polaronic transport regime was previously derived [17] to include the semiclassical Marcus theory [18], the Einstein Smoluchowski equation of diffusive motion [19], and the Einstein relation [19]. For this case, the reorganization energy was computed with the Gaussian 03 package [20] for negative and positive polarons with the UB3LYP functional and a 6-311G** basis set.

Fig. 1 shows the variation of the HOMO–LUMO separation (HLS) or band gap of the different oligoacenes as a function of the number of molecules in the assembly. As a general trend, the HLS decreases as the number of molecules in the assembly increases then reaches a stable value for systems larger than 10 molecular units. This decrease can be easily explained by a progressive evolution from a discrete electronic structure (0D) to a band-like structure (1D) [21]. In addition, a constant decrease of 0.35 eV in HLS from a single molecule to a stable assembly is systematically observed for all the oligoacenes considered. A larger variation is calculated (0.65 eV) for 1-ethyl-naphthalene assembly for shorter intermolecular distance (3.5 Å). This result is directly related to an improved band dispersion that is due to an increasing π-electron overlap between the molecules in the assembly. Finally, the variation of electronic properties of an isolated molecule from ethylbenzene to polyacene is reported in the inset of Fig. 1. From one to eleven benzene rings, we estimate a decrease of 4.45 eV of the HLS value. This change reflects the increasing number of π-electron in longer acene. This variation should progressively converge to the unidimensional band structure limit of polyacene (0.0 eV) if no Peirls distortion occurs [22]. Hence, these results suggest that electronic properties of small oligoacene assemblies can be tailored over a broad range of energy.

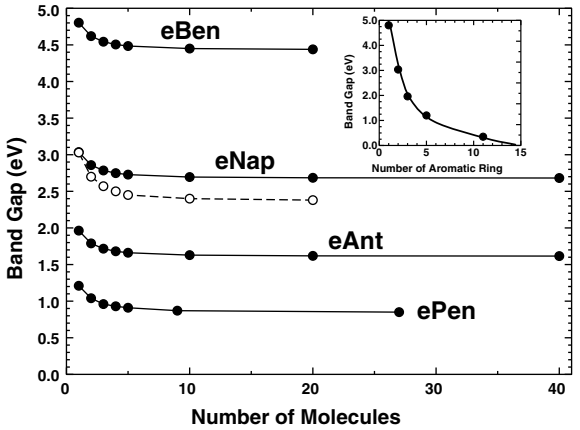


Fig. 1. Variation of the band gap as a function of the number of ethyl-benzene (eBen), 1-ethyl-naphthalene (eNap), 9-ethyl-anthracene (eAnt), 6-ethyl-pentacene (ePen) units in the organic wire. Intermolecular distance was fixed to 3.8 Å except for (eNap) where we also considered 3.5 Å (open circle – dashed line). The inset gives the variation of the HOMO–LUMO separation (band gap) with the number of benzene rings in the isolated molecules.

The electronic structure and transport properties of ethylbenzene (eBen), 1-ethyl-naphthalene (eNap), 9-ethyl-anthracene (eAnt) and 6-ethyl-pentacene (ePen) stacks are compared in Fig. 2. The lower panel shows the density of states of a 10 molecules assembly, while the upper panel gives the calculated transmittance into the different π-resonant channels in the vicinity of Fermi energy (E_F), and the middle panel shows similar results but on a logarithmic scale to emphasize the very large modulation ($>10^{15}$) of the transmittance (conductance) observed in this resonant tunneling transport mechanism. In this mechanism, electrons and holes propagate from

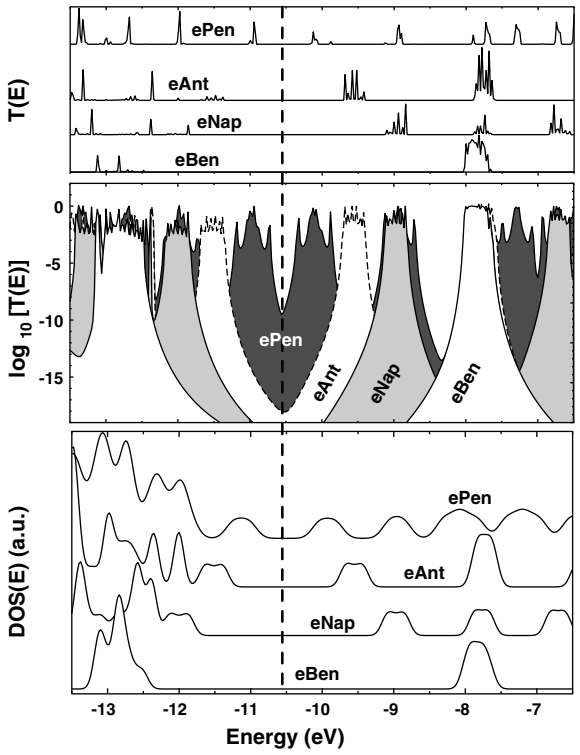


Fig. 2. Electron transport and electronic structure properties of 10 molecules assemblies, ethyl-benzene (eBen), 1-ethyl-naphthalene (eNap), 9-ethyl-anthracene (eAnt), and 6-ethyl-pentacene (ePen) where the intermolecular distance was fixed to 3.8 Å. The upper panel shows the variation of the transmittance while the middle panel shows the results in logarithmic scale. The lower panel gives the density of states (DOS) of the different oligoacene assemblies. Fermi level is indicated by the long vertical dashed line, and is defined with respect to the mid-gap of the assemblies.

a molecule to the next one through a conduction channel which is formed from the combination of π-electron of individual molecules. Hence, molecular π-orbitals combine to form a valence π-stacked band in which the HOMO (top-band) will be an anti-bonding $\pi - \pi = \pi^*$ orbital. Conversely, molecular π^* orbitals mix to form a conduction π-stacked band where the LUMO (bottom-band) is a bonding orbital ($\pi^* + \pi^* = \pi$). Since the molecules in the assembly are not chemically connected but separated by 3.8 Å, and the fact that the only conduction channels available are the π-resonant bands, we can easily understand the very low calculated transmittance at E_F. At this level, the oligoacene assemblies can be considered as a series of individual conductor separated by a 3.8 Å vacuum barrier.

The number and the position of the resonant π-bands are consistent with the calculated density of states (DOS) for the finite 10 units stacks (see Fig. 2) as well as with the periodic 1D band structure (not shown). The upper panel in Fig. 2 shows that the LUMO (conduction) bands give much broader and intense transmittance peaks than the HOMO (valence) bands. The bandwidth of LUMO transmittance peaks is much larger than kT and phonon frequencies. This result suggests that an oligoacene stack would be a better n-type than p-type semiconductor, and where fast band transport can be significant. In addition, the widths of the transmittance peaks of HOMO bands do not appear sufficiently large to expect an efficient band transport: carriers would be strongly perturbed by thermal and vibronic effects [23]. At first glance, this trend sounds surprising since most of experimental works in the field show that active organic materials are hole or p-type semiconductors [24]. Nevertheless, recent works in which specific efforts were deployed to control the chemistry of interfaces show a significantly improved n-type behavior for several organic semiconductors [25].

On the other hand, we are also interested in comparing the band mode conduction to the phonon-assisted hopping mode. In this context, Table 1 gives the calculated values of the interchain transfer integral describing the interaction between adjacent molecules [18], the reorganization energy of negative and positive polarons [27], and the holes and electrons mobilities. The interchain transfer integral which is related to the splittings of the HOMOs for holes (0.4–0.6 eV) and the LUMOs for electrons (0.4–0.5 eV) predicts that holes and electrons might have comparable mobilities in one dimentional stack. The computed reorganization energy for 9-ethyl-anthracene and 6-ethyl-pentacene are in good agreement with those calculated by Coropceanu et al. [17] for anthracene and pentacene molecules. We find that the room-temperature mobility of holes (electrons) increases remarkably from 1.30×10^{-4} cm^2/V s (0.25×10^{-4} cm^2/V s) for ethyl-benzene to 0.91 cm^2/V s (0.68 cm^2/V s) for 6-ethyl-pentacene. The two remaining molecules, 1-ethyl-naphthalene and 9-ethyl-anthracene, have intermediate mobilities. We should emphasized that the calculated mobilities remain a qualitative description of transport properties. Nevertheless, although we have used two different theoretical approaches, both predict very promising transport properties for these small oligoacene assemblies.

In addition to the hopping mode where intramolecular deformations contribute to the transport mechanism, more specifically through a polaronic

Table 1
Estimated values of transfer integrals, reorganization energies, and mobilities for ethyl-benzene, 1-ethyl-naphthalene, 9-ethyl-anthracene and 6-ethyl-pentacene

	Transfer integral (eV)		Polaron reorganization energy (eV)		Mobility ($cm^2/V\,s$)	
Molecule	Hole	Electron	Positive	Negative	Hole	Electron
Ethyl-benzene (eBen)	0.06	0.04	0.98	1.06	0.13×10^{-3}	0.25×10^{-4}
Ethyl-naphthalene (eNap)	0.05	0.04	0.18	0.26	0.48	0.12
Ethyl-anthracene (eAnt)	0.05	0.05	0.16 (0.14)	0.20 (0.20)	0.62	0.38
Ethyl-pentacene (ePen)	0.04	0.04	0.10 (0.10)	0.12 (0.13)	0.91	0.68

The values from the work of Coropceanu et al. [17] are in parenthesis.

defect, we have investigated the influence of the internal structure of the assembly on the band-like transport. For the eNap assembly, we studied the influence of both intermolecular spacing and molecular arrangement within the assembly on their electronic and transport properties. For an assembly of ten molecules, Fig. 3 shows the variation of the band gap in the upper panel, and the fluctuation of transmittance in the lower panel. First, we can clearly see that a compression of the molecular stack contributes to improve π-electron overlap, to increase the dispersion of the π-bands, and to dramatically decrease the HLS. Hence, a compression of 10% within the assembly improves significantly the band dispersion and decreases the band gap by a factor of approximately 2. This result is in agreement with our previous findings on molecular π-stacked system [7], and with other theoretical works on compressed organic crystal [26]. Consequently, these electronic structure changes have a profound impact on the transport where the width and intensity of transmittance peaks drastically increase, more especially for a perfect stacking arrangement.

Besides what is previously shown, more drastic changes are observed when different stacking patterns are considered. In the deformed eNap assembly (see Fig. 3), the molecules were rotated from one to the next by 180° relatively to the ethyl–naphthalene bond or the *y*-axis (see Scheme 1). In this conformation, only one of the two benzene rings is well-aligned along the stacking direction. As a consequence, the π-coupling between molecules decreases as well as the variation in HLS with the number of stacked molecules. It is interesting to note from Fig. 3 that the change in HLS for this deformed eNap stack (0.12 eV) is significantly smaller than the calculated one for an eBen stack (0.35 eV), even though both stacked assemblies have a benzene ring aligned in the stacking direction. A similar picture can be drawn from the transport calculations where three transmission peaks are still observed in the deformed eNap assembly but with smaller intensities and narrower peaks. We can interpret these changes by noting that individual

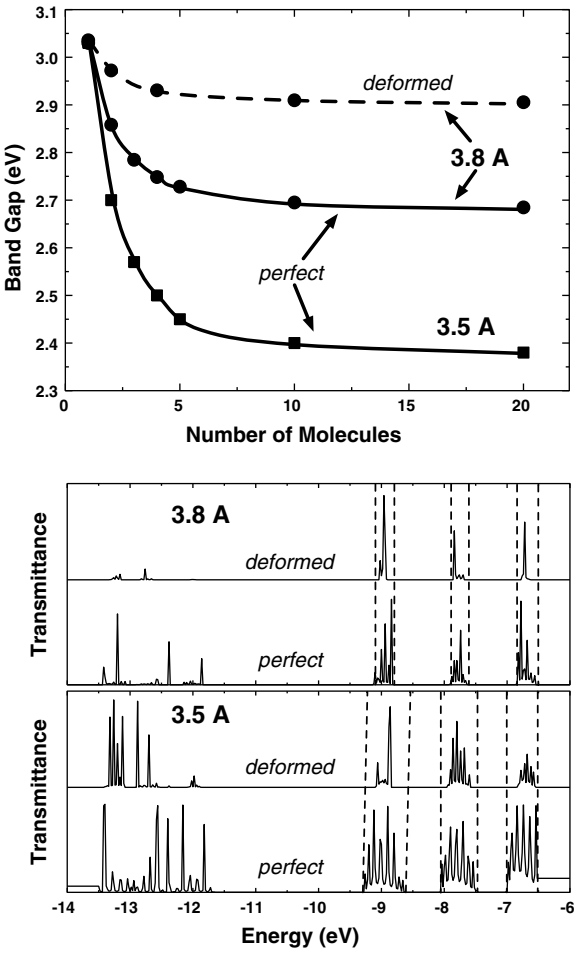


Fig. 3. Influence of molecular conformation and packing density on the electronic and electron transport properties of 1-ethyl-naphthalene assembly. Deformed structure is an assembly in which a successive 180° molecular rotation was considered. The upper panel shows the variation of the band gap as a function of the number of molecular units in the wire. The lower panel gives transmittance for a 10 molecules stack in which the intermolecular distance and the internal structure have been modified.

molecular wavefunction are not drastically perturbed by intermolecular coupling. Delocalized π-wavefunction in isolated molecule remains strongly delocalized once molecules are stacked. It is then clear that a good portion of π-electron in LUMO (HOMO) is not directly participating in the formation of a well-delocalized intermolecular wavefunction over the entire assembly. We may then anticipate the existence of a relatively weak π-electron coupling due to the weak and partial orbital overlap, and finally to a weak dispersion of π-bands in extended systems with such molecular conformation.

In summary, a systematic decrease of 0.35 eV in the band gap is observed in highly organized 1D stacked oligoacene assemblies, independently of the molecular unit. The intermolecular π-electron coupling provides new conduction channels where fast band transport could occur through resonant tunneling mechanism. The agreement found between band-like and charge-hopping results in the transport calculations shows that small oligoacene assemblies would present an interesting source of organic semiconductor. The electronic structure properties can be tailored through the chemical composition of the oligoacene assembly. In highly organized molecular arrangement, we have computed significant band dispersion (≈340 meV), high transmittance ($\overline{T}(E) \sim 1$), and relatively high mobility for holes and electrons (0.1–0.9 $cm^2/V\,s$).

Acknowledgements

This work was supported by the Natural Sciences and Engineering Research Council of Canada (NSERC), and the Ministère du Développement économique et régional (MDER). We are grateful to the Réseau québécois de calcul haute performance (RQCHP) for providing computational facilities. PB thanks NSERC, GCM and École Polytechnique for financial support during this work. BN acknowledges the financial support provided by GCM-RQMP during his sabbatical.

References

[1] D.R. Gamota, P. Brazis, K. Kalyanasundaram, J. Zhang, Printed Organic and Molecular Electronics, Kluwer Academic, Boston, 2004.

[2] (a) M.L. Bushey, A. Hwang, P.W. Stephens, C. Nuckolls, J. Am. Chem. Soc. 123 (2001) 8157;
(b) M.L. Bushey, T.-Q. Nguyen, C. Nuckolls, J. Am. Chem. Soc. 125 (2003) 8264;
(c) M.L. Bushey, A. Hwang, P.W. Stephens, C. Nuckolls, Angew. Chem. Int. Ed. 41 (2002) 2828.

[3] G.P. Lopinski, D.D.M. Wayner, R.A. Wolkow, Nature 406 (2000) 48.

[4] G.A. DiLabio, P.G. Piva, P. Kruse, R.A. Wolkow, J. Am. Chem. Soc. 126 (2004) 16048.

[5] M.R. Linford, P. Fenter, P.M. Eisenberger, C.E.D. Chidsey, J. Am. Chem. Soc. 117 (1995) 3145.

[6] (a) H. Sirringhaus, P.J. Brown, R.H. Friend, M.M. Nielsen, K. Bechgaard, B.M.W. Langeveld-Voss, A.J.H. Spiering, R.A.J. Janssen, E.W. Meijer, P. Herwig, D.M. de Leeuw, Nature 401 (1999) 685;
(b) H. Sirringhaus, R.J. Wilson, R.H. Friend, M. Inbasekaran, W. Wu, E.P. Woo, M. Grell, D.D.C. Bradley, Appl. Phys. Lett. 77 (2000) 406.

[7] A. Rochefort, R. Martel, P. Avouris, Nano Lett. 2 (2002) 877.

[8] A. Rochefort, D.R. Salahub, Ph. Avouris, J. Phys. Chem. B 103 641 (1999).

[9] (a) Y.C. Cheng, R.J. Silbey, D.A. da Silva Filho, J.P. Calbert, J. Cornil, J.L. Brédas, J. Chem. Phys. B 118 (2003) 3764;
(b) J.L. Brédas, D. Beljonne, V. Coropceanu, J. Cornil, Chem. Rev. 104 (2004) 4971.

[10] C.D. Dimitrakopoulos, D.J. Mascaro, IBM J. Res. Dev. 45 (2001) 11.

[11] (a) M. Halik, H. Klauk, U. Zschieschang, G. Schmid, C. Dehm, M. Schütz, S. Maisch, F. Effenberger, M. Brunnbauer, F. Stellacci, Nature 431 (2004) 963;
(b) R. Ruiz, D. Choudhary, B. Nickel, T. Toccoli, K.C. Chang, A.C. Mayer, P. Clancy, J.M. Blakely, R.L. Headrick, S. Iannotta, G. Malliaras, Chem. Mater. 16 (2004) 4497.

[12] R.C. Haddon, X. Chi, M.E. Itkis, J.E. Anthony, D.L. Eaton, T. Siegrist, C.C. Mattheus, T.T.M. Palstra, J. Phys. Chem. B 106 (2002) 8288.

[13] A. Rochefort, A. Beausoleil, Chem. Phys. Lett. 400 (2004) 347.

[14] (a) S. Datta, in: Electronic Transport in Mesoscopic Systems, Cambridge University Press, Cambridge, UK, 1995;
(b) A. Rochefort, Ph. Avouris, F. Lesage, D.R. Salahub, Phys. Rev. B 60 (1999) 13824.

[15] G. Landrum, YAeHMOP (Yet Another Extended Hückel Molecular Orbital Package), Cornell University, Ithaca, NY, 1995.

[16] F. Amy, C. Chan, A. Kahn, Org. Elect. 6 (2005) 85.

[17] V. Coropceanu, M. Malagoly, D.A. da Silva, N.E. Gruhn, T.G. Bill, J.L. Brédas, Phys. Rev. Lett. 89 (2002) 275503.

[18] V. Balzani, A. Juris, S. Campagna, S. Serroni, Chem. Rev. 96 (1996) 759.

[19] P.W. Atkins, Physical Chemistry, fourth ed., Oxford University Press, Oxford, 1990.

[20] M.J. Frisch, G.W. Trucks, H.B. Schlegel, G.E. Scuseria, M.A. Robb, J.R. Cheeseman, J.A. Montgomery Jr., T. Vreven, K.N. Kudin, J.C. Burant, J.M. Millam, S.S. Iyengar, J. Tomasi, V. Barone, B. Mennucci, M. Cossi, G. Scalmani, N. Rega, G.A. Petersson, H. Nakatsuji, M. Hada, M. Ehara, K. Toyota, R. Fukuda, J. Hasegawa, M. Ishida, T. Nakajima, Y. Honda, O. Kitao, H. Nakai, M. Klene, X. Li, J.E. Knox, H.P. Hratchian, J.B. Cross, V. Bakken, C. Adamo, J. Jaramillo, R. Gomperts, R.E. Stratmann, O. Yazyev, A.J. Austin, R. Cammi, C. Pomelli, J.W. Ochterski, P.Y. Ayala, K. Morokuma, G.A. Voth, P. Salvador, J.J. Dannenberg,

V.G. Zakrzewski, S. Dapprich, A.D. Daniels, M.C. Strain, O. Farkas, D.K. Malick, A.D. Rabuck, K. Raghavachari, J.B. Foresman, J.V. Ortiz, Q. Cui, A.G. Baboul, S. Clifford, J. Cioslowski, B.B. Stefanov, G. Liu, A. Liashenko, P. Piskorz, I. Komaromi, R.L. Martin, D.J. Fox, T. Keith, M.A. Al-Laham, C.Y. Peng, A. Nanayakkara, M. Challacombe, P.M.W. Gill, B. Johnson, W. Chen, M.W. Wong, C. Gonzalez, J.A. Pople, Gaussian 03, Revision B.05, Gaussian Inc., Wallingford CT, 2004.

[21] The bandwidth of all periodic oligoacenes stacks obtained from 1D band structure calculations is $\sim$0.35 eV for both HOMO (π) and LUMO (π^*) bands.

[22] S. Kivelson, E.L. Chapman, Phys. Rev. B 28 (1983) 7236.

[23] P.A. Derosa, J.M. Seminario, J. Phys. Chem. B 105 (2001) 471.

[24] C.D. Dimitrakopoulos, P.R.L. Malenfant, Adv. Mater. 14 (2002) 99.

[25] L.L. Chua, J. Zaumseil, J.F. Chang, E.C.W. Ou, P.K.H. Ho, H. Sirringhaus, R.H. Friend, Nature 434 (2005) 194.

[26] P. Puschnig, C. Ambrosch-Draxl, G. Heimel, E. Zojer, R. Resel, G. Leising, M. Kriechbaum, W. Graupner, Synthetic Met. 116 (2001) 327.

[27] T. Keszthelyi, G. Balakrishnan, R. Wilbrandt, W.A. Yee, F. Negri, J. Phys. Chem. A 104 (2000) 9121.

Available online at www.sciencedirect.com
ScienceDirect
Organic Electronics 8 (2007) 8–13
Organic Electronics
www.elsevier.com/locate/orgel

A study of charge transport in a novel electroluminescent poly(phenylene vinylene-co-fluorenylene vinylene) based π-conjugated polymer

Chellappan Vijila [a,*], Almantas Pivrikas [b], Huang Chun [a], Chen Zhikuan [a], Ronald Österbacka [b], Chua Soo Jin [a]

[a] *Institute of Materials Research and Engineering, Opto and Electronics Systems, 3 Research Link, Singapore 117 602, Singapore*
[b] *Department of Physics and Centre for Functional Materials, Åbo Akademi University, Turku, Finland*

Received 18 July 2006; received in revised form 28 September 2006; accepted 2 October 2006
Available online 26 October 2006

Abstract

The charge transport properties in a novel electroluminescent poly{[2-(4′,5′-bis(3″-methylbutoxy)-2′-*p*-methoxy-phenyl)phenyl-1,4-phenylene vinylene]-co-(9,9-dioctyl-2,7-fluorenylene vinylene)} (BPPPV-PF) have been studied using a time-of-flight (TOF) photoconductivity technique. The TOF transients for holes were recorded over a range of temperatures (207–300 K) and electric fields (1.5×10^5–6.1×10^5 V/cm). The hole transport in this polymer was weakly dispersive in nature with a mobility at 300 K of 5×10^{-5} cm^2/V s at 2.5×10^5 V/cm. This increased to 8.4×10^{-5} cm^2/V s at 6.1×10^5 V/cm. The temperature and field dependence of charge mobility has been analyzed using the disorder formalisms (Bässler's Gaussian disorder model (GDM) and correlated disorder model (CDM)). The fit with Gaussian disorder (GDM) model yielded the mobility pre-factor $\mu_\infty = 1.2 \times 10^{-3}$ cm^2/V s, energetic disorder parameter $\sigma = 82$ meV and positional disorder parameter $\Sigma = 1.73$. The average inter-site separation ($a = 7$ Å) and the charge localization length ($L = 3.6$ Å) was estimated by assuming the CDM type charge transport. The microscopic charge transport parameters derived for this polymer are almost identical to the reported values for fully conjugated polymers with high chemical purity. The results presented indicate that the charge transport parameters can be controlled and optimized for organic optoelectronic applications.
© 2006 Elsevier B.V. All rights reserved.

Keywords: Charge transport; Conjugated polymers; PPV derivatives; Time-of-flight photoconductivity; Gaussian disorder model

1. Introduction

Light emitting π-conjugated polymers have attracted significant research interest for display applications due to their ease of processing and flexibility in synthesis. Poly(*p*-phenylene vinylene) (PPV) and its derivatives have excellent electroluminescence properties and have been widely used for polymer light emitting diode (PLED) applications [1–3]. For the development of practical PLEDs with a high quantum efficiency, low operating voltage, and long lifetime, it is required to design processable conjugated polymers with high chemical purity, photoluminescence (PL) efficiency,

* Corresponding author. Tel.: +65 6874 8355; fax: +65 6872 0785.
E-mail address: c-vijila@imre.a-star.edu.sg (C. Vijila).

1566-1199/$ - see front matter © 2006 Elsevier B.V. All rights reserved.
doi:10.1016/j.orgel.2006.10.002

good thermal and oxidation stability, and balance of charge carrier mobility. Some of these can be satisfied by introducing long side chains to the polymer backbone or by controlling the levels of highest occupied molecular orbital (HOMO)/lowest unoccupied molecular orbital (LUMO) energies through chemical modification. For example, the introduction of electron donating or an electron withdrawing side groups to the polymer backbone or interruption of conjugation length through copolymerization techniques can modify solubility and permit tuning of the emission color as well as control of charge carrier mobility [4–7]. Although significant progress has been made on the performance of PPV based PLEDs, there are still a number of issues that need to be solved in order to realize efficient devices with long lifetime [8–10]. The efficiency and operational stability of the devices mainly depend on the behaviour of charge carriers in the active polymer layer; the chemical and structural disorder in the polymer film leads to charge carrier build up in the device and in turn leads to device degradation. It has been reported that the structural defects in PPV derivatives strongly depend on the substitution pattern to the polymer backbone [11]. The biphenylyl substituted PPVs have negligibly small structural disorders compared to other PPV derivatives and thus, they are promising materials for PLEDs with higher efficiency and longer operational lifetime. The degree of disorder in the polymer film can be estimated by investigating their charge transport properties; hence, a thorough understanding of the structure–charge transport properties in these classes of polymers has direct applications to the further development of polymer technology.

Recently, we have reported the charge mobility characteristics of a series of novel biphenylyl substituted PPV derivatives [12]. These PPV derivatives were promising for PLED applications. In this report, we designed an alternating PPV copolymer by introducing a fluorenyl group into the PPV backbone and studied their charge transport properties using the time-of-flight (TOF) photoconductivity technique [13]. The electric field and temperature dependence of charge mobility have been analyzed within the framework of disorder formalisms and obtained the parameters governing the charge transport properties in this polymer. The charge transport parameters obtained are compared with the reported values for the structurally related conjugated polymers.

2. Experimental

2.1. Materials

The copolymer was synthesized by using the Gilch polymerization method [11,14]. A solution of the co-monomer of 2-(4′,5′-bis(3″-methylbutoxy)-2′-*p*-methoxy-phenyl)phenyl-α,α′-dichloro-*p*-xylene and 2,7-dichloromethyl-9,9-dioctylfluorene in anhydrous tetrahydrofuran was added into a solution of 1 M potassium *tert*-butoxide in anhydrous tetrahydrofuran at room temperature with stirring for 24 h, after which 4-(*tert*-butyl)benzyl chloride in tetrahydrofuran was added in one portion. After stirred for another 6 h, the reaction mixture was precipitated in methanol. The resulting yellow precipitates were collected by filtration and dissolved in toluene and reprecipitated from a mixture solvent of methanol and water for two times. The collected polymer was extracted through Soxhlet extractor using methanol followed by acetone to afford poly{[2-(4′,5′-bis(3″-methylbutoxy)-2′-*p*-methoxyphenyl)phenyl-1,4-phenylene vinylene]-co-(9,9-dioctyl-2,7-fluorenylene vinylene)} (BPPPV-PF). The chemical structure of the polymer is shown in Fig. 1.

2.2. Measurements

The polymer was dissolved in chloroform (concentration: 4 mg/ml) and the films were prepared by drop casting onto quartz substrate for the spectral measurements. The absorption and photoluminescence spectra were recorded using a Shimadzu UV 3101PC UV–Vis spectrophotometer and a Perkin Elmer LS 50B luminescence spectrometer, respectively.

For TOF measurements, a thick film of BPPPV-PF was prepared by drop casting technique from chloroform solution (concentration: 4 mg/ml) onto an indium tin oxide (ITO) covered glass slide. The thickness of the polymer film was determined using a surface profiler (KLA-Tencor P10 surface profiler) and found to be 3.29 μm. The TOF measurement system was composed of a pulsed Nd:YAG laser (Quantel Brilliant) operating at the third harmonic generation (wavelength: 355 nm, pulse width <4 ns, pulse repetition rate 1 Hz), a pulse generator (SRS-DG535), a voltage source and a digital oscilloscope (Tekronix, TDS 680B). The sample was housed in a temperature controlled continuous flow cryostat under a vacuum of $\sim 10^{-5}$ mbar. The sample was illuminated from the ITO side of the device and the

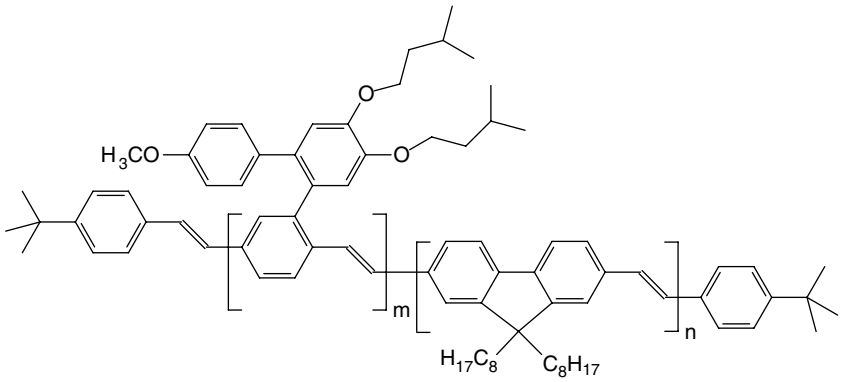


Fig. 1. Chemical structure of the copolymer (BPPPV-PF).

photocurrent under the influence of applied electric field was monitored across a variable resistor ($R = 50\ \Omega$ to $1\ k\Omega$) using an oscilloscope. Care has been taken to ensure that the time constant of the setup is less than the transit time ($RC < t_t$). The laser excitation intensity was adjusted in order to avoid the space charge effects.

3. Results and discussion

The absorption and PL spectrum of the polymer film is shown in Fig. 2. The absorption spectrum shows a broad structure-less band with a maximum at 375 nm (3.3 eV). The PL spectrum was recorded by exciting the sample at 375 nm and the spectrum shows a maximum at 508 nm (2.44 eV) with weak vibronic shoulders at around 537 nm (2.3 eV) and at 574 nm (2.16 eV). The large shift between the absorption and PL spectral maxima indicates the conformational changes in the photo-excited state and/or large spectral diffusion of the excitons through the long conjugated chains. However, the vibronic features and the spectral position of the PL spectrum vary largely with the film morphology, and this is dominated by the film processing conditions. The absence of well-resolved vibronic features in the absorption spectrum precludes the straightforward determination of the Stokes shift of BPPPV-PF copolymer. The band gap of the polymer is found to be ~2.5 eV. The relative photoluminescence quantum efficiency of this polymer in chloroform solution was found to be 42%.

The TOF photocurrent transients for holes were recorded using ITO/polymer interface as the charge carrier generation layer. The linear plots of TOF transients at 300 K are shown in Fig. 3(a) and the respective double logarithmic plots are shown in Fig. 3(b). The transit times were obtained from the inflection points in a double logarithmic plot of photocurrent versus time. The mobilities of the charges were calculated using the relation $\mu = d^2/Vt_{tr}$, where d is the polymer film thickness, V is the applied voltage and t_{tr} is the transit time. It is found that the TOF

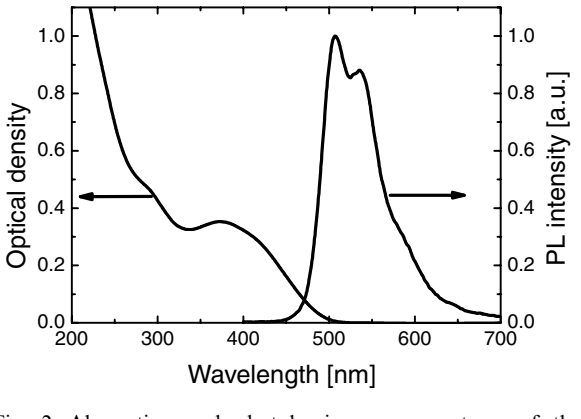


Fig. 2. Absorption and photoluminescence spectrum of the polymer film.

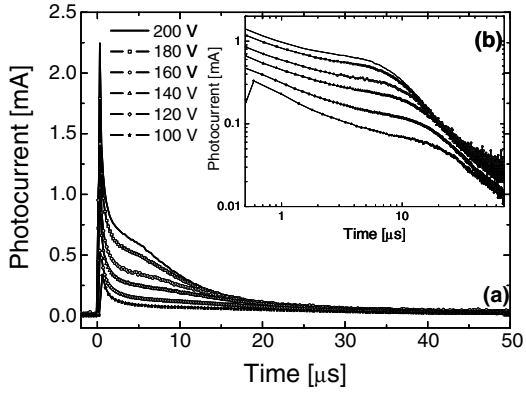


Fig. 3. (a) Linear plots of TOF hole transients in BPPPV-PF film at $T = 300$ K for different applied voltages, film thickness $d = 3.29$ μm. (b) Inset: log–log plot of (a).

transients for holes show dispersive nature of transport for a range of temperatures from 207 K to 300 K. The hole mobility at 300 K was found to be 5×10^{-5} cm^2/V s at an applied electric field of 2.5×10^5 V/cm. To enable the comparison of this value with that of other structurally related polymers, hole mobility values under the same applied electric field were extracted from literature. The hole mobility of this polymer (BPPPV-PF) is approximately one order of magnitude higher than the value reported for MEH-PPV (1.7×10^{-6} cm^2/V s at 2.5×10^5 V/cm) [15], and one order of magnitude smaller than that reported for poly (9,9-dioctylfluorene) (PFO) ($\sim 3 \times 10^{-4}$ cm^2/V s at 2.5×10^5V/cm) [16]. This supports a hypothesis, that the introduction of fluorenyl group to the PPV backbone increases the hole mobility by increasing the rigidity of the backbone.

In order to gain more insight into the hole transport properties of BPPPV-PF, the electric field dependence of hole mobility was studied for a range temperatures from 207 K to 300 K. It was found that the electric field dependence of hole mobility follows the Pool–Frenkel (PF) form [17]:

$$\mu = \mu_{(E=0)} \exp(\gamma E^{1/2}) \tag{1}$$

where $\mu_{(E=0)}$ is the zero field mobility and γ is the slope of the field dependence of charge mobility. Fig. 4 shows the dependence of hole mobility with applied electric field for various temperatures, the solid lines in Fig. 4 are the linear fits according to the Eq. (1). The parameters μ_0 and γ are extracted from the fit and plotted against temperature to further understand the charge transport mechanism in this polymer. It was found that the zero field mobility (μ_0) increases with increasing temperature and the slope

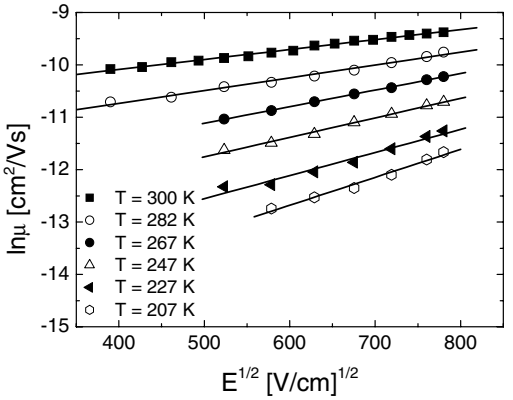


Fig. 4. Variation of the TOF-hole mobility in BPPPV-PF with applied electric field and temperature T, the solid lines are the linear fits according to Eq. (1).

(γ) of the $\ln \mu$ versus $E^{1/2}$ plot decreases with increasing temperature. This behaviour is typical for hopping transport in disordered organic solids.

It is well known that charge transport in disordered organic materials can be described as hopping in a in-homogeneously broadened Gaussian density of localized states, where positional disorder between hopping sites lead to energy disorder. Using the simplest possible model (GDM) Bässler showed that the mobility can be expressed in a functional form as [18]

$$\mu_{\mathrm{GDM}} = \mu_\infty \exp\left[-\left(\frac{2\sigma}{3kT}\right)^2\right] \times \exp\left[C\left\{\left(\frac{\sigma}{kT}\right)^2 - \Sigma^2\right\}E^{1/2}\right] \tag{2}$$

where μ_∞ is the high temperature limit of the mobility, σ is the energetic disorder parameter, Σ is the positional disorder parameter, and C is an empirical constant which reflects the hopping distance that a charge carrier has to overcome to be transferred from one site to another. The energetic disorder parameter σ arises from the distribution of conjugation lengths, while the positional disorder parameter Σ arises from the fluctuations of intermolecular distances or morphological variations. Fig. 5 shows the dependence of logarithmic zero field mobility (μ_0) against $10^6/T^2$, the solid line is a linear fit according to Eq. (2). The parameters obtained from the fit are $\mu_\infty = 1.2 \times 10^{-3}$ cm^2/V s, $\sigma_{\mathrm{GDM}} = 82$ meV. The variation of γ with $(\sigma/kT)^2$ is shown in Fig. 6(a), the parameters Σ and C are obtained from the linear fit and found to be $\Sigma = 1.7$ and $C = 3 \times 10^{-4}$ (cm/V)$^{1/2}$. The obtained values are in good agreement with the values reported for structurally related conjugated polymers.

However, in the GDM model no correlation between the sites is included. It has been argued by Novikov et al. [19] that long-range correlations due to charge–dipole interaction do exist leading to the so called correlated disorder model (CDM). In CDM the mobility can be expressed as

$$\mu_{\mathrm{CDM}} = \mu_\infty \exp\left[-\left(\frac{3\sigma}{5kT}\right)^2\right] \times \exp\left[0.78\left\{\left(\frac{\sigma}{kT}\right)^{3/2} - 2\right\}\sqrt{\frac{eaE}{\sigma}}\right] \tag{3}$$

where a is the inter-site spacing. This model accounts for the charge–dipole interactions in the materials which gives rise to $\ln(\mu) \propto \sqrt{E}$ behaviour

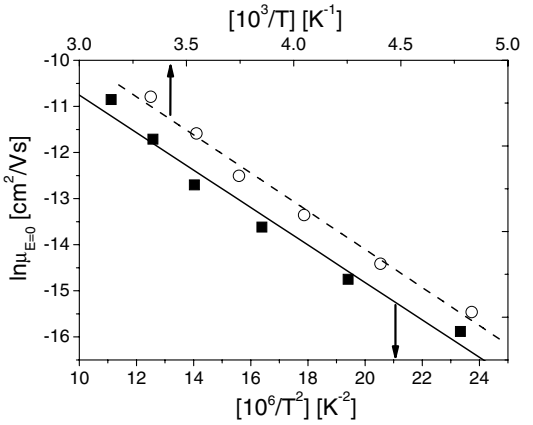


Fig. 5. Temperature dependence of the logarithmic zero field mobility (μ_0) in BPPPV-PF: the plot of $\ln(\mu_0)$ versus $10^6/T^2$ is shown in squares and $\ln(\mu_0)$ versus $10^3/T$ is shown in circles; the solid and dashed lines are the linear fits according to Bässler's GDM model and Arrhenius representation ($\mu = \mu_0 \exp(-\Delta E/kT)$), respectively.

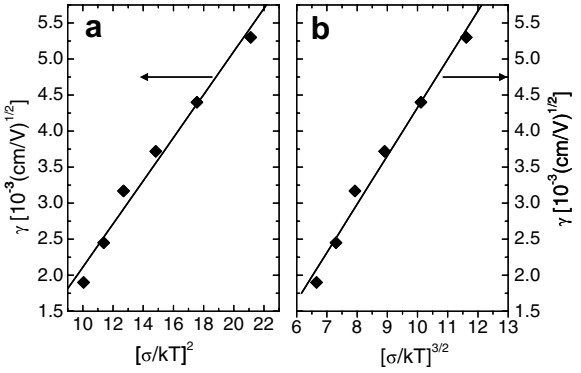


Fig. 6. (a) The slope of the field dependence of mobility (γ) versus $(\sigma/KT)^2$, the solid line is a linear fit according to Eq. (3). (b) The slope of the field dependence of mobility (γ) versus $(\sigma/KT)^{3/2}$, the solid line is a linear fit according to Eq. (4).

over a much broader field range. The difference between the Eqs. (3) and (4) is the predicted temperature dependence of γ. The variation of γ with $(\sigma/kT)^{1.5}$ is shown in Fig. 6(b) and the average site separation a can be obtained from the linear plot according to relation (4). The estimated average site separation 'a' was found to be 7 Å. The energetic disorder parameter σ_{CDM} was calculated from the dependence of logarithmic zero field mobility (μ_0) against $10^6/T^2$ plot (shown in Fig. 5) according to Eq. (3) and found to be 91.5 meV and μ_∞ value was found to be 1.2×10^{-3} cm^2/V s. Using the derived values of σ_{CDM}, μ_∞ and a, the localization length for charges has been estimated using the relation [20]

$$\mu_\infty = \frac{ea^2 \upsilon_{ph}}{\sigma} \exp(-2a/L) \quad (4)$$

where υ_{ph} is phonon frequency for hopping ($\sim 10^{12}$ s^{-1}) and the localization length L estimated was found to be $\sim$3.6 Å. According to the comparative study of hole transport in PPV derivatives reported by Martens et al. [20], the microscopic charge transport parameters obtained for BPPPV-PF is comparable with the parameters obtained for structurally regular, chemically pure conjugated polymer.

The charge transport parameters obtained by fitting the temperature and field dependence of charge mobility using various charge transport models have been summarized in Table 1. Within the temperature range studied, it is not possible to distinguish the dependence of $\ln(\mu_0) \propto -(T_0/T)^2$ from the Arrhenius behaviour: $\mu = \mu_0 \exp(-\Delta E/kT)$ (shown in Fig. 5). The zero field activation energy of $\Delta E = 29$ eV was calculated from the Arrhenius fit. However the mobility pre-factor obtained from the Arrhenius fit does not agree with the values reported for related conjugated polymers. It has also been shown in the literature that the Gaussian disorder formalism is widely accepted to describe the basic features of charge transport in most of the conjugated polymers [21]. Therefore the obtained charge transport parameters based on Gaussian disorder formalisms have been considered for further discussion and the values are compared with the reported values for the structurally related conjugated polymers. The values of mobility pre-factor ($\mu_\infty = 1.2 \times 10^{-3}$ cm^2/V s) and the inter-site hopping constant ($C = 3 \times 10^{-4}$ (cm/V)$^{1/2}$) obtained for BPPPV-PF is in good agreement with the predictions of the Bässler's GDM [22]. The inter-site hopping constant (C) extracted for this polymer (BPPPV-PF) is approximately one order of

Table 1
The charge transport parameters obtained from the fit of temperature and field dependence of charge mobility according to the charge transport models

Charge transport model	Charge transport parameters	BPPPV-PF
Gaussian disorder model	$\mu_{\infty,GDM}$ [cm^2/V s]	1.2×10^{-3}
	C (cm/V)$^{1/2}$	3×10^{-4}
	σ_{GDM} (meV)	82
	Σ	1.73
Correlated disorder model	$\mu_{\infty,CDM}$ [cm^2/V s]	1.2×10^{-3}
	σ_{CDM} (meV)	91.5
	a (Å)	7
	L (Å)	3.6

magnitude smaller than the value reported for MEH-PPV (1.7×10^{-3} (cm/V)$^{1/2}$) [15], but very similar to the value reported for PFO ($\sim 2.5 \times 10^{-4}$ (cm/V)$^{1/2}$) [16]. This indicates the electronic overlap between the adjacent chain segments is effective and is consistent with the large mobility pre-factor obtained for this polymer. It is known that PPVs with bulky biphenylyl substituents can hardly form good packing between polymer backbones. However, the overlapping between the conjugated biphenylyl side chains might be the most possible hopping site for charge transport from one polymer chain to another chain. The average hopping distance for BPPPV-PF is found to be 7 Å. This is consistent with the inter-chain distance (6–8 Å) value reported for the stretch aligned PPV [6].

It is important to note that the BPPPV-PF copolymer shows a weakly dispersive nature of hole transport although the width of the energy disorder ($\sigma_{GDM} = 82$ meV) in this polymer is smaller than the values reported for MEH-PPV ($\sigma_{GDM} = 86$ meV) and for PFO ($\sigma_{GDM} = 103$ meV). The film thickness ($d = 3.29$ μm) may not be enough to reach quasi-equilibrium in BPPPV-PF, which is seen from the transients that show more plateau-like behaviour at higher electric fields. It has been shown in the literature [23–25] that the structural inhomogeneities in the film morphology can significantly alter the nature of charge transport. Hence the observation of weakly dispersive nature of charge transport in BPPPV-PF polymer is attributed to the complex film morphology, the size and distribution of the ordered and non-ordered regions in the thick BPPPV-PF film may be the origin for the dispersion. It can also account for the observation of the $\ln \mu \propto 1/T$ dependence rather than the predicted $1/T^2$ dependence.

4. Conclusion

The charge transport properties of a novel electroluminescent BPPPV-PF copolymer were studied using a TOF photoconductivity method. The dependence of charge mobility on applied electric field and temperature has been analyzed using Gaussian disorder formalisms. The microscopic charge transport parameters were extracted and compared with the reported values for the structurally related conjugated polymers. The results indicate that the charge transport parameters for BPPPV-PF copolymer can be controlled and optimized for organic optoelectronic applications.

Acknowledgement

We gratefully acknowledge Mr. Jeff Gray for valuable discussions.

References

[1] J.H. Burroughes, D.D.C. Bradley, A.R. Brown, R.N. Marks, K. Mackay, R.H. Friend, P.L. Burn, A.B. Holmes, Nature 347 (1990) 539.
[2] Y. Cao, I.D. Parker, G. Yu, C. Zhang, A.J. Heeger, Nature 397 (1999) 414.
[3] H. Becker, H. Spreitzer, W. Kreuder, E. Kluge, H. Schenk, I. Parker, Y. Cao, Adv. Mater. 12 (2000) 42.
[4] S.H. Lee, T. Yasuda, T. Tsutsui, J. Appl. Phys. 95 (2004) 3825.
[5] E. Lebedev, Th. Dittrich, V. Petrova-Koch, S. Karg, W. Brutting, Appl. Phys. Lett. 71 (1997) 2686.
[6] H. Meyer, D. Hararer, H. Naarmann, H.H. Horhold, Phys. Rev. B 52 (1995) 2587.
[7] R.H. Friend, R.W. Gymer, A.B. Holmes, J.H. Burroughes, R.N. Marks, C. Taliani, D.D.C. Bradley, D.A. Dos Santos, J.L. Brédas, M. Lögdlund, W.R. Salaneck, Nature 397 (1999) 121.
[8] Z.K. Chen, W. Huang, L.H. Wang, E.T. Kang, B.J. Chen, C.S. Lee, S.T. Lee, Macromolecules 33 (2000) 9015.
[9] I.N. Kang, D.H. Hwang, H.K. Shim, T. Zyung, J.J. Kim, Macromolecules 29 (1996) 165.
[10] D.M. Johansson, G. Srdanov, G. Yu, M. Theander, O. Inganas, M.R. Anderssson, Macromolecules 33 (2000) 2525.
[11] Z.-K. Chen, N.H.S. Lee, W. Huang, Y.S. Xu, Y. Cao, Macromolecules 36 (2003) 1009.
[12] Vijila Chellappan, Bavani Balakrisnan, Chun Huang, Zhi-Kuan Chen, Chang-Gua Zhen, Mark Dai Joong Auch, Soo Jin Chua, Chem. Phys. Lett. 414 (2005) 393.
[13] P.M. Borsenberger, D.S. Weiss, Organic Photoreceptors for Xerography, Marcel Dekker, New York, 1993.
[14] Chun Huang, Chang-Gua Zhen, Siew Ping Su, Chellappan Vijila, Bavani Balakrisnan, Mark Dai Joong Auch, Kian Ping Loh, Zhi-Kuan Chen, Polymer 47 (2006) 1820.
[15] A.R. Inigo, C.H. Tan, W. Fann, Y.S. Huang, G.Y. Perng, S. Chen, Adv. Mater. 13 (2001) 504.
[16] M. Redecker, D.D.C. Bradley, M. Inbasekaran, E.P. Woo, Appl. Phys. Lett. 73 (1998) 1565.
[17] W.D. Gill, J. Appl. Phys. 43 (1972) 5033.
[18] H. Bässler, Phys. Status Solidi B 175 (1993) 15.
[19] S.V. Novikov, D.H. Dunlap, V.M. Kenkre, P.E. Parris, V. Vannikov, Phys. Rev. B 81 (1998) 4472.
[20] H.C.F. Martens, P.W.M. Blom, H.F.M. Schoo, Phys. Rev. B 61 (2000) 7489.
[21] S.J. Martin, A. Kambili, A.B. Walker, Phys. Rev. B 67 (2003) 165214.
[22] D. Hertel, H. Bässler, U. Scherf, H.H. Horhold, J. Chem. Phys. 110 (1999) 9214.
[23] A.R. Inigo, H.C. Chiu, W. Fann, Y.S. Huang, U.S. Jeng, T.L. Lin, C.H. Hsu, K.Y. Peng, S.A. Chen, Phys. Rev. B 69 (2004) 075201.
[24] A.V. Rakhmanova, E.M. Conwell, Appl. Phys. Lett. 76 (2000) 3822.
[25] A.J. Mozer, Niyazi Sariciftci, Chem. Phys. Lett. 389 (2004) 438.

Available online at www.sciencedirect.com
ScienceDirect
Organic Electronics 8 (2007) 14–20
Organic Electronics
www.elsevier.com/locate/orgel

Energy level alignment regimes at hybrid organic–organic and inorganic–organic interfaces

Slawomir Braun [a,*], Wojciech Osikowicz [a], Ying Wang [b], William R. Salaneck [a]

[a] Department of Physics, Chemistry and Biology – IFM, Linköping University, S-581 83 Linköping, Sweden
[b] E. I. DuPont de Nemours and Co., Inc., P.O. Box 80356, Experimental Station, Wilmington, DE 19880-0356, United States

Received 10 May 2006; received in revised form 9 October 2006; accepted 9 October 2006
Available online 10 November 2006

Abstract

Ultraviolet photoelectron spectroscopy has been used to determine the energy level alignment at interfaces of molecular hole-transporting materials and various conductive substrates. Depending on the work function of the substrate, ϕ_s, a transition between two different energy level alignment regimes has been observed: namely vacuum level alignment and Fermi level pinning. The transition is associated with spontaneous positive charge transfer across the interface to the organic semiconductors above a certain material-specific threshold value of ϕ_s. The charge transfer results in formation of an interfacial dipole of a magnitude that scales with ϕ_s. In the vacuum level alignment regime, the hole-injection barriers scale linearly with ϕ_s, while in the Fermi level pinning regime, these barriers are constant and independent of ϕ_s.
© 2006 Elsevier B.V. All rights reserved.

PACS: 71.20.Rv; 73.20.−r; 73.30.+y; 79.60.−i

Keywords: Energy level alignment; OLED; Hole-transporting materials; Interfaces; Photoelectron spectroscopy; Hole-injection barrier

1. Introduction

Thin film architecture of organic light emitting diodes (OLEDs) encompasses multiple inorganic–organic and organic–organic junctions, the properties of which have a strong impact on device performance. For this reason, much of the effort in organic electronics has been focused on understanding and modification of the electronic properties of the interfaces [1–5]. The most common inorganic–organic interface is comprised of a conductive electrode and an organic hole (electron) transporting layer, often denoted as the HTL (ETL) [6]. At such interfaces, the magnitude of the barrier for charge injection depends on the energy level alignment between the Fermi level of the electrode and the highest (lowest) occupied (unoccupied) molecular orbital HOMO (LUMO) of the transport layer. Under the assumption of common vacuum levels (Shottky-Mott limit) the estimates of the hole-injection barrier E_V^F can be made when ionization potential (IP) of an HTL and the work function (ϕ_s) of an anode are known (see Fig. 1a). Often, due to formation of chemical bonds, charge transfer or a "push-back" effect, the interfacial dipole is formed

* Corresponding author.
E-mail address: slmar@ifm.liu.se (S. Braun).

1566-1199/$ - see front matter © 2006 Elsevier B.V. All rights reserved.
doi:10.1016/j.orgel.2006.10.006

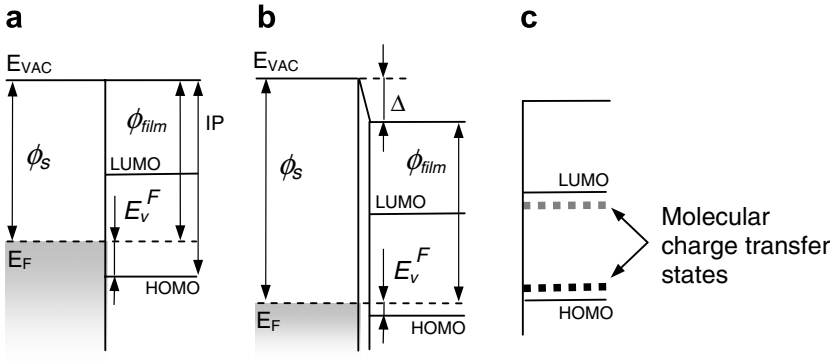


Fig. 1. Energy level diagram for interfaces of organic semiconductor and conducting substrate: (a) vacuum level alignment, (b) vacuum level shift and (c) molecular charge transfer states.

[1,2,5,7,8], which manifests itself as a vacuum level offset (denoted as Δ). This, in turn, negates the assumption inherent in the Shottky-Mott limit and affects E_V^F accordingly, thus determining the magnitude of Δ, as shown in Fig. 1b. Therefore, in the process of developing OLEDs this effect must be taken into account.

The benefit of a good match between electrode work function ϕ_s and the IP of an HTL may be hindered by a negative vacuum level shift that occurs at the corresponding interface. Such a shift pushes the occupied electronic levels away from the substrate Fermi level. This effect seems to be particularly significant for the interfaces with reactive or high work function, atomically clean metal surfaces, *i.e.*, metals with a large surface dipole contribution to the work function [7,9,10]. Polymer-based high work function materials, such as the common electrically conducting polymer PEDOT-PSS [or poly(3,4-ethylenedioxythiophene)-poly(styrene sulfonic acid)], have been reported to lead towards more favorable energy level alignment with hole transporting materials [8,11]. However, significant vacuum level shifts, preventing reduction of hole-injection barrier, have been observed also for polymeric substrates [10].

To gain further understanding of this phenomenon, we have studied the energy level alignment at various interfaces of several common HTL materials and several organic and inorganic substrates. To keep consistency between the substrates, all of them were air exposed (not atomically clean), hence passivated by the presence of hydrocarbons. The molecules chosen span a wide range of IP: CBP (4,4′-*N*,*N*′-dicarbazolyl-biphenyl), IP = 6.1 eV; NPB (*N*,*N*′-bis-(1-naphthyl)-*N*,*N*′-diphenyl1-1,1-biphenyl 1-4,4-diamine), IP = 5.35 eV; and *m*-MTDATA (4,4,4″-tris[3-methyl-phenyl(phenyl) amino]triphenylamine), IP = 5.0 eV. The corresponding chemical structures are depicted schematically in Fig. 2. A range of inorganic and organic materials was chosen for substrates to span wide variation of work functions. In particular, a novel high work function polymer blend PEDOT-PFESA [or poly(3,4-ethylenedioxythiophene)-poly(perfluoroethylene sulfonic acid)] provides substrates with a work function as high as 5.8 eV [12]. Note, that the work function of PEDOT-PFESA exceeds the IPs of *m*-MTDATA

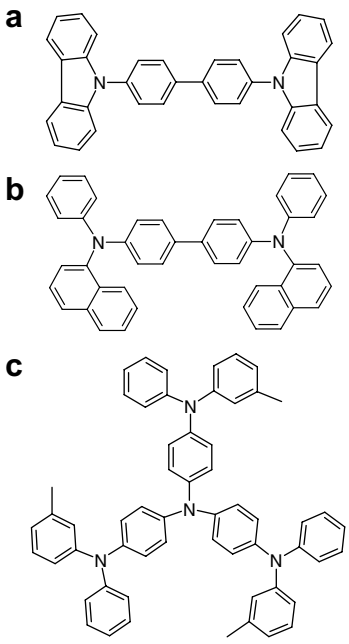


Fig. 2. Chemical structures of the organic molecules studied: (a) CBP, (b) NPB and (c) *m*-MTDATA.

and NPB, which, within Shottky-Mott limit, should correspond to barrier-less injection.

2. Experimental

The various interfaces have been prepared *in situ* under ultra high vacuum (UHV) conditions by physical vapor deposition of the molecular materials. The molecules: CBP (99.9% purity), NPB (99.9% purity), *m*-MTDATA (99.9% purity) were prepared at DuPont. The molecules were evaporated from resistively heated glass Knudsen cell and condensed onto the substrates held at room temperature. The pressure in the vacuum chamber during the growth of the molecular films never exceeded 3×10^{-9} mbar. The deposition rate was set to approximately 3 Å/min, as calibrated from the attenuation of Au(4f) core level line of the substrate, measured by X-ray photoelectron spectroscopy (XPS). The following substrates were used in the study: (as-received) aluminum (with a thin native oxide), $\phi_s = 3.75$–3.85 eV; silicon (with a thin native oxide), $\phi_s = 4.0$–4.1 eV; and gold, $\phi_s = 4.5$ eV; indium tin oxide $\phi_s = 4.5$ (as-received) and cleaned in detergent (Neutracon), acetone and isopropanol, $\phi_s = 4.8$ eV; PEDOT-PSS, $\phi_s = 5.0$–5.2 eV [13]; and PEDOT-PFESA. In case of PEDOT-PFESA, the dispersions with pH 5.2 and pH 1.9 were used, which provided films with work functions of 5.4 eV and 5.8 eV, respectively. The water dispersions of the polymeric materials were obtained from Bayer and Dupont, respectively. The polymeric substrates were prepared by spin coating on ITO.

Ultraviolet photoelectron spectroscopy (UPS) was employed to examine the correlation between the substrate work function and the energy level alignment at the interfaces of HTL. This technique is especially suited for such studies, since it enables direct probing of the occupied valence electronic levels as well as the vacuum levels, and therefore also vacuum level shifts, upon forming the interface. The value of ionization potential (IP) is measured as the onset of HOMO edge versus vacuum level [14]. UPS measurements were performed using monochromatized HeI radiation ($h\nu = 21.2$ eV) in a spectrometer of our own design and construction [15]. The measurement sequence involved characterization of the bare substrates followed by stepwise deposition and characterization of molecular add-layers.

Hole-only devices were fabricated by thermal evaporation of organics and aluminum on patterned indium tin oxide (ITO) coated glass substrates. The ITO thickness is 1400 Å with a sheet resistance of 30 Ω/square. The ITO substrates were cleaned ultrasonically in aqueous detergent solution and rinsed with distilled water. They were subsequently cleaned ultrasonically in acetone, rinsed with isopropanol, and dried in a stream of nitrogen. Immediately before device fabrication the cleaned ITO substrates were treated with O_2 plasma for 3 min. After film deposition, the devices were encapsulated with a glass lid, sealed with epoxy in an argon-filled glove box. *I–V* curves of the encapsulated devices were measured with a Keithley Source Measure Unit.

3. Results and discussion

Fig. 3 shows the dependence of the effective work function of the molecular organic layers (ϕ_{film}) as a function of the known work function of the substrates (ϕ_s), measured by UPS. For values of the substrate work function, ϕ_s, that fall within the intrinsic HOMO–LUMO energy gap of the molecular film, the effective work function of the organic over layer, ϕ_{film}, follows the work function of the substrate (Schottky-Mott limit). The so-called interface slope parameter $S = dE_V^F/d\phi_s$ [16], which is often use to characterize the energy level alignment at the interface, is then unity. The hole-injection barrier follows the changes in the substrate work function. However, when the Fermi level of the substrate approaches energy of HOMO, charge transfer

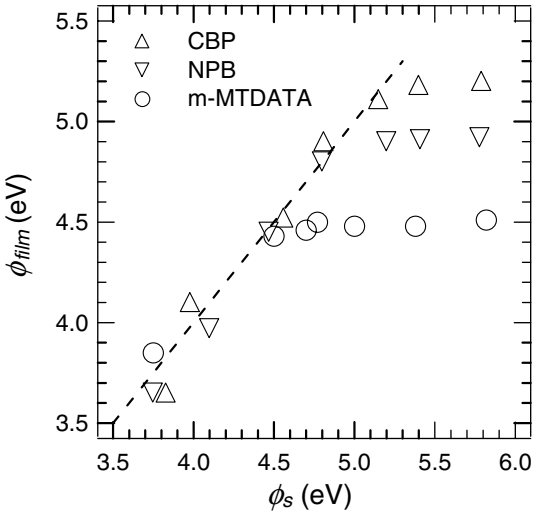


Fig. 3. The work function of the molecular organic layers (ϕ_{film}) versus the work function of the substrates (ϕ_s).

across the interface results in formation of interfacial dipole Δ. In turn, further increase in ϕ_s does not affect ϕ_{film}, instead stronger interfacial dipole is formed. Consequently, the barrier E_V^F remains constant with respect to ϕ_s (slope parameter $S = 0$) and the Fermi level of the substrate remains within the HOMO–LUMO energy gap. Actually, the Fermi level is pinned at a charge transfer state that lies in the vicinity of HOMO energy, as illustrated in Fig. 1c. Note that these charge transfer states would be equivalent to so-called polaronic states in conjugated polymers [17]. The details of the observation that lead to the picture discussed in the paragraph above are presented below.

As shown in Fig. 4, a substantial reduction in the energy difference between the HOMO of NPB and the Fermi level of the substrate is observed for increasing ϕ_s. The barrier for hole-injection decreases from 1.75 eV in the case of Al_xO_y (ϕ_s = 3.75 eV) down to 0.5 eV for ITO ($\phi_s = 4.8$ eV). Within the substrate work function range from 3.75 eV to 4.8 eV, interfaces follow Schottky-Mott limit. The observed energy level alignment indicates a lack of significant interactions at the corresponding interfaces, and is likely related to the inert character of the surfaces of the substrates. This is in apparent contrast to the atomically clean metallic substrates. As reported by Koch et al. [8], deposition of NPB on sputtered-cleaned gold ($\phi_s = 5.1$ eV) results in a negative vacuum level shift of 1.15 eV, and the formation of a hole-injection barrier as large as 1.4 eV. In the case of the NPB/gold interface reported here, no offset in vacuum level is measured, and the hole-injection barrier of 0.9 eV is significantly smaller than that for atomically clean gold. This is in agreement with the recent study by Wan et al. who reported that the contaminated Au substrate with work function ($\phi_s = 4.7$ eV) gives lower injection barrier than the atomically clean Au substrate. The reason for these differences lies in presence of the thin (0.5–1 ML) layer of hydrocarbons on the surface [18], which decreases surface-dipole contribution to the work function of the gold substrate [7]. For such substrate the tail of electrons spilling out from the metal surface into the vacuum is minimized. The important implications are as follows: (i) the initial work function of the substrate ϕ_s is lower (with respect to atomically clean substrate) and corresponds predominantly to the bulk contribution; (ii) the push-back effect is not significant when the film of the organic semiconductor is present, since there is very little (if any) surface contribution to the ϕ_s. Note that these results are important in device fabrication where physical vapour deposition (PVD) is not done under UHV conditions.

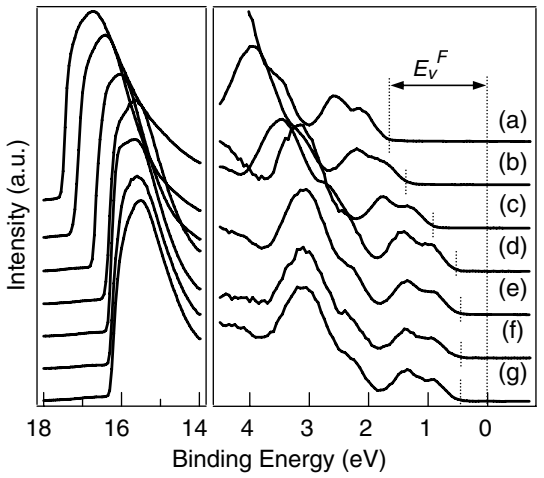


Fig. 4. UPS spectra of thin film of NPB deposited on: (a) aluminum/aluminum oxide – $\phi_s = 3.75$ eV, (b) silicon/silicon oxide – $\phi_s = 4.1$ eV, (c) gold – $\phi_s = 4.5$ eV, (d) ITO – $\phi_s = 4.8$ eV, (e) PEDOT-PSS – $\phi_s = 5.2$ eV, (f) PEDOT-PFESA – $\phi_s = 5.4$ eV, (g) PEDOT-PFESA – $\phi_s = 5.8$ eV. The spectra are referred to the Fermi level of spectrometer at zero binding energy. Hole-injection barrier E_V^F is schematically drawn as the gap between the Fermi level and the leading edge of HOMO.

Within the Shottky-Mott limit, a further increase of the work function of the substrates would lead to further improvement in hole-injection. However, for NPB on PEDOT-PSS ($\phi_s = 5.2$ eV), a substantial deviation from Schottky-Mott limit occurs. In this case, a downward vacuum level shift of 0.3 eV is observed. The hole-injection barrier height changes with respect to that of ITO only by 0.1 eV and is equal to 0.4 eV. This value agrees well with results reported earlier [8]. For large ϕ_s, the magnitude of Δ increases with increasing ϕ_s of the substrates. For interfaces of NPB and PEDOT-PFESA ($\phi_s = 5.4$ eV and 5.8 eV), the values of Δ are −0.5 eV and −0.9 eV, respectively. Meanwhile, HOMO onset stays pinned at the constant distance of about 0.4 eV from the Fermi level, as shown in Fig. 4. In this range of work functions the slope parameter S abruptly changes from unity to zero. The threshold value of ϕ_s, which separates region of so called Fermi level pinning from that of Shottky-Mott limit, is found at about 4.9 eV.

This conclusion is consistent with the I–V data from hole-only devices. We compared the injected current from ITO and PEDOT-PFESA substrates

to NPB using the following hole-only devices: (a) ITO/NPB(200 nm)/Al(100 nm); and (b) ITO/PEDOT-PFESA(50 nm)/NPB(200 nm)/Al(100 nm). In these devices, electron injection from Al to NPB is not feasible due to the high barrier (Al work function – 4.0–4.5 eV; NPB LUMO – 1.4 eV) [19]. The work function for oxygen plasma cleaned ITO is nominally about 4.8 eV. PEDOT-PFESA with a work function of 5.4 eV was deposited by spin-coating, dried, and then moved into vacuum chamber for NPB deposition. The I–V curves for these samples are shown in Fig. 5. We observed only slightly more current injected from PEDOT-PFESA to NPB in spite of its higher work function of 5.4 eV. Based on the HOMO value of 5.35 eV for NPB, we expect ohmic injection from PEDOT-PFESA to NPB. In this regime, the space-charge-limited current (J_{SCLC}) obeys the Mott–Gurney equation, $J_{SCLC} = (9/8)\varepsilon\varepsilon_0\mu V^2/d^3$, where ε is the dielectric constant, ε_0 is the vacuum permittivity, μ is the carrier mobility, V is the applied voltage, and d is the device thickness. At field strength of 4×10^5 V/cm (8 V), taking the mobility of NPB to be 4×10^{-3} cm^2/(V s) (the average of literature reported values [20,21]), dielectric constant to be 3 (typical range for organic is 3–10), J_{SCLC} should be about 10 A/cm^2. The observed current density of PEDOT-PFESA/NPB is only 0.11 A/cm^2, which is about two orders-of-magnitude smaller than the expected space-charged-limited current if injection were ohmic. This result is consistent with the conclusion of UPS study, that the hole-injection barrier at PEDOT-PFESA/NPB interface decreases only slightly (~0.1 eV) with respect to that of ITO/NPB (from 0.5 eV to 0.4 eV). For a purely injection-limited current, a 0.1 eV reduction in barrier would cause ~50 fold increase in current which is not what we observed in Fig. 5. The current injection from ITO and PEDOT-PFESA to NPB therefore lies between the two extremes of space-charge-limited current and injection-limited current.

Similar to the case of NPB, two distinct energy level alignment regimes are observed for CBP (see Fig. 3.). The vacuum level of the molecular film coincides with that of the substrate (Shottky-Mott limit) for ϕ_s smaller than approximately 5.2 eV. Within this regime, the hole-injection barrier E_V^F decreases from 2.3 eV to 0.9 eV, as the ϕ_s is changed from 3.82 eV to 5.15 eV. On the other hand, for both PEDOT-PFESA high work function substrates, the barrier decreases only by about 0.1 eV, despite the work function increase by 0.2 eV and 0.6 eV, as compared to threshold value of 5.2 eV.

The energy level alignment of m-MTDATA follows the patterns seen for NPB and CBP. The threshold work function value above which significant interfacial dipole starts to form is at about 4.5 eV. Above this threshold the interfacial dipole scales directly with increasing ϕ_s while the barrier for hole-injection stays constant at about 0.4 eV. Note that for m-MTDATA and PEDOT-PFESA ($\phi_s = 5.8$ eV) interface, a downward vacuum level

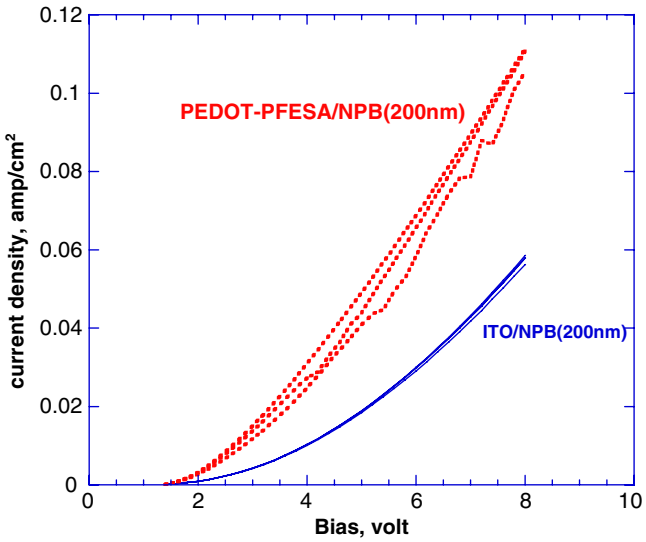


Fig. 5. Hole-only current–voltage curves of two types of devices: solid curves – ITO/NPB(200 nm)/Al(100 nm); dotted curves – ITO/PEDOT-PFESA(50 nm)/NPB(200 nm)/Al(100 nm).

shift as large as 1.3 eV is observed. In the early stages of deposition there is broadening of the photoemission features of *m*-MTDATA located in the low binding energy region. This observation is tentatively interpreted as a result of charge transfer and presence of destabilized HOMO states in the spectrum. However, for low coverages, a signal from the substrate is also present and contributes to the background of the above mentioned spectra. The overlap of the intensities from the substrate and the monolayer (or sub-monolayer) of molecular film makes interpretation of broadening in molecular features, somewhat uncertain.

Recent study by Tsang et al. shows that the change of the electrode from ITO to PEDOT-PSS in the device with *m*-MTDATA as hole transporting layer does not improve hole-injection. At the same time clear improvement is observed for NPB-based devices [22]. This can be explained by the results shown in Fig. 3. Both ITO/*m*-MTDATA and PEDOT-PSS/*m*-MTDATA interfaces fall into Fermi level pinning regime, therefore no improvement in hole-injection is expected. In contrast ITO/NPB interface is in vacuum level alignment regime, while the exchange of electrode to that of PEDOT-PSS results in Fermi level pinning and reduction of the hole-injection barrier across the interface. In other words, the Fermi level pinning regime should correspond to the lowest charge injection barrier (in terms of electronic level alignment) for a given molecular material.

The cases discussed above show clearly that there exist two types of different energy level alignment regimes at the interfaces of HTL and conducting substrates. Negligible vacuum level shifts indicate that, up to a certain threshold ϕ_s value, the interfaces in question exhibit essentially pure Shottky-Mott behavior, *i.e.*, $S = 1$. As a consequence, the barriers for hole-injection scale linearly with ϕ_s. However, for ϕ_s greater than the threshold value, the Fermi level of the substrate is pinned at a charge transfer level of the molecule. Since the charge-transfer state lies in vicinity of HOMO, the magnitude of the threshold value, above which pinning occurs, is higher for the molecules with higher IP.

Observed pinning causes formation of substantial interface charge-transfer dipole. The magnitude of the dipole scales linearly with ϕ_s, while at the same time the barriers for hole-injection remain constant. In other words, by changing ϕ_s the hole-injection barrier can be tuned only to certain value. Any further increase in ϕ_s has little (if any) effect on the charge injection barrier, but results instead in an interfacial dipole layer.

Recently, similar results were reported for interfaces of semiconducting polymers spincoated onto a wide range of organic and inorganic substrates [4]. The effects of interfacial charge transfer have been discussed theoretically earlier [23]. The present results are consistent with these earlier predictions. A model of energy level alignment at the ''atomically clean'' metal–organic and organic–organic interfaces was recently proposed, where the interfacial electronic structure was interpreted in terms of an induced density of interface states (IDIS) [24,25]. For the interfaces of passivated substrates and molecular semiconductors, discussed in this work, the IDIS model does not appear to apply. This can be seen from abrupt change of the slope parameter, S, from 1 to 0 at the transition from vacuum level alignment to Fermi level pinning, when the work function of the substrate exceeds a certain material specific threshold value. In terms of density of states our experiments point to a model where the density of states in the semiconductor band gap peaks at the molecular charge transfer states, but is negligible elsewhere in the gap. Furthermore, for the substrate work function ranging from 4.8 eV to 5.2 eV (see Fig. 3) the formation of either large interfacial dipoles or lack thereof is observed, depending on the molecular semiconductor. Within IDIS model such behaviour of interfaces requires very different strength of the electronic coupling between Fermi states of the same substrate and different molecular semiconductors [18].

The IDIS model has already been considered in the study of the interfaces prepared by *in situ* deposition of TCNQ and TTF. In both cases Fermi level pinning was observed and proposed to originate from a charge exchange between the molecular film and the substrates [26].

4. Summary

Ultraviolet photoelectron spectroscopy has been used to reveal the energy level alignment at the interfaces of molecular organic semiconductors, specifically NPB, CBP and *m*-MTDATA, and various conductive (passivated, not atomically clean) substrates with wide span of the work functions (3.75–5.8 eV). We have consistently observed a transition between two regimes of energy level alignment, namely vacuum level alignment and Fermi level pinning. The later regime results in the

interfacial dipole that scales linearly with the work function of the substrate. Formation of this dipole is associated with spontaneous positive charge transfer across the interface to the molecular charge transfer states of the organic semiconductors. Within the Fermi level pinning regime, the barriers for charge injection are independent of the work function of the substrate, while within the vacuum level alignment regime, the barriers follow Shottky-Mott limit behavior, *i.e.*, they scale linearly with the work function of the substrate. These results show that the hole-injection barriers can be reduced by increasing the work function of the substrate only within certain limits. When the work function of the substrate exceeds the binding energy of the molecular charge transfer states, an interfacial dipole is formed, which inhibits the potential benefit of a high work function electrode.

Acknowledgements

SB has been supported by a contract with E.I. DuPont Corporation, Experimental Station, DE, USA. WO is supported by the European Commission within the Integrated Project NAIMO (No. NMP4-CT-2004-500355). In general, research in Linköping is supported by the Swedish Research Council (VR), the Center for Advanced Molecular Materials, CAMM, and the Center of Organic Electronics (COE). Both centers are funded by the Swedish Foundation for Strategic Research, SSF.

References

[1] H. Ishii, K. Sugiyama, E. Ito, K. Seki, Adv. Mater. 11 (1999) 605.
[2] I.G. Hill, D. Milliron, J. Schwartz, A. Kahn, Appl. Surf. Sci. 166 (2000) 354.
[3] W.R. Salaneck, K. Seki, A. Kahn, J.-J. Pireaux, Conjugated Polymer and Molecular Interfaces: Science and Technology for Photonic and Optoelectronic Applications, Marcel Dekker, New York, 2002.
[4] C. Tengstedt, W. Osikowicz, W.R. Salaneck, I.D. Parker, C.-H. Hsu, M. Fahlman, Appl. Phys. Lett. 88 (2006) 053502.
[5] A. Kahn, N. Koch, W. Gao, J. Polym. Sci. Polym. Phys. 41 (2003) 2529.
[6] C.W. Tang, S.A. VanSlyke, C.H. Chen, J. Appl. Phys. 65 (1989) 3610.
[7] X. Crispin, V. Geskin, A. Crispin, J. Cornil, R. Lazzaroni, W.R. Salaneck, J.-L. Brédas, J. Am. Chem. Soc. 124 (2002) 8131.
[8] N. Koch, A. Kahn, J. Ghijsen, J.-J. Pireaux, J. Schwartz, R.L. Johnson, A. Elschner, Appl. Phys. Lett. 82 (2003) 70.
[9] I.G. Hill, A. Rajagopal, A. Kahn, J. Appl. Phys. 84 (1998) 3236.
[10] N. Koch, A. Elschner, R.L. Johnson, J.P. Rabe, Appl. Surf. Sci. 244 (2005) 593.
[11] A.J. Mäkinen, I.G. Hill, R. Shashidhar, N. Nikolov, Z.H. Kafafi, Appl. Phys. Lett. 79 (2001) 557.
[12] C. Tengstedt, A. Kanciurzewska, M.P. de Jong, S. Braun, W.R. Salaneck, M. Fahlman, Thin Solid Films 515 (2006) 2085.
[13] L. Groenendaal, F. Jonas, D. Freitag, H. Pielartzik, J.R. Reynolds, Adv. Mater. 12 (2000) 481.
[14] W.R. Salaneck, S. Strafström, J.L. Brédas, Conjugated Polymer Surfaces and Interfaces: Electronic and Chemical Structure of Interfaces for Polymer Light Emitting Devices, Cambridge Unversity Press, Cambridge, 1996.
[15] W.R. Salaneck, R. Bergman, J.-E. Sundgren, A. Rockett, T. Motooka, J.E. Greene, Surf. Sci. 198 (1988) 461.
[16] K. Seki, E. Ito, H. Ishii, Synth. Met. 91 (1997) 137.
[17] W.R. Salaneck, R.H. Friend, J.L. Brédas, Phys. Rep. 319 (1998) 231.
[18] A. Wan, J. Hwang, F. Amy, A. Kahn, Org. Electron. 6 (2005) 47.
[19] T. Schwieger, M. Knupfer, W. Gao, A. Kahn, Appl. Phys. Lett. 83 (2003) 500.
[20] P.M. Borsenberger, E.H. Magin, J. Shi, Physica B: Condens. Mat. 217 (1996) 212.
[21] Z. Deng, S.T. Lee, D.P. Webb, Y.C. Chan, W.A. Gambling, Synth. Met. 107 (1999) 107.
[22] S.W. Tsang, S.C. Tse, K.L. Tong, S.K. So, Org. Electron., in press, doi:10.1016/j.orgel.2006.06.002.
[23] P.S. Davids, A. Saxena, D.L. Smith, Phys. Rev. B 53 (1996) 4823.
[24] H. Vázquez, F. Flores, R. Oszwaldowski, J. Ortega, R. Perez, A. Kahn, Appl. Surf. Sci. 234 (2004) 107.
[25] H. Vázquez, W. Gao, F. Flores, A. Kahn, Phys. Rev. B 71 (2005) 041306.
[26] R.J. Murdey, W.R. Salaneck, Jpn. J. Appl. Phys. 44 (2005) 3751.

Available online at www.sciencedirect.com
ScienceDirect
Organic Electronics 8 (2007) 21–28
Organic Electronics
www.elsevier.com/locate/orgel

Influence of polar molecular chain orientation on optical and carrier transport properties of polymer blends

V. Kažukauskas [a,*], V. Čyras [a], M. Pranaitis [a], A. Apostoluk [b,1], L. Rocha [b], L. Sicot [b], P. Raimond [b], C. Sentein [b]

[a] *Department of Semiconductor Physics and Institute of Materials Science and Applied Research, Vilnius University, Saulėtekio 9, Bldg. 3, LT-10222 Vilnius, Lithuania*

[b] *Commissariat à l'Energie Atomique, CEA-Saclay, CEA-DRT-LITEN, DSEN/GENEC/L2C, bât. 451, Laboratoire Cellules et Composants, 91191 Gif-sur-Yvette Cedex, France*

Received 4 May 2006; received in revised form 13 September 2006; accepted 6 October 2006
Available online 2 November 2006

Abstract

We report investigation of optical and electrical properties of poly(9-vinylcarbazole) (PVK) doped with 30 wt% 4-dibutylamino-4′-nitrostilbene (DBANS), depending on the molecular chain orientation of polar DBANS molecules. Orientation of dopant diode-like DBANS dye molecules was achieved by application of a static electric field through the polymer film, while heating the material near its glass transition temperature (T_g). Modification of optical properties due to the orientation was evidenced by the spectral dependencies of absorption coefficient. Appearance of the orientation-induced built-in electrical field was proven optically by the solid electric field induced second harmonic generation (SEFISHG) and electrically by current–voltage (*IV*) characterization. Measurement of the thermally stimulated currents (TSC) spectra demonstrated that carrier transport and trapping are affected, too. Changes of the TSCs induced by orientation were expressed best in the temperature range of 280–290 K. They could be attributed to the thermally activated process with activation energy of about 0.38 eV.
© 2006 Elsevier B.V. All rights reserved.

PACS: 72.80.Le; 73.50.Gr; 73.61.Ph; 81.40.Rs

Keywords: Polymer and organic semiconductors; Molecular chain orientation; Absorption; Carrier transport and trapping; Solid electric field induced second harmonic generation

1. Introduction

Organic electronics is one of the promising and fast developing fields. Particularly, organic-based photovoltaics (PV) can give unique advantages over the traditional silicon based approach from the point of view of production simplicity and convenience.

* Corresponding author. Tel.: +370 672 40208; fax: +370 5 2366003.
E-mail addresses: vaidotas.kazukauskas@ff.vu.lt (V. Kažukauskas), aleksandra.apostoluk@insa-lyon.fr (A. Apostoluk).
[1] Present address: Institut National des Sciences Appliquées de Lyon (INSA Lyon), Laboratoire de Physique de la Matière, LPM CNRS-UMR5511, Domaine Scientifique de la Doua, Bâtiment Blaise Pascal – 7, Avenue Jean Capelle, 69621 Villeurbanne Cedex, France.

1566-1199/$ - see front matter © 2006 Elsevier B.V. All rights reserved.
doi:10.1016/j.orgel.2006.10.004

The components used for organic PV devices are potentially cheap, non-toxic, widely available and can be tailored to suit specific needs (e.g., for selective light harvesting). Manufacturing of organic PV devices is straightforward since low temperature fabrication steps can be used such as screen-printing, ink-jet printing and solution spraying. As compared to present (inorganic) PV technologies, the energy and equipment requirements for producing organic PV devices are thus only minor. Furthermore, such deposition routes are compatible with non-heat resistant substrates such as plastics, allowing high throughput reel-to-reel manufacturing of flexible and lightweight PV modules by integrating well-known thermoplastic processing technologies. Organic photovoltaics could thus become a major technology for sustainable electricity generation in the long term.

Organic solar cells might promise a strong cost reduction if fast improvements of the power efficiency and the lifetime can be achieved. To build up efficient photovoltaic cells, a rectifying junction is necessary to assure effective spatial separation of the photogenerated carriers. One approach to realize such a junction extended over the whole device thickness may be the use of molecular rectification in an oriented amorphous polymer layer incorporating polar molecules. In such layer an internal built-in electric field is introduced and stored forming the structure that behaves as a distributed homojunction within a single polymer film [1,2]. Therefore, excitons photogenerated in the whole volume of the active layer could be more effectively splitted by the built-in field. This field would also assist carrier transport towards the contacts; both these effects leading to the increased device efficiency. Moreover, this principle enables one to avoid the necessity of the deposition of several layers, as in the cases of the Schottky or p–n junctions. The principle relies on the intrinsic polar nature of organic molecules. Oriented polar molecules – the so-called push–pull molecules used in second-order nonlinear optics [3] – are contained inside a polymer binder. Their orientation can be achieved by application of a static electric field through the polymer film, while heating it near the glass transition temperature. Molecular orientation is characterized by an order parameter $\langle \cos^3\theta \rangle$ [4]. Experimentally, it was demonstrated that the current–voltage characteristics of oriented disperse red 1 (DR1) (4-(*N*-(2-hydroxyethyl)-*N*-ethyl)-amino-4′-nitroazobenzene) films grafted onto poly(methyl methacrylate) (PMMA) become strongly asymmetric in an initially symmetric structure [5]. Moreover, molecular order can be controlled using second harmonic generation (SHG). A new method – voltage-dependent SHG – was proposed to probe the internal field induced in the structure. It is called SEFISHG (solid electric field induced second harmonic generation) [6] and was demonstrated to be related to the induced rectification behaviour [7].

On the other hand, device efficiency also depends on carrier transport properties, which are given by carrier mobility and trapping. Engineering of macroscopic devices is necessarily based not only on the technological advances and skills, but also, in the same amount, on the purposeful control of carrier flows, which in their turn are given by microscopic material properties. Both carrier mobility and trapping effects can be foreknown to depend in different manner on molecular chain type and structure and on their orientation, too. Usually, in conjugated polymers charges are severely trapped by defect states. This results in reduced electron or hole mobility and imbalance of electron and hole flows, the equality of which is of primary importance for many modern applications of polymer materials, e.g., light-emitting and harvesting devices. Increase of the carrier mobility after the orientation of diode-like molecules was evidenced by the time of flight (TOF) method [1]. In this paper, we will analyze effect of molecular orientation on the optical, charge transport and trapping properties in the samples of poly(9-vinylcarbazole) (PVK) doped with 30 wt% 4-dibutylamino-4′-nitrostilbene (DBANS).

2. Samples and experiment

We have studied effect of the molecular chain orientation in the samples of PVK (poly(9-vinylcarbazole)) blended with 30 wt% DBANS (4-dibutylamino-4′-nitrostilbene). The chemical structures of the blend of constituents are presented in Fig. 1. The choice of the DBANS molecule was motivated by the facts that it possesses, as DR1, a large ground state dipole moment μ, which is necessary for the efficient DC-field orientation, and is less sensible to disorientation under light illumination than azobenzene dyes. PVK was used because of its high glass transition temperature ($T_g \cong 230$ °C in undoped polymer) which enables more stable orientation as compared to polymers like poly(3-alkylthiophenes) (P3AT) or poly(phenylene vinylene)s

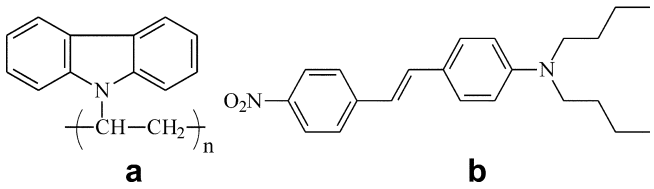


Fig. 1. Molecular structures of the blend constituents: (a) PVK (poly(9-vinylcarbazole)) and (b) DBANS (4-dibutylamino-4′-nitrostilbene).

(PPVs), used in photovoltaic cells. On the other hand, PVK is more conductive than poly(methyl methacrylate) (PMMA).

Samples were prepared by spin coating from the chlorobenzene solutions and were 1–1.3 μm thick. The blend was deposited on an ITO-coated glass substrate. The samples were provided with evaporated Al contacts on the top. The orientation was achieved either by application of constant voltage or by the electric field poling (Corona poling) at the temperature of 394 K – the optimal value found experimentally. The poling time was 15 min. In the first case voltage of 105 V was applied. The reverse bias was used to create polarization field oriented in the forward direction and vice versa. The bias was maintained while cooling the samples down to the room temperature. For Corona poling the +6 kV voltage was applied to the needle electrode. Both methods gave qualitatively similar results.

The effect of molecular orientation of DBANS was evidenced by independent investigations of electrical and optical properties. The UV–Vis absorption spectra of the samples were measured using Lambda 19 Perkin–Elmer spectrometer. The molecular order was controlled using second harmonic (SH) generation, as the SH intensity is directly related to the induced orientation of dipolar molecules [7]. The schematic of the experimental setup is presented in Fig. 2. These measurements enable calculation of the exact value of induced second harmonic coefficient $\chi^{(2)}_{\mathrm{eff}}$ and determination of the internal field stored in an oriented structure [1,2]. Moreover this technique allows for the optimization of the orientation process itself (the applied electric field, temperature, poling duration, cooling conditions, etc.). A sample was mounted so that the ITO coated glass or glass surface faced directly the incident beam. The Q-switched 25-ps duration Nd:YAG laser pulses with the wavelength of 1.064 μm and 10-Hz repetition rate were used for the excitation. The fundamental *p*-polarized infrared light beam impinged onto the sample at non-normal incidence angle passing through the glass substrate and/or the ITO coating and then the polymer layer. The second harmonic signal generated by the sample was detected using a photomultiplier tube (PMT) and integrated by a boxcar. Electrical, charge transport and trapping properties were investigated by the current–voltage (*IV*) characterization and by the thermally stimulated current (TSC) spectroscopy. For the TSC measurements the unexcited samples were cooled down to liquid nitrogen temperature. Later on they were excited for 10 min by the white light from a 100 W halogen lamp. After that the excited samples were heated at a constant rate of 10 K/min with applied bias

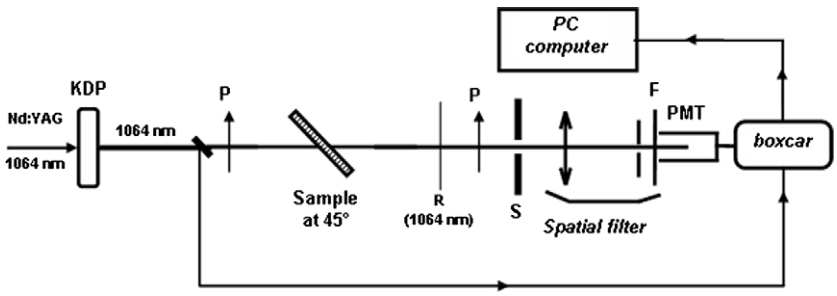


Fig. 2. Experimental set-up for the second harmonic generation studies: Nd :YAG – pulsed ps laser, $\lambda_{\omega} = 1.06$ μm, P – polarizer, R – dielectric mirror for the 1.06 μm beam, S – pinhole, F – interferometric filter at 532 nm; the SHG signal is detected by the photomultiplier (PMT) and registered by a boxcar connected to a PC computer.

assuring extraction of the thermally generated carriers. The dark currents were measured without any excitation. The effective thermal activation energy values were evaluated by the slopes of the curves in log $I \sim 1/T$ representation and the released charge was found by integrating current over time. After each measurement cycle the chain orientation procedure was repeated. For the I–V measurements the voltage step was less than 0.1 V and the duration of the step was long enough to assure the current stabilization between readouts. To prevent the sample polarization by voltage, the I–V measurements were always started from 0 V.

3. Methodical background

To quantitatively analyze the trap parameters by fitting the experimental curves we used a TSC model proposed in [8], as it is described in detail in [9,10]. The kinetics of carrier density at the traps may be described as [8]

$$\frac{dn_t}{dT} = -\frac{f_t n_t}{\beta}\exp\left(-\frac{E_t}{kT}\right). \tag{1}$$

Here, n_t is carrier density at traps with an activation energy E_t, T is temperature, β is a heating rate, k is Boltzmann constant, f_t is a carrier attempt-to-escape frequency. Assuming that f_t is temperature independent and the initial condition is $n_t(T_0) = n_{t0}$, an approximate solution of Eq. (1) can be obtained, that can further be used to calculate the current caused by thermally generated carriers [8]:

$$I = \frac{1}{2}eLAf_t n_{t0} \times \exp\left[-\frac{E_t}{kT} - \frac{f_t kT^2}{\beta(E_t + kT)}\exp\left(-\frac{E_t}{kT}\right)\right]. \tag{2}$$

Here, e is elementary charge, L is a layer thickness, A is a sample area. Eq. (2) can be used to model the single TSC peaks, by choosing the fitting parameters E_t, n_{t0} , and f_t.

Unfortunately, by interpreting experimental results usually the problem arises that no theory adequately explains various transport phenomena in polymers, particularly the electric field and temperature dependencies of drift mobility [11–16]. The most frequently used approaches refer to hopping transport character in disordered organic solids and are based either on a modified Poole–Frenkel (PF) model [12] or a Gaussian disorder model (GDM) [17]. The latter was later extended to include correlation effects [18–20]. In the Poole–Frenkel model the mobility can be described as a field and temperature assisted detrapping process of a carrier from the Coulomb potential of a charged trap. The mobility is given by [12]

$$\mu = \mu_0 \exp\left[-\frac{E_0 - \alpha F^{1/2}}{kT_{\text{eff}}}\right] \tag{3}$$

with

$$1/T_{\text{eff}} = 1/T - 1/T_{\text{R}}, \tag{4}$$

where F is an electric field strength, E_0 is an activation energy of the carrier transport at zero electric field, and T_{R} is the empirical reference temperature at which mobility is supposed to be known.

In the GDM model charge transport in disordered organic conductors is supposed to proceed by means of hopping in a Gaussian site-energy distribution. This density of states (DOS) reflects the energetic spread in the charge transporting levels of chain segments due to fluctuation in conjugation lengths and structural disorder. Within the Gaussian disorder model the mobility is given by [17]

$$\mu(F,T) = \mu_\infty \exp\left[-\left(\frac{2\sigma}{3kT}\right)^2\right]\exp\left\{C\left[\left(\frac{\sigma}{kT}\right)^2 - \Sigma^2\right]\sqrt{F}\right\}. \tag{5}$$

This equation was derived from Monte-Carlo simulations of the hopping processes of charge carriers in a material with energetic (σ) and positional disorder (Σ) described by the Gaussian distribution functions. μ_∞ is the high temperature limit of the mobility and C is a specific parameter that is obtained from the simulations as $C = 2.9 \times 10^{-4}\,(\text{cm/V})^{1/2}$.

Behaviour approximated by both these empirical equations has been observed in many materials. Experimentally, the main difference between both models is the temperature dependence. A consequence of hopping in a Gaussian DOS is the non-Arrhenius behaviour of the mobility [17]. Nevertheless, within the limited temperature range it is practically impossible to discriminate between both dependencies. Furthermore, the simulations of the GDM reproduced the $\ln(\mu) \sim \sqrt{F}$ dependence only in a narrow field range at high fields (10^8 V/m) [16]. Apart from that, both models require many parameters that can be used to fit the experimental data, depending on the preferred model. This causes that actually both approaches can be applied to fit experimental results, basing on the chosen physical mechanism, that in many cases is not known *a priori*

[21]. Therefore, a clear distinction between the two models is not always possible [22].

Moreover, in hopping systems the thermally activated mobility behaviour can cause appearance of the thermally stimulated current maxima [23]. Therefore, in general it is difficult to make a final decision if the results are caused by the change of carrier concentration or their mobility. On the other hand, in the latter case TSC maxima should demonstrate an expressed dependence on the heating rate and applied electric field [23].

4. Results and discussion

The absorption spectra of the PVK–DBANS samples before and after the polarization are presented in Fig. 3. It is clearly seen that the optical density (OD) decreases after the orientation. This is because after orientation process is completed, a part of the polar molecules become oriented perpendicularly to the polymer surface and thus the absorption decreases. The degree of orientation was calculated as $\Delta OD_{max}/OD_{max}$, here ΔOD_{max} is the difference in optical density before and after the polarization at the absorption maximum and OD_{max} is the optical density at the absorption maximum before orientation. The error of the optical density measurement was less than 0.02, the value obtained from the measurement of the calibrated reference filters. The maximum value of the degree of orientation was up to 24%. This value is relatively high as compared to a value of 30% normally reached in grafted polymers [24]. The value of induced second-order susceptibility at saturation $\chi^{(2)}$ was determined from the experimental values of the generated SH intensity and the beam fluencies, using the formula [24]:

$$I_{2\omega}^{\mathrm{SHG}} = \frac{\omega^2 d_{33}^2}{n^2 c^2 10^{\mathrm{OD}}} I_{\omega}^2 L^2, \tag{6}$$

where L is the sample thickness, OD stands for the optical density of the sample at 532 nm and n is the refractive index at 532 nm. The photoinduced nonlinearity $\chi^{(2)}$ deduced from Eq. (6) is 5.72 pm/V for the PVK–DBANS polymer film (the value obtained for the DR1–MMA 35/65 is $\chi^{(2)} = 150$ pm/V [24]). From these results we had also evaluated the average orientation by using the expression: $\chi^{(2)} = N\beta\langle\cos^3\theta\rangle/\varepsilon_0$. Here, N is the density of molecules, β is the molecular hyper polarisability. Taking $N = 1.2\times10^{21}$ cm^{-3} and $\beta = 1.7\times10^{-48}$ cm^3 V^{-2} [3], we obtain the average orientation ratio $\langle\cos^3\theta\rangle = 0.24$, which is in agreement with the ratio calculated from the absorption spectra in Fig. 3.

The photostimulated relaxation of the polar orientation was registered (see Fig. 4). For the studied polymer system a gradual decrease of the SH signal at the room temperature was induced by the illumination with an infrared beam at 1.064 μm wavelength delivered by the Nd:YAG laser at the 10 Hz repetition rate, with the pulse duration of 30 ps and of the intensity of 0.1 mJ per pulse. It was checked before that the polymer films did not bleach under illumination with a strong fundamental beam (1.064 μm). The temporal decay of the SH signal upon IR illumination indicates that the observed decrease of the optical density in absorption

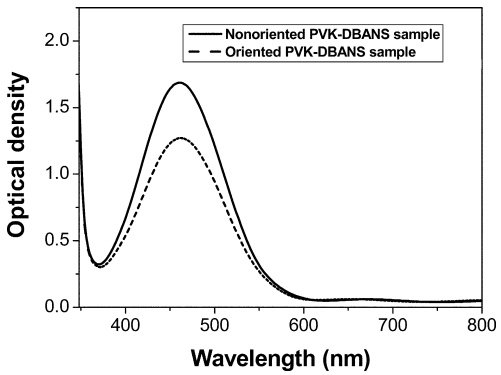


Fig. 3. UV–Vis absorption spectra of the PVK–DBANS polymer film before the orientation by Corona poling process (solid line, OD at the absorption maximum at 462 nm equals to 1.68) and after the Corona poling (dashed line, the OD at 462 nm equals to 1.27).

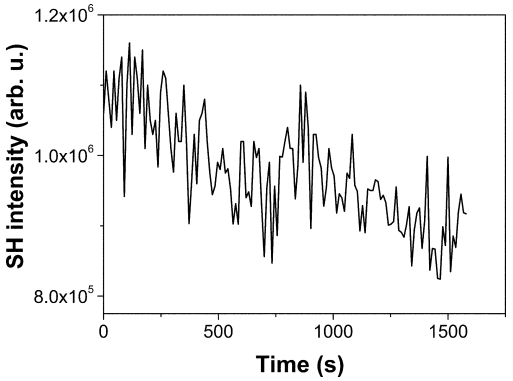


Fig. 4. Temporal decrease of the SH signal generated by the PVK–DBANS, oriented by a Corona poling method. The SH signal decays as the molecular polar order is erased by an infrared beam of the Nd:YAG laser at the 10 Hz repetition rate, with the pulse duration of 30 ps and of the intensity of 0.1 mJ per pulse.

spectrum after orientation is due to the disorientation of the initially oriented molecules in the sample. Thermally induced disorientation is at the origin of the decrease of the SH signal in the studied polymer system. This permits to conclude that this material does not deteriorate chemically under the application of a strong electric field during orientation process.

Appearance of the induced built-in electric field after poling was also proven by the current–voltage (*IV*) characteristics in the dark. To avoid a clearly expressed long living sample polarization by high applied electric fields (as it was also observed in, e.g., MEH-PPV [10,25]), measurements were always started from zero fields, and voltage was increased in small steps of 10 mV allowing sufficient relaxation time between the steps. Under such conditions we did not observe any influence of the molecular orientation at 300 K temperature. On the other hand, at lower temperatures below about 250 K an expressed effect of the molecular orientation was identified, as it is demonstrated in Fig. 5. It can be seen that if molecules were oriented in forward direction, i.e., their dipole field being of the same direction as an external electrical field, creating forward current, a built-in electric field was created in the sample. This field caused the current flow in an opposite direction at low values of the applied reverse bias up to about −3.3 V. Similarly, upon reverse orientation, the built-in field could be compensated by applying about 3.5 V forward bias. Characteristically the observed behaviour can be attributed primarily to the ohmic conduction of the layer volume itself. Meanwhile, e.g., contact effects make only minor influence. This is evidenced by the fact that at 300 K *IV* dependences were linear demonstrating ohmic behaviour at least up to the electric field strength of 4×10^5 V/cm, with the sample resistance being $(3.6–4.2) \times 10^{12}$ Ω and resistivity of about $(1.3–1.7) \times 10^{16}$ Ω cm. This does not enable evaluation neither of contact parameters, nor of carrier mobility, as it would be possible in case of other prevailing current-limiting mechanisms, e.g., thermionic emission over the contact potential barrier, Fowler–Nordheim tunnelling or space-charge-limited currents.

Clear effect of the molecular orientation could be observed also in the thermally stimulated current spectra, as is presented in Fig. 6. In all the cases marked differences are induced by the light excitation in the thermally stimulated regime, as compared to the unexcited dark currents. As far as PVK has an energy gap of 3.49 eV [26], and therefore can hardly be excited by the halogen lamp, the observed excitation effects could be attributed to DBANS. The TSCs had the effective thermal activation energies of about 0.037 eV in the temperature region of 166–240 K. Such small values are most probably caused not by carrier generation from traps, but rather by the thermally stimulated mobility growth. This means that mobility can be varied by light excitation. Changes of the TSCs induced by orientation were expressed best in the temperature range of 260–290 K. In the unoriented and oriented in reverse direction samples a clear current dip appears in this region in contrast to the samples oriented in the forward direction.

As can be seen from Fig. 6, near the room temperature higher conductivity is assured upon light excitation after the orientation in forward direction,

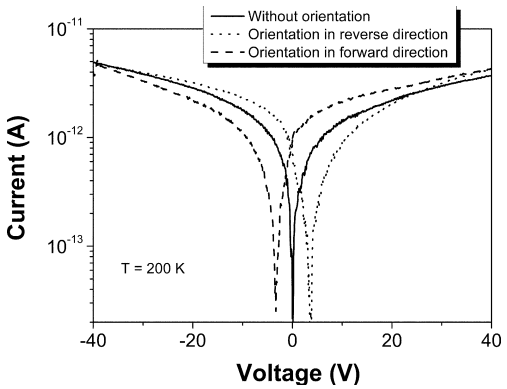


Fig. 5. Current–voltage characteristics, measured at 200 K, depending on the molecular orientation of the sample. Note that here and further the absolute current values are plotted.

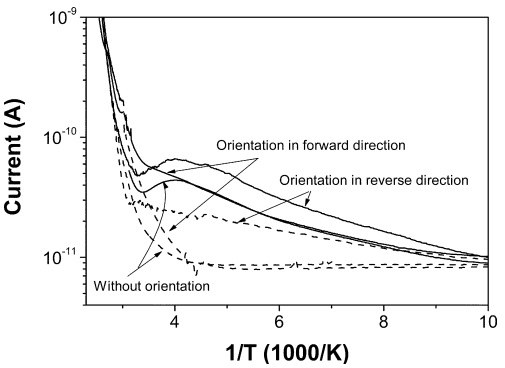


Fig. 6. Thermally stimulated currents (solid lines) and dark currents (dashed curves) depending on the molecular orientation, as indicated in the figure.

what could offer increase of the light-harvesting device efficiency. Therefore, to analyze differences between this case and unoriented sample, we modelled the experimental dependencies by taking into account thermal carrier generation from the trap states as well as their mobility changes given by the Gaussian disorder (GDM) and Poole–Frenkel (PF) approximations according to Eqs. (2)–(5). Results are presented in Fig. 7. Below the curves indicating carrier thermal generation, the trap parameters, i.e., their thermal activation energy and initial filling are presented. Values used for the calculation of mobility effect are as follows:

- *Poole–Frenkel model*: $\mu_0 = 5.40 \times 10^{-11}$ cm^2/V s, $E_0 = 0.152$ eV, $T_R = 1000$ K, $\alpha = 1.95 \times 10^{-4}$ eV (cm/V)$^{1/2}$.
- *Gaussian disorder model*: $\mu_\infty = 1.25 \times 10^{-7}$ cm^2/V s, $\Sigma = 4.9$, $\sigma = 0.039$ eV, $C = 5.00 \times 10^{-4}$ (cm/V)$^{1/2}$.

It is necessary to note that these values used for mobility calculations are only indicative ones, because very similar trends of the curves could be obtained by different sets of parameters. As it is seen from Fig. 7, the important issue is that most fitting parameters were kept unchanged in both cases, evidencing that orientation induces only very definite changes in the thermally stimulated behaviour. These changes relate to the varying influence of the thermally stimulated process with the effective activation energy of about 0.38 eV. This peak appears on the background of the other thermally stimulated process with even higher activation energy, therefore it could be associated not only with thermal carrier generation from the trap state, but also with mobility change.

Notably, the reversely oriented sample exhibits in Fig. 6 the TSC and the dark current both running significantly higher than in other cases. This indicates a noticeably increasing effect of the thermally stimulated mobility. Unfortunately, usually orientation in reverse direction did not give well reproducible results in contrast to the other two cases, therefore additional investigations are necessary to explain its nature. One of the reasons of the steeper mobility increase with temperature could be the necessity for the carriers to overcome higher potential barriers induced by the reverse orientation of molecules.

Above about 310 K the current increase begins with the activation energy of about 0.9 eV. Probably, it can be attributed to the carriers thermally excited over the potential barrier at one of the contacts. Considering the Fermi level of ITO to be at 4.8 eV, the HOMO of the PVK being at 5.64 eV [26], their difference is close to the obtained value.

5. Summary and conclusions

Effects of the molecular chain orientation of diode-like 4-dibutylamino-4′-nitrostilbene (DBANS) molecules blended in poly(9-vinylcarbazole) (PVK) (30–70 wt%, respectively) were investigated by independent optical and electrical methods. To orient the polar DBANS molecules external electric field was applied at the temperature close to the glass transition temperature of the blend material. The value of the photoinduced nonlinearity $\chi^{(2)}$ deduced from the solid electric field induced

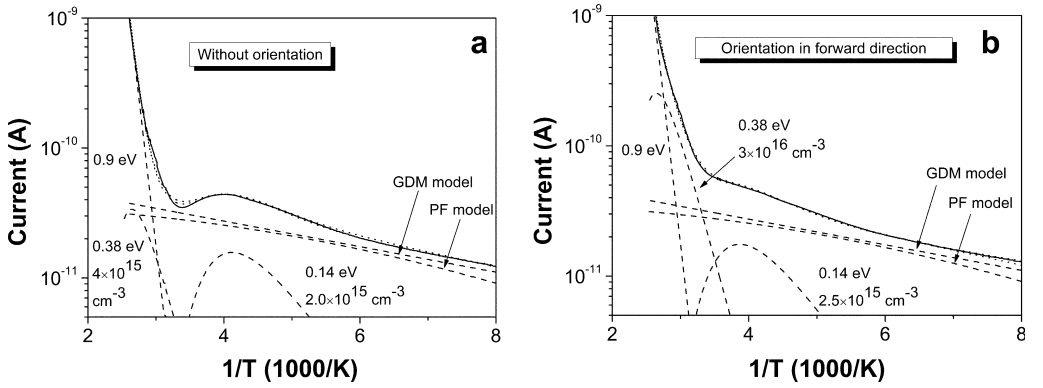


Fig. 7. Fit of the TSCs measured (a) without orientation and (b) after the orientation in forward direction. Experimental curves are presented by solid lines, the fitting curves are plotted by dotted lines, and influences of different thermally activated processes are plotted by dashed lines. Nearby the curves representing carrier thermal generation, trap parameters (thermal activation energy and initial trap filling) are indicated.

second harmonic generation (SEFISHG) method was 5.72 pm/V. Molecular chain ordering perpendicular to the sample surface resulted in a decrease of the optical density of the samples by about 24%.

Carrier transport and trapping effects, as they are influenced by the molecular chain orientation, were investigated by Thermally Stimulated Current spectroscopy and current–voltage characterization. Changes both in *IV* dependencies below about 250 K temperature and the TSC spectra were dependant on the orientation direction of polar DBANS molecules. The TSCs could be modelled by taking into account mobility variation according to the Gaussian disorder and Poole–Frenkel approximations as well as carrier thermal generation from traps. In the temperature region of 166–240 K the effective thermal activation energies of TSC curves were about 0.037 eV. Such small values are most probably caused not by carrier generation from traps, but rather by the thermally stimulated mobility growth. This means that mobility can be varied by light excitation. Changes of the TSCs induced by orientation were expressed best in the temperature range of 280–290 K. The numerical fitting revealed that they could be attributed to the thermally activated process with the activation energy of about 0.38 eV. Above about 310 K the current increase took place with the activation energy of 0.9 eV, that could be caused by the carriers thermally excited over the potential barrier at one of the contacts.

Acknowledgements

The authors acknowledge partial financial support by the European Commission (FP6 MOLYCELL Project, Contract No. SES6-CT-2003-502783), and bilateral support by the EGIDE agency (France) and the Department of Science and Higher Education of the Ministry of Education and Science (Lithuania) within the "Gilibert" Project.

References

[1] C. Sentein, C. Fiorini, A. Lorin, J.-M. Nunzi, Adv. Mater. 9 (1997) 809.
[2] C. Sentein, C. Fiorini, A. Lorin, J.-M. Nunzi, P. Raimond, L. Sicot, Synth. Met. 102 (1999) 989.
[3] J.L. Oudar, J. Chem. Phys. 67 (1977) 446.
[4] K.D. Singer, M.G. Kuzyk, J.E. Sohn, J. Opt. Soc. Am. B 4 (1987) 968.
[5] C. Sentein, C. Fiorini, A. Lorin, J.-M. Nunzi, Synth. Met. 91 (1997) 81.
[6] C. Sentein, C. Fiorini, A. Lorin, L. Sicot, J.-M. Nunzi, Opt. Mater. 9 (1998) 316.
[7] L. Sicot, C. Fiorini, A. Lorin, P. Raimond, C. Sentein, J.-M. Nunzi, Solar Energy Mater. Solar Cells 63 (2000) 49.
[8] J.G. Simmons, G.W. Taylor, Phys. Rev. B 5 (1977) 1619.
[9] G. Kavaliauskienė, V. Kažukauskas, V. Rinkevičius, J. Storasta, J.V. Vaitkus, R. Bates, V. O'Shea, K.M. Smith, Appl. Phys. A 69 (1999) 415.
[10] V. Kažukauskas, Semicond. Sci. Technol. 19 (2004) 1373.
[11] R.G. Kepler, P.M. Beeson, S.J. Jacobs, R.A. Anderson, M.B. Sinclair, V.S. Valencia, P.A. Cahill, Appl. Phys. Lett. 66 (1995) 3618.
[12] W.D. Gill, J. Appl. Phys. 43 (1972) 5033.
[13] P.M. Borsenberger, D.W. Weiss, Organic Photoreceptors for Imaging Systems, Dekker, New York, 1993.
[14] M.A. Abkowitz, Philos. Mag. B 65 (1992) 817.
[15] L.B. Schein, Philos. Mag. B 65 (1992) 795.
[16] P.W.M. Blom, M.C.J.M. Vissenberg, Mater. Sci. Eng. 27 (2000) 53.
[17] H. Baessler, Phys. Status Solidi B 175 (1993) 15.
[18] D.H. Dunlap, P.E. Parris, V.M. Kenkre, Phys. Rev. Lett. 77 (1996) 542.
[19] S.V. Novikov, D.H. Dunlap, V.M. Kenkre, P.E. Parris, A.V. Vannikov, Phys. Rev. Lett. 81 (1998) 4472.
[20] D.H. Dunlap, V.M. Kenkre, P.E. Parris, J. Imag. Sci. Technol. 43 (1999) 437.
[21] W. Bruetting, S. Berleb, A.G. Mueckl, Org. Electron. 2 (2001) 1.
[22] D. Hertel, H. Baessler, U. Scherf, H.H. Hoerhold, J. Chem. Phys. 110 (1999) 9214.
[23] I. Chen, J. Appl. Phys. 47 (1976) 2988.
[24] C. Fiorini, F. Charra, J.-M. Nunzi, P. Raimond, J. Opt. Soc. Am. B 14 (1997) 1984.
[25] V. Kažukauskas, Proc. SPIE 5122 (2003) 163.
[26] Y.Z. Wang, D.D. Gebler, D.J. Spry, D.K. Fu, T.M. Swager, A.G. MacDiarmid, A.J. Epstein, IEEE Trans. Electron Dev. 44 (1997) 1263.

Available online at www.sciencedirect.com
ScienceDirect
Organic Electronics 8 (2007) 29–36
Organic Electronics
www.elsevier.com/locate/orgel

Efficient fluorescent white organic light-emitting diodes with blue-green host of di(4-fluorophenyl)amino-di(styryl)biphenyl

Jwo-Huei Jou [a,*], Chung-Pei Wang [a], Ming-Hsuan Wu [a], Po-Hsuan Chiang [a], Hung-Wei Lin [a], Hao Chun Li [b], Rai-Shung Liu [b]

[a] *Department of Materials Science and Engineering, National Tsing Hua University, Hsin-Chu 30013, Taiwan, ROC*
[b] *Department of Chemistry, National Tsing Hua University, Hsin-Chu 30013, Taiwan, ROC*

Received 15 June 2006; received in revised form 4 October 2006; accepted 15 October 2006
Available online 9 November 2006

Abstract

Efficient fluorescent white organic light-emitting diodes are fabricated with the use of an efficient electro-fluorescence blue-green host material di(4-fluorophenyl)amino-di(styryl)biphenyl, doped with red dye 4-(dicyano-methylene)-2-methyl-6-(julolidin-4-yl-vinyl)-4H-pyran. One resulting two-wavelength white emission device shows a maximum external quantum efficiency of 4.8% and a high power efficiency of 14.8 lm/W with 100 cd/m^2 at 3.8 V. The high efficiency may be attributed to the high electroluminescence character of the host, relatively high host-to-guest energy transfer efficiency, and effective device architecture.
© 2006 Elsevier B.V. All rights reserved.

Keywords: Organic light-emitting diodes; High-efficiency; Fluorescent; White

1. Introduction

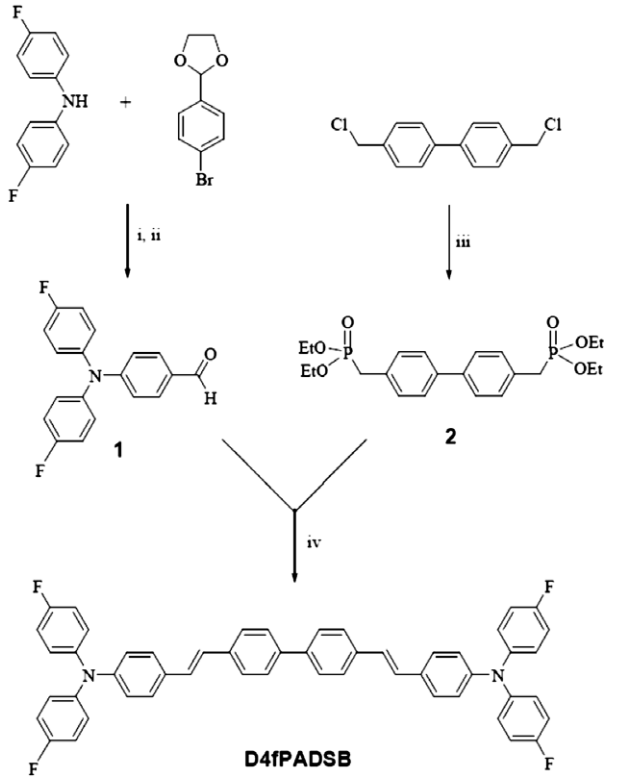
White organic light-emitting diodes (OLEDs) have attracted considerable attention due to their great potential for general purpose illumination [1,2] and flat-panel displays [3,4]. The emitting layer can be made of phosphorescent and/or fluorescent materials [3,5–12]. As reported, the power efficiency of phosphorescent white OLED can reach 36 lm/W, or 57 lm/W with an antireflective coating, while that of fluorescent white polymeric light-emitting diodes is 14–16 lm/W [9]. In comparison, the reported power efficiency of fluorescent white OLED at 100 cd/m^2 is 5.0 lm/W of two-wavelength or 7.2 lm/W of three-wavelength [10,11]. Fluorescent white OLEDs with improved power efficiency are thus being pursued.

To effectively raise power efficiency, the device must be thin, have low carriers injection barriers, and possess effective carriers and excitons confining function [12,13]. More importantly, in the incomplete energy transfer guest-host system [14], the employed light-emitting host must have high electroluminescent (EL) efficiency and exhibit good energy transfer efficiency to the guest.

Accordingly, this study fabricated a high efficiency fluorescent white OLED of two-wavelength

* Corresponding author.
E-mail address: jjou@mx.nthu.edu.tw (J.-H. Jou).

1566-1199/$ - see front matter © 2006 Elsevier B.V. All rights reserved.
doi:10.1016/j.orgel.2006.10.007



i, 2 mmol % $Pd(OAc)_2$, 4 mmol % $(t\text{-}Bu)_3P$, 1.1 eq. t-BuONa, reflux 12 h in toluene
ii, 1 N HCl, acetone
iii, $P(OEt)_3$, 150 , 24 h, 97 %
iv, 2.2 eq. t-BuONa, THF, 20 h, 82 %

Scheme 1. Synthetic protocol of di(4-fluorophenyl)amino-di(styryl)biphenyl (DSB).

using a newly synthesized high electroluminescent blue-green host material of di(4-fluorophenyl)amino-di(styryl)biphenyl (DSB) doped with a red dye. The resulting white OLED has a maximum external quantum efficiency of 4.8% and a high power efficiency of 14.8 lm/W at 100 cd/m^2.

This high electroluminescent blue-green host DSB contains trans-4-diphenyl-amino-stilbene, a derivative of *N*-phenylstilbene. The *N*-phenylstilbene derivatives are generally highly fluorescent due to its effective reduction of cis-trans photoisomerization [15]. However, the introduction of *N*-phenyl substituent to the stilbene framework leads to more planar ground-state geometry, resulting in a less distorted structure with a larger charge-transfer character for the fluorescent excited states, but with an undesired red-shift in the absorption and fluorescent spectra [16]. To tune bluer and enhance fluorescent emission efficiency [17], inert fluoro-substituent is introduced to the Ph2N-containing oligo(arylenevinylene). Scheme 1 shows the structure and synthesis of the new blue-green host DSB.

2. Experimental

2.1. Synthesis of di(4-fluorophenyl)amino-di(styryl)-biphenyl

2.1.1. Synthesis of 4-[bis(4-fluorophenyl)amino]-benzaldehyde

To a toluene solution of bis(4-fluorophenyl)-amine (2.00 g, 9.75 mmol) was added 2-(4-bromophenyl)-1,3-dioxolane (2.23 g, 9.75 mmol), $Pd(OAc)_2$ (43.8 mg, 0.19 mmol), $P(t\text{-}Bu)_3$ (78.9 mg, 0.39 mmol), sodium tert-butoxide (1.03 g, 10.72 mmol). The reaction mixture was stirred under reflux condition at 110 °C for 12 h; after cooling to room tem-

perature, 1 N HCl (20 mL) and acetone (30 mL) were added, stirred for another 1 h; the mixture was extracted with ethyl acetate, washed with aqueous NaCl solution, dried with $MgSO_4$, and concentrated to yield a dark brownish solid. Chromatography (hexanes : EtOAc = 8:1, Rf = 0.30) afforded 4-[bis(4-fluorophenyl)amino]benzaldehyde (1) as a yellowish solid (2.65 g, 88%). 1H NMR ($CDCl_3$, 600 MHz): δ 9.78 (s, 1H), 7.65 (d, $J = 8.2$ Hz, 2H), 7.13–7.11 (m, 4H), 7.03 (t, $J = 8.0$ Hz, 4H), 6.90 (d, $J = 8.2$ Hz, 2H). 13C NMR (CDCl3, 150 MHz): δ 190.3, 160.1 (d, JCF = 244.8 Hz), 153.3, 141.9, 131.4, 129.0, 128.0 (d, JCF = 8.0 Hz), 118.3, 116.7 (d, JCF = 22.7 Hz). HRMS (70 eV): calcd for $C_{19}H_{13}F_2NO$: 309.0965, found: 309.0965. Anal. calcd for $C_{19}H_{13}F_2NO$: C, 73.78; H, 4.24; N, 4.53. found: C, 73.76; H, 4.24; N, 4.54.

2.1.2. Synthesis of tetraethyl biphenyl-4,4′-diylbis(methylene)diphosphonate

To a neat triethylphosphite liquid (3.98 g, 23.89 mmol) was added 4,4′-bis (chloromethyl)-biphenyl (1.50 g, 5.97 mmol). The reaction mixture was stirred at 150 °C for 12 h; after cooling to room temperature, the reaction mixture was purified by bulb to bulb distillation to afford tetraethyl biphenyl-4,4′-diylbis(methylene)diphosphonate (2) as a white solid (2.63 g, 97%). 1H NMR (CDCl3, 400 MHz): δ 7.53 (d, $J = 8.0$ Hz, 4H), 7.36 (d, $J = 8.0$ Hz, 4H), 4.06–4.02 (m, 8H), 3.18 (d, $J = 22.0$ Hz, 4H), 1.26 (t, $J = 6.8$ Hz, 12H). 13C NMR ($CDCl_3$, 100 MHz): δ 139.0, 130.5, 130.0, 126.8, 61.8, 33.1 (d, JCP = 135.8 Hz), 16.1. HRMS (70 eV): calcd for $C_{20}H_{28}O_6P_2$: 426.1361, found: 426.1364. Anal. calcd for $C_{20}H_{28}O_6P_2$: C, 58.15; H, 7.10. found: C, 58.13; H, 7.11.

2.1.3. Synthesis of di(4-fluorophenyl)amino-di(styryl)biphenyl (DSB)

To a THF solution of compound 2 (1.63 g, 3.58 mmol) was added sodium tert-butoxide (0.76 g, 7.91 mmol) at 0 °C. The reaction mixture was stirred under ice bath for 1 h; a THF solution (5 mL) of compound 1 was added. After 20 h, 5 mL of NH_4Cl solution was added. The reaction mixture was extracted with CH_2Cl_2, dried with $MgSO_4$ and evaporated in vacuum. The residue was purified by recrystallization in mixed solution of CH_2Cl_2 and hexane affording DSB (2.14 g, 82%) as a light-green solid. 1H NMR ($CDCl_3$, 600 MHz): δ 7.59 (d, $J = 8.4$ Hz, 4H), 7.54 (d, $J = 8.4$ Hz, 4H), 7.37 (dd, $J = 8.8$, 2.4 Hz, 4H), 7.09 (s, 2H), 7.06–7.03 (m, 12H), 7.02 (s, 2H), 6.99–6.94 (m, 8H). 13C NMR ($CDCl_3$, 150 MHz): δ 158.9 (d, JCF = 241.9 Hz), 147.5, 139.4, 136.6, 131.2, 128.1, 127.4, 127.0, 126.7, 126.5, 126.1 (d, JCF = 7.7 Hz), 122.3, 116.2 (d, JCF = 22.5 Hz).

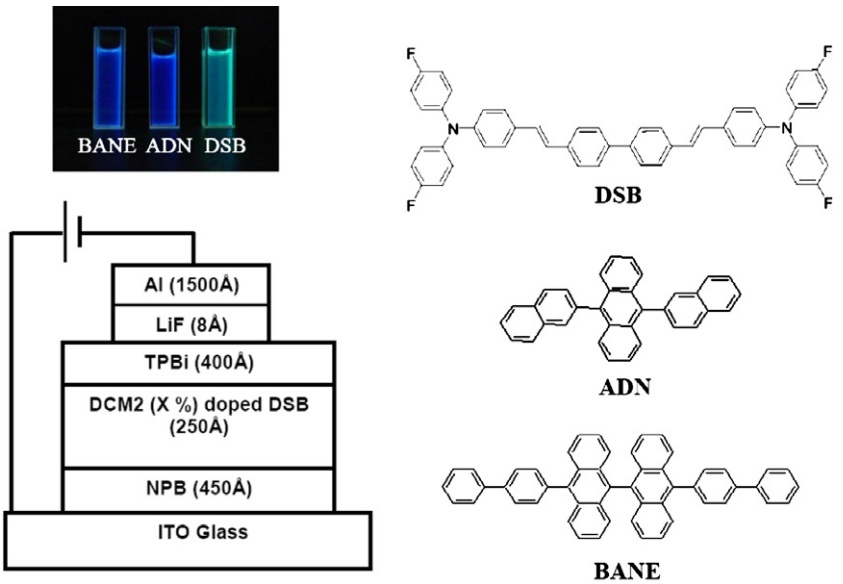


Fig. 1. Schematic illustration of the structure of the two-wavelength fluorescent WOLEDs using the novel blue host DSB, also shown molecular structure of the three blue host. The inset shows solution photoluminescence images of DSB, BANE and ADN in tetrahydrofuran.

HRMS (70 eV): calcd for $C_{52}H_{36}F_4N_2$: 764.2815, found: 764.2811. Anal. calcd for $C_{52}H_{36}F_4N_2$: C, 81.66; H, 4.74; N, 3.66. found: C, 81.63; H, 4.74; N, 3.69.

2.2. Device fabrication

The deposition source of the white emission layer was prepared via solution-mixing [11] as followed. The composing dye and host were first separatively dissolved in tetrahydrofuran. After complete dissolution, the resultant solutions were mixed to form a host solution uniformly dispersed with the desired doping dye. The resulted dye-dispersed host solution was then vacuum-dried at 80 °C for 60 min prior to vapor-deposition.

The device was fabricated by vapor-deposition using an indium tin oxide coated glass substrate (Merck Display Technologies, Ltd.) with a sheet resistance of 13 Ω/square and a thickness of 1250 Å. The substrate was cleaned in ultrasonic baths of detergent, de-ionized water, acetone and isopropyl alcohol in turn, and then treated with the boiling hydrogen peroxide. The resulted substrate was then purged with nitrogen. The respective organic layers and the cathode layer were deposited at 2×10^{-5} Torr using resistively heated tantalum and tungsten boats. All the organic layers were deposited at rates ranging from 1 to 3 Å/s. The 5 Å lithium fluoride and 1500 Å aluminum were subsequently deposited at rates of 0.1 and 10 Å/s, respectively. The emission area of the device was 8 mm^2, and only the luminance in the forward direction was measured.

2.3. Measurement

The luminance and CIE chromatic coordinates of the resulted OLEDs were measured by using Minolta CS-100 luminance-meter. The electro-luminescence and photo-luminescence spectra were measured using a Hitachi F-4500 fluorescence spectrophotometer. The ultraviolet visible (UV–visible) absorption spectra were measured using a Hitachi U-3010 UV–visible spectrophotometer. The highest occupied molecular orbital (HOMO) energy levels of the organic materials studied were calculated from their oxidation potentials measured by a cyclic voltammetry [23], while the corresponding lowest unoccupied molecular orbital energy levels were estimated based on their HOMO energy levels and the lowest-energy absorption edge of the UV–visible

Table 1
Electroluminescent characteristics of the two-wavelength fluorescent WOLEDs with the different blue hosts doped with trace amounts of the red dye

No.	Host	DCM2(%)	Maximum luminance (cd/m^2)	Maximum power/current efficiency (lm/W)/(cd/A)[a]	Power efficiency/current efficiency/driving voltage at 100 cd/m^2			CIE 1931 (x,y) chromatic coordinates at 100 cd/m^2 and 10,000 cd/m^2
					lm/W	cd/A	V	
I	BANE	0	6,500	1.2	0.6	0.8	9.5	(0.155, 0.122) –
		0.10	35,000	6.6	4.8	7.9	5.0	(0.427, 0.433) (0.419, 0.429)
		0.15	40,000	7.8	6.0	9.6	5.1	(0.436, 0.440) (0.428, 0.432)
		0.20	41,500	8.3	7.1	10.0	5.5	(0.464, 0.457) (0.455, 0.452)
II	ADN	0	1,900	0.8	0.3	0.6	8.0	(0.155, 0.102) –
		0.10	12,000	12.8	7.3	10.2	5.5	(0.432, 0.430) (0.401, 0.402)
		0.15	15,300	13.2	8.1	12.1	5.6	(0.457,0.447) (0.412, 0.405)
		0.20	16,500	14.0	9.1	13.8	5.4	(0.487,0.475) (0.440, 0.424)
III	DSB	0	8,550	7.5	6.3	8.0	4.2	(0.188, 0.302) –
		0.10	20,300	15.4	13.7	15.0	3.7	(0.373, 0.421) (0.313, 0.382)
		0.12	22,000	15.7	13.2	14.3	3.7	(0.308, 0.429) (0.341, 0.403)
		0.15	24,600	16.5	14.8	15.6	3.8	(0.424, 0.441) (0.382, 0.420)
		0.20	20,000	16.3	13.9	15.2	3.9	(0.461, 0.459) (0.425, 0.448)

[a] The maximum power/current efficiency is defined as the resultant value obtained at luminance ⩾10 cd/m^2.

absorption spectra. A Keithley 2400 electrometer was used to measure the current–voltage (I–V) characteristics. All the devices were characterized without encapsulation and all the measurements were carried out in the ambient condition.

The resultant blue-green DSB is doped with a red dye of 4-(dicyano-methylene)-2-methyl-6-(julolidin-4-yl-vinyl)-4H-pyran (DCM2) to generate a two-spectrum white emission. To clarify the effects of host materials with different EL efficiency and energy transfer efficiency on device performance, a comparison is made with two other blue light-emitting hosts, namely 1-butyl-9,10-naphthalene-anthracene (BANE) and 9,10-di(2-naphthyl)-anthracene (ADN). Fig. 1 illustrates the device architecture and molecular structures of the three hosts, and the inset shows their solution photoluminescence (PL) images in tetrahydrofuran.

3. Result and discussion

Table 1 lists the effects of different hosts on device EL characteristics. The DSB host composing device, that doped with 0.15% of DCM2, exhibits maximum external quantum efficiency of 4.8% and power efficiency of 16.5 lm/W with 22 cd/m^2 at 2.7 V or 14.8 lm/W with 100 cd/m^2 at 3.8 V, whose CIEx, y coordinates are (0.424, 0.441) at 100 cd/m^2 and (0.382, 0.420) at 10,000 cd/m^2. Meanwhile, the ADN counterpart exhibits maximum external quantum efficiency of 3.7% and power efficiency of 13.2 lm/W with 11 cd/m^2 at 4.5 V or 8.1 lm/W with 100 cd/m^2 at 5.6 V, whose CIEx, y coordinates are (0.457, 0.447) at 100 cd/m^2 and (0.412, 0.405) at 10,000 cd/m^2, and, the BANE counterpart exhibits maximum external quantum efficiency of 3.4% and power efficiency of 7.8 lm/W with 15 cd/m^2 at 3.8 V or 6.0 lm/W with 100 cd/m^2 at 5.1 V, whose CIEx, y coordinates are (0.436, 0.440) at 100 cd/m^2 and (0.428, 0.432) at 10,000 cd/m^2.

All three devices with the different hosts show relatively good efficiency performance owing to having thin device layers, low carriers injection barriers and good carriers and excitons confining function. For example, the energy barriers for injection of holes and electrons to inject the DSB host are 0.16 eV and −0.03 eV, respectively, as shown in Fig. 2 Moreover, the energy barriers for injection of holes and electrons into the ADN host are 0.1 eV and 0.2 eV, respectively, while those for the BANE host are 0.2 eV and 0.1 eV, respectively. From the perspective of hole injection barrier, the best host is ADN (0.1 eV), followed by DSB (0.16 eV), and the least favorable host is BANE (0.2 eV). Whilst, from the viewpoint of electron injection barrier, the best host is DSB (−0.03 eV), followed by BANE (0.1 eV), and finally ADN (0.2 eV). Though the ADN composing device has the lowest hole injection barrier, it has the highest electron injection barrier. On the other hand, the DSB composing device

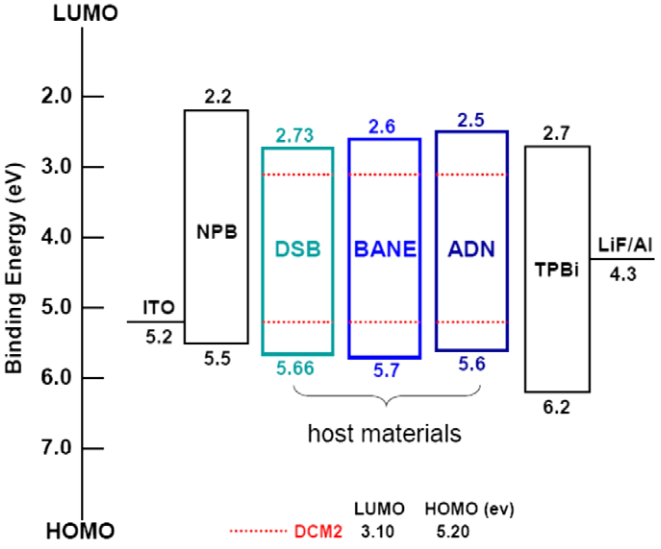


Fig. 2. HOMO/LUMO energy-level diagram of the hole-transporting/emission/electron-transporting trilayered structure of the WOLEDs using the three different hosts.

has no barrier for electron injection though having a slightly higher hole injection barrier than ADN. The better balance between hole and electron injections in the DSB composing device may, at least partly, explain its better device efficiency.

Importantly, the electroluminescent (EL) efficiency of DSB is the highest among all hosts, which is 6.3 lm/W with 100 cd/m^2 at 4.2 V, while those of ADN and BANE at 100 cd/m^2 are 0.3 lm/W at 8.0 V and 0.6 lm/W at 9.5 V, respectively. The resultant better EL efficiency indicates DSB to be a higher EL-efficiency molecule with a sound carrier-mobility, as revealed by its higher current density shown in Fig. 3. The comparatively high EL efficiency of the DSB host itself may also explain the resulting high device efficiency.

The efficiency of energy transfer from host to guest can be revealed by the spectral overlap between the emission of the host and the absorption of the dopant [16]. Fig. 4 shows the solution photoluminescence (PL) spectra of DSB, ADN, and BANE in tetrahydrofuran and the UV–visible absorption spectra of the red dye DCM2. The spectral peaks of the DSB, BANE and ADN hosts are located at 470, 442 and 436 nm, respectively, while that of red dye DCM2 is located at 500 nm. A great-

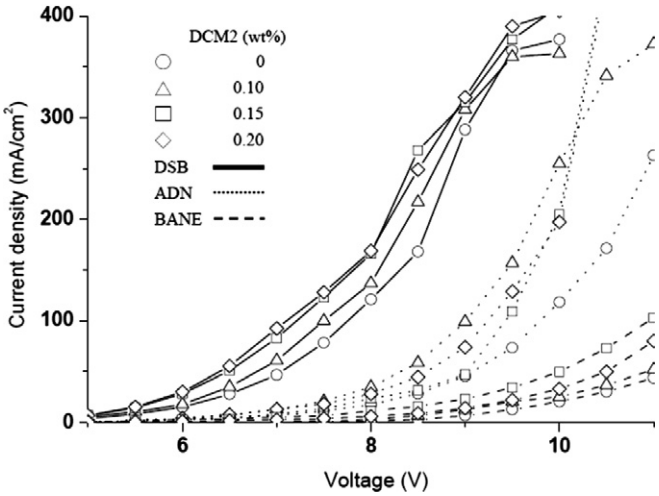


Fig. 3. *J–V* characteristics of the resulted OLEDs, with different hosts with and without the red-dopant DCM2.

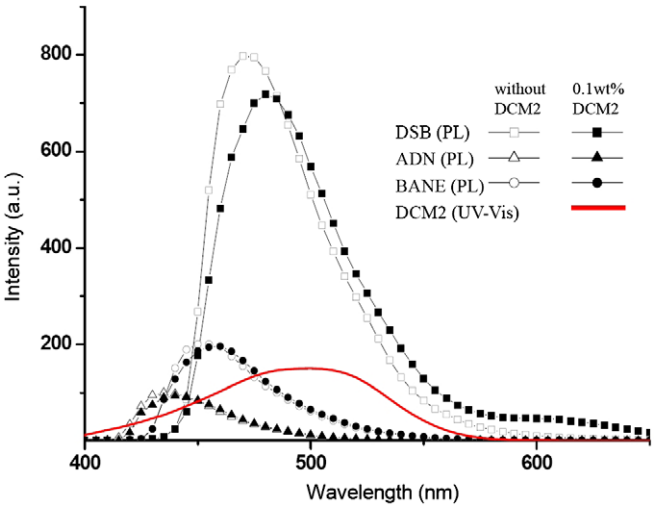


Fig. 4. Photoluminescence spectra of the host molecules of DSB, BANE and ADN with and without the dopant of DCM2, and ultraviolet–visible absorption spectra of the dopant molecule of DCM2.

est spectral overlap is observed between the PL spectrum of DSB and the UV–visible spectrum of DCM2, plausibly indicating a highest Forster energy-transfer efficiency, by realizing that the doping concentration is relatively trace in these devices [17].

Energy transfer efficiency can also be realized via the PL experiments [18–20]. Fig. 4 shows the PL spectra of the three hosts with and without the doping of DCM2. All the PL peaks of the three hosts drop and red-shift on the addition of DCM2, confirming the occurrence of incomplete energy transfer. The decrease in the peak intensity and the extent of red-shift are the most pronounced for the DSB host, indicating a comparatively best energy transfer efficiency. This, coupled with the high electroluminescence efficiency of pure DSB host, the most favorable electron-injection and -confining characteristics, as mentioned above, may explain why the DSB composing device exhibits the highest power efficiency as revealed.

Fig. 5 shows the effect of DCM2 concentration on the power efficiency and luminance of the DSB employed white OLEDs. The maximum luminance

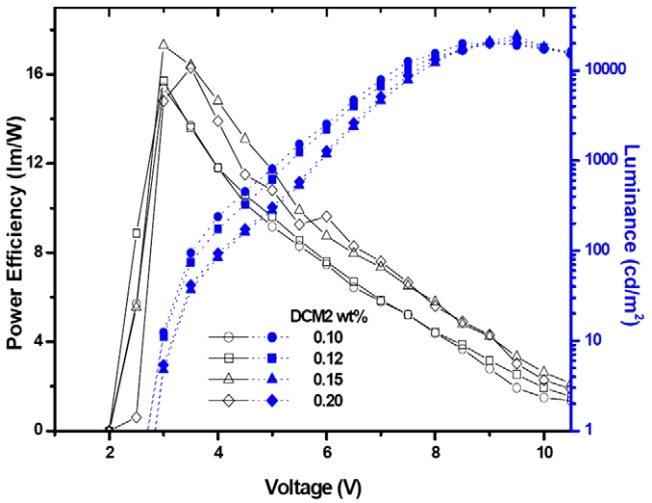


Fig. 5. The effects of the blue emitting host of DSB doped with the different concentration of the red dye of DCM2 on the resulting power efficiency and luminance of the two-wavelength WOLEDs.

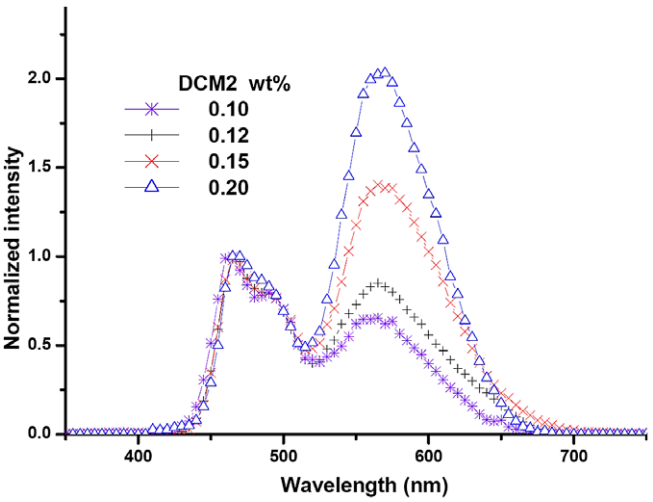


Fig. 6. Doping-concentration effects of the red dye of DCM2 on the electroluminescence spectra of the two-wavelength WOLEDs.

of the resultant device increases with the increase of dopant concentration. Fig. 6 shows the effect of DCM2 concentration on the electroluminescence spectrum. The spectra show two emission peaks at 470 nm from the blue host of DSB and at 560 nm from the red dopant of DCM2. The emission at 10,000 cd/m^2, for example, changes from CIEx, y of (0.283, 0.365) to (0.425, 0.448) as the DCM2 concentration is increased from 0.10% to 0.20%. By doping 0.12% of DCM2, white emission is obtained with a maximum luminance of 22,000 cd/m^2 at 9.5 V and a maximum power efficiency of 15.7 lm/W with 19 cd/m^2 at 2.8 V or 13.2 lm/W with 100 cd/m^2 at 3.7 V. The CIE coordinates of the device blue-shift from (0.385, 0.418) to (0.332, 0.388) as brightness increases from 100 to 10,000 cd/m^2. The power efficiency at 100 cd/m^2, however, decreases from 14.8 to 13.9 lm/W as the DCM2 concentration increases from 0.15% to 0.20%. This decrease may be attributed to the concentration-quenching phenomenon [5], due to the increasing formation of guest molecule aggregates [21], carrier trapping [22] at higher doping-concentrations.

4. Conclusion

To summarize, we have fabricated an efficient fluorescent white organic light-emitting diode with the use of a blue-green host material of DSB, which has a relatively high EL efficiency and fairly good energy transfer efficiency to the red dye of DCM2. Additionally, the device is thin and has a hole-transporting/emission/electron-transporting tri-layered structure with relatively low carrier-injection barriers and efficient carriers and excitons confining function. The resulting two-wavelength white emission device shows a maximum external quantum efficiency of 4.8% and a high power efficiency of 14.8 lm/W with 100 cd/m^2 at 3.8 V.

Acknowledgements

The authors thank Prof. C. H. Cheng of Department of Chemistry, National Tsing Hua University, for help with the EL spectra measurements. The blue hosts of BANE and ADN were provided by Labeltek Inc and Department of Chemistry, National Tsing Hua University, respectively. This work was supported by the University System of Taiwan and National Science Council, Taiwan, Republic of China for financially supporting in part this research under Grants No. 92J0162J4 and NSC92-2216-E-007-027, respectively.

References

[1] A.R. Duggal, J.J. Shiang, C.M. Heller, D.F. Foust, Appl. Phys. Lett. 80 (2002) 3470.
[2] B.W. D'Andrade, S.R. Forrest, Adv. Mater. 16 (2004) 1585.
[3] J. Kido, M. Kimura, K. Nagai, Science 267 (1995) 1332.
[4] Z. Shen, P.E. Burrows, V. Bulović, S.R. Forrest, M.E. Thompson, Science 276 (1997) 2009.
[5] C.W. Tang, S.A. Vanslyke, C.H. Chen, J. Appl. Phys. 85 (1989) 3610.
[6] B.W. D'Andrade, R.J. Holmes, S.R. Forrest, Adv. Mater. 16 (2004) 624.
[7] Y. Shao, Y. Yang, Appl. Phys. Lett. 86 (2005) 073510.
[8] Y.S. Huang, J.H. Jou, W.K. Weng, J.M. Liu, Appl. Phys. Lett. 80 (2002) 2782.
[9] R.F. Service, Science 310 (2005) 1762.
[10] J.H. Jou, Y.S. Chiu, R.Y. Wang, H.C. Hu, C.P. Wang, H.W. Lin, Org. Electron. 7 (2006) 8.
[11] J.H. Jou, Y.S. Chiu, C.P. Wang, R.Y. Wang, H.C. Hu, Appl. Phys. Lett. 88 (2006) 193501.
[12] M. Ikai, S. Tokito, Y. Sakamoto, T. Suzuki, Y. Taga, Appl. Phys. Lett. 79 (2001) 156.
[13] Z.Y. Xie, L.S. Hung, S.T. Lee, Appl. Phys. Lett. 79 (2001) 1048.
[14] R.S. Deshpande, V. Bulovic, S.R. Forrest, Appl. Phys. Lett. 75 (1999) 888.
[15] D.H. Waldeck, Chem. Rev. 91 (1991) 415.
[16] J.S. Yang, S.Y. Chiou, K.L. Liau, J. Am. Chem. Soc. 124 (2002) 2518.
[17] R.M. Gurge, A.M. Sarker, P.M. Lahti, B. Hu, F.E. Karasz, Macromolecules 30 (1997) 8286.
[18] M. Pope, C.E. Swenberg, Electronic Process in Organic Crystals and Polymers, Second ed., Oxford University Press, New York, 1999.
[19] X. Gong, J.C. Ostrowski, D. Moses, G.C. Bazan, A.J. Heeger, Adv. Func. Mater. 13 (2003) 439.
[20] L. Yan, N.J. Watkins, S. Zorba, Y. Gao, C.W. Tang, Appl. Phys. Lett. 81 (2002) 2752.
[21] V. Bulovic, R.S. Deshpande, M.E. Thompson, S.R. Forrest, Chem. Phys. Lett. 308 (1999) 317.
[22] Y.T. Tao, C.W. Ko, E. Balasubramaniam, Thin Solid Films 417 (2002) 61.
[23] S. Janietz, D.D.C. Bradley, M. Grell, C. Giebeler, M. Inbasekaran, E.P. Woo, Appl. Phys. Lett. 73 (1998) 2453.

Available online at www.sciencedirect.com
ScienceDirect
Organic Electronics 8 (2007) 37–43
Organic Electronics
www.elsevier.com/locate/orgel

Degradation of organic light-emitting diodes under different environment at high drive conditions

S. Gardonio [a], L. Gregoratti [a,*], P. Melpignano [b], L. Aballe [a], V. Biondo [b], R. Zamboni [c], M. Murgia [c], S. Caria [c], M. Kiskinova [a]

[a] *Sincrotrone Trieste, Area Science Park, 34012 Trieste, Italy*
[b] *Centro Ricerche Plast-Optica, via Jacopo Linussio 1, 33020 Amaro (UD), Italy*
[c] *Istituto per lo Studio dei Materiali Nanostrutturati dél CNR, via P. Gobetti 101, 40129 Bologna, Italy*

Received 30 June 2006; received in revised form 6 October 2006; accepted 13 October 2006
Available online 7 November 2006

Abstract

The origin of dark spots, crucial for understanding the degradation mechanisms in organic light-emitting diodes (OLEDs), is typically attributed to the penetration of moisture, oxygen and other active atmospheric agents. Employing scanning X-ray photoelectron spectromicroscopy we have investigated the morphology and chemical composition of degraded micro-areas created in OLEDs under different environment. The same confined degradation events, involving decomposition of the ITO film and organic layer and oxidation and delamination of the Al cathode were observed even for devices grown in situ and operated in ultra-high vacuum at pressures lower than 10^{-9} mbar. Our results provide unambiguously prove that 'uncontrollable' imperfections in the fabricated structures are the major cause for ignition of degradation events, whereas external causes related to the air ambient act as efficient promoters.
© 2006 Elsevier B.V. All rights reserved.

PACS: 79.60.−I; 85.60.Jb; 68.37.−d

Keywords: X-ray photoelectron spectra in surface analysis; Light-emitting diodes; Surfaces microscopy; Degradation process

1. Introduction

Intensive investigations on organic light emitting diodes (OLEDs) have been motivated by the eagerness to develop new generation display and lightening devices with low energy consumption [1] and more generally for a new generations of electronic and optoelectronic devices such as the organic light-emitting transistor architectures (OLETs) [2,3] which combined charge transport and light emission in ambipolar organic materials. Recently, current densities of several hundred of ampere per square centimeter [4] have been achieved for OLED opening the possibility to develop electrically pumped organic laser diodes.

The attractive properties of OLEDs are: (i) much higher theoretical efficiency than that of

* Corresponding author. Tel.: +390403758025; fax: +390403758565.
E-mail address: luca.gregoratti@elettra.trieste.it (L. Gregoratti).

1566-1199/$ - see front matter © 2006 Elsevier B.V. All rights reserved.
doi:10.1016/j.orgel.2006.10.005

incandescent, fluorescent and inorganic LED sources currently used in automotive lighting devices and (ii) the ease to generate the desired white and polychromatic radiation by simply replacing some of the molecules in the stack of organic layers or changing the layers architecture [5]. However, there are still technical obstacles to be overcome before OLEDs become a reliable alternative to fluorescent and incandescent lamps. The main unsolved technological issues are operational lifetime, power conversion efficiency and manufacturing costs [5,6]. The increase of operational lifetime is mandatory for OLEDs commercialization and has stimulated many studies focused on the mechanisms responsible for their degradation. Generally the observed loss of OLEDs luminescence is associated with: (i) growth of dark-spots, (ii) catastrophic failure or (iii) intrinsic degradation [7]. The first case is gradual degradation of the device electrodes through formation of non-emissive regions, appearing as dark spots. The catastrophic failure is attributed to electrical shorts resulting in a sudden significant or total loss of luminance due to high leakage current. The intrinsic degradation is a gradual decrease of the brightness without any obvious change in device appearance, most often occurring during device operation.

A lot of efforts have been made to handle the possible causes for degradation. They include strict control of the growth conditions to minimize the contaminations, and proper encapsulations to protect the devices from humidity, oxygen and other active gases in atmospheric ambient, supposed to be responsible for creation of dark spots and catastrophic failures. It has been demonstrated that encapsulation is a fundamental fabrication step, since correlation between OLEDs lifetime (appearance of non-emitting regions) and ambient moisture-level has been found [8,9]. It has been reported to increase the OLEDs lifetime up to several thousand hours. However, many of these values are extrapolated from temperature accelerated tests not being supported by effective measurements yet [10].

Our previous photoemission spectromicroscopy investigation of the topography and chemical composition of the Al cathode surface after degradation of non-encapsulated OLEDs operated in air or under ultra high vacuum (UHV) conditions revealed very similar behaviors [11]. We suggested that imperfections in the morphology of the anode surface, which determines the quality of organic/electrode interface are responsible for the electrical shorts and following degradation. However, the previously studied devices have been exposed to air after fabrication and before operation, thus the external causes, as pollution with contaminants could not be ruled out.

Here we report defect formation in OLEDs grown, kept and operated under ultra high vacuum (UHV) conditions. These devices have not been exposed to air, and thus degradation caused by humidity, oxygen or other gas contaminants can be excluded as possible mechanism for dark spot formation. Comparison with the results from devices exposed to air permit to discriminate the contribution of environment to the degradation processes demonstrating that the intrinsic causes are still to be seriously considered.

2. Experimental

The growth and characterization of the small-molecule-based OLEDs was carried out in the experimental station at the ESCA microscopy beamline at Synchrotron laboratory ELETTRA in Trieste, which consists of three inter-connected UHV chambers [12]. OLEDs were grown in the prototypical structure consisting of: a transparent glass substrate, a transparent ITO bottom anode (160 nm thickness), an α-NPB (*N*,*N*′-bis(naphthalene-1y1)-*N*,*N*′-bis(phenyl)benzidine) hole transport layer (60 nm thickness) an Alq_3(tris(8-hydroxyquinoline aluminium)) electron transport and emissive layer (70 nm thickness) and a highly reflective Al top metal cathode (100 nm thickness). The organic and metallic films were consecutively deposited by thermal evaporation in the preparation chamber (base pressure 1×10^{-7} mbar) of the experimental station. The thickness of the different layers was monitored by a calibrated quartz microbalance. After fabrication the OLEDs were transferred to the inter-connected measurement chamber with base pressure in the 10^{-10} mbar range, hosting the scanning photoemission microscope (SPEM). The pressure after transfer and during measurements was kept in the 10^{-9} mbar range. Measurements of the samples started 30 min after their fabrication. In SPEM the X-ray beam from the synchrotron light source is focused into a small spot of 150 nm diameter by means of a zone plate optics. The photoelectrons are detected and energy filtered by a hemispherical electron analyzer equipped with a 48-channel detector. SPEM measurements can be performed in two

complementary operation modes: imaging and microspot photoelectron spectroscopy (μ-XPS) [13,14]. In the imaging mode, the sample is scanned with respect to the focused beam simultaneously collecting photoelectrons within an energy window, usually corresponding to the elemental core level of interest. In the μ-XPS mode conventional spectra of the energy distribution curve are measured from micro-spot selected from the images, providing detailed information about the local chemical composition. The geometrical setup of the SPEM (normal incidence of the photon beam on the sample and take-off angle of 30°) enhances the surface sensitivity, e.g. the probing depth in the present study using photon energy of 650 eV does not exceed 2 nm. The grazing detection is also more sensitive to the surface topography, resulting in enhancement or shadowing of the photoelectron signal. The topography artifacts provide additional important morphological information and can be handled using well-developed image processing procedures [13,14].

The present study was carried out using a special sample holder constructed to allow simultaneous *in situ* operation and characterization of the OLEDs by SPEM. The composition and morphology of the OLED cathode after fabrication and its evolution during *in situ* operation was monitored from the Al 2p, In 3d and C 1s maps, and the μ-XPS spectra taken in selected areas with energy resolution of 0.2 and 0.35 eV. For deconvolution of the core level spectra we applied a well-developed procedure with Doniach-Sunjic functions convoluted with Gaussians accounting for the experimental resolution and broadening due to different factors [15].

3. Results

The Al 2p maps of the fresh cathode showed a chemically homogeneous and flat surface without visible morphological defects at the length scale of 0.15 μm. Along with the Al 2s and 2p lines the XPS spectrum contains a weak C 1s peak. C is a common contaminant, which cannot be avoided even in the UHV conditions of the preparation chamber during the device fabrication.

The studied OLED samples (emitting area of $2 \times 3\ mm^2$) were DC operated by increasing the

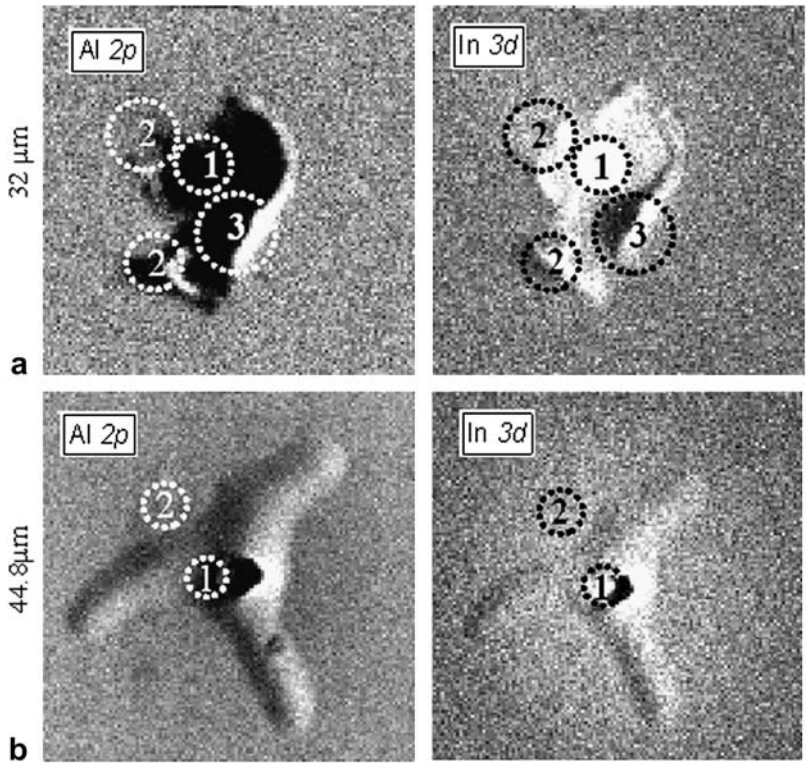


Fig. 1. Al 2p and In 3d maps of a damaged region of the Al cathode layer of an OLEDs: (a) grown, kept and operated under UHV; (b) exposed and operated in air. (1), (2) and (3) indicate the representative regions where XPS μ-spectra measurements were made.

voltage up to 30 V monitoring simultaneously with SPEM the evolution of the Al cathode surface. The device temperature under these conditions remained lower than 350 K, excluding any temperature-related decomposition of the organic layer or ITO anode. Visible damages appear as a localized fracture in the Al cathode. They usually occurred after about 15 min at 30 V, 50 mA/cm^2, 10.000 cd/m^2 (estimated) and do not cease the overall OLED light emission.

The Al 2p map in Fig. 1a illustrates a typical image of a damaged region. It appears as a dark hole ($\sim 14 \times 10\ \mu m^2$) because the Al film is locally disrupted and consequently there is no Al 2p emission. Close inspection of the contrast in the Al 2p map reveals intensity variations around the damaged region of topographic (pieces of disrupted Al film) or 'chemical' origin (attenuation of the Al 2p emission by some species deposited on top), discriminated by comparison with the In 3d map in Fig. 1a. A natural result of disruption of the Al film is exposing the organic and ITO layers below, as demonstrated by the In 3d map in Fig. 1a. The maximum In 3d emission (the brightest spot (1) of $\sim$4 μm in diameter) is at the central part of the hole in the Al cathode. Other brighter areas in the close vicinity of the fracture, such as spot (2), indicate the presence of In deposited on the Al surface, screening the Al 2p emission and appearing darker in the Al 2p map. The In and Al maps contain the same topographic features, resulting from the disruption of the Al film causing local enhancement or shadowing effects [14]. The topographic features can be unambiguously identified in the In map. From the size of the largest shadow (spot (3)) we estimate that the height of fractured Al pieces can reach a few μm.

We did not monitor any swelling and development of bubbles below the Al surface prior fracturing, as observed during degradation of devices exposed to air before operation [11]. For the sake of comparison the Al 2p and In 3d maps of a device degraded during operation in air are shown in Fig. 1b. The topography of the Al map shows three radial swollen protrusions of about 1.4 μm in height meeting at the dark volcano-like hole in the center.

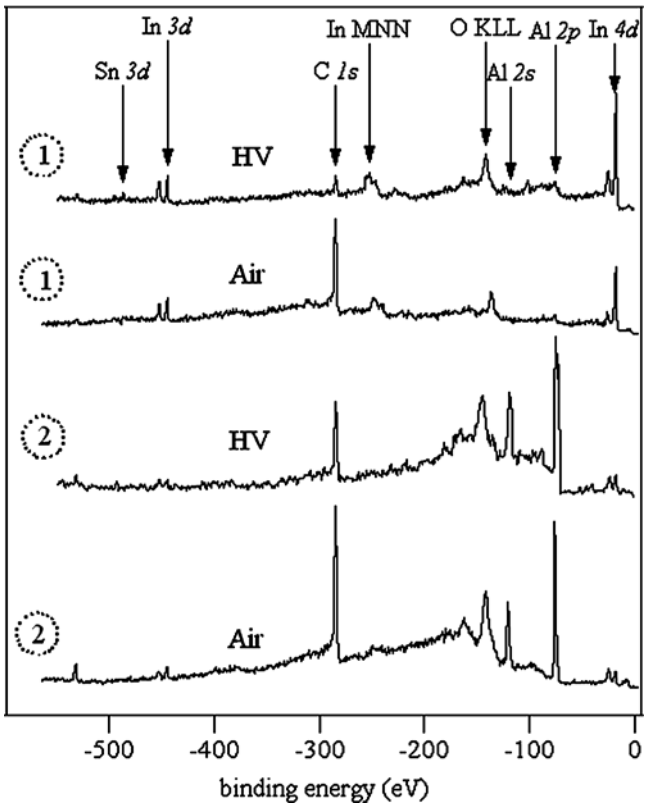


Fig. 2. XPS μ-spectra acquired in regions (1) and (2) indicated in the Al 2p and In 3d maps in Fig. 1 for OLEDS grown, kept and operated under UHV and exposed and operated in air.

Only the left part of the dark hole appears bright in the In 3d map due to strong shadowing by the delaminated Al film. Some In has been deposited on the deformed Al surface around the crater accounting for the inverse contrast in the In and Al maps.

Another distinct difference is the effect of Al cathode fracturing on the partial pressure of the vacuum chamber. For OLEDs, fabricated, kept and operated only under vacuum it did not cause any sensible pressure change in the 10^{-9} mbar range, whereas during fracturing of devices exposed to air prior operation under vacuum we measured a pressure burst up to 10^{-5} mbar when the swollen areas are disrupted.

Detailed information about the chemical composition within the fractured area and the surrounding cathode surface of devices kept in vacuum or exposed in air is provided by the XPS spectra in Figs. 2 and 3, measured in the regions indicated with (1) and (2) in Fig. 1. The spectra in Fig. 2 show for both samples the presence of In, C and O on the Al surface around and inside the fracture, the relative concentration of the elements being distinctively different in the two zones. In the spectra taken in the spot (1) of the In 3d map in the middle of the fractured regions the species containing In are dominant, suggesting that the organic layer has been locally degraded and removed. The 8–10 times lower Sn concentration in ITO than that of In [16–18] accounts for the weak Sn 3d intensity. Along with In, the spectra from both samples taken in close vicinity of the fracture (spot (2)) also show a sensible increase of C indicating that In- and C-containing species have been deposited on the Al cathode. These species can only be a result of local decomposition processes occurring in the ITO and organic layers interface releasing volatile In and C containing products. The major difference between the two samples is in the relative intensity of C 1s line. As expected both representative regions (1) and (2) of a sample exposed and operated in air contains more C, the unavoidable surface contaminant. However, comparing the In 4d/C 1s and Al 2p/C 1s intensity ratios (calculated taking into account the C 1s, In 4d and Al 2p cross-sections at a photon energy of 650 eV [19]), both samples show significantly lower C concentration inside the fractured region. This confirms that locally the organic layer has also been degraded.

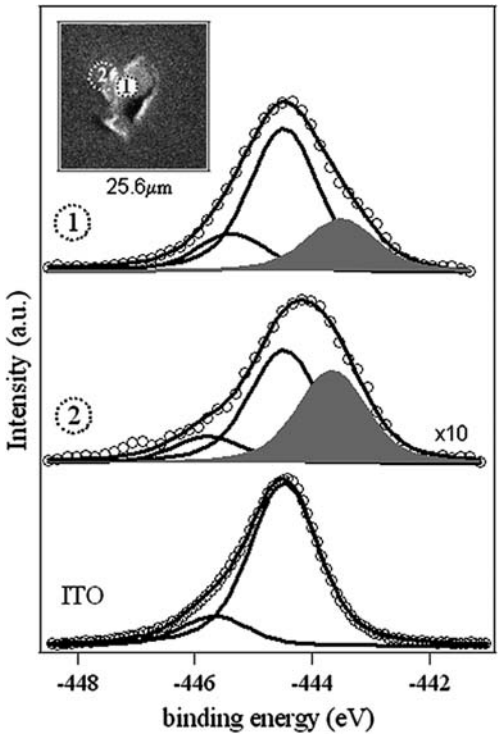


Fig. 3. In $3d_{5/2}$ core level spectra of pristine ITO and taken in regions (1) and (2) indicated in the Al 2p and In 3d maps in Fig. 1a of OLEDs kept and degraded in UHV.

The In $3d_{5/2}$ spectra in Fig. 3 for a device kept and operated under vacuum evidence that the degradation process involves not only fracturing of the Al cathode and local decomposition of the organic layer but also causes reduction of the In_2O_3 phase, the dominant component of the ITO anode. Compared to the In $3d_{5/2}$ spectrum of a pristine ITO (measured before deposition of the organic layer), which requires two components, accounting the different local In coordination [17,20,21], both spectra acquired from the damaged region and from the Al cathode contain a new component at -443.4 ± 0.2 eV, corresponding to metallic In [21]. Apparently the local decomposition of ITO substrate involves a release of volatile O, In and/or InO_x species. The latter can undergo further reduction in contact with the constituents of the organic layer and its decomposition products, which are efficient reducing agents. Part of the volatile species land onto the cathode surface around the fracture.

The Al 2p spectra in Fig. 4, measured on the cathode of the freshly fabricated device and in the vicinity of the fracture created following *in situ* operation in SPEM show that the surface around the fracture exposed to the volatile species has undergone oxidation. The spectra present two components, the narrower corresponding to metallic Al

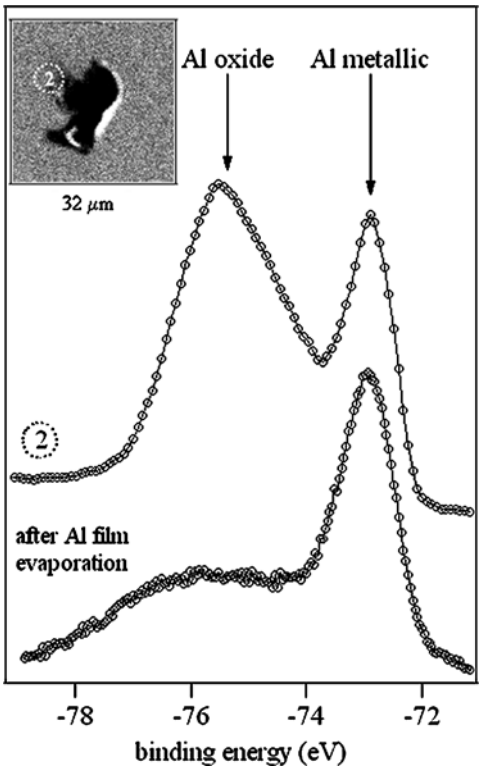


Fig. 4. Al 2p core level μ-spectra acquired on the Al cathode surface for OLEDs kept and degraded in UHV taken in region (2) before and after degradation.

(-72.8 ± 0.2 eV) and a broad one (-75.5 ± 0.2 eV), which accounts for stoichiometric and non-stoichiometric Al oxides [21]. The metallic component dominates the spectra acquired before the OLED operation, where the weak broad oxide feature arises from the unavoidable formation of a thin oxide layer even when the device was kept in the fabrication vacuum chamber at background pressure of 1×10^{-7} mbar. The degradation of OLEDs operated in the SPEM chamber leads to a dramatic increase of the oxide component, apparently as a result of interaction of Al with the volatile decomposition products.

4. Discussion

Comparing the morphology and the chemical composition of the confined degraded regions of OLEDs grown, kept and operated in vacuum with those exposed to air and operated in air or vacuum the differences and similarities can be summarized as follows.

The main difference is in the morphology of the damaged Al cathode and it is clearly evidenced by the Al 2p maps in Fig. 1. When OLEDs have never been exposed to air the degradation leads to a cathode fracture, occurring without any visible prior deformation of the Al film. In the case of OLEDs exposed to air (Fig. 1b) the fracturing is preceded by local swelling induced by bubbles created below the cathode film followed by a volcanic-like explosions disrupting the Al cathode and occurring when our samples were operated at 30 V.

Similar formation of bubbles observed during operation under vacuum of OLEDs exposed to air was attributed to the local overpressure from gases and volatile species released due to decomposition of ITO and organic layers [11]. Since in the present study of OLEDs not exposed to air we did not detect any visible deformations of the cathode prior degradation, the bubble formation is apparently an event occurring only in devices exposed to air where the moisture and oxygen can penetrate through defects of the cathode [9,22,23].

The similarity is that independently of the environment, the final state of degradation is characterized by a confined fracture in the Al cathode, local decomposition of ITO anode and organic layer, and deposition of volatile products on the Al surface around the fractured region. Since the decomposition products include In_xO_y, organic fragments, oxygen, and OH their interaction with the Al cathode also leads to formation of thin Al oxide layers. Before degradation the Al oxide film on the external cathode surface is very thin as shown in Fig. 4, whereas much thicker Al oxide film has grown after degradation in the parts interacting with the released volatile products. This finding is important in order to understand the degradation mechanism because it also concerns the Al surface at the cathode/organic interface, where independently of the ambient conditions Al should be in metallic state. As discussed in Ref. [9] the oxidation of Al at this interface facilitates the cathode delamination. We were not able to detect the oxidative action of the decomposition products for devices exposed to air, because a thick Al oxide film has been already formed naturally on the external cathode surface and the effect of the depositing products is negligible.

Based on the combined microscopy and spectroscopy analysis of OLED samples kept and operated in different ambient condition we propose the following degradation mechanism. When OLEDs are fabricated, kept and operated in ultra-high vacuum only a local increase of the temperature as result of

spikes can lead to dramatic events such as decomposition of the ITO and organic layers leading to delamination of the Al cathode. In the presence of a spike induced current between the electrodes we can estimate an increase of local temperature of several hundreds degrees, sufficient to decompose ITO and the organic layers. The pressure burst of the released volatile In, C and O-containing products, which also interact with Al at the Al/organic interface cause delamination of the cathode. The most probable reason of this failure should be local electrical shorts due to imperfections in the OLED structure, such as defects of structural, topographic or chemical origin at electrode surfaces, which affect the quality of the organic/electrode interface. Such defects are the local weak site where spikes occur, leading to temperature flashes and decomposition events. This mechanism is valid also for devices exposed to air, but in this case the degradation process is further promoted by the oxygen and the moisture that have penetrated inside the OLED structure. The effect of oxygen can be attributed to an increased oxidation rate of Al at the Al/organic interface, whereas according to Schaer et al. [9] the effect of water is more dramatic and is responsible for the deformation of the Al cathode prior fracturing. They suggest that in the presence of a strong electrical field electrochemical reduction of water occurs at the cathode/organic interface, the released H_2, creating bubbles below the cathode. Our observations of cathode swellings and pressure burst during the 'explosion' of the bubbles due to gas overpressures is in accordance with this scenario.

5. Conclusion

The degradation of OLEDs grown, kept and operated in UHV clearly demonstrates that the major cause for the undesired process of dark spot formation is intrinsic. Most likely imperfections in the device structure due to poor material quality and/or non-optimised fabrication conditions act as local spike centers and if gas contamination is strongly reduced they become relevant only at high operation voltages. The degradation results from intense decomposition of the ITO and organic film, caused by local temperature rise during spikes. The released volatile species lead to oxidation and to local delamination of the Al cathode. The similar behavior observed for OLEDs exposed to air show that the oxygen and moisture contamination can strongly accelerate the degradation process, dramatically increasing the probability of failures during operation.

This work was carried out within the EUREKA project E!2541 FOLIA (Flexible Organic Illuminators for the Automotive market) and funded by the Italian MIUR.

References

[1] C.W. Tang, S.A. VanSlyke, Appl. Phys. Lett. 51 (1987) 913.
[2] A. Hepp, H. Heil, W. Weise, M. Ahles, R. Schmechel, H. von Seggern, Phys. Rev. Lett. 91 (2003) 157406.
[3] F. Cicoira, C. Santato, F. Dinelli, M. Murgia, M.A. Loi, F. Biscarini, R. Zamboni, P. Heremans, M. Muccini, Adv. Funct. Mater. 15 (2005) 375.
[4] H. Nakanotani, H. Sasabe, C. Adachi, Appl. Phys. Lett. 86 (2005) 213506.
[5] Organic Light Emitting Diodes for General Illumination Update 2002, Optoelectronics Industry Development Association, 1133 Connecticut Avenue, NW#600, Washington, DC 20036.
[6] R. Farchioni, G. Grosso, Organic Electronics Materials, Springer, 2001.
[7] Hany Aziz, Zoran D. Popovic, Chem. Mater. 16 (2004) 4522.
[8] M.S. Xu, J.B. Xu, H.Z. Chen, M. Wang, J. Phys. D: Appl. Phys. 37 (2004) 2618.
[9] Michel Schaer, Frank Nüesch, Detlef Berner, William Leo, Libero Zuppiroli, Adv. Funct. Mater. 11 (2001) 116.
[10] B. Geffroy, P. le Roy, C. Prat, Polym. Int. 55 (2006) 572, and references therein.
[11] P. Melpignano, A. Baron-Toaldo, V. Biondo, S. Priante, R. Zamboni, M. Murgia, S. Caria, L. Gregoratti, A. Barinov, M. Kiskinova, Appl. Phys. Lett. 86 (2005) 41105.
[12] M. Marsi, L. Casalis, L. Gregoratti, S. Günther, A. Kolomakov, J. Kovac, D. Lonza, M. Kiskinova, J. Electron. Spectrosc. Rel. Phenom. 84 (1997) 73.
[13] S. Gunther, B. Kaulich, L. Gregoratti, M. Kiskinova, Prog. Surf. Sci. 70 (2002) 187.
[14] S. Gunther, A. Kolmakov, J. Kovac, M. Kiskinova, Ultramicroscopy 75 (1998) 35.
[15] S. Doniach, M. Sunjic, J. Phys. C 3 (1970) 285.
[16] M. Yamaquchi, A. Ide-Ektessabi, H. Nomura, N. Yasui, Thin Solid Films 447 (2004) 115.
[17] Y.-S. Kim, Y. –C. Park, S.G. Ansari, B.-S. Lee, H.-S. Shin, Thin Solid Film 426 (2003) 124.
[18] T. Ishida, H. Kobayashi, Y. Nakato, J. Appl. Phys. 73 (1993) 4344.
[19] J.J. Yeh, Atomic Calculation of Photoionization Cross-Sections and Asymmetry Parameters, Gordon and Breach Science Publishers, Langhorne, PE, 1993.
[20] V. Christou, M. Etchells, O. Renault, P.J. Dobson, O.V. Salata, G. Beamson, R.G. Egdell, J. Appl. Phys. 88 (2000) 5180.
[21] NIST XPS Principle Photoelectron lines, http://srdata.nist.gov/xps.
[22] L.S. Liao, J. He, X. Zhou, M. Lu, Z.H. Xiong, Z.B. Deng, X.Y. Hou, S.T. Lee, J. Appl. Phys. 88 (2000) 2386.
[23] Dimitry Kolosov, Douglas S. English, Vladimir Bulovic, Paul F. Barbara, Stephen R. Forrest, Mark E. Thompson, J. Appl. Phys. 90 (2001) 3242.

Available online at www.sciencedirect.com
ScienceDirect
Organic Electronics 8 (2007) 44–50
Organic Electronics
www.elsevier.com/locate/orgel

Patterning effects on poly (3-hexylthiophene) organic thin film transistors using photolithographic processes

Huiping Jia, Erich K. Gross, Robert M. Wallace, Bruce E. Gnade *

Materials Science and Engineering, University of Texas at Dallas, P.O. Box 830688, EC 33, Richardson, TX 75083, United States

Received 11 July 2006; received in revised form 19 October 2006; accepted 23 October 2006
Available online 27 November 2006

Abstract

We explore the effects of conventional photo lithographic patterning of the active layer of poly (3-hexylthiophene) (P3HT) organic thin film transistors (OTFT) on device performance. The performance of the devices was monitored in each step of the patterning process. We successfully developed a patterning process which is compatible with plastic substrates and P3HT as the organic semiconductor. In this process, parylene and atomic layer deposition (ALD) Al_2O_3 were used as capping layers. Al_2O_3 and parylene/P3HT were etched using Al etchant and O_2 plasma reactive ion etching (RIE), respectively. The degradation occurred primarily during the ALD Al_2O_3 deposition and capping layer etching. There was a 30% degradation in mobility, a 1–2× reduction in drive current, and an increase in threshold voltage after the ALD Al_2O_3 deposition. In the capping layer etching, a near 50% degradation in mobility was observed. The patterned devices have a mobility of 0.02 cm^2/V s, which is 1000× better than photo lithographically patterned P3HT OTFTs previously reported in the literature, and comparable to un-patterned P3HT devices.
© 2006 Elsevier B.V. All rights reserved.

PACS: 73.61.Ph; 85.30.Tv

Keywords: Organic thin film transistor; Organic thin film patterning; Photolithography

1. Introduction

The ability to pattern the organic semiconductor active layer in organic devices is often critical. It is required in applications such as color or backlit polymer/organic light emitting diode displays [1,2]. Patterning the active layer reduces cross-talk between adjacent devices. Additionally, parasitic resistance is reduced and leakage current is limited. As a result, the devices have better performance characteristics (I_{ON}/I_{OFF}, for example). Patterning is even more important when OTFTs share a common gate, in which case the leakage through the gate dielectric is significant [3].

There are many ways in which the organic semiconductor films may be patterned. Photolithographic patterning has been used by several groups [2,4–6]. It is a well established method that uses existing tools and processes commonly used within the semiconductor industry. A large area, high resolution lithography system that may be used

* Corresponding author.
E-mail address: gnade@utdallas.edu (B.E. Gnade).

1566-1199/$ - see front matter © 2006 Elsevier B.V. All rights reserved.
doi:10.1016/j.orgel.2006.10.009

for high volume, roll to roll production of organic electronic devices has been demonstrated [7]. Photolithographic patterning will allow relatively complex circuits where multiple layers processes, and modest alignment tolerances are required to meet performance goals. Another promising method is inkjet printing. With this method, the semiconductor is printed only in the desired area, reducing material cost and eliminating the need for subsequent patterning. Printing tools are the subject of extensive research and development, and obstacles such as resolution, printing speed, etc., need to be overcome before commercialization [8–11]. Even though the ultimate goal for organic electronics is to use printing techniques which will not require photolithography, there are a number of applications that will benefit from a robust photolithography process at this time. Photolithographic patterning is needed for device fabrication that incorporates more than one function, for instance integrating capacitors, transistors and diodes in the same device flow. Also, for anything but the simplest single level metal flow, we need to be able to pattern and etch the interlevel dielectric, metal, interconnects, etc., which requires processing on the organic semiconductor. Other processes include laser ablation [1], selective deposition by substrate surface treatment [12,13], and mold printing/pattern transfer [14,15]. Additional details can be found in several recent review papers on organic electronics [8–11].

In this work, we demonstrate a photolithographic patterning process for P3HT OTFTs. We use P3HT as the example because it is one of the most studied solution processed semiconductors. The process described in this paper should apply to other organic semiconductors as well. The challenge when using conventional lithographic patterning is process compatibility with organic semiconductors. Recent reports show a mobility of 6.1×10^{-3} cm^2/V s and 10^{-5} cm^2/V s for photolithographically patterned pentacene and P3HT OTFTs, respectively [4,6]. Considering a typical mobility of 0.1 cm^2/V s and 0.01 cm^2/V s for unpatterned pentacene and P3HT, respectively [8–11], there is a more than two orders of magnitude performance degradation after patterning. Therefore, we focus on how the patterning process impacts device performance in order to develop a process that is compatible with inexpensive plastic substrates, and more importantly, the organic semiconductors.

2. Experimental details

Since the organic semiconductor is sensitive to water, oxygen and solvents, photoresist cannot be applied in direct contact with the organic layer. A protective capping layer must be deposited on top of the organic semiconductor before photoresist processing. Parylene is widely used as a tough, conformal capping material [2]. Another capping material that has been used is water soluble polyvinylalcohol (PVA). Several research groups have reported using PVA or sensitized PVA to pattern pentacene without significant device degradation [5,16,17]. Both parylene and PVA films are permeable to O_2, moisture, and solvents. To prevent the photoresist solvent from diffusing into the organic active layer, an inorganic layer may be deposited on top of the parylene or PVA. Typical inorganic barrier layers are SiO_2, SiN_x, Al_2O_3, or Al [18].

After the capping layers are deposited, the patterning process can be accomplished with wet (inorganic) and dry (organic and active layer) etching. Specifically considering the application of organic devices to flexible electronics, we require that all deposition and etching processes be compatible with plastic substrates, as well as the organic semiconductor being used. This typically means process temperatures of $\leqslant$100 °C. A schematic process flow of the patterning processes is shown in Fig. 1, where a Al_2O_3/parylene capping layer is used.

In order to monitor the device performance during the patterning process, a test chip design shown in Fig. 2 is used. The devices have an interdigitated drain/source layout. Extension lines connect drain/source contacts to the probe pads. The probe pads are masked with tape to prevent any deposition on them, and the devices are probed after each step. The devices were made on a thermal SiO_2/Si substrate with an oxide thickness of 54 nm. Bottom contact structures with channel lengths and widths of 7.5 μm and 4000 μm, respectively were used in this work. The P3HT film thickness was approximately 110 nm. Details regarding the device manufacturing process can be found in Ref. [19].

A Keithley 4200-SCS Semiconductor Characterization System in conjunction with a Cascade Microtech Model Summit Microchamber probe station was used to probe the devices. Other tools used in this work include a Union Carbide model 1030 parylene deposition system for the parylene deposition, a Unaxis 790 PECVD system for the

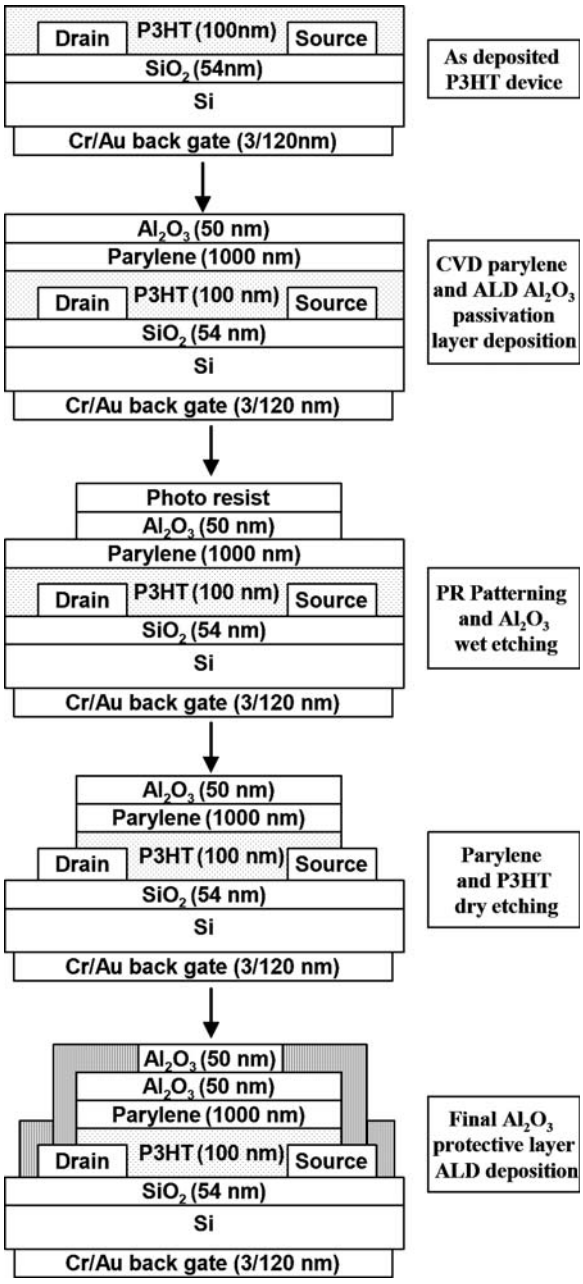


Fig. 1. Schematic patterning process flow on P3HT OTFTs. Al_2O_3/parylene capping layer was used in this process. At the last step, an Al_2O_3 protective layer was ALD deposited after etching.

SiO_2 and SiN_x deposition, a Cambridge NanoTech Inc. Savannah atomic layer deposition (ALD) system for the Al_2O_3 deposition, a Temescal Model BJD-1800 E-beam Evaporator for the Al deposition, and a Technics Series 85 reactive ion etcher (RIE) for the dry etch of parylene and P3HT. The device parameters monitored were drive current,

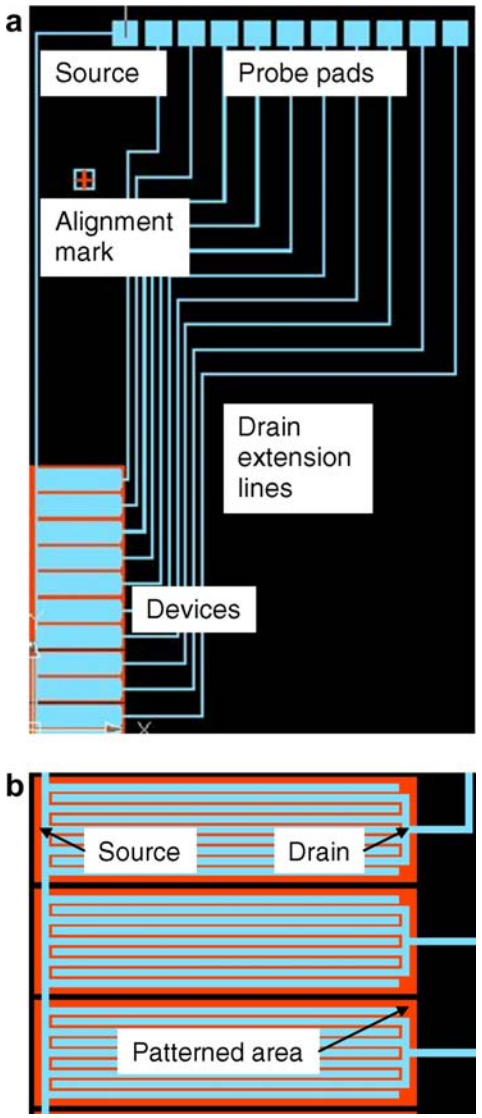


Fig. 2. The schematic layout of the test chips. (a) A quadrant of the test structures. The back side of the Si wafer was used as the gate contact. The devices have a common source. The probe pad size is $150 \times 150\ \mu m^2$. (b) The devices have an interdigitated D/S structure, and a channel length of 7.5 μm and channel width 8×500 μm. The shaded area is where the active layer is patterned.

I_D, at $V_{DS} = V_{GS} = -30$ V, threshold voltage, V_t, on/off ratio, I_{ON}/I_{OFF}, and mobility, μ. The data reported is the average of 10 devices.

3. Results and discussion

First, we tested the deposition of organic capping layers (i.e. parylene and PVA) on the performance of the devices. During the parylene film deposition,

the process chamber was kept at room temperature with a base pressure of 50 mTorr. The deposited film thickness is 1 μm. Although mobility and drive current decreased, and threshold voltage increased after parylene deposition, the variation for each parameter on average was less than 10%, relative to as-deposited devices (see Fig. 3). This confirms that the parylene coating process is compatible P3HT films. The devices capped with PVA films, however, showed dramatic degradation (>10×) in I_D and μ. The PVA film was spin-cast from a 7.5% DI water solution and baked at 95 °C in air for 1 h. This process produced film a thicknesses of 700 nm. Baking the samples at elevated temperatures (105 °C) and in vacuum (730 Torr) for extended periods (3 h) did not improve device performance. The P3HT film appears to have been permanently changed after coating the devices with the PVA water solution. Further investigation and process optimization may be needed if PVA is to be used as a capping layer material.

Next, the parylene coated P3HT devices were photo lithographically patterned. When photoresist (MICROPOSIT S1813) was applied by spin-coating and soft-baked on a 95 °C hot plate for 15 min, the devices degraded 10× in drive current and 5× in mobility (see Fig. 4).

Since polymer films in general are not good barriers for solvents [18], we speculate that the solvent in the photoresist diffused into and severely

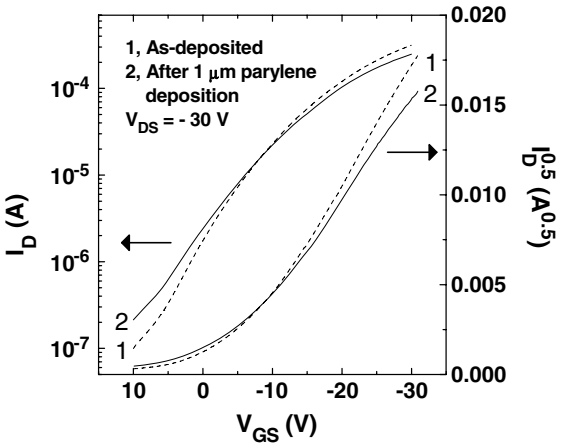


Fig. 3. Compatibility of parylene deposition with P3HT OTFTs, (1), as-deposited OTFT, $I_D = 315$ μA, $V_T = -2.5$ V, $\mu = 0.021$ cm^2/V s, and (2), after 1 μm parylene coating, $I_D = 248$ μA, $V_T = -3.4$ V, $\mu = 0.020$ cm^2/V s. The performance of P3HT OTFTs have less than 10% degradation on average after parylene passivation layer deposition.

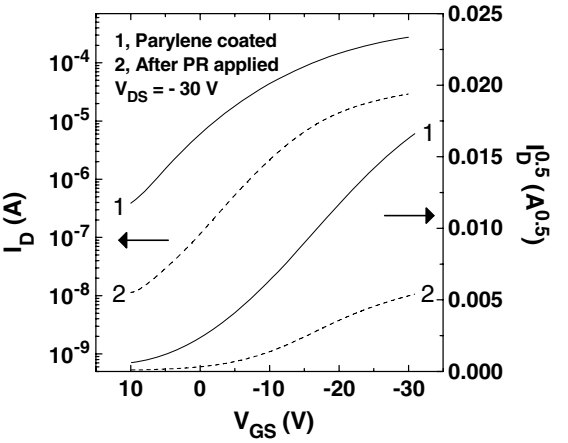


Fig. 4. Degradation of P3HT OTFTs when photo resist was applied on parylene passivated P3HT OTFTs, (1), parylene coated OTFT, $I_D = 270$ μA, $V_T = +2.8$ V, $\mu = 0.016$ cm^2/V s, and (2), after photo resist spin-coating and soft-baking at 95 °C, $I_D = 29$ μA, $V_T = -3.8$ V, $\mu = 0.003$ cm^2/V s.

degraded the devices. To prevent this solvent degradation, a protective inorganic layer may be needed. We considered four materials for this purpose; SiO_2, SiN_x, Al, and Al_2O_3. SiO_2 and SiN_x films were deposited by PECVD at 100 °C. Al was e-beam evaporated at room temperature, and Al_2O_3 was deposited by ALD at 100 °C. All deposition temperatures were compatible with P3HT. Both SiO_2 and Al films (100 nm) showed poor adhesion to parylene. Both films peeled from the parylene surface during photoresist development. The lack of any chemical bonding between the parylene and inorganic films due to the inert parylene surface may be responsible for the lack of adhesion. While the SiN_x films adhere well to parylene, severe degradation was observed following SiN_x deposition (>10×). During the PECVD SiN_x process, SiH_4, NH_3, He, and N_2 were used as carrier or reactant gases. There is an evidence in the literature that ammonia and hydrazine can dedope P3HT semiconductor [20,21]. In another study, it was found that NH_3 reduced/dedoped BF_4^- doped polythiophene and a reduction scheme was proposed [22]. In our study, we speculate that NH_3 defused into the P3HT films during PECVD SiN_x deposition and degraded the devices.

ALD Al_2O_3 was also used as an inorganic capping layer on parylene. The precursors used were trimethylaluminum (TMA) and water. N_2 carrier gas flowed through the chamber at 20 sccm. The deposition was performed at 100 °C with a chamber pressure of 200 mTorr. As can be seen in Table 1

Table 1
The effectiveness of parylene/ALD Al_2O_3 capping layers on P3HT OTFTs

Process step	I_D (μA)	I_{ON}/I_{OFF} (10^3)	V_t (V)	μ (cm^2/V s)
As deposited	252 (23)	1.2 (0.5)	0.4 (2.1)	0.017 (0.001)
After parylene and Al_2O_3 coating	79 (9)	162 (71)	−10.3 (1.0)	0.012 (0.001)
After PR coating	73 (9)	20 (5)	−10.3 (1.1)	0.010 (0.004)
After PR development	73 (12)	16 (5)	−10.5 (1.1)	0.011 (0.001)

The data in this table are the average of 10 devices with the SD included in the parentheses.

and Fig. 5, Al_2O_3 (50 nm) effectively protected the devices. The data in the table is the average of 10 devices with the standard deviation included in the parentheses. The effects of the photolithographic process following the Al_2O_3 deposition were negligible. There is a 30% reduction in mobility and a 1–2× reduction in drive current caused by the Al_2O_3 deposition. Several factors may be responsible to this degradation. While the parylene deposition is process compatible, parylene, as discussed previously, is not a good barrier for water or solvents. During the Al_2O_3 deposition, a small amount of water and TMA may have diffused through the parylene and into the P3HT film. As a result, traps may be introduced and molecular packing/crystalline structure may degrade in some part of the P3HT film [5,23,24], possibly the top layer at the P3HT/parylene interface. The effects of this would resemble those caused by P3HT film thickness reduction, i.e., higher threshold voltage, lower mobility and drive current, and higher on/off ratio, all due to the lower bulk current [19]. Since the Al_2O_3 deposition was done at 100 °C and 200 mTorr vacuum, thermal dedoping may also happen in the P3HT film [25]. The reduction in on/off ratio noted after photo resist coating and developing is caused primarily by increased off current through the exposed contact extension lines.

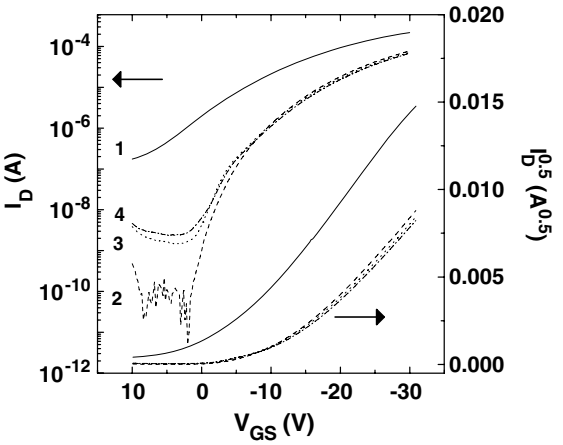


Fig. 5. The effectiveness of parylene/Al_2O_3 capping layer to protect P3HT OTFTs in photolithographic processes. The figure shows the transfer curves ($V_{DS} = -30$ V) of a P3HT OTFT at different stages of the photolithographic processes, (1), as-deposited, (2), after parylene/Al_2O_3 deposition, (3), after photo resist spin-coating, and (4), after photo resist development. Above the threshold voltage, curves 2–4 indicate negligible performance changes after photo resist coating and development. There is a 30% reduction in mobility and a 1–2× reduction in drive current caused by the Al_2O_3 deposition.

As Al_2O_3/parylene double layers can effectively protect the active layer, they were used in a process for patterning P3HT OTFTs (see the process flow in Fig. 1). Initially, the as-deposited devices were probed. After probing, the devices were immediately coated with parylene and Al_2O_3 to prevent doping in the air. In this process, the Al_2O_3 was etched using an Al etchant (Al Etchant type A, Transene Company Inc.) at 50 °C. The etch rate was approximately 10 nm/min. The parylene and P3HT layers were then etched using O_2 plasma reactive ion etching at a rate of 0.1 μm/min. Finally, the devices were coated with an additional 50 nm thick layer of Al_2O_3. The resulting devices exhibited mobilities of 0.02 cm^2/V s (see Table 2 and Fig. 6). The performance of these patterned P3HT devices is, to our knowledge, better than other patterned P3HT devices previously reported, and comparable to unpatterned P3HT devices [6,19]. The performance difference of as-deposited P3HT devices in Tables 1 and 2 is from the non-uniformity of the P3HT film within the wafer.

As can be seen from Table 2 and Fig. 6, the drive current after Al_2O_3 and parylene/P3HT etching changed slightly. The mobility was reduced to approximately 50% that of the pre-etch value, and the threshold voltage was greatly reduced. The patterned area is covered by a parylene/Al_2O_3/photo resist stack, so the effects must have been induced at the edges of the patterned structures where the P3HT and parylene films were exposed to Al

Table 2
The performance evolution of P3HT OTFTs with patterning processes

Process step	I_D (μA)	I_{ON}/I_{OFF} (10^3)	V_t (V)	μ (cm^2/V s)
As deposited	355 (67)	3.3 (0.2)	−1.7 (1.3)	0.028 (0.003)
After parylene and Al_2O_3 coating	176 (22)	2981 (5594)	−10.0 (0.3)	0.025 (0.003)
After Al_2O_3 and P3HT etching	168 (15)	1.4 (0.3)	−2.1 (0.4)	0.014 (0.001)
After Al_2O_3 protective overcoat	187 (19)	38 (6)	−6.8 (0.5)	0.020 (0.002)

The data in this table are the average of 10 devices with the SD included in the parentheses.

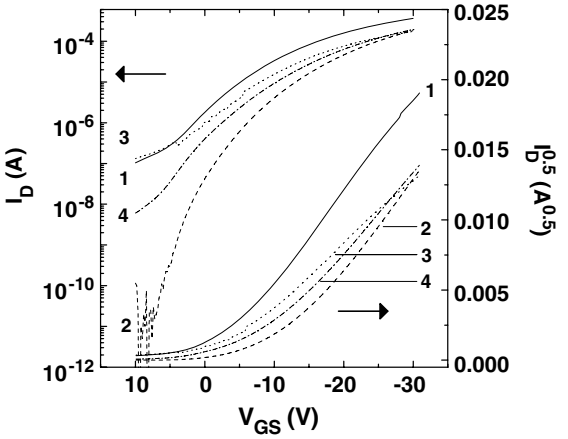


Fig. 6. The performance evolution of P3HT OTFTs with patterning processes. The figure shows the transfer curves ($V_{DS} = -30$ V) of a P3HT OTFT at different stages of the photolithographic patterning processes, (1), as-deposited, (2), after parylene/Al_2O_3 deposition, (3), after wet etch of Al_2O_3 and dry etch of parylene/P3HT, and (4), after a protective Al_2O_3 deposition.

etchant, water, and O_2 plasma during the patterning process. Although the effects are not well understood, the decreased on/off ratio, threshold voltage, and mobility may be partially attributable to higher off current (surface current and bulk current) [19]. The final Al_2O_3 layer deposition caused a recovery of 30% of the mobility and increased the on/off ratio by lowering the off current. Further research is needed to understand the behavior of the devices during etching.

4. Conclusions

In summary, we systematically studied the effects of photolithographic patterning on the performance of P3HT OTFTs. The deposition of parylene is compatible with P3HT OTFTs. A 10% performance decrease was observed after parylene coating. Parylene and ALD Al_2O_3 double capping layers are effective for protecting the P3HT devices during photoresist patterning. Some degradation was seen after Al_2O_3 deposition. There was a 30% degradation in mobility, a 1–2× reduction in drive current, and an almost 10 V increase in threshold voltage. A possible reason for the degradation is the dedoping of the P3HT layer by water and TMA. The drive current after Al_2O_3 and parylene/P3HT etching changed slightly. The mobility was reduced to approximately 50% that of the pre-etch value, and the threshold voltage was greatly reduced. The degradation is partially attributed to the increase in off current resulting from the exposure of the P3HT/parylene and sample surface to the etchant solution. The deposition of an additional Al_2O_3 layer, used as a protective overcoat, on patterned devices recovered 30% of the mobility and increased the on/off ratio by lowering the off current. The resulting patterned P3HT devices have mobilities of 0.02 cm^2/V s. The mobilities associated with these devices are $\sim 10^3\times$ better than those of patterned P3HT OTFTs previously reported and comparable with unpatterned P3HT devices.

Acknowledgements

This work was supported in part by the U.S. Army Soldier Systems Center through Contract No. DAAD-16-00-9732 and DAAD-16-01-C-0026.

References

[1] D.G. Lidzey, M. Voigt, C. Giebeler, A. Buckley, J. Wright, K. Böhlen, J. Fieret, R. Allott, Org. Electr. 6 (2005) 221.
[2] I. Kymissis, C.D. Dimitrakopoulos, S. Purushothanman, J. Vac. Sci. Technol. B 20 (3) (2002) 956.
[3] H. Jia, G.K. Pant, E.K. Gross, E.M. Wallace, B.E. Bruce, Org. Electr. 7 (2006) 16.
[4] J.A. DeFranco, B.S. Schmidt, M. Lipson, G.G. Malliaras, Org. Electr. 7 (2006) 22.
[5] S.H. Han, J.H. Kim, J. Jang, S.M. Cho, M.H. Oh, S.H. Lee, D.J. Choo, Appl. Phys. Lett. 88 (2006) 073519.
[6] F.M. Li, Y. Vygranenko, S. Koul, A. Nathan, J. Vac. Sci. Technol. A 24 (3) (2006) 657.

[7] K. Jain, M. Zemel, M. Klosner, Proc. IEEE 90 (10) (2002) 1681.
[8] M.L. Chabinyc, A. Salleo, Chem. Mater. 16 (2004) 4509.
[9] C. Reese, M. Roberts, M. Ling, Z. Bao, Mater. Today 7 (2004) 20.
[10] M. Ling, Z. Bao, Chem. Mater. 16 (2004) 4824.
[11] H.E. Katz, Chem. Mater. 16 (2004) 4748.
[12] J. Jang, S.H. Han, SID 05 Digest (2005) 12.
[13] M.L. Chabinyc, W.S. Wong, A. Salleo, K.E. Paul, Appl. Phys. Lett. 81 (2002) 4260.
[14] R. Parashkov, E. Becker, T. Riedl, H. Johannes, W. Kowalsky, Adv. Mater. 17 (2005) 1523.
[15] C. Kim, Y. Cao, W.O. Soboyejo, S.R. Forrest, J. Appl. Phys. 97 (2005) 113512.
[16] L. Zhou, S. Park, B. Bai, J. Sun, S. Wu, T.N. Jackson, S. Nelson, D. Freeman, Y. Hong, IEEE Dev. Lett. 26 (2005) 640.
[17] Y. Wang, H. Cheng, Y. Wang, T. Hu, J. Ho, C. Lee, T. Lei, C. Yeh, Thin Solid Film 491 (2005) 305.
[18] J.S. Lewis, M.S. Weaver, IEEE J. Selected Topics Quantum Electron. 10 (2004) 45.
[19] H. Jia, S. Gowrisanker, G.K. Pant, R.M. Wallace, B.E. Gnade, J. Vac. Sci. Technol. A 24 (2006) 1228.
[20] Z. Bao, A. Dodabalapur, A. Lovinger, Appl. Phys. Lett. 69 (1996) 4108.
[21] J.J. Apperloo, R.A.J. Janssen, M.M. Nielsen, K. Bechgaard, Adv. Mater. 12 (2000) 1594.
[22] F. Mohammad, J. Phys. D: Appl. Phys. 31 (1998) 951.
[23] H.L. Gomes, P. Stallinga, M. Cölle, F. Biscarini, D.M. de Leeuw, J. Non-Crystalline Solid 352 (2006) 1761.
[24] D.J. Gundlach, T.N. Jackson, D.G. Schlom, S.F. Nelson, Appl. Phys. Lett. 74 (1999) 3302.
[25] R.H.M. van de Leur, B. de Ruiter, J. Breen, Synth. Met. 54 (1993) 203.

Available online at www.sciencedirect.com
ScienceDirect
Organic Electronics 8 (2007) 51–56
Organic Electronics
www.elsevier.com/locate/orgel

Improved electrical stability and UV emission of zinc oxide thin films prepared by combination of metalorganic chemical vapor deposition technique and post-deposition hydrogen doping

Seung Yeop Myong *, Koeng Su Lim

Division of Electrical Engineering, Department of Electrical Engineering and Computer Science, KAIST, 373-1 Guseong-dong, Yuseong-gu, Daejeon 305-701, Republic of Korea

Received 1 November 2005; received in revised form 25 October 2006; accepted 29 October 2006
Available online 27 November 2006

Abstract

Fourier transform infrared and photoluminescence spectroscopy provide strong evidence that post-deposition hydrogen doping of polycrystalline zinc oxide (ZnO) thin films improves the resistivity by increasing hydrogen-related shallow donors and hydrogen passivation of native defects. Improvement of the electrical stability and UV emission confirm that post-deposition hydrogen doping is a promising method to achieve high quality ZnO thin films for the use as transparent electrodes and/or UV light emitters in thin-film-based optoelectronic devices.
© 2006 Elsevier B.V. All rights reserved.

PACS: 78.55.−m

Keywords: ZnO film; Hydrogen doping; UV emission; Electrical stability; Light-emitting diode

1. Introduction

Zinc oxide (ZnO) materials have attracted great attention due to their unique characteristics. Since Van de Walle theoretically suggested that hydrogen interstitials unintentionally incorporated in ZnO during the deposition act as shallow donors in 2000 [1], a great deal of experimental evidence supporting the existence of hydrogen shallow donors of single-crystal ZnO has been reported [2–8]. Although the majority of research has focused on the role of hydrogen in single-crystal ZnO, the role of hydrogen in polycrystalline ZnO thin films is also very important as these films are commonly used as transparent electrodes in thin-film solar cells and light-emitting diodes (LEDs). In addition, polycrystalline ZnO has the potential to be used as transparent electrodes for thin-film transistor liquid crystal displays (TFT-LCDs) and organic LEDs (OLEDs), provided that its electrical stability can be improved [9]. Our group reported significant improvement in the as-grown electrical conductivity and surface

* Corresponding author. Tel.: +82 42 869 5427; fax: +82 42 869 8530.
E-mail address: myongsy@kaist.ac.kr (S.Y. Myong).

1566-1199/$ - see front matter © 2006 Elsevier B.V. All rights reserved.
doi:10.1016/j.orgel.2006.10.010

roughness of undoped polycrystalline ZnO thin films prepared by the metalorganic chemical vapor deposition (MOCVD) method via an *in situ* post-deposition hydrogen treatment using mercury (Hg)-sensitized hydrogen photodecomposition [10]. The authors demonstrated that hydrogen passivation and surface etching might be effectively employed to improve these parameters. In 1998, we proposed the intentional hydrogen incorporation during the polycrystalline ZnO deposition by combining photo-assisted MOCVD (photo-MOCVD) and Hg-sensitized hydrogen addition [11]. We demonstrated the doping effect of polycrystalline ZnO by hydrogen and remarkably improved electrical stability under an air atmosphere [12]. We have also investigated post-deposition doping of polycrystalline ZnO thin films prepared by the photo-MOCVD technique [13]. Owing to our previous reports mainly concentrated on the electrical and light scattering characteristics, however, more detailed study on the role of hydrogen supported by post-deposition hydrogen doping is requested. Therefore, in this article, we investigate the hydrogen interaction with polycrystalline ZnO and address the advantages of the *in situ* post-deposition hydrogen doping technique in terms of device application.

2. Experimental

Using the MOCVD technique, we prepared nominally undoped polycrystalline ZnO thin films on Corning 7059 glass and c-Si (100) substrates at 140 °C. Bubbled diethylzinc (DEZ) and H_2O were introduced into the reaction chamber using high purity Ar (99.999%) carrier gas. The H_2O/DEZ ratio, chamber pressure, and film thickness were maintained at 18 mol/mol, 7 Torr, and ~1 μm, respectively. *In situ* post-deposition hydrogen doping was performed at the same temperature of 140 °C. The hydrogen flow rate, chamber pressure, and Hg bath temperature were kept at 100 sccm, 1 Torr, and 20 °C, respectively. A low-pressure Hg lamp with resonance lines of 184.9 and 253.7 nm was used as a ultraviolet (UV) light source to decompose Hg-sensitized hydrogen molecules (H_2).

We measured the resistivity, Hall mobility (μ), and carrier concentration (n) at room temperature using the Van der Pauw method. We performed secondary ion mass spectrometry (SIMS) using a magnetic sector ion mass spectrometer CAMECA 4F. The precision for the element level is within 5%. In order to inspect changes in O–H bonding configurations, we performed Fourier transform infrared (FTIR) spectroscopy. An unpolarized He–Ne (maximum power of 4 mW at a wavelength of 633 nm) laser was perpendicularly irradiated to the samples at room temperature. We measured photoluminescence (PL) spectra for nominally undoped ZnO and hydrogen-doped ZnO (ZnO:H) thin films prepared on c-Si (100) substrates at 10 K using a He–Cd laser (typically 40 mW at a wavelength of 325 nm). We examined the crystal orientation via the X-ray diffraction (XRD) measurement. All the films have *c*-axis orientation to [0002], [10 − 10], and [11 − 20] directions. More specifically, the films are highly oriented to the [11 − 20] direction, which displays a pyramid rough surface [14].

Fig. 1 depicts improvement of μ and n of the ZnO and ZnO:H films as a function the hydrogen doping time. Both μ and n enhance with an increase in the hydrogen doping time and then saturate after 60 min.

Fig. 2 shows the evolution of the resistivity of the films at room temperature under a humid air atmosphere (humidity: 60%–80%). The as-grown nominally undoped ZnO film shows a poor resistivity of 1.87 Ω cm. With only 5 min post-deposition hydrogen doping, both μ and n are enhanced by one order of magnitude. Although these parameters increase with the increase in the hydrogen doping time, the extent of the increase monotonously decreases. Thus, the as-grown resistivity gradually decreases with the hydrogen doping time. With hydrogen doping for 60 min, the as-grown resistivity dramatically improves to 4.25×10^{-3} Ω cm. On the other hand, the as-grown resistivity of ZnO

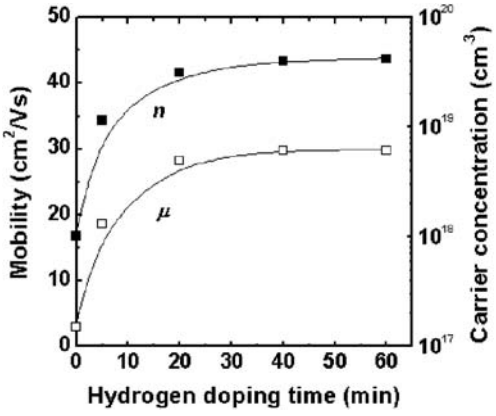


Fig. 1. Variation of the mobility and carrier concentration as a function of the post-deposition hydrogen doping time.

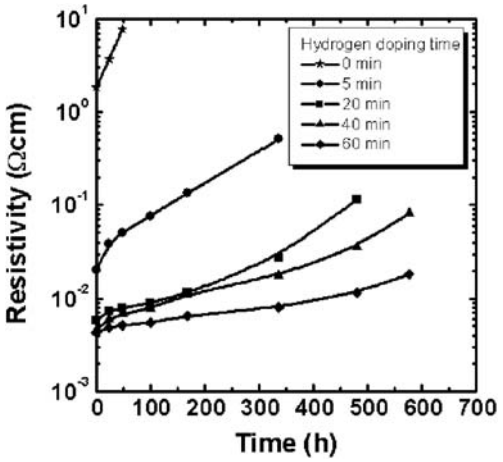


Fig. 2. Evolution of the resistivity for the ZnO:H films under a humid air atmosphere.

progressively decreases with an increase in the time exposed to the air. Notably, we found that the degradation of ZnO:H significantly retarded with the increase in the doping time.

Fig. 3 displays the depth profiles of the films. After hydrogen doping for 60 min, the ratio of Zn/O declines near the surface due to the desorption of oxygen [10,12,13]. H content, meanwhile, almost uniformly increases in the bulk of the ZnO:H film. Together with these elements, we also detect extrinsic impurities such as Al, C, and P. These impurities uniformly distributed in the samples with small content. However, we could not detect any signal corresponding to extrinsic deep acceptors such as Fe, Cu, and Li [15].

Fig. 4 depicts FTIR spectra for the ZnO film and the ZnO:H film with the doping time of 60 min.

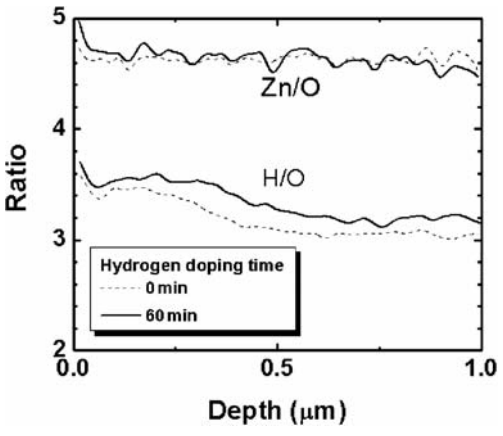


Fig. 3. SIMS depth profiles for the ZnO and ZnO:H films (hydrogen doping time: 60 min).

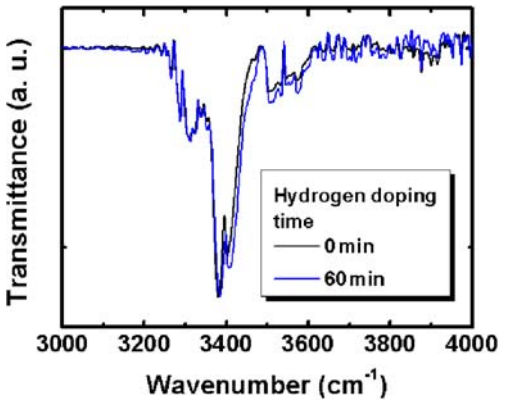


Fig. 4. Comparison of FTIR spectra between the ZnO and ZnO:H films (hydrogen doping time: 60 min). All spectra were measured at room temperature.

Both the films show a broad absorption band in the wave number range of 3200–3620 cm^{-1}, which corresponds to the O–H bond-stretching local vibrational modes (LVMs) of single-crystal ZnO [2–7]. We attribute these absorption lines to a hydrogen passivation of native defects such as zinc vacancies (V_{Zn}) [2,6]; hydrogen shallow donors [1] incorporated in anti-bonding oxygen sites (AB_O) [3] or bond-centers (BC) of O–Zn bonds [2]; and O–H bonds located at grain boundaries [16,17]. We ascribe the invariant lower frequency lines centered in the wavelength range of 3200–3300 cm^{-1} to the LVMs of H-II defects, zinc vacancy (V_{Zn})–H complexes ($V_{Zn}H_2$); two independent O–H bonds consisting of two hydrogen atoms passivate a double charge acceptor, V_{Zn} [2,6]. However, the other absorption bands (wavelength: 3300–3620 cm^{-1}) display the increase in the integrated intensity as a result of hydrogen doping. Thus, intentional post-deposition hydrogen doping increases the quantity of hydrogen-related shallow donors and hydrogen in the grain boundary regions. However, the total increase in O–H bond-stretching LVMs is too small to explain the remarkable improvement of the resistivity. Accordingly, other hydrogen-related shallow donors should be involved in the carrier conduction.

Fig. 5 provides the PL spectra of the ZnO and ZnO:H films measured at 10 K. As shown in Fig. 5a, the near-band-edge (NBE) emission of ZnO can be deconvoluted to four Lorentz peaks. We attribute the highest peak centered at 3.375 eV to the hydrogen-related donor bound-exaction emission (D^oX) [8]. The dominant peak centered at 3.329 eV is due to the two-electron satellite (TES) band [18]. The two-lower energy peaks are

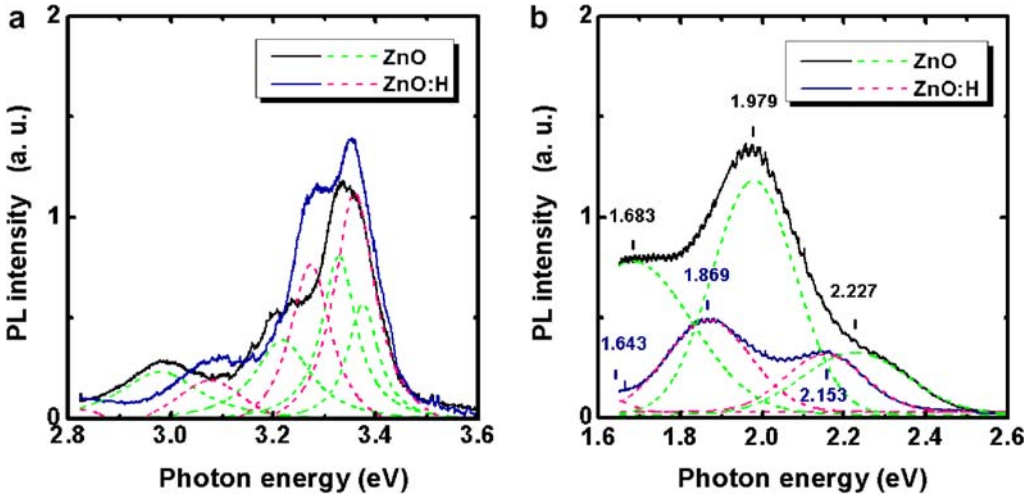


Fig. 5. PL spectra for the ZnO and ZnO:H films (hydrogen doping time: 60 min) measured at 10 K. The dotted lines are the component peaks for the films. (a) near-band-edge emission and (b) visible emission.

phonon replicas. In contrast, the spectrum of ZnO:H is dominated by the (D^oX) line centered at 3.359 eV. Although the peak position of the (D^oX) line shifts to lower energy as a result of hydrogen doping, the highest emission edge is almost unchanged, due to the increase in the full width at half maximum (FWHM) from 73.4 to 99.5 meV. The TES line, meanwhile, shifts to lower energy of 3.274 eV as a result of hydrogen doping and its intensity slightly increases due to the increase in FWHM from 81.8 to 101 meV. All phonon replicas are shifted to lower energies and reduced after hydrogen doping.

Compared to the NBE emission, the films prepared by the MOCVD technique exhibit a pronounced visible emission, as shown in Fig. 5b. The drastic suppression of the green and yellow emissions and the improvement of the NBE UV emission efficiency account for the reduction of nonradiative recombination centers by hydrogen doping [19]. We decomposed the broad lines using three Gaussian peaks. Via hydrogen doping, all emission lines show a redshift and a reduced integrated intensity; peaks of the undoped ZnO film centered at 1.683, 1.979, and 2.227 eV shift to 1.643, 1.869, and 2.153 eV, respectively. As a result of hydrogen doping, the highest energy line at ~2.2 eV decreases slightly mainly due to the decline in FWHM from 306 to 230 meV. However, the two-lower energy lines display a significant reduction. The nature of the visible lines is still being debated since it partly depends on sample deposition conditions. These yellow and green emissions probably originate from native defects, because any Fe, Cu, and Li impurities that act as deep-level acceptors in ZnO are not detectable. From the deep donor level at 0.3 V below the bottom of the conduction band of single-crystal ZnO [20], Ohashi et al. recently demonstrated that the yellow (~2.0 eV) and green (~2.2 eV) emissions are assignable to donor–acceptor-pair (DAP) transitions caused by excitation of electrons from the valence band to the deep level [21]. From the oxygen-deficiency in our polycrystalline ZnO films, we speculate that the oxygen vacancy (V_O) may be a deep-level donor. In this case, the green emission at ~2.2 eV can be explained as the transition between V_O and V_{Zn} donor–acceptor pairs [21]. Since the $V_{Zn}H_2$ defects are invariant after hydrogen doping (see Fig. 4), the small decrease in the green emission is strongly indicative of reduction of active V_O. For the yellow emission at ~2.0 eV, Ohashi et al. suggested Li ions in single-crystal ZnO as the acceptors. However, in our case, the dominant yellow emissions may results from hole capture by neutral V_O [22]. The dramatic reduction of the yellow emissions also indicates the reduction of active V_O.

From Fig. 2, we can observe the improved electrical stability of the ZnO thin films via hydrogen doping. It is well known that under a humid air atmosphere, the electrical conductivity of polycrystalline ZnO decreases due to the reinforced potential barriers at grain boundaries [23]; the chemisorption of oxygen or H_2O vapor through the grain boundaries leads to the degradation of the electrical conductivity by trapping free electrons. Due to the

reinforced potential barriers at grain boundaries, μ severely decreases at the initial stage of the degradation compared to n. Based on the desorption of oxygen in Fig. 3 and the reduction of the visible emission in Fig. 5b, we speculate that post-deposition hydrogen doping disturbs the chemisorption of oxygen or H_2O vapor through the grain boundary regions by inducing a number of hydrogen-related complexes. The V_O–H complex consists of a V_O deep-level donor and a hydrogen atom is the plausible candidate for the remarkable improvement of the as-grown conductivity and reduction of PL visible emission, because it also acts as a shallow donor by capturing a positively charged hydrogen (H^+) [1]. In other words, the V_O deep-level donor can transit to a shallow donor by capturing H^+. However, more detailed research is required for the V_O–H complex. On the other hand, Wolden et al. suggested that effusion of hydrogen from the film is thermally activated process and thereby cause an increase in the resistivity [17]. It is reported that $V_{Zn}H_2$ defects are thermally stable [2] and hydrogen shallow donors in AB_O is clearly less stable [24]. In addition, the BC hydrogen shallow donor is known to the most stable shallow donor [1]. In our previous report [12], it was revealed that ZnO thin films intentionally hydrogen-doped during the deposition were metastable under a humid air atmosphere. However, the resistivity of the ZnO thin films doped by post-deposition H_2-exposure displays a different trend (see Fig. 2). From the continuous evolution of the resistivity, we speculate that at least two different mechanisms are involved in the degradation of the electrical conductivity.

Accordingly, the total concentration of shallow donors (N_D) can be expressed as

$$N_D \propto H^i_{BC} + H^i_{ABo} + H^i_X, \quad (1)$$

where H^i_{BC} is the concentration of BC hydrogen shallow donors and H^i_{ABo} is the concentration of hydrogen interstitial incorporated in AB_O sites. H^i_X is the concentration of other hydrogen-related shallow donors such as the V_O–H complex. Taking into account the potential fluctuations caused by the random distribution of shallow donors, FWHM of the (D^oX) transition is then related to N_D through the following expression [25]

$$\mathrm{FWHM} \propto (N_D r_s)^{1/2}, \quad (2)$$

where r_s is either the Debye or Thomas–Fermi screening radius. The broadening in FWHM of the (D^oX) transition in Fig. 5a also supports our suggestion that H^i_X increases as a result of hydrogen doping.

3. Conclusions

Post-deposition hydrogen doping of polycrystalline ZnO thin films prepared by the MOCVD technique remarkably improves the as-grown conductivity, electrical stability under a humid air atmosphere, and UV emission efficiency. Furthermore, hydrogen doping is easily applicable to ZnO thin-film-based device productions. Accordingly, this hydrogen doping technique is beneficial in terms of achieving high quality ZnO thin films for the use as LEDs.

References

[1] C.G. Van de Walle, Phys. Rev. Lett. 85 (2000) 1012.
[2] E.V. Lavrov, J. Weber, F. Borrnert, C.G. Van de Walle, R. Helbig, Phys. Rev. B 66 (2002) 165205.
[3] M.D. McCluskey, S.J. Jokela, K.K. Zhuraviev, P.J. Simson, K.G. Lynn, Appl. Phys. Lett. 81 (2002) 3807.
[4] C.H. Seager, S.M. Myers, J. Appl. Phys. 94 (2003) 2888.
[5] E.V. Lavrov, Physica B 340–342 (2003) 195.
[6] E.V. Lavrov, F. Börmert, J. Wever, Phys. Rev. B 71 (2005) 035205.
[7] L.E. Halliburton, L. Wang, L. Bai, N.Y. Garces, N.C. Giles, M.K. Callahan, B. Wang, J. Appl. Phys. 96 (2004) 7168.
[8] Y.M. Strzhemechny, J. Nemergut, P.E. Smith, J. Bae, D.C. Look, L.J. Brillson, J. Appl. Phys. Lett. 94 (2003) 4356.
[9] R.G. Gordon, MRS Bull. 25 (8) (2000) 52.
[10] S.J. Baik, J.H. Jang, C.H. Lee, W.Y. Cho, K.S. Lim, Appl. Phys. Lett. 70 (1997) 3516.
[11] S.Y. Myong, S.J. Baik, K.S. Lim, in: Proceedings of the Second World Conference on Photovoltaic Solar Energy Conversion, Vienna, Austria, EC Joint Research Center, Ispra, 1998, pp. 692–695.
[12] S.Y. Myong, K.S. Lim, Appl. Phys. Lett. 82 (2003) 3026.
[13] S.Y. Myong, K.S. Lim, Sol. Energ. Mat. Sol. Cells 86 (2005) 105.
[14] S. Faÿ, L. Feitknecht, R. Schlüchter, U. Kroll, E. Vallat-Sauvain, A. Shah, Sol. Energ. Mat. Sol. Cells 86 (2005) 385.
[15] S.Y. Myong, S.I. Park, K.S. Lim, Thin Solid Films 513 (2006) 148.
[16] X. Li, B. Keyes, S. Asher, S.B. Zhang, S.H. Wei, T.J. Coutts, S.L. Limpijumnong, C.G. Van de Walle, Appl. Phys. Lett. 86 (2005) 122107.
[17] C.A. Wolden, T.M. Barnes, J.B. Baxter, E.S. Aydil, J. Appl. Phys. 97 (2005) 043522.
[18] K. Thonke, Th. Gruber, N. Teofilov, R. Schonfelder, A. Wagg, R. Sauer, Physica B 308–310 (2001) 945.
[19] N. Ohashi, T. Ishigaki, N. Okada, H. Taguchi, I. Sakaguchi, S. Hishita, T. Sekiguchi, H. Haneda, J. Appl. Phys. 93 (2003) 6386.
[20] N. Ohashi, J. Tanaka, T. Ohgaki, H. Haneda, M. Ozawa, T. Tsurumi, J. Mater. Res. 17 (2002) 1529.

[21] N. Ohashi, N. Ebisawa, T. Sekiguchi, I. Sakaguchi, Y. Wada, T. Takenaka, H. Haneda, Appl. Phys. Lett. 86 (2005) 091902.
[22] A. Janotti, Chris G. Van de Walle, Appl. Phys. Lett. 87 (2005) 122102.
[23] S.Y. Myong, K.S. Lim, J. Cryst. Growth 293 (2006) 253.
[24] S.J. Jokela, M.D. McCluskey, Phys. Rev. B 72 (2005) 113201.
[25] T. Makino, Y. Segawa, S. Yoshida, A. Tsukazaki, A. Ohtomo, M. Kawasaki, Appl. Phys. Lett. 85 (2004) 759.

Available online at www.sciencedirect.com
ScienceDirect
Organic Electronics 8 (2007) 57–62
Organic Electronics
www.elsevier.com/locate/orgel

Crosslinkable organic glasses with quadratic nonlinear optical activity

Antonio Carella [a], Roberto Centore [a,*], Loïc Mager [b], Alberto Barsella [b], Alain Fort [b]

[a] *Dipartimento di Chimica, Università degli Studi di Napoli "Federico II", Via Cinthia, 80126 Napoli, Italy*
[b] *IPCMS, UMR CNRS-ULP 7504, 23 Rue du Loess, BP 43, 67034 Strasbourg Cedex, France*

Received 6 September 2006; received in revised form 27 October 2006; accepted 29 October 2006
Available online 21 November 2006

Abstract

In this paper, the use of a pure benzimidazole based dimethacrylic push–pull chromophore has been investigated for the preparation of thin films exhibiting quadratic nonlinear optical (NLO) properties. To stabilize these NLO properties, the chromophore orientation has been frozen in a noncentrosymmetric arrangement by cross-linking the material using thermal polymerization induced by suitable initiators. The films present a very stable quadratic optical activity up to $T = 152$ °C with SHG coefficient d_{33} of 14 pm/V measured at 1.9 μm.
© 2006 Elsevier B.V. All rights reserved.

PACS: 82.35.Ej

Keywords: NLO; Benzimidazole; Cross-linked polymer; SHG

1. Introduction

In the last decade, huge efforts have been deployed to optimize the nonlinear optical (NLO) efficiencies of organic materials functionalised with doped or grafted push–pull chromophores [1–4]. In this context, relatively simple formalisms have been developed as guidelines for the synthesis of push–pull molecules possessing large quadratic hyperpolarizabilities. In the same way, the optimisation of the geometric structure has led to a better efficiency of the poling process by limiting the centrosymmetric chromophore–chromophore interactions. These improvements have led to the elaboration of polymeric materials with high second order nonlinear optical coefficients (r_{33}, d_{33}) [5,6]. However, the temporal stability of such organic NLO materials is still an important challenge. The relaxation of the orientation of the chromophores, inducing the loss of the NLO properties of the polymer, has generally to be improved when looking for applications.

In this work, we have developed an original approach based on a pure crosslinkable NLO chromophore to elaborate a new organic material designed for quadratic optical properties. This

* Corresponding author. Tel.: +39 081 674450; fax: +39 081 674090.
E-mail address: roberto.centore@unina.it (R. Centore).

1566-1199/$ - see front matter © 2006 Elsevier B.V. All rights reserved.
doi:10.1016/j.orgel.2006.10.008

method maximizes the concentration of the NLO-active functions as no NLO-inactive binder is required. Actually, the fully functionalised NLO polymers strategy also limits the amount of binder. But, in general, grafting the chromophore to the polymer chain is achieved in the preliminary synthetic step before any orientation process. As a consequence, the covalent binding of the chromophores to the chain limits their orientational mobility and can therefore restrain the orientation rate and extent [7].

The lifetime of the chromophore orientation, a key feature for the elaboration of efficient materials, mainly depends on the efficiency of freezing chromophore movements in the matrix. For polymeric materials, this can be roughly correlated to the glass transition temperature T_g, a long lifetime being generally associated with high T_g polymers [8–13]. For cross-linked materials [14–17], chromophore motion is limited compared with doped materials and therefore a compromise has to be found between poling and relaxation efficiencies.

The precursor of our material is higher an organic push–pull chromophore functionalised with two crosslinkable functions (see Fig. 1). This molecule, called DIMET, is the only monomer used to obtain the final three-dimensional organic network (organic glass). Thus, one can expect a high efficiency coming from the high chromophore concentration and from the high mobility of small molecules before cross-linking, the long lifetime originating from the high cross-linked nature of the final material.

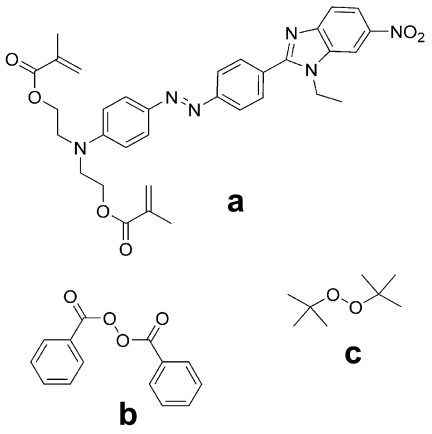


Fig. 1. Molecular scheme of DIMET (a), benzoyl peroxide (b) and *t*-butyl peroxide (c).

We report on the synthesis of this molecule, on the preparation of the NLO material and on some of its specific properties.

2. Results and discussion

The material is obtained from the azo-benzimidazolic chromophore functionalised with two crosslinkable methacrylate groups (see Fig. 1). Except for the radical initiator incorporated in very small quantities (2% wt), the unique component of the material is the chromophore itself. This differs from comparable approaches reported in the literature [14–17] as the present formulation of the material does not include any significant amount of NLO-inactive binder.

Our approach avoids the problems of solubility, segregation or inhomogeneities frequently observed in doped polymers. It is based on the observation that, even if DIMET chromophore can be crystalline at room temperature, it also presents a large overcooling effect for the liquid phase (melting point at 102 °C) preserving the amorphous state over days at room temperature and even after a two hour annealing at 60 °C.

The amorphous structure at room temperature of recently melted DIMET samples has been proved by X-ray diffraction and differential scanning calorimetry (DSC) measurements. The same behaviour has been observed for samples obtained by melting chromophore powders and for samples obtained by evaporation of chloroform DIMET solution. DSC measurements also show that the glassy amorphous chromophore phase has a 37 °C glass transition temperature and that, without initiator, no polymerization occurs up to 250 °C; the degradation temperature, $T_{dec} = 300$ °C, was determined by thermogravimetric analysis.

The amorphous structure and the chemical homogeneity of the precursor material originate the very good optical quality of the final films which is of great importance for optical applications.

The absorption spectrum of DIMET, measured in chloroform, shows a maximum at $\lambda_{max} = 435$ nm and an absorption cut-off at 575 nm. The quadratic nonlinear property of DIMET in chloroform solution has been determined by electric field induced second harmonic generation (EFISHG) technique [18] performed at 1907 nm. In these conditions, the resonance enhancement is limited and there is no re-absorption of the second harmonic signal. The value of 660×10^{-48} esu for the product

$\mu \cdot \beta(2\omega)$, (μ is the ground state permanent dipole moment and β the quadratic hyperpolarizability of the molecule at the second harmonic frequency), has been deduced from the experimental measurements.

Two different formulations were elaborated, their only difference being in the radical initiator. The first one (BP) contains benzoyl peroxide while the second one (*t*BP) relies on *t*-butyl peroxide. The two initiators have a different working temperature. DSC analysis performed on films of chromophores and thermal initiators, in the proper amounts, indicated that decomposition of the latter starts at 85 °C for the BP containing films and at 115 °C for *t*BP films.

Thin amorphous films were deposited on glass substrates by spin coating a DMF solution of DIMET with 2% wt. of thermal initiator. The films have been submitted to poling-polymerization procedures with a first common step at 60 °C for 30 min, followed by a further step at 110 °C for the BP films and 150 °C for the *t*BP ones, maintaining an electric corona potential of 6 kV throughout the entire process. After the polymerization process, the films were no more soluble in DMF.

A preliminary study of poling efficiency as a function of temperature was performed on a film of pure DIMET (i.e. without initiator). As shown in Fig. 2, the second harmonic generation signal (SHG) is stable when the electric field is applied at 30 °C. When the temperature exceeds T_g the signal sharply decreases and finally almost totally vanishes at 60 °C, despite of the presence of the electric field.

Such behaviour could be ascribed to the enhancement of the material electrical conductivity beyond T_g. This phenomenon limits the amount of charges which can be accumulated on the film surface during the poling process, leading to a lower effective electric field and to a poor degree of orientation [19].

When the polymerization is enabled, the electrical conductivity of the system decreases as the degree of polymerization increases and, in this way, it is possible to orient the chromophores even at higher temperatures as those used here (110 °C or 150 °C). Therefore, it is more appropriate to refer to the present situation as a simultaneous poling-polymerization process.

The stability of second order NLO activity in the cross-linked films was checked by applying a temperature ramp (1 °C/min) and measuring the intensity of SHG signals as a function of temperature. The behaviour of the samples containing the two different initiators is shown in Fig. 3.

The depoling temperature T_{dep} is defined as the temperature for which the second harmonic generation signal is half the maximum. Fig. 3 shows that for the BP doped material $T_{dep} = 116$ °C and for

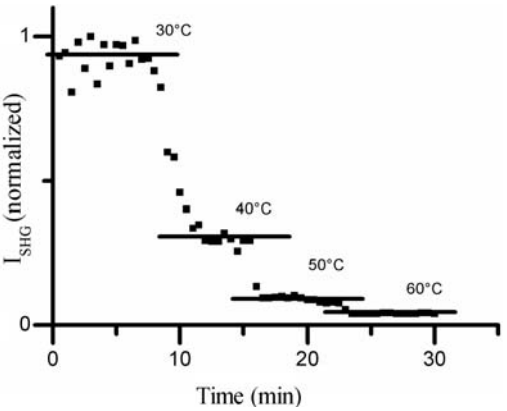


Fig. 2. Normalized SHG signal at four different temperature values for an unpolymerized sample during poling with a corona needle at 4.5 kV.

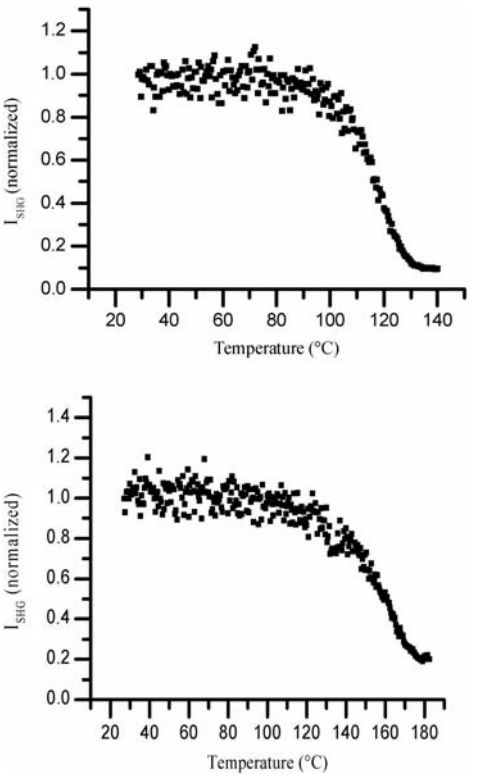


Fig. 3. NLO stability of the film containing BP (up) and *t*BP (down); a ramp of temperature (1 °C/min) was applied and the decay of the SHG signal was observed.

*t*BP doped $T_{dep} = 152$ °C, which indicates its higher stability. This arises from a higher degree of cross-linking reached for *t*BP films, improving the freezing of the chromophore orientation. In fact, on polymerizing a film at constant temperature, the system keeps reacting until the mobility of the molecules involved is sufficiently high. However, as the polymerization goes on, the system hardens more and more, leading to a reduced mobility of the molecules and rate of reaction. In order to have a higher degree of cross-linking and therefore a higher rigidity of the final material, it is then better to start and perform the polymerization at higher temperature. It's noteworthy that the stability of second order NLO activity of our material is higher as compared with other cross-linked systems based on similar approaches [16,17].

The NLO activities of the two different kinds of films, measured by SHG experiments, are comparable and we measured a d_{33} coefficient of 11 pm/V for BP and 14 pm/V for *t*BP. It is worth noticing that in a previous work on polycondensates (polyesters and polyurethanes) containing the same chromophore covalently attached to the polymer chain as side pendant, d_{33} coefficients close to 2 pm/V were measured at $\lambda = 1.536$ μm [20]. By choosing a different approach, i.e. orienting chromophores while they are not yet linked to the polymer, it is possible to reach a higher NLO activity of the material as a consequence of a better efficiency of the poling process.

3. Experimental part

3.1. N,N-bis (2-methacryloxyethyl)-aniline

N,*N*-bis-(2-hydroxyethyl)-aniline (10 g, 0.055 mol) was solved in 10 mL pyridine (0.122 mol). Methacrylic anhydride (23.125 g, 0.15 mol) was slowly added to the solution cooled in an ice-water bath. *N*,*N*-dimethylaminopyridine had been previously added in catalytic amount. The system was left under stirring in the dark for the first 30 min in the ice-water bath and subsequently at room temperature for 24 h. The organic phase was then extracted twice with chloroform (2×100 mL chloroform), washed with water and dried over Na_2SO_4. The solvent was then removed at reduced pressure, obtaining a yellow oil. Yield 65%.

^{1}H-NMR ($CDCl_3$, δ, ppm): 1.926 (s, 6H); 3.684 (t, 4H, $J = 6.4$ Hz); 4.319 (t, 4H, $J = 6.4$ Hz); 5.563 (s, 2H); 6.083 (s, 2H); 6.720–6.815 (m, 3H); 7.196–7.258 (m, 2H).

3.2. 1-Ethyl-2-(4-{[4-Bis(2-methacryloxyethyl) amino]phenylazo}-6-nitro- benzimidazole) (DIMET)

2-(4-aminophenyl)-1-ethyl-6-nitrobenzimidazole (3 g, 10.6 mmol), prepared as previously described [21], was placed in a flask containing 15 mL of water and 2.7 mL 37% HCl; the suspension was cooled to 0–5 °C in an ice-water bath. A solution obtained dissolving $NaNO_2$ (0.797 g, 11.55 mmol) in 5 mL of water was added dropwise to the suspension under stirring. Stirring at low temperature was continued for 30 min after the addition of nitrite solution.

Separately, a water–ethanol solution containing sodium acetate (2.970 g, 0.036 mol) and *N*,*N*-bis-(2-methacryloyloxyethyl)aniline (3.237 g, 10.6 mmol) was prepared. To this solution, cooled in an ice bath and under stirring, the suspension containing the diazonium salt was rapidly added. Immediately the color of solution turned to red and in few seconds, a red precipitated of the azo compound was formed. This compound was collected by filtration and then purified by liquid column chromatography using silica gel as stationary phase and chloroform as eluent. Yield 55%.

Mp: 102 °C.

^{1}H-NMR ($CDCl_3$, δ, ppm): 1.563 (t, 3H, $J = 7.2$ Hz); 1.940 (s, 6H); 3.815 (t, 4 H, $J = 5.6$ Hz); 4.369–4.444 (m, 6H); 5.602 (s, 2H); 6.110 (s, 2H); 6.112 (d, 2H, $J = 8.8$ Hz); 7.853–7.944 (m, 5H); 8.026 (d, 2H, $J = 8.4$ Hz); 8.256 (dd, 1H, $J_1 = 9$ Hz. $J_2 = 2.2$ Hz); 8.415 (d, 1H, $J = 2.2$ Hz).

Elemental analysis calcd. for $C_{33}H_{34}N_6O_6$: C 64.91; H 5.61; N 13.76%. Found: C 64.70; H 5.60; N 13.85%.

4. Physico-chemical characterization

The thermal behaviour of the compounds was studied by differential scanning calorimetry (Perkin–Elmer DSC-7, nitrogen atmosphere, scanning rate 10 K/min), temperature controlled polarizing microscopy (Zeiss microscope, Mettler FP5 microfurnace) and thermo-gravimetric analysis (TA instruments, air, 10 K/min). ^{1}H-NMR spectra were recorded with Varian XL 200 spectrometer. X-ray diffraction patterns were recorded on flat film camera, using Ni filtered Cu Kα radiation.

5. Processing

In a typical procedure a 15 wt% solution containing DIMET and the thermal initiator (chromo-

phore/initiator molar ratio, 98/2) in DMF was spin-coated over a glass substrate ($2.5 \times 2.5\ cm^2$) at 500 rpm for 10 s and subsequently at 1000 rpm for 60 s. Prior to use, the glass was cleaned by treatment with a 5 wt% basic detergent solution in an ultrasonic bath for 30 min, rinsed with distilled water and ethanol and finally treated in an ultrasonic bath for 30 min in methanol and chloroform, respectively. Two different formulations were used to prepare films, differing for the thermal initiators employed. The two thermal initiators employed were benzoyl peroxide (BP) and *t*-butyl peroxide (*t*BP). The typical thickness of the films was found to be around 350 nm.

6. Poling and cross-linking

Films for SHG measurements were poled with a tungsten wire corona electrode ($\Phi = 30\ \mu m$) during cross-linking. Films obtained from the two different formulations were preliminary poled in N_2 atmosphere at 60 °C with an applied voltage of 6 kV for 30 min; then, the films with A formulation were polymerized at 110 °C for 4 h under the electric field and in N_2 atmosphere for the first 2 h, while for films with B formulation the polymerization temperature was 150 °C. The final common step for the two different films was the slow cooling down at room temperature still under electric field. Finally, the field was removed and the samples recovered. The cross-linked films prepared with this procedure are insoluble in chloroform and DMF.

7. Second harmonic generation measurements

The optical nonlinearities of the material are measured using second harmonic generation setup. The pump beam is generated by a Nd:YAG laser emitting 10 ns pulses at 1.064 μm with a 10 Hz repetition rate. Wavelength conversion to 1.9 μm is achieved using a high pressure H_2 Raman cell. The beam is then focalized on the sample and the SHG signal at 950 nm is measured using a photomultiplier equipped by a narrow-band interferometric filter. The setup is used for both measurement of the d_{33} by the Maker fringes method and for the monitoring of the evolution of the SHG efficiency. Measurements were calibrated relative to a quartz crystal slab: the experimental value of $d_{11}^{Quartz} = 1.2 \times 10^{-9}$ esu at 1.06 μm was extrapolated to 1.1×10^{-9} esu at 1.907 μm.

8. Conclusion

We have presented the results of the quadratic NLO activity of thin films obtained by thermopolymerization of a pure chromophore functionalized with di-methacrylate function. The stability and the efficiency of the NLO properties are comparable with those observed for various doped or functionalized polymers described in the literature. However, in our case, as the material precursor is based on a single component with a weak crystallization tendency, segregation and inhomogeneities do not appear and the final material presents a high optical quality. These results demonstrate the validity of our approach. While the d_{33} efficiencies obtained are moderate, we expect further improvements by modifying the molecular properties to increase the hyperpolarizability as well as to limit the material conductivity during the poling step.

Acknowledgement

MIUR of Italy (PRIN 2004) is acknowledged for financial support of this research.

References

[1] D.M. Burland, R.D. Miller, C.A. Walsh, Chem. Rev. 94 (1994) 31.
[2] L. Dalton, Adv. Polym. Sci. 158 (2002) 1.
[3] L. Dalton, Pure Appl. Chem. 76 (2004) 1421.
[4] S.R. Marder, Chem. Commun. (2006) 131.
[5] (5a) S. Liu, M.A. Haller, H. Ma, L.R. Dalton, S.-H. Jang, A.K.-Y. Jen, Adv. Mat. 15 (2003) 603;
(b) J.-W. Kang, T.-D. Kim, J. Luo, M. Haller, A.K.-Y. Jen, Appl. Phys. Lett. 87 (2005) 071109.
[6] (a) C. Weder, P. Neuenschwander, U.W. Suter, P. Pretre, P. Kaatz, P. Günter, Macromolecules 28 (1995) 2377;
(b) T. Pliška, W.-R. Cho, J. Meier, A.-C. Le Duff, V. Ricci, A. Otomo, M. Canva, G. Stegeman, P. Raimond, F. Kajzar, J. Opt. Soc. Am. B 17 (2000) 1554.
[7] V. Ricci, G.I. Stegeman, K. Pong Chan, J. Opt. Soc. Am. B 17 (2000) 1349.
[8] T. Verbiest, D.M. Burland, M.C. Jurich, V.Y. Lee, R.D. Miller, W. Volksen, Macromolecules 28 (1995) 3005.
[9] H.-J. Lee, M.-H. Lee, S.G. Han, H.-Y. Kim, J.-H. Ahn, E.-M. Lee, Y.H. Won, J. Polym. Sci.: Part A: Polym. Chem. 36 (1998) 301.
[10] N. Tsutsumi, M. Morishima, W. Sakai, Macromolecules 31 (1998) 7764.
[11] C. Samyn, T. Verbiest, E. Kesters, K. Van den Broeck, M. Van Beylen, A. Persoons, Polymer 41 (2000) 6049.
[12] K. Van den Broeck, T. Verbiest, J. Degryse, M. Van Beylen, A. Persoons, C. Samyn, Polymer 42 (2001) 3315.
[13] W.N. Leng, Y.M. Zhou, Q.H. Xu, J.Z. Liu, Polymer 42 (2001) 9253.

[14] J.A.F. Boogers, P.Th.A. Klaase, J.J. De Vlieger, D.P.W. Alkema, A.H.A. Tinnemans, Macromolecules 27 (1994) 197.
[15] J.A.F. Boogers, P.Th.A. Klaase, J.J. De Vlieger, A.H.A. Tinnemans, Macromolecules 27 (1994) 205.
[16] S.S.H. Mao, L. Guo, C. Zhang, L. Dalton, A. Chen, S. Garner, W.H. Steier, Chem. Mater. 10 (1998) 146.
[17] C. Zhang, C. Wang, L.R. Dalton, H. Zhang, W.H. Steier, Macromolecules 34 (2001) 253.
[18] K.D. Singer, A.F. Garito, J. Chem. Phys. 75 (1981) 3574.
[19] W. Ren, S. Bauer, S. Yilmaz, W. Wirges, R. Gerhard-Multhaupt, J. Appl. Phys. 75 (1994) 7211.
[20] A. Carella, M. Casalboni, R. Centore, S. Fusco, C. Noce, A. Quatela, A. Peluso, A. Sirigu, Opt. Mater., submitted for publication.
[21] A. Carella, R. Centore, A. Fort, A. Peluso, A. Tuzi, A. Sirigu, Eur. J. Org. Chem. (2004) 2620.

Available online at www.sciencedirect.com
ScienceDirect
Organic Electronics 8 (2007) 63–68
Organic Electronics
www.elsevier.com/locate/orgel

The electronic band alignment on nanoscopically patterned substrates

G. Koller *, B. Winter, M. Oehzelt, J. Ivanco, F.P. Netzer, M.G. Ramsey

Institut für Physik, Karl-Franzens-Universität, Universitätsplatz 5, A-8010 Graz, Austria

Received 9 June 2006; received in revised form 6 November 2006; accepted 7 November 2006
Available online 8 December 2006

Abstract

The electronic level alignment of the organic semiconductor para-sexiphenyl on a nanoscopically patterned substrate was investigated with ultraviolet photoemission spectroscopy, work function measurements and scanning tunnelling microscopy. The results show that for increasing coverage on inhomogeneous surfaces, shifts in electronic level alignment occur, which are due to the change from local to average band alignment. The Cu(1 1 0)–(2 × 1)O stripe phase, used as a model substrate consists of alternating stripes of bare and oxygen passivated copper, with stripe widths of ~35 Å comparable to the sexiphenyl molecular length. In the first molecular layer the electronic bands are clearly aligned to the local surface potential of the specific stripe, resulting in the superposition of two photoemission spectra offset by 1 eV. Beyond two monolayers the valence band spectra clearly indicate a single electronic level alignment, which is determined by the average interface dipole.
© 2006 Elsevier B.V. All rights reserved.

PACS: 73.20.At; 73.63.Rt; 73.22.-f; 68.43.Bc

Keywords: Band alignment; Photoemission; Work function; Sexiphenyl; Copper; Nanostructures

1. Introduction

The worldwide interest in organic semiconducting materials is driven by the wealth of their possible technological applications. At present light emitting and simple electronic devices are on the threshold of being commercially realised, while new applications, such as solar cells and chemical sensors are being explored. Historically, the field of active molecular systems has been evolving from "plastic electronics" through "organic electronics" to "molecular electronics"; that is polymers, better defined as oligomeric films, to the holy grail of single molecule devices. Clearly, an understanding of the electronic level alignment on the molecular scale is vital for molecular electronics, but it can also be important in present day devices as their contact interfaces are unlikely to be uniform on this scale, an intricacy, which may lead to charge trapping at the interface and reduced device performance. The area of such defects can also be on the nanoscale and thus in the order of the here investigated substrate nanostructures.

* Corresponding author. Fax: +43 316 380 9816.
E-mail address: georg.koller@uni-graz.at (G. Koller).

1566-1199/$ - see front matter © 2006 Elsevier B.V. All rights reserved.
doi:10.1016/j.orgel.2006.11.001

One important parameter in organic device performance is the barrier to charge carrier injection, that is the electronic level alignment between the highest occupied (HOMO) and the lowest unoccupied molecular orbital (LUMO) with respect to the Fermi level of the inorganic/metal contact. In our previous work, we investigated this so called molecular band alignment on a variety of chemically different substrates with several highly defined oligomers [1,2]. It is now generally accepted that the electronic alignment of the organic film is determined by the details of the interaction of the first layer of molecules with the contact material and the interface dipole thus formed [1–6]. In this contribution, we explore the local variation in band alignment on a nanoscopically patterned substrate surface by investigating the growth of para-sexiphenyl (p-6P) films, from sub-monolayer to multilayer coverages, with UV-photoemission (UPS), work function (ϕ) measurements and supported by scanning tunnelling microscopy (STM). The substrate used was the mesoscopically patterned oxygen reconstructed Cu(1 1 0) surface. This surface reconstructs to form a substrate consisting of alternating stripes of clean Cu(1 1 0) and (2×1) oxygen reconstructed Cu(1 1 0), the so called Cu–CuO stripe phase, with respective stripe widths in the range of several nanometers depending on the amount of oxygen exposure [7,8]. In this study, we have used an oxygen coverage of 0.25 monolayers (ML), with an average stripe width of 30–40 Å each, as confirmed by STM. The development of the electronic level alignment on this patterned substrate is compared to that on the pure homogenous surfaces: clean copper and the fully reconstructed Cu–(2×1)O surface. On the homogenous surface there is a 1 eV difference in band alignment due to the differences in the interaction of the molecules in their respective monolayers [9]. It will be shown, for sexiphenyl grown on the Cu(1 1 0)–(2×1)O stripe phase, that the photoemission spectra of the first molecular monolayer is a superposition of two spectra offset by this difference in band alignment, clearly reflecting the local differences in the charge injection barrier. In contrast, for the multilayer coverage regime, the valence band spectra clearly indicate a single band alignment, whose energy position is determined by the average interface dipole.

2. Experimental

The experiments were performed in two ultra high vacuum (UHV) (base pressure $<1\times10^{-10}$ mbar) chambers, equipped with an UV-photoemission spectrometer and a scanning tunnelling microscope, described elsewhere [10,11]. In addition both chambers have basic sample cleaning and surface characterisation facilities. The Cu(1 1 0) surface was cleaned by the repeated cycles of Ar^+-ion sputtering and annealing at 800 K. The full Cu(1 1 0)–p(2×1)O reconstruction was made by exposing the clean copper surface to 40 L [1 Langmuir $(L) = 1\times10^{-6}$ Torr sec] of oxygen at 400 K. The Cu–CuO stripe phase was produced by exposing the clean copper to 1.5 L oxygen at 600 K [7,8] and was characterised by STM and work function measurements. The work functions (ϕ), measured by the secondary electron cut-off in normal electron emission, of the substrates were: stripe phase $\phi = 4.6$ eV, clean Cu(1 1 0) $\phi = 4.4$ eV and the fully (2×1)O reconstructed surface $\phi = 4.75$ eV. Sexiphenyl was evaporated from a well degassed molecular evaporator, which allowed film growth in $<5\times10^{-10}$ mbar ambient pressure. The substrate was held at room temperature and nominal growth rates of 1 Å min^{-1} were used, as monitored with a quartz microbalance. In the STM system the clean Cu surface was seen to be completely covered by uniaxially lying molecules at ~3 Å exposure, while in the ARUPS chamber (due to a difference in evaporation geometry) the work function change is completed at nominal 5 Å exposure – these values are considered as the monolayers (ML) in the following.

3. Results and discussion

A 100 Å × 100 Å STM image of the Cu(1 1 0)–(2×1)O striped surface is shown in the insert of Fig. 1, illustrating the alternating stripes of clean copper and (2×1)O reconstructed copper areas with respective diameters of 30–40 Å. It should be noted that the copper atoms are highly mobile at room temperature, causing the fuzzy appear of the copper, while the Cu–(2×1)O stripes can be image with atomic resolution. Fig. 1 shows a 300 Å × 300 Å STM image of this surface after an exposure of 0.8 Å of sexiphenyl, a coverage corresponding to about 0.3 monolayers. At such low exposures the molecules, apparent as bright elongated objects of ~25 Å length in the STM, decorate the clean copper, going first to the Cu–CuO boundary and then covering the clean Cu areas. The molecules are aligned to and are highly mobile along the [0 0 1] substrate azimuth. This mobility is evidenced by the bright stripes that are considerably larger than

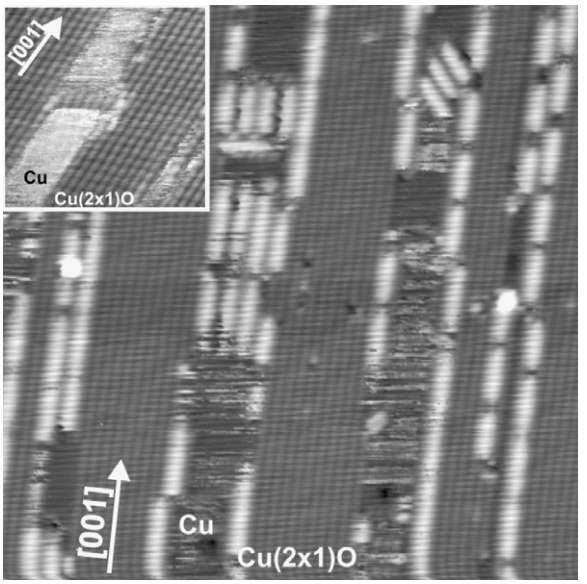


Fig. 1. 300 Å × 300 Å STM image of a Cu(1 1 0)–(2 × 1)O striped surface after deposition of 0.8 Å of sexiphenyl. The insert (100 Å × 100 Å) shows the surface prior to molecular deposition. The [0 0 1] substrate azimuth and the Cu and Cu(2 × 1)O stripes are indicated in both images.

the molecules (25 Å) which, once immobilised in dense structures, can be imaged as individual entities (see for instance the molecules at the top right hand corner). Depending on the stripe width 3–5 molecules, aligned parallel to the stripes, fill one stripe, showing that the underlying surface pattern truly is of molecular dimensions.

Fig. 2a shows a series of UPS spectra of sexiphenyl on a Cu (1 1 0) (2 × 1)O stripe surface as a function of exposure at room temperature. The first monolayer is completed for exposures around 5 Å as determined from the saturation value of the work function. The work function of this monolayer ($\phi =$ 3.8 eV), is approximately the 1:1 area average between the sexiphenyl monolayer work functions on clean Cu (1 1 0) ($\phi = 3.4$ eV) and on the fully (2 × 1)O reconstructed Cu (1 1 0) surface ($\phi =$ 4.3 eV), as shown in Fig. 2b. Since the measured work function is a simple area average of the local work functions [12], we can use them as a simple means to determine the ratio between the copper and Cu(2 × 1)O reconstructed surface areas. It should be noted that the secondary electron cut-offs, used to determine the work function, of all surfaces were sharp and did not show a double cut-off that would reflect the two different local surface potentials. To follow the development of the band align-

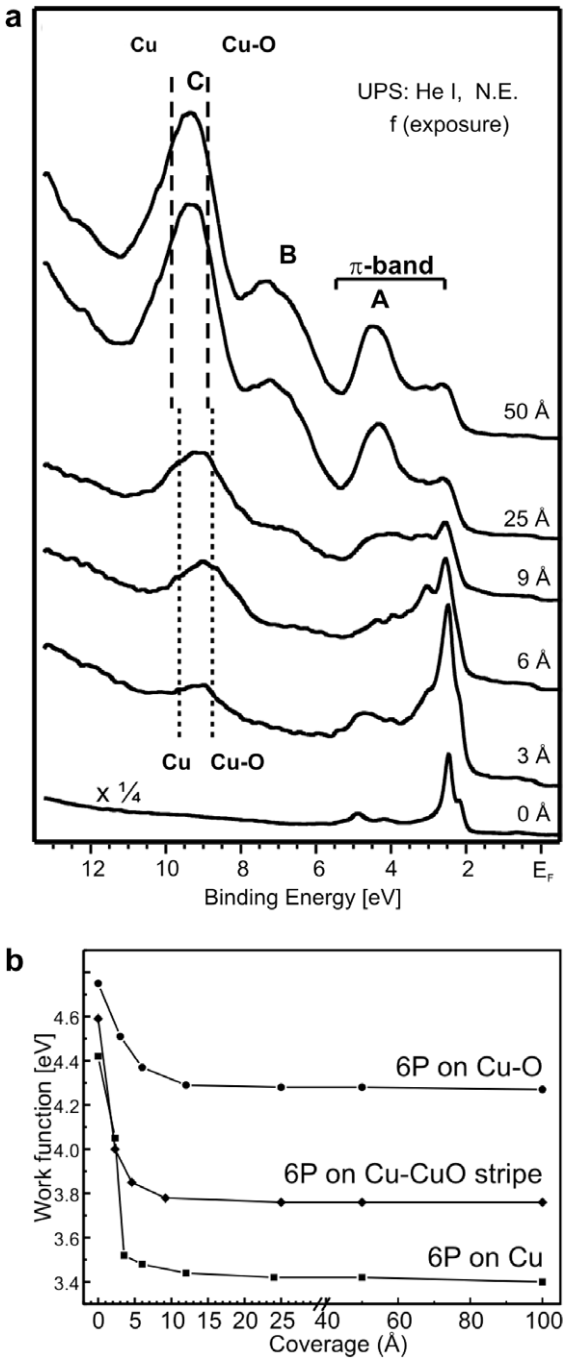


Fig. 2. (a) Normal emission He I UPS spectra from the Cu (1 1 0)–(2 × 1)O stripe phase as a function of sexiphenyl exposure. Photon angle of incidence $\alpha = 60°$. The binding energies of band C of sexiphenyl monolayers and multilayers obtained on clean Cu (1 1 0) and from the fully reconstructed Cu (1 1 0–p(2 × 1)O surface are marked by the dotted and dashed lines, respectively. (b) Development of the work function as function of sexiphenyl coverage on clean Cu(1 1 0) (squares), the fully reconstructed Cu(1 1 0)–p(2 × 1)O (dots) and the Cu (1 1 0) (2 × 1)O stripe phase (diamonds) surfaces.

ment of sexiphenyl on the Cu–CuO stripe phase as a function of film thickness (Fig. 2a), we concentrate on two sexiphenyl bands: band C, which is at high binding energy (9–10 eV) and does not overlap with the copper d-band of the substrate (bottom spectrum of Fig. 2a), and the non bonding π orbitals of band A, which although partially overlapping with the copper d-band, is intense enough to be identified. In addition the binding energies of these bands for the monolayers (dotted lines) and multilayers (dashed lines) observed on the clean and fully (2×1)O reconstructed copper surfaces are also indicated in Fig. 2a. In the UPS spectra of Fig. 2a we can clearly discern two different regimes: For low coverages of up to 9 Å, the molecular orbitals of the UPS spectra appear broad and indistinct. This is particularly apparent for band B, which is completely washed out and the non bonding orbitals of band A, which appear as an indistinct broad step. For coverages beyond 9 Å the molecular features become well defined and distinct and they are energetically positioned between the multilayer spectra on clean copper and that on the fully (2×1)O reconstructed copper (as indicated). It should be noted that after the monolayer is completed, island growth occurs (Stranski–Krastanov growth), as evidenced by the Fermi-edge being visible even at a coverage of more than ten monolayers (50 Å). For the coverages up to 6 Å the measured UPS spectra are a superposition of two spectra, indicating that we observe the two band alignments of p-6P on clean copper and p-6P on Cu(2×1)O. This is illustrated in Fig. 3, where the spectrum of a monolayer coverage on clean Cu(1 1 0) and on the fully reconstructed Cu–(2×1)O surface is compared to a spectrum of a monolayer on the heterogenous striped surface. As indicated in the figure all molecular orbital emissions of the homogenous surfaces are offset by 0.9 eV from each other (equal to the difference in ϕ) due to the differences in the interface dipole. Adding these two spectra results in a composite spectrum (Fig. 3d), which is remarkably similar to the spectrum recorded for the monolayer on the heterogenous Cu–(2×1)O stripe phase (Fig. 3c). This suggests that we do observe the molecular band emissions from the two clearly distinct band alignments and that the sexiphenyl molecules adsorbed on the bare copper stripes feel the local surface potential of the clean copper, while the sexiphenyl molecules on the oxygen reconstructed stripes experience the local surface potential of the Cu(2×1)O surface. In many respects the molecular emissions

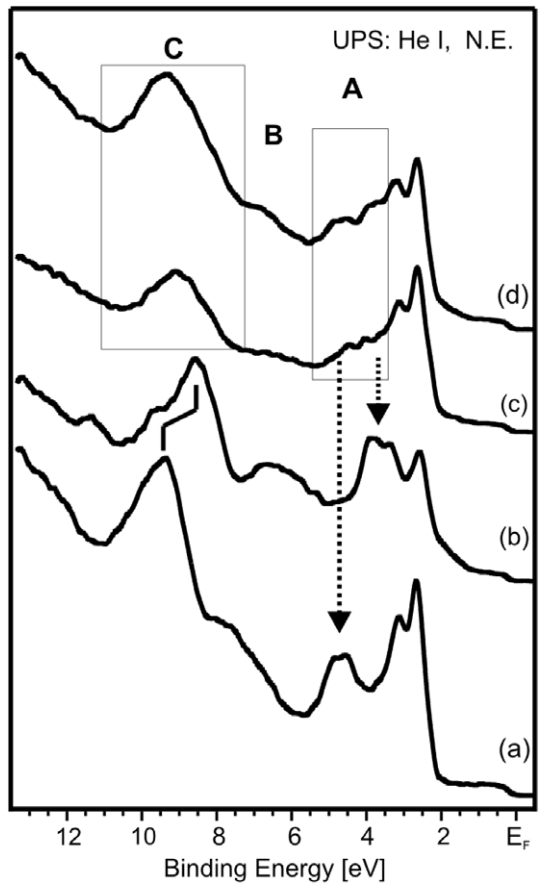


Fig. 3. Normal emission He I UPS spectra of sexiphenyl monolayers on (a) clean Cu (1 1 0) ($\phi = 3.4$ eV), (b) on the fully reconstructed Cu (1 1 0) – p(2×1)O ($\phi = 4.3$ eV) surface and (c) on the Cu (1 1 0) (2×1)O stripe phase ($\phi = 3.8$ eV). (d) Weighted (1:1) sum of (a) and (b). Particular similarities between (c) and (d) of bands A and C are highlighted by boxes, the arrows indicate the position of band A on the homogeneous surfaces.

behave as a local work function probe, similar to the photoemissions of adsorbed Xenon (PAX) technique [12].

For coverages beyond ~ three monolayers on the striped substrate the molecular orbital features become more distinct until the UPS spectrum resembles the usual spectrum of condensed sexiphenyl films as shown in Fig. 4. The binding energy of the molecular orbitals of the multilayers on the striped substrate are situated between those obtained on the homogenous substrates, suggesting that we have a single band alignment with an average offset. In Fig. 4 the bottom two spectra show a nominal 10 ML (50 Å) thick sexiphenyl film on clean copper and on Cu(2×1)O surfaces. It should be noted that the first peak at 2.4 eV binding energy on the clean Cu substrate (shaded in the figure) is not the p-6P

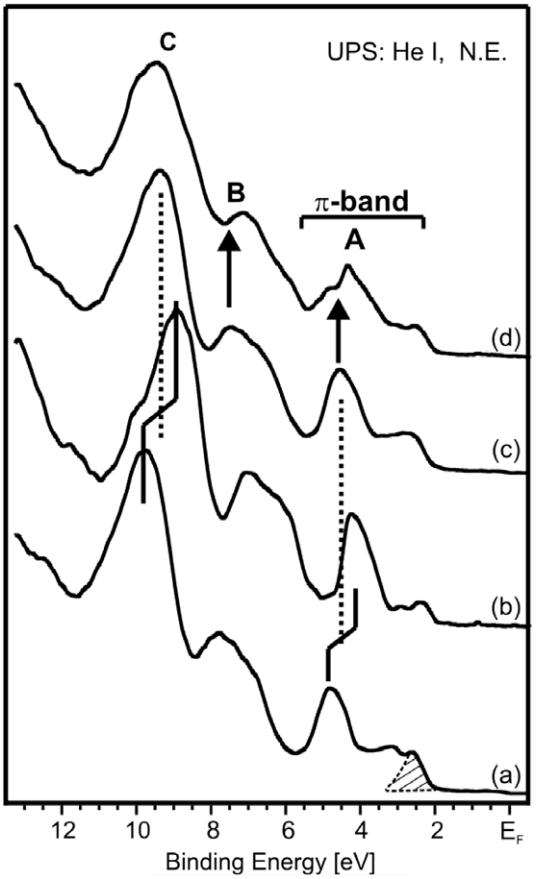


Fig. 4. Normal emission He I UPS spectra of sexiphenyl multilayers on (a) clean Cu (1 1 0) ($\phi = 3.4$ eV), (b) on the fully reconstructed Cu (1 1 0) – p(2 × 1)O surface ($\phi = 4.3$ eV) and (c) on the Cu (1 1 0) (2 × 1)O stripe phase ($\phi = 3.8$ eV). (d) Weighted (1 : 1) sum of (a) and (b). The major differences between (c) and (d) are marked by arrows.

HOMO (which is at 3 eV), but rather stems from the intense copper d-band feature at this energy, which due to the severe islanding on the clean copper substrate is still visible. Comparing the multilayer film spectrum on the striped Cu–CuO substrate to the weighted sum of spectra for multilayers on the homogeneous substrates (cf. 4c and d) shows that they are markedly different and, unlike for the monolayer, the spectra from the multilayer on the striped substrate cannot be due to a superposition of emissions offset by their respective interface dipoles. In particular the orbital emissions of the spectral sum are much broader than the measured spectrum, but the most prominent differences occur in the π-band and band B, as indicated by arrows in the figure. This shows that the sexiphenyl molecules of the higher layers do not feel the local surface potential of the Cu and CuO stripes any longer, but rather are aligned to the average interface potential. Further support for this is given by the fact that all molecular valence band orbitals on the three surfaces shown in Fig. 4, viz. clean Cu (1 1 0), Cu (1 1 0)–p(2 × 1)O, and the Cu–(2 × 1)O stripe phase, have the same binding energy with respect to the vacuum level (ionisation potential IP) of the respective multilayers (e.g. for the HOMO IP = 6.5 ± 0.1 eV, for the non-bonding π-orbitals of band A IP = 8.3 ± 0.1 eV).

The key question is at what layer height the paradigm shift from band alignment to the local interface potential as opposed to band alignment to the average interface potential occurs. From the development of the molecular orbitals as a function of p-6P coverage shown in Fig. 2a it is suggested that this transition occurs around a coverage of 9 Å or about 2 ML. Here the weight of band C has already shifted to its multilayer value and band B has become apparent, although the non bonding orbitals of the π-band A are still broad and indistinct. When taking into account the islanding of the second and higher layers, we expect that a large proportion of the first monolayer is exposed at this coverage. For the area averaging technique of UPS we therefore suggest a superposition of three sexiphenyl spectra: p-6P aligned to the local interface potential of Cu, p-6P aligned to the local interface potential of Cu–(2 × 1)O and p-6P aligned to the average interface potential. This leads us to conclude that this paradigm shift occurs already in the second molecular layer as illustrated in the schematic illustartion of Fig. 5.

4. Summary

Here we have investigated the local band alignment of the organic semiconductor sexiphenyl on the nanopatterned Cu(1 1 0)–(2 × 1)O striped substrate from submonolayer coverages to film thicknesses approaching that of organic electronic devices. The results are summarized in Fig. 5: For the first molecular layer, the electronic bands are clearly aligned to the *local* surface potential of the specific stripe, resulting in the superposition of UPS spectra. Beyond two monolayers the valence band spectra clearly indicate a single electronic level alignment, which is determined by the *average* interface dipole.

The implications of the results on a mundane level are that care must be taken in interpreting orbital shifts with increasing exposure on ill-defined/

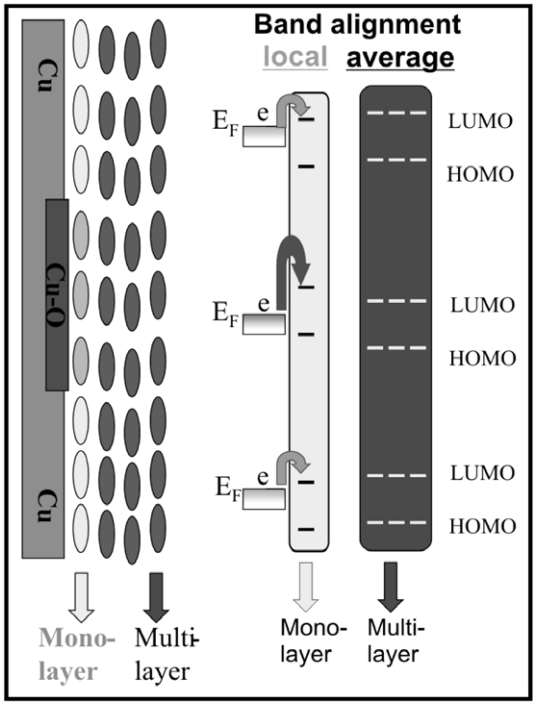


Fig. 5. Schematic illustrating of the observed change from local to average band alignment on the nanopatterned substrate. The shaded discs represent sexiphenyl molecules, with the grey scale indicating the respective band alignment. The curved arrows emphasise the local differences in the barrier height for injection to the first monolayer.

inhomogeneous substrates, such as clean polycrystalline surfaces or even contaminated substrates (consider different crystalline facets can have 0.5 eV difference in work function). The results further imply that future nanopatterned devices will ultimately require thin active organic layers only 1–2 molecules thick. On a more exalted level the capacity to pattern the local surface dipole allows the tailoring of the charge injection ability on the molecular level, a prerequisite for the advent of molecular electronics.

Acknowledgement

This work was supported by the Austrian Science Foundation FWF.

References

[1] G. Koller, R.I.R. Blyth, S.A. Sardar, F.P. Netzer, M.G. Ramsey, Appl. Phys. Lett. 76 (2000) 927.
[2] R.I.R. Blyth, R. Duschek, G. Koller, F.P. Netzer, M.G. Ramsey, J. Appl. Phys. 90 (2001) 270.
[3] I.G. Hill, D. Millron, J. Schwartz, A. Kahn, Appl. Surf. Science 166 (2000) 354.
[4] H. Ishii, K. Sugiyama, E. Ito, K. Seki, Adv. Mat. 11 (1999) 605.
[5] I.G. Hill, A. Rajagopal, A. Kahn, Y. Hu, Appl. Phys. Lett. 73 (1998) 662–664.
[6] G. Koller, F.P. Netzer, M.G. Ramsey, Appl. Phys. Lett. 83 (2003) 563.
[7] K. Kern, H. Niehus, A. Schatz, P. Zeppenfeld, J. George, G. Comsa, Phys. Rev. Lett. 67 (1991) 855.
[8] P. Zeppenfeld, V. Diercks, C. Tölkes, R. David, M.A. Kryzowski, Appl. Surf. Science 59 (1998) 484.
[9] M. Oehzelt, L. Grill, S. Berkebile, G. Koller, F.P. Netzer, M.G. Ramsey, submitted for publication.
[10] G. Koller, R.I.R. Blyth, S.A. Sardar, F.P. Netzer, M.G. Ramsey, Surf. Science 536 (2003) 155.
[11] J. Kraft, M.G. Ramsey, F.P. Netzer, Phys. Rev. B 5384 (1997).
[12] K. Wandelt, Appl. Surf. Science 111 (1997) 1.

Available online at www.sciencedirect.com
ScienceDirect
Organic Electronics 8 (2007) 69–75
Organic Electronics
www.elsevier.com/locate/orgel

Nanostructured semiconductor block copolymers: π–π Stacking, optical and electrochemical properties

Stefan M. Lindner, Nadine Kaufmann, Mukundan Thelakkat *

Makromolekulare Chemie I, Universität Bayreuth, Universitätsstrasse 30, 95440 Bayreuth, Germany

Received 23 December 2005; received in revised form 13 November 2006; accepted 23 November 2006
Available online 19 December 2006

Abstract

The structural and optical properties of semiconductor block copolymers containing triphenylamine as hole transport material and perylene bisimide as dye and electron transport material are reported. The polymers were prepared by nitroxide mediated controlled radical polymerisation and characterized with GPC, DSC, and TGA. The electrochemical properties as determined by cyclic voltammetry show the HOMO and LUMO values of the block copolymers to be −5.23 eV and −3.65 eV, respectively. The perylene bisimide units aggregate by π–π stacking which could be analyzed with wide-angle X-ray scattering. The absorption and fluorescence properties of the perylene bisimide polymers and monomers in solution and film were investigated. It could be shown that they are strongly influenced by intramolecular coupling between different perylene bisimide units in polymers. The block copolymers exhibit a microphase separation on a nanometer scale with a constant perylene bisimide domain width of 13 nm and lengths of up to several micrometers.
© 2006 Elsevier B.V. All rights reserved.

PACS: 84.60.Jt; 87.15.Nn; 73.61.Ph; 78.66.Qn

Keywords: Organic semiconductor block copolymers; Nanostructured bulk heterojunction; Perylene bisimide polymer; Vinyltriphenylamine polymer

1. Introduction

In organic electronic devices the interface between the hole transport material and the electron transport material is crucial for the performance as the charge separation (for organic solar cells) or the charge recombination (for organic light emitting diodes) occurs at this interface. As the exciton diffusion length is only in the order of some nanometers it is very important to get defined nanostructures in this range in the whole of the bulk for photovoltaic devices. The effect of the morphology in some systems has been studied experimentally [1] and by numerical simulations [2]. For this reason several methods were developed to control the thickness of the layers/domains precisely. The first organic heterojunction solar cells [3] were prepared by vacuum deposition, but the layer thickness in two-layer devices was too low to get sufficient absorption. In thicker layers the absorption would be better, but if they are thicker than the exciton diffusion length,

* Corresponding author. Tel.: +49 921 553108; fax: +49 921 553206.
E-mail address: mukundan.thelakkat@uni-bayreuth.de (M. Thelakkat).

1566-1199/$ - see front matter © 2006 Elsevier B.V. All rights reserved.
doi:10.1016/j.orgel.2006.11.002

the excitons cannot reach the interface. The efficiency would therefore not increase. In order to get high absorption with thin layers tandem cells were developed where the layers are adapted to the optical field intensity [4] to maximize the absorption. Another possibility widely used is the blending of polymers or polymers and small molecules. But the exact composition and morphology of such blends is difficult to control as for example, in the PPV–PCBM solar cells two domains occur with one pure PCBM domain and a mixed domain of PPV and PCBM [5,6]. Attempts were earlier carried out to synthesize block copolymers containing PPV and fullerene segments, but a nanoscale morphology could not be observed in these systems, probably due to cross-linking during functionalization with fullerene [7]. We demonstrated that with the use of block copolymers nanostructured domain sizes between the hole and electron transport material can be achieved [8] and this concept can be successfully used for nanostructured bulk heterojunction photovoltaic devices [9,10]. Here we present a detailed study of the morphology of new block copolymers, the effect of molecular stacking in perylene bisimides and their electrochemical properties.

2. Experimental section

2.1. Materials

The initiator **1** and the free nitroxide **2** were synthesized according to literature [11]. The synthetic procedures of the monomers **3** and **5**, and those of the block copolymer **4C** and perylene bisimide homopolymer **7** were already published [7]. The macroinitiators **4A** and **4B** were prepared in a similar manner as **4C**, but varying the ratio of monomer to initiator. The block copolymers **6A**–**C** were synthesized via nitroxide mediated controlled radical polymerisation starting from macroinitiators **4A**–**C**. All solvents were distilled prior to use, anisole (anhydrous) and *o*-dichlorobenzene (anhydrous) were purchased from Aldrich and used as received. Compound **2** was added as a stock solution in the solvent used for the polymerisation.

2.1.1. Poly(4-vinyltriphenylamine) *4A*

The initiator **1** (65.1 mg, 0.2 mmol), the free nitroxide **2** (2.20 mg, 0.01 mmol), the monomer **3** (5.46 g, 20 mmol) and 1 ml anisole were degassed three times and filled with argon. The reaction mixture was heated at 125 °C for 15 min. The polymer was purified by repeated precipitation from THF solution into methanol/acetone (1/1) to yield 350 mg of **4A**.

2.1.2. Poly(4-vinyltriphenylamine) *4B*

The initiator **1** (65.1 mg, 0.2 mmol), the free nitroxide **2** (2.20 mg, 0.01 mmol), the monomer **3** (2.71 g, 10 mmol) and 1 ml anisole were degassed three times and filled with argon. The reaction mixture was heated at 125 °C for 45 min. The polymer was purified by repeated precipitation from THF solution into acetone to yield 2.62 g of **4B**.

2.1.3. Synthesis of PvTPA-bl-PPerAcr *6A*

The macroinitiator **4A** (68 mg), the free nitroxide **2** (0.22 mg, 1 μmol), the PerAcr **5** (825 mg, 1 mmol) and 250 μl *o*-dichlorobenzene were degassed three times and filled with argon. The reaction mixture was heated at 125 °C for 24 h. The polymer was purified by repeated precipitation from chlorobenzene solution into acetone to yield 108 mg of **6A**.

2.1.4. Synthesis of PvTPA-bl-PPerAcr *6B*

The macroinitiator **4B** (264 mg), the free nitroxide **2** (0.22 mg, 1 μmol), the PerAcr **5** (825 mg, 1 mmol) and 250 μl *o*-dichlorobenzene were degassed three times and filled with argon. The reaction mixture was heated at 125 °C for 24 h. The polymer was purified by repeated precipitation from chlorobenzene solution into acetone to yield 385 mg of **6B**.

2.1.5. Synthesis of PvTPA-bl-PPerAcr *6C*

The macroinitiator **4C** (776 mg), the free nitroxide **2** (0.44 mg, 2 μmol), the PerAcr **5** (2970 mg, 3.6 mmol) and 1000 μl *o*-dichlorobenzene were degassed three times and filled with argon. The reaction mixture was heated at 125 °C for 24 h. The polymer was purified by repeated precipitation from chlorobenzene solution into acetone to yield 1857 mg of **6C**.

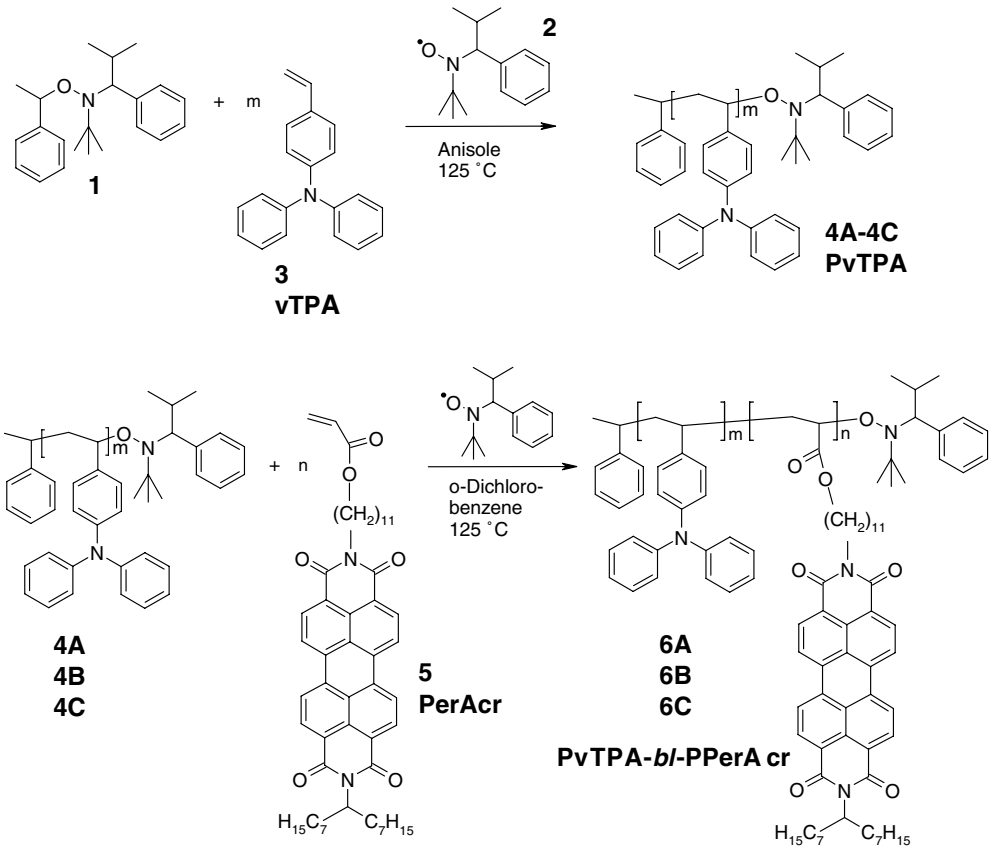
2.2. Instrumentation

The molecular weights of polymers were determined by gel permeation chromatography (GPC) in THF + 0.25 wt% tetrabutylammonium bromide with UV and RI detectors (Waters) using polystyrene standards for calibration. The dye content was determined with ^{1}H NMR spectroscopy using a Bruker AC 250 spectrometer (250 MHz). UV/vis

spectra were recorded using a Hitachi U-3000 spectrometers and fluorescence spectra were recorded using a Shimadzu RF-5301 PC Spectrofluorophotometer. The wide-angle X-ray scattering (WAXS) was performed on a Bruker-AXS D8 Advance in transmission geometry with Cu Kα radiation ($\lambda = 0.154$ nm). The samples were fixed on a tape for the measurement. For the cyclic voltammetry experiments a three-electrode assembly with a glassy carbon working electrode and a $Ag/AgNO_3$ reference electrode was used. THF containing 0.1 M tetrabutylammonium hexafluorophosphate was used as a solvent and each measurement was calibrated with ferrocene as internal standard.

3. Results and discussion

For the synthesis of the block copolymers nitroxide-mediated controlled radical polymerisation NMRP [12] was used (Scheme 1). The advantage of this polymerisation is the controlled nature of polymerisation and the synthesis is metal free, which is especially important for organic electronics. A variety of monomers with different



	macro-initiator	M_n [g/mol]	PDI	wt% of PPer Acr	T_g [°C]	T_m [°C]	TGA$_{-5\%}$ [°C]
4A	-	2440	1.21	-	111	-	311
4B	-	11440	1.11	-	138	-	362
4C	-	15830	1.22	-	144	-	378
6A	**4A**	9220	1.43	73	139	168	390
6B	**4B**	27850	1.47	64	136	194	389
6C	**4C**	26900	1.50	86	-	198	400
7	-	19900	1.65	100	-	190	404

Scheme 1. Controlled radical polymerisation of the macroinitiators **4A**–**4C** and the resulting block copolymers **6A**–**6C**. Overview of the prepared polymers and their properties. **7** is perylene bisimide homopolymer.

functional groups can be used after the monomers were purified by column chromatography to remove any impurities. The monomer used for the first block was 4-vinyltriphenylamine (vTPA **3**) which acts as a hole transport material. The second monomer consists of a perylene bisimide substituted acrylate (PerAcr **5**). The perylene bisimide acts as dye and as electron transport material. They are used due to their thermal, chemical and photochemical stability and they can easily crystallize via π–π stacking to form supramolecular structures [13]. The perylene bisimide is unsymmetrically substituted with an acrylate group for the polymerisation and a swallow-tail substituent [14] for the solubility. The monomer is very well soluble in organic solvents; even in a poor solvent such as hexane it is soluble. The block copolymer **6** consists of an amorphous hole transport block (PvTPA) and a semi-crystalline electron transport block (PPerAcr) which also absorb light intensively in the visible region. Thus all the functions needed for organic solar cells are combined in this one block copolymer. With this approach, not only the ratio of the blocks but also the length of each block can be varied by the polymerisation conditions. In our earlier work [7] we used **4C** as the macroinitiator to build up different lengths of perylene bisimide acrylate blocks, keeping the hole transport segment the same in all the block copolymers. Here different PvTPA macroinitiators **4A**–**4C** with different molecular weights were used as macroinitiators in order to get block copolymers, PvTPA-*b*-PPerAcr **6A**–**C** with different PvTPA chain lengths after the second sequential polymerisation step. The perylene bisimide content is maintained between 60 and 80 wt%, in the range in which nanostructure formation is favoured. Thus, the block copolymers **6A** and **6B** have a comparable ratio of the two blocks, but the molecular weight of each block is very different. The PvTPA block in **6A** has a molecular weight of 2440 g/mol, but 11 440 g/mol in **6B**. In this way, the influence of block lengths, composition and molecular weight on structural and physical properties can be elucidated. In Scheme 1 the molecular weights, polydispersity (from GPC) and the thermal properties (from TGA and DSC) are given. The block copolymers **6A**–**C** exhibit both a glass transition due to the PvTPA block and a melting peak due to PPerAcr segment. The perylene bisimide content was determined from ^{1}H NMR spectroscopy and is also confirmed by UV–vis spectroscopy.

Table 1
Redox potentials and HOMO/LUMO values determined from cyclic voltammetry in solution (Fc: Ferrocene)

Compound	E_{ox1} vs Fc [V]	HOMO [eV]	E_{red1} vs Fc [V]	LUMO [eV]
PvTPA **4**	0.43	−5.23	–	–
PerAcr monomer **5**	–	–	−1.08	−3.72
PerAcr model **8**	1.23	−6.03	−1.09	−3.71
PPerAcr **7**	–	–	−1.17	−3.63
PvTPA-*b*-PerAcr **6**	0.43	−5.23	−1.15	−3.65

The electrochemical properties were determined with cyclic voltammetry. All the measured redox potentials and the HOMO/LUMO values obtained from those are tabulated in Table 1. The measurements were conducted in THF containing 0.1 M tetrabutylammonium hexafluorophosphate as solvent. The HOMO (highest occupied molecular orbital) and LUMO (lowest unoccupied molecular orbital) values were calculated with respect to ferrocene (HOMO: −4.8 eV). The PerAcr **5** monomer as well as the homo and block copolymers have two characteristic reversible reduction peaks of perylene bisimides; the first reduction peaks being at −1.08 V, −1.14 V and −1.15 V, respectively with respect to ferrocene. From these values, the LUMOs can be calculated as −3.72 eV for the monomer **5**, −3.66 eV for the homopolymer **7** and −3.65 eV for the block copolymers **6**. The HOMO value of the PvTPAs **4A**–**C** is −5.23 eV. The polymers **6A**–**C** and **7** are not soluble enough in CH_2Cl_2 to enable the study of the oxidation behaviour of perylene units which take place at higher potentials at which THF is not stable. For this reason we synthesized a highly soluble symmetrical *N*,*N*′-di(1-heptyloctyl)perylene-3,4,9,10-tetracarboxylic bisimide (**8**) as a model system (electrochemically more stable than the monomer **5**) and measured it in CH_2Cl_2 containing 0.1 M tetrabutylammonium hexafluorophosphate. The first reduction peak being at −1.09 V and the first oxidation peak being at 1.23 V with respect to ferrocene, the LUMO can be calculated as −3.71 eV (very similar to those of block copolymer and perylene homopolymer) and the HOMO as −6.03 eV. The electrical gap between these states is 2.32 eV. In the case of block copolymers both the reduction peaks due to the perylene bisimide and the oxidation peak of the triphenylamine can be seen (see Fig. 1). The HOMO and LUMO values were determined as −3.65 eV and −5.23 eV, respec-

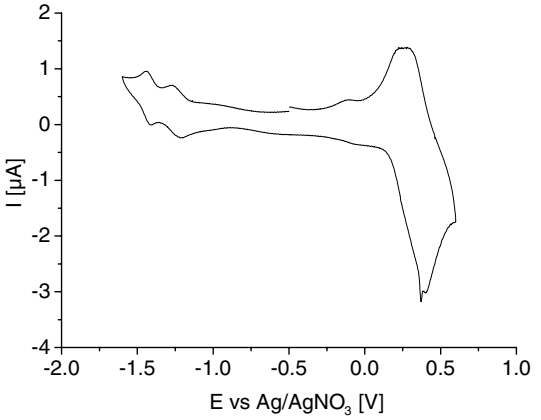


Fig. 1. Example of a cyclic voltammogramm for a block copolymer with two reversible reduction peaks for the perylene bisimide unit and the oxidation of the triphenylamine unit. The spectrum was measured in THF containing 0.1 M tetrabutylammonium hexafluorophosphate.

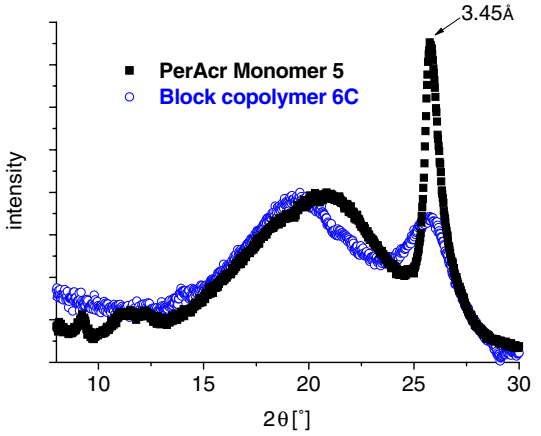


Fig. 2. Wide angle X-ray scattering (WAXS) of the monomer **5** and the block copolymer **6C**.

tively. This results in an electrical band gap of 1.58 eV for the block copolymers which decides the final photovoltage that can be obtained from this system.

Perylene bisimides exhibit a clear tendency to self-alignment via molecular π–π stacking which has a strong influence on their absorption and emission properties. The stacking property was investigated with wide angle X-ray scattering (WAXS) in powder. As an example, in Fig. 2 the spectra of the block copolymer **6C** and the monomer **5** are shown. Besides the amorphous halo, both spectra show a crystalline peak at 25.8° (2θ). The crystallinity is conserved in the block copolymers, only the degree of crystallinity is lower than in **5**. The distance between two perylene bisimide units can be calculated as 3.45 Å which is very similar to the reported values for low molecular weight perylene bisimides [15]. For comparison, the layer distance in graphite is with 3.35 Å only 0.1 Å smaller. The stacking distance of the perylene bisimide is not strongly affected from the swallow-tail substituents which provide the solubility. This fact makes these compounds very promising for electro-optical applications as not only the absorption and emission properties are positively influenced by crystallinity but also the charge carrier mobility.

In order to study the influence of π–π stacking of perylene bisimide units on optical properties, UV–vis and photoluminescence measurements were carried out for the monomer and the various polymers. The difference in the optical properties of the monomer **5** and the homopolymer **7** is shown in Fig. 3a. The UV/vis absorption of the PerAcr monomer **5**

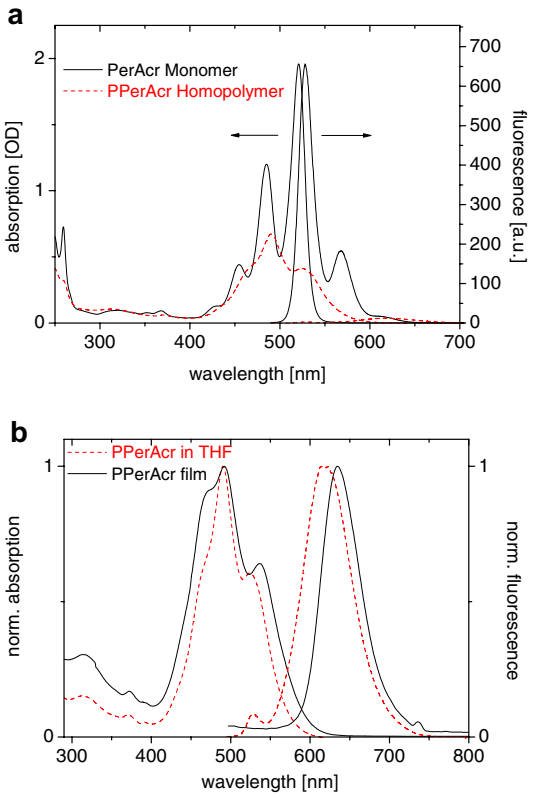


Fig. 3. (a) UV/vis and fluorescence spectra of the monomer PerAcr **5** and the homopolymer PPerAcr **7** in solution. The concentration for the UV/vis measurement is for both samples 0.02 mg/ml THF, (b) normalized UV/vis and fluorescence spectra of the homopolymer PPerAcr in THF solution and in film.

is typical for isolated perylene bisimides without any π–π stacking. In THF the absorption has a maximum at 521 nm with a high extinction coefficient (80 800 cm^2/mmol) and the second vibronic transition is at 485 nm. The monomer has a very strong photoluminescence at 528 nm. As the fluorescence quantum yield for swallow-tail substituted perylene bisimides is quantitative and not considerably affected by oxygen, they can be used as standards for the fluorescence yield [16]. If the UV/vis spectrum of the monomer **5** is compared to the spectrum of the perylene bisimide homopolymer PPerAcr **7** the difference is obvious. The absorption gets broader and the intensities of the transitions change in polymer due to aggregation. The strongest absorption in perylene bisimide polymer **7** is the second vibronic transition at 490 nm. To express this change in the absorption, the quotient of the absorption at the second and the first vibronic transition is introduced. It changes from 0.61 for the monomer **5** to 1.63 for the homopolymer **7** in THF solution. Such optical parameters describe the degree of aggregation in perylene bisimide dyes [17]. It is also influenced by the nature of solvent. The difference in absorption can also be seen as the colour of the monomer **5** changes from yellowish to red for the homopolymer **7**. The intramolecular coupling between the perylene bisimide units occurs in THF solution, which can also be seen from the fluorescence. The fluorescence in the PPerAcr homopolymer is strongly reduced and it is red shifted to 618 nm. This behaviour is analogous to the interchain coupling in conjugated polymers and oligomers [18] but in our case it is an intramolecular coupling of two perylene bisimide units which are attached at the same polymer chain. We assign this behaviour to intramolecular coupling and not to intermolecular coupling as we could not observe any intermolecular aggregates in the GPC experiments. In films the red shift of the absorption is even stronger as can be seen in Fig. 3b and the fluorescence is further red shifted to 634 nm. In block copolymers also such a red shift in absorption is observed; the fluorescence of perylene bisimide being almost completely quenched, most probably due to electron transfer. Therefore the π–π stacking in the perylene bisimide segment is one of the major driving forces which can favour the nanostructure formation in these semiconductor polymers.

The interface between the electron and hole conductor is very important for organic solar cells as only there the exciton separation into a hole and an electron occurs. Block copolymers [19,20] are very interesting for this purpose as it is known that they show microphase separation on a nanometer scale exhibiting different morphologies. We investigated the morphology of the block copolymers **6A**–**6C** by transmission electron microscopy after melting the samples and cooling down to room temperature. In all our block copolymer samples which have a perylene content of 60–80 wt%, elongated nanowire-like structures occur except in **6A**. For

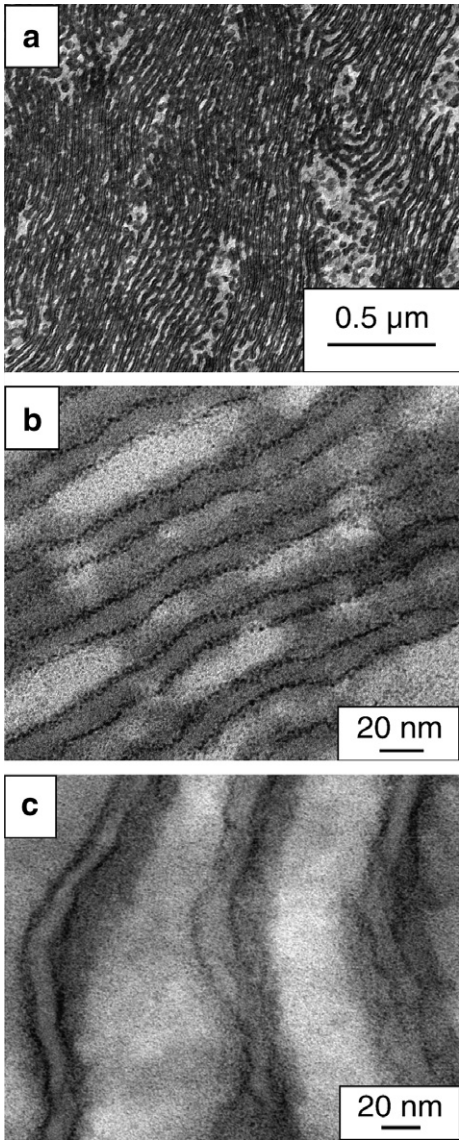


Fig. 4. (a) Overview of a TEM of the block copolymer **6B**, (b) magnification of the nanostructures in **6B**, (c) magnification of the nanostructures in **6C**. Samples were tempered for 1 h at 200 °C, embedded into epoxy resin, cut and stained with RuO_4.

6A as well as for the homopolymer **7** we could not observe any microphase separation using TEM. The building of these wire-like nanostructures seems to be stabilized by the PvTPA block. As in **6A** the PvTPA chain is very short, these structures are not favoured any more, most probably due to lack of enough amorphous domains which promote the segregation. In Fig. 4 the TEMs of the block copolymers **6B** and **6C** are shown. Both block copolymers show a microphase separation. It is interesting to note that both polymers show the same nanowire-like structure. The main driving force for this nanostructure formation is the crystallization of perylene bisimides via π–π stacking. It is important to note that these structures are non-equilibrium structures. In both cases, the perylene bisimide domains have a thickness of 13 nm with a length of up to several micrometers. The triphenylamine domains have no order or defined domain size with respect to the perylene bisimide domains which means that there is a minimal distance between the perylene bisimide wire structures. But the triphenylamine domains are flexible enough to cover also bigger distances. The samples shown here were stained with RuO_4 for approximately 5 min. With longer staining the structures seem to be larger than they actually are. The molecular stacking of the perylene bisimides, which lead to such elongated structures with a constant thickness is still under investigation. In literature there are examples that perylene bisimides together with melamine form hexagonal structures by hydrogen bonds [21,22]. We assume that in the case of the block copolymers **6** the nanostructures are induced by self-assembly of the perylene bisimides. As the domain size in the block copolymers is comparable to the exciton diffusion length these materials are very interesting for organic solar cells.

4. Conclusion

We have shown the controlled synthesis of block copolymers containing a perylene bisimide and a triphenylamine segment using NMRP. The building of these nanostructures is induced by π–π stacking of the perylene bisimides. This stacking could be observed with WAXS. The changes in the optical properties from the monomer to the polymer could be explained as due to intramolecular coupling of the perylene bisimide moieties in polymers. The electrochemical properties together with the microphase separation on a nanometer scale are very interesting for organic electronics as the domain size is in the range of the exciton diffusion length.

Acknowledgements

The financial support for this research work from German Research Council (DFG/SFB 481 – Project B4) is gratefully acknowledged. We also thank Astrid Göpfert, University of Bayreuth, for the TEM measurement.

References

[1] J.K.J. Van Duren, X. Yang, J. Loos, C.W.T. Bulle-Lieuwma, A.B. Sieval, J.C. Hummelen, R.A. Janssen, J. Adv. Funct. Mater. 14 (2004) 425.
[2] K.O. Sylvester-Hvid, S. Rettrup, M. Ratner, J. Phys. Chem. B 108 (2004) 4296.
[3] C.W. Tang, Appl. Phys. Lett. 48 (1986) 183.
[4] J. Xue, S. Uchida, B.P. Rand, S.R. Forrest, Appl. Phys. Lett. 85 (2004) 5757.
[5] S.E. Shaheen, C.J. Brabec, N.S. Sariciftci, F. Padinger, T. Fromherz, J.C. Hummelen, Appl. Phys. Lett. 78 (2001) 841.
[6] H. Hoppe, M. Niggemann, C. Winder, J. Kraut, R. Hiesgen, A. Hinsch, D. Meissner, N.S. Sariciftci, Adv. Funct. Mater. 14 (2004) 1005.
[7] M.H. van der Veen, B de Broer, U. Stalmach, K.I. van de Wetering, G. Hadziioannou, Macromolecules 37 (2004) 3673.
[8] S.M. Lindner, M. Thelakkat, Macromolecules 37 (2004) 8832.
[9] S.M. Lindner, S. Hüttner, A. Chiche, M. Thelakkat, G. Krausch, Angew. Chem., Int. Ed. 45 (2006) 3364.
[10] M. Sommer, S.M. Lindner, M. Thelakkat, Adv. Funct. Mater., in press.
[11] D. Benoit, V. Chaplinski, R. Braslau, C.J. Hawker, J. Am. Chem. Soc. 121 (1999) 3904.
[12] C.J. Hawker, A. Bosman, E. Harth, Chem. Rev. 101 (2001) 3661.
[13] F. Würthner, Chem. Commun. 14 (2004) 1564.
[14] H. Langhals, S. Demmig, T. Potrawa, J. Prakt. Chem. 333 (1991) 733.
[15] E. Hädicke, F. Graser, Acta Cryst. C 42 (1986) 189; E. Hädicke, F. Graser, Acta Cryst. C 42 (1986) 195.
[16] H. Langhals, J. Karolin, L.B.A. Johansson, J. Chem. Soc., Faraday Trans. 94 (1998) 2919.
[17] B.A. Gregg, J. Phys. Chem. 100 (1996) 852.
[18] J. Cornil, A.J. Heeger, J.L. Bredas, Chem. Phys. Lett. 272 (1997) 463.
[19] M.J. Fasolka, A.M. Mayes, Ann. Rev. Mater. Res. 31 (2001) 323.
[20] M.W. Matsen, F.S. Bates, Macromolecules 29 (1996) 1091.
[21] L.E. Sinks, B. Rybtchinski, M. Iimura, B.A. Jones, A.J. Goshe, X. Zuo, D.M. Tiede, X. Li, M.R. Wasielewski, Chem. Mater. 17 (2005) 6295.
[22] J.A. Theobald, N.S. Oxtoby, M.A. Philips, N.R. Champness, P.H. Beton, Nature 424 (2003) 1029.

ORGANIC ELECTRONICS
materials • physics • chemistry • applications

Editors:

Prof. Chihaya Adachi — Center for Future Chemistry, Kyushu University, 744 Motooka, Nishi, Fukuoka 819-0395, Japan. Fax: +81-92-802-3294, e-mail: adachi@cstf.kyushu-u.ac.jp

Prof. Stephen R. Forrest — EECS, MSE, and Physics, University of Michigan, 4080 Fleming Building, 503 Thompson Street, Ann Arbor, MI 48109-1340, USA. Fax: +1-734-763-0085, e-mail: stevefor@umich.edu

Prof. René Janssen — Molecular Materials and Nanosystems, Eindhoven University of Technology, P.O. Box 513, 5600 MB Eindhoven, The Netherlands. Fax: +31 40 2451036, e-mail: r.a.j.janssen@tue.nl

Prof. Josef Salbeck — Macromolecular Chemistry and Molecular Materials Science Department, University of Kassel, Heinrich Plett Strasse 40, D-34123 Kassel, Germany. E-mail: salbeck@uni-kassel.de

Associate Editorial Board:

V.M. AGRANOVICH (Moscow)
Y. CAO (Guangzhou)
A. DODABALAPUR (Austin)
M. FUJIHIRA (Yokohama)
N. PEYGHAMBARIAN (Tucson)
Z. POPOVIC (Mississauga)
W. RIESS (Rüschlikon)
Y. SHIROTA (Osaka)
C. TALIANI (Bologna)
T. TSUTSUI (Fukuoka)
E. UMBACH (Würzburg)

Founding Editors:

Prof. Donal Bradley, Prof. Stephen Forrest, Prof. Norbert Karl and Prof. Kazuhiko Seki

Aims and scope

An interdisciplinary journal on the physics, chemistry, and engineering of materials with applications to organic electronics and optoelectronics, **Organic Electronics** is a primary journal for physicists, material scientists and chemists who are interested in organic electronic devices such as organic light emitting diodes, thin film transistors, photovoltaic cells, etc. Papers suitable for publication in this journal cover such topics as photoconductive and electronic properties of organic materials, film growth and characterization, organic electronic and optoelectronic devices, and applications.

As an important Journal **Organic Electronics** can ensure that your most significant research receives the recognition that it deserves. As a unique publication outlet, uniting the various research disciplines involved, it provides the only forum for both applied and fundamental contributions spanning the many different disciplines addressing electronic applications of organic materials.

Advertising information

Advertising orders and enquiries can be sent to: James Kenney, Commercial Sales, Elsevier, 84 Theobald's Road, London WC1X 8RR, United Kingdom; phone: (+44) (20) 7611 4494; fax: (+44) (20) 7611 4463; e-mail: j.kenney@elsevier.com.

Abstracted/indexed in:

Current Contents: Engineering, Technology and Applied Sciences; El Compendex Plus; Engineering Index; INSPEC; Physics Briefs; Science Citation Index, expanded; Chemistry Citation Index; Current Contents: Physics, Chemistry and Engineering Science. Also covered in the abstract and citation database SCOPUS®. Full text available on ScienceDirect®.

Publication information: *Organic Electronics* (ISSN 1566-1199). For 2007, Volume 8 is scheduled for publication. Subscription prices are available upon request from the Publisher or from the Regional Sales Office nearest you or from this journal's website: (http://www.elsevier.com/locate/orgel). Further information is available on this journal and other Elsevier products through Elsevier's website: (http://www.elsevier.com). Subscriptions are accepted on a prepaid basis only and are entered on a calendar year basis. Issues are sent by standard mail (surface within Europe, air delivery outside Europe). Priority rates are available upon request. Claims for missing issues should be made within six months of the date of dispatch.

Orders, claims, and journal enquiries: please contact the Customer Service Department at the Regional Sales Office nearest you:

Orlando: Elsevier, Customer Service Department, 6277 Sea Harbor Drive, Orlando, FL 32887-4800, USA; phone: (877) 8397126 or (800) 6542452 [toll free numbers for US customers]; (+1) (407) 3454020 or (+1) (407) 3454000 [customers outside US]; fax: (+1) (407) 3631354 or (+1) (407) 3639661; e-mail: usjcs@elsevier.com or elspcs@elsevier.com

Amsterdam: Elsevier, Customer Service Department, P.O. Box 211, 1000 AE Amsterdam, The Netherlands; phone: (+31) (20) 4853757; fax: (+31) (20) 4853432; e-mail: nlinfo-f@elsevier.com

Tokyo: Elsevier, Customer Service Department, 4F Higashi-Azabu, 1-Chome Bldg, 1-9-15 Higashi-Azabu, Minato-ku, Tokyo 106-0044, Japan; phone: (+81) (3) 5561 5037; fax: (+81) (3) 5561 5047; e-mail: jp.info@elsevier.com

Singapore: Elsevier, Customer Service Department, 3 Killiney Road, #08-01 Winsland House I, Singapore 239519; phone: (+65) 6349 0222; fax: (+65) 6733 1510; e-mail: asiainfo@elsevier.com

Printed by Krips BV, Meppel, The Netherlands

ELSEVIER

Available online at www.sciencedirect.com
ScienceDirect
Organic Electronics 8 (2007) v
Organic Electronics
www.elsevier.com/locate/orgel

Publisher's note

Farewell to Professor Seki, Welcome to Professor Adachi

We regret to announce the retirement of Professor Seki from the board of Editors of Organic Electronics. Professor Seki joined the board as a founding editor of the journal in December 2000.

We would like to thank Professor Seki sincerely for his contribution to Organic Electronics, in terms of both editorial work and advising the development of the journal. We wish him well with all future plans.

We are delighted to announce to the readers of Organic Electronics that Professor Adachi has been appointed editor of the journal, replacing Professor Seki as of 15 November 2006.

The contact details of Professor Adachi are:

Professor Chihaya Adachi
Center for Future Chemistry
Kyushu University
744 Motooka, Nishi
Fukuoka 819-0395
Japan

E-mail: adachi@cstf.kyushu-u.ac.jp

Authors are encouraged to submit their papers to one of the editors using the Elsevier Editorial System, the journal's online submission tool at http://ees.elsevier.com/orgele

Please join us in welcoming Professor Adachi to the Organic Electronics editorial team.

The Publisher
December 2006

doi:10.1016/S1566-1199(06)00183-2

Available online at www.sciencedirect.com
ScienceDirect
Organic Electronics 8 (2007) 77–93
Organic Electronics
www.elsevier.com/locate/orgel

Strong exciton–photon coupling in organic materials

R.J. Holmes [a,*], S.R. Forrest [b]

[a] Princeton Institute for the Science and Technology of Materials (PRISM) and the Department of Electrical Engineering, Princeton University, Princeton, NJ 08544, United States
[b] Departments of Electrical Engineering and Computer Science, Physics, and Materials Science and Engineering, University of Michigan, Ann Arbor, MI 48109, United States

Received 3 February 2006; received in revised form 2 May 2006; accepted 11 May 2006
Available online 19 June 2006

Abstract

The study of strong exciton–photon coupling in organic materials has progressed at a rapid pace since the first observation of microcavity polaritons in tetra-(2,6-*t*-butyl)phenol-porphyrin zinc less than 10 years ago. The field is driven by the potential for revolutionary optoelectronic devices based on polaritonic phenomena such as ultrafast optical amplifiers and switches, structures with enhanced nonlinear optical properties, and coherent polariton light emitters, known as polariton lasers. This review examines recent experimental advances related to the general understanding of strong coupling in a range of small molecular weight and polymeric organic materials.
© 2006 Elsevier B.V. All rights reserved.

PACS: 71.36.+c; 71.35.−y; 78.20.−e; 78.30.Jw; 78.67.−n

1. Introduction

The study of organic materials confined to optical microcavities has recently experienced a surge in interest from both experimental [1–21] and theoretical [22–31] standpoints. Strong exciton–photon coupling has garnered special attention in the context of both fundamental investigations into exciton physics, and future optoelectronic devices. Given that electrically pumped lasing in organic materials has yet to be demonstrated [32], the development of coherent light emitting devices based on polariton formation and emission are of particular interest [33–36]. This paper reviews the unique properties of disordered organic materials [25] as they relate to the strongly coupled state determined primarily through recent experimental studies. Strong coupling in crystalline organic materials has, to date only been investigated from a theoretical standpoint [22,30]. Thorough discussions of the deeper theoretical implications of exciton–polariton states in both disordered and ordered materials can be found elsewhere [22–31].

Fermi's Golden Rule states that the rate of spontaneous emission is proportional to the density of photon states at the spatial position of the exciton [37]. Thus, the radiative lifetime of an exciton in an optical microcavity can either be extended or reduced with respect to its lifetime in vacuum. This

* Corresponding author. Present address: Department of Chemical Engineering and Materials Science, University of Minnesota, Minneapolis, Minnesota 55455. Tel.: +1 609 258 7033; fax: +1 609 258 7272.
E-mail address: rholmes@princeton.edu (R.J. Holmes).

1566-1199/$ - see front matter © 2006 Elsevier B.V. All rights reserved.
doi:10.1016/j.orgel.2006.05.005

phenomenon is known as the Purcell effect, and is a feature of weak exciton–photon coupling [38]. The interaction between the exciton and cavity photon is irreversible, since once excited, the exciton cannot transfer its energy back to the cavity. In contrast, the exciton and photon may strongly couple if their respective lifetimes are long in comparison to the interaction time between the two particles. In this case, a quasi-lossless regime is established wherein the system oscillates coherently between the exciton and cavity photon states. The new eigenstates of the system are referred to as microcavity polaritons [39–41]. The microcavity polariton dispersion curve consists of anti-crossed branches separated in energy by the Rabi splitting (Ω) [40,41]. The lifetime condition is equivalent to stating that the linewidth of the exciton and cavity mode resonance must be smaller than the Rabi splitting.

Strong coupling between an exciton and a cavity photon was first demonstrated in GaAs quantum wells by Weisbuch et al. [39]. Subsequent experiments examined polariton photoluminescence (PL), stimulated polariton scattering and the generation of large optical gain in polaritonic systems [33–36,41,42]. Quantum well excitons in inorganic semiconductors are of the Wannier–Mott-type. These extended excited states are weakly bound (~meV) and can have large Bohr radii (>10 nm). The excitonic state has a low saturation density [43] and can generally be ionized at room temperature. These features often limit the observation and study of the strongly coupled state to low temperatures and small excitation densities. Similarly, the low exciton oscillator strength results in small Rabi splittings that are typically $\leqslant$10 meV [41,44]. Resolving such small splittings at room temperature is complicated by thermal broadening that causes the exciton linewidth to exceed the splitting. Nevertheless, there have been multiple reports of strong coupling in inorganic quantum well structures at room temperature with Rabi splittings on the order of the exciton binding energy [45–47]. Microcavities containing GaN active layers with exciton binding energies of ~20 meV have been proposed as a solution to the problem of small exciton binding energies in inorganic semiconductors [48–51]. Recent demonstrations of strong exciton–photon coupling at room temperature in GaN [52,53] have further sparked interest in the use of this system for strongly coupled devices.

Organic materials possess a number of interesting physical properties relevant to strong coupling that contrast those of inorganic semiconductors. In particular, the excitons in organic materials are tightly bound (~1 eV) Frenkel-type states that can have large oscillator strengths [54]. Strong coupling was first demonstrated in organic materials by Lidzey et al. [1] using a spun cast film of tetra-(2,6-*t*-butyl)phenol-porphyrin zinc (4TBPPZn) in polystyrene located in a planar microcavity. This demonstration took place at room temperature, with a Rabi splitting >100 meV. As is typical of organic materials, the excitonic and, hence, polaritonic state is expected to persist even for large exciton densities.

This review is organized as follows. Experimental details relating to general device design considerations and the characterization of the strongly coupled state are outlined in Section 2. Section 3 provides some basic details of microcavity physics and a theoretical basis for interpreting the experimental results of Section 4. This is followed by a discussion of future directions for strong coupling in organic materials in Section 5.

2. Microcavity design and experimental techniques used in exploring exciton–polariton phenomena

In this section, we consider microcavities containing either small molecular weight organics or polymers, in addition to systems that embed a small molecular weight material in a transparent polymer matrix. Unless otherwise noted, polymer films are deposited by spin casting, and small molecular weight materials are deposited by vacuum thermal evaporation at a base pressure of 10^{-7} Torr.

The microcavities considered typically consist of a combination of metallic mirrors and distributed Bragg reflectors (DBR). A DBR contains alternating layers of high and low refractive index dielectric materials selected for maximum index contrast [55]. In organic microcavities, materials such as SiO_2 and LiF have been used as the low index component, while TiO_2, HfO_2, SiN_x, TaO_2 and TeO_2 have been employed as the high index component. Silicon dioxide and SiN_x are deposited on glass or semiconducting substrates using plasma enhanced chemical vapor deposition (PECVD). The high substrate temperatures required for PECVD prevent its use for deposition on the organic material surface. For structures requiring a second, top DBR as opposed to a metal reflector, a gentler deposition technique such as thermal evaporation or rf sputtering can be used. Lithium fluoride and TeO_2, or SiO_2 and TaO_2 can be deposited by high vacuum thermal evaporation to form DBRs without damaging the

underlying organic film [4–6,8,56]. Alternatively, when rf sputtering is used to deposit dielectric layers, low growth rates and plasma powers must be employed to minimize heating and damage to the underlying organic film [13].

The dispersion relation (energy versus in-plane wavevector) of an organic-filled optical microcavity is extracted by measuring the reflection, transmission or luminescent properties of the microcavity as a function of in-plane wavevector [40–42]. For reflectivity and luminescence measurements, the in-plane wavevector can be varied using the angle of reflection or the angle of detection (for luminescence) [57]. For transmission measurements, the wavevector can be varied by changing the microcavity length and, hence, the uncoupled cavity mode dispersion [39]. This is commonly accomplished in inorganic semiconductor systems by intentionally growing a thickness profile into the structure during deposition; this method can also be applied to organic materials.

3. Theory of exciton–polaritons

3.1. Physics of planar microcavities

In inorganic semiconductors, microcavity polaritons have been observed in a variety of cavity structures including planar microcavities [39,41,42,44], and recently, in two-dimensional photonic crystals [58,59]. Strong coupling has also been observed in distributed feedback structures using layered, organic–inorganic perovskites [60,61]. In organic materials, observations have been limited to the use of planar optical microcavities, and we focus our attention on these structures. A planar microcavity is defined as a vertical structure containing an organic material located between two highly reflective mirrors. These mirrors may consist of metallic films or dielectric stacks tailored to form a DBR, and are separated by a distance that yields a cavity resonance [41,55].

To ensure high reflectivity in the DBR stopband, the layer thicknesses must equal $\lambda_0/4n$, where λ_0 is the center wavelength of the stopband in air, and n is the layer refractive index at λ_0. The quarter wavelength condition ensures that successive reflections between layers add constructively to yield a high reflectivity stopband. The reflectivity of the DBR can be calculated as a function of photon energy and angle of incidence using transfer matrices [40,55,62,63]. For a large number of pairs, N, the DBR reflectivity, r_{DBR}, is [40,62]

$$r_{\mathrm{DBR}}(E) = \sqrt{R}\exp(\mathrm{i}\phi_{\mathrm{DBR}}(E)), \tag{1}$$

where the reflectivity at the center of the stopband, R, can be approximated by [40,41,55,62]

$$R = 1 - 4\frac{n_{\mathrm{EXT}}}{n_{\mathrm{Cav}}}\left(\frac{n_{\mathrm{L}}}{n_{\mathrm{H}}}\right)^{2N}, \tag{2}$$

where n_{L}, n_{H}, n_{EXT} and n_{Cav} are the indices of refraction for the low and high index components of the DBR at λ_0, the medium outside of the cavity (i.e. air or glass), and the material located in the cavity, respectively. The corresponding phase (ϕ_{DBR}) has approximately a linear dependence on photon energy, and at normal incidence is [40,55,62]

$$\phi_{\mathrm{DBR}}(E) = \frac{n_{\mathrm{Cav}}L_{\mathrm{DBR}}}{\hbar c}(E - E_{\mathrm{s}}), \tag{3}$$

where E_{s} ($=2\pi c\hbar/(n_{\mathrm{Cav}}\lambda_{\mathrm{S}})$, where c is the speed of light in vacuum, and λ_{S} is the center wavelength of the DBR in the cavity) is the center energy of the stopband, and L_{DBR} is the mirror penetration depth given by [40,55,62]

$$L_{\mathrm{DBR}} = \frac{\lambda_{\mathrm{S}}}{2n_{\mathrm{Cav}}}\frac{n_{\mathrm{L}}n_{\mathrm{H}}}{n_{\mathrm{H}} - n_{\mathrm{L}}}. \tag{4}$$

Here, L_{DBR} depends on both photon polarization and angle of incidence. At normal incidence, L_{DBR} is equal to twice the distance a fixed phase mirror would have to be displaced to produce the same phase delay upon reflection [55,62,64].

The resonant modes of a cavity consisting of a pair of DBRs are solutions to [62]

$$\frac{2n_{\mathrm{Cav}}}{\hbar c}(L_{\mathrm{C}}E + L_{\mathrm{DBR}}(E - E_{\mathrm{s}})) = 2\pi m + \mathrm{i}\ln(R), \tag{5}$$

where m is an integer. The complex energy $E_{\mathrm{m}} - \mathrm{i}\gamma_{\mathrm{m}}$ consists of the real mode energy E_{m} and the cavity mode halfwidth γ_{m}, and is determined by the real and imaginary parts of Eq. (5). Solving for the mode energy yields the real mode frequency [62]:

$$\omega_m = \frac{L_{\mathrm{C}}\omega_{\mathrm{C}} + L_{\mathrm{DBR}}\omega_{\mathrm{S}}}{L_{\mathrm{eff}}} \tag{6}$$

with $\omega_{\mathrm{C}} = m\pi c/(n_{\mathrm{Cav}}L_{\mathrm{C}})$ and $L_{\mathrm{eff}} = L_{\mathrm{C}} + L_{\mathrm{DBR}}$. The cavity mode halfwidth is [62]

$$\gamma_m = \frac{(1-R)\hbar c}{2n_{\mathrm{Cav}}L_{\mathrm{eff}}}. \tag{7}$$

If the DBR (ω_{S}) is centered on ω_{C}, Eq. (6) reduces to $\omega_{\mathrm{m}} = \omega_{\mathrm{C}}$, and the resonant modes of the

microcavity are given by $\omega_m = m\pi c/(n_{Cav}L_C)$ and $L_C = m\lambda_m/2n_{Cav}$.

For planar microcavities consisting of a DBR mirror and a metallic mirror, the penetration depth of the metallic mirror (L_{Metal}) at normal incidence for a photon of wavelength λ is [65]

$$L_{Metal} = \left|\frac{\phi_{Metal}}{4\pi}\lambda\right|, \tag{8}$$

$$\phi_{Metal} = \tan^{-1}\left(\frac{2n_{Cav}n_M}{n_{Cav}^2 - n_M^2 - k_M^2}\right), \tag{9}$$

where ϕ_{Metal} is the phase shift incurred by a photon upon reflection from the metal surface defined in Eq. (9) in terms of the cavity index of refraction and the real and imaginary indices (n_M, k_M) of the metal. Typically, $L_{Metal} \ll L_C$, L_{DBR} and can be ignored when determining the resonant modes of a metal/DBR microcavity.

In a perfectly reflecting planar microcavity, strong photon confinement forces the axial wavevector to be $k_z = \pi/L_C$, such that the dispersion of the cavity mode energy, $E_p(k)$, is [25,41]

$$E_p(k) = \frac{\hbar c}{n_{Cav}}k = \frac{\hbar c}{n_{Cav}}\left[\left(\frac{\pi}{L_C}\right)^2 + k_\parallel^2\right]^{1/2}, \tag{10}$$

where $\hbar$ is Planck's constant divided by 2π, and $k_\parallel$ is the in-plane component of the photon wavevector. Using $k_\parallel = E_p(k)\sin\theta/\hbar c$ [41], Eq. (10) can be rewritten in terms of the photon angle of incidence as [41]

$$E_p(\theta) = E_0\left(1 - \frac{\sin^2\theta}{n_C^2}\right)^{-1/2}, \tag{11}$$

where E_0 is the cut-off energy, θ is the photon angle of incidence, and n_{Cav} is replaced with the effective index of refraction n_C to account for imperfect mirrors. Eq. (11) allows the dispersion of the cavity to be measured experimentally by tracking the cavity mode energy as a function of the photon angle of incidence in reflectivity [57].

3.2. Strong exciton–photon coupling

In this section, we focus our attention on three approaches used to model strong coupling, namely: the semiclassical theory of quantum well (QW) excitons in a semiconductor microcavity [40,62], the coupled oscillator model [41] and a classical, macroscopic linear dispersion theory [25].

The optical response of the QW can be semiclassically treated by using a nonlocal susceptibility [40]. The system is defined as two identical DBRs separated by a distance L_C, with a single QW of negligible width placed at the center of the cavity. This model is frequently applied to treat strong exciton–photon coupling in inorganic quantum well systems. It accounts both for the spatial position of the absorbing QW with respect to the electric field, and also for reflections at the QW/cavity interface. Although the treatment of an organic absorber is often different, this model is helpful in understanding the relationship between the weakly and strongly coupled regimes. Similar to the treatment above, the eigenmodes of the QW-cavity system are found via [40,62,66]:

$$r_{DBR}^2\left[t_{QW}^2 - r_{QW}^2\right]\exp(i2k_zL_C) + 2r_{DBR}r_{QW}\exp(ik_zL_C) = 1, \tag{12}$$

where r_{QW} and t_{QW} are the reflection and transmission coefficients of the embedded QW. For simplicity, we consider only TE polarized radiation [62]:

$$r_{QW} = \frac{i\hbar\Gamma}{\Delta + i\hbar\Gamma}, \quad t_{QW} = 1 + r_{QW}, \tag{13}$$

where Γ is proportional to the exciton oscillator strength, and $\Delta = E - E_{Ex} - i\gamma_{Ex}$, where E_{Ex} is the exciton energy, and γ_{Ex} is the nonradiative exciton broadening [62]. Substitution of Eq. (13) into (12) yields:

$$\frac{\hbar\Gamma}{E - E_{Ex} + i\gamma_{Ex}} = i\frac{1 - r_{DBR}\exp(ik_zL_C)}{1 + r_{DBR}\exp(ik_zL_C)}. \tag{14}$$

Eq. (14) can be solved for the eigenmodes of the coupled system for the case where the QW lies at anti-node of the electric field to approximately yield:

$$(E - E_{Ex} + i\gamma_{Ex})(E - E_m + i\gamma_m) = V^2, \tag{15}$$

where $E_m - i\gamma_m$ is a resonant mode of the nonabsorbing cavity, and the interaction potential, or matrix element V, is defined as [40]

$$V = \sqrt{\frac{1 + \sqrt{R}}{\sqrt{R}}\frac{c\hbar\Gamma}{n_{Cav}L_{eff}}}. \tag{16}$$

The solutions to Eq. (15) are [40]

$$E = \left(\frac{E_{Ex} + E_m}{2}\right) - i\left(\frac{\gamma_{Ex} + \gamma_m}{2}\right) \pm \sqrt{V^2 + \frac{1}{4}[E_{Ex} - E_m - i(\gamma_{Ex} - \gamma_m)]^2}. \tag{17}$$

When the root is real (imaginary), the resonant eigenmodes of the coupled system are split (degenerate), corresponding to strong (weak) exciton–photon coupling [40]. At resonance, ($E_{Ex} = E_m$), the strongly coupled eigenmodes of Eq. (17) are separated in energy by the Rabi splitting, Ω, defined in terms of V as:

$$\Omega = 2\sqrt{V^2 - \frac{1}{4}(\gamma_{Ex} - \gamma_m)^2}, \tag{18}$$

which in the limit of well matched exciton and cavity mode linewidths yields $\Omega = 2V$. From Eq. (17), the strongly coupled regime requires $2|V| > |\gamma_{Ex} - \gamma_m|$ when $E_{Ex} = E_m$. Ideally, the uncoupled exciton and cavity mode should have similar linewidths, and to best resolve the splitting, should be as small as possible [67].

The model of coupled oscillators treats both the exciton and photon as harmonic oscillators with uncoupled energies, E_{Ex} and E_p, respectively. The uncoupled exciton energy is taken as dispersionless, and the uncoupled cavity mode energy is defined by Eq. (11). The oscillators are coupled via an interaction matrix element, V, and the time independent Schrödinger Equation for the system can be written as [41]

$$\begin{bmatrix} E_p & V \\ V & E_{Ex} \end{bmatrix} \begin{bmatrix} \alpha \\ \beta \end{bmatrix} = E \begin{bmatrix} \alpha \\ \beta \end{bmatrix}, \tag{19}$$

which yields a secular determinant that is nearly identical to Eq. (15) with eigenvalues of

$$E = \frac{(E_p + E_{Ex})}{2} \pm \frac{1}{2}\sqrt{(E_p - E_{Ex})^2 + 4V^2}, \tag{20}$$

where α and β are the eigenvector mixing coefficients of the strongly coupled system. In this treatment, we have neglected broadening of the excitonic transition. This dispersion relation can be measured through the angular dependence of E_p via Eq. (11). For well-matched exciton and cavity mode linewidths, the Rabi splitting can be taken as $2V$ (Eq. (18)). In systems where the uncoupled photon and exciton linewidths are poorly matched, Eq. (18) should be employed. Additional corrections depending on the measurement technique must be used when Ω is comparable to the uncoupled linewdiths [40]. It is straightforward to extend Eq. (19) to the case of multiple coupled exciton or photon states [3,15,68–70].

The polariton eigenvalues of Eq. (20) can also be obtained using a classical, macroscopic linear dispersion model. In this case, the cavity medium has a single, dispersionless resonance at E_{ex}, with all other transitions grouped into a background dielectric constant, ε_b. Following Agranovich et al. [25] Maxwell's equations for a transverse electromagnetic wave yields:

$$\frac{\hbar^2 c^2 (k_z^2 + k_\parallel^2)}{E^2} = \varepsilon_b + \frac{A}{E_{Ex}^2 - E^2 - 2iE\gamma_0}, \tag{21}$$

where γ_0 is the total broadening of the excitonic resonance, and A contains the exciton oscillator strength. For $E \sim E_p(k_\parallel) \sim E_{Ex}$,

$$[E - E_p(k_\parallel)][E - E_{Ex} + i\gamma_0] = V^2, \tag{22}$$

where $V = A/4\varepsilon_b$. In the limit of strong coupling and minimal broadening (i.e. $\gamma_0 \ll V$), Eq. (22) has solutions identical to Eqs. (17) and (20).

In Eqs. (16) and (18), the interaction matrix element V and the Rabi splitting are defined using semiclassical theory. The same expressions are obtained when a quantum mechanical treatment of the QW-cavity system is employed [40]. An alternate method for defining these parameters uses a classical, linear dispersion model originally applied to atom-cavity systems that treats the atom (or exciton) as a Lorentzian absorber [71]:

$$\Omega = \left(\frac{\alpha d F \delta_{Ex}\delta_{Cav}}{\pi} - \frac{(\delta_{Ex} - \delta_{Cav})^2}{4}\right)^{1/2}, \tag{23}$$

where α and d are the absorption coefficient and thickness of the active region, δ_{Ex} and δ_{Cav} are the uncoupled exciton and cavity transition full widths at half maxima (FWHM), respectively, and F is the cavity finesse. In this model, the linewidths of the polaritonic features at strongest coupling are equal to the average of the uncoupled cavity and exciton linewidths [71]. While Eq. (23) is qualitatively similar to Eqs. (16) and (18), the linear dispersion model is incomplete as it neglects multiple reflections at the absorber-cavity interface, and does not include the spatial position of the absorber with respect to the optical field. However, these limitations are not as severe in organic materials as they are for inorganic QW structures. The majority of the organic microcavities discussed here are uniformly filled, thus there are no absorber-cavity reflections to consider. The linear dispersion model has been included primarily because it is widely applied to organic microcavity systems, while also offering a convenient starting point for discussions of strong coupling in organic materials.

4. Experimental results

4.1. Reflectivity of strongly coupled organic microcavities

The giant Rabi splittings observed in organic materials were predicted theoretically by Agranovich et al. [22]. Strong exciton–photon coupling was first demonstrated in organic materials experimentally using a metal/DBR microcavity containing a spun cast film of 4TBPPZn in polystyrene [1]. The microcavity was tuned to the highly absorptive Soret band resonance (at $E_{Ex} = 2.88$ eV) of 4TBPPZn, yielding room temperature Rabi splittings up to 160 meV in angularly resolved reflectivity spectra (Fig. 1a). The dependence of the Rabi splitting on the film absorption coefficient (α), and thickness (d) for this structure is shown in Fig. 1b, and follows Eq. (23).

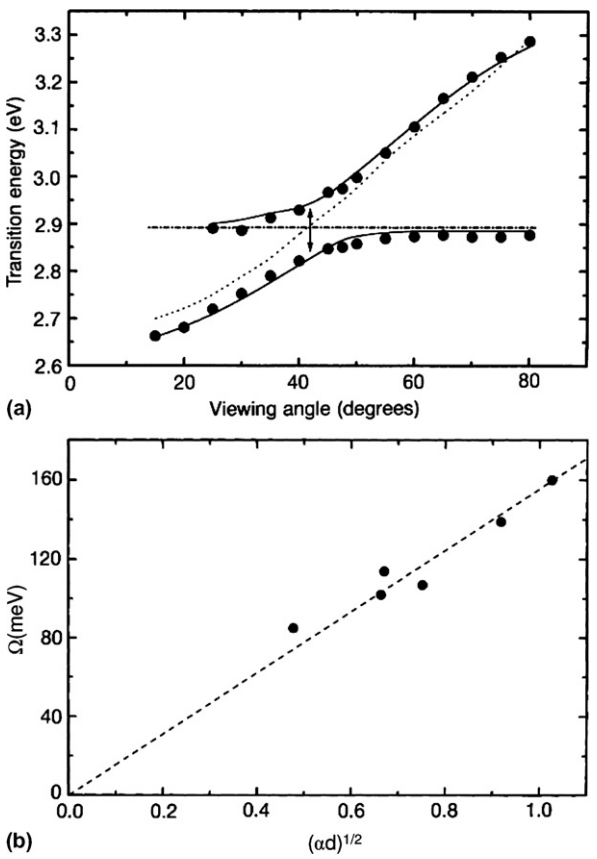


Fig. 1. (a) Dispersion relation for a microcavity containing a film of tetra-(2,6-*t*-butyl)phenol-porphyrin zinc in polystyrene located between a distributed Bragg reflector and a silver mirror. The dispersion was extracted from angularly resolved reflectivity measurements. The solid lines are fits obtained using a transfer-matrix reflectivity model. (b) The dependence of the Rabi splitting (Ω) on the square root of the film absorption. By permission. Copyright, Macmillan Publishers Ltd. [1].

Although capable of large Rabi splittings, 4TBPPZn is not an optimal material for studies of strong coupling since the Soret band does not support a radiative transition. The first studies of polariton emission in organic materials employed luminescent cyanine dyes [2]. Depending on the preparation conditions, cyanine dye films form absorptive J-aggregates [72,73] that are characterized by high exciton oscillator strengths, small Franck–Condon shifts, and absorption and emission linewidths of ~40–60 meV [2]. Fig. 2a shows reflectivity spectra reported by Lidzey et al. [2] that were collected from a microcavity containing 2-2′-dimethyl-8-phenyl-5,6,5′,6′-dibenzothiacarbocyanine chloride in a polyvinylalcohol (PVA) matrix. The resulting dispersion relation (Fig. 2b) exhibits an anti-crossing around the uncoupled exciton energy with a splitting of ~80 meV [2]. Further refinements in microcavity design have led to even larger splittings >200 meV [9,18]. The luminescent properties of polaritons in organic materials are discussed further in Section 4.2.

Schouwink et al. [6] have used cyanine dyes in planar optical microcavities to investigate the dependence of the strongly coupled state on the spatial overlap of the absorbing dye layer and the cavity electric field. This was accomplished by comparing the splitting for three microcavity structures, each with the organic layer located at a different position between SiO_2 spacer layers. The dye, 1,1′-diethtyl-2,2′-cyanine decahydro-closo-decaborate $[(PIC^+)_2B_{10}H_{10}^{2-}]$, was deposited by spin casting without the use of a polymer matrix, and the dispersion relation was extracted from angularly resolved transmission spectra [6]. The splitting is observed to increase as the dye layer is moved closer to an anti-node in the confined optical electric field. The dependence of the splitting on electric field is linear, consistent with a fully quantum mechanical treatment of the light-matter interaction [74].

Observations of strong exciton–photon coupling in spun cast organic materials have extended beyond the Zn-porphyrin and cyanine dye systems. Rabi splittings ranging from 210 to 430 meV have been observed for spun cast films of the σ-conjugated polysilane poly[bis(*p*-butylphenyl)silane] (PBPS, $E_{Ex} = 3.14$ eV) located in metal/DBR microcavities [10,12]. Strong coupling in PBPS overcomes the typically broad exciton linewidths

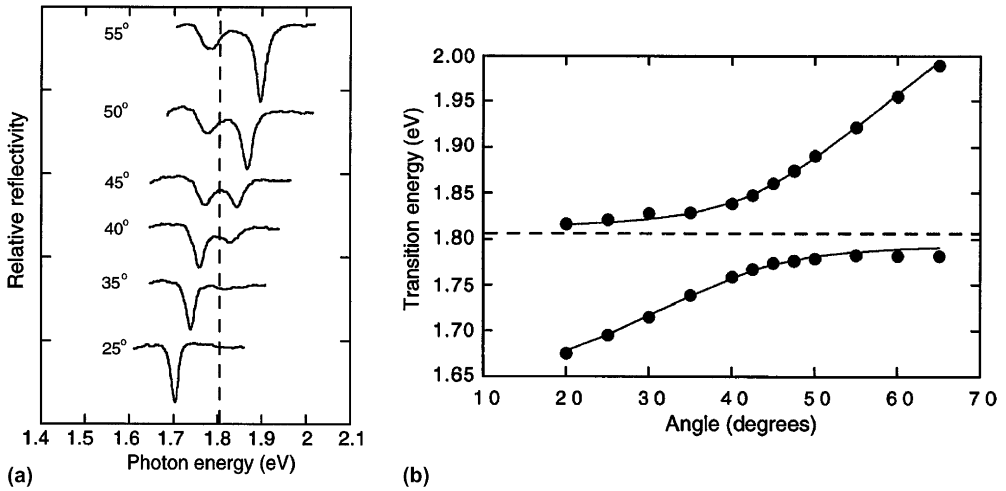


Fig. 2. (a) Reflectivity spectra for a microcavity containing a film of 2-2′-dimethyl-8-phenyl-5,6,5′,6′-dibenzothiacarbocyanine chloride in polyvinylalcohol located between a distributed Bragg reflector and a silver mirror as a function of incident angle. (b) The microcavity dispersion relation extracted from the spectra of (a). The fits (solid lines) are obtained using a transfer-matrix reflectivity model. By permission. Copyright, American Physical Society [2].

associated with conjugated polymers. In PBPS, the large Rabi splitting allows for resolution of the strongly coupled state despite the broad exciton transition linewidth (190 meV) [10]. To our knowledge, PBPS is the only extant demonstration of strong exciton–photon coupling in a neat polymer film, as opposed to the case of a small molecular weight material dispersed in a polymer matrix.

In addition to solution processed systems, strong coupling has also been observed in thermally evaporated small molecular weight materials. Thermal evaporation offers additional control over thin film properties such as morphology [75]. The first observation of strong coupling in a thermally evaporated polycrystalline material used a thin film of 3,4,7,8 napthalenetetracarboxylic dianhydride (NTCDA) located in a metal/DBR microcavity. The absorption spectrum of polycrystalline [76] NTCDA consists of two vibronic transitions at 3.19 ± 0.05 eV (0–0 line) and at 3.39 ± 0.05 eV (0–1 line), with FWHM of (145 ± 5) meV and (138 ± 5) meV, respectively (inset, Fig. 3). These transitions arise from absorption between S_0 and the lowest (0–0) or first (0–1) vibronic level of the S_1 excited state. Coupling between the 0–0 transition and the cavity photon leads to a Rabi splitting of (156 ± 4) meV for a 20 nm thick active layer at room temperature (Fig. 3) [15]. For thicker films, the 0–1 transition becomes sufficiently absorptive to couple to the cavity mode, resulting in photon mediated exciton hybridization (Section 4.3).

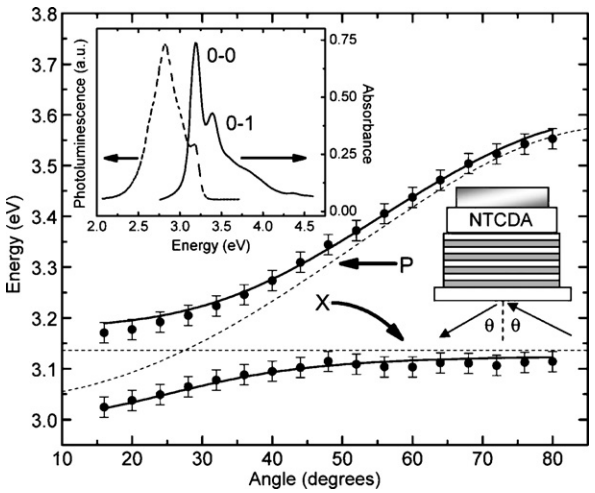


Fig. 3. Dispersion relation extracted from the reflectivity of a microcavity containing a 20 nm thick film of 3,4,7,8 naphthalenetetracarboxylic dianhydride (NTCDA) located between a distributed Bragg reflector and an aluminum mirror. The fits (solid lines) are obtained using a two-level coupled oscillator model. The broken curves indicate the uncoupled photon (P) and exciton (X) dispersion relations. *Inset:* Room temperature photoluminescence and absorbance spectra for a 50 nm thick film of NTCDA. Absorption peaks at 3.19 and 3.39 eV correspond to the 0–0 and 0–1 transitions. By permission. Copyright, American Physical Society [15].

Microcavity polaritons have also been studied in thermally evaporated thin films of the small molecular weight porphyrins namely the phosphor platinum(II) octaethylporphyrin (PtOEP), and the

analogous fluorescent light emitting tetraphenylporphyrin (TPP) [16]. These materials were used to investigate the effect of singlet–triplet intersystem crossing (ISC) [54,77–79] on the strongly coupled state. Metal/DBR microcavities containing a neat film of PtOEP tuned to the lowest energy Q-band [80] transition show a maximum splitting of (140 ± 10) meV in reflection [16]. When PtOEP is doped into a wide energy gap host, the Rabi splitting decreases with doping concentration in accordance with Eq. (23). In TPP, chosen for its structural similarity to PtOEP but lacking the coordinating Pt atom, a maximum splitting of (42 ± 10) meV is obtained [16]. The smaller splitting in TPP is due to the decreased absorption of the Q-band in TPP compared to PtOEP. In Section 4.2, the effect of rapid ISC on polariton PL is analyzed by comparing the cases of PtOEP and TPP.

In analogy to the results of Ref. [1], strong exciton–photon coupling has also been demonstrated to the Soret band of TPP in thermally evaporated thin films [16]. The Soret band of TPP is sufficiently absorptive, such that a neat film located in a resonantly tuned metal/DBR microcavity yields a splitting that exceeds the width of the DBR stopband. To clearly resolve both branches in this case, the film absorbance is reduced by diluting TPP at 20 wt.% in a wide energy gap host, leading to a splitting of (285 ± 20) meV measured in reflectivity [16].

4.2. Photoluminescence from strongly coupled organic microcavities

Polariton PL was first observed in organic materials using metal/DBR microcavities containing 2-2′-dimethyl-8-phenyl-5,6,5′,6′-dibenzothiacarbocyanine chloride ($E_{Ex} = 1.78$ eV) suspended in a spun cast film of PVA [2]. Observations of strong coupling in reflectivity for this particular structure are shown in Fig. 2a and b. Fig. 4a and b show that the PL resulting from surface-normal excitation at 1.96 eV consists of a single feature that tracks the lower branch of the dispersion relation extracted from reflectivity [2]. The absence of PL from the upper branch is attributed to the rapid relaxation of polaritons to the lower branch [2,21].

In later experiments on similar cyanine dyes, cavities were excited below the resonance angle, such that emission from both the upper and lower branches was observed [7,21]. The observed PL corresponds to the polaritonic features observed in reflectivity (Fig. 5a). Both branches radiate at small angles since as the excitonic character of the lower branch decreases, relaxation into it becomes less probable (Fig. 5b) [21]. A similar result is observed for PL from strongly coupled PBPS microcavities [10,12], as well as in strongly coupled InGaAs quantum wells [81].

This general asymmetry in polariton PL intensity between the two branches has been treated quantita-

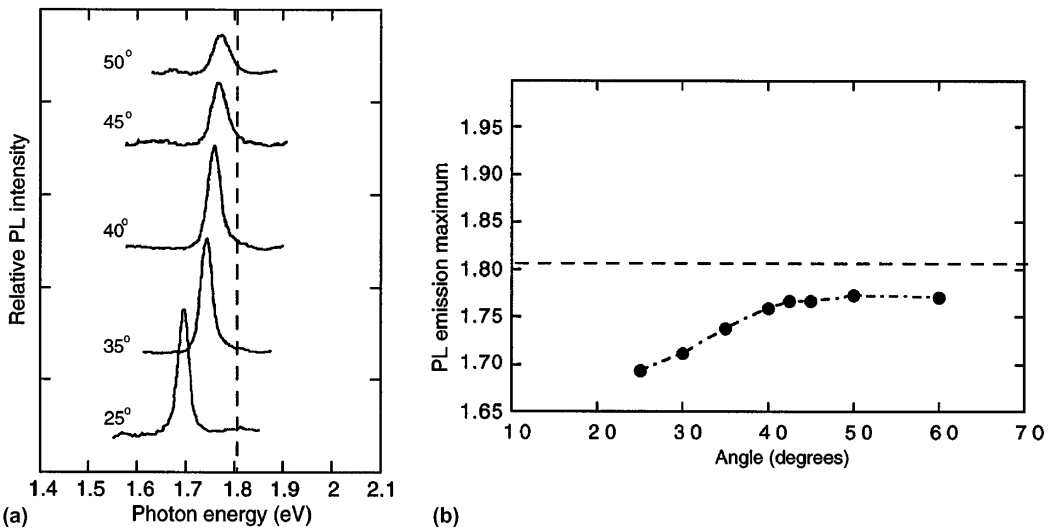


Fig. 4. (a) Photoluminescence spectra collected from the cavity of Fig. 2 as a function of detection angle for excitation at normal incidence. (b) The microcavity dispersion relation extracted from the photoluminescence spectra of (a). By permission. Copyright, American Physical Society [2].

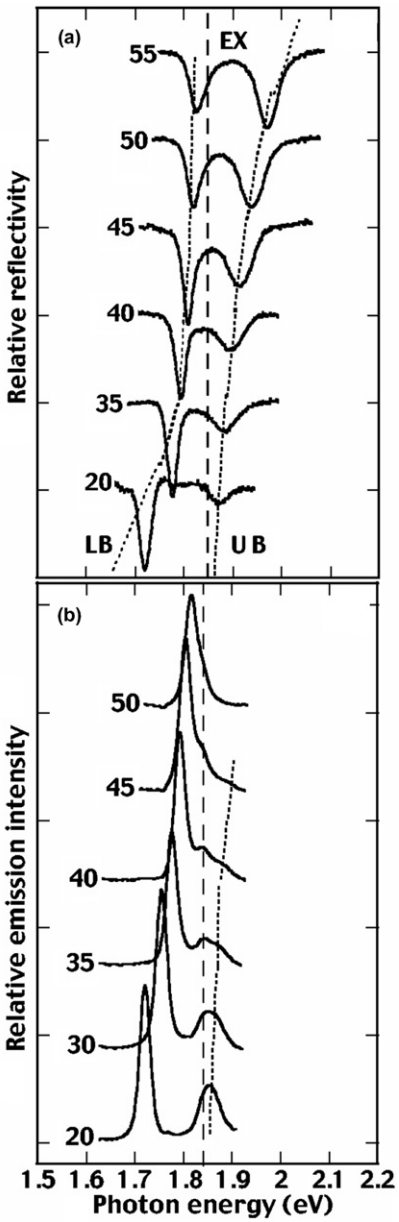


Fig. 5. (a) Reflectivity spectra for a microcavity containing a film of a cyanine dye in polyvinylalcohol located between a distributed Bragg reflector and a silver mirror as a function of incident angle. (b) Photoluminescence spectra obtained for the cavity of (a) as a function of the detection angle for excitation below the resonance angle. By permission. Copyright, American Physical Society [7].

tively using a two-level polariton model in which population transfer between the branches may occur via phonon emission [7]. Using this model to predict PL intensities, Lidzey et al. [7] found good agreement with experiments using the strongly coupled cyanine dye systems.

In strongly coupled structures containing a film of the phosphorescent emitter PtOEP doped into a wide gap host, polariton PL is not observed under nonresonant excitation at 3.04 eV [16]. The only emission from the microcavity is ascribed to phosphorescence from the T_1 triplet level at 1.90 eV [16]. In this case, the strongly coupled state (coupling to the S_1 exciton at 2.30 eV) is not populated under nonresonant excitation. Ideally, nonresonant excitation creates excitons in the S_2 manifold, which then relax into S_1 and strongly couple to the cavity mode. In PtOEP, ISC to the triplet state is sufficiently rapid to convert excited singlets into triplets before relaxation can be completed. In reflectivity, the microcavities are excited with white light, allowing the exciton/polariton state to be directly excited, avoiding the slow relaxation processes. This feature of materials with strong ISC will be discussed further in Section 4.4 as a means of estimating nonradiative decay rates in organic materials.

In contrast to PtOEP, microcavities containing TPP ($E_{Ex} = 1.90$ eV) exhibit PL from both branches of the dispersion curve under nonresonant excitation (3.04 eV) for angles above and below the resonance point (Fig. 6a) [16]. The dispersion curves obtained from reflectivity and PL measurements are in excellent agreement with each other (Fig. 6b). Similar to the case of the cyanine dyes, the upper branch PL is significantly weaker than that originating from the lower branch [16]. In addition, the PL intensity of the upper branch decreases relative to that of the lower branch for increasingly large detection angles. That upper branch PL is less intense than the lower branch PL for all angles, may suggest the existence of phonon-assisted relaxation between the two polariton branches as discussed in Ref. [7]. Also, as suggested in Ref. [2], the decrease in PL intensity from the upper branch with detection angle may result from the generation of polaritons from a relaxed excitonic distribution, implying that only upper branch polaritons lying close to the uncoupled exciton energy can be efficiently populated [2].

4.3. Photon mediated exciton hybridization

When two excitonic resonances are contained within the dispersion of a single cavity mode, all three states (both excitonic transitions and the photon mode) may simultaneously couple. This process is referred to as photon-mediated exciton hybridization, and mixes the character of the excitonic

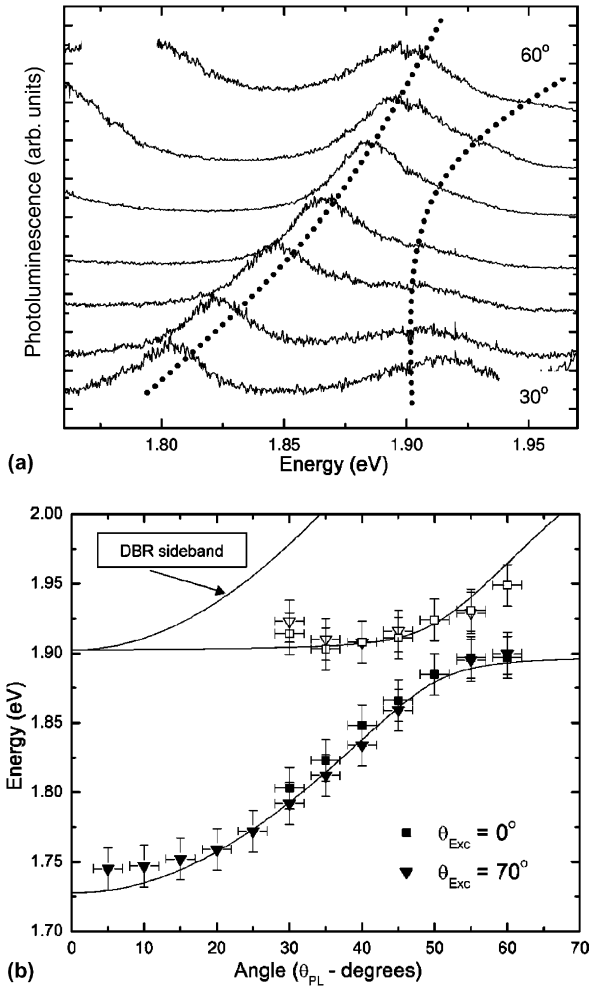


Fig. 6. (a) Photoluminescence spectra for a microcavity containing a film of tetraphenylporphyrin located between a distributed Bragg reflector and an aluminum mirror as a function of incident angle. The broken lines indicate the positions of the upper and lower branch polaritons. (b) The dispersion relation for the microcavity of (a) extracted from the spectra for excitation at both normal incidence and at 70°. The solid lines indicate the positions of polaritonic features extracted from reflectivity spectra. By permission. Copyright, American Physical Society [16].

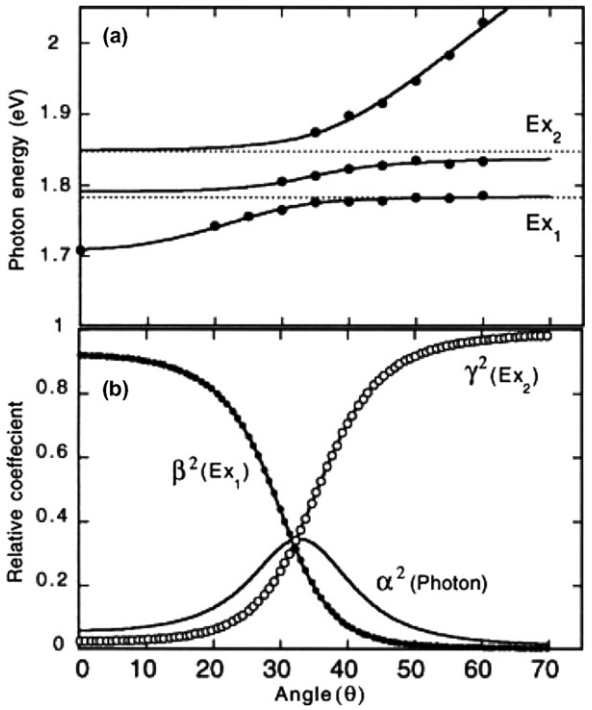


Fig. 7. (a) Dispersion relation for a microcavity containing two cyanine dye layers (broken lines) simultaneously coupling to a common cavity mode. The active layers are spatially separated such that the only interaction between the films is one mediated by the cavity mode. (b) Mixing coefficients $|\alpha|^2$, $|\beta|^2$, and $|\gamma|^2$ extracted from the fits of (a). The middle branch is an equal mixture of both excitons and the photon at an incident angle of $\theta \sim 32°$. By permission. Copyright, AAAS [3].

species. Exciton hybridization in organic materials has been observed between two separate molecular thin films located in a common optical microcavity [3], as well as between the neighboring vibronic transitions of a single molecule [15].

Lidzey et al. [3] first observed hybridization between films of two different cyanine dyes with resonances separated by 60 meV. The resulting three-body dispersion was modeled using a coupled oscillator framework similar to Eq. (19), yielding two branch splittings (Fig. 7a). In this case, the dispersion can be tuned by adjusting the relative concentration (and hence film absorbance) of each cyanine dye. Branch splittings drop from 37 meV and 58 meV to 18 meV and 44 meV for a reduction in the dye concentration from $2.3 \times 10^{20}\,\mathrm{cm}^{-3}$ to $1.2 \times 10^{20}\,\mathrm{cm}^{-3}$, consistent with the reduced film absorbance and, hence, a weaker interaction with the cavity mode. In the less concentrated structure, the middle branch is almost entirely photon-like after interacting with the lowest energy excitonic transition. The mixing coefficients at strongest coupling reflect this reduction in hybridization as the system moves from the case of near perfect mixing (i.e. $|\alpha|^2 = |\beta|^2 = |\gamma|^2$) at high dye concentrations (Fig. 7b), to $|\alpha|^2 = 0.70$ and $|\beta|^2 = |\gamma|^2 = 0.15$ for reduced doping concentrations [3]. This reduction in mixing results from the excitonic separation ($\Delta E \sim 60$ meV) exceeding the respective branch splittings.

Photoluminescence from three-body coupled systems has also been investigated to determine

whether energy transfer can occur between the branches of the dispersion relation [14]. In the cyanine dye based system of Ref. [3], PL is observed from all three branches of the dispersion for angles below the point of maximum mixing. Emission from the upper branch is very weak in comparison to the middle and lower branches, and for angles greater than the resonance point, emission from the upper branch is not observed [14]. It is unclear whether the asymmetry in PL arises as a result of energy transfer between branches.

As has already been discussed, strong coupling to the 0–0 transition is observed for microcavities containing a thin film (20 nm) of the small molecule NTCDA. For larger NTCDA film thicknesses, the absorbance of the 0–1 transition increases and its interaction with the cavity also leads to strong coupling [15]. Branch splittings of $\Omega_{0-0} = (280 \pm 20)$ meV and $\Omega_{0-1} = (100 \pm 20)$ meV for a 40 nm thick film and $\Omega_{0-0} = (360 \pm 20)$ meV and $\Omega_{0-1} = (120 \pm 20)$ meV for a 60 nm thick film are extracted using a coupled oscillator framework (Fig. 8a) [15]. The resulting mixing coefficients at strongest coupling are $|\alpha|^2 = 0.387$ and $|\beta|^2 = |\gamma|^2 = 0.306$ for a 40 nm thick film (Fig. 8b) and $|\alpha|^2 = 0.284$ and $|\beta|^2 = |\gamma|^2 = 0.358$ for a 60 nm thick film [15]. Mixing between all three states is nearly equal in the middle branch, and the excitonic states are hybridized. Thus, due to the large Frenkel exciton oscillator strength of both the 0–0 and 0–1 transitions of NTCDA, hybridization between excitonic transitions separated by $\Delta E \sim 200$ meV can be achieved at room temperature using a single molecular species.

4.4. Estimation of ultrafast relaxation rates in optical microcavities

The hybridization of neighboring vibronic transitions offers a new means to study ultrafast relaxation processes in organic materials. For thick films of NTCDA, strong coupling competes favorably with relaxation from the first excited vibronic state (Fig. 8a), while for a 20 nm thick film, coupling to the 0–1 transition is overcome by relaxation to the ground vibronic state (Fig. 3) [15]. The Rabi period for a 40 nm thick film gives a lower limit estimate of the lifetime of the first excited vibronic state, since at this thickness, the Rabi period is shorter than the vibronic relaxation time. An upper limit estimate can be obtained by calculating the expected Rabi period for a 20 nm thick film based the upper

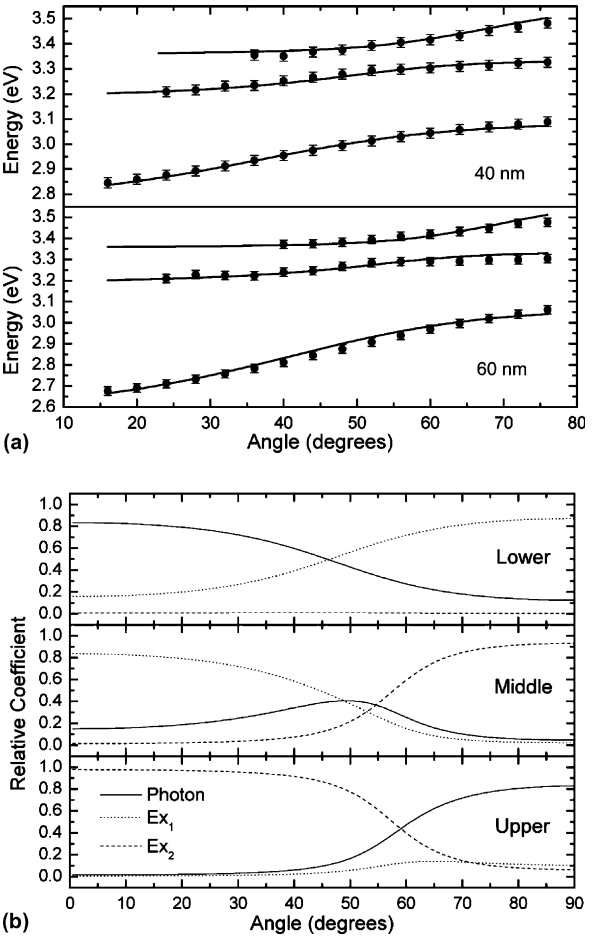


Fig. 8. (a) Dispersion relations extracted for microcavities containing 40 nm and 60 nm thick 3,4,7,8 napthalenetetracarboxylic dianhydride (NTCDA) films. The coupled oscillator model yields splittings of $\Omega_{0-0} = (280 \pm 20)$ meV and $\Omega_{0-1} = (100 \pm 20)$ meV for the 40 nm thick film, and $\Omega_{0-0} = (360 \pm 20)$ meV and $\Omega_{0-1} = (120 \pm 20)$ meV for the 60 nm thick film. (b) Mixing coefficients extracted for each branch from the fits of (a). The middle branch shows significant mixing between both excitons and the cavity photon at an angle $\theta \sim 53°$. By permission. Copyright, American Physical Society [15].

branch splittings observed for 40 and 60 nm thick films (100 meV and 120 meV, respectively) and Eq. (23). Since no coupling is observed to the 0–1 transition in this case, the calculated Rabi period is longer than the vibronic relaxation time. Using Eq. (23), the Rabi splitting for a 20 nm thick film is ~75 meV, corresponding to a Rabi period of ~55 fs. The Rabi splitting of 100 meV for the 40 nm thick case corresponds to a period of ~30 fs. Thus, the relaxation time between the vibronic levels is 30 fs $< \tau_{vib} <$ 55 fs [15]. Ultrafast estimates of similar relaxation processes in organic dyes

yield lifetimes on the order of tens to hundreds of femtoseconds [82–84]. More accurate estimates can be made by measuring the Rabi period as a function of film thickness or concentration (and hence coupling strength) in a transparent host. This technique also permits the estimation of singlet–triplet ISC rates for phosphorescent organic molecules [16].

In Ref. [16], when the concentration of PtOEP in a wide gap host is reduced, the Rabi splitting (period) is observed to decrease (increase). When the Rabi period exceeds τ_{ISC}, coupling should vanish as ISC becomes the dominant relaxation pathway (i.e. $\tau_{ISC} < \tau_{Rabi} = h/\Omega$). For PtOEP, ISC competes with strong coupling when the Rabi splitting is on the order of δ_{Ex} and δ_{Cav}; thus resolving the Rabi splitting becomes difficult when ISC dominates [16]. If the splitting were resolvable at lower concentrations, or if τ_{ISC} were smaller, it would be possible to accurately estimate the ISC time. In such a host–guest system, the crossover concentration (f_x) is defined as the guest concentration at which strong coupling is overcome by relaxation, and hence is no longer observed. An estimate to τ_{ISC} can be extracted from the Rabi splitting at the crossover point f_x giving simply [16]:

$$\tau_{ISC} = \frac{h}{\Omega_x}, \tag{24}$$

where Ω_x is the Rabi splitting calculated at the concentration f_x using Eq. (23). Since this point is not clearly resolved for PtOEP, a lower limit for the ISC transfer time of $\tau_{ISC} \geqslant 100$ fs (corresponding to $f = 0.15$) was estimated. The resolution of this measurement of τ_{ISC} can be improved by employing a phosphor with a shorter τ_{ISC} than PtOEP, leading to the loss of strong coupling at larger (and hence better resolved) values of the Rabi splitting, making the competition with ISC easier to resolve. The challenge with using materials with very short τ_{ISC} (e.g. Ir-based phosphors [78,85]) is that their absorbance spectra consist of several broad and overlapping transitions.

4.5. Alternate cavity designs for strong coupling in organic materials

While microcavities consisting of a DBR bottom mirror and a metallic top mirror are commonly used to study polaritonic phenomena, other microcavity structures have also been used with considerable success. An alternative structure replaces the DBR mirror with a second metallic mirror [9,18]. The quality factor (Q) for the resulting Ag-metal clad cavity is $Q \sim 10$, as reported by Hobson et al. [9]. Regardless, the Rabi splitting for a film of 2,2′-dimethyl-8-phenyl-5,6,5′,6′-dibenzothiacarbocyanine chloride in a PVA matrix was enhanced by a factor of 2.3 over the metal/DBR case to give $\Omega \sim 300$ meV (Fig. 9) [9]. The enhancement results from a significant reduction in the cavity length, since the penetration depth into the DBR mirror is calculated to be 0.87λ, compared to only 10 nm for Ag at $\lambda = 670$ nm. This reduction in cavity length ultimately leads to improved field confinement in the organic film, leading to the pronounced increase in splitting.

It is also straightforward to consider the case of a high finesse, double DBR microcavity. Connolly et al. [11] used a top DBR consisting of alternating layers of TeO_2 ($n = 2.06$) and LiF ($n = 1.36$) deposited by high vacuum thermal evaporation on a layer of zinc tetraphenylporphyrin [56] (ZnTPP) in polystyrene to produce high finesse microcavities with Q-factors between 420 and 600 [11]. In Fig. 10a and b, the Rabi splitting for the structure is reduced slightly (135 meV) in comparison to the case of a microcavity containing 4TBPPZn (160 meV) [1] with a metal/DBR mirror combination. This is due to the LiF/TeO_2 DBR optical penetration depth that increases the cavity length, and reduces the confinement of the field within the organic layer. However, the larger Q-factor leads to a narrower cavity mode linewidth and, hence, a narrower polariton linewidth (Fig. 10a). A measure of the resolution

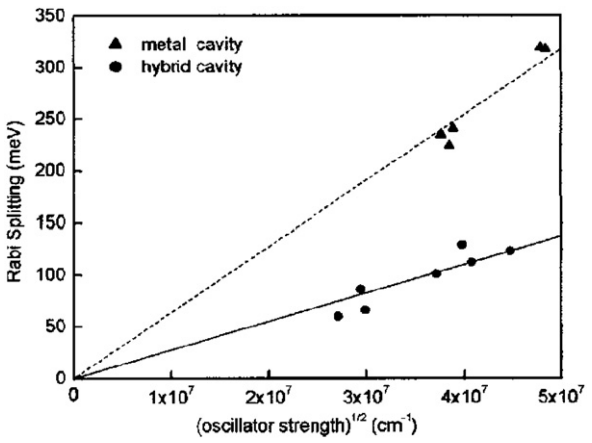


Fig. 9. Rabi splittings for metal-clad and metal-distributed Bragg reflector microcavities as functions of the square root of the oscillator strength. By permission. Copyright, American Institute of Physics [9].

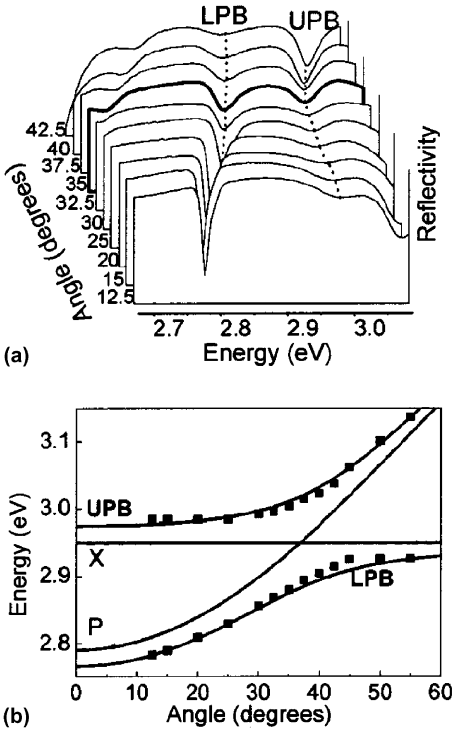


Fig. 10. (a) Reflectivity spectra from a microcavity containing zinc tetraphenylporphyrin located between two distributed Bragg reflectors. (b) The dispersion curve extracted from the reflectivity spectra of (a). The solid lines are fits to a two-level coupled oscillator model. The broken lines indicate the position of the uncoupled exciton (X) and cavity photon (P) energies. By permission. Copyright, American Institute of Physics [11].

of strong coupling is the ratio of the Rabi splitting to the polariton linewidth at resonance. Experimentally, the double DBR microcavity has a polariton linewidth of 45 meV, for a ratio of 3.0. In previous demonstrations using a metal/DBR microcavity, the ratio of the Rabi splitting to the polariton linewidth is between 1.5 and 1.8 [1,2]. This increase in feature resolution comes directly from the increase in the cavity Q.

Beyond modifications of the mirrors, structural modifications that simplify the characterization of the microcavity have also been explored. The first involves the inclusion of a gelatin wedge between the absorbing active layer and the top DBR to facilitate transmission measurements [86]. In this structure, 5-chloro-2-[3-[5[chloro-3-(4-sulfobutyl)-2(3H)-benzothiazolylidene]-1-propenyl]-3-(4-sulfobutyl) benzothiazolium hydroxide, inner salt, compound with triethylamine, was suspended in a compliant gelatin matrix. The gelatin was spun-cast onto the bottom DBR structure, followed by a second, dye-free gelatin film. The top DBR, grown separately on a quartz substrate, was pressed at an angle onto the gelatin film surface, forcing the underlying film into a wedge shape (Fig. 11a). This creates a monotonic variation in the cavity length across the sample, allowing the polariton dispersion to be extracted as a function of position as opposed to angle of incidence. This technique offers fabrication simplicity and the ability to create graded structures for transmission measurements while maintaining a high cavity $Q = 130$. Using this cyanine dye, a splitting of 46 meV was observed in a microcavity containing a gelatin wedge (Fig. 11b).

Another modification to the conventional metal/DBR microcavity structure involves the use of a piezo-controlled, gold-coated optical fiber as the top mirror. This moveable top mirror forms a metal clad cavity with a thin gold bottom mirror, allowing the cavity length to be continuously varied for transmission measurements, with the fiber directing

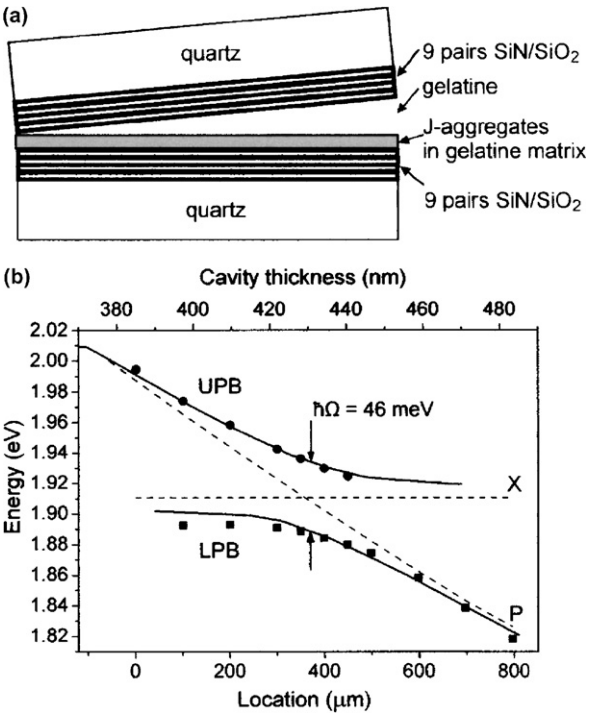


Fig. 11. (a) Schematic of a gelatin-wedge shaped organic microcavity structure. (b) The dispersion curve of the microcavity of (a) extracted from transmission measurements at different points along the sample. The solid lines are fits obtained using a transfer-matrix model. The broken lines correspond to the uncoupled exciton and cavity mode energies as functions of position. By permission. Copyright, American Institute of Physics [86].

light to a monochromator and charge coupled device for detection [19]. The resulting cavity can be tuned over a range of thicknesses from 1.4 μm to 2.6 μm, allowing the detection of two separate anti-crossings corresponding to the first and second longitudinal modes. Strong coupling has been observed in such a structure containing a cyanine dye, and the splitting is observed to decrease with increased cavity length.

4.6. Microcavity polariton electroluminescence

To our knowledge, the population of the strongly coupled state under electrical excitation in inorganic semiconductors has yet to be reported. The difficulty in creating polaritons in inorganic materials arises from the low saturation density and, hence, the low binding energy (1–10 meV) of Wannier–Mott excitons. Since the tightly bound excitons in organic materials do not suffer the same instabilities as their inorganic counterparts, the observation of strong exciton–photon coupling under electrical excitation has been observed in organic materials. Using a Ag-metal clad cavity and a cyanine dye active layer, Tischler et al. [18] observed the polariton dispersion with a Rabi splitting of 265 meV using angularly resolved electroluminescence (see Fig. 12). The use of a layer-by-layer technique to deposit the J-aggregate dye active layer allows for a large absorbance without the need for a thick film [17]. This is an attractive option since in an electrically pumped device, the cavity must include electron and hole transport layers that ultimately reduce the confinement of the optical field to the absorbing layer. The metal clad cavity allows reflectivity and electroluminescence measurements to be performed on the same structure since the silver mirrors also serve as electrical contacts. The dispersion curve observed in reflectivity (Fig. 12a) is consistent with that obtained under electrical excitation (Figs. 12b–d). This observation is significant since it suggests that the strongly coupled state in organic materials may not be adversely affected by the presence of free carriers. Consistent with observations of luminescence in other cyanine dyes, the lower branch electroluminescence is much more intense than for the upper branch.

5. Conclusions and future directions

There has been intense development and study of strong exciton–photon coupling in organic materials since the first observation in 1998. Currently, organic materials are in an excellent position to realize the ultimate goal of electrically pumped, coherent polariton emission. Organic materials possess numerous desirable attributes for application in strongly coupled devices primarily as a result of

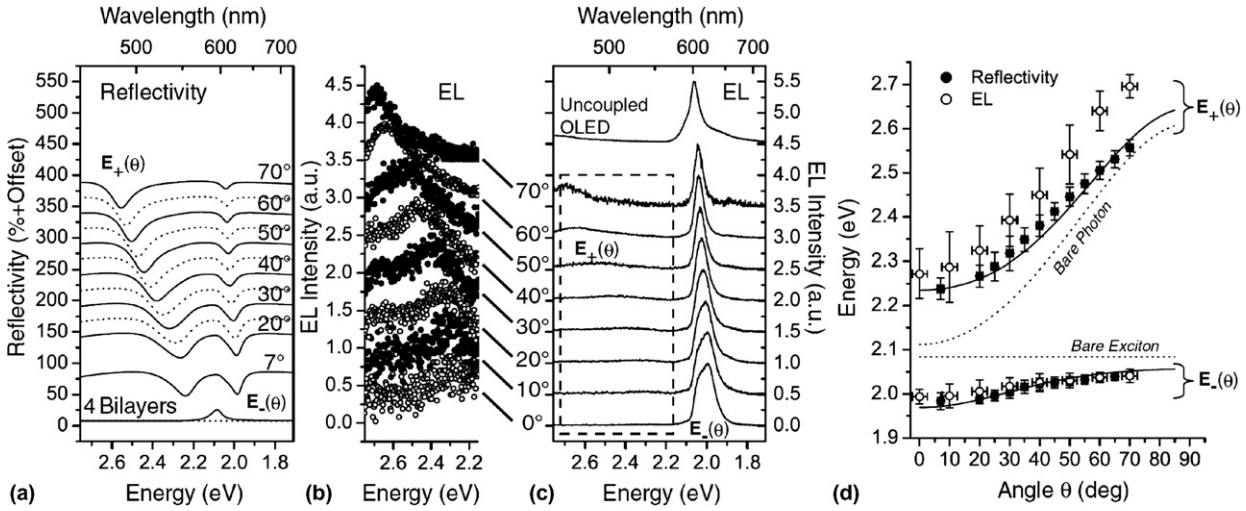


Fig. 12. (a) Reflectivity (transverse electric, TE, polarization) of a metal-clad microcavity designed for electroluminescence measurements as a function of angle. The reflectivity at an incident angle of $\theta \sim 7°$ for a four bilayer cyanine dye film is shown for comparison. (b) Expanded view of the high energy upper polariton branch of the electroluminescence spectra. (c) Electroluminescence spectra normalized to the lower polariton branch peak intensity. The spectrum of an uncoupled light-emitting device is shown for comparison. (d) Microcavity dispersion relation for the device of (a)–(c) with a cavity cut-off energy of 2.11 eV. The fit is generated from the reflectivity data of (a) using a coupled oscillator model with a splitting of 265 meV. By permission. Copyright, American Physical Society [18].

their large exciton binding energies and oscillator strengths. These properties allow for the study of the strongly coupled state at room temperature, even for very large excitation densities. In addition, strong coupling under electrical excitation has already been observed in organic materials; a significant first step in the development of electrically pumped coherent light emitters. This particular area of study must be explored further to gain a better grasp of the influence that charge carriers have on the strongly coupled state. In addition, the behavior of electrically pumped polariton emitters needs to be examined under intense electrical excitation to determine whether a preferential occupation of the $k = 0$ state can be realized; a prerequisite for observations of gain and coherent emission.

In inorganic materials, population of the $k = 0$ state relies on the stimulated scattering of polaritons from states of large energy and wavevector. The scattering rate is typically limited by the polariton "relaxation bottleneck" [42]. When excitons are created off resonance (i.e. excitation leading to the creation of high energy excitons), they first relax by longitudinal optical phonon emission [42]. This process is followed by a slow acoustic phonon emission to populate the high wavevector states of the system. The resulting polaritonic population may relax either by phonon-assistance [42], or by photon emission. Photon emission becomes more probable as the lower branch dispersion becomes more photon-like for small values of the wavevector. The point on the lower branch at which the rate of photon emission overcomes the rate of phonon-assisted relaxation is referred to as the relaxation bottleneck. The bottleneck typically leads to the absence of significant PL for small values of the wavevector and intense PL near the bottleneck due to polariton relaxation by photon emission [42].

In organic materials, it is unclear whether such a bottleneck exists, given the large phonon energies ($\sim$100 meV) and the strong coupling between the exciton and phonon distributions. Theoretical calculations have already clarified the role of large energy molecular optical phonons in facilitating the relaxation of polaritons from states of large wavevector to $k = 0$ [22,31]. Indeed, strongly coupled cyanine dye microcavities have exhibited enhanced resonant Raman scattering [21]; similar experiments might ultimately show the importance of phonon-assisted processes in the generation of coherent light. In addition, the incoherent nature of the strongly coupled state may permit large wavevector polariton states to pump states of low wavevector around $k = 0$. This process circumvents the need for relaxation through a potential bottleneck, and serves as an alternate pathway for the population of the $k = 0$ state [25].

Beyond the interest in strong coupling for coherent light generation and amplification, there is significant application of polaritonic phenomena in organic materials for nonlinear optics beyond the enhancement of resonant Raman scattering [21]. Already, demonstrations have shown the potential for strongly coupled organic microcavities to act as optical switches [13]. The response time for such devices can be ultrafast, given the short lifetime of the polaritonic state.

While the experimental study of microcavity polaritons in organic materials is still in its infancy, it is poised to lead to a more thorough understanding of the molecular excited state, allowing for new and practical device applications. Indeed, additional advances and unique opportunities should continue to drive the field well into the foreseeable future.

Acknowledgements

The authors thank the Air Force Office of Scientific Research (Charles Lee) and Universal Display Corporation for partial financial support of this work.

References

[1] D.G. Lidzey, D.D.C. Bradley, M.S. Skolnick, T. Virgili, S. Walker, D.M. Whittaker, Nature (London) 395 (1998) 53.
[2] D.G. Lidzey, D.D.C. Bradley, T. Virgili, A. Armitage, M.S. Skolnick, S. Walker, Phys. Rev. Lett. 82 (1999) 3316.
[3] D.G. Lidzey, D.D.C. Bradley, A. Armitage, S. Walker, M.S. Skolnick, Science (Washington, DC, 1883) 288 (2000) 1620.
[4] P. Schouwink, H. von Berlepsch, L. Dahne, R.F. Mahrt, Chem. Phys. Lett. 344 (2001) 352.
[5] P. Schouwink, H. von Berlepsch, L. Dahne, R.F. Mahrt, J. Lumin. 94–95 (2001) 821.
[6] P. Schouwink, H. von Berlepsch, L. Dahne, R.F. Mahrt, Chem. Phys. 285 (2002) 113.
[7] D.G. Lidzey, A.M. Fox, M.D. Rahn, M.S. Skolnick, V.M. Agranovich, S. Walker, Phys. Rev. B 65 (2002) 195312.
[8] P. Schouwink, J.M. Lupton, H. von Berlepsch, L. Dahne, R.F. Mahrt, Phys. Rev. B 66 (2002) 081203(R).
[9] P.A. Hobson, W.L. Barnes, D.G. Lidzey, G.A. Gehring, D.M. Whittaker, M.S. Skolnick, S. Walker, Appl. Phys. Lett. 81 (2002) 3519.
[10] N. Takada, T. Kamata, D.D.C. Bradley, Appl. Phys. Lett. 82 (2003) 1812.
[11] L.G. Connolly, D.G. Lidzey, R. Butte, A.M. Adawi, D.M. Whittaker, M.S. Skolnick, R. Airey, Appl. Phys. Lett. 83 (2003) 5377.

[12] R.F. Oulton, N. Takada, J. Koe, P.N. Stravrinou, D.D.C. Bradley, Semicond. Sci. Technol. 18 (2003) S419.
[13] J.-H. Song, Y. He, A.V. Nurmikko, J. Tischler, V. Bulovic, Phys. Rev. B 69 (2004) 235330.
[14] D.G. Lidzey, J. Wenus, D.M. Whittaker, G. Itskos, P.N. Stavrinou, D.D.C. Bradley, R. Murray, J. Lumin. 110 (2004) 347.
[15] R.J. Holmes, S.R. Forrest, Phys. Rev. Lett. 93 (2004) 186404.
[16] R.J. Holmes, S.R. Forrest, Phys. Rev. B 71 (2005) 235203.
[17] M.S. Bradley, J.R. Tischler, V. Bulovic, Adv. Mater. 17 (2005) 1881.
[18] J. Tischler, M.S. Bradley, V. Bulovic, J.-H. Song, A.V. Nurmikko, Phys. Rev. Lett. 95 (2005) 036401.
[19] C.E. Finlayson, G.V. Prakash, J.J. Baumberg, Appl. Phys. Lett. 86 (2005) 041110.
[20] D.N. Krizhanovskii, R. Butte, L.G. Connolly, A.I. Tartakovskii, D.G. Lidzey, M.S. Skolnick, S. Walker, J. Appl. Phys. 93 (2003) 5003.
[21] A.I. Tartakovskii, M. Emam-Ismail, D.G. Lidzey, M.S. Skolnick, D.D.C. Bradley, S. Walker, V.M. Agranovich, Phys. Rev. B 63 (2001) 121302.
[22] V.M. Agranovich, H. Benisty, C. Weisbuch, Solid State Commun. 102 (1997) 631.
[23] V.M. Agranovich, D.M. Basko, G.C. La Rocca, F. Bassani, J. Phys.: Condens. Matter 10 (1998) 9369.
[24] V.M. Agranovich, D.M. Basko, G.C. La Rocca, F. Bassani, Synth. Met. 116 (2001) 349.
[25] V.M. Agranovich, M. Litinskaia, D.G. Lidzey, Phys. Rev. B 67 (2003) 085311.
[26] H. Zoubi, G.C. La Rocca, Phys. Rev. B 72 (2005) 125306.
[27] H. Zoubi, G.C. La Rocca, Phys. Lett. A 339 (2005) 171.
[28] H. Zoubi, G.C. La Rocca, Phys. Rev. B 71 (2005) 235316.
[29] P. Michetti, G.C. La Rocca, Phys. Rev. B 71 (2005) 115320.
[30] M. Litinskaya, P. Reineker, V.M. Agranovich, Phys. Stat. Sol. A 201 (2004) 646.
[31] M. Litinskaya, P. Reineker, V.M. Agranovich, J. Lumin. 119–120 (2006) 277.
[32] M.A. Baldo, R.J. Holmes, S.R. Forrest, Phys. Rev. B 66 (2002).
[33] P.G. Savvidis, J.J. Baumberg, R.M. Stevenson, M.S. Skolnick, D.M. Whittaker, J.S. Roberts, Phys. Rev. Lett. 84 (2000) 1547.
[34] R.M. Stevenson, V.N. Astratov, M.S. Skolnick, D.M. Whittaker, M. Emam-Ismail, A.I. Tartakovskii, P.G. Savvidis, J.J. Baumberg, J.S. Roberts, Phys. Rev. Lett. 85 (2000) 3680.
[35] J.J. Baumberg, P.G. Savvidis, R.M. Stevenson, A.I. Tartakovskii, M.S. Skolnick, D.M. Whittaker, J.S. Roberts, Phys. Rev. Lett. 62 (2000) R16247.
[36] M. Saba, C. Ciuti, J. Bloch, V. Thierry-Mieg, R. Andre, L.S. Dang, S. Kundermann, A. Mura, G. Bongiovanni, J.L. Staehli, B. Deveaud, Nature (London) 414 (2001) 731.
[37] H. Yokoyama, Y. Nambu, T. Kawakami, in: E. Burstein, C. Weisbuch (Eds.), Confined Electrons and Photons: New Physics and Applications, Plenum Press, New York, 1995.
[38] E.M. Purcell, Phys. Rev. 69 (1946) 681.
[39] C. Weisbuch, M. Nishioka, A. Ishikawa, Y. Arakawa, Phys. Rev. Lett. 69 (1992) 3314.
[40] V. Savona, L.C. Andreani, P. Schwendimann, A. Quattropani, Solid State Commun. 93 (1995) 733.
[41] M.S. Skolnick, T.A. Fisher, D.M. Whittaker, Semicond. Sci. Technol. 13 (1998) 645.
[42] M.S. Skolnick, A.I. Tartakovskii, R. Butte, D.M. Whittaker, R.M. Stevenson, IEEE J. Sel. Top. Quant. 8 (2002) 1060.
[43] R. Houdre, J.L. Gibernon, P. Pellandini, R.P. Stanley, U. Oesterle, C. Weisbuch, J. O'Gorman, B. Roycroft, M. Ilegems, Phys. Rev. B 52 (1995) 7810.
[44] G. Khitrova, H.M. Gibbs, F. Jahnke, M. Kira, S.W. Koch, Rev. Mod. Phys. 71 (1999) 1591.
[45] R. Houdre, R.P. Stanley, U. Oesterle, M. Ilegems, C. Weisbuch, Phys. Rev. B 49 (1994) 16761.
[46] T.R. Nelson, J.P. Prineas, G. Khitrova, H.M. Gibbs, J.D. Berger, J.-H. Shin, H.-E. Shin, Y.-H. Lee, P. Tayebati, L. Javniskis, Appl. Phys. Lett. 69 (1996) 3031.
[47] A.R. Pratt, T. Takamori, T. Kamijoh, Appl. Phys. Lett. 74 (1999) 1869.
[48] G. Malpuech, A. Di Carlo, A. Kavokin, J.J. Baumberg, M. Zamfirescu, P. Lugli, Appl. Phys. Lett. 81 (2002) 412.
[49] G. Malpuech, A. Kavokin, F.P. Laussy, Phys. Stat. Sol. A 195 (2003) 568.
[50] J.F. Muth, J.H. Lee, I.K. Shmagin, R.M. Kolbas, H.C. Casey Jr, B.P. Keller, U.K. Mishra, S.P. DenBaars, Appl. Phys. Lett. 71 (1997) 2572.
[51] P. Ramvall, S. Tanaka, S. Nomura, P. Riblet, Y. Aoyagi, Appl. Phys. Lett. 73 (1998) 1104.
[52] R. Butte, G. Christmann, E. Feltin, J.-F. Carlin, M. Mosca, M. Ilegems, N. Grandjean, Phys. Rev. B 73 (2006) 033315.
[53] I.R. Sellers, F. Semond, M. Leroux, J. Massies, P. Disseix, A.-L. Henneghien, J. Leymarie, A. Vasson, Phys. Rev. B 73 (2006) 033304.
[54] M. Pope, C.E. Swenberg, Electronic Processes in Organic Crystals and Polymers, second ed., Oxford University Press, New York, 1999.
[55] L.A. Coldren, S.W. Corzine, Diodes Lasers and Photonic Integrated Circuits, John Wiley and Sons, New York, 1995.
[56] M. Anni, G. Gigli, R. Cingolani, S. Patane, A. Arena, M. Allegrini, Appl. Phys. Lett. 79 (2001) 1381.
[57] R. Houdre, C. Weisbuch, R.P. Stanley, U. Oesterle, P. Pellandini, M. Ilegems, Phys. Rev. Lett. 73 (1994) 2043.
[58] T. Yoshie, A. Scherer, J. Hendrickson, G. Khitrova, H.M. Gibbs, G. Rupper, C. Ell, O.B. Shchekin, D.G. Deppe, Nature (London) 432 (2004) 200.
[59] J.P. Reithmaier, G. Sek, A. Loffler, C. Hofmann, S. Kuhn, S. Reitzenstein, L.V. Keldysh, V.D. Kulakovskii, T.L. Reinecke, A. Forchel, Nature (London) 432 (2004) 197.
[60] T. Fujita, Y. Sato, T. Kuitani, T. Ishihara, Phys. Rev. B 57 (1998) 12428.
[61] M. Shimizu, T. Ishihara, Appl. Phys. Lett. 80 (2002) 2836.
[62] G. Panzarini, L.C. Andreani, A. Armitage, D. Baxter, M.S. Skolnick, V.N. Astratov, J.S. Roberts, A.V. Kavokin, M.R. Vladimirova, M.A. Kaliteevski, Phys. Solid State 41 (1999) 1223.
[63] L.A.A. Pettersson, L.S. Roman, O. Inganas, J. Appl. Phys. 86 (1999) 487.
[64] D.I. Babic, S.W. Corzine, IEEE J. Quantum Electron. 28 (1992) 514.
[65] A. Dodabalapur, L.J. Rothberg, R.H. Jordan, T.M. Miller, R.E. Slusher, J.M. Phillips, J. Appl. Phys. 80 (1996) 6954.
[66] E.L. Ivchenko, M.A. Kaliteevski, A.V. Kavokin, A.I. Nesvizhskii, J. Opt. Soc. Am. B: Opt. Phys. 13 (1996) 1061.
[67] R. Houdre, Phys. Status Solidi B 242 (2005) 2167.

[68] A. Armitage, M.S. Skolnick, A. Kavokin, D.M. Whittaker, V.N. Astratov, G.A. Gehring, J.S. Roberts, Phys. Rev. B 58 (1998) 15367.
[69] J. Wainstain, C. Delalande, G. Gendt, M. Voos, J. Bloch, V. Thierry-Mieg, V. Planel, Phys. Rev. B 58 (1998) 7269.
[70] P.G. Lagoudakis, M.D. Martin, J.J. Baumberg, G. Malpuech, A. Kavokin, J. Appl. Phys. 95 (2004) 2487.
[71] Y. Zhu, D.J. Gauthier, S.E. Morin, Q. Wu, H.J. Carmichael, T.W. Mossberg, Phys. Rev. Lett. 64 (1990) 2499.
[72] E.E. Jelly, Nature (London) 139 (1937) 631.
[73] G. Scheibe, Angew. Chem. 49 (1936) 563.
[74] C. Fabre, in: H. Benisty, J.-M. Gerard, R. Houdre, et al. (Eds.), Confined Photon Systems: Fundamentals and Applications, Springer, Berlin, 1998.
[75] S.R. Forrest, Chem. Rev. 97 (1997) 1793.
[76] S.R. Forrest, M.L. Kaplan, P.H. Schmidt, J. Appl. Phys. 56 (1984) 543.
[77] M.A. Baldo, D.F. O'Brien, Y. You, A. Shoustikov, S. Sibley, M.E. Thompson, S.R. Forrest, Nature (London) 395 (1998) 151.
[78] S. Lamansky, P. Djurovich, D. Murphy, F. Abdel-Razzaq, R.C. Kwong, I. Tsyba, M. Bortz, B. Mui, R. Bau, M.E. Thompson, Inorg. Chem. 40 (2001) 1704.
[79] N.J. Turro, Modern Molecular Photochemistry, University Science Books, Sausalito, 1991.
[80] M. Gouterman, in: D. Dolphin (Ed.), The Porphyrins, vol. 3, Academic Press, New York, 1978, p. 1.
[81] A.I. Tartakovskii, M. Emam-Ismail, R.M. Stevenson, M.S. Skolnick, V.N. Astratov, D.M. Whittaker, J.J. Baumberg, J.S. Roberts, Phys. Rev. B 62 (2000) R2283.
[82] A.J. Taylor, D.J. Erskine, C.L. Tang, Chem. Phys. Lett. 103 (1984) 430.
[83] C.V. Shank, E.P. Ippen, O. Teschke, Chem. Phys. Lett. 45 (1977) 291.
[84] D. Reiser, A. Laubereau, Opt. Commun. 42 (1982) 329.
[85] S. Lamansky, P. Djurovich, D. Murphy, F. Abdel-Razzaq, H.-E. Lee, C. Adachi, P.E. Burrows, S.R. Forrest, M.E. Thompson, J. Am. Chem. Soc. 123 (2001) 4304.
[86] J. Wenus, L.G. Connolly, D.M. Whittaker, M.S. Skolnick, D.G. Lidzey, Appl. Phys. Lett. 85 (2004) 5848.

Available online at www.sciencedirect.com
ScienceDirect
Organic Electronics 8 (2007) 94–113
Organic Electronics
www.elsevier.com/locate/orgel

Solid state cavity QED: Strong coupling in organic thin films

Jonathan R. Tischler [a], M. Scott Bradley [a], Qiang Zhang [b], Tolga Atay [b], Arto Nurmikko [b], Vladimir Bulović [a,*]

[a] *Massachusetts Institute of Technology, Cambridge MA 02139, United States*
[b] *Brown University, Providence RI 02912, United States*

Available online 23 January 2007

Abstract

We review our research efforts to develop solid state integrated devices that operate in the strong coupling limit of cavity quantum electrodynamics (QED) for eventual application in high speed optical switching, optical computing, and quantum computing. Our devices contain *J*-aggregates of (organic) cyanine dyes which, by virtue of their molecular arrangement and strong dipolar coupling, exhibit a collective narrow linewidth high oscillator strength optical transition. Using *J*-aggregates, the strong coupling limit can be reached at room temperature with large coupling strengths (Rabi-splitting >250 meV) in exciton–polariton microcavity structures. We demonstrate that high quality nanoscale thick *J*-aggregate films can be uniformly deposited over macroscopic substrates, engineered at the molecular level, and patterned into single or multi-dimensional photonic bandgap structures. Our unique methods for depositing *J*-aggregates enabled us to structure light emitting devices that demonstrated the first ever electrically pumped polariton emission, uniquely accomplished in room temperature operation. Additionally, we demonstrated critically coupled resonators that concentrate nearly all of the incident light into 5 nm thick *J*-aggregate films, yielding a record high effective absorption constant of 6.8×10^6 cm^{-1} for films with thickness that is less than 1% of the incident light wavelength. Such remarkable optical properties, enabled by scalable deposition techniques, suggest that *J*-aggregates are a unique materials platform on which to demonstrate integrated exciton–polariton devices with the far reaching properties of polaritons in the optical domain.
© 2007 Elsevier B.V. All rights reserved.

PACS: 71.36.+c; 71.35.Aa; 85.60.Jb; 78.40.Me

Keywords: Semiconductor microcavity; Cyanine dye; Optical properties; Multilayer; Polyelectrolytes

1. Introduction

Quantum electrodynamics (QED) is the quantum mechanical description of electromagnetic radiation, matter, and the interaction of the two. Cavity QED is the study and utilization of the quantum interactions between light and matter inside a microcavity optical resonator. When matter inserted inside a microcavity exchanges energy with a resonant mode of the cavity more rapidly than the combined rate at which energy escapes the system either in the form of photons leaving the cavity or the matter wave function losing its phase information [1,2], the strong coupling limit of cavity QED is reached.

* Corresponding author. Tel.: +1 (617) 253 7012; fax: +1 (617) 452 5110.
E-mail address: bulovic@mit.edu (V. Bulović).

1566-1199/$ - see front matter © 2007 Elsevier B.V. All rights reserved.
doi:10.1016/j.orgel.2007.01.008

In this limit, the microcavity and matter form a composite quantum system with two new eigenstates that are superpositions of the initial uncoupled states. The coupled system is governed by quantum effects that rely on or leverage quantum coherence.

The matter component of the coupled system can be a gas of atoms trapped inside the cavity [3], a superconducting qubit [4], or a thin film containing excitons, 2-level-system-like light absorbers, in the form of an inorganic quantum well [5], quantum dot [6,7], or organic material [8,9]. When excitons are used, the superposition states are referred to as exciton–polaritons, as in the experiments discussed in this article.

Applications of strong coupling in atomic and semiconductor systems have led to one-atom zero threshold lasers [10], high gain polariton parametric amplifiers [11], and predictions that strong coupling may play a key role in future quantum information processors [12].

The article is structured in the following way. First, the physics of polaritons is reviewed, and the connection between the oscillator strength of matter and polariton properties is clarified. Crystals of cyanine dyes, known as *J*-aggregates, are then introduced as good candidate materials for room temperature polariton applications because of their very high oscillator strength and consequent optical properties. From there, the methodology for forming *J*-aggregates is described, and the device structures used to demonstrate electrically pumped *J*-aggregate and polariton emission are explained. We describe the reflectivity measurements of polariton effects. Data for our *J*-aggregate organic light-emitting device (OLED) structures are presented, and lastly, electroluminescent spectra of the *J*-aggregate resonant cavity OLED (RC-OLED) are presented as a function of cavity thickness and angle, proving electrically pumped polariton emission. The paper concludes with a discussion of future work, all of which take full advantage of the *J*-aggregate deposition technique we developed in the course of this research.

2. Physics of strong coupling

2.1. Developing an intuitive understanding

What happens when light is trapped in an optical resonator filled with matter (in the form of atoms, excitons or other two level systems) that can exchange energy resonantly with that light? The type of dynamical behavior that is produced depends on the relative rates of the fundamental processes involved. Fundamentally, there are three rates to consider (using notation from [1]):

1. The rate at which the light and matter transfer energy: g.
2. The rate at which light escapes the cavity: κ.
3. The rate at which matter looses its polarization: γ.

When the rate of energy transfer, g, is considerably larger than κ and γ, ($g \gg \kappa$, γ) then strong coupling of the light and matter occurs. In this limit, the light and matter exchange energy periodically (with period $2\pi/g$), for a number of periods before the energy escapes the system. To first order, there is direct analogy between strong coupling and an underdamped LRC (inductor-resistor-capacitor) circuit. The periodic exchange of energy between light and matter is akin to the underdamped LRC circuit exhibiting oscillations in current and voltage before the energy is dissipated in the resistor. The opposite limit, where $g \ll \kappa$, γ, is called the weak coupling limit, because the light and matter trapped in the resonator interact no more strongly with each other than with light or matter outside the system. By way of analogy, this limit is likened to an overdamped LRC circuit, where no ringing occurs because of heavy damping. The main limitation of the analogy is that the LRC circuit is linear while the light matter system is not. Nevertheless, whenever the number of excitations is low, the analogy applies and it can be used to guide intuition.

The physical process responsible for the energy transfer between light and matter is to first order a coupling between dipole and electric field. The energy, E, associated with this coupling is given by $E = \vec{\mu} \circ \vec{E}$, where $\vec{\mu}$ is the dipole moment of the matter component and $\vec{E}$ is the vacuum electric field inside the cavity. The transfer rate, g, is proportional to E, with $g = E/\hbar$.

The periodic exchange of energy between light and matter, at the rate g, directly affects the transmittance and reflectance of the microcavity structure. In particular, in the case where the frequencies of the microcavity resonanace, ω_{cav}, and matter resonance, ω_{ex}, are equal, ($\omega_{cav} = \omega_{ex} = \omega_0$), the transmittance and reflectance spectra both show two new resonances, $\omega_{\pm}$, at frequencies $\omega_{\pm} = \omega_0 \pm g$. This situation is illustrated in Fig. 1

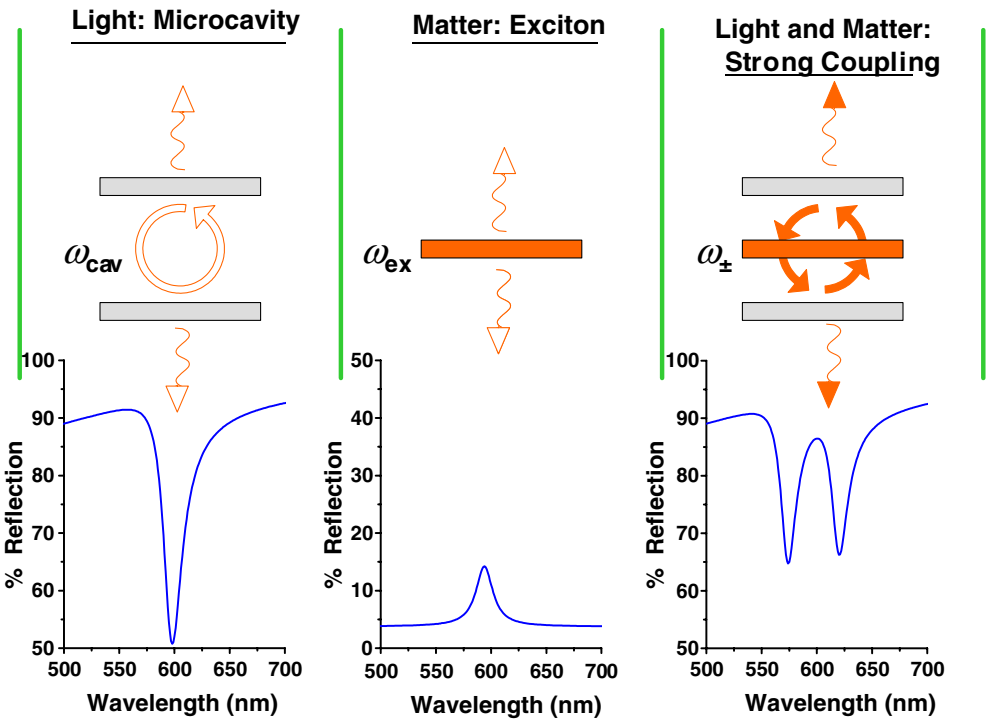


Fig. 1. Reflectance spectra demonstrating consequences of strong coupling between light and matter. The microcavity (light) and matter (exciton layer) possess resonant frequencies of ω_{cav} and ω_{ex}. When strong coupling occurs, the composite system shows new resonances at $\omega_{\pm}$.

for reflectance. Applying the analogy of the underdamped LRC circuit, the two new resonances correspond to the beating of the underdamped (light-matter) oscillator superimposed on the fundamental carrier frequency, ω_0.

2.2. Quantitative model

To gain insight into the physics of strong coupling, we can model the light-matter (photon–exciton) interaction as a two level system (exciton) that is coupled to a simple harmonic oscillator (photon) [13]. The two level system has states: ϕ_1 and ϕ_2 with energies E_1 and E_2, such that the energy difference equals the energy of the exciton transition: $E_2 - E_1 = \hbar\omega_{ex}$. Similarly, the simple harmonic oscillator has states: $|n\rangle$ where $n = 0, 1, 2, \ldots$ with energies of $\hbar\omega_0(n + 1/2)$. Without coupling, the stationary states of the combined system Ψ_n are simply product wavefunctions. The ground state is $\Psi_0 = \phi_1|0\rangle$, and there are two states with one excitation of either one photon $\Psi_1 = \phi_1|1\rangle$ or one exciton $\Psi_2 = \phi_2|0\rangle$, respectively.

Which states, Ψ_n, couple depends on the nature of the coupling interaction. In the case of light-matter interactions, to first order [14], the coupling is due to dipole radiation, which can be represented by the perturbation Hamiltonian $H^{(1)} = -\vec{\mu}\cdot\vec{E}$, where $\vec{\mu} = e\int \phi^*\vec{r}\phi\,\mathrm{d}V$ is the transition dipole moment of the radiator and $\vec{E}$ is the electric field strength of the photon mode, with $\vec{r}$ being the spatial location of the state integrated over the volume V. Since $\vec{r}$ is an odd-parity operator, the perturbation only acts between orthogonal states ϕ_1 and ϕ_2. Similarly, because the action of the exciton corresponds to the creation or annihilation of a photon, the perturbation $H^{(1)}$ only couples states of different quantum number. We can capture this physics in our simplified model by representing $H^{(1)}$ as $H^{(1)} = V_0(\hat{a}' + \hat{a}) * (|\phi_1\rangle\langle\phi_2| + |\phi_2\rangle\langle\phi_1|)$ [13], where $\hat{a}'$ and $\hat{a}$ are creation and annihilation operators, respectively, for photons of energy $\hbar\omega_0$ and V_0 is the magnitude of $H^{(1)}$, which can be tuned by engineering dipole moment and field strength, and is related to g, by $V_0 = \hbar g$. Applying the perturbation $H^{(1)}$ to Ψ_n, we see that Ψ_1 and Ψ_2 couple to each other, while Ψ_0 couples to $\Psi_3 = \phi_2|1\rangle$.

Because of the coupling, the eigenstates of the system are no longer Ψ_n, but rather are superpositions of the states involved in the coupling.

Denoting the new stationary states as Φ_n, the ground state is $\Phi_0 = c_1 * \Psi_0 + c_2 * \Psi_3$, while the first and second excited states, Φ_1 and Φ_2, are rotational superpositions of Ψ_1 and Ψ_2 [13].

Solving for the eigenstates, we can determine the energy levels of the states Φ_0, Φ_1, and Φ_2. The energies of ground state, H_0, and first two excited states, H_1 and H_2, are given by [13]

$$H_0 = \hbar\omega_0 + \frac{1}{2}(E_1 + E_2) - \frac{1}{2}\sqrt{(E_2 - E_1 + \hbar\omega_0)^2 + 4|V_0|^2}$$

and

$$H_1 = \hbar\omega_0 + \frac{1}{2}(E_1 + E_2) - \frac{1}{2}\sqrt{(E_2 - E_1 - \hbar\omega_0)^2 + 4|V_0|^2}$$

$$H_2 = \hbar\omega_0 + \frac{1}{2}(E_1 + E_2) + \frac{1}{2}\sqrt{(E_2 - E_1 - \hbar\omega_0)^2 + 4|V_0|^2}$$

The first excited states of the coupled system, Φ_1 and Φ_2, represent the polariton states of the semiconductor microcavity. The polaritons have both exciton and photon character only near the resonance condition where the exciton and photon energies match. Far away from resonance, the two excited states are essentially equivalent to the first two excited states of the uncoupled exciton–photon system.

To generate one of the polariton states, i.e. either Φ_1 or Φ_2, a quantum of energy equal to the difference in energy between the ground state and excited state must be delivered to the coupled system. Fig. 2 plots these energy differences: $E_- = H_1 - H_0$ and $E_+ = H_2 - H_0$, where:

$$E_\pm = \frac{1}{2}\sqrt{(E_2 - E_1 + \hbar\omega_0)^2 + 4|V_0|^2} \pm \frac{1}{2}\sqrt{(E_2 - E_1 - \hbar\omega_0)^2 + 4|V_0|^2}$$

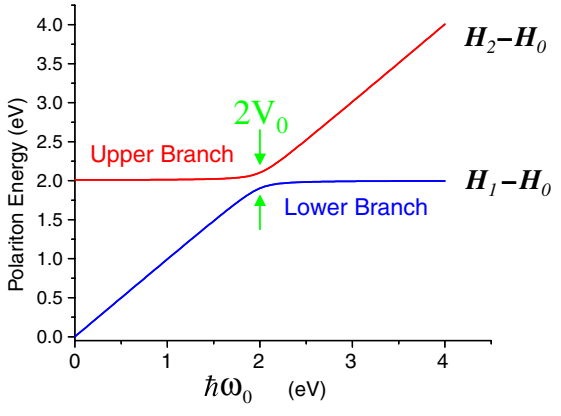


Fig. 2. Upper and lower branches of polariton dispersion curve, as a function of photon tuning, with anti-crossing energy equal to the Rabi-splitting $2V_0 = 0.2$ eV.

This plot is sometimes referred to as a polariton dispersion curve since the bare cavity photon mode energy $\hbar\omega_0$ is related to k-space via the component of the photon mode wave vector perpendicular to the mirrors. The curve representing the amount of energy needed to generate the lower (higher) energy polariton state, $E_-(E_+)$, is referred as the lower (upper) branch polariton curve. We see that the two branches do not cross at the exciton–photon resonance, but instead "repel" each other. The difference in energy between the polariton branches at resonance is the Rabi-splitting, $\hbar\Omega_R$, which is twice the interaction energy V_0, i.e. $\hbar\Omega_R = 2V_0$. Creating the upper polariton requires a quantum of energy at negative detuning approximately equal to the exciton energy since at this detuning, Φ_2 is mostly excitonic, while at positive detuning the energy required is approximately the bare cavity photon energy since at this detuning Φ_2 is mostly photonic.

From the polariton dispersion curve, we are able to relate our model directly to the optical properties of polaritons. At any given cavity tuning, $\hbar\omega_0$, we see that the coupled system responds to two photon energies, and therefore has two absorption peaks. As the system is tuned through resonance these peaks approach each other until the resonance condition at which point they begin to move further away in energy. These absorption peaks also correspond to peaks in the photoluminescent response of the system when the coupled microcavity is excited, and to resonant dips in the reflectivity spectrum as in Fig. 1.

The expressions for $E_\pm$ are greatly simplified by recognizing that the square root term containing the square sum of $\hbar\omega_0$ and $E_2 - E_1$ in the expression for H_0 reduces to:

$$\frac{1}{2}\sqrt{(E_2 - E_1 + \hbar\omega_0)^2 + 4|V_0|^2} \to \frac{1}{2}(E_2 - E_1 + \hbar\omega_0)$$

since the $4|V_0|^2$ term is comparatively small for realistically attainable values of V_0. With this simplification, $E_\pm$ is expressed as

$$E_\pm = \frac{1}{2}(E_2 - E_1 + \hbar\omega_0) \pm \frac{1}{2}\sqrt{(E_2 - E_1 - \hbar\omega_0)^2 + 4|V_0|^2}$$

In the polariton literature, the expression for $E_\pm$ is typically written as

$$E_\pm = \frac{1}{2}(E_{ex} + E_{ph}) \pm \frac{1}{2}\sqrt{(\hbar\Omega_R)^2 + (E_{ex} - E_{ph})^2}$$

where $\hbar\omega_0 \equiv E_{ph}$ is the photon energy, $E_2 - E_1 \equiv E_{ex}$ is the energy difference between the uncoupled levels 1 and 2, which equals the exciton energy, and $2V_0 \equiv \hbar\Omega_R$ is the Rabi-splitting discussed earlier.

In the model so far, the cavity and exciton energies were assumed to be infinitely well-defined, which is unphysical. The impact of the finite linewidths of both the excitonic transition and the photon mode is to broaden the polariton absorption peaks, making observation of the Rabi splitting more difficult.

We can model the line broadening in the frequency domain by first thinking about what the finite line widths of the cavity and exciton mean in the time domain. A finite line width is simply the result of a finite lifetime due to damping of the oscillation in the time domain. On resonance, the two normal modes of the system without damping are:

$$s_{\pm}(t) = A\cos(\omega_{ex} \pm g)t, \quad \text{where } g = V_0/\hbar$$

Given the cavity photon mode damping κ and the exciton damping γ, the two normal modes are now damped oscillations in time [15]:

$$S_{\pm}(t) = Ae^{-(\kappa+\gamma)t/2}\cos(\omega_{ex} \pm g')t$$

$$\text{where now } g' = \sqrt{\left(\frac{V_0}{\hbar}\right)^2 - \frac{1}{4}(\kappa-\gamma)^2}$$

Parenthetically, we see from the g' expression that matching κ and γ, which is analogous to impedance matching, maximizes the coupling and therefore the Rabi-splitting.

By Fourier transforming $S_{\pm}(t)$ and then taking the magnitude squared, we have an expression for the polariton "power" spectrum [15]:

$$S_{\pm}(\omega) = \frac{A_+}{\left(\frac{\kappa+\gamma}{2}\right)^2 + (\omega - (\omega_{ex} + g'))^2} + \frac{A_-}{\left(\frac{\kappa+\gamma}{2}\right)^2 + (\omega - (\omega_{ex} - g'))^2}$$

It is clear from this expression that the polariton spectrum is double peaked so long as the Rabi-splitting $\Omega_R = 2g'$ satisfies the following condition [16]:

$$\Omega_R = 2g' > 0.5(\kappa + \gamma)$$

This condition determines what coupling strength is needed to observe polariton splitting.

Ultimately, the degree of polariton coupling depends on the magnitude of the transition dipole moment $\vec{\mu}$. The quantity $|\vec{\mu}|^2$, however, is experimentally the more accessible metric, since for light-matter interactions where strong coupling does not apply, the quantity $|\vec{\mu}|^2$ governs the relaxation dynamics and linear optical properties. Fermi's Golden Rule gives the rate of decay of the excited state (of the exciton), which is proportional to $|\vec{\mu}|^2$, as [17]:

$$R_{FGR} = \frac{2\pi}{\hbar}\left|\vec{\mu}\cdot\vec{E}\right|^2\rho_{ph}(\hbar\omega_{fi})$$

with the lifetime of the excited state, $\tau_{FGR} = 1/R_{FGR}$ being inversely proportional to $|\vec{\mu}|^2$. Similarly, if the absorption spectrum of the exciton is given by $\alpha(\omega)[\mathrm{cm}^{-1}]$, then it can be shown that [17]:

$$|\vec{\mu}|^2 = \frac{3\varepsilon_0\hbar c}{\pi N}\int\frac{\alpha(\omega)}{\omega}\,d\omega$$

where N is the density of absorbing excitons per unit volume. Fundamentally, $|\vec{\mu}|^2$ represents the variance of the charge distribution of the exciton, and by the fluctuation-dissipation theorem, the fluctuation directly determines the dissipative response of the system [17] (in the perturbative limit of light matter coupling, radiation is indeed dissipative).

It is worth reflecting upon the relation between $|\vec{\mu}|^2$and the absorption coefficient $\alpha(\omega)$. It says that highly absorptive materials make the best candidates for strong coupling, since $V_0 \propto |\vec{\mu}| \propto \sqrt{\alpha_{max}}$. At first glance this concept appears at odds with the notion that in the strong-coupling limit the radiation process is periodic. The consistency comes because, in actuality, the higher the absorption constant of a material the less light intensity is actually lost in the film. The higher $\alpha(\omega)$ is, the more closely the material resembles an ideal radiator (at the frequency ω) with infinitely fast response time to incident electric field of the light, so that the material can in very short distance reflect the light and reject if from penetrating into the film. In the strong coupling limit, higher oscillator strength, due to large absorption, enables the film to respond to its own (virtual) radiation more quickly then the time it takes for that radiation to escape the cavity, and to retransmit this energy back to the photon field before the energy is dissipated via non-radiative pathways. Thus, the enhanced optical response due to high oscillator strength makes the exciton–photon energy transfer process more persistent and the light matter coupling more complete.

To summarize, to achieve strong coupling, the matter component must have a large dipole moment, μ. To achieve strong coupling in a system

where g for a single exciton is low compared to κ and γ, the number of excitons coupled to the cavity mode, N_{ex}, must be increased since for N_{ex} excitons, the coupling [1] $g_{N_{ex}} = g\sqrt{N_{ex}}$. Ideally, the excitonic material should have a very long dephasing time, $T_2 = 2\pi/\gamma$ (T_2 measures the persistence of the polarization). T_2, just like the Q of the cavity, gives an upper limit on how long coherent quantum phenomena will last before dissipation scrambles the phase information.

3. *J*-aggregate thin films

3.1. Physics of J-aggregate formation

The matter component that we utilize to achieve strong coupling are nanoscale thin films of *J*-aggregated dye. *J*-aggregates are luminescent nanostructured ordered arrangements of highly polar cyanine dye molecules that enable strong light-matter interactions to be observed at room temperature [8,18] due to their high oscillator, high absorption coefficient ($\alpha_{max} \approx 10^6\,cm^{-1}$), and room temperature stability. The Rabi-splitting due to *J*-aggregate excitons is typically 1–2 orders of magnitude higher than those using excitons of most other material systems. For example, when *J*-aggregates were incorporated in a metal mirror microcavity [19], polariton emission peaks were separated in energy by more than 300 meV, which corresponds to record high coupling strengths an order of magnitude larger than any Rabi-splitting achieved with inorganic semiconductors. Also, the only reported observation of room temperature polariton photoluminescence [18] utilized *J*-aggregates as the exciton material in the microcavity. This observation was possible because the Rabi-splittings are much larger than room temperature thermal noise (~26 meV), and because *J*-aggregate excitons remain bound at 300 K, unlike inorganic excitons, which ionize into free electrons and holes well below this temperature [11]. We have shown Rabi-splitting of 265 meV [20] at room temperature compared to ~20 meV at 100 K in a CdTe based system [11].

Fig. 3 illustrates the chemical structure of TDBC, an archetypical *J*-aggregate forming cyanine dye. Like TDBC, cyanine dyes are rod-like organic salts in which the lumophore consists of a conjugated polymethine bridge subtended by two highly polar nitrogen rich end-groups. The nitrogen possessing positive charge is equivalently described as electron deficient, acidic or electron accepting and

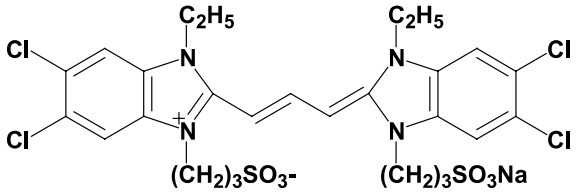


Fig. 3. TDBC, an anionic cyanine dye that readily forms *J*-aggregates in solution and solid state.

the uncharged nitrogen group as electron rich, alkaline or electron donating. Optically, the polymethine bridge acts as a 1-dimensional quantum-wire optical dipole antenna, with the end groups donating (accepting) electron density to (from) the lumophore. Consistent with this description, the transition dipole moment is directed along the polymethine backbone and the dye interacts most strongly with light polarized parallel to this direction [21].

In the *J*-aggregate state, the cyanine dye monomers are closely assembled and specially aligned so that the electron rich nitrogen group of one molecule partially overlaps with the electron deficient nitrogen group of another [22]. This overlap enables the oscillating electron density in one molecule, setup by an optical excitation, to induce similar oscillations in the electron density of nearest neighbor molecules. In this respect, the overlap of side groups can be thought of as the near-field optical-interconnect that couples adjacent molecular oscillators in the *J*-aggregate.

When the molecules couple, the transition dipole moments of the individual molecules add to form a giant dipole oscillator and a new optical transition called a *J*-band [23]. Relative to the monomer, the *J*-band absorption/fluorescence is red-shifted, weakly Stokes shifted, and considerably narrower in energy (50 meV at room temperature). The lifetime of the *J*-band transition is also much faster (~ps) which can lead to an efficient fluorescence process [24]. For example [24], for *J*-aggregating dye THIATS, the dye's quantum efficiency increases from 0.8% to 48.0% (in solution), a factor of 60, as the radiative rate in the aggregate becomes as fast as the non-radiative scattering rates that had hampered the luminescence pathway of the monomer. The fact that the aggregate form of these cyanine dyes is more fluorescent than the monomer runs contrary to the usually accepted rule for organics, which is that aggregates do not fluoresce. As will be described in the subsequent paragraphs,

the discrepancy in quantum efficiency between *J*-aggregates and ordinary amorphous organic aggregates is in the distribution of the oscillator strengths among the energy levels available to the aggregate.

The physical model explaining the optical properties of *J*-aggregates can be built up from an understanding of the interaction of just two dye molecules. When two cyanine dye molecules are in close proximity their transition dipoles will couple, producing a perturbation to the energy levels of the system and causing a mixing of the excited states of the uncoupled molecules. The interaction energy for two dipoles is predictably orientation dependent. This situation is depicted qualitatively in Fig. 4. When the two molecules are aligned tip to tail, then if the transition dipoles are out of phase the energy is higher and the dipole moments cancel, but if the transition dipoles are in phase, the energy is lower and the net transition dipole moment is enhanced by a factor of $\sqrt{2}$.

A similar picture emerges for a *J*-aggregate where there are N molecules in a row, with transition dipoles strongly coupled to one another. The lowest energy excited state corresponds to all N molecules coupling in phase, with the excitation delocalized over all N molecules, and this state also possesses an enhanced transition dipole moment [25]. The redistribution of oscillator strength towards lower energy explains why the *J*-aggregate absorption peak is significantly red-shifted relative to the monomer, typically 50–60 nm, and also why the absorption spectrum tails out asymmetrically towards higher energy. For large N [25]:

$$\mu^2_{J\text{-Agg}} \rightarrow 8(N+1)\mu_0^2/\pi^2 \approx 0.81(N+1)\mu_0^2$$

where μ_0 is the transition dipole of single monomer. The net oscillator strength is proportional to the number of coherently coupled dye molecules: $|\mu_{J\text{-Agg}}|^2 \propto N$, which means the radiative rate for the *J*-aggregate also scales like N, even for a *single* excitation.

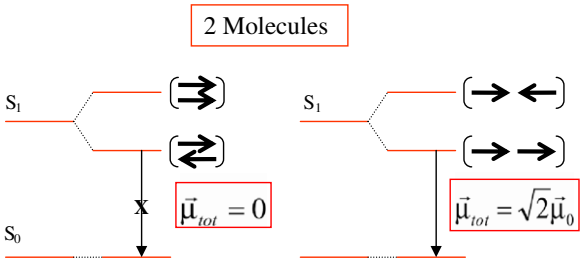


Fig. 4. Energy levels of two molecules interacting via dipole-dipole coupling. The arrows represent the orientation and physical position of the molecular dipoles.

This model also explains the narrowed spectrum of the *J*-aggregate absorption band. The linewidth can be decomposed into homogeneous and inhomogeneous broadening. Higher oscillator strength means the radiative pathway will compete N times better against the non-radiative pathways. Most likely, most of the observable width in the *J*-band is due to inhomogeneous broadening, i.e. the variation of the energy levels of the N coupled dye molecules. In that case, if the monomer exciton transition frequency is ω_M with error $\Delta\omega_M$ (FWHM), the spread in the average energy $\langle\omega_M\rangle$ is statistically reduced to $\Delta\omega_M/\sqrt{N}$, which is the energy spread seen by the *J*-aggregate since it simultaneously involves all N molecules. The linewidth of the *J*-aggregate absorption band is therefore $\Delta\omega_J = \Delta\omega_M/\sqrt{N}$ [26].

3.2. J-aggregate thin film deposition and analysis

J-aggregate thin films are commonly formed using one of three techniques: Langmuir–Blodgett, spin-casting in a polymer matrix, and layer-by-layer (LBL) deposition [27–29]. The last technique is the newest, having first been reported by Fukumoto and Yonezawa [29]. For our electroluminescent devices, we use thin films of *J*-aggregates formed with the LBL deposition method [20]. Our analysis has indicated that LBL *J*-aggregate thin films combine high absorption with low optical scattering and nanometer-scale thickness control [30].

The LBL deposition method has been an active field of materials science research in the past decade since it was first reported by Decher et al. [29,31–37] A basic LBL process consists of dipping a substrate in alternating polycation and polyanion solutions. Substrates undergo these sequential immersions in cationic and anionic solutions (SICAS) in order to build up a thin film, one layer of polymer at a time. The polycations and polyanions can be either strong or weak: strong polyelectrolytes are not pH sensitive, whereas the charge on weak polyelectrolytes depends on the pH of the solvent. The substrates are rinsed between immersions in the polyelectrolytes in order to remove excess polymer. Prior to the deposition, the substrate must be prepared in some manner that allows the first adsorption step to occur.

While the LBL process was developed with polyelectrolytes as both of the thin film constituents,

further work in the 1990s showed that one of the polyelectrolytes could be replaced by a dye molecule or other small, charged component [37]. The only requirement of the charged component was that enough of the component adsorb in the LBL process to reverse the charge on the surface of the substrate. Fukumoto and Yonezawa showed that, by using *J*-aggregating cyanine dyes as one of the charged components, thin films of *J*-aggregates could be built using the LBL process [29]. A schematic of a typical LBL *J*-aggregate thin film grown on glass is shown in Fig. 5 along with the structural formulas of the film constituents. A glass substrate is treated with oxygen plasma to provide a negative surface charge and undergoes multiple immersions in cationic PDAC (poly(diallyldimethylammonium chloride)) and the anionic, *J*-aggregating cyanine dye TDBC (5,6-dichloro-2-[3-[5,6-dichloro-1-ethyl-3-(3-sulfopropyl)-2(3H)- benzimidazolidene]-1-propenyl]-1-ethyl-3-(3-sulfopropyl) benzimidazolium hydroxide, inner salt). Full details of the growth process can be found in the experimental section of a study in which we reported the analysis of optical and morphological properties of LBL *J*-aggregate thin films [30].

LBL *J*-aggregate thin films, when grown on glass, possess remarkable morphological properties, including a layered structure which allows for nanometer-scale thickness variation. These properties are revealed through atomic force microscopy (AFM), which also allows one to gauge the film thickness for optical analysis. Fig. 6 shows the evolution of thin film morphology as substrates undergo increasing numbers of SICAS.

As indicated by the 1.5 SICAS and 2.0 SICAS AFM images in Fig. 6, the surface treatment of a substrate can have significant effects on the build-up of the first few layers in an LBL process. The layered structure of the LBL *J*-aggregate thin films does not appear until after the second dye immersion, likely in part due to using oxygen plasma as a surface treatment as opposed to functionalizing with other molecules. Another notable feature of the film growth progression shown in Fig. 6 is the increase in roughness in the 6.5 and higher SICAS samples. This increase suggests a range in which LBL *J*-aggregate thin films can be grown without significant roughness and with nanometer-scale thickness control.

The optical properties of the LBL *J*-aggregate thin films shown in Fig. 5 can be analyzed through reflectance and transmittance measurements, and together with film thickness estimates provided by AFM measurements, the optical constants of the thin films can be calculated. Fig. 7 shows a propagation and matching matrix model that allows for calculation of transmittances and reflectances of light at varying wavelengths through a structure such as a LBL *J*-aggregate thin film on glass. Using such a model, various methods can be used to obtain the complex index of refraction of the thin film ($\tilde{n} = n + iK$), which is related to the linear thin film absorption constant by the formula $\alpha = 4\pi K(\lambda)/\lambda$. Two such methods were discussed in a previous study [30].

Generally, some of the most reliable (n, K) values are derived by fitting optical data to a model that is compatible with the constraints of the

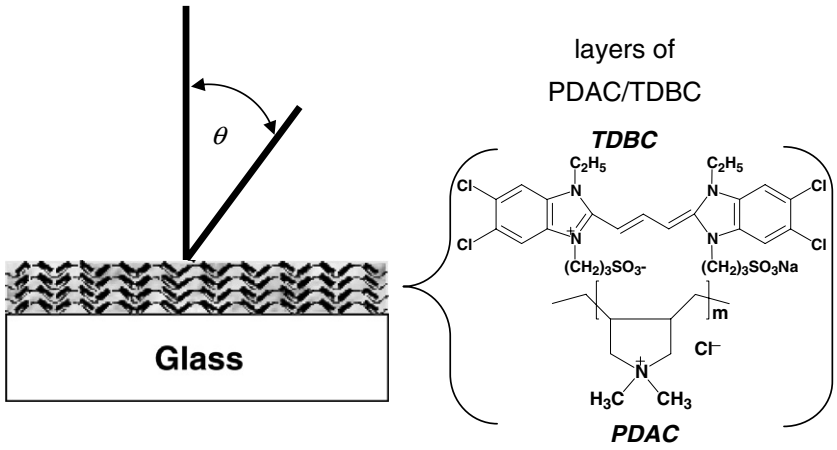


Fig. 5. Layer-by-layer (LBL) *J*-aggregate thin film layer constituents. LBL *J*-aggregate thin films are grown on glass using the polycation PDAC and the anionic, *J*-aggregating cyanine dye TDBC. Optical measurements are taken with the LBL-film side of the sample facing the light beam at a specified angle θ away from the normal [30].

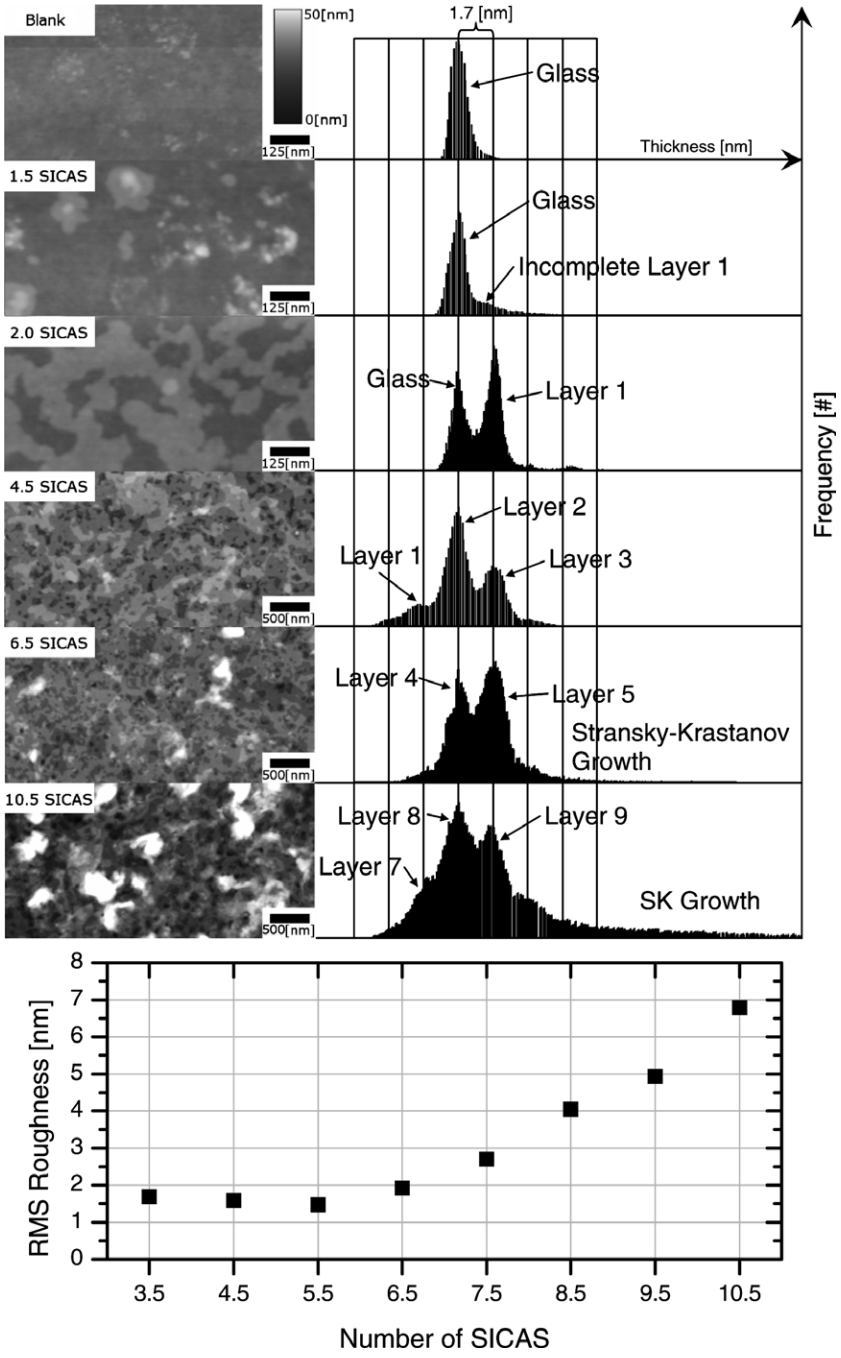


Fig. 6. Atomic force microscope (AFM) images of LBL *J*-aggregate growth with histograms of thickness frequency. Each SICAS consists of a PDAC adsorption step followed by a TDBC adsorption step. N.5 SICAS refers to N SICAS followed by an additional PDAC adsorption step. The AFM images show samples that underwent the indicated number of SICAS. The top three images show that significant PDAC/TDBC layered growth is not evident until 2.0 SICAS. The bottom three images show the build-up of thick layers. The histograms are lined up at the dominant film thicknesses to show that each layer is about 1.7 nm thick, which is the thickness per layer used when modeling the optical constants of the films. The histograms are created from the full 1 μm^2 and 16 μm^2 images for the first three and last three films shown, respectively. The layer numbers indicated in the histograms are based on the progression of layer growth observed in AFM images. The plot shows the roughness profile of films from 3.5 to 10.5 SICAS. At 6.5 SICAS, the dominant growth regime changes from layered to Stransky–Krastanov (SK) type. All images have a vertical scale of 50 nm [30].

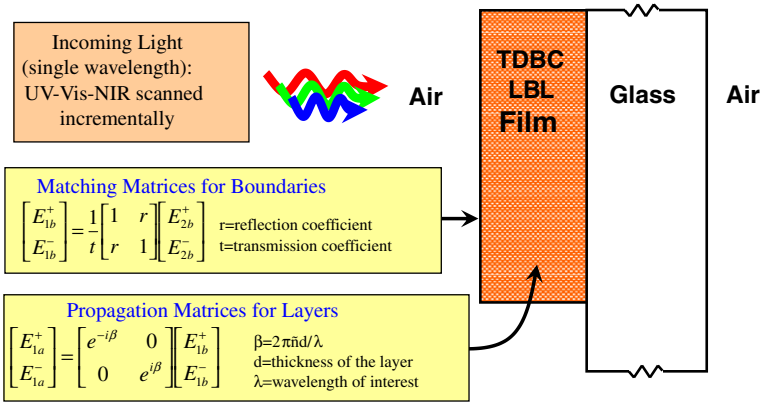


Fig. 7. Propagation and matching matrix model used in analyzing LBL *J*-aggregate thin film samples. Reflectance and transmittance measurements are made using a UV–Vis-NIR spectrometer. Each boundary and layer in the light's path is modeled using the appropriate matrix, with thicknesses provided by AFM measurements. The thin film's index of refraction is the missing parameter to be found using numerical regression.

Kramers–Kronig relations. The Kramers–Kronig relations are based on the causality of an optically excited system. Causality implies that the linear dielectric function, and therefore the complex index of refraction, is analytic on the upper complex frequency plane. This condition allows for the application of Cauchy's Theorem, which in the end results in a relation between the real part of the index of refraction, n, and the imaginary part (extinction coefficient), K [38]. Ultimately, to be exact, the Kramers–Kronig relations require integration to infinite frequency, for which data collection is impossible. Therefore, the contributions outside of the measured frequency range are frequently lumped into some background index of refraction. One of the resulting approximations of the Kramers–Kronig relations is shown in equation for $n(\omega_j)$ [39]:

$$n(\omega_j) \cong n_{\text{offset}} + \frac{2}{\pi} P \int_{\omega_L}^{\omega_U} \frac{\omega K(\omega)}{\omega^2 - \omega_j^2} \, d\omega,$$
$$\omega_L \leqslant \omega_j \leqslant \omega_U$$

n_{offset} refers to the lumped background index due to contributions from outside the measured frequency range, ω_L to ω_U, and P signifies that the integral is the Cauchy Principal value. This expression can be used in a model-free Kramers–Kronig regression algorithm as proposed by Nitsche and Fritz [39]. The advantage of such an algorithm is that it requires no initial model and instead determines the (n, K) that match the optical data provided. We have made frequent use of the model-free Kramers–Kronig regression algorithm along with the model in Fig. 7 in analyzing LBL *J*-aggregate thin films. The results of one such analysis are shown in Fig. 8 along with the optical reflectance and transmittance data used to perform and verify the regression. The peak value of K from the analyzed sample corresponds to an absorption constant of nearly $10^6\ \text{cm}^{-1}$ (at wavelength $\lambda = 593$ nm, $K = 4.5$, hence $\alpha = 4^*\pi^*\ \text{K}/\lambda = 0.96 \times 10^6\ \text{cm}^{-1}$) [30].

Aside from the high peak thin film absorption constant, LBL *J*-aggregate thin films have other notable optical properties as indicated in Fig. 8. The reflectance data shown in Fig. 8a indicate that as thicker films are grown, the full-width at half-maximum (FWHM) of the reflectance band increases, potentially indicating the onset of a polaritonic band gap or increased inhomogeneous broadening of the *J*-aggregate resonant peak. Additionally, the higher energy feature that is visible in the transmittance data in Fig. 8b, as discussed in our previous study, may be due to a polaritonic upper-branch or to a *J*-aggregate vibronic level [30]. The good agreement of the calculated fits in Fig. 8c with the measured data, besides indicating the accuracy of the Kramers–Kronig-derived (n, K) values, also show that there is remarkably low scattering in the 4.5 SICAS film. Scattering would be particularly noticeable in the correspondence of the calculated to the measured transmittance since the Kramers–Kronig regressions for these films were based on reflectance data, which would not be as significantly affected by scattering as transmittance data.

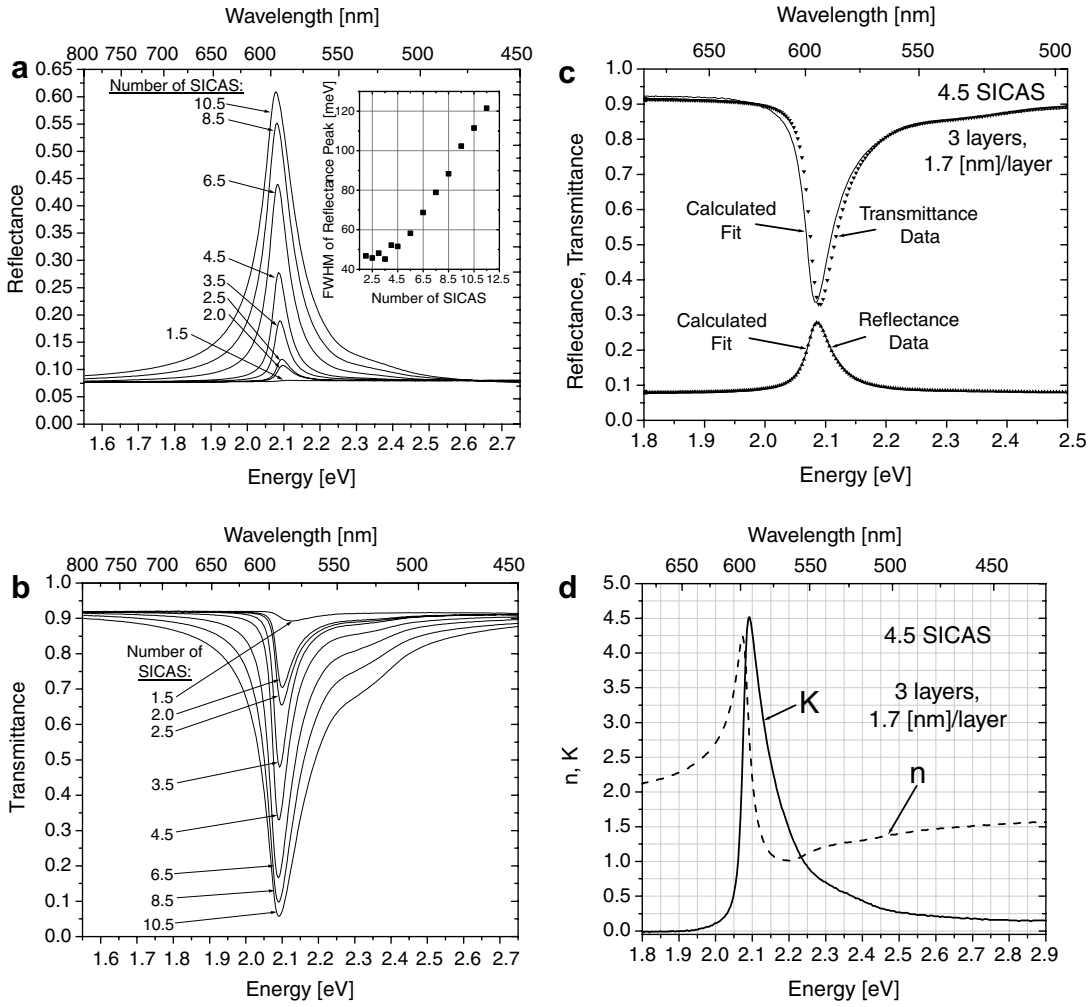


Fig. 8. Optical data and characterization of optical properties for LBL PDAC/TDBC *J*-aggregate films. Plots (a) and (b) show reflectance, R, at $\theta = 7°$ and transmittance, T, at $\theta = 0°$ for a series of samples that underwent different numbers of SICAS. Plot (a, inset) shows the FWHM of the reflectance peak as a function of number of SICAS. Plot (c) shows measured reflectance and transmittance for 4.5 SICAS (5.1 nm thick film, 3 layers with 1.7 nm per layer) and calculated spectra using the (n, K) shown in Plot (d). Plot (d) shows (n, K) for the 4.5 SICAS film in (c) obtained through a Kramers–Kronig (KK) regression based on reflectance data [30].

Further evidence that the increase in the FWHM of the *J*-aggregate reflectance peak is in part due to polaritonic effects can be seen as thicker LBL *J*-aggregate films are formed. Fig. 9 shows the reflectance of a 6 SICAS PDAC/TDBC LBL *J*-aggregate film compared to that of a 31 SICAS film along with photographs of the 31 SICAS film. The 31 SICAS reflectance shows that as the reflectance saturates, two resonant peaks appear, which suggests that two resonances may have been produced by the coupling of the photons of the weak cavity of the thick film to the excitons of the *J*-aggregates in the film.

The photoluminescence (PL) of LBL *J*-aggregate thin films exhibits a narrow FWHM and small Stokes' shift from the absorption, as shown in Fig. 10. The small Stokes' shift is important when considering the use of LBL *J*-aggregate thin films in strong-coupling applications since a large Stokes' shift can contribute to dephasing of the strong coupling. Such dephasing can limit the length of time that interactions between a cavity photon and an exciton occur.

LBL *J*-aggregate thin films exhibit many characteristics that make them well-suited for use in strong-coupling applications. The high absorption

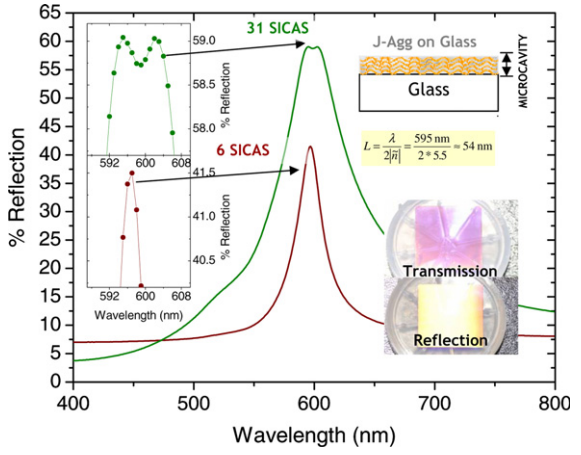


Fig. 9. Reflectance measurements of a 6 SICAS and 31 SICAS PDAC/TDBC LBL *J*-aggregate thin film on glass. The 31 SICAS reflectance shows that broadening of the FWHM eventually leads to the appearance of two resonant peaks in reflection, suggesting that the broadening of the FWHM is due in part to polaritonic effects caused by the formation of a weak cavity in the LBL *J*-aggregate thin film. The inset photographs show the 31 SICAS film in transmission and reflection, exhibiting the strong reflectance around $\lambda = 595$ nm.

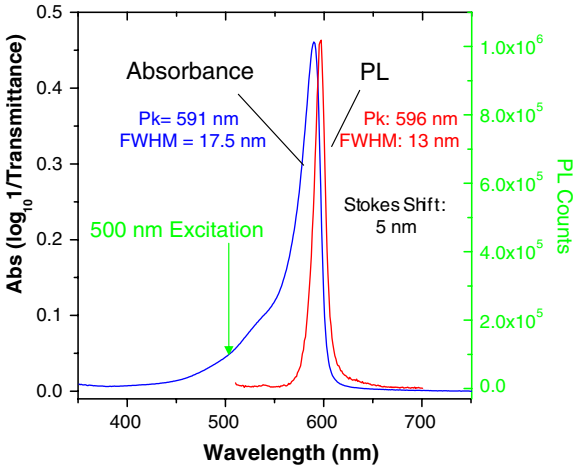


Fig. 10. Photoluminescence (PL) of a LBL PDAC/TDBC *J*-aggregate thin film from excitation at $\lambda = 500$ nm. An absorbance measurement from the same film is shown. Absorbance is defined as $\log_{10}(1/T)$, where T is the measured transmittance. The two plots show the small Stokes' shift of the LBL PDAC/TDBC film and narrow FWHM of the PL.

constant and nanometer-scale thickness controllability achievable with the LBL process allow for the use of very thin *J*-aggregate films with minimal scattering, both of which are important considerations in engineering devices based on the strong coupling of light and matter.

4. *J*-aggregate-based organic light-emitting devices

4.1. *J*-aggregate thin film electroluminescence

We first developed an OLED using *J*-aggregates of cyanine dyes as the emitter material, and then incorporated a similar device structure in a resonant optical microcavity (RC-OLED) to demonstrate polariton emission. The basis for the *J*-aggregate OLED architecture comes from the work of Era et al. [40] Fig. 11 illustrates the structure of our *J*-aggregate OLED. The anode is transparent conducting ITO, and the hole transport layer (HTL) is a polymer film spin-cast on top of the anode. The *J*-aggregate layers are then solution deposited from water. The electron transport layers (ETL), composed of small molecule organics, are thermally evaporated on top of the *J*-aggregates. In this design, the *J*-aggregate layers are concentrated at the cavity antinode, in order to maximize the exciton–photon coupling. Additionally, by not having dispersed dye throughout the device, which can act as electron traps, the electron and hole transport properties of the device are better maintained.

An aromatic polymer is used to make the HTL, instead of a polar conducting polymer, since such films are less likely to be damaged or dissolved during the dip-coating of the *J*-aggregate layers. The polymer chosen is the semiconducting wide-band-gap fluorescent polymer poly-TPD, which is the polymeric form of the TAD used by Era et al. Inserting the HTL between the anode and *J*-aggregate layers improves hole injection and current balance, reduces exciton quenching by the anode contact, and enables placement of the exciton

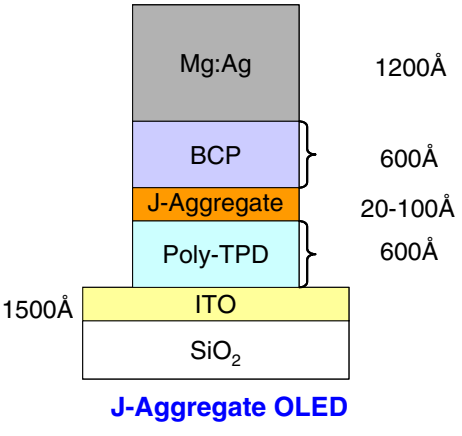


Fig. 11. *J*-aggregate OLED structure.

recombination region precisely at the cavity antinode.

Dip-coating the polyelectrolyte and *J*-aggregate layers on top of poly-TPD relies on the ability of the polyelectrolytes to adsorb to the polymer surface. Typically, a glass or silicon substrate is electrostatically charged via surface treatment techniques like UV-ozone or oxygen plasma to facilitate polyelectrolyte adsorption. Applying such methods would most likely have damaged the fluorescence of poly-TPD. Fortunately, such methods were not necessary because the polymer readily oxidizes, forming polar sites that promote polyelectrolyte adsorption.

The ETL consists of BCP, which also performs the function of a hole blocking layer that confines excitons electrically generated in the *J*-aggregate layers. High Vacuum Sublimation of BCP is performed with angstrom thickness control. Exposing the partial device structure to high vacuum (10^{-7} Torr) environment is also expected to drive off any residual water from the polyelectrolytes, benefiting device current–voltage characteristics and device stability. The cathode of the *J*-aggregate OLED consists of magnesium-silver alloy (Mg:Ag).

Current–voltage (*I–V*) characteristics and optical power output were measured for the *J*-aggregate OLED in operation. The electroluminescence (EL) spectra showed emission peaked at $\lambda = 600$ nm with a 16.5 nm FWHM (Fig. 12). It is significant to note that the EL spectra are independent of the OLED current level, which indicates that the exciton recombination region is entirely in the *J*-aggregate layer. A typical *I–V* curve and external EL quantum

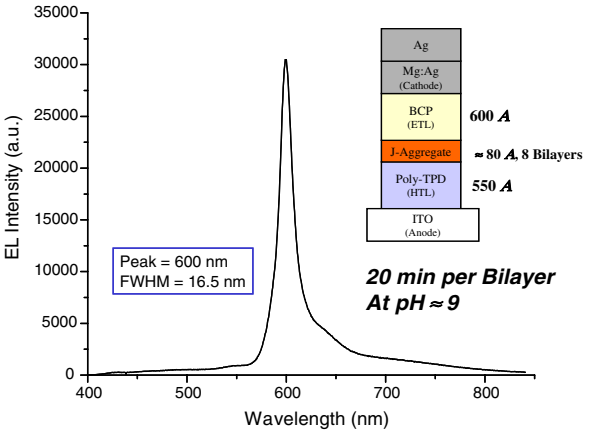


Fig. 12. TDBC *J*-aggregate OLED electroluminescence spectrum.

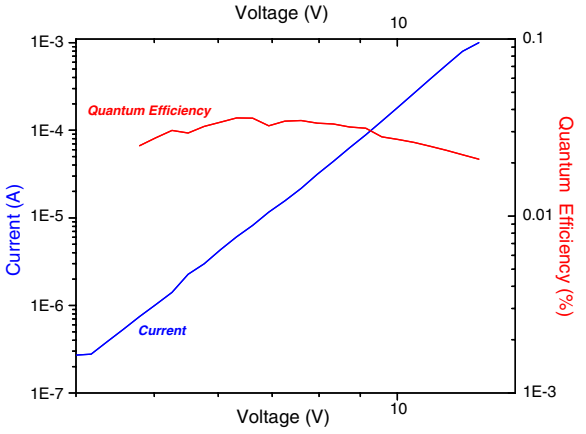


Fig. 13. TDBC *J*-aggregate OLED current–voltage and external quantum efficiency results.

efficiency plot are depicted in Fig. 13, with the maximum efficiency of 0.035%.

4.2. J-aggregate polariton OLED

We recently demonstrated polariton emission from a *J*-aggregate OLED with a similar structure to the one described above, however in the *J*-aggregate polariton OLED, a highly reflective silver mirror was used as the anode in place of ITO in order to form a microcavity [20]. Additionally, the thicknesses of the ETL and HTL were chosen in order to tune the microcavity resonance to that of the *J*-aggregate exciton and to locate the *J*-aggregate layer at the antinode of the cavity [20]. Fig. 14a shows the structure of the *J*-aggregate polariton resonant-cavity OLED (RC-OLED) along with the thicknesses of the constituent layers. The *J*-aggregate layer used was similar to that used in the *J*-aggregated OLED above, consisting of 4 SICAS of the cationic polyelectrolyte PDAC and the anionic *J*-aggregating cyanine dye TDBC. The reflectance of the complete structure is shown in Fig. 14b and exhibits the polaritonic resonances discussed earlier.

Fig. 14b suggests that the device is in the strong coupling limit since the reflectivity of the structure exhibits two resonances split off from the cavity and *J*-aggregate thin film resonance, which is shown for comparison. The large splitting between the resonances is due to strong coupling between the *J*-aggregate exciton ($\lambda = 595$ nm) and photon field of the near resonantly tuned microcavity ($\lambda =$ 587 nm). Because of the strong coupling, the exciton

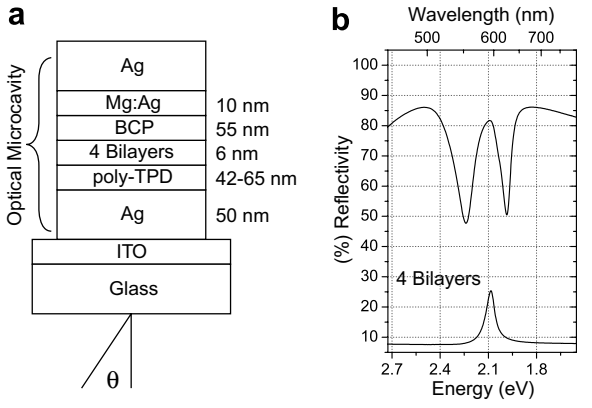


Fig. 14. Structure of *J*-aggregate polariton OLED and reflectance data. (a) Resonant cavity organic light emitting device (RC-OLED) structure, with variable thickness spin-cast poly-TPD layer that tunes microcavity resonance. Metal layers serve as mirrors for the microcavity and as electrical contacts to the device. (b) Reflectivity of RC-OLED with poly-TPD thickness of 54 nm, compared to 4 SICAS film on glass, measured at $\theta = 7°$. The microcavity is tuned to $\lambda = 587$ nm, which is near the resonance of the TDBC *J*-aggregate at $\lambda = 595$ nm [20].

and photon are exchanging energy at a faster rate than the respective dephasing processes, which in this case are primarily dephasing due to spontaneous emission and non-radiative relaxation of the *J*-aggregate exciton and photon dephasing due to light leakage from the cavity [1,2]. Consequently, as described earlier, new eigenstates form with energy levels, $E_{\pm}$, separated from the uncoupled exciton and photon energy levels, E_{ex} and E_{ph}, respectively:

$$E_{\pm} = \frac{E_{ex} + E_{ph}}{2} \pm \frac{1}{2}\sqrt{(\hbar\Omega_R)^2 + (E_{ex} - E_{ph})^2} \qquad (1)$$

The energy separation, $E_+ - E_-$, is dependent on the degree of energy matching between the exciton and photon modes. $\hbar\Omega_R$ is the exciton–photon vacuum Rabi coupling frequency, which increases with the strength of the exciton–photon interaction [2].

Although the reflectivity spectrum shown in Fig. 14b suggests that the RC-OLED structure has indeed reached the strong coupling limit, confirmation of strong-coupling comes from detuning one of the resonances in the exciton–photon system and observing the results. Fig. 15 shows the results in reflectivity and EL measurements of such detuning by changing the thickness of the poly-TPD HTL layer in the RC-OLED, which changes the cavity thickness and therefore detunes the photon energy, E_{ph}.

Fig. 15a shows that the cavity photon energy, E_{ph}, is tuned to the resonance of the *J*-aggregate exciton when the poly-TPD thickness is 54 nm. Fitting the peak energies of the upper and lower branches of the polariton, $E_{\pm}$, to the dispersion curve generated from E_{ph} and Eq. (1) in Fig. 15b shows good agreement between the measured and predicted energies, providing further evidence that the system is in the strong coupling limit. In the EL of Fig. 15c, a spectral shoulder at $\lambda = 610$ nm appears superimposed on the emission spectrum of the E_- state, which could be from *J*-aggregates that are not strongly coupled to the microcavity due to disorder in the layers. Such a shoulder would not be expected to appear in reflectivity since only the transition dipoles parallel to the surface are probed in such a measurement. Fig. 15d shows a magnification of the upper branch in the EL spectra, which in the RC-OLED has a lower emission intensity than the lower branch. Thermalization of the polaritons could account for the lower intensity of $E_+(\theta)$ in the EL spectra.

The energy of the cavity photon can also be changed for a single thickness of the poly-TPD HTL by probing off-normal, since changing θ affects the tuning of E_{ph} according to the dispersion relation [2]:

$$E_{ph}(\theta) = E_0\left(1 - \sin^2\theta/n^2\right)^{-1/2} \qquad (2)$$

where E_0 is the bare cavity resonance at $\theta = 0°$ and n is the refractive index of the cavity spacer layers. E_{ex}, however, remains constant. In particular, for the RC-OLED of Fig. 14c, $E_{ph}(\theta = 0°) = 2.11$ eV, while $E_{ph}(\theta = 80°) = 2.59$ eV (with $n = 1.7$ for the poly-TPD and BCP layers). Fig. 16a–c plot the angular reflectivity and EL spectra for the RC-OLED. Fig. 16d plots the angular dependence of the EL peaks and reflectivity dips together with the calculated dispersion relations for $E_{ph}(\theta)$ and the polariton states $E_{\pm}(\theta)$. Fig. 16e shows the measured and calculated EL and reflectivity dips for the RC-OLED from Fig. 15, where $E_{ph}(\theta = 0°) = 2.05$ eV.

It is notable that in Fig. 16d, at $\theta = 0°$, near resonance for $E_{ph}(\theta)$ and E_{ex}, the polariton branches of the dispersion relation $E_{\pm}(\theta)$ anti-cross in energy, while at larger θ, far away from the resonance condition, they devolve into uncoupled exciton and photon dispersion curves. Such anti-crossing also is seen in Fig. 16e, though at a different angle due to the different thickness of

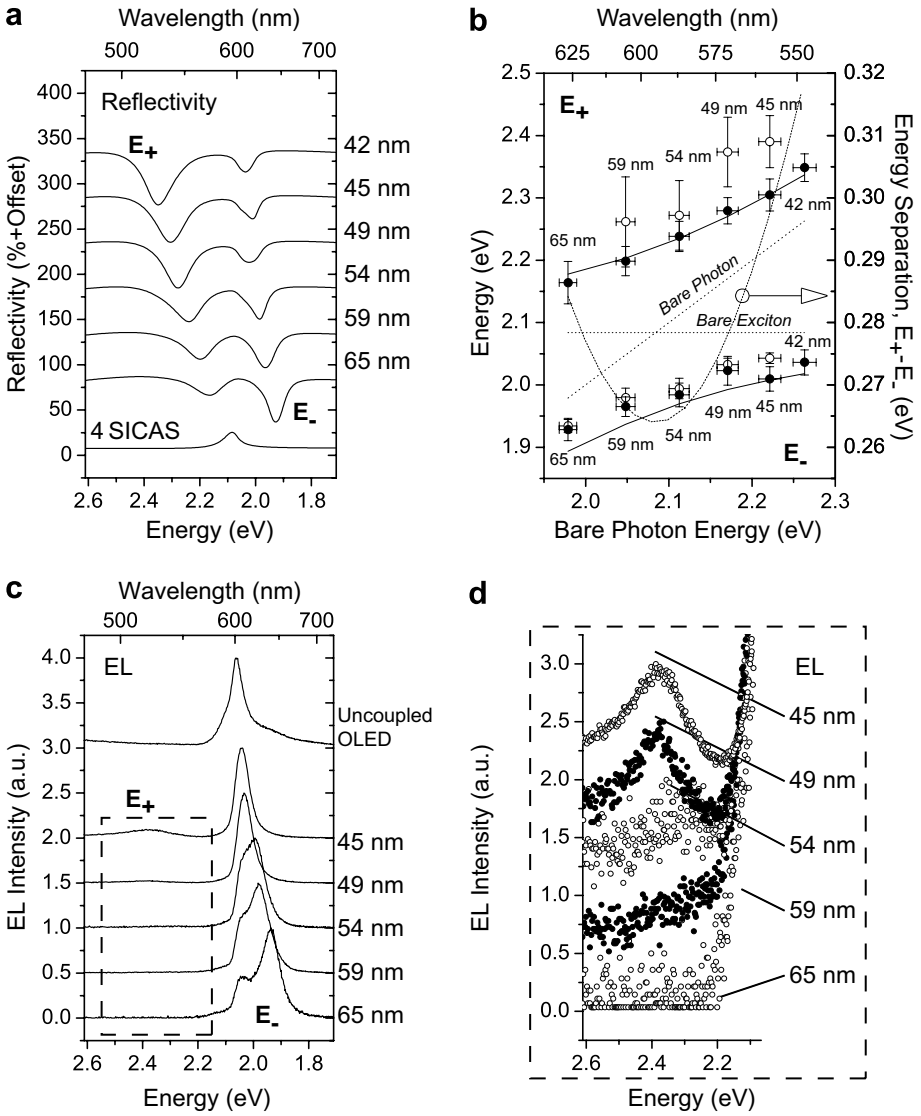


Fig. 15. Normal mode polariton electroluminescence and reflectivity for a series of RC-OLED structures with different microcavity resonance. Cavity resonance is tuned across a 250 meV band, by adjusting the thickness of the poly-TPD layer from 42 nm to 65 nm. (a) Reflectivity at $\theta = 7°$ for a series of RC-OLED structures. Data of successive measurements are offset by 50% points. (b) Resonant peaks in EL (open data points) and resonant dips in reflectivity (solid data points) plotted as a function of the bare (cavity) photon energy exhibit anti-crossing. Fits are generated by the two-state model of Eq. (1) with a Rabi-splitting of $\hbar\Omega_R = 265$ meV. (c) EL spectra at $\theta = 0°$, normalized to the lowest energy peak, E_-. The spectral shoulder at $\lambda = 610$ nm is EL from disordered J-aggregates not strongly coupled to cavity. (d) Expanded view of high-energy portion of EL spectra, normalized to emission of the higher energy polariton peak, E_+, in the $\lambda = 475$ nm to $\lambda = 575$ nm range [20].

the poly-TPD layer. The fits in both Figs. 15 and 16 are generated using a single value for the vacuum Rabi-splitting, $\hbar\Omega_R = 265$ meV. The consistent agreement of the RC-OLED data, across multiple devices and collection angles, with a single value of $\hbar\Omega_R$ in the dispersion relation, further confirms that the RC-OLEDs operate in the strong coupling limit.

Further improvements to the device structure of the RC-OLED could be made by replacing the silver mirrors with DBRs, which would increase the Q of the resulting cavity, reduce dephasing due to losses in the mirrors, and allow for the use of an anode that can better inject holes into the poly-TPD HTL, such as ITO, which has a higher work function than silver.

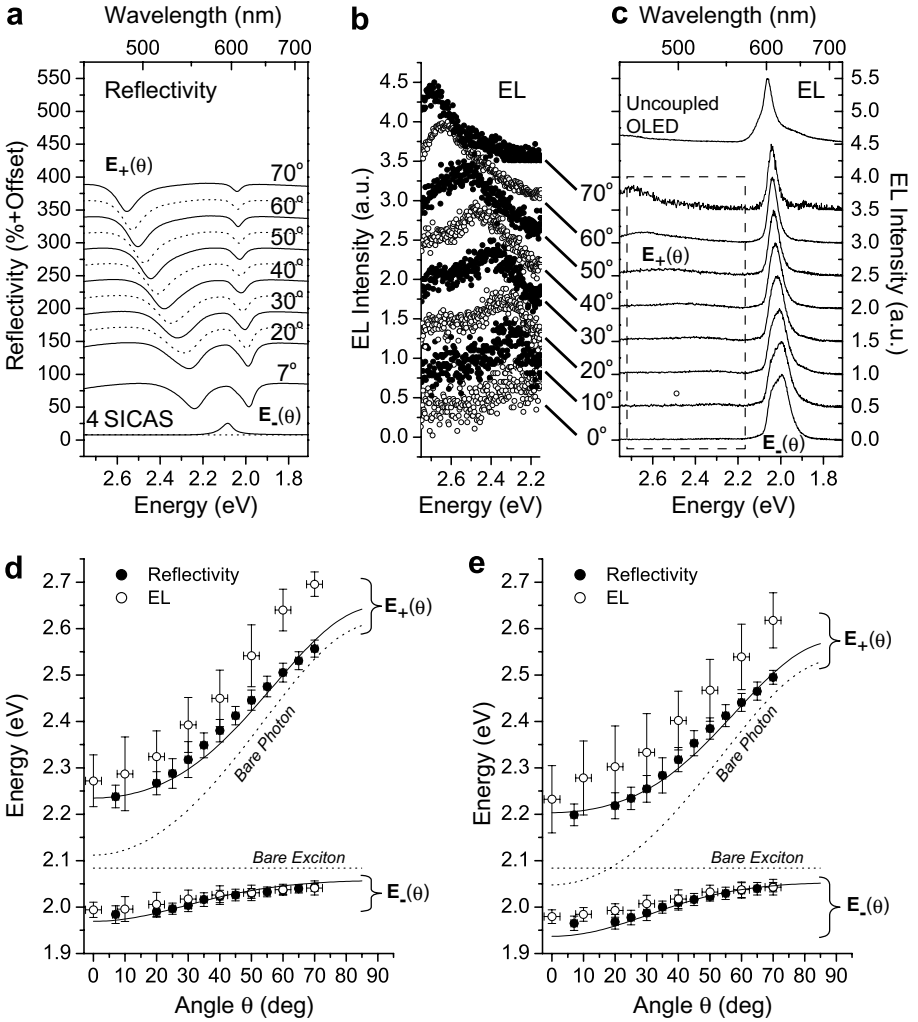


Fig. 16. Angularly resolved polariton electroluminescence and reflectivity measurements for the polariton RC-OLED with poly-TPD thickness of 54 nm, and dispersion relations in (d) and (e) for RC-OLEDs with poly-TPD thickness of 54 nm and 59 nm, respectively. (a) TE polarized reflectivity. Data of successive measurements are offset by 50% points. The reflectivity at $\theta = 7°$ of a 4 SICAS PDAC/TDBC film, is shown for comparison. (b) Expanded view of higher energy portion of the EL spectra, normalized to emission of the higher energy polariton peak, $E_+(\theta)$, in the $\lambda = 450$ nm to $\lambda = 575$ nm range. (c) EL spectra normalized to lower energy polariton peak, $E_-(\theta)$. The EL spectrum at $\theta = 0°$ of an uncoupled OLED is shown for comparison. (d) Polariton angular dispersion relation for RC-OLED of parts (a–c) with $E_{ph}(\theta = 0°) = 2.11$ eV. The fit is generated from reflectivity data in (a) using the two-state model with the coupling interaction, $\hbar\Omega_R = 265$ meV, being independent of angle and the bare (cavity) photon energy following Eq. (2). (e) Polariton angular dispersion relation for RC-OLED with $E_{ph}(\theta = 0°) = 2.05$ eV, and fit with $\hbar\Omega_R = 265$ meV [20].

4.3. Patterned J-aggregate films

To develop integrated photonic devices based on *J*-aggregates we need to develop techniques for generating patterned *J*-aggregate layers. Even simple *J*-aggregate patterns, like those shown in Fig. 17, can be challenging to reproduce, especially when the patterned film must be placed in a complex device structure. To avoid *J*-aggregate crystal damage due to lithograpic patterning and wet/dry etching, we recently demonstrated that microcontact printing (μCP) process can generate *J*-aggregate patterns with better than 1μm line accuracy. The μCP method preserves the optical quality of the deposited *J*-aggregate crystals and facilitates solvent-free incorporation of *J*-aggregate films into a device structure. Reduced exposure of sensitive device materials to solvents present in *J*-aggregate formation helps to improve the stability of devices incorporating LBL *J*-aggregate thin films.

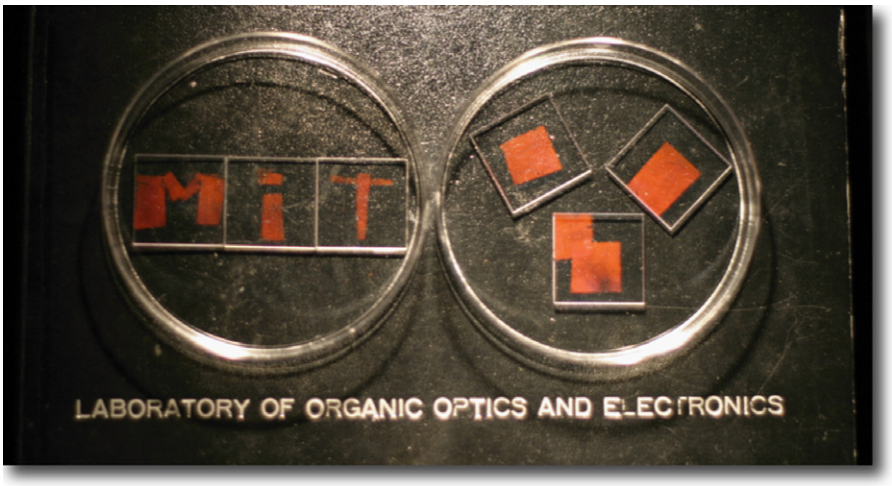


Fig. 17. Patterned PDAC/TDBC *J*-aggregate thin films on glass, formed and deposited through a microcontact printing (μCP) process.

We developed methods for growing LBL *J*-aggregate thin films on PDMS (polydimethylsiloxane) μCP stamps for the purpose of stamping those films into devices. One such method, shown in Fig. 18, involves replacing the strong polycation PDAC with the weak polycation PAH (poly(allylamine hydrochloride)) during the *J*-aggregate growth. The hydrophobic backbone of PAH facilitates adsorption onto hydrophobic surfaces such as PDMS, as described by Park and Hammond [41].

Stamped PAH/TDBC films can be made with large extinction coefficients and nanometer-scale thickness control, similar to PDAC/TDBC LBL *J*-aggregate thin films grown on glass. Fig. 19 shows reflectance and transmittance data from a series of PAH/TDBC films stamped on glass along with the results of Kramers–Kronig regression on the 3 SICAS sample. The plot of the complex index of refraction shows that the 3 SICAS film has a very large peak extinction coefficient of $K = 5.46$ at $\lambda = 594$ nm, which corresponds to a peak thin film absorption coefficient of $\alpha = 1.2 \times 10^6\ \mathrm{cm}^{-1}$. Additionally, the plot of the calculated transmittance along with the measured transmittance shows that, comparable to PDAC/TDBC films grown on glass, there is minimal light scattering in the stamped PAH/TDBC films. The use of other polyelectrolytes for growing *J*-aggregates in solution has been studied extensively, and combined with recent work by Park et al. in studying the growth of LBL polyelectrolyte thin films on hydrophobic surfaces, these studies suggest that stamped LBL *J*-aggregate thin films using various dyes could be achieved through variation of the polyelectrolyte and growth conditions [24,42–46].

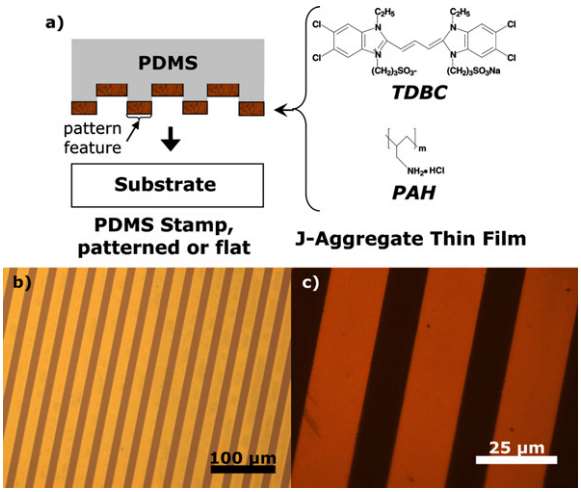


Fig. 18. Microcontact printed *J*-aggregated thin films. (a) Soft lithography schematic and structural formulas of *J*-aggregate thin film constituents. The stamps are either flat or, for soft lithography, patterned PDMS. Patterned PDMS stamps are created by curing PDMS on silicon molds. *J*-aggregate thin films are created in a layer-by-layer (LBL) process in which substrates undergo sequential immersions in cationic and anionic solutions (SICAS). The *J*-aggregating cyanine dye is TDBC, an anionic dye. PAH is directly substituted for PDAC in the *J*-aggregate thin film growth. Optical microscope images of a patterned *J*-aggregate LBL thin film transferred onto glass are shown in (b) and (c). (b) A patterned, 3 SICAS PAH/TDBC film transferred from a patterned PDMS stamp is shown in a reflectance mode image. (c) The same 3 SICAS patterned film is shown in photoluminescence with green light excitation, revealing submicron roughness in pattern definition.

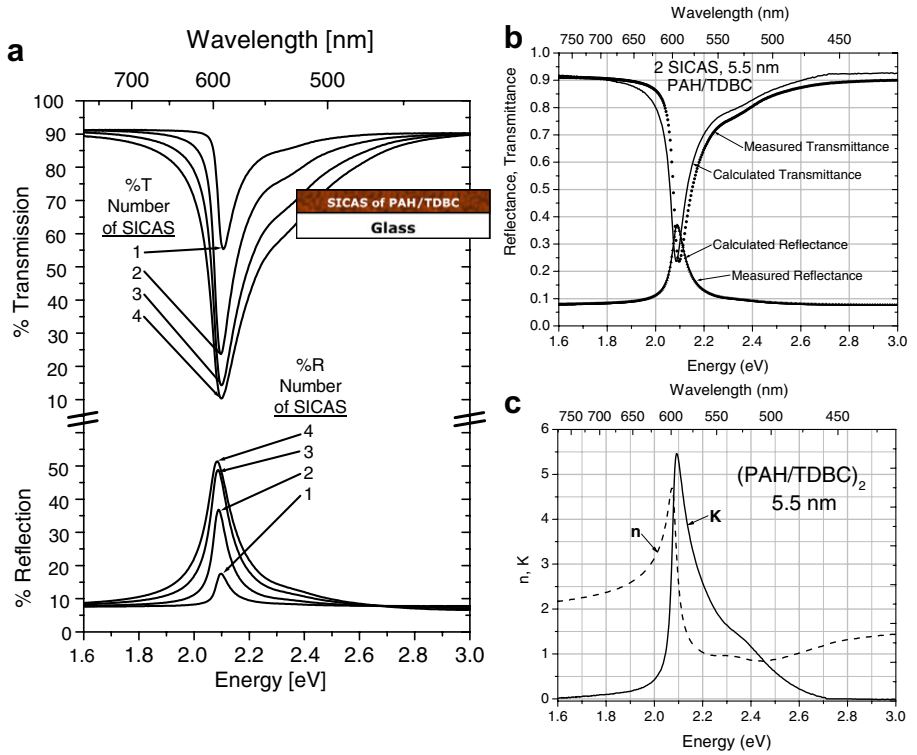


Fig. 19. Measurements and results of KK regression for a series of films formed on PDMS using PAH/TDBC and stamped on glass. (a) Reflectance and transmittance data for stamped films. Due to the overlap of plotted data, the reflectance and transmittance data have been offset for clarity. (b) Measured reflectance and transmittance for 2 SICAS (5.5 nm thick film, measured with AFM) and calculated spectra using the (n, K) shown in Plot (c). (c) Complex index of refraction of the 2 SICAS PAH/TDBC stamped film.

As sketched in Fig. 18a, μCP also enables soft lithography of *J*-aggregate thin films [41,47–53]. The *J*-aggregate LBL thin films are patterned by growing the films on PDMS stamps which are molded on a silicon master to form patterns in PDMS. The films are then stamped onto a substrate, facilitating transfer of *J*-aggregate thin film portions from the raised PDMS surfaces. Fig. 18b and c show a patterned *J*-aggregate thin film initially formed on a molded PDMS stamp and then deposited on glass via stamping.

5. *J*-aggregates in a half-cavity

When constructing a system for demonstrating strong coupling, the natural tendency is to focus primarily on the optical properties of the components, i.e. the excitonic layer and the microcavity, and on the fully integrated composite system to check for Rabi-splitting. Understandably, optical measurements of the half-cavity structure consisting of just one of the two mirrors from the microcavity and the excitonic layer are routinely not reported.

Here, we report the linear optical properties of such a half-cavity thin film structure, in the context of polaritonic devices [54]. The structure, sketched in Fig. 20a, consists of a dielectric Bragg reflector (DBR) as the mirror, a 4.5 SICAS PDAC/TDBC *J*-aggregate film as the excitonic layer, and a spacer layer of transparent material that separates the mirror and absorbing layer by a critical distance. This structure acts as a critically coupled resonator (CCR) capable of absorbing nearly 100% of the light of a particular wavelength that is incident from the excitonic layer side of the device. When light of wavelength $\lambda_c = 591$ nm is incident, the measured reflectance is $R = 2\%$ (Fig. 20b). In contrast, for the DBR with spacer but without the absorbing layer, the reflectance at $\lambda_c = 591$ nm exceeds 95%, showing the dramatic change due to critical coupling. For the same CCR, the transmittance at λ_c is $T = 1\%$. Consequently, 97% of the incident light is absorbed within the *J*-aggregate absorber layer ($d_a/\lambda < 1\%$), corresponding to peak effective absorption coefficient of $\alpha_{eff} = 6.9 \times 10^6\ cm^{-1}$.

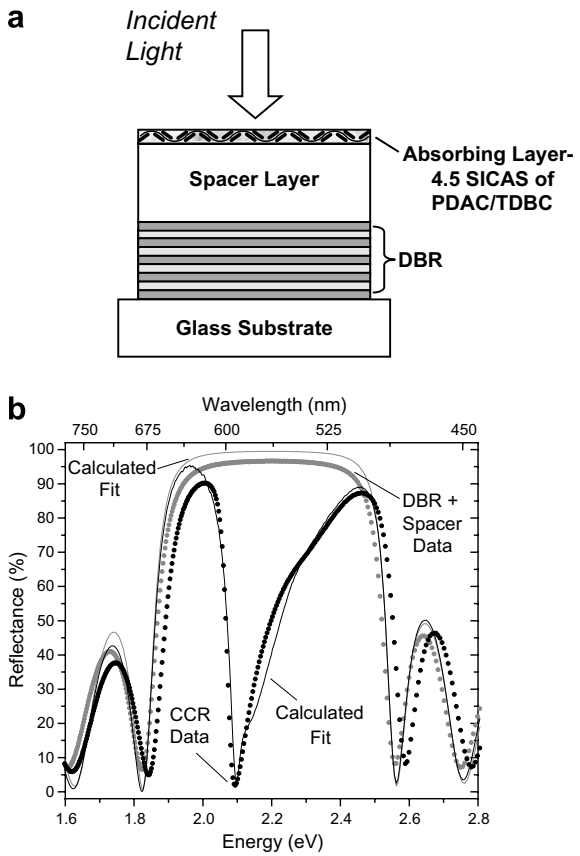


Fig. 20. (a) Critically coupled resonator (CCR) structure. The device consists of a dielectric Bragg reflector (DBR), a transparent spacer layer, and a layer of *J*-aggregate cyanine dye. The DBR consists of 8.5 pairs of sputter coated TiO_2 and Al_2O_3 layers, ending on TiO_2. The spacer layer is an additional sputter coated layer of Al_2O_3. The *J*-aggregate layer consists of the cationic polyelectrolyte, PDAC, and the anionic cyanine dye, TDBC, deposited via sequential immersion into cationic and anionic aqueous solutions (pH = 5.5) utilizing a previously described technique [30]. Reflection and transmission measurements are made with light incident from the *J*-aggregate side of the device. (b) Measured and calculated reflectance for the CCR with $d_s = 90 \pm 1$ nm. Also shown are reflectance data for the dielectric stack consisting of DBR with spacer layer. At $\lambda_c = 591$ nm, the CCR absorbs 97% of incident light [54]. The calculated reflectance is based on the *T*-matrix formalism described in the text. The calculated fit matches the experimentally observed reflectance minimum at $\lambda_c = 591$ nm [54].

The observed critical coupling is numerically confirmed using a wavelength-resolved *T*-matrix simulation (propagation and matching matrices), similar to that shown in Fig. 8d performed to find the index of refraction of a *J*-aggregate thin film on glass. The results of the *T*-matrix simulation for the CCR structure, also shown in Fig. 20b, numerically confirm the observed critical coupling phenomenon. The simulation reproduces critical coupling at $\lambda_c = 591$ nm for a spacer layer thickness $d_s = 90$ nm and odd multiples thereof. It is notable that when d_s is set to a value greater or less than 90 nm, critical coupling does not occur at another wavelength.

Finally, it is especially notable considering the topic of strong coupling that the CCR can be viewed as an integral part of the RC-OLED described above [20].

Conceptually, these structures are a CCR plus a "top" mirror that is separated approximately $\lambda/4$ away from the absorber film of the CCR. The polaritonic bandgap in the RC-OLED, observed as a high reflectance band centered around the uncoupled exciton resonance, follows naturally since there is no optical feedback from the "bottom" mirror, the CCR, to cause a resonant dip in reflectance. Thus, an understanding of the CCR phenomenon can assist in the development of future devices that operate in the strong coupling regime.

6. Conclusion

In the presented studies, we measured the remarkable optical properties of *J*-aggregate thin films and photonic structures that can be realized utilizing them. In particular, we demonstrated an exciton–polariton resonant cavity OLED with large coupling strengths (Rabi-splitting > 250 meV), which functions at room temperature, and a critically coupled resonator that can concentrate nearly all of the incident light into 5 nm thick *J*-aggregate film, yielding a record high effective absorption constant of 6.8×10^6 cm^{-1}. In these studies, the key to demonstrating the high oscillator strength *J*-aggregate films is the layer-by-layer growth method for forming *J*-aggregates. Furthermore, we have presented methods of patterning *J*-aggregate films through microcontact printing that could enable patterning the *J*-aggregates into single or multi-dimensional photonic bandgap structures. From the present rapid progress in use of *J*-aggregate thin films, we believe that *J*-aggregates, which had wide use in the photographic industry of the 20st century, are poised to have a role in the burgeoning integrated photonic industry of the 21st century.

Acknowledgements

This work has been supported in part by the Defense Advanced Research Projects Agency Brown

University Optocenter, the MIT MRSEC Program of the National Science Foundation, and the NSF Interdisciplinary Research Grant. M.S. Bradley acknowledges support of the National Defense Science and Engineering Graduate Fellowship program.

References

[1] H.J. Kimble, in: P.R. Berman (Ed.), Cavity Quantum Electrodynamics, Academic Press, Inc., San Diego, 1994.
[2] M.S. Skolnick, T.A. Fisher, D.M. Whittaker, Semicond. Sci. Technol. 13 (1998) 645.
[3] R.J. Thompson, G. Rempe, H.J. Kimble, Phys. Rev. Lett. 68 (1992) 1132.
[4] A. Wallraff, D.I. Schuster, A. Blais, L. Frunzio, R.S. Huang, J. Majer, S. Kumar, S.M. Girvin, R.J. Schoelkopf, Nature 431 (2004) 162.
[5] C. Weisbuch, M. Nishioka, A. Ishikawa, Y. Arakawa, Phys. Rev. Lett. 69 (1992) 3314.
[6] T. Yoshie, A. Scherer, J. Hendrickson, G. Khitrova, H.M. Gibbs, G. Rupper, C. Ell, O.B. Shchekin, D.G. Deppe, Nature 432 (2004) 200.
[7] J.P. Reithmaier, G. Sek, A. Loffler, C. Hofmann, S. Kuhn, S. Reitzenstein, L.V. Keldysh, V.D. Kulakovskii, T.L. Reinecke, A. Forchel, Nature 432 (2004) 197.
[8] D.G. Lidzey, D.D.C. Bradley, M.S. Skolnick, T. Virgili, S. Walker, D.M. Whittaker, Nature 395 (1998) 53.
[9] V.M. Agranovich, M. Litinskaia, D.G. Lidzey, Phys. Rev. B 67 (2003) 085311.
[10] J. McKeever, A. Boca, A.D. Boozer, J.R. Buck, H.J. Kimble, Nature 425 (2003) 268.
[11] M. Saba, C. Ciuti, J. Bloch, V. Thierry-Mieg, R. Andre, L.S. Dang, S. Kundermann, A. Mura, G. Bongiovanni, J.L. Staehli, B. Deveaud, Nature 414 (2001) 731.
[12] C. Monroe, Nature 416 (2002) 238.
[13] P.L. Hagelstein, S.D. Senturia, T.P. Orlando, Introductory Applied Quantum and Statistical Physics, Massachusetts Institute of Technology, Boston, MA, 2000.
[14] J.S. Townsend, A Modern Approach to Quantum Mechanics, McGraw-Hill, Inc., New York, NY, 1992.
[15] J.J. Licari, L.R. Enlow, Hybrid Microcircuit Technology Handbook, Materials, Processes, Design, Testing and Production, second ed., Noyes Publications, Westwood, NJ, 1998.
[16] Y.F. Zhu, D.J. Gauthier, S.E. Morin, Q.L. Wu, H.J. Carmichael, T.W. Mossberg, Phys. Rev. Lett. 64 (1990) 2499.
[17] P.W. Atkins, R.S. Friedman, Molecular Quantum Mechanics, Oxford University Press, 1997.
[18] D.G. Lidzey, D.D.C. Bradley, T. Virgili, A. Armitage, M.S. Skolnick, S. Walker, Phys. Rev. Lett. 82 (1999) 3316.
[19] P.A. Hobson, W.L. Barnes, D.G. Lidzey, G.A. Gehring, D.M. Whittaker, M.S. Skolnick, S. Walker, Appl. Phys. Lett. 81 (2002) 3519.
[20] J.R. Tischler, M.S. Bradley, V. Bulovic, J.H. Song, A. Nurmikko, Phys. Rev. Lett. 95 (2005) 036401.
[21] T. Kobayashi, K. Misawa, J. Lumin. 72-4 (1997) 38.
[22] S. Kirstein, R. Steitz, R. Garbella, H. Mohwald, J. Chem. Phys. 103 (1995) 818.
[23] S. Kirstein, H. Mohwald, Adv. Mater. 7 (1995) 460.
[24] C. Peyratout, L. Daehne, Phys. Chem. Chem. Phys. 4 (2002) 3032.
[25] M. Vanburgel, D.A. Wiersma, K. Duppen, J. Chem. Phys. 102 (1995) 20.
[26] E.W. Knapp, P.O.J. Scherer, S.F. Fischer, Chem. Phys. Lett. 111 (1984) 481.
[27] D.F. O'Brien, Photogr. Sci. Eng. 18 (1974) 16.
[28] K. Misawa, H. Ono, K. Minoshima, T. Kobayashi, Appl. Phys. Lett. 63 (1993) 577.
[29] H. Fukumoto, Y. Yonezawa, Thin Solid Films 327–329 (1998) 748.
[30] M.S. Bradley, J.R. Tischler, V. Bulovic, Adv. Mater. 17 (2005) 1881.
[31] G. Decher, J.D. Hong, Makromol. Chem. Macromol. Symp. 46 (1991) 321.
[32] G. Decher, J.D. Hong, Ber. Bunsen-Ges. 95 (1991) 1430.
[33] G. Decher, J.D. Hong, J. Schmitt, Thin Solid Films 210–211 (1992) 831.
[34] G. Decher, Science 277 (1997) 1232.
[35] W.B. Stockton, M.F. Rubner, Macromolecules 30 (1997) 2717.
[36] G. Decher, in: G. Decher, J.B. Schlenoff (Eds.), Multilayer Thin Films, Wiley-VCH Verlag GmbH & Co. KGaA, Weinheim, 2002, pp. 1–46.
[37] K. Ariga, Y. Lvov, T. Kunitake, J. Am. Chem. Soc. 119 (1997) 2224.
[38] J.A. Kong, Electromagnetic Wave Theory, EMW Publishing, Cambridge, 2005.
[39] R. Nitsche, T. Fritz, Phys. Rev. B 70 (2004) 195432.
[40] M. Era, C. Adachi, T. Tsutsui, S. Saito, Chem. Phys. Lett. 178 (1991) 488.
[41] J. Park, P.T. Hammond, Adv. Mater. 16 (2004) 520.
[42] C. Peyratout, E. Donath, L. Daehne, J. Photochem. Photobiol. A-Chem. 142 (2001) 51.
[43] C. Peyratout, E. Donath, L. Daehne, Photochem. Photobiol. Sci. 1 (2002) 87.
[44] E. Rousseau, M. Van der Auweraer, F.C. De Schryver, Langmuir 16 (2000) 8865.
[45] E. Rousseau, M.M. Koetse, M. Van der Auweraer, F.C. De Schryver, Photochem. Photobiol. Sci. 1 (2002) 395.
[46] J. Park, P.T. Hammond, Macromolecules 38 (2005) 10542.
[47] A. Kumar, G.M. Whitesides, Appl. Phys. Lett. 63 (1993) 2002.
[48] J.L. Wilbur, A. Kumar, E. Kim, G.M. Whitesides, Adv. Mater. 6 (1994) 600.
[49] A. Kumar, H.A. Biebuyck, G.M. Whitesides, Langmuir 10 (1994) 1498.
[50] B.D. Gates, Q.B. Xu, M. Stewart, D. Ryan, C.G. Willson, G.M. Whitesides, Chem. Rev. 105 (2005) 1171.
[51] M. Geissler, Y.N. Xia, Adv. Mater. 16 (2004) 1249.
[52] Y.N. Xia, J.A. Rogers, K.E. Paul, G.M. Whitesides, Chem. Rev. 99 (1999) 1823.
[53] Y.N. Xia, G.M. Whitesides, Annu. Rev. Mat. Sci. 28 (1998) 153.
[54] J.R. Tischler, M.S. Bradley, V. Bulovic, Opt. Lett. 31 (2006) 2045.

Available online at www.sciencedirect.com
ScienceDirect
Organic Electronics 8 (2007) 114–119
Organic Electronics
www.elsevier.com/locate/orgel

Polarization splitting in organic-based microcavities working in the strong coupling regime

Andrea Camposeo [a,*], Luana Persano [a], Pompilio Del Carro [a], Tersilla Virgili [b], Roberto Cingolani [a], Dario Pisignano [a]

[a] National Nanotechnology Laboratory of CNR-INFM, Distretto Tecnologico ISUFI, Università di Lecce, via Arnesano, I-73100 Lecce, Italy
[b] IFN-CNR, c/o Dipartimento di Fisica, Politecnico di Milano, P.zza Leonardo da Vinci 32, 20132 Milano, Italy

Received 1 February 2006; received in revised form 21 May 2006; accepted 22 June 2006
Available online 20 July 2006

Abstract

The emission features and the polarization splitting are investigated in organic microcavities operating in the strong coupling regime. The microcavity relies on a *J*-aggregate of cyanine dyes as active layer, and on high reflectivity distributed Bragg reflectors, fabricated by low-temperature reactive electron-beam evaporation. The operation of the microcavities in the strong coupling regime is demonstrated both by reflectivity and photoluminescence characterization. A vacuum Rabi splitting in the range 30–100 meV is reported. Important, both polariton branches exhibit a TM–TE polarization splitting depending on the incident angle, θ, and exhibiting a maximum of 35 meV. The angular behaviour of the splitting in the strong coupling regime is investigated and described by the $\sin^2\theta$ dependence predicted by the polarization splitting model.
© 2006 Elsevier B.V. All rights reserved.

PACS: 42.50.Fx; 78.40.Me; 78.66.Qn; 78.67.Pt

Keywords: Organic Microcavity; Strong coupling; Polarization splitting

1. Introduction

Organic semiconductor microcavities, a class of devices in which a semiconductor conjugated layer is embedded between two mirrors, have attracted a lot of attention both from the fundamental and the practical interest viewpoint, for their possible technological applications in advanced optoelectronics [1–3]. In such devices, the optical properties of the active semiconductor layer can be dramatically altered due to quantum electrodynamics (QED) effects [4]. In fact, the light–matter interaction resulting in the absorption and emission of photons does not only depend on the electronic properties of the active molecules, but also on the intensity of the electric field of the incident light, which is determined by the photonic boundary conditions. Among the numerous methods allowing a modification of the boundary conditions (i.e. the control of the resulting emission), the exploitation of photonic crystals is particularly interesting, because it can provide strong confinement of photons in a number of

* Corresponding author. Tel.: +390832298147; fax: +390832 298238.
E-mail address: andrea.camposeo@unile.it (A. Camposeo).

1566-1199/$ - see front matter © 2006 Elsevier B.V. All rights reserved.
doi:10.1016/j.orgel.2006.06.004

dimensions [5]. In particular, one-dimensional photonic crystals, such as vertical microcavities, are the simplest systems where QED effects are observable. The interactions between an organic or inorganic semiconductor in a microcavity and an electromagnetic field can occur under two different regimes, namely, the weak and the strong coupling, respectively. In the strong coupling regime, a cavity-photon couples strongly to an exciton having the same energy and in-plane momentum. The coherent coupled state thus formed is termed a cavity polariton, and can be considered as a mixture of the exciton and cavity-photon modes.

Recently, the strong coupling regime between exciton and photon modes has also been demonstrated for microcavities containing organic materials with large exciton oscillator strengths and relatively narrow line widths, such as porphyrin [6], *J*-aggregated cyanine dyes [7], conjugated polymers [8] and polycrystalline films of small organic molecules [9]. The occurrence of strong coupling is easily identified by the observation of an anticrossing between the cavity photon and the exciton modes that ideally results in resonance in a doublet of cavity polariton states. These exhibit equal linewidth and intensity and are separated by the vacuum Rabi-splitting energy [10,11].

So far, extensive studies have been performed for both inorganic [10] and organic cavity polaritons [12]. In particular, the development of novel architectures exhibiting strong coupling with organics has great importance for the realization of organic optoelectronic devices with featured characteristics [13]. Recently, the enhancement of the optical nonlinearity was observed in a transparent microcavity with all-dielectric mirrors and a *J*-aggregate of cyanine dyes embedded [14] and high-finesse organic microcavities with DBR mirrors have been realized which show quality factors in the range 440–620 [15]. In this work, we report on the fabrication and characterization of an organic semiconductor symmetric microcavity with dielectric mirrors, operating in the strong coupling regime. A novel low-temperature fabrication technique of distributed Bragg reflectors (DBR), that we successfully exploited for the fabrication of vertical cavity organic lasers [16], was applied to the realization of a microcavity with a *J*-aggregate of cyanine dyes as active layer. This organic material is known to have the necessary optical properties for strong coupling operation [7,12]. The devices we fabricated are characterized by a vacuum Rabi splitting in the range 30–100 meV and exhibit a polarization splitting up to 35 meV. Although polarization effects has been extensively studied in GaAs-based microcavites [17] and birefringence-induced polarization splitting was previously observed in microcavities with *J*-aggregates active layer [18], the present work is, to the best of our knowledge, the first extensive experimental investigation of this effect and of its angular behaviour in organic-based microcavities. In particular, we found that both the mode splitting within the lower (LP) and the upper (UP) polariton branch are well described by the $\sin^2(\theta)$ angular dependence predicted by the polarization splitting model, for small ($0 \leqslant \theta \leqslant 20$) and for large ($\theta \leqslant 35$) angles, respectively.

2. Experimental

A scheme of the microcavities is shown in the inset of Fig. 1(b). The technique we developed for the DBRs fabrication has been described in details elsewhere [19] and will be here briefly recalled. The bottom DBR, deposited onto Corning glass substrates is composed by 5.5 pairs of SiO_2 ($d_1 = 127$ nm) and TiO_2 ($d_2 = 83$ nm) layers, used as low-($n_1 = 1.41$) and high-($n_2 = 1.98$) refractive index medium, respectively. The oxide films were deposited from 99.9% purity TiO_2 tablets and SiO_2 disks (Leybold, Germany) at a working pressure of 2.4×10^{-4} mbar. A controlled oxygen atmosphere was accomplished by a gas inlet through a precision needle valve. A blend of an inert transparent matrix polymer (polyvinyl alcohol, PVA) containing a 10 wt.% cyanine dye (Hayashibara Biochemical Labs Inc.) was spin coated on top of the DBR mirror. This blend was spun from a 1:1 mixture of methanol and deionised water. Fig. 1(a) shows the absorption and emission spectrum of the *J*-aggregate forming cyanine dye 2,2′-dimethyl-8-phenyl-5,6,5′,6′-dibenzothiacarbocyanine chloride. The *J*-aggregate shows a strong absorption peak at 1.78 eV with a linewidth of 70 meV. The top mirror, composed by 8.5 pairs was then evaporated on the cavity layer. SiO_x ($d_1 = 127$ nm) and TiO_x ($d_1 = 87$ nm) films were deposited at low temperature (<70 °C), thus preventing any deleterious effect on the optical properties of the active layer. We estimated a quality factor of the empty cavity of 400 by a transfer matrix reflectivity (TMR) model based on the measured mirrors reflectivities. The absorption–reflection properties of the devices at normal incidence were measured by a Cary 5000

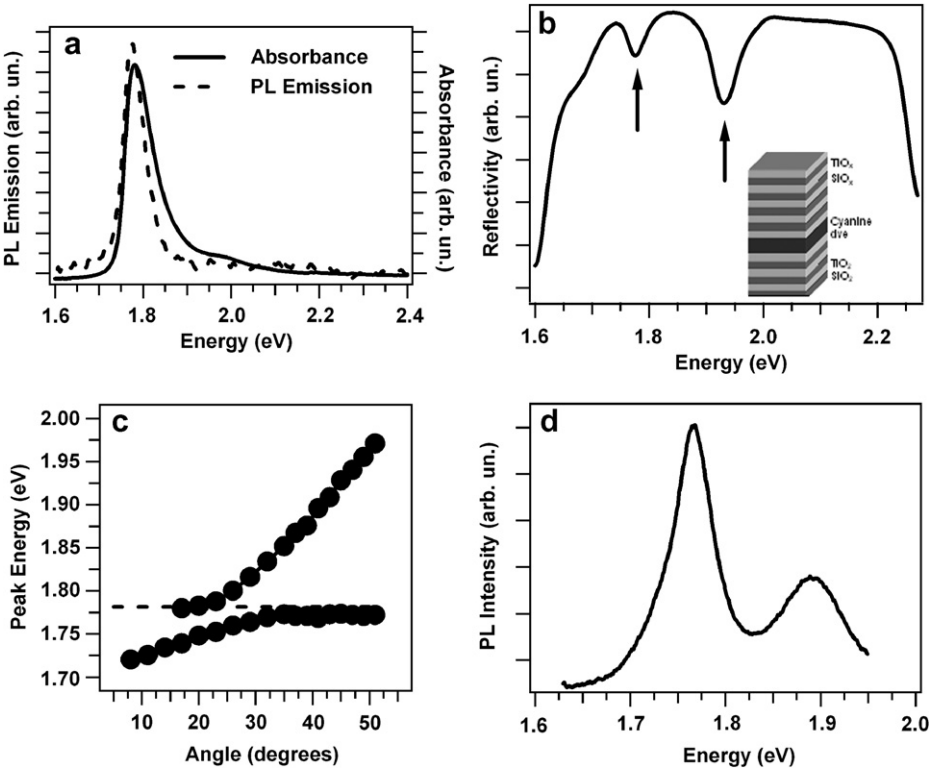


Fig. 1. (a) Absorbance and PL emission of a bare film of *J*-aggregated forming cyanine dye, used in this work. (b) Cavity reflectivity recordered at 45° as a function of incident light energy. The arrows mark the energy of the LP and UP polariton. In the inset a scheme of the monolithic microcavity is reported. (c) Dispersion curves as a function of the incident angle, obtained by reflectivity measurements. The dashed horizontal line indicates the energy of 1.78 eV of a bare film of *J*-aggregate cyanine dye. (d) Photoluminescence spectrum of the cavity excited by a cw He–Ne laser. The sample was excited at normal incidence and photoluminescence recordered at 42°.

spectrophotometer (Varian, Australia). Angle-resolved reflection spectra were obtained by illuminating the samples, mounted on a rotating holder, with a white W halogen lamp and recording the spectrum of the reflected light by a monochromator coupled to a CCD detector. The photoluminescence of the samples was measured by exciting the cavities with a He–Ne cw laser (excitation energy 1.959 eV), with a typical emitting power of 0.3 mW in order to avoid saturation effects [20]. High contrast polarization filters were used to analyze the polarization state of the emitted light. All measurements were carried out at room temperature, in air atmosphere.

3. Results and discussion

A typical reflection spectrum of the fabricated monolithic cavities is displayed in Fig. 1(b), showing the presence of cavity polaritons. The two peaks evidenced by arrows in Fig. 1(b) correspond to the LP and UP polariton branch, respectively, as also indicated by photoluminesence measurements (Fig. 1(d)). The effective strong coupling between the exciton and the cavity-photon modes is indeed confirmed by the characteristic anticrossing behaviour of the two coupled modes dispersion (Fig. 1(c)), obtained by reflectivity angle-tuning measurements. A similar trend was also observed for the photoluminescence measurements. In fact, the cavity mode exhibits an angle dependent resonant energy:

$$E_c(\theta) = E_0\left(1 - \frac{\sin^2(\theta)}{n_{\text{eff}}}\right)^{-1/2} \quad (1)$$

In the previous expression, $E_0 = hc/n_{\text{eff}}L_c$ stands for the photon energy at normal incidence if there is no phase delay in the mirrors, L_c is the cavity thickness and n_{eff} is an effective refractive index of the microcavity system.

Fig. 2 shows the reflectivity spectra (at normal incidence) of three monolithic cavities upon chang-

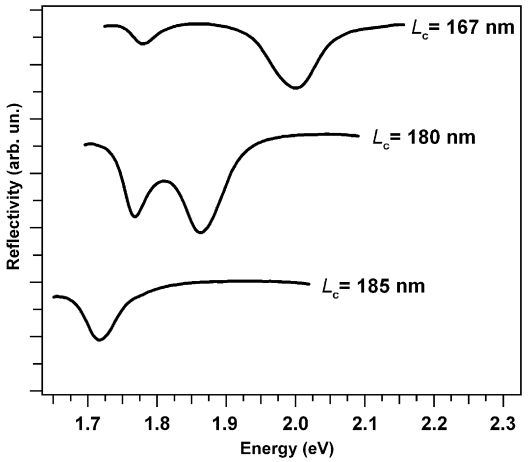


Fig. 2. Dependence of the reflection spectra of the organic-based monolithic microcavities on the thickness of the active layer (spectra acquired at normal incident angle). Spectra are vertically shifted for clarity.

ing the cavity length, L_c, simply by varying the *J*-cyanine thickness in the range 167–185 nm. Exploiting progressively thinner active layers, the blue-shift of the lower energy reflection dip slows down and the peak intensity decreases correspondingly. Vice versa, the blue-shift of the higher energy dip enhances, and its intensity increases upon decreasing the *J*-aggregate thickness. Overall, these results exhibit an anticrossing behaviour in accordance with the expected formation of cavity polaritons, indicating that the exciton–photon system is on resonance at normal incidence for 180 nm-thick *J*-aggregate films. The resulting vacuum Rabi splitting is as large as 100 meV.

In addition, microcavity devices can exhibit polarization effects, such as, for example, polarization mode splitting, observed in the weak coupling regime in a number of organic-based microcavities [21,22]. In the present experiment, we have investigated the polarization state of the cavity polariton through both reflectivity and photoluminescence measurements. Polarization mode splitting arises from different penetration length, L_{DBR}, into the dielectric mirror for TM and TE polarized e.m. fields. It depends on both the incident angle and the polarisation state of the incident light. Moreover, the resonance frequency E_m of a microcavity is dependent on the effective cavity length L_{eff} ($L_{eff} = L_c + L_{DBR}$):

$$E_m = \frac{L_c E_c + L_{DBR} E_s}{L_{eff}} \quad (2)$$

where E_s is the centre of the stop band. In the case of $E_c = E_s$, the microcavity resonance frequency is given by the Fabry–Perot energy E_c, whereas, if E_c is different from E_s, the resonance energy will be polarization dependent with an angular dependence of the resulting energy splitting given by [17]:

$$E_m^{TM}(\theta) - E_m^{TE}(\theta) = A[E_s(0) - E_c(0)]\sin^2(\theta) \quad (3)$$

where A is a constant.

Fig. 3(a) displays the typical reflectivity spectra acquired at a collection angle of 32° with incident TM and TE polarized radiation. The LP (UP) peak is localised at 1.771 (1.837) and 1.761 (1.821) eV for the TM and the TE polarization, respectively. A similar finding characterizes also the emission spectra (Fig. 3(b)), acquired at the same collection angle

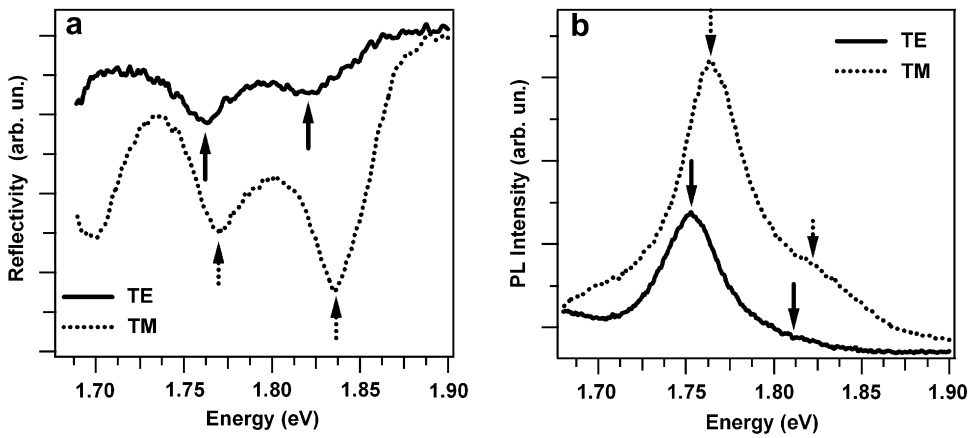


Fig. 3. TM (dotted line) and TE (continuous line) reflection (a) and photoluminescence (b) spectra. The position of the polariton peaks is evidenced by arrows. The acquisition angle was 32°. The peak at low energy is due to a DBR feature.

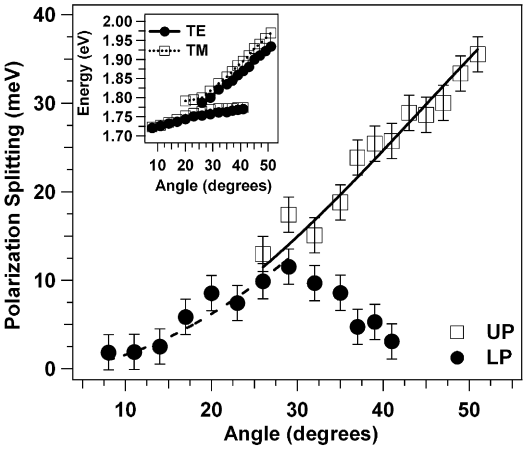


Fig. 4. Polarization splitting by reflectivity measurements, as a function of the incident angle for the LP (filled circles) and UP (empty squares) polariton branches. The dashed and continuous lines are fits to the data with a $\sin^2(\theta)$ function. The inset shows the experimental TM and TE dispersion curves as a function of the incident angle.

(32°). Furthermore, in Fig. 3 the TM polarized peaks are shifted towards higher energies with respect to TE modes, because for the investigated devices the cavity mode energy is lower than the centre of the stop band (Fig. 1(b)). This effect is observed at any incident angle, as evidenced in the inset of Fig. 4, where we plotted the angular polariton dispersion for both TM and TE polarization, obtained by reflectivity measurements. This trend is also observed in the PL measurements, although a quantitative comparison is not straightforward because reflectivity and PL measurements are performed in different points of the same sample and local inhomogeneities of the PVA/*J*-aggregate film [12,18] can affect the emission spectra.

Finally, we note that the $\sin^2(\theta)$ angular dependence of the polarization splitting combined with Eq. (2) provides a similar angular behaviour for the LP polariton at small angles and for the UP polariton at large angles [17]. This is confirmed by the analysis of the angular dependence of the polarization splitting of our microcavities (Fig. 4), showing a polarization splitting increasing as $\sin^2(\theta)$ for the UP branch ($\theta \leqslant 35°$) and for the LP branch at lower angles ($0 \leqslant \theta \leqslant 20$). The found value for the A constant of Eq. (3) is 1.3 ± 0.2. In the angular range where mixed exciton-cavity modes are formed ($25° \leqslant \theta \leqslant 40°$) a non-monotonic behaviour is observed for the LP energy upon increasing θ. The measured trend is similar to the one found for GaAs-based cavities with $In_{0.13}Ga_{0.87}As$ quantum well as active layer [17,23], a behaviour that has been theoretically modelled by a TMR model, taking into account the energy dispersion of the effective refractive index of the structure. We believe that a better understanding of the observed angular dependence can be accomplished by modelling our samples with a TMR model that also includes the energy dispersion of the effective refractive index for TE and TM polarized light [24] and birefringence effects reported in organic microcavities working in the strong coupling regime [18].

4. Conclusions

In conclusion, we fabricated and characterised microcavities with all-dielectric mirrors [14,15], based on *J*-aggregate active layers, which show strong coupling between the photon modes and the excitons of the organics. The characteristic anticrossing angular dispersion of the cavity polaritons was observed by both reflectivity and photoluminescence measurements, with a Rabi splitting in the range 30–100 meV. In addition, we measured a polarization splitting of the cavity polaritons as large as 35 meV, whose angular dependence is well described by the polarization mode splitting modelling for photon-like polaritons. A more quantitative model, describing also the angular range where mixed exciton–photon modes are formed, should also include the dispersion of the structure effective refractive index and birefringence effects of the active layer, which are known to significantly modify the emission properties of organic microcavities in the strong coupling regime [18,25]. Our results show that the strong coupling regime can be also achieved in symmetric microcavities with all-dielectric mirrors, and open the possibility of realizing novel optoelectronic devices based on the unique optical properties of polarized organic cavity polaritons.

References

[1] N. Tessler, G.J. Denton, R.H. Friend, Nature 382 (1996) 695.
[2] P.K.H. Ho, D.S. Thomas, R.H. Friend, N. Tessler, Science 285 (1999) 233.
[3] J.M. Lupton, R. Koeppe, J.G. Műller, J. Feldmann, U. Scherf, U. Lemmer, Adv. Mater. 15 (2003) 1471.
[4] E. Yablonovitch, Phys. Rev. Lett. 58 (1987) 2059.
[5] J.D. Joannopoulos, R.D. Meade, J.N. Winn, in: Photonic Crystals: Molding the Flow of Light, Princeton University Press, Cambridge, MA, 1995.

[6] D.G. Lidzey, D.D.C. Bradley, M.S. Skolnick, T. Virgili, S. Walker, D.M. Whittaker, Nature 395 (1998) 53.
[7] D.G. Lidzey, D.D.C. Bradley, T. Virgili, A. Armitage, M.S. Skolnick, S. Walker, Phys. Rev. Lett. 82 (1999) 3316.
[8] N. Takada, T. Kamata, D.D.C. Bradley, Appl. Phys. Lett. 82 (2003) 1812.
[9] R.J. Holmes, S.R. Forrest, Phys. Rev. Lett. 93 (2004) 186404.
[10] M.S. Skolnick, T.A. Fisher, D.M. Whittaker, Semicond. Sci. Technol. 13 (1998) 645.
[11] R. Houdré, C. Weisbuch, R.P. Stanley, U. Oesterle, P. Pellandini, M. Ilegems, Phys. Rev. Lett. 73 (1994) 2043.
[12] D.G. Lidzey, A.M. Fox, M.D. Rahn, M.S. Skolnick, V.M. Agranovich, S. Walker, Phys. Rev. B 65 (2002) 195312.
[13] J.R. Tischler, M.S. Bradley, V. Bulovic, J.H. Song, A. Nurmikko, Phys. Rev. Lett. 95 (2005) 036401.
[14] J.-H. Song, Y. He, A.V. Nurmikko, J. Tischler, V. Bulovic, Phys. Rev. B 69 (2004) 235330.
[15] L.G. Connolly, D.G. Lidzey, R. Butté, A.M. Adawi, D.M. Whittaker, M.S. Skolnick, R. Airey, Appl. Phys. Lett. 83 (2003) 5377.
[16] L. Persano, P. Del Carro, E. Mele, R. Cingolani, D. Pisignano, M. Zavelani-Rossi, S. Longhi, G. Lanzani, Appl. Phys. Lett. 88 (2006) 121110.
[17] G. Panzarini, L.C. Andreani, A. Armitage, D. Baxter, M.S. Skolnick, V.N. Astratov, J.S. Roberts, A.V. Kavokin, M.R. Vladimrova, M.A. Kaliteevsky, Phys. Rev. B 59 (1999) 5082.
[18] D.N. Krizhanovskii, R. Butté, L.G. Connolly, A.I. Tartakovskii, D.G. Lidzey, M.S. Skolnick, J. Appl. Phys. 93 (2003) 5003.
[19] L. Persano, R. Cingolani, D. Pisignano, J. Vac. Sci. Technol. B 23 (2005) 1654.
[20] R. Houdré, J.L. Gibernon, P. Pellandini, R.P. Stanley, U. Oesterle, C. Weisbuch, J. O'Gorman, B. Roycroft, M. Ilegems, Phys. Rev. B 52 (1995) 7810.
[21] T. Virgili, D.G. Lidzey, D.D.C. Bradley, S. Walker, Synth. Met. 116 (2001) 497.
[22] L. Persano, E. Mele, R. Cingolani, D. Pisignano, Appl. Phys. Lett. 87 (2005) 031103.
[23] D. Baxter, M.S. Skolnick, A. Armitage, V.N. Astratov, D.M. Whittaker, T.A. Fisher, J.S. Roberts, D.J. Mowbray, M.A. Kaliteevski, Phys. Rev. B 56 (1997) R10032.
[24] R. Kumar, A.P. Singh, A. Kapoor, K.N. Tripathi, Opt. Eng. 43 (2004) 2134.
[25] R.F. Oulton, N. Takada, J. Koe, P.N. Stavrinou, D.D.C. Bradley, Semicond. Sci. Technol. 18 (2003) S419–S427.

Available online at www.sciencedirect.com
ScienceDirect
Organic Electronics 8 (2007) 120–126
Organic Electronics
www.elsevier.com/locate/orgel

Optical strong coupling in microcavities containing J-aggregates absorbing in near-infrared spectral range

Jakub Wenus [a,*], Samira Ceccarelli [a], David G. Lidzey [a], Alexei I. Tolmachev [b], Jurii L. Slominskii [b], Julia L. Bricks [b]

[a] *Department of Physics and Astronomy, The University of Sheffield, Hicks Building, Hounsfield Road, Sheffield S3 7RH, United Kingdom*
[b] *Institute of Organic Chemistry, National Academy of Sciences of Ukraine, Murmanskaya ul. 5, Kiev 02094, Ukraine*

Available online 20 July 2006

Abstract

We present strong exciton–photon coupling at near-infrared wavelengths in an organic microcavity containing J-aggregates of a cyanine dye. Strong coupling is resolved using position-tuned transmission measurements, performed at room temperature at a constant angle. Clear anti-crossing around the organic exciton energy (1.57 eV = 789 nm) is observed with a Rabi splitting energy of 68 meV. Such systems will be of significant interest in the creation of hybrid semiconductor structures in which organic and inorganic excitons are electromagnetically coupled. We have also investigated the photostability of the J-aggregates used in the experiments and compare it with other cyanine dyes forming J-aggregates from water-based solutions. Our measurements suggest that the near-infrared dye is exceptionally stable in vacuum, especially at low temperatures.
© 2006 Elsevier B.V. All rights reserved.

1. Introduction

Strong coupling in optical microcavities is a well known phenomenon, having been studied extensively in both inorganic semiconductor [1–5] and organic [6–9] based structures. The effect is manifested by an anti-crossing between the cavity photon and exciton modes evidenced in reflectivity or transmission spectra. In the strong coupling regime the modes form coherent coupled states termed cavity polaritons that have partly photonic and partly excitonic character. The properties of polaritons are interesting not only from the point of view of fundamental physics of light-matter coupling, but also because of their possible applications in ultrafast optical switches, polariton lasers and other sophisticated optoelectronic and photonic devices. The strength of the exciton–photon coupling is characterized by the Rabi splitting energy ($\hbar\Omega_{\mathrm{Rabi}}$), which is a measure of the separation between the polariton branches at resonance. The Rabi splitting energy is often much larger for organic materials due to larger oscillator strength of Frenkel excitons and large chromophore density, both resulting in higher integrated extinction coefficient; $\hbar\Omega_{\mathrm{Rabi}}$ can range from 4 to 10 meV for III–V compound semiconductors (arsenides) [1,3], through 15–40 meV for II–VI compounds [2,4], up to 60 meV for GaN-based semiconductors [5] and even few

* Corresponding author.
E-mail address: j.wenus@sheffield.ac.uk (J. Wenus).

1566-1199/$ - see front matter © 2006 Elsevier B.V. All rights reserved.
doi:10.1016/j.orgel.2006.06.006

hundred meV for organic materials [6–9]. Because of the large binding energy of Frenkel excitons, strong coupling can be observed at room temperature in organic based cavities. This is in contrast to most inorganic semiconductor cavities where such effects are only apparent at lowered temperatures, although recent studies have shown room temperature strong coupling in ZnSe [4] and GaN [5] based microcavities.

Recently there has been a significant interest in hybrid organic–inorganic heterostructures in which the optical or electronic properties of both types of materials are mixed [10–12]. In such structures it should be possible to observe resonant interactions between Frenkel excitons and Wannier-Mott excitons either through short-range Coulomb dipole–dipole interactions at interfaces or via photon-mediated hybridization in strongly-coupled optical microcavities. Such hybrid polaritonic states are expected to combine the large linear absorption of organic excitons, with the large non-linear optical response of inorganic excitons. J-aggregates of cyanine dyes seem to be promising materials for such application, as they have relatively narrow excitonic bands and small Stokes shift between absorption and emission. They often have strong absorption at red and near-infrared wavelengths [13–15] making them suitable systems to be coupled with III–V compound semiconductors. In particular, arsenide-based semiconductors (GaAs/InGaAs/AlGaAs) which have been very widely explored in strongly-coupled microcavities support excitons having optical transitions at wavelengths above ~750 nm. At present, however, we are not aware of reports on strong coupling using organic semiconductors at wavelengths greater than about 695 nm [16]. We therefore present the evidence for optical strong coupling in a microcavity structure where the J-aggregate excitons have a sharp (FWHM ~ 40 meV) absorption band at about 790 nm at room temperature. Such a system is in principle very promising for the creating of hybrid structures by coupling to arsenide-based inorganic semiconductors. Furthermore, we analyze the photostability of the material and compare it with J-aggregates of a similar cyanine dye absorbing at visible wavelengths (~590 nm). We show that the near-infrared J-aggregates appear to be more stable both in air and in vacuum. Moreover, they show very little photo-bleaching when cooled to liquid nitrogen temperatures. This relatively high photostability will be of great potential benefit in possible photonic applications.

2. Experimental methods

Fig. 1 shows chemical structures of the cyanine dyes (U3 (a) and F1 (b)) that we have used in our experiments. Dye F1 (also known as TDBC: 5,6-dichloro-2-[[5,6-dichloro-1-ethyl-3-(4-sulfobutyl)-benzimidazol-2-ylidene]-propenyl]-1-ethyl-3-(4-sulfobutyl)-benzimidazolium hydroxide, inner salt, sodium salt – catalogue reference S0046) was purchased from FEW Chemicals GmbH. It has been used in these experiments as it is a prototypical J-aggregate forming material that has been widely characterized [17,18]. As such it provides an effective 'benchmark' for assessing the stability of J-aggregate containing thin films when used in photonic applications. Dye U3 (3-[(2*Z*)-5-chloro-2-[((3E)-3-{[5-chloro-3-(3-triethylammonium-sulfonatopropyl)-1,3-benzothiazol-3-ium-2-yl]methylene}-2,5,5-trimethylcyclohex-1-en-1-yl) methylene]-1,3-benzothiazol-3(2*H*)-yl] propane-1-sulfonate) was synthesized in the Institute of Organic Chemistry NAS in Kiev, by interaction of two equivalents of 3-(5-chloro-2-methyl-1,3-benzothiazolium-3-yl) propane-1-triethylammonium-sulfonate with 1 equivalent of 1,3-diethoxy-2,5,5-trimethyl-1,3-cyclohexadiene [19] at 145–150 °C in the presence of triethylamine. The dye was recrystallized from methanol with a yield of 32%, having a melting point at 247–248 °C. The maximum absorption of the monomers in methanol is at $\lambda_{max} = 666$ nm with an extinction coefficient $\varepsilon = 21.6 \times 10^4$ l/mol cm. In water the dye forms

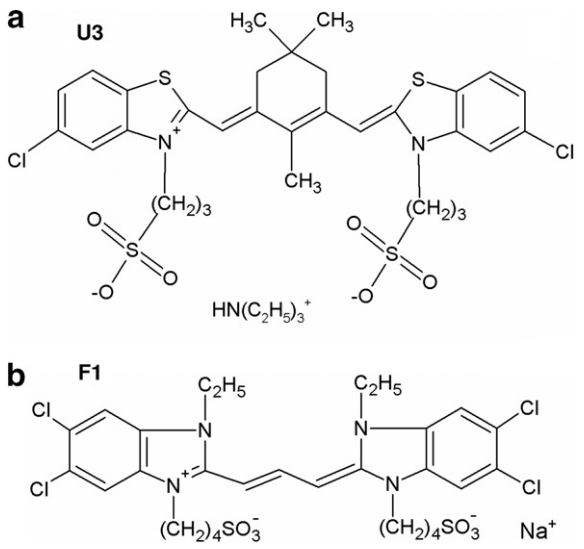


Fig. 1. The chemical structures of cyanine dyes U3 (a) and F1 (b).

J-aggregates, having a maximum absorption at $\lambda_{max} = 790$ nm. The total chemical formula of the dye U3 is: $C_{37}H_{49}Cl_2N_3O_6S_4$ with a molecular weight of 831.6 g/mol. An NMR characterization of the dye is described in Ref. [20].

To process dyes U3 and F1, they were first dissolved in water-based 5% gelatine (purchased from Sigma–Aldrich – catalogue reference 18808) solution at a concentration of 1.5 mg/ml for dye U3 and 3 mg/ml for dye F1. Both solutions were filtered using a 5 μm syringe filter and then spin-coated onto either a quartz slide or a dielectric mirror (DBR). The films of J-aggregates thus formed had a thickness of around 250 nm with similar maximum J-band optical density of around 0.8.

To fabricate microcavity structures, a DBR (coated with the U3 J-aggregate layer) was pressed against another identical dielectric mirror. The DBRs were grown by plasma-enhanced chemical vapor deposition (PECVD) and were composed of twelve pairs of SiO_2 ($n = 1.49$, $d = 143$ nm)/SiN ($n = 1.96$, $d = 109$ nm), exhibiting maximum reflectivity of 99%. This method of lamination is similar to the one that we reported previously for organic microcavities strong-coupled at visible wavelengths [21]. Here however, there is a variable-thickness air-gap between the organic film and the top DBR (as shown schematically in Fig. 5a) with the mirrors being kept in contact using two specially constructed adjustable metal jigs attached to opposite sides of the DBRs. Such a construction (although more bulky), allows us to control the size and shape of the air-gap more precisely. It also prevents the structure from delaminating. This permits us to create a cavity having a linear air-gap thickness gradient of around 50 nm/mm, which permits the relative energy separation between the cavity photon and the exciton to be tuned by changing the relative measurement position.

To characterize the J-aggregated dye films, we have measured their absorbance and photoluminescence (PL) in control films deposited on quartz substrates, as shown in Fig. 2. To generate fluorescence from J-aggregates of dye F1, a GaN laser was used emitting light at 405 nm having a power of 2.5 mW. For the J-aggregates of dye U3, a HeNe laser was used emitting light at 632.8 nm with a power of 1.4 mW. In both cases, the laser beam was focused into a spot of approximately 140 μm diameter equivalent to a power density of $\sim 1.6 \times 10^5$ W/m^2 for dye F1 and $\sim 9.1 \times 10^4$ W/m^2 for dye U3. In all cases, the samples were illuminated at an angle of

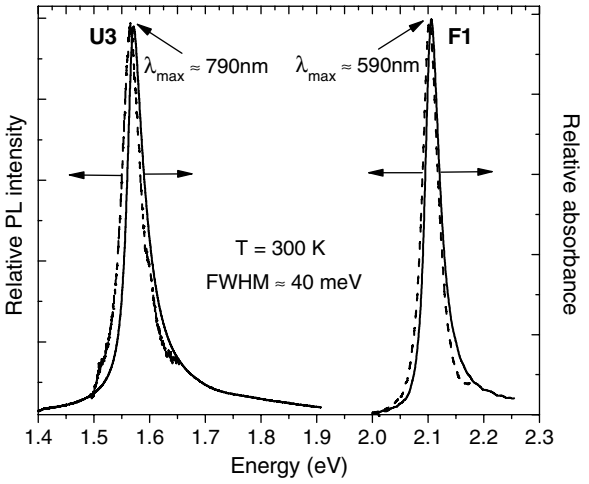


Fig. 2. Absorbance (solid lines) and photoluminescence (dashed lines) of J-aggregates of dyes U3 and F1 suspended in gelatine matrix in a thin ($d = 250$ nm) solid film deposited on a quartz substrate.

20° with fluorescence being collected at normal incidence using an optical light-guide connected to a CCD spectrometer. Note, that it is difficult to accurately determine the absolute power absorbed in the organic layers, as in each case, the J-aggregate absorption at the laser wavelength is small. From Fig. 2 it can be seen that dye F1 shows strong absorption and emission at around 590 nm (2.1 eV) whilst dye U3 is strongly red-shifted, having an absorption and emission at 790 nm (1.57 eV). In both cases, the linewidth of absorption and emission is around 40 meV with a Stokes shift of 6 meV ≈ 3 nm.

3. Photostability of thin J-aggregate films

For technological applications in optoelectronic devices, photostability is a key issue for organic materials, as they often undergo degradation under strong illumination (especially in the presence of oxygen). We have therefore investigated the relative photostability of two different J-aggregates (U3 and F1) in thin gelatine-based solid films deposited on quartz substrates. To do this, the J-aggregate photoluminescence intensity was measured as a function of time under three different conditions: in air at room temperature (~300 K), in vacuum at room temperature and in vacuum at liquid nitrogen temperature (~80 K). The photoluminescence was then tracked for a period of 1 h with measurements taken at 1–3 min time intervals. Fig. 3 shows a comparison of the fluorescence decay of the J-aggregates

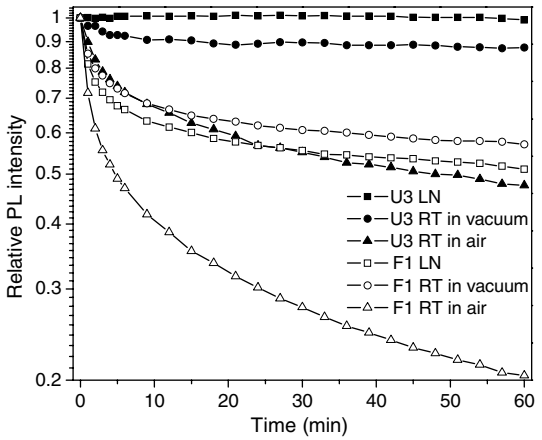


Fig. 3. Relative photoluminescence intensity from J-aggregates of dye U3 (emitting around 790 nm) and F1 (emitting around 590 nm) as a function of time. Here, spectra were recorded under different exposure conditions: at room temperature (RT) in air (indicated by triangles), at room temperature in vacuum (circles) and at liquid nitrogen temperature (LN) in vacuum (squares). The solid symbols correspond to measurements on dye U3 and open symbols correspond to dye F1. The solid lines are guides to the eye.

of dye U3 and J-aggregates of dye F1. The plots show changes in the relative PL intensity of the two materials (displayed on a logarithmic scale) as a function of illumination time.

To analyze the decay of PL, we have split the data set into two time regimes covering the periods of 0–5 min and 20–60 min, where in both cases it could be well fitted with a single exponential function. It was observed that both the materials initially bleach rapidly in air, with a time constant of around 5–15 min. Then, after about 20 min the decay process stabilizes reaching a constant decay rate in the range of 100–200 min (10–20 times slower than during the initial phase). Under vacuum conditions ($\sim 10^{-5}$ mBar) the fluorescence decay is always several times slower than in the air, with time constants in the range of 300–1000 min.

As the excitation power density was not identical for the U3 and F1 films, we cannot directly compare the decay constants of the materials. Our results, however, indicate that the U3 J-aggregates have a relatively enhanced photostability (see Fig. 3). For example, when measured in air, dye F1 decays to 50% of its initial PL intensity almost ten times faster than does dye U3. This relative difference in decay times is significantly larger than the relative difference in the excitation power densities. However, without an accurate measurement of the total radiation flux absorbed by each film, a quantitative comparison cannot be made. We also note that for dye F1, there is no significant difference in the photostability between the measurements taken at room temperature in vacuum and the measurements taken at liquid nitrogen temperature. In fact, the decay in photoluminescence is slightly faster when the dye is cooled to 80 K. The situation is qualitatively different for the J-aggregates of dye U3, where the emission intensity at 80 K is practically constant and there are no short-term signatures of photobleaching. At room temperature under vacuum, dye U3 looses only about 10% of its initial intensity during the first few minutes and then also appears to be exceptionally stable. It is likely that the difference in the photostability of these materials principally originates from their relative reactivity with molecular oxygen. The effect of photo-oxidation of both U3 and F1 is clearly demonstrated by the fact that both dyes are significantly more stable in vacuum than they are in air.

For application of J-aggregates in hybrid organic-inorganic structures, it is important to investigate the properties of organic materials at the low temperatures required to observe excitonic effects in inorganic semiconductors. We have therefore performed temperature-dependent PL measurements between temperatures of 80 K and 300 K on J-aggregates of dyes U3 and F1. Fig. 4 shows the relative changes in the photoluminescence peak

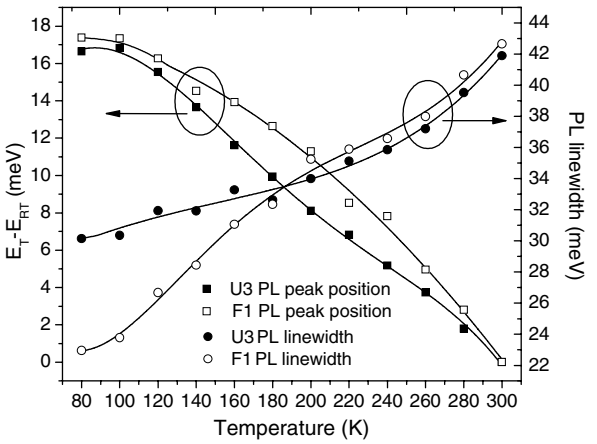


Fig. 4. Relative change in the peak photoluminescence emission energy of the J-aggregate J-band transition (plotted using squares) at temperature $T(E_T)$ compared to room temperature (E_{RT}) and emission linewidth (plotted using circles) for J-aggregates of dyes U3 and F1. Here, data for dye U3 is shown using solid symbols whilst the data for dye F1 is plotted using open symbols. The solid lines are guides to the eye.

emission energy and the emission linewidth measured for the dye U3 (solid points) and F1 (open symbols) at temperature intervals of 20 K. In general, both the materials behave similarly and exhibit a blue-shift in emission coupled with a linewidth narrowing, as the temperature decreases. Although both materials have a similar linewidth at room temperature, it can be seen that at 80 K the emission linewidth of the F1 J-aggregates has narrowed by a factor of two compared to its room temperature value and is equal to 23 meV. This significant reduction in linewidth at low temperatures will be most favorable for the creation of hybrid microcavities, as such photon-induced coupling will in general require organic and inorganic excitons having similar linewidths and oscillator strengths.

4. Strong coupling in near-infrared spectral range

We have studied laminated microcavity structures containing dye U3 (shown schematically in Fig. 5a) using position-resolved transmission measurements. Here, measurements were recorded at a fixed angle of 35°. Fig. 5b shows the transmission plots shifted vertically for clarity. The scan range over which the measurements were taken on the cavity surface was ~1 mm, corresponding to a change in the cavity thickness of ~50 nm. In this particular cavity, as the measurement position was scanned from 300 μm to 1300 μm, the thickness of the optical cavity was reduced, thus tuning the cavity photon mode towards higher energy. It can be seen that the photon mode undergoes anticrossing with the U3 excitons (whose energy is marked by the dashed line). We identify the two polariton branches (the lower polariton branch – LPB and the upper polariton branch – UPB) in the figure. Here, resonance between the exciton and photon occurs at a position corresponding to 800 μm (marked by a thicker line in Fig. 5b). At this point the polariton branches have a similar transmission. In Fig. 5c, we compare the emission intensities from the polariton branches under non-resonant excitation (632.8 nm at normal incidence). Here, the photoluminescence was collected at a fixed angle of 35° from the cavity and is plotted together with the corresponding transmission spectra for three cases: at small negative detuning (position corresponding to resonance −200 μm), at exciton–photon resonance, and at large positive detuning (position corresponding to resonance +400 μm). In all three cases, only the emission from the LPB could be detected, with

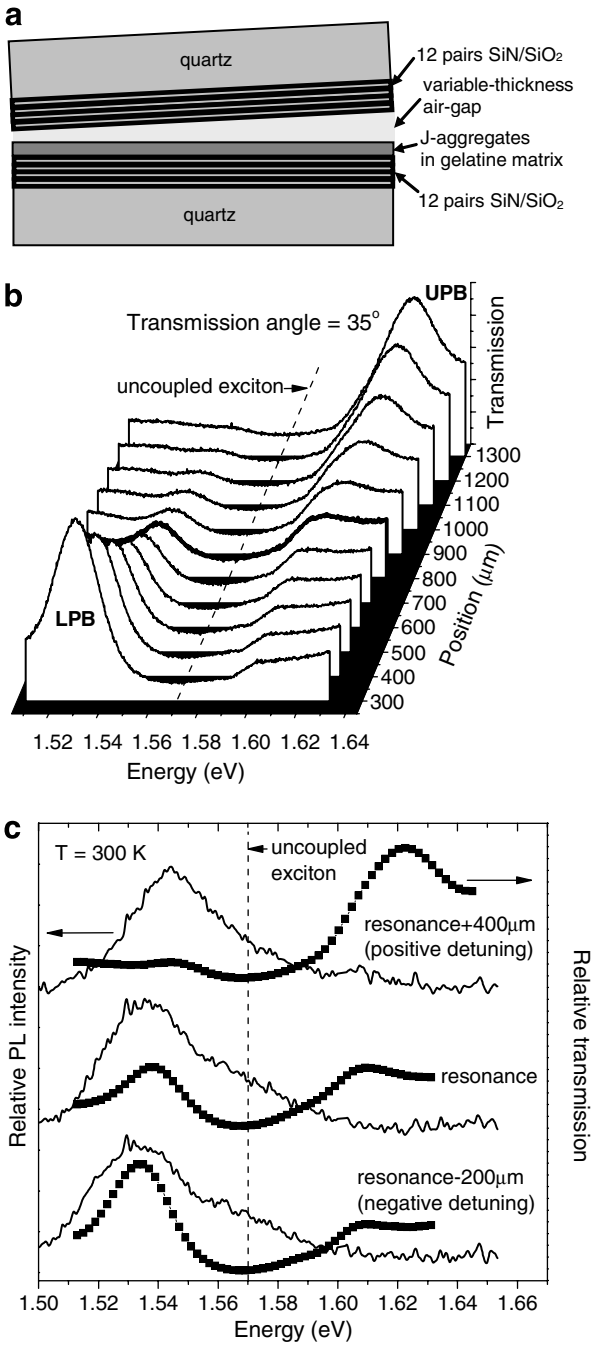


Fig. 5. (a) Schematic structure of the wedge-shaped organic-microcavity. (b) Position-resolved transmission spectra measured at a constant angle of 35° from a laminated organic microcavity containing J-aggregates of the near-infrared cyanine dye U3. The spectrum corresponding to exciton–photon resonance is marked using a thicker line. (c) Photoluminescence (plotted using solid lines) and corresponding transmission (plotted using solid squares) at small negative detuning (bottom curves), at resonance (middle curves) and at large positive detuning (top curves). The plots are shifted vertically for clarity.

a weak emission from the uncoupled excitons being visible at resonance and for negative detunings. This indicates that not all of the excitons are strongly coupled to the optical field; an observation in accordance with other reports on cavities containing J-aggregates of cyanine dyes [15,22]. The strong asymmetry between the UPB and LPB emission intensity has also been observed in other studies of organic microcavities and has been attributed to fast inter-branch population transfer [22].

Anti-crossing is also apparent in the dispersion curves (plotted in Fig. 6) which were constructed from the transmission spectra shown in Fig. 5b. Here it can be seen that the energy separation between the polariton branches at resonance (corresponding to the Rabi splitting energy – $\hbar\Omega$) is equal to 68 meV. It is worth noting that at resonance the polariton branches are not equally separated about the exciton energy (indicated using a dashed horizontal line in Fig. 6). We attribute this behavior to the asymmetry in the absorption line-shape of the J-aggregate excitons [23].

We have performed numerical modeling of our microcavity structure using a transfer matrix reflectivity (TMR) model and compare the results with the experimental data in Fig. 6. Here the solid lines are the theoretical fit to the measured transmission data, which are plotted using square points. The dashed lines predict the dispersion of the uncoupled exciton (X) and photon (P) modes that cross at the point of resonance between the UPB and the LPB. There is a good general agreement between the experimental data and the model, which accurately reproduces the shapes and positions of the polariton branches. We note however, that our model significantly overestimates the Q-factor of the cavity. The value of Q taken directly from measurements is ~60 whilst the TMR model indicates that it should be as high as 300 (assuming negligible optical losses). It is likely that this discrepancy results from the wedged cavity shape as there is a variation in the cavity thickness contained within the measurement area. We estimate the diameter of the white light spot used in the transmission measurements to be about 250 μm, corresponding to a cavity thickness change of almost 13 nm. If we take this broadening mechanism into account, we find that the effective Q-factor of our structure is ~150, indicating that there are optical losses within the cavity that presumably result from scattering.

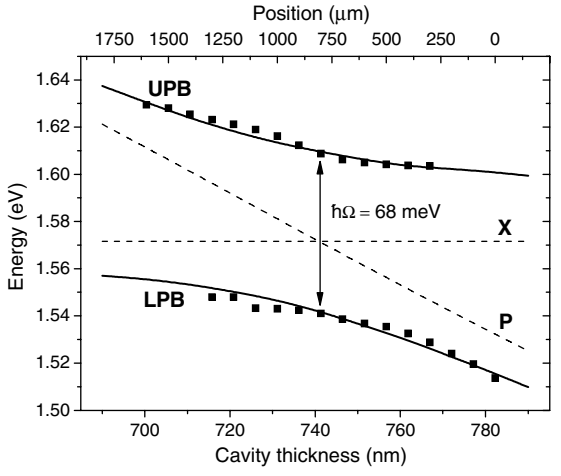


Fig. 6. The energy of the cavity polariton modes as a function of the cavity thickness (bottom axis) and the measurement location (top axis). The points in the figure are the experimentally measured data and the solid lines were calculated using a TMR model. The dashed lines show the energy of the uncoupled exciton (X) and cavity photon (P) modes.

5. Summary

In conclusion, we have demonstrated strong coupling in organic laminated microcavities in the near-infrared spectral range. The structures contained J-aggregates of a new cyanine dye that absorbed and emitted light at about 790 nm. As far as we are aware, this is the lowest energy of organic exciton yet reported to undergo strong coupling in an optical cavity. We believe that this material is very promising for applications in hybrid organic–inorganic heterostructures, as it can be matched to quantum structures fabricated using GaAs/InGaAs/AlGaAs inorganic semiconductor technology. Moreover, the material exhibits a high photostability, especially under vacuum and at low temperatures.

Acknowledgements

The work was financed by the European Commission via the 5th Framework research training network 'HYTEC' (The physics of hybrid organic–inorganic heterostructures for photonics and telecommunications) contract number: HPRN-CT-2002-00315.

References

[1] C. Weisbuch, M. Nishioka, A. Ishikawa, Y. Arakawa, Phys. Rev. Lett. 69 (1992) 3314–3317.

[2] P. Kelkar, V. Kozlov, H. Jeon, A.V. Nurmikko, C.-C. Chu, D.C. Grillo, J. Han, C.G. Hua, R.L. Gunshor, Phys. Rev. B 52 (1995) R5491–R5494.
[3] M.S. Skolnick, T.A. Fisher, D.M. Whittaker, Semicond. Sci. Technol. 13 (1998) 645–669.
[4] A. Pawlis, A. Khartchenko, O. Husberg, D.J. As, K. Lischka, D. Schikora, J. Microelectron. 34 (2003) 439–442.
[5] F. Semond, I. Sellers, F. Natali, D. Byrne, M. Leroux, J. Massies, N. Ollier, J. Leymarie, P. Disseix, A. Vasson, Appl. Phys. Lett. 87 (2005) 021102.
[6] D.G. Lidzey, D.D.C. Bradley, M.S. Skolnick, T. Virgili, S. Walker, D.M. Whittaker, Nature 395 (1998) 53–55.
[7] D.G. Lidzey, T. Virgili, D.D.C. Bradley, M.S. Skolnick, S. Walker, D.M. Whittaker, Opt. Mater. 12 (1999) 243–247.
[8] P.A. Hobson, W.L. Barnes, D.G. Lidzey, G.A. Gehring, D.M. Whittaker, M.S. Skolnick, S. Walker, Appl. Phys. Lett. 81 (2002) 3519–3521.
[9] L.G. Connolly, D.G. Lidzey, R. Butte, A.M. Adawi, D.M. Whittaker, M.S. Skolnick, R. Airey, Appl. Phys. Lett. 83 (2003) 5377–5379.
[10] V.M. Agranovich, G.C. La Rocca, F. Bassani, H. Benisty, C. Weisbuch, Opt. Mater. 9 (1998) 430–436.
[11] H. Abassi, S. Jaziri, R. Bennaceur, Physica E 7 (2000) 686–692.
[12] D.G. Lidzey, J. Wenus, D.M. Whittaker, G. Itskos, P.N. Stavrinou, D.D.C. Bradley, R. Murray, J. Lumin. 110 (2004) 347–353.
[13] T. Tani, in: T. Kobayashi (Ed.), J-aggregates, World Scientific Publishing, Singapore, 1996 (Chapter.9).
[14] V.I. Avdeeva, B.I. Shapiro, Dokl. Phys. Chem. 389 (2003) 77–79.
[15] J. Wenus, L.G. Connolly, D.G. Lidzey, Phys. Status Solid c 2 (2005) 3899–3902.
[16] D.G. Lidzey, D.D.C. Bradley, A. Armitage, S. Walker, M.S. Skolnick, Science 288 (2000) 1620–1623.
[17] H. von Berlepsch, T.C. Böttcher, A. Ouart, C. Burger, S. Dähne, S. Kirstein, J. Phys. Chem. B 104 (2000) 5255–5262.
[18] I.A. Struganova, H. Lim, S.A. Morgan, J. Phys. Chem. B 106 (2002) 11047–11050.
[19] J.L. Slominskii, N.N. Romanov, Z.N. Stezenko, A.I. Tolmachev, Zh. Org. Chem. (Russ.) 15 (1979) 865–868.
[20] ^{1}H NMR spectrum for the dye U3 was recorded on a "Brooker" 300 Hz spectrometer with the following results: %: C, 53.12; H, 5.70; Cl, 8.33; S, 15.18. Calculated, %: C, 53.43; H, 5.94; Cl, 8.53; S, 15.43. ^{1}H NMR in DMSO-d_6, δ, ppm: 1.10 (s, 6H, CH_3), 1.18 (t, $J = 7.1$ Hz, 9H, CH_3), 2.03–2.10 (m, 4H, CH_2), 2.24 (s, 3H, CH_3-meso), 2.63 (t, $J = 6.75$ Hz, 4H, $CH_2SO_3^-$), 2.69 (s, 4H, CH_2), 3.06–3.15 (m, 6H, CH_2N), 4.61 (t, $J = 6.60$ Hz, 4H, CH_2N), 6.63 (s, 2H, CH), 7.38 (d, $J = 8.40$ Hz, 2H, ArH), 7.98 (d, $J = 8.70$ Hz, 2H, ArH), 8.02 (s, 2H, ArH).
[21] J. Wenus, L.G. Connolly, D.M. Whittaker, Maurice S. Skolnick, D.G. Lidzey, Appl. Phys. Lett. 85 (2004) 5848–5850.
[22] D.G. Lidzey, A.M. Fox, M.D. Rahn, M.S. Skolnick, V.M. Agranovich, S. Walker, Phys. Rev. B 65 (2002) 195312.
[23] A. Armitage, D.G. Lidzey, D.D.C. Bradley, T. Virgili, M.S. Skolnick, S. Walker, Synt. Met. 111–112 (2000) 377–379.

Available online at www.sciencedirect.com
ScienceDirect
Organic Electronics 8 (2007) 127–135
Organic Electronics
www.elsevier.com/locate/orgel

Polarization mixing in hybrid organic–inorganic microcavities

Hashem Zoubi *, G.C. La Rocca

Scuola Normale Superiore and CNISM, Piazza dei Cavalieri 7, 56126 Pisa, Italy

Received 1 February 2006; received in revised form 8 September 2006; accepted 9 September 2006
Available online 4 October 2006

Abstract

We use a microscopic theory to study hybrid organic–inorganic microcavities in the strong coupling regime. The optically resonant materials are an anisotropic crystalline organic mono-layer and a semiconductor quantum-well, which are coupled only via the cavity photons. The cavity eigenmodes are the hybrid Frenkel–Wannier–Mott exciton-polaritons. Using the quasi-mode approach, we calculate the hybrid cavity linear optical spectra, i.e. the transmission, reflection, and absorption spectra. In hybrid microcavities the anisotropic organic materials induce a mixing between the TE and TM cavity photon polarizations, and a mixing between the transverse and longitudinal heavy-hole (HH) Wannier–Mott excitons, which is in contrast to the case of ordinary semiconductor microcavities.
© 2006 Elsevier B.V. All rights reserved.

PACS: 71.35.–y; 71.36.+c

Keywords: Hybrid organic–inorganic microcavities; Frenkel excitons; Wannier–Mott excitons; Hybrid cavity polaritons; Polarization mixing; Linear optical spectra

1. Introduction

Recently much progress has been achieved in the fabrication of organic and inorganic microcavities [1]. In the strong coupling regime, the coherent coupling between the cavity photons and the excitons produces the cavity polaritons. The polariton dispersion relation splits into two branches which are separated by the Rabi splitting energy. Much studies, both theoretical and experimental, have been devoted to polaritons in inorganic semiconductor microcavities [2], where in typical quantum-well microcavities the coupling between the Wannier–Mott excitons and the cavity photons yields Rabi splitting values of the order of 10 meV [3]. The main motivation to use organic microcavities is the large oscillator strength of the organic materials. The strong coupling between the Frenkel excitons in organic materials and the cavity photons results in a Rabi splitting which is easily an order of magnitude larger than that of inorganic microcavities [4]. In particular, a strong coupling regime has been observed in an organic microcavity containing disordered J-aggregate molecules of cyanine dye, where the room temperature Rabi splitting is between 80 meV and 300 meV [5]. The recent progress in growing ultrathin organic films, including organic thin-layer crystals, makes the case of microcavities with crystalline organic media of great interest [6]. Furthermore,

* Corresponding author.
E-mail address: zoubi@sns.it (H. Zoubi).

1566-1199/$ - see front matter © 2006 Elsevier B.V. All rights reserved.
doi:10.1016/j.orgel.2006.09.001

organic heterostructures have been grown, as a system of two molecular J-aggregates of cyanine dye mono-layers, which are spatially separated in a microcavity [7], where three cavity polaritons are observed, which are obtained from the mixing of the two Frenkel excitons and the cavity photons.

Crystalline organic microcavities have been investigated by Litinskaia et al. [8] in the framework of the macroscopic approach based on the use of the dielectric tensor, while Balagurov and one of us [9] have calculated the linear optical spectra of such system using a phenomenological uniaxial dielectric tensor and a (4×4) transfer matrix formalism. In our previous paper [10], we have developed a microscopic theory for Frenkel–exciton-polaritons in organic microcavities in the strong coupling regime. Also, in the paper [11] we studied two anisotropic crystalline organic slabs inside a microcavity.

New concepts of hybrid organic–inorganic heterostructures have been suggested by Agranovich et al. [4,12]. They showed that the incorporation of organic and inorganic materials in a microcavity, in the strong coupling regime, results in hybrid Frenkel–Wannier–Mott exciton-polaritons, as the Frenkel excitons in the organic materials and the Wannier–Mott excitons in the inorganic materials are close to resonance to each other and to the cavity photons. In the present paper we study hybrid organic–inorganic microcavities in the linear regime by developing a microscopic theory. The optically resonant materials are an anisotropic organic crystalline mono-layer and a semiconductor quantum-well. No direct interaction exists between the two materials, and they couple only via the cavity photons. In using a microscopic theory, we derive the hybrid polariton dispersion relations and quantum states. Furthermore, we obtain the linear optical spectra of the hybrid organic–inorganic microcavity in applying the quasi-mode approximation, as the cavity is weakly coupled to the external world, and the exciton non-radiative damping in the organic and inorganic materials are included phenomenologically. We emphasize the mixing between the two cavity photon polarizations and the hybridization between the Frenkel and Wannier–Mott excitons, with the mixing between the transverse and longitudinal HH Wannier–Mott excitons.

The paper is organized as follows. In Section 2 the hybrid cavity polaritons are introduced. The linear optical spectra of hybrid microcavities are calculated in Section 3. Conclusions are presented in Section 4.

2. The hybrid Frenkel–Wannier–Mott cavity exciton polaritons

We consider a hybrid organic–inorganic microcavity. The optically resonant materials are an anisotropic organic crystalline mono-layer and a semiconductor quantum-well, which are parallel to each other and parallel to the cavity mirrors. The mono-layer and the quantum-well are located in the center of the cavity, around $z\approx0$, and are separated by a distance L_0, which is smaller than the distance between the cavity mirrors L, namely $L_0\ll L$, see Fig. 1. Moreover, L_0 could easily be large enough to neglect the direct electrostatic interactions between the organic mono-layer and the inorganic quantum well, the range of which is of the order of a few nanometers [13].

First, we represent the cavity photons. The cavity is built of two parallel mirrors, one mirror is at $z=-L/2$, and the other is at $z=L/2$. The electromagnetic field is free in the cavity plane with in-plane wave vector $\mathbf{k}$, and is quantized in the perpendicular z direction, where the wave vector Z component takes the values $k_z=m\pi/L$ with $(m=1,2,3,\cdots)$. For each in-plane wave vector $\mathbf{k}$ there are two possible polarizations: TE transverse electric field which is denoted by (s), and TM transverse magnetic field which is denoted by (p). We assume only one active cavity mode, which is $(m=1)$ and plotted in Fig. 1, the one that is close to resonance with the electronic excitations in the cavity active materials. The cavity mode dispersion relation is

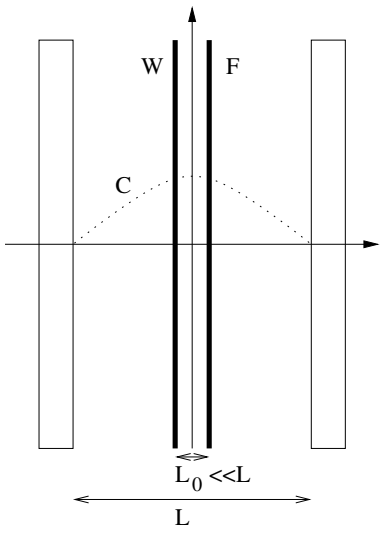


Fig. 1. The hybrid Frenkel–Wannier–Mott microcavity.

$$\omega_k^{\mathrm{C}} = \frac{c}{\sqrt{\epsilon}}\sqrt{k^2 + \left(\frac{\pi}{L}\right)^2}, \tag{1}$$

where $k = |\mathbf{k}|$, and ϵ is the cavity medium dielectric constant.

The cavity photon Hamiltonian is

$$H_{\mathrm{Cav}} = \sum\nolimits_{\mathbf{k}\lambda} \hbar\omega_k^{\mathrm{C}}\ a_{\mathbf{k}\lambda}^{\dagger} a_{\mathbf{k}\lambda}, \tag{2}$$

where $a_{\mathbf{k}\lambda}^{\dagger}$ and $a_{\mathbf{k}\lambda}$ are the creation and annihilation operators of a cavity photon with in-plane wave vector $\mathbf{k}$ and polarization λ, respectively. For the sake of simplicity, we assumed the two photon polarizations to be degenerate, which is not always the case [14].

The organic mono-layer is made of anisotropic molecular crystal with one molecule per unit cell. The Frenkel excitons in the organic crystal mono-layer are represented by the Hamiltonian

$$H_{\mathrm{Fren}} = \sum_{\mathbf{k}} \hbar\omega_{\mathbf{k}}^{\mathrm{F}}\ B_{\mathbf{k}}^{\dagger} B_{\mathbf{k}}, \tag{3}$$

where $B_{\mathbf{k}}^{\dagger}$ and $B_{\mathbf{k}}$ are the creation and annihilation operators of an exciton with in-plane wave vector $\mathbf{k}$, respectively. The exciton dispersion is

$$\omega_{\mathbf{k}}^{\mathrm{F}} = \omega_0 + J_{\mathbf{k}}, \tag{4}$$

where $\hbar\omega_0$ is the excitation energy of a molecule in the mono-layer crystal, and the exciton dispersion is due to the energy transfer among the molecules in the mono-layer. In the limit of long wave lengths, that is $ka \ll 1$, the above dispersion is weak, and of the order of ka, which can be neglected [10]. Then, the interactions between the molecules in the mono-layer only result in a negative energy shift J, namely $\omega^{\mathrm{F}} \approx \omega_0 - J$. The anisotropic material cause a mixing between the two cavity photon polarizations, as will be clear later from the Frenkel exciton-cavity photon coupling.

For the semiconductor quantum-well we take a [0 0 1] grown cubic crystal, and we consider only the HH excitons. The optically active modes for the HH excitons are the (s) transverse excitons and the longitudinal (p) excitons, which are taken relative to the in-plane wave vector $\mathbf{k}$. The Wannier–Mott excitons are represented by the Hamiltonian

$$H_{\mathrm{Wan}} = \sum_{\mathbf{k}\lambda} \hbar\omega_k^{\mathrm{W}}\ C_{\mathbf{k}\lambda}^{\dagger} C_{\mathbf{k}\lambda}, \tag{5}$$

where $C_{\mathbf{k}\lambda}^{\dagger}$ and $C_{\mathbf{k}}$ are the creation and annihilation operators of a ($\lambda = s, p$) exciton with in-plane wave vector $\mathbf{k}$, respectively. The two (s) and (p) exciton energies are assumed to be degenerate neglecting the small k dependent longitudinal-transverse splitting [15]. The exciton dispersion, in the limit of long wave length, is taken to be a parabolic one, which is

$$\omega_k^{\mathrm{W}} = \omega_{\mathrm{W}} + \frac{\hbar k^2}{2m_{\mathrm{W}}}, \tag{6}$$

where m_{W} is the effective mass of the HH Wannier–Mott exciton.

The Frenkel exciton-cavity photon interaction Hamiltonian is

$$V_{\text{Fren-Cav}} = \sum_{\mathbf{k}\lambda} \hbar\left\{f_{\mathbf{k}\lambda}^{\mathrm{F}}\ B_{\mathbf{k}}^{\dagger} a_{\mathbf{k}\lambda} + f_{\mathbf{k}\lambda}^{\mathrm{F}^*}\ a_{\mathbf{k}\lambda}^{\dagger} B_{\mathbf{k}}\right\}. \tag{7}$$

The Frenkel exciton is coupled to the two cavity photon polarizations with the coupling parameter $f_{\mathbf{k}\lambda}^{\mathrm{F}}$. Such a coupling result in a polarization mixing, as we will discuss later. The coupling energy parameters [10] are

$$\begin{aligned}
\hbar f_{\mathbf{k}s}^{\mathrm{F}} &= i\sqrt{\frac{4\pi\hbar\omega_{\mathbf{k}}^{\mathrm{cav}}}{L\epsilon}\frac{\mathcal{N}}{S}}\ \mu_x \sin\phi, \\
\hbar f_{\mathbf{k}p}^{\mathrm{F}} &= \frac{\pi/L}{\sqrt{k^2 + \pi^2/L^2}}\ \sqrt{\frac{4\pi\hbar\omega_{\mathbf{k}}^{\mathrm{cav}}}{L\epsilon}\frac{\mathcal{N}}{S}}\ \mu_x \cos\phi,
\end{aligned} \tag{8}$$

where S is the cavity mirror area, $\mathcal{N}$ is the molecule number in the mono-layer, $\vec{\mu} = (\mu_x, 0, 0)$ is the molecule transition dipole moment which is taken to be in the x direction, and ϕ is the angle between the in-plane wave vector $\mathbf{k}$ and the x axis.

For the Wannier excitons, the (s) exciton is coupled to the (s) cavity photon, and the (p) exciton is coupled to the (p) cavity photon. No polarization mixing exist due to the inorganic materials. The Wannier–Mott exciton-cavity photon interaction Hamiltonian is

$$V_{\text{Wan-Cav}} = \sum_{\mathbf{k}\lambda} \hbar\left\{f_{\mathbf{k}\lambda}^{\mathrm{W}}\ C_{\mathbf{k}\lambda}^{\dagger} a_{\mathbf{k}\lambda} + f_{\mathbf{k}\lambda}^{\mathrm{W}^*}\ a_{\mathbf{k}\lambda}^{\dagger} C_{\mathbf{k}\lambda}\right\}, \tag{9}$$

where $f_{\mathbf{k}\lambda}^{\mathrm{W}}$ is the coupling parameters, (for details see [15]).

The total Hamiltonian reads

$$\begin{aligned}
H = \sum\nolimits_{\mathbf{k}} \hbar\Bigg\{ & \sum_{\lambda} \omega_k^{\mathrm{C}}\ a_{\mathbf{k}\lambda}^{\dagger} a_{\mathbf{k}\lambda} + \omega_k^{\mathrm{F}}\ B_{\mathbf{k}}^{\dagger} B_{\mathbf{k}} \\
& + \sum_{\lambda} \omega_k^{\mathrm{W}}\ C_{\mathbf{k}\lambda}^{\dagger} C_{\mathbf{k}\lambda} + \sum_{\lambda} \left[\left(f_{\mathbf{k}\lambda}^{\mathrm{F}}\ B_{\mathbf{k}}^{\dagger} + f_{\mathbf{k}\lambda}^{\mathrm{W}}\ C_{\mathbf{k}\lambda}^{\dagger}\right) a_{\mathbf{k}\lambda}\right. \\
& \left. + a_{\mathbf{k}\lambda}^{\dagger}\left(f_{\mathbf{k}\lambda}^{\mathrm{F}^*}\ B_{\mathbf{k}} + f_{\mathbf{k}\lambda}^{\mathrm{W}^*}\ C_{\mathbf{k}\lambda}\right)\right] \Bigg\}.
\end{aligned} \tag{10}$$

The coupling is between Frenkel exciton, Wannier–Mott exciton, and cavity photon, which are with the same in-plane wave vector.

The above Hamiltonian is diagonalized to give the polariton Hamiltonian

$$H_{\rm pol} = \sum_{\mathbf{k}} \hbar\Omega_k^r \; A_{\mathbf{k}}^{r\dagger} A_{\mathbf{k}}^r, \tag{11}$$

where the polariton is a coherent superposition of the Frenkel exciton, the transverse and longitudinal Wannier–Mott excitons, and cavity photons of both polarizations. The polariton operator is defined by

$$A_{\mathbf{k}}^r = \sum_{\lambda} X_{\mathbf{k}\lambda}^r \; a_{\mathbf{k}\lambda} + Y_{\mathbf{k}}^r \; B_{\mathbf{k}} + \sum_{\lambda} Z_{\mathbf{k}\lambda}^r \; C_{\mathbf{k}\lambda}. \tag{12}$$

The polariton eigenmodes Ω_k^r and eigenstates $(X_{\mathbf{k}\lambda}^r, Y_{\mathbf{k}}^r, Z_{\mathbf{k}\lambda}^r)$, are the solutions of the matrix equation

$$\begin{pmatrix} \omega_k^{\rm C} - \Omega_k^r & 0 & f_{\mathbf{k}s}^{\rm F} & f_{\mathbf{k}s}^{\rm W} & 0 \\ 0 & \omega_k^{\rm C} - \Omega_k^r & f_{\mathbf{k}p}^{\rm F} & 0 & f_{\mathbf{k}p}^{\rm W} \\ f_{\mathbf{k}s}^{\rm F^*} & f_{\mathbf{k}p}^{\rm F^*} & \omega_k^{\rm F} - \Omega_k^r & 0 & 0 \\ f_{\mathbf{k}s}^{\rm W^*} & 0 & 0 & \omega_k^{\rm W} - \Omega_k^r & 0 \\ 0 & f_{\mathbf{k}p}^{\rm W^*} & 0 & 0 & \omega_k^{\rm W} - \Omega_k^r \end{pmatrix} \times \begin{pmatrix} X_{\mathbf{k}s}^r \\ X_{\mathbf{k}p}^r \\ Y_{\mathbf{k}}^r \\ Z_{\mathbf{k}s}^r \\ Z_{\mathbf{k}p}^r \end{pmatrix} = \mathbf{0}. \tag{13}$$

We get five polariton branches, which are denoted by ($r = 1, 2, 3, 4, 5$).

It is clear that the hybridization is strongly related to the energy difference between the Frenkel and Wannier–Mott excitons, and also on the cavity photon and the excitons detuning energy around zero in-plane wave vector. Strong hybridization will appear around the cavity photon and exciton dispersion intersection points, and it will be very sensitive to the Frenkel excitons and the Wannier–Mott excitons coupling strength with the cavity photons.

For illustration, we numerically calculate the hybrid polariton eigenenergies and eigenstates. We use the following typical numbers for organic and inorganic cavities. For long wave lengths, the Frenkel exciton energy is $\hbar\omega^{\rm F} = 2.1$ eV, and the degenerate transverse and longitudinal Wannier–Mott exciton energy is $\hbar\omega^{\rm W} = 2$ eV, with a weak dependence on k that we neglected. We have a rather large detuning between the two excitons of $\hbar\omega^{\rm F} - \hbar\omega^{\rm W} = 0.1$ eV. For the cavity, the medium dielectric constant is $\epsilon = 4$, and the distance between the mirrors is $L \approx 1500$ Å. Here, the detuning between the cavity photon and the Frenkel exciton at zero in-plane wave vector is close to zero. For the organic and inorganic materials the numbers are chosen in such a way to give the following coupling parameters. The (s) cavity photon and Frenkel exciton coupling parameter is $\hbar f_s^{\rm F} = 0.1$ eV, and the (p) cavity photon and Frenkel exciton coupling parameter is $\hbar f_p^{\rm F} = 0.12$ eV. The (s) cavity photon and the (s) Wannier–Mott exciton coupling parameter is $\hbar f_s^{\rm W} = 0.03$ eV, and the (p) cavity photon and the (p) Wannier–Mott exciton coupling parameter is $\hbar f_p^{\rm W} = 0.05$ eV. In all the coupling parameters, for the long wave length limit, we neglected the weak dependence on the in-plane wave vector.

The five polariton branches are plotted in Fig. 2. It is seen that at large in-plane wave vectors branches (1) and (2) tend to the Wannier–Mott exciton, branch (3) tends to the Frenkel exciton, and the two upper branches tend to states including the cavity photons of both polarizations, in particular the fourth branch is really decouple from the Frenkel exciton. The latter case is similar to that of an anisotropic organic cavity [8,10], where one polariton branch is the specific coherent superposition of both cavity photon polarizations, which does not couple to the Frenkel exciton. To see the hybridization between the Frenkel and the Wannier–Mott excitons in each polariton branch and the cavity photon polarization mixing, we plot the exciton

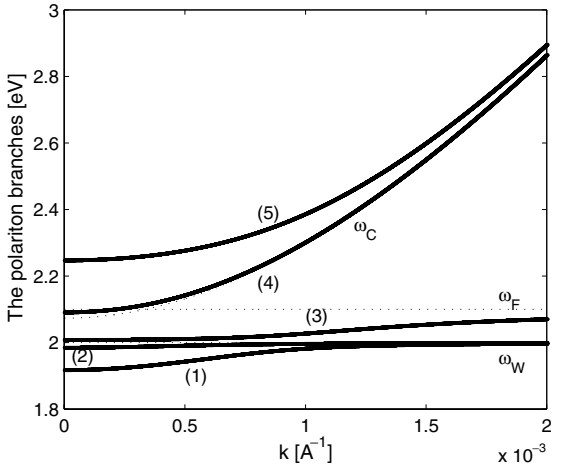


Fig. 2. The five polariton branch energies vs. in-plane wave vector.

and photon weights in each polariton branch. For each (r) branch we plot the (s) cavity photon weight $|X_s^r|^2$, the (p) cavity photon weight $|X_p^r|^2$, the Frenkel exciton weight $|Y^r|^2$, the transverse Wannier–Mott exciton weight $|Z_s^r|^2$, and the longitudinal Wannier–Mott exciton weight $|Z_p^r|^2$. In Fig. 3, for branch (1), a strong hybridization exists at small in-plane wave vectors between the Frenkel and the (s) Wannier–Mott excitons with the (p) cavity photon. Branch (2) weights are plotted in Fig. 4, here a strong mixing exists between the (s) and (p) Wannier–Mott excitons, at small in-plane wave vectors. In Fig. 5, for branch (3), a significant hybridization exists between the Frenkel exciton and the (s) and (p) Wannier–Mott excitons with the (s) cavity photon polarization. Branch (4) weights are plotted in Fig. 6, now there is a significant mixing between the (s) and (p) cavity photon polarizations with a significant hybridization between the Frenkel exciton and the (s) and (p) Wannier–Mott excitons. In Fig. 7 the upper branch weights are plotted. Significant mixing occurs between the (s) and (p) cavity photon polarizations with the Frenkel exciton and a small hybridization with the (s) and (p) Wannier–Mott excitons.

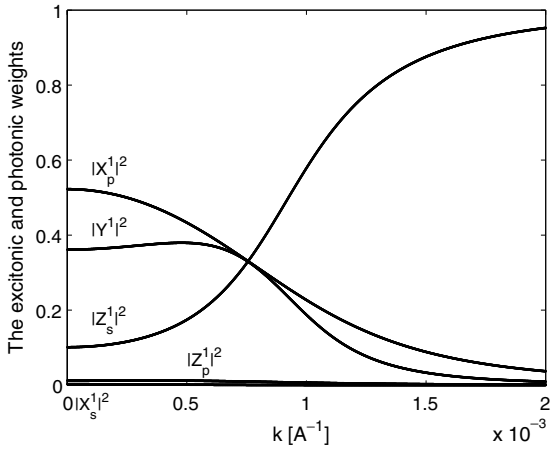


Fig. 3. The Frenkel exciton, the (s) and (p) Wannier–Mott exciton, and the (s) and (p) cavity photon weights vs. in-plane wave vector, in the first polariton branch.

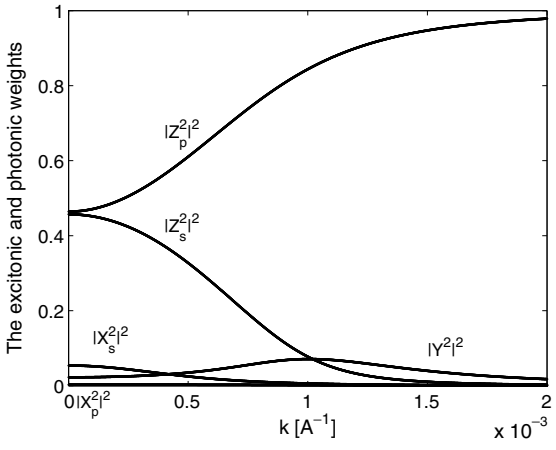


Fig. 4. The Frenkel exciton, the (s) and (p) Wannier–Mott exciton, and the (s) and (p) cavity photon weights vs. in-plane wave vector, in the second polariton branch.

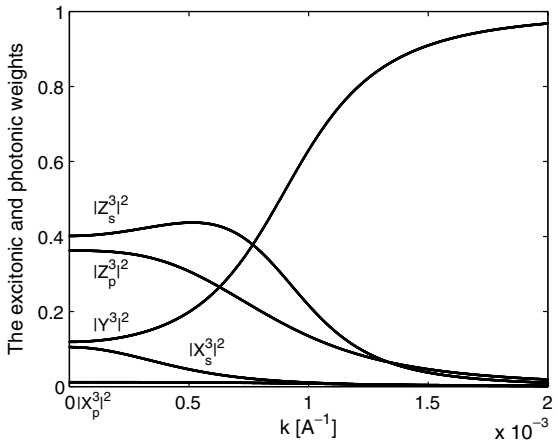


Fig. 5. The Frenkel exciton, the (s) and (p) Wannier–Mott exciton, and the (s) and (p) cavity photon weights vs. in-plane wave vector, in the third polariton branch.

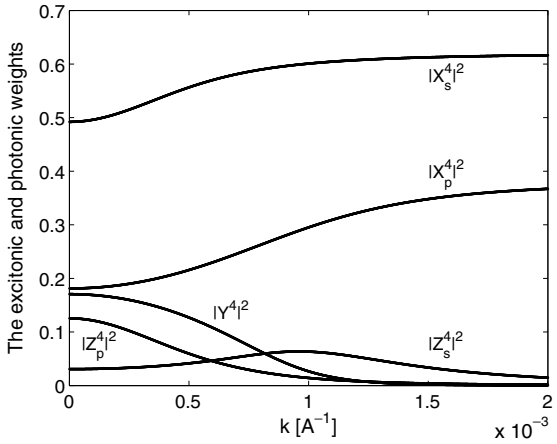


Fig. 6. The Frenkel exciton, the (s) and (p) Wannier–Mott exciton, and the (s) and (p) cavity photon weights vs. in-plane wave vector, in the fourth polariton branch.

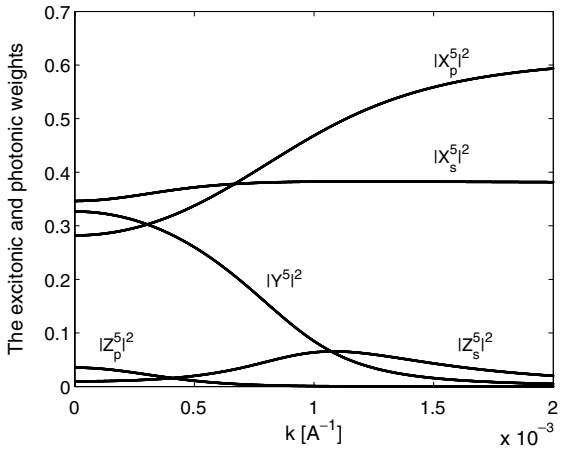


Fig. 7. The Frenkel exciton, the (*s*) and (*p*) Wannier–Mott exciton, and the (*s*) and (*p*) cavity photon weights vs. in-plane wave vector, in the fifth polariton branch.

We conclude, after numerical checking for many different cases, that in general a significant hybridization between the Frenkel and the transverse and longitudinal Wannier excitons, and (*s*) and (*p*) cavity photon polarization mixing, around small in-plane wave vectors, is obtained for systems which are close to zero detuning between the Frenkel exciton and the cavity photon at zero in-plane wave vector, namely for $(\omega_0^{\mathrm{F}} - \omega_0^{\mathrm{C}} \approx 0)$, and for the case in which the energy difference between the Frenkel and Wannier–Mott excitons is close to the Frenkel exciton and the cavity photon coupling energy, namely for $|\omega_0^{\mathrm{F}} - \omega_0^{\mathrm{W}}| \approx |f_{0\lambda}^{\mathrm{F}}|$.

3. Linear optical spectra of hybrid microcavities

To observe the system optical properties we need to couple the cavity with the external world. We do this in applying the quasi-mode approach, which is applicable for high-Q cavities [16]. In this approach the electromagnetic field is divided into two parts, the cavity photons and the external world photons, which are coupled through the cavity non-ideal mirrors. The quasi-mode formalism provides us with two results, first the cavity photon damping out of the cavity into the external radiation field, and second the possibility to include the cavity input and output fields. Furthermore, we include the cavity medium absorption phenomenologically, by taking into account the Frenkel exciton and the Wannier–Mott exciton non-radiative damping rates.

In the frame of the quasi-mode approximation we calculate the hybrid cavity linear optical spectra [10]. In the following we give the transmission, reflection, and absorption coefficients, for the case of (*s*) polarized external input field from the right side. The reflection and transmission coefficients are

$$T_s^{(s)} = \frac{\gamma^2 \left| i\Lambda_{ss} + \gamma\left(\Lambda_{sp}\Lambda_{ps} - \Lambda_{ss}\Lambda_{pp}\right)\right|^2}{|D|^2},$$

$$T_p^{(s)} = R_p^{(s)} = \frac{\gamma^2 |\Lambda_{sp}|^2}{|D|^2}\ ,\ R_s^{(s)} = \frac{\left|1 + i\gamma\Lambda_{pp}\right|^2}{|D|^2}, \tag{14}$$

where

$$|D|^2 = \left|1 - \gamma^2\Lambda_{pp}\Lambda_{ss} + \gamma^2\Lambda_{sp}\Lambda_{ps} + i\gamma\left(\Lambda_{ss} + \Lambda_{pp}\right)\right|^2, \tag{15}$$

and where γ is the cavity photon damping rate, which is related to the cavity mirror reflectivity. We defined the organic cavity matrix

$$\Lambda_{\lambda\mu} = \sum_r \frac{X_\lambda^r X_\mu^{r^*}}{(\omega - \Omega_r + i\Gamma^r)}. \tag{16}$$

The absorption coefficient, A, is obtained from the relation

$$T_s^{(s)} + T_p^{(s)} + R_s^{(s)} + R_p^{(s)} + A^{(s)} = 1. \tag{17}$$

All the results are given for a fixed value of the in-plane wave vector, and with a fixed angles between the in-plane wave vector and the organic and inorganic transition dipole moments, where we dropped k. In the above, Γ^r is the polariton damping rate of branch r, which is given by

$$\Gamma^r = \Gamma_{\mathrm{F}}|Y^r|^2 + \Gamma_{\mathrm{W}}\sum_\lambda |Z_\lambda^r|^2, \tag{18}$$

where Γ_{F} is the Frenkel exciton damping rate in the organic mono-layer, and Γ_{W} is the Wannier–Mott exciton damping rate in the inorganic semiconductor quantum-well which is taken to be equal for the transverse and the longitudinal excitons.

To get the linear optical spectra, beside the results of the previous section, we use the following damping rates: $\hbar\gamma = 0.01$ eV, $\hbar\Gamma_{\mathrm{F}} = 0.01$ eV, and $\hbar\Gamma_{\mathrm{W}} = 0.002$ eV. We choose the in-plane wave vector to be $k = 10^{-4}$ Å^{-1}, with angle of $\phi = \pi/4$ between **k** and the organic molecule transition dipole moment $\vec{\mu} = \mu_x\hat{x}$. Although the input field is (*s*) polarized, the anisotropic organic material gives rise also to (*p*) polarized transmitted and reflected fields. The (*p*) polarized reflection and transmission coefficients are equal, as we consider a cavity with

identical mirrors. Conceptually, the (s) polarized external field excites through the mirror the (s) polarized cavity photon, which is coupled to the anisotropic material, which in turn also excites the (p) polarized cavity photon; such internal photon is finally coupled to the (p) polarized external field through the cavity mirrors to the left and the right sides on equal footing. The (s) polarization transmission is plotted in Fig. 8, the (s) polarization reflection in Fig. 9, the (p) polarization transmission and reflection are in Fig. 10, and the absorption in Fig. 11. The five peaks in the transmission and absorption spectra, and the five dips in the reflection spectrum, correspond to the five hybrid polariton branches. Small transmission and large reflection for the lower branch is obtained for the (s) polarization, which is due the fact the lower branch include only small weight of the (s) cavity photon, as it is clear in Fig. 3. From the spectra it is seen that large transmission and small reflection is obtained for branches which include a significant weights of cavity photons, and large absorption is obtained for branches with large excitonic weights.

For the case of (p) polarized external input field from the right side, the reflection and transmission coefficients are

$$T_p^{(p)} = \frac{\gamma^2 \left| i\Lambda_{pp} + \gamma\left(\Lambda_{sp}\Lambda_{ps} - \Lambda_{ss}\Lambda_{pp}\right)\right|^2}{|D|^2},$$

$$T_s^{(p)} = R_s^{(p)} = \frac{\gamma^2 |\Lambda_{ps}|^2}{|D|^2}, \quad R_p^{(p)} = \frac{|1 + i\gamma\Lambda_{ss}|^2}{|D|^2}. \qquad (19)$$

The absorption parameter, $A^{(p)}$, is obtained from the relation

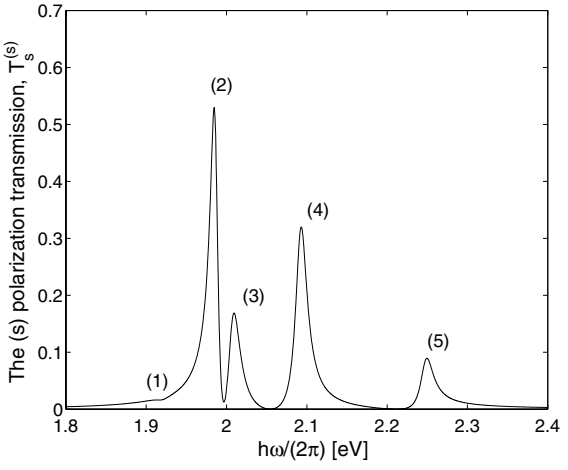


Fig. 8. The (s) polarization transmission $T_s^{(s)}$ vs. energy $\hbar\omega$.

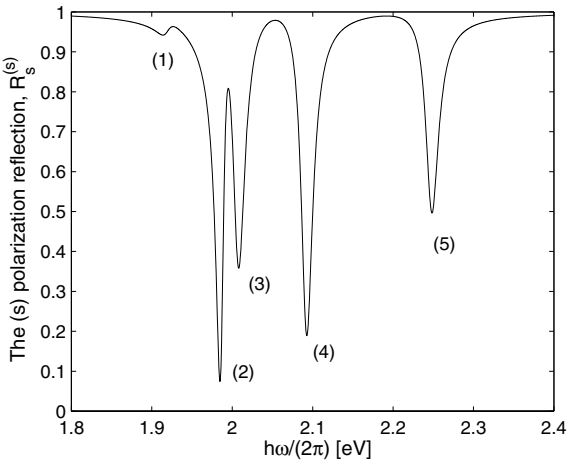


Fig. 9. The (s) polarization reflection $R_s^{(s)}$ vs. energy $\hbar\omega$.

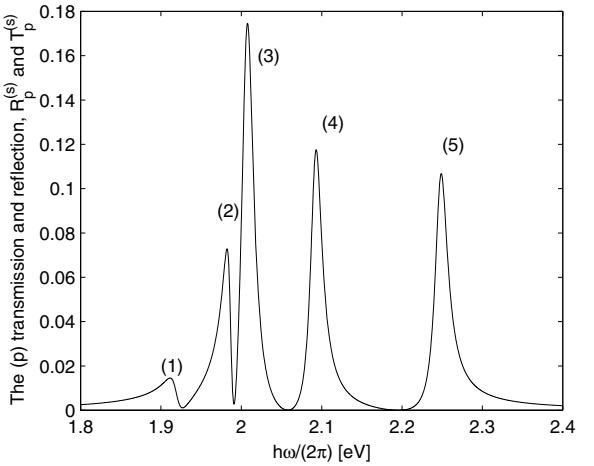


Fig. 10. The (p) polarization transmission and reflection, $T_p^{(s)}$ and $R_p^{(s)}$, vs. energy $\hbar\omega$.

$$T_s^{(p)} + T_p^{(p)} + R_s^{(p)} + R_p^{(p)} + A^{(p)} = 1. \qquad (20)$$

To get the linear optical spectra, we use the same previous numbers. Although the input field is (p) polarized, the organic material gives rise also to (s) polarized transmitted and reflected fields. The (s) polarized reflection and transmission coefficients are equal, as we consider also here a cavity with identical mirrors. The (p) polarization transmission is plotted in Fig. 12, the (p) polarization reflection in Fig. 13, and the absorption in Fig. 14. As before, the five peaks in the transmission and absorption spectra, and the five dips in the reflection spectrum, correspond to the five hybrid polariton branches. Small transmission and large reflection for the second branch is obtained for the (p)

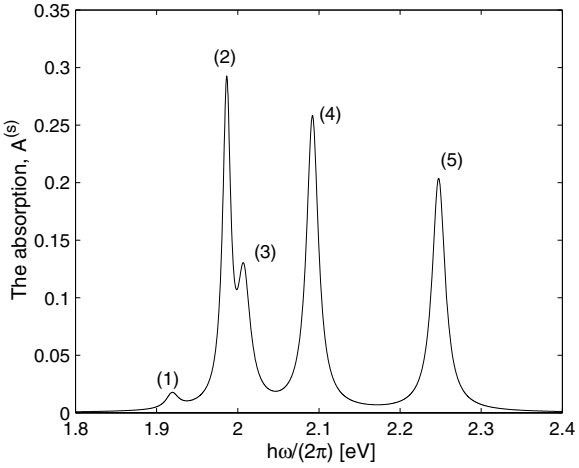


Fig. 11. The absorption $A^{(s)}$ vs. energy $\hbar\omega$.

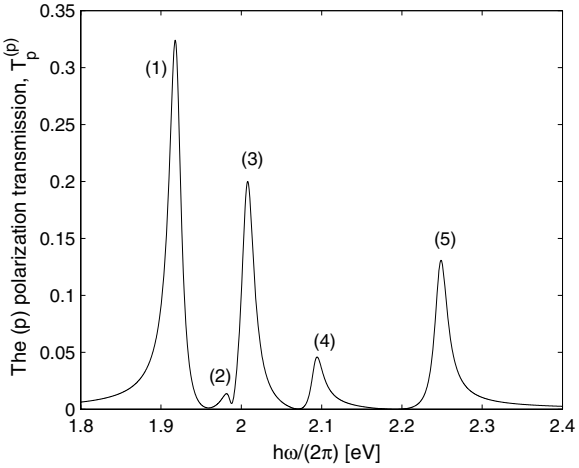


Fig. 12. The (p) polarization transmission $T_p^{(p)}$ vs. energy $\hbar\omega$.

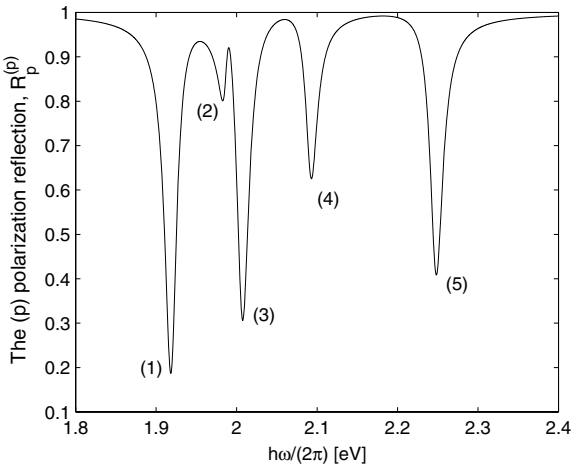


Fig. 13. The (p) polarization reflection $R_p^{(p)}$ vs. energy $\hbar\omega$.

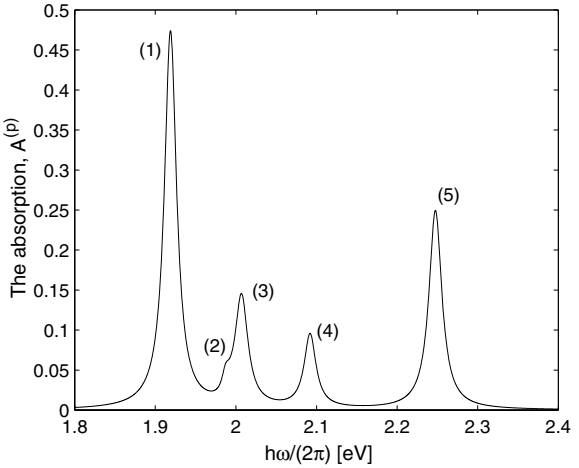


Fig. 14. The absorption $A^{(p)}$ vs. energy $\hbar\omega$.

polarization, which is due the fact the the lower branch include only small weight of the (p) cavity photon, as it is clear in Fig. 4. The second absorption peak is not clearly resolved due to the Frenkel exciton line width. Finally, as it is clear from Eqs. (14,19) the (p) polarization transmission and reflection in the case of (s) polarized incident field are identical to the (s) polarization transmission and reflection in the case of (p) polarized incident field.

4. Conclusions

We have investigated hybrid organic–inorganic microcavities in the strong coupling regime, using a microscopic theory. The hybrid polariton states have been presented, and are shown to be a coherent superposition of the Frenkel excitons in the organic material, the transverse and longitudinal HH Wannier–Mott excitons in the inorganic material, and the cavity photons of both polarizations. The results have been illustrated as plots of the polariton dispersions and the excitonic and photonic weights of the polariton branches. Using the quasi-mode approach to couple the hybrid cavity with the external photons, we have calculated the linear optical response spectra of the hybrid microcavity, including the cavity medium absorption phenomenologically. The transmission, reflection, and absorption spectra have been plotted for different cases. A significant cavity photon polarization mixing is obtained, which is due to the anisotropic organic material. Such a mixing is clear from the (p) polarized reflected and transmitted fields that obtained in the case of only (s) polarized incident

field, and vice versa. Also a significant hybridization between the Frenkel and Wannier–Mott excitons is obtained, with a mixing between the transverse and longitudinal HH Wannier–Mott excitons.

The polarization mixing here considered will be of interest also for quantum optics applications of hybrid microcavities allowing for a more flexible control of the light-matter interactions. Furthermore, the microscopic approach employed here for hybrid microcavities would be the basis for extensions including disorder effects and polariton-polariton interactions, as done for organic and inorganic microcavities [17,18].

Acknowledgements

H.Z. gratefully acknowledge the support of the European Commission via the 5th Framework Research Training Network HPRN-CT-2002-00315 (HYTEC). The authors acknowledge very helpful discussions with Vladimir M. Agranovich.

References

[1] B. Deveaud, A. Quattropani, eds. Electron and Photon Confinement in Semiconductor Nanostructures, (CL course of Enrico Fermi School of Physics, Bologna, 2002). V.M. Agranovich, G.C. La Rocca eds. Organic Nanostructures: Science and Applications, (CXLIX course of Enrico Fermi School of Physics, Bologna, 2001). V.M. Agranovich, G.F. Bassani eds. Electronic Excitations in Organic Based Nanostructures, Thin Films and Nanostructures, 31 (Elsevier, San Diego, 2003).

[2] M.S. Skolnick, T.A. Fisher, D.M. Whittaker, Semicond. Sci. Technol., 13, 645 (1998). Microcavities and Photonic Bandgaps: Physics and Applications, eds. C. Weisbuch and J.G. Rarity (Kluwer, Dordrecht, 1996). Cavity Polaritons, Thin Films and Nanostructures, 32, A. Kavokin, and G. Malpuech, (Elsevier, San Diego, 2003).

[3] C. Weisbuch, M. Nishioka, A. Ishikawa, Y. Arakawa, Phys. Rev. Lett. 69 (1992) 3314.

[4] V. Agranovich, H. Benisty, C. Weisbuch, Solid State Commun. 102 (1997) 631.

[5] D.G. Lidzey, D.D.C. Bradley, M.S. Skolnik, T. Virgili, S. Walker, D.M. Whittaker, Nature 395 (1998) 53.

[6] S.R. Forrest, Chem. Rev. 97 (1997) 1793;
R.J. Holmes, S.R. Forrest, Phys. Rev. lett. 93 (2004) 186404.

[7] D.G. Lidzey, D.D.C. Bradley, A. Armitage, S. Walker, M.S. Skolnik, Science 288 (2000) 1620;
D.G. Lidzey, J. Wenus, D.M. Whittaker, J. Luminescence 110 (2004) 347.

[8] M. Litinskaya, P. Reineker, V.M. Agranovich, Phys. Stat. Sol. (a) 201 (2004) 646.

[9] D.B. Balagurov, G.C. La Rocca, Phys. Stat. Sol. (c) 1 (2004) 518.

[10] H. Zoubi, G.C. La Rocca, Phys. Rev. B 71 (2005) 235316.

[11] H. Zoubi, G.C. La Rocca, Phys. Lett. A 339 (2005) 171.

[12] V.M. Agranovich, G.C. La Rocca, F. Bassani, H. Benisty, C. Weisbuch, Opt. Mater. 9 (1998) 430.

[13] D. Basko, G.C. La Rocca, F. Bassani, V.M. Agranovich, Eur. Phys. B 8 (1999) 353.

[14] G. Panzarini, L.C. Andreani, A. Armitage, D. Baxter, M.S. Skolnick, N.V. Astratov, J.S. Roberts, Phys. Rev. B 59 (1999) 5082;
R.F. Oulton, N. Takada, J. Koe, P.N. Stavrinou, D.D.C. Bradley, Semicond. Sci. Technol. 18 (2003) S419.

[15] L.C. Andreani, Confined Electrons and Photons: New Physics and Devices, in: E. Burstein, C. Weisbuch (Eds.), Plenum Press, New York, 1995.

[16] V. Savona, C. Piermarocchi, A. Quattropani, P. Schwendimann, F. Tassone, Phase Transitions 68 (1999) 169.

[17] P. Michetti, G.C. La Rocca, Phys. Rev. B 71 (2005) 115320; V.M. Agranovich, G.C. La Rocca, Solid State Commun. 135 (2005) 544.

[18] H. Zoubi, G.C. La Rocca, Phys. Rev. B 72 (2005) 125306;
C. Ciuti, V. Savona, C. Piermarocchi, A. Quattropani, P. Schwendimann, Phys. Rev. B 58 (1998) 7926;
G. Khitrova, H.M. Gibbs, F. Jahnke, M. Kira, S.W. Koch, Rev. Mod. Phys 71 (1999) 1591.

Available online at www.sciencedirect.com
ScienceDirect
Organic Electronics 8 (2007) 136–147
Organic Electronics
www.elsevier.com/locate/orgel

Surface plasmon–polariton mediated emission of light from top-emitting organic light-emitting diode type structures

S. Wedge [a,*], A. Giannattasio [b], W.L. Barnes [a]

[a] Thin Films Photonics Group, School of Physics, Stocker Road, University of Exeter, Exeter EX4 4QL, UK
[b] Department of Materials, University of Oxford, Parks Road, Oxford OX1 3PH, UK

Received 6 February 2006; received in revised form 4 July 2006; accepted 7 July 2006
Available online 10 August 2006

Abstract

Surface plasmon–polariton (SPP) modes may act as significant loss channels in organic light-emitting diode devices. We present experimental data illustrating that by the introduction of an appropriately scaled microstructure into a device, some of this lost power may be recovered as light. It is shown that in order to maximize this SPP-mediated light emission in a top-emitting light-emitting diode (TOLED) the plasmon modes associated with the two metal surfaces of the cathode must be coupled together. Data from grating-coupled and index-coupled SPP schemes are presented, and we show that photoluminescence emission from a structure containing a microstructured thin metal film that supports coupled SPPs is at least 50 times more effective than a similar planar structure. Experimental data is also presented from a structure containing a thin metal film whose profile contains a wavelength scale microstructure on a single interface. These data suggest that such a device geometry has the potential to increase the efficiency of top-emitting organic light-emitting devices.
© 2006 Elsevier B.V. All rights reserved.

PACS: 85.60.Jb; 72.80.Le

Keywords: Surface plasmons; Organic light-emitting diodes (OLEDs); Microstructure

1. Introduction

Since it was first demonstrated that organic materials could be used to make organic light-emitting diodes (OLEDs) much work has concentrated on improving the efficiency of these devices. To this end, three main classes of organic materials have been considered for OLED fabrication; conjugated polymers, small molecules and conjugated dendrimers.

The first polymer device utilized poly(*p*-phenylene vinylene) as an emissive material and upon charge injection the resulting electroluminescence (EL) was emitted through a transparent substrate [1]. Subsequent polymer devices have implemented a number of schemes to address both the internal and external efficiency of the device. Methods of increasing internal efficiency have include the use of electron transport layers [2] to aid charge injection and phosphorescent dyes [3] to obtain light

* Corresponding author. Tel.: +44 1392 264157; fax: +44 1392 264111.
E-mail address: s.wedge@exeter.ac.uk (S. Wedge).

1566-1199/$ - see front matter © 2006 Elsevier B.V. All rights reserved.
doi:10.1016/j.orgel.2006.07.003

from otherwise non-radiative triplet states. More recently increases in the external or optical efficiency of polymer devices have been sought by the use of periodic microstructure to scatter waveguided [4] and surface plasmon–polariton (SPP) modes [5] to light.

Initial studies into the use of organic small molecules as light-emitting layers employed the material tris(8-hydroxyquinoline)aluminium (Alq_3) [6]. As with polymer based devices improvements in device efficiency of small molecule OLEDs were sought. Approaches to increase device efficiency have included the addition of low work function materials to the cathode [7], oxygen plasma treatment of the anode [8] and again the use of microstructure to recover power lost to non-radiative modes [5,9]. Small molecule based OLEDs have also been considered where emission takes place through an optically thin metallic cathode [10]. Such top-emitting OLED (TOLED) devices have the capacity to be constructed on opaque silicon substrates. These TOLED devices have two advantages over substrate emitting OLEDs. Firstly, the use of a silicon substrate allows the integration of switching elements into this layer. Secondly, in a substrate emitting OLED between 50% and 80% of the light emission may be waveguided in the organic, anode and substrate layers [11] and the use of an opaque substrate may reduce these loses. As with substrate emitters efficiency improvements have been sought via the use of charge injection layers [12,13], tuning of the thickness of the electrodes [14] and the inclusion of highly reflective anodes [15].

The latest class of materials considered for OLED applications are conjugated dendrimers [16]. Emission of light from dendrimer materials occurs via phosphorescent, as opposed to fluorescence from both polymer and small molecule emitters and thus this class of material has the potential of producing highly efficient devices [17].

Above, it was noted that power dissipated to SPP modes supported by an OLED structure might be recovered as light by the introduction into the structure of a wavelength scale periodic microstructure. Due to the constructional geometry of OLEDs, where an emissive layer is bounded by metallic electrodes the existence of SPP modes is unavoidable. It has been demonstrated that power from the emitter may be lost to SPP modes associated with both the cathode/organic and anode/organic interfaces [18]. In a planar system SPP modes are non-radiative [19] and thus SPP modes may act to limit the efficiency of an OLED device. The power dissipated to SPP modes supported at metal/dielectric interfaces within an OLED depends greatly upon the class of emitter used [20]. This variation in dissipated power is primarily because of the orientation of the dipole moment of the different types of emissive material. For materials where the dipole moment may sample all directions in space on a time scale faster than the excited state lifetime, and are thus effectively isotropic, power is seen to be strongly coupled to SPP modes [21]. This is true of both small molecule and dendrimer emitters. In contrast, the dipole moment of conjugated polymers lie predominantly in the plane of the layers [22] and are therefore less strongly coupled to by SPP modes than either small molecule or dendrimer emitters [20].

The utilization of SPP modes as means to transmit light through thin metal films has been demonstrated in a number of studies [23,24]. In the context of TOLEDs the use of SPPs to augment the emission of light is particularly attractive. Moreover, recently it has been shown that the non-radiative decay of excitons within an emissive layer via coupling to SPP modes supported by TOLEDs may provide a significant loss channel, thus restricting device efficiency [18]. However, the use of SPP modes as a means of mediating light emission from TOLED devices remains relatively little explored. For this reason we examine here a number of schemes in which SPP modes can be used to transport energy across a metal film (cathode). These SPP modes are then scattered to light, from a wavelength scale microstructure. The application of such a device geometry may be of interest commercially and offers some unexpected challenges in understanding the physics involved.

2. Theory

SPPs are trapped surface modes that occur at the interface between a metal and a dielectric and have electromagnetic fields that decay exponentially into both the surrounding media [19]. On a planar surface SPPs are non-radiative in nature, this is due to the wavevector (momentum) of the SPP along the surface, $\boldsymbol{k}_{SPP}$, being greater than that of a photon ($\boldsymbol{k}_0$) in free space of the same frequency. Therefore in a device such as an OLED, in which a metallic cathode is bounded by a dielectric emissive layer, power that is coupled to SPPs is dissipated as heat and therefore lost.

The dispersion of the SPP mode for a simple metal/dielectric interface may be found by solving Maxwell's equations [19] and is given by

$$\boldsymbol{k}_{\mathrm{SPP}} = \boldsymbol{k}_0 \sqrt{\frac{\varepsilon_{\mathrm{d}}\varepsilon_{\mathrm{m}}}{\varepsilon_{\mathrm{d}} + \varepsilon_{\mathrm{m}}}}, \tag{1}$$

where ε_{d} and ε_{m} are the frequency-dependent relative permittivities of the dielectric material and metal, respectively. The non-radiative nature of the SPP may be overcome by the introduction into a device of a wavelength scale periodic microstructure (pitch λ_{g}) [23]. Such a microstructure may act to reduce/augment the momentum (wavevector) of the SPP mode, thus allowing the SPP to Bragg scatter to light according to the relation,

$$\boldsymbol{k}_{\mathrm{SPP}} \pm n\boldsymbol{k}_{\mathrm{g}} = \boldsymbol{k}_0 \sin\theta, \tag{2}$$

where $\boldsymbol{k}_{\mathrm{g}}$ is the grating wavevector ($|\boldsymbol{k}_{\mathrm{g}}| = 2\pi/\lambda_{\mathrm{g}}$), $\boldsymbol{k}_0 \sin\theta$ is in-plane wavevector of the radiated light, θ being the polar angle of the emitted light (see Fig. 2(b)) and n is an integer that defines the order of the scattering process. Here in-plane is the component of the wavevector in the plane of incidence and parallel to the layers of the structure. However, as will be shown below, the recovery of energy dissipated to SPP modes is more complex than the simple scattering process described by Eq. (2).

Emission from a TOLED takes place through a metallic cathode that is often of order 50 nm thick. This thickness is comparable with the decay length of the optical field into the metal so that excitons within the organic emissive material may couple to SPP modes supported at both the metal/organic medium and metal/air interfaces. However, the field of the organic emitter is exponentially attenuated on crossing the metal so that significantly more power is coupled to the SPP supported at the metal/organic interface than to the SPP associated with the metal/air interface [25]. This disparity of coupling strength between SPP supported on either side of a thin metal film is illustrated in Fig. 1 where the emitter has been modelled as an electric dipole at a distance of 20 nm from a 30 nm thick silver film [25]. From Fig. 1 it may be seen that the power dissipated by the emitter to the metal/organic SPP is approximately two orders of magnitude greater than that dissipated to the metal/air SPP. Although the coupling strength between the emitter and the metal/air SPP is relatively weak we will see that the existence of this mode may allow the transfer of energy from the metal/organic interface across the metal. This transfer of energy may be facilitated by coupling together the modes on either side of the metal by means of either grating-coupled or index-coupled SPPs. Here grating-coupling is the matching of the wavevectors of the SPP modes associated with each interface of a thin metal film via a periodic microstructure. Index-coupling is the matching of the SPP wavevectors by matching of the relative permittivities of the two media bounding a thin metal film.

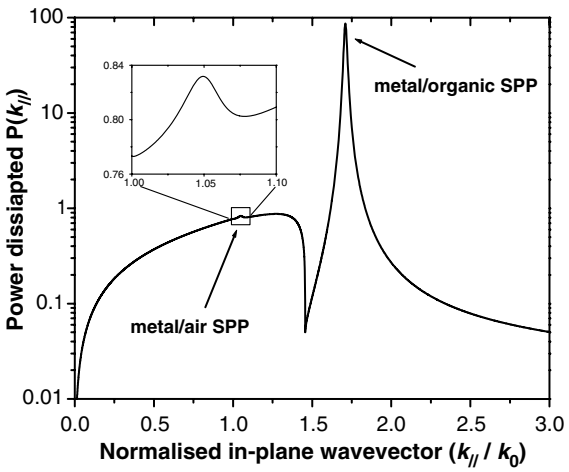


Fig. 1. Calculated power dissipation spectrum on a logarithmic scale for an emitter located in the light-emitting media at a distance of 20 nm from the surface of a 30 nm thick metal film. The large peak at a normalised in-plane wavevector of ~1.7 indicates power being lost to the metal/organic SPP, the inset is an expanded plot (linear scale) of the feature associated with the metal/air SPP.

If a metal is thin enough, of order tens of nanometres, the SPP fields associated with each interface of the metal may span the metal and overlap. Usually the metal film is bounded on either side by media with differing dielectric constants (refractive indices), i.e. an organic emitter and air, so that each of these SPP modes will have different in-plane wavevectors for a given frequency. The two SPP modes will therefore not be able to couple together. In order to couple these modes together, thus enabling energy to be transported across the metal some means must be sought to match the wavevectors of the two modes.

2.1. Grating-coupled SPPs

One method of coupling the SPP modes associated with each side of a thin metal film is SPP grating-coupling [24,26,27]. By adding an appropriately scaled periodic microstructure to the metal the wavevectors of the metal/organic SPP ($\boldsymbol{k}_{\mathrm{SPPorg}}$)

and the metal/air SPP (k_{SPPair}) may be matched when the following condition is satisfied.

$$\pm k_{SPPair} = \pm k_{SPPorg} \pm k_g \quad (3)$$

The metal/air SPP may subsequently be coupled to light, again via the microstructure by satisfying Eq. (2).

2.2. Index-coupled SPPs

Above it was noted that SPPs supported by a metal film bounded by differing refractive indices have different wavevectors. However, if the refractive indices of both bounding media are the same then the two SPP modes are degenerate and may therefore be coupled together [28]. The SPP modes supported by such a system will be coupled across all frequencies and energy may be transferred across the metal film without the need for the addition of a scattering surface. However, a microstructure is required in order to subsequently couple this plasmon energy to light. Below we explore the use of grating-coupled and index-coupled SPPs as a means of recovering energy lost to SPP modes.

3. Sample fabrication

To investigate the emission of light through a thin metal film mediated by SPP modes a number of different samples were constructed and are shown schematically in Fig. 2. Since we were interested here only in the underlying physics of the coupling of the SPP modes to light, it was sufficient to measure the SPP-mediated photoluminescence (PL) emission from an emissive layer through a thin metal film from each of these structures.

The first of these structures (Fig. 2(a)) was a planar control sample and consisted of a 60 nm thick emissive Alq_3 film deposited by thermal evaporation. The Alq_3 layer was subsequently coated with a thermally evaporated silver film (thickness 55 ± 2 nm) again by thermal evaporation under vacuum ($\sim 10^{-7}$ Torr). This structure was used as a reference sample.

The second structure (Fig. 2(b)) was used to investigate the use of a wavelength scale periodic microstructure to scatter SPP modes to light. This sample was similar in construction to the planar control structure (Fig. 2(a)) containing a 60 nm evaporated Alq_3 emissive layer and was coated with a metal film of thickness 55 ± 2 nm. However, the Ag film differed from that used in the above sample

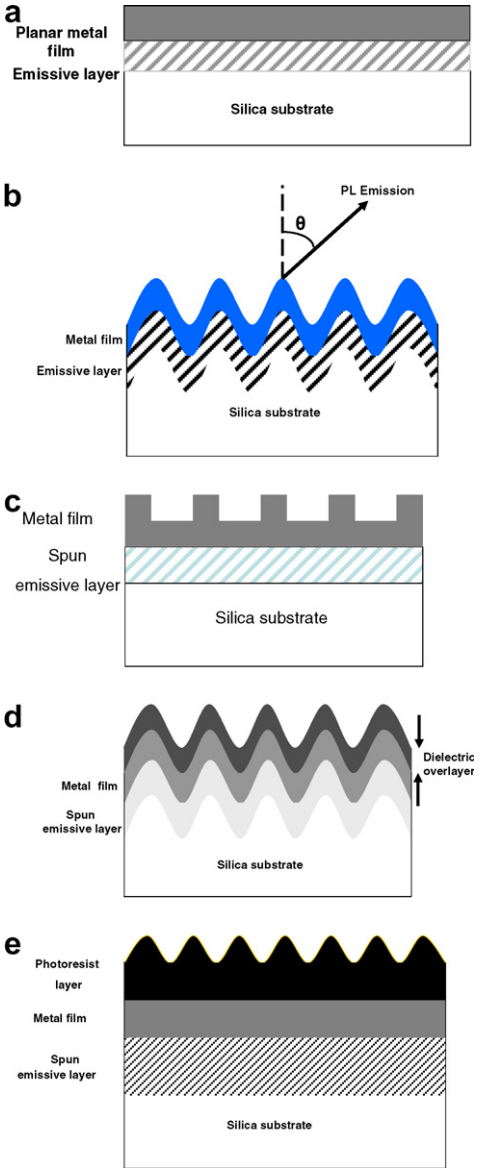


Fig. 2. Schematic representations of the experimental structures used in this study. (a) A 60 nm thick evaporated Alq_3 layer coated with a ~55 nm thick planar silver film. (b) An ~60 nm thick evaporated Alq_3 layer coated with a microstructured ($\lambda_g = 338$ nm) 55 nm thick silver film. (c) A 160 nm thick spun Alq_3 layer coated with a ~50 nm thick silver film where only the metal/air interface has been textured ($\lambda_g = 400$ nm). (d) An ~43 nm thick microstructured ($\lambda_g = 338$ nm) silver film bounded on one side by a 160 nm thick spun Alq_3 film and on the other by a dielectric overlayer (22-tric). (e) An ~55 nm thick planar silver film bounded on one side by a 160 nm spun Alq_3 layer and on the other by an ~100 nm thick microstructured ($\lambda_g = 485$ nm) photoresist overlayer.

in one important respect. The metal film included a wavelength scale microstructure ($\lambda_g = 338 \pm 1$ nm). This microstructure was produced by spin coating

the silica substrate with a ~300 nm thick photoresist (PR) (Shipley Megaposit SPR 700-1.2) film and exposing this film to an interference pattern produced using a 325 nm He–Cd laser. The pattern was chemically developed and then transferred to the silica substrate by reactive-ion etching with a mixture of CHF_3 and O_2 gases. The Alq_3 and silver layers were then in turn deposited on this corrugated substrate.

The third experimental sample (Fig. 2(c)) was constructed in order to examine the emission mediated via SPP modes which were coupled to light from a single scattering surface. The emissive Alq_3 layer differed from that used in the previous samples here being deposited by means of spin coating rather than evaporation. This was achieved by doping a solution of polymethylmethacrylate (PMMA), with Alq_3 (3% by weight) in chloroform. The PMMA/Alq_3 solution was then spin-coated onto the substrate at 4000 rpm the thickness of the resulting film found to be ~160 nm. Subsequently, a silver film of thickness (50 ± 1) nm was thermally evaporated on top of the organic layer. A periodic corrugation was then introduced at the metal/air interface using a focused ion-beam milling system (FEI Nova 600). The corrugation consisted of a grating with square profile having a pitch of 400 nm and a depth of 15 nm; the grating area covered a total of $95\mu m \times 190\ \mu m$.

The next structure studied, shown in Fig. 2(d) was used to study index-coupled SPPs. This sample contained a 43 ± 2 nm thick microstructured metal film ($\lambda_g = 338 \pm 1$ nm) constructed in an identical manner to that used in the sample shown in Fig. 2(b). As with the previous sample, the planar substrate was spin-coated with a solution of PMMA and Alq_3 (3% by weight) in chloroform. Again the thickness of this layer was ~160 nm. The refractive index of this spun emissive layer (~1.46) was less than that of the evaporated Alq_3 film (~1.7). The use of this lower refractive index emitted allowed for a greater choice of media that could be added to the metal/air interface so as to couple the SPP modes supported by the metal film together. This coupling of the SPP modes was achieved by building up layers of a dielectric material at the metal–air interface until the effective refractive indices of the two materials bounding the metal were equal. To this end, monolayers of the material, 22-tricsenoic acid (22-tric) were deposited onto the metal film using the Langmuir–Blodgett (LB) technique [29]. This technique allowed nanometer control of the thickness of the dielectric overlayer, and thus great control over the effective refractive index of the upper air half-space. By increasing the thickness of the dielectric film in this way the effective refractive index at the metal/air boundary could be varied from 1.0 (bare metal) to ~1.58 for a semi-infinite dielectric (22-tric) overlayer thickness. This approach allowed the effective refractive indices of the dielectric material (as seen by the SPP modes) bounding the metal film to be matched by the addition to the metal of a dielectric overlayer of an appropriate thickness.

The final structure studied is shown in Fig. 2(e). The structure consisted of a 55 ± 2 nm thick planar silver film bound on one side by a ~160 nm thick spun Alq_3/PMMA layer. This sample was investigated to explore the use of index-coupled SPP modes further. The other side of the Ag was spin-coated with a PR film, into this film a microstructure was introduced (period $\lambda_g = 485$ nm) using the holographic technique detailed above, the thickness of this microstructured PR film was ~100 nm. The microstructured PR film served two purposes. Firstly, the thickness of the PR film was such that it enabled the effective refractive index of this layer to be matched to the index of the emissive layer, so allowing the SPPs to couple across the metal. Secondly, the microstructure at the PR/air interface enabled the SPP modes supported by the structure to be Bragg scattered to light.

4. Results/analysis

4.1. Modes supported by the structure

Before examining the optical emission from the samples shown in Fig. 2 it was first deemed useful to determine the nature of the various optical modes supported by the structures. This was achieved by measuring the transmittance through the structures as a function of both the angle of incidence and wavelength of the light incident upon the sample. From these data an experimentally derived dispersion map was constructed by converting the collected data to transmittance as a function of both angular frequency and in-plane wavevector. Dispersion maps for TM polarised light incident upon the first two the structures (Fig. 2(a) and (b)) are shown in Fig. 3(a) and (b), respectively. From examination of Fig. 3(a) it may be seen that no modes are supported by this planar structure as the light incident upon the sample is unable to couple to any SPP

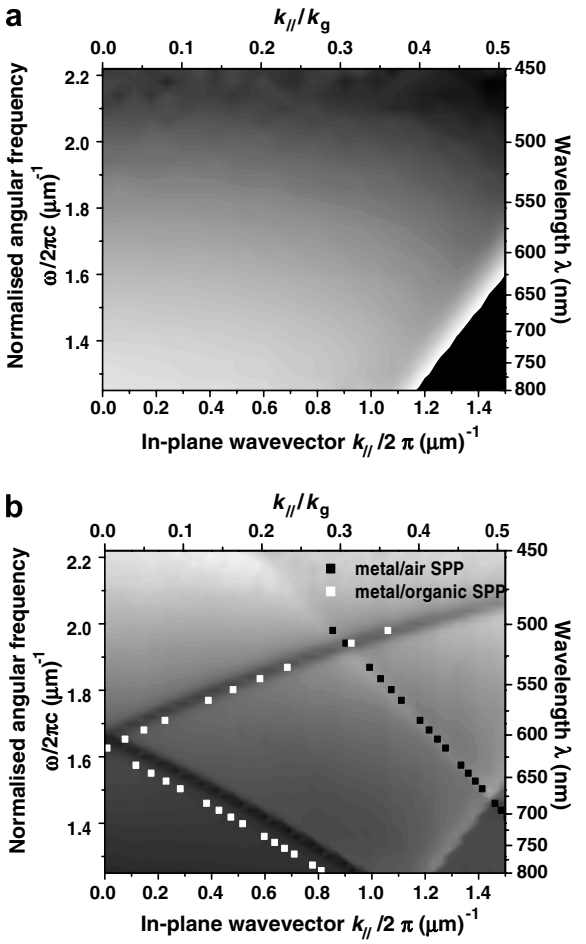


Fig. 3. Dispersion map constructed from experimentally measured transmission data from the experimental samples shown in (a) Fig. 2(a) and (b) Fig. 2(b). Light regions represent high transmission and dark regions represent low transmission. Also shown in (b) is the calculated dispersion of the metal/air (black squares) and metal/organic (white squares) SPPs.

modes due the momentum mismatch mentioned previously. In contrast, from Fig. 3(b) a number of transmission maxima/minima may be seen, these features correspond to incident light coupling to modes supported by the structure. In order to determine the nature of these mode numerical calculations where undertaken.

Using the SPP dispersion relation (Eq. (1)) the in-plane wavevectors of the SPP modes associated with each of the metal interfaces were calculated for a range of angular frequencies (from 1.25 to 2.0 μm^{-1}). The real component of the relative permittivity of silver for each of the values were taken from the literature [30], the relative permittivities of Alq_3 and air were taken to be 2.89 and unity, respectively. By adding/subtracting a grating vector ($\boldsymbol{k}_g$) where appropriate, the in-plane wavevectors of the Bragg-scattered SPPs were calculated. These calculated data are plotted in Fig. 3(b) together with the TM polarised transmittance data. From Fig. 3(b) good agreement may be seen between the calculated SPP in-plane wavevectors and the experimentally measured transmittance data. The transmittance features seen in Fig. 3(b) may therefore be identified as being the result of the TM polarised incident light coupling to SPP modes supported by each of the metal/dielectric interfaces of the structure. (It should be noted that when TE polarised light was incident upon the structure no modes were seen.) Furthermore, as the calculations presented in Fig. 3(b) depend upon the grating vector ($\boldsymbol{k}_g$), this transmission is shown to be result of the SPP modes being Bragg scattering from the microstructured metal film. Note: the discrepancy between the calculated and measured in-plane wavevectors for the metal/organic SPP at lower angular frequencies is due to a single value being used for the relative permittivity of the Alq_3 thus not taking into consideration the dispersion of the refractive index of this layer. Having identified that the samples studied supported SPP modes the structures were further examined in order to see if power coupled to these modes could be recovered as light. To this end PL measurement were taken from each of the structures shown in Fig. 2 and the SPP-mediated emission from each of these samples investigated.

4.2. Photoluminescence measurements

To measure the PL through the silver films each sample was mounted on a rotation stage and the emission measured over a range of polar emission angles θ. The emissive layer was optically pumped through the silica substrate with a 410 nm diode laser, the resulting PL being collected through a small circular aperture that limited the angular acceptance of the emission to approximately 1°. On passing through a polariser, that could be set to pass either TM or TE polarised light, the collected light was focused onto an optical fibre connected to a spectrometer and a charged coupled device (CCD) detector (resolution $\Delta\lambda = 2$ nm). In order to keep the pumping conditions constant the pump angle relative to the sample was maintained constant throughout each experiment.

PL data were measured in the form of emission intensity as a function of both polar emission angle and wavelength, and as with the previous

transmittance data, were converted into the form of a dispersion map. Fig. 4(a) shows the dispersion map constructed from the data measure from the sample shown in Fig. 2(b). The z-axis of this plot represents emission intensity with light regions corresponding to areas of strong emission. From Fig. 4(a) a number of emission maxima may be seen, by comparison with the transmittance data shown in Fig. 3(b) it may be seen that this emission is mediated via the SPP modes previously identified as being associated with each interface of the metal film. These data (Fig. 4(a)) shown that energy lost by excitons within the organic media to SPP modes may be recovered by the introduction into the sample of an appropriate wavelength scale microstructure.

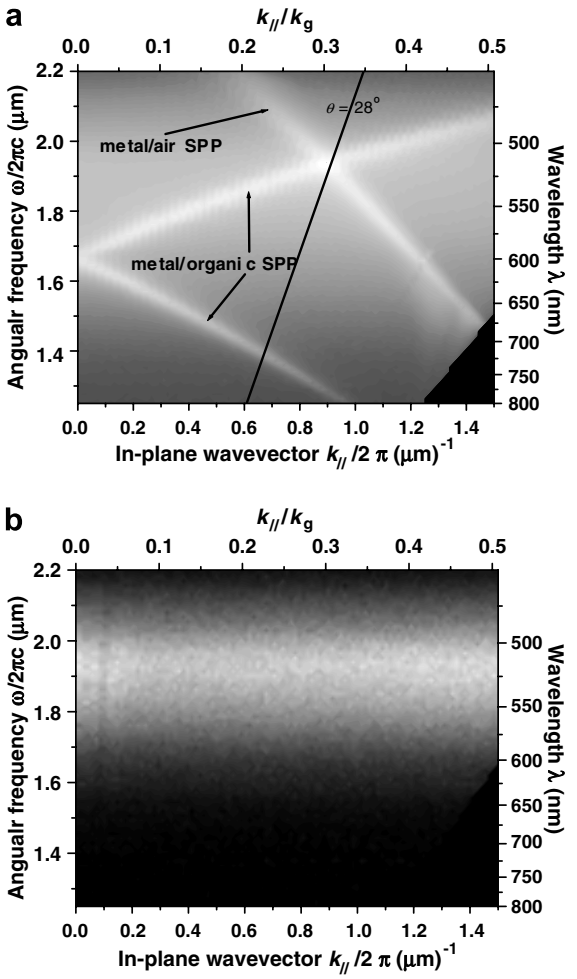


Fig. 4. Dispersion maps constructed from experimentally measured photoluminescence data from the experimental sample shown in (a) Fig. 2(b) and (b) Fig. 2(a). Light regions represent strong emission.

PL measurements were also taken from the planar control sample and these data are shown in Fig. 4(b). From Fig. 4(b) no evidence of PL mediated via SPP modes may be seen. However, the reason for this is not that the structure does not support any SPP modes. In this case the excited emitter may couple to the SPP modes associated with both the metal/organic and metal/air interfaces via the near field [21,31]. The lack of emission from these SPP modes is because the in-plane wavevector of the SPP has no means to match to the in-plane wavevector of photons in air.

To investigate the relative strength of the PL emission from both the metal/organic and metal/air SPP modes individual emission spectra from the samples with planar and microstructured metal films (Fig. 2(a) and (b)) where examined. Fig. 5 shows TM polarised PL spectra measured from the sample with a planar metal film at a polar mission angle of 28° and from microstructured sample at angles of 25°, 28° and 40°. From Fig. 5 a number of features may be seen. For each emission spectrum there is a broad feature with a peak at a wavelength of approximately 520 nm corresponding to the intrinsic emission spectrum of the Alq_3. Additionally for the data collected from the sample with the microstructured metal film a number of sharp emission peaks may be observed. These peaks may be seen to disperse with emission angle, indicative of Bragg scattered modes, they correspond to PL emission mediated via both the metal/organic and metal/air SPP.

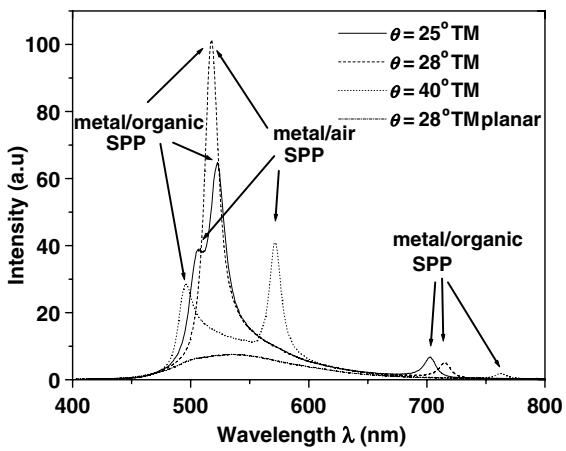


Fig. 5. TM polarised photoluminescence spectra of light emitted from the structure shown in Fig. 2(b) at a polar emission angles θ of 25°, 28° and 40° and from the structure shown in Fig. 2(a) at 28°.

Comparing the SPP-mediated PL from the microstructured sample it can be seen that the relative emission intensities of the metal/organic and metal/air SPPs are approximately equal and seem to depend only upon where the SPP emission peak sits within the Alq_3 intrinsic emission. This appears to be at odds with the data shown in Fig. 1 in which the power coupled to the metal/organic SPP was approximately 100 times greater than the power coupled to the metal/air SPP. To gain an understanding of why this disparity is not seen in the PL emission, the way in which the SPPs may outcouple to light must be considered.

Taking first the SPP mode associated with the metal/organic interface; this mode may couple to light via one of two routes. Firstly, it may be scattered by the microstructure at the metal/organic interface. The light will then be attenuated as it propagates through the metal before emerging into the far-field. Secondly, the microstructure at the metal/air boundary may scatter the mode. In this case it is the attenuated field associated with the metal/organic SPP that is scattered by the microstructure. Emission mediated via either of these two routes is attenuated to a similar degree on crossing the metal film and thus they have a similar amplitude. Recent work [32] has shown that emission via these two out-coupling routes are out of phase with each other, and thus destructively interfere. Therefore, whilst the emitter couples to this mode strongly the resulting emission appears weak.

The emission mediated via the SPP mode associated with the metal/air interface is also attenuated as the power coupled to this mode by the emitter has to cross the metal film. However, this SPP may then scatter from the metal/air interface and emit freely into the far-field. As this emission only occurs by scattering from one interface no cancellation occurs. Thus, whilst this mode is only relatively weakly coupled to by the emitter the intensity of the emission mediated via the metal/air SPP it may be seen to be comparable with that via the metal/organic SPP (Fig. 5).

From the data presented above it may be seen that the introduction into a sample of a wavelength scale microstructure may allow SPP modes to be scattered to light. However, in order to maximize this SPP-mediated emission some means must be sought to overcome the phase cancellation between the two scattering routes open to the metal/organic SPP. One means to achieve this may be to couple the modes associated with the metal/organic and metal/air SPPs together thus allowing energy to be transferred across the metal before being scattered into the far-field. To this end two coupling schemes were considered, grating coupling and index coupling. Also considered was a structure with a thin metal film that was only modulated at one interface. From such a structure SPP modes could only scatter to light from one interface and therefore the phase cancellation route above would be negated.

Fig. 6(a) shows an experimentally derived dispersion map constructed from PL emission measured from the structure shown in Fig. 2(c) [33].

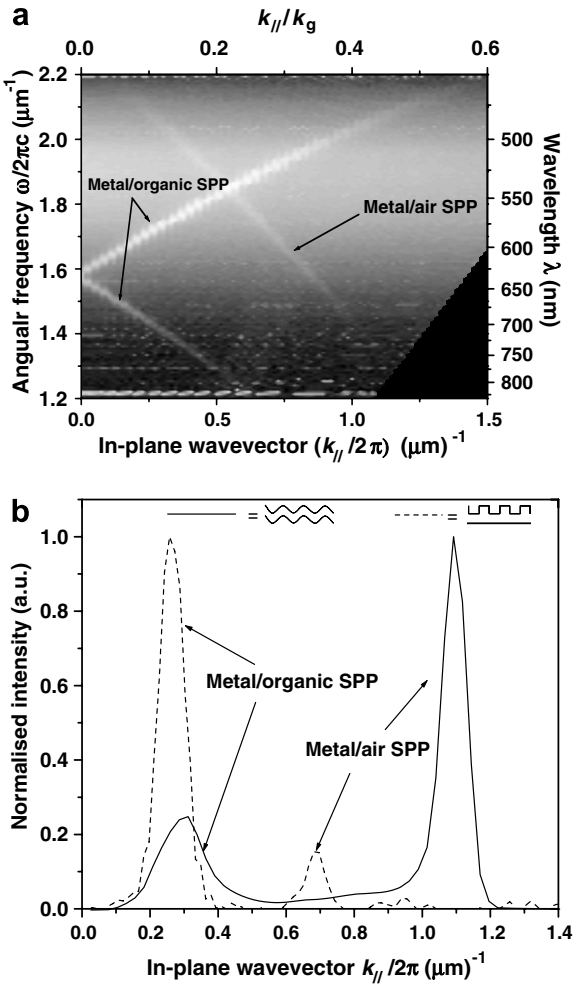


Fig. 6. (a) Dispersion map constructed from TM polarised photoluminescence data from the sample shown in Fig. 2(c) (metal is only textured on top surface the period of grating is 400 nm). (b) Normalised TM polarised photoluminescence intensity measured for two samples shown in Fig. 2(b) (solid line) and (c) (dashed line). Data represented by the solid line were taken at a wavelength of 550 nm, whereas data corresponding to the dashed line were taken at 580 nm.

Comparing these data (Fig. 6(a)) with the corresponding dispersion map constructed from the sample with a symmetrically microstructured metal film (Fig. 4(a)) it may be seen that both plots show evidence of the metal/organic and metal/air SPP modes. There is however one striking difference between the two sets of data, the relative intensity of light mediated via the two SPP modes. From Fig. 4(a) it may be seen that the intensity of the emission mediated by both the metal/organic and metal/air SPPs is very similar in intensity. In contrast the intensity of the emission mediated by the metal/organic SPP is much strong than that emitted by metal/air SPP in Fig. 6(a). This intensity difference is even more evident when the results obtained for the two samples are compared in a single graph, as shown in Fig. 6(b) [33]. These data (Fig. 6(b)) show the normalised PL intensity from each structure plotted as a function of the in-plane wavevector for a given value of angular frequency ($1.82\ \mu m^{-1}$ for the asymmetric structure shown in Fig. 2(c) and $1.72\ \mu m^{-1}$ for the symmetric sample shown in Fig. 2(b)). Fig. 6(b) shows that in the presence of an asymmetric profile of the two interfaces (dashed line) there is a significant increase in PL intensity due to radiative SPPs excited at the metal/organic boundary. These data are consistent with the ideas outlined above, namely that, by removing one of the pathways for emission of the metal/organic SPP, the possibility of destructive interference is removed, resulting in more emission associated with this mode being observed. In turn, this suggests that the efficiency of OLEDs could be increased simply by using a non-conformal geometry for the different metallic interfaces.

The first SPP coupling technique we examined was SPP grating-coupling. From inspection of the PL emission (Fig. 5) from the microstructured sample it may be seen that the maximum emission appears to occur at a wavelength of 518 nm and an emission angle (θ) of 28°. This emission corresponds to the crossing point of the metal/organic and metal/air SPPs and may be seen in Fig. 4(a) at $k_{||} = 0.88\ \mu m^{-1}$ and $\omega = 1.93\ \mu m^{-1}$. Here the wavevectors of the two SPP modes may be matched via scattering from the microstructure satisfying Eq. (3). Energy may therefore be transferred across the metal where it may then scatter to light from the corrugation at the metal/interface (Eq. (2)). However, as this cross-coupled SPP-mediated emission only occurs over a narrow range of emission angles and wavelengths such a scheme may therefore not be best suited to applications such as display devices. Below an alternative SPP coupling scheme is considered.

The second SPP coupling scheme considered was the use of index-coupled SPPs. In this study the SPP modes supported on either side of a metal film were coupled together by the addition to the metal of a dielectric overlayer, see Fig. 2(d). In total nine different dielectric overlayer thicknesses ranging from 26 nm to 198 nm were used with the intensity of the PL emission from the sample measured as a function of dielectric overlayer thickness.

Dispersion maps constructed from the TM polarised PL measured from the samples with dielectric overlayer thicknesses of 46.8 nm, 156.0 nm and 196.8 nm are shown in Fig. 7(a)–(c), respectively [34]. Comparing the position of the SPP mode associated with the metal/air interface from the PL data for the bare microstructured metal sample (Fig. 4(a)) with the same mode for a sample with a dielectric thickness of 46.8 nm (Fig. 7(a)) it may be seen that the addition of the dielectric overlayer causes this mode to shift downwards in frequency. This downshift results from an increase in the wavevector of the SPP mode, given by Eq. (1), associated with the metal/air (now metal/dielectric overlayer-air) boundary as the permittivity at this interface increases with the addition of the dielectric overlayers. This decrease in frequency is seen to continue as the dielectric film thickness is further increased to 156.0 nm (Fig. 7(b)). For dielectric overlayer thicknesses greater than 156.0 nm the position of the metal/dielectric-overlayer/air SPP was seen to remain largely unchanged in frequency (Fig. 7(c)). The observation of two SPP modes with similar frequencies (energies) is consistent with a structure supporting coupled SPP modes and is in agreement with the findings of Gruhlke et al. [27]. In order to determine if the coupling together of the SPP modes supported by the metal film was accompanied by an increase in emission intensity, the PL emission from each of the structures containing a dielectric overlayer was further examined.

For each of the dielectric overlayer thicknesses the PL emission was studied over a range of emission angles (0–40°) and wavelengths (416–806 nm). This was achieved by summing the individual PL spectra obtained at one degree intervals this summed intensity was then plotted as a function of wavelength. The area under each of these curves was then determined by integration to give a mea-

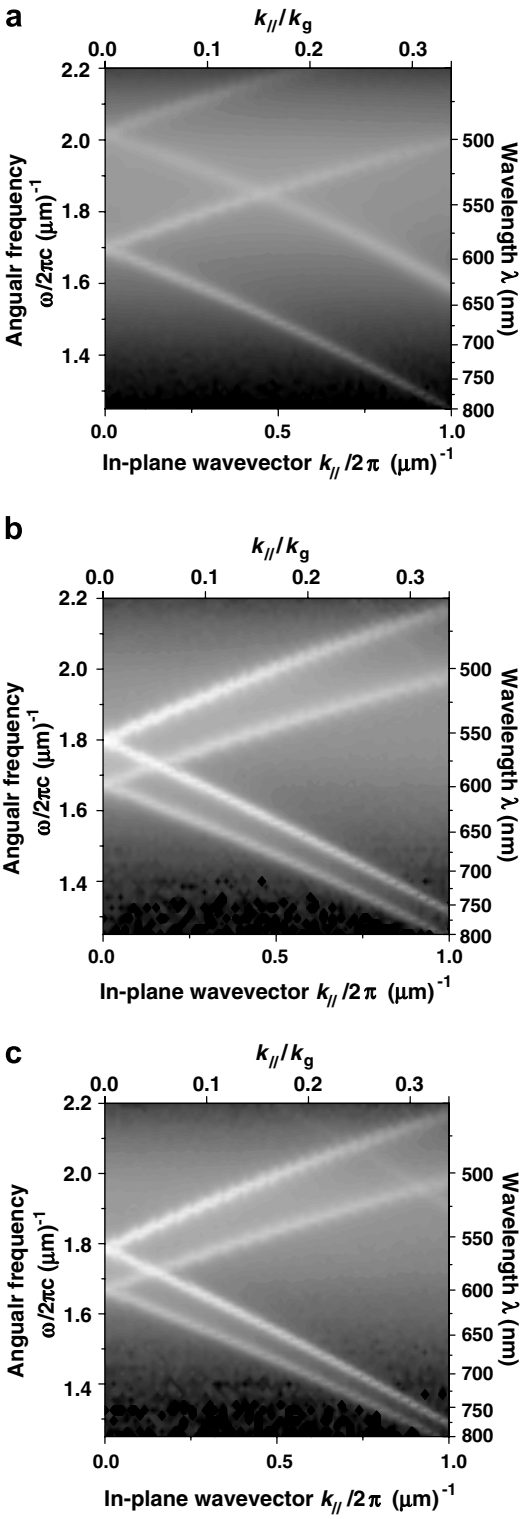


Fig. 7. Dispersion maps showing the TM polarised photoluminescence emission from structures with dielectric overlayer thicknesses of (a) 46.8 nm, (b) 156 nm and (c) 196.8 nm. Light regions indicate areas of strong emission.

sure of the relative emission intensity from each structure.

Fig. 8 shows this integrated emission intensity for both TM and TE polarised emission as a function of dielectric overlayer thickness [34]. Also shown is the integrated TM polarised emission intensity from the planar control sample. From Fig. 8 it may be seen that for dielectric overlayers thicknesses of 26.0–67.6 nm the intensity of the TM polarised PL is the same as that from the microstructured sample with no overlayer, i.e. a bare metal film (to within experimental error). However, as the dielectric overlayer thicknesses further increases the PL emission intensity is seen to increase sharply until a maximum is reached for a dielectric thickness of 156.0 nm. For dielectric overlayer thicknesses greater than ~156.0 nm the emission intensity may be seen to fall. These data (Fig. 8) show the SPP modes are best coupled together for a dielectric overlayer thickness of 156 nm.

For the TE polarised data there were no modes seen for dielectric overlayer thicknesses of less than 114 nm and the data for these samples were approximately equal to the planar structure. For overlayer thickness greater than 114 nm sharp emission features were seen in the PL and corresponded to the recovery of TE polarised waveguided modes associated with the dielectric overlayer. From Fig. 8 it may be seen that for the summed emission associated with the TE polarised emission there was no

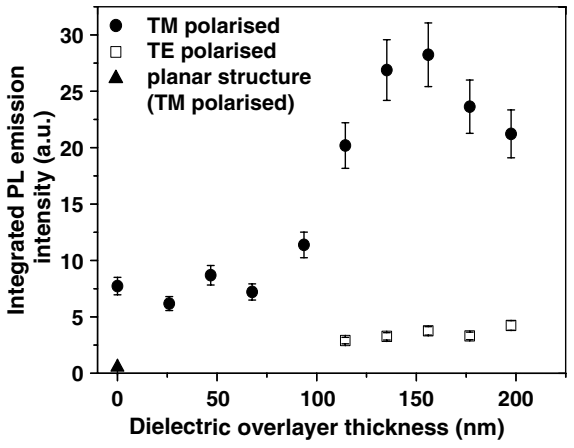


Fig. 8. Integrated intensity of photoluminescence emission as a function of dielectric overlayer thickness from corrugated samples shown in Fig. 2(d). Also shown is the integrated TM polarised photoluminescence emission intensity from a planar control structure (Fig. 2(a)). (Note for dielectric overlayer thicknesses below 114.4 nm no TE polarised emission features were seen.)

increase for dielectric overlayer thicknesses of greater than 114 nm.

The PL data presented in Fig. 8 show that when the SPP modes associated with the metal film are best coupled (dielectric overlayer thickness of 156 nm) the that summed PL emission is ~3 times greater than for a bare microstructure metal film and ~50 times greater than for a planar metal film. However, in term of a commercial device the manufacture of a microstructured metal film may be demanding in terms of fabrication. Below the emission from a device containing a planar metal film which supports coupled SPP and where these modes are scattered to light from a textured dielectric overlayer is examined.

The structure shown in Fig. 2(e) contained a planar metal coated with a microstructured photoresist (PR) film, pitch $\lambda_g = 485 \pm 1$ nm. As noted above this microstructured PR layer served two purposes. Firstly, the thickness of the PR film was such that it enabled the effective refractive index of this layer to be matched to the index of the emissive layer allowing the SPPs to couple across the metal. Secondly, the microstructure at the PR/air interface enabled the SPP modes supported by the structure to be Bragg scattered to light.

Fig. 9 shows the PL emission at an emission angle of 10°, from the samples shown in Fig. 2(a), (b), (d) and (e) labelled planar, grating-coupled, index-coupled and dielectric, respectively [35]. From Fig. 9 it may be seen that the PL from the dielectric and that from the index-coupled samples are comparable. In contrast the PL from the dielectric structure may be seen to be approximately an order of magnitude greater than that from the grating-coupled sample and ~50 times greater than that from the planar structure.

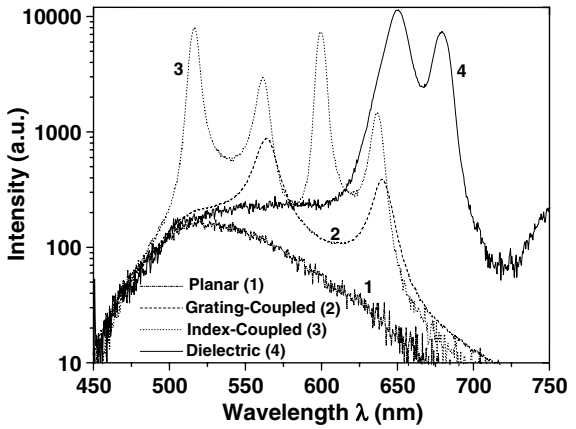


Fig. 9. TM polarised photoluminescence emission spectra measured through the metal film from; planar, grating-coupled, index-coupled and dielectric structures (shown in Fig. 2(a)–(d)), respectively. Each spectrum was measured at a polar emission angle θ of 10°. Note each spectrum has been normalised with respect to the emission spectrum obtained from the planar structure. This normalisation was achieved by fitting the spectra obtained from the three microstructured samples to the spectrum obtain from the planar structure over a wavelength range from 400 nm to 480 nm.

Considering the separation between the Alq_3/PMMA layer and the scattering surface at the PR/air interface (~150 nm) the intensity of the PL from the dielectric structure is remarkable. These data (Fig. 9) illustrate that by introducing an appropriately scaled periodic microstructure into a dielectric film energy lost to SPP modes may be recovered as light.

5. Conclusions

It has been shown that surface plasmon–polariton (SPP) modes supported by a TOLED may provide a significant loss channel thus diminishing the efficiency of the device. The introduction into a structure of an appropriately scale microstructure enables some of this lost power to be recovered as light. However, it has been demonstrated that if this SPP-mediated emission of light is to be optimized careful consideration must be taken over the device geometry. It has been seen that the intensity of light emitted via the SPP mode associated with the metal/organic interface from a metal film that contains a symmetric microstructure is less than might be expected. This is attributed to light mediated via the metal/organic SPP mode that is scattered from the metal/organic interface being in anti-phase with the light mediated from this mode when it is scattered from the metal/air interface and thus leading to cancellation. A thin metal film that incorporates wavelength scale microstructure at a single interface has been used to demonstrate that these phase cancellations may be overcome.

We have also shown that these losses may in part be overcome by selecting a sample geometry that allows the SPP modes associated with either side of a thin metal film to couple, thus enabling energy to be transported across the metal. By the use of grating-coupled and index-coupled SPP modes it has been shown that power might be transported across the metal and that this power may then be scattered to light. However, the emission mediated by grating-coupled SPPs has been seen to occur only

over a narrow range of emission wavelengths and angles and is thus of very limited practical value.

PL emission from a microstructured metal film that supports coupled SPPs has been shown to be ~3 times greater than from a corrugated sample that supports individual SPP modes and ~50 times greater than a similar planar structure. Emission mediated via these index-coupled SPP has been shown to occur across a range of emission angles and wavelengths. We have also shown that similar improvements can be achieved by introducing the microstructure into an overlying dielectric, leaving the metallic cathode planar. This approach should be more compatible with manufacturing processes.

In summary the work presented above has shown that by the careful selection of device geometry power dissipated to otherwise non-radiative SPP modes may be scattered to light. These findings may have the potential to increase the optical efficiency of TOLEDs.

References

[1] J.H. Burroughes, D.D.C. Bradley, A.R. Brown, R.N. Marks, K. Mackay, R.H. Friend, P.L. Burn, A.B. Holmes, Nature 347 (1990) 539.
[2] D. Braun, A.J. Heeger, Appl. Phys. Lett. 58 (1991) 1982.
[3] M.A. Baldo, D. O'Brien, Y. You, A. Shoustiikov, S. Silbey, M.E. Thompson, S. Forrest, Nature 395 (1998) 151.
[4] J.M. Lupton, J. Matterson, I.D.W. Samuel, M.J. Jory, W.L. Barnes, Appl. Phys. Lett. 77 (2000) 3340.
[5] P.A. Hobson, J.A.E. Wasey, I. Sage, W.L. Barnes, IEEE J. Sel. Top. Quantum Electron. 8 (2002) 378.
[6] C.W. Tang, S.A. Van Slyke, Appl. Phys. Lett. 51 (1987) 913.
[7] L.S. Hung, C.W. Tang, M.G. Mason, Appl. Phys. Lett. 70 (1997) 152.
[8] S.A. Van Slyke, C.H. Chen, C.W. Tang, Appl. Phys. Lett. 69 (1996) 2160.
[9] P.A. Hobson, S. Wedge, J.A.E. Wasey, I. Sage, W.L. Barnes, Adv. Mater. 14 (2002) 1393.
[10] V. Buluvic, G. Gu, P.E. Burrows, S.R. Forrest, Nature 380 (1996) 29.
[11] M.-H. Lu, J.C. Sturm, J. Appl. Phys. 91 (2002) 595.
[12] L.S. Hung, C.W. Tang, M.G. Mason, P. Raychaudhuri, J. Madathill, Appl. Phys. Lett. 78 (2000) 544.
[13] S. Han, X. Feng, Z.H. Lu, D. Johnson, R. Wood, Appl. Phys. Lett. 82 (2003) 2715.
[14] M.-H. Lu, M.S. Weaver, T.X. Zhou, M. Rothman, R.C. Kwong, M. Hack, J.J. Brown, Appl. Phys. Lett. 81 (2002) 3921.
[15] Chieh-Wei Chen, Ping-Yuan Hsieh, Huo-Hsien Chiang, Chun-Liang Lin, Han-Ming Wu, Chung-Chih Wu, Appl. Phys. Lett. 83 (2003) 5127.
[16] S.C. Lo, N.A.H. Male, J.P.J. Markham, S.W. Magennis, P.L. Burn, O.V. Salata, I.D.W. Samuel, Adv. Mater. 14 (2002) 975.
[17] T.D. Anthopoulos, M.J. Frampton, E.B. Namdas, P.L. Burn, I.D.W. Samuel, Adv. Mater. 16 (2004) 557.
[18] L.H. Smith, J.A.E. Wasey, W.L. Barnes, Appl. Phys. Lett. 84 (2004) 2986.
[19] H. Raether, Surface Plasmons, Springer-Verlag, Hamberg, 1989.
[20] L.H. Smith, J.A.E. Wasey, I.D.W. Samuel, W.L. Barnes, Adv. Funct. Mater. 15 (2005) 1839.
[21] W.H. Weber, C.F. Eagen, Opt. Lett. 4 (1979) 236.
[22] D. McBranch, I.H. Campbell, D.L. Smith, J.P. Ferraris, Appl. Phys. Lett. 66 (1995) 1175.
[23] R.W. Gruhlke, W.R. Holland, D.G. Hall, Phys. Rev. Lett. 56 (1986) 2838.
[24] R.W. Gruhlke, D.G. Hall, Appl. Phys. Lett. 53 (1988) 1041.
[25] S. Wedge, I.R. Hooper, I. Sage, W.L. Barnes, Phys. Rev. B 69 (2004) 245418.
[26] I. Pockrand, Opt. Commun. 13 (1974) 311.
[27] W. Gruhlke, W.R. Holland, D.G. Hall, Opt. Lett. 12 (1987) 364.
[28] D. Sarid, Phys. Rev. Lett. 47 (1981) 1927.
[29] G.G. Roberts, Langmuir–Blodgett Films, Plenum Press, New York, 1990.
[30] E.D. Palik, Handbook of Optical Constants of Solids, Academic, New York, 1985.
[31] I. Pockrand, A. Brillante, D. Mobius, Chem. Phys. Lett. 69 (1980) 499.
[32] I.R. Hooper, J.R. Sambles, Phys. Rev. B 67 (2003) 235404.
[33] A. Giannattasio, S. Wedge, W.L. Barnes, J. Mod. Opt. 53 (2006) 429.
[34] S. Wedge, S.H. Garrett, I. Sage, W.L. Barnes, J. Mod. Opt. 52 (2005) 833.
[35] S. Wedge, W.L. Barnes, Opt. Exp. 12 (2004) 3673.

Available online at www.sciencedirect.com
ScienceDirect
Organic Electronics 8 (2007) 148–160
Organic Electronics
www.elsevier.com/locate/orgel

Coupled surface plasmon resonance on bimetallic films covered by sub-micrometer polymer gratings

M. Csete [a,*], A. Kőházi-Kis [a], V. Megyesi [a], K. Osvay [a], Zs. Bor [a], M. Pietralla [b], O. Marti [b]

[a] Department of Optics and Quantum Electronics, University of Szeged, H-6720 Szeged, Dóm tér 9, Hungary
[b] Department of Experimental Physics, University of Ulm, D-89069 Ulm, Albert Einstein Allee 12, Germany

Received 6 February 2006; received in revised form 21 June 2006; accepted 22 June 2006
Available online 20 July 2006

Abstract

Angular interrogation investigation of the rotated grating-coupled surface plasmon resonance was performed, via exciting plasmons on special sensing layers by a frequency doubled continuous Nd:Yag laser beam in Kretschmann arrangement. NBK7 glass substrates were evaporated by silver and gold layers having appropriate thicknesses to ensure a narrow plasmon resonance peak. Thin poly-carbonate films spin-coated onto the bimetallic layers were patterned by the fourth harmonic of a pulsed mode Nd:Yag laser applying a master grating-based interference method. The pulsed force mode atomic force microscopic investigation has shown the existence of a surface relief grating and a coexistent adhesion modulation having a period of 416 nm. The conditions of the grating-coupling effect were determined for shallow sub-micrometer polymer gratings, and secondary minima were detected on the resonance curves measured in presence of polymer patterns, according to the calculations. The indispensability of a minimal modulation amplitude and the existence of an optimal rotation angle of the grating grooves with respect to the plasmon propagation direction were experimentally proven. The position of the emerged secondary resonance minimum indicated that the average film thickness was decreased caused by material removal during the structure formation. It was shown by tapping-mode AFM that the sub-micrometer adhesion modulation resulted in periodic adherence of streptavidin in the structure's valleys. The attachment of a small amount of protein was detected based on the shift of the secondary resonance peak. The capability of the polymer grating for sensitivity enhancement was demonstrated, proving that the secondary peak shift is highly sensitive to the protein concentration. The application of the polymer grating covered bimetallic films as transducing layers in novel bio-sensorization method based on rotated grating coupling is proposed.
© 2006 Elsevier B.V. All rights reserved.

PACS: 61.80.Ba; 68.37.Ps; 87.64.Dz; 73.20.Mf

Keywords: Surface plasmon resonance spectroscopy; Grating-coupling; Atomic force microscopy; Protein detection

* Corresponding author. Tel.: +36 62 544 420; fax: +36 62 544 658.
E-mail address: mcsete@physx.u-szeged.hu (M. Csete).

1566-1199/$ - see front matter © 2006 Elsevier B.V. All rights reserved.
doi:10.1016/j.orgel.2006.06.003

1. Introduction

There are new directions in the science devoted to investigate the interaction of light with media containing structures commensurable or smaller then the optical wavelength. The electromagnetic waves propagating at the interface of two materials are very sensitive to the surface-design at the mesoscopic scale. These phenomena offer a possibility to modify the optical properties of materials. A particularly important application is the control of spontaneous emission [1]. The upcoming field ''plasmonics'' investigates, how the presence of individual and periodically arrayed sub-wavelength holes, slits [2,3] and nano-particles [4] influences the propagation of the electromagnetic modes on metal surfaces. The complex periodic metal patterns are highly interesting, since the plasmon localization on nano-scaled sub-structures contributes to the coupling effect caused by the metal gratings. The detailed research of the interaction of metal surfaces and plasmons has proven that the presence of periodic roughness modifies the resonant behavior of plasmons and results in grating-coupling phenomenon, which manifests itself in the development of band gaps [5]. The investigation of the metal gratings has shown that the depth of the modulation and the existence of higher harmonics in the surface structure strongly influence the appearance of the photonic gaps [6]. The effect of the propagation direction of plasmons with respect to the grating grooves, and the conditions of rotated grating-coupling on metal structures are detailed in Ref. [7]. The plasmons can be diffracted also by dielectric structures deposited onto the plasmon carrying metal interfaces, and the grating wave vector mediated coupling was demonstrated on micrometer periodic dielectric patterns [8]. Less attention was devoted to describe the perturbation of the plasmon field by sub-micrometer dielectric structures on metallic surfaces, in spite of their fundamental interest and their new application possibilities.

The plasmon excitation results in intensity enhancement at the surface, therefore many efforts are described in the literature with the purpose to develop bio-sensorization methods based on **S**urface **P**lasmon **R**esonance **S**pectroscopy. The different types of the SPR optical sensors comprise a properly designed transducing medium, and the coupling of the light energy to surface plasmons is usually realized by a prism in Kretschmann configuration, or applying a metal grating. The main detection approaches are the measurement of the resonant momentum of the optical wave including angular or wavelength interrogation of SPR, and the measurement of the intensity of the optical wave near the resonance is also utilized [9].

The application of intact metallic materials is limited by their poor chemical stability and biocompatibility, therefore different pretreatments and over coatings are unavoidable to promote the attachment of bio-molecules on metal surfaces.

Surface plasmon immunoassays were realized on flat metal surfaces covered by antigen-protein films, which made possible the bounding of specific antibodies from solutions [10]. Several SPR sensors are based on the investigation of the metal grating-coupled surface plasmon resonance. It was shown that a gold coated diffraction grating can be applied to couple the light into thiol-pretreated and biotin coated areas, which were periodically arranged on the grating surface itself [11]. The localized surface plasmon resonance was utilized to detect bio-molecule attachment on chemically pretreated, periodically arranged silver nano-particles [12]. The short order nano-hole arrays in metal films allow highly sensitive probing of local indices of refraction, therefore they may be promising in biosensor technology [13].

The review of the literature proves that the transducing medium containing metal layers determines the sensitivity and specificity of the SPR sensors. Polymers are known as materials having good biocompatibility, and it was shown in previous studies, that the UV laser illumination causes surface modifications promoting adherence of bio-molecules [14,15].

In the present work a new type of SPR transducing medium was prepared by generating submicrometer gratings via laser illumination on polymer films coated onto bimetallic layers. The fundamental purpose was to investigate the grating-coupling phenomenon caused by the presence of shallow sub-micrometer dielectric grating on bimetallic film. The excitation of the grating-coupled plasmonic states was realized by combining the prism-based Kretschmann-, and the rotated-grating geometry. The angle-dependent resonance curves were measured at constant wavelength. The influence of the orientation and the modulation amplitude of the polymer grating grooves on the grating-coupling efficiency was determined theoretically and experimentally. AFM investigation was realized to essay the applicability of the structured

polymer layers as sensing surface by mapping the adhesion distribution, and by testing the streptavidin adherence on the grating. Finally the sensitivity of the rotated grating-coupling caused secondary resonance peak to the amount of attached bio-molecules was analyzed.

2. Methods and materials

2.1. Layered substrate preparation

Interferometrically flat NBK7 glass disks (Geodasy) were vacuum evaporated by bimetallic films consisting of silver and gold layers (Optilab). Silver is preferred in sensors, since the narrow resonance curves measurable on this metal result in high signal to noise ratio, but the poor chemical stability limits the applications. The benefits of the gold are the good chemical resistance, and this metal displays higher shift of the resonance angle caused by changes in the ambient layer.

By preparing bimetallic layers having appropriate layer thickness combination, the utilization of the advantages of both metals is possible, and the requirements of the application in bio-sensorization may be fulfilled. The resonance peaks may be narrow, the resonance position is sensitive to optical thickness changes at the surface, and the stability in humid environments is also satisfied [16]. The appropriate layer thickness combinations were determined by transfer-matrix-method calculations based on the Fresnel's equations taking into account the optical constants in Table 1, which are applicable to describe thin metal layers based on Ref. [17]. Further calculations were performed to determine the thickness of a spin-coated **P**oly-**C**arbonate film resulting in plasmon resonance minima at measurable positions.

Table 1
The dielectric constants of the materials composing the investigated layered medium

Material	ε_1	ε_2
NBK7	2.307	0
Ag	−10.0534	0.33799
Au	−5.10288	2.85921
PC	2.53	0
Streptavidin	2.53	0

The dielectric constants from Ref. [17] were used to describe the thin metallic layers.

2.2. Sub-micrometer grating generation on polymer films by laser interference technique

The surface of the poly-carbonate films was structured by laser interference technique. The beam of a Nd:Yag laser ($\lambda = 1064$ nm, $\tau = 10$ ns, $f = 10$ Hz) was frequency quadrupled, and telescopes were built into the green and UV beam-lines to ensure properly large illuminating beam diameter. A spatial filtering was realized to built up noise-free Gaussian intensity distribution in the fourth harmonic of the Nd:Yag laser ($\lambda_{FH} = 266$ nm). A master grating (Spectrogon, PUV 1200) was illuminated by the UV laser light, and the first order diffracted beams were recombined applying an interferometrically polished quartz block [18]. The period of the interference pattern developed in this configuration was half of the master grating constant of $P_{\text{master grating}} = 833$ nm:

$$I(x) = I_{\text{average}}\left(1 + V \cdot \cos\left(\frac{4\pi x}{P_{\text{master grating}}}\right)\right). \qquad (1)$$

It was essential to find the ideal sample plane corresponding to high "V" visibility interference fringes in order to receive a sinusoidal surface relief grating having high modulation amplitude at the period of the interference pattern (Fig. 1a).

2.3. Atomic force microscopical investigation of the laser generated surface structures

A TopoMetriX **A**tomic **F**orce **M**icroscope with **P**ulsed **F**orce **M**ode extension (Witec GMBH) [19] was applied to investigate the effect of the laser treatment conditions on the topographical structure and on the coexistent micromechanical pattern developed on the PC surface. This technique is utilizable to map the adhesion distribution, which has dominant role in the interaction of surface structures and bio-molecules [14,20]. The topography and the adhesion was determined based on the highest repulsive and attractive forces acting on the tip (Nanosensors FMR 22742) at the approach and detachment in case of sinusoidal, low frequency driving force.

2.4. Surface plasmon resonance measurements

A traditional Kretschmann arrangement was built up to investigate the angle-dependent reso-

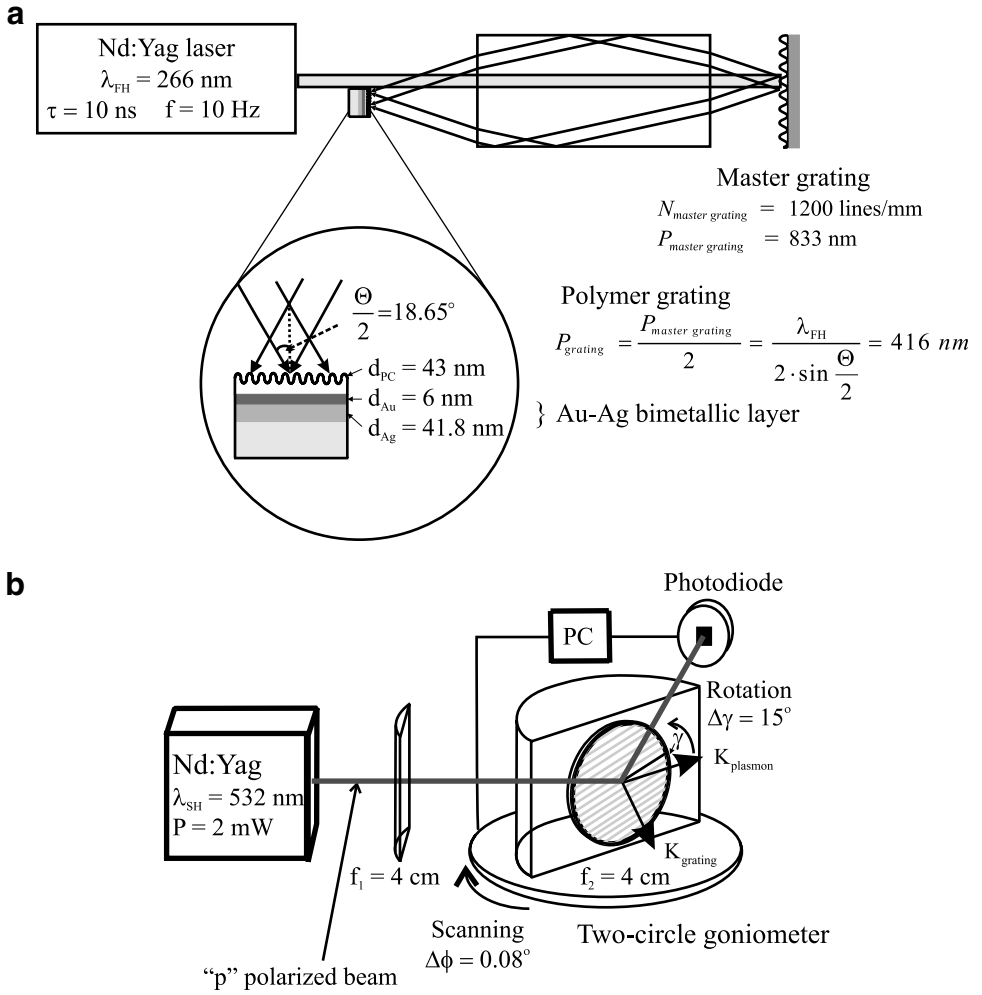


Fig. 1. (a) UV laser based interference technique applied to generate grating on the surface of the poly-carbonate layers spin-coated onto Ag–Au bimetallic films. (b) The Kretschmann arrangement utilized to realize reflectivity versus angle scans. The substrates were rotated to investigate the resonance curves of plasmons excited in bimetallic films coated by structured polymer layer.

nance curves of plasmons excited at constant wavelength in polymer coated bimetallic films (Fig. 1b). The light of a continuous Nd:Yag laser (Intelite, GSLN32-20, $\lambda_{SH} = 532$ nm, 2 mW) illuminated a semi-cylinder (Geodasy), and an additional cylindrical lens was applied to collimate the beams at the sample surfaces. The NBK7 substrates were attached to the half cylinder applying an immersion liquid (Schott). The precision rotation of these optical elements was performed with a resolution of $\Delta\varphi = 0.08°$ on a two-circle goniometer (OWIS, with DMT 65, 2-Ph-SM 240). A simple photodiode (Thorlabs DET110) detected the angle-dependent reflected light.

2.5. Protein seeding

Protein solutions having concentrations of $c_1^{St} = 45$ μg/ml and $c_2^{St} = 30$ μg/ml were prepared by solving streptavidin powder (Jackson Immuno-Research) in Milli-Q water, and PBS was applied to adjust the pH to 7.2. Small amount of 40 μl was dropped from these solutions on untreated and structured PC surface parts and the samples were incubated at 37 °C for 1 h. The substrates were re-immersed in Milli-Q water and placed on a shaker for 15 min, and finally allowed to dry overnight at room temperature. The attached protein was detected by PSIA AFM operating in

tapping-mode, applying NT-MDT tips (NSG11, 5.5 N/m, 150 kHz). The SPR analysis of the protein coated gratings was performed one day after seeding.

3. Results and discussion

3.1. Surface plasmon resonance measurements on untreated films

The NBK7 glass substrates were vacuum evaporated by thicker layer of silver, and very thin gold layer was post-evaporated to build up a sensor-base, according to the pre-calculations.

The SPR measurements realized on the bimetallic films resulted in sharp resonance minimum at $\varphi_{\text{bimetallic}} = 44.8°$. The Fresnel's fit calculation performed taking into account the optical constants summarized in Table 1 revealed $d_{\text{Ag}} = 41.8$ nm and $d_{\text{Au}} = 6$ nm metal layer thicknesses (Fig. 2).

The gold surface was spin-coated after that by poly-carbonate layer, and a shifted resonance position of $\varphi_{\text{primary}}^{\text{untreated}} = 69.04°$ was measured at the central part of the substrate. The intact polymer layer thickness was calculated based on the $\varphi_{\text{primary}}(d_{\text{PC}})$ (Fig. 4b) relationship, which was determined by transfer-matrix-method calculations, taking into account the composition of the underlying bimetallic film. The resonance positions measured in presence of the dielectric layer corresponded to an average PC thickness of $d_{\text{PC}} = 43$ nm. It was experienced that the spin-coating caused $\Delta d_{\text{PC}} = \pm 0.5$ nm thickness distribution of the investigated polymer layer.

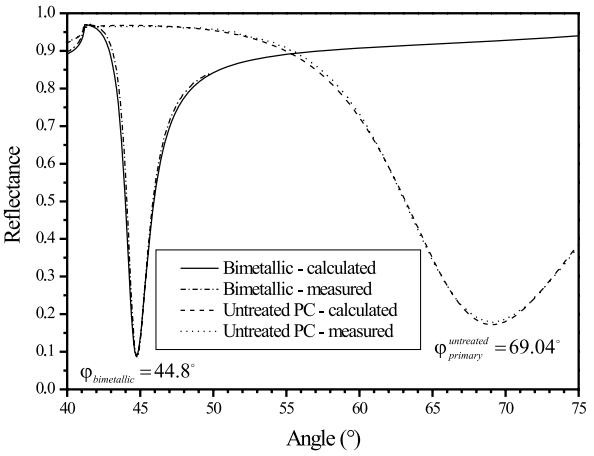


Fig. 2. The comparison of the resonance curves determined by Fresnel's fit calculations and of the resonance peaks measured on the Ag–Au bimetallic layers, and on the untreated poly-carbonate film coated bimetallic layers, respectively. The layer thicknesses resulting in good agreement between the calculations and measurements are: $d_{\text{Ag}} = 41.8$ nm, $d_{\text{Au}} = 6$ nm, and $d_{\text{PC}} = 43$ nm.

3.2. The topography and adhesion on the poly-carbonate surfaces structured by UV laser based two-beam interference

The AFM study of the laser treated polymer layers showed that the period of the surface relief grating was $P_{\text{grating}} = \frac{P_{\text{master grating}}}{2} = 416$ nm (Fig. 3a), and the depth of modulation was tunable in the region of 5–55 nm by increasing the number of laser pulses in the interval of 600–900 of the laser beam having an average intensity of $I_{\text{average}} = 11.48$ mJ/cm^2. The slight mismatch between the directions of the intensity grating determined by the two-beam interference and the orientation of the polarization causes the appearance of a "braided" structure. This sub-structure is a kind of the **L**aser **I**nduced **P**eriodic **S**urface **S**tructures, which develops on solids as a result of the repeated illumination by polarized laser pulses, and may appear at a fluence lower than the material damage threshold [21].

The adhesion images have shown stronger adhesion in the valleys, and the highest attractive forces were measured at the foot of the polymer hills and in the sub-valleys of the LIPSS (Fig. 3b). Based on the results of our previous investigations, the material changes originating from phase transitions and UV light induced photo-degradation contribute to the effect of the surface curvature, and the adhesion patterns caused by low fluence UV laser illumination summarize all of these effects [15,20].

In the present study the polymer films were illuminated by laser beams having relatively high average fluence of $I_{\text{average}} = 11.48$ mJ/cm^2, moreover the intensity may be doubled in case of $V \approx 1$ visibility at the interference maxima. The maximal temperature achievable at the polymer surface was determined by a numerical temperature model calculation described in our previous work [22]. An absorption coefficient of $\alpha_{\text{measured}}^{\text{PC}}(266\text{ nm}) = 3.8 \times 10^4$ cm^{-1} was taken into account, which was determined by measuring the transmission through thin untreated poly-carbonate layers spin-coated onto quartz substrate. We concluded that ablation from the valleys contributed to the material rearrangement accompanying the phase-transitions on the polymer surface. The increase of the PC absorbance caused by repeated UV illumination proba-

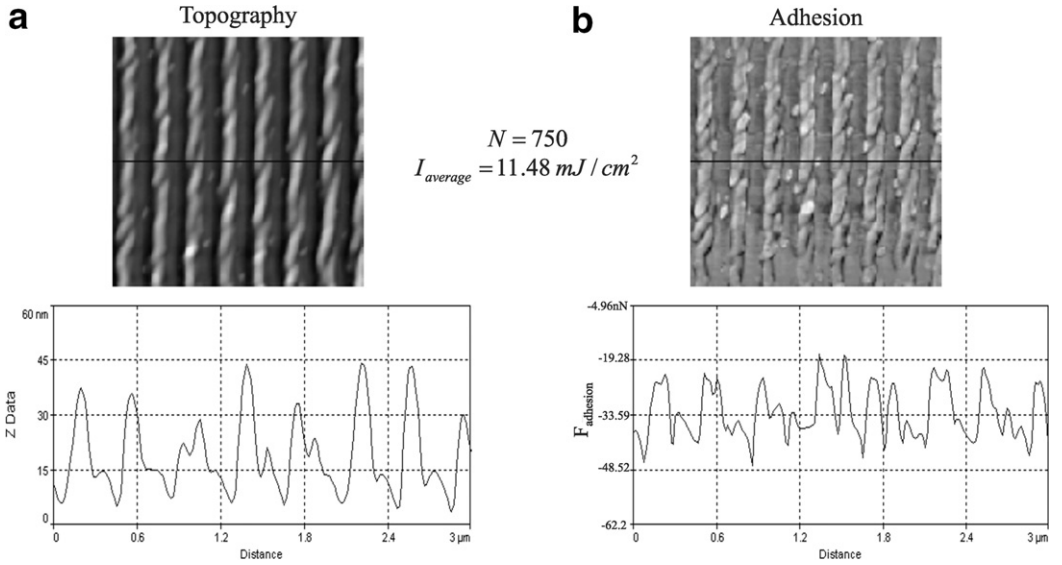


Fig. 3. Pulsed force mode AFM measurements about the (a) topography and (b) adhesion distribution on the polymer-grating generated by $N = 750$ pulses of the fourth harmonic of the Nd:Yag laser beam having an average intensity of $I_{\text{average}} = 11.48\ \text{mJ/cm}^2$.

bly resulted in the enhancement of the rate of ablation.

3.3. The conditions of the grating-coupling on shallow sub-micrometer polymer structures

The fundamental purpose of our work was to analyze the influence of the polymer grating on the plasmon propagation, and to determine the conditions of highly efficient grating-coupling, which may result in the appearance of well defined, deep additional resonance peaks.

As known from the literature, the origin of the resonant behavior of the angular dependence of the reflectance on metals is the excitation of plasmons at the resonance angle, which can be given by the momentum matching condition between photons and surface plasmons. In case of resonance the plasmon wave vector equals with the component of the photon wave vector parallel to the surface, and it can be calculated taking into account the primary resonance minimum of φ_{primary} measurable on flat surfaces [23]:

$$K_{\text{plasmon}} = K_{\text{photon}} = \frac{\omega}{c} \cdot n_{\text{glass}} \cdot \sin \varphi_{\text{primary}}. \tag{2}$$

The periodic roughness causes the broadening of the resonance peaks for all types of surface structures. As a result of our calculations based on the theory of plasmons, three conditions were determined, which has to be fulfilled to result in efficient grating-coupling effect in case of polymer gratings, analogously to the criteria given for metal gratings in the literature [7]:

1. The *period* of the polymer grating has to be appropriately large to ensure a shift in the wave vector smaller than the original plasmon wave vector (Fig. 4a):

$$K_{\text{grating}} = \frac{2\pi}{P_{\text{grating}}} <$$
$$K_{\text{plasmon}} = \frac{2\pi}{\lambda_{\text{SH}}} \cdot n_{\text{glass}} \cdot \sin \varphi_{\text{primary}}. \tag{3}$$

   The polymer structures studied in the present work are commensurable with the wavelength, but this condition is still satisfied.
2. Deep secondary minimum is expected, when the *angle* between the grating grooves and the plasmon propagation direction match the value of

$$\gamma^{n}_{\text{coupling}} = \arcsin\left(n \cdot \frac{K_{\text{grating}}}{2 \cdot K_{\text{plasmon}}}\right), \tag{4}$$

   where "n" indicate the order of the coupling (Fig. 4a). In case of complex polymer grating profiles the coupling efficiency is a continuous function of the rotation angle.

The wave vector of the plasmons, which can be excited via grating-coupling in presence of the polymer grating, can be calculated as the projection of the original wave vector (Fig. 4a):

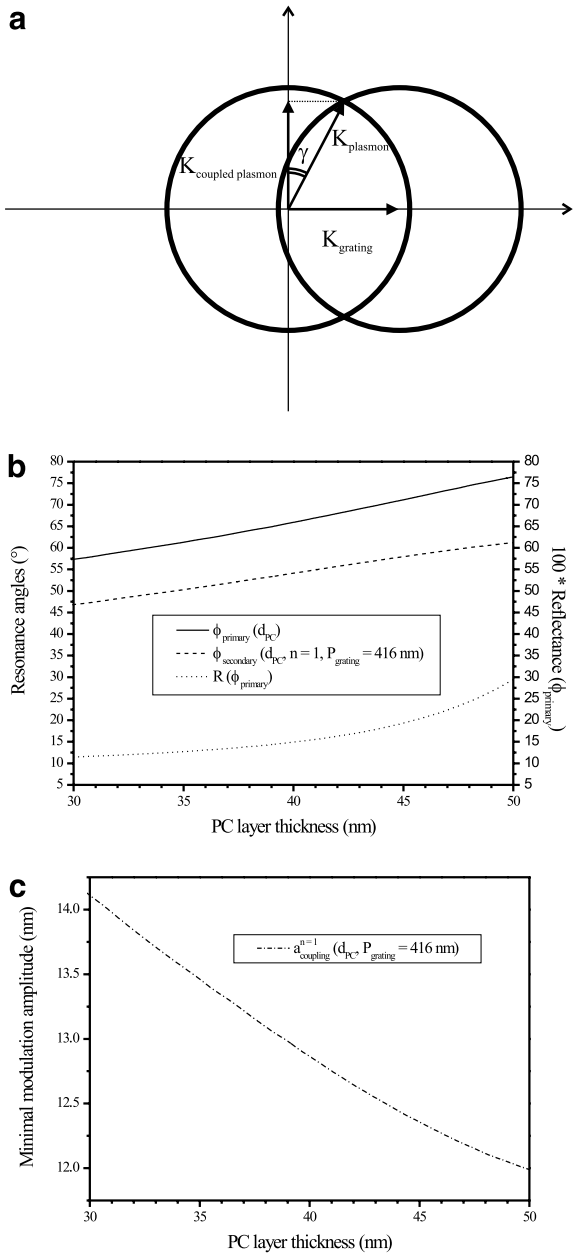


Fig. 4. (a) The rotation geometry resulting in first order grating-coupling. (b) The φ_{primary} resonance angle and the value of the $R(\varphi_{\text{primary}})$ reflectance at the resonance minimum was determined by Fresnel's fit calculations as a function of the PC layer thickness, taking into account the bimetallic film composition of $d_{\text{Ag}} = 41.8$ nm and $d_{\text{Au}} = 6$ nm. The positions of the $\varphi_{\text{secondary}}$ first order secondary minima appearing caused by coupling effect in presence of a polymer grating having a period of $P_{\text{grating}} = 416$ nm were calculated based on Eq. (6) as a function of the polymer layer thickness. (c) The $a^{n=1}_{\text{coupling}}$ minimal modulation amplitude was calculated based on Eq. (7) as a function of the average polymer film thickness. The first order coupling on the polymer grating may result in detectable secondary minimum only in case of a modulation amplitude approximating this value.

$$K^{n}_{\text{coupled plasmon}} = K_{\text{plasmon}} \cos \gamma^{n}_{\text{coupling}}, \tag{5}$$

and the position of the expected secondary resonance minimum may be predicted (Fig. 4b):

$$\varphi^{n}_{\text{secondary}} = \arcsin\left(K^{n}_{\text{coupled plasmon}} \cdot \frac{\lambda_{\text{SH}}}{2\pi \cdot n_{\text{glass}}}\right). \tag{6}$$

3. In our previous SPR studies performed on shallow polymer gratings consisting of lines and droplets the indispensability of a minimal *modulation depth* was confirmed [22], which can be determined as follows (Fig. 4c):

$$a^{n}_{\text{coupling}} = \frac{1}{\sin^2 \gamma^{n}_{\text{coupling}}} \times \frac{\sin \varphi_{\text{primary}} - \sin \varphi^{n}_{\text{secondary}}}{\sin^2 \varphi_{\text{primary}}} \cdot \frac{\sqrt{\varepsilon_{1,\text{PC}}}}{4\frac{2\pi}{\lambda_{\text{SH}}} n_{\text{glass}}}.$$

Based on simple theoretical considerations it can be concluded that the depth of the secondary peak appearing in presence of a grating is influenced by the dependence of the minimal reflectance on the average thickness, and by the ratio of the actual modulation amplitude to the minimal value, calculated for the given secondary resonance position (Fig. 4b and c). The value of the reflectance at the resonance minimum is a monotonically increasing function of the PC layer thickness (Fig. 4b), therefore larger average film thicknesses result in higher intensity at the secondary minimum (i.e., a secondary peak having a smaller depth) in case of appropriately large modulation amplitudes. In contrast: if the modulation amplitude is much larger than the minimal value in case of a grating on thicker film, the larger efficiency of the grating-coupling may result in lower reflected intensity (i.e., deeper secondary peak) at the secondary minimum. This is the reason, why the unambiguous detection of changes in the surface profile can be based on the investigation of the shift of the secondary peak position.

3.4. The grating-coupling determined plasmon resonance curves in presence of shallow sub-micrometer polymer structure

Based on the primary resonance minimum of $\varphi^{\text{untreated}}_{\text{primary}} = 69.04°$ measured on untreated poly-carbonate film we determined the position of the expected secondary minimum, the optimal rotation angle between the grating grooves and the plasmon propagation direction, and the minimal modulation depth (Table 2). The AFM measurements have

Table 2
The **measured** and calculated $\varphi_{primary}$, and $\varphi_{secondary}$ resonance positions; the conditions of the first order optimal grating-coupling: $\gamma^1_{coupling}$ and $a^1_{coupling}$; the measured modulation amplitude: $a_{average}$; the calculated average thickness: $d_{average}$; and the shifts caused by protein adherence: $\Delta\varphi^{30\ \mu g/ml}_{secondary}$ and $\Delta\varphi^{45\ \mu g/ml}_{secondary}$ in case of concentrations of $c^{St}_1 = 45\ \mu g/ml$ and $c^{St}_2 = 30\ \mu g/ml$, respectively

Sample	$\varphi_{primary}$	$\varphi_{secondary}$	$\gamma^1_{coupling}$	$a^1_{coupling}$ (nm)	$a_{average}$ (nm)	$d_{average}$ (nm)	$\Delta\varphi^{30\ \mu g/ml}_{secondary}$	$\Delta\varphi^{45\ \mu g/ml}_{secondary}$
Untreated	**69.04°**	56.5°	26.8°	12.5	0	43		
Untreated + St: 45 μg/ml	**75.76°**					49.3		6.72°
Untreated + St: 30 μg/ml	**74.32°**					47.9	5.28°	
A	62.3°	**51.16°**	28.4°	13.3	17.5–20	36.1		
A + St: 45 μg/ml	67.5°	**55.32°**	27.1°	12.7	<18	41.5		4.16°
B	61.1°	**50.16°**	28.7°	13.5	12.5–15	34.8		
C	62.2°	**51.08°**	28.4°	13.3	25–27.5	36		
C + St: 30 μg/ml	65.6°	**53.88°**	27.5°	12.9	<26	39.7	2.8°	

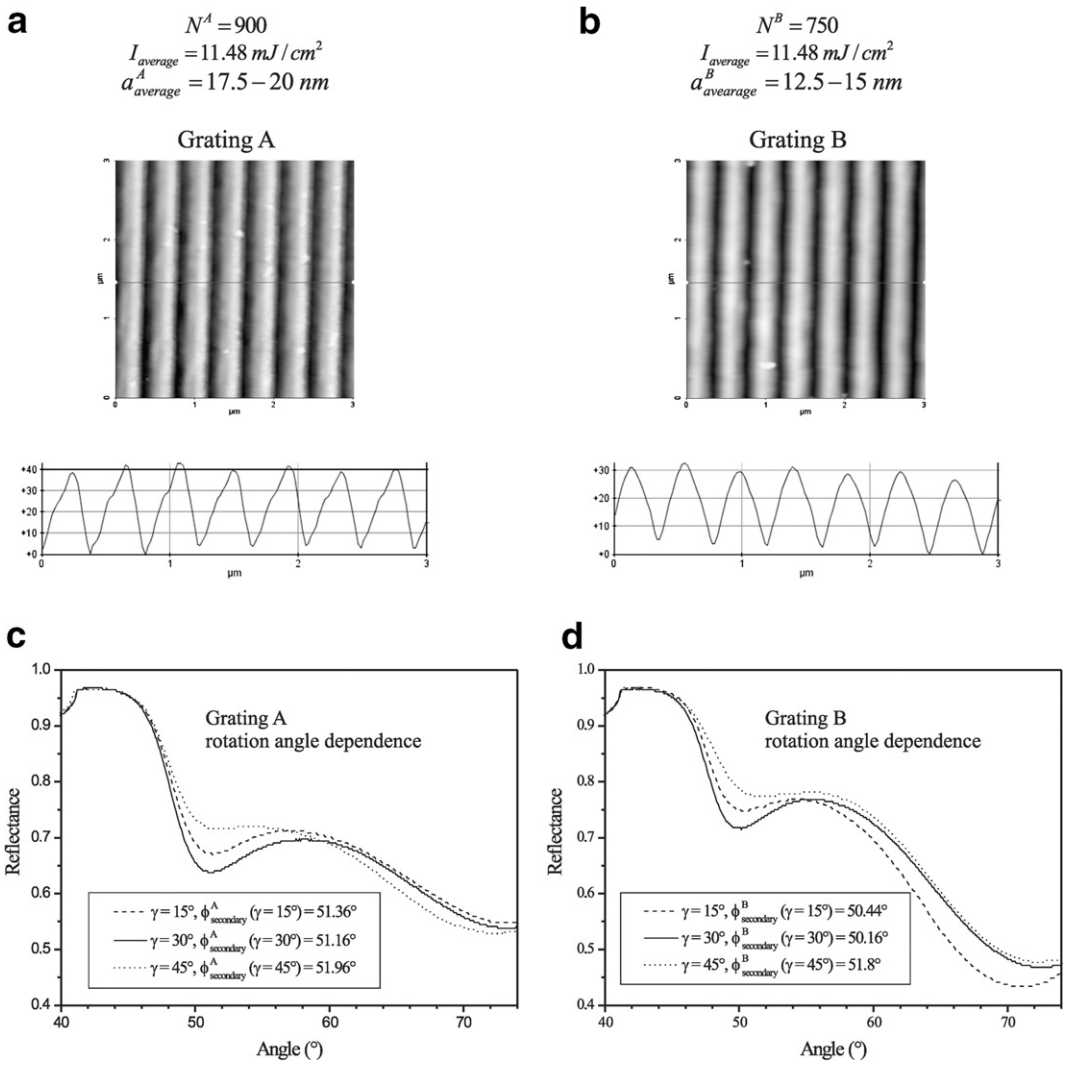


Fig. 5. (a) The topography of the gratings generated by $N^A = 900$ and (b) $N^B = 750$ laser pulses by UV laser beams having an average fluence of $I_{average} = 11.48\ mJ/cm^2$. (c) Surface plasmon resonance curves measured on *Grating A* having a higher modulation amplitude of $a^A_{average} = 17.5–20$ nm, (d) and about the surface pattern on *Grating B* having smaller modulation amplitude of $a^B_{average} = 12.5–15$ nm, after rotating the grating grooves by angles of $\gamma = 15°$, 30° and 45° compared to the plasmon propagation direction.

shown that the $N^{A} = 900$ and $N^{B} = 750$ laser pulses resulted in average modulation depths of $a^{A}_{average} = 17.5$–20 nm and $a^{B}_{average} = 12.5$–15 nm on *Grating A* and *Grating B*, respectively (Fig. 5a and b). Larger part of the treated surface was covered by "braided" grating in case of *Grating A* according to the accumulation nature of the secondary, LIPSS-like structure.

During the SPR measurements the substrates were rotated to modify the angle between the grating grooves and the plasmon propagation in $\Delta\gamma = 15°$ steps. The deepest secondary peaks were identifiable in case of rotation angles of $\gamma = 30°$, i.e., close to the condition of the first order optimal coupling, which was determined based on the primary resonance position measured on untreated film (Fig. 5c and d).

However, the positions of the deepest secondary peaks $\varphi^{A}_{secondary}(30°) = 51.16°$ and $\varphi^{B}_{secondary}(30°) = 50.16°$ were back-shifted compared to the calculated value of $\varphi^{untreated}_{secondary}(26.8°) = 56.5°$. These shifts indicated decrease in the average film thickness and proved that ablation occurred during the grating formation. The average PC thickness on the treated surface parts was calculated based on the interdependence of the positions of the secondary and primary peaks, which was determined for the first order coupling case in presence of the laser generated polymer grating (Fig. 4b). The optimal rotation angles and minimal modulation depths corresponding to the reduced film thickness were also re-calculated, and it was examined, that the rotation angle of $\gamma = 30°$ arranged in the experiments approximated the calculated optimal values (Table 2).

The depth of the secondary peaks was very sensitive to the modulation amplitude, according to the prediction of the theory (Fig. 4c), and the total resonance curve shape was determined by the thickness distribution of the complex surface structure. Very deep secondary peak was detected in case of a modulation amplitude larger than the calculated minimal value on *Grating A* (Fig. 5c). Secondary minima having reduced depth were detected on *Grating B* (Fig. 5d), where the modulation amplitude only approximated the calculated minimal value.

3.5. Protein detection by combined TM AFM and SPR study

In tapping-mode AFM the phase shift between the excitation and response of the cantilever may be used as material dependent signal complementary to the topography [24]. The comparative study of the topographical and phase images collected by TM AFM before and after exposing the polymer gratings to protein solution was realized to distinguish the surface parts covered by biological molecules from the intact polymer grating (Figs. 6a–d and 7a–d).

The AFM images taken about the topography on different parts of the same grating have shown that the modulation amplitude distribution corresponds to the Gaussian intensity distribution of the illuminating beam. The SPR curves measurable on laser generated gratings are influenced by the original thickness of the untreated films, and by the modulation amplitude distribution. In spite of the fact that the laser treated areas were large compared to the diameter of the laser beam applied in SPR measurements, these cumulative effects contribute to the grating-coupling, and the characteristics of the primary and secondary peaks correspond to the unique final thickness distribution of the given grating. In accordance, we experienced that the SPR curves measured on gratings prepared in different experimental conditions are unique. A comparative method based on the analysis of the grating-coupled SPR curves measured on the same polymer grating before and after protein seeding was applied to detect very small amount of bio-molecules adhered on the sub-micrometer structure (Figs. 6e, f and 7e).

Streptavidin seeding was performed from solution having a concentration of $c^{St}_{1} = 45$ μg/ml onto *Grating A*. The comparison of the topographical and phase images made by TM AFM about the central areas containing similar gratings before (Fig. 6a and b) and after (Fig. 6c and d) streptavidin seeding proved that the protein molecule prefer to adhere periodically along the foot of the polymer hills, where the strongest adhesion was detected by PFM AFM method (Fig. 3b). The topographical images have shown that the streptavidin attachment results in the filling of the valleys, causing the increase of the average film thickness and decrease in the average modulation depth (Fig. 6a and c). The plasmon resonance curves indicated that the secondary peaks were shifted to larger angles (Fig. 6e), and the highest shift of $\Delta\varphi^{A+St}_{secondary}(30°, 45\ \mu g/ml) = 4.16°$ was detected at the rotation angle of $\gamma = 30°$ (Fig. 6e and f). During the analyses of the SPR curves it was supposed that the index of refraction of the streptavidin does not differ from that of the PC (Table 1). The average thickness of the protein coated film was calculated

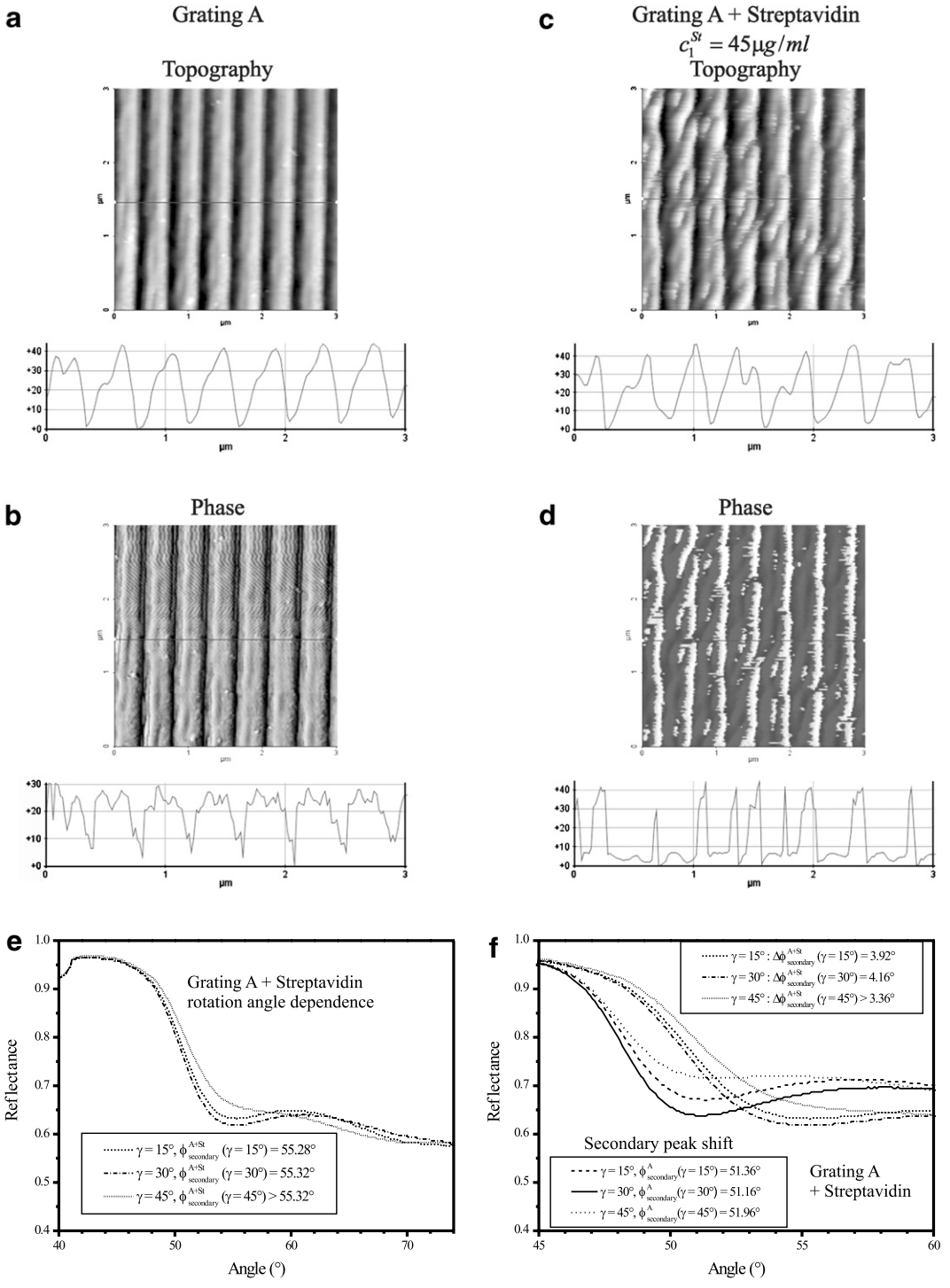


Fig. 6. Tapping-mode AFM pictures about the topography (a, c), and phase (b, d), before and after streptavidin attachment from solution having a concentration of $c_1^{St} = 45$ μg/ml on the polymer *Grating A*. The chemical heterogeneity sensitive phase signal is light at the places, where protein was adhered (d). (e) Surface plasmon resonance curves measured on *Grating A* after streptavidin seeding, and rotating the grating grooves by $\gamma = 15°$, 30° and 45° angles compared to the plasmon propagation direction. (f) The comparison of the secondary resonance peaks measured before and after the protein seeding at different rotation angles.

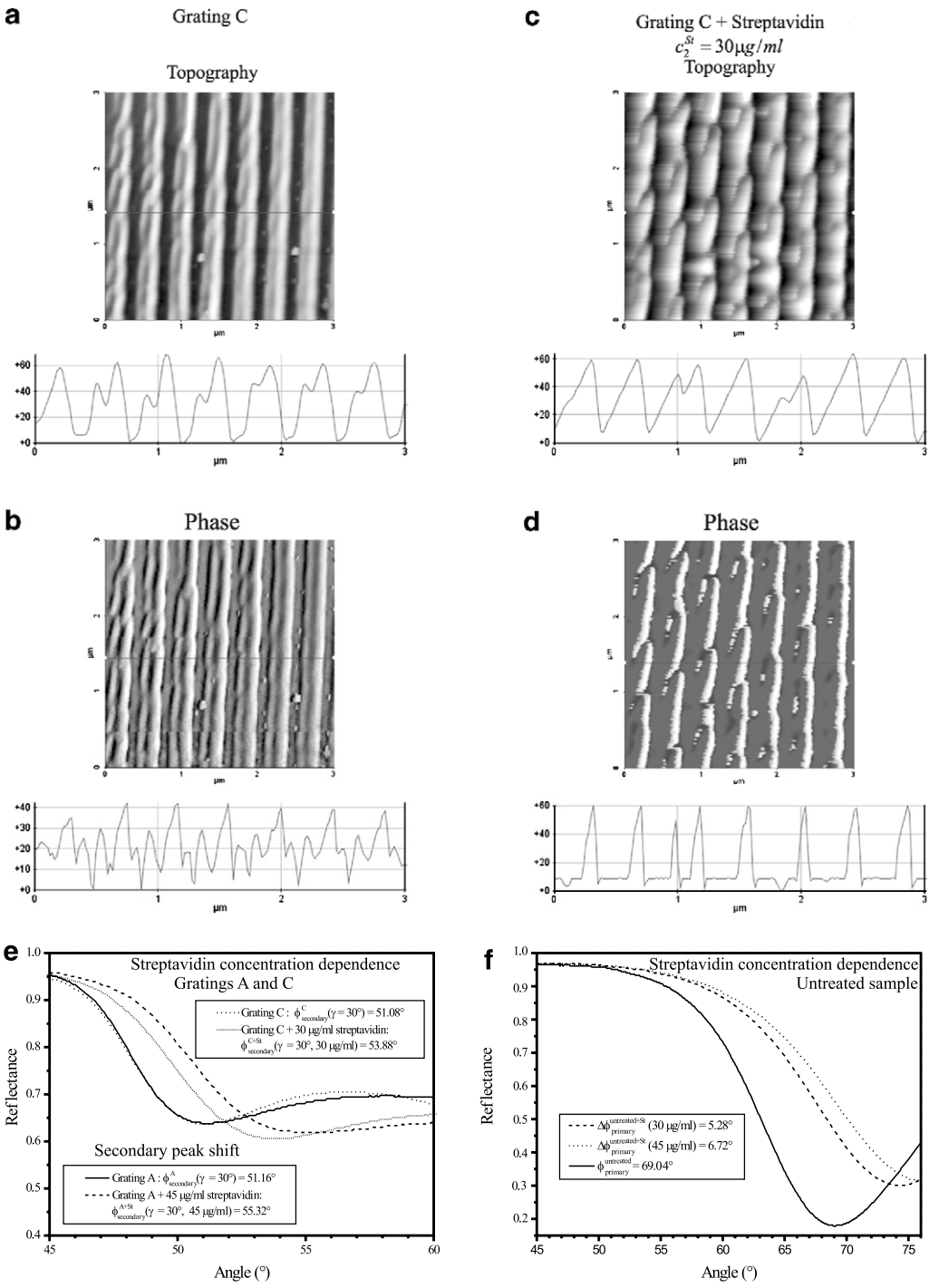


Fig. 7. Tapping-mode AFM pictures about the topography (a, c) and phase (b, d) before and after streptavidin attachment from solution having a concentration of $c_2^{St} = 30$ μg/ml on the polymer *Grating C*. The illumination by $N^C = 950$ laser pulses of a UV Nd:Yag laser beam having a fluence of $I_{average} = 11.48$ mJ/cm^2, resulted in a high modulation amplitude of $a^C_{average} = 25$–27.5 nm (a). The material difference sensitive phase signal is light at the places, where protein was attached (d). (e) Comparison of the shifts of the secondary resonance peaks measured at $\gamma = 30°$ rotation angle, caused by streptavidin attachment from solution having a concentration of $c_1^{St} = 45$ μg/ml on *Grating A*, and caused by adherence from more diluted solvent having a concentration of $c_2^{St} = 30$ μg/ml on *Grating C*. (f) The comparison of the shifts of the primary resonance peak caused by streptavidin seeding from solutions having the $c_1^{St} = 45$ μg/ml and $c_2^{St} = 30$ μg/ml concentrations onto untreated sample.

from the position of the secondary minimum of $\varphi^{A+St}_{secondary}(30^\circ, 45\ \mu g/ml) = 55.32^\circ$, taking into account the dependence of the first order coupling caused secondary minimum on the average PC film thickness (Fig. 4b). The increase of the dielectric film thickness caused by the streptavidin attachment from the solution having a concentration of $c_1^{St} = 45\ \mu g/ml$ was $\Delta d_{PC}^{A+St}(45\ \mu g/ml) = 5.4$ nm.

We investigated the sensitivity of the secondary peak shift to the concentration of the protein, exposing another grating to a streptavidin solution having a concentration of $c_2^{St} = 30\ \mu g/ml$. To minimize the effect caused by the differences between the grating surface profiles, a polymer grating resulting in a secondary minimum in the close proximity of the secondary peak measured on *Grating A* was selected. The *Grating C* was generated by $N^C = 950$ number of laser pulses, which resulted in an average modulation depth of $a^C_{average} =$ 25–27.5 nm. The AFM measurements have shown streptavidin adherence along the foots of the polymer hills, and in the sub-valleys of the secondary structure similarly to the attachment experienced on *Grating A* (Fig. 7a–d). Comparing the positions of the secondary peaks on the resonance curves measured before and after polymer seeding we concluded, that the protein attachment from the more diluted solution on *Grating C* resulted in a shift of $\Delta\varphi^{C+St}_{secondary}(30^\circ, 30\ \mu g/ml) = 2.8^\circ$. This shift was much smaller than the value measured in case of seeding from the solvent having a higher concentration (Fig. 7e). The position of the secondary peak after protein seeding was $\varphi^{C+St}_{secondary}(30^\circ, 30\ \mu g/ml) = 53.88^\circ$, which indicated $\Delta d_{PC}^{C+St}(30\ \mu g/ml) = 3.7$ nm increase in the average dielectric film thickness caused by the streptavidin attachment from the more diluted solution.

We performed protein seeding on untreated surface parts also, and determined the primary resonance peak shifts in case of the above two concentrations (Fig. 7f). The average thickness increase measured after protein adherence from solvents having higher concentration was $\Delta d_{PC}^{untreated+St}(45\ \mu g/ml) = 6.3$ nm, while a slightly reduced enhancement of $\Delta d_{PC}^{untreated+St}(30\ \mu g/ml) =$ 4.9 nm was determined after seeding from solution having smaller concentration.

Comparing the changes of the resonance curves detected on structured and untreated surface parts we can conclude that the $S_{secondary}$ sensitivity of the secondary resonance position shift to the concentration experienced on the gratings, was commensurable with the $S_{primary}$ sensitivity of the primary resonance peak shift, measured on untreated samples:

$$S_{secondary} = \frac{\Delta\varphi^{grating}_{secondary}}{\Delta c} = 0.091\frac{^\circ}{\mu g/ml} \approx S_{primary} = \frac{\Delta\varphi^{untreated}_{primary}}{\Delta c} = 0.096\frac{^\circ}{\mu g/ml}.$$

Taking into account that the $\Delta\varphi_{minima} = \pm 0.08^\circ$ uncertainty in the determination of the resonance minima corresponds to $\Delta S = \pm 0.005\frac{^\circ}{\mu g/ml}$, we can state that the sensitivities equaled within the error of measurement. This cannot be the result of the sensitivity of the secondary peak to the dielectric layer thickness, since the slope of the $\varphi_{secondary}(d_{PC}, n = 1, P_{grating} = 416\ nm)$ curve was much smaller than the slope of $\varphi_{primary}(d_{PC})$ (Fig. 4b). The adhesion modulation mediated adherence on the grating may be responsible for the achievable concentration sensitivity.

The advantages of the rotated grating-coupled SPR detection based on the new transducing medium can be summarized, as follows: (1) the bimetallic layer composition ensured chemical resistance and sharp resonance peaks; (2) the secondary resonance minimum emerging caused by grating coupling was narrower then the primary resonance peak; (3) both of the plasmon field enhancement caused by coupling on polymeric grating, and the periodic adhesion increase caused by the laser treatment occurred in the valleys of the sub-micrometer periodic structure, resulting in additional sensitivity enhancement. Further technical benefit was that the secondary minimum was detectable at smaller angles. Based on the above described results the combined prism- and rotated grating-coupling configuration is proposed to detect bio-molecule attachment via angle interrogation method, monitoring the shift of the grating-coupling caused secondary resonance peak.

The sensitivity may be improved by optimizing the protein–surface interaction via properly designed polymer surface structure. In our present study PC was selected due to the biocompatibility and solubility in harmless solvents of this polymer. The UV pre-treatment of other biocompatible polymers is in progress to investigate the degree of the adhesion enhancement in the structure's valleys, which is key effect to promote selective adherence of bio-molecules from solutions. The above described results proved that the streptavidin attachment

caused well defined shift of the secondary resonance peak. The advantage of this protein is its capability to bind biotinylated specimens from solvents. Further studies are in progress to analyze the concentration sensitivity of the secondary peak shift, and the detectability of the bounded specimens. The modulation-amplitude sensitivity of the grating-coupling efficiency may open detection possibilities in case of very small amount of biomolecules.

4. Conclusion

New type of layered substrates was prepared by the evaporation of Au–Ag bimetallic films having appropriate composition allowing high sensitivity in surface plasmon resonance measurements and ensuring chemical resistance. A polymer layer over-coated onto the bimetallic film was structured by UV laser based interference method to prepare a novel sensing surface. It was shown that the presence of the laser induced grating causes plasmon coupling effect, and the dependence of the grating-coupled secondary resonance peak on the rotation angle and modulation amplitude of the grating was proven theoretically and experimentally. It was experienced that periodic adhesion pattern coexistents on the surface in presence of the laser induced topographical grating. The periodic adhesion-mediated periodic bio-molecule attachment was realized seeding streptavidin from differently concentrated solutions on the structured areas. The most important advantage of the laser induced gratings is that the strong adhesion collect the biomolecules along the foot of the structure's hills, where the field of plasmons coupled by the grating itself is high. The concentration sensitivity of the shift of the secondary resonance position caused by periodic protein attachment proved that the rotated grating-coupled SPR on bimetallic films covered by polymer gratings may be proposed as novel sensing principle.

Acknowledgements

Financial support of this research was provided by the SFB Grant No. 569, and the Hungarian Foundations: OTKA No. TS040759 and M41862. M. Csete would like to thank for the János Bólyai Research Fellowship of the Hungarian Academy of Sciences. We gratefully acknowledge the many discussions with Z. Gingl and B. Heise. We would like to thank to F. Kárpát for metal layer evaporation and to Cs. Vass for the temperature model calculations.

References

[1] E. Yablonovitch, J. Opt. Soc. Am. 10 (1993) 283.
[2] T.W. Ebbesen, H.J. Lezec, H.F. Ghaemi, T. Thio, P.A. Wolff, Nature 391 (1998) 667.
[3] F.J. Garcia Vidal, L. Martin-Moreno, Phys. Rev. B 66 (2002), art. No. 15541.
[4] N. Félidij, J. Aubard, G. Lévi, J.R. Krenn, G. Schider, A. Leitner, F.R. Ausenegg, Phys. Rev. B 66 (2002), art. No. 24540.
[5] W.L. Barnes, T.W. Preist, S.C. Kitson, J.R. Sambles, N.P.K. Cotter, D.J. Nash, Phys. Rev. B 51 (16) (1995) 11164.
[6] B. Fischer, T.M. Fisher, W. Knoll, J. Appl. Phys. 75 (3) (1994) 1577.
[7] W.L. Barnes, T.W. Persist, S.C. Kitson, J.R. Sambles, Phys. Rev. B 54 (9) (1996) 6227.
[8] B. Rothenhausler, W. Knoll, Appl. Phys. Lett. 51 (11) (1987) 783.
[9] J. Homola, S.S. Yee, G. Gauglitz, Sensors Actuators B 54 (1999) 3.
[10] E. Fontana, R.H. Pantell, S. Strober, Appl. Opt. 29 (3) (1990) 4694.
[11] C.E. Jordan, B.L. Frey, S. Kornguth, R.M. Corn, Langmuir 10 (1994) 3642.
[12] C.R. Yonzon, E. Jeoung, S. Zou, G.Z. Schatz, M. Mrksich, R.P.V. Duyne, J. Am. Chem. Soc. 126 (2004) 12669.
[13] P.R.H. Stark, A.E. Halleck, D.N. Larson, Methods 37 (2005) 37.
[14] A.C. Duncan, S. Lazare, Ch. Baquey, Appl. Surf. Sci. 221 (2004) 93.
[15] M. Csete, J. Kokavecz, Zs. Bor, O. Marti, Mater. Sci. Eng. C 23 (2003) 939.
[16] S.A. Zynio, A.V. Samoylov, E.R. Surovtseva, V.M. Mirsky, Y.M. Shirshov, Sensors 2 (2002) 62.
[17] M.A. Ordal, L.L. Long, R.J. Bell, S.E. Bell, R.R. Bell, R.W. Alexander Jr., C.A. Ward, Appl. Opt. 22 (1983) 1099.
[18] H.M. Phillips, D.L. Callahan, R. Sauerbrey, G. Szabó, Z. Bor, Appl. Phys. A 54 (1992) 158.
[19] Th. Stifter, E. Weilandt, O. Marti, Appl. Phys. A 66 (1998) 597.
[20] M. Csete, G. Kurdi, J. Kokavecz, V. Megyesi, K. Osvay, Z. Schay, Zs. Bor, O. Marti, Mater. Sci. Eng. C 26 (2006) 1056.
[21] M. Csete, O. Marti, Zs. Bor, Appl. Phys. A 73 (2001) 521.
[22] M. Csete, Cs. Vass, J. Kokavecz, M. Goncalves, V. Megyesi, Zs. Bor, M. Pietralla, O. Marti, Appl. Surf. Sci. 247 (1–4) (2005) 477.
[23] H. Raether, Surface Plasmons, Springer, Berlin, 1986.
[24] M. Stark, C. Möller, D.J. Müller, R. Guckenberger, Byophys. J. 80 (2001) 3009.

Available online at www.sciencedirect.com
ScienceDirect
Organic Electronics 8 (2007) 161–174
Organic Electronics
www.elsevier.com/locate/orgel

Fabrication of equally oriented pancake shaped gold nanoparticles by SAM-templated OMCVD and their optical response

Anne Kathrena A. Aliganga [a,c], Ingo Lieberwirth [a], Gunnar Glasser [a], Anne-Sophie Duwez [a,b], Yingzhi Sun [c], Silvia Mittler [a,c,*]

[a] *Max Planck Institute for Polymer Research, Ackermannweg 10, D-55128 Mainz, Germany*
[b] *Unité de Chimie et de Physique des Hauts Polymères and Research Center in Micro and Nanoscopic Electronic Devices and Materials (CERMIN), Université catholique de Louvain, Place Croix du Sud 1, B-1348 Louvain-la-Neuve, Belgium*
[c] *Department of Physics and Astronomy, The University of Western Ontario, London, Ont., Canada N6A 3K7*

Available online 12 October 2006

Abstract

The optical response of non-spherical gold nanoparticles not only depends on the size of the objects, but also on their shape and orientation with respect to the polarization direction of the light, exciting the plasmon resonance. This study demonstrates a method to grow non-spherical gold nanoparticles via organometallic chemical vapor deposition (OMCVD) onto planar substrates that are covered by SH-terminated self-assembled monolayers (SAMs). Trimethylphosphinegoldmethyl ($(CH_3)_3PAuCH_3$) is used as the volatile organic precursor. The shape of the deposited particles varies with respect to the nature of the template SAM: disc-like and pancake shaped nanoparticles are fabricated with different aspect rations between the two main axes. UV–vis, AFM, STM, SEM and evanescent waveguide absorption spectroscopy (EWAS) of the OMCVD gold nanoparticles are applied to determine and verify the dimensions and orientation of the nanoparticles in two dimensions. When clusters of nanoparticles are formed, an additional plasmon band with a large red-shift is observed.
© 2006 Elsevier B.V. All rights reserved.

Keywords: SAM; OMCVD; Gold nanoparticles; Aspect ratio; Orientation; Trimethylphosphinegoldmethyl ($(CH_3)_3PAuCH_3$) precursor; Plasmon resonance; Cross-talk; Cluster formation

1. Introduction

The extensive research interest in nanometer-dimension inorganic nanoparticles has been mainly driven by their broad impact on the emerging disciplines of nanoengineering [1], nanoelectronics [2], and nanobioelectronics [3]. Gold nanoparticles, in particular, have been the focus of numerous investigations in recent years because of the promises offered by their optical, electronic, and chemical properties [4]. These nanocluster-based devices have been envisioned as the next generation in electronics miniaturization because of quantum confinement effects that allow tunable electronic, magnetic, and photonic properties [5].

* Corresponding author. Address: Department of Physics and Astronomy, The University of Western Ontario, London, Ont., Canada N6A 3K7. Tel.: + 1 519 661 2111x88592; fax: +1 519 661 2033.
E-mail address: smittler@uwo.ca (S. Mittler).

1566-1199/$ - see front matter © 2006 Elsevier B.V. All rights reserved.
doi:10.1016/j.orgel.2006.09.002

Recent years have also seen a tremendous impact on silver and gold nanoparticles and nanoobjects in biological assays, detection, labeling and sensing. The immobilization of molecules such as recognition sites and the clustering of the nanoparticles into larger agglomerates with a pronounced shift in the plasmon absorption band on nanoparticles in solution are well studied [6].

One of the technological challenges is to fabricate robust and organized assemblies of these nanoscale building blocks [7] where the collective structural properties and functions might be manipulated by the nature, size, position and overall composition of the nanoparticles on a substrate. Among the various techniques developed, self-assembly is quite effective in creating ordered superlattices of nanoparticles by exploiting molecular interactions such as van der Waals forces, chemisorptive bonding, electrostatic interactions, etc. [4,5,8]. A key structural element is a bifunctional bridge, such as an aliphatic dithiol, that links the nanoparticles to the substrate surface and/or allows the layering of nanoparticles. These processes can be achieved by simple beaker chemistry.

Self-assembled monolayers (SAMs) [9] have drawn special attention because their preparation is simple and the resulting films can be densely packed, highly ordered and largely free of defects. In this work, self-assembled monolayers consisting of alkanedithiols are used as templates for the nucleation and growth of nano-sized gold particles.

Several techniques have been explored in the preparation of gold nanoparticles. For instance, colloidal methods, physical vapor deposition processes and template syntheses all currently enjoy varying degrees of popularity. From all these methods, the colloidal approach is undoubtedly the most heavily researched and exploited. Yet, despite numerous successful applications, there are certain limitations to this approach. Issues such as particle stability, orientation of surface bound spherical and non-spherical particles, controlled aggregation and flexibility for further functionalization, continue to be problematic. Although nanoparticles and their superstructures have already given much to chemists, physicists, biologists and material scientists in term of theoretical, experimental and practical considerations, there still remain many possibilities for application and the discovery of new physical effects.

This study presents an alternative method for preparing gold nanoparticles that are covalently attached to a surface [10]. The preparation of Au nanoparticles is done via an organometallic chemical vapor deposition (OMCVD) process where particle growth occurs directly at a functionalized surface. A schematic outline of the preparation of the OMCVD gold on SAMs is presented in Fig. 1.

The OMCVD process offers several advantages aside from the possibility of area selective deposition where nucleation and growth only occur on so-called growth areas [10], it is also economical as the deposition process is done under low vacuum and relatively low temperatures. The aggregation state of the particles can be controlled because the particles are immobilized on the surface and fixed in their morphology. In addition, the OMCVD gold nanoparticles are free and flexible for further functionalization because they are not capped [11].

In order to enhance the design and optimization of photonic applications based on OMCVD gold nanoparticles located at a surface of a transparent substrate, a thorough understanding of the basic properties of the particles is necessary. In this study the size and form of the OMCVD gold nanoparticles are characterized using atomic force microscopy (AFM), scanning tunneling microscopy (STM), scanning electron microscopy (SEM), transmission electron microscopy (TEM), UV–vis spectroscopy and evanescent waveguide absorption spectroscopy (EWAS). This study also emphasizes the non-spherical shape of the particles and their uniform orientation on the substrate which exhibit more interesting and exciting photonic plasmon resonances than spherical particles. This may lead to a

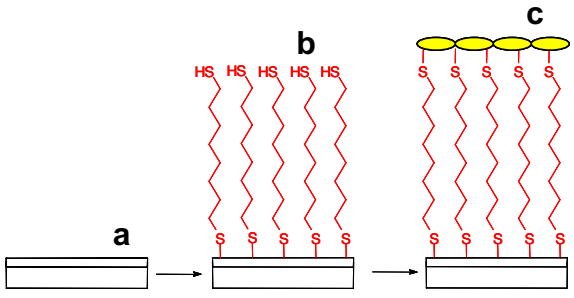


Fig. 1. Schematic outline of the fabrication of gold nanoparticles onto SAMs via the OMCVD process. (a) Preparation of the substrate, e.g. metal-coated glass or mica, bare glass or silicon wafer for silanization, (b) self-assembly process and (c) deposition of gold nanoparticles onto SH- terminated SAMs. (SAM molecules and gold particles are not to scale. Typically a substrate is 1–2 mm thick, the SAM has a thickness around 2–5 nm and the gold nanoparticles can be as thin as 5 Å, but also so large laterally that they form percolated, connected structures on the SAM surface with lengths up to μm and mm.)

greater tunability and tailoring of the plasmon resonance for specific applications.

2. Experimental section

2.1. Au and Au(1 1 1) substrate preparation

Gold (Balzers, 99.99%) was deposited onto BK7 (Schott, Mainz) or freshly cleaved mica substrates (for gold(1 1 1)) using a vacuum coating system (Edwards, FL 400) at $p \leqslant 5 \times 10^{-6}$ mbar. Before deposition, the mica was heated to 650 °C for 3–4 min under N_2 atmosphere for cleaning purposes. It was immediately placed inside the vacuum evaporation machine. The typical evaporation rate was 1 Å/s, and the thickness of the gold film was 60 nm. Prior to the self-assembly process, the freshly evaporated Au on the mica samples was annealed to form large areas with (1 1 1) orientation on the surface. Annealing was carried out at 650 °C for 1 min under a N_2 atmosphere in a tubular oven (Heraeus) and chilled to room temperature under N_2 atmosphere. This method produced flat Au(1 1 1) terraces as large as 300 nm × 300 nm basing from AFM measurements.

2.2. SAM preparation

1,8-Octanedithiol (C8-DT; Aldrich, 97+%), octane thiol (Aldrich, 97+%) and ethanol (Chromasolv®, Riedel-de Haën, 99.9%) were used without further purification. Dithiol-SAMs were prepared by immersing freshly prepared Au substrates in a 1 mM ethanolic solution of the alkanedithiol or the appropriate mixture with octane thiol for approximately 15 h. The samples were then cleaned by rinsing extensively with ethanol, dried with N_2, and stored under inert conditions (sealed in a glass flask under Ar atmosphere).

1-Dodecanethiol (Sigma–Aldrich, product of ATOFINA Chemicals, Inc., 98+% purity) was used without further purification and dissolved in ethanol (Commercial Alcohols Inc., Brampton, ON, puriss) at a concentration of 1 mM. The SAM formation was carried out for 15 h. The samples were then cleaned by rinsing extensively with ethanol and Milli-Q-water (Milli-Q, $\rho > 18$ MΩ cm, Millipore) and dried with N_2.

3-Mercaptopropyltrimethoxysilane (Fluka, 97.0%) was used without further purification for SAMs on silicon wafers, BK7 glass substrates and channel waveguides. Before the silanization process, the substrates were first cleaned by ultra sonication in a 2% solution of Hellmanex (Helma) and Milli-Q-water (Milli-Q, $\rho > 18$ MΩ cm, Millipore) for 20 min each. Pretreatment of the surface with acid or base followed. Glass substrates were immersed in piranha solution (4:1 mixture of concentrated sulfuric acid (H_2SO_4) with hydrogen peroxide (H_2O_2), stored overnight and rinsed thoroughly with Milli-Q-water). (CAUTION! Piranha solution is a strong acid and very reactive. Handle with care. Do not store it especially in a tightly closed container because of danger of explosion.) The substrates were dried in a vacuum at 94 °C for 1–2 h and cooled down at room temperature for further use. For silicon wafer substrates, basic pretreatment on the surface was employed as well: immersing the substrates in a solution containing a 5:1:1 mixture of Milli-Q-water, ammonium hydroxide (NH_4OH) and hydrogen peroxide (H_2O_2), respectively, at 80 °C for 30 min. The substrates were cooled down to room temperature, rinsed thoroughly with Milli-Q-water and dried in a vacuum at 94 °C for 1–2 h and cooled down at room temperature for further use. One percent solution of 3-mercaptopropyltrimethoxysilane (MPTS) in ethanol was prepared and allowed to stand for 30 min for hydrolysis reaction. The cleaned substrate was immersed for 1 h at room temperature. It was rinsed with ethanol and subsequently baked in a vacuum oven at 94 °C for 1 h. The freshly prepared mercaptosilane SAMs were used immediately as substrates for the OMCVD gold nanoparticles.

2.3. Organometallic chemical vapor deposition (OMCVD) of gold onto SAMs

The vapor deposition of $[(CH_3)_3P]AuCH_3$ [12] onto SAMs was carried out in a home built vacuum sealed glass reactor chamber, which contained the SAM sample and a small glass vessel with 20 mg of the gold precursor. The reactor was evacuated ($p_{max} = 2.0 \times 10^{-2}$ mbar) and placed in an oven at 70 °C [10,11]. A 30 min deposition time was employed in this work if not stated otherwise. Subsequently, the SAMs were quickly removed, rinsed with dry ethanol and stored under inert conditions.

2.4. Atomic force microscopy (AFM)

AFM images were acquired using a Nanoscope™ IIIa Atomic Force Microscope (Digital Instruments, Santa Barbara, CA). Imaging was done in

tapping mode at ambient conditions. Silicon nitride cantilevers of 100 μm length (spring constant 0.1 N/m) with integrated sharpened tips (Olympus, Tokyo, Japan) were used.

All AFM tips used to determine the height of the particles were calibrated by imaging colloidal gold with known shape and size as a reference sample. In addition, when comparing gold nanoparticles on mixed SAMs with different ratios, very dilute samples were prepared in order to avoid the tip convolution effects that arise when particles are too close to each other.

2.5. Electron microscopy (SEM and TEM)

SEM measurements were performed using a LEO 1500 field-emission scanning electron microscope (LEO Electron Microscopy Ltd.). Specimens were prepared for transmission electron microscopy (TEM) by peeling off the OMCVD Au film deposited on glass using a cellulose acetate film. Acetone was used to adhere the film onto the surface and was then evaporated. The film containing the peeled-off CVD Au samples was then evaporated with carbon. Samples for TEM analysis were prepared by placing the film containing the nanoparticles on a carbon-coated copper grid. The film was then dissolved using acetone leaving the OMCVD Au nanoparticles on the grid. TEM micrographs were obtained with a Philips CM12 electron microscope operated at 120 keV.

2.6. UV–vis spectroscopy

UV–vis absorption spectra were obtained using Lambda 9 UV/Vis/NIR recording spectrophotometer (Perkin–Elmer). Baseline correction was performed before scanning the samples. SAM films were scanned with clean glass as a reference. For OMCVD Au samples, SAM films were used as a reference.

2.7. Evanescent waveguide absorption spectroscopy (EWAS)

A soda lime glass sample (microscopy slide) with ion exchanged channel waveguides [13,14] of widths 1, 2, 3, 4, 5 and 10 μm located in the surface area were made by exchanging sodium with potassium ions from a potassium nitrate melt at 400 °C through a previously deposited metal mask (patterned by photo lithography technology) in a temperature stabilized three-zone furnace for 60 min. The polished end fires [14] were illuminated via the end fire of a glass fiber and a microscope objective (Newport, 20×) by a white light source (ocean optics, Dunedin, Florida, USA, HL-2000-HP with 20 W output) with an emission spectrum of 360–2000 nm. The light propagated in the channel waveguide as a waveguide mode of either TE or TM polarization (chosen by a polarizer in front of the coupling objective) exhibiting an evanescent field on its free accessible surface. The transmitted light was then collected via a second microscope objective (Newport, 20×) and fed through a second glass fiber into a spectrometer (Ocean optics, Dunedin, Florida, USA, HR-2000 spectrometer). The absorption spectra of the gold nanoparticles recorded this way were normalized by the spectrum of the silanized channel waveguide.

2.8. Quartz crystal microbalance (QCM)

For QCM analysis of the adsorbed gold, deposition experiments were carried out on the front electrode of a quartz crystal microbalance. The overtone-polished, gold-coated AT-cut quartz crystals (Maxtek, Torrance, CA) had an outer diameter of 2.54 cm. The self-assembled monolayer was deposited on the front electrode of the quartz plate in the usual way. The quartz plate was connected to an impedance analyzer (E5100A, Agilent). Resonance frequency and bandwidth were determined by fitting resonance curves to the conductance spectra as described previously [15].

2.9. Spontaneous desorption time-of-flight mass spectrometry (SD-TOF-MS)

The measurements were performed using a linear time-of-flight mass spectrometer in high vacuum at a pressure of about 1×10^{-6} mbar. Atomic and molecular ions from the sample were released by spontaneous desorption, a secondary ion process in which the sample is not bombarded by particles from an external source [16]. Primary ions of adsorbates are field desorbed from the edges of an acceleration grid located in front of the sample. These ions are accelerated towards the sample gaining keV energies. They finally sputter secondary ions from the sample. Spectra of negative secondary ions are recorded using the simultaneously emitted secondary electrons from the sample surface as trigger particles. An acceleration voltage of 9.5 kV was

applied to the sample. The recording time of a spectrum was 20–40 min. Within one spectrum, mass peaks of interest were integrated and normalized with the number of start events with one or more corresponding stop events. This lead to a relative ion yield that allowed for a comparison of intensities of equivalent peaks in different spectra. Fragments of masses *m*/z up to 2000 u can be analyzed by this setup.

2.10. Scanning tunnelling microscopy

STM was performed with a homebuilt scan head in combination with a commercial controller (RHK SPM 1000). PtIr tips were used for imaging. The imaging parameters were 500 mV bias, currents below 100 pA under ambient conditions.

3. Results and discussion

Chemical vapor deposition (CVD) is a method for depositing films of various materials, which involves the thermally induced reaction of a material-containing molecule on a heated surface [17]. First, a volatile precursor is transported into the reactor and to the substrate leading to an adsorption and a surface reaction, whereby the metal is deposited and the by-products are subsequently desorbed. Trough diffusion the metal atoms then form a stable nucleus where subsequent growth occurs. The volatile organometallic precursor used for the OMCVD of gold is trimethylphosphinegoldmethyl ($(CH_3)_3PAuCH_3$), which is known to give pure gold films at low temperatures [17]. The reaction of the precursor to the surface is illustrated in the equations below, where (s) refers to the attachment to the functionalized surface and (g) to a gaseous molecule. The final products of the reaction are solid gold, which is attached to the functionalized surface, and the gaseous products, ethane and trimethylphosphine. When the hydrogen from the nucleating thiol group reacts with the methyl group the final products are solid gold, methane, ethane and trimethylphosphine

$$(CH_3)_3PAuCH_{3(g)} \rightarrow [AuCH_3]_{(s)} + P(CH_3)_{3\,(g)}$$

$$[AuCH_3]_{(s)} + (CH_3)_3PAuCH_{3\,(g)} \rightarrow 2Au_{(s)} + CH_3{-}CH_{3\,(g)} + P(CH_3)_{3\,(g)}$$

or

$$R{-}SH + [AuCH_3]_{(s)} + 2(CH_3)_3PAuCH_{3(g)} \rightarrow R{-}SAu_{3\,(s)} + CH_{4\,(g)}CH_3{-}CH_{3\,(g)} + 2P(CH_3)_{3\,(g)}$$

Depositions of OMCVD gold on SH-terminated SAMs on different substrates, gold(1 1 1), flat silver and silicon wavers, were performed. Fig. 2 shows a (a) STM and an (b) AFM image of the organometallic chemical vapor deposited gold nanoparticles onto C8-DT SAMs on a Au/mica substrate. Pancake-like structures were observed with an average particles' height of approximately 5 Å as obtained from the AFM measurements (Fig. 2b) and lateral diameters of about 5 nm as determined from STM measurements (Fig. 2a), yielding an aspect ratio of 1:10. Quartz crystal microbalance measurements of

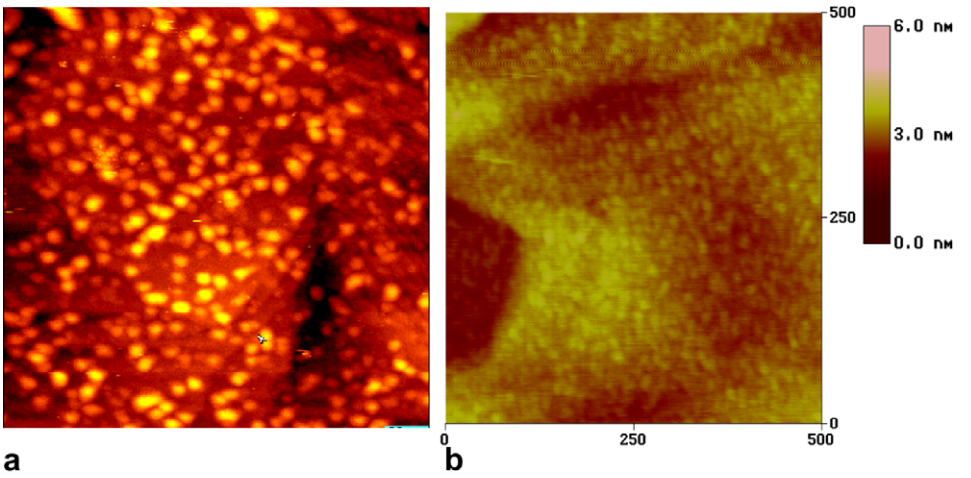


Fig. 2. (a) STM (195 nm × 195 nm) and (b) AFM (500 nm × 500 nm) images of OMCVD gold nanoparticles on a C8-DT SAMs on Au(1 1 1)/mica substrate.

the same samples yielded 1.4×10^{15} atoms/cm^2 as the number of gold atoms per unit area. Employing the QCM results and the corresponding cluster size of about 5 Å in height and 5 nm lateral sizes, an average 35-atom gold cluster is calculated on the C8-DT SAMs on Au/mica.

Fig. 3 shows the AFM results of the gold nanoparticles deposited on C8-DT SAMs on Au(1 1 1)/mica (a), and on flat Ag/mica (b), and on MPTS SAMs/silicon waver (c). The height distribution histograms show a particle distribution of MPTS SAMs/silicon and of C8-DT SAMs on Ag/mica that

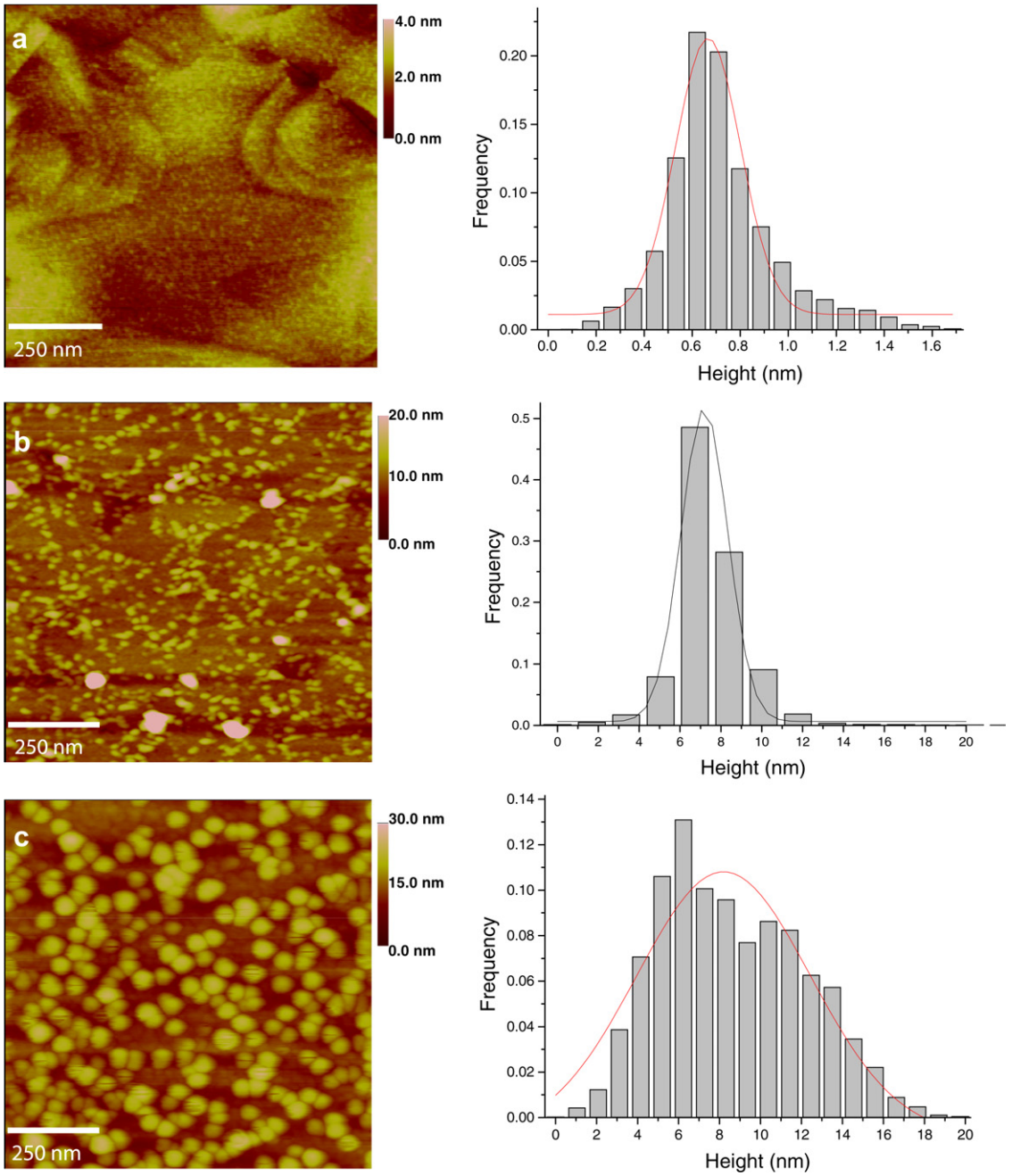


Fig. 3. AFM images of OMCVD gold on –SH-terminated SAMs on different substrates: (a) C8-DT SAMs on Au(1 1 1)/mica, (b) C8-DT SAMs on flat Ag/mica and (c) MPS SAMs on silicon wafer. On the right side of the images are the corresponding height distributions of the gold nanoparticles.

are both very similar with mean height values of about 7.5 nm. While the height of gold nanoparticles on C8-DT SAMs on Au/mica was remarkably low with a mean height of 7 Å. The distribution of the heights is quite broad in all cases, but very much so in the case of MPS SAMs/silicon waver samples.

There are several differences between the various SH-terminated SAMs that can be considered to cause these observations. First, it can be due to the differences in the surface roughness between the substrates, and therefore due to individual orientations of the SH-moieties on the surface. Here Au(1 1 1) substrates show the smoothest surface followed by flat Ag and eventually, the roughest surface is the acid treated silicon wafer substrate: showing approximately 1 Å, 5 Å and 3–5 nm rms values (for a 1 μm × 1 μm area, measured at least at two locations), respectively. Second, the density of free SH-groups on the surface available for the nucleation and growth of the nanoparticles could yield a difference in the nucleation and growth conditions.

Roughness: Considering the differences in surface roughness, it turns out that the more flat the surface is, the more uniform are the growth conditions depicted by the most narrow height distribution of the C8-DT SAM on Au(1 1 1)/mica substrate (Fig. 3a). This is probably due to a more uniform orientation of the terminal SH groups.

Nucleation density: Why is there a difference in nucleation site density between SAMs on Au or on Ag? For instance, the chemisorption of C8-DT SAMs on Ag substrate seems more probable than physisorption [18], while in C8-DT on Au, competition between chemisorption and physisorption occurs. The difference between alkanethiolate SAMs on Au(1 1 1) and Ag(1 1 1) results from an interplay of chemisorption and chain-chain interactions [9]. Silver is more reactive than gold, it forms an oxide spontaneously since its oxidation potential is 1.7 eV lower and its work function 0.6 eV lower than gold. Gold and silver also differ due to effects in the peak-to-valley roughness at their [1 1 1] lattices, 6.0 kcal mol^{-1} for Au(1 1 1) and only 3.3 kcal mol^{-1} for Ag(1 1 1). Therefore, even if a Au(1 1 1) or a Ag(1 1 1) surface is atomically flat, it is energetically heterogeneous, which results in site selective adsorption. And, more site selection will be observed in a Au(1 1 1) surface than in Ag(1 1 1) since the former has a higher peak-to-valley roughness value than the latter. All these differences explain why chemisorption is more probable on Ag surfaces than on Au. When chemisorption is dominant the probability that most of the dithiol molecules will be attached with both of the –SH groups to the surface is enhanced leading to flat lying structures with diminished SH-group density. Therefore, it is possible that the SH density on Ag is smaller in comparison to that of Au and this difference gives a certain effect on the height growth of the nanoparticles.

XPS data (Fig. 4) show the amount of free SH groups in SAMs on Au(1 1 1) (Fig. 4a), Ag (Fig. 4b), and silicon wavers (Fig. 4c). The S 2p spectrum recorded from C8-DT on Au (Fig. 4a) shows two components: one attributed to S–Au and one to free SH. The free SH accounts for 29% of the total amount of sulfur. The spectrum recorded from the C8-DT SAM on Ag (Fig. 4b) shows one additional component which can be attributed to oxidized sulfur species (sulfonates and sulfinates). We can quite confidently state that those species come from the oxidation of Ag–S bonds. We thus have 16% free SH. It is worth mentioning here that sulfur oxidizes more rapidly when it is bound to Ag (a catalytic effect) than when it is in the form of free SH. It is also not surprising that the oxidized species are detected only for the layer adsorbed on Ag and not for the one adsorbed on Au. Oxidation and desorption are known to take place at defect sites (such as domain boundaries, holes) and thus it is more rapidly for more rougher substrates and film containing flat-lying molecules [19]. As for the MPTS layer on silicon wavers (Fig. 4c), we have recorded the S 2s signal (the S 2p signal is not exploitable because it falls in the same energy range than the energy loss peak of Si 2s) and found that only a small amount of sulfur species are free SH (less than 10%). This nucleation site density difference should have a severe effect on the particle height [20].

In order to check this proposed nucleation site density influence, a series of dilution experiments on C8-DT SAMs on Au(1 1 1)/mica were performed. The C8-DT was systematically diluted with octane thiol. Fig. 5 shows the height histograms obtained from AFM images with decreasing amount of C8-DT in the self-assembly solution. By decreasing amount −10% in Fig. 5(a), 5% in Fig. 5(b) to 1% in Fig. 5(c) of C8-DT in the SAM forming solution – the average height rose from 2.4 nm along 3.5 nm to 4.5 nm. Nevertheless, the average amount of deposited gold increases when the amount of C8-DT increases: as seen in Fig. 6 showing relative gold amount data obtained by SD-TOF-MS.

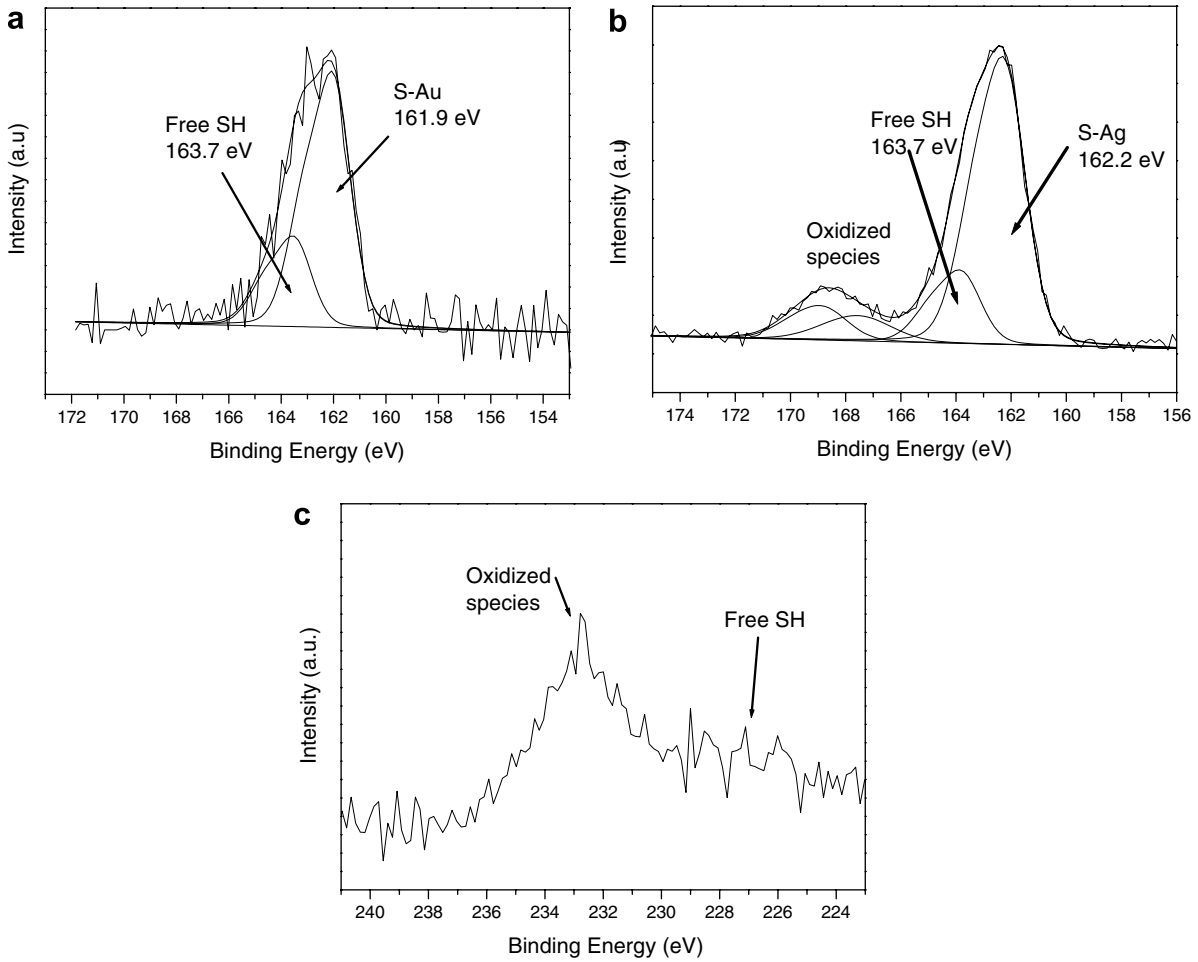


Fig. 4. S 2p XPS spectra of SAMs prepared from C8-DT SAMs on Au (a), Ag (b) and silicon (c) substrates. The lines are the envelopes of doublets (Gaussian–Lorentzian 85–15% linear combination, with an intensity ratio 2:1 and a splitting of 1.18 eV for the $2p_{1/2}$ and $2p_{3/2}$ components) used to fit the spectra. S 2s XPS spectrum of MPTS layer on silicon (c).

Because available nucleation sites compete at a given precursor pressure for each available gold atom the height per present particle increases on average when the amount of competing sites decreases. This is similar but not identical to Ostwald ripening [21]. But still the overall amount of gold decreases. The non-linear curve form in Fig. 6 represents inter alia the non-linear immobilisation probability of a dithiol – monothiol binary mixture. There is essentially no 1:1 relation between the binary composition in the self-assembly solution and the binary composition in the finally formed SAM on the substrate [20,22]. This effect is discussed in detail elsewhere [20].

On the basis of the results of the dilution experiment and the XPS results, we can conclude that the height difference of gold nanoparticles grown on C8-DT SAMs on Au and on Ag is indeed related to the terminal SH group density.

The deposition of OMCVD gold nanoparticles onto SH terminated silane SAMs on glass and silicon wafer substrates are particularly interesting as they allow for simple spectroscopic and electron microscopy analysis of the gold films. They are also advantageous on account of their high rigidity and low cost. Fig. 7 shows the transmission UV–vis spectrum of OMCVD gold (30 min deposition time) on MPTS SAMs/glass. The appearance of the absorption peak around 520–530 nm is consistent with what has already been observed for gold nanoparticles with sizes of about 5–20 nm [22]. This absorption peak is known as the plasmon resonance, and occurs when the incident photon frequencies match with those of the collective

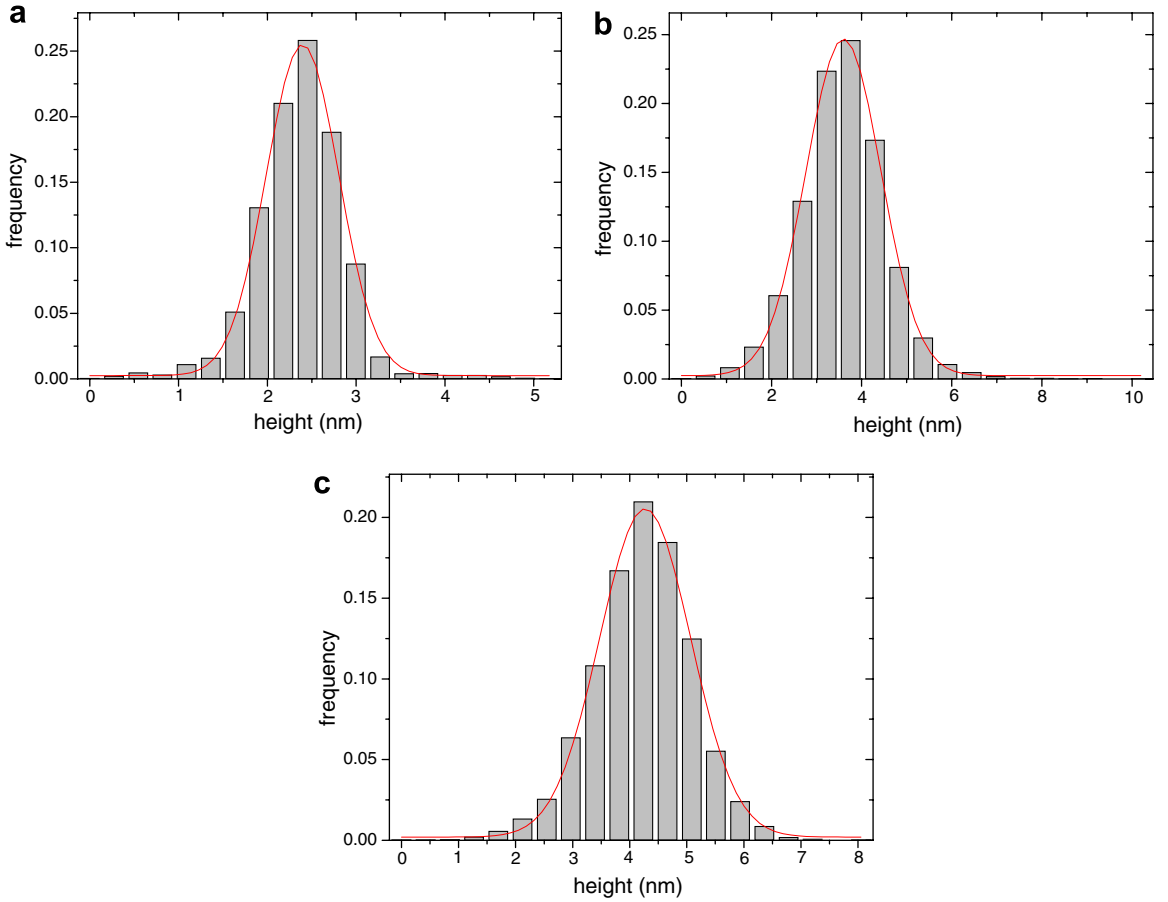


Fig. 5. Height histograms of gold nanoparticles grown on diluted C8-DT SAMs: (a) 10%, (b) 5% and (c) 1% C8-DT in the SAM.

oscillations of the conduction electrons of metal nanoparticles [23,24]. Gold and generally any noble metal nanoparticles exhibit this plasmon absorption band in the visible region. The optical and electronic properties of these metal nanoparticles are dependent on particle size, shape, and environment [4f,25,26]. The spectral width of the nanoparticle

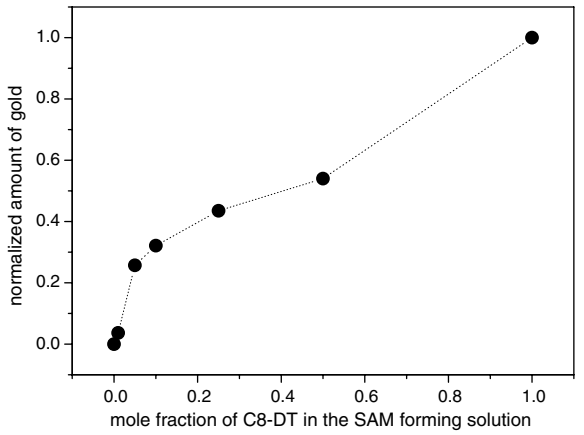


Fig. 6. Normalized amount of gold present on mixed SAMs on gold/glass substrates measured by SD-TOF-MS versus mole fraction × (in the self-assembly solution) of C8-DT in a binary mixture of octane thiol and C8-DT.

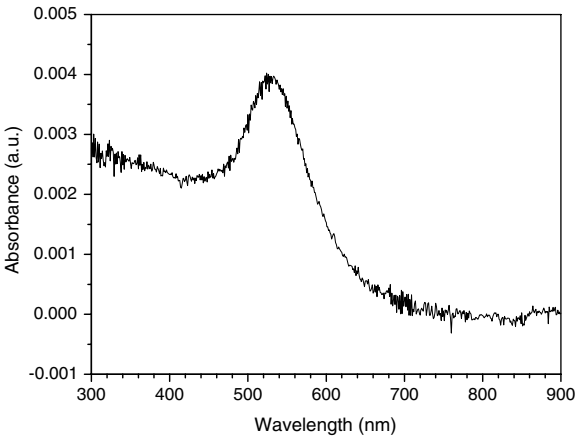


Fig. 7. UV–vis spectra of the OMCVD gold nanoparticles on MPTS SAMs.

ensemble probed is fairly broad in comparison to monodisperse gold nanoparticle samples [26b], representing a fairly broad nanoparticle width distribution. In transmission experiments only the width of the nanoparticle can be probed due to the polarization direction.

In order to have additional shape and size information of the nano-sized OMCVD gold particles, e.g. their lateral dimensions, SEM analysis of gold samples grown on MPTS SAMs on silicon wafers were performed. Fig. 8 shows a corresponding SEM image. The obtained micrograph shows that the particles did not give complete surface coverage during the deposition time employed in this study. It is important to note that in the OMCVD process, size and coverage of the particles on the surface can be controlled by varying the deposition time as demonstrated earlier [27]. The particles occupied approximately 10–20% of the surface area. In addition, the formation of clusters such as dimers, trimers, tetramers and oligomers of gold particles were observed. This is due to statistically appearing too close nucleation sites of the particles when the nanoparticles grow randomly on a SH-functionalized surface. A particle lateral size distribution was measured using a sample of 150 particles. It showed a Gaussian distribution with lateral sizes between 3 and 21 nm and an average lateral size of 12 nm (Fig. 9b).

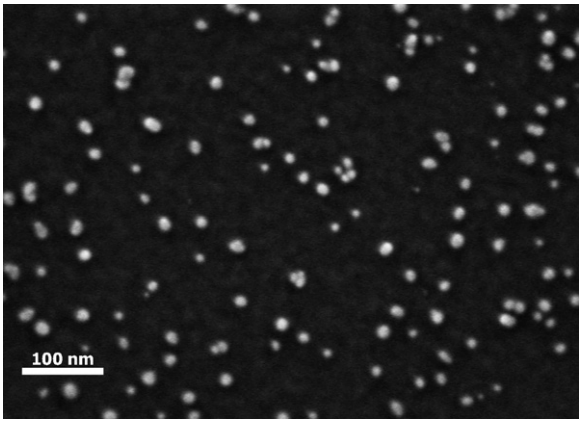


Fig. 8. SEM images of OMCVD gold nanoparticles on MPTS on a silicon waver.

The AFM image of the same sample (Fig. 3c) shows that the lateral size of the particles appeared bigger and denser on the surface compared to the SEM image. This is due to the convolution of the geometry of the sample and the AFM tip. The resulting AFM image features a correct sample height but an overestimated sample width [28]. To have information about the height distribution of the particles, the AFM image was first flattened using the DI software algorithm (excluding the particles from the flattened area), and then analyzed automatically using commercial image processing software (Image Metrology, SPIP). The height extracted from this method was in good agreement with the height determined manually from cross sections. The height data deduced from several such images (~200 particles) is plotted as a histogram (Fig. 9a) from which an average height of 8 nm and a height distribution ranging from 2 to 17 nm was obtained. Combining the average lateral size obtained from SEM analysis and the average height obtained from AFM, pancake-like shaped particles with an average aspect ratio of 8:12 = 2:3 = 1:1.5 were obtained.

Fig. 10 shows a TEM phase-contrast image of an individual nanoparticle from the SAM pealed off after growth for 90 min on a MPTS SAM. This

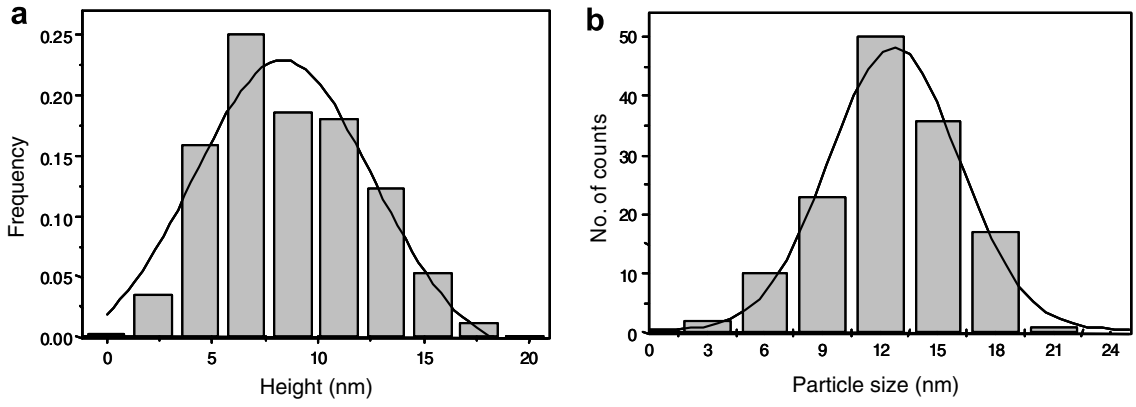


Fig. 9. (a) Height and (b) lateral size distribution of OMCVD gold as obtained from AFM and SEM analysis, respectively.

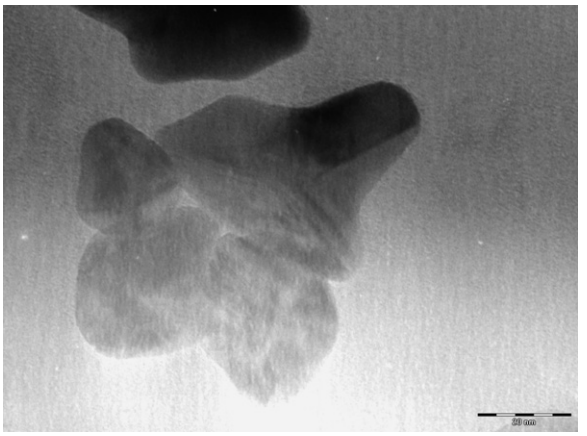


Fig. 10. TEM image of a 90 min OMCVD gold sample showing the crystalline facets of the nanoparticles. Scale: the bar is 30 nm long.

particle shows besides the crystalline facets pointing in the growth direction, a flat peal-off surface from the SAM. The crystalline nature of the nanoparticles [29] means that they may be a promising material for catalysis [30].

We therefore conclude that the particles are pancake-shaped with a large SAM contact area. Fig. 11 shows a schematic representation of pancake-like shaped OMCVD gold nanoparticles grown over 30 min on MPTS SAMs (Fig. 11a), C8-DT SAMs on Au(1 1 1) (Fig. 11b) and on C8-DT SAMs on Ag(1 1 1) (Fig. 11c). This difference in the aspect ratio of the gold nanoparticle structures on different natures of the templating SAMs is not fully understood but it is undoubtedly related to the surface density of available free SH groups and the sample roughness. These two parameters are, in fact, closely related: for a perfectly flat surface, all the free SH groups point towards the outermost part of the film and are accessible. The largest aspect ratio of 1:10, yielding basically a disk-like nanoparticle, is found for the C8-DT layer on Au, i.e. the sample having the highest free SH density and the smoothest surface. The C8-DT on Ag and MPTS on silicon display low and very similar aspect ratios of 1:1.4 and 1:1.5 (the pancakes). C8-DT on Au and Ag is expected to give SAMs of higher quality than the MPTS on silicon. It is well-known that MPTS polymerizes easily and rapidly, giving rise to a polymeric, randomly oriented layer rather than a monolayer with terminal free SH groups oriented towards the outermost part of the film.

An influence on the particle shape of the tilt angle of the respective SAM and therefore the orientation of the SH-group at the surface cannot be deduced here because the used thiols and silanes are too short to yield highly packed and highly oriented SAMs with the typical different tilt angles on Au, Ag and oxide surfaces [9].

Because the nanoparticles are grown in a template approach we should expect all of them to exhibit the same orientation with respect to the

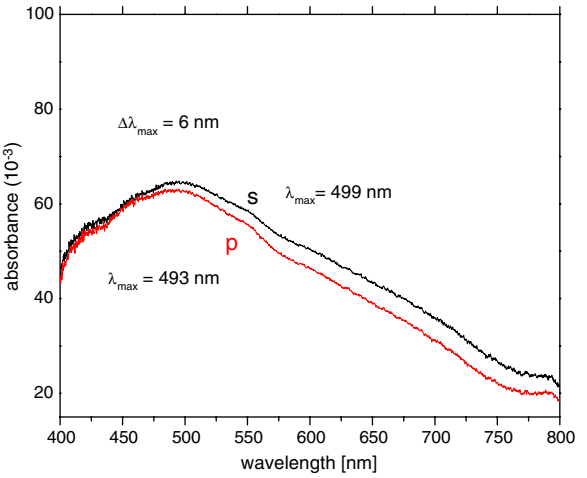


Fig. 12. Evanescent waveguide absorption (EWA) spectra taken in air at s- and p-polarization of a 15 min OMCVD gold nanoparticle sample grown on the MPTS silanized waveguide.

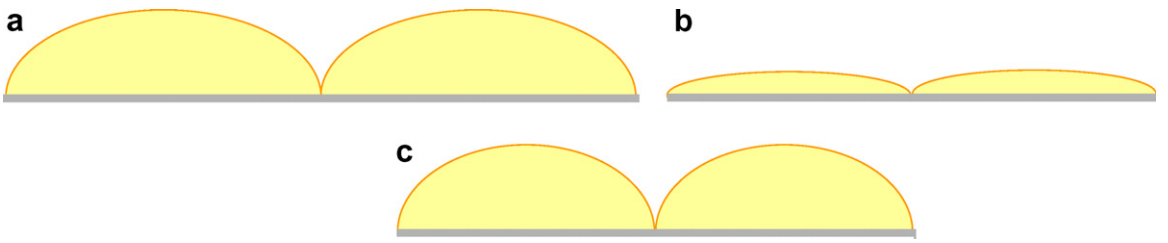


Fig. 11. Schematic illustration of the non-spherical shaped OMCVD gold nanoparticles grown on (a) MPTS SAMs (height of 8 nm and 12 nm lateral size, aspect ratio 2:3 = 1:1.5), (b) on C8-DT SAMs on Au(1 1 1) (0.5 nm and 5 nm for height and lateral size, aspect ratio 1:10) and (c) on C8- DT SAMs on Ag(1 1 1) (height of 7 nm and 10 nm lateral size, aspect ratio 7:10 = 1:1.4).

substrate. A straight forward approach for verification is to look at the spectral position of the plasmon resonance in the plane of and perpendicular to the substrate surface. When the average aspect ratio for gold nanoparticles on a glass substrate is 1:1.5, a smaller height than width, the plasmon band resonance should show a slightly different spectral position when probed with polarization in the plane of and perpendicular to the substrate surface. The in-plane resonance should be slightly red shifted in comparison to the out-of-plane resonance. Fig. 12 shows the absorption spectra taken with EWAS of a 15 min OMCVD gold nanoparticle sample on a silanized waveguide. The TE waveguide mode is s-polarized and probes the particles in plane, whereas the TM waveguide mode is p-polarized and probes the nanoparticles out-of-plane. The plasmon bands were found to be slightly below those of the 30 min samples (Fig. 7) because of the overall reduced particle size. The s-spectrum in Fig. 12 ($\lambda_{max} = 499$ nm) is red shifted by 6 nm in comparison to the p-spectrum ($\lambda_{max} = 493$ nm). This shift is in excellent agreement with size dependent resonance position studies on monodisperse gold nanoparticles [26b]. We also see that both polarization directions depict relatively broad plasmon resonances. This represents the broad height and width distribution of these OMCVD grown nanoparticles.

Fig. 13a and b show the transmission absorption spectra for 60 min and 90 min OMCVD grown gold nanoparticle samples on glass. The plasmon band of the 30 min sample from Fig. 7 (around 520–530 nm) is still present for the 60 min sample, but there is addi-

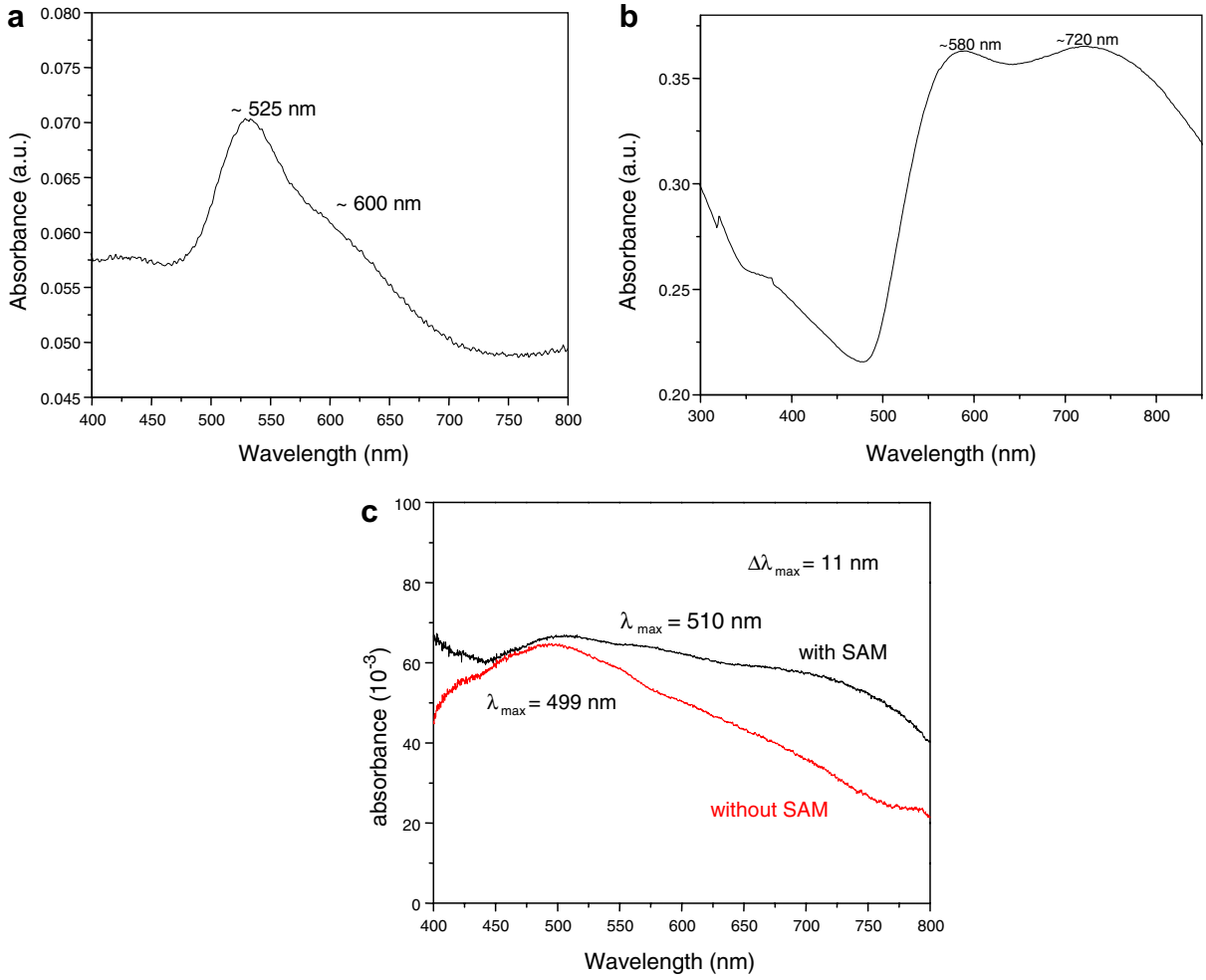


Fig. 13. Transmission absorption spectra of a (a) 60 min and (b) a 90 min OMCVD gold nanoparticle sample. (c) Shows the EWA spectrum in s-polarization in air of a 15 min OMCVD gold nanoparticles sample with a 1-dodecalthiol SAM.

tionally an evolving shoulder at around 600 nm. After 90 min a peak at 580 nm and at 720 nm are present. The transmission spectra essentially probe the lateral size and the coupling between neighboring nanoparticles. As the growth time is increased, so too is the particle size along both the vertical and horizontal directions and the plasmon band should shift accordingly. In addition, the edges of the gold nanoparticles encroach on each other as their in-plane size increases and the empty space between the nanoparticles decreases. The appearance of the shoulder at 600 nm in Fig. 13a is interpreted as the onset of particle-particle cross-talk when the evanescent fields of the nanoparticles in resonance start to overlap and a large red shift is observed [24]. Such a shift is typically associated with cluster formation and has been used in various chemical sensor schemes, e.g. DNA detection [6d]. Here we form random clusters of nanoparticles and, therefore, the absorption spectrum shows the single particle resonance (probably overlapped with the quadrupolar contribution of the single particles and the clusters [24]) and the shifted cluster resonance. Finally, the broad shape of peaks in Fig. 13b is probably a result of the large size and spacing distributions of the particles themselves.

Cluster formation can also be achieved by using small 15 min gold nanoparticles and capping them with an organic layer resulting in enlargement and space filling; in our case we used a SAM made out of 1-dodecanethiol. Fig. 13c shows the s-polarized EWA spectrum of such a sample. Clearly between 700 and 730 nm a shoulder of a red shifted plasmon resonance appears besides the single particle plasmon resonance which is shifted by 11 nm in comparison to the cap-less particles.

As known from various studies [24,31] the field enhancement of the plasmon nanoparticle evanescent field depends strongly on the form of the nanoparticle. In general: as more pointed a metallic nanoobject is, as higher the field enhancement is found right at the tip. In the case of our pancake shaped nanoparticles, we expect to have the highest field enhancement at the margin of the nanoparticles, right there where the interaction between neighboring particles are taking place.

4. Conclusions

We have demonstrated the preparation of crystalline, non-spherical, disk- to pancake-shaped gold nanoparticles using OMCVD. The aspect ratio of the pancake-like structures depends on the nature of the templating SAM. The density of accessible nucleation sites plays a significant role on the shape of the particle and its height growth velocity. With EWA spectroscopy, it could be proven that the non-spherical nanoparticles are, on average, oriented flat on the substrate. Unfortunately the disk-like nanoparticles with the large aspect ratio of 1:10 fabricated on the smooth Au(1 1 1) surface are not accessible for spectroscopic purposes, because they are located on a gold substrate that completely dominates absorption features.

We were able to demonstrate random cluster formation with nanoparticles cross-talking due to the overlap of the evanescent fields both by enlarging the nanoparticles themselves and virtually placing them closer to each other, as well as with capping them with an organic layer, serving the same purpose.

Acknowledgements

The authors like to thank Zhehui Wang, MPI for Polymer Research, Mainz (Germany) for the QCM measurements. The authors want to acknowledge the financial support from the BMBF (Germany) and its Center for Multifunctional Materials, the DFG (Germany), the Academic Development Fund of the University of Western Ontario, the Ontario Photonics Consortium (OPC) through Ontario Research and Development Challenge Fund (ORDCF), NSERC (Canada) and the CRC Program of the Canadian Government for financial support. S.M. also likes to acknowledge the group of George Stegeman at CREOL at University of Central Florida (USA) and Gaetano Assanto, Universita Roma Tre (Italy) for the kind donation of the waveguide sample. A.-S.D. thanks NATO for an Advanced Science Fellowship.

References

[1] (a) K.E. Drexler (Ed.), Nanosystems, Molecular Machinery, Manufacturing and Computation, Wiley, New York, 1992; (b) F.L. Carter, A. Schultz, D. Duckworth, in: F.L. Carter (Ed.), Molecular Electronic Devices, Marcel Decker, New York, 1987, p. 183.
[2] (a) P. Ball, L. Garwin, Nature 355 (1992) 761; (b) G.J. Ashwell (Ed.), Molecular Electronics, Wiley, New York, 1992.
[3] (a) I. Willner, E. Katz, B. Willner, in: H. Baltes, W. Göpel, J. Hesse (Eds.), Sensors Update, vol. 5, Wiley-VCH, Weinheim, 1999, p. 45; (b) W. Göpel, Biosens. Bioelectron. 13 (1998) 723.

[4] (a) X.Y. Zhang, L.D. Zhang, Y. Lei, L.X. Zhao, Y.Q. Mao, J, Mater. Chem. 11 (2001) 1732;
(b) S. Sun, C.B. Murray, D. Weller, L. Folks, A. Moser, Science 287 (2000) 1989;
(c) C.J. Kiely, J. Fink, M. Brust, D. Bethell, D.J. Schiffrin, Nature 396 (1998) 444;
(d) D.I. Gittins, D. Bethell, D.J. Gittins, R.J. Nichols, Nature 408 (2000) 67;
(e) R.G. Osifchin, R.P. Andres, J.I. Henderson, C.P. Kubiak, R.N. Dominey, Nanotechnology 7 (1996) 412;
(f) M.A. Hayat (Ed.), Colloidal Gold. Principles, Methods and Applications, Academic Press, p. 89.
[5] (a) A.P. Alivisatos, Science 271 (1996) 933;
(b) A.P. Alivisatos, J. Phys. Chem. 100 (1996) 13226;
(c) D.L. Feldheim, C.D. Keating, Chem. Soc. Rev. 27 (1998) 1.
[6] (a) A.J. Haes, D.A. Stuart, S. Nie, R.P. Duyne, J. Fluorescence 14 (4) (2004) 355;
(b) K. Aslan, J. Zhang, J.R. Lakowicz, C.D. Geddes, J. Fluorescence 14 (4) (2004) 391;
(c) G.-J. Zhang, R. Möller, R. Kreyschmer, A. Csaki, W. Fritsche, J. Fluorescence 14 (4) (2004) 369;
(d) C. Mirkin, R.L. Letsinger, R.C. Mucic, J.J. Storhoff, Nature 382 (6592) (1996) 607;
(e) M.D. Malinsky, K.L. Kelly, G.C. Schatz, R.P. Van Duyne, J. Am. Chem. Soc. 123 (7) (2002) 1471.
[7] C. Sönnichsen, C.S. Geier, N.E. Hecker, G. Von Plessen, J. Feldmann, H. Ditlbacher, B. Lamprecht, J.R. Krenn, F.R. Aussenegg, V.Z.-H. Chan, J.P. Spartyz, M. Möller, Appl. Phys. Lett. 77 (19) (2000) 2949.
[8] (a) S.J. Chen, Phys. Chem. B 104 (2000) 663;
(b) S.J. Chen, Am. Chem. Soc. 122 (2000) 7420.
[9] A. Ulman, Chem. Rev. 96 (1996) 1533.
[10] P. Wohlfart, J. Weiß, J. Käshammer, C. Winter, V. Scheumann, R. Fischer, S. Mittler-Neher, Thin Solid Films 340 (1999) 274.
[11] S. Busse, J. Käshammer, S. Krämer, S. Mittler-Neher, Sensors Actuators B 60 (1999) 148.
[12] H. Schmidbaur, A. Shiotani, Chem. Ber. 104 (1971) 2821.
[13] (a) M.J. Adams, An Introduction to Optical Waveguides, John Wiley, New York, 1981;
(b) R.G. Hunsperger, Integrated Optics: Theory and Technology, fourth ed., Springer Verlag, Berlin, New York, 1995;
(c) T. Tamir (Ed.), second ed., Integrated Optics, from Topics in Applyied Physics, vol. 7, Springer Verlag, Heidelberg, New York, 1979;
(d) A.W. Snyder, J.D. Love, Optical Waveguide Theory, Chapman and Hall, London, New York, 1983;
(e) R. Syms, J. Cozens, Optical Guided Waves and Devices, McGraw-Hill, Nondon, New York, 1992;
(f) D. Marcuse, Theory of Dielectric Optical Waveguides, second ed., Academic Press, Boston, 1991.
[14] (a) S.I. Najafi, Introduction to Glass Integrated Optics, Artech House, Boston, 1992;
(b) R.V. Ramaswamy, R. Srivastavam, J. Lightwave Technol. 6 (6) (1988) 984.
[15] D. Johannsmann, Macromol. Chem. Phys. 200 (1999) 501.
[16] H. Voit, C. Schoppmann, D. Brandl, Phys. Rev. B 48 (1993) 17517.
[17] M.J. Hampden-Smith, T.T. Kodas, Chem. Vapor Depos. 1 (1995) 8.
[18] M. Cavallini, M. Bracali, G. Aloisi, R. Guidelli, Langmuir 15 (1999) 3003.
[19] G.G. Baralia, A.-S. Duwez, B. Nysten, A.M. Jonas, Langmuir 21 (2005) 6825, and references therein.
[20] A.K.A. Aliganga, A.-S. Duwez, S. Mittler, Organic Electronics 7 (5) (2006) 337.
[21] L. Ratke, P.W. Voorhees, Growth and Coarsening: Ostwald Ripening, Springer, Berlin, New York, 2002.
[22] M. Weisser, J. Käshammer, J. Matsumoto, F. Nakamura, K. Ijiro, M. Shimomura, S. Mittler-Neher, J. Am. Chem. Soc. 122 (2000) 87.
[23] A. Henglein, Langmuir 14 (1998) 6738.
[24] (a) U. Kreibig, M. Vollmer, Optical Properties of Metal Clusters, Springer-Verlag, Berlin, Germany, 1995;
(b) S. Link, M.A. El-Sayed, Int. Rev. Phys. Chem. 19 (2000) 409;
(c) U. Kreibig, L. Genzel, Surf. Sci. 156 (1985) 678;
(d) T. Jensen, L. Kelly, A. Lazarides, G.C. Schatz, J. Cluster Sci. 10 (2) (1999) 295.
[25] K.G. Thomas, J. Zajicek, P.V. Kamat, Langmuir 18 (2002) 3722.
[26] (a) S. Chen, K. Kimura, Langmuir 15 (1999) 1075;
(b) S. Link, M.A. El-Sayed, J. Phys. Chem. B 103 (1999) 4212.
[27] C. Winter, U. Weckenmann, R. Fischer, J. Käshammer, V. Scheumann, S. Mittler, Chem. Vapor Depos. 6 (2000) 199.
[28] P. Markiewicz, M.C. Goh, Langmuir 10 (1994) 5.
[29] A.K.A. Aliganga, F. Xu, W. Knoll, S. Mittler, SPIE 5969 (2005) 0H-1–0H-12.
[30] M.A. El-Sayed, Acc. Chem. Res. 34 (2001) 257.
[31] E. Hao, G.C. Schatz, J.T. Hupp, J. Fluorescence 14 (2004) 331.

Available online at www.sciencedirect.com
ScienceDirect
Organic Electronics 8 (2007) 175–183
Organic Electronics
www.elsevier.com/locate/orgel

Tunable multiline distributed feedback dye laser based on the phenomenon of excitation energy transfer

Rallabandi Sailaja, Prem B. Bisht *

Department of Physics, Indian Institute of Technology Madras, Chennai 600 036, India

Available online 23 January 2007

Abstract

Tunable multiline distributed feedback (DFB) lasing has been observed in the mixture of dyes rhodamine 6G (R6G) and cresyl violet (CV). The dye-pair is pumped by the two pairs of the pump beams derived from a common source at two different angles. A variation in DFB geometry up to seven orders suggests that the third order Bragg diffraction is suitable for such studies. A detailed study at high dye concentrations has been done by steady-state and ps time-resolved spectroscopy. The energy transfer phenomenon and the self-absorption mechanism both, are found to be responsible for the observed tunability and multiline lasing. The threshold energies required for the DFB lasing are also given here.
© 2007 Elsevier B.V. All rights reserved.

PACS: 42.55.Mv; 82.20.Rp; 78.47.+p

Keywords: Dye lasers; State to state energy transfer; Time-resolved optical spectroscopy

1. Introduction

Solid-state organic and polymeric materials are of current interest because of their use in light emitting diodes, field effect transistors and solar cells [1–3]. Organic dyes have broad energy bands. Their emission bands are shifted from the absorption bands (via Stokes' shift) and they can be easily embedded into a host material such as a polymer [4]. The tunability of an organic dye laser is a consequence of the broadened electronic levels. By introducing a frequency selective element in the path of the laser cavity a dye laser can be tuned efficiently [5].

Distributed feedback (DFB) technique can be used to generate tunable sub-nanosecond pulses from longer ones. Fig. 1 shows the schematic of the DFB laser. Lasers with DFB are simple and elegant sources of narrow band, frequency tunable coherent radiation. In case of gain coupled DFB lasers, self-Q-switching leads to transform limited pulses that are 50–100 times shorter than the pump pulse. The feedback is strongly frequency selective and the resonant mode for laser oscillation corresponds to the wavelength that satisfies the Bragg condition [5–12]. Tunability of such lasers is achieved by changing the angle between the two pump beams or by changing the refractive index of the medium, without a need of any frequency selective element in the cavity [13,14].

* Corresponding author. Fax: +91 44 235 2545.
E-mail address: bisht@iitm.ac.in (P.B. Bisht).

1566-1199/$ - see front matter © 2007 Elsevier B.V. All rights reserved.
doi:10.1016/j.orgel.2007.01.006

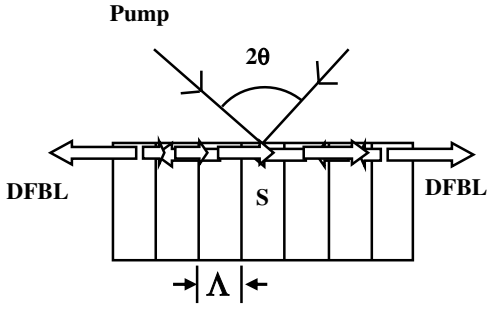


Fig. 1. Schematic of DFB lasers (*DFBL*) satisfying the Bragg condition. Here Λ is the fringe spacing and S represents the gain medium. 2θ Represents the angle between the interfering *Pump* beams (532 nm).

Excitation energy transfer (ET) is a popular mechanism used in photophysics and photobiology [15–21]. Energy transfer dye lasers based on various pumping schemes have also been reported in the literature [22–29]. The dipole–dipole interaction between dissimilar molecules was first considered theoretically by Förster [15]. The excitation energy hoping among donors is known as energy migration. The energy transfer between a donor and an acceptor can be modulated by the energy migration among donors. This modulation of energy transfer depends upon the relative strengths of the interaction between the donor–acceptor (α) and donor–donor (β) molecules, respectively. The efficiency of excitation energy transfer is proportional to the extent of spectral overlap of the fluorescence of the donor and the absorption of the acceptor. Pumping of a dye by using the energy transfer processes can be very efficient for the improvement of the dye laser efficiency and extension of their tuning range.

The mixture of rhodamine 6G (R6G, donor) – cresyl violet (CV, acceptor) is one of the popular energy transfer systems [24–27]. Addition of R6G to CV was reported to have enhanced the lasing efficiency of CV [28]. Lin et al. used a fast vacuum photodiode and an oscilloscope for measuring the fluorescence lifetime of this system [29]. They have reported that this system obeys the Stern–Volmer relation but the rate of excitation transfer calculated from the experiment shows the dominance of resonance transfer due to long range dipole–dipole interaction. Recently, Basheer et al. have reported the pump power dependence and effect of acceptor concentration in prism type geometry [30] in this system. We have used two pairs of pump beams with one fixed at the donor angle, while the other operates at the acceptor angle. We observe that under such geometry by varying the concentration of the acceptor, the tunability of the laser can be easily achieved. A detailed analysis of the excitation energy transfer by steady-state and ps time-resolved measurements shows that the effect of energy migration also contributes to the observed lasing. It is observed that the system follows Förster kinetics of energy transfer at high acceptor concentrations.

2. Experimental

The dyes R6G (Serva) and CV (Serva) were used as received. Spectrograde ethylene glycol was obtained from central drug house (P) Ltd., Mumbai. Different concentrations of dyes prepared in ethylene glycol were stored in a cool place. The second harmonic of a ns Nd: YAG laser (Quanta-Ray, Model INDI-40) of 10 Hz repetition rate was used for pumping the DFBL. The pump beam was split into two beams by using a beam splitter and these two beams were focused onto the dye cell by using a cylindrical lens. Each of these beams was split into two by another beam splitter (Fig. 2). The two beam pairs so obtained were made to interfere in the dye cell at different angles suitable for various orders, or donor and acceptor angles. The sample was kept in a quartz cell of 2 cm length. Lasing spectra from the samples were recorded using a spectrometer (Ocean Optics, S2000).

Absorption spectra of the dyes were recorded using spectrophotometer (JASCO, V570) and steady-state fluorescence spectra of the mixtures were measured with a spectrofluorometer (JASCO,

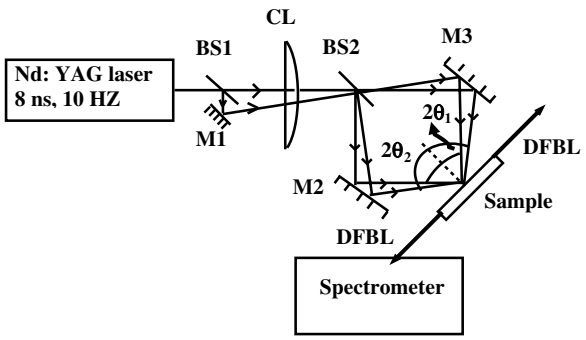


Fig. 2. Experimental set-up for the multiline DFB lasing. BS_1, BS_2 – beam splitters, M_1, M_2 and M_3 – plane mirrors, $2\theta_1$ and $2\theta_2$ correspond to the interfering angles between the pump beam-pairs.

FP-6600). For the time-resolved measurements, a 40 ps pulsed laser at 408 nm (Pilas, Advanced Photonics) was used as an excitation source in a fluorescence microscope. Sample films of ~30 μm thickness were made by taking a drop of the sample on a slide glass and by covering it with a cover glass. Thin samples were necessary to minimize the artifacts of self-absorption. The fluorescence from the samples was collected with a 20X objective lens, passed through a monochromator (Oriel, 772501) and detected by a photomultiplier tube (Hamamatsu, R928). A barrier filter of >420 nm was used to block the scatter from the emission. The fluorescence decays were recorded with the help of time-correlated single photon counting technique [31]. The decay profiles were deconvoluted with the instrument response function (IRF) of the excitation pulse and were fitted with theoretical functions using standard software (TC900, Edinburgh Instruments). The goodness of the fit was estimated by reduced χ^2 and weighted residuals. For a good fit, the value of χ^2 was around one and the residuals were distributed evenly on both sides of the fitted curve.

3. Theory

3.1. Distributed feedback lasers (DFBL)

The rate equations describing the lasing level populations and the photon densities of a DFBL are as follows [6]:

$$\frac{dn(t)}{dt} = I_p(t)\sigma_p[N - n(t)] - \frac{\sigma_e c}{\eta} n(t)q(t) - \frac{n(t)}{\tau_F} \quad (1)$$

$$\frac{dq(t)}{dt} = \frac{(\sigma_e - \sigma_a)c}{\eta} n(t)q(t) - \frac{q(t)}{\tau_{cav}(t)} + \frac{\Omega n(t)}{\tau_F} \quad (2)$$

where N and $n(t)$ are the number densities of the molecules in the ground and in the first excited states, respectively, and q is the number density of the lasing photons. σ_p and σ_e are the cross sections of absorption and stimulated emission at the pump and the lasing wavelengths, respectively. σ_a is the excited state absorption cross section at the lasing wavelength. c is the speed of the light and I_p is the pump photon flux per unit area. η is the refractive index of the dye solution, τ_F is the fluorescence lifetime and Ω is the fraction of spontaneous emission photons which propagate in to the angular and spectral region of the DFBL beam. τ_{cav} is the equivalent cavity decay time. The periodicity of the pump – induced spatial modulation ($\Lambda = \lambda_{pump}/2\sin\theta$) is determined by the angle (2θ) between the two interfering beams and the corresponding lasing wavelength is given by [5],

$$\lambda_{DFBL} = \eta\lambda_{pump}/m\sin\theta \quad (3)$$

where λ_{pump} is the wavelength of the pump laser and m is the order of the Bragg diffraction. The output power from any one end of the DFB laser is given by

$$P_{out} = \left(\frac{1}{2}\right)\frac{hc}{\lambda_{DFBL}}\frac{q(t)lab}{\tau_{cav}(t)} \quad (4)$$

where l, a, and b are the length, height, and skin depth of the gain medium, respectively. The equivalent cavity decay time is given by

$$\tau_{cav}(t) = \frac{\eta l^3}{8\pi^2 c}[n(t)(\sigma_e - \sigma_a)V]^2 \quad (5)$$

here V is the visibility of the interference pattern and the skin depth is given as

$$a = \frac{1}{N\sigma_p} \quad (6)$$

3.2. Excitation energy transfer

The overlap integral (J) between the fluorescence of the donor and the absorption of the acceptor is given as,

$$J = \frac{\int_0^\infty F_D(\bar{\nu})\varepsilon_a(\bar{\nu})d\bar{\nu}/(\bar{\nu})^4}{\int_0^\infty F_D(\bar{\nu})d\bar{\nu}} \quad (7)$$

where $\varepsilon_a(\bar{\nu})$ is the molar decadic extinction coefficient of the acceptor and $F_D(\bar{\nu})$ is the intensity of the donor fluorescence (normalized to unity) at a wavenumber, $\bar{\nu}$. The critical transfer distance (R_{0A}) is given as [19],

$$R_{0A} = \frac{9000(\ln 10)\kappa^2\phi_D J}{128\pi^5 N\eta^4} \quad (8)$$

ϕ_D is the quantum yield of the donor in the absence of the excitation energy transfer, η the refractive index of the medium, κ^2 the molecular orientation factor (=2/3), and N is the Avogadro's number. When the donor and the acceptor, both are fixed in space, the donor fluorescence follows the Förster kinetics of energy transfer and the donor decay function is given by,

$$I_D = I_0 \exp\left[-\frac{t}{\tau_D} - 2\gamma_{DA}(t/\tau_D)^{\frac{1}{2}}\right] \quad (9)$$

The first term corresponds to the unquenched fluorescence lifetime of the donor and the second term is

due to the excitation energy transfer and the parameter γ_{DA} is the reduced concentration defined as,

$$\gamma_{DA} = C_A/C_{0A} \quad (10)$$

here C_A is the acceptor concentration and the C_{0A} is the critical acceptor concentration given by,

$$C_{0A} = (3000/2\pi^{3/2}NR_{0A}^3) \quad (11)$$

In the limit of high donor concentration, when the donor–acceptor interaction (α) is comparable to the donor–donor interaction (β), the donor decay kinetics is modified. The interaction strengths are defined as,

$$\alpha = \frac{1}{\tau_D}(R_{0A})^6 \quad \text{and} \quad \beta = \frac{1}{\tau_D}(R_{0D})^6 \quad (12)$$

where R_{0D} is the critical transfer distance for excitation energy migration between the donors which is obtained from the overlap of the absorption and the fluorescence spectra of the donors.

4. Results and discussion

4.1. Distributed feedback dye lasing

4.1.1. Theoretical simulations

Fig. 3 shows the theoretical simulations for the lasing parameters used for the dyes R6G and CV in ethylene glycol. The input is a Gaussian pulse of pulse width 8 ns. Pump rates of $3.6 \times 10^{24}\ cm^{-2}\ s^{-1}$ and $1.2 \times 10^{23}\ cm^{-2}\ s^{-1}$, respectively, were used to get a single DFBL pulse of pulse width 180 ps from CV and R6G. This indicates ~45 times shortening of the pump pulse. These pump rates were used in the experiments to obtain single DFBL pulses. The required pump rate for CV is ~30 times higher than that for R6G. The peak wavelengths of the experimentally observed DFBL pulses in R6G and in CV (vide infra) have been used in these simulations.

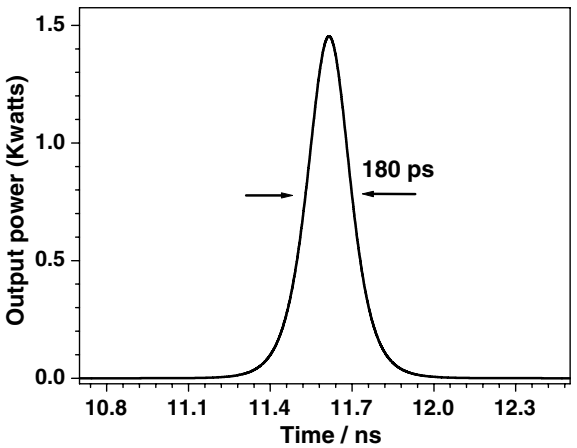


Fig. 3. Theoretical simulations for R6G (pump rate = $4.25 \times 10^{24}\ cm^{-2}\ s^{-1}$, $\lambda_{DFBL} = 571$ nm) for output pulse for input parameters of $\lambda_{pump} = 532$ nm, pulse width = 8 ns with $l = 2$ cm and $b = 0.025$ cm.

4.1.2. Lasing with higher-order Bragg diffraction

We have used pump wavelength of 532 nm. At this wavelength, in the lasing wavelength range of the selected dyes, the lowest working order of Bragg diffraction is limited to $m = 2$. However, to check the lasing threshold, we studied dyes for various orders. Fig. 4a and b gives the spectra of higher order DFB lasing observed in R6G ($m = 7$) and for CV ($m = 5$) independently in ethylene glycol. The threshold energies for various orders of DFBL, their interfering angles, lasing peaks and FWHM are given in Tables 1a and 1b for R6G (donor) and CV (acceptor), respectively. It is seen that the required angle between the two pump beams is smaller as the selected order of the diffraction is higher. The threshold energy increases with the increase in the order of diffraction used to obtain the DFBL. The output energy of the DFBL pulse is observed to be of the order of few μJ. From the measured spectral width of the DFBL pulses the width of the transform limited DFBL pulse can be estimated. CV needs more energy for obtaining DFBL than R6G. It was observed that a weak, unstable lasing from donor was also observed even at $2\theta_1 = 45°$ (angle corresponding to the acceptor lasing wavelength) while no lasing from acceptor was observed at $2\theta_2 = 54°$ (angle corresponding to donor lasing wavelength).

4.1.3. Effect of concentration of acceptor on the DFBL obtained by using two pairs of pump beams

4.1.3.1. Pump beam-pair at donor angle. To benefit from the lower threshold of the pump energy as well as due to ease of geometrical considerations, we work at the third order Bragg diffraction hereafter. Fig. 5 shows the DFB lasing obtained in the donor–acceptor mixture in ethylene glycol ($\eta = 1.431$) pumped at the donor angle. In the mixture the lasing spectra do not show any lasing from acceptor up to 0.1 mM. This is consistent with the observation that even at 1 mM of acceptor no lasing from acceptor was observed at this angle. But when the mixture contains an acceptor concentration of 0.5 mM, lasing from the acceptor was also observed.

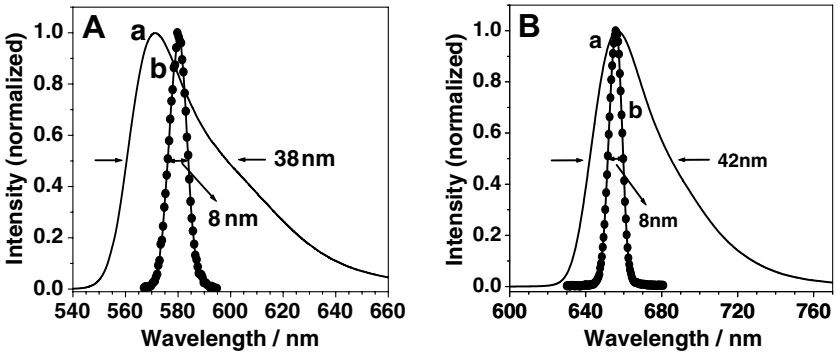


Fig. 4. (a) Fluorescence spectrum (—) and (b) DFB lasing spectrum (-●-) when pumped with the ns Nd: YAG laser. (A) R6G in ethylene glycol (1 mM) (B) CV in ethylene glycol (1 mM).

Table 1a
DFB lasing from the pure donor (R6G, 1 mM) in ethylene glycol at the pump wavelength of 532 nm

Order (m)	Angle (2θ)	λ_{peak} (nm)	FWHM (±0.2 nm)	Threshold energy (μJ)
2	85	576	7.7	50
3	52	580	7.2	60
4	42	579	8.5	70
5	32	582	7.7	80
6	25	580	8.0	90
7	20	581	8.0	100

Table 1b
DFB lasing from the pure acceptor (CV, 1 mM) in ethylene glycol at the pump wavelength of 532 nm

Order (m)	Angle (2θ)	λ_{peak} (nm)	FWHM (±0.2 nm)	Energy (mJ)
2	73	655	8.1	1.5
3	47	654	7.7	2.0
4	35	655	8.5	3.0
5	28	657	7.8	4.5

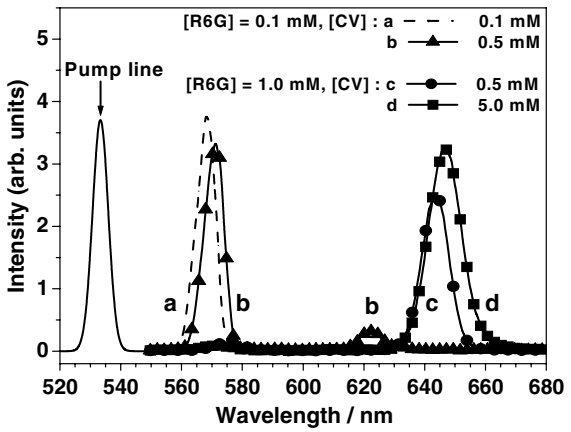


Fig. 5. DFBL observed in mixture when pumped at the donor angle.

This is due to the transfer of energy from donor to the acceptor, as the latter has a relatively weak absorption at 532 nm.

To further increase the acceptor concentration, a higher donor concentration of 1 mM was used. At the acceptor concentration of 1 mM, the observed lasing peak gets red shifted. At a concentration of 5 mM, only lasing from the acceptor was observed. The threshold energies for DFBL in different concentrations of donor and acceptor in the mixture and the FWHM of the observed lasing peaks are given in Table 2. The concentration induced red shift of the lasing peak (tuning) of the acceptor in the mixture is due to the fact that the self-absorption of CV sets in at this concentration.

4.1.3.2. Pump beam pairs at donor and acceptor angles. In the mixture, the lasing from the acceptor at the concentration of 0.5 mM was also observed when pumped at an angle corresponding to the acceptor lasing wavelength. This is possible because at these wavelengths and angle, the amplification is favored by the distributed feedback for the acceptor. When the mixture is pumped by both the pairs of beams (Fig. 6), we observe the dependence of lasing peaks on concentration similar to that observed for the donor angle. We observe that the peaks in this case are more red shifted (by 26 nm) when compared to the pure donor or acceptor cases independently. Under such circumstance, there is also a possibility of amplification of several lines due to the formation of complex gratings in the active medium due to the possibility of selection of several

Table 2
DFB lasing from the donor–acceptor mixture (λ_{pump}: 532 nm, 8 ns)

Energy (mJ)	Concentration (M)		Angle (2θ)	Donor ($2\theta = 54°$)		Acceptor ($2\theta = 45°$)	
	Donor	Acceptor		λ_{peak} (nm)	FWHM (±0.2 nm)	λ_{peak} (nm)	FWHM (±0.2 nm)
0.4	10^{-3}	5×10^{-3}	Donor[a]			647	12.5
			Both[b]			652	10.3
0.7	10^{-3}	5×10^{-4}	Donor[a]	574	10.0	645	10.3
			Both[b]	579	8.8	653	9.6
2.0	10^{-4}	5×10^{-4}	Donor[a]	571	7.3	626	9.1
			Both[b]	572	6.9	626	9.5
3.5	10^{-4}	1×10^{-4}	Donor[a]	568	7.6		
			Both[b]	569	6.8		

[a] Single pair of pump beams with angle corresponding to donor peak.
[b] Two pairs of pump beams with one pair fixed at the angle corresponding to the donor peak, while the other corresponding to the acceptor peak.

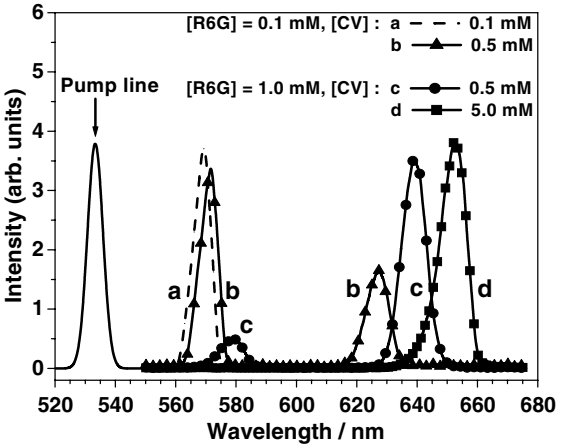


Fig. 6. DFBL observed in mixture when pumped at both the pairs of the pump beams at angles $2\theta_1 = 54°$ and $2\theta_2 = 45°$, respectively.

wavelengths at various possible angles [9]. However, for such a system the multiline lasing is possible when the optical path difference (OPD) between the two pump pairs is less than the coherence length of the pump laser besides the availability of the gain profile. In our case, due to convenience of the experiment, for ns pump laser the OPD (~10 cm) is much larger than the coherence length of the laser [9]. This provides the tuning ability of the DFBL setup by using the energy transfer mechanism in a suitable dye-pair and by choosing appropriate angles for lasing. For various other middle acceptor concentrations it is expected that the peaks are continuously tunable in between the first and the final positions shown in Fig. 6.

Table 2 gives the threshold energies for DFBL in different concentrations of donor and acceptor in the mixture and the FWHM of the observed lasing peaks. The FWHM of all the lasing peaks was observed to be within 7–12 nm. The threshold energy required for lasing became smaller by a factor of 5 as the concentration of the donor was increased from 0.1 mM to 1 mM. This indicates that the increase in the energy transfer rate from donor to acceptor favors the amplification at lower thresholds. A total shift of 26 nm in the peak can be obtained by changing the acceptor concentration from 0.5 mM to 5 mM.

4.2. Mechanism of energy transfer

4.2.1. Steady-state absorption and fluorescence spectra

Fig. 7 shows the absorption and fluorescence spectra of R6G and CV in ethylene glycol. It can be seen that there is an overlap between the fluorescence spectrum of the donor and the absorption spectrum of the acceptor. There is also an overlap between the absorption and fluorescence spectra of the donor or acceptor themselves which indicates a possibility of donor–donor (DD) or acceptor–acceptor (AA) transport of excitation energy at higher concentrations. The overlap integral (J) for donor–acceptor (DA) system was calculated using Eq. (7). The critical transfer distance between the donor and the acceptor (R_{0A}) was calculated using Eq. (8). The value of overlap integral (J_{0D}) and the critical transfer distance for DD system (R_{0D}) were also calculated. The photophysical parameters for this system are given in Table 3.

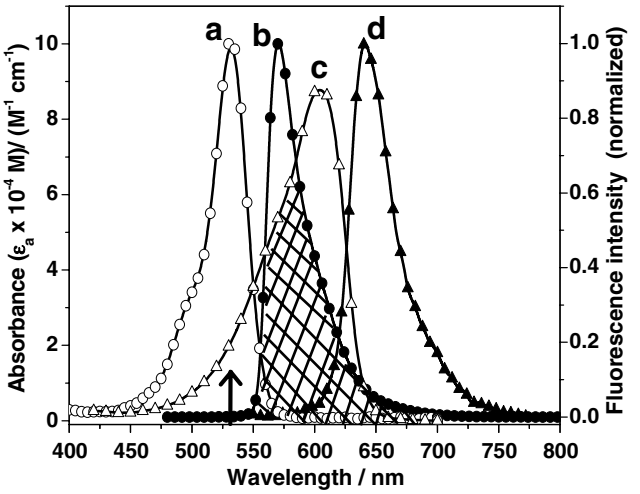


Fig. 7. Steady-state absorption (-○-) (a) and fluorescence spectrum (-●-) (b) of [R6G] = 0.1 mM; absorption (-△-) (c) and fluorescence spectrum (-▲-) of [CV] = 0.1 mM. The shaded region shows the region of overlap. The arrow indicates the pump wavelength chosen for the experiments.

Fluorescence spectra are given in Fig. 8. Excitation wavelength of 532 nm was absorbed mostly by the donor and it is observed that by increasing the concentration of the acceptor the donor fluorescence intensity decreases with an increase in the fluorescence intensity of the acceptor up to a concentration of 1 mM of the acceptor. The reduction in the donor fluorescence is accompanied by an increase in the acceptor fluorescence, which gives the evidence of the energy transfer from R6G to CV.

A red shift of 22 nm was also observed in the acceptor fluorescence maximum with the increase in the acceptor concentration, which is attributed to the effect of radiative migration due to the effect of self-absorption among acceptors. At a concentration of 5 mM of the acceptor, there is no donor fluorescence left and the acceptor fluorescence intensity was also found to be smaller as compared to that at

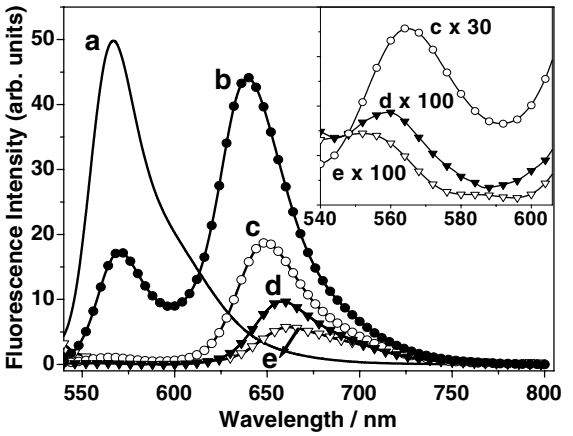


Fig. 8. Fluorescence spectra of [R6G] = 0.1 mM in ethylene glycol at λ_{exc} = 532 nm with varying concentration of CV as: (a) 0 M, (b) 0.1 mM, (c) 0.5 mM, (d) 1 mM, and (e) 5 mM. The inset shows the spectra (c), (d), and (e) on expanded scale for donor fluorescence region.

Table 3
Photophysical parameters for R6G-CV system in ethylene glycol

Donor (R6G)		Acceptor (CV)		J[a] (M^{-1} cm^3)	J_{OD}[b] (M^{-1} cm^3)	R_{OA}[c] (±0.1 Å)	R_{OD}[d] (±0.1 Å)
λ_{abs}[e]	λ_{em}[f]	λ_{abs}	λ_{em}				
530	571	605	641	1.45×10^{-13}	4.0×10^{-15}	52.0	28.6

[a] J is the overlap integral between donor fluorescence and the acceptor absorption.
[b] J_{OD} is the overlap integral between absorption and the fluorescence of donor.
[c] R_{OA} is the critical transfer distance of a donor–acceptor pair.
[d] R_{OD} is the critical transfer distance between two nearest donors.
[e] λ_{abs} is the wavelength of absorption maximum.
[f] λ_{em} is the wavelength of fluorescence maximum.

0.1 mM. The reduction in the intensity of the acceptor can be due to the formation of dimers or higher aggregates with low fluorescence yield. We also observe that there is a blue shift in the donor fluorescence peak with the increase in the acceptor concentration. This is attributed to the radiative transfer of energy from donor to acceptor [32,33].

4.2.2. Time-resolved studies to decipher the energy transfer mechanism

The interaction strengths between the donor–acceptor and that among donors were calculated as $\alpha = 5.8 \times 10^{-42}\ \mathrm{cm^6\ s^{-1}}$ and $\beta = 1.61 \times 10^{-43}\ \mathrm{cm^6\ s^{-1}}$, respectively using Eq. (12). We find that the DA is 36 times stronger than the DD interaction for this system. The fluorescence decay curves of pure R6G and in presence of 5 mM CV, respectively, are shown in Fig. 9. It is seen that while the R6G decay fits to the single exponential function, the mixture shows a good fit with the Förster function. The fluorescence lifetime of R6G is obtained as 3.4 ± 0.1 ns which is consistent with the value reported in the literature [34]. An increase in the concentration of R6G results in the increase in the lifetime to 3.9 ± 0.1 ns. Table 4 gives the parameters obtained from the single exponential fit.

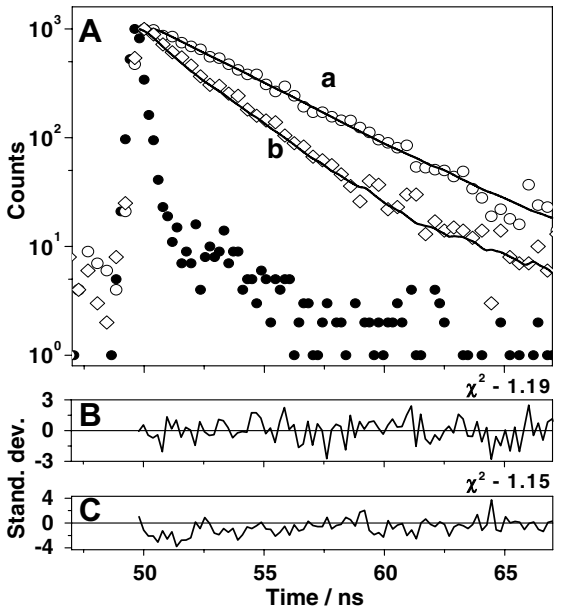


Fig. 9. Panel (A): Fluorescence decay data (○) for [R6G] = 0.1 mM observed at 570 nm (a). The solid line is the single exponential fit. Fluorescence decay data (◇) of [R6G] in the presence of [CV] = 5 mM (b). The solid line represents the Förster fit (Eq. 9). Panels (B) and (C) represent the residuals for the fit (a) and (b), respectively.

Table 4
Analysis of the fluorescence decay data of R6G-CV system in ethylene glycol (λ_{exc}: 408 nm)

[CV] (mM)	Single exponential fit	
	τ_D[a] (±0.1 ns)	χ^2
[R6G] = 0.1 mM		
0	3.4	1.19
0.1	3.5	0.98
0.5	3.2	0.98
1.0	3.1	0.99
5.0	2.2	1.27[b]
[R6G] = 1 mM		
0	3.9	1.18
0.5	3.7	1.15
1.0	3.1	0.94
5.0	2.1	1.20[c]

[a] τ_D is the fluorescence lifetime of the donor.
[b] Förster fit: $\gamma_{DA} = 1.56$, $\chi^2 = 1.15$, $R_{0A} = 51.8 \pm 0.1$ Å.
[c] Förster fit: $\gamma_{DA} = 1.57$, $\chi^2 = 1.05$, $R_{0A} = 51.9 \pm 0.1$ Å.

The fluorescence lifetime of the donor in the mixture was found to follow the single exponential function and its decay time was found to decrease with increase in the concentration of the acceptor. This suggests quenching of the donor fluorescence due to energy transfer.

In ethylene glycol, the calculated rate of material diffusion, ($k_{DA} = 4.1 \times 10^5\ \mathrm{s^{-1}}$) at an acceptor concentration of 1 mM is found to be less than the rate of energy transfer ($k_{et} = 6.6 \times 10^7\ \mathrm{s^{-1}}$). At the acceptor concentration of 5 mM the decay curve deviates from the single exponential nature. The critical transfer distance R_{0A}, was calculated by using the reduced concentration γ_{DA}, obtained from fitting the decay profile. It was observed that this value matches with the spectroscopic value. In case of octanol (viscosity = 8.3 cP) the donor decay has been reported to follow the Förster kinetics [35]. In the present case (ethylene glycol, with viscosity = 16 cP) the system is expected to be free from the contribution of the diffusion.

5. Conclusions

Higher order Bragg diffraction has been used in a dye-pair DFB laser by pumping with two pairs of beams to increase the tunability range. In this system, at higher acceptor concentrations the lasing from the acceptor dominates. The lasing peaks, their FWHM and the threshold pump energies indicate that the threshold energy for DFB lasing decreases with the increase in the concentration of

the donor. The fluorescence lifetime analysis of the donor–acceptor mixture shows that the energy transfer due to long range dipole–dipole interaction is responsible for the observed behavior at high donor and acceptor concentrations.

Acknowledgement

We thank DRDO, New Delhi for the financial assistance.

References

[1] G. Kranzelbinder, G. Leising, Rep. Prog. Phys. 63 (2000) 729.
[2] J.H. Burroughes, D.D.C. Bradley, A.B. Brown, R.N. Marks, K. Mackay, R.H. Friend, P.L. Burns, A.B. Holmes, Nature 347 (1990) 539.
[3] N.S. Sariciftci, L. Smilowitz, A.J. Heeger, F. Wudl, Science 258 (1992) 1474.
[4] M. Berggern, A. Dodabalapur, R.E. Slusher, Z. Bao, Nature 389 (1997) 466.
[5] C.V. Shank, Rev. Mod. Phys. 47 (1975) 649.
[6] Zs. Bor, A. Muller, B. Racz, F.P. Schafer, Appl. Phys. B 27 (1982) 9.
[7] T.Sh. Efendeiv, A. Rubinov, Sov. J. Quant. Elec. 2 (1975) 658.
[8] A. Rubinov, T.Sh. Efendeiv, A.V. Adamushko, Opt. Commun. 20 (1977) 159.
[9] N. Khan, T.A. Hall, Opt. Commun. 228 (2003) 177.
[10] V. Dumarcher, L. Rocha, C. Denis, C. Fiorini, J.-M. Nunzi, F. Sobel, B. Sahraoui, D. Gindre, J. Opt. A: Pure Appl. Opt. 2 (2000) 279.
[11] H. Su, L.F. Luster, J. Phys. D: Appl. Phys. 38 (2005) 2112.
[12] G. Strangi, V. Barna, R. Caputo, A. De Luca, C. Versace, N. Scaramuzza, C. Umeton, R. Bartolina, PRL 94 (2005) 063903-1.
[13] J.E. Bjorkholm, C.V. Shank, Appl. Phys. Lett. 20 (1972) 306.
[14] H. Kogelnik, C.V. Shank, J. Appl. Phys. 43 (1972) 2327.
[15] Th. Förster, Disc. Faraday Soc. 27 (1959) 7.
[16] D.L. Huber, Phys. Rev. B 20 (1979) 2307.
[17] M. Yokota, O. Tanimoto, J. Phys. Soc. Jpn. 22 (1967) 779.
[18] K.K. Pandey, T.C. Pant, Chem. Phys. Lett. 170 (1990) 244.
[19] U. Tripathy, P.B. Bisht, K.K. Pandey, Chem. Phys. 299 (2004) 105.
[20] I.Z. Steinberg, Ann. Rev. Biochem. 40 (1971) 83.
[21] L. Stryer, Ann. Rev. Biochem. 47 (1978) 819.
[22] M.I. Savadatti, S.R. Inamdar, N.N. Math, A.D. Mulla, J. Chem. Soc. Faraday Trans. 82 (1986) 2417.
[23] U. Tsuneno, K. Kajiyama, J. Appl. Phys. 47 (1976) 3563.
[24] S. Speiser, R. Katraro, Opt. Commun. 27 (1978) 287.
[25] O.G. Peterson, B.B. Snavely, Bull. Am. Phys. Soc. 13 (1968) 397.
[26] A. Dienes, M. Madden, J. Appl. Phys. 44 (1973) 4161.
[27] C.E. Moeller, C.M. Verber, A.H. Adelman, Appl. Phys. Lett. 18 (1971) 278.
[28] W. Schmidt, W. Appt, N. Wittekindt, Z. Naturforsch. A 27 (1972) 37.
[29] C. Lin, A. Dienes, J. Appl. Phys. 44 (1973) 5050.
[30] M.B. Ahmed, A. Ramalingam, P.K. Palanisamy, J. Lumin. 105 (2003) 9.
[31] P. Sandeep, P.B. Bisht, J. Chem. Phys. 123 (2005) 204713.
[32] K.C. Jena, P.B. Bisht, Chem. Phys. 314 (2005) 179.
[33] U. Tripathy, P.B. Bisht, K.K. Pandey, Res. Chem. Int. 31 (2005) 649.
[34] A.D. Scully, A. Matsumoto, S. Hirayama, Chem. Phys. 157 (1991) 253.
[35] H.C. Joshi, T.C. Pant, J. Lumin. 39 (1988) 343.

Available online at www.sciencedirect.com
ScienceDirect
Organic Electronics 8 (2007) 184–188
Organic Electronics
www.elsevier.com/locate/orgel

Amplified spontaneous emission in α-phase and β-phase polyfluorene waveguides

Hironobu Azuma, Takashi Kobayashi, Yonggu Shim, Nazim Mamedov [1], Hiroyoshi Naito *

Department of Physics and Electronics, Osaka Prefecture University, 1-1 Gakuen-cho, Sakai, Osaka 599-8531, Japan

Available online 23 January 2007

Abstract

Amplified spontaneous emission (ASE) of α- and β-phase poly(9,9-dioctylfluorene) (F8) based waveguides has been studied and ASE wavelengths have been determined as 451 nm and 468 nm, respectively. β-phase waveguides are found to be with higher net gain and lower light propagation loss as compared to α-phase waveguides. Such important improvement of ASE properties, making β-phase waveguides superior over α-phase counterparts is shown to be achieved at the expense of higher refractive index and photoluminescence quantum efficiency of β-phase F8.
© 2007 Elsevier B.V. All rights reserved.

PACS: 78.20.Ci; 78.45.+h; 78.55.Kz

Keywords: Amplified spontaneous emission; Polyfluorene; Spectroscopic ellipsometry

1. Introduction

Conjugated polymers continue to attract worldwide attention because of low cost, small format optical and electronic device applications such as organic light-emitting diodes (OLEDs), solid-state lasers and thin-film transistors [1–3]. Light amplification in optically pumped thin films of conjugated polymers via amplified spontaneous emission (ASE) has been observed in poly(para-phenylenevinylene), poly(fluorene), and their derivatives and copolymers [2,4–9]. This stems from the fact that the energy-level diagram for stimulated emission in the conjugated polymers is essentially a four-level system [10].

The measurement of ASE has been used to obtain gain and loss coefficients in thin films of conjugated polymers and to identify good gain media for solid-state lasers. Among the conjugated polymers mentioned above, poly(9,9-dioctylfluorene) (F8) exhibits the highest gain because of its high photoluminescence (PL) quantum efficiency, and in addition F8 also exhibits unique properties of good thermal stability and good electron and hole transport properties [3].

F8 exhibits different phases such as amorphous (α), β and crystalline phases [11]. β phase can be induced in α-phase (spin-coated) F8 thin films by cooling α-phase F8 thin films down to 80 K and slowly heating them back up to room temperature

* Corresponding author. Tel.: +81 72 254 9266; fax: +81 72 254 9908.
E-mail address: naito@pe.osakafu-u.ac.jp (H. Naito).
[1] Present address: Baku Institute of Physics, Azerbaijan.

1566-1199/$ - see front matter © 2007 Elsevier B.V. All rights reserved.
doi:10.1016/j.orgel.2007.01.007

[12] or by exposing them to certain solvent vapors [13]. In β phase, F8 polymer chains form a 2_1 helix conformation; the angle between the planes of two adjacent fluorene units is 180°, rendering β-phase F8 highly planar [14]. However, comparative studies of ASE properties between the α-, β- and crystalline phase F8 waveguides have not been made yet. Meanwile, above-listed phases of F8 thin films exhibit distinctive optical properties and the comparative studies are important for optimizing the gain and ASE wavelength. In this paper, we report ASE properties of α- and β-phase F8 waveguides (ASE from crystallized F8 thin films has not been observed).

2. Experiment

The chemical structure of F8 is shown in the inset of Fig. 1. F8 was synthesized via a Suzuki coupling reaction. α- and β-phase F8 planar waveguides were fabricated by spin coating from toluene solutions onto quartz substrates. The β-phase structural conformation of F8 was induced in spin-coated F8 thin films by exposing them to toluene vapor for 24 h [15]. The crystallized phase-F8 waveguides were prepared by annealing spin-coated F8 thin films at 200 °C for 90 min followed by slow cooling to room temperature at 0.5 K/min [11,16].

The optical absorption spectra of F8 waveguides were measured with a JASCO V-570 spectrophotometer. For steady-state PL measurement, a He–Cd laser with $\lambda_{ex} = 32$ nm (Kinmonn, IK3301R-G), and an optical multichannel analyzer with a charge-coupled-device (CCD) detector (Hamamatsu Photonics, PMA11) were used. Ellipsometry measurements were made using a Jobin-Yvon spectroscopic phase modulated ellipsometer (UVISEL-9017TK). For ASE measurements, the waveguides were photopumped at 337 nm with a N_2 laser emitting 4–8 ns pulses at a repetition rate of 1 Hz. A cylindrical lens was used to shape the beam into a narrow stripe of 200 μm × 4 mm. ASE emitted from the edge of the waveguides was detected using CCD.

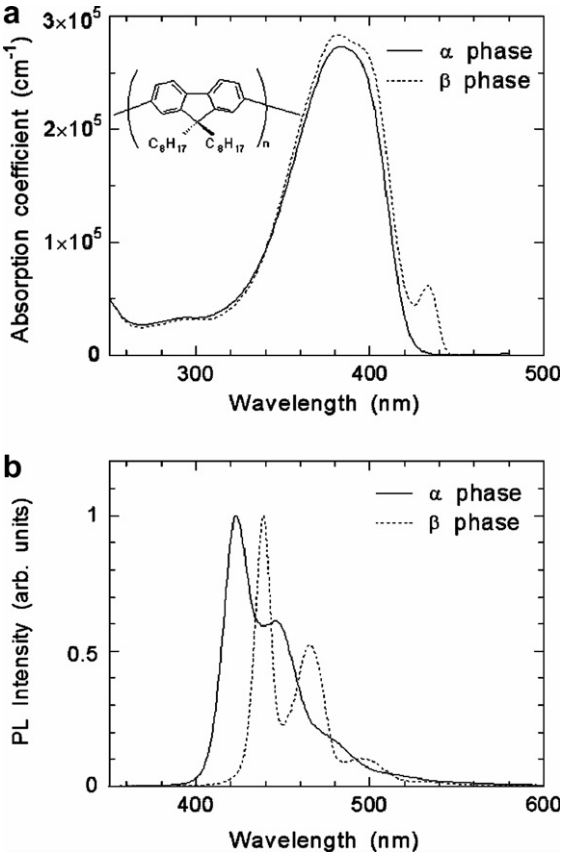


Fig. 1. Absorption (a) and PL spectra (b) of α- and β- phase F8 thin films (inset: the chemical structure of F8).

3. Results and discussion

Fig. 1 shows (a) the absorption and (b) PL spectra of α- and β-phase F8 thin films, respectively. The α-phase F8 thin film exhibits a broad 1Bu exciton absorption band peaked at 390 nm. In PL spectra, a main peak at 423 nm and its vibronic replicas at 447 nm, 476 nm and 502 nm, corresponding to the (0–1), (0–2) and (0–3) vibronic transitions, respectively, are due to excitonic emissions. In addition to the broad 1Bu exciton absorption, the β-phase F8 thin film shows a new absorption peak at 438 nm. In PL spectrum of β-phase F8, the (0–0), (0–1), (0–2) and (0–3) transitions are redshifted by 15–32 nm because of the elongation of effective conjugation length in F8 [15].

Fig. 2 shows the optical constants of α- and β-phase F8 using variable-angle spectroscopic ellipsometry. The optical constants were deduced from the ellipsometric data using a three-phases model (air/F8 thin film/SiO_2 substrate) by neglecting microscopic roughness at the interfaces of air/F8 and F8/substrate. We have observed surface roughness of F8 and substrate surfaces by atomic force miscroscopy, and found that the amplitudes of the roughness at the surfaces are less than 1 nm [8]. Influence of such small roughness on the values of the optical constants shown in Fig. 2 is negligibly small. The refractive index of β-phase F8 in the

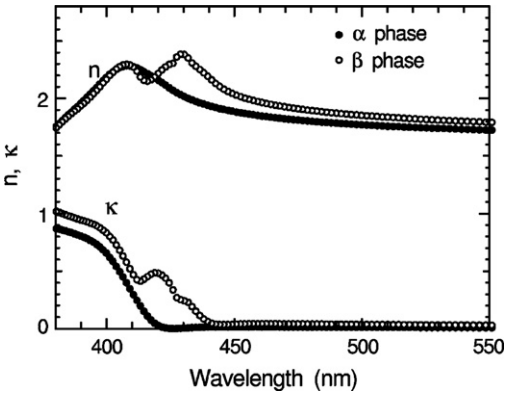


Fig. 2. Refractive index (n) and extinction coefficient (κ) of α- and β-phase F8 thin films.

wavelength range from 420 nm to the 480 nm is higher than that of α-phase F8 because of the new absorption band. The light confinement within β-phase F8 waveguides at ASE wavelengths is thereby improved in comparison with that of α-phase F8 waveguides. Waveguide thicknesses at which only the zero-order transverse electric (TE_0) mode ($m = 0$) is guided are determined from

$$d_{\text{cut-off,TE}} = \frac{\lambda_{\text{ASE}}}{2\pi\sqrt{n_{\text{F8}}^2 - n_{\text{s}}^2}}\left[\tan^{-1}\left(\frac{\sqrt{n_{\text{s}}^2 - n_{\text{a}}^2}}{\sqrt{n_{\text{F8}}^2 - n_{\text{s}}^2}}\right) + m\pi\right], \quad (1)$$

using the data of the optical constants shown in Fig. 2, where n_{F8}, n_{s} and n_{a} are the refractive indices of F8 thin films, substrate and cladding (air), respectively, and m is mode number [17]. The α-phase F8 waveguide cut-off thicknesses for TE_0 mode ($m = 0$) and for TE_1 ($m = 1$) mode are 50 nm and 240 nm, respectively (the β-phase F8 waveguide cut-off thicknesses for TE_0 and TE_1 modes are 40 nm and 200 nm, respectively). We thus chose the α- and β-phase F8 waveguides thickness to be 100 nm at which only TE_0 mode is guided.

Fig. 3 shows normalized emission spectra of (a) α- and (b) β-phase F8 waveguides for different pump energy densities with a constant excitation stripe length of 4 mm. As the pump energy density is increased, the emission spectra become narrower. The spectral narrowing was not observed in crystallized F8 waveguides. The narrowed spectra of α- and β-phase F8 waveguides are located at 451 nm and 468 nm, respectively, which are closed to 0–1 vibrational peaks, reflecting that the stimulated emission is due to quasi-four-level vibronic system [10]. The dependence of the light intensity emitted

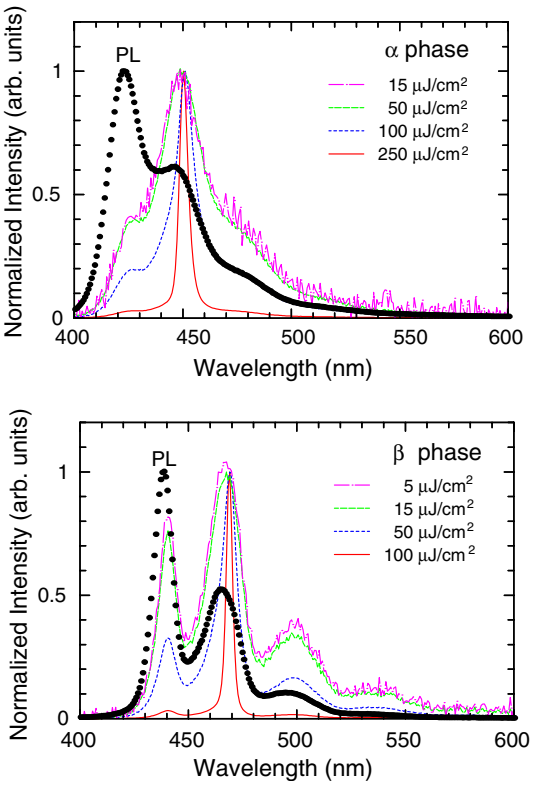


Fig. 3. Normalized emission spectra of (a) α- and (b) β-phase F8 waveguides for different pump energy densities with a constant excitation stripe length of 4 mm. The dotted lines are PL spectra.

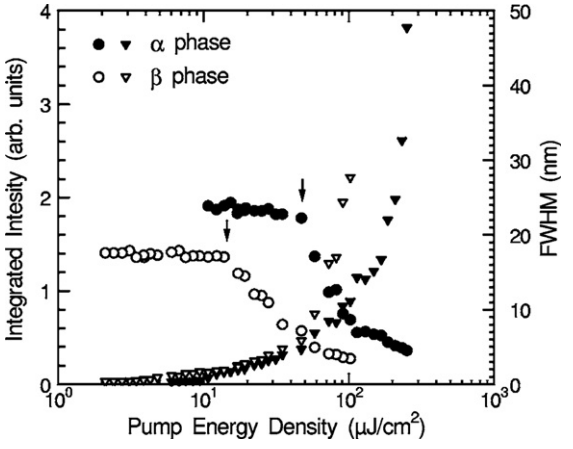


Fig. 4. Pump energy density dependence of the light intensity, emitted from the edge of α- and β-phase F8 waveguides and of FWHM of the ASE spectra.

from the edge of the waveguides and the full width at half maximum (FWHM) of the emission spectra of α- and β-phase F8 waveguides on the pump energy density are shown in Fig. 4. The threshold

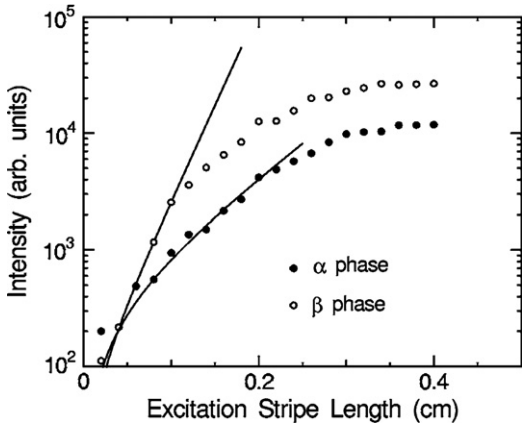


Fig. 5. Dependence of the output intensity at λ_{ASE} on excitation stripe length at pump energy densities of 223 μJ/cm^2. The solid lines are fits to the theoretical prediction (Eq. (2)) for ASE. Note that the points at short excitation stripe lengths, for which gain saturation is not present, were used for the fits.

pump energies are highlighted by the arrows in Fig. 4, and are ~50 μJ/cm^2 and ~15 μJ/cm^2, in α- and β-phase F8 waveguides, respectively. The increase in the pump energy leads to drastic spectral narrowing above the threshold energy densities for ASE, resulting in a spectrum with the FWHMs of 4.5 nm (α phase) and 3.5 nm (β phase).

The dependence of the output intensity at the ASE wavelength, λ_{ASE}, on excitation stripe length at a pump energy density is shown in Fig. 5. The solid lines in the figure are fits to the well-established theoretical expression for ASE, which reads

$$I(\lambda) = \frac{A(\lambda) I_p}{g(\lambda)} (e^{g(\lambda) l} - 1), \quad (2)$$

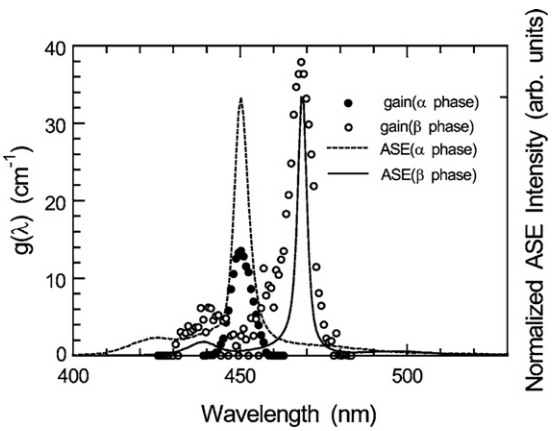


Fig. 6. The open and filled circles are net gain spectra of α- and β-phase F8 waveguides. The solid and dotted lines are normalized ASE spectrum.

where A is a constant related to the cross section for spontaneous emission, I_p is the pump intensity, g is the net gain coefficient, and l is the length of the excitation stripe [18]. Fig. 6 shows the net gain spectra of α- and β-phase F8 waveguides (the fitting of Eq. (2) to the experimental data was carried out at various ASE wavelengths). The maximum net gain coefficients (g_{max}) of α- and β-phase F8 waveguides are 13.5 cm^{-1} ($\lambda_{ASE} = 451$ nm) and 37.9 cm^{-1} ($\lambda_{ASE} = 468$ nm), respectively. The wavelength regions of α- and β-phase F8 waveguides where net gain associated with (0–1) transition is observed are 440–460 nm (α phase) and 450–480 nm (β phase). A previous report has shown that the spectral position of ASE is blue-shifted from 466 nm to 447 nm by simply decreasing F8 waveguide thickness from 100 nm to 36 nm [6]. In Ref. [6], as F8 film thickness is reduced, the spectral position of ASE is not continuously shifted; the ASE wavelength, rather, hops from 468 nm to (452–457) nm. The ASE wavelengths coincide with (0–1) transition energy of β-phase and α-phase F8 thin films. In general, α-phase F8 thin films are formed by spin-coating technique; however, we have found that β-phase F8 is formed beneath air/F8 interface of F8 thin films prepared by spin-coating technique above a certain F8 film thickness [15]. Thus, 20-nm shift in ASE wavelength of F8 reported in Ref. [6] is likely to be due to the structural phase transition induced by reducing spin-coated F8 film thickness.

The loss coefficients of α- and β-phase F8 waveguides are determined from the dependence of the intensity of light emitted at ASE wavelength on the distance x between the edge of the excitation

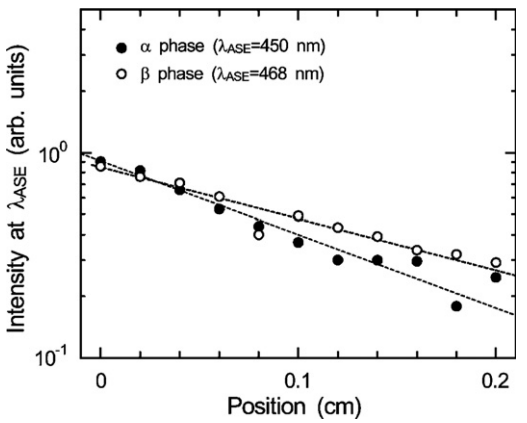


Fig. 7. Dependence of the emission intensity on the length of the nonpumped region between the edge of the excitation stripe and the substrate edge of the waveguide. The pump energy density was 230 μJ/cm^2 and the emission was monitored at λ_{ASE}.

stripe and the edge of the waveguides in Fig. 7. In this experiment, we kept the length of excitation stripe constant ($l = 2$ mm). The loss coefficients α_{loss} of α- and β-phase F8 waveguides within the unpumped region are measured to be 8.2 cm^{-1} and 5.7 cm^{-1} at 230 $\mu J/cm^2$, respectively, using $I = I_0 \exp(-\alpha_{loss} x)$.

The improvement of ASE properties in β-phase F8 waveguides (higher net gain and lower loss coefficient) is obvious in Figs. 6 and 7. The improvement in β-phase F8 results mainly from higher PL quantum efficiency (we have shown PL quantum efficiency of α-phase and β-phase F8 thin films to be 0.37 and 0.70, respectively [11]) as well as stronger light confinement in waveguide slab (higher refractive index as shown in Fig. 2). We analyzed TE mode propagation in F8 slab waveguides, and found that the mode confinement is improved by 13% in β-phase F8 than in α-phase F8 at their ASE wavelengths ($\lambda_{ASE} = 451$ nm for α-phase F8 and $\lambda_{ASE} = 468$ nm for β-phase F8). Thus, higher PL quantum efficiency and stronger light confinement in β-phase F8 do not quantitatively explain the difference in the gain coefficients at λ_{ASE} between α-phase and β-phase F8 (this analysis predicts that the gain coefficient of β-phase F8 is 2.1 times higher than that of α-phase F8, but the gain coefficient of β-phase F8 is 2.8 times higher than that of α-phase F8, as found in Fig. 6). The origin of this disagreement is not known at the present stage.

4. Conclusions

We have carried out ASE and ellipsometry measurements in α-phase and β-phase F8 waveguides. ASE wavelengths of α-phase and β-phase waveguides are 451 nm and 468 nm, respectively: ASE was not observed in crystallized F8 waveguides. The maximum net gain coefficients are 13.5 cm^{-1} and 37.9 cm^{-1}, and the loss coefficients 8.2 cm^{-1} and 5.7 cm^{-1} in α-phase and β-phase waveguides, respectively. Such improvement of ASE properties in β-phase F8 is due to stronger light confinement in the waveguide slab (larger refractive index) and higher PL quantum efficiency of β-phase F8 in comparison with those of α-phase F8.

Acknowledgements

We thank Drs. S. Morishima and T. Ohnishi of Sumitomo Chemical Co. Ltd. for providing the F8 polymer. This work was supported by a Grand-in-Aid for Scientific Research from Japan Society of the Promotion of Science and by a City Area Program of Ministry of Education, Culture, Sports, Science and Technology.

References

[1] J.H. Burroughes, D.D.C. Bradley, A.R. Brown, R.N. Marks, K. Mackay, R.H. Friend, P.L. Burn, A.B. Holms, Nature 347 (1990) 539.
[2] N. Tessler, G.J. Denton, R.H. Friend, Nature (London) 382 (1996) 695.
[3] L.-L. Chua, J. Zaumseil, J.-F. Chang, E.C.-W. Ou, P.K.-H. Ho, H. Sirringhaus, R.H. Friend, Nature (London) 434 (2005) 194.
[4] M.D. McGehee, M.A. Díaz-García, F. Hide, R. Gupta, E.K. Miller, D. Moses, A.J. Heeger, Appl. Phys. Lett. 72 (1998) 1536.
[5] G. Heliotis, R. Xia, D.D.C. Bradley, G.A. Turnbull, I.D.W. Samuel, P. Andrew, W.L. Barnes, Appl. Phys. Lett. 83 (2003) 2118.
[6] G. Heliotis, D.D.C. Bradley, G.A. Turnbull, I.D.W. Samuel, Appl. Phys. Lett. 81 (2002) 415.
[7] H. Takahashi, H. Naito, Thin Solid Films 477 (2005) 53.
[8] H. Takahashi, H. Naito, Curr. Appl. Phys. 6 (2006) 882.
[9] R. Xia, G. Heliotis, Y. Hou, D.D.C. Bradley, Org. Electron 4 (2003) 165.
[10] A. Yariv, Quantum Electronics, Wiley, New York, 1975 (Chapter 10).
[11] K. Asada, T. Kobayashi, H. Naito, Jpn. J. Appl. Phys. 45 (2006) L247.
[12] O.J. Korovyanko, Z.V. Vardeny, Chem. Phys. Lett. 356 (2002) 361.
[13] M. Ariu, M. Sims, M.D. Rahn, J. Hill, A.M. Fox, D.G. Lidzey, M. Oda, J. Cabanillas-Gonzalez, D.D.C. Bradley, Phys. Rev. B 67 (2003) 195333.
[14] M. Fukuda, K. Sawada, K. Yoshino, Jpn. J. Appl. Phys. 28 (1989) L1433.
[15] H. Azuma, K. Asada, T. Kobayashi, H. Naito, Thin Solid Films 509 (2006) 182.
[16] S.H. Chen, H.L. Chou, A.C. Su, S.A. Chen, Macromolecules 37 (2004) 6833.
[17] M. Marcuse, Theory of Dielectric Waveguides, Academic, New York, 1974 (Chapter 1).
[18] A. Yariv, Quantum Electronics, Wiley, New York, 1975 (Chapter 12).

Available online at www.sciencedirect.com
ScienceDirect
Organic Electronics 8 (2007) 189–197
Organic Electronics
www.elsevier.com/locate/orgel

Influences of molecular orientations on stimulated emission characteristics of oligofluorene films

Hao-Wu Lin [a], Chun-Liang Lin [a], Chung-Chih Wu [a,*], Teng-Chih Chao [b], Ken-Tsung Wong [b]

[a] *Department of Electrical Engineering, Graduate Institute of Electro-optical Engineering, and Graduate Institute of Electronics Engineering, National Taiwan University, Taipei 10617, Taiwan, ROC*
[b] *Department of Chemistry, National Taiwan University, Taipei 10617, Taiwan, ROC*

Available online 22 June 2006

Abstract

Efficient luminescence and interesting thermal properties of oligofluorenes provide the opportunity to investigate influences of molecular orientational distributions on characteristics of stimulated emission in organic semiconducting films. While vacuum-deposited terfluorene films exhibit preferential in-plane molecular orientation, they are reoriented and become isotropic with annealing around or above its glass transition temperature. Studies of stimulated emission (amplified spontaneous emission) show that the anisotropic terfluorene films exhibit higher gain and lower threshold than the isotropic films, due to larger confinement of the waveguided mode and larger cross section of stimulated emission. A net gain as high as 78 cm^{-1} (at a pump intensity of ~30 kW/cm^2) and a threshold as low as 0.7 kW/cm^2 were observed. The results suggest that the gain and threshold of stimulated emission in organic semiconducting films could be substantially improved beyond the isotropic case if molecules and their transition dipole moments can be well aligned with the polarization of stimulated emission yet without causing significant loss and emission quenching.
© 2006 Elsevier B.V. All rights reserved.

PACS: 81.10.−h; 78.66.Qn

Keywords: Stimulated emission; Amplified spontaneous emission; Gain; Molecular orientation; Anisotropy; Spectroscopic ellipsometry

1. Introduction

Organic semiconductors have now found wide applications in electronics and optoelectronics, such as organic light-emitting devices, organic thin-film transistors, and organic solar cells, etc. [1–6]. Since observations of stimulated emission in luminescent and semiconducting organic thin films [7–13], they have also been extensively explored as a new class of gain media for solid-state lasers or semiconducting lasing devices. Such organic gain media in general have the advantages of high photoluminescence efficiency, ease of processing, versatility in substrates, and compatibility in integration with other optoelectronic devices. Also, with the variety and the generally wide gain spectra of luminescent

* Corresponding author. Tel.: +886 2 2363 5251x346; fax: +886 2 2367 1909.
E-mail address: chungwu@cc.ee.ntu.edu.tw (C.-C. Wu).

1566-1199/$ - see front matter © 2006 Elsevier B.V. All rights reserved.
doi:10.1016/j.orgel.2006.05.006

organic semiconductors, they have exhibited stimulated emission at wavelengths spanning the whole visible spectra. These promising characteristics of optically pumped organic lasers have thus led to efforts aiming at achieving electrically pumped organic lasers [14–18]. With continuous efforts in pursuing electrically pumped organic lasing, luminescent organic semiconductors with improved characteristics, such as lower thresholds of stimulated emission, enhanced carrier mobilities, and further improved thermal stability, etc., are constantly desired.

As such, recent findings of some intriguing properties of oligofluorenes suggest that they may be of interest for for studies of stimulated emission [19–25]. Appropriate substitutions on C9 of oligofluorenes could render them very high glass transition temperatures (T_g) of >200 °C and high thin-film photoluminescence (PL) quantum yields of 70–90% in neat films. They are electrochemically stable as indicated by both reversible oxidation and reduction. Furthermore, they exhibit unusual non-dispersive ambipolar carrier-transport properties with carrier mobilities over 10^{-2} cm^2/(V s) for both holes and electrons. In this work, we have performed investigations on the stimulated emission characteristics of a terfluorene. Furthermore utilizing interesting thermal properties of the terfluorene, influences of thin-film morphologies (molecular orientational distributions) on such characteristics are also studied.

2. Experimental

The terfluorene (T3, Fig. 1) investigated in this work was synthesized through the Suzuki coupling reaction of 2,7-diboronic ester of 9,9′-diarylfluorene and 2-bromo-9,9-diarylfluorene in the presence of $Pd(PPh_3)_4$ and P^tBu_3 catalysts with high yields (75–83%). Further details of synthesis and chemical analysis had been previously reported [19]. Synthesized T3 molecules were subject to purification by temperature-gradient sublimation before use in this study. Thermal properties of organic compounds were investigated by differential scanning calorimetry (DSC).

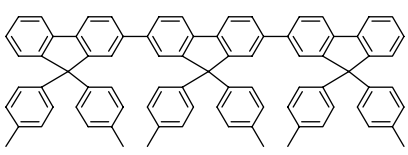


Fig. 1. Molecular structure of T3.

Thin-film samples of organic compounds for optical characterization were deposited on fused silica substrates by vacuum deposition in a high-vacuum chamber. The deposition was performed at a rate of 2–3 Å/s with the substrate held at room temperature. Thicknesses were monitored using a crystal oscillator during deposition and were verified later with ellipsometry. In some cases, the morphology of thin films was varied by annealing. Annealing of thin-film samples was carried out in a nitrogen atmosphere with a computer-controlled heating stage. After annealing, samples were cooled by contact with a metal block held at the room temperature. The PL quantum yield in thin films was determined using a calibrated integrating sphere system [26]. The 325 nm line of the He–Cd laser was used to excite the thin-film sample placed in the sphere that was coupled to a cooled charge-coupled-device (CCD) spectragraph and was purged with dry nitrogen. The quantum yield was determined by comparing the spectral intensities of the laser source and the sample emission.

Variable-angle spectroscopic ellipsometry (VASE) in the reflection and transmission mode was used to study the optical constants, optical anisotropy, and molecular orientation of oligofluorene films [27–30]. Ellipsometry measures the change in polarization of light as a function of incident angle and wavelength. The experimentally determined ellipsometric values are Ψ and Δ, which are related to the ratio of complex reflection coefficients $\widetilde{R}_p$ and $\widetilde{R}_s$ for p- and s-polarized light, respectively, by $\frac{\widetilde{R}_p}{\widetilde{R}_s} = \tan(\Psi)e^{i\Delta}$ or the ratio of complex transmission coefficients $\widetilde{T}_p$ and $\widetilde{T}_s$ for p- and s-polarized light, respectively, by $\frac{\widetilde{T}_p}{\widetilde{T}_s} = \tan(\Psi)e^{i\Delta}$. Optical constants of the materials are then determined by first constructing an optical model of the sample with physically meaningful structural and optical parameters, and then by iteratively adjusting these parameters to obtain the best fit to the measured ellipsometric data, i.e., the fitting with the minimum mean square error (MSE).

Ellipsometry over a wavelength range of 270 nm–1000 nm in steps of 5 nm were performed in air using the J. A. Woollam VASE spectroscopic ellipsometer equipped with a xenon lamp source. The angles of incidence used were between 55° and 75° relative to the surface normal in steps of 5° for reflection ellipsometry and between 40° and 60°

relative to the surface normal in steps of 5° for transmission ellipsometry. Backside of the fused silica substrate was roughened for reflection ellipsometry to eliminate the incoherent backside reflection from the bottom of the substrate. The nonlinear regression analysis of the measured ellipsometric data was performed using the J. A. Woollam WVASE32 software.

Stimulated emission of T3, in the form of amplified spontaneous emission (ASE), was characterized with films of ~100 nm thick deposited on the fused silica, which forms a slab waveguide with SiO_2 on one side and air on the other. The schematic measurement setup is shown in Fig. 2. The third harmonic of a pulsed Nd–YAG laser (355 nm, 10 ns) was used as excitation source for ASE measurements. The energy of pulses was controlled using calibrated neutral density filters. Cylindrical lenses and an adjustable slit were used to shape the excitation beam into a stripe with a width of 1.2 mm and a length of 4 mm on the film, creating a stripe-shaped gain region. The uniformity of the intensity and the width of the stripe were confirmed by a beam profiler. In ASE, the spontaneously emitted photons waveguided along the stripe are amplified via stimulated emission as the pumping intensity is increased beyond a certain threshold. As ASE occurs, most of the light is emitted from the end of the stripe and ASE manifests itself with a sudden narrowing of the emission spectrum and an increase in the intensity of edge emission. The edge emission in the plane of the film was detected at one end of the pump stripe using a fiber bundle connected to a cooled charge-coupled-device (CCD) spectrograph.

The variable-stripe-length (VSL) technique was used to measure the net gain of ASE along the waveguide [31–33], as schematically illustrated in Fig. 3. By varying the length of the pump stripe L yet fixing the pumping intensity, one measures the output intensity $I(\lambda)$ of ASE from one end of the stripe as a function of L. The output intensity $I(\lambda)$ vs. L follows the dependence of:

$$I(\lambda) = \frac{AP_0}{g(\lambda)}(e^{g(\lambda)L} - 1) \quad (1)$$

where A is a constant related to the cross section for spontaneous emission, P_0 is the pump intensity, $g(\lambda)$ is the net gain coefficient, and L is the length of the pump stripe [31–33]. By fitting the experimental data with Eq. (1), one is able to extract the net gain coefficient at the ASE wavelength at a pump intensity.

To measure loss characteristics of the waveguides, the length of the pump stripe was kept constant ($L = 2$ mm) but the distance of the pump stripe itself from the edge of the sample was varied [31–33], as illustrated in Fig. 4. Assuming the emission intensity from the end of the excitation stripe is I_0, the emission from the edge of the sample should decrease as $I = I_0 \exp(-\alpha x)$, where x is the length of the unpumped region between the end of the pump stripe and the edge of the sample and α is the loss coefficient.

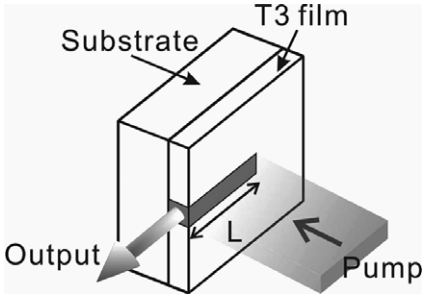


Fig. 3. Schematic setup for measurement of ASE gain.

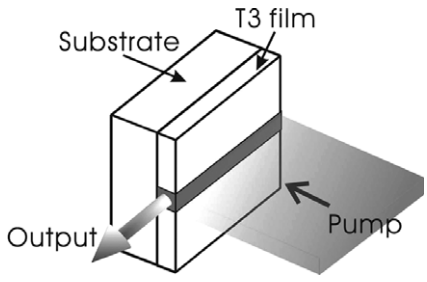


Fig. 2. Schematic setup of ASE measurement.

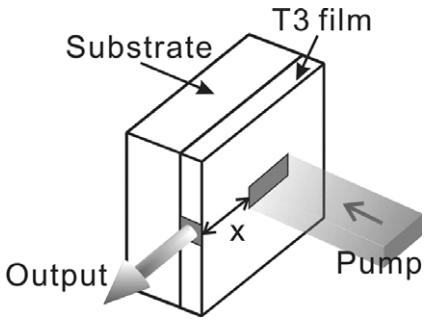


Fig. 4. Schematic setup for measurement of the waveguide loss.

3. Results and discussions

3.1. Thermal properties

Fig. 5 shows the trace of the differential scanning calorimetry (DSC) of T3 molecules. The introduction of rigid aryl substitutions on C9 renders the molecular structure rather steric and bulky. As a consequence, T3 possesses a high glass transition temperature (T_g) of ~200 °C. Thus vacuum-deposited films of T3 are homogeneous and amorphous (as confirmed by X-ray diffraction), and stay morphologically stable well over 100 °C. Interestingly, above T_g, T3 does not show any sign of phase transitions (e.g., crystallization and melting, etc.) up to 400 °C, indicating it be a truly amorphous material and be difficult to crystallize. Indeed, heating a T3 film at a temperature close to or well over its T_g also does not induce apparent changes that can be distinguished by optical microscopy. Further characterization of optical constants of T3 films with spectroscopic ellipsometry, however, reveals that annealing at temperatures close to or above T_g causes significant changes in microscopic morphology (i.e., anisotropic vs. isotropic).

3.2. Optical constants and molecular orientation

In examining optical anisotropy in both the transparent region and the absorption region of the spectrum, due to the high degree of correlation between model parameters for optically anisotropic films, more ellipsometric data other than those from typical reflection ellipsometry at variable angles are required to reduce correlation and to obtain correct results [27–30]. Typical approaches include taking data from samples of different thicknesses (i.e., multi-sample analysis), combining data from reflection ellipsometry and transmission measurements of a sample, or combining data from both reflection and transmission ellipsometry of a sample [29,30]. In this work, anisotropic optical constants of a sample were determined by the combination of reflection and transmission ellipsometry, which in principle is simpler and eliminates the risk of sample-to-sample variation (as may happen in the multi-sample analysis).

Ellipsometric data (both transmission and reflection) measured for a T3 film (~100 nm thick) as-deposited and after annealing are shown in Figs. 6 and 7, respectively. The annealing was performed at 200 °C for 4 min under a dry nitrogen atmosphere, and further annealing induced no more difference in optical properties. After annealing, the sample was then cooled by contact with a metal block held at the room temperature. As clearly

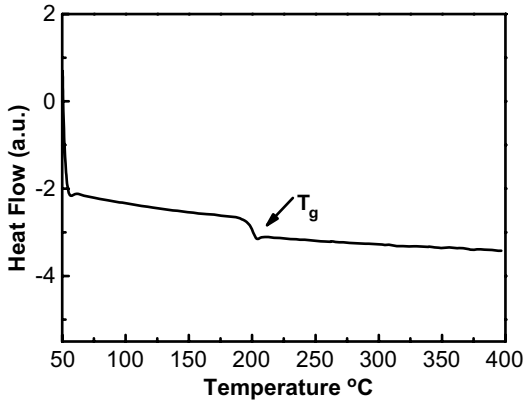


Fig. 5. The DSC trace of T3.

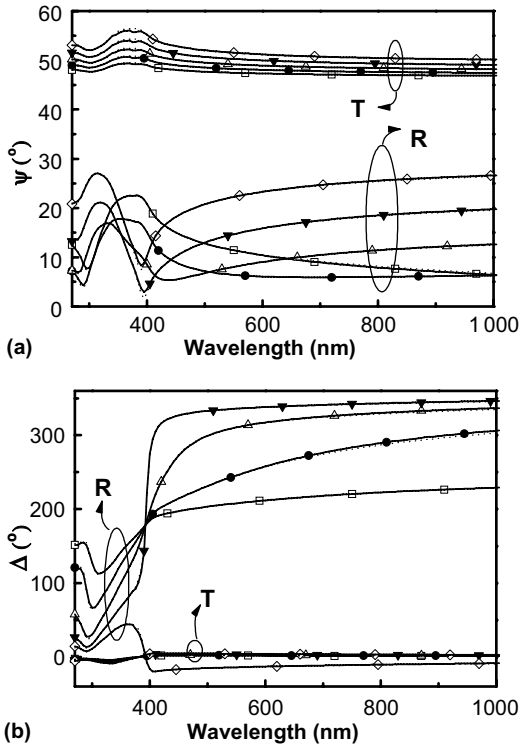


Fig. 6. Measured (solid lines) (a) Ψ and (b) Δ, and the fittings (dashed lines) for reflection ellipsometry (R) at incident angles of 55° (□), 60° (●), 65°(△), 70°(▼), and 75° (◇) and for transmission ellipsometry (T) at incident angles of 40° (□), 45° (●), 50° (△), 55°(▼), and 60° (◇) of an as-deposited T3 film (100 nm). The fitted data (dashed lines) are difficult to identify because of the high quality of the fit.

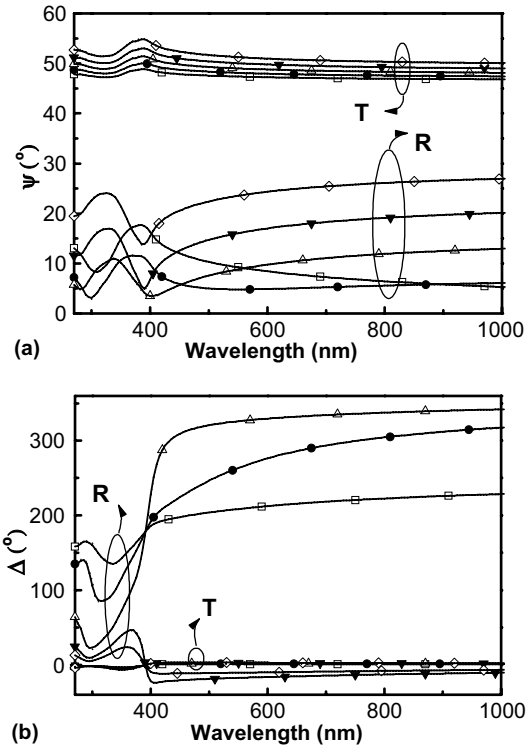


Fig. 7. Measured (solid lines) (a) Ψ and (b) Δ, and the fittings (dashed lines) for reflection ellipsometry (R) at incident angles of 55° (□), 60°(●), 65° (△), 70°(▼), and 75° (◇), and for transmission ellipsometry (T) at incident angles of 40° (□), 45°(●), 50° (△), 55°(▼), and 60° (◇) of an annealed T3 film (100 nm). The fitted data (dashed lines) are difficult to identify because of the high quality of the fit.

shown in Figs. 6 and 7, ellipsometric values (Ψ and Δ) change upon sample annealing. The alteration of such optical properties is not due to degradation or transformation of materials with annealing, since the PL spectra before and after annealing are basically the same and the variation of PL quantum yields as determined with the calibrated integrating sphere system is within the experimental error ($75 \pm 3\%$). Instead, such results indicate changes in microscopic morphology of the T3 film induced with annealing and the sensitivity of ellipsometry in detecting such characteristics.

Since no in-plane anisotropy was observed in polarized optical transmission microscopy and the ellipsometric data were the same when rotating the sample in the plane of the film, in extracting optical constants from the measured ellipsometric data, the films were treated as uniaxially anisotropic with the optical axis along the surface normal. That is, the optical constants are distinguished by those for the ordinary (in-plane) polarization, $n_o + ik_o$, and those for the extraordinary (out-of-plane) polarization, $n_e + ik_e$. The film thickness was first determined using a uniaxially anisotropic Cauchy model to fit the ellipsometric data in the transparent region. A Kramers–Kronig consistent model using a combination of one Cauchy background and several Gaussian oscillators for the ordinary (in-plane) and extraordinary (out-of-plane) optical constants was then constructed to fit the measured ellipsometric data over the whole spectral range [27–30]. Optical constants thus extracted (Figs. 8(a) and (b)) well fitted the experimental ellipsometric data with low MSE values of $\leqslant 2$, as illustrated in Figs. 6 and 7.

As shown in Fig. 8(a), the as-deposited T3 film exhibits significant anisotropy in both refractive index and absorption. The large difference between k_0 and k_e (~4.4:1 at the peak wavelength) indicates preferential orientations of vacuum-deposited T3 molecules parallel to the surface plane, since the transition dipole moment for the $\pi-\pi^*$ transition

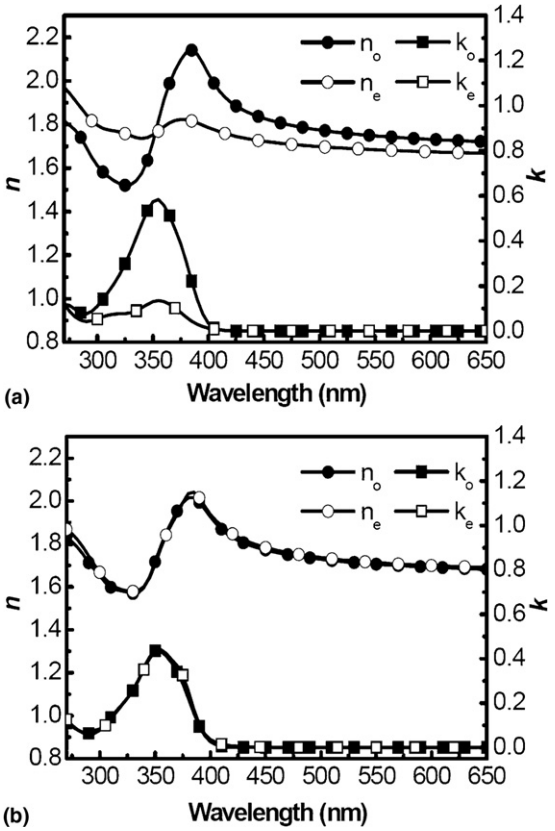


Fig. 8. Ordinary (in-plane) and extraordinary (out-of-plane) optical constants of (a) the as-deposited T3 film, and (b) the annealed T3 film (200 °C, 4 min.).

of oligofluorenes is roughly along the backbone [34]. The optical constants of the annealed T3 film are shown in Fig. 8(b). With annealing, the difference between in-plane and out-of-plane optical constants diminishes and the film becomes optically isotropic. This result suggests that T3 molecules reorient themselves during annealing and eventually take an isotropic orientational distribution, which is then frozen down to the room temperature with the cooling performed. Schematic representation of distributions of molecular orientation in the as-deposited and the annealed films are shown in Figs. 9(a) and (b), respectively. Such a phenomenon shall not be too surprising since T3 is an organic glass. For organic glasses, although there occurs no major morphological change and phase transition across T_g, the viscosity in general would substantially decrease and molecules acquire larger freedom in motion and rotation [35]. Characteristics unique to T3 here, however, are its anisotropy as deposited and its immunity to crystallization above T_g.

3.3. Stimulated emission

To study the influences of molecular orientational distributions on stimulated emission characteristics, ASE of the T3 film (100 nm) as deposited or after annealing was characterized. Figs. 10(a) and (b) show the edge-collected emission spectra from a T3 film as-deposited and after annealing, respectively, at different excitation intensities. At low pump intensities, the emission spectra for both

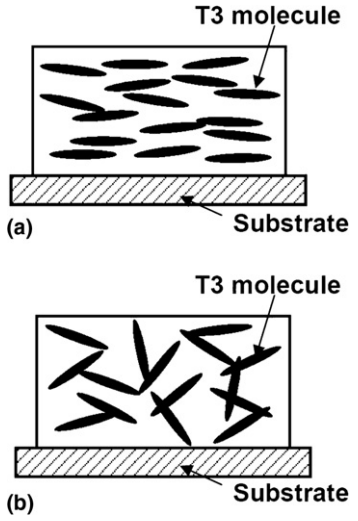


Fig. 9. Schematic illustration of distributions of molecular orientations in (a) the as-deposited and (b) the annealed T3 films.

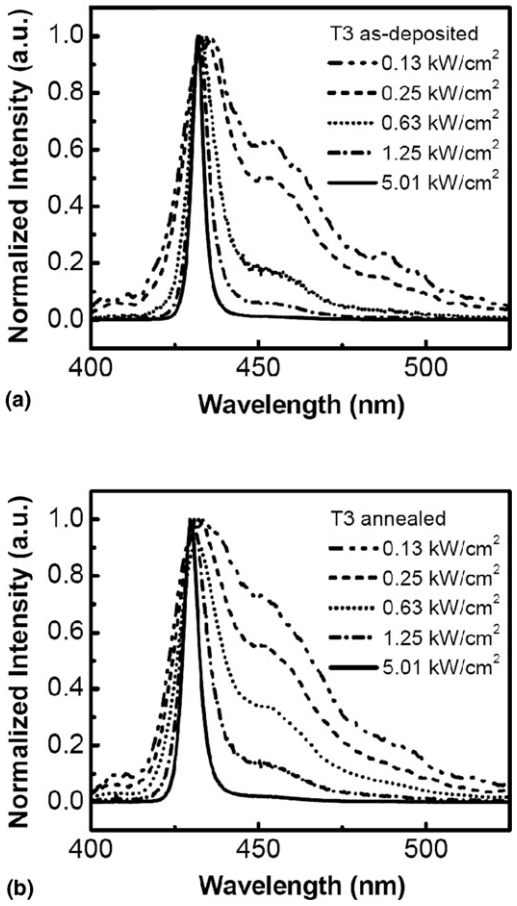


Fig. 10. Normalized edge-detected emission spectra of (a) the as-deposited T3 film, and (b) the annealed T3 film (200 °C, 4 min) at different pump intensities.

cases are broad and exhibit clear vibronic peaks and shoulders at 405 nm (0–0 transition), 430 nm (0–1 transition), 455 nm (0–2 transition), and near 480 nm (0–3 transition), characteristic of spontaneous emission. As the pump energy is increased, the component associated with stimulated emission increases and results in gain narrowing centered at ~430 nm, which coincides with the 0–1 vibronic transition of the T3 spontaneous emission. With increasing the pumping intensities, emission spectra of the as-deposited film narrow faster than those of the annealed film, indicating a lower threshold intensity required for observing ASE in the as-deposited film. Fig. 11(a) shows the corresponding full width at half maximum (FWHM) of emission spectra for these two cases as a function of the pump intensity. As the pump intensity is raised well beyond the threshold values, the intensity at the 430-nm peak grows much more than those at other

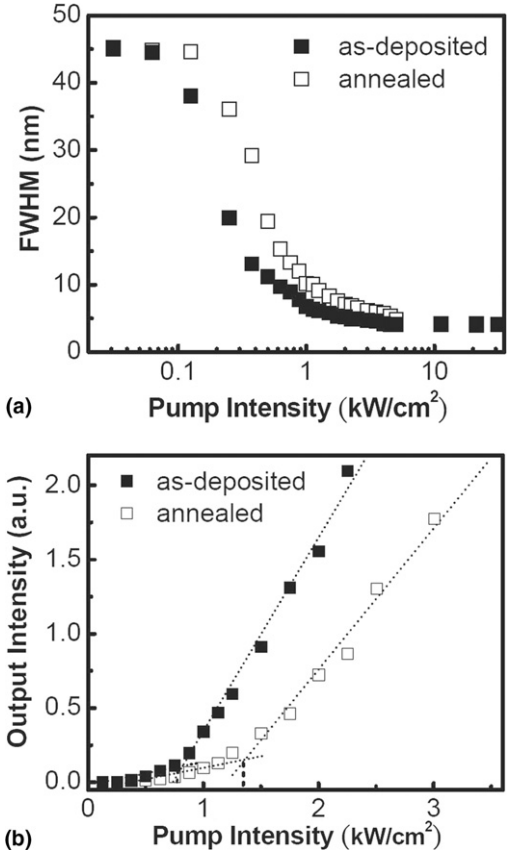


Fig. 11. (a) FWHM of edge-detected emission spectra, and (b) Edge-detected output intensity as a function of the pump intensity for the as-deposited T3 film and the annealed T3 film (200 °C, 4 min.).

wavelengths, resulting in a largely reduced FWHM of <5 nm.

The spectral narrowing is accompanied by the abrupt increase of the edge-detected light intensity (at the ASE wavelength) vs. the excitation intensity, as shown in Fig. 11(b). The abrupt increase of edge emission indicates the onset of stimulated emission along the pumped waveguide region, and thus defines the threshold pump intensity for the ASE to occur. The threshold pump intensities for a film as-deposited and after annealing are ~0.7 kW/cm^2 and ~1.4 kW/cm^2, respectively, which correspond well to pump intensities where strong spectral narrowing occurs. It is noticed that the as-deposited T3 film exhibits a lower ASE threshold than the annealed film.

Stimulated emission of the as-deposited film and the annealed film were further characterized with the variable-stripe-length (VSL) technique (Fig. 3) to measure the net gain of ASE along the waveguide. Fig. 12(a) and (b) show the output intensity at the ASE peak wavelength (symbols) for the as-deposited film and the annealed film, respectively, as a function of the pump stripe-length at different pump intensities. By fitting experimental data using Eq. (1) (represented by dashed lines), the net gain coefficients are determined and are shown in Fig. 13 for both cases. Note that at higher pump intensities, the output intensity saturates at longer excitation lengths. It is typically observed in other solid-state organic gain media as the strongly amplified traveling light induces substantial depletion of the excitations, resulting in gain saturation [36]. Therefore, in the fitting, only subsets of data ($gL < 4$) for which gain saturation is not evident are used. For the as-deposited T3 film, as pumping intensity increases from 1 to 30 kW/cm^2, the net gain increases by nearly two orders of magnitude from 2.6 to 78 cm^{-1}. A net gain of 78 cm^{-1} achieved at a pump intensity of ~30 kW/cm^2 is rather high among those reported for neat semiconducting

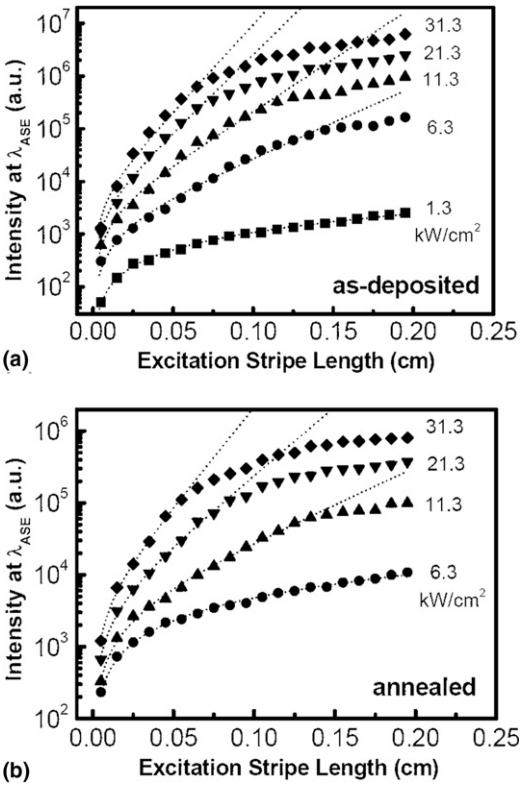


Fig. 12. Measured (symbols) and fitted (lines) emission intensities at the ASE wavelength (symbols) for (a) the as-deposited T3 film, and (b) the annealed T3 film (200 °C, 4 min.) as a function the pump length at several pump intensities.

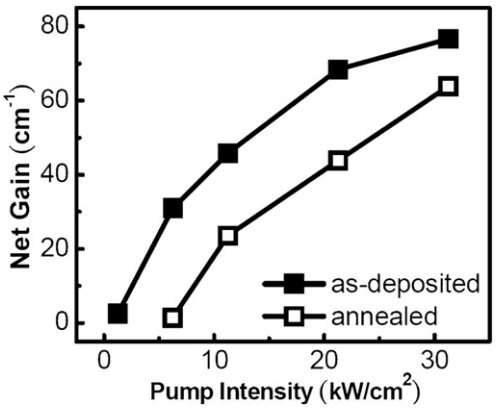


Fig. 13. Net gain coefficients as a function of the pump intensity for the as-deposited and the annealed T3 films.

organic films [31–33]. After annealing, at a same pumping intensity, the net gain becomes substantially lower (15–30 cm^{-1} lower). Such lower net gains explain the higher ASE threshold for the annealed T3 films.

The loss characteristics of the waveguides were also measured using the scheme described in Section 2. Fig. 14 shows the edge-detected emission intensity at the ASE wavelength as a function of the stripe distance from the waveguide edge. By curve fitting the experimental data with an exponential dependence on length, loss coefficients of 7.9 cm^{-1} and 5.7 cm^{-1} are extracted for the as-deposited and the annealed films, respectively. Such values are rather small for neat organic films [31–33], and are close to those reported for host–guest systems in which

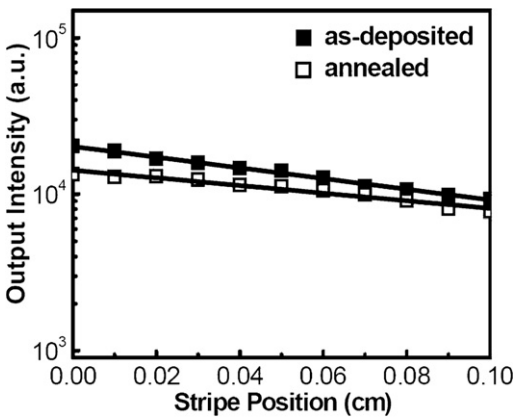


Fig. 14. Measured (symbols) and fitted (lines) edge-detected emission intensities for the as-deposited T3 film and the annealed T3 film as a function of the distance between the end of the excitation stripe and the edge of the substrate.

energy transfer moves the emission away from the absorption tail [9,10]. The slightly lower loss coefficient for the annealed film is due to the lower in-plane absorption (compared to the anisotropic as-deposited film), which would reduce loss resulted from self-absorption.

The lower ASE threshold and the higher net gain of stimulated emission in the anisotropic T3 film than in the isotropic T3 film are worthy of some considerations. To the first order (i.e., neglecting the waveguide loss), the net gain coefficient g roughly has the dependence of $g = \Gamma \times g'$, where g' is the intrinsic material gain and Γ is confinement ratio for the waveguide mode supported by the slab waveguide (i.e., the fundamental transverse electric (TE) mode in the present case) [18,36,37]. As the uniaxially anisotropic T3 film has a higher in-plane refractive index than the isotropic film (by ~0.1–0.15 at emission wavelengths), the waveguide mode (i.e., the fundamental TE mode which has an in-plane polarization) in the anisotropic T3 film sees a larger confinement. As to g', it has the general dependence of $g' = \sigma_{em} \times N_{ex}$, where σ_{em} is the cross section for stimulated emission and N_{ex} represents the population of molecular excited states [38–40]. With nearly same film thicknesses and the stronger in-plane extinction coefficient, the anisotropic T3 film has a slightly higher absorption of the incident excitation than the isotropic film (77% vs. 72%) and thus slightly higher N_{ex}. Since σ_{em} depends on the alignment of the molecular transition dipole moments with the polarization of stimulated emission (i.e., the polarization of the fundamental TE mode) [38], the anisotropic T3 film which has the transition dipole moments preferentially along the surface also has larger σ_{em}. These factors all thus favor a larger net gain of stimulated emission in the anisotropic T3 film even though it has a slightly higher waveguide loss. The results therefore suggest that if in the thin film molecules and their transition dipole moments can be well aligned with the polarization of stimulated emission yet without causing significant loss and emission quenching, the gain and threshold of stimulated emission could be substantially enhanced beyond the isotropic case.

4. Summary

In summary, the efficient luminescence and interesting thermal properties of oligofluorenes provide the opportunity to investigate influences of molecular orientational distributions on characteristics of

stimulated emission in organic semiconducting films. Vacuum-deposited terfluorene films exhibit preferential in-plane molecular orientation, yet with annealing around or above its T_g, the molecules reorient themselves to become isotropic, as examined by spectroscopic ellipsometry. Detailed studies of stimulated emission characteristics, including spectra, intensity, gain and loss, of both the anisotropic and the isotropic films have been performed. Results show that the anisotropic terfluorene films exhibit higher gain for stimulated emission and lower ASE threshold than the isotropic films, due to larger confinement of the waveguided mode and larger cross section of stimulated emission. A net gain as high as 78 cm^{-1} (at a pump intensity of $\sim$30 kW/cm^2), an ASE threshold as low as 0.7 kW/cm^2, and low loss coefficients of 5–8 cm^{-1} for the waveguide were observed. The results suggest that the gain and threshold of stimulated emission in organic semiconducting films could be substantially improved beyond the isotropic case if molecules and their transition dipole moments can be well aligned with the polarization of stimulated emission yet without causing significant loss and emission quenching.

Acknowledgements

The authors would like to acknowledge financial support from National Science Council of Republic of China. C.-L.L. and H.-W.L are also grateful for financial support from MediaTek Fellowship.

References

[1] C.W. Tang, S.A. VanSlyke, Appl. Phys. Lett. 51 (1987) 913.
[2] C.W. Tang, Appl. Phys. Lett. 48 (1986) 183.
[3] J.H. Burroughes, D.D.C. Bradley, A.R. Brown, R.N. Marks, R.H. Friend, P.L. Burns, A.B. Holmes, Nature (London) 347 (1990) 539.
[4] A.A. Shoustikov, Y. You, M.E. Thompson, IEEE J. Sel. Top. Quantum Electron. 4 (1998) 3.
[5] F. Garnier, G. Horowitz, X. Peng, D. Fichou, Adv. Mater. 2 (1990) 592.
[6] T.N. Jackson, Y.-Y. Lin, D.J. Gundlach, H. Klauk, IEEE J. Sel. Top. Quantum Electron. 4 (1998) 100.
[7] F. Hide, M.A. Diáz-Garcia, B.J. Schwartz, M.R. Andersson, Q. Pei, A.J. Heeger, Science 273 (1996) 1833.
[8] N. Tessler, G.J. Denton, R.H. Friend, Nature (London) 382 (1996) 695.
[9] V.G. Kozlov, V. Bulovic, P.E. Burrows, S.R. Forrest, Nature (London) 389 (1997) 362.
[10] M. Berggren, A. Dodabalapur, R.E. Slusher, Z. Bao, Nature (London) 389 (1997) 466.
[11] G.J. Denton, N. Tessler, N.T. Harrison, R.H. Friend, Phys. Rev. Lett. 78 (1997) 733.
[12] S.V. Frolov, M. Liess, P.A. Lane, W. Gellerman, Z.V. Vardeny, M. Ozaki, K. Yoshino, Phys. Rev. Lett. 78 (1997) 4285.
[13] N.D. Kumar, J.D. Bhawalkar, P.N. Prasad, F.E. Karasz, B. Hu, Appl. Phys. Lett. 71 (1997) 999.
[14] V.G. Kozlov, P.E. Burrows, G. Parthasarathy, Appl. Phys. Lett. 74 (1999) 1057.
[15] M.A. Baldo, R.J. Holmes, S.R. Forrest, Phys. Rev. B 66 (2002) 035321.
[16] H. Yamamoto, T. Oyamada, H. Sasabe, C. Adachi, Appl. Phys. Lett. 84 (2004) 1401.
[17] T. Aimono, Y. Kawamura, K. Goushi, H. Yamamoto, H. Sasabe, C. Adachi, Appl. Phys. Lett. 86 (2005) 071110.
[18] M. Pauchard, M. Vehse, J. Swensen, D. Moses, A.J. Heeger, E. Perzon, M.R. Andersson, Appl. Phys. Lett. 83 (2003) 4488.
[19] K.-T. Wong, Y.-Y. Chien, R.-T. Chen, C.-F. Wang, Y.-T. Lin, H.-H. Chiang, P.-Y. Hsieh, C.-C. Wu, C.-H. Chou, Y.-O. Su, G.-H. Lee, S.-M. Peng, J. Am. Chem. Soc. 124 (2002) 11576.
[20] C.C. Wu, T.L. Liu, W.Y. Hung, Y.T. Lin, K.T. Wong, R.T. Chen, Y.M. Chen, Y.Y. Chien, J. Am. Chem. Soc. 125 (2003) 3710.
[21] C.-C. Wu, T.-L. Liu, Y.-T. Lin, W.-Y. Hung, T.-H. Ke, K.-T. Wong, T.-C. Chao, Appl. Phys. Lett. 85 (2004) 1172.
[22] C.-C. Wu, Y.-T. Lin, K.-T. Wong, R.-T. Chen, Y.-Y. Chien, Adv. Mater. 16 (2004) 61.
[23] H.W. Lin, C.L. Lin, C.C. Wu, T.C. Chao, K.T. Wong, Appl. Phys. Lett. 87 (2005) 071910.
[24] L.-Y. Chen, W.-Y. Hung, Y.-T. Lin, C.-C. Wu, Appl. Phys. Lett. 87 (2005) 112103.
[25] C.-C. Wu, W.-G. Liu, W.-Y. Hung, T.-L. Liu, Y.-T. Lin, H.-W. Lin, K.-T. Wong, Y.-Y. Chien, R.-T. Chen, T.-H. Hung, Appl. Phys. Lett. 87 (2005) 052103.
[26] C.-C. Wu, W.-Y. Hung, T.-L. Liu, L.-Z. Zhang, T.-Y. Luh, J. Appl. Phys. 93 (2003) 5465.
[27] R.M.A. Azzam, N.M. Bashara, Ellipsometry and Polarized Light, Amsterdam, North-Holland, 1977.
[28] G.E. Jellison, Thin Solid Films 313–314 (1998) 33.
[29] M. Tammer, A.P. Monkman, Adv. Mater. 14 (2002) 210.
[30] C.M. Ramsdale, N.C. Greenham, Adv. Mater. 14 (2002) 212.
[31] M.D. McGehee, R. Gupta, S. Veenstra, E.K. Miller, M.A. Diaz-Garcia, A.J. Heeger, Phys. Rev. B58 (1998) 7035.
[32] G. Heliotis, D.D.C. Bradley, G.A. Turnbull, I.D.W. Samuel, Appl. Phys. Lett. 81 (2002) 415.
[33] R. Xia, G. Heliotis, D.D.C. Bradley, Appl. Phys. Lett. 82 (2003) 3599.
[34] Y. Geng, A. Trajkovska, D. Katsis, J.J. Ou, S.W. Culligan, S.H. Chen, J. Am. Chem. Soc. 124 (2002) 8337.
[35] K. Naito, A. Miura, J. Phys. Chem. 97 (1993) 6240.
[36] A. Yariv, Quantum Electronics, Wiley, New York, 1975.
[37] M. Pauchard, J. Swensen, D. Moses, A.J. Heeger, E. Perzon, M.R. Andersson, J. Appl. Phys. 94 (2003) 3543.
[38] K. Shimoda, Introduction to Laser Physics, Spinger-Verlag, Berlin Heidelberg, 1986.
[39] X. Liu, C. Py, Y. Tao, Y. Li, J. Ding, M. Day, Appl. Phys. Lett. 84 (2004) 2727.
[40] W. Holzer, A. Penzkofer, S.-H. Gong, A. Bleyer, D.D.C. Bradley, Adv. Mater. 8 (1996) 974.

Available online at www.sciencedirect.com
ScienceDirect
Organic Electronics 8 (2007) 198–205
Organic Electronics
www.elsevier.com/locate/orgel

Large third-order optical nonlinearities of ultrathin films containing octacarboxylic copper phthalocyanine

Chunying He [a,b], Yiqun Wu [b], Guang Shi [a], Wubiao Duan [b], Weina Song [b], Yinglin Song [a,*]

[a] Department of Applied Physics, Harbin Institute of Technology, Harbin 150001, China
[b] Laboratory of Functional Materials, School of Chemistry and Materials Science, Heilongjiang University, Harbin 150080, China

Available online 13 January 2007

Abstract

An ultrathin composite film with alternating layers containing anionic octacarboxylic copper phthalocyanine [$CuPc(COONa)_8$] and cationic polyethylenimine (PEI) has been prepared by the electrostatic layer-by-layer self-assembly technique. The alternating multilayer assemblies of $CuPc(COONa)_8$/PEI were characterized by UV–Vis spectroscopy, showing the regularly consecutive adsorption process. The film surface was smooth and homogeneous as indicated by atomic force microscopy. The closely packed nanoparticles, with the average diameter of 36 nm and the mean interface roughness of 2.984 nm, can be easily seen on the film surface uniformly. Further structure investigation was carried out by using small angle X-ray diffraction. Third-order nonlinear properties of the film and $CuPc(COONa)_8$ aqueous solution were studied by *Z*-scan measurements at 532 nm with 8 ns pulses. The ultrathin film depicted strong nonlinear reverse saturable absorption and excellent self-defocusing performance. The second-order molecular hyperpolarizability γ value of the film was 68 times larger than that of solution sample.
© 2007 Elsevier B.V. All rights reserved.

PACS: 42.65.−k

Keywords: Third-order optical nonlinearity; Electronic self-assembly; Phthalocyanine complexes; *Z*-scan

1. Introduction

Third-order nonlinear optical (NLO) materials have been applied widely in many important technologies including optical recording, optical limiting for sensor protection, photonic switching, optical signal processing and optical computing [1–4]. Therefore, there is intense research interest in developing optical materials with large third-order nonlinearities. Many metallorganic compounds with highly π-conjugated system have large third-order NLO susceptibilities $\chi^{(3)}$ and fast response capability, thus they have been widely used in the devices of photonic switching and modulators [5,6]. Third-order NLO properties of these compounds are influenced by several factors such as π-conjugated electron system, peripheral and axial substituents

* Corresponding author. Tel.: +86 451 86414128; fax: +86 451 86417072.
E-mail address: ylsong@hit.edu.cn (Y. Song).

1566-1199/$ - see front matter © 2007 Elsevier B.V. All rights reserved.
doi:10.1016/j.orgel.2007.01.002

and central metal atom. Enhancement of third-order optical nonlinearities for such compounds with enlarged π-delocalized conjugation system can be explained that π electrons could move freely within the extended π system to produce a large NLO effect [7–9]. Furthermore, Incorporation of functionalized metal atom into organic materials introduces sublevels into the energy hierarchy, which permits electron transition to take place, and naturally enhance $\chi^{(3)}$ value and γ value [10,11]. Besides, variations of molecular electron density caused by metal-ligand charge transfer also improve third-order NLO properties.

During the last two decades, metallophthalocyanine and their derivatives have been extensively studied in the area of nonlinear optics for their third-order NLO properties both in solution and as thin film [12–16]. Most of them possess exceptionally high thermal and chemical stability, ease of fabrication and processing, architectural flexibility, and environmental stability, which make them multipurpose materials for solid-state technology. Phthalocyanine macrocycle, which is a two dimensional π-conjugated system, offers many opportunities for tailoring the electronic and photonic properties through facilitating substitution at peripheral and axial sites and by incorporating different metal atoms into molecular core. Besides, they can aggregate into a variety of supramolecular structures that can be prepared by molecular engineering, and the aggregates usually display outstanding properties. Especially, there is a good window of transparency in the 400–600 nm range, where excited state absorption often occurs. So, they have various utilities for PDT medicine, solar cells, and photoactivators of CD-R discs [17–19].

Many former investigations reveal that the ultrathin film containing phthalocyanine complex often has large $\chi^{(3)}$ which is usually several orders larger than that of solution [20]. In order to exploit the maximum $\chi^{(3)}$ and the second-order molecular hyperpolarizability γ value of metallophthalocyanines and put them into the application, it is necessary to produce the well-defined ultrathin film. Although many techniques have been developed to fabricate uniform nanoscopic film, the layer-by-layer control of composition and thickness is still a challenge. Since the early 1990, Decher [21,22] and his group do much pioneer's work to study the fabrication technique about the electrostatic layer-by-layer (LBL) film and its delicate structure. The electrostatic LBL self-assembly technique is one of the most promising ways for producing ultrathin array composite films because of its simplicity, ease in processability and controlling of thickness and safety to environment. To the best of our knowledge, this is the first study which employs the LBL self-assembly to construct the electrostatic LBL films composed of mononuclear phthalocyanine with excellent third-order NLO properties.

In this paper, the fabrication and characterization of nanostructure multilayer films consisting of anionic $CuPc(COONa)_8$ and cationic polyethylenimine (PEI) via electrostatic LBL self-assembly technique was reported. $CuPc(COONa)_8$ was the candidate as the third-order NLO material, and positively charged PEI was employed as the binder between $CuPc(COONa)_8$ molecule and the substrates. The third-order nonlinear absorptive and refractive effect of the composite film and $CuPc(COONa)_8$ aqueous solution sample was investigated by using the *Z*-scan technique [23]. The film displayed larger third-order optical nonlinearities in comparison with its corresponding aqueous sample. The mechanism for the film improving the third-order NLO properties was investigated.

2. Experimental

2.1. Materials

2,3,9,10,16,17,23,24-octacarboxyl phthalocyanine copper(II) phthalocyanine [$CuPc(COOH)_8$] was synthesized according to the reference [24]. And then $CuPc(COOH)_8$ was reacted with sodium hydroxide solution to obtain the octasodium salt of copper(II) octacarboxylic phthalocyanine [$CuPc(COONa)_8$] aqueous solution. PEI was purchased from Aldrich corp. and used without further purification (PEI; MW 60,000; Aldrich). The quartz slides for the UV–Vis study and for optical nonlinear measurements were sonicated in isopropyl alcohol for 1 h, subsequently washed with deionized water, and then dried with nitrogen. Subsequently, the substrates were immersed in 5 M KOH for 1 min, washed with deionized water to get rid of the residual KOH, and dried with nitrogen for the negatively charged surface. The quartz slides for small angle X-ray diffraction investigation were ultrasonically agitated in a H_2SO_4/H_2O_2 (7:3) mixture for 1 h. After washing and drying, further purification was carried out by using the $H_2O/H_2O_2/NH_3$(5:1:1, v/v/v) mixture.

2.2. Measurements

The multilayer growth process was monitored with Perkin–Elmer Lambda 900 UV/Vis/NIR spectrometer. Small angle X-ray diffraction was performed on the D/MAX-IIIB X-ray diffractometer with Cu Kα radiation at the wavelength of 1.5406 Å. Atomic force microscopic (AFM) image was taken in air at room temperature with nanoscopic III instrument (digital instrument) operating in tapping mode. The linear refractive coefficient of the composite film was determined on an optical ellipsometer (JOBIN YVON UVISEL). The appropriate substrate for AFM experiment was newly peeled mica. The third order NLO properties were measured by the *Z*-scan technique at 532 nm using a Q-switching Nd:YAG laser pulse with pulse width of 8 ns at a 1 Hz repetition rate. The single pulse incident energy for the film and the solution is 15 and 100 μJ, respectively. The input and output energies of the pulses were measured with an energy meter (laser Precision Rjp-735) controlled by computer.

2.3. Preparation of the layer-by-layer films

The chemical structures of phthalocyanine and PEI used for the deposition are shown in Fig. 1. The buildup process of the multilayer films is described as follows (Scheme 1).

The concentration of phthalocyanine solution was fixed at 1 mg/ml, and PEI was diluted to 5 wt% in deionized water. The substrates were dipped in the anionic $CuPc(COONa)_8$ and cationic PEI in turn for 5 min. Various substrates used for the deposition of multilayer films were pre-deposited with three layers of cationic polyelectrolyte prior to deposition of AB to ensure maximum surface charge density and to provide equal surface conditions. After each layer deposition, the substrate was washed with deionized water and dried with a stream of nitrogen gas. Both steps (A → B) were repeated in a cyclic fashion until the desired number of bilayers was obtained.

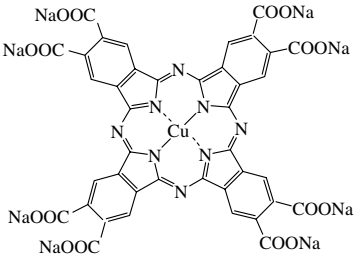
3. Results and discussion

3.1. UV–Vis spectra

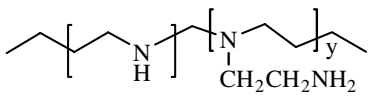
UV–Vis spectroscopy was used to follow the deposition process of multilayer films.

Fig. 2 shows UV–Vis spectra measured during 1–10 bilayer deposition of the film onto the modified solid supports. Both Q-band occurring at about 697 nm and Soret band occurring at about 350 nm originate from the typical absorption which is correlated to $\pi - \pi^*$ transitions from the highest occupied molecular orbital (HOMO) to the lowest unoccupied molecular orbital (LUMO) [25]. The absorbance at both the Soret-band and Q-band increases linearly with the number of bilayers, demonstrating that the successive adsorption of multilayers is a stepwise and regular process. The absorption maximum for Q-band of the multilayer films is red-shifted by 10 nm compared with that of $CuPc(COONa)_8$ aqueous solution, which suggests that phthalocyanine macrocycles are in a face-to-face π-stacking conformation and monomer molecules form aggregates in the densely packed films [26]. In addition, both Q-band and Soret-band of the film are broadened with respect to those of solution probably due to the molecular aggregation [27] and light scattering in the film [28]. The inset plot implies the absorbance of the film at 697 nm versus the number of bilayers. A linear fit yields an average increase of the absorbance of 0.0063 (correlation coefficient $R = 0.9987$) per bilayer, indicating a stepwise and regular process.

Visible polarized spectra were used to study the phthalocyanine molecule orientation in the films.

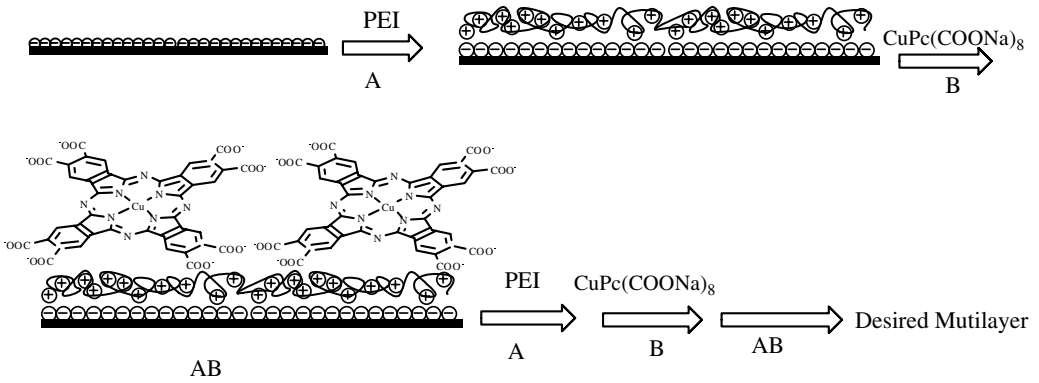


$CuPc(COONa)_8$



Polyethylenimine (PEI)

Fig. 1. Chemical structure of compounds for electrostatic LBL self-assembly.



Scheme 1. Procedure for fabrication of the $CuPc(COONa)_8$/PEI film by alternating deposition.

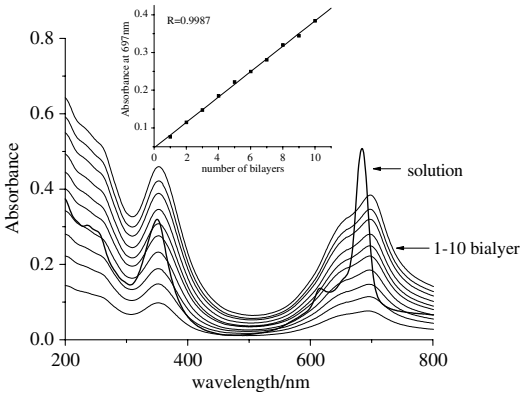


Fig. 2. UV–Vis spectra of $CuPc(COONa)_8$/PEI multilayer films (1–10 bilayers). Inset: the relationship of the absorbance and the number of bilayers.

Fig. 3 shows the polarized spectra of 20 bilayer films at 90° and 45° incidence angles, respectively. The electric vector of the incident light is parallel (p-polarization) and perpendicular (s-polarization) to the plane of the substrates as shown in the figure insert. For the incidence angle of 90°, the polarized absorption spectra, either with the electrical field in the plane of the substrate (s-polarization) or perpendicular to the plane of the substrate (p-polarization), do not alter according to the polarization mode, and no anisotropy was observed for the multilayer films. While at 45°, the position of the Q-band is red-shifted by 3 nm and displays stronger absorption in the s-polarization mode in comparison with the p-polarization mode, meaning that the spectra of the film have polarization dependence at 45°. Because there is no change in the polarized absorption bands at 90° and a large difference in the case of 45°, it can be concluded that the macrocycles of phthalocyanine molecules lie flat relative to the plane of the solid substrates [29–32].

3.2. Atomic force microscopy

The AFM image (Fig. 4) with tapping mode visualizes the surface topography of the 20-bilayer film.

The freshly peeled mica is suitable for the solid support for AFM measurement because the surface

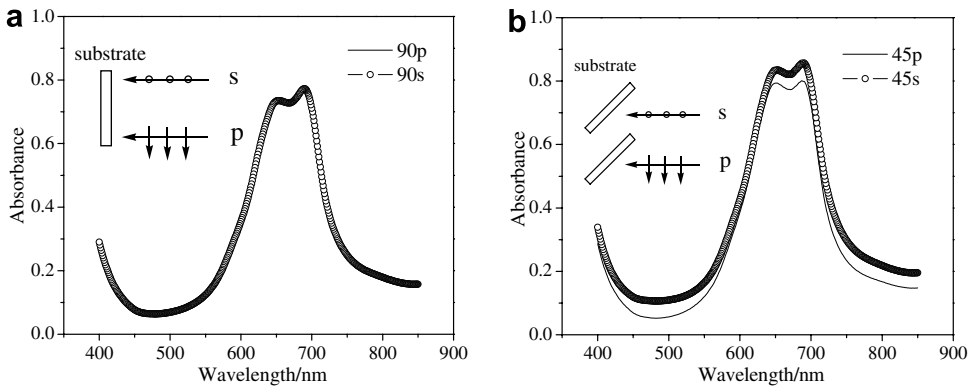


Fig. 3. Polarized UV–Vis absorbance spectra of $CoPc(COONa)_8$/PEI of 20 bilayer at (a) 90° and (b) 45°.

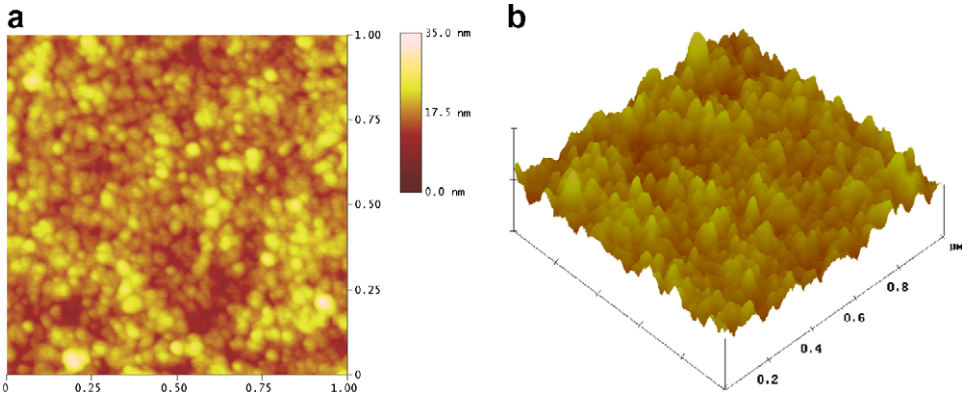


Fig. 4. Tapping mode AFM image of a 20-bilayer CuPc(COONa)$_8$/PEI film on mica in the 1×1 μm region (a) and the corresponding three-dimensional image (b).

of mica is automatically flat and negatively charged (K^+ counter ion). The closely packed nanoparticles having a well-defined spherelike shape can be easily seen on the film surface from the corresponding planar image. The nanostructure particles with the average diameter of 36 nm and the mean interface roughness of 2.984 nm indicate that the film surface is moderately smooth. The area of one particle is much larger than the reported calculated area of one phthalocyanine molecule (about 0.7 nm) [33]. This also proves that nanoscopic aggregates has been formed in the multilayer films. The coverage of the substrate is more than 90%, probably in that pre-deposition with three layers of cationic polyelectrolyte prior to deposition of AB enhances the coverage. The homogenous aggregating units were well-stacked during the deposition of the LBL self-assembly films.

3.3. X-ray diffraction measurements

Further evidence for the multilayer structure is provided by the small angle X-ray diffraction study. Fig. 5 presents X-ray diffraction curve of the 20-bilayer film consisting of CuPc(COONa)$_8$/PEI on the quartz substrate. The diffraction pattern shows the well-defined Kiessig fringes up to scattering angles $2\theta = 2°$, resulting from the interference of X-ray beams reflected at the substrate-film and film-air interfaces [22]. We can conclude from the curve that the film surface is relatively flat and uniform. The total thickness of the 30-bilayer film is about 57.8 nm, which is calculated from the spacing of the peaks. The absorption intensity of the multilayers increases linearly with the number of the layers from the UV–Vis spectra, namely, the thickness of the film increase with the number of deposited bilayers. Thus, average layer is calculated to be about 1.92 nm by division of the total thickness by the number of multilayers. These experiment results, including AFM measurement, linear increase of absorption in the UV–Vis experiment and small angle X-ray study suggest that the self-assembly of highly ordered ultrathin films is rather uniform and in good homogeneity.

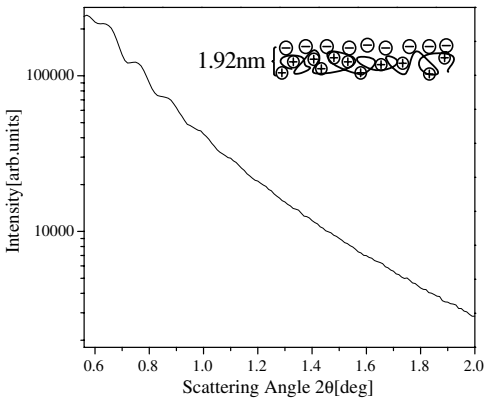


Fig. 5. Small angle X-ray diffraction pattern of a 30-bilayer film of CuPc(COONa)$_8$/ PEI performed on the D/MAX-IIIB X-ray diffractometer with Cu Kα radiation at the wavelength of 1.5406 Å.

3.4. Third-order nonlinear optical measurements

In order to investigate the third-order NLO properties of the 20-bilayer film and CuPc(COONa)$_8$ aqueous solution, *Z*-scan technique was employed. Superior to the other methods, such as degenerate

four-wave mixing (DFWM) and third-harmonic generation (THG), the nonlinear absorption and refraction can be simultaneously determined by Z-scan technique. That is to say, the nonlinear absorption and refraction coefficient can be obtained all together.

The measurements were carried out through the far field sample transmittance of a focused Gaussian beam as a function of the sample position (z) relative to the beam waist. When the aperture is absent, named as open aperture, nonlinear absorption is detected. When an aperture is placed in front of the detector, named as closed aperture, the energy through the aperture contains both nonlinear absorption and nonlinear refraction. Pure nonlinear refraction effect was obtained using division of the normalized closed-aperture data by the normalized open-aperture data.

Fig. 6 shows the open-aperture Z-scan curves of the 20-bilayer film on the quartz substrate at the linear transmittance of 72% and CuPc(COONa)$_8$ aqueous solution in the quartz cell at the linear transmittance of 74%. Both the film sample and aqueous solution sample display reverse saturable absorption. The nonlinear absorption coefficient could be got by fitting the open-aperture normalized transmittance data to the following Eq. (1) [23], which describes the third-order NLO absorption process of the sample:

$$T(z) = \frac{1}{\sqrt{\pi q(z)}} \int_{-\infty}^{\infty} \ln[1 + q(z)] \mathrm{e}^{-\tau^2} \mathrm{d}\tau$$
$$q(z) = \alpha_2^{\mathrm{eff}} I(z) \frac{1 - \mathrm{e}^{-\alpha_0 L}}{\alpha_0} \quad (1)$$

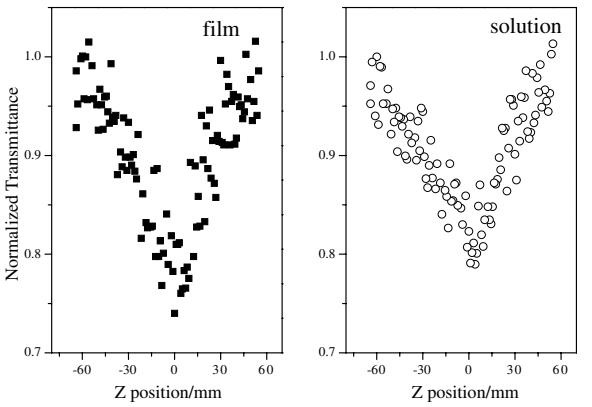


Fig. 6. Open-aperture normalized Z-scan transmittance of CuPc(COONa)$_8$/PEI multilayers and CuPc(COONa)$_8$ aqueous solution measured using 8 nanosecond pulses at 532 nm with $E_0 = 15$ μJ (film), and $E_0 = 100$ μJ (solution).

where T is the normalized energy transmittance, z is the distance of the sample from the focus, α_0 and α_2^{eff} is the linear and effective absorption index, L is the thickness of the film sample, τ is the time, and I is radiation intensity. The nonlinear absorption coefficient β value of the film is 5.83×10^{-5} m/W, indicating a strong reverse saturable arising from the excited state [34]. However, the nonlinear absorption coefficient β of CuPc(COONa)$_8$ solution is 4.91×10^{-10} m/W, which is five orders smaller than that of the film. The third order nonlinear absorption occurs at the valley band of the linear absorption spectra, thereby the resonance enhancement for the two samples may be neglected.

The nonlinear refractive property of the film was assessed from a division of the normalized close aperture data. The normalized close-aperture curve, as shown in Fig. 7 exhibits a peak on the $-z$ side at -13.54 mm and valley on the $+z$ side at 7.10 mm, indicating a self-defocusing effect and a negative refractive index. The peak-valley position of the normalized transmission is asymmetrical to the focus ($z = 0$), which may be caused by the nonlinear scattering due to the surface uniformity degree of the film [35,36].

The third-order nonlinear refractive index, n_2, can be got by fitting the $\Delta T_{\mathrm{p\text{-}v}}$ data of the divided Z-scans using Eq. (2) [37]

$$n_2 = \frac{\alpha_0 \lambda \Delta T_{\mathrm{p\text{-}v}}}{0.812\pi I_0 (1 - s)^{0.25} [1 - \mathrm{e}^{-\alpha_0 L}]} \quad (2)$$

where $\Delta T_{\mathrm{p\text{-}v}}$ is the measured peak-valley transmittance difference from a normalized Z-scan, I_0 is the on-axis peak intensity at the focus ($z = 0$), s is the transmittance of the aperture ahead the detector in absence of a sample. Here, s is 0.14, and $\Delta T_{\mathrm{p\text{-}v}}$ obtained from the nonlinear refractive curve is

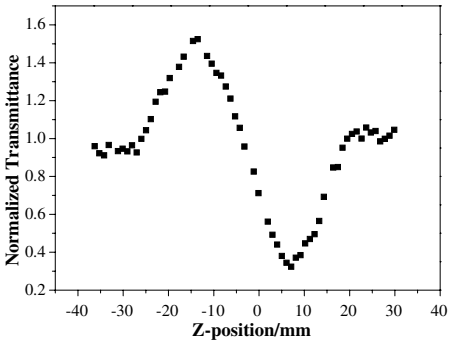


Fig. 7. Close-aperture normalized Z-scan transmittance of CuPc(COONa)$_8$/PEI multilayers measured using nanosecond pulses at 532 nm with $E_0 = 15$ μJ.

Table 1
The third-order NLO parameters of the film and CuPc(COONa)$_8$ aqueous solution at 532 nm

Samples	T_0	n_2 (m^2/W)	β (m/W)	Im$\chi^{(3)}$ (esu)	Re$\chi^{(3)}$ (esu)	$\chi^{(3)}$ (esu)	γ (esu)
Film	0.72	-2.05×10^{-11}	$+5.83\times10^{-5}$	2.87×10^{-6}	2.65×10^{-6}	3.91×10^{-6}	5.25×10^{-27}
Solution	0.74		$+4.91\times10^{-10}$	1.40×10^{-11}		1.40×10^{-11}	7.69×10^{-29}

1.20. The nonlinear refractive index n_2 of the 20-bilayer film is calculated from the Eq. (2) to be -2.05×10^{-11} m^2/W, showing very strong third-order nonlinear refractive effect. But, the nonlinear refractive effect of CuPc(COONa)$_8$ aqueous solution was not observed.

The real and imaginary parts of the third-order nonlinear susceptibility $\chi^{(3)}$ are related to the nonlinear refraction and absorption coefficients:

$$\mathrm{Re}\chi^{(3)} = 2n_0^2\varepsilon_0 c n_2,$$
$$\mathrm{Im}\chi^{(3)} = n_0^2\varepsilon_0 c\beta/k$$

where k is the wave number and c is the speed of light in the vacuum, n_0 is the linear refraction index, equal to 1.7496 for the film sample as determined by an ellipsometer.

The third-order nonlinear susceptibility $\chi^{(3)}$ and the molecular second-order hyperpolarizability γ can be calculated through equations:

$$\chi^{(3)} = \mathrm{Re}\chi^{(3)} + i\mathrm{Im}\chi^{(3)},$$

for the film, γ (esu) $= \frac{1}{N}\chi^{(3)}$ (esu), for phthalocyanine solution, γ (esu) $= \frac{1}{NL^4}\chi^{(3)}$ (esu) where N is the molecular density, $L = (n_0^2+2)/3$ is the local field correction factor.

The CuPc(COONa)$_8$ molecular density in deionized water is calculated to be 7.22×10^{16} cm^{-3}. Since PEI display so weak third-order NLO effect that can be neglected in our experiment, it is reasonable for us to estimate the particle number density only according to the phthalocyanine molecule. The molecular density of phthalocyanine in the film is about 7.45×10^{20} cm^{-3}. The calculated values of the third-order NLO parameters in the 20-bilayer CuPc(COONa)$_8$/PEI film and CuPc(COONa)$_8$ aqueous solution are listed in Table 1. The third-order nonlinear susceptibility $\chi^{(3)}$ is as high as 3.91×10^{-6} esu, which is five orders larger than solution sample. And the molecular hyperpolarizability γ of the film is 5.25×10^{-27} esu, which is about 68 times larger than that of solution sample.

Considering the larger $\chi^{(3)}$ and γ value obtained from the experiments with 20-bilayer film, it is believed that aggregation effect and π–π overlapping between the macrocycles, which are confirmed by AFM images and UV–Vis spectra, enhance the macroscopic third-order nonlinearity of phthalocyanine in the film. This can be further explained that π-electron molecular orbits of macrocycles of in the aggregates should interact with those of its neighbors strongly enough to significantly alter the electronic structure of the system, thus changing nonlinear optical response [38]. On the basis of above results, we consider that the ultrathin film prepared by electrostatic self-assembly technique can enhance notably the third-order nonlinearities of organic materials. This provides a simple and convenient approach to fabricate the composite solid materials with large NLO properties.

4. Conclusions

A novel ultrathin multilayer film with well-defined structure containing anionic CuPc(COONa)$_8$ and cationic PEI on solid supports has been prepared by the electrostatic layer-by-layer self-assembly technique. The third-order nonlinearities of the composite film and CuPc(COONa)$_8$ aqueous solution was investigated using Z-scan technique. The composite film demonstrates very strong reverse saturable absorptive and self-defocusing refractive effect. The molecular hyperpolarizability γ and the third-order nonlinear susceptibility $\chi^{(3)}$ of the film are much larger than that of CuPc(COONa)$_8$ aqueous solution. The ultrathin film can be considered as one of the most promising NLO materials.

Acknowledgement

This work was supported by the Natural Science Foundation of Heilongjiang Province (B2004-05).

References

[1] B. Wei, D.H. Gu, F.X. Gan, SPIE 5060 (2003) 24.
[2] K. Dou, J.Y. Du, E.T. Knobbe, J. Lumin. 83 (1999) 241.
[3] J.W. Perry, K. Mansour, I.–Y.S. Lee, X.–L. Wu, P.V. Bedworth, C.–T. Chen, D. Ng, S.R. Marder, P. Miles, T. Wada, M. Tian, H. Sasabe, Science 273 (1996) 1533.

[4] D. Max Roundhill, P. John, J. Fackler, Optoelectronic Properties of Inorganic Compounds, New York, 1999.
[5] B.K. Teo, Y. Xu, B. Zhong, Y. He, H. Chen, W. Qian, Y. Deng, Y. Zou, Inorg. Chem. 40 (2001) 6794.
[6] M.O. Liu, C.-H. Tai, A.T. Hu, T.-H. Wei, J. Organomet. Chem. 689 (2004) 2138.
[7] T.-H. Wei, T.-H. Huang, T.-T. Wu, P.-C. Tsai, M.-S. Lin, Chem. Phys. Lett. 318 (2000) 53.
[8] Y.Z. Gu, F.X. Gan, S.Q. Wang, H.J. Xu, Opt. Commun. 197 (2001) 501.
[9] J. Schell, D. Ohlmann, D. Brinkmann, R. Levy, M. Joucla, J.L. Rehspringer, J. Chem. Phys. 111 (1999) 5929.
[10] T.C. Wen, I.D. Lian, Synthetic Met. 83 (1996) 111.
[11] C.Y. Tsai, S.P. Chen, T.C. Wen, Chem. Phys. 240 (1999) 191.
[12] Z.Z. Ho, C.Y. Ju, W.M. Hetherington III, J. Appl. Phys. 62 (1987) 716.
[13] H.S. Nalwa, A. Kakuta, Thin Solid Films 253 (1995) 218.
[14] J.S. Shirk, J.R. Lindle, F.J. Bartoli, J. Chem. Phys. 96 (1992) 5847.
[15] J.S. Shirk, J.R. Lindle, F.J. Bartoli, Appl. Phys. Lett. 55 (13) (1989) 1287.
[16] Eva M. Garcia Frutos, Sean M. O'Flaherty, Eva M. Maya, J. Mater. Chem. 13 (2003) 749.
[17] K. Sawada, W.B. Duan, K. Sekitani, K. Satoh, J. Mol. Liq. 119 (2005) 171.
[18] Y.Q. Wu, X. Zuo, Z.M. Chen, D.H. Gu, F.X. Gan, Opt. Commun. 220 (2003) 371.
[19] J. Drechsel, B. Männig, D. Gebeyehu, M. Pfeiffer, K. Leo, H. Hoppe, Org. Electron. 5 (2004) 175.
[20] H. Kanbara, T. Maruno, A. Yamashita, J. Appl. Phys. 80 (7) (1996) 3674.
[21] G. Decher, Science 277 (1997) 1232.
[22] G. Decher, J.D. Hong, J. Schmitt, Thin Solid Film 210/211 (1992) 831.
[23] M. Sheik-Bahae, A.A. Said, T.-H. WEI, D.J. Hagan, E.W. Van Stryland, IEEE J. Quantum. Electron. 26 (4) (1990) 760.
[24] B.N. Achar, G.M. Fohlen, J.A. Parker, J. Polym. Sci. Part A 20 (1982) 1785.
[25] K. Mansour, D. Alvarez, J. Kelly, J. Perry, I. Choong, S.R. Marder, J.W. Perry, SPIE 1853 (1993) 132.
[26] M. Yoneyama, M. Sugi, M. Saito, K. Ikegami, S.-I. Kuroda, S. Iizima, Jpn. J. Appl. Phys. 25 (1986) 961.
[27] J.S. Shirk, G.S. Richard, P. Steven, R. Flom, H. Heckmann, M. Hanack, J. Phys. Chem. A 104 (2000) 1438.
[28] D.M. Guldi, F. Pellarini, M. Prato, C. Granito, L. Troisi, Nanoletters 2 (2002) 965.
[29] M. Rikukawa, M.F. Rubner, Langmuir 10 (1994) 519.
[30] Z.J. Zhang, A.L. Verma, M. Yoneyama, K. Nakashima, K. Iriyama, Y. Ozaki, Langmuir 13 (1997) 4422.
[31] G.F. Xu, Z.N. Bao, J.T. Groves, Langmuir 16 (2000) 1834.
[32] J. Locklin, K. Shinbo, K. Onishi, F. Kaneko, Z.N. Bao, R.C. Advincula, Chem. Mater. 15 (2003) 1404.
[33] M. Fujiki, H. Tabei, Langmuir 4 (1988) 320.
[34] G.Y. Fang, Y.L . Song, Y.X. Wang, X.R. Zhang, C.F. Li, L.C. Song, P.C. Liu, Opt. Commun. 183 (2000) 523.
[35] H.J. Fang, C.M. Du, S.L. Qu, Y.L. Li, Y.L. Song, H.M. Li, H.B. Liu, D.B. Zhu, Chem. Phys. Lett. 364 (2002) 290.
[36] S.L. Qu, H.J. Li, T.Y. Peng, Y.C. Gao, J.R. Qiu, C.S. Zhu, Mater. Lett. 58 (2004) 1427.
[37] C.L. Zhan, D.H. Li, D.Q. Zhang, W. Xu, Y.X. Nie, D.B. Zhu, Opt. Mater. 26 (2004) 11.
[38] E.S. Manas, F.C. Spano, L.X. Chen, J. Chem. Phys. 107 (1997) 707.

Available online at www.sciencedirect.com
ScienceDirect
Organic Electronics 8 (2007) 206–226
Organic Electronics
www.elsevier.com/locate/orgel

Collision of optical solitons in a non-Kerr law media

Anjan Biswas [a,*], Swapan Konar [b]

[a] Department of Applied Mathematics and Theoretical Physics, Delaware State University, 1200 N. DuPont Highway, Dover, DE 19901-2277, USA
[b] Department of Applied Physics, Birla Institute of Technology, Mesra, Ranchi 835 215, India

Available online 18 September 2006

Abstract

The collision of optical solitons in a long haul transmission along trans-oceanic and trans-continental distances is studied in this paper, theoretically and numerically. The solitons travel through optical waveguides in a non-Kerr law media namely the power law, parabolic law and the dual-power law. The numerical results conform to the theoretical development.
© 2006 Elsevier B.V. All rights reserved.

OCIS: 000.3870; 060.2290; 060.2330; 060.4370; 060.4510; 060.5530

AMS classification: 35Q55; 78A60

PACS: 02.30.Ik; 02.30.Jr; 02.60.Cb; 42.65.Tg; 42.81.Dp

Keywords: Kerr law nonlinearity; Non-Kerr law; Solitons; Numerical simulation

1. Introduction

The propagation of solitons through optical fibers has been a major area of research given its potential applicability in all optical communication systems [1–30]. The field of telecommunications has undergone a substantial evolution in the last couple of decades due to the impressive progress in the development of optical fibers, optical amplifiers as well as transmitters and receivers. In a modern optical communication system, the transmission link is composed of optical fibers and amplifiers that replace the electrical regenerators. But the amplifiers introduce some noise and signal distortion that limit the system capacity. Presently the optical systems that show the best characteristics in terms of simplicity, cost and robustness against the degrading effects of a link are those based on intensity modulation with direct detection (IM-DD). Conventional IM-DD systems are based on non-return-to-zero (NRZ) format, but for transmission at higher data rate the return-to-zero (RZ) format is preferred. When the data rate is quite high, soliton transmission can be used. It allows the exploitation of the fiber capacity much more, but the NRZ signals offer very high potential especially in terms of simplicity.

There are limitations, however, on the performance of optical system due to several effects that

* Corresponding author.
E-mail address: biswas.anjan@gmail.com (A. Biswas).

1566-1199/$ - see front matter © 2006 Elsevier B.V. All rights reserved.
doi:10.1016/j.orgel.2006.08.001

are present in optical fibers and amplifiers. Signal propagation through optical fibers can be affected by group velocity dispersion (GVD), polarization mode dispersion (PMD) and the nonlinear effects. The chromatic dispersion that is essentially the GVD when waveguide dispersion is negligible, is a linear effect that introduces pulse broadening generates intersymbol interference. The PMD arises due the fact that optical fibers for telecommunications have two polarization modes, in spite of the fact that they are called monomode fibers. These modes have two different group velocities that induce pulse broadening depending on the input signal state of polarization. The transmission impairment due to PMD looks similar to that of the GVD. However, PMD is a random process as compared to the GVD which is a deterministic process. So PMD cannot be controlled at the receiver. Newly installed optical fibers have quite low values of PMD that is about 0.1 ps/$\sqrt{\text{km}}$.

The main nonlinear effects that arise in monomode fibers are the Brillouin scattering, Raman scattering and the Kerr effect. Brillouin is a backward scattering that arises from acoustic waves and can generate forward noise at the receiver. Raman scattering is a forward scattering from silica molecules. The Raman gain response is characterized by low gain and wide bandwidth namely about 5 THz. The Raman threshold in conventional fibers is of the order of 500 mW for copolarized pump and Stokes' wave (that is about 1 W for random polarization), thus making Raman effect negligible for a single channel signal. However, it becomes important for multichannel wavelength-division-multiplexed (WDM) signal due to an extremely wide band of wide gain curve.

The Kerr effect of nonlinearity is due to the dependence of the fiber refractive index on the field intensity. This effect mainly manifests as a new frequency when an optical signal propagates through a fiber. In a single channel the Kerr effect induces a spectral broadening and the phase of the signal is modulated according to its power profile. This effect is called self-phase modulation (SPM). The SPM-induced chirp combines with the linear chirp generated by the chromatic dispersion. If the fiber dispersion coefficient is positive namely in the normal dispersion regime, linear and nonlinear chirps have the same sign while in the anomalous dispersion regime they are of opposite signs. In the former case, pulse broadening is enhanced by SPM while in the later case it is reduced. In the anomalous dispersion case the Kerr nonlinearity induces a chirp that can compensate the degradation induced by GVD. Such a compensation is total if soliton signals are used.

If multichannel WDM signals are considered, the Kerr effect can be more degrading since it induces nonlinear cross-talk among the channels that is known as the cross-phase modulation (XPM). In addition, WDM generates new frequencies called the Four-Wave mixing (FWM). The other issue in the WDM system is the collision-induced timing jitter that is introduced due to the collision of solitons in different channels. The XPM causes further nonlinear chirp that interacts with the fiber GVD as in the case of SPM. The FWM is a parametric interaction among waves satisfying a particular relationship called phase-matching that lead to power transfer among different channels.

Stabilization of soliton propagation with the aid of nonlinear gain or under combined operation of gain and saturable absorption was recommended by Kodama et al. [20–24]. Thus, in order to model these features in the soliton dynamics, in a practical scenario, the NLSE should be modified by incorporating additional terms. Thus, the concept of control of soliton propagation described by the NLSE with non-Kerr law nonlinearities is new and important developments in the application of solitons for optical communication systems. Because the NLSE, with non-Kerr laws, is not integrable, perturbation methods or numerical techniques have to be applied. Therefore, the control of soliton and interaction of two neighboring solitons incorporating perturbation terms like nonlinear gain, saturable amplification, filtering, higher order dispersion, self-steepening and nonlinear dispersions are going to be addressed in this paper.

2. Governing equations

The dimensionless form of the generalized NLSE is given by

$$iq_Z + \frac{1}{2}q_{TT} + F(|q|^2)q = 0 \tag{1}$$

where Z represents the non-dimensional distance along the fiber while, T represents time in dimensionless form. Also, in (1), F is a real-valued algebraic function and it is necessary to have the smoothness of the complex function $F(|q|^2)q : C \mapsto C$. Considering the complex plane C as a two-dimensional linear space R^2, the function $F(|q|^2)q$ is k times continuously differentiable, so that

$$F(|q|^2)q \in \bigcup_{m,n=1}^{\infty} C^k((-n,n)\times(-m,m);R^2) \tag{2}$$

Eq. (1) is a nonlinear partial differential equation (PDE) of parabolic type that is not integrable, in general. The special case, $F(s) = s$, also known as Kerr law of nonlinearity, is integrable by IST [12]. The IST is the nonlinear analog of Fourier transform that is used for solving the linear partial differential equations. Schematically, the IST and the technique of Fourier transform are similar [12]. The solutions are known as *solitons*.

The general case $F(s) \neq s$ takes (1) away from the IST picture as it is not integrable. In the anomalous dispersion regime [12], the particularly relevant solutions to (1) are called solitons, or non-topological solitons. In a rigorous sense, the pulses of the non-integrable systems are not solitons. However, the term solitons has been used broadly for the solutions of the non-integrable system as well, and this has become common. So, in this paper, the pulses shall be referred to as 'solitons'. Although stationary pulses exist, and some solutions can be written in the analytic form, their behaviour is different from that of the solutions of the cubic NLSE.

In most cases, the interest is confined to a single pulse described by the 1-soliton solution of the NLSE. However, in this paper, the effects of the perturbation terms in NLSE on two soliton interaction will be studied. It is necessary to launch the solitons close to each other for enhancing the information carrying capacity of the fiber. If two solitons are placed close to each other then it can lead to their mutual interaction thus providing a very serious hindrance to the performance of the soliton transmission system. However, the presence of the perturbation terms of the NLSE can lead to the suppression of the two soliton interaction thus solving the problem.

The perturbed NLSE that is going to be studied in this paper for the SSI is

$$\mathrm{i}\frac{\partial q}{\partial Z} + \frac{1}{2}\frac{\partial^2 q}{\partial T^2} + F(|q|^2)q = \mathrm{i}\epsilon R[q, q^*] \tag{3}$$

where

$$R = \delta|q|^{2m}q + \sigma q\int_{-\infty}^{T}|q|^2\,\mathrm{d}t - \alpha\frac{\partial q}{\partial T} + \beta\frac{\partial^2 q}{\partial T^2} - \gamma\frac{\partial^3 q}{\partial T^3} - \mathrm{i}\sigma\frac{\partial^4 q}{\partial T^4} + \lambda\frac{\partial}{\partial T}(|q|^2 q) + \mu q\frac{\partial}{\partial T}\times(|q|^2) \tag{4}$$

In fiber optics ϵ is called the relative width of the spectrum, that arises due to quasi-monochromaticity, and is assumed that $0 < \epsilon \ll 1$. For the perturbation terms given by R in (4), δ represents the coefficient of nonlinear gain, while σ is the coefficient of saturable amplifiers. Also, in (4), m could be 0, 1 or 2. For $m = 0$, there is linear gain, while for $m = 1$ it is called quadratic gain and for $m = 2$, it is quintic gain or gain saturation. The coefficient of β is called the bandpass filtering term. Also, in (4), α is the frequency separation between the soliton carrier and the frequency at the peak of EDFA gain. Moreover, λ is the self-steepening coefficient for short pulses [12] (typically $\leqslant$100 fs), μ is the higher order dispersion coefficient [12] and γ is the coefficient of the third order dispersion [12]. Finally, σ represents the coefficient of fourth order dispersion. It needs to be noted that the coefficients of δ, β and σ represents the non-Hamiltonian perturbation while the remaining terms in (4) represents the Hamiltonian type perturbation.

It is known that the NLSE, as given by (1), does not give correct prediction for pulse widths smaller than 1 ps. For example, in solid state solitary lasers, where pulses as short as 10 fs are generated, the approximation breaks down. Thus, quasi-monochromaticity is no longer valid and higher order dispersion terms come in. If the group velocity dispersion is close to zero, one needs to consider the third order dispersion for performance enhancement along trans-oceanic distances. Also, for short pulse widths where group velocity dispersion changes within the spectral bandwidth of the signal can no longer be neglected, one needs to take into account the presence of the third order dispersion.

Besides these perturbation terms that are considered in this paper, there are various other kinds of perturbation terms that are not considered in this paper. Some of them include the Raman scattering [12], the sixth order dispersion as well as the perturbation terms that arise in the study of quasi-solitons [4]. The quasi-particle theory (QPT) due to these perturbation terms are not yet established for the various non-Kerr law nonlinearities that are considered in this paper. It is still an open problem as yet of today and will be reported in a future publication once the new results are obtained.

Eq. (1), unlike the Kerr law case, does not have infinitely many conserved quantities. In fact, it has as few as three integrals of motion [4]. They are the energy (E) also known as the wave power, linear

momentum (M) and the Hamiltonian (H) that are respectively given by

$$E = \int_{-\infty}^{\infty} |q|^2 \, \mathrm{d}T \tag{5}$$

$$M = \frac{i}{2} \int_{-\infty}^{\infty} (q^* q_T - q q_T^*) \, \mathrm{d}T \tag{6}$$

$$H = \int_{-\infty}^{\infty} \left[\frac{1}{2} |q_T|^2 - f(I) \right] \mathrm{d}T \tag{7}$$

where

$$f(I) = \int_0^I F(\xi) \, \mathrm{d}\xi \tag{8}$$

and the intensity I is given by $I = |q|^2$. One can see that (1) can be written in a canonical form

$$\mathrm{i}q_Z = \frac{\delta H}{\delta q^*} \tag{9}$$

$$\mathrm{i}q_Z^* = -\frac{\delta H}{\delta q} \tag{10}$$

This defines a Hamiltonian dynamical system on an infinite dimensional phase space. It can be analyzed using the theory of Hamiltonian systems. This means that a behaviour of the solution is defined, to a large extent, by the singular points of the system, namely the stationary solutions of (1) and depends on the nature of these points as determined by the stability of its stationary solutions [3].

The QPT of soliton–soliton interaction (SSI) is investigated [3,17–20] and it is proved by virtue of it that the interaction can be suppressed due to nonlinear gain and filters. Also it has been proved that the sliding frequency guiding filters [23–27] leads to the suppression of the SSI. Here, by virtue of the QPT, it will be proved that SSI can be suppressed due to the NLSE given by (1) in presence of the perturbation terms in (2), for Kerr, power, parabolic and dual-power laws.

The soliton solution of (3), for $\epsilon = 0$, although not integrable, for any law of nonlinearity, is assumed to be given in the form

$$q(Z,T) = \eta(Z) g[\zeta(Z)(T - vZ - T_0)] \mathrm{e}^{(-\mathrm{i}\kappa T + \mathrm{i}\omega Z + \mathrm{i}\sigma_0)} \tag{11}$$

where

$$\kappa = -v \tag{12}$$

$$\zeta(Z) = \chi(\eta(Z)) \tag{13}$$

$$\omega(Z) = \psi(\eta(Z), \kappa(Z)) \tag{14}$$

In (11), g represents the shape of the soliton described by the GNLSE and it depends on the type of nonlinearity in (1). The parameters $\eta(Z)$ and $\zeta(Z)$, in (11), respectively, represent the soliton amplitude and width, while $\kappa(Z)$ and $\omega(Z)$ are the frequency and wave number of the soliton respectively while v is the velocity. Also T_0 and σ_0 respectively represent the center of the soliton and center of soliton phase. In (13) and (14), the functional forms, χ and ψ, depend on the type of nonlinearity in (1).

The 2-soliton solution of the NLSE, given by (1), takes the asymptotic form

$$q(Z,T) = \sum_{l=1}^{2} \eta_l(Z) g[\zeta_l(Z)(T - v_l Z - T_l)] \mathrm{e}^{(-\mathrm{i}\kappa_l T + \mathrm{i}\omega_l Z + \mathrm{i}\sigma_l)} \tag{15}$$

with

$$\kappa_l = -v_l \tag{16}$$

$$\zeta_l(Z) = \chi(\eta_l(Z)) \tag{17}$$

$$\omega_l(Z) = \psi(\eta_l(Z), \kappa_l(Z)) \tag{18}$$

where $l = 1, 2$. In the study of SSI, the initial pulse waveform is taken to be of the form

$$q(0,T) = \eta_1 g\left[\zeta_1\left(T - \frac{T_0}{2}\right)\right] \mathrm{e}^{\mathrm{i}\phi_1} + \eta_2 g\left[\zeta_2\left(T + \frac{T_0}{2}\right)\right] \mathrm{e}^{\mathrm{i}\phi_2} \tag{19}$$

which represents the injection of 2-soliton like pulses into a fiber. Here T_0 represents the initial separation of the solitons namely the center-to-center soliton separation. It is to be noted that for $T_0 \to \infty$ (19) represents exact soliton solutions, but for $T_0 \sim \mathrm{O}(1)$ it does not represent an exact 2-soliton solution. The initial pulse form will modify depending on the type of perturbation considered as seen below.

1. *Non-Hamiltonian perturbations*
   For studying the SSI with non-Hamiltonian type perturbations, the case of in-phase injection of solitons with equal amplitudes will be considered. So, without any loss of generality, $\eta_1 = \eta_2 = 1$ and $\phi_1 = \phi_2 = 0$ is chosen so that (19) modifies to

$$q(0,T) = g\left[\zeta_1\left(T - \frac{T_0}{2}\right)\right] + g\left[\zeta_2\left(T + \frac{T_0}{2}\right)\right] \tag{20}$$

2. *Hamiltonian perturbations*
   For studying the SSI with Hamiltonian type perturbations, the case of in-phase injection of solitons with unequal amplitudes will be considered.

So without any loss of generality $\eta_1 = \eta_0$, $\eta_2 = 1$ and $\phi_1 = \phi_2 = 0$ is chosen so that (19) modifies to

$$q(0,T) = \eta_0 g\left[\zeta_0\left(T - \frac{T_0}{2}\right)\right] + g\left[\zeta\left(T + \frac{T_0}{2}\right)\right] \tag{21}$$

where

$$\zeta_0 = \chi(\eta_0) \tag{22}$$

and ζ is given by (13).

The special cases with regards to the four laws of nonlinearity will now be individually discussed in the following four subsections.

2.1. Kerr law

For the case of Kerr law of nonlinearity $F(s) = s$ so that Eq. (3) becomes

$$\mathrm{i}\frac{\partial q}{\partial Z} + \frac{1}{2}\frac{\partial^2 q}{\partial T^2} + |q|^2 q = \mathrm{i}\epsilon R[q, q^*] \tag{23}$$

The 1-soliton solution of (23), for $\epsilon = 0$, that can be obtained by IST has the form [3,4,12]

$$q(Z,T) = \frac{\eta}{\cosh[\zeta(T - vZ - T_0)]}\mathrm{e}^{\mathrm{i}(-\kappa T + \omega Z + \sigma_0)} \tag{24}$$

where

$$\zeta \equiv \chi(\eta) = \eta \tag{25}$$

$$\omega \equiv \psi(\eta, \kappa) = \frac{\eta^2 - \kappa^2}{2} \tag{26}$$

Also, the 2-soliton solution of the NLSE (23), for $\epsilon = 0$ takes the asymptotic form [3,12]

$$q(Z,T) = \sum_{l=1}^{2} \frac{\eta_l}{\cosh[\eta_l(T - v_l Z - T_{0_l})]} \times \mathrm{e}^{\mathrm{i}(-\kappa_l T + \omega_l Z + \sigma_{0_l})} \tag{27}$$

where

$$\zeta_l \equiv \chi(\eta_l) = \eta_l \tag{28}$$

$$\omega_l \equiv \psi(\eta_l, \kappa_l) = \frac{\eta_l^2 - \kappa_l^2}{2} \tag{29}$$

and $l = 1, 2$. The modification of the initial pulse form (19) is given by

$$q(0,T) = \frac{\eta_1}{\cosh\left[\eta_1\left(T - \frac{T_0}{2}\right)\right]}\mathrm{e}^{\mathrm{i}\phi_1} + \frac{\eta_2}{\cosh\left[\eta_2\left(T + \frac{T_0}{2}\right)\right]}\mathrm{e}^{\mathrm{i}\phi_2} \tag{30}$$

The initial pulse form for the two types of perturbations are as follows:

1. *Non-Hamiltonian perturbations*
   In this case, the choice $\eta_1 = \eta_2 = 1$ and $\phi_1 = \phi_2 = 0$, gives

$$q(0,T) = \frac{1}{\cosh\left[\left(T - \frac{T_0}{2}\right)\right]} + \frac{1}{\cosh\left(T + \frac{T_0}{2}\right)} \tag{31}$$

   which represents an in-phase injection of pulses with equal amplitudes.
2. *Hamiltonian perturbations*
   Here, the choice $\eta_1 = \eta_0$, $\eta_2 = 1$ and $\phi_1 = \phi_2 = 0$, gives

$$q(0,T) = \frac{\eta_0}{\cosh\left[\eta_0\left(T - \frac{T_0}{2}\right)\right]} + \frac{1}{\cosh\left(T + \frac{T_0}{2}\right)} \tag{32}$$

   which represents an in-phase injection of pulses with unequal amplitudes.

2.2. Power law

For the case of power law nonlinearity, $F(s) = s^p$ where $0 < p < 2$ to prevent wave collapse [3]. So Eq. (3) modifies to

$$\mathrm{i}\frac{\partial q}{\partial Z} + \frac{1}{2}\frac{\partial^2 q}{\partial T^2} + |q|^{2p} q = \mathrm{i}\epsilon R[q, q^*] \tag{33}$$

In this case, Eq. (33) with $\epsilon = 0$ is not integrable by IST. However, (33), for$\epsilon = 0$, supports solitons of the form [3]

$$q(Z,T) = \frac{\eta}{\cosh^{\frac{1}{p}}[\zeta(T - vZ - T_0)]}\mathrm{e}^{\mathrm{i}(-\kappa T + \omega Z + \sigma_0)} \tag{34}$$

where

$$\zeta \equiv \chi(\eta) = \eta^p\left(\frac{2p^2}{1+p}\right)^{\frac{1}{2}} \tag{35}$$

$$\omega \equiv \psi(\eta, \kappa) = \frac{\zeta^2}{2p^2} - \frac{\kappa^2}{2} \tag{36}$$

The 2-soliton solution of the NLSE (33) with $\epsilon = 0$ takes the asymptotic form

$$q(Z,T) = \sum_{l=1}^{2} \frac{\eta_l}{\cosh^{\frac{1}{p}}[\zeta_l(T - v_l Z - T_{0_l})]}\mathrm{e}^{\mathrm{i}(-\kappa_l T + \omega_l Z + \sigma_{0_l})} \tag{37}$$

where

$$\zeta_l \equiv \chi(\eta_l) = \eta_l^p \left(\frac{2p^2}{1+p}\right)^{\frac{1}{2}} \tag{38}$$

$$\omega_l \equiv \psi(\eta_l, \kappa_l) = \frac{\zeta_l^2}{2p^2} - \frac{\kappa_l^2}{2} \tag{39}$$

In the study of SSI for power law nonlinearity, the initial pulse waveform is assumed to be

$$q(0,T) = \frac{\eta_1}{\cosh^{\frac{1}{p}}\left[\zeta_1\left(T - \frac{T_0}{2}\right)\right]} e^{i\phi_1} + \frac{\eta_2}{\cosh^{\frac{1}{p}}\left[\zeta_2\left(T + \frac{T_0}{2}\right)\right]} e^{i\phi_2} \tag{40}$$

The initial pulse form modifies as follows:

1. *Non-Hamiltonian perturbation*

Here, the choice $\eta_1 = \eta_2 = 1$ and $\phi_1 = \phi_2 = 0$, gives

$$q(0,T) = \frac{1}{\cosh^{\frac{1}{p}}\left[\zeta\left(T - \frac{T_0}{2}\right)\right]} + \frac{1}{\cosh^{\frac{1}{p}}\left[\zeta\left(T + \frac{T_0}{2}\right)\right]} \tag{41}$$

where

$$\zeta = \sqrt{\frac{2p^2}{1+p}} \tag{42}$$

which represents an in-phase injection of pulses with equal amplitudes.

2. *Hamiltonian perturbations*

For this case, the choice $\eta_1 = \eta_0$, $\eta_2 = 1$ and $\phi_1 = \phi_2 = 0$, gives

$$q(0,T) = \frac{\eta_0}{\cosh^{\frac{1}{p}}\left[\zeta_0\left(T - \frac{T_0}{2}\right)\right]} + \frac{1}{\cosh^{\frac{1}{p}}\left[\zeta\left(T + \frac{T_0}{2}\right)\right]} \tag{43}$$

where

$$\zeta_0 = \eta_0^p \left(\frac{2p^2}{1+p}\right)^{\frac{1}{2}} \tag{44}$$

which represents in-phase injection of solitons with unequal amplitudes.

2.3. Parabolic law

For the parabolic law of nonlinearity, $F(s) = s + vs^2$, where the parameter $v > 0$, and so the NLSE is

$$i\frac{\partial q}{\partial Z} + \frac{1}{2}\frac{\partial^2 q}{\partial T^2} + (|q|^2 + v|q|^4)q = i\epsilon R[q, q^*] \tag{45}$$

Eq. (45) is not integrable by the IST. However, (45), for $\epsilon = 0$ supports solitons of the form [3]

$$q(Z,T) = \frac{\eta}{[1 + a\cosh\{\zeta(T - vZ - T_0)\}]^{\frac{1}{2}}} e^{i(-\kappa T + \omega Z + \sigma_0)} \tag{46}$$

where

$$\zeta \equiv \chi(\eta) = \eta\sqrt{2} \tag{47}$$

$$\omega \equiv \psi(\eta, \kappa) = \frac{\eta^2}{4} - \frac{\kappa^2}{2} \tag{48}$$

$$a = \sqrt{1 + \frac{4}{3}v\eta^2} \tag{49}$$

In this paper it will be assumed that $v > 0$ although v could be negative as well. In fact, it is to be noted that for (45), for $\epsilon = 0$, solitons exist for $v \in (-3/4A^2, \infty)$. Also, the 2-soliton solution of the parabolic law takes the asymptotic form [2]

$$q(Z,T) = \sum_{l=1}^{2} \frac{\eta_l}{[1 + a_l\cosh\{\zeta_l(T - vZ - T_l)\}]^{\frac{1}{2}}} \times e^{i(-\kappa_l T + \omega_l Z + \sigma_{0_l})} \tag{50}$$

with

$$\zeta_l \equiv \chi(\eta_l) = \eta_l\sqrt{2} \tag{51}$$

$$\omega_l \equiv \psi(\eta_l, \kappa_l) = \frac{\eta_l^2 - 2\kappa_l^2}{4} \tag{52}$$

$$a_l = \sqrt{1 + \frac{4}{3}v\eta_l^2} \tag{53}$$

In the study of SSI, with parabolic law nonlinearity, the initial pulse waveform is taken to be of the form

$$q(0,T) = \frac{\eta_1}{\left[1 + a_1\cosh\left\{\zeta_1\left(T - \frac{T_0}{2}\right)\right\}\right]^{\frac{1}{2}}} e^{i\phi_1} + \frac{\eta_2}{\left[1 + a_2\cosh\left\{\zeta_2\left(T + \frac{T_0}{2}\right)\right\}\right]^{\frac{1}{2}}} e^{i\phi_2} \tag{54}$$

This initial pulse form modifies as follows:

1. *Non-Hamiltonian perturbation*

Here, the choice $\eta_1 = \eta_2 = 1$ and $\phi_1 = \phi_2 = 0$, gives

$$q(0,T) = \frac{1}{\left[1 + \sqrt{1 + \frac{4}{3}v}\cosh\left\{\sqrt{2}\left(T - \frac{T_0}{2}\right)\right\}\right]^{\frac{1}{2}}} + \frac{1}{\left[1 + \sqrt{1 + \frac{4}{3}v}\cosh\left\{\sqrt{2}\left(T + \frac{T_0}{2}\right)\right\}\right]^{\frac{1}{2}}} \tag{55}$$

which represents an in-phase injection of solitons with equal amplitudes.

2. *Hamiltonian perturbations*

In this case, on setting $\eta_1 = \eta_0$, $\eta_2 = 1$ and $\phi_1 = \phi_2 = 0$, gives

$$q(0,T) = \frac{\eta_0}{\left[1+\sqrt{1+\frac{4}{3}v\eta_0}\cosh\left\{\eta_0\sqrt{2}\left(T-\frac{T_0}{2}\right)\right\}\right]^{\frac{1}{2}}} + \frac{1}{\left[1+\sqrt{1+\frac{4}{3}v}\cosh\left\{\sqrt{2}\left(T+\frac{T_0}{2}\right)\right\}\right]^{\frac{1}{2}}} \tag{56}$$

which represents an in-phase injection of pulses with unequal amplitudes.

2.4. Dual-power law

For the dual-power law nonlinearity, $F(s) = s^p + vs^{2p}$ where in this case, $v < 0$ so that the NLSE is

$$\mathrm{i}\frac{\partial q}{\partial Z} + \frac{1}{2}\frac{\partial^2 q}{\partial T^2} + (|q|^{2p} + v|q|^{4p})q = \mathrm{i}\epsilon R[q, q^*] \tag{57}$$

Eq. (57), for $\epsilon = 0$, is not integrable by IST. However, it supports solitary waves of the form

$$q(Z,T) = \frac{\eta}{[1+a\cosh\{\zeta(T-vZ-T_0)\}]^{\frac{1}{2p}}}\mathrm{e}^{\mathrm{i}(-\kappa T+\omega Z+\sigma_0)} \tag{58}$$

where

$$\zeta \equiv \chi(\eta) = \eta^p\left(\frac{2p^2}{1+p}\right)^{\frac{1}{2p}} \tag{59}$$

$$\omega \equiv \psi(\eta,\kappa) = \frac{\eta^{2p}}{2p+2} - \frac{\kappa^2}{2} \tag{60}$$

$$a = \sqrt{1+\frac{v\zeta^2}{2p^2}\frac{(1+p)^2}{1+2p}} \tag{61}$$

For dual-power law nonlinearity, solitons exist for

$$-\frac{2p^2}{\zeta^2}\frac{1+2p}{(1+p)^2} < v < 0 \tag{62}$$

In this case, the 2-soliton solution of the NLSE (1) takes the asymptotic form

$$q(Z,T) = \sum_{l=1}^{2}\frac{\eta_l}{[1+a_l\cosh\{\zeta_l(T-vZ-T_l)\}]^{\frac{1}{2p}}} \times \mathrm{e}^{\mathrm{i}(-\kappa_l T+\omega_l Z+\sigma_{0_l})} \tag{63}$$

with

$$\zeta_l \equiv \chi(\eta_l) = \eta_l^p\left(\frac{2p^2}{1+p}\right)^{\frac{1}{2p}} \tag{64}$$

$$\omega_l \equiv \psi(\eta_l,\kappa_l) = \frac{\eta_l^{2p}}{2p+2} - \frac{\kappa_l^2}{2} \tag{65}$$

$$a_l = \sqrt{1+\frac{v\zeta_l^2}{2p^2}\frac{(1+p)^2}{1+2p}} \tag{66}$$

In the study of SSI, with dual-power law nonlinearity, the initial pulse waveform is taken to be of the form

$$q(0,T) = \frac{\eta_1}{[1+a_1\cosh\{\zeta_1(T-\frac{T_0}{2})\}]^{\frac{1}{2p}}}\mathrm{e}^{\mathrm{i}\phi_1} + \frac{\eta_2}{[1+a_2\cosh\{\zeta_2(T+\frac{T_0}{2})\}]^{\frac{1}{2p}}}\mathrm{e}^{\mathrm{i}\phi_2} \tag{67}$$

The initial pulse form simplifies as follows:

1. *Non-Hamiltonian perturbation*

In this case, on choosing $\eta_1 = \eta_2 = 1$ and $\phi_1 = \phi_2 = 0$, gives

$$q(0,T) = \frac{1}{\left[1+a_1\cosh\left\{\zeta\left(T-\frac{T_0}{2}\right)\right\}\right]^{\frac{1}{2p}}} + \frac{1}{\left[1+a_2\cosh\left\{\zeta\left(T+\frac{T_0}{2}\right)\right\}\right]^{\frac{1}{2p}}} \tag{68}$$

where ζ is given by (59). Eq. (68) represents an in-phase injection of solitons with equal amplitudes.

2. *Hamiltonian perturbations*

Here, the choice $\eta_1 = \eta_0$, $\eta_2 = 1$ and $\phi_1 = \phi_2 = 0$, leads to:

$$q(0,T) = \frac{\eta_0}{\left[1+a_1\cosh\left\{\zeta_0\left(T-\frac{T_0}{2}\right)\right\}\right]^{\frac{1}{2p}}} + \frac{1}{\left[1+a_2\cosh\left\{\zeta\left(T+\frac{T_0}{2}\right)\right\}\right]^{\frac{1}{2p}}} \tag{69}$$

where

$$\zeta_0 = \eta_0^p\left(\frac{2p^2}{1+p}\right)^{\frac{1}{2p}} \tag{70}$$

which represents in-phase injection of pulses with unequal amplitudes.

3. Analysis

The QPT dates back to 1981 since the appearance of the paper by Karpman and Solov'ev [14]. The mathematical approach to SSI will be studied using

the QPT. Here, the solitons are treated as particles. If two pulses are separated and each of them is close to a soliton they can be written as the linear superposition of two soliton like pulses as [2]

$$q(Z,T) = q_1(Z,T) + q_2(Z,T) \tag{71}$$

with

$$q_l(Z,T) = A_l g[D_l(T-T_l)]\mathrm{e}^{-\mathrm{i}\{B_l(T-T_l)-\delta_l\}} \tag{72}$$

where

$$D_l = \chi(A_l) \tag{73}$$

and $l = 1,2$ while A_l, B_l, D_l, T_l and δ_l are functions of Z. Here, A_l, D_l and B_l do not represent the amplitude, width and the frequency of the full wave form. However, they approach the amplitude, width and frequency respectively for large separation namely if $\Delta T = T_1 - T_2 \to \infty$, then $A_l \to \eta_l$, $D_l \to \zeta_l$ and $B_l \to \kappa_l$. Since the waveform is assumed to remain in the form of two pulses, the method is called the quasi-particle approach. First, the equations for A_l, B_l, T_l and δ_l using the soliton perturbation theory (SPT) [3,12] will be derived. Substituting (71) into (3) yields

$$\mathrm{i}\frac{\partial q_l}{\partial Z} + \frac{1}{2}\frac{\partial^2 q_l}{\partial T^2} = \mathrm{i}\epsilon R[q_l, q_l^*] - F(|q_l + q_{\bar{l}}|^2)|q_l + q_{\bar{l}}| \tag{74}$$

where $l = 1,2$ and $\bar{l} = 3 - l$. By SPT, the evolution equations are

$$\frac{\mathrm{d}A_l}{\mathrm{d}Z} = F_1^{(l)}(A, \Delta T, \Delta\phi) + \epsilon M_l \tag{75}$$

$$\frac{\mathrm{d}B_l}{\mathrm{d}Z} = F_2^{(l)}(A, \Delta T, \Delta\phi) + \epsilon N_l \tag{76}$$

$$\frac{\mathrm{d}T_l}{\mathrm{d}Z} = -B_l - F_3(A, \Delta T, \Delta\phi) + \epsilon Q_l \tag{77}$$

$$\frac{\mathrm{d}\delta_l}{\mathrm{d}Z} = \psi(A_l, B_l) + F_4(A, \Delta T, \Delta\phi) + \epsilon P_l \tag{78}$$

where the functions $F_1^{(l)}$, $F_2^{(l)}$, F_3 and F_4 formulate on using the SPT in (74), with the right side being treated as perturbation terms. The exact form of these functions can be obtained when a specific law of nonlinearity is considered. Also,

$$M_l = h_1(A_l)\int_{-\infty}^{\infty} \Re\{\widehat{R}[q_l, q_l^*]\mathrm{e}^{-\mathrm{i}\phi_l}\} g(\tau_l)\,\mathrm{d}\tau_l \tag{79}$$

$$N_l = h_2(A_l)\int_{-\infty}^{\infty} \Im\{\widehat{R}[q_l, q_l^*]\mathrm{e}^{-\mathrm{i}\phi_l}\} g'(\tau_l)\,\mathrm{d}\tau_l \tag{80}$$

$$Q_l = h_3(A_l)\int_{-\infty}^{\infty} \Re\{\widehat{R}[q_l, q_l^*]\mathrm{e}^{-\mathrm{i}\phi_l}\} \tau_l g(\tau_l)\,\mathrm{d}\tau_l \tag{81}$$

$$P_l = h_4(A_l)\int_{-\infty}^{\infty} \Im\{\widehat{R}[q_l, q_l^*]\mathrm{e}^{-\mathrm{i}\phi_l}\}[g(\tau_l) - \tau_l g'(\tau_l)]\,\mathrm{d}\tau_l \tag{82}$$

where the functions $h_j(A_l)$ for $1 \leqslant j \leqslant 4$ are by virtue of (75)–(78) and the type of nonlinearity that is considered. Also, in (79)–(82), $\Re$ and $\Im$ stands for the real and imaginary parts respectively. Moreover, the following notations are used:

$$\widehat{R}[q_l, q_l^*] = R[q_l, q_l^*] - F(|q_l + q_{\bar{l}}|^2)|q_l + q_{\bar{l}}| \tag{83}$$

$$\tau_l = A_l(T - T_l) \tag{84}$$

$$\phi_l = B_l(T - T_l) - \delta_l \tag{85}$$

$$\Delta\phi = B\Delta T + \Delta\delta \tag{86}$$

$$\Delta T = T_1 - T_2 \tag{87}$$

$$\Delta\delta = \delta_1 - \delta_2 \tag{88}$$

$$A = \frac{1}{2}(A_1 + A_2) \tag{89}$$

$$B = \frac{1}{2}(B_1 + B_2) \tag{90}$$

$$\Delta A = A_1 - A_2 \tag{91}$$

$$\Delta B = B_1 - B_2 \tag{92}$$

Finally, it is assumed that

$$|\Delta A| \ll A \tag{93}$$

$$|\Delta B| \ll 1 \tag{94}$$

$$|\Delta D| \ll D \tag{95}$$

$$A\Delta T \gg 1 \tag{96}$$

$$D\Delta T \gg 1 \tag{97}$$

$$|\Delta A|\Delta T \ll 1 \tag{98}$$

$$|\Delta D|\Delta T \ll 1 \tag{99}$$

From (84)–(92), one can now obtain

$$\frac{\mathrm{d}A}{\mathrm{d}Z} = \epsilon M \tag{100}$$

$$\frac{\mathrm{d}B}{\mathrm{d}Z} = \epsilon N \tag{101}$$

$$\frac{\mathrm{d}(\Delta A)}{\mathrm{d}Z} = F_1^{(1)}(A, \Delta T, \Delta\phi) - F_1^{(2)}(A, \Delta T, \Delta\phi) + \epsilon\Delta M \tag{102}$$

$$\frac{\mathrm{d}(\Delta B)}{\mathrm{d}Z} = F_2^{(1)}(A, \Delta T, \Delta\phi) - F_2^{(2)}(A, \Delta T, \Delta\phi) + \epsilon\Delta N \tag{103}$$

$$\frac{\mathrm{d}(\Delta T)}{\mathrm{d}Z} = -\Delta B + \epsilon\Delta Q \tag{104}$$

$$\frac{\mathrm{d}(\Delta\phi)}{\mathrm{d}Z} = \psi(A_1, B_1) - \psi(A_2, B_2) - B\Delta B + \frac{\Delta T}{2}(F_2^{(1)} + F_2^{(2)}) + \epsilon\Delta P + \epsilon B\Delta Q \tag{105}$$

where

$$M = \frac{1}{2}(M_1 + M_2) \tag{106}$$

$$N = \frac{1}{2}(N_1 + N_2) \tag{107}$$

and ΔM, ΔN, ΔQ and ΔP are the variations of M, N, Q and P which are written as, for example

$$\Delta M = \frac{\partial M}{\partial A}\Delta A + \frac{\partial M}{\partial B}\Delta B \tag{108}$$

assuming that they are functions of A and B only, which is, in fact, true for most of the cases of interest, otherwise, the equations for

$$T = \frac{1}{2}(T_1 + T_2) \tag{109}$$

and

$$\phi = \frac{1}{2}(\phi_1 + \phi_2) \tag{110}$$

would have been necessary. The results in this section, that are derived so far, will now be utilized to show that the SSI can indeed be suppressed in presence of the perturbation terms given by (4) for the four cases of nonlinearity. In all the four types of nonlinearities, the initial conditions for the Kerr law nonlinearity, corresponding to the initial waveform (19), are

$$A = 1, \quad B = 0, \quad \Delta A_0 = 0, \quad \Delta B_0 = 0,$$
$$\Delta T_0 = T_0, \quad \Delta\phi_0 = 0$$

The four laws of nonlinearity are now studied in the following subsections.

3.1. Kerr law

In this case, (72) reduces to

$$q_l(Z,T) = \frac{A_l}{\cosh[D_l(T - T_l)]}\mathrm{e}^{-\mathrm{i}B_l(T-T_l)+\mathrm{i}\delta_l} \tag{111}$$

where

$$D_l \equiv \chi(A_l) = A_l \tag{112}$$

so that (74) transforms to

$$\mathrm{i}\frac{\partial q_l}{\partial Z} + \frac{1}{2}\frac{\partial^2 q_l}{\partial T^2} + |q_l|^2 q_l = \mathrm{i}\epsilon R[q_l, q_l^*] - (q_l^2 q_{\bar{l}}^* + 2|q_l|^2 q_{\bar{l}}) \tag{113}$$

where $l = 1, 2$ and $\bar{l} = 3 - l$ and the separation

$$|q|^2 q = (|q_1|^2 q_1 + q_1^2 q_2^* + 2|q_1|^2 q_2) + (|q_2|^2 q_2 + q_2^2 q_1^* + 2|q_2|^2 q_1) \tag{114}$$

was used based on the degree of overlapping. By SPT, the evolution equations are

$$\frac{\mathrm{d}A_l}{\mathrm{d}Z} = (-1)^{l+1}4A^3\mathrm{e}^{-A\Delta T}\sin(\Delta\phi) + \epsilon M_l \tag{115}$$

$$\frac{\mathrm{d}B_l}{\mathrm{d}Z} = (-1)^{l+1}4A^3\mathrm{e}^{-A\Delta T}\cos(\Delta\phi) + \epsilon N_l \tag{116}$$

$$\frac{\mathrm{d}T_l}{\mathrm{d}Z} = -B_l - 2A\mathrm{e}^{-A\Delta T}\sin(\Delta\phi) + \epsilon Q_l \tag{117}$$

$$\frac{\mathrm{d}\delta_l}{\mathrm{d}Z} = \frac{1}{2}(A_l^2 + B_l^2) - 2AB\mathrm{e}^{-A\Delta T}\sin(\Delta\phi) + 6A^2\mathrm{e}^{-A\Delta T}\cos(\Delta\phi) + \epsilon P_l \tag{118}$$

where

$$M_l = \int_{-\infty}^{\infty} \Re\{\widehat{R}[q_l, q_l^*]\mathrm{e}^{-\mathrm{i}\phi_l}\}\frac{1}{\cosh\tau_l}\,\mathrm{d}\tau_l \tag{119}$$

$$N_l = -\int_{-\infty}^{\infty} \Im\{\widehat{R}[q_l, q_l^*]\mathrm{e}^{-\mathrm{i}\phi_l}\}\frac{\tanh\tau_l}{\cosh\tau_l}\,\mathrm{d}\tau_l \tag{120}$$

$$Q_l = \frac{1}{A_l^2}\int_{-\infty}^{\infty} \Re\{\widehat{R}[q_l, q_l^*]\mathrm{e}^{-\mathrm{i}\phi_l}\}\frac{\tau_l}{\cosh\tau_l}\,\mathrm{d}\tau_l \tag{121}$$

$$P_l = \frac{1}{A_l}\int_{-\infty}^{\infty} \Im\{\widehat{R}[q_l, q_l^*]\mathrm{e}^{-\mathrm{i}\phi_l}\} \times \frac{(1 - \tau_l\tanh\tau_l)}{\cosh\tau_l}\,\mathrm{d}\tau_l \tag{122}$$

and

$$\widehat{R}[q_l, q_l^*] = R[q_l, q_l^*] - i(q_l^2 q_l^* + 2|q_l|^2 q_l^*) \tag{123}$$

The study for the Kerr law case will now be split into the following two subsections.

3.1.1. Non-Hamiltonian perturbations

In presence of non-Hamiltonian perturbation terms, given in, (4), the dynamical system of the soliton parameters, by SPT are

$$\frac{\mathrm{d}A}{\mathrm{d}Z} = \epsilon\delta\frac{\Gamma\left(\frac{1}{2}\right)\Gamma(m+1)}{\Gamma\left(\frac{2m+3}{2}\right)}A^{2m+1} + 2\epsilon\sigma A^2 - \frac{2}{3}\epsilon\beta A(A^2 + 3B^2) \tag{124}$$

$$\frac{\mathrm{d}B}{\mathrm{d}Z} = -\frac{4}{3}\epsilon\beta A^2 B \tag{125}$$

so that by virtue of (102)–(105)

$$\frac{\mathrm{d}(\Delta A)}{\mathrm{d}Z} = 8A^3\mathrm{e}^{-A\Delta T}\sin(\Delta\phi) + \frac{\epsilon\delta}{2^{2m}}\frac{\Gamma\left(\frac{1}{2}\right)\Gamma(m+1)}{\Gamma\left(\frac{2m+3}{2}\right)}\sum_{r=0}^{2m+1}\binom{2m+1}{2r+1} \times (2A)^{2r+1}(\Delta A)^{2m-2r} + 4\epsilon\sigma A\Delta A - 2\epsilon\beta(A^2 + B^2)\Delta A - 4\epsilon\beta AB\Delta B \tag{126}$$

$$\frac{\mathrm{d}(\Delta B)}{\mathrm{d}Z} = 8A^3\mathrm{e}^{-A\Delta T}\cos(\Delta\phi) - \frac{8}{3}\epsilon\beta AB\Delta A - \frac{4}{3}\epsilon\beta A^2\Delta B \tag{127}$$

$$\frac{d(\Delta T)}{dZ} = -\Delta B + \epsilon\sigma \tag{128}$$

$$\frac{d(\Delta\phi)}{dZ} = A\Delta A - \frac{4}{3}\epsilon\beta A^2 B\Delta T \tag{129}$$

where in (126)

$$\binom{n}{r} = \frac{n(n-1)\cdots(n-r+1)}{r(r-1)\cdots 3.2.1} \tag{130}$$

For the fixed point of the dynamical system, given by (126) and (127), with $A = 1$ and $B = 0$, one recovers

$$\beta = 3\sigma + \frac{3\delta}{2}\frac{\Gamma\left(\frac{1}{2}\right)\Gamma(m+1)}{\Gamma\left(\frac{2m+3}{2}\right)} \tag{131}$$

From (128) and (129), one has the coupled system of equations for $\Delta\phi$, the phase difference, and ΔT, the soliton separation, with the fixed point $A = 1$ and $B = 0$ as follows:

$$\frac{d^2(\Delta T)}{dZ^2} + \frac{4}{3}\epsilon\beta\frac{d(\Delta T)}{dZ} + 8e^{-\Delta T}\cos(\Delta\phi) = 0 \tag{132}$$

$$\frac{d^2(\Delta\phi)}{dZ^2} + 2\epsilon(\beta - 2\sigma)\frac{d(\Delta\phi)}{dZ} - \frac{\epsilon\delta}{2^{2m}}\frac{\Gamma\left(\frac{1}{2}\right)\Gamma(m+1)}{\Gamma\left(\frac{2m+3}{2}\right)}\sum_{r=0}^{2m+1}\binom{2m+1}{2r+1} \times \left(\frac{d(\Delta\phi)}{dZ}\right)^{2m-2r} - 8e^{-\Delta T}\sin(\Delta\phi) = 0 \tag{133}$$

where in (132) and (133) β is given by (131). Eqs. (132) and (133) shows that inserting filters produces a damping in both pulse separation and phase difference.

3.1.2. Hamiltonian perturbations

In case of Hamiltonian perturbations of (4), the dynamical system of the soliton parameters is

$$\frac{dA}{dZ} = 0 \tag{134}$$

$$\frac{dB}{dZ} = 0 \tag{135}$$

$$\frac{dT_0}{dZ} = -B - 3\epsilon\gamma B^2 - \frac{\epsilon}{3}\{A^2(3\lambda + 2\mu + 3\gamma) + 3\alpha\} \tag{136}$$

so that by virtue of (102)–(105)

$$\frac{d(\Delta A)}{dZ} = 8A^3 e^{-A\Delta T}\sin(\Delta\phi) \tag{137}$$

$$\frac{d(\Delta B)}{dZ} = 8A^3 e^{-A\Delta T}\cos(\Delta\phi) \tag{138}$$

$$\frac{d(\Delta T)}{dZ} = -\Delta B - \frac{3}{2}\epsilon\gamma B\Delta B - \frac{\epsilon}{6}(3\lambda + 2\mu + 3\gamma)A\Delta A \tag{139}$$

$$\frac{d(\Delta\phi)}{dZ} = A\Delta A \tag{140}$$

Now,

$$A = \frac{1}{2}(A_0 + 1) \tag{141}$$

$$B = 0 \tag{142}$$

$$\Delta A_0 = A_0 - 1 \tag{143}$$

$$\Delta B_0 = 0 \tag{144}$$

$$\Delta T_0 = T_0 \tag{145}$$

$$\Delta\phi_0 = 0 \tag{146}$$

$$\Delta\phi = \Delta\delta \tag{147}$$

so that

$$\frac{d(\Delta T)}{dZ} + \frac{\epsilon}{6}(3\lambda + 2\mu + 3\gamma)\frac{d(\Delta\phi)}{dZ} = -\Delta B \tag{148}$$

For $\Delta B = 0$

$$\Delta T = T_0 - \frac{\epsilon}{6}(3\lambda + 2\mu + 3\gamma)\Delta\delta \tag{149}$$

Now, $T_0 \sim O(1)$ so that $\Delta T \nrightarrow 0$ and thus the pulses do not collide during the transmission.

3.2. Power law

In this case, (72) is

$$q_l(Z,T) = \frac{A_l}{\cosh^{\frac{1}{p}}[D_l(T - T_l)]}e^{-iB_l(T-T_l)+i\delta_l} \tag{150}$$

where

$$D_l \equiv \chi(A_l) = A_l^p\left(\frac{2p^2}{1+p}\right)^{\frac{1}{2}} \tag{151}$$

so that (74) gives

$$i\frac{\partial q_l}{\partial Z} + \frac{1}{2}\frac{\partial^2 q_l}{\partial T^2} = i\epsilon R[q_l, q_l^*] - \left[\sum_{r=0}^{p}\binom{p}{r}q_1^{p-r}q_2^r\right] \times \left[\sum_{r=0}^{p}\binom{p}{r}(q_1^*)^{p-r}(q_2^*)^r\right](q_1 + q_2) \tag{152}$$

Here, the separation

$$|q|^{2p}q = \left[\sum_{r=0}^{p}\binom{p}{r}q_1^{p-r}q_2^r\right] \times \left[\sum_{r=0}^{p}\binom{p}{r}(q_1^*)^{p-r}(q_2^*)^r\right](q_1 + q_2) \tag{153}$$

was used based on the degree of overlapping. By SPT, the evolution equations are

$$\frac{\mathrm{d}A_l}{\mathrm{d}Z} = F_1^{(l)}(A, \Delta T, \Delta\phi; p) + \epsilon M_l \tag{154}$$

$$\frac{\mathrm{d}B_l}{\mathrm{d}Z} = F_2^{(l)}(A, \Delta T, \Delta\phi; p) + \epsilon N_l \tag{155}$$

$$\frac{\mathrm{d}T_l}{\mathrm{d}Z} = -B_l - F_3(A, \Delta T, \Delta\phi; p) + \epsilon Q_l \tag{156}$$

$$\frac{\mathrm{d}\delta_l}{\mathrm{d}Z} = \frac{B_l^2}{2} + \frac{A_l^{2p}}{p+1} + F_4(A, \Delta T, \Delta\phi; p) + \epsilon P_l \tag{157}$$

where for power law

$$M_l = \frac{1}{2-p}\left(\frac{2p^2}{1+p}\right)^{\frac{p-3}{2p}} \frac{\Gamma\left(\frac{1}{p}+\frac{1}{2}\right)}{\Gamma\left(\frac{1}{p}\right)\Gamma\left(\frac{1}{2}\right)} \times \int_{-\infty}^{\infty} \Re\{\widehat{R}[q_l, q_l^*]\mathrm{e}^{-\mathrm{i}\phi_l}\} \frac{1}{\cosh^{\frac{1}{p}}\tau_l}\,\mathrm{d}\tau_l \tag{158}$$

$$N_l = \frac{2}{p}A_l^{p-1}\left(\frac{2p^2}{1+p}\right)^{\frac{p-1}{2p}} \frac{\Gamma\left(\frac{1}{p}+\frac{1}{2}\right)}{\Gamma\left(\frac{1}{p}\right)\Gamma\left(\frac{1}{2}\right)} \times \int_{-\infty}^{\infty} \Im\{\widehat{R}[q_l, q_l^*]\mathrm{e}^{-\mathrm{i}\phi_l}\} \frac{\tanh\tau_l}{\cosh^{\frac{1}{p}}\tau_l}\,\mathrm{d}\tau_l \tag{159}$$

$$Q_l = \frac{1}{A_l^{p+1}}\left(\frac{p+1}{2p^2}\right)^{\frac{p+2}{2p}} \frac{\Gamma\left(\frac{1}{p}+\frac{1}{2}\right)}{\Gamma\left(\frac{1}{p}\right)\Gamma\left(\frac{1}{2}\right)} \times \int_{-\infty}^{\infty} \Re\{\widehat{R}[q_l, q_l^*]\mathrm{e}^{-\mathrm{i}\phi_l}\} \frac{\tau_l}{\cosh^{\frac{1}{p}}\tau_l}\,\mathrm{d}\tau_l \tag{160}$$

$$P_l = \frac{1}{A_l^{p+1}}\left(\frac{2p^2}{p+1}\right)^{\frac{p+1}{2p}} \frac{\Gamma\left(\frac{1}{p}+\frac{1}{2}\right)}{\Gamma\left(\frac{1}{p}\right)\Gamma\left(\frac{1}{2}\right)} \times \int_{-\infty}^{\infty} \Im\{\widehat{R}[q_l, q_l^*]\mathrm{e}^{-\mathrm{i}\phi_l}\} \frac{(1-\tau_l\tanh\tau_l)}{\cosh^{\frac{1}{p}}\tau_l}\,\mathrm{d}\tau_l \tag{161}$$

In addition, the following notations are used:

$$\widehat{R}[q_l, q_l^*] = R[q_l, q_l^*] - \mathrm{i}\left[\sum_{r=0}^{p}\binom{p}{r} q_1^{p-r} q_2^r\right] \times \left[\sum_{r=0}^{p}\binom{p}{r}(q_1^*)^{p-r}(q_2^*)^r\right](q_1+q_2) + i|q_l|^{2p}q_l \tag{162}$$

For the power law, the study will now be split into the following two subsections.

3.2.1. Non-Hamiltonian perturbations

In presence of non-Hamiltonian perturbation terms, given in (4), the dynamical system of the soliton parameters, by virtue of SPT, are

$$\frac{\mathrm{d}A}{\mathrm{d}Z} = \frac{2\epsilon\delta}{2-p}\left(\frac{1+p}{2p^2}\right)^{\frac{1}{2p}} \frac{\Gamma\left(\frac{1}{p}+\frac{1}{2}\right)}{\Gamma\left(\frac{1}{p}\right)} \frac{\Gamma\left(\frac{m+1}{p}\right)}{\Gamma\left(\frac{m+1}{p}+\frac{1}{2}\right)} A^{2m+1} + \frac{\epsilon\sigma}{2-p}\left(\frac{1+p}{2p^2}\right)^{\frac{2p}{p+1}} \frac{\Gamma\left(\frac{1}{p}+\frac{1}{2}\right)}{\Gamma\left(\frac{1}{p}\right)\Gamma\left(\frac{1}{2}\right)} \int_{-\infty}^{\infty} \frac{1}{\cosh^{\frac{2}{p}}\tau}\left(\int_{-\infty}^{\tau} \frac{\mathrm{d}s}{\cosh^{\frac{2}{p}}s}\right)\mathrm{d}\tau A^{3-p} + \frac{2\epsilon\beta}{p^2(2-p)}\left(\frac{2p^2}{p+1}\right)^{\frac{2p-1}{2p}} \frac{\Gamma\left(\frac{1}{p}+\frac{1}{2}\right)}{\Gamma\left(\frac{1}{p}\right)} \frac{\Gamma\left(\frac{p+1}{p}\right)}{\Gamma\left(\frac{p+1}{p}+\frac{1}{2}\right)} A^{2p+1} - \frac{2\epsilon\beta}{2-p}\left(\frac{2p^2}{p+1}\right)^{\frac{1}{2p}} AB^2 - \frac{2\epsilon\beta}{p^2(2-p)}\left(\frac{2p^2}{p+1}\right)^{\frac{2p-1}{2p}} A^{2p+1} \tag{163}$$

$$\frac{\mathrm{d}B}{\mathrm{d}Z} = \frac{4\epsilon\beta}{p^2}\left(\frac{2p^2}{p+1}\right)^{\frac{3p-2}{2p}}\left(\frac{p-2}{p+2}\right)BA^{2p} \tag{164}$$

so that by virtue of (102)–(105)

$$\frac{\mathrm{d}(\Delta A)}{\mathrm{d}Z} = F_1^{(1)}(A, \Delta T, \Delta\phi) - F_1^{(2)}(A, \Delta T, \Delta\phi) + \frac{\epsilon\delta}{2-p}\left(\frac{1+p}{2p^2}\right)^{\frac{1}{2p}} \frac{\Gamma\left(\frac{1}{p}+\frac{1}{2}\right)}{\Gamma\left(\frac{1}{p}\right)} \frac{\Gamma\left(\frac{m+1}{p}\right)}{\Gamma\left(\frac{m+1}{p}+\frac{1}{2}\right)} \times \sum_{r=0}^{2m+1}\binom{2m+1}{2r+1}(2A)^{2r+1}(\Delta A)^{2m-2r} + \frac{\epsilon\sigma}{2-p}\left(\frac{1+p}{2p^2}\right)^{\frac{2p}{p+1}} \frac{\Gamma\left(\frac{1}{p}+\frac{1}{2}\right)}{\Gamma\left(\frac{1}{p}\right)\Gamma\left(\frac{1}{2}\right)} \times \int_{-\infty}^{\infty} \frac{1}{\cosh^{\frac{2}{p}}\tau}\left(\int_{-\infty}^{\tau} \frac{\mathrm{d}s}{\cosh^{\frac{2}{p}}s}\right)\mathrm{d}\tau \times \sum_{r=0}^{2m+1}\binom{3-p}{2r+1}(2A)^{2-p+2r}(\Delta A)^{2r+1} + \frac{\epsilon\beta}{p^2(2-p)}\left(\frac{2p^2}{p+1}\right)^{\frac{2p-1}{2p}} \frac{\Gamma\left(\frac{1}{p}+\frac{1}{2}\right)}{\Gamma\left(\frac{1}{p}\right)} \frac{\Gamma\left(\frac{p+1}{p}\right)}{\Gamma\left(\frac{p+1}{p}+\frac{1}{2}\right)}\tau \times \sum_{r=0}^{2m+1}\binom{2m+1}{2r+1}(2A)^{2r+1}(\Delta A)^{2m-2r} - \frac{2\epsilon\beta}{2-p}\left(\frac{2p^2}{p+1}\right)^{\frac{1}{2p}} AB\Delta B - \frac{\epsilon\beta}{p^2(2-p)}\left(\frac{2p^2}{p+1}\right)^{\frac{2p-1}{2p}}\tau \times \sum_{r=0}^{2m+1}\binom{2m+1}{2r+1}(2A)^{2r+1}(\Delta A)^{2m-2r} \tag{165}$$

$$\frac{\mathrm{d}(\Delta B)}{\mathrm{d}Z} = F_2^{(1)}(A, \Delta T, \Delta\phi) - F_2^{(2)}(A, \Delta T, \Delta\phi)\tau + \frac{4\epsilon\beta}{p^2}\left(\frac{2p^2}{p+1}\right)^{\frac{3p-2}{2p}}\left(\frac{p-2}{p+2}\right)[\Delta BA^{2p} + 2pBA^{2p+1}\Delta A] \tag{166}$$

$$\frac{d(\Delta T)}{dZ} = -\Delta B + 2\epsilon\sigma\left(\frac{A_1^{p+2}}{D_1^3} - \frac{A_2^{p+2}}{D_2^3}\right)\left(\frac{2p^2}{1+p}\right)^{\frac{1}{2}}\frac{\Gamma\left(\frac{1}{p}+\frac{1}{2}\right)}{\Gamma\left(\frac{1}{p}\right)\Gamma\left(\frac{1}{2}\right)} \times \int_{-\infty}^{\infty}\frac{\tau}{\cosh^{\frac{2}{p}}\tau}\left(\int_{-\infty}^{\tau}\frac{ds}{\cosh^{\frac{2}{p}}s}\right)d\tau \quad (167)$$

$$\frac{d(\Delta\phi)}{dZ} = \frac{A_1^{2p} - A_2^{2p}}{p+1} - \frac{4\epsilon\beta}{p^2}\left(\frac{2p^2}{p+1}\right)^{\frac{3p-2}{2p}}\left(\frac{p-2}{p+2}\right)A^{2p}B\Delta T \quad (168)$$

For the fixed point of the dynamical system given by (164) and (165) with $A = 1$ and $B = 0$, one gets

$$\beta = \frac{1}{2\Gamma\left(\frac{2}{p}\right) - \Gamma\left(\frac{1}{p}+\frac{1}{2}\right)} \times \left[\delta(p+1)\frac{\Gamma\left(\frac{2}{p}\right)\Gamma\left(\frac{1}{p}+\frac{1}{2}\right)}{\Gamma\left(\frac{1}{p}\right)}\frac{\Gamma\left(\frac{m+1}{p}\right)}{\Gamma\left(\frac{m+1}{p}+\frac{1}{2}\right)} + \sigma p^2\left(\frac{p+1}{2p^2}\right)^{\frac{(3p-1)(2p+1)}{2p(p+1)}}\frac{\Gamma\left(\frac{2}{p}\right)\Gamma\left(\frac{1}{p}+\frac{1}{2}\right)}{\Gamma\left(\frac{1}{p}\right)\Gamma\left(\frac{1}{2}\right)} \times \int_{-\infty}^{\infty}\frac{1}{\cosh^{\frac{2}{p}}\tau}\left(\int_{-\infty}^{\tau}\frac{ds}{\cosh^{\frac{2}{p}}s}\right)d\tau\right] \quad (169)$$

Thus, from (167) and (168) one gets the coupled system of equations in ΔT and $\Delta\phi$ for the fixed point with $A = 1$ and $B = 0$ as

$$\frac{d^2(\Delta T)}{dZ^2} - \frac{4\epsilon\beta}{p^2}\left(\frac{2p^2}{p+1}\right)^{\frac{3p-2}{2p}}\left(\frac{p-2}{p+2}\right)\frac{d(\Delta T)}{dZ} + F_2^{(1)} - F_2^{(1)} = 0 \quad (170)$$

$$\frac{d^2(\Delta\phi)}{dZ^2} = \frac{2p}{p+1}\left[A_1^{2p-1}\frac{dA_1}{dZ} - A_2^{2p-1}\frac{dA_2}{dZ}\right] \quad (171)$$

where in (170) β is given by (169). From (170), one can observe that there is a damping introduced in the soliton separation and the coefficient of the damping term is positive as $0 < p < 2$.

3.2.2. Hamiltonian perturbations

In presence of Hamiltonian perturbation terms, as given by (4), the dynamical system of the soliton parameters, by virtue of SPT, are

$$\frac{dA}{dZ} = 0 \quad (172)$$

$$\frac{dB}{dZ} = 0 \quad (173)$$

$$\frac{dT_0}{dZ} = -B - \frac{\epsilon}{2}A^2(3\lambda + 2\mu)\frac{\Gamma\left(\frac{1}{2}+\frac{1}{p}\right)}{\Gamma\left(\frac{1}{2}+\frac{2}{p}\right)}\frac{\Gamma\left(\frac{2}{p}\right)}{\Gamma\left(\frac{1}{p}\right)} - \epsilon\left(\mu + 3\gamma B^2\right) + \frac{3\epsilon\gamma D^3}{p^2}\left[\frac{\Gamma\left(\frac{p-1}{p}\right)}{\Gamma\left(\frac{1}{p}\right)}\frac{\Gamma\left(\frac{1}{2}+\frac{1}{p}\right)}{\Gamma\left(\frac{3}{2}+\frac{2}{p}\right)} + 1\right] \quad (174)$$

so that by virtue of (102)–(105),

$$\frac{d(\Delta A)}{dZ} = F_1^{(1)}(A, \Delta T, \Delta\phi) - F_1^{(2)}(A, \Delta T, \Delta\phi) \quad (175)$$

$$\frac{d(\Delta B)}{dZ} = F_2^{(1)}(A, \Delta T, \Delta\phi) - F_2^{(2)}(A, \Delta T, \Delta\phi) \quad (176)$$

$$\frac{d(\Delta T)}{dZ} = -\Delta B - \frac{\epsilon}{4}A\Delta A(3\lambda + 2\mu)\frac{\Gamma\left(\frac{1}{2}+\frac{1}{p}\right)}{\Gamma\left(\frac{1}{2}+\frac{2}{p}\right)}\frac{\Gamma\left(\frac{2}{p}\right)}{\Gamma\left(\frac{1}{p}\right)} - \frac{3\epsilon\gamma}{4p^2}\Delta D[12D^2 + (\Delta D)^2] + \frac{3\epsilon\gamma}{p^2}\Delta D[12D^2 + (\Delta D)^2]\frac{\Gamma\left(\frac{p-1}{p}\right)}{\Gamma\left(\frac{1}{p}\right)}\frac{\Gamma\left(\frac{1}{2}+\frac{1}{p}\right)}{\Gamma\left(\frac{3}{2}+\frac{1}{p}\right)} \quad (177)$$

$$\frac{d(\Delta\phi)}{dZ} = \frac{A_1^{2p} - A_2^{2p}}{p+1} \quad (178)$$

Eq. (178) can be rewritten, by virtue of (105), as

$$\frac{d(\Delta T)}{dZ} = -\Delta B - \frac{\epsilon}{4}(3\lambda + 2\mu) \times f_1\left\{\frac{d(\Delta\phi)}{dZ}\right\}\frac{\Gamma\left(\frac{1}{2}+\frac{1}{p}\right)}{\Gamma\left(\frac{1}{2}+\frac{2}{p}\right)}\frac{\Gamma\left(\frac{2}{p}\right)}{\Gamma\left(\frac{1}{p}\right)} - \frac{3\epsilon\gamma}{4p^2}g_2\left\{\frac{d(\Delta\phi)}{dZ}\right\} + \frac{3\epsilon\gamma}{p^2}f_2\left\{\frac{d(\Delta\phi)}{dZ}\right\}\frac{\Gamma\left(\frac{p-1}{p}\right)}{\Gamma\left(\frac{1}{p}\right)}\frac{\Gamma\left(\frac{1}{2}+\frac{1}{p}\right)}{\Gamma\left(\frac{3}{2}+\frac{1}{p}\right)} \quad (179)$$

For in-phase injection of solitons with unequal amplitudes,

$$A = \frac{1}{2}(A_0 + 1) \quad (180)$$

$$B = 0 \quad (181)$$

$$\Delta A_0 = A_0 - 1 \quad (182)$$

$$\Delta B_0 = 0 \quad (183)$$

$$\Delta T_0 = T_0 \quad (184)$$

$$\Delta\phi_0 = 0 \quad (185)$$

$$\Delta\phi = \Delta\delta \quad (186)$$

so that for $\Delta B = 0$

$$\Delta T = T_0 - \frac{\epsilon}{6}(3\lambda + 2\mu) - \frac{\epsilon}{4}(3\lambda + 2\mu) \times h_1\left\{\frac{\mathrm{d}(\Delta\phi)}{\mathrm{d}Z}\right\}\frac{\Gamma\left(\frac{1}{2}+\frac{1}{p}\right)}{\Gamma\left(\frac{1}{2}+\frac{2}{p}\right)}\frac{\Gamma\left(\frac{2}{p}\right)}{\Gamma\left(\frac{1}{p}\right)} - \frac{3\epsilon\gamma}{4p^2}h_2\left\{\frac{\mathrm{d}(\Delta\phi)}{\mathrm{d}Z}\right\} + \frac{3\epsilon\gamma}{p^2}h_2\left\{\frac{\mathrm{d}(\Delta\phi)}{\mathrm{d}Z}\right\}\frac{\Gamma\left(\frac{p-1}{p}\right)}{\Gamma\left(\frac{1}{p}\right)}\frac{\Gamma\left(\frac{1}{2}+\frac{1}{p}\right)}{\Gamma\left(\frac{3}{2}-\frac{1}{p}\right)} \tag{187}$$

where

$$h_j(s) = \int f_j(s)\,\mathrm{d}s \tag{188}$$

for $j = 1, 2$. Thus

$$\Delta T = T_0 + \mathrm{O}(\epsilon) \tag{189}$$

Now, $T_0 \sim \mathrm{O}(1)$ so that $\Delta T \nrightarrow 0$ and thus the pulses do not collide during the transmission.

3.3. Parabolic law

In this case, (72) yields

$$q_l(Z,T) = \frac{A_l}{[1 + a_l\cosh\{D_l(T - T_l)\}]^{\frac{1}{2}}}\mathrm{e}^{-\mathrm{i}B_l(T-T_l)+\mathrm{i}\delta_l} \tag{190}$$

where

$$D_l \equiv \chi(A_l) = A_l\sqrt{2} \tag{191}$$

By (74), one gets

$$\mathrm{i}\frac{\partial q_l}{\partial Z} + \frac{1}{2}\frac{\partial^2 q_l}{\partial T^2} + (|q_l|^2 + v|q_l|^4)q_l = \mathrm{i}\epsilon R[q_l, q_l^*] - (q_l^2 q_{\bar{l}}^* + 2|q_l|^2 q_{\bar{l}}) - v[q_l^3(q_{\bar{l}}^*)^2 + 2|q_l|^2 q_l^2 q_{\bar{l}}^* + 3|q_l|^4 q_{\bar{l}} + 3|q_l|^2 q_l^* q_{\bar{l}}^2 + 6|q_l|^2|q_{\bar{l}}|^2 q_l] \tag{192}$$

where $l = 1, 2$ and $\bar{l} = 3 - l$. Here, the separation

$$\begin{aligned}|q|^2 q + v|q|^4 q = {} & (|q_1|^2 q_1 + q_1^2 q_2^* + 2|q_1|^2 q_2) \\ & + (|q_2|^2 q_2 + q_2^2 q_1^* + 2|q_2|^2 q_1) \\ & + v[|q_1|^4 q_1 + q_1^3(q_2^*)^2 \\ & + 2|q_1|^2 q_1^2 q_2^* + 3|q_1|^4 q_2 \\ & + 3|q_1|^2 q_1^* q_2^2 + 6|q_1|^2|q_2|^2 q_1] \\ & + v[|q_2|^4 q_2 + q_2^3(q_1^*)^2 \\ & + 2|q_2|^2 q_2^2 q_1^* + 3|q_2|^4 q_1 \\ & + 3|q_2|^2 q_2^* q_1^2 + 6|q_1|^2|q_2|^2 q_2]\end{aligned} \tag{193}$$

was used based on the degree of overlapping. By SPT, the evolution equations are

$$\frac{\mathrm{d}A_l}{\mathrm{d}Z} = F_1^{(l)}(A, \Delta T, \Delta\phi; v) + \epsilon M_l \tag{194}$$

$$\frac{\mathrm{d}B_l}{\mathrm{d}Z} = F_2^{(l)}(A, \Delta T, \Delta\phi; v) + \epsilon N_l \tag{195}$$

$$\frac{\mathrm{d}T_l}{\mathrm{d}Z} = -B_l - F_3(A, \Delta T, \Delta\phi; v) + \epsilon Q_l \tag{196}$$

$$\frac{\mathrm{d}\delta_l}{\mathrm{d}Z} = \frac{A_l^2}{4} + \frac{B_l^2}{2} + F_4(A, \Delta T, \Delta\phi; v) + \epsilon P_l \tag{197}$$

where in this case

$$M_l = h_1^{(1)}(A_l)\int_{-\infty}^{\infty}\Re\{\widehat{R}[q_l, q_l^*]\mathrm{e}^{-\mathrm{i}\phi_l}\} \times \frac{\mathrm{d}\tau_l}{(1 + a_l\cosh\tau_l)^{\frac{1}{2}}}\,\mathrm{d}\tau_l \tag{198}$$

$$N_l = h_2^{(1)}(A_l)\int_{-\infty}^{\infty}\Im\{\widehat{R}[q_l, q_l^*]\mathrm{e}^{-\mathrm{i}\phi_l}\} \times \frac{\sinh\tau_l}{(1 + a_l\cosh\tau_l)^{\frac{1}{2}}}\,\mathrm{d}\tau_l \tag{199}$$

$$Q_l = h_3^{(1)}(A_l)\int_{-\infty}^{\infty}\Re\{\widehat{R}[q_l, q_l^*]\mathrm{e}^{-\mathrm{i}\phi_l}\} \times \frac{\tau_l}{(1 + a_l\cosh\tau_l)^{\frac{1}{2}}}\,\mathrm{d}\tau_l \tag{200}$$

$$P_l = h_4^{(1)}(A_l)\int_{-\infty}^{\infty}\Im\{\widehat{R}[q_l, q_l^*]\mathrm{e}^{-\mathrm{i}\phi_l}\} \times \frac{(1 - a_l\tau_l\sinh\tau_l)}{(1 + a_l\cosh\tau_l)^{\frac{1}{2}}}\,\mathrm{d}\tau_l \tag{201}$$

Also, the following notations are used:

$$\begin{aligned}\widehat{R}[q_l, q_l^*] = {} & R[q_l, q_l^*] - (q_l^2 q_{\bar{l}}^* + 2|q_l|^2 q_{\bar{l}}) \\ & - v[q_l^3(q_{\bar{l}}^*)^2 + 2|q_l|^2 q_l^2 q_{\bar{l}}^* + 3|q_l|^4 q_{\bar{l}} \\ & + 3|q_l|^2 q_l^* q_{\bar{l}}^2 + 6|q_l|^2|q_{\bar{l}}|^2 q_l]\end{aligned} \tag{202}$$

For the parabolic law case, the study will be split into the following two subsections.

3.3.1. Non-Hamiltonian perturbations

In presence of non-Hamiltonian perturbation terms, as given by, (4), the dynamical system of the soliton parameters, by SPT are

$$\frac{dA}{dZ}=\frac{\epsilon\delta A^{2m+1}}{2^m a^{m-1}}F\left(m+1,m+1,m+\frac{3}{2};\frac{a-1}{2a}\right)B\left(\frac{m+1}{p},\frac{1}{2}\right)+\epsilon\sigma a^2\frac{\sqrt{2}}{2}\int_{-\infty}^{\infty}\frac{1}{1+a\cosh\tau}\left(\int_{-\infty}^{\tau}\frac{ds}{1+a\cosh s}\right)d\tau-\epsilon\beta a^2A^3\left[\frac{a^2}{(a^2-1)^{\frac{3}{2}}}\tan^{-1}\sqrt{\frac{a-1}{a+1}}-\frac{1}{2(a^2-1)}\right]-4\sqrt{2}\epsilon\beta\frac{a^2B^2}{\sqrt{a^2-1}}\tan^{-1}\sqrt{\frac{a-1}{a+1}} \quad (203)$$

$$\frac{dB}{dZ}=-\epsilon\beta\frac{\sqrt{2}A^3B}{E}\left[\frac{a^2}{(a^2-1)^{\frac{3}{2}}}\tan^{-1}\sqrt{\frac{a-1}{a+1}}-\frac{1}{2(a^2-1)}\right] \quad (204)$$

where E is the energy of the soliton given by

$$E=\int_{-\infty}^{\infty}|q|^2\,dT=\frac{2\sqrt{2}A}{\sqrt{a^2-1}}\tan^{-1}\sqrt{\frac{a-1}{a+1}} \quad (205)$$

and $F(\alpha,\beta;\gamma;z)$ is the Gauss' hypergeometric function defined as

$$F(\alpha,\beta;\gamma;z)=\frac{\Gamma(\gamma)}{\Gamma(\alpha)\Gamma(\beta)}\sum_{n=0}^{\infty}\times\frac{\Gamma(\alpha+n)\Gamma(\beta+n)}{\Gamma(\gamma+n)}\frac{z^n}{n!} \quad (206)$$

while $B(l,m)$ is the beta function defined as

$$B(l,m)=\int_0^1 x^{l-1}(1-x)^{m-1}\,dx \quad (207)$$

For the fixed point of the dynamical system, given by (203) and (204), with $A=1$ and $B=0$, one recovers

$$\beta=\frac{\sigma\sqrt{2}}{2}\frac{\int_{-\infty}^{\infty}\frac{1}{1+a\cosh\tau}\left(\int_{-\infty}^{\tau}\frac{ds}{1+a\cosh s}\right)d\tau}{\frac{a^2}{(a^2-1)^{\frac{3}{2}}}\tan^{-1}\sqrt{\frac{a-1}{a+1}}-\frac{1}{2(a^2-1)}}+\frac{\delta}{2^m a^{m+1}}\frac{F\left(m+1,m+1,m+\frac{3}{2};\frac{a-1}{2a}\right)B\left(\frac{m+1}{p},\frac{1}{2}\right)}{\frac{a^2}{(a^2-1)^{\frac{3}{2}}}\tan^{-1}\sqrt{\frac{a-1}{a+1}}-\frac{1}{2(a^2-1)}} \quad (208)$$

Thus, one can obtain using, (102)–(105)

$$\frac{d^2(\Delta T)}{dZ^2}+\epsilon\beta G\frac{d(\Delta T)}{dZ}+F_2^{(1)}-F_2^{(2)}=0 \quad (209)$$

where β is given by (208) and $G>0$ represents the coefficient of $-\epsilon\beta\Delta B$ in $d(\Delta B)/dZ=dB_1/dZ-dB_2/dZ$. Now, Eq. (209) shows that there is a damping in the separation of solitons thus proving that there will be a suppression of the SSI in presence of the perturbation terms given by (4).

3.3.2. Hamiltonian perturbations

In presence of Hamiltonian perturbation terms, as given by, (4), the dynamical system of the soliton parameters, by SPT are

$$\frac{dA}{dZ}=0 \quad (210)$$

$$\frac{dB}{dZ}=0 \quad (211)$$

$$\frac{dT_0}{dZ}=-B-\frac{\epsilon\alpha}{E}\frac{2\sqrt{2}A}{\sqrt{a^2-1}}\tan^{-1}\sqrt{\frac{a-1}{a+1}}-\frac{\epsilon\sqrt{2}}{2E}\frac{A^3}{(a^2-1)^{\frac{3}{2}}}(3\lambda+2\mu)\times\left[\sqrt{a^2-1}-2\tan^{-1}\sqrt{\frac{a-1}{a+1}}\right]-3\sqrt{2}\frac{\epsilon\gamma A}{E}\left[\left(\frac{a^4A^2}{2}+\frac{2\kappa^2}{\sqrt{a^2-1}}\right)\tan^{-1}\times\sqrt{\frac{a-1}{a+1}}-\frac{a^2A^2}{4}\sqrt{a^2-1}\right] \quad (212)$$

From (102)–(105) one can now conclude that

$$\frac{d(\Delta A)}{dZ}=F_1^{(1)}(A,\Delta T,\Delta\phi)-F_1^{(2)}(A,\Delta T,\Delta\phi) \quad (213)$$

$$\frac{d(\Delta B)}{dZ}=F_2^{(1)}(A,\Delta T,\Delta\phi)-F_2^{(2)}(A,\Delta T,\Delta\phi) \quad (214)$$

$$\frac{d(\Delta T)}{dZ}=\frac{dT_1}{dZ}-\frac{dT_2}{dZ} \quad (215)$$

$$\frac{d(\Delta\phi)}{dZ}=\frac{1}{2}A\Delta A \quad (216)$$

Eq. (215) can be rewritten as

$$\frac{d(\Delta T)}{dZ}=-\Delta B+\epsilon G(\alpha,\lambda,\mu,\gamma,\sigma)f\left\{\frac{d(\Delta\phi)}{dZ}\right\} \quad (217)$$

where G is the functional form that depends on the said parameters. For in-phase injection of solitons with unequal amplitudes,

$$A=\frac{1}{2}(A_0+1) \quad (218)$$

$$B=0 \quad (219)$$

$$\Delta A_0=A_0-1 \quad (220)$$

$$\Delta B_0=0 \quad (221)$$

$$\Delta T_0=T_0 \quad (222)$$

$$\Delta\phi_0=0 \quad (223)$$

$$\Delta\phi=\Delta\delta \quad (224)$$

so that, one can obtain from (217) and (222)–(224), for $\Delta B=0$,

$$\Delta T = T_0 + \epsilon G(\alpha, \lambda, \mu, \gamma, \sigma) h\left\{\frac{\mathrm{d}(\Delta\phi)}{\mathrm{d}Z}\right\} \tag{225}$$

where

$$h_j(s) = \int f_j(s)\,\mathrm{d}s \tag{226}$$

for $j = 1, 2$. Thus,

$$\Delta T = T_0 + \mathrm{O}(\epsilon) \tag{227}$$

Now, $T_0 \sim \mathrm{O}(1)$ so that $\Delta T \nrightarrow 0$ and thus the pulses do not collide during the transmission.

3.4. Dual-power law

In this case, (72) reduces to

$$q_l(Z,T) = \frac{A_l}{[1 + a_l \cosh\{D_l(T - T_l)\}]^{\frac{1}{2}}} \mathrm{e}^{-\mathrm{i}B_l(T-T_l)+\mathrm{i}\delta_l} \tag{228}$$

where

$$D_l \equiv \chi(A_l) = A_l^p \left(\frac{2p^2}{1+p}\right)^{\frac{1}{2}} \tag{229}$$

Here (74) modifies to

$$\begin{aligned}\mathrm{i}\frac{\partial q_l}{\partial Z} + \frac{1}{2}\frac{\partial^2 q_l}{\partial T^2} = {} & \mathrm{i}\epsilon R[q_l, q_l^*] - \left[\sum_{r=0}^{p}\binom{p}{r} q_1^{p-r} q_2^r\right] \\ & \times \left[\sum_{r=0}^{p}\binom{p}{r} (q_1^*)^{p-r}(q_2^*)^r\right](q_1 + q_2) \\ & - v\left[\sum_{r=0}^{2p}\binom{2p}{r} q_1^{2p-r} q_2^r\right] \\ & \times \left[\sum_{r=0}^{2p}\binom{2p}{r} (q_1^*)^{2p-r}(q_2^*)^r\right](q_1 + q_2)\end{aligned} \tag{230}$$

where the separation

$$\begin{aligned}|q|^{2p}q + v|q|^{4p}q = {} & \left[\sum_{r=0}^{p}\binom{p}{r}\binom{p}{r} q_1^{p-r} q_2^r\right] \\ & \times \left[\sum_{r=0}^{p}\binom{p}{r} (q_1^*)^{p-r}(q_2^*)^r\right](q_1 + q_2) \\ & + v\left[\sum_{r=0}^{2p}\binom{2p}{r} q_1^{2p-r} q_2^r\right] \\ & \times \left[\sum_{r=0}^{2p}\binom{2p}{r} (q_1^*)^{2p-r}(q_2^*)^r\right](q_1 + q_2)\end{aligned} \tag{231}$$

was used based on the degree of overlapping. By SPT, the evolution equations are

$$\frac{\mathrm{d}A_l}{\mathrm{d}Z} = F_1^{(l)}(A, \Delta T, \Delta\phi; v, p) + \epsilon M_l \tag{232}$$

$$\frac{\mathrm{d}B_l}{\mathrm{d}Z} = F_2^{(l)}(A, \Delta T, \Delta\phi; v, p) + \epsilon N_l \tag{233}$$

$$\frac{\mathrm{d}T_l}{\mathrm{d}Z} = -B_l - F_3(A, \Delta T, \Delta\phi; v, p) + \epsilon Q_l \tag{234}$$

$$\frac{\mathrm{d}\delta_l}{\mathrm{d}Z} = \frac{A_l^{2p}}{2p+2} + \frac{B_l^2}{2} + F_4(A, \Delta T, \Delta\phi; v, p) + \epsilon P_l \tag{235}$$

where for the case of dual-power law,

$$M_l = h_1^{(2)}(A_l) \int_{-\infty^\infty} \Re\{\widehat{R}[q_l, q_l^*]\mathrm{e}^{-\mathrm{i}\phi_l}\} \frac{\mathrm{d}\tau_l}{(1 + a_l\cosh\tau_l)^{\frac{1}{2p}}}\,\mathrm{d}\tau_l \tag{236}$$

$$N_l = h_2^{(2)}(A_l) \int_{-\infty^\infty} \Im\{\widehat{R}[q_l, q_l^*]\mathrm{e}^{-\mathrm{i}\phi_l}\} \frac{\sinh\tau_l}{(1 + a_l\cosh\tau_l)^{\frac{1}{2p}}}\,\mathrm{d}\tau_l \tag{237}$$

$$Q_l = h_3^{(2)}(A_l) \int_{-\infty}^{\infty} \Re\{\widehat{R}[q_l, q_l^*]\mathrm{e}^{-\mathrm{i}\phi_l}\} \frac{\tau_l}{(1 + a_l\cosh\tau_l)^{\frac{1}{2p}}}\,\mathrm{d}\tau_l \tag{238}$$

$$P_l = h_4^{(2)}(A_l) \int_{-\infty}^{\infty} \Im\{\widehat{R}[q_l, q_l^*]\mathrm{e}^{-\mathrm{i}\phi_l}\} \frac{(1 - a_l\tau_l\sinh\tau_l)}{(1 + a_l\cosh\tau_l)^{\frac{1}{2p}}}\,\mathrm{d}\tau_l \tag{239}$$

In addition, the following notations are used:

$$\begin{aligned}\widehat{R}[q_l, q_l^*] = {} & R[q_l, q_l^*] + \mathrm{i}|q_l|^{2p}q_l + \mathrm{i}v|q_l|^{4p}q_l \\ & - \mathrm{i}\left[\sum_{r=0}^{p}\binom{p}{r} q_1^{p-r} q_2^r\right] \\ & \times \left[\sum_{r=0}^{p}\binom{p}{r} (q_1^*)^{p-r}(q_2^*)^r\right](q_1 + q_2) \\ & - \mathrm{i}\left[\sum_{r=0}^{2p}\binom{2p}{r} q_1^{2p-r} q_2^r\right] \\ & \times \left[\sum_{r=0}^{2p}\binom{2p}{r} (q_1^*)^{2p-r}(q_2^*)^r\right](q_1 + q_2)\end{aligned} \tag{240}$$

For the case of dual-power law nonlinearity, the study is split into two subsections.

3.4.1. Non-Hamiltonian perturbations

In presence of the perturbation terms, as given by, (4), the dynamical system of the soliton parameters, by SPT, are

$$\frac{dA}{dZ}=\frac{4\epsilon\delta A^{2m+2}}{2^{\frac{m+1}{p}}a^{\frac{m+1}{p}}D}F\left(\frac{m+1}{p},\frac{m+1}{p},\frac{m+1}{p}+\frac{1}{2};\frac{a-1}{2a}\right)B\left(\frac{m+1}{p},\frac{1}{2}\right)+\frac{2\epsilon\sigma A^4}{D^2}\int_{-\infty}^{\infty}\frac{1}{(1+a\cosh\tau)^{\frac{1}{p}}}\left(\int_{-\infty}^{\tau}\frac{ds}{(1+a\cosh s)^{\frac{1}{p}}}\right)d\tau-\frac{4\epsilon\beta A^2}{Da^{\frac{1}{p}}2^{\frac{1}{p}}}\left[D^2F\left(2+\frac{1}{p},\frac{1}{p},\frac{3}{2}+\frac{1}{p};\frac{a-1}{2a}\right)B\left(\frac{1}{p},\frac{3}{2}\right)+B^2F\left(\frac{1}{p},\frac{1}{p},\frac{1}{2}+\frac{1}{p};\frac{a-1}{2a}\right)B\left(\frac{1}{p},\frac{1}{2}\right)\right] \quad (241)$$

$$\frac{dB}{dZ}=-\frac{\epsilon\beta BD^2}{4p^2A^2}\frac{F\left(2+\frac{1}{p},1+\frac{1}{p},2+\frac{1}{p};\frac{a-1}{2a}\right)}{F\left(\frac{1}{p},\frac{1}{p},\frac{1}{2}+\frac{1}{p};\frac{a-1}{2a}\right)}\frac{B\left(1+\frac{1}{p},1\right)}{B\left(\frac{1}{p},\frac{1}{2}\right)} \quad (242)$$

For the fixed point of the dynamical system, given by (241) and (242), with $A=1$ and $B=0$, one recovers

$$\beta=\frac{\delta}{2^{\frac{m}{p}}a^{\frac{m}{p}}}\left(\frac{1+p}{2p^2}\right)^{\frac{1}{p}}\frac{F\left(\frac{m+1}{p},\frac{m+1}{p},\frac{m+1}{p}+\frac{1}{2};\frac{a-1}{2a}\right)}{F\left(2+\frac{1}{p},\frac{1}{p},\frac{3}{2}+\frac{1}{p};\frac{a-1}{2a}\right)}\times\frac{B\left(\frac{m+1}{p},\frac{3}{2}\right)}{B\left(\frac{1}{p},\frac{3}{2}\right)}+\frac{\sigma a^{\frac{1}{p}}}{2^{\frac{p-1}{p}}}\left(\frac{1+p}{2p^2}\right)^{\frac{3}{2p}}\times\frac{1}{B\left(\frac{1}{p},\frac{3}{2}\right)F\left(2+\frac{1}{p},\frac{1}{p},\frac{3}{2}+\frac{1}{p};\frac{a-1}{2a}\right)}\times\int_{-\infty}^{\infty}\frac{1}{(1+a\cosh\tau)^{\frac{1}{p}}}\left(\int_{-\infty}^{\tau}\frac{ds}{(1+a\cosh s)^{\frac{1}{p}}}\right)d\tau \quad (243)$$

Thus, one can obtain using, (102)–(105)

$$\frac{d^2(\Delta T)}{dZ^2}+\epsilon\beta G\frac{d(\Delta T)}{dZ}+F_2^{(1)}-F_2^{(2)}=0 \quad (244)$$

where β is given by (243) and $G>0$ represents the coefficient of $-\epsilon\beta\Delta B$ in $d(\Delta B)/dZ=dB_1/dZ-dB_2/dZ$. Now, Eq. (244) shows that there is a damping in the separation of solitons thus proving that there will be a suppression of the SSI in presence of the perturbation terms given by (4).

3.4.2. Hamiltonian perturbations

In presence of the perturbation terms, as given by, (4), the dynamical system of the soliton parameters, by SPT, are

$$\frac{dA}{dZ}=0 \quad (245)$$

$$\frac{dB}{dZ}=0 \quad (246)$$

$$\frac{dT_0}{dZ}=-B-\epsilon(\mu+3\gamma B^2)-3\frac{\epsilon\gamma D^2}{2p^2}\frac{F\left(2+\frac{1}{p},\frac{1}{p},\frac{1}{p}+\frac{3}{2};\frac{a-1}{2a}\right)}{F}\times\left(\frac{1}{p},\frac{1}{p},\frac{1}{2}+\frac{1}{p};\frac{a-1}{2a}\right)\frac{B\left(\frac{1}{p},\frac{3}{2}\right)}{B\left(\frac{1}{p},\frac{1}{2}\right)}-\epsilon(3\lambda+2\mu)\frac{A^2}{2^{\frac{1}{p}}a^{\frac{1}{p}}}\frac{F\left(\frac{2}{p},\frac{2}{p},\frac{2}{p}+\frac{1}{2};\frac{a-1}{2a}\right)}{F\left(\frac{1}{p},\frac{1}{p},\frac{1}{2}+\frac{1}{p};\frac{a-1}{2a}\right)}\frac{B\left(\frac{2}{p},\frac{1}{2}\right)}{B\left(\frac{1}{p},\frac{1}{2}\right)} \quad (247)$$

From (102)–(105), one can now conclude that

$$\frac{d(\Delta A)}{dZ}=F_1^{(1)}(A,\Delta T,\Delta\phi)-F_1^{(2)}(A,\Delta T,\Delta\phi) \quad (248)$$

$$\frac{d(\Delta B)}{dZ}=F_2^{(1)}(A,\Delta T,\Delta\phi)-F_2^{(2)}(A,\Delta T,\Delta\phi) \quad (249)$$

$$\frac{d(\Delta T)}{dZ}=\frac{dT_1}{dZ}-\frac{dT_2}{dZ} \quad (250)$$

$$\frac{d(\Delta\phi)}{dZ}=\frac{1}{2}A\Delta A \quad (251)$$

For in-phase injection of solitons with unequal amplitudes,

$$A=\frac{1}{2}(A_0+1) \quad (252)$$

$$B=0 \quad (253)$$

$$\Delta A_0=A_0-1 \quad (254)$$

$$\Delta B_0=0 \quad (255)$$

$$\Delta T_0=T_0 \quad (256)$$

$$\Delta\phi_0=0 \quad (257)$$

$$\Delta\phi=\Delta\delta \quad (258)$$

Eq. (250) can be rewritten as

$$\frac{d(\Delta T)}{dZ}=-\Delta B+\epsilon G(\alpha,\lambda,\mu,\gamma,\sigma)f\left\{\frac{d(\Delta\phi)}{dZ}\right\} \quad (259)$$

where G is the functional form that depends on the said parameters. For in-phase injection of solitons with unequal amplitudes, so that for $\Delta B=0$

$$\Delta T=T_0+\epsilon G(\alpha,\lambda,\mu,\gamma,\sigma)h\left\{\frac{d(\Delta\phi)}{dZ}\right\} \quad (260)$$

where

$$h_j(s)=\int f_j(s)ds \quad (261)$$

for $j=1,2$. Thus,

$$\Delta T = T_0 + O(\epsilon) \tag{262}$$

Now, $T_0 \sim O(1)$ so that $\Delta T \nrightarrow 0$ and thus the pulses do not collide during the transmission.

4. Numerical simulation

In this section, the numerical results will support the theoretical analysis of the suppression of SSI. The numerical simulations were carried out for the NLSE using the 2-soliton solution. The code that was written uses the spectral method to integrate the NLSE. The independent parameters that are described in the code are the ones that describe the soliton, namely the soliton amplitude, frequency and the center of mass, while the other parameters, namely the soliton width and the velocity of the soliton, are related to the independent parameters for all the laws of nonlinearity. The initial separation of the solitons were chosen. Subsequently perturbation terms are chosen into two categories namely the Hamiltonian and the non-Hamiltonian types. After this, the Fast Fourier Transform of the profile (envelope) in time is computed. The program proceeds in z step by Picard iteration. The evolution of the nonlinear terms are carried out by computing the convolution integrals. The iterating ceases when the difference in values between successive iterations is sufficiently small, namely $O(h^2)$, where h is the propagation step size.

The following figures describe the suppression of the SSI for various laws of nonlinearity and for both Hamiltonian as well as non-Hamiltonian type perturbation terms as explained in the last section. The value of ϵ in all the cases is taken to be 0.1.

4.1. Kerr law

In case of Kerr law where $F(s) = s$, Eq. (132) shows that for non-Hamiltonian type perturbations there is a damping introduced in the soliton separation as they propagate along the fiber for long distances. This is clearly seen in the following figures. Fig. 1(a)–(c) shows the suppression of SSI for Kerr law nonlinearity with non-Hamiltonian perturbations in presence of saturable amplifiers and nonlinear damping with $m = 0$, 1 and 2, respectively.

Fig. 2 shows the suppression of SSI due to Kerr law nonlinearity in presence of Hamiltonian type perturbations. Without any loss of generality it is only the third order dispersion that is taken to have a non-zero effect. The value of γ is taken to be 0.14 and this shows in Fig. 2 that the suppression of SSI is achieved. It is also an important factor to note that there is a change in the velocity as seen from (136).

4.2. Power law

In case of power law where $F(s) = s^p$, where $0 < p < 2$, Eq. (170) shows that for non-Hamiltonian type perturbations there is a damping introduced in the soliton separation as they propagate along the fiber for long distances. It needs to be noted that when $0 < p < 2$, Eq. (170) has the second term to be positive which is what is needed to have the damping effect introduced for the separation of the solitons. This is seen in the following figures. Fig. 3(a) and (b) show the suppression of SSI for power law nonlinearity with non-Hamiltonian perturbations in presence of saturable amplifiers and nonlinear damping with $m = 1$ and 2, respectively. In both cases, however, p was taken to be 1/2.

Fig. 4 shows the suppression of SSI due to Kerr law nonlinearity in presence of Hamiltonian type perturbations. Here, once again, $p = 1/2$ while $\gamma = 0.14$ and $\lambda = v = 0.5$. Once again, the change in the soliton velocity produces this oblique motion by virtue of (174).

4.3. Parabolic law

In case of parabolic law where $F(s) = s^2 + vs^4$ for constant v, Eq. (209) shows that for non-Hamiltonian type perturbations there is a damping introduced in the soliton separation as they propagate along the fiber for long distances. In Eq. (209), the exact expression for the quantity G cannot be explicitly calculated, but it can be easily seen that $G > 0$. Also, in (209), it needs to be noted that β is given by (208). Thus, the second term in (209), has a positive coefficient and introduces the damping in the soliton separation. Thus, the solitons do not tend to collide during the long distance transmission across the continents and oceans. This fact is reflected in the following figure, where $m = 0$, $\delta = 0.001$, $\sigma = 0.001$ (see Fig. 5).

Fig. 6 shows the suppression of SSI due to parabolic law nonlinearity in presence of Hamiltonian type perturbations. This fact is explained by virtue of (225), where ϵ is small and therefore $\Delta(T) \approx T_0$. It needs to be noted that the function h in (225) cannot be explicitly computed, although the numerical

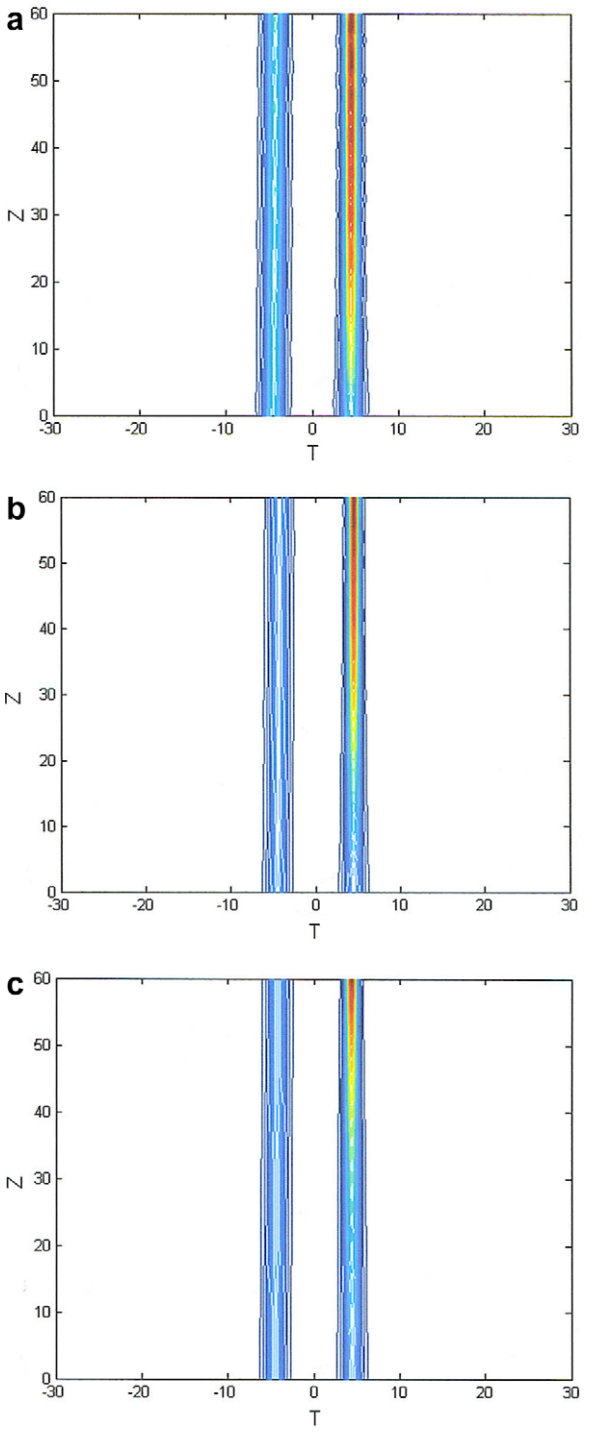


Fig. 1. SSI for $\sigma = \delta = 0.005$. (a) $m = 0$; (b) $m = 1$; (c) $m = 2$. Note that in all cases there is no effect of soliton radiation. The value of β is computed from (131).

results support the analysis. It needs to be noted that the intermittent swelling of the solitons is accounted for by soliton breathing. In the following

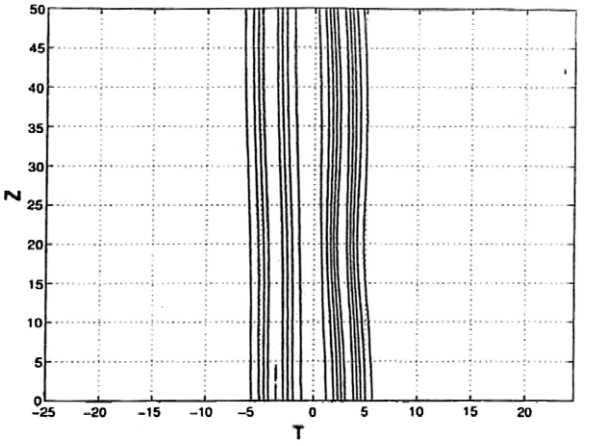


Fig. 2. SSI with $\gamma = 0.14$ and $\lambda = \mu = 0$. Note the oblique motion of the solitons due to (136), but the interaction is suppressed.

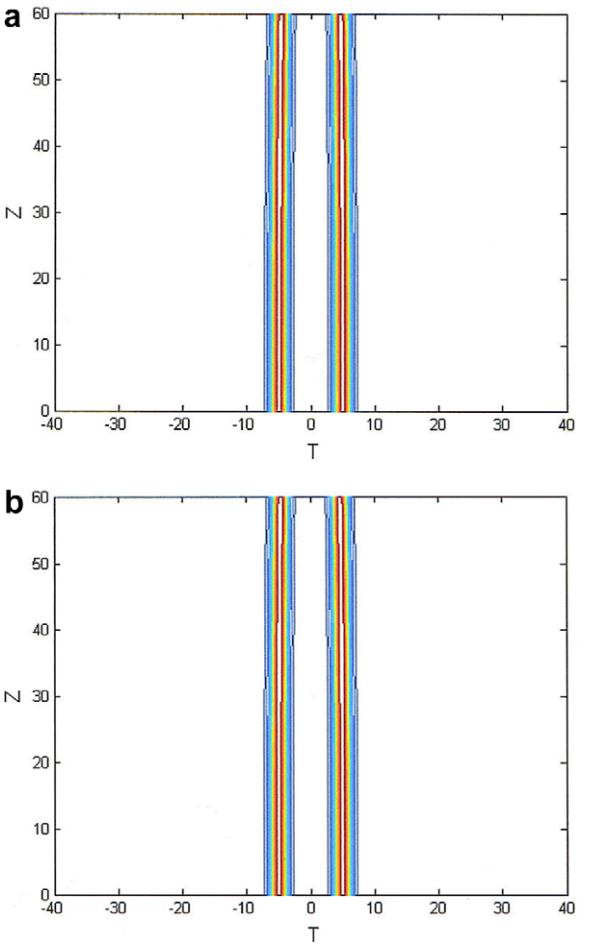


Fig. 3. SSI for $\delta = 0.001$, $\sigma = 0.0$, $p = 1/2$. (a) $m = 1$; (b) $m = 2$. The value of β is obtained from (169). Once again, there is no effect of radiation.

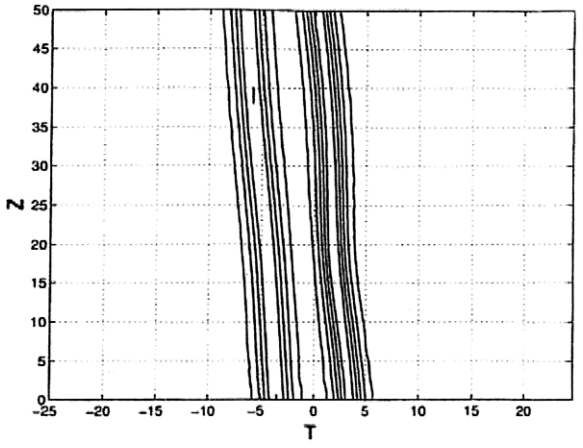


Fig. 4. SSI with $p = 1/2$, $\gamma = 0.14$, $\lambda = v = 0.5$. Again there is the oblique motion due to (174), but the interaction is suppressed.

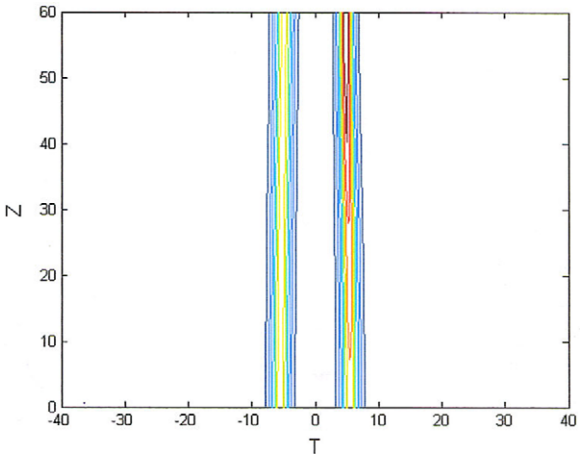


Fig. 5. SSI with $m = 0$, $\delta = 0.001$, $\sigma = 0.001$. β is obtained from (208).

figure, $v = 0.3$, $\alpha = 0.8$, $\gamma = -0.35$, $\sigma = 0.03$. Once again, the oblique motion of the solitons is a consequence of the Hamiltonian perturbations.

4.4. Dual-power law

In case of dual-power law where $F(s) = s^{2p} + vs^{4p}$ for constant $v < 0$, Eq. (244) similarly shows that for non-Hamiltonian type perturbations there is a damping introduced in the soliton separation as they propagate down the fiber for long distances. In Eq. (244), the exact expression for the quantity G cannot be explicitly calculated, but it can be easily seen that $G > 0$. The β is (244) is given by (243). Once the parameters, p,

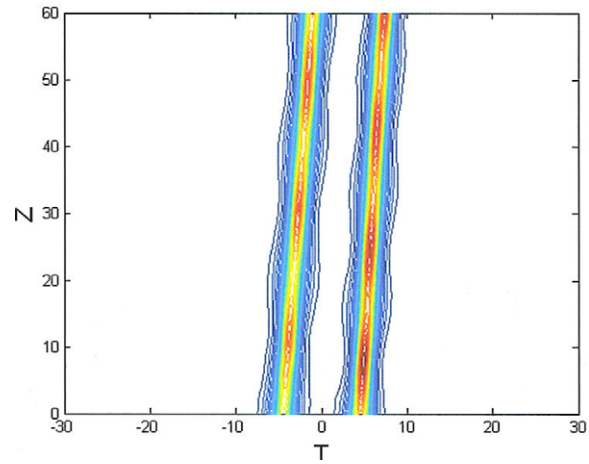


Fig. 6. SSI with $v = 0.3$, $\alpha = 0.8$, $\gamma = -0.35$, $\sigma = 0.03$. The breathing of the solitons is due to the non-zero v and the interaction is suppressed. Also, the oblique motion is due to (212).

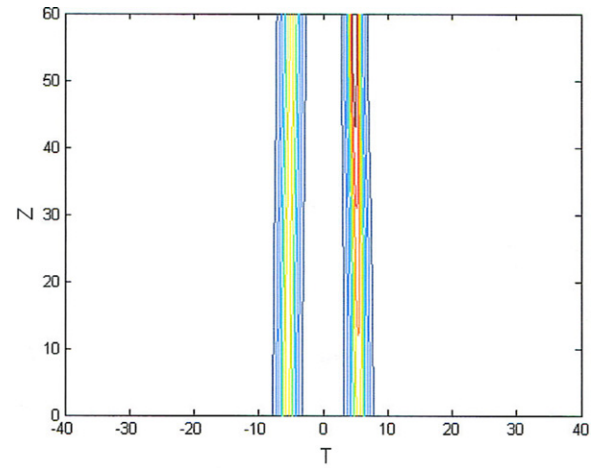


Fig. 7. SSI with $m = 1$, $\delta = \sigma = 0.001$. β is obtained from (243).

m, v, δ, σ are known, β can be obtained at least numerically as there is a non-local term present for β in (243). Thus, with all these issues considered, the solitons tend to stay separated as they propagate long distances down the fiber. This is seen in the following figure where $m = 1$, $\delta = \sigma = 0.001$ (Fig. 7).

Fig. 8 shows the suppression of SSI due to dual-power law nonlinearity in presence of Hamiltonian type perturbations. This fact is explained by virtue of (260) where ϵ is small and therefore, once again, $\Delta(T) \approx T_0$, the initial separation. It needs to be noted that the function h in (225) cannot be explicitly computed, although the numerical results support the

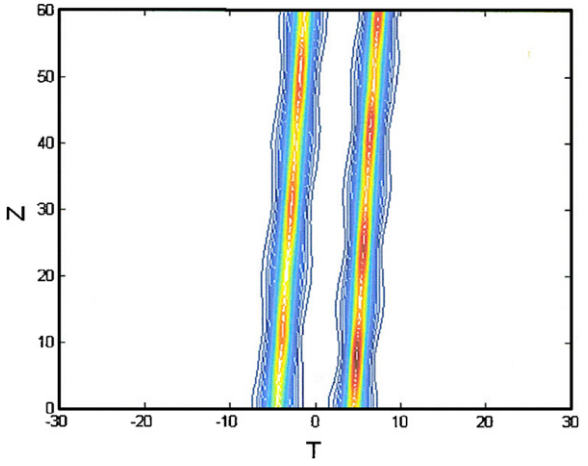


Fig. 8. SSI with $v = 0.5$, $p = 1/2$, $\alpha = 0.8$, $\gamma = -0.25$, $\sigma = 0.05$. $\mu = 0.5$. Again, the oblique motion is due to (247) and there is the soliton breathing.

analysis. One important aspect to note again is that the solitons undergo an oblique motion because of (247). In Hamiltonian perturbations, the amplitude and the frequency of the solitons do not change adiabatically due to the perturbations, however, the center of the soliton undergoes a shift during motion as dictated by (247). Also, one can see the soliton breathing in the numerical simulations. It is guessed that the breathing of the solitons, for parabolic and dual-power law cases, is due to non-zero v. In the following figure, $v = 0.5$, $p = 1/2$, $\alpha = 0.8$, $\gamma = -0.25$, $\sigma = 0.05$ and $\mu = 0.5$ (Fig. 8).

5. Conclusions

This paper talked about the mechanism of the suppression of the collision of optical solitons during their long-haul transmission across the globe. The types of nonlinearities that were considered were Kerr law, power law, parabolic law as well as the dual-power law. The perturbation terms that were considered were both Hamiltonian as well as non-Hamiltonian types. The quasi-particle theory that was developed in this paper was also supported by numerics. Thus, one can achieve performance enhancement by transmitting more than one soliton, in a juxtaposed position, through an optical fiber without any loss of information along the channel.

Acknowledgement

This research for the first author was fully supported by NSF Grant No: HRD-0630388 and the support is sincerely and genuinely appreciated.

References

[1] A.B. Aceves, C.D. Angelis, G. Nalesso, M. Santagiustina, Higher-order effects in bandwidth-limited soliton propagation in optical fibers, Optics Letters 19 (1994) 2104–2106.
[2] V.V. Afanasjev, Interpretation of the effect of reduction of soliton interaction by bandwidth-limited amplification, Optics Letters 18 (1993) 790–792.
[3] A. Biswas, Soliton–soliton interaction in optical fibers, Journal of Nonlinear Optical Physics and Materials 8 (4) (1999) 483–495.
[4] A. Biswas, Quasi-stationary non-Kerr law optical solitons, Optical Fiber Technology 9 (4) (2003) 224–259.
[5] P.L. Chu, C. Desem, Mutual interaction between solitons of unequal amplitudes in optical fibre, Electronics Letters 21 (1985) 1133–1134.
[6] P.L. Chu, C. Desem, Effect of third order dispersion of optical fibre on soliton interaction, Electronics Letters 21 (1985) 228–229.
[7] C. Desem, P.L. Chu, Soliton interactions in presence of loss and periodic amplification in optical fibers, Optics Letters 12 (1987) 349–351.
[8] P.L. Francois, T. Georges, Reduction of averaged soliton interaction forces by amplitude modulation, Optics Letters 18 (1993) 583–585.
[9] T. Georges, F. Favre, Influence of soliton interaction on amplifier noise-induced jitter: a first-order analytical solution, Optics Letters 16 (1991) 1656–1658.
[10] T. Georges, F. Favre, Modulation, filtering and initial phase control of interacting solitons, Journal of Optical Society of America B 10 (1993) 1880–1889.
[11] J.P. Gordon, Interaction forces among solitons in optical fibers, Optics Letters 8 (1983) 596–598.
[12] A. Hasegawa, Y. Kodama, Solitons in Optical Communications, Oxford University Press, 1995.
[13] B. Hermansson, D. Yevick, Numerical investigation of soliton interaction in optical fibers, Electronics Letters 19 (1983) 570–571.
[14] V.I. Karpman, V.V. Solov'ev, A perturbational approach to the two-soliton systems, Physica D 3 (1981) 487–502.
[15] Y. Kodama, K. Nozaki, Soliton interaction in optical fibers, Optics Letters 12 (12) (1987) 1038–1040.
[16] Y. Kodama, M. Romagnoli, S. Wabnitz, Soliton stability and interaction in fiber lasers, Electronics Letters 28 (21) (1992) 1981–1983.
[17] Y. Kodama, S. Wabnitz, Reduction of soliton interaction forces by bandwidth limited amplification, Electronics Letters 27 (21) (1991) 1931–1933.
[18] Y. Kodama, S. Wabnitz, Physical interpretation of reduction of soliton interaction forces by bandwidth limited amplification, Electronics Letters 29 (2) (1993) 226–227.
[19] Y. Kodama, S. Wabnitz, Reduction and suppression of soliton interaction by bandpass filters, Optics Letters 18 (16) (1993) 1311–1313.
[20] Y. Kodama, S. Wabnitz, Analysis of soliton stability and interactions with sliding filters, Optics Letters 19 (3) (1994) 162–164.

[21] M. Nakazawa, H. Kubota, Physical interpretation of reduction of soliton interaction forces by bandwidth limited amplification, Electronics Letters 28 (1992) 958–960.
[22] E. Shiojiri, Y. Fuji, Transmission capability of an optical fibre communication system using index nonlinearity, Applied Optics 24 (1985) 358–360.
[23] I.M. Uzunov, V.D. Stoev, T.I. Tsoleva, *N*-soliton interaction in trains of unequal soliton pulses in optical fibers, Optics Letters 17 (1992) 1417–1419.
[24] I.M. Uzunov, V.D. Stoev, T.I. Tsoleva, Influence of the initial phase difference between pulses on the *N*-soliton interaction in trains of unequal solitons in optical fibers, Optics Communications 97 (5–6) (1993) 307–311.
[25] I.M. Uzunov, M. Gölles, L. Leine, F. Lederer, The effect of bandwidth limited amplification on soliton interaction, Optics Communications 110 (3–4) (1994) 465–474.
[26] I.M. Uzunov, R. Muschall, M. Gölles, F. Lederer, S. Wabnitz, Effect of nonlinear gain and filtering on soliton interaction, Optics Communications 118 (5–6) (1995) 577–580.
[27] I.M. Uzunov, V. Gerdjikov, M. Gölles, F. Lederer, On the description of *N*-soliton interactions in optical fibers, Optics Communications 125 (4–6) (1996) 237–242.
[28] I.M. Uzunov, M. Gölles, F. Lederer, Enhanced sideband instability in soliton transmissions with semiconductor optical amplifiers, Optics Letters 22 (18) (1997) 1406–1408.
[29] S. Wabnitz, Control of soliton train, transmission, storage and clock recovery by cw light injection, Journal of the Optical Society of America B 13 (12) (1996) 2739–2749.
[30] Z. Xu, L. Li, Z. Li, G. Zhou, Soliton interaction under the influence of higher-order effects, Optics Communications 210 (3–6) (2002) 375–384.

Available online at www.sciencedirect.com
ScienceDirect
Organic Electronics 8 (2007) 227–240
Organic Electronics
www.elsevier.com/locate/orgel

Interaction of two different frequency photonic crystal waveguide modes through the resonant excitation of modes on off-channel Kerr nonlinear media

A.R. McGurn *

Department of Physics, Western Michigan University, Kalamazoo, MI 49008-5252, USA

Available online 21 July 2006

Abstract

The properties of two photonic crystal waveguide modes at different frequencies that propagate down a straight photonic crystal waveguide are studied for cases in which the two modes interact with off-channel structures composed of Kerr nonlinear dielectric media. The optical nonlinearity of the off-channel structures mediates an interaction between the two modes that allows the modes to modulate the transmission of each other down the waveguide channel. This interaction and mutual modulation is shown to be pronounced in the case when either of the two waveguide modes resonantly excites a localized mode on the off-channel features formed of Kerr nonlinear media. Cases that are considered are a straight linear dielectric media waveguide with off-channel structures formed as: (a) a single off-channel Kerr site that supports a bound localized electromagnetic mode, (b) multiple off-channel Kerr sites that support a bound intrinsic localized electromagnetic mode, and (c) multiple off-channel Kerr sites that support an intrinsic localized mode that in turn interacts with a semi-infinite waveguide of linear dielectric media. In cases (a) and (b) the effects of resonant excitation of single site and intrinsic localized modes in the Kerr medium on the transmission characteristics are determined. In case (c) the effects of resonant excitation of intrinsic localized modes in the Kerr medium on the transmission characteristics of the two waveguide modes into the infinite and semi-infinite waveguides are studied.
© 2006 Elsevier B.V. All rights reserved.

PACS: 42.70.Qs; 42.81.Dp; 05.45.Yv

Keywords: Photonic crystal waveguides; Intrinsic localized modes; Discrete breathers

1. Introduction

In this paper a theoretical study of the modes of photonic crystal waveguides [1–28] is presented. The focus is on waveguides of linear dielectric media formed in two-dimensional photonic crystals composed of linear dielectric media [1–7,29], and the goal is to study how waveguide modes at two different frequencies interact with one another when off-channel features formed from Kerr nonlinear dielectric media [30–32] are placed near a waveguide channel. A two-dimensional photonic crystal is a periodic array of infinitely long parallel axis dielectric cylinders of circular cross section that are arranged on a two-dimensional periodic lattice

* Tel.: +1 269 387 4950; fax: +1 269 387 4939.
E-mail address: arthur.mcgurn@wmich.edu

1566-1199/$ - see front matter © 2006 Elsevier B.V. All rights reserved.
doi:10.1016/j.orgel.2006.06.008

[1–7,29]. The resulting photonic crystal exhibits a set of frequency pass or stop bands such that light moving in the plane of the lattice either passes through the crystal or is stopped from passing through the crystal depending upon its frequency. Waveguides are introduced into the photonic crystal by replacing a row of its cylinders with cylinders having dielectric properties that confine electromagnetic modes to propagate along the channel (in the plane perpendicular to the cylinder axes) at frequencies in the stop bands of the modes of the bulk photonic crystal [6–17,20–28].

Popular geometries that are treated in the study of photonic crystal waveguides are: (a) sharp waveguide bends [4,5,13,20–23,27], (b) waveguide branchings and couplings of different waveguide channels through various types of joining mechanisms [19–23,25–28], and (c) the interaction of waveguides with off-channel features [13,16–18,26,33–39]. The focus of interest in these structures is for possible applications in photonic or electro-optical designs [40] and the extension of the study of layered optical systems [31,41] to more topologically complex cases.

The interaction of waveguide modes with off-channel features [13,16–18,26,33–39,42–45] was first studied in detail by Noda et al. [16,17] for systems made from linear dielectric media. (See also Refs. [36,37] for some more recent work by others on this problem.) The focus was on the application of the resonant interaction of waveguide modes with localized modes bound on an off-channel site as a means of selectively removing energy from the waveguides and for frequency multiplexing from waveguide channels. For these studies the photonic crystal, the waveguide, and the off-channel sites were all made of linear dielectric media. Simulation studies were shown to give good agreement with experimental data from a variety of waveguide designs. Later the theoretical studies were extended by Cowan and Young [18] and by McGurn [26] to treat the resonant properties of off-channel sites formed of nonlinear media. These studies are based in part on analytical methods. The transmission coefficients of a single waveguide mode were shown to exhibit optical bistability properties arising from the Kerr nonlinearity of the off-channel site. The optical bistability corresponds to multiple solutions for the resonantly excited modes on the off-channel site. In the work of McGurn [26] more complex off-channel features than single site impurities were treated. These included multiple sites that support resonantly excited intrinsic localized modes, and single and multiple sites that connect to a second semi-infinite waveguide. In these later systems transmission into both the infinite waveguide channel and the semi-infinite channel occur. In addition to this analytical work, some other analytical and simulation studies have also recently addressed the optical bistability of nonlinear photonic crystals with linear impurities, nonlinear impurities in photonic crystal waveguides, and more recently nonlinear off-channel features [38,39]. All of the above work treated a single frequency waveguide mode.

In the present work, the interest in off-channel features of Kerr nonlinear media is that the field dependence of their dielectric properties allows two different frequency waveguide modes to interact with one another by a modulation of the site dielectric properties [18,26,30–32]. This modulation can be enhanced in frequency regions at which localized modes on the off-channel features are resonantly excited by one or both of the waveguide modes. In such regions the two waveguide modes can substantially affect one another's propagation down the waveguide formed of linear dielectric media. For example one mode can be used to switch on or off the other mode's propagation down the channel or be used to impress an amplitude modulation on the other. Such an amplitude modulation can be amplified in the waveguide mode to which it is transferred. The two modes can also be used to modulate the intensity of a localized mode bound to the off-channel feature or to transfer a signal to a second waveguide that also interacts with the Kerr off-channel features.

Three different types of off-channel features are treated in this paper. In a first study a single off-channel site of Kerr nonlinear media is treated. This involves an extension of the theory presented in Ref. [26] which was used to study the interaction of a single waveguide mode in the system. A second treatment deals with a cluster of off-channel Kerr sites [26]. In this system the waveguide modes can excite an intrinsic localized mode [14,15,24–28] on the off-channel cluster. In a third treatment a second waveguide of linear dielectric media interacts with the cluster of off-channel Kerr sites so that waveguide modes interacting with the Kerr features can scatter into either the first or second waveguide channels [26]. All of these treatments are, then, extensions of work originally presented in Ref. [26] for waveguide systems propagating a single frequency waveguide mode to now consider two different

interacting frequency modes. For all of the systems studied the emphasis will be on computing the transmission characteristics of the waveguide modes scattering from the Kerr nonlinear media features and the fields resonantly excited on the off-channel Kerr media [26]. For all of the calculations presented a difference equations approach for the description of the electromagnetic modes of the waveguides and off-channel features is used [24,27]. It is based on rewriting the Maxwell's equations for photonic crystals containing waveguide and off-channel features in an integral equation formulation and noting that under certain circumstances the integral equations reduce to a set of difference equations for the electromagnetic fields. This formulation has been discussed in detail in Refs. [24–28] for a square lattice photonic crystal with waveguides along the $[1,0]$ or $[0,1]$ directions for electromagnetic modes with the electric field polarized parallel to the cylinder axes.

The form of the resulting difference equations is

$$E_{n,0} = \gamma[aE_{n,0} + b(E_{n+1,0} + E_{n-1,0})]. \quad (1)$$

In Eq. (1) the waveguide is along the x-axis (i.e., the $[1,0]$ direction of the square lattice) so that $(n,0)$, for n an integer, labels channel sits in the x–y plane, and $E_{n,0}$ is the field in the $(n,0)$ site. The coefficients γ, a, b are defined in Ref. [26]. The factor γ is proportional to the dielectric contrast $\delta\epsilon_{00}$ defined as the dielectric constant of the new dielectric material contained in the replacement cylinders of the waveguide channel subtract the dielectric constant of the material in the original cylinders of the photonic crystal [24,27,28]. The couplings a and b are related, respectively, to averages of the Green's functions (i.e., the Greens functions of the Helmholtz operator describing the electric fields of the modes of the pure photonic crystal) over the same replacement channel site and between closest neighboring replacement channel sites. The couplings a and b depend on the frequency ω and the geometric properties of the bulk photonic crystal. Substituting a plane wave form $E_{n,0} \propto e^{ikn}$ in Eq. (1) gives the dispersion

$$1 = \gamma[a + 2b\cos k] \quad (2)$$

relating a, b, γ and k.

In the solutions presented later, a and b are evaluated at frequencies, ω, in the stop band of a specific realization of a square lattice photonic crystal [24–28] having a lattice constant denoted a_0. The numerical values of a, b, and ω are taken from Refs. [27,28] for the particular bulk photonic crystal that was used in the studies presented in Refs. [14,24–28]. In the following, two waveguide frequencies modes that occur in the same stop band are considered. These have frequencies $\omega_1 a_0/2\pi c = 0.440$ with wavenumber $k_1 = 2.5$ and $\omega_2 a_0/2\pi c = 0.431$ with wavenumber $k_2 = 1.8$. (Note that in the following we add subscripts 1 and 2 on ω, a, b, and k to distinguish the two different waveguide modes.) In this system the relevant parameters of a and b for our considerations are the ratios $b_1/a_1 = 0.0852$, $a_2/a_1 = 0.8953$, and $b_2/a_1 = 0.0701$. These ratios are all that are needed to generate the data presented later in the figures of this paper. For brevity, the reader is referred to the above cited works (and in particular Refs. [27,28]) for the details of the photonic crystal geometry and the generation of the numerical values of the a's and b's. We also note that the value of the parameter γ is taken to be the same for both of the close in frequency modes ω_1 and ω_2 and is determined from the algebraic conditions [24–28] for the existence of a non-zero solution of Eq. (1) for the fields, $\{E_{n,0}\}$. This is also explained in detail in Ref. [24–28].

The order of this paper is as follows: in Section 2 the problem of a waveguide interacting with an off-channel Kerr site is discussed. A number of analytic results are presented showing the bistability properties of the fields and transmission coefficients. In Section 3 the problem of a waveguide interacting with a cluster of off-channel Kerr sites is discussed. The system is shown to exhibit resonance excitation of intrinsic localized modes on the off-channel cluster sites that are associated with transmission anomalies of the waveguide modes. In Section 4 a second waveguide channel is made to interact with the off-channel cluster. The transmission between the various waveguide channels is found to be sharply modulated by the ability to excite intrinsic localized modes on the Kerr components. In Section 5 conclusions are presented.

2. Off-channel site

We consider a straight photonic crystal waveguide of linear dielectric media interacting with a single off-channel site of Kerr nonlinear dielectric medium [18,26]. The waveguide channel is along the x-axis and the off-channel site is located at $(0,m)$ for some $m > 0$. (Fig. 1a presents a schematic figure of the waveguide and off-channel site.) The coupling of the waveguide to the off-channel site

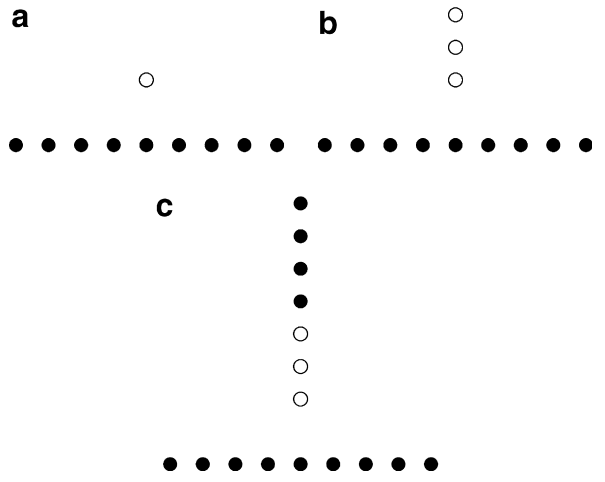


Fig. 1. Schematic plots of (a) A straight infinitely long waveguide of linear dielectric media (closed circles) and an off-channel Kerr impurity (open circle). (b) A straight infinitely long waveguide of linear dielectric media (closed circles) and a cluster of three off-channel Kerr impurity sites (open circles). (c) A straight infinitely long waveguide of linear dielectric media (closed circles) and a cluster of three off-channel Kerr impurity sites (open circles) that in turn connect to a semi-infinite waveguide channel of linear dielectric media (closed circles). Note that only the waveguide channel and off-channel impurity sites are shown. The dielectric cylinders forming the bulk of the photonic crystal are not shown. See Ref. [26] for more details regarding the geometry of the systems used to provide the numerical illustrations of the theory presented in this paper.

can be increased or decreased by changing the separation of the off-channel site and waveguide channel. Modes of two different frequencies ω_1 and ω_2 are sent down the waveguide from infinity and scatter at the off-channel site. The two modes are coupled to one another and to modes localized on the off-channel site through the Kerr nonlinearity of the off-channel site. In the following, the transmission and reflection of the two waveguide modes from the off-channel site are studied along with the fields of the modes resonantly excited at the off-channel site.

The set of difference equations for the fields $E_{i,j}(\omega_1)$ of the mode of frequency ω_1 and the fields $E_{i,j}(\omega_2)$ of the mode of frequency ω_2 are of the form [27]:

$$E_{n,0}(\omega_l) = \gamma_l[a_l E_{n,0}(\omega_l) + b_l(E_{n+1,0}(\omega_l) + E_{n-1,0}(\omega_l))] \tag{3}$$

for $l = 1$ or 2 if $n \leqslant -1$ or if $n \geqslant 1$, with the coupling of the $(0,0)$ waveguide site to the $(0,m)$ off-channel site described by

$$E_{0,0}(\omega_l) = \gamma_l[a_l E_{0,0}(\omega_l) + b_l(E_{1,0}(\omega_l) + E_{-1,0}(\omega_l))] + \gamma_{pl} c_l\Big[1 + \lambda(d_l|E_{0,m}(\omega_l)|^2 + e_l|E_{0,m}(\omega_{l'})|^2)\Big]E_{0,m}(\omega_l), \tag{4}$$

$$E_{0,m}(\omega_l) = \gamma_{pl} a_l\Big[1 + \lambda(d_l|E_{0,m}(\omega_l)|^2 + e_l|E_{0,m}(\omega_{l'})|^2)\Big] \times E_{0,m}(\omega_l) + \gamma_l c_l E_{0,0}(\omega_l) \tag{5}$$

for $(l,l') = (1,2)$ or $(2,1)$. Here $\gamma_1 = \gamma(\omega_1)$, $\gamma_2 = \gamma(\omega_2)$, $a_1 = a(\omega_1)$, $a_2 = a(\omega_2)$, $b_1 = b(\omega_1)$, $\gamma_{p1} = \gamma_p(\omega_1)$, $\gamma_{p2} = \gamma_p(\omega_2)$, etc., and for simplicity when treating ω_1 and ω_2 modes close in frequency $\gamma_1 = \gamma_2 = \gamma$. The result is a set of six difference equations describing the propagation of the two frequency modes down the waveguide.

The incident, reflected, and transmitted fields in the waveguide channel are taken to have planewave forms. Consequently, $E_{n,0}(\omega_l) = u_l e^{ik_l n} + v_l e^{-ik_l n}$ for $n \leqslant 0$, $E_{n,0}(\omega_l) = t_l e^{ik_l n}$ for $n \geqslant 0$, and on the off-channel site $E_{0,m}(\omega_l) = s_l$ for $l = 1$ or 2. In this notation the solutions for the transmission coefficient (i.e., $T_l = |t_l/u_l|^2$) and reflection coefficient (i.e., $R_l = |v_l/u_l|^2$) are

$$T_l = \frac{4\sin^2 k_l}{4\sin^2 k_l + \left[\frac{c_l}{b_l}(r_l - \gamma_l c_l)(1 + 2\frac{b_l}{a_l}\cos k_l)\right]^2} \tag{6}$$

and

$$R_l = \frac{\left[\frac{c_l}{b_l}(r_l - \gamma_l c_l)(1 + 2\frac{b_l}{a_l}\cos k_l)\right]^2}{4\sin^2 k_l + \left[\frac{c_l}{b_l}(r_l - \gamma_l c_l)(1 + 2\frac{b_l}{a_l}\cos k_l)\right]^2} \tag{7}$$

for $l = 1$ or 2. In Eqs. (6) and (7), $r_1 = s_1/t_1$ is a solution of

$$d_1\lambda|t_1|^2|r_1|^2 r_1 + \left[1 + \lambda|t_2|^2 e_1|r_2|^2 - \frac{1}{\gamma_{p1}a_1}\right]r_1 + \frac{\gamma_1 c_1}{\gamma_{p1}a_1} = 0, \tag{8}$$

where t_1 is the amplitude of the transmitted field of frequency ω_1, and $r_2 = s_2/t_2$ is a solution of

$$d_2\lambda|t_2|^2|r_2|^2 r_2 + \left[1 + \lambda|t_1|^2 e_2|r_1|^2 - \frac{1}{\gamma_{p2}a_2}\right]r_2 + \frac{\gamma_2 c_2}{\gamma_{p2}a_2} = 0, \tag{9}$$

where t_2 is the amplitude of the transmitted field of frequency ω_2. Eqs. (8) and (9) are a set of nonlinear coupled equations that represent the interaction of the two waveguide modes at the off-channel site. For the results presented below t_1 and t_2 are taken

to be real, but this is not an essential restriction in applying the above equations.

Before discussing the solutions of the above set of equations for two interacting waveguide modes, it is useful to summarize the results for a single mode [26]. In this case the field amplitudes u_1, v_1, r_1, t_1 describing the ω_1 mode are non-zero and the field amplitudes u_2, v_2, r_2, t_2 describing the ω_2 mode are zero. In Ref. [26] the solution of a single frequency mode was presented. The transmission in Fig. 2b of Ref. [26] for the single mode problem given as a function of the ratio $g = \gamma_p/\gamma$ of the channel parameter γ divided into the off-site parameter γ_p is very similar to the result, presented later in this paper in Fig. 2a, for the ω_1 mode transmission in a case of weak interaction with the ω_2 mode. (Note: in Ref. [26] only one frequency mode was present so no numerical subscripts on γ_p and γ were needed.) It is essentially a type of bistable resonance, and the transmission coefficient of the mode is greatly modified by the mode's interaction with the off-channel site.

The presence of a second mode (at ω_2) in the system allows for new features to appear in the transmission coefficient of the ω_1 mode. These features arise from the change in the dielectric properties of the off-channel site caused by the ω_2 mode fields and can become very large at a scattering resonance of the ω_2 mode with the off-channel site. As will be seen in the later discussions a number of topographical features occur in the ω_1 transmission due to the presence and relative positions in frequency of the resonant scattering of the ω_1 and ω_2 modes with the off-channel site. These can include peaks, dips, and slices that are found in the ω_1 transmission coefficient as a function of $g = \gamma_{p1}/\gamma_1$. To illustrate these affects we treat a simple case of the solutions to Eqs. (3)–(9) in which ω_1 and ω_2 are closely spaced in the same stop band of the photonic crystal. In addition, as the ω_1 mode is our primary focus, Eq. (8) will be treated in the full nonlinearity. The ω_2 mode is, however, of secondary interest so that Eq. (9) will be treated in the linear ($e_2 = d_2 = 0$) limit. This simplifies the numerical solution of Eqs. (8) and (9) but does not affect the semi-quantitative nature of T_1 and R_1 for ω_1 interacting with ω_2 via the off-channel nonlinearity.

In Fig. 2 results are presented for the transmission of the ω_1 mode down the waveguide and past the off-channel site in the presence of the ω_2 mode. The plots are of the transmission coefficient of the ω_1 mode versus $g = \gamma_{p1}/\gamma_1$ for $\lambda t_1^2 = \lambda t_2^2 = 0.00025$ for different ratios of $\gamma_{p2}/\gamma_{p1} = 1.0095$, 1.1034, and 1.1552. The interaction of the two modes through the Kerr nonlinearity of the off-channel site is set in strength by the ratio γ_{p1}/γ_{p2}, and the weak coupling of the waveguide to the off-channel site is chosen such that $c_1/a_1 = c_2/a_1 = 0.02$. (Note: This is the same off-channel coupling as used in the studies presented in Ref. [26] and facilitates a comparison with results in that paper.) In Eq. (8) we have taken $d_1 = e_1 = 1$ as the Kerr interaction should be similar in strength (i.e., of the same order of magnitude) for two modes that are close in frequency. With this parameterization the transmission of the ω_1 mode is found under a proper set of conditions to be greatly affected by the resonant scattering of the ω_2 mode by the mode localized on the off-channel site. We shall see that the importance of the interaction of the modes on each other is found to be dependent on the relative positioning of their resonant interactions with the localized modes that they excite on the off-channel site.

Fig. 2a through d plot the transmission of the ω_1 mode for different ratios $\gamma_{p2}/\gamma_{p1} = 1.0095$, 1.1034, and 1.1552. These different values of γ_{p1}/γ_{p2} correspond, respectively, to different values of $g = 0.955$, 0.874, 0.835 at which the ω_2 mode resonantly scatters from the modes on the off-channel site. The field generated in the off-channel site by resonant excitation with the ω_2 mode changes the Kerr contribution to the dielectric constant of the off-channel site as seen by the ω_1 mode. This affects the ω_1 mode transmission most when the value of g at which the ω_2 resonance occurs is in a region of g for which the ω_1 transmission coefficient is bistable, i.e., for $g = 0.835$. Fig. 2e shows the resonant transmission versus $g = \gamma_{p1}/\gamma_1$ of the ω_2 mode for the three ratios of γ_{p2}/γ_{p1} mentioned above. In each case the ω_2 mode is transmitted down the channel without interference except at the resonant scattering with the off-channel site. Here the transmission of the ω_2 mode is greatly reduced. The transmission of the ω_2 mode does not exhibit bistability as $d_2 = e_2 = 0$.

In Fig. 2a results are shown for the transmission of the ω_1 mode for $\gamma_{p1}/\gamma_{p2} = 1.0095$. The resonant scattering of the ω_2 mode for this case occurs at $g = 0.955$. This is greater than the g value of the resonance in the ω_1 mode and above the range in g of the ω_1 mode bistability. The plot in Fig. 2a displays the characteristic bistability of the transmission plots presented in Ref. [26] for a single frequency waveguide mode incident on the off-channel site. In fact, the effect of the ω_2 mode on the ω_1 resonant

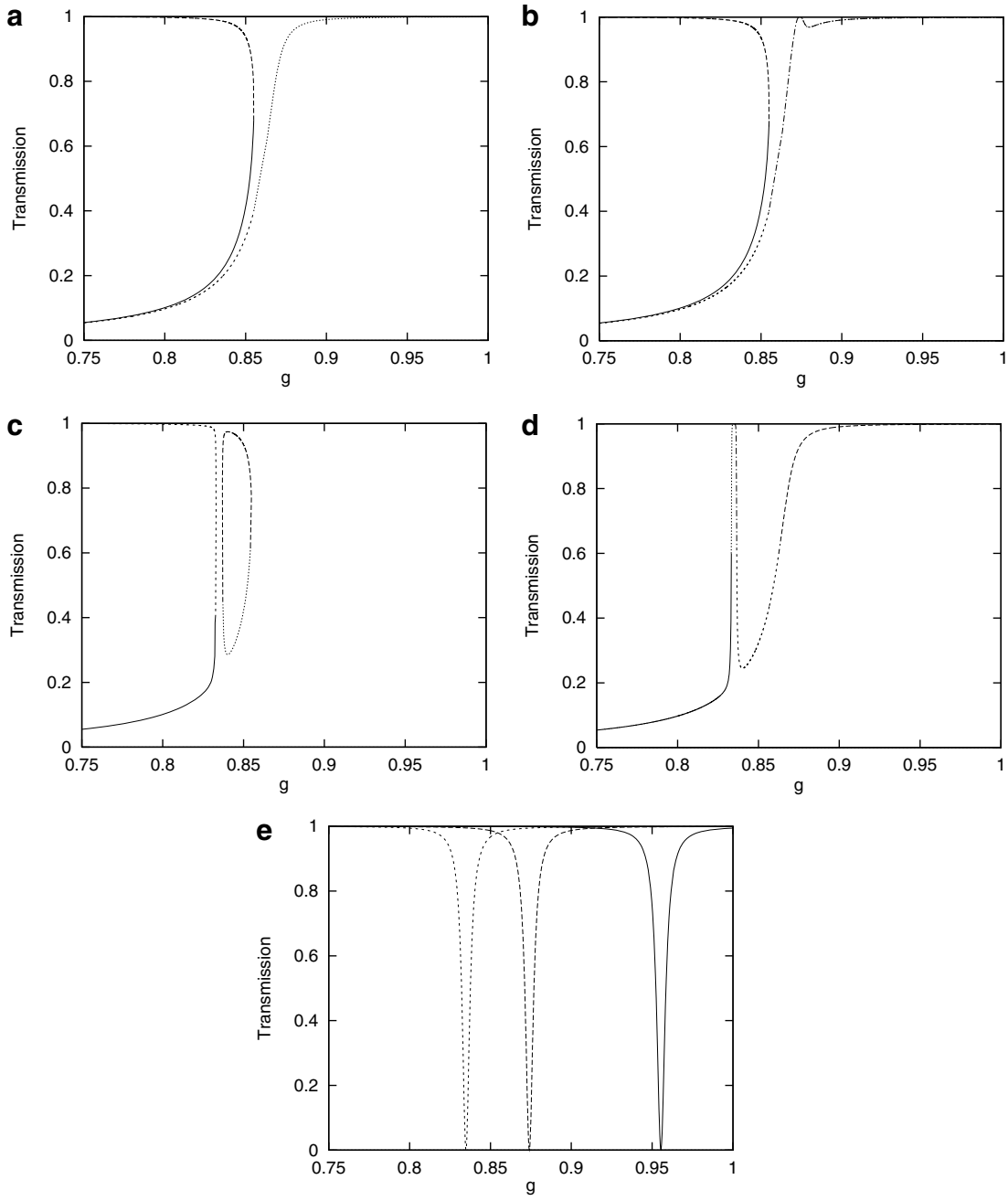


Fig. 2. Plot of the transmission coefficient of the ω_1 mode versus $g = \gamma_{p1}/\gamma_1$ for a waveguide interacting with a Kerr off-channel site. Results are shown for $\gamma_{p2}/\gamma_{p1} =$ (a) 1.0095, (b) 1.1034, (c) 1.1552, and (d) 1.1552. Results for the linear system are presented in (e) showing the linear resonances in the ω_2 mode transmission at $g = 0.955$, 0.874, and 0.835 corresponding to $\gamma_{p2}/\gamma_{p1} = 1.0095$, 1.1034, and 1.1552.

scattering is so small in Fig. 2a that Fig. 2a cannot be distinguished from the transmission plot found in Fig. 2b of Ref. [26] for a single ω_1 mode. For the transmission plot of the ω_1 mode presented in Fig. 2b, $\gamma_{p2}/\gamma_{p1} = 1.1034$. For this case the resonant scattering of the ω_2 mode is seen in Fig. 2e to occur at $g = 0.874$. The resonance in ω_2 affects the transmission of the ω_1 mode only in the neighborhood of $g = 0.874$. This is above and close in g to the position of the resonance of the ω_1 mode but above the region of bistability of the ω_1 mode. Due to its closer proximity to the ω_1 resonance, the effects on the

scattering are greater than those found in Fig. 2a. However, they are not dramatic. The greatest effect on the ω_1 scattering of the ω_2 scattering resonance is found when the resonance occurs in the region of optical bistability of the ω_1 mode. In Fig. 2c and d results are presented for the transmission of the ω_1 mode for $\gamma_{p2}/\gamma_{p_1} = 1.1552$. In this case the resonance in the scattering of the ω_2 mode occurs at $g = 0.835$ which is in the region of ω_1 bistability. For this case the results for the ω_1 mode have been presented on two plots (Fig. 2c and d) that separate the bistable branches of the transmission into results evolving from the left branch in Fig. 2a (results in Fig. 2c) and results evolving from the right branch in Fig. 2a (results in Fig. 2d). In Fig. 2c the region on the left hand side of Fig. 2a that was simply connected has evolved into a two separate simply connected regions. The resonance at $g = 0.835$ has sliced off the two separate simply connected pieces. In Fig. 2d the resonance at $g = 0.835$ has similarly sliced what was a simply connect region into two separate simply connected regions. Since the large effects on the ω_1 transmission are in Fig. 2c and d, we now focus on the properties of the system in this region.

In Fig. 3 results are presented for the field, $r_1 = s_1/t_1$, excited by the ω_1 mode on the off-channel site versus g. The results are for $\gamma_{p2}/\gamma_{p1} = 1.1552$ and correspond to the scattering in Fig. 2c and d. In the plot the field, s_1, is normalized by the transmission amplitude t_1. The positive values of r_1 are for the results presented in Fig. 2c and the negative values of r_1 are for the results in Fig. 2d. The results for $|r_1|$ closest to zero give transmission coefficients near one, while the larger values of $|r_1|$ give small values of the transmission coefficients. The various elements in the bistable scattering observed in Fig. 2c and d can be easily unraveled by using these two last results to correlate r_1 with the transmission as a function of g. In the absence of the ω_2 scattering resonance the slices in the r_1 plots occurring at $g = 0.835$ close up so that the scattering of a single ω_1 mode has one single valued negative r_1 branch and one double valued positive r_1 branch. It is seen from these results that the bistability in the transmission plots in Fig. 2c and d are results of multiple solutions for the resonant fields, r_1, at the impurity site. These multiple solutions for r_1 as functions of g can in turn be significantly affected by changes in the dielectric properties of the off-channel site arising from the r_2 field.

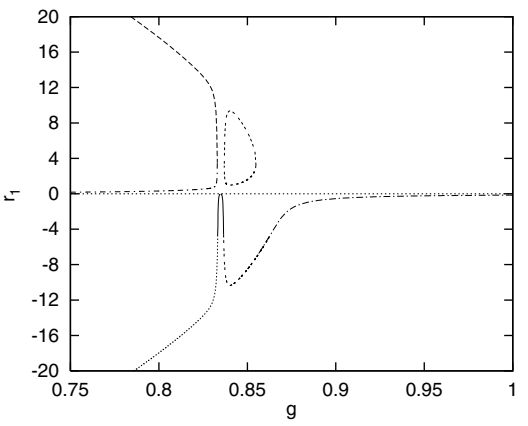


Fig. 3. Plot of r_1 versus $g = \gamma_{p1}/\gamma_1$ for $\gamma_{p2}/\gamma_{p1} = 1.1552$ corresponding to the transmission results shown in Fig. 2c and d.

For two signals of different frequencies sent down the waveguide it is interesting to determine how a small intensity modulation in one signal affects the intensity of the other. This can be done by computing $\frac{\partial|t_1|^2}{\partial|u_2|^2}\Big|_{|u_1|^2}$ where u_1 and u_2 are the incident amplitudes of the modes of frequency ω_1 and ω_2. This gives, for a fixed intensity of the incident ω_1 mode, the rate of change of the intensity of the transmitted ω_1 mode with respect to changes in the intensity of the incident ω_2 mode. A closed form solution for $\frac{\partial|t_1|^2}{\partial|u_2|^2}\Big|_{|u_1|^2}$ can be given as an algebraic expression in the parameters of our theory. (Due to space limitations this was removed from here, but may be presented later as part of another work.) Fig. 4 presents results for this rate as a function of g, considering the case in which $\gamma_{p2}/\gamma_{p1} = 1.1552$ for

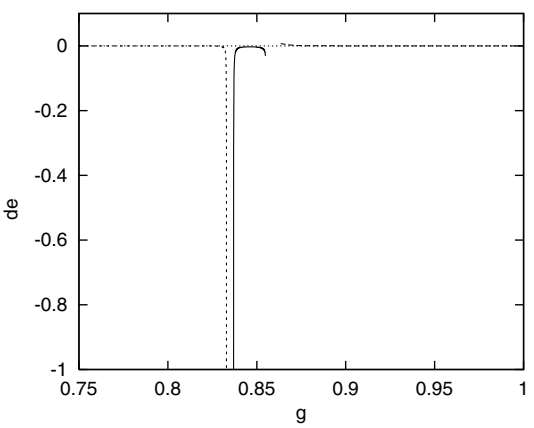


Fig. 4. Plot of $de = \frac{\partial|t_1|^2}{\partial|u_2|^2}\Big|_{|u_1|^2}$ versus g for the transmission results closest to unit transmission in Fig. 2c and d. This describes the amplification of an amplitude modulated signal in the ω_2 mode as it is passed to the ω_1 mode.

the modes in Fig. 2c and d that are closest to a transmission of unity. The modulation is found to be greatest in the vicinity of the ω_2 resonance. It is seen that for a large enough ω_2 resonance, the amplitude modulation in ω_1 can be amplified over that observed in the incident ω_2 mode.

For the results presented earlier, the field on the off-channel site from the ω_2 mode is given by

$$s_2 = \gamma_2 c_2 t_2/(\gamma_{p2} a_2 - 1). \tag{10}$$

This field has a small region in which it exhibits an unphysical singularity at $\gamma_{p2} a_2 = 1$. In a real system the resonantly excited field would be bounded by nonlinear and dissipative effects so that it would become large but bounded. To simulate the effects of a bounded s_2, Eq. (10) can be rewritten to be of the form

$$s_2 = \gamma_2 c_2 t_2 \frac{\gamma_{p2} a_2 - 1}{(\gamma_{p2} a_2 - 1)^2 + \delta^2}, \tag{11}$$

where δ is a parameter that is only important near $\gamma_{p2} a_2 = 1$. This Lorentzian form is of a standard type that one would expect of a bounded resonance and can be view as a type of phenomenological treatment of the resonance. We shall use Eq. (11) to determine the effects of various degrees of limitations on the intensity of r_2 at its resonance.

In Fig. 5 results are presented for the transmission versus g for the system in Fig. 2c and d with Eq. (10) replaced by Eq. (11). Results are shown for $\delta = 0.0$, 0.0012, 0.0015, and 0.002 where $\delta = 0.0$ reproduces the results in Fig. 2c and d. The slicing of the transmission data in Fig. 2c and d due to the unbounded resonant excitation of r_2 is now seen to be changed into regions of rapid change in the transmission as a function of g. The results in Fig. 2c and d represent extrema that the system would evolve into depending on the Q-fact of the ω_2 resonant scattering. The behavior of

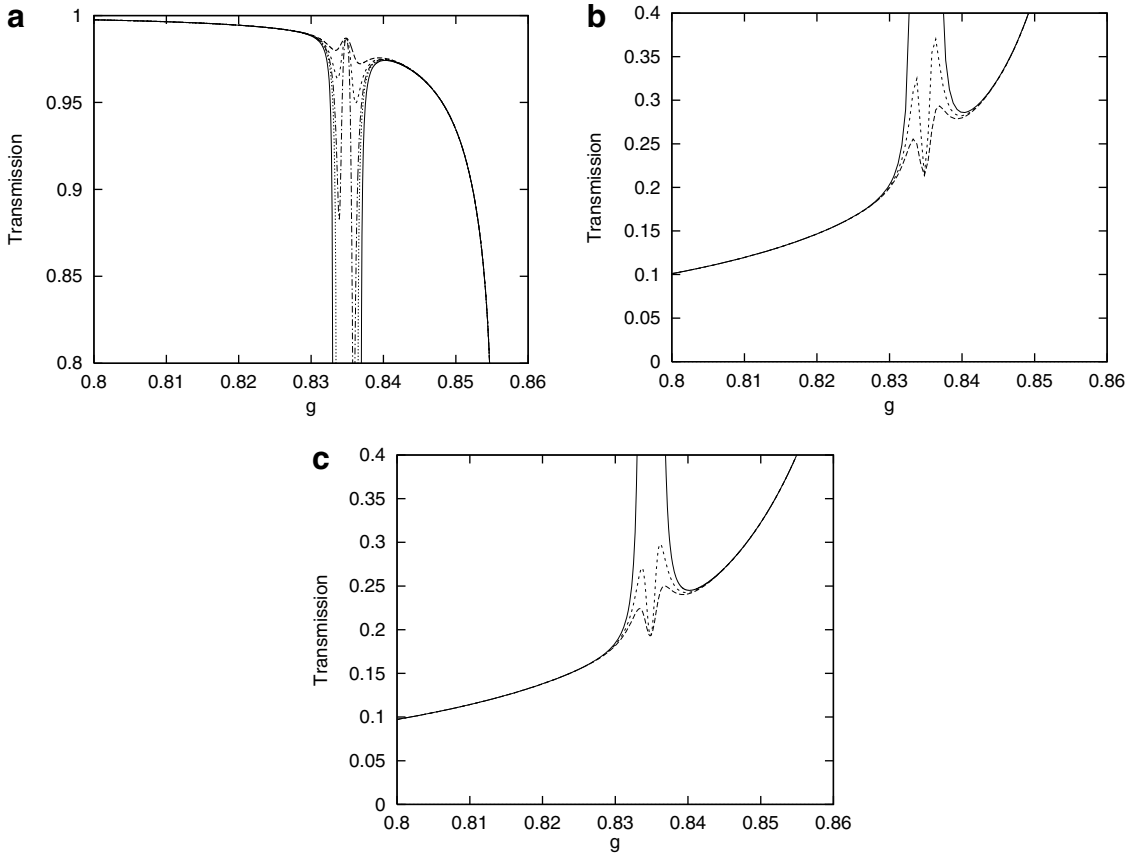


Fig. 5. Plot of the transmission of the ω_1 mode versus g for the system in Fig. 2c and d with Eq. (11) incorporated into the formulation in place of Eq. (10). Results are shown for $\delta = 0.0$, 0.0012, 0.0015, and 0.002. As δ increases from zero the results are found to be increasingly changed from the $\delta = 0.0$ results originally presented in Fig. 2c and d. The results in (a) and (b) are modifications from Fig. 2c and the results in (c) are modifications from Fig. 2d.

experimental systems should range between the results in Figs. 2 and 5.

3. Multiple off-channel sites

In this section the off-channel site problem is modified to treat multiple off-channel sites formed of a Kerr nonlinear dielectric medium [26]. A cluster of a linear array of three off-channel sites is considered [26]. The off-channel cluster is formed in a direction perpendicular to the waveguide and consists of three identical nearest neighbor sites that are weakly connected to the waveguide at the Kerr site closest to the waveguide channel. (See Fig. 1b for a schematic.) This system is of interest because the cluster can support an intrinsic localized mode, and resonant scattering of a waveguide mode from the intrinsic localized mode can be observed. When two waveguide modes of frequencies ω_1 and ω_2 are present the resonant interaction can be easily detuned through the interaction of the ω_2 mode with the Kerr medium in the off-channel sites. The resultant interaction changes the dielectric constant at the Kerr sites and can be effectively used as a type of switching mechanism, turning on and off the ω_1 mode's resonant interaction with the off-channel site.

The system studied is modified from the one described by Eqs. (3)–(5). In this model the waveguide equations in Eqs. (3) and (4) are the same, but Eq. (5) for the interaction of the off-channel site with the waveguide is replaced by

$$\begin{aligned} E_{0,m}(\omega_l) = \gamma_{pl}\Big\{ & a_l\Big[1+\lambda(d_l|E_{0,m}(\omega_l)|^2+e_l|E_{0,m}(\omega_{l'})|^2)\Big] \\ & \times E_{0,m}(\omega_l)+b_l\Big[1+\lambda(d_l|E_{0,m+1}(\omega_l)|^2 \\ & +e_l|E_{0,m+1}(\omega_{l'})|^2)\Big]E_{0,m+1}(\omega_l)\Big\} \\ & +\gamma_l c_l E_{0,0}(\omega_l), \end{aligned} \tag{12}$$

$$\begin{aligned} E_{0,m+1}(\omega_l) = \gamma_{pl}\Big\{ & a_l\Big[1+\lambda(d_l|E_{0,m+1}(\omega_l)|^2 \\ & +e_l|E_{0,m+1}(\omega_{l'})|^2)\Big]E_{0,m+1}(\omega_l) \\ & +b_l\Big[1+\lambda(d_1|E_{0,m}(\omega_l)|^2 \\ & +e_l|E_{0,m}(\omega_{l'})|^2)\Big]E_{0,m}(\omega_l) \\ & +b_l\Big[1+\lambda(d_1|E_{0,m+2}(\omega_l)|^2 \\ & +e_l|E_{0,m+2}(\omega_{l'})|^2)\Big]E_{0,m+2}(\omega_l)\Big\}, \end{aligned} \tag{13}$$

and

$$\begin{aligned} E_{0,m+2}(\omega_l) = \gamma_{pl}\Big\{ & a_l\Big[1+\lambda(d_l|E_{0,m+2}(\omega_l)|^2 \\ & +e_l|E_{0,m+2}(\omega_{l'})|^2)\Big]E_{0,m+2}(\omega_l) \\ & +b_l\Big[1+\lambda(d_l|E_{0,m+1}(\omega_l)|^2 \\ & +e_l|E_{0,m+1}(\omega_{l'})|^2)\Big]E_{0,m+1}(\omega_l)\Big\} \end{aligned} \tag{14}$$

for $(l,l')=(1,2)$ or $(2,1)$. Here the notation used in Eqs. (3)–(5) has been adopted. The resulting eight difference equations for the resonant scattering from the off-channel intrinsic localized mode are now solved. As in Section 2 the focus of the discussions will be on the ω_1 mode and the changes brought about by its weak interaction with the ω_2 mode. Specifically, we will be interested in the resonant scattering of the ω_1 mode from an intrinsic localized mode it excites in the Kerr off-channel sites and how his resonant scattering is changed by interaction with the ω_2 mode. Consequently, to simplify the presentation later in the treatment of the ω_2 mode we shall approximate $d_2 = e_2 = 0$. This approximation has a very small effect on the quantitative nature of the results presented later.

The solution of the difference equations for the waveguide and multiple off-channel site system is obtained using a method similar to that used in Section 2 and in Ref. [26] where the results for a single ω_1 mode in the absence of a second ω_2 mode were presented for the system in Fig. 1b. Planewave forms are used for the incident, reflected, and transmitted fields in the waveguide channel. The fields in the waveguide and off-channel sites are found as the solutions of a set of coupled polynomial equations (obtained from Eqs. (3), (4), (12), (13), and (14)) that are solved numerically. The transmission and reflection coefficients are expressed in terms of the field amplitudes in the waveguide channel.

In Fig. 6 results are shown for the transmission coefficient of the ω_1 mode versus $g = \gamma_{p1}/\gamma_1$ for $\gamma_{p2} = \gamma_{p1}$. The results shown are for fixed $\lambda|E_{0,m+2}(\omega_1)|^2 = 0.001$ and $\lambda|E_{0,m+2}(\omega_2)|^2 = 0.0$ and 0.0000025 where $d_1 = e_1 = 1.0$. The focus is on the effects of increasing $\lambda|E_{0,m+2}(\omega_2)|^2$ on the transmission coefficient associated with the intrinsic localized mode. The resonance associated with the intrinsic localized mode is observed as a sharp dip in the transmission of ω_1 down the waveguide channel in the region $0.5 < g < 0.6$. (Note: Three additional dips in the transmission are found for $g > 0.7$. These are from Fabry–Perot resonances

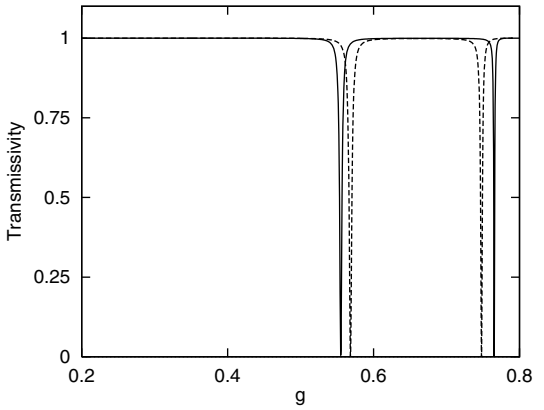


Fig. 6. Plot of the transmission coefficient of the ω_1 mode versus $g = \gamma_{p1}/\gamma_1$ for the off-channel cluster of three Kerr sites. The lowest resonance in g is from the excitation of an intrinsic localized mode and the upper resonance is one of the Fabry–Perot resonances that is renormalized from the $\lambda = 0$ limit. Results are for $\lambda|E_{0,m+2}(\omega_2)|^2 = 0.0$ (solid line) and $\lambda|E_{0,m+2}(\omega_2)|^2 = 0.0000025$ (dashed line). See Fig. 2c of Ref. [26] for the full plot of the transmission in the absence of the ω_2 mode.

that are present in the linear system, i.e., for $\lambda = 0$. The intrinsic localized mode resonance is only present for $\lambda \neq 0$. For a discussion of all of the ω_1 resonances that are present in the system for the resonant scattering of ω_1 in the absences of ω_2 see Ref. [26].) The transmission dip in the region $0.7 < g < 0.8$ is from one of the Fabry–Perot modes that happens to be present in the range of the plot considered.

The transmission of the ω_1 mode down the waveguide as a function of g is found to be sensitive to changes in the intensity of the incident ω_2 field. The presence of the ω_2 mode increases the g at which ω_1 experiences a transmission minima or cutoff due to resonant scattering from the off-channel intrinsic localized mode. This shift is opposite to the shift in g, created by the presence of the ω_2 mode, at which a transmission minima or cutoff in ω_1 arises in Fig. 6 from resonant scattering with the Fabry–Perot mode. Both of these effects have potential switching or amplitude modulating applications for waveguide modes, particularly as the effects shown in this section are much more dramatic than those found in Section 2 for single off-channel sites.

4. Multiple off-channel site with attached semi-infinite waveguide

Not only can off-channel sites be used to modulate the flow of two different waveguide modes through resonant scattering and interactions mediated by their nonlinear dielectric media, but such sites can mediate connections between different waveguide channels [26]. In this section we consider a modification of the problem considered in the previous section. An infinite waveguide of linear dielectric media interacts with three off-channel sites that in turn connect with a semi-infinite waveguide of linear dielectric media. The semi-infinite waveguide is perpendicular to the original infinite waveguide. (See Fig. 1c for a schematic.) Now, associated with the resonant excitation of an intrinsic localized mode and the sharp decrease in the transmission in the infinite waveguide, a transmission peak is observed in the semi-infinite waveguide that can be turned on and off by passing a second, non-resonant, frequency mode down the infinite waveguide.

The equations describing this system are those for the multiple off-channel site problem in the previous section with Eq. (14) replaced by the following three equations [26]:

$$\begin{aligned} E_{0,m+2}(\omega_l) = \gamma_{pl}\Big\{ & a_1\Big[1+\lambda(d_l|E_{0,m+2}(\omega_l)|^2 + e_l|E_{0,m+2}(\omega_{l'})|^2)\Big] \\ & \times E_{0,m+2}(\omega_l) + b_l\Big[1+\lambda(d_l|E_{0,m+1}(\omega_l)|^2 \\ & + e_l|E_{0,m+1}(\omega_{l'})|^2)\Big]E_{0,m+1}(\omega_l)\Big\} \\ & + \gamma_l b_l E_{0,m+3}, \end{aligned} \tag{15}$$

$$\begin{aligned} E_{0,m+3} = {} & \gamma_l[a_l E_{0,m+3}(\omega_l) + b_l E_{0,m+4}(\omega_l)] \\ & + \gamma_{pl} b_l\Big[1+\lambda(d_l|E_{0,m+2}(\omega_l)|^2 \\ & + e_l|E_{0,m+2}(\omega_{l'})|^2)\Big]E_{0,m+2}(\omega_l), \end{aligned} \tag{16}$$

and

$$\begin{aligned} E_{0,m+j} = {} & \gamma_l[a_l E_{0,m+j}(\omega_l) + b_l(E_{0,m+j-1}(\omega_l) \\ & + E_{0,m+j+1}(\omega_l))] \end{aligned} \tag{17}$$

for $j \geqslant 4$. Here again $(l, l') = (1,2)$ or $(2,1)$ and the remaining notation is the same as that used earlier. For the same reasons as in our discussions in the previous two sections we have focused on the ω_1 mode, treating the ω_2 mode in the limit that $d_2 = e_2 = 0$.

The resulting set of difference equations are solve by using standard methods for branching network problems [26]. In the infinite waveguide: $E_{n,0} = u_l e^{ink_l} + r_l e^{-ink_l}$ for $n \leqslant 0$, $E_{n,0} = t_{c,l} e^{ink_l}$ for $n \geqslant 0$. In the semi-infinite waveguide: $E_{0,m+j} = t_{s,l} e^{i(m+j)k_l}$ for $j \geqslant 3$, and in the three Kerr sites $E_{0,m+j} = s_{j,l}\exp(i\theta_{j,l})$ for $j = 0, 1, 2$. Substituting these into the difference equations gives a set of ten nonlinear equations to be solved for all the field amplitudes and phases.

The equations are a set of algebraic forms that exhibit symmetry in the (l, l') set of indices, reducing the set of ten to two sets of five equations that reflect into each other upon rotation of the l and l' indices. (Due to space constraints the list of these algebraic forms has been removed from here. They may be presented elsewhere.) The application of numerical methods yields solutions for $t_{s,l}$, $s_{1,l}$, $s_{0,l}$, $t_{c,l}$, u_l as functions of the waveguide and photonic crystal parameters as discussed below. From these the transmission coefficients in the infinite channel, $|t_{c,l}/u_l|^2$, and the semi-infinite channel, $|t_{s,l}/u_l|^2$, are obtained.

In Fig. 7 results are shown for the transmission coefficient of the ω_1 mode versus $g = \gamma_{p1}/\gamma_1$ for $\gamma_{pl} = \gamma_{p2}$, $e_1 = d_1 = 1$, and $e_2 = d_2 = 0$. The results shown are for fixed $\lambda|E_{0,m+2}(\omega_1)|^2 = 0.001$ and for $\lambda|E_{0,m+2}(\omega_2)|^2 = 0.0$, 0.00001, 0.00009, and 0.00025. In Fig. 7a through c, the structure in the transmission for $g > 0.7$ arises from the interaction with Fabry–Perot modes that are present in the linear system (i.e., for $\lambda = 0$). The structure below $g = 0.7$ arises from resonant interaction with an intrinsic localized mode that is not present in the $\lambda = 0$ limit of the system [26]. Increasing the interaction of the ω_2 mode with the ω_1 mode is seen to push the intrinsic localized mode resonance up into the resonance structure from the Fabry–Perot modes. In Fig. 7d the interaction with the ω_2 has become large enough that the nonlinear resonance coalesces with the Fabry–Perot structure. In Fig. 8 results are presented for the position of the intrinsic localized mode resonance as a function of $\lambda|E_{0,m+2}(\omega_2)|^2$ for the system studied in Fig. 7. It is seen that the g value of the resonance increases with an increasing intensity of the ω_2 fields on the $(0, m+2)$ site.

As in the study of three off-channel Kerr sites treated in Section 3, the systems in Fig. 7 are found to be sensitive to the intensity of the ω_2 waveguide fields. This is particularly true for the case of resonant excitation of an intrinsic localized mode on

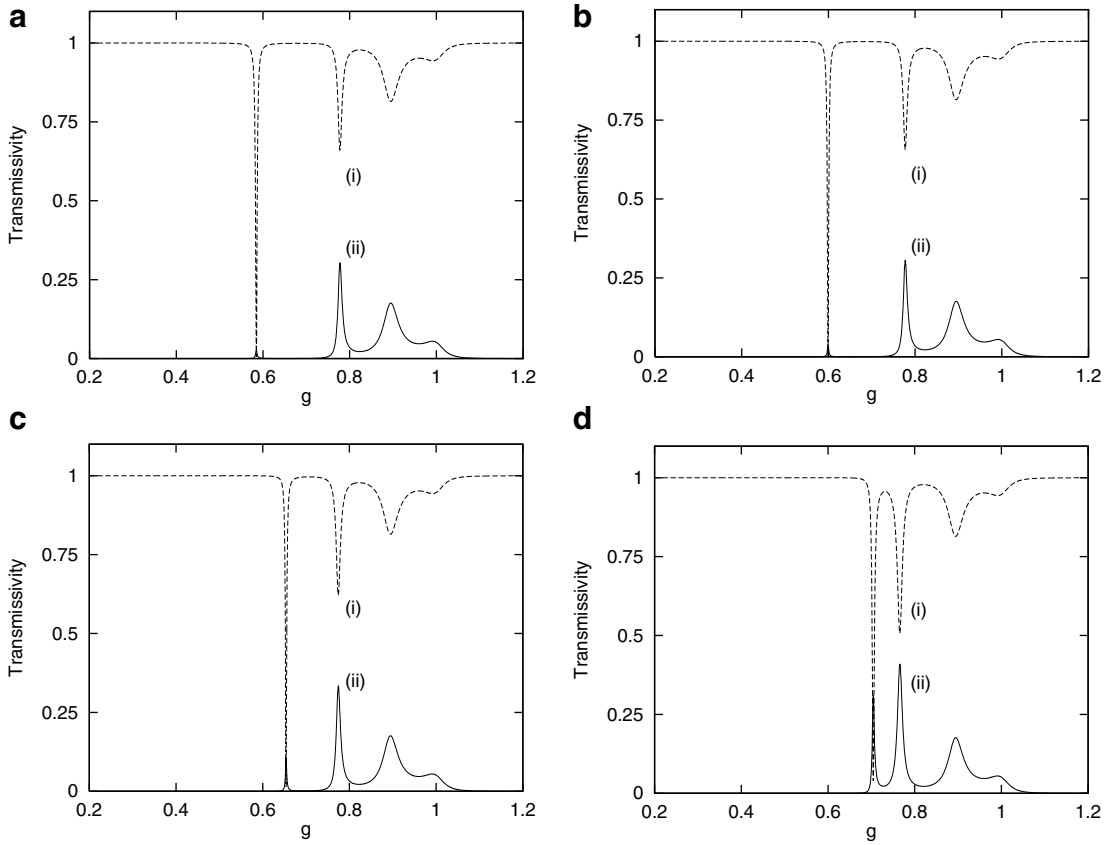


Fig. 7. Plot of the transmission coefficient of the ω_1 mode versus $g = \gamma_{p1}/\gamma_1$ for the off-channel cluster connecting to a semi-infinite waveguide. Results are shown for $\lambda\,|E_{0,m+2}(\omega_2)|^2 =$ (a) 0.0, (b) 0.00001, (c) 0.00009, and (d) 0.00025. The curves labeled (i) are for the transmission into the infinite waveguide, and the curves labeled (ii) are for the transmission into the semi-infinite waveguide.

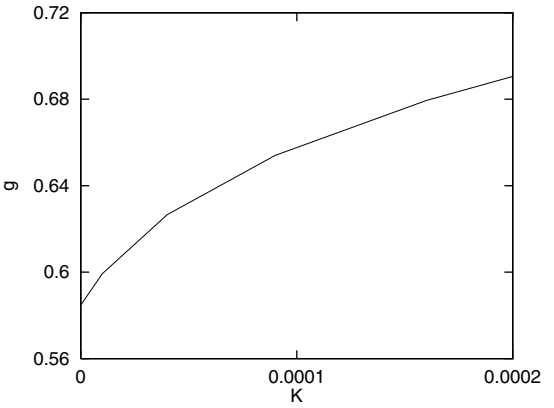


Fig. 8. Plot of $g = \gamma_{p1}/\gamma_1$ at which the intrinsic localized mode resonance occurs as a function of the Kerr term $K = \lambda|E_{0,m+2}(\omega_2)|^2$ for the system in Fig. 7.

the Kerr sites. Here the narrow resonance in g is observed to be easily moved by small ω_2 fields so that the resonant properties of the ω_1 modes quickly change. The resonant interaction of the ω_1 mode with Fabry–Perot modes is less sensitive to the presence of the ω_2 mode and has less potential applications for the switching of waveguide modes between different waveguide channels.

5. Conclusions

A theory is presented for waveguide modes of two different frequencies (ω_1 and ω_2) that travel down a single waveguide and interact with one another due to Kerr nonlinear media off-channel features. The waveguide modes also resonantly excite localized modes on the Kerr off-channel media and this resonant excitation can be used to enhance the interaction of the two waveguide modes with one another or to modulate the fields on the off-channel features.

The treatment is based on a difference equations approach that was used in Ref. [26] to study the behavior of a single waveguide mode of frequency ω_1 interacting with various Kerr off-channel features. (The difference equation approach is an alternative to computer simulations based on finite-difference time-domain methods or finite element approaches [46–50], examples of which were cited in the introduction to this paper. The difference equation approach allows for the expression of the properties of the system in terms of closed formed algebraic expressions.) For a comparison with the earlier treatment presented in Ref. [26] many of the waveguide and off-channel feature geometries treated in Ref. [26] are considered here for similar parameter sets. These are shown to exhibit new transmission anomalies of the ω_1 mode when the ω_1 mode interacts with the ω_2 mode through the Kerr off-channel features.

In the case of a single site Kerr off-channel feature the effects of ω_2 on ω_1 transmission are greatest in the region of parameters in which, in the absence of ω_2, the ω_1 mode exhibits optical bistability. Away from this region the effects of ω_2 on ω_1 transmission are negligible. In the region of ω_1 bistability the ω_2 effects on the fields r_1 at the off-channel site are greatest at the maximum resonant excitation of the r_2 fields on the off-channel site. For the case of multiple Kerr off-channel sites, intrinsic localized modes can be excited on the off-channel features. These can be used to amplitude modulate or to switch on and off the ω_1 mode by modulating the ω_2 mode. For the case of multiple off-channel features that in turn interact with a second waveguide, the intrinsic localized mode on the Kerr cluster can be used to modulate and direct the flow of energy between the two waveguide channels.

It is hoped that this paper will stimulate increased interest in resonant and off-channel interactions for photonic crystal (optical) systems containing Kerr nonlinear media and the diverse optical phenomena they exhibit. Aside from an interest in resonance phenomena as a way of observing enhance nonlinear optical properties, a feature of the above proposed optical systems is their possible technological applications as switches, in amplitude modulation, and in signal amplification. These types of applications are solely dependent on the ability to resonantly excite localized modes in optical media and should be supported in a large class of different types of optical materials. In this regards, recent interest in resonance as a means of enhancing the nonlinearity displayed by systems have been developing in other (non-optical) areas of physics [51–54]. Most of this work has focused on resonances in single frequency mode systems though the work in Ref. [51] on mechanical systems has treated multiple frequency modes. We also note some very recent experimental optical work on resonant interactions of two different frequency photonic crystal waveguide modes using in channel features [55]. In this regards it should be noted that a variety of other schemes have recently been proposed for the observation of optical switching effects in other types of photonic crystal systems [56–59].

Finally, we note that the effects discussed in this paper are generic to all materials that exhibit Kerr

nonlinearity. They rely only on the use of the Kerr interaction to allow a waveguide mode of frequency ω_2 to modulate the dielectric properties seen by a second mode of frequency ω_1. In addition, in some cases the Kerr interaction has been used to cause the medium to support an intrinsic localized mode. The phenomena should display a degree of universality in systems of photonic crystal waveguides. The tendency in recent years has been towards the increasing development of organic materials [60,61], exhibiting nonlinear optical properties that have made them of interest in applications to optical data storage, optical information processing, electro-optic switching, all-optical switching, and in general optical computing and telecommunications systems technologies. This tendency has continued over to photonic crystal research. Particular example of polymer applications in photonic crystals and photonic crystal optical circuits are reviewed in Refs. [62,63] and interesting discussions of nonlinear phenomena in multilayers are found in the reviews by Agranovich, et al. [64,65]. It is hoped that this paper will stimulate the development of types of organic photonic waveguide systems that exhibit the features from nonlinearity that have been discussed here.

References

[1] G. Parker, M. Chalton, Physics World 13 (2000) 8.
[2] P.N. Favennec, Photonic Crystals: Toward Nanoscale Photonic Devices, Springer-Verlag, Berlin, 2005.
[3] F. Zolla, G. Renversez, A. Nicolet, B. Kuhlmey, S. Guenneau, D. Felbacq, Foundations of Photonic Crystal Fibers, World Scientific, New Jersey, 2005.
[4] K. Sakoda, Optical Properties of Photonic Crystals, Springer, Berlin, 2001.
[5] J.D. Joannopoulos, R.D. Meade, J.N. Winn, Photonic Crystals, Princeton University Press, Princeton, 1995.
[6] J.D. Joannopoulos, P.R. Villeneuve, S. Fan, Nature (London) 386 (1995) 143.
[7] C.M. Soukoulis (Ed.), Photonic Band Gaps and Localization, Plenum, New York, 1992.
[8] A. Mekis, J.C. Chen, S. Fan, P.R. Villeneuve, J.D. Joannopoulos, Phys. Rev. B 65 (1996) 77406-1.
[9] M. Loncar, D. Nedeljkovic, T. Doll, J. Vuckovic, A. Scherer, T.P. Pearsall, Appl. Phys. Lett. 77 (2000) 1937.
[10] T. Baba, N. Fukaya, J. Yonekura, Electron Lett. 35 (1999) 654.
[11] M. Notomi, K. Yamada, A. Shinya, J. Takahashi, I. Yokohama, Phys. Rev. Lett. 87 (2001) 253902.
[12] S.Y. Lin, E. Chow, S.G. Johnson, J.D. Joannopoulos, Opt. Lett. 25 (2000) 1297.
[13] A. Chutinan, S. Noda, Phys. Rev. B 62 (2000) 4488.
[14] A.R. McGurn, Chaos 13 (2003) 754.
[15] Y.S. Kivshar, G.P. Agrawal, Optical Solitons, Academic Press, Amsterdam, 2003.
[16] B.S. Song, S. Noda, T. Asano, Science 300 (1996) 1537.
[17] S. Noda, A. Chutinan, M. Imada, Nature (London) 407 (1997) 608.
[18] A.R. Cowan, J.F. Young, Phys. Rev. E 68 (2003) 46606.
[19] D.K. Campbell, S. Rlack, Y.S. Kivshar, Phys. Today 57 (2004) 43.
[20] R.D. Meade, A. Devenyim, J.D. Joannopoulos, O.L. Alerhand, D.A. Smith, K. Kash, J. Appl. Phys. 75 (1994) 4753.
[21] A. Mekis, J.C. Chen, I. Kurland, S. Fan, P.R. Villeneuve, J.D. Joannopoulos, Phys. Rev. Lett. 77 (1996) 3787.
[22] A. Mekis, S. Fan, J.D. Joannopoulos, Phys. Rev. B 58 (1998) 4809.
[23] S. Fan, P.R. Villeneuve, J.D. Joannopoulos, H.A. Haus, Phys. Rev. Lett. 80 (1998) 960.
[24] A.R. McGurn, Phys. Lett. A 251 (1999) 322; A.R. McGurn, Phys. Lett. A 260 (1999) 314.
[25] A.R. McGurn, G. Birkok, Phys. Rev. B 69 (2004) 235105.
[26] A.R. McGurn, J. Phys. CM 16 (2004) S5243.
[27] A.R. McGurn, Phys. Rev. B 53 (1996) 7059; A.R. McGurn, Phys. Rev. B 61 (2000) 13235.
[28] A.R. McGurn, Phys. Rev. B 65 (2002) 75406.
[29] E. Yablonovitch, Phys. Rev. Lett. 58 (1987) 2059.
[30] P.P. Banerjee, Nonlinear Optics, Marcel Dekker, Inc., New York, 2004.
[31] D.L. Mills, Nonlinear Optics, Springer-Verlag, Berlin, 1998.
[32] R.W. Boyd, Nonlinear Optics, Academic Press, Amsterdam, 2003.
[33] M. Okane, S. Kako, S. Noda, Phys. Rev. B 68 (2003) 235110.
[34] Y. Akahane, M. Mochizuki, T. Asano, Y. Tanaka, S. Noda, Appl. Phys. Lett. 82 (2003) 1341.
[35] E. Miyai, S. Noda, J. Opt. Soc. Am. B 21 (2004) 67.
[36] S. Fan, Appl. Phys. Lett. 80 (2002) 908.
[37] S. Fan, W. Suh, J.D. Joannopoulos, J. Opt. Soc. Am. A 20 (2003) 569.
[38] B. Maes, P. Bienstman, R. Baets, J. Opt. Soc. Am. B 22 (2005) 1778.
[39] M.F. Yanik, S. Fan, M. Soljacic, Appl. Phys. Lett. 83 (2005) 2739.
[40] C. Yeh, Applied Photonics, Academic Press, San Diego, 1994.
[41] P. Yeh, Optical Waves in Layered Media, Wiley, New York, 1988.
[42] P.E. Barclay, K. Srinivasan, O. Painter, J. Opt. Soc. Am. B 20 (2003) 2274.
[43] M. Bayindir, E. Ozbay, Appl. Phys. Lett. 81 (2003) 4514.
[44] M. Qui, B. Jaskorzynska, Appl. Phys. Lett. 83 (2003) 1074.
[45] S. Olivier, C. Weisbach, H. Benisty, Opt. Lett. 28 (2003) 2246.
[46] K.S. Yee, IEEE Trans. Antennas Propag. 14 (1966) 302.
[47] A. Taflove, Computational Electrodynamics: the Finite-Difference Time-Domain Method, Arthech House, Boston, 1995.
[48] A. Taflove, Advances in Computational Electrodynamics: the Finite Difference Time-Domain Method, Arthech House, Boston, 1998.
[49] J. Pendy, A. MacKinnon, Phys. Rev. Lett. 69 (1992) 2772.
[50] L.R. Ram-Mohan, Finite Element Boundary Applications in Quantum Mechanics, Oxford University Press, New York, 2002.
[51] A.I. Manevich, L.I. Manevich, The Mechanics of Nonlinear Systems with Internal Resonances, Imperial College Press, London, 2005.
[52] A.E. Miroshnichenko, S. Flach, Chaos 13 (2003) 874.
[53] A.E. Miroshnichenko, S.F. Mingaleev, S. Flach, Y.S. Kivshar, Phys. Rev. E 71 (2005) 26626.

[54] S.W. Kim, S. Kim, Phys. Rev. B 63 (2001) 212301.
[55] T. Tanabe, M. Notomi, S. Mitsugi, A. Shinya, E. Kuramochi, Appl. Phys. Lett. 87 (2005) 151112.
[56] M. Soljacic, M. Ibanescu, S.G. Johnson, Y. Fink, J.D. Joannopoulos, Phys. Rev. E 66 (2002) 055601.
[57] M. Notomi, A. Shinya, S. Mitsugi, G. Kira, E. Kuramochi, T. Tanabe, Opt. Exp. 13 (2005) 2678.
[58] M.F. Yanik, S. Fan, M. Soljacic, J.D. Joannopoulos, Opt. Lett. 28 (2003) 2506.
[59] E. Centeno, D. Felbacq, Phys. Rev. B 62 (2000) R7683.
[60] R. Farchioni, G. Grosso (Eds.), Organic Electronic Materials, Springer, Berlin, 2001.
[61] Ch. Bosshard, K. Sutter, Ph. Pretre, J. Hilliger, M. Florshiemer, P. Kaatz, P. Gunter, Organic Nonlinear Optical Materials, Gordon and Breach Publishers, Basel, 1995.
[62] K. Forberich, S. Riechel, S. Pereira, A. Gombert, K. Bush, J. Feldmann, U. Lemmer, in: K. Busch, S. Lolkes, R.B. Wehrspohn, H. Foll (Eds.), Photonic Crystals, Wiley-VCH, Weinheim, 2004, Chapter 13.
[63] M. Augustin, G. Bottger, M. Eich, C. Etrich, H.-J. Fuch, R. Iliew, U. Hubner, M. Kessler, E.-B. Kley, F. Lederer, C. Liguda, S. Nolte, H.-G. Meyer, W. Morganroth, U. Perchel, A. Petrov, D. Schelle, M. Schmidth, A. Tunnermann, W. Wischmann, in: K. Busch, S. Lolkes, R.B. Wehrspohn, H. Foll (Eds.), Photonic Crystals, Wiley-VCH, Weinheim, 2004, Chapter 15.
[64] V.M. Agranovich, G.C. La Rocca, F. Bassani, in: R. Farchioni, G. Grosso (Eds.), Orangic Electronic Materials, Springer, Berlin, 2001, Chapter 10.
[65] V.M. Agranovich, G.C. La Rocca, F. Bassani, P. Reineker, Pure Appl. Chem. 89 (1997) 1203.

Available online at www.sciencedirect.com
ScienceDirect
Organic Electronics 8 (2007) 241–248
Organic Electronics
www.elsevier.com/locate/orgel

Induced Density of States model for weakly-interacting organic semiconductor interfaces

H. Vázquez [a], F. Flores [a,*], A. Kahn [b]

[a] Departamento de Física Teórica de la Materia Condensada, Universidad Autónoma de Madrid, E-28049 Madrid, Spain
[b] Department of Electrical Engineering, Princeton University, Olden Street, Princeton, NJ 08544, USA

Available online 14 August 2006

Abstract

The Induced Density of Interface States model is revisited and discussed for weakly-interacting organic semiconductor junctions. First, unreactive 'ideal' Au/organic interfaces are analyzed and described as a function of the organic Charge Neutrality Level (CNL) and the slope parameter S_{MO} specific to the case of Au: these values are similar, though not necessarily equal, to those obtained from a fit to reactive and unreactive metal/organic interfaces. Then, using the information provided by the Au/organic cases, we obtain the organic/organic screening parameters and calculate molecular level offsets without any adjustable parameter. The good agreement found between our theoretical results and experimental data for weakly-interacting metal/organic and organic/organic interfaces shows that our analysis in terms of the organic CNL and the corresponding (S_{MO} or S_{OO}) slope parameter provides a consistent and predictive description of the energy level alignment at these interfaces.
© 2006 Elsevier B.V. All rights reserved.

PACS: 73.61.Ph; 73.30.+y; 68.43.Bc

Keywords: Charge neutrality level; Interface states; Energy level alignment; Organic semiconductor; Fermi level pinning; Metal/organic interface; Organic/organic interface

1. Introduction

Research in organic electronics over the past decades has given rise to a series of new organic-based devices, such as light-emitting diodes, thin-film transistors and photovoltaic cells, many of which are based on small-molecule organic materials [1,2]. Since the performance of these devices is ultimately determined by charge injection at interfaces [3,4], the study of metal/organic and organic/organic interfaces is the focus of considerable theoretical and experimental work.

Concerning metal/organic interfaces, the Schottky–Mott model, which consists of the simple alignment of the vacuum levels of the metal and organic material, was soon disproved [5,6], and interface dipoles and partial pinning of the Fermi level were observed. Several models have been proposed to explain this behaviour based on charge transfer between metal and molecule using the organic ionization and affinity levels [7,8], chemical

* Corresponding author.
E-mail address: fernando.flores@uam.es (F. Flores).

1566-1199/$ - see front matter © 2006 Elsevier B.V. All rights reserved.
doi:10.1016/j.orgel.2006.07.006

reaction and formation of gap states [7–11], energetically distributed valence states and band bending [12], orientation of permanent molecular dipoles [13,14], as well as the reduction of the metal work function through the compression of the metal electron tail by the adsorbed molecules [8,15,16] (the 'pillow' effect).

Of these, probably the two most important and frequent mechanisms are chemical reaction at the interface and the 'pillow' effect. Chemically reactive interfaces are abundant and of obvious importance, and are characterized by the formation of metal–molecule bonds and the appearance of chemistry-induced gap states. While methods based on Density Functional Theory can be directly applied to these reacted interfaces, the main drawback is that the outcome of a particular reaction is unpredictable, so that each interface must be studied individually. Moreover, since the results are often very sensitive to the details of the interaction, it is difficult to extrapolate the conclusions to other cases. Thus, knowledge of reactive interfaces is hampered by its advancement in a stepwise manner.

Concerning the 'pillow' effect, the rearrangement of the metal electronic tail by the adsorbed molecules affects the dipole at the interface, effectively reducing the metal work function. Notice that, while the contributions from other mechanisms do not have a definite direction, the 'pillow' effect always tends to reduce the metal work function. This effect has been analyzed theoretically by Crispin et al. [15,17] for chemisorptive interfaces, while for physisorptive junctions, results for small organic molecules [16,18] have demonstrated this effect, though a systematic, quantitative understanding at a fundamental level is still lacking.

In a series of recent papers [19,20], we presented a model based on the Induced Density of Interface States (IDIS), in which the driving mechanism is the tendency of the Charge Neutrality Level (CNL) to align with the metal Fermi level.

While the importance of reactive or interdiffusive metal/organic interfaces is obvious and the effects of chemical reactions or defects cannot be understated, our aim is in fact to focus on the *opposite* class of interfaces: free of the complexity of chemical reactions or defects, which can obscure the understanding of the interface, the study of unreactive, 'ideal' interfaces can unveil the basic fundamental mechanisms governing the Schottky barrier formation. Our aim is to stress that, in the absence of chemical reaction or defects, there is an 'intrinsic' mechanism operating at organic semiconductor interfaces.

At organic heterojunctions, which are weakly-interacting, the vacuum level rule is observed in a number of cases, with notable exceptions exhibiting significant (up to 0.5 eV) interface dipoles. While no consistent explanation for this behaviour had been presented, our model, based on the partial alignment of the CNLs of both organic materials, provided an intuitive, yet general and consistent, explanation for the sign and magnitude of the observed dipoles [21,22].

In this paper, we present a revision of the results of the IDIS model, which we argue is appropriate for understanding the behaviour of weakly-interacting interfaces. Concerning metal/organic junctions, Au is the prototypical case of a non-reactive metal, since its interaction with organic materials has been shown to be very weak. Although the 'pillow' effect is not included in the results presented here, it can be incorporated phenomenologically at this stage through a reduction of the initial metal work function, as will be discussed below.

First, we address Au/organic interfaces and discuss how to extract, using theoretical and experimental information, the CNL of the organic material and the slope parameter (S) of the interface. Here, the values of S are specific to the case of Au and are similar, though not necessarily equal, to the values obtained from several reactive and unreactive metal/organic interfaces [2]. Both the CNL and the S parameter are shown to be related to the interface dipole Δ and the hole injection barrier ϕ_{Bh}.

In addition, given their weak interaction, organic/organic interfaces are studied within our model: the added interest of Au/organic interfaces is the information they provide for understanding organic heterojunctions. A way of obtaining reliable screening parameters, S_{OO}, for the different heterojunctions is presented. It is then shown how these values, together with the CNLs of the organic materials, can be used to calculate molecular level offsets at organic/organic interfaces.

Results for interface dipoles, injection barriers and molecular level offsets are presented for the following organic materials: 3,4,9,10-perylenetetracarboxylic dianhydride (PTCDA), 3,4,9,10-perylenetetracarboxylic bisbenzimidazole (PTCBI), 4,4′,*N*,*N*′-dicarbazolyl biphenyl (CBP), copper phthalocyanine (CuPc), *N*,*N*′-diphenyl-*N*,*N*′-bis(1-naphthyl)-1,1′-biphenyl-4,4′-diamine (α-NPD),

bathocuproine (BCP) and tris-(8-hydroxyquinoline) aluminium (Alq_3). As good quantitative agreement with experiment is found for interface dipoles and injection barriers, our approach provides the first consistent means of understanding the energy level alignment at weakly-interacting organic semiconductor interfaces. Since some values have been slightly modified in light of new data, we consider them to be our most robust and 'up to date' set of results.

2. Discussion of the model

The origin of the concept of CNL can be traced back as early as Pauling and Mülliken. Even though their work focused on quantum atomic properties, such as trends in the periodic table or atom electronegativities, Mülliken proposed considering the average of the ionization (I) and affinity (A) energies an intrinsic property of atoms. Consider, for instance, two atoms having ionization and affinity levels given by I_1, A_1, and I_2, A_2 (Fig. 1). If an electron is removed from 1 and placed at 2, the energy difference is $I_1 - A_2$. Charge transfer in the opposite direction gives $I_2 - A_1$. The difference between both processes yields $I_1 + A_1 - (I_2 + A_2)$, which suggests considering $\frac{I+A}{2}$ as a quantity which characterizes each atom, and whose relative values will determine the direction and magnitude of charge transfer: the atom with the higher (less negative) value of $\frac{I+A}{2}$ donates electrons to the one with the lower (more negative) value. This idea was pursued by Pauling to determine atom electronegativities [23] as a function of $\frac{I+A}{2}$.

In inorganic semiconductors, a generalization of this $\frac{I+A}{2}$ concept which consists on averaging the optical gaps in the Brillouin zone, yields the CNL of the semiconductor. It is well established that the CNL model for inorganic semiconductors can explain the band offsets and Schottky barrier formation associated to the energy level alignment [24]. Concerning organic semiconductors, the average $\frac{I+A}{2}$ was used by Crispin et al. [15,17] to study reactive metal/organic interfaces within a chemisorption approach.

Our model for the induced DOS and CNL for weakly-interacting organic semiconductor interfaces can be regarded as a generalization of the previous cases by considering all molecular levels (rather than just the HOMO and LUMO) and their contribution to the CNL position: the simple $\frac{I+A}{2}$ argument predicts the CNL always at midgap. Instead, for several organic materials, the CNL position is located close to the LUMO [19,20], as the induced DOS is greater around the HOMO, pushing the CNL upper in the gap. Our results for Au/organic and organic/organic interfaces show that a detailed calculation, including the effect of all molecular orbitals, is necessary for a correct determination of interface properties such as induced dipoles and injection barriers.

Within our model, the resonance of molecular states with the metal continuum of states gives rise to a shift and broadening of the molecular levels (see Fig. 2). For the particular case of an energy-independent metal–organic interaction, it can be shown that, for weakly-interacting interfaces, each molecular level is broadened into a Lorentzian function $\frac{\Gamma/2}{(E-E_i)^2+(\Gamma/2)^2}$, where Γ is the broadening of the

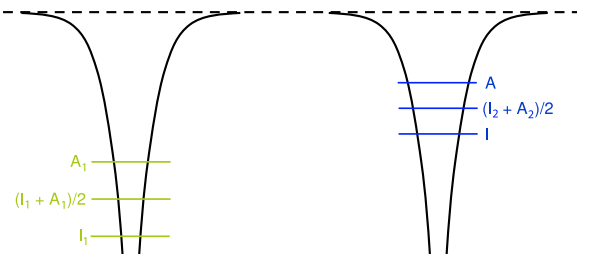


Fig. 1. Ionization (I) and affinity (A) levels for two different atoms. The average $\frac{I+A}{2}$ can be used to determine atom electronegativities.

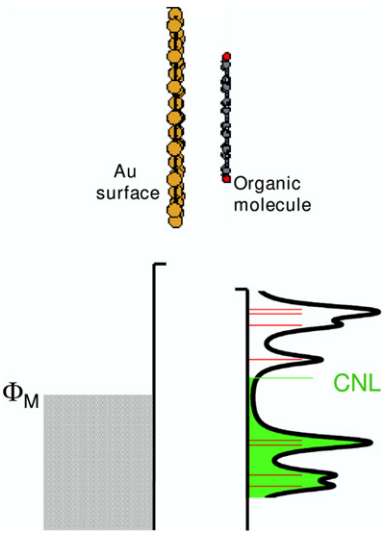


Fig. 2. At weakly-interacting metal/organic interfaces, charge transfer tends to align the organic CNL and metal work function. This gives rise to an induced dipole Δ_{MO} and the partial pinning of the Fermi level in the organic energy gap.

molecular level E_i. The sum of the contributions of the different molecular levels transforms their initial δ-like distribution into a continuum DOS with, in particular, non-negligible values in the former energy gap. By integrating this induced DOS up to the charge of the isolated molecule, the position of the CNL is determined. The relative position of the CNL and metal work function (when measured with respect to a common vacuum level) determines the size and direction of charge transfer. If the organic CNL is higher (less negative) than ϕ_M (as is the case of most organic materials on Au), electrons will be transferred from the molecule to the metal. This initial $\phi_M - CNL$ difference is reduced by the interface slope parameter S_{MO}, which determines how this initial offset is screened at the interface.

The interface Fermi level position and induced dipole can be calculated from Eqs. 1 and 2:

$$E_F - CNL = S_{MO}(\phi_M - CNL) \quad (1)$$

$$\Delta_{MO} = (1 - S_{MO})(\phi_M - CNL) \quad (2)$$

The DOS induced in the gap acts as a buffer for the transferred charge and is thus responsible for the dipole induced at the interface, the degree of Fermi level pinning at the interface and the Schottky barrier formation.

Given their weak interaction, the model was later extended to organic heterojunctions, where it was proposed [21] that the molecular level offset was determined by the relative position of the CNLs of both organic materials. A screening parameter S_{OO}, similar, but not equal to the one introduced for metal/organic interfaces, determines how this initial CNL offset will be screened when the interface is formed. In similarity to metal/organic interfaces, the initial and final CNL differences are related by (see Fig. 3)

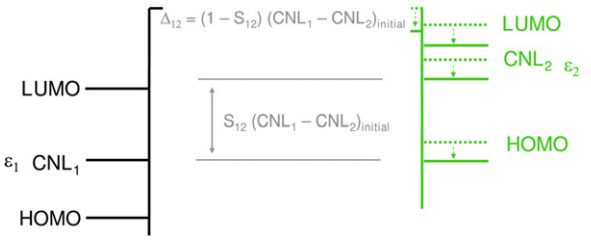


Fig. 3. Energy level alignment at organic heterojunctions: the initial CNL difference is partially screened, resulting in the formation of an interface dipole Δ_{OO} and a smaller final CNL offset.

$$(CNL_1 - CNL_2)_{final} = S_{OO}(CNL_1 - CNL_2)_{initial}, \quad (3)$$

while the induced dipole is

$$\Delta_{OO} = (1 - S_{OO})(CNL_1 - CNL_2)_{initial} \quad (4)$$

Thus, the central quantity in our analysis is the CNL, whose relative position to the metal work function (in the case of metal/organic interfaces) or to the CNL of the other material (at organic heterojunctions) largely determines the interface properties. This initial potential offset is reduced by the S parameter of the interface, whose value reflects the ability of the materials forming the interface to screen electrostatic potential differences. S_{MO} is almost always smaller than S_{OO} because the delocalized electrons in the metal are able to screen the potential difference at the interface efficiently. The screening ability of organic materials, on the other hand, is related to their static dielectric function, as will be commented on below.

3. Au/organic interfaces

Since there is evidence that metals other than Au are reactive or interdiffusive [2], we restrict our discussion to the case of interfaces between organic materials and Au. Au is non-reactive and the junctions formed with organic semiconductors are abrupt, resulting in almost ideal interfaces [7,25–28,11,31].

The electronic structure of the interfaces between Au and PTCDA, PTCBI, CBP and CuPc has been calculated, and the molecular level positions have been appropriately corrected [19,20,29] to account for the underestimation of the gap by DFT and for the band gap reduction due to polarization effects [30]. From the calculated DOS at the interface, CNL positions and values for the S parameter are obtained, which are in good agreement with experiment (see Table 1 and Figs. 4, 5). But whereas the CNL is a robust quantity, whose position is almost independent of the details of the interface, the S parameter is more dependent on the interaction at the interface, in particular through the metal–organic distance. We have taken $S = 0.16$ for PTCDA/Au and PTCBI/Au, as result from our calculations for a metal–organic distance d of 3.2 Å. The CNL position of CBP has been recalculated and is found to be −4.05 eV. Given our previously reported value [20], we consider this figure to have an uncertainty of 0.1 eV. For CuPc/Au, our

Table 1
CNL position, HOMO center (edge) and metal work function, with respect to the vacuum level, as well as theoretical values or fits of the S_{MO} parameter used in the calculations. Comparison between theoretical and experimental interface dipoles and hole injection barriers are given. All energies are given in eV

	−CNL	−IE	$-\phi_M$	S (theortical)	Δ (theortical)	Δ (experimental)	ϕ_{Bh} (theortical)	ϕ_{Bh} (experimental)
PTCDA	4.8	7.3 (6.8)	5.1 [6]	0.16	0.25	0.2 [6]	2.45	2.40 [6]
PTCBI	4.4	6.7 (6.2)	5.0 [7]	0.16	0.50	0.4 [7]	2.20	2.10 [7]
CBP	4.05	6.8 (6.3)	4.9 [10]	0.50	0.43	0.5 [10]	2.33	2.40 [10]
CuPc	4.0	5.7 (5.2)	5.3 [31]	0.30	0.91	1.2 [31]	1.31	1.60 [31]
α-NPD	4.1	6.0 (5.5)	5.14 [32]	0.33	0.70	0.86 [32]	1.56	1.74 [32]
			5.4 [33]		0.87	1.3 [33]	1.47	1.9 [33]
Alq_3	3.65	6.3 (5.8)	5.2 [6]	0.58	0.65	0.65 [6]	1.75	1.75 [6]
BCP	3.65	6.9(6.4)	–	0.42	–	–	–	–

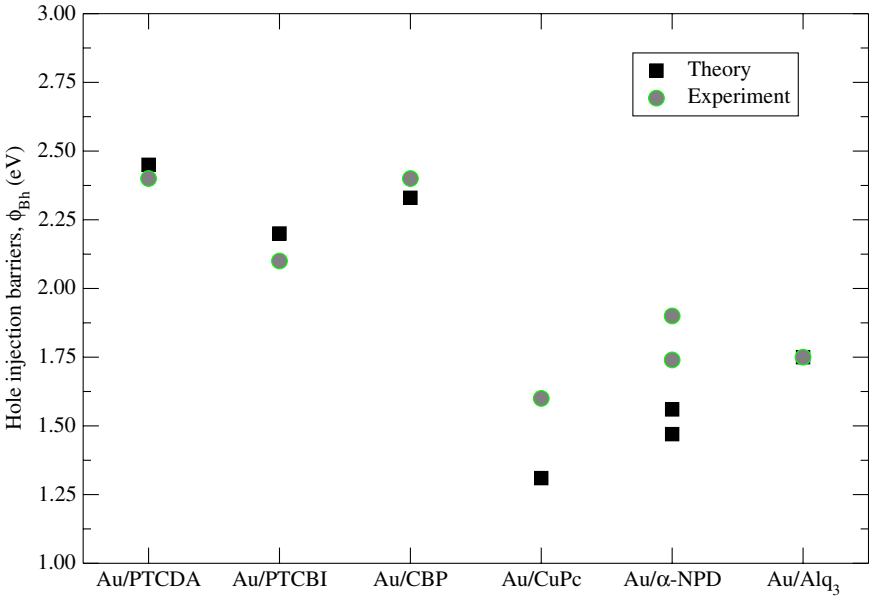


Fig. 4. Comparison of theoretical and experimental injection barriers for Au/organic interfaces, as quoted in Table 1.

choice of $S = 0.3$ ($d \sim 3.6$ Å) needs to be commented on. Experimental studies [31,39] seem to indicate that the molecular level broadening stems from intermolecular interactions, and that the interaction with the Au substrate is weaker than predicted by our model [21] (where a value $d = 3.2$ Å was taken), which would result in narrower CuPc peaks at the interface, and a larger value of S (and possibly d). Considering all this information, we have taken a larger value of S, $S = 0.3$, which is in better agreement with the reported experimental findings. For α-NPD and Alq_3, the CNL positions and the S parameters have been fitted to experimental interface dipoles and Schottky barriers, while maintaining the tendency (relative values) in S observed experimentally over a wide range of reactive and non-reactive metals [2]. In particular, for α-NPD, experimental data for Au/α-NPD interfaces [32,33] yield a low value of S, while geometrical considerations, such as its similarity in molecular structure to CBP, or having its benzene rings less tightly packed than PTCDA, PTCBI or CuPc, suggest that its value cannot be smaller than in these materials. As a compromise, we take $S = 0.3$, with an uncertainty of ± 0.1. Interestingly, we find $S_{Au} \lesssim S_{MO}$, where the latter value is a fit over several reactive and unreactive interfaces, although the reasons for this are unclear at the moment. In the case of BCP, due to the lack of experimental information for Au/BCP interfaces, the calculation and comparison with experiment of interface dipoles and injection barriers cannot be carried out.

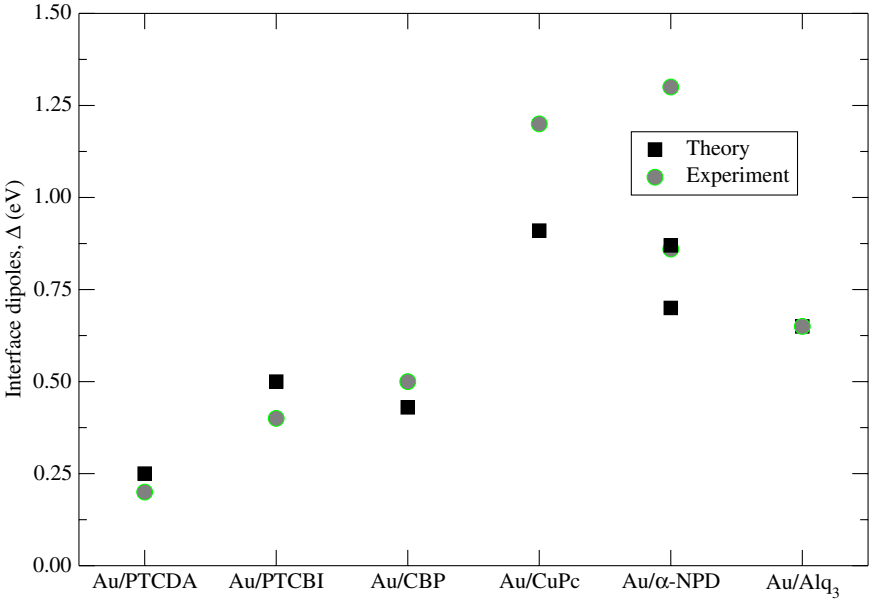


Fig. 5. Calculated and experimental interface dipoles for the Au/organic interfaces considered in this paper.

Instead, the CNL of BCP has been fitted to data from organic heterojunctions (see below).

Table 1 shows CNLs and S parameters for the organic materials considered, and compares the theoretical and experimental values of the interface dipole Δ and hole injection barrier ϕ_{Bh}. Notice that not only the fitted values, as expected, yield good agreement with experiment but so do the theoretical ones, calculated with no aid from external parameters. The agreement in Δ and ϕ_{Bh} is in most cases within 0.1 eV, and the calculated and fitted S values are not necessarily equal though certainly compatible with experimental values derived from a range of several reactive and non-reactive interfaces.

Notice that the 'pillow' effect, not considered in our approach, depends on the S_{MO} parameter, since this reduction of the metal work function is, too, screened by the interface charge. Thus, it can be expected to have a greater impact on those interfaces having larger values of S. Although we are currently working on a proper description of the 'pillow' effect within our formalism, it can nevertheless be immediately incorporated phenomenologically through a modification of the initial work function. As an additional contribution to the interface dipole, which shifts the organic electronic spectrum, it increases the values of Δ and ϕ_{Bh} given in Tables 1, but its effect in Δ (Eq. 1) is proportional to $(1 - S_{MO})$, and can thus be expected to be negligible for interfaces having $S \sim 0$ (as with PTCDA or PTCBI in Table 1), and have a non-negligible impact on those interfaces exhibiting a smaller interfaces screening (Au/Alq_3 is an example). For these systems, we estimate the changes in Δ and ϕ_{Bh} to be no larger than 0.2 eV.

4. Organic/organic interfaces

Since there is evidence that organic/organic interfaces interact only weakly [2], our model for non-reactive Au/organic interfaces can be extended to organic heterojunctions. The calculation of molecular level offsets, as described previously, requires the knowledge of the screening parameter at the heterojunction, S_{OO}. Following Tersoff's proposal for inorganic semiconductors [34], if the potential drop is equally shared by the two organic materials, the screening parameter is given by

$$S_{12} = \frac{1}{2}\left(\frac{1}{\epsilon_1} + \frac{1}{\epsilon_2}\right) \tag{5}$$

However, the static dielectric function in the direction perpendicular to the interface $\epsilon_\perp$ has, to our knowledge, only been measured for PTCDA ($\epsilon_\perp = 1.9$ [35,36]). Using this value as a reference, we propose to make an 'educated guess' of the values of the dielectric function for the other organic materials using Mönch's approximation [37]

$$\left(\frac{1}{S_{Au}} - 1\right) \sim (\epsilon_\perp - 1)^2, \quad (6)$$

where S_{Au} is the metal/organic slope parameter of the corresponding organic material with Au. The results for $\epsilon_\perp$ using this approximation are shown in Table 2. It must be mentioned that they are slightly different from our previously reported values [21,22], especially in the case of CuPc. As was noted before, the case of CuPc is puzzling since experimental results suggest a weak Au–organic interaction and a large value of S_{Au}, while our theoretical calculations (which depend on the Au–CuPc distance d, introduced as an external parameter) point to somewhat smaller values of S_{Au}. We have taken $S_{Au} = 0.3$, corresponding to $d \sim 3.6$ Å, which we believe is a 'middle point' or compromise, compatible with both sets of results. As noted previously [21], different values of $\epsilon_\perp$ introduce small changes in S_{OO} but the main results and trends are not altered, showing the robustness of the results, which depend predominantly on the CNLs.

The values of $\epsilon_\perp$ given in Table 2 enable the calculation of the screening parameters S_{OO}, for organic/organic interfaces. With these, the interface dipoles at the different heterojunctions can be evaluated by inserting S_{OO} into Eq. 4. Table 3 shows the quantitative evaluation and comparison with experimental results for the different interface dipoles for several organic heterojunctions. The sign of the calculated dipoles always agree with the measured values, and the agreement in magnitude is good, in most cases under 0.15 eV.

Recently, a study of the molecular level realignment of organic heterojunctions when one of the materials is p-doped was carried out [38]. The results, analyzed in terms of a doping-induced shift of the CNL of the doped material, show the success of the CNL interpretation of these interfaces and indicate that our set of CNLs is consistent too with the observed behaviour at these doped organic heterojunctions.

Table 2
Values for the Au/organic slope parameter S_{MO} and static dielectric function, obtained using Eq. 6

	S_{Au}	$\epsilon_\perp$
PTCDA	0.16	1.9 [35,36]
PTCBI	0.16	1.90
CBP	0.50	1.39
CuPc	0.30	1.60
α-NPD	0.33	1.56
BCP	0.42	1.46
Alq_3	0.58	1.33

5. Conclusions

In summary, we have presented a model for weakly-interacting interfaces based on the partial alignment of CNLs. An interface parameter, S_{MO} or S_{OO}, plays an important role in determining how efficiently the potential difference at the interface is screened. At weakly-interacting Au/organic interfaces, these values have been calculated for several organic materials (PTCDA, PTCBI, CBP and CuPc), while for others (α-NPD, BCP and Alq_3) they have been fitted to experimental dipoles and injection barriers. This evidence is then used to analyze organic heterojunctions by calculating the corresponding S_{OO} parameters.

The use of either calculated or fitted values of the CNLs and S_{Au} or S_{OO} yields good agreement with experiment in interface dipoles and injection

Table 3
Initial CNL difference, screening parameter S_{OO} and calculated and experimental dipoles (in eV) for different organic heterojunctions

	$(CNL_1 - CNL_2)_{initial}$	S_{12}	Δ (theory)	Δ (experimental)
CuPc/PTCDA	0.80	0.58	0.34	0.4
CuPc/PTCBI	0.40	0.58	0.17	0.1
CuPc/CBP	0.05	0.67	0.02	0.0
CuPc/α-NPD	0.10	0.63	0.04	0.0
PTCDA/Alq_3	−1.15	0.64	−0.42	−0.5
PTCDA/α-NPD	−0.70	0.58	−0.29	−0.1
BCP/Alq_3	0.00	0.72	0.00	0.0
BCP/CBP	0.40	0.70	0.12	0.0
BCP/PTCBI	0.75	0.61	0.30	0.4
BCP/α-NPD	0.45	0.66	0.15	0.0
Alq_3/α-NPD	0.45	0.70	0.14	0.25
Alq_3/CBP	0.40	0.73	0.11	0.1

barriers for different organic interfaces. Moreover, this agreement over a range of different weakly-interacting (Au/organic, organic/organic) interfaces suggests that the values presented here, which have been slightly modified in light of new data [33,31,39], are the most robust and 'up to date', since they compare well over a range of interfaces of different nature.

Our results unambiguously show that the induced DOS and CNL are important quantities, governing the energy level alignment at weakly-interacting organic semiconductor interfaces. Other mechanisms discussed previously, such as chemical reaction and the 'pillow' effect, are presumably small at these weakly-interacting interfaces but could, in any case, be incorporated into our formalism. Moreover, we would like to stress that this is, to our knowledge, the first consistent and *predictive* analysis of this set of interfaces.

Our model has so far been only applied to weakly-interacting interfaces, while reactive or interdiffusive cases are more specific and unpredictable, and need to be studied individually. But since the formulation of our model is general and can include these cases, strongly-interacting or chemisorptive interfaces will be the focus of future work.

Acknowledgments

We gratefully acknowledge financial support by the Consejería de Educación de la Comunidad de Madrid, the Universidad Autónoma de Madrid and the Spanish CICYT under projects MAT 2001-0665, MAT 2004-01271 and NAN-2004-09183-C10-07. Support of this work by the National Science Foundation (DMR-0408589) and the New Jersey Center for Organic Optoelectronics (A.K.) is also acknowledged.

References

[1] C.W. Tang, S.A. van Slyke, Appl. Phys. Lett. 51 (1987) 913.
[2] C. Shen, A. Kahn, I.G. Hill, in: W.R. Salaneck, K. Seki, A. Kahn, J.J. Pireaux (Eds.), Conjugated Polymer and Molecular Interfaces, Marcel Dekker, New York, 2001, pp. 351–400.
[3] J. Campbell Scott, J. Vac. Sci. Technol. A 21 (2003) 521.
[4] Y. Shen, A.R. Hosseini, M.H. Wong, G. George Malliaras, Chem. Phys. Chem. 5 (2004) 16.
[5] S. Narioka, H. Ishii, D. Yoshimura, M. Sei, Y. Ouchi, K. Seki, S. Hasegawa, T. Miyazaki, Y. Harima, K. Yamashita, Appl. Phys. Lett. 67 (1995) 1899.
[6] I.G. Hill, A. Rajagopal, A. Kahn, Y. Hu, Appl. Phys. Lett. 73 (1998) 662.
[7] I.G. Hill, J. Schwartz, A. Kahn, Org. Electron. 1 (2000) 5.
[8] H. Ishii, K. Sugiyama, E. Ito, K. Seki, Adv. Mater. (Weinheim, Ger.) 11 (1999) 605.
[9] C. Shen, A. Kahn, Org. Electron. 2 (2001) 89.
[10] I.G. Hill, A. Rajagopal, A. Kahn, J. Appl. Phys. 84 (1998) 3236.
[11] M. Eremtchenko, D. Bauer, J.A. Schaefer, F.S. Tautz, New J. Phys. 6 (2004) 4.
[12] G. Paasch, H. Peisert, M. Knupfer, J. Fink, S. Scheinert, J. Appl. Phys. 93 (2003) 6084.
[13] S. Kera, Y. Yabuuchi, H. Yamane, H. Setoyama, K.K. Okudaira, A. Kahn, N. Ueno, Phys. Rev. B 70 (2004) 085304.
[14] M. Knupfer, G. Paasch, J. Vac. Sci. Technol. A 23 (2005) 1072.
[15] X. Crispin, V. Geskin, A. Crispin, J. Cornil, R. Lazzaroni, W.R. Salaneck, J.L. Brédas, J. Am. Chem. Soc. 124 (2002) 8131.
[16] P.S. Bagus, V. Staemmler, C. Wöll, Phys. Rev. Lett. 89 (2002) 096104.
[17] X. Crispin, Solar Energy Mater. Solar Cells 83 (2004) 147.
[18] Y. Morikawa, H. Ishii, K. Seki, Phys. Rev. B 69 (2004) 041403(R).
[19] H. Vázquez, R. Oszwaldowski, P. Pou, J. Ortega, R. Pérez, F. Flores, A. Kahn, Europhys. Lett. 65 (2004) 802.
[20] H. Vázquez, F. Flores, R. Oszwaldowski, J. Ortega, R. Pérez, A. Kahn, Appl. Surf. Sci. 234 (2004) 108.
[21] H. Vázquez, W. Gao, F. Flores, A. Kahn, Phys. Rev. B 71 (2005) 041306(R).
[22] H. Vázquez, F. Flores, A. Kahn, Proc. Int. Symp. Super-Funct. Org. Dev. IPAP Conf. Ser. 6 (2005) 1.
[23] L. Pauling, The Nature of the Chemical Bond, third ed., Cornell University Press, 1960 (Chapters 3–8).
[24] F. Flores, C. Tejedor, J. Phys. C 20 (1987) 145.
[25] T.S. Ellis, K.T. Parka, S.L. Hulbert, M.D. Ulrich, J.E. Rowe, J. Appl. Phys. 95 (2004) 982.
[26] P. Fenter, P.E. Burrows, P. Eisenberger, S.R. Forrest, J. Cryst. Growth 152 (1995) 65.
[27] T. Schmitz-Hübsch, T. Fritz, F. Sellam, R. Staub, K. Leo, Phys. Rev. B 55 (1996) 7972.
[28] P. Fenter, F. Schreiber, L. Zhou, P. Eisenberger, S.R. Forrest, Phys. Rev. B 56 (1997) 3046.
[29] R. Oszwaldowski, H. Vázquez, P. Pou, J. Ortega, R. Pérez, F. Flores, J. Phys.: Condens. Matter 15 (2003) S2665.
[30] E.V. Tsiper, Z.G. Soos, W. Gao, A. Kahn, Chem. Phys. Lett. 360 (2002) 47.
[31] H. Peisert, M. Knupfer, T. Schwieger, J.M. Auerhammer, M.S. Golden, J. Fink, J. Appl. Phys. 91 (2002) 4872.
[32] W. Gao, A. Kahn, J. Appl. Phys. 94 (2003) 359.
[33] A. Wan, J. Hwang, F. Amy, A. Kahn, Org. Electron. 6 (2005) 47.
[34] J. Tersoff, Phys. Rev. B 32 (1985) R6968.
[35] Z. Shen, S.R. Forrest, Phys. Rev. B 55 (1997) 10578.
[36] S.R. Forrest, Chem. Rev. (Washington, D.C.) 98 (1997) 1793.
[37] W. Mönch, Appl. Surf. Sci. 92 (1996) 367.
[38] A. Kahn, W. Zhao, W. Gao, H. Vázquez, F. Flores, Chem. Phys. 325 (2006) 129.
[39] M. Knupfer, private communication.

Available online at www.sciencedirect.com
ScienceDirect
Organic Electronics 8 (2007) 249–255
Organic Electronics
www.elsevier.com/locate/orgel

Influence of doping on spin-dependent exciton formation in Alq_3 based OLEDs

Fernando A. Castro [a,b,*], George B. Silva [a], Frank Nüesch [b], L. Zuppiroli [c], Carlos F.O. Graeff [a]

[a] *Departamento de Física e Matemática, FFCLRP – USP, Av. Bandeirantes 3900, 14040-901 Ribeirão Preto-SP, Brazil*
[b] *Empa, Swiss Federal Laboratories for Materials Testing and Research, Laboratory for Functional Polymers, Überlandstr. 129, CH-8600 Dübendorf, Switzerland*
[c] *Laboratoire d'optoélectronique dês matériaux moléculaire, IMX-STI-EPFL, CH-1015 Lausanne, Switzerland*

Available online 20 July 2006

Abstract

We have used electrically detected magnetic resonance (EDMR) to investigate the effect of doping and trapped charges on spin-dependent exciton formation in aluminum(III) 8-hydroxyquinoline (Alq_3) based OLEDs. As dopant we have used 4-(dicyanomethylene)-2-methyl-6-{2-[(4-diphenylamino)-phenyl]ethyl}-4*H*-pyran (DCM-TPA). We observed significant differences (in *g*-factor, ΔH_{pp} and amplitude) between EDMR signals from DCM-TPA doped and undoped devices at room temperature. The signal from the DCM-TPA doped OLED was found to be strongly dependent on temperature, with signal intensity increasing by two orders of magnitude below 200 K. It was attributed to spin-dependent exciton formation, which our results indicate that takes place between a trapped electron in the dopant and a hole from Alq_3, in the current/bias range investigated. The observed differences between doped and undoped devices are discussed in terms of a change in exciton precursor reaction rates and/or decrease in spin coherence time. Preliminary results from rubrene doped OLEDs indicate a similar process.
© 2006 Elsevier B.V. All rights reserved.

PACS: 71.35.−y; 73.40.−c; 76.90.+d; 85.60.Jb

Keywords: Doping; Exciton; OLED; Electrically detected magnetic resonance

1. Introduction

Organic electronics has been the subject of intensive research during the last decade. Since the discovery of the first efficient electroluminescent material aluminum(III) 8-hydroxyquinoline (Alq_3) [1], several organic molecules emitting light from blue to red have been produced. However, due to the intrinsic optical properties of organic solids, these materials often show broad emission spectra with unsatisfactory color purity. For several applications, such as color displays or electrically pumped lasers, not only color tunability is important but also color purity or color saturation is an important

* Corresponding author. Address: Empa, Swiss Federal Laboratories for Materials Testing and Research, Laboratory for Functional Polymers, Überlandstr. 129, CH-8600 Dübendorf, Switzerland. Tel.: +41 44 823 4584; fax: +41 44 823 4012.
E-mail address: fernando.araujo@empa.ch (F.A. Castro).

1566-1199/$ - see front matter © 2006 Elsevier B.V. All rights reserved.
doi:10.1016/j.orgel.2006.06.007

factor. Doping a host matrix with highly fluorescent dyes has proven to be an efficient strategy to achieve narrow emission spectra [2].

Although doping of the electroactive host may bring other advantages, such as increased device lifetime and efficiency [3], the mechanism of light generation is still not fully understood. In particular the process of exciton formation on the doping molecule is subject of debate. While many studies suggest energy-transfer mechanisms [4], others show evidence of charge transfer mechanisms [5].

As a matter of fact, the process of exciton formation itself after charge injection in organic devices is still subject to controversy [6–8], even for undoped materials. One of the main discussions is centered on the relative percentage of singlet and triplet exciton formation. Due to simple spin statistics, one would expect 25% singlets and 75% triplets to be formed, what would limit the efficiency of organic light emitting diodes (OLEDs). However, many experimental and theoretical works [9,10], in particular on conjugated polymers, claimed efficiencies higher than 25%; while other groups claimed singlet generation fraction below this value [11].

We have recently reported the observation of singlet exciton formation probability smaller than 25% for Alq_3-based OLEDs using electrically detected magnetic resonance (EDMR) [8]. Typically, in an EDMR experiment spin level transitions induced by magnetic resonance are measured through changes in device current. The key to EDMR is that many of the processes that lead to charge transport and recombination in semiconductors are strongly dependent on spin selection rules, or the spin states of interacting electrons. One important characteristic of this technique is that it allows the investigation of devices in real working conditions at the same time as it is able to probe the wave functions of unpaired spin sites and its surrounding with higher sensitivity than conventional electron spin resonance (ESR). Although for several years EDMR has been used to characterize inorganic semiconductors [12], only recently Alq_3-based devices have been studied using this and other magnetic resonance related techniques [13,14].

In this work, we used EDMR to investigate the effect of doping and trapped charges on spin-dependent exciton formation. State-of-the-art undoped and DCM-TPA doped Alq_3 based OLEDs were investigated. At room temperature, significant differences were found between EDMR signatures from doped and undoped devices. The signal from DCM-TPA doped OLEDs was found to be strongly dependent on temperature, with signal intensity increasing by two orders of magnitude below 200 K. Our results indicate that exciton formation in these doped devices occurs between an electron trapped in the dopant and a hole in the Alq_3. We discuss these differences in terms of a decrease in spin coherence time, or a change in exciton precursor reaction rates. Preliminary results from rubrene doped OLEDs are also discussed.

2. Experimental

All organic light emitting diodes used in this work were prepared by thermal evaporation in high vacuum ($<5\times10^{-7}$ mbar). Prior to deposition, indium–tin–oxide (ITO) coated glass substrates were cleaned in a sequence of ultrasonic baths using ethanol, acetone, detergent and Milli-Q water, respectively. Then the organic layers were deposited in sequence. For the undoped OLED, used as a reference, the sequence comprises a 10 nm thick copper phthalocyanine (CuPc) layer, used to improve hole injection, followed by a 40 nm thick *N*,*N*′-diphenyl-*N*,*N*′-bis(1-naphthyl)-1,1′biphenyl-4,4″diamine (α-NPD) hole transporting layer and a 60 nm thick Alq_3 electron transporting and emissive layer. Subsequently, a 0.8 nm thick LiF layer was deposited followed by a 100 nm thick Al layer. The doped devices investigated in this work were prepared in the same way, except that instead of the 60 nm Alq_3 layer, a 20 nm thick Alq_3 doped layer (co-evaporation of Alq_3 with 1 wt.% of doping molecules) was deposited followed by a 40 nm thick undoped Alq_3 layer. The doped device structure can be seen in Fig. 1 together with the molecular structures of Alq_3 and the doping molecules used in this work: 4-(dicyanomethylene)-2-methyl-6-{2-[(4-diphenylamino)-phenyl]ethyl}-4*H*-pyran (DCM-TPA) and rubrene.

To avoid air-induced degradation, the devices were directly transferred to an inert gas glove box without being exposed to the atmosphere. Samples with lateral dimensions no greater than 3.0 mm were then contacted and sealed inside an ESR quartz tube.

EDMR measurements were done using a specially designed computer interfaced K-band (24 GHz) spectrometer, in the temperature range from 100 to 300 K. The spin-dependent conductivity changes were measured by modulating the static magnetic field H_0 and using lock-in detection of the current

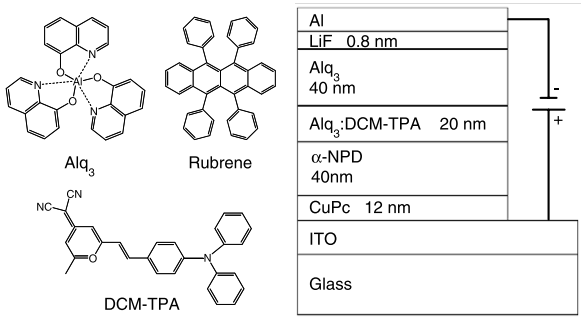


Fig. 1. On the left side: molecular structure of tris-(8-hydroxy quinoline) (Alq_3), 4-(dicyanomethylene)-2-methyl-6-{2-[(4-diphenylamino)-phenyl]ethyl}-4*H*-pyran (DCM-TPA), and rubrene. On the right side: structure of the doped devices used in this work. The undoped device contains a 60 nm thick Alq_3 layer instead of the 20 nm doped layer plus 40 nm Alq_3 layer.

changes. The magnetic-field modulation was typically 133 Hz. The EDMR signal ($\Delta\sigma/\sigma$) is calculated normalizing the current changes: $(I - I_0)/I_0$, where I_0 is the current out of resonance.

Electroluminescence spectra of DCM-TPA doped and Alq_3 undoped OLEDs operating at 0.75 mA/cm^2 were measured using an integrating sphere.

3. Results

Fig. 2 shows the temperature (T) dependence of the EDMR signal amplitude from a DCM-TPA doped OLED (full circles) and an Alq_3 undoped OLED (open squares). For each sample all measurements were performed operating the device at the same bias current. The bias current/voltage was chosen to make sure that the device was always electroluminescent. The general behaviour of $\Delta\sigma/\sigma$ with temperature is different for Alq_3 doped or undoped devices. For the doped OLED a drastic signal decrease is observed for temperatures above 200 K, while the EDMR signal from undoped samples is weakly dependent on T.

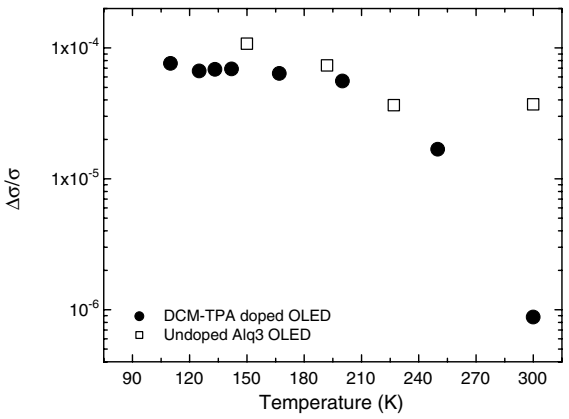


Fig. 2. Amplitude of EDMR signal as a function of temperature for an Alq_3 OLED doped with 1 wt.% DCM-TPA (full circles) and an undoped Alq_3 OLED (open squares).

Since EDMR is measured using a lock-in amplifier, not only the amplitude is measured but also the phase difference with respect to the reference signal. So, if two components have different relaxation times, one expects different phase shifts with respect to the lock-in reference signal and this can be used to separate the EDMR signal components. Detailed information about this procedure can be found on the works by Graeff et al. [8] and Dersch et al. [15]. In Fig. 3 we compare an EDMR signal for the doped device at 110 K and at 250 K showing the signal in both channels 1 and 2 of the lock-in. For $T = 300$ K the signal was too weak. The signal at 250 K was scaled to match the intensity of the one at 110 K for better visualization. Making use of a rotation matrix we changed the phase between channels one and two for each spectrum in order to eliminate the signal from channel 2. In the inset it is shown that this is not possible at 110 K. As a matter

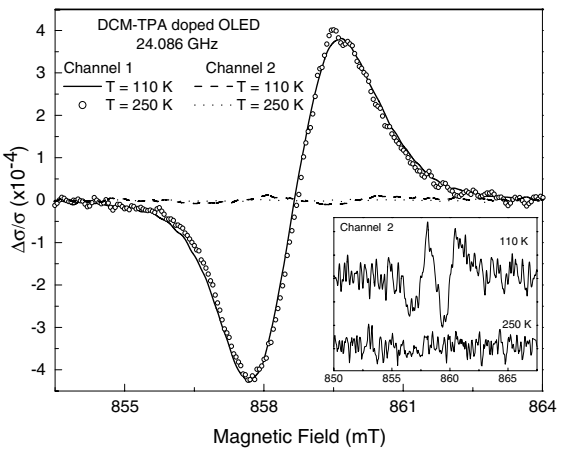


Fig. 3. EDMR spectra of a DCM-TPA doped OLED at 110 K (solid and dashed lines) and at 250 K (open square and dotted line) in both channels 1 and 2 of the lock-in amplifier. The spectrum taken at 250 K was scaled to match the 110 K amplitude for better visualization. The inset shows a magnification of the signals in channel 2, dislocated vertically. For each temperature, the phase between the signals from both channels was changed in order to eliminate the signal in channel 2. Note that a residual signal cannot be eliminated from the spectrum at 110 K.

of fact it was only possible for spectra taken at temperatures above 200 K. This is an indication of a change in spin coherence time with temperature around 200 K, the same "threshold" temperature where a strong decrease in signal amplitude was observed.

Making use of the procedure mentioned above, we noticed that the signal at 110 K can be decomposed into two components one with g-factor of 2.0042 and $\Delta H_{pp} = 1.82 \pm 0.01$ mT (bias independent) and the other with a g-factor of 2.0039 and ΔH_{pp} between 3.00 ± 0.05 and 4.20 ± 0.05 mT (increasing with increasing bias). This signal is similar to the one seen for the undoped OLED, where the signal attributed to holes [8] has $g_h = 2.0042$ and $\Delta H_{pph} = 1.5$ mT and the signal attributed to electrons has $g_e = 2.0032$ and ΔH_{ppe} also dependent on bias, between 2.0 and 3.4 mT. As we recently reported [8], the signal from these Alq_3 undoped OLEDs comes from spin-dependent exciton formation due to different cross sections for anti-parallel and parallel spin pairs prior to exciton formation. In that work, unipolar Alq_3 devices were also investigated, what lead to the conclusion that holes coming from α-NPD were injected in the Alq_3 layer and excitons were formed by a hole and an electron in the Alq_3. In both cases, hole- and electron-only devices, the EDMR signals were at least 25 times less intense than the signal from the OLED.

Although the separation of different contributions to the EDMR signal at 250 K due to different spin-dependent relaxation times was not possible using phase analysis, we fitted the spectra using a sum of Gaussian functions. We did not use the signal of DCM-TPA doped OLED at room temperature, since the signal to noise was not good enough to render a reasonable fit. To decrease the free parameters, we used the g factors obtained from phase analysis of the spectra at low temperatures as "almost" fixed parameters. "Almost" meaning that these values were allowed to fluctuate in a given range around the central value obtained at low temperatures. The signal from the DCM-TPA doped OLED at 250 K could, in this way, be decomposed into two components. One with g-factor of 2.0042 and $\Delta H_{pp} = 1.5 \pm 0.1$ mT and the other with g-factor of 2.0038 and $\Delta H_{pp} = 2.5 \pm 0.1$ mT.

In Fig. 4 typical EDMR spectra are presented for both undoped OLED at room temperature and DCM-TPA doped OLEDs at 250 K. The spectra were scaled to the right-side peak in order to better visualize the spectral differences. We can clearly see

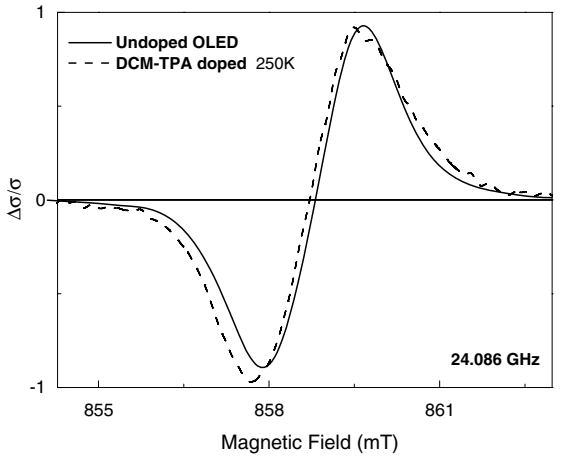


Fig. 4. Typical EDMR spectra of an undoped Alq_3 OLED (full line) at room temperature and of a DCM-TPA doped OLED (dashed line) at 250 K. Signals were scaled to the same value for the right-side peak.

that both g factor and peak-to-peak linewidth (ΔH_{pp}) are different, as well as the signal amplitude (shown in Fig. 2). By comparing the EDMR spectral characteristics of the signals components, the main difference between doped and undoped OLEDs stems from the anion-related signal.

Fig. 5 shows the normalized electroluminescence (EL) spectrum of a DCM-TPA doped OLED and the relative EL spectrum of an undoped OLED, both operating at the same current density at room temperature. The red shift is a clear indication that

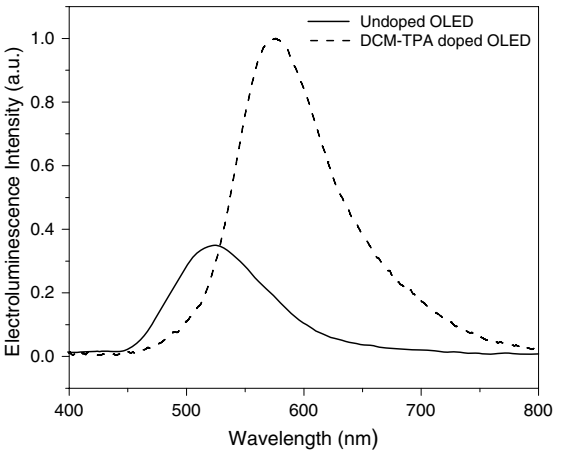


Fig. 5. Normalized electroluminescence spectrum of a DCM-TPA doped OLED (dashed line) and the relative EL spectrum of an undoped Alq_3 OLED at room temperature. Spectra were taken for devices operating at 0.75 mA/cm^2.

light emission is coming from DCM-TPA molecules. Note that the higher EL intensity of the doped sample reflects its higher efficiency [16].

4. Discussion

The results presented above provide two main findings. First, the EDMR signal on DCM-TPA doped samples are strongly dependent on temperature, especially in the transition from room temperature to 200 K, where a two order of magnitude change in signal amplitude is observed. The other important finding is that the spectroscopic characteristics of the signal, g factor and ΔH_{pp}, are distinct from undoped samples.

Our results indicate that the EDMR signal both in undoped and doped samples, are coming from spin-dependent exciton formation. In the following we will discuss possible mechanisms for the strong temperature dependence on doped diodes.

One possibility would be a quench in exciton formation. This is clearly not the case. In fact, the external quantum efficiency of DCM-TPA doped diodes is higher than those found in undoped samples [16]. However, as seen in Fig. 5, the emission color is shifted from green to red. In other words, doping with DCM-TPA is responsible for a strong decrease in the characteristic green emission of Alq_3. One explanation for this effect is that excitons formed in the Alq_3 are energy transferred to the dopant molecule by a Förster mechanism [4]. Another possibility is that electrons are trapped in the dopant which then reacts with a hole in Alq_3, directly forming an exciton [5].

EDMR is not probing the exciton state, but the state just before exciton formation, or in other words its precursor pair [8]. This precursor pair, formed by a cation (hole) and anion (electron) can have different spin states. These states determine the rate at which excitons are formed, and are assumed to be different for spin parallel pairs with respect to spin anti-parallel pair states, as discussed in more detail in [8,7]. Due to the spin conservation rules obeyed in a Förster energy-transfer mechanism, one would expect no change in the EDMR signal, neither in amplitude nor in g-factor and lineshape. In other words, the signal of the doped or undoped samples would be indistinguishable. By contrast, our results show that, under all experimental conditions used, a clear difference in the spectroscopic characteristics (g-factor and ΔH_{pp}) between doped and undoped samples is observed (see Fig. 4). Additionally, a two orders of magnitude change in $\Delta\sigma/\sigma$ occur between 200 K and room temperature. Thus, we have no indication from EDMR that excitons are being formed in Alq_3, in the experimental conditions used. Therefore our results strongly favour electron trapping as the main mechanism for the change in emission color with doping. The fact that the lowest unoccupied molecular orbital (LUMO) of these DCM-TPA molecules is located around 0.48 eV [16] below the LUMO of Alq_3 suggests that the doping molecules are negatively charged prior to exciton formation due to hole transfer from Alq_3. This is also confirmed by numerical modelling, where an important space charge density due to trapped electrons in the doped layers is observed [17].

Why would thus the electron trapping in DCM-TPA quench the EDMR signal at room temperature? At least two mechanisms could be mentioned; both related to a change in the reaction rates of the spin precursor pairs. The signal observed by EDMR related to exciton formation relies on the fact that the reaction rate of anti-parallel spins (R_{AP}) is different from that of parallel (R_P) spins. If they are the same, one has the commonly assumed 75% chance of forming triplet states against 25% of singlet exciton states. The other consequence of this assumption, not so commonly discussed, is that in this case Magnetic Resonance is not useful to probe these states. EDMR, as well as optically detected magnetic resonance, ODMR, can probe systems where R_{AP} and R_P are different. With differences in R_{AP} and R_P there is an increased formation of either triplets or singlet states. In other words, one could have, for example, a 22% probability of singlet exciton formation. Bringing the system into resonance is equivalent to bringing the system to the condition of $R_{AP} = R_P$. In summary, if one assumes that in the DCM-TPA doped Alq_3 at room temperature $R_{AP} = R_P$, bringing the precursor pair spin systems into magnetic resonance condition will have no effect on the triplet or singlet exciton formation rate, in other words, the EDMR or ODMR signal is quenched. At this point one cannot discard this explanation; however one would have to assume that R_{AP} has different temperature dependence than R_P to explain the temperature dependence of $\Delta\sigma/\sigma$.

The second possible explanation for the signal quenching comes from the dynamics of the process. The EDMR as well as the ESR signal amplitude are dependent on the microwave power used (P_μ). For the Alq_3 OLED the dependence is shown in

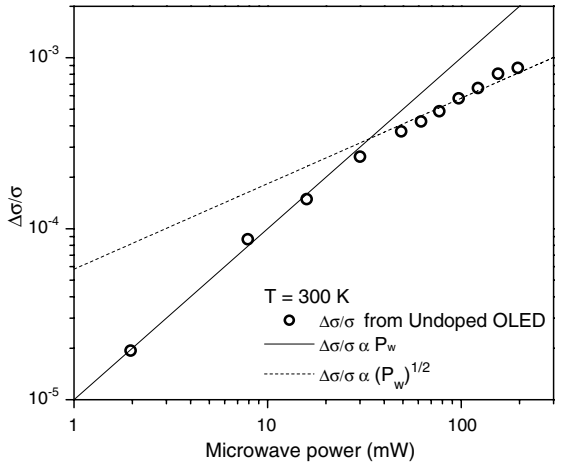


Fig. 6. Amplitude of EDMR signal of an undoped Alq_3 OLED as a function of microwave power intensity (P_w). Dependence change from $\propto P_w$ to $\propto\sqrt{P_w}$ at around 30 mW.

Fig. 6. In this figure one can observe a transition from $\Delta\sigma/\sigma \propto P_\mu$ to $\propto (P_\mu)^{1/2}$ at approximately 30 mW. This behaviour has already been discussed in the literature [18] related to a transition from unsaturated to weakly saturated condition. Kawachi et al., have described in detail the EDMR dependence on power for a-Si:H based transistor. In our previous study on undoped Alq_3 OLEDs [8], we have compared X-band and K-band EDMR lineshape analysis combined with theoretical works on HOMO and LUMO molecular orbital and shown that the lineshape of the cationic and anionic states are dominated by proton hyperfine interaction. In what concerns the broadening mechanisms found in magnetic resonance, in our OLEDs one finds inhomogeneous broadening, as found in a-Si:H. For an inhomogeneously broadened line [18], the dependence of the EDMR signal intensity $\Delta\sigma/\sigma$ at the resonance field H_0 and ΔH_{pp} on the microwave power can be expressed as follows:

$$\Delta\sigma/\sigma \propto \chi_0 H_0 \gamma T_2'' H_1^2 \sqrt{s}, \tag{1}$$

$$\Delta H_{pp} = \frac{2}{\sqrt{3}}\left(\frac{1}{\gamma T_2'}\right), \tag{2}$$

where γ is the gyromagnetic ratio, H_1 is the microwave magnetic field, χ_0 is the static susceptibility and T_2' is defined as

$$\frac{1}{T_2'} = \frac{1}{\sqrt{s}T_2} + \frac{1}{T_2^*}, \tag{3}$$

where T_2^* is the apparent spin–spin relaxation time which reflects the linewidth of the inhomogeneously broadened envelope line far below saturation. The quantity s is the saturation factor defined as

$$s = \frac{1}{1+\gamma^2 H_1^2 T_1 T_2}, \tag{4}$$

where T_1 and T_2 are the spin–lattice and spin–spin relaxation times.

So in the case of DCM-TPA, the signal quenching could result from a strong decrease in $T_{1,2}$ of the anion spin system, or an increase in the exciton precursor reaction rate. By numerical simulation using Eq. (1), it is trivial to calculate that a two order of magnitude change in $\Delta\sigma/\sigma$, implies at least a two order of magnitude change in $T_{1,2}$. In both situations, from what has been discussed, it would be "equivalent" to virtually decrease the applied microwave power. To support this finding one could in fact have made a measurement of $\Delta\sigma/\sigma$ as a function of P_μ. However, this was not possible in a reasonable range due to the weakness of the EDMR signal in the doped sample at room temperature. From simple arguments it is hard to argue why T_1 should decrease so strongly in DCM-TPA. On the other hand, the higher external quantum efficiency observed in DCM-TPA doped OLEDs compared to undoped, could come from an increase in exciton precursor reaction rates, or in other words in a decrease in the spin coherence time. Note that in undoped OLEDs, as in the doped ones below 200 K (Fig. 3), it is not possible to put the signal completely in phase with the reference signal from the lock-in. However, as we have shown, this becomes possible for DCM-TPA doped devices above 200 K. These results are evidence that indeed there is a change in spin coherence time with temperature in the dopant. A detailed explanation of the temperature dependence would involve a detailed understanding of the EDMR spin dynamics.

A few words on the lineshape observed in the doped samples. Through the decomposition of the EDMR signal, we observed that the g-factor for the electron related signal is the most affected, while the hole related signal shows nearly the same g-factor as for the undoped OLED. This observation reinforces the interpretation of DCM-TPA electron trapping. Unfortunately in the case of DCM-TPA there are no theoretical works on cationic and anionic states of this molecule, more importantly inside an Alq_3 matrix. Notice, however, that a broader line should be expected as a response to the more localized nature of the electron trapped in the LUMO state of this molecule. The small g-shift to higher

values with respect to the anionic state in Alq_3 could also be explained by this higher localization. The fact that both components behave differently with temperature is evidence that indeed we are able to probe both spins participating in the spin-dependent exciton formation.

Finally, we have also made some preliminary EDMR studies on rubrene doped Alq_3 OLEDs. The signals show small temperature dependence and very small amplitudes, in the order of 10^{-6}–10^{-7}. Although more studies are necessary to clarify which spin-dependent mechanism is responsible for the signal, we speculate that similarly to what was discussed earlier a decrease in spin coherence time or a change in exciton precursor reaction rates could be responsible for the small signal.

5. Conclusion

We have investigated the effect of doping and trapped charges on spin-dependent exciton formation in Alq_3 based OLEDs using electrically detected magnetic resonance. Strong differences (in g-factor, ΔH_{pp} and amplitude) were found between EDMR signals from DCM-TPA doped and undoped devices at room temperature. The signal from DCM-TPA doped OLED was found to be strongly dependent on temperature, with signal intensity increasing by two orders of magnitude below 200 K. Our results indicate that a direct reaction between a trapped electron in the dopant with a hole from Alq_3 is the main mechanism for exciton formation in the DCM-TPA doped OLEDs, in the current/bias range investigated. The differences, probably due to these trapped states, are discussed in terms of a decrease in spin coherence time or a change in exciton precursor reaction rates. Preliminary results from rubrene doped OLEDs indicate a similar process.

References

[1] C.W. Tang, S.A. VanSlyke, Appl. Phys. Lett. 51 (1987) 913.
[2] A.A. Shoustikov, Y. You, M.E. Thompson, IEEE J. Sel. Top. Quantum Electron. 4 (1998) 3.
[3] M.A. Baldo, M.E. Thompson, S.R. Forrest, Nature 403 (2000) 750.
[4] R.N. Bera, Y. Sakakibara, M. Tokumoto, K. Yase, Jpn. J. Appl. Phys. Part 1 42 (12) (2003) 7379.
[5] X. Gong, J.C. Ostrowski, D. Moses, G.C. Bazan, A.J. Heeger, Adv. Funct. Mater. 13 (6) (2003) 439.
[6] M. Reufer, M.J. Walter, P.G. Lagoudakis, A.B. Hummel, J.S. Kolb, H.G. Roskos, U. Scherf, J.M. Lupton, Nature Mater. 4 (4) (2005) 340.
[7] M. Wohlgenannt, K. Tandon, S. Mazumdar, S. Ramasesha, Z.V. Vardeny, Nature 409 (6819) (2001) 494.
[8] C.F.O. Graeff, G.B. Silva, F. Nüesch, L. Zuppiroli, Eur. Phys. J. E 18 (2005) 21.
[9] J.S. Wilson, A.S. Dhoot, A.J.A.B. Seeley, M.S. Khan, A. Köhler, R.H. Friend, Nature 413 (2001) 828.
[10] D. Beljonne, A.J. Ye, Z. Shuai, J.L. Bredas, Adv. Funct. Mater. 14 (7) (2004) 684.
[11] M. Segal, M.A. Baldo, R.J. Holmes, S.R. Forrest, Z.G. Soos, Phys. Rev. B 68 (7) (2003) 075211.
[12] C.F.O. Graeff, in: H.S. Nalwa (Ed.), Encyclopedia of Nanoscience and Nanotechnology, vol. 2, American Scientific Publishers, Stevenson Ranch, CA, 2004, pp. 1–745.
[13] F.A. Castro, G.B. Silva, L.F. Santos, R.M. Faria, F. Nuesch, L. Zuppiroli, C.F.O. Graeff, J. Non-Cryst. Solids 338–340 (2004) 622.
[14] G. Li, C.H. Kim, P.A. Lane, J. Shinar, Phys. Rev. B 69 (2004) 165311.
[15] H. Dersch, L. Schweitzer, J. Stuke, Phys. Rev. B 28 (1983) 4678.
[16] F. Nüesch, L. Zuppiroli, D. Berner, C. Ma, X. Wang, Y. Cao, B. Zhang, Res. Chem. Intermed. 30 (4–5) (2004) 495.
[17] D. Berner, F. Nuesch, E. Tutis, C. Ma, X. Wang, B. Zhang, L. Zuppiroli, J. Appl. Phys. 95 (7) (2004) 3749.
[18] G. Kawachi, C.F.O. Graeff, M.S. Brandt, M. Stutzmann, Jpn. J. Appl. Phys. 36 (1A) (1997) 121.

Available online at www.sciencedirect.com
ScienceDirect
Organic Electronics 8 (2007) 256–261
Organic Electronics
www.elsevier.com/locate/orgel

Intragap-trapped-carriers enhancement of the low-temperature delayed phosphorescence in Alq_3

I. Bergenti [a], V. Dediu [a], T. Mertelj [a,b,*], M. Murgia [a], A. Riminucci [a], G. Ruani [a], C. Taliani [a]

[a] *Istituto per lo Studio dei Materiali Nanostrutturati ISMN sez. Bologna, Italy*
[b] *University of Ljubljana, Faculty of Mathematics and Physics, Jadranska 19, 1000 Ljubljana, Slovenia*

Received 1 February 2006; received in revised form 8 November 2006; accepted 19 December 2006
Available online 29 December 2006

Abstract

Time resolved electroluminescence of Alq_3 based organic light emitting devices was measured on a millisecond time scale. The millisecond delayed electroluminescence (DEL) was detected at 80 K and 26 K, while no long lived electroluminescence was observed at room temperature. The DEL spectrum consists of two components centered at ~2.3 and ~1.9 eV. The shape of the high energy band is similar to the prompt fluorescence emission peak, although a systematic red shift of about 30 meV is reproducibly found. The low-energy band position corresponds to the phosphorescence of Alq_3. The time decay of both bands is nonexponential, with the low energy band decaying slower. To explain dependencies of intensities of both components on the delay and the injection-current density a mechanism based on enhancement of the triplet-exciton radiative decay by carriers trapped in deep intragap traps is proposed.
© 2006 Elsevier B.V. All rights reserved.

PACS: 78.60.Fi; 85.60.Jb; 71.55.−i; 71.55.Jv

1. Introduction

The emitting properties of aluminium tris(quinoline-8-olate) (Alq_3), one of the most used materials in organic light-emitting devices (OLED), are still *intensively* investigated [1,2,4,3]. Alq_3 is mainly known as a singlet-exciton emitter, while the role of triplet-exciton states remains unclear. A considerable triplet excitons accumulation is expected in Alq_3 based electroluminescent devices due to strong pumping of this state by the electric current injection (~75% of the carrier generated excitons are expected to go to T_1 state [1,5,6]) and very long lifetime compared to that of the singlet excitons. Thus understanding the triplet-exciton state, its properties and its interaction with trapped carriers is of considerable interest to improve OLED operation characteristics.

In the past triplet-exciton properties of Alq_3 were considered only theoretically [7], while experiments were mainly performed in solutions [8,4,9]. Burrows et al. [4] report the Alq_3 triplet energy of 2.17 ±

* Corresponding author. Address: University of Ljubljana, Faculty of Mathematics and Physics, Jadranska 19, 1000 Ljubljana, Slovenia. Tel.: +386 1 477 3313; fax: +386 1 477 3998.
E-mail address: tomaz.mertelj@ijs.si (T. Mertelj).

1566-1199/$ - see front matter © 2006 Elsevier B.V. All rights reserved.
doi:10.1016/j.orgel.2006.12.004

0.1 eV and lifetime less than 50 μs from the phosphorescence spectrum in ethyl iodide glass at temperature 77 K. Indirect experimental methods like exciton diffusion through amorphous Alq_3 thin films indicate the room temperature triplet lifetime of $\tau = 25 \pm 10$ μs and the diffusion coefficient D_T of about 10^{-7}–10^{-8} cm^2/s [10]. Recently phosphorescence was observed in Alq_3-based OLED by measuring the delayed electro(photo)luminescence at low temperatures [1,2,11]. Much longer lifetimes were found in this case (up to 18 ms in the yellowish green Aq_3 [2]).

On the other hand, not only quantitative but even qualitative aspects are still strongly questioned. For example the role of the triplet–triplet exciton annihilation [12] in Alq_3 and intersystem crossing effects [2,13] remain quite unclear in our opinion. In addition, presence of carrier traps [15,14,3] may influence the triplet-exciton population dynamics especially at low temperatures.

In order to better understand these effects we investigated low temperature delayed electroluminescence (DEL) in double organic layer light emitting devices based on Alq_3. We found that presence of carriers trapped in deep intragap traps plays an important role in delayed triplet-exciton phosphorescence of Alq_3 at low temperatures.

2. Experimental

Experiments were carried out on 2.5×3.25 mm^2 ITO/NPB(40 nm)/Alq_3(65 nm)/LiF(2 nm)/Al(40 nm) OLEDs, where ITO and NPB represent indium tin oxide and *N*,*N*′-di(naphthalene-1-yl)-*N*,*N*′-diphenyl-benzidine respectively. NPB and Alq_3 were deposited on commercially available ITO substrates by thermal sublimation from Knudsen cells in ultra high vacuum at a pressure of about 10^{-9} mbar. The deposition rate was ~1 Å/s. The thickness of organics was measured with an Alpha-step thickness meter. LiF was nominally 2 nm thick and it was used to enhance electron injection from Al to Alq_3. During measurements OLEDs were kept in vacuum in a He-flow optical cryostat to enable cooling.

Holes were injected from ITO into NPB which is a good hole-transporting layer. Electrons were injected from Al into Alq_3, which is used as the electron-transporting and electroluminescent layer. At room temperature the EL *switch on* voltage of our devices was about 6 V, a value that is somewhat larger than that reported in literature [3] for similar devices.

OLEDs were powered by an in house built voltage pulse generator, which was triggered by an optical chopper. The pulse generator also generated an adjustable delay between the voltage pulse and the chopper trigger. The voltage pulses were 2.2 ms long with a duty cycle of 12.8%. The OLED voltage and injection current were monitored with a digital oscilloscope (Tektronix TDS-3014). In the following, the delay is defined as the time lag between the falling edge of the voltage pulse and the leading edge of the chopper trigger.

The emitted light was collected by a pair of convex lenses and focused on the input of the fibre optic probe of HAMAMATSU U6039-01 CCD spectrometer. The time resolution of the spectral acquisition was 2 ms.

3. Results

We were unable to detect any long lived DEL at room temperature, presumably because the processes involved were too fast. In order to detect delayed EL spectra the samples were cooled to 80 K and to 26 K. We used 17–24 V voltage pulses depending on temperature and deterioration of samples. The average injected current density was $j \approx 15$ mA/cm^2 during the voltage pulse at 80 K. At 26 K a higher current density of ~50 mA/cm^2 was used to compensate partially for the observed drop in EL intensity. After the voltage was switched off the current decayed on the μs timescale so any capacitance effects on the timescale of interest can be excluded.

The prompt EL spectra, collected by synchronising the voltage pulse to the chopper trigger, were that of the green emitting Alq_3 with a maximum at 2.31 eV. As expected no emission from NPB was observed, since recombination only takes place on the Alq_3 side of the interface. The prompt EL spectra collected at low temperatures were identical to those at room temperature. The intensities of the prompt spectra were two to three orders of magnitude larger than those of the 1 ms delayed EL spectra, depending on the sample.

In Fig. 1 we show prompt and DEL spectra of a fresh sample taken at 80 K. The shape of the DEL spectra is similar to the prompt one, however the peak position is ~30 meV lower in energy. To show in detail the DEL lineshape we plot in Fig. 2a normalised prompt and DEL spectra taken at different delays. Apart from the high-energy-edge red shift which seems virtually independent of the delay,

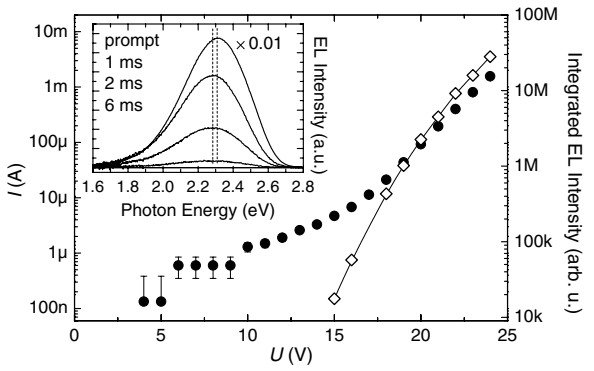


Fig. 1. The current (•) and prompt integrated EL intensity (◊) as functions of voltage at 80 K. Electroluminescence spectra as a function of the delay in a fresh sample at 80 K are shown in the inset.

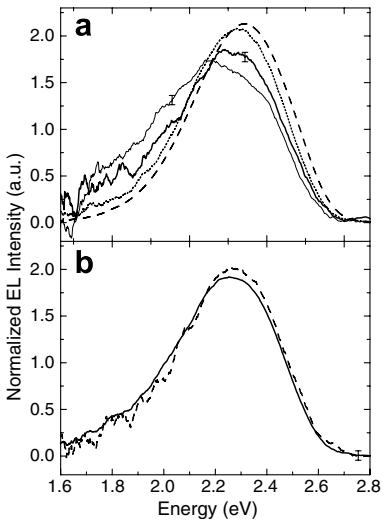


Fig. 2. The EL spectra lineshape dependence as a function of the delay (a) and the injection current at the constant delay of 2 ms (b). In (a) the dashed, dotted and thick lines represent prompt, 2-ms and 6-ms DEL spectra, respectively, while the thin continuous line represents the 6-ms DEL spectrum in a strongly deteriorated sample. In (b) full and dashed lines represent spectra taken with 28 mA/cm^2 and 2.8 mA/cm^2 injection current densities, respectively. Error bars represent the systematic error due to the CCD dark current subtraction for the three weakest intensity spectra. The systematic error for prompt and 2-ms spectra is less than the line thickness.

one can observe a marked increase of the relative spectral intensity below ~2.2 eV with increasing delay and some structure in the lineshape becomes clearly evident below ~2.2 eV. The increase of the low energy spectral intensity and its structure was more pronounced after the samples were deteriorated by prolonged operation and temperature cycling (see Fig. 2a). The deteriorated samples showed a decreased luminance and presence of dark spots in the emissive region.

To distinguish whether the lineshape changes are related to the delay and/or to the DEL intensity we also measured DEL at a constant delay as a function of the ON-pulse injection-current density. We observed no significant changes of the lineshape in this case as shown in Fig. 2b.

4. Data analysis

Due to the obvious structure observed in the low energy part of the DEL spectra and insensitivity of the high energy side of the spectrum to the delay it is very unlikely that the DEL spectra are due to a single process with a complex lineshape. We therefore analyse the spectra in terms of two components. To define the high energy component named A we use the prompt lineshape as a template and properly scale and shift it to fit the high energy edge of the DEL spectra. The low energy component named B corresponds to what remains after subtraction of component A. An example of such decomposition is shown in Fig. 3a. The high energy part of the DEL spectra above ~2.3 eV is remarkably well fit by the shifted prompt lineshape in all samples at all delays at both temperatures. The shift of the prompt lineshape is delay independent and is

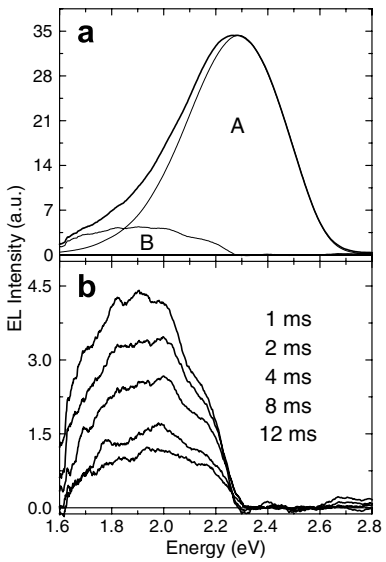


Fig. 3. The decomposition of a spectrum into the high energy component A and low energy component B (a). The delay dependence of the low energy component at 26 K (b).

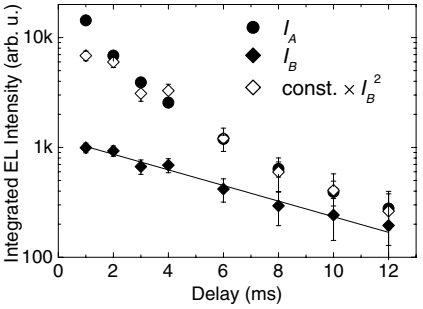


Fig. 4. Integrated intensities of high and low energy components as functions of the delay at 80 K. The full line represents an exponential fit with $\tau = 6.1$ ms. Error bars represent the systematic error due to the CCD dark current substraction.

~30 meV. The delay dependence of component B is shown in Fig. 3b. The lineshape of component B depends on the delay only slightly but varies considerably when the sample deteriorates.

In Fig. 4 we plot the delay dependence of the integrated intensities I_A and I_B of both components. While I_A clearly decays nonexponentially, the decay of I_B is slower than I_A and closer to an exponential decay with a relaxation time of ~6 ms at 80 K and ~10 ms at 23 K. It is interesting to note that the scaled I_B^2 displays a similar nonexponential decay as I_A (see Fig. 4) in all samples and at both temperatures suggesting that the processes responsible for each component are related.

5. Discussion

There are several possible excitations that can contribute to DEL in OLED. It is well known that during the steady injection into Alq_3 electrons and holes form charge transfer excitons within a few tens of nm from the NPB/Alq_3 interface. The excitons relax on a ps timescale to either the lowest energy singlet S_1 or triplet T_1 Frenkel excitons. From here on the S_1 excitons decay radiatively on a 10 ns timescale while the radiative decay of the T_1 excitons is electric-dipole forbidden due to the spin selection rules, so decay proceeds through other slower nonradiative processes on a μs timescale at room temperature. Apart from forming excitons, electrons and holes can also be trapped in and out of the emission region.

At room temperature DEL decays on a μs timescale where the slowest process contributing to DEL is the recombination of the trapped charge governed by diffusion [16]. At lower temperatures the radiative decay of the S_1 exciton is still on the 10 ns timescale, while the nonradiative decay of the T_1 exciton can significantly slow down. Similarly the diffusion of trapped charge is expected to be much slower at low temperatures. Both, the triplet excitons and/or recombination of the trapped charge can contribute to DEL at low temperatures.

Cölle and Gärditz [1] assigned the low energy DEL peak observed in single-layer Alq_3 OLEDs to the direct triplet-exciton phosphorescence. In addition they assign the high energy peak in their DEL spectra to the singlet-exciton fluorescence excited by the triplet-exciton fusion process. From their data they extract an extremely long triplet exciton lifetime of ~8 ms at 30 K.

In our case the experimental results are somehow similar to those of Cölle and Gärditz [1]. The high energy cut-off of component B at ~2.3 eV [17] is very close to the triplet exciton energy which is ~2.1 eV. [4,1,2,13,7], while the spectral signature of component A is that of the singlet-exciton fluorescence. Similarly to reference [1] the delay dependence of intensities of both components at a constant injection-current density j indicates that,

$$I_A(t)|_{j=\text{const.}} \propto I_B(t)^2|_{j=\text{const.}}, \quad (1)$$

which is compatible with the triplet-exciton fusion scenario [1] leading to the singlet-exciton fluorescence origin of component A and the triplet-exciton phosphorescence origin of component B. However, we *fail to observe* consistent behaviour of both intensities when the injection-current density is varied. The lineshape does not change as a function of the injection current density at a constant delay implying

$$I_A(j)|_{t=\text{const.}} \propto I_B(j)|_{t=\text{const.}}, \quad (2)$$

The assignments of Cölle and Gärditz [1] are therefore not compatible with our data since I_A should be proportional to I_B^2 in both cases. Processes leading to component A and component B should be both either monomolecular or bimolecular as indicated by observation (2). Due to the long DEL lifetime a monomolecular origin of the delayed fluorescence (component A) is ruled out. We therefore focus on bimolecular processes only.

An alternative possible assignment of the origin of the two components is based on the recombination of trapped carriers, which are trapped in shallow and deep traps [14,15,3]. In this case the origin of component A is assigned to recombination of carriers trapped in shallow traps:

$$p^+ + p^- \rightarrow S_1 + \text{phonons}; S_1 \rightarrow \hbar\omega_A \quad (3)$$

while the origin of component B is assigned to recombination of carriers trapped in deep traps:

$$p^+ + p_d^- \rightarrow T_1 + \text{phonons}; T_1 \rightarrow \hbar\omega_B \quad (4)$$

The process similar to (4) involving only carriers trapped in shallow traps cannot contribute significantly to component B in comparison to the component A due to a small probability of the radiative triplet decay. However, (i) if $[p_d^-] \gg [p^-]$ and (ii) the carrier recombination from deep traps is limited to the triplet-exciton channel only the relative contribution to component B might be significant. The condition (ii) can only be fulfilled when one of the carriers is in a deep trap and the energy of the carrier pair $p^+p_d^-$ is smaller than the singlet exciton energy.

Both processes (3) and (4) are bimolecular and therefore compatible with injection-current density dependence. However, there is no obvious reason why the decay rate of component A would be twice the decay rate of the component B as experiment indicates (Fig. 4). We therefore consider assignments (3) and (4) very improbable.

Instead, we modify the model of Cölle and Gärditz [1] *and we ascribe component B to a bimolecular process*. We believe that the triplet-exciton phosphorescence may be enhanced by interaction of the exciton with a trapped carrier:

$$p_d + T_1 \rightarrow p_d^* + \hbar\omega_B \quad (5)$$

Here the carrier can take care of the spin conservation by means of exchange interaction. In addition, the presence of the local electric field due to the carrier might increase the spin-orbit coupling for the neighboring triplet excitons. Both mechanisms enhance the probability of photon emission.

It is *essential* that the carrier that contributes to the process (5) is in *a very deep trap*. For such a carrier a more likely non-radiative triplet-exciton quenching process is energetically forbidden allowing the process (5) to take place.

A molecular species corresponding to such a trap should have a large electron affinity (EA). From known values of EA of Alq_3 [19,20] and triplet exciton energy we estimate that EA should be larger than ~3.1 eV. In addition the trap level should be at least the triplet exciton energy above the HOMO of Alq_3. From known ionization potential [19] of ~5.8 eV we estimate that EA of the trap molecule should be smaller than ~3.7 eV. In addition, a radical molecule formed by trapping a carrier should not have an excited state resonant with the triplet exciton energy. This is most likely for small molecular radicals which have only a few excited states [21].

The assignments of component A to the triplet-exciton fusion process and component B to process (5) is in *agreement with all experimental observation*s if we assume that the decay rate of the deep-trapped carrier density $[p_d]$ is negligible. At low temperatures such assumption is plausible. In this case the decay rate of component A is twice the decay rate of component B, and intensities of both components depend on the excitation current density through bimolecular processes.

Existence of very deep intragap states in Alq_3 is supported by observation of a finite subband optical absorption in thin films [18]. The assignment of component B is further supported by its relative intensity enhancement in old deteriorated samples where density of deep carrier traps [3] is expected to increase.

Next we discuss the observed prompt shift of the DEL high-energy edge. At low temperature and ms-delay timescale molecules with the smallest exciton energies are more likely to be occupied by triplet excitons. Fluorescence from singlet excitons created by the fusion process on this molecules has therefore a lower photon energy due to the correlation between the singlet and triplet exciton energy on the same molecule. During electric current injection however, the injected high energy carriers can also form singlet excitons on the molecules with larger excitonic energies resulting in an enhanced fluorescence at the high-energy edge of the spectrum.

Cölle and Gärditz [1] recently investigated DEL in single organic layer Alq_3 OLEDs. The DEL lineshape which they observe is markedly different than in our case and has a well defined double peak structure. The decay of both peaks is clearly exponential on a timescale similar to our case. To check whether the difference is a consequence of the different construction of our device, we measured DEL also in single organic layer Alq_3 OLEDs. Albeit DEL in our single layer OLEDs was significantly weaker it had the same lineshape as in the double layer devices. Since both peaks reported by Cölle and Gärditz are red shifted with respect to our data the origin of the discrepancy could be a different morphology of the emissive Alq_3 layer.

6. Conclusions

We measured the low-temperature delayed electroluminescence in double layer organic light

emitting devices which decays on a ms timescale. The spectra show two component behaviour. The components are centered at ~2.3 and ~1.9 eV. According to previous results [1] the high energy component is assigned to the fluorescence of singlet excitons which are created by fusion of the long-lived triplet excitons. On the basis of the spectral-lineshape injection-current dependency we assign the origin of the low energy component to the intragap-trapped-carrier enhanced phosphorescence of triplet excitons.

Our results are somewhat different from some recently published data [1]. The reason for discrepancy might be a different morphology of the emissive Alq_3 layer.

References

[1] M. Cölle, C. Gärditz, Appl. Phys. Lett. 84 (2004) 3160.
[2] M. Cölle, C. Gärditz, M. Braun, J. Appl. Phys. 96 (2004) 6133.
[3] D.Y. Kondakov, J. Appl. Phys. 97 (2005) 024503.
[4] H.D. Burrows, M. Fernandes, J. Seixas de Melo, A.P. Monkman, S. Navaratnam, J. Am. Chem. Soc. 125 (2003) 15310.
[5] R.H. Friend, R.W. Gymer, A.B. Holmes, J.H. Burroughes, R.N. Marks, C. Taliani, D.D.C. Bradley, D.A. Dos Santos, J.L. Brédas, M. Lögdlund, W.R. Salaneck, Nature 397 (1999) 121.
[6] M. Segal, M.A. Baldo, R.J. Holmes, S.R. Forrest, Z.G. Soos, Phys. Rev. B 68 (2003) 075211.
[7] R.L. Martin, J.D. Kress, I.H. Campbell, D.L. Smith, Phys. Rev. B 61 (2000) 15804.
[8] R. Ballardini, G. Varani, M.T. Indelli, F. Scandola, Inorg. Chem. 25 (1986) 3858.
[9] R.J. Curry, W.P. Gillin, J. Appl. Phys. 88 (2000) 781.
[10] M.A. Baldo, S.R. Forrest, Phys. Rev. B 62 (2000) 10958.
[11] I. Tanaka, Y. Tabata, S. Tokito, Phys. Rev. B 71 (2005) 205207.
[12] J. Partee, E.L. Frankevich, B. Uhlhorn, J. Shinar, Y. Ding, T.J. Barton, Phys. Rev. Lett. 82 (1999) 3673.
[13] M. Cölle, W. Brütting, Phys. Status Solidi (a) 201 (2004) 1095.
[14] A. Hepp, N. von Malm, R. Schmechel, H. von Seggern, Synth. Met. 138 (2003) 201.
[15] H. Fong, K. Lun, S. So, Jpn. J. Appl. Phys. 41 (2002) L1122.
[16] K.O. Cheon, J. Shinar, Phys. Rev. B 69 (2004) 201306, R.
[17] The higher value of the cut-off in comparison to the literature data is probably an artifact of the spectral decomposition into two components. There is no reason that the lineshape of component A would perfectly follow the prompt lineshape.
[18] A. Aziz, K.L. Narasimhan, Synth. Met. 131 (2002) 71.
[19] I.G. Hill, A. Kahn, Z.G. Soos, R.A. Pascal Jr., Chem. Phys. Lett. 327 (2000) 181.
[20] A. Curioni, M. Boero, W. Andreoni, Chem. Phys. Lett. 294 (1998) 263.
[21] Small aluminum oxide clusters [22] Al_xO_y have appropriate EA and could be products of Alq_3 decomposition during OLED operation.
[22] S.R. Desai, H. Wu, C.M. Rohlfing, L-S. Wang, J. Chem. Phys. 106 (1997) 1309.

Available online at www.sciencedirect.com
ScienceDirect
Organic Electronics 8 (2007) 262–271
Organic Electronics
www.elsevier.com/locate/orgel

Novel photofunctions of bilayer composed of p-type phthalocyanine and n-type organic semiconductor as photoelectrodes in the water phase

Toshiyuki Abe [a,*], Keiji Nagai [b,*]

[a] Department of Frontier Materials Chemistry, Hirosaki University, 3 Bunkyo-cho, Hirosaki 036-8561, Japan
[b] Institute of Laser Engineering (ILE), Osaka University, 2-6 Yamada-oka, Suita 565-0871, Japan

Received 31 January 2006; received in revised form 5 January 2007; accepted 7 January 2007
Available online 12 January 2007

Abstract

Novel characteristics of p/n organic bilayers as photoelectrodes working in the water phase were reviewed on the basis of recent examples proposed by us. By applying the bilayer to a photoelectrode in water, an organic solid/water interface can perform photoinduced oxidation/reduction coupled with the conduction of the carriers (*i.e.*, holes/electrons) generated in the interior. This characteristic differs explicitly from that of a single layer where carrier generation occurring at the Schottky interface (solid/water interface) is effective; on the basis of this phenomenon, we found that a more efficient and novel photofunctional interface in water can be formed by means of a p/n organic bilayer. Typically, it is noted that the interface of cobalt phthalocyanine (CoPc, a p-type semiconductor)/water in a p/n bilayer can induce the oxidation of water into O_2 through hole conduction by the CoPc layer under an irradiation of <750 nm, which successfully leads to the photoelectrochemical splitting of water into O_2 and H_2. The utilization of a p/n organic bilayer as the photoelectrode could reveal a new aspect of photoelectrochemical research and technology, particularly areas in which few examples of inorganic semiconducting materials have been reported.
© 2007 Elsevier B.V. All rights reserved.

PACS: 82.47.Jk

Keywords: Perylene; Phthalocyanine; C_{60}; Visible light response; Water splitting; Chemical oxidation/reduction

1. Introduction

Generally, it is known that n-type organic semiconductors are unstable, especially in the presence of oxygen and/or humidity [1,2]. Therefore, careful measurements have been carried out for their characterization. On the other hand, phthalocyanine is one of the most typical p-type organic semiconductors and is chemically stable [3]. For instance, various types of catalyses by phthalocyanines for oxidation have been reported [4]. By combining a p-type conducting material with an n-type conductor, the resulting p/n organic bilayer has been practically

* Corresponding authors. Tel./fax: +81 172 39 3580 (T. Abe), +81 6 6879 8778 (K. Nagai).
E-mail addresses: tabe@cc.hirosaki-u.ac.jp (T. Abe), knagai@ile.osaka-u.ac.jp (K. Nagai).

1566-1199/$ - see front matter © 2007 Elsevier B.V. All rights reserved.
doi:10.1016/j.orgel.2007.01.001

applied to dry-type photodevices such as solar cells, field-effect transistors, and in electroluminescence applications [5]. On the other hand, it has been postulated that organic compounds are not sufficiently stable for application in water (*vide supra*) [6]. Therefore, there are few examples where an organic material of the layered structure is used as a photodevice, especially in the wet condition; however, the p/n organic bilayer can usually perform an efficient visible-light absorption and charge separation.

Dihydrogen (H_2) energy is now attracting a great deal of attention as clean energy. Water photolysis is one of the most promising procedures for yielding H_2. For this process, it is essential to create an efficient solid/water interface to accomplish the photo/chemical energy conversion under solar irradiation. In water photolysis, the oxidation of two water molecules (or two OH^- ions) into O_2 is an important process because it is fundamental and first step for yielding H_2. Considerable efforts have been made to establish a photo/chemical energy conversion system after Honda and Fujishima reported photoelectrochemical water splitting by using a UV-responsive TiO_2 electrode [7]. Considering the theoretical conversion efficiency of solar energy, it is desirable to create a water splitting system that is responsive to visible light across the entire solar spectral region. Inorganic materials (*i.e.*, photocatalysts) have been passively used and investigated for H_2 evolving processes; however, until quite recently, there has been no example in which visible-light energy with a wavelength greater than 600 nm was effective for H_2 evolution [8,9]. Therefore, the design and development of a novel and efficient photodevice that operates in the water phase are vital issues.

As reported recently by the authors, an organic solid/water interface in a p/n organic bilayer was found to be capable of photoinduced oxidation/reduction coupled with photoconduction of the carriers (*i.e.*, holes/electrons) generated in the interior [10–15], where wide visible-light energy with a wavelength of <750 nm is available for the photoinduced reaction at the above mentioned interface. The use of an organic bilayer as a photodevice in the water phase is expected to reveal a new aspect of photoelectrochemical research and technology in which, currently, few examples of inorganic material application exist, thereby emphasizing the importance of investigating and accumulating fundamental knowledge on these potential materials. Based on recent examples proposed by us, this article will introduce the typical characteristics of an organic bilayer that exhibits stable performance for photoinduced reactions in the water phase.

2. Previously investigated molecule-based photoelectrodes in water

Photoelectrochemistry is one of the most promising methods of investigating and establishing a photoenergy conversion system [16]. Molecule-based photoelectrodes have been fabricated using self-assembled monolayers (SAMs) [17–19] and Langmuir–Blodgett (LB) films [20–22]. Such systems can successfully achieve photoinduced charge separation through unidirectional electron transfer; however, the resulting photocurrent has often been identified to have a magnitude of only a few $\mu A/cm^2$. The low output was often attributable to the mono-layered structure capable of only small light absorption by the photoexcitation center. In other words, multi-layered photoexcitation molecules might need to be loaded onto an electrode for fabricating an efficient photoresponsive device. Further, an Ru complex-adsorbed TiO_2 electrode, which is a part of the dye-sensitized photovoltaic cell (called the Grätzel cell), exhibits efficient photoanodic characteristics in an organic phase containing the I_3^-/I^- couple [23]; however, in the water phase, such a dye-sensitized photoelectrode has shown only low photoelectrochemical characteristics because of the instability of the dye in water [24,25]. Therefore, there have been few examples of molecule-based photoelectrodes efficiently leading to photoenergy conversion especially in the water phase.

3. Photoanode of p/n organic bilayer working in the water phase

We aimed to elucidate the chemical reactivity at an organic solid/water interface, for which a simple organic bilayer was applied to a photodevice in the water phase. In our study, all the organic bilayer films were prepared by vapor deposition. For example, when the film was composed of 3,4,9,10-perylenetetracarboxyl-bisbenzimidazole (PTCBI, an n-type semiconductor) coated on an indium-tin oxide (ITO)-coated glass plate and metal-free phthalocyanine (H_2Pc, a p-type semiconductor) coated on top of the PTCBI (denoted as ITO/PTCBI/H_2Pc) [10], photoinduced oxidation was found to occur at the H_2Pc/water interface. For the procedure of photoelectrochemical measurement, refer to the schematic illustration (Fig. 1).

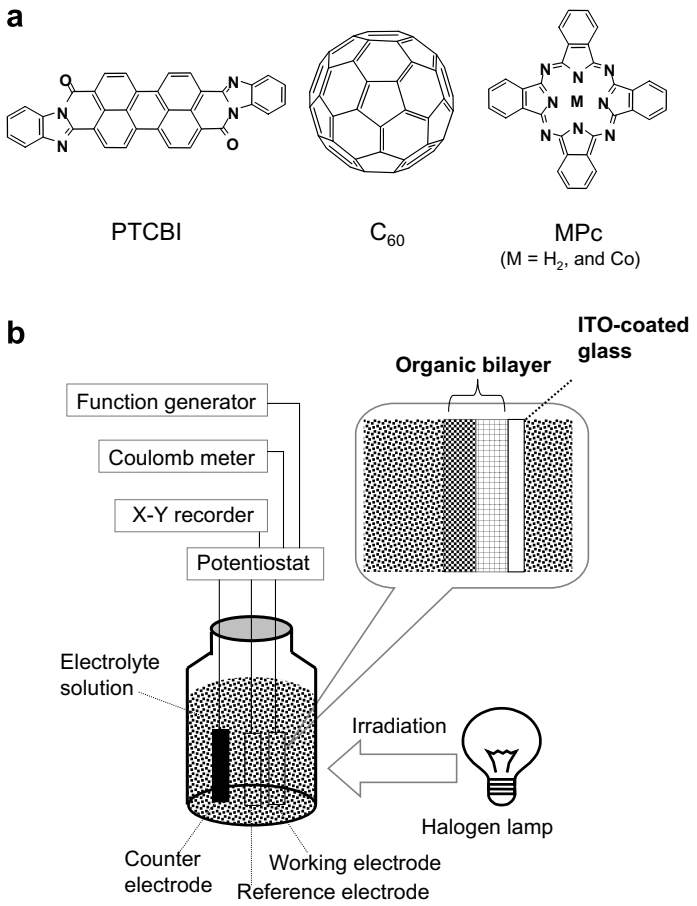


Fig. 1. (a) Chemical structures of organic semiconductor. (b) A schematic illustration of the photoelectrochemical reaction at an organic solid/water interface.

Fig. 2 shows typical cyclic voltammograms (CV) at ITO/PTCBI/H_2Pc under illumination ((a) and (b)) and in the dark (c). When measuring the CVs with (a) and without (b) thiol (electron donor), in the former, a large photoanodic current of $\mu A/cm^2$ order was noticed at potentials more positive than -0.10 V (*vs.* Ag/AgCl). Fig. 2a clearly shows the stable photoelectrochemical response with repeated scans. In a control experiment in the dark (c), no any anodic current can be observed in the presence of thiol. It is unknown whether a small molecule can permeate the organic film; however, when the bilayer was employed as a photoelectrode after soaking it in water for a few days, no change in its photoelectrode characteristics was observed in the experimental.

Fig. 2d shows the CVs measured using a scanning potential from -0.2 V to $+1.2$ V. A noticeable growth in the photocurrent (due to the oxidation of OH^-) was observed at potentials more positive than $+0.6$ V; however, the photoanodic current gradually diminished in subsequent scans, which indicates the decomposition of the organic film. On comparing Fig. 2d with another voltammograms in Fig. 2, the novel photofunction of the organic film in water was observed in potential regions where the film can never decompose. Now, we discuss the stability of the organic film. It is known that in a dry-state device, the application of a thermal stress to the film and an increase in temperature during cell performance lead to a decrease in the photovoltaic characteristics [26,27]. However, in the water phase, such an influence of heat is negligible because water is a medium capable of thermal absorption, thereby resulting in stable film performance. The stability of the film may also be ascribed to the characteristic

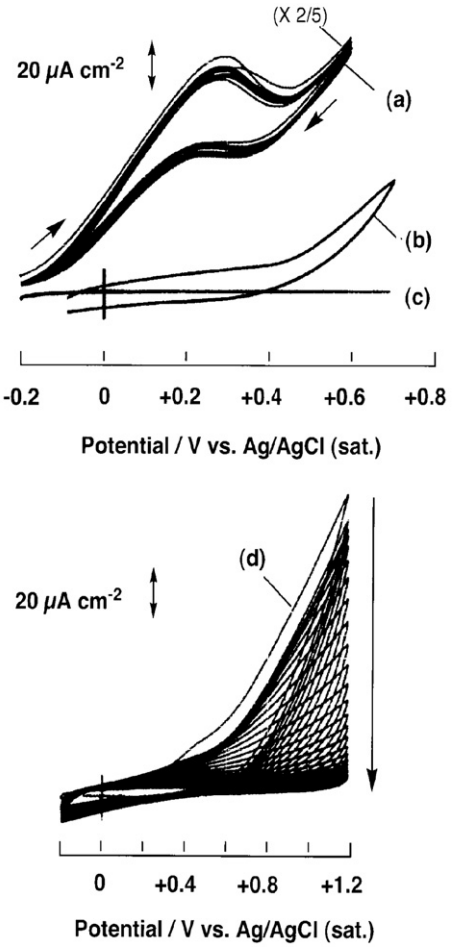


Fig. 2. Cyclic voltammogram (CV) at ITO/PTCBI/H_2Pc under illumination ((a), (b) and (d)) and in the dark (c). In the case of both (a) and (c), thiol (2-mercaptoethanol) of 5×10^{-3} mol dm^{-3} was added. Scan rate, 20 mV s^{-1}; film thickness, 230 nm (PTCBI)/ 50 nm (H_2Pc).

that the consumption of carriers takes place rapidly at the solid/water interface.

Fig. 3 depicts the schematic illustrations together with the photoelectrode characteristics of the p-type semiconductor/water interface in a single layer (a) as well as in a bilayer (b). If an H_2Pc single layer is employed as a photoelectrode, the H_2Pc/water interface must show photocathodic characteristics due to the formation of the Schottky junction, according to Fig. 3a. Therefore, Fig. 2a indicates that the photoinduced oxidation of thiol occurred at the H_2Pc/water interface along with hole conduction through the H_2Pc layer (Fig. 3b). This is a novel example of photoinduced chemical reaction coupled with carrier photogeneration in the interior in a p/n organic bilayer.

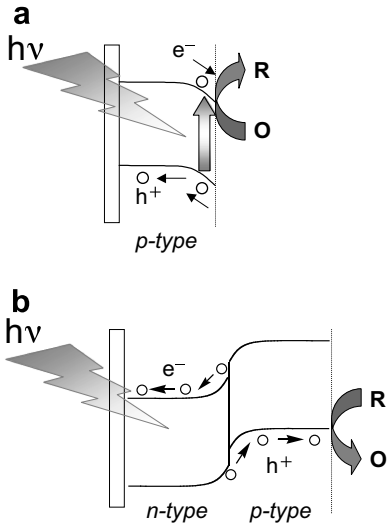


Fig. 3. A schematic illustration of the photoinduced reaction at a p-type semiconductor/water interface in a single layer (a) as well as the p/n bilayer (b). R and O denote reductant and oxidant, respectively.

The action spectrum for the photoanodic current at ITO/PTCBI/H_2Pc was measured in terms of both the irradiation direction of incident light and film thickness (Fig. 4). In summary, the resulting action spectrum was not in agreement with the absorption spectrum of the PTCBI/H_2Pc employed, showing that the present photocurrent generation cannot be induced in visible-light absorption over the entire PTCBI/H_2Pc layer. The monochromatic light irradiation was conducted from the PTCBI side (Fig. 4b), in which the photocurrent was found to be generated over the wavelength employed. In particular, when ITO/PTCBI/H_2Pc of the thin PTCBI layer was used as the photoanode (I in Fig. 4b), the action spectrum was in close agreement with the absorption spectrum of PTCBI. It should also be noted that despite there being no H_2Pc absorption at around 500 nm (Fig. 4a), photocurrent generation could be confirmed. However, in the case of a thick PTCBI layer (II in Fig. 4b), the discrepancy between the action spectrum and the absorption spectrum was apparent. Moreover, the thicker the PTCBI, the larger was the photocurrent. These results indicated that the present photocurrent generation is induced on a wide visible-light absorption by PTCBI bulk, although the action spectra for I as well as II most probably involved the optical filter effect by PTCBI itself. In a separate measurement, when the monochromatic light was irradiated from

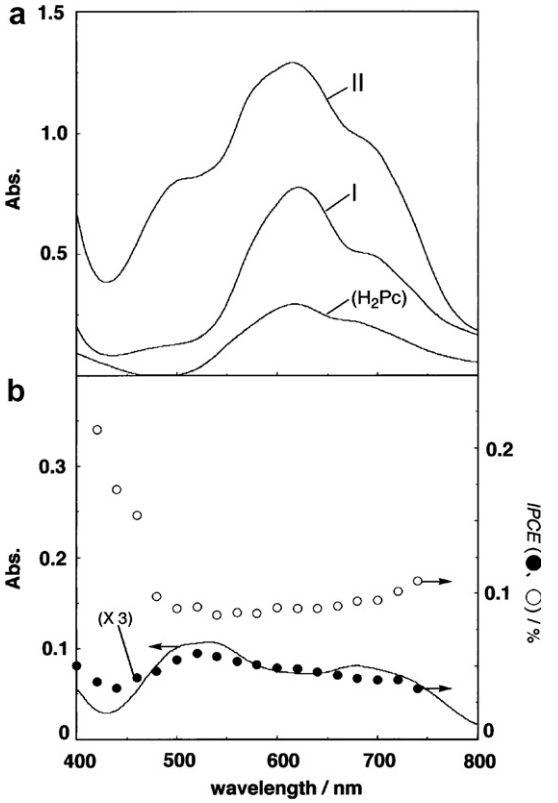


Fig. 4. (a) Absorption spectrum of PTCBI/H_2Pc as well as H_2Pc. Film thickness (I), 30 nm (PV)/60 nm (H_2Pc); film thickness (II), 250 nm (PTCBI)/50 nm (H_2Pc); film thickness (H_2Pc), 30 nm. (b) Action spectrum for photocurrent (● for I, ○ for II) and absorption spectrum (solid line) of PTCBI film (30 nm). Monochromatic light was irradiated from the side of the ITO/PTCBI interface. Applied potential, 0 V; thiol concentration, 1×10^{-3} mol dm^{-3}.

the H_2Pc side, the action spectrum was found to be in close agreement with the transmittance spectrum of H_2Pc, indicating that H_2Pc absorption made little contribution to the present photocurrent generation.

According to the studies on the photovoltaic effect [28–30], the quenching of PTCBI photoluminescence [31], and laser ablation [32–34], the PTCBI/H_2Pc bilayer exhibits charge separation at the p/n interface as follows (Eq. (1))

$$\mathrm{PTCBI} - \mathrm{H_2Pc} + h\nu \rightarrow \mathrm{PTCBI^-} - \mathrm{H_2Pc^+} \quad (1)$$

In particular, the efficient quenching of PTCBI photoluminescence by the H_2Pc layer indicated that the charge separation may be possible by only the absorption of the PTCBI layer [31] (Eq. (2)),

$$\mathrm{PTCBI^*} - \mathrm{H_2Pc} \rightarrow \mathrm{PTCBI^-} - \mathrm{H_2Pc^+} \quad (2)$$

where PTCBI* is the exciton of PTCBI. After the charge separation, the photogenerated carriers of $PTCBI^-$ and H_2Pc^+ can migrate in each layer. Therefore, the present thiol (RS) oxidation, which occur at the H_2Pc/water interface, should be attributed to the photogenerated and migrated H_2Pc^+ (Eq. (3); *cf.*, $RS \rightleftarrows RS^- + H^+$ ($pK_a = 9.7$) [35], $RS^- \rightarrow RS^{\cdot -} + e^-$)

$$\mathrm{H_2Pc^+} + \mathrm{RS^-} \rightarrow \mathrm{H_2Pc} + \mathrm{RS^{\cdot -}} \quad (3)$$

It has been recognized that a vacuum-deposited phthalocyanine film often exhibits a poor electron conductivity in the dark (under electrochemical condition) [36]; that is, the conduction in the H_2Pc layer of PTCBI/H_2Pc can be explained by the photogeneration of H_2Pc^+ acting as a hole carrier according to Eq. (2).

Fig. 5 represents a schematic energy diagram for the oxidation at ITO/PTCBI/H_2Pc. Considering the energy levels of ITO [37], PTCBI [37], and H_2Pc [38], the oxidative power photogenerated at the H_2Pc/water interface is sufficiently high to achieve thiol oxidation (*cf.*, the oxidation potential of H_2Pc is +0.64 V *vs.* SCE [39], which corresponds to ca. +0.69 V *vs.* Ag/AgCl). To our knowledge, this is the first example where thiol oxidation is induced by metal-free phthalocyanine. From Fig. 5, it should also be noted that the H_2Pc/water interface is capable of oxidizing water into O_2 (*cf.*, formal potential for the O_2/OH^- couple, ~+0.44 V *vs.* Ag/AgCl (at pH = 10)); however, the O_2 evolution involving four-electron transfer has not yet been confirmed at the PTCBI/H_2Pc bilayer. Therefore, in order to accomplish O_2 evolution in the bilayer, the H_2Pc surface was modified with an active catalyst. A known amount of IrO_2 was coated onto the H_2Pc surface, followed by a Nafion® coating (ca. 30 nm) to suppress the detachment of IrO_2 from the H_2Pc surface [11]. When the outer surface of H_2Pc in the PTCBI/H_2Pc bilayer was coated with IrO_2, a μA cm^{-2}-order photocurrent was successfully generated to involve the O_2 evolution catalyzed by IrO_2. The energy conversion efficiency for O_2 evolution (~1.0×10^{-2}%, *cf.*, bias potential energy was omitted in the estimation) is considerably low. This implies that the photoelectrode kinetics is dominated by the charge transport process at the solid/liquid interface, which would also be realized by the fact that the catalyst loading required to accomplish the O_2 evolution. The combination of the more active catalyst with the bilayer is one of

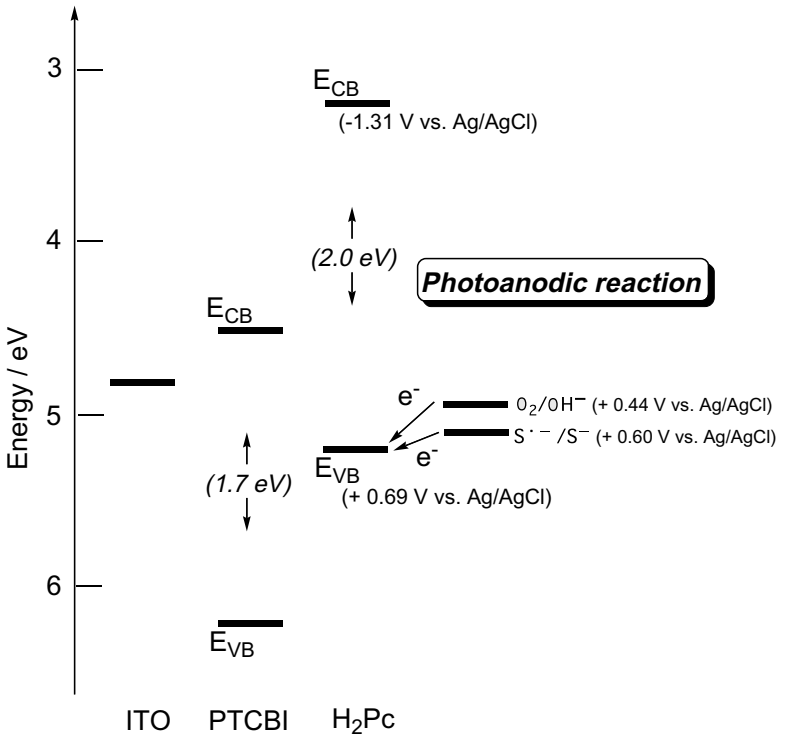


Fig. 5. Schematic energy diagram for photoinduced oxidation at ITO/PTCBI/H_2Pc. E_{VB} and E_{CB} denote the energy levels of the valence band and conduction band, respectively.

the possibilities for creating an efficient solid/water interface with O_2 evolution [40], and the use of this combination would improve the conversion efficiency.

In addition, when H_2Pc was replaced with cobalt(II) phthalocyanine (CoPc), the CoPc/water interface in the PTCBI/CoPc bilayer acted as a novel and advanced photoanode capable of O_2 evolution in the absence of catalyst (such as IrO_2) [12]. Potentiostatic electrolysis at ITO/PTCBI/CoPc was conducted in alkaline water (pH = 11), where a stable and efficient stoichiometric photoelectrochemical water splitting into O_2 and H_2 took place at an applied bias potential lower than the formal potential (ca. +0.38 V *vs.* Ag/AgCl for the O_2/OH^- couple); that is, O_2 evolution, which was related to highly efficient photocatalysis by CoPc, occurred at the photoanode and H_2 was concurrently obtained at the counter electrode. The O_2 amount linearly increased with the electrolysis time when a constant potential of +0.4 V was applied to the bilayer (Fig. 6), showing that a steady water photolysis involving O_2 evolution takes place at the CoPc/water interface. From a mass spectrometric analysis

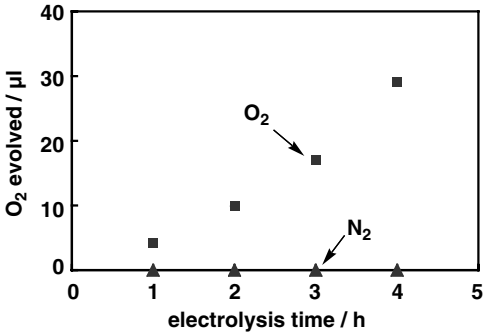


Fig. 6. Time course of the amount of O_2 evolved at ITO/PTCBI/CoPc in an aqueous NaOH solution (pH ~ 11). Applied potential, +0.4 V; film thickness, 160 nm (PTCBI)/90 nm (CoPc). The irradiation was conducted from the PTCBI side.

after the electrolysis, the formation of $^{18}O^{18}O$ from $H_2{}^{18}O$ was confirmed, which evidently shows that the evolved O_2 originates from water. It appears that the oxidative power photogenerated at the CoPc/water interface (+0.69 V *vs.* Ag/AgCl) is sufficiently high to achieve O_2 evolution from OH^- [41]. Although it is also inferred that the level of the valence band (E_{VB}) for H_2Pc is close to that

for CoPc (E_{VB}, 5.07 eV; E_{CB}, 3.75 eV) [38], in the PTCBI/CoPc bilayer, an inner-sphere interaction between the OH^- and the hole-doped CoPc (Co^{III} ion) can be expected to occur especially under the pH condition employed [41]. This phenomenon differs from PTCBI/H_2Pc, which does not lead to O_2 evolution at the solid/liquid interface. This may be a crucial factor in enabling the O_2 evolution to be efficiently induced at the CoPc/water interface. The conventional molecule-based photoelectrodes with highly ordered structures (such as SAMs and LB films) have never been coupled with electron donation from water (or OH^-); however, we have proposed novel examples of water splitting, especially those using layered organic compounds (*i.e.*, PTCBI/H_2Pc + IrO_2, and PTCBI/CoPc) that are responsive to a wide visible-light energy (<750 nm).

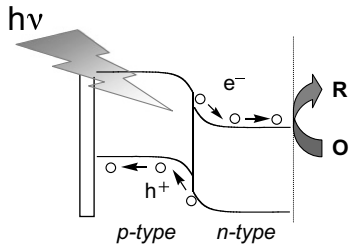


Fig. 7. Schematic illustration for photoinduced reaction at an n-type semiconductor/water interface in the p/n bilayer. R and O denote reductant and oxidant, respectively.

4. Photocathode of p/n organic bilayer working in the water phase

The opposite layer of the PTCBI/H_2Pc on an ITO plate (*i.e.*, ITO/H_2Pc/PTCBI) may exhibit a photocathodic response at the interface of n-type semiconductor/water. In fact, it was shown by voltammetry that a photocathodic current due to $Fe^{III}(CN)_6^{3-}$ reduction occurs at ITO/H_2Pc/PTCBI [13]. However, separate voltammetric studies showed that the photocathodic characteristics of the H_2Pc/PTCBI bilayer are consistent with those of the H_2Pc single layer, indicating that there are pinholes in the PTCBI layer of the bilayer; in other words, H_2Pc is in direct contact with $Fe^{III}(CN)_6^{3-}$ dissolved in water. Thus, it was inferred that the photocathodic current mainly occurs at the H_2Pc

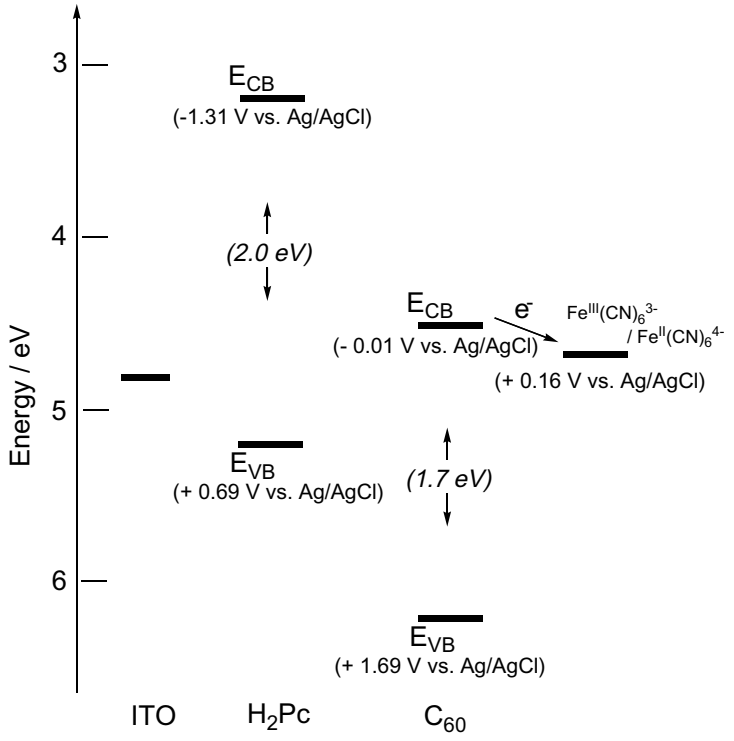


Fig. 8. Schematic energy diagram for photoinduced reduction at ITO/H_2Pc/C_{60}. E_{VB} and E_{CB} denote the energy levels of the valence band and conduction band, respectively.

surface, according to Fig. 3a. However, the action spectrum for the photocathodic current indicated that a broad visible-light absorption (400–750 nm) by PTCBI can also induce photocurrent generation, especially at wavelengths shorter than 500 nm where H_2Pc absorption is absent or relatively weak. This was acceptable based on previous knowledge that the PTCBI exciton alone can contribute to carrier generation through charge separation at the p/n interface [10,11,31]. Therefore, these results revealed the novel photocathodic characteristics at the organic solid/water interface coupled with electron conduction through the n-type semiconductor (Fig. 7), in addition to the ordinary characteristics at the p-type semiconductor/water interface (*cf.*, Fig. 3a).

Since the electron affinity of organic compounds is often low, the number of organic n-type semiconductors is limited; however, fullerene (denoted as C_{60}) is one of the most promising electron conductors. When C_{60} was used in combination with H_2Pc, the C_{60}/water interface in the C_{60}/H_2Pc bilayer also induced the photoinduced reduction of $Fe^{III}(CN)_6^{3-}$, according to Fig. 7 [14]. As shown in Fig. 8, it appeared that the reductive power photogenerated at the C_{60}/water interface is capable of $Fe^{III}(CN)_6^{3-}$ reduction [38,39,42]. The action spectrum for the photocathodic current was measured in terms of the film thickness of the bilayer and compared with the absorption spectrum of the bilayer employed (Fig. 9a and b). The resulting action spectral characteristics were almost consistent with those of the corresponding dry-type cell in which the absorption of the C_{60} layer is mainly effective for photocurrent generation. Similar to the p/n bilayer of the PTCBI layer [10–14], the photocurrent was confirmed to occur at around 500 nm at which no H_2Pc absorption occurs (see Fig. 9a). The previous study on the photovoltaic characteristics of H_2Pc/C_{60} shows that charge separation may be possible by only the absorption of the C_{60} layer [43], which suggests that the photogeneration of carriers in the H_2Pc layer can take place through the migration of the excitation energy of C_{60}. In addition, when comparing the H_2Pc/C_{60} of a thick H_2Pc layer (II) with that of a thin one (I) (*cf.*, the thickness of the C_{60} layer is almost constant), a larger photocurrent was detected in the thinner layer (I), which implies that these action spectra involve the optical filter effect by H_2Pc itself. Considering that the number of photons transmitted to the C_{60} layer can increase with a decrease in the H_2Pc film thickness,

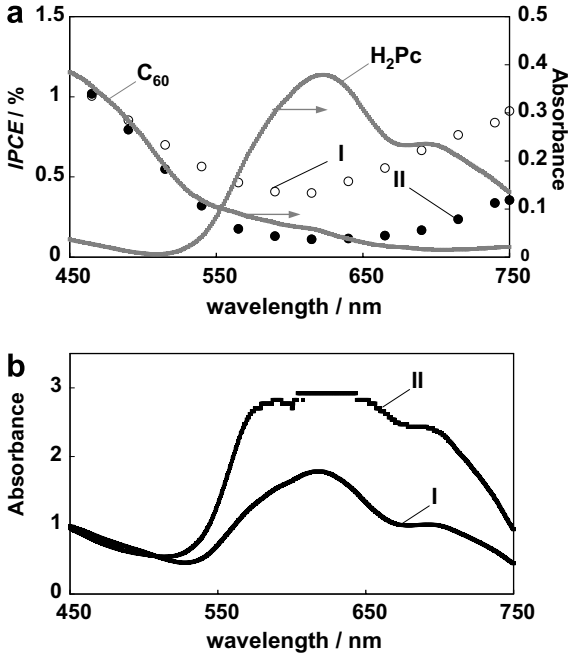


Fig. 9. (a) Action spectra for photocurrent generated at ITO/H_2Pc/C_{60} (○ for I, ● for II), and absorption spectra of C_{60} (15 nm) and H_2Pc (30 nm). Film thickness (I), 90 nm (H_2Pc)/250 nm (C_{60}); film thickness (II), 280 nm (H_2Pc)/215 nm (C_{60}); $K_3Fe(CN)_6$ concentration, 1×10^{-3} mol dm^{-3} (pH 10); applied potential, 0 V (*vs.* Ag/AgCl). (b) Absorption spectra of H_2Pc/C_{60} bilayer for I and II.

Fig. 9a supports that visible-light absorption by C_{60} is essentially effective for photocurrent generation. However, it seems that the resulting action spectra are not consistent with the absorption spectrum of the C_{60} single layer, especially at longer wavelengths where an increase in IPCE values is observed. Although Fig. 9a shows that the H_2Pc layer contributes to the filter effect, visible-light absorption by a thin layer of H_2Pc could also lead to the photocurrent generation. When considering the absorbance (Abs.) of the whole C_{60} layer (for film I) at 515 nm, at which there is little absorption of H_2Pc, the quantum yield ($=IPCE/(1-10^{-Abs.})$) was estimated to be ca. 1.4%, which is of the same order as the corresponding dry-type cell of a H_2Pc/C_{60} bilayer, especially under similar conditions with regard to the irradiated wavelength of monochromatic light as well as the irradiation direction (*cf.*, the film preparation conditions differ in terms of the degree of vacuum, electrode substrate, and film thickness) [43]. The C_{60}/water interface can be one of the most typical examples in which

organic materials efficiently work as a photofunctional interface.

5. Conclusion

The p/n organic bilayer is efficiently responsive to visible light and functions as a stable photoelectrode that works in the water phase. In this bilayer, chemical reaction (oxidation/reduction) at the organic solid/water interface is coupled with photoconduction of the carriers through each layer. This photoelectrode characteristic is based on the photogeneration of carriers in the interior in a p/n organic bilayer, which is distinct from the characteristics of the Schottky interface of a single layer. The p/n organic bilayer creates a molecule-based photofunctional interface that is responsive to a wide visible-light energy of <750 nm. Typically, PTCBI/CoPc is capable of O_2 evolution at the CoPc/water interface; therefore, it exhibits function and stability that is desirable for its application to systems for converting solar energy into hydrogen energy.

In the field of the dry-type photodevices such as solar cells, high energy conversion efficiency has been successfully achieved by controlling the solid (p)/solid (n) interface at which a hybrid planar-mixed molecular heterojunction [44] as well as a codeposited interlayer of the bulk heterojunction are introduced [45,46]. Such treatments were conducted to improve the efficiency for carrier generation at the p/n interface. However, by employing the organic bilayer as a photodevice in the water phase, the authors have recently found that the overall kinetics is dominated by the chemical reaction involving charge/electron transfer at the solid/water interface [15]. Therefore, the fabrication of a more efficient organic material interface is required to obtain improved efficiency in output.

The study on the application of organic bilayers to photodevices in water is now at a nascent stage. A large variety of photoelectrode devices could be fabricated by varying the combinations of both electron and hole conductors. Therefore, it would also become increasingly important to investigate and accumulate fundamental knowledge on a solid/water interface that has potential characteristics. Such a p/n organic bilayer device is extensively and practically applicable to various types of reaction, and its application is expected to reveal a new aspect of photoelectrochemical research and technology, particularly areas in which few examples of inorganic semiconducting materials have been reported.

Acknowledgements

This work was partially supported by Grants-in-Aid for Scientific Research (Nos. 15750110 and 17750118 (T.A.)) and a Grant-in-Aid for Scientific Research in Priority Areas (No. 417 (T.A. and K.N.)) from the Ministry of Education, Culture, Sports, Science and Technology (MEXT) of the Japanese Government.

References

[1] C.D. Dimitrakopoulos, P.R.L. Malenfant, Adv. Mater. 14 (2002) 99.
[2] D.M. de Leeuw, M.M.J. Simenon, A.R. Brown, R.E.F. Einerhand, Synth. Met. 87 (1997) 53.
[3] K-L. Law, Chem. Rev. 93 (1993) 449.
[4] B. Meunier, Chem. Rev. 92 (1992) 1411.
[5] W. Brütting (Ed.), Physics of Organic Semiconductor, Wiley-VCH, Weinheim, 2005.
[6] S.R. Forrest, Chem. Rev. 97 (1997) 1793.
[7] A. Fujishima, K. Honda, Nature 238 (1972) 37.
[8] I. Tsuji, H. Kato, A. Kudo, Chem. Mater. 18 (2006) 1969.
[9] A. Ishikawa, T. Takata, T. Matsumura, J.N. Kondo, M. Hara, H. Kobayashi, K. Domen, J. Phys. Chem. B 108 (2004) 2637.
[10] T. Abe, K. Nagai, M. Kaneko, T. Okubo, K. Sekimoto, A. Tajiri, T. Norimatsu, ChemPhysChem 5 (2004) 716.
[11] T. Abe, K. Nagai, T. Ogiwara, S. Ogasawara, M. Kaneko, A. Tajiri, T. Norimatsu, J. Electroanal. Chem. 587 (2006) 127.
[12] T. Abe, K. Nagai, S. Kabutomori, M. Kaneko, A. Tajiri, T. Norimatsu, Angew. Chem. Int. Ed. 45 (2006) 2778.
[13] T. Abe, K. Nagai, K. Sekimoto, A. Tajiri, T. Norimatsu, J. Electroanal. Chem. 583 (2005) 327.
[14] T. Abe, K. Nagai, K. Sekimoto, A. Tajiri, T. Norimatsu, Electrochem. Commun. 7 (2005) 1129.
[15] T. Abe, K. Nagai, H. Ichinohe, T. Shibata, A. Tajiri, T. Norimatsu, J. Electroanal. Chem. 599 (2007) 65.
[16] M. Kaneko, I. Okura (Eds.), Photocatalysis, Kohdansha-Springer Verlag, Tokyo, 2002.
[17] T. Hasobe, H. Imahori, P.V. Kamat, T.-K. Ahn, S.-K. Kim, D. Kim, A. Fujimoto, T. Hirakawa, S. Fukuzumi, J. Am. Chem. Soc. 127 (2005) 1216.
[18] H. Ma, M.-S. Kang, Q.-M. Xu, K.-S. Kim, A.K.-Y. Jen, Chem. Mater. 17 (2005) 2896.
[19] A.D. Schwab, D.E. Smith, B. Bond-Watts, D.E. Johnston, J. Hone, A.T. Johnston, J.C. de Paula, W.F. Smith, Nano Lett. 4 (2004) 1261.
[20] S. Yang, L. Fan, S. Yang, J. Phys. Chem. B 108 (2004) 4394.
[21] M. Sakomura, K. Ueda, M. Fujihira, Chem. Commun. (2004) 2392.
[22] S. Isoda, Y. Hanazato, K. Akiyama, S. Nishimura, S. Ueyama, Thin Solid Films 441 (2003) 277.
[23] B. O'Regan, M. Grätzel, Nature 353 (1991) 737.

[24] P. Liska, N. Vlachopoulos, M.K. Nazeeruddin, P. Comte, M. Grätzel, J. Am. Chem. Soc. 110 (1988) 3686.
[25] B. O'Regan, J. Moser, M. Anderson, M. Grätzel, J. Phys. Chem. 94 (1990) 8720.
[26] F. Padinger, T. Fromherz, P. Denk, C.J. Brabec, J. Zrttner, H. Hierl, N.S. Sariciftci, Synth. Met. 121 (2001) 1605.
[27] J.M. Kroon, M.M. Wienk, W.J.H. Verhees, J.C. Hummelen, Thin Solid Films 403–404 (2002) 223.
[28] C.W. Tang, Appl. Phys. Lett. 48 (1986) 183.
[29] T. Morikawa, C. Adachi, T. Tsutsui, S. Saito, Nippon Kagaku Kaishi (1990) 962.
[30] D. Wöhrle, L. Kreienhoop, G. Schnurpfeil, J. Elbe, B. Tennigkeit, S. Hiller, D. Schlettwein, J. Mater. Chem. 5 (1995) 1819.
[31] K. Nagai, Y. Fujimoto, H. Shiroishi, M. Kaneko, T. Norimatsu, T. Yamanaka, Chem. Lett. (2001) 354.
[32] K. Nagai, K. Morishita, H. Yoshida, T. Norimatsu, N. Miyanaga, Y. Izawa, T. Yamanaka, Synth. Met. 121 (2001) 1445.
[33] K. Nagai, H. Yoshida, T. Norimatsu, N. Miyanaga, Y. Izawa, T. Yamanaka, Appl. Surf. Sci. 197 (2002) 808.
[34] K. Nagai, T. Norimatsu, N. Miyanaga, T. Yamanaka, Fus. Sci. Technol. 41 (2002) 257.
[35] S. Surdhar, D.A. Armstrong, J. Phys. Chem. 90 (1986) 5915.
[36] A. Eizing, A. Van der Putten, W. Visscher, E. Barendrecht, J. Electroanal. Chem. 200 (1986) 313.
[37] A. Yakimov, S.R. Forrest, Appl. Phys. Lett. 80 (2002) 1667.
[38] R.O. Loutfy, Y.C. Cheng, J. Chem. Phys. 73 (1980) 2902.
[39] A.B.P. Lever, E.R. Milaeva, G. Speier, in: C.C. Leznoff, A.B.P. Lever (Eds.), Phthalocyanines, vol. 3, VCH Publishers Inc., New York, 1993, p. 1.
[40] T. Abe, M. Kaneko, Prog. Polym. Sci. 28 (2003) 1441.
[41] J.H. Zagal, M.A. Gulppi, C. Depretz, D. Lelièvre, J. Porphyrins Phthalocyanines 3 (1999) 355.
[42] P. Peumans, S.R. Forrest, Appl. Phys. Lett. 79 (2001) 126.
[43] K. Murata, S. Ito, K. Takahashi, B.M. Hoffman, Appl. Phys. Lett. 68 (1996) 427.
[44] J. Xue, S. Uchida, B.P. Rand, S.R. Forrest, Appl. Phys. Lett. 85 (2004) 5757.
[45] S. Uchida, J. Xue, B.P. Rand, S.R. Forrest, Appl. Phys. Lett. 85 (2004) 4218.
[46] K. Suemori, T. Miyata, M. Yokoyama, M. Hiramoto, Appl. Phys. Lett. 86 (2005) 063509.

Available online at www.sciencedirect.com
ScienceDirect
Organic Electronics 8 (2007) 272–285
Organic Electronics
www.elsevier.com/locate/orgel

Polymeric light emitting properties and structural relationships of fluorene-based conjugated copolymers containing various hole transporting derivatives

Jong-Hwa Park, Nam Sung Cho, Young Kwan Jung, Hoon-Je Cho, Hong-Ku Shim *, Hyoseok Kim, Yoon Sup Lee

Department of Chemistry (BK21), Korea Advanced Institute of Science and Technology (KAIST), 373-1 Guseong-dong, Yuseong-gu, Daejeon 305-701, Republic of Korea

Available online 18 September 2006

Abstract

A series of new fluorene-based alternating polymers (PF-CZ50, PF-DPA50, PF-PXZ50, PF-PZB50) composed of comonomers containing well-known hole-transporting moieties, namely carbazole, diphenylamine, phenoxazine, and phenothiazine, respectively, were synthesized via Suzuki coupling reactions. The molecular structures of the polymers were characterized with ^{1}H NMR spectroscopy and elemental analysis, and their photophysical, electrochemical, and electroluminescence properties were investigated. The absorption and photoluminescence (PL) emission maxima of the copolymers in the solid state varied depending on which hole-transporting unit was present. Although the polymers' LUMO levels are similar, the differences between their HOMO levels mean they have different hole-transportation properties. Light-emitting devices using the polymers as emitting layers were fabricated with ITO/PEDOT:PSS/polymer/Ca/Al configurations. The emitted light of these polymers ranged from yellowish green to red for the sequence PF-CZ50, PF-DPA50, PF-PXZ50, and PF-PZB50. Especially, PF-PXZ50 and PF-PZB50 emitted almost pure red with good brightness. The planarity of the hole-transporting moieties in the polymers is the main factor affecting the efficiency of these electroluminescence (EL) devices. The planarity of each hole-transporting moiety was calculated by computational analysis using the ab initio Hartree–Fock (HF) with the split-valence 6-31G* basis set. As the magnitude of the non-planarity of the hole-transporting moieties increased, it was found that the EL quantum efficiency of the polymers was enhanced. Compared to PF-CZ50 containing planar carbazole moieties, PF-DPA50 containing a non-planar diphenylamine moiety showed better EL performances without a significant change of the emitting color. In the case of PF-PXZ50 and PF-PZB50, their emission color was red-shifted, and the EL quantum efficiency of their LED devices was enhanced, with respect to the result for PF-CZ50, because of their extra heteroatoms (oxygen and sulfur respectively), which bend the molecules and strengthen their activities as electron donors.
© 2006 Elsevier B.V. All rights reserved.

PACS: 78.60.Fi

Keywords: PLED; Carbazole; Phenoxazine; Phenothiazine; Polyfluorene

* Corresponding author. Tel.: +82 42 869 2827; fax: +82 42 869 2810.
E-mail address: hkshim@kaist.ac.kr (H.-K. Shim).

1566-1199/$ - see front matter © 2006 Elsevier B.V. All rights reserved.
doi:10.1016/j.orgel.2006.08.002

1. Introduction

Polymer light-emitting diodes (PLEDs) have attracted much scientific and technological research interest since their first discovery in 1989 [1], and are now emerging as commercial products. Electroluminescent conjugated polymers have a number of advantages over inorganic or organic small molecules for use in LEDs: better processability, lower operating voltages, faster response times, lower production costs, and high flexibility. Furthermore, electroluminescent conjugated polymers provide the possibility of uniformly covering large areas by inexpensive solution processing techniques such as spin coating, and their optical and electrical properties can be fine-tuned by varying their structures [2,3].

For full color displays, red, green, and blue light-emitting polymers with low turn-on and operating voltages, high luminescence efficiencies, and stability are required. Among the various methods for color tuning, covalently attaching a chromophore to the polymer has been the most widely used because aggregation and excimer formation is prevented, and efficient energy transfer from the polymer main backbone chromophores to the dye chromophores easily confines the singlet excitons. If two chromophores with different energy band gaps are copolymerized, energy transfer occurs from the moiety with the larger band gap to that with the smaller band gap, and emission from the latter dominates [4–6].

Polyfluorene (PF) has been selected for the polymer backbone, because of its large band gap, high photoluminescence quantum efficiency, good thermal stability as well as good solubility and film-forming property. Numerous PFs with various comonomers have been developed with a view to obtaining stable, highly efficient, red, green, and blue emitters [7–13].

Many studies of the introduction of charge-transporting moieties into π-conjugated polymers for efficient LEDs have been reported [14–17]. It is known that the hole mobilities of most emissive π-conjugated polymers are generally orders of magnitude larger than their electron mobilities [18]. Nevertheless, it is important to investigate the effects of hole-transporting derivatives on efficient PLEDs, because improving the charge injection and the balance of charge carriers are crucial factors deciding the efficiencies of PLEDs. The most well-known hole-transporting moieties are aromatic amines [19,20]. Aromatic amines possess low ionization potentials, which facilitate the formation of cation radicals (holes) [15]. Recently, phenoxazine [21,22] and phenothiazine [11,23] derivatives have attracted considerable research interest in diverse electronic applications. Due to their extra heteroatoms, they are strong electron donors which give rise to unique electro-optical properties. In addition, their non-planar ring structures impede π-stacking aggregation and intermolecular excimer formation in the polymer main-chains [11].

In this paper, we report the effects of the incorporation of various aromatic amines – carbazole, diphenyl amine, phenoxazine and phenothiazine – into π-conjugated polymer main-chains. We determined the variations of the color tunability, electrochemical properties, and EL efficiency of the polymers with the non-planarity of the fused aromatic amines by carrying out optical and electronic measurements, and computational analysis. We conclude that the planarity of the hole-transporting material is an important factor in PLED efficiency.

2. Experimental section

2.1. Measurements

^{1}H and ^{13}C NMR spectra were recorded on a Bruker AVANCE 400 spectrometer with tertramethylsilane as an internal reference. Elemental analysis was performed using EA-1110-FISONS elemental analyzer. The number- and weight-average molecular weight of the polymer was determined by gel permeation chromatography (GPC) on Waters GPC-150C instrument using tetrahydrofuran (THF) as eluent and monodisperse polystyrene as standard. UV–vis spectra were measured by using a Jasco V-530 UV/vis Spectrometer. PL spectra were measured by using Spex Fluorolog-3 spectrofluorometer. Cyclic voltammetry measurement was performed on an AUTOLAB/PGSTAT12 at room temperature with a three-electrode cell in a solution of 0.1 M tetrabutylammonium tetrafluoroborate in anhydrous acetonitrile at room temperature under nitrogen gas with a scan rate of 50 mV/s. The working electrode was polymer coated platinum, the counter electrode was a platinum wire, and the reference electrode was $Ag/AgNO_3$ (0.10 M) which was separated by a diaphragm. The measurements were calibrated using ferrocene as a standard. Mass spectra were obtained with an Autospec ultra spectrometer and a MALDI-TOF mass spectrometer Voyager-DESTR. FT-IR spectra

were obtained using a Nicolet model 800 spectrometer with samples prepared as KRS-5 pellets.

2.2. Device fabrication and characterization

A hole injection layer of poly(3,4-ethylenedioxythiophene) (PEDOT) doped with poly(styrenesulfonic acid) (PSS) (PEDOT:PSS, Bayer Al 4083) was spin-coated onto the pre-patterned ITO anode and dried. Polymer solution was then spin-coated onto the PEDOT:PSS layer and dried. Ca/Al (100 nm/100 nm) cathode was vacuum-deposited onto the polymer film through shadow mask at a pressure below 1×10^{-6} Torr, yielding an active area of 0.04 cm^2. For PLED measurements, EL spectra were obtained with a Minolta CS-1000. The current–voltage–luminance characteristics were measured with a current–voltage source (Keithley 238) and a luminescence detector (Minolta LS-100).

2.3. Computational details

The geometries of monomers were optimized using the ab initio Hartree–Fock (HF) with the split-valence 6-31G* basis sets. Molecular orbital energy levels of the HOMO and LUMO for monomers computed at the DFT level of theory with the B3LYP functional [24] using HF optimized geometries (B3LYP/HF). To obtain more reliable energy levels which include some account of electron correlation, DFT using the B3LYP functional was used with the 6-31G* basis set. All calculations described here were carried out with the GAUSSIAN 03 program [25].

2.4. Materials

Carbazole, diphenyl amine, phenoxazine, phenothiazine, 4-bromophenylacetonitrile, 1-bromohexane, potassium *tert*-butoxide, phosphoryl trichloride, *N*,*N*-dimethylformamide (99.8%, anhydrous), 2,7-dibromofluorene, 1-bromooctane, *t*-butyllithium (1.7 M in hexane), 2-isopropoxy-4,4,5,5-tetramethyl-1,3,2-dioxaborolane and Aliquat® 336 were purchased from Aldrich. Tetrakis (triphenylphosphine)palladium(0) was purchased from DNF Solution Co. Solvents with analytical-grade were used during the whole experiments, and all chemicals were used without further purification. 2,7-dibromo-9,9-dioctylfluorene() was synthesized according to procedures outlined in the literature [26].

2.5. Synthesis of 10-n-hexylcarbazole (*1a*)

1-Bromohexane (16.56 g, 100.36 mmol), carbazole (10 g, 59.80 mmol), sodium hydroxide (20.0 g, 500 mmol), and dimethylsulfoxide (DMSO) (150 mL) were placed in a 500 mL two-neck round-bottom flask, and then this mixture was stirred for 1 day at room temperature. The resulting mixture was extracted with EA/brine and then dried with $MgSO_4$. After filtering, the solvent was evaporated. The resulting solid was recrystallized in methylene chloride and methanol. The product yield was 69% (10.37 g). ^{1}H NMR ($CDCl_3$, ppm) δ 8.10 (d, 2H), 7.45 (m, 4H), 7.21 (t, 2H), 4.29 (t, 2H), 1.86 (m, 2H), 1.31 (m, 6H), 0.85 (t, 3H). ^{13}C NMR ($CDCl_3$, ppm) δ 140.356, 125.492, 122.757, 120.350, 118.604, 108.282, 42.898, 31.515, 28.835, 26.883, 22.483, 14.087. Anal. Calcd for $C_{18}H_{21}N$: C, 86.01; H, 8.42; N, 5.57. Found: C, 86.39; H, 8.01; N, 5.81.

2.6. Synthesis of n-hexyldiphenylamine (*1b*)

It was synthesized according to the procedure of 1a. Yellowish liquid was obtained after purification by column chromatography with hexane. The product yield was 81%. ^{1}H NMR ($CDCl_3$, ppm) δ 7.27 (t, 4H), 7.03 (m, 6H), 3.72 (t, 2H), 1.71 (m, 2H), 1.37 (m, 6H), 0.92 (m, 3H), ^{13}C NMR ($CDCl_3$, ppm) δ 148.054, 129.187, 120.951, 52.311, 32.100, 27.367, 27.029, 22.624, 14.327. Anal. Calcd for $C_{18}H_{23}N$: C, 85.32; H, 9.15; N, 5.53 Found: C, 85.42; H, 10.20; N, 6.46. Electron-impact mass spectrometry (EIMS) *m*/*z*: 253.17 Calcd.: 253.18.

2.7. Synthesis of 10-n-hexylphenoxazine (*1c*)

It was synthesized according to the procedure of 1a. White solid was obtained. The product yield was 71%. ^{1}H NMR (DMSO-d_6, ppm) δ 6.78 (m, 2H), 6.60 (m, 6H), 3.48 (t, 2H), 1.47 (m, 2H), 1.32 (m, 6H), 0.83 (m, 3H), ^{13}C NMR (DMSO-d_6, ppm) δ 140.478, 135.201, 130.089, 127.482, 112.680, 110.014, 44.105, 30.945, 26.146, 24.878, 22.403, 14.004. Anal. Calcd for $C_{18}H_{21}NO$: C, 80.86; H, 7.92; N, 5.24. Found: C, 81.03; H, 7.75; N, 5.59.

2.8. Synthesis of 10-n-hexylphenothiazine (*1d*)

It was synthesized according to the procedure of 1a. The resulting liquid was purified by column chromatography. The product yield was 67% (9.53

g). ^{1}H NMR (DMSO-d_6, ppm) δ 7.12 (m, 4H), 6.88 (m, 4H), 3.75 (t, 2H), 1.57 (m, 2H), 1.30–1.13 (m, 6H), 0.74 (t, 3H). ^{13}C NMR (DMSO-d_6, ppm) δ 145.05, 127.97, 127.51, 122.81, 116.24, 48.20, 31.78, 27.45, 26.94, 23.48, 16.08. Anal. Calcd for C_{18}H21NS: C, 76.28; H, 7.47; N, 4.94; S, 11.31. Found: C, 76.90; H, 7.65; N, 6.02; S, 10.11. EIMS *m*/*z*: 283.14 Calcd.: 283.14.

2.9. Synthesis of 9-n-hexylcarbazole-3, 6-dicarbaldehyde (**2a**)

A 500 mL three necked flask containing 26.2 mL (340 mmol) of anhydrous DMF was cooled in an ice bath. To this solution, 25.6 mL (279 mmol) of phosphorous oxychloride was added dropwisely for 30 min. Compound 1a (7 g, 27.85 mmol) in 30 mL of 1,1,2-trichloroethane was added to the above solution and heated to ca. 90 °C for 2 days. This solution was cooled to room temperature, poured into ice water, and neutralized to pH 6–7 by dropwise addition of saturated aq. sodium hydroxide solution. The mixture was extracted with EA/water. The organic layer was dried with anhydrous $MgSO_4$ and then concentrated under a reduced pressure. The crude product was purified by column chromatography. A white solid was obtained (5.6 g, 65%). ^{1}H NMR ($CDCl_3$, ppm) δ 10.04 (s, 2H), 8.83 (s, 2H), 8.01 (d, 2H), 7.80 (d, 2H), 4.46 (t, 2H), 1.69 (m, 2H), 1.16 (m, 6H), 0.73 (t, 3H) ^{13}C NMR ($CDCl_3$, ppm) 191.415, 144.715, 129.598, 127.858, 124.235, 123.104, 109.723, 43.763, 31.376, 28.838, 26.788, 22.421, 14.488. Anal. Calcd for $C_{20}H_{21}NO_2$: C, 78.15; H, 6.89; N, 4.56. Found: C, 77.21; H, 6.67; N, 4.65. EIMS *m*/*z*: 307.12 Calcd.: 307.16.

2.10. Synthesis of 4,4′-hexylimino-bisbenzaldehyde (**2b**)

It was synthesized according to the procedure of 2a. Yellowish liquid was obtained. The product yield was 55%. ^{1}H NMR ($CDCl_3$, ppm) δ 9.86 (s, 2H), 7.77 (d, 4H), 7.12 (d, 4H), 3.82 (t, 2H), 1.68 (m, 2H), 1.27 (m, 6H), 0.85 (t, 3H), 0.73 (t, 3H) ^{13}C NMR ($CDCl_3$, ppm) 190.345, 151.727, 131.446, 130.381, 120.515, 52.351, 31.010, 27.525, 26.204, 23.089, 14.274. Anal. Calcd for $C_{20}H_{23}NO_2$: C, 77.64; H, 7.49; N, 4.53. Found: C, 76.20; H, 7.11; N, 4.84. EIMS *m*/*z*: 309.15 Calcd.: 309.17.

2.11. Synthesis of 10-n-hexylphenoxazine-3, 7-dicarbaldehyde (**2c**)

It was synthesized according to the procedure of 2a. Greenish solid was obtained. The product yield was 56%. ^{1}H NMR (DMSO-d_6, ppm) δ 9.66 (s, 2H), 7.41 (dd, 2H), 7.03 (d, 2H), 6.91 (d, 2H), 3.71 (t, 2H), 1.53 (m, 2H), 1.29 (m, 6H), 0.84 (t, 3H) ^{13}C NMR ($CDCl_3$, ppm) 189.639, 144.829, 137.322, 131.125, 129.489, 128.405, 114.640, 111.519, 44.655, 31.394, 26.387, 24.973, 22.555, 14.031. Anal. Calcd for $C_{20}H_{21}NO_3$: C, 74.28; H, 6.55; N, 4.33. Found: C, 74.48; H, 6.47; N, 4.91.

2.12. Synthesis of 10-n-hexylphenothiazine-3, 7-dicarbaldehyde (**2d**)

It was synthesized according to the procedure of 2a. A bright yellow solid was obtained (4.3g, 71%). ^{1}H NMR ($CDCl_3$, ppm) δ 9.78 (s, 2H), 7.63 (q, 2H), 7.54 (2, 2H), 6.91 (d, 2H), 3.89 (t, 2H), 1.79 (q, 2H), 1.43 (m, 2H), 1.28 (m, 4H), 0.85 (m, 3H). ^{13}C NMR ($CDCl_3$, ppm) δ 189.79, 148.84, 131.93, 130.10, 128.35, 124.36, 115.51, 48.46, 31.24, 26.56, 26.33, 22.47, 13.89. Anal. Calcd for $C_{20}H_{21}NO_2S$: C, 70.77; H, 6.24; N, 4.13; S, 9.45. Found: C, 69.50; H, 6.35; N, 4.93; S, 9.61. EIMS *m*/*z*: 339.12 Calcd.: 339.13.

2.13. 3,6-Bis[2-(4′-bromophenyl)-2-cyanovinyl]-9-hexylcarbazole (**3a**)

Compound **2a** (3 g, 9.76 mmol), 4-bromophenylacetonitrile (7.65 g, 39.04 mmol), and methanol (100 mL) were placed in a 250 mL two-neck round-bottom flask at room temperature. A catalytic amount of potassium *tert*-butoxide in methanol was added into this mixture. After 12 h, the bright yellow solid was filtered and dried. The resulting solid was recrystallized in methylene chloride and methanol, and then the solid was dried in vacuo. The resulting product yield was 42% (2.7 g). ^{1}H NMR (DMSO-d_6, ppm) δ 8.72 (s, 2H), 8.13 (d, 2H), 8.08 (s, 2H), 7.73 (d, 2H), 7.67 (m, 8H), 4.45 (t, 2H), 1.88 (m, 2H), 1.29 (m, 6H), 0.82 (t, 3H). ^{13}C NMR ($CDCl_3$, ppm) δ 143.05, 142.09, 133.85, 132.09, 127.57, 127.11, 125.41, 123.01, 122.89, 122.68, 118.53, 109.62, 106.89, 43.54, 31.43, 28.92, 26.84, 22.48, 13.97. Anal. Calcd for $C_{36}H_{29}Br_2N_3$: C, 65.17; H, 4.41; N, 6.33. Found: C, 65.32; H, 4.54; N, 6.32. MALDI-TOF *m*/*z*: 663.00 Calcd.: 661.07.

2.14. Bis{4-[2-(4′-bromophenyl)-2-cyanovinyl]-phenyl}-hexylamine (**3b**)

It was synthesized according to the procedure of 3a. The bright yellow solid was obtained. The product yield was 35%. ^{1}H NMR ($CDCl_3$, ppm) δ 7.83 (d, 4H), 7.52 (m, 8H), 7.42 (s, 2H), 7.10 (d, 4H), 3.80 (t, 2H), 1.69 (m, 2H), 1.31 (m, 6H), 0.85 (t, 3H). ^{13}C NMR ($CDCl_3$, ppm) δ 148.86, 141.76, 133.85, 132.13, 131.03, 127.19, 126.92, 122.80, 120.75, 118.27, 107.22, 52.34, 31.52, 27.50, 26.64, 22.60, 13.99. Anal. Calcd for $C_{36}H_{31}Br_2N_3$: C, 64.98; H, 4.70; N, 6.31. Found: C, 65.74; H, 4.67; N, 6.53.

2.15. 3,7-Bis[2-(4′-bromophenyl)-2-cyanovinyl]-10-hexylphenoxazine (**3c**)

It was synthesized according to the procedure of 3a. The bright red solid was obtained. The product yield was 41%. ^{1}H NMR ($CDCl_3$, ppm) δ 7.50 (dd, 8H), 7.36 (d, 2H), 7.17 (d, 4H), 6.47 (d, 2H), 3.48 (t, 2H), 1.63 (m, 2H), 1.36 (m, 6H), 0.90 (t, 3H). ^{13}C NMR ($CDCl_3$, ppm) δ 144.49, 140.76, 134.33, 133.66, 132.11, 127.20, 127.12, 126.71, 122.80, 118.10, 115.64, 111.57, 106.93, 44.30, 31.49, 26.50, 22.64, 14.04. Anal. Calcd for $C_{36}H_{29}Br_2N_3O$: C, 63.64; H, 4.30; N, 6.18. Found: C, 64.22; H, 4.35; N, 6.39.

2.16. 3,7-Bis[2-(4′-bromophenyl)-2-cyanovinyl]-10-hexylphenothiazine (**3d**)

It was synthesized according to the procedure of 3a. The bright red solid was obtained. The product yield was 65%. ^{1}H NMR (DMSO-d_6, ppm) δ 7.93 (s, 2H), 7.85 (d, 2H), 7.72–7.64 (m, 10H), 7.20 (d, 2H), 3.97 (t, 2H), 1.70 (m, 2H), 1.41 (m, 2H), 1.27 (m, 4H), 0.83 (m, 3H). ^{13}C NMR (DMSO-d_6, ppm) δ 145.12, 141.45, 133.20, 132.00, 129.43, 128.29, 127.69, 127.40, 122.07, 122.03, 117.86, 115.94, 1.6.35, 47.04, 30.75, 25.89, 25.65, 22.05, 13.79. Anal. Calcd for $C_{36}H_{29}Br_2N_3S$: C, 62.17; H, 4.20; N, 6.04; S, 4.61. Found: C, 61.82; H, 4.34; N, 6.01; S, 4.88.

2.17. Synthesis of 2,7-Bis(4,4,5,5,-tetramethyl-1,3,2-dioxaborolan-2-yl)-9,9′-dioctylfluorene (**5**)

To a solution of 2,7-dibromo-9,9′-dioctylfluorene (7.0 g, 12.8 mmol) in THF (120 mL) at −78 °C was added, by syringe, 33.79 mL (57.42 mmol) of *t*-butyllithium (1.7 M in hexane). The mixture was stirred at −78 °C for 2 h. 2-Isopropoxy-4,4,5,5,-tetramethyl-1,3,2-dioxaborolane (7.97 mL, 38.4 mmol) was added to the solution, and the resulting mixture was stirred at −78 °C for 1 h and warmed to room temperature and stirred for 40 h. The mixture was poured into water, extracted with dichloromethane and dried over $MgSO_4$. The solvent was removed by solvent evaporation, and the residue was purified by several re-precipitation in hexane to provide 4.82 g (59%) of the product as a white solid. ^{1}H NMR ($CDCl_3$, ppm) δ 7.78 (d, 2H), 7.72 (s, 2H), 7.70 (d, 2H), 1.97 (m, 4H), 1.37 (s, 24H), 1.18-0.99 (m, 20H), 0.79 (t, 6H), 0.53 (m, 4H). ^{13}C NMR ($CDCl_3$, ppm) δ 150.45, 143.89, 133.62, 128.89, 119.35, 83.69, 55.16, 40.07, 31.76, 29.91, 29.18, 29.13, 24.92, 23.57, 22.57, 14.05. Anal. Calcd for $C_{41}H_{64}B_2O_4$: C, 76.64; H, 10.04. Found: C, 77.00; H, 10.17.

2.18. General polymerization procedure [9]

Into 100 mL two-neck flask were added 1.56 mmol of dibromo compounds (3a, 3b, 3c, or 3d) and 1.56 mmol of 2,7-bis(4,4,5,5-tetramethyl-1,3,2-dioxaborolan-2-yl)-9,9-dioctylfluorene in 25 mL of anhydrous toluene. Water soluble Pd(0) complex (0.02 g), tetrakis(triphenylphosphine)palladium (1 mol%) was transferred into the mixture in dry box. Subsequently, 2 M aqueous sodium carbonate (5.4 mL, 10.7 mmol) deaerated for 30 min and the phase transfer catalyst, Aliquat®336 (several drops) in toluene purged under nitrogen for 1 h was transferred via cannula. The reaction mixture was stirred at 80 °C for 3 days and then the excess amount of bromobenzene, the end capper, dissolved in 1 mL of anhydrous toluene was added and stirring continued for 12 h. The reaction mixture is cooled to about 50 °C, added slowly to a vigorously stirred mixture of 200 mL of methanol. The polymer fibers are collected by filtration and re-precipitation from methanol and acetone. The polymers are purified further by washing for 2 days in a Soxhlet apparatus with methanol and acetone to remove oligomers and catalyst residues, and column chromatographied with a chloroform solution of the polymer. The re-precipitation procedure in chloroform/methanol is then repeated a several times. The resulting polymers were soluble in common organic solvents. The yield was 58–81%.

2.19. Poly{9,9-dioctylfluorene-2,7-diyl-co-3,6-bis(2-phenyl-2-cyanovinyl)-9-hexylcarbazole-4′,4′-diyl} (PF-CZ50)

2,7-bis(4,4,5,5-tetramethyl-1,3,2-dioxaborolan-2-yl)-9,9-dioctylfluorene (5) (0.50 equiv.) and CZ (3a)

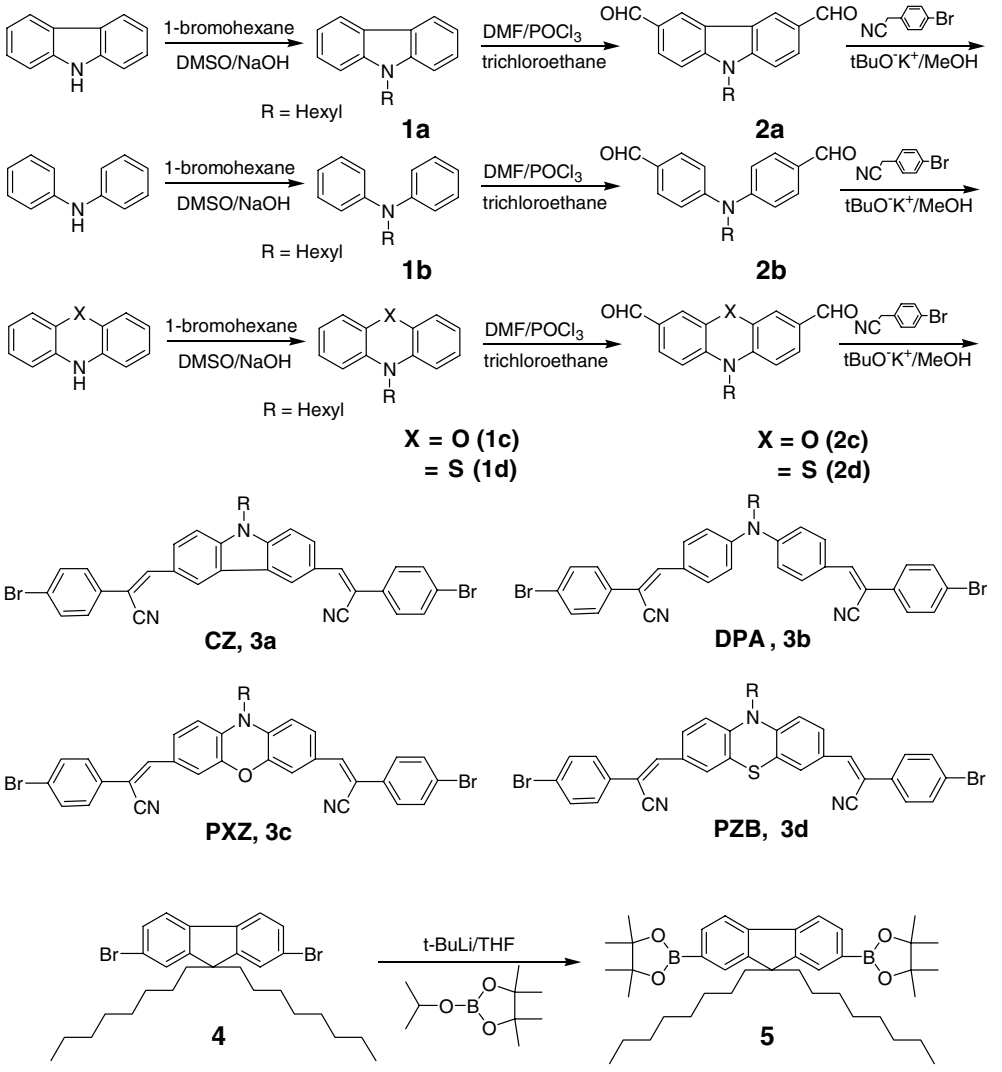
(0.50 equiv.) were used in this polymerization. ^{1}H NMR ($CDCl_3$, ppm) δ aromatic and vinylene; 8.80–7.43 (22H), aliphatic; 4.30–4.10 (2H), 2.06–0.70 (~45H). Element Anal. Found: C, 85.96%; H, 8.74%; N, 4.35%.

2.20. Poly{9,9-dioctylfluorene-2,7-diyl-co-bis{4-[2-(4′-bromophenyl)-2-cyanovinyl]-phenyl}-hexylamine-4′,4′-diyl} (PF-DPA50)

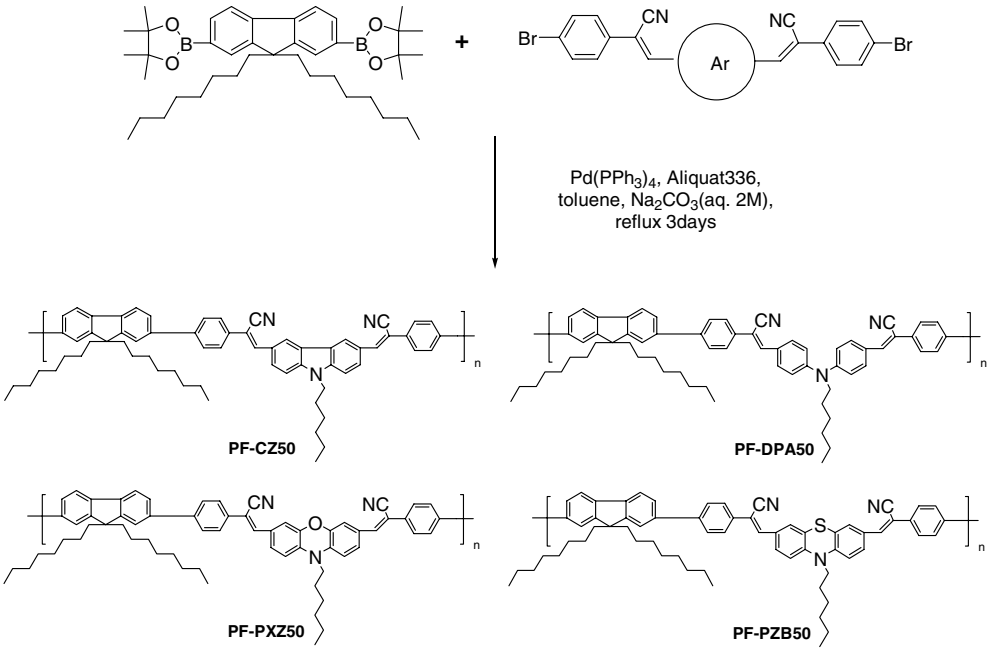
2,7-bis(4,4,5,5-tetramethyl-1,3,2-dioxaborolan-2-yl)-9,9-dioctylfluorene (5) (0.50 equiv.) and DPA (3b) (0.50 equiv.) were used in this polymerization. ^{1}H NMR ($CDCl_3$, ppm) δ aromatic and vinylene; 8.05–6.90 (24H), aliphatic; 3.90–3.71 (2H), 2.05–0.70 (~45H). Element Anal. Found: C, 86.89%; H, 8.32%; N, 4.62%.

2.21. Poly{9,9-dioctylfluorene-2,7-diyl-co-3,7-bis(2-phenyl-2-cyanovinyl)-10-hexylphenoxazine-4′,4′-diyl} (PF-PXZ50)

2,7-bis(4,4,5,5-tetramethyl-1,3,2-dioxaborolan-2-yl)-9,9-dioctylfluorene (5) (0.50 equiv.) and PXZ (3c) (0.50 equiv.) were used in this polymerization. ^{1}H NMR ($CDCl_3$, ppm) δ aromatic and vinylene; 7.80–6.50 (22H), aliphatic; 3.55–3.30 (2H), 2.10–0.55 (~45H). Element Anal. Found: C, 83.79%; H, 8.09%; N, 4.50%.



Scheme 1. Synthetic routes of the monomers.



Scheme 2. Synthetic routes of the polymers.

2.22. Poly{9,9-dioctylfluorene-2,7-diyl-co-3,7-bis(2-phenyl-2-cyanovinyl)-10-hexylphenothiazine-4′,4′-diyl} (PF-PZB50)

2,7-bis(4,4,5,5-tetramethyl-1,3,2-dioxaborolan-2-yl)-9,9-dioctylfluorene (5) (0.50 equiv.) and PZB (3d) (0.50 equiv.) were used in this polymerization. ^{1}H NMR ($CDCl_3$, ppm) δ aromatic and vinylene; 8.80–7.30 (22H), aliphatic; 4.17–3.67 (2H), 2.12–0.76 (∼45H). Element Anal. Found: C, 82.98%; H, 7.80; N, 3.80; S, 4.78 (see Scheme 1 and 2).

3. Results and discussion

3.1. Synthesis and characterization of the polymers

All the copolymers were found to be soluble in common organic solvents. Each copolymer was easily spin-coated onto an ITO substrate, and was found to produce transparent and homogeneous thin films. The number average molecular weights (M_n) and the weight average molecular weights (M_w) of the copolymers were determined with gel permeation chromatography using polystyrene standards, and found to range from 11,000 to 34,000 (M_n) and from 22,000 to 58,000 (M_w), respectively, with polydispersity indexes (PDI) ranging from 1.7 to 2.7. The yields of the copolymers ranged from 58% to 81%. All the copolymers were end-capped with bromobenzene via Suzuki copolymerizations. The polymerization results for the synthesized copolymers are summarized in Table 1. The molecular structures of polymers were confirmed by FT-IR spectroscopy. The most distinctive functional group of the polymers which can be confirmed with IR spectroscopy is cyano group. The cyano group produces a medium-intensity, sharp band in the triple-bond region of the spectrum (2270–2210 cm^{-1}), and conjugation with double bonds or aromatic rings moves this absorption to lower frequency. As a result, the absorption band due to stretching of cyano groups in the polymers typically appears at 2210 cm^{-1}.

3.2. Optical and photoluminescence properties

Fig. 1 shows the normalized UV–vis absorption and PL emission spectra of the polymers in the chloroform solution. In solution, the energy transfer from the higher energy segment to the lower energy

Table 1
Polymerization Results

Copolymers	M_w	M_n	PDI (M_w/M_n)	Yield (%)
PF-CZ50	58,000	34,000	1.7	58
PF-DPA50	26,000	12,000	2.2	63
PF-PXZ50	22,000	11,000	2.0	71
PF-PZB50	65,000	24,000	2.7	81

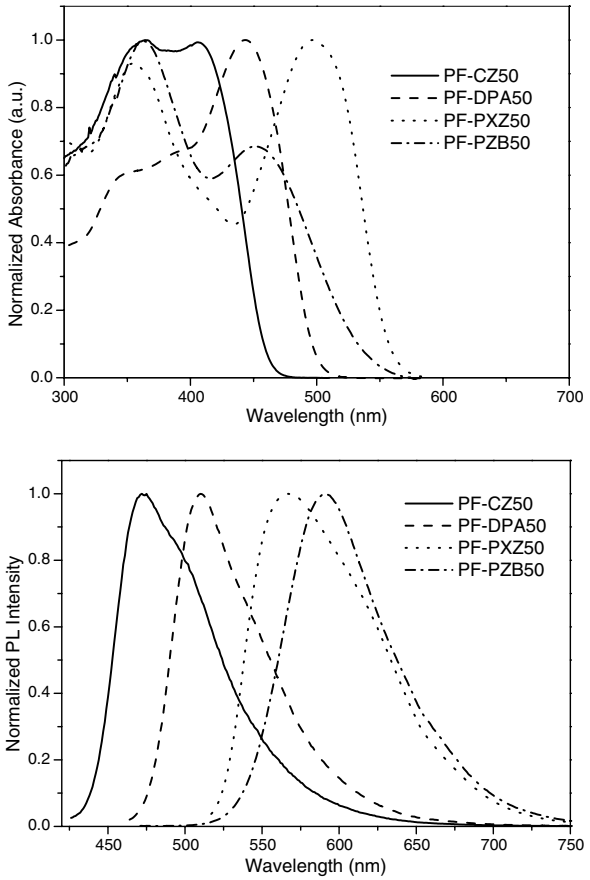


Fig. 1. UV–vis absorption and PL spectra of the polymers in the chloroform solution.

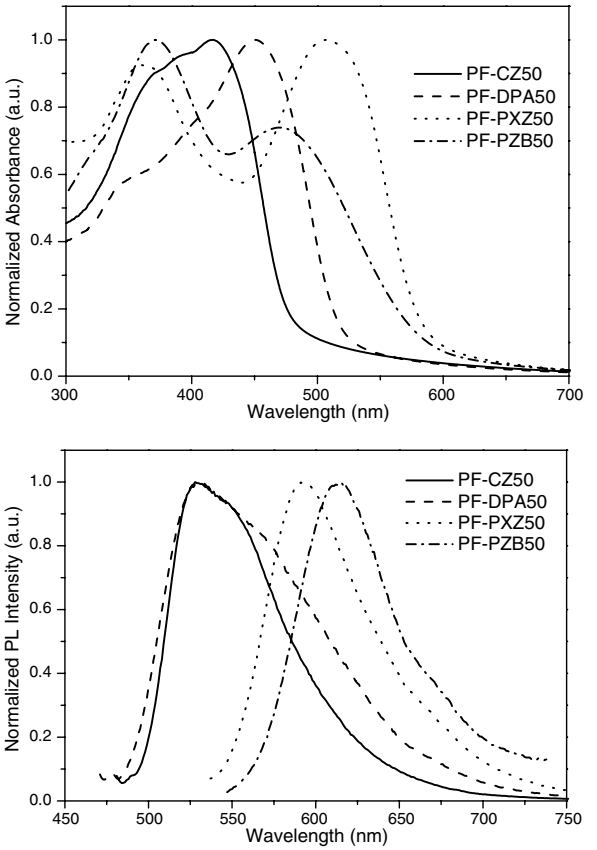


Fig. 2. UV–vis absorption and PL spectra of polymers as films.

site occurs mainly along the polymer chain. In other words, the intramolecular energy transfer occurs from the excitons created on the fluorene backbone to the N-containing comonomer units in the solution state. In the film, all of the polymers exhibit two absorption peaks, as shown in Fig. 2. The peak near 380 nm is due to the fluorene unit, and the other peak above 410 nm is due to the comonomer unit. The spectral characteristics of the alternating copolymers vary significantly with the hole-transporting moiety. The absorption maxima were found to be shifted to longer wavelengths in the sequence PF-CZ50, PF-DPA50, PF-PZB50, and PF-PXZ50. Interestingly, only in the case of PF-PZB50 was the maximum absorption peak due to the fluorene unit bigger than the peak due to the N-containing comonomer unit.

The film of the poly(9,9-dioctylfluorene-2,7-diyl) (PDOF) homopolymer exhibits PL emission maxima at 420 and 440 nm [9]. These two strong and sharp peaks are not present in the PL spectra of the copolymers, as shown in Fig. 2. In contrast, the emission peaks due to the N-containing comonomer units dominate the PL spectra of the copolymers, indicating that the inclusion of these units quenches the PDOF emission. These large red-shifts in the PL maxima arise because the conjugation lengths of the copolymers are longer than that of PDOF. The PL emission maxima of the copolymers PF-CZ50, PF-DPA50, PF-PXZ50, and PF-PZB50 were found at 528, 529, 593, and 614 nm, respectively. In the case of PF-DPA50, its PL emission maximum was found to be almost identical compared to that of PF-CZ50. Comparing to PF-PZB50, the absorption spectrum of PF-PXZ50 was slightly red-shifted with respect to that of PF-PZB50, but its PL emission spectrum was blue-shifted with respect to that of PF-PZB50. These results suggest that energy transfer from the fluorene unit to the PZB comonomer unit may be more efficient than to the PXZ comonomer unit.

Both the absorption and the emission spectra of the film state are more red-shifted and broader than those of the solution state, because of the increased

Table 2
Spectroscopy data

Copolymers	λ_{max} (nm)					CIE coordinates (x, y)
	UV-sol[a]	UV-film[b]	PL-sol[a]	PL-film[b]	EL emission	
PF-CZ50	364, 406	417	472	528	547	(0.37, 0.49)
PF-DPA50	443	451	510	529	531	(0.43, 0.54)
PF-PXZ50	355, 497	362, 507	567	593	592	(0.58, 0.42)
PF-PZB50	362, 451	369, 469	591	614	614	(0.63, 0.36)

[a] Measured in chloroform solution.
[b] Measured as thin films onto fused quartz plates.

Table 3
Electrochemical data

Copolymers	$\lambda_{onset,abs}$ (nm)	E_g (eV)[a]	E_{HOMO} (eV)[b]	E_{LUMO} (eV)[c]
PF-CZ50	477	2.60	−5.67	−3.07
PF-DPA50	517	2.40	−5.44	−3.04
PF-PXZ50	582	2.13	−5.23	−3.10
PF-PZB50	580	2.14	−5.26	−3.12

[a] Calculated from the film state absorption onset wavelength.
[b] Calculated regarding the first oxidation potential of Ferrocene as −4.8 eV.
[c] Estimated by subtraction of the optical band-gap from the electrochemically determined HOMO level.

Table 4
Orbital energies (in eV) from the B3LYP/HF calculations for monomers

	HOMO	B3LYP/HF LUMO	E_g
F-CZ	−5.46	−1.87	3.59
F-DPA	−5.43	−1.98	3.45
F-PXZ	−5.02	−1.94	3.08
F-PZB	−5.19	−2.01	3.18

intermolecular interactions between neighboring molecules in the film state. The polymers having more planar structure showed large shift of emission maxima. The emission maximum of PF-CZ50 in the film state was 56 nm red-shifted than that of the solution state. This shift is more than two times larger than that of the other polymers – PF-PXZ50 (26 nm), PF-PZB50 (23 nm), PF-DPA50 (19 nm). The more non-planar moieties are efficient for impeding π-stacking aggregation and intermolecular excimer formation which is related to the improvement of the overall external quantum efficiency of an LED devices. Table 2 lists all the spectroscopy data of the polymers.

3.3. Electrochemical properties of the polymers

Cyclic voltammetry (CV) was employed to investigate the redox behavior of the polymers and to estimate their HOMO and LUMO energy levels. The electrochemical data for the polymers are listed in Table 3. To convert the measured redox behavior

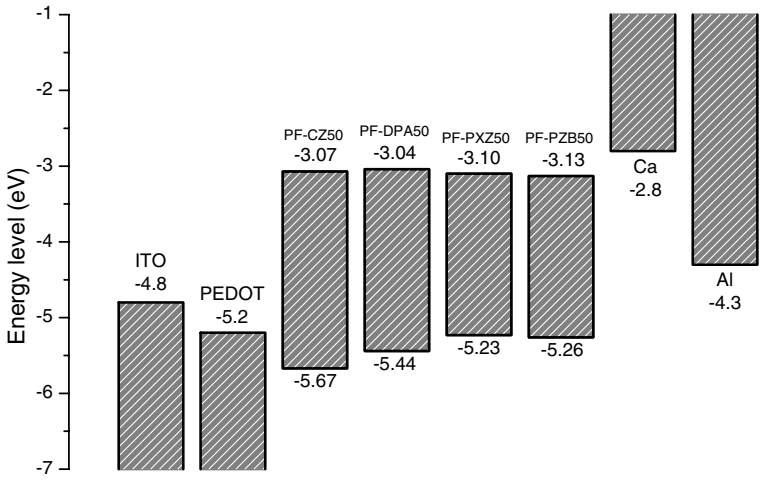


Fig. 3. Energy level diagram for the polymers.

into estimates of the HOMO and LUMO levels, we used an empirical relationship based on detailed comparison of valence effective Hamiltonian calculations and experimental electrochemical measurements, assuming that the energy level of ferrocene/ferrocenium is 4.8 eV below the vacuum level [27,28].

In general, the fluorene copolymers only exhibit oxidation curves, because they are intrinsic p-type semiconductors [29]. As expected, we were unable to record cathodic scans for these polymers. The LUMO energies of these copolymers were estimated from their optical band gaps (taken as the absorption onsets of the UV–vis spectra of the polymer films) and the HOMO energies. Using this approach, we estimated the energy band gaps of PF-CZ50, PF-DPA50, PF-PXZ50, and PF-PZB50 to be 2.60, 2.40, 2.13, and 2.14 eV, respectively, as shown in Fig. 3. The incorporation of electron-rich hole-transporting materials and cyano moieties into the copolymers thus leads to higher HOMO and lower LUMO levels than those found for PDOF [30]. The HOMO energy levels of the copolymers vary significantly with the use of different hole-transporting moieties, whereas their LUMO energy levels are almost identical. It is worth to note that the incorporation of hole-transporting moieties into the polymers affects their HOMO energy levels and enhances their hole-transportation properties. The HOMO levels of PF-PXZ50 and PF-PZB50 were −5.23 and −5.26 eV, respectively. Thus when highly electron-negative atoms such as oxygen and sulfur are incorporated into the hole-transporting moieties as the bridge atoms between the two aromatic rings, their activities as electron donors are enhanced by the extra lone-pair of electrons.

We also studied the energy levels from computational point of view. In Table 4 the computed HOMO and LUMO energies of the monomers (a 9,9′-dioctylfluorene monomer with an attached N-containing comonomer) were obtained at the B3LYP level of theory using HF optimized geometries. Energies computed using the B3LYP method are more accurate than those obtained with the HF method because the effects of electron correlation are included in the B3LYP method. The HOMO energy levels of the monomers were very similar to those of the polymers obtained with CV, although the computed LUMO levels of the monomers were about 1 eV higher than the electrochemical LUMO energy levels of the polymers. The sequence of energy band gaps predicted with the computational analysis was almost identical to the sequence obtained with CV.

3.4. Electroluminescence properties

To test the performances of the copolymers in real devices, we fabricated double-layered LED devices with ITO/PEDOT-PSS/polymer/Ca/Al configurations. The EL spectra of the copolymers are similar to their corresponding PL spectra, as shown in Fig. 4. The characteristics of the PLED devices are summarized in Table 5, and the chromaticity

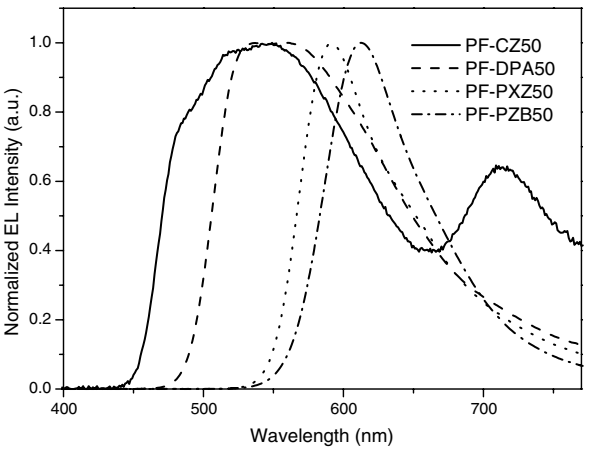


Fig. 4. Electroluminescence (EL) spectra of the polymers.

Table 5
Characteristics of the PLED devices

Polymers	V_{on} (V)[a]	L_{max} (cd/m^2, voltage)[b]	Luminance efficiency (cd/A, voltage)	Ex. quantum efficiency[c] (%, voltage)
PF-CZ50	6.6	(101, 16.4)	(0.03, 10.4)	(0.02, 10.4)
PF-DPA50	3.5	(520, 9.2)	(0.08, 6.4)	(0.04, 6.4)
PF-PXZ50	3.1	(508, 9.2)	(0.07, 6.4)	(0.04, 6.0)
PF-PZB50	3.2	(3440, 11.2)	(0.37, 6.4)	(0.43, 6.4)

[a] Turn-on voltage required for 1 cd/m^2.
[b] Maximum luminance.
[c] External quantum efficiency.

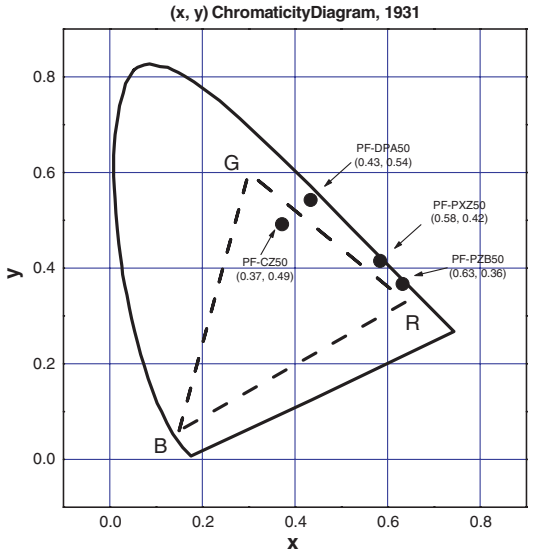


Fig. 5. CIE coordinates (x, y) of the polymers (NTSC, solid line).

values of the polymers are shown in Fig. 5. In the case of the PF-CZ50 device, there was an extra emission peak at about 710 nm and the turn-on voltage was found to be much higher (6.6 eV) than that of the other polymers due to the electroplex emission. Although the origin of electroplex emission has not yet been clearly explained, it is thought to be due to the interactions of a polymer segment at the excited state with its neighboring segment at the ground state of the same polymer and a different polymer, respectively [31,32]. The electroplex emission severely degrades the EL efficiency. In the case of the PF-PXZ50 and PF-PZB50 devices, their EL emission maxima were found to exhibit at 592 nm and 614 nm, respectively. As shown in Fig. 5, the chromaticity coordinates of PF-PZB50 and PF-PXZ50 are (0.63, 0.36) and (0.58, 0.42), respectively, which means that they are good candidates for use as the red-emitting layers in polymer LED and photovoltaic devices.

In Figs. 6 and 7, the luminance and external quantum efficiencies respectively of the LED devices are shown. To explain the differences in their efficiencies, we considered the different geometries of the comonomer units. In Table 6, the angles of planarity of each of the comonomers are summarized. Whereas PF-DPA50 contains dicyclic diphenyl amine moieties, PF-CZ50, PF-PXZ50 and PF-PZB50 contain tricyclic rings. Firstly, comparing tricyclic carbazole ring with dicyclic diphenyl amine moieties, the only structural difference between PF-CZ50 and PF-DPA50 is in their planarity. As

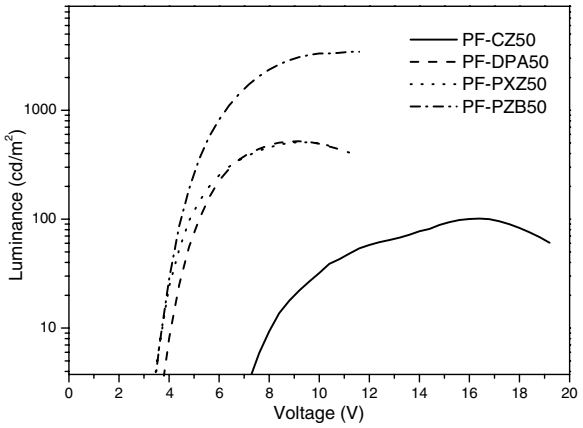


Fig. 6. Voltage–luminance curves of the devices.

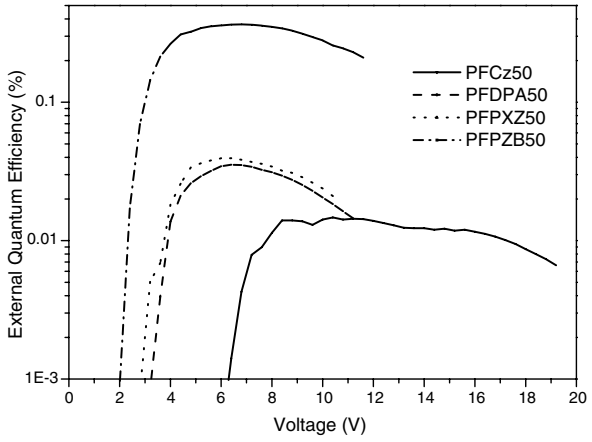


Fig. 7. Voltage-external quantum efficiency characteristics of the devices.

shown in Fig. 8, monomer CZ is highly planar, whereas monomer DPA is highly non-planar. Since both monomers do not contain extra heteroatom, we conclude that the more non-planar structure a polymer has, the higher its efficiency is, as shown in Fig. 7. It is likely that a highly non-planar structure impedes π-stacking aggregation and intermolecular excimer formation [11]. Secondly, comparing tricyclic rings, in comparison to PF-CZ50, PF-PXZ50 and PF-PZB50 have extra heteroatoms (oxygen and sulfur, respectively) bridging the two aromatic rings, so they are much more non-planar than PF-CZ50. PF-PZB50 has a particularly non-planar structure because sulfur is a much bulkier atom than oxygen, as shown in Fig. 9. The trend in efficiency matches the trend in planarity: as the non-planarity of the polymers increases, their external quantum efficiency is enhanced. Additionally,

Table 6
The angles of planarity of the comonomers

Comonomer	CZ	DPA	PXZ	PZB
Angle (°)[a]	0	76	19	31

[a] The angles are those between the two benzene rings attached to the nitrogen atom.

we also have to consider the electronic properties of sulfur and oxygen. The phenoxazine and phenothiazine rings which contain extra heteroatoms are much stronger electron-donating moieties than carbazole. [33] Due to the lone pair of electrons in phenoxazine and phenothiazine, conjugation ranges

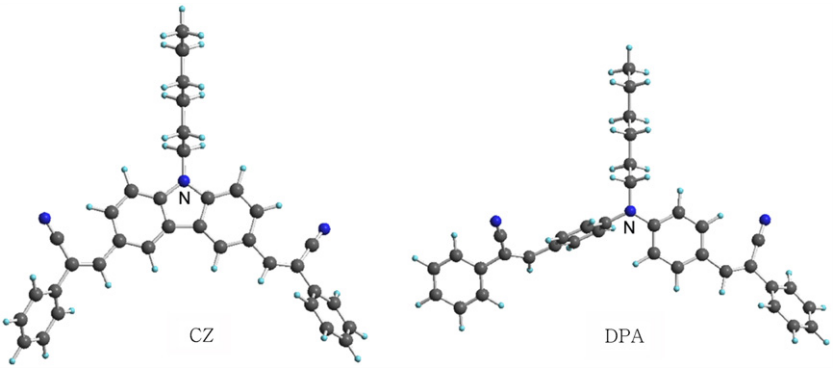


Fig. 8. Comparison of the geometries of CZ and DPA, obtained with HF/6-31G* calculations.

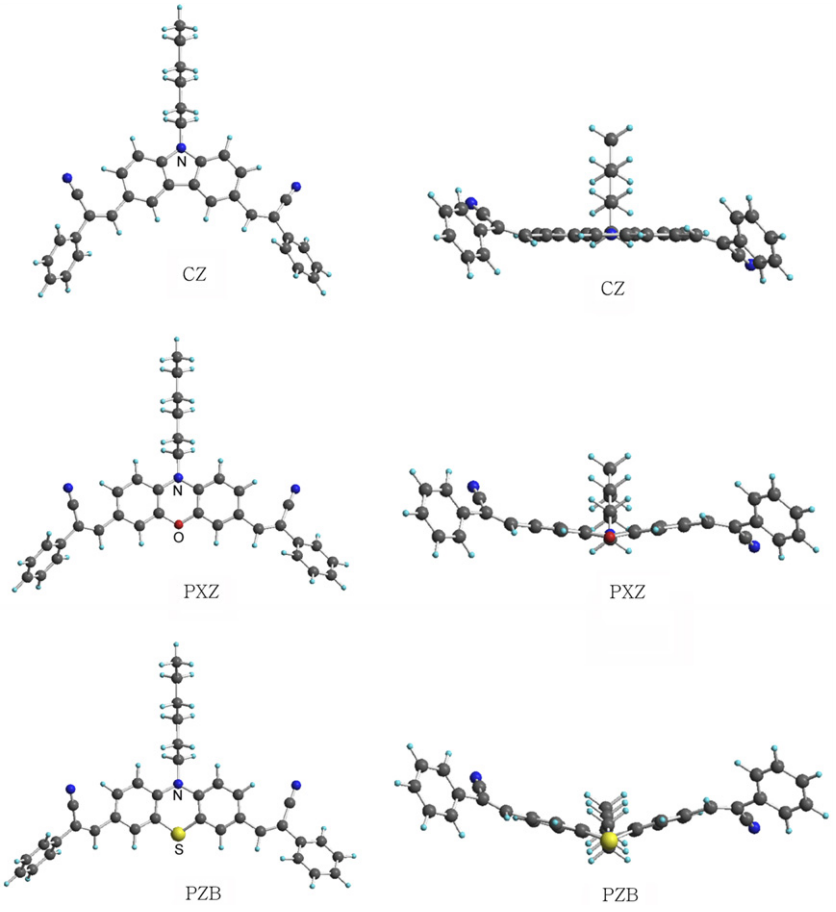


Fig. 9. Comparison of the geometries of CZ, PXZ, and PZB, obtained with HF/6-31G* calculations.

of PF-PXZ50 and PF-PZB50 are also extended. [34] Therefore phenoxazine and phenothiazine moieties enhance the polymers' hole-transportation properties and thereby enhance their EL efficiencies. Moreover, in the case of PF-PZB50, sulfur is much larger atom than oxygen is so that it enhances π-electron overlap along the polymer main chains. Also phenothiazine chromophores are much more effective in lowering the ionization potential and band gap than other hole-transporting chromophores. As shown in Fig. 3, the LUMO level of PF-PZB50 is lowest. The lower LUMO level is, the easier electron charge carrier transports from cathode. The S-containing copolymer, PF-PZB50, exhibits improved charge carrier mobility with respect to that of its oxygen analogue of PF-PXZ50 due to the electron-donating property of sulfur. For these reasons, the device of PF-PZB50 exhibits the best performance.

4. Conclusions

New conjugated fluorene-based copolymers, PF-CZ50, PF-DPA50, PF-PXZ50, and PF-PZB50 containing hole-transporting moieties were synthesized with Pd(0)-catalyzed Suzuki coupling polymerizations. The PL emission maxima of the copolymers in the film state were found at 528, 529, 593, and 614 nm, respectively. The HOMO levels of the polymers with different hole-transporting moieties vary significantly. The incorporation of different hole-transporting moieties affects the HOMO energy levels of the polymers and varies their hole-transportation properties. Conventional polymeric LED devices using the polymers as emitting layers were fabricated in ITO/PEDOT:PSS/polymer/Ca/Al configurations. PF-CZ50 exhibits electroplex emission in its EL spectrum. The EL emission maxima of PF-PXZ50 and PF-PZB50 were found at 592 nm and 614 nm, respectively, which indicates that these polymers are good candidates for use as red-emitting layers in PLED and photovoltaic devices. The trend in the non-planarity of the comonomers was determined with computational analysis and found to match the trend in their EL efficiencies. As the non-planarity of the polymers increases, the external quantum efficiency of the polymers is enhanced. The highly non-planar PF-PZB50 exhibits better performance when used in an EL device than the planar PF-CZ50. Stronger electron donating ability due to extra heteroatom in PF-PXZ50 and PF-PZB50 also influences device performance drastically.

Acknowledgement

We gratefully acknowledge financial support from the Center for Advanced Functional Polymers through Korea Science and Engineering Foundation (KOSEF) and BK21.

References

[1] J.H. Burroughes, D.D.C. Bradley, A.R. Brown, R.N. Marks, K. Mackay, R.H. Friend, P.L. Burns, A.B. Holmes, Nature 347 (1990) 539.
[2] A. Kraft, A.C. Grimsdale, A.B. Holmes, Angew. Chem. Int. Ed. 37 (1998) 402.
[3] H.-K. Shim, J.I. Jin, Adv. Polym. Sci. 158 (2002) 1942.
[4] T. Ahn, H.-K. Shim, Macromol. Chem. Phys. 202 (2001) 3180.
[5] Q. Hou, Y. Xu, M. Yuan, J. Peng, Y. Cao, J. Mater. Chem. 12 (2002) 2887.
[6] C. Ego, D. Marsitzky, S. Becker, J. Zhang, A.C. Grimsdale, K. Müllen, J.D. MacKenzie, C. Silva, R.H. Friend, J. Am. Chem. Soc. 125 (2003) 437.
[7] E. Lim, B.-J. Jung, H.-K. Shim, Macromolecules 36 (2003) 4288.
[8] H.-J. Cho, B.-J. Jung, J. Lee, N.S. Cho, H.-K. Shim, Macromolecules 36 (2003) 6704.
[9] N.S. Cho, D.-H. Hwang, B.J. Jung, E. Lim, J. Lee, H.-K. Shim, Macromolecules 37 (2004) 5265.
[10] J. Lee, H.-J. Cho, N.S. Cho, B.-J. Jung, H.-K. Shim, Macromolecules 37 (2004) 8523.
[11] X. Kong, A.P. Kulkarni, S.A. Jenekhe, Macromolecules 36 (2003) 8992.
[12] S. Beaupre, M. Leclerc, Adv. Funct. Mater. 12 (2002) 192.
[13] R. Yang, R. Tian, J. Yan, Y. Zhang, J. Yang, Q. Hou, W. Yang, C. Zhang, Y. Cao, Macromolecules 38 (2005) 244.
[14] A.P. Kulkarni, C.J. Tonzola, A. Babel, S.A. Jenekhe, Chem. Mater. 16 (2004) 4556.
[15] P. Strohriegl, J.V. Grazulevicius, Adv. Mater. 14 (2002) 1439.
[16] P. Herguth, X. Jiang, M.S. Liu, A.K.-Y. Jen, Macromolecules 35 (2002) 6094.
[17] F.-I. Wu, P.-I. Shih, C.-F. Shu, Y.-L. Tung, Y. Chi, Macromolecules 38 (2005) 9028.
[18] H. Antoniadis, M.A. Abkowitz, B.R. Hsieh, Appl. Phys. Lett. 65 (1994) 2030.
[19] E. Lim, B.-J. Jung, H.-K. Shim, J. Polym. Sci. Part A: Polym. Chem. 44 (2006) 243.
[20] Y.J. Pu, M. Soma, J. Kido, H. Nishide, Chem. Mater. 13 (2001) 3817.
[21] Y. Zhu, A.P. Kulkarni, S.A. Jenekhe, Chem. Mater. 17 (2005) 5225.
[22] D.-H. Hwang, J.-D. Lee, M.-J. Lee, C. Lee, Curr. Appl. Phys. 5 (2005) 244.
[23] R.Y. Lai, X. Kong, S.A. Jenekhe, A.J. Bard, J. Am. Chem. Soc. 125 (2003) 12631.
[24] A.D. Becke, J. Chem. Phys. 98 (1993) 5648.
[25] M.J. Frisch et al., Gaussian 03, Revision C.02, Gaussian, Inc., Wallingford CT, 2004.
[26] M. Ranger, D. Rondeau, M. Lerlerc, Macromolecules 30 (1997) 7686.

[27] J.L. Brédas, R. Silbey, D.S. Boudreaux, R.R. Chance, J. Am. Chem. Soc. 105 (1983) 6555.
[28] J. Pommerehne, H. Vestweber, W. Guss, R.F. Mahrt, H. Bässler, M. Porsch, J. Daub, Adv. Mater. 7 (1995) 551.
[29] Y. Zhu, A. Babel, S.A. Jenekhe, Macromolecules 38 (2005) 7983.
[30] S. Janietz, D.D.C. Bradley, M. Grell, C. Giebeler, M. Inbasekaran, E.P. Woo, Appl. Phys. Lett. 38 (2005) 7983.
[31] N.S. Cho, D.-H. Hwang, B.-J. Jung, J. Oh, H.Y. Chu, H.-K. Shim, Synth. Met. 143 (2004) 277.
[32] Y.-Z. Lee, X. Chen, M.-C. Chen, S.-A. Chen, J.-H. Hsu, W. Fann, Appl. Phys. Lett. 79 (2001) 308.
[33] S.A. Jenekhe, L.D. Lu, M.M. Alam, Macromolecules 34 (2001) 7315.
[34] T.–Y. Wu, Y.J. Chen, J. Polym. Sci. Part A: Polym. Chem. 40 (2002) 4452.

Available online at www.sciencedirect.com
ScienceDirect
Organic Electronics 8 (2007) 286–291
Organic Electronics
www.elsevier.com/locate/orgel

Intrachain confinement of excitons and radiative recombination in polyaniline grains

O.P. Dimitriev *, V.V. Kislyuk, P.S. Smertenko

Institute of Semiconductor Physics, National Academy of Sciences of Ukraine, Pr. Nauki 45, Kiev 03028, Ukraine

Received 1 February 2006; received in revised form 30 June 2006; accepted 12 July 2006
Available online 14 August 2006

Abstract

Suppression of the benzenoid-to-quinoid excitonic transition (BQET) and enhancement of the quantum yield of photoluminescence (PL) at ~390 nm has been observed in grained films of the emeraldine base (EB) of polyaniline. The major PL band from the EB films with the grained morphology was relatively narrow, with FWHM of about 1020 cm^{-1}, followed by vibronic overtones the intensity of which was dependent on the mode of the PL excitation. The change of the film morphology, where instead of grains large aggregates were formed, leaded to the recovery of the absorption band corresponding to the BQET and quenching of the emission, respectively. It is suggested that the origin of PL in EB films is due to the distorted polymer chains in EB grains where the ring torsion angle of benzenoid group in respect to the adjacent quinoid group increases, thus resulting in the suppressed BQET and enhanced emission.
© 2006 Elsevier B.V. All rights reserved.

PACS: 61.43.−j; 78.55.Kz; 78.66.Qn

Keywords: Polyaniline; Conformational changes; Morphology; Excitonic transition; Photoluminescence

1. Introduction

Electronic excitations that yield radiative recombination of the excited electron-hole pair in polyaniline (PANI) has been a subject of investigations, because of potential application of this effect in organic light-emitting diodes (OLEDs) [1–6]. It has been shown that the leucoemeraldine (LE) form of PANI possesses photoluminescence (PL) in the visible with the band maximum near 400 nm. This property has been used to demonstrate that LE films are able to emit light under applied electric field, i.e., they possess electroluminescence (EL) [2].

On the other hand, some controversial results have been reported in respect to the EB form of PANI. It was shown that the EB form of PANI does not possess PL when it is dissolved, for example, in *N*-methyl-pyrrolidinone (NMP). This is due to the fact that the EB chains contain both reduced benzenoid and oxidized quinoid units. The benzenoid units are responsible for the emission properties, while the quinoid groups cause the intrachain charge migration due to the benzenoid-to-quinoid excitonic transition (BQET) [1–6] and, therefore, act as excitation traps and quench the PL emission. However, EB films cast from the solution are able to emit light at

* Corresponding author.
E-mail address: dimitr@isp.kiev.ua (O.P. Dimitriev).

1566-1199/$ - see front matter © 2006 Elsevier B.V. All rights reserved.
doi:10.1016/j.orgel.2006.07.005

~400 nm, similar to that shown by LE films. Such an effect of EB films was suggested to occur due to a partial phase separation of the EB form into LE and pernigraniline base (PB) phases of PANI, respectively [1,7,8], where the LE phase was responsible for the PL emission. However, such an explanation was in controversy with the electronic absorption spectra of EB films which could not be presented as a superposition of the LE and PB phases that should result in the relative reduction and blue shift of the BQET band of EB at ~630 nm to that of PB at ~530 nm [9], because the LE phase does not have the BQET band. Moreover, there was no evidence that the phase separation in EB is thermodynamically favorable, because it is known that both LE and PB phases of PANI are unstable in air, and the former spontaneously oxidizes, while the latter degrades due to hydrolysis under environmental humidity [10,11]. It appears that the PL ability of EB films requires alternative explanation. The purpose of this work is to provide such an alternative.

Recently, we have synthesized various complexes of the EB and transition metal salts and observed that the complex films have different morphologies depending on the inorganic salt used [12]. Some evidences have been obtained to show that the grained morphology of the films is consistent with the compact-coil chain conformation of the polymer molecules in the grain, while the morphology of extended aggregates is consistent with the expanded-coil conformation [13]. A similar difference in the film morphology can be observed also in films of pristine EB if they were prepared under certain conditions. In this work, we show that there is a correlation between the film morphology which is dependent on the intrinsic chain conformation and emission properties of the EB chains.

2. Experimental

2.1. Sample preparation

PANI in the EB oxidation form (the average molecular weight $M_w = 65000$) was obtained from the Institute of Physical Chemistry (Kiev), where it was synthesized by a standard chemical polymerization procedure. The EB powder was dissolved in NMP to prepare a stock solution with concentration of 1 wt%, followed by sonication and filtering of the solution to remove undissolved particles. Films of EB were prepared by drop casting of 10 μl of the solution onto quartz or glass plates. Films with different morphology were obtained by variation of the EB concentration in the stock solution.

2.2. Measurements

For optical measurements, the films were prepared on quartz plates. Electronic absorption spectra were recorded in the transmission mode, bare quartz plate served as a reference, using a 'SPECORD M40' spectrophotometer.

Luminescence was stimulated either by a xenon lamp through a LOMO grate monochromator or by a nitrogen laser ($\lambda_{exc} = 337$ nm). The emission was registered through another LOMO grate monochromator equipped with a photomultiplier tube counter, and an amplitude discriminator. The final spectra were corrected for the spectral sensitivity of the registering system.

Film surface morphology was studied by atomic force microscopy (AFM), using a commercial microscope from Park Scientific (USA) and standard Si_3N_2 cantilevers. The AFM measurements were performed in air and at room temperature. The images were measured in contact mode by working in constant force mode. The effective repulsive measuring force of 10 nN was small enough not to destroy the investigated films.

3. Results and discussion

Two types of PANI films have been prepared. The first type of films had a grained morphology. These films were prepared from diluted solutions of EB in NMP. It was found that drop-casting of the EB solutions with concentration in the range of 0.1–0.25 wt% with slow evaporation of the solvent at ambient conditions provided the grained structure of the films. As has been concluded in our previous works [13,14] on the base of the kinetics of the film formation, the tendency to form precipitate in a solution, electronic and IR spectra, the polymer molecules in these films have a compact-coil conformation. This was suggested to be due to the fact that the film is formed initially by single molecules which predominate in the diluted solution and where intramolecular interactions prefer the polymer–polymer intermolecular interactions. AFM images showed that a structure of these films consists of grains with size of several tens of nanometers (Fig. 1a).

The second type of films showed a morphology called here as that of large aggregates (Fig. 1b).

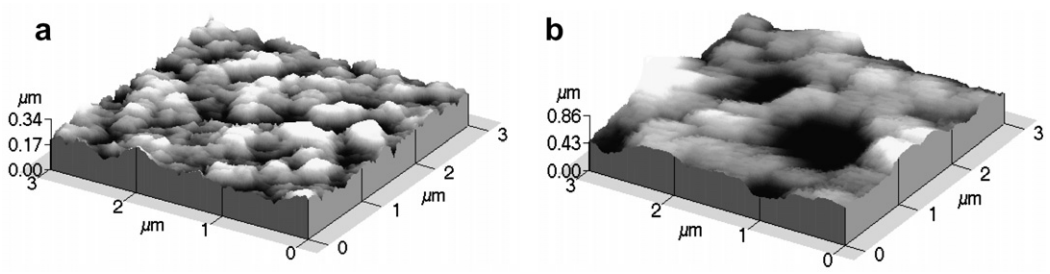


Fig. 1. AFM images of EB films drop-cast from (a) diluted and (b) concentrated NMP solutions.

These films were prepared by drop-casting from more concentrated EB solutions. It was found that the EB solutions with concentration in the range of 0.5–1.0 wt% can provide such a structure. The polymer molecules in films with the morphology of large aggregates have a more expanded-coil conformation [13,14]. The main reason of that is that the molecules in these films are well-blended with NMP and their conformation, therefore, is more similar to that of molecules in the NMP solution. There is no full understanding how the molecules interact with each other in the film. According to the standard models they can be presented either as collapsed coils or as interpenetrating statistical coils [15], the both models allow solvation of the chains because the coils are not the close packed formations. A slow process of the film formation in our experiments favors the latter model, therefore the term 'large aggregates' should be equivalent here to that of 'interpenetrating coils'. It should be noted also that the above-mentioned values of concentrations are not absolute to distinguish between films with the grained and aggregated morphology, because a mixture of single molecules and aggregates can be observed in NMP solution with concentration of EB as low as 0.005 wt% [16]. It is obvious, however, that the ratio of single molecules to aggregates increases as the solution concentration decreases.

Electronic absorption of EB solutions consists of two absorption bands located at ~320 and 638 nm. The first one is attributed to the benzenoid π–π^* transition and the second to the BQET, respectively [17,18]. Electronic absorption spectra of films with different morphologies (Fig. 2) showed a difference in the BQET band positions and a different intensity ratio of bands corresponding to the π–π^* transition and the BQET, respectively. In the case of films with the aggregate morphology the spectrum is more similar to the solution spectrum of EB, i.e., the position of BQET band is at ~625 nm, and its intensity is comparable with that of the π–π^* transition band

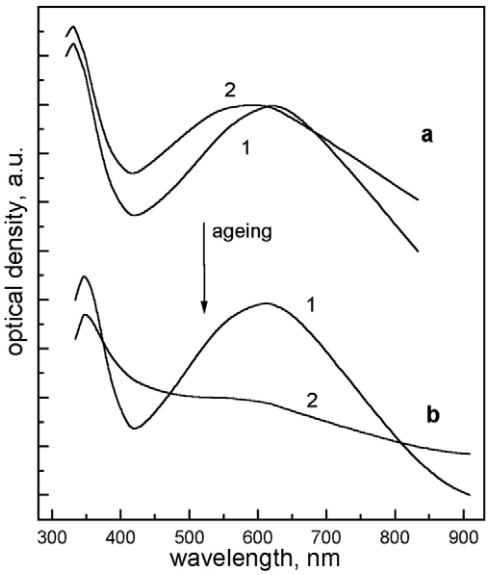


Fig. 2. Electronic absorption spectra of (a) as-prepared EB films and (b) the same films several months later. (1) film with the morphology of large aggregates, (2) film with the grained morphology.

(Table 1). On the other hand, a spectrum of films with the grained morphology demonstrated that the BQET is blue-shifted and suppressed (Fig. 2 and Table 1). The blue shift of BQET in electronic absorption spectra of EB films, as was shown in our previous work [19] and as discussed above, can be attributed to the compact-coil conformation of the EB molecules, where a change in the torsion angle of the benzenoid rings in respect to the quinoid rings and/or interaction of the approaching chromophore groups inside the polymer coil occurs. Suppressed intensity of the BQET band means also suppression of the excitonic migration in the polymer chain.

PL emission spectra of EB films showed a major emission band at ~390 nm (Fig. 3). This is consistent with results published in the literature (see, for example, [1,2]). However, it was found that the

Table 1
The visible band position and the ratio of intensities of the π–π^* transition to the visible band in electronic absorption spectra of polyanilines

Identification of the sample	Absorption maximum in the visible (nm)	UV/Vis absorption band intensity ratio
EB solution	638	1.18:1
Solution of EB + PB + LB (66:17:17)	619	1.69:1
Solution of EB + PB + LB (64:18:18)	618	1.73:1
Solution of EB + PB + LB (1:1:1)	595	2.52:1
Solution of PB + LB (1:1)	530	3.54:1
PB solution	530	1.45:1
As-prepared aggregated film of EB (our experiment)	625	1.24:1
Aged aggregated film of EB	614	1.10:1
As-prepared grained film of EB (our experiment)	592	1.73:1
Aged grained film of EB	~552, band smeared	2.40:1

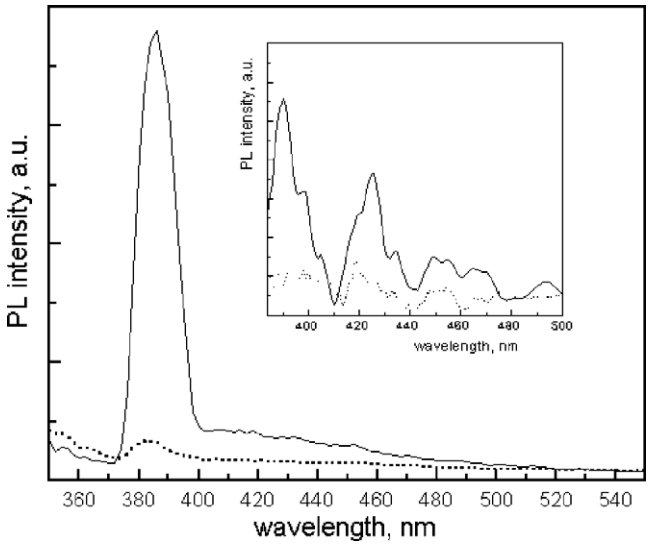


Fig. 3. PL emission spectra of EB films with the morphology of large aggregates (dotted curves) and the grained morphology (solid curves). The excitation wavelength is $\lambda_{exc} = 330$ nm from xenon lamp for spectra on main figure and $\lambda_{exc} = 337$ nm from laser for spectra on insert.

structure of the PL band is dependent on the film morphology. EB films with the grained morphology revealed a relatively high PL intensity with the narrow PL band whose full width at half maximum (FWHM) is about $\sim$1020 cm^{-1}. EB films with the morphology of large aggregates showed much lower PL intensity and a more broaden PL band. It should be noted that the spectra in Fig. 3 have been measured in the same geometry of the samples, however, amount of the polymer material in the grained film was at least two times lower as compared with the film which has the aggregate morphology, because these were prepared from solutions of different concentration, so the relative difference in the PL intensity of a unit mass of the material should be more than one order of magnitude.

The other difference in PL spectra of EB films with the grained and aggregate morphologies is a different contribution of vibronic overtones to the long wavelength emission tail. It has been found, first, that the contribution of vibronic overtones can be dependent on the mode of PL excitation, for example, by xenon lamp or laser (Fig. 3). Second, it seems that such a contribution in respect to the major PL band is higher for films with the aggregate morphology; this may be the reason of some confusion in the literature showing the major PL emission of EB films at longer wavelengths [1,2].

It was a subject of discussion in the literature what is the mechanism of the PL emission from EB films. It has been unequivocally established that the chromophore responsible for the emission of

PANI is a benzenoid group, this fact is consistent with a similar PL emission of aniline near 400 nm [6], whereas the presence of the quinoid groups leads to quenching of the PL due to the BQET process. However, it has not been taken into account that the long-range exciton migration along the PANI chain is affected by geometrical factors such as the ring torsion angle between neighboring phenyl rings [20–25]. Particularly, Harigaya [20] has calculated that the ring torsion effect in PANI is quite significant due to the large torsion angle and a large number of bonds whose hopping integrals are modulated by torsion. Another possible factor is chain defects the number of which should increase in the distorted chain and which act to confine the exciton migration length. For example, Zhang et al. [26] have shown that the BQET becomes suppressed as the EB chain becomes smaller in length. Namely, the intensity ratio of the absorption bands corresponding to the π–π^* transition and the BQET progressively increases as one goes from the EB polymer to the EB 16-mer and tetramer, being 1.18, 1.90, and 3.08, respectively, with a subsequent blue shift of the BQET.

Thus, our results allow us to put forward an alternative explanation of the origin of PL in EB films. As has been shown above, the emission originates mainly from PANI grains which represent a compact-coil conformation of the polymer molecules. In such a grain, the equilibrium configuration of a free polymer coil is strongly distorted, leading to changes in the absorption spectrum (Fig. 2). Such a change cannot be assigned to the phase separation of the EB into LE and PB. Simple calculations using molar absorption coefficient of all three phases of PANI from Ref. [27] allow us to simulate the behavior of electronic spectra of EB solution on gradual separation of the EB into PB and LB phases (Fig. 4). The comparison of these data with electronic spectra of the grained EB films leads to the conclusion that these films do not represent the phase separated blends of EB, PB and LB. For example, the as-prepared grained film showed the absorption ratio of the UV band to the visible band being 1.73 which is characteristic of the EB polymer partially separated into PB and LB with molar fractions of EB + PB + LB as 64:18:18 (Table 1). However, such a mixture demonstrates the absorption maximum at 618 nm in the visible, which is far different from that at 592 nm demonstrated by the film. The aged grained film showed the absorption ratio of the UV band to the visible band being 2.40 which is close to that of the mixture of EB + PB + LB with molar ratio of 1:1:1; however, the wavelength position of the visible band and the overall spectrum shape is far different from the

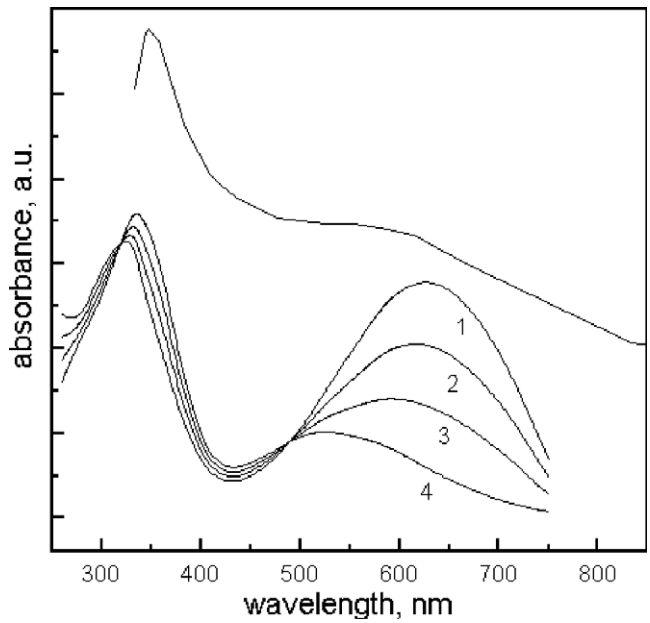


Fig. 4. Change in absorption spectra of the EB solution upon its phase separation into PB and LB phases: 1-EB (100%); 2-EB + PB + LB (66% + 17% + 17%); 3-EB + PB + LB (33.3% + 33.3% + 33.3%); 4-PB + LB (50% + 50%). Isosbestic points at 318 and 490 nm can be seen. The upper spectrum is that of the aged grained EB film which is shifted for clarity.

spectral features of the above mixture (Fig. 4). Therefore, the more plausible reason for the above spectral changes in grained EB films is a ring torsion that reduces the conjugation length and suppresses the BQET, respectively. Suppression of the exciton formation then favors the radiative recombination. Such a conclusion is consistent with observation of the enhanced PL emission in other polymers, for example, poly(3-alkyl)thiophenes upon their compact-coil conformation in a poor solvent [28]. Moreover, the distorted PANI chain is probably a reason of the suppressed vibronic modes observed in PL spectra of the grained films. Particularly, this result is consistent with an overall decrease of intensity of vibration modes observed in IR spectra of the grained films of PANI complexes [13].

4. Conclusions

It has been found that PL of EB films is strongly dependent on the film morphology. It has been shown that the PL emission originates mainly from the polymer grains. It is suggested that the polymer chain is greatly distorted in such a grain, where the ring torsion angle increases. Such a distortion suppresses intramolecular migration of exciton, leads to the diminishing BQET band in the electronic absorption spectra, and to the enhanced quantum yield of the PL emission. Thus, the PL emission phenomenon in EB films is associated with the distorted polymer chain.

Acknowledgements

The AFM images have been performed in the framework of a DAAD fellowship at Potsdam University. The assistance of Mrs. Strilchuk in measurements of PL spectra is gratefully acknowledged.

References

[1] J.Y. Shimano, A.G. MacDiarmid, Synth. Met. 123 (2001) 251.
[2] S.A. Chen, K.R. Chuang, C.I. Chao, H.T. Lee, Synth. Met. 82 (1996) 207.
[3] M.K. Ram, G. Mascetti, S. Paddue, E. Macciohi, C. Nicolini, Synth. Met. 89 (1997) 63.
[4] Y. Son, H.H. Patterson, C.M. Carlin, Chem. Phys. Lett. 162 (1989) 461.
[5] M. Wan, J.J. Yang, Appl. Polym. Sci. 55 (1995) 399.
[6] K. Kim, L.B. Lin, J.M. Ginder, T.L. Gustafson, A.J. Epstein, Synth. Met. 50 (1992) 423.
[7] H.S. Lee, K.R. Chuang, S.A. Chen, P.K. Wei, J.H. Hsu, W.S. Fann, Macromolecules 28 (1995) 7645.
[8] V.F. Ivanov, O.L. Gribkova, S.V. Novikov, A.A. Nekrasov, A.A. Isakova, A.V. Vannikov, G.B. Meshkov, I.V. Yaminsky, Synth. Met. 152 (2005) 153.
[9] J.G. Masters, Y. Sun, A.G. MacDiarmid, Synth. Met. 41 (1991) 715.
[10] J.M. Leng, R.P. McCall, K.R. Cromack, Y. Sun, S.K. Manohar, A.G. MacDiarmid, A.J. Epstein, Phys. Rev. B 48 (1993) 15719.
[11] G.E. Asturias, A.G. MacDiarmid, R.P. McCall, A.J. Epstein, Synth. Met. 29 (1989) E157.
[12] O.P. Dimitriev, Macromolecules 37 (2004) 3388.
[13] O.P. Dimitriev, P.S. Smertenko, B. Stiller, L. Brehmer, Synth. Met. 149 (2005) 187.
[14] O.P. Dimitriev, O.N. Kopylov, in preparation.
[15] V.P. Privalko, Molecular building and properties of polymers, Khimija, Leningrad, 1986.
[16] T.A.P. Seery, M. Angelopoulos, K. Levon, A. Seghal, Synth. Met. 84 (1997) 79.
[17] A.P. Monkman, D. Bloor, G.C. Stevens, J.C.H. Stevens, J. Phys. D: Appl. Phys. 20 (1987) 1337.
[18] D.S. Boudreaux, R.R. Chance, J.F. Wolf, L.W. Shacklette, J.L. Bredas, B. Themas, J.M. Andre, R. Silbey, J. Chem. Phys. 85 (1986) 4584.
[19] O.P. Dimitriev, Synth. Met. 122 (2001) 315.
[20] K. Harigaya, Chem. Phys. Lett. 281 (1997) 319.
[21] J.M. Ginder, A.J. Epstein, Phys. Rev. B 41 (1990) 10674.
[22] J.L. Bredas, C. Quattrocchi, J. Libert, A.G. MacDiarmid, J.M. Ginder, A.J. Epstein, Phys. Rev. B 44 (1991) 6002.
[23] F. Zuo, R.P. McCall, J.M. Ginder, M.G. Roe, J.M. Leng, A.J. Epstein, G.E. Asturias, S.P. Ermer, A. Ray, A.G. MacDiarmid, Synth. Met. 29 (1989) E445.
[24] M.G. Roe, J.M. Ginder, R.P. McCall, K.R. Cromack, A.J. Epstein, T.L. Gustafson, M. Angelopoulos, A.J. MacDiarmid, Synth. Met. 29 (1989) E425.
[25] A.P. Monkman, P. Adams, A. Milton, M. Scully, S. Pomfret, A.M. Kenwright, Mol. Cryst. Liq. Cryst. 236 (1993) 189.
[26] W.J. Zhang, J. Feng, A.G. MacDiarmid, A.J. Epstein, Synth. Met. 84 (1997) 119.
[27] J.G. Masters, Y. Sun, A.G. MacDiarmid, Synth. Met. 41 (1991) 715.
[28] S. Lee, J.Y. Lee, H. Lee, Synth. Met. 101 (1999) 248.

ORGANIC ELECTRONICS
materials • physics • chemistry • applications

Editors:

Prof. Chihaya Adachi — Center for Future Chemistry, Kyushu University, 744 Motooka, Nishi, Fukuoka 819-0395, Japan. Fax: +81-92-802-3294, e-mail: adachi@cstf.kyushu-u.ac.jp

Prof. Stephen R. Forrest — EECS, MSE, and Physics, University of Michigan, 4080 Fleming Building, 503 Thompson Street, Ann Arbor, MI 48109-1340, USA. Fax: +1-734-763-0085, e-mail: stevefor@umich.edu

Prof. René Janssen — Molecular Materials and Nanosystems, Eindhoven University of Technology, P.O. Box 513, 5600 MB Eindhoven, The Netherlands. Fax: +31 40 2451036, e-mail: r.a.j.janssen@tue.nl

Prof. Josef Salbeck — Macromolecular Chemistry and Molecular Materials Science Department, University of Kassel, Heinrich Plett Strasse 40, D-34123 Kassel, Germany. E-mail: salbeck@uni-kassel.de

Associate Editorial Board:

V.M. AGRANOVICH (Moscow)
Y. CAO (Guangzhou)
A. DODABALAPUR (Austin)
M. FUJIHIRA (Yokohama)
N. PEYGHAMBARIAN (Tucson)
Z. POPOVIC (Mississauga)
W. RIESS (Rüschlikon)
Y. SHIROTA (Osaka)
C. TALIANI (Bologna)
T. TSUTSUI (Fukuoka)
E. UMBACH (Würzburg)

Founding Editors:

Prof. Donal Bradley, Prof. Stephen Forrest, Prof. Norbert Karl and Prof. Kazuhiko Seki

Aims and scope

An interdisciplinary journal on the physics, chemistry, and engineering of materials with applications to organic electronics and optoelectronics, **Organic Electronics** is a primary journal for physicists, material scientists and chemists who are interested in organic electronic devices such as organic light emitting diodes, thin film transistors, photovoltaic cells, etc. Papers suitable for publication in this journal cover such topics as photoconductive and electronic properties of organic materials, film growth and characterization, organic electronic and optoelectronic devices, and applications.

As an important Journal **Organic Electronics** can ensure that your most significant research receives the recognition that it deserves. As a unique publication outlet, uniting the various research disciplines involved, it provides the only forum for both applied and fundamental contributions spanning the many different disciplines addressing electronic applications of organic materials.

Advertising information

Advertising orders and enquiries can be sent to: James Kenney, Commercial Sales, Elsevier, 84 Theobald's Road, London WC1X 8RR, United Kingdom; phone: (+44) (20) 7611 4494; fax: (+44) (20) 7611 4463; e-mail: j.kenney@elsevier.com.

Abstracted/indexed in:

Current Contents: Engineering, Technology and Applied Sciences; El Compendex Plus; Engineering Index; INSPEC; Physics Briefs; Science Citation Index, expanded; Chemistry Citation Index; Current Contents: Physics, Chemistry and Engineering Science. Also covered in the abstract and citation database SCOPUS®. Full text available on ScienceDirect®.

Publication information: *Organic Electronics* (ISSN 1566-1199). For 2007, Volume 8 is scheduled for publication. Subscription prices are available upon request from the Publisher or from the Regional Sales Office nearest you or from this journal's website: (http://www.elsevier.com/locate/orgel). Further information is available on this journal and other Elsevier products through Elsevier's website: (http://www.elsevier.com). Subscriptions are accepted on a prepaid basis only and are entered on a calendar year basis. Issues are sent by standard mail (surface within Europe, air delivery outside Europe). Priority rates are available upon request. Claims for missing issues should be made within six months of the date of dispatch.

Orders, claims, and journal enquiries: please contact the Customer Service Department at the Regional Sales Office nearest you:

Orlando: Elsevier, Customer Service Department, 6277 Sea Harbor Drive, Orlando, FL 32887-4800, USA; phone: (877) 8397126 or (800) 6542452 [toll free numbers for US customers]; (+1) (407) 3454020 or (+1) (407) 3454000 [customers outside US]; fax: (+1) (407) 3631354 or (+1) (407) 3639661; e-mail: usjcs@elsevier.com or elspcs@elsevier.com

Amsterdam: Elsevier, Customer Service Department, P.O. Box 211, 1000 AE Amsterdam, The Netherlands; phone: (+31) (20) 4853757; fax: (+31) (20) 4853432; e-mail: nlinfo-f@elsevier.com

Tokyo: Elsevier, Customer Service Department, 4F Higashi-Azabu, 1-Chome Bldg, 1-9-15 Higashi-Azabu, Minato-ku, Tokyo 106-0044, Japan; phone: (+81) (3) 5561 5037; fax: (+81) (3) 5561 5047; e-mail: jp.info@elsevier.com

Singapore: Elsevier, Customer Service Department, 3 Killiney Road, #08-01 Winsland House I, Singapore 239519; phone: (+65) 6349 0222; fax: (+65) 6733 1510; e-mail: asiainfo@elsevier.com

Printed by Krips BV, Meppel, The Netherlands

ELSEVIER

Available online at www.sciencedirect.com
ScienceDirect
Organic Electronics 8 (2007) iii
Organic Electronics
www.elsevier.com/locate/orgel

Retraction Notice

Retraction notice to: "Properties of organic light-emitting diodes by aluminum cathodes modification using Ar^+ ion beam" [Org. Electron. 6 (4) (2005) 149–160]

Soon Moon Jeong, Won Hoe Koo, Sang Hun Choi, Hong Koo Baik *

Department of Metallurgical Engineering, School of Materials Science and Engineering, Yonsei University, 134 Shinchon-dong, Seodaemun-ku, Seoul 120-749, Republic of Korea

This article is retracted at the request of the editors as it is a duplication of a paper that has already appeared in at least nine other publications. As such this article represents a severe abuse of the scientific publishing system. It has wasted the time of many reviewers and also wastes costly journal space which is explicitly reserved for publishing original, not self-plagiarized work. *Organic Electronics* takes a very strong view on this matter. The editors want to inform our readership and authors, that those who publish multiple copies of their papers in *Organic Electronics* and elsewhere will lose their rights to further publication in this journal.

DOI of original article: 10.1016/j.orgel.2005.03.010
* Corresponding author. Tel.: +82 2 2123 2838; fax: +82 2 312 5375.
E-mail address: thinfilm@yonsei.ac.kr (H.K. Baik).

1566-1199/$ - see front matter © 2007 Elsevier B.V. All rights reserved.
doi:10.1016/j.orgel.2007.02.006

Available online at www.sciencedirect.com
ScienceDirect
Organic Electronics 8 (2007) vii–viii
Organic Electronics
www.elsevier.com/locate/orgel

Editorial

Special issue on coupled states of excitons, photons, and plasmons in organic structures

Coupling of the excited states of organic films with modes of optical cavities can lead to lasing action in the weak coupling limit or exciton-polariton phenomena in strongly coupled systems. Lasing action in organic semiconducting thin films has been actively pursued over the last decade with goals of demonstrating tunable light sources for applications such as high sensitivity chemical probes and organic photonic integrated circuits, and with emphasis on design of electrically pumped organic lasing structures. In the field of strongly coupled organic-optical cavity systems, researchers are in pursuit of thresholdless lasing, quantum computing, electromagnetically induced transparency, and related manifestations of room temperature cavity quantum electrodynamics. Related work on coupling of organic excited states to the plasmon modes of metals, metal nanocrystals, and inorganic semiconductor nanocrystals (quantum dots), complements the above studies by investigating near-field phenomena. Today's experimental demonstrations suggest tomorrow's practical optoelectronic devices that reconcile the demands and balance the opportunity of coupled optical and electronic phenomena in room temperature organic structures.

This special issue gives a broad overview of the topics of current interest.

The issue starts with a comprehensive review by Holmes and Forrest of the strong coupling phenomena in thin film structures containing organic molecules of high absorption coefficient. Molecular thin films with a record-high absorption constant are examined in the paper by Tischler et al. that uses J-aggregated cyanine dyes. The J-aggregate multilayers in optical half-cavities are used to demonstrate critically coupled resonators capable of absorbing nearly all of the incident light in 6 nm thick films, enabling unprecedented directing of optical energy to a $\lambda/100$ thick optical films. Surrounding the J-aggregate films with a complete optical cavity leads to the strong coupling phenomena that is manifested at room temperature and for different optical polarizations in optically pumped all-dielectric microcavities of Camposeo et al., in optically pumped laminated microcavities containing infra-red (790 nm peak wavelength) J-aggregates of Wenus et al., and in electrically pumped metal-mirror structures of Tischler et al. The strong coupling in hybrid organic–inorganic microcavities of organic material Frenkel excitons, inorganic material Wannier–Mott excitons, and cavity photons of both polarizations are theoretically examined in the paper of Zoubi and La Rocca.

Coupling of the metal plasmon modes to the optical transitions of molecules and cavities is a topic of several papers including the work of Wedge et al. that methodically demonstrates surface plasmon-polariton mediated emission of light in patterned metal/organic thin film structures. Metal electrode micro-patterns enable scattering of the otherwise non-radiative surface plasmon-polariton modes and recovery of their energy as light, suggesting use of such coupled structures in surface-emitting (transparent) organic light emitting devices (LEDs). Coupling of the plasmon mode resonance of a metal bi-layer film to an overlayer of a polymer grating is experimentally and numerically investigated by Csete et al., demonstrating utility of the structure as a bio-sensor. Fabrication of shaped gold nanoparticles by SAM templating, and influence of

1566-1199/$ - see front matter © 2007 Elsevier B.V. All rights reserved.
doi:10.1016/j.orgel.2007.01.005

nanoparticle clustering on the plasmon resonance are the topic of the study of Aliganga et al.

The subset of papers that examine weak light-matter coupling in lasing and amplified structures starts with a paper by Sailaja and Bisht who examine optical output of tunable multiline distributed feedback dye lasers containing a mixture of two optically active organic dyes. The authors show that the relative dye concentration controls the inter-dye exciton energy transfer and the emitted light self-absorption, with the consequence on the lasing threshold. Azuma et al. study the amplified spontaneous emission (ASE) in α-phase and β-phase polyfluorine waveguides, noting differences in ASE that are dependent on the polymer refractive index and the luminescence quantum efficiency. Similarly, the paper of Lin et al. demonstrate the ASE difference in isotropic and oriented oligofluorine films, concluding that ASE gain and threshold of stimulated emission in organic semiconducting films can be improved by aligning the molecular transition dipole moments with the polarization of the stimulated emission field.

Experimental measurements of the optical non-linear response of molecular organic materials and theoretical descriptions of use of the optical non-linearities in coupling different optical waveguided modes are discussed in the next subset of papers. Experiments of He et al. examine the non-linear optical response of phtalocyanine-based molecular organic thin films. The analysis paper of Biswas uses perturbation methods and numerical techniques to treat non-linearities (such as nonlinear gain, saturable amplification, filtering, higher order dispersion) responsible for interaction of two neighboring optical solitons propagating through an optical fiber. Analogously, McGurn considers interaction of two optical modes of different frequencies that propagate along a straight photonic crystal waveguide. The waveguide is surrounded by off-channel structures composed of Kerr non-linear dielectric that mediate interaction between the two optical modes and allow the modes to modulate the transmission of each other down the waveguide. Theoretical studies, such as those of Biswas and McGurn, highlight the power of numerical analysis in optimizing light transmitting structures containing non-linear media.

The interaction of free and trapped charge carriers with excitonic and polaronic states of molecular thin films are examined in the next subset of papers. The first of these, by Vázques et al., presents a model of the induced density of states at the non-chemically-reacted metal/organic interfaces and demonstrates the predictive power of the model by comparing its prediction to the experimental measurements of energy level alignment at these interfaces. Formation of excitons from free/trapped charge precursors is investigated by Castro et al. in a series of neat and doped fluorescent molecular organic devices, using the electrically detected magnetic resonance, with change is structure and temperature affecting the spin coherence time or exciton precursor reaction rates. Paper by Bergenti et al. examines the low temperature phosphorescence of an archetypical amorphous molecular organic thin film and ascribes the delayed phosphorescence spectral signatures to the enhancement of triplet–exciton radiative decay interaction with trapped charge carriers. Nagai and Abe in their paper discus use of photoilluminated organic heterojunctions that efficiently dissociate excitons, generate charge, and, when in contact with water, can facilitate production of O_2.

Paper by Park et al. makes a connection between the planarity of the hole-transporting moieties in four fluorine-based alternating polymers and the electronic properties of the polymer films, which are manifested in performance of polymer light emitting devices (LEDs). Analogously, Dimitriev et al. associate morphological changes in molecular organic films they examine with the enhanced self-localization of excitons, which is manifested in the change of the film photoluminescence spectra.

Vladimir Bulović
Massachusetts Institute of Technology,
77 Massachusetts Ave, Cambridge,
Massachusetts 02139,
USA
E-mail address: bulovic@mit.edu

Chihaya Adachi
Center for Future Chemistry,
Kyushu University,
744 Motooka,Nishi,
Fukuoka 819-0395,
Japan
E-mail address: adachi@cstf.kyushu-u.ac.jp

Available online 20 January 2007

Available online at www.sciencedirect.com
ScienceDirect
Organic Electronics 8 (2007) 293–299
Organic Electronics
www.elsevier.com/locate/orgel

Light extraction from OLEDs for lighting applications through light scattering

R. Bathelt [a], D. Buchhauser [b,c], C. Gärditz [a,b], R. Paetzold [b,*], P. Wellmann [a]

[a] Department of Material Science VI, University Erlangen-Nuremberg, Martensstraße 7, 91058 Erlangen, Germany
[b] Siemens AG, CT MM1, Guenther Scharowsky Street 1, 91052 Erlangen, Germany
[c] Department of Experimental Physics, University of Freiberg, Leipzigerstrasse 23, 09599 Freiberg, Germany

Received 18 July 2006; received in revised form 11 October 2006; accepted 28 November 2006
Available online 22 December 2006

Abstract

OLEDs are gaining increasing interest for lighting applications as large-area light sources. Their lifetime and overall efficiency can be increased by the optimization of light outcoupling.

In this article, scattering films on the viewer's side of the substrate to increase the outcoupling efficiency of OLEDs for lighting applications are examined. Experimental results show that the increase of outcoupling efficiency is dependent from the absolute number of scattering particles in the matrix.

Theoretical considerations expect an increase of outcoupling efficiency of up to 70%. Experimental results yield an increase of outcoupling efficiency of about 22%. A software model based on raytracing to simulate light outcoupling from OLEDs through a scattering layer is introduced to gain a deeper understanding of the light extraction mechanism. We found that the scattering anisotropy factor g determined using the Henyey–Greenstein phase function and the effective absorbance of the OLED device have strong impact on outcoupling efficiency.
© 2006 Elsevier B.V. All rights reserved.

PACS: 78.20.Bh; 85.60.Jb; 78.35.+c; 72.80.Le

Keywords: OLED; Lighting; Outcoupling enhancement; Light scattering; Simulation; Raytracing

1. Introduction

Organic light emitting diodes (OLEDs) are potential candidates for next-generation flatpanel-display applications. With increasing efficiency and lifetime, lighting applications are becoming another focus of interest [1]. For the latter, optimised light extraction efficiency is of particular interest. The typical design of a polymer-based OLED is made up of two layers of active polymer between a metallic cathode and a transparent anode on glass substrate. These active layers consist of a hole-transporting layer and the light emitting polymer (LEP). The light from the LEP must go through the device layers to be emitted. Assuming isotropic emission from the LEP and using Snell's Law with typical values for indices of

* Corresponding author. Tel.: +49 9131 7 33611.
E-mail address: ralph.paetzold@siemens.com (R. Paetzold).

1566-1199/$ - see front matter © 2006 Elsevier B.V. All rights reserved.
doi:10.1016/j.orgel.2006.11.003

refraction of the device layers one can calculate that, due to reflections at the interfaces within the OLED, only 30% of the light produced is emitted.

In the past years an extensive discussion took place concerning surface modification [2–4] to improve light outcoupling from organic and inorganic LEDs using ordered structures at the interface to air like e.g. micro spheres [5] or lenses [6]. At the interface to the active layers e.g. mesa structures [7] or distributed bragg-reflectors [8] were examined. Concerning lighting applications these approaches often have a serious effect on the emitted spectrum or radiation distribution. Another approach is the use of random structures to achieve light scattering like sanding of the surface to air [3,9] or application of an aerogel [10]. These approaches have a merely corrective effect on the emission concerning lighting purposes. In [14] light extraction through a scattering film has been examined using the radiative transport theory.

In this article, we introduce a computer simulation program based on a statistical approach and ray-tracing to gain a deeper understanding of the outcoupling mechanism of light from an OLED through a scattering layer.

Therefore freestanding scattering films were fabricated and attached to white emitting OLEDs in order to address the issue of light extraction efficiency. Light reflected at the internal interfaces is lost due to absorption in the OLED stack, respective emission from the substrate edges [11]. By changing photon trajectory randomly, all substrate light modes are recycled by scattering films. Hence, photons reflected at the interface to air may be redirected to the OLED surface, increasing the total light extraction probability and OLED efficiency. Using scattering films on the viewer's side of the substrate, solely glass or polymer foil substrate modes may be extracted to the viewer. Layer modes (modes confined within the emitting material), however, are not accessible in this approach. From a theoretical point of view, an increase of light outcoupling efficiency of up to 70% may be achievable in this approach.

The paper is organized in the following way: first, we address the model, the parameters and simplifications taken into account in the creation of the simulation program. In the experimental part we describe the determination of the model input parameters, foil production and the measurement of the impact of scattering films on OLED emission. In the last parts we compare the simulation results with the experimental results.

2. Simulation

The ray-tracing computer simulation tool uses a Monte-Carlo component to simulate light outcoupling from an OLED by means of a scattering film.

Using the MIE-Theory [12], one can calculate the scattering anisotropy exactly using particle size and the indices of refraction of particle and matrix. However, this process may be difficult. The Henyey–Greenstein

$$P_{\mathrm{HG}}(\cos\vartheta) = \frac{1-g^2}{4\pi(1+g^2-2g\cos\vartheta)^{\frac{3}{2}}}$$

phase function [13], is an approach on light scattering, which is widespread because of simplifications as to which the properties of the scattering system are summarized to the scattering anisotropy factor g. This factor is experimentally accessible. It is defined in between -1 and 1. The values "-1", "0", "1" mean mirror-like backscattering, isotropic scattering, and no change in photon trajectory respectively. Only g factors >0, which imply forward scattering, are examined in this article, as non-reflecting particles are used.

The Henyey–Greenstein distribution of a scattering event is being modeled statistically through a Monte-Carlo approach. The resulting angular distribution of scattered photons depends on the g-factor. The frequency of scattering depends on the mean free pathway between two scattering events and film thickness.

The software models an OLED consisting of active polymer and ITO, summarized to one layer with index of refraction n_{LEP} of 1.7, substrate glass with n_{g} of 1.5 and attached scattering layer.

Fig. 1 sketches typical paths of photons in this simulated OLED. Path 1 shows a photon confined within the LEP by reflection at the interface LEP/substrate and at the mirror like cathode. It is finally recognized as side emission from the LEP. Path 2 shows a photon that is reflected back into the device at the interface to air after some scattering events. Path 3 shows a photon that is finally extracted to the viewer after some reflections at the interface to air and scattering events where it has been redirected back to the surface. Path 4 shows a photon that is scattered back into the OLED stack where it may be absorbed or reflected back to the scattering layer depending on the effective absorbance of the OLED. Combinations of these sketched paths are possible as well. Back-reflection at the interface

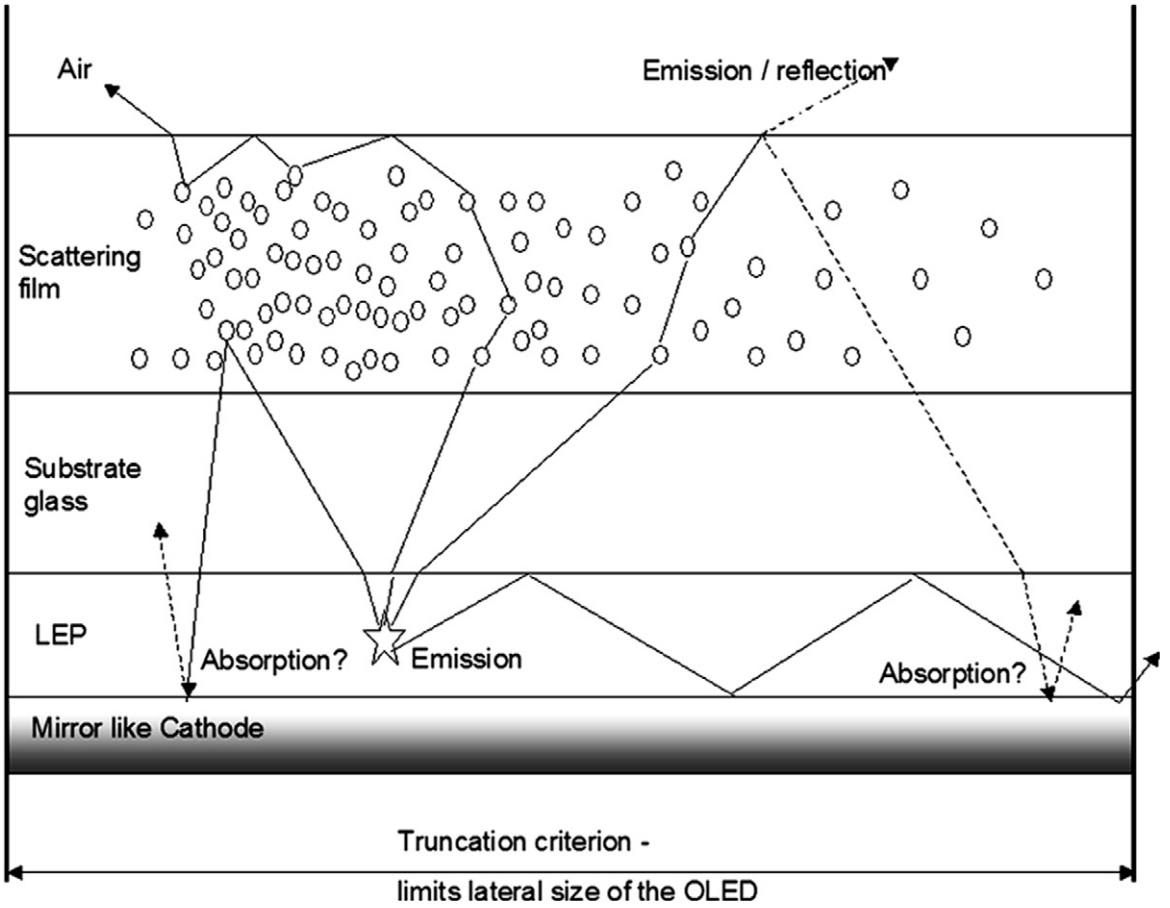


Fig. 1. Sketch of typical ways of photons in the simulated OLED. A description is given in the text.

to air is the major loss mechanism at a low concentration of scattering particles, while backscattering is the major loss mechanism at high concentrations. This indicates that an optimum exists between these extremes.

As proposed elsewhere [14], the following six input parameters are taken into account in our simulation tool. (1) The absorption coefficient of the matrix material of the scattering film α. (2) The mean free pathway between two scattering events X_f, which depends on particle concentration and size. (3) Thickness of the scattering film x. (4) The index of refraction of the matrix material n_m is required to calculate the change of propagation direction through refraction at the layer interfaces and the critical angle for reflection using Snell's law. (5) The probability of backscattered photons to be absorbed in the active layers of the OLED or at the metallic cathode is summarized in the parameter of effective absorbance A_e. (6) The scattering anisotropy factor g of the scattering system describes the "strength" of an average scattering event following the Henyey–Greenstein phase function.

Nine simplifications are applied to the model. (1) The angular distribution of the emission of the LEP is assumed to be isotropic. However, interference effects can be incorporated by choosing suitable emission characteristics. (2) A truncation criterion limits the lateral size of the OLED. Photons crossing this limit are always being recognized as waveguided in the respective layer. (3) All interfaces are assumed to be even. (4) LEP and ITO are summarized to be one layer with $n_{LEP} = 1.7$. (5) The OLED emission is assumed to be azimuthally symmetric (2D case). (6) Dispersion and (7) interference effects are not taken into account. (8) The scattering particles are assumed to be randomly distributed in the matrix and (9) equal in size.

As result of the simulation, angularly resolved distributions of photons in the respective layers

are obtained and the amount of photons that are absorbed in, or emitted from the side of the respective layer.

3. Experiment

Scattering films were produced by dispersing thin-walled hollow polymer micro spheres in an acrylate-based resist, which is used as matrix material. All samples were prepared via doctor blading of the mixture on a glass substrate. After UV curing the film is removed from the substrate. The absorption coefficient of the scattering layer was determined by measuring the transmission of unloaded films with different thickness using a Perkin-Elmer Lambda 35 spectrophotometer. The absorption coefficient α is found to be (0.35 ± 0.04) cm^{-1} at 550 nm. The index of refraction of the matrix material was measured using wavelength resolved ellipsometry. The index of refraction of the matrix material n_m is determined to vary between 1.51 at 400 nm up to 1.47 at 780 nm. Please note: the refractive index close to the one of glass (1.5) ensures a good transfer of photons from glass to the matrix. The average particle size of (10 ± 2) μm was determined via measuring the diameter of a number of scattering particles in the matrix using an optical microscope. As the differences of refractive indices of polymers are small in most cases, it can be assumed that the main scattering process takes place at the interface between particle shell and particle hollow core rather than at the interface of matrix and polymer particle sphere. The effective absorption A_e of the OLED used was measured using the reflectivity accessory of the Lambda 35 spectrophotometer and found to be (20 ± 10)%. Light scattering was determined by transilluminating a freestanding scattering film with a collimated beam of light emitted from a white inorganic LED. The angular distribution of the scattered light in forward direction was determined angularly resolved using a PR 650 spectrophotometer from Spectra Scan™. The scattering anisotropy factor g is then calculated via fit of the Henyey–Greenstein Phase function on the measurement. The g-factor of the system is found to be (0.85 ± 0.05).

To investigate the effect of scattering films on outcoupling, films with differing weight loadings of polymer spheres and differing thickness were prepared and successively applied to a white emitting polymer-based OLED (120 nm PEDOT, 80 nm LEP, active area about 2 cm^2) that exhibited lambertian emission characteristics.

The spectrum of the OLED without a scattering layer applied was measured angularly resolved using the PR 650 spectrophotometer. Directly afterwards a scattering layer was applied using optical gel and the measurement was repeated. The ratio of the intensity with and without scattering layer yields a parameter referred to as outcoupling enhancement in the following.

The average of the outcoupling enhancement over the visible spectrum and all angles leads to the overall outcoupling enhancement. The scattering foil was removed after the measurement and the intensity of the OLED was measured again to exclude fluctuations of the OLED intensity during the measurement. Integrating sphere measurements are used as references.

4. Experimental results

Scattering films with particle concentrations of 5, 15, 25, 40 and 50 wt.% and thickness between 40 and 300 μm were produced and their impact on outcoupling was measured as described above.

Fig. 2 shows a decreasing overall enhancement with increasing film thickness for high particle concentrations (50 wt.%), while the situation is vice versa for low particle concentrations (5 wt.%). A maximum enhancement of about 22% is observed. It shifts to lower film thickness with increasing particle concentration. This result indicates a correspondence between particle concentration and film thickness. If a matrix system with negligible absorption is used, the scattering ability gets independent from the scattering film thickness (Fig. 2b). It only depends from the number of particles per area, i.e. if a thin film with high load or a thick film with low load is used, same results can be obtained if the absolute number of particles per area is identical. Consequently, it does not matter if the optimum outcoupling efficiency is achieved by adjusting the concentration of scattering particles, or through adjusting the pathway in the film by thickness or by observation angle.

Another result is concerning the microcavity-effect, which is common in OLEDs based on broadband emitters. With increasing observation angle it usually exhibits a blue-shift based on destructive interference of the red part of the spectrum [15].

Fig. 3 shows the CIE 1931 y coordinate of the color of the emitted light for different observation angles. Without scattering film it oscillates. With applied scattering film and increasing particle load

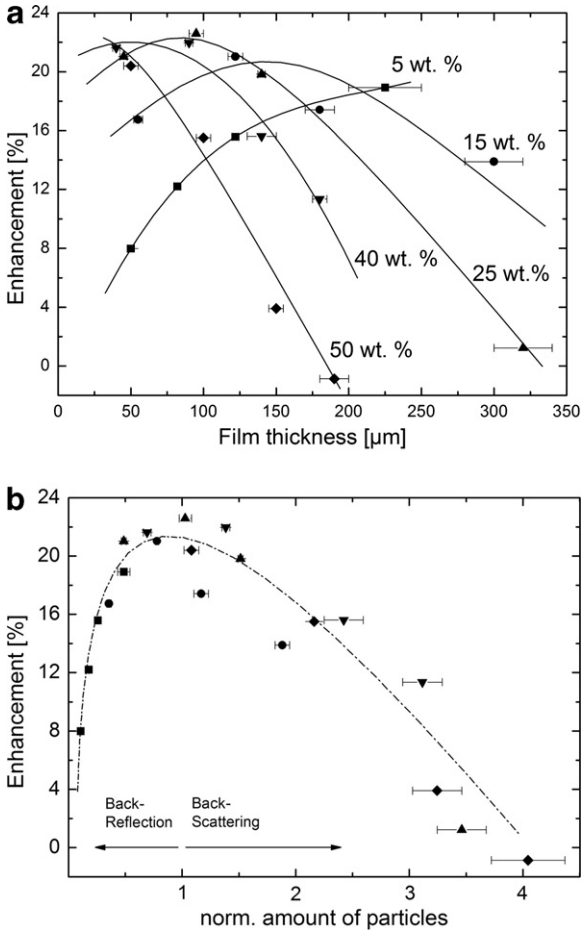


Fig. 2. (a) Shows the overall outcoupling enhancement plotted over film thickness for different weight loadings. (b) Shows these results plotted over the normalized amount of particles per area. A description is given in the text. Plotted lines are guidelines for the eye only.

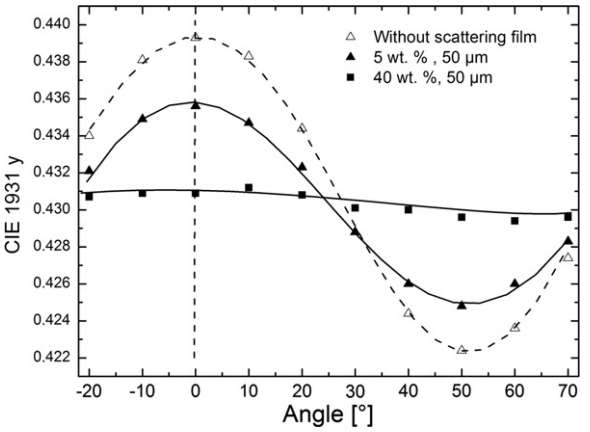


Fig. 3. Impact of scattering films on the angle-dependent microcavity-effect. Through angular intermixing of different modes the microcavity-effect is reduced and almost vanishes at a sufficiently high particle load. The CIE 1931 x - coordinate is not displayed as it exhibits only minor angle-dependency. Plotted lines are guidelines for the eye only.

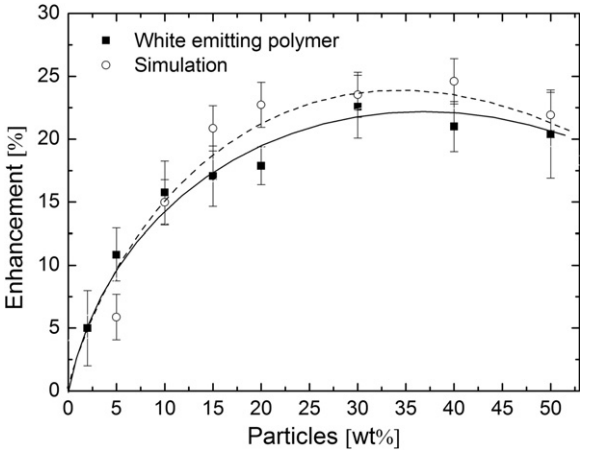


Fig. 4. Squares (solid line) denote the experimentally determined overall outcoupling enhancement, as described in part III. Maximum enhancement is found at a particle load of about 30 wt.% for scattering films with 50 µm thickness. Open circles (dashed line) denote simulation results for the respective input parameters. Plotted lines are guidelines for the eye only.

the oscillation is reduced and it almost vanishes at a particle load of 40 wt.% through increasing angular intermixing of modes with different wavelength.

5. Simulation results

The simulation was executed with the input values stated in part III. Fig. 4 shows the simulation results using open circles and – using squares – the measured outcoupling enhancement for scattering foils with 50 µm thickness and different particle concentrations. Measurement and simulation exhibit a maximum outcoupling efficiency of about 22% at a particle load of about 35 wt.%.

The angular resolved light output of a white emitting OLED with attached scattering films, one with high, and one with a rather low amount of particles is examined in Fig. 5.

Symbols denote the measured values of the normalized light intensity emitted in the respective angle. Lines denote the simulation results. At high particle concentrations (open circles, 25 wt.%), the highest output is found in forward direction and backscattering increases to higher angles. As the optimum is exceeded in forward direction, outcoupling efficiency decreases to higher angles as

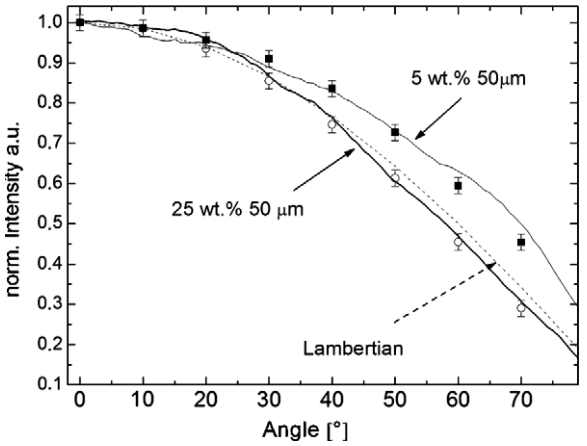


Fig. 5. Symbols denote measured values of the normalized light intensity in the respective angle. Lines denote the simulation results for the corresponding input values of thickness and particle load. Additionally, a lambertian emission characteristic (dashed) is shown.

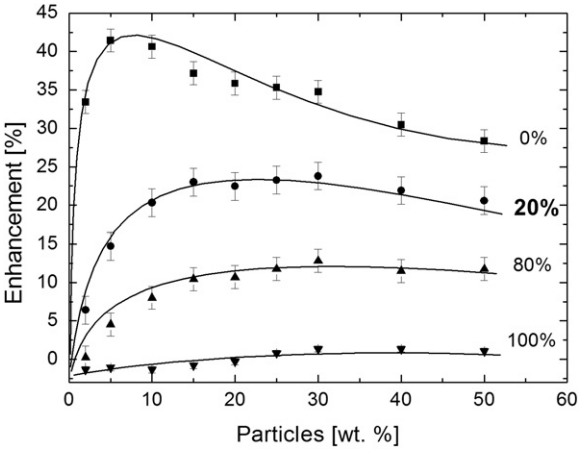


Fig. 6. Impact of effective OLED absorbance on outcoupling efficiency. The plot of 20% denotes the simulation result for the measured value of OLED absorbance. Plotted lines are guidelines for the eye only.

indicated by the weak undershoot from lambertian. At low amounts of scattering particles, the behavior is vice versa. Around relatively low amounts (5 wt.%) of particles (squares), a stronger overshoot from lambertian behavior is observable. This is due to more optimal numbers of scattering events at higher angles because of a more optimal way length in the film than in forward direction. These deviations from lambertian disappear towards very low amounts of particles (<1 wt.%, 50 µm) and are generally relatively weak at high amounts of particles (>25 wt.%, 50 µm).

The good agreement between simulation and experimental results in Figs. 4 and 5 shows clearly that our raytracing algorithm simulates outcoupling efficiency and angular distribution of the emission correctly quite well.

To find optimal film compositions, simulation runs with varied input parameters were performed (Figs. 6 and 7). The most relevant input parameters are thus identified by the software model. We found that the effective absorbance A_e and the g factor have the strongest impact on outcoupling efficiency.

During the variation of one parameter, all other parameters are fixed at their measured value. The thickness of the scattering film is set to 50 µm.

Fig. 6 shows that the effective absorbance of the OLED A_e has high impact on outcoupling. The measured value is 20%. Reduction of OLED absorbance leads to a significantly increased maximum outcoupling enhancement. At low OLED absorbance, the maximum efficiency is found at a low particle concentration. A possible reason is, that in this case back-reflection is a much weaker loss mechanism than absorption in the scattering film. With constant α, film absorbance is reduced through a lower way length in it because of lower amounts of scattering particles.

Fig. 7 shows the impact of the g factor on outcoupling. We found values between 0.6 and 0.8 to be optimal for high outcoupling efficiency. With increasing g factor the maximum moves to higher particle loads, which might be due to a weaker redirection effect of a single scattering event at a high g factor.

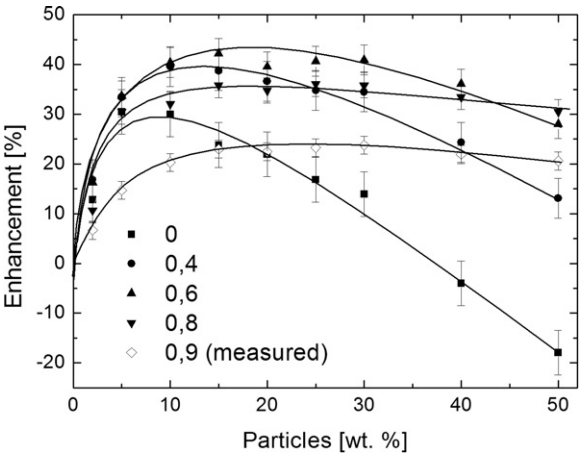


Fig. 7. Impact of the g-factor on outcoupling efficiency. The plot for the value 0.9 denotes the simulation result for the measured value. Plotted lines are guidelines for the eye only.

With all other parameters at their measured value, the simulation predicts an increase of the maximum outcoupling enhancement from 22% at a g factor of 0.9 to about 40%, which is consistent with [14], at a g factor of 0.7. As the g factor can be tuned more easily by choosing a suitable system of matrix and particle, this parameter is the best approach on outcoupling, rather than the device parameter of effective absorbance A_e.

6. Summary

In this contribution we have explained the differences between theoretical estimation and experimental result in the attempt to improve OLED outcoupling efficiency through scattering. We have gained a deeper understanding of the outcoupling mechanism through a computer simulation based on raytracing. After experimental determination of the input parameters we found that the outcoupling enhancement depends mainly on the absolute number of scattering particles per area in the respective system of matrix material and particle. It could be demonstrated that the simulation tool describes outcoupling enhancement and angular distribution of the emission correctly to a great extend.

Finally, light scattering offers inherent advantages like a more constant color over all observation angles and encryption of small defects [11].

References

[1] A. Bergh, G. Crawford, A. Duggal, R. Haitz, The promise and challenge of solid-state lighting, Phys. Today 54 (2001) 12.
[2] Bergh, Saul, Method of manufacturing surface textured high-efficiency radiating devices and devices therefrom, US. Pat. 3,739,217, 1973.
[3] M. Scheffel, A. Hunze ,J. Birnstock, J. Blässing, W. Rogler, G. Wittmann, A. Winnacker, Enhanced light extraction by substrate modification of organic electroluminescent devices in: Proceedings of Eur. Conf. Org. Elect. Related Phenomena'01, 158 2001.
[4] Windisch, Heremans, Knobloch, Kiesel, Dohler, Dutta, Borghs, Light emitting diodes with 31% external quantum efficiency by outcoupling of lateral waveguide modes, Appl. Phys. Lett. (1999) 74, p. 2256–2258.
[5] T. Yamasaki, K. Sumioka, T. Tsutsui, Organic light emitting device with an ordered monolayer of silica microspheres as a scattering medium, APL 76 (2000) 1243–1245.
[6] S. Moeller, S.R. Forrest, Improved light out-coupling in organic light emitting diodes employing ordered microlens arrays, J. Appl. Phys. 91 (2002) 3324–3327.
[7] G. Gu, D.Z. Garbuzov, P.E. Burrows, S. Venkatesh, S.R. Forrest, M.F. Thomson, High-external-quantum-efficiency organic light emitting devices, Opt. Lett. 22 (1997) 396–398.
[8] J.M. Lupton, B.J. Matterson, I.D.W. Samuel, M.J. Jory, W.L. Barnes, Bragg scattering from periodically microstructured light emitting diodes, APL 77 (2000) 3340–3342.
[9] M.H. Lu, C.F. Madison, J.C. Sturm, Tech. Dig. Int. Electron. Dev. Meeting 607 (2000).
[10] T. Tsutsui, M. Yahiro, H. Yokogawa, K. Kawano, M. Yokoyama, Doubling coupling-out efficiency in organic light emitting devices using a thin silica aerogel layer, Adv. Mater. 13 (2001) 1149–1152.
[11] C. Gaerditz, R. Paetzold, D. Buchhauser, R. Bathelt, G. Gieres, C. Tschamber, A. Hunze, K. Heuser, A. Winnacker, J. Amelung, D. Kunze, OLED lighting based on white broadband polymer emitters, Proc. SPIE 5937 (2005) 59370L.
[12] Bergmann-Schaefer, Lehrbuch der Experimentalphysik, Bd. III „Optik", 9. Auflage, de Gruyter, Berlin, 1993.
[13] L.G. Henyey, J.L. Greenstein, Diffuse radiation in the Galaxy, Astrophys. J. 93 (1941) 70–83.
[14] J.J. Shiang, T.J. Faircloth, A.R. Duggal, Experimental Demonstration of increased organic light emitting device output via volumetric light scattering, J. Appl. Phys. 95 (2004) 2889–2895.
[15] H. Becker, S.E. Burns, N. Tessler, R.H. Friend, Role of optical properties of metallic mirrors in microcavity structures, J. Appl. Phys. 81 (1997) 2825–2829.

Available online at www.sciencedirect.com
ScienceDirect
Organic Electronics 8 (2007) 300–304
Organic Electronics
www.elsevier.com/locate/orgel

Metal contacts in thin-film transistors

P. Stallinga *, H.L. Gomes

Universidade do Algarve, Facudade de Ciencias e Tecnologia, Campus de Gambelas, 8005-139 Faro, Portugal

Received 9 December 2005; received in revised form 24 July 2006; accepted 29 November 2006
Available online 22 December 2006

Abstract

The effects of metal contacts on the electrical characteristics in thin-film transistors are discussed. It is found that the effects of these contacts are twofold. First, a constant potential that can range from zero to some volts (half the bandgap) is added to the entire channel. Second, a residual barrier is formed with a height that depends on the bias, and is in the order of tens of meV when a current is present. It is shown that these predicted effects are in agreement with experimental observations.
© 2006 Elsevier B.V. All rights reserved.

PACS: 85.30.De; 85.30.Tv

Keywords: Thin film field-effect transistors; Amorphous silicon; Organic semiconductors; Two-dimensional electronics; Contact effects

Thin film field-effect transistors (TFTs) are made from the deposition of a thin active layer on top of an insulator. Because of the flexibility in design – the insulator and active layer do not have to be necessarily of the same material – they have taken a tremendous leap in recent years. Most commonly made from (amorphous) silicon on silicon oxide [1], with applications in active matrix displays, modern devices also include organic materials. Such materials can be made flexible as well as transparent or emitting light in the full range of colors. Together with the low cost of production, this extended the number of possible applications; unique devices are possible [2–4].

Thin-film transistors (TFTs) are transistors in which the active current-carrying layer is a thin film, in contrast to MOS-FET transistors where the currents are in the bulk of the material. The use of organic materials allows for a fabrication of the devices by printing techniques, thereby largely reducing the cost. Disadvantages of TFTs are a lower quality (crystallinity) of the active layer resulting in a lower mobility of charge carriers and therefore lower switching speeds. For this reason, TFTs find main applications in which the switching speed is not crucial, for instance in active matrix displays. Future applications also include flexible electronics, an area only feasible with (organic) TFTs. From bottom to top, a typical TFT consists of (1) a substrate giving support to the device, (2) a metal, or highly doped semiconductor taking the role of the gate electrode, (3) an insulator separating the gate from the active layer (4) metallic contacts serving as drain and source electrodes for injection and collecting of charges, and (5) the active semiconductor

* Corresponding author.
E-mail address: pjotr@ualg.pt (P. Stallinga).

1566-1199/$ - see front matter © 2006 Elsevier B.V. All rights reserved.
doi:10.1016/j.orgel.2006.11.004

layer. In some TFT geometries, the source–drain electrodes are deposited on top of the active layer, both geometries having their pros and cons. Finally, some TFTs have an additional capping layer to protect the device from external influences (diffusion of impurities, such as water, etc.). While originally made from CdS and CdSe, the most widely used and best studied devices are TFTs of (amorphous) silicon on silicon oxide [1].

One of the problems encountered in TFTs is the way to describe the effects of the metallic contacts. TFTs are normally described in the framework of the metal-oxide-semiconductor field-effect transistor (MOS-FET) model [5]. It is then common to attribute all deviations from MOS-FET behavior to the effects of the contacts, sometimes also generically termed contact resistance, although the effects include much more than simple ohmic resistance. Contact effects are well studied in the MOS-FET model and a multitude of reports exist to describe them, see for example the summary of Vega [6]. Some attempts exist to extend the theory to TFTs as well, see for example Necliudov et al. [7] and Hamadani and Natelson [8].

To compare, in a standard MOS-FET the contacts are made from the same material as the channel, but with a different doping type. Once an inversion channel of free charge is induced, the conduction and valence bands have aligned across the device from source to drain and no energetic barriers exists for the injection of carriers into the channel. Modern thin-film transistors, even when made from (amorphous) silicon, often have metallic contacts. Thus, when a channel is induced a barrier might still exist.

The active layer in a TFT is best treated as two-dimensional. This is applicable to thin-film transistors and thick FETs when in accumulation (when the charge in the channel is of the same type as the majority carriers in bulk material). The latter is true because, in the absence of electronic states to store immobile charge of the correct sign, all induced charge is mobile charge and therefore necessarily close to the interface since there is nothing opposing the pulling force of the electric field. To give an idea of how thick a channel in a MOS-FET is when in accumulation, or what the minimum thickness for the active layer in a TFT is and still function properly. For a device, with an oxide (insulator) thickness of 200 nm, operating at 1 V gate bias (with drain and source grounded), the induced charge density in the channel is $0.17\,\mathrm{mC/m^2}$. Assuming that the active layer is made of silicon with an effective density of valence band states of $N_V = 1.06 \times 10^{19}\,\mathrm{cm^{-3}}$ [9], the induced charge can easily fit in a monatomic layer. This explains why the measured mobility in TFTs is normally found to be independent of layer thickness after the first monolayer [10,11] and why the first layer and the interface with the insulator plays a key role in the device properties. As a result, we can imagine all densities of charge and states as true two-dimensional entities, without loss of accuracy [12].

In the current work, we describe the metallic TFT contacts when the device is in accumulation. We describe a p-channel accumulation device, but with the appropriate changes it is equally applicable to n-channel accumulation devices. As an immediate observation it can be stated that, when the device is working in accumulation, there are no depletion zones at the contacts and they can therefore not be treated as Schottky barriers, as is common for metallic contacts in MOS-FETs.

Fig. 1 shows a cross section of a TFT with the definitions used in the current work. As mentioned above, we consider the active layer as truly two-dimensional, where, at any point x along the channel, the local charge density $\rho(x)$ is directly linked to the local potential $V(x)$:

$$\rho(x) = C_{ox}[V(x) - V_g], \tag{1}$$

with C_{ox} the insulator capacitance density and V_g the bias at the gate. The implications of rigorously maintaining this relation will now be demonstrated.

Fig. 2 shows a schematic energy diagram of an unbiased metal–semiconductor–metal system. Because of the difference in Fermi level, E_{Fm} in the metal and E_{Fs} in the semiconductor (with ΔE_F defined as the difference), the system can gain energy by transferring electrons, in the case of Fig. 2 from semiconductor to metal (or holes from metal to semiconductor). The conventional buildup of space charge by uncompensated ionized acceptors or donors via Poisson's equation as in Schottky barriers does not take place due to the non-existence of

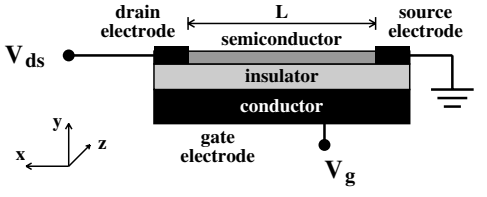


Fig. 1. Cross section of a thin-film FET (TFT) with the definitions used in the current work.

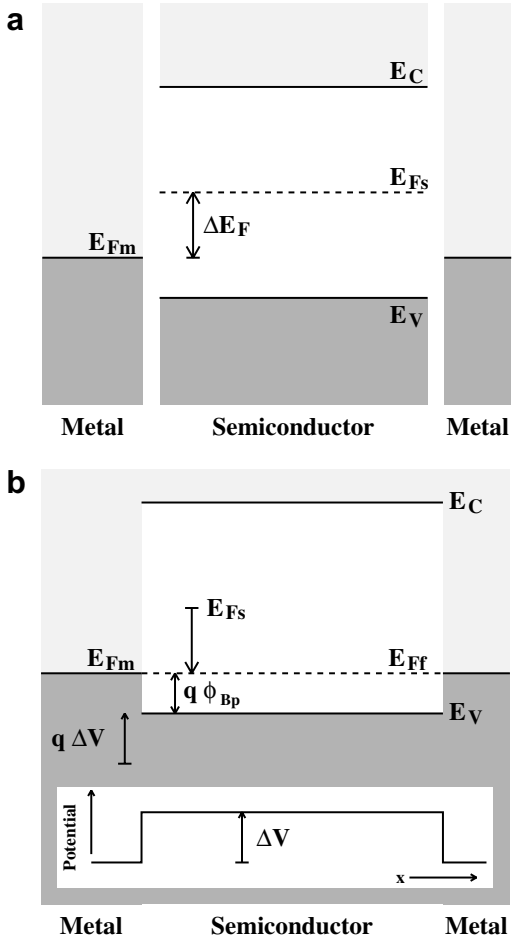


Fig. 2. Schematic energy diagram of a metal-contact TFT before (a) and after (b) contact. The parameters are: E_{Fm}, Fermi level in the metal; E_{Fs}, Fermi level in semiconductor before contact; E_{Ff}, Fermi level in semiconductor after contact; E_{C} and E_{V}, conduction band and valence band respectively; ΔV, voltage drop at the interface and equal to the voltage in the channel, as shown in the inset.

such impurities ionizable with the correct sign. Instead, the charge flowing into the channel is solely comprised of free holes. As a first effect, the holes cause a change of the Fermi level from E_{Fs} to E_{Ff} according to the Boltzmann relation:

$$p = N_{\mathrm{V}} \exp[(E_{\mathrm{V}} - E_{\mathrm{Ff}})/kT], \tag{2}$$

with N_{V} the effective (two-dimensional) density of valence band states, E_{V} the energy of an electron in the valence band, k Boltzmann's constant, T the absolute temperature and E_{Ff} the final position of the Fermi level. As a second effect, the new free holes are adding a potential to the channel (and to all energy levels in the channel) via Eq. (1),

$$\Delta V = qp/C_{\mathrm{ox}}, \tag{3}$$

with q the elementary charge. The free-hole density and thus the potential are constant over the entire length of the channel, because any gradient in either will cause a redistribution of the charges until the gradients disappear. At steady state, the only solution is a homogeneous distribution of holes and a constant voltage in the channel. The two effects, changing the Fermi level and increasing the in-channel potential, continue, until the Fermi levels have lined up, $E_{\mathrm{Ff}} = E_{\mathrm{Fm}}$. Combining the above two equations, with the definition of ΔE_{F}, the potential in the channel will be given by

$$\Delta V = \frac{kT}{q} W\left(\frac{q}{kT} A\right), \tag{4}$$

with W the Lambert-W function, and A equal to

$$A = \frac{qN_{\mathrm{V}}}{C_{\mathrm{ox}}} \exp\left(\frac{E_{\mathrm{V}} - E_{\mathrm{Fm}}}{kT}\right). \tag{5}$$

At the same time, a residual barrier $q\phi_{\mathrm{Bp}}$, equal to the difference in Fermi level and valence band in the semiconductor, exists at the contacts. Combination of Eqs. (1) and (2) yields,

$$q\phi_{\mathrm{Bp}} = -kT \ln\left(\frac{C_{\mathrm{ox}}(\Delta V - V_{\mathrm{g}})}{qN_{\mathrm{V}}}\right) \tag{6}$$

This barrier height thus depends on the bias V_{g}. When the bias is changed, the density of free holes changes and the Fermi level depth changes and the barrier height with it.

The easiest way to measure the height of the barrier is via the temperature dependence of the drain–source current. However, this necessitates the existence of a channel and thus free holes. Free holes imply that the Fermi level in the active layer is close to the band edge. The Fermi level depth being equal to the barrier height (see Fig. 2) then tells us that the measured barrier height is always rather small, in the order of tens of meV. We can thus give an estimate for the measured barrier height by substituting typical values for the parameters: $N_{\mathrm{V}} = 1.06 \times 10^{16}\ \mathrm{m}^{-2}$, $C_{\mathrm{ox}} = 170\ \mu\mathrm{F/m}^2$, $V_{\mathrm{g}} = -1$ V and $T = 300$ K yields about 60 meV for the barrier height. For the same reason, the barrier height, when measured by current, is independent of the type of metal used for the contact, since it depends only on the final Fermi level depth; at most, a slightly different threshold voltage results.

An observation can also be made for the in-channel potential ΔV. It can take values ranging from

zero up to the volts range. For intrinsic materials, even a tiny amount of charge in the channel can shift the Fermi level substantially and it is thus possible that the effect is nearly completely absorbed by a shift of the Fermi level, $E_{Fs} - E_{Ff} \approx \Delta E_F$, and $\Delta V \approx 0$. On the other hand, in a system where the Fermi level is pinned, for instance in doped semiconductors, the effect is mainly a voltage drop at the contact, $\Delta V \approx \Delta E_F/q$ and this can easily be in the volts range.

Summarizing, the metal contacts of a TFT working in accumulation cause two effects: (i) the building up of an in-channel potential that can be in the volts range and (ii) the formation of a residual barrier, with a height that depends on the gate bias and, when measured, is of the order of some tens of meV.

Relevant in view of this, are the experimental results reported in literature. Yagi et al. report on a gate-bias-dependent barrier with, for a certain bias, an activation energy of 80 meV [13] which is very close and easily within the range of the prediction above. Note that the devices of Yagi have top electrodes, a slightly different geometry compared to the bottom electrode devices presumed here. Apparently, the difference between the two geometries is not important enough and the model still applicable.

Concerning the in-channel potential predicted above, relevant is the voltage profiling experiment of Bürgi et al. [14]. They measured a potential in the channel, in the absence of bias, with an order of magnitude as described in the current work. Others report similar Kelvin probe experiments, but without presenting the most relevant zero-bias results.

Some observations have to be made about the limitations of the model. First of all, in Eq. (2), the Boltzmann approximation to the full Fermi-Dirac distribution has been used. This simplification is done to make the idea more understandable and make it analytically solvable. For Fermi levels close to – or resonant with – the valence band, this approximation is no longer valid. Note however that for such systems, the barrier height goes to zero and the effects of the contacts disappear completely.

Moreover, even a negative barrier height is predicted for large biases. The model thus loses applicability for such conditions. What happens for large biases is that all available states N_V are occupied by holes and saturation is thus expected for the transfer curves. As long as such saturation is not observed, the model is apparently applicable. In practice what will happen is that when the states in the first monolayer are depleted, the second layer (if present) starts getting filled. This layer is slightly more distant from the gate electrode and feels a slightly different capacitance and a different charge–voltage relation exists, compared to Eq. (1). To a good approximation, when the insulator is much thicker than a monolayer, it can be imagined that the DOS is simply multiplied by a factor 2 and then 3, etc. The simplified model presented only describes non-degenerate cases for low biases. Moreover, in practice it is expected that burning through the oxide occurs long before depletion of the valence band sets in, especially for thicker devices.

It was stated that no band bendings occur at the contacts. This is not entirely true. Band bendings can occur, but the spatial extent is rather small. To give an idea, were a classical Schottky barrier analysis used [9], with a density of states of $N_V = 10^{19}\,\mathrm{cm}^{-3}$, and a voltage drop at the contacts of $V_{bi} = 1$ V, this gives a space charge region of 8 nm. (Note that the value of N_V was used instead of N_D because the space charge is caused by free holes rather than ionized donors). In this regime, the tunneling will dominate over thermionic emission and the band bending region does not impede carrier injection. In fact, this strategy is normally followed to make ohmic contacts, where inter-diffusion of material at the interface is stimulated so as to allow for a high density of space charge and a small band bending region.

In summary, we have shown here, based on a single assumption of treating the active layer of thin-film transistor as a two-dimensional entity, the effects of the contacts. The idea is that if a current is present, however tiny, as long as it is observable, there must be free charge in the channel and consequently, the Fermi level must be somewhere close to the states responsible for conduction (for simplicity, these states are considered band states). Because on the other side the Fermi level is equal to the top of the Fermi sea, the barrier is rather small and injection to these conduction states are never a limiting process.

This work is relevant because it applies to all TFTs with any combination of active layer and contact metal, as long as the transistor is working in accumulation and band bendings are either absent or limited in size. Finally, it has to be pointed out that the theory described is for pure metal–semicon-

ductor–metal structures, with homogeneous materials and abrupt interfaces. Any diffusion or reaction taking place at the interface can undermine the validity. In fact, the current level of technology of organic TFTs makes most of them probably of a non-ideal type. Moreover, the workfunction of the metal can cause the semiconductor to go into depletion instead as the above described accumulation, in which case a threshold voltage is expected to exist, turning the device into a normally-off FET. Only after overcoming this threshold voltage does the theory apply.

Acknowledgement

This work has been financed by Portuguese grant POCTI/FAT/47956/2002 and POSC research unit CEOT.

References

[1] M.J. Powell, IEEE Trans. Electron Dev. 36 (1989) 2753.
[2] S.R. Forrest, Nature 428 (2004) 911.
[3] C.D. Sheraw, L. Zhou, J.R. Huang, D.J. Gundlach, T.N. Jackson, M.G. Kane, I.G. Hill, M.S. Hammond, J. Campi, B.K. Greening, J. Franci, J. West, Appl. Phys. Lett. 80 (2002) 1088.
[4] H. Sirringhaus, N. Tessler, R.H. Friend, Science 280 (1998) 1741.
[5] G. Horowitz, Adv. Mat. 10 (1998) 365.
[6] R.A. Vega, IEEE Trans. Electron Dev. 53 (2006) 866.
[7] P.V. Necliudov, M.S. Shur, D.J. Gundlach, T.N. Jackson, J. Appl. Phys. 88 (2000) 6594.
[8] B.H. Hamadani, D. Natelson, Appl. Phys. Lett. 84 (2004) 443.
[9] S.M. Sze, Physics of Semiconductor Devices, second ed., Wiley & Sons, New York, 1981.
[10] T. Muck, V. Vagner, U. Bass, M. Leufgen, J. Geurts, L.W. Molenkamp, Synth. Met. 146 (2004) 317.
[11] F. Dinelli, M. Murgia, P. Levy, M. Cavallini, F. Biscarini, D.M. de Leeuw, Phys. Rev. Lett. 92 (2004) 116802.
[12] P. Stallinga, H.L. Gomes, Synth. Met., accepted for publication.
[13] I. Yagi, K. Tsukagoshi, Y. Aoyagi, Appl. Phys. Lett. 84 (2004) 813.
[14] L. Bürgi, H. Sirringhaus, R.H. Friend, Appl. Phys. Lett. 80 (2002) 2913.

Available online at www.sciencedirect.com
ScienceDirect
Organic Electronics 8 (2007) 305–310
Organic Electronics
www.elsevier.com/locate/orgel

Bright and efficient white stacked organic light-emitting diodes

J.X. Sun, X.L. Zhu, H.J. Peng, M. Wong, H.S. Kwok *

Center for Display Research and Department of Electronic and Computer Engineering, The Hong Kong University of Science and Technology, Clear Water Bay, Kowloon, Hong Kong

Received 27 July 2006; received in revised form 10 November 2006; accepted 27 November 2006
Available online 8 January 2007

Abstract

High brightness and efficient white stacked organic light-emitting diodes have been fabricated by connecting individual blue and red emissive units with the anode–cathode layer (ACL) consisting of LiF (1 nm)/Ca (25 nm)/Ag (15 nm). Use 1,3-bis(carbazol-9-yl)benzene (mCP):bis(3,5-difluoro-2-(2-pyridyl)phenyl-(2-carboxypyridyl) iridium III (FirPic) as the blue emitter and tris(8-hydroxy-quinolinato)aluminium (Alq_3):4-(dicyanomethylene)-2-*tert*-butyl-6-(1,1,7,7-tetramethyljulolidin-4-yl-vinyl)-4H-pyran (DCJTB) as the red emitter, white light emission with CIE coordinates of (0.32, 0.38) was obtained at a driving voltage of 26 V with a luminance of 40,000 cd/m^2. By replacing the red fluorescent emitter with a phosphorescent one, the color coordinates were improved to (0.33, 0.31). The peak external quantum efficiency was enhanced from 5.3% (at 28.2 mA/cm^2) to 10.5% (at 1.4 mA/cm^2) as well.
© 2006 Elsevier B.V. All rights reserved.

PACS: 78.60.Fi; 78.66.Bz; 78.66.Qn; 85.60.Jb

Keywords: White organic light-emitting diode; Stacked; High efficiency

White organic light-emitting diode (OLED) has been widely investigated due to its potential application in making full-color OLED display as well as in next-generation light source [1–3]. However, for the conventional single-unit OLED, the peak efficiency is often achieved at low current density level (e.g., 0.01 mA/cm^2) and hence low brightness, remaining a drawback to solid-state lighting [4]. In contrast, stacked OLED (SOLED) with N (N: integer) emissive units is showing N times luminous efficiency as high as that of the conventional single-unit device [5–7]. It is easy to achieve high efficiency at high luminance because that the driving current density is only approximately $1/N$ of that of the single-unit device to achieve the same luminance while still maintaining a high efficiency. This feature makes such white SOLED (WSOLED) more attractive for lighting. So far reports on WSOLED are rather limited [8–11].

Recently, we have successfully developed an efficient anode–cathode layer (ACL) for connecting two adjacent emissive units in SOLED [12]. In the present report, we shall introduce a WSOLED using this ACL. The ACL consists of LiF (1 nm)/Ca (25 nm)/Ag (15 nm) and can function quite well after CF_4-plasma treatment of the Ag layer for efficient

* Corresponding author.
E-mail addresses: sjxaa@ust.hk (J.X. Sun), eekwok@ust.hk (H.S. Kwok).

1566-1199/$ - see front matter © 2006 Elsevier B.V. All rights reserved.
doi:10.1016/j.orgel.2006.11.006

hole injection [13]. Here it is used to connect a blue and red emissive unit to produce the WSOLED. The blue and red emissive units are *N*,*N*′-bis(naphthalen-1-yl)-*N*,*N*′-bis(phenyl)-benzidine (NPB)/1,3-bis(carbazol-9-yl)benzene (mCP): bis(3,5-difluoro-2-(2-pyridyl)phenyl-(2-carboxypyridyl) iridium III (FirPic)/2,2′,2″-(1,3,5,-benzinetriyl)-tris(1-phenyl-1-H-benzimidazole (TPBi) and NPB/tris(8-hydroxyquinolinato)aluminium (Alq_3):4-(dicyanomethylene)-2-*tert*-butyl-6-(1,1,7,7-tetramethyljulolidin-4-yl-vinyl)-4H-pyran (DCJTB)/2,9-dimethyl-4,7-diphenyl-1,10-phenanhroline (BCP), respectively. Efficient white light with a CIE coordinates of (0.32, 0.38) was obtained under a driving voltage of 26 V with the luminance of 40,000 cd/m^2. A correlated color temperature (CCT) of 5796 K and a color rendering index (CRI) of 67 are calculated from this spectrum [14–16]. The external quantum efficiency (EQE) is peaked at 5.3% at a driving voltage of 15.1 V with current density of 28.2 mA/cm^2. By using a red phosphorescent emissive unit consisting of NPB/mCP: bis(2-benzo[*b*]thiophen-2-yl-pyridine) (acetylacetonate) iridium (III) (Btp_2Ir(acac))/BCP, the WSOLED showed a more saturated white light emission with CIE coordinates of (0.33, 0.31). The peak EQE was improved to 10.5% as well.

Glass coated with 75 nm indium-tin oxide (ITO) was used as the substrate for the WSOLED. The sequence of pre-cleaning prior to loading into the surface treatment chamber consisted of soaking in ultra-sonic detergent for 30 min, spraying with deionized (DI) water for 10 min, soaking in ultra-sonic DI water for 30 min and baking for 1 h. The organic materials were commercially available from LumTec Corp. and used as received. All the thin films were prepared by thermal evaporation in a four-chamber deposition system with the base pressure lower than 10^{-6} Torr. The schematic architecture of the WSOLED along with the chemical structures of the organic materials used here is shown in Fig. 1. The structure of the WSOLED in this work is ITO/NPB (40 nm)/mCP:FirPic (30 nm, 10wt%)/TPBi (30 nm)/LiF (1 nm)/Ca (25 nm)/Ag (15 nm)/NPB (50 nm)/Alq_3:DCJTB (30 nm, 1.5wt%)/BCP (20 nm) or NPB (60 nm)/mCP:Btp_2Ir(acac) (30 nm, 6wt%)/BCP (30 nm)/LiF (1 nm)/Ca (20 nm)/Ag (80 nm). Doping was achieved by co-evaporation from two separated sources. The typical deposition rates of organic thin films, LiF and metals were 0.1–0.15 nm/s, 0.03–0.04 nm/s and 0.3–0.4 nm/s, respectively, which were monitored by quartz oscillators *in situ*. The active area of bottom and top devices are both defined by a shadow mask and is 18 ± 1 mm^2.

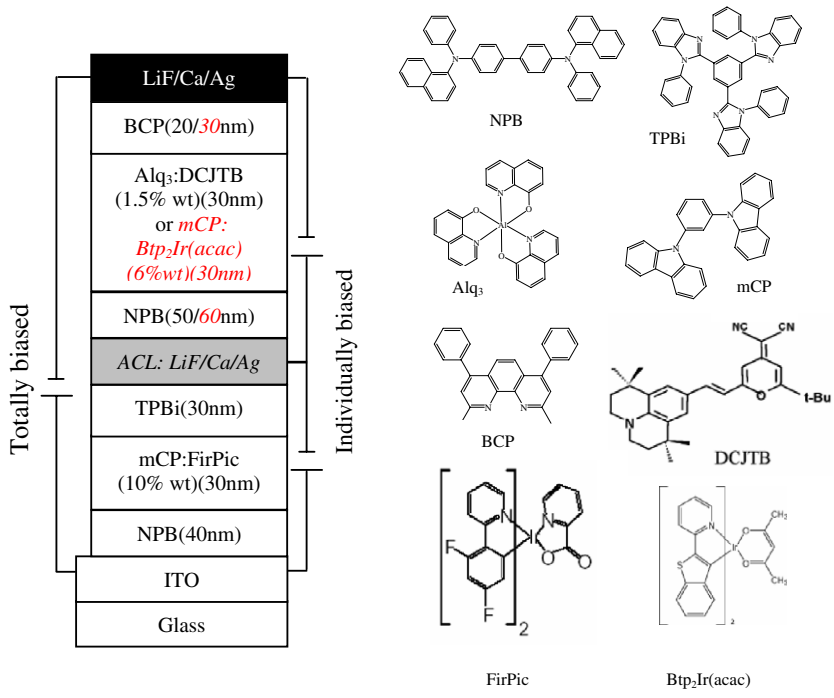


Fig. 1. Structure of the WSOLED along with the molecular structures of organic materials used in this work.

The luminance–current density–voltage (L–J–V) characteristics of the devices were recorded simultaneously with a semiconductor parameter analyzer (HP4145B) and a large diameter (25 mm) silicon photodiode mounted 2 mm above the measured device. The edge emission from the substrate was not captured due to the use of black paste on the edge. The EQE was measured at the same time under the assumption of Lambertian emission profile. The electroluminescent (EL) spectral characterization and the luminance calibration of the photodiode were carefully performed with a Photo-Research PR650 spectrometer. All measurements were carried out under ambient atmosphere without device encapsulation.

As known to us, to achieve efficient light emission from SOLED, the intermediate connecting layers shall have enough transparency as well as less absorption [17,18]. Here we checked the reflectance/transmittance characteristics of Ca (25 nm)/Ag (15 nm) double layers, which are the major constituent of our ACL. Transmittance and reflectance spectra of Ca/Ag double layers on glass substrate were obtained with UV/VIS spectrophotometer – Perkin–Elmer (model: Lambda 20). Acceptable transmittance over 60% and residual reflectance lower than 15% in the wavelength range of 450–620 nm were measured for Ca/Ag double layers, making it suitable as the intermediate layers in our WSOLED (see Fig. 2). Indeed, Ca/Ag double layers show much higher transmittance compared to Ag layer only in the visible range as described in the previous report [19].

In order to study the emission properties of individual units as well as in tandem, we patterned the middle electrode such that it can be connected externally. Fig. 3 shows the normalized EL spectra of the bottom blue unit and top red unit under different driving voltages. It can be seen that the EL spectra of the individual emissive unit are almost unchanged with the increase of driving voltages. As a result, the CIE coordinates of the individual blue and red emission from respective bottom and top unit are shifted very little with the change of the driving voltage as shown in Fig. 4. It is obvious that if the two emissive units are biased in a proper ratio, white light emission can be achieved. Fig. 5 shows the total output spectrum with the individually emissive bottom blue unit and top red units biased at 6 V and 8 V, respectively. It is simply a sum of the spectra in Fig. 3.

Fig. 6 shows the EL spectra of the WSOLED with only the top and bottom electrodes connected to the power source. The ACL is not connected and functions as an electron injector for the bottom

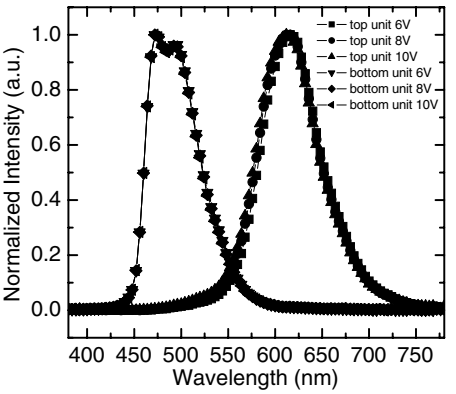


Fig. 3. Normalized EL spectra of bottom blue unit and top red unit under different driving voltages.

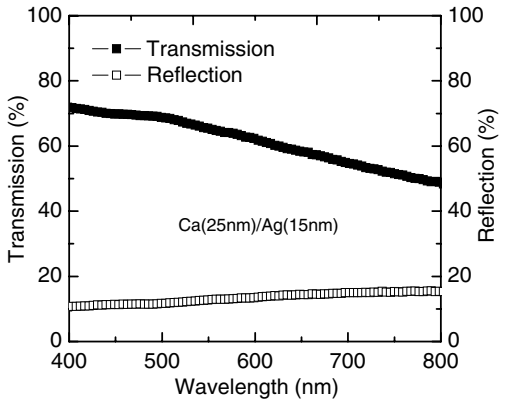


Fig. 2. Transmission and reflection spectra of Ca (25 nm)/Ag (15 nm) double layers.

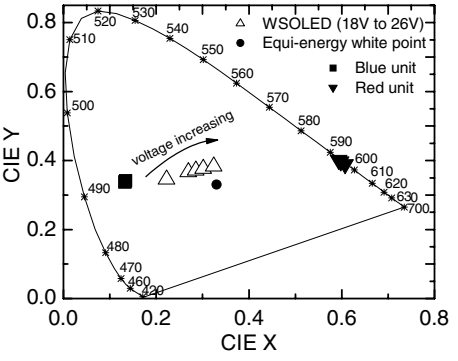


Fig. 4. The CIE coordinates of bottom blue unit, top red unit and total WSOLED at different driving voltages.

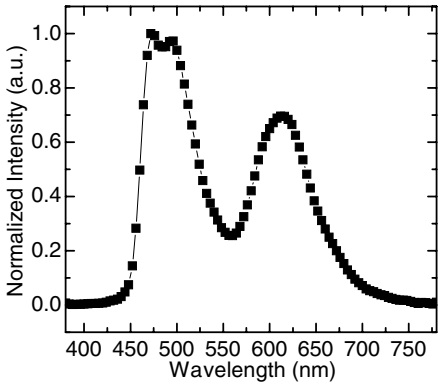


Fig. 5. Total EL spectrum with bottom and top units at 6 V and 8 V, respectively.

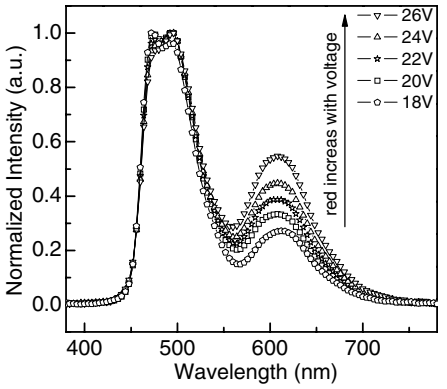


Fig. 6. EL spectra of the WSOLED under different driving voltages.

unit and a hole injector for the top unit. The EL spectra are plotted for different driving voltages. The CIE coordinates are gradually close to equi-energy white point (0.33, 0.33) with the increase of driving voltages, as indicated in Fig. 4. The two peaks at ~472 nm and ~612 nm correspond to emission from FirPic and DCJTB, respectively. When the driving voltage is increased, it is found that the red emission from the top unit increases more than the bottom blue unit. It results in a better white color at higher bias. To investigate this tendency, we try to calculate the ratio of the height of blue emission peak to that of red emission peak based on the relation between radiance and luminance [20],

$$\int \mathrm{Le}(\lambda) \times K(\lambda)\mathrm{d}\lambda = L \tag{1}$$

where, $\mathrm{Le}(\lambda)$ is the radiance in W/sr m^2, $K(\lambda)$ is ocular response curve for cones, L is the luminance in cd/m^2. In this work, the $\mathrm{Le}(\lambda)$ for the blue light from FirPic and red light from DCJTB can be easily measured by the PR650. Additionally, as shown in Fig. 3, the normalized EL spectra of the blue and red emissive units are constant and do not change with applied voltage. Therefore, we can easily get the relative height of blue and red peaks by evaluating

$$P_{\mathrm{B}} \int \mathrm{Le}_{\mathrm{B}}(\lambda) \times K(\lambda)\mathrm{d}\lambda = L_{\mathrm{B}} \tag{2}$$

$$P_{\mathrm{R}} \int \mathrm{Le}_{\mathrm{R}}(\lambda) \times K(\lambda)\mathrm{d}\lambda = L_{\mathrm{R}} \tag{3}$$

where, P_{B} and P_{R} are the height of the peaks in the EL spectra for blue and red emission from FirPic (472 nm) and DCJTB (612 nm), respectively. $\mathrm{Le}_{\mathrm{B}}(\lambda)$ and $\mathrm{Le}_{\mathrm{R}}(\lambda)$ are the normalized radiance for blue and red light.

In the WSOLED, the current flowing through the two emissive units is continuous, thus it is straightforward to predict the ratio of the peak heights based on the separately measured luminous efficiency vs. current density curves of the respective blue and red units. Since $L_{\mathrm{B}}/L_{\mathrm{R}} = \eta_{\mathrm{B}}/\eta_{\mathrm{R}}$, where η_{B} and η_{R} are the luminous efficiency of blue and red emission respectively, using Eqs. (2) and (3), we can get:

$$\frac{P_{\mathrm{B}}}{P_{\mathrm{R}}} = 1.47555\frac{\eta_{\mathrm{B}}}{\eta_{\mathrm{R}}} \tag{4}$$

The experimental results on η_{B} and η_{R} are shown in Fig. 7. Using Eq. (4) and the results shown in Fig. 7, we can calculate the $P_{\mathrm{B}}/P_{\mathrm{R}}$ ratio under different current driving conditions. Fig. 8 shows the peak ratio of blue to red emission vs. current density

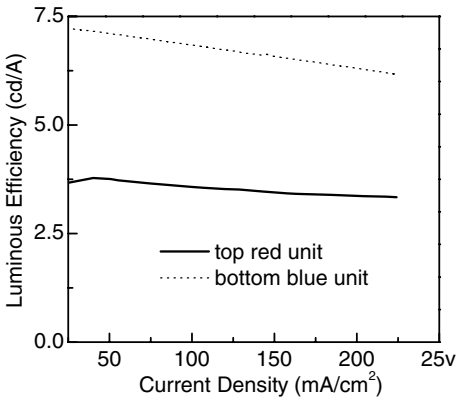


Fig. 7. The experimental curves of luminous efficiency vs. current density of top red unit and blue bottom unit individually biased for calculation.

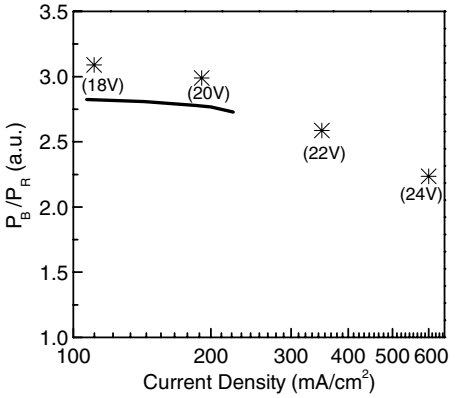


Fig. 8. The peak ratio of blue to red emission in the WSOLED, together with the experimental results denoted as asters.

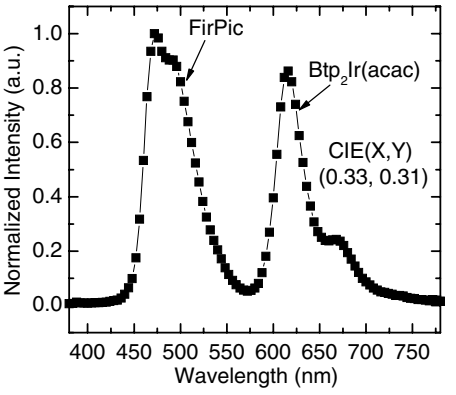


Fig. 9. EL spectra of the alternative WSOLED at a driving voltage of 17 V.

curve in the WSOLED. The calculated curve shows that indeed the ratio of blue to red decreases with current density. Also, the measured results, denoted as asterisks in Fig. 8, agree reasonably well with the calculated values. It is noteworthy that, based on Eq. (4), it is difficult to achieve comparable blue and red in this device due to the mismatch in efficiencies. However, it is still possible to obtain white light emission from this device. For example, at the bias of 26 V, white light with CIE coordinates of $(0.32, 0.38)$ is achieved, with a luminance of 40,000 cd/m^2. Brighter light with even better color purity can be expected at higher voltages. Of course, breakdown of the stacked device is a problem. The EQE of the whole device peaks at 5.3% at a driving voltage of 15.1 V. The relatively low EQE can be attributed to the use of red fluorescent dopant material DCJTB.

To overcome these problems, we replace the red fluorescent emissive unit with the red phosphorescent one consisting of NPB (60 nm)/mCP:Btp_2Ir(acac) (30 nm, 6wt%)/BCP (30 nm). This emitter can offer a comparable efficiency as the blue emissive unit in our experiment. Again, we measured the EL spectra of two individual units (not shown here) and calculated the P_B/P_R ratio. In this case, we can have:

$$\frac{P_B}{P_R} = 0.86496\frac{\eta_B}{\eta_R} \tag{5}$$

From Eq. (5), it is seen that it will be much easier to implement saturated white light emission from this alternative device architecture. Experimentally, purer white light with CIE coordinates of $(0.33, 0.31)$ is indeed achieved, together with a higher external quantum efficiency of 7.8% at a current density of 39.4 mA/cm^2 and luminance of 4450 cd/m^2.

Fig. 9 shows the EL spectra of this WSOLED at the driving voltage of 17 V. It can be seen that the two peaks from FirPic and Btp_2Ir(acac) are comparable in height and therefore results in a purer white light with CIE coordinate of $(0.33, 0.31)$. At this driving voltage, the WSOLED gives a luminance of 4450 cd/m^2. However a CCT of 5899 K and rather poor CRI of 13 were calculated from the spectrum [14–16], making it unsuitable for possible lighting application. It is understood that the large distance of two peaks from respective narrow blue and red emission and valley formed in-between cause the unfavorable CRI. However, it is not the intrinsic limitation of the concept of WSOLED with our ACL because alternative favorable emissive units can be freely chosen to meet the requirements.

Fig. 10 shows the overall EL characteristics of the WSOLED. Fig. 10a shows the current density and luminance vs. voltage curves, while Fig. 10b shows the power efficiency and external quantum efficiency vs. voltage curves. The driving voltage is relatively high due to the large stack structure. The EQE is peaked at 10.5% at the driving voltage of 11.2 V with a current density of 1.4 mA/cm^2 and luminance of 273 cd/m^2. As can be seen, the power efficiency of current WSOLED is still low, e.g., at a luminance of 1000 cd/m^2, the power efficiency is only 3.31 m/W. Clearly, further investigation is needed to improve the power efficiency by reducing the operating voltages. As well, the lifetime of this WSOLED needs to be studied.

In summary, efficient white stacked organic light-emitting diodes using a novel ACL to connect the

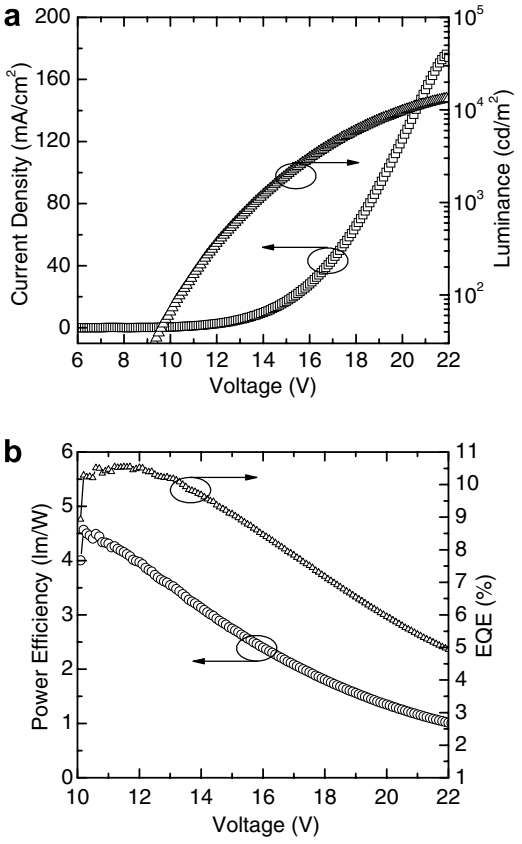


Fig. 10. (a) Luminance and current density vs. voltage, (b) power efficiency and external quantum efficiency vs. voltage curves of the WSOLED.

blue and red emissive units have been demonstrated. In one implementation using singlet red emitter, very high brightness (40,000 cd/m^2) white light with CIE coordinates of (0.32, 0.38) was achieved. A correlated color temperature (CCT) of 5796 K and a color rendering index (CRI) of 67 are obtained. In another implementation using a red phosphorescent emissive unit, a much purer white light emission with CIE coordinates of (0.33, 0.31) as well as better EQE are achieved. This latter efficient white light was achieved at only 17 V with a luminance of 4450 cd/m^2.

Acknowledgements

This work was supported by the Hong Kong Government Innovation and Technology Fund.

References

[1] B.W. D'Andrade, R.J. Holmes, S.R. Forrest, Adv. Mater. (Weinheim, Ger.) 16 (2004) 624.
[2] H. Kanno, Y. Sun, S.R. Forrest, Appl. Phys. Lett. 86 (2005) 263502.
[3] S. Tokito, T. Iijima, T. Tsuzuki, F. Sato, Appl. Phys. Lett. 83 (2003) 2459.
[4] H. Kanno, N.C. Giebink, Y. Sun, S.R. Forrest, Appl. Phys. Lett. 89 (2006) 023503.
[5] T. Matsumoto, T. Nakada, J. Endo, K. Mori, N. Kavamura, A. Yokoi, J. Kido, Soc. Info. Displ. Sympos. Digest 34 (2003) 979.
[6] L.S. Liao, K.P. Klubek, C.W. Tang, Appl. Phys. Lett. 84 (2004) 167.
[7] C.C. Chang, S.W. Hwang, C.H. Chen, J.F. Chen, Jpn. J. Appl. Phys. 43 (9A) (2004) 6418.
[8] T. Matsumoto, T. Nakada, J. Endo, K. Mori, N. Kawamura, A. Yokoi, J. Kido, in: Proceedings of IDMC'03, vol. 413, 2003.
[9] C.C. Chang, S.W. Hwang, H.H. Chen, C.H. Chen, J.F. Chen, in: Proceedings of IDW'04, vol. 1285, 2004.
[10] C.C. Chang, J.F. Chen, S.W. Hwang, C.H. Chen, Appl. Phys. Lett. 87 (2005) 253501.
[11] H. Kanno, R.J. Holmes, Y. Sun, S.K. Cohen, S.R. Forrest, Adv. Mater. (Weinheim, Ger.) 18 (2006) 339.
[12] J.X. Sun, X.L. Zhu, H.J. Peng, M. Wong, H.S. Kwok, Appl. Phys. Lett. 87 (2005) 093504.
[13] H.J. Peng, X.L. Zhu, J.X. Sun, Z.L. Xie, S. Xie, M. Wong, H.S. Kwok, Appl. Phys. Lett. 87 (2005) 173505.
[14] Y. Ohno, in: Proceedings of SPIE Fourth International Conference on Solid State lighting, Denver, CO, 2004, vol. 5530, 2004, pp. 88–98.
[15] W. Davis, Y. Ohno, in: Proceedings of SPIE Fifth International Conference on Solid State Lighting, Bellingham, WA, 2005, vol. 5941, 2005, p. 59411G.
[16] Y. Ohno, Opt. Eng. 44 (11) (2005) 111302.
[17] G. Gu, G. Parthasarathy, P.E. Burrows, P. Tian, I.G. Hill, A. Kahn, S.R. Forrest, J. Appl. Phys. 86 (1999) 4067.
[18] P.E. Burrows, G. Gu, S.R. Forrest, E.P. Vicenzi, T.X. Zhou, J. Appl. Phys. 87 (2000) 3080.
[19] R.B. Pode, C.J. Lee, D.G. Moon, J.I. Han, Appl. Phys. Lett. 84 (2004) 4614.
[20] W.J. Mooney, Optoelectronic Devices and Principles, Prentice-Hall International, Inc., London, UK, 1991.

Available online at www.sciencedirect.com
ScienceDirect
Organic Electronics 8 (2007) 311–316
Organic Electronics
www.elsevier.com/locate/orgel

High gain in hybrid transistors with vanadium oxide/tris(8-hydroxyquinoline) aluminum emitter

Mingdong Yi [a], Shunyang Yu [a], Chengang Feng [a,b], Tong Zhang [b], Dongge Ma [a,*], M.S. Meruvia [c], Ivo A. Hümmelgen [c,*]

[a] State Key Laboratory of Polymer Physics and Chemistry, Changchun Institute of Applied Chemistry, Graduate School of the Chinese Academy of Sciences, Chinese Academy of Sciences, Changchun 130022, PR China
[b] National Key Laboratory of Integrated Optoelectronics, Jilin University, Changchun 130012, PR China
[c] Group of Organic Optoelectronic Devices, Departamento de Física, Universidade Federal do Paraná, Caixa Postal 19044, 81531-990 Curitiba PR, Brazil

Received 19 May 2006; received in revised form 27 September 2006; accepted 29 November 2006
Available online 4 January 2007

Abstract

We report the electrical characterization of hybrid permeable-base transistors with tris(8-hydroxyquinoline) aluminum as emitter layer. These transistors were constructed presenting an Al/n-Si/Au/Alq_3/V_2O_5/Al structure. We investigate the influence of the V_2O_5 layer thickness and demonstrate that these devices present high common-base and common-emitter current gain, and can be operated at very low driving voltages, lower than 1 V, in both, common-base and common-emitter modes.
© 2006 Elsevier B.V. All rights reserved.

PACS: 81.07.Pr; 73.40.Vz; 85.30.De

Keywords: Hybrid permeable-base transistors; Tris(8-hydroxyquinoline) aluminum emitter; High gain

1. Introduction

Organic and hybrid transistors are attracting attention due to potential applications in organic displays [1]. Since the green emitter tris(8-hydroxyquinoline) aluminum (Alq_3) probably received more attention than any other small molecular emitter for organic light-emitting diodes (LEDs) applications [2,3], it would be highly desirable to use this material in transistors aiming compatibility between LED and transistor production processes and materials, simplifying production processes and reducing costs.

Hybrid organic/inorganic semiconductor–metal–semiconductor transistors presenting nearly-ideal base transport factor were demonstrated by Meruvia et al. [4], solving a problem that has plagued inorganic semiconductor-metal-semiconductor devices [5]. The base transport factor is the fraction

* Corresponding authors. Tel.: +86 431 5262357; fax: +86 431 5262873.
E-mail addresses: mdg1014@ciac.jl.cn (D. Ma), iah@fisica.ufpr.br (I.A. Hümmelgen).

1566-1199/$ - see front matter © 2006 Elsevier B.V. All rights reserved.
doi:10.1016/j.orgel.2006.11.005

of charge carriers emitted by the emitter that crosses the base being collected by the collector. Their devices have a thin Au base layer deposited on top of n-type Si substrate. The emitter is composed by C_{60} and Al, sequentially deposited on top of the Au layer, resulting in a device that emits electrons from the C_{60} through the Au layer with enough energy to allow collection via the Si collector.

Alq_3 based transistors applications were very limited by relatively low currents and high operational voltages [6]. But quite recently, hybrid Alq_3-based devices allowing higher operational current densities at low voltages were reported by Yi et al. [7]. These Al/n-Si/Au/Alq_3/Al permeable base transistors (PBTs) showed high common-base current gain $\alpha_0 \equiv \frac{\partial I_C}{\partial I_E}$ [8], which were demonstrated to be dependent on base thickness (I_C is the collector current and I_E the emitter current). These devices were constructed in vertical architecture because this structure implies short channel lengths [9], a condition which is relevant due to lower charge carrier mobility in organic semiconductors. In the vertical architecture, the charge transport paths through the organic semiconductors are determined by layers thickness.

Despite the advantages of high α_0 and low operational voltages, the Alq_3-based devices reported by Yi et al. [7] presented unsatisfactory characteristics when operating in the common-emitter mode, like difficulty of obtaining high and reproducible values of common emitter current gain $\beta = \frac{\partial I_C}{\partial I_B}$ [8], characteristics that are required in applications involving amplification.

Recently, Zhu et al. [11] and Chu et al. [12] demonstrated that a V_2O_5 layer between metal and organic semiconductor can be used to improve OLEDs and field effect transistors performance, mostly facilitating charge carrier injection into the organic semiconductor layer.

In this article, we report the preparation and characterization of PBTs with Au base and Alq_3 emitter, investigating the consequences of the introduction of a thin (between 1 and 3 nm thick) V_2O_5 layer between Al and Alq_3 in the emitter, demonstrating a significant improvement in device performance.

2. Experimental

Transistors in this study were prepared using *n*-type Si (100) substrate with resistivity between 1 and 10 Ω cm. The Si substrate was etched in a 5% HF solution to remove surface oxide and an Al was applied to the unpolished side to form the ohmic contact. The transistors were prepared evaporating a thin layer of Au as the base at a rate of 0.5 nm/s on the Si substrate, which also acts as transistor collector. The emitter consists of Alq_3 deposited onto Au/Si by thermal sublimation at a rate of 0.4 nm/s at a pressure of 10^{-6} Torr, followed by V_2O_5 (supplied by Aldrich) evaporation at a rate of 0.1 nm/s. Al contact strips were evaporated on top of the V_2O_5 to produce devices of ~9 mm^2 active area. Rigorously, despite designating this layer as V_2O_5, it is probable that after evaporation the stoichiometry and oxidation state of the vanadium is altered. Layers thickness and deposition rate were monitored using a quartz oscillator. The n-Si/Au/Alq_3/V_2O_5/Al device structure, except by the additional V_2O_5 layer, and measurement circuit are analogous to those given elsewhere [4,9,10].

We also prepared ITO/Ca(80 nm)/Alq_3(70 nm)/V_2O_5(1.5 nm)/Al(120 nm) devices following the procedures described above to investigate the influence of the V_2O_5 on injection characteristics of the Al/Alq_3 interface.

Electrical characterization of the transistors was always carried out in the dark using two Keithley 2400 units. The common-base current characteristics were determined by measuring the collector current I_c as a function of the potential in the collector V_{cb} at constant emitter-current I_e. The current source controlled the emitter potential V_{be} in order to maintain the selected emitter current I_e. The common-emitter characteristics were determined measuring I_c as a function of the potential difference between the collector and the emitter V_{ce}. The following sign convention will be adopted throughout the text: when electrons are injected at the emitter and leave from the collector, I_e and I_c are positive, $V_{cb} > 0$ means that the base/collector Au/n-Si Schottky junction is reverse-biased, $V_{be} > 0$ means that the base is positively biased with respect to emitter, and $V_{ce} > 0$ means collector positively biased with respect to the emitter.

3. Results and discussion

The insertion of the V_2O_5 layer between Al and Alq_3 favors the injection of negative charge carriers. To demonstrate it, we show the comparison of the electrical characteristics of ITO/Ca(80 nm)/Alq_3 (70 nm)/V_2O_5/Al(120 nm) devices with different V_2O_5 thicknesses and ITO/Ca(80 nm)/Alq_3-

(70 nm)/Al(120 nm) devices. When the Al is negatively biased with respect to ITO, these devices behave like electron-only devices. This occurs because the potential barrier for holes at the Ca/Alq_3 interface due to the difference between Alq_3 highest occupied molecular orbital (5.7–5.9 eV)[3] and Ca work function (~2.9 eV) is too high to allow non-negligible hole injection. In Fig. 1, we present these current–voltage $I(V)$ characteristics, where it can be seen that the insertion of the V_2O_5 layer implies an increase in the current density, which is more pronounced for the thinner layer. Since the Alq_3 layer has the same thickness, it can be deduced that the Al/V_2O_5 contact more efficiently injects electrons into the Alq_3 than Al does.

V_2O_5 is usually applied for positive charge carrier injection improvement [11–13]. Considering that the valence-band and conduction-band edges are respectively at −4.7 and −2.4 eV with respect to vacuum level [14], this oxide should not contribute to electron injection improvement from Al into Alq_3, as evidenced by the simplified energy levels structure of the used materials presented in Fig. 2. But we are not sure about the vanadium oxide structure and vanadium valence after film deposition, since there are principal oxides with oxidation states +5, +4, +3 and +2 and a number of other identified phases with intermediate composition [15], which may introduce energy states at different energy levels, possibly introducing transitory host-states for

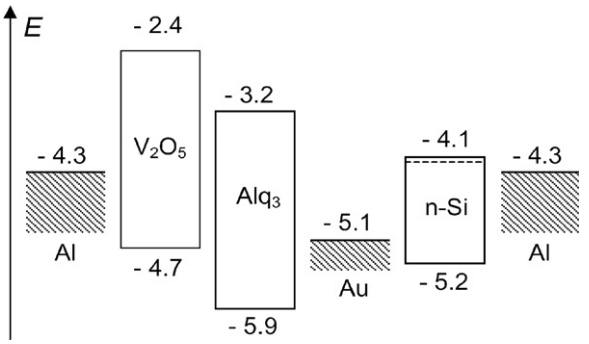


Fig. 2. Simplified energy scheme of the materials used in device production. The electron energy values E are measured with respect to vacuum level. These are in case of metals, Fermi levels, in case of Alq_3, HOMO and LUMO levels, in case of V_2O_5 and n-Si, valence and conduction band, with the dashed line indicating the position of the Fermi level in n-Si.

electrons in the Al to Alq_3 charge injection process. By this way, the major role in the electron injection improvement would be displayed by defects, rather than stoichiometry deposited V_2O_5.

The common-base characteristics of an Al(300 nm)/n-Si/Au(20 nm)/Alq_3(70 nm)/V_2O_5(1.5 nm)/Al(120 nm) can be shown in Fig. 3. For increasingly negative V_{cb}, there is a rapid increase in negative I_c, a behavior expected for Au/n-Si Schottky junctions. For positive V_{cb}, a saturation of I_c is observed at $I_c \cong I_e$, plus a contribution of a leakage current I_1^{bc} between base and collector, which can be neglected because it is quite small. This leakage current is independent

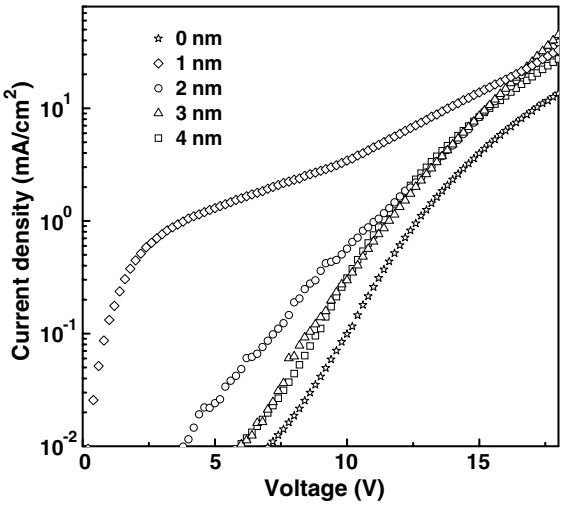


Fig. 1. Electrical characteristics of ITO/Ca(80 nm)/Alq_3(70 nm)/V_2O_5/Al(120 nm) and ITO/Ca(80 nm)/Alq_3(70 nm)/Al(120 nm) devices for different V_2O_5 thickness values. Al is negatively biased with respect to ITO.

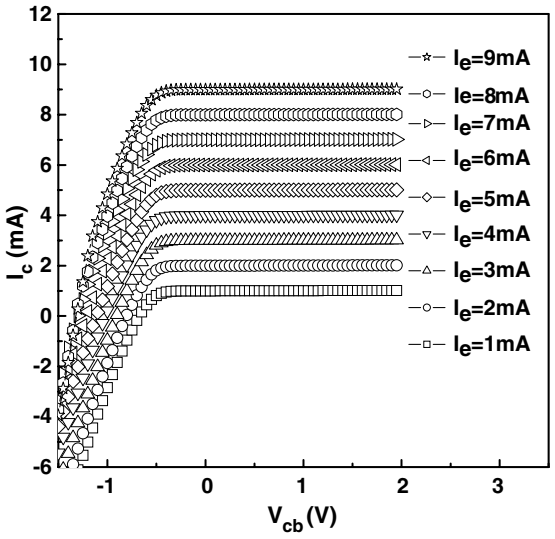


Fig. 3. Common-base characteristics of an Al(300 nm)/n-Si/Au(20 nm)/Alq_3(70 nm)/V_2O_5(1.5 nm)/Al(120 nm) device.

on the particular value of I_e since the variation of I_c in the entire $V_{cb} > 0$ range corresponds to the variation of I_e. Additionally, if I_c is plotted against I_e (see Fig. 4) for different V_{cb} values, the dependence is linear and the angular coefficient is $\alpha_0 = \frac{\partial I_c}{\partial I_b} \cong 1$, indicating that almost all electrons injected by the emitter are able to cross the base, being collected by the collector.

An important characteristic of our transistors can be shown in Fig. 5. The voltage required to achieve current levels of the order of 1 mA/mm^2 is lower than 1 V, which implies low power dissipation in the emitter layer. This characteristic is especially important in case of organic and hybrid devices, because organic materials are more sensible to high temperatures than their inorganic counterparts and heat dissipation constitutes a general problem if higher integration is aimed.

Like in previously reported devices without V_2O_5 layer [7], Al(300 nm)/n-Si/Au(20 nm)/Alq_3(70 nm)/V_2O_5(1.5 nm)/Al(120 nm) devices show permeable-base characteristics, since at constant I_e, we observe that $\frac{\partial V_{be}}{\partial V_{cb}} \approx 1$, indicating that the base is not able to shield the emitter from electric field changes between base and collector [9], as can be seen in Fig. 6. This result is consistent with the existence of pinholes in the metallic base layer, which are indeed observed in atomic-force-microscopy images, as exemplified in Fig. 7. This image shows several metal grains, demonstrating that the surface is not flat, as well as some pinholes (dark regions).

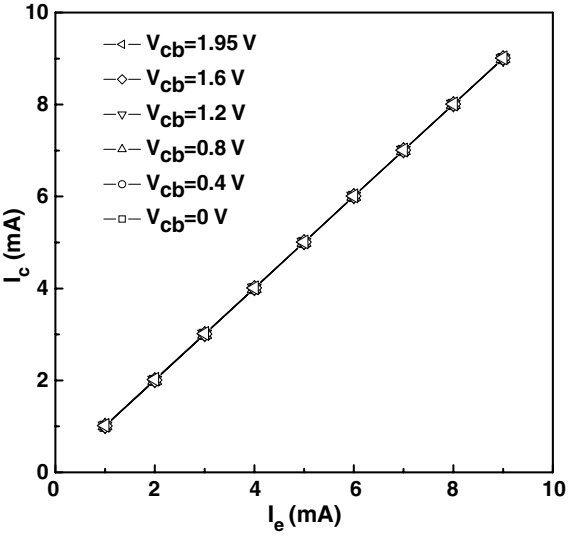


Fig. 4. Dependence of I_c on I_e of an Al(300 nm)/n-Si/Au(20 nm)/Alq_3(70 nm)/V_2O_5(1.5 nm)/Al(120 nm) device.

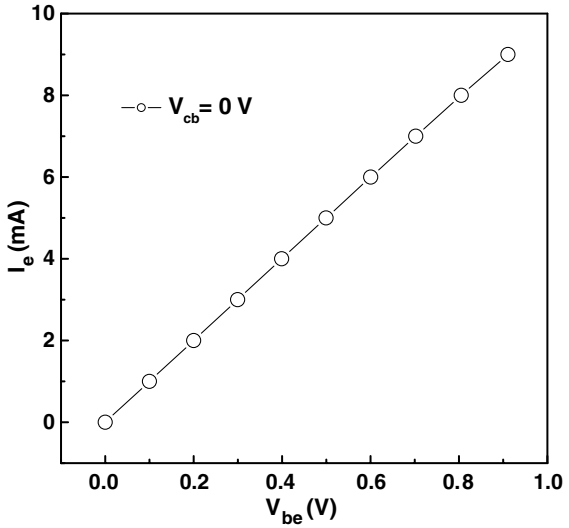


Fig. 5. Dependence of I_e on V_{be} of an Al(300 nm)/n-Si/Au(20 nm)/Alq_3(70 nm)/ V_2O_5(1.5 nm)/Al(120 nm) device.

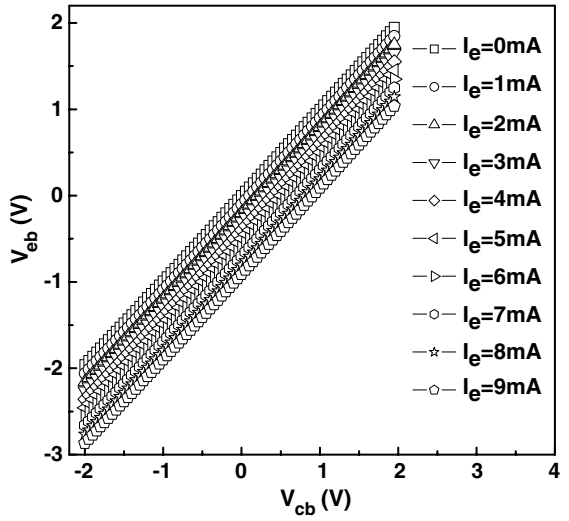


Fig. 6. Dependence of V_{eb} on V_{cb}, for constant I_e, of an Al(300 nm)/n-Si/Au(20 nm)/Alq_3(70 nm)/V_2O_5(1.5 nm)/Al(120 nm) device.

In Fig. 8a, we present the common-emitter mode characteristics of an Al(300 nm)/n-Si/Au(20 nm)/Alq_3(70 nm)/V_2O_5(1.5 nm)/Al(120 nm) device. Due to the high collector current even for $I_b = 0$, these data are replotted in Fig. 8b in the form $I_c - I_1^{ec}$ as a function of V_{ce}, where I_1^{ec} is the leakage current between emitter and collector, to allow visualization of the separation between curves of different I_b.

In Fig. 9, we present a plot of $I_c - I_1^{ec}/I_b$ as a function of V_{ce}. It can be clearly seen that these

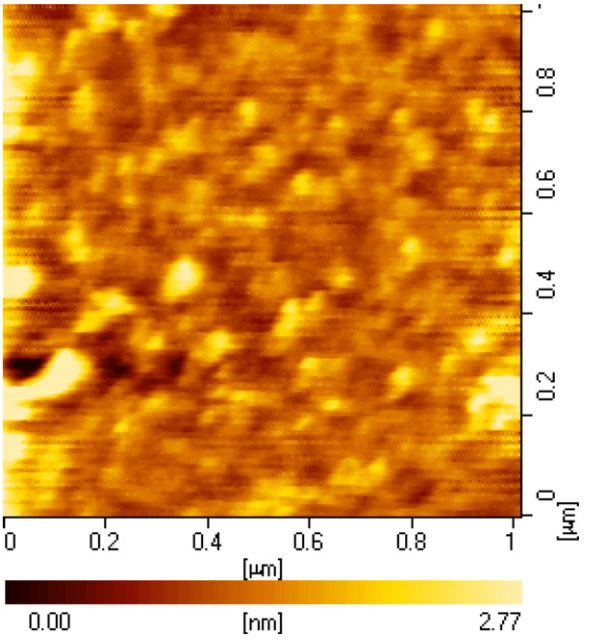


Fig. 7. AFM image of the base layer surface.

devices show high gain for low base currents, but as I_b increases the increasing rate of I_c tends to be lower, almost tending to a saturation in $I_c - I_1^{ec}$ (Fig. 8b) and consequently, to a stabilization of $I_c - I_1^{ec}/I_b$ (Fig. 7) at a lower level.

The charge carrier transport to or from the base, either to collector or to emitter, is hindered by some kind of transport barrier, since the differential resistance $R_d = \left(\frac{\partial I}{\partial V}\right)^{-1}$ for transport between emitter and collector is the lowest one when two terminal measurements are compared, as can be shown in Fig. 10. It is consistent with the permeable base character suggesting again that the potential barrier from charge transfer from emitter to collector is much lower than the potential barrier between emitter and base. This difference in the differential resistance was also observed in Ag/C_{60}/PEDOT:PSS/n-Si [PEDOT:PSS: Poly(3,4-ethylenedioxythiophene): poly(styrenesulfonate) blend] devices reported by Rossi et al. [16], where common-emitter current gain at reasonable voltage levels could also be observed, but showing reproducibility limitations.

Taking the observations listed above, it seems plausible to indicate that easy charge carrier injection in the emitter and thin emitter in order to avoid high emitter resistance, i.e., low emitter operational voltage, and a thin base in order to allow high base transport factor, are the basic requirements for high

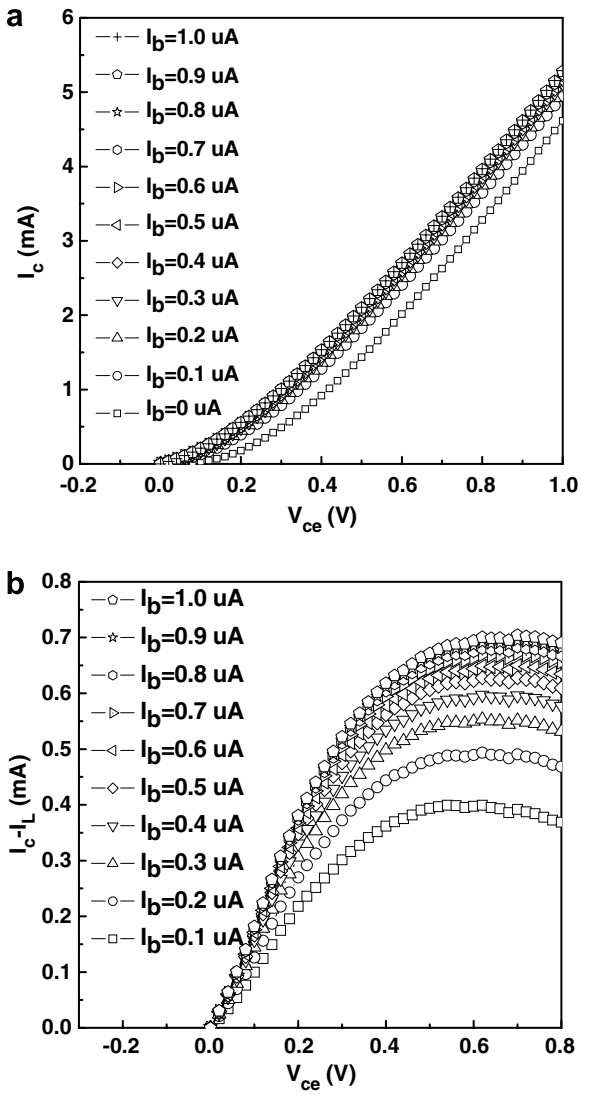


Fig. 8. (a): Common-emitter characteristics of an Al(300 nm)/n-Si/Au(20 nm)/Alq_3(70 nm)/V_2O_5(1.5 nm)/Al(120 nm) device; (b) same data as in (a), but deducing the collector current for $I_b = 0$.

common-emitter current gain at low voltages. Additionally, our observations suggest that easy injection in the emitter is important for reproducible common-emitter current gain realization.

When the V_2O_5 layer thickness is changed in Al(300 nm)/n-Si/Au(20 nm)/Alq_3(70 nm)/V_2O_5/Al(120 nm) devices (we made devices with 1.0, 2.0 and 3.0 nm thick V_2O_5 layer), the essential characteristics of the devices remain unchanged. However, devices with thicker V_2O_5 usually present higher common-emitter current gain, but concomitantly show a higher dispersion of common-emitter

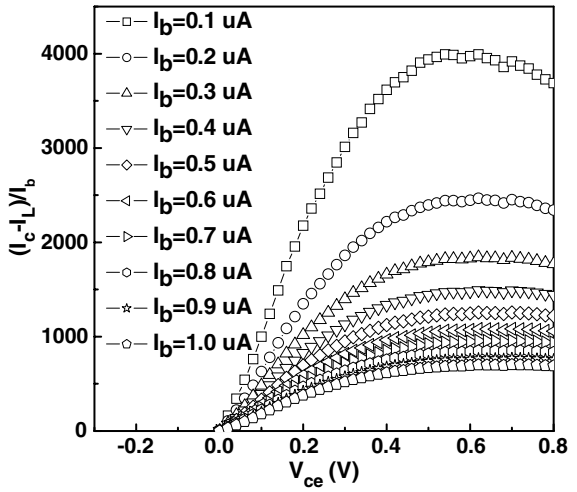


Fig. 9. Common-emitter current gain of an Al(300 nm)/n-Si/Au(20 nm)/Alq_3(70 nm)/V_2O_5(1.5 nm)/Al(120 nm) device.

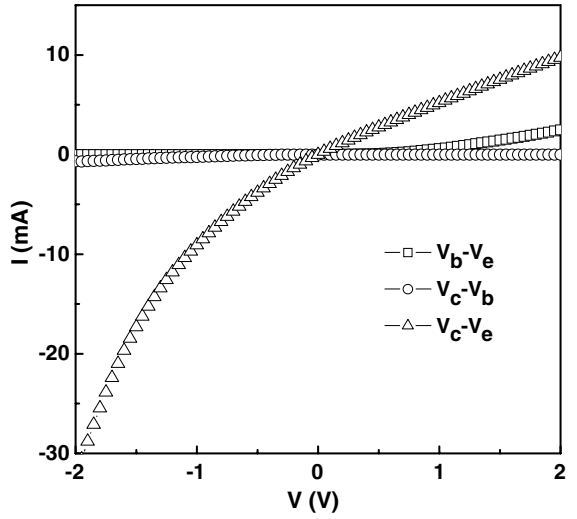


Fig. 10. Two terminal electrical measurements between emitter, base and collector of an Al(300 nm)/n-Si/Au(20 nm)/Alq_3(70 nm)/V_2O_5(1.5 nm)/Al(120 nm) device.

current gain values, if nominally similar devices are compared.

4. Conclusion

We report the production of hybrid permeable-base transistors with emitter layers of Alq_3. In order to improve the charge carrier injection characteristics of Alq_3 based hybrid transistors, a V_2O_5 layer was introduced before Al deposition on top of the Alq_3, resulting in Si/Au/Alq_3/V_2O_5/Al structures, which operate at low voltages presenting high common-emitter current gains.

Acknowledgements

The authors thank the Hundreds Talents program of Chinese Academy of Sciences, National Natural Foundation of China (50573075), National Science Fund for Distinguished Young Scholars of China (50325312), the Ministry of Science and Technology of China (973 Program No. 2002CB6-13403), and the Brazilian institutions CNPq, Renami/CNPq and Instituto do Milênio/CNPq for research grants.

References

[1] S. Fujimoto, K. Nakayama, M. Yokoyama, Appl. Phys. Lett. 87 (2005) 133503.
[2] C.W. Tang, S. VanSlyke, Appl. Phys. Lett. 51 (1987) 913.
[3] J. Shinar, V. Savvateev, in: J. Shinar (Ed.), Organic Light-Emitting Diodes, Springer, 2004.
[4] M.S. Meruvia, I.A. Hümmelgen, M.L. Sartorelli, A.A. Pasa, W. Schwarzacher, Appl. Phys. Lett. 84 (2004) 3978.
[5] S.M. Sze, High-Speed Semiconductor Devices, Wiley, New York, 1990.
[6] S. Zorba, Y. Gao, Appl. Phys. Lett. 86 (2005) 193508.
[7] M. Yi, S. Yu, D. Ma, C. Feng, T. Zhang, M.S. Meruvia, I.A. Hümmelgen, J. Appl. Phys. 99 (2006) 106102.
[8] K.N.G. Kwok, Complete Guide to Semiconductor Devices, Wiley, New York, 2002.
[9] M.S. Meruvia, I.A. Hümmelgen, Adv. Funct. Mater. 16 (2006) 459.
[10] M.S. Meruvia, A.R.V. Benvenho, I.A. Hümmelgen, J.A. Gómez, C.F.O. Graeff, R.W.C. Li, L.H.J.M.C. Aguiar, J. Gruber, Phys. Status. Solidi. A 202 (2005) R158.
[11] X.L. Zhu, J.X. Sun, H.J. Peng, Z.G. Meng, M. Wong, H.S. Kwok, Appl. Phys. Lett. 87 (2005) 153508.
[12] C.W. Chu, S.H. Li, C.W. Chen, S. Shrotriya, Y. Yang, Appl. Phys. Lett. 87 (2005) 193508.
[13] T.-H. Chen, Y. Liou, T.J. Wu, J.Y. Chen, Appl. Phys. Lett. 87 (2005) 243510.
[14] V. Shrotriya, G. Li, Y. Yao, C.-W. Chu, Y. Yang, Appl. Phys. Lett. 88 (2006) 073508.
[15] N.N. Greenwood, A. Earnshaw, Chemistry of the Elements, Pergamon, Oxford, 1990, p. 1144.
[16] L. Rossi, M.S. Meruvia, I.A. Hümmelgen, W. Schwarzacher, A.A. Pasa, J. Appl. Phys. 100 (2006) 024504.

Available online at www.sciencedirect.com
ScienceDirect
Organic Electronics 8 (2007) 317–324
Organic Electronics
www.elsevier.com/locate/orgel

Control of emission outcoupling in liquid-crystalline fluorescent polymer films

Tae-Woo Lee [a,*], O Ok Park [b], Young Chul Kim [c,*]

[a] Samsung Advanced Institute of Technology, Mt. 14-1 Nongseo-Dong, Giheung-Gu, Yongin-Si, Gyeonggi-Do 449-712, Republic of Korea
[b] Department of Chemical and Biomolecular Engineering, Korea Advanced Institute of Science and Technology, 373-1 Guseong-Dong, Yuseong-Gu, Daejeon 305-701, Republic of Korea
[c] College of Environment and Applied Chemistry, Kyung Hee University, 1 Sochen-ri, Giheung-Gu, Yongin-Si, Gyeonggi-Do 449-701, Republic of Korea

Received 27 February 2006; received in revised form 4 December 2006; accepted 10 December 2006
Available online 29 December 2006

Abstract

We report the improvement of light outcoupling efficiency of thermally annealed thin liquid crystalline light-emitting polymer films. Unlike the generally observed phenomena from thermally annealed fluorescent polymer films, in the liquid-crystalline fluorescent polymer (LCFP) films, the transverse electric waveguide mode was suppressed due to the light scattering by liquid-crystalline domains in the film. In addition, the optical anisotropy of the annealed LCFP was increased. As a result, the light extraction of photoluminescence and electroluminescence emission in the annealed LCFPs was enhanced by ~2 times because the emitted light loss by waveguide was minimized. This approach to improve light extraction by forming scattering domains inside the LCFP film gives an insight to improve the outcoupling efficiency of the EL devices in the viewpoint of the material design and film morphologies without employing external geometric device structures.
© 2006 Elsevier B.V. All rights reserved.

PACS: 73.71.Ph; 74.25.Gz

Keywords: Electroluminescence; Emission outcoupling; Liquid crystalline polymer film; Thermal annealing

1. Introduction

Since the first report of polymer light-emitting diode (PLED) based on poly(*p*-phenylenevinylene) in 1990 [1], PLED is rapidly approaching commercialization to full color flat or flexible panel display. However, their poor luminescent efficiency as well as operation instability still remains significant hindrances to their commercialization in full color panel displays. Therefore, improving the external quantum efficiency (η_{ex}) of organic/polymer LEDs is one of the key issues in recent researches of organic LEDs because the internal quantum efficiency (η_{in}) is the intrinsic property of an emitting material and it is now close to the theoretical limit

* Corresponding authors. Tel.: +82 31 280 6765; fax: +82 31 280 6725.
E-mail addresses: taew.lee@samsung.com, taew.lee@yahoo.co.kr (T.-W. Lee), kimyc@khu.ac.kr (Y.C. Kim).

1566-1199/$ - see front matter © 2006 Elsevier B.V. All rights reserved.
doi:10.1016/j.orgel.2006.12.003

[2,3]. η_{ex} can be further improved by increasing the light outcoupling efficiency (ξ) in the devices ($\eta_{ex} = \xi\eta_{in}$) [4,5]. ξ in conventionally constructed organic LEDs is usually as low as ~20% [4,5]. In other words, almost 80% of the light generated in the device is lost due to waveguiding and total internal reflection in the glass substrate generally used in organic LEDs as well as due to re-absorption [4,5]. Therefore, various methods to overcome external efficiency limitations have been proposed to date: for example, introduction of a corrugated surface for Bragg scattering [6], two-dimensional photonic crystals [7], ordered microlens array [8], and self-organized photonic structure of a thin polymer film [9] in the device. The common feature of above methods is to expand the escape cone of the substrate and to suppress the waveguide mode by adding additional photonic structures outside or inside the device. Thus they all need additional patterning processes. In this work, however, we report the enhancement of outcoupling of photoluminescence (PL) and electroluminescence (EL) from liquid-crystalline blue-emitting polymer films by forming liquid crystalline domains inside the film via thermal annealing at nematic–isotropic phase transition temperature (T_{NI}) without employing additional photonic structures. Once liquid crystalline multi-domains by thermal annealing at T_{NI} have been grown inside liquid-crystalline thin films, they can effectively suppress the waveguide mode. As a result, the waveguiding loss of emitted light is reduced due to the light scattering and thus higher external device efficiency is obtained. This approach gives an insight to improve the outcoupling efficiency in the viewpoint of material design and film morphology without using external geometric device structures.

The thermal treatment of EL polymer films at higher temperatures above the glass transition temperature of the material is known to induce interchain emission species and lowering of fluorescence efficiency [10,11]. When the thermal annealing was done before the metal electrode deposition, the device gave a little lower efficiency but demonstrated higher operating stability due to the enhanced packing density of polymer chains [12]. Therefore, if we can obtain a higher external luminous efficiency from the devices comprising thermally annealed polymer emitting films, the device stability at the same luminance can also be further improved since the driving current is lowered for the same device. Nowadays, blue polymer LEDs still have much poorer operational stability compared with the green and red devices. Therefore, it is quite necessary to develop highly stable blue-emitting polymers to expedite the commercialization of full color PLED displays. As a prospective blue-emitting material for PLEDs, polyfluorenes (PFs) have been investigated because they display extremely high luminescence efficiencies with emission wavelengths primarily in the blue spectral region. In addition, polarized electroluminescence from aligned liquid crystalline PFs can be realized [13,14]. However, it has been reported that PFs generate undesired excimer emission [15] or keto emission (a lower energy emission due to keto-defect) [16] due to the strong chain interaction when the PF films were annealed above the glass transition temperature. In contrast, we found that the thermal annealing of LCFP films can improve the outcoupling efficiency of luminescence without generating strong excimer emission or keto emission.

2. Experimental

The PBSDHFS films with varying thickness were spincast from the chlorobenzene solution. The PL spectra of the specimens were measured using an ISS PC1 photon counting spectrofluorometer. The thermal characteristics and the liquid crystallinity of poly(2,7-bis(*p*-stiryl)-9,9′-di-*n*-hexylfluorene sebacate) (PBSDHFS) were examined by employing a Perkin Elmer Pyris 1 differential scanning calorimeter and a Leitz Ortholux II polarized optical microscope equipped with a hot stage, respectively. The films are also spincast on the top of the O_2-plasma-treated indium-tin-oxide (ITO)-coated glass substrates for EL devices. The film thicknesses were averaged after measuring several times by a TENCOR P-10 surface profiler and controlled to be constant. The thickness was calibrated from the UV absorbance for unannealed and annealed films, independently. Aluminum was deposited on the top of the blend film under a high vacuum (10^{-6} torr) and used as the cathode. EL spectra were measured using an ISS PC1 Photon Counting Spectrofluorometer. The spectroscopic refractive index was determined using a dual-beam reflectometer SCI, FilmTek 4000.

The PBSDHFS/poly(9,9-di-*n*-hexyl fluorenediyl-vinylene-*alt*-1,4-phenylenevinylene) (PDHFPPV) blend (98:2 by wt.) films were spincast from the chrolobenzene solution for amplified spontaneous emission study and were photo-pumped with 1 Hz,

800 ps pulses at 337.1 nm generated by a nitrogen laser. The pumping energy was controlled using a set of calibrated neutral density filters. The pumping beam was focused on $1 \times 5\ mm^2$ of the specimen and the emission from the film edge was collected by a Minolta CS1000 spectrofluorometer.

3. Results and discussion

A fluorene-based light-emitting polymer, PBSDHFS was synthesized as reported elsewhere [17] and its chemical structure is shown in Fig. 1a. PBSDHFS showed liquid crystallinity with the glass transition temperature of 48 °C and the T_{NI} of 103 °C as illustrated in Fig. 1b.

We annealed the PBSDHFS films with different thicknesses at 103 °C and then investigated their fluorescence characteristics as a function of the film thickness. The annealing was carried out in a vacuum oven to reduce chemical oxidation where the oven temperature was slowly increased from room temperature to 103 °C for 30 min and kept at 103 °C for 30 min. Before annealing, the film is amorphous and does not have liquid crystalline domains. We did not observe any fluorescence from the unannealed pristine films via a cross polarized fluorescence optical microscope as Fig. 2a shows. But after annealing, the formation of the nematic liquid crystal domain of PBSDHFS was observed by the cross-polarized fluorescence optical microscope as Fig. 2b shows [18]. Actually, although we tried to figure out the liquid crystalline domain size after thermal annealing with the function of the film thickness, we could not observe the domain size clearly due to the resolution limit of the optical microscope. In addition, the cross-polarized fluorescence from the annealed thin films of 50–100 nm thickness was not clearly observed. However, as the film thickness increases above 100 nm, it was getting easier to observe the liquid-crystalline

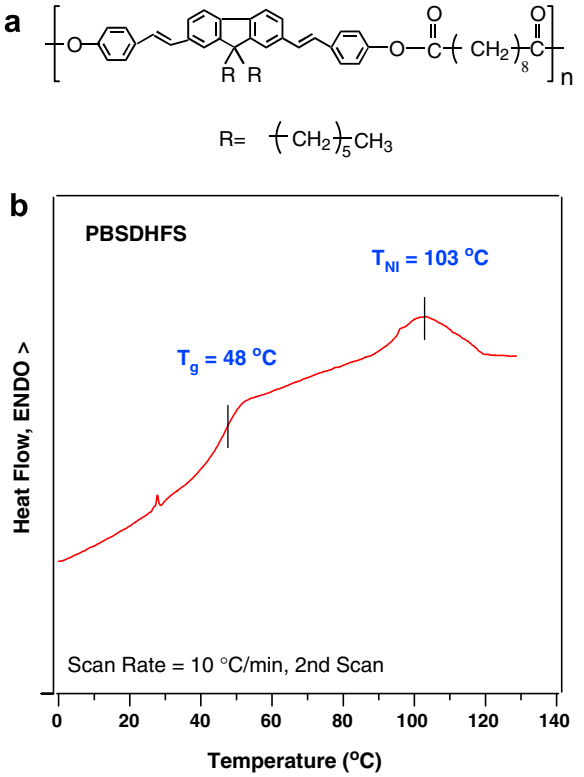


Fig. 1. (a) The chemical structure of poly(2,7-bis(*p*-stiryl)-9,9′-di-*n*-hexylfluorene sebacate) (PBSDHFS). (b) The glass transition temperature (T_g) and the nematic-to-isotropic transition temperature (T_{NI}) determined by differential scanning calorimetry. The PBSDHFS film showed liquid crystallinity with the glass transition temperature of 48 °C and the nematic-to-isotropic transition temperature of 103 °C.

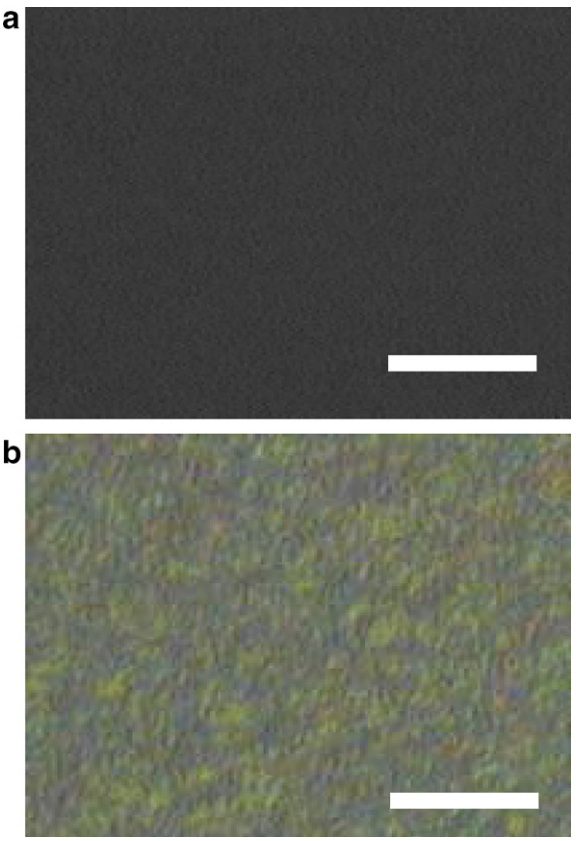


Fig. 2. The cross-polarized fluorescence microscope images for: (a) the unannealed film; (b) the annealed film. The film thickness was ~200 nm. The scale bars are 10 μm.

multi-domains from the cross-polarized fluorescence microscope. Therefore, we speculate that the domain size could increase linearly as the film thickness increase. To find out another evidence of the multi-domain formation, we tried to observe the surface morphology by atomic force microscopy as Fig. 3 shows. Unlike the generally observed surface phenomena for the thermally annealed amorphous films (i.e. smoother surface) [10], the thermally annealed PBSDHFS films have more rough surface than the pristine film, which implies that liquid crystalline multi-domains are formed. The more precise morphological observation of the growth of the nematic liquid crystalline domains in the two-dimensionally confined thin film geometry with varying the film thickness is currently our research topic.

We observed the PL intensities from the films at 90° with respect to the excitation monochromatic light incident on the film at 40° without using an integration sphere in order to compare relatively the outcoupled light intensity of the annealed films

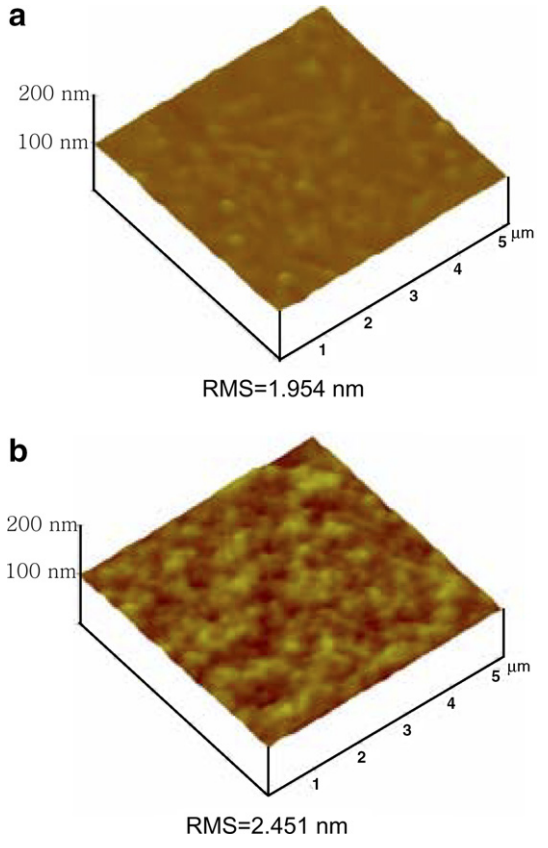


Fig. 3. Atomic force microscope images for: (a) the unannealed film; (b) the annealed film. The film thickness was ~200 nm.

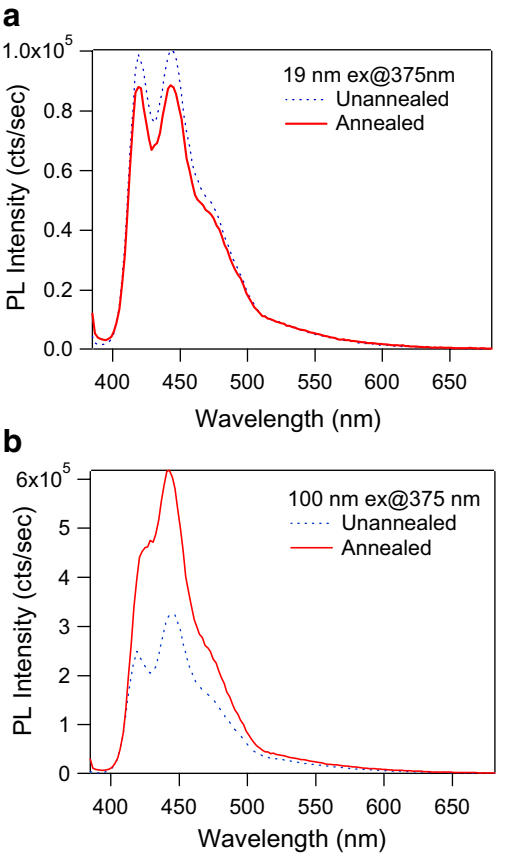


Fig. 4. The PL Spectra of the PBSDHFS films before and after the annealing at 103 °C, measured while being excited at 375 nm: (a) the 19 nm-thick film and (b) the 100 nm-thick film.

with that of the unannealed film. By the thermal annealing, the PL intensity of the 19 nm-thick PBSDHFS film was decreased by ~10% (Fig. 4a), which was generally observed in annealed fluorescent polymer films [10]. The PL intensity reduction comes from the interchain interactions in the annealed films [10]. For the 100 nm-thick film, however, the PL intensity was almost doubled after the thermal annealing (Fig. 4b). In addition, we did not observe any undesired spectral broadening over lower energy emission band that had been observed for polyfluorenes due to the excimers or keto defects formation [15,16]. It is worth noting that the full-width at half maximum (FWHM) of the PL spectrum was reduced from 58 to 46 nm by the annealing.

We plotted the PL intensity of the PBSDHFS films as a function of the film thickness before and after the annealing as Fig. 5a shows. The ratio of the PL intensities measured before and after the

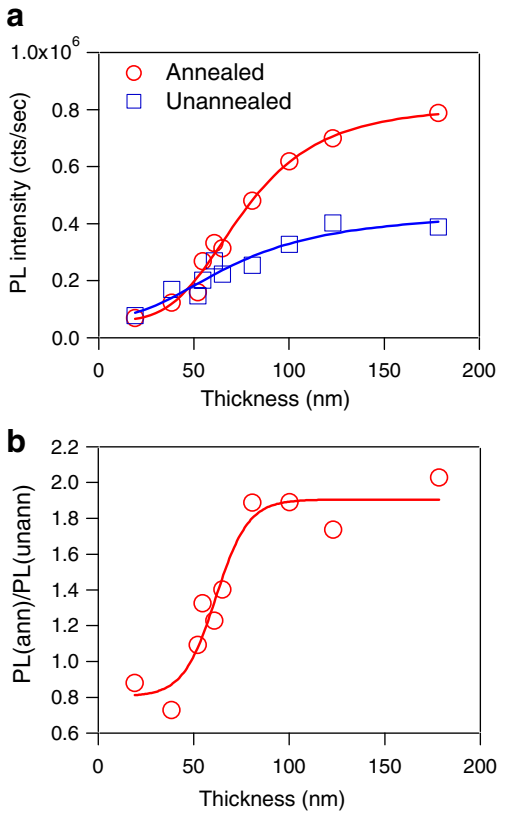


Fig. 5. (a) The PL intensities of the PBSDHFS films before and after the annealing as a function of the film thickness. (b) The ratio of the PL intensities measured before and after the annealing as a function of the film thickness.

annealing was also shown as a function of the film thickness in Fig. 5b. The PL intensity ratio tends to increase as the film thickness exceeds ~50 nm and then saturates after the thickness reaches ~80 nm where the PL intensity is almost doubled. We consider this PL intensity increase by the annealing originates from the liquid-crystalline nature of the film material because the liquid-crystalline domains in the PBSDHFS films will grow up by annealing. The PL intensity increase for the films thicker than 50 nm indicates that the light scattering by the domains starts to be effective when the film thickness exceeds ~50 nm to suppress the waveguide mode. The light scattering inside the film waveguide changes the direction of the propagating light to escape the waveguide. We found that the cut-off thickness of the zero-order transverse electric (TE) mode waveguiding ($d_{c,TE}$) is close to 50 nm. $d_{c,TE}$ is expressed by the following equation that represents the zero-order TE-mode of waveguiding [19].

$$d_{c,TE} = \frac{\lambda}{2\pi\sqrt{n_p^2 - n_s^2}} \tan^{-1}\left(\sqrt{\frac{n_s^2 - n_c^2}{n_p^2 - n_s^2}}\right) \quad (1)$$

where n_p, n_s, and n_c are the refractive indices of the polymer (PBSDHFS), substrate (glass), and cladding layer (air), respectively, and λ is the wavelength. $d_{c,TE}$ was obtained to be 54 nm from the Eq. (1) with the known parameters ($n_s = 1.5$, $n_c = 1.0$, $n_p = 1.83$ at 430 nm). Therefore, the light scattering within the waveguide becomes effective when the film is thicker than the $d_{c,TE}$ of 54 nm. This implies that although the film is much thinner than the wavelength of visible light, the lateral dimension of the nematic liquid crystal domains may grow to be large enough to scatter visible light in the TE-mode waveguiding along the substrate. The detailed growth mechanism of the lateral liquid crystalline domain size inside the confined geometry and the estimation of the lateral liquid crystalline domain size with the function of film thickness are beyond the scope of this paper and currently another research subject. Our approach is unique in that the fluorescent film itself acts as a light scattering medium as a single polymer film without adding an optical structure or a layer on the surface. Other approaches using Bragg scattering in a laterally corrugated microstructures [6] or phase separated microstructures by self-organization using a polymer blend [9] cause a rough device surface which can be a potential source to deteriorate a device long-term stability due to uneven electric field.

In order to confirm the suppression of the waveguide mode in the EL device, we fabricated the devices of the structure of indium-tin-oxide (ITO)/PBSDHFS/Al with the annealed and unannealed PBSDHFS films. As Fig. 6a shows, the EL intensity of the device based on the annealed film was also doubled at the same bias voltage (11 V) and the FWHM of the EL spectrum was also narrowed. To date, we have generally observed that the EL devices based on thermally annealed EL film above the glass transition temperature have shown lower device quantum efficiency [10], However, as the inset of Fig. 6b shows, the maximum EL quantum efficiency of the device with the annealed film is ~2.8 times higher than that of the one with the unannealed film although the current versus voltage characteristics are similar as shown in Fig. 6b. Without any geometrical modification of the device, the outcoupling of the light intensity could be enhanced by the formation of the lateral liquid crystalline

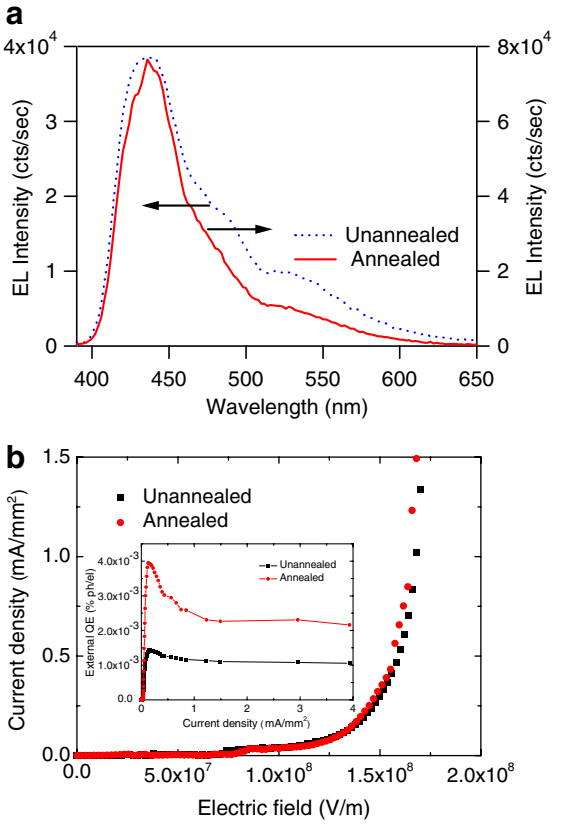


Fig. 6. (a) The EL spectra of the ITO/PBSDHFS/Al devices based on the annealed and unannealed PBSDHFS films, measured at the operating voltage of 11 V. (b) The current density versus electric field characteristics of the ITO/PBSDHFS/Al devices. The inset shows the external EL quantum efficiency (Q.E.) as a function of the current density. The 100 nm PBSDHFS film became thinner (95 nm) after thermal annealing. Thus we showed electric field (V/m) on the x axis.

domains via the thermal annealing only. Beside the fact that we doubled the extracted light intensity, the device operation lifetime also can be much more improved if we drive the device at the lowered current density for the same luminance level. For example, when we apply 2.0 as the conversion acceleration factor of the lifetime for the half reduction of the luminance level, the device lifetime can be 4 times improved [20,21]. Therefore, this simple light extraction method can be useful to improve the efficiency and the lifetime of the polymer LEDs based on LCFPs.

In order to reconfirm that the waveguide mode was suppressed by the formation of the liquid crystalline domain via the annealing, we examined the edge emission from the annealed and unannealed films. The excitation geometry is shown in Fig. 7a. When we photo-excited the 15 nm-thick film before and after the annealing, the PL intensity was a little lowered after the annealing but the PL spectrum remained almost unchanged, which are very similar to the results shown in Fig. 4a. This indicates that the PL characteristics of the edge emission from the films thinner than $d_{c,TE}$ are not different from those of the normal emission. In contrast, the PL intensity of the edge emission from the 100 nm-thick annealed film was much lower than that from the unannealed film of the same thickness as Fig. 7c shows, which suggests that the waveguide mode was largely suppressed due to the light scattering inside the annealed film. The amplified spontaneous emission from the edge of the thin fluorescent films on the substrates with low refractive index such as glass or quartz has been reported to date [18,22,23]. We observed a low-threshold amplified spontaneous emission (~20 nJ/cm^2/pulse) in the blend film of PBSDHFS with 2 wt% PDHFPPV as Fig. 7d shows [17]. However, with the annealed LCFP film, we did not observe the amplified spontaneous emission at a very high excitation energy (600 μJ) due to the waveguide mode suppression while the unannealed film showed a gain narrowing even at much lower excitation energy (~24 nJ). This also supports that the waveguide mode is largely suppressed in the annealed LCFP films due to light scattering by the liquid crystalline domains. Thus the amplified spontaneous emission of the annealed fluorescent film on glass can not occur since emitting light can not effectively travel the film slab waveguide.

We also tried to observe optical anisotropy of the LCFP film before and after the thermal annealing. As Fig. 8 shows, it is interesting to observe that the film anisotropy (Δn) was increased after thermal annealing although the overall refractive index values were reduced. Hence, the total intensity coupled out of the device increases when the emitters are aligned in the plane compared with an isotropic orientation [5]. This is possibly because that annealing changes the director orientation of the annealed liquid crystalline films. We optically simulated the outcoupled luminescence yield from the device when we assume that the emitting dipoles aligned only in the plane (i.e. no out-of-plane emitting dipoles). In this case, the luminescence yield was improved by ~49% compared with the perfect isotropic orientation [24]. Other literature also reported that the ~58% improvement of outcoupling efficiency for Al

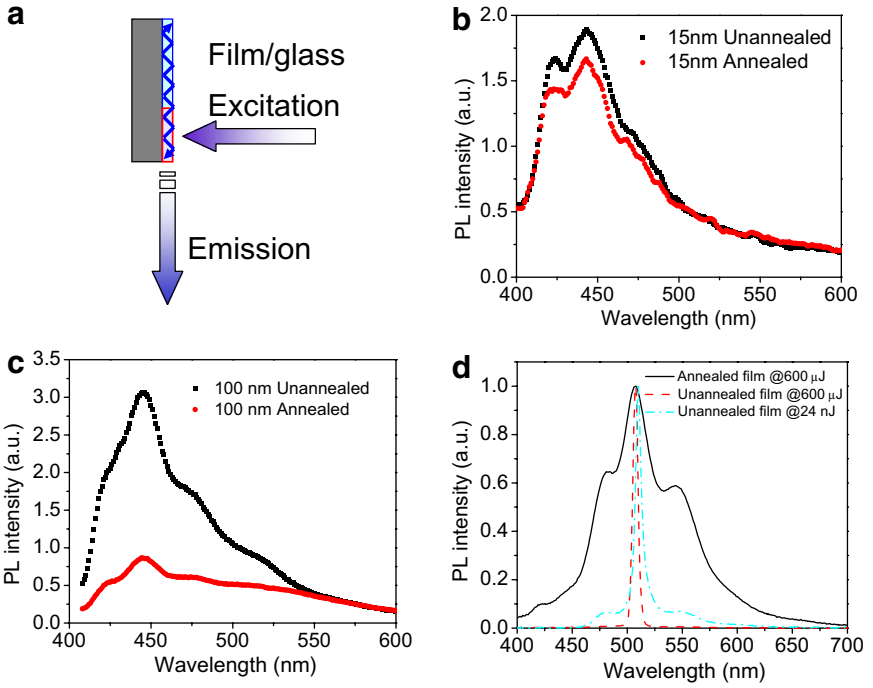


Fig. 7. The PL characteristics of the edge emissions from the PBSDHFS films before and after the annealing measured while exciting the films at the normal incident angle: (a) the 15 nm-thick film excited by the 370 nm monochromatic beam; (b) the 100 nm-thick film excited by the 370 nm monochromatic beam; (c) the 100 nm-thick film excited by the 337.1 nm pulsed N_2 laser. The film contains 2 wt% of PDHFPPV.

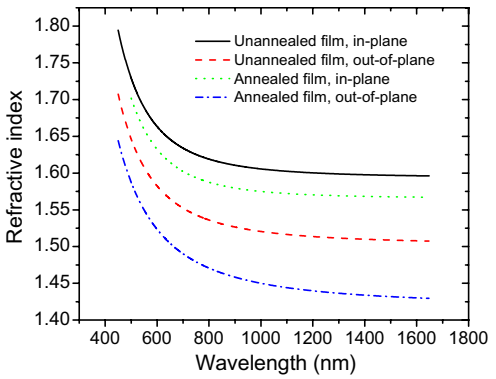


Fig. 8. The in-plane and out-of-plane refractive index with the function of the wavelengths for the unannealed and annealed films.

devices based on the emitting film with only in-plane dipoles compared with that with the isotropic dipoles [5]. Although, in the annealed film (with liquid crystalline domain), the emitting dipoles was more aligned in the plane compared with those in the unannealed film (without liquid crystalline domain), the outcoupled light improvement by the difference in optical anisotropy between the unannealed and the annealed film should be much less than ~49%. Therefore, the ~2 time improvement in light extraction mainly originated from the light scattering inside the films due to the multi-domains.

4. Conclusion

Thermal annealing for fluorescent polymers, especially polyfluorene derivatives, generally give rise to the generation of a lower energy emission (excimer or keto emission) and the lower fluorescence yield. However, we found that the improvement of light outcoupling efficiency above the cut-off thickness of TE waveguide can be realized in thin LCFP films by the formation of the liquid crystalline domains via thermal annealing. The TE waveguide mode was suppressed due to the light scattering by liquid-crystalline multi-domains in the film. As a result, the external PL and EL efficiency was enhanced by ~2 times above the cut-off thickness of TE waveguide mode. This approach to form liquid crystalline multi-domains in LCFP film by thermal annealing gives an insight to

improve the light extraction yield in the EL devices in the viewpoint of material design and film morphology without employing external geometric device structures.

Acknowledgements

We acknowledge Prof. B.J. Schwartz for helpful discussion and Dr. H. Jeong for optical calculation. This work was supported by Grant No. R01-2005-000-10852-0 from the Basic Research Program of the Korea Science & Engineering Foundation.

References

[1] J.H. Burroughes, D.D.C. Bradley, A.R. Brown, R.N. Marks, K. Mackay, R.H. Friend, P.L. Burns, A.B. Holmes, Nature 347 (1990) 539.
[2] C. Adachi, M. Baldo, S.R. Forrest, M.E. Thompson, J. Appl. Phys. 90 (2001) 5048.
[3] Y. Cao, I.D. Parker, G. Yu, C. Zhang, A.J. Heeger, Nature 397 (1999) 414.
[4] S.R. Forrest, D.D.C. Bradley, M.E. Thompson, Adv. Mater. 13 (2003) 1043.
[5] J.-S. Kim, P.K.H. Ho, N.C. Greenham, R.H. Friend, J. Appl. Phys. 88 (2000) 1073.
[6] (a) B.J. Matterson, J.M. Lupton, A.F. Safonov, M.G. Salt, W.L. Barnes, I.D.W. Samuel, Adv. Mater. 13 (2001) 123; (b) J.M. Ziebarth, A.K. Saafir, S. Fan, M.D. McGehee, Adv. Funct. Mater. 14 (2004) 451.
[7] Y.R. Do, Y.C. Kim, Y.-W. Song, C.-O. Cho, H. Jeon, Y.-J. Lee, S.-H. Kim, Y.-H. Lee, Adv. Mater. 15 (2003) 1214.
[8] S. Möller, S.R. Forrest, J. Appl. Phys. 91 (2002) 3324.
[9] (a) G. Fichet, N. Corcoran, P.K.H. Ho, A.C. Arias, J.D. MacKenzie, W.T.S. Huck, R.H. Friend, Adv. Mater. 16 (2004) 1908; (b) N. Corcoran, P.K.H. Ho, A.C. Arias, J.D. Mackenzie, R.H. Friend, G. Fichet, W.T.S. Huck, Appl. Phys. Lett. 85 (2004) 2965.
[10] T.-W. Lee, O.O. Park, Adv. Mater. 12 (2000) 801.
[11] (a) S.A. Jenekhe, J.A. Osaheni, Science 265 (1994) 765; (b) S.A. Jenekhe, Adv. Mater. 7 (1995) 309.
[12] (a) J. Kim, J. Lee, C.W. Han, N.Y. Lee, I.-J. Chung, Appl. Phys. Lett. 82 (2003) 4238; (b) T.-W. Lee, M.-G. Kim, S.Y. Kim, S.H. Park, O. Kwon, T. Noh, T.-S. Oh, Appl. Phys. Lett. 89 (2006) 123505.
[13] M. Grell, W. Knoll, D. Lupo, A. Meisel, T. Miteva, D. Neher, H.-G. Nothofer, U. Scherf, A. Yasuda, Adv. Mater. 11 (1999) 671.
[14] M. Grell, D.D.C. Bradley, Adv. Mater. 11 (1999) 895.
[15] J.-I. Lee, G. Klaerner, R.D. Miller, Chem. Mater. 11 (1999) 1093.
[16] E.J.W. List, R. Guentner, P.S. de Freitas, U. Scherf, Adv. Mater. 14 (2002) 374.
[17] Y.C. Kim, H.N. Cho, D.Y. Kim, J.M. Hong, N.W. Song, D. Kim, C.Y. Kim, Polymer (Korea) 24 (2000) 211.
[18] Y.C. Kim, T.-W. Lee, O.O. Park, C.Y. Kim, H.N. Cho, Adv. Mater. 13 (2001) 646.
[19] M. Marcuse, Theory of Dielectric Waveguides, Academic, New York, 1974 (Chapter 1).
[20] J. Burroughes, PLED: A Display Technology, ASIA DISPLAY/IMID'04, 23–27 August 2004, Daegu, Korea, Session 11.3.
[21] Although we did not test the operational stability with a function of time, we found that the annealed devices are more stable against the electrical current. The unannealed devices failed at the current density of 1.34 mA/mm^2. However, the annealed devices endured even higher current density (7.62 mA/mm^2).
[22] R. Gupta, M. Stevenson, A. Dogariu, M.D. McGehee, J.Y. Park, V. Srdanov, A.J. Heeger, Appl. Phys. Lett. 73 (1998) 3492.
[23] T.-W. Lee, O.O. Park, D.H. Choi, H.N. Cho, Y.C. Kim, Appl. Phys. Lett. 81 (2002) 424.
[24] The calculation was done by the optical simulator, Haemosu which was developed in Samsung SDI.

Available online at www.sciencedirect.com
ScienceDirect
Organic Electronics 8 (2007) 325–335
Organic Electronics
www.elsevier.com/locate/orgel

Photoinduced absorption spectroscopy on MDMO-PPV:PCBM solar cells under operation

Ton Offermans, Stefan C.J. Meskers *, René A.J. Janssen

Molecular Materials and Nanosystems, Department of Chemical Engineering and Chemistry, Eindhoven University of Technology, P.O. Box 513, 5600 MB, Eindhoven, The Netherlands
Dutch Polymer Institute (DPI), P.O. Box 902, 5600 AX Eindhoven, The Netherlands

Received 14 August 2006; received in revised form 1 December 2006; accepted 15 December 2006
Available online 22 December 2006

Abstract

Near-steady-state photoinduced absorption (PIA) spectroscopy is employed to study the charge carrier dynamics in polymer:fullerene (poly[2-methoxy-5-(3′,7′-dimethyloctyloxy)-1-4-phenylene vinylene]: 1-(3-methoxycarbonyl)-propyl-1-phenyl-[6,6]C_{61}; MDMO-PPV:PCBM) solar cells under operating conditions. Artifacts in the PIA spectra originating from thermal heating of the aluminum electrode and from interference of incoming and reflected light waves are analyzed. PIA signals from functioning devices are studied as a function of applied bias and temperature and complemented with photocurrent measurements under identical conditions. Comparison between photocurrent and PIA measurements shows that PIA mainly probes trapped cationic charge carriers while the photocurrent samples mobile carriers. The number density of trap sites is estimated at 10^{17} cm^{-3} and trapped carriers can be stabilized by applying a reverse bias potential over the device.
© 2007 Elsevier B.V. All rights reserved.

PACS: 73.50.Gr; 73.50.Pz; 72.20.Ee; 73.50.Lw

Keywords: Plastic solar cells; Photoinduced absorption; Photocurrent; Charge generation; Photovoltaics

1. Introduction

Photoinduced charge transfer from MDMO-PPV to PCBM takes place on the femtosecond time scale [1–4]. Recombination of the metastable charge pair created at the interface of the two materials by back transfer is a much slower process and takes place at a far longer time scale [5]. This difference has been utilized with success in fabricating photovoltaic devices based on these materials [6]. High external quantum efficiencies have been reported for these devices [7]. The dynamical behavior of charge carriers in films of MDMO-PPV:PCBM has been studied extensively by photoinduced absorption (PIA) spectroscopy, which, in principle, provides information on the number of photogenerated charge carrier and their (average) lifetime [8–11]. PIA studies on films of the MDMO-PPV:PCBM blend indicate that the recombination dynamics is limited by thermally activated detrapping of the positive polarons [9,11,12].

* Corresponding author. Tel.: +31 40 2473723; fax: +31 40 2451036.
E-mail address: s.c.j.meskers@tue.n (S.C.J. Meskers).

1566-1199/$ - see front matter © 2007 Elsevier B.V. All rights reserved.
doi:10.1016/j.orgel.2006.12.002

Recently, the recombination dynamics in functioning PPV:PCBM-solar cell devices has been investigated, probing the surviving charge carrier density either optically [13–15] or electrically via extraction through contacts [16–19]. The two detection methods are complementary as not all photo induced charge carriers may be extractable in a bulk hetero junction and while not all charge carriers may be detectable optically especially if they are in close vicinity of the metal electrode. Nevertheless, at low temperature both detection methods confirm the presence of a fraction of long-lived charge carriers.

Here we will present PIA measurements on the MDMO-PPV:PCBM solar cell under operation. The choice of an aluminum electrode in these devices is motivated by the fact that with the Al electrode the highest efficiencies are reported [20]. It will be shown however that the presence of the aluminum back electrode introduces artifacts in PIA measurements on devices. By careful choice of the experimental parameters these artificial contributions can be suppressed allowing one to probe the charge carrier density by optical means. Comparison with the complementary photocurrent measurements on the devices reveals that the subset of photogenerated carriers that are extracted via the electrodes differ in dynamical behavior from the charge carriers that are probed optically. We conclude that PIA predominantly probes charge carriers that are trapped on a limited number of trap sites.

2. Experimental

2.1. Device preparation

The photovoltaic devices were prepared using glass substrates with patterned indium tin oxide (ITO). After careful scrubbing, cleaning, and UV-ozone treatment, a 100 nm thin layer of poly(3, 4-ethylenedioxythipophene):poly(styrene sulfonate) (PEDOT:PSS) (Baytron P, H.C. Starck) was applied by spin coating, followed by the 1.0×10^2 nm composite layer of poly[2-methoxy-5-(3′,7′-dimethyloctyloxy)-1-4-phenylene vinylene]:1-(3-methoxycarbonyl)-propyl-1-phenyl-[6,6]C_{61} (MDMO-PPV:PCBM) in a 1:4 wt ratio from a chlorobenzene solution. The metal back electrode of LiF (1 nm) and Al (150 nm) was evaporated at 5×10^{-6} mbar through a shadow mask. The active area of the devices under study was 0.095 cm^2.

2.2. PIA spectroscopy and photocurrent measurements

Near-steady-state PIA spectra were recorded, by exciting the material under study with 2.71 eV photons from a mechanically modulated Ar^+ laser (3 mm beam diameter, modulation frequency 37 or 77 Hz). The resulting change in transmission (ΔT) of continuous, broad band probe light from a tungsten halogen source (intensity 0.4 W/cm^2) was monitored with a phase-sensitive lock-in amplifier after dispersion by a grating monochromator and detection using Si, InGaAs, and cooled InSb detectors (Fig. 1). The PIA ($-\Delta T/T$) was calculated directly from the change in transmission after correction for the photoluminescence.

For measurements on devices, the intensity of the probe light was recorded after reflection at the back aluminum electrode of the device. During the measurement the device was held under dynamic vacuum. The photocurrent induced by the modulated laser radiation was recorded simultaneously with the near steady state induced absorption by measuring the amplitude of the oscillating voltage over a probe resistance R_s (0.02 Ω) connected in series with the device using a lock-in amplifier (Fig. 1). During the photocurrent measurement the device is also illuminated by the continuous probe light used to record the PIA. The driving voltage over the device was applied using a Keithley 2400 source-measuring unit.

Photoinduced absorption measurement on the ns time scale were recorded by exciting the sample with

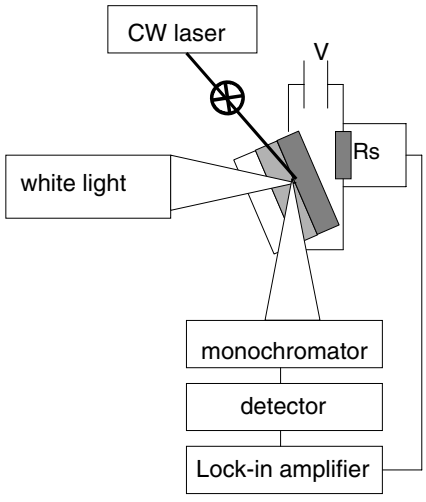


Fig. 1. Schematic of the setup used.

pulses of 2.76 eV photons (pulse width 4 ns, repetition rate 10 Hz) obtained from an optical parametric oscillator (OPO), pumped by the third harmonic of a Nd-YAG laser. An intensified CCD camera was used to record the reflection of a tungsten–halogen probe light on the metal electrode of the device. The probe light was dispersed by a spectrograph and signal acquisition by the camera was gated electronically. To obtain differential reflection spectra, the probe light was recorded at the delay time of interest and then the reference reflection at a 20 ms delay. For small acquisition delays, the transmission spectra were corrected for a very small residual fluorescence.

3. Experimental considerations

3.1. Thermotransmission and thermoreflection of thin Al layers

In this section the influence of an aluminum layer on the PIA spectrum of an MDMO-PPV film is investigated with the purpose to validate induced absorption measurements in which the probe light is reflected by an evaporated Al layer (reflection geometry).

To analyze the problems involved we start with measurements on a neat MDMO-PPV film. Excitation of the polymer leads to long-lived triplet excitations which can be probed by near-steady-state PIA at 80 K. Fig. 2 illustrates the transmission PIA signal for a 40 nm thick film, featuring the characteristic triplet–triplet absorption band at 1.35 eV. This signal is accompanied by a bleaching of the ground state absorption (2.2 eV). The weak absorption at 0.5 eV is normally not associated with the triplet excited state and most likely originates from a small number of photogenerated charges which are formed with low probability. For thick MDMO-PPV films (100 nm) coated with a semi-transparent aluminum layer (15 nm) both the bleaching and the 1.3 eV band are observable, but in addition a band at 1.5 eV appears in the transmission PIA. For thin films (40 nm) with evaporated Al aluminum (15 nm) both the triplet–triplet signal at 1.3 eV and the bleaching have disappeared completely and are replaced by a band with a maximum at 1.5 eV. The absence of a bleaching band suggests that in this case the long-lived excitation probed at 1.5 eV is not associated with the MDMO-PPV polymer. Further analysis reveals that the transmission PIA signal lags 45° behind in phase with respect to the excitation, showing in-phase (X) and 90° out-of-phase components (Y) of the same shape and equal magnitude (see Fig. 3). These signals closely resemble published data for the

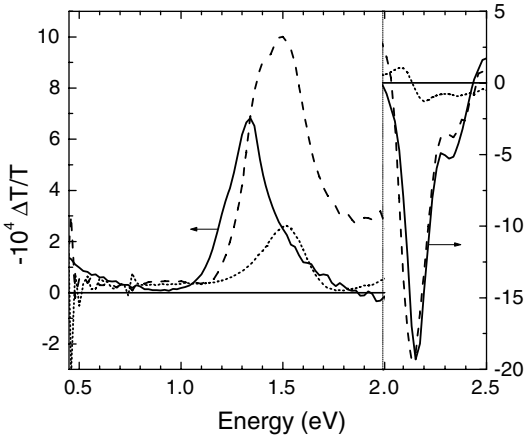


Fig. 2. PIA spectra of MDMO-PPV films of different thickness (40 nm, dotted line; 100 nm, dashed line) on glass with a thin (15 nm) Al top layer recorded at 80 K with excitation at 2.71 eV photon energy, 50 mW intensity and a modulation frequency of 37 Hz, compared to the spectrum of MDMO-PPV (40 nm) on glass without Al top layer (solid line).

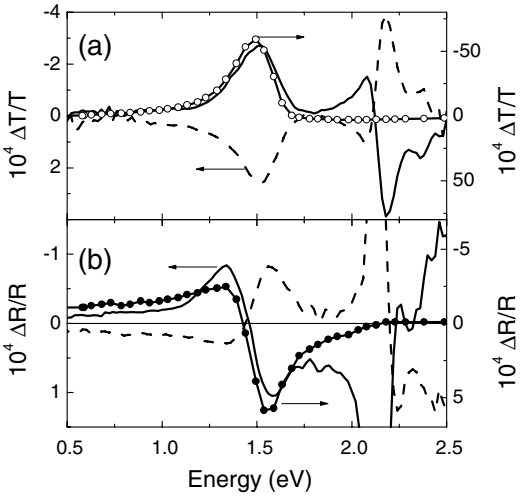


Fig. 3. PIA spectra in transmission (a) and reflection (b) of glass/MDMO-PPV (40 nm)/Al (15 nm) recorded at 80 K with excitation at 2.71 eV photon energy and 50 mW intensity through glass using a modulation frequency of 37 Hz. The solid line is the X component, the dashed line the Y component of the signal. The thermotransmission (a) and thermoreflection (b) signals of a 29 nm thick Al film at 120 K are shown with open ($\Delta T/T$) and closed ($\Delta R/R$) circles (data taken from Ref. [21]. Here about 1.5 W of modulated power was dissipated in a sample with 0.25 cm^2).

thermotransmission effect of thin aluminum layers [21] (Fig. 3a).

Thermotransmission describes the change in transmission of light through a thin Al layer brought about by a change in temperature of the metal layer. For Al, an intense thermotransmission feature is observed near 1.5 eV coinciding with an interband transition of this metal.

A variation in the temperature of an Al layer can also results in a change in reflectivity near the spectral position of the interband transition (thermoreflection). In Fig. 3b the available literature data [21] for this effect are reproduced. For the thin MDMO-PPV/Al layers we have measured the change in reflection of white probe light upon laser excitation and the relative differential reflectivity ($\Delta R/R$) bears again a strong resemblance to the thermoreflection signal of Al. In the polymer/Al layers photoexcitations on the polymer will eventually decay with the photon energy being converted into heat. This will result in a small periodic variation of the temperature of the Al layer upon illumination with the modulated Ar^+ laser beam giving rise to the thermotransmission and thermoreflection effects mentioned above. Eventually, the heat in the polymer and the thin Al layer will diffuse into the thick glass substrate.

Assuming a one-dimensional heat diffusion process, the periodic temperature variation ΔT in the thin surface layers on top of the much thicker glass substrate can be approximated by [22]:

$$\Delta T(t,\omega) = \frac{l_0(\omega) W_0}{SK\sqrt{2\mathrm{i}}} \mathrm{e}^{\mathrm{i}\omega t} \tanh\left(\sqrt{2\mathrm{i}}(l/l_0(\omega))\right) \qquad (1)$$

Here W_0 denotes the amplitude of the modulation of the optical power absorbed by the polymer, ω the frequency of the modulation, S the illuminated area, K the thermal conductivity of glass and l the thickness of the supporting glass slide. Finally $l_0(\omega)$ represents a characteristic length given by $l_0(\omega) = (2K/s\rho\omega)^{1/2}$ with s the heat capacity of glass and ρ its density. For sufficiently high frequencies, (1) predicts that the thermo transmission signal, which is proportional to ΔT, varies as $1/\sqrt{\omega}$ with the frequency and lags behind 45° in phase with respect to the modulated heat source. Under the experimental conditions applied here, one expects a temperature modulation in the Al layer on the order of 1 K. The modulation in temperature results in an optical signal with a long lifetime, decaying according to a power law ($1/\sqrt{t}$) after pulsed excitation [22]. Because of this slow decay the thermotransmission/reflection effect may be expected to dominate over the induced absorption features resulting from (charged) excitations on the polymer on long times scales (or low modulation frequencies) if the excitations on the polymer decay exponentially ($\sim \mathrm{e}^{-t}$) or bimolecularly ($\sim 1/t$). In order to minimize the contribution of the Al layer to the induced absorption measurements, we have resorted to reflection measurements probing the induced absorption near the zero-crossing of the thermoreflection close to 1.45 eV.

3.2. 'Dead layer' effect with evaporated Al electrodes

One other complication in measuring PIA on devices based on thin polymer films in reflection geometry, is the wavelength dependent modification of the probability for photon absorption resulting from the destructive interference of the incoming and reflected probe light by the metal electrode deposited on the polymer films.

To illustrate the problem we have measured PIA on a MDMO-PPV:PCBM film spin-coated on glass. When the Al layer is deposited on the other side of the glass (blend/glass/Al), PIA can be measured in reflection geometry, showing the well known absorption bands of the radical cation of MDMO-PPV at 0.5 and 1.4 eV (Fig. 4). The spectrum obtained is virtually identical to that obtained in a transmission measurement. However, when the Al layer is deposited on the MDMO-PPV:PCBM (glass/MDMO-PPV:PCBM/Al) the induced absorption spectrum is different. Compared with the transmission spectrum, the low energy absorption band at 0.5 eV in reflection is now strongly suppressed with respect to the 1.4 eV band which in turn is reduced relative to the bleaching signal at 2.2 eV. Also a relatively small contribution from thermoreflection at 1.5 eV may be discerned for the glass/MDMO-PPV:PCBM/Al sample (Fig. 4).

When light is reflected by a metal surface, a 180° phase shift occurs resulting in destructive interference between the incoming and outgoing wave so that the requirement of zero electric field in the metal can be satisfied [23,24]. The destructive interference results in a 'dead layer' near the metal surface with low values for the amplitude of electromagnetic fields. The thickness of this zone depends on the wavelength of the light and the refractive index n of the film and is typically $\lambda/4n$. When a polymer layer of thickness d is spin-coated directly on top of the metal layer, absorption of light by photoinduced excitations will be severely suppressed

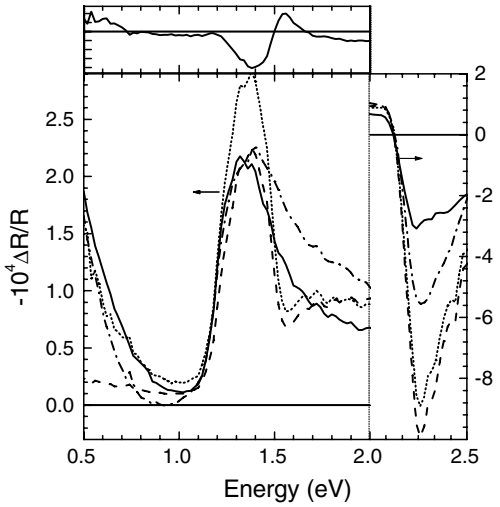


Fig. 4. Photoinduced absorption measurements of the MDMO-PPV:PCBM (1:4) blend spin coated on glass. The measurements performed in reflection mode. Solid line pertains to a blend/glass/Al structure, the dashed line to a glass/blend/Al structure. The dotted line shows the spectrum for the glass/blend/Al after correction using Eq. (2) (see text). The dash-dotted line shows transmission PIA measurements on parts of the blend/glass/Al structure not covered by Al. The uppermost panel shows the differences between the induced absorption in the blend/glass/Al structure and glass/blend/Al structure after correction using Eq. (2) and normalization. The residual resembles the thermoreflection signal in Fig. 3b.

for those probe wavelengths for which $\lambda/4n > d$. For wavelengths <700 nm and assuming $d = 0.1$ μm and $n = 2$, suppression of absorption is not severe, which is consistent with well known applications of electro-optical methods using *visible* light to study thin film organic devices with metal electrodes. However, for light with wavelength $\lambda > 1500$ nm, the suppression is much stronger and this will cause the low-energy absorption band of the radical cation of MDMO-PPV to be reduced substantially in photoinduced measurements on glass/MDMO-PPV:PCBM/Al structures. For the (near)infrared spectral region where the polymer does not absorb light, it is possible to correct for this effect by dividing the absorption measured at a certain wavelength (λ) by the square of the amplitude of the electric field $\boldsymbol{E}$ of the standing electromagnetic wave near the metal surface, integrated over the film thickness d and over a time interval $(0, T)$ [23]:

$$\int_0^T \int_0^d \left(E_i \sin\left(\omega t - \frac{2\pi n x}{\lambda}\right) - E_r(n, n_{Al}, k_{Al}) \times \sin\left(\omega t + \frac{2\pi n x}{\lambda}\right) - \delta(n, n_{Al}, k_{Al})\right)^2 dx\, dt \qquad (2)$$

where n is the wavelength dependent refractive index of the film and λ the wavelength of the probe light in air. The blend contains 80 wt% PCBM, which has a refractive index close to 1.8 in the wavelength region of interest [25,26], and therefore the correction (1) has been carried out with $n = 2$. The factor E_r describes the amplitude of the electric field of the reflected wave; the term $\delta(n, n_{Al}, k_{Al})$ represents the deviation of the phase shift of the reflected wave from the expected 180° [27]. It depends on the wavelength dependent, complex refractive index of the aluminum [28]. As our correction is mainly intended for a spectral region where the polymer composite layer hardly absorbs, we have neglected the imaginary part of the refractive index of the polymer film. After application of the correction, the low energy band is recovered and the spectrum matches the spectrum of the glass/blend sample (Fig. 4). In addition, the contribution due to the thermoreflection effect becomes visible in the plot of the residuals.

In this analysis we have assumed that the quasi-particles giving rise to the induced absorption are distributed evenly throughout the illuminated area of the film. One may argue that the high optical density of the film at the excitation wavelength and the interference between the incoming excitation beam and the ray reflected at the metal back electrode, will cause photoexcitations to occur predominantly near the transparent electrode. However, the time-scale of the experiment discussed here is quite long (ms), which allows for diffusion of photogenerated charges away from the site at which their parent photon was originally absorbed.

In summary, even though the PIA of a MDMO-PPV:PCBM blend measured in reflection shows only one major absorption band at 1.4 eV, and may be mistakenly interpreted as due to triplet excitations, the data are fully compatible with MDMO-PPV radical cations as the absorbing species. A contribution of triplet excitations, which show only absorption near 1.4 eV, does not need to be invoked to explain the deformed induced absorption spectra measured in reflection.

4. Modelling

Here we analyze a simplified model, providing a joint description of the photocurrent and the photo-induced absorption in the photovoltaic device. The model is illustrated in Fig. 5. Here, charge generation and recombination take place at the interface between a MDMO-PPV rich and a PCBM rich

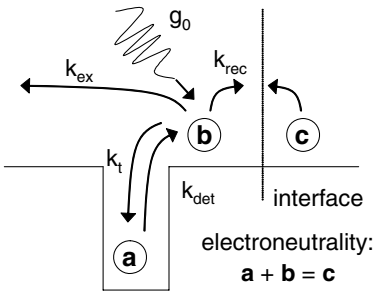


Fig. 5. Scheme illustrating the kinetic model describing trapped holes a, free holes b and electrons c at the interface of donor and acceptor material. Rate parameters involved: generation g_0, carrier extraction k_{ex}, bimolecular carrier recombination k_{rec}, trapping k_t and detrapping k_{det}.

domain. The positive charge carriers reside in the MDMO-PPV phase and can either be mobile or trapped with number densities b and a, respectively. The negative charge carriers (c) reside at the opposite site of the interface between polymer and fullerene. In this model mobile carries b are generated upon illumination with rate g_0 and can be extracted with a rate k_{ex}. A positive and a negative carrier can recombine in a bimolecular process characterized by rate constant k_{rec}. For simplicity we assume electroneutrality so that for the number densities a, b and c the relation $a + b = c$ holds. Mobile carriers may also get trapped (rate k_t) on a trap site, which are presented with a number density n_0. All trap sites are taken to be identical in energy and each trap can only be occupied by a single carrier. To account for trap filling we introduce an additional factor $(1 - a/n_0)$ in the rate for trapping of mobile carriers representing the fraction of *unoccupied* trap sites. Trapped carriers can be detrapped via thermal activation (rate k_{det}). Because of the low modulation frequency, we apply the steady-state approximation during the illumination periods and this gives the following equations for the number density of trapped positive carriers a:

$$\frac{da}{dt} = k_t\left(1 - \frac{a}{n_0}\right)b - k_{det}a = 0 \Longleftrightarrow a = \frac{k_t b n_0}{k_{det}n_0 + k_t b} \quad (3)$$

Here b denotes the number density of mobile holes. For this species the following steady state relation holds:

$$\frac{db}{dt} = g_0 + k_{det}a - k_t\left(1 - \frac{a}{n_0}\right)b - k_{ex}b - k_{rec}bc = 0 \quad (4)$$

Relation (4) can be simplified taking into account the cancellation of trapping and detrapping terms as expressed in (3). Furthermore, the number density of electrons c can be eliminated using the electro-neutrality condition $a + b = c$:

$$g_0 + k_{ex}b - k_{rec}b(a + b) = 0 \quad (5)$$

Combining (3) and (5) we obtain a cubic equation for the number density of mobile carriers b, which can be solved by standard methods. We assume that trapped and mobile carriers are indistinguishable by absorption spectroscopy so that the differential reflection signal will be proportional to the total number density of holes $(a + b)$. The photocurrent is given by $k_{ex}b$.

5. Results

In this section we present PIA measurements on devices measured in reflection as discussed above. The measurements will be complemented with recordings of the photocurrent under the same conditions. Finally we will investigate the dependence of the optical and electrical signal on the power of the incident excitation light.

5.1. Photoinduced absorption

PIA spectra of a MDMO-PPV:PCBM photovoltaic device with aluminum back contact are shown in Fig. 6 for three different values of the externally applied voltage. The spectra were measured between 1.0 and 2.5 eV in reflection mode at low temperature

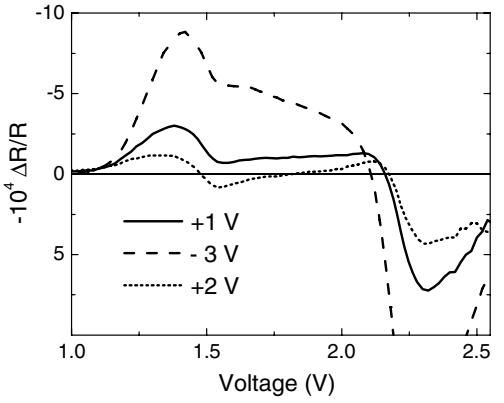


Fig. 6. Photoinduced absorption spectra in reflection mode at applied bias of +1 V (solid line), −3 V (dashed line) and +2 V (dotted line) of a glass/ITO/PEDOT/MDMO-PPV:PCBM(1:4)/LiF/Al photovoltaic device. Excitation at 2.71 eV, 25 mW and 77 Hz modulation. $T = 80$ K.

(80 K) and are not corrected for the reduced induced absorption at long wavelength. At high reverse bias (Al electrode charged positive) the induced absorption band at 1.4 eV and the bleaching of the MDMO-PPV ground state absorption at 2.1 eV indicate the presence of MDMO-PPV radical cations. Upon raising the bias from −3 to +1 V, the intensity of both the induced absorption and the bleaching band decrease, indicating a lower concentration of cations. At a forward bias of +2 V, virtually no radical cation absorption is observed and the spectrum is dominated by the thermoreflection feature of the Al electrode. The bias dependence of the radical cation absorption band in the devices was studied further by measuring the intensity of the absorption band at the zero-crossing of the thermoreflection near 1.47 eV for different temperatures (Fig. 7a). A continuous decrease of the absorption signal is found when increasing the applied voltage from −2 to +3 V. Upon increasing the temperature to 150 K, the induced absorption does not change much. At 295 K, however, the PIA signal under reverse bias is significantly lower than at 80 K. At bias voltages >+1.5 V the signals are found to converge for the different temperatures and approach zero.

In Fig. 7b we show the phase angle of the induced absorption with respect to the modulated excitation as a function of voltage. At reverse bias, the signal is found to be 180° out of phase with the laser light indicating that the charge carriers have a lifetime significantly shorter than the modulation period (13 ms). Under bias voltages V larger than the open circuit voltage ($V_{OC} \cong +1$ V) of the photovoltaic device, the optical signal becomes very small, and scatter in the data for the phase angle becomes apparent. Under these conditions, where the optical signal almost vanishes, the relative weight of the contributions stemming from the imperfect suppression of the thermoreflection contribution and random noise are more important in determining the recorded phase angle than for reverse bias voltages.

Probing the PIA signal at 1.47 eV, we find that for applied voltages over the device in the range −3 to +2 V, the PIA is virtually independent of the excitation modulation frequency. This is consistent with the charge carriers having a lifetime much shorter than the shortest modulation period applied (0.3 ms). Under these circumstances, the PIA signal is proportional to the time averaged number density of charge carriers in the film. In order to monitor

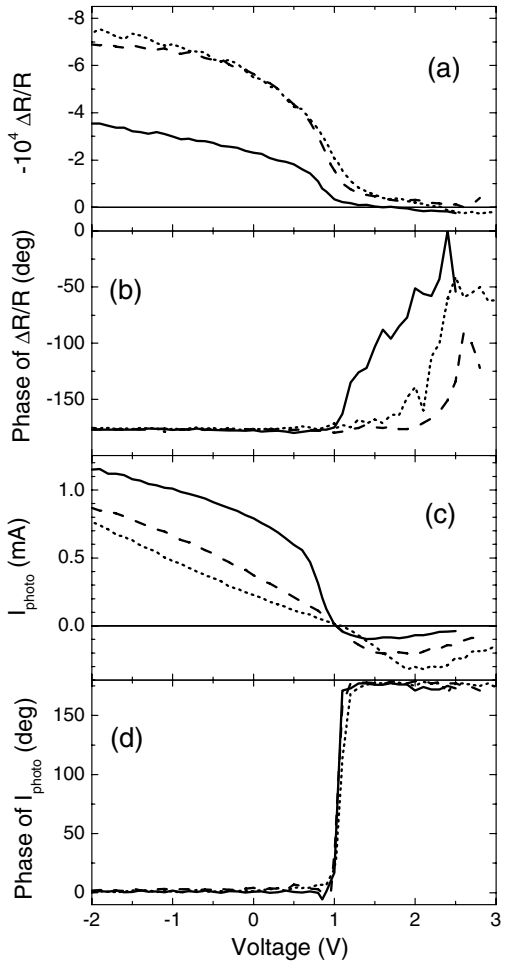


Fig. 7. Near-steady-state photoinduced absorption of a glass/ITO/PEDOT/MDMO-PPV:PCBM(1:4)/LiF/Al photovoltaic device measured in reflection mode as function of applied voltage at $T = 295$ K (solid), 150 K (dashed) and 80 K (dotted) probed at photon energies corresponding to the zero crossing of the thermoreflection (1.47 eV at 80 K). Excitation at 2.71 eV, 25 mW, 77 Hz modulation. (a) Component of the PIA signal that is in phase with the excitation modulation. (b) Phase angle of the induced absorption signal. (c) In-phase component of the photocurrent. (d) Phase angle of the photocurrent.

the decay of the photoinduced carriers as a function of applied bias, we have measured PIA in the reflection geometry in the ns time domain using pulsed methods. In Fig. 8 we show the results, monitoring the intensity of the bleaching band at 2.2 eV in a reflection geometry at low temperature (80 K). When applying a forward bias voltage ($V = +1$ or +2 V), we observe a power law decay ($t^{-\alpha}$, $\alpha = -0.5$) consistent with earlier studies [9,10]. When a reverse bias voltage is applied, a deviation from the power law decay is observed corresponding to an enhanced absorption at $t > 10^2$ ns. At

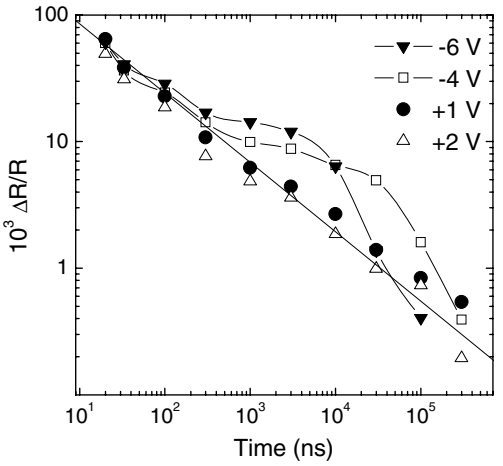


Fig. 8. Decay of the photoinduced bleaching of a glass/ITO/PEDOT/MDMO-PPV:PCBM(1:4)/LiF/Al photovoltaic device in reflection mode at 2.1 eV photon energy as a function of time for different applied voltages, see inset. Excitation 2.76 eV, pump fluence $\sim$1 mJ/cm^2, $T = 80$ K. The straight line represents a power law decay $\propto t^{-\alpha}$ with $\alpha = 0.55$.

longer times the induced absorption rapidly drops, which may be related to extraction of carriers from the device.

These experiments indicate that the enhancement of the PIA signal under application of reverse bias voltage as observed in the modulation experiments (Fig. 6) results, at least in part, from an extension of the lifetime of carriers in the microsecond time domain.

5.2. Photocurrent

In the setup used for measurement of the near steady state PIA in reflection, the photocurrent generated by the modulated excitation beam can be recorded simultaneously with the induced absorption, providing a complementary data set for exactly the same experimental conditions. Fig. 7c shows the photocurrent as a function of applied voltage. Starting at a reverse bias voltage of -2 V, we observed a steady decrease of the photocurrent upon raising the bias voltage. Also upon lowering the temperature the magnitude of the photocurrent drops. For $V < +1.0$ V the phase angle between the photocurrent and the excitation modulation is close to 0° (Fig. 7d). This shows that the average time interval needed to collect a carrier after generation is much shorter than the modulation period used (13 ms). When the bias applied crosses the open circuit voltage $V_{OC} = +1.0$ V, the photocurrent changes sign and for $V > V_{OC}$ the phase angle is close to 180°, again indicating that carrier extraction occurs rapidly in comparison with the modulation period. The absolute magnitude of the photocurrent decreases again when the bias voltage is raised above +1.2 V ($T = 295$ K) or above +2 V ($T = 80$ K). This shows that a loss mechanism for photogenerated carriers is operative at higher forward bias voltages.

The external quantum efficiency (EQE) of the photovoltaic device under study can be estimated from the laser intensity (25 mW excitation intensity with 2.71 eV photons) and the photocurrent current at room temperature under short circuit conditions (0.8 mA), yielding an EQE of 0.2. This estimate takes into account that the photocurrent as measured using the lock-in amplifier represents a root-mean-square amplitude around a time averaged value. The EQE decreases upon lowering the temperature and reaches values of 0.09 at 150 K and 0.05 at 80 K.

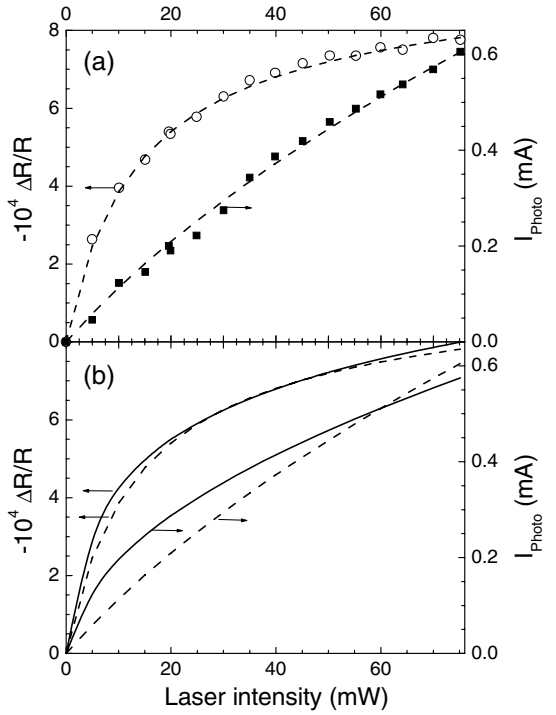


Fig. 9. (a) Intensity dependence of the photoinduced absorption measured in reflection at 1.47 eV photon energy under short circuit conditions at 80 K. Intensity dependence of the photocurrent density under identical conditions. Excitation at 2.71 eV, with 77 Hz modulation. (b) Model calculation of the induced absorption and photocurrent using Eqs. (3) and (5) and the parameter sets 1 (solid line) or 2 (dashed line) from Table 1.

5.3. Intensity dependence of the photocurrent and the induced absorption under short circuit conditions

In Fig. 9 the photocurrent and the PIA signals under short circuit conditions at 1.47 eV and 80 K are plotted against the intensity of the modulated excitation source. The photocurrent shows a linear dependence on intensity I when $I < 35$ mW. A sublinear dependence is observed at higher intensities. The sublinear dependence above 35 mW can be approximated by $(I/I_0)^{3/4}$ which was derived for space charge limited photocurrents [29]. The PIA signal shows a much stronger deviation from linearity and above intensities of 35 mW it seems to approach a saturation limit. The different intensity dependencies of the photocurrent and PIA signal indicate that the two techniques probe to two different subsets of charge carriers. With near-steady-state PIA trapped carriers are probed and with the photocurrent the non-trapped carriers.

6. Discussion

In this section we first discuss the dependence on the applied voltage of the photocurrent and the induced absorption as shown in Fig. 6. This will then be followed by a discussion of the intensity dependence of the photocurrent and the photo-induced absorption.

The first point to be addressed concerns the small photocurrent and induced absorption observed for applied voltages higher than the open circuit voltage. Given the large injection current for voltages V above V_{OC}, recombination of photogenerated charges with injected charges may explain the low concentration of photogenerated carriers and thus the small PIA signals [13,14]. The observations of a rise of the photocurrent upon lowering the temperature in the forward bias regime, may then be rationalized in terms of suppression of the recombination with injected carriers at low temperature. This may result from, e.g. a lower density of injected charge carriers at low temperature due to injection barriers or a lower value for the bimolecular recombination constant k_{rec}. In addition to this recombination mechanism, reduction of the photocurrent may also result from screening of the electric field in the polymer layer by a relatively large number of injected charge carriers trapped at the PEDOT electrode [30,31].

When applying reverse bias voltages ($V < +1$ V) we find that the induced absorption increases upon lowering the temperature while the photocurrent decreases. Qualitatively, this could be interpreted in terms of a shift in the equilibrium between trapped and mobile carriers in favor of the trapped species. An interesting observation for the reverse bias regime is that at all three temperatures used the induced absorption rises when the applied bias gets more negative. Concurrently, the photocurrent also increases upon lowering the voltage. The latter observation can be rationalized by a higher rate for carrier extraction k_{ex} at more negative bias. However, in the model sketched in Fig. 5, a higher value for k_{ex} will result in a smaller stationary number density of photogenerated carriers for more negative bias voltages contradicting the experimentally observed rise in the induced absorption due to charge carriers. To resolve this contradiction, the increase in k_{ex} must be counterbalanced by the voltage dependence of another parameter. Possible options include a voltage dependent generation rate g_0 [32] and a stabilization of trapped carriers as expressed by and increase of k_t/k_{det} at more negative bias voltage. Concerning the first option, we note that for bias voltages near V_{OC} we still observe a considerable charge carrier induced absorption indicating that the voltage dependence of the generation rate is not so strong as to suppress the generation of carriers completely under conditions where the internal electric field is very small. The second option is supported by the PIA measurements in the ns–μs time domain (Fig. 8), which show an increase in the lifetime of the photogenerated carriers at reverse bias voltages. Experimental evidence supporting the stabilization of electron–hole pairs by an externally applied electric field can be found in literature [33–40] but, interestingly, it has also been reported that applied electric fields can enhance the rate of charge recombination in polymer-C_{60} mixtures [41]. One of the possible ways to interpret the stabilization of trapped carriers by an electric field is to assume that the trapped cationic carriers on the MDMO-PPV are accompanied by an anionic carrier on the PCBM at close distance, forming an Coulombically bound electron–hole pair.

By introducing trapped carriers into the model, we can account for the different intensity dependence of the induced absorption and the photocurrent solving Eq. (5). This is illustrated in Fig. 9b, where we show simulation results for two different sets of parameters (See Table 1). In the first set, the rate of charge generation (g_0) is taken to be proportional to the flux of incident photons (I_0)

Table 1
Parameters used in numerical simulation of the induced absorption and photocurrent as a function the intensity of laser excitation involving Eqs. (3) and (5)

Parameter	Set 1	Set 2
g_0	$0.75I_0$	$0.075I_0$
n_0 (cm^{-3})	2×10^{17}	2×10^{17}
k_t/k_{det}	1×10^{2}	8×10^{2}
k_{ex} (s^{-1})	2×10^{6}	1×10^{7}
k_{rec} ($cm^3\ s^{-1}$)	7×10^{-9}	8×10^{-9}

The rate of charge carrier generation g_0 is expressed in terms of the flux of incident photons, I_0 (see text).

multiplied by factor of 0.75 to describe the probability for absorption of an incident photon. This estimate is based on the optical density of a corresponding film without the metal electrode (0.3), multiplied by two to take into account the reflection of light at the back electrode. From the magnitude of the parameter k_t/k_{det} we estimate that the trap sites are quite shallow with the change in free energy (ΔG) upon trapping of a mobile carrier approximately equal to 0.03 eV. From the value of the parameter k_{ex}, we can calculate the time needed for extraction of a carrier by taking the inverse of its value. The time interval thus calculated is indeed much shorter that the modulation period in the experiments (13 ms) and therefore compatible with the small phase angles observed for the photocurrent. In the simulations the curvature of the photocurrent signal is larger than in the experiment and therefore we are overestimating the effect of bimolecular recombination between photogenerated charge carriers. A likely reason for this is that our model does not include a monomolecular or pseudo-monomolecular loss mechanism and therefore the limited efficiency of the device can only be accounted for via bimolecular recombination. A very simplified way to incorporate monomolecular decay is to equate the generation rate g_0 to only a fraction of the number of absorbed photons, assuming that the other charge carriers recombine geminately within a short time interval after photon absorption. In parameter set 2, g_0 is taken to be 0.1 times the number of absorbed photons. The resulting charge generation rate ($0.075I_0$,) is in qualitative agreement the measured EQE of 0.05 at low temperature. The second parameter set gives a satisfactory simulation of the power dependence of the photocurrent. With this set, the depth of the traps and the extraction time for the carriers are of the same order of magnitude as with parameter set 1.

In modeling the induced absorption we have assumed a value of $10^{-15}\ cm^2$ for the absorption cross-section for a charge carrier on the MDMO-PPV. This estimate is based on the following reasoning. In the PIA spectra in Fig. 4, the intensity of the bleaching band corresponding to the transition between the ground state and the lowest excited singlet state (S_0–S_1) is comparable to the intensity of the 1.4 eV absorption band of the MDMO-PPV. The absorption cross-section for the S_0–S_1 transition in the polymer can be estimated from studies on oligomers of OPV and approaches $10^{-15}\ cm^2$ [42]. With this estimate of the absorption cross-section, we then find that the number density of trap sites is on the order of $10^{17}\ cm^{-3}$.

7. Conclusions

PIA measurements on MDMO-PPV:PCBM bulk-heterojunction solar cells can be performed under working conditions. Two artifacts are identified complicating the measurement on devices with an aluminum electrode: (i) the thermoreflection effect of this metal. This can be suppressed by detecting near the zero crossing of the thermoreflection close to 1.4 eV photon energy; (ii) the wavelength dependent modification of the probability for photon absorption resulting from the destructive interference of the incoming and reflected probe light by the metal electrode. Incidentally, this latter effect is also of importance when optimizing the probability for photon absorption in thin layer photovoltaics with polymers absorbing in the near-infrared as active material.

PIA measurements on devices provide data on the charge carrier density in the device and are complementary to photocurrent measurements. The combination of both experimental techniques provides detailed information on the charge carrier dynamics and reveals that at least two different kinds of cationic charge carriers have to be distinguished: mobile and trapped ones. The presence of trapped carriers may be taken as typical for photovoltaic devices based on disordered materials.

Acknowledgements

We thank Dr. Martijn Wienk and Dr. Paul van Hal for valuable discussions. The work of TO forms part of the research programme of the Dutch Polymer Institute (DPI), project DPI#324. The PCBM used for this research was obtained as a generous

gift from the group of Prof. J.C. Hummelen, Groningen University, The Netherlands. The research of SCJM has been made possible by a fellowship of the Royal Dutch Academy of Arts and Sciences.

References

[1] C.J. Brabec, G. Zerza, G. Cerullo, S. De Silvestri, S. Luzzati, J.C. Hummelen, S. Sariciftci, Chem. Phys. Lett. 340 (2001) 232.
[2] B. Kraabel, J.C. Hummelen, D. Vacar, D. Moses, N.S. Sariciftci, A.J. Heeger, F. Wudl, J. Chem. Phys. 104 (1996) 4267.
[3] B. Kraabel, D. McBranch, N.S. Sariciftci, D. Moses, A.J. Heeger, Phys. Rev. B 50 (1994) 18543.
[4] N.S. Sariciftci, L. Smilowitz, A.J. Heeger, F. Wudl, Science 258 (1992) 1474.
[5] G. Yu, J. Gao, J.C. Hummelen, F. Wudl, A.J. Heeger, Science 270 (1995) 1789.
[6] C.J. Brabec, F. Padinger, J.C. Hummelen, R.A.J. Janssen, N.S. Sariciftci, Synth. Met. 102 (1999) 861.
[7] S.E. Shaheen, C.J. Brabec, N.S. Sariciftci, F. Padinger, T. Fromherz, J.C. Hummelen, Appl. Phys. Lett. 78 (2001) 841.
[8] J. Nelson, Phys. Rev. B: Condens. Matter 67 (2003) 155209.
[9] A.F. Nogueira, I. Montanari, J. Nelson, J.R. Durrant, C. Winder, N.S. Sariciftci, C. Brabec, J. Phys. Chem. B 107 (2003) 1567.
[10] T. Offermans, S.C.J. Meskers, R.A.J. Janssen, J. Chem. Phys. 119 (2003) 10924.
[11] I. Montanari, A.F. Nogueira, J. Nelson, J.R. Durrant, C. Winder, M.A. Loi, N.S. Sariciftci, C. Brabec, Appl. Phys. Lett. 81 (2002) 3001.
[12] T. Offermans, S.C.J. Meskers, R.A.J. Janssen, Chem. Phys. 308 (2004) 125.
[13] C. Arndt, U. Zhokhavets, G. Gobsch, C. Winder, C. Lungenschmied, N.S. Sariciftci, Thin Solid Films 451–452 (2004) 60.
[14] C. Winder, C. Lungenschmied, G. Matt, N.S. Sariciftci, A.F. Nogueira, I. Montanari, J.R. Durrant, C. Arndt, U. Zhokhavets, G. Gobsch, Synth. Met. 139 (2003) 577.
[15] T. Offermans, S.C.J. Meskers, R.A.J. Janssen, Org. Electron. 7 (2006) 213.
[16] A.J. Mozer, N.S. Sariciftci, L. Lutsen, D. Vanderzande, R. Österbacka, M. Westerling, G. Juska, Appl. Phys. Lett. 86 (2005) 112104.
[17] A.J. Mozer, G. Dennler, N.S. Sariciftci, M. Westerling, A. Pivrikas, R. Osterbacka, G. Juska, Phys. Rev. B. 72 (2005) 035217.
[18] G. Dennler, A.J. Mozer, G. Juška, A. Pivrikas, R. Österbacka, A. Fuchsbauer, N.S. Sariciftci, Org. Electron. 7 (2006) 229.
[19] T. Offermans, S.C.J. Meskers, R.A.J. Janssen, J. Appl. Phys. 100 (2006) 074509.
[20] V.D. Mihailetchi, P.W.M. Blom, J.C. Hummelen, M.T. Rispens, J. Appl. Phys. 94 (2003) 6849.
[21] R. Rosei, D.W. Lynch, Phys. Rev. B 5 (1972) 3883.
[22] S.C.J. Meskers, J.K.J. van Duren, R.A.J. Janssen, J. Appl. Phys. 92 (2002) 7041.
[23] H. Hänsel, H. Zettl, G. Krausch, R. Kisselev, M. Thelakkat, H.-W. Schmidt, Adv. Mater. 15 (2003) 2056.
[24] P. Peumans, A. Yakimov, S.R. Forrest, J. Appl. Phys. 93 (2003) 7.
[25] N.K. Persson, H. Arwin, O. Inganas, J. Appl. Phys. 97 (2005) 034503.
[26] M.S. Dresselhaus, G. Dresselhaus, P.C. Eklund, J. Mater. Res. 8 (1993) 2054.
[27] R.W. Pohl, Optik und Atomphysik, Springer, Berlin, 1976.
[28] E.D. Palik, Handbook of Optical Properties of Solids, Academic Press, London, 1998.
[29] V.D. Mihailetchi, J. Wildeman, P.W.M. Blom, Phys. Rev. Lett. 94 (2005) 126602.
[30] H. Frohne, C.R. McNeill, P.C. Dastoor, Appl. Phys. Lett. 85 (2004) 1042.
[31] P.J. Brewer, P.A. Lane, A.J. DeMello, D.D.C. Bradley, J.C. DeMello, Adv. Funct. Mater. 14 (2004) 562–570.
[32] L.J.A. Koster, V.D. Mihailetchi, R. Ramaker, P.W.M. Blom, Appl. Phys. Lett. 86 (2005) 123509.
[33] V. Arkhipov, H. Bässler, E. Emelyanova, D. Hertel, V. Gulbinas, L. Rothberg, Macromol. Symp. 212 (2004) 13.
[34] H.J. Snaith, I.B. Malone, C.M. Ramsdale, R.H. Friend, N.C. Greenham, in: Z.H. Kafafi, P.A. Lane (Eds.), Proceedings of SPIE, Denver, 2004, vol. 5520, University of Denver, Denver, CO, 2004, pp. 26–35.
[35] S. Barth, D. Hertel, Y.H. Tak, H. Bässler, H.H. Hörhold, Chem. Phys. Lett. 274 (1997) 165.
[36] M. Esteghamatian, Z.D. Popovic, G. Xu, J. Phys. Chem. 100 (1996) 13716.
[37] V.D. Mihailetchi, L.J.A. Koster, J.C. Hummelen, P.W.M. Blom, Phys. Rev. Lett. 93 (2004) 216601.
[38] P. Peumans, S.R. Forrest, Chem. Phys. Lett. 398 (2004) 27.
[39] B. Schweitzer, V.I. Arkhipov, H. Bässler, Chem. Phys. Lett. 304 (1999) 365.
[40] M. Reufer, M.J. Walter, P.G. Lagoudakis, B. Hummel, J.S. Kolb, H.G. Roskos, U. Scherf, J.M. Lupton, Nat. Mater. 4 (2005) 340.
[41] M. Liess, Z.V. Vardeny, P.A. Lane, Phys. Rev. B 59 (1999) 11503.
[42] E. Peeters, A.M. Ramos, S.C.J. Meskers, R.A.J. Janssen, J. Chem. Phys. 112 (2000) 9445.

Available online at www.sciencedirect.com
ScienceDirect
Organic Electronics 8 (2007) 336–342
Organic Electronics
www.elsevier.com/locate/orgel

Effects of polar functional groups and roughness topography of polymer gate dielectric layers on pentacene field-effect transistors

Kwonwoo Shin, Sang Yoon Yang, Chanwoo Yang, Hayoung Jeon, Chan Eon Park *

Polymer Research Institute, Department of Chemical Engineering, Pohang University of Science and Technology (POSTECH), Pohang 790-784, Republic of Korea

Received 21 August 2006; received in revised form 7 December 2006; accepted 15 December 2006
Available online 8 January 2007

Abstract

The present study analyzed the effects of the polar functional groups and rough topography of the gate dielectric layer on the characteristics of pentacene field-effect transistors. For this purpose, prior to deposition of the organic semiconductor, we introduced polar functional groups and created a rough topography onto the poly(methylmethacrylate)/Al_2O_3 gate dielectric layer using oxygen plasma treatment, and controlled the number of polar groups using an aging process. The mobility decrease observed after oxygen plasma treatment ranged from 0.2 to <0.01 cm^2/V s and was related to the many polar functional groups and the rough topography of the gate dielectric, which formed localized trap states in the band gap and created disorder in the crystal structure. In addition, the electric dipole of the polar groups and the fixed interface charges induced a positive shift of the threshold voltage and an increase in the off-state current. After aging of the oxygen plasma-treated gate dielectrics, the reduced number of polar groups led to greatly enhanced charge mobility, a less positive shift of the threshold voltage, a lower off-state current, and lower activation energy compared to layers without aging. However, the mobility still remained lower than for layers without plasma treatment owing to the rough topography of the gate dielectric.
© 2007 Elsevier B.V. All rights reserved.

PACS: 72.20.Jv; 72.80.Le

Keywords: Pentacene; Trap; Mobility; Polar groups; Roughness of gate dielectric; Oxygen plasma

1. Introduction

The use of organic field-effect transistors (FETs) in many potential applications, such as radio-frequency identification tags [1,2], displays [3,4], chemical sensors [5–7], etc., can be accelerated by the improvement of device performances such as

* Corresponding author. Tel.: +82 54 279 2269; fax: +82 54 279 8298.
E-mail address: cep@postech.ac.kr (C.E. Park).

1566-1199/$ - see front matter © 2007 Elsevier B.V. All rights reserved.
doi:10.1016/j.orgel.2006.12.007

the charge carrier mobility and the switching speed. These properties are correlated to interface phenomena between the organic active layer and the gate dielectric layer, which are significantly influenced by the surface characteristics of the gate dielectric. The presence of functional groups and the roughness topography of compounds used as gate dielectrics have dramatic effects on the morphology of organic semiconductor materials and the electrical characteristics of FETs. There have been many studies about the effects of the surface characteristics of gate dielectrics, but only a few of polymer gate dielectric layers [8–15]. Poly(methylmethacrylate) (PMMA) is a polymer substance commonly used in gate dielectrics [15–17]. In this study the effects of polar functional groups and the roughness topography of PMMA gate dielectric layers were analyzed by applying oxygen (O_2) plasma treatment on the gate dielectric and measuring the temperature-dependent mobility for pentacene FETs.

If a polymer gate dielectric is treated with O_2 plasma, the polymer chains on the surface are broken and surface polar functional groups containing oxygen, such as –OH, –CO–, –OCO–, and –COOH, are created. As a result, the surface polarity and surface energy of the gate dielectric are increased, and the etched polymer surface shows roughened topography [18–21]. The extent of these changes during plasma treatment is dependent on the O_2 plasma treatment conditions. A longer treatment time results in a greater number of polar functional groups and a much roughened gate dielectric surface. If a plasma-treated gate dielectric with such polar functional groups is exposed to dry air, the polar functional groups diffuse into the gate dielectric layer to reduce its surface polarity and energy [19–21]. During this aging process, almost no changes occur in the morphology of the gate dielectric surface. Thus, this can show the effect of polar functional groups of the PMMA gate dielectric without changing the other gate dielectric properties.

In our experiment, the surface properties of PMMA/Al_2O_3 gate dielectric layers were controlled using O_2 plasma treatment and an aging process. Even though a PMMA single layer can be used as gate dielectric layer for pentacene FET, the PMMA/Al_2O_3 hybrid gate dielectric is superior in insulation and uniform electrical characteristics. It also minimizes possible changes in the bulk properties of the gate dielectric, such as leakage current through the gate dielectric layer and capacitance, during the O_2 plasma treatment.

2. Experiments

All the gate dielectrics used had a dual layer structure of an upper PMMA layer and a lower anodized Al_2O_3 layer. The lower Al_2O_3 layer was fabricated by anodizing the surface of an aluminum gate electrode in aqueous ammonium phosphate solution, created by neutralizing 0.1 M phosphoric acid to pH 6 with 0.1 M ammonium hydroxide. The resulting Al_2O_3 had a thickness of approximately 100 nm when the voltage applied was 80 V. The upper PMMA layer was produced by spin coating of 3 wt.% PMMA in toluene at a spin speed of 4000 rpm. The PMMA thickness was approximately 120 nm with an rms roughness of approximately 0.7–0.9 nm. The structure of the gate dielectric and a schematic structure of the FET are shown in Fig. 1. The prepared gate dielectric layer was dried for over 1 day in a vacuum oven at 80 °C, and then treated with O_2 plasma. Some of the O_2 plasma-treated gate dielectrics were aged for 1 week in a 60 °C convection oven. D0s, D20s and D40s denote gate dielectrics which were O_2 plasma-treated for 0, 20, and 40 s, respectively. DA20s (DA40s) is the aged gate dielectric after O_2 plasma treatment for 20 s (40 s).

A pentacene film was deposited onto the gate dielectric layer at a deposition rate of 0.2–0.3 Å/s with a substrate temperature of room temperature. The fabrication of a pentacene FET with top-contact geometry was completed by evaporating gold

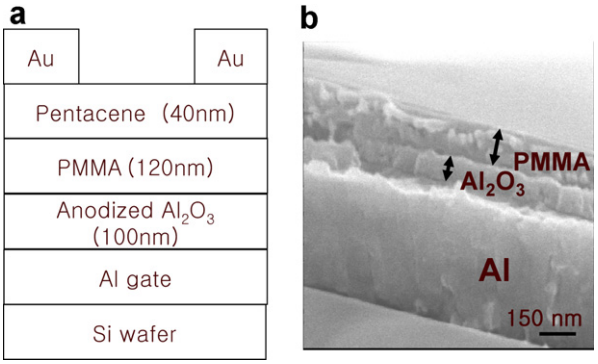


Fig. 1. (a) Schematic structure of pentacene FET. (b) Scanning electron micrograph (SEM) of the dual-layer gate dielectric. The lower Al_2O_3 layer was obtained by anodizing an aluminum gate electrode and the upper PMMA layer was formed by spin-coating.

through a shadow mask to define the source and drain electrodes. P0s, P20s (PA20s) and P40s (PA40s) denote pentacene FETs with D0s, D20s (DA20s), D40s (DA40s) as gate dielectric layers, respectively.

The gate dielectric surface and morphologies of the pentacene films were analyzed by atomic force microscopy (AFM; Multimode IIIa, Digital Instruments) operating in tapping mode. Synchrotron X-ray diffraction (XRD) analyses for pentacene films on the prepared gate dielectrics were performed at 10C1 beam line of Pohang Accelerator Laboratory (PAL). The electrical properties of the FETs were characterized using a semiconductor characterization system (Keithley 2400 and 236). The activation energy for charge transport was obtained by measuring mobilities changes in the range of temperature from 80 K to room temperature, using a cryostat system with liquid nitrogen.

3. Results and discussion

To examine the changes in surface properties of PMMA/Al_2O_3 gate dielectrics resulting from O_2 plasma treatment and aging, we investigated the surface morphology of each specimen using AFM. When the O_2 plasma treatment time was increased, the surface was etched to a greater extent and roughened, as shown in Fig. 2. An increase in PMMA roughness induced by O_2 plasma treatment was reported in previous experiments [18,19], but its extent is slightly different, depending on the experimental conditions. In our case, the gate dielectric did not show much increase in roughness topography with plasma treatment time up to 20 s. However, the topography after 40 s of treatment became much rougher, even if the rms roughness obtained from AFM analysis remained at approximately 0.7–0.9 nm. The topography of the roughness formed by O_2 plasma etching is very different from that formed by spin coating on an underlying rough substrate. The O_2 plasma-etched surface is rough with sharp, pointed ends and edges. In contrast, the roughness after spin-coating has a smoothly curved surface. This discrepancy can induce very different effects on the pentacene film morphology and the electrical properties of FETs.

The changes in surface energy after O_2 plasma treatment were calculated by measuring the contact angles of water and diiodomethane. The contact

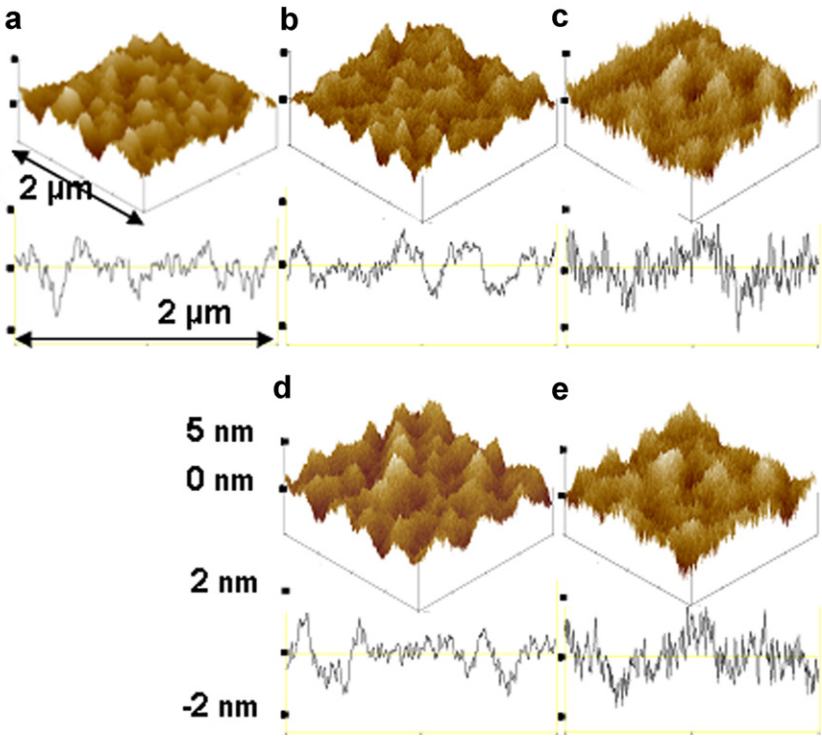


Fig. 2. Tapping-mode AFM topographic images of the dual layer gate dielectric surfaces: (a) D0s; (b) D20s; (c) D40s; (d) DA20s; and (e) DA40s. The upper and lower images show the three-dimensional and the cross-sectional view of the gate dielectrics, respectively.

angle is influenced by the polar functional groups and roughness of the gate dielectric. The calculated surface energy increased from 47 to 68 mJ/m^2. This is because the introduced polar functional groups and the enlarged surface area increased the surface energy of the gate dielectric. When O_2 plasma-treated gate dielectrics were aged, the surface energy decreased to approximately 52–55 mJ/m^2 after sufficient aging. However, AFM analyses indicate that almost no change occurred in the surface topography of the gate dielectric layers as a result of the aging process, as shown in Fig. 2. Therefore, the surface energy change on aging process mainly originates from a reduction in the number of polar functional groups. The surface energy of each gate dielectric is shown in Fig. 5c.

Fig. 3a–c show the morphologies of pentacene films on D0s, D20s, and D40s, respectively. As the O_2 plasma treatment time increased, the grain size of pentacene film decreased. The decrease in gain size can be attributed to the increased surface energy and the roughened gate dielectric layer from O_2 plasma treatment. Fig. 3d and e show the morphologies of pentacene films on DA20s and DA40s. Since surface topography does not change during aging process, the smaller grains on D20s (D40s) than those on DA20s (DA40s) indicate that the higher surface energy of the gate dielectrics can disturb the crystallization of pentacene.

However, a smaller grain was still observed in the pentacene film on DA40s, even though the surface energy of DA40s was reduced by aging process. This suggests that the sharply edged and pointed surface also restricts the crystallization of pentacene. In our previous study [15], we already reported that the

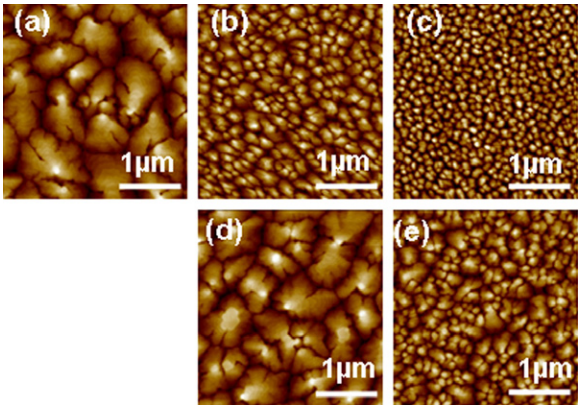


Fig. 3. Tapping-mode AFM topographic images of 40 nm thick pentacene films on: (a) gate dielectrics D0s, (b) D20s, (c) D40s, (d) DA20s, and (e) DA40s.

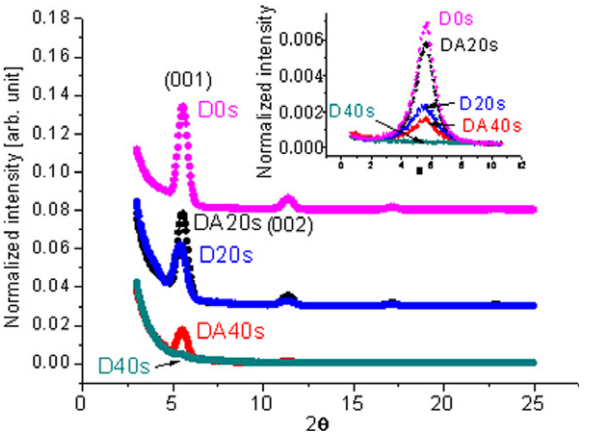


Fig. 4. Out-of-plane X-ray diffraction profiles of 10 nm thick pentacene films on gate dielectrics with O_2 plasma treatment time and the aging process.

smoothly curved roughness (R_q: 0.45–1.51 nm) prepared by spin-coating polymer films on an underlying rough surface did not cause a noticeable reduction in grain size in pentacene film. Therefore, these two results demonstrate that the morphology of pentacene film can be mainly determined by the topographical characteristics of roughened surface rather than by the rms roughness itself of polymer gate dielectrics.

The out-of-plane XRD profiles in Fig. 4 exhibit series of diffraction patterns of pentacene films grown on the various gate dielectrics shown in Fig. 2. Each peak corresponding to (00l) indicates that pentacene thin films on the gate dielectrics with various topographies and surface energies have thin-film phase characterized by d_{00l}-spacing of 15.5 Å. The variation of peak intensity shows that the ordering of the layered crystal structure is dependent upon O_2 plasma treatment time and aging process of gate dielectrics. To compare the ordering of each specimen, the rocking curve measurement was carried out on (002) peaks as shown in the inset of Fig. 4. The highest peak intensity in the rocking curve was observed in pentacene films grown on D0s, and a dramatic decrease of peak intensity of pentacene films appeared as O_2 plasma treatment time increased (see the rocking curves of D20s and D40s in the inset of Fig. 4). The implication of this result is that the O_2 plasma treatment on the PMMA dielectrics decreases the out-of-plane ordering of pentacene molecules in thin film. The lower intensity of rocking scan of D20s (D40s) than that of DA20s (DA40s) reveals that the reduction of out-of-plane ordering is caused by the polar func-

tional groups introduced from O_2 plasma treatment, because both dielectrics have similar topographies but different surface energy. Also, DA40s with lowered surface energy has lower intensity of rocking scan than DA20s, which indicates that the rough topography with sharp and pointed edges also decreases the ordering of pentacene molecules in the film. Therefore, the peak disappearance on D40s can be attributed to both the highest surface energy and the pronounced rough topography of gate dielectric layer, resulting in severely disturbed ordering of pentacene molecules.

To examine the effects of polar functional groups and the roughness topography of the gate dielectrics on the electrical characteristics of the pentacene FETs, we obtained the transfer characteristics of pentacene FETs, such as mobility, threshold voltage, and sub threshold swing. Also, by measuring mobilities at different temperature, we calculated the activation energy (E_A), which indicates the distribution of the widths of the localized trap states [8], and the trap-free mobility (μ_0) from the Arrhenius relation $\mu = \mu_0 \exp(-E_A/kT)$.

In cases for which plasma treatment was carried out without aging, i.e., P20s and P40s, the mobility at room temperature fell sharply to approximately 0.01 cm^2/V s, the threshold voltage (V_{th}) and turn-on voltage (V_{on}) shifted positively, and the off-state current (I_{off}) and subthreshold swing (SS) increased, as shown in Fig. 5. Temperature-dependent mobility measurements revealed a linear relationship between $\ln(\mu)$ and $1/T$ for all samples, which indicates the occurrence of thermally activated transport. As a result of the O_2 plasma treatment, E_A increased from 59.5 to 108.1 meV, as shown in Fig. 6.

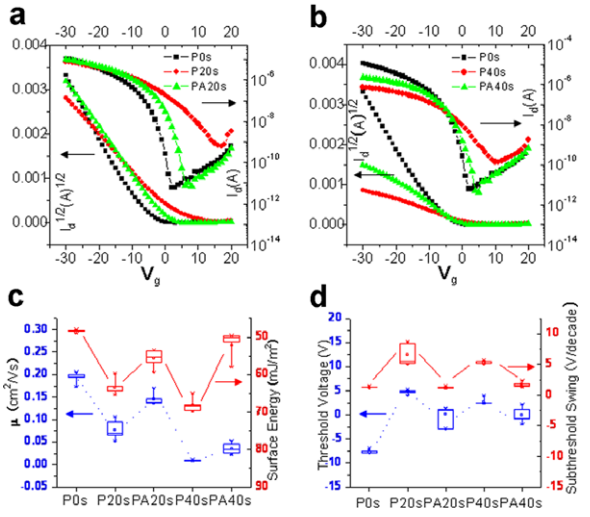


Fig. 5. Electrical characteristics of pentacene FETs depending on O_2 plasma treatment time and the aging process: (a), (b) the transfer curves for pentacene FETs; (c) the change of charge mobility of pentacene FETs and surface energy of gate dielectrics; and (d) the change of threshold voltage and subthreshold swing of pentacene FETs.

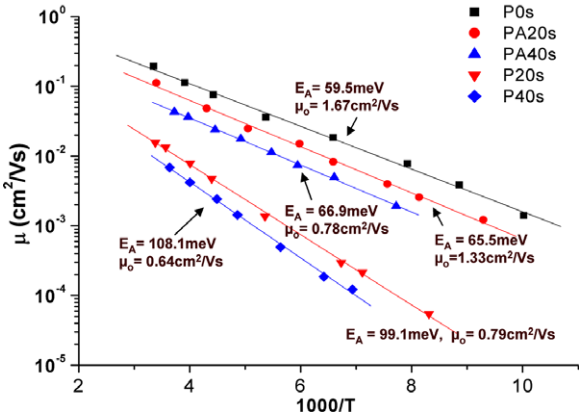


Fig. 6. Temperature-dependent charge mobility measurements, in which a linear relationship between $\ln(\mu)$ and $1/T$ was revealed for all samples, indicating the occurrence of thermally activated transport. The activation energy (E_A) and the trap-free mobility (μ_0) were determined from the Arrhenius relation $\mu = \mu_0 \exp(-E_A/kT)$.

The decrease in mobility resulting from O_2 plasma treatment is partly caused by the formation of many hole trap states in the band gap [8,22]. The electric dipoles of the polar functional groups and interface charges that arise in the gate dielectric layer as a result of the O_2 plasma treatment induce split energy levels in the band gap and broaden the Gaussian distribution of the energy levels around the HOMO level edge. As a consequence, energy levels are formed that can function as hole trap states in the band gap [23]. Thus, the width of the localized trap state increases, as reflected in the increase in E_A [8], so trap filling at bias values below V_{th} and the capacitance of trapped interface charges result in an increase in SS. This result exactly coincides with the results of simulations reported by Bolognesi et al. and Scheinert et al., who examined the relationships between interface traps and transfer curve behavior [24,25].

The decrease in mobility also originates from the decrease in μ_0, as shown by Fig. 6. The increased level of crystal imperfections, the smaller grain size, and the resulting restriction of charge transport in

the charge channel lead to a decrease in μ_0. The polar functional groups and rough topography of the gate dielectrics can hinder the diffusion of pentacene molecules and result in the production of smaller grains. Moreover, the sharp, pointed ends and valleys in the topography disturb the growth of pentacene crystals, resulting in many defects and vacancies in the pentacene film. Grain boundaries, crystal defects, and rough interfaces can restrict the flow of charges and cause scattering [8,9]. According to Steudel et al., a rough topography also produces valley effects that result in a pronounced decrease in μ_0 [11].

Regarding the positive shift of V_{th} and V_{on} in the transfer curve shown in Fig. 5, the electric dipoles and fixed interface charges produced by the plasma treatment cause a surface potential change that induces a bending of the HOMO level at the interface and increases the carrier density in the channel, which have the same effect as applying a negative gate bias [24–28]. As a result, many mobile charges are present at zero gate bias, so a more positive gate voltage is needed to switch off the FET. In addition, the increased number of carriers and the broad potential distribution of the gate dielectric layer result in an increase in I_{off}.

However, the transfer curves indicate that the positive shifts in V_{th} and V_{on} and the increase in I_{off} for P40s are smaller than those for P20s. As shown in Fig. 6, longer plasma treatment time induces more and deeper trap states, which reduce the number of mobile carriers, resulting in a smaller positive shift of V_{th} and V_{on} and a smaller increase in I_{off}. In the study by Yang et al., O_2 plasma treatment ($t > 30$ s) was found to induce deep trap states in the band gap [28]. The simulations carried out by Bolognesi et al. and Scheinert et al. examined the effect of the depth of trap states on the transfer characteristics, and their conclusions support our experimental results [24,25]. This phenomenon can also be related to lower μ_0. The rough topography of the gate dielectric in P40s reduces μ_0, as shown in Fig. 6, and the resulting lowered charge mobility induces smaller positive shifts of V_{th} and V_{on} and a smaller increase in I_{off}.

On the other hand, in PA20s and PA40s using aged gate dielectrics, the fewer polar functional groups in the gate dielectrics reduce bending of the HOMO level at the interface, thus inducing smaller positive V_{th} and V_{on} values than for P20s and P40s, as shown in Fig. 5. The fewer split energy states around the HOMO edge that result from a less polar surface, homogeneous chemical state, and resulting increased ordering of pentacene reduce the number of trap states, and leads to higher mobility and lower E_A, SS, and I_{off}. However, the mobility in PA40s is still lower than that of PA20s, although they have similar E_A values. This is because the rougher topography of the gate dielectric is maintained even after aging, as is the disturbed crystallization of pentacene. Accordingly, it is presumed that the low trap-free mobility in PA40s is caused by scattering at the rough interface [8] and the roughness valley effect [11] rather than by the formation of trap states.

The effects of the surface properties of the gate dielectrics and the grain boundaries on the distribution of trap states have been intensively studied by many groups. In our experiments, both the surface properties of the gate dielectric and the grain size were changed by plasma treatment and aging of the gate dielectrics. Aging of the gate dielectrics resulted in a decrease in E_A and SS and an increase in the grain size of pentacene, however, the results for PA20s and PA40s, with similar surface energy but different topographies, show that the gate dielectric topography did not change E_A and SS, even though the samples had pentacene of different grain sizes. Thus, the distribution of trap states is determined more by the polar functional groups on the gate dielectric than by its topography. This result also indicates that the distribution of trap sites is not localized in the grain boundaries of the pentacene film.

4. Summary

This study analyzed the effects of polar functional groups and a rough topography of polymer gate dielectrics on the characteristics of FETs. As a result of O_2 plasma treatment and aging of PMMA/Al_2O_3 gate dielectrics, we identified several mobility-reducing factors, i.e., polar functional groups, interface charges, and rough topography. Surface polar groups and surface polarity led to a smaller grain size, a greater number of trap states, and a positive shift of the threshold voltage. Rough topography of the dielectric surface reduced the grain size and the trap-free mobility. Analysis showed that O_2 plasma treatment and aging could change the surface energy of PMMA to a wider range, and the effects of polar functional groups on different surface topography could be examined.

Acknowledgement

This work was supported by Grant No. RTI04-01-04 from the Regional Technology Innovation Program of the Ministry of Commerce, Industry, and Energy (MOCIE) of Korea.

References

[1] P.F. Baude, D.A. Ender, M.A. Haase, T.W. Kelly, D.V. Muyres, S.D. Theiss, Appl. Phys. Lett. 82 (2003) 3964.
[2] H. Klauk, M. Halik, U. Zschieschang, E.F. Ute, G. Schmid, C. Dehm, Appl. Phys. Lett. 82 (2003) 4175.
[3] A. Dodabalapur, Z. Bao, A. Makhija, J.G. Laquindanum, V.R. Raju, Y. Feng, H.E. Katz, J. Rogers, Appl. Phys. Lett. 73 (1998) 142.
[4] H. Sirringhaus, N. Tessler, R.H. Friend, Synth. Met. 102 (1999) 857.
[5] B. Crone, A. Dodabalapur, A. Gelperin, L. Torsi, H.E. Katz, A.J. Lovinger, Z. Bao, Appl. Phys. Lett. 78 (2001) 2229.
[6] C. Bartic, A. Campitelli, S. Borghs, Appl. Phys. Lett. 82 (2003) 475.
[7] L. Wang, D. Fine, A. Dodabalapur, Appl. Phys. Lett. 85 (2004) 6386.
[8] D. Knipp, R.A. Street, A.R. Völkel, Appl. Phys. Lett. 82 (2003) 3907.
[9] D. Knipp, R.A. Street, A. Völkel, J. Ho, J. Appl. Phys. 93 (2003) 347.
[10] S.E. Fritz, T.W. Kelley, C.D. Frisbie, J. Phys. Chem. B 109 (2005) 10574.
[11] S. Steudel, S. De Vusser, S. De Jonge, D. Janssen, S. Verlaak, J. Genoe, P. Heremans, Appl. Phys. Lett. 85 (2004) 4400.
[12] L.A. Majewski, R. Schroeder, M. Grell, P.A. Glarvey, M.L. Turner, J. Appl. Phys. 96 (2004) 5781.
[13] T.W. Kelley, L.D. Boardman, T.D. Dunbar, D.V. Muyres, M.J. Pellerite, T.P. Smith, J. Phys. Chem. B 107 (2003) 5877.
[14] S.Y. Yang, K. Shin, C.E. Park, Adv. Funct. Mater. 15 (2005) 1806.
[15] K. Shin, C. Yang, S.Y. Yang, H. Jeon, C.E. Park, Appl. Phys. Lett. 88 (2006) 072109.
[16] A.-L. Deman, J. Tardy, Org. Electron. 6 (2005) 78.
[17] S. Uemura, A. Komukai, R. Sakaida, T. Kawai, M. Yoshida, S. Hoshino, T. Kodzasa, T. Kamata, Synth. Met. 153 (2005) 405.
[18] C. Jinan, L. Fuzhi, L. Baoming, Y.K. Daniel, Langmuir 20 (2004) 10919.
[19] M.R. Sanchis, V. Blanes, M. Blanes, D. Garcia, R. Balart, Eur. Polym. J. 42 (2006) 1558.
[20] L. Carrino, W. Polini, L. Sorrentino, J. Mater. Process. Technol. 153–154 (2004) 519.
[21] K.S. Kim, C.M. Ryu, C.S. Park, G.S. Sur, C.E. Park, Polymer 44 (2003) 6287.
[22] A.R. Völkel, R.A. Street, D. Knipp, Phys. Rev. B 66 (2002) 195336.
[23] J. Veres, S.D. Ogier, S.W. Leeming, D.C. Cupertino, S.M. Khaffaf, Adv. Funct. Mater. 13 (2003) 199.
[24] A. Bolognesi, M. Berliocchi, M. Manenti, A.D. Carlo, P. Lugli, K. Lmimouni, C. Dufour, IEEE Trans. Electron Dev. 51 (2004) 1997.
[25] S. Scheinert, G. Paasch, M. Schrödner, H.-K. Roth, S. Sensfuss, Th. Doll, J. Appl. Phys. 92 (2002) 330.
[26] K.P. Pernstich, S. Haas, D. Oberhoff, C. Goldmann, D.J. Gundlach, B. Batlogg, A.N. Rashid, G. Schitter, J. Appl. Phys. 96 (2004) 6431.
[27] J. Takeya, T. Nishikawa, T. Takenobu, S. Kobayashi, Y. Iwasa, T. Mitani, C. Goldmann, C. Krellner, B. Batlogg, Appl. Phys. Lett. 85 (2004) 5078.
[28] Y.S. Yang, S.H. Kim, S.C. Lim, J.-I. Lee, J.H. Lee, L.-M. Do, T. Zyung, Appl. Phys. Lett. 83 (2003) 3939.

Available online at www.sciencedirect.com
ScienceDirect
Organic Electronics 8 (2007) 343–348
Organic Electronics
www.elsevier.com/locate/orgel

Fine tuning hole injection for high-performance polyfluorene-based blue emitting device by adjusting work function of anode via deposition of CF_x layer with proper ionization potential on indium tin oxide

Chung-Chin Hsiao, Chih-Hao Chang, Hsin-Hung Lu, Show-An Chen *

Chemical Engineering Department, National Tsing-Hua University, Hsinchu 30043, Taiwan, ROC

Received 25 July 2006; received in revised form 5 December 2006; accepted 21 December 2006
Available online 17 January 2007

Abstract

By introducing CF_x thin film as hole injection layer on top of indium tin oxide (ITO) anode via plasma polymerization of CHF_3, the device with poly(9,9-dioctylfluorene) (PFO) as emitting layer, ITO/CF_x(35 W)/PFO/CsF/Ca/Al, is prepared. At the optimal C/F atom ratio using the radio frequency power 35 W, the device performance is optimal having the maximum current efficiency 3.1 cd/A and maximum brightness 8400 cd/m^2. This is attributed to a better balance between hole and electron fluxes, resulting from a decrease in hole injection barrier as manifested by ultraviolet photoelectron spectroscopy and scanning surface potential microscopy.
© 2007 Elsevier B.V. All rights reserved.

Keywords: Polymer light-emitting diode; Scanning surface potential microscopy; Poly(9,9-dioctlyfluorene); Plasma polymerization of CHF_3

1. Introduction

The interfaces between emitting conjugated polymer and electrodes are central to the physics of polymer light-emitting diode (PLED) [1], since a mismatch between polymer's highest occupied molecular orbital (HOMO) and lowest unoccupied molecular orbital (LUMO) with work functions of the electrodes can lead to poor charge injections into the device. To minimize carrier (hole or electron) injection barrier of PLED, many efforts have been attempted [2–11]. For example, by using alkaline metal fluoride (LiF [2], LiF/Ca [3], CsF [4], or CsF/Ca [4]) or its composite as the cathode, the electron injection barrier can be reduced to enhance electron injection. For improving hole injection, various treatments for indium tin oxide (ITO) as the anode have also been reported, including a coating with self-assembled monolayer (SAM) based on 4,4′-bis[(*p*-trichlorosilylpropylphenyl)phenylamino] biphenyl (TPD–Si_2) [5], wet aquaregia treatment [6], UV ozone treatment [7], and low pressure oxygen

* Corresponding author. Tel.: +886 3 571 0733; fax: +886 3 573 7798.
E-mail address: sachen@che.nthu.edu.tw (S.-A. Chen).

1566-1199/$ - see front matter © 2007 Elsevier B.V. All rights reserved.
doi:10.1016/j.orgel.2006.12.008

plasma treatment [8]. Besides, inserting an interlayer between ITO and emitting polymer as hole transport layer has been widely adopted, including polystyrenesulfonic acid-doped poly(3,4-ethylene dioxythiophene) (PEDOT-PSS) [9,10] or PSS-doped polyaniline [10,11]. For organic light-emitting diodes (OLEDs), anode modification with plasma polymerized CHF_3 has been found to improve hole injection due to a reduce of hole injection barrier and a generation of interfacial dipole [12,13]. However, application of such modification on ITO for PLEDs does not appear in literature.

Here we present that three different CF_x layers: CF_x(20 W), CF_x(35 W), and CF_x(50 W) formed by plasma polymerization of CHF_3 based on the different radio frequency (rf) powers: 20, 35, and 50 W on an indium tin oxide surface for poly(9,9-dioctylfluorene) (PFO)-based light-emitting diodes can control the extent of enhancement in hole injection. This is due to the fact that they have the different ionization potentials (IPs): 5.7, 5.6, and 5.3 eV, respectively. In addition, we found that introducing a CF_x(35 W) layer for the device, ITO/CF_x(35 W)/(PFO)/CsF/Ca/Al, can lead to a high device performance with the maximum current efficiency 3.1 cd/A and maximum brightness 8400 cd/m^2. The high device performance is attributed to a better balance between hole and electron fluxes, resulting from a dramatic enhancement in hole injection and better wetting by converting the ITO surface from hydrophilic to hydrophobic provided by the CF_x deposition. The effect of enhancing hole injection of the present CF_x layers is different from that in our previous work, in which we found that the thin CF_x layer has a hole blocking effect in the MEH-PPV device, ITO/CF_x/MEH-PPV/Ca/Al, due to a presence of interfacial dipole at the CF_x/MEH-PPV interface [14].

2. Experiment

The PFO we used was synthesized via the Ni[0] mediated Yamamoto-coupling reaction [15]. Its weight averaged molecular weight (M_w) relative to polystyrene standards was 262,000 Dalton (M_n = 160,000 Dalton; PD = 1.6) as determined by use of gel permeation chromatography. The preparation procedures for the devices are as follows. The ITO glass plate was cleaned sequentially with isopropyl alcohol, acetone, deionized water/H_2O_2/NH_4OH (volume ratio = 5:1:1), and deionized water. Then, it was exposed to oxygen plasma at a power of 50 W and a pressure of 200 mTorr for 5 min with a base pressure 3×10^{-6} Torr in a plasma generator chamber of a parallel electrode type. The plasma polymerization of CF_x layer was carried out in the same chamber with the precursor CHF_3 at 150 mTorr and the different powers, 20, 35, and 50 W, by using a 13.56 MHz rf power generator, which are designated as CF_x(20 W), CF_x(35 W), and CF_x(50 W) layers, respectively. A thin layer (~100 nm) of PFO was spin-coated onto the CF_x-modified ITO from its solution in THF (8 mg/mL) in an Ar glove box. On top of the PFO layer, a thin layer of cesium fluoride (CsF, 1.5 nm) covered with a protecting layer of aluminum (about 100 nm) as the cathode was deposited in a vacuum thermal evaporator through a shadow mask at a pressure of less than 2×10^{-6} Torr. The device with CF_x-modified ITO using the different power 20, 35, 50 W (ITO/CF_x(20, 35, or 50 W)/PFO/CsF/Al) are designated as CF_x(20 W)-, CF_x(35 W)-, and CF_x(50 W)-device, respectively, while that without CF_x layer as bare device (ITO/PFO/CsF/Al). For a comparison purpose, we also introduced the PEDOT-PSS (Baytron P CH 8000 with a conductivity of 10^{-5} S/cm from Bayer) as the hole transport layer (15 nm) to fabricate the device, (ITO/PEDOT/PFO/CsF/Al), which is designated as PEDOT device. Finally, for reducing electron injection barrier, we also fabricate the two devices, ITO/PEDOT/PFO/CsF/Ca/Al and ITO/CF_x(35 W)/PFO/CsF/Ca/Al, by evaporating CsF (1.5 nm), Ca (3.5 nm), and finally Al (100 nm) in sequence. The active area of device is about 12 mm^2. *I–V* characteristics of the devices were measured using a KEITHEY-238 source meter and brightness measured with a TOPCON BM-8 luminance meter. The current efficiency of the device in cd/A was obtained by dividing current density from its corresponding brightness.

3. Results and discussion

The thicknesses of the CF_x(20 W), CF_x(35 W), and CF_x(50 W) layers are estimated to be all about 15 Å using an ellipsometric spectrometer (from Jobin Yvon). The deposition of the CF_x layer has changed the ITO surface from hydrophilic to hydrophobic and reduced the difference in surface energy between ITO and PFO surface, as evidenced by measurements of aqueous contact angles for bare ITO, ITO/PEDOT-PSS, PFO, and the three CF_x(20 W), CF_x(35 W), and CF_x(50 W) layers surfaces to give 22°, 33°, 83°, 89°, 86°, and 85°,

respectively. It means that there are higher interfacial affinities between these three CF_x-modified ITOs and PFO surface. Besides, the individual hydrophobic CF_x-modified ITO also provides the hydrophobic PFO with a larger contact area due to a better wetting [6,16,17].

For the devices with the same cathode CsF/Al, Fig. 1 shows the electroluminescence (EL) spectra and the Commission Internationale d'Eclairage $(CIE)_{x,y}$ color coordinate of the bare, PEDOT, CF_x(20 W)-, CF_x(35 W)-, and CF_x(50 W)-devices at the applied voltage 10 V; there appears no obvious difference in color coordinate. The performances of these five devices are shown in Fig. 2. Their maximum current efficiencies are 0.1, 1.3, 1.4, 1.8, and 1.2 cd/A, and their maximum brightnesses are 65, 1800, 8100, 7800, and 3660 cd/m^2, respectively. The present CF_x(20 W) and CF_x(35 W) devices have higher brightnesses as compared to other PLEDs with PFO and CsF/Al or Ca/Al as the cathode [5,18,19]. From the *I–V* characteristics (Fig. 2a), we can find that the CF_x(20 W)-, CF_x(35 W)-, and CF_x(50 W)-devices have higher current density than the bare and PEDOT devices, suggesting that all these three CF_x layers can improve the hole injection, which leads to a better balance between hole and electron fluxes in these three CF_x-modified devices. The improvements of hole injection are likely due to the decrease in hole injection barriers between PFO and these three CF_x-modified ITOs as also reflected in the lower turn-on voltages 3.2, 3.5, and 3.6 V as compared to the bare and PEDOT devices 4.4 and 3.7 V, respectively (referenced to 0.2 cd/m^2).

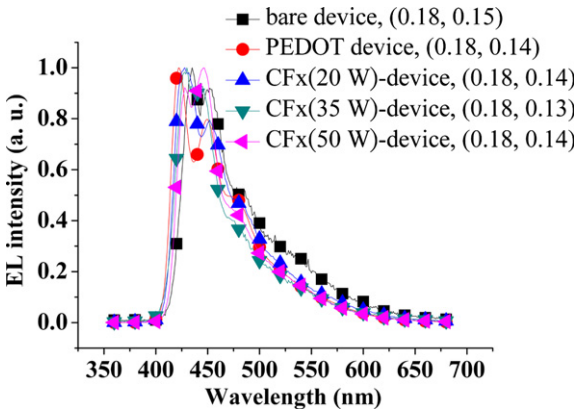


Fig. 1. Electroluminescence spectra of the bare device (ITO/PFO/CsF/Al), PEDOT device (ITO/PEDOT/PFO/CsF/Al), CF_x(20 W)-, CF_x(35 W)-, and CF_x(50 W)-devices (ITO/CF_x(20, 35, or 50 W)/PFO/CsF/Al) at the applied voltage 10 V.

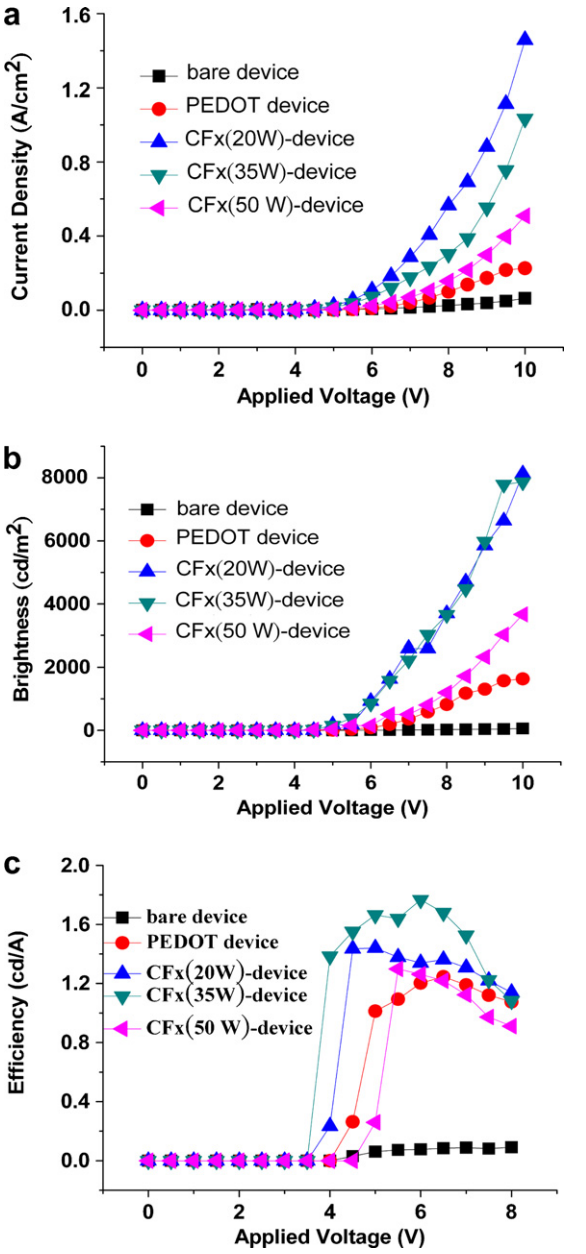


Fig. 2. Three curves of the current density–applied voltage (a), brightness–applied voltage (b), and current efficiency–applied voltage (c) for the bare device, PEDOT device, CF_x(20 W)-, CF_x(35 W)-, and CF_x(50 W)-device. The cathode CsF/Al is used for all the devices.

To support this further, we use the ultraviolet photoelectron spectroscopy (UPS, from Thermo Electron Corporation) to measure the work functions of bare ITO and PEDOT, the ionization potentials (IPs) of these three CF_x layers on ITO, and the HOMO level of PFO, which are 4.9, 5.1, 5.7, 5.6, 5.3 and 5.8 eV, respectively. And, we observe

that there is no obvious interfacial dipole at these three CF_x/PFO interfaces, which is different from our previous work as that there is interfacial dipole having hole blocking effect at the CF_x/MEH-PPV interface [14] as to be revealed in more detail in the next paragraph. Therefore, the corresponding hole injection barriers in the bare, PEDOT, and CF_x(20 W)-, CF_x(35 W)-, and CF_x(50 W)-devices are 0.9, 0.7, 0.1, 0.2, and 0.5 eV, respectively. It also explains that the sequence of the current densities and maximum brightnesses from large to small is CF_x(20 W)-, CF_x(35 W)-, CF_x(50 W)-, PEDOT, and bare devices. We also quantitatively determine the relation between the F/C atom ratio and the ionization potential of these three CF_x layers as listed in Table 1. For the former, a X-ray photoelectron spectrometer from Thermo Electron Corporation is used and the original XPS results are given in Supplementary data. We find that the lower rf power we use, the higher F/C atom ratio and IP of the CF_x layer has, which indicates that using different rf power can control the composition and IP of the CF_x layers and the hole injection barrier in PFO-based device.

The reason for similar CF_x anodes with the different behaviors of the interfacial dipole to PFO and MEH-PPV is charge transfer [20] and permanent dipole [21]. Tengstedt et al. suggested that charges are transferred across the interface to form the interfacial dipole if the anode work function is greater than the positive polaron/bipolaron formation energy for the light-emitting polymer [20], which explains why there is an interfacial dipole at the CF_x/MEH-PPV interface (the work function of this CF_x-modified ITO in our previous article, 5.55 eV, is larger than the HOMO level of the MEH-PPV, 5.0 eV [14]), but not at the CF_x/PFO interface (the work function of the CF_x-modified ITO we present here, 5.3–5.7 eV, is smaller than the HOMO level of the PFO, 5.8 eV). Besides, the permanent dipole might exist at the CF_x/MEH-PPV interface resulting from the polar ether group of the side chain in MEH-PPV [21]. On the contrary, there is no polar group in the PFO.

Table 1
The ionization potential and the F/C atom ratio of the three CF_x layers

CF_x layer	Ionization potential (eV)	F/C ratio
CF_x(20 W)	5.7	1.51
CF_x(35 W)	5.6	1.47
CF_x(50 W)	5.3	1.33

We also apply scanning surface potential microscopy (SSPM) [22] to measure the local work function of the different treated ITO, just cleaned-ITO, O_2 plasma–ITO, CF_x(50 W)–ITO, CF_x(35 W)–ITO, and CF_x(20 W)–ITO as shown in Fig. 3. The average local work functions of these five ITO surfaces are 4.70, 5.05, 5.36, 5.55, and 5.64 eV, respectively (all are within a variation below 0.005 eV), which are close to the results from the above UPS data. In addition, we observed that their maximum differences are 0.185, 0.09, 0.03, 0.04, and 0.03 eV (from the raw data of SSPM), indicating that the CF_x films not only increase the work function of the ITO but also decrease the difference in local work function of ITO.

To assure that whether introducing CF_x layer provides an improvement in hole injection, we fabricated the five hole-only devices, ITO/PFO/Au, ITO/PEDOT/PFO/Au, ITO/CF_x(50 W)/PFO/Au, ITO/CF_x(35 W)/PFO/Au, and ITO/CF_x(20 W)/PFO/Au, in which electron injection from the cathode is blocked by the high work function cathode, Au layer, to prove the enhancement of hole injection by CF_x layers. From their I–V curves shown in Fig. 4, the hole current densities of the device with CF_x(20 W)- and CF_x(35 W)–ITO are both larger than those of the device with PEDOT by 2 orders of magnitude and the device with bare ITO by 3–4 orders of magnitude, while that of the device with CF_x(50 W)–ITO is slightly larger than that of

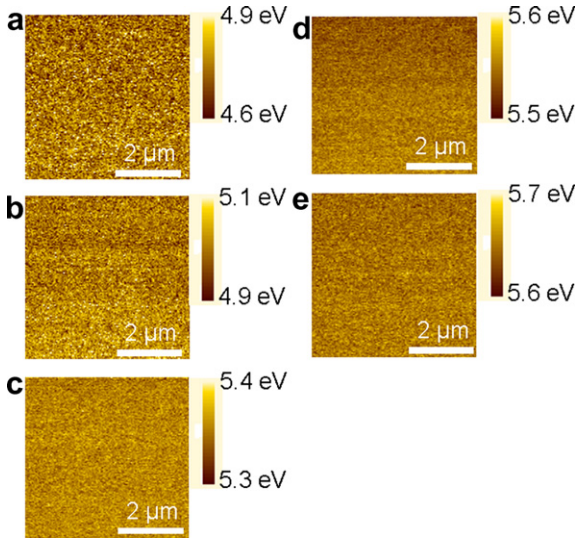


Fig. 3. Scanning surface potential microscopy (SSPM) images of the different treated-ITO surfaces: just cleaned-ITO (a), O_2 plasma–ITO (b), CF_x(50 W)–ITO (c), CF_x(35 W)–ITO (d), and CF_x(20 W)–ITO (e).

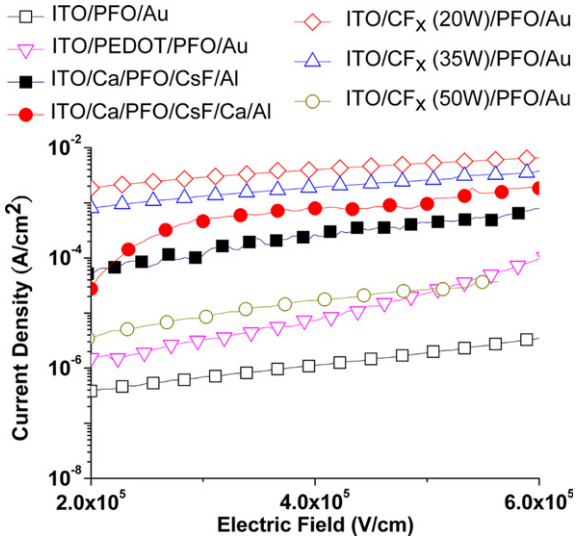


Fig. 4. Comparison of injection characteristics of hole-only devices having the structures: ITO/PFO/Au, ITO/PEDOT/PFO/Au, ITO/CF_x(20 W)/PFO/Au, ITO/CF_x(35 W)/PFO/Au, and ITO/CF_x(50 W)/PFO/Au and those of electron-only devices having the structures: ITO/Ca/PFO/CsF/Al and ITO/Ca/PFO/CsF/Ca/Al.

the device with PEDOT. The improvement in hole injection is due to the fact that the hole injection barriers among the three CF_x-modified hole-only devices are indeed decreased by the CF_x layers. In order to understand the relative values of hole and electron fluxes, we also fabricated two electron-only devices, ITO/Ca/PFO/cathode (using CsF/Al and CsF/Ca/Al), in which hole injection from the anode is blocked by the low work function anode, Ca. As shown in Fig. 4, we observed that the latter device has electron current density higher than the former device and its level is close to the hole-only device with CF_x(35 W). It can be expected that a use of CF_x(35 W) on ITO as anode and CsF/Ca/Al as cathode would provide a bipolar device with optimal performance. Fig. 5 shows that it is just the case, for which the maximum current efficiency and brightness, and turn-on voltage are 3.1 cd/A, 8400 cd/m^2, and 3.1 V, respectively. Its $CIE_{x,y}$ color coordinate of the EL spectra (not shown here) of this device is [0.18, 0.15] at the applied voltage 10 V. To the best of our knowledge, this device has high current efficiency and brightness comparable to or higher than other PLEDs using PFO and other dialkyl-substituted PFs as light-emitting layer in the literatures (maximum brightness 7000 cd/m^2 [5], maximum current efficiency 1.96 cd/A [23]).

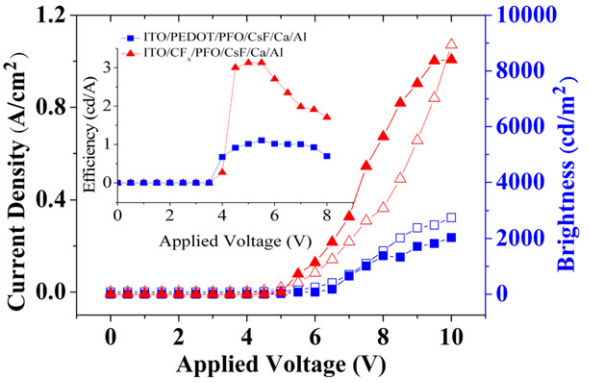


Fig. 5. Current density–applied voltage–brightness curves for the devices, ITO/PEDOT/PFO/CsF/Ca/Al and ITO/CF_x(35 W)/PFO/CsF/Ca/Al; the close and open symbols are for brightness and current density, respectively. Brightnesses and current densities of the devices, ITO/PEDOT/PFO/CsF/Ca/Al and ITO/CF_x(35 W)/PFO/CsF/Ca/Al are ■, ▲, □, and △, respectively. The inset is current efficiency–applied voltage curves.

4. Conclusion

In summary, we have demonstrated that we can control the extent of enhancement in hole injection in the PFO-based devices by using CF_x layers based on different radio frequency powers. We have also demonstrated that a dramatic enhancement of hole injection and thus a better balance between hole and electron fluxes are achieved in the present device, ITO/CF_x(35 W)/PFO/CsF/Ca/Al, which results in a high current efficiency (3.1 cd/A) and high brightness (8400 cd/m^2).

Acknowledgements

We thank the financial supports from the Ministry of Education (Project 91E-FA04-2-4A) and from the National Science Council (Project NSC 95-2752-E007-005 (and 008)-PAE).

Appendix A. Supplementary data

Supplementary data associated with this article can be found, in the online version, at doi:10.1016/j.orgel.2006.12.008.

References

[1] J.H. Burroughes, D.D.C. Bradley, A.R. Brown, R.N. Marks, K. Mackay, R.H. Friend, P.L. Burns, A.B. Holmes, Nature 347 (1990) 539.
[2] R.B. Fletcher, D.G. Lidzey, D.D.C. Bradley, S. Walker, M. Inbasekaran, E.P. Woo, Synth. Met. 111–112 (2000) 151.

[3] T.M. Brown, R.H. Friend, I.S. Millard, D.J. Lacey, J.H. Burroughes, F. Cacialli, Appl. Phys. Lett. 79 (2001) 174.
[4] T.M. Brown, R.H. Friend, I.S. Millard, D.J. Lacey, T. Butler, J.H. Burroughes, F. Cacialli, J. Appl. Phys. 93 (2003) 6159.
[5] H. Yan, Q. Huang, J. Cui, J.G.C. Veinot, M.M. Kern, T.J. Marks, Adv. Mater. 15 (2003) 835.
[6] F. Li, H. Tang, J. Shinar, O. Resto, S.Z. Weisz, Appl. Phys. Lett. 70 (1997) 2741.
[7] S.K. So, W.K. Choi, C.H. Cheng, L.M. Leung, C.F. Kwong, Appl. Phys. A: Mater. Sci. Process. 68 (1999) 447.
[8] J.S. Kim, R.H. Friend, F. Cacialli, Appl. Phys. Lett. 74 (1999) 3084.
[9] T.M. Brown, J.S. Kim, R.H. Friend, F. Cacialli, R. Daik, W.J. Feast, Appl. Phys. Lett. 75 (1999) 1679.
[10] S.A. Carter, M. Angelopoulous, S. Karg, P.J. Brock, J.C. Scott, Appl. Phys. Lett. 70 (1997) 2067.
[11] J.C. Scott, S.A. Carter, S. Karg, M. Angelopoulous, Synth. Met. 85 (1997) 1197.
[12] L.S. Hung, L.R. Zheng, M.G. Mason, Appl. Phys. Lett. 78 (2001) 673.
[13] S.W. Tong, C.S. Lee, Y. Lifshitz, D.Q. Gao, S.T. Lee, Appl. Phys. Lett. 84 (2004) 4032.
[14] C.C. Hsiao, C.H. Chang, T.H. Jen, M.C. Hung, S.A. Chen, Appl. Phys. Lett. 88 (2006) 033512.
[15] H.H. Lu, C.Y. Liu, T.H. Jen, J.L. Liao, H.N. Tseng, C.W. Huang, M.C. Hung, S.A. Chen, Macromolecules 38 (2005) 10829.
[16] R.F. Bianchi, A.J.F. Carvalho, M.A. Pereira-da-Silva, D.T. Balogh, R.M. Faria, Mater. Sci. Eng. C 24 (2004) 595.
[17] J.S. Kim, R.H. Friend, F. Cacialli, J. Appl. Phys. 86 (1999) 2774.
[18] M.K. Fung, S.L. Lai, S.W. Tong, M.Y. Chan, C.S. Lee, S.T. Lee, W.W. Wu, M. Inbasekaran, J.J. O'Brien, Appl. Phys. Lett. 81 (2002) 1497.
[19] K.H. Weinfurtner, H. Fujikawa, S. Tokito, Y. Taga, Appl. Phys. Lett. 76 (2000) 2502.
[20] C. Tengstedt, W. Osikowicz, W.R. Salaneck, I.D. Parker, C.H. Hsu, M. Fahlman, Appl. Phys. Lett. 88 (2006) 053502.
[21] N. Koch, A. Kahn, J. Ghijsen, J.J. Pireaux, J. Schwartz, R.L. Johnson, A. Elschner, Appl. Phys. Lett. 82 (2003) 70.
[22] S.H. Chen, J. Appl. Phys. 97 (2005) 073713.
[23] K.H. Weinfurtner, H. Fujikawa, S. Tokito, Y. Taga, Appl. Phys. Lett. 76 (2000) 2502.

Available online at www.sciencedirect.com
ScienceDirect
Organic Electronics 8 (2007) 349–356
Organic Electronics
www.elsevier.com/locate/orgel

New hole blocking material for green-emitting phosphorescent organic electroluminescent devices

Sung Ouk Jung [a], Yun-Hi Kim [a,*], Soon-Ki Kwon [a,*], Hyoung-Yun Oh [b], Jung-Hwan Yang [b]

[a] *School of Nano-Advanced Materials and Engineering Research Institute, Department of Chemistry, Gyeongsang National University, Jinju 660-701, Republic of Korea*
[b] *LG Elite, Umeon-Dong, Seoul, Republic of Korea*

Received 10 May 2006; received in revised form 4 December 2006; accepted 21 December 2006
Available online 29 December 2006

Abstract

The new amorphous molecular material, 2,5-bis(4-triphenylsilanyl-phenyl)-[1,3,4]oxadiazole, that functions as good hole blocker as well as electron transporting layer in the phosphorescent devices. The obtained material forms homogeneous and stable amorphous film. The new synthesized showed the reversible cathodic reduction for hole blocking material and the low reduction potential for electron transporting material in organic electroluminescent (EL) devices. The fabricated devices exhibited high performance with high current efficiency and power efficiency of 45 cd/A and 17.7 lm/W in 10 mA/cm^2, which is superior to the result of the device using BAlq (current efficiency: 31.5 cd/A and power efficiency: 13.5 lm/W in 10 mA/cm^2) as well-known hole blocker. The ITO/DNTPD/α-NPD/6% Ir(ppy)$_3$ doped CBP/2,5-bis(4-triphenylsilanyl-phenyl)-[1,3,4]oxadiazole as both hole blocking and electron transporting layer/Al device showed efficiency of 45 cd/A and maximum brightness of 3000 cd/m^2 in 10 mA/cm^2.
© 2007 Elsevier B.V. All rights reserved.

Keywords: Amorphous material; Hole blocking; Electron transporting; Oxadiazole; Phosphorescent

1. Introduction

The application of organic light-emitting devices (OLEDs) has reached a full-color display due to the advanced technology in organic materials and device processes since encourage breakthroughs [1–4]. However, some important and fundamental challenges remain, including maximization of the external quantum efficiency [5]. A major factor responsible for low device external quantum efficiency is unbalance of charge carriers in emissive materials. Most of electroluminescent (EL) materials favor injection and transport of holes rather than electrons, and therefore, the recombination of charges takes place near the cathode resulting in quenching of the excitons produced. The use of an additional hole blocking/electron transport layer between the cathode and the organic layer helps not only to block the holes passing on to the

* Corresponding authors. Tel.: +82 55 751 5296; fax: +82 55 753 6311.
E-mail addresses: ykim@gsnu.ac.kr (Y.-H. Kim), skwon@gsnu.ac.kr (S.-K. Kwon).

1566-1199/$ - see front matter © 2007 Elsevier B.V. All rights reserved.
doi:10.1016/j.orgel.2006.12.005

cathode but also to inject electrons by tunneling effect, thus increasing the efficiency and stability of such devices [6].

It is reported that hole-blocking materials for use in organic EL devices should fulfill several requirements [5,7,8]. The material must have a wide energy band-gap, a deep (high ionization potential) highest occupied molecular orbit and lowest unoccupied molecular orbit should be closely aligned with that of ETL. And, it should be readily sublimable, forming uniform amorphous films. In order to develop of fulfilling several requirements, many research groups reported that low molar mass compound or polymeric structures containing π electron deficient heterocyclic moieties such as oxadiazole, triazole, triazine, quinoline, or quinoxaline and electron deficient boron-containing or aluminum-containing amorphous materials have been utilized as a hole blocking layer and electron transporting layer [9–19]. Among them, BAlq with T_g of 92 °C and BCP with T_g of 124 °C were widely used [11]. However, a hole blocking layer and electron transporting layer still require improvement for efficient OLEDs.

Molecular and polymeric 1,3,4-oxadiazole (OXD) derivatives are the most widely studied classes of electron injection and/or hole-blocking materials, mainly because of their electron affinity and high ionization potential as well as high photoluminescence quantum yield, and good thermal and chemical stabilities [9,20–24].

In the present study, we design, synthesis, and characterization of amorphous molecular material, 2,5-bis(4-triphenylsilanyl-phenyl)-[1,3,4]oxadiazole (BTSO), that functions as good hole blocker as well as both hole blocker and electron transporting layer in the phosphorescent devices. Based on the concepts that the incorporation of rigid moieties increases glass transition temperatures (T_g) and that the enlargement of molecular size enhances the stability of the amorphous glassy state, triphenylsilylphenyl groups were introduced into the parent oxadiazole.

2. Experiment

2.1. Materials

All reagent and solvents were purchased from Aldrich Chemical Co. and Fluka. Only analytical grade quality chemicals were used. Spectroscopic grade $CHCl_3$ (Aldrich) was used for all absorption and emission experiments. All other compounds were used as received.

2.1.1. Synthesis of (4-bromophenyl)triphenylsilane

28.4 g (0.085 mol) of 2.5 M *n*-BuLi was added in the 20 g (0.085 mol) of 1,4-dibromobenzene ether solution at −78 °C. After addition, the mixture was stirred 1 h at room temperature. 30 g (0.101 mol) of triphenylsilyl chloride was added in the monolithiated 1,4-dibromobenzene at −70 °C. After stirring for 12 h, the crude product was filtered and washed with H_2O and hexane. The product was obtained by recrystallization (m.p.: 169 °C. Yield: 17.16 g, 85%). ^{1}H NMR (500 MHz, $CDCl_3$) δ (ppm): 7.59–7.53 (8H, m), 7.45–7.40 (11H, m). FT-IR (KBr, cm^{-1}): 3062 cm^{-1} (aromatic C–H), 1483 cm^{-1} (aromatic C–Si), 1061 cm^{-1} (aromatic C–Br).

2.1.2. 4-Triphenylsilanylbenzoic acid

17.5 g (0.063 mol) of 2.5 M *n*-BuLi was added in the 20 g (0.053 mol) of (4-bromophenyl)triphenylsilane ether solution at −78 °C. After addition, the mixture was stirred 1 h at room temperature. 7 g (0.159 mol) of CO_2 was added in the lithiated 4-bromophenyltriphenylsilane. After stirring for 4 h, the crude product was filtered and washed with water and hexane (m.p.: 198 °C. Yield: 15.57 g, 85%). ^{1}H NMR (500 MHz, $CDCl_3$) δ (ppm): 8.1 (2H, d), 7.7 (2H, d), 7.61–7.58 (6H, d of d), 7.5–7.4 (9H, m). FT-IR (KBr, cm^{-1}): 3451 cm^{-1} (acid OH), 3062 cm^{-1} (aromatic C–H), 1695 cm^{-1} (acid C═O), 1483 cm^{-1} (aromatic C–Si).

2.1.3. Synthesis of bis(4-tripenylsilanyl-benzo)-hydrazide

15 g (0.041 mol) of 4-triphenylsilanylbenzoic acid was reacted with thionyl chloride for 3 h. 4-Triphenylsilanylbenzoyl chloride was obtained after removing of unreacted thionyl chloride. The obtained 4-triphenylsilanylbenzoyl chloride was reacted with triethylamine and 0.67 g (0.0135 mol) of hydrazine monohydrate in the co-solvent of methylene dichloride and H_2O for 3 h at room temperature. The crude product was filtrated and recrystallized in the ethanol (m.p.: 235 °C. Yield: 5.2 g, 51%). ^{1}H NMR (500 MHz, $CDCl_3$) δ (ppm): 8.69 (2H, s), 7.85 (4H, d), 7.58–7.56 (16H, m), 7.45–7.37 (18H, m). FT-IR (KBr, cm^{-1}): 3223 cm^{-1}(NH), 3068 cm^{-1} (aromatic C–H), 1622 cm^{-1} (aromatic C═O), 1485 cm^{-1} (C–Si).

2.1.4. Synthesis of 2,5-bis(4-triphenylsilanyl-phenyl)-[1,3,4]oxadiazole

5 g (6.60 mmol) of bis(4-tripenylsilanyl-benzo)-hydrazide and 10 g of thionyl chloride was reacted

in the toluene and refluxed for 10 h. After removing of unreacted thionyl chloride, the mixture was extracted with methylene dichloride. After drying with $MgSO_4$ and removing the solvent, the crude product was purified by following column with methylene dichloride and hexane, recrystallization with ethanol (m.p.: 215 °C. Yield: 3.47 g, 72%). ^1H NMR (500 MHz, $CDCl_3$) δ (ppm): 8.3 (d of d, 4H), 7.8 (d of d, 4H), 7.6–7.5 (m, 12H), 7.4–7.3 (m, 18H). FT-IR (KBr, cm^{-1}): 3068 cm^{-1}(aromatic C–H), 1478 cm^{-1} (aromatic C–Si), 1020 and 980 cm^{-1} (oxadiazole). Elemental analysis: Calcd. for $C_{50}H_{38}N_2O_1Si_2$: C, 81.1; H, 5.14; N, 3.78; O, 2.16; Si, 7.82. Found: C, 80.95; H, 5.12%.

2.2. Instrument

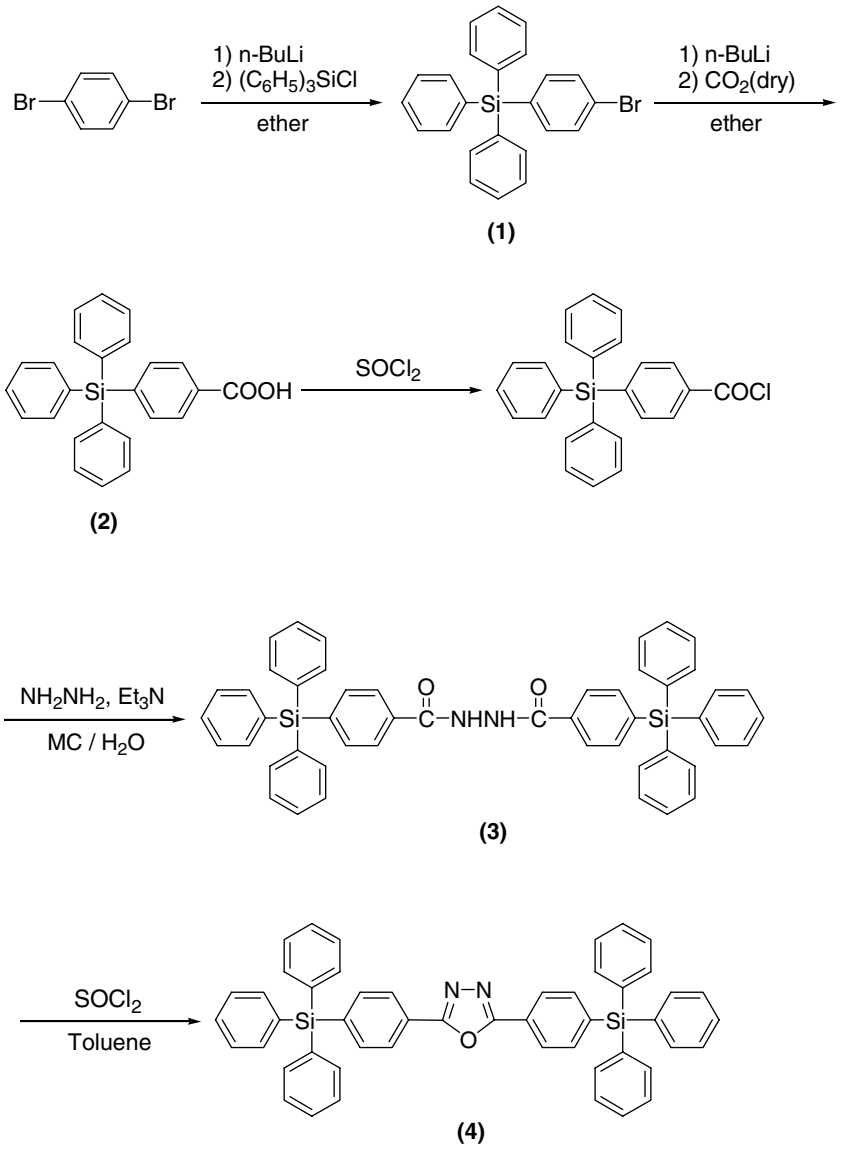
^1H NMR spectra were recorded using a Bruker AM-500 spectrometer, and chemical shifts are reported in ppm units with tetramethylsilane as internal standard. FT-IR spectra were obtained with a Bomem Michelson series FT-IR spectrometer and UV–Vis absorption spectra were obtained in chloroform on a Shimadzu UV-3100 spectrophotometer. Melting points were determined using an Electrothermal Mode 1307 digital analyzer. Thermal analysis was carried out on a Dupont TGA 2100 thermogravimetric analyzer in a nitrogen atmosphere at a rate of 10 °C/min. The photoluminescence spectra were recorded on a Perkin–Elmer LS-50 fluorometer utilizing a lock-in amplifier system with a chopping frequency of 150 Hz. Elemental analyses were performed by Leco Co. CHNS-932. Redox potentials of the compounds were determined by cyclic voltammetry (CV) using a BAS 100B electrochemical analyzer with a scanning rate at 100 mV/s. The compound coated Pt disc was measured in a three electrode compartment cell with a Pt wire counter electrode and a $Ag/AgNO_3$ (0.1 M) reference electrode. The electrolyte was 0.1 M Bu_4NClO_4 solution in anhydrous acetonitrile, and the cell was purged with argon. Ferrocene was used for potential calibration (all reported potentials are referenced against Ag/Ag^+) and for reversibility criteria.

Fabrication of EL devices: EL devices were fabricated by successive vacuum deposition of the organic materials onto an ITO-coated glass substrate at a deposition rate of 0.1 nm/s at 10^{-6} Torr. Then Al was deposited onto the organic layer. The evaporation rate and the thickness of the film were measured with a quartz oscillator. OLED performance was studied by measuring the current–voltage–luminescence (I–V–L) characteristics, EL, and PL spectra at room temperature. I–V–L characteristics, EL spectra and CIE color coordinates were measured with a Keithley SMU238 and Spectrascan PR650. EL spectra of the devices were measured utilizing a diode array rapid analyzer system (Professional Scientific Instrument Corp.). Fluorescence spectra of the solutions in chloroform were measured using a spectrofluorimeter (Shimadzu Corp.).

3. Results and discussion

The synthetic route of material is shown in Scheme 1. The mono-lithiated 1,4-dibromobenzene was reacted to give (4-bromo-phenyl)-triphenylsilane. 4-Triphenylsilanyl-benzoic acid was obtained from the reaction of lithiated (4-bromo-phenyl)triphenylsilane and CO_2. After 4-triphenylsilanyl-benzoic acid was reacted with thionyl chloride, 4-triphenylsilanyl-benzoyl chloride was reacted with hydrazine in the triethylamine, methylene dichloride and water to give bis(4-triphenylsilanyl-benzo)-hydrazide. BTSO was obtained by the dehydration of bis(4-triphenylsilanyl-benzo)hydrazide with good yield. The obtained BTSO was confirmed by various spectroscopic analyses such as NMR, IR, mass and elemental analysis. The thermal properties of BTSO were evaluated by means of thermogravimetric analysis (TGA) and differential scanning calorimetry (DSC) in a nitrogen atmosphere. Thermal analysis of BTSO reveals its high thermal stability. The decomposition temperature of it, corresponding to 5% weight loss upon heating in TGA, is around 400 °C for BTSO. The DSC of BTSO exhibits a distinct glass transition around 99 °C. This result indicates that rigid and bulky tetraphenylsilyl group having tetrahedral molecular skeleton in BTSO might mitigate the intermolecular interactions among the molecules in the solid state [25,26]. As a consequence, BTSO is able to form homogeneous and stable amorphous film by thermal evaporation which is a basic requirement for material to be used as hole blocking material in OLEDs.

Cyclic voltammetry (CV) was used to study reversible redox behavior and electrochemical stability and to obtain information about HOMO and LUMO energy values of hole and electron transport materials and to examine the barriers for charge injection. By means of an internal redox standard, ferrocene/ferrocenium for each measurement, the HOMO and LUMO energy levels were



Scheme 1.

determined from redox potentials. In order to estimate the charge injection barriers with respect to used anode (ITO) and cathode (Al) in LED configurations, the HOMO and LUMO values of the materials were determined by tacking the value of −4.8 eV as the HOMO energy level for the Fc standard system with respect to zero vacuum level as known in the literature [27,28]. Fig. 1 shows cyclic voltammograms for the cathodic reduction of BTSO. The half-wave reduction potential ($E^{red}_{1/2}$) of the compound was −1.0 V. The result indicate that the electron accepting property of the compound, which is stronger than those of boron derivatives ($E^{red}_{1/2} = -2.5$ V) and that of Alq_3 ($E^{red}_{1/2} = -2.01$ V) [1,29,30]. Thus, the obtained BTSO fulfill not only the requirement of reversible cathodic reduction for hole blocking material in organic EL devices but also the requirement of low reduction potential for electron transporting material in EL devices.

Fig. 2 shows the electronic absorption of BTSO. The BTSO showed absorption maximum at 296 nm. The optical energy band gap of BTSO was estimated to be 3.88 eV from the energy threshold of its electronic absorption spectrum. Based on the reduction potential, the LUMO energy level of BTSO was estimated to be −3.0 eV. The HOMO

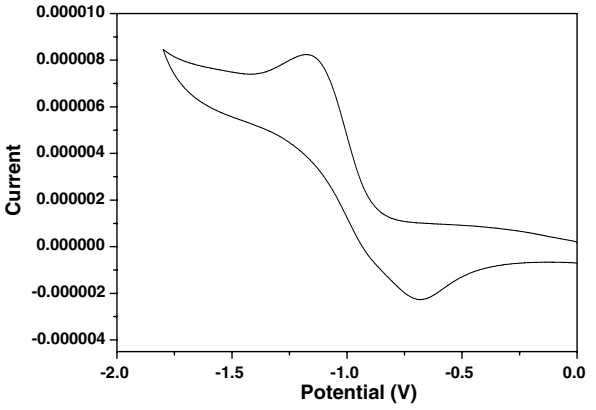


Fig. 1. Cyclic voltammogram for the cathodic reduction of BTSO.

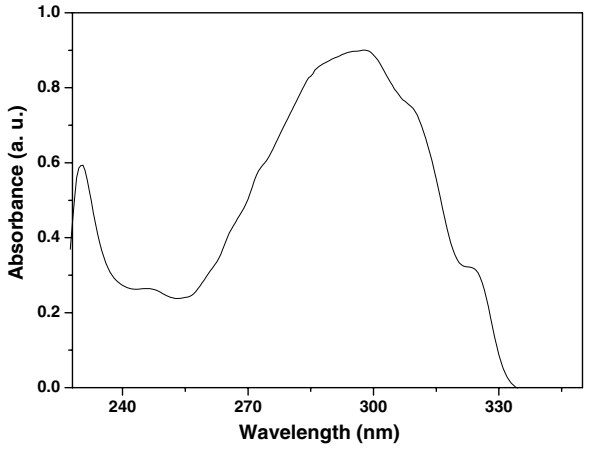


Fig. 2. The UV-absorption spectrum of BTSO in $CHCl_3$ solution.

energy level of BTSO is approximately 6.88 eV, as estimated from its optical band gap. Although the HOMO level of BTSO is obtained by the optical band gap and the LUMO level, the HOMO level is comparable with BCP which is well known for suitable hole blocking layer due to its large HOMO level (HOMO = 6.4 eV) [19,20]. From the results of HOMO and LUMO level, the obtained BTSO is expected to have not only function as good hole blocker but also double function as good hole blocker and good electron transporter.

All devices were fabricated by high vacuum thermal evaporation. The devices consisted of an indium tin oxide anode (120 nm), a 60 nm DNTPD (*N*,*N*′-[*p*-di(*m*-tolyl)aminophenyl]-*N*,*N*′-diphenyl benzidine), a 40 nm α-NPD (*N*,*N*′-di(naphtyl)-*N*,*N*′-diphenyl bendizine) hole transporting layer, a 30 nm of 4,4′-bis(*N*-carbazoyl)biphenyl (CBP) doped with 6% of $Ir(ppy)_3$ emissive layer, a 10 nm hole blocking layer, 30 nm Alq_3 electron transporting layer, and Al cathode. Fig. 3 shows the voltage–current density (*V*–*J*) and current density–luminescence (*J*–*I*) characteristics of the ITO/DNTPD/α-NPD/6% $Ir(ppy)_3$ doped CBP/BTSO as hole blocking/Alq_3/Al device and ITO/DNTPD/α-NPD/6% $Ir(ppy)_3$ doped CBP/BAlq as hole blocking/Alq_3/Al device. For the same voltage, the device with BTSO as hole blocker showed lower current density than that of the device with BAlq. On the other hand, in the same current density, the device with the BTSO as hole blocker showed higher luminance than that of device with BAlq. From the results, it is suggested that BTSO effectively blocked hole without leakage current. Moreover, the triplet energy of BTSO was

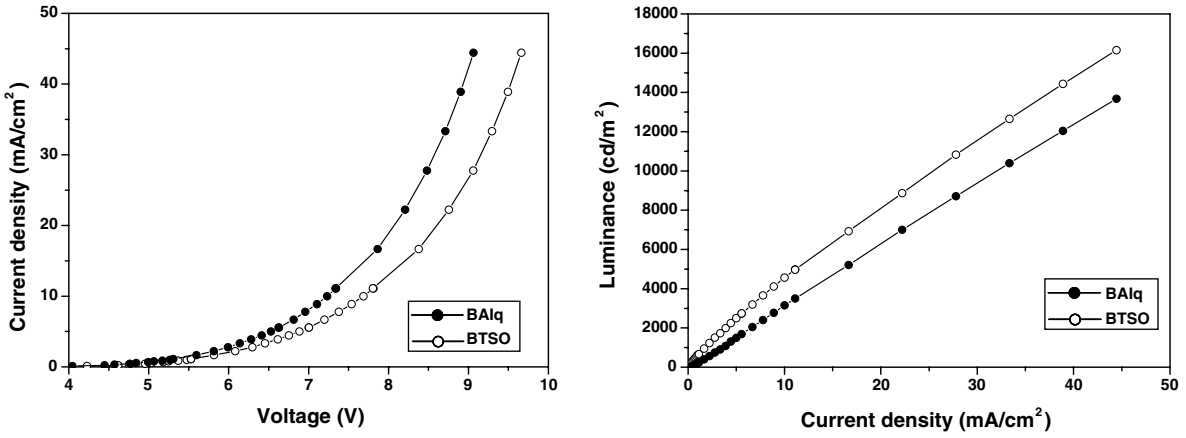


Fig. 3. The voltage–current density (*V*–*J*) (a) and current density–luminescence (*J*–*I*) (b) characteristics of the ITO/DNTPD/α-NPD/6% $Ir(ppy)_3$ doped CBP/BTSO/Alq_3/Al device and ITO/DNTPD/α-NPD/6% $Ir(ppy)_3$ doped CBP/BAlq/Alq_3/Al device.

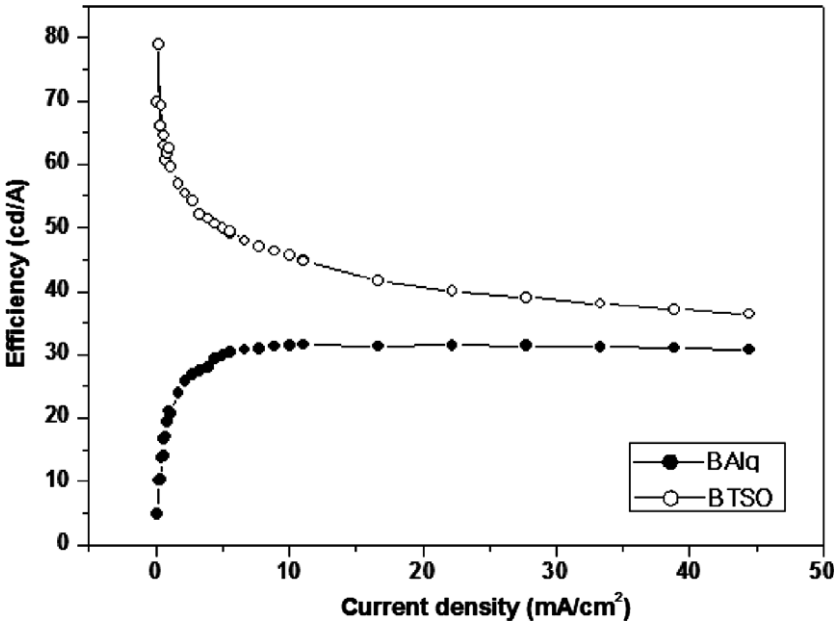


Fig. 4. The current density–current efficiency curve of the ITO/DNTPD/α-NPD/6% Ir(ppy)$_3$ doped CBP/BTSO/Alq$_3$/Al device and ITO/DNTPD/α-NPD/6% Ir(ppy)$_3$ doped CBP/BAlq/Alq$_3$/Al device.

measured to 2.85 eV. Thus, the large triplet level can be possible blocking of exciton, too. Fig. 4 shows the current density–current efficiency curve of devices. The efficiency of the device with BTSO as hole blocker showed higher than that of device with BAlq as well-known hole blocker. Especially, in the 10 mA/cm^2 which is current for driving of active device, the efficiency of the device with BTSO as hole blocker was 45 cd/A while the efficiency of the device with BAlq as hole blocker was 31.5 cd/A. The power efficiency of the device with BTSO as hole blocker was 17.7 lm/W at 10 mA/cm^2. It is proved that the obtained BTSO is effective hole blocker. The high performance of BTSO as hole blocker may be due to easy electron injection (low lying LUMO) and low lying HOMO level.

In Fig. 5, the EL spectra of the devices were compared. The device provides a main EL peak at 516 nm and additional small shoulder peak around 540 nm, indicating the emission from Ir(ppy)$_3$ triplets. The EL spectrum of device with BTSO as hole blocker was very similar with that of device with BAlq. The emitting color of device with BTSO as hole blocker showed the green emission $(x, y) = (0.296, 0.64)$ at 10 mA/cm^2 in CIE (Commission Internationale de l'Eclairage) chromaticity coordinates. The color purity of the device with BTSO as hole blocker was similar with that of BAlq $(x, y) = (0.295, 0.637)$.

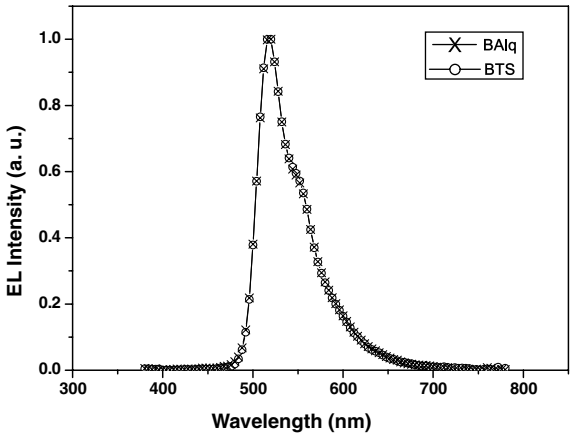


Fig. 5. The electroluminescent (EL) spectra of the ITO/DNTPD/α-NPD/6% Ir(ppy)$_3$ doped CBP/BTSO/Alq$_3$/Al device and ITO/DNTPD/α-NPD/6% Ir(ppy)$_3$ doped CBP/BAlq/Alq$_3$/Al device.

For the studying of the double function of BTSO, we studied the device performance by varying the thickness of BTSO as hole blocking layer and Alq$_3$ as electron transporting layer. Table 1 summarized the results of device performance. Although BTSO layer is gradually increased instead of Alq$_3$ layer as electron transporting layer, the device performance is not changed. Fig. 6 showed voltage and efficiency characteristics of ITO/DNTPD/α-NPD/6% Ir(ppy)$_3$ doped CBP/BTSO as hole blocking and electron transporting layer/Al device. In the

Table 1
Summary of the performance of BTSO based OLEDs

	$X = 50$	$X = 100$
$Y = 350$	10.75 V at 10 mA/cm^2, 3002 cd/m^2	
$Y = 200$	10.18 V at 10 mA/cm^2, 2915 cd/m^2	
$Y = 150$	10.97 V at 10 mA/cm^2, 3111 cd/m^2	10.38 V at 10 mA/cm^2, 3286 cd/m^2
$Y = 100$	10.75 V at 10 mA/cm^2, 3108 cd/m^2	10.10 V at 10 mA/cm^2, 3315 cd/m^2
$Y = 50$	11.04 V at 10 mA/cm^2, 3008 cd/m^2	10.33 V at 10 mA/cm^2, 3225 cd/m^2
$Y = 0$	8.21 V at 10 mA/cm^2, 1606 cd/m^2	

The device configuration is DNTPD (X Å)/NPD (350 Å)/CBP + Ir(ppy)3 (8 wt%) (200 Å)/BTSO(Y Å)/Alq_3 (350–Y Å)/Al.

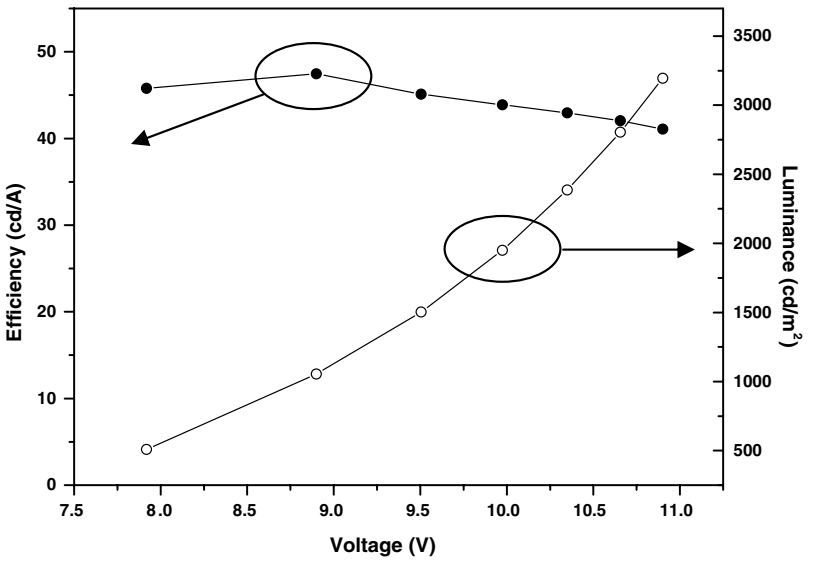


Fig. 6. Voltage and efficiency characteristics of ITO/DNTPD/α-NPD/6% $Ir(ppy)_3$ doped CBP/BTSO/Al device by using BTSO as hole blocking and electron transporting layer.

10 mA/cm^2, the device efficiency and maximum brightness was 45 cd/A and 3000 cd/m^2, respectively. From the results, it is also proved that BTSO effectively performed dual function as hole blocker and electron transporter. The good electron transporting ability of BTSO may be due to oxadiazole unit, which is well-known electron transporting material.

4. Conclusion

A bis(tetraphenylsilylated)-oxadiazole-containing amorphous molecular material that function as effective hole blocker as well as effective electron transporting material has been created. It forms uniform amorphous thin film by vacuum deposition without recrystallization. It is characterized by high oxidation potentials, low lying HOMO and LUMO level, large HOMO–LUMO energy gap and large triplet level. The synthesized BTSO has been proven to function as excellent hole blockers, enabling the fabrication of high-performance phosphorescent EL device. The fabricated devices exhibited high performance with high current efficiency and power efficiency of 45 cd/A and 17.7 lm/W in 10 mA/cm^2, which is superior to the result of the device using BAlq as well-known hole blocker. Furthermore, BTSO was proven to dual function as electron transporter as well as good hole blocker. ITO/DNTPD/α-NPD/6% $Ir(ppy)_3$ doped CBP/BTSO as hole blocking and electron transporting layer/Al device also showed high performance with high efficiencies of 45 cd/A in 10 mA/cm^2.

Acknowledgments

This work was supported by Korea Research Foundation Grant (KRF-2000-005-D00251), and LG Electronics and Ministry of Commerce, Industry and Energy (00014756).

References

[1] M. Kinoshita, H. Kita, Y. Shirota, Adv. Funct. Mater. 12 (2002) 780.
[2] Y. Shirota, J. Mater. Chem. 10 (2000) 1.
[3] M.R. Robinson, S. Wang, A.J. Heeger, G.C. Bazan, Adv. Funct. Mater. 11 (2001) 413.
[4] J.C. Ostrowski, R.A. Hudaok Jr., M.R. Robinson, S. Wang, G.C. Bazan, Chem. Eur. J. 7 (2001) 4500.
[5] C. Wang, G.-Y. Jung, Y. Hua, C. Pearson, M.R. Bryce, M.C. Petty, A.S. Batsanov, A.E. Goeta, J.A.K. Howard, Chem. Mater. 13 (2001) 1167.
[6] C. Jonda, M. Huppauff, Chem. Mater. 10 (1998) 3620.
[7] K. Okumoto, Y. shirota, Chem. Mater. 15 (2003) 699.
[8] X. Duan, Z. Jiang, G. Yu, P. Lu, Y. Liu, X. Xu, D. Zhu, Thin Solid Films 478 (2005) 121.
[9] M. Strukelj, F. Papadimitrakopoulos, T.M. Miller, L.J. Rothberg, Science 267 (1995) 1969.
[10] T. Yamamoto, J. Polym. Sci. Part A: Polym. Chem. 34 (1996) 997.
[11] B.A. Andrade, S.R. Forrest, A.B. Chwang, Appl. Phys. Lett. 83 (2003) 3858.
[12] T. Yamamoto, K. Sugiyama, T. Kushida, T. Inoue, T. Kambara, J. Am. Chem. Soc. 118 (1996) 3930.
[13] H.Q. Tang, H.X. Liao, L.H. Zhu, Chem. Phys. Lett. 381 (2003) 605.
[14] R. Fink, C. Frenz, M. Thelakkat, H.-W. Schmidt, Polym. Prep. 38 (1997) 323.
[15] J. Kido, C. Ontaki, K. Hongawa, K. Oknyama, K. Nagai, Jpn. J. Appl. Phys. 32 (1993) L917.
[16] C. Adachi, R.C. Kwong, S.R. Forrest, Org. Electron. 2 (2001) 37.
[17] R.C. Kwong, M.R. Nugent, L. Michaiski, T. Ngo, K. Rajan, Y.-J. Tung, M.S. Weaver, T.X. Zhou, M. Hack, M.E. Tomson, S.R. Forrest, J.J. Brown, Appl. Phys. Lett. 81 (2002) 162.
[18] P.E. Burrows, S.R. Forrest, T.X. Zhou, L. Michalski, Appl. Phys. Lett. 76 (2000) 2493.
[19] I.G. Hill, A. Kahn, J. Appl. Phys. 86 (1999) 4515.
[20] D.C. Shin, J.H. Ahn, Y.H. Kim, S.K. Kwon, J. Polym. Sci. Polym. Chem. 38 (2000) 3086.
[21] Y.H. Kim, S.K. Kwon, J. Appl. Polym. Sci. 100 (2006) 2151.
[22] J. Battenhausen, P. Strohrigel, Adv. Mater. 8 (1996) 507.
[23] C. Adachi, T. Tustui, S. Saito, Appl. Phys. Lett. 55 (1989) 1489.
[24] H. Zhang, B. Seggern, H.W. Kraabel, A. Schmidt, A.J. Heeger, Synth. Met. 72 (1995) 185.
[25] J.U. Kim, H.B. Lee, J.S. Shin, Y.H. Kim, Y.K. Joe, H.Y. Oh, C.G. Park, S.K. Kwon, Synth. Met. 27 (2005) 150.
[26] X. Ren, J. Li, R.J. Holmes, P.I. Djurovich, S.R. Forrest, M.E. Thompson, Chem. Mater. 16 (2004) 4743.
[27] Y.H. Kim, D.C. Shin, S.H. Kim, C.H. Ko, H.S. Yu, Y.S. Chae, S.K. Kwon, Adv. Mater. 13 (2001) 1690.
[28] Y.H. Kim, H.C. Jung, S.H. Kim, K.Y. Yang, S.K. Kwon, Adv. Funct. Mater. 15 (2005) 1799.
[29] Y. Shirota, Y. Kuwabara, H. Inada, T. Wakimoto, H. Nakada, Y. Yonemoto, S. Kawami, K. Imai, Appl. Phys. Lett. 65 (1994) 807.
[30] Y. Shirota, Y. Kuwabara, D. Okuda, R. Okuda, H. Ogawa, H. Inada, T. Wakimoto, H. Nakada, Y. Yonemoto, S. Kawami, K. Imai, J. Lumin. 72 (1997) 985.

Available online at www.sciencedirect.com
ScienceDirect
Organic Electronics 8 (2007) 357–366
Organic Electronics
www.elsevier.com/locate/orgel

Blue electroluminescence of silyl substituted anthracene derivatives

Takashi Karatsu [a,*], Reiko Hazuku [a], Michihiro Asuke [b], Atsuko Nishigaki [b,1], Shiki Yagai [b], Yoshiyuki Suzuri [c], Hiroshi Kita [c], Akihide Kitamura [b]

[a] Graduate School of Science and Technology, Chiba University, 1-33 Yayoi-cho, Inage-kn, Chiba 263-8522, Japan
[b] Department of Materials Technology, Faculty of Engineering, Chiba University, 1-33 Yayoi-cho, Inage-kn, Chiba 263-8522, Japan
[c] Konica Minolta Technology Center, Inc., 1 Sakura-chou, Hino, Tokyo 191-8511, Japan

Received 23 February 2006; received in revised form 25 December 2006; accepted 28 December 2006
Available online 24 January 2007

Abstract

The substitution of the bulky substituents, such as the triphenylsilyl groups, on the 9,10-positions of anthracene produced a remarkable increase in Φ_f, and the substituents controlled the intermolecular stacking by diminishing the electroplex formation and inter- and intra-molecular photochemical reactions. Organic light-emitting diode (OLED) devices composed of these anthracene derivatives showed highly pure blue electroluminescence (EL).
© 2007 Elsevier B.V. All rights reserved.

PACS: 85.60.Jb; 78.55.Kz; 33.20.−t; 33.50.−j; 33.50.Dq

Keywords: Electroluminescence; Blue color; Silylanthracene; Steric effect of dopant

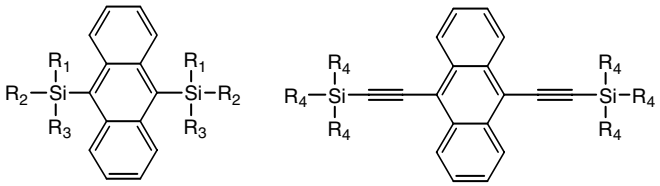
1. Introduction

Recently, efficient light emitting materials applicable for organic electroluminescent (EL) materials have been actively investigated. Especially, electrophosphorescent iridium and platinum complexes have attracted much attention as green and red emitting materials because of their marvelous device performance [1–6]. However, for a blue device, the materials for such a device are still under development, and low molecular weight materials are still useful for blue-emission.

In this study, the photophysical characteristics of the silylanthracenes were investigated to determine their suitability as candidates for such materials. Anthracene (Ant) was the first material producing an EL. However, it has problems with its photophysical and photochemical properties. Therefore, its performance is inferior for practical applications [7–11]. However, Ant and its derivatives have still been attracting attention from the viewpoint of application and basic science. For the recent rapid developments in organic electronic devices, the importance of molecular stacking control and

* Corresponding author. Tel.: +81 43 290 3366; fax: +81 43 290 3039.
E-mail address: karatsu@faculty.chiba-u.jp (T. Karatsu).
[1] Present address: Faculty of Science, Toho University, Miyama 2-2-1, Funabashi, Chiba, 274-8510 Japan.

1566-1199/$ - see front matter © 2007 Elsevier B.V. All rights reserved.
doi:10.1016/j.orgel.2006.12.009



Me3: R_1, R_2, R_3=CH_3
Me2Ph: R_1, R_2=CH_3, R_3=Ph
MePh2: R_1=CH_3, R_2, R_3=Ph
Ph3: R_1, R_2, R_3=Ph

Me3E: R_4=CH_3
Ph3E: R_4=Ph

Scheme 1.

adding a new functionality, such as charge transporting abilities, etc., are increasing [12–18].

The lowest singlet excited state, Ant undergoes about a 30% fluorescence and 70% intersystem crossing to the triplet state [19]. The excited state Ant has the potential to react with another Ant molecule through the excimer to produce the [4 + 4] cyclization adduct [20], react with oxygen to give the endoperoxide and then produce anthraquinone and other products [21]. Those products are usually non-emissive.

Our strategies to design materials for an OLED are very simple, i.e., the introduction of bulky substituent on the 9,10-position of Ant. This strategy produces a significant increase in the fluorescence quantum yield (Φ_f) as well as preventing intermolecular stacking that decreases the device lifetime and color purity. It has been reported that the introduction of silyl groups at the 9,10-positions of Ant results in a significant increase of Φ_f [22–26], which is rationally explained by the alteration of the relative position of the energy levels of S_1 and T_2 governing the efficiency of the intersystem crossing (Φ_{isc}) and Φ_f [27]. In addition to the energy level positioning, these silyl groups are useful for introducing a bulky substituent to control the molecular stacking since the typical Si–C bond (1.90 Å) is longer than the C–C bond (1.54 Å) [28]. There have been many reports using twisted structures to design hole transporting aryl amines, and there have been some similar attempts including the introduction of bulky substituents as the emitting dopant [17,18]. However, the introduction of bulky substituents through the C–C bond results in bending of the Ant plane due to steric hindrance, which in turn induces intramolecular cyclization between the 9- and 10-positions of the Ant that produces a non-emissive Dewer-benzene-type product [29]. A spherical shape prevents stacking of the molecules, intermolecular exciplex/electroplex formation, and therefore, photochemical cycloaddition. The formation and emission of the electroplex formed between the dopant molecule and host molecule or polymers, and their formation affect the color purity and lifetime of the device [30–39]. The molecular design proposed here would be one of the methods to control the formation of the electroplex. Anthony and us have already reported that an OLED device consisting of ethynylanthracene derivatives emit a green EL [40,41]. X-ray crystallography showed perpendicular alignment of the silylethynylanthracene molecules [41a] which decreased the stacking. Silylethynyl groups produce a higher radiative rate constant, but a decreased EL efficiency by self-absorption due to a small Stokes shift. In this paper, their photophysical characteristics are compared to those of the silylanthracenes. In addition, after changing the bulkiness of the substituents by four silylanthracenes, the performance of the OLEDs were compared.

The compounds examined in this study were anthracenes having silyl or silylethynyl groups, trimethylsilyl-(**Me3**), dimethylphenylsilyl-(**Me2Ph**), methyldiphenylsilyl-(**MePh2**), triphenylsilyl-(**Ph3**), trimethylsilylethynyl-(**Me3E**), and triphenylsilylethynyl-(**Ph3E**) on their 9,10-positions (Scheme 1). Compounds containing silane atoms have been widely investigated, from the interest in their charge transportability and high triplet energies, those are important for the host of the electrophosphorescent device [42–45].

2. Results and discussion

2.1. Photophysical characteristics in solution

Fig. 1 shows the absorption and emission spectra of **Me3**, **Me2Ph**, **MePh2**, **Ph3**, **Me3E** and **Ph3E** in cyclohexane. In the absorption spectra of the **Me3–Ph3** series, the molar extinction coefficients

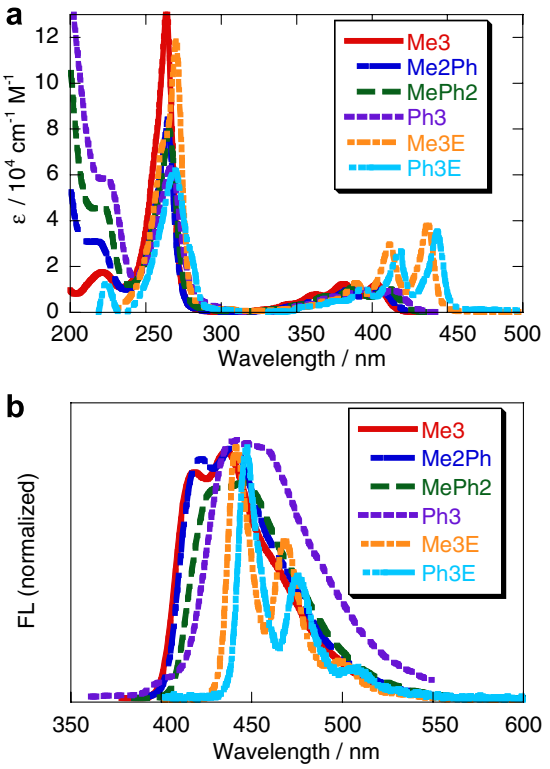


Fig. 1. Absorption (a) and fluorescence (b) spectra of 9,10-bissilylanthracenes in cyclohexane.

(ε) of ^1L_a band around 400 nm were not affected by the substituents. The ε of the ^1B_b band around 260 nm decreased and the ^1C_b band around 230 nm increased upon increasing the bulkiness of the substituent. The absorption maximum of the ^1L_a band of **Ph3E** shifts by 6 nm in comparison with that of **Me3E**, and much larger shifts (30–40 nm) were observed for the **Me3–Ph3** group. The molar extinction coefficient of these bands of **Me3E** and **Ph3E** are twice as high as those of **Me3–Ph3**. This well coincides with the increased transition momentum of this band (along short axes of Ant) However, a much smaller shift was observed for the ^1B_b band and the order of magnitude of ε is non-definitive by substitution.

Fig. 1b shows the fluorescence spectra in argon-purged cyclohexane. Kyushin et al. revealed an increased fluorescence quantum yield (Φ_f) by substitution of the silyl groups on Ant [23]. There are numerous reports concerning this point for Ant derivatives and for the parent Ant molecules. Kellogg estimated the energy levels of T_2 (26050 cm^{-1}) from the data for the phosphorescence 0,0 band and $T_2 \leftarrow T_1$ absorption band [27]. This is quite close to the fluorescent S_1 state

Table 1
Absorption and fluorescence characteristics

Compounds	$\lambda^{abs}_{0,0}$ (nm)	$\lambda^{f}_{0,0}$ (nm)	Stokes shift (cm^{-1})	τ_S (ns)	Φ_f	k_f (10^7 s^{-1})
Ant	375	379	281	4.90[a]	0.36[a]	7.4
Me3	403	418	891	12.1	0.92	7.6
Me2Ph	406.5	422	904	10.4	0.85	8.2
MePh2	410	432	1242	9.85	0.88	8.9
Ph3	413.5	443	1582	10.5	0.77	7.3
Me3E	473	441	208	5.92	0.85	14
Ph3E	443	447	202	4.97	0.84	17

[a] Values from Ref. [1].

(26,700 cm^{-1}), and the relative energy level of the S_1 and T_2 states determines Φ_f and the intersystem crossing quantum yield (Φ_{isc}). Though there are many data for the relation of the energy levels and the yields for the Ant derivatives [27,46], it is hard to apply such a technique to the present case because no phosphorescence was observed for the silylanthracenes and silylethynylanthracenes.

Table 1 summarizes the photophysical characteristics of Ant and its derivatives examined in argon-purged cyclohexane. The fluorescence lifetime (τ_s) and Φ_f have relationships with the radiative and intersystem crossing rate constants as shown in the following equations (1)–(3) and therefore, derived as shown in Table 1:

$$\tau_S = \frac{1}{k_f + k_{isc}} \quad (1)$$

$$\Phi_f = \frac{k_f}{k_f + k_{isc}} \quad (2)$$

$$k_f = \frac{\Phi_f}{\tau_S} \quad (\Phi_f = k_f \tau_S) \quad (3)$$

The characteristic parameters in Table 1 are plotted in Fig. 2. An increase in Φ_f and elongation of τ_S, without a change in k_f between Ant and **Me3–Ph3** indicates that a decrease in the intersystem crossing rate is an important factor. Due to the fact that the main deactivation paths of Ant are the fluorescence and intersystem crossing, a decrease in the intersystem crossing rate constant without changing the fluorescence radiative decay rate constant elongates τ_S and enlarges Φ_f. However, for **Me3E** and **Ph3E**, an increased k_f and slight decrease in k_{isc} becomes the main factor for a large Φ_f. The increasing k_f is explained by the large transition momentum (μ). Since the momentum μ is proportional to the molar absorptivity, molecules having a large ε generally show a large k_f [47]. In the present system, ε of the

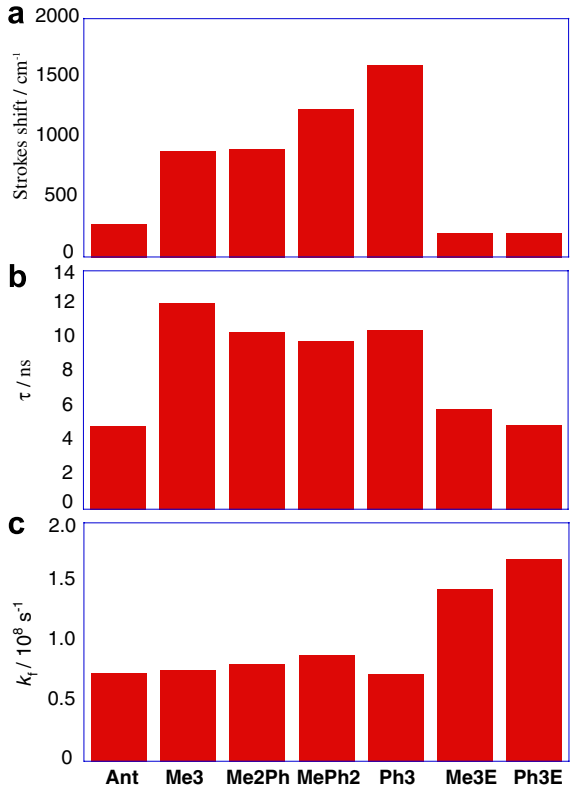


Fig. 2. Stokes shift (a), fluorescence lifetime (b), and radiative rate constant of anthracene derivatives in argon-purged cyclohexane.

^1L_a band of **Me3E** and **Ph3E** are more than twice as large as Ant and **Me3–Ph3**. A small Stokes shift also provides a better overlap of the wave functions.

Table 2 summarizes the redox potentials of **Me3–Ph3** obtained by cyclic voltammetry in argon-purged acetonitrile using a Ag^+/AgCl electrode as a reference. All the potentials were determined by the peak potentials since the voltammograms were found to be irreversible. Since the oxidation and reduction potentials correspond to the HOMO and LUMO energy levels, respectively, the lowest excitation energies can be estimated by the ΔE ($=E_{ox} - E_{red}$), which can be converted to wavelengths. The substitution of the bulky triphenylsilyl groups increased the HOMO and LUMO energy levels based on the redox potential measurements, however, the influence is not very significant for HSOMO of the excited molecules, since the bond lengths in the excited state are more elongated than those in the ground state. Therefore, the Stokes shift values observed during the fluorescence measurement shown in Table 1 were in the order of the expected steric hindrance.

Table 2
Redox potentials measured in acetonitrile

Compds	E_{red} (V)[a]	E_{ox} (V)[a]	ΔE (V)	ΔE (kJ mol^{-1})	λ[b] (nm)
Me3	−1.15	1.55	2.80	64.6	443
Me2Ph	−1.24	1.69	2.93	67.6	423
MePh2	−1.27	1.67	2.94	67.8	422
Ph3	−1.34	1.63	2.97	68.5	418

[a] Ag^+/AgCl as a reference electrode.
[b] Calculated by ΔE values derived from redox potentials.

2.2. Performance of OLED devices

Fig. 3 shows the typical configuration in a fabricated multilayer OLED device and molecular structures of the used materials. Fig. 4 shows the electroluminescence (EL) spectra from a device fabricated with 5% **Me3–Ph3** as the dopant in CBP (host). The concentration of the dopant in CBP is estimated by monitoring the co-sublimation rates by a couple of quartz oscillator thickness meter. The EL spectra were measured with a 10-V driving voltage. The emission spectral peaks shifted to a longer wavelength by increasing the dopant concentrations from 1.3% to 5.0%, and almost lost the vibrational fine structures compared with those measured in cyclohexane, and this partial disappearance of the highest energy emission band is due to self-absorption. The power efficiency of the 5% and 1.3% doped devices were 1.2 and 0.75 lm/W at 5 V, respectively, however, no difference was observed at a 15 V applied voltage. In addition, the external quantum efficiency behaves similarly. The external quantum efficiency was 1.6% and 1.2% at the 0.07 mA/cm^2 low current density for the 5% and 1.3% doping devices, respectively. This difference disappeared at a current density greater than 100 mA/cm^2. In all cases, a pure blue EL was observed. Their CIE (Commission Internationale de L'Éclairage) chromaticity coordinates are shown in the inset of Fig. 4. Especially, the coordinate of **Ph3** (x, $y = 0.155$, 0.145) is close to pure blue. The side band slightly affected the color coordinate shift in the green direction. Devices composed of **Me3E** and **Ph3E** without using a host and hole transporting layer were reported, and they give a green EL with a significant amount of self-absorption [30].

Fig. 5a–d show the basic properties of OLED devices composed of **Ph3**. Characterization of the devices was performed using the semilogarithmic

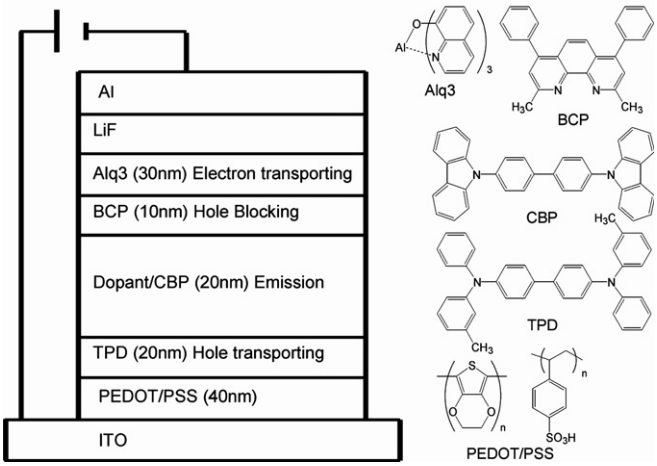


Fig. 3. Schematic cross section of the multilayered OLED device and chemicals used for fabrication.

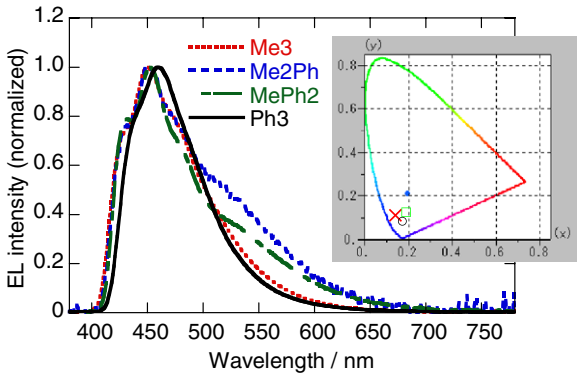


Fig. 4. EL spectra for **Me3–Ph3** (5% doped in CBP) at 10 V applied voltage. Inset is CIE chromaticity coordinates of EL devices, **Me3** (○), **Me2Ph** (●), **MePh2** (□), and **Ph3** (×) at 10 V applied voltage.

current versus voltage plot (a), the double logarithmic luminance versus current density plot (b), the logarithmic current density versus external quantum efficiency plot (c), and the relationship of power efficiency vs. driving voltage plot (d). These behaviors showed the reversibility versus the up and down change in the voltage or current. No significant difference between four devices (**Me3–Ph3**) was observed for the double logarithmic luminance versus current density plot in Fig. 5b, however, the behaviors shown in Fig. 5a, c and d are classified into two groups, i.e., **Me3** + **Ph3** and **Me2Ph** + **MePh2**. The current density (Fig. 5a), external quantum efficiency (Fig. 5c), and power efficiency (Fig. 5d) of the **Me3** and **Ph3** groups takes higher values for lower applied voltages or current densities. This may be related to the molecular shape and formation of the electroplex.

Table 3 shows the performance of the 10-V driven devices containing 5% **Me3–Ph3** as the dopant. Their external quantum efficiencies were ca. 1%, and the highest case is ca. 2% for **Ph3** (Fig. 5c). They are lower than the theoretical efficiency (5%), even dopants having fluorescence quantum yields near unity. This may be explained by the low recombination probability between hole and electron at the interface area, and details will be explained later.

In Fig. 4, the EL spectra of **MePh2** and **Me2Ph** have a tail around 500 nm. These new emission sub-bands appeared around 500 nm for **MePh2**, **Me2Ph**, and **Me3**. These sub-bands strongly appeared relative to the usual fluorescence around 450 nm at low driving voltages. The relative intensities (I_{500nm}/I_{450nm}) decreased by increasing the driving voltage, and also the intensity changes showed a reversibility versus the driving voltages. The typical driving voltage dependence of the EL spectra of a device composed of **Me3** is shown in Fig. 6a. No such luminescence was observed for **Ph3**. The origin of such an emission sub-band was investigated by the following controlled experiments.

First, the possibility that this emission come from Alq3 was examined. Since Alq3 shows fluorescence around 500 nm, therefore, we fabricated a device without the Alq3 layer, and if the hole blocking layer is insufficient, the device may exhibit a green fluorescence. However, no effect on the spectral change was observed as shown in Fig. 6b. Second, complexzation between the dopant **Me3** and host CBP were examined. **Me3** and CBP were co-evaporation on a

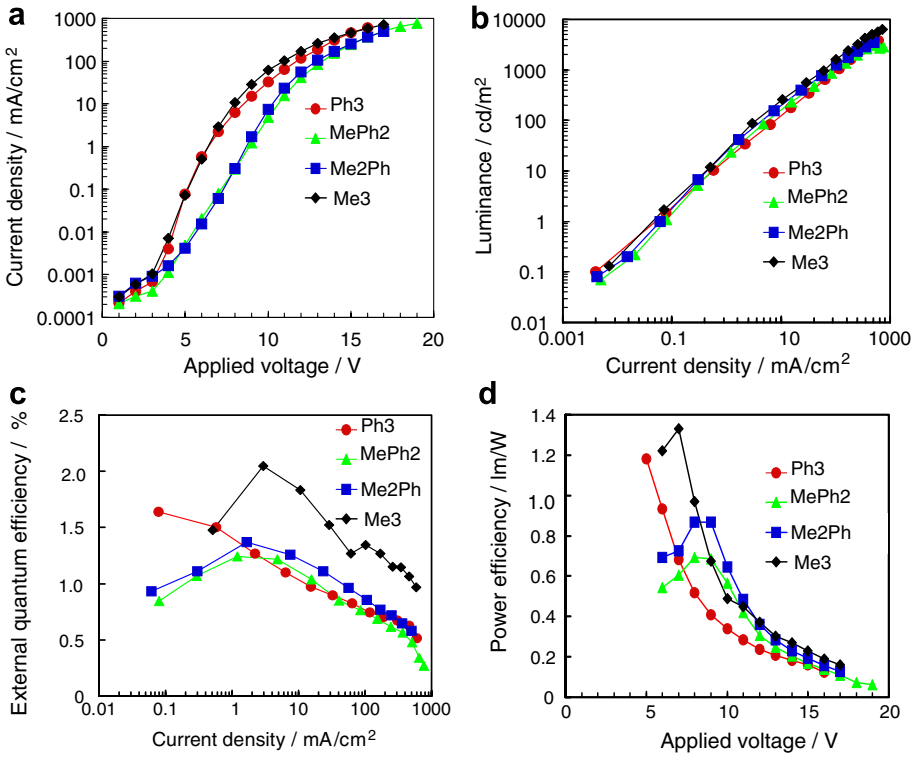


Fig. 5. Characterization of devices, semilogarithmic current versus voltage plot (a), double logarithmic luminance versus current density plot (b), logarithmic current density versus external quantum efficiency plot (c), and power efficiency vs. driving voltage plot (d).

Table 3
Performance of devices fabricated by 5% doping concentration in CBP at 10 V driving voltage

Dopant	Current density (mA/cm^2)	Luminance (cd/m^2)	External quantum efficiency (%)	Current efficiency (cd/A)	Power efficiency (lm/W)	λ_{max} (nm)	Color coordinate (x, y)
Me3	61.2	950	1.27	1.55	0.49	450	0.162, 0.151
Me2Ph	7.48	154	1.26	2.06	0.65	451	0.193, 0.213
MePh2	4.76	85.6	1.20	1.80	0.56	453	0.189, 0.186
Ph3	32.5	349	0.90	1.08	0.34	460	0.155, 0.145

quartz plate and the photoluminescence (PL) was examined. The PL spectra obtained after various excitation wavelengths and their excitation spectra were measured and are shown in Fig. 7. However, the emission sub-band could not be observed by photoexcitation.

The reason for this EL driving voltage dependence is not clear at this moment. However, this interesting voltage reversibility could be tentatively explained as follows. Extremely low concentration aggregates or exciplexes, which are difficult to observe by photoexcitation, between the dopant and host, or dopant and charge transporting materials at the interface (dopant and TPD or BCP), were more efficiently produced the EL at a lower driving voltage. The exciplex has a higher charge or excitation energy accepting ability but has lower EL efficiency. However, these sites are saturated under the condition of a higher applied voltage, i.e., higher current density, and emitting area shifts into central part of emitting layer from the interface. This produce exciton of dopant more efficiently, that has higher EL efficiency than exciplex. The difference in this interesting voltage reversibility between the substrate is mainly explained by the bulkiness of the silyl groups, because of no signifi-

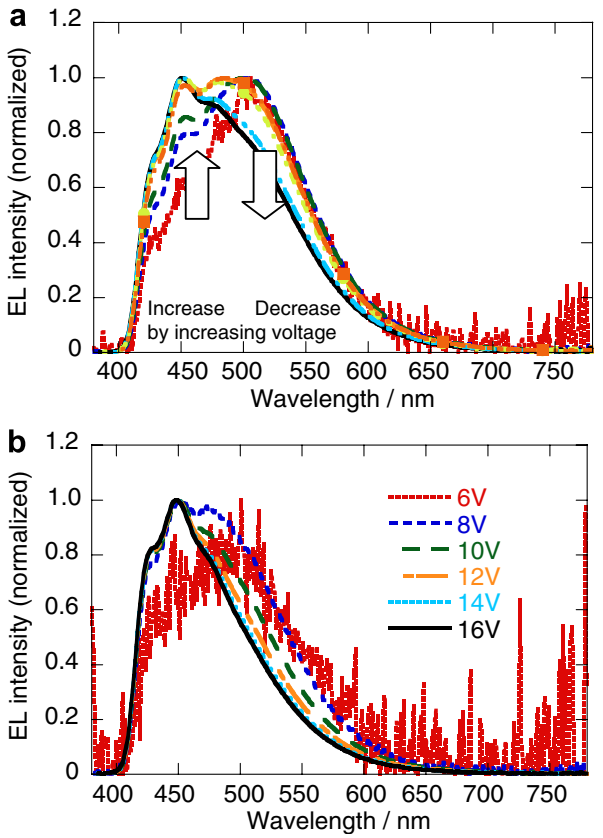


Fig. 6. EL spectra of **Me3**; driving voltage was shifted up and down (a), and the same reversible change was observed without the Alq3 layer (b).

cant difference in the optical spectral data and redox potentials. Fig. 8a and b show the space filling models of **Me3** and **Ph3** based on their DFT calculation results, respectively (for **Me3**, this was similar to the reported X-ray crystallographic structure [22]). Not

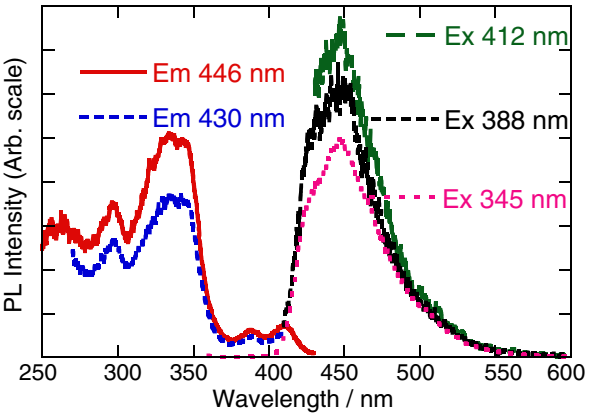


Fig. 7. PL spectra and excitation spectra of CBP and **Me3** deposited on a quartz plate.

only both surfaces of Ant are completely covered by two triphenylsilyl groups for **Ph3**, but also the spherical shape prevents the stacking. The phenyl groups may act as spacers without reducing charge recombination probability as a dopant. Our several attempts to produce a single crystal to measure X-ray crystallography were unsuccessful.

The higher external quantum efficiency of **Ph3** at smaller current density than others (Fig. 5c, left side) and the largest drop of the efficiency of **Me3** imply that the exciplex formation at the interface is inefficient for **Ph3**, and this agrees well with the above consideration.

There have been some reports on driving voltage dependent EL spectral change. This might be applicable to the device that changes color by the driving voltage. The experiments designed to elucidate the mechanism and develop such a device are currently underway.

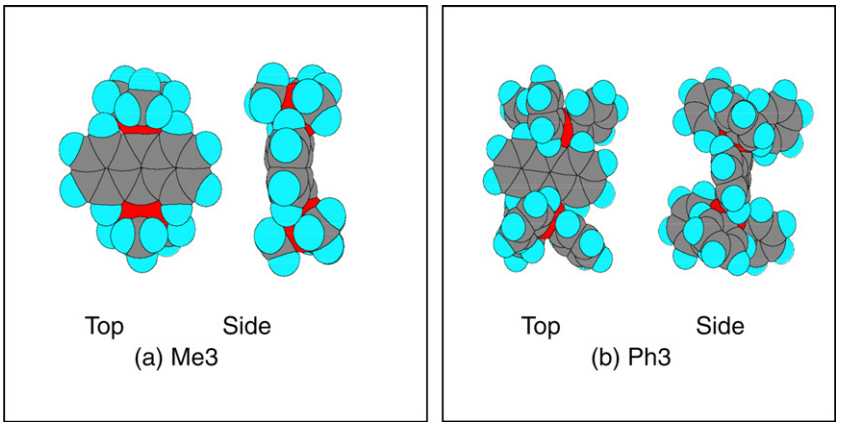


Fig. 8. Side and top views of space-filling models of **Me3** and **Ph3** optimized by DFT/B3LYP(6-31G*) method.

3. Experimental

3.1. Materials

In a typical run, 2.988 g (8.893 mmol) of 9,10-dibromoanthracene to which 8.0 ml (53.0 mmol) of tetramethylenediamine (TMEDA) was added in 72 ml of dry THF and 24 ml of dry ether, was lithiated with 17.9 mmol of *n*-BuLi at −50 to −60 °C. A 2.25 ml (17.9 mmol) aliquot of chlorosilanes was then added to give 9,10-bissilylanthracenes using a reported method [23]. The reaction mixture was poured into benzene and washed with water, and the organic layer was isolated and dried over sodium sulfate. After evaporation of the solvent, the product was isolated by flash column chromatography using hexane (**Me3**), hexane:benzene = 10:2 (**Me2Ph**), hexane:benzene = 2.2:1 (**MePh2**), and hexane: $CHCl_3$ = 1:2 (**Ph3**) mixture. The compounds were purified by crystallization in hexane or a hexane:benzene mixture. The yield was usually 3.3–25%. The ^{1}H NMR spectra were recorded using a JEOL LA400 spectrometer.

3.1.1. 9,10-Bis(trimethylsilyl)anthracene (*Me3*)

^{1}H NMR ($CDCl_3$, TMS), $\delta = 0.67$ (s, 18 H, –CH_3), 7.386 (d, $J = 6.766$, 2H, Ar–H), 7.394 (d, $J = 6.766$, 2H, Ar–H), 8.354 (d, $J = 6.765$, 2H, Ar–H), 8.362 (d, $J = 6.765$, 2H, Ar–H).

3.1.2. 9,10-Bis(dimethylphenylsilyl)anthracene (*Me2Ph*)

Yield was 0.099 g (0.222 mmol, 15.1%). ^{1}H NMR ($CDCl_3$, TMS), $\delta = 0.869$ (s, 12 H, –CH_3), 7.253 (d, $J = 6.283$, 2H, Ar–H), 7.262 (d, $J = 7.008$, 2H, Ar–H), 7.33–7.38 (m, 6H, Ph–H), 7.62–7.64 (m, 4H, Ph–H), 8.279 (d, $J = 7.007$, 2H, Ar–H), 8.288 (d, $J = 7.007$, 2H, Ar–H). Anal. Calcd for $C_{30}H_{30}Si_2$: C, 80.66; H, 6.77%. Found: C, 80.46; H, 6.71%.

3.1.3. 9,10-Bis(methyldiphenylsilyl)anthracene (*MePh2*)

Yield was 0.068 g (0.119 mmol, 11.1%). ^{1}H NMR ($CDCl_3$, TMS), $\delta = 1.08$ (s, 6 H, –CH_3), 6.995 (d, $J = 6.765$, 2H, Ar–H), 7.004 (d, $J = 7.007$, 2H, Ar–H), 7.34–7.39 (m, 12H, Ph–H), 7.57–7.59 (m, 8H, Ph–H), 8.087 (d, $J = 6.766$, 2H, Ar–H), 8.095 (d, $J = 7.008$, 2H, Ar–H). Anal. Calcd for $C_{40}H_{34}Si_2$: C, 84.16; H, 6.00%. Found: C, 83.94; H, 6.03%.

3.1.4. 9,10-Bis(triphenylsilyl)anthracene (*Ph3*)

Yield was 1.735 g (2.5 mmol, 25%). m.p. 108 °C. ^{1}H NMR ($CDCl_3$,TMS), $\delta = 6.778$ (d, $J = 7.007$, 2H, Ar–H), 6.786 (d, $J = 6.766$, 2H, Ar–H), 7.24 – 7.41 (m, 12H, Ph–H), 7.63 – 7.66 (m, 18H, Ph–H), 8.037 (d, $J = 7.007$, 2H, Ar–H), 8.047 (d, $J = 6.766$, 2H, Ar–H). Anal. Calcd for $C_{50}H_{38}Si_2$: C, 86.41; H, 5.51%. Found: C, 86.15; H, 5.65%.

3.2. Spectroscopy

Absorption spectra and fluorescence spectra were measured in spectroscopic grade c-hexane or acetonitrile (Dotite) using a V-570 spectrophotometer (JASCO) and an FP-6600 (JASCO) or an F-4010 spectrofluorimeter (Hitachi), respectively. For the fluorescence measurements, the sample solutions were purged with dry argon for at least 15 min prior to the measurements. The fluorescence lifetime was measured using a Horiba NAES-550 single-photon counting spectrofluorimeter.

3.3. Cyclic voltammetry

Cyclic voltammetry was performed using a Hokuto Denko (HABF1510m) potentio-galvanostat with Ag^+/AgCl as the reference electrode and (n-Bu)$_4$NBF$_4$ as the supporting electrolyte in argon-purged acetonitrile.

3.4. Fabrication and Characterization of OLED devices

The OLED devices were fabricated using a vacuum evaporation instrument (ULVAC VPC-1100), and evaluated by a Minolta chromaticity luminance meter, ES-300. The PEDOT/PSS layer was used to increase the surface flatness. TPD and Alq3 were used as hole and electron transporting materials, respectively. The BCP layer was inserted between Alq3 and the emission layer as a hole blocking layer to prevent Alq3 emission. Typically, each layer was formed by the following thicknesses on an ITO coated plate glass, PEDOT 40 nm/TPD 20 nm/dopant-CBP 30 nm/BCP 10 nm/Alq3 30 nm/LiF 0.5 nm/Al.

The **Me2Ph** sample showed some decomposition during the evaporation, and this was confirmed by a TGA measurement.

4. Conclusions

In conclusion, the 9,10-bissilylanthracenes have a significant potential as fluorescent materials, and a pure-blue electroluminescence was obtained for the device fabricated using **Ph3** as a dopant. The substitution by silyl groups produced a drastic increase in the fluorescence efficiency. The large Stokes shift of the fluorescence λ_{max} by the substitution of the silyl groups are a result of the combination of destabilization of the ground state energy levels by steric hindrance of the bulky substituent and stabilization in the excited state.

For the **Me3**, **Me2Ph**, and **MePh2**, a new emission sub-band was observed on the lower energy side at a lower driving voltage. The appearance of this electroplex emission is reproducible versus the applied voltage. This emission band was not observed during photoluminescence of the device. This may be attributed to the low concentration of molecular stacking formed at the interface, and a different emission efficiency of electroluminescence and photoluminescence from those stacked molecules. For **Me3E** and **Ph3E**, the substitution by silyl groups increased the radiative rate constant.

Finally, our strategy of introducing bulky substituents at the 9,10-position of Ant is effective for improving the OLED performance.

Acknowledgements

The authors thank Prof. Shogo Shimadzu for the TGA measurements. This work was supported by a Grant-in-Aid for Scientific Research (No. 17350090) and a Scientific Research on Priority Areas (417, No. 17029013) from the Ministry of Education, Culture, Sports, Science, and Technology (MEXT) of the Japanese Government, and Chiba University President's Grant to T.K.

References

[1] M.A. Baldo, S. Lamansky, P.E. Burrows, M.E. Thompson, R.S. Forrest, Appl. Phys. Lett. 75 (1999) 4.
[2] M.A. Baldo, M.E. Thompson, S.R. Forrest, Nature 403 (2000) 750.
[3] M.A. Baldo, D.F. O'Brien, Y. You, A. Shoustikov, S. Sibley, M.E. Thompson, S.R. Forrest, Nature 395 (1998) 151.
[4] D.F. O'Brien, M.A. Baldo, M.E. Thompson, S.R. Forrest, Appl. Phys. Lett. 74 (1999) 442.
[5] A.B. Tamayo, B.D. Alleyne, P.I. Djurovich, S. Lamansky, I. Tsyba, N.N. Ho, R. Bau, M.E. Thompson, J. Am. Chem. Soc. 123 (2003) 7377.
[6] T. Karatsu, T. Nakamura, S. Yagai, A. Kitamura, K. Yamaguchi, Y. Matsushima, T. Iwata, Y. Hori, T. Hagiwara, Chem. Lett. 32 (2003) 886.
[7] G. Fleet, G.F. Kirkbright, C.J. Pickford, Talanta 15 (1968) 556.
[8] D.F. Williams, M. Schadt, Proc. Lett. (1970) 476.
[9] D.F. Williams, M. Schadt, J. Chem. Phys. 53 (1970) 3480.
[10] I.Z. Gränacher, H.P. Schwob, E. Baldinger, Solid State Commun. (1967) 5825.
[11] J. Dresner, A.M. Goodman, Proc. Lett. (1970) 1868.
[12] X.H. Zhang, M.W. Liu, O.Y. Wong, C.S. Lee, H.L. Kwong, S.T. Lee, S.K. Wu, Chem. Phys. Lett. 369 (2003) 478.
[13] M.-T. Lee, H.-H. Chen, C.-H. Liao, C.-H. Tsai, C.H. Chen, Appl. Phys. Lett. 85 (2004) 3001.
[14] Z.L. Zhang, X.Y. Jiang, W.Q. Zhu, X.Y. Zheng, Y.Z. Wu, S.H. Xu, Synthetic Met. 137 (2003) 1141.
[15] N.P.H. Nam, S.W. Cha, B.-S. Kim, S.-H. Choi, D.S. Choi, J.-I. Jin, Synthetic Met. 130 (2002) 271.
[16] J. Shi, C.W. Tang, Appl. Phys. Lett. 80 (2002) 3201.
[17] S. Shirai, J. Kido, Chem. Lett. (2002) 386.
[18] T.-H. Liu, W.-J. Shen, C.-K. Yen, C.-Y. Iou, H.-H. Chen, B. Banumathy, C.H. Chen, Synthetic Met. 137 (2003) 1033.
[19] (a) S.L. Murov, I. Carmichael, G.L. Hug, Handbook of Photochemistry, Marcel Dekker, Inc., New York, 1993;
(b) I.B. Berlman, Handbook of Fluorescence Spectra of Aromatic Molecules, Academic Press, New York, 1971.
[20] (a) H. Bouas-Laurent, A. Castellan, J.-P. Desvergne, Pure Appl. Chem. 52 (1980) 2633, and references therein;
(b) H. Bouas-Laurent, J.-P. Desvergne, Photochromism Molecules and Systems, in: H. Durr, H. Bouas-Laurent (Eds.), Elsevier, Amsterdam, 1990.
[21] H.H. Wasserman, J.R. Schaffer, J.L. Cooper, J. Am. Chem. Soc. 94 (1972) 4991, and references therein.
[22] H. Bock, M. Ansari, N. Nagel, R.F.C. Claridge, J. Organometal. Chem. 501 (1995) 53.
[23] (a) K. Kyushin, M. Ikarugi, M. Goto, H. Hiratsuka, H. Matsumoto, Organometallics 15 (1996) 1067;
(b) H. Suzuki, S. Satoh, Y. Kimata, A. Kuriyama, Chem. Lett. (1995) 451.
[24] (a) H. Maeda, T. Maeda, K. Mizuno, K. Fujimoto, H. Shimizu, M. Inoue, Chem. Eur. J. 12 (2006) 824;
(b) H. Maeda, Y. Inoue, H. Ishida, K. Mizuno, Chem. Lett. (2001) 1224.
[25] H. Shizuka, Y. Sato, Y. Ueki, M. Ishikawa, M. Kumada, J. Chem. Soc., Faraday Trans. l 80 (1984) 341.
[26] H. Shizuka, H. Obuchi, M. Ishikawa, M. Kumada, J. Chem. Soc., Faraday Trans. l 80 (1984) 383.
[27] R.E. Kellogg, J. Chem. Phys. 44 (1966) 411.
[28] J.Y. Corey, The Chemistry of Organic Silicon Compounds, Part 1, in: S. Patai, Z. Rappoport (Eds.), John Wiley & Sons, 1989.
[29] V.V. Minaylov, V.S. Gurman, A. Vorobiev, A. Kh, J. Photochem. Photobiol. A: Chem. 87 (1995) 67, and references therein.
[30] X. Chen, J.-L. Liao, Y. Liang, M.O. Ahmed, H.-E. Tseng, S.-A. Chen, J. Am. Chem. Soc. 125 (2003) 636.
[31] J. Kalinowski, G. Giro, M. Cocchi, V. Fattori, R. Zamboni, Chem. Phys. 277 (2002) 387.
[32] Z. Zhang, G. Li, Y.M.J. Shen, Mater. Chem. Phys. 82 (2003) 613.
[33] M.A. Baldo, S. Lamansky, P.E. Burrows, M.E. Thompson, S.R. Forrest, Appl. Phys. Lett. 75 (1999) 4.

[34] H. Cao, X. Gao, C.-H. Huang, Appl. Surf. Sci. 161 (2000) 443.
[35] G. Gadret, G. Ruani, M. Cavallini, F. Biscarini, M. Murgia, R. Zamboni, G. Giro, M. Cocchi, V. Fattori, T. Loontjens, J. Thies, D.A. Leigh, A.F. Morales, R.F. Mahrt, Appl. Surf. Sci. 175–176 (2001) 369.
[36] Y.-M. Wang, F. Teng, Z. Xu, Y.-B. Hou, S.-Y. Yang, L. Qian, T. Zhang, D.-A. Liu, Appl. Surf. Sci. 236 (2004) 251.
[37] J. Kalinowski, G. Giro, M. Cocchi, V. Fattori, P.D. Marco, Appl. Phys. Lett. 76 (2000) 2352.
[38] G. Giro, M. Cocchi, J. Kalinowski, P.D. Marco, V. Fattori, Chem. Phys. Lett. 318 (2000) 137.
[39] N.S. Cho, D.-H. Hwang, B.-J. Jung, J. Oh, H.Y. Chu, H.-K. Shim, Synthetic Met. 143 (2004) 277.
[40] T. Karatsu, R. Hazuku, D. Nishioka, S. Yagai, N. Kobayashi, A. Kitamura, J. Photopolym. Sci. Technol. 18 (2005) 65.
[41] (a) C.A. Landis, S.R. Parkin, J.E. Anthony, Jpn. J. Appl. Phys. 44 (2005) 3921;
(b) S.A. Odom, S.R. Parkin, J.E. Anthony, Org. Lett. 5 (2003) 4245.
[42] R.J. Holmes, B.W. D'Andrade, S.R. Forrest, X. Ren, J. Li, M.E. Thompson, Appl. Phys. Lett. 83 (2003) 3818.
[43] S.A. Manhart, A. Adachi, K. Sakamaki, K. Okita, J. Ohshita, T. Ohno, T. Hamaguchi, A. Kunai, J. Kido, J. Organomet. Chem. 592 (1999) 52.
[44] A. Adachi, J. Ohshita, T. Ohno, A. Kunai, S.A. Manhart, K. Okita, J. Kido, J. Appl. Organometal. Chem. 13 (1999) 859.
[45] E. Kobayashi, J. Jiang, H. Ohta, J. Furukawa, J. Polymer Sci. Part A: Polymer Chem. 28 (1990) 2641.
[46] (a) E. Bowen, J. Sahu, J. Chem. Phys. 63 (1959) 4;
(b) W. Ware, B. Baldwin, J. Chem. Phys. 43 (1965) 1194;
(c) R. Bennett, P. McCartin, J. Chem. Phys. 44 (1966) 1969;
(d) E. Lim, J. Laposa, J. Yu, J. Molec. Spec. 19 (1966) 412.
[47] N.J. Turro, Modern Molecular Photochemistry, Benjamin/Cummings Pub. Inc., Menlo Park, 1978.

Available online at www.sciencedirect.com
ScienceDirect
Organic Electronics 8 (2007) 367–381
Organic Electronics
www.elsevier.com/locate/orgel

Optimization, preparation, and electrical short evaluation for 30 cm^2 active area dual conjugated polymer electrochromic windows

Venkataramanan Seshadri [a], Javier Padilla [b], Humeyra Bircan [a], Bijan Radmard [c], Russell Draper [d], Mike Wood [d], Toribio F. Otero [b], Gregory A. Sotzing [a,*]

[a] *Department of Chemistry and the Polymer Program, 97, N. Eagleville Road, University of Connecticut, Storrs, CT-06269-3136, USA*
[b] *Centro de Electroquimica y Materiales Inteligentes, C/Carlos III s/n, Campus Alfonso XIII, Universidad Politecnica de Cartagena, 30203, Spain*
[c] *Triton Systems Inc., 200, Turnpike Road, Chelmsford, MA-01824, USA*
[d] *Night Vision and Electronic Sensors Directorate, Ft Belvoir, VA-22060, USA*

Received 2 December 2005; received in revised form 19 December 2006; accepted 2 January 2007
Available online 20 January 2007

Abstract

Solid-state electrochromic devices, based on poly-(3,6-bis(2-(3,4-ethylenedioxy)thienyl)-*N*-methylcarbazole) (PBEDOT-NMCz) and poly((3,4-ethylenedioxy)thiophene) (PEDOT), having 30 cm^2 active switching area, low voltage consumption, photopic contrasts of ca. 30% and switching speeds as low as 0.6 s, were prepared and studied. A special design of electrochemical cell allowed us to electrodeposit films of conducting polymer over large areas. Photopolymerization of the gel is a fast and straightforward way to assemble sealed and solid-state devices. Addition of different amounts of plastizicer to a photopolymerizable PEO-based gel electrolyte enhanced switching speed performance over approximately two orders of magnitude. Cyclic voltammetry was shown as a tool to evaluate shorcircuited devices.
© 2007 Published by Elsevier B.V.

PACS: 82.45.Wx

Keywords: Conjugated polymer; Electrochromics; Smart windows; PEDOT; Solid-state devices

1. Introduction

Electrochromism is defined as the ability to change the optical properties of a material upon application of a potential. The tunability of the optical properties of conjugated polymers as a function of potential makes them very useful electrochromic materials. Some that advantages conjugated polymers possess include a wide range of color tunability, ease of processing, low operational voltages and extraordinary color retention.

Both organic and inorganic materials have been used to design and construct electrochromic devices [1–6], that work as electrochemical cells. One of the

* Corresponding author. Tel.: +1 860 486 4619; fax: +1 860 486 4745.
E-mail address: sotzing@mail.ims.uconn.edu (G.A. Sotzing).

1566-1199/$ - see front matter © 2007 Published by Elsevier B.V.
doi:10.1016/j.orgel.2007.01.004

simplest configurations for an EC device consists of a four layer assembly: a transparent electronic conductive film, usually indium doped tin oxide (ITO) on glass or polyethylene terephthalate (PET), a coating of the electrochromic (EC) material, an ionically conductive layer, and another transparent electronic conductive film on glass or PET. Typically, the use of only one electroactive film in an EC device translates to a short device life time. This is due to the lack of a second electroactive film on the counter electrode to complete the redox process, ion shuttling, in the cell, leading to degradative reactions at the electrode. This issue has been alleviated by the use of dual-type configurations [7–10], in which an additional electroactive layer is added on the counter electrode in the assembly to accommodate ion shuttling. This additional layer could also be EC and therefore could be used to obtain mixed colored states, or enhance contrast by using electrochromic materials with complementary optical characteristics.

The ability of an electrochromic device to switch between an optically transparent and an optically dense state has gained much attention due to its potential for insertion into applications including eyewear and the automotive industry. For example, materials with the above characteristics could be applied as intelligent windows capable of providing constant light intensity irrespective of external illumination. Conjugated polymers have been proposed and demonstrated as potential candidates for rearview mirrors that eliminate glare, smart optical attenuation systems which could be useful in architectural windows for privacy and conservation of energy, goggles, and for helmet mounted displays [5,11,12].

The properties of the human eye are key factors in the development of these devices since there are substantial differences in the way we perceive the visible light under different conditions. There are two kinds of light receptors in human eye: rods and cones. The former is sensitive to even small amounts of radiation but cannot perceive the different colors and, therefore, are primarily used under low illumination. The latter yields perceptions of different colors, but requires more radiation intensity to be activated and, therefore, are predominantly used in well illuminated conditions. The scotopic vision refers to situations wherein the rods are used and photopic vision is the use primarily of the cones. In the two different situations, the eye is most sensitive to a different wavelength. For photopic vision, the eye is most sensitive to light at 555 nm. Each wavelength of the visible spectrum has a relative weight in terms of how well it is perceived by the eye. The relative values for each wavelength have been standardized by the Commission Internationale de l'Eclairage (CIE) [13,14].

The above mentioned applications have the potential to be in close proximity to the human eye and could be exposed to relatively high temperature. Therefore, for safety purposes, incorporation of liquid electrolytes should be avoided. To move away from liquid electrolytes, several ionically conductive gels composed of polymethylmethacrylate (PMMA) with low vapor pressure plasticizers [13–18] and polyethylene oxide (PEO) based polymer electrolytes have been reported [19,20]. PEO based polymers are known to be excellent for dissolving lithium salts without allowing crystallization even operating at fairly low temperatures [21]. Apart from safety, solid-gel electrolytes increase the operating life of devices due to the absence of solvent evaporation. One practice is to form the polymer electrolyte layer in a device by solvent casting. A more practical approach towards preparing large area devices is to photopolymerize an acrylate functionalized low molecular weight PEO in the presence of photoinitiator [22,23]. For the applications sought after for EC windows, the polymer electrolyte has to be both ionically conductive and have a high level photopic transmission.

Herein, we report the fabrication of relatively large area, 30 cm^2, electrochromic windows based on the dual conjugated polymer approach using photopolymerized polymeric electrolytes. Both the anodically and cathodically coloring conjugated polymers used in these electrochromic windows were electrochemically prepared on ITO coated glass and on PET films. Several issues regarding electrochemical generation of the conjugated polymers on these surfaces are discussed. Furthermore, we report the effect of adding plasticizers to the gel-electrolyte on the EC device switching response. Finally, a significant problem that is encountered for production of larger area devices compared to smaller area (<5 cm^2) devices is electrical shorting. Electrical shorts will decrease the ability of the electrochromic device to maintain a colored state under open circuit conditions and therefore will significantly increase the power consumption. Herein, we report the use of cyclic voltammetry and cyclic voltammetry with resistors in parallel to evaluate shorting of EC devices.

2. Experimental

2.1. Materials

3, 4-Ethylenedioxythiophene (EDOT) and 3,6-dibromocarbazole were purchased from Aldrich. EDOT was distilled under reduced pressure before use to obtain a clear and colorless liquid. Bis (3,4-ethylenedioxythiophene)-*N*-methylcarbazole (BEDOT-NMCz) was synthesized by reported procedure [24]. The only exception was that 3,6-Dibromo-*N*-methylcarbazole was obtained in near quantitative yields by running the reaction for longer times (~12 h) at room temperature. Acetonitrile was procured from Fisher scientific and freshly distilled over calcium hydride (from ACROS). Lithium trifluoromethanesulfonate (LITRIF), poly (ethyleneglycol) ethylether methacrylate (MA), poly(ethyleneglycol) diacrylate (DA) and 2,2-dimethoxy-2-phenyl-acetophenone (DMPAP) were purchased from Aldrich and used as received. Glass beads (diameter 50–100 μm) were purchased from Polysciences Inc. 3 in. × 3 in. (58 cm^2) indium doped tin oxide (ITO) coated glass of 0.028 thickness and a nominal surface resistance of 15–25 Ω/sq and ITO coated polyethylene terephthalate rolls with a nominal resistance of 40–60 Ω/sq were purchased from Delta technologies.

2.2. Instrumentation

Both CHI 400 and CHI 660A potentiostats (CH instruments) were used both for the electropolymerization of EDOT and BEDOT-NMCz and study of EC devices. A Perkin–Elmer UV lambda 900 spectrophotometer was used for optical studies.

2.3. Electrochemical polymerization to prepare conjugated polymers

A special cell was designed for the electropolymerization of EDOT and BEDOT-NMCz onto 58 cm^2 ITO coated substrates. The area of the ITO that was coated with conjugated polymer was approximately 30 cm^2 using our electrochemical cell configuration (Fig. 1).

PEDOT was deposited electrochemically onto 58 cm^2 ITO glass from an acetonitrile solution containing 20 mM EDOT and 0.1 M LITRIF at 1.3 V (vs a non-aqueous Ag/Ag^+ reference, 0.456 V vs NHE). PBEDOT-NMCz was deposited onto 58 cm^2 ITO coated PET from a 1 mM BEDOT-NMCz solution containing 0.1 M LITRIF at 0.7 V (vs Ag/Ag^+) and further reduced to the pale yellow neutral form at −0.8 V (vs Ag/Ag^+). Both the polymers were thoroughly washed with acetonitrile, dried and stored in a dessicator until the construction of the device.

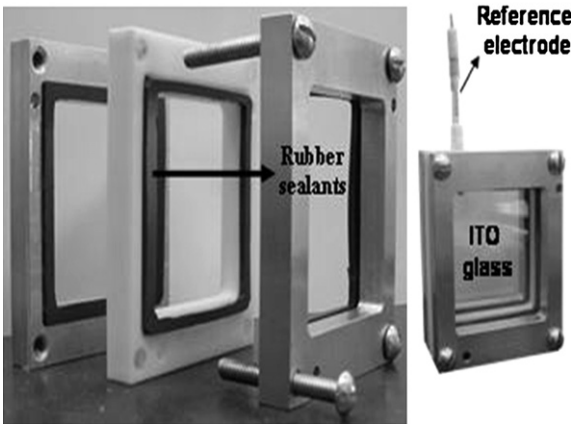


Fig. 1. Electrochemical cell used for the polymerization of the conjugated polymers (*insert shows the assembled electrochemical cell*).

2.4. Construction of device

The gel electrolyte was composed of a poly(ethylene glycol) based acrylate macromonomer, photoinitiator, plasticizer, glass beads and the electrolyte to compensate for the charge injected into or extracted from the conducting polymer. The ionic conductivity of lithium-PEO has been reported to be at a maximum for a Li/O ratio of 0.04 and hence the composition of the gel electrolyte with no plasticizer was prepared with this ratio [25]. Since we intended to study the effect of plasticizer alone, the salt concentration was kept constant in all the compositions. The different compositions of the gel electrolyte used in this study are shown in Table 1.

Approximately 0.5 ml of the gel electrolyte solution was poured onto the PEDOT coated ITO glass and the PBEDOT-NMCz coated PET-ITO was placed over it with conducting surfaces facing each other. The glass beads dispersed in the gel electrolyte help prevent electrical shorting. The two electrodes were gently hand pressed together to remove any trapped air-bubbles and to squeeze out excess gel electrolyte solution. Polymerization of the macromonomer, MA or DA in the presence of photoinitiator DMPAP, was carried out under UV light [365 nm, 5.8 mW/cm^2] for 15 min.

Table 1
Different composition of gels

MA (g)	DA (g)	Propylene carbonate (g)	DMPAP (mg)
10	0	0	25.0
9.0	0	1.0	22.5
8.0	0	2.0	20.0
7.0	0	3.0	17.5
6.0	0	4.0	15.0
5.0	0	5.0	12.5
0	10	0	25.0
0	9.0	1.0	22.5
0	8.0	2.0	20.0
0	7.0	3.0	17.5
0	6.0	4.0	15.0
0	5.0	5.0	12.5

*1.0 g LITRIF and 5 mg of 50–100 μm glass beads were used in all compositions.

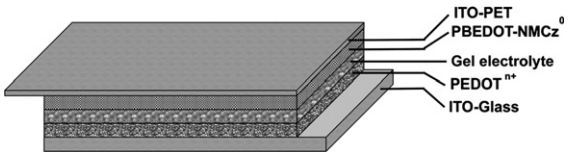


Fig. 2. Cutaway of a solid-state electrochromic device.

Completion of curing of the monomers was monitored through the loss of C=C stretching intensity in the IR and also via NMR of $CDCl_3$ extracts of the gel electrolyte. The device was hermetically sealed using a polyurethane based UV curable resin. Fig. 2 shows a cutaway of a solid-state electrochromic device.

The quality of the seal was tested by immersing the devices into a slightly acidified aqueous solution containing an iron (III) thiocyanate complex. Devices not sealed were totally delaminated within a couple of minutes. The gel electrolyte cracked completely with uptake of water and became intensely colored due to the absorbed dye. There was no observed change in switching response with respect to speed or contrast for well sealed devices after subjecting the devices to reduced pressure of 0.1 torr at 75 °C.

3. Results and discussion

3.1. Electropolymerization process on ITO

For nearly all electrochromic windows, ITO coated surfaces have been utilized as the optically transparent electrode (OTE). Recently, Reynolds et al. reported the use of PEDOT/PSS as the OTE [26]. Generally, ITO has a significantly larger resistance than metal and hence electropolymerization onto its surface will lead to more non-uniform films for larger substrate size due to a drop in the potential/electric field along the surface from the electrical contact point. Non-uniformity of conjugated poly-

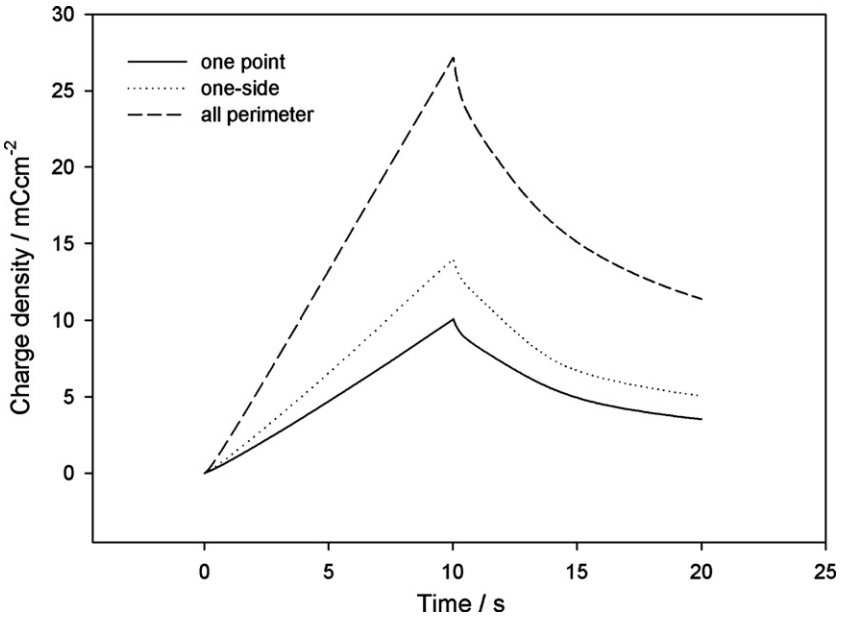


Fig. 3. Chronocoulometric data obtained during polymerization of EDOT using metallic contact at one point (solid-line), one-side (dotted line), and whole perimeter (dashed line) of the ITO glass.

mer coating will be more pronounced for materials that exhibit a higher surface resistance than ITO, such as PEDOT-PSS.

With 58 cm^2 ITO coated glass plates, the conjugated polymer film uniformity issue was addressed by means of covering the perimeter of the ITO coated glass plate with an adhesive copper tape used as the electrical contact. As a result, we obtained more uniform deposition of conjugated polymer films. Furthermore, as observed in the chronocoulometry (Fig. 3), an increase in the charge density (i.e., rate of polymer deposition) was observed for a given time during electrochemical polymerization of EDOT onto ITO glass by increasing the area of metallic contact on the ITO glass viz. single point, one side, and whole perimeter.

Relationship between polymerization time and consumed charge density in the process, related to

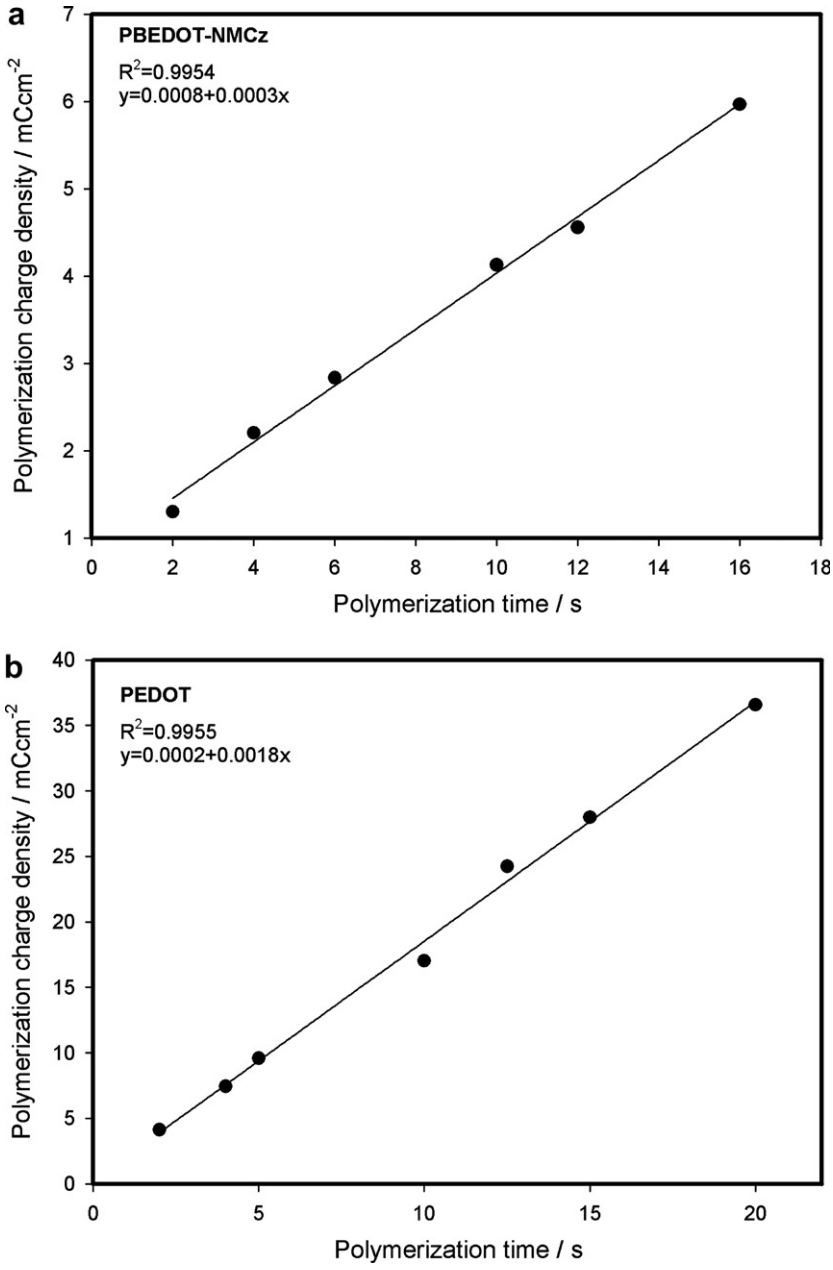


Fig. 4. Relationship between charge density and polymerization time for preparation of (a) PBEDOT-NMCz and (b) PEDOT films.

the amount of polymer created, was found to be linear (Fig. 4a,b).

3.2. Optical characteristics of PEDOT and PBEDOT-NMCz

PEDOT is a very well known, and cathodically coloring conductive polymer reported in several electrochromic device applications [9–11,22,27,28]. PEDOT switches between a transparent sky blue in its oxidized state to a deep blue in the neutral state with a maximum absorbance centered at ca. 620 nm. PBEDOT-NMCz was prepared by Sotzing et al[24] and was reported to switch from a pale yellow in the neutral form to a deep blue in its oxidized form (λ_{max} in oxidized form = 570 nm). Since PBEDOT-NMCz has a higher optical density in the oxidized state, it is anodically coloring and complementary to PEDOT when on the counter electrode. Spectra of both polymers were taken in their reduced and oxidized forms and are shown in Fig. 5.

3.3. Photopic behavior of PEDOT and PBEDOT-NMCz

In order to have an accurate metric for the optical contrast change as a function of switching the EC device, photopic contrast values were determined for the devices. Generally, in the area of EC devices, optical values for switching a device have either been reported at the λ_{max} of the electrochromic or have been reported at the wavelength for maximum sensitivity, 555 nm, for the eye. Although the maximum sensitivity is at 555 nm under daylight conditions, we feel it is most appropriate to report the optical switching data as photopic contrasts across the entire visible spectrum. The equation used for converting a typical visible spectrum to a photopically weighted spectrum is given as:

$$T_{\text{photopic}} = \frac{\int_{380}^{720} T(\lambda)\cdot S(\lambda)\cdot P(\lambda)\mathrm{d}\lambda}{\int_{380}^{720} S(\lambda)\cdot P(\lambda)\mathrm{d}\lambda} \quad (1)$$

where $T(\lambda)$ is the spectral transmittance of the device under test, $S(\lambda)$ is the normalized spectral emittance of a 6000 °K blackbody and $P(\lambda)$ is the normalized spectral response of the eye.

In order to obtain the contrast characteristics of both polymers used in the construction of the devices, we prepared a series of films of PEDOT and PBEDOT-NMCz varying charge densities. The transmittance spectrum of PEDOT in the neutral and oxidized forms was recorded at −1.2 V and − 0.15 V (vs Ag/Ag^{+}), respectively. Similarly, the neutral and oxidized form transmittance spectra of

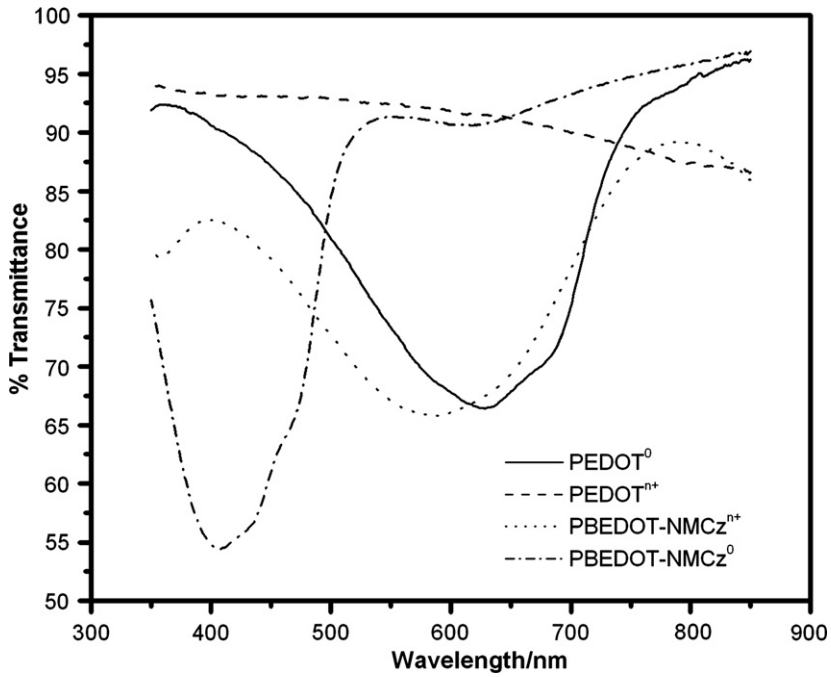


Fig. 5. Transmittance spectra of PEDOT and PBEDOT-NMCz in the visible region.

PBEDOT-NMCz on ITO coated glass were obtained at −0.7 V and 0.2 V (vs Ag/Ag^{+}), respectively. It should be noted that the transmittance values reported are for the conjugated polymers where the absorption of the substrates was subtracted. The photopic transmittance in the clear and dark states and the photopically weighted contrast, i.e., difference between the values in the clear and dark states, were calculated. The relationships between contrast and charge density for conjugated polymer film preparation for each polymer are shown in Fig. 6a and b.

The photopic contrast for PBEDOT-NMCz was found to increase from ca. 15% for a charge density for polymer film preparation of 1 mC/cm^2 to an almost constant value of ca. 20%. This value was found to be constant beyond a charge density of ca. 2.5 mC/cm^2, while both the clear and dark state

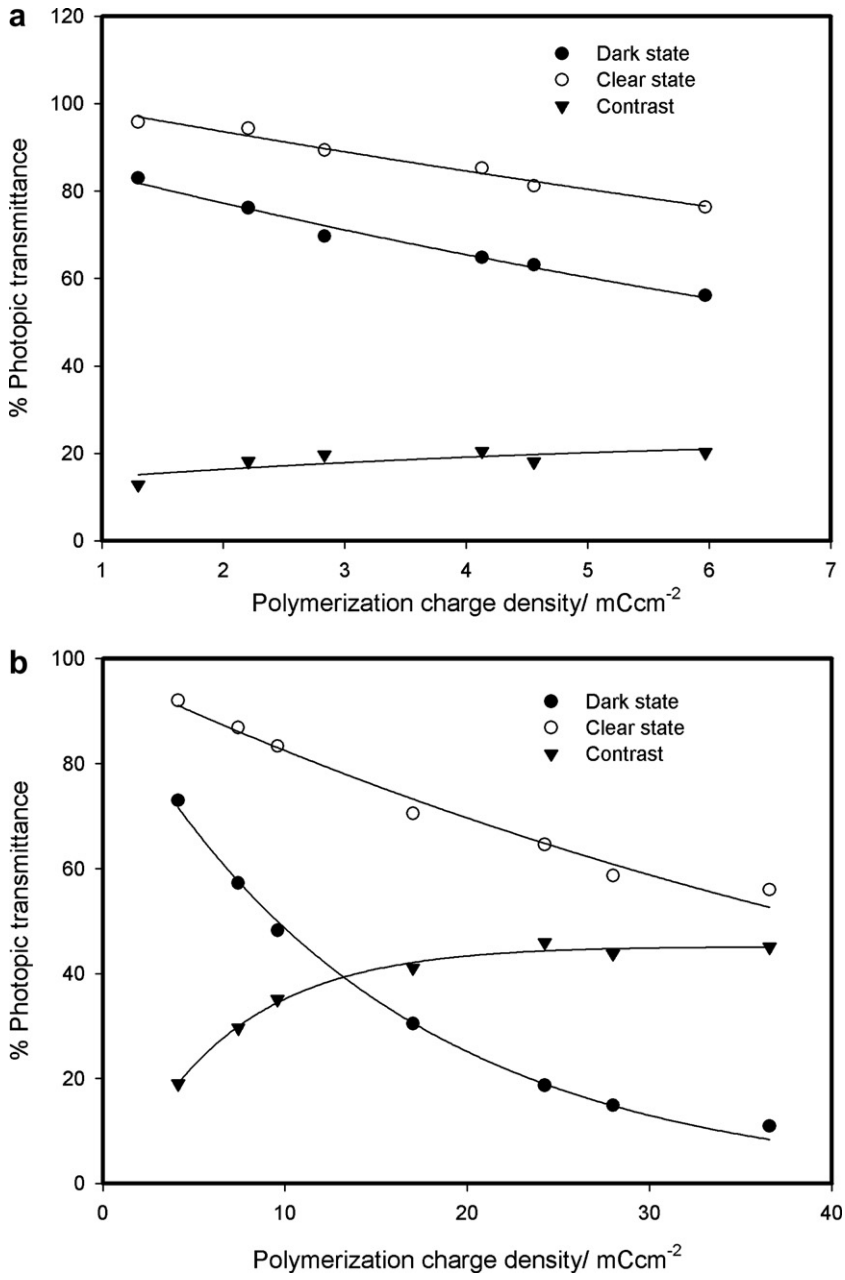


Fig. 6. Relationship between charge density and contrast for (a) PBEDOT-NMCz and (b) PEDOT.

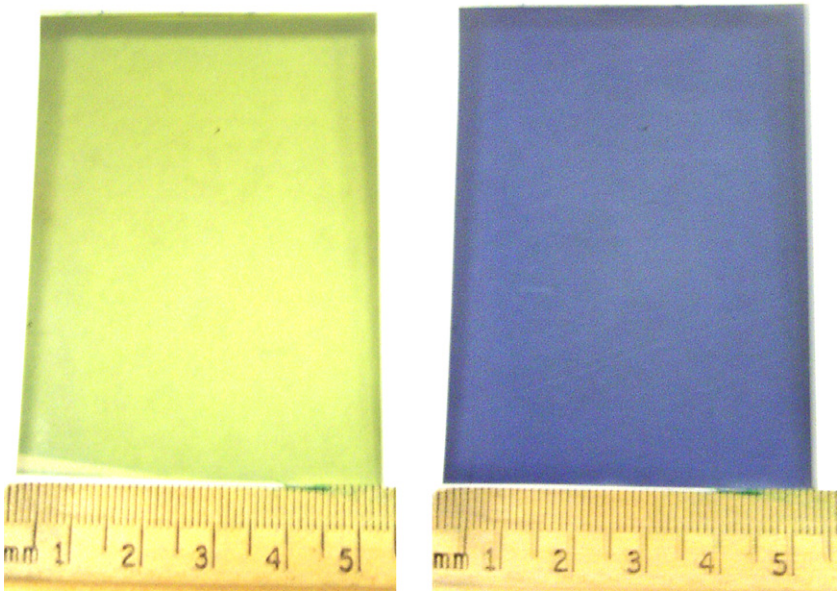


Fig. 7. PEDOT//PBEDOT-NMCz dual polymer solid-state device with an electrochromic area of ~30 cm^2 in the clear (65% transmittance) and dark state (30%).

photopic transmittance values were found to decrease with increasing polymerization charge densities. For PEDOT, a more dramatic increase in photopic contrast of 20% for a charge density of 4 mC/cm^2 to about ca. 45% for charge densities >24 mC/cm^2 was observed. For practical application, the transmittance for the clear state should be high in order to serve usefully in low to moderate illumination conditions while still maintaining the maximum contrast between the two states.

In order to optimize contrast in a dual conjugated polymer configuration, we prepared a series of polymer films on small ITO sheets (2.1×0.7 cm) with polymerization charge densities ranging from ca.3 to 28 mC/cm^2 for PEDOT and from ca.1 to 5.5 mC/cm^2 for PBEDOT-NMCz. We then combined each of one type film with the opposing conjugated polymer films. The photopic transmittances and contrasts were then determined, after submitting each combination to -1 and 1.4 V potential steps in a 0.1 M LITRIF acetonitrile solution. We found that the best contrast, around 40% (41.9 and 81.4% transmittance in dark and clear state, respectively), would be exhibited for an EC device consisting of PEDOT and PBEDOT-NMCz prepared with polymerization charge densities of ca. 10 mC/cm^2 and 2 mC/cm^2, respectively. Contrasts were calculated subtracting electrolyte and glass contribution.

3.4. Photopic contrasts for assembled EC devices

Since the end user perceives the device as a whole, it is important that the cell itself without the conjugated polymer be highly transmissive throughout the visible region. The device with the configuration shown in Fig. 2 without the PBEDOT-NMCz and PEDOT EC layers exhibited 80% photopic transmission. It is important to note that since the relationship between transmittance and absorbance is logarithmic, different architectures for a device will produce, ultimately, different contrast values when the same EC materials are utilized since the device minus EC materials will have different photopic transmissions. Assembled devices with the polymerization conditions described above resulted in ca. ~30% (65% photopic transmittance in the clear state, 34% in dark state). Inclusion of the solid electrolyte and glass absorbance account for the 10% loss in maximum contrast calculated above. Fig. 7 shows pictures of the solid-state EC device in the bleached and colored states corresponding to photopic transmittance values of ca. 65 and 34%. The photopically weighted transmittance results of this device in the clear and dark state are shown in Fig. 8.

Optimized devices were used for the after-mentioned switching studies.

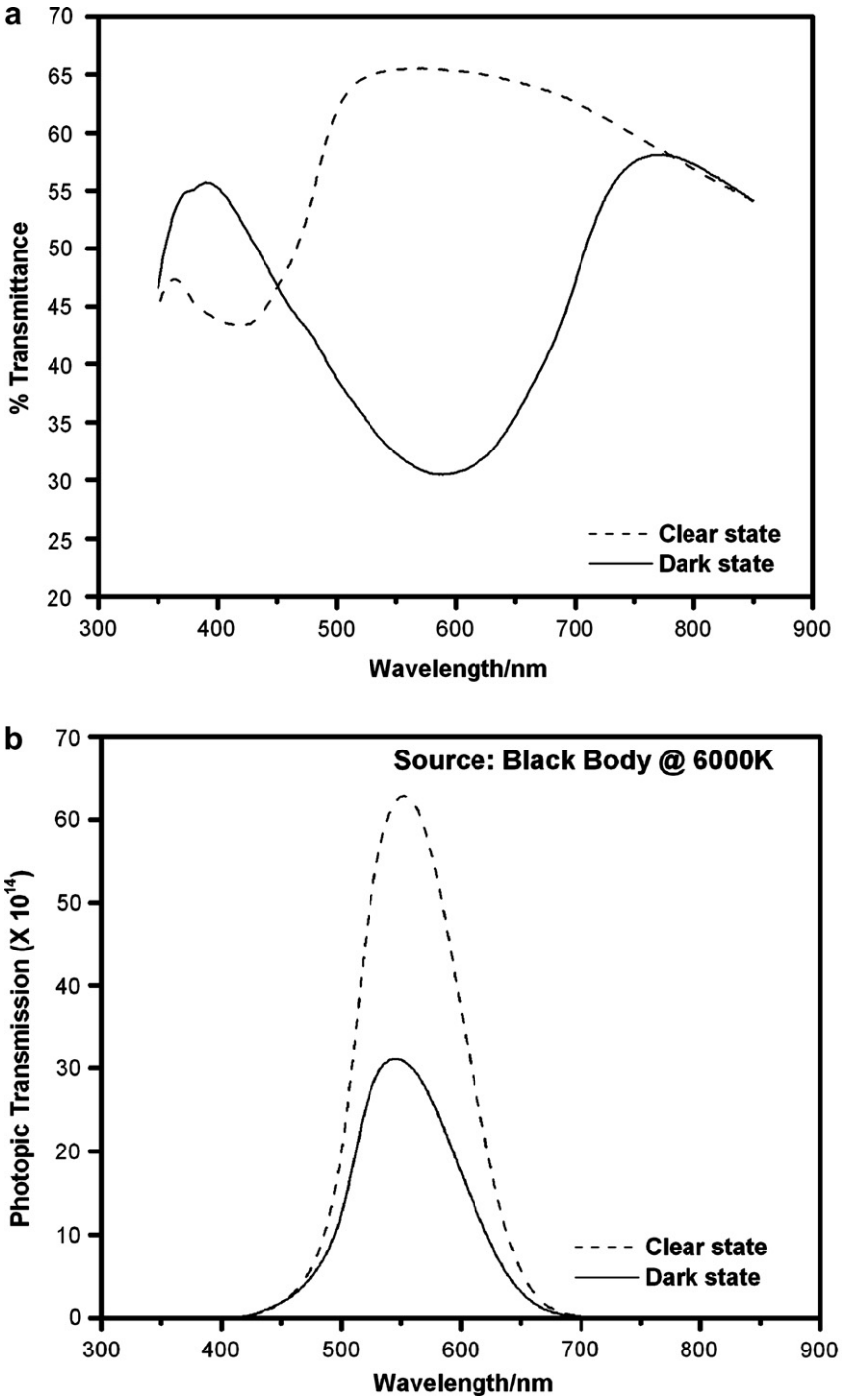


Fig. 8. Device spectrum in comparison with the photopically weighted transmittance spectrum of a solid-state device in the clear and dark state.

3.5. Operating potentials of solid-state devices

Cyclic voltammograms of the solid-state devices were obtained using a two electrode configuration with the counter electrode and reference electrode shorted. PEDOT coated ITO-glass was connected as the shorted counter electrode/reference electrode pair. Fig. 9 shows the cyclic voltammogram of a

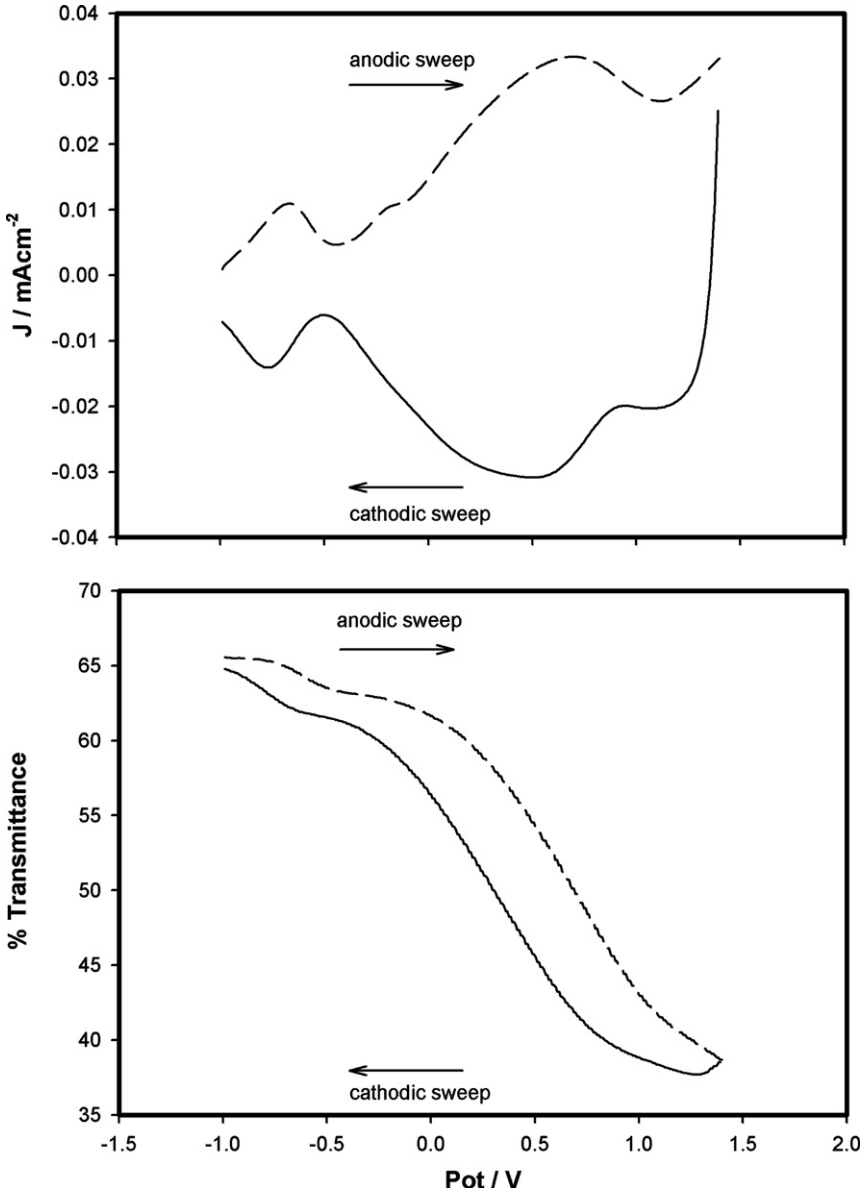


Fig. 9. Current (top) and change in percent transmittance (bottom) for a dual polymer solid-state device measured as a function of the applied potential (referenced against PEDOT containing electrode).

dual polymer solid-state device obtained at a scan rate of 100 mV/s and its corresponding change in photopic percent transmittance. As the device is scanned from −1 V to 1.4 V the device goes from a clear to a dark state. At −1 V (i.e., clear state) PEDOT is in the conductive oxidized state and PBEDOT-NMCz is in the insulating neutral state and at a potential of 1.4 V when the device is dark PEDOT is neutral and PBEDOT-NMCz is oxidized. During the reverse scan the change in percent T did not retrace the original path obtained during the forward scan indicating a hysteresis. This phenomenon was also observed at very low scan rate ca. 10 mV/s for all the gel–electrolyte compositions and in the absence of polyelectrolyte using 10 mM LITRIF-PC solution[1]. Thus, this hysteresis is a function of the dual conjugated polymer system as

[1] Devices property sealed were made with liquid solution inside (10 mM LITRIF in propylene carbonate) substituing the solid–gel electrolyte.

opposed to the physical composition of the electrolyte (solid or liquid).

An inherent asymmetry or hysteresis between the anodic and cathodic processes is a usual phenomenon observed in redox processes of conjugated polymers. Energetic differences between doping and dedoping processes, related to asymmetric structural changes necessary to complete them, have been proposed as a possible explanation [29]. As the change in transmittance is directly related to the redox processes, with the creation or depletion of intermediate energy levels in the band gap, the hysteresis in the observed spectral response is inherent to the conjugated polymer.

Device cycling between −1 and 1.4 V was optimal due to no observed loss in photopic contrast. In general, EC devices were found to exhibit stable switching responses with respect to contrast and switch speed for ca. 90000 cycles between −1 and 1.4 V [30].

3.6. Switch speed optimization

Several solutions based on MA or DA and LITRIF mixed with different amounts of plasticizer, PC, were used for the preparation of polymeric electrolytes. Solutions containing pure MA or DA, or with 10, 20, 30, 40, 50 weight percent PC were prepared for this study. A solution of 10 mM LITRIF in PC was also used to study the differences between liquid and polymeric electrolyte. Potential steps between −1 to 1.4 V in the two electrode configuration were applied to devices constructed with these electrolytes, and both charge and transmittance (at 555 nm) were recorded to determine the switching speed. Here, we define switching speed as the amount of time it takes for the device to attain 90% of its end charge or transmittance value. Surprisingly, without PC plasticizer, DA was found to exhibit a faster response than MA as shown in Fig. 10. It would be expected that a crosslinked polyelectrolyte system, such as DA would have a lower mobility of polymer chains and, therefore, an EC device constructed from it would exhibit a slower response compared to a polyelectrolyte consisting of linear polymer such as the one prepared from MA. Both DA and MA showed similar switching speeds with MA being slightly faster when mixed with PC plasticizer. A large effect is noticed in going from 0 to 20% PC plasticizer in both cases. The switching speed with MA improves from 90 sec to 2 sec and the switching speed for DA improves from 10 sec to 2 sec. Increasing the plasticizer content to 30, 40 and 50% by weight marginally improves the switching speed in both cases by approximately 1 sec (Fig. 11a and b). The use of PC/LITRIF alone only allowed for a further decrease of response speed of approximately

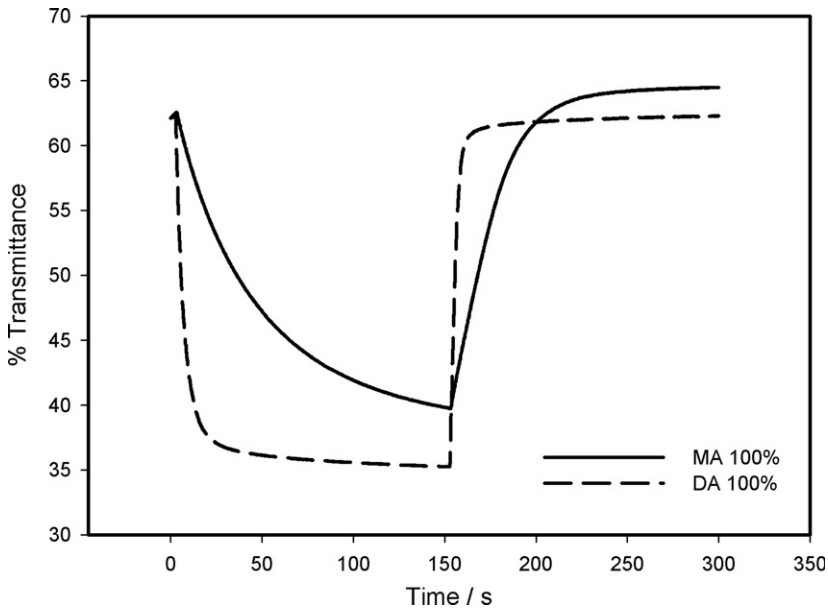


Fig. 10. Percent Transmittance change at 555 nm during potential stepping experiments for devices containing pure MA and DA as electrolytes.

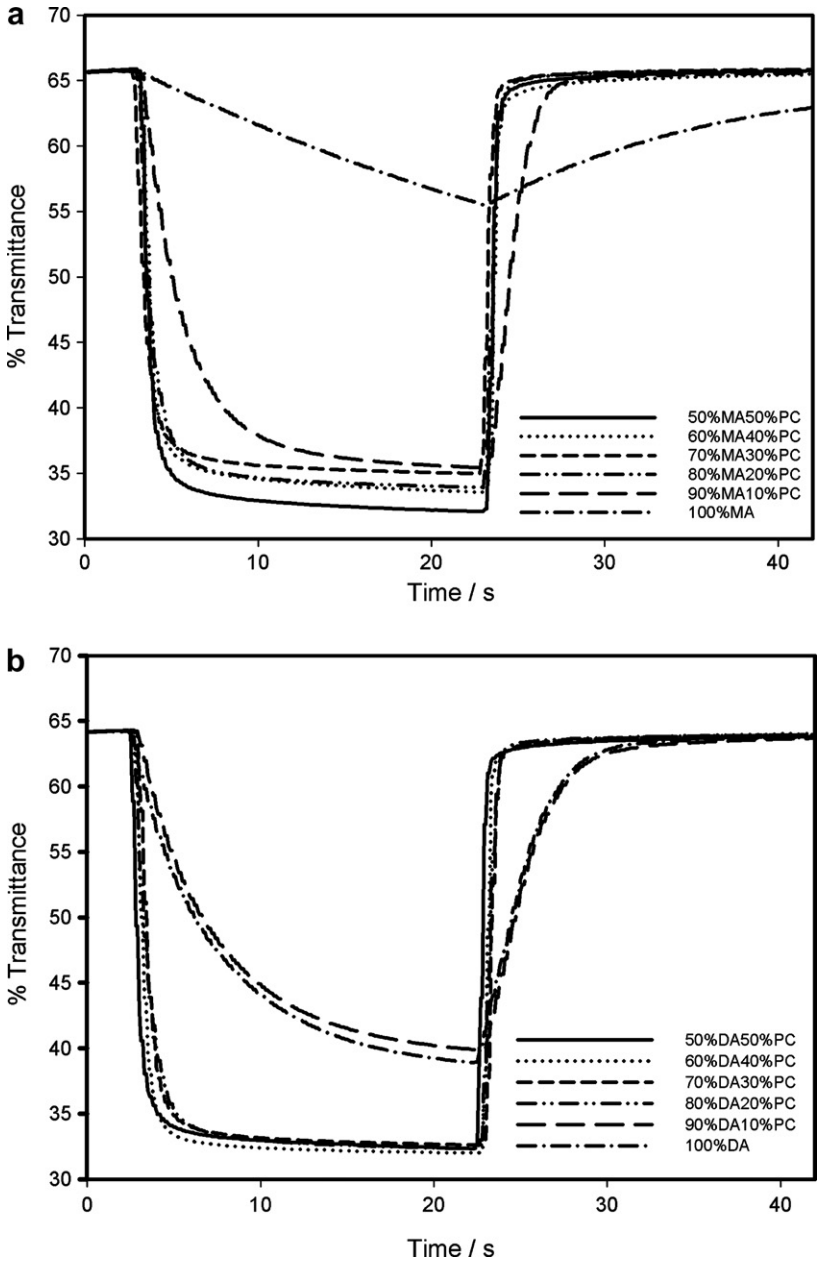


Fig. 11. Percent Transmittance change at 555 nm for different electrolytes, (a) MA and (b) DA during constant potential stepping between −1 and 1.4 V.

0.3 sec in comparison to polyelectrolytes containing >20% by weight PC. Table 2 tabulates the response speed to attain the electrochromic state as a function of changing electrolyte composition.

A general observation was that the switch response speed from the colored to bleached states was faster than the switch speed observed in going from the bleached to colored state. In some cases, this difference was almost a factor of two. The dual conjugated polymer configuration implies that in going from the bleached to color state, PEDOT is transitioning from its oxidized to its neutral form whereas PBEDOT-NMCz is transitioning from its reduced to oxidized form. Although the non-symmetrical switching speeds observed could be attributed to the differences in conductivities between

Table 2
Switching speeds for bleached to colored state transitions and vice-versa for different gel electrolyte compositions

Gel electrolyte composition	Switching speed (sec)	
	(Coloring)	(Bleaching)
100% MA	95.5	48.6
100% DA	15.9	7.8
50%MA 50%PC	1.5	0.9
60%MA 40%PC	1.8	0.9
70%MA 30%PC	2.2	1.1
80%MA 20%PC	2.4	1.5
90%MA 10%PC	6.3	3.1
50%DA 50%PC	1.6	0.8
60%DA 40%PC	1.5	1.1
70%DA 30%PC	2	1.2
80%DA 20%PC	2.4	1.5
90%DA 10%PC	10.6	5.6

the oxidized and reduced state of PEDOT, or compaction–relaxation processes delaying the oxidation process of PBEDOT-NMCz [31,32], the fact that both polymers are involved in undergoing redox processes simultaneously make it difficult to propose a single explanation.

3.7. Leakage current and device memory

Leakage current will have a significant effect on color retention capability in open circuit and, therefore, the power consumption of conjugated polymer EC devices [33]. Apart from the ability of the conjugated polymer to retain a particular optical state, engineering of the device plays a crucial role for long color retention times. Solid-state devices based on conjugated polymers are similar to capacitors (fast discharge batteries or supercapacitors) in that they store electrical charge when a potential is applied and the device is then placed in open circuit [34]. In both the bleached and colored states, one of the conjugated polymers is in a positively charged state and short-circuiting between the two electrodes would result in leakage of charge thus resulting in a corresponding loss of the optical state. In our device assembly, one of the electrodes is an ITO coated thin PET film having a tendency to curl at the edges which in some cases results in a short between both electrodes thereby leading to the incapability of the device to hold its colored state when potential is no longer applied. This was experimentally confirmed by purposefully discharging the charge on one polymer to the other via a conducting wire connecting the two electrodes while observing a loss in the optical state. Cyclic voltammetry was a useful and rapid procedure to identify shorted devices. Fig. 12 shows a series of cyclic voltammograms obtained with different known resistors in parallel to a non-shorted device.

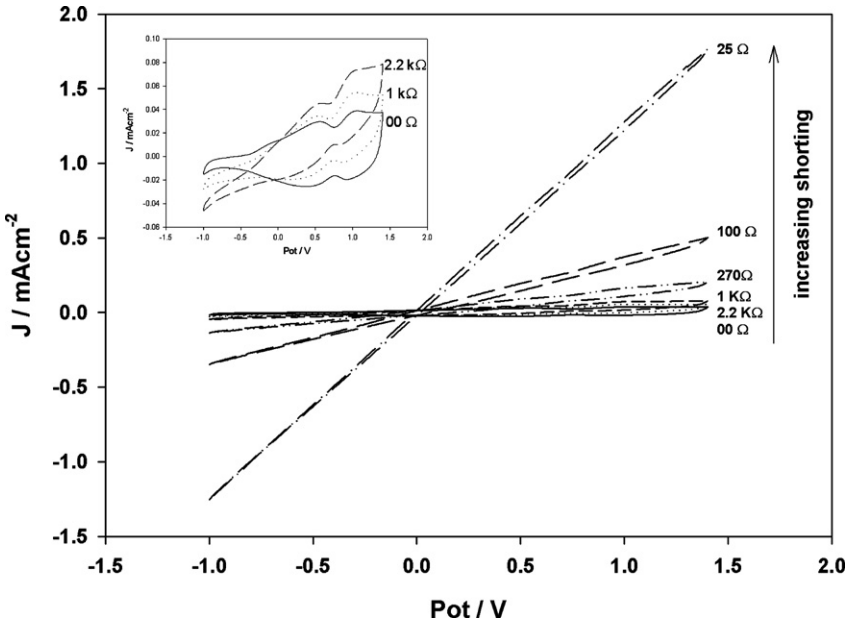


Fig. 12. Cyclovoltammograms of a solid-state electrochromic device with different known resistors: $\infty\Omega$ (i.e., device without any additional resistance), 2.2 kΩ, 1 kΩ, 270 Ω, 100 Ω and 25 Ω in parallel. First three are zoomed for clarity.

The current passing through the combination of the device and resistor in a parallel fashion was found to increase with a decreasing resistance value of the resistor connected in parallel to the device, and the shape of the voltammograms becomes closer to that expected from a pure resistance. The connection of the resistor in parallel did not affect the transmittance of the device in either the bleached or colored state. From this, it was determined that cyclic voltammetry is a useful tool for determining the internal structure of the device and for deducing its long term actuation. A shorted device will offer less capability to retain optical density over time and, thereby, will consume more power for operation.

Fig. 13 shows the optical tunability and memory retention of an EC solid-state device at different potentials. The solid-state device initially held at −1.1 V was pulsed to various potentials viz., −1 to 1.4 V and the power was turned off after 10 sec of pulse width while the transmittance data at 555 nm was gathered for another 2 min. Except for a small increase (about 1–2%) in the percent T just after turning off the potential the device was held at different colored states for up to 24 h. As observed in Fig. 13, the drop in percent T between −1 and −0.2 V is very gradual whereas a more substantial drop in photopic percent T is observed between −0.2 and 0.8 V.

In general, EC devices in the bleached state under ambient light conditions held their transparency for up to 4 days under open circuit conditions indicating resistance of the device to photo-oxidation. No change in the charge or optical switching response, viz. change in initial contrast was observed at the end of this experiment.

4. Conclusions

EC windows with an active switching area of approximately 30 cm^2 were prepared and studied. Several issues involved with the scale up of EC windows have been addressed herein including coating evenness of the conjugated polymer from an electrochemical deposition process, evaluation of optical contrast using photopic contrast, optimization of polymerization charge density for optical contrast, the effect of switching speed upon varying polyelectrolyte composition and the ability to rapidly screen and evaluate contact resistance of an EC device using cyclic voltammetry. It was determined that for coating relatively large area electrochromics sufficient for the manufacture of EC eyewear using an electro-deposition process it is necessary to have a

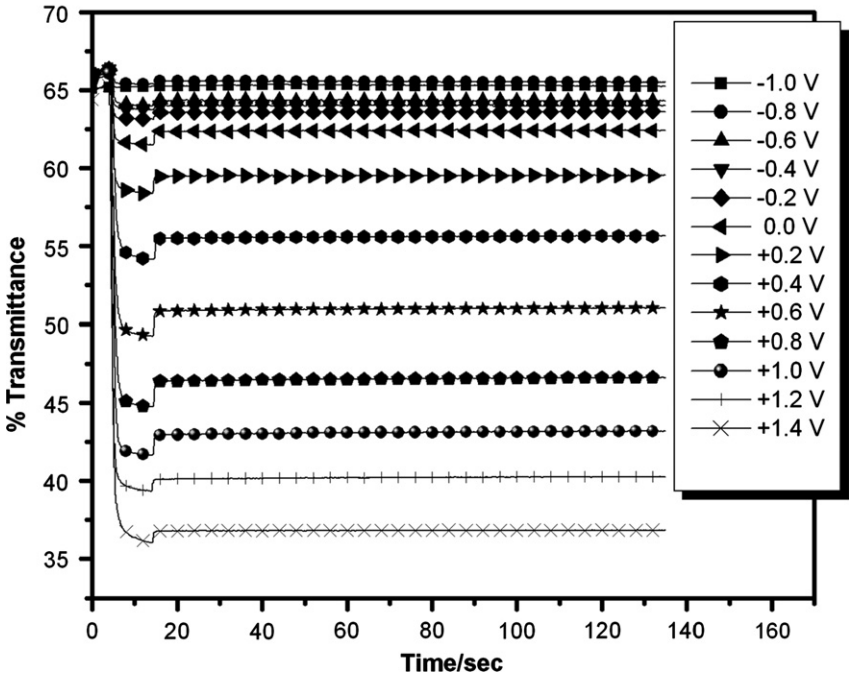


Fig. 13. Optical tunability of a PEDOT//PBEDOT-NMCz solid-state device at different potentials and the ability of the device to hold the different optical states after turning off the power supply. (*The transmittance was measured at* 555 nm).

highly conductive perimeter in order to achieve film uniformity. For dual conjugated polymers, the optical contrast as a function of polymerization charge density for each conjugated polymer can be used in order to determine an optimal combination for maximum optical contrast. Photopic contrast values, a true measure for what the eye will see during daylight operation, is a realistic metric for EC windows. Values reported at 555 nm are several percentage values different for photopically weighted values and values reported at λ_{max} can be in error as high as 50%. Membranes of monoacrylate terminated polyethylene oxide are worse than polyethylene oxide with two acrylate end groups in an all-solid polyelectrolyte; whereas, both function to approximately the same switching speeds with PC as a plasticizer to levels between 20% and 50%. A large issue with relatively large area electrochromics is the higher potential for these devices to be electrically shorted in comparison to small area devices. With this in mind, we have shown that cyclic voltammetry in conjunction with resistors placed in parallel can be utilized to evaluate the extent of shorting. A shorted device will offer less capability to retain optical density over time and, thereby, will consume more power for operation. Fast responses times and long term stability of the bleached and colored states under open circuit were obtained.

Acknowledgements

Sotzing would like to thank the National Science Foundation (DMR-0502928) for partial support of this work. Javier Padilla and Toribio F. Otero thank for the financial support of Spanish Ministry of Education and Science (through project BQ-2001-0477) and Seneca Foundation (through PI-25/00827/FS/01). Sotzing and Triton Systems Inc. would like to thank Night Vision and Electronic Sensors Directorate (NVESD) for their financial support (Contract No. W909MY-04-C-0007).

References

[1] A.A. Argun, P.H. Aubert, B.C. Thompson, I. Schwendeman, C.L. Gaupp, J. Hwang, N.J. Pinto, D.B. Tanner, A.G. Macdiarmid, J.R. Reynolds, Chemistry of Materials 16 (2004) 4401–4412.
[2] C.G. Granqvist, Solar Energy Materials and Solar Cells 60 (2000) 201–262.
[3] K. Hyodo, Electrochimica Acta 39 (1994) 265–272.
[4] R.J. Mortimer, Electrochimica Acta 44 (1999) 2971–2981.
[5] D.R. Rosseinsky, R.J. Mortimer, Advanced Materials 13 (2001) 783–793.
[6] P.R. Somani, S. Radhakrishnan, Materials Chemistry and Physics 77 (2003) 117–133.
[7] A.S. Ribeiro, D.A. Machado, P.F.D. Filho, M.A. De Paoli, Journal of Electroanalytical Chemistry 567 (2004) 243–248.
[8] A.M. Rocco, M.A. DePaoli, A. Zanelli, M. Mastragostino, Electrochimica Acta 41 (1996) 2805–2816.
[9] S.A. Sapp, G.A. Sotzing, J.L. Reddinger, J.R. Reynolds, Advanced Materials 8 (1996) 808–811.
[10] S.A. Sapp, G.A. Sotzing, J.R. Reynolds, Chemistry of Materials 10 (1998) 2101–2108.
[11] J.C. Gustafssoncarlberg, O. Inganas, M.R. Andersson, C. Booth, A. Azens, C.G. Granqvist, Electrochimica Acta 40 (1995) 2233–2235.
[12] R.D. Rauh, Electrochimica Acta 44 (1999) 3165–3176.
[13] G. Wyszecki, W.S. Stiles, Color Science: Concepts and Methods, Quantitative date and formulae, John Wiley & Sons, New York, 1982.
[14] D.B. Judd, G. Wyszecki, Color in Business, Science and Industry, John Wiley & Sons, New York, 1967.
[15] S.A. Agnihotry, Pradeep, S.S. Sekhon, Electrochimica Acta 44 (1999) 3121–3126.
[16] H.J. Byker, Electrochimica Acta 46 (2001) 2015–2022.
[17] P. Georen, G. Lindbergh, Electrochimica Acta 49 (2004) 3497–3505.
[18] S.S. Sekhon, Deepa, S.A. Agnihotry, Solid State Ionics 136 (2000) 1189–1192.
[19] F.B. Dias, L. Plomp, J.B.J. Veldhuis, Journal of Power Sources 88 (2000) 169–191.
[20] W.A. Gazotti, M.A.S. Spinace, E.M. Girotto, M.A. De Paoli, Solid State Ionics 130 (2000) 281–291.
[21] W.H. Meyer, Advanced Materials 10 (1998) 439–448.
[22] H.W. Heuer, R. Wehrmann, S. Kirchmeyer, Advanced Functional Materials 12 (2002) 89–94.
[23] M.K. Song, J.Y. Cho, B.W. Cho, H.W. Rhee, Journal of Power Sources 110 (2002) 209–215.
[24] G.A. Sotzing, J.L. Reddinger, A.R. Katritzky, J. Soloducho, R. Musgrave, J.R. Reynolds, Chemistry of Materials 9 (1997) 1578–1587.
[25] R.K. Gupta, H.Y. Jung, C.M. Whang, Journal of Materials Chemistry 12 (2002) 3779–3782.
[26] A.A. Argun, A. Cirpan, J.R. Reynolds, Advanced Materials 15 (2003) 1338–1341.
[27] D. DeLongchamp, P.T. Hammond, Advanced Materials 13 (2001) 1455–1459.
[28] H.C. Ko, S.A. Park, H.S. Lee, Synthetic Metals 143 (2004) 31–35.
[29] H. Grande, T.F. Otero, Journal of Physical Chemistry B 102 (1998) 7535–7540.
[30] R.S. Draper, M.V. Wood, B. Radmard, K. Mahmud, P. Schuler, G.A. Sotzing, V. Seshadri, W. Mino, J. Padilla, T.F. Otero, Cockpit and Future Displays for Defense and Security Proceedings of the SPIE (2005).
[31] T.F. Otero, H.J. Grande, J. Rodriguez, Journal of Physical Chemistry B 101 (1997) 3688–3697.
[32] T.F. Otero, M. Bengoechea, Langmuir 15 (1999) 1323–1327.
[33] N.A. O'Brien, J. Gordon, H. Mathew, B.P. Hichwa, Thin Solid Films 345 (1999) 312–318.
[34] K.H. Heckner, A. Kraft, Solid State Ionics 152 (2002) 899–905.

Available online at www.sciencedirect.com
ScienceDirect
Organic Electronics 8 (2007) 382–388
Organic Electronics
www.elsevier.com/locate/orgel

Novel approach for energy band diagram and barrier heights in metal/organic structures

Il-soo Park *, Soonryong Park, Junsik Oh, Joohwa Lee

CTO CAE Team, Samsung SDI Co., Ltd., 428-5 Gongse-Dong, Giheung-Gu, Yongin-City, Gyungki-Do 449-902, Republic of Korea

Received 18 August 2006; received in revised form 4 January 2007; accepted 9 January 2007
Available online 15 January 2007

Abstract

We propose a new method for obtaining the Fermi-level aligned energy band diagram and the electron and hole barrier heights in metal/organic structure. It is obtained from the known metal work function, vacuum level shift at metal/organic interface, and orbital states of organic material. This theory has two assumptions: (i) metal work function can be deviated from the original one at metal/organic interface and (ii) the energetic disorders of transport sites in interfacial layer are broadened and the broadening is related to the change of the metal work function. Our theoretical results are verified by using a conventional drift–diffusion model. This new approach to electrical characteristic simulation is applied to Mg:Ag/Alq_3/Mg:Ag, Mg:Ag/Alq_3/Al, and Mg:Ag/Alq_3/LiF/Al structures and then the current–voltage curves are consistent with experimental ones. From these results, we conclude that the above two assumptions are reasonable. Also we find that built-in potential and intrinsic carrier density are very important besides barrier heights in order to obtain more accurate current–voltage characteristics.
© 2007 Elsevier B.V. All rights reserved.

PACS: 71.20.Rv; 73.40.Ns; 73.61.Ph; 79.60.Jv

Keywords: Fermi-level alignment; Vacuum level shift; Band diagram; Barrier height; Built-in potential

1. Introduction

In order to obtain the current–voltage (J–V) characteristics in organic light emitting diodes (OLEDs), we have to know the charge transport in organic bulk; the charge injection at organic/organic (O/O) and metal/organic (M/O) interface. The charge transport in organic bulk is characterized by the mobility using Poole–Frenkel model or Bässler's Gaussian disorder model [1,2]. The charge injection at O/O interface can be obtained by the probability adopting Gaussian disorder concept [3]. For the M/O interface, it is generally known that the charge injection is described by using Richardson–Schottky (RS) thermionic emission or Fowler–Nordheim tunneling model. The current density by the RS thermionic emission is then written as [1,4]

$$J_{\mathrm{RS}} = A^* T^2 \exp\left[-\left(\phi_{\mathrm{B}} - \sqrt{e^3 F/4\pi\varepsilon}\right)/(k_{\mathrm{B}}T)\right], \quad (1)$$

* Corresponding author. Tel.: +82 31 2884285; fax: +82 31 2884289.
E-mail address: ilsoo.park@samsung.com (I.-s. Park).

1566-1199/$ - see front matter © 2007 Elsevier B.V. All rights reserved.
doi:10.1016/j.orgel.2007.01.003

where A^* is the modified Richardson constant, ϕ_B is the injection barrier height, e is the electronic charge, F is the electric field, ε is the permittivity, k_B is Boltzmann's constant, and T is the temperature. Here, the injection barrier heights for electron and hole (ϕ_e and ϕ_h) play an important role in the device design because the power efficiency with l m/W unit in OLEDs can be increased by the charge balance through the optimization of the barrier heights.

If we use the Schottky–Mott rule related to metal/semiconductor (M/S) interface, ϕ_e (ϕ_h) corresponds to $\Phi_M - \chi$ ($IE - \Phi_M$), where Φ_M, χ, and IE are metal work function, electron affinity, and ionization energy of the solid [5]. However, we cannot apply the Schottky–Mott rule at M/O interface due to the vacuum level shift (Δ), which can be observed using ultraviolet photoemission spectroscopy (UPS) [5,6]. Thus, Δ has to be considered for the suitable ϕ_e and ϕ_h.

Fig. 1 shows the energy band diagram using three parameters obtained from UPS, Φ_M, IE of organic material, and Δ at M/O interface. Here, χ is given by using the known energy gap (E_g) of organic material. For typical organic materials, it is not clear whether a sufficient amount of charges is available to achieve the band bending [7]. However, the band bending effect in M/O structure is usually neglected due to the extremely small number of thermally generated carriers in organic layer with typically large wide band gap (2–3 eV) [8,9]. Therefore, in the case of undoped organic materials, where the band bending effects are negligible, ϕ_e and ϕ_h can be modified as $\Phi_M - \chi - \Delta$ and $IE - \Phi_M + \Delta$, respectively.

It is noted that most of organic materials have the intrinsic characteristic except for an intentional doping case. Fermi-energy level (E_f) is thus located near the band center. However, as illustrated in Fig. 1, organic material has the E_f locating near the lowest unoccupied molecular orbital (LUMO) or the highest occupied molecular orbital (HOMO) levels just like having an extrinsic characteristic. Also, we can easily observe the unfixed E_f in organic material when only the metal contact is changed in M/O structure [5,9]. The question for Fermi-level alignment at M/O structure is occurred due to the lack of interface information, and then the ambiguity appears in energy band diagram.

In the present study, we propose a new method for obtaining the energy band diagram in M/O structure and calculating the electron and hole barrier heights using the known parameters (Φ_M, Δ, χ, IE). The proposed energy band diagram satisfies two conditions: (i) Φ_M and E_f in organic material are aligned and (ii) the intrinsic characteristic in undoped organic material holds. This theory is accomplished by the assumptions of the changeable Φ_M and broadened energetic disorder of transport sites in interfacial layer. This theory is verified by comparing simulation results with experimental J–V data for Mg:Ag/Alq_3/Mg:Ag, Mg:Ag/Alq_3/Al, and Mg:Ag/Alq_3/LiF/Al structures.

2. Theory

2.1. Energy band diagram and barrier heights

Fig. 2 shows the energy band diagram using a proposed method in order to obtain the electron

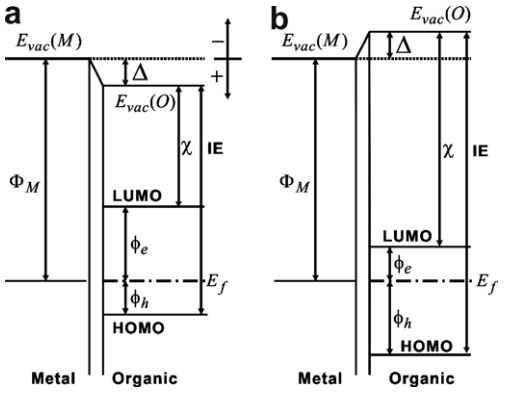


Fig. 1. Conventional energy band diagrams in metal/organic structure.

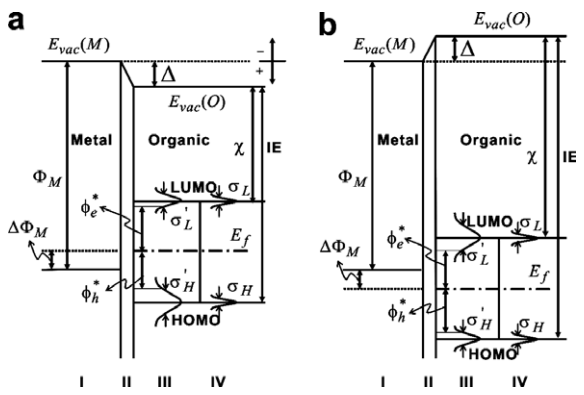


Fig. 2. Proposed energy band diagrams in metal/organic structure.

and hole barrier heights. Hereafter, those barrier heights are named as the effective electron and hole barrier heights (ϕ_e^* and ϕ_h^*). Here, we use only the four parameters Φ_M, Δ, χ, IE as in the case of Fig. 1. It is noted that E_f is located near the band center, and therefore the intrinsic characteristic of organic material is preserved. The proposed method is depicted as follows.

For M/S structure, the carriers in semiconductor are occupied in gap states at its interface, and then the equilibrium state is achieved through the band banding in semiconductor. Meanwhile, for M/O structure, the equilibrium state is reached by Δ at its interface (region II in Fig. 2). It is known that Δ appears due to the charge transfer, chemical reaction, and surface dipole [5]. In order to achieve the equilibrium state, Δ generally moves upward when Φ_M is close to the LUMO level, and vice versa.

The solid line in region I is the original Φ_M, the reference energy in UPS experiment. Because Δ is often not enough for reaching equilibrium state through Fermi-level alignment, additional changes are needed in both the metal and the organic material. Then, Φ_M can be moved upward or downward due to the push-back of electron cloud into the metal surface or surface dipole [6]. Φ_M is aligned with the original E_f of organic material, and then the change of Φ_M can be expressed as

$$\Delta\Phi_M = \left|(\Delta + \chi + E_g/2) - \Phi_M\right|. \tag{2}$$

However, the new Φ_M (dot line in region I) leads to two kinds of physically unacceptable results: (i) the built-in potential (V_{bi}) becomes always 0 V regardless of the metal and (ii) ϕ_e and ϕ_h are always the same.

For V_{bi}, we can explain as follows: The change of the Φ_M occurred in metal surface and can be considered as an additional vacuum level shift. The schematic diagram is depicted in Fig. 3. Fig. 3a shows a conventional V_{bi} ($V_{bi} = \Phi_{M1} - \Phi_{M2}$) in M/S structure. Fig. 3b illustrates V_{bi} in M/O structure using additional vacuum level shifts at anode and cathode interface (Δ_{m1}, Δ_{m2}), where $V_{bi} = \Delta_{m1} + \Delta_{m2}$. The V_{bi}s for the two cases are the same assuming that the applied voltage initially drops at M/O interface. Therefore, the schematic diagrams at $V = V_{bi}$ in M/S/M and M/O/M structures are also the same (Fig. 3c).

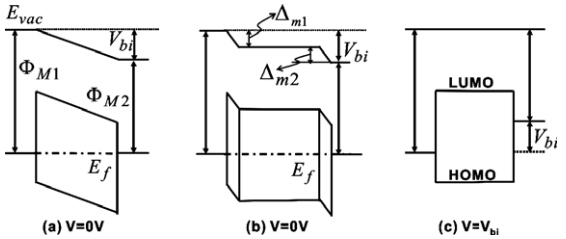


Fig. 3. Schematic illustration of the built-in potential for (a) $V = 0$ V in M/S/M, (b) $V = 0$ V in M/O/M, and (c) $V = V_{bi}$ in M/S/M and M/O/M structures.

For the barrier heights, we can presume that the additional change occurred in the region III (interfacial layer). The interfacial layer is supposed to have a broadened energetic disorder of transport sites in HOMO and LUMO. Indeed, Baldo and Forrest show the broadness of energetic disorder in interfacial layer using Monte-Carlo simulation [10]. Therefore, ϕ_e and ϕ_h change to new ones (ϕ_e^* and ϕ_h^*).

Meanwhile, it is not expected that there are the same changes in the broadness of energetic disorder in each transport state of HOMO and LUMO. We estimate that the more change occurs in state closer to the original Φ_M due to the orbital overlap, and assume that the broadening effect keeps the center of the HOMO (or LUMO) considering the negligible band bending. This change can be derived by the relative position of the original Φ_M compared to HOMO and LUMO levels, and then the energetic disorder of the first layer (σ') in interfacial layer is written as

$$\sigma'_H = \sigma_H + 2\Delta\Phi_M \cdot (\Phi_M - \chi)/E_g, \tag{3a}$$

$$\sigma'_L = \sigma_L + 2\Delta\Phi_M \cdot (IE - \Phi_M)/E_g, \tag{3b}$$

where σ is the original energetic disorder of transport sites, and subscripts H and L denote HOMO and LUMO, respectively.

The final results, the effective barrier heights for electron and hole can be expressed as

$$\phi_e^* = (E_g - \sigma'_L)/2, \tag{4a}$$

$$\phi_h^* = (E_g - \sigma'_H)/2. \tag{4b}$$

Here, σ'_L and σ'_H are more and more decreased as closer to the region IV with σ_L and σ_H. However, in forward bias, the hole experiences ϕ_h^* at anode, and electron ϕ_e^* at cathode and carriers can transport through a negligible barrier in the interfacial layer. Therefore, we can use ϕ_e^* and ϕ_h^* as ϕ_B in Eq. (1). Meanwhile, in order to obtain J–V characteristic, we use a conventional drift–diffusion model which is depicted in the next chapter.

2.2. Simulation method

The numerical framework for our steady state simulation is based on a conventional drift–diffusion model. All parameters are scaled and symbolized by bar. The scaling factors are summarized in Table 1. The electrical characteristics are described with the following scaled equations:

$$\nabla \cdot (\nabla \bar{V}) = -(\bar{p} + \bar{p}_t - \bar{n} - \bar{n}_t), \quad (5)$$

$$\nabla \bar{J}_p + \bar{R} = 0, \quad (6)$$

$$\nabla \bar{J}_n - \bar{R} = 0, \quad (7)$$

$$\bar{J}_p = -\bar{\mu}_p(\bar{p}\nabla \bar{V} + \nabla \bar{p}), \quad (8)$$

$$\bar{J}_n = -\bar{\mu}_n(\bar{n}\nabla \bar{V} - \nabla \bar{n}), \quad (9)$$

$$\bar{R}_{pn} = (\bar{\mu}_p + \bar{\mu}_n)\bar{p}\bar{n}, \quad (10)$$

where V is the potential energy, R is the recombination rates, μ is the mobility, and p, n are the hole and electron densities. Subscripts, p, n, t mean hole, electron, and trap, respectively. The distribution of carriers and J–V curves can be obtained by self-consistent calculation using Eqs. (5)–(10).

In the above calculation, additional information is needed: (i) boundary condition, (ii) injection model, and (iii) mobility model. Here, Schottky contact boundary condition [11] is adopted and the potential energy at anode and cathode (V_{anode} and $V_{cathode}$) can be modified as:

$$V_{anode} = (\phi_h - E_g/2 + eV_{appl})/e, \quad (11a)$$

$$V_{cathode} = (E_g/2 - \phi_e)/e, \quad (11b)$$

where V_{appl} is the externally applied bias and e is the elementary charge. Meanwhile, Scott's injection model [12] is employed as

$$J_{INJ} = 4\psi^2 N_0 e\mu F \exp(-\phi_B^*/k_B T) \exp(f^{1/2}), \quad (12a)$$

$$\psi(f) = f^{-1} + f^{-1/2} - f^{-1}(1 + 2f^{1/2})^{1/2}, \quad (12b)$$

$$f = e^3 F/[4\pi\varepsilon(k_B T)^2], \quad (12c)$$

Table 1
Scaling factors

Quantity	Symbol	Value
Length	x	$\sqrt{\varepsilon k_B T/e^2 N}$
Potential energy	V	$k_B T/e$
Carrier density	N	$10^{14}/cm^3$
Diffusivity	D	1 cm^2/s
Mobility	μ	D/V
Recombination rate	R	DN/x^2
Current density	J	qDN/x
Time	t	x^2/D

where N_0 is the density of charge hopping sites, ψ is a slowly varying function of electric field, and f represents the usual Schottky barrier lowering effect. Here, we used $N_0 = 10^{21}/cm^3$ and $\varepsilon = 3.5 \times 8.854 \times 10^{-14}$ farad/cm. For mobility model, the field dependent mobility at room temperature from Bässler's Gaussian disorder model [2] is used and expressed as [3]

$$\mu(F)_{RT} = \mu_{0,RT} \cdot \exp(C_{RT} \cdot \sqrt{F}). \quad (13)$$

3. Results and discussion

In order to verify the formula for ϕ_e^* and ϕ_h^*, simulated results have to be compared to experimental results. Then, J–V curves as well as Φ_M, Δ, χ, IE are needed in M/O/M structure. We refer to only Baldo and Forrest's paper [10], because the literature containing all those information is scarce.

Fig. 4 shows a quantitative comparison between experimental and simulated J–V results for Mg:Ag/Alq_3/Mg:Ag structure. The material properties of Alq_3 are listed in Table 2. The other used parameters and discussions are as follows:

(i) A (dot line): If Δ at M/O interface is not considered, $\phi_e = 1.1$ eV and $\phi_h = 2.1$ eV using Φ_M of Mg:Ag (3.7 eV) and χ, IE of Alq_3 (2.6 eV, 5.8 eV). In this case, the electron and hole injections are difficult due to the high electron and hole barriers, and then only ohmic current is shown by the thermally generated intrinsic carrier density (n_i).

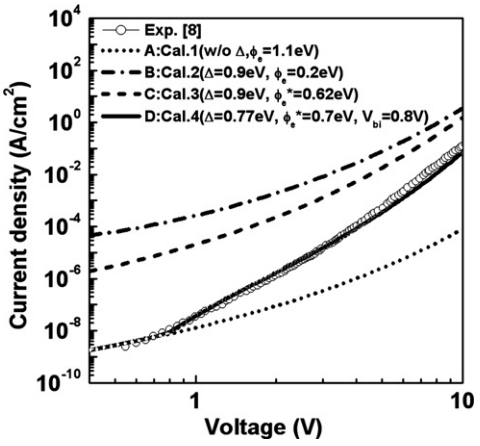


Fig. 4. Comparison of experimental and calculated J–V results according to simulation conditions in Mg:Ag/Alq_3/Mg:Ag structure.

Table 2
Material Properties for Alq_3

Parameters	Value
Electron affinity (eV)	2.6
Ionization energy (eV)	5.8
Trap density (cm^{-3})	10^{20}
Trap energy level (eV)	0.37
Energetic disorder (eV)	0.13
Electron mobility	$\mu_{0,RT} = 5.0 \times 10^{-6}$ $C_{RT} = 9.5 \times 10^{-3}$
Hole mobility	$\mu_{0,RT} = 5.0 \times 10^{-7}$ $C_{RT} = 6.0 \times 10^{-3}$

The parameters $\mu_{0,RT}$ and C_{RT} are given in $cm^2/V\,s$ and $(cm/V)^{1/2}$, respectively.

(ii) B (dash dot line): If we consider Δ at M/O interface, $\phi_e = \Phi_M - \chi - \Delta = 0.2$ eV using $\Delta = 0.9$ eV [10]. In this case, the current density is not injection-limited due to the low electron barrier and we cannot find ohmic current. Therefore, the current density is much higher than the experimental one.

(iii) C (dash line): From (2)–(4), $\phi_e^* = 0.62$ eV using $\Delta = 0.9$ eV. The current density in this case becomes lower than that in the case B, but is still much higher than the experimental one.

(iv) D (solid line): We can fit the result for the C case by the change of n_i, Δ, and V_{bi}. The current density at low voltage region can be fitted by n_i, the injection current density is controlled by ϕ^* using Δ, and the voltage axis in J–V curve is shifted by V_{bi}. Here, we use $n_i = 10^7/cm^3$, $\phi_e^* = 0.7$ eV using $\Delta = 0.77$ eV, and $V_{bi} = 0.8$ V. Then, the calculation result coincides with the experimental one. The increase of energetic disorder of HOMO and LUMO states at interfacial layer leads the decrease of E_g, and then n_i can be changed. For Δ, various experimental values in the same M/O structure appeared, for example ± 0.3 eV deviation is shown [10]. It can come from the difficulty in UPS analysis and a different

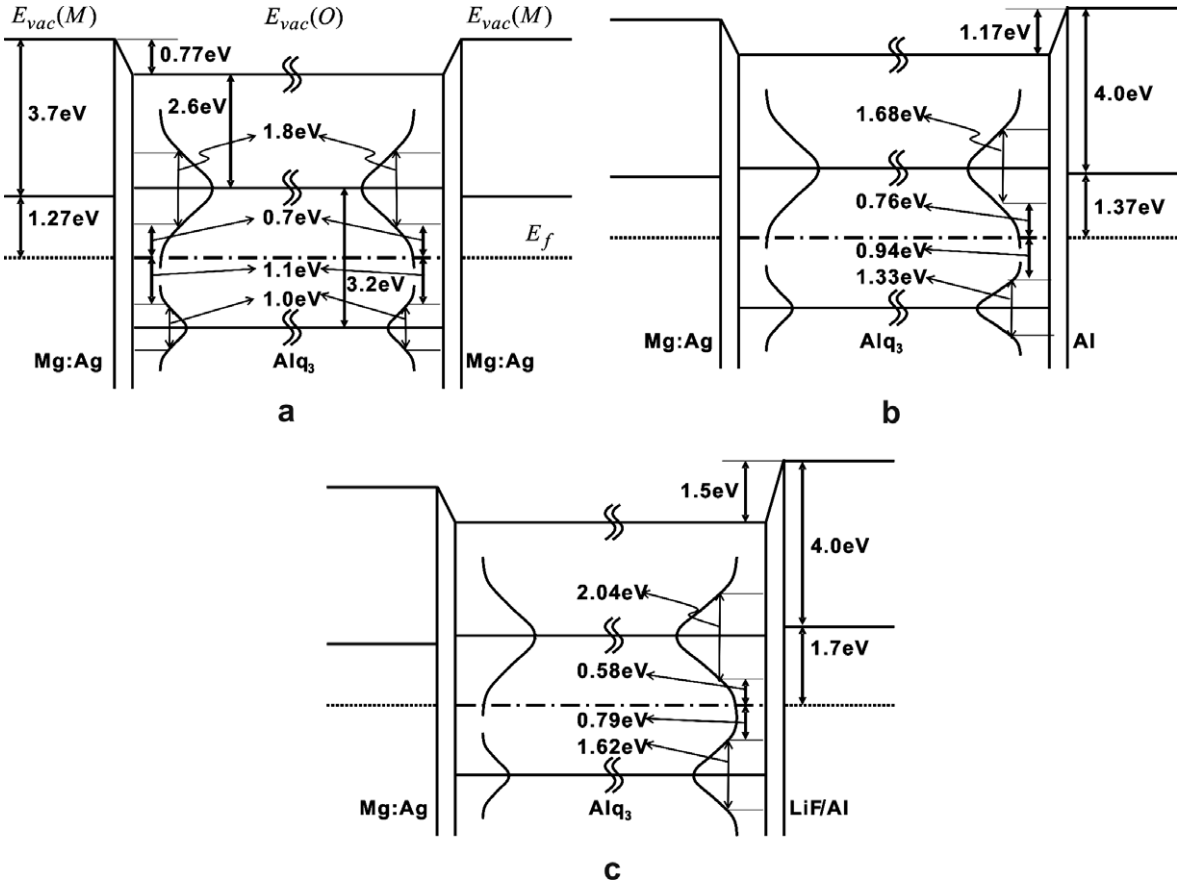


Fig. 5. Energy band diagram for obtaining the effective barrier heights in (a) Mg:Ag/Alq_3/Mg:Ag, (b) Mg:Ag/Alq_3/Al, and (c) Mg:Ag/Alq_3/LiF/Al.

experimental situation. Meanwhile, if the same metal is used for anode and cathode, V_{bi} is 0 V considering V_{bi} is flat band voltage. However, V_{bi} can be deviated from the difference of the two metal work functions due to the charge accumulation near the electrodes, dipole layer, and chemical reactions at M/O interface [13,14].

Fig. 5 shows the energy band diagram for effective barrier heights in (a) Mg:Ag/Alq_3/Mg:Ag, (b) Mg:Ag/Alq_3/Al, and (c) Mg:Ag/Alq_3/LiF/Al structures. In all cases, it is noted that Fermi-level alignment is achieved and ϕ_e^* and ϕ_h^* are easily obtained by the assumptions of the changeable Φ_M and broadened energetic disorder in interfacial layer.

For Mg:Ag/Alq_3/Al and Mg:Ag/Alq_3/LiF/Al cases, we obtain J–V curves using the same method as in the Mg:Ag/Alq_3/Mg:Ag case. The results are shown in Fig. 6 and used fitting parameters are listed in Table 3. The current density of Mg:Ag/Alq_3/LiF/Al case is higher than that of Mg:Ag/Alq_3/Al case due to the low electron barrier height ($\phi^*_{e_{Alq_3/LiF/Al}} = 0.58$ eV, ($\phi^*_{e_{Alq_3/Al}} = 0.76$ eV)). Meanwhile, if the fitting parameters in Table 3 are examined, we can estimate that the deviation of V_{bi} is related to Δ and $\Delta\Phi_M$. Namely, the deviation of V_{bi} originates from the interface of M/O as the above mentioned paper [13,14].

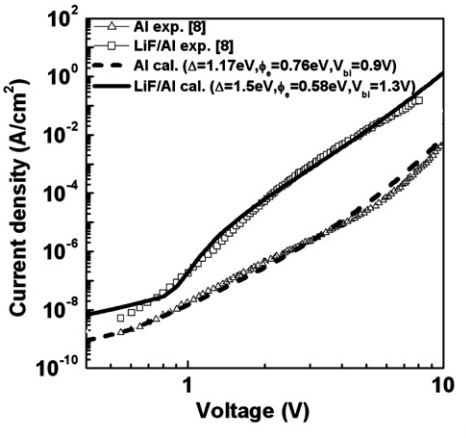


Fig. 6. Comparison of experimental and calculated J–V results in Mg:Ag/Alq_3/Al, and Mg:Ag/Alq_3/LiF/Al.

Table 3
Fitting parameters

M/O	Δ (eV)	$\Delta\Phi_M$ (eV)
Mg:Ag/Alq_3	0.77	1.27
Al/Alq_3	1.17	1.37
Al/LiF/Alq_3	1.5	1.7
M/O/M	V_{bi}	n_i (cm^{-3})
Mg:Ag/Alq_3/Mg:Ag	0.8	1×10^7
Mg:Ag/Alq_3/Al	0.9	5×10^6
Mg:Ag/Alq_3/LiF/Al	1.3	3×10^7

4. Conclusions

In metal/organic/metal structure, we show a novel approach for Fermi-level aligned energy band diagram and barrier heights for electron and hole by the assumptions of the changeable Φ_M and broadened energetic disorder in interfacial layer. Our theoretical results are verified by using a conventional drift–diffusion model with fitting parameters (intrinsic carrier density, vacuum level shift, and built-in potential). The simulated current–voltage curves are consistent with experimental ones for Mg:Ag/Alq_3/Mg:Ag, Mg:Ag/Alq_3/Al, and Mg:Ag/Alq_3/LiF/Al cases. From these results, we conclude that the above two assumptions are reasonable. Also, we find that built-in potential and intrinsic carrier density are very important besides barrier heights in order to obtain more accurate current–voltage characteristics.

Meanwhile, we estimate that built-in potential is related to vacuum level shift and the change of metal work function at metal/organic interface, but cannot find clear evidence for the origin of deviation of built-in potential. Therefore, the mechanisms for the origin of built-in potential have to be further investigated.

References

[1] W. Brütting, S. Berleb, A.G. Mückl, Org. Electron. 2 (2001) 1.
[2] H. Bässler, Phys. Stat. Sol. (b) 175 (1993) 15.
[3] J. Staudigel, M. Stößel, F. Steuber, J. Simmerer, J. Appl. Phys. 86 (1999) 3895.
[4] I.Y. Goliney, Synth. Met. 111–112 (2000) 359.
[5] A. Kahn, N. Koch, W. Gao, J. Polymer Science B polymer physics 41 (2003) 2529.
[6] H. Ishii, K. Sugiyama, E. Ito, K. Seki, Adv. Mater. 11 (1999) 605.
[7] H. Yamane, Y. Yabuuchi, H. Fukagawa, S. Kera, K.K. Okudira, N. Ueno, J. Appl. Phys. 99 (2006) 093705.
[8] W. Gao, A. Kahn, Org. Electron. 3 (2002) 53.
[9] H. Ishii, N. Hayashi, E. Ito, Y. Washizu, K. Sugi, Y. Kimura, M. Niwano, Y. Ouchi, K. Seki, Phys. Stat. Sol. (a) 201 (2004) 1075.

[10] M.A. Baldo, S.R. Forrest, Phys. Rev. B 64 (2001) 085201.
[11] S. Selberherr, Analysis and Simulation of Semiconductor Devices, Springer-Verlag, Wien, New York, 1984.
[12] J.C. Scott, G.G. Malliaras, Chem. Phys. Lett. 299 (1999) 115.
[13] G.G. Malliaras, J.R. Salem, P.J. Brock, C. Scott, Phys. Rev. B 58 (1998) R13411.
[14] B. Bohnenbuck, E. von Hauff, J. Parisi, C. Deibel, V. Dyakonov, J. Appl. Phys. 99 (2006) 024506.

Available online at www.sciencedirect.com
ScienceDirect
Organic Electronics 8 (2007) 389–395
Organic Electronics
www.elsevier.com/locate/orgel

Micromolding in capillaries and microtransfer printing of silver nanoparticles as soft-lithographic approach for the fabrication of source/drain electrodes in organic field-effect transistors

Alexander Blümel [a,1], Andreas Klug [a,1], Sabrina Eder [a], Ullrich Scherf [b], Erik Moderegger [c], Emil J.W. List [a,*]

[a] *Christian Doppler Laboratory Advanced Functional Materials, Institute of Solid State Physics, Graz University of Technology, Petersgasse 16, A-8010 Graz, Austria and Institute of Nanostructured Materials and Photonics, JOANNEUM RESEARCH, A-8160 Weiz, Austria*

[b] *Bergische Universität Wuppertal, Makromolekulare Chemie, Germany*

[c] *AT&S Austria Technologie und Systemtechnik AG, A-8700 Leoben, Austria*

Received 24 November 2006; received in revised form 7 January 2007; accepted 13 January 2007
Available online 12 February 2007

Abstract

Within the past years there has been much effort in developing and improving new techniques for the processing of advanced functional materials used in promising applications like micro-optics or organic electronics. Much attention has been paid to solution-based techniques, which enable low-cost processing and new possible developments like flexible displays or inkjet printed electronics. An alternative approach to inkjet printing is soft-lithography, which is a collective term for a number of non-photolithographic techniques and has become an important tool for the micron-sized structuring of materials.

Here we report on the use of micromolding in capillaries (MIMIC) and microtransfer printing (μTP) as two soft-lithographic techniques for the fabrication of silver source/drain electrodes in well-performing bottom-gate/bottom-contact organic field-effect transistors (OFETs) with poly(3-hexylthiophene) as active layer material.

While MIMIC combines solution-processability with high lateral resolution for highly accurate patterns, μTP is the miniaturized counterpart to conventional letterpress printing.

The performance of the OFETs fabricated with these techniques is similar to devices based on conventional gold source/drain electrodes with well-defined source-to-drain current saturation and a linear behavior at low drain voltages suggesting a low contact resistance and hence good carrier injection from the silver electrodes into the organic semiconductor.

© 2007 Elsevier B.V. All rights reserved.

* Corresponding author. Present address: Christian Doppler Laboratory Advanced Functional Materials, Institute of Solid State Physics, Graz University of Technology, Petersgasse 16, A-8010 Graz, Austria. Tel.: +43 316 873 8468.
E-mail address: e.list@TUGraz.at (E.J.W. List).

[1] The authors have contributed equally to the presented publication.

1566-1199/$ - see front matter © 2007 Elsevier B.V. All rights reserved.
doi:10.1016/j.orgel.2007.01.009

PACS: 61.46.Df; 72.80.Le; 81.65.Cf; 85.30.Tv; 85.40.Hp

Keywords: Micromolding in capillaries; Microtransfer printing; Silver nanoparticles; Soft-lithography; Organic field-effect transistors

1. Introduction

Soft-lithography is a non-photolithographic approach for structuring materials on the micro- and nanometer scale. In recent years, a large number of publications in various fields such as microelectronics (micro-wires [1], organic light-emitting devices (OLEDs) [2], organic field-effect transistors (OFETs) [3]) or biology (patterned cell growth [4]) underlines its flexibility and applicability in many different areas.

There are several soft-lithographic techniques utilizing different principles like capillary action (micromolding in capillaries (MIMIC)) [5,6] or self assembly of molecules (microcontact printing (μCP)) [7]. The use of an elastomeric stamp peeled from a rigid master is the common element of all these techniques. This stamp is used for structuring different materials with processes both similar to and quite different from conventional pattern printing. A detailed introduction into soft-lithography, its techniques and its applications is given by G.M. Whitesides and co-workers [8,9].

For the soft-lithographic fabrication of micron-sized silver structures, μCP, for instance, was applied [10], where patterned self-assembled monolayers (SAMs) act as etching resist on an evaporated silver substrate. Furthermore, inkjet printing of solution-processable silver, either as organo-complex precursor or as dispersed nanoparticles, was successfully demonstrated for the fabrication of organic field-effect transistors [11].

OFETs have been in the focus of research since the late 1980's [12,13]. Today their performance, determined by parameters such as field-effect mobility, on/off-current ratio and switch-on voltage, is similar to that of thin film transistors (TFTs) based on amorphous silicon. Compared to the latter, OFETs have the great advantage that the applied materials allow for low-cost, solution-based processing techniques at low temperatures.

Various methods for the fabrication of source/drain electrodes have been applied, such as vacuum evaporation and sputtering (in combination with shadow masks or lift-off techniques [14]), inkjet printing [11,15–17], electrochemical polymerization of monomers [18], screen printing [19], photochemical patterning [20], MIMIC [21] and μCP [22]. Non-solution-processed techniques typically are more expensive and require sophisticated instrumentation.

Here we report on the use of MIMIC for the fabrication of source/drain electrodes based on a solution-processable silver nano-dispersion (CABOT AG-IJ-G-100-S1) [23] in well-performing bottom-gate/bottom-contact organic field-effect transistors. By making use of a system of capillaries between a stamp and a substrate, this technique combines the advantage of solution-processability with high lateral resolution for accurate patterns. Depositing a droplet of the desired material at one end of a capillary makes the liquid enter the microchannel due to capillary action.

In addition, we apply microtransfer printing (μTP), the miniaturized counterpart to conventional letterpress printing, as a means to fabricate OFET source/drain electrodes based on the same silver nano-dispersion as used for the MIMIC devices. Here the stamp is set onto an inking pad so that the protruding surfaces of the stamp come into contact with the dispersion. With the inked stamp the silver fluid is directly transferred to the substrate.

Our results show that both techniques have the potential to be applied on industrial scale, since the stamp material and the nano-dispersion are commercially available and the process itself leaves room for improvement.

2. Experimental

For MIMIC stamps spin-cast, exposed and developed photoresist films (Microposit 1813, obtained from Shipley) were used as master structures. In contrast, for the fabrication of μTP stamps suitable master structures were directly printed onto transparency sheets using a conventional 600 dpi office laser printer.

For the preparation of the stamp polydimethylsiloxane (PDMS) (Sylgard 184 from Dow Corning) was processed according to standard procedures.

As substrates n^{++}-Si wafer pieces (dimensions: 25 mm × 25 mm) with a 247 nm thick, thermally grown SiO_2 layer were used. The highly n-doped

Si served as common gate electrode, the SiO_2 layer as gate dielectric.

For MIMIC the Si/SiO_2 substrates were pre-treated with an O_2-plasma in a home-made plasma chamber and put in deionized water to obtain a hydrophilic surface. Then the stamp was placed onto the substrate to make conformal contact. Two droplets of the silver nano-dispersion (CABOT AG-IJ-G-100-S1) [23] were deposited near the open ends of the capillaries. Due to capillary action the channels were filled with the liquid, which is a very slow process depending on parameters like height, width and length of the microchannel as well as dynamic viscosity, surface tension of the carrier fluid and advancing contact angles on both the substrate and the stamp. The sample was stored under ambient conditions until the filling process was completed. After sample curing at 150 °C for 1 h the stamp was removed carefully and the structures were characterized by optical microscopy.

For μTP the first step was the fabrication of an ''inking pad'', for which a small amount of the silver nano-dispersion (CABOT AG-IJ-G-100-S1) [23] was drop-cast onto a microscope slide. The dispersion spread over a large area due to the hydrophilic glass surface. For more accurate printing the inking pad was stored in ambient conditions for several hours to increase viscosity by evaporation of low-boiling components of the silver nano-dispersion. After inking the stamp it was put onto a glass slide for 4–5 times to get rid of excess ink and obtain well-defined structures. Then the actual printing process was performed either by placing the stamp onto the Si/SiO_2 substrate for approximately 3 s or leaving it there and baking substrate and stamp for 2 h at 80 °C. Both methods typically resulted in defined source/drain electrodes. After removing the stamp, the samples were baked (again) at 150 °C for 1 h.

As active layer material the well-established conjugated polymer regioregular poly(3-hexylthiophene) (P3HT, $M_n = 37\,900$, $M_w = 53\,700$) was applied. Alkyl-substituted thiophenes are known to dissolve well in solvents like chloroform and yield charge-carrier mobilities up to 0.1 cm^2/Vs, depending on the material and the processing conditions [24]. An amount of P3HT was heated at 120 °C in high vacuum for several hours in order to (a) remove the H_2O film on the surface of the polymer chains resulting from air humidity and (b) dedope the material [25,26]. Then the polymer was quickly transferred into an argon glove box in the hot state, where it was dissolved in spectrally clean chloroform ($CHCl_3$, concentration: 2 mg/ml).

The substrates with the pre-defined MIMIC and μTP source/drain structures were baked at 110 °C in vacuum for 1 h to remove the H_2O-film on the surface.

In order to complete the bottom-gate/bottom-contact OFETs, the P3HT solution was deposited under inert conditions by drop-casting (MIMIC structures) and spin-casting (μTP structures, spin parameters: 1500 rpm, 40 s). Due to the hydrophilization of the substrate in the MIMIC process spin-coating P3HT from chloroform solutions did not yield homogenous films. Therefore, drop-casting was applied for MIMIC devices and spin-casting only for μTP OFETs.

After the deposition the layers were dried in argon at 50 °C for 10 min. A frame was scratched around every single device within the P3HT layer in order to reduce parasitic leakage currents both across the gate dielectric and within the organic semiconducting layer. Finally a baking step was performed where the devices were heated at 180 °C for 1.5 h under high vacuum. Before and after scratching the P3HT layer as well as after the baking procedure the devices were analyzed in argon atmosphere with an E5262A parameter analyzer from Agilent Technologies.

3. Results and discussion

Fig. 1 schematically depicts the process flow for the fabrication of the source/drain electrodes by means of both MIMIC and μTP. The micrographs of the realized structures are shown as well. Details on the individual process steps are given in the experimental section.

The MIMIC silver electrodes were well-defined showing high lateral resolution, which was confirmed by investigating single lines with atomic force microscopy (AFM). Fig. 2 shows an example of a corresponding AFM image, where the electrode height was determined to approximately 600 nm (for comparison, the capillary height was ~1.3 μm).

The cross-sectional shape differed slightly from the rectangular shape of the master, as the top of the electrodes showed a height depression of approximately 60 nm with respect to their edges. This was ascribed both to sagging of the stamp and diffusion of the carrier fluid into the stamp [27]. The resistivity of the material was determined

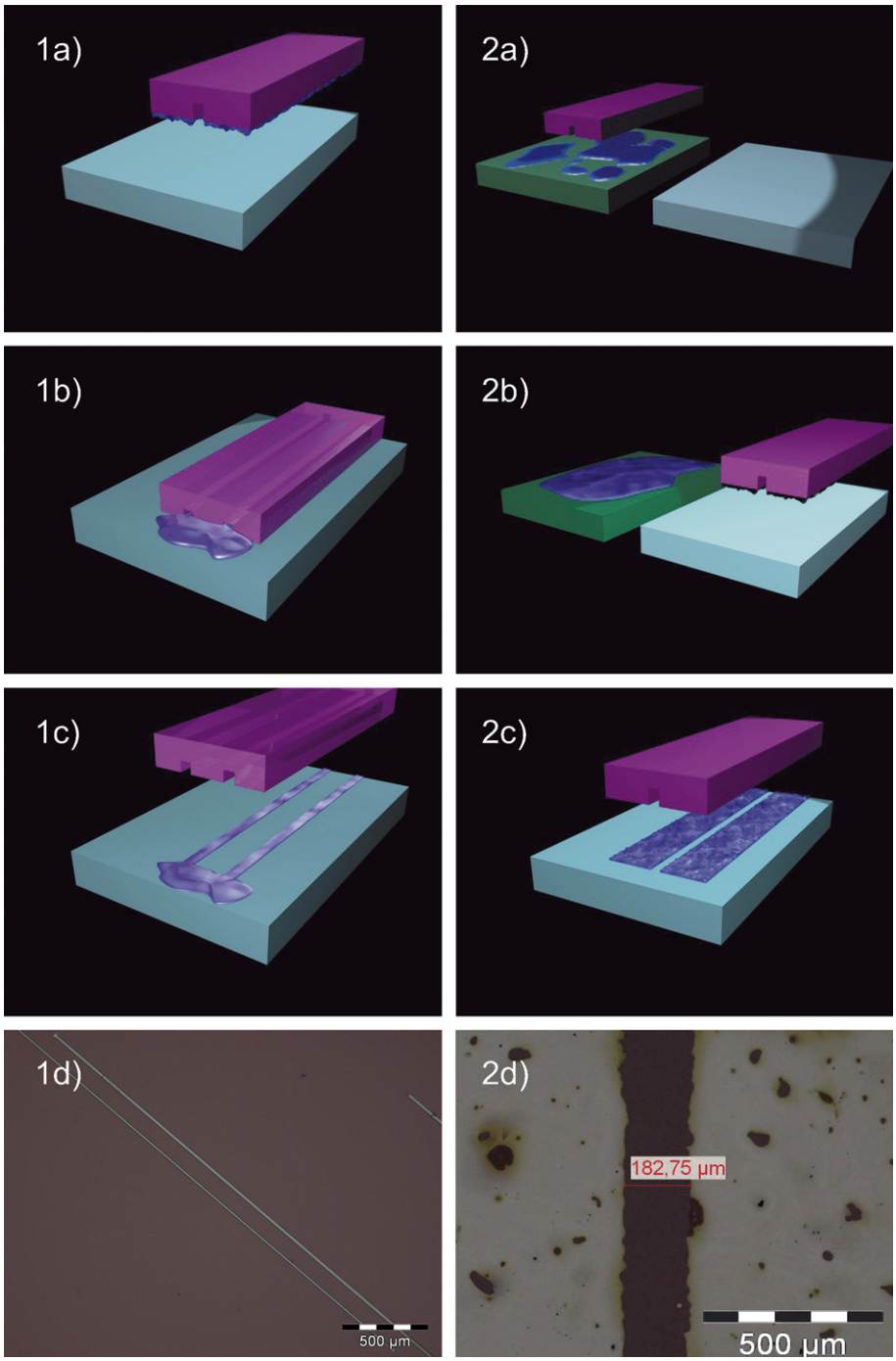


Fig. 1. Process flow and realized structures of source/drain electrodes fabricated by means of micromolding in capillaries (1a–1d) and microtransfer printing (2a–2d); 1a: stamp and substrate, 1b: silver nano-dispersion entering the microchannels due to capillary action, 1c: cured silver pattern on the substrate forming source/drain electrodes, 1d: optical micrograph of typical MIMIC electrodes after curing; 2a: inking pad, substrate and stamp, 2b: inking pad, substrate and inked stamp, 2c: transferred silver pattern forming source/drain electrodes, 2d: optical micrograph of typical µTP electrodes after curing.

to 20 µ Ω cm, which is significantly above the value of 1.49 µ Ω cm for bulk silver [28].

In 1998, Rogers et al. reported the use of MIMIC for the fabrication of polyaniline and carbon

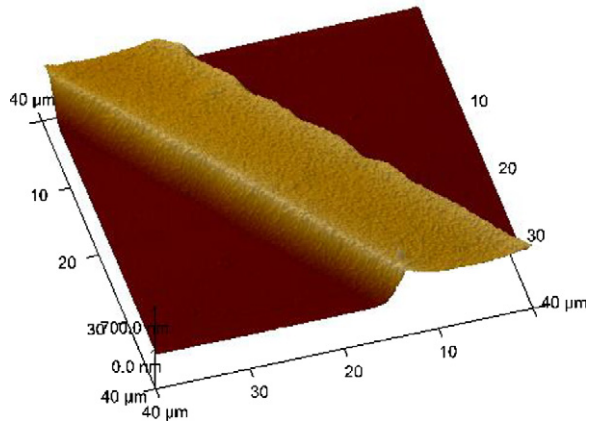


Fig. 2. 3D-AFM height image (tapping mode) of a silver line obtained with micromolding in capillaries.

source/drain electrodes [21], which were structured as squares (dimensions: 1 mm × 1 mm). In contrast, in the present work single silver lines (approximately 10–15 µm width) were used as electrodes. Aside from the geometric approach, further items differing from the work mentioned above [21] were the use of silver nanoparticles for increased conductivity and the better-developed source-to-drain current saturation behavior of the devices, also ascribed to the larger channel lengths.

The source/drain structures obtained with microtransfer printing exhibited regions of incomplete pattern transfer (see 2d in Fig. 1). The rather high edge roughness can be attributed to the different approach in master production, as the lateral dimensions of the photoresist masters for MIMIC stamps were too small for the µTP process. Therefore, laser-printed masters with lower lateral resolution were used instead. Furthermore, the applied nano-dispersion was optimized for inkjet printing and hence exhibited a too low dynamic viscosity to yield well-defined µTP structures.

Nevertheless, one major advantage of microtransfer printing is that electrode structuring is performed in a single and fast step, while MIMIC is a very time-consuming procedure related to capillary action (see Refs. [5,6]).

Fig. 3 depicts the output and transfer characteristics of a well-performing MIMIC device after the baking procedure. They clearly do not reveal a quadratic behavior of the source-to-drain current I_D with respect to the gate voltage V_G in the saturation regime. This is ascribed both to the inhomogenous P3HT layer obtained by drop-casting and the hydrophilization of the substrate. High trap-densi-

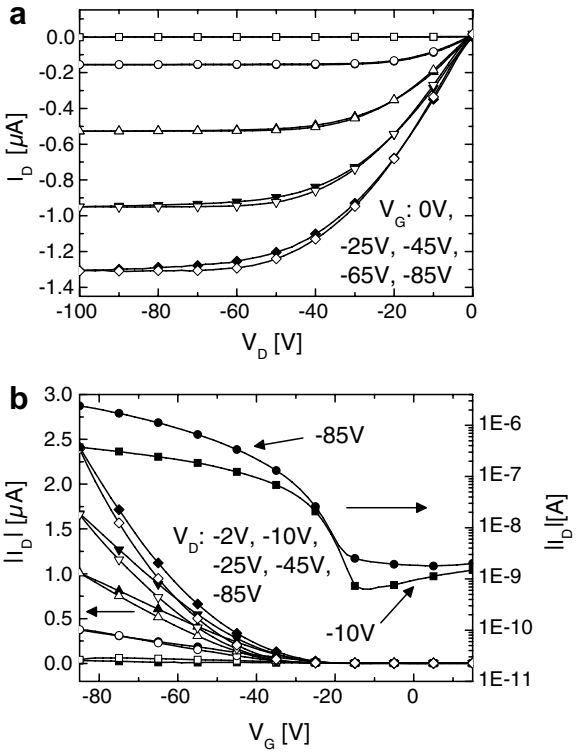


Fig. 3. (a) Output and (b) transfer characteristics of a MIMIC device after baking at ~180 °C for 90 min (channel length $L = 94$ µm, channel width $W = 1920$ µm); measured in argon; filled symbols: sweeps from positive to negative voltages; open symbols: reverse sweep.

ties within the active layer and near the semiconductor/dielectric interface lead to a reduction of the channel current with time due to charge-carrier trapping mechanisms, an effect which becomes stronger when V_G is increased (gate-bias stress) [29,30].

Gate-bias stress is also responsible for the fact that I_D at a particular drain voltage V_D and (high) V_G is larger in the transfer characteristics than in the corresponding output characteristics. Furthermore, gate-bias stress implies that the hysteresis typically is larger in the transfer characteristics than in the output characteristics.

From the semilogarithmic plot of the transfer characteristics (Fig. 3b) the switch-on voltage of the transistor is determined to approximately −15 V, which is rather large and also a sign of the presence of high trap densities at the semiconductor/dielectric interface and within the semiconductor bulk. Compared with the current–voltage characteristics obtained before device baking (not

shown), the switch-on voltage in Fig. 3 is shifted to more negative values and the channel current is reduced. This is attributed to dedoping of the active layer material [25,26]. By device baking the magnitude of hysteresis was strongly reduced as well, in particular in the transfer characteristics, which mirrors a better morphology of the heated polymer film.

The mobility in the saturation regime, calculated directly from the transfer characteristics in Fig. 3 using Eq. (1), was $\sim 4 \times 10^{-3}$ cm^2/Vs (at $V_G = -60$ V and $V_D = -85$ V), well in the range expected for disordered P3HT.

$$I_{Dsat} = \frac{W}{2L} \mu C_i (V_G - V_0)^2 \quad (1)$$

I_{Dsat}: source-to-drain current in the saturation regime, W: channel width, L: channel length, μ: field-effect mobility, C_i: dielectric capacitance per unit area, V_0: threshold voltage.

The on/off-current ratio of the MIMIC device in Fig. 3 was determined to approximately 10^3. The rather linear behavior of I_D at low drain voltages and the well-defined current saturation suggest that contact resistance is small in these devices so that charges are well injected from the silver MIMIC electrodes into the P3HT. However, in OFETs with larger channel lengths (here $L = 94$ μm) the influence of contact resistance generally is reduced due to the larger channel resistance [15,16].

Fig. 4 shows the output and transfer characteristics of a well-performing μTP OFET after the baking procedure. The current saturation is well observable as with the MIMIC OFETs. However, in contrast to the latter, the μTP OFETs showed a superquadratic behavior of the source-to-drain current with respect to the gate voltage. This is expected when trap densities are rather low and when the field-effect mobility increases with gate bias, as commonly observed with conjugated polymers like P3HT [31]. The lower trap densities are ascribed both to the spin-casting process (more homogenous, thinner films than drop-casting) and the absence of the substrate hydrophilization. The more homogenous and thinner films were also responsible for the fact that the effects of the baking procedure mentioned above were weaker than with the MIMIC OFETs.

The lower trap densities in the μTP devices are also confirmed by the smaller difference of the channel current values in the output and transfer characteristics at a particular working point, by the smaller

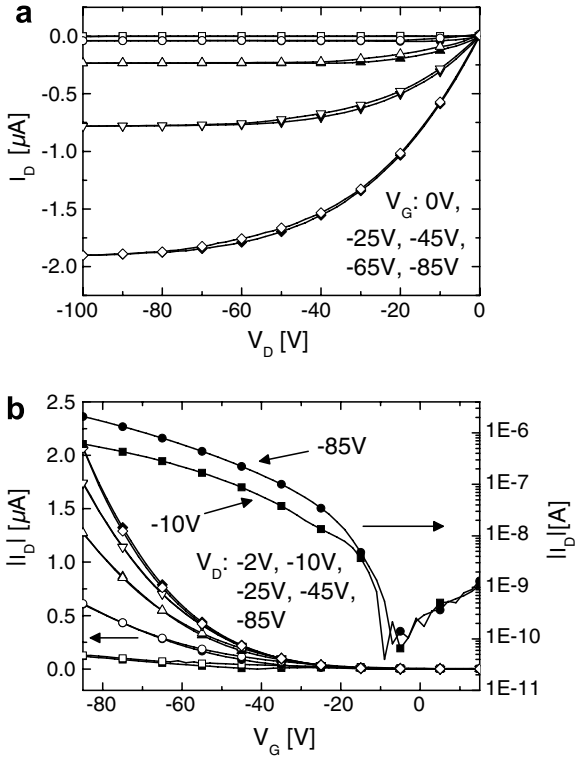


Fig. 4. (a) Output and (b) transfer characteristics of a μTP device after baking at ~180 °C for 90 min (channel length $L = 159$ μm, channel width $W = 5814$ μm); measured in argon; filled symbols: sweeps from positive to negative voltages; open symbols: reverse sweep.

magnitude of hysteresis in the transfer characteristics (same measurement speed as with the MIMIC OFETs) and by the lower absolute value of the switch-on voltage ($V_{SO} \sim -9$ V). The thinner, spin-cast P3HT film implies a lower number of free charge carriers within its bulk, which explains the about one order of magnitude smaller off-current observed with the μTP OFETs (compare Fig. 3b and Fig. 4b). Accordingly, the on/off-current ratio of the μTP OFETs (10^3–10^4) is a little larger than that of the MIMIC OFETs.

The mobility in the saturation regime determined from Eq. (1) was in the same range ($\sim 2 \times 10^{-3}$ cm^2/Vs at $V_G = -60$ V and $V_D = -85$ V).

Similar to the MIMIC OFETs, the linear behavior of I_D at low drain voltages and the well-observable current saturation suggest low contact resistance between the silver μTP electrodes and the P3HT. Again, the influence of contact resistance on device characteristics is rather low compared to channel resistance when channel lengths are large (here $L = 159$ μm) [15,16].

With both MIMIC and μTP OFETs, gate leakage currents were in the same range (smaller than 5×10^{-8} A).

4. Conclusions

In summary, we have shown that the soft-lithographic techniques micromolding in capillaries (MIMIC) and microtransfer printing (μTP) can be applied for the structuring of solution-processable silver for source/drain electrodes in organic field-effect transistors. The attained performance is comparable with OFETs based on commonly used gold source/drain electrodes. The well-observable source-to-drain current saturation and the linear behavior at low drain voltages suggest a low contact resistance and hence good carrier injection from both the MIMIC and μTP electrodes into the P3HT.

Tuning of the ink parameters such as solid content, dynamic viscosity and surface tension will improve the process flow, decrease the process time and yield more accurate and smaller structures, which altogether will be crucial for industrial scale applications. In addition, after the deposition of the electrodes with MIMIC the substrate should be hydrophobized, for instance, by applying a non-polar self-assembled monolayer, which would facilitate the applicability of spin-casting for better film morphology.

With these improvements, micromolding in capillaries and microtransfer printing could become standard methods in OFET fabrication.

Acknowledgements

The CDL-AFM greatfully acknowledges AT&S AG for the continuous support, the ISOTEC project cluster for (projects N702 and N706) for financial support and austriamicrosystems AG for providing the substrates.

References

[1] F. Zhang, T. Nyberg, O. Inganas, Nano Lett. 2 (2002) 1373.
[2] Y. Koide, M.W. Such, R. Basu, G. Evmenenko, J. Cui, P. Dutta, M.C. Hersam, T.J. Marks, Langmuir 19 (2003) 86.
[3] P. Cosseddu, A. Bonfiglio, Appl. Phys. Lett. 88 (2006) 023506.
[4] R.S. Kane, S. Takayama, E. Ostuni, D.E. Ingber, G.M. Whitesides, Biomaterials 20 (1999) 2363.
[5] E. Kim, Y. Xia, G.M. Whitesides, J. Am. Chem. Soc. 118 (1996) 5722.
[6] A. Blümel, Diploma Thesis. Graz University of Technology; 2005.
[7] J.L. Wilbur, A. Kumar, H.A. Biebuyck, E. Kim, G.M. Whitesides, Nanotechnology 7 (1996) 452.
[8] Y. Xia, G.M. Whitesides, Angew. Chem., Int. Ed. 37 (1998) 550.
[9] Y. Xia, G.M. Whitesides, Annu. Rev. Mater. Sci. 28 (1998) 153.
[10] Y. Xia, N. Venkateswaran, D. Quin, J. Tien, G.M. Whitesides, Langmuir 14 (1998) 363.
[11] S. Gamerith, A. Klug, H. Scheiber, U. Scherf, E. Moderegger, E.J.W. List, Adv. Funct. Mat., in press.
[12] H. Koezuka, A. Tsumura, T. Ando, Synth. Met. 18 (1987) 699.
[13] A. Tsumura, H. Koezuka, T. Ando, Synth. Met. 25 (1988) 11.
[14] T. Miyazaki, K. Kobayashi, K. Ishida, S. Hotta, T. Horiuchi, K. Matsushige, H. Yamada, J. Appl. Phys. 97 (2005) 124503.
[15] Andreas Klug, Diploma Thesis, Graz University of Technology; 2005.
[16] S. Gamerith, PhD thesis, Graz University of Technology; 2006.
[17] H. Sirringhaus, T. Kawase, R.H. Friend, T. Shimoda, M. Inbasekaran, W. Wu, E.P. Woo, Science 290 (2000) 2123.
[18] R. Parashkov, E. Becker, G. Ginev, T. Riedl, H.-H. Johannes, W. Kowalsky, J. Appl. Phys. 95 (2004) 1594.
[19] Z. Bao, Y. Feng, A. Dodabalapur, V.R. Raju, A.J. Lovinger, Chem. Mater. 9 (1997) 1299.
[20] C.J. Drury, C.M.J. Mutsaers, C.M. Hart, M. Matters, D.M. de Leeuw, Appl. Phys. Lett. 73 (1998) 108.
[21] J.A. Rogers, Z. Bao, V.R. Raju, Appl. Phys. Lett. 72 (1998) 2716.
[22] J. Tate, J.A. Rogers, C.D.W. Jones, B. Vyas, D.W. Murphy, W. Li, Z. Bao, R.E. Slusher, A. Dodabalapur, H.E. Katz, Langmuir 16 (2000) 6054.
[23] <http://www.cabot-corp.com>.
[24] C.D. Dimitrakopoulos, P.R.L. Malenfant, Adv. Mater. 14 (2002) 99.
[25] R.H.M. Van der Leur, B. De Ruiter, J. Breen, Synth Met. 54 (1993) 203.
[26] B.A. Mattis, P.C. Chang, V. Subramanian, Mat. Res. Soc. Symp. Proc. 771 (2003) L10.35.
[27] C.R. Martin, I.A. Aksay, J. Mater. Res. 20 (2005) 1995.
[28] Ch. Weißmantel, C. Hamann, Grundlagen der Festkörperphysik, Auflage, vol. 4, Johann Ambrosius Barth Verlag, Heidelberg/Leipzig, 1995.
[29] A. Schoonveld, Transistors based on ordered organic semiconductors, PhD Thesis, University of Groningen, Netherlands; 1999.
[30] C. Goldmann, C. Krellner, K.P. Pernstich, S. Haas, D.J. Gundlach, B. Batlogg, J. Appl. Phys. 99 (2006) 034507.
[31] A.R. Brown, C.P. Jarrett, D.M. de Leeuw, M. Matters, Synth. Met. 88 (1997) 37.

Available online at www.sciencedirect.com
ScienceDirect
Organic Electronics 8 (2007) 396–400
Organic Electronics
www.elsevier.com/locate/orgel

Reverse biased annealing: Effective post treatment tool for polymer/nano-composite solar cells

Ajay K. Pandey [a,*], J.-M. Nunzi [a,1], H. Wang [b], C.C. Oey [b], A.B. Djurišić [b], M.H. Xie [b], Y.H. Leung [b], K.K.Y. Man [b], W.K. Chan [b]

[a] *Equipe CSPVP, Laboratoire POMA,UMR CNRS 6136, Université d'Angers,49045 Angers, France*
[b] *University of Hong Kong, Pokfulam Road, Hong Kong*

Received 27 March 2006; accepted 7 February 2007
Available online 14 February 2007

Abstract

Hybrid organic solar cells using nano-porous TiO_2 infiltrated with MEH-PPV were made and characterized under standard AM 1.5 G solar illumination. Reverse biased annealing was performed on the fabricated cells as a post treatment and origin of the counter-diode was investigated by illuminating the cells through a UV-blocking filter. Treated devices deliver increased open circuit voltage and short circuit current density values, leading to significant increase in cell performances.
© 2007 Elsevier B.V. All rights reserved.

PACS: 72.20.Jv; 72.80.Le; 73.22.−f; 72.40.+w; 72.80.Tm

Keywords: Hybrid solar cells; Titanium dioxide; Nano-composite

1. Introduction

Motivated by the highly efficient TiO_2 based dye sensitized solar cells where a liquid electrolyte is required to initiate the electrochemical conversion of solar radiation, organic–organic and organic–inorganic hybrid cells have emerged as an alternative to realize cheap and clean conversion of solar energy into electricity [1–4]. Solar cells based on organic donors with metal oxide electron acceptors have been investigated by different research groups; while the majority reports on using different morphological TiO_2 layers in combination with polymeric donors such as MEH-PPV [4–7]. Nano-porous TiO_2 appears to be the most promising as it offers larger surface area than TiO_2 prepared by conventional sol–gel techniques [5]. In case of MEH-PPV based devices: relatively lower photocurrent and formation of a counter-diode under illumination appears to be the limiting factor behind poor efficiency. Different modifications have been proposed in order to improve devices efficiency [5,8,9]. Song et al. after incorporating a layer of PEDOT:PSS reported a power conversion efficiency $\eta = 0.49\%$ at $50\ mW\ cm^{-2}$ with short circuit current density $J_{SC} = 0.64\ mAcm^{-2}$ [5]. Recently Ravirajan

* Corresponding author.
E-mail addresses: ajay.pandey@univ-angers.fr (A.K. Pandey), nunzijm@post.queensu.ca (J.-M. Nunzi).
[1] Present address: Departments of Chemistry and Physics, Queen's University, Kingston K7L 3N6, Ontario, Canada.

1566-1199/$ - see front matter © 2007 Elsevier B.V. All rights reserved.
doi:10.1016/j.orgel.2007.02.003

et al., adopting the same strategy, reported a better short-circuit current close to 2 $mAcm^{-2}$ at 100 mW cm^{-2} resulting in $\eta = 0.58\%$ with an optimized device structure [8]. Takahashi et al. after blending DCM into MEH-PPV reported 0.47% power conversion efficiency [9]. Our systematic studies on cells made by MEH-PPV–filled TiO_2 nano-composites reveal that using biased annealing as post treatment and avoiding the UV part of the solar radiation spectrum can eliminate the counter-diode leading to significant improvement of cell performances.

2. Experimental

ITO coated glass substrates purchased from Merck with 15 Ω/square sheet resistance were selectively patterned by wet chemical etching and subsequently cleaned with ethanol and acetone followed by multiple rinsing in de-ionized water. Cleaned substrates were dried at 120 °C for one hour inside an oven. Highly porous TiO_2 layers consisting of a 3D interconnected network of anatase crystallites were processed on the ITO substrates. The titanium interconnected network was prepared as follows: Poly (styrene-block-ethylene oxide) (PS-*b*-PEO) was used as a templating agent, while titanium tetraisopropoxide (TTIP) was used as a TiO_2 precursor; A solution of 1% w/v PS-*b*-PEO (Polymer Source Inc., $M_w/M_n = 1.04$ polydispersity, 25,300 g/mol average molecular weight, 75:25 (PS:PEO) weight ratio) was prepared in toluene and aged overnight; A solution of 2.5% w/v of TTIP (99.999%, Aldrich Chemical Co.) in toluene were prepared; The PS-*b*-PEO and TTIP mixed solutions with different volume fractions were aged for 5 min before spin coating onto the ITO; Films of 40 nm thickness were obtained by spin coating; The films were finally calcinated by heating at 1 °C /min rate up to 200 °C, 300 °C, or 400 °C in atmosphere (relative humidity ~50%). Annealing in air is necessary in order to convert the titanium precursor into TiO_2 and to eliminate organic components of the film. It was observed that before annealing the films show featureless surface. Annealing at 200 °C starts to reveal the TiO_2 interconnected network. At 300 °C, large part of the film is converted to TiO_2. The best results were obtained for 400 °C.

The mechanism of formation of the porous TiO_2 interconnected network is as follows. Upon mixing the block copolymer and TTIP solutions, ethylene oxide segments will form crown-ether-type complexes with titanium ion. Since this will lower the solubility of the PEO block in toluene, the phase separation of the block copolymer will be affected. The conversion of the Ti containing organic material into TiO_2 is accomplished by annealing at 400 °C in air.

Transmission electron microscope (TEM) image in Fig. 1a was obtained using a JEOL 2010F microscope. Titania nano-porous layers, with average pore size of ~8 nm, were thus fabricated on top of transparent ITO conducting layers. To build the

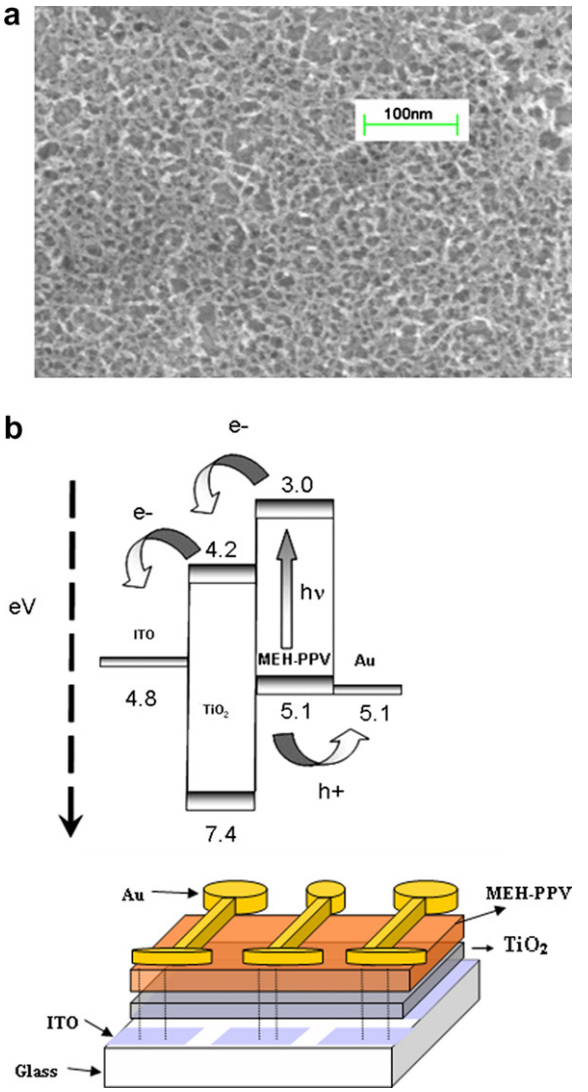


Fig. 1. (a) TEM image of the fabricated TiO_2 nano-porous layer with ~10 nm average pore-size and (b) energy-level diagram and device geometry of the TiO_2: MEH-PPV solar cells. Long tail in the device structure was used for connecting the circular devices. Small ITO strips down under were used as contact pad for the tails whereas the bigger one serves as common cathode for all three devices.

solar cells, a 50 nm layer of MEH-PPV (American Dye Source, Inc.) was spin coated from 8 mg/ml xylene solutions on top of the titania porous layers, followed by overnight annealing at 100 °C inside a vacuum oven. Prior to MEH-PPV deposition, the titania coated substrates were kept for 90 min inside a UV-Ozone cleaner (Jelight 42-220, 28 W/cm^2). Thirty nanometers of gold was finally evaporated as an anode through a proper shadow mask inside a BOC-Edwards evaporator in an argon filled MBraun 200B glove-box, defining an active device area of 0.32 cm^2 with three devices on each substrate. Our multilayer device configuration ITO/40 nm TiO_2/50 nm MEH-PPV/ 30 nm Au is depicted in Fig. 1b. Also shown in Fig. 1b is the energy-level diagram with respective HOMO-LUMO levels of the TiO_2 and MEH-PPV showing energetically favorable charge transfer and collection mechanisms.

Current–voltage (J–V) characteristics in the dark and under illumination were measured using a Keithley 236 source measurement unit with an AM 1.5 solar simulator (Steuernagel Solar constant 575). The devices were illuminated through the transparent ITO, serving as a cathode in our device structure. Annealing was performed by directly putting the biased/un-biased devices inside an oven (Buchi). A Keithley 236 SMU was used to apply the static reverse bias at different stages. All measurements were done under argon atmosphere with less than 0.1 ppm oxygen and moisture. The same set of reference devices were used for all post treatments.

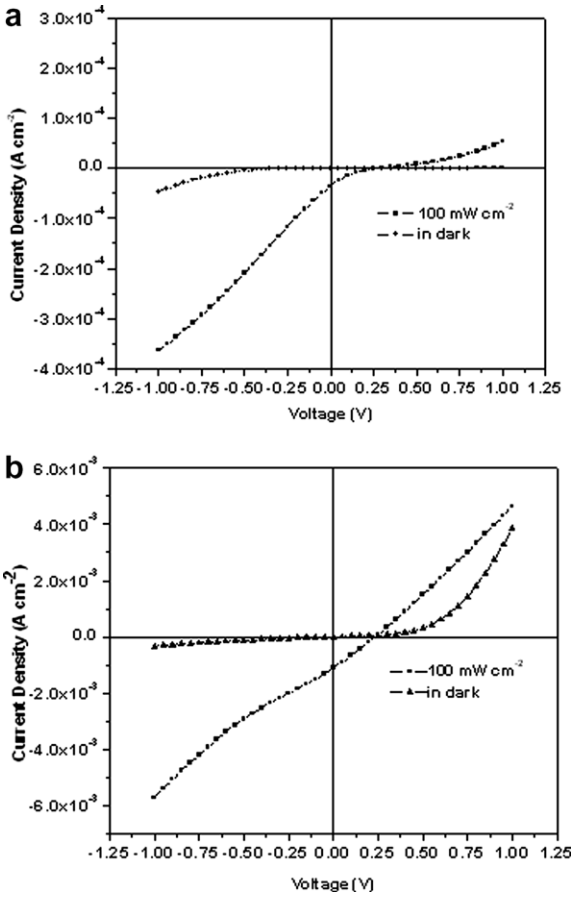


Fig. 2. J–V characteristics of the ITO/TiO:MEH-PPV/Au cells: (a) untreated cells in the dark (filled circles) and under 100 mW cm^{-2} AM1.5 illumination (filled squares); (b) after 5 min annealing at 250 °C in dark (filled triangles) and under 100 mW cm^{-2} AM1.5 illumination (filled squares).

3. Results and discussion

Fig. 2a shows the J–V characteristics of the hybrid cells measured in dark and under AM 1.5 G solar illumination at 100 mW cm^{-2}. The open circuit voltage, V_{OC} and the short-circuit current density J_{SC} measured for as fabricated cells were 250 mV and 36 μAcm^{-2}, respectively. Following the metal-insulator-metal (MIM) picture an open circuit voltage of 300 mV is expected as it comes from the difference in the work function of gold and ITO (see Fig. 1b). This may not be the case for low open circuit observed in our device structure as high open circuit voltage is a typical characteristic of MEH-PPV based bulk-heterojunction (BHJ) devices [10] which appears to be controlled by difference of the HOMO and LUMO of the respective donor and acceptor composition [11]. A direct comparison with efficient polymer-BHJ cannot be made in this case as in BHJ a spontaneous nano scale phase separation favors the device performance [12] whereas with porous TiO_2 the concern lies in to achieve a uniform filling of the nano pores with the polymer [13]. This may result in formation of dead ends for either kind of charge carriers breaking the percolation. In such a situation the unfilled pores can behave as charge traps which can prevent significant charge transfer because electron transfer from the MEH-PPV to the isolated network would result in charge buildup on local sites, which can lead to bimolecular recombination causing low shunt resistance [14]. The cell performance also suffers from appearance of counter-diode under illumination which too is apparently responsible for reduced V_{OC} and poor fill factor FF = 0.15. In relation to the small average pore size (~8 nm) of the porous TiO_2 layer, we attribute the low V_{OC} and

J_{SC} values in such cells to the poor filling of the polymer inside the TiO_2 network. In order to improve the polymer infiltration, cells were annealed at a higher temperature: 250 °C for 5 min. J_{SC} increased to 1.11 mAcm^{-2} after annealing but V_{OC} remained almost unchanged at 230 mV, yielding 0.07% efficiency (Fig. 2b). Annealing has been known to induce order of crystallization in polymer chains which reflects in the increased current observed here [15]. Moreover, it is also reported that crystallization prevents the efficient pore filling in TiO_2 layers [13] leading to improper interfacial contacts between the TiO_2 and the polymer which appears the case behind no increase in V_{OC} in our annealed cells.

Further treatment consisted in static biased annealing of the cells. It is indeed well established that an external static electric field can help aligning polar molecules, which can in turn increase significantly the open circuit voltage and efficiency of polymer solar cells [16]. Nano-porous TiO_2 is commonly used as a sensor for high temperature CO detection [17] and we suspect that adsorbed carbonates created during calcination cover our TiO_2 surfaces. For static field reverse bias was preferred as the diode conducts large current in forward bias regime. To prevent the device damage, cells were biased and annealed at relatively lower temperature at 100 °C in steps of −1 V under reverse bias up to −4 V for 10 min at each bias. Degradation occurred above −5 V. The changes induced after bias annealing were stable and reproducible as the above treated devices stored during 2 months under argon atmosphere delivered almost identical response, with only a slight decrease in V_{OC}. Fig. 3a shows the evolution of the cell characteristics treated under different biases. Significant increase in J_{SC} as well as V_{OC} is observed after each treatment. The effect of biased annealing on the photovoltaic parameters is summarized in Table 1. Devices treated at −4 V had more than doubled V_{OC} and an order of magnitude larger J_{SC}. Fill factor also increased from 0.15 to 0.29 and the cells delivered up to 0.08% efficiency with significantly reduced counter-diode in the J–V curves. No significant increase in V_{OC} and J_{SC} as well as FF was observed on the unbiased cells on the same substrate. This indicates the improvement is not a signature of annealing and it comes from the effect of external applied filed.

Counter-diode appearance under illumination in the J–V characteristics is commonly seen in reports on hybrid MEH-PPV based cells [5,18]. It is commonly believed to appear from the poor carrier selective nature of the electrodes used, as the TiO_2 network can probably get connected across the electrodes in such device geometries. To suppress such connection, we also made devices with 5–10 nm

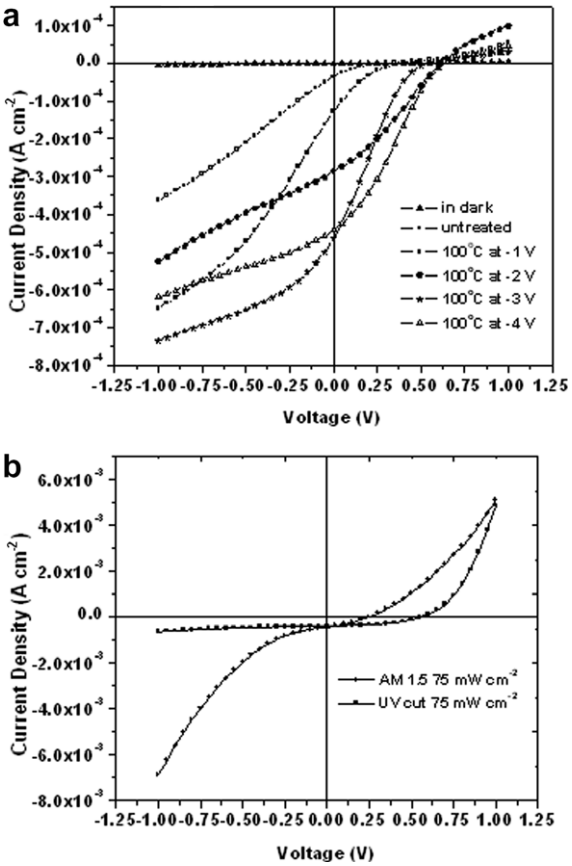


Fig. 3. (a) J–V characteristics under 100 mW cm^{-2} AM 1.5 G illumination of devices annealed at $T = 100$ °C for 10 min under −1 V (filled squares); followed by for 10 min under −2 V (filled pentagons); followed by for 10 min under −3 V (filled stars) and 10 min under −4 V (open triangles); and untreated devices in the dark (filled triangles). (b) J–V characteristics under 75 mW cm^{-2} AM 1.5 G illumination (filled circles) and 75 mW cm^{-2} illumination through a 475 nm UV-blocking filter (filled squares).

Table 1
Summary of the photovoltaic parameters of the ITO/TiO_2:MEH-PPV/Au solar cells treated by reverse bias annealing under different biases

Bias (V)	V_{OC}(mV)	J_{SC}(mA cm^{-2})	FF	η (%)
0	250	0.03	0.15	<0.01
−1	350	0.12	0.18	<0.01
−2	600	0.28	0.27	0.04
−3	500	0.46	0.20	0.05
−4	600	0.44	0.29	0.08

Table 2
Device performances obtained on cutting the UV-solar radiation

Intensity (mW cm^{-2})	V_{OC} (mV)	J_{SC} (mAcm^{-2})	FF	η (%)
75	291	0.42	0.32	0.04
75 (UV-cut)	668	0.37	0.46	0.13

CuPc layer before evaporation of the gold electrode on top of MEH-PPV (result not shown) but there were no signs of improvement. This suggests that the counter-diode originates from the ITO/TiO_2 interface. In order to substantiate our assumption, we measured cell performances under a fixed illumination of 75 mW cm^{-2} with and without cutting the UV portion of the AM 1.5 spectrum; TiO_2 indeed absorbs a significant portion of the UV-spectrum. This was done by using a 475 nm UV-blocking filter. We observe complete disappearance of the counter-diode behavior when the filter is used in Fig. 3b: larger fill factor FF = 0.47 and V_{OC} = 0.67 mV yield improved conversion efficiency $\eta = 0.13\%$ (see Table 2). It must be noticed that the J_{SC} of 0.34 mAcm^{-2} was observed even after blocking the significant portion of the polymer absorption profile. A higher value is indeed achievable using the appropriate UV-cut filter. This is comparable to other available reports on TiO_2/polymer hybrid solar cells [7,9,19], as reviewed recently [20]. According to the energy diagram in Fig. 1b, no counter-diode should originate from the TiO_2 – ITO interface. However, owing to surface states and impurities, nano-porous TiO_2 is not expected to have strictly the same Fermi level as bulk TiO_2 and large shifts of the Fermi have been predicted and observed previously [21], particularly when exposed to UV [22], which is likely to be at the origin of our UV-activated counter-diode.

4. Conclusion

We demonstrated reverse bias annealing as an effective post treatment tool for polymer: nanocomposite solar cells, as it permits to orient localized dipoles along the electric-field direction. A counter-diode behavior was identified as originating from the ITO/TiO_2 interface owing to UV-absorption from TiO_2. Blocking the UV portion of the solar spectrum significantly improves the J–V characteristics of the devices, owing to an increased fill factor. We believe that present study bears the potential to be used as a post treatment for solid state dye sensitized solar cells as well.

Acknowledgements

We acknowledge the France/Hong Kong Joint Research Scheme project F-HK25/03T, and the PROCORE program of the ministry of foreign affairs in France (No. 07799XM) for supporting our research. POMA also thanks the Nanosciences – Nanotechnologies ACI program *OxTi-Photobatterie* for support.

References

[1] B. O'Regan, M. Grätzel, Nature (London) 353 (1991) 737.
[2] J. Xue, S. Uchida, P.R. Barry, S.R. Forrest, Appl. Phys. Lett. 84 (16) (2004) 3014.
[3] R.-R. Marisol, K. Kyungkon, L.C. David, Appl. Phys. Lett. 87 (2005) 83506.
[4] W.J.E. Beek, M.M. Wienk, R.A.J. Janssen, Adv. Mater. 16 (2004) 1009.
[5] M.Y. Song, J.K. Kim, A.Y. Kim, Synth. Meter. 137 (2003) 1387.
[6] K.M. Coakley, M.D. McGehee, Appl. Phys. Lett. 83 (2003) 3380.
[7] A.J. Breeze, Z. Schlesinger, S.A. Carter, P.J. Brock, Phys. Rev. B 64 (2001) 125205.
[8] P. Ravirajan, D.D.C. Bradley, J. Nelson, S.A. Haque, J.R. Durrant, H.J.P. Smit, J.M. Kroon, Appl. Phys. Lett. 86 (2005) 143101.
[9] K. Takahashi, K. Seto, T. Yamaguchi, J.-I. Nakamura, C. Yokoe, K. Murata, Chem. Lett. 33 (2004) 1042.
[10] S. Alem, R. Bettignies, J.-M. Nunzi, M. Cariou, Appl. Phys. Lett. 84 (2004) 2178.
[11] C.J. Brabec, A. Cravino, D. Meissner, N.S. Sariciftci, T. Fromherz, M.T. Rispens, L. Sanchez, J.C. Hummelen, Adv. Funct. Mater. 11 (2001) 374.
[12] H. Hoppe, M. Niggemann, C. Winder, J. Kraut, R. Heisgen, A. Hinsch, D. Miessner, N.S. Sariciftci, Adv. Funct. Mater. 14 (2004) 1005.
[13] L. Schmidt-Mende, M. Grätzel, Thin Solid Films 500 (2006) 296.
[14] A.C. Arango, S.A. Carter, P.J. Brock, Appl. Phys. Lett. 74 (1999) 1698.
[15] F. Padinger, R.S. Rittberger, N.S. Sariciftci, Adv. Funct. Mater. 13 (2003) 85.
[16] C. Sentein, C. Fiorini, A. Lorin, J.M. Nunzi, P. Raimond, L. Sicot, Synth. Meter. 102 (1999) 989.
[17] N.O. Savage, S.A. Akbar, P.K. Dutta, Sensor. Acta. B 72 (2001) 239;
T. Anukunprasert, C. Saiwan, E. Traversa, Sci. Technol. Adv. Mater. 6 (2005) 359.
[18] H. Wang, C.C. Oey, A.B. Djurišić, K.K.Y. Man, W.K. Chan, M.H. Xie, Y.H. Leung, P.C. Chui, A. Pandey, J.-M. Nunzi, Appl. Phys. Lett. 87 (2005) 23507.
[19] P. Ravirajan, S.A. Haque, J.R. Durrant, D. Poplavskyy, D.D.C. Bradley, J. Nelson, J. Appl. Phys. 95 (2004) 1473.
[20] C.C. Oey, A.B. Djurišić, H. Wang, K.K.Y. Man, W.K. Chan, M.H. Xie, Y.H. Leung, A. Pandey, J.-M. Nunzi, P.C. Chui, Nanotechnology 17 (2006) 706.
[21] I. Mora-Sero, J. Bisquert, NanoLett. 3 (2003) 945.
[22] M. Jakob, H. Levanon, P.V. Kamat, NanoLett. 3 (2003) 353.

Available online at www.sciencedirect.com
ScienceDirect
Organic Electronics 8 (2007) 401–406
Organic Electronics
www.elsevier.com/locate/orgel

A flexible polymer memory device

Liang Li [a], Qi-Dan Ling [a], Siew-Lay Lim [a], Yoke-Ping Tan [b], Chunxiang Zhu [b], Daniel Siu Hhung Chan [b], En-Tang Kang [a,*], Koon-Gee Neoh [a]

[a] Department of Chemical and Biomolecular Engineering, National University of Singapore, 10 Kent Ridge, Singapore 119260, Singapore
[b] SNDL, Department of Electrical and Computer Engineering, National University of Singapore, 119260 Singapore, Singapore

Received 3 April 2006; received in revised form 1 February 2007; accepted 1 February 2007
Available online 13 February 2007

Abstract

A flexible polymer memory device is demonstrated in a sandwich structure of polypyrrole/P6FBEu/Au. Conductance switching at a voltage of about 4 V, with an ON/OFF current ratio up to 200, was observed in this flexible memory device. At the low-conductivity state, current density–voltage (J–V) characteristics of the device were dominated by a charge injection current. At the high conductivity state, J–V characteristics were dominated by a space-charge-limited current. Both the ON and OFF states are stable up to 10^6 read cycles at a read voltage of 1 V. The device can be used as a write-once read-many-times (WORM) memory with good electronic stability.
© 2007 Elsevier B.V. All rights reserved.

PACS: 61.82.Pv; 73.00.Oo; 85.30.De; 85.65.+h

Keywords: Polypyrrole; Lanthanide polymer complex; Flexible memory device; WORM

1. Introduction

Due to the rapid development of information technology, considerable attention has been paid to overcome the miniaturization challenges facing the traditional Si, Ge, and GaAs semiconductor industry [1]. Organic materials are potential candidates for future molecular-scale device applications [2]. Several types of organic electronics and devices, including light-emitting diodes [3], transistors [4], photovoltaic cells [5] and switches [6], have been realized. Recently, flash-type memory and write-once read-many-times (WORM)-type memory based on polymeric materials have also been demonstrated [7,8]. Polymer memories exhibit simplicity in structure, good scalability, low-cost potential, 3D stacking capability and large capacity for data-storage. Rather than encoding "0" and "1" as the amount of charge stored in a cell in silicon devices, polymer memory stores data, for instance, based on the high and low-conductivity response to an applied voltage [9]. Electroactive polymers and organics are usually deposited by ink-jet printing, spin-coating or vacuum evaporation on a variety of rigid metal, metal oxide and inorganic substrates in the fabrication of memory and other devices [7–10]. The use of conductive polymer films [11–13]

* Corresponding author. Tel.: +65 6516 2189; fax: +65 6779 1936.
E-mail address: cheket@nus.edu.sg (E.-T. Kang).

1566-1199/$ - see front matter © 2007 Elsevier B.V. All rights reserved.
doi:10.1016/j.orgel.2007.02.002

as substrate electrodes offers an opportunity for the preparation of flexible devices.

In this work, we report on a flexible polymer memory device based on the conjugated copolymer of 9,9-dihexylfluorene and benzoate with chelated europium–thenoyltrifluoroacetone ligand complex (P6FBEu, structure shown in Fig. 1a [14]). A conducting polypyrrole (PPy) film is used as the flexible substrate for the memory device, instead of the rigid metal or metal oxide electrodes commonly reported in the memory architectures [7,8,10]. Conductance switching, with an ON/OFF current ratio up to 200, was observed in this flexible memory device.

2. Experimental

2.1. Preparation and characterization of P6FBEu

The copolymer, P6FBEu, containing both the electron–donor (9,9′-dihexylfluorene) and electron-acceptor (europium complex) groups, was synthesized via the Suzuki coupling copolymerization, hydrolysis of the benzoate units, and post-chelation [14]. The Eu complex is known to exhibit memory effects [15]. The number-average molecular weight of P6FBEu was around 41 800, with a polydispersity index of about 2.70 and a Eu weight content of 3.61%, corresponding to a molar ratio of 0.92/0.08 for the dihexylfluorene units to the benzoate units containing the Eu complex. From cyclic voltammetry, the energies for the highest occupied molecular orbital (E_{HOMO}) and the lowest unoccupied molecular orbital (E_{LUMO}) of P6FBEu were calculated to be -5.66 eV and -3.23 eV, respectively. P6FBEu exhibited good thermal stability, with an onset decomposition temperature above 310 °C, and a glass transition temperature of about 120 °C. With long alkyl substituents on the fluorene group, P6FBEu was soluble in common organic solvents, such as THF, toluene and chloroform. It could be

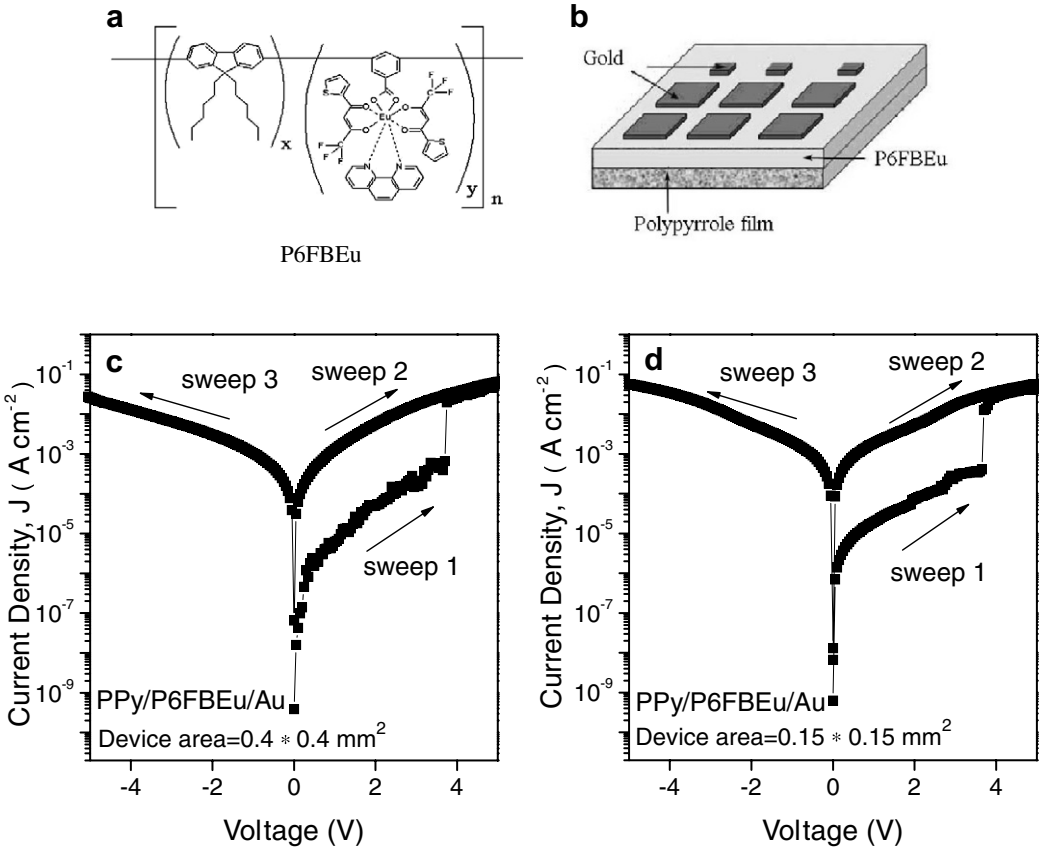


Fig. 1. (a) Molecular structure of the conjugated copolymer P6FBEu having the composition of x:y = 0.92:0.08. (b) Schematic diagram of the memory devices consisting of a thin film (~50 nm) of P6FBEu sandwiched between a flexible PPy film substrate (~40 μm in thickness) and gold top electrodes (~0.2 μm in thickness). J–V characteristics of the (c) PPy/P6FBEu/Au device with a 0.4×0.4 mm^2 gold electrode and (d) with a 0.15×0.15 mm^2 gold electrode.

cast into transparent and uniform thin films from solutions. Ionic aggregation and phase separation associated with the rare earth complex [16] were absent in the present copolymer film because the Eu complexes were covalently bonded to the polymer chains.

2.2. Fabrication and characterization of the devices

As shown in Fig. 1b, the flexible memory device has the simple structure of a P6FBEu film (~50 nm in thickness) sandwiched between a PPy bottom electrode (~40 μm in thickness) and a gold top electrode (~0.2 μm in thickness) (PPy/P6FBEu/Au). For the fabrication of the memory device, the PPy substrate was electrochemically polymerized in an electrolyte solution of pyrrole and toluene-4-sulfonic acid in acetonitrile containing 1 vol.% water, as reported in the literature [17]. A toluene solution of P6FBEu (10 mg/ml) was spin-coated onto PPy film of conductivity of about 60 S cm^{-1}, followed by solvent removal in a vacuum chamber at 10^{-5} Torr and 50 °C for 12 h. Gold top electrodes of 0.4×0.4 mm^2 and 0.15×0.15 mm^2 in areas were thermally evaporated onto the polymer surface at about 10^{-7} Torr using a shadow mask. The devices were characterized on a Hewlett–Packard 4156A semiconductor parameter analyzer equipped with an Agilent 16440A SMU/pulse generator under ambient conditions.

3. Results and discussion

The conductance switching effect of the flexible PPy/P6FBEu/Au memory device is shown in the current density–voltage (J–V) characteristics in Fig. 1c and d, for active device areas of 0.4×0.4 mm^2 and 0.15×0.15 mm^2, respectively. Initially, the as-fabricated PPy/P6FBEu/Au device was in its low-conductivity state (OFF state). The current density in the low-voltage range (0–4 V) on the first sweep was low, in the orders of 10^{-6}–10^{-5} A/cm^2, at 1 V. J increases progressively with the applied voltage (sweep 1). When a switching threshold voltage of about 4 V was applied, an abrupt increase in J from 10^{-4} to 10^{-2} A/cm^2 was observed, indicating the device transition from a low-conductivity state (OFF state) to a high conductivity state (ON state). This electrical transition from the OFF state to the ON state served as the "writing" process for the memory device. The device exhibited good stability in this high-conductivity state during the subsequent forward and reverse voltage scans. It remained in the ON-state even after turning off the power and in the subsequent voltage scans: sweep 2 (0 to +5 V) and sweep 3 (0 to −5 V). This flexible memory device could not be returned to the low-conductivity state by turning off the power and application of a reverse bias of the same magnitude (sweep 3, from 0 to −5 V) after it had been switched on. Thus, this device exhibits the write-once read-many-times (WORM) memory behavior. The memory device based on P6FBEu and flexible PPy film substrate is able to achieve an ON/OFF current ratio of about 200, which is comparable to those of the contemporary single layer molecular switching devices [18]. As shown in Fig. 1c and d, the current density and WORM memory effect of this flexible memory device are independent of the metal electrode area. Thus, contributions from the filament effect [19] and dielectric breakdown to the observed memory behaviour of P6FBEu can be ruled out.

It is well known that the lanthanide complexes distinguish themselves from the transition metal complexes by a high (up to 12, due to larger ionic radii) and variable coordination number (3–12, due to weaker crystal fields) [20]. The coordination number of the europium complex in P6FBEu is 8. Thus, it is an electron-deficient complex and can act as an electron acceptor [21,22]. The device based on P6FBEu was in its low-conductivity state in the low voltage range during the first sweep (0 to +5 V) since there were not much free charge carriers in P6FBEu before all the traps were filled. When the voltage was increased to the switching threshold voltage of about 4 V, the conjugated polymer became doped by the high electric field. The charge carriers can now migrate freely and the device is switched from the low-conductivity state to the high conductivity state. For P6FBEu, the neighboring fluorene groups can only assume a "shoulder-to-shoulder" conformation through position 2 and 7 (Fig. 1a) due to the rigid nature of the π-bond and steric hindrance. It is difficult for the fluorene groups to form insulating charge transfer complexes [10] with the europium complexes. Charge in polyfluorene composites with internal donor/acceptor heterojunction can be separated and migrated through the conjugated system. P6FBEu can thus retain its doped state. As a result, the device based on P6FBEu remains in the high conductivity state even after turning off the power (sweep 2) and does not return to the low-conductivity state upon applying a negative bias (sweep 3).

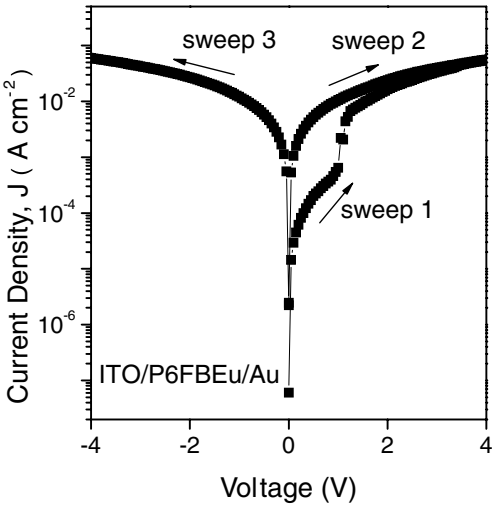


Fig. 2. J–V characteristics of the ITO/P6FBEu/Au device.

As a comparison, a similar device having the structure of ITO/P6FBEu/Au was also fabricated. The J–V characteristics of the ITO/P6FBEu/Au device are shown in Fig. 2. The ITO/P6FBEu/Au device switches from the low-conductivity (OFF) state to the high-conductivity (ON) state at about 1 V, with an ON/OFF current ratio of about 80 (sweeps 1 and 2). As indicated by the J–V curve of the ITO/P6FBEu/Au device, it cannot be returned to the OFF state by the application of a reverse bias of the same magnitude (sweep 3) after it has been switched on, and is thus also a WORM device similar to the PPy/P6FBEu/Au device.

The use of flexible PPy substrate in the memory device, instead of the rigid ITO glass, has resulted in an increase in the switching voltage. The phenomena may have resulted from the difference in surface resistance of the PPy film and ITO glass substrate. The surface resistance of PPy film is about $10^3\,\Omega\,\mathrm{sq}^{-1}$ while the surface resistance of ITO glass is about $20\,\Omega\,\mathrm{sq}^{-1}$. Furthermore, the mobility of charge carriers in PPy films is very slow [23]. Thus, a high field is required to drive the charge carriers in a PPy film. Taking into account of the high surface resistance and low-carrier mobility in PPy, a higher switch-on voltage is required for the PPy/P6FBEu/Au device than for the ITO/P6FBEu/Au device. In ITO/P6FBEu/Au and PPy/P6FBEu/Au devices, the lowest energy barrier (0.56 eV) is between the work function (Φ) of Au (−5.1 eV) and the highest occupied molecular orbital (HOMO) of P6FBEu, indicating that hole injection from Au into the HOMO of P6FBEu (corresponding to Au as the anode), is the favored process. Electron injection from ITO ($\Phi = -4.8$ eV) or PPy ($\Phi = -4.5$ eV) [24,25] into the lowest unoccupied molecular orbital (LUMO) of P6FBEu will be much more difficult because of the high energy barrier (1.57 eV for ITO, or 1.27 eV for PPy). Thus only hole injection dominates the conduction process.

To further understand the device transition from the OFF state to the ON state in WORM-type memory behavior, the J–V curves in both states were analyzed in terms of theoretical models. For the OFF-state, the J–V curve can be fitted by the Schottky emission model [26]:

$$J \propto T^2 \exp\left(+a\sqrt{V}/T - q\phi_B/kT\right),$$

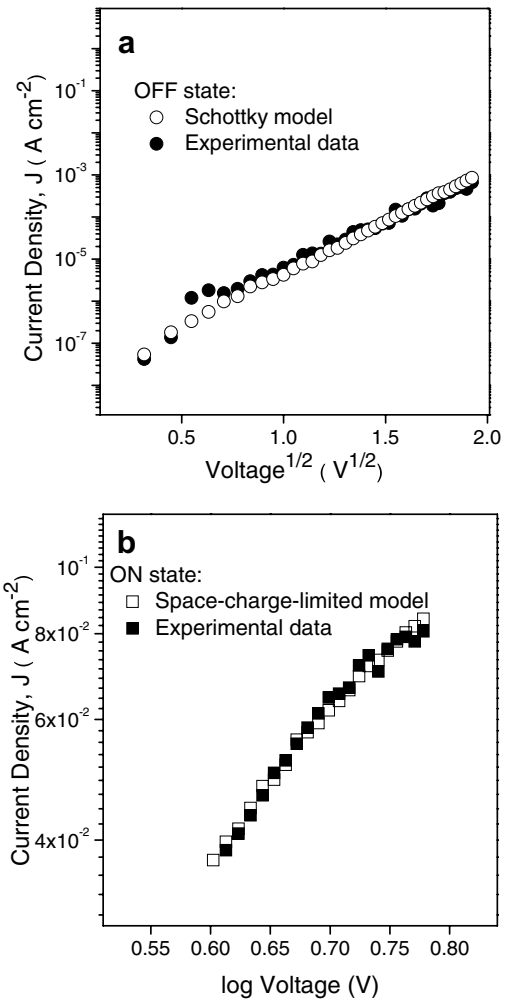


Fig. 3. Experimental and fitted J–V curves of the PPy/P6FBEu/Au device: (a) OFF state with the Schottky emission model and (b) ON state with a combination of the space-charge-limited model and the Ohmic model (the former is predominant).

wherein, T is room temperature (298 K), $a = \sqrt{q/(4\pi\varepsilon_i d)}$, ϕ_B is the barrier height, ε_i is the dynamic permittivity of the insulator, and d is the film thickness. As shown in Fig. 3a, the current before the transformation from the OFF state to the ON state was controlled by charge injection from the electrode. For the ON state, the J–V curve can be simulated by a combination of the space-charge-limited model and the Ohmic model as follows [26]:

$$J \propto \frac{8\varepsilon_i \mu V^2}{9d^3} + V\exp(-c/T),$$

wherein, μ is the mobility of carriers and c is a positive constant independent of V or T. The J–V characteristic in Fig. 3b suggests that, after the electrical transition, the current through the device changed from a charge injection current to a predominantly space-charge-limited current [27].

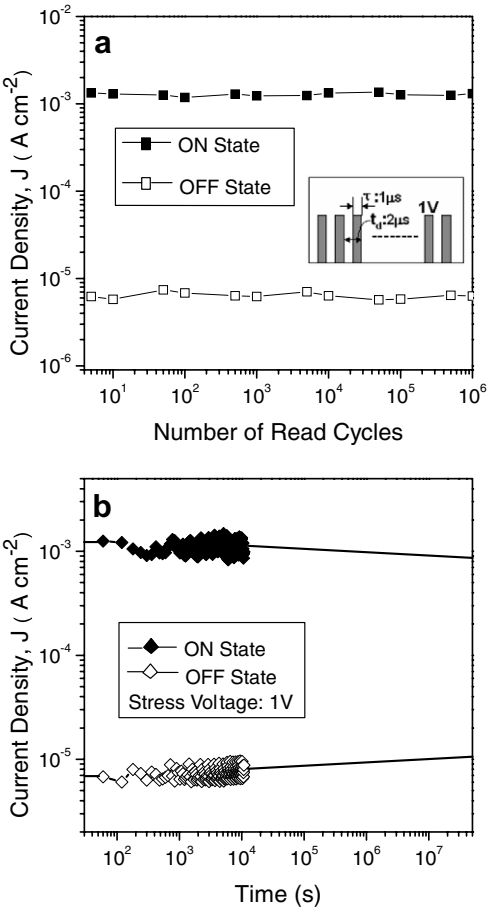


Fig. 4. (a) Effect of read cycles on the ON and OFF states in the PPy/P6FBEu/Au device. (b) Stability of the PPy/P6FBEu/Au device in either ON or OFF state under a constant stress at 1 V.

Besides the switching capability, stability is always an important issue in memory device performance. The performance of the WORM device based on PPy/P6FBEu/Au was evaluated under ambient conditions. First, the effect of continuous read pulses (with a read voltage of 1 V) on the ON and OFF states was investigated. More than one million read cycles were conducted on the PPy/P6FBEu/Au device. As shown in Fig. 4a, no current degradation was observed for the ON and OFF states. Thus, both states are insensitive to read cycles. The stability of the device under a constant stress of 1 V is shown in Fig. 4b. An ON/OFF current ratio of about 10^2 can be maintained when projected to one year.

4. Conclusions

In summary, a flexible polymer memory device is demonstrated in a sandwich structure of PPy/P6FBEu/Au. Conductance switching at a voltage of about 4 V, with an ON/OFF current ratio up to 200, was observed in this flexible memory device. After the device was switched to the high conductivity state, it remained in the ON state even when swept negatively. The device can be used as a write-once read-many-times (WORM) memory with good electronic stability. With the advantage of the flexible and conductive PPy substrate, the present polymer WORM memory is expected to meet the demand for data storage in memory devices of unique spatial construct or architecture.

References

[1] C. Li, D.H. Zhang, X.L. Liu, S. Han, T. Tang, C.W. Zhou, W. Fan, J. Koehne, J. Han, M. Meyyappan, A.M. Rawlett, D.W. Price, J.M. Tour, Appl. Phys. Lett. 82 (2003) 645.
[2] A.P. Kulkarni, C.J. Tonzola, A. Babel, S.A. Jenekhe, Chem. Mater. 16 (2004) 4556.
[3] D. Dini, Chem. Mater. 17 (2005) 1933.
[4] F. Garnier, R. Hajlaoui, A. Yassar, P. Srivastava, Science 265 (1994) 684.
[5] M. Granstrom, K. Petritsch, A.C. Arias, A. Lux, M.R. Andersson, R.H. Friend, Nature 395 (1998) 257.
[6] J. Isaksson, C. Tengstedt, M. Fahlman, N. Robinson, M. Berggren, Adv. Mater. 16 (2004) 316.
[7] J. Ouyang, C.W. Chu, C.R. Szmanda, L.P. Ma, Y. Yang, Nat. Mater. 3 (2004) 918.
[8] S. Moller, C. Perlov, W. Jackson, C. Taussig, S.R. Forrest, Nature 426 (2003) 166.
[9] A. Stikeman, Technol. Rev. 105 (2002) 31.
[10] Q.D. Ling, Y. Song, S.J. Ding, C.X. Zhu, D.S.H. Chan, D.L. Kwong, E.T. Kang, K.G. Neoh, Adv. Mater. 17 (2005) 455.
[11] H. Shirakawa, Angew. Chem. Int. Ed. 40 (2001) 2575.

[12] A.G. MacDiarmid, Angew. Chem. Int. Ed. 40 (2001) 2581.
[13] A.J. Heeger, Angew. Chem. Int. Ed. 40 (2001) 2591.
[14] Q.D. Ling, E.T. Kang, K.G. Neoh, W. Huang, Macromolecules 36 (2003) 6995.
[15] Z.M. Liu, A.A. Yasseri, J.S. Lindsey, D.F. Bocian, Science 302 (2003) 1543.
[16] D.L. Tao, Y.Z. Xu, F.S. Zhou, B.G. Huang, N. Duan, T. Zhang, H. Shen, Z.H. Xu, Z. Xu, J.J. Wang, X.Q. Zhang, F.X. Guo, X.X. Liu, D.F. Xu, J.G. Wu, S.R. Xu, Thin Solid Films 436 (2003) 281.
[17] L. Cen, K.G. Neoh, Y.L. Li, E.T. Kang, Biomacromolecules 5 (2004) 2238.
[18] A. Bandyopadhyay, A.J. Pal, Appl. Phys. Lett. 82 (2003) 1215.
[19] H.K. Henish, W.R. Smith, Appl. Phys. Lett. 24 (1974) 589.
[20] T. MoellerGmelin Handbook of Inorganic Chemistry, vol. 39 (D3), Springer-Verlag, New York, 1981.
[21] C.J. Liang, Z.R. Hong, X.Y. Liu, D. Zhao, W.L. Li, J.B. Peng, J.Q. Yu, C.S. Lee, S.T. Lee, Thin Solid Films 359 (2000) 14.
[22] H. Xin, M. Guang, F.Y. Li, Z.Q. Bian, C.H. Huang, K. Ibrahim, F.Q. Liu, Phys. Chem. Chem. Phys. 4 (2002) 5895.
[23] K. Kaneto, Thin Solid Films 393 (2001) 249.
[24] P.S. Abthagir, R. Saraswathi, J. Appl. Polym. Sci. 81 (2001) 2127.
[25] R. Gupta, S.C.K. Misra, B.D. Malhotra, N.N. Beladakere, S. Chandra, Appl. Phys. Lett. 58 (1991) 51.
[26] S.M. Sze, Physics of Semiconductor Devices, Wiley, New York, 1981.
[27] C.A. Mills, D.M. Taylor, A. Riul, A.P. Lee, J. Appl. Phys. 91 (2002) 5182.

Available online at www.sciencedirect.com
ScienceDirect
Organic Electronics 8 (2007) 407–414
Organic Electronics
www.elsevier.com/locate/orgel

Atomic layer deposited Al_2O_3 as a capping layer for polymer based transistors

S. Ferrari [a,*], F. Perissinotti [a], E. Peron [a], L. Fumagalli [b], D. Natali [b], M. Sampietro [b]

[a] *Laboratorio MDM-CNR-INFM, Via Olivetti 2, 20041 Agrate Brianza (Mi), Italy*
[b] *Politecnico di Milano, Dipartimento di Elettronica e Informazione, Via Golgi 40, 20133 Milano, Italy*

Received 13 December 2006; received in revised form 31 January 2007; accepted 1 February 2007
Available online 14 February 2007

Abstract

The strong sensitivity of organic/polymeric semiconductors to the exposure to O_2 and H_2O atmospheres makes the use of capping layers mandatory for the realization of stable devices based on such materials. In this paper we explore the realization of inorganic capping layers by atomic layer deposition (ALD) that provides smooth and pinhole-free films with a great potential as passivation layer for organic based devices. We show that the deposition of Al_2O_3 on transistors based on poly-3 hexyltiophene (P3HT) allows to obtain air stable devices. Whereas the growth of Al_2O_3 directly on the P3HT layer leads to a rough interface and significant intermixing between the oxide and the polymer, which results in a deterioration of transistor performances, an interlayer of a poly-alcohol such as poly-vinylphenol interposed between the Al_2O_3 and the P3HT gives a well defined Al_2O_3/polymer interface without degradation of the hole mobility. Transistors capped with Al_2O_3/PVP are very stable in air, with no appreciable differences in the electrical characteristics when measured in vacuum or in air. In addition no significant degradation of the transistors electrical properties was detected even after one month of air exposure.
© 2007 Elsevier B.V. All rights reserved.

PACS: 68.35.Ct; 68.35.Fx; 68.37.Lp; 73.50.−h; 73.61.Ph

Keywords: Organic thin film transistor; Capping; Atomic layer deposition; Aluminum oxide

1. Introduction

Due to the sensitivity of organic active materials to water and oxygen [1,2], organic based devices require the development of efficient encapsulating layers. Encapsulation by means of polymer layers such as cross-linked poly-vinyl alcohol [3–5] improves the lifetime of organic field effect transistors (OTFT) devices, yet the use of inorganic materials such as oxides [6] or nitrides [7] provides stronger resistance giving more effective permeation barriers against oxygen and moisture. Among different passivating layers, the Al_2O_3 shows excellent gas permeation properties [8–10]. For this reason in this paper we investigate its application as capping layer for OTFT.

* Corresponding author. Tel.: +39 039 6036383; fax: +39 039 6881175.
E-mail address: sandro.ferrari@mdm.infm.it (S. Ferrari).

1566-1199/$ - see front matter © 2007 Elsevier B.V. All rights reserved.
doi:10.1016/j.orgel.2007.02.004

The deposition of Al_2O_3 on polymeric materials has been studied by different groups for various applications such as adhesion layer for organic based low-k dielectrics [11] and gas permeation barriers [12–14] most notably for OLED [15,8]. The preferred technique for the deposition of Al_2O_3 on polymers is atomic layer deposition, by using trimethyl aluminum (TMA) and H_2O as aluminum and oxygen precursors, respectively [16,17,12], or plasma enhanced ALD, by using oxygen or ozone instead of the H_2O as oxygen precursor [18,15,14]. Following the standard model of the ALD growth mechanism of Al_2O_3 on inorganic surfaces, the TMA is reacting at the surface hydroxyl groups in a self-limiting reaction. When the process is carried out on polymers lacking reactive groups, the TMA should be adsorbed physically into the polymer and the reaction with the H_2O should take place inside the polymer. This results in broad Al_2O_3/polymer interfaces [16,17]. Therefore the use of ALD deposited Al_2O_3 as an encapsulating layer directly on the polymeric semiconductor is problematic since it is expected that AlO_x is included into the semiconducting layer and degrades its electrical properties. In this paper we studied the mechanism of ALD Al_2O_3 growth on the polymeric semiconductor poly-3 hexyltiophene (P3HT), and the effect of the growth process on the electrical properties of transistors based on P3HT. We elaborate a strategy to prevent Al_2O_3 diffusion into the P3HT layer by proper engineering of the polymeric layer. We will provide a structural and chemical characterization of the Al_2O_3/polymers stacks by using transmission electron microscopy (TEM) and time of flight secondary ion mass spectrometry (ToF-SIMS) respectively, while electrical characterization on capped and uncapped transistors shows the effect of the capping layer on the electrical properties of the semiconductor.

2. Experimental details

The transistors schematized in Fig. 1 were prepared by a conventional optical lithography process. The gate dielectric is a thermally grown SiO_2 100 nm thick on a Si $p+$, that acts as a common gate. Source and drain were made by patterning Au lines by photo-lithography. Channel width varied from 3 μm to 18 μm. The SiO_2 surface in the transistor channel was functionalized with dimethyl-dichlorosilane prior to P3HT deposition to improve the mobility. Regioregular poly 3-hexyltiophene (RR-P3HT) (Aldrich) was fractionated and purified by a sequence of organic solvent extraction (molecular weight = 52000 g/mol, poly dispersity = 2.0). RR-P3HT films were spin-coated from a 0.5% wt/wt solution in chloroform in order to achieve a thickness of about 30 nm. Poly-vinyl alcohol (PVP) or poly(methylmethacrylate) (PMMA) were spin cast from ethyl-acetate on the RR-P3HT films at a concentration of 0.4% wt/wt. The resulting thickness of the PVP and of the PMMA are around 10 nm as verified by X-ray reflectivity (data not shown), so that the total thickness of the P3HT/PVP(PMMA) stack is about 40 nm.

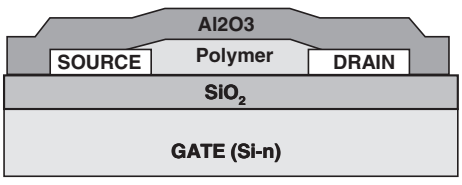


Fig. 1. Scheme of the encapsulated organic field effect transistor.

The Al_2O_3 films were grown by Atomic Layer Deposition (ALD) in a flow type (F-120 ASM-Microchemistry) reactor. TMA and H_2O were used as aluminum and oxygen precursors, respectively. For each film, 600 pulse/purge cycles were programmed in order to achieve a thickness of about 50 nm. During the growth, the pressure in the reactor was between 4 mbar and 6 mbar and the substrate temperature was kept at 125 °C. For the chemical and structural characterization of interfaces, Al_2O_3/polymers stacks were deposited on flat SiO_2 substrates. ToF-SIMS depth profiling and imaging was performed using and ION-TOF IV instrument equipped with two ion guns. Sputtering was performed using Cs^+ at 0.5 keV, while Ga^+ at 25 keV were used for the generation of the analyzed negative ions. High resolution TEM images where collected by means of a Leo 922 Omega EFTEM operating at 200 KV. Electrical measurements were performed in vacuum at 10^{-5} mbar after about 24 h of permanence in vacuum, and in ambient air, using a Keithley 4200 Modular DC source/monitor.

3. Results and discussion

3.1. Deposition on bare P3HT layer

The growth of Al_2O_3 by ALD on bare P3HT is expected to follow a mechanism analogous to other polymers such as poly-ethylene [16,17]. Due to the absence of highly reactive functional groups in the polymer, the nucleation process of Al_2O_3 during

the ALD process takes place throughout a relatively thick layer of the polymer. In fact the porosity of the P3HT allows the physisorption of the TMA precursor during the growth process, that upon exposure to H_2O forms aluminum hydroxide nuclei that in turn evolve into a compact film.

A TEM cross-section of the Al_2O_3/P3HT stack is shown in Fig. 2. The bright area corresponds to the low electron density layer made by the P3HT, while the darker one on top corresponds to the Al_2O_3. The P3HT layer is between 5 nm and 7 nm thinner with respect to its thickness before the Al_2O_3 deposition (measured by means of XRR, data not shown). The interface between the Al_2O_3 and the P3HT is broad due to a very strong roughness. The transition between the two layers is extended over approximately 10 nm. In the P3HT layer are visible dark regions, that indicate the presence of clusters of aluminum oxide or hydroxide. At the interface between the P3HT and the substrate is observed a dark band related to a higher density of clusters in this area. The accumulation of aluminum oxide at the bottom interface can be explained considering that during the oxide growth the precursors are penetrating into the polymeric layer down to the bottom interface, where they find an higher density of sites for nucleation and growth that are provided by the SiO_2 substrate.

Fig. 3 shows a ToF-SIMS profile of the Al_2O_3/P3HT stack. The AlO^- signal is a marker of the

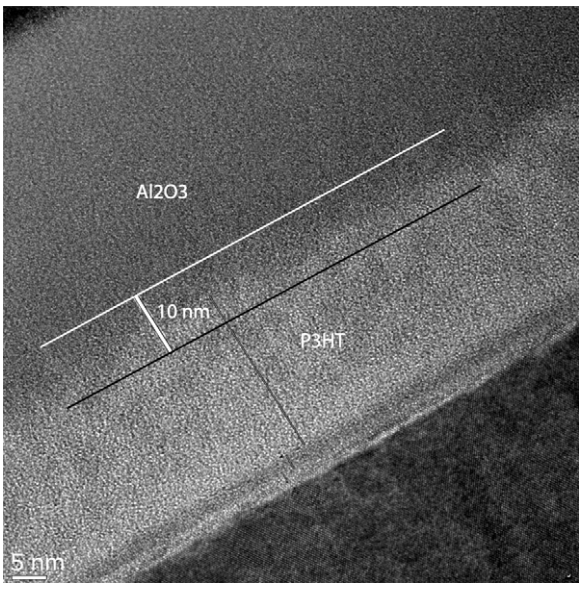


Fig. 2. TEM cross-section of a P3HT/Al_2O_3 stack on Si substrate.

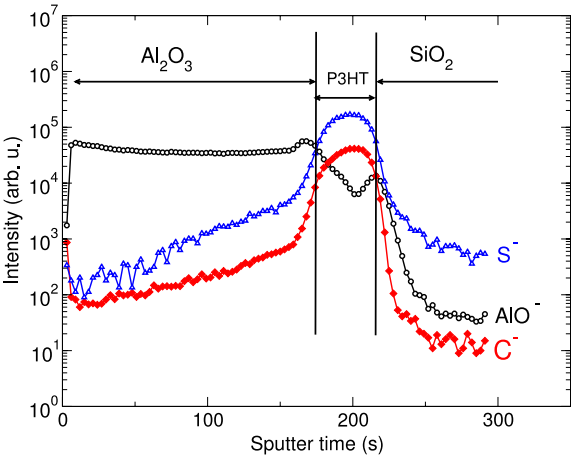


Fig. 3. ToF-SIMS profile of a Al_2O_3/P3HT stack on SiO_2.

Al distribution, while C and S are indicative of the presence of the P3HT polymer. The AlO^- signal decreases slowly into the P3HT layer and it shows a peak at the P3HT/substrate interface. The relatively high AlO^- intensity inside the P3HT confirms the results of the TEM analysis related to the presence of aluminum oxide clusters, while the peak at the interface confirms the accumulation of aluminum oxide at the P3HT/substrate interface. The C signal inside the Al_2O_3 layer relates partly to residual carbon from the TMA precursor in the ALD process and partly to residues of the polymer that are out-diffusing into the oxide layer. The S signal arises exclusively from the P3HT polymer and shows a long tail into the oxide layer as well. We conclude that during the film growth a fraction of the polymer migrates into the oxide film or that a polymer degradation process takes place leading to sulfur and carbon residuals moving into the Al_2O_3 layer.

3.2. Use of interlayers with reactive groups

Polymers carrying functional groups reactive toward the TMA are expected to show a different behavior as compared to the P3HT. Indeed the reaction of the TMA with functional groups prevents its diffusion inside the polymer layer, and consequently favors the formation of sharp interfaces. For this reason, we deposited polymers carrying reactive functional groups on top of the P3HT layer to act as Al_2O_3 diffusion barrier. Materials have to satisfy various requisites such as strong reactivity with TMA, stability in contact with P3HT, high glass

transition temperature and thermal stability to stand the thermal budget during the Al_2O_3 growth. In addition, the protecting polymer should be spin-coated from a solvent that is not destroying the underlying P3HT layer. The TMA reacts with several functional groups, such as alcohols, carbonyl and carboxyl groups. We selected two different polymers that were often used as dielectrics in OFET, in particular the poly-vinyl-phenole (PVP) [19,20] and the poly-methyl-metacrylate (PMMA) [21,22]. The PVP shows high glass transition temperature (above 130 °C) and is soluble in ethyl-acetate where P3HT is not. Also the carboxyl groups of the poly-metylmetacrilate (PMMA) are expected to react with the TMA [23], and it shows a relatively high glass transition temperature [24].

Fig. 4a and b shows the ToF-SIMS profile of the Al_2O_3/PMMA/P3HT and Al_2O_3/PVP/P3HT stacks, respectively. The comparison of the ToF-SIMS profile of the Al_2O_3/PMMA/P3HT stack of Fig. 4 a with the one of the Al_2O_3/P3HT of Fig. 3 demonstrates that PMMA is reducing the interdiffusion between the polymer and the oxide. S signal is absent in the Al_2O_3 layer, while the C signal is low and constant, meaning that no P3HT can be found inside the oxide. The C signal intensity is the same found in the Al_2O_3 films grown on silicon, and is attributed to a residue from the growth process. From a rough estimate its concentration should be lower than 0.1 atomic %. In addition the AlO^- signal drops faster at the interface with the polymer. Yet, Al segregation at the polymer/substrate interface is still observed, as seen from the AlO^- peak at such interface.

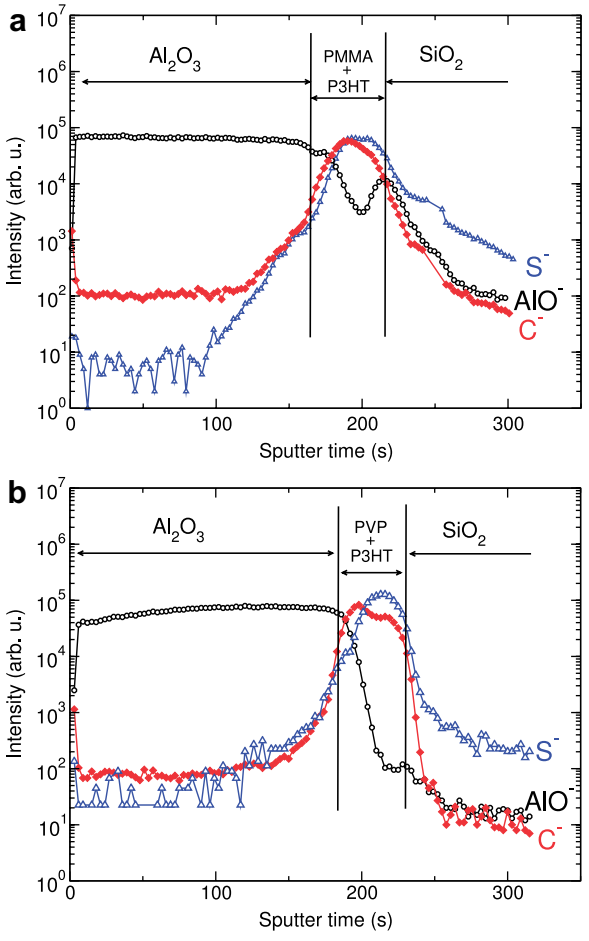


Fig. 4. ToF-SIMS profile of the Al_2O_3/PMMA/P3HT stack (a) and of the Al_2O_3/PVP/P3HT stack (b).

In the case of the Al_2O_3/PVP/P3HT layer, the AlO^- signal drops abruptly over three orders of magnitude at the interface with the polymer, approaching its background level, meaning that this polymer forms a sharper interface with the Al_2O_3. Also in this case C and S signals, flat and with low intensity, confirm the absence of P3HT inside the oxide layer. The difference in the behavior of the PMMA and the PVP is not easy to explain since, based on the reactivity of carboxylic and alcoholic groups with TMA, we would expect similar results for the two polymers [23]. On the other hand, the tendency of the TMA to diffuse deeply into the PMMA during the ALD process has been observed earlier by Wilson et. al. [17], and it was explained with a large free volume characteristic of the PMMA. According to this scenario TMA is free to penetrate into the PMMA layer and absorb into the P3HT layer where it might subsequently react with H_2O and form a broad interface. PVP is eventually much more compact and this prevents the TMA diffusion into the underlying P3HT layer. The reaction of the PVP hydroxyl groups in addition proceeds quickly and irreversibly, giving rise to the formation of an Al–O bond and elimination of CH_4 [25].

Given the results from ToF-SIMS analyses, we focused our attention on the Al_2O_3/PVP/P3HT system and investigated the nature of the interfaces by TEM analyses. Fig. 5 shows the TEM cross-section of the Al_2O_3/PVP stack deposited on a Si substrate, to specifically address the properties of the Al_2O_3/PVP interface. The interface is well defined, with a sharp contrast between the oxide and the polymer regions. In addition the interfacial roughness is extremely limited, with no indication of those Al_2O_3 inclu-

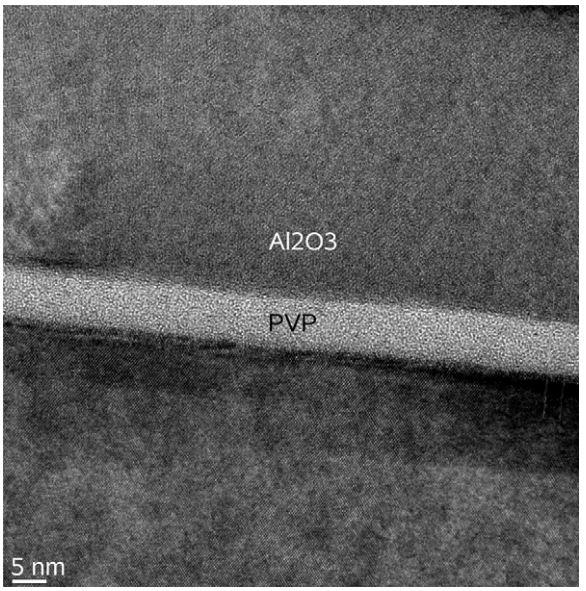


Fig. 5. TEM cross-section of a Al_2O_3/PVP on Si substrate.

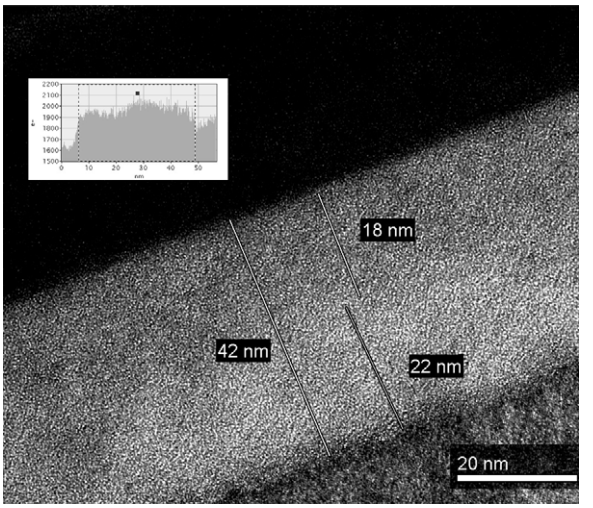


Fig. 7. Detail of the polymeric layer in the TEM cross-section of the Al_2O_3/PVP/P3HT stack shown in Fig. 6 (contrast has been enhanced). The inset shows the contrast profile of the picture.

sions that were apparent in the Al_2O_3/P3HT stack. The morphology of the Al_2O_3/PVP interface is therefore quite different from the Al_2O_3/P3HT one, confirming the ToF-SIMS observation.

The whole triple stack Al_2O_3/PVP/P3HT TEM cross-section is shown in Fig. 6 and shows that the Al_2O_3/PVP interface is identical to the one of Fig. 5. We can therefore conclude that the PVP is an excellent barrier against the diffusion of Al_2O_3, thanks to the reactivity of the OH functional groups that react with the TMA during the ALD process and prevent its diffusion into the polymer matrix. Further insights on the Al_2O_3/PVP/P3HT stack can be gained by enhancing the TEM image contrast and focusing the interest on the polymeric layer as shown in Fig. 7, where we can see that the polymeric layer is composed by two phases showing different brightness. The inset of Fig. 7 shows the contrast profile of the picture. The darker phase can be associated to the PVP while the brighter one is related to the P3HT. We can observe that even though the two layers remain well separated, the interface is relatively rough, meaning that a non negligible phase mixing occurs in proximity of the PVP/P3HT interface. Such mixing is due to the thermal budget used during the growth of the ALD Al_2O_3 films. Indeed we have carried out ToF-SIMS studies on the surface composition of the PVP/P3HT stack as deposited and upon annealing (data not shown) and we have observed the appearance of a sulfur peak at the surface when the stack is heated at the temperature used during ALD growth process (125 °C).

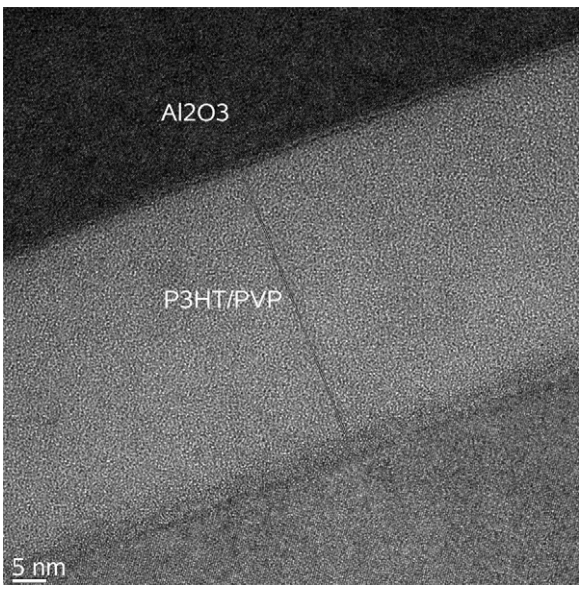


Fig. 6. TEM cross-section of a Al_2O_3/PVP/P3HT stack on Si substrate.

3.3. Electrical characterization of TFT capped with ALD Al_2O_3

The effect of the Al_2O_3 layer on the electrical properties of OTFT having the structure shown in

Table 1
Mobility and I_{on}/I_{off} of the transistor uncapped, capped with Al_2O_3 and capped with the Al_2O_3/PVP stack

Sample	μ ($cm^2\ V^{-1}\ s^{-1}$)	I_{on}/I_{off}
Uncapped	1×10^{-2}	10^6
Capped with Al_2O_3	0.87×10^{-3}	50
Capped with Al_2O_3/PVP stack	1.1×10^{-2}	30

Fig. 1 was studied by comparing devices uncapped, capped with Al_2O_3 and capped with Al_2O_3/PVP. The mobilities of the transistors measured in vacuum are reported in Table 1, while the output and transfer characteristic curves are shown in Figs. 8 and 9 respectively. The uncapped device has a hole mobility of 10^{-2} cm^2/Vs and an on/off ratio of about 10^6, typical values for spin cast high MW P3HT. Output characteristic curves, reported in Fig. 8a, show a well defined saturation region.

When the device is capped by Al_2O_3, a degradation in the mobility of almost an order of magnitude occurs (Table 1). This could be correlated with the diffusion of the Al_2O_3 into the P3HT layer that might introduce trapping states into the semiconductor and increase the structural disorder. It is worth noting that the accumulation of AlO_x and therefore the increase of disorder, is maximum at the P3HT/substrate interface, as shown in Fig. 2, exactly where the transistor channel is located. The on/off ratio is lowered by almost four orders of magnitude: as a consequence the tendency to reach the saturation regime decreases, as can be seen in Fig. 8b. The drop of the on/off ratio can be related to the high doping caused by the Al_2O_3 clusters embedded in the P3HT layer. Such clusters are carrying OH groups and physisorbed H_2O molecules that are trapped in the layer during the ALD growth process. Such species can act as dopant, increasing the off current of the transistor [1].

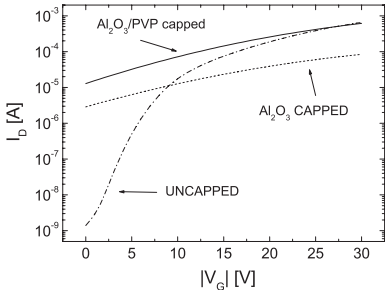


Fig. 9. Transfer characteristic curves of the transistor uncapped (dash dot line), capped with Al_2O_3 (dashed line) and capped with the Al_2O_3/PVP stack (solid line). Measurements performed in vacuum, channel length 3 μm. Drain voltage −30 V.

As shown in Table 1, when the Al_2O_3/PVP stack is employed as capping layer, no degradation of the mobility with respect to the uncapped device occurs, thanks to the suppression of the Al_2O_3 diffusion into the P3HT operated by the PVP interlayer, as shown above (see Fig. 6). On the other hand, the on/off ratio is still very low, because of the flowing of non negligible currents in the off state, and thus the tendency to reach the saturation is limited (Fig. 8c). The fact that the mobility is unaffected by the capping while the on/off ratio decreases significantly, can be explained as follows. According to the TEM and ToF-SIMS analyses (Figs. 6 and 4b) the PVP and the P3HT, although remaining in two different layers, form a broad interfacial region. We can assume that the PVP induces high conductivity in the PVP/P3HT interfacial region either directly, through the doping of the polar groups of the PVP or indirectly, through the residual water which remains into the PVP, which is highly hygroscopic, and which is subsequently released into the P3HT. This results in a high off current. On the other hand the transistor channel that is located at the bottom interface therefore far from the PVP/

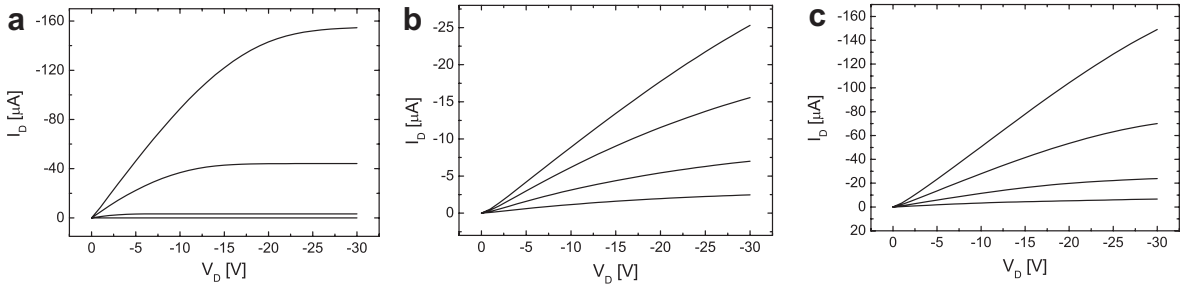


Fig. 8. External characteristics of the transistor uncapped (a), capped with Al_2O_3 (b) and capped with PVP/Al_2O_3 stack (c). Measurements performed in vacuum, channel length 6 μm. Gate voltage ranging from 0 V to −30 V in steps of 10 V.

P3HT interface is unaffected by the presence of the PVP, thus preserving its high mobility.

The situation is summarized in Fig. 9: the uncapped and the Al_2O_3/PVP capped device reach the same maximum current, but the former has a far lower off current. The device capped with Al_2O_3 alone resembles the one capped with the Al_2O_3/PVP stack, but with currents which are one order of magnitude lower.

Finally we tested the capping layer properties of Al_2O_3 on our TFT devices. We measured the transfer characteristic curves of transistors in ambient air with the ones in vacuum. We can observe that in air a high doping of the uncapped device occurs through moisture and oxygen adsorption, which results in an intolerable low on/off ratio of about 3, as shown in Fig. 10. On the contrary, the Al_2O_3/PVP capped transistor is exceptionally robust to air exposure as its transfer characteristic curves measured in vacuum and in air almost superimpose as shown in Fig. 11. In addition, this device was measured after 30 days of continuous air exposure: apart from a slight degradation of the on current, we measured a negligible variation in the off current (from 43 μA to 57 μA). This confirms the exceptional properties of the ALD deposited of thin Al_2O_3 films as oxygen and moisture barrier as demonstrated earlier [9]. Even though interface engineering and more complex formulation of the interlayer should be considered to develop a capping process that preserves completely the performances of the OFET, this result demonstrates the great capabilities of Al_2O_3 as capping layer and as oxygen/moisture barrier for organic based thin film transistor.

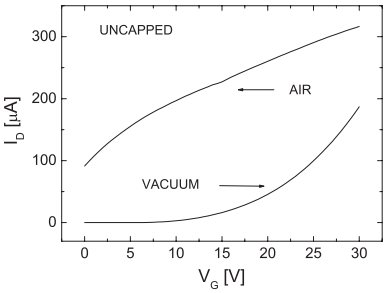


Fig. 10. Transfer characteristic curves of the uncapped transistor ($L = 6$ μm) measured in air and in vacuum. Drain voltage −30 V.

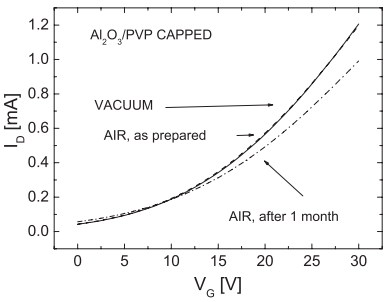


Fig. 11. Transfer characteristic curves of the Al_2O_3/PVP capped transistor in vacuum (solid line), in air just after preparation (dashed line), and after 30 days of air exposure (dash dot line) ($L = 3$ μm). Drain voltage −30 V.

4. Conclusions

In conclusion we have shown the effectiveness of ALD Al_2O_3 layers as capping for OTFT. Whereas the deposition of Al_2O_3 directly on the P3HT layer causes the oxide to grow inside the polymer with a significant degradation of the hole mobility, the use of an organic interlayer with alcohol functional groups such as PVP prevents Al_2O_3 inclusion thus providing no mobility degradation together with long term stability of the OTFT in air.

Acknowledgements

This work was supported financially by Fondazione CARIPLO, through PROTEO project. The authors are indebted with Giovanna Scarel and Luca Lamagna for the ALD growth, Claudia Wiemer for assistance in XRR analysis and Mario Alia for device fabrication from MDM Laboratory, with Alberto Bolognesi and Paolo Di Gianvincenzo from CNR-ISMAC for P3HT purification, with Sergio Masci from Politecnico di Milano for wafer bonding and Giuseppe Pavia from STMicroelectroncis for TEM analysis.

References

[1] S. Hoshino, M. Yoshida, S. Uemura, T. Kodzasa, N. Takada, T. Kamata, K. Yase, Journal of Applied Physics 95 (9) (2004) 5088–5093.
[2] D. Li, E.-J. Borkent, R. Nortrup, H. Moon, H. Katz, Z. Bao, Applied Physics Letters 86 (4) (2005) 042105.
[3] S.H. Han, J.H. Kim, J. Jang, S.M. Cho, M.H. Oh, S.H. Lee, D.J. Choo, Applied Physics Letters 88 (7) (2006) 073519.
[4] C.D. Sheraw, L. Zhou, J.R. Huang, D.J. Gundlach, T.N. Jackson, M.G. Kane, I.G. Hill, M.S. Hammond, J. Campi, B.K. Greening, J. Francl, J. West, Applied Physics Letters 80 (6) (2002) 1088–1090.
[5] J.-H. Lee, K. G-H, S.-H. Kim, S.-C. Lim, Y.-S. Yang, J. Oha, J.-O. Youka, J. Jang, T. Zyunga, Current Applied Physics 5 (2005) 348–350.

[6] W.H. Koo, S.M. Jeong, S.H. Choi, H.K. Baik, S.M. Lee, S.J. Lee, Journal of Physical Chemistry B 108 (49) (2004) 18884–18889.
[7] S. Koul, Y. Vygranenko, F. Li, A. Sazonov, A. Nathan, Material Research Society Symposium Proceedings 871E (2005) 19.4.1.
[8] S.-H.K. Park, J. Oh, C.-S. Hwang, J.-I. Lee, Y.S. Yang, H.Y. Chu, Electrochemical and Solid-State Letters 8 (2) (2005) H21–H23.
[9] M.D. Groner, S.M. George, R.S. McLean, P.F. Carcia, Applied Physics Letters 88 (5) (2006) 051907.
[10] A. Erlat, B. Henry, J. Ingram, D. Mountain, A. McGuigan, R. Howson, C. Grovenor, G. Briggs, Y. Tsukahara, Thin Solid Films 388 (1–2) (2001) 78–86.
[11] J.W. Elam, C.A. Wilson, M. Schuisky, Z.A. Sechrist, S.M. George, Journal of Vacuum Science and Technology B 21 (3) (2003) 1099–1107.
[12] M.D. Groner, F.H. Fabreguette, J.W. Elam, S.M. George, Chemistry of Materials 16 (2004) 639–645.
[13] P.F. Carcia, R.S. McLean, M.H. Reilly, M.D. Groner, S.M. George, Applied Physics Letters 89 (3) (2006) 031915.
[14] E. Langereis, M. Creatore, S.B.S. Heil, M.C.M. van de Sanden, W.M.M. Kessels, Applied Physics Letters 89 (8) (2006) 081915.
[15] S.J. Yun, Y.-W. Ko, J.W. Lim, Applied Physics Letters 85 (21) (2004) 4896–4898.
[16] J.D. Ferguson, A.W. Weimer, S.M. George, Chemistry of Materials 16 (26) (2004) 5602–5609.
[17] C.A. Wilson, R.K. Grubbs, S.M. George, Chemistry of Materials 17 (23) (2005) 5625–5634.
[18] S.J. Yun, J.W. Lim, J.-H. Lee, Electrochemical and Solid-State Letters 7 (1) (2004) C13–C15.
[19] H. Klauk, M. Halik, U. Zschieschang, G. Schmid, W. Radlik, W. Weber, Journal of Applied Physics 92 (9) (2002) 5259–5263.
[20] H.G.O. Sandberg, T.G. Backlund, R. Osterbacka, H. Stubb, Advanced Materials 16 (13) (2004) 1112–1115.
[21] J.A. Rogers, Z. Bao, A. Makhija, P. Braun, Advanced Materials 11 (9) (1999) 741–745.
[22] S. Uemura, A. Komukai, R. Sakaida, T. Kawai, M. Yoshida, S. Hoshino, T. Kodzasa, T. Kamata, Synthetic Metals 153 (1–3) (2005) 405–408.
[23] A. Hooper, G.L. Fisher, K. Konstadinidis, D. Jung, H. Nguyen, R. Opila, R.W. Collins, N. Winograd, D.L. Allara, Journal of the American Chemical Society 121 (1999) 8052–8064.
[24] M. Na, S.-W. Rhee, Organic Electronics 7 (2006) 205–212.
[25] S. Akhter, X.-L. Zhou, J.M. White, Applied Surface Science 37 (1989) 201–216.

Available online at www.sciencedirect.com
ScienceDirect
Organic Electronics 8 (2007) 415–422
Organic Electronics
www.elsevier.com/locate/orgel

Investigation of turn-on voltage shift in organic ferroelectric transistor with high polarity gate dielectric

C.A. Nguyen *, P.S. Lee, S.G. Mhaisalkar

School of Materials Science and Engineering, Nanyang Technological University, Blk N4.1, #B3-02, Nanyang Avenue, Singapore 639798, Singapore

Received 29 November 2006; accepted 31 January 2007
Available online 13 February 2007

Abstract

Large positive shifts of turn-on voltage V_{to} were observed in ferroelectric organic thin film transistor using P(VDF-TrFE) copolymer (57–43 mol%) as gate insulator during OFF to ON state sweeping. The shift of the transfer characteristic up to +25 V is attributed to the accumulation of mobile charge carriers (holes) in pentacene layer even during the device OFF state. The observed phenomena were first discussed on the basis of a negative surface potential created by the dipole field of a polar dielectric and trap states in an organic semiconductor layer. It was however found that these were unable to fully address the observed strong V_{to} shift due to the presence of large polarization in the P(VDF-TrFE) layer. A mechanism of negative polarization-compensating charges which are injected to the insulator region next to the semiconductor layer was proposed and examined to understand the phenomenon. The turn-on voltage is found to change with different magnitude of positive voltage pulses, and corresponds to different amount of charges injected for compensation. Time measurement of drain current shows a transient decaying behavior when gate bias is switched from positive to negative polarity which confirms the trapping of negative charges in the insulator.
© 2007 Elsevier B.V. All rights reserved.

PACS: 72.80.Le; 85.30.Tv; 77.22.Ej; 77.80.−e; 77.84.−s

Keywords: Ferroelectric polymer; P(VDF-TrFE); Ferroelectric FET; Organic transistors; Threshold voltage

1. Introduction

Ferroelectric copolymers [1] have been recently studied for the application in non-volatile memory for organic electronics [2–6]. The memory functionalities are resulted from the polarizability of dipoles in the organic layer that serves as the gate insulator in the field effect transistors. Two of the copolymers which have been reported as gate dielectrics in ferroelectric transistors are Poly(vinylidene fluoride-trifluoroethylene), P(VDF-TrFE), and Nylon poly(*m*-xylylene adipamide), MXD6. While PVDF copolymers are usually in semicrystalline form, MXD6 has been reported for ferroelectric-like properties but in amorphous state [6,7]. Transistor

* Corresponding author.
E-mail addresses: acnguyen@pmail.ntu.edu.sg (C.A. Nguyen), pslee@ntu.edu.sg (P.S. Lee).

1566-1199/$ - see front matter © 2007 Elsevier B.V. All rights reserved.
doi:10.1016/j.orgel.2007.01.010

devices with spin-coated thin film of both materials have shown good memory functionalities of high ON/OFF ratio at zero gate voltage, long current retention time and high programming cycles.

The memory function is obtained by the manipulation of surface conductivity in the semiconductor layer due to the ferroelectric remnant polarization. It is realized by the existence of two turn-on (or threshold) voltages of opposite signs, and hence a hysteresis of drain current in the transfer characteristic curve. As the coercive voltages of the ferroelectric film (voltages at which polarization reversal occurs) have equal amplitude, the above-mention magnitude of turn-on voltages are ideally expected to be similar. Gate insulators modified with self assembled monolayers (SAM) have recently been reported to exhibit positive turn-on voltage shift during transistor sweeping between OFF to ON state due to the non-switchable dipole's field [8,9] and semiconductor trap states [10]. This suggests that organic transistors using insulating PVDF copolymer films are likely to exhibit similar behavior during switching which is critical in memory operation and has not been previously addressed.

In this study, we fabricated ferroelectric field effect transistors using P(VDF-TrFE) copolymer as the gate insulator with pentacene as the organic semiconducting layer. We have for the first time observed the strong effect of turn-on voltage shift in the device's transfer characteristic and aimed to investigate this phenomenon in P(VDF-TrFE)/pentacene transistors.

2. Experimental

Indium doped tin oxide (ITO) glass slides were cleaned by standard process (acetone, methanol, deionized water) in ultrasonic bath and blown dry with Nitrogen gas. Copolymer P(VDF-TrFE) of 57–43 mol%, respectively, was used as purchased without further purification and dissolved in 2-butanone. The solution was then filtered using pore size of 0.45 μm and subsequently spin-coated onto the ITO substrates to form a 1.2 μm thick film. Film thickness was measured by Surface Profiler. The samples were annealed in Nitrogen ambient at 140 °C for 2 h to enhance the film crystallinity [11] and adhesion to the ITO surface. Circular gold electrodes of 1.5 mm diameter were deposited by thermal evaporation onto the film to form metal–insulator–metal (MIM) capacitors. Hysteric polarization was measured from the MIM device using a Radiant Ferroelectric tester HVS6000 with high voltage options and subjecting the devices to a triangular signal frequency of 2 Hz. The dielectric constant of the used polymer was extracted from capacitance measured on the same device using HP4284 LCR Analyzer at 1 MHz, 15 mV AC amplitude at zero DC voltage. Pentacene (Sigma Aldrich) was purified by temperature gradient sublimation in vacuum at 10^{-3} Torr and then deposited by thermal evaporation onto the copolymer film. Pentacene evaporation was done at 5×10^{-5} Pa vacuum and rate of 0.1–0.2 Å/s to result 80 nm thick film. Pure gold (99.99%) was evaporated in 9×10^{-5} Pa vacuum through shadow mask to form top contacts for source and drain. The transistor dimensions are of 500 μm gate width and 150 μm length. Electrical measurement of transistors was done with two connected Keithley 2400 Sourcemeter units to apply drain and gate voltage and measure drain and gate leakage current in dark N_2 ambient. The transfer characteristics (I_D–V_G) of the transistors were done by sweeping the gate voltage from positive value corresponding to the depletion state of the pentacene transistor (OFF state) to the negative value – accumulation state (ON state), and reversed to show the current hysteresis.

3. Results and discussion

Crystalline structure of the spin-coated copolymer film was first characterized using X-ray diffraction (XRD) as the polarization properties are strongly dependent on the presence of ferroelectric phase in the thin film. Fig. 1 reveals the co-existence of both ferroelectric and paraelectric phase in crystalline phase which is observed by the double peak at around 19°. This doublet is resulted from both diffraction of the paraelectric (α) phase (18.5°) and ferroelectric (β) phase (19.7°) [12]. From the diffracting intensity, the paraelectric phase exists in a comparable amount compared to the ferroelectric counterpart. This is probably due to the more stable energetic state of the trans-gauche bond in comparison to the all trans bond [13] and is consistent with previous report [12]. The broadening of the base line in the XRD spectra indicates the coexistence of the amorphous phase. This shows that the spin-coated copolymer film has a semicrystalline structure. It is possible that the fast evaporation of the 2-butanone solvent (the boiling point of 80 °C) during the spinning affected the mobility of long polymer chains

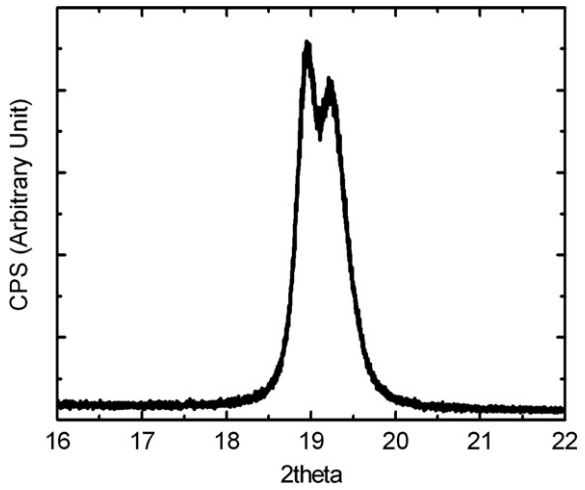


Fig. 1. Crystalline structure of P(VDF-TrFE) spin-coated thin film.

and allowed only a limited time for the large molecules to pack into high order phase.

Polarization data of the spin-coated copolymer thin film are presented in Fig. 2 (tested device structure is shown in the inset) with a typical hysteresis loop. The remnant polarization value is |6| μC/cm^2 and the coercive voltage is |70| V (∼|58.3| MV/m). The highest reported remnant value for a P(VDF-TrFE) copolymer of around 57 mol% VDF is maximum of |7| μC/cm^2 and the coercive field is generally |50| MV/m [14] for samples that had been thermally and mechanically treated to obtain a higher order structure. A remnant value of |6| μC/cm^2 as obtained in this study is reasonably good

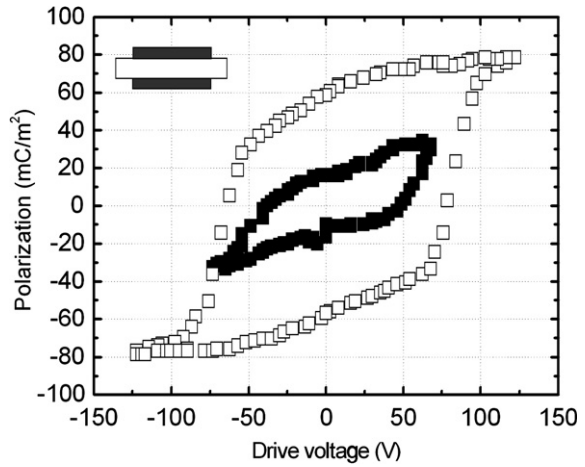


Fig. 2. Polarization hysteresis (*P–E*) curve of a metal–insulator–metal (MIM) capacitor structure of P(VDF-TrFE). Inset shows the MIM device structure with spin-coated P(VDF-TrFE) film sandwiched between ITO and Gold electrode.

for spin-coated thin films. Using the reported value (|50| MV/m), the corresponding coercive voltage of the copolymer film in this work should have a value of |60| V (film thickness of 1.2 μm), which is smaller than the measured value. The difference is likely due to voltage drop across very thin interfacial layers between the copolymer and the metal electrodes.

From Fig. 2, a difference of 2 μC/cm^2 between remnant polarization (P_R) and the spontaneous polarization (P_S) is observed, which results in the non-square shape of the *P–E* curve. Bolten et al. ascribed the loss polarization to a reversible process that exists concurrently with the irreversible polarization in thin film samples [16]. It has been also well recognized that local charge compensation of polarization is necessary to maintain the matter neutrality [17]. There are three types of contribution to the polarization properties of semicrystalline PVDF homopolymers, namely permanent polarization of dipoles in crystalline phase, frozen-in polarization in the amorphous state and the Maxwell–Wagner amorphous–crystalline interfacial polarization [18]. It has clearly linked the loss polarization observed in the *P–E* curve to the electrical properties of the amorphous state and the interfacial states. The compensating charges to the dipolar polarization in these two states can, hence, be treated as trapped charge existing in the gate dielectric layer of the transistor device. The trapped charges are either created or released during the voltage sweeping at the transistor gate. As a result, interpretation of ferroelectric transistor's operation would require the understanding of the electrical behaviors not only from the dipolar polarization but also the trapped charges due to charge compensation.

Bottom-gate ferroelectric FET device is shown in Fig. 3a and the corresponding I_D–V_D curve is shown in Fig. 3b. The device was observed to operate in accumulation mode of p-type transistor, in which holes are the hopping charge carriers. The copolymer layer is also seen to operate as an excellent gate dielectric layer. The mobility of the device (μ_{FE}) is determined to be 0.05 cm^2/V s in the saturated regime following the equation:

$$I_{D,sat} = \frac{W}{2L} C_{FE} \mu_{FE} (V_G - V_T)^2. \quad (1)$$

The capacitance C_{FE} of the dielectric layer was measured as described above to have value of 15.7 nF/cm^2 and dielectric constant ε is calculated to be 17. Recently, there have been a few reports from Naber et al. describing the ferroelectric transistor

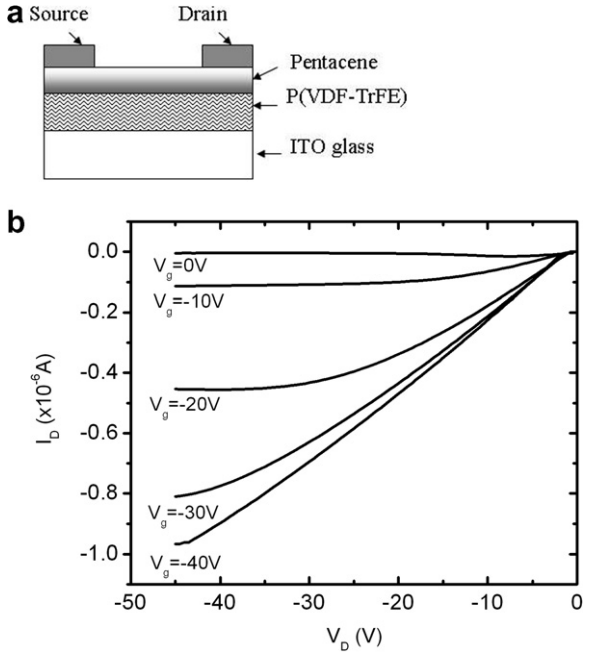


Fig. 3. Bottom gate ferroelectric thin film transistor with top source/drain contacts. Transistor device structure (a). I_D–V_D curve (b).

using similar P(VDF-TrFE) copolymer but with higher composition of VDF component, e.g. 65 mol%VDF [2–4]. It is interesting to note that the copolymer with higher VDF composition possesses a higher value of remnant polarization (74 mC/cm^2) but of a lower dielectric constant (calculated to be 11) than the one used in this study ($\varepsilon = 17$). The difference in the remnant value is due to the different amount of dipoles while higher dielectric constant of the copolymer in this case is due to the higher composition of Fluorine atoms from the trifluoroethylene groups in the gate dielectric.

The transfer characteristics (I_D–V_G) in the linear regime were obtained by sweeping the gate bias to values higher than the coercive voltages of the ferroelectric copolymer as shown in Fig. 4. The device was measured in nitrogen ambient inside a dark glove box to minimize the degradation of pentacene due to effect of air and moisture during bias stressing time. Before the transfer characteristic measurement, a voltage of +100 V was applied to program the device to OFF state. The gate bias was then swept from +100 V to −100 V and back, with a same drain voltage of −30 V. The I_D–V_G curve shows a current hysteresis following a clockwise direction which is consistent with the hysteretic data reported in [2–4,6]. It indicates the current retention behavior is due to the dipolar polarization by the ferroelectric dielectric rather than charge trapping mechanism. In the current hysteresis which is caused by charge trapping, the hysteresis would be observed in the opposite manner in which the drain

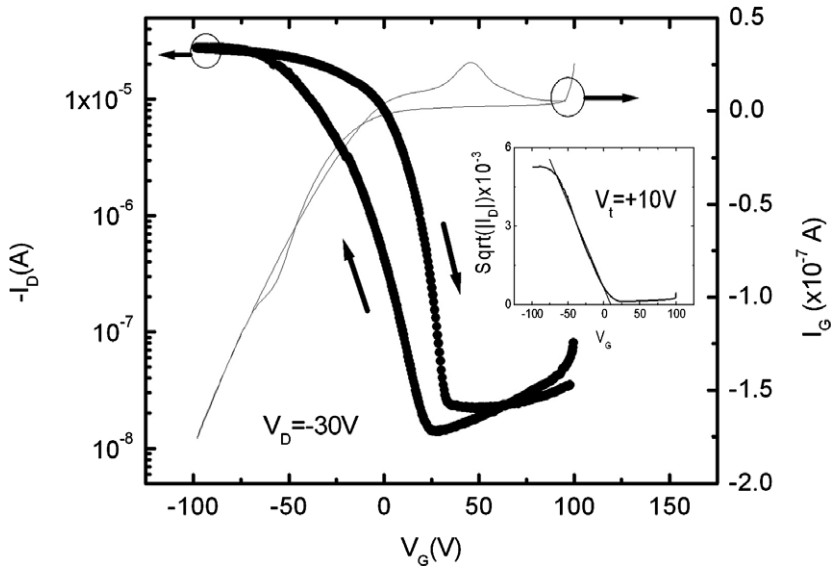


Fig. 4. Transfer characteristic curve I_D–V_G with turn-on voltage $V_{to} = +25$ V and gate leakage profile I_G–V_G of the ferroelectric transistor. Inset shows the $\sqrt{I_D}$ vs. V_G curve, threshold voltage $V_t = +10$ V. Gate current I_G is obtained concurrently with drain current I_D during transfer characteristic measurement.

current in the reversed sweeping is smaller than that of the first sweeping for the same gate voltage with the same gate voltage looping direction [19,20].

A significantly positive shift of turn-on voltage V_{to}, which is the gate voltage at which the drain current starts to increase exponentially, can be observed in the first sweeping cycle (+100 V to −100 V). In previous reports [2–4,21], the devices were shown to switch on by negative gate biases. While the negative turn-on voltage shows the complete operation in accumulation mode of the device, the observed positive V_{to} in this study implicates a possibly critical charge trapping mechanism [7,8]. Because of the positive shift of V_{to} in the first sweeping cycle, the ratio of On/Off current at 0 V zero gate bias is deteriorated as observed (less than two-order difference). This prompts for a more in-depth understanding in the characteristic behavior of ferroelectric PVDF copolymer as a gate dielectric in organic memory FET devices.

In terms of p-type FET devices, a positive turn-on voltage is usually associated with device working in depletion mode. In this experiment, before the I_D–V_G curve was taken, gate voltage of +100 V was applied to keep the device in OFF state. This voltage ensured all the dipoles aligned into the direction (pointing up, away from the gate) that would not accumulate holes in the pentacene layer. The device was then measured from OFF to ON state by sweeping gate voltage from +100 V to −100 V. If the pentacene layer is free from hole accumulations, a negative gate voltage higher than the coercive field (around −60 V) is expected to switch the polarization and turn the device on as similar to Ref. [2]. The large positive turn-on voltage V_{to} observed in I_D–V_G graph of Fig. 4 clearly indicated significant hole accumulation (p-doping) in the pentacene layer. As the device was characterized in inert and dark ambient, it is therefore reasonable to believe that the P(VDF-TrFE) layer has a significant negative surface potential which is sufficient to induce hole accumulation in pentacene channel even during the OFF state of the device (e.g. gate voltage gradually drops from +100 V to zero).

Similarly observed V_{to} shifts (or I_D–V_G behavior) have been investigated for pentacene transistor devices with self-assembled monolayer (SAM) of similar chemical functional groups on thermal oxides used as gate dielectric [8,9]. A large positive shift in turn-on voltage of about +60 V for device modified with 1H,1H,2H,2H-Perfluorooctyl trichlorosilane having the highest number of F atoms in the functional end-group was recorded. By reducing the number of atoms but still keeping F in the functional group, a positive V_{to} shift was still observable at near +50 V in the case of Trichloro(3,3,3-trifluoropropyl)silane [8]. This was attributed to the effect of the SAM's dipole field and the increasing of trap states in the interfacial layer next to gate insulator. By applying their proposed model to the transfer curve in our experiment, the mobile charge carrier density induced by the surface dipoles of P(VDF-TrFE) layer is estimated to be 2.45×10^{12} cm^{-2}, corresponding to a charge amount of 0.39 μC/cm^2. The total trap states are deduced from the threshold voltage above the turn-on voltage to be 1.47×10^{12} cm^{-2}, or equivalent charge amount of 0.24 μC/cm^2. The results are surprisingly in good agreement with findings from Ref. [8] as well as from simulation model in Ref. [9]. Direct measurement on the top surface of a (PVDF-TrFE) film (20–50 nm thick on graphite substrate) also resulted in a negative potential of −40 mV [15]. The negative surface field can induce accumulation in the gate channel even without gate bias application. This explains the high drain current obtained during the device OFF state.

It is noted that combination of the above findings can only yield up to carrier charge of 0.63 μC/cm^2 in the channel. Using the model by Miller and McWhorter [22] with adjustments for device operating in accumulation mode, it had been found that the remnant value of the surface charge density yielded up to a quarter of the remnant polarization charge [2]. For the remnant polarization of 6 μC/cm^2 for the copolymer film in this case, the remnant surface charge density by the dipolar polarization could yield up to 1.5 μC/cm^2 that is about twofold larger than the estimated total charge density of 0.63 μC/cm^2. Therefore, as the device is switched to OFF state, the total dipole field should be sufficient to compensate for all the defects described above and shift the turn-on voltage back to the negative value corresponding to negative coercive field. Another possible charge trapping mechanism caused by surface roughness of the gate insulator is also considered. The surface roughness R_{ms} of the P(VDF-TrFE) layer in this work was measured by Atomic Force Microscopy to be 15 nm, which falls within the range for semicrystalline copolymer thin film. Positive threshold voltage has previously been observed for organic transistor with rough gate dielectric layer (RMS up to 10 nm) but the magni-

tude was small ($V_t \approx +2$ V) and did not depend on the dielectric roughness values [23]. The combination of the mentioned mechanisms, hence, cannot fully account for such a large turn-on voltage shift that has been observed.

For a complete explanation for the large positive V_{to} shift, compensating charge injection into P(VDF-TrFE) layer during switching due to different potentials at gate and drain electrode is examined. The right axis of Fig. 4 shows the gate current profile of the same device which was recorded concurrently as the drain current was measured. The large value of the gate current (up to 1.75×10^{-7} A) obtained only during the ON state of the device is due to the leakage current through the semiconductor during accumulation. This occurred as the pentacene layer was not patterned that possibly created leaking paths between gate and source/drain electrodes. Apart from the current due to leaky paths, gate current in a ferroelectric transistor could also originate from the polarization reversal, e.g. displacement current (appears as peaks in the gate current curve Fig. 4). This contributes to the non-zero gate current during the device OFF state.

At the start of gate voltage sweeping (+100 V, OFF to ON state), the gate and drain current closely mimic each other showing a sudden drop from the initial value. At the beginning of this sweeping, the relative potential difference between the gate and drain was largest and the positive current spike at the gate indicates negative charges were injected to the P(VDF-TrFE) layer to compensate for the polarization buildup at beginning of the sweeping cycle. It has been reported that the Fermi level located at a position much nearer to the unoccupied conduction band for an ultra-thin P(VDF-TrFE) film likely favors electron injection or removal from the film [15,24]. As PVDF copolymer is a wide band-gap insulator, the injected electrons were unlikely to be conducted to the positive ITO electrode but rather remained trapped at region near to the interface with pentacene. Combining the negative compensating trapped charges with the possible effects of dipole field and trap states discussed above, these defects could result in a gate field that overcome the reducing applied positive field and turn the transistor on at positive gate voltage. As gate voltage crossed zero and the device reached complete accumulation state, the trapped charges were released as the gate voltage now (−100 V) was more negative compared to the drain voltage (−30 V). No charge trapping should occur during the accumulation and as gate voltage returned to zero because of the existence of holes in the pentacene region near the interface. The drop of drain current from accumulation at −100 V to zero gate voltage is related to the release of non-switchable charges in the semicrystalline P(VDF-TrFE) film which is similar to the behavior of polarization in P–E curve (Fig. 2).

To observe the control of V_{to} shift, I_D–V_G curve measurements were done on a device ($L = 100$ μm, $W = 2000$ μm) after it was subjected to different positive pulsing gate voltages at fixed source-drain voltage $V_{DS} = -5$ V (Fig. 5a). The transfer characteristic was measured right after the application of pulsing voltages and started from gate voltage of

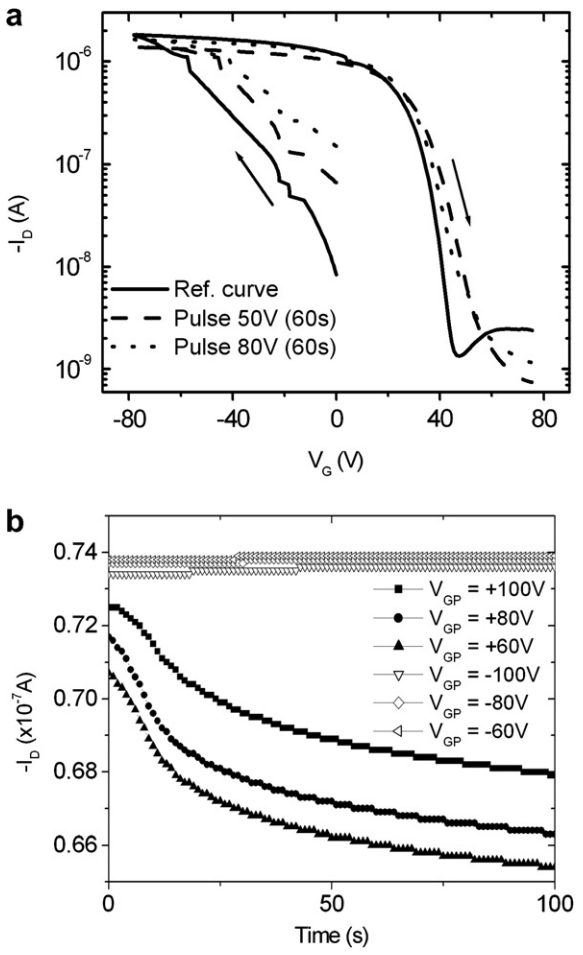


Fig. 5. (a) I_D–V_G curves measured right after the application of different positive gate voltage pulses, (b) Decaying drain current profile as measured from time-domain with the application of different gate voltage pulses V_{GP} followed by a gate bias of −60 V.

Table 1
Calculated trapped charge density from Eq. (2) and data in Fig. 5a

	I_D ($V_G = 0$ V) (A)	σ_{trap} (cm^{-2})
Reference curve (no pulsing)	8.38×10^{-9}	5.25×10^{12}
Pulse 50 V	6.61×10^{-8}	4.125×10^{13}
Pulse 80 V	1.49×10^{-7}	9.375×10^{13}

0 V. It can be clearly seen that V_{to} (as determined by extrapolating from current value at 0 V gate) was strongly dependent on the magnitude of positive voltage applied at the gate. Different pulse duration (up to 60 s) at each voltage showed little effects on the V_{to} shift (data not shown). This indicates the negative charge trapping process in the P(VDF-TrFE) layer is a long and irreversible process. The relationship of I_D and V_{DS} shown in Eq. (2) was used to estimate the remnant charge density (σ) in the transistor device (linear regime was assumed as the device had been turned on due to the V_{to} shift). The results calculated from current values obtained by sweeping-up direction in Fig. 5a are shown in Table 1.

$$I_D = q\mu \frac{W}{L} \sigma |V_{DS}|. \quad (2)$$

As discussed above, the effective remnant polarization by the P(VDF-TrFE) layer is about 1.5 μC/cm^2, or corresponding to a surface charge density of 9.4×10^{12} cm^{-2}. From Table 1, it can be seen that the charge trapping upon the application of a positive pulse voltage is much higher than the surface charge amount resulted by the remnant polarization. The amount of the excessive trapped charges in the copolymer dielectric layer is believed to result from the buildup of ferroelectric polarization which is contributed from the conductivity in the P(VDF-TrFE) layer [25]. This process was observed to occur at much slower speed as compared to the fast ferroelectric polarization (in microseconds range) and involved compensation charges in the non-ferroelectric (amorphous and paraelectric) phase in the semicrystalline thin film.

To confirm the presence of negative trapped charges, time domain measurement was applied to the same device as shown in Fig. 5b. Positive pulse voltage of different amplitudes was applied to the gate for 100 s followed by a fixed −60 V pulse to measure the behavior of the drain current. As discussed above, the application of a positive bias to the gate leads to different surface charge densities in the channel caused by the trapped charges in the P(VDF-TrFE) layer. By applying a negative voltage to the gate right after the pulse, partial amount of the negative charges should be detrapped [26]. As this occurred, the decaying hole population in the channel would led to the decrement of drain voltage in the same manner. One may argue about the presence of the dipoles in the P(VDF-TrFE) layer that pointed towards the gate to enhance accumulation of holes in the pentacene channel. However, the results in Table 1 show a much higher concentration of trapped charges as compared to the accumulated charges by the dipoles. This, hence, indicates a more dominant effect of trapped charges. Another time-domain experiment using negative voltage pulses and followed by $V_G = -60$ V (Fig. 5) showed no changes observed in the drain current after the pulse period. This agrees with the consistency of the I_D–V_G (Fig. 5a) curve swept from ON to OFF direction and evidently supports the negative charges trapping during the OFF to ON sweeping cycle.

4. Conclusion

We have fabricated ferroelectric thin film transistor using pentacene as semiconducting layer and P(VDF-TrFE) copolymer as gate insulator. The transistor devices exhibited a generally observed clockwise hysteresis of drain current during the sweeping of gate voltage, which indicates the memory effects by dipole moment in P(VDF-TrFE) layer. Large positive turn-on voltage shift up to +25 V was obtained as gate bias was swept from OFF to ON state. We found that the observed large V_{to} shift cannot be fully accounted based on factors such as surface dipole field, trap states in semiconductor, and surface roughness due to high remnant dipolar polarization of P(VDF-TrFE). Our investigations revealed a significant contribution of the negative charge compensation for polarization, which is the dominant mechanism to account for the large V_{to} shift in addition to other factors. The presence of negative charges is confirmed by time-domain measurement of drain current that shows decaying behavior which is resulted from decrement of hole population in the channel region. Carrier charge density at zero-gate bias is calculated and shows dependence on the positive voltage applied to the device that leads to changes in V_{to} shift. Optimization to obtain good control over the transistor turn-on voltage is necessary to improve the ON/

OFF memory window and the stability of signal current so that the favorable application of ferroelectric transistor can be realized.

Acknowledgements

One of the authors, C. A. Nguyen, would like to acknowledge the research scholarship awarded by Nanyang Technological University. This work is supported by A*Star Grant No. M47070011.703012.

References

[1] A.J. Lovinger, Science 220 (1983) 1115.
[2] R.C.G. Naber, C. Tanase, P.W.M. Blom, G.H. Gelinck, A.W. Marsman, F.J. Touwslager, S. Setayesh, D.M. De Leeuw, Nature Mater. 4 (2005) 243.
[3] G.H. Gelinck, A.W. Marsman, F.J. Touwslager, S. Setayesh, D.M. de Leeuw, R.C.G. Naber, P.W.M. Blom, Appl. Phys. Lett. 87 (2005) 092903.
[4] R.C.G. Naber, B. De Boer, P.W.M. Blom, D.M. De Leew, Appl. Phys. Lett. 87 (2005) 203509.
[5] K.N. Narayanan Unni, R. de Bettignies, S. Dabos-Seignon, J.M. Nunzi, Appl. Phys. Lett. 85 (2004) 1823.
[6] R. Schroeder, L.A. Majewski, M. Grell, Adv. Mater. 16 (2004) 633.
[7] R. Schroeder, L.A. Majewski, M. Voigt, M. Grell, Mater. Res. Soc. Symp. Proc. 830 (2005) D6.19.1.
[8] K.P. Pernstich, S. Haas, D. Oberhoff, C. Goldmann, D.J. Gundlach, B. Batlogg, A.N. Rashid, G. Schitter, J. Appl. Phys. 96 (2004) 6431.
[9] S. Kobayashi, T. Nishikawa, T. Takenobu, S. Mori, T. Shimoda, T. Mitani, H. Shimotani, N. Yoshimoto, S. Ogawa, Y. Iwasa, Nature Mater. 3 (2004) 317.
[10] J. Veres, S.D. Ogier, S.W. Leeming, D.C. Cupertino, S.M. Khaffaf, Adv. Funct. Mater. 13 (2003) 199.
[11] T. Furukawa, H. Matsuzaki, M. Shiina, Y. Tajitsu, Jpn. J. Appl. Phys. 24 (1985) L661.
[12] A.J. Lovinger, G.T. Davis, T. Furukawa, M.G. Broadhurst, Macromolecules 15 (1982) 323.
[13] H. Su, A. Strachan, W.A. Goddard III, Phys. Rev. B 70 (2004) 064101.
[14] T. Furukawa, Adv. Coll. Int. Sci. 71–72 (1997) 183.
[15] X. Chen, H. Yamada, T. Horiuchi, K. Matsushige, Jpn. J. Appl. Phys. 38 (1999) 3932.
[16] D. Bolten, U. Böttger, R. Waser, J. Appl. Phys. 93 (2003) 1735.
[17] M.G. Broadhurst, G.T. Davis, A.S. DeReggi, S.C. Roth, R.E. Collins, Polymer 23 (1982) 22.
[18] D. Rollik, S. Bauer, R. Gerhard-Multhaupt, J. Appl. Phys. 85 (1999) 3282.
[19] C.H. Seager, D.C. McIntyre, W.L. Warren, B.A. Tuttle, Appl. Phys. Lett. 68 (1996) 2660.
[20] M.W.J. Prins, S.E. Zinnemers, J.F.M. Cillessen, J.B. Giesbers, Appl. Phys. Lett. 70 (1997) 458.
[21] R.C.G. Naber, M. Mulder, B. De Boer, P.W.M. Blom, D.M. De Leeuw, Organic Electron. 7 (2006) 132.
[22] S.L. Miller, P.J. McWhorter, J. Appl. Phys. 72 (1992) 5999.
[23] S. Steudel, S. De Vusser, S. De Jonge, D. Janssen, S. Verlakk, J. Genoe, P. Heremans, Appl. Phys. Lett. 85 (2004) 4400.
[24] J. Choi, P.A. Dowben, S. Pebley, A.V. Bune, S. Ducharme, Phys. Rev. Lett. 80 (1998) 1328.
[25] H. von Seggern, S.N. Fedosov, Appl. Phys. Lett. 81 (2002) 2830.
[26] G. Gu, M.G. Kane, J.E. Doty, A.H. Firester, Appl. Phys. Lett. 87 (2005) 234512.

Available online at www.sciencedirect.com
ScienceDirect
Organic Electronics 8 (2007) 423–430
Organic Electronics
www.elsevier.com/locate/orgel

Non-equilibrium effects on electronic transport in organic field effect transistors

Lars Mattias Andersson *, Olle Inganäs

Biomolecular and Organic Electronics, Department of Physics, Chemistry and Biology, Linköping University, S-581 83 Linköping, Sweden

Received 9 November 2006; received in revised form 2 February 2007; accepted 2 February 2007
Available online 13 February 2007

Abstract

Non-ideal behavior in organic field effect transistors, in particular threshold voltage drift and light sensitivity, is argued to be due to intrinsic carrier dynamics. The discussion is based on the theory for hopping transport within a Gaussian density of states. Carrier concentration is shown to be of fundamental importance, and the time required to reach equilibrium at different bias is responsible for device behavior, with implications for mobility evaluation. Experimental results from various conjugated polymers in a field effect transistor illustrate the theory.
© 2007 Elsevier B.V. All rights reserved.

PACS: 73.50.Gr; 73.61.Ph; 85.30.De; 85.30.Tv

Keywords: Organic field-effect transistors (OFETs); Conjugated polymer; Hysteresis; Charge transport; Gaussian disorder model; Bias stress

1. Introduction

Recent studies have addressed the non-ideal behavior of organic field effect transistors (OFET), in the form of hysteresis, threshold voltage shift and relaxation of various forms. Several physical mechanisms have been suggested, some of them related to extrinsic phenomena, such as water dipoles in the organic layer [1,2] or interface states at the semiconductor/insulator interface [3]. Additionally, many devices have exhibited photosensitivity [4], which in turn has been possible to link to the non-ideal effects [5]. Here it will be argued that some aspects of the non-ideal behavior, including the light sensitivity, are possible to explain and model by considering the implications of hopping transport in a Gaussian density of states (DOS), thus indicating an intrinsic mechanism. A Gaussian DOS is not a requirement but is, as will be shown, close enough to reality and simple to work with. Furthermore, extrinsic phenomena are certainly not insignificant, and probably dominating in many cases, but this does not affect the basic argumentation here as extrinsic contributions can be considered simply as alterations of the shape of the DOS. A good example of this is the concept of "traps". This term is frequently used to describe a state, coupled to some extrinsic influence such as impurities, where

* Corresponding author. Tel.: +46 13 281253.
E-mail address: matan@ifm.liu.se (L.M. Andersson).

1566-1199/$ - see front matter © 2007 Elsevier B.V. All rights reserved.
doi:10.1016/j.orgel.2007.02.001

a carrier located in the trap will not easily move. Since a Gaussian is an exponential function there will certainly be intrinsic states at the same energy and with the same function as extrinsic traps.

A major motivation for this work comes from the use of OFETs as a tool for mobility evaluation of thin organic films where it is important to be able to track small variations in mobility and correlate these to device performance. Hysteresis and memory effects leave ample room for arbitrary evaluation of data, and the discrepancies between published mobility evaluations of several materials are large. Most of this is likely due to differences in material synthesis and device fabrication, or to established influences on transport behavior such as charge carrier concentration or field dependence. There is, however, also a possibility to influence mobility values obtained from OFETs on an order of magnitude scale by simply varying the measurement speed or ambient illumination. By considering this problem in the context of a well-established theory for electronic transport in disordered systems, it is possible to explain many finer nuances of OFET performance and to thus develop a more physically motivated measurement protocol. The discussion in this paper is mostly on a phenomenological level and is based on measurements on about 20 different materials of both polarities during several years. All the results in the experimental section are representative for many materials, but are selected because they emphasize points in the discussion. This means that other materials exhibit the same behavior but possibly to a lesser extent.

The key idea is based on the fact that a considerable time is required to reach energetic equilibrium within the wide density of discrete sites of a disordered system when the carrier concentration is switched between low, as in an off-state transistor channel, and very high, as in an on-state transistor channel. With the typical disorder and carrier concentrations present in OFETs, there will be a significant number of carriers in low energy states with a high occupancy of spatially and energetically contiguous states. These carriers are virtually immobile and the non-ideal behavior of organic FETs is here linked to the time dynamics of their transport.

2. Experimental

The materials used here have mainly been designed for use as active layers in organic photovoltaic cells and are thus not very high performing

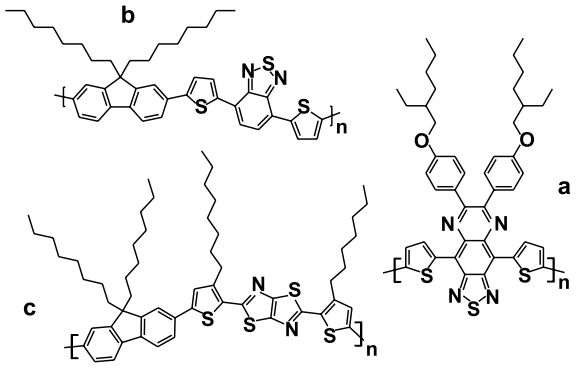


Fig. 1. Chemical structure of (a) PDAD-1, (b) APFO-3 and (c) APFO-16.

transistor materials. As example systems, a low band gap polymer based on donor–acceptor–donor (D–A–D) segments of thiophene – [1,2,5]thiadiazolo[3,4-g]quinoxaline – thiophene (PDAD-1), a higher band gap polymer which is a co-polymer comprising D–A–D segments of thiophene – 2,1,3-benzothiadiazole – thiophene and fluorene (APFO-3), and a similar polymer with a thiazolo[5,4-d]thiazole acceptor segment (APFO-16) (Fig. 1a–c) as active layer on an inorganic substrate has been used. Similar polymers can be found in the literature [6]. There is no specific reason for this choice of polymers other than the availability of measurement data. Other polymers, co-polymers or fullerene derivatives have been measured upon, with the same qualitative results.

Substrates were made from thermally oxidized highly doped p-type silicon wafers with thermally evaporated gold electrodes patterned by lithography. Chromium was used as a buffer layer for the gold and the oxide had a thickness of 100 nm. Electrodes were fabricated in a multiple finger configuration with channel lengths (L) between 9 and 37 μm and widths (W) between 2 and 16 mm. The active layer was spin coated from a chloroform solution of a few grams of polymer per liter at 1000 rpm, resulting in films with an estimated thickness of about 100 nm.

Characterization has been done under vacuum ($\approx 10^{-6}$ Torr) and in air on a Keithley 4200 semiconductor parameter analyzer and a HP4156A semiconductor parameter analyzer. Repeated, continuous or time delayed, cyclic measurements have been made with either cyclic tests on the 4200 or in repeat mode on the 4156 A. Where appropriate the repetitions have been allowed to continue until a stable measurement has been obtained. Typically

an integration time of 20 ms and a potential step of 1 or 2 V have been used resulting in measurement times of about 1 s. Drain-source potential is always equal to the maximum V_G used and is in the range 30–50 V. Mobilities were calculated using Eq. (3) where I_D denotes drain-source current, V_G gate voltage and C_i gate dielectric capacitance per unit area. All mobility comparisons are based on the maximum values for outgoing (off to on) sweeps.

$$\mu = \left(\frac{\partial\sqrt{I_D}}{\partial V_G}\right)^2 \frac{2L}{WC_i} \tag{1}$$

A tungsten halogen lamp in conjunction with an Oriel Instruments MS 257 monochromator configured to have a full width at half maximum of about 7 nm was used as a monochromatic light source and neutral density filters were used to control the intensity for white light. Monochromatic light intensity varies strongly with more than one order of magnitude in the wavelength range used here. Where appropriate this was compensated by simple normalization of measured data with the intensity versus wavelength spectra of the monochromator.

3. Results and discussion

To simplify the discussion we make some definitions regarding the state of a device and the different relaxation processes that are present. A device that is un-biased and at equilibrium is labeled as a ''recovered device''. A device that is not at equilibrium and that has been under considerable bias is labeled as ''stressed device''. The time to reach equilibrium after increasing the carrier concentration is labeled ''equilibration time'' and this is different from ''recovery time'' which is the time required for a stressed device to return to its recovered state. Both the equilibration and recovery time are associated with relaxation processes and are collectively labeled as relaxation times.

From a device perspective three cases can illustrate the time dynamics of energetic relaxation: (1) turning on a recovered device. (2) Turning off a stressed device. (3) Turning on a stressed device that has not been allowed enough time to fully recover. Fundamentally these three cases correspond to: (1) rapidly going from a low to a high carrier concentration with an average energy higher than at equilibrium and then slowly approaching the equilibrium density of occupied states (ODOS). (2) Rapidly removing all the mobile carriers in the high carrier concentration equilibrium ODOS and then very slowly removing the immobile carriers. (3) Rapidly increasing the carrier concentration from intermediate to high and then approach equilibrium. In addition to the expected threshold voltage [7] of an unbiased device, there will thus also be a bias and time dependent part directly proportional to the number of immobile carriers determined by the width of the DOS. The recovery time is longer than the equilibration time due to the predominantly energetically upward jumps of the recovery process.

Electrical transport in conjugated organic systems can be successfully modeled using hopping transport through localized states with a Gaussian energy distribution [8], where the DOS is described by Eq. (1) and the jump rate between states by Eq. (2). The σ_{DOS} denotes the width of the DOS and is indicative of the disorder in the system. E is energy. Eq. (2) is the product of a prefactor v_0, an electronic wave function overlap factor where γ is the inverse of the decay length of the localized wave functions and ΔR_{ij} is the distance between sites i and j with energy ε_i and ε_j, respectively, and a Boltzmann factor for jumps upward in energy. Further information can be found in [8].

$$g(E) = \frac{1}{\sqrt{2\pi}\sigma_{DOS}} \exp\left(-\frac{E^2}{2\sigma_{DOS}^2}\right) \tag{2}$$

$$v_{ij} = v_0 \exp(-2\gamma\Delta R_{ij}) \begin{cases} \exp\left(-\frac{\varepsilon_i-\varepsilon_j}{kT}\right); & \varepsilon_j > \varepsilon_i \\ 1; & \varepsilon_j < \varepsilon_i \end{cases} \tag{3}$$

Both static properties, such as temperature dependence, and dynamic properties, such as transient features, can be rationalized through the theory. Experimentally, dynamic aspects have generally only been considered for stacked sample types, where an active layer is sandwiched between two electrodes, such as in time of flight (TOF) measurements [8], and not for OFETs, where measurements are typically done in a planar configuration and on longer time scales.

The fundamental issue is illustrated in Fig. 2, which shows five consecutive transfer scans for an APFO-16 based device in air and in vacuum. In both cases the first scan reveals a low threshold voltage and consecutive scans that appear to have a significantly higher threshold voltage. All scans show hysteresis and for the subsequent scans this is much larger than the shift in outgoing threshold voltage. This would then correspond to first turning on a

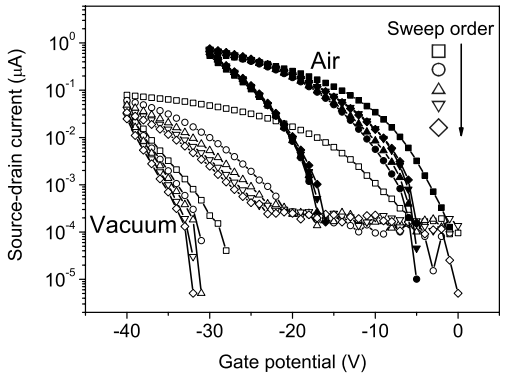


Fig. 2. Typical transfer characteristics. Different bias for illustrative purposes only. Filled symbols measured in air and open symbols in vacuum. Active layer is APFO-16.

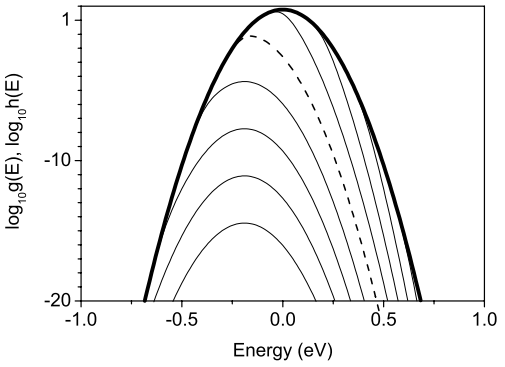


Fig. 3. Normalized 70 meV wide Gaussian density of states ($g(E)$, thick envelope line) and density of occupied states ($h(E)$) for different Fermi levels (carrier concentrations). The dashed line corresponds to 0.01 carriers per site.

recovered device and then cycling the device in a stressed state that eventually reaches a semi equilibrium based on the measurement conditions, where some carriers are trapped in low energy states. The main argument here is that these low energy states does not need to be deep traps caused by extrinsic impurities. A sufficiently wide DOS of discrete hopping sites would have the same effect. Normalization of the curves shows that the hysteresis is larger in air than in vacuum but that the general behavior is retained. There are indications that water is indeed a cause of hysteresis as reported [1] but not the only one. Indeed the hysteresis is directly proportional to the humidity and will decrease in dry gas atmosphere such as nitrogen or oxygen. The higher mobility of the sample in air is likely due to oxygen doping.

Most non-idealities, such as hysteresis and photo-activity in an OFET, can be traced back to an unstable threshold voltage. The threshold voltage can in turn be shown to be dependent on the carrier concentration [9] and, as suggested here, thus be time-dependent through the energetic relaxation of the ODOS. When the carrier concentration of a device is increased, the added carriers are initially taken to be randomly distributed. This is not necessarily the case and not really a requirement as non-equilibrium should be sufficient, but, again, is a useful simplification. The equilibrium ODOS for different carrier concentrations are determined by the DOS and the Fermi distribution function. Dynamics are related to hopping events. All aspects of the discussion is valid for both n- and p-type materials and all devices, irrespective of polarity, are assumed to be of enhancement type with a finite threshold voltage such that a forward bias is required for operation. All carrier concentrations are given in terms of carriers per site.

A 70 meV wide DOS and calculated equilibrium ODOS for carrier concentrations between 10^{-16} and 1 at room temperature are shown in Fig. 3. The width of the DOS is chosen based on results obtained for similar materials [10]. At very low carrier concentrations there are plenty of unoccupied sites available at all energies and all the carriers are mobile. When the carrier concentration is increased, more and more carriers are located in almost completely filled states at low energies. To find an available state it is then required of all the carriers in the almost filled low energy states to make a jump upward in energy. Since almost all states are filled for a relatively wide range of energies these jumps must be to states with a significantly higher energy; the jump rate is then so low that the carriers in these states can be considered immobile. For a carrier concentration of 1 there are obviously no sites available and all carriers are immobile. Barring the extremely high carrier concentrations close to 1, most of the carriers are still mobile and have a mobility that is proportional to the average energy of the equilibrium ODOS as has been established elsewhere [8,11]. The Fermi level is a convenient and useful first order limit for the number of immobile carriers, even though the real limit should be at a lower energy. All carriers below the Fermi level are thus considered immobile in this approximation. The dashed line in Fig. 3 corresponds to a concentration of 0.01, which is reasonable for an OFET in its on-state [11]. At this concentration and DOS width, 15% of the carriers are below the Fermi level and the contribution of

these carriers to the threshold voltage of a device is significant. The ratio of immobile to total number of carriers will change with both carrier concentration and width of the DOS. A plot of the density of immobile carriers as a function of carrier concentration is found in Fig. 6.

Due to the time and bias dependence of the threshold voltage imposed on disordered systems subject to hopping transport proposed here, and the time and bias dependence on mobility described elsewhere [8,11,12], the evaluation of experimental data is difficult. The macroscopic mobility is related to the average energy of the ODOS [8] and will, for a step-wise increase in carrier concentration, decrease with time as equilibrium is approached.

Even though direct extraction of dynamic properties through FET mobility measurements is not possible, or at least very difficult, qualitative observations can be done. By varying the delay time between change in bias and measurement it is possible to observe the expected decrease in mobility with increased time and this is shown in Fig. 4b, where mobility is plotted against the delay time per step of the i/v sweep. The measurement itself takes about 0.2 ms per measurement point. Because the evaluation is done from transfer characteristics where the gate potential is increased in many steps, in this case 21, it is not possible to directly obtain the equilibration time from this type of measurement.

Band gap illumination changes the relaxation times in a device by changing the carrier generation and recombination rates. The average energy of a photo-excited carrier is higher than that of an equilibrium carrier in the transistor channel. Immobile

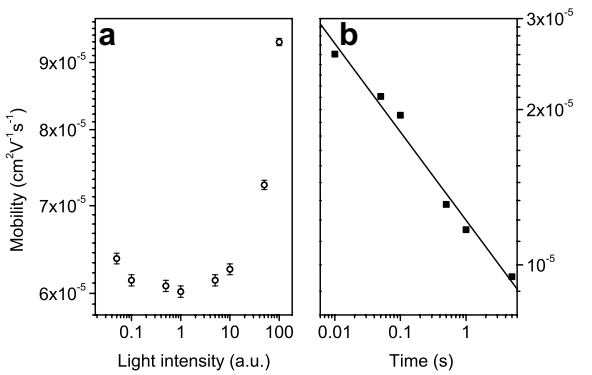


Fig. 4. Mobility as a function of (a) light intensity and (b) delay time between potential application and measurement, including linear fit for PDAD-1. Error bars in (a) indicate evaluation uncertainties.

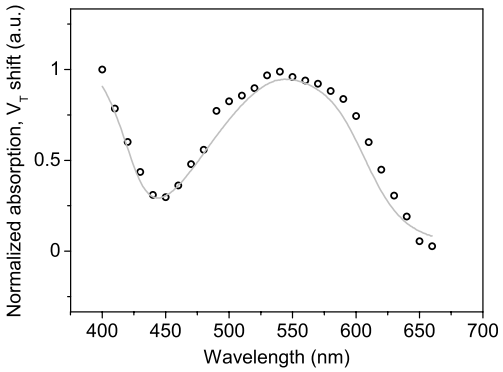


Fig. 5. Normalized absorption from transmission measurements for an APFO-3 film and threshold shifts for an APFO-3 device with illuminated channel. Actual threshold shifts are up to 10 V.

carriers in the channel thus have a probability to be replaced with mobile photo generated carriers. This means that on-state equilibrium is delayed and that the recovery time is decreased.

In terms of the quasi equilibrium obtained during continuously repeated transfer curve scanning, the impact of incident light can be visualized through the outgoing threshold voltage. Fig. 5 shows the shift in threshold voltage, referenced to the stressed dark value and normalized for lamp intensity, superimposed on the absorption spectrum of the active layer for an APFO-3 device, and this shows that the polymer absorption is directly correlated to the threshold voltage shift. A larger shift in the figure corresponds to a smaller threshold voltage of the device and is consistent with other experimental observations found in the literature [5]. In this case, the threshold shift is due to the decrease in recovery time caused by the incident light.

The influence of light on the equilibration time can be seen through transfer characteristic measurements at different light intensities if the relaxation time of the system in the dark is longer than the measurement time. When the relaxation time and measurement are close there will be a corresponding maximum in hysteresis. At this point the risk of underestimating mobility from a transfer characteristic is the highest. Experimentally, it should thus be possible to observe a weak minimum in a mobility versus light intensity plot, if the conditions are appropriate (Fig. 4a). As the light intensity is increased from zero the hysteresis increases and the mobility appears to decrease. When the relaxation times are increased further with even higher light intensity, the whole measurement is done at

elevated energy and the mobility is therefore higher than its equilibrium value. The decrease in mobility in this case is only perceived, as it is an artifact from a shifting threshold voltage. Since a complete measurement cycle takes about 3 s it can be inferred that the time constant of the system is somewhat faster than this in the dark considering that the minimum occurs at around 1 in relative intensity. All data in Fig. 4 are from PDAD-1 devices. Other materials, such as [6,6]-phenyl-C_{61}-butyric acid methylester, yield a larger underestimate of mobility due to hysteresis but show only a small increase in mobility at available higher light intensities.

For the PDAD-1 system and these measurement conditions, the underestimate of mobility due to hysteresis is small, less than 10%, and the overestimate due to elevated carrier energies is less than a factor of 2. Other circumstances may give larger differences. As a side note it can be mentioned that the difference in current between low and high light intensity is large, but this is mainly due to the rather large difference in threshold voltage between the two cases. The difference in mobility values between the time and light dependence measurements in Fig. 4b and a, is a good indication of typical differences between samples and measurement occasions.

Static properties are easier to quantitatively correlate than the dynamic properties. A good example is the implications of stress on threshold voltage. Since the recovery time is very long, it is possible to obtain the threshold shift as a function of stress potential by making two transfer measurements separated by a stress cycle. In this case the measurement itself must be fast compared to the equilibration time, so that only the low carrier concentration limit of the threshold voltage is measured. By calculating the trapped carrier concentration as a function of carrier concentration for a given value of σ_{DOS}, and fitting the experimental data it is possible to obtain the carrier concentration in the device. The relationship between threshold shift, stress potential, trapped carrier concentration and carrier concentration is given by Eq. (4), where n_s is the Fermi distribution function, ΔV_T is the threshold shift and V_{stress} is the stress potential.

$$\frac{\Delta V_T}{V_{stress}} = \frac{\int_{-\infty}^{E_F} n_s g(E)}{\int_{-\infty}^{\infty} n_s g(E)} \quad (4)$$

Fig. 6 shows threshold shift versus stress potential for a real device, and each data point represents the difference in threshold voltage between two transfer measurements separated by a stress cycle

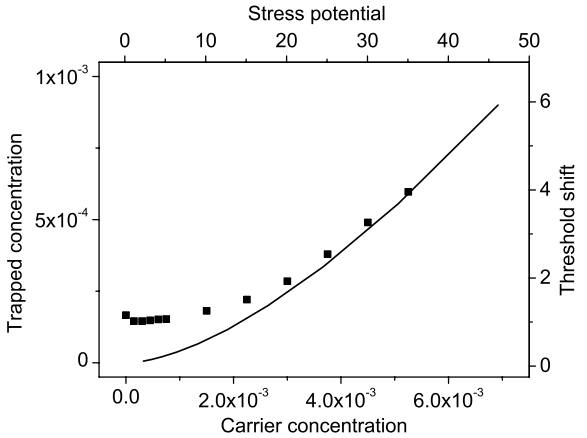


Fig. 6. The correlation between experimental potentials and theoretical carrier concentrations according to Eq. (4). Solid squares are experimental data and line is theoretical prediction. Potentials are experimental values and concentrations are from data fitting. PDAD-1 is the active layer.

of 1 s duration at the indicated gate stress voltage with source and drain both at 0 V. For low stress potentials there is a shift of 1 V, caused by stress from the measurement itself. The solid line is the theoretical prediction, assuming equilibrium, and shows the number of carriers below the Fermi level versus the total number of carriers (Eq. (4), right hand side, $\sigma_{DOS} = 70$ meV.). At high potentials the shift in threshold voltage follows an approximately $V^{1.6}$ dependence on stress potential with slightly larger exponents for smaller σ_{DOS} and smaller ditto for larger σ_{DOS}. For relevant distribution widths, the exponent varies between close to 1 and around 2.5. By fitting the experimental data to the theoretical calculation both total and trapped carrier concentrations of the device can be obtained. The carrier concentrations for the real device obtained in this way are very reasonable, and at higher stress voltages where the effects of the measurement itself become small, the fit is excellent. It is thus possible to calculate the carrier concentration of a device without the need for any guesswork regarding site density and channel volume if the DOS is known. At higher stress potentials the recovery time becomes prohibitively long, so that proper recovery is not easily guaranteed. It is also possible to fit the experimental data in Fig. 6 with larger values for σ_{DOS}. Indeed, with a σ_{DOS} of around 100 meV it is also possible to attain a good fit, with the difference being that the obtained carrier concentrations in the device is about one order of magnitude

smaller. A narrower σ_{DOS} does not provide a good fit, which suggests that the true value may be somewhat larger than 70 meV. One reason for this might be that the 70 meV width has been obtained for a different but similar material in a diode configuration. The variation in σ_{DOS} between different materials of the same family is usually small but there might be issues with the evaluation [13] and there might be a difference in the DOS between the two sample geometries.

4. Conclusions

Using a transistor transfer curve to extract mobility has the following consequences: (a) the mobility and threshold voltage *are* increasing with bias during the measurement. (b) The mobility *is* initially higher than at equilibrium and decreases with time during the equilibration. (c) The mobility will *appear* lower due to the increasing threshold voltage during the equilibration. Hysteresis in a transfer curve is influenced by all of these effects. It is not possible to resolve the different contributions through a single i/v measurement without elaborate modeling. Indeed, even with the aid of models and several different measurements, the OFET is unsuitable for determining the relevant relaxation times with any accuracy. A better way of measuring the equilibration time is through photo-charge extraction with linearly increasing voltage (CELIV). Such a measurement on a polythiophene indicates that the equilibration time of an ensemble of randomly distributed carriers is on the 10–100 ms timescale for low concentrations [14]. This timescale is one or two orders of magnitude smaller than the tentative estimates for the PDAD-1 transistors made here by way of varying measurement delays and by association with the minima in the mobility versus light intensity plot. Reasons for this difference between two materials could be a larger disorder and differences in mobility and carrier concentrations. Although not very easy to prove, this difference is still plausible since the relaxation time varies over many orders of magnitude depending on the amount of disorder [8]. The fact that many of the lower energy states are almost filled could also conceivably lead to longer relaxation times, especially if there is some long-range correlation in the site energy distribution. The recovery time for many of the experimental systems in this paper is several hours, and since devices have to be stressed to investigate the progress of the recovery this attribute is also difficult to measure accurately. This timescale is very long compared to that of the equilibration, but since all carrier jumps in this case is against the potential energy this is expected. Furthermore, the contribution from extrinsic traps could be more significant for this process and the extrinsic traps are, by definition, associated with a larger time constant. Suffice to say, the time dependence may influence device characterization on a parameter analyzer, since these operate on the same timescale.

The implications of time dependence of the ODOS coupled with high carrier concentration effects for mobility measurements through transfer characteristics on FETs vary between systems. In some cases the effects are significant and calculated mobilities can vary on the order of magnitude scale between different measurement conditions. More often the variations are smaller and in some systems possibly irrelevant. For device applications the threshold shifts also means that the channel current of a device can vary quite strongly with time. Furthermore it is important to note that the absence of significant hysteresis in a transfer characteristic does not necessarily translate into a correct equilibrium measurement, as it can also rather be a sign of non-equilibrium. If thermal annealing of organic thin films is assumed to decrease disorder, and hence the width of the DOS, the theory predicts a decrease in hysteresis since a more narrow DOS has a lower ratio of immobile to total carriers, as reported in the literature [15].

Summarizing the proposed theory, it has been shown that much of the non-ideal behavior observed in organic FETs can be considered as an, at least in part, intrinsic property related to the DOS. A high carrier concentration in a sufficiently wide Gaussian DOS leads to a very high occupancy of the lower energy states and carriers in those states are immobile. Immobile carriers contribute to the threshold voltage of a device and the time dynamics of the immobile carriers is responsible for the non-ideal behavior. Recovery times can be long and hysteresis should be expected in OFETs with high carrier concentrations. The influence of light and thermal annealing on hysteresis is consistent with the model. Transfer characteristics based mobility calculations can be both significantly over- and underestimated. By considering the effects of a time dependent ODOS it is possible to set up mobility measurements with sound physical justification and thus eliminating one significant contribution

to the frequent discrepancies of the research field. We also note that this explanation could be relevant to inorganic FETs with amorphous semiconductors if the DOS is small and wide. We predict that there will not be any significant effects in ambipolar devices such as light emitting diodes, due to the simultaneous presence of electrons and holes and their continuous recombination occurring in such devices. Therefore the suggested theory explains the intrinsic non-equilibrium effects in OFETs, is consistent with existing theories of transport in OLEDs, and constitutes an advance compared to existing theories of electronic transport in disordered organics in devices.

Acknowledgements

This work has been supported by the Swedish Science Council (VR) and COE, the Center of Organic Electronics, funded by the Strategic Research Foundation. We thank Wendimagegn Mammo and Mats R. Andersson, Chalmers University of Technology for polymer samples.

References

[1] C. Goldmann, D.J. Gundlach, B. Batlogg, Evidence of water-related discrete trap state formation in pentacene single-crystal field-effect transistors, Applied Physics Letters 88 (6) (2006) 063501.

[2] H.L. Gomes et al., Electrical instabilities in organic semiconductors caused by trapped supercooled water, Applied Physics Letters 88 (8) (2006) 082101.

[3] I. Torres, D.M. Taylor, E. Itoh, Interface states and depletion-induced threshold voltage instability in organic metal-insulator-semiconductor structures, Applied Physics Letters 85 (2) (2004) 314–316.

[4] S. Dutta, K.S. Narayan, Nonexponential relaxation of photoinduced conductance in organic field effect transistors, Physical Review B 68 (12) (2003) 125208.

[5] A. Salleo, R.A. Street, Light-induced bias stress reversal in polyfluorene thin-film transistors, Journal of Applied Physics 94 (6) (2003) 4231 (vol 94, pg 471, 2003).

[6] C. Kitamura, S. Tanaka, Y. Yamashita, Design of narrow-bandgap polymers. Syntheses and properties of monomers and polymers containing aromatic-donor and o-quinoid-acceptor units, Chemistry of Materials 8 (2) (1996) 570–578.

[7] G. Horowitz et al., The concept of "threshold voltage" in organic field-effect transistors, Advanced Materials 10 (12) (1998) 923–927.

[8] H. Bassler, Charge transport in disordered organic photoconductors – a Monte-Carlo simulation study, Physica Status Solidi B-Basic Research 175 (1) (1993) 15–56.

[9] O. Tal et al., Threshold voltage as a measure of molecular level shift in organic thin-film transistors, Applied Physics Letters 88 (4) (2006) 043509.

[10] A. Gadisa et al., Stoichiometry dependence of charge transport in polymer/methanofullerene and polymer/C-70 derivative based solar cells, Organic Electronics 7 (4) (2006) 195–204.

[11] R. Coehoorn et al., Charge-carrier concentration dependence of the hopping mobility in organic materials with Gaussian disorder, Physical Review B 72 (15) (2005) 155206.

[12] C. Tanase et al., Unification of the hole transport in polymeric field-effect transistors and light-emitting diodes, Physical Review Letters 91 (21) (2003) 216601.

[13] W.F. Pasveer et al., Unified description of charge-carrier mobilities in disordered semiconducting polymers, Physical Review Letters 94 (20) (2005) 206601.

[14] R. Osterbacka et al., Mobility and density relaxation of photogenerated charge carriers in organic materials, Current Applied Physics 4 (5) (2004) 534–538.

[15] F. Dinelli et al., Thermal annealing effects on morphology and electrical response in ultrathin film organic transistors, Synthetic Metals 146 (3) (2004) 373–376.

Available online at www.sciencedirect.com
ScienceDirect
Organic Electronics 8 (2007) 431–438
Organic Electronics
www.elsevier.com/locate/orgel

Device and circuit simulation of printed polymer electronics

Matthias Bartzsch [a,*], Heiko Kempa [b], Michael Otto [c], Arved Hübler [a], Dirk Zielke [d]

[a] Chemnitz University of Technology, Institute for Print and Media Technology, Reichenhainer Strasse 70, D-09107 Chemnitz, Germany
[b] Fraunhofer Institute Reliability and Microintegration, Branch Lab Chemnitz Reichenhainer Strasse 88, D-09126 Chemnitz, Germany
[c] Printed Systems GmbH Altchemnitzer Strasse 27, D-09120 Chemnitz, Germany
[d] University of Applied Sciences Bielefeld, Department of Electrical Engineering and Information Technologies, Wilhelm-Bertelsmann-Strasse 10, D-33602 Bielefeld, Germany

Received 23 October 2006; received in revised form 8 February 2007; accepted 13 February 2007
Available online 20 February 2007

Abstract

For the electrical simulation of all printed polymer circuits an AIM-SPICE model was developed, which is based on an a-silicon approach. By fitting the parameters to the behaviour of our polymer devices, we obtain a model, which allows to model all-printed polymer transistors and circuits.
© 2007 Elsevier B.V. All rights reserved.

PACS: 72.80.Le; 85.40.−e; 85.30.Tv

Keywords: Organic electronics; Printed electronics; Device simulation; Organic field effect transistor (OFET)

1. Introduction

The technology for printed organic electronics has rapidly developed in recent years. First devices and circuits for applications like RFID have been presented [1,2]. Due to intrinsic drawbacks of organic materials compared to their inorganic counterparts in terms of electronic properties, future applications are foreseeable in fields where low-cost manufacture is more important than extremely high performance [3]. Mass printing technologies are most promising in this context, as their main advantage compared to other fabrication methods, e.g. lithographic structuring used in silicon-based industry, is the possibility to produce a huge amount of samples with one printing form [4].

To avoid a ''trial and error strategy'' which would involve the fabrication of many different printing forms, it is helpful to have some reliable and easy to use simulation tools for printed circuits at hand. By means of simulations the device and circuit layout can be verified and optimized without performing a large number of cost and time consuming experiments. In order to support our daily work in roll-to-roll printing of organic circuits, we have developed an easy to use and easy to parameterize model which describes the static and dynamic

* Corresponding author. Tel.: +49 (0) 371 531 32126; fax: + 49 (0) 371 531 23619.
E-mail address: matthias.bartzsch@mb.tu-chemnitz.de (M. Bartzsch).

1566-1199/$ - see front matter © 2007 Elsevier B.V. All rights reserved.
doi:10.1016/j.orgel.2007.02.005

behaviour of organic devices and circuits with sufficient accuracy.

2. Experimental

Our transistors and circuits were fabricated solely by means of fast, continuous mass-printing processes on a printing machine which was especially designed and set up for the purpose of printing electronic devices (Fig. 1). The machine is capable of all conventional mass-printing techniques due to its modular setup, i.e. offset, flexographic and gravure printing and has a small web width of 35 mm in order to work with small amounts of experimental materials.

The thin-film transistors (TFTs) are built up in top-gate configuration on a PET-substrate. Source and drain electrodes are offset printed from a re-formulation of a water-based dispersion of poly-(3,4-ethylenedioxythiophene) doped with poly-(styrene-sulfonate) (PEDOT:PSS, Baytron P®). Poly(9,9-dioctylfluorene-co-bithiophene) (F8T2) solved in xylene was gravure printed as semiconducting layer. For the gate dielectric a double layer approach with a low-k and a high-k dielectric was used [5]. Veres et al. [6] found that a semiconductor/low-k dielectric interface shows superior properties in terms of field effect mobility compared to semiconductor/high-k dielectric interfaces. This effect has also been observed in our device setup [5]. However, due to the high roughness of our source/drain structures, an additional layer of a high-k dielectric material has been deposited on top of the low-k dielectric in order to guarantee sufficient insulation and capacitance. A combination of gravure and flexographic printing processes was used to deposit the dielectrics. The gate electrodes were manually dispensed from carbon black. Details of the involved printing processes will be described elsewhere [7].

The transistors had a channel length of 100 μm and a channel width of 30,000 μm. In order to demonstrate the applicability of our model for logic circuits we have chosen a seven-stage ring oscillator as a demonstrator (Fig. 2). The ring oscillator incorporated eight inverter stages, where one of them was used as a buffer stage for uncoupling of the signal. Each inverter stage consisted of a load and a drive transistor with a channel width of 6000 μm and 30,000 μm, respectively. The channel length was 100 μm for both the load and the drive transistor.

Standard characterizations of the individual TFTs and inverter stages were carried out using two Keithley source meters, whereby the measured transistors and inverters, respectively, were electrically separated from the surrounding circuitry. The ring oscillator signal was traced with a Keithley source meter controlled by an appropriate software, making use of its large input impedance. All measurements were carried out in a Suess Microtech probe station.

Fig. 3 shows the output characteristics variation of the D-TFTs of an oscillator circuit. The variation of approx. 25% in the output characteristics is mainly a consequence of two effects. The first one is the non-uniformity of the semiconducting layer which causes voids because of wetting problems. Because of this effect the effective channel width is reduced. The second effect that influences the varia-

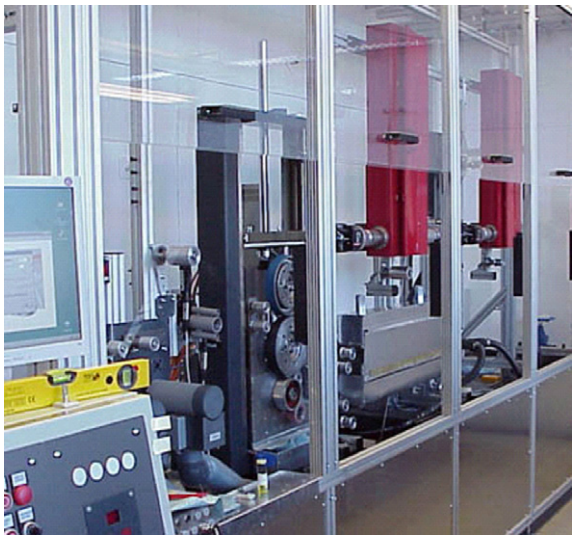


Fig. 1. Laboratory printing machine for the fabrication of all-printed electronic devices.

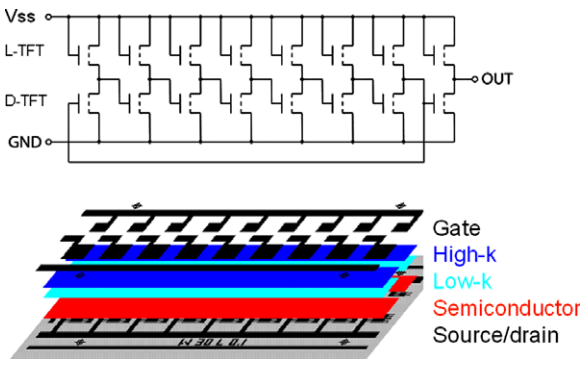


Fig. 2. Circuitry of the seven-stage ring oscillator (top) and schematic of a printed ring oscillator (bottom).

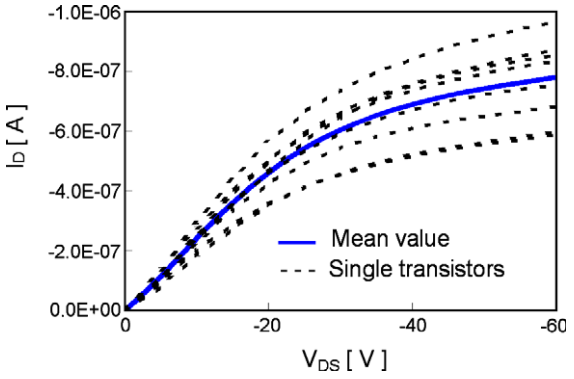


Fig. 3. Output characteristics of the D-TFTs at $V_{GS} = -60$ V.

tion of transistor characteristics is the variation in the thickness of the insulating layer.

2.1. Device model

For the simulation of the behaviour of organic field effect transistors (OFETs) usually a common set of equations known as gradual channel (or Shockley) approximation is used. Within this framework, the drain current (I_D) can be described as function of the drain/source voltage (V_{DS}) and the gate/source voltage (V_{GS}):

$$I_D = \begin{cases} 0 & |V_{DS}| < |V_{TH}| \\ \mu \cdot \frac{\varepsilon_0 \varepsilon_r}{t_{ox}} \cdot \frac{W}{L} V_{DS} \left(V_{GS} - V_{TH} - \frac{V_{DS}}{2} \right) & |V_{GS} - V_{TH}| > |V_{DS}| \\ \mu \cdot \frac{\varepsilon_0 \varepsilon_r}{t_{ox}} \cdot \frac{W}{2 \cdot L} \cdot (V_{GS} - V_{TH})^2 & |V_{GS} - V_{TH}| < |V_{DS}| \end{cases} \quad (1)$$

where μ is the mobility, t_{ox} and ε_r the thickness and relative dielectric constant of the gate oxide, V_{TH} the threshold voltage and W and L are the channel width and length.

This model describes the above threshold region well, as long as the source/drain-contact exhibits ohmic characteristics [8]. However, for the subthreshold behaviour of an OFET the parasitic effects like surface traps and gate-voltage-dependent mobility have to be considered.

A number of physical approaches which describe the carrier concentration in different organic semiconductors have been reported [8–11]. However, the parameters for these models are hard to determine and the models are unhandy for circuit simulations. On the other hand, there are papers, which show that the behaviour of organic semiconductors is similar to that of amorphous silicon [12–14]. For this reason we attempt to describe our printed TFTs with an a-silicon model developed by Lee et al. [15]. It is based on the assumption that the drain current I_D is composed of two contributions, i.e.

$$I_D = I_{leakage} + I_{ab} \quad (2)$$

One of them is due to the accumulation of carriers (I_{ab}), while the other one is due to the intrinsic conductivity of the organic semiconductor ($I_{leakage}$). An inversion of carriers is not included in this model as this effect is not observed in a-silicon as well as in organic semiconductors.

The accumulation current I_{ab} can be calculated from the carrier concentration n_s. The carrier concentration n_s is composed of the free carrier concentration n_{sa} and the carriers from deep traps n_{sb}

$$n_s = \frac{n_{sa} \cdot n_{sb}}{n_{sa} + n_{sb}} \quad (3)$$

In order to calculate the free carrier concentration, the carrier equilibrium approach is used

$$n_{sa} = \frac{\varepsilon_0 \varepsilon_r \cdot V_{gte}}{e \cdot t_{ox}} \left(\frac{V_{gte}}{\mathrm{VAA}} \right)^{\mathrm{GAMMA}} \quad (4)$$

where e is the elementary charge, VAA the characteristic voltage for field effect mobility and GAMMA the power law mobility parameter. V_{gte} is given by

$$V_{gte} = \frac{\mathrm{VMIN}}{2} \left[1 + \frac{V_{gt}}{\mathrm{VMIN}} + \sqrt{\mathrm{DELTA}^2 + \left(\frac{V_{gt}}{\mathrm{VMIN}} - 1 \right)^2} \right] \quad (5)$$

where VMIN is the convergence parameter, DELTA the transition width parameter and

$$V_{gt} = V_{GS} - V_{TH} \quad (6)$$

In order to determine the trap carrier concentration n_{sb} a special approach for a-silicon [15] is used. The conductivity of the channel g_{chi} can be calculated using the carrier concentration n_s,

$$g_{chi} = e \cdot n_s \cdot W \cdot \mu / L \quad (7)$$

Taking into account the resistance of the drain and source areas (RD and RS), the effective conductivity g_{ch} is given by

$$g_{ch} = \frac{g_{chi}}{1 + g_{chi}(\mathrm{RS} + \mathrm{RD})} \quad (8)$$

so that the contribution of the drain current I_{ab} can be written as

$$I_{ab} = g_{ch} V_{dse} (1 + \mathrm{LAMDA} \cdot V_{ds}) \quad (9)$$

with

$$V_{\mathrm{dse}} = \frac{V_{\mathrm{DS}}}{\left[1 + \left(V_{\mathrm{DS}}/V_{\mathrm{SATE}}\right)^{M}\right]^{1/M}} \tag{10}$$

and

$$V_{\mathrm{SATE}} = \mathrm{ALPHASAT} \cdot V_{\mathrm{gte}} \tag{11}$$

where LAMBDA is the output conductance parameter, M the knee shape parameter and ALPHASAT the saturation modulation parameter.

The leakage current I_{leakage} is due to the intrinsic conductivity of the organic semiconductor and can be described as

$$I_{\mathrm{leakage}} = \mathrm{SIGMA0} \cdot V_{\mathrm{DS}} \tag{12}$$

where SIGMA0 is the minimum leakage current parameter.

2.2. Parameter extraction

The simulations of our devices were carried out using the Spice-version of AIM-Software. The software includes various TFT models for amorphous as well as for poly-silicon. For our purpose the AFET 15 model was used, which was originally developed for amorphous silicon TFTs.

The parameters for the AFET 15 model were determined in two steps. Firstly, the mobility was calculated from the measured output and transfer characteristics. In order to do so, the mobility is derived from Eq. (1):

$$\mu = \frac{\partial I_{\mathrm{DS}}}{\partial V_{\mathrm{G}}} \frac{L}{WC_{\mathrm{i}}V_{\mathrm{DS}}} \quad \text{for } |V_{\mathrm{GS}} - V_{\mathrm{TH}}| > |V_{\mathrm{DS}}| \tag{13}$$

and

$$\mu = \left(\frac{\partial\sqrt{I_{\mathrm{DS}}}}{\partial V_{\mathrm{G}}}\right)^{2} \frac{2L}{WC_{\mathrm{i}}} \quad \text{for } |V_{\mathrm{GS}} - V_{\mathrm{TH}}| < |V_{\mathrm{DS}}| \tag{14}$$

The mean value of the mobility of the D-TFTs is shown in Fig. 4. The mobility strongly depends on the gate voltage, a behaviour which is often reported for organic [16,17] as well as for a-silicon [11] TFTs.

In a second step the parameter extractor of AIM-Spice was used to fit the whole parameter set for the AFET 15 model. While the AFET 15 model is valid for n-semiconductors, it had to be taken into account that F8T2 is a p-type semiconductor, i.e. all currents and voltages had to change sign. The obtained values for the fit parameters are summarized in Table 1.

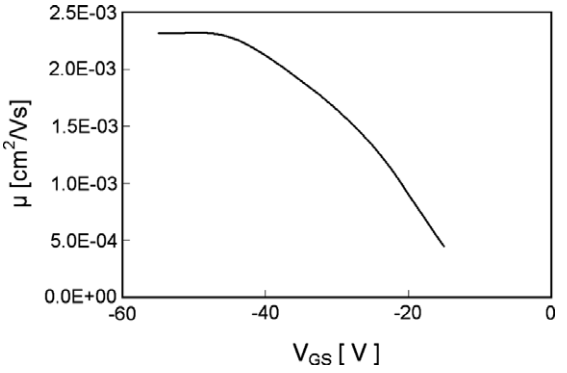


Fig. 4. Mean value of the mobility of the D-TFTs as a function of the gate voltage.

Table 1
Fitted model parameters

Parameter	Value	Description
μ	1.66×10^{-3} cm^2/Vs	Mobility
Alphasat	0.48	Saturation modulation parameter
Lambda	0.0042 V^{-1}	Output conductance parameter
M	2.88	Knee shape parameter
Defo	0.6 eV	Dark fermi level position
V_{FB}	−65.60 V	Flat band voltage
V_0	0.14 V	Characteristic voltage for deep states
V_{TH}	2.97 V	Threshold voltage
SIGMA0	1.19×10^{-3} A	Minimum leakage current parameter

With these values, a good agreement between simulation and experimental results could be achieved. Figs. 5 and 6 show the output and transfer characteristics, respectively, of the F8T2-model-TFT and the means of the measured values of the drive transistors.

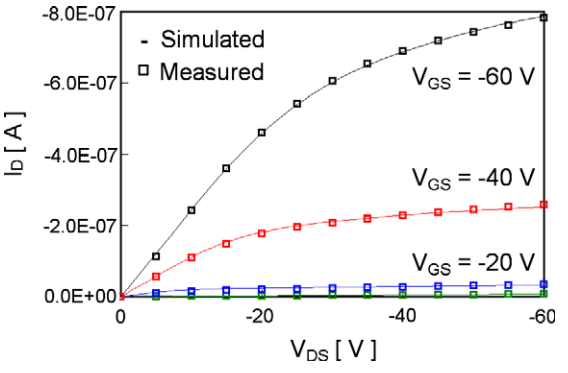


Fig. 5. Simulated and measured output characteristics of a typical D-TFT.

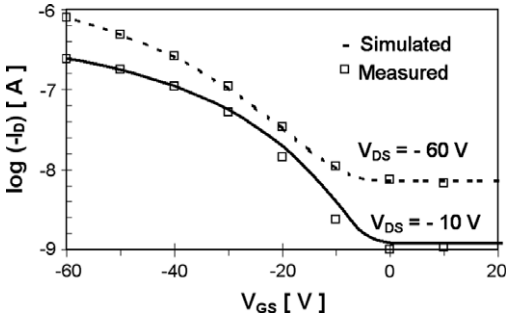


Fig. 6. Simulated and measured transfer characteristics of a typical D-TFT.

2.3. Circuit simulations

For the purpose of circuit simulations the TFT-model was extended with parasitic gate/source and gate/drain resistors and capacities in order to describe the non ideal organic insulator (Fig. 7). Furthermore it was necessary to parameterize the leakage current.

In order to calculate the parasitic elements as functions of the channel width and length, the following linear approaches were used

$$C_{GS} = C_{GD} = C_I \cdot W \cdot F \tag{15}$$

$$R_{GS} = R_{GD} = \frac{R_I}{W \cdot (F + L)} \tag{16}$$

$$\mathrm{SIGMA0} = \mathrm{sigma_I}\frac{W}{L} \tag{17}$$

Here, W, L and F are the channel width and length and the finger width, respectively of the TFT. The obtained fit parameters are summarized in Table 2.

Using the described transistor model, a single inverter stage was simulated. The SPICE model of an inverter is shown in Fig. 8. Fig. 9 shows the simulated as well as the measured characteristics. Although the agreement of the simulation with the experimental results is satisfactory, unfortunately

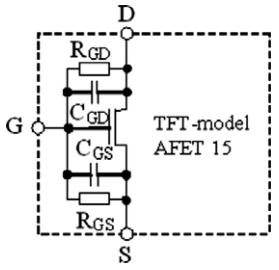


Fig. 7. Equivalent circuit of the F8T2-TFT.

Table 2
AFET 15 model parameter fit for a F8T2 transistor

Parameter	Value
R_I	198 kΩ m^2
C_I	7.1 μF/m^2
Sigma$_I$	3.97×10^{-13} A

```
*************** Inverter ***************************
XL1  1 1 3 tr_ l1=100u w1=6000u  f1=200u
XD1  3 4 0 tr_ l1=100u w1=30000u f1=200u
RL 3 0          11G
V_VSS          1 0 -40Vdc
V_VIN          4 0 -40Vdc
************ F8T2 TFT-Modell ********************
.SUBCKT tr_ 1 2 3 PARAM: L1=100u W1=30000u F1=200u
M         1 2 3 0 TFT_1 l=L1 w=W1
C1          2 3 (7.1u *F1*W1)
R1          2 3 (198k*/W1/(L1+F1))
C2          2 1 (7.1u*F1*W1)
R2          2 1 (198k*/W1/(L1+F1))
.model TFT_1 PMOS level=15 alphasat=0.477524 defo=0.6 +
delta=5 emu=0.02 el=0.1 eps=4 epsi=30 gamma=1e-10
+ gmin=1e+023 iol=0 kvt=-0.01 lambda=0.00415455
+ m=2.88474 muband=1.65e-007 rd=70000 rs=70000
+ sigmao=(3.97e-013*W1/L1) tnom=27
+ tox=2.7e-005 vaa=1e+009 vdsl=7 vfb=-65.5993 vgsl=7
+  vmin=0.3 vo=0.141822 vto=2.96861
.ENDS
```

Fig. 8. SPICE model for an inverter with F8T2-TFTs.

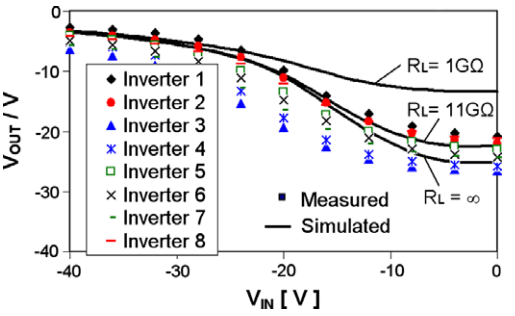


Fig. 9. Measured inverter transfer characteristics and simulations with different load resistances.

there is a large variation of the characteristics among different inverters, which is due to the variation of the transistor characteristics (see Fig. 3). However, it can be seen from Fig. 9 that the H-level of the inverter is strongly depending on the output load. Obviously, an 11 GΩ load resistance is approx. equal to the input resistance (which is determined by the gate/source resistance) of a following inverter stage.

The results of a simulation of a chain of 7 interconnected inverters are shown in Figs. 10 and 11 for supply voltages of −40 and −80 V, respectively. Simulated transfer characteristics after the 1st,

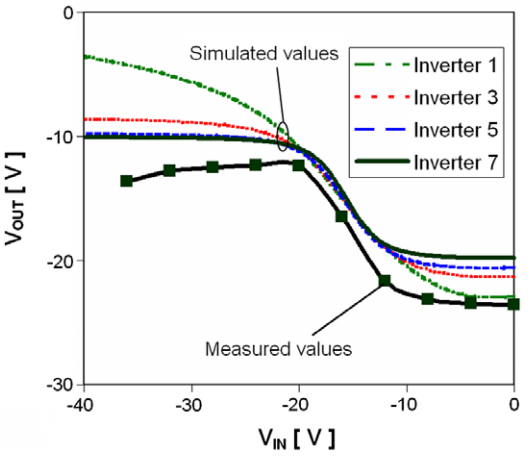


Fig. 10. Transfer characteristics of 7 interconnected inverters at $U_{SS} = -40$ V.

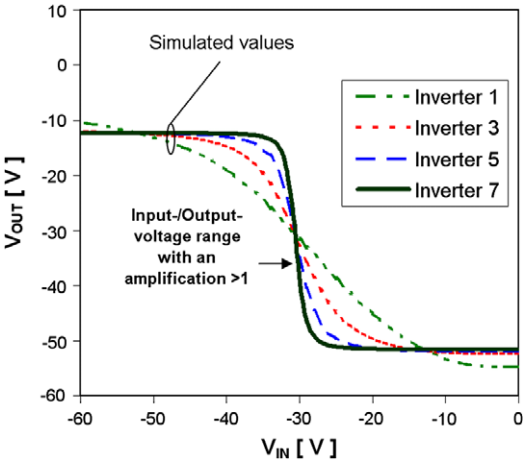


Fig. 11. Simulated transfer characteristics of 7 interconnected inverters at $U_{SS} = -80$ V.

2nd, ..., 7th inverter stages are plotted. For comparison, the measured characteristics after 7 inverters is included in Fig. 10.

For a supply voltage of 40 V (Fig. 10) there is hardly any interval in which the inverter gain (the slope of the output characteristics, dV_{out}/dV_{in}) is higher than 1. Therefore, the inverter chain does not work as an amplifier and no oscillation can be sustained. This situation is different for a supply voltage of −80 V (Fig. 11). Here the output swing of inverter 7 is higher than the input swing (the gain is higher than 1) within the input voltage range of −12 to −52 V. In this interval the amplification after all inverter stages is higher than one (the maximum gain is about 10) and, thus, if the output of

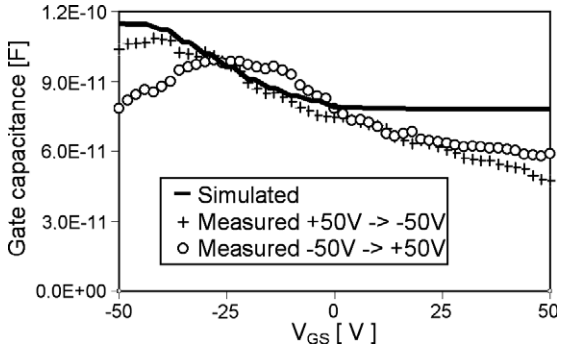


Fig. 12. *CV*-measurement of the gate capacitance of a typical D-TFT.

inverter 7 is fed back into the input of inverter 1, the circuit is oscillating with this amplitude (see Fig. 13). Provided that the amplification of the inverter chain is greater then one, the oscillator frequency is strongly dependent on the gate capacitance, which results from two contributions. One contribution is the overlap capacitance between the gate and the drain/source electrode structures and the second contribution is the gate-channel capacitance. Fig. 12 shows the quasistatically measured gate capacitance of a typical D-TFT. It can be seen that the capacitance is strongly dependent on the gate/source-voltage. However, the low gate capacitance at positive gate voltages reflects the overlap capacitance, whereas the increase of the gate capacitance towards negative gate voltages is due to the channel capacitance, which increases upon accumulation of charge carriers.

The initial increase of the capacitance when measured towards positive gate voltages (circles in Fig. 12) is due to a measurement artifact which is based on the initial load of the capacitor during the start phases. This initial load to a voltage of −60 V has not been completely finished, when the *CV*-measurement is started. Thus, the first measurement points are corrupted by the initial load current. Another artifact is the significant decrease for higher (positive) voltages which can not be explained yet and is also not seen in simulation. Nevertheless, the simulated *CV*-curve, which is also plotted in Fig. 12, is in reasonable agreement with the experimental data, at least for negative gate voltages. This result confirms our approach to use the a-silicon trap distribution model [15].

Using the F8T2 transistor model we were able to simulate the printed ring oscillator circuit and predict the supply voltage that is needed for the oscilla-

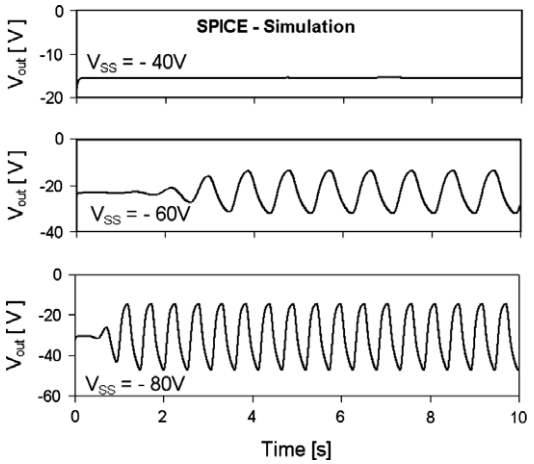


Fig. 13. Spice simulation of a 7 stage ring oscillator for different supply voltages for $R_L = \infty$.

tion. In Fig. 13 the simulated output signal is shown. The amplitude of the oscillation is in a good agreement with the prediction from the static simulations (see Figs. 10 and 11). However the amplitude of the measured output signal is lower (Fig. 14). The reason for this deviation could be an input resistance of our measurement equipment, which we estimate to be approx. 1 GΩ. This load on the output of the oscillator can be responsible for the lower oscillation amplitude and a slightly higher frequency.

Table 3 shows the simulated and measured frequencies and amplitudes of our ring oscillator for different load resistance. A reasonable agreement between simulated and measured values can be observed.

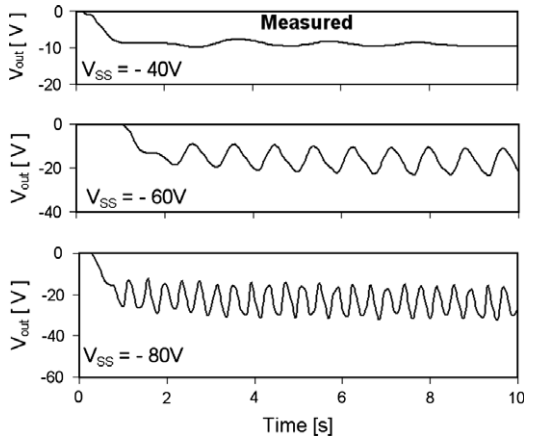


Fig. 14. Measured output signal of a 7 stage ring oscillator for different supply voltages.

Table 3
Comparison of simulated and measured frequency and amplitude of a seven-stage ring oscillator

Supply voltage	Simulated				Measured	
	$R_L = \infty$		$R_L = 1$ GΩ			
	f in Hz	$V_{O,PP}$ in V	f in Hz	$V_{O,PP}$ in V	f in Hz	$V_{O,PP}$ in V
−40 V	–	–	–	–	–	–
−60 V	1.1	20	1.2	11	1.1	11
−80 V	1.8	35	2.1	25	2.5	17

3. Conclusions

We have developed an easy to use model in order to describe the behaviour of printed organic circuits which is based on an existing model for a-silicon [15]. With the model it is possible to simulate device parameters of printed transistors and inverters with high accuracy. Furthermore, more complex circuits can be easily simulated both in terms of static and dynamic behaviour. Qualitative agreement with experimental data is obtained in this case, however some quantitative deviations occur which are subject to future study. We have also used the model for devices based on poly(3-hexylthiophene) (P3HT) and poly(triarylamin) (PTAA) with similar results.

Future development of circuit simulation should be aimed at the requirements of the fabrication of more complex circuits. Furthermore, it is desirable to model the trap-behaviour with a specific polymer-related approach, taking advantage of the parameters having a physical background and thus allowing for an understanding of the interrelation of technological changes and parameter variations.

References

[1] Philips, Philips Demonstrates World-first Technical Feasibility of 13.56-MHz RFID Tags Based on Plastic Electronics, Press Release, 2006, February 6.
[2] W. Clemens et al., From polymer transistors toward printed electronics, J. Mater. Res. 19 (2004) 1963.
[3] J.R. Sheats, Manufacturing and commercialization issues in organic electronics, J. Mater. Res. 19 (2004) 1974.
[4] A.C. Huebler et al., High volume printing technologies for the production of polymer electronic structures, Proc. Polytronic (2002) 172.
[5] D. Zielke et al., Polymer-based organic field-effect transistor using offset printed source/drain structures, Appl. Phys. Lett. 87 (2005) 123508.
[6] J. Veres, S.D. Ogier, G. Lloyd, D. de Leeuw, Gate insulators in organic field-effect transistors, Chem. Mater. 16 (2004) 4543.

[7] A.C. Huebler et al., Org. Electr., accepted for publication.
[8] G. Horrowitz, M. Hajlaoui, R. Hijlaoui, Temperature and gate voltage dependence of hole mobility in polycrystalline oligothiophene thin film transistors, J. Appl. Phys. 87 (2000) 4456.
[9] S. Scheinert, G. Paasch, Fabrication and analysis of polymer field-effect transistors, Phys. Status Solidi (A) (6) (2004) 1263.
[10] S. Scheinert, G. Paasch, M. Schroedner, H.-K. Roth, S. Sensfuß, Th. Doll, Subthreshold characteristics of field effect transistors based on poly(3-dodecylthiophene) and an organic insulator, J. Appl. Phys. 92 (2002) 330.
[11] S. Cherian, C. Donley, D. Mathine, L. LaRussa, W. Xia, N. Armstrong, Effects of field dependent mobility and contact barriers on liquid crystalline phthalocyanine organic transistors, J. Appl. Phys. 96 (2004) 5638.
[12] Th. Lindner, G. Paasch, S. Schreinert, in: 48th International Scientific Colloquium, Technical Digest, Ilmenau, Germany, September 2003.
[13] F. Schauer, Temperature dependent field effect in organic-based thin film transistor and its spectroscopic character, J. Appl. Phys. 86 (1999) 524.
[14] P.V. Necliudov, M.S. Shur, D.J. Gundlach, T.N. Jackson, Modeling of organic thin film transistors of different designs, J. Appl. Phys. 88 (2000) 6594.
[15] K. Lee, M. Shur, T. Fjeldly, T. Ytterdal, Semiconductor Device Modeling for VLSI, Prentice Hall, 1993, 1993.
[16] G. Horowitz, R. Hajlaoui, D. Fichou, A. El Kassmi, Gate voltage dependent mobility of oligothiophene field-effect transistors, J. Appl. Phys. 85 (1999) 3202.
[17] R. Brown et al., Synthetic Met. 88 (1997) 37.

Available online at www.sciencedirect.com
ScienceDirect
Organic Electronics 8 (2007) 439–444
Organic Electronics
www.elsevier.com/locate/orgel

The CDW and SDW in interchain coupled quasi-one-dimensional organic ferromagnet

L. Zhao *, J. Wang, K. Gong

Department of Physical Science and Technology, Wuhan University of Technology, Wuhan 430070, People's Republic of China

Received 18 September 2006; received in revised form 12 February 2007; accepted 19 February 2007
Available online 23 February 2007

Abstract

Based on a theoretical model proposed for interchain coupled quasi-one-dimensional organic ferromagnet, the effects of the electron–phonon coupling and electron–electron interactions on the CDW and SDW of the system are studied. It is found that the strong electron–phonon coupling will decrease the amplitude of the SDW, which is unfavorable to the ferromagnetic ground state of the system. Moreover, with increasing of the inter-site electron–electron interaction, the system will transfer from a strong SDW state into a strong CDW state, which will weaken the mediating function of the antiferromagnetic SDW along the main chain, and accordingly affect the ferromagnetic coupling intensity between the spins of the side radicals, and finally weaken the stability of the ferromagnetic state in the system.
© 2007 Elsevier B.V. All rights reserved.

PACS: 75.50.Dd; 75.30.Fv; 73.61.Ph

Keywords: Organic ferromagnet; Charge density wave (CDW); Spin density wave (SDW)

1. Introduction

In the past decade and more, great effects have been aimed at the design and synthesis a new class of ferromagnetic materials based on molecular rather than metallic or ionic lattices [1–9]. Several organic ferromagnets, such as *p*-NPNN [1], DTDA [2] have been successfully synthesized. Since the known cases of ferromagnetism always involve spin of either d or f electrons, which play an essential role in the forming of ferromagnetic correlation, the mechanism of ferromagnetic ordering in organic solids containing no d or f electrons at all is, therefore, a considerable challenge and has attracted considerable attention.

Ovchinnikov and Spector [10,11] proposed a simplified structure as schematically shown in Fig. 1 (single chain) to demonstrate the ferromagnetic ordering in organic ferromagnet. The main chain consists of carbon atoms each with a π electron and R represents a kind of side radicals containing an unpaired electron. Fang, Liu, and Yao [12] proposed a theoretical model to describe this kind of quasi-one-dimensional organic ferromagnets and obtained a ferromagnetic ground state, in which a parallel spin arrangement of the unpaired electrons at side radicals can be gained and there exists an

* Corresponding author.
E-mail address: lizhao_2001@yahoo.com.cn (L. Zhao).

1566-1199/$ - see front matter © 2007 Elsevier B.V. All rights reserved.
doi:10.1016/j.orgel.2007.02.007

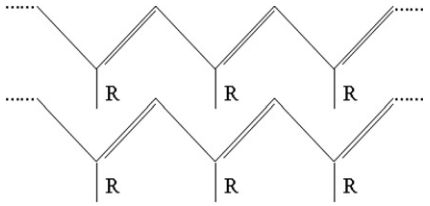


Fig. 1. Two neighboring chains of a quasi-1D organic ferromagnet.

antiferromagnetic spin density wave along the main chain. Considering the interchain electron transfer between the corresponding sites on the nearest chains, Wang and Yao [13] developed an interchain coupled model to deal with two neighboring organic ferromagnetic chains. In this paper, the CDW and SDW in the interchain coupled model will be studied. The model Hamiltonian and numerical method are given in Section 2. The results and discussions are presented in Section 3.

2. The hamiltonian and numerical method

We consider two neighboring chains (as shown in Fig. 1). The Hamiltonian employed in our study is given by:

$$\widehat{H} = \widehat{H}_1 + \widehat{H}_2 + \widehat{H}_3 + \widehat{H}_4 \tag{1}$$

$$\widehat{H}_1 = -\sum_{jl\sigma}[t_0 + \gamma(u_{jl} - u_{jl+1})](c^+_{jl\sigma}c_{jl+1\sigma} + \text{H.c.}) + \frac{\kappa}{2}\sum_{jl}(u_{jl} - u_{jl+1})^2 \tag{2}$$

$$\widehat{H}_2 = U\sum_{jl} n_{jl\alpha}n_{jl\beta} + V\sum_{jl\sigma\sigma'} n_{jl\sigma}n_{jl+1\sigma'} \tag{3}$$

$$\widehat{H}_3 = J_0\sum_{jl}\mathbf{S}_{jlR}\cdot\mathbf{S}_{jl}\Delta_l \tag{4}$$

$$\widehat{H}_4 = -\sum_{l\sigma}[T_1 + (-1)^l T_2](c^+_{1l\sigma}c_{2l\sigma} + c^+_{2l\sigma}c_{1l\sigma}) \tag{5}$$

The first term $\widehat{H}_1$ describes the intrachain hoppings of the π electrons on each main chain, the electron–phonon interaction and the distortion of the lattice. Where $c^+_{jl\sigma}(c_{jl\sigma})$ is the creation (annihilation) operator for a π electron with spin σ on the lth site of the jth chain, $\sigma(=\alpha,\beta)$ labels the direction of spin where α and β denote up and down spin, respectively, t_0 is the hopping integral of the π electrons along each main chain when there is no dimerization, α_0 is the electron–phonon coupling constant, u_{jl} is the displacement of the lth lattice site of the jth main chain, κ is the elastic constant of the lattice.

The second term $\widehat{H}_2$ describes the Hubbard on-site electron–electron repulsion of π electrons (the first term in $\widehat{H}_2$) and the inter-site electron–electron Coulomb repulsion of π electrons (the second term in $\widehat{H}_2$), U and V are electron repulsion constants and $n_{jl\sigma} = c^+_{jl\sigma}c_{jl\sigma}$.

The third term $\widehat{H}_3$ describes the antiferromagnetic correlation between the spin $\mathbf{S}_{jl}$ of π electron and the residual spin $\mathbf{S}_{jlR}$ of the side radical R. $J_0(>0)$ is the coupling constant. Δ_l defines the connection of the radicals, if the carbon atom on the lth site connects with side radical, then $\Delta_l = 1$; otherwise $\Delta_l = 0$.

The fourth term $\widehat{H}_4$ describes the interchain coupling. T_1 and T_2 are the hopping integrals from site l of the first chain to the corresponding site l of the second chain. Since the side radicals only connects with even site in each chain (as shown in Fig. 1), the interchain transfer integrals should be unsymmetrical with respect to even sites and odd sites as shown in the Eq. (5).

The term $\mathbf{S}_{jlR}\cdot\mathbf{S}_{jl}$ in Eq. (4) can be rewritten as

$$\mathbf{S}_{jlR}\cdot\mathbf{S}_{jl} = S^z_{jlR}S^z_{jl} + \frac{1}{2}\left[S^+_{jlR}S^-_{jl} + S^-_{jlR}S^+_{jl}\right] \tag{6}$$

where S^z_{jl} and S^+_{jl} are the Pauli spin matrix:

$$S^z_{jl} = \frac{1}{2}(n_{jl\alpha} - n_{jl\beta}), \quad S^+_{jl} = c^+_{jl\alpha}c_{jl\beta},$$
$$S^-_{jl} = c^+_{jl\beta}c_{jl\alpha} \tag{7}$$

Then we use the mean-field approximation to divide $n_{jl\sigma}$ and S^z_{jl} as follows:

$$n_{jl\sigma} = \langle n_{jl\sigma}\rangle + \Delta n_{jl\sigma} \tag{8}$$

$$S^z_{jlR} = \langle S^z_{jlR}\rangle + \Delta S^z_{jlR} \tag{9}$$

Here $\langle\cdots\rangle = \langle G|\cdots|G\rangle$ is the average with respect to the ground state $|G\rangle$, $\Delta n_{jl\sigma}$ and ΔS^z_{jlR} are fluctuations from the average values.

It is convenient to cast all quantities into dimensionless form as:

$$h = \frac{\widehat{H}}{t_0}, \quad u = \frac{U}{t_0}, \quad v = \frac{V}{t_0}, \quad j_0 = \frac{J_0}{t_0},$$
$$t_1 = \frac{T_1}{t_0}, \quad t_2 = \frac{T_2}{t_0}, \quad \lambda = \frac{2\gamma^2}{t_0\pi\kappa},$$
$$y_{jl} = (-1)^l(u_{jl} - u_{jl+1})\gamma/t_0 \tag{10}$$

Using the self-consistent iterative method and self-consistent field Hartree–Fock approximation, we can numerically solve the Schrödinger equation of the system:

$$h\sum_{jl\sigma} Z^\sigma_{\mu jl}c^+_{jl\sigma}|0\rangle = \varepsilon_\mu\sum_{jl\sigma} Z^\sigma_{\mu jl}c^+_{jl\sigma}|0\rangle \tag{11}$$

where $|0\rangle$ is the true electron vacuum state, ε_μ denotes the μth eigenvalue of Eq. (11), $Z^\sigma_{\mu jl}$ is the expansion coefficient. From Eq. (11) we can get the iterative equations of the system:

$$
\begin{aligned}
&-[1+(-1)^l y_{jl}]Z^\sigma_{\mu jl+1} - \left[1+(-1)^{l-1}y_{jl-1}\right]Z^\sigma_{\mu jl-1} \\
&+\frac{1}{2}J_0\Delta_l\langle S^Z_{jlR}\rangle(\delta_{\sigma\alpha}-\delta_{\sigma\beta})Z^\sigma_{\mu jl} + u\sum_{\substack{\mu'\\(occ)}}\left[Z^{\bar\sigma}_{\mu' jl}\left(Z^{\bar\sigma}_{\mu' jl}\right)^*\right]Z^\sigma_{\mu jl} \\
&-\left[t_1+(-1)^l t_2\right]\left(Z^\sigma_{\mu 2l}\delta_{j1}+Z^\sigma_{\mu 1l}\delta_{j2}\right) \\
&+v\sum_{\substack{\sigma'\mu'\\(occ)}}\left[Z^{\sigma'}_{\mu' jl+1}(Z^{\sigma'}_{\mu' jl+1})^* + Z^{\sigma'}_{\mu' jl-1}(Z^{\sigma'}_{\mu' jl-1})^*\right]Z^\sigma_{\mu jl} \\
&=\varepsilon^\sigma_\mu Z^\sigma_{\mu jl}\quad (j=1,2)
\end{aligned}
\tag{12}
$$

Here $\bar\sigma = \alpha\delta_{\beta\sigma}+\beta\delta_{\alpha\sigma}$. The dimerization y_{jl} can be obtained by minimizing the total energy of the system with respect y_{jl}:

$$
y_{jl} = \pi\lambda(-1)^l\left[\sum_{\substack{\mu\sigma\\(occ)}} Z^\sigma_{\mu jl}Z^\sigma_{\mu jl+1} - \frac{1}{N}\sum_l\sum_{\substack{\mu\sigma\\(occ)}} Z^\sigma_{\mu jl}Z^\sigma_{\mu jl+1}\right] \tag{13}
$$

Here, the periodic boundary conditions are used, N is the number of sites along each main chain, and (occ) means those states occupied by electrons. The distribution of charge density $\langle n_{jl}\rangle$ and spin density δn_{jl} can be expressed in terms of the expansion coefficients $Z^\sigma_{\mu jl}$ as:

$$
\langle n_{jl}\rangle = \langle n_{jl\alpha}\rangle + \langle n_{jl\beta}\rangle = \sum_{\substack{\mu\sigma\\(occ)}} Z^{\sigma *}_{\mu jl}Z^\sigma_{\mu jl}. \tag{14a}
$$

$$
\delta n_{jl} = \frac{1}{2}\left(\langle n_{jl\alpha}\rangle - \langle n_{jl\beta}\rangle\right) = \frac{1}{2}\sum_{\substack{\mu\sigma\\(occ)}}\left(Z^{\alpha *}_{\mu jl}Z^\alpha_{\mu jl} - Z^{\beta *}_{\mu jl}Z^\beta_{\mu jl}\right). \tag{14b}
$$

The energy eigenvalue ε^σ_μ and the expansion coefficients $Z^\sigma_{\mu jl}$ can be obtained from Eqs. (12)–(14) self-consistently. The starting geometry in the iterative optimization process is usually the one with $y_{jl}=0$ and $\langle n_{jl\alpha}\rangle = \langle n_{jl\beta}\rangle = 1/2$. The criterion for terminating the optimization is that the differences are less than 10^{-6} for the y_{jl},$\langle n_{jl\alpha}\rangle$ and $\langle n_{jl\beta}\rangle$ between two successive iterations.

3. Results and discussion

We now consider two neighboring chains each with 60 carbon atoms and 30 side radicals shown in Fig. 1. In order to study the ground state, we always fill the π electrons in the possible lowest levels in every iterative step. In the following numerical calculation, we assume the parameters $j_0 = 0.5$, $t_1 = 0.1$, $t_2 = 0.05$. Since it is clear that for $j_0 \neq 0$, the total energy of an isolated chain is the lowest when $\langle S^z_{jlR}\rangle = \pm 0.5$ [12], we choose $\langle S^z_{jlR}\rangle = 0.5$ in this paper.

First, we discuss the collective effects of electron–phonon coupling and inter-site electron–electron interaction on the charge density, spin density and ferromagnetic ordering of the system. Here, the on-site electron–electron interaction u is assumed to be 1.0. Fig. 2a shows the amplitude of the antiferromagnetic SDW along the main chains, which is expressed as δn_{jl}, as a function of the inter-site electron–electron interaction v with different electron–phonon couplings. Curves a, b, c and d correspond to $\lambda = 0.2$, 0.3, 0.4 and 0.5, respectively. From Fig. 2a, one can find that with increasing of λ, the amplitude of the SDW will decrease, and for different electron–phonon couplings, the amplitude of the SDW all will experience a sharp decline when v is larger than a critical value v_c. Since the parallel spin arrangement of the unpaired electrons at side radicals is mediated by the SDW along the main chain [12], the strong electron–phonon coupling and inter-site electron–electron interaction will weaken the stability of the ferromagnetic ordering in the system. Fig. 2b shows the amplitude of the CDW along the main chains, which is expressed as $\langle n_{jl}-1\rangle$, versus the inter-site electron–electron interaction v with different electron–phonon couplings. It is clear that

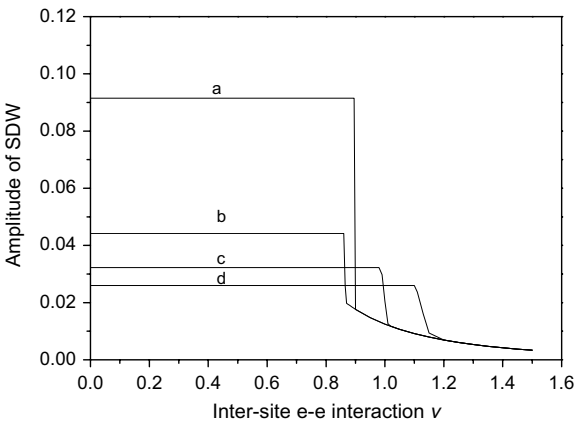


Fig. 2a. The amplitude of the SDW versus the inter-site electron–electron interaction v with different electron–phonon couplings. Curves a: $\lambda = 0.2$; b: $\lambda = 0.3$; c: $\lambda = 0.4$; and d: $\lambda = 0.5$.

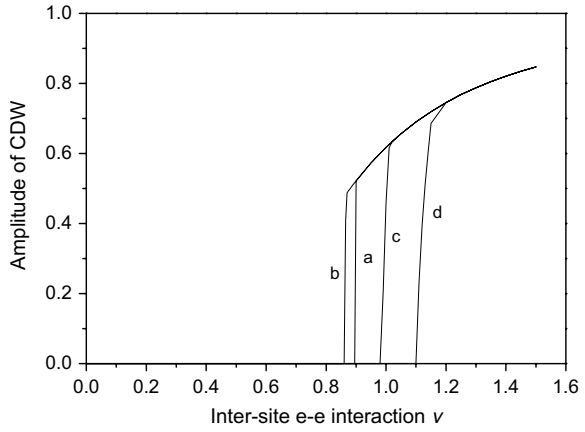


Fig. 2b. The amplitude of the CDW versus the inter-site electron–electron interaction v with different electron–phonon couplings. Curves a: $\lambda = 0.2$; b: $\lambda = 0.3$; c: $\lambda = 0.4$; and d: $\lambda = 0.5$.

when $v > v_c$, a strong CDW along the main chains will appear in the system. In addition, the electron–phonon coupling has an impact on the critical value v_c. In our study, when λ varies from 0.3 to 0.5, the v_c will become larger although the electron–phonon coupling will decrease the amplitude of the SDW. Fig. 3 gives the spin density and charge density along the main chain when $\lambda = 0.2$ and $v = 0.5(<v_c)$(a); $v = 1.4(>v_c)$(b), which exhibits the strong SDW state and CDW state in the system respectively when the v are at the different sides of the v_c.

Then, we discuss the effects of the electron–electron interactions on the CDW and SDW along the main chain when the electron–phonon coupling $\lambda = 0.2$. Figs. 4a and 4b respectively show the amplitude of the antiferromagnetic SDW and CDW along the main chains as a function of the inter-site electron–electron interaction v with different on-site electron–electron interactions. Curves a, b and c correspond to $u = 0.5$, 1.0 and 1.5, respectively. From Fig. 4, one can see that the amplitude of the SDW will significantly increase with increasing of u, and whatever the on-site electron–electron interaction u is, the inter-site electron–electron interaction v will reach a critical point v_c, at which a transfer from the strong SDW state to strong CDW state will happen in the system. Moreover, the strong on-site electron–electron interaction will make the critical value v_c become larger.

As for the influence from the interchain interactions on the ground state of the system, our calcula-

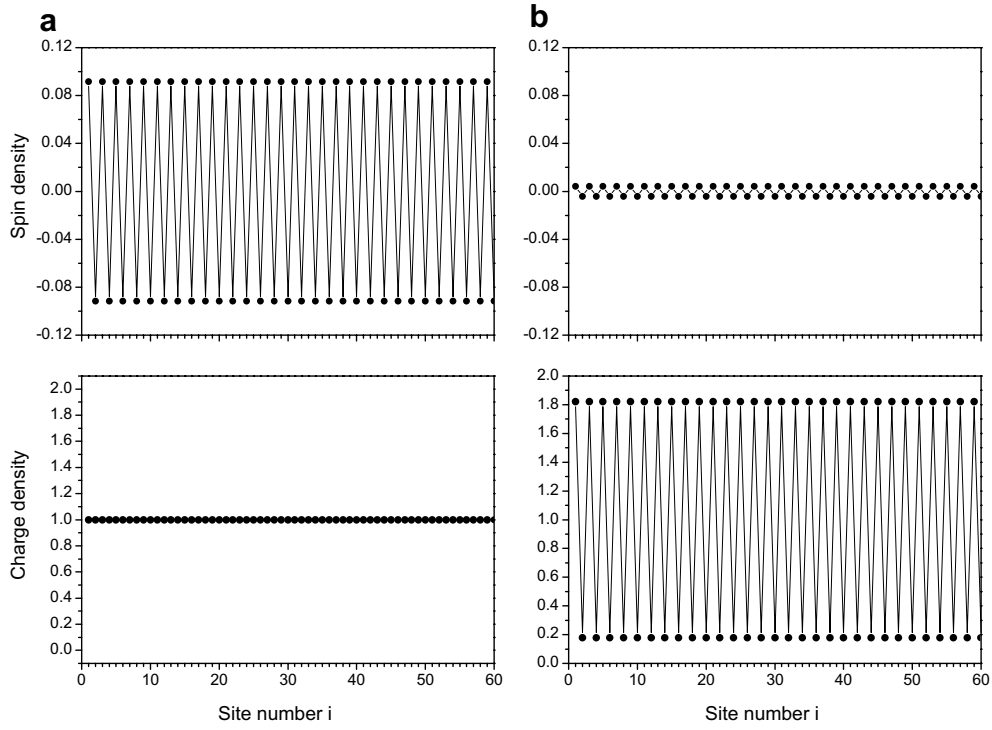


Fig. 3. Spin density and charge density along the main chain when $\lambda = 0.2$ and $v = 0.5 < v_c$ (a) and $v = 1.4 > v_c$(b).

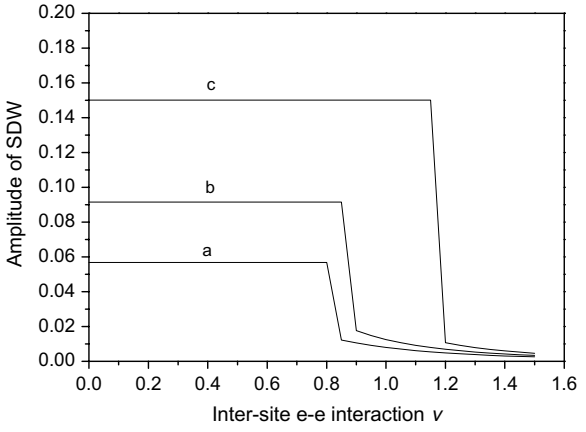


Fig. 4a. The amplitude of the SDW versus the inter-site electron–electron interaction v with different on-site electron- electron interactions. Curves a: $u = 0.5$; b: $u = 1.0$; and c: $u = 1.5$.

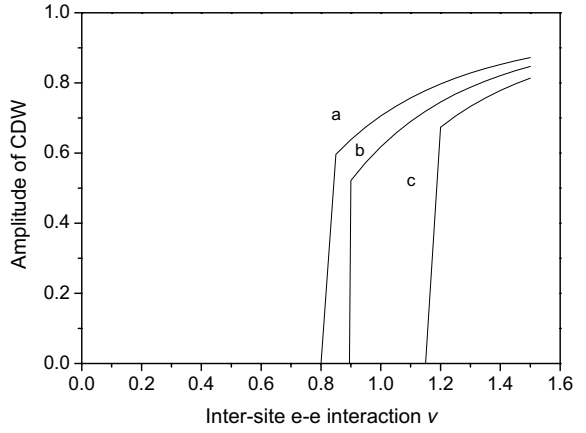


Fig. 4b. The amplitude of the CDW versus the inter-site electron–electron interaction v with different on-site electron-electron interactions. Curves a: $u = 0.5$; b: $u = 1.0$; and c: $u = 1.5$.

tion shows that whatever the interchain coupling parameters t_1 and t_2 are, there also exists a critical value of the inter-site electron–electron interaction, at which the system will experience a transfer from the strong SDW state to strong CDW state. However, the interchain coupling parameter t_1 has no obvious influence on the amplitude of the SDW along the main chain and the critical value of inter-site electron–electron interaction, while the strong interchain coupling parameter t_2 will significantly decrease the amplitude of the SDW and has an obvious influence on the critical value of inter-site electron–electron interaction, which is unfavorable to the ferromagnetic ground state in the system.

In conclusion, we have studied the distribution of the charge density and spin density in the interchain coupled organic ferromagnet with electron–phonon coupling and electron–electron interactions. It is shown that strong electron–phonon coupling and inter-site electron–electron interaction are unfavorable to the ferromagnetic ordering in the system, while the on-site electron–electron interaction makes the ferromagnetic ground state more stable. Whatever the electron–phonon coupling and on-site electron–electron interaction are, there exists a critical value of the inter-site electron–electron interaction, at which the system will experience a transfer from the strong SDW state to strong CDW state. The role played by the on-site electron–electron interaction in maintaining the stability of the ferromagnetic state is contrary to that played by the inter-site electron–electron interaction and there exists a competition with each other.

Acknowledgement

The authors are grateful to Professor W.Z. Wang for helpful discussion. This work is supported by the Natural Science Foundation of Hubei Province, P.R. China under the Grant No. 2004ABA102.

References

[1] M. Takahashi, P. Turek, Y. Nakazawa, M. Tamura, K. Nozawa, D. Shiomi, M. Ishikawa, M. Kinoshita, Discovery of a quasi-one-dimensional organic ferromagnet, *p*-NPNN, Phys. Rev. Lett. 67 (1991) 746–748.

[2] R. Chiarelli, M.A. Novak, A. Rassat, J.L. Tholence, A ferromagnetic transition at 1.48 K in an organic nitroxide, Nature 363 (1993) 147–149.

[3] M.M. Matsushita, A. Izuoka, T. Sugawara, T. Kobayashi, N. Wada, N. Takeda, M. Ishikawa, Hydrogen-bonded organic ferromagnet, J. Am. Chem. Soc. 119 (1997) 4369–4379.

[4] Y. Pontillon, T. Akita, A. Grand, K. Kobayashi, E. Lelievre-Berna, J. Pécaut, E. Ressouche, J. Schweizer, Experimental and theoretical spin density in ferromagnetic molecular complex presenting interheteromolecular hydrogen bonds, J. Am. Chem. Soc. 121 (1999) 10126–10133.

[5] W. Fujita, K. Awaga, Room-temperature magnetic bistability in organic radical crystals, Science 286 (1999) 261–262.

[6] J.A. Crayston, J.N. Devine, J.C. Walton, Conceptual and synthetic strategies for the preparation of organic magnets, Tetrahedron 56 (2000) 7829–7857.

[7] T. Makarova, B. Sundqvist, R. Höhne, P. Esquinazi, Y. Kopelevich, P. Scharff, V.A. Davydov, L.S. Kashevarova, A.V. Rakhmanina, Magnetic carbon, Nature 413 (2001) 716–718.

[8] A. Rajac, J. Wongsriratanakul, S. Rajac, Magnetic ordering in an organic polymer, Science 294 (2001) 1503–1505.

[9] D. Luneau, Molecular magnets, Curr. Opin. Solid State Mat. Sci. 5 (2001) 123–129.
[10] Yu.V. Korshak, T.V. Medvedeva, A.A. Ovchinnikov, V.N. Spector, Organic polymer ferromagnet, Nature (London) 326 (1987) 370–372.
[11] A.A. Ovchinnikov, V.N. Spector, Organic ferromagnets. New results, Synthetic Met. 27 (1988) B615–B624.
[12] Z. Fang, Z.L. Liu, K.L. Yao, Theoretical model and numerical calculation for quasi-one-dimensional organic ferromagnet poly-BIPO, Phys. Rev. B49 (1994) 3916–3919; Z. Fang, Z.L. Liu, K.L. Yao, Spin configuration of π-electrons in quasi-one-dimensional organic ferromagnets, Phys. Rev. B51 (1995) 1304–1307.
[13] W.Z. Wang, Z.L. Liu, K.L. Yao, Interchain coupling model for quasi-one-dimensional ferromagnets, Phys. Rev. B55 (1997) 12989–12994.

Available online at www.sciencedirect.com
ScienceDirect
Organic Electronics 8 (2007) 445–449
Organic Electronics
www.elsevier.com/locate/orgel

Small-molecular organic solar cells with C_{60}/Al composite anode

M.L. Wang, Q.L. Song, H.R. Wu, B.F. Ding, X.D. Gao, X.Y. Sun, X.M. Ding, X.Y. Hou *

Surface Physics Laboratory (National Key Laboratory) and Advanced Materials Laboratory, Fudan University, Shanghai 200433, China

Received 16 November 2006; received in revised form 3 March 2007; accepted 4 March 2007
Available online 12 March 2007

Abstract

By adopting C_{60}/Al composite anode and an inverted device structure of ITO/Alq_3/C_{60}/CuPc/C_{60}/Al, we have achieved a power conversion efficiency of 0.78% under 75 mW/cm^2 AM1.5G simulated illumination and a shelf lifetime of 950 h from unencapsulated organic solar cells. The improved stability is attributed to efficient protection of the C_{60} layer in the inverted structure. Replacing the C_{60}/Al anode with C_{60}/Au anode in the inverted structure, produces a power conversion efficiency of 0.64%, comparable to that of the device with C_{60}/Al anode. This indicates that the property of the composite electrode is mainly determined by the thin C_{60} layer. Use of C_{60}/Al composite anode to fabricate inverted organic light-emitting devices gives rise to an efficiency of the device comparable to that of conventional devices.
© 2007 Elsevier B.V. All rights reserved.

PACS: 84.60.Jt; 73.50.Pz; 85.60.Bt

Keywords: C_{60}/Al composite electrode; Inverted device structure; Long lifetime; Interfacial layer; Organic light-emitting devices (OLEDs)

1. Introduction

Great progress in the power conversion efficiency of organic solar cells [1–3] has been distinguishing this technology as a promising cost-effective alternative to silicon-based solar cells. However, despite extensive studies on these devices, the lifetime of organic solar cells to date is too short to meet the requirement for practical applications, especially when the cells are unencapsulated [4–6]. For the cells based on copper phthalocyanine (CuPc)/fullerene (C_{60}) heterojunction structures, a very likely reason for their degradation is the decrease of C_{60} conductivity upon oxygen permeation [4–6]. By using a new buffer layer of tris-8-hydroxy-quinolinato aluminum (Alq_3) to replace conventionally used bathocuproine (BCP), the lifetime of the device with conventional structure of indium tin oxide (ITO)/CuPc/C_{60}/buffer/aluminium (Al) has been improved from less than one hour to about 60 h [4]. The improvement of the device stability has been attributed to the more effective block against water/oxygen and better stability of Alq_3 than BCP. However, C_{60} is still vulnerable by oxygen permeation in devices with the conventional structure. Recently, an inverted structure of acceptor/donor instead of donor/acceptor in organic solar cells has been developed [7–9]. The lifetime of the

* Corresponding author. Tel./fax: +86 21 65103617.
E-mail address: xyhou@fudan.edu.cn (X.Y. Hou).

1566-1199/$ - see front matter © 2007 Elsevier B.V. All rights reserved.
doi:10.1016/j.orgel.2007.03.001

inverted gold-on-top anode polymer solar cells was improved to be about 2 weeks as compared to less than one day for conventional cells under ambient air conditions without encapsulation, and high stability of gold in an oxidizing environment was considered the main reason for that. For such kind of solar cells, a top anode with high work function is needed. Au meets the requirement of high work function while Al does not due to its low work function of 4.3 eV [10]. However, it was demonstrated that the work function of Al could be modified by evaporating a thin C_{60} layer on Al, resulting in a value about 5.2 eV [11,12]. Thus C_{60}/metal composite electrode would be suitable as an anode in inverted solar cells.

In this article, we present an organic solar cell of inverted structure ITO/Alq_3/C_{60}/CuPc/C_{60}/Al with C_{60}/Al composite electrode as the anode. Shelf lifetime (the time that power conversion efficiency (η_p) degrades to 50% of its initial value) of about 950 h has been achieved for the devices without encapsulation. The η_p reaches 0.78% under AM1.5G (air mass 1.5 global) 75 mW/cm^2. Replacing the C_{60}/Al anode with C_{60}/Au anode in the inverted structure, produces a power conversion efficiency of 0.64%, comparable to that of the device with C_{60}/Al anode. Use of C_{60}/Al composite anode to fabricate inverted organic light-emitting devices (OLEDs) gives rise to an efficiency of the devices comparable to that of conventional OLEDs. We thus confirm that different from Al, the C_{60}/Al composite electrode is suitable as anode in inverted organic semiconductor devices.

2. Experiment

The cells with inverted structure ITO/Alq_3 (2 nm)/C_{60} (40 nm)/CuPc (20 nm)/C_{60} (5 nm)/metal were fabricated on pre-cleaned glass substrates coated with transparent conducting ITO. The sheet resistance of ITO was about 17 Ω/square. The substrate was heated to 150 °C in air after solvent cleaning and then loaded into a high vacuum chamber ($\sim 5 \times 10^{-6}$ Pa) without UV-ozone treatment. A 2 nm-thick Alq_3 layer was used as the buffer layer between ITO and C_{60}, while a 5 nm C_{60} layer was used as the buffer layer between CuPc and top metal. The top metal electrode of Al or Au was in situ deposited with a shadow mask. The OLEDs with inverted structure ITO/Al (5 nm)/LiF (0.6 nm)/Alq_3 (50 nm)/NPB (30 nm)/C_{60} (5 nm)/Al (100 nm) were fabricated in the same way. The organic solar cells and the OLEDs were of area 9 mm^2, with 3-mm-wide ITO stripes over-crossed by 3-mm-wide top metal stripes. Power conversion efficiency was measured under illumination of an Oriel solar simulator producing the AM1.5G spectrum. The intensity of the simulator output was measured with a calibrated broadband optical power meter (verified by a standard crystalline silicon solar cell). The current–voltage (I–V) characteristics of solar cells were measured by Keithley 2400 and the I–V characteristics of OLEDs were measured by Keithley 236 and Keithley 2000. The investigated devices were kept in air at room temperature during the whole measurement procedure without any encapsulation.

3. Results and discussion

Fig. 1 shows the I–V characteristics of solar cells ITO/Alq_3 (2 nm)/C_{60} (40 nm)/CuPc (20 nm)/C_{60} (x nm)/Al (100 nm) ($x = 5$ nm, device A; $x = 0$ nm, device B). Under the irradiation of simulated sunlight, the open circuit voltage (V_{oc}), short circuit current (I_{sc}) and the fill factor (FF) of device A are 0.434 V, 3.46 mA/cm^2 and 38.8%, respectively, resulting in η_p of 0.78%. The V_{oc}, I_{sc} and η_p of device B are 0.02 V, 0.03 mA/cm^2 and 0.0003%, respectively. The I–V curves also show that V_{oc} is negative and I_{sc} is positive for device A, while V_{oc} is positive and I_{sc} is negative for device B, and hence the polarities of the two devices are opposite to each other, indicating that the built-in electric fields are opposite in the two devices. Incorporating 5 nm C_{60} layer, which is the sole difference between device A and device B, should be the cause of the opposite polarity in the two devices and also for the improved performance of device A. In previous work [11,12], it was demonstrated that, by evaporating a C_{60} monolayer onto Al, the work function of Al could be modified to a value about 5.2 eV. Also, Al deposited on C_{60} can lead to similar charge transfer and interface dipole formation [13,14]. That means the C_{60}/Al composite electrode acts as an anode in device A, resulting in a built-in electric field pointing from ITO (work function is between 4.4 eV and 4.7 eV [15,16]) to the C_{60}/Al composite electrode, shown in the inset of Fig. 1(a). For solar cells with C_{60}/CuPc heterojunction, the photoexcitated excitons split at the C_{60}/CuPc interface, leaving electrons at the C_{60} layer side while the holes at the CuPc layer side. Since in device A the built-in electric field is pointing from ITO to Al, the field will drive the free electrons toward the ITO cathode

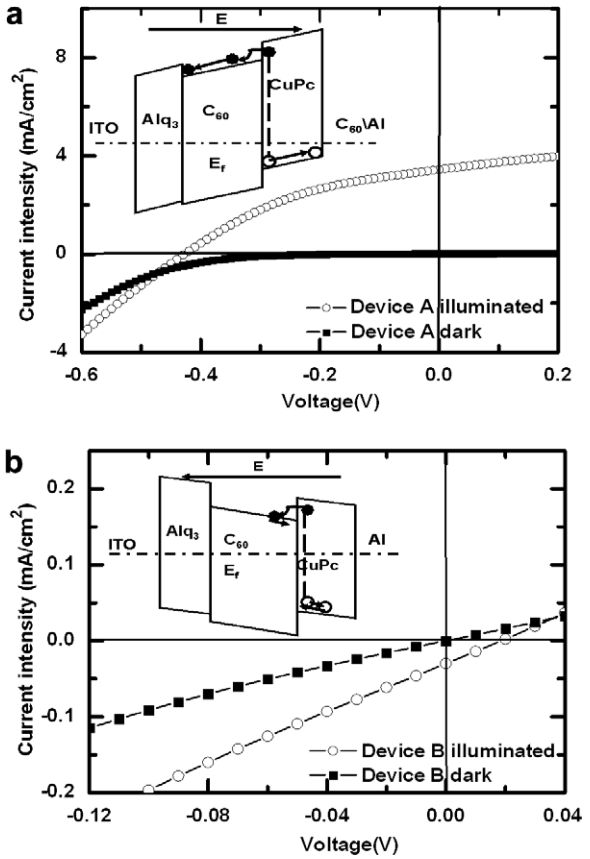


Fig. 1. (a) I–V characteristics of device A (ITO/Alq_3 (2 nm)/C_{60} (40 nm)/CuPc (20 nm)/C_{60} (5 nm)/Al (100 nm)). (b) I–V characteristics of device B (ITO/Alq_3 (2 nm)/ C_{60} (40 nm)/CuPc (20 nm)/Al(100 nm)). The inset shows the energy diagram of the two devices.

and holes toward the C_{60}/Al composite anode, resulting in effective separation of electrons and holes, and leading to effective carrier collection by the electrodes and a large current density of 3.46 mA/cm^2. In device B with ITO and Al as electrodes, the difference in work function of ITO and Al results in a built-in electric field pointing from Al to ITO, as shown in the inset of Fig. 1(b). Thus the field will drive the electrons toward the Al electrode and holes toward the ITO electrode, causing the free carriers to accumulate and recombine at the C_{60}/CuPc interface, where they are generated, resulting in inefficient carrier collection by the electrodes, and leading to a poor performance of device B.

Fig. 2 shows the degradation of normalized η_p of device A with C_{60}/Al anode, compared to that of the conventional device C of structure ITO/CuPc (30 nm)/C_{60} (40 nm)/Alq_3 (6 nm)/Al [4]. The shelf

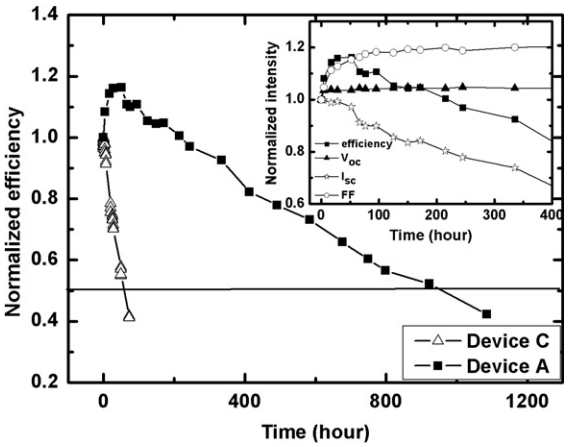


Fig. 2. Normalized power conversion efficiency of device A and device C (ITO/CuPc (30 nm)/C_{60} (40 nm)/Alq_3 (6 nm)/Al (100 nm)) versus time. The inset shows the degradation of V_{oc}, I_{sc} and FF of device A.

lifetime of device A without encapsulation is about 950 h. Device C, although characterized by a higher η_p of 2.1%, achieved a shelf lifetime of only 61 h. Another feature of the degradation curve is that the η_p of the device with inverted structure increases initially, reaching the maximal increment of about 16% at around 52 h, and then decreases gradually. For organic solar cells made from CuPc/C_{60} heterojunctions, one of the most important factors for cell degradation is the decrease of C_{60} conductivity upon oxygen permeation [4,6]. In the conventional structure of ITO/CuPc/C_{60}/Alq_3/Al, oxygen permeates first into C_{60} and then into CuPc; thus the performance of C_{60} is influenced in a very short time and η_p decreases continuously. In contrast, oxygen first permeates through the whole CuPc layer then into the C_{60} layer in device A, because C_{60} is buried under CuPc; thus the permeation of oxygen into C_{60} is postponed. Since the power conversion efficiency of a cell is the product of I_{sc}, V_{oc} and FF, in order to clarify which one is mainly responsible for the η_p degradation of these cells, degradations of I_{sc}, V_{oc} and FF of device A are all plotted in the inset of Fig. 2. It can be seen that I_{sc} decreases continuously and slowly, which decreases to 40% in about 950 h; V_{oc} is stable and shows no degradation, while FF keeps increasing during the time, especially in the first 52 h, indicating that the degradation of η_p is mainly due to the degradation of I_{sc} in device A. Additionally, because the increase of FF exceeds the slight decrease of I_{sc} in the first 52 h, the η_p increases in this period. Such initial increase of η_p has not been observed in conventional devices [4],

while in previous work of BCP-based solar cells with inverted gold-on-top anode structure [9], such increase of η_p was also observed, which was primarily contributed by the increase of V_{oc}. In our group the initial increase of η_p caused by increase of V_{oc} in inverted solar cells with Au anode was also observed [17]. Thus the initial increase of η_p of solar cells with C_{60}/Al anode or Au anode acts differently. The underlying mechanisms need further investigation.

Modifying the ITO cathode by 2 nm Alq_3 is very important for maximizing η_p of device A. Fig. 3 shows the *I–V* characteristics of device D with structure of ITO/C_{60} (40 nm)/CuPc (20 nm)/C_{60} (5 nm)/Al (100 nm), without the thin Alq_3 interfacial layer. Under the irradiation of simulated sunlight, V_{oc}, I_{sc} and FF of device D are 0.14 V, 1.35 mA/cm^2 and 26.4%, respectively. This results in η_p of 0.06%, which is much lower than that of device A ($\eta_p = 0.78\%$), as mentioned above. Compared to device A, the rectification ratio of device D is weakened considerably without the insertion of 2 nm Alq_3 interfacial layer. At the voltage of 0.5 V, the ratio was about 24 for device A but only about 1 for device D. Direct contact of C_{60} with ITO can increase the work function of ITO [18], resulting in a reduced work function difference between ITO and C_{60}/Al composite electrode, and in turn weakening the built-in electric field in device D. These lead to the bad performance of device D. Insertion of 2 nm Alq_3 layer can separate C_{60} from ITO, preventing them from direct contacting. Additionally, theoretical [19] and experimental [20] results showed that surface dipoles can be formed to lower the work function of electrodes upon Alq_3 deposition on some metal surfaces. Surface dipoles may be formed between Alq_3 and ITO, resulting in reduced work function of ITO, and in turn strengthening the built-in electrical field, leading to better carrier collection by the electrodes. Meanwhile, the hole injection barrier from ITO to C_{60} under positive bias is enhanced and this could be responsible for the better rectification of device A.

The distinct difference of performance of C_{60}/Al composite electrode and Al electrode in inverted solar cells and the great improvement of performance after insertion of 2 nm Alq_3 between ITO and C_{60} layer demonstrate that the contact of C_{60} layer with metal electrode has great influence on the performance of devices. We replaced C_{60} (5 nm)/Al (100 nm) with C_{60} (5 nm)/Au (20 nm) and fabricated inverted solar cells with structure of ITO/Alq_3 (2 nm)/C_{60} (40 nm)/CuPc (20 nm)/C_{60} (5 nm)/ Au (20 nm). Fig. 4 shows the *I–V* characteristics in the dark and under simulated sunlight. I_{sc} of 3.46 mA/cm^2 and η_p of 0.64% were obtained, comparable with these of device A. The direction of I_{sc} is from ITO to Au, which means the built-in electrical field points from ITO to Au, similar to that in device A. This demonstrates that the Fermi-level is pinned by the thin C_{60} interfacial layer, and in turn the built-in electric field is mainly determined by the thin C_{60} interfacial layer and is insensitive to the materials of metal electrode.

In inverted OLEDs (ITO/electron transporting layer/emitting layer/hole transporting layer/anode), Au [21,22], Ag/TeO_2 [23] and WO_3/Al [24] have been used as anodes. As mentioned above, C_{60}/Al

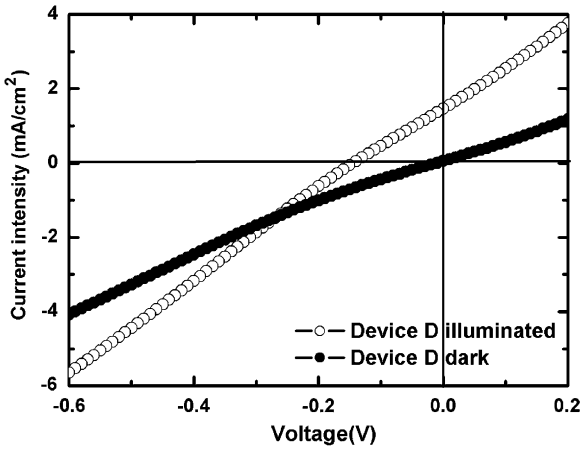


Fig. 3. Dark and illuminated *I–V* characteristics of device D ITO/C_{60} (40 nm)/CuPc (20 nm)/C_{60} (5 nm)/Al (100 nm).

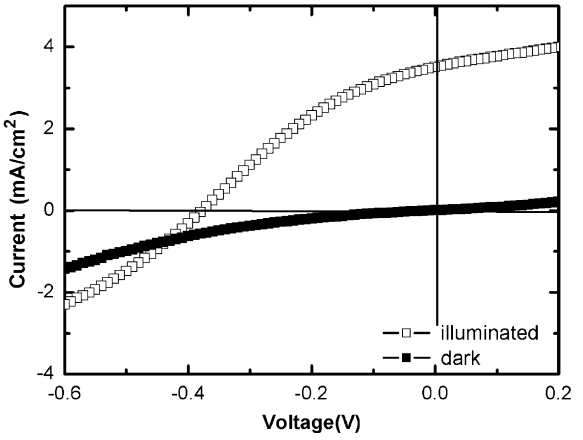


Fig. 4. Dark and illuminated I–V characteristics of the device with structure of ITO/Alq_3 (2 nm)/C_{60} (40 nm)/CuPc (20 nm)/C_{60} (5 nm)/Au (20 nm).

is suitable as anode in inverted organic solar cells. Thus it would also be suitable as an anode in inverted OLEDs.We have used ITO/Al (5 nm)/LiF as cathode, and C_{60}/Al or Al as anode to fabricate devices ITO/Al (5 nm)/LiF (0.6 nm)/Alq_3 (50 nm)/NPB (30 nm)/C_{60} (x nm)/Al (100 nm) ($x = 5$ nm, device E; $x = 0$ nm, device F). Device E shows a luminance of 7000 cd/m^2 under bias 12 V while device F shows almost no luminance (only 10 cd/m^2 under bias 12 V). The maximum current efficiency is 1.8 cd/m^2 and power efficiency is 1 lm/W of device E, comparable with conventional devices. Under 12 V bias, device E shows a current intensity of 390 mA/cm^2 compared to device F of 65 mA/cm^2, which demonstrates that C_{60}/Al composite electrode has much better hole injection ability than that of Al electrode. Thus the C_{60}/Al composite electrode can also be used as the anode in inverted OLEDs to effectively inject holes into organic layers. Moreover, C_{60}/Al composite electrode can be used in devices that require a high work function electrode.

4. Conclusions

In summary, we have used C_{60}/Al composite electrode as anode and fabricated inverted organic solar cells, achieving an efficiency of 0.78% and a shelf lifetime of over 950 h without encapsulation. The improvement of lifetime can be mainly attributed to the inverted structure, which provides a more efficient protection of the C_{60} layer. Inverted organic solar cells with C_{60}/Au composite anode have been fabricated with an efficiency of 0.64%, indicating that Fermi-level is pinned by the thin C_{60} layer. In addition, C_{60}/Al composite electrode has been used in inverted OLEDs, and the efficiency of the device is comparable to that of conventional devices. Therefore C_{60}/Al is suitable as anode in a variety of organic semiconductor devices.

Acknowledgements

This work is supported by CNKBRSF and the National Natural Science Foundation of China.

References

[1] P. Peumans, S.R. Forrest, Appl. Phys. Lett. 79 (2001) 126.
[2] J. Xue, B.P. Rand, S. Uchida, S.R. Forrest, Adv. Mater. 17 (2005) 66.
[3] G. Li, V. Shrotriya, J. Huang, Y. Yao, Y. Yang, Nat. Mater. 4 (2005) 864.
[4] Q.L. Song, F.Y. Li, H. Yang, H.R. Wu, X.Z. Wang, W. Zhou, J.M. Zhao, X.M. Ding, C.H. Huang, X.Y. Hou, Chem. Phys. Lett. 416 (2005) 42.
[5] P. Peumans, S.R. Forrest, Appl. Phys. Lett. 80 (2002) 338.
[6] S. Heutz, P. Sullivan, B.M. Sanderson, S.M. Schultes, T.S. Jones, Sol. Energy Mater. Sol. Cells 83 (2004) 229.
[7] J. Rostalski, D. Meissner, Sol. Energy Mater. Sol. Cells 63 (2000) 37.
[8] L. Sicot, B. Geffroy, A. Lorin, P. Raimond, C. Sentein, J.-M. Nunzi, J. Appl. Phys. 90 (2001) 1047.
[9] Y. Sahin, S. Alem, R. Bettignies, J.M. Nunzi, Thin Solid Films 476 (2005) 340.
[10] S. Son, S.-H. Yoon, J.-G. Jang, M.-S. Kang, S.-Y. Jeon, in: SID International Symposium Digest of Technical Papers 35 (2004) 52.
[11] A.J. Maxwell, P.A. Bruhwiler, D. Arvanitis, J. Hasselstrom, Phys. Rev. B 57 (1998) 7312.
[12] J.Y. Lee, Appl. Phys. Lett. 88 (2006) 73512.
[13] A.F. Hebard, C.B. Eom, Y. Iwasa, K.B. Lyons, G.A. Thomas, D.H. Rapkine, R.M. Fleming, R.C. Haddon, Julia M. Philips, J.H. Marshall, R.H. Eick, Phys. Rev. B 50 (1994) 17740.
[14] D.W. Owens, C.M. Aldao, D.M. Poirier, J.H. Weaver, Phys. Rev. B 51 (1995) 17068.
[15] Y. Park, V. Choong, Y. Gao, B.R. Hsieh, C.W. Tang, Appl. Phys. Lett. 68 (1996) 2699.
[16] Ji Cui, Anchuan Wang, Nikki L. Edleman, Jun Ni, Paul Lee, Neal R. Armstrong, Tobin J. Marks, Adv. Mater. 13 (2001) 1476.
[17] Q.L. Song, M.L. Wang, E.G. Obbard, X.Y. Sun, X.M. Ding, X.Y. Hou, C.M. Li, Appl. Phys. Lett. 89 (2006) 251118.
[18] II-Hwa Hong, Min-Woo Lee, Young-Mo Koo, Hyein Jeong, Tae-Shick Kim, Ok-Keun Song, Appl. Phys. Lett. 87 (2005) 063502.
[19] S. Yanagisawa, Y. Morikawa, Chem. Phys. Lett. 420 (2006) 523.
[20] U. Zerweck, C. Loppacher, L.M. Eng, Nanotechnology 17 (2006) S107.
[21] H.W. Choi, S.Y. Kim, W.-K. Kim, J.-L. Lee, Appl. Phys. Lett. 87 (2005) 082102.
[22] L. Hou, F. Huang, W. Zeng, J. Peng, Y. Cao, Appl. Phys. Lett. 87 (2005) 153509.
[23] C.-W. Chen, C.-L. Lin, C.-C. Wu, Appl. Phys. Lett. 85 (2004) 2469.
[24] Ta-Ya Chu, Jenn-Fang Chen, Szu-Yi Chen, Chao-Jung Chen, Chin H. Chen, Appl. Phys. Lett. 89 (2006) 53503.

Available online at www.sciencedirect.com
ScienceDirect
Organic Electronics 8 (2007) 450–454
Organic Electronics
www.elsevier.com/locate/orgel

Letter

Low-voltage organic thin film transistors with hydrophobic aluminum nitride film as gate insulator

Hsiao-Wen Zan [a,b,*], Kuo-Hsi Yen [a,b], Pu-Kuan Liu [a,b], Kuo-Hsin Ku [c], Chien-Hsun Chen [c], Jennchang Hwang [c]

[a] *Department of Photonics and Institute of Electro-Optical Engineering, National Chiao Tung University, 1001, Ta Hsueh Road, Hsinchu 300, Taiwan, ROC*
[b] *Department of Photonics and Display Institute, National Chiao Tung University, Taiwan*
[c] *Department of Materials Science and Engineering, National Tsing Hua University, Taiwan*

Received 21 June 2006; received in revised form 6 December 2006; accepted 15 December 2006
Available online 22 December 2006

Abstract

This paper reports on the low-voltage (<5 V) pentacene-based organic thin film transistors (OTFTs) with a hydrophobic aluminum nitride (AlN) gate-dielectric. In this work, a thin (about 50 nm), smooth (roughness about 0.18 nm) and low-leakage AlN gate dielectric is obtained and characterized. The AlN film is hydrophobic and the surface free energy is similar to the organic or the polymer films. The demonstrated AlN–OTFTs were operated at a low-voltage (3–5 V). A low-threshold voltage (−2 V) and an extremely low-subthreshold swing (~170 mV/dec) were also obtained. Under low-voltage operating conditions, the on/off current ratio exceeded 10^6, and the field effect mobility was mobility was 1.67 cm^2/V s.
© 2006 Elsevier B.V. All rights reserved.

Keywords: OTFTs; AlN; Pentacene; High-*k*; Sputtering; Contact angle; Surface energy

1. Introduction

Organic thin-film transistors have been proposed for use in various applications in displays and flexible electronics [1,2]. However, the high operating-voltage remains a limitation on organic transistors. Capacitance is important in lowering the operating voltage. A larger capacitance is well known to accumulate more carriers and turn on transistors at lower voltage. Two approaches have been proposed to increase the gate capacitance: to reduce the thickness of the gate-dielectric [3] and to use a high-*k* material as a gate-dielectric [4]. Nevertheless, controlling gate leakage is an additional difficulty [5]. As well as the increase in capacitance, the surface polarity (hydrophilic or hydrophobic) of the gate-dielectric is an important factor. Many researchers have shown that polymer dielectrics are suitable for organic film deposition because they have similar surface energies to those of organic films. The

* Corresponding author. Address: Department of Photonics and Institute of Electro-Optical Engineering, National Chiao Tung University, 1001, Ta Hsueh Road, Hsinchu 300, Taiwan, ROC. Tel.: +886 3 5712121x52922; fax: +886 3 5716631.
E-mail address: hsiaowen@mail.nctu.edu.tw (H.-W. Zan).

1566-1199/$ - see front matter © 2006 Elsevier B.V. All rights reserved.
doi:10.1016/j.orgel.2006.12.001

dielectric polarity is altered by the self-assembled monolayer (SAM) on inorganic dielectrics. Inorganic dielectrics with lower surface energy offer improved device performance; such surfaces reduce the number of interface traps in OTFTs [6,7].

This work presents AIN film as the gate dielectric for OTFTs. The AlN film is known to have high chemical and physical stability, as well as high dielectric permittivity [8]. In this study, the AlN film was hydrophobic and the surface energy was similar to that of the pentacene film. Moreover, the AlN film can be deposited at 150 °C by using RF-sputtering system. High breakdown voltage and low-leakage-current can be obtained. This letter also presents the favorable switching characteristics of AlN–OTFTs.

2. Experimental

AlN film was deposited at low-temperature (150 °C) by a radio-frequency (RF) sputtering system [9]. For AlN-deposition, the n^+-Si wafer was used as the substrate. The wafer was rinsed in the deionization water, and was then immersed in the acetone with ultrasonic clean. Consequently, the wafer was dipped in dilute HF solution ($HF:H_2O = 1:100$) to remove the native oxide from the Si wafer. Finally, the wafer was transferred to the RF-sputtering system immediately. The system was then pumped down to a base pressure of under 2×10^{-6} Torr before gas was admitted. Mixed argon and nitrogen gas was monitored by mass flow controllers (MFC). The AlN films were deposited at a total pressure of 2.5 mTorr. All the relevant experimental details have been published elsewhere [9]. After the AlN films were deposited, pentacene film was deposited through the shadow mask. The pentacene material obtained from Aldrich without any purification was directly placed in the thermal coater for deposition. The substrate was heated to 70 °C during the deposition at a pressure of around 1×10^{-6} Torr. The thickness of the pentacene film was about 100 nm and the deposition rate was around 0.5 Å/s, monitored by a quartz crystal oscillator. Then, Au was deposited as the source/drain electrodes on the pentacene film. The thickness of the electrode pad was 1000 Å. The channel width and length were defined as 600 μm and 100 μm. Metal–insulator–semiconductor (MIS) – Au/AlN/Si was also fabricated to analyze the gate leakage and the dielectric properties. The area of the Au pad was 500×500 μm^2. All electrical characteristics were measured using Agilent 4156 and Agilent 4284 analyzers.

3. Results and discussion

In our previous investigation, the AlN film was deposited at a higher substrate temperature [9]. The AlN film has a grain-structure and is highly *c*-axis oriented. If the AlN film is deposited at high temperature to form the gate-dielectrics, the grain boundaries will affect the surface roughness and reduce the uniformity. The grain boundaries commonly serve as leakage paths. Since the dielectric roughness and leakage are critical in OTFT fabrication, in this work, AlN was deposited at a lower substrate temperature (150 °C). Fig. 1(a) reveals the AFM image of the 150 °C AlN film. Unlike a high-temperature AlN film [9], the 150 °C AlN film was smooth. The surface roughness was only 0.18 nm. Fig. 1(b) presents the scanning electron microscopic (SEM) image to verify the dielectric quality. In the 150 °C sputtered AlN film (with a thickness of around 50 nm), no significant surface irregular and pinholes were observed. The fluctuation of dielectric thickness is appeared; it may result in performance variation when OTFT size is reduced to micro-scale. The 150 °C AlN film had favorable surface properties. The dielectric properties were also examined. The measured capacitance of the MIS structure was approximately 104 nF/cm^2. Fig. 1(c) shows the gate-leakage, which was as low as $\sim 10^{-8}$ A/cm^2 in an electric field of 1 MV/cm.

In this investigation, OTFTs were fabricated with thin AlN film (thickness is about 50 nm, dielectric constant is about 6) as gate-dielectric. Fig. 2(a) presents the transfer characteristics. The AlN–OTFTs can be operated at a relatively low-voltage (~5 V). The on/off current ratio was about 10^6; the threshold voltage was only −2.1 V; the field effect mobility was 1.67 cm^2/V s. The subthreshold swing was 170 mV/decade. The magnitude approached the theoretical minimum, ~60 mV/decade ($kT/q \cdot \ln(10)$) [7]. Fig. 2(b) shows the output characteristics, the AlN–OTFT were operated in the saturation region at low-drain bias (~3 V). Since the subthreshold swing represents the interface quality and the trap behavior, [10] the maximum interface trap density is given by the approximation, [11]

$$N_{SS} = \left[\frac{S \cdot \log(e)}{kT/q} - 1\right] \cdot \frac{C_i}{q}$$

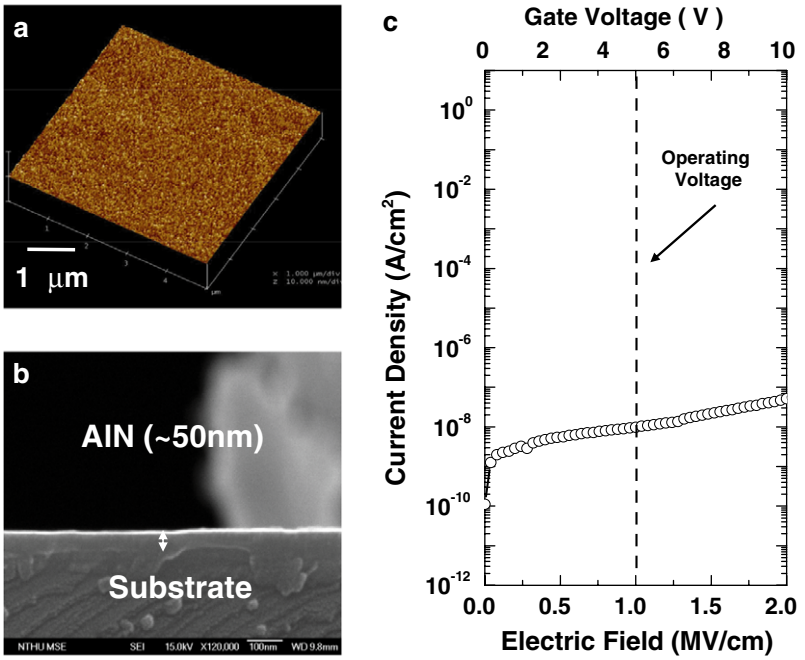


Fig. 1. (a) The AFM image shows the 150 °C AlN film, and the scanning size is $5 \times 5\ \mu m^2$. (b) The SEM image is the cross-section view of the AlN film on substrate. (c) The leakage current of the Au–AlN–Si structure as a function of the electric field and gate voltage.

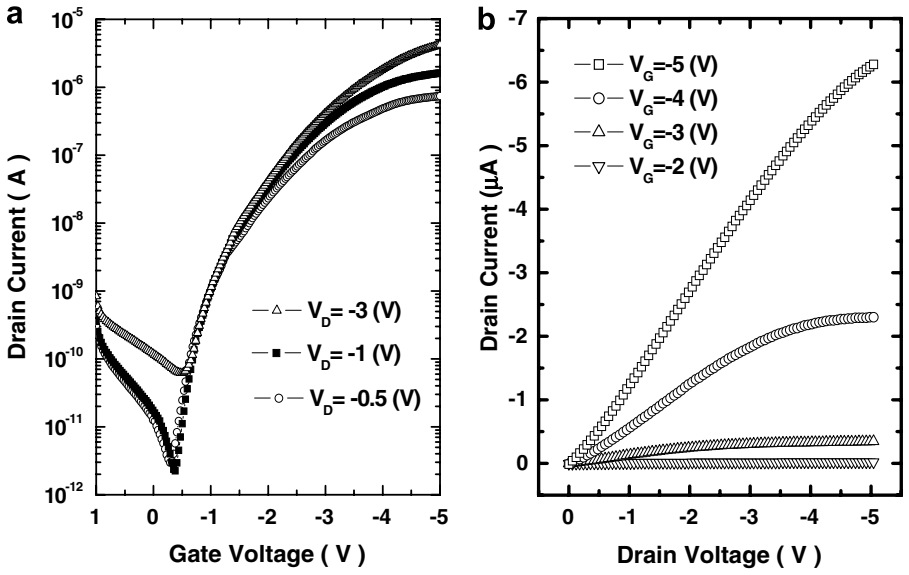


Fig. 2. (a) The transfer characteristics of OTFTs with AlN gate dielectric. (b) The corresponding output characteristic.

where S is the subtheshold swing; C_i is the capacitance per unit area; k is Boltzmann's constant, and T is the absolute temperature. Substituting $C_i = 104\ \mathrm{nf/cm^2}$ and $S = 170\ \mathrm{mV/decade}$ yields an approximate interface trap density in the devices of $1.2 \times 10^{12}\ \mathrm{cm^{-2}\,eV^{-1}}$. To the authors' limited knowledge, this value is close to the lowest reported for organic transistors [3,7,12].

The organic/dielectric interface defects strongly affect the performance of OTFTs. Surface polarity is key to reducing the interface defect. SAM-treatment and a polymer dielectric are widely employed

to change the polarity of the surface. Researchers have recently demonstrated that interface defects can be minimized by changing the dielectric polarity [6,7,13]. Accordingly, the AlN surface polarity was determined herein. The modified Fowkes' equation for the surface polarity in terms of the surface energy is introduced [14]

$$(1+\cos\theta)\gamma_L = 2(\gamma_S^d\gamma_L^d)^{1/2} + 2(\gamma_S^p\gamma_L^p)^{1/2}$$

where θ is the contact angle between probing liquid and the solid surface; γ_L is the total surface free energy of the probing liquid; γ_L^d is the dispersion component, and γ_L^p is the polarity component. Based on this approximation, the total surface free energy of the solid surface is,

$$\gamma_S = \gamma_S^d + \gamma_S^p$$

where the total surface free energy γ_S is the sum of γ_L^d (dispersion component) and γ_L^p (polar component). The surface free energy can be calculated by measuring the contact-angle between the solid surface and the different probing liquids. As shown in Fig. 3(a)–(c), the optical images of various liquid drops on the 150 °C AlN films were captured using a CCD camera. The water–AlN, ethylene glycerol–AlN and di-iodo-methone–AlN contact angles were $72.9° \pm 5°$, $60.7° \pm 4°$ and $43.8° \pm 2°$, respectively. The Owens-Wendt-Rabel and Kaelble's method [14] yields an estimated surface energy of AlN of 38.3 (mJ/m^2). As stated in Table 1; compared to the inorganic dielectrics, the AlN had a low-surface free energy [15,16]. The surface free energy was unusually lower than those of polymer dielectrics [17,18], pentacene, [19] and the HMDs-treated SiO_2 [20]. It was close to that of OTS-treated SiO_2 [20]. The particular characteristic differs from those of the other ceramic-based dielectrics. According to Chou et al. investigation [21], the deposited pentacene film is composed of both orthorhombic and triclinic pentacene. The "dielectric" surface free energy matched to the "orthorhombic pentacene film" (38 mJ/m^2) is the key factor to the high mobility OTFTs. It is believed that the voids and the

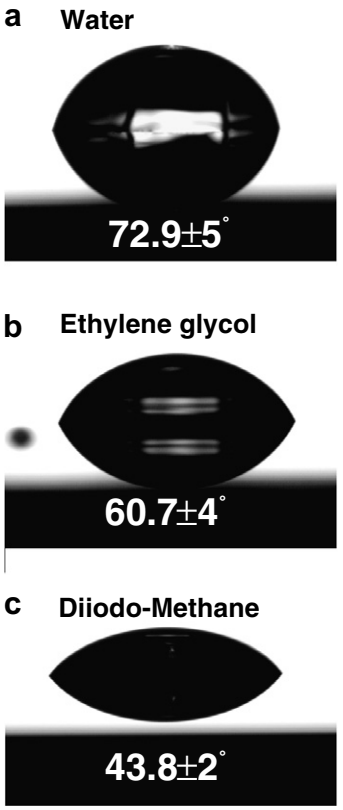


Fig. 3. (a) The water, (b) ethylene glycol, and (c) di-iodo-methane drops on the 150 °C AlN film for the surface-energy measurement. Each value below the drop indicates the contact-angle between the liquid drop and the AlN film. The entire optical images were captured from the CCD camera.

Table 1
Contact-angle measurements and the corresponding surface free energy of the commonly used dielectrics in the OTFTs fabrication

Substrate	Contact angle between liquid and sample			Surface free energy (mJ/m^2)	Reference
	D.I. water	Glycerol	Di-iodo-methane		
Al_2O_3	20–37			68–78	[15]
Si_3N_4	20–30			55–60	[16]
SiO_2	35.7	22.4	25.1	60	[20]
PVA	53.9	54		46.3	[17]
HMDs + SiO_2	53.7	53.7	43.9	45.4	[20]
PVP-copolymer	50–60			42	[18]
Pentacene				38,42–48	[19], [21]
AlN	72.9 ± 5	60.7 ± 4	43.8 ± 2	38.3	This work
OTS + SiO_2	78.9	81.8	43.9	34.9	[20]

incompletely stacked layers, which limited the carrier transport in the pentacene film, are reduced due to the match of surface energy [22]. In this study, the surface free energy of AlN agrees very well with that of the orthorhombic pentacene film, but not to the triclinic pentacene film [23]. Based on these arguments, the high performance AlN–OTFT is attributed to the match of orthorhombic pentacene film with AlN.

4. Conclusions

An AlN film was used as the gate dielectric for OTFTs. The pinhole free, smooth and extremely thin AlN film can be deposited by the RF-sputtering system at 150 °C. This low-temperature deposition process enables the potential application on polymer substrates. The dielectric leakage was significantly low, and the AlN has a surface free energy that is similar to that of the pentacene film. The transfer and output characteristics demonstrate that the AlN–OTFT has potential application in low-voltage and rapid-switching organic transistors.

Acknowledgements

The authors thank for the financial supporting from National Science Council (NSC) of the Republic of China, Taiwan (Contract No. NSC-95-2221-E-009-228) and the Ministry of Economic Affairs of the Republic of China, Taiwan (Contract No. MOEA-95-EC-17-A-07-S1-046) for financially supporting this research. Coworkers from Advanced Displays Labs of NCTU Display Institute are appreciated, as supported by AU Optronics Corp.

References

[1] Kazumasa Nomoto, Nobukazu Hirai, Nobuhide Yoneya, Noriyuki Kawashima, Makoto Noda, Masaru Wada, Jiro Kasahara, IEEE Trans. Electron Dev. 52 (2005) 1519.
[2] Qing Cao, Zheng-Tao Zhu, Maxime G. Lemaitre, Ming-Gang Xia, Appl. Phys. Lett. 88 (2006) 113511.
[3] Marcus Halik, Hagen Klauk, Ute Zschieschang, Gunter Schmid, Christine Dehm, Markus Schutz, Steffen Maisch, Franz Effenberger, Markus Brunnbauer, Francesco Stellacci, Nature (London) 431 (2004) 963.
[4] A.L. Deman, J. Tardy, Org. Electron. 6 (2005) 78.
[5] Guangming Wang, Daniel Moses, Alan J. Heeger, Hong-Mei Zhang, Mux Narasimhan, R.E. Demaray, J. Appl. Phys. 95 (2004) 316.
[6] Bo-Tan Wu, Yan-Kuin Su, Ming-Lung Tu, An-Chang Wang, You-Sian Chen, Yu-Zung Vhiou, Yii-Tay Chiou, Chun-Hsun Chu, Jpn. J. Appl. Phys. 44 (2005) L2783.
[7] M. McDowell, I.G. Hill, J.E. McDermott, S.L. Bernasek, J. Schwartz, Appl. Phys. Lett. 88 (2006) 073505.
[8] Laurie Valbin, Laure Sevely, Serge Spirkovitch, Proc. SPIE 4174 (2000) 154.
[9] C.-M. Yeh, C.H. Chen, J.-Y. Gan, C.S. Kou, J. Hwang, Thin Solid Films 483 (2005) 6.
[10] Christopher R. Newman, C. Daniel Frisbie, Demetrio A. da Silva Filho, Jean-Luc Bredas, Paul C. Ewbank, Kent R. Mann, Chem. Mater. 16 (2004) 4436.
[11] K.N. Narayanan Unni, Sylvie Dabos-Seignon, Jean-Michel Nunzi, J. Phys. D: Appl. Phys. 38 (2005) 1148.
[12] L.A. Majewski, R. Schroeder, M. Grell, Adv. Mater. 17 (2005) 192.
[13] G. Nunes Jr., S.G. Zane, J.S. Meth, J. Appl. Phys. 98 (2002) 104503.
[14] Kui-Xiang Ma, Chee-Hin Ho, Furong Zhu, Tai-Shung Chung, Thin Solid Films 371 (2000) 140.
[15] Flavio de Paula Santos, Elson de Campos, Marcelo Costa, Francisco Cristovao Lourenco Melo, Roberto Yzumi Honda, Rogerio Pinto Mota, Mater. Res. 6 (2003) 353.
[16] Myung M. Sung, G. Jonathan Kluth, Roya Maboudian, J. Vac. Sci. Technol. A 17 (2) (1999) 540.
[17] Tuncer Caykara, Serkan Demirci, Mehment S. Eroglu, Olgun Guven, J. Polym. Sci.: Part B: Polym. Phys. 44 (2006) 426.
[18] Hagen Klauk, Marcus Halik, Ute Zschieschang, Gunter Schmid, Wolfgang Radlik, Wemer Weber, J. Appl. Phys. 92 (2002) 5259.
[19] M. Yoshida, S. Uemura, T. Kodzasa, T. Kamata, M. Matsuzawa, T. Kawai, Syn. Met. 137 (2003) 967.
[20] Sang Chul Lim, Seong Hyun Kim, Jung Hun Lee, Mi Kyung Kim, Do Jin Kim, Taehyoung Zyung, Syn. Met. 148 (2005) 75.
[21] Wei-Yang Chou, Chia-Wei Kuo, Horng-Long Cheng, Yi-Ren Chen, Fu-Ching Tang, Feng-Yu Yang, Dun-Yin Shu, Chi-Chang Liao, App. Phys. Lett. 89 (2006) 112126.
[22] Sang Yoon Kwonwoo, Kwonwoo Shin, Chan Eon Park, Adv. Funct. Mater. 15 (2005) 1806.
[23] L.F. Drummy, D.C. Martin, Adv. Mater. 17 (2005) 903.

Available online at www.sciencedirect.com
ScienceDirect
Organic Electronics 8 (2007) 455–459
Organic Electronics
www.elsevier.com/locate/orgel

Letter

Improved pentacene device characteristics with sol–gel SiO_2 dielectric films

T. Cahyadi [a,c], H.S. Tan [a], E.B. Namdas [a], S.G. Mhaisalkar [a,*], P.S. Lee [a], Z.-K. Chen [b], C.M. Ng [c], F.Y.C. Boey [a]

[a] *School of Materials Science and Engineering, Nanyang Technological University, Block N4.1, Nanyang Avenue, Singapore 639798, Singapore*
[b] *Institute of Materials Research and Engineering, 3 Research Link, Singapore 117602, Singapore*
[c] *Chartered Semiconductor Manufacturing Ltd., 60 Woodlands, Industrial Park D, Street 2, Singapore 738406, Singapore*

Received 13 November 2006; received in revised form 20 December 2006; accepted 20 December 2006
Available online 29 December 2006

Abstract

The interfacial interactions between semiconductors and gate dielectrics have a profound influence on the device characteristics of field effect transistors (FETs). This paper reports on the concept of introducing a sol–gel SiO_2 as inorganic capping layer to significantly improve device characteristics of pentacene-based FETs. The smoother film surfaces of sol–gel SiO_2 (1.9 Å root-mean-square) induced larger pentacene grain sizes, and led to hole mobilities of 1.43 cm^2/Vs, on–off ratio of 10^7, and a subthreshold swing of 102 mV/decade when operating at −20 V.
© 2006 Elsevier B.V. All rights reserved.

PACS: 72.80.Le; 81.20.Fw; 82.35.Gh; 85.30.Tv

Keywords: Pentacene; Field effect transistors; Sol–gel; Dielectrics

1. Introduction

Research into organic field effect transistors (OFETs) has gained great interest because of their potential applications in low-cost and large area electronics [1–7]. For pentacene-based FETs, better device performances have been achieved by tuning the film deposition rate, substrate temperature, material purity, and substrate surface. However, the electronic transport, in particular the role of semiconductor–dielectric interfacial interactions, of the polycrystalline films is still poorly understood [3–5]. Thermally grown SiO_2 as the gate dielectric is a widely used substrate for the growth of pentacene, mainly due to its superior electrical properties. However, for large area electronics applications, organic electronics on glass or flexible foil substrates, solution processed organic or inorganic dielectrics are imminent [6].

Candidates for large area compatible inorganic dielectrics are sputtered silicon oxide, sputtered Al_2O_3, or plasma-enhanced chemical vapor deposited

* Corresponding author. Tel.: +65 6790 4626; fax: +65 6790 9081.
E-mail address: Subodh@ntu.edu.sg (S.G. Mhaisalkar).

1566-1199/$ - see front matter © 2006 Elsevier B.V. All rights reserved.
doi:10.1016/j.orgel.2006.12.006

(PECVD) silicon nitride and silicon oxide. These dielectrics require complex and expensive processes, higher temperatures, and are not compatible with low-cost, solution processed methodologies. Solution processed organopolysilsesquioxane glass resins (GR) as gate dielectrics, with moderate improvement in device characteristics, have been reported [7]. Sol–gel based process high-k dielectrics have also been proposed [8,9], however concerns over roughness [10] and interfacial compatibility with pentacene remain [11]. The present paper reports on the possibility of using sol–gel SiO_2 film as a capping/surface modification layer that can significantly improve FET device characteristics. Electrical properties between pentacene on thermally grown SiO_2 and sol–gel SiO_2 bi-layer films are compared. Bi-layer approaches have been shown to allow effective modification of bottom layer topography without being limited by the chemistry required for self-assembled monolayer (SAM) functionalization, while simultaneously fine-tuning the dielectric surface [12]. The surface of the sol–gel SiO_2 film was found to be smoother than thermally grown SiO_2, resulting in planarization of dielectric surface roughness. This results in higher mobility of up to 1.43 cm^2/Vs for pentacene on sol–gel SiO_2 due to larger grain size.

2. Experimental details

Sol–gel SiO_2 films with excellent uniformity were prepared by a two-step acid–base catalyst procedure and spin coating. This process allows the completion of polycondensation at low temperatures and the development of silica networks during drying and post-treatment [13]. Sol–gel solutions were prepared by mixing tetraethylorthosilicate (TEOS, 99.9% purity), ethanol, ammonium hydroxide, deionized water and concentrated HCl. In the first step, TEOS, ethanol, water, and HCl were stirred at room temperature for 90 min in the following molar ratios: 1:10:3.5:0.003. Three drops of the base catalyst (0.1 M NH_4OH) was then added to the above solution. Solution was aged under constant stirring at room temperature for 3 days.

The pentacene FETs were fabricated on n-type Si/thermally grown SiO_2 (450 Å). All substrates were cleaned by wet cleaning procedures (Piranha solution, SC2, and SC1). Sol–gel SiO_2 solution was spin-coated (2000 rpm) on the substrate to form the bi-layer dielectric sample (Fig. 1, Device II). Sol–gel films were dried at ambient conditions at 60 °C and were further heated at 100 °C, 10^{-7} mbar, before pentacene deposition. The 500 Å pentacene (sublimed once) film was evaporated under a vacuum of 10^{-7} mbar. During the deposition, the substrate temperature was held at 100 °C and the deposition rate was sustained at 0.5 Å/s. Gold source and drain layers were patterned using a shadow mask. The thickness of the sol–gel SiO_2 film was 3900 Å. The capacitance of 76.7 and 17.1 nF/cm^2 was measured on uni-layer (Fig. 1, Device I) and bi-layer structures respectively, through the capacitance–voltage method using HP4284 LCR meter. The transistor characteristics were measured using Keithley 4200 semiconductor parameter analyzer. All electrical measurements were done in Desert Cryogenics probe station with a base pressure of 5×10^{-5} mbar.

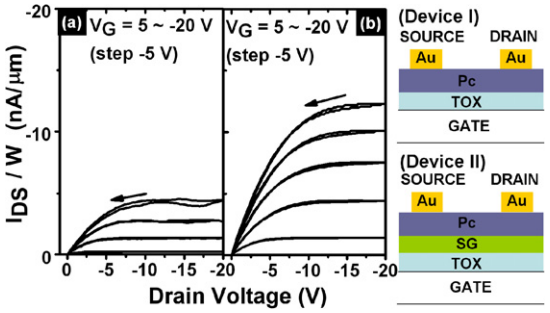


Fig. 1. Drain current–drain voltage (I_{DS}–V_{DS}) curves obtained from pentacene-based FETs with (a) thermally grown SiO_2 uni-layer film (Device I), (b) sol–gel SiO_2-thermally grown SiO_2 bi-layer film (Device II). [Gate = n-type Si wafer, TOX = thermally grown SiO_2, SG = sol–gel SiO_2, Pc = pentacene].

3. Results and discussion

Contrary to that of the reference FETs, saturation of the drain current was not observed in bi-layer FETs (Fig. 1b). This can be attributed to the reduced electric field across the gate dielectric in the bi-layer FETs as compared to the uni-layer devices (Fig. 1a). At $V_G = -20$ V, the gate electric fields were 0.98 MV/cm and 4.44 MV/cm in the bi-layer TFT and uni-layer FETs respectively, calculated using the equivalent oxide thickness (EOT). Therefore, the channel saturation that typically ensues at high electric fields had not occurred in the bi-layer FETs. Despite its lower gate dielectric field, bi-layer FETs display higher I_{DS} than that of uni-layer FETs.

Saturation mobility, μ_{sat}, may be extracted from the saturation region of the transfer characteristics (Fig. 2) as follows:

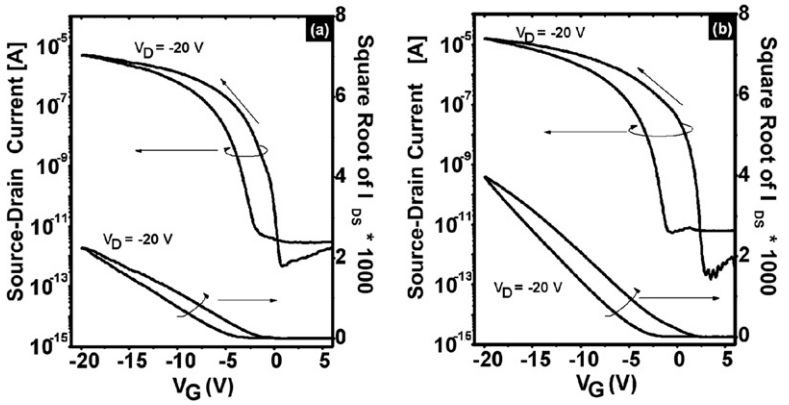


Fig. 2. Log $(-I_{DS}) - V_G$ and $\sqrt{I_{DS}} - V_G$ plots obtained for pentacene FETs with (a) thermally grown SiO_2 uni-layer film, (b) sol–gel SiO_2-thermally grown SiO_2 bi-layer film.

$$\mu_{sat} = \frac{2I_{DS}L}{C_i W(V_G - V_{Th})^2}$$

where I_{DS} is the drain current, C_i is the insulator capacitance, V_G and V_{Th} are the gate and threshold voltage, respectively, and W and L are the channel width and length, respectively. The mobilities thus calculated are 0.11 cm^2/Vs and 1.43 cm^2/Vs for uni-layer and bi-layer FETs, respectively. The on–off current ratio of bi-layer FETs was about three times than that of the uni-layer TFT (Table 1). The subthreshold swings (*s.s*) and threshold voltages (V_{Th}) for the bi-layer devices were 102 mV/decade and −0.23 V; whereas those for the uni-layer devices were 400 mV/decade and −1.24 V respectively, despite lower bi-layer FET capacitances (C_i). The improvements in subthreshold swings and V_{Th} suggest improved pentacene–dielectric interfaces for the bi-layer FETs.

For both FETs, similar hysteresis characteristics were observed and agrees favorably with recent reports by other research groups [12,14–16]. The gate-swing hysteresis is attributable to electron traps (electrochemical traps such as surface hydroxyl groups [17]) at the organic-channel/inorganic-dielectric interface, where the trapping and detrapping of electrons is likely to occur during the bias swing.

Hysteresis in Si MOSFET technology is known due to the impurities and trapped charges, such as hydroxyl groups that can capture electrons [18], at the semiconductor–dielectric interface and/or those in the bulk of the dielectric, as well as the inherent properties of the dielectric [19]. In a recent study [20], a bi-layer dielectric employed in the fabrication of FETs yielded evidence of the hysteresis being bulk-related rather than interface-related. Similar off-currents observed in the present study suggest that moisture and ions, if any, are trapped inside the bulk of sol–gel SiO_2 films as opposed to the surface. If moisture were adsorbed on the film and crevices between the pentacene grains, increased trap densities would ensue. The moisture traps would capture charges in the channel under operation, leading to an increase in the conductivity between source and drain when the device is in the off-state, resulting in increased off currents [21].

From the capacitance value of 17.1 nF/cm^2, the dielectric constant k for the bi-layer dielectrics was calculated to be ~9, which is much higher than the dielectric constant for thermally grown SiO_2 ($k = 3.9$). Higher k values have been reported for TEOS based sol–gel materials due to absorption of moisture [22]. The trapping of moisture can occur in closed or open pore structures. Porosity in the form of closed cells can prevent adsorption and

Table 1
Room temperature transfer characteristics

	μ_{sat} (cm^2/Vs)	V_{Th} (V)	*s.s* (mV/decade)	I_{on} (μA) @ ($V_G - V_{Th} = -18$ V)	I_{on}/I_{off}	I_G (pA) @ ($V_G = -20$ V)	C_i (nF/cm^2)
Uni-layer FET	0.11	−1.24	400	−5.03	1.21×10^7	−9.53	76.6
Bi-layer FET	1.43	−0.23	102	−13.85	3.78×10^7	−7.03	17.1

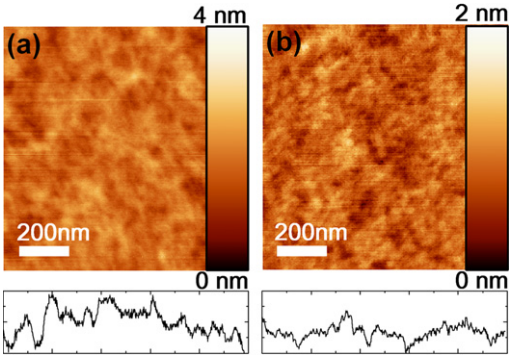


Fig. 3. AFM scans for (a) wet thermally grown SiO_2 film and (b) sol–gel SiO_2 film of bi-layer structure. The area size of the images was $1 \times 1\ \mu m^2$. Line scans were scaled to the same z-axis ($z = 2$ nm) and x-axis ($x = 1\ \mu m$) to aid better comparison.

diffusion of moisture and contaminations, so that films with closed-pores are less likely to cause electrical problems than those with open-pore structures.

Scanning electron microscopy (SEM) observations, not shown here, and atomic force microscopy (AFM) images (Fig. 3b) revealed a negligible distribution of pores and crack-free surface. This suggested a closed-pore structure of the sol–gel SiO_2 films used in the bi-layer FETs. Cracking and shrinkage commonly associated with ORMOSIL type materials [23] due to the breakage of the single and double carbon bonds were not observed in this study primarily because of the slow heating rates and considerably lower temperatures (60 °C) employed in this investigation. The resulting surface roughnesses of sol–gel SiO_2 film of the bi-layer structure and thermally grown SiO_2 film, as measured by AFM (Fig. 3), were ~1.9 Å and ~3.1 Å, respectively.

One order of increase in mobility with decreasing surface roughness, has been reported [16]. Increasing dielectric roughness is thought to reduce carrier mobility, possibly through interfacial scattering [6,24] or obstructing charge movement due to valleys [25].

Morphological studies of the pentacene layers grown on sol–gel and thermal SiO_2 exhibited grain sizes of ~1.0 μm and 0.5 μm, respectively (Fig. 4). Roughness is known to inhibit the growth of uniform, large crystal domains of polycrystalline materials [16].

The improved device performance of the bi-layer FETs may be attributed to an increased carrier density due to presence of polar molecules in the dielectric, increased grain sizes of pentacene, and smoother surface of sol–gel that improved the ordering of the first few monolayers of pentacene providing the hopping sites for the carriers to move easily through the channel. The contributions of these factors and interfacial/deep level trap effects are being published elsewhere.

4. Conclusions

In summary, we report improved FET performance by employing an inorganic capping layer to form a bi-layer dielectric. This sol–gel based capping layer that is free of cracks and porosity results in improved mobilities, subthreshold swings, without compromising leakage and current on–off ratios. Similar solution processed dielectrics can potentially be employed to provide improved semiconductor–dielectric interfaces on a wide variety of substrates

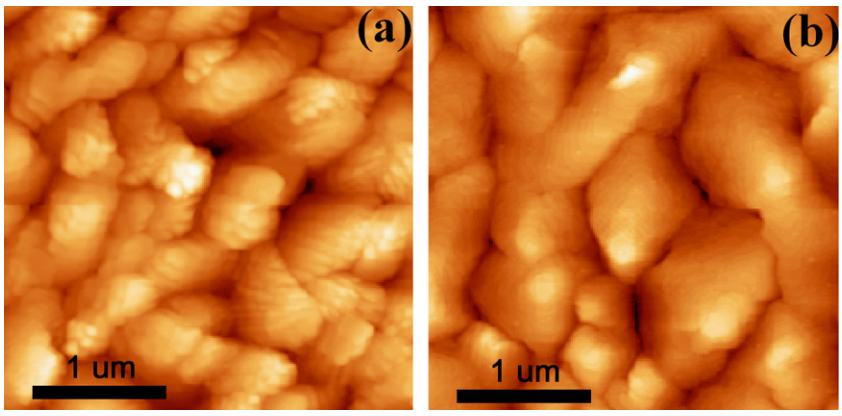


Fig. 4. (a) Morphology of pentacene film on thermally grown SiO_2 and (b) on sol–gel SiO_2-thermally grown SiO_2 bi-layer film. The scanned area is $2.5 \times 2.5\ \mu m^2$.

that may be used for large area electronic applications.

Acknowledgements

The authors thank Prof. Ananth Dodabalapur, UT Austin for useful suggestions and discussions. We also acknowledge Dr. Lap Chan (Chartered Semiconductor Manufacturing Ltd.), and Chartered Semiconductor Manufacturing for its technical support regarding the experiment. This research was supported by Nanyang Technological University, Singapore and Agency of Science Technology and Research, Singapore.

References

[1] G. Horowitz, J. Mater. Res. 19 (2004) 1946.
[2] C.D. Dimitrakopoulos, P.R.L. Malenfant, Adv. Mater. 14 (2002) 99.
[3] S.F. Nelson, Y.-Y. Lin, D.J. Gundlach, T.N. Jackson, Appl. Phys. Lett. 93 (1998) 1854.
[4] R.A. Street, D. Knipp, A.R. Völkel, Appl. Phys. Lett. 80 (2002) 1658.
[5] S. Verlaak, V. Arkipov, P. Heremans, Appl. Phys. Lett. 82 (2003) 745.
[6] D. Knipp, R.A. Street, A.R. Völkel, Appl. Phys. Lett. 82 (2003) 3907.
[7] Z. Bao, V. Kuck, J.A. Rogers, M.A. Paczkowski, Adv. Funct. Mater. 12 (2002) 526.
[8] C.D. Dimitrakopoulos, I. Kymissis, S. Purushothaman, D.A. Neumayer, P.R. Duncombe, R.B. Laibowitz, Adv. Mater. 11 (1999) 1372.
[9] C.D. Dimitrakopoulos, S. Purushothaman, J. Kymissis, A. Callegari, J.M. Shaw, Science 283 (1999) 822.
[10] C. Yang, K. Shin, S.Y. Yang, H. Jeon, D. Choi, D.S. Chung, C.E. Park, Appl. Phys. Lett. 89 (2006) 153508.
[11] J. Veres, S. Ogier, G. Llyod, Chem. Mater. 16 (2004) 4543.
[12] M.-H. Yoon, C. Kim, A. Facchetti, T.J. Marks, J. Am. Chem. Soc. 128 (2006) 12851.
[13] M. Langlet, C. Vautey, J. Sol–Gel Sci. Technol. 13 (1998) 743.
[14] G. Gu, M.G. Kane, J.E. Doty, A.H. Firester, Appl. Phys. Lett. 87 (2005) 243512.
[15] D.K. Hwang, K. Lee, J.H. Kim, S. Im, J.H. Park, E. Kim, Appl. Phys. Lett. 89 (2006) 093507.
[16] S.E. Fritz, T.W. Kelley, C.D. Frisbie, J. Phys. Chem. B 109 (2005) 10574.
[17] L.-L. Chua, J. Zaumseil, J.-F. Chang, C.-W. Ou, P.K.-H. Ho, H. Sirringhaus, R.H. Friend, Nature 434 (2005) 194.
[18] E.H. Nicollian, J.R. Brews, MOS (Metal Oxide Semiconductor) Physics and Technology, Wiley, New York, 1982.
[19] D.K. Schroder, Semiconductor Material and Device Characterization, second ed., Wiley, New York, 1998.
[20] S.Y. Park, M. Park, H.H. Lee, Appl. Phys. Lett. 85 (2004) 2283.
[21] Y. Qiu, Y. Hu, G. Dong, L. Wang, J. Xie, Y. Ma, Appl. Phys. Lett. 83 (2003) 1644.
[22] S. Yu, T.K.S. Wong, X. Hu, M.S. Yong, J. Sol–Gel Sci. Technol. 35 (2005) 69.
[23] K.A. Vorotilov, V.A. Vasiljev, M.V. Sobolevsky, A.S. Sigov, J. Sol–Gel Sci. Technol. 13 (1998) 467.
[24] D. Knipp, R.A. Street, A.R. Völkel, J. Ho, J. Appl. Phys. 93 (2003) 347.
[25] S. Steudel, S.D. Vusser, S.D. Jonger, D. Janssen, S. Verlaak, J. Genoe, P. Heremans, Appl. Phys. Lett. 85 (2004) 4400.

Available online at www.sciencedirect.com
ScienceDirect
Organic Electronics 8 (2007) 460–464
Organic Electronics
www.elsevier.com/locate/orgel

Letter

High mobility, low voltage polymer transistor

Hyewon Kang, Keon-kook Han, Jeong-Eun Park, Hong H. Lee *

School of Chemical Engineering, Seoul National University, Seoul 151-744, Republic of Korea

Received 29 January 2007; received in revised form 3 March 2007; accepted 7 March 2007
Available online 19 March 2007

Abstract

We introduce a polymer transistor that operates with low supply voltage and yet has a field-effect mobility higher than the mobilities reported for low voltage polymer transistors. A simple plasma oxidation of the gate metal to form a thin (3.74 nm) top metal oxide layer in the gate metal is involved in the fabrication that acts as the gate dielectric. With ultrathin gate dielectrics, the variation in the dielectric thickness and the surface roughness scattering can severely limit the mobility attainable. The plasma oxidation under certain conditions produces a very smooth oxide surface, leading to the high mobility.
© 2007 Elsevier B.V. All rights reserved.

PACS: 73.40.Qv; 73.61.Ng; 85.30.Tv

Keywords: Organic thin-film transistor; Low-voltage operation; Poly(3-hexylthiophene); Aluminum oxide; Plasma oxidation; High mobility

Thin-film transistors (TFTs) based on small molecule organics and polymers have received much attention since the mid nineties [1,2] and applications to integrated circuits [3] and active-matrix display [4] have been reported. Of these, the best electrical performance has mainly been obtained with small molecule semiconductor of pentacene. Carrier mobilities higher than 1 $cm^2 V^{-1} s^{-1}$ have been achieved with vacuum deposited pentacene as the active layer and silicon dioxide as the gate dielectric [5]. With polymer semiconductors, the mobility has reached 0.2 $cm^2 V^{-1} s^{-1}$ using poly(3-hexylthiophene) (P3HT) as the active layer and silicon oxide as the gate dielectric [6], which is close to the mobility attainable with amorphous silicon. However, the operating voltage exceeds 20 V.

While the performance of the polymer based TFT (PTFT) is poorer than that of the small molecule semiconductor TFT, the low-cost wet processing that is made possible with polymer, which does not require expensive vacuum equipment along with inexpensive synthesis of the materials, has helped to push the trend toward more utilization of polymer semiconductors. Polymer transistors are of interest for a variety of large area applications as in displays, including flexible ones, sensors and electronic bar codes. With non-photolithographic techniques such as ink-jet printing, circuits, paper-like display and flexible circuits have been fabricated [7–9].

* Corresponding author. Tel.: +82 2 880 7403; fax: +82 2 878 5043.
E-mail address: honghlee@snu.ac.kr (H.H. Lee).

1566-1199/$ - see front matter © 2007 Elsevier B.V. All rights reserved.
doi:10.1016/j.orgel.2007.03.004

There are two major performance aspects of the polymer transistor that need to be improved for practical applications. One is lower power consumption that is related to lower operating voltage. The other is higher device speed that has to do with higher carrier mobility. Recent studies have shown that the operating voltage, typically 20 V or higher, can be reduced to around 2 V or lower. Utilizing the concept from small molecule transistors [10,11] self-assembled monolayer (SAM) (dielectric thickness of 2.6 nm) [12] and polymer dielectric (CPVP-C6) (dielectric thickness of 10–20 nm) [13] have been used as the gate dielectric to lower the operating voltage of polymer transistor. For the PTFT with a single layer of SAM [12], the field-effect mobility was reported to be 5.0×10^{-3} $cm^2 V^{-1} s^{-1}$ with an on/off ratio of 2×10^2. With CPVP-C6 [13], the mobility was 4.0×10^{-3} $cm^2 V^{-1} s^{-1}$ with an on/off ratio of about 10^2. A thin silicon oxide formed on the gate metal (thickness of 3.5 nm) on which SAM was deposited was also used [14] for polymer transistor. The mobility in this case was also about 0.01 $cm^2 V^{-1} s^{-1}$. In all three cases, the operating voltage is less than 2 V.

It is known that with ultrathin gate dielectrics, the variation in dielectric thickness [15] and the roughness scattering of charge carriers [16] can severely limit the mobility. Unlike pentacene, which is vapor-deposited, the solvent used in depositing polymer semiconductor such as P3HT creates roughness [17] even when the solvent does not dissolve the underlying polymer or organic. A dry transfer technique [18] can help alleviate this problem. In addition, the SAM deposited on the gate can create a thickness variation in terms of effective dielectric thickness and also roughness problems with or without penetration of the semiconducting polymer, which could be construed as the reasons for the low mobility reported for SAM dielectrics with polymer semiconductor.

Plasma oxidation has been used for pentacene transistors not only for the gate dielectric [19] but also for a better wettable gate surface for subsequent coating of polymer dielectric [20]. The low voltage pentacene transistor fabricated with the dielectric of plasma-oxidized gate metal showed a high current leakage with an on–off ratio of 8.76×10^3, which compares with typical on–off ratio of over 10^5 for pentacene transistors. This high current leakage is presumably due to the high surface roughness created when the gate metal was oxidized for more than 10 min.

In this work, we introduce a polymer transistor that operates with supply voltages less than 2 V and yet the mobility is 0.017 $cm^2 V^{-1} s^{-1}$. This mobility is the highest ever reported for the low voltage polymer transistors based on ultrathin dielectric materials. The mobility is affected by a number of factors such as film deposition method, molecular weight and regioregularity of semiconducting layer, etc. However, the dielectric is also an important factor that determines the mobility. Fabricating the polymer transistor involves a simple plasma oxidation of the gate metal to form a very thin (3.74 nm) oxide dielectric in the gate metal. The roughness of the surface of the oxidized gate metal goes through a minimum with increasing oxide thickness and the oxide with this minimum roughness is utilized as the gate dielectric.

The polymer TFTs fabricated in this work are of bottom-gate and top-contact type with P3HT as its semiconductor and a thin oxidized layer of aluminum gate as its dielectric, the device structure of which is shown in Fig. 1. On cleaned glass substrate, aluminum was deposited by thermal evaporation through a shadow mask at a rate of 15 Å/s to define the gate electrode. An oxygen plasma was used for the oxidation of the gate metal that is 50 nm thick at a power of 75 W, a flow rate of 10 sccm, and a pressure of 0.2 torr. The oxidation time was varied from 30 s to 15 min in the experiment to obtain a range of the aluminum oxide thickness. Metal insulator–metal capacitors were fabricated to determine the capacitance. The capacitance was measured at three different voltages between 1 V and −1 V and two frequencies (10^2 and 10^5 Hz) (Precision LCR Meter, Agilent, 4284 A). All the data were in the range of 83.5–84.5 nF, yielding an average capacitance of 1.4 μF/cm^2 for the gate area of 0.06 cm^2.

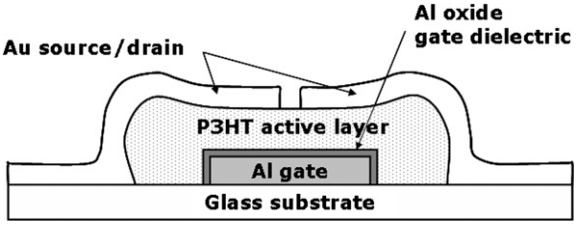


Fig. 1. Structure of polymer (P3HT) TFT with plasma-oxidized ultrathin dielectric. The dielectric layer was prepared by oxygen plasma treatment of thermally evaporated Al gate surface. The P3HT active layer was drop-casted on the aluminum oxide. The source and drain were formed by thermal evaporation through shadow mask.

It yields an aluminum oxide dielectric constant of about 5.9 which is lower than the typical value of around 9. It is known that the dielectric constant of a thin film decreases with decreasing film thickness [21]. Onto this gate with an oxidized top layer, P3HT layer was formed in a glove box filled with argon by drop casting a 0.3 wt% P3HT (Aldrich Company, $M_w = 87{,}000$) solution in toluene. No further processing such as annealing or patterning was involved. The source and drain electrodes were formed by thermal evaporation of gold through a shadow mask to define the channel that is 120 μm long and 3 mm wide.

Oxygen plasma has been used to treat an insulator surface prior to depositing an active semiconductor. For instance, a silicon oxide surface was treated with oxygen plasma before depositing P3HT [22]. The thickness of the oxidized top layer in the aluminum gate, as determined by ellipsometry (L2W15S830, Stokes Waferskan Ellipsometer), is given in Fig. 2 as a function of time under the plasma conditions stated earlier. The bar shows the range of 6 data points, 2 data points each from 3 samples. As expected, the oxide thickness increases linearly with time initially, the period representing the kinetically-controlled oxidation regime. As is well known in silicon oxidation [23], this linear regime is followed by a gradual increase with time that corresponds to the parabolic regime that represents diffusion-controlled oxidation. It is noted that the native oxide thickness is about 2 nm.

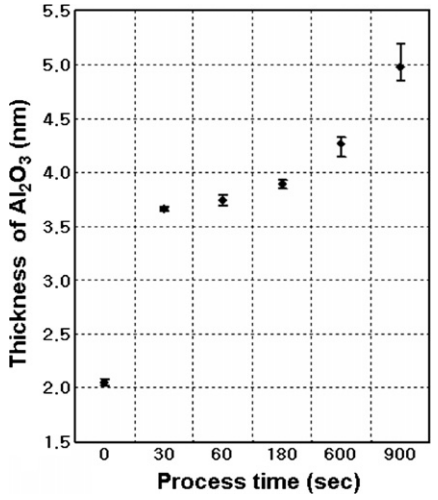


Fig. 2. Thickness of the aluminum oxide gate dielectric as a function of plasma oxidation time. Oxygen plasma was used at a power of 75 W, a flow rate of 10 sccm, and a pressure of 0.2 torr. The bar shows the range of six measurements.

With the PTFT fabricated, the carrier mobility in the linear region was determined on the basis of the following relationship [24]:

$$I_D = \frac{Z\overline{\mu}_n C_i}{L}\left[(V_G - V_T)V_D - \frac{V_D^2}{2}\right] \quad (1)$$

where I_D is the drain current, Z and L are the channel width and length, respectively, $\overline{\mu}_n$ is the effective mobility, C_i is the capacitance per unit area, V_G is the gate voltage, V_T is the threshold voltage, and V_D is the drain voltage. The mobility was determined at the source–drain voltage, V_{DS}, of −1 V and the field-effect mobility determined from Eq. (1) is 0.017 $cm^2\ V^{-1}\ s^{-1}$. The transfer characteristics of the polymer transistor with the oxide thickness or

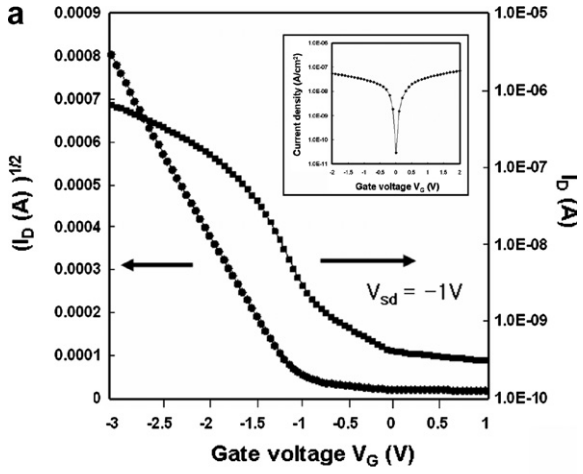


Fig. 3. Electrical characteristics of P3HT TFTs with ultrathin aluminum oxide gate dielectric. The thickness of the oxide layer is 3.74 nm. (a) Electrical transfer characteristics of the device with drain voltage of −1 V. The inset shows gate leakage. (b) Electrical output characteristics of the device for various gate voltages.

the dielectric thickness of 3.74 nm are shown in Fig. 3a. The on–off current ratio is 3.6×10^3. The threshold and subthreshold voltages are −0.8 V and 0.45 V, respectively. The subthreshold voltage was obtained from the data in the linear region of the transfer curve in Fig. 3a according to its definition [25] by reading the currents at −1 V and −1.45 V. This subthreshold voltage of 450 mV/decade is quite low. The output characteristics of the polymer transistor are given in Fig. 3b for various levels of the gate voltage.

The plasma oxidation time has been found to have a profound effect on the device performance. When the oxidation time is less than 30 s, the transistor did not function as a transistor. Furthermore, the yield was poor because of too thin a dielectric layer. When the time exceeds 3 min, no saturation occurred and the transistor was unstable in that it gave different characteristics each time it was turned on. However, the polymer transistor operated satisfactorily when the oxidation time was larger than 30 s and less than 2 min. The best performance was realized for 1 min of plasma oxidation. Because of the dielectric thickness variation and surface roughness scattering that are known to limit the mobility attainable for ultrathin dielectrics, the surface roughness was examined by atomic force microscopy (AFM). Shown in Fig. 4 are the three dimensional AFM images of the oxide surfaces for native oxide and for the oxides of the aluminum gate grown by oxygen plasma under the plasma conditions stated earlier, and the corresponding sectional height profiles for the oxidation times of zero (Fig. 4a), 1 min (Fig. 4b) and 3 min (Fig. 4c). For the native oxide in Fig. 4a (thickness of 2.0 nm), the root mean square (RMS) roughness is about 0.56 nm. When it is plasma-oxidized for 1 min, the RMS roughness reduced to 0.26 nm but then it increased to 1.03 nm when oxidized for 3 min, the roughness going through a minimum as the oxidation time is increased. The initial reduction in the roughness can be explained in terms of oxidation regimes discussed earlier. The protruding parts of the oxide layer are oxidized or grow in thickness in the diffusion-limited regime where the growth is relatively slow due to its relatively thicker oxide layer whereas the receding parts of the oxide layer are in the kinetically-controlled regime where the growth is relatively fast, resulting in evening out the roughness. As the thickness increases, all parts of the oxide layer grow in the diffusion-limited regime. The emergence of nanocolumns with increasing roughness in Fig. 4c is presumably due to the stress generated by the volume expansion accompanying the transformation from metal to metal oxide.

The low-voltage operation of organic and polymer transistors has been made possible by introduction of ultrathin dielectrics. For this thin dielectrics, the thickness of which is less than, say 5 nm, as in

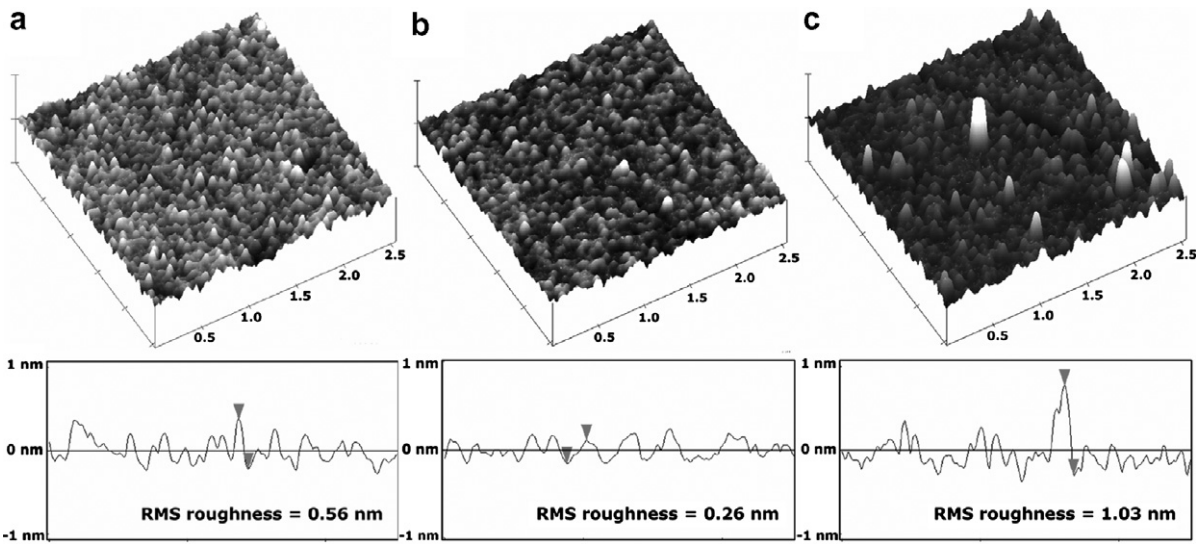


Fig. 4. Atomic force microscopy (AFM) images of aluminum oxide surface. Upper frames show three-dimensional images and the lower the corresponding sectional profiles. (a) Surface of native oxide. (b) Surface of plasma-oxidized aluminum at the oxidation time of 1 min. (c) Surface of plasma-oxidized aluminum at the oxidation time of 3 min.

SAM (2.6 nm) and plasma-oxidized metal oxide (3.8 nm), the variation of the dielectric thickness would be one of the significant factors affecting the mobility. A theoretical study [15] on the mobility of silicon transistor, for example, showed that for ultrathin gate oxide (<10 nm), a change in thickness variation from 0.1 nm to 0.4 nm results in a close to one and half orders of magnitude decrease in the mobility. A recent study [16] revealed that the charge scattering at the gate–insulator interface caused by the dielectric roughness, known as remote-surface-roughness scattering, can reduce the mobility significantly when the dielectric layer is ultrathin. In the plasma-oxidized metal oxide formed in the native metal, the interface should be smooth and continuous unlike the interface created when a dielectric is deposited on a gate surface, which should minimize the mobility reduction due to the roughness scattering. Unlike pentacene, which is vapor-deposited, the solvent used in depositing polymer semiconductor such as P3HT creates roughness [17] even when the solvent does not dissolve the underlying polymer or organic. In addition, when a SAM is used as a dielectric, there are vacant spaces between adsorbed SAM, the air in the space acting as the dielectric for the space. Therefore, the thickness variation in terms of effective dielectric thickness, putting aside the orientation effects of the adsorbed SAM, would be present. Although the properties and casting method of the semiconducting layer affect the mobility, the combination of the solvent-induced roughness and the thickness variation could be construed as the main factors for the low mobility reported for the SAM-based polymer transistors.

In the polymer transistor with the plasma-oxidized dielectric reported here, therefore, it is natural that the best mobility obtained was for the transistor with the smallest oxide surface roughness. It is of interest to note that the smallest roughness corresponds to the time where the transition occurs from kinetically-controlled to diffusion-controlled oxidation. While the high mobility, low voltage polymer transistor reported here is based on the aluminum gate that is plasma-oxidized, the same approach should be applicable to other gate metals.

References

[1] F. Garnier, R. Hajlaoui, A. Yassar, P. Srivastava, Science 265 (1994) 2684.
[2] A. Dodabalapur, L. Torsi, H.E. Kats, Science 268 (1995) 270.
[3] B. Crone, A. Dodabalapur, Y.-Y. Lin, R.W. Filas, Z. Bao, A. LaDuca, R. Sarpeshkar, H.E. Katz, W. Li, Nature 403 (2000) 521.
[4] H. Sirringhaus, N. Tessler, R.H. Friend, Science 280 (1998) 1741.
[5] C.D. Sheraw, L. Zhou, J.R. Huang, D.J. Gundlach, T.N. Jackson, M.G. Kane, I.G. Hill, M.S. Hammond, J. Campi, B.K. Greening, J. Francl, J. West, Appl. Phys. Lett. 80 (2000) 1088.
[6] G. Wang, J. Swensen, D. Moses, A.J. Heeger, J. Appl. Phys. 93 (2004) 6137.
[7] H. Sirringhaus, T. Kawase, R.H. Friend, T. Shimoda, M. Inbasekaran, W. Wu, E.P. Woo, Science 290 (2000) 2123.
[8] J.A. Rogers, Science 291 (2001) 1502.
[9] J.A. Rogers, Z. Bao, A. Makhija, P. Braun, Adv. Mater. 11 (1999) 741.
[10] P. Fontaine, D. Goguenheim, D. Deresmes, D. Vuillaume, Appl. Phys. Lett. 62 (1993) 2256.
[11] M. Halik, H. Klauk, U. Zschieschang, G. Schmid, C. Dehm, M. Schütz, S. Maisch, F. Effenberger, M. Brunnbauer, F. Stellacci, Nature 431 (2004) 963.
[12] Y.D. Park, D.H. Kim, Y. Jang, M. Hwang, J.A. Lim, K. Cho, Appl. Phys. Lett. 87 (2005) 243509.
[13] M.-H. Yoon, H. Yan, A. Facchetti, T.J. Marks, J. Am. Chem. Soc. 127 (2005) 10388.
[14] L.A. Majewski, M. Grell, Synthetic Met. 151 (2005) 175.
[15] J. Walczak, B. Majkusiak, Microelectron. Eng. 59 (2001) 417.
[16] S. Saito, K. Torii, Y. Shimamoto, S. Tsujikawa, H. Hamamura, O. Tonomura, T. Mine, D. Hisamoto, T. Onai, J. Yugami, M. Hiratani, S. Kimura, Appl. Phys. Lett. 84 (2004) 1395.
[17] J. Park, S.Y. Park, S.-O. Shim, H. Kang, H.H. Lee, Appl. Phys. Lett. 85 (2004) 3283.
[18] J. Park, S.-O. Shim, H.H. Lee, Appl. Phys. Lett. 86 (2005) 073505.
[19] K.D. Kim, C.K. Song, Appl. Phys. Lett. 88 (2006) 233508.
[20] K. Han, S.W. Lee, H.H. Lee, Appl. Phys. Lett. 88 (2006) 233509.
[21] H. Quajji, A. Sylvestre, E. Defaÿ, K. Raouadi, F. Jomni, in: Electronics Packaging Technology Conference, Proceedings of 7th, 2005, p. 740.
[22] S.K. Park, Y.H. Kim, J.I. Han, D.G. Moon, W.K. Kim, IEEE Trans. Electron Dev. 49 (2002) 2008.
[23] B.E. Deal, A.S. Grove, J. Appl. Phys. 36 (1965) 3770.
[24] R.F. Pierret, Semiconductor Device Fundamentals, Addison-Wesley Publishing Company, 1996.
[25] S.M. Sze, Physics of Semiconductor Devices, second ed., John Wiley & Sons, 1981.

ORGANIC ELECTRONICS
materials • physics • chemistry • applications

Editors:

Prof. Chihaya Adachi — Center for Future Chemistry, Kyushu University, 744 Motooka, Nishi, Fukuoka 819-0395, Japan. Fax: +81-92-802-3294, e-mail: adachi@cstf.kyushu-u.ac.jp

Prof. Stephen R. Forrest — EECS, MSE, and Physics, University of Michigan, 4080 Fleming Building, 503 Thompson Street, Ann Arbor, MI 48109-1340, USA. Fax: +1-734-763-0085, e-mail: stevefor@umich.edu

Prof. René Janssen — Molecular Materials and Nanosystems, Eindhoven University of Technology, P.O. Box 513, 5600 MB Eindhoven, The Netherlands. Fax: +31 40 2451036, e-mail: r.a.j.janssen@tue.nl

Prof. Josef Salbeck — Macromolecular Chemistry and Molecular Materials Science Department, University of Kassel, Heinrich Plett Strasse 40, D-34123 Kassel, Germany. E-mail: salbeck@uni-kassel.de

Associate Editorial Board:

V.M. AGRANOVICH (Moscow)
Y. CAO (Guangzhou)
A. DODABALAPUR (Austin)
M. FUJIHIRA (Yokohama)
N. PEYGHAMBARIAN (Tucson)
Z. POPOVIC (Mississauga)
W. RIESS (Rüschlikon)
Y. SHIROTA (Osaka)
C. TALIANI (Bologna)
T. TSUTSUI (Fukuoka)
E. UMBACH (Würzburg)

Founding Editors:

Prof. Donal Bradley, Prof. Stephen Forrest, Prof. Norbert Karl and Prof. Kazuhiko Seki

Aims and scope

An interdisciplinary journal on the physics, chemistry, and engineering of materials with applications to organic electronics and optoelectronics, **Organic Electronics** is a primary journal for physicists, material scientists and chemists who are interested in organic electronic devices such as organic light emitting diodes, thin film transistors, photovoltaic cells, etc. Papers suitable for publication in this journal cover such topics as photoconductive and electronic properties of organic materials, film growth and characterization, organic electronic and optoelectronic devices, and applications.

As an important Journal **Organic Electronics** can ensure that your most significant research receives the recognition that it deserves. As a unique publication outlet, uniting the various research disciplines involved, it provides the only forum for both applied and fundamental contributions spanning the many different disciplines addressing electronic applications of organic materials.

Advertising information

Advertising orders and enquiries can be sent to: James Kenney, Commercial Sales, Elsevier, 84 Theobald's Road, London WC1X 8RR, United Kingdom; phone: (+44) (20) 7611 4494; fax: (+44) (20) 7611 4463; e-mail: j.kenney@elsevier.com.

Abstracted/indexed in:

Current Contents: Engineering, Technology and Applied Sciences; El Compendex Plus; Engineering Index; INSPEC; Physics Briefs; Science Citation Index, expanded; Chemistry Citation Index; Current Contents: Physics, Chemistry and Engineering Science. Also covered in the abstract and citation database SCOPUS®. Full text available on ScienceDirect®.

Publication information: *Organic Electronics* (ISSN 1566-1199). For 2007, Volume 8 is scheduled for publication. Subscription prices are available upon request from the Publisher or from the Regional Sales Office nearest you or from this journal's website: (http://www.elsevier.com/locate/orgel). Further information is available on this journal and other Elsevier products through Elsevier's website: (http://www.elsevier.com). Subscriptions are accepted on a prepaid basis only and are entered on a calendar year basis. Issues are sent by standard mail (surface within Europe, air delivery outside Europe). Priority rates are available upon request. Claims for missing issues should be made within six months of the date of dispatch.

Orders, claims, and journal enquiries: please contact the Customer Service Department at the Regional Sales Office nearest you:

Orlando: Elsevier, Customer Service Department, 6277 Sea Harbor Drive, Orlando, FL 32887-4800, USA; phone: (877) 8397126 or (800) 6542452 [toll free numbers for US customers]; (+1) (407) 3454020 or (+1) (407) 3454000 [customers outside US]; fax: (+1) (407) 3631354 or (+1) (407) 3639661; e-mail: usjcs@elsevier.com or elspcs@elsevier.com

Amsterdam: Elsevier, Customer Service Department, P.O. Box 211, 1000 AE Amsterdam, The Netherlands; phone: (+31) (20) 4853757; fax: (+31) (20) 4853432; e-mail: nlinfo-f@elsevier.com

Tokyo: Elsevier, Customer Service Department, 4F Higashi-Azabu, 1-Chome Bldg, 1-9-15 Higashi-Azabu, Minato-ku, Tokyo 106-0044, Japan; phone: (+81) (3) 5561 5037; fax: (+81) (3) 5561 5047; e-mail: jp.info@elsevier.com

Singapore: Elsevier, Customer Service Department, 3 Killiney Road, #08-01 Winsland House I, Singapore 239519; phone: (+65) 6349 0222; fax: (+65) 6733 1510; e-mail: asiainfo@elsevier.com

Printed by Krips BV, Meppel, The Netherlands

ELSEVIER

Available online at www.sciencedirect.com
ScienceDirect
Organic Electronics 8 (2007) 465–479
Organic Electronics
www.elsevier.com/locate/orgel

Probing individual nanoscale organic light-emitting diodes with atomic force electroluminescence microscopy and bridge-enhanced nanoscale impedance microscopy

Liam S.C. Pingree [a,1], Matthew T. Russell [b], Brian J. Scott [b,2], Tobin J. Marks [a,b,*], Mark C. Hersam [a,*]

[a] *Department of Materials Science and Engineering, Northwestern University, Evanston, IL 60208-3108, United States*
[b] *Department of Chemistry, Northwestern University, Evanston, IL 60208-3113, United States*

Received 9 January 2007; received in revised form 21 February 2007; accepted 25 February 2007
Available online 4 March 2007

Abstract

Two recently developed atomic force microscopy (AFM) techniques are used to characterize the impedance and charge transport/emission characteristics of *individually addressed* micro- and nano-scale organic light-emitting diodes (OLEDs). To fabricate independent diodes at this length scale, a suspended silicon nitride membrane shadow mask scheme is employed with semiconductor processing and electron beam lithography. This approach enables the fabrication of individually addressable OLEDs ranging in size from microns down to hundreds of nanometers. Atomic force electroluminescence microscopy (AFEM) and bridge enhanced nanoscale impedance microscopy (BE-NIM) are used to characterize these devices. AFEM offers real-time nanometer-scale spatial resolution mapping of simultaneously acquired current, topography, and light emission data while BE-NIM enables real-time impedance spectroscopy studies of functioning OLEDs. These two AFM techniques are shown to be capable of analyzing device-to-device response variations across a broad range of length scales and to provide unique quantification of intra-array device variations.
© 2007 Elsevier B.V. All rights reserved.

PACS: 81.07.Pr; 72.80.Le; 42.70.Jk

Keywords: OLEDs; Conductive atomic force microscopy; Impedance spectroscopy; Sub-micron; Interface traps; Spatial variations

1. Introduction

Over the past two decades, organic light-emitting diodes (OLEDs) have evolved from laboratory curiosities [1] into commercial products [2]. More recently, OLEDs have received considerable attention as the advantages of low-cost fabrication, wide color range, low power consumption, and flexibility

* Corresponding authors. Address: Department of Materials Science and Engineering, Northwestern University, Evanston, IL 60208-3108, United States. Tel.: +1 847 491 2696; fax: +1 847 491 7820.
E-mail addresses: t-marks@northwestern.edu (T.J. Marks), m-hersam@northwestern.edu (M.C. Hersam).
[1] Present address: Department of Chemistry, University of Washington, Seattle, WA 98195-1700, United States.
[2] Present address: Hewlett-Packard Corp., San Diego, CA 92127, United States.

1566-1199/$ - see front matter © 2007 Elsevier B.V. All rights reserved.
doi:10.1016/j.orgel.2007.02.008

have become evident [3,4]. As issues of short device lifetimes [4,5], organic layer instabilities [6,7], power and light out-coupling inefficiencies [8,9], and high manufacturing costs [10,11] have been addressed, OLEDs have proliferated in low-cost portable electronic products. However, fabrication costs for large-area displays [12,13], encapsulation [3,4], large area non-uniformities [4,11], and the short lifetimes of blue emitters [13,14] continue to present challenges.

With the aforementioned attractions, arrays of sub-μm OLEDs hold promise as alternative high-quality light sources in sensors [15,16] or as redundant pixels in displays [4]. However, the accurate characterization of *individual* sub-μm devices has yet to be achieved due to various technical challenges. Furthermore, sub-μm OLED array fabrication is complicated by the limitations inherent in traditional shadow masking or lithographic fabrication schemes [11]. Shadow masks are employed to pattern all or part of conventional OLED arrays during vacuum deposition of the organic layers and/or cathode due to the incompatibility of such organic materials with conventional lithography techniques. However, the fabrication of suitable shadow masks is complicated by the stringent requirements placed on the mask materials such as chemical inertness, thermally stability, rigidity, and ease of patterning features with sub-μm dimensions. Alternative lithographic approaches to sub-μm OLED array fabrication have typically relied on selective deposition of insulating layer patterns on the OLED anode (tin-doped indium oxide, ITO) either by micro-contact printing or by resist-based lithography techniques to define device size prior to active organic layer deposition [17–22]. However, such anode patterning techniques incur the risk of spatially non-uniform device response [17,19].

The characterization of individual sub-μm OLEDs fabricated by any technique also poses significant challenges. Although shadow mask patterning of OLED cathodes can be utilized to define arrays of sub-μm diodes, direct on-substrate addressing schemes can require very intricate and fragile masks. When devices are defined by a patterned insulating layer as discussed above, the cathode covers a significant portion of the patterned area, resulting in a single cathode addressing multiple OLEDs in parallel. In lithographically patterned OLEDs of this type [17–24], similar response characteristics have been reported for the patterned arrays and individual macro-scale diodes [19–24]. However, to extract single OLED characteristics, this approach assumes that each diode in the array measured in parallel responds identically, both electrically and optically. In other words, this approach probes the average performance of an ensemble of sub-μm OLEDs without measuring the performance of the component sub-μm OLEDs. Thus, information on spatial and performance variations, as well as their statistics, has not previously been available for sub-μm OLED arrays.

In this contribution, we report a new suspended silicon nitride membrane shadow mask technique for the fabrication of individually addressed micro- and nano-scale organic light-emitting diodes (OLEDs) and two new atomic force microscopic (AFM) approaches for spatially mapping and correlating, down to the nanometer scale, the topology, charge transport, electroluminescence, and impedance characteristics of the individual OLEDs. The first technique, atomic force electroluminescence microscopy (AFEM) [25,26], couples a photomultiplier tube with conductive AFM to enable simultaneous spatial mapping of light emission, current, and quantum efficiency. The second technique, bridge enhanced nanoscale impedance microscopy (BE-NIM) [27], couples conductive AFM with a lock-in-amplifier to monitor variations in the sample impedance while using an electronic bridge to enhance sensitivity. With the unique combination of AFEM and BE-NIM, direct current (DC) and frequency-dependent alternating current (AC) charge transport and electroluminescence data are efficiently gathered from arrays of sub-μm OLEDs.

These fabrication and AFM techniques are augmented by an impedance spectroscopy technique capable of quantitatively monitoring the electronic trap density at the OLED cathode/organic interface [28]. Through analysis of frequency-dependent OLED complex conduction, it has been shown that the parasitic role of traps in macroscopic OLEDs can be suppressed by passivation of the ITO surface with self-assembled adhesion/injection layers prior to deposition of the active organic layers and cathode. The signature of this passivation effect is a negative capacitance (NC) that acts in series with the capacitive behavior of the electronic traps [29]. The source of NC is the accumulation of space charge in the device, and the interplay between NC and the magnitude of the parasitic trap capacitance enables characterization of the trap density at this buried interface. When coupled with BE-NIM,

these techniques enable the probing of this key OLED interface with sub-micron resolution.

As noted above, a novel shadow masking approach is implemented in this study to fabricate individually addressable sub-micron OLEDs. Electron beam lithography (eBL) and reactive ion etching (RIE) are used to fabricate shadow masks capable of creating diodes ranging in diameter from 250 nm to 10 μm. This new shadow mask approach is highly customizable, allowing arbitrary patterns of variable size and tunable array pitch. Current–voltage–luminescence (*I–V–L*) measurements of individual OLEDs are acquired with AFEM, demonstrating the capabilities of this technique as well as revealing informative device-to-device response variations. The frequency-dependent impedance properties of the micron-scale OLEDs are further examined with BE-NIM, demonstrating the application of the technique to organic optoelectronic devices and providing additional inter-device impedance uniformity information. In the discussion section, the potential sources of these spatial variations are briefly evaluated.

2. Experimental

Fabrication of suspended membrane silicon nitride shadow masks is accomplished using the sequence of steps outlined in Fig. 1. Single side polished silicon ⟨100⟩ wafers are used as received (Fig. 1a). Low pressure chemical vapor deposition (LP-CVD) is used to grow a ~150 nm thick low-stress (50–100 MPa) silicon nitride (Si_3N_4) film on both sides of the wafer (Fig. 1b). Plasma-enhanced chemical vapor deposition (PECVD) can also be used to grow Si_3N_4 films, however the higher quality, lower stress LPCVD films better withstand the subsequent processing conditions [30]. Both film types are grown in a class 1000 clean room. The unpolished side of the wafer is then coated with photoresist (Clariant AZ 1518), baked at 90 °C for 2.0 min (Fig. 1c), and photolithographically patterned with an array of boxes. Development (4:1H_2O:Clariant AZ 400K) for 1.0 min, followed by a post-bake at 90 °C for 1.5 min (Fig. 1d), yields wafers which are then etched in a RIE chamber to remove the exposed Si_3N_4 (PlasmaLab 80+ RIE, 35 SCCM CF_4, 75 mTorr base pressure, 200 W). The RIE etched wafers are then sonicated in acetone to remove the photoresist, blown dry with nitrogen, and immersed in an aqueous KOH solution (33 wt.%, ~90 °C) for 3–5 h to anisotropically etch the Si wafer, stopping at the Si_3N_4 layer on the other side. The resulting suspended silicon nitride membranes are rinsed with copious amounts of deionized water and blown dry with nitrogen (Fig. 1e).

Next, electron beam resist (MicroChem Nano 495 PMMA C9) is spin-coated onto the cleaned suspended membranes and baked (180 °C for 2.0 min) (Fig. 1f). Then, eBL of an array of boxes is performed with a FEI Quanta sFEG scanning electron microscope ($<1.0\times10^{-5}$ Torr, 30 kV beam energy),

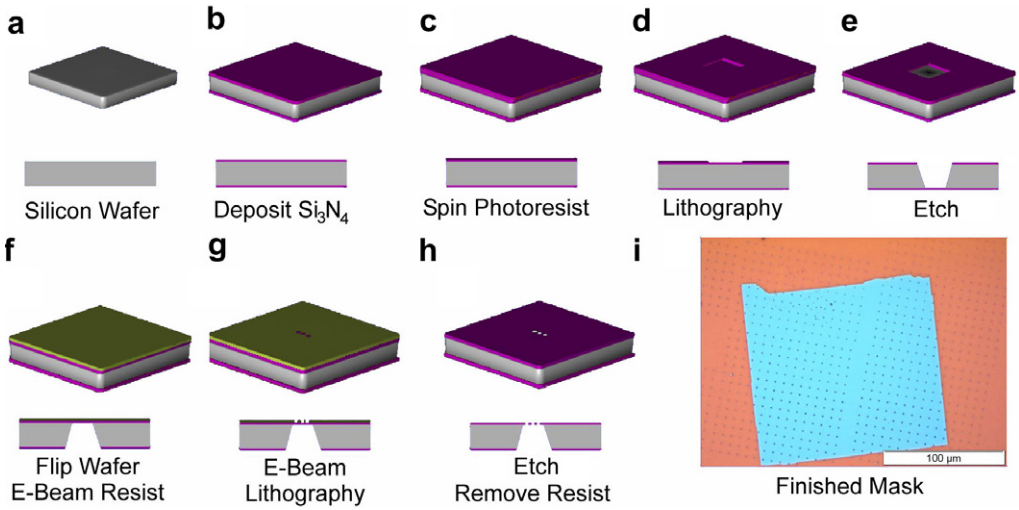


Fig. 1. Procedure for fabrication of eBL-patterned suspended membrane shadow masks. (a) Starting from a polished ⟨100⟩ Si wafer, (b) LP-CVD Si_3N_4 growth, (c–d) photolithographic patterning, (e) RIE and KOH etch, (f–g) eBL patterning, (h) final RIE etch and cleaning to yield (i), the finished shadow mask.

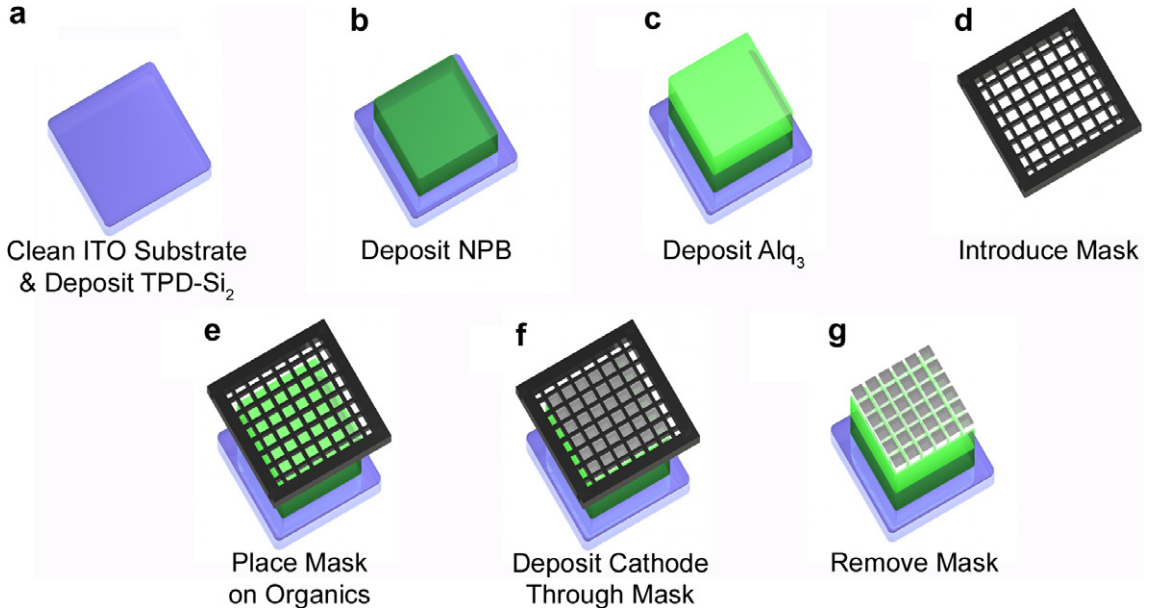


Fig. 2. Procedure for fabrication of individually addressable sub-μm OLEDs. (a) Starting from cleaned, TPD-Si_2 coated ITO, (b) NPB is thermally deposited, (c) followed by Alq_3. (d–e) The patterned suspended membrane shadow mask is placed on the organic heterostructure and, (f) an Al–Au or Ag cathode is thermally deposited, (g) completing the device upon mask removal.

and the patterned membranes are developed (1:1 methyl isobutylketone:2-propanol) and blown dry with nitrogen (Fig. 1g). Next, the eBL patterned suspended membranes are placed in an RIE and etched to remove the exposed silicon nitride (35 SCCM CF_4, 5 SCCM O_2, 75 mTorr base pressure, 200 W). Next, the membranes are placed in acetone to remove the electron beam resist, and then in an aqueous KOH solution (33 wt.%, ~25 °C) for ~12 h to ensure a complete etch (Fig. 1h). After the final KOH etch, the suspended membranes are again rinsed with copious amounts of deionized water and blown dry with nitrogen (Fig. 1i).

In additional to eBL, focused ion beam milling (FIB) of the suspended membranes can alternatively be used to define the patterned region. The procedure for FIB is similar to the steps portrayed in Fig. 1a–g, but instead of the final RIE etch, the suspended membranes are patterned with a FIB instrument (Hitachi FIB 2000-A, 30 kV beam energy). The patterned electron beam resist is used to locate the suspended silicon nitride membrane in the FIB. An array of boxes is then fabricated, and after patterning, the suspended membranes are subjected to the same acetone rinse and room temperature KOH etch as the eBL-patterned suspended membranes (Fig. 1h).

The OLEDs in this study are fabricated following the procedure outlined in Fig. 2 [31]. Briefly, ITO-coated glass substrates, purchased from thin film devices are cleaned and treated with a TPD-Si_2 (4,4′-bis[(*p*-trichlorosilylpropylphenyl)phenylamino]-biphenyl) adhesion/injection SAM reagent following an established procedure (Fig. 2a) [32,33]. Then, 35 nm of the hole-transport layer NPB (*N*,*N*′-di-(naphthyl)-*N*,*N*′-diphenyl-1,1′-biphenyl-4,4′-diamine) [34] (Fig. 2b) and 51 nm of the electron transport/emissive layer Alq_3 (Aldrich 99.995%, tris(8-hydroxyquinalato)aluminum(III)) (Fig. 2c) are sequentially thermally deposited (1.5–2.0 Å/s) onto the ITO surface. Prior to deposition, both NPB and Alq_3 are purified by triple gradient vacuum sublimation. The FIB or eBL patterned suspended membranes (Fig. 2d) are subsequently placed into conformal contact with the Alq_3 layer (Fig. 2e). The cathodes are nominally either 100–200 nm of Ag or 60 nm of Al (Aldrich 99.9999%), coated with a 12 nm Au passivating layer as noted below. All metals are deposited thermally at 1.5 Å/s and ~10^{-6} Torr. Depositions are performed without exposure to ambient conditions in separate evaporation chambers within a double glove box to avoid contamination. The actual thicknesses of the final cathodes are often somewhat less (5–50%, dependent upon

cathode size) than stated above due to shielding by the shadow mask, as confirmed by AFM.

The OLEDs are probed with one of two modified conductive atomic force microscope (cAFM) techniques [35], AFEM and BE-NIM. To address submicron OLEDs, substantial modifications have been made to the originally reported AFEM experimental set-up [25]. First, an improved PMT holder is introduced and an independent PMT (Hamamatsu 7400P) and high voltage power supply are employed. To minimize the effects of spurious light entering the PMT, a self-contained 4-piece PMT/filter holder has also been designed. This design accommodates a Peltier cooling system, allowing PMT operation at ~1 °C and reducing the dark current by more than one order of magnitude. Each joint is fitted with a custom Viton® gasket to minimize light leakage. Furthermore, Viton® O-rings are also used between the two filter/housing interfaces, the filter/filter interface, and the two PMT/housing interfaces. An Andover 500 nm high pass filter and an Omega Optical custom low pass filter with a cut-off wavelength of 585 nm and an optical density (OD) of 12–16 (transmission of 40–60%) are mounted to the front of the PMT housing. The performance of the low-pass filter is confirmed to be >OD 8 using a 5 mW He–Ne laser and an optical power meter. All AFEM results are acquired with a PMT temperature of 1.2 °C and a dew point of less than −20.0 °C in a nitrogen environment.

To further improve the optical noise floor of the present AFEM instrument, the following experimental procedure is used. First, specific OLED devices are located using standard contact mode techniques under zero applied bias. Once a particular device is located, the scan size is reduced sequentially by 50% until a 500 nm × 500 nm image of the device is obtained. The AFEM probe is then placed on the center of the device by "scanning" a 0 Å × 0 Å area. This arduous procedure is required due to the open-loop nature of the piezoscanner on the ThermoMicroscopes CP-II research AFM. At this point, the z-feedback loop is turned off while the tip deflection is actively monitored. To maintain a constant force, the z-piezo position is manually adjusted until a stable deflection is achieved. The beam bounce laser is subsequently turned off via an external switch, and bias sweeps are begun. Note that although ultra-dense optical filters are used to protect the PMT from stray reflections from the beam bounce laser, once device sizes decrease below 300 nm × 500 nm, these precautions no longer provide a sufficiently low optical noise floor due to the limited wavelength separation of the OLED emission (532 nm) and the wavelength of the beam-bounce laser (675 nm).

To obtain the spectroscopic impedance data, a new digital approach to BE-NIM is employed. Briefly, two impedance spectra are obtained for each device: one with the AFM probe in contact with the OLED and the second with the probe lifted ~100 nm from the sample surface. In the first spectrum, a measure of the device impedance in parallel with the fringe capacitance is obtained, and in the second an independent measure of the fringe capacitance is recorded. Once the resistance and reactance are calculated from the acquired phase shift and current magnitude data for both spectra, the impedance spectrum of the OLED can be calculated through:

$$Z_{\text{sample}}(f) = \frac{Z_{\text{fringe}}(f) * Z_{\text{total}}(f)}{Z_{\text{fringe}}(f) - Z_{\text{total}}(f)} \quad (1)$$

In Eq. (1), $Z_{\text{sample}}(f)$ is the impedance of the OLED as a function of frequency and $Z_{\text{total}}(f)$ and $Z_{\text{fringe}}(f)$ are the calculated impedances from the respective spectra discussed above. Although the signal-to-noise ratio is slightly decreased through the use of the digital bridge, the acquisition of impedance data across a wide range of frequencies without bridge-tuning is possible.

From the impedance spectra acquired using BE-NIM, a qualitative analysis of the ITO/NPB interface trap density can be obtained via a previously reported technique [28]. Briefly, the interplay of intrinsic OLED NC behavior at low frequencies and the slow time-constant capacitive nature of electronic traps at the NPB/ITO interface [29,31] causes the observed NC magnitude to vary with the trap density. As traps become more prevalent, the influence of their capacitive behavior becomes more pronounced. This can be readily observed in the derivative of resistance with respect to frequency (dR/df), since dR/df is negative in the case of dominant capacitance and positive in the case of dominant NC. As shown previously [28], the variations in dR/df are most prevalent in the frequency range of 10^3–10^4 Hz. In the case of thoroughly cleaned ITO surfaces passivated with TPD-Si_2, positive values of dR/df were observed over this frequency range, whereas in the case of an OLED fabricated on solvent-cleaned ITO surfaces, only negative values of dR/df are observed for all frequencies. Devices fabricated on ITO surfaces cleaned with

an oxygen plasma exhibit an intermediate value of dR/df. In each of these devices, the measured value of dR/df directly reflects the expected variation in trap density at the NPB/ITO interface, illustrating the unique capability of this technique to directly assess interfacial trap density in a fully functional and operating OLED. When this method of analysis is combined with BE-NIM data, spatial variations in trap density are directly observed.

3. Results

The original AFEM configuration for OLEDs utilized an Al cathode with a Au passivating layer to prevent oxidation of the Al beneath the AFEM tip [25]. To facilitate fabrication and remove the potential for misalignment of the cathode layers, especially as device size is decreased, a single-layer cathode that is not subject to oxidation is preferred. Although the work function of Ag is 0.5 eV greater than that of Al [36], it has been identified as a suitable cathode alternative [37,38]. No adverse consequences from the increase in driving biases required to overcome this small change in work function have been observed over the timescales of these studies. To confirm that the change in cathode material does not alter diode performance and to verify the performance of the modified AFEM instrument, AFEM was performed on an array of 36 μm^2 Ag cathode devices driven at 20 V (Fig. 3). Regions of decreased current flow (Fig. 3a) and light emission (Fig. 3b) are readily discernable near the top of the scan in agreement with previous results [25]. Since decreased values of light emission and

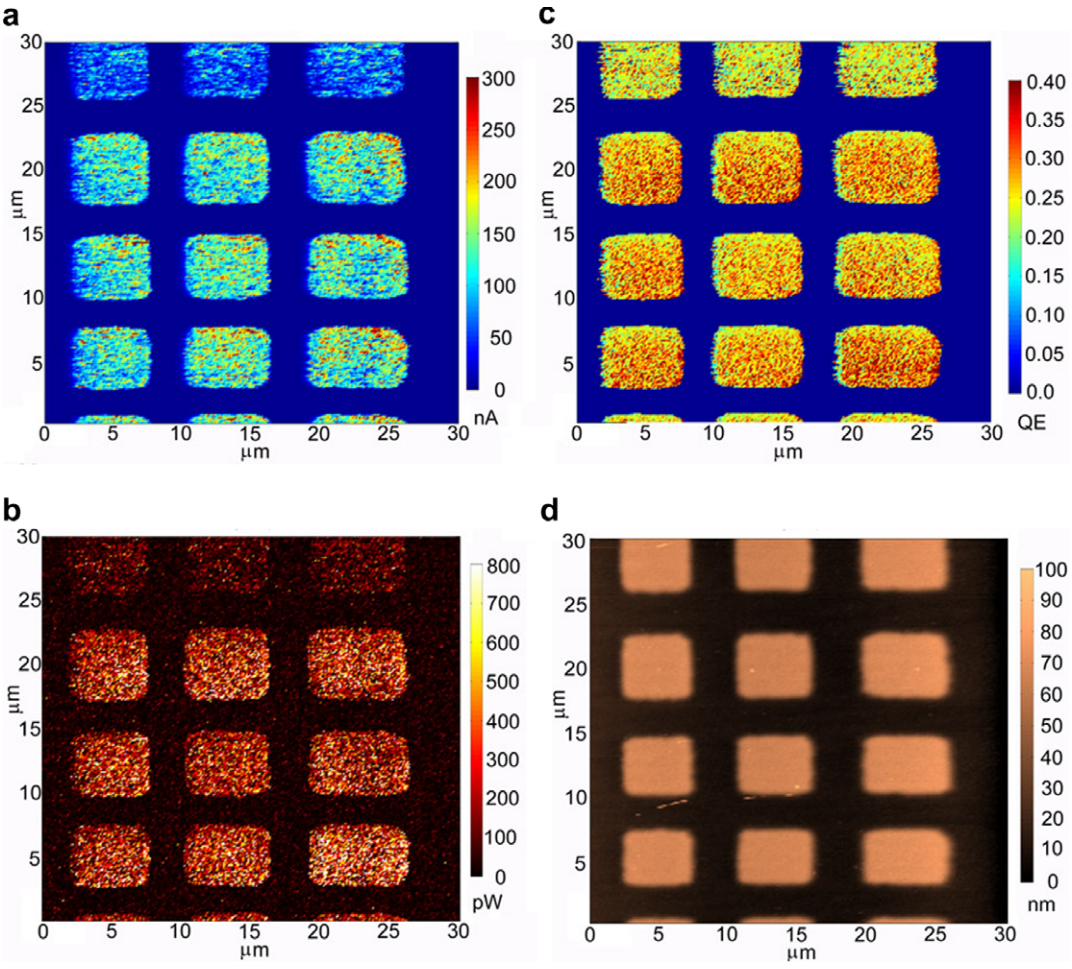


Fig. 3. AFEM results from Ag cathode OLEDs patterned via a TEM grid shadow mask. Images were acquired at 20 V. (a) Current flow through the AFM probe, (b) light emission map, (c) spatial map of quantum efficiency, reported in percent, and (d) topography. (a–d) were acquired simultaneously.

current flow occur on the same devices, only subtle variations in the quantum efficiency are found (Fig 3c). These results illustrate the importance of both small devices and the use of AFEM, since such variations may not be directly observable, nor can they be quantified in a macroscopic device. Since the characteristics of the transport are still averaged over the entire cathode area in this figure, the resolution of the technique is limited to 36 μm^2 in this case. However, dramatic improvements in resolution can be achieved using smaller devices.

The importance of decreased device size is clearly illustrated in Fig. 4, which contains a current map of 1.5 μm diameter devices on a 2.5 μm pitch acquired at 12 V by conductive AFM. In this result, inter-device response variations are readily identified. Thus, the "hotspot" in the middle of the image reveals that variations in device response properties exist on the 8–20 μm scale. To rule out the possibility that this apparent hotspot is simply due to a variation in the contact resistance between the AFM probe and the OLED cathodes, the same region was re-imaged 10 times (the final image of the series is shown in Fig. 4). The persistence of the hotspot over those 10 scans verifies that the observed current enhancement is an inherent property of the OLED array.

To demonstrate AFEM resolution and to map the spatial distribution of the observed OLED variations, large arrays of 300 nm × 500 nm OLEDs were fabricated with the suspended membrane shadow mask technique and examined with AFEM. As seen clearly in Fig. 5, which is a series of 30 μm × 30 μm scan areas, variations are observed in both the spatial maps of emission intensity and the spatial maps of current flow. These variations are observed at both the nanoscale, as seen in the inter-device variations, and at the microscale, demonstrated through the large regions of similar behavior evident in the array, exemplified in Fig. 5f, where there is a region of enhanced performance stretching from the upper-left to the lower-right corners of the images. These results suggest that there are long-length scale (10s of μms) variations in the density of interface traps or other performance-altering defects present in these devices. The likely sources of these defects are discussed later in the text. Unlike the subtle variations in the quantum efficiencies observed in Fig. 1, the range of quantum efficiencies observed in Fig. 5g and h appears to be much greater. These variations can be attributed to a transition from injection-limited transport to space charge-limited transport in these devices resulting from the drastic decrease in current flow [39]. This change in transport mechanism directly affects quantum efficiencies, as devices are less efficient in the injection-limited regime due to decreased hole accumulation and the subsequent reduction in the recombination rate [40,41].

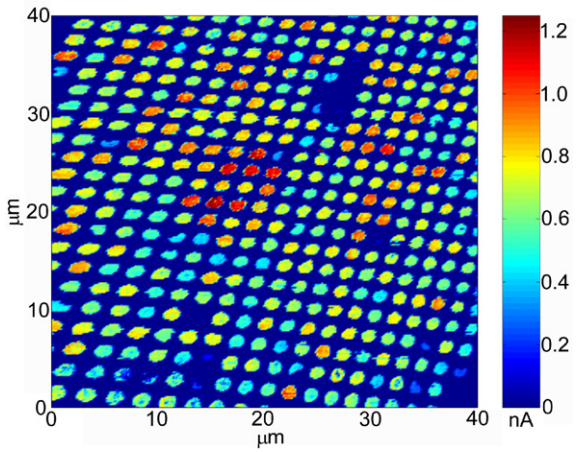


Fig. 4. Conductive AFM spatial map of current flow through an array of 1.5 μm OLEDs on a 2.5 μm pitch. Image was acquired under an applied bias of 12 V.

Since each small OLED is characterized independently, a large data sampling can be rapidly acquired for further analysis of inter-device variations. Histograms are shown in Fig. 6 for the average current flow through (Fig. 6a), light emission (Fig. 6b), and quantum efficiencies (QE) (Fig. 6c) from 758 individually addressed 300 nm × 500 nm diodes biased at 22.5 V. The average values are calculated by summing the values for every pixel on a given device and dividing by the number of pixels comprising that device. The nature of this behavior is also discussed later in the text.

As with the 300 nm × 500 nm diodes, arrays of 250 nm × 250 nm diodes were also fabricated with the new suspended membrane shadow masks. A typical *I–V–L* plot for an individual 250 nm × 250 nm OLED is shown in Fig. 7. To limit the optical noise generated by the beam-bounce laser, AFEM was performed in the spectroscopy mode, where the AFEM tip was fixed on a single device. The laser was subsequently shut off once the feedback loop was turned off, and the tip/sample contact force was stabilized. Subsequently, low-noise *I–V–L* curves were generated. To our knowledge, this is the smallest OLED individually addressed and characterized to date.

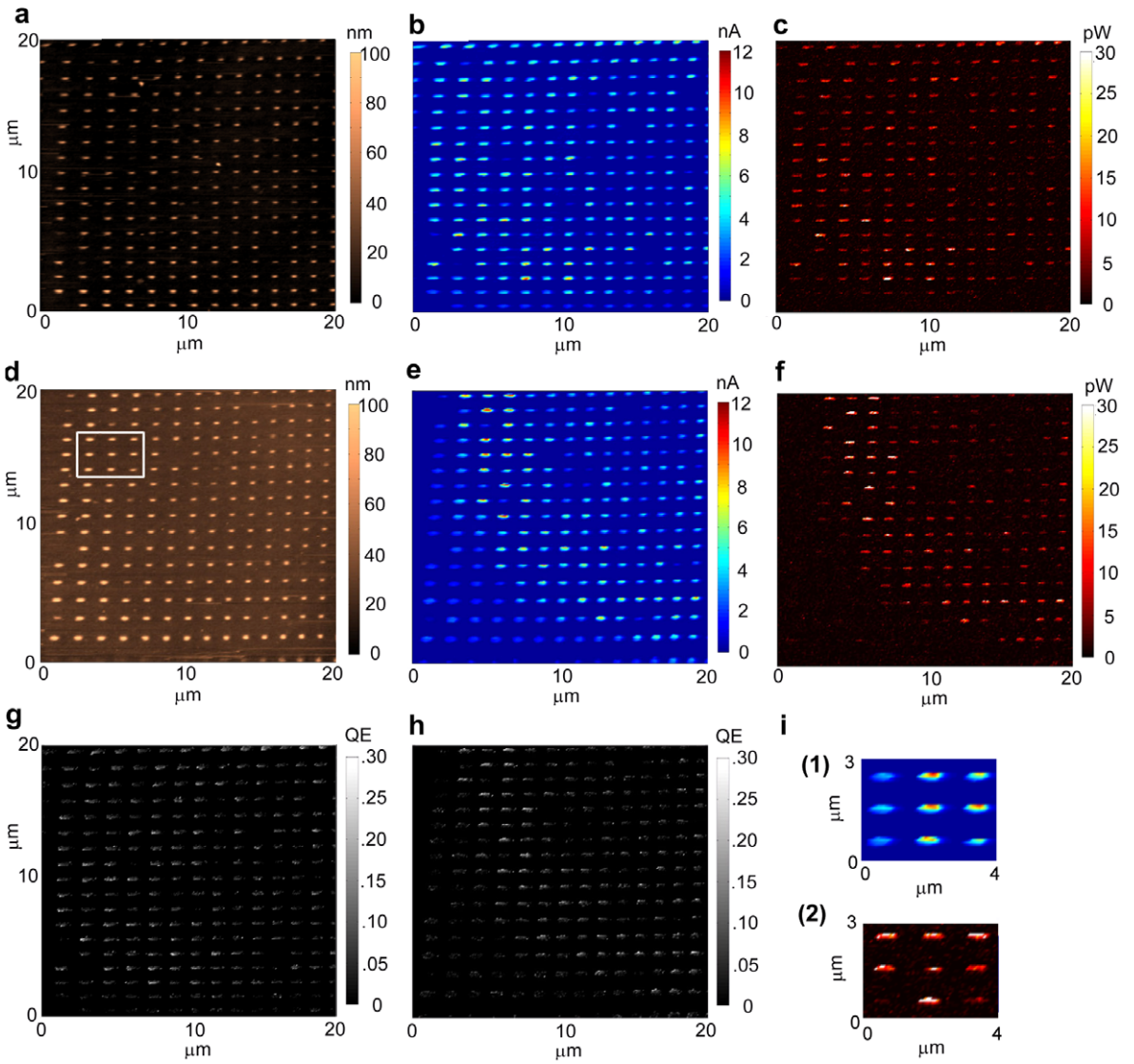


Fig. 5. AFEM images of two regions of an array of 300 nm × 500 nm devices under an applied bias of 22.5 V. (a and d) topography, (b and e) current, (c and f) emitted light, and (g and h) quantum efficiency [g is the efficiency map for a, b, and c]. Both neighbor-to-neighbor fluctuations and regional variations are evident, with regional variations occurring over a 10–20 μm range. (i) higher-resolution images from e (i 1) and f (i 2) of the region denoted by the white box in (d). The color scales used in i are unaltered from e and f.

To determine if any variations in frequency dependent impedance accompany the fluctuations in emission and current properties, AFEM and BE-NIM were consecutively applied to the same devices. First, AFEM was performed over a 30 μm × 30 μm region of 36 μm^2 devices to locate devices with varying current densities and emissive characteristics. These measurements were carried out with Al–Au cathodes under a 12 V applied bias. Al–Au cathodes were chosen to improve the stability of the tip/sample contact during subsequent frequency sweeps. As seen in Fig. 8b and c, two devices with significantly attenuated performance are observed. Impedance spectroscopy of these two devices, as well as one device with more representative performance, was subsequently performed with BE-NIM. The numbers on the topography image (Fig. 8a) correspond to the device labels in the subsequent impedance plots (Fig. 9). There are no observed variations in the topographies across these three devices, and the effects of the passivating Au layer are easily discernable in the spatial maps of current flow in Fig. 8b.

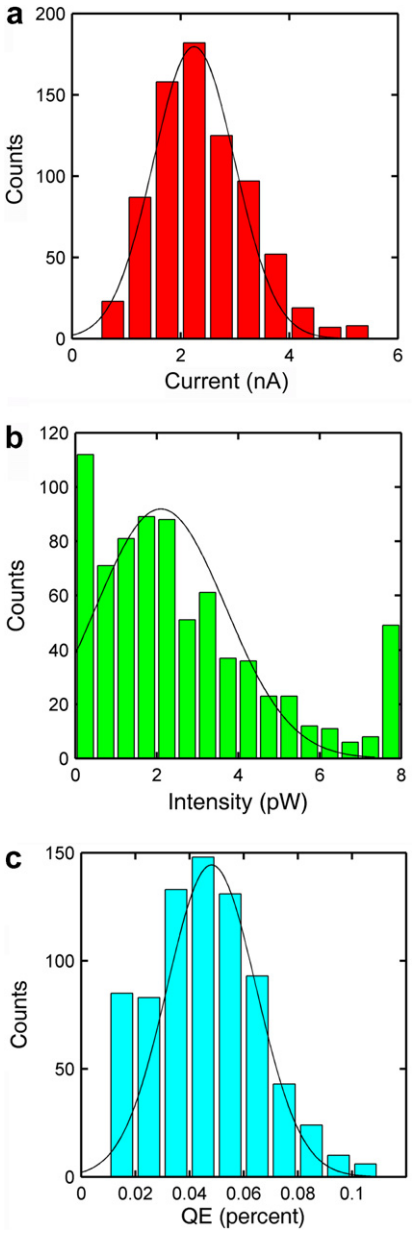


Fig. 6. Histograms of (a) current flow (red in webversion), (b) light emission (green in webversion), and (c) quantum efficiencies (QE, teal in webversion) for 758 individually addressed 300 nm × 500 nm OLEDs gathered from scan areas shown in Fig. 5 and additional areas. The black lines are fitted Gaussian distributions.

BE-NIM frequency sweeps were subsequently performed on the aforementioned three devices under a 13 V DC offset with a 150 mV_{RMS} amplitude dither. Following data acquisition, differential capacitance, reactance, and resistance vs. frequency plots, as well as a Cole–Cole diagram were generated. From the reactance vs. frequency plot in Fig. 9a, the similarities in RC time constants are clear. Subsequent equivalent circuit modeling reveals that a capacitance of 40 fF can be used with resistances of 330 MΩ, 360 MΩ, and 300 MΩ to model the RC behavior of devices 1, 2, and 3, respectively, where the resulting modeled behavior is shown as solid lines in Fig. 9a. These results suggest that the observed performance variations cannot be attributed to an alteration in the location of the accumulated charge, as the capacitance remains constant between the devices, regardless of their performance. This uniform inter-device capacitance also suggests that there is no discernable variation in the position of the space charge with decreasing device size under an applied bias [39]. This is confirmed through a simple calculation of capacitance based on the 36 μm^2 area and the 51 nm thickness (Alq_3 thickness), resulting in a capacitance of 26 fF, which is of the proper order of magnitude and does not account for 3D effects that act to increase the capacitance of the device [42]. The values of resistance also can be confirmed through ohm's law where a 13 V DC bias and a 330 MΩ resistance suggests a DC current flow of ~40 nA. This is in agreement with the values shown for device 1 in Fig. 8. Although the capacitance remains constant across these three devices, a strong variation in the NC magnitude is evident in the resistance vs. frequency plot, the Cole–Cole diagram, and the differential capacitance vs. frequency plots, as seen in Fig. 9b–d. As previously discussed, this behavior can be attributed to variations in the trap density at the NPB/ITO interface.

4. Discussion

The sub-micron and nanoscale OLED arrays in Figs. 4 and 5 were patterned with the suspended membrane shadow mask technique outlined above. This approach offers several advantages over traditional lithographic techniques for patterning sub-μm OLED arrays. For example, photolithography or soft-contact printing of insulating layers at length scales below 1 μm necessitates the use of photomasks or Si masters, respectively, both of which are expensive and time-consuming to fabricate. For each change in diode size or array pitch, a new photo mask or Si master would be required, further increasing the cost and time required to create different pitches and diode sizes. Furthermore, neither conventional photolithography nor soft

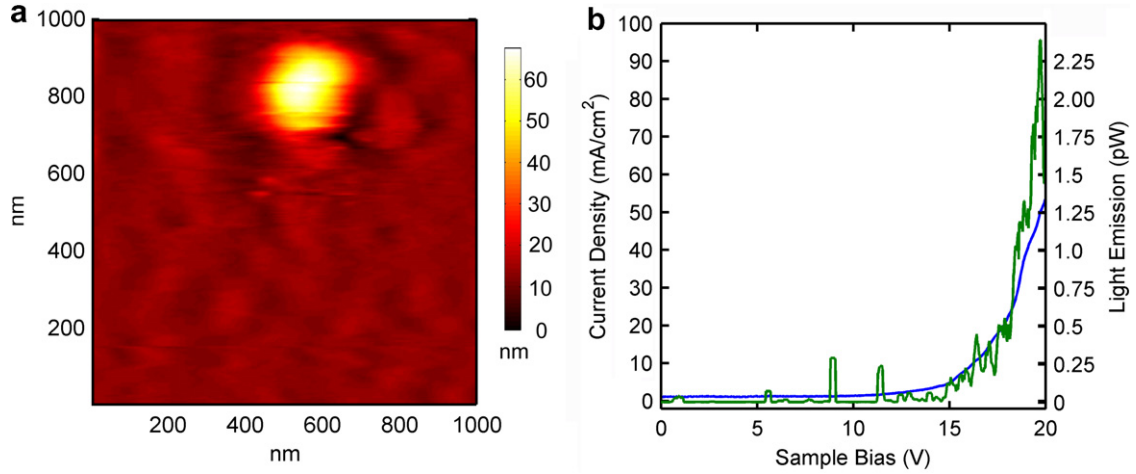


Fig. 7. AFEM image of a single 250 nm × 250 nm OLED fabricated with a patterned suspended membrane shadow mask. (a) Topography, and (b) *I–V–L* response data for the diode. The current density is represented as a blue line and light emission is represented in green.

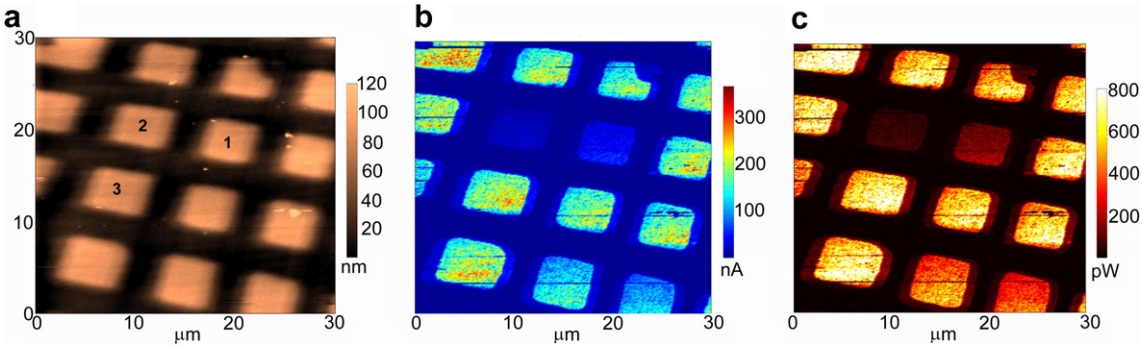


Fig. 8. AFEM results from Al–Au cathode devices patterned by a TEM grid shadow mask gathered at 12 V. The numbering in topographic image (a) corresponds to the device numbers in Fig. 9.

contact printing has a resolution comparable to the sub-20 nm resolution of eBL.

The use of eBL also enables the suspended membrane shadow masking scheme (Fig. 2) to pattern OLEDs in a variety of shapes and sizes. Although circular OLEDs have been patterned throughout this work, there is no fundamental limitation prohibiting the generation of other shapes and/or complex patterns. The ability to tailor the dimensions of the resulting holes using eBL readily provides suspended membranes with holes ranging in size from tens of microns to hundreds of nanometers. Furthermore, the spacing or pitch between neighboring diodes can also be tuned with exquisite control. An additional advantage of the new suspended membrane shadow mask technique is the ability to reuse the membranes. A single patterned membrane can often be reused 10 times or more times before discarding. If the membrane becomes clogged with metal from the cathode deposition, a quick (10 s) dip in *aqua regia* is sufficient to remove the deposited material without membrane damage. Recycling of eBL patterned masks minimizes the time and cost associated with eBL, giving the shadow mask approach an additional advantage over single-run lithographic patterning of sub-μm insulating features on anode surfaces using eBL [19,22].

As stated earlier, a major limitation of the shadow mask approach for patterning sub-micron and nanoscale OLEDs has been the ability to address the resulting diodes. The small sizes coupled with the low current flow within each diode renders probing and characterizing tiny OLEDs extremely challenging. For this purpose, AFEM is an incisive

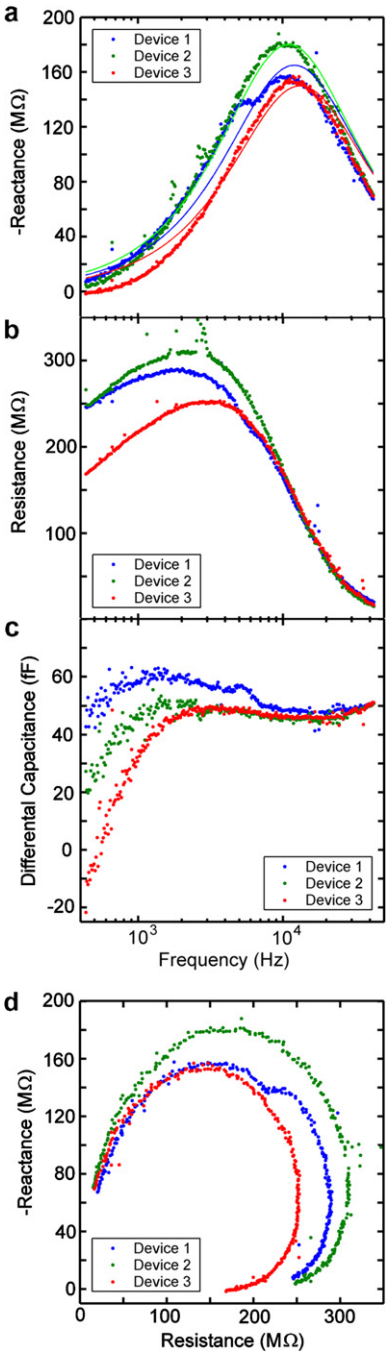


Fig. 9. Impedance sweeps gathered on individual 6 μm × 6 μm OLEDs, as labeled in Fig. 8a. (a) Reactance vs. frequency, showing little device-to-device variation in the RC time constant. The solid lines represent the modeled RC behavior discussed in the text. (b) Resistance vs. frequency plot, illustrating clear variations on the order of the magnitude of NC. (c) Differential capacitance vs. frequency, showing variability in the onset frequency of negative values of capacitance. (d) Cole–Cole diagram, again, showing large device-to-device variations on the order of the magnitude of NC.

technique for precise addressing of individual nanoscale OLEDs. OLEDs ranging in size from tens of micrometers to hundreds of nanometers have been individually addressed, and low-noise *I–V–L* measurements have been demonstrated at all size scales. Furthermore, meaningful statistics can be generated for the *individual* diodes comprising an array. Thus, the statistics in Fig. 6a indicate device-to-device variations *within* the sub-μm OLED array. For this array, the distribution of diode currents is found to be essentially Gaussian, with a mean value of 2.10 ± 0.15 nA and a standard deviation of 0.75 nA. Although a Gaussian distribution appears to only loosely fit the light intensity distribution (Fig. 6b), a mean of 2.1 ± 0.15 pW with a standard deviation of 1.59 pW is calculated over the array. In a similar fashion, the distributions of quantum efficiencies can also be loosely fit to a Gaussian distribution with a mean of $0.045 \pm 0.005\%$ with a standard deviation of 0.0165%. The distribution in current flow through the diodes is not paralleled in the non-Gaussian distribution of light emission values for the same array. Thus, 114 OLEDs exhibit an average emission intensity of less than 0.5 pW. In contrast, Fig. 6a indicates that every diode in the array passes an average of *at least* 0.5 nA of current, and less than 1% of the diodes pass, on average, more than 5.0 nA. This also suggests that device shorting is an unlikely cause of decreased emission, since higher currents would be expected. Instead, a variety of other factors are likely responsible. These trends are further paralleled in the distribution of quantum efficiencies, as similar deviations in the fit can be found in both the light emission and quantum efficiency data as the QE and emission tend towards zero. However, the standard deviation (as a fraction of the mean) is much less for the quantum efficiency than for the emission data. We have previously reported similar trends in micron-scale devices [35], suggesting that inter-device variation continues to be related to injection/contact variations and not to variations in recombination efficiencies or local quenching defects even as the devices size decreases.

The complex nature of the observed OLED response variations is further illuminated in the AFEM spectroscopy mode data since it facilitates collection and observation of the *I–V–L* response variations from the 250 nm × 250 nm diodes. Variations in the slopes of these plots correspond to different electroluminescence efficiencies [38,43], and clearly demonstrate the existence of device-to-device variations on the nanometer scale. Interestingly,

when these results are compared to previously reported *average* *I–V–L* data for similar micron-[25] and macro-scale OLEDs [32], strong similarities in the shapes of the *I–V–L* response, emission intensity per unit area, and current densities are observed. However, cross-comparison of macro-, micron-, and nano-scale devices indicates that the magnitude of inter-device variations increases with decreasing device size, highlighting the importance of small defects, which become more prevalent as the individual device size decreases.

Additional evidence for device-to-device OLED variability at the sub-μm scale is evident in threshold voltages. From the *I–V–L* characteristics of individual devices in an array of twelve 500 nm × 500 nm OLEDs, threshold voltage *variations* on the order of 4–5 V are observed (Fig. 10) [44]. Further analysis of the two diodes circled in black reveals variations in the *I–V–L* slopes of ~20%. Such non-uniformity in neighboring diodes could have detrimental effects in sensors or displays since regions of dimmer pixels or of increased potential to maintain constant current flow would occur. In comparison, commercial liquid crystal displays for medical applications have pixel-to-pixel luminescence variations of 25% or more [45].

These conclusions are further confirmed by the BE-NIM results in Fig. 9 and the subsequent trap density analysis [28]. These results suggest that defects and/or variations in the organic layers, interfaces, or the anode surface occur over the μm scale and can be correlated with variations in the trap density and/or work function at the ITO/NPB interface. Furthermore, since these experiments were performed without aging the devices, dark spot nucleation and growth is an unlikely source of these intensity variations [46]. Since dark spots are the only OLED defect reported to date having a similar size, the present results suggest that another mechanism may be operative. Although large scale variations in performance occur over ~50–500 μm^2 regions, inter-device performance is fairly uniform within these regions, providing additional support to the theory that additional mechanisms for device attenuation are present.

Device-to-device variations similar to the above have also been observed in other micron and submicron OLED arrays. In some reports, a tentative explanation for the variations was provided [17–19], while in others, no explanation was offered [22,24,47,48]. There are several difficulties in interpreting single-diode behavior for small OLEDs addressed in parallel. Often the device architecture has not enabled individual diode addressing. Data collected for an array addressed in this manner are therefore the collective response of *all* diodes addressed in parallel, averaging out any inherent variations, analogous to macroscopic device measurements. Furthermore, larger diodes are commonly averaged with smaller diodes to boost the signal-to-noise ratio during *I–V–L* measurements, further compounding this issue. These shortcomings are avoided by shadow mask fabrication of individual OLEDs and by addressing the diodes with AFEM and BE-NIM. The signal-to-noise ratios of the PMT and current pre-amplifier are well below the signal levels for single nanoscale diodes, as evident in Fig. 5, eliminating the need for averaging over multiple diodes. This enables extraction of true *single-diode* behavior and provides a quantitative means to examine inter-diode variations.

Attempts were made to in the present study to minimize device-to-device variations by using known ITO cleaning procedures [29], optimal deposition rates [49], extensive pumping cycles [50], triply gradient-sublimed organic materials [10], ultra-pure cathode materials, and TPD-Si_2 treated ITO [32]. Variations remain despite these procedures, and there are several plausible explanations. First is the role of ITO intrinsic and extrinsic surface irregularities, suggested by the BE-NIM results (Fig. 9). It is known that different ITO cleaning procedures yield dramatically different ITO surface states [51–53] and that organic solvent cleaning results in higher levels of carbon contamination than does oxygen or an ozone plasma cleaning [54,55]. Recent impedance spectroscopy studies indicate that unintentional carbon contamination increases device impedance and the subsequent driving voltages required to obtain the desired luminance [28,29,31]. There are also inherent sources of local heterogeneity within the ITO film itself, in addition to surface contamination, which could give rise to inter-device response fluctuations. Substantial conductivity variations over freshly cleaned ITO surfaces suggest the existence of inherent 'hotspots' in polycrystalline ITO films [56]. These 'hotspots' are approximately the size of the nanoscale OLEDs in this study, so their role in contributing to inter-device variations is possible.

Furthermore, subtle fluctuations in the ITO surface roughness may also contribute to increased variability in device performance at micron and nanometer length scales. Contact mode AFM

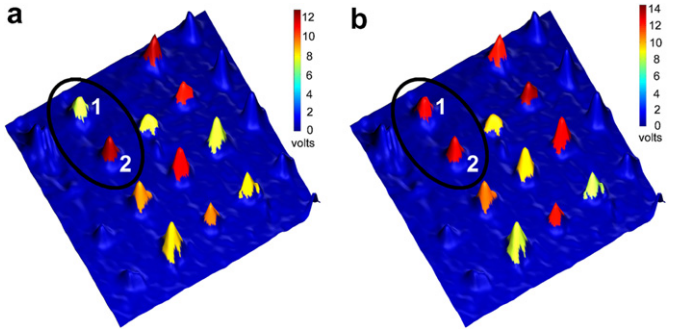


Fig. 10. Array of twelve 500 nm × 500 nm OLEDs fabricated with a patterned suspended membrane shadow mask. (a) Turn-on voltage for the start of current flow, (b) turn-on voltage for the start of light emission. The scan window is 7 μm × 7 μm.

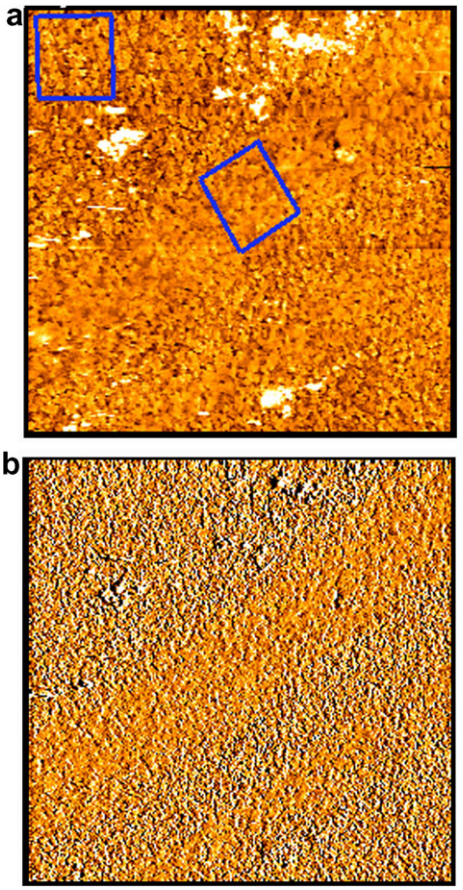


Fig. 11. Contact mode AFM images of the TPD-Si_2 modified ITO surface used throughout these studies. (a) A 10 μm × 10 μm scan exhibiting both smooth and rough regions. The surface roughness in the blue box in the upper left is 6.00 $Å_{RMS}$, whereas the roughness in the center box is 4.07 $Å_{RMS}$. (b) Error signal map of the same region shown in (a), more clearly exhibiting the regional roughness variations.

images of the ITO substrates treated with a TPD-Si_2 SAM reveal such features. A 10 μm × 10 μm AFM image is shown in Fig. 11a, demonstrating the occurrence of distinct rough and smooth regions. Roughness analysis from the two regions denoted by the blue boxes show a surface roughness of 6.00 $Å_{RMS}$ in the upper left region and 4.07 $Å_{RMS}$ in the central region. These regional variations are more distinct in Fig. 11b, a map of the AFM error signal. From larger area scans and scan montages, these smooth regions extend for ~30 μm and are ~5 μm wide. The shape and size of these roughness variations are very similar to the size of the regional variations in the current flow and light intensity observed in Fig. 5, suggesting that variations in the ITO surface roughness variations as small as 1.9 $Å_{RMS}$ may result in measurable variations in the electronic performance. These results are supported by previous studies of macroscopic OLED performance as a function of ITO surface roughness [57,58].

5. Conclusions

The shadow mask approach to small OLED fabrication reported here offers flexibility not afforded by many alternative lithographic routes that pattern insulating layers on OLED ITO anodes. Suspended membrane shadow masks with openings as small as 250 nm have been successfully fabricated and utilized to pattern comparably sized OLEDs. Additionally, advances in AFEM allow characterization of individual nanoscale devices with low noise and high precision. For the first time, statistics *within* an array of sub-μm OLEDs have been generated and examined. Furthermore, the ability to extract buried interface properties of individual OLED pixels has been demonstrated using BE-NIM. These results provide evidence for significant OLED-to-

OLED response variations within small arrays of sub-μm diodes. Through the combination of AFEM and BE-NIM, these variations can be quantified, better understood, and thus minimized in future generations of sub-micron OLED pixel arrays.

Acknowledgements

This work was supported by the NASA Institute for Nanoelectronics and Computing under Award Number NCC 2-1363 and the NSF under Award Number DMR-0134706. The authors also acknowledge the use of the facilities supported by the Northwestern University MRSEC (NSF DMR-0520513). The eBL work was performed in the EPIC facilities of the NUANCE Center at Northwestern University. The NUANCE Center is supported by the NSF-NSEC, NSF-MRSEC, Keck Foundation, State of Illinois, and Northwestern University. Finally, the authors thank J. Li for providing the TPD-Si_2.

References

[1] C.W. Tang, S.A. Van Slyke, Appl. Phys. Lett. 51 (1987) 913.
[2] O. Graydon, Opto Laser Europe (April) (2003) 5.
[3] J.K. Borchardt, Mater. Today 7 (2004) 42.
[4] J.N. Bardsley, IEEE J. Select. Top. Quantum Elect. 10 (2004) 3.
[5] P.E. Burrows, V. Bulovic, S.R. Forrest, L.S. Sapochak, D.M. McCarty, M.E. Thompson, Appl. Phys. Lett. 65 (1994) 2922.
[6] X. Xu, G. Yu, Y. Liu, D. Zhu, Displays 27 (2006) 24.
[7] E.-M. Han, L.-M. Do, N. Yamamoto, M. Fujihira, Thin Solid Films 273 (1996) 202.
[8] M.A. Baldo, M.E. Thompson, S.R. Forrest, Nature 403 (2000) 750.
[9] S. Tokito, Y. Taga, T. Tsutsui, Synth. Met. 91 (1997) 49.
[10] D.A. Pardo, G.E. Jabbour, N. Peyghambarian, Adv. Mater. 12 (2000) 1249.
[11] M.B. Wolk, Opt. Eng. 94 (2005) 307.
[12] D.B. Chrisey, A. Piqué, R.A. McGill, J.S. Horwitz, B.R. Ringeisen, D.M. Bubb, P.K. Wu, Chem. Rev. 103 (2003) 553.
[13] J.R. Sheats, J. Mater. Res. 19 (2004) 1974.
[14] E. Holder, B.M.W. Langeveld, U.S. Schubert, Adv. Mater. 17 (2005) 1109.
[15] V. Savvate'ev, Z. Chen-Esterlit, J.W. Aylott, B. Choudhury, C.-H. Kim, L. Zou, J.H. Friedl, R. Shinar, J. Shinar, R. Kopelman, Appl. Phys. Lett. 81 (2002) 4652.
[16] B. Choudhury, R. Shinar, J. Shinar, Proc. SPIE 5214 (2004) 64.
[17] Y. Koide, M.W. Such, R. Basu, G. Evmenenko, J. Cui, P. Dutta, M.C. Hersam, T.J. Marks, Langmuir 19 (2003) 86.
[18] Y. Koide, Q. Wang, J. Cui, D.D. Benson, T.J. Marks, J. Am. Chem. Soc. 122 (2000).
[19] F.A. Boroumand, P.W. Fry, D.G. Lidzey, Nano Lett. 5 (2004) 67.
[20] T. Nyberg, F. Zhang, O. Inganäs, Nanotechnology 13 (2002) 205.
[21] Y.-C. Kim, Y.R. Do, Opt. Exp. 13 (2005) 1598.
[22] H. Yamamoto, J. Wilkinson, J.P. Long, K. Bussman, J.A. Christodoulides, Z.H. Kafafi, Nano Lett. 5 (2005) 2485.
[23] D. Suh, H.H. Lee, J. Vac. Sci. Tech. B 22 (2004) 1123.
[24] S.P. Price, J. Henzie, T.W. Odom, Small 3 (2007) 372.
[25] L.S.C. Pingree, M.C. Hersam, M.M. Kern, B.J. Scott, T.J. Marks, Appl. Phys. Lett. 85 (2004) 344.
[26] L.S.C. Pingree, M.M. Kern, B.J. Scott, T.J. Marks, M.C. Hersam, TMS Lett. 1 (2004) 127.
[27] L.S.C. Pingree, M.C. Hersam, Appl. Phys. Lett. 87 (2005) 233117.
[28] L.S.C. Pingree, M.T. Russell, B.J. Scott, T.J. Marks, M.C. Hersam, Thin Solid Films 515 (2007) 4783.
[29] L.S.C. Pingree, M.T. Russell, T.J. Marks, M.C. Hersam, J. Appl. Phys. 100 (2006) 044502.
[30] J. Yota, J. Hander, A.A. Saleh, J. Vac. Sci. Technol. A 18 (1999) 372.
[31] L.S.C. Pingree, B.J. Scott, M.T. Russell, T.J. Marks, M.C. Hersam, Appl. Phys. Lett. 86 (2005) 073509.
[32] J. Cui, Q. Huang, J.C.G. Veinot, H. Yan, Q. Wang, G.R. Hutchison, A.G. Richter, G. Evmenenko, P. Dutta, T.J. Marks, Langmuir 18 (2002) 9958.
[33] Q. Huang, G.A. Evmenenko, P. Dutta, P. Lee, N.R. Armstrong, T.J. Marks, J. Am. Chem. Soc. 127 (2005) 10227.
[34] T. Yamamoto, M. Nighiyama, Y. Koie, Tetrahedron Lett. 39 (1998) 2367.
[35] For a review of conductive atomic force microscopy, please see M.E. Greene, C.R. Kinser, D.E. Kramer, L.S.C. Pingree, M.C. Hersam, Micro. Res. Tech. 64 (2004) 415.
[36] Electron work function of the elements, in: Lide, D.R. (Ed.), CRC Handbook of Chemistry and Physics (Internet Version), Taylor and Francis, Boca Raton, 2006.
[37] M. Stössel, J. Staudigel, F. Steuber, J. Simmerer, A. Winnacker, Appl. Phys. A 68 (1999) 387.
[38] S.K. So, W.K. Choi, C.H. Cheng, L.M. Leung, C.F. Kwong, Appl. Phys. A 68 (1999) 447.
[39] W. Brutting, S. Berleb, A.G. Muckl, Org. Electron. 2 (2000) 1.
[40] J. Kalinowski, N. Camaioni, P. Di Marco, V. Fattori, A. Martelli, Appl. Phys. Lett. 72 (1998) 513.
[41] K. Book, V.R. Nikitenko, H. Bassler, A. Elschner, J. Appl. Phys. 89 (2001) 2690.
[42] T. Sakurai, K. Tamaru, IEEE Trans. Electron. Dev. 30 (1983) 183.
[43] I.-M. Chan, W.-C. Cheng, F.C. Honga, Appl. Phys. Lett. 80 (2002) 13.
[44] This image was created by using topography relief as the 3-D information, and overlaying a color-map corresponding to the threshold voltages of the individual devices acquired through the *I–V–L* measurements.
[45] T. Kimpe, A. Xthona, P. Matthijs, L.D. Paepe, J. Digital Imag. 18 (2005) 209.
[46] J. McElvain, H. Antoniadis, M.R. Hueschen, J.N. Miller, D.M. Roitman, J.R. Sheats, R.L. Moon, J. Appl. Phys 80 (1996) 6002.
[47] S. Kiyohara, M. Fujiwara, F. Matsubayashi, K. Mori, Jpn. J. Appl. Phys. 44 (2005) 3686.

[48] A. Bolognesi, C. Botta, S. Yunus, Thin Solid Films 492 (2005) 307.
[49] C.B. Lee, A. Uddina, X. Hua, T.G. Andersson, Mater. Sci. Eng. B 112 (2004) 14.
[50] A. Böhler, S. Dirr, H.-H. Johannes, D. Ammermann, W. Kowalsky, Synth. Met. 91 (1997) 95.
[51] J.S. Kim, P.K.H. Ho, D.S. Thomas, R.H. Friend, F. Cacialli, G.-W. Bao, S.F.Y. Li, Chem. Phys. Lett. 315 (1999) 307.
[52] I.-M. Chan, F.C.-N. Hong, Thin Solid Films 444 (2003) 254.
[53] H.-T. Lu, M. Yokoyama, J. Cryst. Growth 260 (2004) 186.
[54] K. Sugiyama, H. Ishii, Y. Ouchi, K. Seki, J. Appl. Phys 87 (2000) 295.
[55] C. Donley, D. Dunphy, D. Paine, C. Carter, K. Nebesny, P. Lee, D. Alloway, N.R. Armstrong, Langmuir 18 (2002) 450.
[56] Y.-H. Liau, N.F. Scherer, K. Rhodes, J. Phys. Chem. B 105 (2001) 3282.
[57] G. Wantz, L. Hirsch, N. Huby, L. Vignau, J.F. Silvain, A.S. Barriere, J.P. Parneix, Thin Solid Films 485 (2005) 247.
[58] Y.H. Tak, K.B. Kim, H.G. Park, K.H. Lee, J.R. Lee, Thin Solid Films 411 (2002) 12.

Available online at www.sciencedirect.com
ScienceDirect
Organic Electronics 8 (2007) 480–486
Organic Electronics
www.elsevier.com/locate/orgel

Ring oscillator fabricated completely by means of mass-printing technologies

A.C. Huebler [a,e], F. Doetz [b], H. Kempa [a,*], H.E. Katz [c], M. Bartzsch [a], N. Brandt [a], I. Hennig [b], U. Fuegmann [a], S. Vaidyanathan [d], J. Granstrom [d], S. Liu [d], A. Sydorenko [d], T. Zillger [e], G. Schmidt [a], K. Preissler [a], E. Reichmanis [d], P. Eckerle [b], F. Richter [b], T. Fischer [a], U. Hahn [a]

[a] *Institute for Print and Media Technology, Chemnitz University of Technology, 09107 Chemnitz, Germany*
[b] *BASF AG, 67056 Ludwigshafen, Germany*
[c] *Department of Materials Science and Engineering, Johns Hopkins University, 3400 North Charles Street, 103 Maryland Hall, Baltimore, MD 21218, USA*
[d] *Bell Laboratories, Alcatel-Lucent, Murray Hill, NJ 07974, USA*
[e] *Printed Systems GmbH, 09125 Chemnitz, Germany*

Received 2 October 2006; received in revised form 26 February 2007; accepted 28 February 2007
Available online 12 March 2007

Abstract

We report on the first successful fabrication of an integrated circuit solely by means of fast, continuous mass-printing technology. Our demonstration object is a seven-stage ring oscillator which delivers an ac-signal with a frequency of approximately 4 Hz. The process speed of the order of 1 m/s demonstrates the high potential of mass-printing techniques for the production of low-cost electronics. By identifying major technological issues that occur upon printing of electronic circuits, routes for further development are clarified.
© 2007 Elsevier B.V. All rights reserved.

PACS: 72.80.Le; 77.84.Jd; 85.30.Tv

Keywords: Printed electronics; Mass-printing; Integrated circuit

1. Introduction

During the last years, research has increasingly concentrated on the processing of functional polymers for the development of electronic devices. Researchers hope to realize extremely cost-effective applications on flexible substrates, such as plastic foils or paper in the future, in order to equip and embellish many daily life products as "smart objects". Among other functions, it is primarily electronic circuits based on organic field effect transistors (oFETs) that are of interest. In the last years, a great number of methods for the processing of

* Corresponding author. Tel.: +49 371 531 35 693; fax: +49 371 531 835 693.
E-mail address: heiko.kempa@mb.tu-chemnitz.de (H. Kempa).

1566-1199/$ - see front matter © 2007 Elsevier B.V. All rights reserved.
doi:10.1016/j.orgel.2007.02.009

material layers necessary for oFET circuits have been proposed which are frequently borrowed from traditional electronics production (e.g. Refs. [1–10]).

However, the solubility and dispersibility of functional polymers in various solvents suggest applying them as formulated inks which can be deposited into patterned layers by means of printing techniques. Some research groups have adapted methods from printed circuit board production, such as screen printing and pad printing [11–14], while many other groups have used inkjet printing [15–18]. By combining these methods in different ways, it has been possible in the past to show that comparatively complex circuits based on organic semiconductors with hundreds [7] or even thousands [19] of transistors are possible and that microsecond switching speeds can be achieved [11,20]. Furthermore, there are ring oscillator circuits for which exclusively polymer materials were used [1,9,11,12,15], not only for the semiconductor but also for the conductive source/drain and gate electrodes as well as for the gate dielectric. Completely printed single transistors and ring oscillators produced by pad printing [11,12] and inkjet [15–17] have been reported.

Compared to the approaches mentioned so far, mass-printing technologies bring very special challenges. The traditional technologies of offset, gravure and flexographic printing are currently primarily used for the production of newspapers, books, packaging etc. and have a 10^3–10^6 times higher productivity than other printing methods [21]. Typical printing speeds range from 2 m/s to 15 m/s. With respect to a future mass production of polymer electronics, it is a key issue to use solely these mass-printing methods for a successive deposition of different layers. So far, these printing methods as well as the necessary printing machines have only been optimized for visual image properties. Printing materials with electronic functions imposes more stringent requirements on the methods, machines as well as ink chemistry and rheology [22], which go beyond the current state of today's printing technologies.

2. Experimental

While the preparation of oFETs from solution has already become a routine technique [15], the actual deposition of thin semiconductive or dielectric layers by means of additive printing methods still remains challenging. We therefore believe that the key task in printed electronics is represented by the transfer of processing steps from the laboratory using solution deposition techniques like spin coating and casting to the printing machine. A ring oscillator consisting of several inverter stages is considered to be a useful example of testing logic capability in integrated circuits [12]. By presenting a fully printed oscillator the general concept of printed electronics can be proven. Furthermore, potential risks and bottlenecks of the approach can be identified.

Fig. 1 shows the setup of our oFETs together with the used materials and printing methods. An oFET top gate architecture was chosen primarily because the first deposition step of source and drain contacts requires the highest resolution and can be accomplished most easily on a plain and defined substrate like a smooth polyester foil (PET) rather than on a printed multilayer surface with significant roughness. Our substrate is a commercially available (Dupont Tejin) PET foil with a surface roughness of 8 nm. In order to assure dimensional stability the foil is pre-shrunk by means of thermal and mechanical stress. The foil is subject to a standard in-line corona treatment before the source/drain structures are offset-printed on top of it.

The channel length of the transistor representing the distance between source and drain electrodes was set to $L = 0.1$ mm, and the channel width $W = 30$ mm and $W = 6$ mm for the load and driver transistors, respectively. However, no attempts were made so far to further reduce the channel length so as to obtain a significantly increased inverter



layer	material	method
1 substrate	PET	-
2 source/drain	PEDOT:PSS	offset
3 semiconductor	F8T2	gravure
4 low-k dielectric	BuS*	gravure
5 high-k dielectric	Luxprint	flexo
6 gate	Ag-ink	flexo

Fig. 1. Layer setup of the printed oFETs together with the used materials and printing methods, respectively (* BuS: butadiene–styrene-copolymer).

frequency [2]. The electrodes are made of a commercially available, water-based dispersion of poly(3,4-ethylenedioxythiophene) doped with poly(styrenesulfonate) (PEDOT:PSS), Baytron P® of H.C. Starck, that is reformulated in order to make it offset-printable [23]. In particular, the viscosity of the material was adjusted to 40 Pa s, which falls into the range of conventional offset inks.

Offset printing is an especially attractive method among the mass-printing methods for patterning of the source and drain electrodes, due to the comparatively simple and inexpensive printing form fabrication. At the same time it shares the high resolution and layer quality of gravure printing. Taking into account that the layout of the source and drain electrodes largely determines the overall circuit setup and performance, offset printing of this layer allows for quick changes of the circuit layout.

A basic challenge for the circuit fabrication is the morphology of the source/drain electrode structure. The offset printing process in its currently applied manner results in very inhomogeneous layers with an average layer thickness of approximately 600 nm with the observed local layer thickness varying between 50 nm and 3 μm throughout the printed structure [23,24]. The reasons for these specific layer properties as well as strategies to improve them are subject to intensive, ongoing studies. However, functional integrated circuits could be built up on this kind of electrode structure [23].

In addition to the uniformity, the absolute value of the conductivity, which is approximately 13 kΩ/sq. and thereby significantly above the ones typically achieved with PEDOT:PSS (the sheet resistance of spin coated layers can be as low as 2 kΩ/sq. [25,26]), is also affected by this phenomenon. Furthermore, a gate dielectric thickness of several μm is necessary for sufficient insulation of the source/drain level from the gate electrode. Most commonly, a thin dielectric layer is incorporated in organic field-effect transistors with electrodes made of metals like gold by means of e.g. photolithography [27,28]. Clearly, this approach could not be followed here due to the inhomogeneous nature of the source and drain layer.

As the active semiconducting layer we used a THF-formulation of commercially available poly(9,9-dioctyl-fluorene-co-bithiophene) (F8T2) of American Dye Source, which exhibits field effect mobilities of up to 10^{-2} cm^2/V s after high temperature alignment [15] although the limited stability of F8T2 in such devices has been reported [29,30]. The high mobility state of F8T2 was achieved due to a phase transition into a nematic liquid crystalline phase upon heating above 265 °C [15]. However, the integration of such a high temperature alignment within the printing process would be technologically very challenging due to the necessity of using flexible substrates (polyester foil in our case) and the high process speed. Therefore, the mobility of the printed semiconductor is about one order of magnitude smaller compared to the one achieved with high temperature alignment on a glass substrate (see below). We believe that the enhancement of the mobility of printed semiconductors is rather a task of a joint development of material and process.

The viscosity of the semiconductor solution is low (<∼20 mPa s), which is typical for organic semiconductors. On the other hand the semiconductor has the highest requirements in terms of layer quality. Gravure printing is known to handle low viscosity inks and deposit high-quality layers. Therefore, gravure printing is the best suited method for the preparation of the semiconductor.

The semiconductor is applied by means of a carefully adjusted gravure printing process which results in high-quality, patterned layers. The gravure printing form cells had a pyramidal form and a depth of 25 μm. The process parameters such as cell pattern and cell depth of the printing form, shape, angle and pressure of the squeegee and pressure between the printing form and the adjacent cylinder were empirically optimized for an optimum performance of the semiconducting layer in the oFET-configuration.

We have chosen a double layer structure for the gate dielectric, where a low permittivity material (low-k) is in contact with the semiconductive layer and a high permittivity material (high-k) lies on top of the low-k. As previously demonstrated, the incorporation of a low-k layer leads to an enhancement of the field-effect mobility of more than one order of magnitude [27,28].

Our low-k material is a fully hydrogenated linear copolymer of styrene and butadiene [31] with a molecular weight of $M_n = 120{,}000$ and a narrow polydispersity of 1.1. It was synthesized by anionic copolymerization in cyclohexane using butyllithium as an initiator. Hydrogenation was achieved by high pressure (50–250 bar) and platinum on activated carbon as a catalyst. There was substantially no molar mass degradation during the hydrogenation. The glass transition temperature of the resulting copolymer was −60 °C and 138 °C for the soft

and hard phases, respectively. The material displays good solubility in alkane solvents as hexane and heptane.

In the experiment referred to here, we used a solution in hexane, which was deposited by means of gravure printing in a similar process as the semiconductor. Again, the low viscosity of the solution (<~20 mPa s) and the high quality requirements of the semiconductor–dielectric interface have led to the choice of this method. The material exhibited very good film forming in this process, which was proofed by the fact that the gravure printed layers showed similar performance in oFETs compared to spin coated layers.

The high-*k* material was a commercially available, printable $BaTiO_3$-suspension, Luxprint 8153® of DuPont (viscosity 10–20 Pa s) which was thinned with ethanol. The material was applied by means of flexographic printing on top of the low-*k* layer, whereby extremely low pressure between the printing form and the substrate was applied (the so-called "kiss-print"). Both the thinning of the dispersion and the choice of the printing method have turned out to be effective to overcome intrinsic wetting and adhesion problems when printing a high-*k* (i.e. polar) material on top of a low-*k* (i.e. non-polar) material. Especially the application of sufficiently low pressure upon imprint is not possible with the other mass-printing methods. Furthermore, a layer thickness of the high-*k* dielectric sufficient for insulation of the gate electrodes from the source and drain electrodes is most easily achieved with flexographic printing.

The circuits are completed by flexographic printing of the gate electrodes from a printable silver ink of Precisia. Again, the necessity of applying low pressure in order to avoid a destruction of the underlying layers determined the choice of the method. As all underlying layers are naturally patterned due to the additive printing methods used for deposition, formation of the interconnects (vias) between individual transistors is straightforward upon printing of the gate level.

3. Results and discussion

Fig. 2 shows the circuitry used for our ring oscillator and a photographic image of a printed circuit. It consists of seven inverter stages and an additional output buffer stage. Neither level shifters nor any specific circuitry features were incorporated. Each inverter stage consists of a load (L-) transistor with a channel width $W = 6$ mm and a drive (D-) transistor with a channel width $W = 30$ mm. Fig. 3 shows the output characteristics of a typical *D*-transistor. The charge carrier mobility of this device $\mu = 1.3 \times 10^{-3}$ cm^2/V s, determined by standard procedure [32] from the slope of the linear range, the on/off-ratio 320, taken at a drain-source voltage of −60 V and at gate-source voltage of 0 V (off-

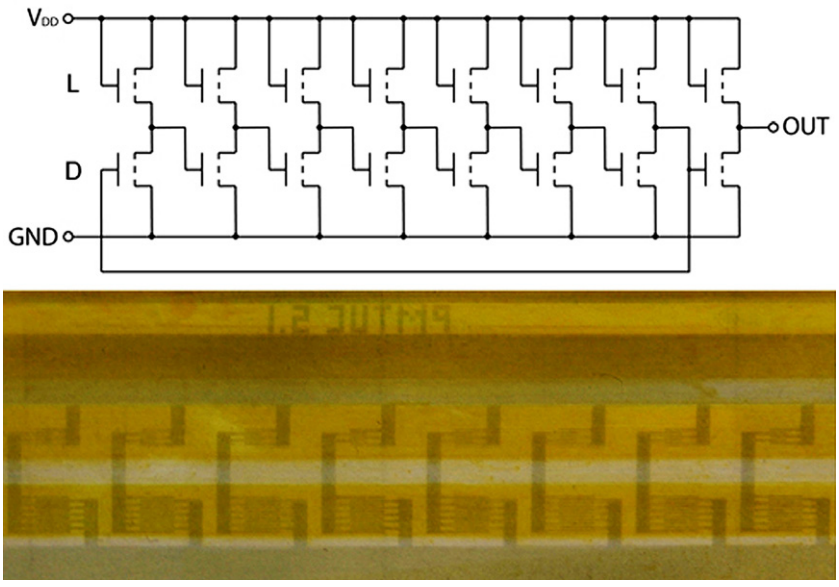


Fig. 2. Circuitry of the seven-stage ring oscillator and photographic image of a fully-printed circuit.

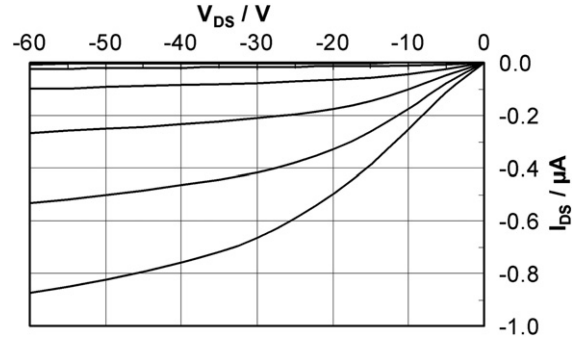


Fig. 3. Output characteristics of a typical D-transistor. The curves are taken at gate-source voltages of $-60, -50, \ldots, 10$ V (bottom to top), respectively.

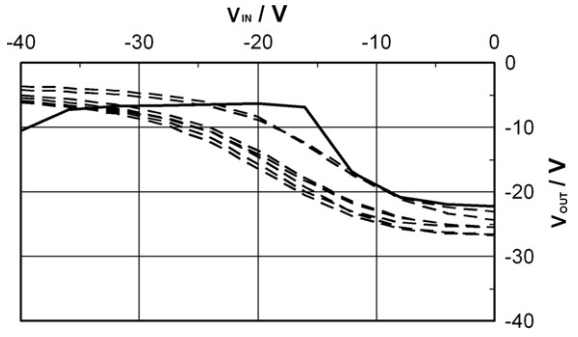


Fig. 4. Static transfer curves of individual inverter stages of a printed circuit (dashed lines) and of seven inverter stages connected in series (solid line).

state) and -60 V (on-state), respectively. For comparison, the mobility $\mu = 4.0 \times 10^{-3}\,\mathrm{cm^2/V\,s}$ and the on/off-ratio 2700 were measured in a typical D-transistor built up on identical source and drain electrode structures by means of spin coating. A detailed study shows that the performance loss appears upon printing of the semiconductor, while no significant changes occur upon printing of the subsequent layers. Obviously, the process parameters for printing (and/or post-treatment) of the semiconductor are not yet fully optimized compared to the spin coating process.

For reasons of the proof of the concept, no systematic studies were carried out so far on how single process parameters of the printing processes for the individual layers influence the layer properties and thereby the performance of the devices. This is mainly due to the large number of process parameters and their complex interactions in printing. Clearly, such studies remain an important experimental task in order to improve the circuit performance.

However, the main challenge turned out to be the uniformity of the transistor properties, which are reflected in the uniformity of the individual inverter stages with respect to each other. In Fig. 4 the transfer characteristics of seven inverter stages of a printed circuit are plotted together with the static transfer characteristics of all stages connected in series. Thereby, the level of uniformity achieved is demonstrated. When a supply voltage $V_{DD} = -40$ V is applied, the ring oscillator starts oscillating. In Fig. 5 the tracking of the output signal at a supply voltage of -40 V is shown. The frequency increases with $|V_{DD}|$ and eventually reaches 3.9 Hz at -80 V, as shown in Fig. 6.

Clearly, this frequency is significantly below those which are expected to be necessary for realistic

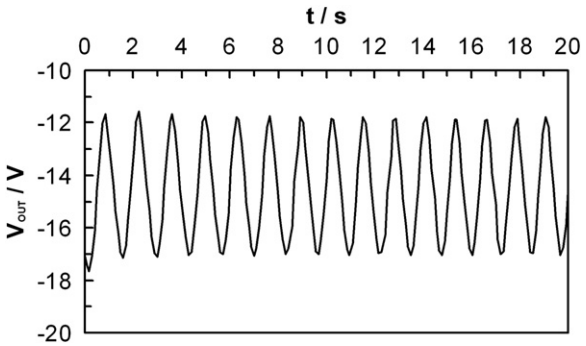


Fig. 5. Dynamic output signal of a printed ring oscillator at a supply voltage $V_{DD} = -40$ V.

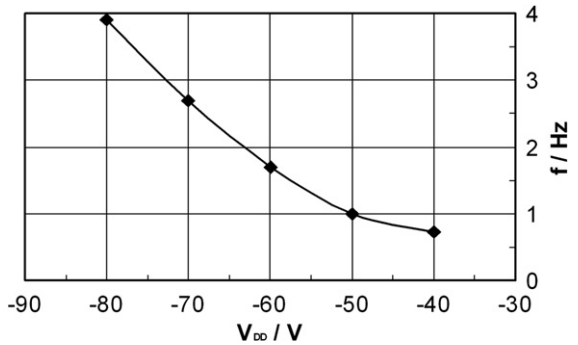


Fig. 6. Oscillation frequency of a printed ring oscillator as a function of the supply voltage.

applications of printed electronics. However, the purpose of our experiment was to demonstrate feasibility of mass-printing technology to fabricate all-printed integrated circuits. We would like to point out, that no process steps that break the continuity and lower the overall speed of the process, e.g. wet chemical developing or lithographic steps,

are involved in the preparation of the circuits presented here and all printing steps were performed at speeds of the order of 1 m/s.

The frequency of the circuits is mainly a function of the channel length, which in turn is determined by the resolution of printing of the source/drain-electrodes, and the charge-carrier mobility, which is a property of the semiconductor/dielectric-interface [2]. We believe that reduction of the critical feature size within the printing process combined with the introduction of higher mobility materials will lead to significantly increased operational frequencies of printed transistors and integrated circuits thereof within the near future.

4. Conclusions

In summary, we have set up a fast, continuous printing process for the fabrication of integrated circuits that consist of several interconnected organic field-effect transistors. We have identified the major challenges that need to be overcome in order to improve the performance of all-printed circuits. In particular, it is highly desirable to enhance the conductivity, uniformity and resolution of the source and drain electrodes. This will in turn facilitate the introduction of single-layer dielectrics and a wider choice of higher-mobility semiconductors, and lead to higher frequency, lower operating voltage, and increased reliability.

Finally, we believe that the demonstration of integrated circuits prepared solely by means of mass-printing technology is an important step towards the development of organic electronics into realistic applications as it paves the way for highly productive fabrication of electronic devices from organic functional materials.

Acknowledgements

We thank D. Zielke for valuable discussions and G. Schlegel, D. Kuehnrich, M. Dinter, K. Reuter, S. Wagner, C. Walther, V. Boerner, S. Grenz, C. Rahnfeld, J. Ahner and T. Szusdziara for technical support.

References

[1] F. Garnier, R. Hajlaoui, A. Yassar, P. Srivastava, Science 265 (1994) 1684.
[2] A.R. Brown, A. Pomp, C.M. Hart, D.M. de Leeuw, Science 270 (1995) 972.
[3] C.J. Drury, C.M.J. Mutsaers, C.M. Hart, M. Matters, D.M. de Leeuw, Appl. Phys. Lett. 73 (1998) 108.
[4] J.A. Rogers, Z. Bao, A. Makhija, P. Braun, Adv. Mater. 11 (1999) 741.
[5] P. Mach, S.J. Rodriguez, R. Nortrup, P. Wiltzius, J.A. Rogers, Appl. Phys. Lett. 78 (2001) 3592.
[6] U. Zschieschang, H. Klauk, M. Halik, G. Schmid, C. Dehm, Adv. Mater. 15 (2003) 1147.
[7] G.B. Blanchet, Y.-L. Loo, J.A. Rogers, F. Gao, C.R. Fincher, Appl. Phys. Lett. 82 (2003) 463.
[8] P.R. Parashkov, E. Becker, S. Hartmann, G. Ginev, D. Schneider, H. Krautwald, T. Dobbertin, D. Metzdorf, F. Brunetti, C. Schildknecht, A. Kammoun, M. Brandes, T. Riedl, H.-H. Johannes, W. Kowalsky, Appl. Phys. Lett. 82 (2003) 4579.
[9] G.H. Gelinck, T.C.T. Geuns, D.M. de Leeuw, Appl. Phys. Lett. 77 (2000) 1487.
[10] W. Fix, A. Ullmann, J. Ficker, W. Clemens, Appl. Phys. Lett. 81 (2002) 1735.
[11] W. Clemens, W. Fix, J. Ficker, A. Knobloch, A. Ullmann, J. Mater. Res. 19 (2004) 1963.
[12] A. Knobloch, A. Manuelli, A. Bernds, W. Clemens, J. Appl. Phys. 96 (2004) 2286.
[13] Y. Wu, Y. Li, B.S. Ong, P. Liu, S. Gardner, B. Chiang, Adv. Mater. 17 (2005) 184.
[14] J.A. Rogers, Z. Bao, V.R. Raju, Appl. Phys. Lett. 72 (1998) 2716.
[15] H. Sirringhaus, T. Kawase, R.H. Friend, T. Shimoda, M. Inbasekaran, W. Wu, E.P. Woo, Science 290 (2000) 2123.
[16] T. Kawase, H. Sirringhaus, R.H. Friend, T. Shimoda, Adv. Mater. 13 (2001) 1601.
[17] N. Stutzmann, R.H. Friend, H. Sirringhaus, Science 299 (2003) 1881.
[18] B.-J. de Gans, P.C. Duineveld, U.S. Schubert, Adv. Mater. 16 (2004) 203, and references therein.
[19] B. Crone, A. Dodabalapur, Y.-Y. Lin, R.W. Filas, Z. Bao, A. Laduca, R. Sarpeshkar, H.E. Katz, W. Li, Nature 403 (2004) 521.
[20] T.W. Kelley, P.F. Baude, C. Gerlach, D.E. Ender, D. Muyres, M.A. Haase, D.E. Vogel, S.D. Theiss, Chem. Mater. 16 (2004) 4413.
[21] H. Kipphan (Ed.), Handbook of Print Media, Springer, Berlin, 2001.
[22] A. Huebler, U. Hahn, W. Beier, N. Lasch, T. Fischer, in: Proceedings of the 2nd International IEEE Conference on Polymers and Adhesives in Microelectronics and Photonics, Zalaegerszeg, Hungary, 2002, p. 172.
[23] D. Zielke, A.C. Hübler, U. Hahn, N. Brandt, M. Bartzsch, U. Fügmann, T. Fischer, Appl. Phys. Lett. 87 (2005) 123508.
[24] N. Brandt, T. Fischer, U. Fügmann, U. Hahn, A. Hübler, D. Zielke, Presented at the International Symposium on Technologies for Polymer Electronics, Rudolstadt, Germany, 2004.
[25] S. Ashizawa, R. Horikawa, H. Okuzaki, Synth. Met. 153 (2005) 5.
[26] S.K.M. Jönsson, J. Birgerson, X. Crispin, G. Greczynski, W. Osikowicz, A.W. Denier van der Gon, W.R. Salaneck, M. Fahlman, Synth. Met. 139 (2003) 1.
[27] J. Veres, S. Ogier, S. Leeming, D. Cupertino, S.M. Khaffaf, G. Lloyd, Proc. SPIE 5217 (2003) 147.

[28] J. Veres, S. Ogier, S. Leeming, D. Cupertino, S.M. Khaffaf, Adv. Func. Mater. 13 (2003) 199.
[29] A. Salleo, R.A. Street, J. Appl. Phys. 94 (2003) 471.
[30] H. Kempa, K. Reuter, M. Bartzsch, U. Hahn, A.C. Huebler, D. Zielke, M. Forster, U. Scherf, in: Proceedings of the 5th International IEEE Conference on Polymers and Adhesives in Microelectronics and Photonics, Wroclaw, Poland, 2005. p. 67.
[31] K. Knoll, US-Pat. 2004/0132943, 2004.
[32] A.R. Brown, C.P. Jarret, D.M. de Leeuw, M. Matters, Synth. Met. 88 (1997) 37.

Available online at www.sciencedirect.com
ScienceDirect
Organic Electronics 8 (2007) 487–497
Organic Electronics
www.elsevier.com/locate/orgel

Conductance switching, hysteresis, and magnetoresistance in organic semiconductors

J.H. Wei [a,*], S.J. Xie [a], L.M. Mei [a], J. Berakdar [b], YiJing Yan [c,*]

[a] School of Physics and Microelectronics, Shandong University, Jinan 250100, China
[b] Max-Planck Institut für Mikrostrukturphysik, 06120 Halle, Germany
[c] Department of Chemistry, Hong Kong University of Science and Technology, Kowloon, Hong Kong, China

Received 5 November 2005; received in revised form 27 January 2007; accepted 28 February 2007
Available online 12 March 2007

Abstract

The controllability of charge transport through an organic molecular spin-valve system is theoretically investigated on the basis of a Su–Schrieffer–Heeger model combined with the non-equilibrium Green's function formalism. We show how the formation of polaron in the organic sub-structure leads to a hysteretic conductance switching, via sweeping either the bias voltage or the electrochemical potential. We further obtain an exponential dependence of the magnetoresistance as a function of the applied bias voltage. The implications of calculated results in relation to experiments and device applications are addressed and commented.
© 2007 Elsevier B.V. All rights reserved.

PACS: 85.75.−d; 73.61.Ph; 71.38.Ht

Keywords: Conductance switching; Hysteresis; Giant magnetoresistance; Organic spintronics

1. Introduction

Due to their compatibility in processing and tunability in electronic properties, π-conjugated organic semiconductors (OSEs) have been utilized broadly for various device applications [1–5]. Recent progress in the field of OSE electronics has revealed a number of technologically important transport characteristics, such as current rectification [6], Coulomb blockade [7], Kondo resonance [8], negative differential resistance (NDR) [9–12], bistable switching [13–19], and giant magnetoresistance [20,21].

An OSE system is characterized by not only its electronic structure but also its strong electron–phonon (e–ph) coupling that induces polarons [22,23]. In view of charging-induced conformational change [14,24], the formation of non-equilibrium polaron should be a reasonable mechanism of the conductance switching and/or NDR in OSE electronics. This idea is first shown theoretically by Galperin et al. [25] with a simplified model, in which the molecular wire consists of a single electronic state coupled with a single Brownian oscillator.

* Corresponding authors.
E-mail addresses: wjh@sdu.edu.cn (J.H. Wei), yyan@ust.hk (Y. Yan).

1566-1199/$ - see front matter © 2007 Elsevier B.V. All rights reserved.
doi:10.1016/j.orgel.2007.03.002

Apparently, the Su–Schrieffer–Heeger (SSH) model [26] renders a more realistic description of an OSE system. It captures the essential characteristic of a conjugated molecule, where the strong e–ph coupling leads it to the polaron charged states and dimerized ground state. Indeed, the SSH model has been remarkably successful in the study of the electronic conductivity and optical phenomena in π-conjugated OSEs. In addition to conducting polymers, the SSH model has also been extended to molecular systems [27,28], carbon nanotubes [29], and DNA molecules [30]. We have recently [31] exploited this model for an OSE system, and demonstrated that a NDR may appear due to the annihilation of a predoped polaron; i.e., an equilibrium charge transfer state that may exist before applying the external bias voltage. The resulting NDR can also be spin-polarization sensitive, leading to a magnetoresistance significantly larger than 100%.

In this work, we elucidate the possibility of a polaron mechanism for the bistable switching and hysteresis in OSE nanostructures, and further for the giant magnetoresistance in OSE spin-valve devices where ferromagnetic metal electrodes are used. More importantly, we highlight that these technologically important properties are likely achievable by a wide range of OSE systems. To do that, moderate/typical values of the SSH parameters will be adopted in this work to avoid the formation of predoped polarons mentioned earlier. Besides the model and its parameters for the OSE spin-valve nanostructure of study, Section 2 presents also the transport theory based on the Keldysh non-equilibrium Green's function (NEGF) formalism [32–34], together with its implementation to the evaluation of current in response to linear sweeping bias voltage. Hysteretic conductance switchings controlled via bias voltage and via an electrochemical means are then numerically investigated in Sections 3 and 4, respectively. The giant magnetoresistance property of OSE spintronic structures is addressed in Section 5. Finally, we conclude in Section 6.

2. Model and theory

2.1. A Su–Schrieffer–Heeger static polaron model

We adopt a non-degenerate SSH Hamiltonian for the isolate OSE system [20,30],

$$H_{\mathrm{OSE}} = \sum_{n,\sigma}\{\epsilon_0 c^+_{n,\sigma}c_{n,\sigma} - [t_0 - (-1)^n t_1 - \alpha_0(u_{n+1} - u_n)] \times (c^+_{n,\sigma}c_{n+1,\sigma} + c^+_{n+1,\sigma}c_{n,\sigma})\} + \frac{K_0}{2}\sum_n (u_{n+1} - u_n)^2. \quad (1)$$

Here, $c^+_{n,\sigma}$ ($c_{n,\sigma}$) denotes the creation (annihilation) operator of an electron at the nth site with spin σ of the OSE system. The e–ph coupling induced on-site lattice displacement parameters $\{u_n\}$ are treated classically and will be determined in a self-consistent manner to be described later (cf. Section 2.2). The input parameters involved in Eq. (1) are the on-site energy ϵ_0, zero-displacement hopping integral t_0, non-degeneracy parameter t_1, electron–phonon coupling α_0, and lattice elastic constant K_0.

For the electrodes, we choose two symmetrical 3d ferromagnetic (FM) transition metals; each of them is described by a one-dimensional tight-binding Hamiltonian with the Stoner-like exchange term [35],

$$H_{\mathrm{FM}} = \sum_{n,\sigma}\{\epsilon_{\mathrm{f}} d^+_{n,\sigma}d_{n,\sigma} + t_{\mathrm{f}}(d^+_{n,\sigma}d_{n+1,\sigma} + d^+_{n+1,\sigma}d_{n,\sigma})\} - \sum_n J_{\mathrm{f}}(d^+_{n,\uparrow}d_{n,\uparrow} - d^+_{n,\downarrow}d_{n,\downarrow}). \quad (2)$$

Here, $d^+_{n,\sigma}$ ($d_{n,\sigma}$) denotes the creation (annihilation) operator of a 3d-electron at the nth site with spin σ of the metal electrode; ϵ_{f} is the on-site energy of a metal atom, t_{f} the nearest neighbor transfer integral, and J_{f} the Stoner-like exchange integral.

The coupling between the OSE and each of the FM electrodes is described by a tight-binding hopping integral,

$$t_{\mathrm{c}} = \beta(t_{\mathrm{f}} + t_0). \quad (3)$$

Here, β is the OSE–FM binding parameter, which for simplicity is set to be spin-independent. However, charge transport can be spin dependent. According to the two-current description, the total current arises from the majority-spin (up-spin) and the minority-spin (down-spin) of the 3d electrons of the FM electrodes [36]. We also neglect the spin-flip processes during the spin-dependent charge transport that takes place between the FM electrodes.

The above simple model for the molecule–metal coupling allows us to focus on the effects of OSE molecular system on the spin-dependent transport.

2.2. Non-equilibrium Green's function formalism

The quantum transport, in terms of the conductance switching, hysteresis and giant magnetoresistance behaviors of the model FM/OSE/FM system, will be calculated by means of the NEGF approach, based on the Keldysh formalism [5,32–34]. To proceed, the infinite FM/OSE/FM system is divided into three distinct regions: The central scattering region (S) that consists of the OSE together with a few metal atoms attached to each of its ends [34], and two semi-infinite FM electrodes (L and R) that serve as charge reservoirs and also set the temperature and electron distribution of the junction in the steady state. As results, the Hamiltonian for the whole system is mapped onto a 3×3 block matrix,

$$H_{\rm total}=\begin{pmatrix} H_{\rm L} & H_{\rm LS} & 0\\ H_{\rm SL} & H_{\rm S} & H_{\rm SR}\\ 0 & H_{\rm RS} & H_{\rm R}\end{pmatrix}, \tag{4}$$

with $H_{\rm L}$, $H_{\rm S}$, and $H_{\rm R}$ being the isolated Hamiltonians for the L-electrode, the central scattering S-region, and the R-electrode, respectively, while $H_{\rm LS}=H_{\rm SL}^{\dagger}$ and $H_{\rm RS}=H_{\rm SR}^{\dagger}$ the couplings between them.

The applied electric potential bias V does not change the electronic structure of L and R leads, but just shifts their energy levels by $eV/2$ and $-eV/2$, respectively. This leads to the electron distribution function $f(E,\mu_\alpha)\equiv[{\rm e}^{(E-\mu_\alpha)/k_{\rm B}T}+1]^{-1}$, where $\mu_{\rm L/R}=\mu_{\rm eq}\pm eV/2$, with $\mu_{\rm eq}=E_{\rm F}$ being the Fermi energy of the FM electrode. In contrast to the electrodes, the effect of applied bias on the S-region is characterized by the electric potential function $\Phi(x)$. With the boundary conditions of $\Phi(x_1)=V/2$ and $\Phi(x_{N_{\rm S}})=-V/2$, it shifts the nth-site energy by $-e\Phi(x_n)$ in the S-region. As it is correlated with the electronic and lattice structures of OSE, $\Phi(x)$ should be evaluated together with the S-region density matrix and lattice distortion in a self-consistent manner, which will be elaborated soon [cf. Eqs. (10)–(12)].

Eliminating the L- and R-electrodes degrees of freedom results in the NEGF of the central S-region [33],

$$G(E)=\frac{1}{E-H_{\rm S}+e\Phi(x)-\sum_{\rm L}(E)-\sum_{\rm R}(E)+{\rm i}0_+}. \tag{5}$$

The effect of L- or R-electrode coupling is incorporated via the self-energy,

$$\sum_{\alpha}(E)=H_{{\rm S}\alpha}\frac{1}{E-H_\alpha+{\rm i}0_+}H_{\alpha{\rm S}};\quad \alpha={\rm L},\ {\rm R}. \tag{6}$$

In particular, $\Gamma_{\rm L/R}(E)\equiv{\rm i}[\sum_{\rm L/R}(E)-\sum_{\rm R/L}^{\dagger}(E)]$ amounts to the electrode coupling-induced broadening function.

The electron transmission probability function reads in terms of the NEGF at a finite bias as [33]

$$T(E,V)={\rm Tr}[\Gamma_{\rm L}(E)G(E)\Gamma_{\rm R}(E)G^{\dagger}(E)]. \tag{7}$$

The electric current can then be evaluated as [33,37,38]

$$I=\frac{2e}{h}\int_{-\infty}^{\infty}T(E,V)[f(E,\mu_{\rm L})-f(E,\mu_{\rm R})]\,{\rm d}E. \tag{8}$$

We shall show later that the above expression remains practically valid in the evaluation of current under the quasi-steady-state voltage sweeping condition; cf. the comments to the end of this subsection.

The NEGF determines also the density of states $D(E)$ and the density matrix ρ in the S-region [34]. They are given, respectively, by

$$D(E)=\frac{\rm i}{2\pi}{\rm Tr}[G(E)-G^{\dagger}(E)], \tag{9}$$

and

$$\rho=\frac{1}{2\pi}\sum_{\alpha={\rm L,R}}\int_{-\infty}^{\infty}f(E,\mu_\alpha)[G(E)\Gamma_\alpha(E)G^{\dagger}(E)]\,{\rm d}E. \tag{10}$$

The number of carrier electrons in the S-region is $N={\rm Tr}(\rho S)$, with S denoting the overlap integral matrix that reduces to the unit matrix if an orthogonal basis set is used.

We are now in the position to complete the self-consistent evaluation of the NEGF. The involving electric potential function $\Phi(x)$ in Eq. (5) is related to the charge density, and the latter depends further on the steady-state lattice distortion at a given finite applied electric potential bias.

Let us start with the Poisson equation that relates $\Phi(x)$ and the on-site charge $\{\rho_{nn}\}$,

$$\nabla^2\Phi(x)=-\sum_n\frac{\rho_{nn}}{\varepsilon_0}\delta(x_n-x). \tag{11}$$

Here, ε_0 denotes the vacuum permittivity, and $x_n=(n-1)a+u_n$, with a being the e–ph coupling-free lattice constant and set to be 0.122 nm. The e–ph coupling-induced on-site lattice displacement is of the boundary conditions of $u_1=u_{N_0}=0$. To solve the Poisson equation we introduce $\Phi(x)=$

$(0.5 - x/L)V + \delta\Phi(x)$, with L denoting the S-region length. $\delta\Phi(x)$ satisfies the same Poisson equation, but with the boundary conditions of $\delta\Phi(x_1) = \delta\Phi(x_{N_0}) = 0$. It can be readily evaluated in terms of the on-site charge $\{\rho_{nn}\}$ via the method of images, in which $\delta\Phi(x)$ is a sum of the individual image contributions from all point charges. To avoid the infinity associated with point charges, we follow the Appendix 3 of Ref. [39] and analytically integrate the usual electrostatic potential within the small area around each point charge separately.

Consider now the lattice distortion, which plays an important role in determining the properties of OSE due to the strong e–ph interactions. For a steady or quasi-steady state, the lattice distortion is assumed to catch up with the variation of charges under a slow voltage sweep condition treated in this work. In this case, the OSE lattice distortion can be determined in terms of the density matrix elements via the Hellman–Feynman variation theorem of $0 = \partial E_S/\partial u_n = \partial \mathrm{Tr}(H_S\rho)/\partial u_n$. It is that

$$2\alpha_0(\rho_{n,n-1} - \rho_{n+1,n}) + K_0(2u_n - u_{n-1} - u_{n+1}) = 0. \tag{12}$$

Eqs. (10)–(12) constitute a set of coupled equations for solving ρ, $\Phi(x)$ and $\{u_n\}$ in a self-consistent manner by iteration. The converged result in the electric potential $\Phi(x)$ is then used to determine the NEGF of Eq. (5), and then the I–V characteristics of Eq. (8). The most time consuming part of the aforementioned self-consistent evaluation is Eq. (10). The involving integrand is non-zero over a broad energy range and often has sharp structures that makes Eq. (10) numerically challenging. To facilitate this problem, let

$$\rho \equiv \rho_{\mathrm{eq}} + \delta\rho, \tag{13}$$

where

$$\rho_{\mathrm{eq}} = \frac{1}{2\pi}\sum_{\alpha=\mathrm{L,R}}\int_{-\infty}^{\infty} f(E,\mu_{\mathrm{eq}})[G_{\mathrm{eq}}(E)\Gamma_\alpha(E)G_{\mathrm{eq}}^\dagger(E)]\,\mathrm{d}E \tag{14}$$

is the equilibrium density matrix, and $\delta\rho$ the non-equilibrium correction. The evaluation of ρ_{eq} requires a broad energy range and couples only with Eq. (12) as $V = 0$ is implied. The involving integration will be tackled by taking the advantage of the contour integration technique [34,40]. On the other hand, the non-equilibrium correction $\delta\rho$ involves the self-consistent determination, together with Eqs. (11) and (12). It will be evaluated directly, as the integration is now required only for a limited energy range, where the integrands in Eqs. (10) and (14) differ significantly. This is the same situation as the evaluation of current [Eq. (8)], and can thus be carried out with a fine grid. Note that ρ_{eq} is naturally real but $\delta\rho$ may not, unless a real basis set functions is employed. This is the case of this work, and the resulting ρ does assume a real matrix.

To conclude this subsection, let us comment on the quasi-steady-state condition that will be applied in this work for the evaluation of I–V characteristics subject to a sweeping voltage of $V(t) = V_0 \pm V't$. Here, $V_0 = 0$ or $V_{\max}$ for the sweeping up (+) or down (−) direction, respectively; $V' > 0$ denotes the constant rate of bias sweeping, which is typically 0.01–0.1 V/s in experiments. In our calculations of the quasi-steady-state current of interest, we set $V' = 0.1$ V/s. Note that all experimental observations of the correlated electron and lattice degrees of freedom on the OSE are functionals of density matrix ρ. As the bias sweeping is linear, one can map the time evolution of density matrix onto the bias sweeping one, $\rho(t) \to \rho(V)$. Starting from $\rho(t = 0)$, the density matrix evolution is then evaluated via $\rho(t + \Delta t) = \rho(t) + \langle\Delta\rho(t)\rangle_T$, where the second term denotes the time average of $\Delta\rho(t)$ over the range of $[t,t + T]$. with T being the measurement duration (set to be $T = 1$ s) under the quasi-steady-state condition. The corresponding $I(t) \to I(V)$ in each of the measurement time interval is then formally the same as Eq. (8).

2.3. Model parameters

Reasonable values for the model parameters must be determined from other sources, such as the band structure calculations and/or experimental current–voltage (I–V) characteristics. In this study, the FM electrodes are chosen to be cobalt metal. With its experimental 3d-band structure and Fermi energy of $E_F = -4.9$ eV [21,41], the tight-binding parameters for the Co metal in Eq. (2) are determined as $t_f = 1.5$ eV, $J_f = 1.45$ eV, and $\epsilon_f = -6.5$ eV. The parameters of the OSE in Eq. (1) are chosen as $\epsilon_0 = -5.5$ eV, $t_0 = 2.5$ eV, $t_1 = 0.04$ eV, $\alpha_0 = 5.0$ eV/Å, and $K_0 = 21.0$ eV/Å^2. These are the modified values from those of a typical conducting polymer, but lead to a relatively large band gap, which is about 2.8 eV for the OSE length of $N_0 = 10$ sites considered in this work. In a realistic OSE molecule, the on-site energy ϵ_0 can

be site-dependent and also can be adjusted by applying a gate voltage [4]. The OSE–Co metal binding parameter β affects the magnitude of current sensitively, but it is hardly controlled due to the weak interaction. In the calculations, one can adjust it so that the calculated I–V curve is of about the same amplitude of the measured one. We find that choosing $\beta = 0.25$ for the conductance switching via applied voltage sweep and $\beta = 0.5$ for that via electrochemical potential sweep will produce the current in the magnitude of nA for some nanosize molecules reported experimentally [13–19].

For a self-consistent evaluation of quantum transport based on the NEGF formalism, the central scattering S-region is chosen such that its Green's function can properly represent the bulk property at the boundary. For the coupling parameters given above, it is sufficient to have the S-region a total of $20 + 10 + 20$ sites; i.e., to include 20 Co electrode atoms to each end of the model OSE of length $N_0 = 10$. For the OSE–Co binding parameter used in this work, it is found that the OSE subsegment is charge neutral in the absence of applied bias ($V = 0$). Changing the relative energy levels of OSE with respect to electrodes may lead to intra-regional charge transfer, forming a preexisting (charged) polaron state in the OSE before applying bias voltage [31].

Fig. 1 depicts the band structures of the OSE and the Co metal electrodes at a low temperature ($T = 11$ K). This figure summarizes the model parameters adopted in this work (except for β which in this figure is set to zero). For the OSE, the evaluated band gap is about 2.8 eV, which well reproduces the band diagram of the organic spin-valve system in a recent experiment [21]. For the Co electrodes, our calculation is consistent with the real material [41], showing a completely filled 3d band and a half-filled 3d band for the majority-spin (up-spin) and the minority-spin (down-spin) electrons, respectively.

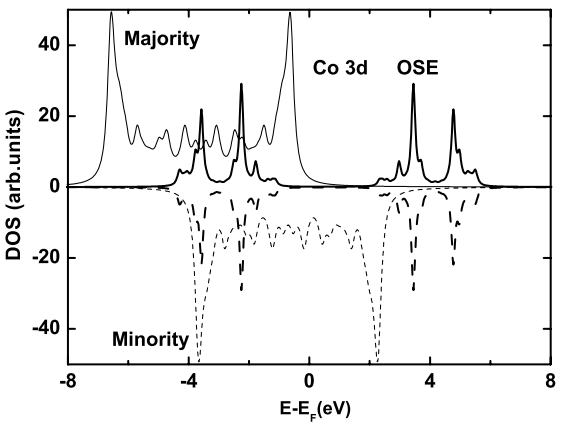


Fig. 1. Density of states of Co 3d band and OSE structure at 11 K. The solid (dashed) lines correspond to majority (minority) electronic bands. The thick (thin) curves are for OSE (Co), with the phenomenological Lorentzian width of 0.15 eV being included.

Quantitative simulations of experiment results [21,42–44] may need to incorporate the spin dynamics, such as spin-flip, diffusion and accumulation, which are however not included in this work. Despite of its simplicity, we shall show soon that the present model possesses some interesting properties that can highlight the important transport mechanism in relation to experiments.

3. Hysteretic conductance switching via bias voltage sweep

In this section we report the hysteretic bistable switching I–V behavior of the model Co/OSE/Co structure. In contact with experimental reality [13,18], the bias sweep rate in our calculations is fixed at a representing value of 0.1 V/s, at which the quasi-steady-state condition is reasonably satisfied.

There are two distinct transport measurement configurations, parallel (P) and antiparallel (AP), with respect to the relative magnetization orientation of two FM electrodes. Generally, in the two-current model, both the majority–majority and minority–minority (or majority–minority and minority–majority) transports are permitted in the P (or AP) configuration. However, for the cobalt electrodes in the present work, the full-filled up-spin electrons cannot transport in P-configuration under a positive bias voltage $V > 0$ and the charge carriers are only the half-filled down-spin electrons. Contrary, the charge carriers in AP-configuration under $V > 0$ are only the up-spin electrons, driven from the full-filled majority-spin band of L-electrode to the half-filled minority-spin band of R-electrode of opposite magnetization orientation.

Fig. 2 depicts the resulting hysteretic I–V characteristic in P-configuration. The bias sweep directions are indicated with the arrows. The OSE nanostructure is shown to have an insulating state and two conducting states in the indicated sweeping bias range. These conducting states are switched on (off), respectively, at 1.5 ± 0.2 V (0.75 ± 0.2 V)

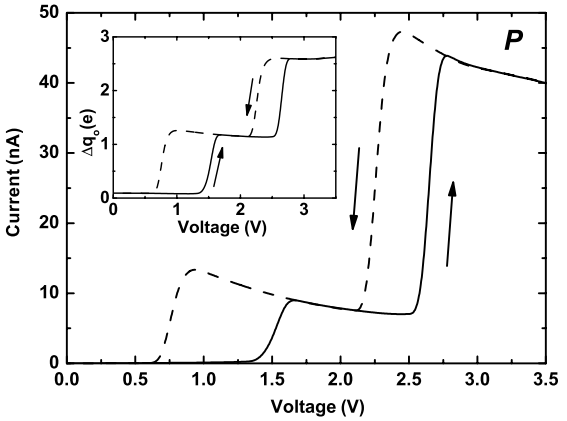


Fig. 2. The hysteretic current as the function of sweeping bias potential for the model OSE in junction with Co electrodes in the parallel configuration. The linear voltage sweep rate is at 0.1 V/s. The inset is the bias voltage-induced charge variation in the OSE substructure. The OSE–Co metal binding parameter $\beta = 0.25$.

and 2.6 ± 0.1 V (2.1 ± 0.1 V) in the sweep up (down) direction. The voltage-triggered two-step hysteretic conductance switching has been observed experimentally in some molecular nanojunction systems [18], often associating with voltage-triggered molecular confirmation change. On the other hand, that observed in Fig. 2, according to the e–ph coupling Hamiltonian used here (cf. Section 2), can only be of polaron in nature. The inset in Fig. 2 shows the sweeping bias-induced charge modification Δq_0 within the OSE sub-structure. The synchronization between the Δq_0–V and I–V curves demonstrates clearly that the two voltage-triggered conducting states have $1.15e$ and $1.44e$ charges, respectively. These are negatively charged polaron states, with the clear evidence of the e–ph coupling induced lattice distortion being presented soon (cf. Fig. 3).

To further elaborate what happens to the conductance bistability of the OSE nanostructure, Fig. 3 depicts the transmission function and lattice distortion for the bistable states, exemplified with the P-configuration at $V = 1$ V (cf. Fig. 2). The resulting window between μ_L and μ_R for the electric transmission $T(E)$, as indicated in Fig. 3a, clearly distinguishes between the conducting state (solid curve) and the insulation state (dash curve). Note that the lattice distortions in Fig. 3b are reported in terms of the e–ph coupling induced bond length variation $y_n = u_{n+1} - u_n$ between nearest neighbors. The dashed curve there for the insulating state is effectively the same as the equilibrium ($V = 0$)

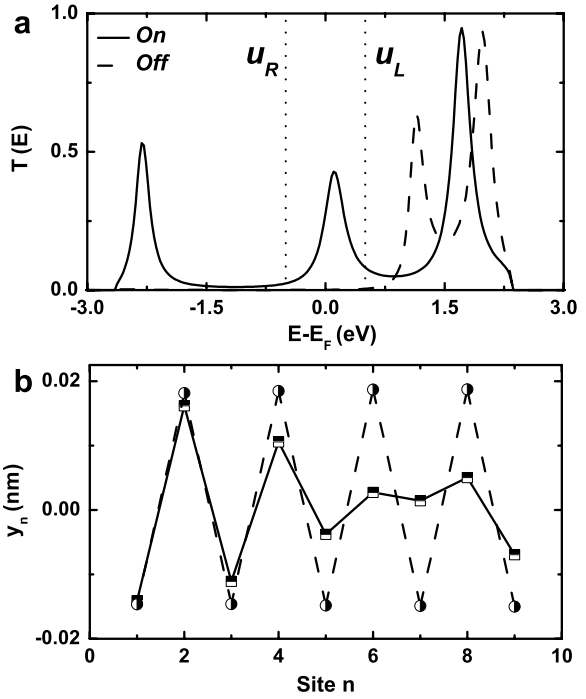


Fig. 3. Bistable switched-on (solid-curves) and switched-off (dashed-curves) states for the P-configuration at bias voltage $V = 1.0$ V. (a) Transmission coefficient of down spin electrons. The vertical dot lines indicate the window between μ_L and μ_R for the charge transmission. (b) Lattice distortion $y_n \equiv u_{n+1} - u_n$ of the OSE substructure.

lattice distortion. In contrast, the solid curve in Fig. 3 demonstrates that a charged polaron state is formed in the conducting state toward the right-side of the OSE-substructure due to the external bias-induced spatial symmetry broken.

The polaron mechanism for the observed hysteretic conduction switching behavior in Fig. 2 can now be summarized as follows. In the equilibrium state ($V = 0$), the OSE substructure is charge neutral, with its lowest-unoccupied and highest-occupied molecular orbital (LUMO and HOMO) electronic wave functions delocalized over the entire S-region. The chemical potentials of electrodes are the same as the Fermi energy, $\mu_L = \mu_R = E_F$, locating in between the LUMO and HOMO levels of the OSE; no current is observed and the OSE is in an insulating state. Applying a positive bias $V > 0$, which elevates $\mu_L = E_F + eV/2$ and depresses $\mu_R = E_F - eV/2$, drives electron transport from L-electrode to R-electrode through the unoccupied levels of OSE substructure. Since the two bistable conductance states in Fig. 2 are of the same physical origin, let us focus on the first one for illustration.

As the sweep-up voltage approaches to the vicinity of the LUMO level, electron starts to migrate into the OSE, followed by the e–ph coupling-induced reorganization that leads to the formation of polaron. In other words, $V_{on} = 2(E_{LUMO} - E_F)/e$ defines the switch-on voltage of the first conducting state. However, as the OSE gets charged, the e–ph coupling-induced reorganization process occurs, forming a polaronic gap state that serves as the first conducting state in Fig. 2. The fact that $E_{polaron} < E_{LUMO}$ due to the reorganization accounts therefore for the observed hysteresis, since $V_{off} = 2(E_{polaron} - E_F)/e$ is the switch-off voltage in the down-sweep direction. In the case of study here, $V_{on} \approx 1.5$ V and $V_{off} \approx 0.75$ V (cf. Fig. 2). The reorganization energy of the negatively charged polaron gap state can be obtained as $E_{LUMO} - E_{polaron} = e(V_{on} - V_{off})/2 \approx 0.37$ eV.

Fig. 4 depicts the hysteretic I–V characteristics and the corresponding charge modifications for the AP-configuration of the electrode magnetization directions. Similar to the P-configuration, the two-step hysteretic conductance switching behavior appears also here. This observation indicates that the hysteresis itself is originated from the OSE due to the polaron formation, regardless the contact is magnetic and nonmagnetic in this aspect. However, in the present Co/OSE/Co model study, the hysteresis curves in the AP-configuration are narrower than those in the P-configuration. This difference gives us an additional handle by using a magnetic contact on the conductance control since one can alter from the P- to the AP-configuration of magnetization by applying an external magnetic field, especially when the electrode is made of soft magnetic material.

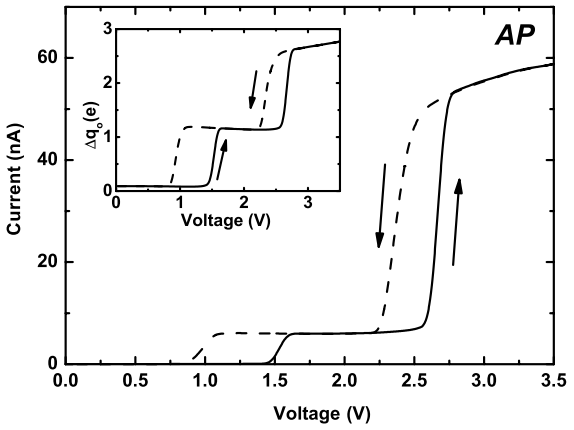


Fig. 4. Same as Fig. 2 but for the antiparallel configuration of the Co electrodes.

4. Hysteretic conductance switching via electrochemical potential sweep

We now turn to another type of conductance switching, controlled by sweeping the Fermi energy [or ϵ_f effectively in Eq. (2)] of both electrodes simultaneously via an electrochemical means, or equivalently sweeping the gate voltage via an microelectronic means that adjusts the on-site energy of the OSE. Here, the bias voltage is kept fixed at a small value to open a transmission window between μ_L and μ_R. For instance, in the experiment of He et al. [18], the current through Au–polyaniline–Au nanoelectronic junctions was measured under a linear sweep of the electrochemical potential at a fixed bias voltage of 20 mV. The fast conductance switching behaviors of the electrochemical system is closely related to chemical and biosensor applications [18,45], while the gate voltage modulation is of great importance for the organic transistors and memories [16,46]. They share the same mechanism; i.e. the control of the polaron (reduced/oxidized) state of the molecule by electrochemical potential or gate voltage, and can therefore be qualitatively illustrated with the same model. As discussed earlier, the polaron formation is responsible to the conductance switching. It arises from the coupling between the electronic states of the OSE near the LUMO energy and that of the metal leads near μ_α ($\alpha = L, R$). When μ_α approaches to the polaron energy level (which is lower than the LUMO of the ground state) an abrupt change of current occurs.

In the following calculations, we fix the electrochemical potential sweeping rate at 0.1 eV/s that supports the quasi-steady-state condition. As described to the end of Section 2.2, Eq. (8) together with Eqs. (10)–(12) are used again for the evaluation of the quasi-steady-state current as the time-averaged one in the interval of every second.

Fig. 5 shows the dependence of the charge transport current on a sweeping of the electrochemical potential E_P, in terms of its difference from the initial Fermi level E_F (=4.9 eV) of the metal leads in the P-configuration of electrodes. The bias voltage between the electrodes is kept at a constant value of 20 mV. The OSE–Co metal binding parameter is $\beta = 0.25$ in Fig. 5a and $\beta = 0.5$ in Fig. 5b, respectively. While the value of β affects the magnitude of

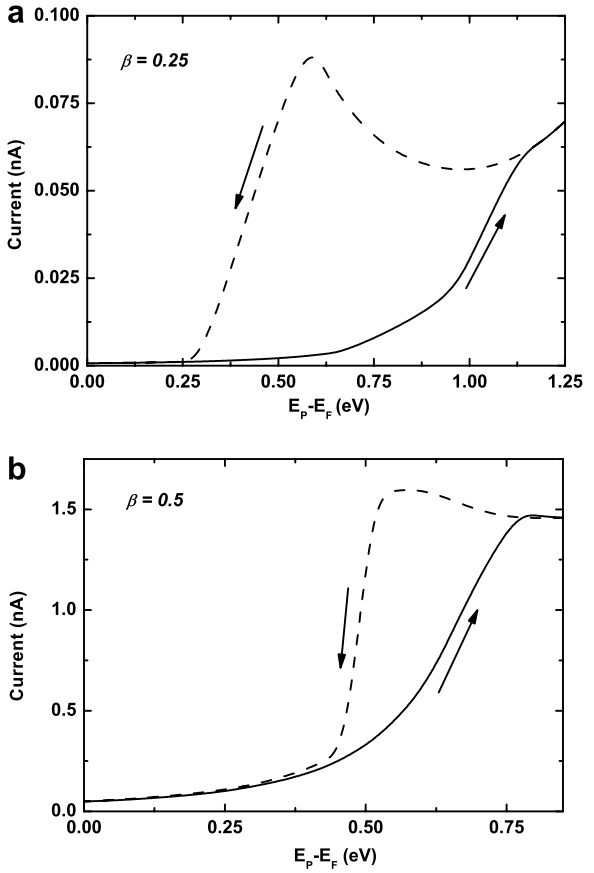


Fig. 5. The hysteretic current as the function of sweeping electrochemical potential for the model OSE in junction with Co electrodes in the parallel configuration, at the fixed bias voltage of $V = 20$ mV. The OSE–Co binding parameter: (a) $\beta = 0.25$ and (b) $\beta = 0.5$, respectively. The initial Fermi level $E_F = 4.9$ eV.

current, the hysteretic behavior of conductance switching is shown to be an intrinsic character of the OSE, regardless the details of OSE–electrode coupling. Making in contact with the experimental output of current, which is of nA in magnitude for a nanosized molecule [16,18], $\beta = 0.5$ is favored for the calculations of the potential-dependent conductance switching behavior.

As shown in Fig. 5b, enhancing the potential leads to a rapid increase of the current during $E_P - E_F \sim 0.5$ eV and 0.75 eV, as the OSE switches from the insulating to the conducting state. The hysteresis behavior here is attributed to the formation of a *bipolaron* state that localizes two electrons in the OSE region. The formation of a bipolaron (not depicted here) is further confirmed with various OSE chain lengths of $N_0 = 10$–40.

The electrochemical potential-dependent charge transport behavior is similar to its bias voltage-dependent counterpart. In both cases, the same physical mechanism; i.e., the polaron-assisted charge transport is operational. A similar phenomenon is also found for the AP-configuration of electrodes.

The potential dependent spin-polarized charge transport through OSE has been studied theoretically by Xie et al. [35] in the context of the ground-state properties of ferromagnetic metal/conjugated polymer interface. The conclusions there are that electrons can transfer to the polymer and form bipolarons from the magnetic layer through an interfacial coupling by adjusting the relative chemical potentials of the contact and the polymer. This conjecture is confirmed by the present calculations.

5. Magnetoresistance effects

Now we address the magnetoresistance property of the model Co/OSE/Co spin-valve system, measured as

$$\mathrm{MR} = \frac{R_{\mathrm{AP}} - R_{\mathrm{P}}}{R_{\mathrm{AP}}}. \tag{15}$$

Here, R_{AP} (R_{P}) denotes the electric resistance with the antiparrellel (parallel) magnetization orientation of two FM electrodes. To study that, we turn on the conductance of OSE by choosing $E_P = E_F + 0.8$ eV (cf. Fig. 5), and calculate the steady-state currents [Eq. (8) with Eqs. (10)–(12)]. The resulting I–V characteristics of the model Co/OSE/Co spin-valve device in the conducting state for both the P- and AP-configurations of electrodes are shown in Fig. 6, and the corresponding MR behavior in the inset. The I–V characteristics for the P-configuration exhibits roughly a linear behavior (with $R_P \approx 17$ MΩ) and can be considered as a metallic phase. In contrast, for the AP-configuration the current increases much slower and is non-linear as the bias voltage increases. The resulting MR shown in the inset of Fig. 6 decays nearly exponentially as the applied bias voltage increases from $V = 0$ where MR ≈ 100% to $V = 0.5$ V where MR = 60%. The relatively large MR here in comparing with the typical experimental values may partially be attributed to the fact that our model system does not include spin-flip processes. As shown in Fig. 6, R_P is almost constant for the range of voltage reported here; thus, the bias-dependence of MR is governed by the R_{AP} in the AP-configuration, where the charge

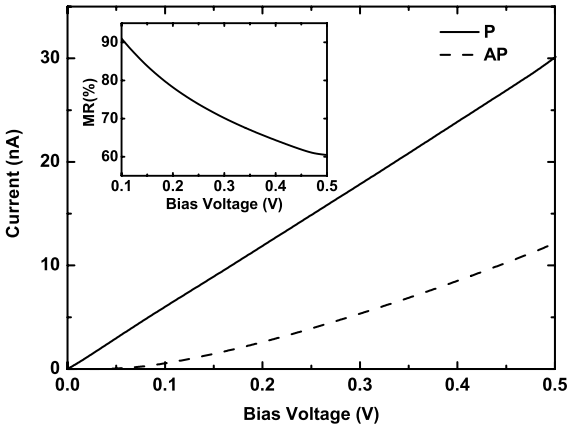


Fig. 6. The I–V characteristic of the OSE spintronics at the conducting state, with the electrochemical potential of $E_P = E_F + 0.8$ eV, in the parallel (solid curve) and antiparallel (dashed curve) configurations. The inset is the MR as the function of bias voltage.

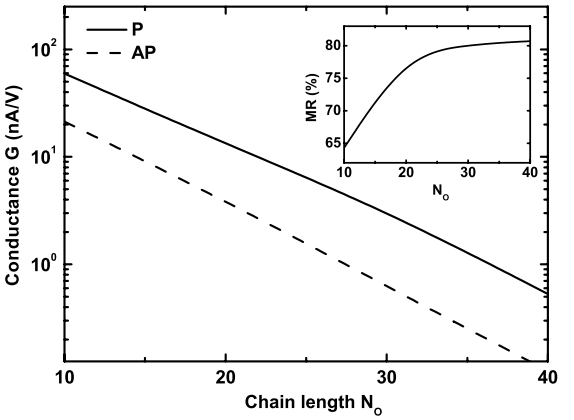


Fig. 7. The length dependence of the conductance in the parallel (solid curve) and antiparallel (dashed curve) configurations, at the bias voltage of $V = 0.4$ V. The inset is the corresponding length dependence of the MR.

carriers in $V > 0$ are the up-spin electrons driven from the full-filled (majority) band of the L-electrode to the half-filled (minority) band of the R-electrode (cf. Fig. 1). As the up-spin electrons traverse the polaron level of the OSE barrier, the electric resistance R_{AP} decreases progressively as the bias voltage increases, resulting in the MR of an appearance of exponential decay.

We now turn to the effect of OSE length on the transport, which has been considered so far only with the fixed value of $N_0 = 10$. The experimental conductance often decreases exponentially as the length of the molecular chain increases [47]. The length-dependent conductance can be investigated theoretically with the help of the equilibrium Green's function formalism [48], and the exponential length dependence of the conductance characterizes the coherent transport [49]. Fig. 7 depicts our theoretical results using the NEGF formalism at the bias voltage $V = 0.4$ V. The evaluated conductances do show near exponential dependences, for both the P- and the AP-configuration. The latter decays faster, leading to the non-uniform OSE-length dependence of MR, as shown in the inset of Fig. 7.

6. Summary and concluding remarks

In summary, we have investigated the spin-dependent charge transport in organic spintronics devices, on the basis of the SSH model combined with the NEGF formalism. We have demonstrated the polaron mechanism for the conductance switching, which can be controlled either by an appropriate bias voltage (Section 3) or by changing the electrode electrochemical potential (Section 4). Despite of its dependence on the electrode property, the conductance switching is generally a property of nanosize organic semiconductors. To have a one- or two-step conductance switching, it is not necessary for the lead to be magnetic. It is believed that the two-step conductance switching can be observed even in some nanostructures with nonmagnetic or paramagnetic electrodes. However, using magnetic electrodes does offer an additional handle on the conductance control (see the discussion to the end of Section 3); thus it has potential applications in organic electronics. We have also studied the behavior of magnetoresistance (Section 5). The calculated magnetoresistance shows an exponential decay as the applied bias voltage increases in the $V > 0$ region. The dependence of the magnetoresistance on the length of molecular junction is also addressed.

It is worth to mention here that a decay behavior of MR has been reported experimentally in an LSMO/OSE(Alq_3)/Co spin-valve device, where the MR has a maximal value at $V \approx 0$ and decreases exponentially as the applied voltage increases [21]. Similar decay behavior is also observed for OSEs with magnetic tunnel junctions with LSMO and Co or CoFe electrodes [50,51]. These experiments are for layer devices with the OSE thicknesses that may lead to the spin-dependent transport of diffusive. The spin diffusion can be incorporated

phenomenologically into the present model to account for the relatively fast decay behavior observed experimentally. It is however beyond the scope of this paper and will be considered elsewhere.

The present calculations are done for the steady or quasi-steady state electric transport. The dynamical polaron effects that are not considered in this work may be importance for the transport in organic spintronics, especially in the presence of a time-dependent external field. Some theoretical investigations have been devoted to this issue. The method used there is the wave-packet evolution approach [52] or non-adiabatic time-dependent Schrödinger equation method [53]. The resulting transport mechanism depends rather sensitively on the time scale of the electronic motion than that of the lattice distortion. Increasing the lattice vibrational frequency, the transport can change from electron-like to polaron-like behavior. The strong lattice fluctuation may also lead to the polaron transport mechanism even in the low phonon-frequency regime [52]. Nevertheless, the polaron mechanism studied in this work for the hysteretic conductance switching and giant magnetoresistance is expected to remain at least qualitatively valid.

Acknowledgement

Support from the National Natural Science Foundation of China (Nos. 10474056 and 10234010) and the Research Grants Council of the Hong Kong Government (No. 605105) is gratefully acknowledged.

References

[1] R. Farchioni, G. Grosso, Organic Electronic Materials, Springer Press, Berlin, 2001.
[2] R.H. Friend, R.W. Gymer, A.B. Holmes, J.H. Burroughes, R.N. Marks, C. Taliani, D.D.C. Bradley, D.A.D. Santos, J.L. Brédas, M. Lögdlund, W.R. Salaneck, Nature 397 (1999) 121.
[3] D. Voss, Nature 407 (2000) 442.
[4] S. Datta, Nanotechnology 15 (2004) S433.
[5] A.R. Rochal, V.M. García-Suárez, S.W. Bailey, C.J. Lambert, J. Ferrer, S. Sanvito, Nat. Mater. 4 (2005) 335.
[6] R.M. Metzger, J. Mater. Chem. 10 (2000) 55.
[7] R.P. Andres, T. Bein, M. Dorogi, S. Feng, J.I. Henderson, C.P. Kubiak, W. Mahoney, R.G. Osifchin, R. Reifenberger, Science 272 (1996) 1323.
[8] W. Liang, M.P. Shores, M. Bockrath, J.R. Long, H. Park, Nature 417 (2002) 725.
[9] I. Kratochvilova, M. Kocirik, A. Zambova, J. Mbindyo, T.E. Malloukc, T.S. Mayer, J. Mater. Chem. 12 (2002) 2927.
[10] K. Walzer, E. Marx, N.C. Greenham, R.J. Less, P.R. Raithby, K. Stokbro, J. Am. Chem. Soc. 126 (2004) 1229.
[11] A.M. Rawlett, T.J. Hopson, I. Amlani, R. Zhang, J. Tresek, L.A. Nagahara, R.K. Tsui, H. Goronkin, Nanotechnology 14 (2003) 377.
[12] N.P. Guisinger, M.E. Greene, R. Basu, A.S. Baluch, M.C. Hersam, Nano Lett. 4 (2004) 55.
[13] C.P. Collier, G. Mattersteig, E.W. Wong, Y. Luo, K. Beverly, J. Sampaio, F.M. Raymo, J.F. Stoddart, J.R. Heath, Science 289 (2000) 1172.
[14] Z.J. Donhauser, B.A. Mantooth, K.F. Kelly, L.A. Bumm, J.D. Monnell, J.J. Stapleton, D.W. Price Jr., A.M. Rawlett, D.L. Allara, J.M. Tour, P.S. Weiss, Science 292 (2001) 2303.
[15] M.A. Reed, J. Chen, A.M. Rawlett, D.W. Price, J.M. Tour, Appl. Phys. Lett. 78 (2001) 3735.
[16] C. Li, W. Fan, B. Lei, D. Zhang, S. Han, T. Tang, X. Liu, Z. Liu, S. Asano, M. Meyyappan, J. Han, C. Zhou, Appl. Phys. Lett. 84 (2004) 1949.
[17] F. Chen, J. He, C. Nuckolls, T. Roberts, J.E. Klare, S. Lindsay, Nano Lett. 5 (2005) 503.
[18] H.X. He, J.H. Zhu, N.J. Tao, J. Am. Chem. Soc. 123 (2001) 7730.
[19] A.S. Blum, J.G. Kushmerick, D.P. Long, C.H. Patterson, J.C. Yang, J.C. Henderson, Y.X. Yao, J.M. Tour, R. Shashidhar, B.R. Ratna, Nat. Mater. 4 (2005) 167.
[20] V. Dediu, M. Murgia, F.C. Matacotta, C. Taliani, S. Barbanera, Solid State Commun. 122 (2002) 181.
[21] Z.H. Xiong, D. Wu, Z.V. Vardeny, J. Shi, Nature 427 (2004) 821.
[22] T. Holstein, Ann. Phys. 8 (1959) 325.
[23] T. Holstein, Ann. Phys. 8 (1959) 343.
[24] J.M. Seminario, A.G. Zacarias, J.M. Tour, J. Am. Chem. Soc. 122 (2000) 3015.
[25] M. Galperin, M.A. Ratner, A. Nitzan, Nano Lett. 5 (2005) 125.
[26] W.P. Su, J.R. Schrieffer, A.J. Heeger, Phys. Rev. B 22 (1980) 2099.
[27] H.J. Torii, J. Phys. Chem. A 104 (2000) 413.
[28] H. Ness, S.A. Shevlin, A.J. Fisher, Phys. Rev. B 63 (2001) 125422.
[29] J.H. Wei, S.J. Xie, S.G. Wang, M.L. Mei, Phys. Lett. A 292 (2001) 207.
[30] E.M. Conwell, S.V. Rakhmanova, Proc. Natl. Acad. Sci. USA 97 (2000) 4556.
[31] J.H. Wei, S.J. Xie, L.M. Mei, J. Berakdar, Y.J. Yan, New J. Phys. 8 (2006) 82.
[32] L.V. Keldysh, Zh. Eksp. Teor. Fiz. 47 (1964) 1515 [Sov. Phys. JETP 20 (1965) 1018].
[33] S. Datta, Electronic Transport in Mesoscopic Systems, Oxford University Press, New York, 1995.
[34] M. Brandbyge, J.L. Mozos, P. Ordejón, J. Taylor, K. Stokbro, Phys. Rev. B 65 (2002) 165401.
[35] S.J. Xie, K.H. Ahn, D.L. Smith, A.R. Bishop, A. Saxena, Phy. Rev. B 67 (2003) 125202.
[36] A. Fert, J. Phys. C: Solid State Phys. 2 (1969) 1784.
[37] R. Landauer, IBM J. Res. Dev. 1 (1957) 223.
[38] R. Landauer, Philos. Mag. 21 (1970) 863.
[39] M.J. McLennan, Y. Lee, S. Datta, Phys. Rev. B 43 (1991) 13846.
[40] A.R. Williams, P.J. Feilbelman, N.D. Lang, Phys. Rev. B 26 (1982) 5433.

[41] D.A. Papaconstantopoulos, Handbook of the Band Structure of Elemental Solids, Plenum Press, New York, 1986.
[42] Z.G. Yu, M.A. Berding, S. Krishnamurthy, Phys. Rev. B 71 (2005) 060408(R).
[43] P.P. Ruden, D.L. Smith, J. Appl. Phys. 95 (2004) 4898.
[44] Z.G. Yu, M. Flatté, Phys. Rev. B 66 (2002) 201202(R).
[45] A.O. Solak, L.R. Eichorst, W.J. Clark, R.L. McCreery, Anal. Chem. 75 (2003) 296–305.
[46] B.Q. Xu, X.Y. Xiao, X.M. Yang, L. Zang, N.J. Tao, J. Am. Chem. Soc. 127 (2005) 2386.
[47] S. Wakamatsu, S. Fujii, U. Akiba, M. Fujihira, Ultramicroscopy 97 (2003) 19.
[48] Y. Asaiand, H. Fukuyama, Phys. Rev. B 72 (2005) 085431.
[49] Y.J. Yan, H.Y. Zhang, J. Theor. Comput. Chem. 1 (2002) 225.
[50] J.M. De Teresa, A. Barthélémy, A. Fert, J.P. Contour, R. Lyonnet, F. Montaigne, P. Seneor, A. Vaurès, Phys. Rev. Lett. 82 (1999) 4288.
[51] J. Hayakawa, K. Ito, S. Kokado, M. Ichimura, A. Sakuma, M. Sugiyama, H. Asano, M. Matsui, J. Appl. Phys. 91 (2002) 8792.
[52] Z.G. Yu, D.L. Smith, A. Saxena, A.R. Bishop, Phys. Rev. B 59 (1999) 16001.
[53] C.Q. Wu, Y. Qiu, Z. An, K. Nasu, Phys. Rev. B 68 (2003) 125416.

Available online at www.sciencedirect.com
ScienceDirect
Organic Electronics 8 (2007) 498–504
Organic Electronics
www.elsevier.com/locate/orgel

Electronic, morphological and transport properties of 6,13-pentacenequinone thin films: Theory and experiments

P. Parisse *, S. Picozzi, L. Ottaviano

CNR-INFM and Dipartimento di Fisica, Università degli Studi dell'Aquila, I–67010 Coppito, L'Aquila, Italy

Received 9 January 2007; received in revised form 3 March 2007; accepted 7 March 2007
Available online 23 March 2007

Abstract

We investigated the electronic, morphological and transport properties of 6,13-pentacenequinone thin films grown by vacuum thermal evaporation gram on silicon oxide (native and thermally grown) substrates at room temperature using X-ray photoemission spectroscopy, atomic force microscopy and in situ transport measurements. The chemical properties of the molecule have been characterized by high resolution C1s, O1s and Valence Band X-ray photoemission as a function of the thickness and the photoemission peaks were interpreted on the basis of density functional theory calculations. The photoemission analysis of the above mentioned regions reveals characteristic features (namely a double peak on C1s due to the six inequivalent carbon atoms, a single peak on O1s at binding energy of 531.3 eV and a feature centered at 3.7 eV assigned to a convolution of the highest occupied molecular orbitals). Atomic force microscopy measurements show an initial amorphous wetting layer with a subsequent island growth in two different crystalline phases, namely the bulk crystal phase and a metastable substrate induced phase. Finally, electrical measurements evidence the insulating character of 6,13-pentacenequinone films with a resistivity $\rho \geqslant 5 \times 10^6\ \Omega\,\mathrm{m}$.
© 2007 Elsevier B.V. All rights reserved.

PACS: 61.66.Hq; 68.55.Ac; 79.60.Dp; 71.15.Mb; 68.37.Ps

Keywords: Organic compounds; Thin film structure and morphology; Photoelectron spectroscopy; Density functional theory; Atomic force microscopy

1. Introduction

The investigation and the understanding of the structural, electronic and transport properties of organic molecules are of great interest for their potential application in molecular electronics. Low cost, flexible, nano-sized devices are the ultimate goal of the research in nano and microelectronics. Several applications (OTFTs, OLEDs, Schottky diodes, solar cells) have been studied in recent years [1–5] and pentacene is undoubtedly one of the most promising candidates for device integration, due to its high mobility and capability to form stable crystalline films [6–15]. An open issue on this material is the effect of structural defects and chemical impurities on the electronic and transport properties and the relevance of purity of crystals and films has been stressed in several works [15–20]. The most

* Corresponding author. Tel.: +39 0862 433097; fax: +39 0862 433033.
E-mail address: pietro.parisse@aquila.infn.it (P. Parisse).

1566-1199/$ - see front matter © 2007 Elsevier B.V. All rights reserved.
doi:10.1016/j.orgel.2007.03.007

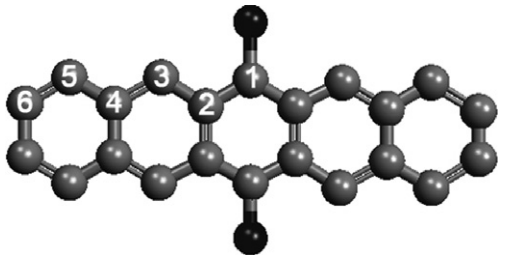


Fig. 1. Schematic drawing of PQ molecule. Gray balls are C atoms, black balls O atoms. Hydrogens not shown.

common chemical impurity of pentacene is 6,13-pentacenequinone ($C_{22}H_{12}O_2$, hereafter PQ). This oxidized form of pentacene (the structure is reported in Fig. 1) belongs to the family of linear para-quinones used as industrial dyes and pigments. Its optical and structural properties in the bulk crystal phase are known in literature [21–23]. PQ is an insulator with an electrical breakdown field of about 3 MV/cm and relative dielectric constant ε_r of 3.5, as measured on single crystals [24], and has been used very recently as gate dielectric in excellent pentacene single crystal FETs [25,26]. The interface properties of PQ/pentacene are of technological interest and a possible application in the field of organic heterostructures has been recently presented in a work in which the electronic properties of interfaces of PQ and pentacene thin films on SiO_2 and Ag(1 1 1) surfaces are showed [27]. Anyhow, there is a lack of knowledge about the basic properties of thin films of PQ. Only few years ago the structural and optical properties of PQ thin films have been studied for the application in UV detectors due to its photoluminescence properties [28,29] and very recently a Low Energy Electron Microscopy and Diffraction study of the growth of PQ thin films on Si(1 1 1)-7 × 7 has been reported [30].

In our work we present our theoretical and experimental investigations on thin films grown by means of Vacuum Thermal Evaporation on native silicon oxide surfaces. First, we report high resolution X-ray Photoemission analysis of C1s and O1s core levels and Valence Band as a function of the film thickness, and we compare them with accurate Density Functional Theory (DFT) simulations on an isolated PQ molecule. Then we report our detailed study of the morphological and transport properties upon increasing of the film thickness as evidenced by Atomic Force Microscopy (AFM) and *I–V* measurements.

2. Experimental and computational details

6,13-Pentacenequinone (Aldrich chemicals) was deposited in a ultra high vacuum chamber (base pressure = 1×10^{-9} Torr) by vacuum thermal evaporation from a quartz crucible held at 180 °C. The evaporation rate was 5 Å/min (as monitored by a quartz crystal micro-balance) for all the samples. The substrates were cleaned by sonication in ethanol and acetone before placement in the UHV system, and heated to 300 °C in vacuum prior to the deposition of PQ. Tapping Mode AFM measurements are performed ex situ in air with a Digital D5000 equipped with Nanoscope IV controller using commercial silicon nitride cantilevers (cantilever resonance frequency = 70 kHz for "soft" organic samples). X-ray photoemission spectra have been acquired in situ with an Al monochromatized source, $h\nu = 1486.6$ eV, with a PHI hemispherical analyzer. All spectra have been acquired with a pass energy of 5.85 eV and a corresponding overall experimental resolution (Half Width at Half Maximum, HWHM) of 0.15 eV. Current–voltage measurements on gold prepatterned samples (see Ref. [19]) were carried out in situ at RT with a Keithley source measure unit, model number 236. The *I–V* curves have been acquired by varying every 0.5 s the voltage at steps of 0.05–0.2 V.

Our simulations were performed within the Density Functional Theory framework, using the Generalized Gradient Approximation (GGA) to the exchange–correlation potential [31]. The all-electron non-relativistic DMol3 (density functional for theory and molecules [32]) method was used, based on a localized atom-centered numerical polarized basis set employed for the wave function expansion, with a finite size basis cut-off of 9.0 a.u. Scalar relativistic effects were introduced using a local-pseudopotential [33].

3. Results and discussion

In Fig. 2 we report our XPS investigation on PQ films deposited onto native silicon oxide surface. Panels (a)–(c) show the evolution of the C1s (a) and O1s (b) core level and Valence Band (c) spectra as a function of the film thickness, whereas in panels (d) and (f) we report the corresponding peak analysis based on DFT calculation on a PQ isolated molecule. Calculations of the electronic structure of isolated molecules are a relevant tool to predict the behaviour of molecular crystals. In fact, in their

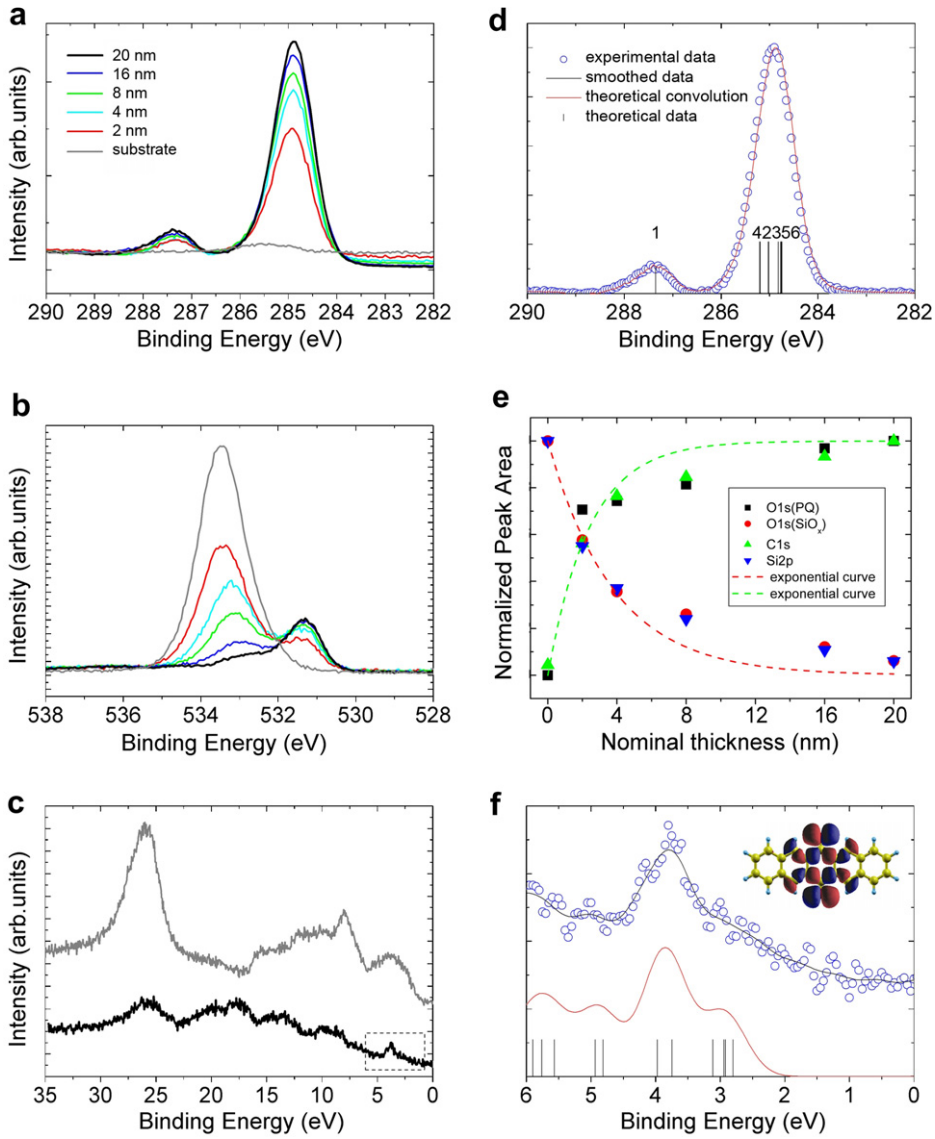


Fig. 2. Evolution of the C1s (a), O1s (b) and Valence Band (c) spectra, as a function of the thickness of PQ film on native silicon oxide. (d) Experimental Photoemission spectrum of 20 nm PQ film and raw and convoluted theoretical data of C1s. (e) Evolution of the normalized peak areas of the C1s, Si2p, O1s(PQ) and O1s(SiO_x) as a function of the nominal thickness. Dashed lines represent the exponential trends for a layer-by-layer growth. (f) Experimental Photoemission spectrum of 20 nm PQ film and raw and convoluted theoretical data of Valence Band. In the inset of panel (f) is shown the wavefunction plot of the HOMO of isolated PQ molecule (isosurface at 0.1 e/Å^3). (For interpretation of the reference in colour in this figure legend, the reader is referred to the web version of this article.)

aggregate state, organic molecules are bonded by weak van der Waals interactions and therefore their molecular levels are not so much influenced by the crystalline packing. So, our calculations of the PQ electronic structure can be very useful to assign the spectral features of photoemission spectroscopy, or absorption and fluorescence measurements on PQ thin films or single crystals. The experimental C1s core level (Fig. 2(a)) evidences the presence of two distinct peaks centered at 284.9 and 287.3, even in the thinnest considered film. The two peaks have a Full Width Half Maximum (FWHM) of 1.0 eV and 0.7 eV, respectively, and do not show multiplet structure. Nonetheless, considering that the FWHM of cleaved HOPG C1s spectrum acquired with the same system settings is 0.6 eV, we can attribute the experimental broadening of the C1s core level to a sum of the different components due to six

inequivalent C atoms in PQ (see Fig. 1), as also observed for pentacene in the gas phase [34]. These components give rise to different energy levels shifted one with respect to the other: namely the 1C component at 287.3 eV of Binding Energy (BE), 4C at 285.2 eV, 2C at 285.0 eV, 3C at 284.8 eV, 5C and 6C at 284.7 eV, as shown in Fig. 2(d) (vertical bars) [35]. In fact, the convolution of gaussians with same $\sigma = 0.3$ eV (solid line) centered at the above mentioned levels accurately fit the experimental spectrum (circles) and allows to unequivocally identify the chemical shifts in BE for the inequivalent C atoms. Moreover, analyzing the peak intensities and the peak areas of the features at 284.9 and 287.3 eV, we find a ratio C–C/C–O of 10 ± 1, in excellent agreement with those predicted by DFT calculations. In Fig. 2 panel (b) we report the O1s XPS spectrum. The O1s shows in two main components around 533.0 and 531.3 eV BE . The evolution as a function of the thickness suggests to assign the component centered at 531.3 eV to the C–O bonds of PQ and the component at 533.0 to the Si–O bond in the native silicon oxide substrate [36]. This assignment is supported by the comparison between the experimental spectrum and the theoretical data (not shown): this allows to assign unequivocally the component centered at 531.3 eV to the C–O bonds of PQ. Moreover, a more accurate fit of the data allows to distinguish two components at 533.0 and 531.8 eV BE, respectively due to SiO_2 and SiO bonds [36,37]. This is a sign of a nonstoichiometric oxide and then of a more reactive and defective surface. The presence of the components due to the substrate, even for a PQ 20 nm thick film, is a sign of a noncomplete coverage typical of an island growth (the XPS analysis for this film also shows the presence, not reported here, of the Si2p peak). In order to clarify this latter statement, in Fig. 2 panel (e) we report the evolution of the C1s(PQ), O1s(PQ), O1s(SiO_x) and Si2p normalized peak areas as a function of the nominal thickness. It is interesting to note that the PQ components (squares and triangles, respectively black and green on the web colour version) scale accordingly one to another, as well as the substrate components (circles and reverse triangles, respectively red and blue on the web colour version). In case of a perfect layer by layer growth the carbon and oxygen signal relative to the PQ film (the attenuation of the substrate (O1s(SiO_x) and Si2p) signal) would scale according to an exponential trend $e^{-\alpha x}$ $(1 - e^{-\alpha x})$, respectively [38]. As evident from the plot of the normalized peak areas shown in Fig. 2(e), all the trends deviate significantly from exponential curves (dashed lines) for thicknesses of more than 2 nm, then following a linear trend. This indicates an amorphous wetting layer of PQ molecules (responsible of the initial exponential behaviour) followed by a subsequent island growth (explaining the linear trend).

The Valence Band spectra of the clean substrate (grey line) and of the 20 nm PQ film (black line) are shown in Fig. 2(c). The two spectra are clearly different and evidence the decrease in intensity of the O2s level (25.6 eV) and the comparison of an evident feature around 3.7 eV. We show in Fig. 2(f) the zoomed area (dashed rectangle in panel (c)) of the Valence Band (VB) (circles and solid line, respectively blue and black in the web colour version). Our results are in excellent agreement with the UPS spectra of same thickness PQ film on native silicon oxide testifying the high purity of our films [27]. In this work the peak around 3.7 eV is assigned to derive from the PQ Highest Occupied Molecular Orbital (HOMO). On the basis of our DFT calculations, we can assign the spectral features observed in their work to a convolution of the occupied levels (vertical bars) and not only to a single level, as shown in Fig. 2 where a convolution of gaussians ($\sigma = 0.3$ eV) centered around the molecular levels is also reported.

The agreement between the theoretical convolution and the experimental curve is quite good and suggests that PQ is weakly bonded in thin films. In the inset of Fig. 2(f) we report the HOMO state. We observe that the HOMO is strongly localized at the center of the molecule and the main contribution to the wavefunction comes from the p orbital of the O atoms. The LUMO state (not shown) is more delocalized over the entire molecule with a prominent contribution of the p orbital of the C1 (the carbon bonded with O). Both states denote localization around the central ring: this is due to the electronegative nature of the O atom. Comparing the PQ HOMO with respect to that of pentacene [39–41], we note that the pentacene orbitals are more delocalized over the entire molecule. This delocalization produces a lowering of the HOMO–LUMO gap (the experimental optical gap of pentacene is 1.82 eV versus 2.94 eV for PQ [28,29,42]) and an increase of the overlap between orbitals in their crystalline stacks and therefore a strong intermolecular interaction (in PQ the concentration of charge near the oxygens favors the repulsion between adjacent molecules). The different shape of PQ and

pentacene HOMO and LUMOs can also modify the interaction of the molecule with substrates changing in such a way the growth type and the morphology of thin films.

In fact, the investigation of the morphological properties of PQ thin films as a function of the thickness confirms such theoretical predictions. In Fig. 3 we report the results for a 5 nm thin film on a silicon native oxide surface. We clearly observe in such AFM images that PQ grows in an island mode, in line with the XPS indication. The presence of an initial wetting layer is not evident in such images, but analyzing the roughness of the dark zones we observe a root mean square (rms) roughness of 3.1 ± 0.5 Å. Considering that for clean substrates we have a rms roughness of 0.8 Å, we believe that this higher value can be explained by the presence of a layer of randomly oriented PQ molecules, according to the XPS results (Fig. 2 panel (e)). Fig. 3(a) shows the nucleation of islands with no defined shape and submicrometer dimension. Such compact islands are believed to be at this first stage amorphous-like, accordingly to the observations made in Ref. [30]. The growth is clearly non dendritic, at variance with pentacene at the same growth conditions [43]. Moreover, similar thick films of pentacene show a complete coverage of the substrate surface [44]. A different sticking coefficient on the surface and weaker molecule-molecule interactions (in line with XPS and DFT results) can explain this difference in the growth, consistently with a diffusion limited aggregation model [45,46]. In fact, a sticking coefficient lower than one and a weak molecule-molecule interaction can lead to the growth of drop-like instead of dentritic islands. By analyzing more accurately the islands (Fig. 3 panel (b)), we observe that they appear atomically flat with some prominent areas indicating the nucleation of the subsequent layer (as can be seen on the left upper edge and on the lower edge of the island). Fig. 3 panel (c) shows a zoomed image at one of these step edges. The analysis of the height histogram (panel (d)) shows an interplanar distance of 13 ± 2 Å comparable with the interplanar distance ($d = 12.7$ Å) of a metastable phase due to substrate-induced strain, as already reported in [28,29]. Upon increase in the thickness of the film, we did not observe the complete coverage of the substrate, even at the 50 nm nominal thickness film (see Fig. 4 panels (a) and (b)). However, we note an evolution of the islands in two different shaped grains, needle (flat) shaped and almost pyramidal (mounds) shaped, probably due to the two distinct

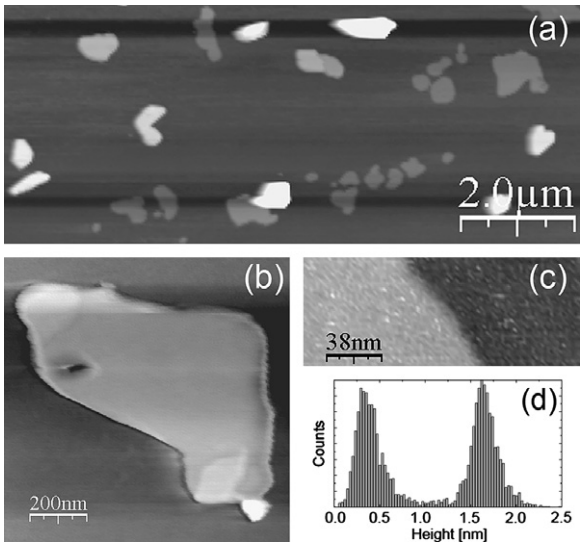


Fig. 3. (a–b) AFM images of the 5 nm film of PQ on native oxide SiO_2/Si(100) surface. (c–d) Zoomed image of a terrace on a island and relative height histogram.

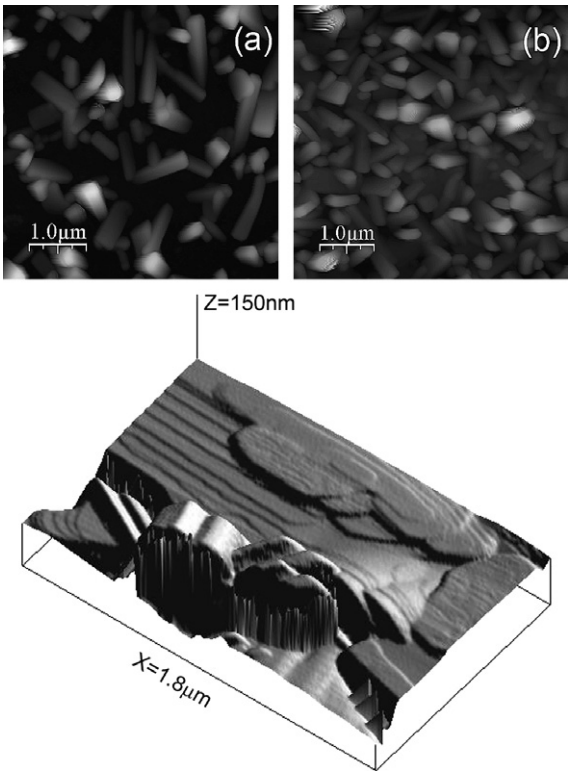


Fig. 4. 5×5 μm^2 AFM images of 20 nm (a) and 50 nm (b) PQ film on 100 nm thermally grown SiO_2/Si(100). Bottom panel: Three-dimensional AFM image of 100 nm nominal thickness PQ film on native oxide SiO_2/Si(100).

phases reported by Hwang et al., namely the bulk crystal phase (spacing between (0 0 1) planes is 17.79 Å) and the above mentioned metastable phase [47]. We note that the percentage of mounds area with respect to the flat areas increases with the thickness of the film but the flat areas seems to be predominant for thickness $\leqslant$50 nm. We also note that the flat areas, even at higher thicknesses, (see bottom panel of Fig. 4, nominal 100 nm) show a stacking of planes with an interplanar distance of 13 ± 2 Å. Thus we assigned the flat areas to the metastable phase and the mounds areas to the bulk crystal phase, at variance with the assignments made in Ref. [28].

In view of the application of PQ as gate dielectric or in organic heterostructures, it is of technological interest to study the transport properties of such thin films and check their resistivity. The morphological data suggest us to perform electrical measurements only on the 50–100 nm films (under our growth conditions the film is not continuous at lower thickness). Our electrical measurements, performed in vacuum with the same apparatus used in Ref. [19] for pentacene thin films, on 50 and 100 nm PQ films evidence no changes of I–V characteristics with respect to the clean patterned substrate (the overall resistance was of around 10^4 GΩ). This allows to estimate a lower boundary for the PQ resistivity of $\rho \geqslant 5 \times 10^6\ \Omega\,\mathrm{m}$ [48]. Subsequent exposure to air does not evidence remarkable changes in the I–V characteristics, confirming the insulating character of the PQ films.

4. Conclusions

We have reported a comprehensive study of the morphological, transport and electronic properties of thin films of 6,13-pentacenequinone. The study of the photoemission lines of PQ thin films reveals on C1s, O1s and Valence Band regions characteristic features (namely a double peak at 284.9 and 287.3 eV of binding energy, a peak at 531.3 eV and a feature centered at 3.7 eV assigned to a convolution of the last occupied molecular orbitals), that are a fingerprint of the presence of this molecule. All the photoemission features have been also commented separating the effects of the inequivalent atoms according to DFT calculations of the electronic structure of the PQ molecule: this could help the interpretation of site adsorption of PQ molecule. Moreover this study evidences strong differences with respect to the pentacene electronic properties: such different features could be used in a PQ/pentacene interface study as an easy tool to identify the relative quantity and the presence of the two molecules. A careful morphological analysis clearly shows an initial amorphous wetting layer and a subsequent island growth in two different shaped grains attributed to two distinct crystallographic phases, namely bulk crystal phase and a metastable substrate-induced phase. AFM measurements clearly show that the metastable phase is predominant at thicknesses lower than 100 nm. Therefore, the electronic and transport properties of such thick films are to be assigned to this specific crystalline phase. We call for further X-ray diffraction analyses for a better understanding of the structural parameters of such phase. Moreover AFM images show that, under our growth conditions, an almost continuous film is reached only for thickness higher than 50 nm. Such thick films have been proved to be insulating with a lower boundary for the resistivity of $\rho \geqslant 5 \times 10^6\ \Omega\,\mathrm{m}$, as checked by electrical measurements. All these information on the basic properties of PQ films can be very useful for possible applications in the field of organic heterostructures and for the future design and optimization of all organic devices (e.g. optimization of the PQ dielectric film thickness versus leakage currents in OTFTs).

Acknowledgements

Helpful discussion with Fabio Bussolotti and Adriano Verna and experimental support from Maurizio Passacantando are acknowledged. This work was supported with grants from MIUR (Italian Ministry for the University and Research) fondo COFIN2004.

References

[1] C. Reese, M. Roberts, M. Ling, Z. Bao, Mater. Today 7 (9) (2004) 20.
[2] Z. Bao, Adv. Mater. 12 (2000) 227.
[3] C.D. Dimitrakopoulos, P.R.L. Malenfant, Adv. Mater. 14 (2002) 99.
[4] J.L. Bredas, J.P. Calbert, D.A. da Silva Filho, J. Cornil, Proc. Natl. Acad. Sci. USA 99 (2002) 5804.
[5] G. Horowitz, Adv. Mater. 10 (1998) 365.
[6] Y.Y. Lin, D.J. Gundlach, T.N. Jackson, S.F. Nelson, IEEE Trans. Electron Dev. 44 (1997) 1325.
[7] L. Wang, D. Fine, T. Jung, D. Basu, H. von Seggern, A. Dodabalapur, Appl. Phys. Lett. 85 (2004) 1772.
[8] M. Daraktchiev, A. von Mhlenen, F. Nesch, M. Schaer, M. Brinkmann, M.-N. Bussac, L. Zuppiroli, New J. Phys. 7 (2005) 133.

[9] S.S. Kim, Y.S. Choi, K. Kim, J.H. Kim, S. Im, Appl. Phys. Lett. 82 (2003) 639.
[10] C. Voz, J. Puigdollers, I. Martn, D. Munoz, A. Orpella, M. Vetter, R. Alcubilla, Solar Energy Mater. Solar Cells 87 (2005) 567.
[11] C.C. Mattheus, A.B. Dros, J. Baas, G.T. Oostergetel, A. Meetsma, J.L. de Boer, T.T.M. Palstra, Synth. Met. 138 (2003) 475.
[12] R. Ruiz, D. Choudary, B. Nickel, T. Toccoli, K.-C. Chang, A.C. Mayer, P. Clancy, J.M. Blakely, R.L. Headrick, S. Iannotta, G.G. Malliaras, Chem. Mater. 16 (2004) 4497.
[13] F.-J. Meyer zu Heringdorf, M.C. Reuter, R.M. Tromp, Nature 412 (2001) 517.
[14] A.C. Mayer, R. Ruiz, R.L. Headrick, A. Kazimirov, G.G. Malliaras, Org. Elec. 5 (2004) 257.
[15] O.D. Jurchescu, J. Baas, T.T.M. Palstra, Appl. Phys. Lett. 84 (2004) 3061.
[16] A. Vollmer, O.D. Jurchescu, I. Arfaoui, I. Salzmann, T.T.M. Palstra, P. Rudolf, J. Niemax, J. Pflaum, J.P. Rabe, N. Koch, Eur. Phys. J. E 17 (2005) 339.
[17] A. Vollmer, H. Weiss, S. Rentenberger, I. Salzmann, J.P. Rabe, N. Koch, Surf. Sci. 600 (2006) 4004.
[18] O.D. Jurchescu, J. Baas, T.T.M. Palstra, Appl. Phys. Lett. 87 (2005) 052102.
[19] P. Parisse, S. Picozzi, M. Passacantando, L. Ottaviano, Org. Elec. 7 (2006) 403.
[20] J.H. Kang, D. da Silva Filho, J.L. Bredas, X.-Y. Zhu, Appl. Phys. Lett. 86 (2005) 152115.
[21] A.V. Dzyabchenko, V.E. Zavodnik, V.K. Belsky, Acta Cryst. B35 (1979) 2250.
[22] T. Itoh, Chem. Rev. 95 (1995) 2351.
[23] T.C. Wen, C.J. Tiao, L.C. Hwang, C.Y. Tsai, Synth. Met. 92 (1998) 235.
[24] This value of the relative dielectric constant, reported in Refs. [25,26], is referred to a measurement performed in a sandwich type geometry with the electric field along the *c*-axis of the crystal.
[25] O.D. Jurchescu, M. Popinciuc, B.J. van Wees, T.T.M. Palstra, Adv. Mater. 19 (2007) 688.
[26] O.D. Jurchescu, Ph.D. Thesis, RuG, 2006.
[27] N. Koch, I. Salzmann, R.L. Johnson, J. Pflaum, R. Friedlein, J.P. Rabe, Org. Elec. 7 (2006) 537.
[28] D.K. Hwang, K. Kim, J.H. Kim, S. Im, D.-Y. Jung, E. Kim, Appl. Phys. Lett. 85 (2004) 5568.
[29] D.K. Hwang, K. Kim, J.H. Kim, D.-Y. Jung, E. Kim, S. Im, Appl. Surf. Sci. 244 (2005) 615.
[30] A. Al-Mahboob, J.T. Sadowski, T. Nishihara, Y. Fujikawa, Q.K. Xue, K. Nakajima, T. Sakurai, Surf. Sci. 601 (2007) 1311.
[31] J.P. Perdew, K. Burke, M. Ernzerhof, Phys. Rev. Lett. 77 (1996) 3865.
[32] B. Delley, J. Chem. Phys. 92 (1990) 508;
B. Delley, J. Chem. Phys. 113 (2000) 7756.
[33] B. Delley, Int. J. Quantum Chem. 69 (1998) 423.
[34] M. Alagia, C. Baldacchini, M.G. Betti, F. Bussolotti, V. Carravetta, U. Ekstrom, C. Mariani, S. Stranges, J. Chem. Phys. 122 (2005) 124305.
[35] In order to correct the well known DFT failures in predicting strongly localized and correlated core levels, Binding Energy values of C1s (Valence Band) are multiplied by a scale factor of 1.35 (1.2) and then rigidly shifted to fit the experimental ones.
[36] J.F. Moulder, W.F. Stickle, P.E. Sobol, K.D. Bomben, Handbook of X-ray Photoelectron Spectroscopy, Perkin-Elmer Corporation, 1992.
[37] T.P. Nguyen, S. Lefrant, J. Phys.: Condens. Mat. 1 (1989) 5197.
[38] S. Sohnchen, S. Lukas, G. Witte, J. Chem. Phys. 121 (2004) 525.
[39] G.A. de Wijs, C.C. Mattheus, R.A. de Groot, T.T.M. Palstra, Synth. Met. 139 (2003) 109.
[40] A. Troisi, G. Orlandi, J. Phys. Chem. B 109 (2005) 1849.
[41] R.G. Endres, C.Y. Fong, L.H. Yang, G. Witte, Ch. Woll, Comput. Mater. Sci. 29 (2004) 362.
[42] J. Lee, S.S. Kim, K. Kim, J.H. Kim, S. Im, Appl. Phys. Lett. 84 (2004) 1701.
[43] P. Parisse, M. Passacantando, L. Ottaviano, Appl. Surf. Sci. 252 (2006) 7469.
[44] T. Schwieger, X. Liu, D. Olligs, M. Knupfer, Th. Schmidt, J. Appl. Phys. 96 (2004) 5596.
[45] R. Ruiz, B. Nickel, N. Koch, L.C. Feldman, R.F. Haglund Jr., A. Kahn, F. Family, G. Scoles, Phys. Rev. Lett. 67 (2003) 125406.
[46] P. Meakin, in: H.E. Stanley, N. Ostrowsky (Eds.), On Growth and Form, Martinus Nijhoff, Boston, MA, 1986, p. 120.
[47] Ancillary X-ray diffraction measurements on 100 nm thick film reveal the presence of both crystalline phases with relative intensities comparable with those reported in Refs. [26,27].
[48] The resistivity value obtained here for the thin film is, affected by grain boundary effects, as showed by the morphological investigation. Such effects largely influence the transport and we believe that PQ bulk crystals may show a different behaviour.

Available online at www.sciencedirect.com
ScienceDirect
Organic Electronics 8 (2007) 505–512
Organic Electronics
www.elsevier.com/locate/orgel

Growth enhancement and field emission characteristics of one-dimensional 3,4,9,10-perylenetetracarboxylic dianhydride nanostructures on pillared titanium substrate

Shich-Chang Suen [a], Wha-Tzong Whang [a,*], Fu-Ju Hou [b], Bau-Tong Dai [b]

[a] *Department of Materials Science and Engineering, National Chiao Tung University, 1001 Ta Hsueh Road, Hsinchu 30050, Taiwan, ROC*
[b] *National Nano Device Laboratories, No. 26, Prosperity Road I, Science-based Industrial Park, Hsinchu, Taiwan, ROC*

Received 8 January 2007; received in revised form 7 March 2007; accepted 12 March 2007
Available online 19 March 2007

Abstract

We have utilized the π–π interactions between 3,4,9,10-perylenetetracarboxylic dianhydride (PTCDA) molecules and temperature-induced morphology changes to synthesize one-dimensional (1D) nanostructures of PTCDA on a heated (ca. 100 °C) titanium substrate through vacuum sublimation. Because of the pillared Ti structures and the presence of reactive Ti–Cl sites, the titanium substrate played a crucial role in assisting the PTCDA molecules to form 1D nanostructures. The average diameter of the nanofibers deposited on the Ti-CVD substrate, a Ti substrate formed by chemical vapor deposition (CVD), at 100 °C was ca. 84 nm, with lengths ranging from 100 nm to 3 μm. When the PTCDA nanofibers were biased under vacuum, the emission current remained stable. The turn-on electric field for producing a current density of 10 $\mu A/cm^2$ was 8 V/μm. The maximum emission current density was 1.3 mA/cm^2, measured at 1100 V ($E = 11$ V/μm). From the slope of the straight line obtained after plotting $\ln(J/E^2)$ versus $1/E$, we calculated the field enhancement factor β to be ca. 989. These results demonstrate the PTCDA nanofibers have great potential for applicability in organic electron-emitting devices.
© 2007 Elsevier B.V. All rights reserved.

PACS: 79.70.+q; 81.07.Nb; 85.35; 81.16.Dn; 72.80.Le

Keywords: PTCDA; Nanofibers; Field Emission; Morphology; Pillared titanium

1. Introduction

3,4,9,10-Perylenetetracarboxylic dianhydride (PTCDA) is one of the most intensively studied materials for organic electronic and optoelectonic applications [1,2]. Investigations into its bulk properties, such as its photoconductivity [3], carrier transport [4], and electroluminescence [5], have led to PTCDA's rapid development for applications in light emitting devices [6], field effect transistors [7], and solar cells [8]. Recently, a number of π-stacking organic molecules, including tris(8-hydroxyquinoine)aluminum [9], (7,7,8,8-tetracyanoquinodimethane)silver [10], coronene [11], anthracene [12], perylene [12], and copper phthalocyanine (CuPc)

* Corresponding author. Tel.: +886 3 5726111x31873; fax: +886 3 5724727.
E-mail address: wtwhang@mail.NCTU.edu.tw (W.-T. Whang).

1566-1199/$ - see front matter © 2007 Elsevier B.V. All rights reserved.
doi:10.1016/j.orgel.2007.03.003

[13], have been demonstrated to form one-dimensional (1D) nanostructures readily under milder conditions than those used typically to prepare analogous structures from inorganic compounds. Moreover, most of these organic 1D nanostructures possess excellent field emission characteristics when biased in a vacuum chamber. Because the morphology of planar π-stacked PTCDA molecules on various substrates can be altered through modification of the processing temperature – i.e., granular morphologies at room temperature, island morphologies at high temperature [14–19] – we suspected that PTCDA might form 1D structures under certain conditions. In this paper, we present nanofibers having high aspect ratios formed using a relatively low-temperature (100 °C) process and describe the significant effect that the Ti substrate formed by plasma enhancement chemical vapor deposition (PECVD) has on the 1D structural growth. We also evaluate the field emission characteristics of the PTCDA nanofibers synthesized directly on Ti metal films. The results open up an interesting area of study and suggest potential further applications.

2. Experimental procedure

PTCDA films were grown through vacuum sublimation in a thermal coater at a base pressure of ca. 3×10^{-6} torr. A commercial powder of PTCDA (Aldrich) was sublimed onto various substrates, including Ti and Au, from a heated crucible. The crucible temperature of ca. 100 °C corresponded to a deposition rate of 1 Å/s, as determined using a quartz crystal microbalance. To study the effect that altering the temperature had on the film morphology, the substrate temperature (T_{sub}) was maintained at 25, 80, 100, or 120 °C. The Au substrate was prepared by depositing an Au film on a Si (100) substrate through electron-beam gun evaporation (physical vapor deposition; PVD). We denote this substrate as "Au-PVD". The Ti substrate was prepared by depositing a Ti film on a Si (100) substrate using the PECVD technique. This sample is denoted as "Ti-CVD". Details of the PECVD process have been reported elsewhere [20]. It mainly utilizes titanium tetrachloride ($TiCl_4$) to react with H_2 and form a metallic Ti film in a plasma-generating chamber. A Ti substrate deposited using the sputter technique (a variation on PVD) was also prepared to ascertain the effect that the substrate has on forming the PTCDA nanofibers. We denote this substrate as "Ti-PVD".

Structural investigations were performed using a JEOL JSM-6500F scanning electron microscope (SEM). The profiles and fine structures of the nanostructures were imaged and analyzed using a JEOL JEM-2010F high-resolution transmission electron microscope (HRTEM) equipped with an Oxford energy dispersive spectrometer. The substrate morphologies were investigated using a Veeco D5000 atomic force microscope (AFM). The concentration of trace elements was determined using an ATOMIKA TXRF-8030W total reflection X-ray fluorescence (TXRF) spectrometer. The field emission measurements were performed in a vacuum chamber (ca. 10^{-6} torr) where a cylindrical copper electrode (diameter: 2.2 mm) was positioned above the sample surface at a distance of 100 μm. A Keithley 237 instrument was used to measure the emission current of the PTCDA nanofibers as a function of the sweep bias.

3. Results and discussion

PTCDA molecules tend to form island morphologies on various substrates at elevated temperatures [14–19]. To determine the growth conditions necessary to prepare PTCDA nanofibers, we deposited PTCDA onto Ti and Au substrates at various temperatures and assessed the film morphologies by means of SEM.

Figs. 1a–h display SEM topographic images of PTCDA films deposited on Au and Ti-CVD substrates under various temperatures. At room temperature, the film morphology on the Au substrate was that of contiguous granular structures having an average grain size of 45 nm (Fig. 1a). As the substrate temperature increased, we observed typical temperature-induced morphological changes [19,21]; i.e., Figs. 1b–d indicate that the film morphologies changed from grains to facets and finally to separated islands upon increasing the temperature. According to Krause et al., PTCDA films deposited at room temperature are metastable. When PTCDA is deposited at elevated temperatures, or when PTCDA-coated substrates are annealed at high temperatures, the adsorbate contains a sufficient amount of energy to diffuse to already existing crystallite sites in an energetically favorable process [14,15]. Such morphological changes may also occur through strain relaxation mechanisms [21]. As a result of strong chemisorption, the first layer of PTCDA is strained, such that the molecules adsorbed onto larger island sites have

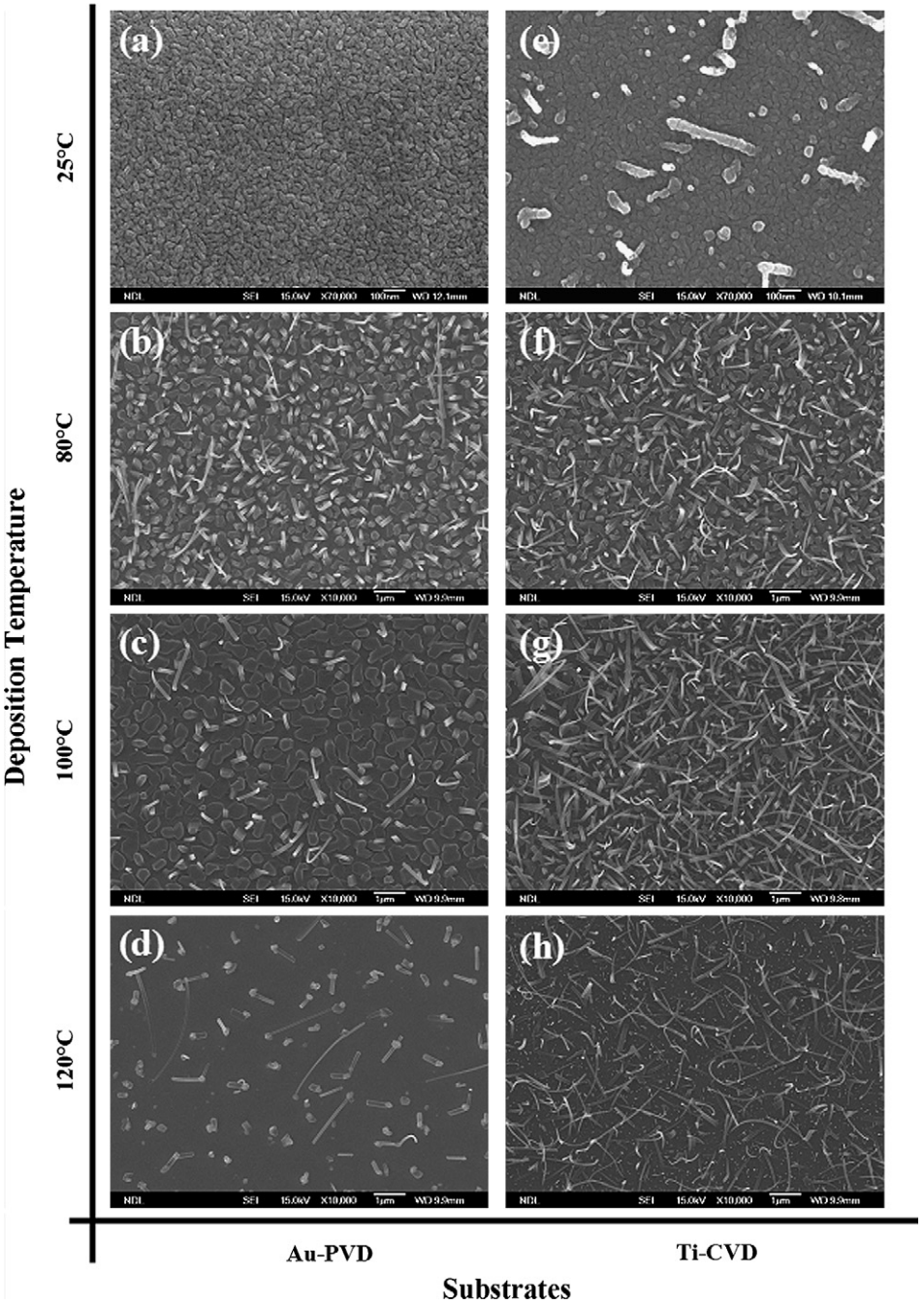


Fig. 1. Top-view SEM images of PTCDA layers deposited on an Au substrate at values of T_{sub} of (a) 25, (b) 80, (c) 100, and (d) 120 °C and on a Ti substrate at values of T_{sub} of (e) 25, (f) 80, (g) 100, and (h) 120 °C. To discern the subtle difference between samples deposited at room temperature, the images of (a) and (e) have been magnified by 70,000 times, whereas the others have been magnified only 10,000 times.

lower energies than those adsorbed onto smaller island sites, and therefore Stranski–Krastanov (SK) growth help to relax this strain [18,22]. When the temperature increases, the islands grow at the expense of the number of crystallites, and the space between the islands extends gradually. Moreover, portions of the adsorbate desorb from the substrate, resulting in decreasing island density. Among our SEM images, we also observed needle- and belt-like structures lying on the Au substrate. According to

the S-type growth model [16], these structures result from homogeneous nucleation, i.e., the PTCDA molecules combined prior to adsorbing on the substrate. Under these circumstances, the adsorbate formed elongated needles through stacking of additional molecules along the needle's axis.

Figs. 1e–h present the PTCDA film morphologies on the Ti-CVD substrate at the same set of temperatures. In this case, we observed that many more of the needle-like structures existed on the Ti-CVD substrate than they did on the Au substrate. The cause of this change in film morphology is very subtle. Herein we suggest two possibilities. First, according to the film growth mechanism, the adsorbate usually diffuses to the step edges of terraces [23]; thus, the substrate morphology plays an important role as a template. In Fig. 1e, we observe a preformed 1D nanostructure having a diameter of 30 nm that looks like a string of beads. After examining the morphology of the pure Ti-CVD substrate with AFM, we realized that this threaded bead structure existed on the Ti-CVD substrate prior to the formation of the PTCDA film, suggesting that the Ti pillar morphology might induce and enhance the formation of 1D nanostructures of PTCDA. The other possibility is that when the Ti film was deposited using $TiCl_4$ as a liquid source precursor, incompletely reacted $TiCl_4$ probably remained on the Ti film; i.e., some of the Ti surface atoms were still bonded to chlorine atoms. Because $TiCl_4$ and $TiCl_3$ are strongly Lewis acidic (electrophilic) groups [24], such units might provide sites for reacting with PTCDA adsorbate molecules. Table 1 displays the trace element concentration of the Ti-CVD substrate, as determined using TXRF spectrometry. We observe indeed the existence of chlorine atoms on the Ti-CVD substrate (ca. 9 at%). Consequently, when depositing PTCDA at high temperature, the presence of reactive Ti–Cl sites might lead to the preference for deposition of PTCDA and form nanofiber structures.

Comparing Figs. 1d and h, which display images of the materials prepared at a temperature at which some of the PTCDA molecules re-evaporated from the substrate ($T_{sub} = 120$ °C), the number of nanostructures present on the Ti-CVD substrate is greater than that on the Au substrate. We ascribe this phenomenon partly to the dianhydride groups of PTCDA bonding more strongly to the reactive Ti substrate than to the inert Au substrate. This observation is consistent with the UPS results reported by Hirose et al. [25,26]

To confirm our assumption that the nanofibers formed relatively easier on the Ti-CVD substrate as a result of the substrate template effect operating in conjunction with the presence of reactive Ti–Cl sites, we used PVD to prepare another Ti substrate to compare its behavior with that of the Ti-CVD substrate. The Ti-CVD and Ti-PVD films both exhibited hexagonal structures, as characterized using grazing incident X-ray diffraction (GID). Figs. 2a and b display topographic SEM images of the PTCDA films, which we deposited simultaneously, at a value of T_{sub} of 100 °C, onto both the Ti-CVD and Ti-PVD substrates. Both substrates are Ti but with distinct PTCDA film morphologies, it reveals that some other factors besides the crystal structure enhance the growth of the PTCDA nanofibers. Figs. 3a and b present the initial morphologies of the Ti-CVD and Ti-PVD substrates, respectively, prior to deposition of PTCDA. The image of the Ti-PVD surface indicates that it had a smooth topography with a root mean square roughness of 1.3 nm, a value that is quite normal for a sputtered metal film. In contrast, the image for the Ti-CVD sample indicates that pillared structures existed, with a root mean square roughness as high as 25.5 nm. Based on the theory that the adsorbate has a greater tendency to diffuse toward and grow along the step edge, we attribute the enhanced growth of the 1D nanostructures on Ti-CVD primarily to its abrupt pillar-shaped morphology. When we deposited PTCDA on the heated Ti-CVD substrate, the mobile adsorbate molecules shifted location to the vicinity of the Ti pillars and grew around them.

The results of the TXRF analyses for both substrates (Table 1) further support our hypotheses. Although we detected chlorine atoms (ca. 9 at.%) on the Ti-CVD substrate, none could be detected on the Ti-PVD substrate. As mentioned previously, $TiCl_x$ species are highly reactive Lewis acids – for example, some are used as Ziegler–Natta catalysts for olefin polymerization [27]. If the reactive Ti–Cl sites of our substrate act as anchor sites of the first set of deposited PTCDA molecules, subsequent

Table 1
The concentration of trace elements on Ti-CVD substrate and Ti-PVD substrate

Element	Ti-CVD substrate concentration ± sigma (10^{10} atoms/cm^2)	Ti-PVD substrate Concentration ± sigma (10^{10} atoms/cm^2)
Ti	673940.55 ± 6619.29	255681.04 ± 2469.12
Cl	60211.44 ± 700.33	Not detected

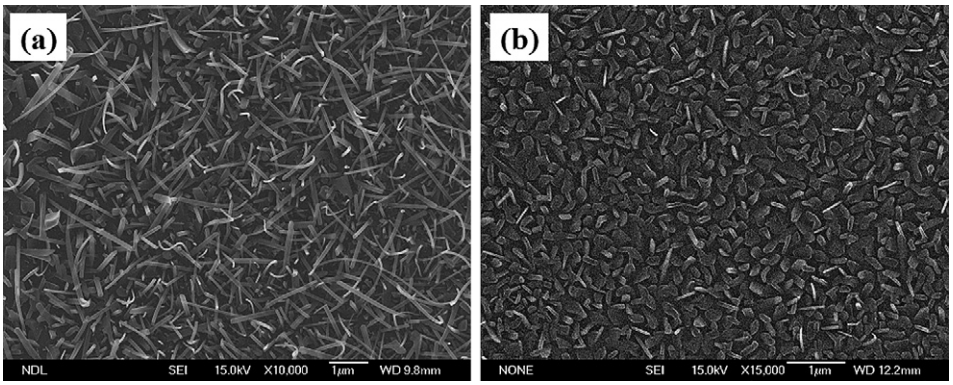


Fig. 2. Top-view SEM images of PTCDA layers deposited on (a) Ti-CVD and (b) Ti-PVD at values of T_{sub} of 100 °C.

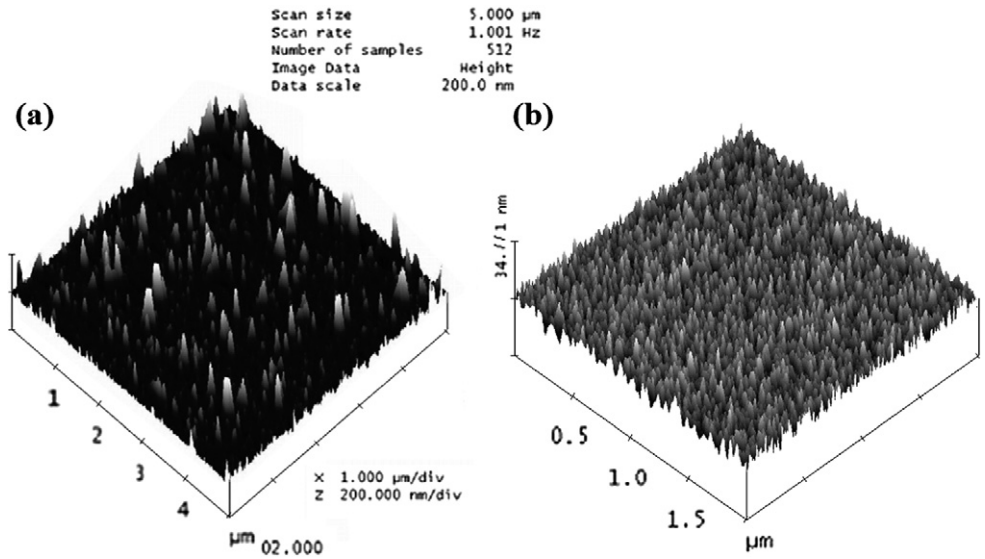


Fig. 3. AFM images of the (a) Ti-CVD (image area: 5×5 μm^2; height: 200 nm) and (b) Ti-PVD (image area: 2×2 μm^2; height: 34.77 nm) substrates.

molecules will deposit upon them through π–π interactions to develop 1D nanostructures. We are presently undertaking further studies to verify the exact details of this reaction mechanism.

Fig. 4 presents side-view SEM images of the PTCDA nanofibers deposited on the Ti-CVD substrate at a value of T_{sub} of 100 °C. The average diameter of these nanofibers was ca. 84 nm, with lengths ranging from 100 nm to 3 μm. The nanofibers stand with angles on the Ti substrate as a result of repulsive forces among nuclei, which led to a parallel-displaced conformation and resulted in tilted columnar structures [28].

Fig. 5a presents an HRTEM image of a single PTCDA nanofiber, having a diameter of 22 nm, that was formed at a value of T_{sub} of 100 °C on the Ti-CVD substrate. In Fig. 5b, the high-magnification image displays fringes that are orientated in short-range order at the edges of the nanofiber, but entangled randomly within the nanofiber. The electron diffraction pattern presented in the inset of Fig. 5a displays only amorphous rings, rather than distinct diffractive spots, suggesting an insignificant degree of crystallinity. In addition, we did not observe any catalyst at the tip of the fiber, similar with previous results of other organic nanofibers [11,13]. Therefore, the growth mechanism is dissimilar to that of carbon nanotubes (CNTs), which require a catalyst surface to enhance the decomposition of the hydrocarbon reactants, forming a super-

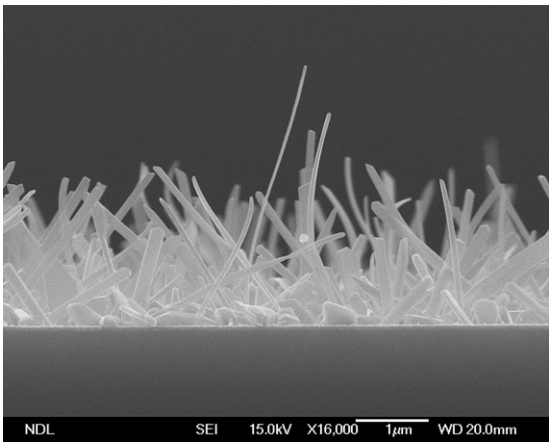


Fig. 4. Side-view SEM images of PTCDA nanofibers deposited on the Ti-CVD substrate at a value of T_{sub} of 100 °C.

saturated solution of carbon and catalyst, which finally precipitates carbon atoms and extrudes the walls [29].

Interestingly, although most of the PTCDA nanofibers were amorphous and included no catalyst, certain nanofibers did contain titanium atoms within them. Fig. 5c presents an image of a PTCDA nanofiber having a diameter of ca. 12 nm. This nanofiber possessed a heterogeneous structure, as indicated by the arrow. When selected area diffraction (SAD) was performed, a distinct diffraction pattern was observed, as shown in the inset of Fig. 5c. We examined this heterogeneous structure further through the use of energy dispersive spectroscopy (EDS), with which we found peaks associated with Ti atoms. Fig. 5d presents a magnified image of the heterogeneous structure, which shows that Ti atoms arranged in an ordered manner within the nanofiber, accompanied by amorphous carbon atoms located around the outer region. This observation further supports our mechanism for the growth of PTCDA nanofibers. Parts of the PTCDA nanostructure grew along the Ti pillars and, in some cases, they grew around these pillars. The highly electronegative chlorine atoms on the Ti surface attract electrons and weaken the bonding between Ti atoms; consequently, some of the chlorine-bound Ti atoms ($TiCl_x$) might desorb from the surface at

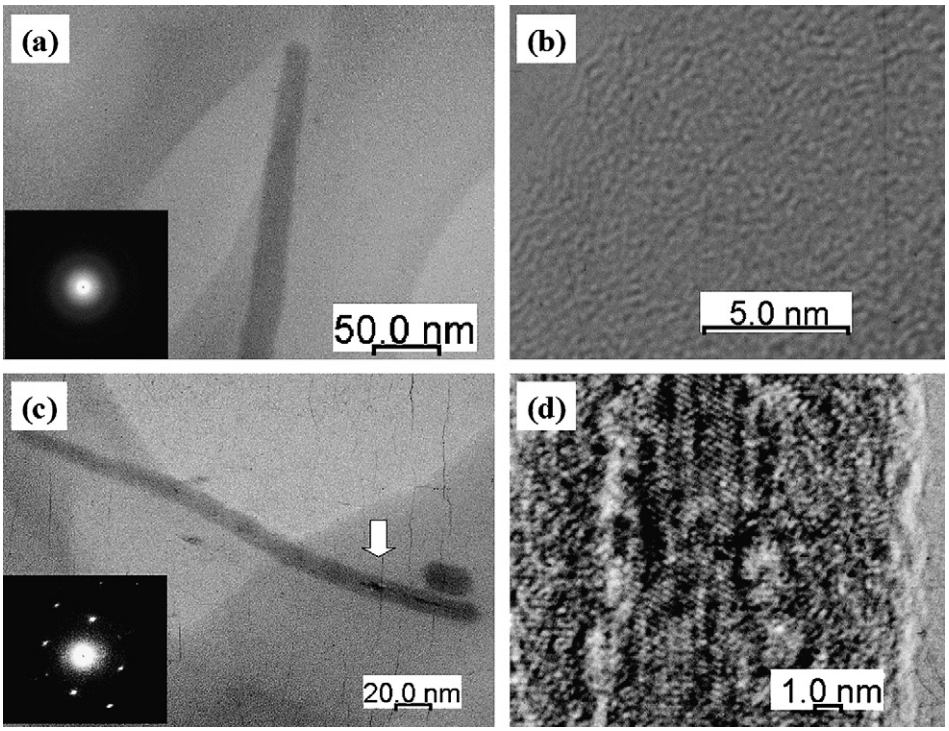


Fig. 5. (a) HRTEM image of a single PTCDA nanofiber formed on the Ti-CVD substrate at a value of T_{sub} of 100 °C. Inset: The corresponding electron diffraction pattern. (b) A magnified image of the nanofiber in (a), displaying its amorphous structure. (c) HRTEM image of a single Ti-included PTCDA nanofiber (diameter: 12 nm). The corresponding electron diffraction pattern in the inset displays Ti atoms within the fiber. (d) Magnified image of the nanofiber in (c), highlighting the heterogeneous region, which exhibits a crystallized structure.

high temperature. Because Ti atoms have a great tendency to react with the anhydride groups of PTCDA [25], desorbed $TiCl_x$ species might react with incoming PTCDA adsorbate units to form Ti-included PTCDA nanofibers.

Field emission characterization of the PTCDA nanofibers synthesized on a heated (100 °C) Ti-CVD substrate was performed under vacuum (5×10^{-6} torr) by placing a cylindrical Cu electrode (diameter: 2.2 mm) at a distance of 100 μm above the surface of the sample. The Cu electrode was connected to the source monitor unit (SMU) of a Keithley 237 instrument, and the titanium substrate beneath the PTCDA nanofibers was grounded. Fig. 6 presents the emission current density (J) as a function of the applied field (E). The turn-on field required for the PTCDA nanofibers to produce a current density of 10 μA/cm^2 was 8 V/μm. The maximum emission current density of 1.3 mA/cm^2 occurred at a potential of 1100 V ($E = 11$ V/μm). This performance is better than that of the CuPc nanofibers that we reported previously [13]. From the point of view of electron injection, the electron affinity (4.6 eV) of PTCDA [30] is close to the work function (4.33 eV) of the Ti substrate [31]; thus, electrons are able to transfer from the Ti substrate to the PTCDA nanofibers much more readily than they could from an Au substrate (5.1 eV) to CuPc nanofibers (3.1 eV). Furthermore, the strong bonding between the Ti substrate and the dianhydride groups of PTCDA molecules provides a better interface for electron injection [25].

The Fowler–Nordheim (FN) theory is most commonly used to model the emission of cold electrons from a conductor under a strong field [32]. By plotting $\ln(J/E^2)$ versus $1/E$, one can obtain a straight line, the slope of which can be used to deduce the field enhancement factor (β) [33]. The inset of Fig. 6 indicates that the plot of $\ln(J/E^2)$ versus $1/E$ is a straight line, implying that the field emission from these nanofibers follows FN theory. From the values of the work function of bulk PTCDA (4.6 eV) and the slope of the fitted line (−64.21 V/μm), we calculated the field enhancement factor β of the PTCDA nanofibers to be 989 cm^{-1}. This value is smaller than determined for a CNT film (1000–3000 cm^{-1} for a 125-μm inter-electrode distance) [34], presumably because of the different length-to-radius (L/r) ratios of the 1D nanostructure, as has been discussed elsewhere [9]. As compared with similar π-stacked organic 1D nanostructure, AlQ_3 nanowires, the field enhancement factor of the PTCDA nanofibers is higher than the value of AlQ_3 nanowires ($\beta = 275$ cm^{-1}) [9]. Although the L/r ratio of the AlQ_3 nanowires ($L/r = 5.5$ μm/20 nm = 275) was higher than that of the PTCDA nanofibers ($L/r = 2.2$ μm/84 nm = 26), the lower work function of AlQ_3 (3.0 eV) relative to that of PTCDA (4.6 eV) limits the deduced value of β according to the formula $\beta = B\phi^{3/2}/\text{slope}$, where $B = 6.83 \times 10^9$ V m^{-1} eV$^{-3/2}$ [8,33]. This result reveals that the geometric shape and intrinsic properties of the emitter both influence the field enhancement effect.

Fig. 7 displays the emission current stability of the PTCDA nanofibers when biased at 1000 V ($E = 10$ V/μm) for 1600 s. The mean current density was ca. 0.5 mA/cm^2 with a perturbation of less than

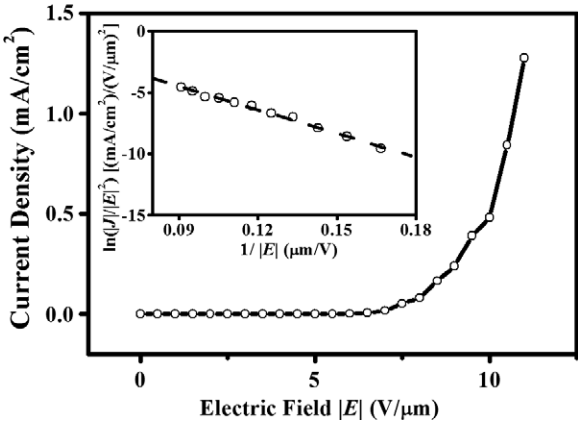


Fig. 6. Field emission $J - E$ curve of the PTCDA nanofibers. Inset: Corresponding FN plot.

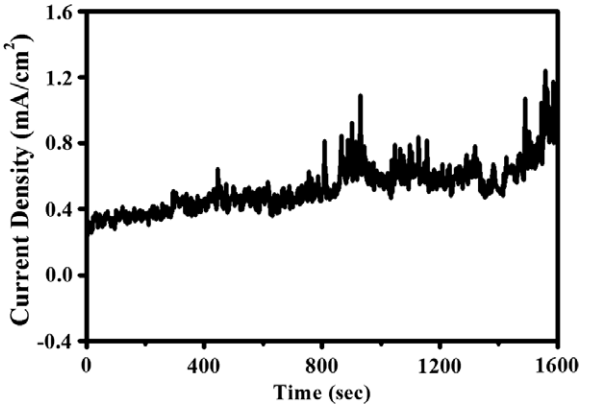


Fig. 7. Emission current of the PTCDA nanofibers plotted at a constant voltage.

one order of magnitude. The increasing tendency of emission current might result from the training effect [35,36] that some contaminants have been expelled after biasing the nanofibers for a period of time. The field emission current did not decay during the stability measurements, demonstrating that the PTCDA organic nanofibers is suitable for applications as electron-emitting devices.

4. Conclusions

In this study, we observed the temperature-induced morphological changes that occurred to PTCDA on Au, Ti-PVD, and Ti-CVD substrates. Owing to the presence of pillared Ti structures and Ti–Cl reactive sites, PTCDA nanofibers grew much more readily on the Ti-CVD substrate than on the Au and Ti-PVD substrates. A stable emission current was measured when the PTCDA nanofibers were biased under vacuum. The turn-on field required to produce a current density of 10 $\mu A/cm^2$ was 8 V/μm. The maximum emission current density was 1.3 mA/cm^2, measured at $E = 11$ V/μm. From the slope of the straight line obtained after plotting $\ln(J/E^2)$ versus $1/E$, we calculated the field enhancement factor β to be ca. 989. These results demonstrate an alternative application of PTCDA as an electron-emitting device and open up an interesting area of study of the anisotropic carrier transfer in 1D organic nanostructure.

Acknowledgements

We thank the National Science Council of the Republic of China for supporting this research financially under Contract No. NSC 95-2221-E-009-121. We are also grateful for the technical support provided by the National Nano Device Laboratories.

References

[1] S.R. Forrest, Chem. Rev. 97 (1997) 1793.
[2] M. Eremtchenko, J.A. Schaefer, F.S. Tautz, Nature 425 (2003) 602.
[3] N. Karl, J. Marktanner, R. Stehle, W. Warta, Synth. Met. 41–43 (1991) 2473.
[4] W. Warta, N. Karl, Phys. Rev. B 32 (1985) 1172.
[5] C.W. Tang, S.A. VanSlyke, Appl. Phys. Lett. 51 (1987) 913.
[6] H.P. Wagner, A. DeSilva, Phys. Rev. B 70 (2004) 235201.
[7] A. Dodabalapur, H.E. Katz, L. Torsi, Adv. Mater. 8 (1996) 853.
[8] K. Triyana, T. Yasuda, K. Fujita, T. Tsutsui, Thin Solid Films 477 (2005) 198.
[9] J.J. Chiu, C.C. Kei, T.P. Perng, W.S. Wang, Adv. Mater. 15 (2003) 1361.
[10] H. Liu, Q. Zhao, Y. Li, Y. Liu, F. Lu, J. Zhuang, S. Wang, L. Jiang, D. Zhu, D. Yu, L. Chi, J. Am. Chem. Soc. 127 (2005) 1120.
[11] S.C. Suen, W.T. Whang, B.W. Wu, Y.F. Lai, Appl. Phys. Lett. 84 (2004) 3157.
[12] H. Liu, Y. Li, S. Xiao, H. Gan, T. Jiu, H. Li, L. Jiang, D. Zhu, D. Yu, B. Xiang, Y. Chen, J. Am. Chem. Soc. 125 (2003) 10794.
[13] S.C. Suen, W.T. Whang, F.J. Hou, B.T. Dai, Org. Electron. 7 (2006) 428.
[14] B. Krause, A.C. Dürr, K. Ritley, F. Schreiber, H. Dosch, D. Smilgies, Phys. Rev. B 66 (2002) 235404.
[15] B. Krause, A.C. Dürr, F. Schreiber, H. Dosch, O.H. Seeck, J. Chem. Phys. 119 (2003) 3429.
[16] M. Möbus, N. Karl, J. Crystal Growth 116 (1992) 495.
[17] M. Stöhr, M. Gabriel, R. Möller, Surf. Sci. 507–510 (2002) 330.
[18] L. Chkoda, M. Schneider, V. Shklover, L. Kilian, M. Sokolowski, C. Heske, E. Umbach, Chem. Phys. Lett. 371 (2003) 548.
[19] Th. Wagner, A. Bannani, C. Bobisch, H. Karacuban, M. Stöhr, R. Gabriel, R. Möller, Org. Electron. 5 (2004) 35.
[20] J. Hu, M. Ameen, G. Leusink, D. Webb, J.T. Hillman, Thin Solid Films 308–309 (1997) 589.
[21] P. Fenter, F. Schreiber, L. Zhou, P. Eisenberger, S.R. Forrest, Phys. Rev. B 56 (1997) 3046.
[22] B. Krause, F. Schreiber, H. Dosch, A. Pimpinelli, O.H. Seeck, Europhys. Lett. 65 (2004) 372.
[23] F. Schreiber, Phys. Status Solidi 201 (2004) 1037.
[24] J. McMurry, third ed.Organic Chemistry, Brooks/Cole, 1992, p. 55.
[25] Y. Hirose, A. Kahn, V. Aristov, P. Soukiassian, V. Bulovic, S.R. Forrest, Phys. Rev. B 54 (1996) 13748.
[26] Y. Hirose, A. Kahn, V. Aristov, P. Soukiassian, Appl. Phys. Lett. 68 (1996) 217.
[27] A.F. Hill, Organotransition Metal Chemistry, Wiley-Inter-Science, New York, 2002, p. 136.
[28] J.D. Wright, Molecular Crystals, second ed., Cambridge University Press, 1995, p. 22.
[29] V. Vinciguerra, F. Buonocore, G. Panzera, L. Occhipinti, Nanotechnology 14 (2003) 655.
[30] A. Rajagopal, C.I. Wu, A. Kahn, J. Appl. Phys. 83 (1998) 2649.
[31] H. Wu, S.R. Desai, L.S. Wang, Phys. Rev. Lett. 76 (1996) 212.
[32] R.H. Fowler, L. Nordheim, Proc. Royal Soc. London Ser. A 119 (1928) 626.
[33] V.V. Zhirnov, C. Lizzul-Rinne, G.J. Wojak, R.C. Sanwald, J.J. Hren, J. Vac. Sci. Technol. B 19 (2001) 87.
[34] J.M. Bonard, J.P. Salvetat, T. Stöckli, W.A. de Heer, L. Forró, A. Châtelain, Appl. Phys. Lett. 73 (1998) 918.
[35] J.M. Bonard, N. Weiss, H. kind, T. Stöckli, L. Forró, K. Kern, A. Châtelain, Adv. Mater. 13 (2001) 184.
[36] S.K. Patra, G.M. Rao, J. Appl. Phys. 100 (2006) 024319.

Available online at www.sciencedirect.com
ScienceDirect
Organic Electronics 8 (2007) 513–521
Organic Electronics
www.elsevier.com/locate/orgel

Effects of different electroplated gate electrodes on electrical performances of flexible organic thin film transistor and flexibility improvement

Y.G. Seol, J.G. Lee, N.-E. Lee *

School of Advanced Materials Science and Engineering and Center for Advanced Plasma Surface Technology, Sungkyunkwan University, Suwon, Kyunggi-do 440-746, Republic of Korea

Received 2 September 2006; received in revised form 7 March 2007; accepted 8 March 2007
Available online 19 March 2007

Abstract

Various electroplated metal gate electrodes (Ni, Cu, and Au) on flexible polyimide (PI) substrates were applied to the fabrication of inverted staggered pentacene organic thin film transistors (OTFTs). The metal gate electrodes additively electroplated onto the patterned negative photoresist mask on the Cu(seed)/Cr(adhesion) layers sputter-deposited on the O_2-plasma-treated PI substrates were effective in obtaining good adhesion between the metal gate electrode and organic substrate. It was found that the reduction in the surface roughnesses of the electroplated metal gate and of the subsequently deposited PVP (poly-4-vinyl phenol) gate dielectric layers was a critical factor in improving the device performance. The Ni-gated OTFT exhibited the best electrical characteristics, with a field-effect mobility of $\cong 0.2\ cm^2/V\text{-}s$ and a current on/off ratio of $\cong 10^3$, due to the better chemical stability of the Ni electrode and the smoother surface of the PVP layer on the Ni electrode, as compared to the OTFTs with PVP/Cu or PVP/Au gates. The results of the flexibility test showed that the field-effect mobility and current on/off ratio were not changed significantly when the OTFTs were subjected to 10,000 cyclic bendings with a bending radius of 6 mm in tension mode (outward bending).
© 2007 Elsevier B.V. All rights reserved.

PACS: 72.20.Jv; 82.35.Gh; 85.30.Tv

Keywords: Organic thin film transistor; Pentacene; Electroplating; Polyimide; Flexible devices

1. Introduction

A wide variety of organic semiconductor materials, including pentacene, thiophene oligomers, and regio-regular poly(3-hexylthiophene) (P3HT) polymer, have been investigated for the fabrication of thin film transistors (TFTs) on various substrates [1–23]. The highest performance among the various OTFTs (organic TFTs) with a field-effect mobility of $1.5\ cm^2/V\text{-}s$ has been reported for pentacene organic semiconductors on a silicon substrate [21]. One of the advantages of OTFTs is that they can be used for flexible electronic devices, including radio-frequency identification tags (RFIDs) [1–4],

* Corresponding author. Tel.: +82 32 290 7398; fax: +82 31 290 7410.
E-mail address: nelee@skku.edu (N.-E. Lee).

1566-1199/$ - see front matter © 2007 Elsevier B.V. All rights reserved.
doi:10.1016/j.orgel.2007.03.005

low-cost sensors [5–7], and flexible displays [1,3,8–12].

In order to realize flexible electronic systems utilizing OTFTs on polymer substrates, the good mechanical flexibility of each layer and excellent adhesion between the layers without delamination and cracking during repetitive bending are essential. Using all organic layers in flexible devices may allow them to have acceptable mechanical flexibility [20]. However, the performances of all-organic TFTs in high-frequency, high-resolution or high-power systems on very large substrates can be restricted by the low conductivity of the organic conductor electrodes and interconnects (as low as 200 S/cm compared to $>10^5$ S/cm of Al and Cu), provided that the device performance is not already limited by the field-effect mobility [4,20]. In such cases, designing the metal electrodes and interconnect lines might be restricted by the difficulty in depositing films with a large thickness, fine pitch-size, good adhesion, and precise edge profile. For practical applications of flexible devices, it is necessary to improve the adhesion of the metallic electrodes to the polymeric substrate. In this respect, electroplated metal electrodes on plasma-treated polymer substrates are very useful in obtaining strong adhesion between the electrodes and the substrates [24–26]. Electroplated gate electrodes, therefore, can be a competitive candidate for OTFT applications requiring large area coverage, structural flexibility, low temperature processing and, especially, low processing cost.

In this work, various organic thin film transistors (OTFTs) were fabricated using pentacene as the semiconducting layer, cross-linked PVP (poly-4-vinyl phenol) as the gate dielectric layer, and electroplated metals (Au, Ni, or Cu) as the gate electrodes on flexible polyimide (PI) substrates and their electrical performances were compared. For the fabrication of the gate metal electrode, we utilized the micro-scale metallization approach on a flexible PI substrate, previously reported by our group [25,26], by an additive electroplating process capable of producing conductive metal lines with a fine pitch-size down to ≅4 μm and a high aspect-ratio of ≅4. It was found in this study that controlling the surface roughnesses of the gate electrodes and of the subsequently deposited gate dielectric layer is critical in obtaining high-performance OTFT devices. The electroplated gate electrodes on the polyimide substrate could be successfully integrated into a metal-gated pentacene TFT, resulting in a field-effect mobility of ≅0.2 cm^2/V-s and a current on/off ratio (I_{on}/I_{off}) of ≅10^3 for the Ni-gated OTFT.

2. Experimental

Fig. 1a shows a schematic of the inverted-staggered (bottom-gated) pentacene TFT fabricated in this work. The devices were fabricated by varying the diverse process and geometrical variables, such as the electroplating, gate electrode materials, patterning of the gate dielectric, pentacene thermal evaporation, layer thickness and channel length. The channel length (L) ranged between 10 and 110 μm, and the channel width (W) was 800 μm. PI film (Du Pont; Kapton®) with a thickness of 125 μm was used as the substrate.

An Au, Cu, or Ni gate electrode was electroplated on the adhesion (Cr)/seed (Cu) layers sputter-deposited on the O_2-plasma-treated PI substrates using a negative photo-resist (KMPR, Kayaku Micro Chem Corp.) mask pattern defined by photolithography. The detailed experimental procedures used for the plasma surface-treatment of the PI substrates can be found in Ref. [24]. And the experimental details used for sputter deposition

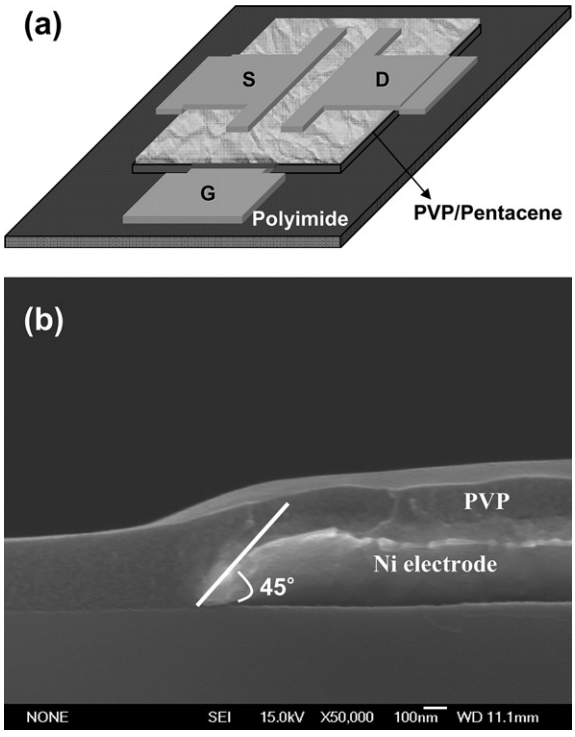


Fig. 1. (a) Structure of OTFT, and (b) FE-SEM image of spin-coated PVP layers coated at the edge of the electroplated Ni gate electrode.

of the adhesion(Cr)/seed(Cu) layers, negative photoresist patterning, electroplating, and selective removal of the Cr/Cu layers were described elsewhere [25,26]. To improve the smoothness of the surface of the electroplated Cu, Au, and Ni gate electrodes, pulsed dc electroplating was used. The electroplating conditions including the temperature of the electrolyte and the current density were optimized for the purpose of reducing the surface roughness of the electroplated gate electrodes. The edge shape of the electroplated metal electrode was controlled with a positive slope of ≅45°, in order to enhance the integrity between the layers, by using a negative-sloped mask for electroplating [for an example, see Fig. 1b].

After the electroplating of the gate electrodes with a thickness of 230–260 nm, cross-linked PVP with a thickness in the range of 250–300 nm was spin-coated on the electroplated metal gate electrodes in order to act as an organic gate dielectric layer. To prepare the organic gate insulator, PVP and a cross-linking agent (CLA), poly(melamine-co-formaldehyde), were mixed with the solvent, propylene glycol monomethyl ether acetate (PGMEA). The patterning of the PVP gate dielectric layer was carried out by chemical dry etching using a negative PR (KMPR) mask in an $O_2/N_2/CF_4$ microwave plasma.

A pentacene active layer with a thickness of ≅75 nm was deposited by thermal evaporation in a vacuum chamber at a typical working pressure of less than 5×10^{-6} Torr, while keeping the substrate temperature at 80–100 °C and the deposition rate near to 0.1 nm/s. No further purification or sublimation of the purchased pentacene (Aldrich Chemical Company) was performed. Gold source/drain (S/D) electrodes with a thickness of ≅100 nm were formed by thermal evaporation using a shadow mask.

The surface morphologies of the layers of the fabricated devices were examined by atomic force microscopy (AFM) in contact mode. To check the adhesion of the electrodes, flexibility tests were performed by bending the fabricated devices in tension and/or compression modes with a bending radius ranging from 3 to 6 mm. The tested devices were examined by optical microscopy, FE-SEM (field-emission scanning electron microscopy), and dual beam-FIB (focused ion-beam) FE-SEM (NOVA 200), in order to examine the delamination and cracking of the layers. The electrical characterization of the OTFTs before and after the flexibility test was carried out in an ambient atmosphere using a HP 4145B semiconductor parameter analyzer.

3. Results and discussion

The electrical performance of the OTFT devices with electroplated metal gate electrodes and PVP gate dielectric was measured under ambient conditions without any protection after their preparation. The I_{SD} (source–drain current) – V_{SD} (source–drain voltage) output characteristics were determined by varying the applied V_{SD} from 0 to −40 V, while also varying the V_G (gate voltage) from 0 to −40 V in steps of −4 V. The field-effect mobility μ was calculated in the saturation region with the following equation:

$$I_{SD(sat.)} = (WC_i/2L)\mu(V_G - V_T)^2, \quad (1)$$

where μ is the field-effect mobility, C_i the capacitance per unit area of the insulator, and V_T is the threshold voltage.

The typical output characteristics of the OTFT devices with the electroplated Ni, Cu, and Au electrodes are shown in Fig. 2a–c, respectively. The plots of the transfer characteristic, $(I_{SD})^{1/2}$ versus V_G, for the devices at $V_{SD} = -40$ V are shown in Fig. 2 as the insets. The Ni-gated device [$L = 40$ μm] in Fig. 2a shows that the μ and V_T values were 0.2 cm^2/V-s and −2.7 V, respectively. The drain current on/off ratio, I_{on}/I_{off}, was ≅10^3. Fig. 2b shows the typical I–V characteristics of the Cu-gated device [$L = 40$ μm]. The device has a μ value of 0.1 cm^2/V-s, a V_T of −1.2 V and an I_{on}/I_{off} of ≅10^2, as obtained from Eq. (1). The smaller I_{on}/I_{off} and field-effect carrier mobility of the Cu-gated device compared to those of the Ni-gated OTFT is presumably due to the poor ordering and slightly smaller grain size of the pentacene layer, as will be discussed later. In the case of the Cu-gated OTFT, when a V_{DS} and V_G larger than −20 V were applied, delamination occurred between the semiconductor and the Au S/D electrodes. Therefore, the I–V characteristics of the Au-gated device [$L = 30$ μm] shown in Fig. 2c were obtained by applying V_{DS} and V_G values of up to −20 V. This device shows the smallest field-effect carrier mobility of 0.01 cm^2/V-s, as compared to that of the Ni-gated or Cu-gated device, and a threshold voltage of 1.5 V and I_{on}/I_{off} of 10. The off-current, I_{off}, was ≅0.4 μA at $V_{DS} = -40$ V, which indicates that there exists a relatively high bulk current.

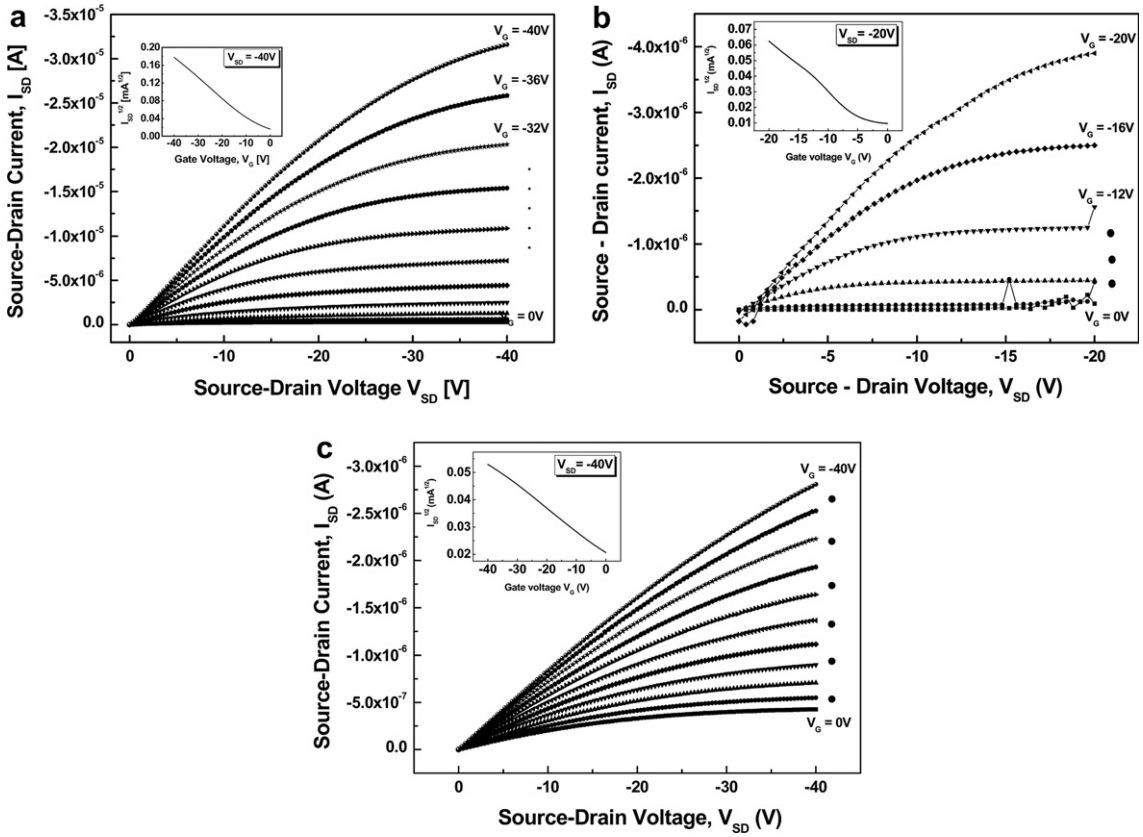


Fig. 2. (a) The I_{SD}–V_{SD} output and transfer characteristics, $(I_{SD})^{1/2}$ versus V_{GS}, obtained at $V_{SD} = -40$ V of the fabricated device ($L = 40$ μm) with the electroplated Ni gate electrode. The V_{SD} was varied from 0 to −40 V and V_G was varied from 0 to −40 V in steps of −4 V. (b) The I_{SD}–V_{SD} output and transfer characteristics, $(I_{SD})^{1/2}$ versus V_{GS}, obtained at $V_{SD} = -20$ V of the fabricated device ($L = 40$ μm) with the electroplated Cu gate electrode. The V_{SD} was varied from 0 to −20 V and V_G was varied from 0 to −20 V in steps of −4 V. (c) The I_{SD}–V_{SD} output and transfer characteristics, $(I_{SD})^{1/2}$ versus V_{GS}, obtained at $V_{SD} = -40$ V of the fabricated device ($L = 30$ μm) with the electroplated Au gate electrode. The V_{SD} was varied from 0 to −40 V and V_G was varied from 0 to −40 V in steps of −4 V.

In order to understand the effect of the gate metal on the device characteristics, the surfaces of the electroplated gate metals and the spin-coated PVP layers were characterized by AFM and the typical images of the PVP surfaces are shown in Fig. 3a–c. The typical rms (root-mean-squared) surface roughness of the electroplated Ni, Cu, and Au layers ranged from 3.9 to 8.7 nm, increasing in that order. As shown in Fig. 3a, the surface of the cross-linked PVP gate dielectric layers on the Ni gate electrode is smoothened out and shows an rms roughness of 0.33 nm. A similar surface morphology was observed for the PVP layer on the Cu electrode, but with a larger surface roughness of ≅0.91 nm, as seen in Fig. 3b. The surface morphology of the spin-coated PVP layers on the Au electrodes shown in Fig. 3c shows that it has a rougher surface than that of the Ni or Cu electrode, with a surface roughness of ≅3.56 nm. In Fig. 3d, the rms surface roughness values of the PVP layers on the different gate electrodes are plotted. The surface roughness increased in the order of the Ni, Cu, and Au electrodes. Even though the surface roughness of the PVP gate dielectric layers was significantly reduced compared to that of the metal electrode surface, the surface roughness of the PVP layers followed the same tendency as that of the corresponding metal electrodes.

The measured surface morphologies of the PVP layers on the different electroplated gate electrodes patterned by photolithography and chemical dry etching showed slightly larger features on the PVP/Au gate compared to those on the PVP/Ni and PVP/Cu gates. For example, an increase in the surface roughness of the patterned PVP layer on the Ni electrode from ≅0.33 nm to ≅1.37 nm

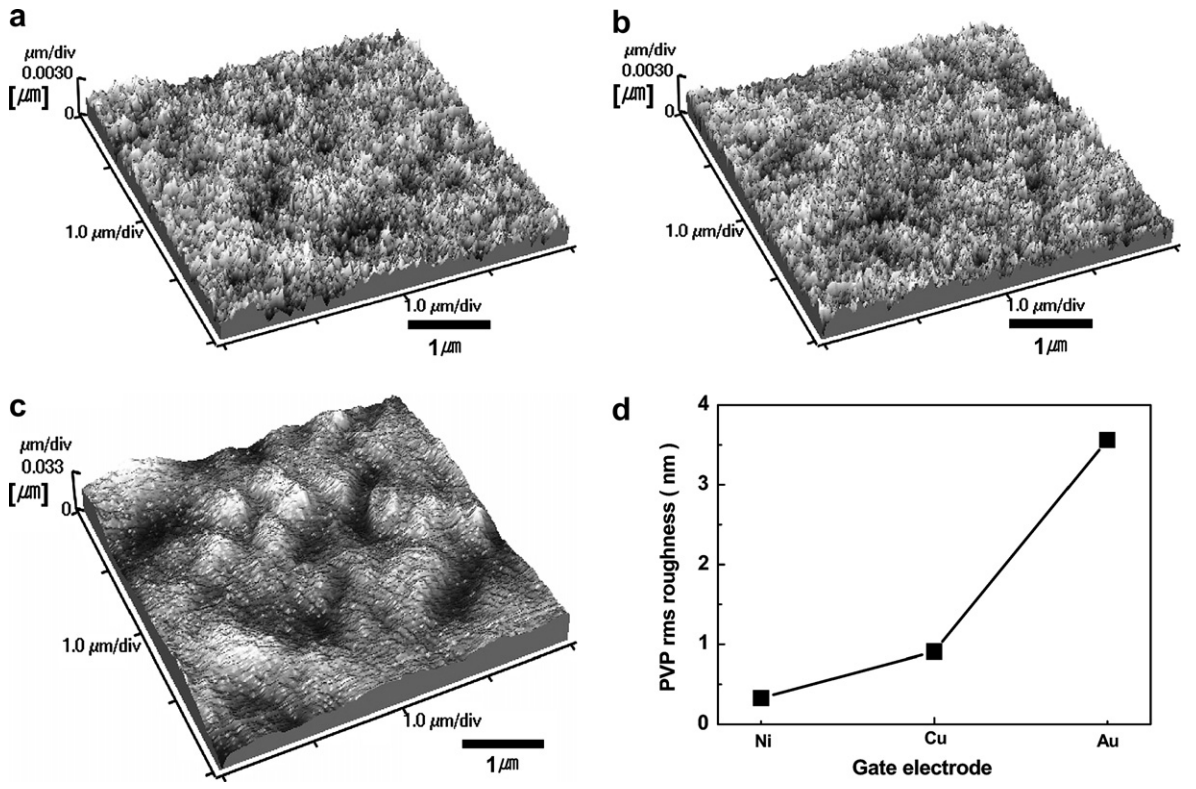


Fig. 3. AFM images of spin-coated cross-linked PVP dielectric layer on (a) electroplated Ni gate electrode [rms roughness of 0.33 nm], (b) electroplated Cu gate electrode [rms roughness of 0.91 nm], and (c) electroplated Au gate electrode [rms roughness of 3.56 nm] (d) rms surface roughness values of the PVP layers on electroplated Ni, Cu, and Au gate electrodes.

[not shown here] was observed after patterning. The increase in the surface roughness after the patterning of the PVP layers is presumably due to the damage that occurred during the process of removing the PR etch mask using solvent [27,28].

Interestingly, the field-effect carrier mobility values for the different gate metals shown in Fig. 4, obtained from the data in Fig. 1, were well correlated with the rms surface roughness of the PVP layers, indicating that a larger gate dielectric roughness leads to a lower field-effect mobility. This observation is probably related to the difference in the pentacene microstructure which is affected by the surface morphologies of the PVP layers, as shown in Fig. 5. The $I_{on/off}$ data plotted together with the field-effect mobilities in Fig. 4 also show that the $I_{on/off}$ values are related to the surface roughness of the different electroplated electrodes. In the case of the Au gate metal, impurities on the electroplated Au electrode may also affect the device performance characteristics, such as the high level of the drain off-current, as discussed below. Relatively low field-effect mobility and current on–off ratio in this work, compared to the reported values in the other literatures [22,23], is presumably attributed to larger surface roughness caused by the use of electroplated gate electrodes and higher leakage current of the gate dielectric layers used in this work, respectively.

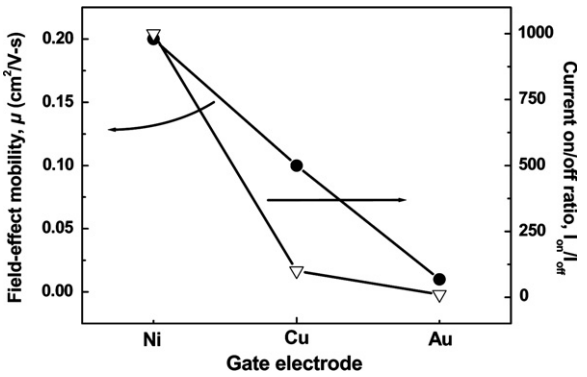


Fig. 4. Field-effect mobilities μ and current on/off ratios $I_{on/off}$ for the devices with the different gate electrodes.

In order to understand the effect of the gate dielectric roughness on the device characteristics, the typical AFM surface morphologies of the 75-

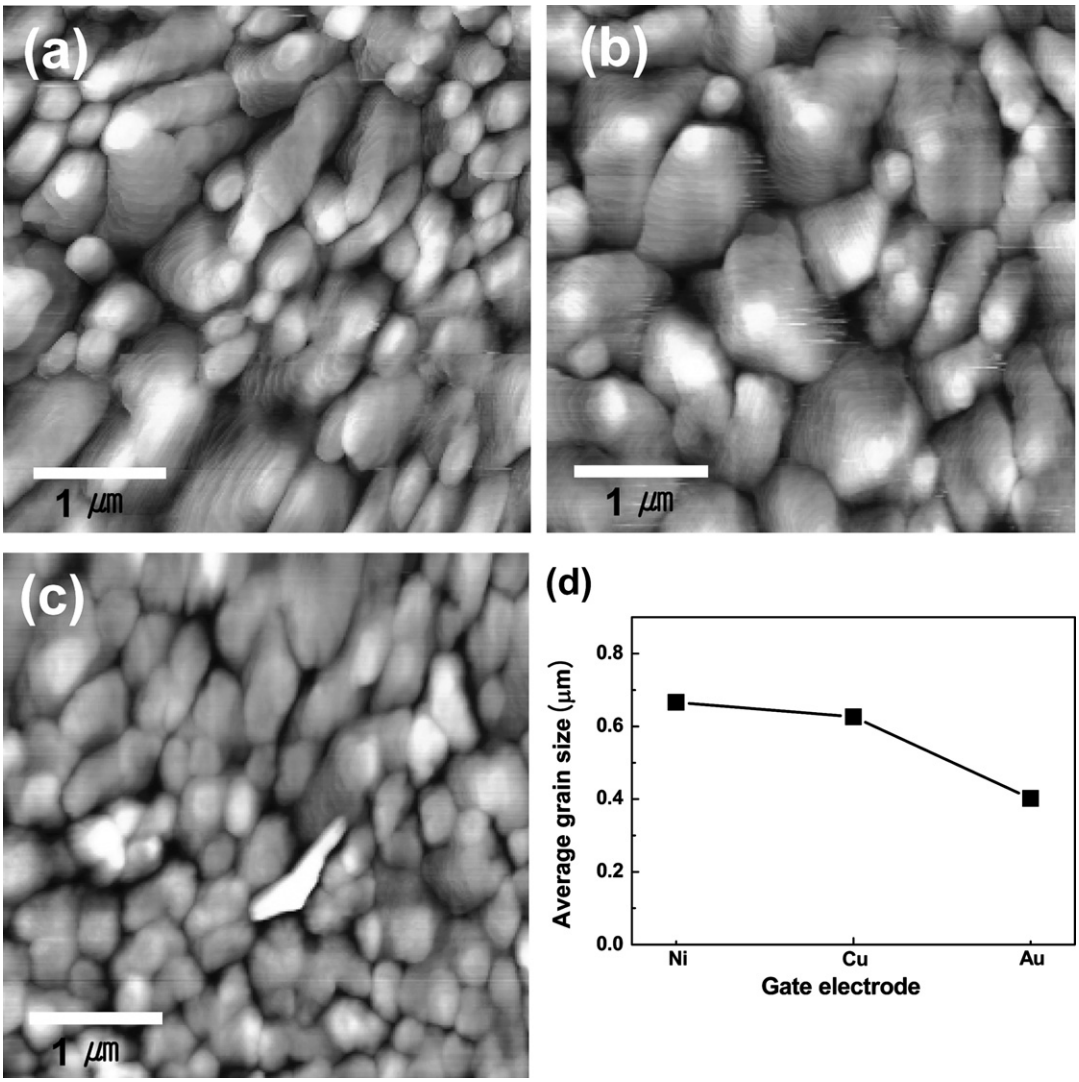


Fig. 5. AFM images of the pentacene layers deposited on the (a) PVP/Ni, (b) PVP/Cu, (c) PVP/Au gates, and (d) average grain size of the pentacene layers on the different gates.

nm-thick pentacene layers on the PVP dielectric on the Ni, Cu, and Au electrodes were also obtained and are shown in Fig. 5a–c, respectively. As shown in Fig. 5d, the average grain size of the pentacene layers decreased in the order of the PVP/Ni, PVP/Cu, and PVP/Au gates. Furthermore, the interconnectivity of the pentacene grains seems to be better for the pentacene on the PVP/Ni gate as compared to that on the PVP/Cu and PVP/Au gates. The increased roughness of the metal gate and, in turn, of the PVP gate dielectric layer, leads to the pentacene layer having a smaller grain size, which is similar to the observations of the effect of the gate dielectric roughness made by two other research groups [29,30]. The difference between this experiment and these previously reported experiments [29,30] is that, in these previous experiments, gate dielectric layers with different surface roughnesses were deposited on the same gate electrode. The reduced grain size of the active pentacene layers can contribute to the reduced carrier mobility, presumably due to an increase in the amount of trap states [31], scattering by grain boundaries [32] and surface scattering [33]. A rougher dielectric surface leads to more defects and voids that can act as traps at the semiconductor–dielectric interface [31]. The roughness of the interface also affects the ordering of the organic semiconductor molecules during the

formation of the active layer [13,34–36]. In consequence, the field-effect carrier mobility decreases as the interface roughness increases, due to the interface traps and poor molecular ordering. This poor ordering probably impedes the movement of the charge carriers through the semiconductor layer and the interface region, due to the scattering and transfer of the momentum of the carriers to the phonons in the organic semiconductor [13]. The surface scattering of the hole carriers near the rough interface between the gate dielectric and metal electrode can contribute to the trapping of the carriers in the roughness "valleys" [29].

In the case of the PVP/Au gates, the impurities that diffused into the PVP gate dielectric layer from the surface of the electroplated Au may have contributed to the increase in the off-current, I_{off}. We previously demonstrated the effect of impurities such as Na, S, and Cu (which diffused from the seed layer) in the electroplated Au source and drain surfaces on the device performances of top-gated P3HT TFTs [37]. These impurities may cause an increase in the off-current, and in turn a decrease in the I_{on}/I_{off} value, due to the increased bulk current in the organic semiconductor caused by the diffusion of the impurities through the PVP dielectric layer from the electroplated Au gate electrode.

In order to evaluate the adhesion between the layers in the device and the effects of cyclic bending on the device characteristics, a flexibility test was carried out for the Ni-gated OTFT devices on the plasma-treated or non-treated PI surface, by bending the device in cyclic tension and compression mode or in cyclic tension mode only, with bending radii of 3 and 6 mm. The bending direction of the device, i.e. the direction of induced strain, was perpendicular to the direction of the channel, i.e. the carrier transport.

When 10,000 repetitive bendings in tension mode only (outward bending) with a bending radius of 6 mm were applied to the devices on the plasma-treated or non-treated PI substrate, the μ and I_{on}/I_{off} values were not significantly changed and no cracks were observed on the device surfaces. When the bending radius was reduced to 3 mm in cyclic tension mode, however, some cracks appeared in the Ni gate electrode area of the tested devices on the non-treated PI substrate, whereas no cracks appeared on the plasma-treated PI substrate. However, the device characteristics of the Ni gate electrode were not changed significantly, in spite of the presence of the cracks.

When the cyclic bending test was performed using alternating tension and compression, 20 times each, with a bending radius of 3 mm, the μ and $I_{on/off}$ values for the device on the non-treated PI substrate were decreased by 0.7% and 90%, respectively. For the devices on the plasma-treated PI substrate, the extent of the degradation in the electrical properties was similar. In order to see the effects of the alternative tension and compression of the devices on the non-treated and plasma-treated PI substrates, the structural integrity was examined. The optical microscopy images [not shown here] showed the presence of cracks in the Ni gate elec-

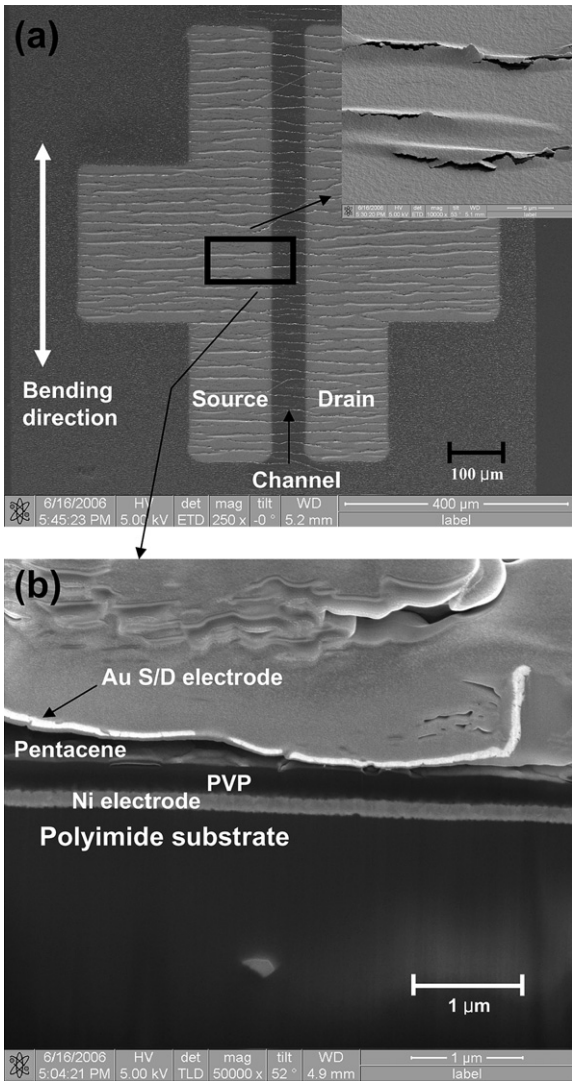


Fig. 6. FE-SEM images of the devices after cyclic bending in alternating tension and compression mode with a bending radius of 3 mm. (a) Top-view and (b) cross-sectional view.

trodes for the devices on both PI substrates. However, the bending test for the device on the non-treated substrate resulted in delamination at the interface of the Ni electrode/PI substrate. The top-view FE-SEM image [Fig. 6a] of the device fabricated on the plasma-treated PI substrate shows the cracking of the Ni electrode layers in the channel and source/drain regions. The direction of the cracks is parallel to the channel direction. The cross-sectional image of the device after the bending test obtained by dual-beam FIB FE-SEM in Fig. 6b shows the occurrence of delamination at the interface between the Au source/drain electrode and pentacene layer. However, the images of the Ni electrode/PI substrate and the PVP/Ni electrode interfaces in Fig. 6b still show good integrity of the interfaces, indicating that the plasma treatment of the polyimide substrate was effective in obtaining good interfacial adhesion. These results indicate that the plasma treatment of the PI substrate is effective in improving the adhesion between the metal gate electrode and the flexible substrate, even though the electrical performances of the devices seem to be primarily affected by the cracks and delamination of the Au S/D electrodes. The adhesion strength between the Au S/D electrode and the pentacene layer, therefore, needs to be improved.

4. Conclusion

The experimental results in this work showed how the different electroplated gate metal electrodes affect the electrical performance of the OTFTs. A rougher gate electrode and resulting larger roughness of the PVP gate dielectric surface led to lower electrical performances due to reduced the field-effect mobility caused by a decrease in the grain size of the pentacene layers. Therefore, the electroplating process that controls the initial surface roughness of the electroplated metal electrode is very important for fabricating OTFTs with high electrical performance.

In this work, we utilized a reliable, low-cost and large-area compatible process, which is similar to that used in FPCB (flexible printed circuit board) technology, in which metal wiring is incorporated on a flexible polyimide substrate using an additive metallization. In this technology, the use of the metal electrodes electroplated on adhesion layers deposited on the plasma-treated polymer surface might enable one to obtain reliable devices on a flexible substrate, as regards their mechanical flexibility during repetitive cyclic bending. Furthermore, the interconnect lines can be formed using the same approach. Therefore, active devices such as OTFTs might be integrated into advanced FPCB technologies using electroplating to form the electrodes and interconnect lines.

Acknowledgements

This work was supported in part by the Korea Science and Engineering Foundation (Grant No. 2005-0563-000) and in part by the Center of Excellence program of the Korea Science and Engineering Foundation (Grant No. R-11-2000-086-0000-0).

References

[1] J.R. Sheats, J. Mater. Res. 19 (2004) 1974.
[2] P.F. Baude, D.A. Ender, M.A. Haase, T.W. Kelley, D.V. Muyres, S.D. Thesis, Appl. Phys. Lett. 82 (2003) 3964.
[3] T.W. Kelley, P.F. Baude, C. Gerlach, D.F. Ender, D. Muyres, M.A. Haase, D.E. Vogel, S.D. Theiss, Chem. Mater. 16 (2004) 4413.
[4] W. Clemens, W. Fix, J. Ficker, A. Knobloch, A. Ullmann, J. Mater. Res. 19 (2004) 1963.
[5] B. Crone, A. Doadbalapur, A. Gelperin, L. Torsi, H.E. Katz, A.J. Lovinger, Z. Bao, Appl. Phys. Lett. 78 (2001) 2229.
[6] L. Torsi, N. Cioffi, C.D. Franco, L. Sabbatini, P.G. Zambonin, T. Bleve-Zacheo, Solid-State Electron. 45 (2001) 1479.
[7] T. Someya, T. Sekitani, S. Iba, Y. Kato, H. Kawaguchi, T. Sakurai, Proc. Natl. Acad. Sci. 101 (2004) 9966.
[8] J.A. Rogers, Z. Bao, A. Dodabalapur, IEEE Electron. Dev. Lett. 21 (2000) 100.
[9] P. Mach, S.J. Rodriguez, R. Nortrup, P. Wiltiuz, J.A. Rogers, Appl. Phys. Lett. 78 (2001) 3592.
[10] C.D. Sheraw, L. Zhou, J.R. Huang, D.J. Gunbdlich, T.N. Jackson, M.G. Kane, I.G. Hill, M.S. Hammond, J. Campi, B.K. Greening, J. Francl, J. West, Appl. Phys. Lett. 80 (2002) 1088.
[11] Y.-H. Kim, S.-K. Park, D.-G. Moon, W.-K. Kim, J.-I. Han, Displays 25 (2004) 167.
[12] B. Comiskey, J.D. Albert, H. Yshizawa, J. Jacobson, Nature 394 (1998) 253.
[13] H. Sirringhaus, P.J. Brown, R.H. Friend, M.M. Nielsen, K. Bechgaard, B.M.W. Langeveld-Voss, A.J.H. Spiering, R.A.J. Janssen, E.W. Meijer, P. Herwig, D.M. de Leeuw, Nature 401 (1999) 685.
[14] C.D. Dimitrakopuls, D.J. Mascaro, IBM J. Res. Dev. 45 (2001) 11.
[15] Z. Bao, A. Dodabalapur, A.J. Lovinger, Appl. Phys. Lett. 69 (1996) 4108.
[16] G. Wang, T. Hirasa, D. Moses, A.J. Heeger, Synth. Met. 146 (2004) 127.
[17] S.K. Park, Y.H. Kim, J.I. Han, D.G. Moon, W.K. Kim, M.G. Kwak, Synth. Met. 139 (2003) 377.
[18] M.M. Ling, Z. Bao, Chem. Mater. 16 (2004) 4824.

[19] J.-F. Chang, B. Sun, D.W. Breiby, M.M. Nielsen, T.I. Solling, M. Giles, I. McCulloch, H. Sirringhaus, Chem. Mater. 16 (2004) 4772.
[20] H. Rost, J. Ficker, J.S. Alonso, L. Leenders, I. McCulloch, Synth. Met. 145 (2004) 83.
[21] S.F. Nelsona, Y.-Y. Lin, D.J. Gundlach, T.N. Jackson, Appl. Phys. Lett. 72 (1998) 1854.
[22] H. Klauk, M. Halik, U. Zschieschang, F. Eder, G. Schmid, C. Dehm, Appl. Phys. Lett. 82 (2003) 4175.
[23] H.S. Byun, Y.-X. Xu, C.K. Song, Thin Solid Films 493 (2005) 278.
[24] S.H. Kim, S.W. Na, N.-E. Lee, Y.W. Nam, Y.-H. Kim, Surf. Coat. Technol. 200 (2005) 2072.
[25] S.H. Cho, S.H. Kim, N.-E. Lee, H.M. Kim, Y.W. Nam, Thin Solid Films 475 (2005) 68.
[26] S.H. Cho, S.H. Kim, J.G. Lee, N.-E. Lee, Microelectron. Eng. 77 (2005) 116.
[27] J. Park, S.-O. Shim, H.H. Lee, Appl. Phys. Lett. 86 (2005) 073505.
[28] J. Park, S.Y. Park, S.-O. Shim, H. Kang, H.H. Lee, Appl. Phys. Lett. 85 (2004) 15.
[29] S. Steudel, S. De Vusser, S. De Jonge, D. Janssen, S. Verlaak, J. Genoe, P. Heremans, Appl. Phys. Lett. 85 (2004) 4400.
[30] J. Puigdollers, C. Voz, A. Orpella, R. Quidant, I. Martín, M. Vetter, R. Alcubilla, Org. Electron. 5 (2004) 67.
[31] A.R. Volkel, R.A. Street, D. Knipp, Phys. Rev. B 66 (2002) 195336.
[32] S. Valletta, L. Marincci, P. Heremans, Appl. Phys. Lett. 82 (2003) 745.
[33] A. Valletta, L. Mariucci, G. Fortunato, Appl. Phys. Lett. 82 (2003) 3119.
[34] I. Kymissis, C.D. Dimitrakopoulos, S. Purushothaman, IEEE Trans. Electron. Dev. 48 (2001) 1060.
[35] D.J. Gundlach, L. Jia, T.N. Jackson, IEEE Electron. Dev. Lett. 22 (2001) 571.
[36] C. Yang, F.P. Orfino, S. Holdcroft, Macromolecules 29 (1996) 6510.
[37] J.G. Lee, Y.G. Seol, N.-E. Lee, Thin Solid Films 515 (2006) 805.

Available online at www.sciencedirect.com
ScienceDirect
Organic Electronics 8 (2007) 522–528
Organic Electronics
www.elsevier.com/locate/orgel

The electronic structure of Ni-phthalocyanine/metal interfaces studied by X-ray and ultraviolet photoelectron spectroscopy

F. Petraki, V. Papaefthimiou, S. Kennou *

Department of Chemical Engineering, University of Patras and FORTH-ICE/HT, Gr-26504 Rion, Patras, Greece

Received 26 July 2006; received in revised form 8 February 2007; accepted 9 March 2007
Available online 19 March 2007

Abstract

Nickel phthalocyanine (NiPc) thin films were grown stepwise on polycrystalline gold and silver substrates and the formed interfaces were characterized by X-ray and ultraviolet photoelectron spectroscopies (XPS, UPS). The variation of the XPS core level binding energy with NiPc film thickness yields information about band bending and interface dipoles. The valence band structure of the NiPc thin films was determined by UPS and exhibits four main features at binding energies 1.50 eV, 3.80 eV, 6.60 eV and 8.85 eV, respectively. The NiPc highest occupied molecular orbital (HOMO) cut-off was measured at ~1.00 eV from the analyzer Fermi level and from the measured work function change of the growing NiPc film a final work function value for NiPc was estimated at 3.90 ± 0.10 eV. The main C1s peak of the NiPc film (~5.0 nm) consists of two components at 284.8 eV (C–C bonds), 286.2 eV (C–N bonds) reflecting photoemission from multiple carbon sites within the molecule and a satellite at 287.9 eV, whereas the Ni2p and N1s peaks appear at ~855.9 eV and ~399.3 eV, respectively and are due to Ni–N bonds. The energy level diagrams of the NiPc/Au and NiPc/Ag interfaces were determined from a combination of the XPS and UPS results, yielding a hole injection barrier of 0.90 ± 0.10 eV for both substrates.
© 2007 Elsevier B.V. All rights reserved.

PACS: 73.20.At; 78.40.Me; 79.60.−i

Keywords: NiPc; XPS; UPS; Metals; Interface; Energy diagrams; Work function

1. Introduction

Semiconducting organic materials have received increasing attention in recent years due to their successful application in optical and electronic devices. Phthalocyanines (Pcs) is a family of medium sized organic molecules. These materials are already widely used in gas sensor technology and in electronic devices [1–3] because of their beneficial properties such as thermal, chemical and photochemical stability, layered like growth mode when deposited onto metallic substrates and advantageous optical and electronic properties. Their thermal stability makes them suitable for formation of thin films by thermal sublimation. In general Pcs and MPcs are

* Corresponding author. Tel.: +30 2610 996324; fax: +30 2610 993255.
E-mail address: kennou@iceht.forth.gr (S. Kennou).

1566-1199/$ - see front matter © 2007 Elsevier B.V. All rights reserved.
doi:10.1016/j.orgel.2007.03.006

classified as p-type semiconductors characterized by low mobility and low carrier concentration [4].

PCs that have already attracted most interest are metal-free phthalocyanine (H_2Pc) and its metal derivative copper phthalocyanine (CuPc). CuPc (pure and fluorinated) and the interfaces that it forms with different substrates have been extensively investigated with several techniques and have been already successfully applied as buffer layers in OLEDs and as active layers in OFETs [5–10].

Nickel phthalocyanine (NiPc) is an organic semiconductor with a relatively high mobility value ($\sim 1 \times 10^{-5}\ m^2\ V^{-1}\ s^{-1}$) [11], compared with the equivalent for other MPcs ($7.6 \times 10^{-9}\ m^2\ V^{-1}\ s^{-1}$ for ZnPc [12], $3 \times 10^{-7}\ m^2\ V^{-1}\ s^{-1}$ for PbPc [13], $10^{-8}\ m^2\ V^{-1}\ s^{-1}$ for CuPc [14]), which makes it a promising candidate for the development of future electronic devices. There are several studies of the electrical properties of NiPc thin films for transistors and photovoltaic devices [15–19], but only few investigations for the interfaces of NiPc with metals, Si and HOPG [18–20], although the role of the interfaces is crucial in the device performance. In this work we investigate the electronic properties of the interface of NiPc with polycrystalline gold and silver, which are used as electrode materials in organic devices, by core level X-ray photoemission (XP) and valence band ultraviolet photoemission (UP) Spectroscopies. The results are compared with those for CuPc adsorption on gold and silver substrates.

2. Experimental

The experiments were carried out in a multichamber UHV system (base pressure $\sim 2 \times 10^{-10}$ mbar) which allows the preparation of interfaces with high purity and controlled thickness [21].

Commercial NiPc powder from Alfa Aesar was evaporated in the preparation chamber, from a home made deposition source kept at 425 °C, after purification in UHV by heating at 150 °C for about 15 h [21]. The pressure during the stepwise evaporation of NiPc films was less than 5×10^{-8} mbar. The substrates, polycrystalline Au and Ag foils, were cleaned by Ar^+ sputtering at room temperature and subsequent annealing. For sputtering, an argon pressure of 5×10^{-6} mbar, an accelerating voltage of 5 keV and an incidence angle of 45° were used. During sputtering the substrate temperature was $T_{Au} = 430$ °C and $T_{Ag} = 200$ °C. The cleanliness of the substrates was checked by XPS. A small persistent residual signal of chemisorbed oxygen could be detected only in the case of the Ag foil, which is more reactive than Au. The coverage of oxygen on Ag is calculated by the equation [22]

$$I_{Ag3d} = I^{\infty}_{Ag3d}\{1 - \Phi_O + \Phi_O \exp[-\alpha_o/\lambda_O(E_{Ag3d})]\}$$

which gives the signal of the Ag substrate covered by a fractional monolayer Φ_O of oxygen in the absence of inelastic scattering. From the kinetic energy $E(Ag3d)$ of the $Ag3d_{5/2}$ peak the attenuation length for the photoelectrons in an oxide matrix $\lambda_O(E_{Ag3d}) = 2.35$ nm and the atomic radius α_O of oxygen, a small concentration of 0.25 ML was determined.

After each deposition step the surface of the sample was characterized by XPS and UPS. The XPS measurements were carried out with a non-monochromatic AlKα source at 1486.6 eV while for UPS measurements the HeI (21.22 eV) excitation line was used. The binding energy scale of the spectrometer was calibrated by the $Au4f_{7/2}$ core level (84.00 ± 0.05 eV) for clean Au. The XPS resolution measured by the full width at half maximum (FWHM) of the $Au4f_{7/2}$ was 1.7 eV for a constant pass energy of 97 eV. A negative bias of 12.28 V was applied to the sample during UPS measurements in order to separate sample and analyzer high binding energy cut-offs and estimate the absolute work function value from the ultraviolet photoemission spectra. The analyzer resolution is determined from the width of the Au Fermi edge and it is found 0.16 eV.

The film thickness was estimated by XPS from the attenuation of the substrate peak intensity (Au4f for the NiPc/Au interface and Ag3d for the NiPc/Ag interface) due to the NiPc overlayer formation (increasing C1s) assuming a layer by layer growth mode for small coverage [22]. The average film thickness, d, was calculated assuming that the attenuation of the substrate signal, Au4f, follows the exponential relation

$$I_{Au4f}/I^0_{Au4f} = \exp\left(-d/\lambda^{NiPc}_{(Au4f)}\right)$$

where I^0_{Au4f} is the Au4f peak intensity measured for the clean metallic surface and $\lambda^{NiPc}_{(Au4f)}$ is given for organic compounds by [22]

$$\lambda^{organic}_{(Au4f)} = (10^3/\rho) \times (49E^{-2} + 0.11E^{0.5}) = 26\ \text{Å}$$

where E is the kinetic energy of the Au4f photoelectrons and the density ρ has been taken approximately equal to 1.64 g cm^{-3} as specified for CuPc [23]. The same equations were used for the estimation of the organic film thickness at the NiPc/Ag

interface, using the I^0_{Ag3d}, the Ag3d peak intensity measured for the clean metallic surface and the kinetic energy of the Ag3d photoelectrons, in order to calculate the $\lambda^{NiPc}_{(Ag3d)}$. The Fermi level position and the work function of the metallic substrates were determined by the onset and the cut-off of the UP spectra, respectively.

3. Results and discussion

Fig. 1 presents the variation of the C1s peak with organic film thickness for the: NiPc/Au (a) and NiPc/Ag (b) interfaces. All XPS C1s peaks were normalized to the same height and were fitted with Lorentzian and Gaussian functions after the subtraction of a Shirley-type background [24]. The C1s peak attributed to NiPc appears after the first deposition and its intensity increases as the organic film grows, whereas the binding energy exhibits a small upward shift. The C1s peak for the 5.0 nm organic film was resolved into three components, reflecting photoemission from multiple sites within the molecule (Fig. 2). The binding energies (BEs) of the XPS C1s components for the bulk organic overlayer are: 284.8 eV for the aromatic carbon of benzene rings, 286.2 eV for pyrrole carbon linked to nitrogen and 287.9 eV, which can be attributed to satellite of the main peak in agreement with studies of NiPc films deposited onto nickel stubs [25]. The BE and FWHM of the Au4f and Ag3d peaks of the metallic substrates remain stable, while the intensity of these peaks gradually decreases upon deposition. The absence of additional components in the C1s peak and also at Au4f and Ag3d core levels (not shown) indicates that the formed interfaces are abrupt without chemical interactions or interfacial states. The N1s XPS peak of the organic film has a lower intensity than the C1s peak because of the atomic ratio N/C (=8/32) in the NiPc molecule. The N1s peak of the NiPc film (5.0 nm) appears at 399.3 eV binding energy with a FWHM of 1.85 eV and Ni2$p_{3/2}$ at 855.9 eV.

Fig. 3 shows the binding energies of the XPS C1s peak as the NiPc film thickness grows. At the NiPc/Au interface there is a total shift of 0.45 eV towards higher binding energies for a 7.0 nm thick film. Up to 1.0 nm thick film of NiPc there is a 0.30 eV shift and for thicker organic films a further shift of 0.15 eV is observed. In the case of the NiPc/Ag interface only a small total shift of 0.10 eV towards higher binding energies could be detected. The origin of these binding energy shifts will be discussed later in combination with the UPS results.

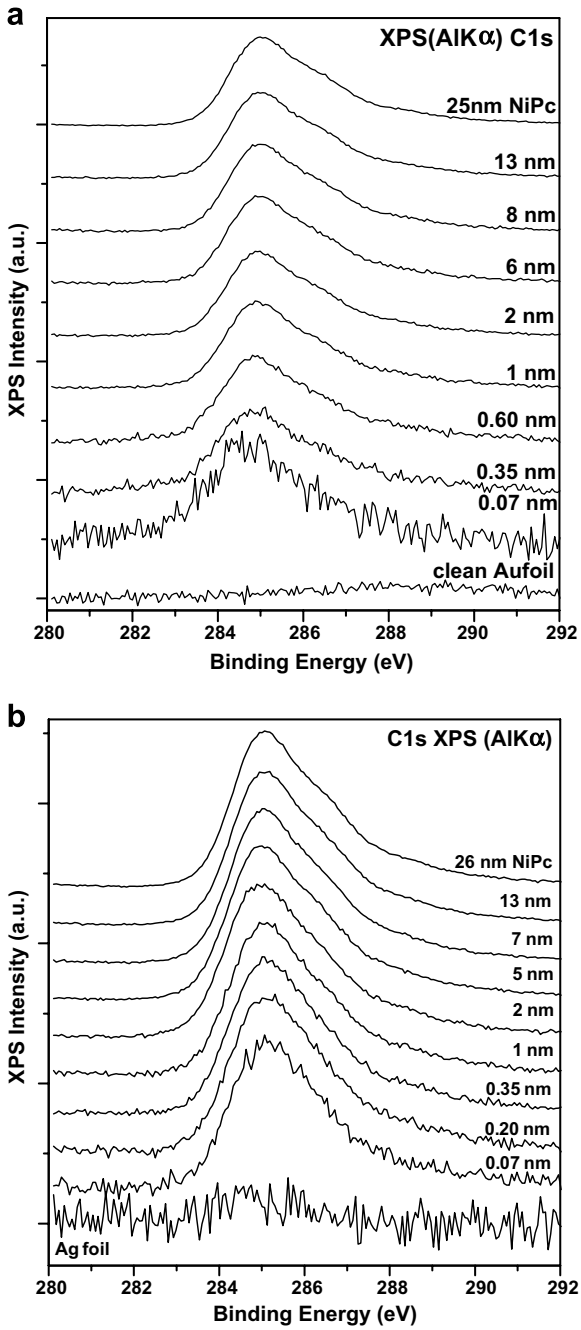


Fig. 1. Evolution of XPS C1s peak of the NiPc on (a) Au and (b) Ag during interface formation.

Fig. 4 shows the changes of the UP spectra of the NiPc/Au and NiPc/Ag interfaces with increasing organic film thickness. Fig. 4a shows the change of the UP spectra of the NiPc/Au interface. The bottom spectrum represents the clean Au substrate, which is dominated by the Au5d orbital emission features. The metallic Fermi edge cut-off is clearly visible.

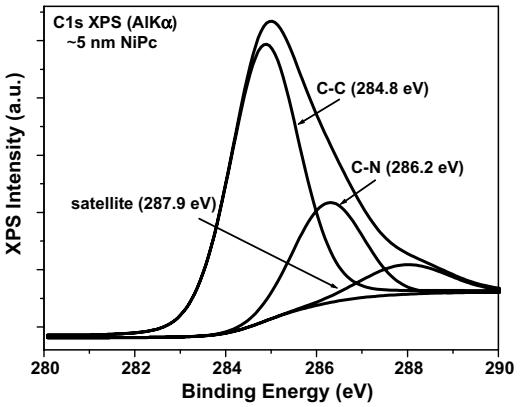


Fig. 2. Analysis of the XPS C1s peak for a 5.0 nm thick NiPc film.

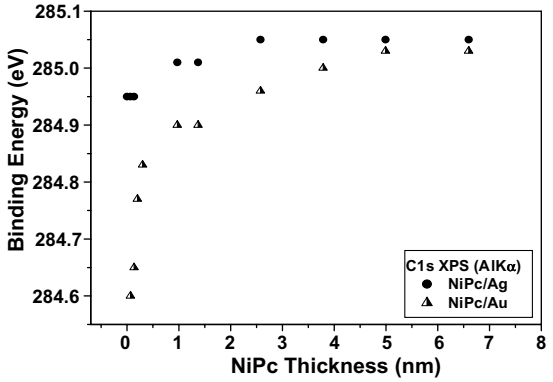


Fig. 3. XPS binding energy of C1s peak versus NiPc thickness for NiPc/Au and NiPc/Ag interfaces.

After a submonolayer NiPc coverage (one monolayer ~0.35 nm [26]) new features appear and, as the coverage increases, those of Au5d are gradually attenuated. At a film thickness of about 2.0 nm the NiPc specific characteristics are fully developed and those of the substrate are completely covered.

Fig. 4b shows the UPS results for the variation of the valence band of the NiPc/Ag interface during depositions. The bottom spectrum mainly represents the Ag4d orbital emission features of Ag [27]. Similar to the NiPc/Au interface, after deposition of about 2.0 nm of NiPc the metallic Fermi edge cut-off and the Ag4d valence band characteristic features are completely covered by the specific characteristics of the NiPc film. From these spectra, the band structure of the substrate and the organic film is determined, the organic HOMO (highest occupied molecular orbital) position is identified and the work function of both the substrate and

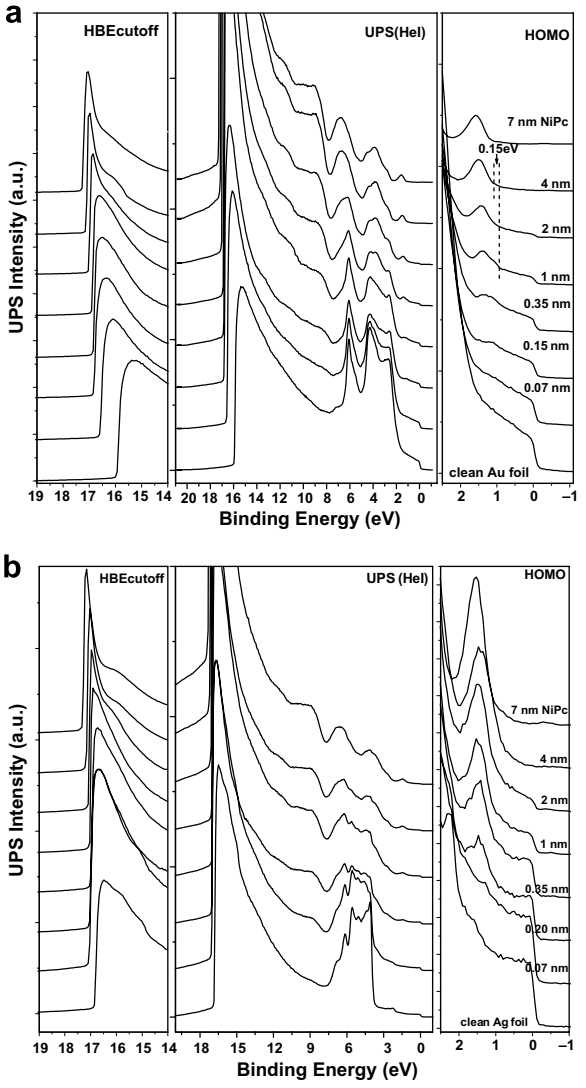


Fig. 4. HeI UP spectra of the (a) NiPc/Au and (b) NiPc/Ag interface. The full spectra are shown in the center part. On the left, the high binding energy cut-off regions of the spectra are shown normalized to allow better comparison. On the right, the development of the HOMO peak with increasing organic thickness is shown magnified for clarity.

the organic film is measured. In both systems, NiPc/Au and NiPc/Ag, the HOMO cut-off of the NiPc overlayer is found to be 1.00 ± 0.05 eV, similar to the value for CuPc films deposited onto Au [9]. The HOMO position in both interfaces exhibits a small shift of 0.15 eV towards higher binding energies with increasing film thickness between 1.0 nm and 7.0 nm.

The valence band structure of the NiPc overlayer exhibits four distinct features at BEs 1.50 eV, 3.80 eV, 6.60 eV and 8.85 eV, respectively. The

valence band shape between 0 and 6 eV corresponds to the d-electron state of the central metal atom and results from the interaction of metal d-electrons with the four central N atoms, in agreement with theoretical calculations of NiPc valence band structure [28,29] and experimental observations of the valence band of NiPc on metallic substrates by XPS [20]. The intensity of the upper UP spectra in the 6–12 eV range is attributed to orbitals from benzene and pyrrole which are common to all Pc molecules. Substitution of one metal atom has only minor influence on the electronic structure of the upper valence band features [29].

From the UP spectrum the work function of both the substrate and the organic film can be measured by subtracting the total width of the UP spectra from the HeI photon energy (21.22 eV). For the clean polycrystalline Au substrate a work function of 5.20 ± 0.05 eV was found in agreement with literature [30]. In the case of polycrystalline Ag a work function of 4.40 ± 0.05 eV was measured, higher than that found in the literature (4.26 ± 0.02 eV) [30] due to the small amount of absorbed oxygen. Fig. 5 shows the variation of the work function versus the thickness of the NiPc film deposited on Au and Ag. For both curves an initial fast decrease is observed at the early stages of the deposition, whereas as the film thickness increases the rate of decrease becomes smaller. The total decrease of the work function is 1.20 eV for Au and 0.42 eV for Ag, yielding a work function for the NiPc overlayer equal to 4.00 ± 0.05 eV on both surfaces if the organic Fermi position is taken to be aligned with that of the metal. Taking the organic Fermi level

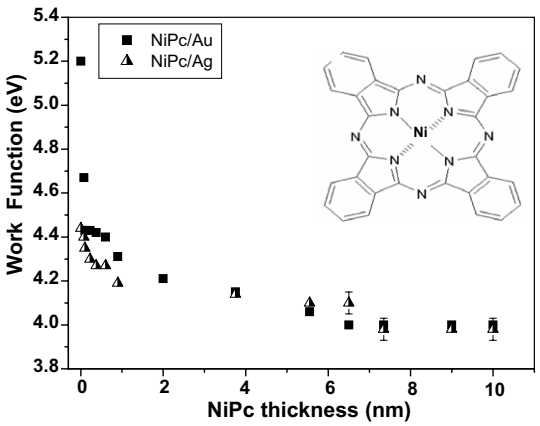


Fig. 5. The variation of high BE cut-off, which corresponds to work function, as the NiPc layer increases. The NiPc molecule is shown in the inset.

at mid-gap would result in a slightly lower work function of the organic film (3.80 ± 0.05 eV) assuming a transport gap of 2.40 eV [29].

The initial binding energy increase of ~0.30 eV in Fig. 3, for the C1s XPS peak in NiPc/Au films up to 1.0 nm is attributed to the decreasing effect of metal screening [7,31]. The metallic conductive substrate has the ability to screen the photohole generated in the organic molecule for ultra thin films, while for higher coverage this is done exclusively and less effectively by the organic material. For NiPc films thicker than 1.0 nm the small observed shift of 0.15 eV in the C1s binding energy, as well as the same energetic shift of the HOMO position in the UPS (Fig. 4), is attributed to band bending [6] although a possible effect of a gradual structural rearrangement of the NiPc molecule in going from near monolayer to a multilayer coverage cannot be excluded [7]. The origin of the band bending is the change of the electrostatic potential during the equilibration of the chemical potentials of the materials in contact and its small magnitude is explained in terms of the very small number of charge carriers in the NiPc organic semiconductor. Similar behavior has been reported for CuPc on polycrystalline gold [9]. From the XPS data, the total band bending is $V_b = 0.15 \pm 0.05$ eV for the NiPc/Au interface, while the total work function change is $\Delta\Phi = 1.20 \pm 0.05$ eV. Thus, the interface dipole (eD) is equal to

$$\mathrm{eD} = \Delta\Phi - V_b = (1.20 - 0.15)\ \mathrm{eV} = 1.05 \pm 0.10\ \mathrm{eV}.$$

The ionization potential can be calculated by

$$I = \mathrm{e}\Phi_{(\mathrm{NiPc})} + \mathrm{HOMO}_{\text{cut-off}} = (4.00 + 1.00)\ \mathrm{eV} = 5.00 \pm 0.10\ \mathrm{eV}$$

similar to the value for CuPc (5.05 eV) [6]. In order to determine the barrier Φ_{bh} between the Au Fermi level and the HOMO cut-off of the thick NiPc overlayer, it is necessary to calculate the offset between them. Since the Fermi level is defined to be zero, the hole injection barrier (Φ_{bh}) at the interface is determined from the UPS spectrum at a coverage of 5.0 nm by

$$\Phi_{bh} = \mathrm{HOMO}_{\text{cut-off}} - V_b = (1.00 - 0.15)\ \mathrm{eV} = 0.85 \pm 0.10\ \mathrm{eV}.$$

The energy difference between HOMO and LUMO taken from electronic structure calculations is $E_g =$ 2.40 eV [29]. Thus, the electron injection barrier is

$$\Phi_{be} = \Phi_{bh} - E_g = (0.85 - 2.40)\ \text{eV} = -1.55 \pm 0.10\ \text{eV}.$$

For the NiPc/Ag interface, the small observed shift of 0.10 eV of the XPS core levels and the corresponding shift of the HOMO binding energy at higher coverage can be also attributed to band bending or to structural effects at the interface. The screening effects are less important in this case most likely due to the presence of adsorbed oxygen which decreases the metal charge density for screening. Thus, taking the band bending as $V_b = 0.10 \pm 0.10$ eV, the interface dipole $eD = 0.30 \pm 0.10$ eV, the ionization potential $I = 5.00 \pm 0.10$ eV, the hole injection barrier $\Phi_{bh} = 0.90 \pm 0.10$ eV and the electron injection barrier is $\Phi_{be} = -1.50 \pm 0.10$ eV.

Fig. 6a and b shows the energy level diagrams at the NiPc/Au and NiPc/Ag interfaces as derived from the combination of the photoemission results. In both interfaces the Φ_{be} and Φ_{bh} values are found quite similar. The significant difference of the work function between Au and Ag affects only the interface dipole, since no chemical interaction was observed in both interfaces. The formation of the interface dipole has been the subject of detailed study in recent years and several mechanisms have been proposed to account for its magnitude [6,32–34]. In view of the non reactive character of both interfaces studied here, as evidenced by the absence of additional components of either the organic or the substrates in XPS, mechanisms based on extended charge transfer and strong chemisorptive bond formation leading to interface states and eD almost independent of metal work function can be excluded. The most plausible mechanism for both NiPc/Au and NiPc/Ag, involves the local rearrangement of the electron cloud at the metal surface induced by the presence of the organic molecules, possibly coupled with a redistribution of the electron density within the organic molecule itself even under physisorption conditions. The net outcome of this rearrangement could be to push the tailing part of the electronic cloud towards the metal resulting in an effectively positive charging of the vacuum side and a lowering of the vacuum level and the work function.

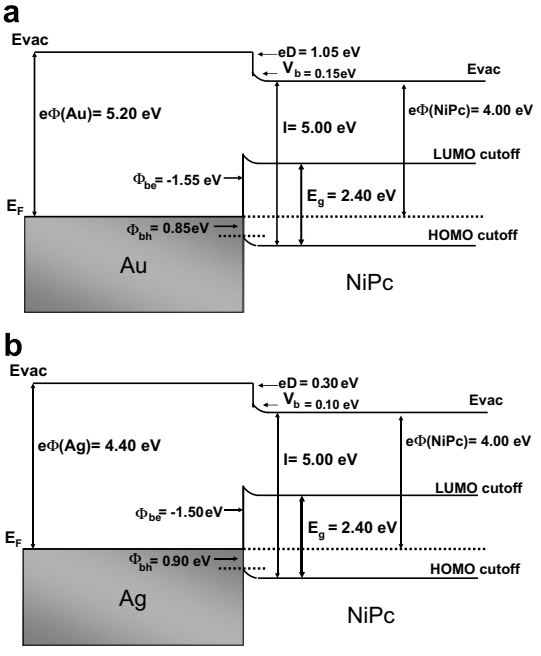


Fig. 6. Schematic energy level diagrams of the NiPc/Au and NiPc/Ag interfaces.

4. Summary

The electronic structure of the NiPc/Au and NiPc/Ag interfaces has been investigated using core and valence level photoemission spectroscopy. Both interfaces are non-reactive. The initial observed total upward binding energy shift of 0.30 eV of the NiPc XPS core levels in the NiPc/Au interface is attributed to the weakening of the screening effects induced by the metallic substrate for organic film thickness up to 1.0 nm. The additional small shift (0.15 eV) in thicker organic overlayers NiPc/Au, as well as the small overall observed shift of 0.10 eV for the NiPc/Ag interface are attributed to band bending, although possible structural effects accompanying the transition from near monolayer to thicker NiPc films cannot be excluded. In both interfaces, the NiPc valence band specific characteristics have fully developed for 2.0 nm of organic film thickness and those of the substrate are completely covered. The NiPc valence band exhibits four main peaks at 1.50 eV, 3.80 eV, 6.60 eV and 8.85 eV binding energy. The HOMO cut-off of the NiPc film on both substrates is found equal to 1.00 ± 0.05 eV in agreement with electronic structure calculations, which leads to similar hole injection barriers around 0.90 eV. The main difference in the two substrates is in the interface dipole value, which is significantly larger for NiPc/Au (1.05 eV) compared with NiPc/Ag (0.30 eV) due to the larger work function of the Au foil.

References

[1] T.S. Shafai, T.D. Anthopoulos, Thin Solid Films 398–399 (2001) 361, and references therein.
[2] H.S. Majumdar, A. Bandyopadhyay, A.J. Pal, Org. Electron. 4 (2003) 39.
[3] C. Clarisse, M.T. Riou, J. Appl. Phys. 69 (5) (1991) 3324.
[4] R.D. Gould, Coordin. Chem. Rev. 156 (1996) 237.
[5] H. Peisert, M. Knupfer, J. Fink, Appl. Phys. Lett. 81 (13) (2002) 2400.
[6] G. Paasch, H. Peisert, M. Knupfer, J. Fink, J. Appl. Phys. 93 (10) (2003) 6084.
[7] H. Peisert, M. Knupfer, T. Schwieger, J.M. Auerhammer, M.S. Golden, J. Fink, J. Appl. Phys. 91 (8) (2002) 4872.
[8] C. Shen, A. Kahn, J. Appl. Phys. 90 (9) (2001) 4549.
[9] H. Peisert, M. Knupfer, T. Schwieger, G.G. Fuentes, D. Olligs, J. Fink, J. Appl. Phys. 93 (12) (2003) 9683.
[10] S.M. Tadayyon, H.M. Grandin, K. Griffiths, P.R. Norton, H. Aziz, Z.D. Popovic, Org. Electron. 5 (2004) 157.
[11] T.G. Abdel-Malik, R.M. Abdel-Latif, A.E. El-Samahy, S.M. Khalil, Thin Solid Films 256 (1995) 139.
[12] G.D. Sharma, S.G. Sangodkar, M.S. Roy, Mater. Sci. Eng. B41 (1996) 222.
[13] S. Gravano, A.K. Hassan, R.D. Gould, Int. J. Electron. 70 (1991) 477.
[14] R.D. Gould, J. Phys. D: Appl. Phys. 9 (1986) 1785.
[15] R.Ben. Chaabane, G. Guillaud, M. Gamoudi, Thin Solid Films 296 (1997) 145.
[16] P.D. Hooper, M.I. Newton, G. McHale, M.R. Willis, Semicond. Sci. Technol. 12 (1997) 455.
[17] G. McHale, M.I. Newton, P.D. Hooper, M.R. Willis, Opt. Mater. 6 (1996) 89.
[18] L. Ottaviano, S. Di Nardo, L. Lozzi, M. Passacantando, P. Picozzi, S. Santucci, Surf. Rev. Lett. 4 (1) (1997) 59.
[19] L. Ottaviano, S. Di Nardo, L. Lozzi, M. Passacantando, P. Picozzi, S. Santucci, Surf. Sci. 373 (1997) 318.
[20] H. Höchst, A. Goldmann, S. Hüfner, H. Malter, Phys. Status Solidi B 76 (1976) 559.
[21] A. Siokou, V. Papaefthimiou, S. Kennou, Surf. Sci. 482–485 (2001) 1186.
[22] D. Briggs, M.P. Seah, Practical Surface Analysis, second ed., Wiley, New York, 1996.
[23] A. Hoshino, T. Takenaka, H. Miyaji, Acta Crystallogr. B 59 (2003) 393.
[24] D.A. Shirley, Phys. Rev. B 5 (1972) 4709.
[25] R.J. Ewen, C.L. Honeybourne, J. Phys.: Condens. Mat. 3 (1991) S303.
[26] T.S. Ellis, K.T. Park, J. Appl. Phys. 95 (3) (2004) 982.
[27] R. Schlaf, P.G. Schroeder, M.W. Nelson, B.A. Parkinson, C.D. Merritt, L.A. Crisafulli, H. Murata, Z.H. Kafafi, Surf. Sci. 450 (2000) 142.
[28] F.W. Kutzler, D.E. Ellis, J. Chem. Phys. 84 (2) (1986) 1033.
[29] B. Bialek, I.G. Kim, J.I. Lee, Synth. Met. 129 (2002) 151.
[30] A.W. Dweydari, C.H.B. Mee, Phys. Status Solidi A 27 (1975) 223.
[31] K. Jacobi, Phys. Rev. B 38 (9) (1988) 6291.
[32] H. Ishii, K. Sugiyama, E. Ito, K. Seki, Adv. Mater. 11 (1999) 605.
[33] J.C. Scott, J. Vac. Sci. Technol. A 21 (2003) 521.
[34] D. Cahen, A. Kahn, E. Umbach, Mater. Today 8 (2005) 32.

Available online at www.sciencedirect.com
ScienceDirect
Organic Electronics 8 (2007) 529–534
Organic Electronics
www.elsevier.com/locate/orgel

Color stable white organic light-emitting diode based on a novel triazine derivative

Bo Qu, Zhijian Chen *, Feng Xu, Huayu Cao, Zhihao Lan, Ziyao Wang, Qihuang Gong *

State Key Laboratory for Artificial Microstructures and Mesoscopic Physics, Department of Physics, Peking University, Beijing 100871, People's Republic of China

Received 10 October 2006; received in revised form 23 January 2007; accepted 26 March 2007
Available online 2 April 2007

Abstract

A novel red–orange emitting material with a branched molecular structure, 2,4,6-tris[2-(*N*-ethyl-3-carbazole)carboxethenyl]-1,3,5-*s*-triazine (TC3), has been synthesized and characterized using UV–visible, photoluminescence (PL) and electroluminescence (EL) spectroscopy. White EL devices were fabricated using TC3 as a red–orange emitter and 8-hydroxyquinolinolato lithium (Liq) as a blue–green emitter. *N*,*N*-bis(3-methylphenyl)-*N*,*N*-diphenylbenzidine (TPD) as the adjustor for charge carrier mobility was introduced between the two emitting layers to improve the stability of the white emission color on bias voltage. The EL devices of ITO/poly(*N*-vinylcarbazole) (PVK):TC3 (56 nm)/TPD (5 nm)/Liq (30 nm)/Mg:Ag exhibited good quality white emission. The Commission Internationale De L'Eclairage chromaticity coordinates are (0.34, 0.39) and are stable on the bias voltage.
© 2007 Elsevier B.V. All rights reserved.

PACS: 78.55.Kz; 78.60.Fi; 78.66.Qn

Keywords: White-light-emitting; Organic electroluminescence; *s*-Triazine

1. Introduction

Organic light-emitting diodes (OLEDs) have attracted much attention since the pioneering work of Tang and Van Slyke [1], owing to their extensive applications [2–7]. Nowadays, more and more research groups have devoted time to the investigation of white organic light-emitting diodes (WOLEDs) due to their applications in low-cost back lighting in liquid-crystal displays, full-color displays combined with color filters and various lightings [8–13]. However, the emission color of WOLEDs is usually changed with the varying bias voltage, which has restricted the practical application of WOLEDs. Therefore, much effort has been devoted to the research of bright and color-stable white organic light-emitting diodes.

In this study, we successfully synthesized a new three-branched octupolar molecule material,

* Corresponding authors. Tel.: +86 10 62754990; fax: +86 10 62756567.
E-mail addresses: zjchen@pku.edu.cn (Z. Chen), qhgong@pku.edu.cn (Q. Gong).

1566-1199/$ - see front matter © 2007 Elsevier B.V. All rights reserved.
doi:10.1016/j.orgel.2007.03.009

2,4,6-tris[2-(*N*-ethyl-3-carbazole)carboxethenyl]-1,3,5-*s*-triazine (TC3), and used it as a red–orange emitter to fabricate WOLEDs. The star-like structure of the molecule can effectively enhance the steric hindrance; thus TC3 had less concentration quenching effect and stable red–orange emission could be obtained even from an undoped single-layer device. The EL properties of WOLEDs based on TC3 and a blue–green emitter of 8-hydroxyquinolinolatolithium (Liq) were investigated in detail. A TPD layer inserted between the PVK:TC3 and Liq layers can effectively balance the hole and electron current while the electric field increases and achieve the inalterable Commission Internationale De L'Eclairage (CIE) coordinates of white emission at various voltages. The full width at half maximum (FWHM) of the white EL spectra is more than 200 nm, which covers the visible region. These properties are beneficial for application in displays.

2. Experimental

2.1. Synthesis

The synthesis process as well as the chemical structure of TC3 are shown in Scheme 1. The molecule of TC3, assembled from an *s*-triazine ramification node acting as an acceptor group, vinylene conjugated connectors and *N*-ethylcarbazoles as donor peripheral groups, was synthesized by alkaline condensation reactions between *N*-ethyl-3-carbazolecarboxaldehyde and 2,4,6-trimethyl-1,3,5-*s*-triazine, which were synthesized according to the literature [14,15]. TC3 was synthesized according to the following procedure. Under refluxing temperature, a solution of 2,4,6-trimethyl-1,3,5-*s*-triazine (0.2 g, 0.0016 mol) in 15 mL methanol was added dropwise into a 100-mL flask containing methanol (30 mL), *N*-ethyl-3-carbazolecarboxaldehyde (1.07 g, 0.0048 mol) and potassium hydroxide (0.2 g) for about 2 h. The reaction mixture was refluxed for a further 72 h and then the solvent was removed in vacuo. The residue was purified by column chromatography on silica gel using benzene/ethanol (10/1) as eluent.

2,4,6-Tris[2-(N-ethyl-3-carbazole)carboxethenyl]-1,3,5-s-triazine

^{1}H NMR ($CDCl_3$) δ (ppm): 8.55 (d, 3H), 8.45 (d, 3H), 8.15 (d, 3H), 7.86 (q, 3H), 7.53 (t, 3H), 7.46 (q, 6H), 7.30 (t, 3H), 7.19 (d, 3H), 4.43 (q, 6H), 1.48 (t, 9H). Calculated for $C_{51}H_{42}N_6$: C, 82.93%; H, 5.69%; N, 11.38%. Found: C, 82.39%; H, 5.77%; N, 11.78%.

TC3 is a promising red–orange emitting material for OLEDs. Liq has superior electron-transporting properties and is also an excellent material for blue–green emitting EL devices [16]. Liq was synthesized from the dehydration reaction of lithium hydroxide and 8-hydroxyl quinoline. WOLEDs were fabricated based on TC3 and Liq.

2.2. OLED fabrication and characterization

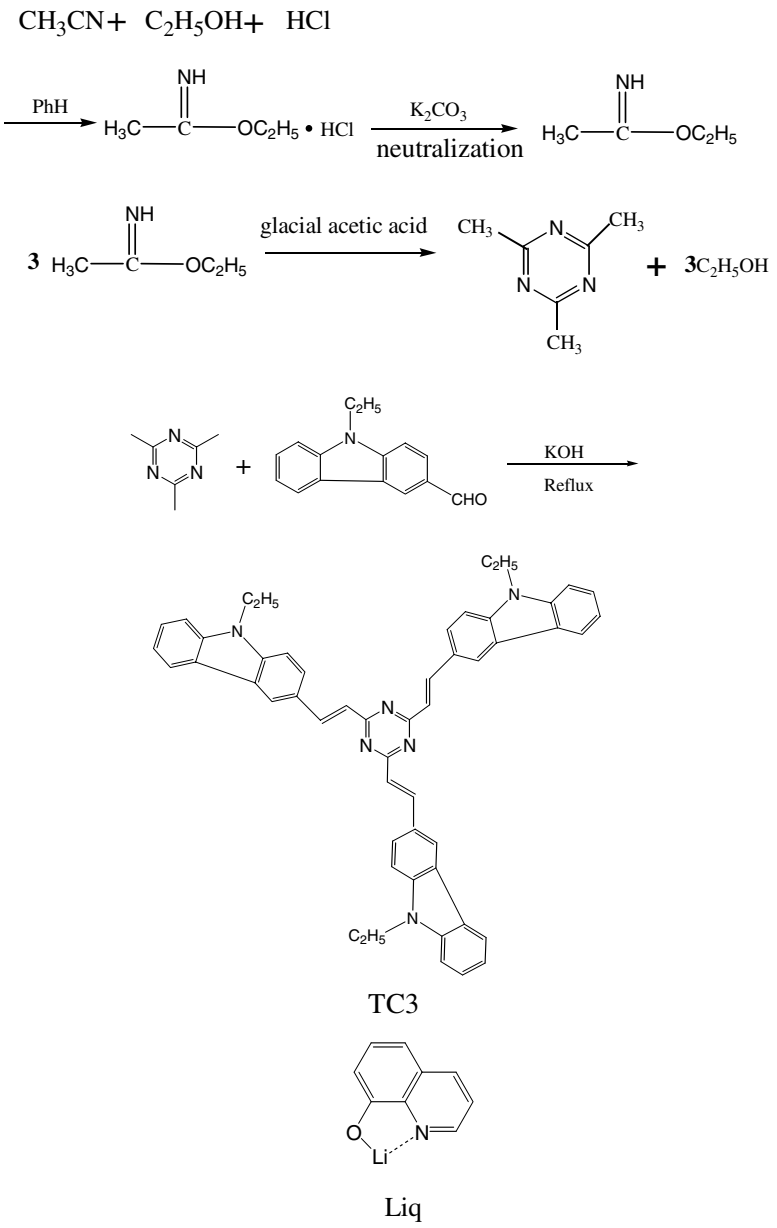
In order to study the EL properties of TC3, two devices, a single-layer device of indium tin oxide (ITO)/TC3 (35 nm)/Mg:Ag, and a double-layer device of ITO/poly(9-vinylcarbazole) (PVK):TC3 (weight ratio 1:1, 46 nm)/2,9-dimethyl-4,7-diphenyl-1,10-phenanthroline (BCP, 10 nm)/Mg:Ag were fabricated.

White organic light-emitting diodes were fabricated, and the structures were as follows:

Device I: ITO/PVK:TC3 (weight ratio 4:1, 56 nm)/Liq (30 nm)/Mg:Ag.
Device II: ITO/PVK:TC3/TPD (5 nm)/Liq/Mg:Ag.

ITO-coated glasses with a sheet resistance of $<15\ \Omega$ per square were pretreated with ultrasonic cleaning using detergent, distilled water, acetone and anhydrous ethanol, respectively, and then were dried by nitrogen gas. TC3 (or PVK:TC3) was dissolved in chloroform (6 mg/ml) and deposited onto the ITO substrates by spin-coating technique with a rotary speed of 2000 rpm. The thickness was measured using a Jobin Yivon UVISEL ellipsometer. The PVK blending in the TC3 molecule can decrease the fluorescence quenching of TC3 [17,18]. Liq serving as the electron-injecting and blue–green emitting layer, and *N*,*N*-bis(3-methylphenyl)-*N*,*N*-diphenylbenzidine (TPD) serving as the hole-transporting layer [6,19] were formed by vacuum evaporation at 3.4×10^{-6} Torr. Finally, 150 nm-thick layers of magnesium and silver (weight ratio: approximately 10:1) were thermally evaporated as cathodes without breaking the vacuum. The thicknesses of all vacuum evaporation layers were controlled by quartz crystal microbalance.

The devices' performance was studied by measuring the Luminescence–current–voltage (*L*–*I*–*V*) characteristics, EL spectra and the corresponding CIE coordinates, which were evaluated by a



Scheme 1. Synthesis of TC3 and chemical structure of Liq.

Photo-Research 650 and a current–voltage meter. None of the devices were encapsulated, and measurements were carried out at room temperature under ambient conditions.

3. Results and discussion

3.1. Electrochemical properties of TC3 and Liq

The lowest unoccupied molecular orbital (LUMO) and highest occupied molecular orbital (HOMO) energy levels could be obtained from the measurements of the absorption spectra and cyclic voltammetry (CV) curves. Fig. 1 shows typical UV–vis absorption and photoluminescence (PL) spectra of TC3 in a dilute solution of chloroform and in the film state (the thickness was 35 nm). The absorption maximum of TC3 in dilute solution occurred at 394 nm, while the absorption maximum of TC3 film occurred at 403 nm with a shoulder peak at 503 nm, which showed a red shift (9 nm) with respect to the solution. Fig. 2 (inset) shows

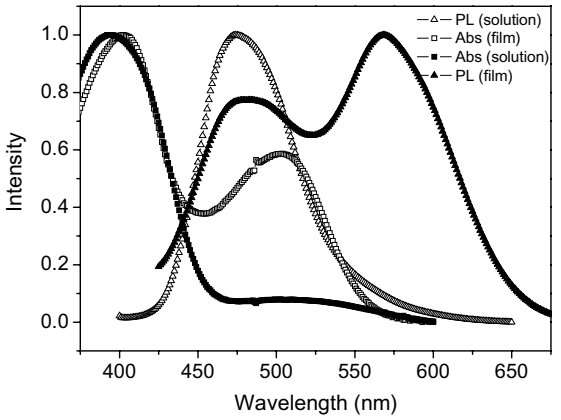


Fig. 1. Absorption and PL spectra of TC3.

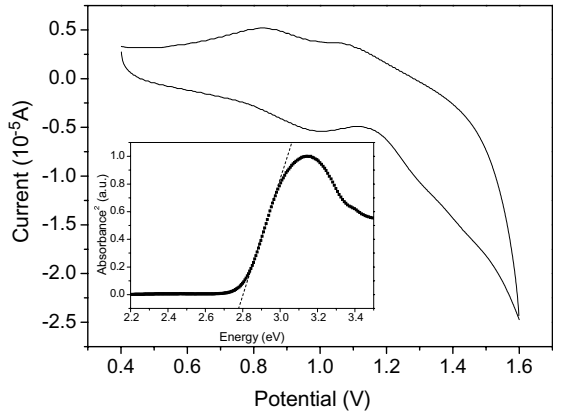


Fig. 2. Cyclic voltammograms of TC3; scan rate: 100 mV/s. Inset: absorbance squared versus the photon energy extrapolated linearly to zero absorption determining the optical band gap.

the absorbance squared versus the photon energy of TC3 in solution. The optical band gap (E_g) of TC3 could be determined to be 2.77 eV by the extrapolation of the linear region to zero absorption [20]. The PL spectrum of TC3 in dilute solution peaked at 474 nm, and the FWHM was only about 69 nm. The PL spectrum of TC3 film showed two peaks at 483 nm and 569 nm, which were assigned to the monomer and excimer emissions [19,21], respectively. Cyclic voltammetry (CV) was carried out using an electrochemical workstation, and the CV curve of TC3 is shown in Fig. 2. TC3 was dissolved in an electrolyte solution of 50 mM Bu_4NClO_4 in dichloroethane against Ag/Ag^+ using the method proposed by Janietz and Bradley [22]. The HOMO level of TC3 was estimated to be about −5.2 eV under vacuum level by CV curve with platinum (Pt) wire, glassy carbon and Ag/AgCl used as the counter electrode, the working electrode and the reference electrode, respectively. Then the LUMO level of TC3 was evaluated to be −2.4 eV by the subtraction of E_g from the HOMO level.

According to the description in previous literature [16], the E_{HOMO} and E_{LUMO} values for Liq are −5.58 and −3.15 eV, respectively. Moreover, Liq shows an absorption maximum at 259 nm and an emission peak (PL) centered at 485 nm.

3.2. Electroluminescence

The electroluminescence properties of the ITO/TC3/Mg:Ag and ITO/PVK:TC3/BCP/Mg:Ag devices are shown in Fig. 3. The single-layer device exhibited the red–orange emission of TC3 with the peak centered at 620 nm, and the FWHM of the EL spectrum was about 136 nm. The double-layer device gave red–orange emission, peaked at the wavelength of 604 nm and the FWHM was about 108 nm, which was narrower than that of the single-layer device, due to less excimer emission from the low-concentration TC3. Therefore, TC3 can be used as a red–orange emitter in white EL devices.

White emission was obtained from white EL Devices I and II. The energy levels of the devices are shown in Fig. 4 and the EL spectra are shown in Fig. 5. EL spectra ranging from 400 to 750 nm, which completely covered the total visible region, were obtained. The blue–green emission was from Liq, and the red–orange emission was from TC3. One of the major problems in white EL devices is that the emission color changes in different bias voltages. The profiles of EL spectra of Device I

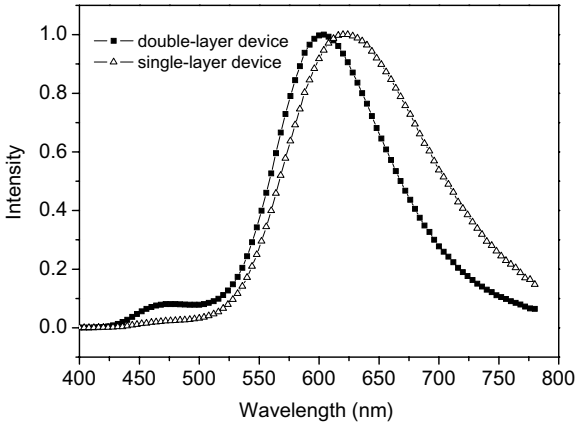


Fig. 3. EL spectra of ITO/TC3/Mg:Ag and ITO/PVK:TC3/BCP/Mg:Ag.

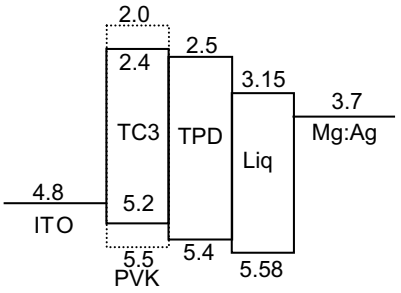


Fig. 4. HOMO and LUMO levels of TC3, PVK, TPD, Liq, ITO and Mg:Ag with respect to vacuum level.

varied when the bias voltage increased. The Liq layer was not superior in hole transportation, and the holes were blocked by the Liq layer at low bias voltage; thus the red emission was dominant. With the increase of the electric field, more holes could be transported into the Liq layer and the blue–green emission from Liq became stronger, and then the emission color was different at various bias voltages.

In order to improve the stability of color emission at different bias voltages, a TPD layer was introduced between the TC3 and Liq layers in Device II. TPD is an excellent hole transporter and its HOMO energy level is between those of TC3 and Liq; therefore TPD can help holes to be injected into Liq at low bias voltage. TPD balances hole and electron currents in whole layers and improves the stability of white EL spectra on bias voltages. More detailed experiments are required to solve the mechanism of TPD stabilizing emission color. The dependence of the EL property on the thickness of the TPD layer was studied and experimental data confirmed that the device with a 5-nm TPD layer exhibited the best performance. Unaltered EL spectra were observed at various voltages in Device II as shown in Fig. 5.

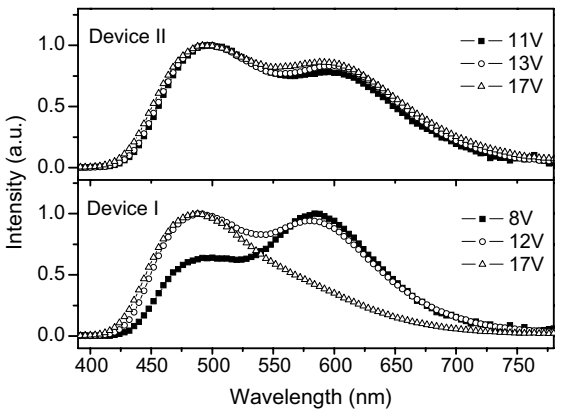


Fig. 5. EL spectra of Devices I and II at various voltages.

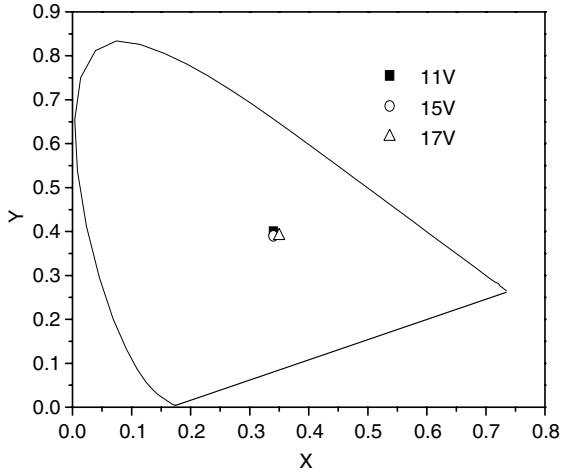


Fig. 6. CIE chromaticity diagram of Device II.

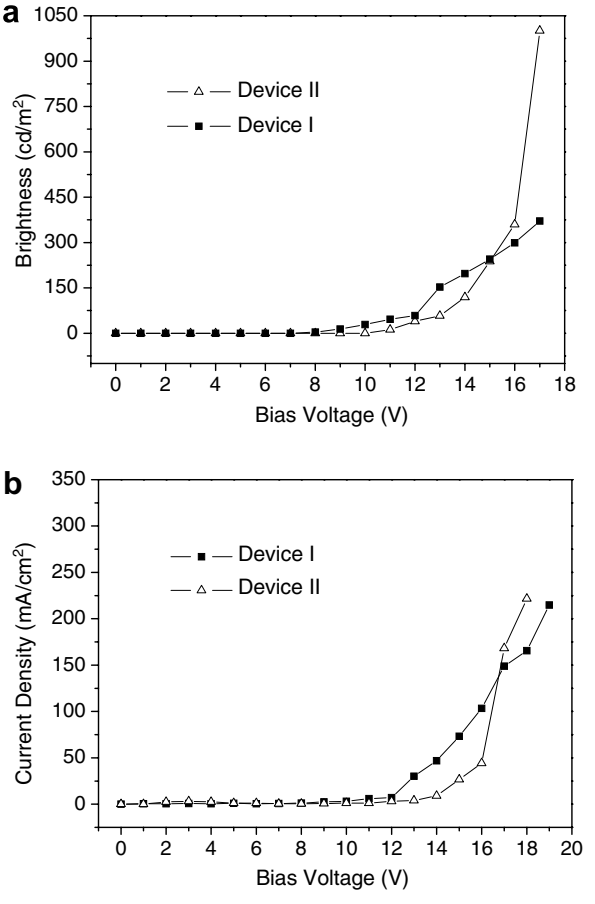


Fig. 7. (a) *B–V* characteristics of Devices I and II; and (b) *I–V* characteristics of devices.

The CIE chromaticity coordinates of Device II were (0.34, 0.40) for 11 V, (0.34, 0.39) for 15 V and (0.35, 0.39) for 17 V, as clearly shown in Fig. 6. The coordinates all belonged to the white region of the CIE chromaticity diagram [9,10,12] and they were relatively constant of bias voltage, which is beneficial to their application in white illumination and displays.

The brightness–voltage (B–V) and current density–voltage (I–V) of the two devices are shown in Fig. 7. The forward current increased with increasing forward bias voltage and the curves showed typical diode characteristics. The current density of Device II was lower than that of Device I below the bias voltage of 17 V. Furthermore, the maximal brightness of 1001 cd/m^2 coming from Device II was obtained at a bias voltage of 17 V, as shown in Fig. 7a. The maximal efficiency of Device II was calculated to be 1.46 cd/A. The experimental results imply that the TPD layer plays an important role in devices to achieve stable WOLEDs.

4. Conclusion

A new organic material, TC3, was successfully synthesized by alkaline condensation reaction. We demonstrated a bright and color stable white organic light-emitting diode based on red–orange emitting TC3, hole-transporting TPD and blue–green emitting Liq. The maximum brightness of 1001 cd/m^2 coming from the WOLED was measured at the driving voltage of 17 V. Moreover, the CIE coordinates of the white-emitting device was stable on bias voltage.

Acknowledgements

This work was supported by the National Natural Science Foundation of China under Grant Nos. 60407004, 10674011 and 10521002, and the National Basic Research Program under Grant No. 2007CB307001. The authors would like to thank Mr. Zhong Chen of the College of Chemistry and Molecular Engineering for his kind assistance in the measurement of the CV spectra.

References

[1] C.W. Tang, S.A. Van Slyke, Appl. Phys. Lett. 51 (1987) 913.
[2] K. Ziemelis, Nature 399 (1999) 408.
[3] K.M. Vaeth, K.F. Jensen, Appl. Phys. Lett. 71 (1997) 2091.
[4] B. Qu, Z.J. Chen, F. Xu, et al., Mater. Lett. 60 (15) (2006) 1927.
[5] C.D. Muller, A. Falcou, Nature 421 (2003) 829.
[6] J.H. Burroughes et al., Nature (London) 347 (1990) 539.
[7] Jing-hua Niu, Wen-lian Li, Han-zhi Wei, et al., J. Phys. D: Appl. Phys. 38 (2005) 1136.
[8] Fangzhong Shen, Feng He, Dan Lu, et al., Semicond. Sci. Technol. 21 (2006) L16.
[9] Benjamin C. Krummacher, Vi-En Choong, Mathew K. Mathai, et al., Appl. Phys. Lett. 88 (2006) 113506.
[10] Mingtao Li, Wenlian Li, Lili Chen, et al., Appl. Phys. Lett. 88 (2006) 091108.
[11] Hanzhi Wei, Wenlian Li, Mingtao Li, et al., Appl. Surf. Sci. 252 (2006) 2204.
[12] Do-Hoon Hwang, Moo-Jin Park, Changhee Lee, Synth. Met. 152 (2005) 205.
[13] Guoli Tu, Chongyu Mei, Quanguo Zhou, et al., Adv. Funct. Mater. 16 (2006) 101.
[14] C.S. Fred, P.J. Gracea, Org. Chem. 26 (1961) 2778.
[15] H.K. Jung, C.L. Lee, J.K. Lee, Thin Solid Films 401 (2001) 111.
[16] Christoph Schmitz, Hans-Werner Schmidt, Mukundan Thelakkat, Chem. Mater. 12 (2000) 3012.
[17] Z.Q. Bian, D.Q. Gao, K.Z. Wang, et al., Thin Solid Films 460 (1–2) (2004) 237.
[18] K.S. Yang, H.K. Shin, C. Kim, et al., Synth. Met. 152 (1–3) (2005) 245.
[19] C. Weder, M.S. Wrighton, Macromolecules 29 (1996) 5157.
[20] I. Seguy, P. Jolinat, P. Destruel, et al., J. Appl. Phys. 89 (10) (2001) 5442.
[21] R. Pizzoferrato, T. Ziller, A. Micozzi, et al., Chem. Phys. Lett. 414 (2005) 234.
[22] S. Janietz, D. Bradley, Appl. Phys. Lett. 73 (1998) 2453.

Available online at www.sciencedirect.com
ScienceDirect
Organic Electronics 8 (2007) 535–539
Organic Electronics
www.elsevier.com/locate/orgel

Efficient red phosphorescence polymer light-emitting diodes with dual function polymer

Yunhua Xu, Bo Liang, Junbiao Peng *, Qiaoli Niu, Wenbo Huang, Jian Wang

Institute of Polymer Optoelectronic Materials and Devices, South China University of Technology, Key Laboratory of Specially Functional Materials, Ministry of Education, Guangzhou 510640, China

Received 6 December 2006; received in revised form 20 March 2007; accepted 26 March 2007
Available online 14 April 2007

Abstract

The efficient red phosphorescence polymer light-emitting diodes (PLEDs) based on aluminum (Al) cathode were demonstrated. The devices composed of neutral aminoalkyl substituted polyfluorene, poly[(9,9-bis(3′-(*N*,*N*-dimethylamino) propyl)-2,7-fluorene)-*alt*-2,7-(9,9-dioctylfluorene)] (PFN) as the host and bis(1-(3-(9,9-dimethyl-fluorene-2-yl)phenyl)isoquinoline-C2,*N*′) iridium (III) (3-(pyridin-2′-yl)-1,2,4-triazole) [Ir(DMFPQ)$_2$pt] as the dopant. High external quantum efficiency of 5.6% (at 16.8 V) and a luminance of 1400 cd/m^2 (at 19.6 V) were obtained from the device with Al cathode only. The performances (quantum efficiency and luminance) of the devices could be comparable to those of the devices with a low work-function metal cathode (such as calcium and barium). We believe that the reason for the high performances was due to the effective electron injection from Al into PFN.
© 2007 Elsevier B.V. All rights reserved.

PACS: 72.80.Le; 78.60.Fi; 85.60.Jb

Keywords: Polymer red light-emitting diode; Electron injection; High work-function metal cathode

1. Introduction

Polymer light-emitting diodes (PLEDs) have been extensively investigated due to their great potential applications in full color displays and solid-state lighting sources [1–3]. Significant progress has been made on improving performances and understanding of the fundamental electroluminescence (EL) processes. However, the performances, such as efficiency and operating lifetime, do not yet meet commercial application requirements. One of effective methods to improve the EL efficiency is to balance holes and electrons injected from their respective electrodes. Generally, most of conjugated polymers are p-type semiconductors [4], and holes in the EL processes are major carriers. Many works focus on improving electron injection and transportation in PLEDs. Low work-function metal cathodes, such as barium (Ba) and calcium (Ca), are commonly utilized to enhance electron injection through efficiently reducing the barrier height at the interface of cathode and

* Corresponding author. Tel.: +86 20 87114535; fax: +86 20 87110606.
E-mail address: psjbpeng@scut.edu.cn (J. Peng).

1566-1199/$ - see front matter © 2007 Elsevier B.V. All rights reserved.
doi:10.1016/j.orgel.2007.03.012

emissive polymer, leading to high EL efficiencies [2,5–7]. Unfortunately, low work-function metals are extremely sensitive to oxygen and moisture, so the device fabrication must be processed in an inert gas or the device has to be encapsulated carefully to keep its EL stability. So far, many salts or oxides (alkaline earth metal salts and some oxides), such as LiF, CsF, Al_2O_3, NaCl, and Cs_2CO_3 have been developed as the interfacial layer between Al cathode and emissive layer for enhancing electron injection [8–15]. Cao et al. obtained high performance PLEDs by blend of a surfactant with emissive polymers [16]. Recently, Huang et al. [17,18], Wu et al. [19,20] and Liang et al. [21] demonstrated that the performances of PLEDs with high work-function cathodes (such as Ag and Au) were significantly improved by adding a thin layer of polyfluorene copolymers with an aminoalkyl group between emissive polymer layer and the cathode.

In this work, we report an efficient red phosphorescent polymer light-emitting diodes composing of PFN blend with the triplet compound of bis(1-(3-(9,9-dimethyl-fluorene-2-yl)phenyl)isoquinoline-C2,N') iridium (III) (3-(pyridin-2′-yl)-1,2,4-triazole) [Ir(DMFPQ)$_2$pt] as the active layer and Al as the cathode. Since PFN functioned as both host and electron injection, the PLEDs show high performances of external quantum efficiency (over 5%) and luminous (1400 cd/m^2). To the best of our knowledge, it is the first report on the device with the dual function polymer.

2. Experimental details

Fig. 1 shows the chemical structures of PFN and Ir(DMFPQ)$_2$pt. The synthesis and characteristics of PFN and Ir(DMFPQ)$_2$pt were reported elsewhere [17,21]. Indium tin oxide (ITO) coated glass with sheet resistance of 15–20 Ω/□ was used as substrate. Prior to the device fabrication, the ITO substrates underwent a wet-cleaning course in an ultrasonic bath, in sequence of acetone, detergent, deionized water, and isopropanol. After cleaning, a thin anode buffer layer of PEDOT:PSS [poly(ethylendioxythiophene):poly(styrene sulfonic acid), Baytron P4083, Bayer AG] was spin-coated onto the substrates and dried via baking in a vacuum at 80 °C for 12 h. A 40 nm thick layer of PVK [poly(*N*-vinylcarbazole), Aldrich] was subsequently spin-cast onto the top of the PEDOT:PSS buffer layer from chlorobenzene solution to serve as a hole-transporting layer. On the top of that, the polymer emitting layer was spin-coated from PFN + Ir(DMFPQ)$_2$pt or PFN + Ir(DMFPQ)$_2$pt + + 30 wt% PBD (PBD:[2-(4-biphenylyl)-5-(4-tert-butylphenyl)-1,3,4-oxadiazole]) xylene solution at desired Ir(DMFPQ)$_2$pt ratios to form a 80 nm thick film. Surface profiler (Tencor Alfa-Step 500) was used to determine the thickness of the polymer films. Finally, a layer of 200 nm thick Al or a thin layer of Ba (4 nm thick) with a 200 nm thick Al capping layer was thermally deposited through a shadow mask (defined active area of 0.15 cm^2) in a vacuum chamber at a base pressure of $<3 \times 10^{-4}$ Pa. The layer thickness was monitored upon deposition through a crystal thickness monitor (Sycon). The device fabrication, except PEDOT:PSS coating, was carried out in a N_2 atmosphere dry-box (Vacuum Atmosphere Co.)

Current density (J)–voltage (V)–luminance (L) data were collected by a Keithley 236 source measurement unit and a silicon photodiode calibrated by PR-705 SpectraScan Spectrophotometer (Photo Research). External EL quantum efficiency (QE_{ext}) was obtained by measuring the total light output in all directions in an integrating sphere (IS-080, absphere). The photoluminescence (PL) and EL spectra were recorded by the Spectrophotometer (PR-705) under the drive of the power source (Keithley model 2400 programmable voltage–current source).

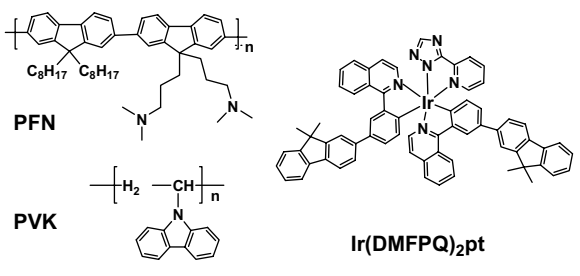


Fig. 1. Chemical structures of PFN, PVK, and Ir(DMFPQ)$_2$pt.

3. Results and discussion

PFN has a large band gap (3.47 eV) determined by the cyclic voltammetry (CV) [17], which was expected to be a good host for phosphorescent materials. Fig. 2a shows the PL spectrum of PFN film and the absorption spectrum of Ir(DMFPQ)$_2$pt, exhibiting clearly overlap between them and suggesting Förster energy transfer from PFN to Ir(DMFPQ)$_2$pt. Fig. 2b shows the PL spectra of the films of PFN doped with various concentrations of Ir(DMFPQ)$_2$pt. All PL spectra show two types of emission peaks, one locates

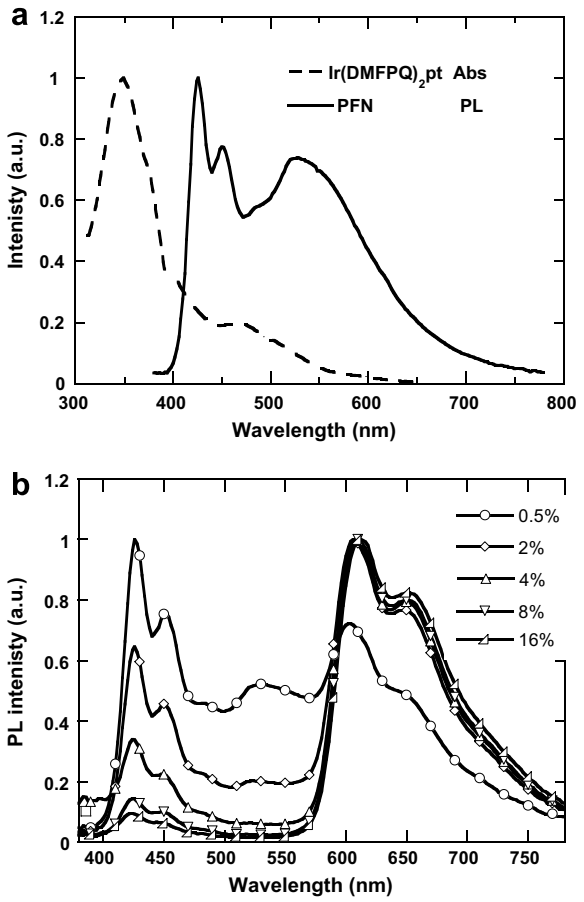


Fig. 2. (a) PL spectrum of PFN and the absorption spectrum of $Ir(DMFPQ)_2pt$ and (b) PL spectra of PFN films doped with various concentration of $Ir(DMFPQ)_2pt$.

in the range of 420–550 nm originated from PFN, the other is in 610–650 nm from $Ir(DMFPQ)_2pt$. As the concentration of $Ir(DMFPQ)_2pt$ increases from 0.5 wt% to 16 wt%, the blue band emission from PFN decreases significantly, suggesting that the efficient energy transfer occurs from PFN to $Ir(DMFPQ)_2pt$.

Fig. 3 shows the EL spectra of the PLEDs consisting of PFN doped with various concentrations of $Ir(DMFPQ)_2pt$. The EL spectra are remarkably different from the PL spectra (Fig. 2b). In the EL spectra, the blue band emission from PFN is nearly completely quenched even at low concentration of $Ir(DMFPQ)_2pt$ of 0.5 wt%; however, in the PL spectra, the blue band emission from PFN is still strong even at the high concentration of $Ir(DMFPQ)_2pt$ of 16%. The remarkable difference between the PL and EL spectra in the doped systems is ascribed to the charge trapping effect in the EL processes [2,22].

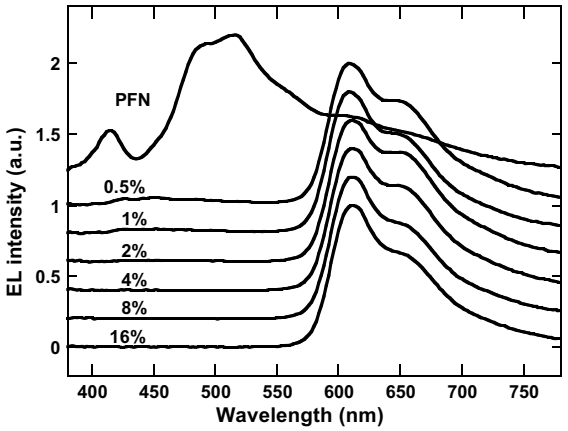


Fig. 3. EL spectra of the devices with different doping concentrations of $Ir(DMFPQ)_2pt$.

The efficiency–current density–luminance characteristics of the devices (the structure is ITO/PEDOT/PVK/PFN:$Ir(DMFPQ)_2pt$/Al, defined as Al-device) with different doping concentrations of $Ir(DMFPQ)_2pt$ are illustrated in Fig. 4. The EL efficiencies were strongly depended on the doping concentration of $Ir(DMFPQ)_2pt$, and increase with the concentration from 0.5 wt% to 4 wt%, and drop dramatically when the concentration exceeds 4 wt%. The efficiency decay at high doping concentrations is believed to be due to triplet–triplet annihilation [23]. The highest external quantum efficiency of 5.6% (at 16.8 V) and luminance of 1400 cd/m^2 (at 19.6 V) were obtained from the devices with 4 wt% doping concentration of $Ir(DMFPQ)_2pt$.

In order to investigate the electron injection from Al cathode into PFN, a kind of controlled devices with the structure of ITO/PEDOT/PVK/PFN:PBD (30 wt%):$Ir(DMFPQ)_2pt$ (4 wt%)/Ba/Al (defined as Ba/Al-device) were fabricated. The PBD here serves as both electron injection from the cathode and electron transportation in PFN films. The same EL spectra were observed from the devices with either Al or Ba/Al cathode, implying that the different cathodes do not influence on the exciton recombination zone. Table 1 summarized the performances of Al-device and Ba/Al-device. Clearly, both Al-device and Ba/Al-device with or without PBD dopant, all exhibit almost same quantum efficiency.

The current (I)–voltage (V) characteristics of the Ba/Al-device and Al-device are shown in Fig. 5. The Ba/Al-device has a lower turn-on voltage than that of Al-device, which is agreement with the fact that the barrier height between PFN and Ba is smaller

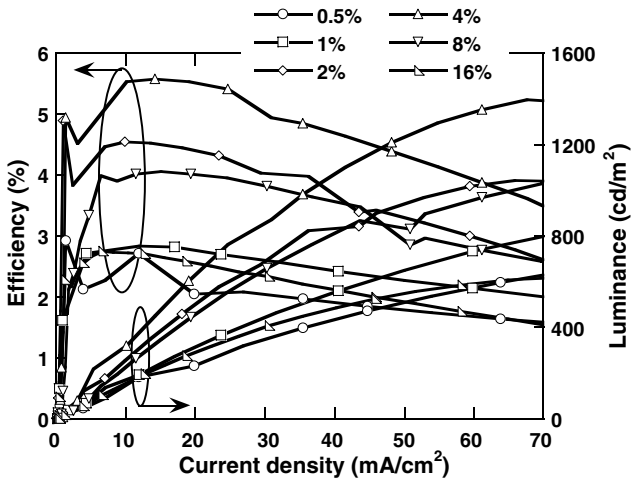


Fig. 4. Efficiency–current density–luminance characteristics of PLEDs with different doping concentrations of $Ir(DMFPQ)_2pt$.

Table 1
EL performances of the devices with the structure of ITO/PEDOT/PVK/Host:$Ir(DMFPQ)_2pt$ (4 wt%)/cathode

Host	Cathodes	Turn-on voltages (V)	Maximum efficiencies				Maximum luminance (cd/m^2)
			Quantum efficiencies (%)	Luminous efficiencies (cd/A)	Bias (V)	Current (mA/cm^2)	
PFN + 30% PBD	Ba/Al	11.5	5.7	3.4	14.5	6.7	1417
	Al	14	5.6	3.5	16.8	12.0	1400
PFN	Ba/Al	12.5	5.5	3.4	15.1	16.0	980
	Al	14.5	5.4	3.4	17.2	6.0	1100

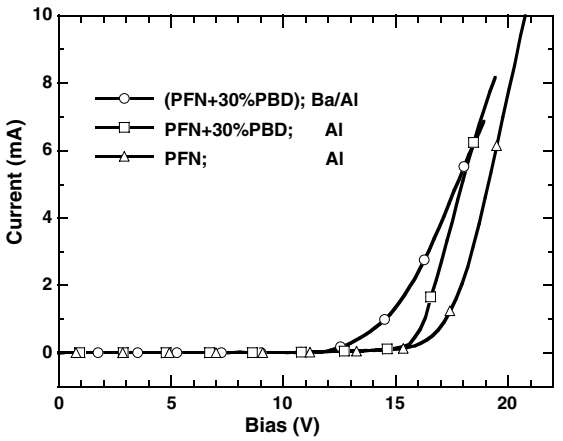


Fig. 5. Current–voltage characteristics of PLEDs with different hosts: PFN and PFN + PBD (30 wt%) and different cathodes: Al and Ba/Al.

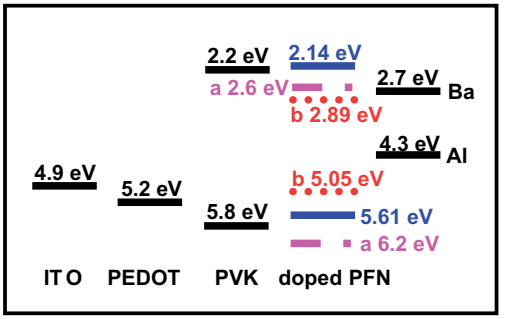


Fig. 6. Energy levels of the materials used in this paper: (a) PBD and (b) $Ir(DMFPQ)_2pt$ and the work-functions of the electrodes. (HOMO and LUMO energy levels of PVK and PBD referred to Refs. [24,25].)

than that between PFN and Al (Fig. 6). Although Fig. 6 exhibits large barrier height between PFN and Al, both kinds of devices have a similar efficiencies, as shown in Table 1. The fact reveals a mechanism that electrons are able to inject into PFN layer efficiently from the Al cathode. The mechanism could be explained via the formation of dipole layer. To the devices with PFN thin layer attached to the Al cathode, the mechanism of a dipole formation at

the interface between PFN/Al was proposed and confirmed by using small-angle X-ray diffraction [19,20]. The dipole layer was formed due to an interaction between the polarizable PFN and Al atoms, and can remarkably reduce the electron injection barrier height. As a result, efficient electron injection occurs from the Al cathode and the high performance device was realized.

In addition, the devices with PBD dopant can reduce turn-on voltage, implying PBD indeed benefits for improving electron injection from Al cathode and transport in PFN layer.

4. Conclusion

Efficient red emission phosphorescent PLEDs with high work-function metal cathode of Al have been demonstrated. PFN functioned as both host and electron injection layer, while Ir-compound of $Ir(DMFPQ)_2pt$ was the emitter. The highest external quantum efficiency and luminance of 5.6% and 1400 cd/m^2, respectively, were obtained. Probably, it was an available way that using PFN to fabricate PLEDs to enhance performances, simplify technique and improve stability of devices without using Ba or Ca.

Acknowledgements

The authors acknowledge the financial support from the National "973" Project of China (Grant No. 2002CB613405), the National Natural Science Foundation of China (under the Grant Nos. 50573024 and 50433030), the Key Project of Chinese Ministry of Education (Grant No. 104208) and the Doctorate Foundation of South China University of Technology.

References

[1] R.H. Friend, R.W. Gymer, A.B. Holmes, J.H. Burroughes, R.N.D.A. Dos Santos, J.L. BreÂ das, M. LoÈ gdlund, W.R. Salaneck, Nature 397 (1999) 121.
[2] X. Gong, M.R. Robinson, J.C. Ostrowski, D. Moses, G.C. Bazan, A.J. Heeger, Adv. Mater. 14 (2002) 581.
[3] Anil R. Duggal, J.J. Shiang, Donald F. Foust, Larry G. Turner, William F. Nealon, Jake C. Bortscheller, SID'05 Digest, 2005, p. 28.
[4] A.J. Heeger, I.D. Parker, Y. Yang, Synth. Met. 67 (1994) 23.
[5] D. Braun, A.J. Heeger, Appl. Phys. Lett. 58 (1991) 1982.
[6] Y. Cao, G. Yu, I.D. Parker, A.J. Heeger, J. Appl. Phys. 88 (2000) 3618.
[7] C. Jiang, W. Yang, J. Peng, S. Xiao, Y. Cao, Adv. Mater. 16 (2004) 537.
[8] L.S. Hung, C.W. Tang, M.G. Mason, Appl. Phys. Lett. 70 (1997) 152.
[9] G.E. Jabbour, B. Kippelen, N.R. Armstrong, N. Peyghambarian, Appl. Phys. Lett. 73 (1998) 1185.
[10] F. Li, H. Tang, J. Anderegg, J. Shinar, Appl. Phys. Lett. 70 (1997) 1233.
[11] S.J. Kang, D.S. Park, S.Y. Kim, C.N. Whang, K. Jeong, S. Im, Appl. Phys. Lett. 81 (2002) 2581.
[12] Q. Xu, J. Ouyang, Y. Yang, T. Ito, J. Kido, Appl. Phys. Lett. 83 (2003) 4695.
[13] H.-M. Lee, K.-H. Choi, D.-H. Hwang, L.-M. Do, T. Zyung, J.-W. Lee, J.-K. Park, Appl. Phys. Lett. 72 (1998) 2382.
[14] X.Y. Deng, W.M. Lau, K.Y. Wong, K.H. Low, H.F. Chow, Y. Cao, Appl. Phys. Lett. 84 (2004) 3522.
[15] T.-F. Guo, F.-S. Yang, Z.-J. Tsai, T.-C. Wen, S.-N. Hsieh, Y.-S. Fu, Appl. Phys. Lett. 87 (2005) 013504.
[16] Y. Cao, G. Yu, A.J. Heeger, Adv. Mater. 10 (1998) 917.
[17] F. Huang, H. Wu, D. Wang, W. Yang, Y. Cao, Chem. Mater. 16 (2004) 708.
[18] F. Huang, L. Hou, H. Wu, X. Wang, H. Shen, W. Cao, W. Yang, Y. Cao, J. Am. Chem. Soc. 126 (2004) 9845.
[19] H. Wu, F. Huang, Y. Mo, W. Yang, D. Wang, J. Peng, Y. Cao, Adv. Mater. 16 (2004) 1826.
[20] H. Wu, F. Huang, J. Peng, Y. Cao, Org. Electron. 6 (2005) 118.
[21] B. Liang, C. Jiang, Zhao Chen, X. Zhang, H. Shi, Y. Cao, J. Mater. Chem. 16 (2006) 1281.
[22] Y. Xu, J. Peng, J. Jiang, W. Xu, W. Yang, Y. Cao, Appl. Phys. Lett. 87 (2005) 193502.
[23] R.A. Negres, X. Gong, J.C. Ostrwski, G.C. Bazan, D. Moses, A.J. Heeger, Phys. Rev. B 68 (2003) 115209.
[24] L. Berthelot, J. Tardy, M. Garrigues, P. Cremillieu, J. Joseph, B. Masenelli, Opt. Mater. 12 (1999) 261.
[25] C.-H. Kim, J. Shinar, Appl. Phys. Lett. 80 (2002) 2201.

Available online at www.sciencedirect.com
ScienceDirect
Organic Electronics 8 (2007) 540–544
Organic Electronics
www.elsevier.com/locate/orgel

Electrical conductivity of organic single-nanofiber devices with different contact materials

Henrik H. Henrichsen [a], Jakob Kjelstrup-Hansen [b,*], Daniel Engstrøm [a], Casper H. Clausen [a], Peter Bøggild [a], Horst-Günter Rubahn [b]

[a] *MIC – Department of Micro and Nanotechnology, NanoDTU, Technical University of Denmark, Building 345 east, DK-2800 Kgs. Lyngby, Denmark*
[b] *Mads Clausen Institute, University of Southern Denmark, Alsion 2, DK-6400 Sønderborg, Denmark*

Received 30 November 2006; received in revised form 26 March 2007; accepted 27 March 2007
Available online 4 April 2007

Abstract

The electrical characteristics of morphologically completely defined individual *para*-hexaphenylene (p6P) nanofibers are investigated with different electrode materials Au, Al, and Cr. Simple quadratic fitting of the *I–V* measurements along the Mott–Gurney law results in a large range of mobility values, suggesting that the tested contact materials lead to injection limited conduction. We find that Au exhibit the best charge injection properties. A method for fabricating single-nanofiber devices with different anode and cathode materials is applied, with the aim of investigating the electroluminescent properties.
© 2007 Elsevier B.V. All rights reserved.

PACS: 72.80 Le; 73.40.Sx

Keywords: Organic nanofibers; Mobility; Mott–Gurney; *para*-Hexaphenylene; Electrical contact; Micromanipulation

1. Introduction

Within the last two decades, research in organic light emitting devices (OLEDs) has been driven by the perspectives of making cheap and efficient light sources [1]. While the current commercial interest goes in the direction of making displays and artificial lighting [2], the miniaturization perspectives of such devices could be integrated light sources in optoelectronic chips or in on-chip optical analysis of chemical or biological samples [3]. Nanoscale OLEDs have been demonstrated recently [4,5]. In both studies electron beam lithography techniques were used to define the active area.

Light generation requires recombination of electrons and holes from the lowest unoccupied molecular orbital (LUMO) and highest occupied molecular orbital (HOMO) levels, respectively. Optimizing the efficiency of this process involves balancing the hole and electron currents. As a first approximation, this can be attempted by choosing appropriate cathode and anode materials, which

* Corresponding author. Tel.: +45 65 50 16 85; fax: +45 65 50 16 54.
E-mail address: jkh@mci.sdu.dk (J. Kjelstrup-Hansen).

1566-1199/$ - see front matter © 2007 Elsevier B.V. All rights reserved.
doi:10.1016/j.orgel.2007.03.010

have equal injection barriers to the LUMO and HOMO levels of the organic material, respectively. This, however, does not account for factors such as the difference in electron and hole mobilities and variations in the interface between the organic material and different electrode materials. Thus, an experimental comparison of electrode materials is highly relevant.

In contrast to the previously reported nanoscale OLEDs based on amorphous materials [4,5], this study focuses on quasi-crystalline nanofiber structures i.e. composed of highly oriented molecules stacked in a crystal structure [6]. The high crystal order results in preferred electrical conduction along the long nanofiber axis [7,8], and a highly polarized photoluminescence output in the blue region of the spectrum [9]. A similar electroluminescence spectrum is anticipated based on studies of a p6P thin film [10]. The nanofibers have shown lasing [11] and waveguiding [12] properties and by chemical engineering of the molecular building blocks, it is possible to design nanofibers with specific properties such as frequency doubling [13]. This makes the nanofibers promising candidates for electro-optical components. We have recently demonstrated that it is possible to electrically contact individual nanofibers using a shadow mask evaporation technique [14].

In this work we investigate the electrical properties of devices based on self-assembled p6P nanofibers [6] with different contact materials with the aim of finding suitable electrodes for obtaining electroluminescence. By analysis of a large number of samples compared to Ref. [14], we find that the data are inconsistent with a well-defined mobility as should be expected from bulk limited conduction. Hence, we suggest that the charge transport is instead injection limited.

2. Experimental

The organic nanofibers are epitaxially grown by evaporating p6P molecules from a Knudsen cell onto a freshly cleaved (0001) muscovite mica surface [6]. In order to investigate an individual nanofiber, some of the nanofibers are transferred to a target substrate, which is a 35 μm wide and 1 μm thick silicon dioxide support elevated some μm above a silicon substrate by under-etching. The transfer is accomplished by dispersing nanofibers in an appropriate liquid and using a micropipette to deposit a droplet of the nanofiber dispersion onto the silicon dioxide structure [15]. When the liquid

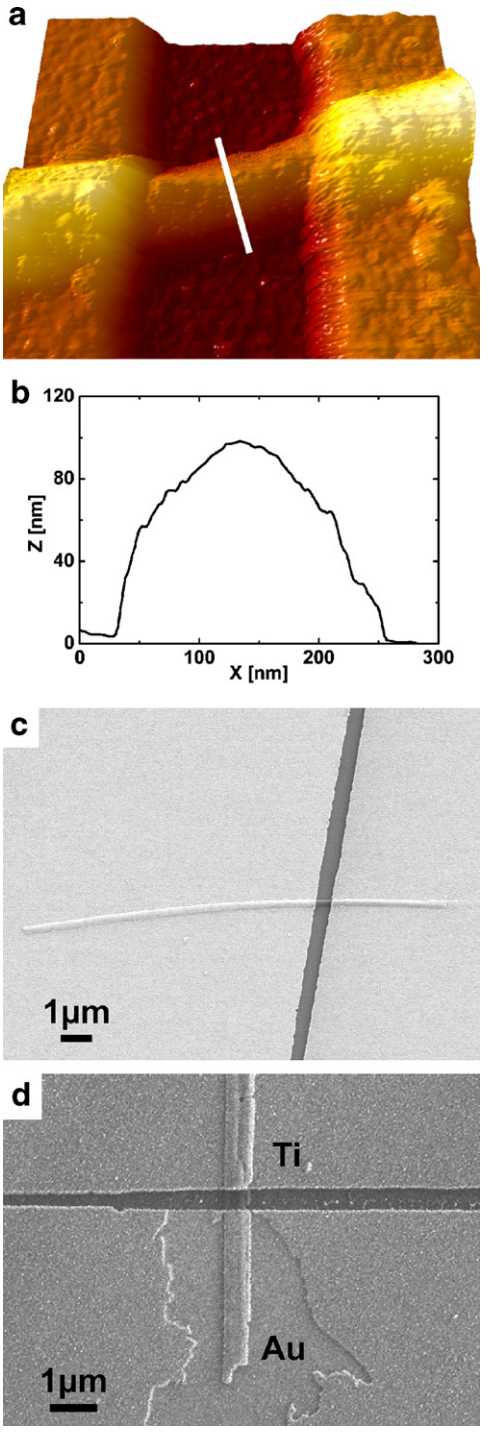


Fig. 1. Organic nanofiber devices. (a) 1 μm by 1 μm tapping mode AFM image of the device topography. (b) Cross section of the active part of the nanofiber at the line indicated in (a). (c) SEM image of a p6P nanofiber on a silicon dioxide support with electrodes separated by the shadow of a silicon wire mask. (d) SEM image of a p6P nanofiber on a silicon dioxide support with two different electrode metals.

evaporates, the nanofibers remain on the surface, out of which one will be used for a device. Using a micromanipulation setup and a microfabricated manipulation tool, a silicon nanowire is placed across the silicon dioxide support to function as a shadow mask during subsequent metal deposition [16]. After metal deposition the silicon nanowire is removed and the device is contacted by ultrasonically attaching bonding wires. Fig. 1 shows scanning electron microscope (SEM) and atomic force microscope (AFM) images of nanofiber devices.

Devices with two different electrode materials were fabricated by adding an extra shadow mask. After placement of the silicon nanowire across the p6P nanofiber, a small flake of silicon was placed adjacent to the silicon nanowire, only covering the organic nanofiber on one side of the silicon nanowire. Then the first electrode material was deposited. After removing the small flake of silicon, the second electrode was deposited. The silicon nanowire was then removed by nanomanipulation and bonding wires were attached [16]. Fig. 1d shows a device with electrodes made from different materials through this double shadow mask technique.

The current–voltage characteristics were measured using a custom-built, LabVIEW-based measurement setup, where the voltage is controlled by a 16-bit National Instruments DAQ card which also reads out the current measured by a Stanford Research SR 570 current amplifier. In cases where the supply voltage must be higher than the 10 V limit of the DAQ card, a Delta Elektronika ES075-2 voltage supply was used to amplify the voltage. In order to determine the dimensions of the active part of the nanofiber between the contacts, the height was measured with a Veeco CP-II AFM in tapping mode, and an SEM was used to measure the length and width in order to avoid problems with AFM tip convolution effects.

3. Results

More than 150 devices have been fabricated, but only 23 of these shows a characteristic that can be interpreted as conduction through the nanofiber. Typical failures are short circuits (failure in the shadow mask method) or open circuits (failure in the contacts). A typical current density versus voltage (J–V) measurement is shown in Fig. 2a.

The parabolic dependence of the last part of the J–V characteristics suggests that conduction occurs in the space-charge limited regime (SCL) [17]. In the

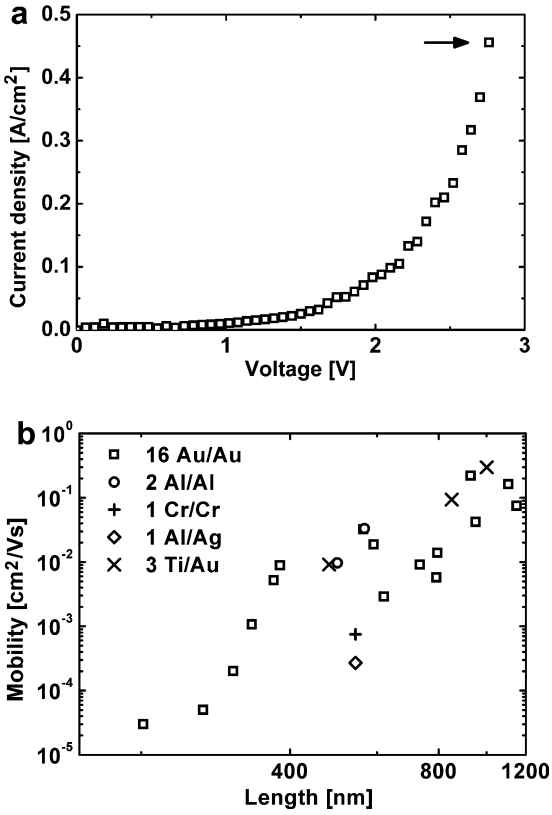


Fig. 2. (a) Typical J–V characteristic of a p6P nanofiber device with Au electrodes. The arrow indicates the last sample point, used to extract a lower limit mobility value. (b) The estimated lower limit of carrier mobility values for all 23 working devices versus device length assuming SCL conduction. The 620 nm long device was also used in [14]. If the assumption of SCL conduction is fulfilled, the estimated values of mobility should not show any length dependence, whereas contact effects introduce a seeming length dependence in the estimates indicating contact-limited conduction.

SCL regime the maximum current density J is given by the Mott–Gurney law [18]:

$$J = \frac{9\varepsilon_r\varepsilon_0\mu V^2}{8L^3}, \tag{1}$$

where L is the device length, the mobility μ is a constant, and the relative dielectric constant ε_r is estimated to 1.9 [12]. Eq. (1) provides an upper limit to the current density that can flow in a single carrier device. Any additional effects such as carrier traps or interface barriers will only decrease the current density below this value. We can therefore extract a lower limit of the carrier mobility by rearranging Eq. (1), inserting the highest obtained current density, and using the widths and lengths obtained from SEM and the heights obtained from

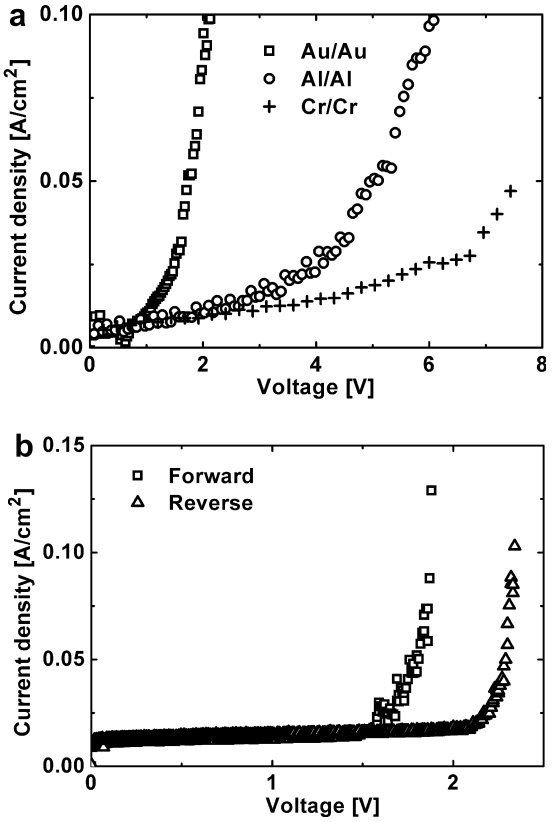


Fig. 3. Current density versus voltage, sweeping from zero volts. (a) Devices with three different contact metals: Au/Au (930 nm long), Al/Al (500 nm long) and Cr/Cr (540 nm long) showing different onset voltages. (b) Forward and reverse voltage sweep of a Ti (cathode)/Au (anode) contacted device.

AFM measurements [17]. The lower limit mobility determined this way for the working devices is plotted in Fig. 2b as a function of L.

Selected J–V measurements on devices with different contact materials are shown in Fig. 3.

4. Discussion

Due to the considerable sample to sample variations, we fabricated and investigated a large number of samples to form a reasonable basis for interpretation. Most of the devices were made with Au contacts since Au does not oxidize and has a low barrier to hole injection compared to the other electrode metals (work functions: Al: 4.28 eV, Cr: 4.5 eV, Au: 5.1 eV) [19].

The current in the nanofiber devices can either be injection limited or bulk limited, i.e. the electrical characteristics are determined either by contact barriers or by the nanofiber "bulk", where bulk limited conduction is assumed to obey the Mott–Gurney law (1). In order to determine which of these two is applicable, we have investigated the measured data under the assumption of bulk limited conduction by extracting values of the lower limit of carrier mobility. Since carrier mobility is an intrinsic parameter, the strong length dependence in Fig. 2b suggests that these devices are not dominated by bulk limited transport. Presumably the contact barriers are too large for SCL conduction; the conduction is injection limited and the devices fail due to electrical breakdown at the contacts before the current reaches the SCL regime. It is suggested that the electrode/organic interface significantly influences the J–V characteristics. A similar investigation of mobility has been conducted on tetracene crystals by de Boer et al. [17], also observing large variations in the resulting minimum mobilities. Therefore, if a good estimate of the mobility is to be found with the Mott–Gurney law, other contact materials with lower injection barriers to p6P must be used.

Although the measurements cannot give a definite value of carrier mobility in p6P nanofibers, it is still possible to extract useful information from the J–V characteristics. The typical characteristics for devices with different contact metals (Fig. 3a) show a rather clear dependence of onset voltage on the contact metal. Fig. 3a can qualitatively be explained by the different metal work functions and the way they line up with the HOMO (~6.0 eV) and LUMO (~2.9 eV) levels [20] of the organic material. In a first approximation, the barrier to electron or hole injection is the difference between the work function and the LUMO and HOMO levels, respectively. With this interpretation, Au has the lowest barrier (0.9 eV), and therefore exhibits the lowest onset voltage. Aluminium has a larger barrier of ~1.4 eV for electron injection, while Cr has the largest barrier (1.6 eV for electrons and 1.5 eV for holes) and therefore the largest onset voltage. A qualitative agreement between contact barrier and onset value is observed.

Next we have investigated the J–V characteristic of a nanofiber with electrodes made from two different materials. As described in the introduction, efficient electroluminescence requires different anode and cathode materials to obtain sufficiently high hole and electron injection, respectively. This experiment was made to investigate if the shadow mask technique can be extended to different anode and cathode materials, separated by a small gap. With Au and Ti used as anode (hole emitting) and cathode

(electron emitting) material, respectively, no electroluminescence was observed. This could be due to a significant difference in injection barrier height for the two contacts. Nevertheless, the asymmetric characteristics with an onset voltage significantly larger under reverse bias than under forward bias (Fig. 3b), suggests that the method for applying different contact materials is working. Devices with the same electrode materials show forward and reverse symmetry.

Considerable DC current offsets can be observed in the J–V characteristics in Fig. 3 as also observed with a p6P thin film [21]. The DC offset was found to increase in proportion to the voltage sweeping speed, which indicates a capacitive origin. Our device structure consists of two relatively large electrodes, which act as a capacitor. This capacitor, which schematically is in parallel to the nanofiber, limits the maximum measurement speed but does not appear to disturb the measurement more than adding a constant offset value.

5. Summary and outlook

A large number of single p6P nanofiber devices were fabricated with either Al, Cr, Au or Au + Ti electrodes. From typical J–V characteristics it is concluded that Au shows much better charge injection than any of the other investigated metals. The double shadow mask technique demonstrated in Ref. [15] can facilitate the use of different cathode and anode materials, which is here demonstrated to lead to asymmetric electrical characteristics indicating a difference in injection barriers. A material with low work function is needed to match the characteristic of Au in order to balance the hole and electron injection in a light emitting device. The space-charge limited regime is not reached and the current is injection limited. Therefore the Mott–Gurney law can only be used to make a rough estimate of the lower limit charge carrier mobility in the organic nanofibers. For space-charge limited conduction, small contact barriers are needed. For example by using a low work function metal, such as Sm, it is possible to obtain low electron injection barriers to p6P [20].

A possible method of estimating the mobility, avoiding the problem of injection limited conduction, is to use time-of-flight spectroscopy where effects from contact barriers are avoided [17]. However, our device geometry hinders the application of this method, in which photocarriers must be generated at one electrode. This is typically done by photoexcitation through a transparent back contact in a layered device structure. An approach to examining the contact barriers could be to investigate the temperature dependence of the J–V characteristics, which could provide a better understanding of the injection mechanism [22].

Acknowledgements

HGR is grateful to the Danish research agencies SNF and FTP for financial support.

References

[1] R. Meerheim, K. Walzer, G. He, M. Pfeiffer, K. Leo, Proc. SPIE 6192 (2006) 100.
[2] P. Wellmann, M. Hofmann, O. Zeika, A. Werner, J. Birnstock, R. Meerheim, G.F. He, K. Walzer, M. Pfeiffer, K. Leo, J. Soc. Inf. Display 13 (2005) 393.
[3] Y. Huang, X.F. Duan, C.M. Lieber, Small 1 (2005) 142.
[4] F.A. Boroumand, P.W. Fry, D.G. Lidzey, Nano Lett. 5 (2005) 67.
[5] H. Yamamoto, J. Wilkinson, J.P. Long, K. Bussman, J.A. Christodoulides, Z.H. Kafafi, Nano Lett. 5 (2005) 2485.
[6] F. Balzer, H.-G. Rubahn, Appl. Phys. Lett. 79 (2001) 3860.
[7] H. Yanagi, S. Okamoto, T. Mikami, Synth. Met. 91 (1997) 91.
[8] H. Yanagi, S. Okamoto, Appl. Phys. Lett. 71 (1997) 2563.
[9] F. Balzer, H.-G. Rubahn, Adv. Funct. Mater. 15 (2005) 17.
[10] M. Klemenc, F. Meghdadi, S. Voss, G. Leising, Synth. Met. 85 (1997) 1243.
[11] F. Quochi, F. Cordella, R. Orru, J.E. Communal, P. Verzeroli, A. Mura, G. Bongiovanni, A. Andreev, H. Sitter, N.S. Sariciftci, Appl. Phys. Lett. 84 (2004) 4454.
[12] F. Balzer, V.G. Bordo, A.C. Simonsen, H.-G. Rubahn, Phys. Rev. B 67 (2003). Art. No. 115408.
[13] J. Brewer, M. Schiek, A. Lützen, K. Al-Shamery, H.-G. Rubahn, Nano Lett. 6 (2006) 2656.
[14] J. Kjelstrup-Hansen, H.H. Henrichsen, P. Bøggild, H.-G. Rubahn, Thin Solid Films 515 (2006) 827.
[15] J. Brewer, C. Maibohm, L. Jozefowski, L. Bagatolli, H.-G. Rubahn, Nanotechnology 16 (2005) 2396.
[16] J. Kjelstrup-Hansen, S. Dohn, D.N. Madsen, K. Mølhave, P. Bøggild, J. Nanosci. Nanotechnol. 6 (2006) 1995.
[17] R.W.I. de Boer, M. Jochemsen, T.M. Klapwijk, A.F. Morpurgo, J. Niemax, A.K. Tripathi, J. Pflaum, J. Appl. Phys. 95 (2004) 1196.
[18] M.A. Lampert, P. Mark, Current Injection in Solids, Academic Press, New York, 1970.
[19] H.B. Michaelson, J. Appl. Phys. 48 (1977) 4729.
[20] N. Koch, E. Zojer, A. Rajagopal, J. Ghjisen, R.L. Johnson, G. Leising, J.-J. Pireaux, Adv. Funct. Mater. 11 (2001) 51.
[21] S. Tkaczyk, I.V. Kityk, Appl. Surf. Sci. 241 (2005) 287.
[22] V.I. Arkhipov, E.V. Emelianova, Y.H. Tak, H. Bässler, J. Appl. Phys. 84 (1998) 848.

Available online at www.sciencedirect.com
ScienceDirect
Organic Electronics 8 (2007) 545–551
Organic Electronics
www.elsevier.com/locate/orgel

Dissociation of sexithiophene on Al(1 1 1) surface

J. Ivanco [a,b,*], F.P. Netzer [a], M.G. Ramsey [a]

[a] Institute of Physics, Surface and Interface Physics, Karl-Franzens University Graz, Universitätsplatz 5, A-8010 Graz, Austria
[b] Institute of Physics, Slovak Academy of Sciences, Vrbovská cesta 102, SK-921 01 Piešťany, Slovakia

Received 23 September 2006; received in revised form 28 March 2007; accepted 29 March 2007
Available online 5 April 2007

Abstract

The growth of sexithiophene ultra-thin films on an atomically clean Al(1 1 1) surface has been investigated by angle-resolved ultraviolet photoemission spectroscopy. Although sexithiophene on Al(1 1 1) represents a weakly interacting system, sexithiophene molecules were found to dissociate even below room temperature, presumably via reactive sites. The mechanism is distinctly different to that claimed on the reverse system, i.e. aluminum evaporated on thiophene oligomers films, where isolated aluminum atoms were reported to covalently bond to thiophene rings and thus dramatically affect the molecule geometry and the conjugation. The effect of the insertion of an ultra-thin separator film of sexiphenyl, on the dissociation of sexithiophene was also examined.
© 2007 Elsevier B.V. All rights reserved.

PACS: 81.05.Hd; 79.60.−i; 68.43.−h; 73.30.+y

Keywords: Organic semiconductors; Oligothiophenes; Metal–organic interfaces; Heterojunctions; Ultraviolet photoelectron spectroscopy; Work function

1. Introduction

The performance of molecular devices relies on both bulk properties of conjugated organic films and their interfaces with a contacting material. In particular, understanding and controlling the interfaces represents an ongoing challenge to realizing the full potential of organic electronics. The sequence of the contact formation is relevant: organics-on-contact material and contact material-on-organics usually represent different problems. The former approach is mostly adopted in structural and morphological studies of molecular films employing the substrate in the role of a growth template, while the latter one focuses on a stable planar metal contact formation on the top of an organic film. Junction characteristics of a particular organic film and metal are not yet predictable from the nature of the metal. The interaction at the interface, which is specific for every system, dramatically affects the interfacial electronic structure and therefore understanding this interaction is crucial for the control of transport properties/charge injection of contacts.

Both pioneering [1] and recent [2] attempts to employ sexithiophene and polythiophene thin films,

* Corresponding author. Present address: Institute of Physics, Technical University Chemnitz, D-09107 Chemnitz, Germany. Tel.: +49 371 531 36729; fax: +49 371 531 21819.
E-mail address: jan.ivanco@physik.tu-chemnitz.de (J. Ivanco).

1566-1199/$ - see front matter © 2007 Elsevier B.V. All rights reserved.
doi:10.1016/j.orgel.2007.03.011

respectively, as active layers in organic field-effect transistors justify the ongoing studies on these relevant systems. Since aluminum is among the most common contact metallizations, several theoretical [3–6] and experimental studies [7–9] on the formation of aluminum layers on thiophene oligomers films have been reported. Theoretical investigations on the reaction of aluminum with terthiophene indicate that aluminum atoms covalently bond to the α-carbons of thiophene monomers and thus form complexes. The reaction, which presumes the supply of isolated aluminum atoms, heavily distorts the molecular geometrical structure and thus disrupts its π conjugation. In contrast, vibrational [10], valence band photoemission and desorption [11,12] studies on (bi)thiophene films condensed at liquid nitrogen temperature on Al(1 1 1) surface suggested a weakly interacting system where the covalent bonding between thiophene and aluminum can be excluded. These results lead to the question of whether the isolated Al atoms are *per se* more reactive to the thiophenes than those at the surface of the bulk metal.

In this work, we present examinations on sexithiophene films grown at different temperatures on the Al(1 1 1) surface. It is shown that the conjugation of a sexithiophene molecule deposited at liquid nitrogen temperature distorts upon warming-up to room temperature in spite of the absence of isolated aluminum atoms. The effect of the insertion of a molecular spacer layer between the 6T and Al(1 1 1), an ultra-thin film of sexiphenyl (6P), will be illustrated and discussed.

2. Experimental

The film growth and photoemission characterization were carried out *in situ* in a UHV VG-ADES 400 angle resolving ultraviolet photoemission spectrometer (ARUPS) with a base pressure less than 10^{-10} mbar. The samples could be cooled down to liquid nitrogen temperature (LNT, about 90 K) and resistively heated. The movable hemispherical analyser enables the variation of the electron take-off angle with respect to surface normal and to the photon incident angle of an unpolarized HeI (21.2 eV) radiation. A resolution of 80 meV as measured via the Fermi edge width (in the intensity range from 10% to 90%) of the clean Al(1 1 1) at LNT has been employed. Work functions were measured using the secondary electron cut-off of spectra in normal emission with the sample biased by −9 V.

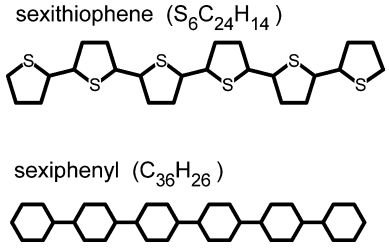


Fig. 1. Schematic formulae of sexithiophene and sexiphenyl.

The system was also equipped with facilities for low energy electron diffraction (LEED) and Auger electron spectroscopy (AES).

The Al(1 1 1) single crystals was cleaned by cycles of sputtering with 1 keV Ar^+ ions at room temperature (RT) followed by annealing for 5 min at about 700 K. Both the surface order and cleanliness were checked before applying the molecules by LEED and UPS, respectively; both a sharp LEED pattern and a featureless valence band, the latter being otherwise extremely sensitive to the surface contamination, classified the Al(1 1 1) surface for interface studies.

Sexithiophene (Syncom, B.V.) and sexiphenyl (Tokyo Chemical Industry Co., Ltd.) are unsubstituted π-conjugated oligomers of benzene and thiophene, respectively, build up by six aromatic rings joined together in *para* positions (Fig. 1). Both were deposited from a thoroughly outgassed specially designed evaporator such that the pressure in the system remained in the low 10^{-10} mbar range during the film growth. The exposures were monitored by a water-cooled quartz microbalance and are given in terms of nominal thickness using the 6T and 6P density of 1.55 g/cm^3 [13] and 1.29 g/cm^3 [14]. The typical growth rates used were 1.5 ± 0.5 Å/min. It is worth noting that a thickness of ∼3–4 Å and ∼25 Å would correspond to complete monolayers (ML) formed by molecules either lying parallel (flat-on) or perpendicular (“end-on”) to the substrate, respectively.

3. Results

3.1. The 6T/Al(1 1 1) interface

Fig. 2 shows the evolution of photoemission spectra of the clean Al(1 1 1) surface upon increasing coverage of 6T grown at LNT. The valence band of the 6T qualitatively corresponds to spectra reported previously [15–17]. Particularly for small coverages,

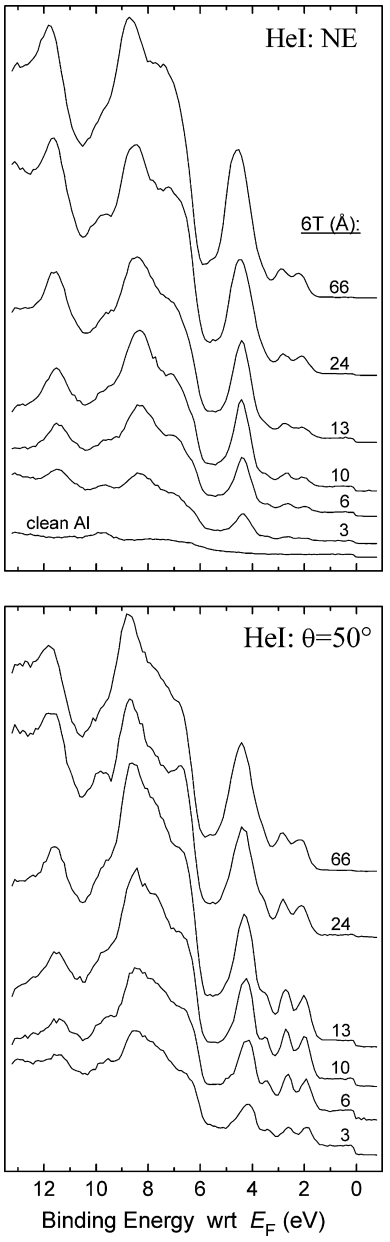


Fig. 2. Photoemission spectra of 6T layers grown at LNT on the atomically clean Al(1 1 1) taken at normal emission (NE) (upper panel) and 50° (lower panel). The nominal film thickness is indicated in Å.

the spectra are strongly angular dependent, which is apparent on the well-resolved π band. Both the photoemission intensity evolution with the coverage and the angular dependence suggest that the 6T molecules are lying down [18]. While the Fermi edge is still visible for the 24 Å-thick film, it is not observed anymore for the 66 Å-thick film. This indicates islands on monolayers (Stranski–Krastanov) molecular film growth at LNT.

The π stabilization, i.e. the differential shift of molecular π orbitals induced by the interaction between molecules and the substrate surface, is a measure of the molecule-substrate bond strength. Apart from being somewhat better resolved, the spectra of the lying monolayer at LNT are identical to those of the thick multilayer films both in terms of orbital energy position and angular effects in the orbital emissions. This indicates that the screening from the substrate and intermolecular screening are similar, which in turn indicates a weak bonding to the substrate. In other words, there is no evidence for any strong covalent bond or charge transfer from the substrate.

Fig. 3 illustrates the work function evolution with the 6T coverage of films grown at LNT (full circles). The work function drops abruptly with the 6T thickness up to about 6 Å and remains near constant upon further deposition. Such dependence is typical for the layer-by-layer (Frank-Van der Merwe) and Stranski–Krastanov molecular film growth, where the work function of the substrate drops near linearly up to the coverage corresponding

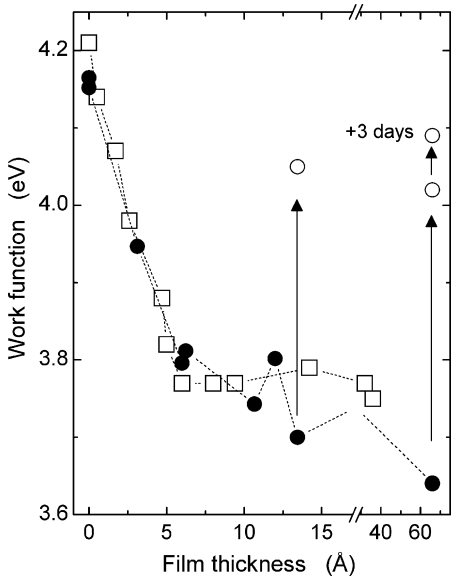


Fig. 3. Work function diagrams of 6T (circles) and 6P (squares) films on Al(1 1 1). The 6T and 6P films were grown at LNT and RT, respectively. The empty circles represent values after warmings-up as indicated by the arrows. The value labeled "+3 days" was obtained after the storage of the sample for three days in UHV at RT. Straight dotted lines serve as guidelines only.

to 1–2 ML due to an interfacial dipole formation, and it does not change with further coverage. The work function decrease of about 0.4 eV corresponds to the interfacial dipole similar to that observed for thiophene and bithiophene on Al(1 1 1) [11]. Parenthetically we note that aluminum is not a low work function metal, as it is sometimes regarded [5,7,8,19]. Its work function of about 4.2 eV for Al(1 1 1) falls rather in the "middle" range of metal work functions. However, the work function of aluminum is very sensitive to the amount of the chemisorbed oxygen with a total drop for the oxygen-saturated surface by more than 1 eV. A low work function of aluminum would indicate surface contamination (its partial oxidation), which will considerably modify its reactivity [20,21].

The 6T has been found to be stable on other studied surfaces like SiO_x [17], TiO_2(1 1 0) [18], Cu(1 1 0), and Cu(1 1 0)–(2 × 1)O [22], whether grown at RT or elevated temperatures up to 400 K. In contrast, the RT-grown sexithiophene films on Al(1 1 1) displayed a progressive degradation within several tens of minutes. The same effect – particularly manifested in the smearing-out of the upper π band and an increase in the background – occurs upon overnight warming-up of the LNT-grown sexithiophene films. This is illustrated in Fig. 4, where the valence band of the clean Al(1 1 1) surface taken at a take-off angle of 50° (curve *a*), the LNT-growth of 13 Å-thick sexithiophene film recorded at normal emission (curve *b*), and with a take-off angle of 50° (curve *c*), and after warming-up to RT (curve *d*) are shown. Note that the spectra are referenced to the vacuum level by adjusting to the work functions of the respective films, and thus the HOMO position of about 5.8 eV gives the ionization potential of the sexithiophene thin film. The 6T film warmed-up to RT does not display any dependence on the take-off angle. Notably, the spectra of the 6T films kept at RT in UHV on Al(1 1 1) progressively degraded over several days till the π-band signature was eliminated. This was particularly manifested in the disappearance of the HOMO, -1, and -2 orbitals, which have their principle weight on the α-carbons of the molecule [16]. The thicker films (66 Å) showed virtually the same degradation of the valence band upon warming-up to RT; moreover the Fermi edge, entirely eliminated at LNT, reappeared suggesting the formation of islands.

The work function returns almost to the original substrate work function upon overnight warming-up to RT as indicated by empty circles in Fig. 3.

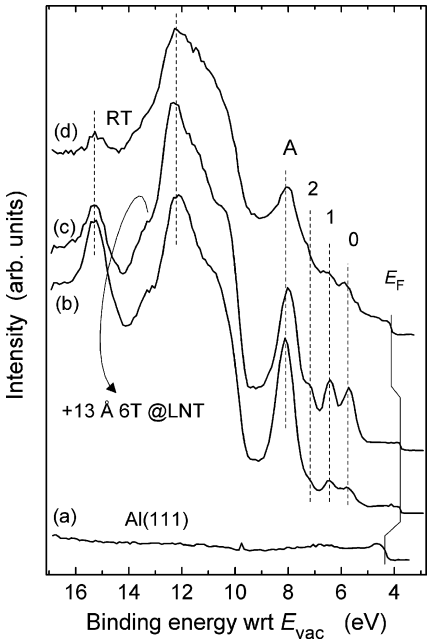


Fig. 4. Photoemission spectra of clean Al(1 1 1) measured at a take-off angle of 50° (curve *a*), and after the growth of 13 Å of 6T at LNT taken at normal emission (curve *b*) and take-off angle of 50 ° (curve *c*), and after warming-up to RT at take-off angle of 50 ° (curve *d*). The spectra are referenced to the vacuum level. Positions of Fermi edges for particular spectra are indicated. The highest individual π orbitals HOMO, HOMO-1, and HOMO-2 are labeled 0, 1, and 2, respectively. The nonbonding π orbitals are labeled *A*.

Apparently, the increase of the work function is not due to dewetting of the Al(1 1 1) surface since the integral intensity of the valence band of the 6T does not change much, i.e. it corresponds to 1–2 monolayer coverage. It rather reflects the change of the interfacial dipole due to the dissociation of the 6T molecule at the interface. The change of the interfacial dipole is evidenced by the fact that work function change on warming to RT (0.3–0.4 eV) is also reflected in the same shift of the whole 6T spectrum with respect to the Fermi level (Fig. 4).

The 6T degradation is not due to a radiation damage induced by the photoemission measurement itself, since no degradation was observed in films exposed to the HeI irradiation over the course of many hours at LNT. In contrast, a degradation of 6T films grown at Al(1 1 1) at RT was apparent after tens of minutes whether irradiated by HeI or not (the UPS characterization lasted only several minutes). The gradual changes in the work function upon warming-up were observed to commence

already above ~160 K with concomitant degradation of the photoemission spectra. The 6T degradation is neither due to a contamination; the 6T films prepared on other surfaces (SiO_x[17], TiO_2(1 1 0) [18], and Cu(1 1 0)) under the same conditions and in the identical UHV system were stable.

3.2. The 6T/6P/Al(1 1 1) interface

A possible way to avoid the dissociation of 6T molecules could be the insertion of a stable ultra-thin organic spacer layer between the 6T and Al(1 1 1) to prevent their intimate contact. We have employed sexiphenyl (6P) as a separator since the 6P/Al(1 1 1) interface is stable up to at least 430 K [23–25], 6P forms a stable dense ordered monolayer on Al(1 1 1) [23,25], and the interfacial dipole on Al(1 1 1), i.e. the Al(1 1 1) work function change (Fig. 3, squares) [24], is comparable to that of the 6T on Al(1 1 1).

Fig. 5 shows the valence band evolution during the Al(1 1 1) + 6P + 6T heterostructure formation.

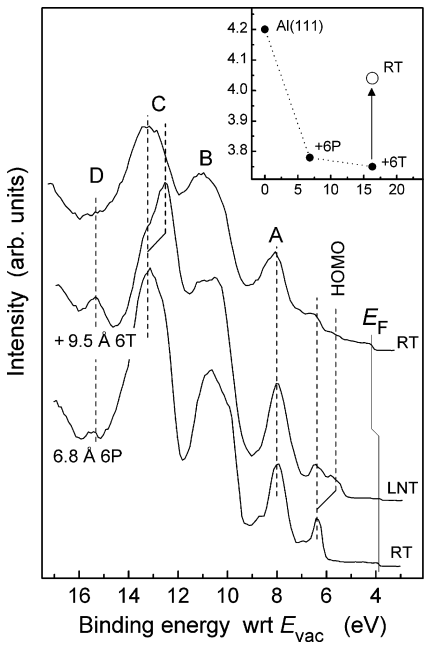


Fig. 5. Photoemission spectra during the Al(1 1 1) + 6.8 Å 6P + 9.5 Å 6T heterolayer formation. The 6P layer and 6T layers were grown at RT and LNT, respectively. The top spectrum shows the effect of warming-up to RT. The inset presents the work function diagram of the heterostructure during its formation (full symbols) and after warming-up (empty symbol). Straight dotted lines serve as guidelines only.

The spectra were collected at a take-off angle of 50°, where the particular HOMOs are well pronounced. Nominal coverages of both 6P and 6T correspond to about two and three monolayers of lying molecules, respectively, and given the evolution of the photoemission intensity, the growth proceeds by layerwise fashion. Note that the Al(1 1 1) surface is fully covered by 6P (~2 ML) and the work function is saturated, i.e. no work function change is expected upon further deposition of molecules. This is actually what is observed upon addition of 9.5 Å of 6T (see the inset in Fig. 5). That 6T on 6P does not lead to any additional work function change indicates the absence of a dipole at the organic/organic (6P/6T) interface. Addition of 6T onto 6P has replaced the 6P valence band spectrum by the 6T one indicating the laminar growth. Although of similar shape and bandwidth, the π bands do not coincide because the ionization potential of the 6T is lower by about 0.6 eV compared to that of the 6P [26,27]. As a result, the addition of 6T onto 6P shifts the HOMO of the system by about 0.7 eV. Besides the π band, the fingerprints of the 6T are clearly distinguishable also in the bands labeled *B*, *C*, and *D*.

Upon warming-up to RT (the top spectrum in Fig. 5), features related to 6T strongly diminish and the spectrum resembles more that of the 6P layer (this is best distinguished via comparison of the bands *C*, *D*, and to some extent of the π band) combined with the spectrum of remnants of the 6T (compare to curve *d* in Fig. 4). We note that the 6T features vanish completely for the same heterostructure formed by single 6P and 6T monolayers. The disappearance of 6T-related features of the Al + 6P + 6T heterostructure could be the result of islanding of the 6T on the 6P – this is suggested by the reappearance of the Fermi edge. However, if the 6T islanding was uniquely responsible, the work function would remain rather constant since it should correspond to the work function of the 6P spacer layer, which is itself stable on the Al(1 1 1) [23–25]. Yet, as it is shown in the inset of Fig. 5, the work function increases similarly to that of the single 6T film on Al(1 1 1) (Fig. 3). This suggests that the interfacial dipole is modified in the same way as if the 6T were in intimate contact with Al(1 1 1). Here, the work function change also corresponds to the shift of the spectrum (Fig. 5). We therefore, believe that the separator made of 6P apparently does not prevent the dissociation of the 6T molecules; the heterostructure becomes unstable

at RT in that the layer-by-layer morphology breaks down exposing the Al interface to the upper 6T layer while 6P presumably forms islands on the 6T film. The latter is deduced from the facts that 6P intensity becomes smaller in comparison with intensity of the pristine 6P film grown directly on the Al(1 1 1) surface and the 6T-related features were not eliminated completely.

4. Discussion

The studies on the reaction between aluminum and thiophene-based films performed on the reverse system (Al evaporated onto the organic film) in reality deal with the reaction between isolated Al atoms and individual molecules [3–9]. During the thermal deposition of aluminum, the temperature of the impinging aluminum atoms might be argued to enhance their reaction with the organic film, thus inducing the formation of Al/thiol complexes. Here, such kinetics-promoted effects are eliminated by measuring upon warming-up of the LNT-grown 6T on the Al(1 1 1).

It should be noted that the argon ion sputtering of the Al(1 1 1) surface at RT produces adatoms and vacancy clusters and induces the growth of adatom islands [28]. However, the adatom coverage becomes negligible after the annealing at 700 K [29], the temperature applied for the surface preparation here. Thus, the Al(1 1 1) surface employed in this study can be considered being free of isolated Al adatoms.

6T molecules have been observed to fragment spontaneously at RT on Si(1 0 l0)–2×1 surfaces [30] and we suggest a similar process occurs on the Al(1 1 1) surface. Here, fragmentation is supported by two facts: firstly, the antibonding orbitals HOMO, -1, and -2 (labeled 0, 1, and 2, respectively, in Fig. 4), which are the result of the interaction between six monomer units, gradually vanish, while, secondly, the nonbonding orbitals (labeled *A* in Fig. 4), which are independent of the number of thiophene units [15], remain without significant variation of either energy or intensity. This suggests that the conjugation has been destroyed. If the 6T molecules were dissociated into thiophene and bithiophene oligomers, these would be absent at RT as both molecules are reported to adsorb molecularly and desorb intact from Al(1 1 1) at 156 and 255 K, respectively [11]. In contrast, in this study the break-up products appear to remain on the Al(1 1 1) surface: this is indicated by the carbon and sulfur that were observed by AES even after the annealing up to 700 K (both the amount and element ratio corresponding to about one 6T monolayer coverage).

The observed variations of the electronic properties of sexithiophene molecules on the atomically clean Al(1 1 1) surface suggest that a realistic 6T/Al(1 1 1) interface is thermodynamically unstable. It is important to remember that the 6T molecular film at RT dissociates gradually over a period of tens of minutes although the film thickness is only 1–2 monolayers, with most of molecules in intimate contact with the Al(1 1 1) surface. A flash of such a thin LNT-grown film to RT (the entire cycle, i.e. the warming-up to RT and cooling down to LNT, lasted about 10 min) has not affected the work function within the experimental accuracy of 0.1 eV and resulted only in a marginal deterioration of the 6T-valence band. Thus, the activation energy of the dissociation plays a minor role and a further rate-limited reaction parameter, strongly dependent on the temperature, must be involved. The following mechanism can be proposed: The Al(1 1 1) surface is unreactive to 6T except for a fractional area acting as reactive sites, e.g. step edges, kinks or other defect sites, which facilitate the dissociation of molecules. For a particular catalytic system, the dissociation rate is determined by the concentration of active sites and the arrival rate, i.e. the diffusion constant of a molecule. If the former is very low, the latter becomes the limiting factor for the molecule dissociation. The mechanism is similar to that proposed for a weakly interacting system such as the 6T on H-passivated Si(1 0 0)–(2×1) surface, where STM examinations indicate highly mobile 6T molecules diffusing at RT over surface till they are captured by reactive defect sites [30]. In our case, the 6T molecules, which are deposited at LNT directly on the reactive sites may dissociate on a very short time scale, these however only represent a small fraction of the population, and are thus not observable by the area-averaging photoemission technique.

In terms of the interaction, the model is consistent with the weakly interacting (bi)thiophene/Al(1 1 1) systems, where no break-up products were reported [11] in spite of the relatively high desorption temperature of bithiophene of 255 K. This can be explained by the high warming-up rate employed in desorption studies. In other words, the bithiophene molecules desorb before they reach a reactive surface site for dissociation.

5. Conclusions

Sexithiophene films grown on the Al(1 1 1) at LNT and RT have been characterized by ultraviolet photoemission spectroscopy. While the 6T films grown at LNT were stable and no strong chemical bonds at the interface were detected, the 6T films grown at RT gradually deteriorated up to a point where their conjugation was eventually lost. Given the very slow degradation of the ultra-thin films and an absence of isolated aluminum atoms, it has been concluded that the dissociation of the 6T occurs on reactive surface sites attainable via the diffusion of the molecules. The origin of the reactive sites has not been investigated here, yet the reaction mechanism, which leads to the dissociation of sexithiophene molecules on the atomically clean Al(1 1 1) surface, is distinct from the mechanism claimed for reverse systems (i.e., aluminum-on-thiophene oligomers film). Further, the insertion of an ultra-thin sexiphenyl layer between the sexithiophene layer and Al(1 1 1) does not prevent the dissociation of the 6T molecules, because the heterostructure is morphologically unstable at room temperature.

Acknowledgements

This work was supported by the Austrian Science Foundation (FWF). Gratitude is also expressed to A. Fleming for his careful readings of the manuscript.

References

[1] G. Horowitz, D. Fichou, X.Z. Peng, Z.G. Xu, F. Garnier, Solid State Commun. 72 (1989) 381.
[2] W. Porzio, S. Destri, M. Pasini, A. Bolognesi, A. Angiulli, P. Di Gianvincenzo, D. Natali, M. Sampietro, M. Caironi, L. Fumagalli, S. Ferrari, E. Peron, F. Perissinotti, Mater. Sci. Eng. C 26 (2006) 996.
[3] M. Boman, S. Stafström, J.L. Brédas, J. Chem. Phys. 97 (1992) 9144.
[4] M. Boman, H. Ågren, S. Stafström, J. Phys. Chem. 99 (1995) 16597.
[5] V. Parente, G. Pourtois, R. Lazzaroni, J.-L. Brédas, G. Ruani, M. Murgia, R. Zamboni, Adv. Mater. 10 (1998) 319.
[6] J.M. Maud, Synth. Met. 101 (1999) 597.
[7] P. Dannetun, M. Boman, S. Stafström, W.R. Salaneck, R. Lazzaroni, C. Fredriksson, J.L. Brédas, R. Zamboni, C. Taliani, J. Chem. Phys. 99 (1993) 664.
[8] W.R. Salaneck, S. Stafström, J.-L. Brédas, Conjugated Polymer Surfaces and Interfaces, Cambridge University Press, Cambridge, 1996.
[9] F. Baier, F.v. Ludowig, A. Soukopp, C. Väterlein, J. Laubender, P. Bäuerle, M. Sokolowski, E. Umbach, Opt. Mater. 12 (1999) 285.
[10] R. Duschek, R.I.R. Blyth, M.G. Ramsey, F.P. Netzer, Surf. Sci. 439 (1999) 211.
[11] R.I.R. Blyth, F. Mittendorfer, J. Hafner, S.A. Sardar, R. Duschek, F.P. Netzer, M.G. Ramsey, J. Chem. Phys. 114 (2001) 935.
[12] S.K. Sengupta, H. Ahn, J.E. Whitten, Surf. Sci. 520 (2002) 207.
[13] B. Servet, S. Ries, M. Trotel, P. Alnot, G. Horowitz, F. Garnier, Adv. Mater. 5 (1993) 461.
[14] K.N. Baker, A.V. Fratini, T. Resch, H.C. Knachel, W.W. Adams, E.P. Socci, B.L. Farmer, Polymer 34 (1993) 1571.
[15] H. Fujimoto, U. Nagashima, H. Inokuchi, K. Seki, Y. Cao, H. Nakahara, J. Nakayama, M. Hoshino, K. Fukuda, J. Chem. Phys. 92 (1990) 4077.
[16] M. Lögdlund, P. Dannetum, C. Fredriksson, W.R. Salaneck, J.L. Brédas, Phys. Rev. B 53 (1996) 16327.
[17] J. Ivanco, J.R. Krenn, M.G. Ramsey, F.P. Netzer, T. Haber, R. Resel, A. Haase, B. Stadlober, G. Jakopic, J. Appl. Phys. 96 (2004) 2716, Errata 97 (2005) 099904.
[18] J. Ivanco, T. Haber, J.R. Krenn, F.P. Netzer, R. Resel, M.G. Ramsey, Surf. Sci. 601 (2007) 178.
[19] C. Shen, A. Kahn, J. Schwartz, J. Appl. Phys. 89 (2001) 449.
[20] J. Ivanco, B. Winter, F.P. Netzer, M.G. Ramsey, L. Gregoratti, M. Kiskinova, Appl. Phys. Lett. 85 (2004) 585.
[21] B. Winter, S. Berkebile, J. Ivanco, G. Koller, F.P. Netzer, M.G. Ramsey, Appl. Phys. Lett. 88 (2006) 253111.
[22] S. Berkebile, personal communication.
[23] B. Winter, J. Ivanco, F. Netzer, M. Ramsey, Thin Solid Films 433 (2003) 269.
[24] J. Ivanco, B. Winter, F.P. Netzer, M.G. Ramsey, Adv. Mater. 15 (2003) 1812.
[25] B. Winter, J. Ivanco, I. Salzman, R. Resel, F.P. Netzer, M.G. Ramsey, Langmuir 20 (2004) 7512.
[26] R. Telesca, H. Bolink, S. Yunoki, G. Hadziioannou, P.Th. Van Duijnen, J.G. Snijders, H.T. Jonkman, G.A. Sawatzky, Phys. Rev. B 63 (2001) 155112.
[27] K. Seki, U.O. Karlsson, R. Engelhardt, E.-E. Koch, W. Schmidt, Chem. Phys. 91 (1984) 459.
[28] C. Busse, H. Hansen, U. Linke, T. Michely, Phys. Rev. Lett. 85 (2000) 326.
[29] C. Polop, H. Hansen, C. Busse, T. Michely, Phys. Rev. B 67 (2003) 193405.
[30] R. Lin, M. Galili, U.J. Quaade, M. Brandbyge, T. Bjørnholm, A. Degli Esposti, F. Biscarini, K. Stokbro, J. Chem. Phys. 117 (2002) 321.

Available online at www.sciencedirect.com
ScienceDirect
Organic Electronics 8 (2007) 552–558
Organic Electronics
www.elsevier.com/locate/orgel

Novel organic inverters with dual-gate pentacene thin-film transistor

Jae Bon Koo [a,*], Chan Hoe Ku [a,b], Jung Wook Lim [a], Seong Hyun Kim [a]

[a] IT Convergence and Components Laboratory, Electronics and Telecommunications Research Institute, Yuseong, Daejeon 305-700, Republic of Korea
[b] Information Display Department, Kyung Hee University, Seoul 130-701, Republic of Korea

Received 31 August 2006; received in revised form 28 February 2007; accepted 3 April 2007
Available online 14 April 2007

Abstract

We report on the fabrication and characterization of dual-gate pentacene organic thin-film transistors (OTFTs) with plasma-enhanced atomic-layer-deposited (PEALD) 150 nm thick Al_2O_3 as a bottom-gate dielectric and PEALD 200 nm thick Al_2O_3 as a top-gate dielectric. The V_{th} of dual-gate OTFT has changed systematically with the application of voltage bias to top-gate electrode. When voltage bias from −10 V to 10 V is applied to top gate, V_{th} changes from 1.95 V to −9.8 V. Two novel types of the zero drive load logic inverter with dual-gate structure have been proposed and fabricated using PEALD Al_2O_3 gate dielectrics. Because the variation of V_{th} due to chemical degradation and the spatial variation of V_{th} are inherent in OTFTs, the compensation technology by dual-gate structure can be essential to OTFT applications.
© 2007 Elsevier B.V. All rights reserved.

PACS: 72.80.Le

Keywords: Organic thin-film transistor; Organic inverter; Pentacene; Threshold voltage; Dual-gate; PEALD

1. Introduction

Organic thin-film transistors (OTFTs) are being extensively studied for their potential use in flexible low-cost electronic circuits and switching devices for active-matrix displays [1,2]. The pentacene-based OTFTs have received considerable attention in recent years due to their superior electrical properties such as high field-effect mobility and large on/off current ratio [1,2]. To date, it was of great interest to increase field-effect mobility and downsize the channel length of the transistor for the organic circuits of high switching speed [3].

Inverter is a basic building block used in organic integrated circuits. Complementary technology leads to lower power dissipation, higher noise margin, better stability and easier design of the circuit. Although organic complementary inverters were recently demonstrated using a solution-processed ambipolar OTFT [4] and the integration of both p- and n-type OTFTs on the same substrate [5], most of the OTFT-based circuits reported to date used p-type transistor only because of unstable and easily degraded n-type OTFT. There are two

* Corresponding author. Tel.: +82 42 860 5470; fax: +82 42 860 5202.
E-mail address: kjb0706@etri.re.kr (J.B. Koo).

1566-1199/$ - see front matter © 2007 Elsevier B.V. All rights reserved.
doi:10.1016/j.orgel.2007.04.001

types of inverter built with only p-type transistors [6]. One is called zero drive load logic inverter (D-inverter), as the load transistor has the source connected to gate. In the case of zero drive load logic inverter, depletion and enhancement mode characteristics are needed for load and driver transistor, respectively. The other is called diode-connected load logic inverter (E-inverter) which has two transistors with enhancement mode characteristics. The former has some advantages such as wider swing range, higher gain, lower power dissipation, and higher noise margin as compared to the latter.

Threshold voltage (V_{th}) is an important parameter that needs to be controlled to ensure both low power consumption and proper operation of organic circuits. The voltage transfer characteristics (VTCs) of D-inverter such as swing range and inversion voltage ($V_{inversion}$) from low output voltage ($V_{out\,low}$) to high output voltage ($V_{out\,high}$) depend on V_{th} and on-current of the driver transistor [6,7]. The different V_{th} values in the same substrate which are necessary for fabricating D-inverter are not easily attainable. Until now, the variation of transistor dimension W/L (channel width/length) was an established solution for fabricating the load transistor of depletion mode and the driver transistor of enhancement mode in the same substrate [6]. Haddock et al. [3] presented a comprehensive study of short channel effects in OTFT and reported that as the channel length is reduced, the shift from enhancement mode to depletion mode is observed. In silicon metal-oxide-semiconductor field effect transistors (MOSFETs), V_{th} can be easily controlled by changing the doping level of semiconductor. However, the control of V_{th} by doping is not available for OTFT yet.

Recently, the results on the control of V_{th} of pentacene and polymer OTFTs with dual-gate (DG) structure were reported by Someya [8], Gelinck [9], and Morana [10]. The change of V_{th} of OTFT with DG structure was successfully understood by an analysis of electrostatic potential [8–10]. The remaining issues on the development and the mass-production of practical OTFTs are the improvement of passivation performance and the control of electrical parameters such as V_{th} and on-current. These problems can be simultaneously solved using DG OTFT. Furthermore, the DG geometry adapts to different bias configurations and offers higher flexibility of operation with respect to single-gate devices; Each bottom- and top-gate electrode can apply voltage biases to channel layer independently.

The result that the OTFT with plasma-enhanced atomic-layer-deposited (PEALD) Al_2O_3 gate dielectric shows superior electrical properties was recently reported by authors [11]. PEALD Al_2O_3 is believed to be a promising candidate for the gate dielectric of low-voltage and high-gain inverter. In this work, the DG pentacene OTFTs with PEALD Al_2O_3 as gate dielectrics were fabricated and a possibility of controlling V_{th} with DG structure was presented. The electrical properties of DG OTFTs were systematically evaluated and then they were utilized to fabricate the novel D-inverters with high performances.

2. Experimental

Pentacene OTFTs with DG structure were fabricated on a Corning 1737 glass substrate. The cross-sectional structure and bias configuration of the DG OTFT are schematically shown in Fig. 1. A bottom-gate electrode (G1), 50 nm thick Ti, was deposited in an e-beam evaporator. PEALD Al_2O_3 was deposited at 150 °C to form a 150 nm thick bottom-gate dielectric layer, using trimethylaluminum (TMA) precursors and O_2 gas mixed with N_2 gas. The breakdown field of 9 MV/cm and capacitance (C_{bottom}) of 41 nF/cm^2 were obtained. More detailed results on the electrical properties and process conditions of our PEALD Al_2O_3 gate dielectric were reported elsewhere [12]. For the source (S) and drain (D) electrodes, an Au (80 nm)/Ti (3 nm) double layer was used. The Al_2O_3 surface was treated with hexamethyldisilazane (HMDS) as the self-organizing material, which had been used to improve the quality of the organic/dielectrics interface [13]. Before spin coating of HMDS, in order to remove organic contaminants, UV–ozone treatment was carried out for 10 s; the duration of the treatment was established after preliminary tests with various treatment times. After spin coating of HMDS at 3000 rpm, post baking was performed on a hot plate at 150 °C for 30 min. Pentacene was purchased from Aldrich Chemical Co. and was purified using train sublima-

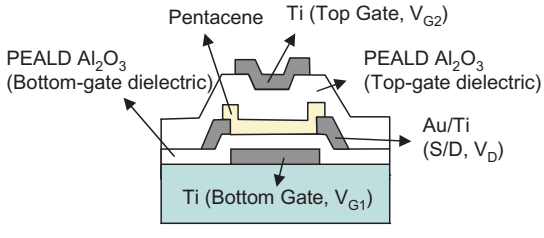


Fig. 1. Schematic structure of dual-gate OTFT device.

tion method at 1.33×10^{-5} Pa or lower. The pentacene thin-films were deposited by thermal evaporation at 70 °C. The deposition rate was 0.1 nm/s and the total deposited thickness was 60 nm.

On top of the pentacene layer, a 200 nm thick PEALD Al_2O_3 film was deposited at 100 °C ($C_{top} = 26.9$ nF/cm^2). The PEALD Al_2O_3 film deposited at 100 °C is a newly developed passivation material without damage on pentacene layer by authors [14]. Finally, a 50 nm thick Ti film was deposited to form a top-gate electrode (G2). After the electrical properties of the DG OTFT in the individual device were systematically evaluated, the novel D-inverters were designed based on the transfer characteristics of the individual transistor. Pattering for the integration of the inverters was done by the deposition of each layer through a shadow mask and their VTCs were investigated. The transfer characteristics of OTFT and the VTCs of inverter were characterized using Keithley 4200 semiconductor parameter analyzer in the dark at room temperature.

3. Results and discussion

Directly after the pentacene deposition, the transfer and output characteristics were measured to determine the performance of the initial OTFT prior to the formation of top-gate dielectric and top-gate electrode. Fig. 2a shows the transfer characteristics of the initial OTFT with $W/L = 200/50$ μm. The initial OTFT had a saturation mobility of 0.06 cm^2/Vs, a V_{th} of −0.83 V, a subthreshold swing (SS) of 0.47 V/decade, and an on/off current ratio of 1×10^6. The drain current–voltage characteristics of the initial OTFT as a function of the gate voltage exhibited good current saturation as well as a negligible contact resistance, as presented in Fig. 2b.

After top-gate dielectric, PEALD Al_2O_3, was coated on top of the pentacene active layer and then top-gate electrode was deposited on the Al_2O_3, two types of OTFT are available; As a matter of convenience, we designated the OTFT of which bottom-gate electrode was swept and top-gate electrode was floating to bottom-gate OTFT and vice versa to top-gate OTFT. From the bottom-gate OTFT with 150 nm thick PEALD Al_2O_3 as a gate dielectric as shown in Fig. 2a, saturation mobility, V_{th}, SS, and on/off current ratio were obtained as 0.03 cm^2/Vs, −2.8 V, 0.48 V/decade, and 5×10^5, respectively. The PEALD Al_2O_3 deposition as a top-gate dielectric layer slightly degraded device performances

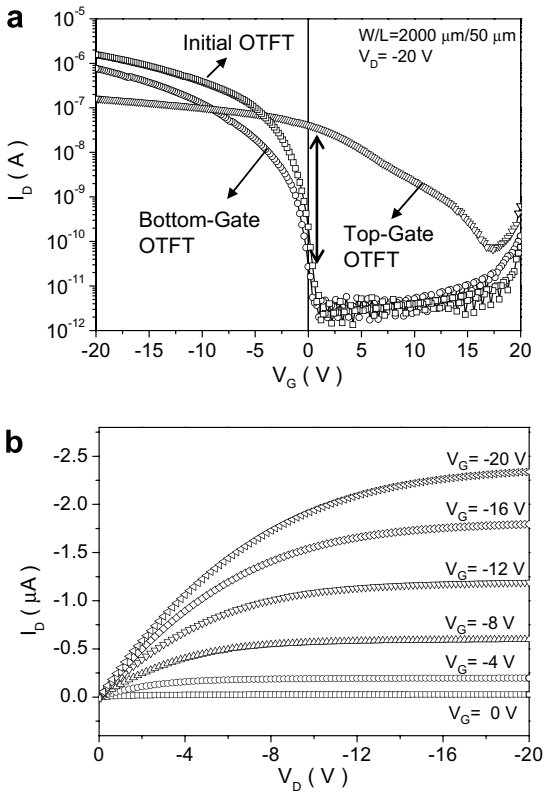


Fig. 2. (a) Transfer characteristics of the initial OTFT, the bottom-gate OTFT, and the top-gate OTFT and (b) drain current–drain voltage characteristics of the initial OTFT as a function of gate voltage.

and resulted in a slight shift of V_{th} to negative direction and a decrease of mobility. When the top gate was swept from 20 V to −20 V, the top-gate OTFT with 200 nm thick PEALD Al_2O_3 as a gate dielectric had a saturation mobility of 0.005 cm^2/Vs, a V_{th} of 11.6 V, a SS of 3.3 V/decade, and an on/off ratio of 2.3×10^4. The large difference of drain current (I_D) at gate voltage $V_G = 0$ V as depicted by an arrow in Fig. 2a was obtained, which can be essential for making D-inverter. I_D at $V_G = 0$ V of the bottom-gate OTFT was 10^{-11} A and that of the top-gate OTFT was 10^{-7} A.

Fig. 3 shows the transfer curves of the DG OTFT with the change of top-gate bias (V_{G2}) and the dependence of V_{th} on V_{G2}. When V_{G2} was 0 V, the transfer curves of first and second scan were exactly identical. Based on these successive scans, it was concluded that there is no bias-stress effect in our devices which consists of a progressive shift of the V_{th} toward negative gate voltage as the gate electrode is biased [15,16] and the stability of our device is enough for testing the control of V_{th} using

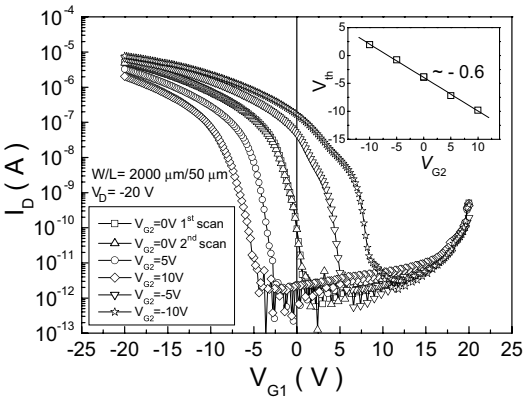


Fig. 3. The change of transfer characteristics of the dual-gate OTFT with PEALD 150 nm Al_2O_3 as a bottom-gate dielectric and PEALD 200 nm Al_2O_3 as a top-gate dielectric when the top-gate bias (V_{G2}) is changed from −10 V to 10 V in steps of 5 V. The inset shows the dependence of V_{th} on V_{G2} for the dual-gate OTFT.

the top-gate bias. When V_{G2} was changed from −10 V to 10 V in steps of 5 V, V_{th} was systematically shifted from 1.95 V to −9.8 V.

The shift of transfer curve can be explained by the body effect in a Si MOSFET [17]. In a bulk device, the body effect is defined as the dependence of the V_{th} on the substrate bias. In a DG OTFT, it is similarly defined as the dependence of the V_{th} of the bottom-gate OTFT on the top-gate bias. The V_{th} as a function of top-gate bias can be predicted from the following equation [18]:

$$\frac{dV_{th}}{dV_{G2}} = -\frac{C_{pen}C_{top}}{C_{bottom}(C_{pen}+C_{top})} \cong -\frac{C_{top}}{C_{bottom}}, \qquad (1)$$

where C_{bottom}, C_{pen}, and C_{top} are the capacitances of the bottom-gate dielectric, pentacene semiconductor, and top-gate dielectric, respectively. From the DG OTFT as shown in Fig. 3, the measured slope of dV_{th}/dV_{G2} was −0.6, which is in agreement with the theoretically predicted value ($-C_{top}/C_{bottom} = -0.66$). The controllable shift of V_{th} and turn-on voltage in pentacene OTFTs by the use of organosilances with different functional groups was recently reported [19,20]. Although V_{th} of OTFT can be controlled by modifying the surface of gate dielectric layer with self –assembled monolayer (SAM) [19,20], such approaches are still far from practical use due to the reliability of manufacturing process and the instability in moisture on SAM coating. The DG OTFT investigated in this work gives a more practical alternative for artificially controlling V_{th} and on-current.

Based on the electrical properties of the bottom-gate, top-gate, and DG OTFT in the individual device, two novel types of the D-inverter with DG structure are proposed. The one (Type-I) is the integrated structure with a top-gate OTFT as a load transistor and a bottom-gate OTFT as a driver transistor and the other (Type-II) is the integrated structure with a single-gate OTFT as a load transistor and a DG OTFT as a driver transistor. Fig. 4 shows the cross-sectional structures and bias configurations for two novel types of D-inverter. In the case of D-inverter, the W/L of load transistor must be larger than that of driver transistor in order to make load transistor more depletion type [3,6]. However, the load and the driver transistor with the same W/L (=2000/50 μm) were connected as shown in Fig. 4 because the Type-I has a top-gate load transistor with depletion mode as shown in Fig. 2a and the Type-II has a DG driver transistor being able to control V_{th} with the change of V_{G2} as shown in Fig. 3. Contacts and via holes for the integration of these structures were formed by the deposition of each layer through a shadow mask.

The transfer characteristics of the bottom- and top-gate OTFT measured in the inverter circuit are shown in Fig. 5a, which were actually used as the load transistor or the driver transistor in the two novel inverters. The V_{th} of the bottom-gate OTFT was 3.8 V and that of the top-gate OTFT was 11.5 V. As compared to those of the individual transistors in Fig. 2a, the V_{th} of the bottom-gate OTFT was shifted to positive V_G direction but that of the top-gate OTFT was similar. While the on-current of the bottom-gate OTFT was decreased, that of the top-gate OTFT was slightly increased. The reason for this difference between the individual device and the circuit is not clear. The unintentional process parameter variations such as the exposure to humidity prior to the deposition of top gate dielectric may be one of possible causes. Because the variation of V_{th} due to chemical degradation and the spatial variation of V_{th} are inherent in OTFTs, the V_{th} compensation technology described in this work, dual-gate method, can be essential to OTFT applications. The difference of V_{th} depending on storage time and the variation of manufacturing parameter can be also compensated by applying a different voltage bias to the top-gate electrode of DG OTFT.

Fig. 5b shows the VTCs of the Type-I inverter as schematically presented in Fig. 4a. When the input voltage (V_{in}) was changed from 0 V to −10 V at

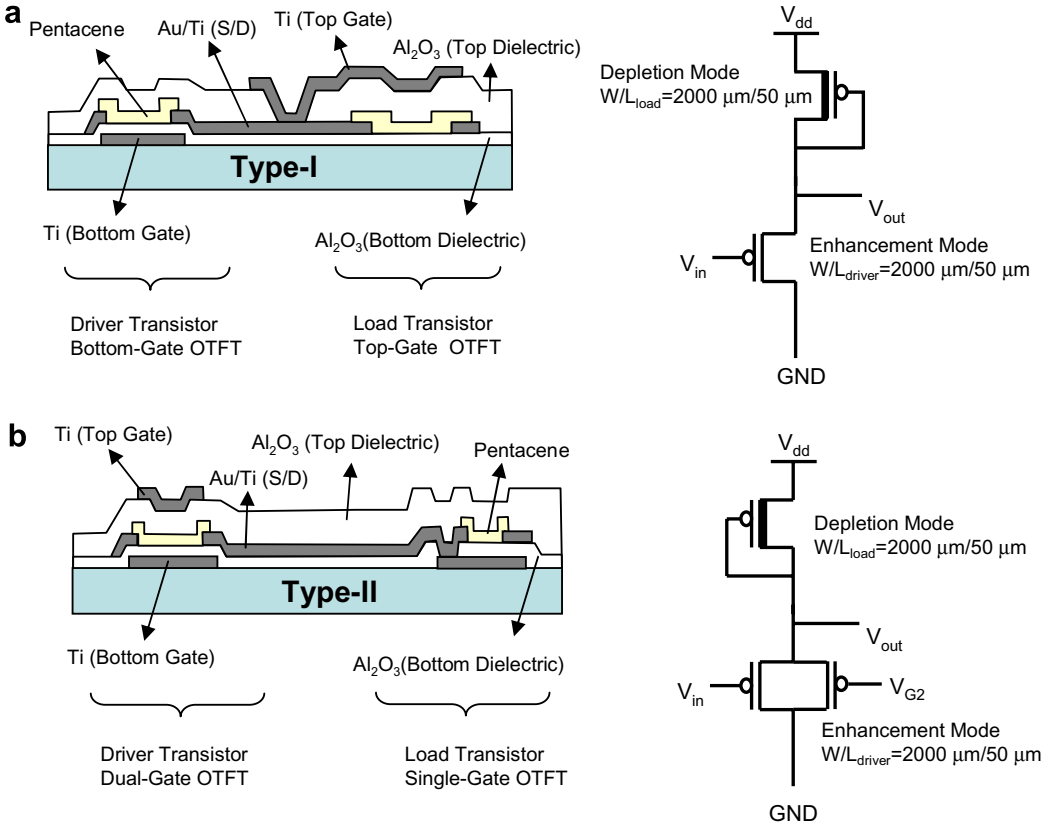


Fig. 4. The schematic cross-sectional structures and bias configurations of (a) the Type-I and (b) the Type-II D-inverter.

supply voltage (V_{dd}) of −1 V, −2 V, −3 V, −5 V, −7 V, and −10 V, the Type-I inverter was suitably operated. The gain defined as the maximum value of $(dV_{out}/dV_{in})V_{dd=-10\,V}$ was 1.5 and $V_{inversion}$ defined as the input voltage at $V_{in} = V_{out}$ was around −5 V. The suitable operation of the Type-I inverter at low V_{dd} is attributed to the significant difference of I_D at $V_G = 0$ V even though that in the inverter circuit as depicted by an arrow in Fig. 5a was decreased as compared to that in the individual device in Fig. 2a. The VTCs of the Type-II inverter are shown in Fig. 5c. The gain at $V_{dd} = -10$ V was 1.3 and $V_{inversion}$ was − 4.6 V. $V_{out\,low}$ is mainly determined by V_{dd} and $V_{out\,high}$ depends on V_{th} or on-current of the driver transistor [6]. Furthermore, the position of $V_{inversion}$ also depends on V_{th} of the driver transistor [6,7]. When negative and positive voltage bias were applied to top-gate electrode, the VTCs were shifted toward positive and negative V_{in} direction, respectively. The shift of the VTCs of the Type-II inverter with the change of V_{G2} was due to the positive or negative V_{th} shift of the driver transistor induced by the body effect of DG OTFT. Consequently, the shift of V_{th} of the driver transistor resulted in the shift of $V_{inversion}$ of the Type-II inverter. The VTCs at negative V_{G2} showed the increase of swing range because of the positive shift of the V_{th} and the increase of on-current of the driver transistor as shown in Fig. 3. Because the V_{th} and on-current of the driver transistor could be controlled by DG structure, the VTC of the Type-II inverter such as $V_{inversion}$ and swing range was systematically changed as shown in Fig. 5c.

In fact, the Type-I inverter was a by-product obtained from the fabrication of DG OTFT. We could successfully fabricate the Type-I inverter due to the significant difference of I_D at $V_G = 0$ V. The VTCs of the Type-I inverter are not controlled artificially and its successful operation entirely depends on the device characteristics of bottom- and top-gate OTFT, while those of the Type-II inverter with DG driver transistor can be controlled by applying different voltage bias to top-gate electrode. Although there is a trade-off due to the complexity of fabrication and driving, the inverter with both

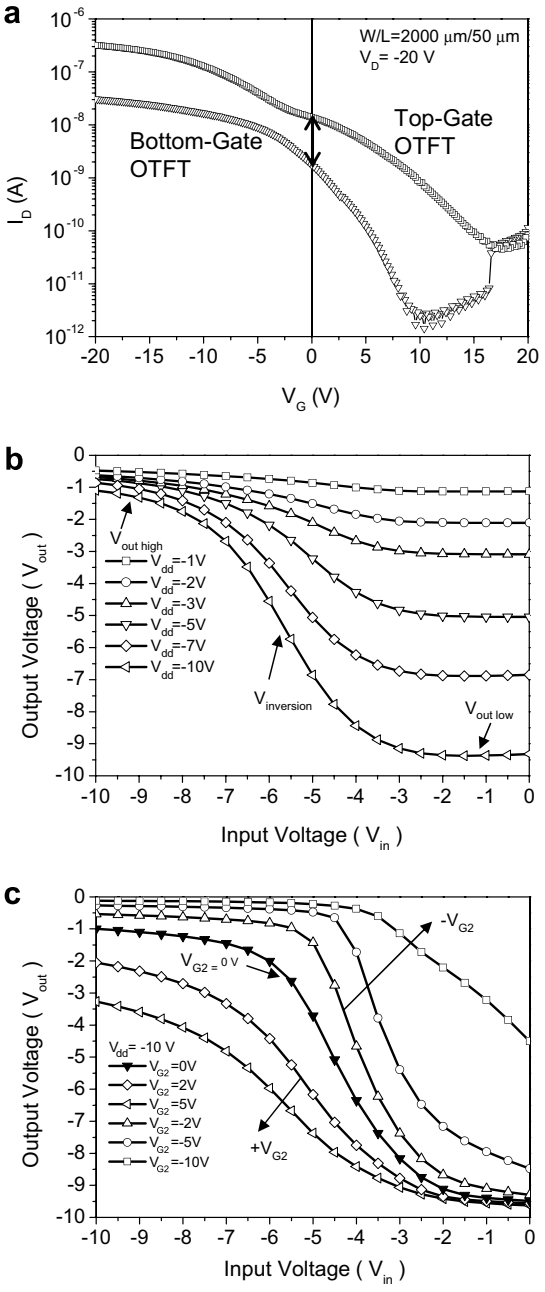


Fig. 5. (a) The transfer characteristics of the bottom- and top-gate OTFT measured in the inverter circuit. (b) The voltage transfer characteristics of the Type-I D-inverter composed of a bottom-gate driver transistor and a top-gate load transistor as a function of supply voltage (V_{dd}) and (c) the voltage transfer characteristics of the Type-II D-inverter composed of a dual-gate driver transistor and a single-gate load transistor as a function of top-gate bias (V_{G2}).

DG driver transistor and DG load transistor may be an ultimate and ideal structure with respect to controllability. If DG OTFTs are used in complicated organic integrated circuits such as a ring oscillator and a shift register, more symmetric characteristics, higher gain, better noise margin, lower power dissipation can be obtained.

Recently, Takamiya et al. [21] tried to use DG OTFT for fabrication of organic circuits. The V_{th} control technology using a back gate was applied to compensate for the shift of V_{th} due to chemical degradation of the OTFTs and to achieve a reliable circuit operation. Sekitani et al. [22] also reported that the operation voltage (V_{dd}) of organic CMOS inverter with DG structure was significantly reduced and the gain was enhanced. Polyimide and parylene were used as bottom- and top-gate dielectric for the fabrication of their DG OTFT, respectively [21,22]. The fabrication of the DG pentacene OTFT with PEALD 150 nm thick Al_2O_3 as a bottom-gate dielectric and 300 nm thick parylene as a top-gate dielectric was reported by authors [23]. Unfortunately, the devices showed severe depletion mode characteristics due to degradation during parylene deposition. Consequently, the VTC of the D-inverter has a fatal problem that V_{in} range is not compatible to the V_{out} range. Nevertheless, that work was a first trial to apply DG OTFT structure to organic inverter, reporting that the VTCs of an inverter with a DG driver transistor and a single-gate load transistor, specifically, $V_{inversion}$ and swing range were artificially controlled by changing the voltage bias of the top-gate electrode [23]. In this work, replacing parylene with PEALD Al_2O_3 deposited at 100 °C as a top-gate dielectric, both the Type-I inverter with a bottom-gate driver transistor and a top-gate load transistor and the Type-II inverter with a DG driver transistor and a single-gate load transistor were successfully fabricated and then based on the transfer characteristics of the DG OTFT, the VTCs of those D-inverters could be systematically controlled.

4. Conclusions

In summary, the DG OTFT with PEALD 150 nm thick Al_2O_3 as a bottom-gate dielectric and 200 nm thick Al_2O_3 as a top-gate dielectric was fabricated. The V_{th} of DG OTFT was systematically shifted from 1.95 V to −9.8 V when V_{G2} was changed from −10 V to 10 V. The Type-I inverter with a bottom-gate driver transistor and a top-gate load transistor and the Type-II inverter with a DG driver transistor and a single-gate load transistor were newly proposed and fabricated using PEALD Al_2O_3 gate dielectrics. The present work suggests

that the DG OTFT geometry can supply high flexibility of operation with respect to single-gate devices for organic circuits and it is an applicable and useful structure for the fabrication of practical OTFTs and inverters. It is believed that an additional advantage of the DG OTFT is the increase of passivation performance owing to the use of the top-gate dielectric and electrode layer on top of the pentacene active layer. We have also confirmed the increase of shelf-storage life time of DG OTFT as compared to single-gate OTFT and that will be reported separately.

Acknowledgement

This work has been supported financially by Korean Ministry of Science and Technology through the NRL program.

References

[1] C.D. Dimitrakopoulos, P.R.L. Malenfant, Adv. Mater. 14 (2002) 99.
[2] G. Horowitz, Adv. Mater. 10 (1998) 365.
[3] J.N. Haddock, X. Zhang, S. Zheng, Q. Zhang, S.R. Marder, B. Kippelen, Org. Electron. 7 (2006) 45.
[4] E.J. Meijer, D.M. De Leeuw, S. Setayesh, E. van Veenendaal, B.-H. Huisman, P.W.M. Blom, J.C. Hummelen, U. Scherf, T.M. Klapwijk, Nat. Mater. 2 (2003) 678.
[5] S.D. Vusser, S. Steudel, K. Myny, J. Genoe, P. Heremans, Appl. Phys. Lett. 88 (2006) 162116.
[6] E. Cantatore, E.J. Meijer, in: Proceedings of the 29th European Solid-State Circuits Conference ESSCIRC, 2003, p. 29.
[7] A. Dodabalapur, J. Baumbach, K. Baldwin, H.E. Katz, Appl. Phys. Lett. 68 (1996) 2246.
[8] S. Iba, T. Sekitani, Y. Kato, T. Someya, H. Kawaguchi, M. Takamiya, T. Sakurai, S. Takagi, Appl. Phys. Lett. 87 (2005) 23509.
[9] G.H. Gelinck, E. van Veenendaal, R. Coehoorn, Appl. Phys. Lett. 87 (2005) 73508.
[10] M. Morana, G. Brest, C. Brabec, Appl. Phys. Lett. 87 (2005) 153511.
[11] J.B. Koo, J.W. Lim, S.H. Kim, S.J. Yun, C.H. Ku, S.C. Lim, J.H. Lee, Thin Solid Films 515 (2007) 3132.
[12] J.W. Lim, S.J. Yun, Electrochem. Solid-State Lett. 7 (2004) F45.
[13] I. Yagi, K. Tsukagoshi, Y. Aoyagi, Appl. Phys. Lett. 86 (2005) 103502.
[14] J.H. Lee, S.H. Kim, J.B. Koo, C.H. Ku, S.C. Lim, J.W. Lim, S.J. Yun, J. Jang, T. Zyung, J. Kor. Phys. Soc. 49 (2006) 1148.
[15] A. Salleo, R.A. Street, J. Appl. Phys. 94 (2003) 471.
[16] R.A. Street, A. Salleo, M.L. Chabinyc, Phys. Rev. B 68 (2003) 85316.
[17] S. Dimitrijev, Understanding Semiconductor Devices, second ed., Oxford University Press, New York, 2000.
[18] T. Ernst, S. Cristoloveanu, Gerard Ghibaudo, T. Ouisse, S. Horiguchi, Y. Ono, Y. Takahashi, K. Murase, IEEE Trans. Electron. Dev. 50 (2003) 830.
[19] S. Kobayashi, T. Nishikawa, T. Takenobu, S. Mori, T. Shimoda, T. Mitani, H. Shimotani, N. Yoshimoto, S. Ogawa, Y. Iwasa, Nat. Mater. 3 (2004) 317.
[20] K.P. Pernstich, S. Haas, D. Oberhoff, C. Goldmann, D.J. Gundlach, B. Batlogg, A.N. Rashid, G. Schitter, J. Appl. Phys. 96 (2004) 6431.
[21] M. Takamiya, T. Sekitani, Y. Kato, H. Kawaguchi, T. Someya, T. Sakurai, Solid-state circuits, in: IEEE International Conference Digest of Technical Papers, 2006, p. 1060.
[22] K. Hizu, T. Sekitani, Y. Shimada, J. Otsuki, M. Takamiya, T. Sakurai, T. Someya, in: Spring Meeting of Materials Research Society, M10.59, 2006.
[23] J.B. Koo, J.W. Lim, S.H. Kim, C.H. Ku, S.C. Lim, J.H. Lee, S.J. Yun, Y.S. Yang, Electrochem. Solid-State Lett. 9 (2006) G320.

Available online at www.sciencedirect.com
ScienceDirect
Organic Electronics 8 (2007) 559–565
Organic Electronics
www.elsevier.com/locate/orgel

On the switching mechanism in Rose Bengal-based memory devices

Fredrik L.E. Jakobsson [a,*], Xavier Crispin [a], Michael Cölle [b], Michael Büchel [b], Dago M. de Leeuw [b], Magnus Berggren [a]

[a] Department of Science and Technology (ITN), Linköping University, S-60174 Norrköping, Sweden
[b] Philips Research Laboratories, High Tech Campus 4 (WAG11), 5656 AE Eindhoven, The Netherlands

Received 5 March 2007; received in revised form 30 March 2007; accepted 6 April 2007
Available online 19 April 2007

Abstract

Impedance switching has been observed in many organic devices, but the mechanism is still a matter of debate. Reliable switch devices consisting of an organic layer of Rose Bengal derivatives sandwiched in between indium tin oxide and aluminum electrodes were fabricated. Modifying the chemical nature of the organic layers and visualizing the temperature distribution in the organic memory rule out several mechanisms. It is shown that the memory effect originates from filamentary switching.
© 2007 Elsevier B.V. All rights reserved.

PACS: 72.80.Le; 85.65.+h; 85.30.−z

Keywords: Impedance switching; Resistance switching; Filaments; Rose Bengal; Indium tin oxide; Aluminum

1. Introduction

The field of organic electronics has had a tremendous progress in the last decade. While organic light emitting diodes has entered the commercial market, the performance of organic transistors and photovoltaic devices are closing in on market demands. What the field is still lacking is a viable organic memory alternative to traditional silicon based technologies. The driving force for organic memory devices is the possibility of low-cost production through solution processing and high integration densities when scaling down towards the molecular dimension.

A wide range of reversible and bistable impedance switch phenomena have been reported. A few examples include resistance switching in charge transfer materials [1–3], switching of charge traps in diodes [4] and dynamic doping/dedoping or displacement of ions [5–7]. Switching by the reversible formation of conducting filaments through a low-conducting matrix film has been studied over the past four decades, both in inorganic [8–12] as well as in organic [13–15] materials. Recently, filamentary switching was observed in a wide range of semiconducting organic materials [16–18], including

* Corresponding author. Tel.: +46 11 363215; fax: +46 11 363270.
E-mail address: freja@itn.liu.se (F.L.E. Jakobsson).

1566-1199/$ - see front matter © 2007 Elsevier B.V. All rights reserved.
doi:10.1016/j.orgel.2007.04.002

organic electroluminescent diodes [19], revitalizing the discussion of the topic.

Switching in devices based on 4,5,6,7-tetrachloro-2′,4′,5′,7′-tetraiodofluoresein (Rose Bengal) sodium salt sandwiched between indium tin oxide (ITO) and aluminum electrodes was first reported by Bandyopadhyay et al. [20–22]. The origin of the switching has been proposed to be an electro-reduction [20] and/or a conformational change of the molecule [22]. Recently, Karthäuser et al. [23] also reported switching phenomenon in devices based on Rose Bengal. The last authors presented strong evidence that the switching is due to the growth of metallic filaments from the electrodes rather than to a molecular effect. However, due to the great difference in current density levels between their devices and the devices of other investigators, they could not rule out the possibility of an intrinsic switching of Rose Bengal.

In this report, we present results that strongly supports that there is only one switch mechanism in Rose Bengal memory devices. The importance of the organic layer is investigated by varying the chemical nature of the material. Finally the heat dissipation in the device during operation is recorded and scrutinized.

2. Experimental

In this study we have used Rose Bengal sodium salt (RBI, Fig. 1a), Rose Bengal bis(triethylammonium) salt (RBII, Fig. 1a), Rose Bengal lactone (RBIII, Fig. 1b) and Fluorescein lactone (FL, Fig. 1c). All molecules were used as received from Sigma–Aldrich without further purification. RBI and RBIII were dissolved in methanol (4 mg/ml), RBII was dissolved in 1-propanol (4 mg/ml and 8 mg/ml) and FL was dissolved in tetrahydrofuran (THF, 4 mg/ml). To ensure high film quality the solutions were filtered with a 0.1 μm filter.

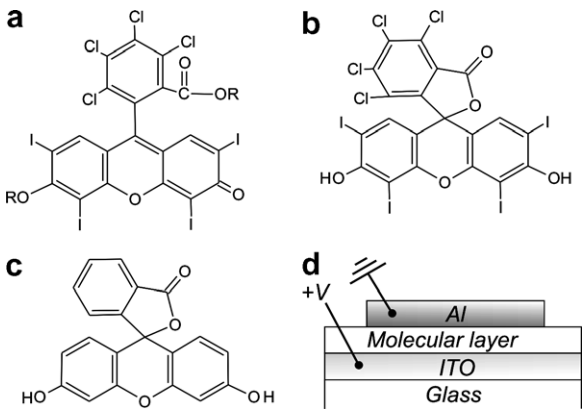


Fig. 1. Chemical structure of Rose Bengal sodium salt ($R = Na^+$) and Rose Bengal bis(triethylammonium) salt ($R = [NH(C_2H_5)_3]^+$): (a) Rose Bengal lactone (b) and Fluorescein lactone (c). In d the device structure is shown.

ITO substrates precoated on glass were used as bottom electrodes. The substrates were carefully cleaned in acetone and isopropanol. When methanol or THF solutions were used, the substrates were further cleaned in an O_2-plasma to ensure a hydrophilic surface. All organic films were spin cast on top of the clean substrate at 2000 rpm for 30 s, resulting in film thickness between 10 nm and 30 nm as measured with ellipsometry and atomic force microscopy (AFM). Finally aluminum top electrodes of a thickness of 100 nm were deposited through a shadow mask ($P \sim 10^{-6}$ mbar), resulting in an active device area of 5 mm^2. The device structure is shown in Fig. 1d.

All electrical measurements were conducted in vacuum ($P < 10^{-4}$ mbar) in a Janis Corp. cryogenic probe station using a HP4155B parameter analyzer unless stated differently in the text. The voltage was applied on the ITO electrode and was swept at 0.5 V/s, while the current was sensed on the grounded aluminum electrode. The applied voltage was cycled and increased incrementally until repeatable switching was observed. The low- and high-impedance states are denoted the ON- and OFF-state, respectively. Furthermore, a write- or erase-operation denotes setting the device in the ON- or OFF-state, respectively.

Write- and erase-time measurements were performed by first programming the device with an applied voltage of −4 V or +4 V using the parameter analyzer to set the device in the OFF- or the ON-state, respectively. Then a positive- or negative-pulse, with amplitude of 4 V and varying pulse width, was applied using an Agilent 33120A arbitrary waveform generator together with a custom-made amplifier, in order to switch back the device to the ON- or OFF-state, respectively. A 10 Ω resistor in series with the applied signal was used to eliminate detrimental current spikes and the integrity of the pulse was verified with an Agilent 54832D oscilloscope. The state of the device was probed before and after the pulse by applying a voltage of −0.5 V. The switching time was defined as the write- or erase-pulse width at which switching was no longer observed.

IR camera measurements were performed using a Thermosensorik CMT 284 SM IR camera with a real time lock-in system in ambient atmosphere. Before each image was recorded the device was programmed with an applied voltage of +4 V or −4 V to set the device in the ON- or the OFF-state, respectively. The IR camera image was acquired using a considerably lower voltage (typically −0.5 V square waveform at 1 Hz for 60 s). The lower voltage ensured that the state of the component was not disturbed during the readout and the square wave signal enabled the use of lock-in technique to improve resolution.

3. Results

When operating a pristine device, the *J–V* behavior evolves in three stages as illustrated in Fig. 2 for a RBII-based device. Firstly, at low voltages the device starts in a very high impedance state ($\sim 10^8\ \Omega$) without any switching. Secondly, as the voltage is increased above approximately 2 V, of either polarity, the current increases dramatically and repeatable hysteresis emerges upon further cycling of the voltage. The device is switched to ON- and OFF-states by applying a positive (V_{write}) and negative (V_{erase}) voltage, respectively. The impedance in the ON (Z_{ON}) and OFF (Z_{OFF}) states depends on V_{write} and decreases irreversibly when V_{write} is increased. This behavior was pronounced in thicker films as shown in the inset of Fig. 2. Those two first stages correspond to the initialization of the switch device and are independent of starting sweep direction.

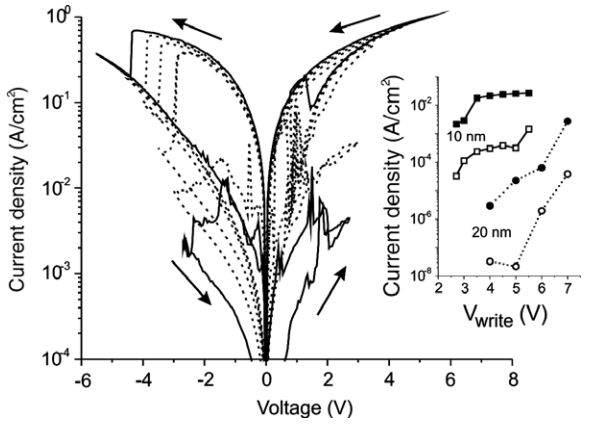


Fig. 2. Hysteresis behavior for increasing maximum sweep voltages in the ITO/RBII/Al devices with a RBII film thickness of 10 nm. The *J–V* behavior of the uninitialized devices with very high impedance is not shown. The inset shows the variation of the ON (full symbols) and OFF (open symbols) currents with respect to the thickness of the RBII layer. The currents in the inset were measured at −0.5 V and −1 V for the 10 nm (squares) and 20 nm (circles) thick films, respectively.

Thirdly, at higher V_{write} (>3.5 V), Z_{ON} and Z_{OFF} becomes only weakly dependent on V_{write} and the device becomes reliable. At this stage V_{erase} has the character of a distinct threshold with a magnitude lower than, but depending on, V_{write}. As V_{write} is increased V_{erase} is shifted towards larger negative voltages. The switching could be repeated more than 50 times and the states were retained for more than 24 h. In the ON-state the *J–V* behavior is nearly ohmic, i.e. linear for either polarity of the applied voltage. This indicates negligible barrier for charge injection in both directions as well as high conductivity of the material between the electrodes.

The reported current density levels for RB devices vary over orders of magnitude between different investigators. Bandyopadhyay et al. have reported current densities in the order of 1 mA/cm^2 in the ON state [20], while Karthäuser et al. [23] and Jakobsson et al. [24] have measured three orders of magnitudes higher current density. However, as mentioned above and shown in Fig. 2, the current density is actually strongly dependent on both the RB film thickness and V_{write}. Consequently, in the devices presented in this report, the current density could be varied over the range reported by previous investigators.

3.1. A look at previous hypothesis

If the switching from the OFF to the ON state is due to an electro-reduction of RB [20], i.e. an electrochemical reaction, the negative charge of the reduced RB molecule has to be compensated for by a nearby cation. The origin of this counterion has not been explained.

The Rose Bengal salts (RBI and RBII) contains an abundance of cations (Na^+ and $[NH(C_2H_5)_3]^+$, respectively) that might be mobile. In an applied field these ions might migrate, causing a concentration gradient and consequently a doping profile towards the cathode [5,25]. This is utilized in electrochemical light-emitting cells and result in an asymmetric *J–V* behavior, with efficient charge injection only when the field is applied in the forward direction in the formed p–n junction. Furthermore, the doping gradient is not stable and decays when the applied electric field is removed as the ions

diffuse back to their original homogeneous distribution. Since, the Rose Bengal devices display symmetric J–V behavior and the states are stable, we conclude that the switching is not due to rearrangement of intrinsic ions.

A possible source for extrinsic counter ions is In^{3+}, diffusing into the organic layer from the ITO bottom electrode. Such diffusion is well documented and is believed to be one of the failure mechanisms in organic light emitting diodes [26–29]. In this case the reduction of RB is not necessarily limited by the intrinsic ion distribution and a uniform reduction could potentially be achieved.

In water, the $[NH(C_2H_5)_3]^+$ cation has an ionic mobility 1.5 times lower than Na^+ ions [30]. It is therefore reasonable to assume that the former cation has lower mobility than the later also in the Rose Bengal films. If the mobility of intrinsic ions is important for the switching event, a certain difference in RBI and RBII device behavior is expected. However, the J–V behavior of RBI and RBII is similar as is shown in Fig. 3. The removal of water in organic films is known to decrease the ionic mobility by several orders of magnitude [31,32]. Therefore the measurements were performed both after storage in vacuum ($P = 5 \times 10^{-6}$ mbar) for 72 h and in 40% relative humidity, but the J–V behavior were identical in the two cases.

To further test the importance of ions we measured the write- and the erase-time. Devices based on ionic motion typically have a switching speed in the order of tens of ms [5,6]. However, the write time for an initialized RBII device is shorter than

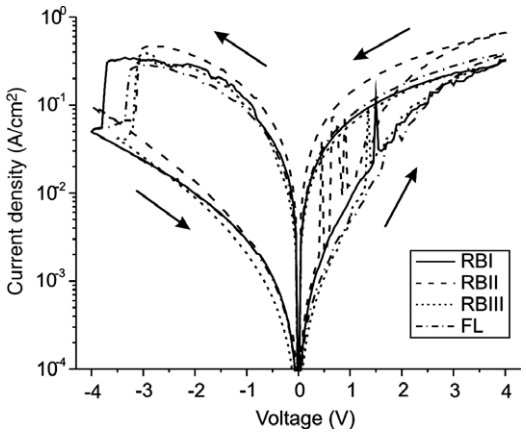


Fig. 3. Hysteresis in the J–V curve of ITO/molecular layer/Al devices, where the molecular layer consists of Rose Bengal sodium salt (RBI), Rose Bengal bis(triethylammonium) salt (RBII), Rose Bengal lactone (RBIII) or Fluorescein (FL).

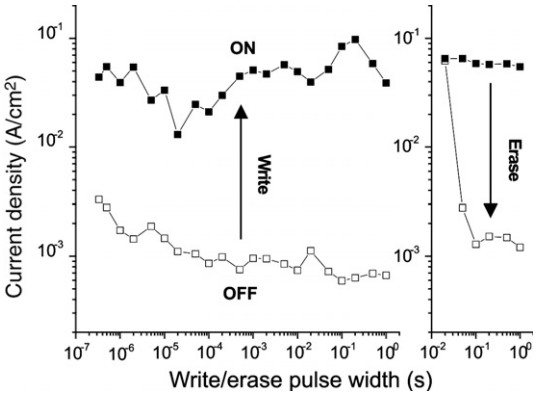


Fig. 4. Write-(left) and erase-(right) time measurement for a RBII device. The readout current in the figure is measured at −0.5 V. The slight increase in the OFF current to the left is attributed to degradation. The write time is shorter than 500 ns, while the erase time is ~50 ms.

the limit of the measurement setup, i.e. 500 ns, while the erase time is in the order of ms (see Fig. 4). The measurements were performed both in vacuum and in 40% relative humidity and the switching speed was independent on atmosphere. The sub-microsecond write time rules out long-range ionic motion as an important factor for the switching. Ionic motion on the atomic scale could be very fast and can probably not be completely ruled out.

The switching has been proposed to be due to a conformational change within the molecule [22]. In the neutral RBI and RBII, the fused three-ring part and the chlorinated phenyl ring are twisted due to steric hindrance [33]. The twist angle between those two moieties is expected to be reduced for the negatively charged RBI molecule due to the presence of a double bond character between the aromatic moieties. On the contrary, in RBIII the cyclic ester ring (lactone) connecting the chromophore and xanthene moieties locks the molecule and prevents conformational changes [33]. The electrical behavior of RBIII is similar to RBI and RBII (see Fig. 3), indicating that a conformational change induced by electroreduction is not the cause of the switching phenomena.

Since, RB carries both a donor and an acceptor group, another hypothesis for the switch mechanism is an intramolecular electron transfer from the donor group (xanthene) to the acceptor group (chlorinated phenyl) at high electric fields. RB would act as an intrinsic charge transfer salt. To further test this hypothesis, devices were fabricated with fluorescein (Fig. 1), a molecule completely

devoid of acceptor groups. Note also that fluorescein is lactonic as well; hence it is not expected to change conformation. The switching behavior is identical to the behavior of the RB devices (see Fig. 3), indicating that the switching is not likely due to any (internal) charge transfer phenomenon.

3.2. Hot spot observations

The above-mentioned results point out that switching is insensitive to the chemical nature of the molecular film. This indicates that the electrodes play an active role in the switch mechanism, for example via filamentary switching. Here we use the word filament for local areas with high current densities. If the current is conducted through conducting filaments the resistive heat dissipation should be localized to the areas containing the filaments, rather than being homogenous across the devices area [19]. The dissipated heat was therefore measured using a high-resolution IR camera focused on the Al top electrode, with the device both in the ON and in the OFF state. On the left-hand-side of Fig. 5, the device is in the ON state, with an approximate device current of 1 mA (at −0.5 V), and a hot spot is clearly visible. In the middle, the device has been switched off, resulting in a current of only 40 μA (at −0.5 V), and the hot spot has disappeared. On the right-hand side, the device is switched ON again. Surprisingly, the hot spot appears at the same position as previously observed.

The background temperature over the device stressed with 4 V is approximately 25 °C, while the average temperature of the area within a radius of 100 μm from the center of the hot spot is 55 °C. Due to heat diffusion in the electrodes, the true size of the conducting filament is smaller, although not easily measurable. Note the presence of a large circular area in the bottom ITO electrode, which is attributed to the lower heat conductivity of ITO compared to Al, resulting in less effective heat dissipation. Assuming that the majority of the current is carried through an area with a radius of 100 μm, the current density through the hot spot is 80 A/cm^2 at 4 V. This is one order of magnitude higher than typical break down current densities in organic materials operated under continuous wave and of similar geometry [34,35].

4. Discussion

Several observations indicate that the switching mechanism cannot be due to burn-off of conducting filaments as has been suggested for other materials [8]. First, the switching in RB devices depends on the polarity of the applied voltage. Second, the appearance of the hot spot in the same position indicates that the switching is a reversible process. Finally, the J–V curves are reproducible without any apparent discontinuities as would be expected in the case of a break-down-like mechanism.

Cölle et al. [19] have shown that the Al top electrode is the origin of filamentary switching in devices using materials typically employed in organic light emitting diodes. In our device, an aluminum electrode is used and thus can be involved as well in the switch mechanism. In order to investigate if the ITO electrode is also playing a role in the switching a clean ITO surface was contacted directly with beryllium copper (BeCu) probe tips, i.e. without the presence of an organic layer or a top electrode, similar to the experiments performed by

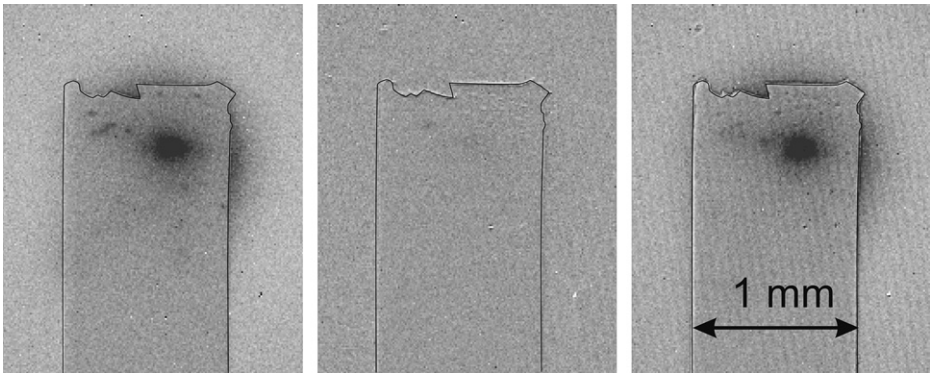


Fig. 5. IR camera images of the device in ON state (left), OFF state (middle) followed by ON state (right). For clarity the edge of the top electrode is marked with a black line. The width of the device is 1 mm, indicating a hot spot diameter less than 100 μm.

Karthäuser et al. [23]. In this case, a similar switching appears again (full line in Fig. 6) despite the electrode geometry difference and absence of the molecular layer. This observation has two possible implications for RB based switch devices: the switch mechanism in the ITO/BeCu-device is either a probing effect or it originates from a phenomenon at the ITO surface, which has an impact on the switching mechanism of the ITO/RB/Al device.

In order to ensure that the switching effect was not merely an effect of probing on ITO, two neighboring devices were connected in series (sketch in Fig. 6), with the electrical contact made only to the Al electrodes. Since, the distance between the Al electrodes (~1 mm) is much larger than the RB film thickness (~10 nm), the current passes through the RB film of both devices via the ITO. Hence, the devices were connected in opposite direction, corresponding to a device layout of Al/RB/ITO/RB/Al. As expected, the J–V behavior of the combined component (circles in Fig. 6) is a superposition of the J–V behavior of two single RB devices (Fig. 3) connected in series and opposite direction. This rules out that the effect is only due to the probe contact to ITO, and that the effect really originates from the device.

A few observations of the initialization process are worth highlighting: (i) the impedance is irreversibly changed by several orders of magnitude; (ii) the process is independent on the polarity of the applied voltage as well as the level of humidity (vacuum of $P = 5 \times 10^{-6}$ mbar or 40% humidity at atmospheric pressure); and (iii) the process is smooth without any discontinuous step in the current as the voltage is increased. Note also that we have not measured the speed of the initialization process. Hence, it might be slower than the actual switching event.

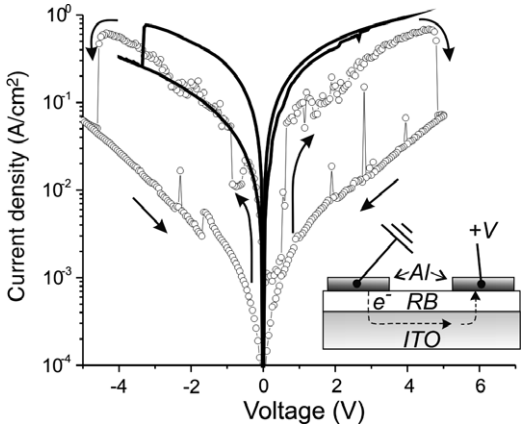


Fig. 6. Switching of the current between the BeCu probe tip and ITO (full line) and switching of two devices coupled in series by only probing on the Al top electrodes (open circles). Note that the scales in the lateral and vertical directions are very different. While width and spacing of the Al electrodes is 1 mm, the thickness of the RB layer is only 10 nm.

The initialization could consist of the formation of the filaments, either through an electrochemical process or through electro-migration. Electrochemical formation of filaments has been proposed where metal ions migrate from the anode through an intermediate layer [36–38]. When the ions reach the cathode they become reduced, resulting in the build-up of a metallic path towards the anode. However, this kind of process is polarity dependent and consequently when the polarity of the applied voltage is reversed the filament is dissolved. Since, the initialization of Rose Bengal devices is polarity independent, this is most likely not the process.

Electro-migration is well-known in Al [39] and has also been reported for ITO [40,41]. Hence, formation of filaments could be achieved by electro-migration from either the Al or the ITO electrode, depending on polarity of the applied voltage.

Another possibility is that the current is not transported through the organic material at all but through pinholes in the film that is already present in the pristine device. Considering the very low thickness of the organic layer the latter is not unlikely, even though such pinholes have not been observed when investigating the film with AFM. Also, the very high current density estimated above through the hot spots indicates that the current is not carried through the organic film. The initialization in such case could correspond to modification of the metal oxide at either electrode, possibly assisted by resistive heating.

5. Conclusions

By varying the chemical nature of the organic layer, we have demonstrated that the switching mechanism in Rose Bengal sodium based memory devices is not an intrinsic molecular effect. The apparent discrepancies in data between different investigators can be explained in terms of maximum voltage applied to the device as well as organic film thickness. IR camera images confirm the existence of switchable hot spots due to the existence of highly conducting filaments. When probing directly on top of the ITO substrate switching is also observed, indicating that ITO might be partly responsible for the switching.

Acknowledgements

The authors at Linköping University gratefully acknowledge The Swedish Foundation for Strategic Research (COE@COIN), VINNOVA, The Royal Swedish Academy of Sciences and The Swedish Research Council for financial support of this project. The authors at Philips Research Laboratories gratefully acknowledge the financial support received from the EC (project PolyApply IST-IP-507-507143).

References

[1] T. Oyamada, H. Tanaka, K. Matsushige, H. Sasabe, C. Adachi, Appl. Phys. Lett. 83 (2003) 1252.
[2] R.S. Potember, T.O. Poehler, D.O. Cowand, Appl. Phys. Lett. 34 (1979) 405.
[3] C. Sato, S. Wakamatsu, K. Tadokoro, K. Ishii, J. Appl. Phys. 68 (1990) 6535.
[4] P. Andersson, N.D. Robinson, M. Berggren, Adv. Mater. 17 (2005) 1798.
[5] J.H.A. Smits, S.C.J. Meskers, R.A.J. Janssen, A.W. Marsman, D.M. de Leeuw, Adv. Mater. 17 (2005) 1169.
[6] F. Verbakel, S.C.J. Meskers, R.A.J. Janssen, Chem. Mater. 18 (2006) 2707.
[7] S. Patil, Q. Lai, F. Marchioni, M. Jung, Z. Zhu, Y. Chen, F. Wudl, J. Mater. Chem. 16 (2006) 4160.
[8] E.L. Cook, J. Appl. Phys. 41 (1970) 551.
[9] Y. Kawamura, Y. Kashiwaba, T. Ikeda, Jpn. J. Appl. Phys. 21 (1982) 429.
[10] A.G. Steventon, J. Phys. D.: Appl. Phys. 8 (1975) 120.
[11] M. Shatzkes, M. Av-Ron, R.M. Anderson, J. Appl. Phys. 45 (1974) 2065.
[12] D.F. Weirauch, Appl. Phys. Lett. 16 (1970) 72.
[13] H. Carchano, R. Lacoste, Y. Segui, Appl. Phys. Lett. 19 (1971) 414.
[14] Y. Segui, B. Ai, H. Carchano, J. Appl. Phys. 47 (1976) 140.
[15] L.F. Pender, R.J. Fleming, J. Appl. Phys. 46 (1975) 3426.
[16] C.-H. Tu, Y.-S. Lai, D.-L. Kwong, Appl. Phys. Lett. 89 (2006) 062105.
[17] C.-H. Tu, Y.-S. Lai, D.-L. Kwong, IEEE El. Dev. Lett. 27 (2006) 354.
[18] Y.-S. Lai, C.-H. Tu, D.-L. Kwong, Appl. Phys. Lett. 87 (2005).
[19] M. Cölle, M. Büchel, D.M. de Leeuw, Organ. El. 7 (2006) 305.
[20] A. Bandyopadhyay, A.J. Pal, J. Phys. Chem. B 107 (2003) 2531.
[21] A. Bandyopadhyay, A.J. Pal, Appl. Phys. Lett. 82 (2003) 1215.
[22] A. Bandyopadhyay, A.J. Pal, Appl. Phys. Lett. 84 (2004) 999.
[23] S. Karthäuser, B. Lüssem, M. Weides, M. Alba, A. Besmehn, R. Oligschlaeger, R. Waser, J. Appl. Phys. 100 (2006) 094504.
[24] F.L.E. Jakobsson, X. Crispin, M. Berggren, Appl. Phys. Lett. 87 (2005) 063503.
[25] J.-H. Shin, S. Xiao, L. Edman, Adv. Funct. Mater. 16 (2006) 949.
[26] M.P. de Jong, D.P.L. Simons, M.A. Reijme, L.J. van Ijzendoorn, A.W. Denier van der Gon, M.J.A. de Voigt, H.H. Brongersma, R.W. Gymer, Synth. Met. 110 (2000) 1.
[27] S. Takemura, H. Kato, Y. Nakajima, Appl. Surf. Sci. 144–145 (1999) 360.
[28] S.T. Lee, Z.Q. Gao, L.S. Hung, Appl. Phys. Lett. 75 (1999) 1404.
[29] H. Kato, S. Takemura, Y. Nakajima, J. Appl. Phys. 81 (1997) 7313.
[30] D.R. Lide (Ed.), CRC Handbook of Chemistry and Physics, Taylor and Francis, Boca Raton, 2007.
[31] J.J. Fontanella, M.C. Wintersgill, R.S. Chen, Y. Wu, S.G. Greenbaum, Electrochimica Acta 40 (1995) 2321.
[32] A. Johansson, Å. Lauenstein, J. Tegenfeldt, J. Phys. Chem. 99 (1995) 6163.
[33] J.J.M. Lamberts, D.C. Neckers, Tetrahedron 41 (1985) 2183.
[34] H. Yakamoto, H. Kasajima, W. Yokoyama, H. Sasabe, C. Adachi, Appl. Phys. Lett. 86 (2005) 083502.
[35] H. Nakanotani, T. Oyamada, Y. Kawamura, H. Sasabe, C. Adachi, Jpn. J. Appl. Phys. 44 (2005) 3659.
[36] S. Ssenyange, H. Yan, R.L. McCreery, Langmuir 22 (2006) 10689.
[37] T. Sakamoto, H. Sunamura, H. Kawaura, T. Hasegawa, T. Nakayama, M. Aono, Appl. Phys. Lett. 82 (2003) 3032.
[38] S. Kaeriyama, T. Sakamoto, H. Sunamura, M. Mizuno, H. Kawaura, T. Hasegawa, K. Terabe, T. Nakayama, M. Aono, IEEE J. Solid-State Circ. 40 (2005) 168.
[39] B.H. Cumpston, K.F. Jensen, Appl. Phys. Lett. 69 (1996) 3941.
[40] X. Zhou, J. He, L.S. Liao, M. Lu, X.M. Ding, X.Y. Hou, X.M. Zhang, X.Q. He, S.T. Lee, Adv. Mater. 12 (2000) 265.
[41] J. He, X. Zhou, J.R. Cao, K.L. Wang, L.S. Liao, Z.B. Deng, X.M. Ding, X.Y. Hou, S.T. Lee, Thin Solid Films 363 (2000) 240.

Available online at www.sciencedirect.com
ScienceDirect
Organic Electronics 8 (2007) 566–574
Organic Electronics
www.elsevier.com/locate/orgel

Effects of thin film processing on pentacene/C_{60} bilayer solar cell performance

Jihua Yang, Thuc-Quyen Nguyen *

Center for Polymers and Organic Solids, Department of Chemistry and Biochemistry, University of California, Santa Barbara, CA 93106, USA

Received 28 December 2006; received in revised form 3 April 2007; accepted 11 April 2007
Available online 18 April 2007

Abstract

Solar cells based on pentacene/C_{60} bilayer heterojunctions have been fabricated with a structure of ITO/poly(styrenesulfonate) (PEDOT:PSS)/pentacene (40 nm)/fullerene (C_{60})(40 nm)/2,9-dimethyl-4,7-diphenyl-1,10-phenanthroline (BCP) (10 nm)/Al. The effect of pentacene crystalline domain size on performance was investigated by controlling the pentacene deposition rate. The devices show improved light-to-electricity conversion efficiencies from 0.49% to 1.12% under an AM 1.5 solar simulator (100 mW/cm^2), when the pentacene evaporation rate is in a range of 5 Å/s–0.5 Å/s. Atomic force microscopy (AFM) measurements show that the pentacene films deposited by a slow evaporation rate have larger crystalline domains and a fewer amorphous domains, compared to films obtained by faster evaporation rates. Upon thermal annealing at 200 °C for 1 min, there is merging of pentacene crystalline domains. These changes in film morphology impact the charge separation at the donor/acceptor interface and the hole and electron mobilities, and hence, directly affect the device performance.
© 2007 Elsevier B.V. All rights reserved.

PACS: 72.40.+w

Keywords: Pentacene; C_{60}; Solar cell; Film morphology; Film processing; Thermal annealing; Hole and electron mobilities

1. Introduction

Organic solar cells have attracted a great deal of attention in the past few years [1–5]. Potentially, they offer low-cost, light weight, and flexible devices, compared to photovoltaics based on traditional inorganic semiconductors. Additionally, via the chemical synthesis/modification control of organic materials one can obtain films with a broad absorption range to optimize overlap with the solar spectrum and desirable energy levels to minimize power loss. Furthermore, organic materials offer the possibility of taking advantage of simple fabrication technologies, such as spin-coating or thermal evaporation.

Photoexcitation of an organic solid generates excitons which are neutral electron-hole pairs bound by Coulombic forces. For efficient exciton dissociation/charge separation process, bulk heterojunction (the active material is a blend of the

* Corresponding author. Tel.: +1 805 893 4851; fax: +1 805 893 4120.
E-mail address: quyen@chem.ucsb.edu (T.-Q. Nguyen).

1566-1199/$ - see front matter © 2007 Elsevier B.V. All rights reserved.
doi:10.1016/j.orgel.2007.04.005

electron donor with electron acceptor materials) [1,6–9] and bilayer heterojunction (the active material comprises an electron acceptor layer on top of an electron donor layer) [2,3,10–12] device structures have been used. The difference in electron affinities and/or ionization potentials of the donor and acceptor materials in their corresponding phases provides the driving force for exciton dissociation into charge carriers at the interfaces. The primary advantage of the bulk heterojunction morphology is the large donor–acceptor interface area, however the two phases must form bicontinuous networks that transport charge carriers to the electrodes. Such active layer structures are used mainly in conjugated polymer-based solar cells fabricated from solution methods. In the bilayer heterojunction structure, the charge separation is limited to a single donor–acceptor interface region but the separated charge carriers can be transported efficiently through the donor and acceptor layers to the corresponding electrodes. This device structure is suitable for solar cells based on small molecular materials.

Solar cells from copper or zinc phthalocyanine/C_{60} [13,14] and oligo(*p*-phenylene vinylene)/C_{60} [15,16] have been demonstrated. In recent years, pentacene has been demonstrated to be a good choice of hole transporting material for small molecule-based solar cells [17–19] due to its high hole mobility and to the excellent body of work in the literature describing its electronic properties [20–26]. Several factors influence the performance of small molecule-based solar cells, including substrate surface treatment, substrate temperature, level of impurities, depositing conditions, testing conditions, film morphology, molecular packing in ordered regions, and charge mobility. Thermal annealing has been found to improve efficiencies in some cases, most likely as a result of increased crystallinity and reduction of traps/defects [6,9,27]. In this contribution, we investigate the effects of pentacene deposition rate and thermal annealing temperature on the crystalline domain size, the film morphology, the electron and hole mobilities, and the performance of pentacene/C_{60} bilayer heterojunction devices.

Photovoltaic devices were fabricated with a structure consisting of indium–tin-oxide glass (ITO)/poly(3,4-ethylenedioxythiophene)/poly(styrenesulfonate)(PEDOT:PSS)/pentacene/fullerene(C_{60})/2,9-dimethyl-4,7-diphenyl-1,10-phenanthroline (BCP)/Al. The thicknesses of the pentacene and C_{60} layers are 40 nm each and are within the range expected for the exciton diffusion length [3,18]. As shown in Fig. 1, the higher energy of the lowest unoccupied orbital (LUMO) of pentacene (donor) relative to C_{60} (acceptor) results in conditions suitable for photoinduced electron transfer. The absorption spectrum of pentacene/C_{60} bilayer covers the wavelength range from 400 nm to 700 nm.

The *I–V* characteristics of annealed ITO/PEDOT:PSS/pentacene (40 nm)/C_{60} (40 nm)/BCP (10 nm)/Al devices with different pentacene evaporation rates measured under AM 1.5 solar illumination of 80 mW/cm^2 are shown in Fig. 2. For the

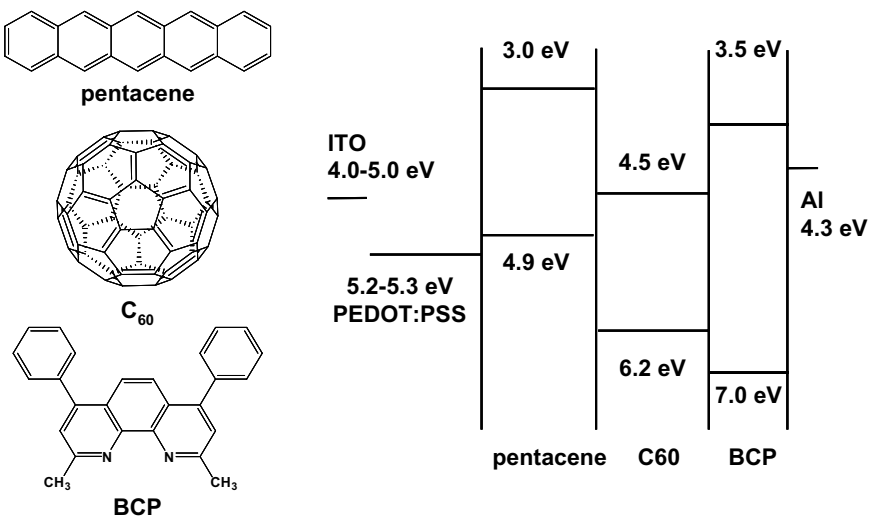


Fig. 1. Molecular structures and energy levels of the ITO/PEDOT/pentacene/C_{60}/BCP/Al device.

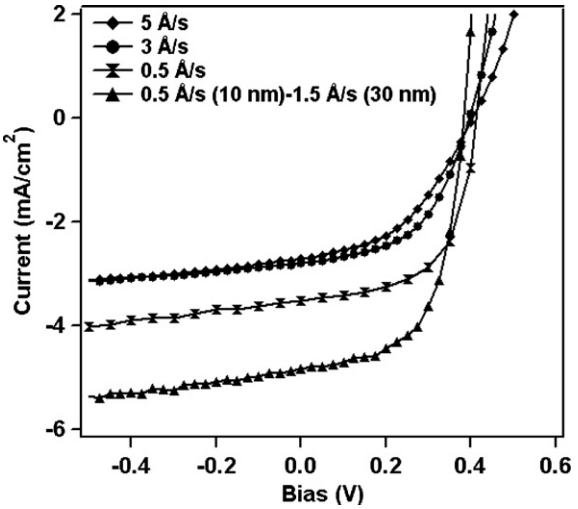


Fig. 2. *I–V* curves of the annealed ITO/PEDOT/pentacene (40 nm)/C_{60} (40 nm)/BCP (10 nm)/Al devices, with different pentacene layer deposition rates: 5 Å/s (diamond symbols), 3 Å/s (circular symbols), 0.5 Å/s (cross symbols), and 0.5 Å/s for the first 10 nm and 1.5 Å/s for the following 30 nm (triangular symbols). All devices were annealed at 200 °C for 1 min.

device fabricated with an evaporation rate of 5 Å/s, the short-circuit current density (J_{sc}) is 2.71 ± 0.13 mA/cm^2 and the open-circuit voltage (V_{oc}) is 0.41 V. The fill factor (FF), defined as $J_{mpp}V_{mpp}/J_{sc}V_{oc}$($J_{mpp}$ and V_{mpp} are the current and voltage in the maximum power point of the *I–V* curve in the 4th quadrant), is 0.44 ± 0.02. The resulting light conversion efficiency, $\eta = (FFJ_{sc}V_{oc})/I_L$, is 0.49 ± 0.03%. When the pentacene deposition rate is reduced to 3 Å/s, the J_{sc} and the V_{oc} do not change significantly: 2.80 ± 0.18 mA/cm^2 and 0.40 ± 0.01 V, respectively. However, both the FF and η increase to 0.51 ± 0.03 and 0.58 ± 0.03%, respectively. Possible reasons why J_{sc} and V_{oc} show no apparent change but the FF and η increase with the reduced evaporation rate are a reduction of charge trap density at pentacene/C_{60} interface and within the pentacene layer and variations in interfacial resistances, recombination rates, and field-dependent geminate pair dissociation.

When the pentacene deposition rate was further reduced to 0.5 Å/s, the J_{sc} increases to 3.53 ± 0.16 mA/cm^2 and the V_{oc} increases very little but the efficiency is enhanced over 50%, compared to cell fabricated with a 5 Å/s deposition rate. The most significant improvement in performance was obtained when the pentacene layer was deposited in two steps: ~0.5 Å/s for the first 10 nm and ~1.5 Å/s for the following 30 nm (triangular symbols, Fig. 2). As shown in Table 1, while the V_{oc} has a small reduction of about 30 mV–0.38 V, the J_{sc} is increased to 4.83 ± 0.15 mA/cm^2, which is almost double the J_{sc} from the fast deposition rates (3 and 5 Å/s). The FF also increased to 0.61 ± 0.03 from 0.44 ± 0.02. The device efficiency increases significantly from 0.49 ± 0.03% to 1.12 ± 0.03%. Fig. 3 shows the absorption spectrum of the glass/PEDOT/pentacene (40 nm, 0.5 Å/s for the first 10 nm and 1.5 Å/s for the following 30 nm)/C_{60} (40 nm) sample and the photocurrent action spectrum of the PEDOT/pentacene (40 nm, 0.5 Å/s for the first 10 nm and 1.5 Å/s for the following 30 nm)/C60 (40 nm)/BCP (10 nm)/Al device. The pentacene has its main absorption region in 540–700 nm, with the highest peak at 670 nm. C_{60} has strong absorption in the region of 400–540 nm. Therefore, the absorption region of the pentacene/C_{60} bilayer film is well matched with the visible region of the solar spectrum. In the photocurrent action spectrum of the device, the electronic transitions of pentacene are clearly distinguished at 670 nm, 630 nm, 582 nm, and 449 nm. The maximum photocurrent contribution of pentacene is from the shoulder absorption peak at 630 nm rather than the maximum absorption peak at 670 nm. This difference may be the result of the interference and filter effects.

The photocurrent response in the 400–540 nm region arises from photoexcitation of the C_{60} layer; thus, the C_{60} layer should have a contribution to the device photovoltaic effect. We examined devices with ITO/PEDOT/C_{60} (85 nm)/BCP (10 nm)/Al structures and the efficiency was only ~0.05%. The

Table 1
The photovoltaic device characteristics at various pentacene deposition rates for annealed devices

Pentacene evaporation rate	I_{sc} (mA/cm^2)	V_{oc} (V)	FF	η (%)
5 Å/s	2.71 ± 0.13	0.41 ± 0.00	0.44 ± 0.02	0.49 ± 0.03
3 Å/s	2.80 ± 0.18	0.40 ± 0.01	0.51 ± 0.03	0.58 ± 0.03
0.5 Å/s	3.53 ± 0.16	0.43 ± 0.00	0.57 ± 0.02	0.87 ± 0.03
0.5 Å/s (10 nm) – 1.5 Å/s (30 nm)	4.83 ± 0.15	0.38 ± 0.00	0.61 ± 0.01	1.12 ± 0.03

The devices were annealed at 200 °C for 1 min.

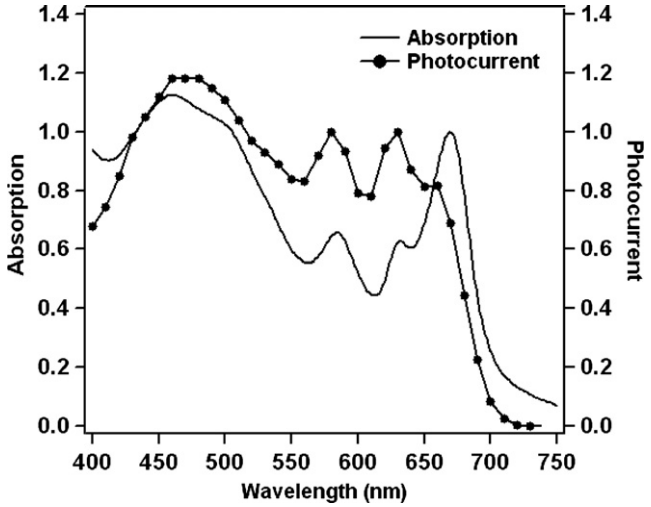


Fig. 3. The absorption spectrum of glass/PEDOT/pentacene (40 nm, 0.5 Å/s for the first 10 nm and 1.5 Å/s for the following 30 nm)/C_{60} (40 nm) and photocurrent action spectrum of ITO/PEDOT/pentacene (40 nm, 0.5 Å/s for the first 10 nm and 1.5 Å/s for the following 30 nm)/C_{60} (40 nm)/BCP/Al.

photocurrent from C_{60} photoexcitation should involve dissociation of the C_{60} exciton at the pentacene interface. From Fig. 1, the HOMO energy level offset between pentacene and C_{60} provides a driving force of 1.0–1.3 eV. As a result, the hole and electron are efficiently separated and transported in the pentacene and C_{60} layers and reach their respective electrodes. Pentacene can play two roles: electron donor when it absorbs light and hole acceptor when the C_{60} is photoexcited. A similar model was proposed to optimize the performance of device based on donor–acceptor bilayer heterojunctions [28]. Photocurrent from excitation of electron acceptors was also observed in different solar cell configurations [9,18,29]. Here it should be noted that our device efficiencies are likely to be further improved if the materials are more rigorously purified. We used commercially available pentacene and C_{60} without any purification, which likely contain impurities that can act as carrier traps [30] or/and scattering centers [31] reducing hole mobility and hence device efficiency.

To gain insight into the dependence of device performance on pentacene deposition rate, AFM was used to examine film morphologies. Generally, the size of a crystal is determined by its growth rate: the faster the growth rate, the smaller the crystal size and the higher the number of grain boundaries [32]. Additionally, the degree of disorder and defects increases with faster rates. Fig. 4 shows the surface topography of pentacene films deposited onto the ITO/PEDOT:PSS substrates at 5 Å/s, 3 Å/s, 0.5 Å/s, and 0.5 Å/s for 10 nm and 1.0 Å/s for the remain 30 nm. The films comprise crystalline domains (grains) with layer structures and isolated fiber-like domains with lamellar structures similar to the topography of samples deposited on SiO_2 surfaces [23,33–35]. The layer structure results from the herringbone stacking with the pentacene long-axis oriented perpendicular to the substrate, whereas the lamellar structure comprises molecules that lie flat on the surface with high degree of disorder [33]. The lamellar structures are only observed to grow on top of the crystalline grains and not on the bare substrate. Thus, the layer structure and the lamellar structure are also called the *thin film phase* and the *bulk phase*, respectively [35].

Several differences are observed from the films prepared at various deposition rates. The surface of the film deposited at 5 Å/s displays small grain sizes and a large number of fiber-like domains. The coexistence of the two types of crystalline grains has been observed in pentacene films deposited on SiO_2 surface by molecular beam deposition at a fast speed and low substrate temperature [33] and by thermal evaporation [35]. Reducing deposition rates decreases the fiber-like domains and these domains almost disappear in the film deposited at 0.5 Å/s for 40 nm and 0.5 Å/s for the first 10 nm and 1.5 Å/s for the following 30 nm. In addition, the length of the crystalline grains is typically ~300–400 nm in films deposited at 5 and 3 Å/s and

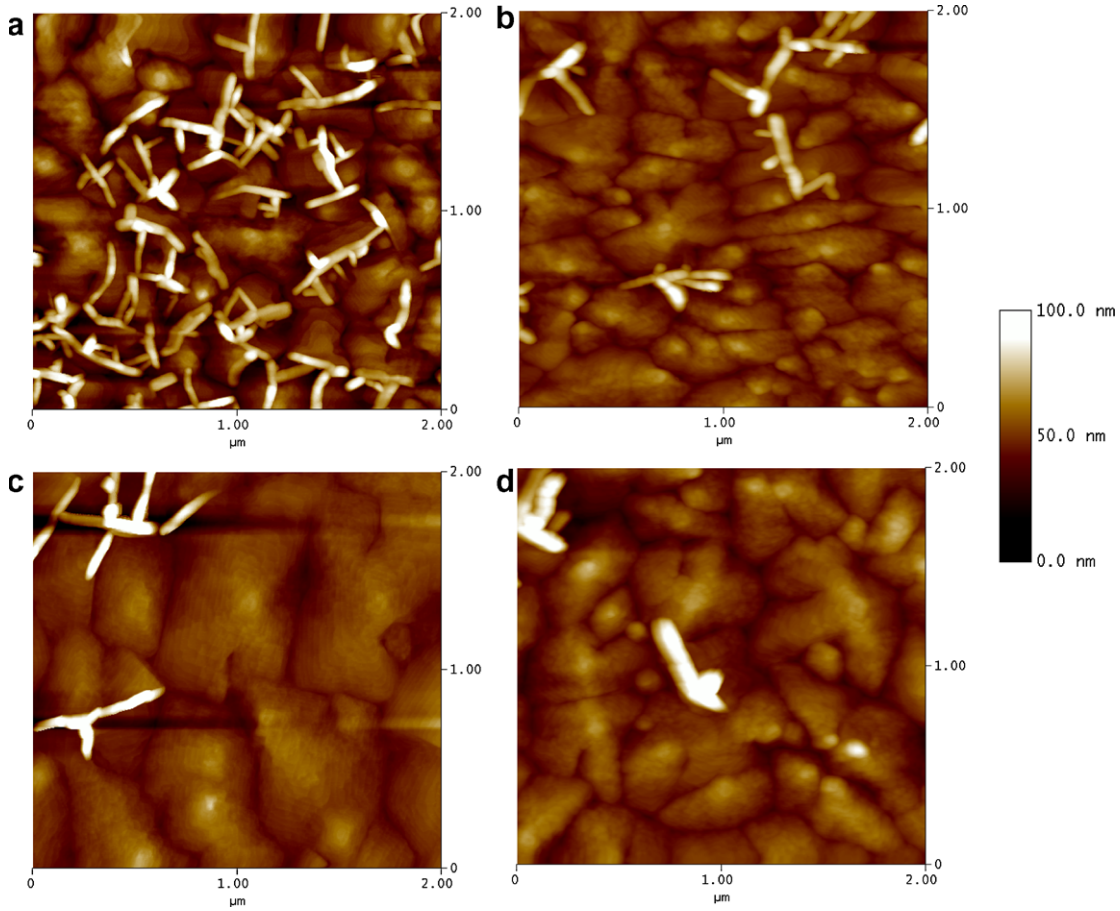


Fig. 4. AFM images of the pentacene films (40 nm) on the ITO/PEDOT substrates evaporated at various rates: (a) 5 Å/s, (b) 3 Å/s, (c) 0.5 Å/s, and (d) 0.5 Å/s for the first 10 nm and 1.5 Å/s for the following 30 nm.

increases to 800 nm in films deposited at 0.5 Å/s. When pentacene molecules arrive on a surface, they rearrange and pack in a herringbone fashion to form small two-dimensional islands/nucleation sites. The nucleation density depends strongly on the type of the substrate used and the deposition rate. The faster the deposition rate, the higher the nucleation sites, and as a result, the grain size is smaller. As more pentacene molecules arrive, the islands grow larger and the second layer begins to form on top of the initial layer; the process continues until grains with dome shapes cover the entire surface [36]. Comparing the slow single (0.5 Å/s for 40 nm) and double step (0.5 Å/s and 1.5 Å/s) deposition rates, one observes that the grain sizes from the double step deposition and show a high degree of dendritic structures. Our results indicate that the formation of the first few layers determines the grain size thus, the importance of initial slow deposition rate. However, if the subsequent deposition occurs too quickly, films may form with a large number of defects, including voids and amorphous disordered domains.

AFM analysis provides insight for understanding the differences in device performance as a function of deposition rate. There is a direct correlation between film morphology and device performance. Pentacene films obtained via a fast deposition rate provide a larger surface area, and hence, a larger interface with the C_{60} layer. Such features may be desirable for increasing exciton dissociation. However, the lamellar grains in the pentacene layer are highly disordered. This fact, coupled with the presence of a larger number of grain boundaries and the induced defects reduce the charge carrier (hole) mobility [34,37]. Therefore, the currents at the reverse bias and J_{sc} are smaller than those in devices fabricated by slow deposition rates. On the other hand, the pentacene layer from low deposition rate has large grain sizes and less grain boundary defects

and disorder domains, thus, the hole mobility is likely higher, as indicated by the significantly increased current in the reverse bias and J_{sc} compared to the films formed by fast deposition. Following this reasoning, devices fabricated at 0.5 Å/s should have highest efficiency, but this is not the case. The reason for this unexpected result may be that the grain size is large but there is less dendritic-like structures at the interface, giving rise to a reduced donor–acceptor interface area. Thus, a delicate balance must be reached.

Heating devices at 200 °C has been shown to increase molecular order and to improve the performance of devices with a ITO/PEDOT:PSS/pentacene/C_{60}/CsF/Al structure [27]. However, the surface morphology has not been examined. Annealing at 100 °C or 150 °C has also been reported but the device performances are lower than for devices annealed at 200 °C. Similar results were obtained in our studies. In our devices, the efficiency was 0.78% before annealing and increased to 1.12% after annealing for the slow deposition films. Molecules thus rearrange within the film and at the interface with C_{60}. Fig. 5 shows the AFM images of a pentacene film deposited at 0.5 Å/s for 10 nm followed by 1.5 Å/s for 30 nm before and after annealing at 100 °C, 150 °C, and 200 °C for 1 min. Annealing the pentacene film at 250 °C shows loss of material via sublimation. At 100 °C and 150 °C, there is no apparent change in morphology. Heating to 200 °C leads to a smoother film surface, the lamellar domains merge into crystalline grains and the boundaries between the pentacene grains are less pronounced (Fig. 5d). These morphology studies are in agreement with the report by Malliaras et al. on the dependence of the device performance on annealing temperatures [27].

The film morphology of C_{60} was also examined. Fig. 6 shows the AFM images of a 40 nm thick C_{60} film deposited onto glass/ITO/PEDOT/pentacene

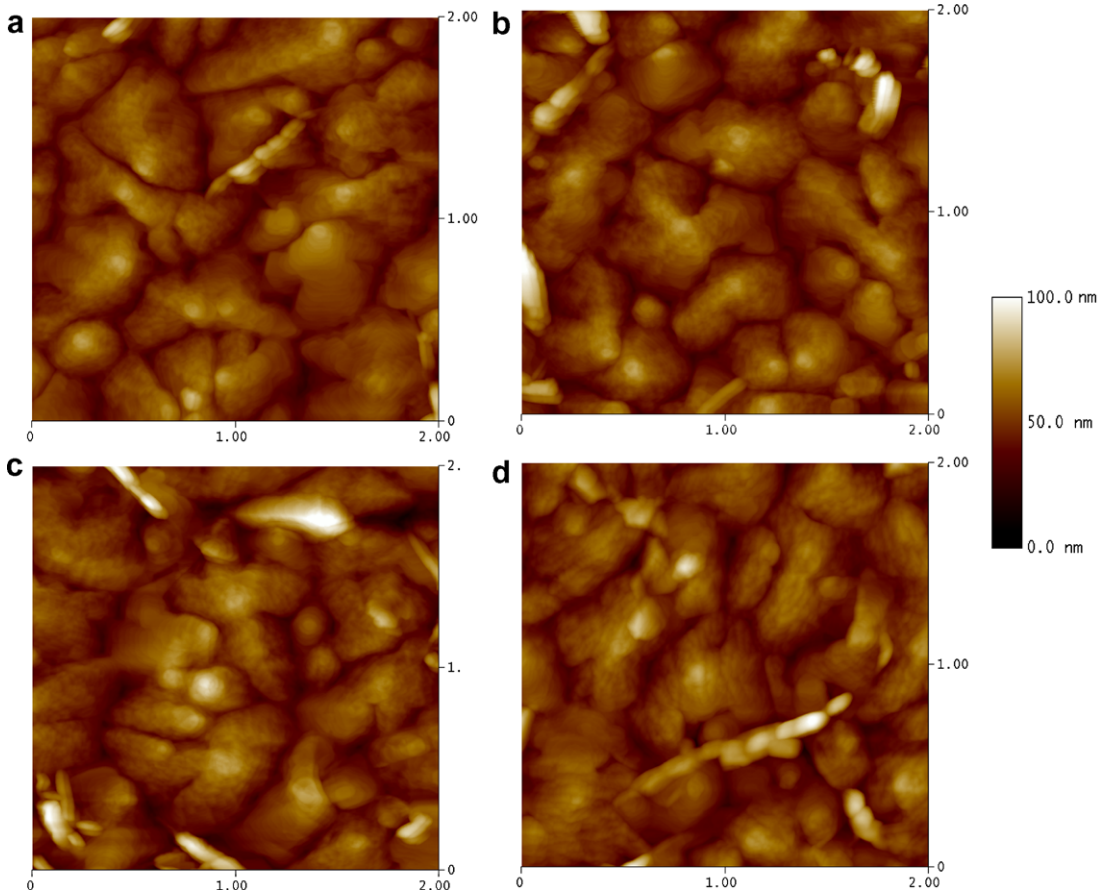


Fig. 5. AFM images of the pentacene films on the ITO/PEDOT substrates evaporated at 0.5 Å/s for the first 10 nm and 1.5 Å/s for the following 30 nm before annealing (a), after the thermal annealing at 100 °C (b), at 150 °C (c), and at 200 °C (d) for 1 min.

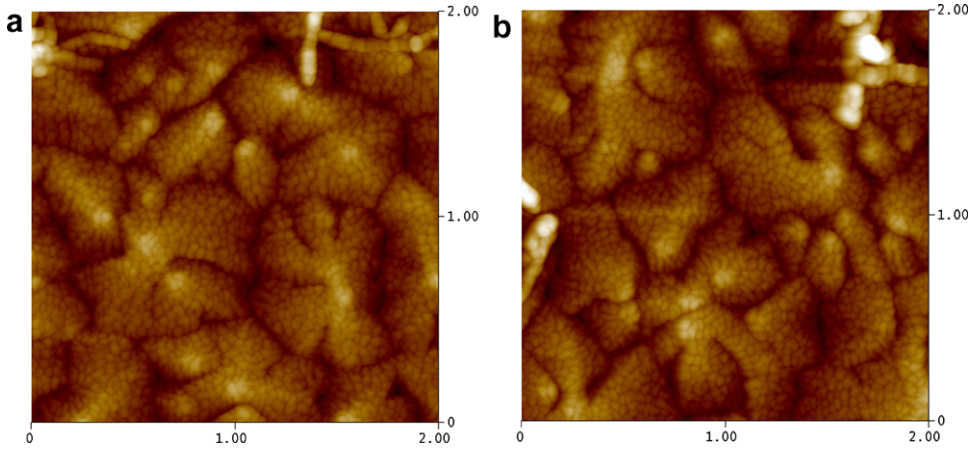


Fig. 6. AFM images of unannealed (a) and annealed (b) glass/ITO/PEDOT/pentacene (40 nm)/C_{60} (40 nm thick) samples. The sample was annealed at 200 °C for 1 min.

(40 nm) before and after annealing. The films were deposited at 0.3 Å/s. The surface morphology of the C_{60} deposited onto a pentacene layer is very different from the C_{60} deposited onto ITO-coated glass substrate. Indeed, that the C_{60} morphology is controlled by pentacene "substrate" emphasizes that the pentacene morphology plays a dominant role in determining device efficiency. The C_{60} film is described by small grains of approximately 30 nm in width. Upon thermal annealing, there is no obvious change in the film morphology. It should be noted, however, that annealing C_{60} film at 177 °C and higher temperatures increases the film order as observed by high-resolution electron-energy-loss spectroscopy [38] and by thin film X-ray diffraction [39].

To confirm that changes in film morphology upon thermal annealing lead to improvements in charge mobility, hole-only and electron-only devices were fabricated as follows: ITO/PEDOT/pentacene (0.5 Å/s for 10 nm and 1.5 Å/s for 80 nm)/Au and Al/C_{60} (0.3 Å/s for 122 nm)/Al. The hole and electron mobilities can be calculated from the space charge limited current (SCLC) densities using Child's law: [40–42]

$$j_{\mathrm{SCLC}} = \frac{9}{8}\varepsilon_r \varepsilon_0 \mu \frac{V^2}{L^3}$$

where ε_r is the dielectric constant of the material, ε_0 is the permittivity of the free space, L is the distance between the electrodes or the film thickness, and V is the voltage applied. Fig. 7 compares the dark J–V properties of the hole-only and electron-only devices before (open circles) and after annealing at 200 °C for 1 min (solid circles). All devices show three current–voltage response regions: ohmic regime ($J \propto V$), space charge limited current ($J \propto V^2$), and trap-filled region ($J \propto V^l$, $l > 2$), as indicated by the solid fitting lines. The hole and electron mobilities were calculated from the space charge limited current region. The hole mobility is 1.4×10^{-4} cm^2 V^{-1} s^{-1} for the as-prepared hole-only device. After annealing at 200 °C for 1 min, the hole mobility increases to 3.5×10^{-4} cm^2 V^{-1} s^{-1}. Fig. 7b shows the dark J–V characteristics of the electron-only device before and after annealing. The electron mobility increases from 2.2×10^{-3} cm^2 V^{-1} s^{-1} to 6.4×10^{-3} cm^2 V^{-1} s^{-1} upon thermal annealing supporting the idea of increased order in the film.

In summary, we investigated the effects of pentacene deposition rate and thermal annealing on the film morphology, the charge carrier mobilities, and the performance of pentacene/C_{60} bilayer solar cells. There is a direct correlation between the film morphology and the device performance. The films prepared by two-step evaporation (0.5 Å/s for the first 10 nm and 1.5 Å/s for the following 30 nm) have larger crystalline domains and a lower number of defects (lamellar domains and grain boundaries) than films prepared at faster rates; therefore, the device efficiency increases from 0.49% to 1.12%. Annealing quickly at 200 °C reduces grain boundaries, defects, and the density of the interface trap states by forming a more intimate pentacene/C_{60} interface. Additionally, thermal annealing increases the film crystallinity, resulting in higher hole and electron mobilities. The improvement in the hole mobility, the charge transfer, and electron mobility

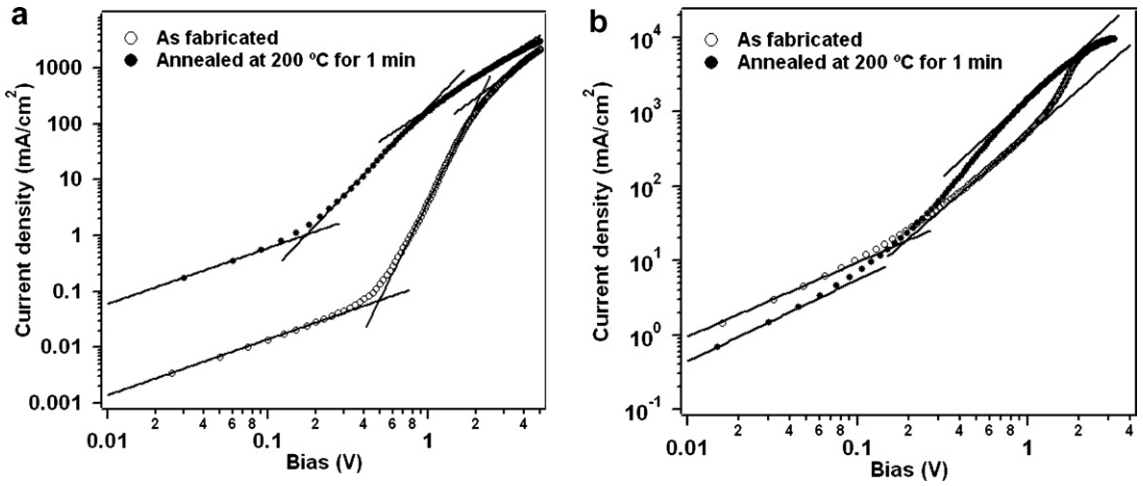


Fig. 7. (a) Dark J–V curves of the ITO/PEDOT/pentacene (90 nm)/Au (hole-only device) and (b) Al/C_{60} (122 nm)/Al (electron-only device) devices before (open circles) and after the thermal annealing at 200 °C for 1 min (solid circles). The pentacene layer was deposited at 0.5 Å/s for the first 10 nm and 1.5 Å/s for the following 80 nm. The C_{60} layer was deposited at 0.3 Å/s.

leads to an increase in the device efficiency from 0.78% to 1.12%. The increase in the crystalline domains at slow evaporation rates and reduction in the grain boundaries upon annealing can be visualized by AFM. Reversing the device structure (ITO/C_{60}/pentacene/Al) where pentacene is deposited onto the C_{60} surface may further change the film morphology as well as the donor–acceptor interface. The pentacene crystalline domain size depends strongly on the polarity and mechanical properties of the underlying substrate. ITO substrates are hydrophilic and hard whereas the C_{60} surface is hydrophobic and soft. Pentacene tends to form larger domains on Si/SiO_2 treated with a self-assembled monolayer of octadecyltrichlorosilane (OTS). Overall, processing conditions can be used to control the film quality, and hence, the device performance. Combining material purification, processing conditions, thermal treatment, and device engineering is likely to further improve the device efficiency.

2. Experimental

Pentacene and BCP were purchased from Aldrich. C_{60} was obtained from BuckyUSA. All the organic materials were used as received. The ITO-coated glass substrates (Thin film Devices, Anaheim, CA) were ultrasonically cleaned for 15 min in isoprophyl alcohol and then acetone. The ITO-coated glass substrates were treated by UV/O_3 for 30 min and immediately, a PEDOT:PSS layer was spin coated onto the ITO-coated glass substrates with a thickness ca. 40 nm, and then heated at 140 °C for 10 min in air. Then the ITO/PEDOT:PSS substrates were transferred into the thermal evaporator to deposit the organic layers and Al electrode. The PEDOT:PSS layer was used to smooth the ITO. The BCP layer was inserted between C_{60} and Al to provide a exciton blocking layer [18,43].

The organic layers were deposited in a high vacuum chamber (Angstrom engineering), $\sim 10^{-7}$ Torr. The film thickness of each layer was controlled by a quartz crystal monitor. The 40 nm pentacene layer was deposited at a rate of 5 Å/s, 3 Å/s, 0.5 Å/s for the first 10 nm and 1.5 Å/s for the following 30 nm, and 0.5 Å/s. The thickness of the pentacene layer is ca. 40 nm as measured by AFM. Then, C_{60} was deposited on top of pentacene layer at a rate of 0.3 Å/s to give the total thickness of 80 nm. Next, a BCP layer of 10 nm was evaporated at 2 Å/s. Then the Al cathode of 100 nm was deposited at a rate of 3 Å/s using a shadow mask to give a device area of 4.9 mm^2. The devices were not exposed to air and were characterized in a nitrogen glovebox at room temperature. The thermal annealing process was done inside an inert atmosphere of a glovebox. A hotplate was set at 200 °C and after it reached 200 °C, the devices were placed on top for 1 min and then removed immediately from the hot plate to cool down to the ambient temperature. Several annealing temperatures were used but the temperature that yielded the highest device efficiencies

was 200 °C in an agreement with the literature reported [27]. Current–voltage (I–V) measurements were conducted with a Keithley 2602 source-measure unit. The photocurrent was obtained under AM 1.5 solar illumination of 100 mW/cm^2 (I_L) from Xenon lamp (150 W Oriel). Calibrated silicon solar cells and photodiodes and pentacene solar cells were measured and referenced to a solar simulator at Konarka Technologies.

For charge mobility measurements, hole-only and electron-only devices were fabricated: ITO/PEDOT/pentacene (0.5 Å/s for 10 nm and 1.5 Å/s for 80 nm)/Au and Al/C_{60} (0.3 Å/s for 122 nm)/Al. The hole and electron mobilities were calculated using the space charge limiting current (SCLC) model.

Tapping mode AFM images were obtained in air using the MultiMode microscope and the Nanoscope IIIa controller (Veeco Inc.). Doped silicon probes with a spring constant of 1–5 N/m and a resonant frequency of 75 kHz (Budget Sensors) were used. All images were collected in air under ambient conditions.

Acknowledgements

This work is supported by the ONR Young Investigator Program and the UCSB startup fund.

References

[1] G. Yu, J. Gao, J.C. Hummelen, F. Wudl, A.J. Heeger, Science 270 (1995) 1789.
[2] C.W. Tang, Appl. Phys. Lett. 48 (1986) 183.
[3] P. Peumans, A. Yakimov, S.R. Forrest, J. Appl. Phys. 93 (2003) 3693.
[4] C.J. Brabec, N.S. Sariciftci, J.C. Hummelen, Adv. Funct. Mater. 11 (2001) 15.
[5] C.J. Brabec, A. Cravino, D. Meissner, N.S. Sariciftci, T. Fromherz, M.T. Rispens, L. Sanchez, J.C. Hummelen, Adv. Funct. Mater. 11 (2001) 374.
[6] D. Chirvase, J. Parisi, J.C. Hummelen, V. Dyakonov, Nanotechnology 15 (2004) 1317.
[7] J. Drechsel, B. Männig, D. Gebeyehu, M. Pfeiffer, K. Leo, H. Hoppe, Organic Electron. 5 (2004) 175.
[8] M. Granström, K. Petritsch, A.C. Arias, A. Lux, M.R. Andersson, R.H. Friend, Nature 395 (1998) 257.
[9] P. Peumans, S. Uchida, S.R. Forrest, Nature 425 (2003) 158.
[10] A. Yakimov, S.R. Forrest, Appl. Phys. Lett. 80 (2002) 1667.
[11] G.P. Kushto, W. Kim, Z.H. Kafafi, Appl. Phys. Lett. 86 (2005) 093502.
[12] B.P. Rand, J. Xue, F. Yang, S.R. Forrest, Appl. Phys. Lett. 87 (2005) 233508.
[13] Jiangeng Xue, Soichi Uchida, Barry P. Rand, Stephen R. Forrest, Appl. Phys. Lett. 84 (2004) 3013.
[14] D. Gebeyehu, B. Maennig, J. Drechsel, K. Leo, M. Pfeiffer, Sol. Energy Mater. Sol. Cells 79 (2003) 81.
[15] W. Geens, J. Poortmans, S.C. Jain, J. Nijs, R. Mertens, S.C. Veenstra, V.V. Krasnikov, G. Hadziioannou, Sol. Energy Mater. Sol. Cells 61 (2000) 43.
[16] A. El-ghayoury, A.P.H.J. Schenning, P.A. van Hal, C.H. Weidl, J.L.J. van Dongen, R.A.J. Janssen, U.S. Schubert, E.W. Meijer, Thin Solid Films 403–404 (2002) 97.
[17] G.K.R. Senadeera, P.V.V. Jayaweera, V.P.S. Perera, K. Tennakone, Sol. Energy Mater. Sol. Cells 73 (2002) 103.
[18] S. Yoo, B. Domercq, B. Kippelen, Appl. Phys. Lett. 85 (2004) 5427.
[19] S. Yoo, B. Domercq, B. Kippelen, J. Appl. Phys. 97 (2005) 103706.
[20] S.P. Park, S.S. Kim, J.H. Kim, C.N. Whang, S. Im, Appl. Phys. Lett. 80 (2002) 2872.
[21] Rui He, X. Chi, Aron Pinczuk, D.V. Lang, A.P. Ramirez, Appl. Phys. Lett. 87 (2005) 211117.
[22] G.B. Blanchet, C.R. Fincher, M. Lefenfeld, J.A. Rogers, Appl. Phys. Lett. 84 (2004) 296.
[23] C.D. Dimitrakopoulos, P.R.L. Malenfant, Adv. Mater. 14 (2002) 99.
[24] S.J. Kang, Y. Yi, C.Y. Kim, K. Cho, J.H. Seo, M. Noh, K. Jeong, K.-H. Yoo, C.N. Whang, Appl. Phys. Lett. 87 (2005) 233502.
[25] S.H. Jin, C.A. Lee, K.D. Jung, H. Shin, B.-G. Park, J.D. Lee, IEEE Electron Dev. Lett. 26 (2005) 903.
[26] J. Lee, S.S. Kim, K. Kim, J.H. Kim, S. Im, Appl. Phys. Lett. 84 (2004) 1701.
[27] A.C. Mayer, M.T. Lloyd, D.J. Herman, T.G. Kasen, G.G. Malliaras, Appl. Phys. Lett. 85 (2004) 6272.
[28] S. Sun, Z. Fan, Y. Wang, J. Haliburton, J. Mater. Sci. 40 (2005) 1429.
[29] C.J. Brabec, Sol. Energy Mater. Sol. Cells 83 (2004) 273.
[30] Y.S. Yang, S.H. Kim, J.-I. Lee, H.Y. Chu, L.-M. Do, H. Lee, J. Oh, T. Zyung, Appl. Phys. Lett. 80 (2002) 1595.
[31] O.D. Jurchescu, J. Baas, T.T.M. Palstra, Appl. Phys. Lett. 84 (2004) 3061.
[32] G. Horowitz, R. Hajllaoui, D. Fichou, A. El. Kassmi, J. Appl. Phys. 85 (1999) 3202.
[33] H. Yanagisawa, T. Tamaki, M. Nakamura, K. Kudo, Thin Solid Films 464–465 (2004) 398.
[34] D.J. Gundlach, Y.Y. Lin, T.N. Jackson, S.F. Nelson, D.G. Schlom, IEEE Electron Dev. Lett. 18 (1997) 87.
[35] I.P.M. Bouchoms, W.A. Schoonveld, J. Vrijmoeth, T.M. Klapwijk, Synth. Met. 104 (1999) 175.
[36] F.-J. Meyer zu Heringdorf, M.C. Reuter, R.M. Tromp, Nature 412 (2001) 517.
[37] J.G. Laquindanum, H.E. Katz, A.J. Lovinger, A. Dodabalapur, Chem. Mater. 8 (1996) 2542.
[38] J. Schmidt, M.R.C. Hunt, P. Miao, R.E. Palmer, Phys. Rev. B 56 (1997) 9918.
[39] J. Gong, G. Ma, E. Xie, C. Xu, G. Wang, G. Chen, Mater. Lett. 25 (1995) 185.
[40] T. Siegrist, C. Kloc, J.H. Schon, B. Batlogg, R.C. Haddon, S. Berg, G.A. Thomas, Angew. Chem. Int. Ed. 40 (2001) 1732.
[41] N.F. Mott, R.W. Gurney, Electronic Processes in Ionic Crystals, Oxford University Press, London, 1948.
[42] M.A. Lampert, P. Mark, Current Injection in Solids, Academic Press, New York, 1970.
[43] P. Peumans, S.R. Forrest, Appl. Phys. Lett. 79 (2001) 126.

Available online at www.sciencedirect.com
ScienceDirect
Organic Electronics 8 (2007) 575–583
Organic Electronics
www.elsevier.com/locate/orgel

Electron transport through polycyclic hydrocarbon molecules: A study of shot noise contribution to the power spectrum

Santanu K. Maiti *

Theoretical Condensed Matter Physics Division, Saha Institute of Nuclear Physics, 1/AF, Bidhannagar, Kolkata-700 064, India

Received 28 December 2006; received in revised form 1 April 2007; accepted 11 April 2007
Available online 19 April 2007

Abstract

We study electron transport characteristics through some polycyclic hydrocarbon molecules attached with two metallic electrodes by the use of Green's function technique. Here we do parametric calculations based on the tight-binding model to investigate the transport properties through such molecular bridges. In this context we also discuss noise power of the current fluctuations and focus our attention on the shot noise contribution to the power spectrum. The electron transport characteristics are significantly influenced by (a) the length of the molecules, (b) the interference effects and (c) the molecule-to-electrodes coupling strength.
© 2007 Elsevier B.V. All rights reserved.

PACS: 73.23.−b; 73.63.Rt; 73.40.Jn; 81.07.Nb

Keywords: Polycyclic molecules; Interference effects; Conductance; *I–V* characteristic and Shot noise

1. Introduction

The advancements in nanoscience and technologies prompting a growing number of researchers across multiple disciplines to attempt to devise innovative ways for decreasing the size and increasing the performance of microelectronic circuits. One possible route is based on the idea of using molecules and molecular structures as functional devices. During 1970s Aviram and Ratner [1] first studied theoretically the electron transport characteristics in molecular bridge systems. Later several numerous experiments [2–6] have been carried out on electron transport through molecules placed between two non-superconducting electrodes with few nanometer separation. From experimental developments, theory can give a better insight in understanding the new mechanism of conductance but yet the complete knowledge of the conduction mechanism in this scale is not well understood even today. Molecular transport properties in such systems are characterized by several important factors. First one, of course, is the quantization of energy levels associated with the identity of the molecule itself and the quantum interference of electron waves [7–12] associated with the geometry that the molecule adopts within the junction. Second are the different parameters of the Hamiltonian that describe the

* Tel.: +91 33 2337 5345; fax: +91 33 2337 4637.
E-mail address: santanu.maiti@saha.ac.in

1566-1199/$ - see front matter © 2007 Elsevier B.V. All rights reserved.
doi:10.1016/j.orgel.2007.04.004

molecular system, the electronic structure of the molecule and the molecular coupling with the side attached electrodes. To design molecular electronic devices with specific properties, it is important to study structure-conductance relationships and in a very recent work Ernzerhof et al. [13] have presented a general design principle and performed several model calculations to demonstrate the concept. The knowledge of current fluctuations (of thermal or quantum origin) also gives many key ideas for fabrication of efficient molecular devices. Blanter and Büttiker [14] have described elaborately how the lowest possible noise power of the current fluctuations can be determined in a two-terminal conductor. The steady state current fluctuations so-called shot noise is a consequence of the quantization of charge and it can be used to obtain information on a system which is not directly available through conductance measurements. The noise power of the current fluctuations provides an additional important information about the electron correlation by calculating the Fano factor (F) which directly informs us whether the magnitude of the shot noise achieves the Poisson limit ($F = 1$) or the sub-Poisson ($F < 1$) limit.

There exist different *ab initio* methods for the calculation of conductance [15–20] through a molecular bridge system. At the same time the tight-binding model has been extensively studied in the literature and it has also been extended to DFT transport calculations [21]. The study of static density functional theory (DFT) [22] within the local-density approximation (LDA) to investigate the electronic transport through nanoscale conductors, like atomic-scale point contacts, has met with nice success. But when this similar theory applies to molecular junctions, theoretical conductances achieve larger values compared to the experimental predictions and these quantitative discrepancies need extensive study in this particular field. In a recent work, Sai et al. [23] have predicted a correction to the conductance using the time-dependent current-density functional theory since the dynamical effects give significant contribution in the electron transport, and illustrated some important results with specific examples. Similar dynamical effects have also been reported in some other recent papers [24,25], where authors have abandoned the infinite reservoirs, as originally introduced by Landauer, and considered two large but finite oppositely charged electrodes connected by a nanojunction. Our aim of this article is to reproduce an analytic approach based on the tight-binding model to characterize the electronic transport properties through some polycyclic hydrocarbon molecules and focus our attention on the effects of (a) the length of the molecules, (b) the molecule-to-electrodes coupling strength and (c) the quantum interferences in such transport. Here we utilize a simple parametric approach [26–36] for these calculations. The model calculations are motivated by the fact that the *ab initio* theories are computationally too expensive, while, the model calculations by using the tight-binding formulation are computationally very cheap and also provide a worse insight to the problem. In our present study attention is drawn on the qualitative behavior of the physical quantities rather than the quantitative ones. Not only that, the *ab initio* theories do not give any new qualitative behavior for this particular study in which we concentrate ourselves.

We organize this article specifically as follows. Section 2 describes, very briefly, the methodology for the calculation of the transmission probability (T), current (I) and the noise power of current fluctuations (S) through a molecule sandwiched between two metallic electrodes by means of the Green's function technique. In Section 3, we study the behavior of the conductance as a function of the injecting electron energy, the current and the noise power of its fluctuations as a function of the

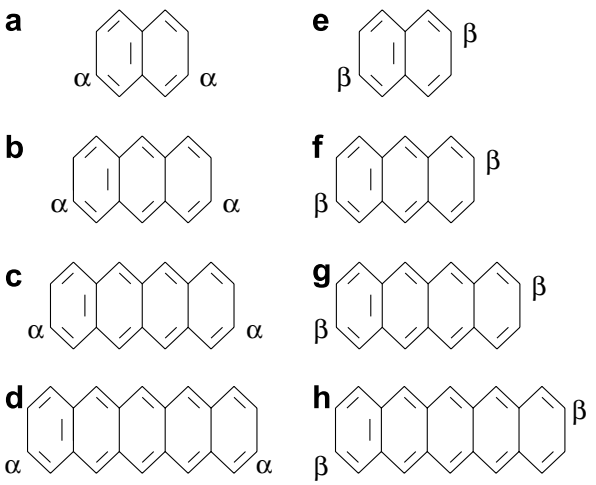


Fig. 1. Schematic view of four polycyclic hydrocarbon molecules those are attached with the two electrodes, the source and the drain, in *cis* (α–α) and *trans* (β–β) configurations by thiol (sulfur–hydrogen i.e., S–H bond) groups. These four molecules are defined as: napthalene (two rings), anthracene (three rings), tetracene (four rings) and pentacene (five rings).

applied bias voltage for the different polycyclic hydrocarbon molecules (Fig. 1). Finally, we summarize our investigations in Section 4.

2. Theoretical formulation

In this section we briefly describe the formulation of the transmission probability (T), conductance (g), current (I) and the noise power of its fluctuations (S) of a molecule (schematically represented as in Fig. 1), which is attached with the two metallic electrodes, by using the Green's function technique.

At low voltage and low temperature the conductance g of the molecule is given by the Landauer conductance formula [37]

$$g = \frac{2e^2}{h} T \tag{1}$$

where the transmission probability T is written in this form [37]

$$T = Tr[\Gamma_S G_M^r \Gamma_D G_M^a] \tag{2}$$

where G_M^r (G_M^a) is the retarded (advanced) Green's function of the molecule and Γ_S (Γ_D) describes its coupling with the source (drain). The Green's function of the molecule is expressed as

$$G_M = (E - H_M - \Sigma_S - \Sigma_D)^{-1} \tag{3}$$

where E is the energy of the injecting electron and H_M is the Hamiltonian of the molecule which can be written in the tight-binding model within the non-interacting picture like

$$H_M = \sum_i \epsilon_i c_i^\dagger c_i + \sum_{\langle ij \rangle} t(c_i^\dagger c_j + c_j^\dagger c_i) \tag{4}$$

where ϵ_i's are the site energies and t is the nearest-neighbor hopping strength. In Eq. (3), Σ_S and Σ_D correspond to the self-energies due to coupling of the molecule with the two electrodes. Now all the informations about the molecule-to-electrodes coupling are included into these two self-energies and are described through the use of Newns–Anderson chemisorption theory [26,27].

The current passing across the molecule can be considered as a single electron scattering process between the two reservoirs of charge carriers. The current–voltage relation can be obtained from the expression [37]

$$I(V) = \frac{e}{\pi\hbar} \int_{-\infty}^{\infty} (f_S - f_D) T(E)\, dE \tag{5}$$

where the Fermi distribution function $f_{S(D)} = f(E - \mu_{S(D)})$ with the electrochemical potentials $\mu_{S(D)} = E_F \pm eV/2$. For the sake of simplicity, here we assume that the entire voltage is dropped across the conductor–electrode interfaces and this assumption does not greatly affect the qualitative aspects of the I–V characteristics. This assumption is based on the fact that the electric field inside the molecule, especially for short molecules, seems to have a minimal effect on the conductance–voltage characteristics. On the other hand for quite longer molecules and high bias voltage, the electric field inside the molecule may play a more significant role depending on the internal structure of the molecule [38], but yet the effect is too small.

The noise power of the current fluctuations is calculated from the following expression [14]

$$S = \frac{2e^2}{\pi\hbar} \int_{-\infty}^{\infty} [T(E)\{f_S(1 - f_S) + f_D(1 - f_D)\} + T(E)\{1 - T(E)\}(f_S - f_D)^2]\, dE \tag{6}$$

where the first two terms of this equation correspond to the equilibrium noise contribution and the last term gives the non-equilibrium or shot noise contribution to the power spectrum. By calculating the noise power of the current fluctuations we can evaluate the Fano factor F, which is essential to predict whether the shot noise lies in the Poisson or the sub-Poisson regime, through the relation [14]

$$F = \frac{S}{2eI} \tag{7}$$

For $F = 1$, the shot noise achieves the Poisson limit where no electron correlation exists between the charge carriers. On the other hand for $F < 1$, the shot noise reaches the sub-Poisson limit and it provides the information about the electron correlation among the charge carriers.

In this article we study our results at very low temperature (5 K), but the qualitative behavior of all the results are invariant up to some finite temperature (~300 K). For simplicity we take the unit $c = e = h = 1$ in our present calculations.

3. Results and their interpretation

In this section we investigate the characteristic properties of the conductance as a function of the injecting electron energy, current and the noise power of its fluctuations as a function of the applied bias voltage for four different polycyclic

hydrocarbon molecules (Fig. 1). These molecules are defined as napthalene (two rings), anthracene (three rings), tetracene (four rings) and pentacene (five rings), respectively. To emphasize the interference effects on the electron transport, here we attach the electrodes (the source and the drain) to the molecules in the two distinct configurations. One is so-called the *cis* configuration, denoted by the position α–α (see the first column of Fig. 1) and the other one is so-called the *trans* configuration which is defined by the notation β–β (see the second column of Fig. 1). By contacting the molecules with the electrodes in these two different ways we can control very nicely the interference conditions of the electron waves traversing through the two arms of the molecular rings, and, we will see that the electron transport properties are significantly affected by these interference effects. In the actual experimental set-up, the electrodes are generally constructed from the gold and the molecules are attached with these electrodes by thiol (sulfur–hydrogen i.e., S–H bond) groups in the chemisorption technique where the sulfur atoms remove and the hydrogen atoms reside.

We will study the behavior of the electron transport characteristics through the polycyclic hydrocarbon molecules in the two distinct regimes. One is so-called the weak-coupling regime defined as $\tau_{S(D)} \ll t$ and the other one is the higher-coupling regime which is defined as $\tau_{S(D)} \sim t$, where τ_S and τ_D are the hopping strengths of the molecules with the source and the drain, respectively. In our calculations, the parameters for these two regimes are chosen as $\tau_S = \tau_D = 0.5$, $t = 3$ (weak-coupling) and $\tau_S = \tau_D = 2.5$, $t = 3$ (higher-coupling). Here we take the site energy $\epsilon_i = 0$ for all the sites of the molecules.

In Fig. 2, we plot the conductance (g) as a function of the injecting electron energy (E) for the molecules attached with the electrodes in the *cis* configuration. Fig. 2a–d correspond to the results for the napthalene, anthracene, tetracene and pentacene molecules, respectively, where the solid curves correspond to the results for the weak-coupling limit and the dotted curves denote the results in the limit of higher molecular coupling. In the weak molecular coupling limit, the conductance shows very sharp resonance peaks (solid curves in Fig. 2) for some specific energy values, while, for all other energies it almost drops to zero. At these resonances the conductance g achieves the value 2, and accordingly, the transmission probability T goes to unity, since from the Landauer conductance formula we

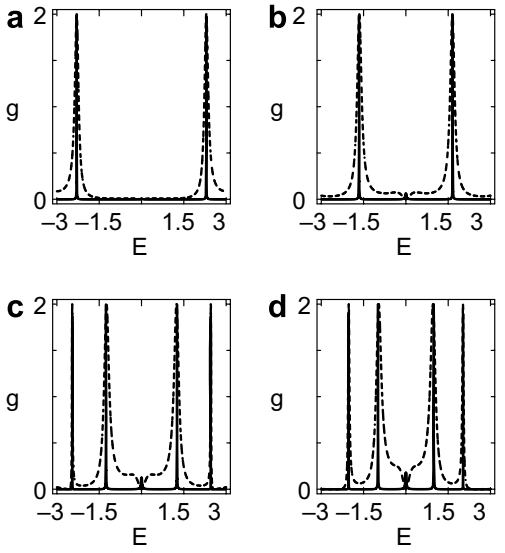


Fig. 2. Conductance g as a function of the electron energy E for the molecules attached with the electrodes in the *cis* configuration. (a–d) Correspond to the results for the napthalene, anthracene, tetracene and pentacene molecules, respectively. The solid and the dotted curves denote the weak- and the higher-coupling limits, respectively.

get $g = 2T$ (see Eq. (1) with $e = h = 1$ in our present calculations). These resonance peaks are associated with the energy eigenvalues of the corresponding molecule and hence more resonance peaks appear with the increment of the length of the molecule. Thus it can be emphasized that the conductance spectrum manifests itself the energy eigenvalues of the molecule. Now with the increase of the molecular coupling strength, the widths of these resonance peaks get enhanced substantially, as shown by the dotted curves in Fig. 2. This is due to the substantial broadening of the molecular energy eigenvalues in the limit of higher molecular coupling. The contribution for this broadening of the energy levels comes from the imaginary parts of the two self energies Σ_S and Σ_D, respectively [37]. Thus for the higher-coupling limit, the electron conducts across the molecules for the wide range of energies, while, a fine tuning in the energy scale is necessary to get the electron conduction through the molecules in the limit of weak molecular coupling. Therefore, it can be predicted that the molecule-to-electrodes coupling strength has a significant role in the determination of the electron conduction through the molecular bridges.

Fig. 3 corresponds to the conductance-energy characteristics for the molecules attached with the

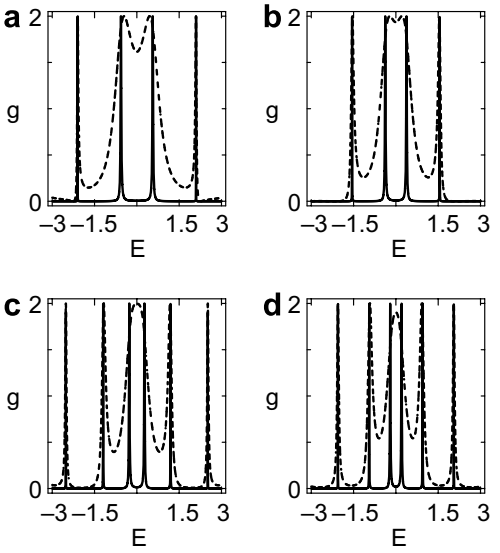


Fig. 3. Conductance g as a function of the electron energy E for the molecules attached with the electrodes in the *trans* configuration. (a–d) Correspond to the results for the napthalene, anthracene, tetracene and pentacene molecules, respectively. The solid and the dotted curves denote the weak- and the higher-coupling limits, respectively.

electrodes in the *trans* configuration where, Fig. 3a–d represent the results for the napthalene, anthracene, tetracene and pentacene molecules, respectively. The solid and the dotted curves correspond to the same meaning as in Fig. 2. Similar to the case of Fig. 2, here we also get the sharp resonance peaks in the conductance spectra for the weak-coupling limit (see the solid curves of Fig. 3), and, they (resonance peaks) become broadened in the limit of higher molecular coupling (see the dotted curves of Fig. 3). The explanations for such behaviors are the same as we discuss earlier. From this figure (Fig. 3), it is observed that both for the weak- and the higher-coupling limits, more resonance peaks appear in the conductance spectra i.e., we get more resonating energy eigenstates compared to the results obtained for the *cis* configuration (Fig. 2). This feature can be explained as follows. When the molecule is attached with the electrodes, its energy eigenvalues get modified by the two self-energies Σ_S and Σ_D, respectively. The self-energies contain the real and the imaginary parts, where the real part corresponds to the energy shift and the imaginary part gives the broadening of the molecular energy levels [37]. By changing the positions of the two electrodes from one configuration to the other i.e., either from the *cis* to the *trans* configuration or inverse of that, the molecular energy levels are shifted in different ways and accordingly, we get more/less resonating energy eigenstates in the scale of the energy E. This situates different resonance peaks in the conductance spectra for the two different cases (see Figs. 2 and 3). Another significant observation is that in the higher-coupling case, the probability amplitude for getting the electron across the molecular ring in the *trans* configuration is much greater than that of the *cis* configuration for most of the energy values, except at the resonance peaks where the amplitudes are same ($T = 1$) for both these two configurations. This is solely due to the quantum interference effects of the electron waves traversing through the different arms of the molecular rings. This can be explained very simply from the standard interpretation of the quantum mechanical theory. The electrons are carried from the source to the drain through the molecules and the electron waves propagating along the two arms of the molecular ring may suffer a relative phase shift between themselves. Accordingly, there might be constructive or destructive interference due to superposition of the electronic wave functions along the various pathways. Therefore, the probability amplitude of the electron across the molecule becomes either large or small. So electron transmission is strongly affected by the quantum interference and can be controlled by the molecule-to-electrodes interface structure. It is observed that the qualitative features of the g–E characteristics are in good agreement with the experimental results. Now these interference effects can be visible much more clearly by investigating the current–voltage (I–V) characteristics across the molecules and in the forthcoming parts we will describe the current and the noise power of its fluctuations as a function of the applied bias voltage for both the *cis* and the *trans* configurations.

Both the current (I) and the noise power of its fluctuations (S) are calculated from the integration procedure of the transmission function (T), as given in Eqs. (5) and (6). The behavior of the transmission function is exactly similar to that of the conductance variation as shown in Figs. 2 and 3, differ only in magnitude by the factor 2 since we get $g = 2T$ from the Landauer conductance formula (Eq. (1)). In Fig. 4, we plot the current and the noise power of its fluctuations as a function of the applied bias voltage for the different molecular bridges in the limit of weak-coupling where the molecules are attached with the electrodes in the *cis* configuration. Fig. 4a–d

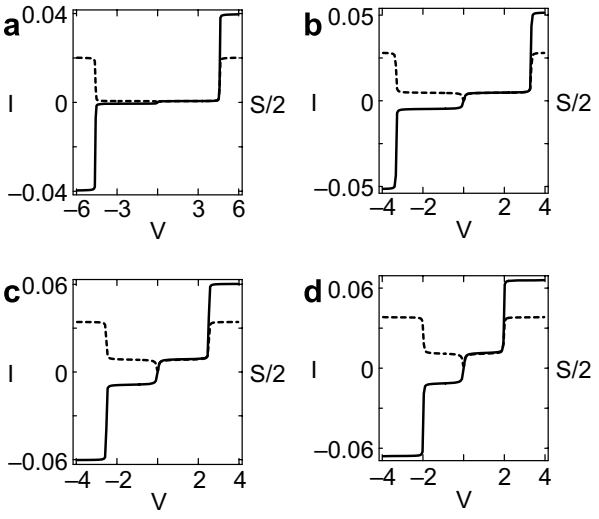


Fig. 4. Current I (solid curve) and the noise power of its fluctuations S (dotted curve) as a function of the applied bias voltage V for the molecules attached with the electrodes in the *cis* configuration in the limit of weak molecular coupling. (a–d) Correspond to the results for the napthalene, anthracene, tetracene and pentacene molecules, respectively.

correspond to the results for the napthalene, anthracene, tetracene and pentacene molecules, respectively. The solid and the dotted curves denote the current and the noise power, respectively. Current shows the staircase-like behavior with sharp steps as a function of the applied bias voltage. This is due to the sharp resonance peaks in the conductance spectra (see the solid curves of Fig. 2), since the current is evaluated from the integration method of the transmission function T. With the increase of the applied bias voltage, the electrochemical potentials on the electrodes are shifted gradually and finally cross one of the molecular energy levels. Therefore, a current channel is opened up and a jump in the current–voltage characteristic curve appears. More steps appear as we increase the length of the molecule associated with the molecular resonance states. For all these bridges the current amplitudes are very small and they are comparable with each other (solid curves of Fig. 4). Another significant observation is that the threshold bias voltage of the electron conduction through the bridge decreases gradually with the increase of the length of the molecule. Thus by controlling the length of the molecule we can tune the threshold bias voltage which provides a key idea for fabrication of efficient molecular switch. Now in the study of the noise power of the current fluctuations for these molecular bridges in this weak-coupling limit (dotted curves of Fig. 4) we see that the shot noise goes from the Poisson limit ($F = 1$) to the sub-Poisson limit ($F < 1$) as long as we cross the first step in the current-voltage characteristics. This reveals that the electrons are correlated after the tunneling process has occurred. Here the electrons are correlated only in the sense that one electron feels the existence of the other according to the Pauli exclusion principle, since we have neglected all other electron–electron interactions in our present formalism. Another important observation is that the amplitudes of the noise power in the sub-Poisson region for all these bridges are almost invariant. These results emphasize that in the limit of weak-coupling the noise power of the current fluctuations within the sub-Poisson limit remains in the same level independent of the length of the molecule.

The characteristic properties of the current and the noise power of its fluctuations are also very interesting for these molecular bridges (molecules attached with the electrodes in the *cis* configuration) in the limit of higher molecular coupling. The results are represented in Fig. 5 where, Fig. 5a–d correspond to the results for the same molecular bridges as given in Fig. 4, respectively. The solid and the dotted curves denote the same meaning as in Fig. 4. It is observed that the current varies quite

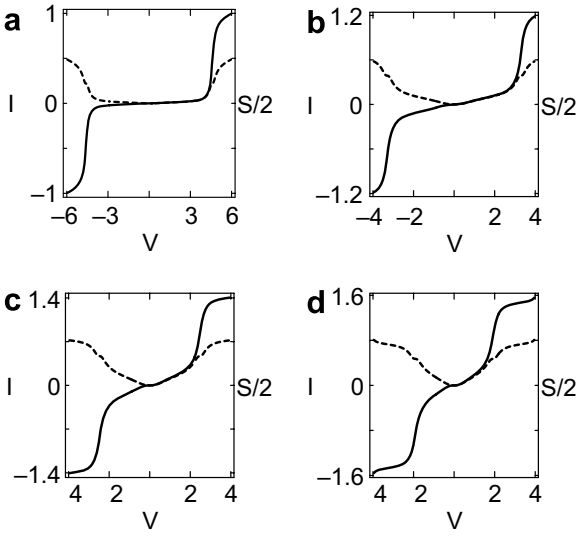


Fig. 5. Current I (solid curve) and the noise power of its fluctuations S (dotted curve) as a function of the applied bias voltage V for the molecules attached with the electrodes in the *cis* configuration in the limit of higher molecular coupling. (a–d) Correspond to the results for the napthalene, anthracene, tetracene and pentacene molecules, respectively.

continuously (solid curves of Fig. 5) with the applied bias voltage V. This is due to the broadening of the resonance peaks in this higher-coupling limit (see the dotted curves of Fig. 2) as the current is computed from the integration procedure of the function T. The remarkable observation is that the current amplitudes get enhanced quite significantly compared to the current amplitudes observed for the molecular bridges in the weak-coupling limit (see the solid curves of Fig. 4). This can be emphasized very simply by noting the areas under the curves in the conductance spectra for these two coupling cases (Fig. 2). It is also noted here that the current amplitude increases gradually as we increase the length of the molecule for this higher-coupling limit. Now in the determination of the noise power of the current fluctuations, we see that the shot noise makes a transition from the Poisson limit ($F = 1$) to the sub-Poisson limit ($F < 1$) after some critical value of the applied bias voltage (see the dotted curves of Fig. 5). This critical value of the bias voltage decreases gradually as we increase the length of the molecule so that the shot noise goes faster to the sub-Poisson limit for the longer molecules. Therefore, it predicts that the electron correlation is much more significant for the molecules with higher length than that of the shorter ones. In this limiting case we also see that, like as in the weak-coupling case, the amplitudes of the noise power in the sub-Poisson regime for all these bridges are almost comparable to each other.

Now focus our attention on the current and the noise power of its fluctuations for the molecules attached with the electrodes in the *trans* configuration. In Fig. 6, we plot the current and the noise power for the molecules attached with the electrodes in the *trans* configuration in the limit of weak molecular coupling. Fig. 6a–d correspond to the results for the napthalene, anthracene, tetracene and pentacene molecules, respectively. The solid and the dotted curves represent the same meaning as in Figs. 4 and 5. Like as in the *cis* configuration, for the weak-coupling limit here we also see that the current shows staircase-like behavior with sharp steps (see the solid curves of Fig. 6) as a function of the applied bias voltage and the shot noise makes a transition from the Poisson limit to the sub-Poisson limit as we cross the first step in the I–V curves (see the dotted curves of Fig. 6). The explanations of such behaviors are the same as before. The strange observation is that the current amplitudes for all these molecular bridges get enhanced quite significantly, though we are in the weak-coupling limit, compared to the current amplitudes obtained for these molecules in the *cis* configuration. This is solely due to the quantum interference effects of the electron waves traversing through the different arms of the molecular rings (Fig. 1). Thus interference effects play significant role in the determination of the current through the molecular bridges. Here also, like as in Fig. 4, the noise power of the current fluctuations lies in the same level within the sub-Poisson limit (see the dotted curves of Fig. 6), independent of the length of the molecule.

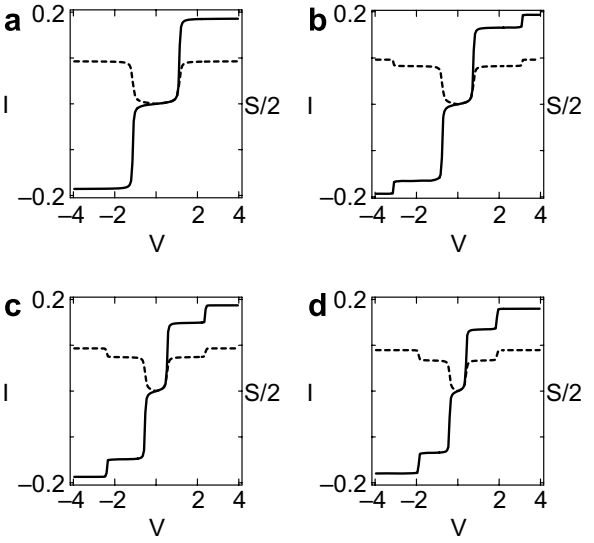


Fig. 6. Current I (solid curve) and the noise power of its fluctuations S (dotted curve) as a function of the applied bias voltage V for the molecules attached with the electrodes in the *trans* configuration in the limit of weak molecular coupling. (a–d) Correspond to the results for the napthalene, anthracene, tetracene and pentacene molecules, respectively.

Fig. 7 displays the results for the molecular bridges (molecules attached with the electrodes in the *trans* configuration) in the limit of higher-coupling, where, Fig. 7a–d correspond to the same molecules as in Fig. 6. The current varies continuously (solid curves of Fig. 7) with the bias voltage V for all these bridges, similar to the results studied earlier for the bridges in the *cis* configuration (solid curves of Fig. 5). For this higher-coupling limit the current amplitudes are also very large than the results obtained for the bridges in the *cis* configuration with higher molecular coupling and the explanation for such kind of behavior is the same as we describe earlier. Here it is observed that the current amplitude decreases gradually as we increase the length of

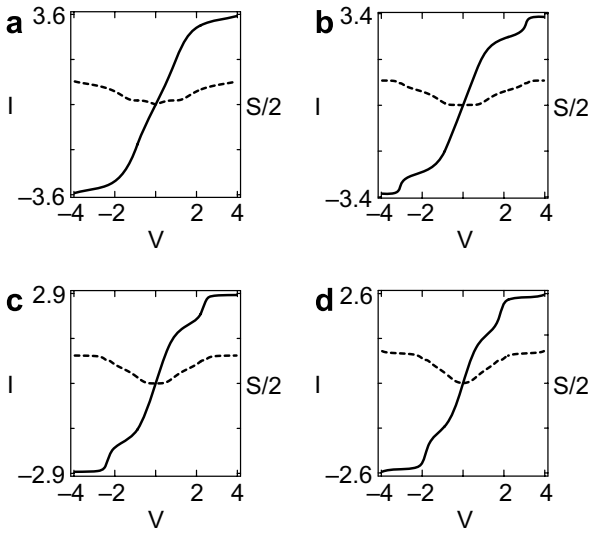


Fig. 7. Current I (solid curve) and the noise power of its fluctuations S (dotted curve) as a function of the applied bias voltage V for the molecules attached with the electrodes in the *trans* configuration in the limit of higher molecular coupling. (a–d) Correspond to the results for the napthalene, anthracene, tetracene and pentacene molecules, respectively.

the molecule, in contrary to the results predicted in Fig. 5. Our calculations of the noise power of the current fluctuations for such bridges provide that there is no such possibility of transition from the Poisson limit to the sub-Poisson limit since the shot noise already achieves the sub-Poisson limit (see the dotted curves of Fig. 7), momentarily as we switch on the bias voltage. Accordingly, for such bridges in this limit of molecular coupling the electron correlation is highly significant. Thus we can predict that the noise power of the current fluctuations strongly depends on the molecule-to-electrode interface structures and as well as the molecule-to-electrodes coupling strength.

4. Conclusion

In summary of this article, we have introduced parametric calculations based on the tight-binding model to investigate the electron transport properties through some polycyclic hydrocarbon molecules attached with two metallic electrodes. We have shown that the electron transport properties are significantly affected by (a) the length of the molecules, (b) the quantum interference effects and (c) the molecule-to-electrodes coupling strength. All the results described here provide several key ideas for fabrication of efficient molecular devices.

The conductance shows sharp resonance peaks for the weak-coupling limit (solid curves of Figs. 2 and 3), while, they get broadened in the limit of higher molecular coupling (dotted curves of Figs. 2 and 3). This increment of the resonance widths is due to the broadening of the molecular energy levels, where the contribution comes from the imaginary parts of the self energies Σ_S and Σ_D [37].

The quantum interference effects on the electron transport have been clearly described by studying the current–voltage characteristics. Both for the *cis* and the *trans* configurations, in the limit of weak molecular coupling, the current gets the staircase-like behavior with sharp steps (solid curves of Figs. 4 and 6). On the other hand it varies quite continuously with the applied bias voltage in the limit of higher molecular coupling (solid curves of Figs. 5 and 7). The most remarkable observation is that by increasing the molecular coupling strength one can enhance the current amplitude quite significantly. We can also tune the current amplitude in a controllable way by varying the molecule-to-electrodes interface structures associated with the quantum interference effects.

In the study of the noise power of the current fluctuations, we have seen that it strongly depends on the molecule-to-electrodes interface structures and as well as the molecular coupling strength. In the weak-coupling case both for the *cis* and the *trans* configurations, the shot noise makes a transition from the Poisson limit ($F = 1$) to the sub-Poisson limit ($F < 1$) as we cross the first step in the I–V characteristics (dotted curves of Figs. 4 and 6) which reveals that the electrons are correlated with each other after the tunneling process has occurred. Quite similarly in the higher-coupling limit for the molecular bridges in the *cis* configuration, the shot noise makes a transition from the Poisson limit to the sub-Poisson limit beyond some critical value of the applied bias voltage V (dotted curves of Fig. 5). On the other hand for the molecules attached with the electrodes in the *trans* configuration and in the limit of higher-coupling, there is no such possibility of transition from the Poisson limit to the sub-Poisson limit as the shot noise already lies in the sub-Poisson limit momentarily as we switch on the bias voltage (dotted curves of Fig. 7), and accordingly, for such cases the electron correlation is very much significant.

Throughout our discussions we have used several approximations by neglecting the effects of the electron–electron interaction, all the inelastic scattering

processes, the Schottky effect, the static Stark effect, etc. More studies are expected to take into account all these approximations for our further investigations.

References

[1] A. Aviram, M. Ratner, Chem. Phys. Lett. 29 (1974) 277.
[2] R.M. Metzger et al., J. Am. Chem. Soc. 119 (1997) 10455.
[3] C.M. Fischer, M. Burghard, S. Roth, K.V. Klitzing, Appl. Phys. Lett. 66 (1995) 3331.
[4] J. Chen, M.A. Reed, A.M. Rawlett, J.M. Tour, Science 286 (1999) 1550.
[5] M.A. Reed, C. Zhou, C.J. Muller, T.P. Burgin, J.M. Tour, Science 278 (1997) 252.
[6] T. Dadosh, Y. Gordin, R. Krahne, I. Khivrich, D. Mahalu, V. Frydman, J. Sperling, A. Yacoby, I. Bar-Joseph, Nature 436 (2005) 677.
[7] M. Magoga, C. Joachim, Phys. Rev. B 59 (1999) 16011.
[8] J.-P. Launay, C.D. Coudret, in: A. Aviram, M.A. Ratner (Eds.), Molecular Electronics, New York Academy of Sciences, New York, 1998.
[9] R. Baer, D. Neuhauser, Chem. Phys. 281 (2002) 353.
[10] R. Baer, D. Neuhauser, J. Am. Chem. Soc. 124 (2002) 4200.
[11] R.H. Goldsmith, M.R. Wasielewski, M.A. Ratner, J. Phys. Chem. B 110 (2006) 20258.
[12] M. Ernzerhof, H. Bahmann, F. Goyer, M. Zhuang, P. Rocheleau, J. Chem. Theory Comput. 2 (2006) 1291.
[13] M. Ernzerhof, M. Zhuang, P. Rocheleau, J. Chem. Phys. 123 (2005) 134704.
[14] Y.M. Blanter, M. Büttiker, Phys. Rep. 336 (2000) 1.
[15] S.N. Yaliraki, A.E. Roitberg, C. Gonzalez, V. Mujica, M.A. Ratner, J. Chem. Phys. 111 (1999) 6997.
[16] M. Di Ventra, S.T. Pantelides, N.D. Lang, Phys. Rev. Lett. 84 (2000) 979.
[17] Y. Xue, S. Datta, M.A. Ratner, J. Chem. Phys. 115 (2001) 4292.
[18] J. Taylor, H. Gou, J. Wang, Phys. Rev. B 63 (2001) 245407.
[19] P.A. Derosa, J.M. Seminario, J. Phys. Chem. B 105 (2001) 471.
[20] P.S. Damle, A.W. Ghosh, S. Datta, Phys. Rev. B 64 (2001) R201403.
[21] (a) M. Elstner et al., Phys. Rev. B 58 (1998) 7260;
(b) T. Frauenheim et al., J. Phys.: Condens. Matter 14 (2002) 3015.
[22] (a) P. Hohenberg, W. Kohn, Phys. Rev. 136 (1964) B864;
(b) W. Kohn, L.J. Sham, Phys. Rev. 140 (1965) A1133.
[23] N. Sai, M. Zwolak, G. Vignale, M.D. Ventra, Phys. Rev. Lett. 94 (2005) 186810.
[24] N. Bushong, N. Sai, M.D. Ventra, Nano Lett. 5 (2005) 2569.
[25] M.D. Ventra, T.N. Todorov, J. Phys.: Condens. Matter 16 (2004) 8025.
[26] V. Mujica, M. Kemp, M.A. Ratner, J. Chem. Phys. 101 (1994) 6849.
[27] V. Mujica, M. Kemp, A.E. Roitberg, M.A. Ratner, J. Chem. Phys. 104 (1996) 7296.
[28] M.P. Samanta, W. Tian, S. Datta, J.I. Henderson, C.P. Kubiak, Phys. Rev. B 53 (1996) R7626.
[29] M. Hjort, S. Stafström, Phys. Rev. B 62 (2000) 5245.
[30] S.K. Maiti, Phys. Lett. A 362 (2007) 225.
[31] S.K. Maiti, Chem. Phys. 331 (2007) 254.
[32] S.K. Maiti, Physica E 36 (2007) 199.
[33] S.K. Maiti, Phys. Scr. 75 (2007) 62.
[34] S.K. Maiti, Physica B 394 (2007) 33.
[35] S.K. Maiti, Solid State Commun. 142 (2007) 398.
[36] S.K. Maiti, Tuning of electron transport through molecular bridge systems: a study of shot noise, IJQC, in press.
[37] S. Datta, Electronic Transport in Mesoscopic Systems, Cambridge University Press, Cambridge, 1997.
[38] W. Tian, S. Datta, S. Hong, R. Reifenberger, J.I. Henderson, C.I. Kubiak, J. Chem. Phys. 109 (1998) 2874.

Available online at www.sciencedirect.com
ScienceDirect
Organic Electronics 8 (2007) 584–590
Organic Electronics
www.elsevier.com/locate/orgel

(Organic) Switching phenomenon in lateral structures: Tuning by gate voltage

Biswanath Mukherjee, Amlan J. Pal *

Department of Solid State Physics, Indian Association for the Cultivation of Science, Kolkata 700 032, India
Centre for Advanced Materials, Indian Association for the Cultivation of Science, Kolkata 700 032, India

Received 18 January 2007; received in revised form 27 March 2007; accepted 18 April 2007
Available online 3 May 2007

Abstract

We have fabricated devices based on copper phthalocyanine (CuPc) that exhibited electrical bistability and switching phenomenon. Apart from sandwiched structures, coplanar (lateral) electrodes or field-effect transistor structures have also been characterized. The observation of switching and memory phenomenon in lateral structures with Au/Au electrode combination primarily rules out (1) migration of metal ions into the organic materials, (2) metal filament formation through a redox-driven process, and (3) electroreduction of the molecules as possible mechanisms of electrical bistability in CuPc. The existence two conducting state and bistability have been explained in terms of trapping and detrapping of carriers in the molecular layer. Furthermore, the lateral structures show possibilities to tune switching processes through the bias of the base (gate) electrode.
© 2007 Elsevier B.V. All rights reserved.

PACS: 85.65.+h; 73.40.Sx; 73.61.Ph

Keywords: Memory phenomenon; Conductance switching; Lateral structures; Organic semiconductors

1. Introduction

Molecular electronic materials with electrically bistable states have raised a rapidly growing interest for potential application in ultra high-density non-volatile memory elements [1–4]. They are now being considered as an alternative to the inorganic resistive-switching material for future information storage media. Apart from non-volatile memory elements, devices with volatile memory [5] are also crucial in fabricating switching devices. The switching devices exhibit two conducting states at any voltage. In devices, where no bias is needed to retain the high-conducting state, the switching is termed as memory switching [6–8]. In threshold switching, on the other hand, a bias is needed to retain the high-conducting state [2,9]. A variety of molecular electronic junctions have been investigated over the recent years with the general objective of investigating charge transfer through the molecules. Most of the studies to date involve metal/molecule/metal

* Corresponding author. Tel.: +91 33 24734971; fax: +91 33 24732805.
E-mail address: sspajp@iacs.res.in (A.J. Pal).

1566-1199/$ - see front matter © 2007 Elsevier B.V. All rights reserved.
doi:10.1016/j.orgel.2007.04.008

sandwich structures based on covalent or electrostatic bonds between the molecule and metals [6,10]. It is generally accepted that both the molecular structure and the contact between metal and molecule are important to the junction conductance. In addition to the molecular structure, the metal work function and the metal–molecule bonds are expected to significantly affect the electron transport through the junction [4].

There has been a debate about the exact mechanism of conductance switching. It is now believed that the mechanism may depend on the (molecular) system chosen. The mechanisms so far proposed to explain the electrical bistability in organic molecule include conformational change [11,12], electroreduction of the molecule [6,7], migration of metal-ions into the organic material [13,14], metal filament formation [15,16]. Oxide layer grown during the top/bottom electrode (Al) evaporation might also help in switching the material to the high state.

In the present work, we took a lateral approach. We have fabricated devices with a common organic semiconductor in a coplanar electrode configuration. Such a coplanar (lateral) or field-effect transistor (FET) structure with films deposited on a gate insulator would also provide an additional parameter, namely gate voltage, which may tune or control the characteristics of electrical bistability.

2. Experimental

Copper phthalocyanine (CuPc), purchased from Aldrich Chemical Co., was used without further purification. To fabricate sandwiched-structure devices, indium tin oxide (ITO) and gold (Au) coated glass substrates were used as bottom electrodes. CuPc was thermally evaporated at a pressure below 10^{-5} torr. Aluminum (Al), thermally evaporated in vacuum through a mechanical mask, was the top electrode. Active area and thickness of a device were 6 mm^2 and 150 nm, respectively. To fabricate lateral structures, Au or Al was thermally evaporated on glass or SiO_2 coated (oxide thickness = 300 nm) *n*-Si wafers with a mechanical mask before depositing CuPc through thermal evaporation. The interdigitated electrode pattern had a channel length of 11 μm and width of 30 mm. The structures on oxide coated Si were used in the FET mode. Schematic representations of the sandwiched- and the lateral structures are shown in the inset of respective figures.

To study electrical and dielectrical characteristics, sandwiched and lateral structures were kept in a shielded vacuum chamber. Measurements were carried out at room temperature. Current–voltage (*I–V*) characteristics of the devices were recorded with Keithley 6517A electrometer and also with a Yokogawa 7651 programmable d.c. source and a Keithley 486 picoammeter. For the sandwiched structures, bias was applied with respect to the top Al electrode. Voltage step was 0.01–0.05 V, and scan speed varied between 10 and 500 mV/s. Impedance spectroscopy of the devices was recorded with a Solartron 1260 Impedance Analyzer. Amplitude of ac test voltage was 100 mV rms, and the frequency range of measurement was 1 Hz to 12 MHz (8 points/decade). Corrections for the external leads and contacts with them were carried out by measuring short-circuit and open-circuit condition cases. Some of the lateral structures with a bottom (gate) electrode were characterized with usual FET configuration. Bias was applied with respect to one on the top electrodes (source). The instruments were controlled by a PC via a general-purpose interface bus (GPIB). All the measurement was carried out with LabView/SMaRT softwares. Scanning tunneling microscope (STM) measurements were carried out with a Nanosurf easyScan2 controller in a non-contact (tunneling) mode under ambient condition.

3. Results and discussion

3.1. Sandwiched structures

A schematic representation of an Au/CuPc/Al sandwich-structure is shown in the inset of Fig. 1. *I–V* characteristics were measured by scanning the bias in a loop, e.g., from 0 to $+V_{Max}$ to $-V_{Max}$ to $+V_{Max}$ and so on. We have varied the amplitude of V_{Max} to generate a range of *I–V* characteristics. Fig. 1 shows *I–V* characteristics of the device under three consecutive voltage loops. The device exhibits electrical bistability in a reproducible manner. The as-fabricated device was initially in the low conducting (off) state. At a critical bias (threshold voltage V_{Th}), the current suddenly jumps to a higher value. When the bias is scanned towards from $+V_{Max}$ to 0 V, the high-conducting state is retained and the device current at any voltage during the sweep from $+V_{Max}$ to 0 V remains several orders higher in magnitude as compared to that during the initial sweep from 0 to $+V_{Max}$. Finally, when the bias is

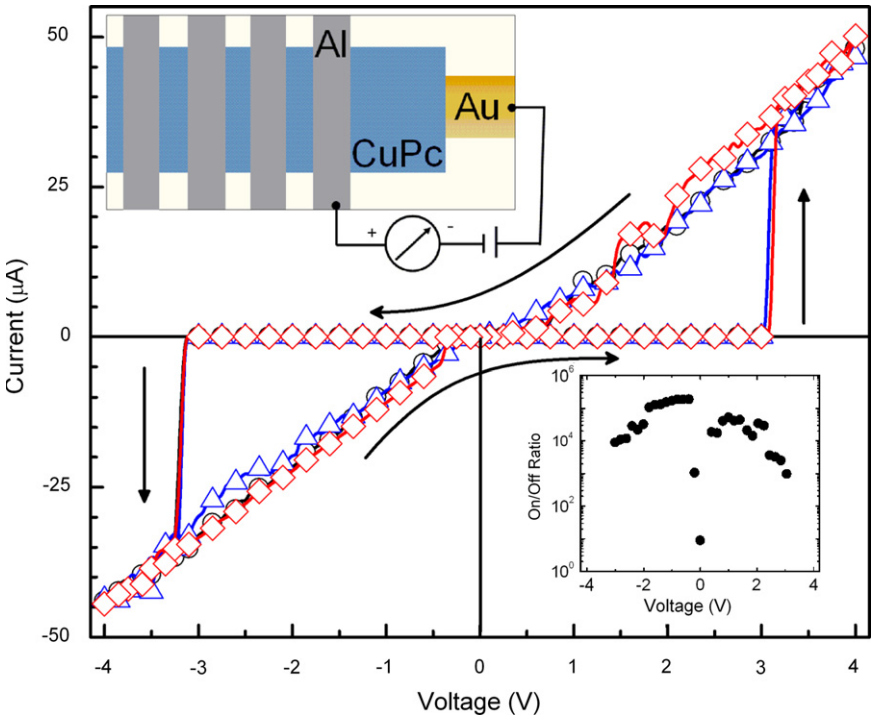


Fig. 1. Typical *I–V* characteristics of Au/CuPc/Al device for two voltage sweeps. Three consecutive loops are shown in the figure. Arrows show the direction of voltage sweep. Upper inset shows the schematic diagram of the device structure and the lower one shows the voltage dependence of On/Off ratio.

completely withdrawn (by applying 0 V), the device switches back to the original low-conducting state. Similar bistability is observed also in the reverse bias section of *I–V* characteristics. The magnitude of V_{Th} remains the same in both bias modes and does not depend on the work-function of hole-injecting electrode (CuPc is a predominantly hole conductor). This may infer that the threshold-switching is a voltage-driven process. Fig. 1 shows that the *I–V* characteristics are reversible in nature – that is, the threshold switching is reproducible over many cycles. The On/Off ratio, the ratio between the currents in the high- and low-conducting states, reached more than 10^5 (inset of Fig. 1). The ratio however depends on the voltage at which it is measured.

Conductance switching in organic materials depends on the type of molecule-electrode combination chosen. Molecules may be electroreduced to exhibit a high-conducting state [6,7]. As compared to the molecular conformation of the pristine low-conducting state, another energetically stable conformer may also have a higher scale of conductance [11,17]. Diffusion of metals during top electrode deposition may results in metal-filaments in sandwiched structures resulting in enhanced current flow through the filaments [18]. When metals with low reduction-potential are used, metals-filaments are formed through a redox-driven process [15]. When the high-conducting state arises due to the metal-filaments, the switching process cannot be termed as a molecular phenomenon, which is required to increase the density of memory bits for future applications. In the following, we will present results from lateral structures that will exclude some of the above-mentioned mechanisms in CuPc based devices.

3.2. Lateral structures

I–V characteristics of CuPc in lateral structures with similar metal electrodes are presented in Fig. 2a and b. A schematic representation of the structure is shown in the inset of Fig. 2a. The figures represent Au/CuPc/Au and Al/CuPc/Al cases, respectively on glass substrates. Both the cases exhibit threshold-switching over many cycles. The nature of *I–V* characteristics is similar to that observed in sandwiched structures. The threshold voltage of switching, V_{Th} does not depend on the

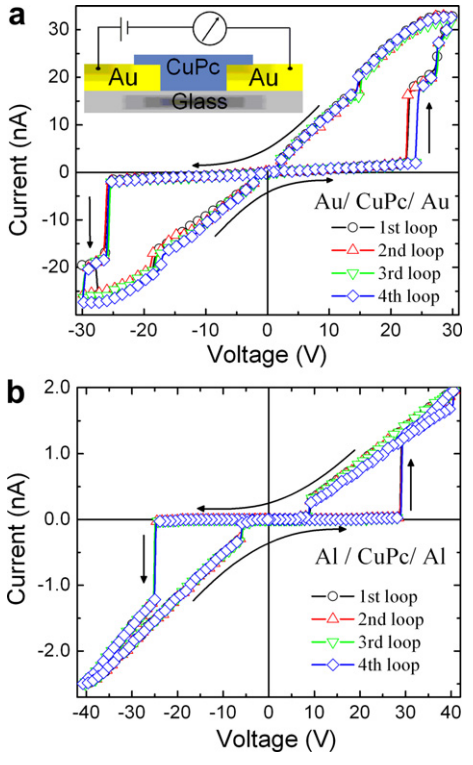


Fig. 2. *I–V* characteristics of (a) Au/CuPc/Au and (b) Al/CuPc/Al device in coplanar electrode configuration. Interelectrode separation was 150 μm. Four consecutive loops are shown in both the cases. Inset of (a) shows the schematic representation of the device.

work-function of the metals in lateral structures. It is however higher as compared to that in the sandwich-structure configuration. This is due to large inter-electrode separation in the lateral structure as compared to that in the sandwiched ones suggesting that the threshold-switching may be a voltage/field-driven process. We have used two different interelectrode separations. When the separation is lower, the V_{Th} also becomes lower. This indicates that the threshold-switching in CuPc may be a field-assisted process.

Since CuPc was vacuum evaporated on patterned lateral electrodes with an inter-electrode separation of 150 μm, a possibility of metal ion diffusion during device fabrication can be excluded. Also, the contribution of any oxide barrier on switching phenomenon can be overruled as the switching is observed in Au/CuPc/Au lateral electrode configuration. In Al/CuPc/Al case, where some oxide layer may form on the electrodes, the nature of threshold switching is very similar to that in the Au/CuPc/Au case. The overall current (at any voltage) in case of Al/CuPc/Al device is an order of magnitude lower as compared to that of the Au/CuPc/Au device. This can be due to the insulating oxide layer formed on Al electrodes. Since CuPc is a hole-conducting material, higher barrier height with the highest occupied molecular orbitals (HOMO) in Al-based devices (as compared to that with Au electrodes) may also yield lower current in the former structure. Under ambient condition, the device showed similar reproducible electrical behavior. However, the overall current becomes a little higher and the threshold voltage for switching a little lower as compared to the measurements performed in vacuum. (For a typical Au/CuPc/Au device, the switching voltages in vacuum and under ambient condition are 22 and 16 V, respectively; the corresponding currents being 23 and 33 nA, respectively.) Under ambient condition, oxygen may get adsorbed and partly fill the trap sites of CuPc resulting in an increase in conductivity.

The observation of electrical bistability with gold electrodes further excludes the possibility of metal filament formation upon diffusion of metal cations. Such a redox-driven filament formation generally occurs in devices based on metals with low oxidation potential (silver or copper, for example) [15]. To further confirm the absence of metal filaments in the active CuPc layer, we have measured *I–V* characteristics in the (non-contact) tunneling mode. Here we have used a platinum/iridium (Pt/Ir) tip of a STM so that in the voltage range of measurement, electrons tunnel from the STM tip to the organic layer and finally transport to the base electrode (Au). In such a tunneling mode, any possibility of redox-driven filament formation in the CuPc layer is inherently excluded due to the high reduction potential of Pt/Ir. Moreover, a non-contact mode of operation will hinder formation of metal filaments in the bulk of the CuPc film at such a low voltage regime. *I–V* characteristics of CuPc on Au electrode with Pt/Ir tip in a voltage loop are shown in Fig. 3. Here also, the film shows electrical bistability. During the initial scan from 0 to $+V_{Max}$, the device current was low (off-state). At a suitable forward bias (1.0 V), the film switched to a high-conducting state and current reaches the limit of the instrument. During the sweep towards 0 V, the device persisted in its high-conducting state. Current at a voltage during the sweep towards 0 V is an order higher than that during the initial sweep (towards $+V_{Max}$).

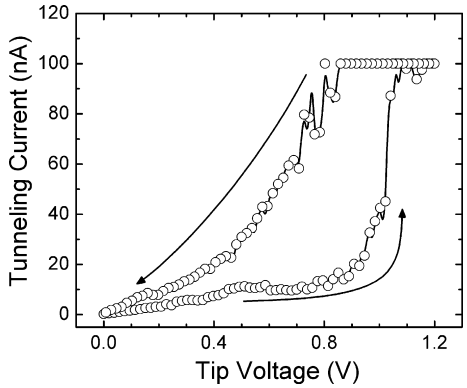


Fig. 3. *I–V* characteristics of a vacuum deposited CuPc film on Au substrates measured with a Pt/Ir tip of a STM. The directions of voltage sweep are shown in the figure.

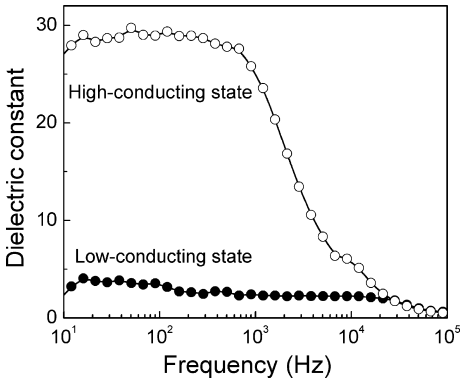


Fig. 4. Frequency response of dielectric constant of CuPc in their high- and low-conducting states in an Au/CuPc/Al sandwich structure configuration. Measurements were carried out at 0.5 V d.c. bias after the high- and low-states were induced by applying +3.5 V and 0 V, respectively.

The results presented in Figs. 2 and 3 hence confirm that the electrical bistability observed in CuPc based devices is due to some inherent property of the molecules. The switching is hence truly a molecular phenomenon. The threshold-switching can be explained in the following way: with application of a bias, charges are injected and trapped in the organic molecules. With increase in bias voltage, more and more traps are filled up. As the bias exceeds a threshold voltage, all the traps get filled, and the conductivity of the molecule switches to a high-value (on-state). With decrease in bias, the trapped charges remain confined within the molecular site retaining the high-conducting state of the molecules. Finally, when the device is shorted (by applying 0 V), molecules become detrapped leading to the low-conducting off-state. Similar trapping/detrapping processes occur also in the reverse bias direction.

3.3. Dielectric properties

To get further insight on the mechanism of electrical bistability, we have carried out impedance spectroscopy of devices based on CuPc. Devices in their low- and high-conducting states were probed by measuring complex impedance as a function of frequency at 0.5 V d.c. bias. Suitable biases induced the low- and the high-conducting states prior to probing by impedance spectroscopy. Relative dielectric constant of CuPc in an Au/CuPc/Al sandwich structure, calculated following the parallel combination of a resistor and a capacitor ($C_P - R_P$) model, is plotted in Fig. 4. The figure shows that there is a large increase in dielectric constant of the active material due to the transition from a low- to a high-conducting state. Such a large increase in dielectric constant reflects increased charge storage in the high-conducting state of the devices [19]. It should be possible if charge confinement occurred in the CuPc molecules as has been put forwarded from the *I–V* characteristics.

3.4. Memory phenomenon

Memory phenomenon in devices based on lateral structure of CuPc, namely Au/CuPc/Au one, has been tested for read-only memory (ROM) and random-access memory (RAM) applications. For a ROM application, a device was monitored under electrical stress. The current under 15 V probe voltage is plotted in Fig. 5a as a function of time for both the high- and low-states. Here, the device was switched to the two states by applying 35 (for 10 s) and 0 V, respectively. The states of the devices were "read" by measuring current under 15 V for three hours. While probing the high-state, the device was never shorted (by applying 0 V) before and during the measurement. The figure shows that the current under probe voltage for the high-conducting state is two orders in magnitude higher as compared to the current when the low-state is probed by the same voltage. While the response of the low-state remains very steady, the response for the high-conducting state shows some decay. The two states are clearly distinguishable even after 3 h of continuous probing. Such ROM applications were also observed in the sandwiched (ITO/CuPc/Al) and the Al-based lateral (Al/CuPc/Al) structures. The

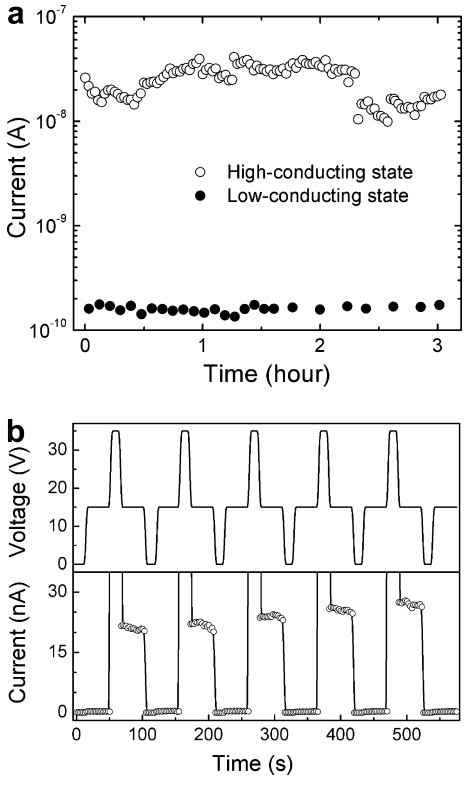


Fig. 5. (a) ROM and (b) RAM applications of a device based on Au/CuPc/Au lateral structure. The states were induced by +35 V and 0 V, respectively and probed by 15 V. Absolute values of current are plotted for comparison as a function of time. In (b), "write-read-erase-read" voltage sequence for the RAM application are shown in upper panel.

On/Off ratio, obtained from the time response of the two states, mostly matched that from the *I–V* characteristics.

Reversibility of memory phenomenon in these devices can best be studied under a "write-read-erase-read" (WRER) pulse sequence. In such a voltage-pulse sequence in cycles, the high- and low-conducting states are induced ("write" and "erase", respectively) repeatedly and the states are monitored or "read" in between. We have characterized the devices under such a voltage sequence for hours. A section of the voltage sequence and corresponding current for an Au/CuPc/Au lateral structure are shown in Fig. 5b. Here also, a +35 and a 0 V pulse (width = 10 s) were applied to "write" the high-state and "erase" to a low-conducting one, respectively. The states were probed or "read" by measuring device current under 15 V. Here also, during probing the high-state the device was never shorted by applying 0 V. The figure shows that the magnitude of device current under "read" voltage is much higher during probing the high-conducting state as compared to that for the low-one. The results hence show that the two states of the devices can be flip-flopped and probed for rewritable or RAM applications. Additionally, we have observed WRER performance in both the ITO/CuPc/Al and Au/CuPc/Al structures.

3.5. Tuning by "gate" voltage

The observation of memory phenomenon in lateral structures opens up a possibility of tuning the bistability through a new parameter, namely the "gate" voltage [20]. As in the case of FET structures, the active CuPc layer has now been deposited on an oxide-coated metal ("gate"). While measuring *I–V* characteristics between the lateral electrodes, bias has been applied to the gate. Fig. 6 shows source-to-drain current (I_{DS}) versus source-to-drain voltage (V_{DS}) characteristics of CuPc film deposited on SiO_2-coated *n*-Si substrate. Au, deposited on the SiO_2 coated *n*-Si substrate through an interdigitated mask, formed the two electrodes with an inter-electrode separation (channel length) of 11 μm. In Fig. 6, the I_{DS} versus V_{DS} characteristics without any bias at the *n*-Si gate show electrical bistability. The bistability is similar to that observed in laterals structures on glass substrate, which has been presented in Fig. 2a. The switching voltage is, however, expectedly lower in this case due to shorter channel length. When bias was scanned in multiple loops, the switching phenomenon in the $I_{DS} - V_{DS}$ characteristics showed a high degree of reproducibility (not shown in the figure for clarity). Fig. 6 further shows that with a bias at the gate electrode (V_G),

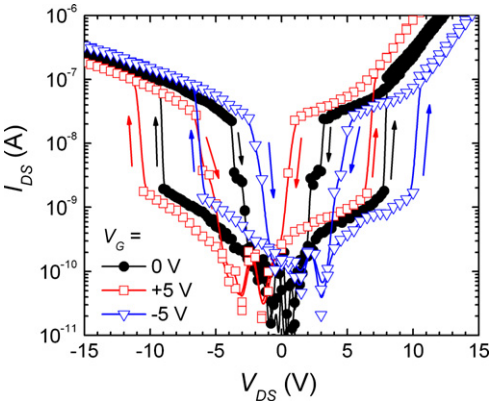


Fig. 6. *I–V* characteristics of an Au/CuPc/Au lateral structure deposited on SiO_2-coated *n*-Si substrate with different gate voltages. Arrows show the direction of voltage sweep.

the threshold voltage of switching changes. With gate bias, the $I_{DS} - V_{DS}$ characteristics, which were mostly symmetric at $V_G = 0$ V condition, becomes highly asymmetric with direction of bias between the top electrodes (V_{DS}). Both the threshold voltages respond to the V_G in the opposite sense. That is, at a positive V_G, the device switches at a lower V_{Th} in the positive and at a higher (magnitude of) V_{Th} in the negative bias directions. Fig. 6 shows that at $V_G = 5$ V condition, the device switches at −10.5 and +6.5 V. The threshold voltages with $V_G = -5$ V are, on the other hand, −5.9 and +9.9 V. It seems that a factor of gate voltage gets subtracted to the threshold voltages of switching in the devices. Such a correspondence could be due to formation of depletion/conductive region in the channel between the two gold electrodes. Here a negative V_G results a depletion region in the channel leading to an increase in resistance of the channel. In this case, higher bias is hence required to achieve conductance switching. With a positive V_G, a conductive channel forms enhancing carrier conduction and resulting in a decrease in V_{Th} of switching. In the negative V_{DS} region, a positive V_G depletes the channel yielding higher resistance and hence requiring higher (magnitude of) threshold voltage to produce conductance switching. The saturation current also depends on the V_G. While a conductive channel yields higher (magnitude of) saturation current, a depleted channel expectedly offers lower source-to-drain saturation current. The I_{DS}–V_{DS} characteristics above V_{Th} hence resemble that of typical FET structures.

4. Conclusions

In conclusion, we have shown electrical bistability and memory phenomenon in CuPc-based lateral structures. The observation of threshold-switching in such lateral structures with Au as the electrodes, migration of metal ions or metal filament formation due to redox reaction in the CuPc layer can be ruled out as possible mechanisms for electrical bistability in the present system. From the current–voltage characteristics and dielectric spectroscopy, we propose charge confinement in the organic materials as a possible mechanism for the observed threshold-switching in CuPc. With lateral structures on oxide coated doped-Si wafers (as gate oxide and gate electrode, respectively), we could tune threshold switching through the gate voltage. The new parameter (gate voltage) provided a novel route to optimize conductance switching to suit a need.

Acknowledgements

The authors acknowledge Dr. Henrik Sandberg of VTT Technical Research Centre of Finland for kindly providing the interdigitated mask. B.M. acknowledges financial support from CSIR (F. No. 2-56/2002(I) EU.II). The Department of Science and Technology, Government of India supported the work through Projects SP/S2/M-44/99 and SR/S2/RFCMP-02/2005.

References

[1] S. Moller, C. Perlov, W. Jackson, C. Taussig, S.R. Forrest, Nature 426 (2003) 166.
[2] D. Ma, M. Aguiar, J.A. Freire, I.A. Hümmelgen, Adv. Mater. 12 (2000) 1063.
[3] J.C. Scott, Science 304 (2004) 62.
[4] B. Mukherjee, A.J. Pal, Org. Electron. 7 (2006) 249.
[5] J. McGinness, P. Corry, P. Proctor, Science 183 (1974) 853.
[6] A.O. Solak, S. Ranganathan, T. Itoh, R.L. McCreery, Electrochem. Solid-State Lett. 5 (2002) E43.
[7] A. Bandhopadhyay, A.J. Pal, J. Phys. Chem. B 107 (2003) 2531.
[8] M. Kushida, H. Inomata, H. Miyata, K. Harada, K. Saito, K. Sugita, Jpn. J. Appl. Phys. 42 (2003) L622.
[9] L. Ma, S. Pyo, J. Ouyang, Q. Xu, Y. Yang, Appl. Phys. Lett. 82 (2003) 1419.
[10] C.P. Collier, G. Mattersteig, E.W. Wong, Y. Luo, K. Beverly, J. Sampaio, F.M. Raymo, J.F. Stoddart, J.R. Heath, Science 289 (2000) 1172.
[11] Z.J. Donhauser, B.A. Mantooth, K.F. Kelly, L.A. Bumm, J.D. Monnell, J.J. Stapleton, D.W. Price Jr., A.M. Rawlett, D.L. Allara, J.M. Tour, P.S. Weiss, Science 292 (2001) 2303.
[12] P.A. Lewis, C.E. Inman, Y. Yao, J.M. Tour, J.E. Hutchison, P.S. Weiss, J. Am. Chem. Soc 126 (2004) 12214.
[13] C.-H. Tu, Y.-S. Lai, D.-L. Kwong, Appl. Phys. Lett. 89 (2006) 062105.
[14] J. Ouyang, C.-W. Chu, D. Sieves, Y. Yang, Appl. Phys. Lett. 86 (2005) 123507.
[15] S. Ssenyange, H. Yan, R.L. McCreery, Langmuir 22 (2006) 10689.
[16] M. Cölle, M. Büchel, D.M. de Leeuw, Org. Electron. 7 (2006) 305.
[17] A. Bandyopadhyay, A.J. Pal, Appl. Phys. Lett. 84 (2004) 999.
[18] M. Lauters, B. McCarthy, D. Sarid, G.E. Jabbour, Appl. Phys. Lett. 87 (2005) 231105.
[19] A. Bandyopadhyay, A.J. Pal, J. Phys. Chem. B 109 (2005) 6084.
[20] R.C.G. Naber, C. Tanase, P.W.M. Blom, G.H. Gelinck, A.W. Marsman, F.J. Touwslager, S. Setayesh, D.M. de Leeuw, Nature Mater. 4 (2005) 243.

Available online at www.sciencedirect.com
ScienceDirect
Organic Electronics 8 (2007) 591–600
Organic Electronics
www.elsevier.com/locate/orgel

Interface states in polyfluorene-based metal–insulator–semiconductor devices

M. Yun [a], S. Gangopadhyay [a], M. Bai [b], H. Taub [b], M. Arif [b], S. Guha [b,*]

[a] Department of Electrical and Computer Engineering, University of Missouri, Columbia, MO 65211, United States
[b] Department of Physics and Astronomy, University of Missouri, Columbia, MO 65211, United States

Received 24 January 2007; received in revised form 16 April 2007; accepted 17 April 2007
Available online 29 April 2007

Abstract

Hybrid metal–insulator–semiconductor structures based on ethyl-hexyl substituted polyfluorene (PF2/6) as the active polymer semiconductor were fabricated on a highly doped p-Si substrate with Al_2O_3 as the insulating oxide layer. We present detailed frequency-dependent capacitance–voltage (C–V) and conductance–voltage characteristics of the semiconductor/insulator interface. PF2/6 undergoes a transition to an ordered crystalline phase upon thermal cycling from its nematic-liquid crystalline phase, confirmed by our atomic force microscope images. Thermal cycling of the PF2/6 films significantly improves the quality of the (PF2/6)/Al_2O_3 interface, which is identified as a reduced hysteresis in the C–V curve and a decreased interface state density (D_{it}) from $\sim 3.9 \times 10^{12}$ eV^{-1} cm^{-2} to $\sim 3.3 \times 10^{11}$ eV^{-1} cm^{-2} at the flat-band voltage. Interface states give rise to energy levels that are confined to the polymer/insulator interface. A conductance loss peak, observed due to the capture and emission of carriers by the interface states, fits very well with a single time constant model from which the D_{it} values are inferred.
© 2007 Elsevier B.V. All rights reserved.

PACS: 61.41.+e; 72.80.Le; 73.61.Ph; 84.37.+q

Keywords: MIS diode; Polyfluorene; Capacitance–voltage characteristics

1. Introduction

In recent years, the use of organic π-conjugated polymers (PCM) have become very attractive for building electronic devices such as active matrix displays, photovoltaic cells, and organic integrated circuits due to their low-cost solution processing [1]. Although there have been significant improvements in PCM-based optoelectronic devices, there are still many open issues that need to be fully addressed before commercialization of such devices can begin. A few of them include low carrier mobility and stability in PCMs compared with their inorganic counterparts and interface traps which can dramatically impact the electronic properties of PCM-based devices [2]. The development of a suitable device structure and self-organized high quality polymeric semiconductor thin films as well as the structure-property relationship of these polymers are critical issues for enhancing the performance of PCM-based

* Corresponding author. Tel.: +1 573 884 3687.
E-mail address: guhas@missouri.edu (S. Guha).

1566-1199/$ - see front matter © 2007 Elsevier B.V. All rights reserved.
doi:10.1016/j.orgel.2007.04.007

devices. Among conjugated polymers, polyfluorenes (PFs) are good candidates for light-emitting displays and field-effect transistors (FETs) due to their efficient blue emission, relatively high charge carrier mobility [3], and excellent chemical and thermal stability [4,5].

The quality of an interface between an insulator and a semiconducting polymer determines the performance of polymer FETs. In particular, trapped and interfacial charges have significant impact on the performance of organic light-emitting diodes (LEDs) and FETs resulting in voltage instability and delay time of electroluminescence at low operation voltages. Early organic electronic devices have utilized hybrid structures; inorganic materials such as a thermally grown SiO_2 gate insulator on a degenerately-doped silicon substrate were combined with a semiconducting polymer [6]. Many recent works focus on organic insulators to form a high quality interface with PCM [7] or to have a specific role such as a one carrier (hole or electron) device or an inversely doped (*n*-doped) semiconducting polymer. The importance of an interface for practical device operation and applications is demonstrated in a recent publication by Chua et al. [8]. They have shown that the utilization of a specific hydroxyl-free gate insulator produces *n*-channel FET conduction in several conjugated polymers. Thus, the role of the gate insulator has most commonly been regarded as the layer affecting semiconductor morphology.

Al_2O_3, which has a great potential as a high-dielectric constant (high-*k*) gate dielectric, has a variety of advantages in FETs due to its low leakage characteristics [9]. The oxide capacitance increases due to its higher dielectric constant resulting in a reduction of the threshold voltage and lower power dissipation. In addition, high-*k* dielectric materials can partially compensate for the relatively low carrier mobility of semiconducting polymers [10], and further enhance the switching speed of FETs [11].

In this paper, the effect of thermal cycling on a semiconducting polymer, poly[bis(2-ethyl)hexylfluorene] (PF2/6), is investigated using a metal–insulator–semiconductor (MIS) diode structure by means of capacitance and conductance measurements. By transforming the PF2/6 films to a semicrystalline phase, the interface properties of (PF2/6)/Al_2O_3 can be significantly improved compared to the as-grown polymer in MIS structures shown in a recent work by Yun et al. [12]. Detailed analysis of the data following the Nicollian and Goetzberger [13] methodology clearly demonstrates the role of interface traps and the influence of thermal annealing on device performance, which are vital requirements for the fabrication of PF2/6-based FETs. Although we do not infer the values of mobilities from this work, our current–voltage (*I–V*) measurements from PF2/6-based LED structures demonstrate that the perpendicular mobilities are enhanced by more than an order of magnitude in annealed films [14].

This paper is organized as follows: Section 2.1 describes the structure and morphology of the polymer, PF2/6, followed by the experimental details and methodologies in Section 2.2. In Section 3, we present our results and discussion of capacitance–voltage (*C–V*) and conductance–voltage (*G–V*) measurements; Section 3.1 describes the Schottky–Mott analysis from the *C–V* characteristics; and, in Section 3.2, we present a detailed analysis of the interface trap densities. In Section 4, we draw our conclusions.

2. Experiment

2.1. Structure and morphology

The MIS structures were fabricated using a derivative of the PF family, PF2/6, as the active semiconducting material. PFs are attractive due to their facile processing characteristics, allowing uniaxial chain orientation which result in linearly polarized emission [15]. Almost all PFs are characterized by side chains substituted at the bridging carbon that can cause a rich array of mesomorphic behavior with the appearance of the nematic-liquid crystalline (*n*-LC) phase. PF2/6, in particular, has an unusual structure-property relationship: despite the molecular-level disorder that is inherent due to two possible enantiomers and limited number of isomers, thermally annealed PF2/6 films exhibit an ordered hexagonal phase. The PF2/6 chains self-consistently average to a five-fold helix. These soft, hairy-rod brushlike polymers further self-organize into a three-chain unit cell [16], which yields a well ordered semicrystalline hexagonal phase with coherence lengths exceeding 50 nm [5].

The PF2/6 used in this work has $M_n = 88{,}000$ g/mol and $M_w = 130{,}000$ g/mol; its synthesis is reported elsewhere [17] and chemical structure is shown in Fig. 1(a). Depending on the forming conditions, PF2/6 may be glassy or semicrystalline at room temperature, with a nominal glass transition

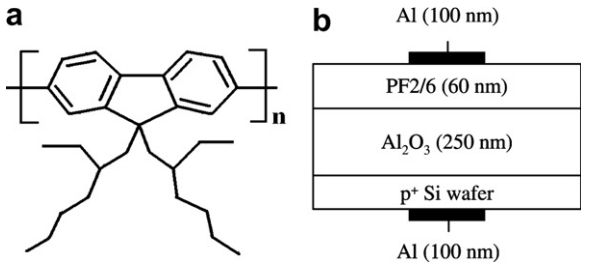


Fig. 1. (a) Chemical structure of poly[bis(2-ethyl)hexylfluorene] (PF2/6); (b) schematic diagram of the configuration of Al/p^+–Si/Al_2O_3/(PF2/6)/Al polymer MIS diode.

temperature (T_g) for the amorphous component at 80 °C and a crystalline to *n*-LC phase transition just above 160 °C. Work by Tanto et al. [5] shows that bulk PF2/6 (powder) has some resemblance to the hexagonal phase at the onset and at T_g there is a distinct structural evolution to the hexagonal phase. Upon cooling the polymer from its *n*-LC phase the X-ray diffraction pattern shows sharp Bragg peaks indicative of improved long-range order. To ascertain whether these features are observed in thin PF2/6 films cast from toluene (that are used in our MIS structures), we measured the atomic force microscopy (AFM) images from two films: one as-grown and the second thermally annealed (with the same conditions that we used in our MIS structures).

For the AFM studies, PF2/6 films were spin-coated on silicon wafers, which were cleaned using procedures described elsewhere [18]. The concentration of the PF2/6 solutions and the recipe for spincoating were the same as used in our MIS structures (described below). A detail of the annealing process is also described in Section 2.2. The AFM measurement was performed with a Nanoscope IIIa (Veeco Instruments, Inc.) operating in the tapping mode. Commercial ultra-sharp, rectangular silicon cantilevers made by Micromasch ($250 \times 35 \times 1.7\ \mu m^3$) were used having a nominal spring constant of ~0.35 N/m and a resonance frequency of ~33 kHz. We simultaneously recorded AFM topography and phase images. Fig. 2 shows the topography and phase images of the as-grown (a, b) and annealed sample (c, d). The annealed samples clearly show an increase in the particle size with an average particle footprint area of $\sim 10^4\ nm^2$. The rms roughness of the two samples for $1\ \mu m \times 1\ \mu m$ area increased from ~1.4 nm in the as-grown sample to ~2.9 nm in the annealed sample. Since annealing promotes crystallization to an ordered hexagonal phase and its coherence length is in excess of 50 nm [5], each grain in the image most probably reflects a single domain of PF2/6 with a loss of coherence about halfway across each domain due to disorder effects. We point out that since our processing temperature reached only 150 °C, the annealed film may not have fully crystallized.

2.2. Methodology

Polymer MIS diodes were fabricated with PF2/6 as the electronically active polymeric semiconductor layer and Al_2O_3 as an inorganic insulator layer grown on p^+-Si. Highly p-doped (100) silicon wafers employed as the bottom gate electrode, with resistivity of 0.001–0.005 Ω-cm, were etched via the modified Shiraki process [19] prior to the Al_2O_3 growth. This method chemically removed the native oxide and produces an atomically flat, hydrogen terminated surface that prevents the re-growth of oxide upon exposure to air. After drying under nitrogen, a Kurt J. Lesker AXXIS electron-beam system was utilized to first deposit the Al back-side contact (100 nm) on p^+-Si substrate. A 250 nm thick Al_2O_3 film was then grown, using Al_2O_3 pellets as source material, by e-beam evaporation onto the p^+-Si where the Si substrate was heated to 50 °C. Oxygen backfill was applied by flowing oxygen at 4 sccm and the working pressure was held at 5×10^{-5} Torr during the film deposition.

After wet-cleaning of p^+-Si/Al_2O_3 substrate in an ultrasonic bath with acetone and isopropyl alcohol, the PF2/6 films were prepared by spincoating onto the Al_2O_3 layer, at a speed of 2500 rpm, from a toluene solution (10 mg/ml) that was first filtered through a 0.45 μm filter. The thickness of the film was measured as ~60 nm. All thickness measurements were done ex situ with a J.A. Woollam variable angle spectroscopic ellipsometer. After spincoating, the PF2/6 films were baked at 50 °C for 20 min to remove any traces of the solvents used. The samples were then immediately loaded into a thermal evaporator for the top Al contact which was evaporated through a shadow mask. The three processes: spincoating, baking, and evaporation were performed in a nitrogen filled glove box system (from M. Braun Inc.) with oxygen and water levels below 1 ppm. The cross-sectional device configuration fabricated was Al/p^+–Si/Al_2O_3/(PF2/6)/Al as shown in Fig. 1b, and the device area was determined by scanning electron microscopy to be $4.9 \times 10^{-4}\ cm^2$.

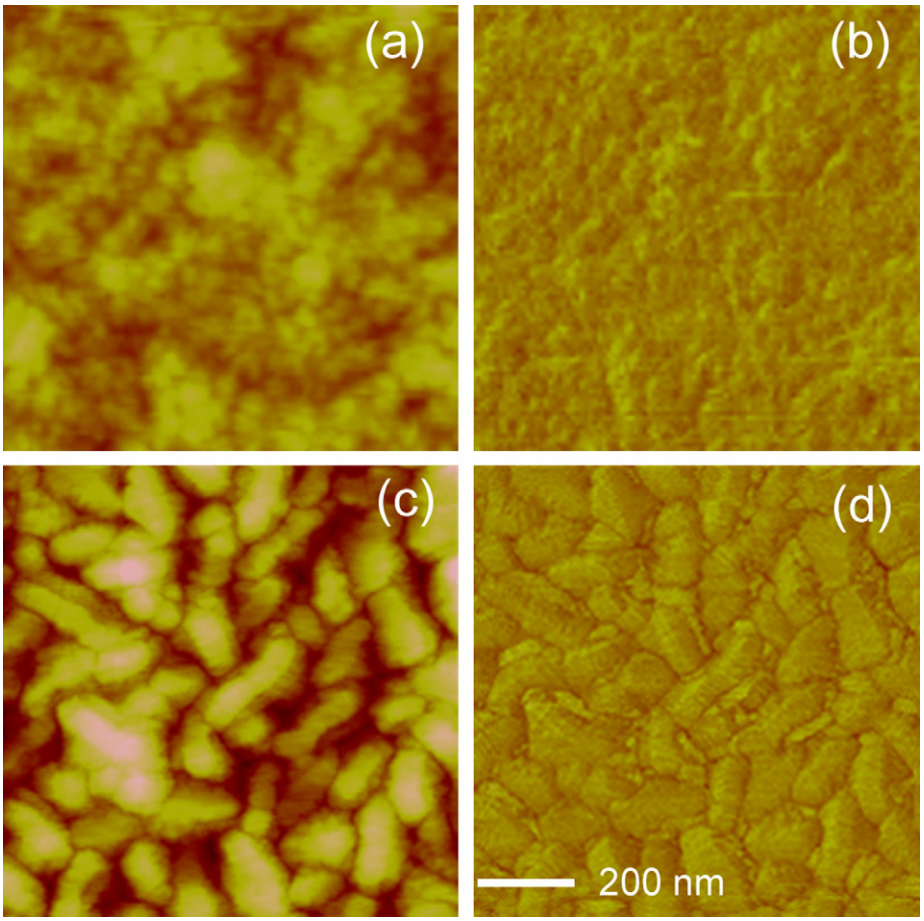


Fig. 2. AFM topography and phase images of PF2/6 deposited on Si wafers before and after annealing. (a) Topography image of the as-deposited sample; (b) phase image of the as-deposited sample; (c) topography image of the annealed sample, and (d) phase image of the annealed sample.

Thermal cycling of PF2/6 films was done prior to the evaporation of the top Al contact. After spin-coating the PF2/6 layer on top of Al/p^+–Si/Al_2O_3, the samples were transferred to a high vacuum (10^{-7} Torr) annealing chamber to prevent the possible doping of the silicon substrate due to the long duration of the thermal treatment. Since PF2/6 shows a very slow crystallization process, the samples were first raised slowly to 80 °C (close to T_g) and held for 10–15 h. This was followed by raising the temperature close to the *n*-LC phase temperature of the polymer (150 °C) at 2 °C/min. The samples were then cooled back to room temperature at 1 °C/min, after which the top contacts were evaporated for the MIS structures. We further checked the *C–V* characteristics of a control sample (p-Si/Al_2O_3/Al) that was annealed under the same conditions to ensure that the changes observed in our PF2/6-based MIS structures are not due to the changes between the silicon and Al_2O_3 interface.

Electrical measurements of the polymer MIS diodes were carried out at room temperature in air using a probe station. *C–V* and *G–V* dependence of the devices were achieved over a frequency range from 1 kHz to 1 MHz using a precision HP 4284 LCR meter which is controlled by a computer program written in LabView®. For the *C–V* measurements the devices were biased from −15 V to 40 V by varying the sweep rates from 55 mV/s to 11 V/s. Since the wide-gap semiconducting polymer shows a deep depletion capacitance, by decreasing the sweeping time a deep depletion capacitance in the *C–V* curve may be obtained (not shown here). We allowed optimal holding times to achieve thermal equilibrium since the polymer MIS cannot adequately recover from deep depletion for short

holding times. This was followed by reverse biasing for hysteresis measurements. The C–V and G–V profiles were corrected for the possible presence of series resistance (R_S) [20]. Corrected capacitance (C_c) and corrected equivalent parallel conductance (G_c) at a particular frequency are given by

$$C_c = \frac{(G_m^2 + \omega^2 C_m^2) C_m}{a^2 + \omega^2 C_m^2} \quad \text{and} \tag{1}$$

$$G_c = \frac{(G_m^2 + \omega^2 C_m^2) a}{a^2 + \omega^2 C_m^2}, \tag{2}$$

where C_m and G_m are the measured capacitance and the equivalent parallel conductance across the two terminals of the MIS diodes, respectively, ω is the ac signal frequency, and $a = G_m - (G_m^2 + \omega^2 C_m^2) R_S$. For the best high frequency fit, R_S was found to be 191 Ω for an as-grown sample and 130 Ω for an annealed sample, respectively.

3. Results and discussion

3.1. Schottky–Mott analysis

The capacitance of a polymer MIS can be changed by accumulating, depleting, and inverting charges in the semiconductor at the interface with the insulator. A negative potential causes holes to be accumulated at the insulator/semiconductor interface forming a thin layer which behaves like a parallel plate capacitor. When the semiconductor layer is depleted, the capacitance falls owing to the formation of a depletion region at the insulator/semiconductor interface. When the gate bias is increased sufficiently to invert the surface, an inversion layer is created and the value of the capacitance strongly depends on the applied frequency. This last inversion layer is typically not observed in polymer semiconductors, which is also confirmed by theory [21]; the very long relaxation time of the minority carriers precludes the presence of the polymer inversion at practical time scales.

Fig. 3 exhibits a typical C–V characteristic curve with hysteresis at 1 MHz for both as-grown and annealed samples. Although these plots are shown for one frequency, similar measurements were performed for a range of frequencies; the magnitude of the hysteresis for both samples was independent of the applied frequency at room temperature but dependent on the sweeping rate as discussed later in this Section. For consistency, we checked that the results presented here represent typical data

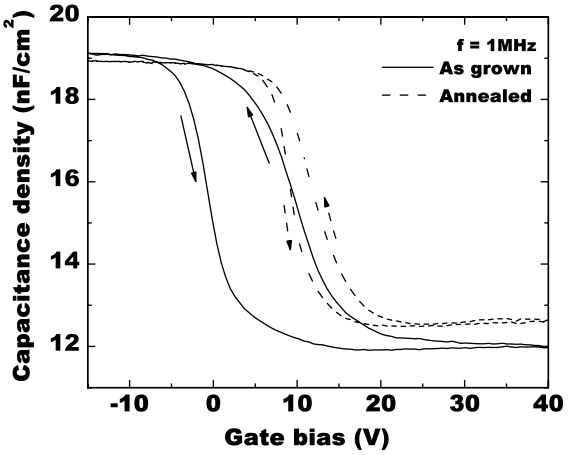


Fig. 3. Hysteresis curves of both the as-grown sample (solid line) and annealed sample (dashed line) at constant frequency of 1 MHz with sweeping rate of 55 mV/s. The arrows indicate the sweep direction of the gate bias voltage.

measured from more than five MIS diodes. The shape of the C–V curves for both samples reveals typical p-type behavior of the PF2/6 MIS diode. This is inferred from a higher capacitance in the accumulation region at negative bias (with the maximum capacitance being given by the insulator capacitance) and a lower capacitance value in the depletion region at positive bias (with minimum capacitance produced by the series sum of insulator capacitance and the capacitance associated with the maximum depletion layer). We observe full deep deletion capacitance in both samples when sweeping times are very short.

The inversion-charge generation time in polymer MIS is much slower compared to the applied high frequency in our C–V measurements. This implies that the polymer MIS does not have enough time to generate minority carriers to form an inversion layer and as a result the depletion region reaches a maximum depth where the high frequency capacitance still relies on the majority carrier position and distribution.

Typically, the bias sweep from negative to positive voltage and in the reverse direction display the same amount of hysteresis (Δ). Brown et al. [22] have attributed such a hysteresis in P3HT-based MIS structures to slow carrier trapping (relaxation) or to the migration of low-mobility dopant ions towards the accumulation layer. Recently, Lindner et al. have shown by detailed numerical simulations that the origin of the hysteresis in organic devices is a combination of mobile species and trap recharging [23]. Thus, in our case, the hysteresis and related

phenomena originate from charge trapping at or near the interface between the polymeric semiconductor and the gate insulator as well as from ambient oxygen and moisture. The counterclockwise nature of hysteresis is usually attributed to a positive carrier injection into the semiconducting PF2/6 layer with subsequent charge trapping [24]. The nature of the observed hysteresis is the same for the as-grown and annealed samples, albeit greatly reduced in the latter.

In comparing the as-grown with the annealed PF2/6-based MIS structures, there are two important features to be noted in the C–V characteristics. First, the shape of C–V curves is similar in both samples although the accumulation and depletion capacitance values are changed after thermal annealing: a slight decrease in the accumulation capacitance and a slight enhancement of the depletion capacitance is seen for the annealed sample. Most probably this arises from the Si/Al_2O_3 interface; a similar change is seen in our control sample. Second, at 1 MHz, annealing the polymer films substantially reduces the hysteresis from 9 V (as seen for the as-grown sample) to 3 V. We measured the thickness and the dielectric constant of PF2/6 films cast on bare Si and PF2/6 films sandwiched between Al/(PF2/6)/Al metal–insulator–metal (MIM) structures for both as-grown and annealed films. No changes in the thickness and the dielectric constant ($k = 2.6 \pm 0.1$) are seen. This suggests that the crystalline domains in the PF2/6 layer (after annealing) fill up the open trap charge centers, decreasing charge migration in the film and resulting in a reduction of the hysteresis.

By using the relationship, $N_t = C_{ox}\Delta/q$, where N_t is the trapped charge, C_{ox} is the accumulation capacitance density of the insulator, Δ is the hysteresis, and q the elementary charge, we find that N_t decreases from 1.1×10^{12} cm^{-2} in the as-grown sample to 3.5×10^{11} cm^{-2} in the annealed sample. These values maybe overestimated due to the unexpected mobile ions. To ensure that the above results originate from annealing (crystallization) of the PF2/6 film and not from the insulator, we checked the hysteresis from two control samples (p-Si/Al_2O_3/Al), one as-grown and the other annealed under the same conditions as our polymer MIS structures. There are virtually no changes in the hysteresis of the C–V curves in the two samples. [Δ is 0.4 V in as-grown and 0.35 V in annealed]. This is not surprising since 150 °C is a relatively low temperature for modification of the structural properties of Al_2O_3. Hence, we conclude that the decrease in N_t in the annealed sample is an effect of the crystallization of the PF2/6 layer.

Typical frequency dependence of the C–V curves for both the samples measured at selected frequencies is shown in Fig. 4 in the forward (−15 V to 40 V) direction with a slow sweeping rate (55 mV/s). A fast sweeping rate of C–V measurements show a deep depletion capacitance (not shown here) due to the long relaxation time of carriers in the polymer. The C–V curves of the annealed sample are characterized by relatively steeper transition region from a maximum capacitance to a minimum capacitance compared to the as-grown sample. The positively shifted flat-band voltage (V_{FB}) with annealing indicates the creation of negative charges in the oxide layer. These charges consist of trapped charges in the Al_2O_3 layer that most probably diffuse from the PF2/6 film on the application of a high gate voltage. The negligible variation of flat-band voltage shift with annealing in our control samples indicates that these charges are not from bulk Si or Si/Al_2O_3 interface. Since a large flat-band voltage shift is the origin of a large threshold voltage in FET structures, we will attempt to reduce the flat-band voltage shift upon annealing of the polymer in the future, using a surface treatment of the Al_2O_3 or H_2 annealing.

The frequency dispersion (FD) in the accumulation region is greater for the as-grown sample compared to the annealed one. The origin of the FD in this region is most probably due to a different response of trapped and mobile charges between

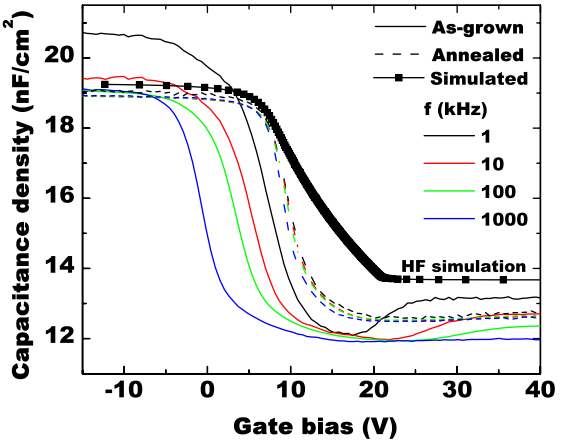


Fig. 4. Frequency dependence of the capacitance–voltage characteristics of the as-grown sample (solid line) and annealed sample (dashed line). Frequencies shown are 1, 10, 100 kHz and 1 MHz right to left, respectively. The high frequency simulated curve is denoted by black squares.

the interface region and bulk, which can be directly related to the long lifetimes and low carrier generation rates for carriers in disordered organic semiconductors [25]. Detailed reasons for FD in the accumulation region of as-grown samples were discussed by Yun et al. [12]. The transition region in the as-grown sample also shows a large FD, which arises from a large number of interface traps in this sample compared to the annealed film. This is discussed in more detail in the next section. We point out that in our previous work the C–V measurements were done using a fast sweep and the FD in the deep depletion region was negligible [12].

Slower sweep rates result in induced traps [21] in the insulator or insulator/semiconductor interface of the as-grown sample, which result in larger hysteresis (not shown here). This sample shows an increasing depletion capacitance below 100 kHz (Fig. 4). These enhanced values result from a combination of the capacitance associated with induced traps and single time constant traps (discussed in Section 3.2) that reside at the polymer–insulator interface.

The annealed sample, on the other hand, does not show any increased capacitance in the depletion region due to fewer traps in the insulator and at the insulator/semiconductor interface. To obtain further insight into the nature of the capacitance (whether it is full depletion or inversion), we simulated a high frequency C–V curve as shown by the black squares in Fig. 4. The simulations were carried out at infinite frequency assuming that the oxide thickness is much greater than the maximum depletion width. With the intrinsic carrier concentration n_i calculated from the effective density of states: $N_C = 10^{19}\,\mathrm{cm}^{-3}$, $N_V = 4\times10^{21}\,\mathrm{cm}^{-3}$ [14] energy gap $E_G = 2.8$ eV, doping density $= 8.8\times10^{17}\,\mathrm{cm}^{-3}$ at 1 kHz, and $V_{FB} = 6$ V from the experimental C–V curve, we simulated the high frequency C–V curve using exact-charge analysis [26]. Since the minimum capacitance of the annealed sample in our experimental data is lower than the simulated one, PF2/6 MIS diodes do not reach the inversion region and shows a depletion capacitance.

Overall, compared to the as-grown sample, the annealed sample shows a reduced hysteresis, very small FD in the depletion region, and a reduced stretching of the C–V curve about the voltage axis (Figs. 3 and 4). These characteristics can be attributed to a reduced interface trap density indicating a better interface quality between Al_2O_3 and PF2/6 as discussed in Section 3.2.

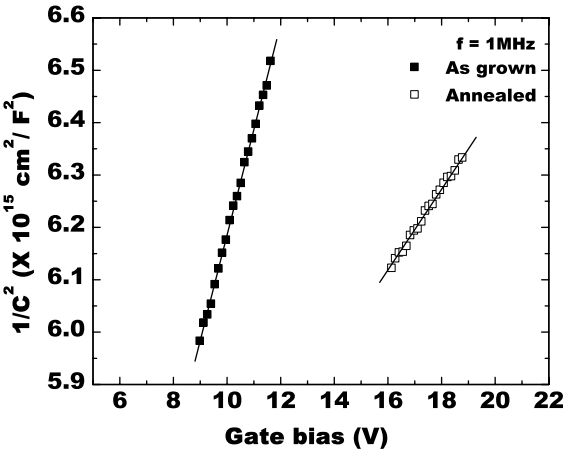


Fig. 5. $1/C^2$ versus gate bias voltage curves of as-grown and annealed samples at test frequency of 1 MHz, derived from the depletion region C–V curves in Fig. 3.

A closer inspection of the C–V curves suggests charge carrier localization in the bulk of the polymer. As a first step, we extract the unintentional doping density from a plot of $1/C^2$ versus V as shown in Fig. 5. We use the depletion region at 1 MHz sample frequency for the plots. The slopes correspond to the localized doping concentration. This is derived from the standard Schottky–Mott analysis [24] where the doping concentration in a p-type semiconductor can be extracted in the depletion region via

$$\frac{\partial\left(\frac{1}{C^2}\right)}{\partial V} = \frac{2}{q\varepsilon_0\varepsilon_{\mathrm{semi}}N_A}; \tag{3}$$

C is the capacitance density in the depletion region, V is the gate bias, ε_0 is the dielectric constant of vacuum, $\varepsilon_{\mathrm{semi}}$ is the relative dielectric constant of PF2/6, and N_A is the concentration of localized charges which react slowly to the testing frequency [27]. The slopes of $1/C^2$ versus V are slightly different for the as-grown and the annealed sample. Using the dielectric constant of PF2/6 as 2.6, and the slopes from Fig. 5 in Eq. (3), N_A for the as-grown and the annealed samples are $4.3\times10^{17}\,\mathrm{cm}^{-3}$ and $9.1\times10^{17}\,\mathrm{cm}^{-3}$ at 1 MHz, respectively. N_A as a function of the frequency is plotted for both samples in Fig. 6.

The p-type nature of PF2/6 arises most probably from structural and oxygen-induced defects that can stabilize mobile radical cations [28]. The slight enhancement of N_A maybe related to the morphological changes in the polymer film upon annealing; thermal cycling of PF2/6 results in a closed-pack

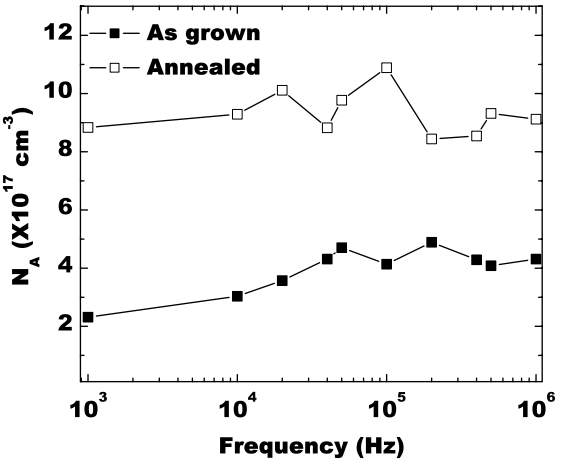


Fig. 6. Extracted doping density (N_A) plotted as a function of measured frequency in the as-grown sample and the annealed one.

formation of the polymer chains where the side chains are nested pairwise. However, the exact mechanism is still not understood since the thicknesses of the films remain almost the same before and after annealing. Annealing also results in an enhancement of the charge carrier mobility perpendicular to the insulator as in the recent work by Grecu et al. [29]. This has been independently verified by determining the hole mobilities from PF2/6-based LED structures using I–V characteristics under space charge limited conduction; the carrier mobilities are enhanced by more than an order of magnitude [14].

3.2. Interface states

An MIS diode can be described by a series capacitance of the insulator and depletion layer of the semiconductor as schematically shown in Fig. 7. The appropriate equivalent circuit is modeled as the connection in series of the insulator (R_{ins}, C_{ins}), semiconductor (R_s, C_s) and small contact resistance associated with the electrodes (R_l). This is the simplest model; for a full description of the dielectric response of MIS structures models taking into account the time constant dispersion in bulk polymer should be considered [25,30]. Since this work compares the semiconductor/insulator interfacial properties of two samples, we use the simple circuit model shown in Fig. 7, assuming that the correction terms are the same for both samples.

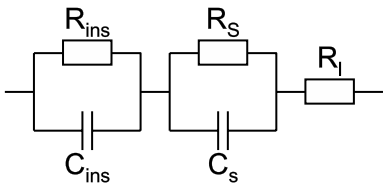


Fig. 7. Equivalent circuit model of resistors and capacitors for contacts, semiconductor and insulator.

Fig. 8a and b shows the measured loss of conductance per angular frequency (G_m/ω) as a function of the gate bias for five selected frequencies. Distinct conductance peaks are observed for both samples because of the ac loss due to the capture and emission of carriers by the interface traps. The peak of the G_m/ω versus V curve shifts negatively with increasing frequency, which is consistent with the shift of the flat-band voltage of the corresponding C–V curves. The height of the loss peak denotes the number of interface traps at a given frequency [31]. Since the loss peak height of the annealed sam-

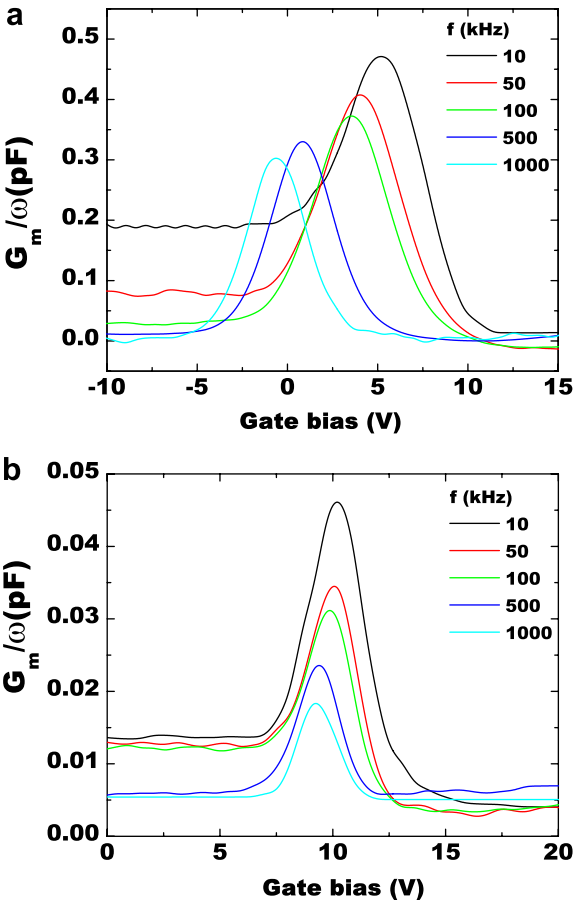


Fig. 8. Frequency dependence of the measured conductance loss (G_m/ω) as a function of gate bias voltage for (a) as-grown and (b) annealed samples.

ple (Fig. 8b) is substantially reduced compared to the as-grown sample, it suggests a reduction in the interface traps. Also, the stretch of G_m/ω versus V profiles for the as-grown sample reflects the stretching of C–V curves, seen in Fig. 4. The rise in conductance in the accumulation region for the as-grown sample is due to the presence of high series resistance effects.

Although there is considerable on-going work with fabrication and characterization of polymer MIS diodes [10,27,29], there is almost no published work on the analysis of polymeric semiconductor/insulator interface trap states. To investigate the effect of annealing on the interface, we focused on the interface trap charges (also known as interface states). Among several techniques available for estimating the interface trap density (D_{it}), the conductance technique involving point-by-point determination of interface trap density throughout the depletion region gives reliable D_{it} values. We have utilized the method proposed by Nicollian and Goetzberger [13,20] to calculate the equivalent parallel conductance (G_p). The measured capacitance and conductance are used to extract G_p in the depletion region as given by

$$\frac{G_p}{\omega} = \frac{\omega C_{ox}^2 G_m}{G_m^2 + \omega^2 (C_{ox} - C_m)^2}. \quad (4)$$

To calculate D_{it} using G_p, two models were employed: (a) the single time constant (STC) model, where G_p/ω is given by

$$\frac{G_p}{\omega} = \frac{qD_{it}\omega\tau}{(1+\omega^2\tau^2)}, \quad (5)$$

where τ is the time constant of the interface state; and (b) the continuum of states model, where

$$\frac{G_p}{\omega} = \frac{qD_{it}}{2\omega\tau}\ln(1+\omega^2\tau^2). \quad (6)$$

The maximum value of G_p/ω occurs at $\omega\tau = 1$ using Eq. (5) and $\omega\tau = 1.98$ for Eq. (6). At each fixed bias, the maximum value of G_p/ω is plotted against frequency, and the peak maximum and the corresponding frequency are recorded. These values are then substituted into Eqs. (5) and (6) to evaluate D_{it} and to generate the theoretical G_p/ω versus frequency plots. Fig. 9 represents G_p/ω versus frequency for the as-grown and annealed MIS structures at biases of -1 V and 8 V flat band voltages, respectively. The continuous lines (bold and dotted) denote the theoretical curves generated using Eqs. (5) and (6). The filled circles represent the experimental data. The equivalent parallel capacitance versus frequency agrees well with the STC model (indicated by solid lines) over the entire range of gate biases for both samples.

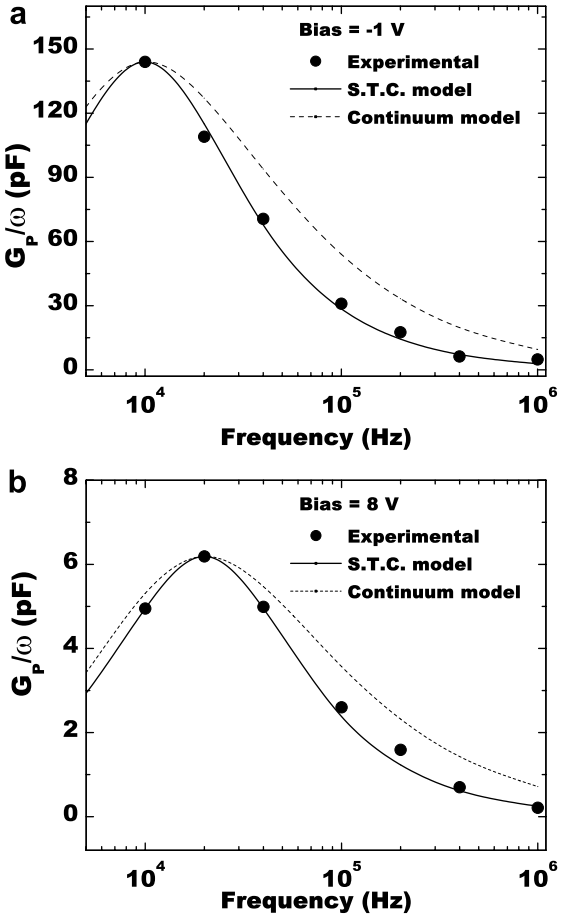


Fig. 9. Equivalent parallel conductance (G_p/ω) versus frequency at a fixed bias of -1 V for (a) the as-grown sample, and at 8 V for the (b) annealed sample. Both curves match the single-time constant model.

The calculated D_{it} values versus gate bias are plotted for the as-grown and annealed sample in Fig. 10. Thermal annealing improves the quality of interface between (PF2/6)/Al_2O_3 layer as identified by a reduction of the interface trap density from $\sim 3.9 \times 10^{12}\ eV^{-1}\ cm^{-2}$ to $\sim 3.3 \times 10^{11}\ eV^{-1}\ cm^{-2}$ at the flat-band voltage. The lower value of D_{it} for the annealed sample is in agreement with the small frequency dispersion shown in Fig. 4. Thus, thermal cycling of PF2/6 from its n-LC phase to room temperature results in large crystalline domains reducing the interface trap densities at the (PF2/6)/Al_2O_3 interface.

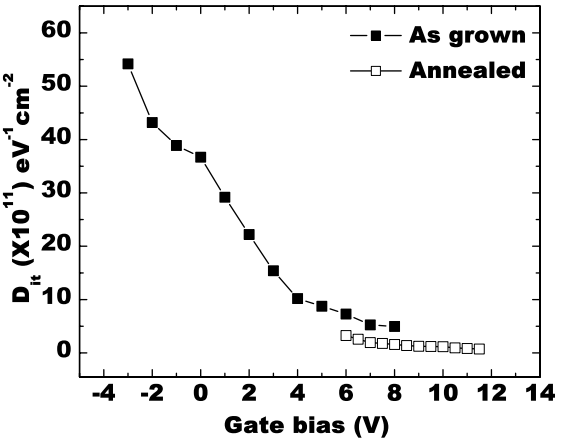


Fig. 10. Plot of the interface state density (D_{it}) as a function of the gate bias voltage as determined by the conductance method for as-grown and annealed samples.

4. Conclusions

In conclusion, we have shown the influence of thermal cycling of PF2/6-based MIS diode on the interface properties using *C–V* and *G–V* measurements. Thermal cycling of PF2/6 films on Si substrates results in particles with an average footprint area of $\sim 10^4$ nm^2, as evident from the AFM images. This results in a reduction of the open charge centers and a decrease of charge migration into the polymer layer in MIS structures, thus reducing the magnitude of hysteresis in the *C–V* curves. In addition, annealing reduces the interface trap density at the (PF2/6)/Al_2O_3 interface and frequency dispersion in depletion region of the *C–V* curve. Further, enhanced charge carrier density in the annealed film is attributed to the morphological changes in the PF2/6 film as it goes through crystallization. The high quality interface of Al_2O_3/annealed (PF2/6) enables its application in high performance FETs and other organic devices.

Acknowledgements

The authors gratefully acknowledge the support of this work through the National Science Foundation (NSF) under Grant No. ECS-0523656. The thin film deposition system used for device fabrication was purchased from an instrumentation award from the NSF (DMR-0413601). One of us (HT) acknowledges the NSF (DMR-0411748) for partial support of this work. We thank Ulli Scherf and Frank Galbrect for donation of the PF2/6 sample.

References

[1] H. Sirringhaus, T. Kawase, R.H. Friend, T. Shimoda, M. Inbasekaran, W. Wu, E.P. Woo, Science 290 (2000) 15.
[2] W. Riess, H. Riel, T. Beierlein, W. Brütting, P. Müller, P.F. Seidler, IBM J. Res. Dev. 45 (2001) 77.
[3] H. Sirringhaus, R.J. Wilson, R.H. Friend, M. Inbasekaran, W. Wu, E.P. Woo, M. Grell, D.D.C. Bradley, Appl. Phys. Lett. 77 (2000) 406.
[4] M.T. Bernius, M. Inbasekaran, J. O'Brien, W. Wu, Adv. Mater. 12 (2000) 1737.
[5] B. Tanto, S. Guha, C.M. Martin, U. Scherf, M.J. Winokur, Macromolecules 37 (2004) 9438.
[6] J.M. Shaw, P.F. Seidler, IBM J. Res. Dev. 45 (2001) 3.
[7] J. Veres, S. Ogier, G. Lloyd, D. de Leeuw, Chem. Mater. 16 (2004) 4545.
[8] L.-L. Chua, J. Zaumseil, J.-F. Chang, E.C.-W. Ou, P.K.-H. Ho, H. Sirringhaus, R.H. Friend, Nature 434 (2005) 194.
[9] E.P. Gusev, M. Copel, E. Cartier, I.J.R. Baumvol, C. Krug, M.A. Gribelyuk, Appl. Phys. Lett. 76 (2000) 176.
[10] G. Wang, D. Moses, A.J. Heeger, H.-M. Zhang, M. Narasimhan, R.E. Demaray, J. Appl. Phys. 95 (2004) 316.
[11] M. Raja, N. Sedghi, S.J. Higgins, W. Eccleston, Mater. Res. Soc. Proc. 734 (2003) B9.1..
[12] M. Yun, R. Ravindran, M. Hossain, S. Gangopadhyay, U. Scherf, T. Bünnagel, F. Galbrecht, M. Arif, S. Guha, Appl. Phys. Lett. 89 (2006) 013506.
[13] E.H. Nicollian, A. Goetzberger, Bell Syst. Tech. J. 46 (1967) 1055.
[14] M. Arif, M. Yun, S. Gangopadhyay, K. Ghosh, L. Fadiga, F. Galbrecht, U. Scherf, S. Guha, Phys. Rev. B 75 (2007) 195202.
[15] M. Grell, D.D.C. Bradley, Adv. Mater. 11 (1999) 895.
[16] M. Knaapila, K. Kisko, B.P. Lyons, R. Stepanyan, J.P. Foreman, O.H. Seeck, U. Vainio, L.-O. Pålsson, R. Serimaa, M. Torkkeli, A.P. Monkman, J. Phys. Chem. B 108 (2004) 10711.
[17] U. Scherf, E.J.W. List, Adv. Mater. 14 (2002) 477.
[18] S. Trogisch, M.J. Simpson, H. Taub, U.G. Volkmann, M. Pino, F.Y. Hansen, J. Chem. Phys. 123 (2005) 154703.
[19] A. Ishizaka, Y. Shiraki, J. Electrochem. Soc. 133 (1986) 666.
[20] E.H. Nicollian, J.R. Brews, MOS Physics and Technology, Wiley, New York, 1982.
[21] S. Scheinert, G. Paasch, S. Pohlmann, H.-H. Hörhold, R. Stockmann, Solid-State Electron. 44 (2000) 845.
[22] J. Brown, H. Sirringhaus, M. Harrison, M. Shkunov, R.H. Friend, Phys. Rev. B 63 (2001) 125204.
[23] Th. Linder, G. Paasch, S. Scheinert, J. Appl. Phys. 98 (2005) 114505.
[24] S.M. Sze, Physics of Semiconductor Devices, second ed., Wiley Interscience, New York, 1981.
[25] I. Torres, D.M. Taylor, J. Appl. Phys. 98 (2005) 073710.
[26] R.F. Pierret, Semiconductor Device Fundamentals, first ed., Addison-Wesley, Boston, 1996.
[27] N. Zhao, O. Marinov, G.A. Botton, M.J. Deen, B.S. Ong, Y. Wu, P. Liu, IEEE Trans. Electron Dev. 52 (2005) 2150.
[28] A. Cravino, N.S. Sariciftci, Nat. Mater. 2 (2003) 360.
[29] S. Grecu, M. Roggenbuck, A. Opitz, W. Brütting, Org. Electron. 7 (2006) 314.
[30] I. Torres, D.M. Taylor, E. Itoh, Appl. Phys. Lett. 85 (2004) 314.
[31] D.-G. Park, H.-J. Cho, K.-Y. Lim, C. Lim, I.-S. Yeo, J.-S. Roh, J.W. Park, J. Appl. Phys. 89 (2001) 6275.

Available online at www.sciencedirect.com
ScienceDirect
Organic Electronics 8 (2007) 601–605
Organic Electronics
www.elsevier.com/locate/orgel

Exciton diffusion length of tris (dibenzoylmethane) mono (phenanthroline) europium (III) measured by photocurrent and absorption as a function of wavelength

M.R. Black *, C. Chavez, E. Brosha

Los Alamos National Laboratory, International, Space, and Response Division, P.O. Box 1663, Los Alamos, NM 87545, United States

Received 9 January 2006; received in revised form 23 April 2007; accepted 24 April 2007
Available online 10 May 2007

Abstract

Ideally, the exciton diffusion length in an organic photovoltaic is comparable to the optical penetration depth, i.e., the inverse of the absorption coefficient. In most organic materials, the exciton diffusion length is up to several orders of magnitude smaller than the absorption penetration depth – resulting in lower energy conversion efficiencies. In metal-organic materials, the exciton lifetime has been predicted to be large due to strong spin orbit coupling. This increased lifetime may lead to increased exciton diffusion. One particular metal-organic material, tris (dibenzoylmethane) mono (phenanthroline) europium (III) or Eu-DM, is especially interesting for photovoltaic applications as it is soluble in toluene and therefore can be spun-on and processed inexpensively. Using photocurrent and optical absorption as a function of wavelength, the exciton diffusion length of spun-on Eu-DM was measured to be 250 ± 8 Å, for optical excitation wavelengths in the range $350\ \text{nm} < L < 450\ \text{nm}$. A long tail in the photocurrent and absorption spectra indicate a weakly allowed transition in this energy range. Possible implications of this tail are discussed.
© 2007 Published by Elsevier B.V.

PACS: 72.40.+W; 73.20.Mf; 73.50.Pz; 78.20.Jq; 78.30.Jw; 78.66.Qn

Keywords: Exciton; Photovoltaics; Metal-organic; Diffusion length; Solar cell; Organo-metallic

1. Introduction

Third generation solar cells promise lower cost, greater efficiency, and/or increased functionality over first generation (single crystal silicon) and second generation (polycrystalline, thin film, and microcrystalline) photovoltaics [1]. The possible contenders for third generation photovoltaics include photovoltaics made from organic materials. This type of solar cell will likely have the advantage that it can be processed inexpensively, rapidly, and on flexible surfaces. Although many scientists are researching organic materials for LEDs and much of the acquired knowledge from their research can be applied to solar cells, solar cells have unique requirements separate from those of LEDs that must also be met.

* Corresponding author. Tel.: +1 505 667 9419; fax: +1 505 606 1515.
E-mail address: marcie@alum.mit.edu (M.R. Black).

1566-1199/$ - see front matter © 2007 Published by Elsevier B.V.
doi:10.1016/j.orgel.2007.04.011

Unlike inorganic materials, where an absorbed photon creates an electron and a hole, within organic materials a bound electron hole pair or exciton is created. Since the exciton is charge neutral, the exciton can only diffuse (and not drift), throughout the material. Most excitons that disassociate do so at an interface, so the exciton must diffuse to an interface and then disassociate into an electron and a hole. The electron and hole can then drift to opposite contacts producing photocurrent. As a result, material properties required for efficient organic excitonic solar cells include: strong optical absorption, large exciton diffusion length, and high carrier mobility. This study focuses on measuring the exciton diffusion length within a particular organic material.

In general, excitons are one of two types, singlets or triplets. Since the ground state is a singlet, transitions to and from the excited singlet state conserve spin and are therefore optically allowed. Hence, they tend to have large absorption coefficients, an advantage for solar cells. At the same time, they exhibit small exciton diffusion lengths, a disadvantage for excitonic solar cells. Transitions between the ground state and the first excited triplet state do not conserve spin and are therefore not optically allowed. Hence, triplet states have very large exciton lifetimes and therefore are likely to have long exciton diffusion lengths. On the other hand, triplet excitons have very weak optical absorption.

In metal organic materials, the presence of the metal increases spin–orbit coupling and results in the mixing of the singlet and triplet states (e.g. [2,3]). The spin–orbit coupling in metal organic materials can lead to singlet-like and triplet-like exciton states that are both partially optically allowed and have long exciton lifetimes. Since the exciton diffusion length is proportional to the square root of the product of the diffusion coefficient and the lifetime, the mixing of the triplet and singlet exciton states may also lead to long exciton diffusion lengths.

Since metal organics are suspected to have large exciton diffusion lengths, we choose a metal-organic film for this study. For solar cell applications, low cost is imperative, and so spin coating has a distinct advantage over evaporation. As a result, this study concentrated on metal-organic films which could be dissolved in a solvent and hence be spin coated onto a surface. In particular, the exciton diffusion length of tris (dibenzoylmethane) mono (phenanthroline) europium (III) (Eu-DM) is investigated (see Fig. 1).

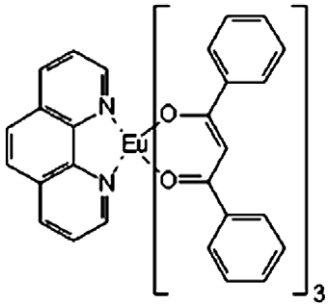


Fig. 1. A molecule of tris (dibenzoylmethane) mono (phenanthroline) europium (III) (Eu-DM).

2. Experimental

Glass was used as a substrate for the devices, and was first cleaned by a solvent rinse of acetone, toluene, and IPA and then followed by a 5 min oxygen plasma ash. The glass substrates were subsequently transferred into a glove box filled with argon at atmospheric pressure and were not exposed to air for the duration of the experiment. Next, a 150 Å thin layer of aluminum (Al) was thermally evaporated onto the glass slide. The pressure during the evaporation was between 1×10^{-7} and 5×10^{-7} Torr and the rate was kept near 2 Å s^{-1}. The sample was then removed from the evaporator and Eu-DM was spin coated onto the Al at 1000 rpm for 90 s from a solution of 25 mg of Eu-DM (H.W. Sands OPA9808) in 1 ml of toluene. Samples were also prepared by evaporating Eu-DM, and results were similar to the spin-coated samples. However, only the spun-on samples are presented. Both the evaporated and spin coated Eu-DM were found to be amorphous by X-ray diffraction. Prior to spin coating, in order to ensure full dissolution of the Eu-DM in the toluene, the solution was heated to 50 °C for an hour and then cooled to room temperature. Following spin coating, another layer of Al was evaporated onto the sample. Since the surface of the Eu-DM is not as smooth as the plain glass, a thicker layer is needed for the back contact than the front contact to ensure a continuous film. Therefore, the back Al layer was made slightly thicker, 450 Å. To avoid the Al deposition throughout the Eu-DM film and shorting out the top and bottom contacts, the Al deposition was kept below 2 Å s^{-1} and the pressure was strictly kept in the low 10^{-7} Torr range. A schematic of the device is shown in the inset of Fig. 3.

To avoid exposing the sample to air, the photocurrent was measured inside a cryostat at room

temperature. A 50 W tungsten lamp was used with an Acton Research Corporation Spectra Pro 2300i monochromator. The photocurrent was amplified using a Stanford Research System model SR570 current preamplifier, and detected using a Stanford Research Systems SR830 lock-in amplifier at a frequency of 100 Hz. The photocurrent was normalized to the intensity of the incident light as measured by a calibrated photodector. Absorption spectra were taken using a Hewlett Packard 8452 diode array spectrometer in air. The same sample for the photocurrent measurement was used for the absorption measurements, but the absorption spectrum was taken in an area of the sample that was masked off, and thus did not have a metal coating. Glass is used as the background spectra.

3. Results

The most common method of measuring exciton diffusion lengths is to use photoluminescence quenching. Both glass and gold were tested as quenching surfaces for photoluminescence quenching. Glass did not quench the excitons in Eu-DM, and hence the quenching experiment on glass substrates did not yield useful information. Gold surfaces acted as efficient quenching sites, but Eu-DM films on gold exhibited metal enhanced exciton quenching. As a result, the simple method of finding the exciton diffusion length by plotting the photoluminescence intensity as a function of sample thickness and finding the x-intercept could not be used for Eu-DM on gold. Metal enhanced exciton quenching is well understood (e.g. [4]), and so a set of samples with different thicknesses on gold could be used to find the exciton diffusion length, but many samples with different thicknesses are required to accurately resolve the effects of metal enhanced exciton quenching. Hence, this study utilizes another method of determining the exciton diffusion length.

The exciton diffusion length also can be derived from the photocurrent and absorption spectra as a function of wavelength, provided several assumptions are made [5,6]; the current is limited by exciton diffusion to contacts, the exciton diffusion is proportional to the space derivative of the exciton distribution, and the metal surfaces are perfect exciton quenchers so that the exciton densities at the surfaces are approximately zero. In order to help ensure that the current is limited by exciton diffusion, we choose aluminum as our metal contact, since it is a poor electron and hole injector. This minimizes any photocurrent resulting from carrier injection from the metal to the organic film. The exciton distribution can be solved from the continuity equation using only the optical absorption coefficient and the exciton diffusion length. The exciton density distribution $n(E,z)$ is then

$$n(E,z) = \frac{\alpha\eta I/D}{\beta^2-\alpha^2}\left[\left(\frac{e^{\beta L}-e^{-\alpha L}}{e^{-\beta L}-e^{\beta L}}\right)e^{-\beta z} - \left(\frac{e^{-\beta L}-e^{-\alpha L}}{e^{-\beta L}-e^{\beta L}}\right)e^{\beta z}+e^{-\alpha z}\right], \quad (1)$$

where η is the exciton generation efficiency, α is the optical absorption length at the incident photon energy, $1/\beta$ is the exciton diffusion length, I is the incident light flux, L is the sample thickness, z is the distance into the device, and D is the exciton diffusion constant. The current is then found by the diffusion equation

$$J(E,z) = -D\left.\frac{dn(E,z)}{dz}\right|_{z=0,L}. \quad (2)$$

The calculation is greatly simplified if the photocurrent is dominated by exciton dissociation at only one contact. In order to test if this is the case in our devices, the photocurrent was measured for both front and back side illumination (see Fig. 2). It was expected that front side illumination would yield larger photocurrent since the front aluminum is thinner (150 Å) than the back side aluminum (450 Å). Hence, more light should transmit through the front side than the back side. However, more photocurrent was produced when the sample was illuminated from the back side. In addition, since

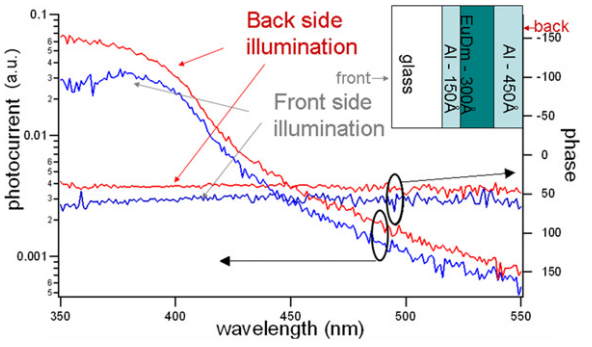


Fig. 2. A plot of the photocurrent and phase of an Al/Eu-DM/Al device with both front and backside illumination. The phase of the photocurrent is very similar for the two illumination directions, while the photocurrent intensity is slightly larger for backside illumination.

the phase of the photocurrent from front and back side illumination is very similar (see Fig. 2), we can conclude that the same surface is dominating the photocurrent regardless of the direction of illumination. If the device were perfectly symmetric, switching the direction of illumination will switch the direction of the current and hence result in a difference in phase of 180° for the two directions of illumination. Since more photocurrent was observed from backside illumination and since only one side was dominating the photocurrent, we concluded that exciton disassociation at the back contact dominated the photocurrent. This was easily explained by the larger surface roughness of the back Eu-DM/Al interface compared to the front Eu-DM/Al interface. The larger surface roughness provided a larger exciton disassociation area and therefore more efficient exciton disassociation.

Fig. 3 compares the photocurrent and absorption spectra of a device. The photocurrent follows the absorption fairly closely. Interestingly, both have a long tail from 420 to 550 nm. This tail could result from disorder or could indicate the presence of a weakly allowed state which also contributes to the photocurrent. One possible explanation for the tail in the absorption and photocurrent spectra is that the triplet-like excitons are directly being excited by the incident light and contributing to the photocurrent. However, more research into the absorption mechanism in this energy range is needed before conclusions can be made as to the origin of the tail.

Since the backside dominates the photocurrent in our sample, we can simplify Eqs. (1) and (2) for front side illumination if we can assume that the exciton diffusion length is smaller than the sample thickness (300 Å). Thus,

$$J \propto \frac{\alpha \exp(-\alpha L)}{\beta - \alpha}, \tag{3}$$

and the exciton diffusion length is determined by finding the x-intercept on a graph of $1/[J\exp(\alpha L)]$ vs. $1/\alpha$ [7]. A similar calculation can be done for backside illumination. However, in order to obtain a simple equation, the additional assumption that $\alpha L \gg 1$ must be made. For our sample and the energy range of interest, this assumption is not accurate; hence only front side illumination is shown.

Fig. 4 plots $1/[J\exp(\alpha L)]$ as a function of $1/\alpha$ for the photocurrent measured using front side illumination. Part of the graph is linear, as expected if all the assumptions are met. The linear region of the graph results from data taken between 350 and 420 nm. The exciton diffusion length derived from this data is 248 ± 8 Å. For wavelengths above 420 nm, the graph is non-linear, indicating that one of the aforementioned assumptions is incorrect for this energy range, or that the absorption or photocurrent measurements are not accurate for this energy range. Many possible reasons could explain why the graph is non-linear in this regime. The most probable cause is that the absorption length is longer than the sample thickness and therefore the method is not valid in this case. Theoretically, Eq. (3) could be rederived without any assumption of the exciton diffusion length relative to the sample thickness and then this new equation could be fitted to the data to obtain the exciton diffusion length. Using Eqs. (1) and (2), without making any assumptions as to the exciton diffusion length relative to the sample thickness, the current from the backside can be calculated as

$$J \propto \frac{\alpha}{\beta^2 - \alpha^2}\left[-\beta\left(\frac{2 - e^{-\beta L - \alpha L} - e^{\beta L - \alpha L}}{e^{-\beta L} - e^{\beta L}}\right) - \alpha e^{-\alpha L}\right].$$

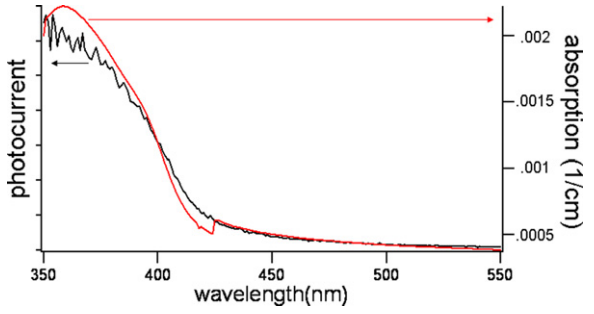


Fig. 3. Photocurrent and absorption as a function of wavelength for an Eu-DM device and film respectively. The photocurrent and absorption track each other and both exhibit a tail in the long wavelength side.

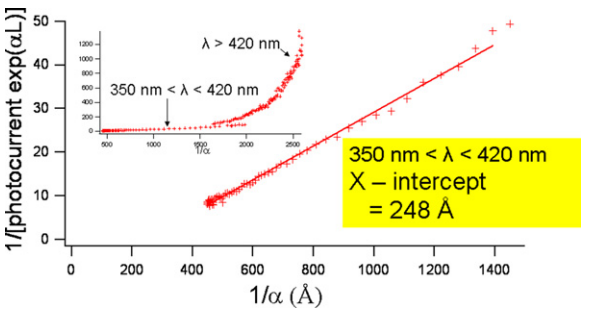


Fig. 4. $1/[J\exp(\alpha L)]$ as a function of $1/\alpha$. For the wavelength range between 350 and 420 nm, the x-intercept gives an exciton diffusion length of 248 Å.

When this new equation is derived and then fitted to the data, the data fits well. Unfortunately, even with the new equation, this method is expected to be inaccurate when the absorption length is very small. However, ignoring the limits of this method and fitting the data to find the exciton diffusion length in the low energy range, an exciton diffusion length much longer than the sample thickness is derived. Within this wavelength range, the absorption and photocurrent have a low energy tail, so it is possible that the photocurrent and absorption result from direct coupling into a triplet-like state which should have a weak absorption and a very large exciton diffusion length. However, significantly more research needs to be conducted to accurately identify the absorption and photocurrent mechanisms in Eu-DM.

Table 1 compares the exciton diffusion length of Eu-DM, as determined from this study, with exciton diffusion lengths of other materials. The exciton diffusion length of Eu-DM is comparable to other small molecule systems which were evaporated or sublimated, and the diffusion length is larger than the spin coated polymer films. The large exciton diffusion lengths expected for metal-organic films were not observed in this study. However, the energy at which the large exciton diffusion length states exist in Eu-DM could very likely be outside the energy range of this measurement and another method of measuring exciton diffusion would need to be employed.

Table 1
Exciton diffusion lengths, the method of deposition, and the corresponding references

Material	Lex (Å)	Deposition method	Refs.
Eu-DM	250 ± 8	Spin coated	This work
PTCBI	30 ± 3	Sublimation/evaporation	[8]
PTCDA	880 ± 60	Evaporation	[5]
PPEI	25,000	Evaporated	[9]
CuPc	100 ± 30	Sublimation/evaporation	[8]
	680 ± 200	Evaporation	[10]
C60	400 ± 50	Sublimation/evaporation	[8]
	141	Sublimation	[11]
Alq3	200	Evaporation	[12]
	210	Evaporation	[13]
PPV	70 ± 10	Spin coated	[14]
	120 ± 30	Spin coated	[10]
PEOPT	47	Spin coated	[11]
	50	Spin coated	[15]

PTCBI = 3,4,9,10-perylenetetracarboxylic bis-benzimidazole, PTCDA = 3,4,9,10-perylenetetracarboxylic dianhydride, PPEI = Perylene bis(phenethylimide), CuPc = copper phthalocyanine, Alq3 = tris(8-hydroxyquinoline) aluminum, PPV = poly(phenylene–vinylene), PEOPT = poly (3-(4′-(1″,4″,7″-trioxaoctyl)-phenyl)thiophene).

4. Conclusion

The exciton diffusion length of spin coated Eu-DM films was measured by analyzing the photocurrent and absorption as a function of wavelength. For exciton wavelengths between 350 and 420 nm, the exciton diffusion length is 250 ± 8 Å. This is comparable to other small molecule systems and larger than spin coated polymers. The expected large enhancement of the exciton diffusion length resulting from the spin–orbit coupling in Eu-DM was not observed, but likely occurs at lower incident photon energies than those energies for which the method employed in this paper is valid.

Acknowledgements

The authors thank Brian Crone for his feedback on this work, help in setting up equipment, and supervision of this project. We also acknowledge Ian Campbell, Marc Baldo, and Vladimir Bulovic for useful discussions. This research was supported by the Los Alamos National Laboratory Directed Research and Development Program.

References

[1] Martin A. Green, Third Generation Photovoltaics, Springer, 2003.
[2] Vicki Cleave, Goghan Yahioglu, Pierre Le Barny, Richard H. Friend, Nir Tessler, Adv. Mater. 11 (4) (1999) 285–288.
[3] Marc Baldo, Michael Segal, Phys. Stat. Sol. (a) 201 (6) (2004) 1205–1214.
[4] R.R. Chance, A. Prock, R. Silbey, in: I. Prigogine, Stuart A. Rice (Eds.), Advances in Chemical Physics XXXVII, Wiley, New York, 1978, p. 1.
[5] V. Bulovic', S.R. Forrest, Chem. Phys. 210 (1996) 13–25.
[6] C.L. Yang, Z.K. Tang, W.K. Ge, J.N. Wang, Z.L. Zhang, X.Y. Jian, Appl. Phys. Lett. 83 (9) (2003) 1737–1739.
[7] V. Bulovic, S.R. Forrest, Chem. Phys. Lett. 238 (1995) 88–92.
[8] Peter Peumans, Aharon Yakimov, Stephen R. Forrest, J. Appl. Phys. 93 (7) (2003) 3693–3723.
[9] Brian A. Gregg, Julian Sprague, Mark W. Peterson, J. Phys. Chem. B 101 (1997) 5362–5369.
[10] Thomas Stübinger, Wolfgang Brütting, J. Appl. Phys. 90 (7) (2001) 3632–3641.
[11] Leif A.A. Pettersson, Lucimara S. Roman, Olle Inganäs, J. Appl. Phys. 86 (1) (1999) 487–496.
[12] C.W. Tang, S.A. VanSlyke, C.H. Chen, J. Appl. Phys. 85 (9) (1989) 3610–3616.
[13] V.E. Choong, Y. Park, Y. Gao, M.G. Mason, C.W. Tang, J. Vac. Sci. Technol. A 16 (3) (1998) 1838–1841.
[14] J.J.M. Halls, K. Pichler, R.H. Friend, S.C. Moratti, A.B. Holmes, Appl. Phys. Lett. 68 (22) (1996) 3120–3122.
[15] M. Theander, A. Yartsev, D. Zigmantas, V. Sundström, W. Mammo, M.R. Andersson, O. Inganäs, Phys. Rev. B 61 (19) (2000) 12957–12963.

Available online at www.sciencedirect.com
ScienceDirect
Organic Electronics 8 (2007) 606–614
Organic Electronics
www.elsevier.com/locate/orgel

Energy level alignment and morphology of interfaces between molecular and polymeric organic semiconductors

F.J. Zhang [a,b], A. Vollmer [c], J. Zhang [b], Z. Xu [a], J.P. Rabe [b], N. Koch [b,*]

[a] *Key Laboratory of Luminescence and Optical Information, Ministry of Education, Institute of Optoelectronic Technology, Beijing Jiaotong University, Beijing 100044, China*
[b] *Institut für Physik, Humboldt-Universität zu Berlin, Newtonstr. 15, D-12489 Berlin, Germany*
[c] *Berliner Elektronenspeicherring-Gesellschaft für Synchrotronstrahlung m.b.H., Albert-Einstein-Str. 15, D-12489 Berlin, Germany*

Received 17 January 2007; received in revised form 1 April 2007; accepted 27 April 2007
Available online 23 May 2007

Abstract

Ultraviolet photoelectron spectroscopy (UPS) was used to determine the energy level alignment at organic–organic conductor–semiconductor and semiconductor–semiconductor hetero-interfaces that are relevant for organic optoelectronic devices. Such interfaces were formed by *in situ* vacuum sublimation of small molecular materials [C_{60} and pentacene (PEN)] and *ex situ* spin-coating of poly(3-hexylthiophene) (P3HT), all on the common substrate poly(3,4-ethylenedioxythiophene)/poly(styrenesulfonate) (PEDOT:PSS). We found that the deposition sequence had a significant impact on the interface energetics. The hole injection barrier (HIB) of C_{60} on PEDOT:PSS could be changed from 1.0 eV (moderate hole injection) to 1.7 eV (good electron injection) by introducing a layer of P3HT. The HIB of P3HT/PEDOT:PSS was increased by 0.35 eV due to an interfacial PEN layer. However, PEN deposited on PEDOT:PSS and P3HT/PEDOT:PSS exhibited the same value. These observations are explained by material-dependent dipoles at the interfaces towards PEDOT:PSS and substrate dependent inter-molecular conformation.
© 2007 Elsevier B.V. All rights reserved.

PACS: 73.20.−r; 73.61.Ph; 68.37.Ps

Keywords: Organic semiconductors; Interfaces; Photoelectron spectroscopy; Atomic force microscopy

1. Introduction

The physico-chemical properties of interfaces in organic optoelectronic devices, such as organic light emitting diodes (OLEDs), organic photovoltaic cells (OPVCs), and organic thin film transistors (OTFTs), largely determine device function and performance [1–5]. For instance, the importance of the energy level alignment at organic–metal interfaces has been pointed out in many studies [6–8]. However, comparably little is known about the energy level alignment at organic–organic hetero-interfaces [9–15], which is essential for further understanding and optimizing organic devices. Such hetero-interfaces are ubiquitous in modern devices, in order to facilitate efficient charge recombination (in OLEDs)

* Corresponding author. Tel.: +49 3020937819; fax: +49 3020937632.
E-mail address: norbert.koch@physik.hu-berlin.de (N. Koch).

1566-1199/$ - see front matter © 2007 Elsevier B.V. All rights reserved.
doi:10.1016/j.orgel.2007.04.010

or charge separation (in OPVCs). Even fewer studies exist on interfaces formed between molecular and polymeric organic semiconductor interfaces [16], despite the potentially interesting structures resulting from that particular material combination. Here, we present studies on the energy level alignment at interfaces between two molecular materials (C_{60} and pentacene) and one polymeric organic semiconductor [poly(3-hexylthiophene)], with the conducting organic polymer mixture poly(3,4-ethylenedioxythiophene)/poly(styrenesulfonate) as common substrate. These prototypical organic materials are representative for the use in present OPVCs and OTFTs. Ultraviolet photoemission spectroscopy (UPS) was used to assess the relative positions of the highest occupied levels of the organic materials relative to the substrate Fermi-level, and the magnitude of interface dipoles. Furthermore, we investigated the influence of the deposition sequence of a polymer and a molecular material pair on the interface energetics, which has not been reported to date. Complementary investigations by atomic force microscopy (AFM) revealed that also the sample morphology was strongly influenced by the deposition sequence.

2. Experimental

Indium-tin-oxide (ITO) coated glass substrates (with a sheet resistivity 30 Ω/sq.) were cleaned by ultrasonication in acetone, ethanol and deionized water. An aqueous dispersion of poly(3,4-ethylenedioxythiophene):poly(styrenesulphonate) (Baytron P CH8000®, H.C. Starck GmbH & Co. KG) was spin-coated onto ITO/glass substrates and annealed at 200 °C for 5 min in ambient air. These conducting polymer/ITO stacks were used as substrates throughout this study. P3HT (Aldrich) was spin-coated (600 rounds per minute) *ex situ* from chloroform solution (0.2 mg/ml). Pentacene (Aldrich) and C_{60} (Aldrich) were evaporated from resistively heated pinhole sources in a preparation chamber directly attached to the analysis chamber of the experimental setup used for photoemission experiments (SurIcat at beamline PM4) at the synchrotron light source BESSY Gmbh (Berlin). The chemical structures of the used materials are shown in Fig. 1. The molecular film thickness was monitored with a quartz microbalance, and a typical evaporation rate of 0.2 nm/min was used. Photoemission spectra were collected with a hemispherical energy analyzer (Scienta SES 100) set to an energy resolution of 100 meV. The photon energy was 35 eV or 45 eV, as indicated in the respective spectra shown below. The secondary electron cutoff (for determination of sample work function and molecular ionization energy) was measured with −10.00 V sample bias. The positions of the low binding energy photoemission onsets and the secondary electron cutoffs were determined by the intersection of the tangents to peaks at the half-width position and the baseline.

The morphology of molecule-on-polymer and polymer-on-molecule heterostructures was investigated *ex situ* by atomic force microscopy (AFM), using a multimode nanoscope IV (Veeco) operated in tapping mode.

3. Result and discussion

3.1. C_{60} on PEDOT:PSS

First, C_{60} was deposited onto PEDOT:PSS/ITO in steps of increasing thickness. UPS spectra at each step were recorded as shown in Fig. 2a, with the Fermi-level (E_F) as binding energy (BE) reference. For 1 nm C_{60} on PEDOT:PSS, the emission from PEDOT:PSS was already strongly attenuated, and the characteristic photoemission of the valence levels of the organic material became apparent. The low BE onset of the highest occupied molecular orbital (HOMO) was found 1.1 eV below E_F. Increasing the overlayer thickness to 10 nm resulted in a 0.1 eV rigid shift of C_{60} levels towards lower BE. This shift was paralleled by the secondary

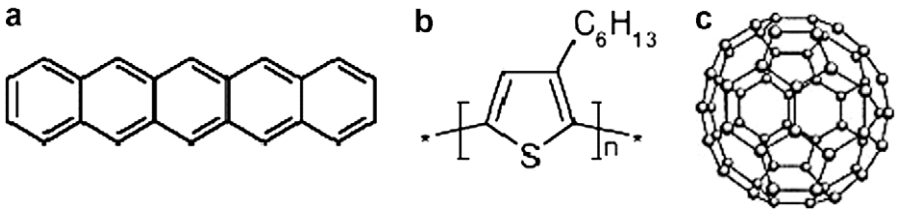


Fig. 1. Chemical structure of (a) pentacene, (b) P3HT, and (c) C_{60}.

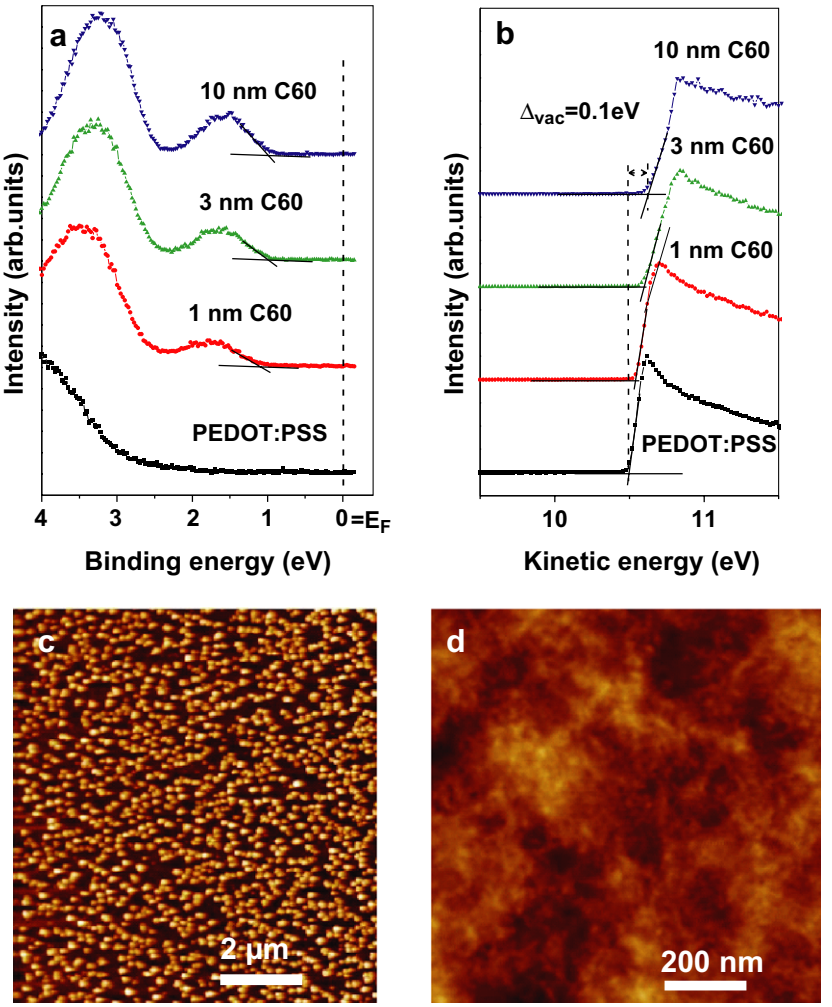


Fig. 2. (a) Valence region and (b) secondary electron cutoff photoemission spectra ($h\nu = 35$ eV) for increasing coverage of C_{60} on PEDOT:PSS/ITO. The intersections of the baselines with the tangents to the photoemission features are shown, indicating how the position of the low BE photoemission onset and the secondary electron cutoff was determined. AFM micrographs of (c) 10 nm C_{60} on PEDOT:PSS (120 nm height scale), and (d) PEDOT:PSS/ITO (10 nm height scale).

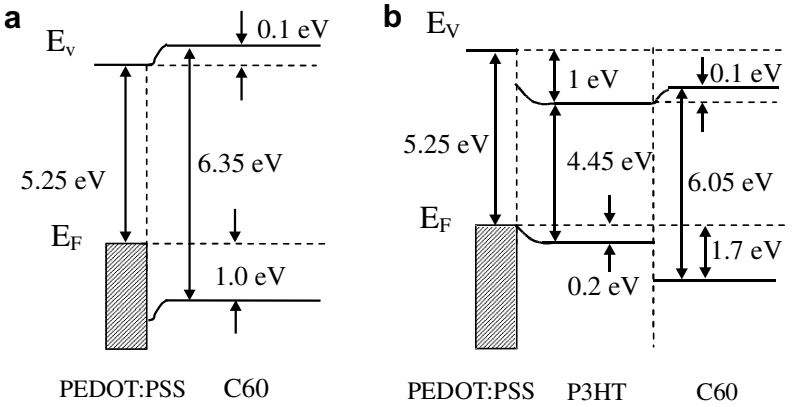


Fig. 3. Schematic energy level diagrams of the interfaces (a) C_{60}/PEDOT:PSS, and (b) C_{60}/P3HT/PEDOT:PSS. The vacuum level shift across the interface and the ionization energy of C_{60} must be regarded as lower limits, as uncovered PEDOT:PSS surface patches may yield too low work function values (see text).

electron cutoff, as shown in Fig. 2b. Thus, an interface dipole between C_{60} and PEDOT:PSS of +0.1 eV was formed, which is very close to the limit of vacuum level alignment. One might speculate that molecular level bending away from the direct interface to the conducting polymer was observed [6], since most of the 0.1 eV shift occurred between 3 nm and 10 nm of C_{60} nominal coverage. However, AFM images for 10 nm C_{60}/PEDOT:PSS (Fig. 2c and d) revealed that the film formed by C_{60} was not homogeneous, and rather small area islands with large heights were formed (pronounced island growth), compared to the rather smooth PEDOT:PSS surface. As a consequence, even at 10 nm nominal C_{60} thickness possibly bare PEDOT:PSS surface areas still existed, making a clear-cut statement on molecular level bending unattainable at this point. The ionization energy (IE) of C_{60} determined under these experimental conditions was 6.35 eV, which must be regarded as lower limit, as the secondary electron cutoff is an area-averaged measure of the sample work function. Conse-

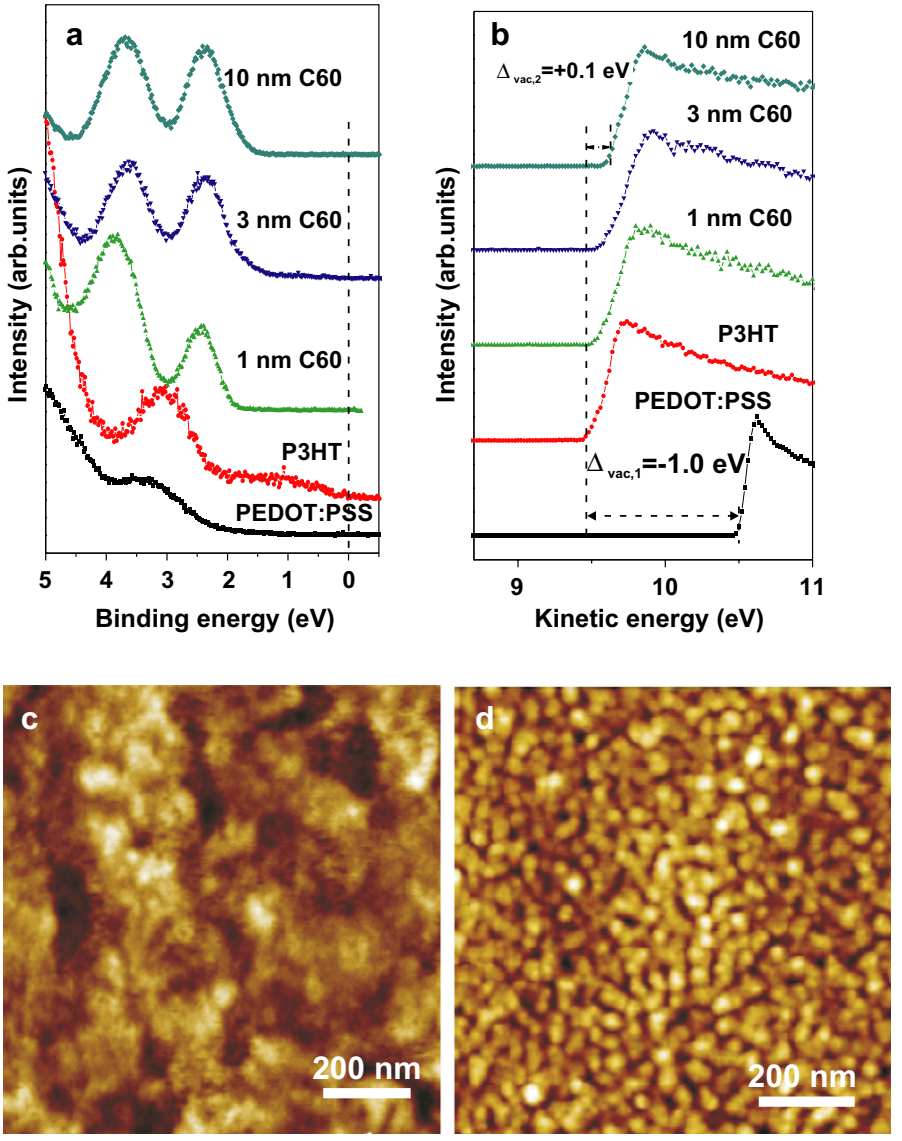


Fig. 4. (a) Valence region and (b) secondary electron cutoff photoemission spectra ($h\nu = 45$ eV) for increasing coverage of C_{60} on P3HT/PEDOT:PSS. AFM micrographs of (c) P3HT/PEDOT:PSS (10 nm height scale), and (d) 10 nm C_{60} on P3HT/PEDOT:PSS (25 nm height scale).

quently, contributions from still uncovered PEDOT:PSS (see above) lead to too low values for work function and ionization energy. A schematic diagram of the electronic structure for C_{60}/PEDOT:PSS summarizes these results (Fig. 3a). Note that only occupied levels are shown in all schematics, as unoccupied levels cannot be determined from UPS and consequently would posses a considerable error bar [15].

3.2. C_{60} on P3HT/PEDOT:PSS

Now we turn towards C_{60} deposited on P3HT pre-covered PEDOT:PSS. To start with, we discuss the P3HT/PEDOT:PSS interface. AFM showed that the P3HT morphology (Fig. 4c) closely resembled that of pristine PEDOT:PSS, and no detailed structures were observed on a nanoscopic scale. The appearance of crystalline grains for P3HT has been reported, however, on a flat Si-oxide substrate [17,18]. The hole injection barrier for P3HT was found to be only 0.2 eV from UPS (bottom-most curve in Fig. 4a), and a larger interface dipole of −1.0 eV was observed (Fig. 4b). This indicates that this interface is in the limiting case of Fermi-level pinning, due to the fact that P3HT polaronic levels determine the position of E_F within the energy gap of the polymer [19–21], leading to interfacial charge

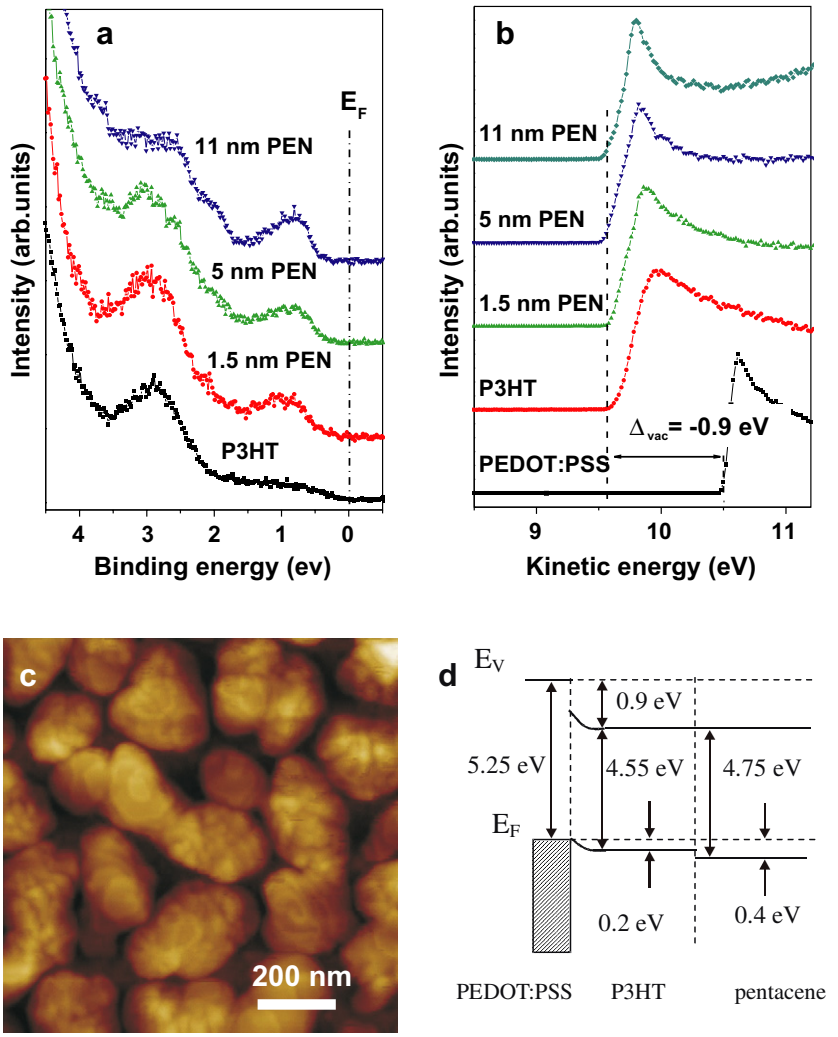


Fig. 5. (a) Valence region and (b) secondary electron cutoff photoemission spectra ($h\nu = 35$ eV) for increasing coverage of pentacene (PEN) on P3HT/PEDOT:PSS. (c) AFM micrograph of 11 nm pentacene on P3HT/PEDOT:PSS (30 nm height scale). (d) Schematic energy level diagram of the interface pentacene/P3HT/PEDOT:PSS.

transfer (positive charges on P3HT) that gives rise to the large interface dipole. Alternatively, due to the low ionization energy obtained for this P3HT film of *ca.* 4.45 eV, P3HT might undergo a similar charge exchange reaction at the PEDOT:PSS surface that was proposed for pentacene (ionization energy: *ca.* 5.0 eV) [22]. When depositing C_{60} onto P3HT/PEDOT:PSS, we observed the appearance of C_{60} photoemission features and an attenuation of P3HT signal, similar to C_{60} on PEDOT:PSS. However, the position of the energy levels was markedly different. The HOMO onset of C_{60} on P3HT/PEDOT:PSS was *ca.* 1.7 eV below E_F, and did not change as function of C_{60} thickness. The secondary electron cutoff position exhibited a shift of + 0.1 eV (= interface dipole) towards higher kinetic energy, *i.e.*, almost vacuum level alignment occurred at the C_{60}/P3HT interface. The ionization energy of C_{60} on P3HT/PEDOT:PSS was thus determined to be 6.05 eV, in agreement with literature [23]. This value is smaller than that of C_{60} on PEDOT:PSS, which could be due to the presence of still uncovered PEDOT:PSS surfaces patches (see Section 3.1). Note that the morphology of C_{60}/P3HT was markedly smoother than that for C_{60}/PEDOT:PSS (Fig. 4d).

The key result here is that the alignment of C_{60} energy levels relative to E_F was increased by 0.7 eV, by simply pre-coating PEDOT:PSS with a thin film of P3HT. This translates into PEDOT:PSS being a moderate hole injecting contact for C_{60}, while P3HT/PEDOT:PSS is a good electron injecting contact, which becomes strikingly evident when comparing the schematic energy level diagrams of the two different interfaces (Fig. 3a and b). Responsible for this is the charge transfer at the P3HT/PEDOT:PSS interface, which introduces a large interface dipole. C_{60} deposited onto P3HT/PEDOT:PSS aligns its levels relative to P3HT (essentially vacuum level alignment), but the effective substrate work function has already been decreased by the P3HT/PEDOT:PSS interface dipole of −1.0 eV.

3.3. Pentacene on P3HT/PEDOT:PSS

UPS spectra for increasing pentacene (PEN) coverage on P3HT/PEDOT:PSS are shown in Fig. 5a and b. In comparison to the P3HT/PEDOT:PSS shown in Fig. 2 the vacuum level shift was 0.1 eV smaller, which may indicate slight differences in the polymer film morphology; however, the valence band onset was not changed, and the overall reproducibility for other P3HT/PEDOT:PSS samples was better than 0.1 eV in our case. Most of the spectral features of P3HT disappeared already after 1.5 nm PEN coverage, and PEN features dominated for higher coverage. In particular, a clear peak evolves at *ca.* 0.9 eV BE, which is derived from the PEN HOMO. The low BE onset of the pentacene HOMO was 0.4 eV below E_F for all thicknesses, while the low BE onset of the P3HT valence band was 0.2 eV below E_F. No change in the position of the secondary electron cutoff was observed upon PEN deposition (Fig. 5b), indicating that vacuum level alignment prevails at the PEN/P3HT interface. The ionization energy of PEN was 4.75 eV. Such small values have been reported before for PEN films where the long molecular axes are oriented almost perpendicular to the substrate surface [15,24]. This type of molecular orientation was corroborated for the present sample by AFM (Fig. 5c), where individual step-heights corresponding to the length of a pentacene molecule (*ca.* 1.5 nm) were measured. Also, the PEN morphology on P3HT closely resembles that observed for PEN on PEDOT:PSS [22]. The schematic energy level diagram of PEN/P3HT/PEDOT:PSS interface is shown in Fig. 5d.

3.4. P3HT on pentacene/PEDOT:PSS

In order to investigate whether molecule-on-polymer and polymer-on-molecule interfaces exhibit the same energy level alignment, we first established that pentacene thin films are not significantly altered by treatment with the solvent used for P3HT. We

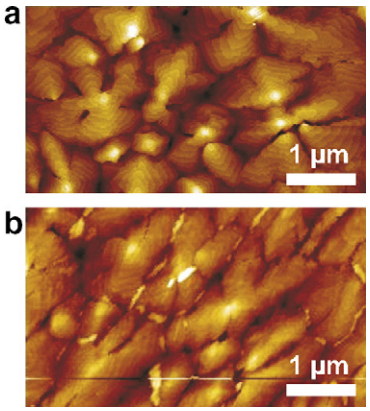


Fig. 6. AFM micrographs of 10 nm pentacene on native silicon oxide (a) before, and (b) after $CHCl_3$ treatment (40 nm height scale).

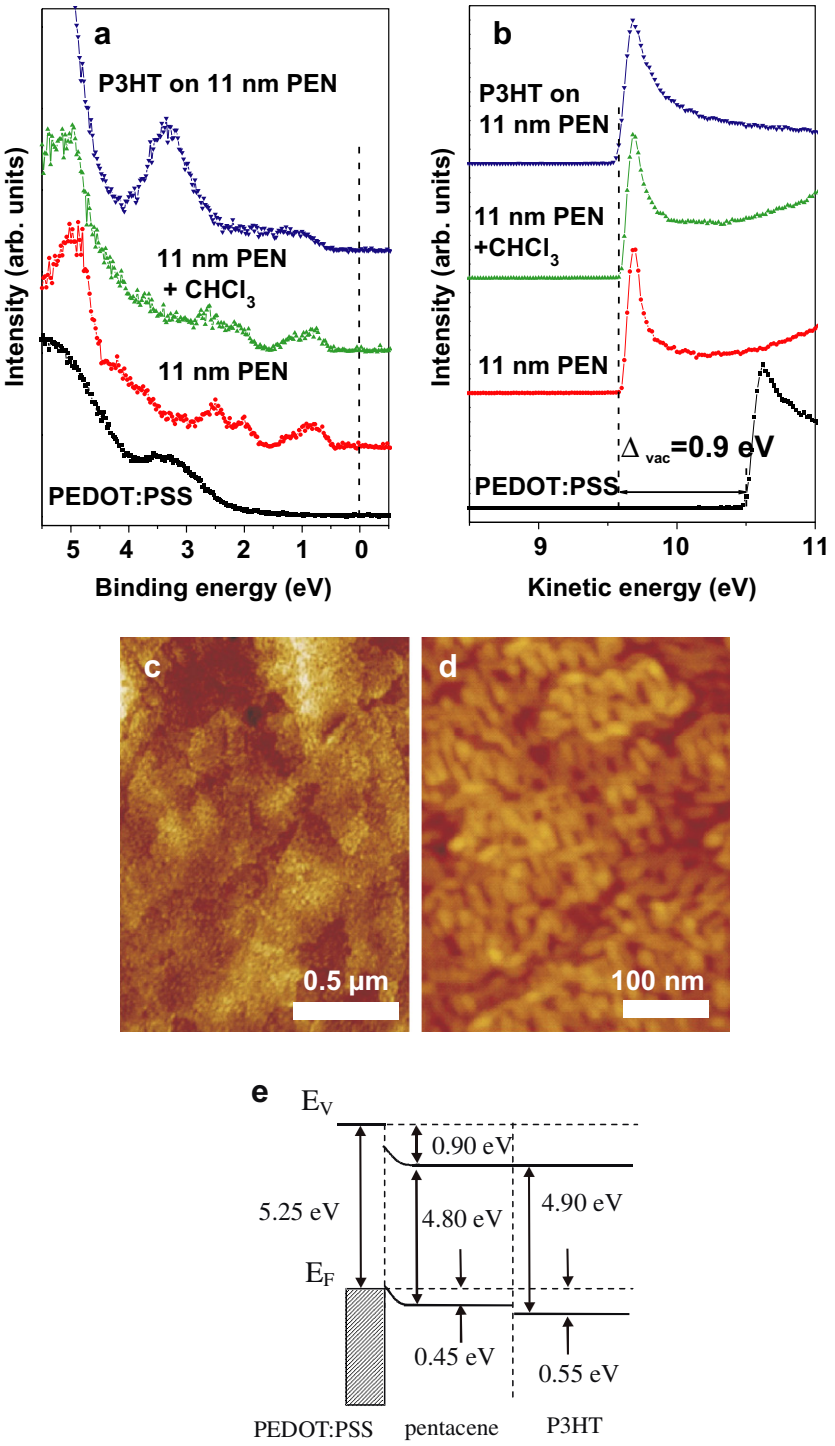


Fig. 7. (a) Valence region and (b) secondary electron cutoff photoemission spectra ($h\nu = 35$ eV) for 11 nm pentacene (PEN) on PEDOT:PSS before and after $CHCl_3$ treatment, and for P3HT spin-coated on top of pristine 11 nm PEN/PEDOT:PSS. (c) and (d) AFM micrographs of P3HT spin-coated onto 11 nm pentacene/PEDOT:PSS (15 nm height scale). (e) Schematic energy level diagram of the interface P3HT/pentacene/PEDOT:PSS.

simulated P3HT spin-coating onto PEN by employing identical spin-coating parameters (600 rpm) for chloroform alone. AFM showed that only minor changes of the PEN thin film morphology (for bet-

ter visibility with native silicon oxide as substrate) occurred, and the typical molecular step-heights were measured before and after $CHCl_3$ treatment (Fig. 6). Yet, some PEN probably was dissolved by $CHCl_3$ under our experimental conditions, as indicated by the fringed island edges. However, the solubility of PEN in $CHCl_3$ is very low, since even after soaking such PEN samples in copious amounts of $CHCl_3$ for 5 min removed only *ca.* 30% of the film mass (not shown).

Notably, also the electronic structure of the pentacene/PEDOT:PSS interface was not altered by $CHCl_3$ treatment (spin-coating of the solvent). The valance and secondary electron cutoff spectra for PEN on PEDOT:PSS before and after $CHCl_3$ treatment were virtually identical (Fig. 7a and b), and reproduced already published values for hole injection barrier (0.45 eV) and interface dipole (−0.9 eV) [22].

Consequently, spin-coating P3HT from $CHCl_3$ solution onto a PEN film should yield reliable photoemission results on the polymer-on-molecule electronic structure. In fact, UPS showed that vacuum level alignment at the P3HT/PEN interface prevailed (as was the case for PEN/P3HT), as no shift of the secondary electron cutoff occurred (Fig. 7b). However, the P3HT valence band onset was found 0.55 eV below E_F, *i.e.*, at 0.35 eV higher BE than for P3HT/PEDOT:PSS. At the same time, the ionization energy for the polymer-on-molecule case was 4.90 eV (compared to 4.45 eV and 4.55 eV for P3HT/PEDOT:PSS; see above). This change of ionization energy by ~0.4 eV is attributed to a different inter-molecular arrangement within P3HT on the molecular film substrate. This is supported by AFM images, which show that – in contrast to P3HT/PEDOT:PSS – small crystallite-like grains existed in the polymer overlayer (Fig. 7d). Larger scale images reveal that the P3HT film continuously covered the pentacene substrate, and the individual PEN steps could still be discerned (Fig. 7c). The energy levels at the P3HT/PEN/PEDOT:PSS interface are summarized in Fig. 7e.

4. Conclusions

The energy level alignment and morphology of interfaces formed between two molecular (C_{60}, PEN) and one polymeric (P3HT) organic semiconductors was investigated by UPS and AFM. As common substrate for all experiments the conducting polymer PEDOT:PSS was used. We found that the hole injection barrier for C_{60} was drastically larger on P3HT pre-coated PEDOT:PSS (1.7 eV) compared to pristine PEDOT:PSS (1.0 eV). This was facilitated by a large dipole (−1.0 eV) formed at the P3HT/PEDOT:PSS interface underneath the C_{60} layer. This effect of deposition-sequence-dependent energy level alignment needs to be considered when using multi-heterolayers in organic functional devices.

On the other hand, the hole injection barrier for pentacene was hardly affected by pre-coating PEDOT:PSS with P3HT (0.40 on P3HT/PEDOT:PSS *vs.* 0.45 eV on PEDOT:PSS). We attribute this to the fact that pentacene shows virtually the same interfacial dipole when deposited on PEDOT:PSS as does P3HT, and to a similar growth of PEN on both polymeric substrates. However, the valence band onset of P3HT was closer to E_F on PEDOT:PSS (0.2 eV) compared to PEN pre-covered PEDOT:PSS (0.55 eV). The ionization energy of P3HT on PEN/PEDOT:PSS was increased by almost the same amount. This was explained by different P3HT inter-molecular packing on the two substrates, which was corroborated by the observation by AFM of a disordered P3HT film on PEDOT:PSS and nanoscopic P3HT-related crystallites on PEN/PEDOT:PSS.

Acknowledgements

The authors thank H.C. Starck GmbH & Co. KG for providing PEDOT:PSS. This work was supported by the Sfb448 (DFG), the 863 project of the National High Technology Research and Development Program of China (No. 2006AA03Z0412), the 973 project of the National Grand Fundamental Research Program of China (No. 60576016), and the *Excellent Doctor's Science and Technology Innovation Foundation* of Beijing Jiaotong University (48011). NK acknowledges financial support by the Emmy Noether-Program (DFG).

References

[1] C.W. Tang, S.A. van Slyke, Appl. Phys. Lett. 51 (1987) 913.
[2] M. Pope, C.E. Swenberg, Electronic Processes in Organic Crystals and Polymers, Oxford University Press, Oxford, 1999.
[3] R.H. Friend, R.W. Gymer, A.B. Holmes, J.H. Burroughes, R.N. Marks, C. Taliani, D.D.C. Bradley, D.A. Dos Santos, J.L. Bredas, M. Löglund, W.R. Salaneck, Nature 397 (1999) 121.
[4] G. Hadziioannou, P.F. van Hutten (Eds.), Semiconducting Polymers, Wiley-VCH, Weinheim, 2000.

[5] B. Mazhari, Org. Electron. 6 (2005) 229.
[6] H. Ishii, K. Sugiyama, E. Ito, K. Seki, Adv. Mater. 11 (1999) 605.
[7] W.R. Salaneck, K. Seki, A. Kahn, J.-J. Pireaux (Eds.), Conjugated Polymer and Molecular Interfaces: Science and Technology for Photonic and Optoelectronic Applications, Marcel Dekker, New York, 2001.
[8] A. Kahn, N. Koch, W.Y. Gao, J. Polym. Sci. B 41 (2003) 2529.
[9] A. Rajagopal, C.I. Wu, A. Kahn, J. Appl. Phys. 83 (1998) 2649.
[10] S. Berleb, W. Brütting, G. Paasch, Synth. Met. 122 (2001) 37.
[11] W.Y. Gao, A. Kahn, Appl. Phys. Lett. 82 (2003) 4815.
[12] S.C. Veenstra, H.T. Jonkman, J. Polym. Sci. B 41 (2003) 2549.
[13] H. Vazquez, W. Gao, F. Flores, A. Kahn, Phys. Rev. B 71 (2005) 041306.
[14] O.V. Molodtsova, T. Schwieger, M. Knupfer, Appl. Surf. Sci. 252 (2005) 143.
[15] N. Koch, I. Salzmann, R.L. Johnson, J. Pflaum, R. Friedlein, J.P. Rabe, Org. Electron. 7 (2006) 537.
[16] A. Rajagopal, N. Koch, J. Ghijsen, K. Kaeriyama, R.L. Johnson, G. Leising, J.-J. Pireaux, Metallized Plastics 7 (2001) 1.
[17] S. Chao, K. Lee, J. Yuan, G.M. Wang, D. Moses, A.J. Heeger, J. Appl. Phys. 100 (2006) 114503.
[18] A. Zen, M. Saphiannikova, D. Neher, J. Grenzer, S. Grigorian, U. Pietsch, U. Asawapirom, S. Janietz, U. Scherf, I. Lieberwirth, G. Wegner, Macromolecules 39 (2006) 2162.
[19] C. Tengstedt, W. Osikowicz, W.R. Salaneck, I.D. Parker, C.H. Hsu, M. Fahlman, Appl. Phys. Lett. 88 (2006) 053502.
[20] S. Rentenberger, A. Vollmer, E. Zojer, R. Schennach, N. Koch, J. Appl. Phys. 100 (2006) 053701.
[21] N. Koch, A. Vollmer, Appl. Phys. Lett. 89 (2006) 162107.
[22] N. Koch, A. Elschner, J.P. Rabe, R.L. Johnson, Adv. Mater. 17 (2005) 330.
[23] S. Hasegawa, T. Miyamae, K. Yakushi, H. Inokuchi, K. Seki, N. Ueno, J. Electron Spectrosc. Relat. Phenom. 88–91 (1998) 891.
[24] H. Fukagawa, H. Yamane, T. Kataoka, S. Kera, M. Nakamura, K. Kudo, N. Ueno, Phys. Rev. B 73 (2006) 245310.

Available online at www.sciencedirect.com
ScienceDirect
Organic Electronics 8 (2007) 615–620
Organic Electronics
www.elsevier.com/locate/orgel

Letter

Top gate pentacene thin film transistor with spin-coated dielectric

Taegeun Kwon, Changhoon Baek, Hong H. Lee *

School of Chemical and Biological Engineering, Interdisciplinary Program in Nano-Science and Technology, Seoul National University, Seoul 151-742, Republic of Korea

Received 27 January 2007; received in revised form 17 March 2007; accepted 19 March 2007
Available online 28 March 2007

Abstract

Fabrication of top gate pentacene thin film transistor (TFT) is made possible with spin-coatable dielectrics by the technique presented here. Such fabrication has been impractical because of the ill effects a solvent can have on pentacene. A bilayer of pentacene on insulator that are coated on a mold is transferred to a glass substrate on which source and drain electrodes are defined. In the transfer process, pentacene is automatically patterned. This fabrication method allows for the channel length to be as small as photolithography would permit.
© 2007 Elsevier B.V. All rights reserved.

PACS: 85.30.Tv

Keywords: Organic thin film transistor; Top gate; Pentacene; Spin-coated dielectric; Transfer patterning; Grain size

Pentacene thin film transistor (TFT) has come a long way since its introduction in the early 1990s [1,2]. The use of these TFTs for flat panel display [3] and integrated circuits [4] has already been demonstrated. To fabricate the TFT, pentacene has to be patterned. Typically, a shadow mask is used to define the active area. However, the resolution is limited and it is difficult to apply the method over large area.

To overcome the shortcomings of the shadow mask method, lamination techniques with [5] and without [6,7] light exposure have been introduced. Recently, a transfer patterning technique [8] has been introduced. In this technique, pentacene is deposited on a patterned "rigiflex" mold [9] and the pentacene on the raised part of the mold that corresponds to the desired active area is directly transferred from the mold to the gate dielectric of the TFT. While the method is simple, the surface on which pentacene is deposited is limited to that of the mold material and thus the freedom to choose a surface for larger pentacene grain size is lost. To remove the restriction, a gate dielectric of choice needs to be coated on the mold and then pentacene is deposited on the coated dielectric. When this bilayer of pentacene on dielectric is transfer-patterned, the usual bottom gate TFT cannot be fabricated since then the transferred bilayer will have

* Corresponding author. Tel.: +82 2 880 7403; fax: +82 2 878 5043.
E-mail address: honghlee@snu.ac.kr (H.H. Lee).

1566-1199/$ - see front matter © 2007 Elsevier B.V. All rights reserved.
doi:10.1016/j.orgel.2007.03.008

dielectric on pentacene. Therefore, a top gate TFT results.

While we were initially motivated to have the freedom to choose any dielectric for larger grain size, we were also inspired by the prospect that a top gate pentacene TFT can be fabricated with solution-based dielectrics such as polymer dielectrics that can be dip- or spin-coated. Low cost manufacturing is the main driving force for solution-processing. Consequently, polymer dielectrics and sol-derived dielectrics [10] are sought after to replace vapor-deposited gate dielectrics. This push for solution-based gate dielectric is inherently incompatible with top gate pentacene transistor because a solution that is coated on pentacene can lead to damaging the underlying pentacene. It is, therefore, not surprising that there are only a handful of articles [11–13] on top gate pentacene TFT. The performance of the device, however, is poor because of the deleterious effects a solvent can have on pentacene.

In this letter, we present a method of fabricating top gate pentacene TFT with solution-based gate dielectric. Pentacene can be deposited on any dielectric of choice such that the grain size can be manipulated. The active area of pentacene is defined automatically when a bilayer of pentacene on dielectric is transferred to a substrate.

The procedure involved in fabricating top gate pentacene TFT is schematically illustrated in Fig. 1. A rigiflex mold, which is poly(urethaneacrylate) (PUA) [14] in this case, is prepared in which the raised part of the mold corresponds to the active area. The UV-curable, PUA mold material is obtained from Minuta Tech in Korea and used as received. The PUA mold material consists of a functionalized prepolymer with acrylate group, a photoinitiator, and a radiation-curable releasing agent for the surface activity. The liquid mixture was drop-dispensed onto a master pattern. A flexible and transparent polyethyleneterephthalate (PET) film was brought into contact with the liquid mixture. Subsequently, it was exposed to UV ($\lambda =$ 250–400 nm) for a few tens of seconds through the transparent backplane (dose = 100 mJ/cm^2). After the UV curing, the mold was peeled away from the master mold. The backplane film for the hard mold is a 188-μm-thick adhesive PET film (PET primed with polyurethane, SKC Co., Korea) that allows a degree of flexibility. The cured mold can be used repeatedly for the patterning without any deformation problem of the mold if there is no contamination from the experimental environment. Onto the mold, fluorinatedethylenepropylene (FEP) is thermally deposited to a thickness of 30 nm at a deposition rate of <1 Å/s at room temperature to form an interface with a low work of adhesion. To overcome the problem of wetting the low energy surface, enough solution drops are dispensed on the substrate to cover the whole surface prior to spin-coating. The dielectric of 10 wt.% poly(methylmethacrylate) (PMMA) (MW 16,000) in toluene is then spin-coated on the FEP deposited surface at 3000 rpm for 30 s, followed by deposition of pentacene by thermal evaporation to a thickness

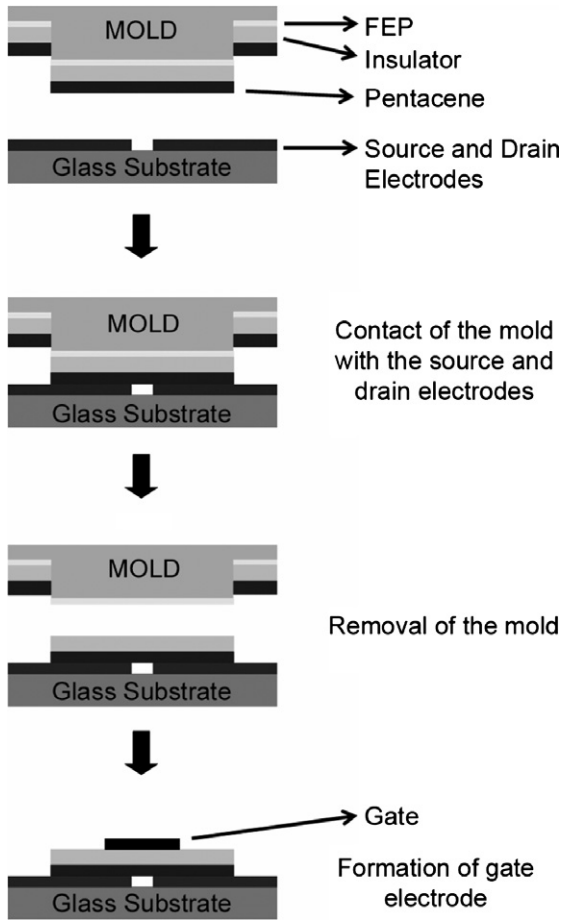


Fig. 1. Schematic illustration of the procedure for fabricating top gate pentacene TFT. To prepare a mold for the transfer to follow, FEP is vapor-deposited on the patterned mold, followed by spin coating of polymer dielectric, and then by vapor-deposition of pentacene. This prepared mold is brought into contact with the substrate on which source and drain electrodes are patterned. Slight pressing and heating are applied for the transfer, after which the mold is removed. The gate is then defined by vapor deposition with a shadow mask, completing the fabrication.

of 100 nm at a deposition rate of <0.5 Å/s at room temperature. The spin-coating conditions are such that the dielectric layer is 1 μm thick. A cleaned glass substrate is also prepared on which the gold source and drain electrodes are patterned by thermal evaporation with a shadow mask. The channel width and length are 3000 and 120 μm, respectively. The mold with the coated layers is brought into contact with the glass substrate. Manual alignment was used to ensure that the raised part of the mold is aligned with the gold electrodes. A pressure less than 1 MPa is applied at 80 °C for several minutes to transfer the bilayer of pentacene on dielectric to the glass substrate. The bilayer of pentacene and PMMA on the protruding part of the mold is transferred to the substrate where the gold source and drain electrodes are patterned. The mold is then simply removed, resulting in the transfer. The height of the raised part of the mold is much larger than the thickness of spin-coated PMMA. As a consequence, the PMMA coated on the edges of the side walls is very thin, facilitating relatively easy tearing at the edges when the transfer is made. Because the work of adhesion at the FEP-dielectric interface is the lowest, clean separation takes place at the interface. The work of adhesion at an interface can be calculated based on contact angle measurements with two probe liquids [15,16]. The aluminum gate is then defined by thermal evaporation through a shadow mask, completing the fabrication of top gate pentacene TFT. All the metal and organic semiconductor films in both devices were deposited by thermal evaporation at room temperature under a vacuum of 10^{-6} Torr.

The transfer patterning results of the pentacene/PMMA bilayer are shown in Fig. 2. A tilted micrograph by scanning electron microscopy (SEM) in Fig. 2a shows the pentacene/PMMA bilayer that was transferred across the channel formed by the source and drain electrodes on a glass substrate. To clearly show that the bilayer bridges the electrodes rather than follows the contour of the electrodes, a bit of space was allowed between the edge of the electrodes and that of the bilayer, the dark horizontal line being the edge of the bilayer (1000 nm thick PMMA + 100 nm thick pentacene). As a result, the lower part of the channel is bare and the upper part in the figure is covered with the bilyer, the darkish slanted vertical strip being the channel. Simple bilayer transfer pattering is demonstrated in Fig. 2b–d. Shown in Fig. 2b is an optical image of the master pattern of 4 μm size square holes made on silicon wafer. A PUA mold was prepared from the master and the mold was

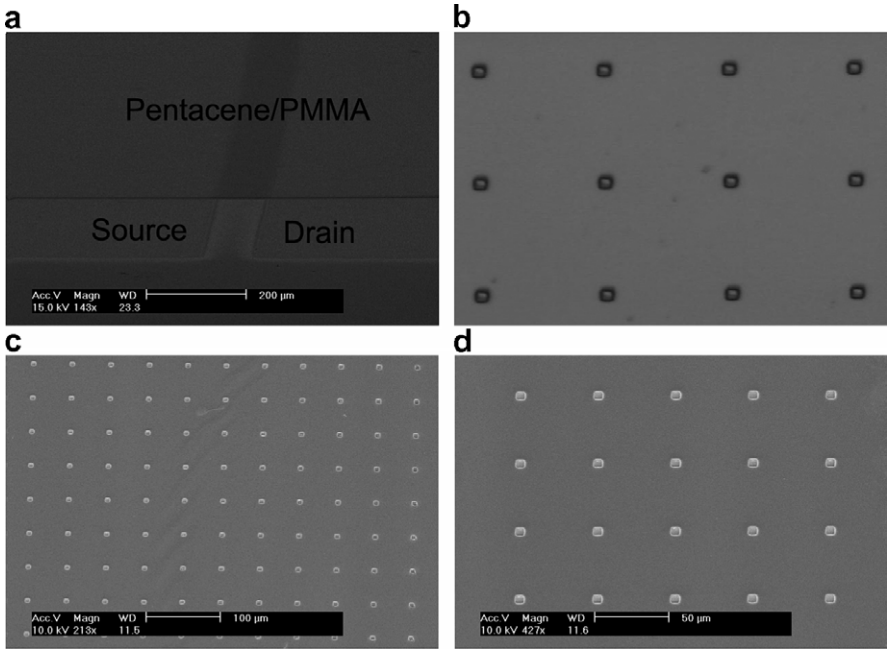


Fig. 2. Results of transfer patterning of bilayer of pentacene on insulator: (a) SEM image of the bilayer that was transferred across the channel between source and drain, (b) optical image of Si master with an array of 4 μm boxes, (c) SEM image of the bilayer transferred using the master in (b) and (d) enlarged image of (c).

coated with PMMA followed by pentacene. Fig. 2c shows the boxes of the bilayer formed on a glass substrate by the transfer from the mold to the substrate and Fig. 2d is an enlarged image of Fig. 2c.

It should be noted here that an advantage of top gate TFT over bottom gate TFT is that the channel length can be defined as small as photolithography allows. In the top gate structure, the source and drain electrodes are made on glass substrate and therefore the conventional photolithography can be used for the patterning. A definitive comparison between top and bottom gate transistors has not been made in the literature.

To compare the electrical performance, a reference device was also fabricated by the conventional shadow mask method. Since pentacene would be damaged in the process of coating PMMA solution on pentacene for the top gate TFT, the bottom gate structure was used instead for the reference. The materials and deposition conditions were the same as for the top gate TFT except that pentacene is patterned using the shadow mask method for the reference device. The current–voltage characteristics of both the top gate device fabricated with the transfer method (black squares) and the bottom gate reference device fabricated with the shadow mask method (gray dots) are shown in Fig. 3a. For the transfer curves, the gate voltage V_G was scanned from 10 V to −100 V with a fixed source–drain voltage, V_{SD}, at −100 V. The same transfer curves plotted in terms of $I_D^{1/2}$ vs V_G are shown in Fig. 3b. The output curves for various gate voltages are given in Fig. 3c for the top gate TFT fabricated with the transfer method and in Fig. 3d for the bottom-gate reference device. For the effective mobility, μ_e, the following relationship in the saturation region was used

$$I_D = \frac{1}{2}\mu_e C_i \frac{W}{L}(V_G - V_T)^2 \quad (1)$$

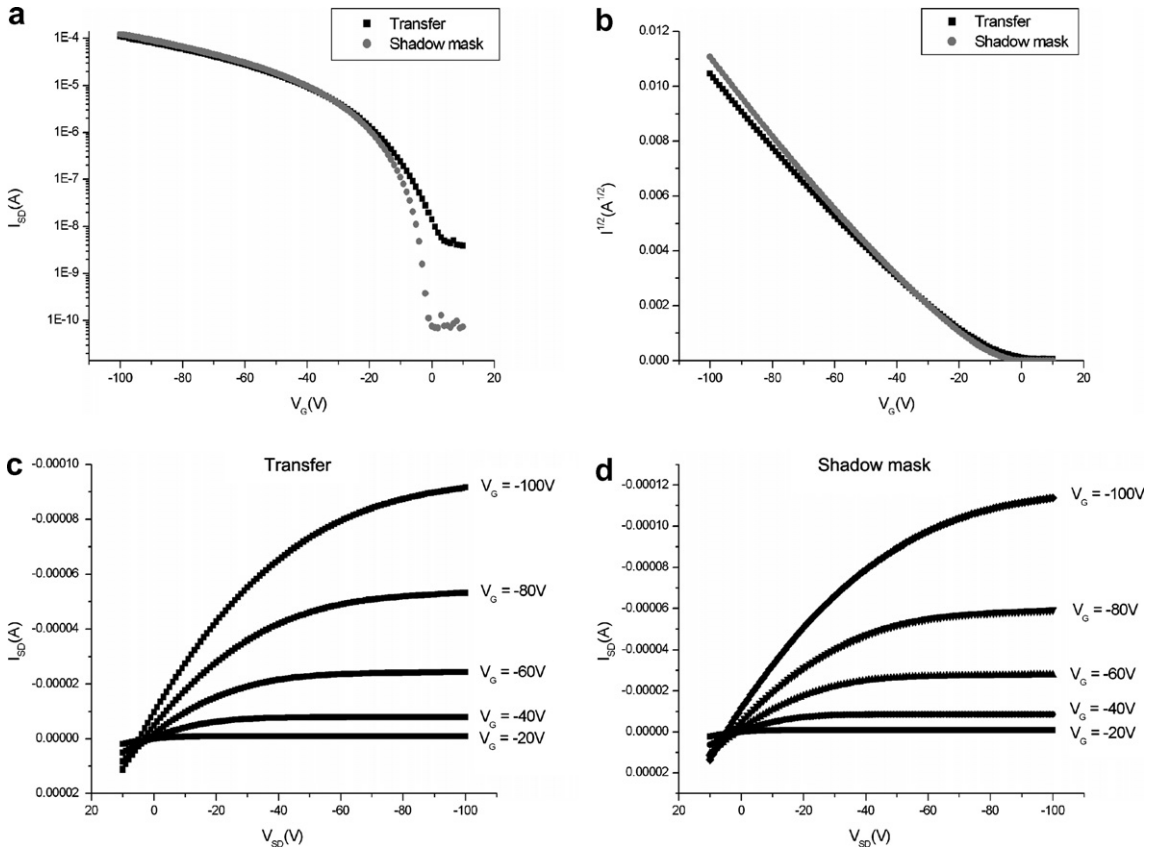


Fig. 3. Electrical characteristics of OTFTs: (a) $\log I_D$ vs V_G for the reference device (gray dots) fabricated by conventional thermal evaporation with shadow mask and for the device (black squares) fabricated by the transfer method. The source–drain voltage is −100 V, (b) $I_D^{1/2}$ vs V_G for both OTFTs for a fixed source–drain voltage of −100 V, (c) I_D vs V_{SD} for the device fabricated by the transfer method and (d) I_D vs V_{SD} for the reference device.

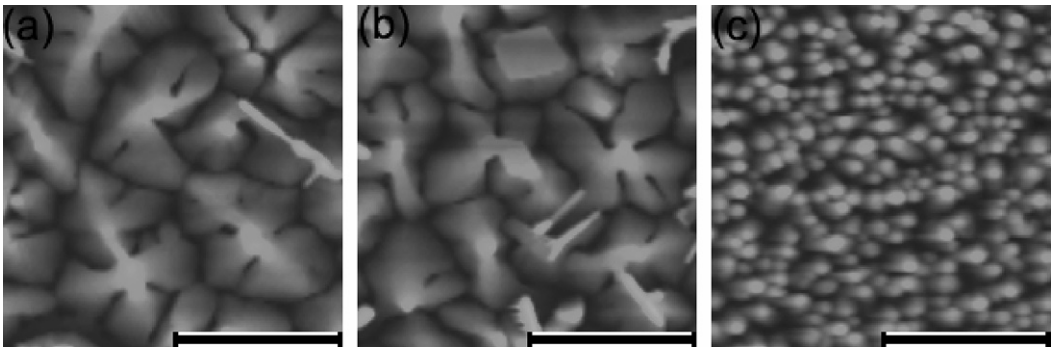


Fig. 4. AFM images of pentacene morphology and grains: (a) pentacene film thermally evaporated on PMMA film, (b) thermally evaporated on PUA mold and (c) thermally evaporated on PMMA film that was coated on FEP deposited PUA mold. The scale bar in all the images is 1 μm long.

where I_D is the drain current density, W and L are the channel width (3000 μm) and channel length (120 μm), respectively, and C_i is the insulator capacitance (5.3 nF/cm^2), and V_G and V_T are the gate and threshold voltage, respectively. The mobility thus determined is 0.18 cm^2/V s for the top gate TFT whereas it is 0.21 cm^2/V s for the reference. For the top gate TFT, the threshold voltage and on- and off-state currents are -13 V, 1.1×10^{-4} A, and 3.9×10^{-9} A, respectively, such that the on–off current ratio is 2.8×10^{4} whereas those for the reference are -16 V, 1.2×10^{-4} A, and 7.3×10^{-11} A, respectively, with the on–off ratio of 1.6×10^{6}. The electrical characteristics are essentially similar. However, the leakage current at the off-state is higher by more than one order of magnitude than the reference device and any difference between the two devices are mainly due to the high off-state current of the device that was fabricated with the transfer method. This high off-current is believed due to trapped air/particle at the interface or roughness caused by less than perfect wetting of the PMMA solution on the low energy surface of FEP, the exact cause of which has not yet been resolved.

One of the motivations for the top gate TFT was to have the freedom to choose any dielectric or to tailor the surface so that the grain size of pentacene can be manipulated. When the direct pentacene transfer method is used, the surface on which pentacene is deposited is restricted to that of the mold, which is PUA in this case. Shown in Fig. 4 are the images of pentacene grains by atomic force microscopy (AFM). The AFM image in Fig. 4a, which is for the pentacene film deposited on PMMA by thermal evaporation, shows a larger grain size when compared with the grain size in Fig. 4b for the film deposited on PUA film. As expected, the image in Fig. 4c for the film deposited on PMMA that was coated on FEP deposited PUA mold shows a grain structure similar to that in Fig. 4a. Because of this larger grain size, the mobility of the top-gate pentacene TFT device is higher (0.18 cm^2/V s) than that of the device fabricated by the direct transfer method [5] (0.07 cm^2/V s).

In summary, the fabrication of top gate pentacene TFTs is now made possible with the technique introduced here even when the gate dielectric is solution-based material such as polymeric dielectrics. The top gate TFTs with spin-coatable dielectrics have been impractical to fabricate because of the deleterious effects a solvent can have on pentacene. With this advent of the capability to fabricate top gate pentacene TFTs, the source and drain electrodes can be patterned by photolithography and as such the channel length can be made as small as photolithography would allow. Unlike the direct transfer method presented earlier for pentacene patterning [5], the technique introduced here allows tailoring of dielectric surface so as to maximize the pentacene grain size in the course of patterning pentacene. This capability would open the door to routine fabrication and use of top gate pentacene TFTs, which has so far been impractical because of the solvent effects. Although pentacene and PMMA were used for the semiconductor and insulator of TFT, the same approach should be applicable to other organic semiconductors and insulators.

References

[1] G. Horowitz, X.-Z. Peng, D. Fichou, F. Garnier, Synthetic Metals 51 (1992) 419.

[2] C.D. Dimitakopoulos, A.R. Brown, A. Pomp, J. Appl. Phys. 80 (1996) 2501.
[3] P. Mach, S.J. Rodirguez, R. Nortrup, P. Wiltzius, J.A. Rogers, Appl. Phys. Lett. 78 (2001) 3592.
[4] M. Ahles, R. Schmechel, H. Seggern, Appl. Phys. Lett. 87 (2005) 113505.
[5] G.B. Blanchet, Y.-L. Loo, J.A. Rogers, F. Gao, C.R. Fincher, Appl. Phys. Lett. 82 (2003) 463.
[6] D.R. Hines, S. Mezhenny, M. Breban, E.D. Williams, Appl. Phys. Lett. 86 (2005) 163101.
[7] M. Ofuji, A.J. Lovinger, C. Kloc, T. Siegrist, A.J. Maliakal, H.E. Katz, Chem. Mater. 17 (2005) 5748.
[8] S.Y. Park, T. Kwon, H.H. Lee, Adv. Mater. 18 (2006) 1861.
[9] S.-J. Choi, P.J. Yoo, S.J. Baek, T.W. Kim, H.H. Lee, J. Am. Chem. Soc. 126 (2004) 7744.
[10] K.K. Han, S.Y. Park, M.J. Kim, H.H. Lee, Appl. Phys. Lett. 87 (2005) 253502.
[11] E. Becker, R. Parashkov, G. Ginev, D. Schneider, S. Hartmann, F. Brunetti, T. Dobbertin, D. Metzdorf, T. Riedl, H.-H. Johannes, W. Kowalsky, Appl. Phys. Lett. 83 (2003) 4044.
[12] T. Cui, G. Liang, Appl. Phys. Lett. 86 (2005) 064102.
[13] M.J. Panzer, C.R. Newman, C.D. Frisbie, Appl. Phys. Lett. 86 (2005) 103503.
[14] P.J. Yoo, S.J. Choi, J.H. Kim, D. Suh, S.J. Baek, T.W. Kim, H.H. Lee, Chem. Mater. 16 (2004) 5000.
[15] Z. Wang, J. Zhang, R. Xing, J. Yuan, D. Yan, Y. Han, J. Am. Chem. Soc. 125 (2003) 15278.
[16] J. Rhee, Ph.D thesis, Cathode Patterning for Organic Light-Emitting Diodes, Seoul National University, 2004 (Chapter 3).

Available online at www.sciencedirect.com
ScienceDirect
Organic Electronics 8 (2007) 621–624
Organic Electronics
www.elsevier.com/locate/orgel

Letter

A polymer light-emitting diode as an optical communication light source

Iain A. Barlow [a], Theo Kreouzis [b], David G. Lidzey [a,*]

[a] Department of Physics and Astronomy, The University of Sheffield, Hicks Building, Hounsfield Road, Sheffield S3 7RH, United Kingdom
[b] Department of Physics, Queen Mary, University of London, Mile End Road, London E1 4NS, United Kingdom

Received 3 April 2007; accepted 11 April 2007
Available online 19 April 2007

Abstract

We demonstrate improvements in the electroluminescence switching rate of polymer light-emitting diodes by reducing their active area. We explore the frequency response of devices having a range of sizes and show that LED's having an active area of 0.02 mm^2 can be modulated at 16 MHz. The emission from our devices peaks at around 540 nm and thus falls within a transmission window of plastic optical fibers, suggesting possible applications of polymer LED's as low cost optical communication sources.
© 2007 Elsevier B.V. All rights reserved.

PACS: 42.82.Ds; 78.60.Fi; 85.60.Jb

Keywords: Conjugated polymer; Light-emitting; Transient electroluminescence; Optical communication

1. Introduction

Light-emitting diodes capable of fast EL switching are finding application as electro-optic conversion devices for short range local area networks based on plastic optical fibers (POF's). A recently commercialized POF network technology [1] used in motor vehicle airbag deployment, is capable of a data rate of 10 Mb/s and utilizes inorganic LED's working at $\lambda = 650$ nm. In-vehicle local area networks are eventually anticipated to provide data buses for key vehicle functions such as steer and brake-by-wire as well as multimedia entertainment, with future systems predicted to reach data transfer rates of up to 400 Mb/s [2].

Nanosecond transient electroluminescence of small area organic LED's has in fact been demonstrated at low duty cycles [3–8]. However the high operating voltages and low bit-rates used in previous studies would not be suitable for practical optical communication systems. Recent work has shown that a blue emitting organic LED, based on a low molecular mass organic dye [9], had a 50% cutoff frequency of approximately 30 MHz. However, such devices had an emission peak of 430 nm, a wavelength not well matched to plastic optical fiber transmission windows at 510 and 570 nm [10]. Although such an emission wavelength

* Corresponding author. Tel.: +44 (0) 114 222 3501; fax: +44 (0) 114 222 3555.
E-mail address: d.g.lidzey@sheffield.ac.uk (D.G. Lidzey).

1566-1199/$ - see front matter © 2007 Elsevier B.V. All rights reserved.
doi:10.1016/j.orgel.2007.04.003

can be easily met using molecular dyes such as Alq_3, this material is not well suited for fast switching, as its fluorescence decay lifetime is relatively slow, being 12–16 ns [11,12].

To address this issue, we have developed an efficient conjugated polymer based LED having a peak emission wavelength of 538 nm which is more closely matched to a POF transmission window. By reducing device area, we demonstrate device switching at 16 MHz. Although the conjugated polymer used in our work has a relatively low charge carrier mobility, such performance would be suitable for low bit rate communication systems. Significant improvements in switching rates could be readily achieved by using higher mobility conjugated polymers.

2. Experimental procedure

The green emitting polymer that we have used is based on a polyfluorene copolymer which is a proprietary "LUMATION™" polymer termed K2. The absorption and photoluminescence spectra of K2 and the device electroluminescence spectrum are shown in Fig. 1. Using time-correlated single-photon counting measurements we have determined the fluorescence decay lifetime of K2 to be 2 ns. LED devices were fabricated on 30×30 mm ITO coated glass substrates with a sheet resistance of 20 Ω/□. Each LED structure had an ITO anode coated by a 50 nm poly(3,4-ethylenedioxythiophene):poly(styrene sulfonate) film to enhance hole injection which was coated by a 70 nm thick layer of K2. The PEDOT:PSS (Baytron P VP CH 8000) was purchased from H.C. Starck. The K2 polymer was spin cast from toluene solution onto the PEDOT:PSS and baked at 100 °C for 1 h. A device cathode was coated onto the K2, and was composed of a 20 nm thick layer of Ca capped by 50 nm of Ag.

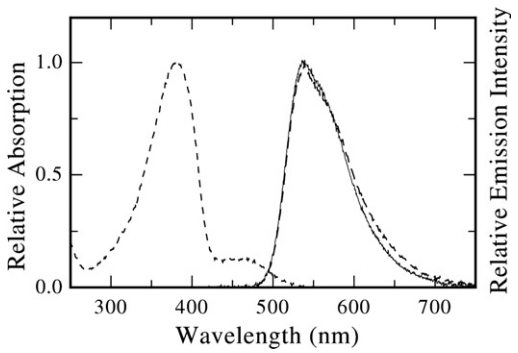


Fig. 1. Absorption (short dash) and photoluminescence (long dash) spectra of K2 polymer and device EL spectrum (solid line).

To explore the effect of device active area on the EL switching rate, we have varied the overlap area between anode and cathode contacts. Here, the ITO surface was photolithographically patterned and subsequently etched with HCl to create anode strips having widths of 3 mm or 70 μm. The LED cathode was deposited onto the K2 polymer through a shadow mask, creating a strip having a width of between 6 mm and 320 μm. The active area of devices was thus defined by the electrode overlap, forming devices having active areas of 0.02, 9 and 18 mm^2.

Devices were encapsulated in a nitrogen glovebox with a glass cover slip held in place by UV curing epoxy glue. For pulsed measurements, LED's were driven with an Agilent Technologies 8114A rectangular pulse generator with 7 ns rise and fall times. The EL response was detected by a fast photo-multiplier tube (Electron Tubes 9079B) with a response time of 1.8 ns. A Tektronix 3052B digital oscilloscope was used to simultaneously record the voltage and EL pulses. All transient results presented are the average of 64 oscilloscope traces.

Time-of-flight measurements were performed on a 600 nm thick spin-coated K2 device that was UV epoxy encapsulated. The sample employed semitransparent Al electrodes and had an identical pixel geometry to the 18 mm^2 light-emitting devices.

3. Results and discussion

Fig. 2 shows current–voltage–luminance characteristics of three different devices, having active

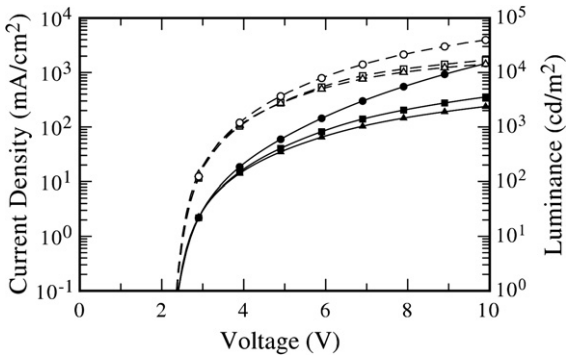


Fig. 2. Current–voltage–luminance characteristics for 0.02 mm^2 (circles), 9 mm^2 (squares) and 18 mm^2 (triangles) devices. Open shapes on dashed lines are voltage–luminance and closed shapes on solid lines are voltage–current density.

areas of 0.02, 9 and 18 mm^2. As the active area of the device is reduced, surprisingly, we find that the devices sustain a higher current density and emit more intense electroluminescence. The efficiency of the LED's is not however a strong function of area, with all devices having a maximum efficiency of 7.1 ± 0.7 cd/A. The reason for this apparent area dependence of current density results from the fact that the smaller area LED's have a proportionally greater resistance compared to the serial resistance of the anode and cathode stripes that comprise part of the external circuit. This results in the voltage dropped across the polymer layers being relatively larger for smaller area devices. We have measured the total serial electrode resistance of our devices as a function of area and find, for example, that for an applied voltage of 5 V, almost exactly 5 V is dropped across the active layer of a 0.02 mm^2 LED compared with 4.3 V across an 18 mm^2 device.

The RC time constant of the LED equivalent circuit can be approximated by R_sC [3], where R_s represents the resistance of the electrode strips and the external circuit and C is the device capacitance. We have determined the capacitance of the 9 and 18 mm^2 devices using an impedance analyzer operating at subthreshold dc bias voltages with an ac test signal of 50 mV at a frequency of 10 kHz. Significant carrier injection is not anticipated and thus we extract the "intrinsic" capacitance of the device. The measured capacitance of the 9 and 18 mm^2 devices was 3.4 and 6.8 nF, respectively. This agrees well with the calculated capacitances of 3.3 and 6.8 nF, assuming a value of 3 for the relative permittivity, ϵ_r, of the emitting polymer [13] and the PEDOT:PSS layer functions as part of the anode and does not contribute to capacitance [8]. Unfortunately we could not accurately determine the capacitance of the 0.02 mm^2 device, however if we assume a similar polymer thickness, we estimate that its capacitance is 8.5 pF. We calculate the overall time constant of the LED (including the resistance of the external circuit) to be 3.4 ns, 545 ns and 1.23 μs for the 0.02, 9 and 18 mm^2 devices, respectively.

The delay between the application of the applied voltage pulse and the onset of EL is often referred to as the turn-on delay. The EL turn-on delay is demonstrated in Fig. 3a. This turn-on delay results from two effects [6]: firstly, the time to charge the device to the threshold voltage for bipolar injection and secondly, the time taken for charge carriers to drift from the electrodes to the emission zone. As it can be seen from Fig. 3a, reducing the device area significantly reduces the turn-on delay which can be partly attributed to a reduced RC time constant. In particular, the delay time is reduced from 320 ns for the 18 mm^2 LED to 11 ns for the 0.02 mm^2 device. We have also determined the initial fast EL rise time for our devices (here defined as the time taken for the LED to switch between 10% and 90% of its steady state brightness). Again we see a reduction in rise time as the device active area is reduced, being 180 ns for the 0.02 mm^2 device compared to 410 ns for the 18 mm^2 device. We believe that this reduction in rise time for small

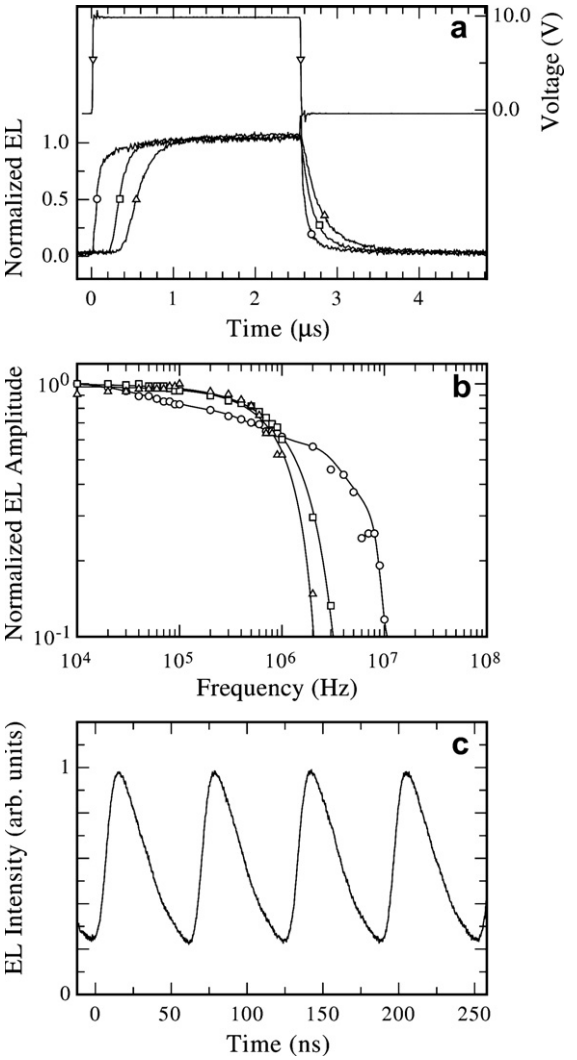


Fig. 3. (a) EL response of the 0.02 (○), 9 (□) and 18 mm^2 (△) devices to an applied 10 V, 2.5 μs pulse (▽), (b) frequency response of the devices (symbols are as before and the lines are a guide for the eye), and (c) EL response of the 0.02 mm^2 device to a 10 V, 10 ns pulse width, 16 MHz repetition frequency square wave.

area LED's also occurs as a consequence of the fact that a proportionally larger voltage is dropped across the emitting polymer film, which increases the injected current density and thus reduces the saturation time, as demonstrated by Nikitenko et al. [14].

Fig. 3b shows the frequency response of the different area devices, with all devices driven at a voltage of 10 V and 50% duty cycle. We define the EL amplitude as the difference between the maximum and minimum intensity of the EL pulse. As the device area is reduced, it can be seen that the roll-off frequency increases. The 0.02 mm^2 device, having the shortest turn-on delay and fastest initial rise has a roll-off frequency approximately 5 times greater than the largest (18 mm^2) device.

The *RC* time constant for the 0.02 mm^2 device is much smaller than the fast initial EL rise, indicating that the transient EL is dominated by the carrier transport properties of the emitting polymer. Our preliminary time-of-flight measurements have revealed a hole mobility of 3×10^{-5} cm^2/Vs measured at a field of 4.2×10^5 V/cm. This hole mobility is comparable to that of another Dow green emitting polymer [15]. The hole mobility of K2 is thus relatively low compared to other conjugated polymer materials that have hole mobilities up to 3×10^{-3} cm^2/Vs at a field of 2.5×10^5 V/cm [16]. We therefore anticipate that faster switching rates can be expected through the use of conjugated polymers having higher carrier mobilities.

4. Conclusion

The highest frequency at which we could successfully modulate EL at a 50% duty cycle was 10 MHz with a power output of 0.36 μW per pulse. Faster modulation can be achieved by using a reduced duty cycle to address the device. For example, Fig. 3c shows the EL response of the 0.02 mm^2 device driven by an applied pulse of 10 ns duration (excluding 7 ns rise and fall times) at a repetition frequency of 16 MHz and voltage of 10 V. Note that this pulse rate is limited by our driving electronics and not the LED itself. Here the temporal width (at half-maximum) of each EL pulse is 33 ns.

We have therefore demonstrated that reducing the active area of the LED has the effect of reducing device capacitance which in turn reduces the *RC* charging time and therefore the turn-on delay. We have used such devices to create optical pulses of 33 ns width at a repetition rate of 16 MHz. By improving the mobility of the active conjugated polymer and reducing device thickness, we believe that further improvements in device switching speed can be anticipated.

Acknowledgements

The authors wish to thank A.R. Buckley (Micro-Emissive Displays Ltd.) for useful discussions, A.J. Cadby for fluorescence decay lifetime measurements, M.J. Stevenson for help with obtaining spectra and The Dow Chemical Company for provision of the LUMATION™ polymer. This work was funded by EPSRC Grant No. (GR/R25712) "High performance light sources based on polymer light-emitting diodes".

References

[1] J. Lambkin, in: Optics and Laser Europe, April 2006, p. 23.
[2] T. Freeman, in: Fibre Systems Europe in association with Lightwave Europe, May 2004, p. 14.
[3] D. Braun, D. Moses, C. Zhang, A.J. Heeger, Appl. Phys. Lett. 61 (26) (1992) 3092–3094.
[4] N.T. Harrison, N. Tessler, C.J. Moss, K. Pichler, R.H. Friend, Opt. Mater. 9 (1–4) (1998) 178–182.
[5] C. Hosokawa, H. Tokailin, H. Higashi, T. Kusumoto, Appl. Phys. Lett. 63 (10) (1993) 1322–1324.
[6] M. Ichikawa, J. Amagai, Y. Horiba, T. Koyama, Y. Taniguchi, J. Appl. Phys. 94 (12) (2003) 7796–7800.
[7] N. Tessler, N.T. Harrison, R.H. Friend, Adv. Mater. 10 (1) (1998) 64.
[8] J. Wang, R.G. Sun, G. Yu, A.J. Heeger, J. Appl. Phys. 91 (4) (2002) 2417–2422.
[9] H. Kajii, T. Tsukagawa, T. Taneda, Y. Ohmori, J. Phys. D 35 (12) (2002) 1334–1337.
[10] A.J. Shaw, A.L. Bradley, J.F. Donegan, J.G. Lunney, IEEE Photonic. Technol. L 16 (9) (2004) 2006–2008.
[11] C.W. Tang, S.A. VanSlyke, C.H. Chen, J. Appl. Phys. 65 (9) (1989) 3610–3616.
[12] I. Sokolik, R. Priestley, A.D. Walser, R. Dorsinville, C.W. Teng, Appl. Phys. Lett. 69 (27) (1996) 4168–4170.
[13] D.J. Pinner, R.H. Friend, N. Tessler, J. Appl. Phys. 86 (9) (1999) 5116–5130.
[14] V.R. Nikitenko, Y.H. Tak, H. Bassler, J. Appl. Phys. 84 (4) (1998) 2334–2340.
[15] D. Poplavskyy, W.C. Su, F. So, J. Appl. Phys. 98 (1) (2005) 014501.
[16] M. Redecker, D.D.C. Bradley, M. Inbasekaran, W.W. Wu, E.P. Woo, Adv. Mater. 11 (3) (1999) 241.

Available online at www.sciencedirect.com
ScienceDirect
Organic Electronics 8 (2007) 625–630
Organic Electronics
www.elsevier.com/locate/orgel

Letter

Energy level alignment and interface states at α-sexithiophene/Ag interfaces

Mandy Grobosch *, Martin Knupfer

IFW Dresden, Postfach 270116, D-01171 Dresden, Germany

Received 22 January 2007; received in revised form 19 April 2007; accepted 19 April 2007
Available online 25 April 2007

Abstract

We present a combined X-ray and ultraviolet photoemission study of the interface between the thiophene based organic semiconductor α-sexithiophene (6T) and silver. Thermally evaporated organic films were deposited in several steps without breaking the vacuum on polycrystalline silver foils. Subsequently, the films were characterized via photoemission spectroscopy. These series of spectra allowed the determination of the energy level alignment at the interface. Our results provide evidence that chemical interaction takes place between flat lying α-6T molecules and the silver surface resulting in interface electronic levels. From the observed well defined molecular orbitals we have analyzed the energy level alignment and have found an interface dipole of −0.7 eV and a hole injection barrier of about 1.8 eV.
© 2007 Elsevier B.V. All rights reserved.

PACS: 79.60.−i; 79.60.Bm; 79.60.Jv

Keywords: Energy level alignment; Sexithiophene; Interfaces; Photoemission spectroscopy

1. Introduction

In recent years, molecular organic semiconductor materials have been extensively studied due to their high application potential in electronic and optoelectronic devices. Thiophene based materials are a prominent member of the organic semiconductors, and for instance, organic field effect transistors (OFETs) on the basis of different thiophenes are characterized by high performance and a large potential for application [1–4]. The charge transport in organic electronic devices critically depends on the interface properties between the organic semiconductor material and the metal electrode. Deposition of organic semiconductor material on metal surfaces often results in the formation of a rather large interface dipole, a situation which is not fully understood yet [5–12]. Optimization of device performance however requires detailed knowledge of the interface electronic properties. In this contribution, we present studies of the organic/metal interface between α-sexithiophene and polycrystalline silver using core level X-ray photoemission spectroscopy and valence band ultraviolet photoemission spectroscopy. 6T has been chosen as a model representative for thiophene based systems, and silver is

* Corresponding author.
E-mail address: m.grobosch@ifw-dresden.de (M. Grobosch).

1566-1199/$ - see front matter © 2007 Elsevier B.V. All rights reserved.
doi:10.1016/j.orgel.2007.04.006

one of the few metals that also is expected to allow reasonable electron injection in these organic semiconductors. We observe the formation of an interface dipole of −0.7 eV and a large hole injection barrier of 1.8 eV. Importantly, our results indicate a chemical interaction between the thermally deposited α-6T and silver which causes interface states that might negatively impact charge transport across those interface.

2. Experimental

The photoemission experiments were performed using a commercial PHI 5600 spectrometer which was equipped with two monochromatic light sources. Photons with an energy of 1486.6 eV from an Al Kα source for X-ray photoemission spectroscopy (XPS) and photons from a He lamp with a photon energy of 21.21 eV for ultraviolet photoemission spectroscopy (UPS) are provided. The ultraviolet photoemission spectra including the secondary electron cutoff were measured applying a bias voltage of −5 V. The UPS spectra have been corrected for the contributions of He satellite radiation. By analyzing the width of a Ag Fermi edge the total energy resolution of the spectrometer was determined to be about 350 meV (XPS) and 100 meV (UPS), respectively. The binding energy scale was aligned by measuring the Fermi edge (0 eV binding energy) and the Ag $3d_{5/2}$ emission (368.3 eV binding energy) of a silver substrate. The used polycrystalline silver foils were cleaned by several cycles of Ar^+-sputtering (3 keV, 10^{-8} mbar). After the cleaning of the silver foils we have used X-ray photoemission spectroscopy to check their surface composition. We did not observe any sign of contaminations. We have used polycrystalline silver foils to simulate the conditions in fabrication of organic devices. In a preparation chamber (base pressure 5.5×10^{-10} mbar), which is attached to the spectrometer system, thin films of α-sexithiophene (purchased from Sigma Aldrich) with different thickness were prepared by in situ thermal evaporation on these polycrystalline silver foils. Typical evaporation rates were between 1 and 2.5 Å/min. Subsequently, the films were transferred to the measurement chamber (base pressure 10^{-10} mbar) without breaking the vacuum and characterized taking a full range XPS spectrum. The number of impurities in the films was very small and below the detection limit of XPS due to the ultra high vacuum conditions during the preparation process. We have estimated the thickness of the individual sexithiophene layers by monitoring the attenuation of the intensity of the Ag $3d_{5/2}$ substrate peak due to the organic overlayer. According to Seah and Dench [13] we have calculated the mean free path of electrons in α-sexithiophene films to be about 2.45 nm, for the kinetic energy of 1119 eV (Ag $3d_{5/2}$ signal from the substrate) and a sexithiophene density of 1.50 g/cm^3 [14,15]. We note that this procedure of thickness determination is only correct for a layer by layer growth of the organic film. If the organic film does not grow uniformly, this method undervalues the film thickness.

3. Results and discussion

Fig. 1 displays the measured C1s core level spectra of the α-sexithiophene films after a consecutive deposition onto the polycrystalline silver foil. For all thicker α-6T layers a clear fine structure in the C1s emission is visible. Going to lower coverage the fine structure starts to smear out and is lost for very low (0.3 nm) thicknesses. This fine structure, in the form of two equal components arises from the two different binding sites of the carbon atoms in the α-sexithiophene molecule [16–18]. The component at the lower binding energy site (C_C) corresponds to carbon atoms bonded on other

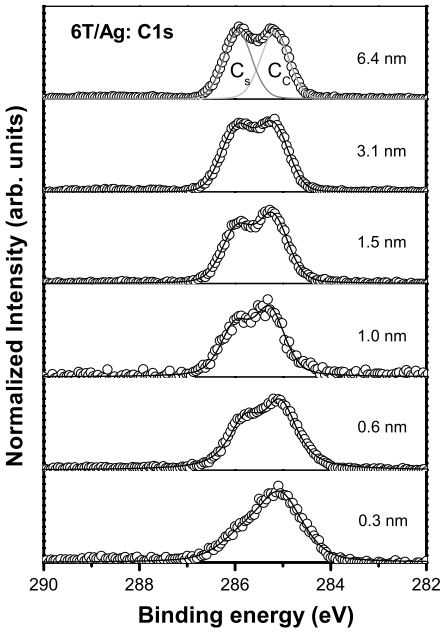


Fig. 1. Evolution of the C1s core level spectra with increasing α-6T layer thickness on Ag.

carbon atoms only. The second component (C_S) at the higher binding energy side of the C1s core level spectra results from the two carbon atoms in the thiophene rings that are attached to sulfur. The energy position of the C_S-component at 285.9 eV is in good agreement with the peak position of other sulfur containing organic materials [16,19,20]. The observed fine structure in the C1s core level spectra of α-sexithiophene is in very good agreement with previous results for other thiophene based organic materials [16–18]. The binding energy of the C1s core level as measured using the C_C component remains vitually constant by increasing the α-6T film thickness. The peak shape however significantly varies between thin and thick 6T layers. This peak shape change suggests a different chemical environment of the carbon atoms in thick and thin 6T films on silver, which could be due to a chemical interaction of the sexithiophene molecules with silver within the first molecular layer. This aspect will be discussed in more detail below.

The behaviour of the S2p core level revealing the two spin orbit split components $S2p_{3/2}$ and $S2p_{1/2}$ is shown in Fig. 2 for increasing α-6T film thicknesses. These data are in good correspondence to previous photoemission studies of other thiophenes [17,18,21–24]. Fig. 2 depicts that the binding energy of the S2p doublets changes by about 0.4 eV on going from very thin to thick 6T films, which is in contrast to the virtually constant binding energy of the C1s core excitations. We attribute this shift to a larger screening of the S2p core level of molecules close to the silver surface. Such a shift now in general can be due to partial electron transfer from silver to 6T in the initial or the final state of our experiment. This in turn can also explain the lower spectral weight at the binding energy associated to the C_C component for C1s emission from very thin 6T films, since such a charge transfer would render the two carbon sites more equivalent. From our core level studies alone, it is not possible to distinguish the two cases, initial or final state charge transfer, but we will see below that there is chemical interaction leading to the formation of interface induced electronic levels, which clearly demonstrates that there is charge transfer in the initial state.

We now turn to the results of our valence band photoemission studies. The left panel of Fig. 3 depicts the secondary electron cutoff which is a measure for the work function of the metallic substrate as well as of the organic overlayer. The work func-

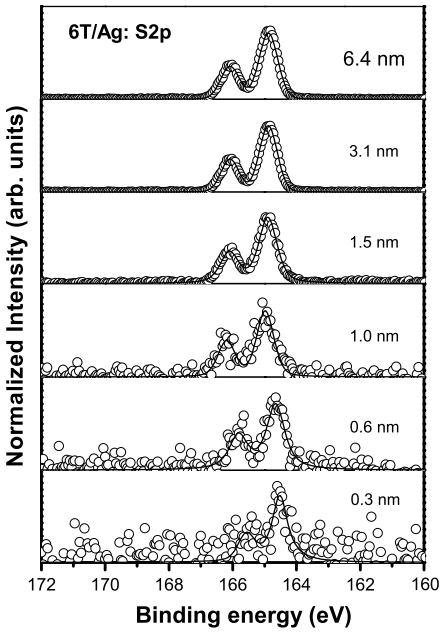


Fig. 2. Evolution of the S2p core level spectra with increasing α-6T layer thickness on Ag.

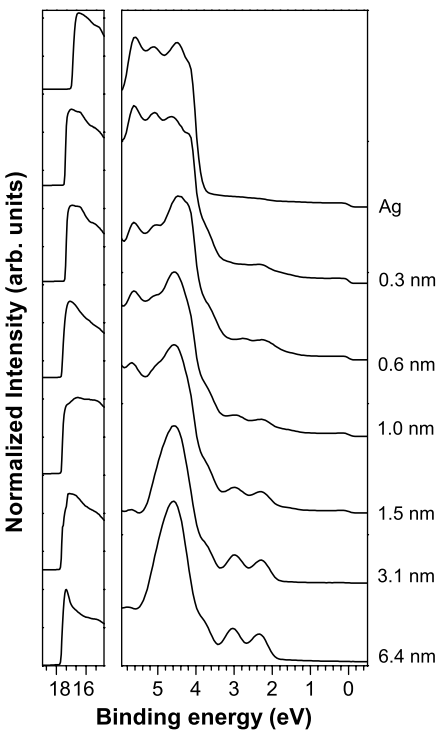


Fig. 3. Right panel: Ultraviolet photoemission spectra of α-6T films deposited on polycrystalline silver as a function of film thickness. Left panel: Corresponding high-binding energy cutoff of the UPS spectra.

tion of the metallic silver surface used in our studies was measured to be $\Phi_M = 4.2$ eV within an absolute error of 0.1 eV. This is in good agreement with previously reported values for polycrystalline silver surfaces [25–27]. Upon the initial deposition of α-6T we can observe an abrupt and rigid shift of the work function (about 0.4 eV) while with further increase in the α-6T film thickness it remains essentially constant. We deduce that the α-6T/Ag interface is characterized by a rather large interface dipole confined to a thin interfacial region. Additionally, the abrupt change in the work function is a clear indication for the formation of a first, most likely closed monolayer of α-sexithiophene on silver. Such abrupt changes of the work function were previously also reported for thiophene based molecular systems on gold [17,18,23,28,29], as well as for overlayers consisting of other organic molecular systems grown layer by layer on metal substrates [30]. We therefore conclude that 6T grows on polycrystalline silver via the formation of an essentially closed first monolayer. Moreover, the thickness range of the abrupt work function change strongly indicates that the 6T molecules lie flat in this first monolayer, which is in agreement with conclusion drawn previously for other metal surfaces [17,21,22,31–34]. The right panel of Fig. 3 depicts the evolution of the valence band features of α-6T deposited on silver referenced to the thickness of the organic overlayer. The valence band spectra for the sputtered Ag surface show a prominent Fermi edge defining the binding energy axis. The lowest lying peak structures of 6T arise at 1.8, 2.4, and 3.8 eV. The full development of the main spectral features of α-sexithiophene is reached at an organic overlayer thickness above 3.1 nm. Up to this thickness the characteristic Ag structures are suppressed but still visible. The first two features are attributed to the two highest occupied molecular orbitals, HOMO and HOMO-1, respectively. The peak in the energy range of 4–5 eV is attributed to localized, non-bonding π-states. In comparison to recent photoemission studies of α-sexithiophene, the valence band structure is in good agreement with formerly reported results [17,35–38]. A direct measure of the hole injection barrier at the interface is possible using the spectral onset of the valence band features. The low binding energy emission edge of the valence band onset was determined by linear extrapolation. The hole injection barrier across the α-6T/Ag interface is found to be 1.8 eV. Moreover, considering the exciton binding energy E_b in 6T of about 0.4 eV [39,40] and the onset of electron–hole excitations E_{eh} of about 2.2 eV [41,42], the band gap of 6T can be obtained to be $E_g = E_{eh} + E_b$, and thus the electron injection barrier at the Ag/6T interface would be about 0.8 eV.

Fig. 4 shows a direct comparison of the valence band data for very thin and thick 6T films. From this figure its becomes clear that the α-sexithiophene valance band features are much broader for the thin films and, in addition, a small feature at about 1.4 eV is visible. This clearly indicates that there is interaction between Ag and 6T molecules in contact to the silver surface. The additional feature at 1.4 eV binding energy suggests the formation of an interface related electronic level due to a chemical interaction, a negative charge transfer from silver to 6T, which parallels the situation for other organic molecular semiconductors in contact to silver [27,43].

The energy level alignment for the metal/organic interface between the organic semiconductor α-sexithiophene and silver is summarised in Fig. 5. This interface is characterized by the presence of a quite large interface dipole of about −0.7 eV. We note that such high interface dipoles have been reported previously for other interfaces between oligothiophenes and metals [17,23,26,28,29,44,45]. In general, such quite large interface dipoles are also found for many further organic/metal interfaces [5–7]. The interface dipole at metal/organic interfaces can be caused by more than one contribution [5–7,9,10,46], which are: (i) a reduction of the metal work function upon the adsorption of the organic

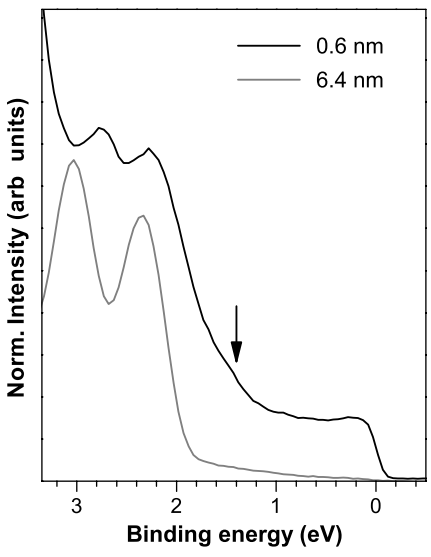


Fig. 4. UPS spectra for 0.6 and 6.4 nm α-sexithiophene film thickness. The arrow marks the interface electronic state.

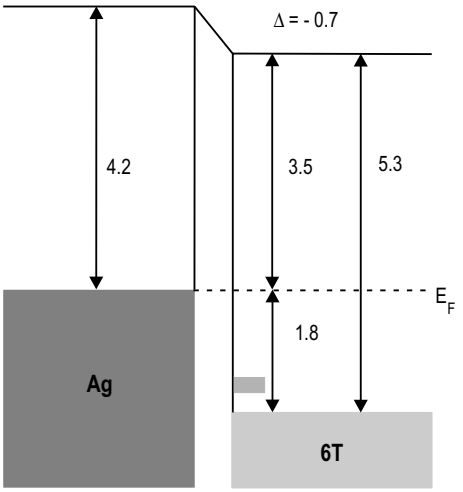


Fig. 5. Schematic energy level diagram of the α-6T/Ag interface obtained from the ultraviolet photoemission studies. The energy values are given in eV.

molecules [47–52], (ii) the chemical interaction between the α-6T molecules and the silver surface, and (iii) an induced density of states defining the charge neutrality level of the organic semiconductor which pin the Fermi level close to the charge neutrality level [46,53–55]. In the case of the α-6T/Ag interface discussed here, the observed interface states can pin the interface Fermi level and in this way also predominantly determine the interface energy level alignment.

4. Summary

We have performed X-ray and ultraviolet photoemission studies of the metal/organic interface between the organic semiconductor α-sexithiophene and polycrystalline silver. From our data we can conclude a chemical interaction at this interface resulting in the formation of interface electronic levels. Furthermore we have found a large interface dipole of about −0.7 eV and the energetic barrier for hole injection has been estimated to be about 1.8 eV, while the electron injection barrier is about 0.8 eV. The interface states might have considerable impact on the charge transport properties across the 6T/Ag interface since they can act as traps for the charge carriers.

Acknowledgements

Technical support by R. Hübel, R. Schönfelder, S. Leger is gratefully appreciated. We acknowledge financial support by the Deutsche Forschungsgemeinschaft under No. KN393/5.

References

[1] G. Horowitz, J. Mater. Res. 19 (2004) 1946–1962.
[2] W. Clemens, I. Fix, J. Ficker, A. Knobloch, A. Ullmann, J. Mater. Res. 19 (2004) 1963–1973.
[3] S. Scheinert, G. Paasch, Phys. Stat. Sol. (a) 6 (2004) 1263–1301.
[4] A.B. Chwang, C.D. Frisbie, J. Phys. Chem. B 104 (2000) 12202–12209.
[5] H. Ishii, K. Sugiyama, E. Ito, K. Seki, Adv. Mater. 11 (1999) 605–625.
[6] W.R. Salaneck, K. Seki, A. Kahn, J.J. Pireaux, Conjugated Polymer and Molecular Interfaces: Science and Technology for Photonic and Optoelectronic Applications, Marcel Dekker, New York, 2002.
[7] W.R. Salaneck, M. Fahlman, J. Mater. Res. 19 (2004) 1917–1923.
[8] D. Cahen, A. Kahn, Adv. Mater. 15 (2003) 271–277.
[9] M. Knupfer, H. Peisert, Phys. Stat. Sol. (a) 201 (2004) 1055–1074.
[10] M. Knupfer, G. Paasch, J. Vac. Sci. Technol. A 23 (2005) 1072–1077.
[11] A. Kahn, N. Koch, W. Gao, J. Polym. Sci. B 41 (2003) 2529–2548.
[12] D. Cahen, A. Kahn, E. Umbach, Mater. Today 8 (2005) 32–41.
[13] M.P. Seah, W.A. Dench, Surf. Interface Anal. 1 (1979) 2–11.
[14] B. Servet, S. Ries, M. Trotel, P. Alnot, G. Horowitz, F. Garnier, Adv. Mater. 5 (1993) 461–464.
[15] D. Oeter, C. Ziegler, W. Göpel, Synth. Met. 61 (1993) 147–150.
[16] G.J. Herrera, G.J. Whitten, Synth. Met. 128 (2002) 317–324.
[17] T. Schwieger, X. Liu, H. Peisert, B. Adolphi, N. Kiriy, M. Knupfer, J. Appl. Phys. 97 (2005) 123712.
[18] X. Liu, M. Knupfer, B.H. Huisman, Surf. Sci. 595 (2005) 165–171.
[19] G. Koller, F.P. Netzer, M.G. Ramsey, Surf. Sci. 421 (1999) 353–361.
[20] M.G. Ramsey, G. Koller, I. Kardinal, F.P. Netzer, Surf. Sci. 352–354 (1996) 128–132.
[21] K.M. Baumgärtner, M. Volmer-Uebing, J. Taborski, P. Bäuerle, E. Umbach, Berichte der Bunsengesellschaft 95 (1991) 1488–1495.
[22] A. Nambu, H. Kondoh, I. Nakai, K. Amemiya, T. Ohta, Surf. Sci. 530 (2003) 101–110.
[23] J.E. Lyon, A.J. Cascio, M.M. Beerbom, R. Schlaf, Y. Zhu, S.A. Jenekhe, Appl. Phys. Lett. 88 (2006) 222109.
[24] A.J. Cascio, J.E. Lyon, M.M. Beerbom, R. Schlaf, Y. Zhu, S.A. Jenekhe, Appl. Phys. Lett. 88 (2006) 062104.
[25] H.B. Michaelson, J. Appl. Phys. 48 (1977) 4729–4733.
[26] A.J. Mäkinen, I.G. Hill, M. Kinoshita, T. Noda, Y. Shirota, Z.H. Kafafi, J. Appl. Phys. 91 (2002) 5456–5461.
[27] T. Schwieger, H. Peisert, M. Knupfer, Chem. Phys. Lett. 384 (2004) 197–202.
[28] X. Liu, M. Knupfer, L. Dunsch, A. Tabet, H. Hartmann, Org. Electron. 7 (2006) 107–113.
[29] M. Knupfer, X. Liu, Surf. Sci. 600 (2006) 3978–3981.

[30] T.S. Ellis, K.T. Park, S.L. Hulbert, M.D. Ulrich, J.E. Rowe, J. Appl. Phys. 95 (2004) 982–988.
[31] P. Väterlein, M. Schmelzer, J. Taborski, T. Krause, F. Viczian, M. Bässler, R. Fink, E. Umbach, W. Wurth, Surf. Sci. 452 (2000) 20–32.
[32] S. Terada, T. Ykokoyama, M. Sakano, A. Imansishi, Y. Kitajima, M. Kiguchi, Y. Okamoto, T. Ohta, Surf. Sci. 414 (1998) 107–117.
[33] R. Li, P. Bäuerle, E. Umbach, Surf. Sci. 331–333 (1995) 100–104.
[34] G. Yoshikawa, M. Kiguchi, S. Ikeda, K. Saiki, Surf. Sci. 559 (2004) 77–84.
[35] H. Fujimoto, U. Nagashima, H. Inokuchi, K. Seki, Y. Cao, H. Nakahara, J. Nakayama, M. Hoshino, K. Fukuda, J. Chem. Phys. 92 (1990) 4077–4092.
[36] N. Koch, G. Heimel, J. Wu, E. Zojer, R.L. Johnson, J.-L. Brédas, K. Müllen, J.P. Rabe, Chem. Phys. Lett. 413 (2005) 390–395.
[37] C.E. Heiner, J. Dreyer, I.V. Hertel, N. Koch, H.-H. Ritze, W. Widdra, B. Winter, Appl. Phys. Lett. 87 (2005) 093501.
[38] A. Chandekar, J. Whitten, Synth. Met. 150 (3) (2005) 259–264.
[39] L.M. Blinov, S.P. Palto, G. Ruani, C. Taliani, A.A. Tevosov, S.G. Yudin, R. Zamboni, Chem. Phys. Lett. 232 (1995) 401–406.
[40] I.G. Hill, A. Kahn, Z.G. Soos, R.A. Pascal Jr., Chem. Phys. Lett. 327 (2000) 181–188.
[41] M. Knupfer, T. Pichler, M.S. Golden, J. Fink, M. Murgia, R.H. Michel, R. Zamboni, C. Taliani, Phys. Rev. Lett. 83 (1999) 1443–1446.
[42] P. Lang, F. Kouki, J. Roger, J. Martinez, G. Horowitz, F. Garnier, Synth. Met. 101 (1999) 536–537.
[43] V. Shklover, S. Schmitt, E. Umbach, F.S. Tautz, M. Eremtchenko, Y. Shostak, J.A. Schaefer, M. Sokolowski, Surf. Sci. 482–485 (2001) 1241–1248.
[44] F. Baier, F. von Ludowig, A. Soukopp, C. Väterlein, J. Laubender, P. Bäuerle, M. Sokolowski, E. Umbach, Opt. Mater. 12 (1999) 285–290.
[45] A.J. Mäkinen, I.G. Hill, T. Noda, Y. Shirota, Z.H. Kafafi, Appl. Phys. Lett. 78 (5) (2001) 670–672.
[46] H. Vázquez, W. Gao, F. Flores, A. Kahn, Phys. Rev. B 71 (2005) 041306.
[47] X. Crispin, V. Geskin, A. Crispin, J. Cornil, R. Lazzaroni, W.R. Salaneck, J.-L. Brédas, J. Am. Chem. Soc. 124 (2002) 8131–8141.
[48] X. Crispin, Sol. Energy Mater. Sol. Cells 83 (2004) 147–168.
[49] K. Wandelt, Appl. Surf. Sci. 111 (1997) 1–10.
[50] L. Yan, N.J. Watkins, S. Zorba, Y.L. Gao, C.W. Tang, Appl. Phys. Lett. 81 (2002) 2752–2754.
[51] H. Peisert, M. Knupfer, J. Fink, Appl. Phys. Lett. 81 (2002) 2400–2402.
[52] N. Koch, A. Kahn, J. Ghijsen, J.J. Pireaux, J. Schwartz, R.L. Johnson, A. Elschner, Appl. Phys. Lett. 82 (2003) 70–72.
[53] A. Kahn, W. Zhao, W. Gao, H. Vázquez, F. Flores, Chem. Phys. 325 (2006) 129–137.
[54] H. Vázquez, R. Oszwaldowski, P. Pou, J. Ortega, R. Pérez, F. Flores, A. Kahn, Europhys. Lett. 65 (2004) 802–808.
[55] H. Vázquez, F. Flores, R. Oszwaldowski, J. Ortega, R. Pérez, A. Kahn, Appl. Surf. Sci. 234 (2004) 107–112.

Available online at www.sciencedirect.com
ScienceDirect
Organic Electronics 8 (2007) 631–634
Organic Electronics
www.elsevier.com/locate/orgel

Letter

Growth of quaterrylene thin films on a silicon dioxide surface using vacuum deposition

Ryoma Hayakawa [a], Matthieu Petit [a], Yutaka Wakayama [a,b,*], Toyohiro Chikyow [a]

[a] *Advanced Electronic Materials Centre, National Institute for Materials Science, 1-1 Namiki, Tsukuba, Ibaraki 305-0044, Japan*
[b] *Nanoscale Quantum Conductor Array Project, ICORP, JST, 1-1 Namiki, Tsukuba, Ibaraki 305-0044, Japan*

Received 15 May 2007; received in revised form 10 July 2007; accepted 17 July 2007
Available online 8 August 2007

Abstract

Quaterrylene molecules, which have a planar and highly π-conjugated chemical structure, were deposited on a SiO_2 surface, and their thin film structures, including surface morphology and molecular orientation, were examined by atomic force microscopy (AFM) and X-ray diffractometry (XRD). AFM observations revealed the grain size and surface roughness to be closely dependent on the substrate temperature in the range from 27 °C to 200 °C. Particularly at a substrate temperature of 140 °C, grain sizes of up to 6 μm and low surface roughness of 1.67 nm were successfully obtained in the 8 ML-thick film. XRD measurements of the quaterrylene thin film revealed (0 0 *l*) Bragg reflections, corresponding to a spacing of 1.89 nm. This value coincides with the average height of the terraces of the stepped structure observed in the AFM images. These results clearly demonstrate the quaterrylene molecules to have an upright orientation and that thin films grow as layered structures on the surface. From the full width of half maximum (FWHM) of the XRD rocking curve, the degree of alignment of the molecular planes (mosaicity) was estimated to be 0.09°, which shows that the film has a highly ordered structure.
© 2007 Elsevier B.V. All rights reserved.

PACS: 68.55.Jk; 73.61.Ph; 81.15.Ef; 81.15.Kk

Keywords: Organic semiconductor; Thin film growth; Crystal orientation; Grain size; X-ray diffractometry; Atomic force microscopy

The development of electronic devices based on organic semiconductor thin films, such as organic field effect transistors (OFETs) [1,2], has made them an interesting and competitive alternative to conventional silicon-based devices for applications in which large areas are required at low production cost. Their low processing temperature and compatibility with flexible substrates give them the potential to open new fields of applications. Planar aromatic molecules, such as oligothiophenes and pentacene, have emerged as promising candidates for applications in organic electronics, since they can grow as films with high crystalline order and

* Corresponding author. Tel.: +81 29 860 2000; fax: +81 29 860 4796.
E-mail address: WAKAYAMA.Yutaka@nims.go.jp (Y. Wakayama).

1566-1199/$ - see front matter © 2007 Elsevier B.V. All rights reserved.
doi:10.1016/j.orgel.2007.07.007

exhibit a high carrier mobility of up to 0.1–8 cm^2/eV [3–5].

Several factors can suppress carrier mobility: crystal disorder, grain boundaries and non-uniform overlap of π-orbitals. To solve these issues and improve carrier mobility, it is essential to design molecules with specific chemical structures and to control the crystalline orientation and surface morphology of organic thin films. First of all, organic molecules with an extensive and independent π-conjugated electron system should be chosen, since π-electron conjugation plays an important role in carrier transport. The second important point is molecular packing in the crystal. Many aromatic molecules have herringbone (edge-to-face) configurations, arising from intermolecular CH–π interactions, in which the overlapping of π-conjugated electrons is limited. Therefore, highly stacked systems with face-to-face configurations are needed to enhance the π-orbital overlap. The third key approach is to obtain an organic thin film with an upright molecule orientation on the SiO_2 surface, since the first few monolayers of the molecular thin film work as a transistor channel. Finally, increasing the grain size of organic thin films is another important requirement. This is because carrier scattering at grain boundaries limits the carrier mobility of organic thin films. Two-dimensional growth, with the molecules adopting a layered configuration, is thus advantageous for obtaining large grain sizes.

The quaterrylene molecule is worthy of attention in this context because it has a planar chemical structure and a more expansive π-conjugated electron system than pentacene, which is widely adopted in OFETs, as shown in Fig. 1(a). Basically, the quaterrylene crystal is composed of an edge-to-face configuration with an angle of 73.2° overall [6,7], as seen in many aromatic molecules. However, a couple of molecules occupy one lattice point, showing face-to-face packing, as shown in Fig. 1(b). The intermolecular distance is 0.37 nm, which enhances intermolecular π–π interaction in organic crystals [8].

In this paper, we describe the growth of quaterrylene thin films on SiO_2 surface. The thin film structure, including grain size, molecular orientation and surface morphology, were investigated using XRD and AFM measurements.

Quaterrylene thin films were deposited using a vacuum deposition technique with a base pressure below 5×10^{-7} Pa. As a substrate, we used silicon dioxide grown using a chemical treatment as

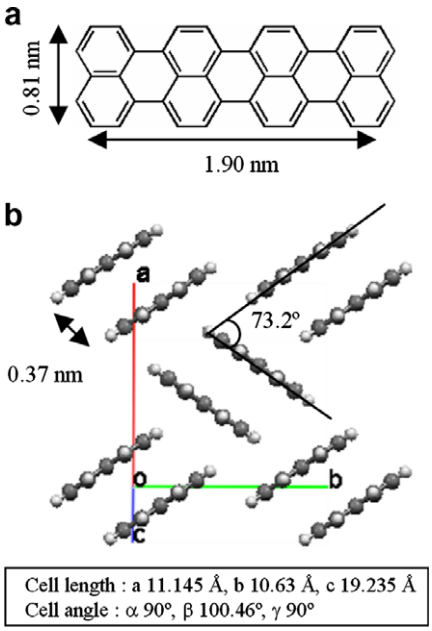


Fig. 1. (a) Chemical structure and (b) crystal structure of quaterrylene molecules.

described in Shiraki's method on n-type Si(0 0 1) substrate [9]. The thickness of the silicon dioxide film was estimated as 1.8 ± 0.2 nm by X-ray refractivity. In this experiment, a glass pipe with a heater was placed between a Knudsen cell and the substrate to guide molecules effectively onto the substrate and precisely control the flux rate [10]. The substrate temperature varied from 27 °C to 200 °C. The flux rate of molecules onto the substrate was fixed at 0.02 monolayer(ML)/min, and molecules were deposited for 7 h. The crystal structure and surface morphology were analyzed using XRD (Bruker, D8 Discover) and AFM (SII, SPI4000) systems.

Fig. 2(a) shows AFM images of quaterrylene thin films grown at substrate temperatures ranging from 27 °C to 200 °C. Both grain size and surface roughness show a clear dependence on the substrate temperature. Peculiarly, the substrate temperature of 140 °C was found to be a critical temperature. The grain size of the quaterrylene thin films increased with increasing substrate temperature up to 140 °C and changed little above that. The surface roughness initially decreased with increasing substrate temperature, then started increasing at 140 °C. In addition, the film thickness of 8 ML was constant up to 140 °C, showing that all molecules adsorbed on the substrate. However, it also reduced above

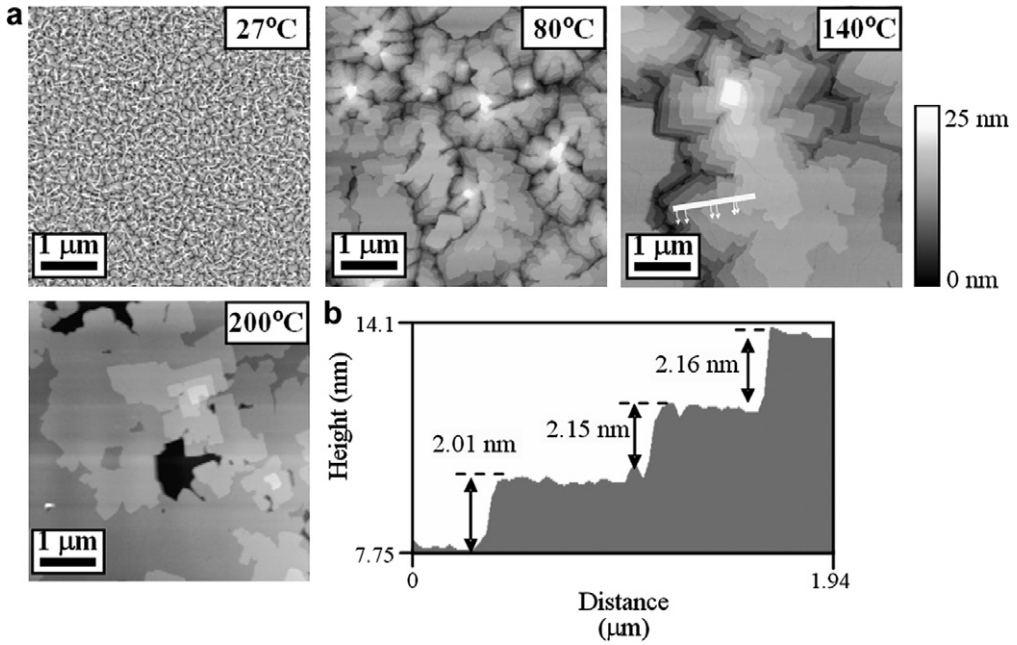


Fig. 2. (a) AFM images of quaterrylene thin films formed at substrate temperatures ranging from 27 to 200 °C. (b) Topographic profile of quaterrylene thin film with a thickness of 8 ML grown at 140 °C.

140 °C. Finally, quaterrylene molecules were only slightly adsorbed onto the SiO_2 surface at 200 °C, although surface morphology seems to improve in AFM image shown in Fig. 2(a). These results were caused by the balance of the adsorption and desorption rates of the molecules on the substrate. That is, desorption of molecules from the substrate was enhanced above 140 °C. Optimization of substrate temperature at 140 °C achieved a grain size of up to 6 μm and a surface roughness as low as 1.67 nm, which are key properties for efficient charge transport. This large grain size equals or exceeds that of pentacene thin films, which have been extensively studied for use in OFETs [11,12]. Quaterrylene thus has a great advantage over pentacene. The AFM images also revealed that the films grew in a layer-by-layer manner throughout the temperature range. As seen from the topographic profile of the film grown at 140 °C, as shown in Fig. 2(b), the average height of the terraces was 2.10 nm, which coincides with the long-axis of the quaterrylene molecules. This result shows that a layered structure of standing-up molecules was formed on the surface.

XRD measurements were carried out to obtain a more detailed structural analysis of the quaterrylene thin film. Fig. 3 shows the XRD pattern of the films with a thickness of 8 ML. The quaterrylene thin film

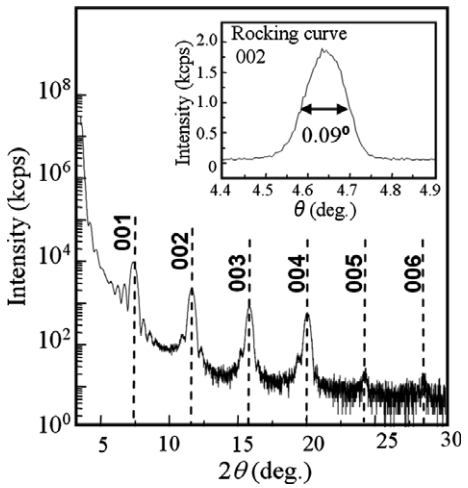


Fig. 3. XRD pattern of quaterrylene thin film with a thickness of 8 ML grown at the substrate temperature of 140 °C on a silicon oxide surface. The rocking curve is also shown in the inset.

exhibited (00*l*) Bragg reflections up to the sixth order, corresponding to a spacing of 1.89 nm. The Kiessing fringes and Laue oscillation, coinciding with the thickness of quaterrylene thin film, were also clearly observed at small angles below $2\theta = 2.5°$ and around the Bragg reflections, respectively. These results provide evidence that the quaterrylene thin film grows with high structural

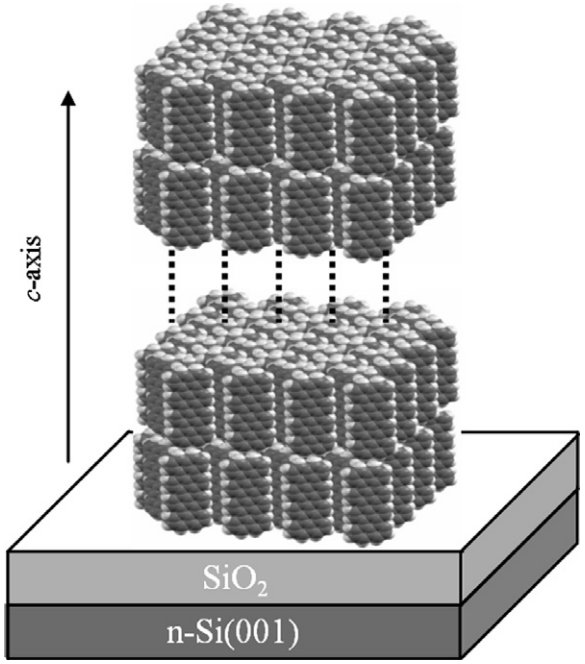


Fig. 4. Simplified scheme illustrating the structure of quaterrylene thin film.

order and smooth surface morphology. Furthermore, this lattice constant value of 1.89 nm, estimated from XRD measurement, agrees with the average height of the terraces shown in Fig. 2(b), which further demonstrates their molecular orientation: the molecules have a standing-up orientation and are aligned perpendicularly to the surface as illustrated in Fig. 4. This result is different from the orientation of the quaterrylene thin films grown on Au(1 1 1) reported in previous paper. Franke et al. reported that the quaterrylene thin film had a lying down orientation on Au(1 1 1) [7]. This origin is due to the difference of the electron density on substrate. The electron density on SiO_2 surface is lower than that on Au(1 1 1). Therefore, the molecule–molecule interaction between neighboring molecules is dominant over the molecule-substrate interaction, enhancing that the film has a standing-up orientation on SiO_2 surface.

From the FWHM of the rocking curve shown in the inset of Fig. 3, the degree of alignment of the molecular planes (mosaicity) was estimated to be 0.09°. These results show that the film is also highly ordered, which is another key property for efficient charge transport.

In summary, quaterrylene thin films were formed on a SiO_2 surface by vacuum deposition, and their structures were then examined using XRD and AFM systems. Quaterrylene films with a grain size of up to 6 μm and a low surface roughness of 1.67 nm were successfully obtained by growing at a substrate temperature of 140 °C, which led to a layered structure with upright orientation being formed on the silicon oxide surface. XRD measurements confirmed that the quaterrylene films grew with a standing-up structure, since 0 0 *l* Bragg reflections that corresponded to a spacing of 1.89 nm were observed. Our results demonstrate the potential usefulness of quaterrylene and the importance of precise optimization of growth conditions, which could deliver the high carrier mobility required for OFETs.

References

[1] S.R. Forrest, Nature 428 (2005) 911.
[2] G. Witte, C. Woll, J. Mater. Res. 19 (2004) 1889.
[3] T.W. Kelley, P.F. Baude, C. Gerlanch, D.E. Ender, D. Muyres, M.A. Haase, D.E. Voge, S.D. Theiss, Chem. Mater. 16 (2004) 4413.
[4] V. Podzorov, S.E. Sysoev, E. Loginova, V.M. Pudalov, M.E. Gershenson, Appl. Phys. Lett. 83 (2003) 3504.
[5] H. Sirringhaus, R.H. Friend, X.C. Li, S.C. Moratti, A.B. Holmes, N. Feeder, Appl. Phys. Lett. 71 (1997) 3871.
[6] T. Maeda, T. Kobayashi, T. Nemot, S. Isoda, Philos. Mag. B 81 (2001) 1659.
[7] R. Franke, S. Franke, C. Wagner, T. Dienel, T. Fritz, S.C.B. Mannsfeld, Appl. Phys. Lett. 88 (2006) 161907.
[8] J.P. Luis, A. Minoia, H. Ujii, C. Rovira, J. Cornil, S.D. Feyter, R. Lazzaroni, D.B. Amabilino, J. Am. Chem. 128 (2006) 12602.
[9] A. Ishizaka, Y. Shiraki, J. Electrochem. Soc. 133 (1986) 666.
[10] H. Sasaki, Y. Wakayama, T. Chikyow, E. Barrena, H. Dosh, K. Kobayashi, Appl. Phys. Lett. 88 (2006) 08197.
[11] I. Yagi, K. Tsukagoshi, Y. Aoyagi, Appl. Phys. Lett. 86 (2005) 103502.
[12] T. Minari, T. Nemoto, S. Isoda, J. Appl. Phys. 96 (2004) 769.

Available online at www.sciencedirect.com
ScienceDirect
Organic Electronics 8 (2007) 635–639
Organic Electronics
www.elsevier.com/locate/orgel

Letter

Enhanced light extraction from organic light-emitting devices by using microcontact printed silica colloidal crystals

Feng Li *, Xiao Li, Junhu Zhang, Bai Yang *

Key Lab for Supramolecular Structure and Materials of Ministry of Education, Jilin University, 2699 Qianjin Avenue, Changchun, 130012, PR China

Received 27 March 2007; received in revised form 23 May 2007; accepted 6 June 2007
Available online 13 June 2007

Abstract

One simple method to increase the light extraction from organic light-emitting devices by using microcontact printed silica colloidal crystals is demonstrated. A close-packed hexagonal silica microsphere arrays is pressed into poly(vinyl alcohol) layer that is spin-coated on the opposite side of the indium–tin–oxide-coated glass substrate. This structure has the similar characteristics of microlens arrays. By using the silica microspheres with the diameters of 400 and 1000 nm those were half pressed into poly(vinyl alcohol), the luminance efficiencies of the devices in the normal direction are increased by a factor of 1.6 and 1.3 at the current density of 7.0 mA/cm^2 compared to that of the device using flat glass substrate, respectively, and the shapes of emission spectra exhibit almost no angle dependence.
© 2007 Elsevier B.V. All rights reserved.

PACS: 78.60.Fi; 72.80.Le; 85.60.Jb; 42.79.Bh

Keywords: Organic light-emitting devices; Light extraction; Light outcoupling; Silica microsphere arrays

1. Introduction

Organic light-emitting devices (OLEDs) have attracted wide interest due to their applications not only for flat panel displays but also for illumination. Because of the good properties such as ultra thin, light weight, environmentally protective, and actually the planar light source, the OLEDs are considered as one of the candidates of the next-generation planar light source. For illumination application, "the ultimate goal is to demonstrate a device that has an efficiency exceeding that of florescent bulbs, which are among the most power-efficient illumination sources available" [1]. Though the internal quantum efficiency of OLEDs has almost reach 100% by employing phosphorescent materials and carefully designing the device structures [2,3], almost 70–80% of the generated light cannot escape from the OLEDs due to the total internal reflection at the interface between the indium–tin–oxide (ITO) anode and glass (or glass and air). Therefore, there is a large room for improving the light extraction from OLEDs to reach the goal above. There are several methods to increase the light extraction that include introducing rough or

* Corresponding authors. Tel.: +8643185168492; fax: +8643185193421.
E-mail addresses: lifeng01@jlu.edu.cn (F. Li), byangchem@jlu.edu.cn (B. Yang).

1566-1199/$ - see front matter © 2007 Elsevier B.V. All rights reserved.
doi:10.1016/j.orgel.2007.06.001

textured surfaces [4], mesa [5], microcavities [6], periodic or photonic-crystals [7–12] structures, and adding a scattering layer [13,14] or a low refractive index layer [15] to the devices. However, most of them often accompany problems such as an undesirable angle dependent emission spectra, costly or complex processing. Madigan et al. propose applying millimeter-sized hemispherical lens to the back side of the glass substrate, which avoids many shortcomings above [16]. Whereas, this method is not practical because it is difficult to align each OLED to the large lenses. An improvement is to use arrays of microlens introduced by Moller et al. [17] and developed by Wei et al. [18] and Sun et al. [19]. In these works, a mold (Si or glass) was firstly made by the standard photolithographic method, then a polymer sheet of microlens arrays was formed in the mold and subsequently transferred to the surface of the glass substrate [17,18] or the polymer sheet of microlens arrays was formed directly on the glass substrate through the mold [19]. The method using arrays of microlens does not need alignment with the OLEDs and avoids the problem of angle dependent emission, so seems more practical. Even so, searching simpler method to increase the light extraction is still interesting and important.

In this work, we demonstrate one simple method to increase the light extraction by using microcontact printed silica colloidal crystals. A close-packed hexagonal silica microsphere arrays was pressed into poly(vinyl alcohol) (PVA) layer that was spin-coated on the opposite side of the ITO glass substrate. This structure has the similar characteristics of microlens arrays and called quasi-microlens arrays here. The merits of this method are no photolithographic process is needed and easy synthesis of the microspheres with the diameters ranged from 100 nm to 1400 nm. The luminance efficiencies in the normal direction are increased by a factor of 1.6 and 1.3 and the shapes of the emission spectra exhibit almost no angle dependence by using the quasi-microlens arrays composed by the silica microspheres with the diameters of 400 and 1000 nm compared to those of the flat glass substrate, respectively.

2. Experimental methods

The silica microspheres were synthesized by the method of Stober et al. [20] and were separated by centrifuge. Monodisperse silica microspheres were assembled into colloidal crystals on the silicon wafer by the evaporation of suspension [21,22]. Through using the lift-up soft lithography we reported [23], a single layer of close-packed microspheres was transferred to the surface of the elastomeric polysimethylsiloxane (PDMS) stamp. A film of PVA (about 200 nm) was spin-coated on the opposite side of the ITO-coated glass substrate. After that, the PDMS stamp containing the silica microspheres was brought into contact with the PVA-coated substrate under a pressure of about 0.2×10^5 Pa and the system was heated at 100 °C for 1.5 h. The PDMS stamp was then carefully peeled away and the silica microspheres were transferred into the PVA. The full process took about three hours to be finished and is illustrated in Fig. 1. The ITO-coated glass substrates with the silica microsphere arrays and a control sample without the silica microsphere arrays were loaded into the multiple source organic molecular beam deposition system, respectively, and the organic and metal materials were vapor deposited at a background pressure of 6×10^{-4} Pa. The structure of these devices was ITO/*N*,*N*-diphenyl-*N*,*N*-bis(1-naphthyl)-(1,1-biphenyl)-4,4-diamine (NPB) (60 nm)/tri-(8-Hydroxyquinoline)aluminum (Alq_3) (70 nm)/LiF (0.5 nm)/Al (100 nm), where NPB is used as the hole-transporting layer and Alq_3 as the electron-transporting as well as light-emitting layer. The shadow masks were used to define the electrode areas and to make several 4 mm^2 devices per substrate. The luminance, current–voltage characteristics and electroluminescent spectra were measured by panel-display luminancemeter, Keithley model

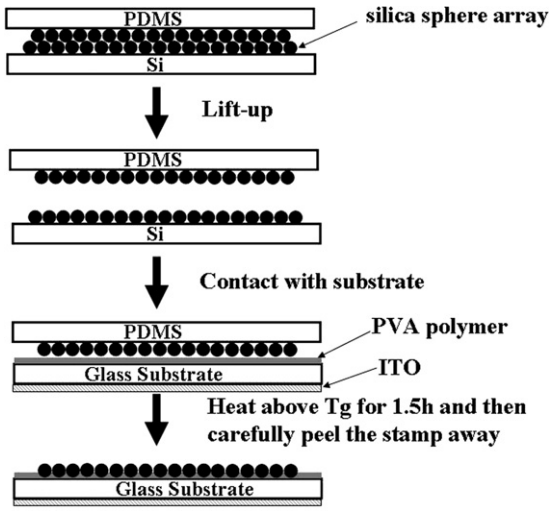


Fig. 1. Illustration of the process to fabricate the quasi-microlens arrays for OLEDs.

2400 and charge-coupled device (CCD) spectrograph. The angular dependence of light emission was tested by putting the sample vertically on the center of one rotation stage.

3. Results and discussion

The refractive index of PVA is 1.53 measured by a variable-incidence-angle spectroscopic ellipsometer, which is very close to the value of the glass substrate and the silica microspheres. So the refraction and reflection effect at the glass-PVA and PVA-silica microspheres interface can be neglected. The glass substrate, PVA and silica microspheres compose a structure that has the similar function of microlens arrays, as shown in Fig. 2a. Fig. 2b shows the scanning electron micrograph (SEM) of silica microspheres monolayer colloidal crystal on the PVA-coated glass substrate fabricated using our method. As clearly can be seen, silica microspheres are highly ordered in the hexagonal-packed arrays, which reflects the perfect transfer of the ordered arrays of microsphere from the colloidal crystal to a PDMS surface and at last to the PVA-coated glass substrate. The uniformity of microspheres is good, and the diameter difference is less than 20 nm among the most microspheres on one substrate.

Fig. 3 shows the luminance efficiency in the normal direction of OLEDs as a function of the current density. The maximum luminance efficiencies are 5.4, 4.3 and 3.3 cd/A for the OLEDs with the silica microsphere arrays of ∅400, 1000 nm and the control device, respectively. The enhancement of luminance efficiencies are 1.6 and 1.3 at the current density of 7.0 mA/cm^2 for the OLEDs with the silica microsphere arrays of ∅400 and 1000 nm, respectively.

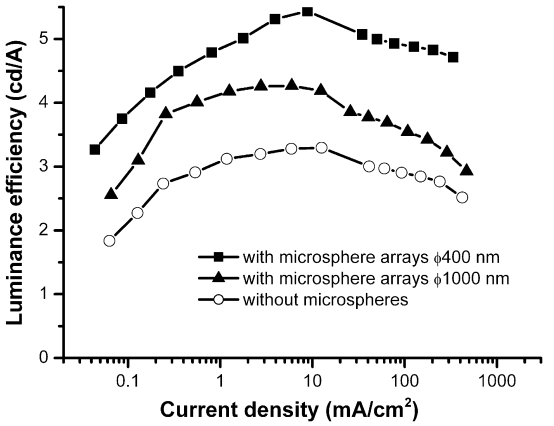


Fig. 3. The luminance efficiency in the normal direction of OLEDs with and without the silica microsphere arrays as a function of the current density, respectively.

Fig. 4 shows the electroluminescent (EL) spectra of the OLED with the silica microsphere arrays (diameter: 400 nm) at the current density of 30 mA/cm^2 as a function of viewing angle. The detail about the experimental configuration and the definition of viewing angle are shown in the inset of Fig. 4. In order to avoid the influence of the edge emission at the large viewing angle, the edges of the

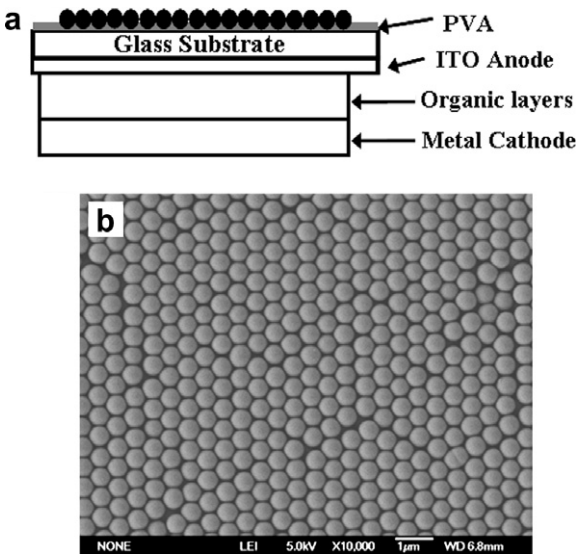


Fig. 2. (a) The OLEDs structures with the quasi-microlens arrays on the substrate. (b) SEM image of the silica microspheres colloidal crystal on the PVA-coated glass substrate.

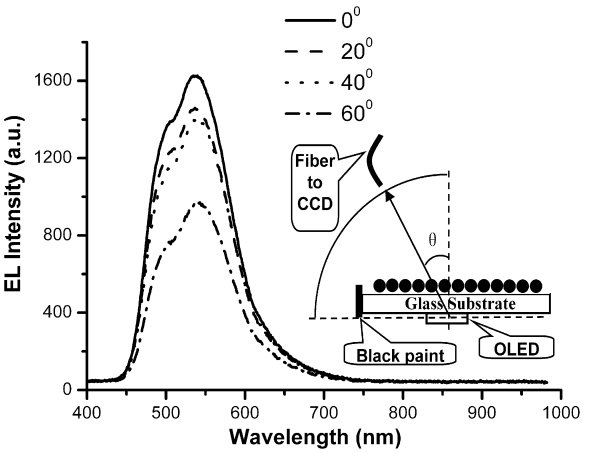


Fig. 4. The electroluminescent (EL) spectra taken at the current density of 30 mA/cm^2 of the OLED with the silica microsphere arrays (diameter: 400 nm) as a function of viewing angle. Inset: the detail about the experimental configuration and the definition of viewing angle.

device is coated by the black paint. The diameter of the fiber connected to the CCD is 400 μm and distance between the device and fiber is about 7 cm, so the solid angle to collect the surface emission of the device is less than 1 sr. The shapes of the spectra do not vary with viewing angle and are identical with those of the control device, indicating that the scattering effect can be neglected here, otherwise the scattering of the silica microspheres can result in the variation of EL spectra with viewing angle [13].

Fig. 5 shows the normalized peak intensity of EL spectra as a function of the viewing angle for OLEDs with the silica microsphere arrays of ∅400 and 1000 nm and the control device at the current density of 30 mA/cm^2, respectively, and the definition of viewing angle is shown in the inset of Fig. 4. The intensities of the emission from the control device are smaller than those of the Lambertian emission at all the viewing angles, however, the intensities of the emission from the OLEDs with the silica microsphere arrays are smaller than those of the Lambertian emission at the small viewing angles and larger than those when the viewing angles exceed 25° and 50° for the silica microspheres of ∅400 and 1000 nm, respectively. The intensities of the emission from the OLEDs with the silica microsphere arrays are larger than those of the control device at all viewing angles. The characteristics mentioned above consist with the OLEDs using the microlens arrays reported before [19] and exclude the possibility of the anti-reflective-film induced enhancement of light extraction, because in that case the light intensities at higher viewing angles are reduced instead of being increased.

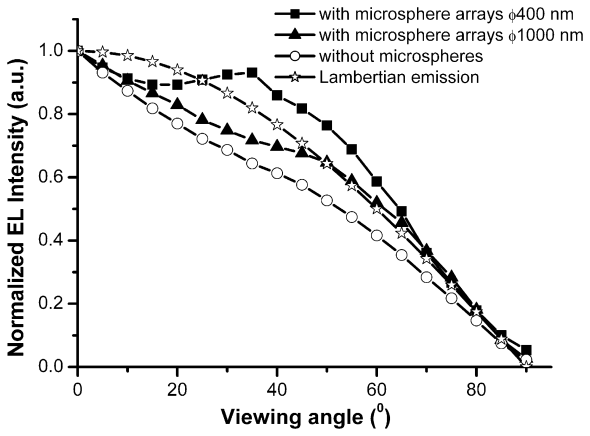


Fig. 5. The normalized peak intensity of EL spectra taken at the current density of 30 mA/cm^2 as a function of the viewing angle for OLEDs with and without silica microsphere arrays, respectively. The definition of viewing angle is shown in the inset of Fig. 4.

It should be noted that in the previous work [17–19], the diameters of used microlens are all larger than 5 μm and the microlens with diameters near the wavelength of light emitted from the OLEDs can not be made due to the limitation of the standard photolithographic technique. In this work, the experimental results indicate that both the microspheres with the diameter of the micrometer order and the diameter near the wavelength of light emitted from the OLEDs can increase the light extraction.

4. Conclusions

In summary, we use microcontact printed silica colloidal crystals to fabricate a quasi-microlens arrays structure for OLEDs and the photolithographic process is not needed in the full process. The luminance efficiencies in the normal direction for the OLEDs with the double layer structure of ITO/NPB/Alq_3/LiF/Al are increased by 1.6 and 1.3 times through using the quasi-microlens arrays with the diameters of 400 and 1000 nm, respectively. The experimental results indicate that both quasi-microlens arrays with the diameter of the micrometer order and the diameter near the wavelength of light emitted from the OLEDs can increase the light extraction.

Acknowledgements

We are grateful for financial support from Ministry of Science and Technology of China (Grant No.: 2002CB6134003), National Nature Science Foundation of China (Grant No.: 20534040) and the program for Changjiang Scholars and Innovative Research Team in University (No. IRT0422).

References

[1] B.W. D'andrade, R.J. Holmes, S.R. Forrest, Adv. Mater. 16 (2004) 624.
[2] C. Adachi, M.A. Baldo, M.E. Thompson, S.R. Forrest, J. Appl. Phys. 90 (2001) 5048.
[3] Y. Sun, N.C. Giebink, H. Kanno, B. Ma, M.E. Thompson, S.R. Forrest, Nature 440 (2006) 908.
[4] I. Schnitzer, E. Yablonovitch, C. Caneau, T.J. Gmitter, A. Scherer, Appl. Phys. Lett. 63 (1993) 2174.
[5] G. Gu, D.Z. Garbuzov, P.E. Burrows, S. Venkatesh, S.R. Forrest, M.E. Thompson, Opt. Lett. 22 (1997) 396.
[6] J. Gruner, R. Cacialli, R.H. Friend, J. Appl. Phys. 80 (1996) 207.

[7] J. Feng, T. Okamoto, S. Kawata, Opt. Lett. 30 (2005) 2302.
[8] B.J. Matterson, J.M. Lupton, A.F. Safonov, M.G. Salt, W.L. Barnes, I.D.W. Samuel, Adv. Mater. 13 (2001) 123.
[9] Y.R. Do, Y.C. Kim, Y. Song, C. Cho, H. Jeon, Yong-Jae Lee, S. Kim, Yong-Hee Lee, Adv. Mater. 15 (2003) 1214.
[10] J.M. Ziebarth, A.K. Saafir, S. Fan, M.D. McGehee, Adv. Funct. Mater. 14 (2004) 451.
[11] M. Fujita, K. Ishihara, T. Ueno, T. Asano, S. Noda, H. Ohata, T. Tsuji, H. Nakada, N. Shimoji, Jpn. J. Appl. Phys. 44 (2005) 3669.
[12] C. Liu, V. Kamaev, Z.V. Vardeny, Appl. Phys. Lett. 86 (2005) 143501.
[13] T. Yamasaki, K. Sumioka, T. Tsutsui, Appl. Phys. Lett. 76 (2000) 1243.
[14] J.J. Shiang, T.J. Faircloth, A.R. Duggal, J. Appl. Phys. 95 (2004) 2889.
[15] T. Tsutsui, M. Yahiro, H. Yokogawa, K. Kawano, M. Yokoyama, Adv. Mater. 13 (2001) 1149.
[16] C.F. Madigan, M.H. Lu, J.C. Sturm, Appl. Phys. Lett. 76 (2000) 1650.
[17] S. Moller, S.R. Forrest, J. Appl. Phys. 91 (2002) 3324.
[18] Mao-Kuo Wei, I-Ling Su, Yi-Jia Chen, M. Chang, Hong-Yi Lin, Tung-Chuan Wu, J. Micromech. Microeng. 16 (2006) 368.
[19] Y. Sun, S.R. Forrest, J. Appl. Phys. 100 (2006) 073106.
[20] W. Stober, A. Fink, J. Colloid Interface Sci. 26 (1968) 62.
[21] R. Micheletto, H. Fukuda, M. Ohtsu, Langmuir 11 (1995) 3333.
[22] X. Yan, J. Yao, G. Lu, X. Chen, K. Zhang, B. Yang, J. Am. Chem. Soc. 126 (2004) 10510.
[23] J. Yao, X. Yan, G. Lu, K. Zhang, X. Chen, L. Jiang, B. Yang, Adv. Mater. 16 (2004) 81.

ORGANIC ELECTRONICS
materials • physics • chemistry • applications

Editors:

Prof. Chihaya Adachi — Center for Future Chemistry, Kyushu University, 744 Motooka, Nishi, Fukuoka 819-0395, Japan. Fax: +81-92-802-3294, e-mail: adachi@cstf.kyushu-u.ac.jp

Prof. Stephen R. Forrest — EECS, MSE, and Physics, University of Michigan, 4080 Fleming Building, 503 Thompson Street, Ann Arbor, MI 48109-1340, USA. Fax: +1-734-763-0085, e-mail: stevefor@umich.edu

Prof. René Janssen — Molecular Materials and Nanosystems, Eindhoven University of Technology, P.O. Box 513, 5600 MB Eindhoven, The Netherlands. Fax: +31 40 2451036, e-mail: r.a.j.janssen@tue.nl

Prof. Josef Salbeck — Macromolecular Chemistry and Molecular Materials Science Department, University of Kassel, Heinrich Plett Strasse 40, D-34123 Kassel, Germany. E-mail: salbeck@uni-kassel.de

Associate Editorial Board:

V.M. AGRANOVICH (Moscow)
Y. CAO (Guangzhou)
A. DODABALAPUR (Austin)
M. FUJIHIRA (Yokohama)
N. PEYGHAMBARIAN (Tucson)
Z. POPOVIC (Mississauga)
W. RIESS (Rüschlikon)
Y. SHIROTA (Osaka)
C. TALIANI (Bologna)
T. TSUTSUI (Fukuoka)
E. UMBACH (Würzburg)

Founding Editors:

Prof. Donal Bradley, Prof. Stephen Forrest, Prof. Norbert Karl and Prof. Kazuhiko Seki

Aims and scope

An interdisciplinary journal on the physics, chemistry, and engineering of materials with applications to organic electronics and optoelectronics, **Organic Electronics** is a primary journal for physicists, material scientists and chemists who are interested in organic electronic devices such as organic light emitting diodes, thin film transistors, photovoltaic cells, etc. Papers suitable for publication in this journal cover such topics as photoconductive and electronic properties of organic materials, film growth and characterization, organic electronic and optoelectronic devices, and applications.

As an important Journal **Organic Electronics** can ensure that your most significant research receives the recognition that it deserves. As a unique publication outlet, uniting the various research disciplines involved, it provides the only forum for both applied and fundamental contributions spanning the many different disciplines addressing electronic applications of organic materials.

Advertising information

Advertising orders and enquiries can be sent to: James Kenney, Commercial Sales, Elsevier, 84 Theobald's Road, London WC1X 8RR, United Kingdom; phone: (+44) (20) 7611 4494; fax: (+44) (20) 7611 4463; e-mail: j.kenney@elsevier.com.

Abstracted/indexed in:

Current Contents: Engineering, Technology and Applied Sciences; El Compendex Plus; Engineering Index; INSPEC; Physics Briefs; Science Citation Index, expanded; Chemistry Citation Index; Current Contents: Physics, Chemistry and Engineering Science. Also covered in the abstract and citation database SCOPUS®. Full text available on ScienceDirect®.

Publication information: *Organic Electronics* (ISSN 1566-1199). For 2007, Volume 8 is scheduled for publication. Subscription prices are available upon request from the Publisher or from the Regional Sales Office nearest you or from this journal's website: (http://www.elsevier.com/locate/orgel). Further information is available on this journal and other Elsevier products through Elsevier's website: (http://www.elsevier.com). Subscriptions are accepted on a prepaid basis only and are entered on a calendar year basis. Issues are sent by standard mail (surface within Europe, air delivery outside Europe). Priority rates are available upon request. Claims for missing issues should be made within six months of the date of dispatch.

Orders, claims, and journal enquiries: please contact the Customer Service Department at the Regional Sales Office nearest you:

Orlando: Elsevier, Customer Service Department, 6277 Sea Harbor Drive, Orlando, FL 32887-4800, USA; phone: (877) 8397126 or (800) 6542452 [toll free numbers for US customers]; (+1) (407) 3454020 or (+1) (407) 3454000 [customers outside US]; fax: (+1) (407) 3631354 or (+1) (407) 3639661; e-mail: usjcs@elsevier.com or elspcs@elsevier.com

Amsterdam: Elsevier, Customer Service Department, P.O. Box 211, 1000 AE Amsterdam, The Netherlands; phone: (+31) (20) 4853757; fax: (+31) (20) 4853432; e-mail: nlinfo-f@elsevier.com

Tokyo: Elsevier, Customer Service Department, 4F Higashi-Azabu, 1-Chome Bldg, 1-9-15 Higashi-Azabu, Minato-ku, Tokyo 106-0044, Japan; phone: (+81) (3) 5561 5037; fax: (+81) (3) 5561 5047; e-mail: jp.info@elsevier.com

Singapore: Elsevier, Customer Service Department, 3 Killiney Road, #08-01 Winsland House I, Singapore 239519; phone: (+65) 6349 0222; fax: (+65) 6733 1510; e-mail: asiainfo@elsevier.com

Printed by Krips bv, Meppel, The Netherlands

ELSEVIER

Available online at www.sciencedirect.com
ScienceDirect
Organic Electronics 8 (2007) 641–647
Organic Electronics
www.elsevier.com/locate/orgel

Improving the efficiency of light-emitting diode based on a thiophene polymer containing a cyano group

S. Cheylan [a,*], H.J. Bolink [b], A. Fraleoni-Morgera [c], J. Puigdollers [d], C. Voz [d], I. Mencarelli [c], L. Setti [c], R. Alcubilla [d], G. Badenes [a]

[a] *ICFO – Institut de Ciencies Fotoniques, Mediterranean Technology Park, Av. del Canal Olímpic s/n, 08860 Castelldefels (Barcelona), Spain*
[b] *Instituto de Ciencia Molecular, Universidad de Valencia, P.O. Box 22085, 46071 Valencia, Spain*
[c] *Departamenti de Quimica Industriale e Materiali, Universite di Bologna – V. Risorgimento 4, 40136 Bologna, Italy*
[d] *Departamento de Ingeniería Electrónica, Universidad Politécnica de Cataluña – UPC, Campus Nord Edifici C4, c/Jordi Girona 1-3, 08034 Barcelona, Spain*

Received 12 February 2007; received in revised form 23 April 2007; accepted 26 April 2007
Available online 5 May 2007

Abstract

We report on the overall improvement of a single layer organic light-emitting diode device based on poly{[3-hethylthiophene]-co-3-[2-(*p*-cyano-phenoxy)ethyl]thiophene} or namely PTOPhCN. This polymer was recently developed by adding a cyano group as a side-chain substituent of the thiophenic backbone onto the main polymer chain and showed promising results for light-emitting diode devices. Using an improved device layout, bright red electroluminescence was obtained at 4 V and showed a luminance of about 400 cd/m^2 at 8 V with current densities in the order of 6000 A/m^2.
© 2007 Elsevier B.V. All rights reserved.

PACS: 42.70.−a; 82.35.Cd; 85.60.Jb

Keywords: Organic light-emitting diodes; Polymer; Thiophene; Cyano group; Luminance efficiency

1. Introduction

Organic light-emitting diodes (OLEDs) have been investigated intensively for the past decade or so. A variety of approaches are being investigated to improve their quantum efficiency and lifetime. Extensive work has been done on the surface properties of the most commonly used anode, a layer of indium tin oxide (ITO), modified by chemical and physical treatments. Such treatments have been shown to affect the electrode work function, the surface energy, the morphology, the sheet resistance and therefore the OLEDs efficiency and lifetime [1–4]. Another approach consists in modifying the metal used for the cathode, such as using a mixture of metals such as Ba/Al or Mg/Ag [5] in order to improve the electron injection, or increasing its transparency to improve the output efficiency of

* Corresponding author. Tel.: +34 93 553 4033; fax: +34 93 553 4000.
E-mail address: stephanie.cheylan@icfo.es (S. Cheylan).

1566-1199/$ - see front matter © 2007 Elsevier B.V. All rights reserved.
doi:10.1016/j.orgel.2007.04.009

the device. At present, devices exhibiting charge transport layers (hole or electron), or buffer layers such as SiO_2 or LiF for the electron injection improvement [6–8], are commonly reported for their high efficiency and lifetime. Finally, substantial performance enhancement may be obtained directly modifying the properties of the active organic material by way of rational design of the chemical structure of the photoactive material. For example, adding a functional group to the main polymer chain, or using polymer blends, have resulted in highly efficient devices [9–12]. Following this line of research, we have synthesized a novel thiophene-based polymer by adding a functional cyano group to its side-chain and investigated its potential use in OLEDs [13]. Among all the conjugated polymers developed in the past years for device application, polythiophene was selected due to its high chemical stability and structural tailorability, which can be usefully exploited to design proper structures for the targeted aims (color emission, physical properties such as glass transition temperatures, etc.) [14]. The cyano group (CN) has been widely reported to provide high electron affinity [10], a characteristic which is highly desirable for OLED applications because it allows the use of more stable metal electrodes (e.g. aluminium) for electron injection.

In our earlier work [11], we demonstrated that this novel thiophene-based polymer bearing a cyano group in its side-chain, namely PTOPhCN, showed promise for OLED applications. Orange-red photoluminescence (PL) was observed for either spin coated films or chloroform-based solution of the polymer. In addition, red electroluminescence (EL) was obtained for a single layer device, although the EL threshold voltage was high, i.e. about 28 V.

This work presents the progress obtained on the use of PTOPhCN as the active layer for OLED. Inserting charge injection layers at the electrode-organic interface, we can now report electroluminescence at 4 V with a high current density of the order of 6000 A/m^2, and a luminance of about 400 cd/m^2. The insertion of a PEDOT-PSS layer between the anode and the organic layer improved the hole injection and transport, while a more appropriate cathode was used for the electron injection. Compared to linear polythiophenes reported in the literature and used in our reference device, OLEDs using the PTOPhCN polymer show a significant improvement in luminance and hence in current efficiency of 0.08 cd/A which is, to our knowledge, the best result reported so far for an "all-thiophene" electroluminescent polymer.

2. Experimental

Poly{[3-hethylthiophene]-co-3-[2-(*p*-cyano-phenoxy)ethyl]thiophene} abbreviated as PTOPhCN was prepared by oxidative polymerization. Such synthesis enables to obtain in a cheap and easy way gram quantities of the polymer, which chemical structure can be seen in Fig. 1a. For extensive details on the chemical synthesis, refers to [13,15]. PTOPhCN was dissolved in chloroform at 5 mg/mL and thoroughly purged with N_2(g). Before spin coating the solutions were filtered over a 0.45 μm PTFE filter. Thin films were prepared from the chloroform based-solution via spin coating on patterned ITO coated glass plates. The ITO glass plates were extensively cleaned, using a sequence of soap, water and isopropanol ultrasonic washing steps and just before the deposition of the organic film were exposed to UV-Ozone for 20 min. A 100 nm thick PEDOT-PSS (HCStarck) hole injection layer was first deposited followed by an 80 nm thick layer of the light-emitting polymer. Ba (5 nm) and Al (80 nm) were used as cathode for the devices, which were evaporated under vacuum ($<1 \times 10^{-6}$ mbar). Devices were characterised in an inert atmosphere (<0.1 ppm H_2O and O_2). Film thickness was deter-

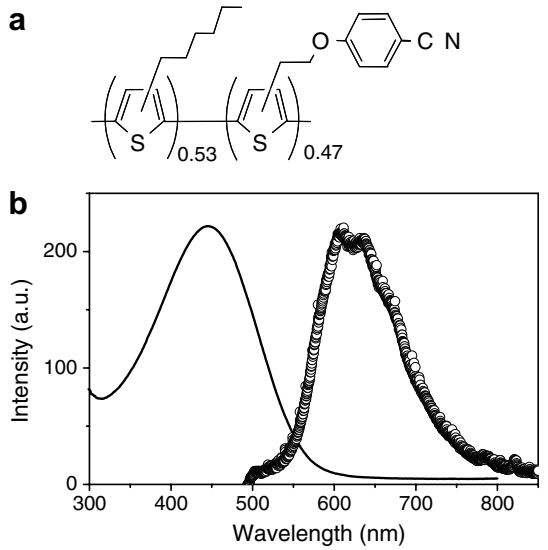


Fig. 1. (a) Chemical structure of PTOPhCN. (b) Optical absorption (—) and emission (○) spectra of a 220 nm thick spin coated layer of PTOPhCN.

mined using an Ambios XP1 profilometer. Current density and luminance versus voltage were measured using a Keithley 2400 source meter, and a photodiode coupled to a Keithley 6485 picoampmeter using a Minolta LS100 to calibrate the photocurrent. An Avantes luminance spectrometer was used to measure the EL spectrum. The quantum yield measurements were performed in N_2 ambient, using the quantum yield measurement system model C9920-01 from HAMAMATSU, for a thin layer of polymer spin coated on quartz substrates. The system is made up of an excitation light source that uses a xenon lamp and a monochromator, an integration sphere and a multi-channel spectrometer.

3. Results and discussion

3.1. Photophysical characteristics

Details about the chemical synthesis and the structural properties of the polymer can be found in previous works [13–16]. Fig. 1b shows the absorption and photoluminescence spectra of PTOPhCN for a spin coated layer about 220 nm thick. From the absorption edge, an optical band gap of 2.0 eV may be estimated, which corresponds to orange emission. The PL spectrum shows evident structuration and differs markedly from the absorption one, which is broad and misses any trace of sharp peaks and/or shoulders. In particular, two sharp peaks at 609 nm and 636 nm, with the presence of a bump around 665 nm, are visible, which origin is still under investigation. An important parameter for emitting organic materials is their luminous efficiency, i.e. the ratio between the number of photons of light radiated from the material and the number of photons of light absorbed by the material. The luminescence quantum yield of a thin layer of PTOPhCN was measured to be about 0.08 (8%). Such a low result is consistent with the well known relatively poor photoluminescence efficiency of these compounds [17,18]. As a final observation on the absorption and emission properties of PTOPhCN, from Fig. 1b a large Stokes' shift of 0.75 eV between the PL and the Absorption is evident, with a low self-absorption, which makes this material also a promising candidate for laser applications.

To investigate the structure of the deposited layer, X-ray diffraction (XRD) measurements were conducted on a thick 300 nm film of PTOPhCN spin-coated on a glass substrate (not shown here), measured as-deposited. No sharp peaks due to the diffraction by a crystalline structure of the X-rays were present, leading to conclude that the structure of the PTOPhCN layer as deposited is amorphous.

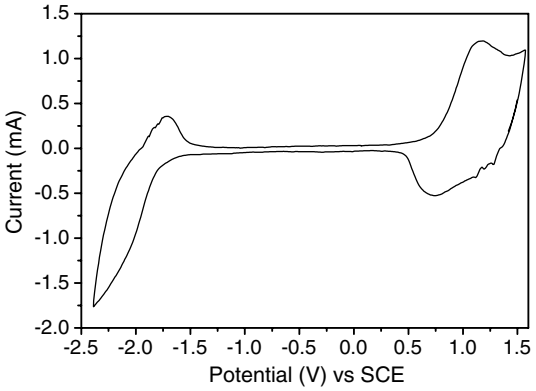


Fig. 2. Cyclovoltammetric response of a thin film of PTOPhCN (about 150 nm) deposited on a Pt slide, with a voltage sweep of 50 mV/s. HOMO level at −5.1 eV and LUMO level at −2.6 eV were calculated. The electrochemical bandgap is of 2.5 eV.

In order to have an indication on the energy levels of PTOPhCN, electrochemical measurements have also been performed on a spin-coated thin film (about 150 nm) of the polymer. As is visible from Fig. 2, the polymer showed clear oxidation and reduction onsets at 0.73 and −1.75 V, respectively. Based on the most recent literature considerations on the subject [16], the expressions:

$$E_{\mathrm{LUMO}} = -\mathrm{e}(E^{\mathrm{red}}_{\mathrm{onset}} + 4.4)$$
$$E_{\mathrm{HOMO}} = -\mathrm{e}(E^{\mathrm{ox}}_{\mathrm{onset}} + 4.4)$$

have been used to calculate the absolute HOMO and LUMO levels. This resulted in HOMO and LUMO levels of PTOPhCN of −5.1 and −2.6 eV, respectively. From these values an electrochemical bandgap of 2.5 eV was found.

3.2. Current density– voltage – luminance characteristics

A single layer light-emitting device was fabricated using PTOPhCN as the active material, with a 220 nm thick layer and Al electrodes [13]. For this device EL was reported for a voltage around 28 V, with current densities of the order of 2500 A/m^2 which resulted in low power efficiency. In order to improve the efficiency, various changes in the device layout were examined. Fig. 3 shows the current density (J) versus the applied voltage (V_{applied}) curves of

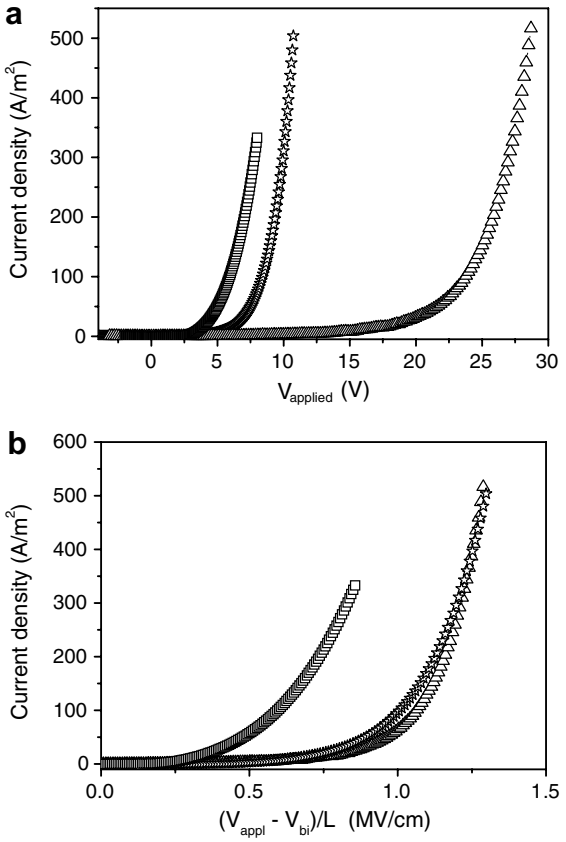


Fig. 3. Curves of current density J as a function of applied voltage $V_{applied}$ (a) and $(V_{applied} - V_{bi})/L$ (b) of the thiophene-based diode structures ITO/PTOPhCN/Al with a layer of PTOPhCN of around 220 nm (△) and 80 nm (*). Also shown is the measurement for a device with an 80 nm thick layer of PTOPhCN, with Ba/Ag as material used for the electrode (□). V_{bi} was calculated using Ref. [29] with values of the work function of metals from the literature and values of the energy level of PTOPhCn from electrochemistry.

the basic device previously mentioned as well as of a device with a thin active layer of about 80 nm. As can be seen, the use of a thinner layer leads to a dramatic lowering of the operating voltage of the device (threshold voltage going from 12 V down to 5 V). Furthermore, the EL was observed at around 15 V for the thinner device instead of 28 V. As the data in Fig. 3b clearly demonstrates, this decrease in voltage threshold is purely associated with the layer thickness as the electric field strength is constant for both devices. Indeed, the curves of current density plotted as a function of $(V_{applied} - V_{bi})/L$ fall nearly on top of each other, indicating that the device is contact limited instead of space charge limited as there is no change in E over the distance due to the enhanced charge injection at higher fields [19]. Various reports have dealt with the improvement of device performance with decreasing thickness of the active layer [20,21], thus consolidating this interpretation.

The current is controlled almost exclusively by holes injected at the ITO contact, due to the high energy barrier of about 1.8 eV present at the PTOPhCN/Al interface for the electron injection. The electron injecting contact plays no real part in determining the J/V characteristics of the device, but is the limiting factor for the device efficiency in terms of luminance. In order to remediate this unbalanced charge distribution in the device, to improve the electron injection and to increase the luminance, a third device was fabricated using Ba/Ag electrode instead of Al electrode. As mentioned previously, although Al is widely used as the cathode material due to its stability and processability, its injection efficiencies are generally inferior to those of Ba/Ag, Mg/Ag or Ca cathodes. In that case, the use of Ba/Ag as a cathode should increase significantly the electron injection in the device, as Ba has a work function of about 2.7 eV, while Al has a work function of 4.4 eV. Therefore, the metal electrode was changed from Al to Ba/Ag (Ag is used to protect the oxidation-sensitive Ba contact) for a diode structure with a thin 80 nm of PTOPhCN whose J/V characteristic can be seen in Fig. 3 as well. When Ba/Ag is used as the electrode instead of Al, current densities of around 330 A/m^2 and luminance of 20 cd/m^2 are reached at 4 V. Such an increase in current density and luminance concurs with an increased injection of electrons due to the reduced energy barrier at the polymer/cathode interface, leading to a better charge balance and therefore better radiative recombination rate. Fig. 3b exhibits a change in the current density curves as a function of $(V_{applied} - V_{bi})/L$ when Ba is used as an electrode. This result corroborates that a PTOPhCN-based device with ITO and Al as electrodes is injection limited, while now, using a Ba electrode instead of Al, one contact of the device is no longer limited. Furthermore, it has been reported that adding a thin Ba layer, the distance from the excitons in the PTOPhCN layer to the metallic electrode is increased, thus resulting in a reduced energy transfer from the excitons to the metal electrode, improving the light output efficiency of the device [22].

Finally, a standard step in OLED fabrication in order to improve the overall efficiency of the devices is to use a thin intermediate layer of PEDOT-PSS

between the ITO and the active organic layers. Extensive studies have been carried out and report that this thin uniform layer has several beneficial effects. It can planarise the otherwise rough ITO surface, modify its wetting properties for subsequent organic layer deposition and increase the anode work function thus facilitating the hole injection [7,20,22]. Fig. 4 displays the J/V and L/V curves for the following diodes structures: ITO/PTOPhCN/Ba/Ag (device A) and ITO/PEDOT-PSS/PTOPhCN/Ba/Ag (device B), with a PTOPhCN layer of around 80 nm for both devices. The data obtained with a diode based on a linear standard polythiophene (P3HT) of similar thickness is also added in order to compare the efficiency. Indeed, in this work, the addition of a PEDOT-PSS layer also resulted in higher current densities, around 6000 A/m^2 at 8 V, as well as an equally strong increase in luminance, from 20 cd/m^2 for a single layer device up to 400 cd/m^2 for the device with the PEDOT-PSS hole injection layer. The higher current densities obtained show that the PEDOT-PSS layer improved the hole injection from the anode as expected. The concurrent increase in luminance shows that sufficient electrons are present in the device to recombine with the added holes, resulting in a higher recombination rate. A better charge balance has hence been reached.

Fig. 5 shows the normalized photoluminescence and electroluminescence spectra taken at room temperature of a thin film of the thiophene-based polymer. The EL spectrum was obtained for an applied bias of 5 V, for the device structure ITO/PEDOT-PSS/PTOPhCN/Ba/Ag, with a PTOPhCN layer of around 80 nm, while the PL spectra were obtained for a layer of about 220 nm. Both EL and PL spectra exhibit similar characteristics, with a good overlap, peaking around 600 nm. The EL spectrum actually contains a small artefact at 650 nm from the experimental set-up. At 5 V, the luminance from

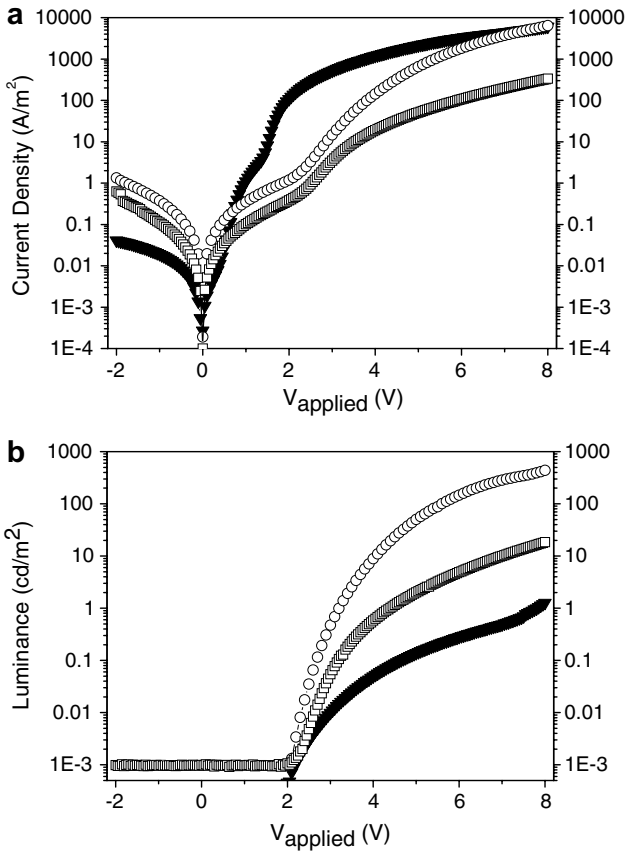


Fig. 4. Current density (a) and luminance (b) as a function of $V_{applied}$ for the following diode structure: ITO/PTOPhCN/Ba/Ag (□) as well as the diode structure ITO/PEDOTPSS/PTOPhCN/Ba/Ag (○), with a PTOPhCN layer of around 80 nm. The data obtained with a similar structure diode based on P3HT (▲) are also added for comparison.

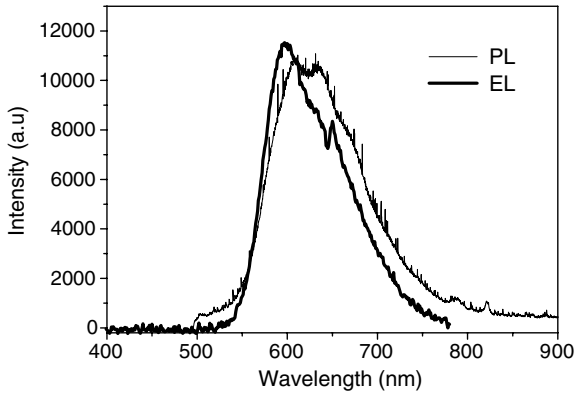


Fig. 5. Room temperature photoluminescence and electroluminescence of the thiophene-based diode structure: ITO/PEDOT-PSS/PTOPhCN/Ba/Ag, with a PTOPhCN layer of around 80 nm. The electroluminescence spectrum was obtained for an applied bias of 5 V.

the EL signal is about 30 cd/m^2 and the maximum luminance obtained at 8 V is 400 cd/m^2. Efficiency of the order of 0.08 cd/A for current densities of about 1000 A/m^2 were obtained for our PTOPhCN-based devices, which represents very promising results for electroluminescent devices based on polythiophenes. Indeed so far, luminous efficiencies of about 0.08–0.12 cd/A have been reported for such devices [23,24]. For example, Barta et al. reported efficiencies of up to 0.28% (0.12 cd/A) for regioregular poly(alkylthiophenes) but this was achieved at high applied voltages of around 38 V [23]. Other regiorandom polythiophene-based devices showed luminous efficiencies ranging from 0.0004 cd/A (for LB layers of P3HT) [24] to 0.08 cd/A (for a pristine uretane-substituted polythiophene, PURET) [25], up to values of 0.66 cd/A for dye-doped PURET [25]. Furthermore, a similar device based on synthesized P3HT (regioregular, 94% head to tail) was also fabricated and its luminuous efficiency obtained is about 0.002 cd/A, confirming that better device performance is obtained while using PTOPhCN as the active layer of the device. The I/V and L/V curves of this device are shown in Fig. 4. In any case PTOPhCN being a regiorandom polythiophene, it is expected that its charge transport ability would be limited by its intrinsialy disordered structure (and indeed, the polymer is amorphous in its solid state [13]).

From a practical point of view, an EL device should possess not only a high brightness but also a low operation current density. Therefore, although PTOPhCN-based devices show appreciable performances, there is still room for improvements in terms of optimizing their luminance efficiency. Nevertheless, this new polythiophene shows a significant increase in efficiency compared to previously reported polythiophenes, indicative of the gain that can be obtained by further optimizing the chemical structure and device optimization.

Now, looking at the effect of the CN group on the polymer properties, it could seem at first that its role is to increase the electron affinity of the polymer. Indeed, in many cyano-substituted polymers, such as for example CN-MEH-PPV, this is the case [26,27]. However, in PTOPhCN the cyano group is not linked to the backbone via conjugated bonds, hence a direct conjugative effect is not expected to take place. On the other hand, for other thiophene-based polymers substituted in side-chain with a polar moiety through an ethylenic spacer, NMR and reactivity evidences show that some kind of electronic communication between the backbone and the polar moiety is present, in the solvated state [28]. In view of this, the found enhancement of EL given by the presence of the OPhCN group may be ascribed to (i) a possible electronic effect transmission through the ethylenic spacer, (ii) a spatial vicinity of the polar moiety to the backbone, or to a combination of the two factors. At this stage of our investigations it is not possible to find out if these or other factors are the ones influencing the device behaviour and more investigation is underway to clarify this point. However, it did not escape from our notice that the mentioned possible mechanism of EL enhancement could have interesting consequences for clarifying the basic behaviour of organic electronics-based systems and devices.

4. Conclusion

A new orange-red light-emitting thiophene-based polymer (PTOPhCN) containing a cyano group in the side-chain has been used in OLED devices. A successful electroluminescent diode based on a single organic layer was fabricated, showing bright EL around 4 V for a luminance of 20 cd/m^2. Introducing a PEDOT-PSS layer resulted in an overall improvement of the device, with luminance of about 400 cd/m^2 and current densities of about 6000 A/m^2 at 8 V, giving a maximum luminous efficiency of 0.08 cd/A. Although such device shows good efficiency in terms of luminance, it still exhibits current densities too high for being used in practical devices and further optimization of the device is underway.

To our knowledge, due to the easy synthesis, good filmability, redox potentials and device performance, this is the best 'all-thiophene' electroluminescent polymer described so far. The presence of the cyano group as a side-chain substituent of the polymer plays without any doubt a role in determining its interesting performances, but wether this is due to a direct conjugative effect exerted on the backbone, or to other factors such as spatial vicinities of polar groups, still remains to be completely clarified, and work is underway in this sense.

Acknowledgements

S.C. and H.J.B. acknowledge support from the Spanish Government, from the Ramon y Cajal program. This work was carried out with the financial support of the Spanish Ministry of Education and Science through grants TEC2005-02716/MIC, TEC2006-10665/MIC and the European Commission through the European Network of Excellence PHOREMOST (FP6-511616).

References

[1] J.-S. Kim, F. Cacialli, R.H. Friend, Thin Solid Films 445 (2003) 358.
[2] J.-S. Lim, P.-K. Shin, Appl. Surf. Sci. 253 (2003) 3828.
[3] S. Jung, N.G. Park, M.Y. Kwak, B.O. Kim, K.H. Choi, Y.J. Cho, Y.K. Kim, Y.S. Kim, Opt. Mater. 21 (2002) 235.
[4] T.P. Nguyen, P. Le Rendu, N.N. Dinh, M. Fourmigué, C. Mézière, Synth. Met. 138 (2003) 229.
[5] M.Y. Chan, S.L. Lai, F.L. Wong, O. Lengyel, C.S. Lee, S.T. Lee, Chem. Phys. Lett. 371 (2003) 700.
[6] S.T. Zhang, Z.J. Wang, J.M. Zhao, Y.Q. Zhan, Y. Wu, Y.C. Zhou, X.M. Ding, X.Y. Hou, Appl. Phys. Lett. 84 (2004) 2916.
[7] D. Xu, Z. Deng, X. Li, Z. Chen, C. Liang, Appl. Surf. Sci. 253 (2007) 3378.
[8] H. Kanno, N.C. Giebink, Y. Sun, S.R. Forrest, Appl. Phys. Lett. 89 (2006) 023503.
[9] G. Gigli, M. Anni, M. Theander, R. Cingolani, G. Barbarella, L. Favaretto, O. Inganäs, Synth. Met. 119 (2001) 581.
[10] M.-T. Lee, H.-H. Chen, C.-H. Liao, C.-H. Tsai, C.H. Chen, Appl. Phys. Lett. 85 (2004) 3301.
[11] J.M. Xu, S.C. Nq, H.S.O. Chan, Macromolecules 34 (2001) 4314.
[12] T.-Q. Nguyen, I.B. Martini, J. Liu, B.J. Schwartz, J. Phys. Chem. B 104 (2000) 237.
[13] S. Cheylan, A. Fraleoni-Morgera, J. Puigdollers, C. Voz, L. Setti, R. Alcubilla, G. Badenes, Thin Solid Films 497 (2006) 16.
[14] J.C. Gustafsson-Carlberg, O. Inganäs, M.R. Andersson, C. Booth, A. Azens, C.G. Granqvist, Electrochim. Acta 40 (1995) 2233.
[15] A. Fraleoni-Morgera, C. Della-Casa, M. Lanzi, P. Costa-Bizzarri, Macromolecules 36 (2003) 8617.
[16] W.-C. Wu, C.-L. Liu, W.-C. Chen, Polymer 47 (2006) 527, and references therein.
[17] F. Cacialli, Synth. Met. 76 (1996) 145.
[18] N.C. Greenham, I.D.W. Samuel, G.R. Hayes, R.T. Philips, Y.A.R.R. Kessener, S.C. Moratti, A.B. Holmes, R.H. Friend, Chem. Phys. Lett. 241 (1995) 89.
[19] B.K. Crone, P.S. Davids, I.H. Campbell, D.L. Smith, J. Appl. Phys. 84 (1998) 833.
[20] P.W.M. Blom, C. Tanase, D.M. de Leeuw, R. Coehoom, Appl. Phys. Lett. 86 (2005) 092105.
[21] I.D. Parker, J. Appl. Phys. 75 (1994) 1656.
[22] F. Li, Appl. Phys. Lett. 70 (1997) 1233.
[23] P. Barta, F. Cacialli, R. Friend, M. Zagórska, J. Appl. Phys. 84 (1998) 6279.
[24] A.J. Pal, T.P. Ostergard, R.M. Osterbacka, J. Paloheimo, H. Stubb, IEEE J. Sel. Top. Quant. Electron. 4 (1998) 137.
[25] A. Kaur, M.J. Cazeca, S.K. Sengupta, J. Kumar, S.K. Tripathy, Synth. Met. 126 (2002) 283.
[26] M. Cheng, Y. Xiao, W.-L. Yu, Z.-K. Chen, Y.-H. Lai, W. Huang, Thin Solid Films 363 (2000) 110.
[27] M.M.D. Ramos, H.M.G. Correia, R. Mendes Ribeiro, A.M. Stoneham, Synth. Met. 147 (2004) 281.
[28] A. Fraleoni-Morgera, C. Della-Casa, P. Costa-Bizzarri, M. Lanzi, A. Missiroli, Macromolecules 38 (2005) 3170.
[29] W. Brütting (Ed.), Physics of Organic Semiconductors, WILEY-VCH Verlag GmbH & Co KGaA, 2005.

Available online at www.sciencedirect.com
ScienceDirect
Organic Electronics 8 (2007) 648–654
Organic Electronics
www.elsevier.com/locate/orgel

Organic field-effect transistors and memory elements using deoxyribonucleic acid (DNA) gate dielectric ☆

Philipp Stadler [a], Kerstin Oppelt [a], Thokchom Birendra Singh [a,*], James G. Grote [b], Reinhard Schwödiauer [c], Siegfried Bauer [c], Heidi Piglmayer-Brezina [d], Dieter Bäuerle [d], Niyazi Serdar Sariciftci [a]

[a] *Linz Institute of Organic Solar Cells (LIOS), Physical Chemistry, Johannes Kepler University Linz, A-4040 Linz, Austria*
[b] *Air Force Research Laboratory, Materials and Manufacturing Directorate, AFRL/MLPS, Wright Patterson Air Force Base, OH 45433-7707, USA*
[c] *Soft Matter Physics (SOMAP), Johannes Kepler University Linz, A-4040 Linz, Austria*
[d] *Institut für Angewandte Physik, Johannes Kepler University Linz, A-4040 Linz, Austtria*

Received 2 April 2007; received in revised form 3 May 2007; accepted 6 May 2007
Available online 24 May 2007

Abstract

Deoxyribonucleic acid (DNA) bio-polymers derived from fish waste products are employed as gate dielectric in n-type methanofullerene as well as p-type pentacene based organic field-effect transistors working at low voltage levels and low gate leakage currents. Based on the large hysteresis in the transfer characteristics, operation of the transistor as a non-volatile memory element is shown. Practically hysteresis free operation of DNA based transistors is obtained at low voltage levels by adding an additional aluminium oxide blocking layer between the organic semiconductor and the DNA gate dielectric.
© 2007 Elsevier B.V. All rights reserved.

PACS: 85.30.Tv; 72.80.Le; 73.61.Ph

Keywords: Deoxyribonucleic acid; Organic transistors; Hysteresis; Organic dielectric; Persistent polarization

1. Introduction

Organic insulators and semiconductors are very attractive for use in low cost electronic products that can be produced for example by printing techniques on large area and flexible substrates [1]. In early reports on organic electronic devices inorganic insulating materials, such as thermally grown SiO_2, were used as gate dielectric. Later on, organic insulators were employed as gate dielectrics in organic

☆ This work is supported by Air Force Research Laboratory, Materials and Manufacturing Directorate AFRL/ML, the Asian Office of Advanced Research and Development AOARD, the Air Force Office of Scientific Research AFOSR and the European Office of Aerospace Research&Development EOARD.
* Corresponding author.
E-mail address: birendra.singh@jku.at (T.B. Singh).

1566-1199/$ - see front matter © 2007 Elsevier B.V. All rights reserved.
doi:10.1016/j.orgel.2007.05.003

field-effect transistors (OFETs) for a number of reasons. Organic dielectric materials are often solution-based and allow low-temperature processing steps. High permittivity, optical transparency and chemical compatibility with a large number of other materials are further advantages of some organic gate dielectrics [2,3]. Both bottom and top gate structures were realized, some of them operating at low voltage levels. All solution-processed printed OFETs utilizing polyester as gate dielectric (1.5 μm thick, insulator capacitance per area, $C_i = 1.5\ \text{nF cm}^{-2}$) [4] were reported by several groups. Large efforts were devoted to printed electronics with organic dielectrics during the last years [5–7], an example being ''all-polymer'' integrated circuits [8,9]. By producing ultra-thin insulating layers with a large insulating capacitance per area, C_i and a large dielectric breakdown voltage, low voltage operating OFETs were achieved [10]. Most of the organic dielectrics which possess a rather high permittivity typically cause a significant hysteresis in the transfer characteristics when used as gate dielectric in organic transistors. Recent work has localized the origin of this hysteresis to the movement of mobile charges/ions, and to the presence of trapping/detrapping mechanisms in the dielectric/semiconductor interface [9,10], but a clear microscopic picture of the processes that cause hysteresis in OFET's is still lacking. Persistently polarizable gate dielectrics, such as space charge electrets and ferroelectric polymers can be used for ''non-volatile memory elements'' (memOFETs). In memories advantage is made of the hysteresis in the transfer characteristics to store one bit of digital information per transistor [11,12]. A major breakthrough has been the recent demonstration of fast switching in electret based devices [13] on the order of only μs. However, the voltage level for switching was on the order of 100–200 V, so the question remains if devices can be made with a programming voltage of around 10 V [14].

Here, we address especially the problem of reducing the programming voltage in OFET memory elements. Our structures are based on the biomolecule, deoxyribonucleic acid (DNA), which we employ as dielectric layer in solution-processed n-type bio-organic OFET (BiOFET) memory elements based on methanofullerenes. We also show how such transistors can be made to work without significant hysteresis effects, by adding an additional blocking layer between the organic semiconductor and the DNA dielectric.

2. Organic field-effect transistors with DNA gate dielectrics

Deoxyribonucleic acid (DNA)-based bio-polymers were recently described [15] for optoelectronic applications, such as organic light emitting diodes (OLEDs) [16], for cladding layers in waveguides, as a host material in active waveguide structures in electro-optical devices [17], and also as gate dielectric in organic field-effect transistors (OFET) [18]. Purified DNA is modified through a cationic surfactant (hexadecyltrimethyl ammonium chloride-CTMA) cation exchange reaction to enhance solubility, processing and stability. Additionally, the molecular weight can be tailored to suit the application through sonication [19]. For the present device fabrication, 300 kDa molecular weight DNA were used. Simplified energy band diagrams are shown in Figs. 1a and b for the organic semiconductors pentacene [20] and 1-(3-methoxycarbonyl)propyl-1-phenyl[6,6]C_{61} (PCBM) [12,21], with DNA–CTMA as gate dielectric and Au as gate electrode, in the absence of a bias potential and interface dipoles. DNA–CTMA has a large band gap energy of 4.7 eV. Injecting electrons into its LUMO level has a very large injection barrier of $[\phi_b(e^-) \sim 4.1\ \text{eV}]$ [16] with gold as electrodes. Although one would expect that the injection of holes from gold into the HOMO of DNA seems possible with an injection barrier of $[\phi_b(h^+) \sim 0.6\ \text{eV}]$, our previous studies showed DNA–CTMA to be a good gate dielectric for high performance pentacene based (p-type) BiOFETs [18]. FETs corresponding to Fig. 1a would be n-type and both Fig. 1b and c would be p-type. However, injected or inherent, the presence of mobile charges in DNA–CTMA is inevitable, so here we also introduce a thin charge blocking layer of Al_2O_3, [22] (see Fig. 1c) to allow for a hysteresis free operation of DNA based transistors.

3. Device preparation and morphological characterization

Borosilicate glasses were cut into 15 mm × 15 mm size. After cleaning with acetone and Hellmanex (Hellma GmbH and Co.) in an ultrasonic bath, a 0.5 mm × 15 mm area of Cr/Au gate electrode was evaporated on the surface. DNA–CTMA, with a molecular weight of 300 kDa, was dissolved in butanol at a weight ratio of 1:10 and spin-deposited under ambient conditions at 1500 rpm. The average thickness was about 1–1.1 μm with estimated dielec-

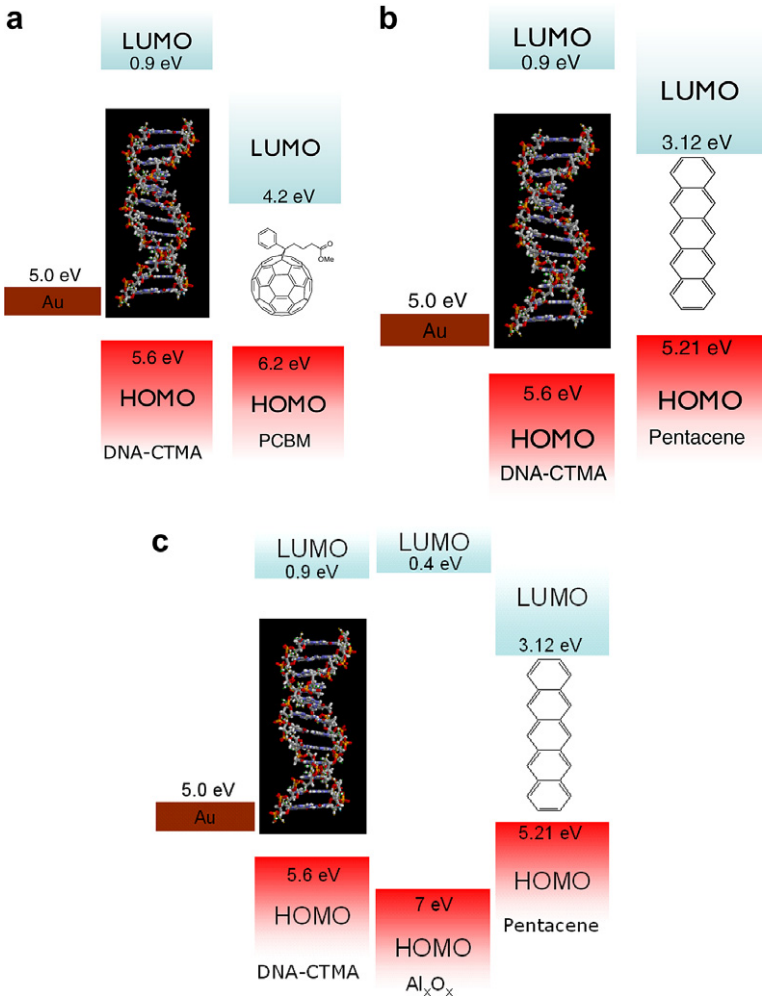


Fig. 1. (a) Simplified energy band diagram of a MIS structure of Au/deoxyribonucleic acid (DNA)/1-(3-methoxycarbonyl)propyl-1-phenyl[6,6]C_{61} (PCBM), (b) simplified energy band diagram of MIS structure Au/deoxyrebonucleic acid (DNA)/pentacene and (c) simplified energy band diagram of MIS structure Au/deoxyrebonucleic acid (DNA)/Al_2O_3/pentacene. It is to be noted here that energy levels of the respective layers without taking into account of interface dipoles are taken respectively from Ref. [22].

tric constant of 7.8–8. PCBM semiconductor thin-films were spin-deposited inside a glove box at a spin rate of 1500 rpm, from 3% weight ratio of PCBM in chlorobenzene resulting a thickness of 50–70 nm. Pentacene was used as received from Sigma–Aldrich. Organic thin-films of Pentacene were grown at a rate of 0.2–0.3 Å/s at room temperature at a base vacuum of 10^{-6} mbar using a Leybold Univex 350. The source to substrate height was about 0.5 m. The Al_2O_3 charge blocking layer was deposited in a commercial high vacuum chamber (Pfeiffer, classic 500) by electron beam evaporation of Al_2O_3 (purity 99.99%). The deposition rate was about 5 Å/s. For all metal-insulator-metal (MIM), metal-insulator-semiconductor (MIS) and BiOFET devices, Cr/Au electrodes were used a bottom electrode (gate). For MIM structures, with DNA–CTMA as the insulator, a 40 nm thick Au electrode was employed as the top electrode. For MIS structures, with DNA–CTMA/PCBM, a 40 nm thick LiF/Al electrode was employed as the top contact. For all BiOFETs, LiF/Al and Au were use as the source–drain contact for both the PCBM and Pentacene semiconductors, respectively. For all BiOFETs, the channel length L of the device was 35–40 μm and the channel width was $W = 3$ mm, giving a W/L ratio of 70. All the device electrical characterization was carried out under an argon environment inside the glove box. An Agilent E5273A with a two source-measure unit instrument

was employed for the steady state current–voltage measurements. All measurements were performed at a typical scan rate as stated above. For quasi-static capacitance–voltage measurements, we used a HP 4248 A precision LCR meter at a typical scan rate with a hold time of 2.5 s. An Alpha-A high performance frequency analyzer (Novocontrol), along with a high voltage booster HVB 1000_156/0 (Novocontrol), were used for low frequency dielectric spectroscopy. The surface morphology and thicknesses of the bio-organic dielectric and semiconducting organic thin-films were measured under ambient conditions with a Digital Instrument Dimension 3100 atomic force microscope.

The surface morphology of low molecular weight DNA–CTMA (300 kDa), revealed a surface roughness < 5 nm in such films as shown in Fig. 2a. Figs. 2b and c depict smooth PCBM film on top of DNA–CTMA film and pentacene crystallites on the DNA–CTMA layers. For comparison, larger crystallites of pentacene are usually obtained when using more common organic dielectrics as bottom gate layer [23].

4. Experimental results

Before studying transistor structures, capacitance voltage measurements were performed on MIS structures. The MIS structures consist of PCBM spin-coated on top of DNA–CTMA. For the metal electrode in the MIS device we have chosen Cr/Au as a bottom as well as top electrodes. Measurements of the capacitance versus bias voltage are shown at a frequency of 66 Hz for different sweep rates of the bias voltage. The ac-voltage signal level was set to 0.5 V. As expected for dielectrics with mobile charge carriers, hysteresis loops are evident in the capacitance C versus bias field (Fig. 3), which enlarge when decreasing the sweep rate of the bias voltage. The hysteresis observed in the capacitance of the MIS sample, further depends on the maximum bias level applied and also strongly on the device temperature.

Based on the observations from the MIS structure, we expect that BiOFET's with PCBM films spin-coated on DNA–CTMA (see bottom gate BiOFET device scheme in the inset of Fig. 4) also reveal a large hysteresis in the current–voltage characteristics. Fig. 4a shows the output characteristics of BiOFETs with LiF/Al source–drain electrodes. This demonstrates an n-channel BiOFET. Since we used electron-injecting contacts, LiF/Al, a p-channel

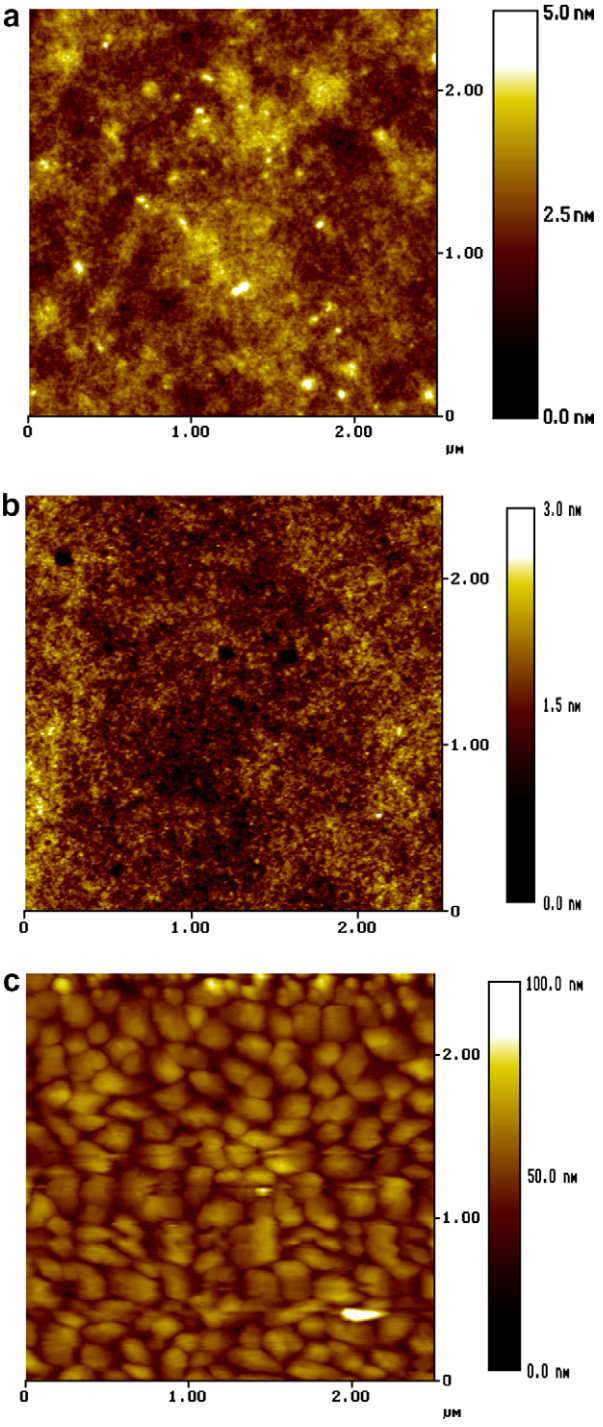


Fig. 2. (a) AFM topographical images (2.5 μm × 2.5 μm) of spin-coated 1 μm thick film of 300 kDa molecular wt. DNA–CTMA. Height scale indicating surface roughness of around 3 nm is also shown. (b) AFM topographical images (2.5 μm × 2.5 μm) of 100 nm spin-coated film of PCBM on DNA–CTMA and (c) AFM topographical images (2.5 μm × 2.5 μm) of 50 nm film of pentacene evaporated on DNA–CTMA.

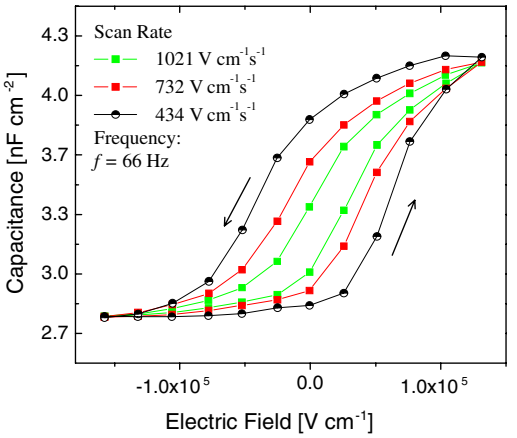


Fig. 3. Quasi-static capacitance-electric field curves for the MIS structures in (at 66 Hz) at different sweep/scan rate (dV_{Gate}/dt) as indicated. Larger hysteresis with slower scan rates are found.

BiOFET with PCBM as a semiconductor is not expected due to large hole injection barrier [$\phi_b(h^+) = 1.2$ eV] from these electrodes into PCBM [24]. $I_{Drain,Sat}$ can be as high as 4–5 μA, for a channel length of 35 μm and width of 3 mm and for $V_{Drain} = 20$ V and $V_{Gate} \approx 10$ V. This is promising when compared to standard organic dielectric based PCBM OFETs with an operating voltage in the range of >60 V [12]. The lower operating voltage of the n-channel BiOFET is even clearer from its transfer characteristics as shown in Fig. 4b. The threshold voltage, V_t, is found to be different from standard PCBM OFETs using other organic gate dielectrics, even though the thickness of the dielectrics and other device parameters are similar [12]. The gate leakage currents in our devices are on the order of 10^{-9} A (for $V_{Gate} = 10$ V), not exceedingly large values typically also found in other OFET's. Mobilities for the semiconductors are not given, since they are affected by the large hysteresis in the transfer characteristics of the transistors.

In the present case, a drain current on the order of 10^{-10} A in the off-state can be modulated by the gate by four-orders of magnitude, reaching a saturated I_{Drain} of 10^{-6} A with an applied $V_{Gate} < 10$ V. In analogy to the capacitance vs. electric field measurements, one can also clearly observe a large hysteresis with a shift of $V_t \approx 7$ V. The results reported here are obtained at a scan rate of 12.4 mV s^{-1} and a hold time of 2.5 s to obtain a data point. More than 20 different devices were measured and we found a deviation of about 20% in V_t when all measurements are performed with a scan rate of 12.4 mV s^{-1}. However, a large shift in $V_t \approx 7$ V for the return curve

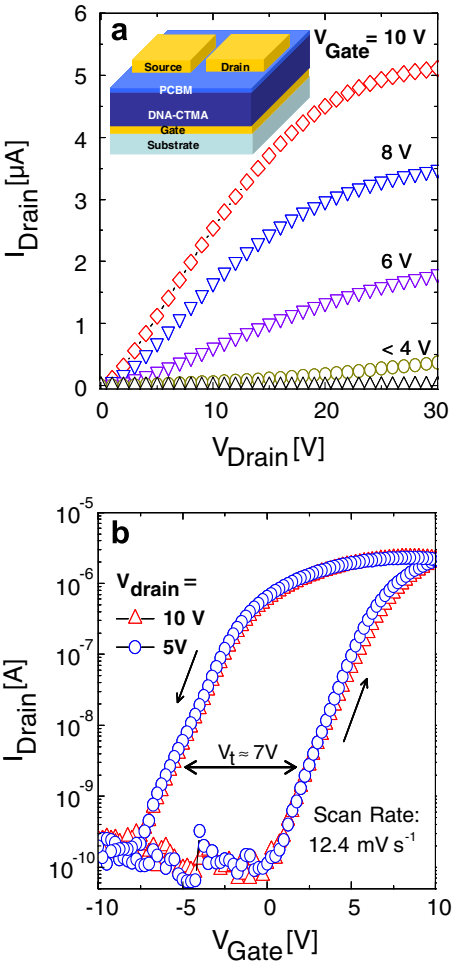


Fig. 4. (a) Output characteristics of solution-processed low voltage operating BiOFET with voltage step of 1 V/s and (b) transfer characteristics of BiOFET. All measurements are performed with steps of 12.4 mV s^{-1}. Note: gate current characteristics of the BiOFET, also plotted, correspond to the right scale of the graph.

is clearly seen in transfer characteristics. This shift in V_t is towards negative V_{Gate} with respect to ideal PCBM OFETs based on standard organic dielectrics and is towards the same direction as it appears in polyvinyl alcohol electret based OFET [12]. Fig. 4b shows that $I_{Drain,Sat}$ is bistable around $V_{Gate} = 0$ V. In Fig. 5 $I_{Drain,Sat}$ is measured for a gate voltage pulse V_{Gate} applied for 200 s. Note the pulse voltage level is only around 20 V, thereby demonstrating that voltage levels can be reduced to values of practical interest. However, the programming time is still an obstacle to be addressed in further work. After switching off the voltage pulse, the current decays, after 800 s the current is still more than one order

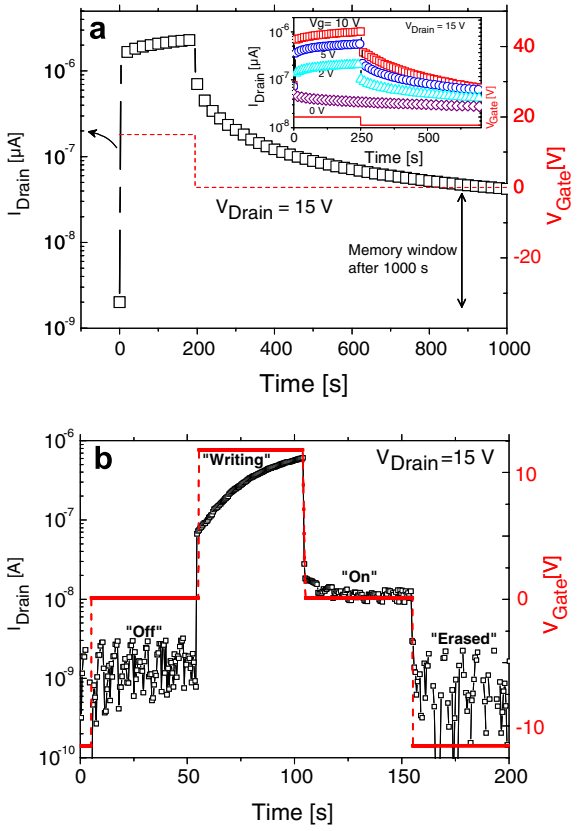


Fig. 5. Transient response characteristics of BiOFETs (a) indicating a long retention time Inset: Transient decay characteristics of BiOFET with different gate bias condition (b) as a memory element with an applied gate voltage pulse showing memory "off", "on", "write" and "erase". Note: Gate voltage pulse height is shown in right hand scale of each graph.

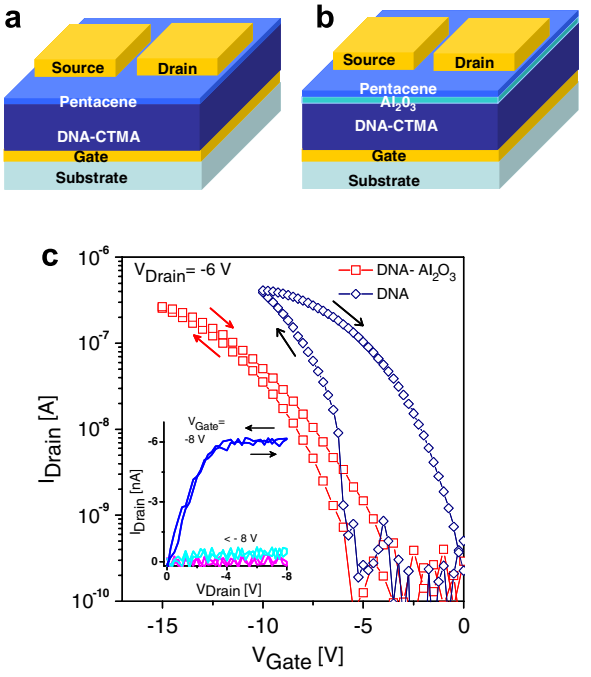


Fig. 6. Transfer characteristics of BiOFET with pentacene as a semiconductor with DNA–CTMA single layer as a dielectric and with additional Al_2O_3 charge blocking layer. Inset: Output characteristics of BiOFET with pentacene as semiconductor with DNA–CTMA single layer as a dielectric and with additional Al_2O_3 charge blocking layer.

of magnitude larger than the off current. It is also evident in the Fig. 5a that the relaxation of the current slows down, so we expect a sizable memory even after much larger times. The inset of Fig. 5a shows the retention time measurement as a function of V_{Gate}. $I_{Drain,Sat}$ can be depleted upon applying a depletion voltage as shown in Fig. 5b. For the measured $I_{Drain,Sat}$ one can define four states: "off", "write", "on" and "erase". By applying alternating V_{Gate} pulse cycles function as a memory element is shown.

While hysteresis is desired in memory applications of OFET's, it is not wanted in transistors used for the amplification of signals in circuits. Therefore it is desirable to indicate pathways for obtaining hysteresis free DNA based transistors. By introducing a charge blocking layer at the interface between the semiconductor and the insulator [25] others have shown that hysteresis effects can be minimized. In our BiOFET a 50 nm thick layer of Al_2O_3 is deposited on the semiconductor layer before the DNA–CTMA is applied. As semiconductor pentacene was chosen, and the characteristics of devices with and without Al_2O_3,charge blocking layer are summarized in Fig. 6. The pentacene based BiOFETs show a significantly reduced hysteresis when the charge blocking layer is introduced, in comparison to the device without charge blocking layer. The inset in Fig. 6 shows the BiOFET output characteristic for a device with a charge blocking layer. Note that there is no hysteresis observed in the forward and reverse bias sweep, This observation further supports our working assumption that interface charging between the organic insulator and organic semiconductor is responsible for the hysteresis effect in DNA OFET transfer characteristics.

5. Conclusions

In this work we have presented the use of DNA–CTMA-based bio-polymers as gate dielectric in low voltage operating BiOFETs. The hysteresis present

in the devices is found to depend on the gate voltage sweep rate. The hysteresis is probably caused by charged species present in the DNA polymer. By introducing a charge blocking layer at the interface between the insulator/semiconductor the hysteresis is reduced.

Acknowledgements

The authors acknowledge the work done by Professor Naoya Ogata, CIST in making salmon DNA available for our BiOFET research. We also wish to acknowledge the support of the Air Force Research Laboratory, Materials and Manufacturing Directorate (AFRL/ML), the Asian Office of Advanced Research and Development (AOARD), the Air Force Office of Scientific Research (AFOSR) the European Office of Aerospace Research & Development (EOARD) and the Austrian Foundation for Advancement of Science (FWF) (No. S9711-N08). These authors thank Dr. Joshua Hagen for his technical assistance and fruitful discussions.

References

[1] (a) Th.B. Singh, N.S. Sariciftci, Ann. Rev. Mater. Res. 36 (2006) 199;
(b) H. Sirringhaus, Adv. Mater. 17 (2005) 2411;
(c) C.D. Dimitrakopoulos, P.R.L. Malenfant, Adv. Mater. 14 (2002) 99;
(d) G. Horowitz, J. Mater. Res. 19 (2004) 1946.

[2] (a) J. Veres, S. Ogier, G. Lloyd, D. de Leeuw, Chem. Mat. 16 (2004) 4543;
(b) J. Veres, S.D. Ogier, S.W. Leeming, D.C. Cupertino, S.M. Khaffaf, G. Lloyd, Proc. SPIE 5217 (2003) 147.

[3] A. Facchetti, M.H. Yoon, T.J. Marks, Adv. Mater. 17 (2005) 1705.

[4] (a) X. Peng, G. Horowitz, D. Fichou, F. Garnier, Appl. Phys. Lett. 57 (1990) 2013–2015;
(b) F. Garnier, R. Hajlaoui, A. Yassar, P. Srivastava, Science 265 (1994) 1684;
(c) M. Halik, H. Klauk, U. Zschieschang, T. Kriem, G. Schmid, W. Radlik, K. Wussow, Appl. Phys. Lett. 81 (2002) 289.

[5] H. Klauk, M. Halik, U. Zschieschang, G. Schmid, W. Radlik, J. Appl. Phys. 92 (2002).

[6] R. Parashkov, E. Becker, G. Ginev, T. Riedl, H.H. Johannes, W. Kowalsky, J. Appl. Phys. 95 (2004) 1594–1596.

[7] J. Park, S.Y. Park, S. Shim, H. Kang, H.H. Lee, Appl. Phys. Lett. 85 (2004) 3283–3285.

[8] H. Sirringhaus, T. Kawase, R.H. Friend, T. Shimoda, M. Inbasekaran, W. Wu, E.P. Woo, Science 290 (2000) 2123.

[9] H.E. Huitema, G.H. Gelinck, E. Van Veenendaal, E. Cantatore, F.J. Touwslager, L.R.R. Schrijnemakers, J.B. Ph. H. Van der Putten, T.C.T. Geuns, M.J. Beenhakkers, P.J.G. Vam Lieshout, R.W. Lafarre, D.M. De Leeuw, B.J.E. Vam Rens, IDW 1663 (2003).

[10] M.J. Panzer, C.D. Frisbie, Appl. Phys. Lett. 88 (2006) 203504.

[11] H.E. Katz, X.M. Hong, A. Dodabalapur, R. Sarpeshkar, J. Appl. Phys. 91 (2002) 1572.

[12] Th.B. Singh, N. Marjanoviæ, G.J. Matt, N.S. Sariciftci, R. Schwödiauer, S. Bauer, Appl. Phys. Lett. 85 (2004) 5409.

[13] K. Baeg, Y. Noh, J. Ghim, S. Kang, H. Lee, D. Kim, Adv. Mater. 18 (2006) 3179.

[14] G. Gelinck, Nature 445 (2007) 268.

[15] L. Wang et al., Chem. Mat. 13 (4) (2001) 1273–1281.

[16] J.A. Hagen, W.X. Li, J.G. Grote, A.J. Steckl, Appl. Phys. Lett. 88 (2006) 171109.

[17] E.M. Heckman, J.G. Grote, F.K. Hopkins, P.P. Yaney, Appl. Phys. Lett. 89 (2006) 181116.

[18] Th.B. Singh, N.S. Sariciftci, James G. Grote, Frank K. Hopkins, J. Appl. Phys. 100 (2006) 024514.

[19] E.M. Heckman, J.A. Hagen, P.P. Yaney, J.G. Grote, F.K. Hopkins, Appl. Phys. Lett. 87 (2005) 211115.

[20] Y.Y. Lin, D.J. Gundlack, S.F. Nelson, T.N. Jackson, IEEE Electr. Dev. Lett. 18 (1997) 606.

[21] N. Koch et al., Appl. Phys. Lett. 82 (2003) 70.

[22] M. Hong, J. Kwo, Electr. Chem. Soc. Trans. 1 (2006) 41.

[23] Th.B. Singh, F. Meghdadi, S. Günes, N. Marjanović, G. Horowitz, P. Lang, S. Bauer, N.S. Sariciftci, Adv. Mater. 17 (2005) 2315.

[24] C. Lungenschmied, G. Dennler, H. Neugebauer, N.S. Sariciftci, E. Ehrenfreund, Appl. Phys. Lett. 89 (2006) 223519.

[25] Ch. Lee et al., Appl. Phys. Lett. 88 (2006) 252102.

Available online at www.sciencedirect.com
ScienceDirect
Organic Electronics 8 (2007) 655–661
Organic Electronics
www.elsevier.com/locate/orgel

Fabrication of vertical channel top contact organic thin film transistors

Yi Chen *, Ishiang Shih

Department of Electrical and Computer Engineering, McGill University, 3480 University Street, Montreal, Que., Canada H3A 2A7

Received 22 March 2007; received in revised form 4 May 2007; accepted 8 May 2007
Available online 25 May 2007

Abstract

Vertical channel top contact (TC) organic thin film transistors (OTFTs) have been successfully realized on Si substrates with SiO_2 as gate insulators and P3HT(poly ~3-hexylthiophene) as organic semiconductors. The active channel region was defined by a steep step through a Si etching method. Source and drain metal contacts were deposited by vacuum evaporation through a shadow mask at a high tilting angle. Top contact transistors with channel lengths 5 μm can be fabricated with a relatively simple and efficient (yield >85%) fabrication process with only two photolithography steps (two photo masks) while no need for high-resolution and precision alignment for channel definition. Measurement results showed that the vertical channel BC (bottom contact) devices have compatible performance with planar BC devices. However, vertical channel TC transistors showed improved performance with double field effect mobilities and three times larger current ON/OFF ratios than vertical channel BC devices.
© 2007 Elsevier B.V. All rights reserved.

PACS: 73.61.Ph

Keywords: Organic thin film transistors; Vertical channel; Field effect mobility; Top contact; Bottom contact

1. Introduction

Recently, organic thin film transistors (OTFTs) have attracted considerable research interests due to their promising potentials for low-cost flexible display applications. A top contact (TC) electrode structure has been widely used since it provides much better performance than bottom contact (BC) OTFT devices [1–3]. However, these top contact electrodes in the previously reported work are usually realized by metal deposition through shadow masks, which results in bulky devices with channel lengths around a few hundred microns [1–3]. In order to reduce the transistor size for practical applications, several attempts have been made to modify the device structure of OTFTs. Among them, vertical channel structure has emerged as a promising candidate for smaller channel devices. They either used the so-called embossing technique to "microcut" into the substrate [4] or tried to control and align source/drain contacts to the edge of

* Corresponding author. Tel.: +1 514 398 5492; fax: +1 514 398 4470.
E-mail address: Yi.chen2@mail.mcgill.ca (Y. Chen).

1566-1199/$ - see front matter © 2007 Elsevier B.V. All rights reserved.
doi:10.1016/j.orgel.2007.05.004

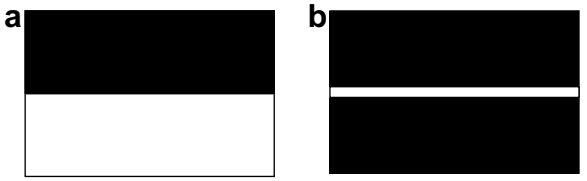


Fig. 1. Photo masks used for photolithography process in this work: (a) Mask#1 for Si etching to form steep steps and (b) mask#2 to open gate windows for the growth of thin gate oxide.

photoresist, creating the vertical sidewalls as transistor channels [5,6].

In the present work, we fabricated OTFTs with channels defined by a steep step created by silicon etching. OTFTs with top contacts and channel lengths around 5 μm can be easily fabricated. Furthermore, the last step to form source and drain contacts was performed by vacuum evaporation of metals through a shadow mask at a high titling angle to the substrate. So, the channel was left open without the need for further photolithography, precise alignment and etching for channel definition. The main purpose for our work in utilizing vertical structure for the channel is to realize top contact small channel devices with relatively simple and efficient fabrication method. Although currently we can only reduce the channel length to 5 μm, it is believed that by controlling the Si etching time more precisely, devices with smaller channel lengths ($L \sim 1$ μm) can be realized. OTFTs with bottom contact electrodes and planar structure were also fabricated for comparison purpose. And the measurement results further confirmed that TC devices

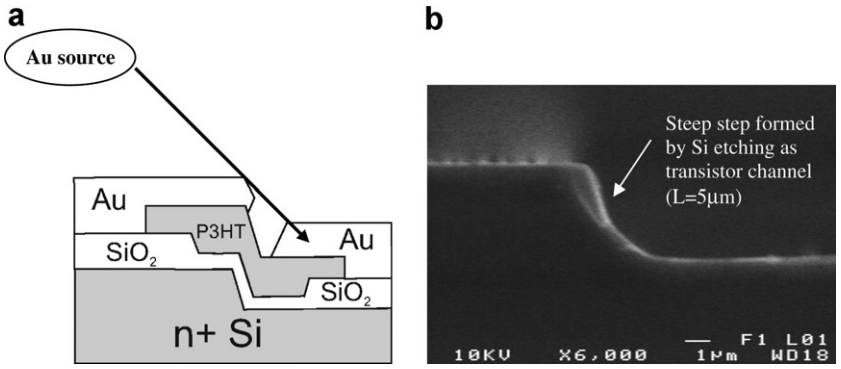


Fig. 2. (a) Schematic device structure of a top contact vertical channel transistor. (b) A SEM image of a 5 μm steep step after the etching of Si.

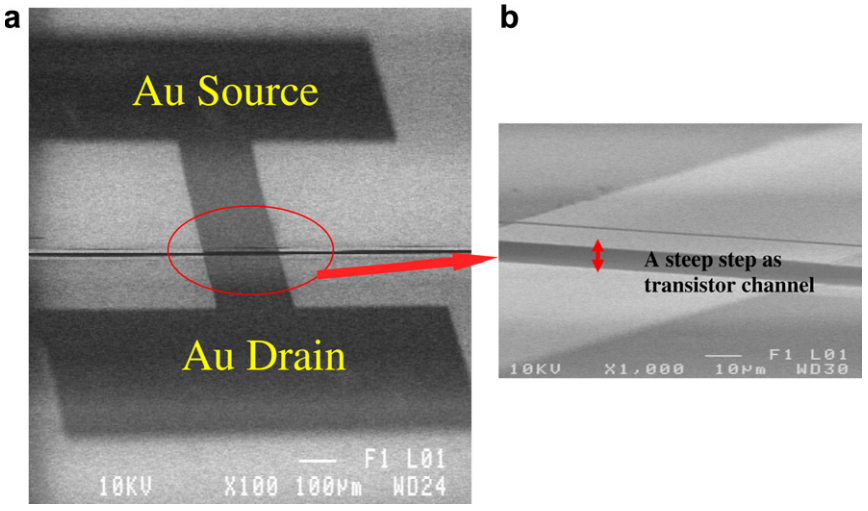


Fig. 3. SEM images of (a) an as-fabricated transistor and (b) enlarged view of channel region.

had better performance than BC devices which is in agreement with results from other researchers [1–3].

2. Experimental

Transistors were fabricated on heavily doped n type Si substrates, with thermally grown SiO_2 as gate insulators. First, the Si substrate was thermally oxidized, followed by a photolithography process with mask#1 (Fig. 1a) to define the step (channel) region. Then SiO_2 on the unwanted region was etched away with buffered HF solution, while the remaining SiO_2 served as the mask for the subsequent Si etching step. After that, the sample was immersed into a Si etching solution with the mixture of HNO_3, CH_3COOH and HF to create the steep step. After etching, SiO_2 on the whole sample was removed by the buffered HF solution, then wet oxidation was performed again to re-grow the thick SiO_2. Next, photolithography was performed again with mask#2 (Fig. 1b) to open the window in thick SiO_2 region followed by the dry oxidation for the growth of thin gate oxide. The thermally grown oxides are about 0.5 μm for thick field oxide and 0.1 μm for thin gate oxide. Then source and drain contacts (Au) were vacuum evaporated at a high

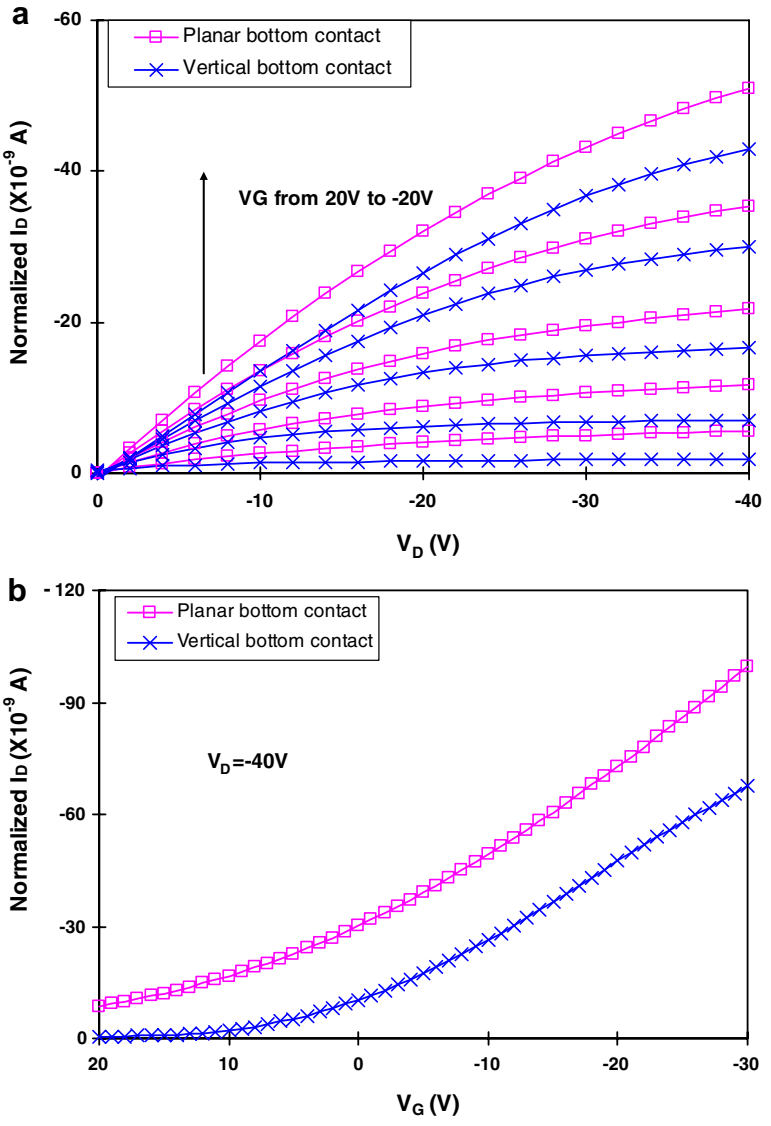


Fig. 4. Typical I–V characteristics of vertical bottom contact and planar bottom contact devices: (a) I_D–V_D and (b) I_D–V_G.

tilting angle to the substrate through a shadow mask. As a result, the step region was left open as transistor channels. For TC devices, regio-random P3HT(poly~3-hexylthiophene) with 0.3% by weight dissolved into toluene, serving as organic semiconducting layer, was spun-coated onto the substrate before metallization, while for BC devices, metallization was performed before the spin-coating of P3HT. Fig. 2a shows the last fabrication step of metallization and the resulting structure for a top contact device. By eliminating the conventional channel definition step which usually requires high-resolution photolithography process and precise alignment, the entire fabrication process only needs two masks and is relatively simple with pretty high yield (>85%). In order to determine precisely the height of the etched step, one test sample fabricated under the same condition was cleaved and the cross section was examined at 90° viewing angle under SEM. It is seen from Fig. 2b that the channel L is about 5 μm. Meanwhile, Fig. 3 showed the SEM images of an as fabricated transistor. The transistors have two different dimensions: $L/W = 5\ \mu m/200\ \mu m$ and $L/W = 5\ \mu m/100\ \mu m$.

For comparison purpose, transistors with three different contact configurations were fabricated

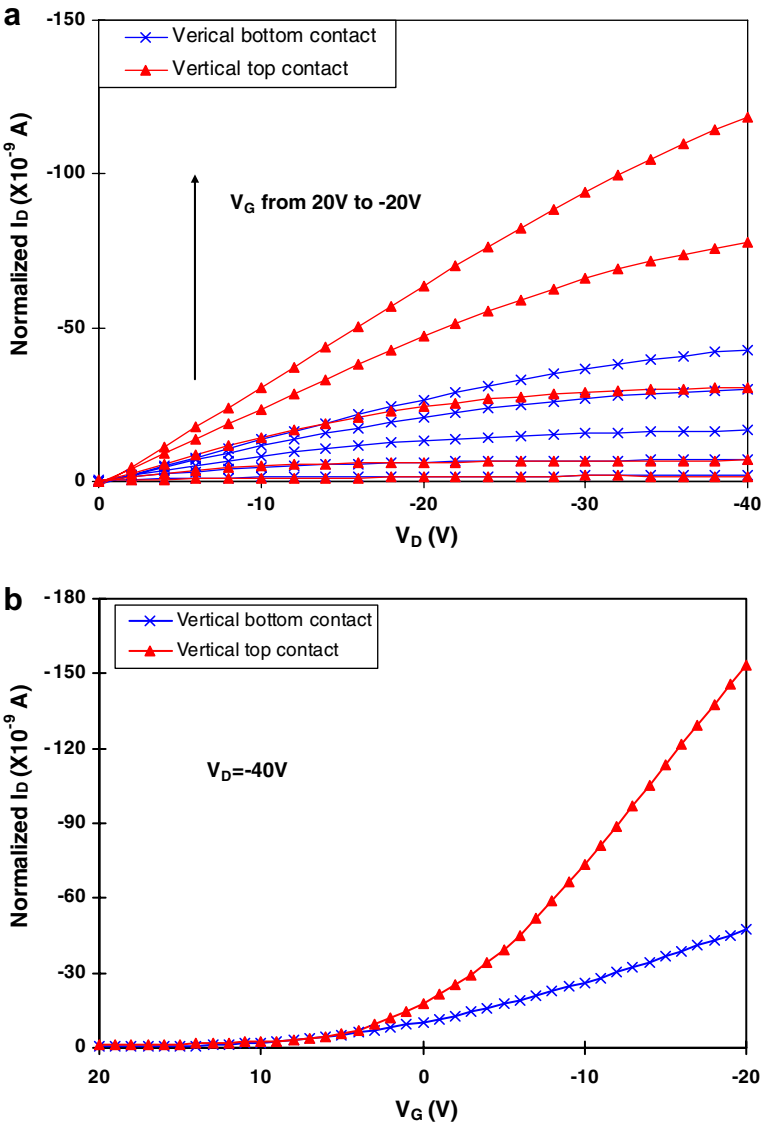


Fig. 5. Typical I–V characteristics of vertical bottom contact and vertical top contact devices: (a) I_D–V_D and (b) I_D–V_G.

under the same condition, including top and bottom contact devices with vertical channels and bottom contact devices with planar channels. For planar bottom contact devices, the channel lengths and widths are 20 μm and 630 μm.

After fabrication, current–voltage characteristics of the transistors were measured with an HP 4145A semiconductor parameter analyzer under air without further treatment.

3. Results and discussion

The devices showed clear p-type transistor behavior with gate voltage modulation. The filed effect mobilities were extracted from $I_D^{1/2}$ vs. V_G curves according to the following equation [7]:

$$\sqrt{I_D} = \sqrt{\frac{W}{2L}\mu_{eff}C_{ox}} \quad (V_G - V_T) \tag{1}$$

where I_D is the drain current W is the channel width and L is the channel length; μ_{eff} is field effect mobility; C_{ox} is gate oxide capacitance per unit area; V_G is gate voltage and V_T is threshold voltage.

The typical I–V characteristics of planar BC transistors versus vertical BC transistors were shown in Fig. 4. While Fig. 5 showed the I–V characteristics of vertical BC and vertical TC transistors. Because

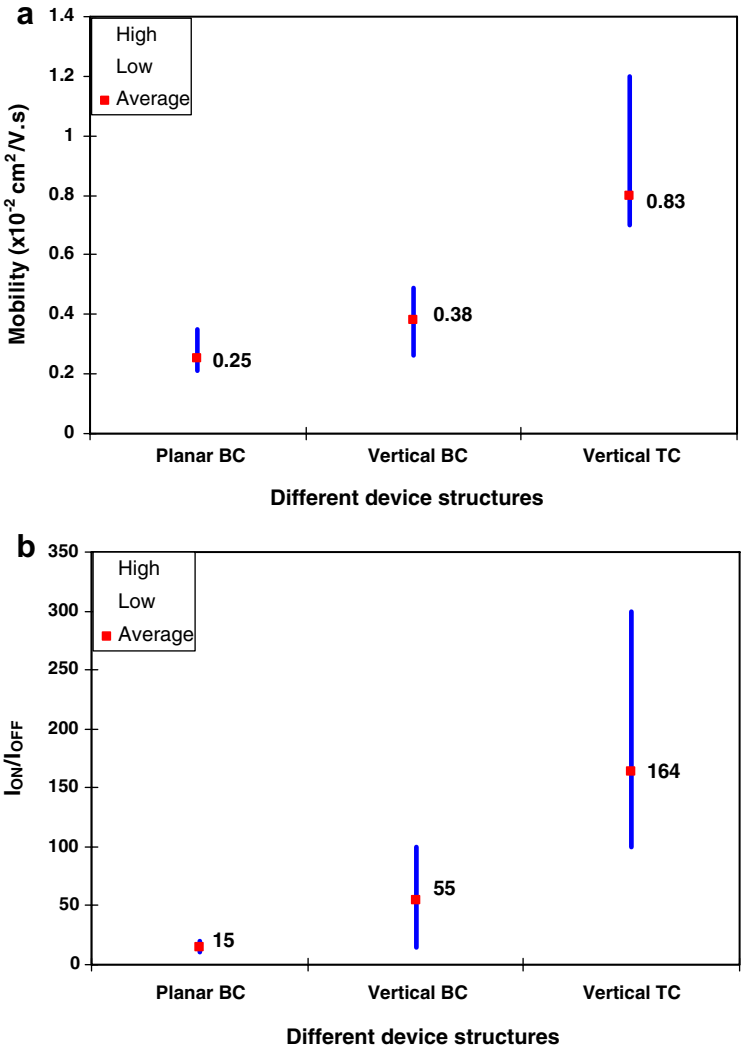


Fig. 6. (a) Field effect mobility for devices with different structures; (b) ON/OFF current ratios for devices with different structures.

devices have different dimensions, for easier comparison, all I_D values have been normalized to L/W.

The field effect mobilities of transistors with different structures were calculated according to Eq. (1) and plotted in Fig. 6a. While their ON/OFF current ratios were obtained as the drain current I_D at $V_G = -20$ V and $V_D = -40$ V over I_D at $V_G = 20$ V and $V_D = -40$ V, which were shown in Fig. 6b.

It is clear from Fig. 6 that vertical channel BC devices have better performance than planar devices since although they have compatible field effect mobility around 3×10^{-3} cm^2/V s, vertical channel BC devices have much higher ON/OFF current ratios 55 compared to only 15 for planar BC devices. Furthermore, vertical channel TC devices have improved performance with the highest mobility $\mu_{av} = 8.3 \times 10^{-3}$ cm^2/V s, which is about three times larger than devices with planar BC structures. The average ON/OFF current ratio of vertical TC devices is 164, which is about 10 times higher than that of planar BC devices. These results have been repeated more than once during our fabrication and measurement. Although the performance of these P3HT based organic TFTs did not represent the state of art devices, we believe this can be greatly improved by adding a passivation layer (such as SiO_2 or SiN_x) after the fabrication to protect the organic semiconductors from oxygen and water rich environment. It is noted again the purpose of this work is to demonstrate the novel and simple Si etching method to fabricate top contact small channel devices. The reason for the above results is explained below:

1. Vertical BC devices versus planar BC devices: For planar BC devices, the source/drain Au contacts were patterned by an additional photolithography and etching process. For the vertical channel BC devices, however, the photolithography and etching process has been eliminated due to the adoption of a shadow mask. Hence, the chance of surface contamination has been greatly reduced. This results in vertical channel BC devices with improved performance and higher ON/OFF current ratios.
2. Vertical TC devices versus vertical BC devices: Because of the relatively large bandgap and high ionization energy of organic materials, they usually form Schottky barriers with metals. To circumvent this problem, high work function metals such as Au are commonly used as source/drain contacts. However, some research groups have also pointed out that even the use of Au cannot guarantee an ohmic contact between Au/P3HT [8,9]. We believe that the contact resistance of TC devices should have been greatly reduced when Au was evaporated on top of the P3HT films due to the unintentional doping of P3HT resulting from the diffusion of Au atoms into P3HT films. This conclusion is consistent with reports from some other groups [1–3]. A more recent study on another organic semiconductor-pentacene also proved that TC devices had much smaller contact resistance than BC devices [10]. So, we conclude that the reduction in contact resistance of TC devices is the main reason for much better improvement of device performance.

4. Summary

In summary, vertical channel top contact organic thin film transistors with channel lengths around 5 μm have been fabricated with a simple and efficient silicon etching method combined with high tilting angle metallization. The average mobility of vertical channel TC transistors with P3HT is about 8.3×10^{-3} cm^2/V s. We believe that using the same method, transistor size can be further shrink down to 1 μm or even smaller with more precise control of Si etching.

References

[1] D.J. Gundlach, L. Zhou, J.A. Nichols, T.N. Jackson, P.V. Necliudov, M.S. Shur, An experimental study of contact effects in organic thin film transistors, J. Appl. Phys. 100 (2006) 024509.
[2] R.A. Street, A. Salleo, Contact effects in polymer transistors, Appl. Phys. Lett. 81 (2002) 2887.
[3] I. Kymissis, C.D. Dimitrakopoulos, S. Purushothaman, High-performance bottom electrode organic thin-film transistors, IEEE. Trans. Electron. Dev. 48 (2001) 1060.
[4] N. Stutzmann, R.H. Friend, H. Sirringhaus, Self-aligned vertical-channel polymer field-effect transistors, Science 299 (2003) 1881.
[5] R. Parashkov, E. Becker, S. Hartmann, G. Ginev, D. Schneider, H. Krautwald, T. Dobbertin, D. Metzdorf, F. Brunetti, C. Schildknecht, A. Kammoun, M. Brandes, T. Riedl, H.-H. Johannes, W. Kowalsky, Vertical channel all-organic thin-film transistors, Appl. Phys. Lett. 82 (2003) 4579.
[6] K. Yutani, K. Nakayama, M. Yokoyama, Fabrication of vertical organic field effect transistor at the edge of patterned photoresist, Mol. Cryst. Liq. Cryst. 444 (2006) 197.
[7] G. Horowitz, P. Delannoy, An analytical model for organic-based thin-film transistors, J. Appl. Phys. 70 (1991) 469.

[8] L. Bu Rgi, H. Sirringhaus, R.H. Friend, Noncontact potentiometry of polymer field-effect transistors, Appl. Phys. Lett. 80 (2002) 1913.
[9] D.B.A. Rep, A.F. Morpurgo, T.M. Klapwijk, Doping-dependent charge injection into regioregular poly(3-hexyl-thiophene), Org. Electron. 4 (2003) 201.
[10] Paul V. Pesavento, Kanan P. Puntambekar, C. Daniel Frisbie, John C. McKeen, P. Paul Ruden, Film and contact resistance in pentacene thin-film transistors: dependence on film thickness electrode geometry and correlation with hole mobility, J. Appl. Phys. 99 (2006) 094504.

Available online at www.sciencedirect.com
ScienceDirect
Organic Electronics 8 (2007) 662–672
Organic Electronics
www.elsevier.com/locate/orgel

Stably anodic green electrochromic aromatic poly(amine–amide–imide)s: Synthesis and electrochromic properties

Cha-Wen Chang, Guey-Sheng Liou *

Functional Polymeric Materials Research Laboratory, Department of Applied Chemistry, National Chi Nan University, 1 University Road, Puli, Nantou Hsien 545, Taiwan, ROC

Received 9 February 2007; received in revised form 12 May 2007; accepted 12 May 2007
Available online 24 May 2007

Abstract

A series of new poly(amine–amide–imide)s with pendent 4-methoxy-substituted triphenylamine (TPA) units having inherent viscosities of 0.35–0.45 dL/g were prepared from various aromatic bis(trimellitimide)s and the 4-methoxy-substituted triphenylamine-based aromatic diamine, 4,4′-diamino-4″-methoxytriphenylamine (**I**), by direct polycondensation. All the polymers are readily soluble in polar organic solvents. Flexible and amorphous films of these poly(amine–amide–imide)s could be obtained by solution-casting, and showed excellent thermal stability, 10% weight-loss temperatures in excess of 515 °C, and char yields at 800 °C in nitrogen higher than 58% associated with high glass-transition temperatures (297–305 °C). These polymers exhibited a maximum UV–vis absorption at 302–304 nm with fluorescence emission maxima around 360–376 nm in *N*-methyl-2-pyrrolidinone (NMP) solution. The hole-transporting and electrochromic properties were examined by electrochemical and spectroelectrochemical methods. Cyclic voltammograms of the poly(amine–amide–imide) films cast onto an indium–tin oxide (ITO)-coated glass substrate exhibit a reversible oxidation at 0.79–0.80 V vs. Ag/AgCl in acetonitrile solution, and reveal good stability of electrochromic characteristics with a color change from yellow to green at applied potentials ranging from 0.00 to 0.95 V. These anodically polymeric electrochromic materials not only showed excellent reversible electrochromic stability with good green coloration efficiency (CE = 395 cm^2/C) but also exhibited high contrast of optical transmittance change ($\Delta T\%$) up to 78% in 768 nm. After over 100 cyclic switches, the polymer films still exhibited stable electrochromic characteristics.
© 2007 Elsevier B.V. All rights reserved.

Keywords: Poly(amine–amide–imide)s; Triphenylamine; Electrochromic materials; Coloration efficiency

1. Introduction

Electrochromism can be defined as the reversible change in optical properties of a material resulting from electrochemically induced redox states. Color changes are commonly between a transparent state, where the chromophore only absorbs in the UV region, and a colored state or between two colored states in a given electrolyte solution. The electrochromic material may exhibit several colors and be termed polyelectrochromic. Electrochromic

* Corresponding author.
E-mail address: gsliou@ncnu.edu.tw (G.-S. Liou).

1566-1199/$ - see front matter © 2007 Elsevier B.V. All rights reserved.
doi:10.1016/j.orgel.2007.05.002

anti-glare car rear-view mirrors have already been commercialized, with other proposed applications of electrochromic materials including their use in controllable light-reflective or light-transmissive devices for optical information and storage, sunglasses, protective eyewear, and aircraft canopies for the military, and glare-reduction systems for offices and smart windows used in cars and buildings [1–3].

The first studies and commercial interests in electrochromic materials started with inorganic compounds such as tungsten trioxide (WO_3) and iridium dioxide (IrO_2) [4]. Later, organic materials (i.e., viologens, metallophthalocyanines and conjugated polymers) have received more attention than inorganics for electrochromic applications because of the different colors observed with these compounds while switching among their redox states [1,5,6]. Although conjugated polymers (CPs) in particular have several advantages over inorganic compounds; i.e., outstanding coloration efficiency, fast switching ability, high stability, fine-tuning of the band gap (and the color) through chemical structure modification, multiple colors with the same material [7], thin film flexibility, and cost effectiveness, they have not received enough attention in terms of applications. One of the main reasons for this was the deficient third leg (green) of color space in conjugated polymers (CPs) until first report about a green-colored neutral conjugated polymer (CP) was published [8]. For green color, at least two chromophores are required that absorb at red and blue wavelengths in the neutral form, and should also deplete together when the polymer is oxidized.

Aromatic polyimides are an important class of high performance materials because of their excellent thermo-oxidative stability, mechanical strength, electrical properties, and solvent resistance. However, the intractable characteristics have been major problems as a result of high melting point and insolubility. To overcome this drawback, various copolyimides and polymer-structure modification have been developed [9]. For example, a poly(amide–imide) (PAI) has been developed as an alternative material offering a compromise between excellent thermal stability and processability. Another common approach for increasing solubility and processability of polymers without sacrificing high thermal stability is the introduction of bulky, packing-disruptive groups into the polymer backbone [10–17]. A number of PAIs have been synthesized through two main routes: via amide–imide-forming reaction from trimellitic anhydride, and through amide-forming reaction from imide-containing monomers such as imide-preformed dicarboxylic acid or their acid chlorides [18]. One of the more facile approaches to prepare PAIs with high molecular weights is the direct polycondensation between imide-bearing dicarboxylic acids with aromatic diamines following the Yamazaki–Higashi phosphorylation technique [19–22]. The direct polycondensation route avoids using moisture-sensitive acid chlorides or isocyanates and provides significant advantages in laboratory preparation of PAIs as well as aromatic polyamides. Recently, we have reported some TPA-containing polyamides and polyimides from 4,4′-diamino-4″-*N*-carbazolyltriphenylamine [23,24], 4,4′-dicarboxy-4″-*N*-carbazolyltriphenylamine [25], and 4,4′-dicarboxy-4″-methoxytriphenylamine [26], respectively. Because of the incorporation of bulky, propeller-shaped TPA units along the polymer backbone, all the polymers were amorphous with high thermal stability, good solubility in many aprotic solvents, and thin-film-forming capability. Recently, we have initiated a study to obtain TPA-containing anodic electrochromic polymers which exhibited green light in the oxidized state and were transparent in the neutral state [27–30].

The anodic oxidation of TPA in aprotic solvents has been well studied [31]. The oxidation product, the TPA radical cation, is not stable and the following chemical reaction produces tetraphenylbenzidine by tail to tail (*para* position) coupling, with the loss of two protons per dimer. When the phenyl groups were incorporated by electron-donating substituents at the *para*-position of TPA, the coupling reactions were greatly prevented that afforded stable radical cations [32,33]. In this article, we therefore synthesized a diamine, 4,4′-diamino-4″-methoxyltriphenylamine (**I**), and its derived poly(amine–amide–imide)s containing TPA groups with electron-rich pendent 4-methoxy phenyl ring which permits tuning the solubility and redox potential of the polymers. The general properties such as solubility and thermal properties are described. The electrochemical and electrochromic properties of these polymers are also described herein and are compared with those of structurally related ones from 4,4′-diaminotriphenylamine without 4-methoxy substituent.

2. Experimental

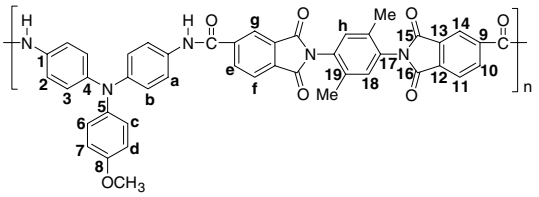
2.1. Synthesis

2.1.1. Materials

A 4-methoxy-substituted TPA-containing aromatic diamine, 4,4′-diamino-4″-methoxytriphenylamine (I), was synthesized by the cesium fluoride-mediated condensation of *p*-anisidine with 4-fluoronitrobenzene, followed by palladium-catalyzed hydrazine reduction of the dinitro intermediate according to a previously reported procedure [34–36]. 4,4′-Diaminotriphenylamine (mp = 186–187 °C) [37], 2,5-Bis(trimellitimido)toluene [38] (**II-M**), 1,4-bis (trimellitimido)-2,5-dimethylbenzene [39] (**II-2M**), and 1,4-bis(trimellitimido)-2,5-dichlorobenzene [40] (**II-2Cl**) were prepared as previously reported procedures. *N*,*N*-dimethylacetamide (DMAc) (TEDIA), *N*,*N*-dimethylformamide (DMF) (ACROS), *N*-methyl-2-pyrrolidinone (NMP) (TEDIA), pyridine (Py) (TEDIA), and triphenyl phosphite (TPP) (ACROS) were also used as received. Tetrabutylammonium perchlorate (TBAP) (ACROS) was recrystallized twice from ethyl acetate and then dried under vacuum prior to use. All other reagents were used as received from commercial sources.

2.1.2. Polymer synthesis through direct polycondensation via the phosphorylation reaction

The synthesis of poly(amine–amide–imide) **PAI-2M** is used as an example to illustrate the general synthetic route: A mixture of 0.382 g (1.25 mmol) of diamine, 4,4′-diamino-4″-methoxytriphenylamine (**I**), 0.606 g (1.25 mmol) of 1,4-bis(trimellitimido)-2,5-dimethylbenzene (**II-2M**), 0.30 g of calcium chloride, 0.9 mL of triphenyl phosphite, 1.2 mL of pyridine, and 5 mL of NMP was heated with stirring at 105 °C for 3 h. The obtained polymer solution was poured slowly into 300 mL of stirred methanol giving rise to a stringy, fiber-like precipitate that was collected by filtration, washed thoroughly with hot water and methanol, and dried under vacuum at 100 °C. Reprecipitations from DMAc into methanol were carried out twice for further purification. The inherent viscosity of the obtained poly(amine–amide–imide) **PAI-2M** was 0.45 dL/g, measured at a concentration of 0.5 g/dL in NMP at 30 °C. ^{1}H NMR (DMSO-d_6, δ, ppm): 2.10 (s, 6H, CH_3), 3.75 (s, 3H, OCH_3), 6.97–7.05 (m, 8H, $H_d + H_b + H_c$), 7.48 (s, 2H, H_h), 7.73 (d, 4H, H_a), 8.15 (d, 2H, H_f), 8.42 (d, 2H, H_e), 8.48 (s, 2H, H_g), 10.59 (s, 2H, NH–CO). ^{13}C NMR (DMSO-d_6, δ, ppm): 17.2 (CH_3), 55.5 (OCH_3), 115.2 (C^7), 122.0 (C^2), 122.6 (C^{14}), 122.9 (C^3), 124.0 (C^{11}), 126.7 (C^6), 131.4 (C^{18}), 131.7 (C^{17}), 132.1 (C^1), 133.3 (C^{19}), 134.0 (C^{13}), 134.6 (C^{10}), 135.0 (C^4), 140.3 (C^{12}), 140.7 (C^5), 144.2 (C^9), 155.9 (C^8), 163.4 (NH–CO), 166.5 (C^{15}), 166.7 (C^{16}). Anal. Calcd. for $(C_{45}H_{31}N_5O_7)_n$ $(753.76)_n$: C, 71.71%; H, 4.15%; N, 9.29%. Found: C, 69.70%; H, 4.28%; N, 9.11%. The other poly(amine–amide–imide)s were synthesized by an analogous procedure.



2.1.3. Preparation of the films

A solution of polymer was made by dissolving about 0.7 g of the poly(amine–amide–imide)s sample in 10 mL of DMAc, and the homogeneous solution was poured into a 9-cm diameter glass culture dish which was heated at 90 °C for 2 h and 160 °C for 8 h to slowly release the solvent under vacuum. The obtained flexible films were about 50–70 μm in thickness and were used for inherent viscosity tests, solubility tests, and thermal analyses.

2.2. Measurements

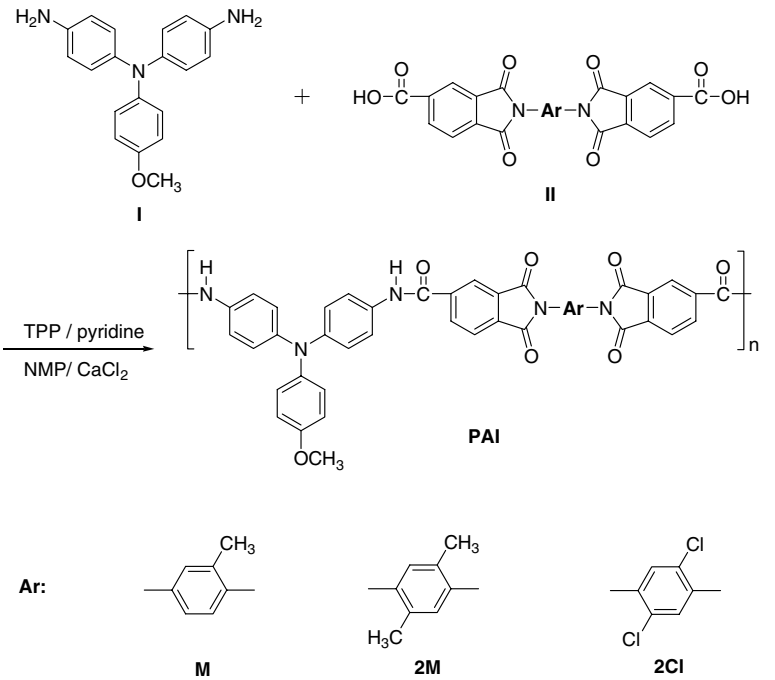
Infrared spectra were recorded on a PerkinElmer RXI FT-IR spectrometer. ^{1}H and ^{13}C NMR spectra were measured on a Bruker Avance 300 MHz FT-NMR system. Elemental analyses were run in an Elementar VarioEL-III. Wide-angle X-ray diffraction (WAXD) measurements of the polymer films were performed at room temperature (≈25 °C) on a Shimadzu XRD-7000 X-ray diffractometer (40 kV, 20 mA) with a graphite monochromator, using nickel-filtered Cu-Kα radiation. Ultraviolet–visible (UV–vis) spectra of the polymer films were recorded on a Varian Cary 50 Probe spectrometer. Thermogravimetric analysis (TGA) was conducted with a PerkinElmer Pyris 1 TGA. Experiments were carried out on approximately 6–8 mg film samples heated in flowing nitrogen or air (flow

rate = 40 cm^3/min) at a heating rate of 20 °C/min. DSC analyses were performed on a PerkinElmer Pyris 1 DSC at a scan rate of 20 °C/min in flowing nitrogen (20 cm^3/min). Electrochemistry was performed with a CHI 611B electrochemical analyzer. Voltammograms are presented with the positive potential pointing to the left and with increasing anodic currents pointing downwards. Cyclic voltammetry was performed with the use of a three-electrode cell in which ITO (polymer films area about 0.7 cm × 0.5 cm) was used as a working electrode. A platinum wire was used as an auxiliary electrode. All cell potentials were taken with the use of a homemade Ag/AgCl, KCl (sat.) reference electrode. Absorption spectra in the spectroelectrochemistry experiments were measured with a HP 8453 UV–Visible spectrophotometer. Coloration efficiency is derived from the equation: $\eta = \Delta OD/Q$, ΔOD is optical density change at specific absorption wavelength and Q is ejected charge determined from the *in situ* experiments. Photoluminescence spectra were measured with a Jasco FP-6300 spectrofluorometer. The fluorescence quantum yields (Φ_{PL}) of polymer solution were determined in toluene against quinine sulfate (ACROS) in 1 N $H_2SO_{4(aq)}$ as the standard ($\Phi_{PL} = 0.546$).

3. Results and discussion

3.1. Polymer synthesis

A series of new intrinsic alternating 4-methoxy-substituted TPA-containing poly(amine–amide–imide)s were successfully prepared from the diamine, 4,4′-diamino-4″-methoxytriphenylamine (**I**), and various aromatic diimide–diacids by the direct polycondensation reaction using triphenyl phosphite and pyridine as condensing agents (Scheme 1). The polymerization proceeded homogeneously throughout the reaction and afforded highly viscous polymer solutions, and precipitated in a tough fiber-like form when pouring the resultant polymer solutions into methanol. The obtained poly(amine–amide–imide)s had inherent viscosities in the range of 0.35–0.45 dL/g, and the formation of these polymers was confirmed by elemental analysis, IR, and NMR spectroscopy. Fig. 1 shows a typical IR spectrum for poly(amine–amide–imide) **PAI-2M**, and exhibits characteristic IR absorption bands of the amide group at 3371 (N–H) and 1655 cm^{-1} (amide carbonyl), imide absorption bands at 1777 (asymmetrical C=O), 1721 (symmetrical C=O), 1358 (C–N), and 726 cm^{-1} (imide ring deforma-



Scheme 1. Synthesis of poly(amine–amide–imide)s.

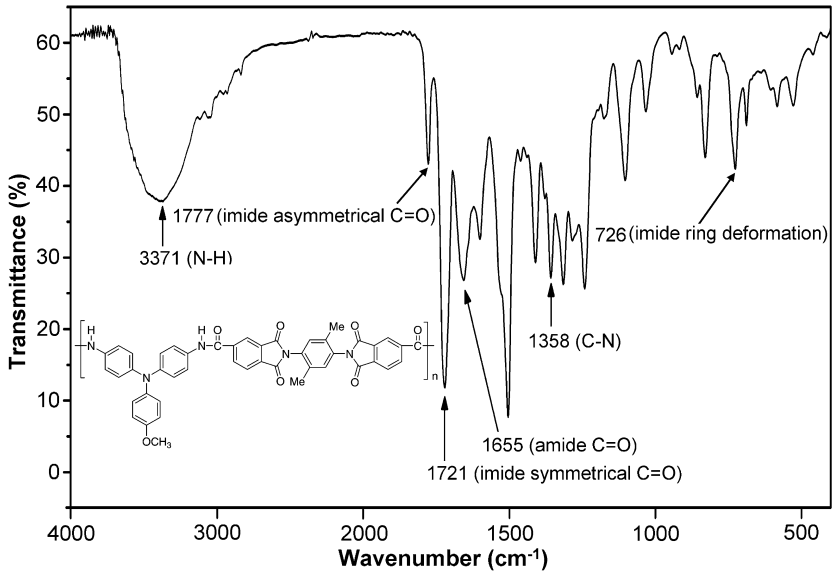


Fig. 1. IR spectrum (film) of poly(amine–amide–imide) **PAI-2M**.

tion). Fig. 2 shows a typical set of ^{1}H and ^{13}C NMR spectra of **PAI-2M** in deuterated dimethyl sulfoxide (DMSO-d_6), where all the peaks have been readily assigned to the hydrogen and carbon atoms of the recurring unit. Assignments of each carbon and proton are assisted by the two-dimensional H–H COSY and C–H HMQC NMR spectrum shown in Figs. 3 and 4, and these spectra agree well with the proposed molecular structure of **PAI-2M**. For a comparative study, a referenced poly(amine–amide–imide) **PAI-2M′** was also synthesized from 4,4′-diaminotriphenylamine and the corresponding diimide–diacid **II-2M**.

3.2. Polymer properties

3.2.1. Basic characterization

As indicated by the (WAXD) patterns shows in Fig. 5, all the polymers were essentially amorphous. The qualitative solubility of the amorphous poly(amine–amide–imide)s in various solvents is shown in Table 1. These polymers show excellent solubility in aprotic dipolar solvents such as NMP, DMAc, DMF, and DMSO, and even in less polar *m*-cresol. The solubility behavior of the **PAI-2M** was compared with the **PAI-2M′** derived from 4,4′-diaminotriphenylamine and corresponding diimide–diacid **II-2M** in Table 1. The enhanced solubility of **PAI-2M** can be attributed to the introduction of bulky pendent 4-methoxytriphenylamine group in the repeat unit.

The results of inherent viscosity and thermal properties of the poly(amine–amide–imide)s are summarized in Table 2. The obtained polymers have inherent viscosities in the range of 0.35–0.45 dL/g and could afford flexible polymer films. Their 10% weight-loss temperatures in nitrogen and air are recorded in the range of 515–525 and 525–555 °C, respectively. The amount of carbonized residue (char yield) of these polymers in nitrogen atmosphere is more than 58% at 800 °C. The high char yields of these polymers can be ascribed to their high aromatic content. The softening temperatures (T_s) of the polymer film samples are determined by the TMA method with a loaded penetration probe. They are obtained from the onset temperature of the probe displacement on the TMA trace. A typical TMA thermogram for poly(amine–amide–imide) **PAI-2Cl** is illustrated in Fig. 6. In all cases, the T_s values obtained by TMA are comparable to the T_g values measured by the DSC experiments (Table 2).

3.2.2. Optical and electrochemical properties

The optical and electrochemical properties of the poly(amine–amide–imide)s are investigated by UV–vis, photoluminescence spectroscopy, and cyclic voltammetry, and the results are summarized in Table 3. These polymers exhibit strong UV–vis absorption bands at 302–304 nm in NMP solution, which are assignable to the π–π^* transition resulting from the conjugation between the aromatic rings

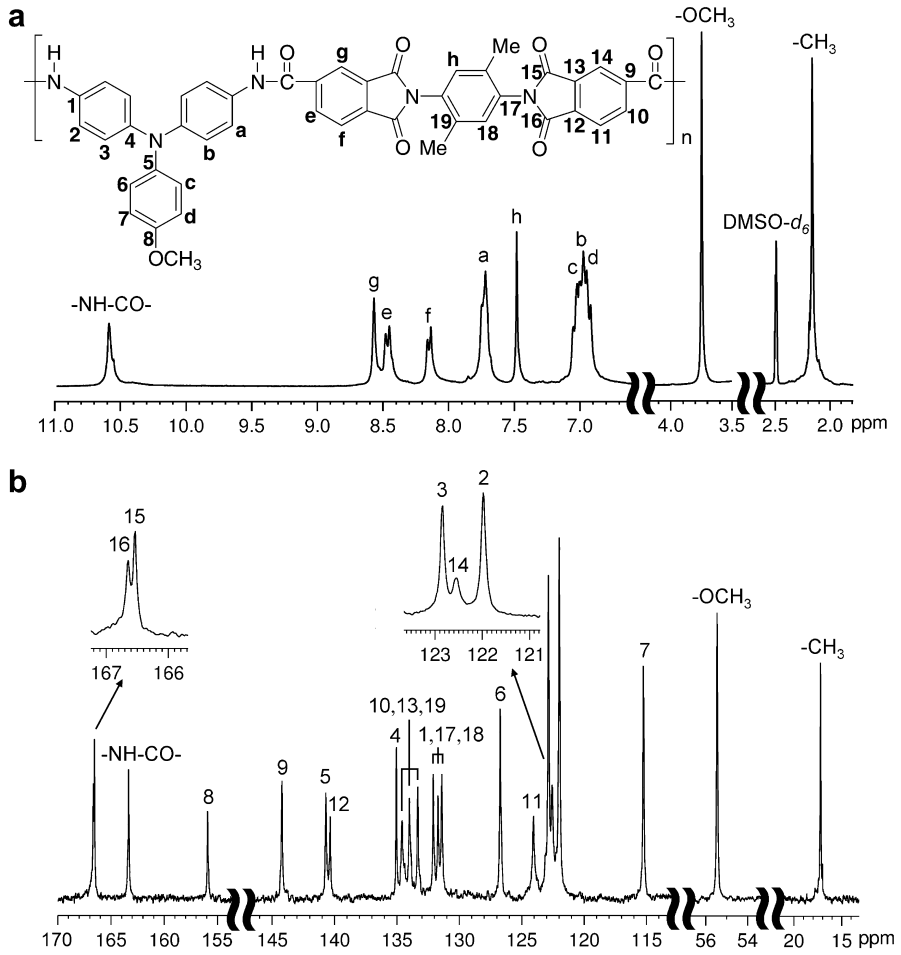


Fig. 2. (a) ^{1}H NMR and (b) ^{13}C NMR spectra of poly(amine–amide–imide) **PAI-2M** in DMSO-d_6.

and nitrogen atoms. In solid state, the UV–vis absorptions of poly(amine–amide–imide)s are nearly identical and show absorbance around 301–312 nm. These 4-methoxy-substituted TPA-based poly(amine–amide–imide)s exhibited fluorescence emission maxima around 360–376 nm in NMP solution with extremely low fluorescence quantum yield ranging from 0.02% for **PAI-2Cl** to 0.06% for **PAI-M** due to intramolecular charge transfer self-quench effect. The polymer films are measured for optical transparency using UV–vis transmittance spectroscopy and the cut-off wavelengths (absorption edge: λ_0) in the range of 476–496 nm.

The redox behavior of the poly(amine–amide–imide)s **PAI** and **PAI′** series have been investigated by cyclic voltammetry conducted for the cast film on an ITO-coated glass substrate as working electrode in dry acetonitrile (CH_3CN) containing 0.1 M of TBAP as an electrolyte under nitrogen atmosphere. The typical cyclic voltammograms for **PAI-2M** (with 4-methoxy-substituted) and **PAI-2M′** (without 4-methoxy-substituted) are shown in Fig. 7 for comparison. Electrochemical oxidation (or p-doping) of the polymer **PAI-2M** started at about 0.66 V (E_{onset}) with a reversible oxidation processes at $E_{1/2}$ (average potential of the redox couple peaks) 0.79 V vs. Ag/AgCl. After continuous 100 cyclic scans between 0.0 and 1.04 V, the polymer films still exhibited excellent electrochemical stability. The oxidation of **PAI-2M** occurred at nitrogen center of TPA unit, which is incorporated by electron-donating methoxyl substituents at the *para*-position of phenyl rings in a propeller-like geometry. The introduction of electron-donating methoxyl substituents into the *para*-position of TPA not only greatly stabilize the cationic radicals but also lower the oxidation

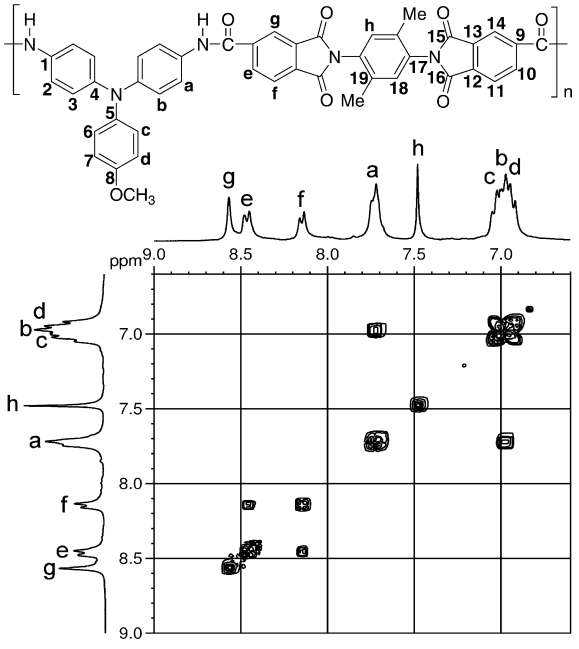


Fig. 3. H–H COSY spectra of poly(amine–amide–imide) **PAI-2M** in DMSO-d_6.

potentials of the electroactive poly(amine–amide–imide)s **PAI** as compared with the corresponding **PAI′** without methoxyl substituent. The energy of

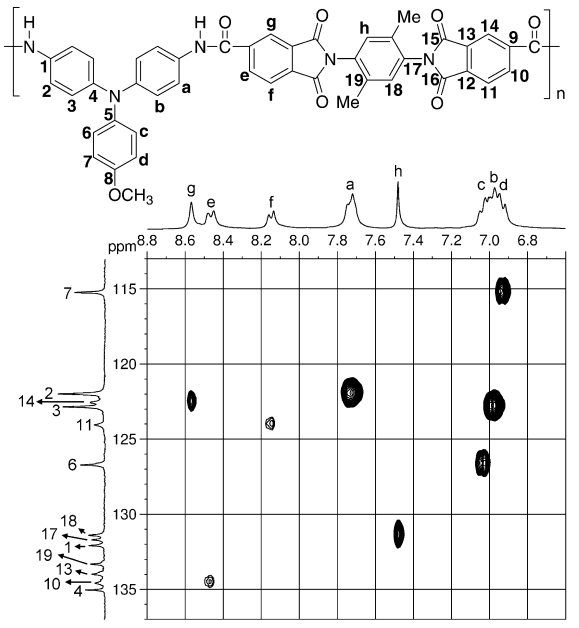


Fig. 4. C–H HMQC spectra of poly(amine–amide–imide) **PAI-2M** in DMSO-d_6.

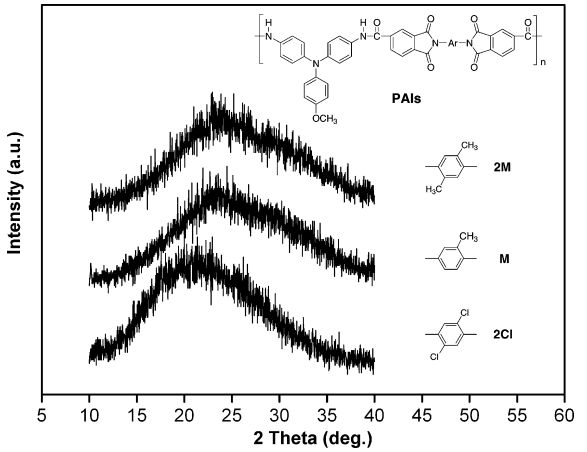


Fig. 5. WAXD patterns of poly(amine–amide–imide) films.

the highest occupied molecular orbital (HOMO) and lowest unoccupied molecular orbital (LUMO) levels of the investigated polymers could be determined from the oxidation onset or half-wave potentials and the onset absorption wavelength of polymer films, and the results are also listed in Table 3. For example, the oxidation half-wave potential for **PAI-2M** has been determined as 0.79 V ($E_{onset} = 0.66$ V) vs. Ag/AgCl. The external ferrocene/ferrocenium (Fc/Fc^+) redox standard $E_{1/2}$ (Fc/Fc^+) is 0.44 V vs. Ag/AgCl in CH_3CN. Assuming that the HOMO energy for the Fc/Fc^+ standard is 4.80 eV with respect to the zero vacuum level, the HOMO energy for poly(amine–amide–imide) **PAI-2M** has been evaluated to be 5.15 eV.

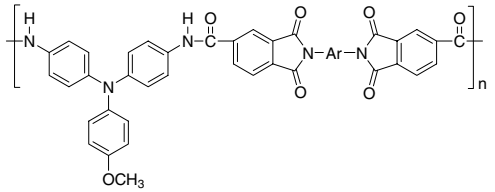
3.2.3. Electrochromic characteristics

Electrochromism of the poly(amine–amide–imide) thin films was examined by optically transparent thin-layer electrode (OTTLE) coupled with a UV–vis spectroscopy. The electrode preparation and solution condition were identical to those used in cyclic voltammetry. The typical electrochromic transmittance spectra of poly(amine–amide–imide) **PAI-2M** are shown in Fig. 8. When the applied potentials increased positively from 0.00 to 0.95 V, the peak of absorption at 312 nm, characteristic for neutral form for poly(amine–amide–imide) **PAI-2M** decreased gradually, while two new bands grew up at 395 and 768 nm, respectively. The new spectrum patterns were assigned as that of the cation radical poly(amine–amide–imide) **PAI-2M**, by electron removal from the lone pair electron of nitrogen atom on the TPA structure. Meanwhile,

Table 1
Solubility[a] of aromatic poly(amine–amide–imide)s

Polymer code[b]	Solvents						
	NMP	DMAc	DMF	DMSO	*m*-Cresol	THF	$CHCl_3$
PAI-M	++	++	++	++	–	–	–
PAI-2M	++	++	++	++	–	–	–
PAI-2Cl	++	++	++	++	–	±	–
PAI-2M′	+	+	+	+	–	–	–

++: Soluble at room temperature; +: soluble on heating; ±: partial soluble; −: insoluble even on heating.
[a] The solubility was determined by using 1 mg sample in 1 mL of solvent.
[b] **PAI** series:



.**PAI′** series:

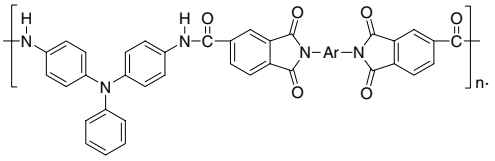


Table 2
Inherent viscosities and thermal properties of aromatic poly(amine–amide–imide)s

Polymer code	η_{inh}[a] (dL/g)	T_g (°C)[b]	T_s (°C)[c]	T_d at 5% weight loss (°C)[d]		T_d at 10% weight loss (°C)[d]		Char yield (wt.%)[e]
				N_2	Air	N_2	Air	
PAI-M	0.45	305	301	490	505	525	555	62
PAI-2M	0.45	303	281	485	480	515	525	58
PAI-2Cl	0.35	297	301	475	480	515	525	61

[a] Measured at a polymer concentration of 0.5 g/dL in NMP at 30 °C.
[b] Midpoint temperature of baseline shift on the second DSC heating trace (rate 20 °C/min) of the sample after quenching from 400 °C.
[c] Softening temperature measured by TMA with a constant applied load of 10 mN at a heating rate of 10 °C/min.
[d] Decomposition temperature, recorded via TGA at a heating rate of 20 °C/min and a gas-flow rate of 30 cm^3/min.
[e] Residual weight percentage at 800 °C in nitrogen.

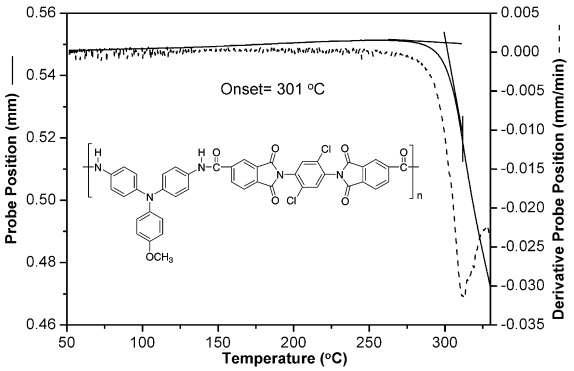


Fig. 6. TMA curve of poly(amine–amide–imide) **PAI-2Cl** with a heating rate of 10 °C/min.

complementary color of the **PAI-2M** film changed from yellow to green with high contrast of optical transmittance change ($\Delta T\%$) up to 78% at 768 nm (as shown in Fig. 8).

The color switching times were estimated by applying a potential step, and the absorbance profiles were followed (Fig. 9). The switching time was defined as the time that required for reach 90% of the full change in absorbance after applying potential. Thin films from poly(amine–amide–imide) **PAI-2M** would require 3.0 s at 0.95 V for switching absorbance at 395 and 768 nm and 2.5 s for bleaching. The color switching times of **PAI-2M** are also shown in Fig. 9. After over 100

Table 3
Optical and electrochemical properties for poly(amine–amide–imide)s

Index	Solution λ (nm)[a]			Film λ (nm)				$E_{1/2}$/V (vs. Ag/AgCl in CH_3CN)		E_g[e] (eV)	HOMO[f] (eV)		LUMO[g] (eV)	
	Abs max	PL_{max}[b]	Φ_F (%)[c]	$\lambda\lambda_0$[d]	Abs max	Abs onset[e]	PL_{max}[b]	$E_{1/2}$	E_{onset}		$E_{1/2}$	E_{onset}	$E_{1/2}$	E_{onset}
PAI-M	302	360	0.06	494	308	417	–	0.79	0.67	2.97	5.15	5.03	2.18	2.06
PAI-2M	304	376	0.05	476	312	427	–	0.79	0.66	2.90	5.15	5.02	2.25	2.12
PAI-2Cl	303	374	0.02	496	301	416	–	0.80	0.66	2.98	5.16	5.02	2.18	2.04
PAI-2M′	308	363	0.08	444	325	413	–	0.93	0.77	3.00	5.29	5.13	2.29	2.13

[a] Polymer concentration of 10^{-5} M in NMP at room temperature.
[b] Excited at the absorption maximum for both the solid and solution states. –: No discernible PL_{max} was observed.
[c] The quantum yield in dilute solution was calculated in an integrating sphere with quinine sulfate as the standard ($\Phi_F = 0.546$).
[d] The cutoff wavelength from the UV–vis transmission spectra of polymer films.
[e] The data were calculated by the equation: gap $= 1240/\lambda_{onset}$ of polymer film.
[f] The HOMO energy levels were calculated from cyclic voltammetry and were referenced to ferrocene (4.8 eV).
[g] LUMO = HOMO − E_g.

cyclic scans, the polymer films still exhibited good stability of electrochromic characteristics. The high electrochromic coloring efficiency ($\eta = \Delta A/Q$) ranging from 395 cm^2/C for first cycle to 379 cm^2/C for

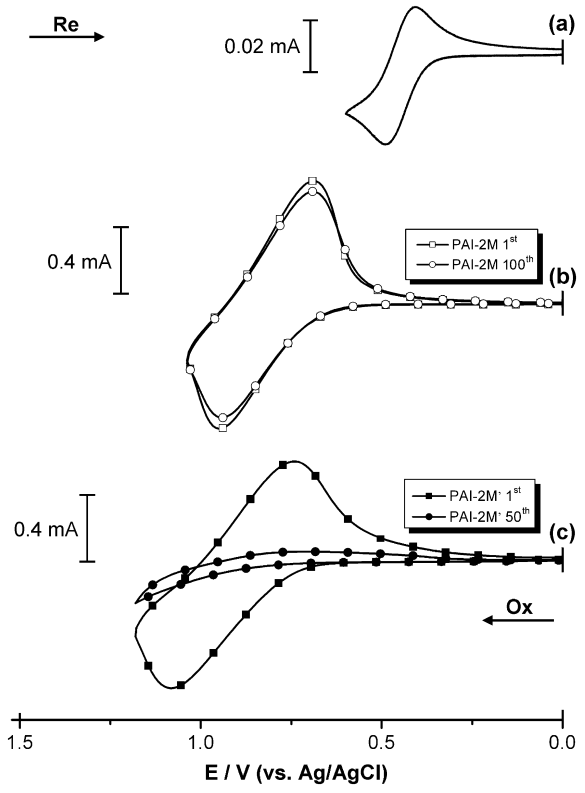


Fig. 7. Cyclic voltammograms of (a) ferrocene, (b) poly(amine–amide–imide) **PAI-2M** and (c) **PAI-2M′** films onto an indium–tin oxide (ITO)-coated glass substrate over 100 and 50 cyclic scanning in CH_3CN containing 0.1 M TBAP at scan rate = 0.05 V/s.

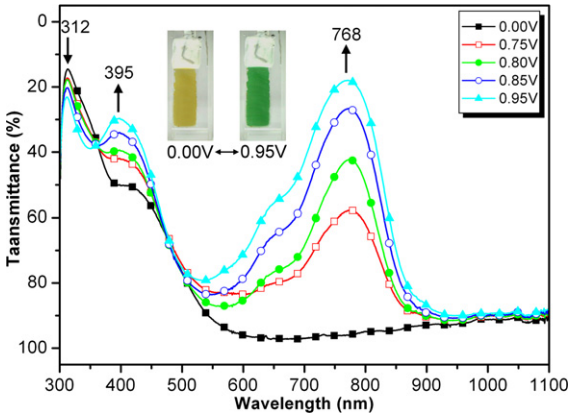


Fig. 8. Electrochromic behavior of poly(amine–amide–imide) **PAI-2M** thin film (in CH_3CN with 0.1 M TBAP as the supporting electrolyte) at (■) 0.00 (□) 0.75 (●) 0.80 (○) 0.85 (▲) 0.95.

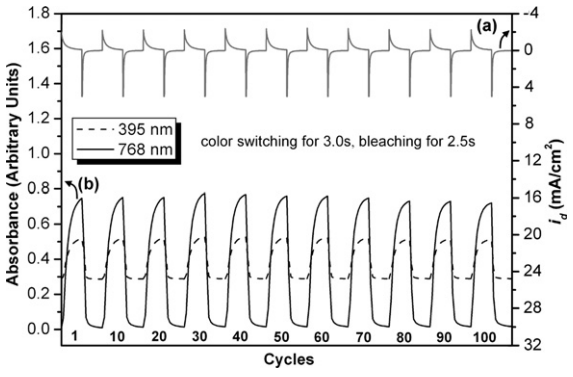


Fig. 9. (a) Current consumption and (b) potential step absorptometry of polyamide **PAI-2M** (in CH_3CN with 0.1 M TBAP as the supporting electrolyte) by applying a potential step (0 V ↔ 0.95 V), (coated area: 1 cm^2) and cycle time 10 s for coloration efficiency from 395 cm^2/C (first cycle) to 379 cm^2/C (100th cycle).

Table 4
Coloration efficiency with optical and electrochemical properties of poly(amine–amide–imide) **PAI-2M**

Cycles[a]	ΔA_{768}[b]	Q (mC cm^{-2})[c]	η (cm^2 C^{-1})[d]	Decay (%)[e]
1	0.738	1.86	395	0.0
20	0.738	1.88	392	0.8
40	0.754	1.92	391	1.0
60	0.744	1.94	382	3.3
80	0.716	1.88	380	3.8
100	0.703	1.85	379	4.0

[a] Times of cyclic scan by applying potential steps: $0.00 \leftrightarrow 0.95$ (V vs. Ag/Ag$^+$).
[b] Optical density change at 768 nm.
[c] Ejected charge, determined from the in situ experiments.
[d] Coloration efficiency is derived from the equation: $\eta = \Delta A/Q$.
[e] Decay of coloration efficiency after cyclic scans.

100th cycle and decay of the **PAI-2M** were calculated [41] and the results are summarized in Table 4.

4. Conclusions

A series of stable anodic green electrochromic poly(amine–amide–imide)s with high contrast of optical transmittance change ($\Delta T\%$) up to 78% in 768 nm have been readily prepared from the diamine, 4,4′-diamino-4″-methoxytriphenylamine (**I**), and various aromatic diimide–diacids via the direct phosphorylation polycondensation. Because of the incorporation of electron-donating methoxy substituents at the *para*-position of TPA, not only the electrochemical oxidative coupling reactions could be greatly prevented that afforded stable cationic radicals but also lower the oxidation potentials of the electroactive poly(amine–amide–imide)s. In additional to enhanced solubility and thin film formability, high T_g values, and good thermal stability, these anodically polymeric electrochromic materials also showed excellent continuous cyclic stability of electrochromic characteristic with good coloration efficiency from 395 cm^2/C for first cycle to 379 cm^2/C for 100th cycles, changing color from the yellow neutral form to the green oxidized forms when scanning potentials positively from 0.00 to 0.95 V. After over 100 cyclic switches, the polymer films still exhibited excellent reversibility of electrochromic characteristics. Thus, the 4-methoxy-substituted TPA-based poly (amine–amide–imide)s could be good candidates as anodic electrochromic materials due to their proper oxidation potentials, excellent electrochemical and thermal stability.

Acknowledgement

The authors are grateful to the National Science Council of the Republic of China for its financial support of this work.

References

[1] P.M.S. Monk, R.J. Mortimer, D.R. Rosseinsky, Electrochromism: Fundamentals and Applications, VCH, Weinheim, 1995.
[2] M. Green, Chem. Ind. 17 (1996) 641.
[3] R. Mortimer, J. Chem. Soc. Rev. 26 (1997) 147.
[4] W.C. Dautremont-Smith, Displays 3 (1982) 3.
[5] R.J. Mortimer, Electrochim. Acta 44 (1999) 2971.
[6] K. Bange, T. Gambke, Adv. Mater. 2 (1990) 10.
[7] (a) A. Kumar, D.M. Welsh, M.C. Morvant, F. Piroux, K.A. Abboud, J.R. Reynolds, Chem. Mater. 10 (1998) 896;
(b) G. Sonmez, I. Schwandemann, P. Schottland, K. Zong, J.R. Reynolds, Macromolecules 36 (2003) 639;
(c) S.A. Sapp, G.A. Sotzing, J.R. Reynolds, Chem. Mater. 10 (1998) 2101;
(d) B.C. Thompson, P. Schottland, K. Zong, J.R. Reynolds, Chem. Mater. 12 (2000) 1563.
[8] (a) G. Sonmez, C.K.F. Shen, Y. Rubin, F. Wudl, Angew. Chem. Int. Ed. Engl. 43 (2004) 1498;
(b) G. Sonmez, H.B. Sonmez, C.K.F. Shen, R.W. Jost, Y. Rubin, F. Wudl, Macromolecules 38 (2005) 669;
(c) G. Sonmez, H.B. Sonmez, C.K.F. Shen, F. Wudl, Adv. Mater. 16 (2004) 1905.
[9] (a) G.S. Liou, Y.L. Yang, Y.O. Su, J. Polym. Sci. Part A: Polym. Chem. 44 (2006) 2587;
(b) S.H. Hsiao, Y.M. Chang, W.C. Chen, G.S. Liou, Polym. Sci. Part A: Polym. Chem. 44 (2006) 4579.
[10] Y. Imai, High Perform. Polym. 7 (1995) 337.
[11] Y.R. Imai, Funct. Polym. 30 (1996) 3.
[12] (a) S.H. Hsiao, C.T. Li, Macromolecules 31 (1998) 7213;
(b) S.W. Lee, S.I. Kim, B. Lee, W. Choi, B. Chae, S.B. Kim, M. Ree, Macromolecules 36 (2003) 6527;
(c) S.W. Lee, S.I. Kim, B. Lee, H.C. Kim, T. Chang, M. Ree, Langmuir 19 (2003) 10381;
(d) S.I. Kim, M. Ree, T.J. Shin, J.C. Jung, J. Polym. Sci.: Part A: Polym. Chem. 37 (1999) 2909.
[13] G.S. Liou, J. Polym. Sci. Part A: Polym. Chem. 36 (1998) 1937.
[14] G.C. Eastmond, J. Paprotny, R.S. Irwin, Polymer 40 (1999) 469.
[15] G.C. Eastmond, M. Gibas, J. Paprotny, Eur. Polym. J. 35 (1999) 2097.
[16] D.S. Reddy, C.H. Chou, C.F. Shu, G.H. Lee, Polymer 44 (2003) 557.
[17] B.Y. Myung, C.J. Ahn, T.H. Yoon, Polymer 45 (2004) 3185.
[18] Y. Imai, Synthesis of polyamideimides, in: M.K. Ghosh, K.L. Mittal (Eds.), Polyimides: Fundamentals and Applications, Marcel Dekker, New York, 1996, p. 49.
[19] N. Yamazaki, M. Matsumoto, F. Higashi, J. Polym. Sci. Polym. Chem. Ed. 13 (1975) 1375.
[20] S.H. Hsiao, C.P. Yang, Makromol. Chem. 190 (1989) 2119.
[21] S.H. Hsiao, C.P. Yang, J. Polym. Sci. Polym. Chem. 28 (1990) 1149.

[22] S.H. Cheng, S.H. Hsiao, T.H. Su, G.S. Liou, Polymer 46 (2005) 5939.
[23] G.S. Liou, H.W. Chen, H.J. Yen, J. Polym. Sci. Part A: Polym. Chem. 44 (2006) 4108.
[24] G.S. Liou, S.H. Hsiao, H.W. Chen, J. Mater. Chem. 16 (2006) 1831.
[25] G.S. Liou, S.H. Hsiao, N.K. Huang, Y.L. Yang, Macromolecules 39 (2006) 5337.
[26] G.S. Liou, N.K. Huang, Y.L. Yang, Polymer 47 (2006) 7013.
[27] S.H. Cheng, S.H. Hsiao, T.H. Su, G.S. Liou, Macromolecules 38 (2005) 307.
[28] T.H. Su, S.H. Hsiao, G.S. Liou, J. Polym. Sci. Part A: Polym. Chem. 43 (2005) 2085.
[29] G.S. Liou, S.H. Hsiao, T.H. Su, J. Mater. Chem. 15 (2005) 1812.
[30] G.S. Liou, S.H. Hsiao, T.H. Su, J. Polym. Sci. Part A: Polym. Chem. 43 (2005) 3245.
[31] E.T. Seo, R.F. Nelson, J.M. Fritsch, L.S. Marcoux, D.W. Leedy, R.N. Adams, J. Am. Chem. Soc. 88 (1966) 3498.
[32] L. Hagopian, G. Kohler, R.I. Walter, J. Phys. Chem. 71 (1967) 2290.
[33] A. Ito, H. Ino, K. Tanaka, K. Kanemoto, T. Kato, J. Org. Chem. 67 (2002) 491.
[34] Y. Nishikata, S. Fukui, M. Kakimoto, Y. Imai, K. Nishiyama, M. Fujihira, Thin Solid Films 296 (1992) 210.
[35] K.Y. Chiu, T.X. Su, J.H. Li, T.H. Lin, G.S. Liou, S.H. Cheng, J. Electroanal. Chem. 575 (2005) 95.
[36] C.W. Chang, G.S. Liou, S.H. Hsiao, J. Mater. Chem. 17 (2007) 1007.
[37] Y. Oishi, H. Takado, M. Yoneyama, M. Kakimoto, Y. Imai, J. Polym. Sci. Part A: Polym. Chem. 28 (1990) 1763.
[38] C.P. Yang, G.S. Liou, C.C. Yang, N.W. Tseng, Polym. Bull. 42 (1999) 1.
[39] C.P. Yang, G.S. Liou, C.C. Yang, S.H. Chen, Polym. Bull. 43 (1999) 21.
[40] C.P. Yang, G.S. Liou, S.Y. Chang, S.H. Chen, J. Appl. Polym. Sci. 73 (1999) 271.
[41] R.J. Mortimer, J.R. Reynolds, J. Mater. Chem. 15 (2005) 2226.

Available online at www.sciencedirect.com
ScienceDirect
Organic Electronics 8 (2007) 673–682
Organic Electronics
www.elsevier.com/locate/orgel

Effect of substituents on the properties of indolo[3,2-*b*]carbazole-based hole-transporting materials

Hua-Ping Zhao [a], Xu-Tang Tao [a,*], Ping Wang [b], Yan Ren [a], Jia-Xiang Yang [c], Yun-Xing Yan [a], Chun-Xue Yuan [a], Hui-Jun Liu [a], De-Chun Zou [b], Min-Hua Jiang [a]

[a] *State Key Laboratory of Crystal Materials, Shandong University, Jinan 250100, PR China*
[b] *Department of Polymer Science and Engineering, College of Chemistry, Peking University, Beijing 100871, PR China*
[c] *Department of Chemistry, Anhui University, Hefei 230039, PR China*

Received 3 January 2007; received in revised form 19 March 2007; accepted 10 May 2007
Available online 24 May 2007

Abstract

Three new compounds based on indolo[3,2-*b*]carbazole,2,8-bis(4-diphenylaminophenyl)-5,11-di-*n*-octylindolo[3,2-*b*]carbazole (**BTOICZ**), 2,8-bis(9,9′-di-*n*-butylfluorenyl)-5,11-di-*n*-octylindolo[3,2-*b*]carbazole (**BFOICZ**) and 2,8-bis[*N*-(*n*-butyl)carbazolyl]-5,11-di-*n*-octylindolo[3,2-*b*]carbazole (**BCOICZ**), as hole-transporting materials have been synthesized by Suzuki coupling reaction. The effects of substituents on the optical, thermal and electrochemical properties of indolo[3,2-*b*]carbazole derivatives have been studied carefully. Electroluminescent (EL) devices using these compounds as hole-transporting layer in combination with Alq_3 as electron-transporting and emitting layer have been fabricated and characterized. The devices based on **BTOICZ** or **BFOICZ** showed green emission at 526 nm, while the device based on **BCOICZ** emitted very weak light. The turn-on voltages are 4.1 and 5.4 V for **BTOICZ** and **BFOICZ**, respectively. The maximal luminance efficiencies are 0.738 and 0.767 lm/W for **BTOICZ** and **BFOICZ**, respectively. The difference of the EL performances of these compounds reveals that the substituent effects have great effect on the hole-transporting performance of the indolo[3,2-*b*]carbazole-based compounds.
© 2007 Elsevier B.V. All rights reserved.

PACS: 73.61.Ph; 78.40.Me; 78.55.Kz; 78.60.Fi; 81.15.Ef; 81.20.Ka; 85.60.Jb

Keywords: Indolo[3,2-*b*]carbazole; Synthesis; Substituent effect; Hole-transporting properties

1. Introduction

Organic light-emitting diodes (OLEDs) have attracted a great deal of attention due to their potential use in full color flat-panel displays [1–3]. OLEDs are emerging as an attractive display technology which has the potential to offer cheap materials, low power consumption, high brightness, and a wide viewing angle [4,5]. Generally, OLEDs are composed of functionally divided organic multi-layers, a hole-transporting, an emitting, and an electron

* Corresponding author. Fax: +86 531 88574135.
E-mail address: txt@icm.sdu.edu.cn (X.-T. Tao).

1566-1199/$ - see front matter © 2007 Elsevier B.V. All rights reserved.
doi:10.1016/j.orgel.2007.05.001

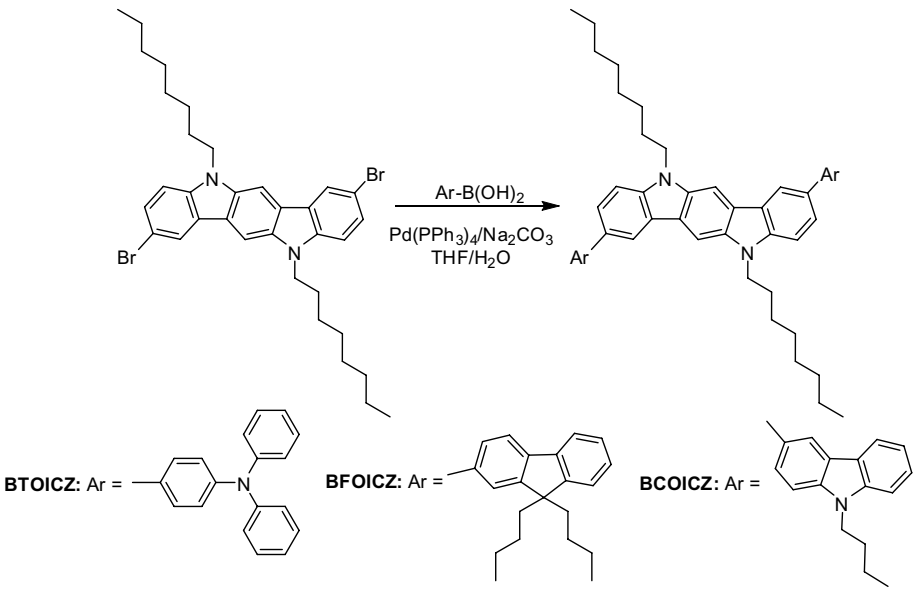
transporting layers sandwiched between two electrodes. Charge carriers (holes and electrons) are injected and transported from the anode and cathode, and are recombined in the emitting layer to emit light [5,6]. The primary role of the hole-transporting layer is to assist the hole injection from the anode into the light-emitting layer and block electrons within this layer, transporting the holes to the emitting layer, thus maximizing the recombination probability of the injected carriers [7–12]. The materials used as hole-transporting materials should be good hole conductors and possess good mechanical, thermal and electrochemical properties. Much efforts have been paid to develop efficient hole-transporting materials and to understand the relationships of structure-property [13–18]. Although the triarylamine-containing compounds such as TPD (*N*,*N*′-di-*m*-tolyl-*N*,*N*′-diphenyl-1,1′-biphenyl-4,4′-diamine) are the most widely used hole-transporting materials and exhibit excellent hole-transporting characteristics, they generally produces amorphous films with poor morphological stability [19,20]. The reason can be attributed to the thermal instability of the hole-transporting layers [21,22]. On the other hand, many compounds containing carbazole units are often effective hole-transporting materials because the nitrogen atom in the carbazole ring bestows an electron-donating ability, and possess better morphological stability and thermal durability [23]. Therefore, indolo[3,2-*b*]carbazole derivatives have attracted great interest as a new kind of hole-transporting materials in recent years [24,25].

In this contribution, three new hole-transporting molecules have been designed and synthesized, namely 2,8-bis(4-diphenylaminophenyl)-5,11-di-*n*-octylindolo[3,2-*b*]carbazole (**BTOICZ**), 2,8-bis (9,9′-di-*n*-butylfluorenyl)-5,11-di-*n*-octylindolo[3,2-*b*]-carbazole (**BFOICZ**) and 2,8-bis[*N*-(*n*-butyl)carbazolyl]-5,11-di-*n*-octylindolo[3,2-*b*]carbazole (**BCOICZ**), by introducing triphenylamine/fluorenyl/carbazolyl groups to 2,8-positions of indolo[3,2-*b*]carbazole. Their optical, thermal and electrochemical properties are reported. EL devices using these compounds as hole-transporting layers have been fabricated and characterized to study the substituent effect on the hole-transporting performances of the indolo[3,2-*b*]carbazole-based compounds.

2. Experimental

2.1. Chemicals and instruments

2,8-Dibromo-5,11-di-*n*-octylindolo[3,2-*b*]carbazole was synthesized by double Fischer indolization, followed by ring closure cyclization, and then alkylated with alkyl bromide and NaH in DMF [26]. 4-(Diphenylamino)phenylboronic acid, 9,9′-di-*n*-butylfluorenyl-2-boronic acid and *N*-(*n*-butyl)carbazolyl-3-boronic acid were prepared according to



Scheme 1. Synthesis of **BTOICZ**, **BFOICZ** and **BCOICZ**.

the literature [27–29]. The 400 MHz ^{1}H NMR and ^{13}C NMR spectra were obtained on a Bruker AV400 spectrometer. Elemental analyses were performed with a PE2400 elemental analyzer. The electrospray mass spectrograph was determined on API 4000 LC–MS/MS system (APCI source). UV–Vis spectra were measured on a TU-1800SPC spectrophotometer. The fluorescence spectra measurements were performed with a Hitachi 4500 FL spectrophotometer. Thermal gravimetric analysis (TGA) and differential scanning calorimetry (DSC) measurements were carried out under a nitrogen atmosphere at a heating rate of 20 °C/min from 20 °C to 320 °C, with a Perkin–Elmer Diamond thermogravimetric analyzer and a Perkin–Elmer Diamond DSC thermal analysis system, respectively. Electrochemical measurements were used to determine HOMOs of the materials with an EG&G model 283 electrochemical system. A platinum-disk working electrode, a platinum-wire auxiliary electrode, and an Ag/AgCl reference electrode were used in a three-electrode configuration with 0.1 mol/L Bu_4NClO_4

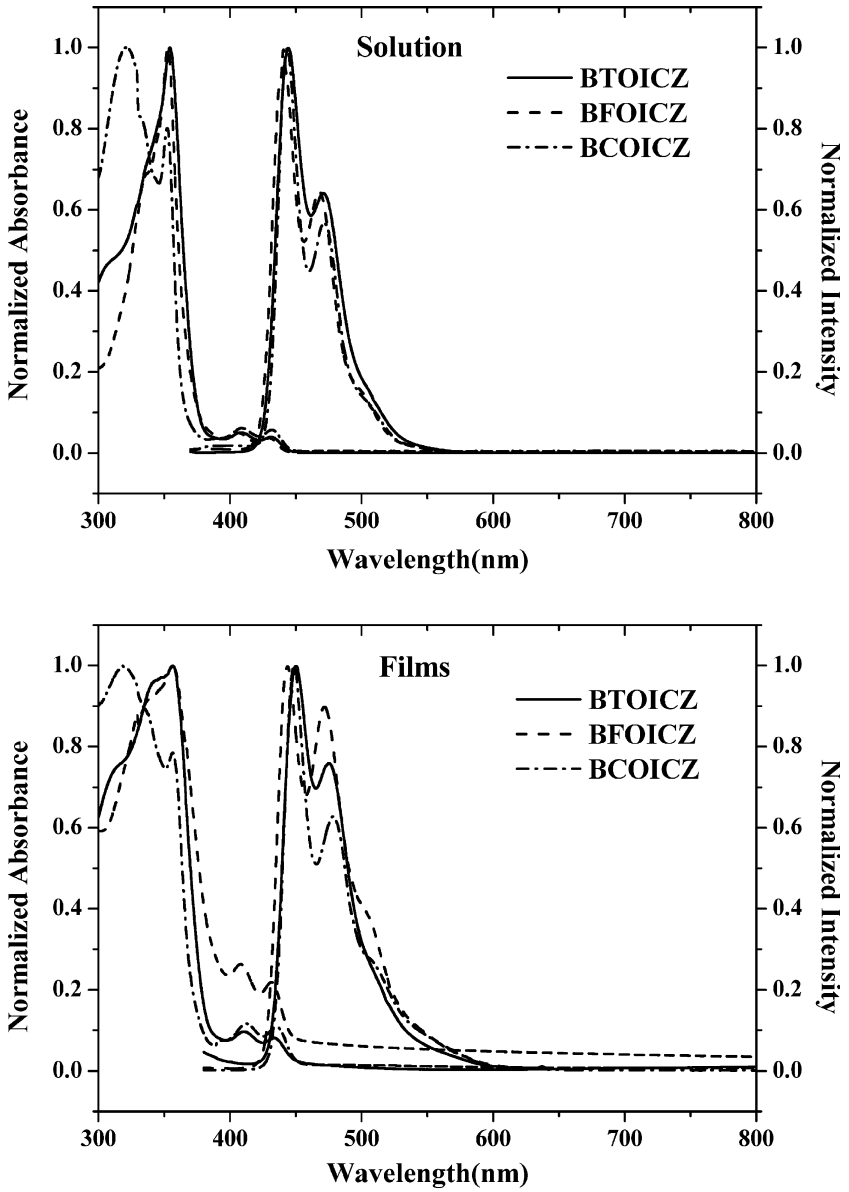


Fig. 1. UV–Vis absorption and PL spectra of the compounds in solution and solid films.

Table 1
Optical properties of **BTOICZ**, **BFOICZ** and **BCOICZ**

Compounds	λ_{ab}^{max} (nm)		λ_{em}^{max} (nm)		E_g^{opt} (eV)
	Solution	Film	Solution	Film	
BTOICZ	354.5	356.5	444	450	3.22
BFOICZ	352.5	355.5	441	444	3.19
BCOICZ	321.5	319	443	448	3.31

(in dichloromethane) as supporting electrolyte. The scan speed is 50 mV/s.

2.2. Synthesis

The synthetic sequences for the preparation of the three molecules are shown in Scheme 1.

2,8-Bis(4-diphenylaminophenyl)-5,11-di-*n*-octylindolo[3,2-*b*]carbazole (**BTOICZ**). 2,8-Dibromo-5,11-di-*n*-octylindolo[3,2-*b*]carbazole, 0.958 g (1.5 mmol); 4-(diphenylamino)phenylboronic acid, 1.04 g (3.6 mmol); tetrakis-(triphenylphosphine)palladium, 0.116 g (0.1 mmol); 20 mL THF and 10 mL (2 M) sodium carbonate aqueous solution under nitrogen, were added to a three-necked flask equipped with a magnetic stirrer, a reflux condenser, and a nitrogen input tube. The reaction mixture was refluxed in an oil bath under nitrogen. A yellow-brown product was obtained after heating and stirring for 24 h. The mixture was cooled to room temperature, extracted with 100 mL dichloromethane, washed with water and dried over anhydrous sodium sulfate. Then the solvent was removed under reduced pressure. The crude product was chromatographed on silica gel using petroleum/dichloromethane (2:1) as eluent. Compound **BTOICZ** was obtained as a yellow powder in a yield of 46%. Anal. Calc. for $C_{70}H_{70}N_4$: C, 86.91; H, 7.29; N, 5.79. Found: C, 86.47; H, 7.22; N, 5.70%. ^{1}H NMR ($CDCl_3$, 400 MHz) δ: 0.82–0.86 (m, 6H), 1.25–1.49 (m, 20H), 1.95–1.98 (m, 4H), 4.41 (t, 4H, $J = 7.2$ Hz), 6.99–7.30 (m, 24H), 7.44 (d, 2H, $J = 8.4$ Hz), 7.64 (d, 4H, $J = 8.6$ Hz), 7.71 (dd, 2H, $J = 8.4$ Hz, $J = 1.6$ Hz), 8.04 (s, 2H), 8.39 (d, 2H, $J = 1.6$ Hz). ^{13}C NMR ($CDCl_3$, 100.62 MHz) δ: 13.60, 22.15, 26.98, 28.44, 28.76, 29.00, 31.38, 43.04, 98.47, 108.11, 117.87, 122.14, 122.56, 122.87, 123.63, 124.16, 124.41, 127.43, 128.75, 130.55, 136.04, 136.35, 140.54, 145.76, 147.44. APCI-MS: m/z calculated for $C_{70}H_{70}N_4$: 967.33, Found: 968.3.

Table 2
Performance of ITO/HTL/Alq_3/Mg:Ag/Ag devices

HTL	**BTOICZ**	**BFOICZ**
Activating voltage (V)[a]	4.1	5.4
Maximum external quantum efficiency (%)	0.383	0.451
Maximum brightness (cd m^{-2})	19,473.9[c]	11,915.2[d]
Maximum current efficiency (cd A^{-1})	1.610	1.901
Maximum luminescence efficiency (lm W^{-1})	0.738	0.767
EL maximum/nm[b]	526	526
CIE coordinates[b], x and y	0.313 and 0.554	0.308 and 0.562

[a] Recorded at 1 cd m^{-2}.
[b] Recorded at 8 V.
[c] Recorded at 15 V.
[d] Recorded at 15.5 V.

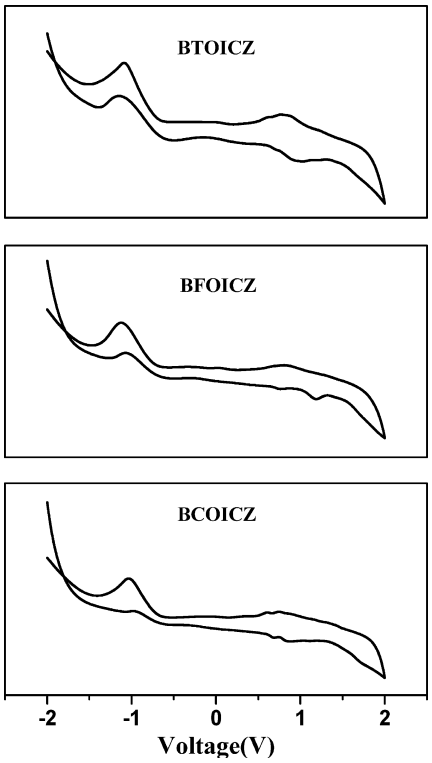


Fig. 2. Cyclic voltammograms for BTOICZ, BFOICZ and BCOICZ in CH_2Cl_2 with 0.1 mol/L Bu_4NClO_4 as supporting electrolyte and at a scan rate is 50 mV/s.

2,8-Bis(9,9′-dibutylfluorenyl)-5,11-di-*n*-octylindolo[3,2-*b*]carbazole (**BFOICZ**). This was obtained by a similar approach as for **BTOICZ** (yield: 42%). Anal. Calc. for $C_{76}H_{92}N_2$: C, 88.32; H, 8.97; N, 2.71. Found: C, 88.02; H, 8.82; N, 2.51%. ^{1}H NMR ($CDCl_3$, 400 MHz) δ: 0.72 (t, 12H, $J = 7.3$Hz), 0.84–0.87 (m, 6H), 1.10–1.50 (m, 34H), 2.02–2.09 (m, 14H), 4.48 (t, 4H, $J = 7.1$ Hz), 7.25–7.37 (m, 6H), 7.52 (d, 2H, $J = 8.4$ Hz), 7.71–7.83 (m, 10H), 8.13 (s, 2H), 8.50 (d, 2H, $J = 1.5$ Hz). ^{13}C NMR($CDCl_3$, 100.62 MHz) δ: 13.37, 13.58, 22.14,

22.67, 25.60, 26.99, 28.46, 28.76, 29.01, 31.37, 39.86, 43.06, 54.61, 98.59, 108.16, 118.24, 119.10, 119.40, 121.16, 122.41, 122.62, 122.93, 124.93, 125.57, 126.27, 131.59, 136.12, 138.98, 140.61, 140.71, 140.80, 150.44, 150.92.

2,8-Bis[*N*-(*n*-butyl)carbazolyl]-5,11-di-*n*-octylindolo[3,2-*b*]carbazole (**BCOICZ**). This was obtained by a similar approach as for **BTOICZ** (yield: 71%). Anal. Calc. for $C_{66}H_{74}N_4$: C, 85.85; H, 8.08; N, 6.07. Found: C, 85.85; H, 8.10; N, 5.94%. ^{1}H NMR ($CDCl_3$, 400 MHz) δ: 0.84–0.88(m, 6H), 0.98–1.01(m, 6H), 1.28–1.31(m, 12H), 1.41–1.54(m, 12H), 1.89–1.95(m, 4H), 2.01–2.05(m, 4H), 4.36–4.39 (t, 4H, $J = 7.1$ Hz), 4.46–4.49(t, 4H, $J = 7.1$ Hz), 7.25–7.29(m, 2H), 7.44–7.53(m, 8H), 7.84–7.90(m, 4H), 8.13(s, 2H), 8.22(d, 2H, $J = 7.7$ Hz), 8.47(d, 2H, $J = 1.6$ Hz), 8.54(d, 2H, $J = 1.6$ Hz). ^{13}C NMR($CDCl_3$, 100.62 MHz) δ: 13.44, 13.58, 20.14, 22.14, 27.02, 28.49, 28.76, 29.03, 30.73, 31.38, 42.51, 43.06, 98.48, 108.10, 108.30, 108.37, 118.23, 118.36, 118.43, 119.97, 122.62, 122.64, 122.95, 122.99, 125.09, 125.13, 132.11, 133.14, 136.09 139.05, 140.35, 140.46. APCI-MS: *m*/*z* calculated for $C_{66}H_{74}N_4$: 923.32, Found: 924.3.

2.3. Devices fabrication and characterization

Double-layer devices were fabricated with a configuration of indium tin oxide (ITO)/HTL(50 nm)/Alq_3(50 nm)/Mg:Ag(10:1, 150 nm)/Ag(10 nm), in which the indolo[3,2-*b*]carbazole derivatives were used as hole-transporting layers (HTL) and Alq_3 was used as the electron-transporting and emitting layer. The ITO glass was cleaned in ultrasonic baths of detergent, deionized water and acetone in sequence, and followed oxygen plasma cleaning. The organic films and metal electrode were sequentially deposited on the substrate by thermal evaporation under a vacuum of 10^{-6} Torr. The deposition rates were 2–3 Å/s for the organic materials and 5–7 Å/s for the cathode metals. The emitting area of the device was 4 mm^2. The thickness of films was measured by a Dektak surface profilometer. The EL spectra and current–voltage–luminance (*J*–*L*–*V*) characteristics were measured with a Spectrascan PR 650 photometer and a computer-controlled DC power supply. All the measurements of the devices were carried out under ambient conditions.

3. Results and discussion

3.1. Synthesis and characterization

Scheme 1 shows the synthetic route of the designed compounds. All the three compounds were readily synthesized by Suzuki coupling reaction, using 2,8-dibromo-5,11-di-*n*-octylindolo[3,2-*b*]carbazole with the corresponding boronic acids, with good yields. These compounds can dissolve in common organic solvents, allowing these compounds to be easily purified by column chromatography and other methods. All the obtained compounds were

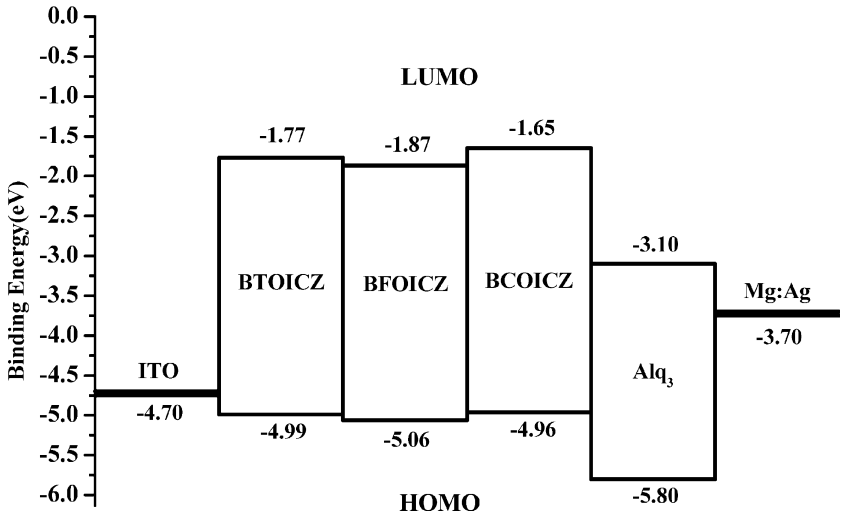


Fig. 3. Energy-level diagram of OLED components.

characterized by ^{1}H NMR, ^{13}C NMR, MS and elemental analysis. Differential scanning calorimetry (DSC) measurements were carried out from 20 °C to 320 °C under a nitrogen atmosphere with a heating rate of 20 °C/min, and the DSC curves showed sharp melting endotherm peaks at 243 °C for **BTOICZ**, 205 °C for **BFOICZ** and 202 °C for **BCOICZ**, respectively. Both BTOICZ and BFOICZ showed glass transition phenomena upon the heating process, and the glass transition temperatures (T_g) are 92 °C (**BTOICZ**) and 79 °C (**BFOICZ**), respectively, while **BCOICZ** has not been observed the glass transition phenomenon upon heating process from 20 °C to 320 °C. Although the long alkyl chains at N-5 and N-11 positions can effectively enhance the solubility of the product, the glass transition temperatures are greatly decreased at the same time compared with those containing rigid aryl groups at N-5 and N-11 positions [24,25]. All of these compounds have no obvious crystallization features, implying that they have excellent amporphous stability. Thermogravimetric analysis (TGA) measurements gave the thermal decomposition temperatures (T_d) 459 °C for **BTOICZ**, 420 °C for **BFOICZ** and 453 °C for **BCOICZ**, indicating that all of them possess good thermal stability.

3.2. Photophysical properties

The absorption and photoluminescence spectra of **BTOICZ**, **BFOICZ** and **BCOICZ** in dichloromethane and solid films are shown in Fig. 1. All the corresponding spectral data are summarized in Table 1. These compounds have similar absorption and emission properties, indicating that the introductions of different substituted groups have little effect on the energy levels of the molecular excited states with respect to those of the unsubstituted indolo[3,2-*b*]carbazole molecule. From the absorption and PL spectra in dichloromethane solution, the Stokes shifts are 90, 88, and 121 nm for **BTOICZ**, **BFOICZ** and **BCOICZ**, respectively. Compared to their spectra in the solution, the absorption and emission spectra of the solid films of the three compounds are little red-shifted. The broadened edge at the longer wavelength region can be ascribed to the intermolecular excimer formation and the twisted substituted groups with respect to the indolo[3,2-*b*]carbazole core [30]. This twist is helpful for decreasing intermolecular interaction in the aggregated state. The optical band gaps calculated from the absorption edges of the solid films are 3.22 eV for **BTOICZ**, 3.19 eV **BFOICZ** for and 3.31 eV for **BCOICZ**, respectively (see Table 2).

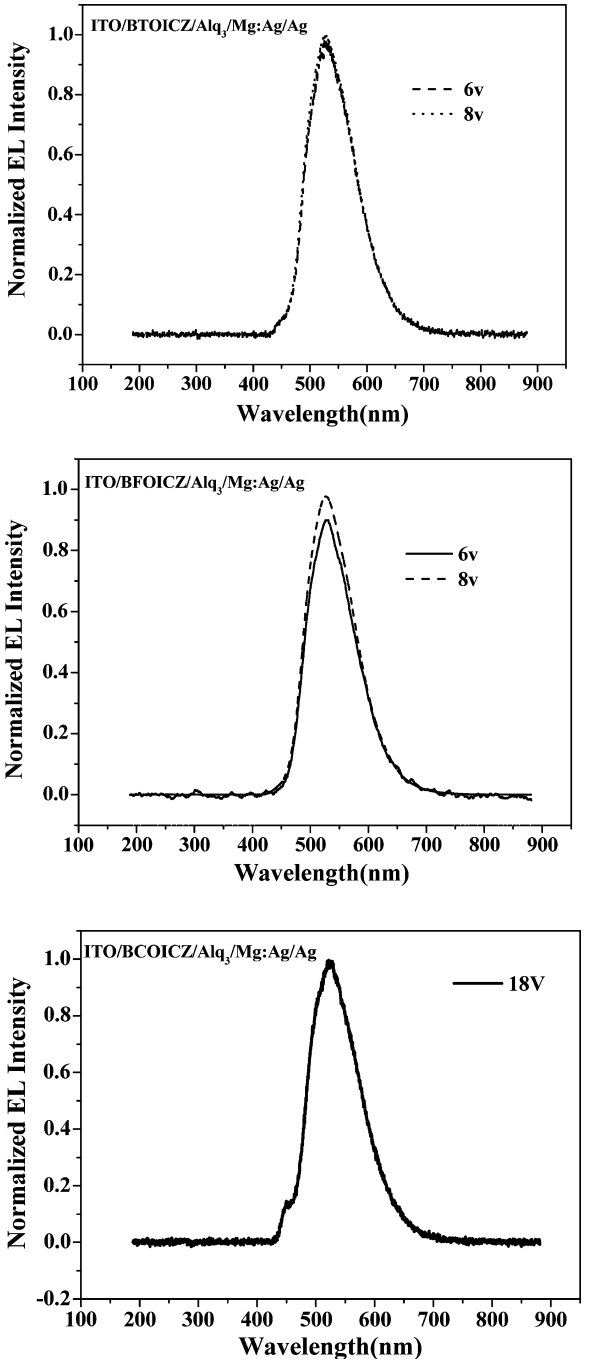


Fig. 4. EL spectra of devices reported at different applied voltages.

3.3. Electrochemistry

We performed cyclic voltammetry (CV) measurements of the indolo[3, 2-*b*]carbazole based compounds using Ag/AgCl as an internal standard. According to the cyclic voltammograms (Fig. 2), the onset potentials of oxidation are 0.61 V for **BTOICZ**, 0.68 V for **BFOICZ** and 0.58 V for **BCOICZ**, respectively. Therefore, the HOMO energy levels are −4.99 eV for **BTOICZ**, −5.06 eV for **BFOICZ** and −4.96 eV for **BCOICZ**, respectively. All the compounds have low energy barrier between the work function of ITO (−4.70 eV) and the HOMO energy levels, indicating that these compounds can be expected to have excellent hole-injecting performances. The LUMO energy levels calculated by subtraction of the optical band gaps from the HOMO energy levels are −1.77, −1.87 and −1.65 eV, respectively. All the compounds possess higher LUMO energy levels than those of other normal electron-blocking materials. Therefore, these compounds may be used as effective electron-blocking layer, which block electrons to escape from the emitting layer to the anode and then

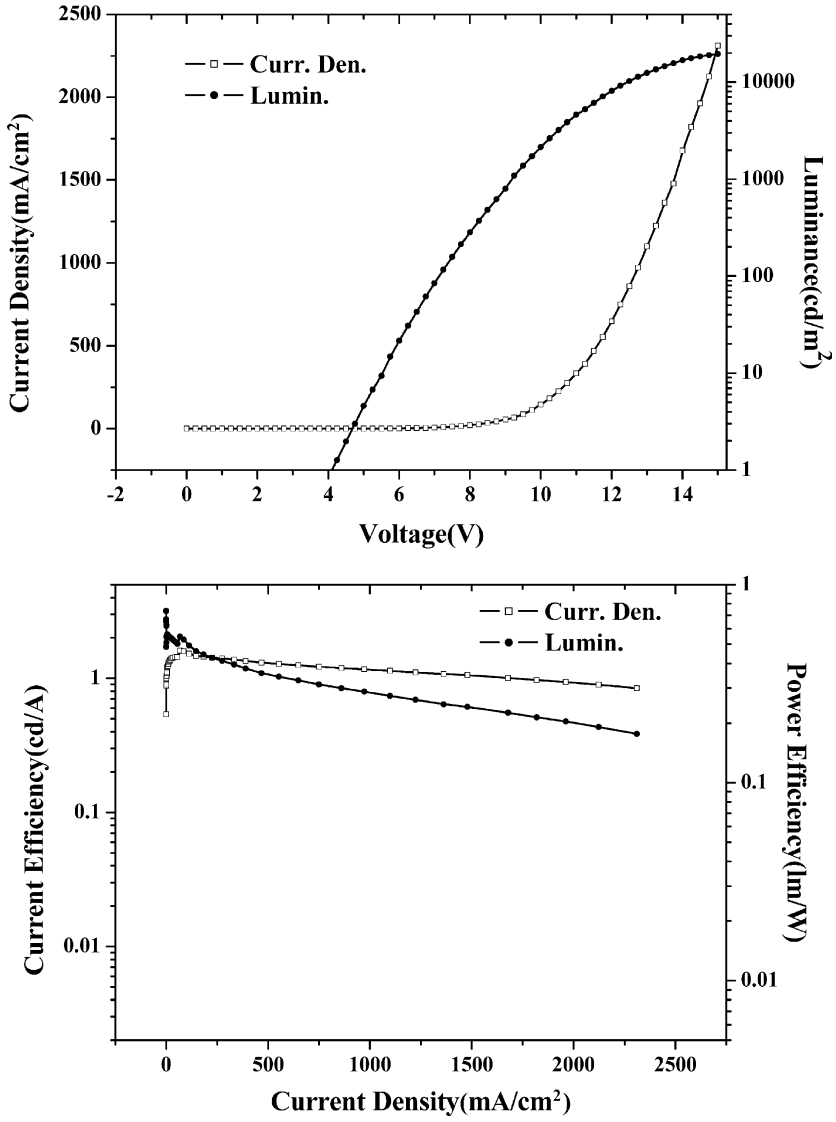


Fig. 5. The current density–luminance–voltage characteristics and the current efficiency–current density characteristics of the EL device of **BTOICZ**.

improve the efficiency of the devices, especially the electrophosphorescense based OLEDs [30]. Fig. 3 shows the energy-level diagram of the different layers in the OLEDs composed of these materials. The energy barrier between the HOMO energy level of **BCOICZ** (−4.96 eV) and the work function of ITO (−4.70 eV) is 0.26 eV, which is lower than that of **BTOICZ** (0.29 eV) and **BFOICZ** (0.36 eV). Thus, the hole-injection from ITO into **BCOICZ** is easier than those of into the other two compounds.

3.4. Electroluminescence properties

To understand the capability of **BTOICZ**, **BFOICZ** and **BCOICZ** as hole-transporting layers (HTL), double-layer EL devices were fabricated with the configuration ITO/HTL (50 nm)/Alq_3 (50 nm)/Mg:Ag (10:1, 150 nm)/Ag (10 nm). In the devices, **BTOICZ**, **BFOICZ** and **BCOICZ** was used as hole-transporting layer, respectively, and Alq_3 was used as both the electron-transporting and the emitting layer. Green emissions were observed in

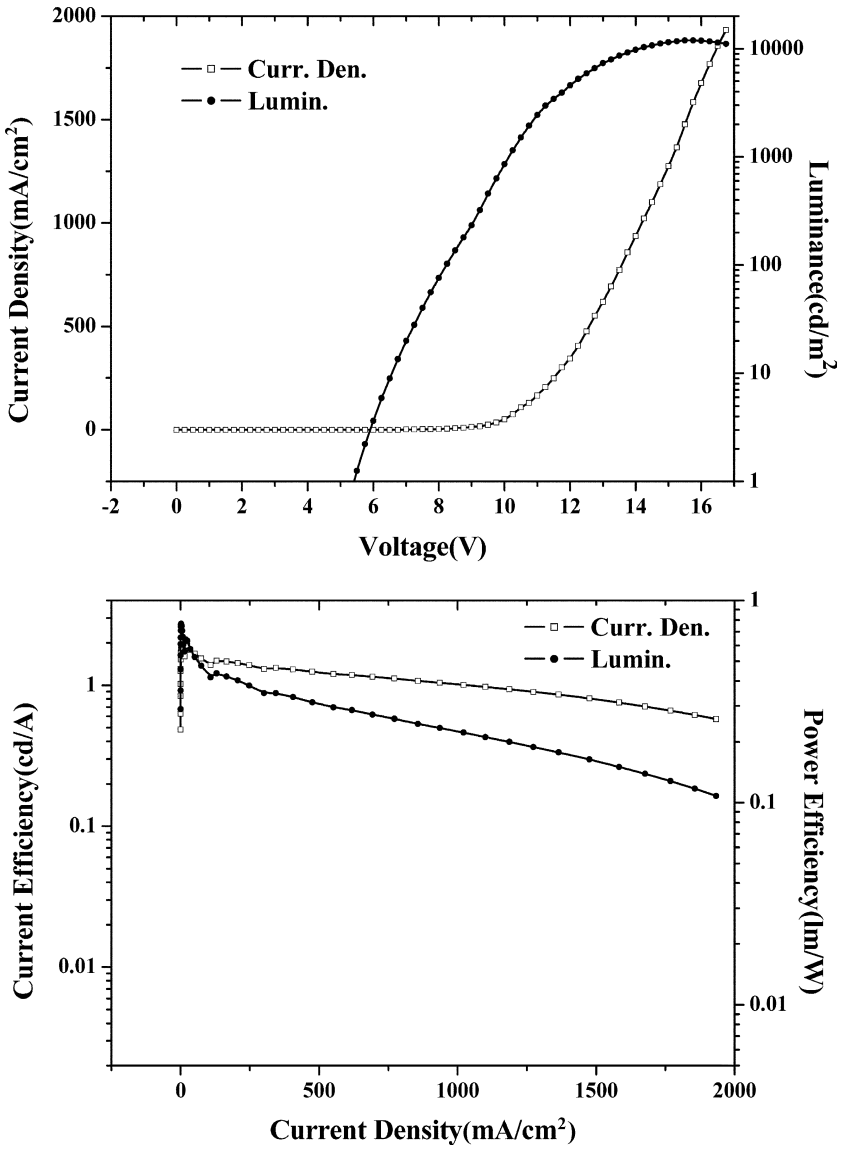


Fig. 6. The current density–luminance–voltage characteristics and the current efficiency–current density characteristics of the EL device of **BFOICZ**.

the devices based on **BTOICZ** and **BFOICZ**, while very weak light was emitted from the device based on **BCOICZ** when being applied high voltage. Fig. 4 illustrates the EL spectra of the devices based on **BTOICZ**, **BFOICZ** or **BCOICZ** as HTL, respectively, recorded at different applied voltages. Green emissions from Alq_3 with a peak at 526 nm suggested that the charge recombination was localized in the Alq_3 layer and **BTOICZ** or **BFOICZ** acts primarily as hole transporters without causing exciplex formation at the interface with Alq_3. This result should be attributed to the proper HOMO energy levels of **BTOICZ** and **BFOICZ** which are favorable for hole injection from ITO to the indolo[3,2-*b*]carbazole derivatives layer and then transportion to the Alq_3 layer. Similarly, the proper high LUMO energy levels of **BTOICZ** and **BFOICZ** block electron injection from Alq_3 to themselves (see Fig. 3). In Fig. 6, there two peaks located at 448 nm and 522 nm, respectively, in the EL spectra of the device based on **BCOICZ**. The main peak located at 522 nm is the emission of Alq_3, while the shoulder peak located at 448 nm, which is similar to the emission of **BCOICZ** in solid film, is the emission of **BCOICZ**. This phenomena indicates that the charge recombination was localized not only in the Alq_3 layer but also in the **BCOICZ** layer.

The current density–luminance–voltage (*J–L–V*) characteristics and the efficiency-current density characteristics of the devices using **BTOICZ/BFOICZ** as hole-transporting material are shown in Fig. 5 and 6, respectively. The devices exhibit a low turn-on voltage of 4.1 (**BTOICZ)** and 5.4 V (**BFOICZ)**, respectively, which is partly attributed to the low energy barrier between anode (ITO) and HTL [31]. The maxima brightness of the devices is 19,473.9 cd/m^2 (at 15 V) using **BTOICZ** as hole transfer layer and 11,915.2 cd/m^2 (at 15.5 V) using **BFOICZ** as hole transfer layer, while the maxima current efficiencies are 1.61 cd/A and 1.90 cd/A for the device using **BTOICZ** and **BFOICZ** as hole transfer layer, respectively. The current efficiencies of the devices remain almost constant with current density up to 2000 mA/cm^2. This may suggest that the EL devices based on the indolo[3,2-*b*]carbazole derivatives as hole-transporting materials will be thermally stable. Both devices using **BTOICZ** and **BFOICZ** as hole transfer layers have similar power efficiencies, which are 0.738 and 0.767 lm/W, respectively. The current density–luminance–voltage (*J–L–V*) characteristics of the devices using **BCOICZ** as hole-transporting material is shown in Fig. 7. The turn-on voltage of the device is 15 V, which is much higher than that of devices using **BTOICZ** and **BFOICZ** as hole transfer layer. The maxima brightness of the devices is only 3.7 cd/m^2 at 18 V. This may due to that the charge recombination was mainly localized in the **BCOICZ** layer, and only a very few holes and electrons were recombined in Alq_3 layer. The poor EL performance of the device based on **BCOICZ** as hole-transporting materials, compared with that of the devices based on

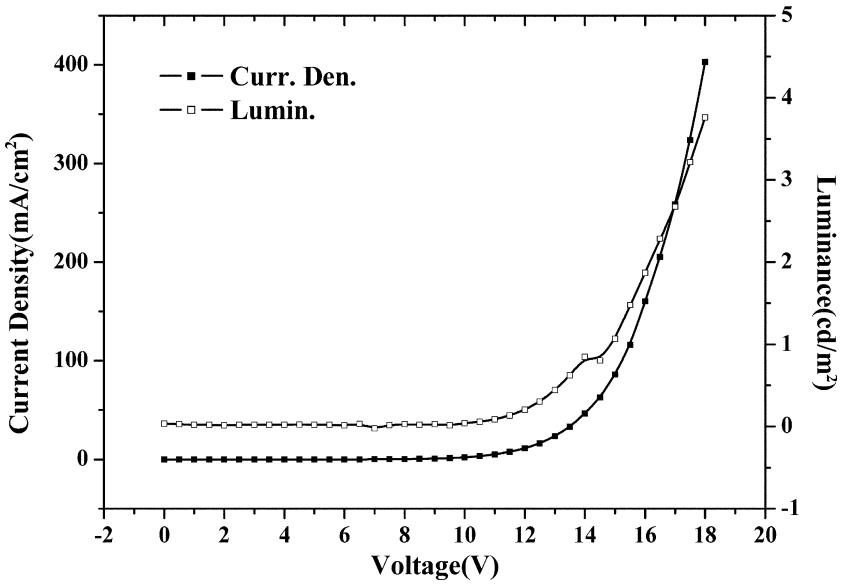


Fig. 7. The current density–luminance–voltage characteristics of the EL device of **BFOICZ**.

BTOICZ or **BFOICZ**, indicates that the hole-transporting capability of **BCOICZ** is much poorer than that of **BTOICZ** or **BFOICZ**. The results indicated that the different substituted groups have great influence on the hole-injecting and transporting performances of the compounds based on indolo[3,2-*b*]carbazole.

4. Conclusions

Three new compounds based on indolo[3,2-*b*]carbazole, **BTOICZ, BFOICZ** and **BCOICZ**, as hole-transporting materials have been synthesized and characterized. The EL results indicate that **BTOICZ** and **BFOICZ** possess excellent hole-transporting properties with low activating voltage and high brightness, while **BCOICZ** exhibits very poor hole-transporting capability in the same device configuration. These substituent groups have little influence on the optical properties of the compounds, but have great influence on the hole-transporting performance in the EL devices. Therefore, excellent hole-transporting materials based on indolo[3,2-*b*]carbazole can be obtained through strategic substitution.

Acknowledgements

We thank the State National Natural Science Foundation of China (Grant Nos. 50323006, 50325311, 50590403 and 50603011) and 973 program of PR China (Grant Nos. 2004CB619002 and 2002CB613405) for financial support.

References

[1] C.W. Tang, S.A. VanSlyke, Appl. Phys. Lett. 51 (1987) 913.
[2] R.H. Friend, R.W. Gymer, A.B. Holmes, J.H. Burroughes, R.N. Marks, C. Taliani, D.D.C. Bradley, D.A. Dos Santos, J.L. Bredas, M. Logdlund, W.R. Salaneck, Nature 397 (1999) 121.
[3] S.R. Forrest, Org. Electron. 4 (2003) 45–48.
[4] A. Kraft, A.C. Grimsdale, A.B. Holmes, Angew. Chem. Int. Ed. 37 (1998) 402.
[5] H. Aziz, Z.D. Popovic, N.X. Hu, A.M. Hor, G. Xu, Science 283 (1999) 1900.
[6] M. Strukelj, F. Papadimitrakopoulos, T.M. Miller, L.J. Rothberg, Science 267 (1995) 1969.
[7] A. Higuchi, H. Inada, Y. Shirota, Adv. Mater. 3 (1991) 549.
[8] Y. Kuwabara, H. Ogawa, H. Inada, N. Noma, Y. Shirota, Adv. Mater. 6 (1994) 677.
[9] K. Katsuma, Y. Shirota, Adv. Mater. 10 (1998) 223.
[10] H. Inada, Y. Shirota, J. Mater. Chem. 3 (1993) 319.
[11] Y. Shirota, Y. Kuwabara, H. Inada, T. Wakimoto, H. Nakada, Y. Yonemoto, S. Kawami, K. Imai, Appl. Phys. Lett. 65 (1994) 807.
[12] M. Thelakkat, H. Schmidt, Adv. Mater. 10 (1998) 219.
[13] H. Tanaka, S. Tokito, Y. Taga, A. Okada, J. Chem. Soc. Chem. Commun. 2175 (1996).
[14] S. Tokito, H. Tanaka, A. Okada, Y. Taga, Appl. Phys. Lett. 69 (1996) 878.
[15] S.A. Van Slyke, C.H. Chen, C.W. Tang, Appl. Phys. Lett. 69 (1996) 2160.
[16] B.E. Koene, D.E. Loy, M.E. Thompson, Chem. Mater. 10 (1998) 2235.
[17] D.F. O'Brien, P.E. Burrows, S.R. Forrest, B.E. Koene, D.E. Loy, M.E. Thompson, Adv. Mater. 10 (1998) 1108.
[18] P.J. Low, M.A.J. Paterson, D.S. Yufit, J.A.K. Howard, J.C. Cherryman, D.R. Tackley, R. Brook, B. Brown, J. Mater. Chem. 15 (2005) 2304.
[19] C. Adachi, K. Nagai, N. Tamoto, Appl. Phys. Lett. 66 (1995) 2679.
[20] M. Stolka, J.F. Janus, D.M. Pai, J. Phys. Chem. 88 (1984) 4707.
[21] P.F. Smith, P. Gerroir, S. Xie, A.M. Hor, Z. Popovic, M.L. Hair, Langmuir 14 (1998) 5946.
[22] P. Fenter, F. Schreiber, V. Bulovic, S.R. Forrest, Chem. Phys. Lett. 277 (1997) 521.
[23] Q. Zhang, J. Chen, Y. Chen, L. Wang, D. Ma, X. Jing, F. Wang, J. Mater. Chem. 14 (2004) 895.
[24] N.X. Hu, S. Xie, Z. Popovic, B.S. Ong, A.M. Hor, S. Wang, J. Am. Chem. Soc. 121 (1999) 5097.
[25] N. Hu, S. Xie, Z.D. Popovic, B. Ong, A. Hor, Synth. Met. 111–112 (2000) 421.
[26] L.N. Yudina, J. Bergman, Tetrahedron 59 (2003) 1265.
[27] M.Y. Chou, M. Leung, Y.O. Su, C.L. Chiang, C.C. Lin, J.H. Liu, C.K. Kuo, C.Y. Mou, Chem. Mater. 16 (2004) 654.
[28] D. Katsis, Y.H. Geng, J.J. Ou, S.W. Culligan, A. Trajkovska, S.H. Chen, L.J. Rothberg, Chem. Mater. 14 (2002) 1332.
[29] Y. Li, J. Ding, M. Day, Y. Tao, J. Lu, M. D'iorio, Chem. Mater. 16 (2004) 2165.
[30] V.I. Adamovich, S.R. Cordero, P.I. Djurovich, A. Tamayo, M.E. Thompson, B.W. D'Andrade, S.R. Forrest, Org. Electron. 4 (2003) 77.
[31] S. Okutsu, T. Onikubo, M. Tamano, T. Enokida, IEEE Trans. Electron Dev. 44 (1997) 1302.

Available online at www.sciencedirect.com
ScienceDirect
Organic Electronics 8 (2007) 683–689
Organic Electronics
www.elsevier.com/locate/orgel

Four-wavelength white organic light-emitting diodes using 4,4′-bis-[carbazoyl-(9)]-stilbene as a deep blue emissive layer

C.H. Jeong *, J.T. Lim, M.S. Kim, J.H. Lee, J.W. Bae, G.Y. Yeom

Department of Advanced Materials Science and Engineering, SungKyunKwan University, Suwon, Gyonggi-Do 440-746, Republic of Korea

Received 13 June 2006; received in revised form 5 March 2007; accepted 17 May 2007
Available online 26 May 2007

Abstract

White organic light-emitting diodes (WOLEDs) with four wavelengths were fabricated by using three doped layers, which were obtained by separating recombination zones into three emitter layers. Among these emitters, blue emissions with two wavelengths (456 and 487 nm) were occurred in the 4,4′-bis(carbazoyl-(9))-stilbene (BCS) host doped with a perylene dye. Also, a green emission was originated from the tris(8-quinolinolato)aluminum (III) (Alq_3) host doped with a green fluorescent of 10-(2-benzothiazolyl)-1,1,7,7-tetramethyl-2,3,6,7-tetrahydro-1H,5H,11H-[1]benzopyrano [6,7,8-*ij*]-quinolizin-11-one (C545T) dye. Finally, an orange emission was obtained from the *N*,*N*′-bis(1-naphthyl)-*N*,*N*′-diphenyl-1,1′-biphenyl-4,4′-diamine (NPB) host doped with a 4-(dicyanomethylene)-2-*tert*-butyl-6-(1,1,7,7-tetramethyljulolidyl-9-enyl)-4H-pyran (DCJTB) dye. The white light could be emitted by simultaneously controlling the emitter thickness and concentration of fluorescent dyes in each emissive layer, resulting in partial excitations among those three emitter layers. Electroluminescent spectra of the device obtained in this study were not sensitive to driving voltage of the device. Also, the maximum luminance for the white OLED with the CIE coordinate of (0.34, 0.34) was 56,300 cd/m^2 at the applied bias voltage of 11.6 V. Also, its external quantum and the power efficiency at about 100 cd/m^2 were 1.68% and 2.41 lm/W, respectively.
© 2007 Elsevier B.V. All rights reserved.

PACS: 79.60.Fr; 78.55.Kz; 85.60.Pg

Keywords: WOLED; White emission; BCS; Energy transfer; Carrier trapping; Doping

1. Introduction

In the last few years, white light emission of organic light-emitting diodes (OLEDs) has become increasingly popular as one of the major methods to fabricate full-color display combined with red-green-blue (RGB) color filters, as a flat panel display backlight, and as general solid-state lighting applications [1].

In order to obtain white light emission from the OLEDs, the simultaneously excitation of more than one molecular species in different emissive layers is required because the luminescence of a single organic molecule does not span the entire visible spectrum. White-light emission can be obtained by mixing two complementary colors (e.g., red/bluish-green,

* Corresponding author. Tel.: +82 31 299 6562; fax: +82 31 299 6565.
E-mail address: hyuny517@skku.edu (C.H. Jeong).

1566-1199/$ - see front matter © 2007 Elsevier B.V. All rights reserved.
doi:10.1016/j.orgel.2007.05.005

blue/orange, or green/magenta) or three primary colors (red, green, and blue) from small-molecules and/or polymers [1–10].

White light emission is mainly achieved by modifying the spectral characteristics of OLEDs. First, a doping method [2] using a luminescent dye can be used to occur energy transfer from the host to the dopant, or to take place carrier trapping directly at a dopant site [3]. Thus, by using two or three layers doped with different dyes, white light emission can be obtained [1,3–7]. Second, the spatial tuning of the exciton recombination zone can be used by a carrier-blocking layer that preferentially blocks one type of carrier between the hole-transporting layer (HTL) and electron-transporting layer (ETL). Controlling the thickness of this blocking layer enables exciton formation in both the HTL and ETL. If the layers themselves are emissive or contain lumophore dopants, simultaneous emission from the two layers can be achieved, leading to the appropriate color balance. Third, white light emission can be induced by confining each exciton of RGB into different wells of organic multiple quantum-well structures (MQWs), in which the injected carrier distributes in different light-emitting wells [8]. And last, the formation of either excimers (among homolayers) or exciplexs (among heterolayers) can lead to the white emission [1]. These are due to the complicated intermolecular interactions between donor and acceptor consisted of two blue-emitting organic molecules of different electron affinities. Among the above technologies for white emission, first two methods have been used most widely in obtaining white light emission.

For the application of white OLEDs (WOLEDs), the following four issues need to be resolved. One is the shift of color with the increase of the applied bias voltage, due to the movement of carrier recombination zone over the light emitting layers. Second is the mismatch of a luminance and luminous efficiency among the sub pixels of RGB colors as a function of the life time. Third is the achievement of a stable green light among RGB colors by preventing cascade energy transfer between the emissive multilayers [9]. The last is the improvement of the luminous efficiencies further for commercialization. Therefore, the unchangeable color coordinates and the stable exciton recombination with respect to the applied bias voltage in the emitting layers are essential in the successful performance of WOLEDs.

In this study, to obtain highly efficient and highly stable WOLEDs, the OLEDs generating four-wavelength lights (deep blue, bluish-green, deep green, and orange color) were fabricated and their device characteristics were investigated. Especially, to introduce strong blue emission at 450 nm to WOLED, 4,4′-bis(carbazoyl-(9))-stilbene (BCS) doped with perylene system was used [11]. Also, to emit deep green emission at 520 nm more effectively and to obtain a device with less color shift with increasing applied voltage, a novel WOLED device structure composed of three layered hetero-structure multilayer preventing cascade energy transfer [1,6–10] was developed. In these devices, high emission efficiencies could be obtained by controlling either the thickness or the doping concentration of the multiple-doped layers.

2. Experimental

Fig. 1 exhibits molecular structures of the organic materials of the WOLEDs investigated in this study. Among the organic materials, BCS which emits blue light was synthesized by using a two-step route containing processes such as a nucleophilic displacement reaction and a conventional McMurry coupling reaction [12].

Fig. 2a shows the schematic configuration of the WOLEDs used in this study. The multilayered WOLED with three different emissive layers was composed of glass/tin-doped indium oxide (ITO, 120 nm)/2-TNATA (35 nm)/NPB (10 nm)/NPB

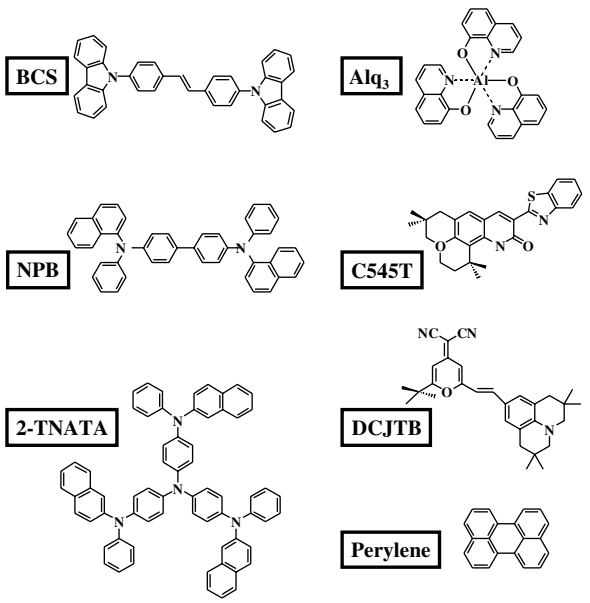


Fig. 1. Molecular structures of the organic materials used in this study.

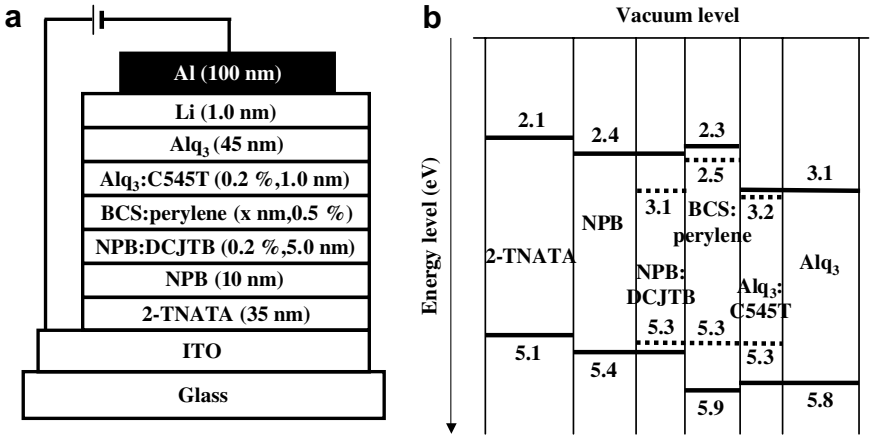


Fig. 2. (a) Schematic diagram of the device structure and (b) energy levels of the organic materials used in this study.

(5.0 nm):DCJTB (0.2 wt%)/BCS (x nm, $x = 10$, 8, and 6, respectively):perylene (0.5 wt%)/Alq_3 (1.0 nm):C545T (0.2 wt%)/Alq_3 (45 nm)/Li (1.0 nm)/Al (100 nm). ITO (anode) coated on the glass (0.7 mm) has the sheet resistance of about 10 Ω/□. Here, Alq_3 is tris(8-quinolinolato) aluminum (III), C545T is 10-(2-benzothiazolyl)-1,1,7,7-tetramethyl-2,3,6,7-tetrahydro-1H,5H,11H- [1] benzopyrano [6,7,8-*ij*]-quinolizin-11-one, NPB is *N*,*N*′-bis(1-naphthyl)-*N*,*N*′-diphenyl-1,1′-biphenyl-4, 4′-diamine, and DCJTB is 4-(dicyanomethylene)-2-*tert*-butyl-6-(1,1,7,7-tetramethyljulolidyl-9-enyl)-4H-pyran.

In the WOLEDs, the 4,4′,4″-tris(2-naphthylphenyl-1-phenylamino)triphenylamine (2-TNATA) and NPB layers are used as the hole-injecting layer (HIL) and HTL, respectively. Three emitter layers were used to emit different colors by doping a dopant into the host. The NPB layer doped with the DCJTB dye was used to emit orange color. The BCS layer doped with the perylene dye acted as both the deep blue and bluish-green emitter. The Alq_3 layer doped with the C545T was used as the deep green emitter. Alq_3, lithium (Li), and aluminum (Al) were used as the ETL, as the electron-injecting layer (EIL), and as the cathode, respectively.

Before loading ITO coated on the glass into a deposition chamber, ITO coated on the glass was cleaned with detergents and deionized water, and dried in the oven at the temperature of 120 °C for 2 h. Devices were fabricated by evaporating both organic materials and metal at the rate of 0.05–0.2 nm/s onto the ITO coated on glass substrate, sequentially at the pressure below 1×10^{-6} Torr. Doping in each emitting layer was simultaneously carried out by co-evaporating both the host and dopant. The emissive active area of the devices was 2×2 mm^2.

Current–voltage–luminance characteristics were measured using a source-measure unit (2400, Keithley Instrument). The intensities from the emission of WOLEDs devices were measured by the photocurrent induced on the silicon photodiodes using a picoammeter (485, Keithley Instrument). The photoluminescence excitation (PLE) and photoluminescence emission (PL) spectra of the deposited OLED materials were measured using luminescence spectrometer (AMINCO Bowman series2, Thermo Spectronic). The electroluminescent (EL) spectra of the as-fabricated devices were measured by optical emission spectroscopy (PCM-420, SC Technology).

3. Results and discussion

As shown in Fig. 2a, WOLEDs investigated in this study are composed of glass/ITO (120 nm)/2-TNATA (35 nm)/NPB (10 nm)/NPB (5.0 nm):DCJTB (0.2 wt%)/BCS (x nm):perylene (0.5 wt%)/Alq_3 (1.0 nm):C545T (0.2 wt%)/Alq_3 (45 nm)/Li (1.0 nm)/Al (100 nm).

The light emission from the dopant molecules in all emissive layers are known to be occurred by either energy transfer or carrier trapping [13]. In general, a significant spectral overlap, i.e. overlap of the host emission and the dopant absorption is a key requirement for the efficient energy transfer, whereas for the efficient hole or electron trapping, the HOMO/LUMO energy levels of the dopant must fall within the energy gap of the host. Fig. 2b shows the energy levels (the ionization

potential (IP) and the electron affinity (EA)) of 2-TNATA as HIL, NPB as HTL, NPB doped with DCJTB as the orange-emitting layer, BCS doped with perylene as the blue-emitting emitter, Alq_3 doped with C545T as the green-emitting emitter, and Alq_3 as ETL, respectively. As shown in the energy levels of the three emissive layers of Fig. 2b, the HOMO/LUMO of all fluorescent dopant exists within those of the corresponding host. Specially, among the three emissive layers, the BCS doped with perylene is expected to have some hole trapping effect. This is because the IP energy level (5.3 eV) of perylene is located well within the energy gap of the BCS, therefore, it can function as a deep trap in the perylene doped BCS layer. In addition, an electron injection from the C545T doped Alq_3 layer would be expected to be efficiently injected to a dopant rather than the host. This is attributed to the electron injection barrier between Alq_3 (EA: 3.1 eV) and BCS (EA: 2.3 eV) is higher than that between Alq_3 and perylene (EA: 2.5 eV). However, it does not mean that there will be no emission by the energy transfer effect (Foster energy transfer) which is enhanced by the overlapping between the absorption spectrum of the perylene as an acceptor and the emission spectrum of the BCS host as a donor [14]. Therefore, PLE and PL spectra of BCS thin film as well as the PL spectra of BCS doped with perylene were investigated.

Fig. 3 shows the PLE and PL spectra of BCS thin film as well as the PL spectra of BCS doped with perylene (0.5%). As shown in the figure, PLE and PL spectral peaks of BCS were located at 360 and 430 nm, respectively. Also, BCS doped with perylene showed the PL spectrum with two peaks located at 456 and 487 nm, showing the emission characteristic by perylene rather than BCS. Mi et al. [15] reported that the PL spectrum of perylene has two peaks at 446 and 472 nm and its absorption spectrum at 412 and 436 nm. Therefore, it can be seen that the PL spectrum of BCS is largely overlapped with the absorption peak of perylene, which is the condition of EL by Foster energy transfer. Therefore, not only the hole trapping but also Foster energy transfer play an important role in the EL spectrum from the perylene doped BCS layer even though it is difficult to tell currently which is more responsible for the EL spectra observed.

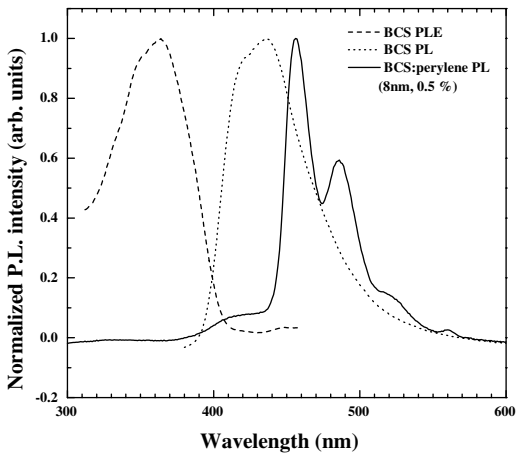


Fig. 3. PLE and PL spectra of BCS thin film and BCS doped with perylene (0.5%) thin film (dash line: BCS PLE, dot line: BCS PL, and solid line: BCS doped with perylene PL, respectively).

In the OLEDs, the luminous efficiency and life time of an emissive layer can be generally improved by doping a dopant into the host layer. Also the emission spectra of the DCM-series (for example: DCJTB, DCM2 [16], etc.) doped layers are generally red-shifted from yellow to deep red with increasing the dopant concentration in an organic solid due to the solid-state solvation effect (SSSE) [14]. However, in the case of doping DCM2 to Alq_3, the external quantum efficiency (η_{ext}) and power efficiency (η_{PE}) are decreased with increasing dopant concentration or increasing a doped-layer thickness when the doping concentration and the thickness of a doped layer are higher than 0.5 wt% and 10 nm, respectively, due to the concentration quenching and hole trapping processes. As a result, the current will be decreased by the reduction of a hole mobility in this layer [17]. For the perylene and C545T doped system, when the dopant concentration is higher than 1 wt%, due to the planar structure of the dopant molecules, the aggregation between molecules is increased. Therefore, EL studies show that, if the dopant concentration is higher the 1 wt%, a shoulder at the long-wavelength edge of emission spectrum begins to grow resulting in undesirable hue shift or lowering its luminance efficiency due to concentration quenching [15,18,19]. Therefore, in this study, to improve a luminous efficiency of the WOLEDs, the emissive layers with low dopant concentration were used. Dopant concentrations of DCJTB as an orange, perylene as a blue, C545T as a green dye in each host layer were 0.2, 0.5, and 0.2 wt%, respectively. Also, as shown in the device configuration of Fig. 2a, the thickness for all emissive layers was optimized within the thickness of 10 nm.

In order to tune to the balanced white emission, EL characteristics at the luminance of 100 cd/m^2 was measured as a function of the thickness of BCS doped with perylene between 6 and 10 nm and the results are shown in Fig. 4a. Table 1 also shows photometric properties and a thickness of BCS doped with perylene of 0.5 wt%. Here, for Device 1, Device 2, and Device 3 shown in Table 1, the thicknesses of the BCS doped with perylene layer were 10, 8, and 6 nm, respectively. Among those three devices, the balanced white emission was obtained through Device 2. The EL spectrum of Device 2 was composed of two blue peaks of 456 and 487 nm, one green peak of 518 nm, and one orange peak of 560 nm. And these peaks were originated from the three emissive layers doped with low concentration dopants. Two blue peaks of 456 and 487 nm composing of the EL spectra are generated by the dopant excitation through both by Foster energy transfer and by carrier trapping at the dopant site (as mentioned in Figs. 2 and 3) because the EL spectrum of the OLED having BCS as the emissive layer should have the maximum peak at the wavelength of 425 nm [11]. Also, similar to the EL result of the perylene-doped OLED investigated by other researchers, two blue peaks instead of one blue peak could be obtained [15]. The green peak at 518 nm is estimated to be occurred by carrier trapping at the C545T molecule site or by the energy transfer from Alq_3 to C545T [18–20]. Meanwhile, the orange peak at 560 nm is estimated to be generated by either partial energy transfer from NPB to DCJTB (about 550 nm) due to the incompletely overlaps between the emission spectrum of NPB and the absorption spectrum of DCJTB, or the carrier trapping effect at the DCJTB site [6,16].

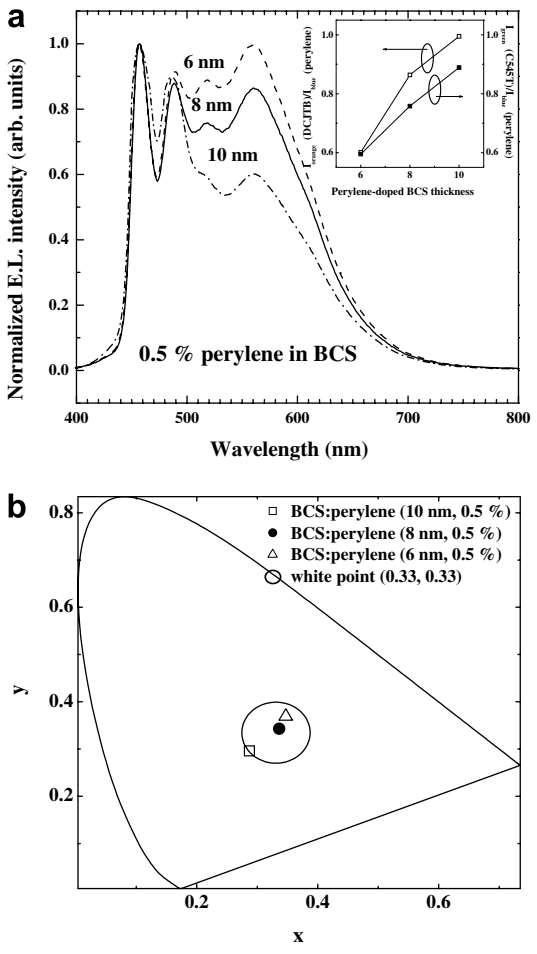


Fig. 4. (a) Effect of the BCS deped with perylene thickness on the normalized EL spectra of the devices composed of glass/ITO (120 nm)/2-TNATA (35 nm)/NPB (10 nm)/NPB (5.0 nm): DCJTB (0.2 wt%)/BCS (x nm):perylene (0.5 wt%)/Alq_3 (1.0 nm): C545T (0.2%)/Alq_3 (45 nm)/Li (1.0 nm)/Al (100 nm) ($x = 10$ (dash dot line), 8 (solid line), 6 (dash line), respectively), at the applied bias voltage of about 7 V (corresponding to the luminance of 100 cd/m^2). Inset: variation of the EL intensity ratios of I_{orange}(DCJTB)/I_{blue}(perylene) (open square) and I_{green} (C545T)/I_{blue}(perylene) (closed square) as a function of BCS doped with perylene thickness. (b) The CIE chromaticity diagram for the same devices.

The inset of Fig. 4a shows the variation of the EL intensity ratios of I_{orange} (DCJTB)/I_{blue} (perylene) and I_{green} (C545T)/I_{blue} (perylene) as a function in the BCS doped with perylene thickness. As shown in the figure, the decrease of the perylene doped BCS layer thickness from 10 to 6 nm increased the intensity ratios of I_{orange} (DCJTB)/I_{blue} (perylene) and I_{green} (C545T)/I_{blue} (perylene). In fact, more exciton recombination was occurred in the DCJTB and C545T as the BCS doped with perylene thickness was decreased. This is attributed to energy levels of the BCS material having a high electron-blocking property from the Alq_3 doped with C545T layer to NPB doped with DCJTB layer and a hole blocking property from the NPB doped with DCJTB layer to Alq_3 doped with C545T layer as shown in the energy level in Fig. 2b. Therefore, as the perylene doped BCS layer thickness was decreased, the green- and orange-emission intensities were increased compared to the blue one. In addition, as the thickness of perylene doped BCS layer was decreased, the wavelength range of the white EL spectra was slightly broaden. Fig. 4b shows the corresponding Commission Internationale d'Eclairage (CIE) chromaticity coordinates for the EL spectra of Devices 1–3. The CIE chromacity

Table 1
Turn-on voltage (V_T), current density (J), power efficiency (η_{PL}), external quantum efficiency (η_{ext}), CIE coordinate, and maximum luminance (L_{max}) of WOLEDs for various thickness (t) of BCS doped with perylene

	Device 1	Device 2	Device 3
Thickness of the perylenedoped BCS layer (x nm, 5 wt%)	10	8	6
V_T[a]	3.2	3.2	3.2
J (mA/cm^2)[b]	2.38	2.25	2.17
η_{PL} (lm/W)[b]	2.00	2.41	2.61
η_{ext} (%)[b]	1.42	1.68	1.72
CIE coordinates[b]	(0.29, 0.30)	(0.34, 0.34)	(0.35, 0.37)
L_{max} (cs/m^2)	55,200 at 11.8 V	56,300 at 11.6 V	55,300 at 11.4 V

[a] The turn-on voltage was measured at the luminance of 0.1 cd/m^2.
[b] The data were measured at 100 cd/m^2.

coordinates for Devices 1–3 at the luminance of 100 cd/m^2 were (0.29, 0.30), (0.34, 0.34), and (0.35, 0.37), respectively. Therefore, Device 2 is the closest to white point of (0.33, 0.33) among the WOLEDs investigated.

Fig. 5 shows white EL spectra as a function of the applied bias voltage for Device 2 having 8 nm-thick BCS doped with perylene (0.5 wt%) and the inset of Fig. 5 exhibits the CIE coordinates for corresponding EL spectra. As shown in the inset of Fig. 5, as the voltage increased from 4 (the corresponding luminance of 1.40 cd/m^2) to 9 V (1610 cd/m^2), the corresponding CIE chromaticity coordinates of EL spectra showed nearly unchangeable characteristic within the range of (0.34–0.35, 0.34–0.35). This stability of the coordinates obtained in our devices is attributed to the stable exciton recombination in each emissive layer for the bias voltages investigated.

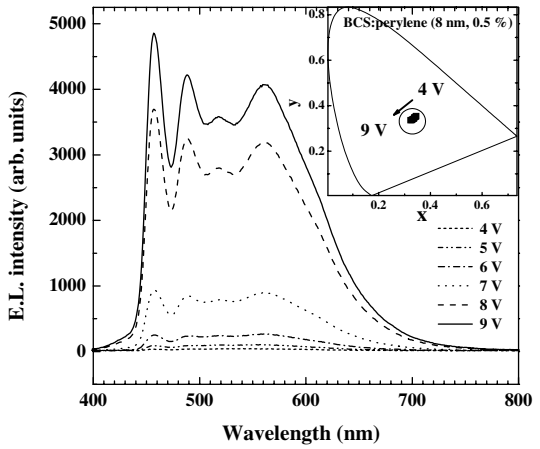


Fig. 5. Spectral variation as a function of the applied bias voltage (4–9 V) for Device 2. The inset shows the corresponding CIE chromaticity coordinates for the same device. The white point is CIE chromaticity coordinates of (0.33, 0.33).

Fig. 6a shows the current density (J) and luminance (L) of the Devices 1–3 as a function of applied bias voltage. The maximum luminance of the devices are also shown in Table 1. As shown in Fig. 6a and Table 1, the maximum luminance (L_{max}) were 55,200 (11.8), 56,300 (11.6), and 55,300 cd/m^2 (11.4 V) for Device 1, Device 2, and Device 3, respectively. And the turn-on voltages at the luminance of 0.1 cd/m^2 for Devices 1–3 were 3.2, 3.2, and 3.2 V, respectively. Also, as the perylene-doped BCS thickness was increased in the OLEDs, the current density at the same applied bias voltage was slightly increased. Especially for the operating voltage was lower than 3 V, when the thickness of the perylene doped BCS was 6 or 8 nm, the $J-V-L$ characteristics were similar each other and showed good properties, however, when the thickness was 10 nm, the current–voltage characteristic was a little degraded. Even though the device operating mechanism needs more investigation, the change of electrical properties appears to be related to the high hole-blocking and high electron-blocking properties of BCS.

Fig. 6b shows the power efficiency (η_{PE}) and external quantum efficiency (η_{ext}) as a function of current density (J) for Devices 1–3. Device 2 having the CIE coordinate close to the white point exhibited η_{PE} of 2.25 lm/W at the luminance of about 100 cd/m^2. The η_{PE} values at about 100 cd/m^2 for Device 1 and Device 3 were 2.00 and 2.61 lm/W, respectively. Also, the values of η_{ext} for Devices 1–3 were 1.42%, 1.68%, and 1.72%, respectively. Therefore, as the thickness of perylene doped BCS layer was decreased, η_{PE} and η_{ext} of the device were increased. Therefore, the luminous efficiencies, that is, both η_{PE} and η_{ext} were the highest for Device 3 among Devices 1–3. The differences of the luminous efficiencies obtained in our devices are also believed

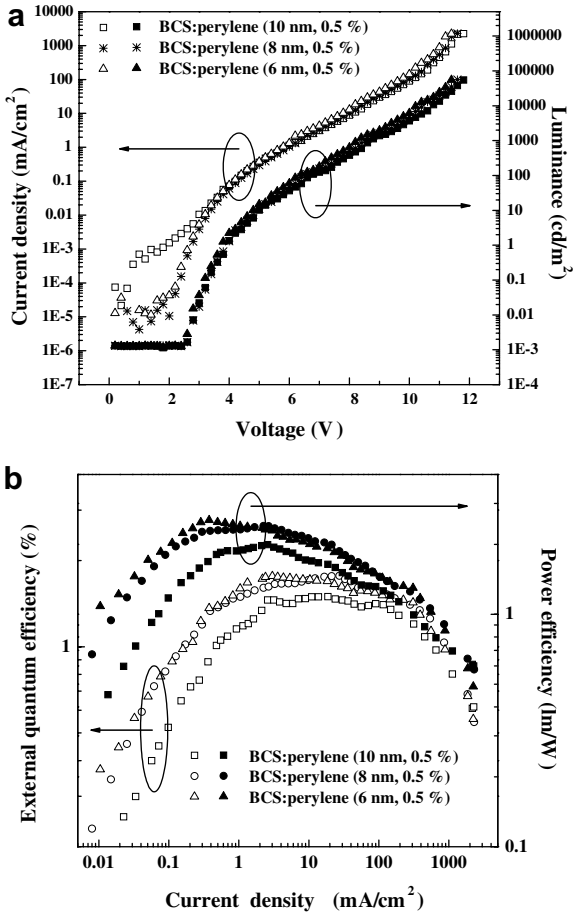


Fig. 6. (a) Current density–voltage–luminance characteristics for Devices 1–3 composed of glass/ITO (120 nm)/2-TNATA (35 nm)/NPB (10 nm)/NPB (5 nm):DCJTB (0.2 wt%)/BCS (*x* nm):perylene (0.5 wt%)/Alq_3(1.0 nm):C545T (0.2 wt%)/Alq_3 (45 nm)/Li (1.0 nm)/Al (100 nm) (square: 10, star: 8, and triangle: 6, respectively). (b) External quantum efficiency and power efficiency as a function of current density for the same devices (square: 10, circle: 8, and triangle: 6, respectively).

to be closely related to the carrier-blocking property.

4. Conclusions

Four-wavelength emitting WOLEDs were successfully fabricated by using three doped emissive layers and by separating each recombination zone in the three emitter layers. Also, the very bright and highly efficient WOLEDs with the L_{max} exceeding 55,000 cd/m^2 and with the η_{PE} of up to 2.62 lm/W could be demonstrated. The white light was originated from the partial excitation of fluorescent dyes composing the doped systems by controlling the layer thickness and concentration of each fluorescent dye in the emissive layers. EL spectra of the white light-emitting device investigated in this study were not highly sensitive to deriving voltages investigated in this study, therefore, the color coordinates of the devices were well within white range with increasing the bias voltage. The WOLED device with the CIE coordinate of (0.34, 0.34) showed the maximum luminance of 56,300 cd/m^2 and at the luminance of about 100 cd/m^2, η_{ext} and η_{PE} of the devices were 1.68% and 2.41 lm/W, respectively.

Acknowledgements

This work was supported by the National Research Laboratory Program (NRL) of the Ministry of Science and Technology and by the Ministry of Commerce, Industry and Energy (MOCIE).

References

[1] B.W. D'Andrade, S.R. Forrest, Adv. Mater. 16 (2004) 1585.
[2] C.W. Tang, S.A. Van Slyke, C.H. Chen, J. Appl. Phys. 65 (1989) 3610.
[3] J. Kido, W. Ikeda, M. Kimura, K. Nagai, Jpn. J. Appl. Phys. 35 (1996) L394.
[4] J. Kido, M. Kimura, K. Nagai, Science 267 (1995) 1332.
[5] R.H. Jordan, A. Dodabalapur, M. Strukelj, T.M. Miller, Appl. Phys. Lett. 68 (1996) 1192.
[6] R.S. Deshpande, V. Bulovic, S.R. Forrest, Appl. Phys. Lett. 75 (1999) 888.
[7] C.W. Ko, Y.T. Tao, Appl. Phys. Lett. 79 (2001) 4234.
[8] Z.Y. Zie, Y.Q. Li, J. Feng, J.S. Huang, Y. Wang, C.N. Li, S.Y. Liu, J.C. Shen, Synth. Metals 106 (1999) 71.
[9] M. Berggren, A. Dodabalapur, R.E. Slusher, Z. Bao, Nature 389 (1997) 466.
[10] J. Liu, Q. Zhou, Y. Cheng, Y. Geng, L. Wang, D. Ma, X. Jing, F. Wang, Adv. Mater. 17 (2005) 2974.
[11] H.S. Woo, S.J. Cho, T.W. Kwon, D.K. Park, J. Korean Phys. Soc. 46 (2005) 981.
[12] T. Mukaiyama, T. Sato, J. Hanna, Chem. Lett. 10 (1973) 1041.
[13] D.M. Roundhill, J.P. Fackler, Optoelectronic Properties of Inorganic Compounds, Plenum Press, 1999.
[14] M. Anni, G. Gigli, V. Paladini, R. Cingolani, G. Barbarella, L. Favaretto, G. Sotgiu, M. Zambianchi, Appl. Phys. Lett. 77 (2000) 2458.
[15] B.X. Mi, Z.Q. Gao, C.S. Lee, S.T. Lee, H.L. Kwong, N.B. Wong, Appl. Phys. Lett. 75 (1999) 4055.
[16] V. Bulovic, A. Shoustikov, M.A. Baldo, E. Bose, V.G. Kozlov, M.E. Thompson, S.R. Forrest, Chem. Phys. Lett. 287 (1998) 455.
[17] K.O. Cheon, J. Shinar, Appl. Phys. Lett. 81 (2002) 1738.
[18] C.H. Chen, C.W. Tang, Appl. Phys. Lett. 79 (2001) 3711.
[19] K. Yamashita, J. Futenma, T. Mori, T. Miutani, Synth. Metals 111–112 (2000) 87.
[20] J. Littman, P. Martic, J. Appl. Phys. 72 (1992) 1957.

Available online at www.sciencedirect.com
ScienceDirect
Organic Electronics 8 (2007) 690–694
Organic Electronics
www.elsevier.com/locate/orgel

Contact resistance between pentacene and indium–tin oxide (ITO) electrode with surface treatment

Dong-Jin Yun, Dong-Kyu Lee, Hwan-Ki Jeon, Shi-Woo Rhee *

Laboratory for Advanced Molecular Processing (LAMP), Department of Chemical Engineering, Pohang University of Science and Technology (POSTECH), San 31 Hyojadong, Namgu, Pohang 790-784, Republic of Korea

Received 10 December 2006; received in revised form 18 May 2007; accepted 26 May 2007
Available online 5 June 2007

Abstract

Contact resistance between indium–tin oxide (ITO) electrode and pentacene was studied by transmission line method (TLM). Organic solvent cleaned, inorganic alkali cleaned, and self-assembled monolayer (with OTS: octadecyltrichlorosilane) modified ITO electrode structures were compared. Pentacene layer of 300 Å thickness was vacuum deposited on patterned ITO layer at 70 °C with a deposition rate of 0.3 Å/s. Alkali cleaned and SAM modified ITO gave a lower contact resistance of about $6.34 \times 10^4\ \Omega\,cm^2$ and $1.88 \times 10^3\ \Omega\,cm^2$, respectively than organic solvent cleaned ITO of about $6.58 \times 10^5\ \Omega\,cm^2$. Especially with the SAM treatment, the work function of ITO increased closer to the highest occupied molecular orbital (HOMO) level of pentacene, which lowers the injection barrier between ITO and pentacene. It was also believed that pentacene morphology was improved on SAM modified ITO surface due to the lowering of the surface energy. We could obtain the low contact resistance with SAM treatment which is comparable to the measured value of gold–pentacene contact, $1.86 \times 10^3\ \Omega\,cm^2$. This specific contact resistance is still much higher than that of amorphous silicon thin film transistor ($0.1–30\ \Omega\,cm^2$).
© 2007 Elsevier B.V. All rights reserved.

PACS: 73.40.Cg; 72.80.Le; 82.45.Xy; 73.30.+y

Keywords: Contact resistance; Organic thin film transistor; Pentacene; Indium–tin oxide; Work function

1. Introduction

For organic thin film transistors (OTFT), research effort has been focused on improving electrical properties of the semiconductor as well as the gate dielectric and conducting electrodes. The mobility of OTFT with pentacene was improved up to 1.5 cm^2/Vs and on/off ratio was also improved up to 10^5 [1,2]. Despite the considerable progress made in recent years to improve the performance of organic TFTs, many of the design, material, and process parameters are still poorly understood and poorly controlled. One such part is contact resistance between metal electrode and organic semiconductor. With decreasing device dimensions, the contact resistance as a part of the total device resistance will dominate compared with channel resistance and therefore will play an important part

* Corresponding author. Tel.: +82 54 279 2265; fax: +82 54 279 8619.
E-mail address: srhee@postech.ac.kr (S.-W. Rhee).

1566-1199/$ - see front matter © 2007 Elsevier B.V. All rights reserved.
doi:10.1016/j.orgel.2007.05.006

in device operations. Unlike in field effect transistors based on single-crystalline silicon, polycrystalline silicon, or hydrogenated amorphous silicon, the source and drain contacts in organic TFTs are not easily optimized by conventional processes, such as semiconductor doping or metal alloying. Consequently, the speed of organic integrated circuits may be limited by the contact resistance, not by the intrinsic carrier mobility of the organic semiconductor. Interface properties between electrode and semiconductor are critical factors for good TFT performance and work function modification of the metal surface to lower the barrier and removal of impurities such as native oxide have been studied to lower the contact resistance [3,4]. As a contact metal, gold, silver, calcium and palladium [2,5–7] were studied. It has been known that gold has a work function of 5.1 eV, which is close to the HOMO (highest occupied molecular orbital) level of pentacene, 5.2 eV. Thus the hole injection barrier is expected to be low for gold with pentacene. To date, gold showed best result but the material may not be preferred in real application due to the cost and patterning problem. On the other hand, ITO (indium–tin oxide) is widely used as a transparent conducting material in optical devices like organic light emitting diode and solar cell [8]. In this case, the contact property of ITO with organic layer is also a major concern for efficient carrier injection [9]. As is shown in Figs. 3 and 4, ITO has a work function of 4.5–4.7 eV and the barrier for hole injection to pentacene is higher than gold. To improve contact properties between organic semiconductors and metal electrodes, modification of the drain and source contacts with conductive polymer or charge transfer compounds was proposed [9,10]. Reduction of energy barrier at the electrode interface can be achieved in different ways. One approach is to increase the electrode work function by grafting a self-assembled monolayer (SAM) of molecules that possess a permanent dipole moment onto the ITO surface [7,8]. Enhancement of the carrier injection and the luminescence efficiency in optical device by SAMs was studied [8].

In this work, we measured the contact resistance between ITO and pentacene with TLM (transmission line method) for the first time and compared with gold contact metal. We tried organic solvent cleaned, inorganic alkali cleaned, and self-assembled monolayer (with OTS: octadecyltrichlorosilane) modified ITO electrode structures.

2. Experimental

Octadecyltrichlorosilane (OTS) and pentacene were purchased from Aldrich Chemical Co. and ITO (In_2O_3:SnO_2 = 90:10 wt%) coated glass was supplied by Samsung Corning Co. We used two different sets of processing techniques for treating the surface of the ITO substrates, before the deposition of pentacene active layer by evaporation, wet cleaning and self-assembled monolayer (OTS) deposition. Before the ITO surface treatment, ITO was patterned with photolithography and etching as shown in Fig. 1, with length (d) of 0.1 cm and width of 0.7 cm. For wet cleaning, we adopted two different processes. One is the ultrasonic degreasing where the substrate was washed in an ultrasonic bath of acetone for 30 min, followed by the IPA (isopropyl alcohol) washing for 30 min at room temperature. The other one is washing in a solution of NH_4OH (70 wt%), H_2O_2 (30 wt%) and distilled water in a ratio of 1:4:20 (RCA cleaning SC-1). The substrate was first dipped into the solution at 60 °C for 30 min, and then rinsed twice in distilled water. In order to eliminate the traces of water, we then rinsed in IPA and all substrates were then dried in a flow of nitrogen.

The SAM modified ITO substrates were prepared by the immersion of ITO-glass substrates in octadecyltrichlorosilane (OTS) solutions (concentration of

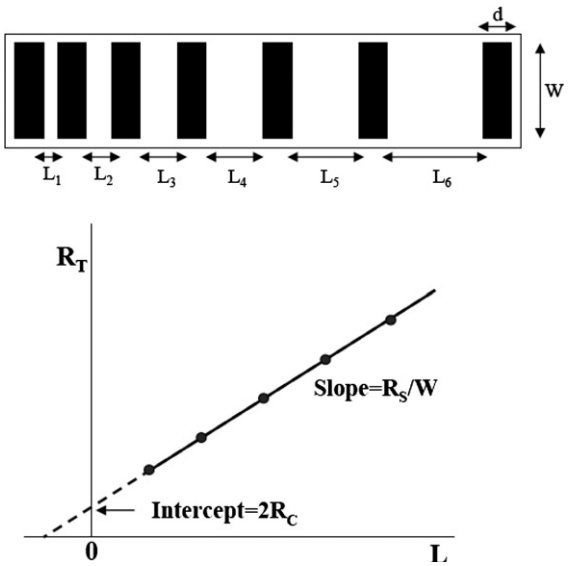


Fig. 1. Structure of ITO lines on glass substrate for the measurement of the contact resistance between ITO and pentacene with transmission line method (TLM).

0.02 mM), for 1.5 h. They were then washed with chloroform and ethanol and dried in a high purity argon filled glove box. To compare ITO electrodes with gold, we also made patterned gold substrates for TLM. Au/Ti (100 nm/3 nm) electrode (length (d): 0.1 cm, width (W): 0.25 cm) patterns with inter spacing of 55, 60, 65, 70, 75, 80 and 85 μm were made on a glass substrate using a shadow mask in an e-beam evaporator at room temperature. Ti layer was used as a glue layer to promote the adhesion of gold on glass. Pentacene film was deposited at 70 °C with a deposition rate of 0.3 Å/s in an organic molecular beam deposition system at 2×10^{-6} torr. 0.5 cm of total electrode width was covered with 300 Å thick pentacene film leaving 0.2 cm of ITO for probe contact. I–V measurement between adjacent ITO lines was done with E5270A (Agilent technology). We obtained the work function of ITO electrode by using ultraviolet photoelectron spectroscopy (UPS, Escalab 220IXL) with a He(I) emission of 21.2 eV. Surface energy was calculated from the contact angle measurement with water and diiodomethane droplets.

3. Results and discussion

The contact resistance between ITO electrode and pentacene was measured with transmission line method (TLM). The TLM pattern is shown in Fig. 1. Total resistance (R_T) as a function of the distance L between electrodes is

$$R_T = R_S \cdot L/W + 2R_C \quad (1)$$

where R_T is the total resistance between two contacts, R_C is the contact resistance, R_S is the sheet resistance of the pentacene layer, L is the electrode spacing, and W is the width of the electrode covered with pentacene (0.5 cm). Fig. 2 shows the total resistance measured as a function of the electrode spacing and from the half of the intercept value, the contact resistance (R_C) can be calculated. From the slope of the curve, R_S can be calculated. The specific contact resistance (ρ_C) can be calculated from [11,12]

$$\rho_C = \frac{R_C^2 W^2}{R_S}, \quad (2)$$

where R_C and R_S were determined from Eq. (1). Specific contact resistance is independent of the system geometry and this value can be compared for different materials used in thin film transistors.

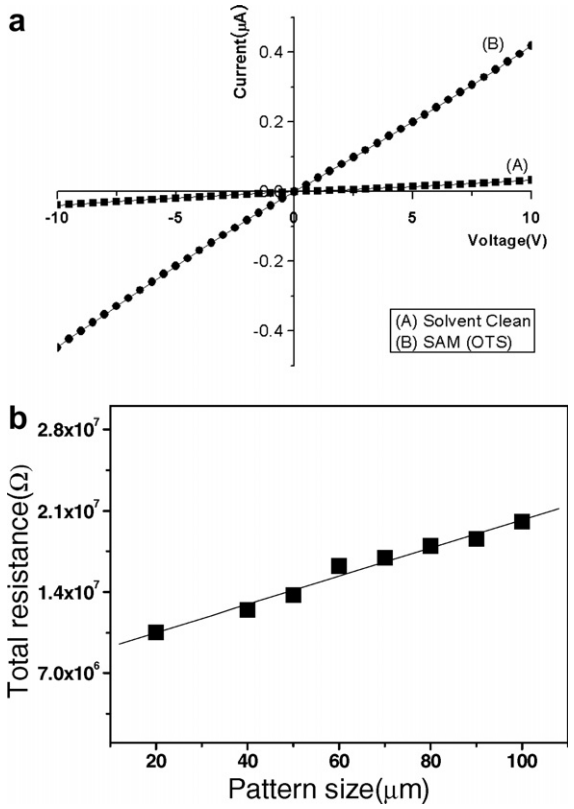


Fig. 2. (a) I–V curve graph of bare ITO and SAM treated ITO where spacing between electrodes is 20 μm and (b) plot of the total resistance (R_T) versus the spacing (L) measured with the transmission line method (TLM). ITO was covered with self-assembled monolayer of OTS (octadecyltrichlorosilane).

Measured value of contact resistance, sheet resistance of pentacene and specific contact resistance are summarized in Table 1. We used two wet cleaning methods for surface treatment of ITO. Organic solvent cleaned ITO showed contact resistance of $1.32 \times 10^9\ \Omega$ and RCA cleaned ITO showed $9.34 \times 10^8\ \Omega$. Sheet resistance of pentacene does not change appreciably for different growth surfaces. Specific contact resistance calculated from Eq. (2) was 6.58×10^5 and $6.34 \times 10^4\ \Omega\,cm^2$ for organic solvent cleaned and RCA cleaned ITO, respectively. Organic solvent cleaning method could only eliminate organic contaminants from ITO surface and RCA cleaning method could remove metallic impurity. RCA cleaning gave lower resistance than simple organic cleaning. SAM modified ITO gave the lowest specific contact resistance of $1.88 \times 10^3\ \Omega\,cm^2$ which is comparable to the contact resistance of gold and pentacene of $1.86 \times 10^3\ \Omega\,cm^2$. The SAM on the ITO enhances the hole injection abilities of this electrode by increasing the

Table 1
Sheet resistance of pentacene and contact resistance and specific contact resistance measured with transmission line method for the pentacene film deposited on various ITO surfaces

Surface treatment	Contact resistance (Ω)	Sheet resistance R_S (Ω/□)	Specific contact resistance ρ_C (Ω cm^2)
Organic cleaning	2.04×10^8	1.58×10^{10}	6.58×10^5
RCA cleaning	5.48×10^7	1.18×10^{10}	6.34×10^4
SAM (OTS)	1.10×10^7	1.60×10^{10}	1.88×10^3
Au (no cleaning)	2.21×10^7	1.64×10^{10}	1.86×10^3

Deposition temperature was at 70 °C and deposition rate was 0.3 Å/s.

work function [13] and hence reducing the resistance between ITO and pentacene. Also the growth of pentacene on low energy surface is more favorable for the property of the active layer. Other advantages are the increased adhesion between the ITO and organic layers due to the addition of the SAM [14]. Also there are less adsorbed molecules on the surface of the ITO (e.g. oxygen, water, hydrocarbons) as they are competing with SAM. Table 2 shows the contact angle and surface energy for bare ITO and OTS deposited ITO substrates. The contact angles were measured by the KRUSS drop shape analysis system DSA 10 Mkz with sessile drop measurement. The measurements were repeated more than 10 times for each surface and their average values were recorded. DI-water contact angles of the bare ITO and SAM treated ITO substrate were 48° and 104°, respectively, which indicates that surface energy of the substrate can be obviously reduced when OTS SAM was coated. Surface energy can be calculated from the relationship between the contact angles of deionized water and diiodomethane droplets using Fowkes method [15]. The pentacene molecule grown on substrate with low surface energy tends to align vertically, which leads to the higher mobility and increase in the grain size on the ITO electrode [16]. Several studies have demonstrated that trap density is lower and performance is significantly increased when pentacene has a large grain size with little grain boundaries which form trapping sites [17]. The vertical alignment of pentacene with increased grain size on ITO electrode seems to lower the contact resistance between ITO and pentacene.

Table 2
Contact angle and surface energy of bare ITO and SAM treated ITO

Surface treatment	DI-Water (°)	Diiodomethane (°)	Surface energy (mJ/m^2)
No cleaning	48	33	54.728
SAM (OTS)	104	60	29.343

Source/drain electrode with work function close to the HOMO level of the p-type semiconductor can form ohmic contact with low barrier. In this case, there is a possibility that a low contact resistance can be obtained [18]. As shown in Fig. 3a, ITO makes ohmic contact to pentacene even though there is a schottky barrier in the interface between ITO and pentacene. Because of schottky barrier,

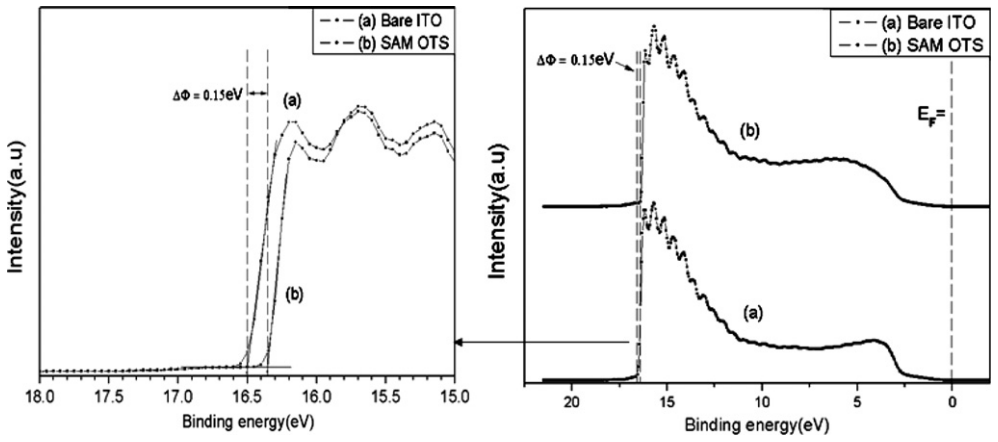


Fig. 3. UPS spectra of (a) bare ITO and (b) ITO with self-assembled monolayer of OTS (octadecyltrichlorosilane).

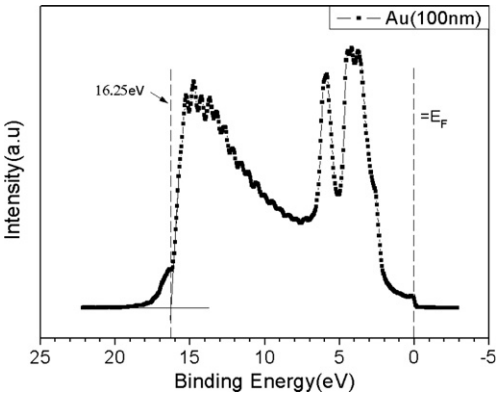


Fig. 4. UPS spectra of gold (Au).

contact resistance of as-deposited ITO has a high value of $\sim 10^5\ \Omega\,cm^2$. Schottky barrier could be lowered by the work function increase with SAM treatment. Fig. 3b shows UPS of bare ITO and OTS treated ITO and Fig. 4 shows UPS of bare Gold. The work function of each surface can be estimated by calculating the UPS spectra width [19]. The work function of bare ITO is known to be 4.7 eV [20]. From UPS measurement, the work function of the bare ITO was 4.7 eV, and SAM treated ITO was 4.85 eV. The dipole moment of the SAM material increased the work function of ITO closer to the HOMO level of pentacene (5.2 eV) and the work function of gold (4.95 eV). The work function increase with insertion of self-assembled monolayer could lower the contact resistance as confirmed from the measurement.

4. Conclusion

We measured the contact resistance between ITO and pentacene with transmission line method (TLM). ITO (indium–tin oxide) surface was wet cleaned with organic solvent or alkali solution. Self-assembled monolayer (SAM) modified ITO surface was also tried. Organic cleaning had negligible effect on the reduction of the contact resistance but alkali cleaning could reduce the resistance. SAM modified ITO gave the lowest specific contact resistance of $1.88 \times 10^3\ \Omega\,cm^2$ which is comparable to the contact resistance of gold and pentacene of $1.86 \times 10^3\ \Omega\,cm^2$. SAM on ITO surface lowered the surface energy of ITO substrate which can improve pentacene morphology grown on it. Also the energy barrier between ITO and pentacene was lowered due to the work function increase with SAM on ITO. The contact resistance of ITO and pentacene or gold and pentacene is still very high compared to amorphous silicon TFT of about 0.1 to $30\ \Omega\,cm^2$ [17] and much effort is needed in this regard.

Acknowledgements

This research was supported by the Korea Science and Engineering Foundation (KOSEF) through the National Research Laboratory Project.

References

[1] B.C. Shekar, J. Lee, S.W. Rhee, Kor. J. Chem. Eng. 21 (2004) 267.
[2] G. Horowitz, J. Mater. Res. 19 (2004) 1946.
[3] H.H. Busta, J.E. Pogemiller, R.W. Standley, K.D. Mackenzie, IEEE Trans. Electro. Dev. 36 (1989) 2883.
[4] H.F. Bare, G.W. Neudeck, IEEE Electro. Dev. Lett. 7 (1986) 431.
[5] J.M. Beebe, V.B. Engelkes, L.L. Miller, C.D. Frisbie, J. Am. Chem. Soc. 124 (2002) 11268.
[6] P.V. Pesavento, R.J. Chesterfield, C.R. Newman, C.D. Frisbie, J. Appl. Phys. 96 (2004) 7312.
[7] P.V. Necliudov, M.S. Shur, D.J. Gundlach, T.N. Jackson, Solid-State Electro. 47 (2003) 259.
[8] L. Zhu, H. Tang, Y. Harima, K. Yamashita, Y. Aso, T. Otsubo, J. Mater. Chem. 12 (2002) 2250.
[9] J. Morgado, N. Barbagallo, A. Charas, M. Matos, L. Alcacer, F. Cacialli, J. Phys. D: Appl. Phys. 36 (2003) 434.
[10] I.H. Campbell, J.D. Kress, R.L. Martin, D.L. Smith, N.N. Barashkov, J.P. Feraris, Appl. Phys. Lett. 71 (1997) 3528.
[11] M. Obata, T. Sakuda, K. Abe, R. Hayashibe, K. Kamimura, Surf. Coat. Technol. 180 (2004) 136.
[12] S. Oussalah, B. Djezzar, R. Jeisian, Solid-State Electro. 49 (2005) 1617.
[13] C. Ganzorig, K.J. Kwak, K. Yagi, M. Fujihira, Appl. Phys. Lett. 79 (2001) 272.
[14] B. Tao, C. Xian-Hua, Wear 261 (2006) 730.
[15] A.J. Kinloch, Adhesion and Adhesives, Chapman and Hall, London, 1987, p. 29.
[16] S.Y. Yang, K.W. Shin, C.E. Park, Adv. Funct. Mater. 15 (2005) 1806.
[17] I. Kymissis, IEEE Trans. Electro. Dev. 48 (2001) 1060.
[18] P.C. Rusu, G. Brocks, Phys. Rev. B 74 (2006) 073414.
[19] D. Cahen, A. Kahn, Adv. Mater. 15 (2003) 271.
[20] C.R. Kagan, P. Andry, Thin Film Transistors, Marcel Dekker, New York, 2003 (Chapter 3).

Available online at www.sciencedirect.com
ScienceDirect
Organic Electronics 8 (2007) 695–701
Organic Electronics
www.elsevier.com/locate/orgel

Magnetic field release of trapped charges in poly(fluorenylenevinylene)s

Michelle S. Meruvia [a], José A. Freire [a], Ivo A. Hümmelgen [a,*], Jonas Gruber [b], Carlos F.O. Graeff [c]

[a] *Group of Organic Optoelectronic Devices, Departamento de Física, Universidade Federal do Paraná, Caixa Postal 19044, 81531-990 Curitiba-PR, Brazil*
[b] *Instituto de Química, Universidade de São Paulo, Caixa Postal 26077, 05513-970 São Paulo-SP, Brazil*
[c] *Departamento de Física, FC, Universidade Estadual Paulista, 17033-360 Bauru-SP, Brazil*

Received 30 January 2007; received in revised form 23 April 2007; accepted 26 May 2007
Available online 16 June 2007

Abstract

We have measured the effect of an applied magnetic field on the current through thin films of two different organic conjugated polymers that have previously shown to exhibit magnetoresistance, poly(9,9-dioctyl-1,4-fluorenylenevinylene) and poly(9,9-dioctyl-2,7-fluorenylenevinylene). The results show that the magnetic field releases trapped charges from inside the material and enhances the current. We have also performed optical absorption experiments on these polymer films under applied voltage and magnetic field. The results show that the magnetic field produces a change in the optical absorption in the low-energy range associated with deep traps and only under conditions when these traps are likely charged. These two results provide a strong case for the release of trapped charges caused by the magnetic field as being the cause of the magnetoresistance in these polymers and possibly in other organic materials where magnetoresistance was recently observed.
© 2007 Elsevier B.V. All rights reserved.

PACS: 72.80.Le; 81.05.Lg; 85.70.Kh

Keywords: Magnetoresistance; Conjugated polymers; Aggregates

The use of organic conjugated materials in electronic or optoelectronic devices have been firmly established in recent years. There are now numerous examples of their use in light emitting diodes [1–3], transistors [4–7], photovoltaic cells [8–10] and memory devices [11–13]. To extend this range of applications it would be interesting to have magnetic field control of the transport properties of these materials. This perspective seemed a little dim for the materials commonly used in the above mentioned applications because these are free of magnetic atoms and no mechanism has been presented so far whereby the magnetic field could have a marked influence in their transport properties. It came as a

* Corresponding author. Tel./fax: +55 41 33613645.
E-mail address: iah@fisica.ufpr.br (I.A. Hümmelgen).

1566-1199/$ - see front matter © 2007 Elsevier B.V. All rights reserved.
doi:10.1016/j.orgel.2007.05.007

grateful surprise the report of a measurable magnetoresistance (MR) in (non-magnetic) metal–organic material–metal sandwich structures and on organic material based transistors. Some of the reported MR being as high as 100% for a field of 200 mT [14].

Besides the technological appeal of these results is the basic scientific question: what effect can a magnetic field of the order of 100 mT have on the transport properties of a non-magnetic, disordered, conjugated material sandwiched between two non-magnetic metallic electrodes? Here we report two experiments aimed at answering this question and argue that our results point toward the release of trapped charges induced by the magnetic field as the cause of the observed magnetoresistance. This mechanism for MR is probably unique to disordered organic materials and is related to the presence of aggregates embedded in an amorphous matrix.

MR of both signs have been observed in π-conjugated polymers [14–18] and in small molecular weight conjugated molecules [19,20] using either a simple metal/organic/metal sandwich device or a transistor geometry, with the organic material as the emitter and p-type silicon and tin as the collector and base, respectively. In Ref. [16], where some of the results were gathered and summarized, it was suggested that the MR in all these materials might share a common origin due to the observed universality of the (normalized) $\Delta R/R$ versus B curves. The experiments discussed in Ref. [16] also indicated that the cause of the phenomena was very likely not linked to: electronic spin, electrodes, impurities or excitonic recombination effects.

In Refs. [18,20] some points in favor and against the excitonic mechanism were further discussed and in Ref. [21] a spin–orbit coupling mechanism was discussed.

The present paper adds important experimental information to the ongoing discussion on the origin of the MR effect in conjugated systems. We selected two conjugated polymers that have previously shown to exhibit negative MR, poly(9,9-dioctyl-1,4-fluorenylenevinylene), PDO14FV, and, poly(9,9-dioctyl-2,7-fluorenylenevinylene), PDO27FV. These polymers (see the structures in Fig. 1) were synthesized following procedures already published [22,23].

We devised a transport experiment and an optical absorption experiment which helps to understand the origin of the MR in these polymers. Both experiments involved the combined application of voltage and magnetic field in a setup shown

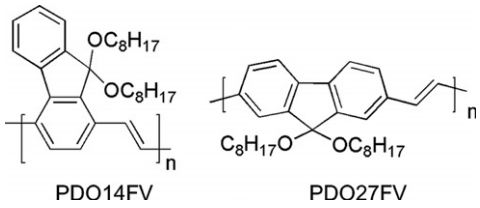


Fig. 1. Molecular structure of poly(9,9-dioctyl-1,4-fluorenylenevinylene), PDO14FV, and poly(9,9-dioctyl-2,7-fluorenylenevinylene), PDO27FV.

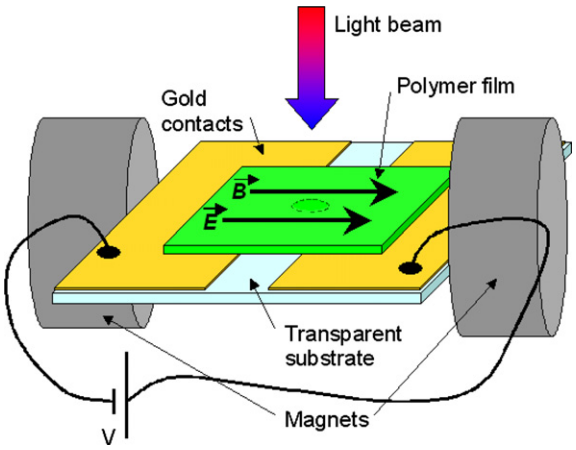


Fig. 2. Experimental setup used for both transport and absorption spectroscopy measurements.

in Fig. 2. Two Au-contacts were deposited on top of an 18 mm by 18 mm glass substrate by evaporation at 10^{-6} torr, the gap between the contacts was 3 mm. The polymer film, either PDO14FV or PDO27FV, was deposited on top of the contacts by spin-coating, using a 5 mg/ml solution in $CHCl_3$. A pair of removable permanent magnets provided the source of the magnetic field. Using a Hall probe, the magnetic field strength in the polymer region was measured to be 50 mT. Although the sample geometry used may not be optimal for transport measurements in low charge carrier mobility materials due to the large gap between the contacts, it allows simultaneous optical and transport measurements to be made in the presence of a magnetic field.

In the first experiment we wanted to observe the transient current response to a sudden change in the magnetic field. First the voltage was turned on and off at different times then the magnetic field was applied and removed. The transient current signal, see Fig. 3a, shows that the current response to the turning on of the magnetic field is much slower that the current response to its turning off. The MR reports so far have concentrated on the steady state

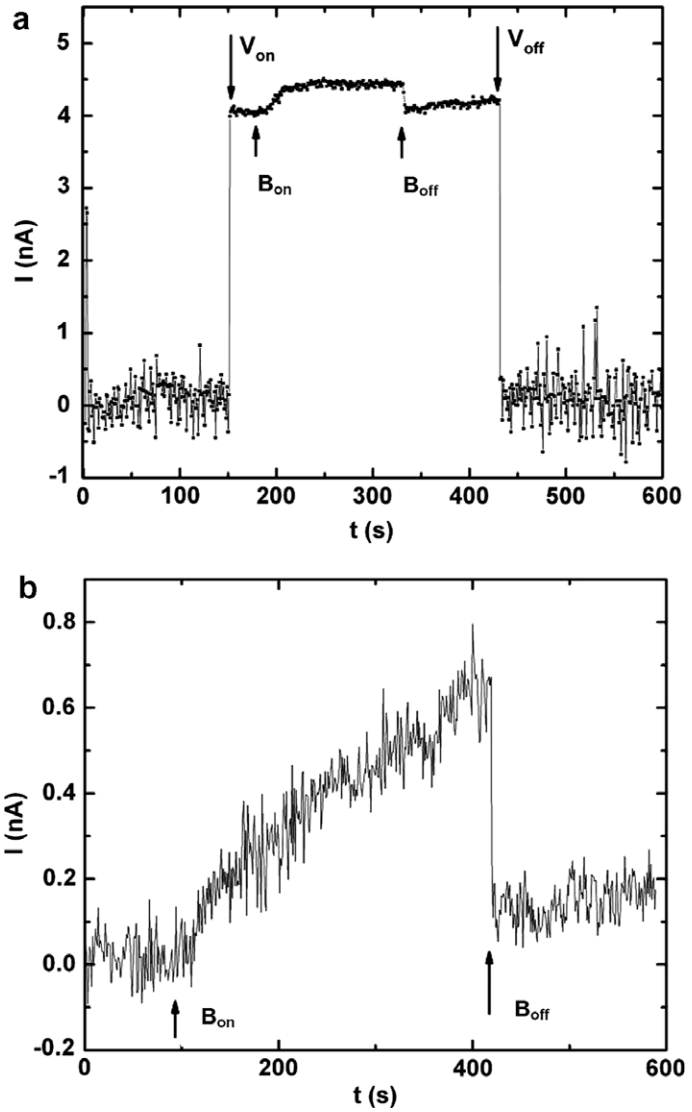


Fig. 3. (a) Time-dependence of the current when the voltage, 10 V, is switched on (V_{on}) and off (V_{off}). During the period of application of the voltage, the magnetic field of 50 mT, was applied (B_{on}) and removed (B_{off}); (b) time-dependent current in a sample that was submitted to 50 V during 10 min. before starting the measurement. At $t = 0$ the voltage was switched off. The magnetic field of 50 mT was applied (B_{on}) and removed (B_{off}) at the times indicated.

current change with the magnetic field, ignoring the important information contained in the transient current. In Fig. 3b the sample was submitted to a bias of 50 V for 10 min before starting the current measurement. At $t = 0$ the voltage was switched off and the magnetic field was applied at $t \sim 100$ s and removed at $t \sim 400$ s. Even in the absence of an applied voltage, the presence of a magnetic field gives rise to a current signal. Again, the current response to the turning on of the magnetic field is slower than the response to its turning off. If the voltage is not applied at $t < 0$ the effect cannot be observed. Various questions can be raised from this last result: (i) what is the role of the applied voltage at $t < 0$?, (ii) if there is no applied voltage at $t > 0$, how can there be current through the sample when just the magnetic field is applied? (iii) what is the magnetic field effect on the carriers? Some possible answers can be provided: (i) the previously applied voltage has charged some deep traps in the system and the result shown in Fig. 3b is the effect of the magnetic field on these trapped charges, (ii) the previously applied voltage created a non-uniform space charge distribution inside the sample and a built-in

voltage is present at $t > 0$, (iii) the applied magnetic field promoted the release of trapped charges in the system and these charges, driven by the built-in voltage, are the ones responsible for the observed current.

The range of voltage values used corresponds to low electric field strengths only if the rigid band approximation is assumed. In the case of a semiconductor with traps, the possibility of formation of depletion layers close to the interfaces and other space charge effects in the bulk, must be considered. These charge accumulations cause the electric field to be non-uniform and to attain very high values at some points inside the sample, particularly in the vicinity of the electrodes. Considering this we avoided higher voltages in order to minimize the risk of breakdown and/or electromigration and consequently, sample degradation. Further, constraints for high voltages were imposed by the experimental setup.

It is worth mentioning that the excitonic-hyperfine mechanism proposed for the MR [18,20] would have difficulties in explaining this current rise at zero applied voltage given that this mechanism depends on electron and holes being injected from the electrodes to explain the magnetic field effect on the current.

The conclusion to be drawn from Fig. 3b is that the rise in the current is due to trapped charges being released from inside the sample by the magnetic field. It is not unreasonable to suppose that the current increase seen in Fig. 3a, and hence the MR in the polymers studied here, is also due to the same effect.

In addition to these transport measurements, an optical absorption experiment was carried out and provided further evidence that trapped charges are indeed affected by the magnetic field. The results reported below correspond to a PDO14FV sample of thickness 350 nm and a PDO27FV sample of thickness 708 nm. The thicknesses were determined using a surface profiler. Qualitatively similar results were also observed for samples of different thicknesses. The samples together with the removable magnet (~50 mT) were fitted inside a UV/Vis spectrometer. The Au-contacts were connected to a voltage source allowing the spectroscopic measurements to be carried out simultaneously with an applied voltage, in the presence or absence of a magnetic field. The measurements could be performed without changing the position of the sample inside the spectrometer, so as to avoid spectral variations due to a change in the sample region being probed.

We have measured the absorption spectra of PDO14FV and PDO27FV samples under different conditions: (i) without applied voltage ($V = 0$) and without applied magnetic field ($B = 0$); (ii) with $V = 0$ and $B \neq 0$; (iii) with $V \neq 0$, $B = 0$; (iv) simultaneously $V \neq 0$ and $B \neq 0$; (v) $V \neq 0$ immediately before recording the spectrum with $B \neq 0$ and $V = 0$; and (vi) $B \neq 0$ immediately before recording the spectrum with $V \neq 0$ and $B = 0$. We observed changes in the absorption spectrum only in the cases (iv) and (v) above, namely, when V and B are simultaneously applied during spectral measurement and when the spectral measurements are performed at $B \neq 0$ and $V = 0$, but in samples submitted to $V \neq 0$ immediately before the spectral measurements. Additionally, to exclude all possibilities of spurious effects, we measured the spectra of samples with the substrate and Au-contacts, but without the polymer film, under all conditions listed above. Fig. 4 presents the absorbance data of the PDO27FV (Fig. 4a) and PDO14FV (Fig. 4b) samples as prepared ($V \neq 0$ and $B = 0$) and the absorbance variation observed upon simultaneous application of the electric and magnetic fields ($V \neq 0$ and $B \neq 0$). A small, but well-defined and reproducible reduction in the absorption could be observed in both samples in the spectral region of the low-energy absorption edge.

The low-energy absorption edge corresponds to the lowest energetic transitions allowed in these polymers, which involve high lying highest occupied molecular orbital (HOMO) levels and low lying lowest unoccupied molecular orbital (LUMO) levels. These energy levels are usually associated with aggregates [24], regions of sub-micron size where some degree of morphological order is achieved as a result of chain–chain interaction. These aggregates are surrounded by amorphous polymer and act as deep trapping centers for both holes and electrons, they are present in a wide variety of organic systems [24].

The decrease in absorbance caused by the magnetic field only occurs when these aggregates are charged. The conclusion to be drawn from this experiment is that the magnetic field has a direct influence on the excitation energy of charged aggregates. Both this effect and the release of trapped charges seen in the transport experiment have in common that they both involve the effect of a 50 mT magnetic field on charged aggregates.

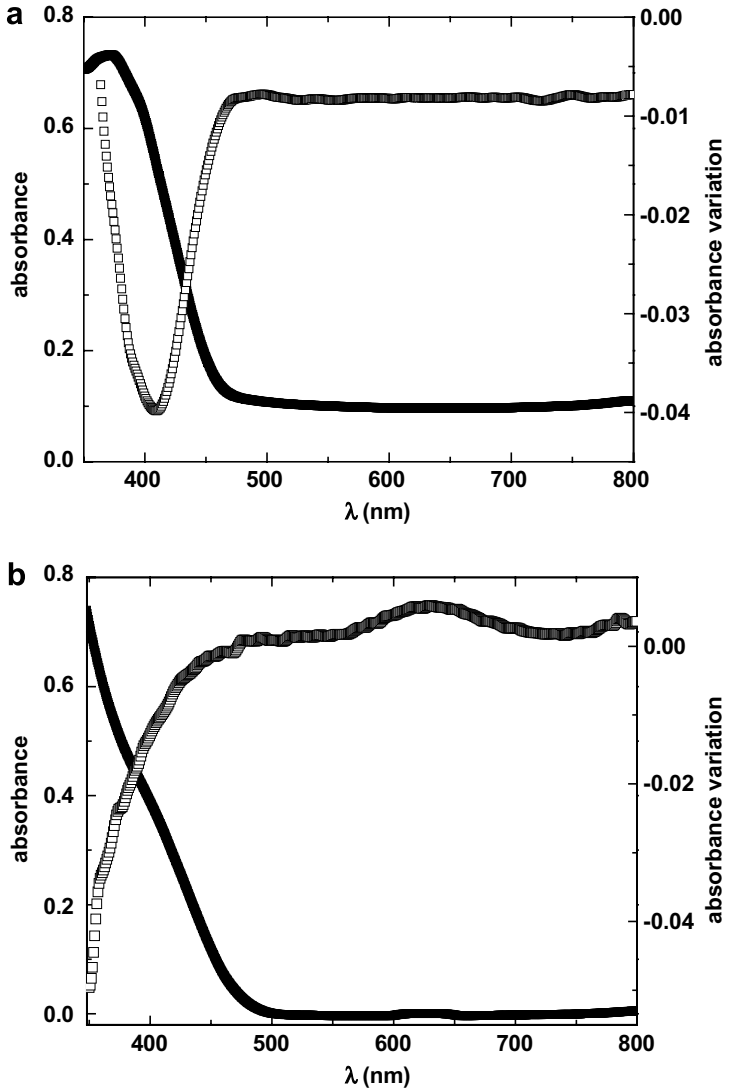


Fig. 4. (a) Absorption spectrum of a 708 nm thick film of PDO27FV (full symbols) and the observed variation after simultaneous application of $V = 5$ V and $B = 50$ mT (open symbols); (b) absorption spectrum of a 350 nm thick film of PDO14FV (full symbols) and the observed variation after simultaneous application of $V = 5$ V and $B = 50$ mT (open symbols).

In search for the physical mechanism behind the magnetic field effect on charged aggregates we begin by noting the energy scale associated with a 50 mT magnetic field. The cyclotron energy, $\hbar eB/m_e$, is 6×10^{-6} eV if one uses the bare electron mass, ignoring the fact that inside the aggregate the effective mass is probably larger than m_e. This is the order of magnitude of the energy shift promoted by the field on single-particle energy levels. Clearly this cannot account for the release of trapped charges or for the change in absorbance. To explain the trapped charge release one would need a shift of the order of $kT \sim 25$ meV, because such an energy shift would produce a significant change in the thermal hopping rate from the trap to the amorphous region. Next we note that the magnetic length associated with this field, $l_B = \sqrt{\hbar/eB}$, is 115 nm. Any quantum state of dimensions larger than l_B will shrink in the direction perpendicular to the field in an effect well-known in the physics of doped semiconductors [25]. If the aggregates in our samples have sizes ranging from 100 nm to 400 nm, like the ones reported in Ref. [24], their quantum states are likely affected by the field. However, the energy

argument still holds and, if one ignores electron–electron repulsion inside the aggregate, the energy shifts will still be of the order of 10^{-6} eV. However, it is not a good approximation to neglect the electronic repulsion inside the aggregates given that they are charged when both transport and absorbance experiments display the magnetic field effect. The order of magnitude of the Coulomb energy of an aggregate of linear dimension L is e^2/L, using $L \sim 200$ nm we obtain $e^2/L \sim 7.2$ meV. This suggests that a magnetic field as low as 50 mT can affect the Coulomb energy inside charged aggregates and produce an energy shift in the meV range. One may worry that the strength of the Coulomb repulsion renders the aggregate wave-functions incompressible for a magnetic field of 50 mT, the wave-functions would simply deform themselves so as to minimize the gain in energy. However, the linear combination of quasi one-dimensional electronic wave-functions found in conjugated materials do not have much room to accommodate themselves in, therefore, we suggest that the nature of the electronic states found in conjugated materials may be crucial for the proposed mechanism to work. Needless to say, only an electronic structure calculation can validate the proposed mechanism.

The energy barrier for a hop from an aggregate with N carriers to the neutral amorphous region is $\Delta E = [E_{ag}(N-1) + E_{am}(1)] - [E_{ag}(N) + E_{am}(0)]$, where $E_{ag(am)}(N)$ is the total energy of the aggregate (amorphous) region with N carriers. Assuming that the energy of the amorphous region does not change with the field, one must have an increase in the charging energy of the aggregate, $E_{ag}(N) - E_{ag}(N-1)$, with the field in order to have the barrier reduced and the charge released. Note that the charging energy scales with N. Given the energy scale of the Coulomb energy and the fact that the aggregates may contain quite a few elementary charges, it is not unreasonable to expect that the shrinkage of the aggregate wave-functions caused by the magnetic field may cause the charging energy to change by a few tens of meV. The decrease in the barrier for hopping out of the aggregate due to the magnetic field could explain our transport experiment results. The slow increase of the current due to the turning on of the magnetic field and the fast decrease due to the turning off implies that the charge detrapping happens slower than the charge retrapping. The absorbance reduction could be due to a decrease in the amount of charge per aggregate and/or due to a direct change in the charged aggregate excitation energy.

The above mentioned shrinkage of the electronic wave-functions is well understood in the case of the hydrogenic-like states [25], the situation in an anisotropic aggregate is more involved. The effect of the magnetic field on the Coulomb repulsion will depend on the aggregate charge, shape, orientation relative to the field and degree of order. It is not unconceivable that one may find cases where instead of an increase in the Coulomb repulsion one finds a decrease, this would be important to test the applicability of this mechanism to other organic systems where a positive MR was observed. We are in urgent need of an electronic structure calculation of a model charged aggregate subjected to a magnetic field.

In brief we have obtained two experimental evidences that the magnetic field affects the energy of charged trapping centers in the polymers PDO14FV and PDO27FV. The transport experiment showed that the field releases trapped charges from inside the polymers and the optical absorption experiment showed a distinct decrease in the absorbance in the low-energy range associated with deep traps and only under conditions when these traps are likely charged. We suggested a scenario for the MR in these materials whereby the magnetic field modifies the energy of the many-body state of the charged aggregates causing an alteration in the balance between the trapping and detrapping of charges. This scenario may well be applicable to the MR observed in other conjugated systems given that the presence of aggregates is rather common in disordered organic systems. Since aggregate dimensions and distribution depends on material, substrate and preparation process, the proposed mechanism helps to understand the dispersion of MR values reported so far in the literature. An independent verification of the existence of aggregates in samples where MR is measured is a necessary step to check the validity of this scenario.

Acknowledgements

The authors would like to thank the Brazilian agencies CNPq, FAPESP, IM^{2}C and Renami for research grants.

References

[1] C.W. Tang, S.A. Vanslyke, Appl. Phys. Lett. 51 (1987) 913.

[2] R.H. Friend, R.W. Gymer, A.B. Holmes, J.H. Burroughes, R.N. Marks, C. Taliani, D.D.C. Bradley, D.A.D. Santos, J.L. Brédas, M. Löglund, Nature 397 (1999) 121.
[3] S.R. Forrest, Nature 428 (2004) 911.
[4] D.J. Gundlach, Y.Y. Lin, T.N. Jackson, S.F. Nelson, D.G. Schlom, IEEE Electron Device Lett. 18 (1997) 87.
[5] H. Sirringhaus, P.J. Brown, R.H. Friend, M.M. Nielsen, K. Bechgaard, B.M.W. Langeveld-Voss, A.J.H. Spiering, R.A.J. Janssen, E.W. Meijer, P. Herwig, D.M. de Leeuw, Nature 401 (1999) 685.
[6] M. Shtein, J. Mapel, J.B. Benziger, S.R. Forrest, Appl. Phys. Lett. 81 (2002) 268.
[7] C.D. Dimitrakopoulos, P.R.L. Malenfant, Adv. Mater. 14 (2002) 99.
[8] M. Granstrom, K. Petritsch, A.C. Arias, A. Lux, M.R. Andersson, R.H. Friend, Nature 395 (1998) 257.
[9] C.J. Brabec, N.S. Sariciftci, J.C. Hummelen, Adv. Funct. Mater. 11 (2001) 15.
[10] P. Peumans, S. Uchida, S.R. Forrest, Nature 425 (2003) 158.
[11] D. Ma, M. Aguiar, J.A. Freire, I.A. Hümmelgen, Adv. Mater. 12 (2000) 1063.
[12] D.M. Taylor, C.A. Mills, J. Appl. Phys. 90 (2001) 306.
[13] M. Mushrush, A. Facchetti, M. Lefenfeld, H.E. Katz, T.J. Marks, J. Am. Chem. Soc. 125 (2003) 9414.
[14] M.S. Meruvia, A.R.V. Benvenho, I.A. Hümmelgen, R.W.C. Li, L.H.J.M.C. Aguiar, J. Gruber, Solid State Commun. 139 (2006) 27.
[15] T.L. Francis, Ö. Mermer, G. Veeraraghavan, M. Wohlgenannt, New J. Phys. 6 (2004) 185.
[16] Ö. Mermer, G. Veeraraghavan, T.L. Francis, Y. Sheng, D.T. Nguyen, M. Wohlgenannt, A. Köhler, M.K. Al-Suti, M.S. Khan, Phys. Rev. B 72 (2005) 205202.
[17] M.S. Meruvia, A.R.V. Benvenho, I.A. Hümmelgen, J.A. Gómez, C.F.O. Graeff, R.W.C. Li, L.H.J.M.C. Aguiar, J. Gruber, Phys. Stat. Sol. A 202 (2005) R158.
[18] Y. Sheng, T.D. Nguyen, G. Veeraraghavan, Ö. Mermer, M. Wohlgenannt, S. Qiu, U. Scherf, Phys. Rev. B 74 (2006) 045213.
[19] Ö. Mermer, G. Veeraraghavan, T.L. Francis, M. Wohlgenannt, Solid State Commun. 134 (2005) 631.
[20] V.N. Prigodin, J.D. Bergeson, D.M. Lincoln, A.J. Epstein, Synth. Met. 156 (2006) 757.
[21] Y. Sheng, D.T. Nguyen, G. Veeraraghavan, Ö. Mermer, M. Wohlgenannt, Phys. Rev. B 75 (2007) 035202.
[22] J. Gruber, R.W.C. Li, L.H.J.M.C. Aguiar, A.R.V. Benvenho, R. Lessmann, I.A. Hümmelgen, J. Mater. Chem. 15 (2005) 517.
[23] J. Gruber, R.W.C. Li, L.H.J.M.C. Aguiar, T.L. Garcia, H.P.M. de Oliveira, T.D.Z. Atvars, A.F. Nogueira, Synth. Met. 156 (2006) 104.
[24] B.J. Schwartz, Annu. Rev. Phys. Chem. 54 (2003) 141.
[25] B.I. Shklovskii, A.L. Efros, in: Electronic Properties of Doped Semiconductors, Springer-Verlag, Berlin, 1984.

Available online at www.sciencedirect.com
ScienceDirect
Organic Electronics 8 (2007) 702–708
Organic Electronics
www.elsevier.com/locate/orgel

Control of molecular orientation of organic p–i–n structures by using molecular templating effect at heterointerfaces

Takeaki Sakurai [a,*], Ryosuke Fukasawa [a], Kazuhiro Saito [b], Katsuhiro Akimoto [a]

[a] *Institute of Applied Physics, University of Tsukuba, 1-1-1 Tennodai, Tsukuba, Ibaraki 305-8573, Japan*
[b] *Research Center for Photovoltaics, National Institute of Advanced Industrial Science and Technology (AIST), Central 2, 1-1-1 Umezono, Tsukuba, Ibaraki 305-8568, Japan*

Received 31 March 2006; received in revised form 12 April 2007; accepted 12 June 2007
Available online 23 June 2007

Abstract

Structural control of the organic intrinsic layer (i-layer), which consists of a mixture of p- and n-type organic semiconductor materials, and the organic p–i–n triple-layer structure has been investigated. Significant modification of these structures, which used metal-free phthalocyanine (H_2Pc) and 3,4,9,10-perylene tetracarboxylic dianhydride (PTCDA) as the p- and n-type materials, respectively, was observed by introducing a modification layer deposited on a glass substrate. The orientation of the molecular planes of both H_2Pc and PTCDA in the i-layer (H_2Pc:PTCDA mixture) and p–i–n structure (H_2Pc/i-layer/PTCDA) formed onto a PTCDA modification layer was parallel to the substrate surface. On the other hand, when H_2Pc was used as the modification layer, the orientation of the molecular planes in the i-layer was found to be random. These results indicate that the internal structure of the organic mixed-layer is strongly affected by the organic layer-substrate interface. The enhancement in optical absorption observed for the orientation controlled p–i–n structure suggests the importance of the control of molecular orientation for improving the optical properties in organic device structures.
© 2007 Elsevier B.V. All rights reserved.

PACS: 61.10.Nz; 68.65.Ac; 78.66.Qn; 81.15.Ef

Keywords: Molecular orientation; Template layer; Crystal growth; Organic p–i–n structure

1. Introduction

The device efficiency of organic photovoltaic (PV) cells has drastically improved in the past 10 years due to improvements in the materials and device structures [1,2]. In particular, organic p–i–n structures, which contain an intrinsic layer (i-layer) between p- and n-type layers, have significantly contributed to the progress of organic PV cells due to the high density of the p/n interface at which the carrier generation resulting from exciton decomposition proceeds smoothly [3,4]. However, the i-layer, which consists of a mixture of p- (donor) and n-type (acceptor) organic semiconductor materials, has a high electric resistance because of its random and disordered structure [5]. It has been reported that the nanostructures in the i-layer can be controlled by heat treatment for improving the efficiency of

* Corresponding author. Tel.: +81 29 853 6150; fax: +81 29 853 5205.
E-mail address: sakurai@bk.tsukuba.ac.jp (T. Sakurai).

1566-1199/$ - see front matter © 2007 Elsevier B.V. All rights reserved.
doi:10.1016/j.orgel.2007.06.004

PV cells [6]. Therefore, it is very important to control the internal structure of the i-layer in order to obtain organic PV cells with high device efficiency.

Recently, Heutz and coworkers reported the effect of the surface modification of a glass substrate on the molecular orientation of metal-free phthalocyanine (H_2Pc) films by using a 3,4,9,10-perylene tetracarboxylic dianhydride (PTCDA) template layer [7]. Further, we have found that the PTCDA layer controls the stacking direction of H_2Pc orientated parallel to the surface of the glass substrate, even when the thickness of the PTCDA layer is only 5 Å [8]. This result suggests that the properties of the interface between H_2Pc films and the substrate play an important role in molecular orientation. It is evident that the performance of organic semiconductor devices strongly depends on the molecular orientation and regularities [9,10]. Therefore, it is important to clarify the effect of the template layer on the molecular orientation of both the i-layer and the p–i–n structure. In this work, we studied this effect by using H_2Pc and PTCDA as the p- and n-type materials, respectively. It was found that the orientation of the molecular planes of both H_2Pc and PTCDA in a H_2Pc:PTCDA mixed layer (i-layer) deposited on a PTCDA template layer was parallel to the surface of the substrate. Moreover, the H_2Pc layer deposited on the H_2Pc:PTCDA/PTCDA/glass structure, which corresponds to the p–i–n structure, showed an arrangement of molecular planes parallel to the substrate surface. The molecular orientation of H_2Pc and PTCDA in the i-layer is strongly affected by the template layer and the aggregated structures of the PTCDA in the i-layer.

2. Experimental

H_2Pc, PTCDA, and the i-layer (mixture of H_2Pc and PTCDA) were deposited on glass (Corning 7059) and SiO_2/Si(001) substrates by organic molecular beam deposition (OMBD) with a base pressure of 1.5×10^{-9} torr. The organic source materials were purified three times by the gradient sublimation method and charged into Knudsen cells. The glass substrates were cleaned in ultrasonic baths of acetone and ethanol and then dried under a nitrogen flow before loading them into an OMBD chamber. The SiO_2/Si substrate was fabricated by depositing SiO_2 on Si(001) wafers by electron beam evaporation. After a thin PTCDA or H_2Pc template layer was grown, 50–300-nm-thick H_2Pc:PTCDA mixed layers (i-layers) were deposited onto it. In all the deposition processes, the sample holder was held at room temperature. The deposition rate was measured using a quartz oscillator placed near the substrate holder; this rate was maintained below 0.3 Å/s.

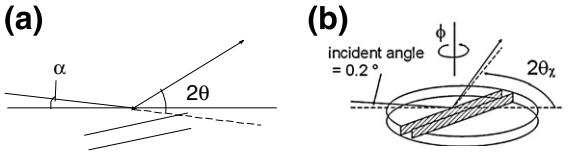


Fig. 1. X-ray diffraction geometry: (a) Seemann–Bohlin configuration (incident angle: α) and (b) grazing incidence X-ray diffraction.

X-ray diffraction (XRD) and grazing incidence X-ray diffraction (GIXD) analyses were performed using a thin film X-ray diffractometer (Rigaku RINT2100 In-plane) with a CuKα source ($\lambda = 1.54$ Å); the configurations adopted in these analyses are shown in Fig. 1. In the XRD analysis, we used the Seemann–Bohlin geometry (incident angle $\alpha = 0.2°$) to examine the out-of-plane lattice periodicity [8,11]. In this measurement, the diffraction plane is inclined at θ–α to the surface. However, the diffraction intensity of the organic films increased markedly with an increase in the X-ray irradiation area induced by the glancing-angle incidence [8,11]. From the GIXD analysis, the lattice periodicity of which direction is parallel to the substrate surface is obtained. Therefore, the three-dimensional crystalline structure could be observed in these measurements. The absorption spectrum in the visible region was obtained from transmittance and reflectance measurements using a Jasco Ubest V-570 system. SEM images were obtained using a Jeol JSM-6700F system with an electron beam acceleration voltage of 5 kV. In the SEM measurement, we used 10-nm-thick SiO_2/Si(001) instead of a glass substrate, to prevent the electrical charging of the substrate.

3. Results and discussion

Fig. 2a shows the XRD profiles of 270-nm-thick H_2Pc:PTCDA (volume ratio = 1:1) mixed layers formed on 8.5-nm-thick template layers of (i) H_2Pc and (ii) PTCDA; the corresponding GIXD profiles are shown in Fig. 2b. For the mixed layer deposited on the H_2Pc template layer, we observed α-H_2Pc (200) and α-H_2Pc (400) diffraction peaks

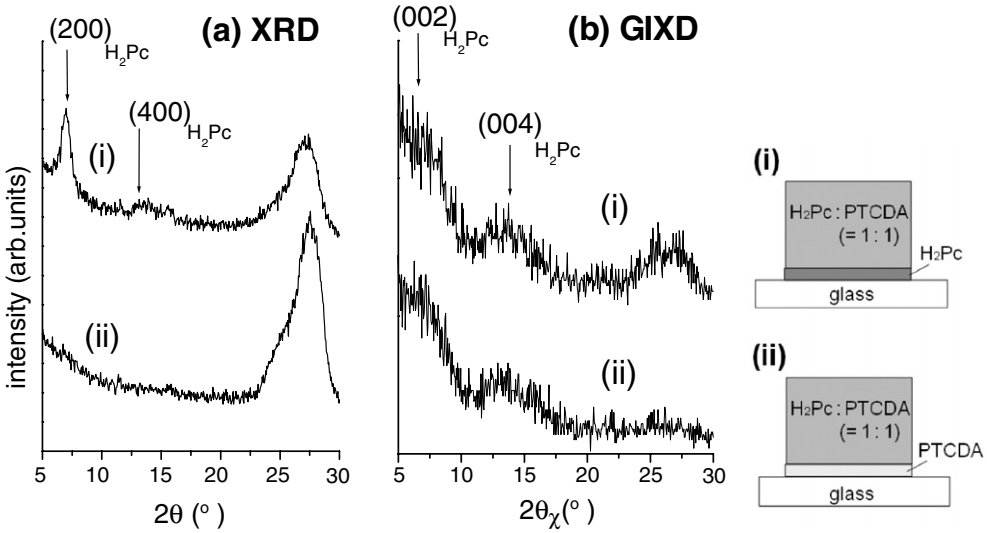


Fig. 2. (a) XRD profiles of 270-nm-thick H_2Pc:PTCDA (volume ratio = 1:1) mixed layers formed on 8.5-nm-thick template layers of (i) H_2Pc and (ii) PTCDA. (b) GIXD profiles of samples shown in (a).

at $2\theta = 6.9°$ and 13.8° in the XRD profiles, respectively, as shown in Fig. 2a (i). Further, we observed α-H_2Pc (002) and α-H_2Pc (004) diffraction peaks at $2\theta_\chi = 7.3°$ and 14.6° in the GIXD profiles, respectively, as shown in Fig. 2b (i). These results indicate that aggregation of H_2Pc, which results in the formation of α-H_2Pc crystals, occurs in the mixed layer deposited on the H_2Pc template layer. Besides these peaks, we observed a peak at $2\theta = 27°$ in the XRD profiles and a peak at $2\theta_\chi = 27°$ in the GIXD profiles. These peaks correspond to a lattice spacing of ~3.3 Å and are in good agreement with the distance between the facing molecular planes of α-H_2Pc [7]. Because the diffraction peak at $2\theta(2\theta_\chi) = 27°$ appeared both in XRD and GIXD, the molecular planes of H_2Pc were not aligned in the mixed layer deposited on the H_2Pc layer. On the other hand, for the mixed film deposited on the PTCDA layer, no α-H_2Pc (200) and α-H_2Pc (400) diffraction peaks were observed in the XRD profile, although a peak was observed at $2\theta = 27°$, as shown in Fig. 2a (ii). Further, no peak was observed at $2\theta_\chi = 27°$ in the GIXD profile, although α-H_2Pc (002) and α-H_2Pc (004) diffraction peaks were observed at $2\theta_\chi = 7.3°$ and 14.6°, respectively, as shown in Fig. 2b (ii). These results indicate that the orientation of the molecular planes of H_2Pc in the mixed layer deposited on the PTCDA template layer is parallel to the substrate surface. The PTCDA molecules in the mixed layers, on the other hand, were found to be aggregated and formed a structure consisting of stacked molecular planes, as observed in the optical absorption spectra, which will be explained in a subsequent paragraph (Fig. 4). Furthermore, it was confirmed that PTCDA deposited on the H_2Pc template layer exhibits a parallel arrangement of its molecular planes [7]. From these results, it is possible to say that the molecular planes of both H_2Pc and PTCDA in the mixed layer deposited on PTCDA are parallel to the substrate surface, and the diffraction peak at $2\theta = 27°$, seen in Fig. 2a (ii), might also originate from the distance between the facing molecular planes of PTCDA (~3.2 Å), which is almost the same as that in α-H_2Pc [12]. Thus, the molecular orientation of H_2Pc and PTCDA in the mixed layer is strongly affected by the template layer.

Fig. 3 shows the XRD profiles of 270-nm-thick H_2Pc:PTCDA mixed layers with volume ratios of (a) 1:1, (b) 2:1, and (c) 4:1 deposited on 8.5-nm-thick PTCDA template layers. For the H_2Pc:PTCDA mixed layers with volume ratios of 1:1 and 2:1, we observe a peak only at $2\theta = 27°$, suggesting that the molecular planes of both H_2Pc and PTCDA are parallel to the substrate surface, as shown in Figs. 3a and b, respectively. On the contrary, for the H_2Pc:PTCDA mixed layer with the volume ratio of 4:1 (H_2Pc:PTCDA (4:1)), an α-H_2Pc (200) diffraction peak was observed at $2\theta = 6.7°$ in the XRD profile, which is observed when the orientation of the α-H_2Pc molecular plane is perpendicular to the surface. These results suggest

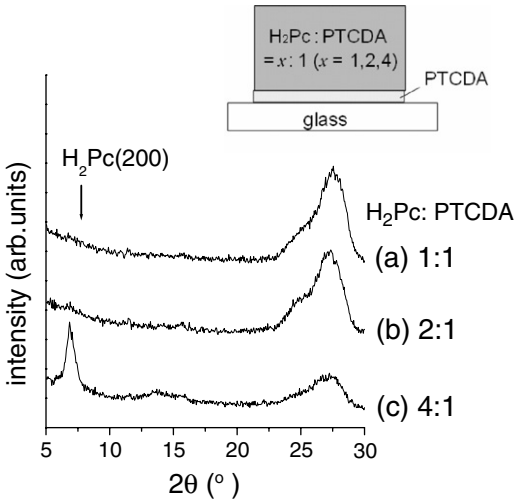


Fig. 3. XRD profiles of 270-nm-thick H_2Pc:PTCDA mixed layers with volume ratios of (a) 1:1, (b) 2:1, and (c) 4:1 formed on 8.5-nm-thick PTCDA template layers.

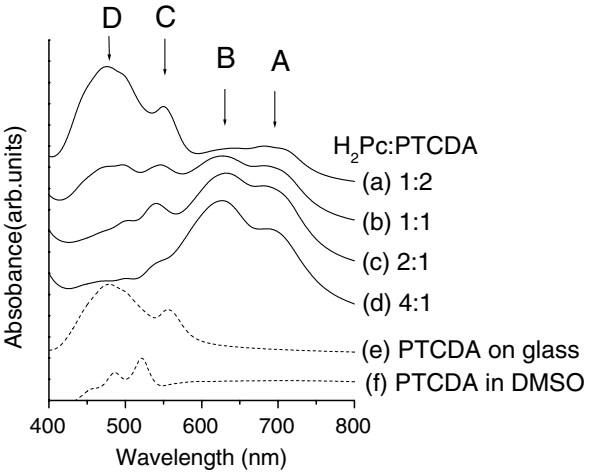


Fig. 4. Optical absorption spectra of 270-nm-thick H_2Pc:PTCDA mixed layers with volume ratios of (a) 1:2, (b) 1:1, (c) 2:1, and (d) 4:1 formed on 8.5-nm-thick PTCDA template layers. For comparison, the absorption spectra of PTCDA film on glass, which corresponds to the absorption spectrum of a PTCDA crystal, and those of PTCDA dissolved in dimethylsulfoxide (DMSO), which corresponds to the single-molecule spectrum, are shown in (e) and (f), respectively.

that the orientation of the molecular plane of H_2Pc and/or PTCDA in H_2Pc:PTCDA (4:1) mixed layers is random, even if a PTCDA template layer is introduced between the mixed layer and the glass substrate; therefore, the internal structure is important for controlling the molecular orientation of the mixed layer.

Fig. 4 shows the optical absorption spectra of 270-nm-thick H_2Pc:PTCDA mixed layers with volume ratios of (a) 1:2, (b) 1:1, (c) 2:1, and (d) 4:1 deposited on 8.5-nm-thick PTCDA template layers. The absorption by the PTCDA template layer was subtracted from the spectra by using data from reference samples. In these spectra, peaks A and B are attributable to the absorption band of H_2Pc, and peaks C and D to that of PTCDA [13,14]. As shown in Figs. 4a–d and f, we observe that the height ratio of peak D to peak C decreases with decreasing volume ratios of PTCDA to H_2Pc and finally approaches the absorption spectra of single PTCDA molecules, as observed for PTCDA dissolved in dimethylsulfoxide (DMSO) [13]. This phenomenon is observed when the aggregation size of PTCDA is reduced due to a variation in the interaction of the overlapping π-electron systems between facing molecular planes of PTCDA [13]. On the other hand, we also observe an increase in the height ratio of peak B to peak A with the volume ratio of H_2Pc to PTCDA, and these profiles finally approach that of bulk crystalline α-H_2Pc [14]. Therefore, these results suggest that the aggregation sizes of these molecules vary with the mixing ratio. We believe that such a variation in the aggregation size and structure of PTCDA in H_2Pc:PTCDA mixed layers affects the molecular orientation of their molecular planes.

As for the H_2Pc:PTCDA (1:1) mixed layers, it is evident that both H_2Pc and PTCDA are aggregated with individual molecules, and their cohesive structures exhibit the bulk crystal structures of α-H_2Pc and PTCDA, respectively, as shown in Fig. 4b. Moreover, the molecular orientation of both H_2Pc and PTCDA in the mixed layers can be controlled by using the PTCDA template layer, as indicated by the XRD profiles shown in Fig. 3a. These results suggest that such aggregated structures of PTCDA in H_2Pc:PTCDA (1:1) mixed layers have a templating effect on H_2Pc, and aggregates of both H_2Pc and PTCDA are stacked on the substrate surface in keeping with the templating effect of the lowest H_2Pc and PTCDA layer, as illustrated in Figs. 5a and b, respectively. On the other hand, the aggregation size of PTCDA decreased in the H_2Pc:PTCDA (4:1) mixed films, as shown in Fig. 4d. It has already been reported that the orientation properties of an H_2Pc layer deposited on a PTCDA/glass structure deteriorates with a decrease in the PTCDA layer thickness [8]. Therefore, it can be stated that the aggregated structures and sizes of the molecules of both PTCDA and H_2Pc in the mixed layer are

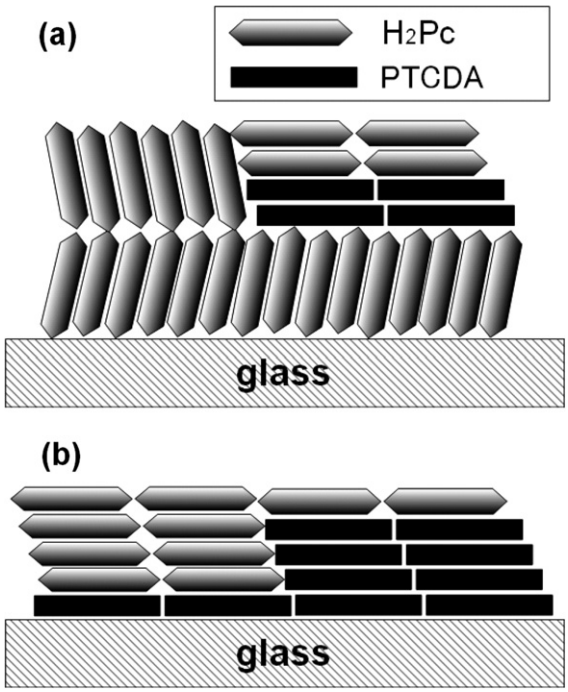


Fig. 5. Schematic illustration of the growth of the H_2Pc:PTCDA mixed layer deposited on (a) H_2Pc template layer: stacking direction of the H_2Pc molecular planes in the mixed layer is random, (b) PTCDA template layer: the molecular planes of both H_2Pc and PTCDA are parallel to the substrate surface.

important in controlling the crystal structure of the mixed layer.

Fig. 6 shows the XRD profiles of (a) H_2Pc:PTCDA (volume ratio = 1:1, thickness = 50 nm)/H_2Pc (10 nm), (b) H_2Pc (300 nm) deposited on structure (a), (c) H_2Pc:PTCDA (50 nm)/PTCDA (10 nm), and (d) H_2Pc (300 nm) deposited on structure (c). For both the H_2Pc:PTCDA layer and the H_2Pc/H_2Pc:PTCDA heterostructure deposited on the H_2Pc template layer, we observed an α-H_2Pc (200) peak at $2\theta = 6.7°$, indicating that the molecular plane of α-H_2Pc is perpendicular to the surface, while the peak at $2\theta = 27°$ suggests that the molecular plane of α-H_2Pc (and PTCDA) is parallel to the surface, as shown in Figs. 6a and b, respectively. On the other hand, we observed a peak only at $2\theta = 27°$ for both the H_2Pc:PTCDA layer and the H_2Pc/H_2Pc:PTCDA heterostructure formed on the PTCDA template layer, as shown in Figs. 6c and d, respectively. It is well known that the molecular orientation of H_2Pc is strongly affected by the interfacial structure. Therefore, these results suggest that the H_2Pc layer deposited on the H_2Pc:PTCDA mixed layer was affected by the molecular orientation of the mixed layer. Moreover, the H_2Pc layer deposited on the H_2Pc:PTCDA/PTCDA/glass structure, which corresponds to the p–i–n structure, showed an arrangement of molecular planes parallel to the substrate surface. Therefore, it is concluded that the molecular orientations of the H_2Pc layer, H_2Pc:PTCDA mixed layer, and PTCDA layer in a

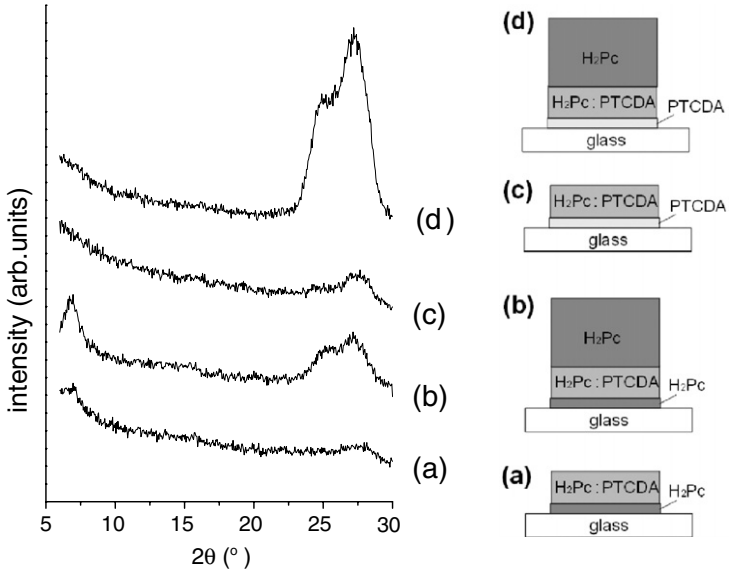


Fig. 6. XRD profiles of (a) H_2Pc:PTCDA (volume ratio = 1:1, thickness = 50 nm)/H_2Pc (10 nm), (b) H_2Pc (300 nm) deposited on structure (a), (c) H_2Pc:PTCDA (50 nm)/PTCDA (10 nm), and (d) H_2Pc (300 nm) deposited on structure (c).

p–i–n structure can be controlled by modification of the substrate surface.

Fig. 7 shows the cross-sectional SEM images of H_2Pc (75 nm)/H_2Pc:PTCDA (volume ratio = 1:1, thickness = 15 nm) double-layer structures deposited on 10-nm-thick (a) H_2Pc and (b) PTCDA template layers. For the H_2Pc/H_2Pc:PTCDA/H_2Pc triple-layer structure, fibril structures, which grew randomly from the substrate surface, are observed in the cross-sectional image shown in Fig. 7a. It is well known that the crystal feature of H_2Pc generally reveals a fibril structure growing in the stacking direction of the molecular plane (*b*-axis orientation) [8,15]. Therefore, the SEM results indicate that the molecular plane of H_2Pc is randomly grown on the H_2Pc:PTCDA/H_2Pc double-layer structure. On the other hand, for the H_2Pc/H_2Pc:PTCDA/PTCDA structure, vertical columnar structures are observed in the cross-sectional image shown in Fig. 7b. Therefore, the stacking direction of the molecular planes of H_2Pc on the H_2Pc:PTCDA/PTCDA structure is aligned perpendicular to the substrate surface. These SEM results are consistent with the XRD results shown in Fig. 6.

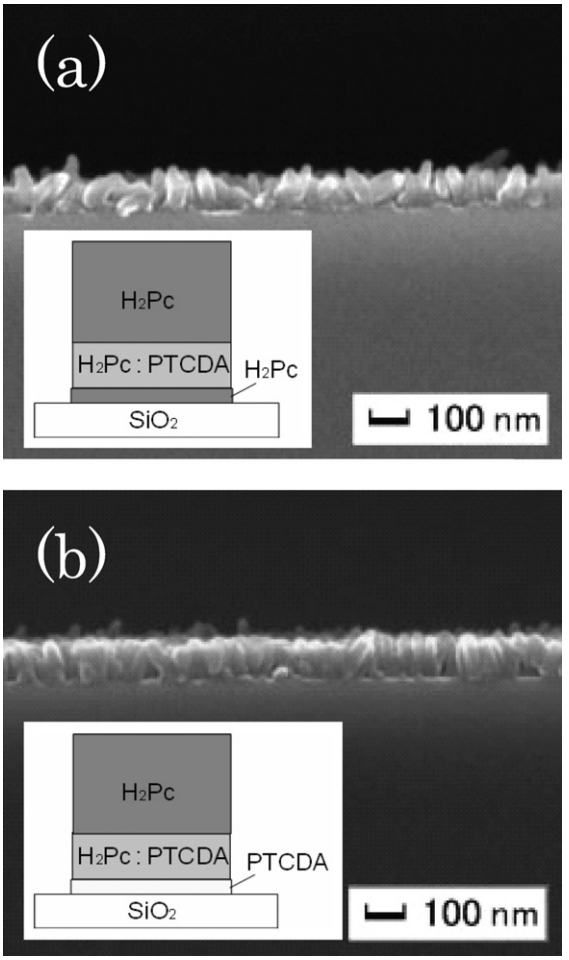


Fig. 7. Cross-sectional SEM images of H_2Pc (75 nm)/H_2Pc:PTCDA (volume ratio = 1:1, thickness = 15 nm) double-layer structures formed on 10-nm-thick (a) H_2Pc and (b) PTCDA template layers.

Fig. 8 shows the optical absorption spectra of H_2Pc (200 nm)/H_2Pc:PTCDA (volume ratio = 1:1, thickness = 65 nm) double-layer structures deposited on 8.5-nm-thick (a) H_2Pc and (b) PTCDA template layers. It was observed that the absorption coefficient of the samples was increased by the PTCDA template layer. It is obvious that the transition moment of intramolecular excitation in H_2Pc exists in the direction of the molecular plane, and the absorption intensity, I, is proportional to

$$I \propto \cos^2 \gamma,$$

where γ is the angle between the electric vector of the incident light and the π–π* transition moment [16]. In an arrangement with light at normal incidence, the absorption intensity is amplified in a parallel arrangement between the molecular plane and the substrate surface. As discussed, the molecular planes of H_2Pc in the H_2Pc/H_2Pc:PTCDA double-layer structures deposited on PTCDA are parallel to the substrate surface. Therefore, its higher optical absorption can be attributed to the parallel arrangement of H_2Pc. Thus, the control of molecular orientation is one of the most important issues in the improvement of the optical properties of organic optoelectronic device structures such as p–i–n triple-layer structures.

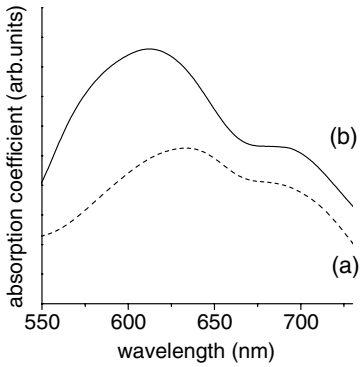


Fig. 8. Optical absorption spectra of H_2Pc (200 nm)/H_2Pc:PTCDA (volume ratio = 1:1, thickness = 65 nm) double-layer structures formed on 8.5-nm-thick (a) H_2Pc and (b) PTCDA template layers.

4. Conclusion

We have investigated a method to control the molecular orientations of H_2Pc:PTCDA mixed layers and p–i–n triple-layer structures by using a template layer. In the case when a PTCDA template layer is introduced between a H_2Pc:PTCDA (1:1) mixed layer and a glass substrate, the orientation of the molecular planes of both H_2Pc and PTCDA in the mixed layer is parallel to the substrate surface. On the other hand, in the case of a H_2Pc template layer, the orientation of the molecular planes of both H_2Pc and PTCDA in the mixed layer is found to be random. These results indicate that the molecular orientation of H_2Pc and PTCDA in mixed layers is strongly affected by the template layer. On the other hand, a degradation of the orientation properties is observed in the H_2Pc:PTCDA (4:1) mixed layer; therefore, the control of the internal structure of the mixed layer is necessary for orientation control. We observe that the H_2Pc layer deposited on the H_2Pc:PTCDA/PTCDA/glass structure, which corresponds to a p–i–n structure, shows an arrangement of molecular planes parallel to the substrate surface. Further, the optical properties in these layers are significantly affected by the molecular orientation. Therefore, it is important to control the organic film/substrate interface for device applications.

Acknowledgements

The Japanese Ministry of Education, Culture, Sports, Science and Technology is gratefully acknowledged for the Grant-in-Aid for Young Scientists (B) (No. 17760246) in support of this work. This study was also performed as a research project supported by the Nissan Science Foundation.

References

[1] P. Peumans, A. Yakimov, S.R. Forrest, J. Appl. Phys. 93 (2003) 3693.
[2] C.J. Brabec, N.S. Sariciftci, J.C. Hummelen, Adv. Funct. Mater. 11 (2001) 15.
[3] M. Hiramoto, H. Fujiwara, M. Yokoyama, Appl. Phys. Lett. 58 (1991) 1062.
[4] J. Xue, S. Uchida, B.P. Rand, S.R. Forrest, Appl. Phys. Lett. 85 (2004) 5757.
[5] T. Taima, M. Chikamatsu, Y. Yoshida, K. Saito, K. Yase, Appl. Phys. Lett. 85 (2004) 6412.
[6] K. Suemori, T. Miyata, M. Yokoyama, M. Hiramoto, Appl. Phys. Lett. 86 (2005) 063509.
[7] S. Heutz, R. Cloots, T.S. Jones, Appl. Phys. Lett. 77 (2000) 3938.
[8] T. Sakurai, S. Kawai, J. Shibata, R. Fukasawa, K. Akimoto, Jpn. J. Appl. Phys. 44 (2005) 1982.
[9] M. Pope, C. Swenberg, Electronic Processes in Organic Crystals and Polymers, second ed., Oxford Univ. Press, New York, 1999.
[10] M. Ofuji, K. Ishikawa, H. Takezoe, K. Inaba, K. Omote, Appl. Phys. Lett. 86 (2005) 062114.
[11] S. Suzuki, T. Kosaka, S. Sato, M. Saito, E. Matsubara, Y. Waseda, Phys. Status Solidi A 161 (1997) 193.
[12] S.R. Forrest, P.E. Burrows, E.I. Haskal, F.F. So, Phys. Rev. B 49 (1994) 11309.
[13] H. Proehl, T. Dienel, R. Nitsche, T. Fritz, Phys. Rev. Lett. 93 (2004) 097403.
[14] O.E. Sieicken, M.M. Van Tilborg, M.F.M. Roks, R. Hendriks, W. Drenth, R.J.M. Nolte, J. Am. Chem. Soc. 109 (1987) 4261.
[15] M. Ofuji, K. Inaba, K. Omote, H. Hoshi, Y. Takanishi, K. Ishikawa, H. Takezoe, Jpn. J. Appl. Phys. 42 (2003) 7520.
[16] O.D. Gordan, M. Friedrich, D.R.T. Zahn, Thin Solid Films 455–456 (2004) 551.

Available online at www.sciencedirect.com
ScienceDirect
Organic Electronics 8 (2007) 709–717
Organic Electronics
www.elsevier.com/locate/orgel

Photochemical reactions in organic semiconductor thin films

Sebastian Scholz [a,*], Cathrin Corten [b], Karsten Walzer [a], Dirk Kuckling [b], Karl Leo [a]

[a] Institut für Angewandte Photophysik, Technische Universität Dresden, D-01062 Dresden, Germany
[b] Fachrichtung Chemie und Lebensmittelchemie, Technische Universität Dresden, D-01062 Dresden, Germany

Received 17 January 2007; received in revised form 1 June 2007; accepted 12 June 2007
Available online 16 June 2007

Abstract

We investigate the dissociation and the photochemical behavior of different organic semiconductor materials typically employed in organic light emitting diodes (OLED) and other organic electronic devices, using laser desorption/ionization time-of-flight mass spectrometry (LDI-TOF-MS). The study is subdivided into two parts: The first part is an investigation of several hole conductive materials from the class of triarylamines commonly used in OLEDs and organic solar cells. Upon LDI measurements, this class of materials does not show any photochemical reactions. The second part of the work deals with two typical electron conductive materials: tris(8-hydroxyquinolinato)-aluminum (Alq_3) and 4,7-diphenyl-1, 10-phenanthroline (BPhen). These materials show photochemical reactions in terms of oligomerization. The individual reaction pathways will be discussed in detail. We compare these reactions by further studying two similar molecules (1,1′-biphenyl-4′-oxy)bis(8-hydroxy-2-methylquinolinato)-aluminum (BAlq) and bathocuproine (BCP). Finally, we discuss a possible relation of the results to degradation mechanisms taking place in organic devices.
© 2007 Elsevier B.V. All rights reserved.

PACS: 78.30.Jw; 78.40.Fy; 81.15.Ef; 81.40.-z; 82.45.Wx; 82.50.Nd; 82.80.Ms

Keywords: Organic semiconductors; Degradation; Decomposition; Laser desorption; Photochemical reaction; LDI-TOF-MS

1. Introduction

Since Tang and VanSlyke [1] reported the first efficient organic light emitting diode (OLED), the field of organic electronics and optoelectronics has attracted a tremendous attention. Within the last few years, very high efficiencies were reached for OLEDs [2–4]. The focus of research has turned meanwhile to the increase of device lifetime. For this reason, the investigation of degradation mechanisms and pathways is of vital interest for the further development of organic electronics, covering the fields of OLEDs, organic solar cells, transistors and others. Depending on the type of application, often operating times of several ten thousand hours and more are required. For some devices, such as red OLEDs, the lifetime issue is nearly solved [5]. Other applications require further work in this field.

* Corresponding author. Tel.: +49 351 463 39190; fax: +49 351 463 37065.
E-mail address: sebastian.scholz@iapp.de (S. Scholz).

1566-1199/$ - see front matter © 2007 Elsevier B.V. All rights reserved.
doi:10.1016/j.orgel.2007.06.002

Several studies have been carried out over the last few years [6–14] revealing different degradation mechanisms for OLEDs.

In this paper, we focus on the chemical behavior of relevant organic semiconductor materials upon laser desorption/ionization under an applied positive high voltage, using the method of matrix assisted laser desorption/ionization time-of-flight mass spectrometry (MALDI-TOF-MS). This method is usually used for analyzing polymeric chains and proteins [15,16]. Soltzberg et al., e.g., used the method of MALDI to analyze freshly made and aged OLEDs by removing the OLED material from the substrate and mixing it with a matrix material [17]. The main advantage of the laser desorption/ionization (LDI) technique is the detection of chemical compounds via their mass-to-charge ratio even at very low concentrations, which allows to apply it to thin films without using additional matrix material. Other techniques for thin film analysis of organic semiconductor devices are, e.g., dynamic secondary ion mass spectrometry (SIMS) [11,13,18], Rutherford back scattering (RBS) [19], X-ray photoelectron spectroscopy (XPS) [20], and radiotracer measurements [12] to detect responses related to specific atoms. In contrast, the LDI technique allows the detection of undestroyed charged molecules, their fragments, the observation of donor–acceptor interactions between different substances, and the analysis of reaction products of photochemical reactions. Impurities like unreacted reactants or by-products can be detected, and their potential to act as donor or acceptor materials in thin layers can be studied [21]. For this reason, we study a selection of typical organic semiconductor compounds commonly used in organic devices. The photochemical reactions we discuss in this paper focus on the dimerization of the well-known molecules BPhen and Alq_3. We discuss possible reaction pathways of both substances and compare the dimerization of Alq_3 with the non-dimerization of BAlq as a similar electron transporting, aluminum-based organic compound under the same photochemical conditions. Further, we have a look on BCP, a near relative of BPhen as a proof of the reaction pathway which is expected for the oligomerization of BPhen.

In this work, we try to correlate the reactions caused by the highly intense laser excitation pulse in the LDI experiment with molecular long-term degradation under OLED operation. It is known from several OLED studies that (to a certain extent) free holes can cross electron conductive materials in organic devices. Thus, in electron transporting layers, hole densities in the order of $10^{13}\,cm^{-3}$ [22] to $10^{16}\,cm^{-3}$ can be reached [23]. In the current work we explain that high hole densities are responsible for the degradation of the adjacent hole blocking layers inside the OLED. Up to now, no data about the reaction of positively charged electron transport molecules are known. To compare the results of the LDI experiment with OLED data, we will now estimate the amount of holes created in the LDI experiment. Upon LDI excitation, per pulse 2×10^{14} photons (120 μJ, 337 nm) interact with the electron transporting hole blocking layer consisting of BPhen. Zenobi and Knochenmuss [24] showed that the primary ionization mechanism in LDI is two photon absorption (TPA), creating positively charged species. From literature, we know the TPA cross section σ_{GM} of similar organic molecules ranging from 0.1 GM (1.0×10 to $50\,cm^4\,s\,photon^{-1}\,molecule^{-1}$) to 800 GM [25–27]. Following the calculation of Lin, the number of photons absorbed by the TPA process can be calculated to 3×10^{15} photons/cm^3 for the value of 1 GM, when using typical values of our experiment: $\rho_{BPhen} = 1.244$ g/mol, $E_{LASER} = 120$ μJ, laser spot size $10^{-4}\,cm^2$ [25]. Thus, we estimate hole densities of 1.5×10^{14}–2.5×10^{18} holes cm^{-3}. This is in a similar order of magnitude as in the OLED discussed above. However, heating effects due to heavy light absorption may cause increased reaction constants for possible degradation reactions, leading to accelerated degradation, which allows us to analyze degradation products in a detectable quantity.

2. Experimental

All organic layers were prepared by thermal evaporation of the material of interest onto commercial MALDI targets (MTP multi probe adapter target from Bruker Daltonics, Germany) in an ultrahigh vacuum system. The deposition rate of the organic compounds was 0.3–0.4 Å/s for all layers. This rate is also common for device preparation (OLEDs, solar cells). The targets were cleaned (sonication in acetone and ethanol) and dried under a stream of nitrogen. For analytical reasons, the targets for the electron conductive materials BPhen and Alq_3 were cleaned by the same sonication procedure, wetted with isopropanol, and dried under ambient conditions to exploit the alkaline impurities (especially sodium) from isopropanol as adducts for the ionic complexes.

The following materials were used in this study: From the group of hole transporters, we investigated several triarylamines: *N*,*N*,*N*′,*N*′-tetrakis(4-methoxyphenyl)-benzidine (MeO-TPD), 4,4′-bis[(1-naphthyl)phenylamino]-1,1′-biphenyl (NPD), 2,2′,7,7′-tetrakis(*N*,*N*-diphenylamino)-9,9′-spirobifluorene (Spiro-TAD), 4,4′,4″-tris(carbazol-9-yl)triphenylamine (TCTA), *N*,*N*′-di(4-(2,2-diphenyl-ethen-1-yl)-phenyl)-*N*,*N*′-di(4-methylphenylphenyl)benzidine (PV-TPD), ([1,1′:4′,1″:4″,1‴-quaterphenyl]-4,4‴-di[1-naphthyl(phenyl)]- diamine (4P-NPD), 4,4′-bis(*N*,*N*-diphenylamino)-tetraphenyl (4P-TPD) and 2,7-bis(*N*-phenyl-*N*-(4′*N*,*N*-diphenylamino-biphenyl-4-yl))-9,9-dimethyl-fluorene (Di-TPD). Further, we studied 4,7-diphenyl-1,10-phenanthroline (BPhen), bathocuproine (BCP), tris(8-hydroxyquinolinato)-aluminum (Alq_3) and 1,1′-biphenyl-4′-oxy)-bis(8-hydroxy-2-methylquinolinato)-aluminum (BAlq) as typical electron conductive materials. In Fig. 1, the structures of all materials are displayed together with their monoisotopic masses in the dimension of g/mol.

The samples prepared in the vacuum system were subsequently mounted under nitrogen atmosphere and inserted into the MALDI-TOF sample chamber within less than 30 s of handling in air. The LDI mass spectra were obtained using a Bruker Daltonics Biflex IV MALDI-TOF instrument in positive detection mode with an applied high voltage of 19 kV between the target and the aperture of the time-of-flight analyzer (see Fig. 2). The excitation inside this system occurred via a laser with

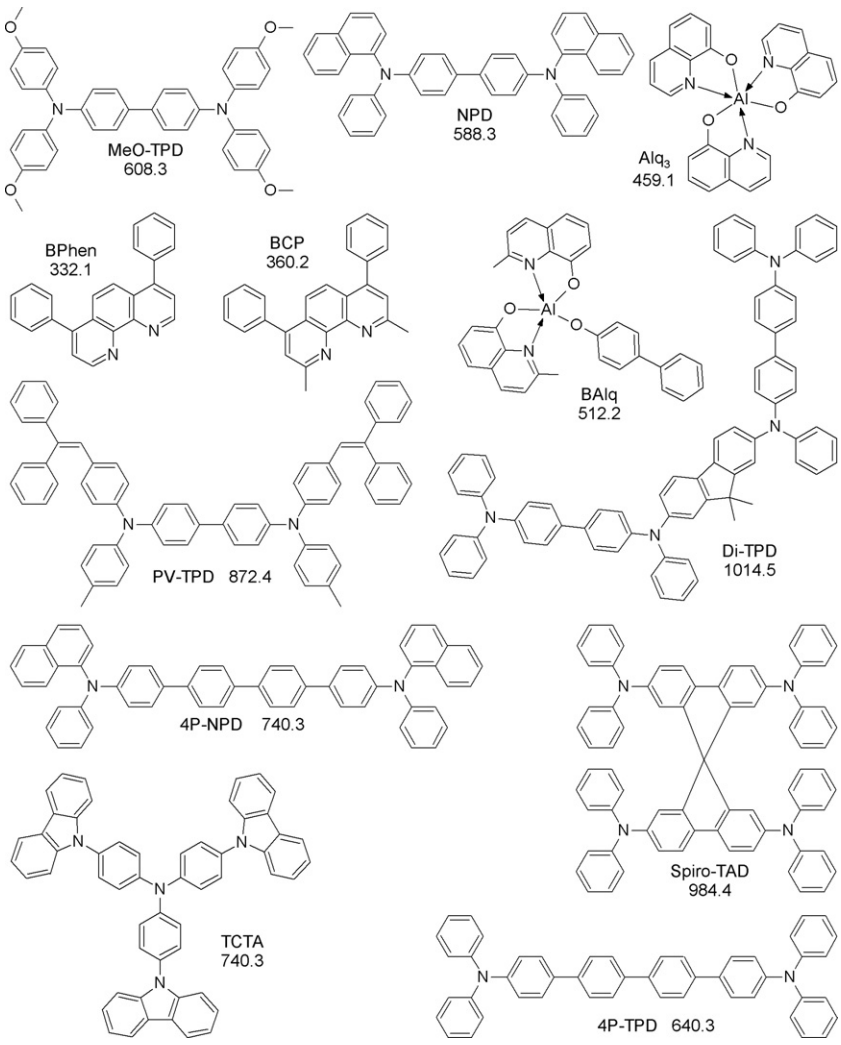


Fig. 1. Chemical structures of the materials studied and their monoisotopic mass in g/mol.

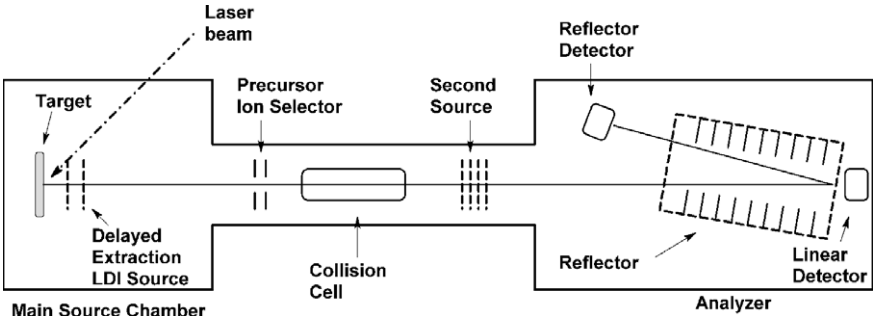


Fig. 2. Scheme of a LDI-TOF-TOF-MS setup with a precursor ion selector for the parent ion selection and a collision cell for post source fragmentation.

$\lambda = 337$ nm and a maximum output energy of 400 μJ, a spot size of 0.01 mm^2 and a pulse duration of 3–5 ns. The spectra were obtained by using the lowest possible laser energy to ionize/desorb the molecules and to prevent the material from fragmentation. While already a single laser pulse would be enough to collect a spectrum, to enhance the signal-to-noise ratio all spectra shown in this work have been averaged over 60 measurements collected at three different sample positions. For calibration, polyethylene oxide (PEO) from Sigma Aldrich with a molecular weight of 2000 g/mol was used under standard conditions. To measure the LDI-TOF-TOF mass spectra of BPhen and Alq_3, an Autoflex TOF/TOF tandem mass spectrometer (Bruker) was used. After excitation and ionization via identical laser pulses as in the LDI-TOF instrument, the selected parent ions cross the argon collision gas where they fragment. During the tandem mass measurement, the reflector voltage is reduced stepwise to guide the fragments through the second time-of-flight analyzer to the detector.

3. Results and discussion

3.1. LDI-TOF-MS of triarylamines used as hole transporting materials in OLEDs

In Figs. 3 and 4, we show LDI-TOF mass spectra of different triarylamines commonly used as hole transporting and electron blocking materials in organic light emitting devices or organic solar cells. Fig. 3 shows the spectra of MeO-TPD, NPD, TCTA and Spiro-TAD, while Fig. 4 presents data of PV-TPD, 4P-NPD, 4P-TPD and Di-TPD. As expected, the mass spectra of all triarylamines show a strong generation of the corresponding positively charged molecules and, therefore, the electron donating

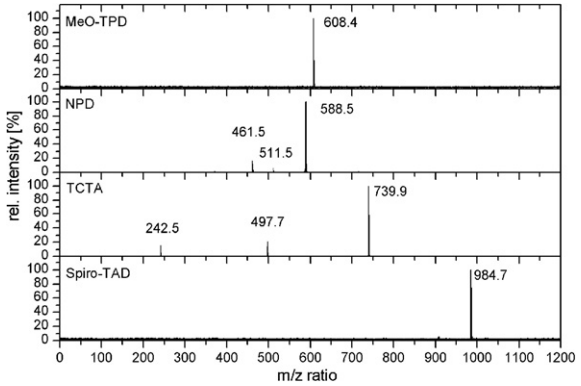


Fig. 3. LDI-TOF-MS spectra of MeO-TPD, NPD, TCTA, and Spiro-TAD. While NPD and TCTA suffer a fragmentation, the TPD-like molecules MeO-TPD and Spiro-TAD remain undestroyed by the UV-light pulse.

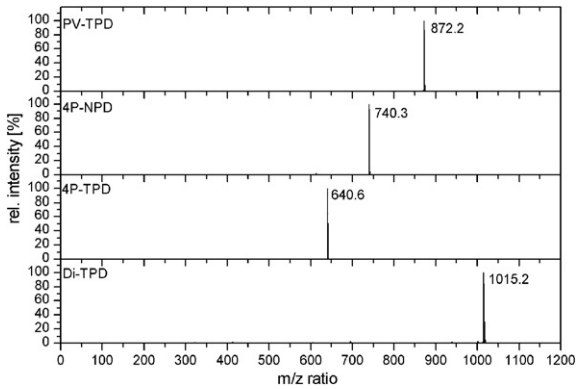


Fig. 4. LDI-TOF-MS spectra of PV-TPD, 4P-NPD, 4P-TPD, and Di-TPD. All materials are detected without fragmentation or further reactions.

character of the materials. The spectra were obtained by using the lowest possible laser energy (individual for each material) to ionize/desorb the compounds with the goal to avoid fragmentation.

For example, MeO-TPD with the monoisotopic mass of 608.267 g/mol shows a mass-to-charge ratio of 608.41, indicating the detection of the charged molecule $[MeO\text{-}TPD]^+$.

The intensity of the signal in the mass-to-charge spectra depends on the energy input into the material. Enhancement of intensity is possible either by increase of the laser energy or of the layer thickness to improve light absorption and to take advantage of the intermolecular effect of charge transfer. Further, the absorption coefficient of the organic material under investigation at the wavelength of excitation defines the level of excitation [28]. The laser energy and the high voltages applied in the time-of-flight analyzer lead to a compound-specific fragmentation pattern of the materials. It is also possible to distinguish between compounds with the same mass-to-charge ratio by analyzing their fragmentation patterns. Besides the main mass peak, the spectrum of NPD ($m/z = 588.5$) shows two other signals which are caused by the loss of a phenyl ($m/z = 511.5$) or a naphthyl group ($m/z = 461.5$). This reveals that the nitrogen–carbon bond of the naphthyl group is the weakest bond in the molecule, as is also known from semi-empirical calculations on NPD [29,30]. In the spectrum of TCTA, besides the main peak, also the positively charged carbazol unit at $m/z = 242.5$ and the positively charged first fragment of TCTA ($m/z = 497.7$) are observed. This is the result of the bond scission between 4-(carbazol-9-yl)phenyl and the diarylamine residue of the molecule. Our hypothesis is that hole transporting materials form positively charged molecules without further (photo chemical) reactions. To prove this, a broad range of further triarylamines was investigated. The spectra of Spiro-TAD, PV-TPD, 4P-NPD, 4P-TPD and Di-TPD (Figs. 3 and 4) show the molecular ions of the materials without further reactions. All these materials show no pronounced fragmentation because of their high number of vibrational degrees of freedom. The higher intensities of fragmentation signals in the NPD and TCTA spectra lead to the assumption that these materials suffer a stronger fragmentation in the excited state and may therefore dissociate even under a low intensity of UV-light irradiation.

3.2. Photo-induced dimerization of BPhen

As shown in Figs. 5 and 6, the electron conducting materials BPhen (332.13 g/mol), BCP (360.16 g/mol) and BAlq (512.17 g/mol) possess no detectable stable cationic molecular species during laser irradiation and time-of-flight analysis. Detectable complexes of electron transporting materials consist mostly of a molecule plus a proton ($[molecule + H]^+$) and in the presence of alkaline metals of a positively charged alkaline adduct ($[molecule + alkaline\ metal]^+$). The alkaline metal adducts are well observable in the spectra of BPhen (Fig. 5) and in the insets of the Alq_3 and BAlq spectra (Fig. 6). The sodium adduct creation was forced by wetting the MALDI target with the solvent isopropanol (for synthesis) without drying under a nitrogen stream, such that

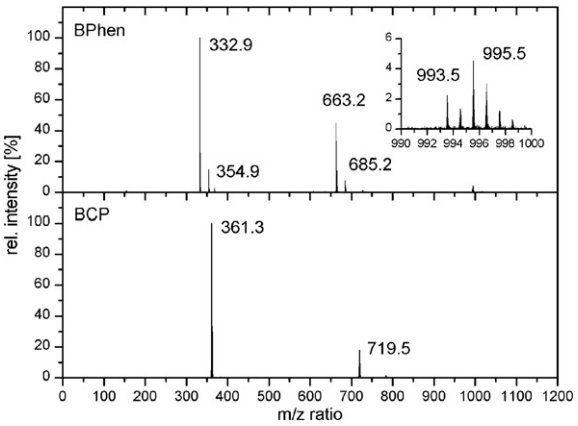


Fig. 5. LDI-TOF-MS spectra of BPhen and BCP. As a result of a chemical reaction, dimers are seen for both materials. In contrast to BCP, BPhen shows additional adducts with sodium as a result of a special treatment of the target. The inset of the BPhen spectra shows two different kinds of trimers.

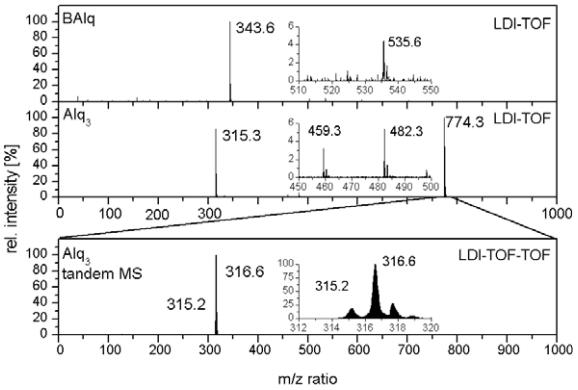


Fig. 6. LDI-TOF-MS spectra of BAlq and Alq_3, and the LDI-TOF-TOF-MS fragmentation spectrum of Alq_3 of the extracted parent ion $[Al_2O_5]^+$ at $m/z = 774.3$. The insets of BAlq and Alq_3 show the expanded regions of the assumed cationic species and their sodium adducts, where the inset of the tandem MS spectra shows the isotopic pattern of the observed fragment.

the alkaline impurities remained on the target. Nitrogen stream dried samples do not show alkaline adducts, as it is seen in the spectrum of BCP (Fig. 5). In addition, oligoaggregates of the materials BPhen and BCP are observed as we will describe next.

Let us first analyze the spectrum of BPhen. This electron transporting material shows two positively charged complexes $[BPhen + H]^+$ at 332.9 and $[BPhen + Na]^+$ at 354.9 (Fig. 5). The peaks at the mass-to-charge ratios of 663.2 and 685.2 correspond to products of a photochemical dimerization reaction stimulated by the laser irradiation. In Fig. 7, we suggest three possible pathways of a photochemical dimerization reaction, starting in both cases from a neutral and an excited positively charged BPhen molecule. The BPhen dimer detected at the mass-to-charge ratio of 663.2 is attributed to the mass of a positively charged intermediate (**1**) of the reaction to the neutral dimer molecule (**2**), which has a satellite caused by a sodium complex at $m/z = 685.2$. This is the reaction via the most likely pathway 1. Additionally, the signal at the mass-to-charge ratio of 663.2 can be explained as the protonated species of (**2**). The two dimers (**1**) and (**2**) were distinguished by further experiments using tandem mass spectrometry, where the generated dimers are broken into characteristic fragments by an additional time-of-flight scan after crossing a collision gas. In the first step of the photochemical reaction, one BPhen molecule is oxidized and the ion reacts with the *para* position of a phenyl ring at another BPhen molecule (pathway 1). We assume that the reaction does not occur via the pathway 2 because of the sterically hindered *ortho* position at the phenyl ring. The expected reaction pathway 3 might occur via the nucleophilic position 2 of the 1,10-phenanthroline basic structure of BPhen. However, this reaction does not take place, as we demonstrate at the similar molecule bathocuproine (BCP), where position 2 of the 1,10-phenanthroline basic structure is substituted with a methyl group ($R = CH_3$). Bathocuproine oligomerizes in the same way like BPhen, even without losing the methyl group. This can be seen in Fig. 5, where only the protonated molecule $[BCP + H]^+$ at $m/z = 361.3$ and the BCP dimer (**1a**) at $m/z = 719.5$ are seen. A signal around $m/z = 705$, indicating the dimer (**3a**), is not observable. Additionally, the absence of a trimeric BCP species and the lower signal of the BCP dimer (**1a**) in contrast to the BPhen dimer (**1**) show the sterically hindering effect. Not only the methyl group, even the phenyl rings act as sterically hindering groups, shown in the drawing of Fig. 7.

In a second step, a rearrangement of electron pairs can occur in the charged dimerized BPhen molecule (**1**), whereby a substitution on the neighbored position 2 or 6 occurs. The trimers of BPhen at 993.5 and 995.5 are built by similar reactions like the dimers. A neutral BPhen forms an adduct (995.5) with a charged dimer (**1**) of BPhen. Besides this, it is also possible that the molecule detected at 993.5 is the reaction product formed between the dimer (**2**) and a monomeric BPhen. Comparing the spectra of BCP and BPhen, the generation of BCP dimers is less pronounced than BPhen dimers, and trimers are not detected at all in the BCP layer. These results confirm the model of the sterically hindered reaction of this oligomerization.

We conclude that generated holes may cause a chemical reaction in a BPhen layer. Obviously, the high energy of the laser makes it possible to increase

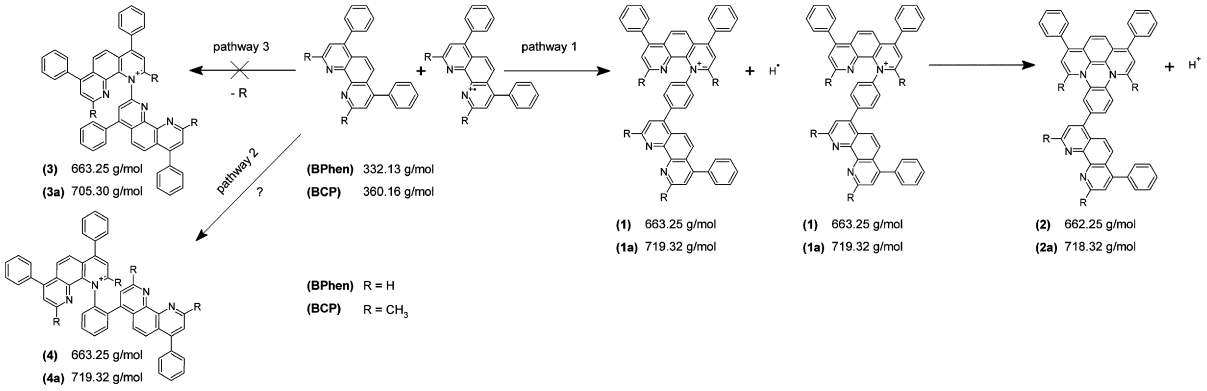


Fig. 7. Dimerization reactions of BPhen ($R = H$) and BCP ($R = CH_3$) after a short laser pulse excitation and an applied positive high voltage by LDI experiments.

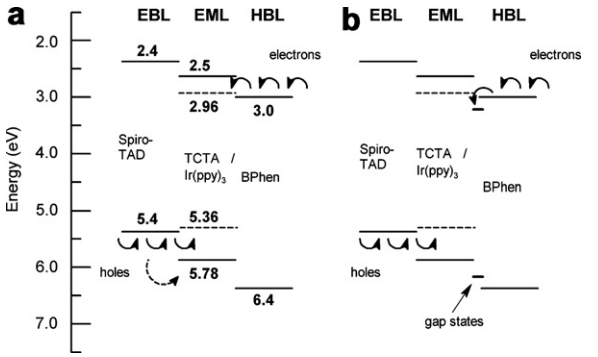


Fig. 8. (a) Energy diagram of the emission zone of a typical OLED comprising an electron blocking layer (EBL), an emission layer (EML) and a hole blocking layer (HBL). (b) After an electro-chemical reaction of BPhen, the EML–HBL interface has additional gap states which may lead to electron trapping and, thus, will reduce exciton creation on the emitter material (energy levels after [3,33]).

the reaction constant of the BPhen dimerization in a rigorous way and, therefore, it allows us to study a detectable amount of reaction products. In a typical OLED architecture [31], holes will cross the emission layer (EML) and reach the hole blocking layer (HBL) [32] (Fig. 8(a)). These holes will cause a reaction or even an excitation of the HBL material. Even a very small amount of reacted molecules will create charge traps at the EML/HBL interface. By looking at the different species studied in this work it is seen that the intermediate reaction product (**1**) is positively charged and will act as a trap for electrons. The dimer (**2**) has a lower lying lowest unoccupied molecular orbital (LUMO) as compared to the monomer, because of its expanded π-electron system and will therefore create gap states on the BPhen interface (Fig. 8(b)). Thus, the LUMO of the dimer may be energetically below the triplet state of the emitter material, such that a certain amount of excitons will not recombine radiatively.

3.3. Chemical reactions of positively charged Alq_3 molecules

Alq_3 as an electron transporter is well known to be an unstable material under hole transporting conditions in organic light emitting devices [12,34], where the reaction products of Alq_3 quench the fluorescence of the active material (Alq_3) [7]. A quenching of emission was also shown under ambient conditions, were Alq_3 reacts with oxygen and water and form different oxygen containing aluminum(III) 8-hydroxyquinoline species [35]. With aid of the LDI-TOF-MS technique, another possible quenching species can be pointed out (Fig. 6): Alq_3 shows a clear behavior of dissociation by losing one of its oxygen containing ligands during laser irradiation of the LDI-TOF-MS experiment by forming the fragment $[Alq_2]^+$ at $m/z = 315.3$, even under water and oxygen free conditions. We assume that this excitation-caused dissociation is reversible under OLED operation conditions, due to the fact that the reaction products stay nearby, so that after charge recombination, the products may recombine. At this point, we should mention that Papadimitrakopoulos et al. found by cyclovoltammetric measurements an irreversible oxidation of Alq_3 in dimethylformamide (DMF), where the reduction remains reversible [35].

The signal of the mass-to-charge ratio of Alq_3 at 459.3 can be seen in the spectrum as well (see inset), although with a small intensity, which leads to the conclusion that Alq_3 can be oxidized (Fig. 6). This positively charged molecule is stable for the short timescale of the LDI-TOF measurement which agrees with the slightly hole transporting properties of this material. At $m/z = 482.3$, the sodium adduct of Alq_3 is visible, which is typical for electron conducting materials. In a positively charged environment, after the LDI laser pulse, a further reaction between the fragment $[Alq_2]^+$ and another Alq_3 molecule leads to a rearrangement from a fourfold and a sixfold coordinated species to a fivefold coordinated molecule, containing two aluminum core atoms $[Al_2q_5]^+$ (see Fig. 9). This charged molecule is seen in the Alq_3 spectrum of Fig. 6 at $m/z = 774.3$. From tandem MS measurements, we know that the $[Al_2q_5]^+$ signal of a Alq_3 layer shows $[Al_2q_5]^+$ as the parent ion and $[Alq_2]^+$ as the only fragment after crossing the collision gas. The tandem mass spectrum in Fig. 6 shows $[Alq_2]^+$ at $m/z = 315.2$ and with higher intensities as an obviously protonated, one time charged, species at $m/z = 316.6$. This leads to the conclusion that $[Al_2q_5]^+$ is a twofold five times coordinated species. The dimerization reaction will shift the reversible dissociation of Alq_3 to the reaction products and increases the dimer concentration with operational time. This will also increase the concentration of free chinoline ions and their reaction products. This agrees well with earlier findings [5,10,21,35]. The positively charged dimers may also act as charge traps, and, therefore, as luminescence quenchers.

Now, we will look on a similar aluminum based semiconductor electron transporting material,

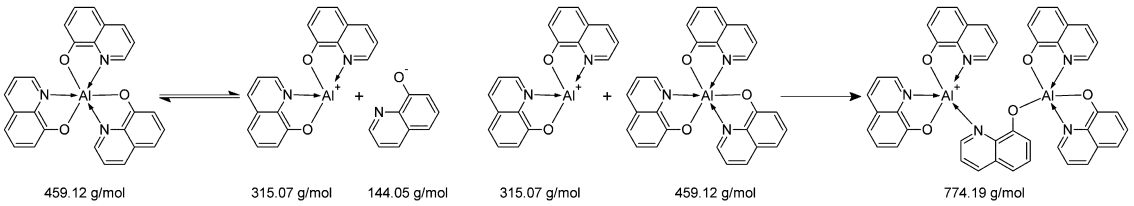


Fig. 9. Suggested reaction scheme of the fragmentation and dimerization reactions of Alq_3 after a short laser pulse under an applied high positive bias as used in the LDI experiments.

BAlq. It is known as stable hole blocking material in OLEDs [5]. BAlq has a fivefold coordination sphere, comparable with the coordination structure of $[Al_2q_5]^+$ around its two aluminum cores. As seen in the inset of Fig. 6, the LDI-TOF-MS spectrum of BAlq shows the sodium adduct of BAlq only with low intensity, while oxidized BAlq is not seen at all. The first fragment is seen as main peak in the mass spectrum at $m/z = 343.6$, originating from the loss of the *p*-phenylphenolate ligand. This ligand has a more ionic character than the 8-hydroxy-2-methylquinolinate ligands, due to the fact that the HOMO is localized nearly exclusively on the *p*-phenylphenolate [36]. During light irradiation, an electron is excited from the HOMO of the *p*-phenylphenolate ligand to the LUMO, which is located at the 8-hydroxy-2-methylquinolinate ligand. Therefore, the aluminum complex detaches the *p*-phenylphenolate ligand (Fig. 10). In contrast, in Alq_3, the HOMO and LUMO are located on the same ligand. Because the *p*-phenylphenolate ligand has just one binding site, no further reaction may occur and the reaction remains reversible. Therefore, BAlq does not form charged dimers, which act as luminescence quenchers.

We conclude that under hole transport conditions in organic devices, BAlq and Alq_3 undergo a reversible chemical reaction with an equilibrium state. However, while in Alq_3 the reaction is irreversibly shifted to the product side due to the further reaction to a dimer of Alq_3, BAlq is stable. BAlq containing devices are therefore much more stable under hole transporting conditions, since the *p*-phenylphenolate ligand and the fivefold coordinated ligand sphere prevent such a dimerization, and the dissociation of the BAlq complex remains reversible. This explains the extremely high OLED lifetime reached with BAlq as host and EBL [5,36].

4. Conclusions

By means of the LDI-TOF-MS technique, we studied different organic semiconductor materials commonly used in OLEDs with regard to their photochemical reactions, induced by UV-laser light irradiation, under the influence of a positive bias voltage. We found that triarylamines, known as good hole transporting compounds, are unreactive under UV-light irradiation and hole transport conditions. They form stable, positively charged molecules in the mass-to-charge analysis, as expected for this group of materials. Dissociation may occur at excited or charged molecules, which was shown by the spectra of NPD and TCTA. In contrast, the electron transporting materials BPhen, BCP and Alq_3 show photo-induced chemical reactions during the LDI-TOF measurements. The analysis of their LDI-TOF-MS spectra allows an additional understanding of the underlying degradation mechanisms, which may occur in electrically driven organic semiconductor devices. We studied possible reaction pathways and the different stages of dimer-

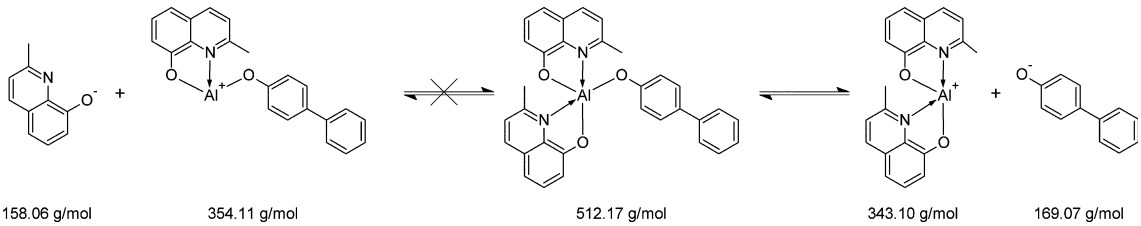


Fig. 10. Fragmentation of BAlq. No further reactions are observed after the short laser pulse under applied high positive bias as used in the LDI experiments.

ization of the well-known electron transport material BPhen and compared these to the results with its analog BCP, showing the degradation of the two materials under hole transporting conditions. With aid of the LDI-TOF-MS spectra, we were able to uncover the fragmentation and further dimerization of positively charged Alq_3. By comparison to BAlq, another aluminum containing organic compound, it was possible to understand why BAlq is stable against hole transport while Alq_3 degrades.

Acknowledgements

The authors thank NOVALED AG for financial support, Horst Hartmann and Ansgar Werner for helpful discussions and the Forschungszentrum Rossendorf for the use of the MALDI-TOF-TOF set-up.

References

[1] C.W. Tang, S.A. VanSlyke, Appl. Phys. Lett. 51 (1987) 913.
[2] J. Birnstock, A. Lux, M. Ammann, P. Wellmann, M. Hofmann, T. Stübinger, SID Int. Symp. Digest Tech. Papers XXXVII (2006) 1866.
[3] G. He, M. Pfeiffer, K. Leo, M. Hofmann, J. Birnstock, R. Pudzich, J. Salbeck, Appl. Phys. Lett. 85 (2004) 3911.
[4] D. Tanaka, H. Sasabe, Y.J. Li, S.J. Su, T. Takeda, J. Kido, Jap. J. Appl. Phys. Pt. 2 46 (1–3) (2007) L10.
[5] R. Meerheim, K. Walzer, M. Pfeiffer, K. Leo, Appl. Phys. Lett. 89 (2006) 061111.
[6] H. Aziz, Z.D. Popovic, Chem. Mater. 16 (2004) 4522.
[7] H. Aziz, Z.D. Popovic, N.-X. Hu, A.-M. Hor, G. Xu, Science 283 (1999) 1900.
[8] Z.D. Popovic, H. Aziz, N.-X. Hu, A. Ioannidis, P.N.M. dos Anjos, J. Appl. Phys. 89 (2001) 4673.
[9] F. Steuber, J. Staudigel, M. Stössel, J. Simmerer, A. Winnacker, H. Spreitzer, F. Weissörtel, J. Salbeck, Adv. Mater. 12 (2000) 130.
[10] M. Müller-Wiegand, G. Georgiev, E. Oesterschulze, T. Fuhrmann, J. Salbeck, Appl. Phys. Lett. 81 (2002) 4940.
[11] S.T. Lee, Z.Q. Gao, L.S. Hung, Appl. Phys. Lett. 75 (1999) 1404.
[12] M. Scharnberg, J. Hu, J. Kanzow, K. Rätzke, R. Adelung, F. Faupel, C. Pannemann, U. Hilleringmann, S. Meyer, J. Pflaum, Appl. Phys. Lett. 86 (2005) 024104.
[13] W. Song, Z. Li, S.K. So, Y. Qiu, Y. Zhu, L. Cao, Surf. Interface Anal. 32 (2001) 102.
[14] L. Ke, S.-J. Chua, K. Zhang, N. Yakovlev, Appl. Phys. Lett. 80 (2002) 2195.
[15] K. Tanaka, Angew. Chem. Intl. Ed. Engl. 42 (2003) 3860.
[16] M.W.F. Nielen, Mass Spectrom. Rev. 18 (1999) 309.
[17] L.J. Soltzberg, J.D. Slinker, S. Flores-Torres, D.A. Bernards, G.G. Malliaras, H.D. Abruna, J.-S. Kim, R.H. Friend, M.D. Kaplan, V. Goldberg, J. Am. Chem. Soc. 128 (2006) 7761.
[18] A. Delcorte, S. Hermans, M. Devillers, N. Lourette, F. Aubriet, J.-F. Muller, P. Bertrand, Appl. Surf. Sci. 231 (2004) 131.
[19] M.P. de Jong, L.J. van Ijzendoorn, M.J.A. de Voigt, Appl. Phys. Lett. 77 (2000) 2255.
[20] L.S. Hung, L.S. Liao, C.S. Lee, S.T. Lee, J. Appl. Phys. 86 (1999) 4607.
[21] J. Drechsel, A. Petrich, M. Koch, S. Pfützner, R. Meerheim, S. Scholz, K. Walzer, M. Pfeiffer, K. Leo, SID Int. Symp. Digest Tech. Papers XXXVII (2006) 1692.
[22] T. Ogawa, D.-C. Cho, K. Kaneko, T. Mori, T. Mizutani, Thin Solid Films 438–439 (2003) 171.
[23] D. Berner, H. Houili, W. Leo, L. Zuppiroli, Phys. Status Solidi A 202 (2005) 9.
[24] R. Zenobi, R. Knochenmuss, Mass Spectrom. Rev. 17 (1998) 337.
[25] T.-C. Lin, S.-J. Chung, K.-S. Kim, X. Wang, G.S. He, J. Swiatkiewicz, P.N. Prasad, Adv. Polym. Sci. 161 (2003) 157.
[26] S. Härtner, H.-C. Kim, N. Hampp, J. Photochem. Photobiol. A 187 (2007) 242.
[27] S.-i. Kato, T. Matsumoto, M. Shigeiwa, H. Gorohmaru, S. Maeda, T. Ishis-i, S. Mataka, Chem. Eur. J. 12 (2006) 2303.
[28] D.A. Allwood, R.W. Dreyfus, I.K. Perera, P.E. Dyer, Appl. Surf. Sci. 109–110 (1997) 154.
[29] R.Q. Zhang, C.S. Lee, S.T. Lee, Appl. Phys. Lett. 75 (1999) 2418.
[30] B.C. Lin, C.P. Cheng, Z.P.M. Lao, J. Phys. Chem. A 107 (2003) 5241.
[31] G. He, O. Schneider, D. Qin, X. Zhou, M. Pfeiffer, K. Leo, J. Appl. Phys. 95 (2004) 5773.
[32] Y. Kijima, N. Asai, S.-i. Tamura, Jap. J. Appl. Phys. 38 (1999) 5274.
[33] S. Watanabe, Y. Agata, D. Tanaka, J. Kido, J. Photopolym. Sci. Technol. 18 (2005) 83.
[34] Z.D. Popovic, H. Aziz, IEEE J. Sel. Top. Quant. Electron. 8 (2002) 362.
[35] F. Papadimitrakopoulos, X.-M. Zhang, D.L. Thomsen III, K.A. Higginson, Chem. Mater. 8 (1996) 1363.
[36] T.-Y. Chu, Y.-S. Wu, J.-F. Chen, C.H. Chen, Chem. Phys. Lett. 404 (2005) 121.

Available online at www.sciencedirect.com
ScienceDirect
Organic Electronics 8 (2007) 718–726
Organic Electronics
www.elsevier.com/locate/orgel

High-performance pentacene field-effect transistors using Al_2O_3 gate dielectrics prepared by atomic layer deposition (ALD)

Xiao-Hong Zhang [a], Benoit Domercq [a], Xudong Wang [b], Seunghyup Yoo [a], Takeshi Kondo [c], Zhong Lin Wang [b], Bernard Kippelen [a,*]

[a] *Center for Organic Photonics and Electronics (COPE), School of Electrical and Computer Engineering, Georgia Institute of Technology, Atlanta, GA 30332, United States*
[b] *Center for Organic Photonics and Electronics (COPE), School of Materials Science and Engineering, Georgia Institute of Technology, Atlanta, GA 30332, United States*
[c] *Center for Organic Photonics and Electronics (COPE), School of Chemistry and Biochemistry, Georgia Institute of Technology, Atlanta, GA 30332, United States*

Received 6 April 2007; received in revised form 13 June 2007; accepted 19 June 2007
Available online 5 July 2007

Abstract

High-performance pentacene field-effect transistors have been fabricated using Al_2O_3 as a gate dielectric material grown by atomic layer deposition (ALD). Hole mobility values of 1.5 ± 0.2 cm^2/V s and 0.9 ± 0.1 cm^2/V s were obtained when using heavily *n*-doped silicon (n^+-Si) and ITO-coated glass as gate electrodes, respectively. These transistors were operated in enhancement mode with a zero turn-on voltage and exhibited a low threshold voltage (< -10 V) as well as a low sub-threshold slope (<1 V/decade) and an on/off current ratio larger than 10^6. Atomic force microscopy (AFM) images of pentacene films on Al_2O_3 treated with octadecyltrichlorosilane (OTS) revealed well-ordered island formation, and X-ray diffraction patterns showed characteristics of a "thin film" phase. Low surface trap density and high capacitance density of Al_2O_3 gate insulators also contributed to the high performance of pentacene field-effect transistors.
© 2007 Elsevier B.V. All rights reserved.

PACS: 85.30.Tv; 72.80.Le; 77.55.+f; 81.15.−z

Keywords: Organic field-effect transistors (OFETs); Atomic layer deposition (ALD); Al_2O_3; Pentacene; ITO

1. Introduction

Organic field-effect transistors (OFETs) have recently gained attention as building blocks for electronic applications that can greatly benefit from low-cost, large-area fabrication and flexible form factors, such as radio-frequency identification tags

* Corresponding author. Tel.: +1 404 385 5163; fax: +1 404 385 5162.
E-mail address: Kippelen@ece.gatech.edu (B. Kippelen).

1566-1199/$ - see front matter © 2007 Elsevier B.V. All rights reserved.
doi:10.1016/j.orgel.2007.06.009

(RFID) [1], drivers for electronic paper [2] and driving circuits for flat panel displays (FPDs) [3]. To achieve high-performance OFETs, development of suitable gate dielectric materials in addition to high-mobility organic semiconductors is important. Preferably, dielectric materials should have a high dielectric constant (κ) and should be processible into thin high-quality, defect-free films to form OFETs with a reduced operating voltage, fast switching speed, and large on/off ratio. Low deposition temperature is also desirable to allow for fabrication on plastic substrates. Atomic layer deposition (ALD) is a deposition technique that allows for the deposition of highly conformal, defect-free dielectric layers at relatively low temperature [4–7]. Dielectric films grown by ALD have a high resistivity and good barrier properties, and therefore are excellent candidates for gate insulators. The deposition process is simple, low-cost, and compatible with various substrates made from different materials and with irregular shapes [4,5]. Oxide layers fabricated by ALD have also been studied as O_2/H_2O barriers for organic light-emitting diodes [8]. However, to date ALD technology has had limited success in fabricating dielectric materials suitable for OFET applications [9,10].

Here, we report on the fabrication of high-performance pentacene OFET devices using a 200 nm-thick film of Al_2O_3 grown by ALD as the gate dielectric material. We first characterized the dielectric and the surface properties of Al_2O_3 thin films grown by ALD. We then fabricated OFETs on heavily *n*-doped silicon (n^+-Si) substrates (serving also as the gate electrode) with both, 200 nm-thick films of Al_2O_3 grown by ALD and thermally-grown SiO_2, as the gate dielectrics. The latter was used as a reference control sample. Finally, we used the conformational aspect of ALD to fabricate high-performance OFETs on a substrate with a large surface roughness: ITO-coated glass substrate.

2. Deposition and characterization of Al_2O_3 gate insulators

A Savannah100 ALD system from Cambridge Nanotech Inc. was used to deposit Al_2O_3 dielectric films on n^+-Si substrates ($5 \times 10^{-3}\ \Omega\,cm$) and on ITO-coated glass substrates (Colorado Concept Coatings, 60 Ω/sq.). ITO-coated glass substrates were cleaned in an ultrasonic bath using, successively, soapy water, deionized water, acetone, and reagent alcohol for 15 min each, and then dried under nitrogen. The n^+-Si substrates were cleaned in a mixture of H_2SO_4/H_2O_2, and a buffered oxide etchant (1:6 diluted HF in H_2O) was used to remove the natural oxide. Immediately before being loaded into the ALD deposition system, substrates underwent O_2 plasma treatment in a plasma asher for 10 min at low power. This plasma treatment is known, not only to remove organic residues and other contaminants from surfaces, but also to increase the concentration of surface hydroxyl groups and the amount of absorbed aluminum precursor [11]. Al_2O_3 films were deposited at 100 °C using alternating exposures of $Al(CH_3)_3$ and H_2O vapor at a deposition rate of approximately 1 Å per cycle. Each deposition cycle (one monolayer) lasted 24 s, yielding a total deposition time of 13.3 h for 2000 cycles. The thickness of the Al_2O_3 films was measured by a stylus profilometer (Dektak 6M by Veeco) and found to be about 200 nm.

We characterized the dielectric properties of Al_2O_3 films (200 nm) grown on ITO-coated glass using parallel plate capacitors of various plate areas ranging from $3.1 \times 10^{-3}\ cm^2$ to $2.4 \times 10^{-1}\ cm^2$. The capacitors were fabricated by sandwiching a 200 nm-thick Al_2O_3 film between an ITO electrode and a 100 nm-thick Al electrode. For each of the 12 devices, capacitance and dissipation factor (loss tangent) were measured at 1.0 V_{RMS} as a function of frequency from 20 Hz to 1 MHz with an Agilent 4284A precision LCR meter. The dielectric constant (κ) of Al_2O_3 at 1 kHz was determined to be 7.5 ± 0.2 (calculated from the linear dependence of capacitance as a function of device area $C_{OX} = \varepsilon_o k/t$, where ε_o is the permittivity in vacuum, t is the thickness, and κ is the dielectric constant). This result is comparable to the value obtained by Groner [5]. The current density vs. voltage characteristic presented in Fig. 1a shows that a 200 nm-thick Al_2O_3 film is an excellent insulator with a leakage current density less than 200 nA/cm^2 under an applied field of 2 MV/cm over a contact area of 0.016 cm^2. Notably, these values are small considering the large surface roughness of ITO-coated glass. Dissipation factors for all devices were measured in the range of 10^{-3}. Furthermore, the capacitance density C_{OX} was stable up to a relatively high frequency of 1 MHz, as shown in Fig. 1b.

In addition to dielectric properties, the chemical and physical surface properties of dielectrics including surface wetting properties, surface roughness, and surface defect density are also important

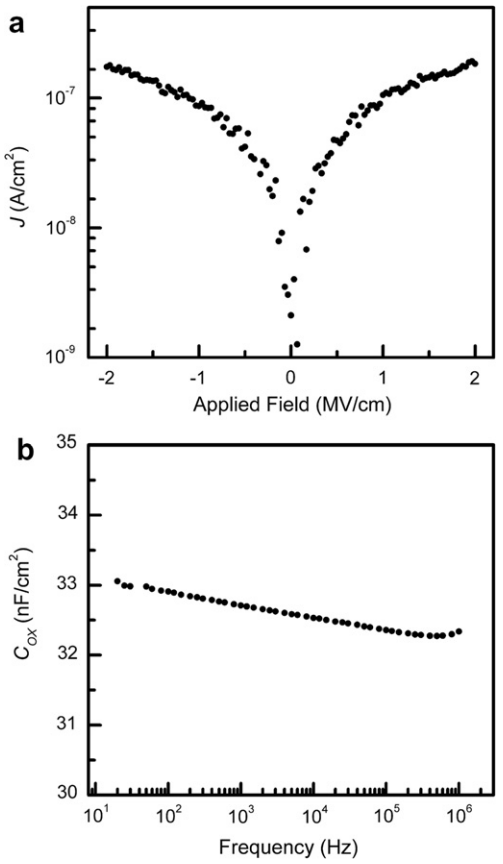


Fig. 1. (a) Current density (J) vs. applied field characteristics and (b) capacitance density (C_{OX}) vs. frequency characteristics of capacitors prepared with ALD-grown Al_2O_3 dielectric materials on ITO-coated glass substrates.

parameters that affect the electrical performance of OFETs, through the morphology/structural ordering of organic semiconductor films and the charge transport at the dielectric/semiconductor interface. To characterize the surface properties, first, an element analysis of Al_2O_3 films was done by energy dispersive spectrometry (EDS). No other elements other than Al, O, and elements from the substrates (e.g., Si, In, and Sn) were detected over a test area of $10\ \mu m \times 10\ \mu m$. Then, the surface morphology of Al_2O_3 on both n^+-Si substrates (smooth) and on ITO-coated glass (rough) was investigated by AFM (Digital Instruments NanoScope™ Scanning Probe Microscopes). The results were compared with thermally-grown SiO_2 on n^+-Si substrates as shown in Fig. 2. The root-mean-square (RMS) surface roughness of the 200 nm-thick Al_2O_3 film on an n^+-Si substrate was estimated to be 4.3 Å when measured over an area of $1\ \mu m \times 1\ \mu m$ (Fig. 2 left), which is almost identical to that of the 200 nm-thick SiO_2 film thermally-grown on an identical n^+-Si substrate 4 Å (Fig. 2 center). With an ITO-coated glass substrate, the RMS surface roughness of a 200 nm-thick film of Al_2O_3 was increased up to 12 Å (Fig. 2 right), which is comparable to the value of the substrate prior to deposition.

So far, we have obtained high-quality Al_2O_3 dielectric insulators with a dielectric constant ($\kappa = 7.5$) almost twice that of SiO_2. Although, high-κ dielectric insulators are desirable for reducing operating voltage of OFETs, Veres et al. have reported that high-κ dielectrics usually contain polar functional groups that can increase the energetic disorder at the interface, which results in a higher localization of the charge carriers and reduced field-effect mobility in polymer OFETs [12,13]. Recent studies based on organic single-crystal transistors have attributed the dependence of mobility on dielectric polarizability to the coupling/interaction force between the charged carriers in the organic conducting channel and the ionic lattice of the dielectric [14,15]. To minimize the effect of dielectric polar functional groups and other surface charges on the organic conducting channel, the surfaces of all oxides were passivated with an octadecyltrichlorosilane (OTS) self-assembled monolayer (SAM) just before the deposition of pentacene. It is well established that SAMs applied on the interfaces in OFETs allow for better control of the morphology and properties of the organic semiconducting material. The OTS SAMs were formed by dipping the substrates in a 5 mM toluene solution of OTS for 30 min after the substrates were oxygen-plasma treated for two minutes. The static aqueous contact angle measurement showed that after the treatment, the previously hydrophilic surfaces of both dielectric materials became hydrophobic. A contact angle of 91–92° was obtained from OTS-treated Al_2O_3 on both smooth surface (n^+-Si) and rough surface (ITO-coated glass), indicating that a uniform self-assembled OTS monolayer with long alkyl chains was formed. This value is slightly lower than that of OTS-treated SiO_2 on n^+-Si (112°). This can be attributed to a lower concentration of oxygen atoms of Al_2O_3 and a different SAM formation mechanism compared with SiO_2 [16,17].

3. Fabrication and characterization of OFETs with Al_2O_3 gate insulators

OFETs were fabricated using 200 nm-thick Al_2O_3 on n^+-Si (T1), 200 nm-thick SiO_2 on n^+-Si

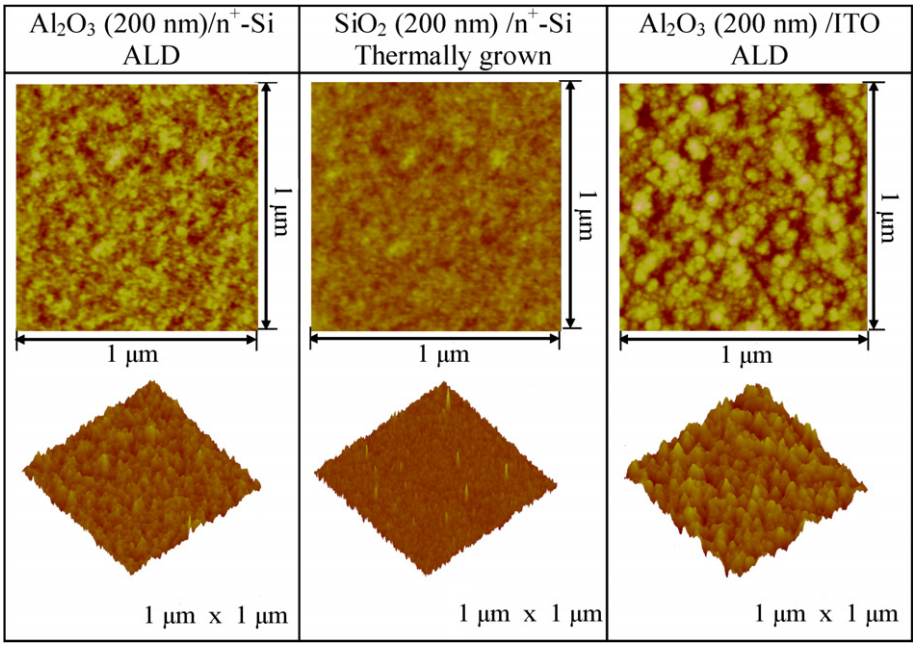


Fig. 2. AFM images (1 μm × 1 μm) of a 200 nm-thick Al_2O_3 film grown by ALD on n^+-Si substrates (left, with a data scale of 5 nm), a 200 nm-thick film of thermally-grown SiO_2 on n^+-Si substrates (center, with a data scale of 5 nm) and a 200 nm-thick Al_2O_3 film grown by ALD on ITO coated-glass substrates (right, with a data scale of 10 nm).

(T2, the reference sample), and 200 nm-thick Al_2O_3 on ITO-coated glass (T3). All oxide surfaces were treated with OTS SAMs as described above and n^+-Si and ITO acted as gate electrodes, respectively. All three types of transistors were top-contact devices (as shown in Fig. 3a for T1 and T2, and Fig. 3b for T3). The transistors were fabricated by evaporating a 60 nm-thick film of pentacene on

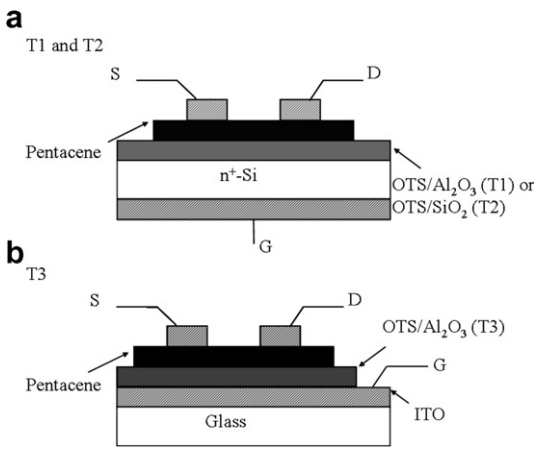


Fig. 3. Diagram of the OFET device geometries for transistors T1 and T2 (a) and T3 (b), where S, D and G stand for source, drain and gate, respectively.

different substrates (T1, T2, and T3) followed by the patterned deposition of a 40 nm-thick Au film capped with a 100 nm-thick Al film to serve as top source/drain electrodes through a shadow mask. Here, a thin Au film was inserted to form a quasi-ohmic contact between pentacene and the source/drain electrodes. Ti/Au (10 nm/100 nm) backside metallization was used as the external gate contact in T1 and T2. Prior to deposition, pentacene (Aldrich) was purified using gradient zone sublimation, and then deposited at a deposition rate of 0.3 Å/s, as measured by a crystal monitor. The temperature and pressure during deposition were 25 °C and 2×10^{-8} Torr, respectively. The samples were transferred in a vacuum-tight vessel without being exposed to atmospheric conditions into a nitrogen glove box (O_2, $H_2O < 0.1$ ppm) for electrical testing. The electrical measurements were performed using an Agilent E5272A source/monitor unit in a dark environment.

The surface morphology of the pentacene films on different substrates (T1, T2, and T3) was characterized using AFM as shown in Fig. 4. The growth of pentacene films on all three OTS-treated substrates exhibited high structural order and displayed island formation, but no dendrite-like crystal

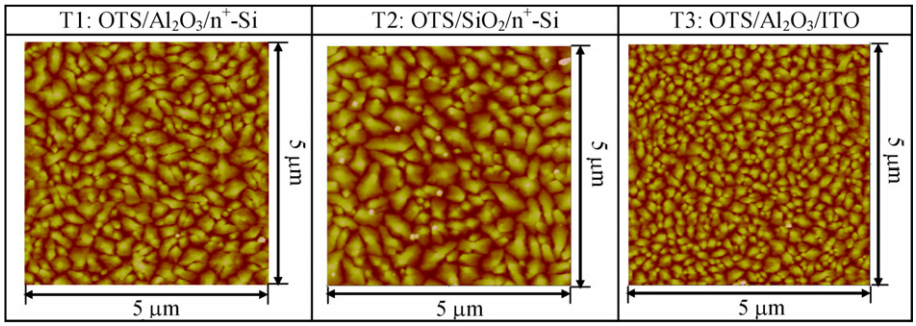


Fig. 4. AFM images (5 μm × 5 μm) of a 60 nm-thick pentacene film on an OTS-treated 200 nm-thick Al_2O_3 film (T1, with n^+-Si as substrates and gate electrodes), on an OTS-treated 200 nm-thick SiO_2 film (T2, with n^+-Si as substrates and gate electrodes) and on an OTS-treated 200 nm-thick Al_2O_3 film (T3, with ITO-coated glass as substrates and gate electrodes).

formation was observed. However, the grain size greatly varied from the substrates with different surface energy and surface roughness. Therefore, although the RMS roughness on T1 and T2 are comparable (see Fig. 2), the grain size was slightly reduced on T1 where its aqueous contact angle is lower. A further reduction in grain size can be seen in T3 due to its larger roughness (12 Å) compared to T1 and T2 [18,19]. The larger grain size of pentacene films on T2 may be due to the residual polar groups on SiO_2, like silanols [20].

Intermolecular layer spacing of pentacene films was determined by X-ray diffraction (XRD). As shown in Fig. 5, the diffraction spectrum of island films consisted of crystalline peaks with a first diffraction peak at $2\Theta = 5.74°$, corresponding to "thin film" spacing of 15.4 Å, and the presence of higher order peaks (up to 4 or 5) was observed on the smooth substrates (T1, T2). The lattice spacing corresponds to a tilt of the molecules of 17.1° to the surface normal, assuming a triclinic single-crystal structure. The presence of a "bulk" phase of pentacene with a spacing of 14.4 Å was not observed for films reported here. Peak intensity and number of higher-order reflections mirrored the grain size of the crystalline structure observed in AFM images: films with larger grains showed higher intensity and more higher-order reflections. With smaller crystalline grain size (Fig. 4), the peak intensity of T1 was slightly lower than that for T2. In comparison, the grain size was reduced and then the peak intensity was decreased in T3 due to its large substrate surface roughness, as discussed by Steudel [18] and Fritz [19].

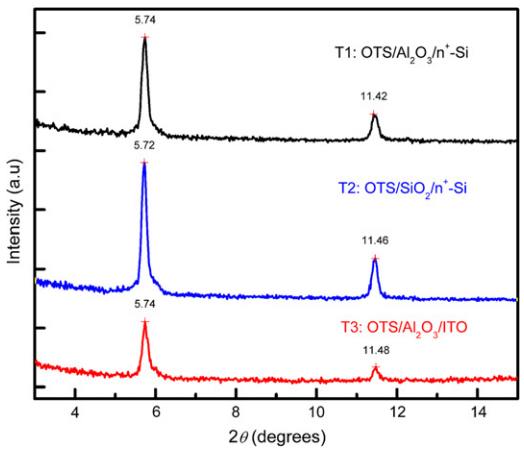


Fig. 5. XRD patterns of a 60 nm-thick pentacene film on an OTS-treated 200 nm-thick Al_2O_3 film (T1, with n^+-Si as substrates and gate electrodes), on an OTS-treated 200 nm-thick SiO_2 film (T2, with n^+-Si as substrates and gate electrodes) and on an OTS-treated 200 nm-thick Al_2O_3 film (T3, with ITO-coated glass as substrates and gate electrodes).

Pentacene transistors were characterized in the saturation regime defined by standard MOSFET models. To explore the influence of the different dielectrics (Al_2O_3 and SiO_2) on device performance, transistors T1 and T2 with a channel length $L = 65 \pm 5$ μm and a channel width $W = 590 \pm 90$ μm were compared. These two types of transistors had similar properties such as substrate surface roughness, pentacene morphology, and structural ordering as discussed earlier. Fig. 6 shows the output characteristics in Fig. 6a (drain-source current I_{DS} vs. drain-source voltage V_{DS} for increasing values of gate-source voltage V_{GS}) and transfer characteristics in Fig. 6b ($-I_{DS}$ vs. V_{GS} plotted on a logarithmic scale and $\sqrt{|I_{DS}|}$ vs. V_{GS}, at $V_{DS} = -30$ V) for the two transistors. Field-effect

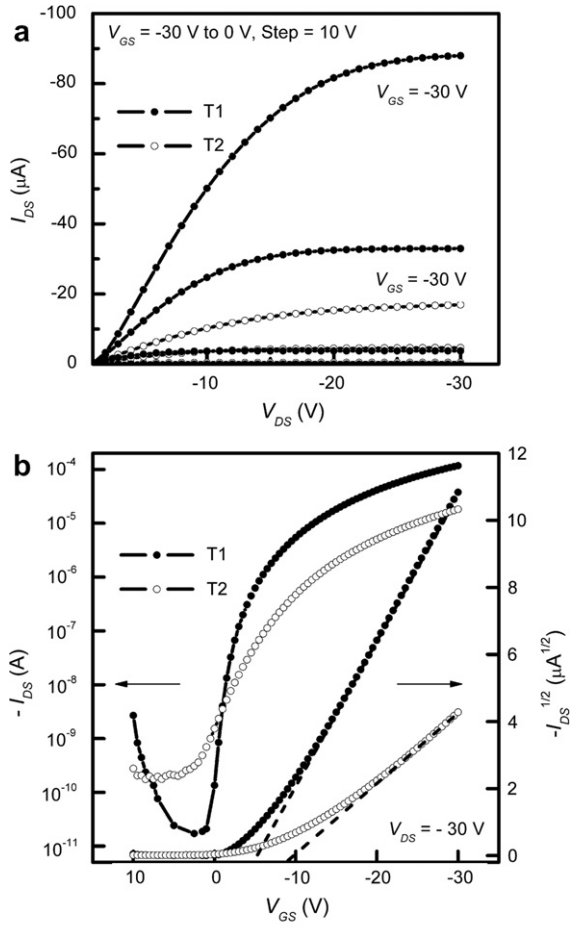


Fig. 6. (a) Output characteristics (I_{DS} vs. V_{DS}) at several values of the gate voltage (V_{GS}) and (b) transfer characteristics ($-I_{DS}$ vs. V_{GS} plotted on a logarithmic scale and $\sqrt{|I_{DS}|}$ vs. V_{GS}) at $V_{DS} = -30$ V for devices ($W = 590 \pm 90$ μm, $L = 65 \pm 5$ μm) with a 60 nm-thick thick pentacene film on an OTS-treated 200 nm-thick Al_2O_3 film (T1) and an OTS-treated 200 nm-thick SiO_2 film (T2), with n^+-Si as substrates and gate electrodes.

mobilities and threshold voltages were calculated in the saturation regime by fitting the $\sqrt{|I_{DS}|}$ vs. V_{GS} data to the square law:

$$I_{DS} = \mu C_{OX} \frac{W}{2L} (V_{GS} - V_T)^2 \quad (1)$$

where μ is the field-effect mobility, C_{OX} is the capacitance density of the gate dielectric insulator, V_T is the threshold voltage, and W (width) and L (length) are the dimensions of the semiconductor channel defined by the source and drain electrodes.

A field-effect mobility of 1.5 ± 0.2 cm^2/V s was extracted for the T1 transistors while the T2 transistors had a lower carrier mobility of 0.6 ± 0.1 cm^2/V s. With Al_2O_3 ($\kappa = 7.5$) as gate insulators, the capacitance density of the gate insulator in T1 transistors was as high as 32.7 nF/cm^2 as compared to 17.3 nF/cm^2 in T2 transistors. Consequently, the saturation current (−88 μA) in T1 transistors was almost five times larger than that (−17 μA) obtained from T2 transistors as shown in Fig. 6a. The higher mobility and current obtained from T1 transistors can be correlated with the morphology of pentacene film and the dielectric/surface properties of OTS-treated Al_2O_3: first, compared with pentacene films on T2 (OTS-treated SiO_2), a reduced grain size and a well-ordered island formation of pentacene films on OTS-treated Al_2O_3 (T1) indicate a higher interconnection and tighter packing (with improved contact) between grains, which could lead to more efficient charge transport and enhance the drain current in the channel [21]. Secondly, with OTS SAMs on the surface, the surface disorder induced by the polar groups from high-κ dielectric surface (Al_2O_3 in our case) can be minimized. This is confirmed by the zero turn-on voltage V_{TO} shown on the transfer curve in Fig. 6b, indicating that no net fixed charges exist at the semiconductor/insulator interface. By using gate insulators with higher dielectric constant, a higher concentration of the charge carriers is accumulated in the channel for the same gate voltage and the Fermi level moves towards the band edge. The trapping states located in the 'gap' are filled and consequently a higher density of injected carriers is free to move with the microscopic mobility associated with carriers in the delocalized states. Thus, the use of high-κ dielectrics not only lowers the operating voltage, but also improves the mobility. This increase in mobility can be superlinear, as observed in this study, since it is due to the cumulative process of carriers becoming available at higher energies as the lower energy traps are filled. Using dielectric films with comparable thickness but having different dielectric constants, Dimitrakopolous et al. have demonstrated that the mechanism responsible for enhancing TFT carrier mobility is related to the carrier density in the channel region rather than the gate electric field [22].

Along with a zero turn-on voltage V_{TO}, a low threshold voltage of -7 ± 2 V and a subthreshold slope of 0.6 V/decade were extracted for T1. A high on/off current ratio of 6×10^6 was also obtained for T1, measured between the "on" current value at $V_{GS} = -30$ V and the "off" current at $V_{GS} = 0$ V, both with $V_{DS} = -30$ V. On the other hand, T2 showed a positive turn-on voltage V_{TO} of 5 V with a threshold voltage of -9 ± 2 V. Thus the transis-

tors were operated in the depletion mode instead of the enhancement mode as in T1, and consequently they could only be switched off by applying a positive gate bias. In addition, a higher sub-threshold slope of 3 V/decade and a lower on/off ratio of 10^5 were obtained for T2. The "off" current in T2 was 10 times higher than that in T1. These significant improvements in subthreshold slope, turn-on voltage (threshold voltage) and "off" current seen in T1 transistors can be attributed to a lower charge trap density at the pentacene/dielectric interface. We can estimate the maximum interfacial trap density $N_{\text{trap}}^{\max}$ from Eq. (2): [23,24]

$$N_{\text{trap}}^{\max} = \frac{C_{\text{OX}}}{q}\left[\frac{qS\log e}{k_{\text{B}}T} - 1\right] \tag{2}$$

where k_{B} is Boltzmann's constant, T is temperature, q is the electronic charge, e is the base of the natural logarithm, C_{OX} is the capacitance density of the gate insulator and S is the subthreshold slope in V/decade. Calculated from Eq. (2), the trap density at the OTS-treated Al_2O_3 (T1) surface was as low as $1.8 \times 10^{12}\ \text{cm}^{-2}$. A much higher value of trap density ($5.2 \times 10^{12}\ \text{cm}^{-2}$) was obtained from OTS-treated SiO_2 (T2) surface. This higher value can explain the positive turn-on voltage, larger subthreshold slope, and higher "off" current observed in T2. However, this calculated trap density value for OTS-treated SiO_2 is comparable to previously reported values for bare SiO_2 [23]. The interfacial traps are usually due to surface imperfections such as oxygen (OH groups), water molecules or mobile ions. It has been shown that silanol groups on SiO_2 cannot be completely passivated by self-assembled alkyl layers [25]. The residual silanol groups can trap electrons with protons and release H_2, therefore forming negative charges and inducing a positive shift in V_{TO} [20]. The electrical parameters we discussed here for transistors T1 and T2 along with those of the transistors T3 to be discussed next are summarized in Table 1.

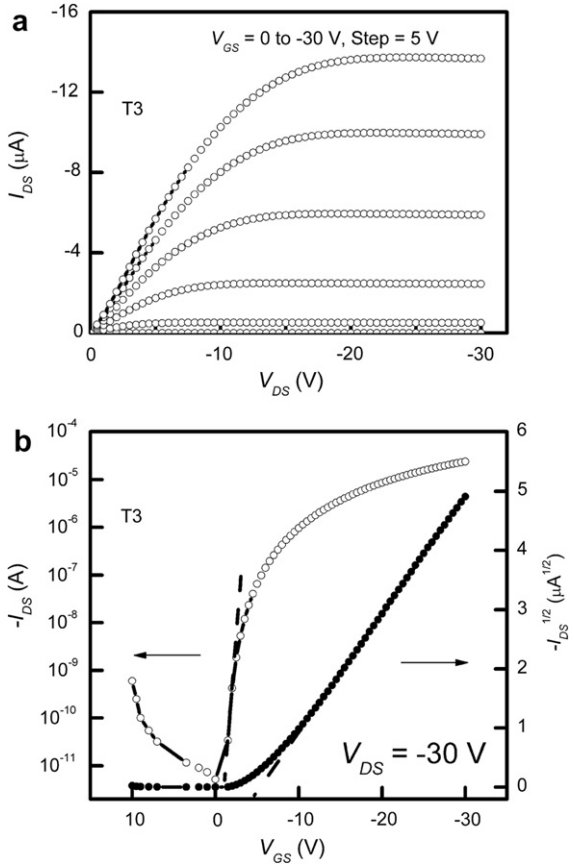


Fig. 7. (a) Output characteristics (I_{DS} vs. V_{DS}) at several values of the gate voltage (V_{GS}) and (b) transfer characteristics ($-I_{\text{DS}}$ vs. V_{GS} plotted on a logarithmic scale and $\sqrt{|I_{\text{DS}}|}$ vs. V_{GS}) at $V_{\text{DS}} = -30$ V for devices ($W = 550 \pm 50$ μm, $L = 185 \pm 5$ μm) with a 60 nm-thick pentacene film on an OTS-treated 200 nm-thick Al_2O_3 film with ITO as substrates and gate electrodes (T3).

The output characteristics and transfer characteristics of T3 transistors were shown in Figs. 7a and 7b, respectively. Even though the substrate ITO-coated glass had a relatively large surface roughness (see Fig. 2), a high field-effect mobility of $0.9 \pm 0.1\ \text{cm}^2/\text{V s}$ was obtained in the saturation region for T3 (Fig. 7b) with a channel length

Table 1
Summary of the electrical parameters for pentacene transistors T1, T2, and T3

Transistors	t (nm)	C_{OX} (nF/cm^2)	μ (cm^2/V s)	V_{T} (V_{TO}) (V)	S (V/decade)	$N_{\text{trap}}^{\max}$ ($\times 10^{12}$ cm^{-2})	$I_{\text{on/off}}$
T1: OTS/Al_2O_3/n^+-Si	200	32.7	1.5 ± 0.2	-7 ± 2 (0)	0.6	1.8	6×10^6
T2: OTS/SiO_2/n^+-Si	200	17.3	0.6 ± 0.1	-9 ± 2 (5)	3	5.2	10^5
T3: OTS/Al_2O_3/ITO	200	32.7	0.9 ± 0.1	-6 ± 1 (0)	0.5	1.4	10^6

t: thickness of gate dielectric insulator, C_{OX}: capacitance density, μ: carrier mobility, V_{T}: threshold voltage, V_{TO}: turn-on voltage, S: subthreshold slope, $N_{\text{trap}}^{\max}$: maximum interfacial trap density, $I_{\text{on/off}}$: on/off current ratio.

$L = 185 \pm 5$ μm and a channel width $W = 550 \pm 50$ μm. This value of mobility ranks to date as the highest known mobility reported for pentacene-based OFETs on ITO-coated glass [26]. This indicates that the contribution of higher carrier density to the field-effect mobility is dominant compared to the adverse effect of the substrate roughness on the morphology and transport. In addition to the high-mobility values, T3 transistors exhibited superior electrical characteristics similar to those of T1: a turn-on voltage V_{TO} of zero volts, a threshold voltage of -6 ± 1 V, and a subthreshold slope of 0.5 V/decade, as extracted from the transfer characteristic curve (Fig. 7b). The maximum trap density was estimated to be 1.4×10^{12} cm^{-2}, which is again close to the value estimated for T1. The consistency of trap density across the same type of oxide surface further confirms that Al_2O_3 has fewer trapping sites. A high on/off current ratio larger than 10^6 was also obtained from T3. Since pentacene growth, and thus OFETs made of it, can be affected by the roughness of dielectric layers underneath as demonstrated by Fritz et al. [19], the high performance of T3 transistors demonstrates the effectiveness of employing an Al_2O_3 layer grown by ALD technique as a dielectric for inherently rough substrates.

4. Conclusions

In summary, we have utilized atomic layer deposition (ALD) to grow Al_2O_3 gate dielectric insulators and obtained high-performance pentacene OFETs. OFETs fabricated on n^+-Si wafers and ITO-coated glass were operated in enhancement mode with a zero turn-on voltage, and exhibited large carrier mobility and a low threshold voltage, as well as a low subthreshold slope and a large on/off current ratio. Atomic force microscopy (AFM) images of pentacene films on Al_2O_3 revealed well-ordered island formation, and X-ray diffraction patterns showed characteristics of a "thin film" phase. Low trap density and high capacitance density of Al_2O_3 gate insulators also contributed to the high performance of pentacene field-effect transistors. The results of this work not only demonstrate that gate dielectrics grown by ALD present a viable alternative to dielectrics from traditional deposition techniques, but also show that the ALD dielectrics can result in improved electrical performance of transistors even on substrates with high roughness. The latter will become an increasingly critical issue in future for most flexible substrates of interest.

Acknowledgements

This material is based upon work supported in part by the STC Program of the National Science Foundation under Agreement Number DMR-0120967, by the Office of Naval Research. This work was performed in part at the Microelectronics Research Center at Georgia Institute of Technology, a member of the National Nanotechnology Infrastructure Network, which is supported by the NSF (Grant ECS- 03–35765).

References

[1] V. Subramanian, J.M.J. Frechet, P.C. Chang, D.C. Huang, J.B. Lee, S.E. Molesa, A.R. Murphy, D.R. Redinger, S.K. Volkman, Proc. IEEE 93 (7) (2005) 1330.
[2] G.H. Gelinck, H.E.A. Huitema, E. van Veenendaal, E. Cantatore, L. Schrijnemakers, J.B.P.H. van der Putten, T.C.T. Geuns, M. Beenhakkers, J.B. Giesbers, B.-H. Huisman, E.J. Meijer, E.M. Benito, F.J. Touwslager, A.W. Marsman, B.J.E. van Rens, D.M. de Leeuw, Nat. Mater. 3 (2) (2004) 106.
[3] L. Zhou, A. Wanga, S.-C. Wu, J. Sun, S. Park, T.N. Jackson, Appl. Phys. Lett. 88 (8) (2006) 083502/1.
[4] J.E. Crowell, J. Vac. Sci. Technol. B: Microelectron. Nanometer Struct. 21 (5 suppl.) (2003) 88.
[5] M.D. Groner, F.H. Fabreguette, J.W. Elam, S.M. George, Chem. Mater. 16 (4) (2004) 639.
[6] M. Leskela, M. Ritala, Angew. Chem., Int. Ed. 42 (45) (2003) 5548.
[7] L. Niinistö, J. Päiväsaari, J. Niinistö, M. Putkonen, M. Nieminen, Phys. Statu Solid A 201 (7) (2004) 1443.
[8] A.P. Ghosh, L.J. Gerenser, C.M. Jarman, J.E. Fornalik, Appl. Phys. Lett. 86 (22) (2005) 223503.
[9] H.J. Kim, S.J. Kang, D.S. Park, K.B. Chung, M. Noh, C.N. Whang, M.H. Cho, J. Kor. Phys. Soc. 45 (4) (2004) 935.
[10] J.B. Koo, S.H. Kim, J.H. Lee, C.H. Ku, S.C. Lim, T. Zyung, Synth. Met. 156 (2–4) (2006) 99.
[11] R.L. Puurunen, J. Appl. Phys. 97 (12) (2005) 121301.
[12] J. Veres, S.D. Ogier, S.W. Leeming, D.C. Cupertino, S.M. Khaffaf, Adv. Funct. Mater. 13 (3) (2003) 199.
[13] J. Veres, S. Ogier, G. Lloyd, D. de Leeuw, Chem. Mater. 16 (23) (2004) 4543.
[14] I.N. Hulea, S. Fratini, H. Xie, C.L. Mulder, N.N. Iossad, G. Rastelli, S. Ciuchi, A.F. Morpurgo, Nat. Mater. 5 (12) (2006) 982.
[15] V. Coropceanu, J.-L. Bredas, Nat. Mater. 5 (12) (2006) 929.
[16] L.N. Mitchon, J.M. White, Langmuir 22 (15) (2006) 6549.
[17] Y. Wang, M. Lieberman, Langmuir 19 (4) (2003) 1159.
[18] S. Steudel, S. De Vusser, S. De Jonge, D. Janssen, S. Verlaak, J. Genoe, P. Heremans, Appl. Phys. Lett. 85 (19) (2004) 4400.
[19] S.E. Fritz, T.W. Kelley, C.D. Frisbie, J. Phys. Chem. B 109 (21) (2005) 10574.

[20] M.-H. Yoon, C. Kim, A. Facchetti, T.J. Marks, J. Am. Chem. Soc. 128 (39) (2006) 12851.
[21] S.Y. Yang, K. Shin, C.E. Park, Adv. Funct. Mater. 15 (11) (2005) 1806.
[22] C.D. Dimitrakopoulos, S. Purushothaman, J. Kymissis, A. Callegari, J.M. Shaw, Science 283 (5403) (1999) 822.
[23] M. McDowell, I.G. Hill, J.E. McDermott, S.L. Bernasek, J. Schwartz, Appl. Phys. Lett. 88 (7) (2006) 073505.
[24] A. Rolland, J. Richard, J.P. Kleider, D. Mencaraglia, J. Electrochem. Soc. 140 (12) (1993) 3679.
[25] D.L. Angst, G.W. Simmons, Langmuir 7 (10) (1991) 2236.
[26] J.-M. Choi, D.K. Hwang, J.H. Kim, S. Im, Appl. Phys. Lett. 86 (12) (2005) 123505.

Available online at www.sciencedirect.com
ScienceDirect
Organic Electronics 8 (2007) 727–734
Organic Electronics
www.elsevier.com/locate/orgel

Field-effect transistors based on poly(3-hexylthiophene): Effect of impurities

Mathieu Urien [a], Guillaume Wantz [a,*], Eric Cloutet [b], Lionel Hirsch [a], Pascal Tardy [a], Laurence Vignau [a], Henri Cramail [b], Jean-Paul Parneix [a]

[a] *Université Bordeaux 1, Laboratoire de l'Intégration, du Matériau au Système (IMS), CNRS (UMR 5218), Site ENSCPB, 16 avenue Pey Berland, 33607 Pessac Cedex, France*
[b] *Université Bordeaux 1, Laboratoire de Chimie des Polymères Organiques (LCPO), CNRS (UMR 5629), ENSCPB, 16 avenue Pey Berland, 33607 Pessac Cedex, France*

Received 12 April 2007; received in revised form 13 June 2007; accepted 14 June 2007
Available online 21 June 2007

Abstract

Organic field-effect transistors (OFETs) based on regioregular poly(3-hexylthiophene)s (P3HT)s have been studied as a function of the amount of impurities in the active polymer. P3HTs have been synthesized via a nickel-initiated cross-coupling polymerization and successively purified by a series of Soxhlet extractions with methanol, hexane and chloroform. At each stage, the amount of impurities was quantified by means of ^{1}H nuclear magnetic resonance (NMR) spectroscopy, Rutherford backscattering spectroscopy (RBS) and particle induced X-ray emissions (PIXE). Traces of Ni, Cl, Mg, Ca, Fe and Zn could be detected in non-fully purified P3HTs. The presence of impurities in the different fractions of P3HT is shown to affect not only the characteristics of the OFETs but also the photovoltaic performances.
© 2007 Elsevier B.V. All rights reserved.

PACS: 72.80.Le; 71.20.Rv; 85.30.Tv; 71.55.Jv

Keywords: Field-effect transistor; Poly(3-hexylthiophene); Purity; Nuclear analysis

1. Introduction

Semi-conducting polymers have gained increasing interest over the last few years due to their potential applications in organic electronics such as organic photovoltaic cells (OPVs), organic light emitting diodes (OLEDs), and organic field-effect transistors (OFETs). Among these polymers, regioregular poly(3-hexylthiophene) (rr-P3HT) is widely studied because of its good solubility, processability, chemical stability and excellent electronic properties. For instance, photovoltaic cells with power conversion efficiency of about 5% have been obtained using P3HT/fullerene derivative blends [1]. Concerning OFETs, P3HT is one of the most promising solution processable material with a high hole mobility [2,3]. It is believed that for electronic applications, the level of chemical purity required is extremely high because the presence of impurities even in very low amount can have considerable

* Corresponding author. Tel.: +33 540006630; fax: +33 540006631.
E-mail address: guillaume.wantz@ims-bordeaux.fr (G. Wantz).

1566-1199/$ - see front matter © 2007 Elsevier B.V. All rights reserved.
doi:10.1016/j.orgel.2007.06.003

effects on the electronic properties of materials. In inorganic semi-conductors, impurities play a significant role due to the wide delocalization of charge carriers. For organic semi-conductors, charge carriers are localized on molecules and the influence sphere radius of impurities is reduced in comparison with their inorganic homologues. However, traces of impurities in semi-conducting polymers have been found to seriously affect the electronic properties [4,5]. In this paper, we aim to investigate the influence of impurities in rr-P3HT on OFETs characteristics. The presence of impurities was determined by various techniques (*i.e.* ^{1}H Nuclear Magnetic Resonance, ^{1}H NMR; Rutherford Backscattering Spectroscopy, RBS; and Particle Induced X-ray Emission, PIXE) during the different steps of purification and extraction of a home-made rr-P3HT. In parallel OFETs were built and studied in order to better correlate the relationship between their characteristics and the level of purity of the semi-conducting polymer matrix.

2. Synthesis and purifications of regioregular P3HTs (rr-P3HTs)

Highly regioregular poly(3-hexylthiophene)s (rr-P3HTs) were synthesized by the Grignard metathesis method (GRIM), which has been described by McCullough and colleagues [6] as being a very good way to achieve such polymers. P3HTs with 97% of regioregularity, determined from the ^{1}H NMR spectra, have been reported in the literature [7]. The synthesis, which is described hereafter (Fig. 1) is a nickel-catalyzed cross-coupling polymerization and proceeds by a chain-growth mechanism [8]. The polymer was purified by consecutive washings using the Soxhlet technique with methanol and hexane, respectively. The final P3HT was isolated from the chloroform solution. At each stage of the purification process, aliquots were removed and analyzed to determine their composition with size exclusion chromatography (SEC), ^{1}H NMR analyses and also nuclear analyses, *i.e.* Rutherford Backscattering Spectroscopy (RBS) and Particle Induced X-ray Emission (PIXE). A series of samples have thus been collected directly from the Soxhlet filter after the polymer had been washed. Thus F1 was the crude material received precipitated from the reaction mixture in methanol; F2 is P3HT that has been washed with methanol; F3 is P3HT that has been washed with hexane; and F4 is the remaining P3HT recovered from the Soxhlet filter by chloroform distillation.

3. Composition analyses

It is noteworthy that a large list of compounds can be present in the crude product and remain after several washings depending on the solvent strength. One can cite for instance remnants of monomer (2,5-dibromo-3-hexylthiophene), catalyst (Ni(dppp)Cl_2), secondary products (e.g. 2-bromo-3-hexylthiophene, 5-bromo-3-hexylthiophene, *tert*-butane and magnesium chloride) and low molecular weight P3HTs. All these species must be eliminated by the successive washings in order to obtain a pure material suitable for electronic applications.

SEC traces (in THF, polystyrene calibration) of F1, F2, F3 and F4 are shown in Fig. 2 and values are summarized in Table 1. F2, F3 and F4 traces

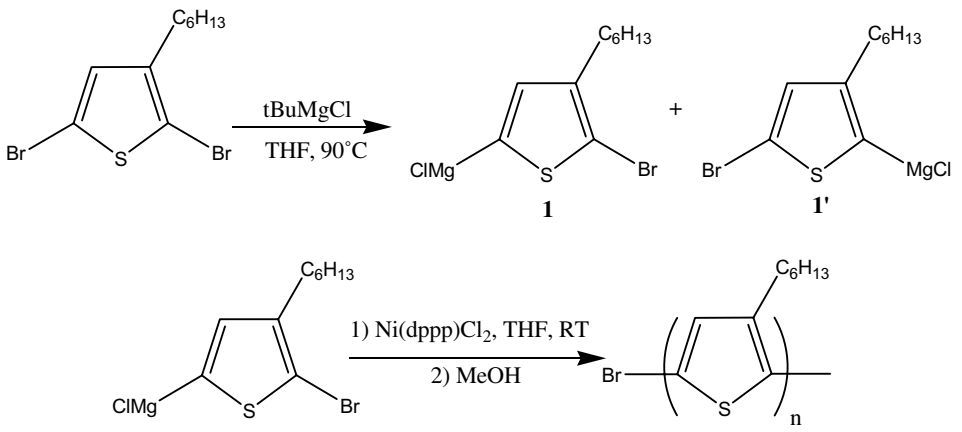


Fig. 1. Synthesis of high-regioregular P3HT.

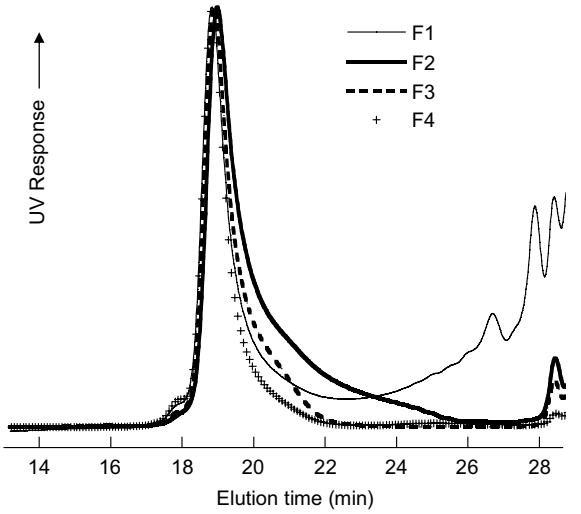


Fig. 2. SEC traces of F1, F2, F3 and F4 (in THF as eluent).

Table 1
Analysis of each fraction: $\overline{M_n}$ and PDI $\left(\frac{\overline{M_w}}{\overline{M_n}}\right)$ from SEC analyses (in THF, PS calibration); [S]/[Br] ratio from RBS data

	F1	F2	F3	F4
M_n (g/mol)	16,000	9300	17,900	21,100
PDI	1.21	1.47	1.26	1.17
[S]/[Br]	2	75	76	147

show a main peak and a negligible shoulder at higher molecular weight due to a few coupling reactions occurring after methanol quenching [9]. Besides these peaks, F1 presents many minor oligomers at 26 and 27 min elution time. A non-regular increase in molecular weights is observed between F1 (raw material) and F4 (final material). Indeed, a surprising high molecular weight of 16,000 g/mol is obtained for F1 (crude material). This value can be explained taking into account that the calculated values were taken over a range included only the main peak and not oligomers. Therefore one can propose that the molecular weight found for F1 is overestimated because it does not take account of low molecular weight impurities. Concerning the other fractions, as expected an increase of the molecular weight is observed between F2 (9300 g/mol) and F4 (21,100 g/mol). This means that low molecular weight P3HTs have been removed during the washings. Moreover, SEC spectra (Fig. 2) show shrinkage of polymer peak and thus a decrease of the polydispersity index between F2 and F4 (Table 1). That was also confirmed by the SEC analysis of the fraction isolated from the hexane solution which showed low molecular weight polymers of 2000 g/mol (PDI ~ 1.48).

^{1}H NMR spectra have been recorded for each fraction, as shown in Fig. 3. It should be noted that the spectrum of F1 shows many minor peaks, due both to the presence of residual starting materials, and oligomers with high degrees of chain irregularities caused by the GRIM reaction, which is known to promote single irregularities at chain ends [10]. In particular, F1 spectrum shows signals at 2.5 ppm and 6.6–6.9 ppm that can be assigned, respectively, to methylene and hetero-arylene protons of the remaining monomer. Conversely, F2, F3 and F4 spectra are similar to a typical P3HT ^{1}H NMR spectrum [7] and show no side peak or impurities. In F4 spectrum all peaks could be assigned to the different protons of the expected P3HT structure. In fact, the peak at 7.0 ppm, assigned to the P3HT backbone proton at position 4 (see Fig. 3) or the peak at 2.8 ppm, assigned to the α methylene protons of the hexyl chains, are used as probes to quantify the regioregularity of the P3HT. This allowed us to confirm that all P3HT samples were highly regioregular (*i.e.* regioregularity above or equal to 97%).

In addition to ^{1}H NMR spectroscopy, nuclear analyses were carried out in order to search for heavy elements. Indeed, they can play the role of defects in the material. Each fraction (F1, F2, F3

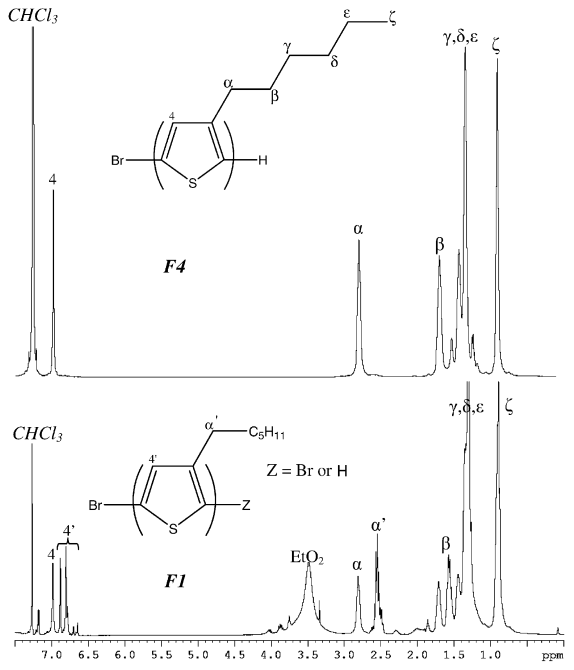


Fig. 3. ^{1}H NMR spectra (400 MHz, in $CDCl_3$) of F4 and F1.

and F4) has been analyzed by Rutherford Backscattering Spectroscopy (RBS) and Particle Induced X-ray Emission (PIXE) [11–14]. Such nuclear analyses are rarely used in the case of polymeric semi-conductors. Erwin et al. carried out RBS studies of an as received P3HT to reveal the presence of zinc and bromine [15]. On the one hand, RBS and PIXE are used to analyse the polymer purity. On the other hand, we demonstrate for the first time that these techniques can be useful to evaluate the molecular weight as well as the degree of polymerization of P3HT. While ^{1}H NMR spectroscopy did not reveal any difference between fractions F2, F3 and F4, RBS and PIXE analyses clearly show a variation of the composition as a function of purification steps. Fig. 4 shows PIXE spectra of F1, F2, F3 and F4 (normalized on the bremstrahlung). Spectra have been shifted for clarity. Strong differences are observed between those spectra unveiling the efficiency of the purification process. Indeed concerning F1, lots of elements are detected as the sulphur and the bromine. S and Br are the only heavy elements present in the final material (F4). Nickel, chlorine, magnesium, calcium, iron, and zinc are detected by PIXE. While Ni, Cl and Mg are involved in the polymer synthesis (monomer, reagent and catalyst), Ca, Fe and Zn have no reason for being present and are probably impurities ensuing from reagents and solvents, which were used as received without further purification. PIXE spectrum of F2 clearly shows a strong decrease of Br amount comparing to F1. It indicates that a part of species containing Br is soluble in MeOH (monomers and/or oligomers). Cl and Ca peaks have vanished on F2 spectrum. Ni, Zn, Fe and Mg are still present on the F3 spectrum. These latter elements are only removed on the F4 spectrum, except traces of iron. The final P3HT (F4) does not contain impurities detectable by RBS and PIXE techniques. Only sulphur and bromine are present as heavy elements in the polymer. Sulphur obviously comes from thiophene moieties and Br is the end group of the synthesized P3HT, as previously seen (see Fig. 1). Consequently the ratio [S]/[Br], evaluated from RBS spectra, can be used to determine the degree of polymerization (DP) of the polymer and therefore the absolute molecular weight. Table 1 summarizes the evolution of that ratio for each step of purification. [S]/[Br] increases significantly from F1 to F4. It indicates that species containing Br, as monomers or reaction intermediaries, have been removed. Since the molecular weight of a hexylthiophene unit is 166 g/mol and that the ratio [S]/[Br] or degree of polymerization is DP = 147, the molecular weight of the final P3HT (F4) can be calculated as about 24,400 g/mol, which is consistent with the molecular weight determined by SEC analysis (21,100 g/mol). RBS thus turns out to be a suitable technique to determine the molecular weight of the polymers without any need of standard samples.

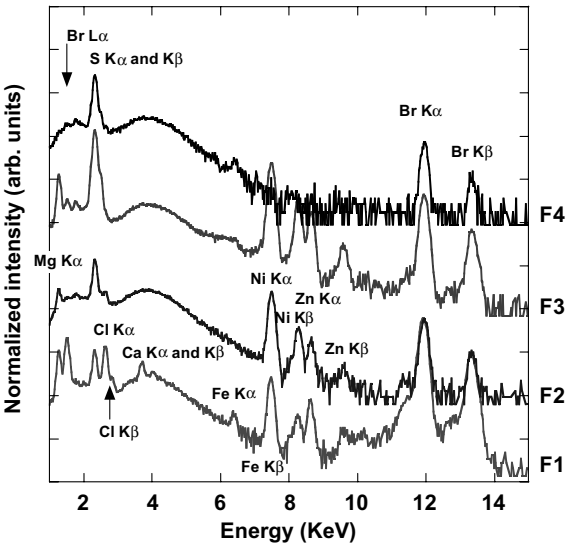


Fig. 4. PIXE spectra of F1 (raw material), F2 (MeOH wash), F3 (hexane wash) and F4 (final material).

4. Organic field-effect transistors

Field-effect transistors have been prepared from each fraction of P3HT. The OFETs were manufactured using an experimental procedure previously described by Nunzi and colleagues. [16]. The geometry is bottom-gate of ITO strips and gold drain and source electrodes evaporated on top of P3HT through a shadow mask to create a 40 μm-long and 3 mm-wide channel. Fig. 5 shows the typical characteristics of OFETs based on the initial raw material F1 (a) and the final purified polymer F4 (b). The final compound shows normal FET behaviour with well defined linear and saturation regimes. At zero volt gate bias, the drain–source current is low, leading to an on/off ratio of 125 (defined between gate voltage of −100 V and 0 V). With the raw material, the drain current at zero gate bias is significantly high, leading to a very low on/off ratio of 8. With intermediates F2 and F3, OFETs show characteristics which are very similar to the one of F1 with on/off ratios in the same order of

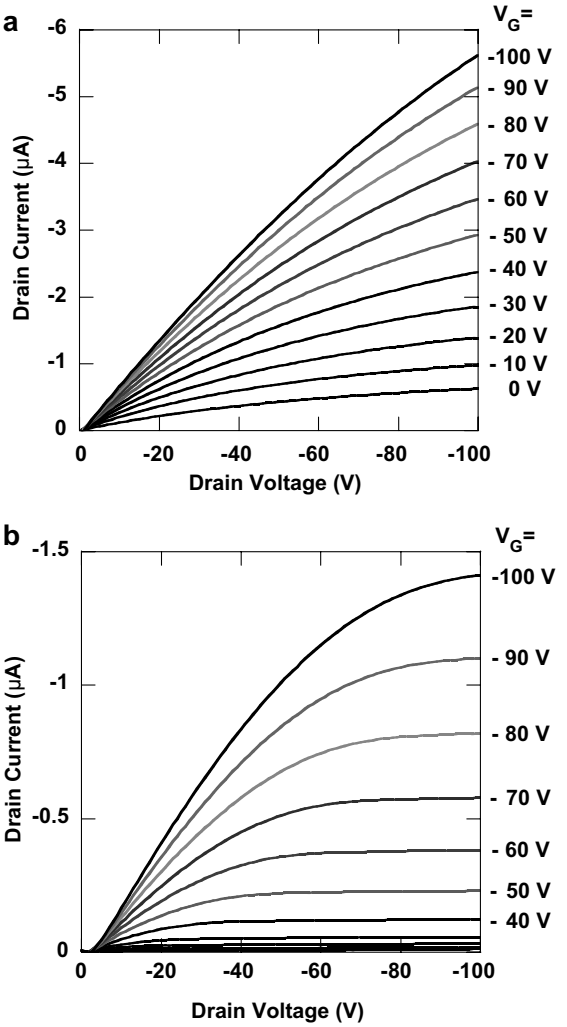


Fig. 5. Typical FET characteristics obtained with the raw material F1 (a) and the fully purified polymer F4 (b).

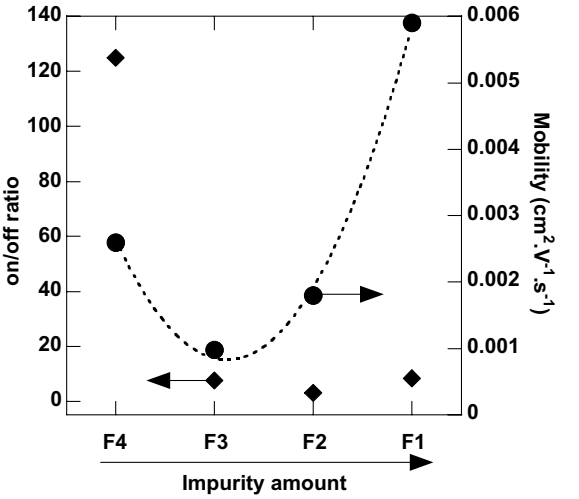


Fig. 6. Field-effect mobility calculated from the linear regime and on/off ratios of OFETs as a function of polymer fraction, *i.e.* as a function of the amount of polymer impurities (the dashed line is a guide for eye). On/off ratios are calculated as the ratio of drain currents between $V_G = -100$ V and $V_G = 0$ V at a constant $V_D = -100$ V.

magnitude. On/off ratios are plotted in Fig. 6 as a function of polymer purity. They have been calculated as the ratio of drain currents between $V_G = -100$ V and $V_G = 0$ V at a constant $V_D = -100$ V. Such a behaviour has already been reported elsewhere [5,17,18]. It is believed that impurities act as dopant moieties to make the P3HT partially conductive in the channel. As a consequence, such a conductive behaviour induces a parasitic "ohmic" current between drain and source [19]. It is interesting to note that such a chemical doping is observed in F1, F2 and F3. Only F4 show normal saturation behaviour. During the first washing, removing species containing Br (monomers), Cl (catalyst and $MgCl_2$) or Ca from F1 does not lead to a reduction of doping. Removing oligomers from F2 does not help either. But, finally, removing Ni, Zn, Fe and Mg containing species has a major impact on the doping effects decrease.

With such unusual saturations of OFETs, mobilities were not evaluated using the saturation regime model but by using the linear regime theory at low drain voltage following [20]:

$$I_D = \frac{W \cdot C_i}{L} \mu_{FE} \left(V_G - V_T - \frac{V_D}{2} \right) V_D \quad (1)$$

where I_D is the drain current, W and L are the width and length of the channel, respectively, C_i is the capacitance of polyimide $C_i = 2.8$ nF cm^{-2}; V_G, V_T and V_D are gate, threshold and drain voltages, respectively. Results are plotted in Fig. 6 as a function of polymer fraction, *i.e.* as a function of the amount of impurities. The mobility varies between 10^{-3} and 6.10^{-3} cm^2 V^{-1} s^{-1} and the evolution is non-regular. However, a similar behaviour has been described by Jiang et al. concerning the mobility in polymers that were chemically doped on purpose [21,22]. Once again, our results are consistent with doping effects due to impurities. Arkhipov et al. have theoretically described the effect of doping on the mobility of semi-conducting polymers [23,24]. They have demonstrated that the doping of disordered materials is ambivalent. On the one hand, it increases the concentration of charge carriers and lifts the Fermi level. On the other hand, it creates additional deep Coulombic traps of the opposite polarity

to induce energy disorder due to potential fluctuations. Doping of polymers in OFETs can also increase the mobility as it can reduce the injection barrier for holes at the metal/P3HT interface [25]. Here, the considered mobility is based on field-effect only. In their study, Jiang et al. mainly worked on electrochemistry measurements and observed a very strong effect of doping on the mobility values. However, it has been demonstrated that field-effect mobilities are less affected than the electrochemical ones [26]. This is the reason why, in our study, the mobility is only slightly dependent on the amount of impurities. The molecular weight (M_w) of the polymer must also be considered. Indeed, it has been demonstrated that P3HT's molecular weight has an influence on OFETs features and mobility [27,28]. Usually, mobility increases with molecular weight mainly because in a high M_w polymer, there is a formation of an amorphous inter-lamellar zone, which enables charge carrier transfer from one crystalline lamella of P3HT to another [29]. In our study, we can consider that the increase in M_w between F1 and F4, *i.e.* respectively, from 16,000 g/mol to 21,000 g/mol is negligible in regards to the mobility changes. The latter can only be attributed to the impurities present in the synthesized P3HTs. To date, organic photovoltaic cells based on P3HT are of the most promising solution-processed devices that have been made [1]. In this work, raw and fully purified P3HT fractions (F1 and F4) have been used as electron donor in photovoltaïc cells based on blends with PCBM (1:1 wt/wt). Like OFETs, the cells performances were found strongly dependent on the impurity content. F1 and F4 exhibit a power conversion efficiency of 0.001% and 1.21%, respectively, without any optimization of the devices in terms of thickness and post-treatments. Such a strong drop is certainly due to impurities rather than any modification of mobility in P3HT. The impurities play a critical role in P3HT:PCBM blends since they act both as dopants and as recombination centres.

5. Experimental part

5.1. Materials

2,5-Dibromo-3-hexylthiophene, *tert*-butylmagnesiumchloride, Ni(dppp)Cl_2, were used as received without further purification. THF was dried and distilled over CaH_2 and sodium/benzophenone, respectively. Methanol, hexane and chloroform used for Soxhlet extractions were used as received without purifications. All reactions were carried out under a dry nitrogen atmosphere, using flame-dried glassware. All materials were purchased from *Aldrich*.

5.2. Synthesis of high-regioregular poly(3-hexylthiophene): ''McCullough method''

A dry three-neck flask was charged with 2,5-dibromo-3-hexylthiophene (0.5 g, 1.5 mmol) and anhydrous THF (15 mL). A 2 M solution of butyl magnesium chloride (0.75 mL, 1.5 mmol) in diethylether (Et_2O) was added via a syringe, and the reaction mixture was gently refluxed for 90 min. The reaction mixture was allowed to cool down to room temperature, time at which Ni(dppp)Cl_2 (0.013 g, 0.023 mmol) was added to the reaction mixture. The polymerization was allowed to proceed for 15 min at room temperature and under stirring. The reaction mixture was then poured into methanol to precipitate the polymer and concentrated by rotary evaporation. The polymer powder was then poured into an extraction thimble and washed by sequential Soxhlet technique with methanol and hexane. After many cycles, the impurities which are soluble, respectively, in methanol and hexane were concentrated in the distillation flask. Soxhlet washings have been carried out during 24 h for each solvent. The polymer was then isolated from the chloroform solution and finally recovered by evaporation of chloroform by rotary evaporation.

5.3. Materials characterizations

^{1}H NMR spectra were recorded using a *Bruker AC-400 NMR* spectrometer at room temperature. Size exclusion chromatography (SEC) analyses were performed at room temperature in THF with a set-up consisting of a WATERS 880-PU pump and a series of three microstyragel columns with pore sizes of 10^3, 10^5 and 10^6 Å. The elution of the filtered samples was monitored using simultaneous UV and RI detection. The elution time were converted to molecular weights using a calibration curve based on narrow polydispersity PS standards.

RBS and PIXE measurements were performed at the Centre d'Etudes Nucléaires de Bordeaux Gradignan (CENBG) AIFIRA platform. Samples were prepared by drop casting the polymer on pure carbon substrates from an *ortho*-dichlorobenzene (ODCB) solution. For RBS studies, a 2 MeV $^4He^+$ monokinetic $\Delta E_0/E_0 = 10^{-5}$ incident beam was used. A silicon surface barrier detector with an

energy resolution of 13.5 keV, measured with a ^{241}Am source, and a collecting solid angle $d\Omega = 2.8$ msr, checked with a Al_2O_3/Al anodized thin film, was used for RBS studies. The detection angle was $\theta_L = 160°$. PIXE measurements were performed with a 2.5 MeV $^1H^+$ incident beam. The ionic current was set at 0.5 nA. A liquid nitrogen-cooled *Canberra* silicon detector was used. For both RBS and PIXE, the signal was recorded via a low capacitance charge amplifier and the samples were biased at 200 V to trap the secondary electrons. The diameter of both $^4He^+$ and $^1H^+$ incident beams is typically about 1 mm.

5.4. OFETs fabrication and characterization

OFETs were made using the following procedure. Indium tin oxide (ITO) coated glass slides (12 Ω/square), from *Merck Display*, were used as substrates. The ITO was selectively etched and cleaned. Before deposition of the polyimide dielectric, an adhesion promoter (VM-651, from *HD Microsystems*) was spin-coated on the substrate from a 50% water solution. Then, the substrates were baked at 120 °C in an oven for 15 min. Gate dielectric films were deposited from polyimide (PI-2555, from *HD Microsystems*). The films were softly baked in an oven at 120 °C for 30 min followed by curing at 200 °C for 30 min. Gate dielectric thickness is 1 μm. P3HT was then spin-coated onto the sample at 2000 rpm creating a 70 nm layer from a wt. 2% *o*-dichlorobenzene solution. To complete the OFET structure, gold source and drain electrodes were thermally evaporated onto the P3HT layer through a shadow mask under secondary vacuum (10^{-6} mbar) to create a 40 μm-long and 3 mm-wide channel. OFETs were then stored and characterized under inert atmosphere in a nitrogen glove box ($[O_2]$ and $[H_2O] < 1$ ppm). Contacts were taken using a prober (*Karl Suss PM5*). Current–voltage curves were recorded using a *Keithley 4200 SCS*.

6. Conclusion

Regioregular poly(3-hexylthiophene)s have been synthesized via a nickel-initiated cross-coupling polymerization and successively purified by a series of soxhlet extractions with methanol, hexane and chloroform giving rise to a series of P3HT fractions F1 to F4. The content of impurities such as residual monomers, catalyst and reactants has been determined by NMR, SEC and nuclear analysis (RBS and PIXE). Traces of Ni, Cl, Mg, Ca, Fe and Zn have been identified within the raw product. Interestingly, after purification the removal of all heavy metals was complete and the quantification of the ratio [S]/[Br] allowed us to determine the molecular weight of P3HT. It was shown in good agreement with the values obtained from SEC results using PS standards. OFETs based on each fraction of P3HT have been studied. They show a strong dependence on the amount of impurities with a low on/off ratio for devices based on non-fully purified materials because of chemical doping. The slight mobility variation is consistent with the fact that metallic impurities act as dopant moieties. It is also reported that photovoltaic properties of P3HTs are significantly sensitive to impurities.

Acknowledgments

This work was supported by the "Région Aquitaine", the STII Department of French CNRS (ELORGA platform). The authors thank Roger Hiorns for his help in the preparation of this manuscript and the CENBG team for their help in RBS and PIXE studies.

References

[1] M. Reyes-Reyes, K. Kim, D.L. Carroll, Applied Physics Letters 87 (2005) 083506.
[2] H. Sirringhaus, Advanced Materials 17 (2005) 2411–2425.
[3] B.H. Hamadani, D. Natelson, Applied Physics Letters 84 (2004) 443.
[4] S.S. Pandey, W. Takashima, S. Nagamatsu, T. Endo, K. Kaneto, IEICE Transactions on Electronics E83C (2000) 1088.
[5] Y. Chen, I. Shih, S. Xiao, Journal of Applied Physics 96 (2004) 454–458.
[6] M.C. Iovu, M. Jeffries-EL, E.E. Sheina, J.R. Cooper, R.D. McCullough, Polymer 46 (2005) 8582.
[7] R.D. McCullough, Advanced Materials 10 (1998) 193.
[8] M.C. Iovu, E.E. Sheina, R.R. Gil, R.D. McCullough, Macromolecules 38 (2005) 8649.
[9] R. Miyakoshi, A. Yokoyama, T. Yokozawa, Macromolecular Rapid Communications 25 (2004) 1663.
[10] R.C. Hiorns, A. Khoukh, B. Gourdet, C. Dagron-Lartigau, Polymer International 55 (2006) 608.
[11] J.W. Mayer, E. Rimini, Ion Beam Handbook of Material Analysis, Academic Press Inc., 1977.
[12] W.K. Chu, J.W. Mayer, M.A. Nicolet, Backscattering Spectroscopy, Academic Press Inc., 1978.
[13] J.F. Ziegler, W.K. Chu, Atomic Data and Nuclear Data Tables 13 (1974) 463.
[14] L. Hirsch, F. Natali, P. Moretto, A.-S. Barrière, D. Byrne, F. Semond, J. Massies, N. Grandjean, N. Antoine-Vincent, J. Leymarie, Physica Status Solidi A 195 (2003) 502.

[15] M.M. Erwin, A.V. Kadavanich, J. McBride, S. Pennycook, S.J. Reosenthal, European Physical Journal D 16 (2001) 275–277.
[16] K.N. Narayanan Unni, S. Dabos-Seignon, J.-M. Nunzi, Journal of Physics D: Applied Physics 38 (2005) 1148–1151.
[17] G. Lloyd, M. Raja, I. Sellers, N. Sedghi, R. Di Lucrezia, S. Higgins, B. Eccleston, Microelectronic Engineering 59 (2001) 323–328.
[18] H. Kokubo, T. Yamamoto, H. Kondo, Y. Akiyama, I. Fujimura, Japanese Journal of Applied Physics 42 (2003) 6627–6628.
[19] G. Horowitz, Advanced Materials 8 (1996) 177–179.
[20] G. Horowitz, Advanced Materials 10 (1998) 365–377.
[21] X. Jiang, Y. Harima, K. Yamashita, Y. Tada, J. Ohshita, A. Kunai, Chemical Physics Letters 364 (2002) 616–620.
[22] X. Jiang, R. Patil, Y. Harima, J. Ohshita, A. Kunai, Journal of Physical Chemistry B 109 (2005) 221–229.
[23] V.I. Arkhipov, P. Heremans, E.V. Emelianova, G.J. Adriaenssens, H. Bässler, Applied Physics Letters 82 (2003) 3245–3247.
[24] V.I. Arkhipov, P. Heremans, E.V. Emelianova, H. Bässler, Physical Review B 71 (2005) 045214.
[25] B.H. Hamadani, H. Ding, Y. Gao, D. Natelson, Physical Review B 72 (2005) 235302.
[26] H. Shimotani, G. Diguet, Y. Iwasa, Applied Physics Letters 86 (2005) 022104.
[27] J.-M. Verilhac, G. LeBlevennec, D. Djurado, F. Rieutord, M. Chouiki, J.-P. Travers, A. Pron, Synthetic Metals 156 (2006) 815–823.
[28] A. Zen, M. Saphiannikova, D. Neher, J. Grenzer, S. Grigorian, U. Pietsch, U. Asawapirom, S. Janietz, U. Scherf, I. Lieberwirth, G. Wegner, Macromolecules 39 (2006) 2162–2171.
[29] M. Brinkmann, P. Rannou, Advanced Functional Materials 17 (2006) 101–108.

Available online at www.sciencedirect.com
ScienceDirect
Organic Electronics 8 (2007) 735–742
Organic Electronics
www.elsevier.com/locate/orgel

Efficient fluorescent white organic light-emitting diodes using co-host/emitter dual-role possessed di(triphenyl-amine)-1,4-divinyl-naphthalene

Jwo-Huei Jou *, Ming-Hsuan Wu, Chung-Pei Wang, Yung-Sheng Chiu, Po-Hsuan Chiang, Huei-Ching Hu, Ren-Yang Wang

Department of Materials Science and Engineering, National Tsing Hua University, Hsin-Chu 30013, Taiwan, ROC

Received 8 March 2007; received in revised form 30 May 2007; accepted 17 June 2007
Available online 5 July 2007

Abstract

Efficient fluorescent white organic light-emitting diodes with low carrier-injection barriers were fabricated with device structure of indium tin oxide/*N,N′*-bis-(1-naphthy)-*N,N′*-diphenyl-1,1′-biphenyl-4-4′-diamine/white emission layer/1,3,5-tris(*N*-phenyl-benzimidazol-2-yl)benzene/lithium fluoride/aluminium. By blending in the blue host of 1-butyl-9,10-naphthalene-anthracene in the emissive layer an efficient electro-luminescent greenish-blue co-host of di(triphenyl-amine)-1,4-divinyl-naphthalene, with the doping of a trace amount of red dye of 4-(dicyano-methylene)-2-methyl-6-(julolidin-4-yl-vinyl)-4*H*-pyran, bright and colour-stable white emission with high power-efficiency of 14.6 lm/W at 100 cd/m^2 or current efficiency of 19.2 cd/A at 300 cd/m^2 or 18.7 cd/A at 10,000 cd/m^2 was obtained. The resulted synergistic increase in brightness and efficiency may be attributed to the presence of cascading new routes with comparatively lower electron injection barrier.
© 2007 Published by Elsevier B.V.

PACS: 73.40.Lq; 73.50.−h; 73.61.Ph; 73.63.−b

Keywords: Organic light-emitting diodes; White; Co-host; High-efficiency

1. Introduction

White organic light-emitting diodes (OLEDs) have attracted increasing attention for having great potential for use in high quality display [1–3] and area illumination [4,5], especially since relatively high power efficiency phosphorescent white OLEDs have been fabricated [6–8]. Instead of having a maximum 100% internal quantum efficiency in phosphorescent dopants [9], fluorescent dopants posses only a maximum of 25% [10], resulting in an inherently poorer luminescent efficiency in fluorescent devices. Although the efficiency of fluorescent white OLEDs is sufficient to fabricate some displays [11], the extension to more competitive display applications as well as next-generation area illumination demands a much higher efficiency.

* Corresponding author. Tel.: +886 3 5742617; fax: +886 3 5719524.
E-mail address: jjou@mx.nthu.edu.tw (J.-H. Jou).

1566-1199/$ - see front matter © 2007 Published by Elsevier B.V.
doi:10.1016/j.orgel.2007.06.010

The efficiency of white OLEDs relies on device thickness, carrier injection barriers, carriers and excitons confinement, and host-to-guest energy transfer [7]. The generation of a strong blue emission is crucial to the entire efficiency performance [8]. Especially for systems employing blue light-emitting host, the efficiency markedly varies with the use of hosts with different electro-luminescent efficiencies [12]. The introduction of a proper co-host may enhance the efficiency performance [13,14]. The task in generating a brighter and more efficient white emission with high colour-stability hence becomes difficult since nearly all these factors must be taken into consideration in fabrication, especially when some of them are competing against each other. By varying the host in a given device structure, for example, favouring the injection of hole into the emissive layer by minimizing the corresponding hole-injection-barrier frequently maximize the electron injection barrier, greatly limiting the injection of electron, and vice versa.

Here, we demonstrate the fabrication of efficient fluorescent white OLEDs with effective carriers and excitons confinement, efficient host-to-guest energy transfer, and, especially, low carrier-injection-barriers, by using a blue host of 1-butyl-9,10-naphthalene-anthracene (BANE) or a greenish-blue host of di(triphenyl-amine)-1,4-divinyl-naphthalene (DPVP), doped with red dye of 4-(dicyano-methylene)-2-methyl-6-(julolidin-4-yl-vinyl)-4*H*-pyran (DCM2) in the emissive layer of a device composing 125 nm indium tin oxide/45nm *N,N*′-bis-(1-naphthy)-*N,N*′diphenyl-1,1′-biphenyl-4-4′-diamine (NPB)/30 nm white emission layer/40 nm 1,3,5-tris(*N*-phenyl-benzimidazol-2-yl)benzene (TPBi)/1 nm lithium fluoride/150 nm aluminium. By further blending in the red dye-doped blue host BANE the greenish-blue DPVP, markedly bright and efficient fluorescent white emission is obtained.

2. Experimental

2.1. Device fabrication

All the guest and host molecules were vapour-deposited in one single layer using deposition sources prepared by a solution-mixing method, whose detailed experimental procedures are presented elsewhere [12]. The device was fabricated using an indium tin oxide coated glass substrate (Merck Display Technologies, Ltd.) with a sheet resistance of 13 Ω/□ and a thickness of 1250 Å. The substrate was cleaned in ultrasonic baths of detergent, de-ionized water, acetone and isopropyl alcohol in turn, and then treated with the boiling hydrogen peroxide. The resulted substrate was then purged with nitrogen. The respective organic layers and the cathode layer were deposited at 2×10^{-5} Torr using resistively heated tantalum and tungsten boats. All the organic layers were deposited at rates ranging from 1 to 3 Å/s. The 5 Å lithium fluoride and 1500 Å aluminium were subsequently deposited at rates of 0.1 and 10 Å/s, respectively. The emission area of the device was 8 mm^2, and only the luminance in the forward direction was measured.

2.2. Measurement

The luminance and CIE chromatic coordinates of the resulted OLEDs were measured by using Minolta CS-100 luminance-meter. The electro-luminescence and photo-luminescence spectra were measured using a Hitachi F-4500 fluorescence spectrophotometer. The ultraviolet visible (UV–Vis) absorption spectra were measured using a Hitachi U-3010 UV–Vis spectrophotometer. The highest occupied molecular orbital (HOMO) energy-levels of the organic materials studied were calculated from their oxidation potentials measured by a cyclic voltammetry, while the corresponding lowest unoccupied molecular orbital (LUMO) energy levels were estimated based on their HOMO energy-levels and the lowest-energy absorption edge of the UV–Vis absorption spectra. A Keithley 2400 electrometer was used to measure the current–voltage (*I–V*) characteristics. All the devices were characterized without encapsulation and all the measurements were carried out in the ambient condition.

3. Result and discussion

By using the blue BANE as host, for example, the energy barrier is 0.2 eV for holes to inject from the hole-transporting layer (HTL) to the emissive layer (EML), while 0.1 eV for electrons to inject from the electron-transporting layer (ETL) to the EML. These two carrier barriers are comparatively low, effectively facilitating the injection of carriers to the emissive layer, forming one fundamental base of an efficient OLED.

The efficiency further depends on the amount of excitons generated in the emission zone, which in turn depends on recombination probability of the

carriers [15]. Effectively confining the carriers within the emissive layer can greatly enhance the recombination probability and, likewise, the generation of excitons [16,17]. The effectiveness of hole-confinement is dependent on the difference in HOMO level between the EML and the ETL, [18] which is 0.5 eV by using BANE host. The 0.5 eV energy barrier is relatively high, effectively preventing hole to further transport away from the emissive layer.

Similarly, the effectiveness of electron-confinement is dependent on the difference in LUMO level between the EML and the HTL. The LUMO of the NPB-composing HTL is 0.4 eV higher than that of the BANE host, forming an effective electron-blocking barrier. Both of these high carrier-blocking barriers would greatly enhance recombination probability and consequently result in high-efficiency, as evidenced in the white OLED with blue BANE doped with 0.1 wt% DCM2. The resultant maximum current efficiency is 9.6 cd/A and maximum power efficiency is 6.5 lm/W, both with a white emission of 12 cd/m^2 at 4.5 V (Table 1).

The efficiency of dye-doped fluorescent white OLEDs also relies on energy transfer from the host to the guest(s) [19], which can be investigated according to the overlapping area of the ultraviolet visible (UV–Vis) absorption spectra of the guest and the photo-luminescence (PL) spectra of the host [20] and the difference in PL spectra between the host with and without the dopant [14,21,22]. As shown in Fig. 2, great overlap is seen between the UV–Vis absorption spectra of DCM2 and the PL spectra of BANE, indicating the possibility of an efficient energy transfer. As shown in Fig. 3, the PL peak of BANE host had markedly decreased as 0.1 wt% DCM2 is added, indicating the occurrence of an efficient energy transfer.

By using DPVP as host, the energy barrier for holes to transport from the HTL layer to DPVP is −0.2 eV, forming a trap instead of barrier for holes. Meanwhile, the electron injection barrier is 0.47 eV, comparatively higher than the 0.1 eV of the BANE counterpart. This apparently is unfavourable to the injection of electrons. On the other hand, the use of DPVP host forms an ideal hole-blocking barrier with an energy barrier of 0.9 eV. Contrarily, its electron-blocking barrier is 0.03 eV, which is too low to effectively confine the electrons in the emissive layer, which explains why the DPVP-composing device (E) shows higher current density but lower current efficiency, as compared with the BANE counterpart (D) (Fig. 4). As a result, the electron-blocking function would be replaced by the ETL/DPVP interface. Nevertheless, since the hole-blocking barrier is relatively much higher, barely any hole can jump across the DPVP/ETL interface before the entering of electrons, and carrier recombination would still occur within the emissive layer, but very likely markedly shifting to the EML/ETL interface.

By doping in DPVP with the same weight amount of DCM2, the resultant maximum current efficiency is 6.6 cd/A with 88 cd/m^2 at 3 V, which is significantly lower than that of the BANE counterpart, which is 9.6 cd/A. The comparatively lower current efficiency confirms that significant portions of the carriers transport through the device without

Table 1
Composition effect of the mixed host of the blue BANE with the greenish-blue DPVP on the electro-luminescent characteristics of the resulted white OLEDs

No.	Weight ratio			Turn-on voltage[a] (V)	Maximum luminance/voltage (cd/m^2) (V)	Maximum power/current efficiency[b] (lm/W) (cd/A)		CIE coordinates (x, y) at 100 cd/m^2 and 10,000 cd/m^2	
	BANE	DPVP	DCM2						
A	100	–	–	5.2	6500/11.5	1.0	2.6	(0.16, 0.12)	–
B	–	100	–	3.0	7600/8.0	4.0	4.4	(0.21, 0.41)	–
C	–	–	100	6.5	420/13.5	0.02	0.1	(0.64, 0.34)	–
D	100	–	0.10	4.0	24,100/10.0	6.5	9.6	(0.38, 0.39)	(0.38, 0.38)
E	–	100	0.10	2.7	19,300/7.5	6.9	6.6	(0.36, 0.43)	(0.37, 0.43)
F	100	10	–	3.1	36,600/8.5	11.2	14.3	(0.19, 0.33)	(0.19, 0.33)
G	100	5	0.10	3.3	43,400/9.5	11.0	14.5	(0.36, 0.43)	(0.35, 0.42)
H	100	10	0.10	3.1	56,000/9.5	16.0	19.2	(0.36, 0.43)	(0.34, 0.41)
I	100	15	0.10	3.1	60,600/9.0	15.3	18.0	(0.37, 0.43)	(0.35, 0.43)
J	100	20	0.10	2.9	53,200/9.0	13.5	17.5	(0.38, 0.44)	(0.38, 0.45)
K	100	25	0.10	2.6	20,100/8.5	11.9	15.8	(0.38, 0.45)	(0.40, 0.46)

[a] The turn-on voltage is defined herein as the resultant value obtained at luminance $\geqslant$ 1 cd/m^2.
[b] The maximum power and current efficiency are defined as the resultant values obtained at luminance $\geqslant$ 10 cd/m^2.

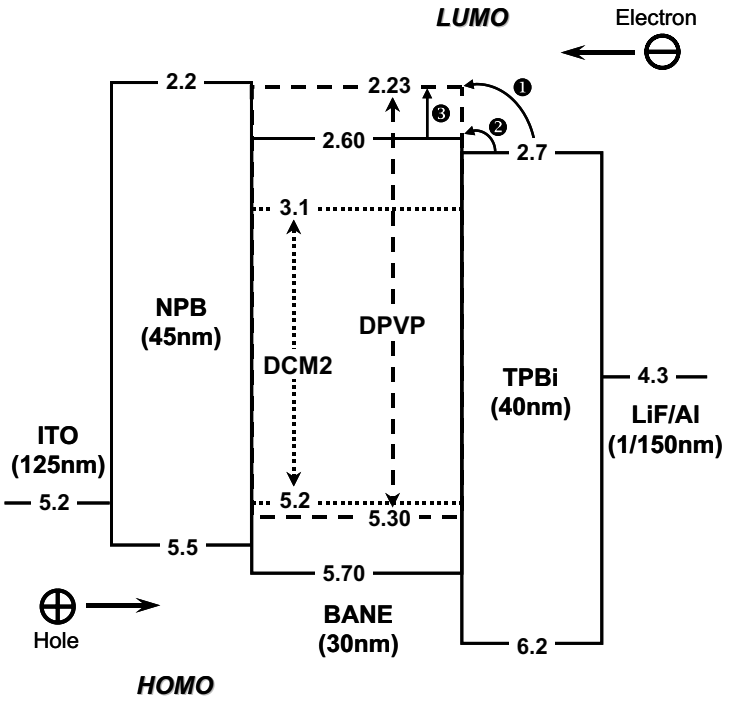


Fig. 1. Schematic illustrations of the HOMO/LUMO energy-level alignment of the studied white OLED with the blue BANE host or the greenish-blue DPVP host doped by the red dye of DCM2. Cascading routes (2) and (3) with lower electron injection barriers to DPVP are formed by using mixed host of BANE with DPVP.

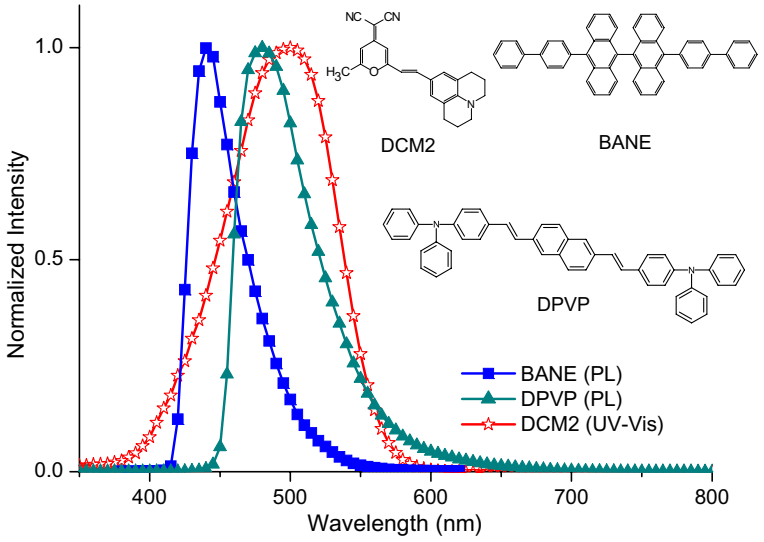


Fig. 2. Photo-luminescence spectra of the host molecules of BANE and DPVP and UV–Vis absorption spectrum of the guest molecule of DCM2. Their chemical structures are shown in inset.

recombination due to its comparatively poorer electron-blocking function mentioned above. However, its maximum power efficiency is 6.9 lm/W at 88 cd/m^2 at 3 V, which is slightly greater than the maximum power efficiency of 6.5 lm/W for the BANE counterpart. This may be mainly attributed to the fact that DPVP-composing device has a lower driving voltage, besides having a higher electro-lumines-

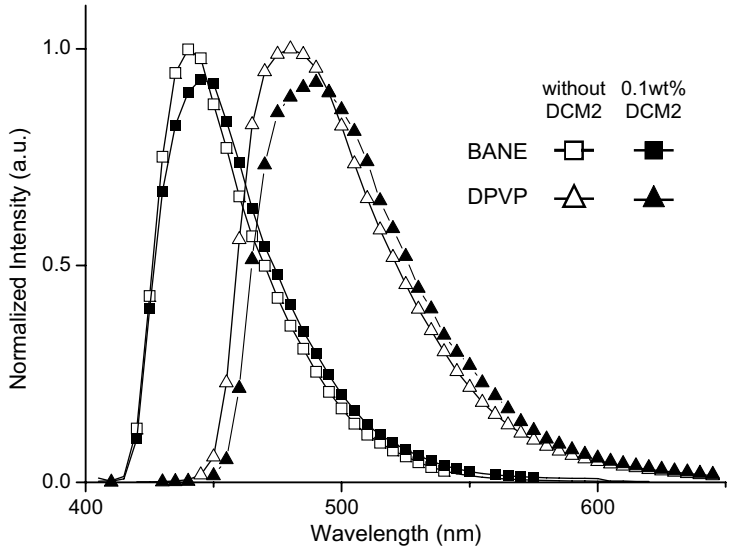


Fig. 3. Photo-luminescence spectra of the host molecules of BANE and DPVP with and without the dopant of DCM2.

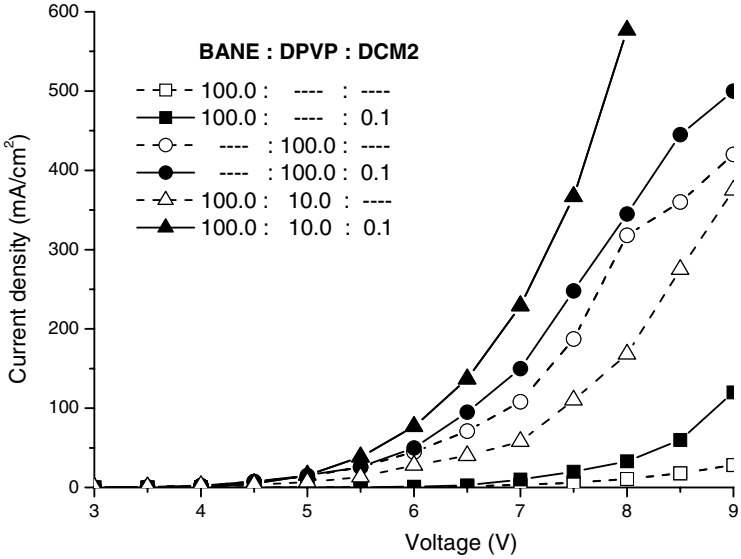


Fig. 4. *J–V* characteristics of the resulted OLEDs, with different hosts and mixed host with and without the red-dopant DCM2.

cent efficiency. Additionally, energy transfer between DPVP and red dye DCM2 is more effective than that between BANE and DCM2, as indicated by the comparatively greater overlapping area between the UV–Vis absorption spectra of the red dye DCM2 and the PL spectra of the DPVP host (Fig. 2). Though DPVP has a higher electron injection barrier than BANE, its resultant better power efficiency indicates DPVP to be a higher EL-efficiency molecule with a sound carrier-mobility, as revealed by its higher current density shown in Fig. 4.

More importantly, the PL spectrum markedly red-shifts as DCM2 is added, and the decrease of the PL peak of DPVP is greater than that of BANE, indicating that DPVP is a more efficient host than BANE for DCM2. Besides, DPVP is electro-luminescence more efficient than BANE. As seen in Table 1, its maximum power efficiency is 4.0 lm/W (Device B), while 1.0 lm/W for BANE (Device A).

The current or power efficiency is markedly improved by using mixed hosts of BANE with DPVP. The presence of a significant portion of BANE host can effectively improve the poor electron-confining problem of the DPVP co-host. Additionally, the resultant mixed host system provides lower barriers to the entering electron. As the route (1) shown in Fig. 1, the 0.47 eV electron injection barrier to the DPVP host is the highest among all the carrier-injection-barriers mentioned above. By blending the two hosts together, the electrons coming from the ETL gain one additional route with two smaller energy barriers to enter the DPVP host; i.e. that it is 0.1 eV to first enter the BANE host (route 2) and then 0.3 eV to further enter the DPVP host (route 3). Since there is no energy barrier for holes to enter into the DPVP host (−0.2 eV), the holes and electrons can easily recombine. Hence, more excitons would form on the high electro-luminescent DPVP host. Accordingly, the resulted DPVP/BANE binary host composing devices show synergistic increase in brightness and efficiency (Fig. 3). A brightest emission of 60,600 cd/m^2 is observed for the device with the binary host with a DPVP to BANE weight ratio of 15:100, while it is 24,100 cd/m^2 for the single BANE host composing device and 19,300 cd/m^2 for the DPVP counterpart.

A greatest efficiency improvement is observed for the device with the binary host with a DPVP to BANE weight ratio of 10:100, whose maximum power efficiency is 16 lm/W with 14 cd/m^2 and 0.08 mA/cm^2 at 3.5 V. The power efficiency is 14 lm/W at 100 cd/m^2 with a driving voltage of 4.7 V. Its maximum current efficiency is 19.2 cd/A with 300 cd/m^2 and 1.5 mA/cm^2 at 4.5 V (Table 1). At 10,000 cd/m^2, it shows a best-reported current efficiency of 18.7 cd/A with 57.7 mA/cm^2 at 7.5 V.

Similar increments in brightness and efficiency are observed in the devices composing the binary hosts but without the DCM2 dopant. A brightest, most efficient greenish-blue emission is obtained when the weight ratio of DPVP to BANE is 10:100. Its maximum brightness is 36,600 cd/m^2, more than two times the total brightness of the two devices composing the pure BANE and the pure DPVP, which are 6500 cd/m^2 and 7,600 cd/m^2, respectively. The maximum power efficiency is 11.2 lm/W for the binary host composing device, compared with 1.0 lm/W and 4.0 lm/W for the ones with pure BANE host and pure DPVP host, respectively.

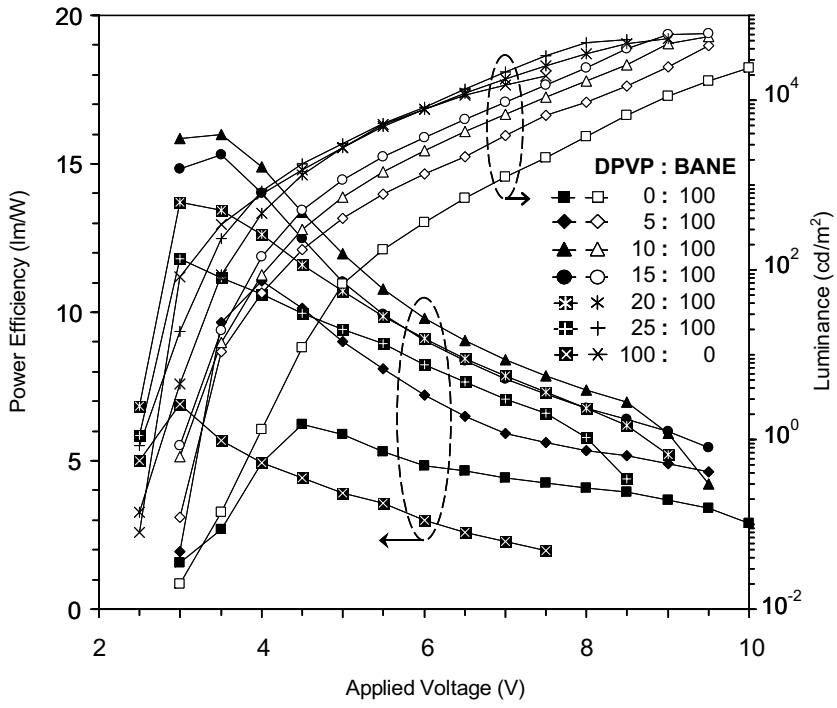


Fig. 5. Composition effects of DPVP on the power efficiency and luminance of the resulted white OLEDs with DPVP/BANE binary hosts doped with 0.1 % DCM2.

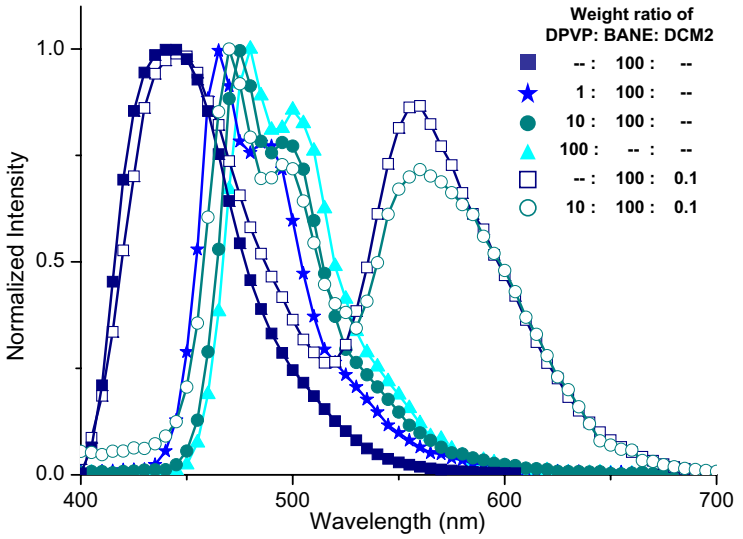


Fig. 6. Doping effect of the greenish-blue DPVP on the resultant electro-luminescent spectra of the blue BANE host composing OLEDs. Also shown are the electro-luminescent spectra of 0.1 wt% DCM2 doped white OLEDs with the pure BANE host (white square) and the BANE/DPVP mixed host (white circle). (For interpretation of the references to colour in this figure legend, the reader is referred to the web version of this article.)

As DPVP weight percentage increases from 9 to 100, the efficiency consistently decreases from 11.2 to 4.0 lm/W for the devices without the DCM2 dopant, and it decreases from 16.0 to 6.9 lm/W for those with the DCM2 dopant. This may be attributed to the relatively poorer electron-confinement function of the DPVP-composing device. More electrons would easily jump from EML to HTL without recombining with holes as DPVP content increases, resulting in a lower efficiency with lower brightness, as shown in Fig. 5.

Frequently, emissive colour of white OLEDs somewhat varies with the variation of brightness or applied voltage. For examples, as brightness increases from 100 cd/m^2 to 10,000 cd/m^2, the colour of the device with 0.1% DCM2 in pure BANE slightly blue-shifts from (0.38, 0.39) to (0.38, 0.38), while that with 0.1% DCM2 in pure DPVP slightly red-shifts from (0.36, 0.43) to (0.37, 0.43). As revealed in the literature [21], the external quantum efficiency for OLEDs doped with higher concentration of red dye markedly decreases as current density increases due to the quenching of the singlet-excited state of the dopant, which may explain why some white emission would blue-shift as brightness increases. The red-shift observed in the latter case indicates that exciton-quenching is more pronounced on the greenish-blue DPVP, which, in turn, explains why the colour variation systematically changes from blue-shift to red-shift as the weight ratio of DPVP to BANE is increased from 5:100 to 25:100 for Devices from G to K (Table 1).

The electro-luminescent (EL) spectra markedly shifts from the blue emission of BANE toward the greenish-blue emission of DPVP as 1% DPVP is doped into the pure BANE, as shown in Fig. 6. The emission shift is more pronounced by doping 9 wt% DPVP. The great increment in greenish-blue emission reveals that most excitons have been formed on the greenish-blue DPVP molecules, another proof for the cascading routes (routes 2 and 3) to be favourable to the injection of more electrons to DPVP.

4. Conclusion

To conclude, colour-stable, high-efficiency fluorescent white OLEDs are fabricated by forming a hole-transporting/white emission/electron-transporting tri-layered structure with low carrier-injection-barriers and an effective carriers confinement. Properly blending in the blue host BANE an efficient electro-luminescent and emitter/co-host dual-role possessed greenish-blue DPVP generates in the device structure cascading new routes with lower electron injection barrier, resulting in synergistic electro-luminescent performance with a maximum power efficiency of 16 lm/W at 14 cd/m^2 or

14.6 lm/W at 100 cd/m^2 and maximum current efficiency of 19.2 cd/A at 300 cd/m^2.

Acknowledgements

We thank Professor C.H. Cheng of Department of Chemistry, National Tsing Hua University, for his help with the EL spectra measurements, and Labeltek for providing the blue BANE and greenish-blue DPVP studies. This work was supported by National Science Council, Taiwan, People's Republic of China for financially supporting in part this research under NSC 95-2221-E-007-128-MY3.

References

[1] J. Kido, M. Kimura, K. Nagai, Science 267 (1995) 1332.
[2] Z. Shen, P.E. Burrows, V. Bulović, S.R. Forrest, M.E. Thompson, Science 276 (1997) 2009.
[3] M. Ricks, M. Boroson, J. Ludwicki, A. Arnold, Society for Information Display Boston, USA, 2005, p. 826.
[4] A.R. Duggal, J.J. Shiang, C.M. Heller, D.F. Foust, Appl. Phys. Lett. 80 (2002) 3470.
[5] B.W. D'Andrade, S.R. Forrest, Adv. Mater. 16 (2004) 1585.
[6] B.W. D'Andrade, M.E. Thompson, S.R. Forrest, Adv. Mater. 14 (2002) 147.
[7] B.W. D'Andrade, R.J. Holmes, S.R. Forrest, Adv. Mater. 16 (2004) 624.
[8] R.F. Service, Science 310 (2005) 1762.
[9] C. Adachi, M.A. Baldo, M.E. Thompson, S.R. Forrest, J. Appl. Phys. 90 (2001) 5048.
[10] M.A. Baldo, D.F. O'Brien, Y. You, A. Shoustikov, S. Sibley, M.E. Thompson, S.R. Forrest, Nature 395 (1998) 151.
[11] Y.S. Huang, J.H. Jou, W.K. Weng, J.M. Liu, Appl. Phys. Lett. 80 (2002) 2782.
[12] J.H. Jou, C.P. Wang, Y.S. Chiu, R.Y. Wang, H.C. Hu, Appl. Phys. Lett. 88 (2006) 193501.
[13] X. Yang, D. Neher, T.K. Daubler, Adv. Mater. 16 (2004) 161.
[14] X. Gong, J.C. Ostrowski, D. Moses, G.C. Bazan, A.J. Heeger, Adv. Funct. Mater. 13 (2003) 439.
[15] S. Miyata, H.S. Nalwa, Organic Electroluminescent Materials and Devices, Gordon and Breach Publishers, Tokyo, Japan, 1997 (Chapter 1).
[16] M. Ikai, S. Tokito, Y. Sakamoto, T. Suzuki, Y. Taga, Appl. Phys. Lett. 79 (2001) 156.
[17] Z.Y. Xie, L.S. Hung, S.T. Lee, Appl. Phys. Lett. 79 (2001) 1048.
[18] J.H. Jou, Y.S. Chiu, R.Y. Wang, H.C. Hu, C.P. Wang, H.W. Lin, Org. Electron. 7 (2006) 8.
[19] C.W. Tang, S.A. VanSlyke, C.H. Chen, J. Appl. Phys. 65 (1989) 3610.
[20] M. Pope, C.E. Swenberg, Electronic Process in Organic Crystals and Polymers, second ed., Oxford University Press, New York, 1999.
[21] L. Yan, N.J. Watkins, S. Zorba, Y. Gao, C.W. Tang, Appl. Phys. Lett. 81 (2002) 2752.
[22] J.H. Jou, C.P. Wang, M.H. Wu, P.H. Chiang, H.W. Lin, H.C. Li, R.S. Liu, Org. Electron. 8 (2007) 29.

Available online at www.sciencedirect.com
ScienceDirect
Organic Electronics 8 (2007) 743–748
Organic Electronics
www.elsevier.com/locate/orgel

Organic–inorganic hybrid materials as solution processible gate insulator for organic thin film transistors

Chaun Gi Choi, Byeong-Soo Bae *

Laboratory of Optical Materials and Coating (LOMC), Department of Materials Science and Engineering, Korea Advanced Institute of Science and Technology (KAIST), Daejeon 305-701, Republic of Korea

Received 17 September 2006; received in revised form 12 June 2007; accepted 19 June 2007
Available online 30 June 2007

Abstract

We synthesized organic–inorganic hybrid materials (hybrimers) using a simple non-hydrolytic sol–gel reaction and applied the materials as gate insulators in organic thin film transistors (OTFTs). The hybrimer thin films had smooth and hydrophobic surfaces, and were stable with solvents. In addition, the hybrimer thin films had good electrical properties such as low leakage current and high dielectric strength. The performance of the OTFT with hybrimer gate insulator fabricated by drop casting of regioregular poly(3-hexylthiophene) (P3HT) was similar to that of OTFT with hexamethyldisilazane (HMDS) treated thermally grown SiO_2. The hysteresis of RR-P3HT based OTFT with hybrimer gate insulator was negligible.
© 2007 Elsevier B.V. All rights reserved.

PACS: 81.07.Pr; 85.30.Tv; 73.61.−r; 77.55.+f; 68.55.-a

Keywords: Organic thin film transistors; OTFTs; Organic–inorganic hybrid materials; Hybrimer gate insulators; P3HT organic semiconductor

1. Introduction

Organic thin-film transistors (OTFTs) have attracted a great deal of attention and have been utilized for integrated circuits and driving circuits for active matrix displays [1,2], sensors [3], and RFIDs [4] because OTFTs have many advantages for flexible electronics such as low temperature processibility, low cost, and flexibility compared with conventional Si technology. The performance of the OTFTs using a small molecule or polymer semiconductors is comparable to that obtained with hydrogenated amorphous silicon, which is being used for active matrix liquid-crystal displays.

Since field-induced carriers are confined to a very thin region close to the interface of the gate insulator and organic semiconductor [5], it is important to choose proper materials and to control the surface of the gate insulator to obtain a better performance of the OTFT. In order to improve the performance of the OTFT, the gate insulator requires such characteristics as a high dielectric constant, a

* Corresponding author. Tel.: +82 428694119; fax: +82 428693310.
E-mail address: bsbae@kaist.ac.kr (B.-S. Bae).

1566-1199/$ - see front matter © 2007 Elsevier B.V. All rights reserved.
doi:10.1016/j.orgel.2007.06.006

low leakage current, and a smooth surface [6]. For flexible electronics using plastic substrates, it is also preferred for gate insulators to be capable of being prepared by a solution process because they are desirable to be easily formed at low temperature. Hence, many solution processible polymer thin films have been used as the gate insulator in the OTFT instead of using inorganic insulators [6,7]. However, polymer gate insulators have limits to their practical use due to their restricted dielectric properties and low thermal stability.

The sol–gel derived siloxane based organic–inorganic hybrid materials (hybrimers), in which inorganic and organic components are intimately linked at the molecular scale by a covalent bond, have been widely studied with respect to new dielectric materials for applications in optics and electronics [8,9]. Such materials combine the characteristics of both glass and polymers, and they improve the thermal and mechanical properties of the final materials to be applied. By a suitable selection of precursors and optimization of processing parameters, we can easily control the properties of hybrimers such as dielectric constant, thermal stability, refractive index, surface roughness, and hydrophobicity [8,10] Especially, the methacrylate hybrimers synthesized using a precursor of methacryloxypropyl trimethoxysilane (MPTMS) have been widely investigated for many optical applications, since they show good optical characteristics and are photo-patternable, allowing easy fabrication for micro-optical devices. Thus, the hybrimers can be applied to the gate insulators in the OTFTs since they can control a wide range of electrical and surface properties with high thermal stability and are photo-patternable, as well as solution processible for easy fabrication of the OTFT. Recently, Bao et al. [11] reported that silsesquioxane based materials, which are another type of hybrid materials, could be potential candidates for gate insulators in low cost and low process temperature OTFTs.

In this study, we report on solution processible hybrimers as gate insulators to fabricate solution processed OTFTs with regioregular poly(3-hexylthiophene) (RR-P3HT) organic semiconductor. The photo-patternable hybrimers, which contain oligosiloxanes nanoclusters grafted by photo-polymerizable methacryl radicals, were synthesized using a simple non-hydrolytic sol–gel reaction. Electrical characteristics and surface properties of the hybrimer thin films were examined. In addition, the performance of the fabricated OTFT with hybrimer gate insulator was also investigated.

2. Experimental

We synthesized hybrimer resins containing oligosiloxanes grafted by methacryl radicals using a simple non-hydrolytic sol–gel reaction as shown in Fig. 1a. Methacryloxypropyl trimethoxysilane (MPTMS, Aldrich) and diphenylsilanediol (DPSD, TCI) were used as precursors without further purification, and barium hydroxide monohydrate ($Ba(OH)_2{\cdot}H_2O$, Aldrich) was used as a catalyst to promote a condensation reaction between the two precursors. The total proportion of MPTMS and DPSD together was 1:1 molar ratio. Detailed fabrication procedures, as well as structure and properties of the methacrylate hybrimer, were reported in previous report [10]. The hybrimer thin films were deposited on indium tin oxide (ITO) coated glass (sheet resistance of 15 Ω/□). The ITO coated glasses were cleaned with acetone, isopropylalcohol (IPA), and de-ionized (DI) water in ultrasonic, and were then exposed to oxygen plasma for 5 min at 200 W to remove organic contamination and to improve the wettability of hybrimers solution. The synthesized hybrimer resins were diluted with propylene glycol monomethyl ether acetate (PGMEA). The solutions were filtered through a 0.22 μm pore size polytetrafluoroethylene (PTFE) membrane syringe filter and spin cast at a spin rate of 5000 rpm for 30 s on the ITO coated glass. The deposited films were exposed to UV light ($\lambda = 365$ nm, Hg lamp) for 1 min 30 s and thermally cured at 150 °C for 2 h in air condition.

The electrical properties of the hybrimer thin films, such as dielectric constant and leakage current density, were measured using Al/hybrimers thin film/ITO structures with an HP4194A (Agilent Technologies) impedance/gain analyzer and a Keithley 237 source-measure unit (Keithley). We measured the surface roughness and water contact angle of the hybrimers thin films using atomic force microscopy (AFM) (XE/100,PSIA) and a contact angle analyzer (Phoenix 150, SEO), respectively.

OTFTs with the bottom contact geometry were fabricated. Gold was thermally evaporated on either hybrimer gate insulator/ITO or the hexamethyldisilazane (HMDS)-treated thermally grown SiO_2 on Si wafer (resistivity of 0.01 Ωcm) through a shadow mask to form source and drain electrodes. The OTFTs had a channel length of 50 μm and channel width of 3000 μm. RR-P3HT was used as received from Rieke Metals (Lincoln, USA) without further purification. Since the charge carrier mobility is

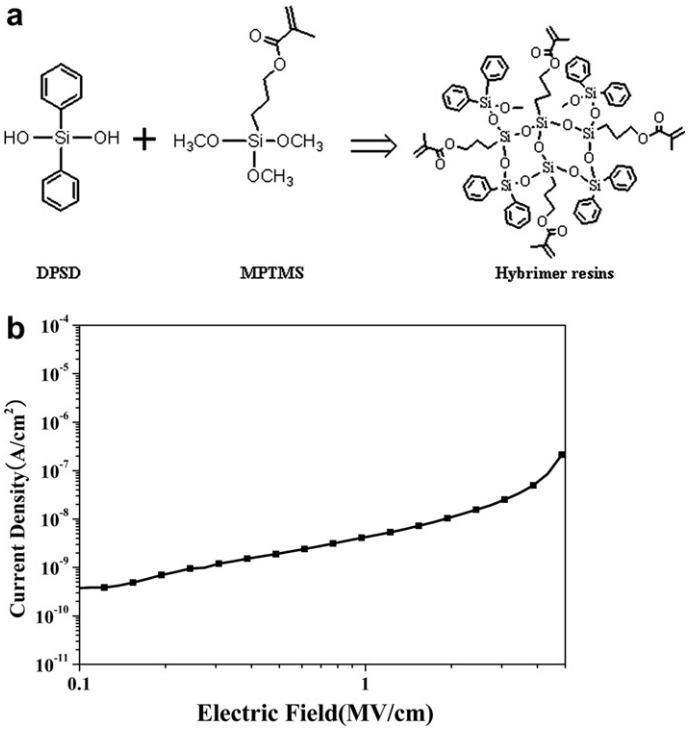


Fig. 1. (a) Schematic synthesis diagram of hybrimers by sol–gel reaction of DPSD and MPTMS, and (b) leakage current density of hybrimer thin film for the MIM structure.

enhanced when the evaporation rate of solvents is low [12], RR-P3HT was dissolved in chlorobenzene (concentration of 0.2 wt%). The solution was filtered through a 0.22 μm pore size PTFE membrane syringe filter, drop cast on the substrate in a nitrogen atmosphere. The thin films were dried overnight (10–12 h) at 100 °C in a vacuum oven. Electrical characteristics of the fabricated OTFTs were measured using an HP 4155 A semiconductor parameter analyzer (Agilent Technologies) under ambient laboratory conditions. In order to investigate the hysteresis of RR-P3HT based OTFT with hybrimer gate insulator, capacitance–voltage (C–V) characteristics were measured using metal–insulator–semiconductor (MIS) structure, Au/RR-P3HT/hybrimer gate insulator/ITO, with an HP4194A (Agilent Technologies) impedance/gain analyzer. The voltage was swept with 0.5 V step, starting from +40 V to −40 V and returning to +40 V at 100 kHz.

3. Results and discussion

The deposited hybrimer thin films were dense and pinhole free, as determined by scanning electron microscope (SEM, JEOL). In addition, the adhesion of the hybrimer films on the ITO coated glass was excellent. The dielectric constant (ε_r) of the hybrimer thin film is ~3.1 at 100 kHz calculated from the thickness and capacitance. The ε_r of hybrimer is lower than that of SiO_2 ($\varepsilon_r = 3.9$). The low ε_r is attributed to the nonpolar phenyl group of DPSD and symmetrical structures of hybrimers.

Fig. 1b shows the dependence of leakage current density (J) of hybrimer thin film on the applied electric field (E) at room temperature. The leakage current density at 1 MV/cm of the hybrimer thin film is 4.1 nA/cm^2 and the dielectric strength of the hybrimer thin film, which was measured at current density of 10^{-6} A/cm^2 is about 5 MV/cm. The leakage current density and the dielectric strength of the hybrimer thin film are much better than those of the commonly used solution-processable polymer gate insulators in OTFT [13–15]. Polymer gate insulators were reported to have the relatively high leakage current density of $\sim 10^{-7}$ A/cm^2 at 1 MV/cm and the low dielectric strength of typically 0.1 ~ 1 MV/cm [16]. This is due to the fact that they cannot yield conformal and pin-hole free film, and also a number of the polymers possess hydroxyl groups which act as trap sites [17].

Hybrimer thin film was fabricated by the condensation reaction between two precursors and by the polymerization of the methacryl groups. The condensation reaction between the methoxy groups of MPTMS and hydroxyl groups of DPSD forms the oligosiloxane networks. Oligosiloxane networks are cross-linked via polymerization under UV irradiation due to the photosensitivity of methacryl groups in MPTMS, which allowing the hybrimer thin film to be more dense and robust. Since the non-hydrolytic sol–gel reaction to fabricate the hybrimer does not use the water which is necessary to hydrolyze the precursor, there are few hydroxyl groups in the hybrimer gate insulator [10]. The formation of totally cross-linked 3-dimensional networks and few hydroxyl groups in hybrimer gate insulator give the low leakage current density and high dielectric strength of hybrimer thin film.

It is well known that the surface energy and surface roughness of the gate insulator play important roles in the performance of OTFT [7,15,16,18]. The gate insulators should have smooth and hydrophobic surface, and chemical stabilities with the solvents used to dissolve RR-P3HT. The water contact angle of the hybrimer thin film was as high as ~80°, which indicates that it has a hydrophobic surface. The hydrophobic surface of the hybrimer thin film is attributed to the methacryl and phenyl groups grafted to the oligosiloxanes networks. The hydrophobic characteristics of hybrimer film can remove the additional works such as self assemble monolayers treatment to improve the performance of OTFTs.

The solvent used in the solution processing of the organic semiconductor layer affects the underlying polymer gate insulators and, consequently, affects the device performance significantly [15]. The hybrimer thin films were treated with various solvents, which can dissolve the RR-P3HT, to examine the chemical stabilities of the hybrimer thin films although the solvents could not dissolve the hybrimer thin films. Fig. 2 shows the AFM surface images of the hybrimer thin films as deposited and after dipping in the solvent for 5 min and drying the solvents. The as-deposited hybrimer thin film shows a smooth surface with a RMS roughness of 0.38 nm. The hybrimer solution fills up the valley region on the rough ITO substrate during the spin coating due to the low viscosity of the solution, which makes ITO surface planar. This is consistent with other groups' results using polymer to flatten the ITO surface [19,20]. The RMS roughness of the solvent treated thin films is around 0.3–0.4 nm, which is almost identical with as deposited hybrimer thin films. Thus, we concluded that the hybrimer thin films are stable with the solvents for RR-P3HT due to the cross-linked 3-dimensional networks consisting of inorganic and organic networks.

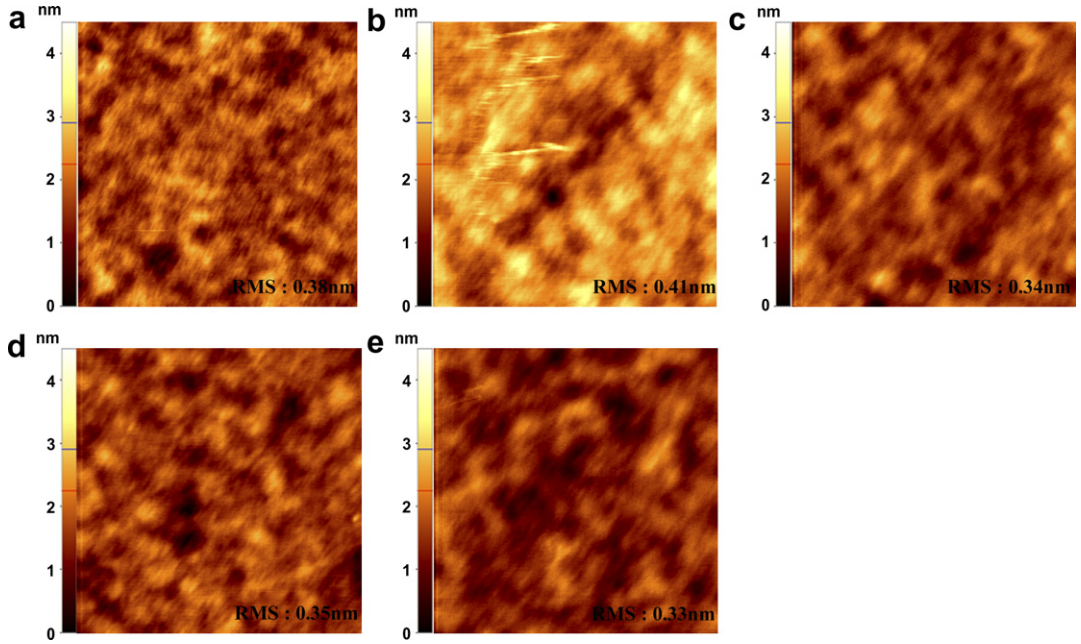


Fig. 2. AFM surface images of the hybrimer thin films (a) as deposited, and after treated with (b) chlorobenzene, (c) *p*-xylene, (d) trichloroethylene, and (e) toluene. All images are 5 μm × 5 μm in size.

One major problem in using polymeric gate insulators is the hysteresis problem. It is desirable that the hysteresis of OTFTs is as small as possible for organic circuit applications. Fig. 3 shows C–V hysteresis behavior of hybrimer gate insulator in MIS structure at 100 kHz is negligible. It is well known the hysteresis of OTFTs with polymeric gate insulator is caused by two mechanisms: (1) slow polarization of the dipolar groups or molecules such as hydroxyl groups in the gate insulator and/or (2) charge injection from gate, movement, and storage in gate insulator [21]. Thus, we conclude that the small hysteresis is attributed to the hydrophobic surface which prevents the water from penetrating into the gate insulator [22], the low contents of hydroxyl groups which act as electron traps in the gate insulators, and low leakage current density of hybrimer gate insulator.

RR-P3HT based OTFTs with the bottom contact geometry were fabricated to investigate the performance of the OTFTs with either the hybrimer gate insulators or HMDS-treated thermally grown SiO_2. Fig. 4 shows the transfer characteristics of the OTFTs with the hybrimer gate insulator and the HMDS-treated thermally grown SiO_2. The electrical performance parameters are summarized in Table 1. The carrier mobility was determined from a plot of $(-I_D)^{1/2}$ vs. V_G on the basis of the following relationship in the saturation regime:

$$I_D = \frac{WC_i}{2L}\mu(V_G - V_{th})^2 \quad (1)$$

where I_D is the drain current, W and L are the channel width and length, respectively, μ is the field-effect mobility, C_i is the capacitance per unit area,

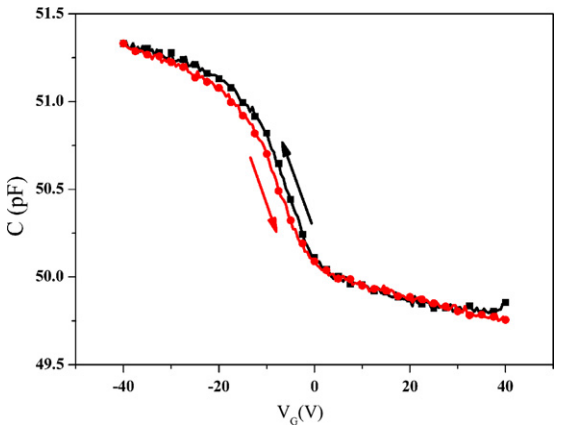


Fig. 3. C–V hysteresis behavior of hybrimer gate insulator in MIS structure. RR-P3HT was drop cast on the hybrimer gate insulator.

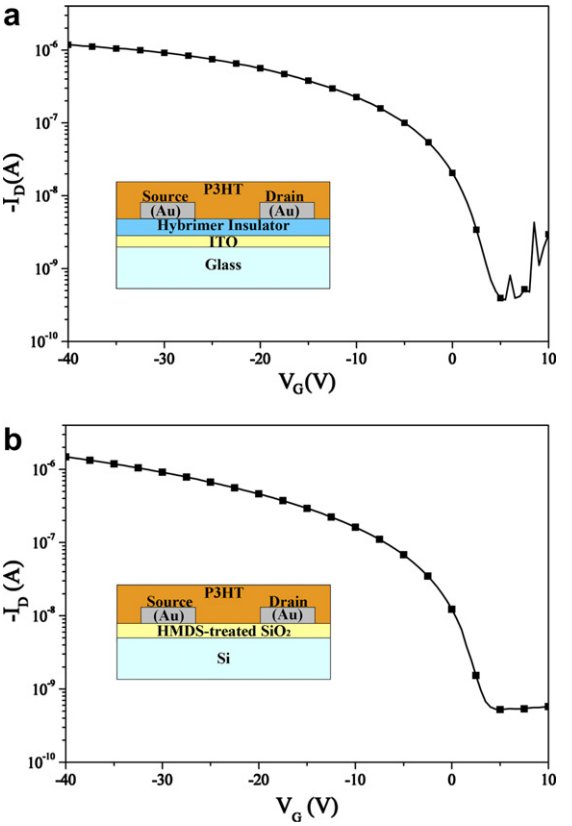


Fig. 4. Transfer characteristics of RR-P3HT based OTFT (a) with hybrimer gate insulator and (b) with HMDS-treated SiO_2 gate insulator. Inset: the schematic transistor structure with different gate insulators.

Table 1
Electrical performance of OTFTs with the hybrimer gate insulator and HMDS-treated thermally grown SiO_2

Insulators	μ (cm^2/V s)	V_{th} (V)	S (V/dec.)	On/off ratio
Hybrimer gate insulator	4.6×10^{-3}	5.0	2.3	3.2×10^3
HMDS-treated thermally grown SiO_2	2.8×10^{-3}	4.6	2.4	2.8×10^3

and V_{th} is the threshold voltage. The saturation regime mobility was determined at drain–source voltage (V_D) of −40 V. The measured capacitance of the hybrimer gate insulator and SiO_2 was 7.2 nF/cm^2 and 10 nF/cm^2 at 100 kHz, respectively. The subthreshold slope, S, is defined as the voltage required to increase the drain current by a factor of 10. Since the surface properties of hybrimer gate insulators are analogous to that of HMDS-treated SiO_2 such as the hydrophobicity and surface roughness, the

OTFT with hybrimer gate insulator shows similar electrical performance to that of the OTFT with HMDS-treated thermally grown SiO_2.

4. Conclusion

We synthesized the hybrimers using a non-hydrolytic sol–gel reaction of MPTMS and DPSD and characterized the electrical and surface properties of hybrimer thin film for the low temperature and solution-processable gate insulator in OTFTs. The hybrimer thin film had a low dielectric constant of 3.1 at 100 kHz, low leakage current density of 4.1 nA/cm^2 at 1 MV/cm, high dielectric strength of 5 MV/cm, a smooth and hydrophobic surface, and chemical stability against the solvent for dissolving RR-P3HT. The *C–V* hysteresis of MIS capacitor with hybrimer gate insulator is negligible due to the hydrophobic surface, the low contents of hydroxyl groups, and low leakage current density of hybrimer gate insulator. The performance of the OTFT with hybrimer gate insulator was similar to that of OTFT with HMDS treated SiO_2.

Acknowledgement

This work was financially supported by the Basic Research Program (Grant No. R01-2003-000-10125-0) of the Korea Science and Engineering Foundation (KOSEF). Byeong-Soo Bae acknowledges the financial support of the LG Yonam Foundation for his visit to Flexible Display Center at Arizona State University.

References

[1] G.H. Gelink, H.E. Huitema, E. van Veenendaal, E. Cantatore, L. Schrijnemakers, J.B.P.H. Van Der Putten, T.C.T. Geuns, M. Beenhakkers, J.B. Giesbers, B.-H. Huisman, E.J. Meijer, E.M. Benito, F.J. Touwslager, A.W. Marsman, B.J.E. Van Rens, D.M. de Leeuw, Nat. Mater. 3 (2004) 106.
[2] C.D. Sheraw, L. Zhou, J.R. Huang, D.J. Gundlach, T.N. Jackson, M.G. Kane, I.G. Hill, M.S. Hammond, J. Campi, B.K. Greening, J. Francl, J. West, Appl. Phys. Lett. 80 (2002) 1088.
[3] Z.-T. Zhu, J.T. Mason, R. Dieckmann, G.G. Malliaras, Appl. Phys. Lett. 81 (2002) 4643.
[4] P.F. Baude, D.A. Ender, M.A. Haase, T.W. Kelley, D.V. Muyres, S.D. Theiss, Appl. Phys. Lett. 82 (2003) 3964.
[5] G. Wang, D. Moses, A.J. Heeger, H.-M. Zhang, M. Narasimhan, R.E. Demaray, J. Appl. Phys. 95 (2004) 316.
[6] A. Facchetti, M.-H. Yoon, T.J. Marks, Adv. Mater. 17 (2005) 1705.
[7] J. Veres, S. Ogier, G. Lloyd, D.D. Leeuw, Chem. Mater. 16 (2004) 4543.
[8] (a) E.S. Kang, T.H. Lee, B.S. Bae, Appl. Phys. Lett. 81 (2002) 1438;
(b) O.H. Park, S.Y. Seo, J.H. Shin, B.S. Bae, Appl. Phys. Lett. 82 (2003) 2787;
(c) W.S. Kim, K.S. Kim, Y.J. Eo, K.B. Yoon, B.S. Bae, J. Mater. Chem. 15 (2005) 465;
(d) D.J. Kang, W.S. Kim, B.S. Bae, Appl. Phys. Lett. 87 (2005) 21106;
(e) D.J. Kang, J.K. Kim, B.S. Bae, Optics Express 12 (2004) 3947.
[9] R. Buestrich, F. Kahlenberg, M. Popall, P. Dannberg, R. Müller-Fiedler, O. Rösch, J. Sol–Gel. Sci. Technol. 20 (2001) 181.
[10] (a) Y.J. Eo, T.H. Lee, S.Y. Kim, J.K. Kang, Y.S. Han, B.S. Bae, J. Polym. Sci. Polym. Phys. 43 (2005) 827;
(b) Y.J. Eo, J.H. Kim, J.H. Ko, B.S. Bae, J. Mater. Res. 20 (2005) 401.
[11] Z. Bao, V. Kuck, J.A. Rogers, M.A. Paczkowski, Adv. Func. Mater. 12 (2002) 526.
[12] J.-F. Chang, B. Sun, D.W. Breiby, M.M. Nielsen, T.I. Sölling, M. Giles, I. McCulloch, H. Sirringhaus, Chem. Mater. 16 (2004) 4772.
[13] H. Klauk, M. Halik, U. Zschieschang, G. Schmid, W. Radlik, W. Weber, J. Appl. Phys. 92 (2002) 5259.
[14] S.W. Pyo, D.H. Lee, J.R. Koo, J.H. Kim, J.H. Shim, J.S. Kim, Y.K. Kim, Synth. Met. 154 (2005) 141.
[15] J. Park, S.Y. Park, S.-O. Shim, H. Kang, H.H. Lee, Appl. Phys. Lett. 85 (2004) 3283.
[16] L.L. Chua, P.K.H. Ho, H. Sirringhaus, R.H. Friend, Adv. Mater. 16 (2004) 1609.
[17] S. Jeong, D. Kim, S. Lee, B.-K. Park, J. Moon, Appl. Phys. Lett. 89 (2006) 092101.
[18] S. Steudel, S.D. Vusser, S.D. Jonge, D. Janssen, S. Verlaak, J. Genoe, P. Heremans, Appl. Phys. Lett. 85 (2004) 4440.
[19] G. Wantz, L. Hirsch, N. Huby, L. Vignau, J.F. Silvain, A.S. Barriere, J.P. Parneix, Thin Solid Films 485 (2005) 247.
[20] C.S. Kim, S.J. Jo, J.B. Kim, S.Y. Ryu, J.H. Noh, H.K. Baik, S.J. Lee, K.M. Song, Semicond. Sci. Technol. 22 (2007) 691.
[21] G. Gu, M.G. Kane, Proc. SPIE 6336 (2006) 63360H.
[22] T. Jung, A. Dodabalapur, R. Wenz, S. Mohapatra, Appl. Phys. Lett. 87 (2005) 182109.

Available online at www.sciencedirect.com
ScienceDirect
Organic Electronics 8 (2007) 749–758
Organic Electronics
www.elsevier.com/locate/orgel

Electrical stability of pentacene thin film transistors

Amare Benor, Arne Hoppe, Veit Wagner, Dietmar Knipp *

School of Engineering and Science, Jacobs University Bremen, 28759 Bremen, Germany

Received 14 February 2007; received in revised form 1 May 2007; accepted 18 June 2007
Available online 29 June 2007

Abstract

The influence of environmental conditions on the device operation and the stability of polycrystalline pentacene thin film transistors (TFTs) were investigated. Electrical in-situ and ex-situ measurements of staggered pentacene TFTs were carried out to study the influence of dry oxygen and moisture on the device stability. The transistors were fabricated by organic molecular beam deposition on thermal oxide dielectrics. Oxygen exposure of the pentacene films lead to the creation of acceptor-like states in the bandgap. The acceptor-like states cause a shift of the onset of the drain current towards positive gate voltages. The charge carrier mobility and the on/off ratio of the transistor are not affected by the acceptor-like states. Furthermore, the acceptor-like states have an influence on the stability of the TFTs. Devices exposed to oxygen exhibit a shift of the threshold voltage upon prolonged biasing. Transistors characterized under vacuum conditions (no oxygen exposure) do not exhibit a shift of the threshold voltage (bias stress effect) as a consequence of prolonged biasing. The experimental results show a clear correlation between the device behavior upon oxygen exposure and the stability of the devices. The shift of the onset voltage upon oxygen exposure correlates with the shift of the threshold voltage upon prolonged bias. The influence of dry oxygen on the onset voltage, the threshold voltage, and the electrical stability will be described. Furthermore, the influence of bias stress on the operation of organic circuits like an active matrix addressed OLED displays will be discussed.
© 2007 Elsevier B.V. All rights reserved.

PACS: 72.80.Le; 73.40.Qv; 73.61.Ph

Keywords: Pentacene; Thin film transistors; Electronic transport; Electronic defects

1. Introduction

Electronics based on organic and polymer materials has gained considerable attention in recent years. The interest in organic electronics can be attributed to the emerging demands in novel display media (active and passive) on low cost and/or flexible substrates. The progress has been caused by distinct improvements of material and device properties [1–4].

Of organic and polymeric materials, pentacene ($C_{22}H_{14}$) has demonstrated one of the highest charge carrier mobilities [1]. Hole carrier mobilities of $>3.0\ cm^2/Vs$ were reported for polycrystalline pentacene TFTs by Kelly et al. [1] and Klauk et al. [4]. Thus organic TFTs are of potential interest for application like backpanels of displays or

* Corresponding author.
E-mail address: d.knipp@jacobs-university.de (D. Knipp).

1566-1199/$ - see front matter © 2007 Elsevier B.V. All rights reserved.
doi:10.1016/j.orgel.2007.06.005

organic radio frequency identification tags (organic RFID tags). However, the realization of active matrix addressed displays or RFID tags require the fabrication of highly stable TFTs [5,6]. In particular the threshold voltage has to be stable to allow the realization of complex organic circuitry. Small variations of the threshold voltage might have a significant influence on the operation of displays or organic RFID tags. The change of the threshold voltage is usually caused by bias stress effects. Such effects occur for most thin film transistor fabricated at low temperatures. Bias stress effects have been observed for amorphous silicon [5,7], polycrystalline silicon, organic [8–11] and polymeric TFTs [12,13]. Several investigations reveal that the threshold voltage is strongly affected by bias stress and environmental conditions [3,8–13]. To gain insights in the electronic transport and stability of polycrystalline pentacene TFTs electrical in situ and ex situ measurements were carried out. The influence of environmental conditions on the device operation was studied by exposing the TFTs to dry oxygen and moisture.

The fabrication of the pentacene TFTs will be described in Section 2 of the paper. The experimental results will be presented in Section 3, which is divided in four subsections. In the first subsection the electrical characteristic of pentacene TFTs under ambient conditions will be described. Electrical measurements of pentacene transistors under different bias stress conditions will be described in Section 3.2. In Section 3.3 the influence of contacts on the operation of organic transistors will be investigated. The influence of environmental conditions and bias stress on the device operation of organic circuits like pixel drivers for organic light emitting diode (OLED) displays will be described in Section 3.4. Different strategies how to minimize the influence of environmental conditions on the device operation will be discussed in Section 4. The work will be summarized in Section 5.

2. Fabrication of organic thin film transistors

The pentacene films were deposited using an organic molecular beam deposition (OMBD) system. Silicon and glass substrates where used upon which staggered thin film transistors were fabricated. A cross section of a pentacene thin film transistor (TFT) with bottom drain and source electrodes is shown in Fig. 1b. In the first step a metal gate electrode was prepared on the glass substrate. The thickness of the gate electrode is typically 100 nm. The gate dielectrics were realized by inorganic dielectrics like plasma enhanced chemical vapor deposited (PECVD) silicon oxide, silicon nitride [15,17] or organic dielectrics like polyvinylphenol (PVP) [4] or benzocyclobutene (BCB) [16]. Transistors characterized under vacuum conditions were prepared on prepatterned oxidized silicon wafers. The use of silicon substrates significantly simplifies the evaluation of the materials and the devices. The gate dielectrics were formed by 50–100 nm thick thermal oxide. The source and drain electrodes of the TFTs were defined by optical lithography.

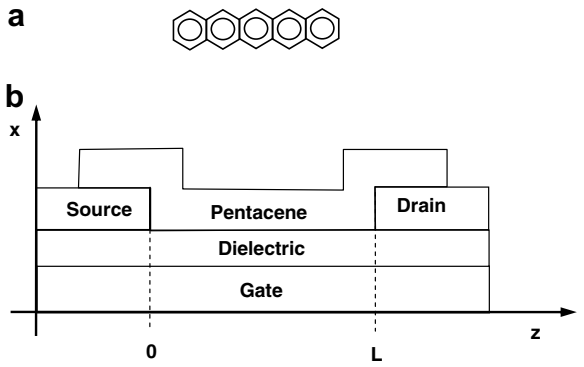


Fig. 1. Molecular structure of pentacene (a) and schematic cross section of a staggered polycrystalline pentacene thin film transistor with bottom drain and source contacts (b).

In order to improve the adhesion of the gold source and drain contacts on the substrate a 3 nm thick titanium film was evaporated prior to the deposition of gold. The pentacene molecules (Fig. 1a) were deposited at a deposition rate of 0.5 Å/s. The source material was two times sublimation purified before depositing the molecules at a base pressure of 5×10^{-6} Pa. The films were prepared at a constant substrate temperature of 70 °C. The source temperature was kept constant at 275 °C while depositing the pentacene films. The pentacene layer has a thickness of 10–15 nm. The channel length of the device ranges from 5 to 150 μm. To improve the device performance of the TFTs the dielectrics were treated by hexamethyldisilazane (HMDS) prior to the deposition of the pentacene film. Self-assembled monolayers (SAMs) like HMDS change the surface wetting properties of the dielectric and the growth of the organic film. A detailed description of the preparation of self-assembled monolayers and the influence of the SAMs on the device performance of organic thin film transistors is given in Ref. [18].

3. Results

3.1. Pentacene TFTs under ambient conditions

The transfer characteristics of a pentacene TFT with a channel length of 20 μm and a width to length ratio (W/L) of 10,000 is shown in Fig. 2. The transistor was measured under ambient conditions. The pentacene film has a thickness of 10 nm. The pentacene film was prepared on top of an HMDS treated thermal oxide gate dielectric with a thickness of 50 nm. The transistors exhibit a charge carrier mobility of 0.4–0.6 cm^2/V s, a threshold voltage of −2.0 V and an on/off ratio of more than 8 orders of magnitude. Furthermore, the transistor exhibits a pronounced subthreshold region and a positive onset of the drain current. Such behavior is typical for polycrystalline pentacene TFTs characterized under ambient conditions [1–4,8–11,15–17,20]. Numerical simulations of the electrical transistor characteristic indicate that the shift of the onset of the drain current is caused by acceptor-like states deep in the bandgap [10,16,19,20]. The acceptor-like states are supposed to be created by oxygen or –OH molecules that are incorporated in the organic film [21,22].

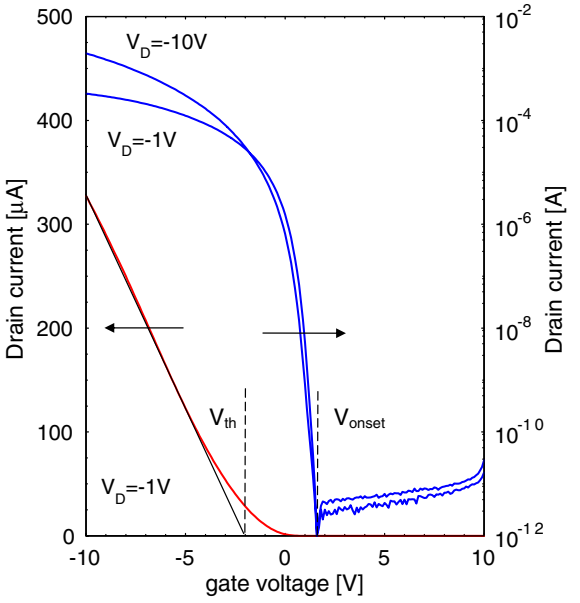


Fig. 2. Transfer characteristic of a pentacene TFT measured under ambient conditions (ex-situ measurement). The transistor has a channel length of 20 μm and a channel width to channel length ratio of 10,000.

3.2. Influence of bias stress on device behavior

Stability transistor operation is essential for the realization of organic integrated circuits. In particular variations of the threshold voltage have a distinct influence on the operation of OLED displays or organic radio frequency identification tags (RFID). Major sources of instabilities are bias stress effects, which leads to a change of the threshold voltage over time. Such effects are well known for inorganic and organic TFTs prepared at low temperatures. The threshold voltage shift for amorphous and polycrystalline silicon TFTs has been extensively investigated [5,7]. The effect can arise from slow trapping in the dielectric and/or surface states at the semiconductor/dielectric interface, or defect creation in the semiconductor. So far few papers have been published addressing these issues in organic thin film transistors [3,8–10,12,13,17].

Bias stress effects are closely related to the electronic structure of the organic films. The electronic structure is again related to impurities in the film, which are affected by environmental conditions. Therefore, it can be expected that environmental conditions have a strong effect on the stability of organic thin film transistors. To avoid the influence of environmental conditions on the device behavior the bias stress experiments were carried out under high vacuum conditions ($\sim 10^{-6}$ Pa). The transfer characteristics of a pentacene TFT with a channel length of 40 μm and a width to length ratio (W/L) of 4000 is shown in Fig. 3. The solid line in Fig. 3 represents the initial transfer characteristic of the transistor. The sample exhibits a hole mobility of 0.5 cm^2/V s and a subthreshold slope of 0.2 V/decade using a 50 nm thick silicon oxide gate dielectric. After measuring the initial transfer and output characteristics (0 min, unstressed device) the pentacene transistors were stressed for 10 min, 30 min, 90 min and 180 min at different gate and drain voltages. Afterwards regular measurements of the I/V curves were carried out. Interestingly no change of the device characteristic was observed after stressing the devices up to 180 min. The bias stress experiment was repeated after exposing the devices to dry oxygen. The concentration of dry oxygen in the system was controlled by the pressure in the high vacuum chamber. The transfer characteristic of a pentacene TFT after exposure to oxygen (before applying bias stress) is shown in Fig. 3 (dashed line). The oxygen exposure results in a shift of the onset of the drain current towards positive gate voltages.

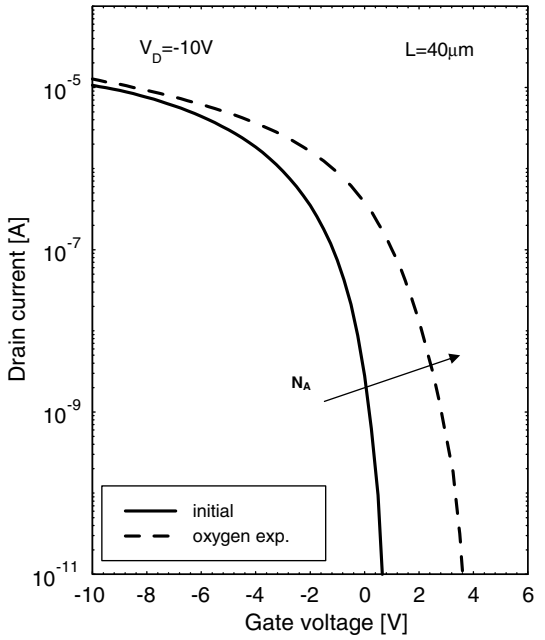


Fig. 3. Electrical in situ measurements of the transfer characteristic of a pentacene TFT for a drain voltage of $V_D = -10$ V. The transistor with a channel length of 40 µm was measured in vacuum (solid line) and after exposure to dry oxygen (dashed line) leading to the formation of acceptor-like states, N_A, in the pentacene film.

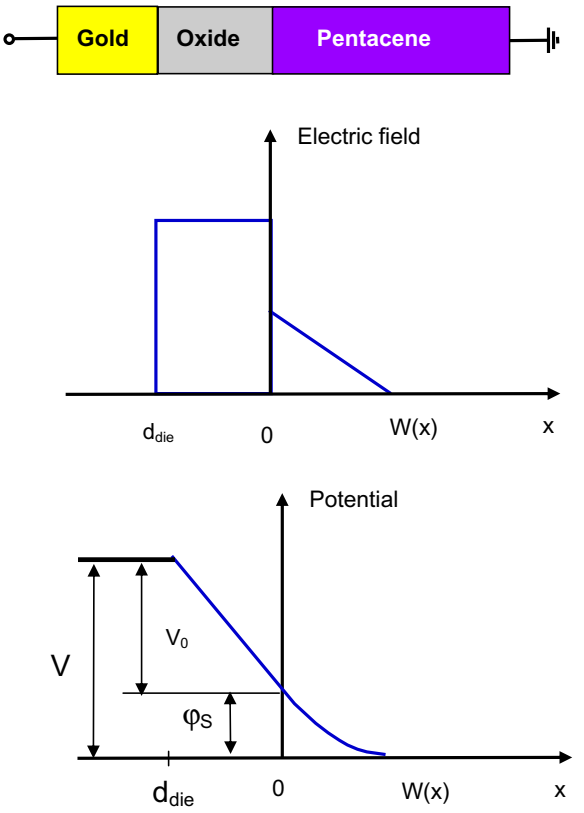


Fig. 4. Schematic cross section of a pentacene metal oxide semiconductor (MOS) structure and the corresponding electric and potential distribution.

The charge carrier mobility and the threshold voltage of the transistors were not affected by the oxygen contamination. The onset voltage was shifted by 2.8 V. Furthermore, the oxygen exposure leads to a slight increase of the subthreshold slope. The shift of the drain current onset is caused by acceptor-like states deep in the bandgap [10,16,19,20]. The concentration of acceptor-like states in the film can be determined by analyzing the MOS structure of the pentacene transistor. A schematic cross section of a pentacene MOS is shown in Fig. 4. The voltage applied to the MOS structure is equal to $V = V_0 + \varphi_S$, where V_0 is the voltage drop across the dielectric and φ_S corresponds to the band bending at the interface (surface potential) due to the influence of the impurities. The voltage drop across the dielectric and the surface potential can be determined by the classical theory for Metal Oxide Semiconductor (MOS) structures [23]. By analyzing the band bending of the semiconductor the doping concentration can be determined by

$$N_A = \frac{\varepsilon_0}{d_{pen}} \cdot \frac{V_{onset} - V_{fb}}{q} \left[\frac{\varepsilon_{pen}}{d_{pen}} + \frac{\varepsilon_{die}}{d_{die}} \right] \quad (1)$$

where $\varepsilon_0 \cdot \varepsilon_{pen}$ and $\varepsilon_0 \cdot \varepsilon_{die}$ are the permittivities of the pentacene film and the gate dielectric, d_{pen} and d_{die} are the thicknesses of the pentacene film and the gate dielectric. q is the elementary charge. The voltage V can be substituted by $V_{onset} - V_{fb}$, where V_{onset} is the gate voltage for which an onset of the drain current is observed and V_{fb} is the flatband voltage. As $\varepsilon_{pen}/d_{pen}$ is significantly small than $\varepsilon_{die}/d_{die}$ Eq. (1) can be simplified to

$$N_A = \frac{C_G}{d_{pen}} \cdot \frac{V_{onset} - V_{fb}}{q}, \quad (2)$$

where C_G is the gate capacitance, which is calculated by $C_G = \varepsilon_0 \cdot \varepsilon_{die}/d_{die}$. Eq. (2) is valid if the complete organic film is depleted. The voltage $V_{onset} - V_{fb}$ can be determined by comparing unexposed and exposed transistors. The unexposed sample is used as a reference to determine the flatband voltage. Such approach was already suggested by Meijer et al. [24] for polymer TFTs and Knipp et al. [25] for small molecule based TFTs. Based on the experimental results an acceptor

concentration of 1.5×10^{18} cm^{-3} was estimated for a transistor with a channel length of 40 μm.

After exposing the device to oxygen the devices were stressed for 10 min, 30 min, 90 min, and 180 min. The transfer characteristics after stressing the transistor in the on-state are shown in Fig. 5. The drain voltage was kept constant at −10 V and the gate voltage was fixed at $V_G = -20$ V. Due to bias stress the transfer curves were shifted towards negative gate voltages. The charge carrier mobility, the on/off ratio and the subthreshold slope of the transistor are not affected by the bias stress experiment. The bias stress results in a threshold voltage shift of 0.7 V towards negative gate voltages. The opposite behavior is observed if the transistor is bias stressed in the off-state (positive gate voltage). As a consequence the threshold voltage shifts towards positive gate voltage. The data in Fig. 5 represents typical bias stress data. The devices were stressed several times in the on- and the off-state before extracting the shift of the threshold voltage from the transfer characteristic.

A summary of the bias stress experiment for different transistors under positive and negative bias is given in Fig. 6. The shift of the threshold voltage is plotted as a function of time (linear (Fig. 6a) and logarithmic time scale (Fig. 6b)). Fig. 6a and b show the shift of the threshold voltage for pentacene TFTs with a channel length of 40 μm, 115 μm and 140 μm. All devices have the same channel width of 4000 μm. We observed that the shift of the threshold voltage due to bias stress is channel length dependent. The shift is more pronounced for TFTs which shorter channels.

The shift of the threshold voltage as a function of time can be described by the following stretching exponential model [14,26], which is typically used

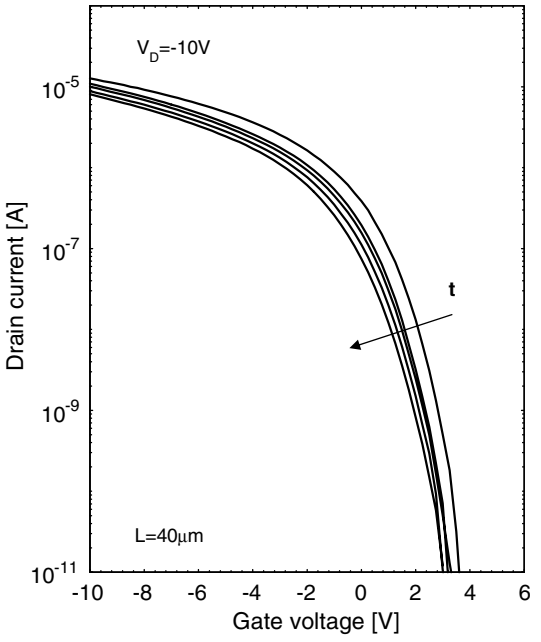


Fig. 5. Measured transfer curve of a pentacene TFT with a channel length of 40 μm after applying bias stress to the device. The transfer curves were measured after 0 min, 10 min, 30 min, 90 min and 180 min of prolonged bias stress. The transistor was stressed in the on-state. The drain voltage was kept constant at −10 V and the gate voltage was fixed at $V_G = -20$ V.

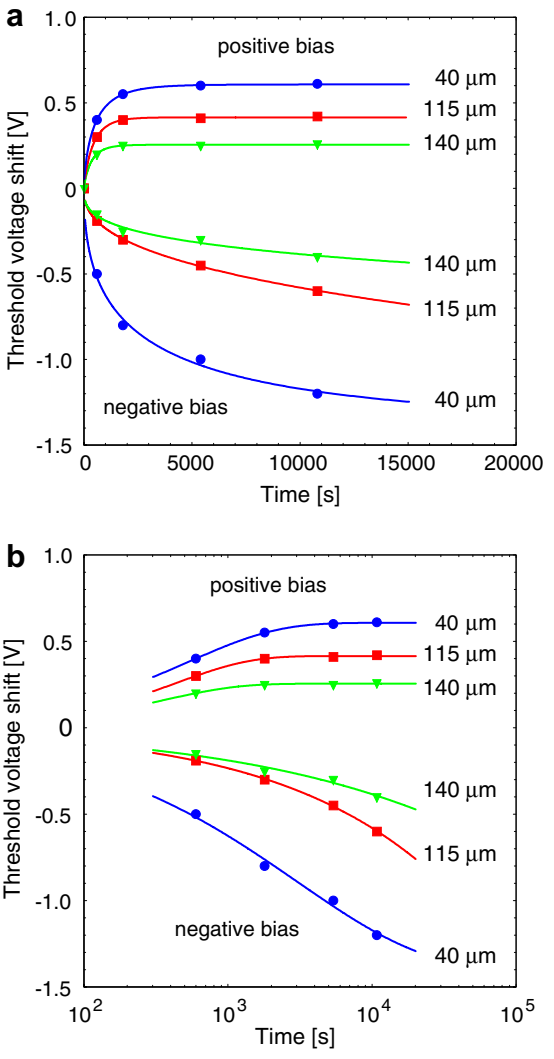


Fig. 6. Measured shift of the threshold voltage of pentacene TFTs for different channel length after applying bias stress. The devices were exposed to oxygen before carrying out the measurement.

to describe bias stress effects in amorphous silicon TFTs:

$$\Delta V_T \propto (V_G - V_T) \cdot \left(1 - \exp\left(-\left(\frac{t}{\tau}\right)^{\gamma}\right)\right). \quad (3)$$

The parameter t corresponds to the stress time, and γ is a stretching factor. The time constant τ depends on the material and device parameters. The shift of the threshold voltage is described very well by Eq. (3). The marks in Fig. 6a and b represent the experimental data, whereas the solid lines correspond to the fit of the data. For positive gate bias the stretching factor increases with increasing channel length from $\gamma = 0.7$ to 0.85. The opposite behavior is observed for the time constant τ, which decreases with increasing channel length from $\tau = 540$ s to 360 s. For negative bias stress and increasing channel length the stretching factor γ increases from 0.32 to 0.40. For negative voltages the time constant, τ, is 100–1000 times higher than the time constant for positive bias voltages.

Other models including power law models have been proposed in literature in order to account for the threshold voltage shift upon prolonged bias stress [3,17]. However, the experimental data in Fig. 6 can only be described by the stretching exponential model. For positive bias stress the threshold voltage converges towards an upper bound. Only the stretching exponential model accounts for such behavior. The situation is different for negative gate bias stress. Here the experimental data does not show a lower bound.

The experimental results reveal that electronic defects are created during the oxygen exposure of the device. During the bias stress experiment, which was carried out under vacuum conditions, the defect states are charged or recharged, but no additional defects are created. Subsequently the threshold voltage converges towards an upper bound for positive bias stress. Further measurements have to be carried out for negative bias stress. It remains open whether a lower bound for the threshold voltage exists.

Measurements under different biasing conditions show that the shift of the threshold voltage increases with increasing bias stress applied to the gate and the drain electrodes.

Similar experiments carried out under ambient conditions (oxygen plus moisture exposure) exhibit a more pronounced shift of the threshold voltage [17]. However, the fundamental trend remains the same. The threshold voltage shifts towards positive (negative) gate voltages, if the device is stressed at positive (negative) gate voltages [17]. Bias stress experiments carried out under ambient conditions do not exhibit an upper bound for the threshold voltage, which reveals that electronic defects are charged or recharged and new defects are created during the stress experiment [17].

After stressing the devices for 180 min and characterizing the samples the gate and drain electrodes were grounded. The transfer curves of the TFT were measured periodically over a period of days to obtain the threshold voltage. Measurements show that the threshold voltage of the transistor recovers. The threshold voltages shifts back towards the threshold voltage, which was obtained after exposing the sample to dry oxygen. However, further measurements are needed to study long term bias stress effects. Recent investigations of polymer TFTs shows that it is necessary to distinguish between permanent and reversible shifts of the threshold voltage [27,28].

3.3. Influence of contacts on the stability of pentacene transistors

The stability of organic transistors is influenced by the structural properties of the organic film. Pentacene films with increased structural order are less susceptible to bias stress and environmental influences. Therefore, staggered transistors using bottom drain and source electrodes are less stabile than thin film transistors with top drain and source electrodes. The pentacene film close to the contacts of the bottom drain and source transistors exhibit an increased structural disorder, so that the overall stability is reduced [25].

In the case of bottom drain and source contacts the structural order of organic films can be increased by modifying the surface property of the contacts and/or the channel region by self-assembled monolayers (SAMs). The gold electrodes can be treated by using eicosanethiol, hexadecanethiol, 2-Mercapto-5-nitrobenzimidazole, thiophenol, or 4-nitrothiophenol self-assembled monolayers prior to the deposition of the pentacene film. All these SAMs comprise of –SH (thiol) head groups, which bond to the gold surface. Subsequently the growth of pentacene on the metal electrodes and close to the metal electrodes is improved. Fig. 7 shows a schematic cross section of a device structure, which was treated by self-assembled monolayers. The silicon oxide dielectric was treated by hexamethyldisilazane (HMDS), whereas the gold electrodes

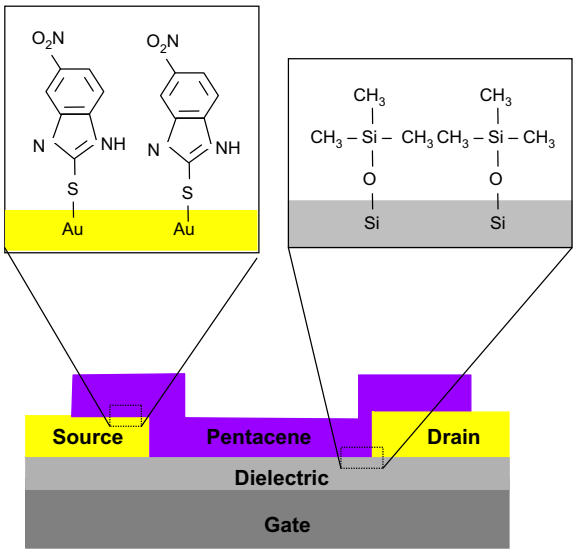


Fig. 7. Schematic cross section of a staggered pentacene transistor with bottom drains and source contacts. The bottom drain and source contacts (gold) were treated by eicosanethiol and the gate dielectric (silicon oxide) by hexamethyldisilazane self-assembled monolayer (SAM) prior to the deposition of the pentacene film.

were treated by 2-Mercapto-5-nitrobenzimidazole (MNB). The corresponding atomic force microscope image is shown in Fig. 8b. The pentacene film was prepared according to the deposition conditions described in Section 2. The pentacene film is highly ordered in the channel and the contact region. Pentacene films on pure gold surfaces are disorder and the pentacene molecules are lying flat on the gold surfaces. An atomic force microscope image of a pentacene film prepared on a pure gold electrode is shown in Fig. 8a. The pentacene film has a thickness of 10 nm. The channel region was treated by HMDS, whereas the gold electrode was untreated. A comparison of transistors with treated and non-treated bottom drain and source electrodes are shown in Fig. 9. The channel of the transistors is 20 μm long. Both devices were exposed to dry oxygen before measuring the transistor. Only the device with untreated gold electrodes exhibits a shift of the onset voltage due to the oxygen exposure. The onset voltage of the transistor with pretreated bottom and source electrodes does not exhibit a change of the onset voltage due to the oxygen exposure. Furthermore, the SAM treatment has an influence on the threshold voltage. The threshold voltage of the transistors with untreated drain and source electrodes is higher. The charge carrier mobility of pentacene TFTs with treated drain and source electrodes is

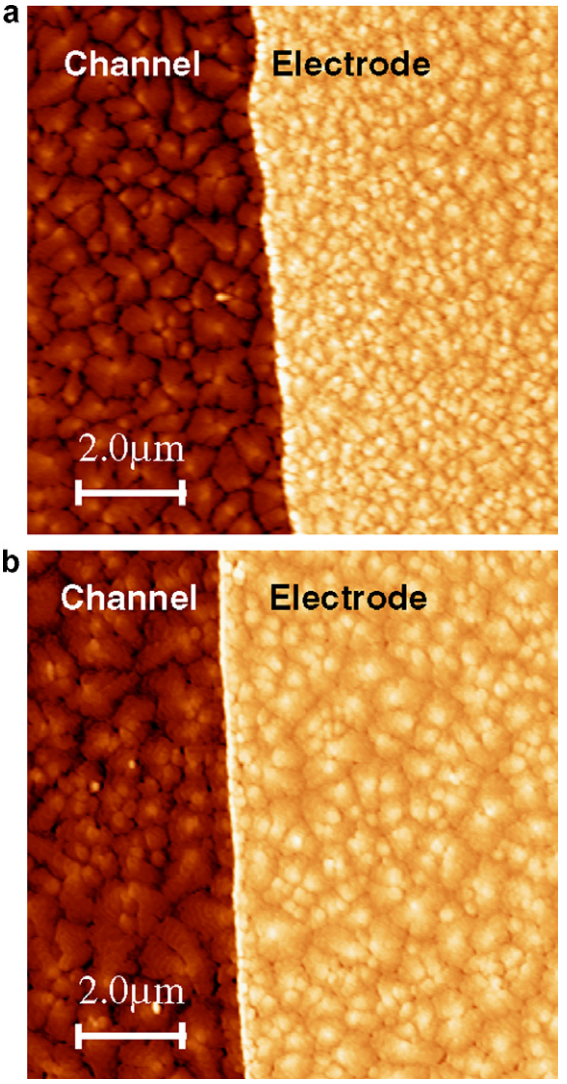


Fig. 8. Atomic force microscope image of a pentacene film prepared on a silicon dioxide substrate and gold drain/source electrodes. The gate dielectric (silicon oxide) was pretreated by a hexamethyldisilazane self-assembled monolayer (SAM) prior to the deposition of the pentacene film. In the drain/source region the pentacene film was prepared on pure gold (a) and 2-Mercapto-5-nitrobenzimidazole (MNB) pretreated gold (b).

increased in comparison to transistors with treated electrodes. In particular short channel transistors exhibit a distinct increase of the charge carrier mobility by 30–50%.

3.4. Influence of transistor stability on the performance of organic circuits

In the following the influence of bias stress on the performance of organic integrated circuits will be

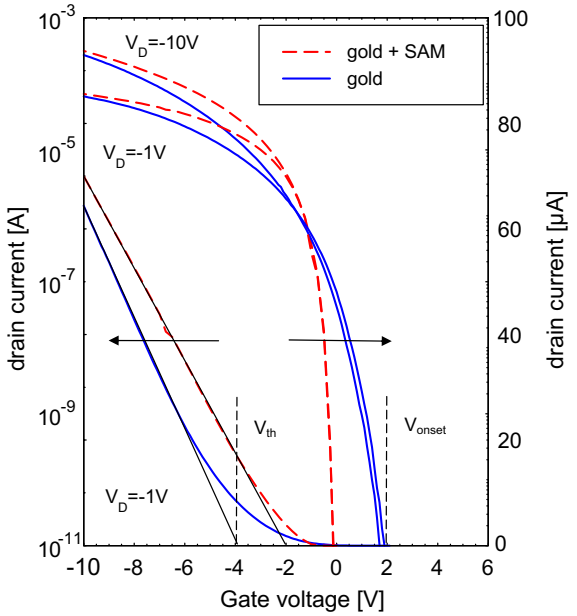


Fig. 9. Transfer characteristic of pentacene thin film transistors prepared on a silicon dioxide substrate with bottom drain and source electrodes. The pentacene films were prepared on pure gold and 2-Mercapto-5-nitrobenzimidazole (MNB) pretreated gold drain and source electrodes.

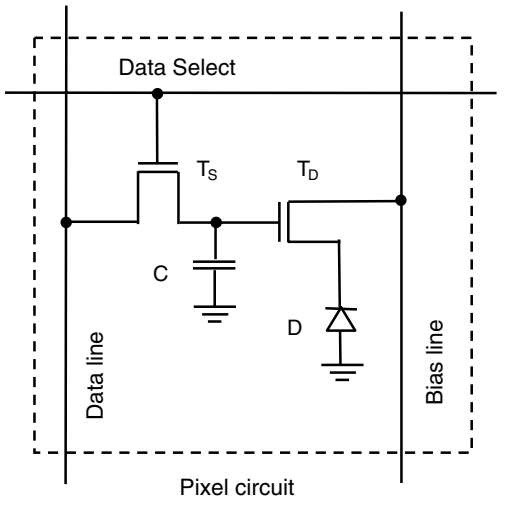


Fig. 10. Circuit of an organic light emitting diode (OLED) pixel using a two-transistor configuration.

investigated. As an example an OLED pixel driver will be used. A simple two-transistor ($2T$) OLED pixel circuit is shown in Fig. 10 [14]. The pixel circuit comprises of a select transistor, T_s, which transfers the input signal (charge) from the external drive electronics to the storage capacitor in the pixel. The charged on the storage capacitor, C, is used to bias the drive transistor T_D. It is assumed that the drive transistors can be described by the classical transistor equation

$$I_D = k \cdot \frac{W}{L} \cdot \mu \cdot C_G \cdot (V_G - V_T)^m \quad (4)$$

where μ is mobility, W and L are the TFT channel width and length. If the drain voltage, V_D, is smaller than $V_G - V_T$ the parameter m is equal to 1 and the TFT operates in the linear region. Under such conditions the prefactor k is equal to V_D. If the drain voltage $V_D \geqslant V_G - V_T$ the transistors operates in the saturation region. Subsequently the parameter m is equal 2 and the prefactor k is equal to 1/2.

In the following the transistor operates as a drive transistor in an organic pixel circuit [14]. It was assumed that a certain drain current variation ($\Delta I_D/I_D$) can be tolerated without having a negative effect on the image quality of the display. Thus the following relationship between the threshold voltage shift and the variation of the drain current can be derived:

$$\Delta V_T = -(V_G - V_T) \cdot \frac{\Delta I_D}{m \cdot I_D}. \quad (5)$$

The parameter m is equal 1 in the linear and equal to 2 in the saturation region. In the saturation mode of operation it can be assumed that $V_G - V_T$ is small, for example, $V_G - V_T$ is equal to -1 V. If a variation of the drain current by 10% can be tolerated by the display, a maximum variation of the threshold voltage by 50 mV can be determined. In the linear region of operation the term $V_G - V_T$ is going to be larger, for example -5 V. Subsequently a threshold voltage variation of 500 mV can be tolerated by the display. In general, the requirements in terms of the threshold voltage stability are high in the saturation region, whereas the requirements in the linear region are distinctly lower. Therefore, a variation of the threshold voltage by 500 mV in the linear region of operation defines the minimum requirement in terms of the threshold voltage stability.

4. Discussion

The stability of the devices is a very important requirement for the application of organic thin film transistors. In particular the stability of the threshold voltage is of major importance for the realization of organic integrated circuits. In general the

change of the threshold voltage due to bias stress is caused by charge trapping or recharging of defect states in the dielectric, trapping and slow release of carriers in existing deep states in the semiconductor (bulk or interface), or a reversible structural change in the semiconductor that creates new traps. The fact that bias stress is only observed after exposing a pentacene TFT to dry oxygen indicates that trapping of charges in the dielectric can be excluded as a source of the threshold voltage shift. The results reveal that recharging of electronic defects in the channel material causes the threshold voltage shift. In order to account for the shift of the threshold voltage in Fig. 6 a defect density of more than $1.5–6 \times 10^{17}\,\mathrm{cm}^{-3}$ is required. Furthermore, the defects need to be acceptor-like for positive bias stress and donor-like for negative bias stress. First principle pseudopotential density function calculations of –O and –OH defects in pentacene shows that such impurities lead to the creation of electronically active gap states [22]. In the case of oxygen such defect are located 0.18 eV (donor-like states) and 0.62 eV (acceptor-like states) relative to the valence band maximum. Further electrical measurements including temperature dependent electronic transport measurements and/or numerical simulations are needed to determine the energy level and the concentration of the defect states.

A comparison of the experimental results presented in this paper with other results published in literature indicates that the shift of the threshold voltage due to bias stress is relatively small [3,5,8–13,17]. However, the shift of the threshold voltage does not fulfill the requirements defined for a drive transistor in an OLED display. The shift of the threshold voltage due to bias stress exceeds the required limits in the linear and the saturation mode of operation. As the actual bias stress induced shift of the threshold voltage (Eq. (3)) and the maximum tolerable threshold voltage shift (Eq. (5)) scale with $V_G - V_T$ further aspects have to be taken into account when deciding on the mode of operation of the drive transistor. It should be mentioned that the requirements in terms of OLED pixel circuits are very high. Polycrystalline silicon TFTs are typically used as pixel circuits as the devices are very stable. In terms of other displays like active matrix addressed liquid crystal (AMLCD) displays or reflective displays the requirements are not as high. For such applications the stability of pentacene TFTs is sufficient [29]. Preliminary bias stress measurements carried out under vacuum conditions (no oxygen exposure) do not exhibit a change of the device characteristic upon prolonged bias stress (180 min.). These results underline the importance of effective encapsulation concepts, which prevent the exposure to oxygen and moisture. However, the experimental results show that very efficient encapsulation concepts are needed, as the device already exhibit distinct changes of the device characteristics for rather low levels of oxygen.

5. Summary

The influence of environmental conditions on the device operation and the stability of staggered polycrystalline pentacene thin film transistors (TFTs) with bottom drain and source contacts were investigated. In-situ and ex-situ measurements of pentacene TFTs were carried out to study the effect of oxygen contamination on the operation and the stability of pentacene TFTs. Oxygen exposure leads to a shift of the onset of the drain current towards positive gate voltage. The charge carrier mobility, the threshold voltage and the on/off ratio are not affected by the oxygen exposure. The shift of the onset voltage is caused by acceptor-like states created in the film. The experimental results show a clear correlation between the shift of the onset voltage and the stability of the devices. A shift of the onset voltage upon oxygen exposure is correlated with a shift of the threshold voltage upon prolonged bias stress. The shift of the threshold voltage upon prolonged bias stress is larger for short channel devices, whereas long channel devices exhibit a small shift of the threshold voltage upon prolonged bias stress. Applying self-assembled monolayers can help to reduce the sensitivity towards oxygen and therefore, the bias stress induced shift of the threshold voltage. The example of a pixel driver of an organic light emitting display was investigated in terms of the required device stability. A simple relationship between the acceptable variation of the drive current and the maximum shift of the threshold voltage was derived. The simple estimation reveals that efficient encapsulation concepts are needed to use pentacene TFTs in complex organic integrated circuits. Measurements under vacuum conditions do not show bias stress induced changes of the threshold voltage, which underlines the huge potential of organic transistors for a variety of applications.

Acknowledgement

We gratefully acknowledge the financial support by the Deutsche Forschungsgemeinschaft (DFG) Project No. Wa1039/2-2 within SP1121.

References

[1] T.W. Kelley, P.F. Baude, C. Gerlach, D.E. Ender, D. Muyres, M.A. Haase, D.E. Vogel, S.D. Theiss, Chem. Mater. 16 (2004) 4413.
[2] G. Horowitz, Organic thin film transistors: from theory to real devices, J. Mater. Res. 19 (2004) 1946.
[3] D. Knipp, R.A. Street, B. Krusor, R.B. Apte, J. Ho, SPIE 466 (2001) 8.
[4] H. Klauk, M. Halik, U. Zschieschang, G. Schmid, W. Randlik, W. Weber, J. Appl. Phys. 92 (2002) 5259.
[5] R.A. Street (Ed.), Technology and Applications of Amorphous Silicon, Springer Series in Material Science, Science, vol. 37, Springer-Verlag, Berlin, 2000.
[6] S. de Vusser, J. Genoe, P. Heremans, IEEE Trans. Elec. Dev. 53 (2006) 601.
[7] C.-S. Chiang, J. Kanicki, K. Takechi, Jpn. J. Appl. Phys. 37 (1998) 4704.
[8] P.V. Necliudov, M. Shur, D.J. Gundlach, T.N. Jackson, Mater. Res Soc. Symp. Proc. 660 (2001).
[9] H.L. Gomes, P. Stallinga, F. Biscarini, D.M. de Leeuw, T. Muck, J. Geurts, L.W. Molenkamp, V. Wagner, Appl. Phys. Lett. 84 (2004) 3184.
[10] A.R. Völkel, R.A. Street, D. Knipp, Phys. Rev. B 66 (2002) 195336.
[11] D. Knipp, T. Muck, A. Benor, V. Wagner, J. Non-Cryst. Solids 352 (2006) 1774.
[12] A. Salleo, F. Endicott, R.A. Street, Appl. Phys. Lett. 86 (2005) 263505.
[13] A. Salleo, R.A. Street, Phys. Rev. B 70 (2004) 235324.
[14] A. Nathan, D. Striakhilev, R. Chaji, S. Ashtiani, C.-H. Lee, A. Sazonov, J. Robertson, W. Milne, Mater. Res. Soc. Symp. Proc. 910 (2006).
[15] S. Steudel, S.D. Vusser, S.D. Jonge, D. Janssen, S. Verlaak, J. Genoe, P. Heremans, Appl. Phys. Lett. 85 (2004) 4400.
[16] D. Knipp, R.A. Street, A.R. Völkel, P. Kumar, Synth. Met. 155 (2005) 485.
[17] D. Knipp, R.A. Street, B. Krusor, J. Ho, J. Appl. Phys. 93 (2003) 347.
[18] A. Facchetti, M.-H. Yoon, T.J. Marks, Adv. Mater. 17 (2005) 1705.
[19] S. Scheinert, G. Paasch, Th. Doll, Synth. Met. 139 (2003) 233.
[20] K.P. Pernstich, D. Oberhoff, C. Goldmann, B. Batlogg, J. Appl. Phys. Lett. 89 (21) (2006) 213509.
[21] A. Vollmer, O.D. Jurchescu, I. Arfaoui, I. Salzmann, T.T.M. Palstra, P. Rudolf, J. Niemax, J. Pflaum, J.P. Rabe, N. Koch, Eur. Phys. J. E 17 (2005) 339–343.
[22] J.E. Northrup, M.L. Chabinyc, Phys. Rev. B 68 (2003) 041 202.
[23] M. Shur, Physics of Semiconductor Devices, Prentice Hall, Englewood Cliffs, NJ, USA, 1990.
[24] E.J. Meijer, C. Detcheverry, P.J. Baesjou, E. van Veenendaal, D.M. de Leeuw, T.M. Klapwijk, J. Appl. Phys. 93 (2003) 4831.
[25] D. Knipp, A. Benor, V. Wagner, T. Muck, J. Appl. Phys. 101 (2007) 044504.
[26] M.J. Powell, C. van Berkel, J.R. Hughes, Appl. Phys. Lett. 54 (1989) 1323.
[27] J. Genoe, S. Steudel, S. De Vusser, S. Verlaak, D. Janssen, P. Heremans, in: Proc. 34th Eur. Solid-State Device Research Conf. – ESSDERC 2004, Leuven, Belgium, 2004, p. 413.
[28] R. A Street, M.L. Chabinyc, F. Endicott, B. Ong, J. Appl. Phys. 100 (2006) 114518.
[29] G.H. Gelinck, H.E A. Huitema, E. van Veendaal, E. Cantatore, L. Schrijnemakers, J.B.P.H. van der Putten, T.C.T. Geuns, M. Beenhakkers, J.B. Giesbers, B.-H. Huisman, E.J. Meijer, E.M. Benito, F.J. Touwslager, A.W. Marsman, B.J.E. van Rens, D.M. de Leeuw, Nature Mater. 3 (2004) 106–110.

Available online at www.sciencedirect.com
ScienceDirect
Organic Electronics 8 (2007) 759–766
Organic Electronics
www.elsevier.com/locate/orgel

Air stability of n-channel organic transistors based on nickel coordination compounds

Hiroshi Wada, Tomohiro Taguchi, Bunpei Noda, Takuya Kambayashi, Takehiko Mori *, Ken Ishikawa, Hideo Takezoe

Department of Organic and Polymeric Materials, Tokyo Institute of Technology, 2-12-1 O-okayama, Meguro-ku, Tokyo 152-8552, Japan

Received 10 May 2007; received in revised form 25 May 2007; accepted 20 June 2007
Available online 3 July 2007

Abstract

A series of tetraphenyl nickel dithiolene complexes, **1**, are prepared, and the air stability of the n-channel organic field-effect transistors (OFET) is investigated. The fluoro and trifluoromethyl derivatives with reduction potentials higher than 0 V afford reasonably air-stable n-channel OFET. Metallic organic charge-transfer complex (TTF)(TCNQ) (TTF: tetrathiafulvalene and TCNQ: tetracyanoquinodimethane) is used as source and drain electrodes, and realizes n-channel transistor properties even when Al electrodes do not work.
© 2007 Elsevier B.V. All rights reserved.

PACS: 73.61.Ph

Keywords: Organic transistor; Metal complex; n-Channel; Charge-transfer complex

1. Introduction

Organic field-effect transistors have attracted a great deal of attention due to the potential applications to large area and flexible devices [1]. Although satisfactory p-channel FET characteristics have been achieved by various compounds such as polyacenes and oligothiophenes, good n-channel organic materials for OFETs are relatively limited [2]. C_{60} and naphthalene tetracarboxy dianhydride derivatives are known as representative n-channel OFET semiconductors as well as a variety of fluoro and trifluoromethyl compounds, and some of them show very high performance [2]. These n-channel OFETs are, however, usually not very stable in air, though several air-stable compounds have been known [2d,2f]. It has been reported that n-type organic semiconductors are unstable with respect to oxidations by H_2O and O_2, which take place at redox potentials of −0.66 V and 0.57 V (vs. SCE), respectively [3]. Compounds with reduction potentials to the monoanionic (1-) states higher than the former (−0.66 V) is reported to be stable in air [4], as represented by F_{16}CuPc (copper hexadecafluoro phthalocyanine) [2d]. However, even these n-type semiconductors are not always stable depending on the conditions. Reduction potentials higher than the latter (0.57 V) are realized only in an extremely

* Corresponding author. Tel.: +81 3 5734 2427; fax: +81 3 5734 2876.
E-mail address: mori.t.ae@m.titech.ac.jp (T. Mori).

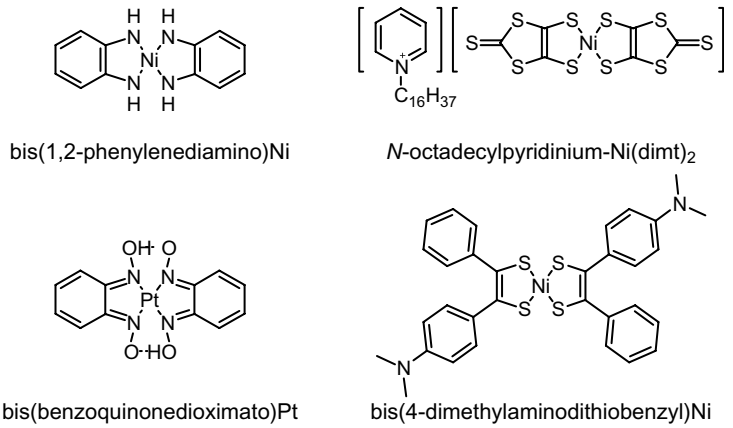
1566-1199/$ - see front matter © 2007 Elsevier B.V. All rights reserved.
doi:10.1016/j.orgel.2007.06.007

strong electron acceptor. In this connection, metal coordination compounds are promising because metal complexes show a wide variety of redox potentials in comparison with pure organic compounds. There are several metal coordination compounds that have been used for OFET (Scheme 1). In addition to copper phthalocyanine, which is a well-known p-channel material [5], bis(1,2-phenylenediamino)Ni has been reported to show p-channel characteristics [6]. In addition to F_{16}CuPc [2d], n-channel characteristics have been observed in *N*-octadecylpyridinium Ni(dmit)$_2$ (dmit: 4,5-dimercapto-1,3-dithiole-2-thione) and bis(benzoquinonedioximato)Pt [7]. Ambipolar OFET has been also reported in bis(4-dimetylaminodithiobenzyl)Ni [8]. We have reported that a tetraphenyl nickel dithiolene complex exhibits n-channel characteristics (**1a** in Scheme 2) [9]. Interestingly, a nickel diamino compound, coordinated by four nitrogen atoms (Scheme 1), is a strong electron donor and works as a p-channel semiconductor, while a nickel dithiolene compound with four-sulfur coordination is a strong electron acceptor and achieves an n-channel OFET. Since OFET of **1a** is still not very stable in air, we have prepared a series of tetraphenyl nickel dithiolene complexes substituted at the phenyl groups (Scheme 2). These compounds have exhibited n-channel FET properties, and particularly the air stability is improved in the compounds with fluoro substituents. Here we report correlation between the redox potentials and the air stability of the OFETs in these materials.

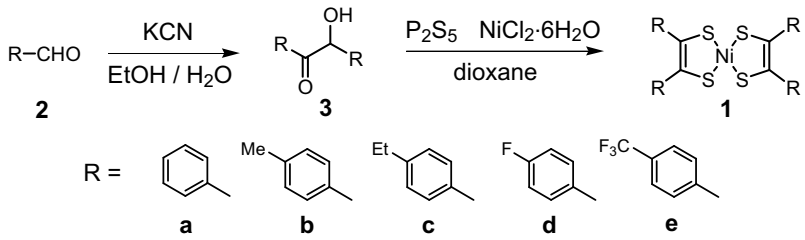
2. Results and discussion

2.1. Syntheses and electrochemistry

The substituted tetraphenyl nickel dithiolene complexes have been investigated as dyes [10]. Except for commercially available "bis(dithiobenzyl)nickel" **1a**, the nickel dithiolene compounds are prepared according to the two-step sequence (Scheme 2) similarly to [10]. Compounds **3** are prepared from aromatic aldehydes by the benzoin condensation [11]. Although the yield of the benzoin condensation is excellent for the non-substituted benzaldehyde, the fluorine substituted compounds result in relatively low yields. Accordingly the ben-



Scheme 1. Metal complexes showing FET characteristics.



Scheme 2. Preparation of bis(dithiobenzyl)nickel derivatives.

zoins **3** are purified by vacuum distillation. The second step proceeds smoothly for non-fluoro derivatives **1b** and **1c**, but precipitates are not easily obtained for the fluoro derivatives **1d** and **1e**. In these cases, stirring under air for a few days affords the desired precipitation. This may be related to the relatively high oxidation potentials of these compounds. The ethyl derivative **1c** is a previously unknown compound. All obtained compounds are purified by sublimation, giving black microcrystals.

The redox potentials are measured by cyclic voltammogram as summarized in Fig. 1. These compounds are reduced to the monoanionic (1-) states at around 0 V; these compounds are moderately strong acceptors. The introduction of fluoro or trifluoromethyl groups enhances the acceptor ability. The shift of the redox potential in the trifluoromethyl compound is larger than that in the fluoro compound. In contrast, the methyl substitution slightly decreases the acceptor ability. These redox potentials correspond to the LUMO levels at about 4.4–4.6 eV [12]; these values are a little larger than the work function of Al (4.3 eV), so that good electron injection from Al electrodes is expected.

2.2. Thin-film morphology and crystal structure

Thin films of the nickel complexes are made by vacuum evaporation on SiO_2 substrates. The AFM images are shown in Fig. 2. The non-fluorinated compounds, **1a**, **1b** and **1c**, show no large continuous domains or terraces, but have fibril-like structures. For **1a**, relatively large microcrystals are observed, and there are few flat parts. On the contrary, **1c** enlarges the continuous area, and obscures the boundaries between microcrystals and flat parts. Accordingly the ethyl substitution improves the thin-film property. The thin film of **1d** does not show fibril-like structure like the alkyl derivatives, but shows a smooth but inhomogeneous pattern. Compound **1e** shows continuous surface with no clear grain boundary. In general, fluoro compounds (**1d** and **1e**) afford much improved thin films.

In the X-ray diffraction (XRD) measurement, clear peaks are observed only for **1c** and **1e**. Observed diffraction peaks of **1c** and **1e** correspond to the *d*-spacings of 15.9 Å and 16.2 Å, respectively. The molecular lengths are 20.1 Å and 16.3 Å from the geometry-optimized molecular orbital calculation. Accordingly the tilt angle is 38° for **1c**, while the molecules are approximately perpendicular to the substrate for **1e**. The alkyl and CF_3 groups seem to improve the molecular packing and the film morphology. The difference of the tilt angles, however, suggests that the molecular arrangement varies as a sensitive function of the end groups.

Single crystal X-ray crystal structure analysis has been carried out for **1d** (Fig. 3) [13]. The central nickel dithiolene part has a bent structure owing to the strong dimerization, similarly to the previously reported crystal structure of **1a** [14]. The space group ($P\bar{1}$) is, however, different from **1a** ($P2_1/n$). This is because all dimers in **1d** are arranged parallel

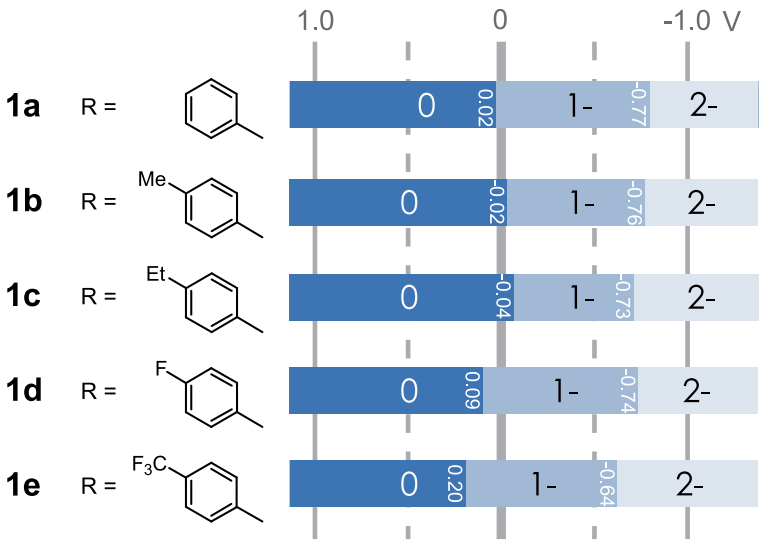


Fig. 1. Redox potentials $E^{1/2}$ of the nickel complexes (vs. Ag/AgCl).

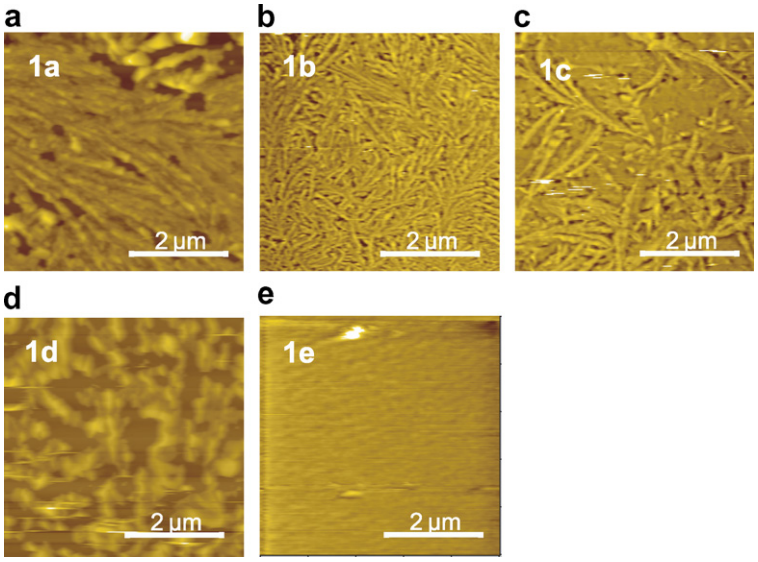


Fig. 2. AFM images of nickel complexes. (a)–(e) correspond to **1a**–**e**.

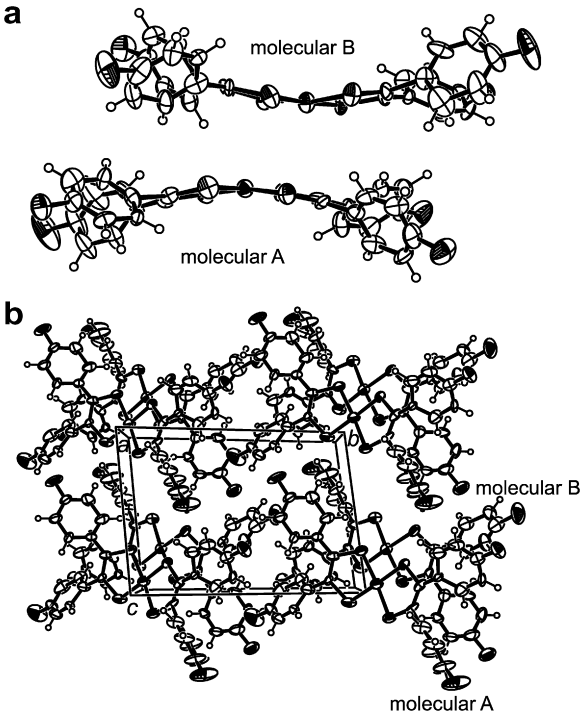


Fig. 3. Crystal structure of **1d**. (a) The dimer, and (b) the projection along the *a* axis.

to each other, whereas the molecules in **1a** are tilted alternately. The phenyl groups are out of the central dithiolene part, making dihedral angles of 12.7°, 19.5°, 30.4°, and 58.7° for Molecule A and 24.5°, 52.0°, 52.3° and 83.4° for Molecule B.

2.3. FET characteristics

Bottom-contact type FETs have been fabricated on SiO_2 substrates. An organic charge-transfer complex (TTF)(TCNQ) as well as Al is used as source and drain electrodes. (TTF)(TCNQ) is a metallic complex, and has been used as source and drain electrodes in single-crystal OFETs [15]. We can expect a good contact between the electrodes and the active layer, because both are composed of organic materials [16]. In addition, the Fermi level of (TTF)(TCNQ) is higher than Au, and electron injection is possible [15].

The FET performance is summarized in Table 1. OFETs of all compounds have shown n-channel characteristics, though the mobilities are in the order of 10^{-4}–10^{-6} cm^2/V s. Since in our study of TTF derivatives, dimerized compounds have not shown transistor properties [17], it is rather surprising that these strongly dimerized compounds show transistor properties. The presence of the out-of-plane phenyl groups is disadvantageous to the molecular packing and the FET properties, resulting in the observed moderate mobility values. This, however, facilitates the vacuum evaporation, and consequently all these compounds show FET properties. In comparison with our previous report on **1a** [9], the mobility values are improved. For **1b**, (TTF)(TCNQ) electrodes have given much better results than Al electrodes. For **1c**–**1e**, OFET properties have been observed only for (TTF)(TCNQ) electrodes.

Table 1
FET performance of bis(dithiobenzyl)nickel and their derivatives

Compound	Electrodes	Electron mobility $cm^2/V\,s$ (air)	Electron mobility $cm^2/V\,s$ (vacuum)	On/off ratio (air/vacuum)	V_t (air/vacuum) (V)
1a	Al	3.0×10^{-6}	2.0×10^{-5}	$10^2/10^2$	68/10
1b	Al	–	1.3×10^{-5}	$-/2\times10^2$	–/4.0
	(TTF)(TCNQ)	–	1.3×10^{-4}	$-/2\times10^2$	–/ 45
1c	(TTF)(TCNQ)	–	6.0×10^{-5}	$-/10^4$	–/ 27
1d	(TTF)(TCNQ)	9.0×10^{-5}	5.0×10^{-5}	20/30	7/−10
1e	(TTF)(TCNQ)	6.6×10^{-6}	6.4×10^{-6}	10/<10	−69/−110

Output characteristics of these nickel complexes in vacuum are shown in Fig. 4, where characteristics after 5 min air exposure are also depicted for (d) **1a**, (f) **1d**, and (h) **1e**. These figures are arranged in the order of the acceptor strength. In vacuum, good saturation properties are observed for all compounds. Remarkable difference is observed in the measurements in air. Output characteristics of **1d** and **1e** show good saturation properties which are basically the same as the vacuum measurements (Fig. 4f and h). Compound **1e** exhibits a decrease of the off-current in air, showing better characteristics in air than in vacuum. Output characteristics become more unstable with decreasing the acceptor ability. The measurement for **1a** is depicted in Fig. 4d, but for **1c** and **1d**, the FET properties are similarly lost in air. The air stability seems to change abruptly between **1a** and **1d**. For all compounds, p-channel characteristics are not observed even in air.

As depicted in Fig. 5, there is a good correlation between the threshold voltage and the redox potentials. When the redox potential shifts to positive, making the molecule stronger acceptors, the threshold voltage becomes more negative. The change of the former of 0.25 V induces a more than 100 V change of the latter. The threshold voltage is not naively determined by the potential difference, but by the barriers at the junctions.

Since **1d** and **1e** are considerably air-stable, we have investigated time dependence of the transistor characteristics after exposure to air. As shown in Fig. 6, the threshold voltage gradually increases in air. Compound **1d** loses FET properties within 1 h. The FET of **1e** degrades during several hours, but this drop stops at about 10 h. We have observed almost the same n-channel FET properties even after more than 37 days as those after 10 h.

Air-stable n-channel OFETs have been reported for F_{16}CuPc, naphthalene tetracarboxy diimide, and a hybrid dmit complex [2c,2e,4]. The LUMO level of F_{16}CuPc is reported to be 4.61 V [18], which corresponds to the redox potential of +0.17 V. Therefore, F_{16}CuPc is an acceptor as strong as the present compound **1e**. The reduction potentials of tetracarboxy diimides are about −0.5 V [19]. Although the fluoro compounds are expected to have a little higher redox potentials, these compounds are not very strong acceptors. In addition, FET of TCNQ (redox potential: +0.18 V) is reported to maintain its activity for days [2b]. The results obtained in the present work, together with the previous observations, indicate that organic acceptors with positive redox potentials have a good chance of showing reasonably air-stable FET properties, and the threshold to the stability is about 0 V. These observations suggest the possibility to much improved air stability in n-channel OFET.

3. Experimental

Bis(dithiobenzyl)nickel **1a** was purchased from Tokyo Kasei, and used after sublimation.

3.1. Preparation of benzoin derivatives *3b–e*

In a flask were placed benzaldehyde derivative **2**, EtOH, and 0.16 equivalent of potassium cyanide dissolved in water. The mixture was refluxed for 3 h. The resulting mixture was washed with water and the solvent was removed by evaporation. The obtained pale yellow oil was distilled under vacuum condition, giving a pale yellow solid.

3.2. Preparation of bis(dithiobenzyl)nickel derivative *1b–e*

Benzoin derivative **3** was refluxed with 1.4 equivalent of P_2S_5 in dioxane for 1 h. To the cooled and filtered reaction solution 0.5 equivalent of $NiCl_2\cdot6H_2O$ dissolved in water were added, then the mixture was refluxed for 1 h. After cooling, black crystals of the complex were formed and

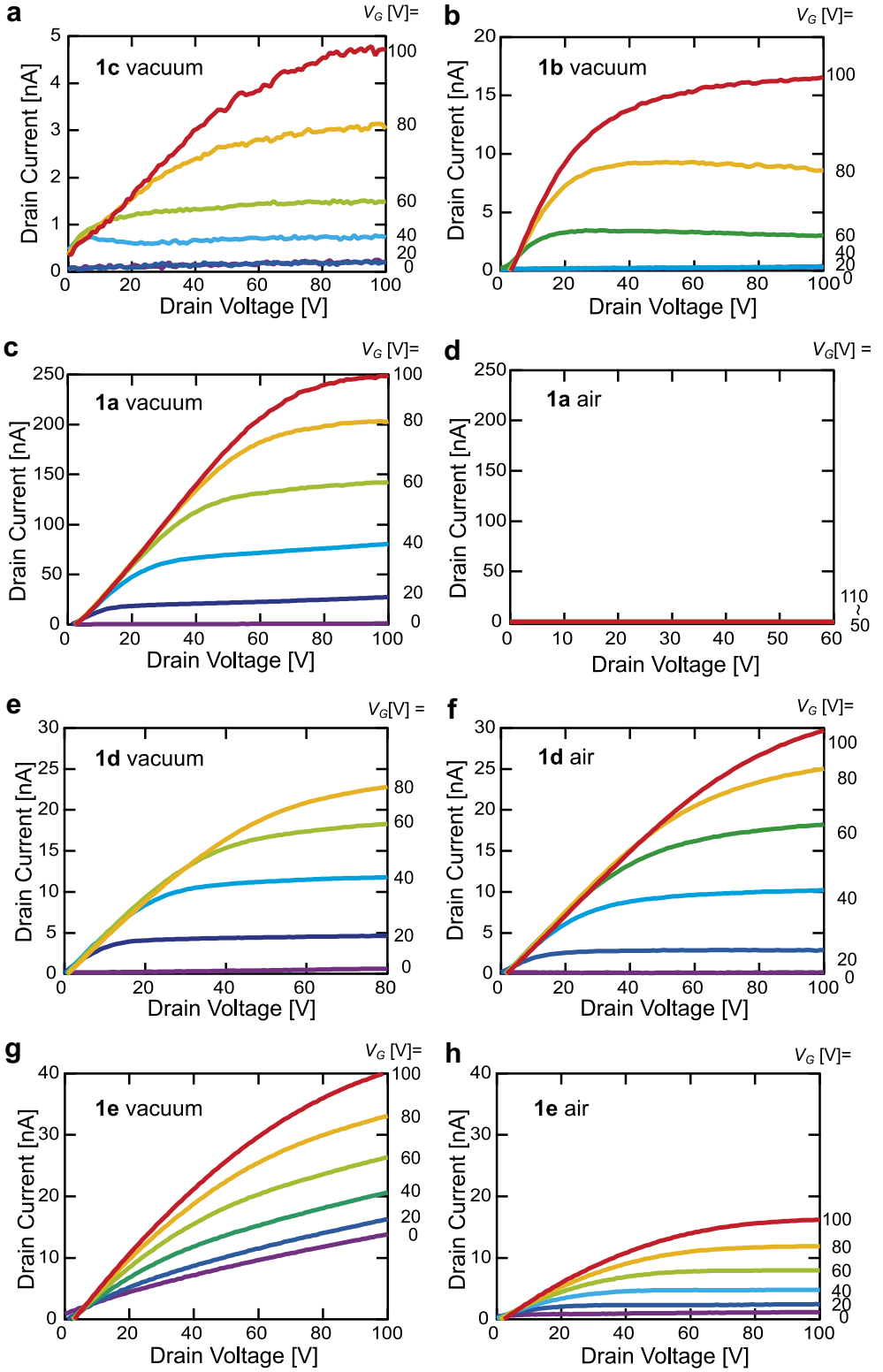


Fig. 4. Output characteristics of OFETs with Al electrodes for **1a** and (TTF)(TCNQ) electrodes for **1b**–**e**.

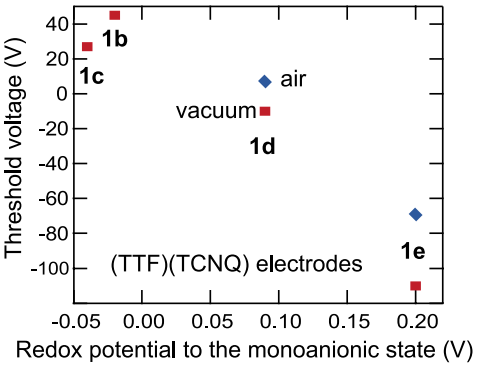


Fig. 5. Correlation between the threshold voltages for (TTF)(TCNQ) electrodes, and the redox potentials to the monoanionic state.

collected by filtering the solution, giving a black solid. The product was purified by sublimation.

The redox potentials were measured by a Yanaco VMA-010 cyclic voltammetric analyzer. All electrochemical measurements were conducted on a glassy carbon working electrode vs. Ag/AgCl in benzonitrile containing tetrabutylammonium hexafluorophosphate as a supporting electrolyte.

AFM images of the evaporated thin films on the Si/SiO_2 substrates were taken with a SII scanning probe microscope system SPI3800N and SPA 300 by using a Si_3N_4 cantilever. Scanning range of the thin films was 5×5 μm. X-ray diffraction profiles of organic thin films deposited on the Si/SiO_2 substrates were obtained with a Phillips X'Pert-MPD-OEC PW3050 with a monochromated Cu Kα radiation ($\lambda = 1.541$ Å) at room temperature using the θ–2θ technique for $2° \leqslant 2\theta \leqslant 30°$. The single-crystal X-ray data of the nickel complex **1d** were collected on a Rigaku AFC-7R diffractometer with a rotating anode X-ray generator with graphite monochromated Mo Kα radiation at room temperature and using the 2θ–ω scan technique to a maximum 2θ of 60°. The structure was solved by the direct method (SIR 92) and refined by full-matrix least-squares analysis.

Bottom-contact type FETs were fabricated on heavily doped n^+-Si substrates with 300 nm thermally grown SiO_2. Powder of (TTF)(TCNQ) in a crucible was thermally deposited ($<10^{-5}$ Torr) through a shadow mask on the substrates. Al electrodes were similarly deposited. Subsequently, the substrates were loaded into an evaporator and the nickel complexes were evaporated under high-vacuum conditions ($<10^{-6}$ Torr) to thickness of approximately 50–100 nm. The substrate temperature was kept at room temperature during the deposition and the measurement. The channel dimensions were W/L (μm/μm) = 2000/100 for **1b**–**1e** except for 6000/50 (vacuum) and 1000/20 (air) for **1a**. The FET properties were measured by a Keithley 4200-SCS semiconductor parameter analyzer. The measurements in air were carried out by using an OYAMA manual prober system model TB-2-H-200, and the *in situ* measurements were done by connecting the device by using copper wires and silver paste. In the measurement under vacuum, the substrates were once taken out from the evaporation chamber and transferred to a measurement chamber, and kept under vacuum overnight. Mobilities (μ) were estimated from the transfer characteristics in the saturation regime ($V_{ds} = 60$ V)

$$I_{ds} = \frac{WC\mu}{2L}(V_g - V_t)^2, \quad (1)$$

where C (13.3 nF/cm^2) was the oxide capacitance, and V_g was the gate voltage. The threshold voltage

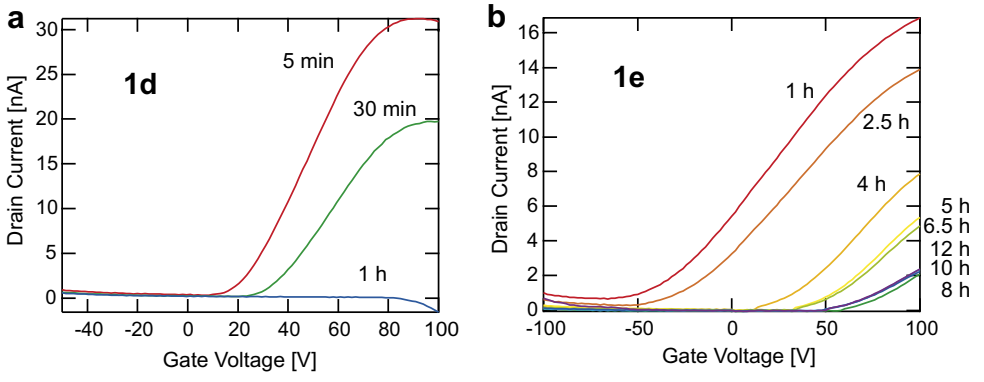


Fig. 6. Time dependence of the transfer characteristics in air in (a) **1d** and (b) **1e**.

V_t was estimated from the intercept of the linear section of the plot of V_g vs. $(I_d)^{1/2}$.

Acknowledgement

This work was partly supported by Grant-in Aid for Scientific Research (No. 15073211 and No. 18350095) from the Ministry of Education, Culture, Sports, Science and Technology.

References

[1] (a) Z. Bao, Adv. Mater. 12 (2000) 227;
(b) H.E. Katz, S.L. Gilat, Acc. Chem. Res. 34 (2001) 359;
(c) C.D. Dimitrakopoulos, P.R.L. Malenfant, Adv. Mater. 14 (2002) 99;
(d) C.R. Kagan, P. Andy, Thin-Film Transistors, Marcel Dekker, New York, 2003.

[2] (a) C.R. Newman, C.D. Frisbie, D.A. da S. Filho, J.L. Brédas, P.C. Ewbank, K.R. Mann, Chem. Mater. 16 (2004) 4436;
(b) A.R. Brown, D.M. de Leeuw, E.J. Lous, E.E. Havinga, Synth. Met. 66 (1994) 257;
(c) J.G. Laquindanum, H.E. Katz, A. Dodabalapur, A.J. Lovinger, J. Am. Chem. Soc. 118 (1996) 11331;
(d) Z. Bao, A.J. Lovinger, J. Brown, J. Am. Chem. Soc. 120 (1998) 207;
(e) H.E. Katz, J. Johnson, A.J. Lovinger, W. Li, J. Am. Chem. Soc. 122 (2000) 7787;
(f) H.E. Katz, A.J. Lovinger, J. Johnson, C. Kloc, T. Siegrist, W. Li, Y.-Y. Lin, A. Dodabalapur, Nature 404 (2000) 478;
(g) P.R.L. Malenfant, C.D. Dimitrakopoulos, J.D. Gelorme, L.L. Kosbar, T.O. Graham, Appl. Phys. Lett. 80 (2002) 2517;
(h) S. Ando, J. Nishida, H. Tada, Y. Inoue, S. Tokito, Y. Yamashita, J. Am. Chem. Soc. 127 (2005) 5336;
(i) S. Ando, R. Murakami, J. Nishida, H. Tada, Y. Inoue, S. Tokito, Y. Yamashita, J. Am. Chem. Soc. 127 (2005) 14996;
(j) Naraso, J. Nishida, D. Kumaki, S. Tokito, Y. Yamashita, J. Am. Chem. Soc. 128 (2006) 9598.

[3] D.M. de Leeuw, M.M.J. Simenon, A.R. Brown, R.E.F. Einerhand, Synth. Met. 87 (1997) 53.

[4] T.D. Anthopoulos, G.C. Anyfantis, G.C. Papavassiliou, D.M. de Leeuw, Appl. Phys. Lett. 90 (2007) 122105.

[5] (a) Z. Bao, A.J. Luvinger, A. Dodabalapur, Appl. Phys. Lett. 69 (1997) 3066;
(b) R. Zeis, T. Siegrist, Ch. Kloc, Appl. Phys. Lett. 86 (2005) 022103.

[6] S. Noro, H. Chang, T. Takenobu, Y. Murayama, T. Kanbara, T. Aoyama, T. Sassa, T. Wada, D. Tanaka, S. Kitagawa, Y. Iwasa, T. Akutagawa, T. Makamura, J. Am. Chem. Soc. 127 (2005) 10012.

[7] (a) C. Pearson, A.J. Moore, J.E. Gibson, M.R. Bryce, M.C. Petty, Thin Solid Films 244 (1994) 932;
(b) K. Sakai, T. Hasegawa, M. Ichikawa, Y. Taniguchi, Chem. Lett. 35 (2006) 302.

[8] E.C.P. Smits, T.D. Anthopoulos, S. Setayesh, E. van Veenendaal, R. Coehoorn, P.W.M. Blom, B. de Boer, D.M. de Leeuw, Phys. Rev. B 73 (2006) 205316.

[9] T. Taguchi, H. Wada, T. Kambayashi, B. Noda, M. Goto, T. Mori, K. Ishikawa, H. Takezoe, Chem. Phys. Lett. 421 (2006) 395.

[10] (a) H. Shiozaki, H. Nakazumi, Y. Nakado, T. Kitao, Chem. Lett. 16 (1987) 2393;
(b) H. Nakazumi, H. Shiozaki, T. Kitao, Chem. Lett. 18 (1989) 1027;
(c) H. Shiozaki, H. Nakazumi, T. Morikawa, Y. Sato, T. Kitao, Bull. Chem. Soc. Jpn. 63 (1990) 646;
(d) H. Shiozaki, H. Nakazumi, Y. Takamura, T. Kitao, Bull. Chem. Soc. Jpn. 63 (1990) 2653.

[11] B.S. Furniss, A.J. Hannaford, P.W.G. Smith, A.R. Tatchell, Vogel's Textbook of Practical Organic Chemistry, fifth ed., Longman, Harlsow, UK, 1989, p.1045.

[12] H. Meng, L. Zheng, A.J. Lovinger, Bo-Cheng Wand, P.G.V. Patten, Z. Bao, Chem. Mater. 15 (2003) 1778.

[13] Crystallographic data for **1d**: $C_{28}H_{16}F_4NiS_4$, $F_w = 615.37$, triclinic, space group $P\bar{1}$, $a = 10.469(3)$, $b = 14.179(3)$, $c = 10.033(4)$ Å, $\alpha = 90.10(2)°$, $\beta = 107.46(3)°$, $\gamma = 69.92(2)°$, $V = 1325.7(7)$ Å^3, $Z = 2$, $D_{calc} = 1.542$ g cm^{-3}, and $R/R_w = 0.043/0.045$ for 3742 independent reflections.

[14] D. Sartain, M.R. Truter, J. Chem. Soc. (1967) 1264.

[15] (a) Y. Takahashi, T. Hasegawa, Y. Abe, Y. Tokura, N. Nishimura, G. Saito, Appl. Phys. Lett. 86 (2005) 063504;
(b) Y. Takahashi, T. Hasegawa, Y. Abe, Y. Tokura, G. Saito, Appl. Phys. Lett. 88 (2006) 073504.

[16] K. Shibata, H. Wada, K. Ishikawa, H. Takezoe, T. Mori, Appl. Phys. Lett. 90 (2007) 193509.

[17] B. Noda, H. Wada, M. Katsuhara, I. Aoyagi, T. Mori, T. Kambayashi, K. Ishikawa, H. Takezoe, Multifunctional Conducting Molecular Materials, in: G. Saito, F. Wudl, R.C. Haddon, K. Tanigaki, T. Eoki, H.E. Katz, M. Maesato (Eds.), RSC Publishing, Cambridge, 2007, p. 286.

[18] H. Wang, J. Wang, X. Yan, J. Shi, H. Tian, Y. Geng, D. Yan, Appl. Phys. Lett. 88 (2006) 133508.

[19] G.M. Kheifets, N.V. Martyushina, T.A. Mikhailova, N.V. Khromov-Borisov, J. Org. Chem. USSR 13 (1977) 1159.

Available online at www.sciencedirect.com
ScienceDirect
Organic Electronics 8 (2007) 767–772
Organic Electronics
www.elsevier.com/locate/orgel

Organic thin-film transistors with reduced photosensitivity

Chiao-Shun Chuang [a], Fang-Chung Chen [b,*], Han-Ping D. Shieh [b]

[a] Department of Photonics and Institute of Electro-optical Engineering, National Chiao Tung University, Hsinchu 300, Taiwan
[b] Department of Photonics and Display Institute, National Chiao Tung University, Hsinchu 300, Taiwan

Received 31 January 2007; received in revised form 22 June 2007; accepted 25 June 2007
Available online 27 July 2007

Abstract

Organic thin-film transistors with a minimal threshold voltage shift and a more stable photocurrent under illuminated conditions can be made by embedding titanium dioxide (TiO_2) nanoparticles into a polymer dielectric layer. While the studies of pentacene morphology using atomic force microscopy and X-ray diffraction have shown similar results before and after embedding the TiO_2 into the dielectric layer, it has been found that the presence of TiO_2 nanoparticles is essential. The reduced photosensitivity can be attributed to the recombination centers induced by the TiO_2 nanopartilces and this can enhance substantially the recombination process of the electrons trapped in the channel.
© 2007 Elsevier B.V. All rights reserved.

PACS: 82.35.Np; 85.30.Tv

Keywords: Organic; Photosensitivity; Nanoparticle; Dielectrics; Thin-film transistors

1. Introduction

Currently, there is increased interest in thin-film transistors made of organic materials due to their great potential applications in low-cost and flexible electronics, such as smart cards, radio-frequency identification (RFID) tags and paper-like displays [1–6]. A level of performance by organic thin film transistors (OTFTs) comparable to that of amorphous silicon (a-Si) has been achieved. For example, a field-effect mobility higher than 1 $cm^2/V\,s$ and with several orders of on–off ratio has been demonstrated for OTFTs based on pentacene. While the intrinsic properties of organic semiconductors and the device physics of OTFTs have been studied extensively, their reliability and photoresponse levels have not received much attention until recently [7–12]. Moreover, methods to lower photosensitivity and to improve device stability have received considerably less attention.

On the other hand, the photosensitivity of OTFTs is a critical issue for driving applications in displays, such as liquid–crystal displays (LCDs) [12]. For instance, pentacene has high level of photo absorption in the visible range, which is due to its high oscillator strength and low energy between its highest occupied molecular orbital (HOMO) and its lowest unoccupied molecular orbital (LUMO): around 1.7 eV. Therefore, light from backlight modules may pass through the OTFTs and cause

* Corresponding author. Tel.: +886 3 5131484; fax: +886 3 5735601.
E-mail address: fcchen@mail.nctu.edu.tw (F.-C. Chen).

1566-1199/$ - see front matter © 2007 Elsevier B.V. All rights reserved.
doi:10.1016/j.orgel.2007.06.012

a serious threshold voltage (V_{th}) shift [12]. As a result, OTFTs usually cannot be turned off effectively when the gate bias is set at zero under illumination [10–12]. In this work, one method to reduce photosensitivity and to enhance device stability has been reported. To put it simply, by blending the polymer dielectrics with titanium dioxide (TiO_2) nanoparticles, the V_{th} shift is minimized and the output current becomes more stable under white light illumination. This improvement can be attributed to the recombination centers induced by the TiO_2 nanoparticles. Moreover, by reducing the photosensitivity, the pentacene-based OTFTs has the potential to drive the circuits without a noticeable V_{th} shift and with no light shield. Finally, the device reported in this work will greatly facilitate the making of more reliable transparent organic electronics: an area which has received much attention recently [13,14].

2. Experimental

Titanium oxide with a rutile structure ($k = 114$) was used as the high-dielectric component in the nanocomposite dielectrics [15,16]. The device structure is shown in Fig. 1a. Poly-4-vinylphenol (PVP) and poly(melamine-*co*-formaldehyde) methylated were dissolved in propylene glycol monomethyl ether acetate (PGMEA), blended with TiO_2 nanoparticles, whose surface was further modified with organosiloxane to enhance their solubility (Ishihara Sangyo Kaisha LTD., Japan) [16]. The solution was then spin-coated onto the indium–tin-oxide (ITO) patterned glass substrates and ITO was used as the gate electrodes. The resulting film was further thermally annealed to 200 °C. Then, the thermally evaporated pentacene was used as the semiconducting layer for the OTFTs. Next, gold was thermally evaporated as the source and drain electrodes. The channel length (L) and width (W) of the devices were 100 and 2000 μm, respectively. To suppress the degradation of the on–off ratio after adding the nanoparticles, the insulator was further overcoated with a very thin-layer of poly(α-methylstrylene) (PαMS) by spin-coating from a diluted toluene solution (0.1 wt%). Due to the robustness of the cross-linked polymers, the underlayer was not affected by this process [16]. The film thickness and roughness were measured using a DI 3100 series atomic force microscope (AFM). The current–voltage (I–V) characteristics of the OTFTs were measured with a HP 4156A semiconductor parameter analyzer. The illumination light source was a standard Hg lamp. All measurements were performed under the atmosphere.

3. Results and discussion

The transfer characteristics of the devices before and after the modification of the PαMS are shown in Fig. 2a. The extracted mobility of the PVP device following the conventional field effect transistor model is 0.1 $cm^2 V^{-1} s^{-1}$. The threshold voltage and subthreshold slope are 0.5 V and 2.9 V/decade, respectively. Initially, the on–off ratio was about 1.0×10^4, but after the addition of a thin layer of the low-κ material, PαMS, the subthreshold swing became smaller, the on–off ratio was improved by one order; while the mobility was almost unchanged.

The controllable threshold voltages and turn-on voltages in pentancene TFTs have been demonstrated by using different organosilanes with various functional groups as the self-assembled monolayers (SAMs) on the SiO_2 insulators [17,18]. To quantify the device characteristics, the turn-on voltage (V_{to})

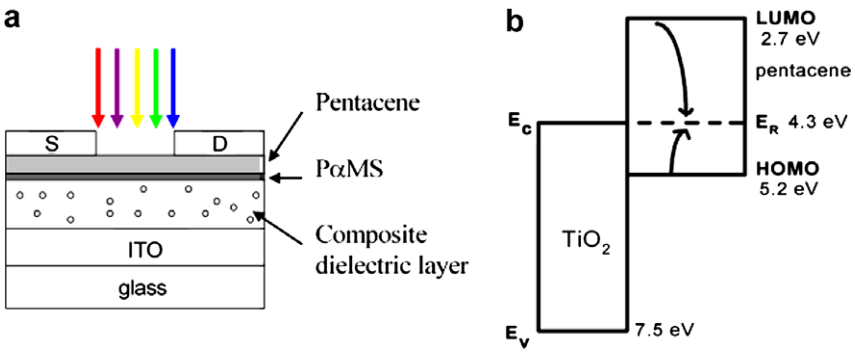


Fig. 1. (a) The device structure of the OTFTs in this study and (b) energy band diagram of pentacene and TiO_2.

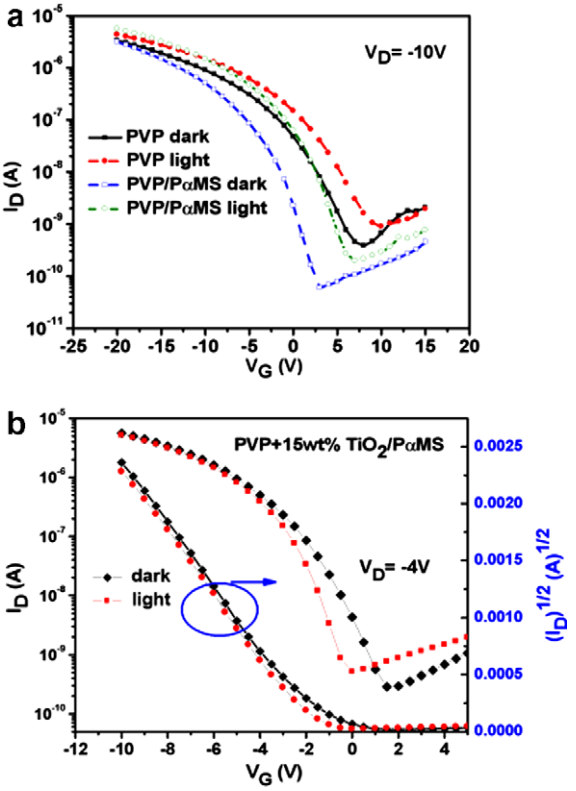


Fig. 2. Transfer curves for devices in the dark and under illumination with (a) cross-linked PVP and cross-linked PVP/PαMS double layers as the dielectric insulators and (b) PVP + 15 wt% TiO_2 as the gate insulator.

is defined as the gate voltage at which the drain current starts to increase exponentially; while the transistor is in a flat-band position [18,19]. The built-in electric field resulting from the polar SAM molecules induces mobile charges which alters the threshold voltage [17,18]. In this study, the water contact angle on the cross-linked PVP surface is 69.0°, while the angle on PαMS is 86.7°. This indicates that cross-linked PVP is much more polar than PαMS. Similarly, the high polarity of cross-linked PVP, which is attributable to its hydroxyl groups, may also explain the high surface polarization which causes the higher mobile charge density. Consequently, as shown in Fig. 2a, the V_{th} and V_{to} are more positive when compared with those of devices with a PαMS thin-film. Such phenomena suggest the presence of a dipole field at the pentacene/dielectrics interface [18]. However, after applying a low-κ PαMS onto the PVP, the V_{to} shifts from 7.5 V to 2.5 V. This change implies a lower free charge density at the interface. The non-polar properties of PαMS prevent surface polarization, thereby reducing the charge density in the conducting channel at $V_g = 0$ V.

While the device was under white illumination (10 mW/cm^2), the threshold voltages and V_{to} of both the devices shifted toward the position direction, the off-current became stronger (Fig. 2a). In addition, the subthresold swings also increased. It has been suggested that the photogenerated electron–hole pairs increase the off-state current dramatically [11,12]. However, while the holes can flow out through the drain electrode under the electrical field, the electrons may be trapped at the grain boundaries of the pentacene, and/or the insulator/pentacene interface, resulting in a positive shift in the V_{th} [11,12].

A change in the behavior of the devices was observed upon blending the TiO_2 nanoparticles into the gate dielectrics. Fig. 2b shows the transfer characteristics of the device in the dark and under illumination. In the dark, the threshold voltage becomes lower because of the use of an insulator with a higher dielectric constant. while the subthresold swing also decreases to about 1 V/decade. Such phenomena are quite consistent with previous reports on OTFTs with adopted high-κ insulators [5]. Upon illumination, instead of a positive shift, the V_{to} comes closer to 0 V, the subthresold swing becomes even better. The changes of the V_{th} and subthresold swing are exactly *opposite* to those of the devices with PVP and PVP/PαMS (Fig. 2a) as the gate dielectrics. The electric parameters of the devices have been summarized in Table 1.

To explain the different behaviors of the devices represented in Fig. 2, several experiments have been conducted which attempt to identify the possible mechanisms involved. First, from the surface morphology analysis using an AFM, it has been shown that the morphology of pentacene is quite similar on the surfaces of both the neat cross-linked PVP and the nanocomposite with the thin PαMS film (Fig. 3) [16]. Furthermore, the X-ray diffraction patterns of the pentacene deposited on the neat cross-linked PVP, the PαMS, the nanocomposite with additional PαMS, all reflect the so-called "thin-film" phase structure [20]. Consequently, the morphology change is not likely to be the mechanism which causes the different device behaviors upon blending the nanoparticles.

The above mentioned observation is also probably due to the processes occurring at the ITO–insulator interface. In order to determine whether the effect is due to the interface, heavy n-type doped

Table 1
Electrical parameters in this study

Device	Mobility ($cm^2/V\,s$)	Dielectric constant	Insulator thickness (nm)	Ci (nF/cm^2)	V_{th} (V)	S.S. (V/decade)	On–off ratio
PVP dark	0.10 ± 0.02	4.3 ± 0.1	290	13.1	0.5	2.9	9×10^3
PVP light	0.10 ± 0.02	4.3 ± 0.1	290	13.1	4.5	3.2	4×10^3
PVP/PαMS dark	0.13 ± 0.02	4.2 ± 0.1	290	12.8	−4.3	1.8	9×10^4
PVP/PαMS light	0.14 ± 0.01	4.2 ± 0.1	290	12.8	0.2	2.1	5×10^4
PVP/TiO_2/PαMS dark	0.40 ± 0.05	10.5 ± 0.3	270	34.1	−2.8	1.1	5×10^4
PVP/TiO_2/PαMS light	0.40 ± 0.05	10.5 ± 0.3	270	34.1	−2.9	0.9	2×10^4

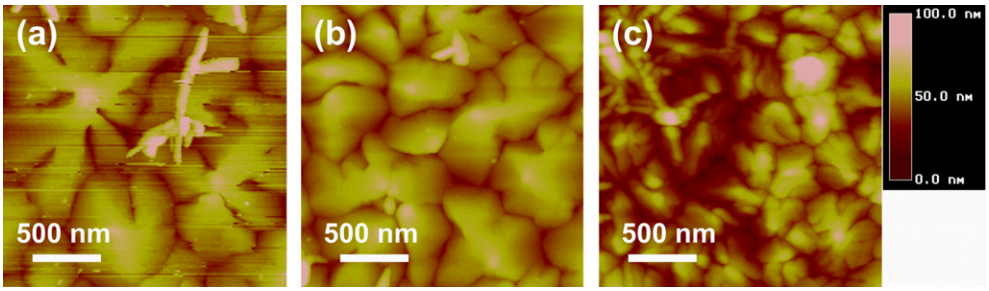


Fig. 3. AFM images of pentacene on (a) cross-linked PVP, (b) PaMS/cross-linked PVP and (c) PaMS/TiO2 nanoparticles + cross-linked PVP.

Si and SiO_2 were used in the devices as the gate electrode and the dielectrics, respectively (Fig. 4). The SiO_2 surface was further modified with a nanocomposite (15% TiO_2 in PVP)/PαMS bi-layer. However, the device with TiO_2 exhibited similar behavior (that is, a negligible V_{th} shift), which implies that the mechanism is not relevant to the different processes of the gate electrodes. On the other hand,

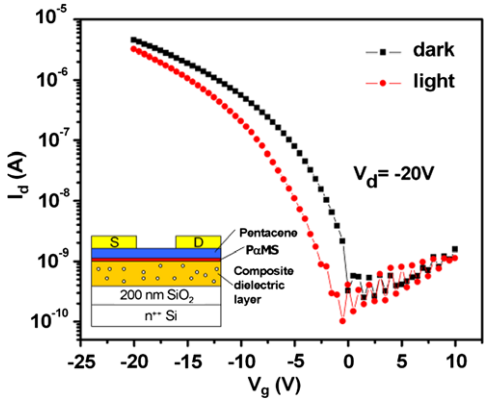


Fig. 4. Transfer characteristics of the device with n-doped Si/SiO_2 as the substrate in the dark and under illumination. The inset shows the device structure.

the present of TiO_2 nanoparticles in the gate insulator seems essential to minimize the effect of white illumination for the device.

The results strongly indicate that the blending of TiO_2 nanoparticles is an important part of the mechanism. The present of TiO_2 nanoparticles probably induces the recombination of the centers in the channel. As seen in Fig. 1b, because of the conduction band of TiO_2 and/or the energy levels induced locate between the HOMO and LUMO of the pentacene, they may behave like recombination centers; thereby releasing the trapped electrons. Consequently, upon illumination, the excess electrons can be eliminated more easily and the V_{th} shift is suppressed.

Stress tests on the three different devices were also performed to further understand the effects of the TiO_2 nanoparticles. The typical stress-test results of the devices, both in the dark and under illumination, used in this study are shown in Fig. 5. For the device with a neat cross-linked PVP as an insulator, the field-induced current and/or photocurrent increased steadily over time. This result was consistent with the previous report [8,12]. It has already been indicated that the absorption of water molecules in cross-linked PVP enhances surface polarization, thus

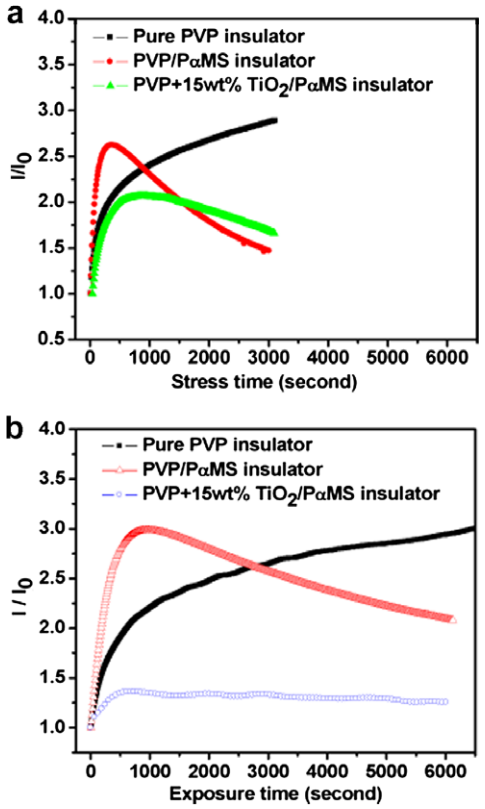


Fig. 5. The normalized time-dependent current of the devices (a) in the dark; and (b) under illumination. The devices with PVP and PVP/PαMs as the dielectric layers were biased at $V_g = -10$ V and $V_d = -10$ V; while the device with 15 wt% TiO_2 nanoparticles was measured at $V_g = -5$ V and $V_d = -4$ V.

the accumulation of extra charges increases the current and results in a positive shift of V_{th} [8]. However, after modification with PαMS, the current increased initially, but then, decreased with time. Since PαMS is non-polar, the surface polarization probably was found to be inhibited. In addition, it was also found that the hydrophobic PαMS may also retard water absorption. Consequently, after the initial sharp increase, the increase of photocurrent is relieved and the current decreases again, probably due to the natural device decay [8].

On the other hand, a more stable current was observed after the introduction of TiO_2 nanoparticles in the dark (Fig. 5a). Furthermore, upon white-light illumination, although an initial increase in photocurrent was also observed, the magnitude was much smaller (Fig. 5b). The device only exhibited a very small current decay. The more stable photocurrent may further confirm the presence of recombination centers introduced by the TiO_2 nanoparticles dispersed in the organic insulator; the latter can suppress the electron trapping. Without the recombination centers, the trapped electrons will cause a dramatic increase in current.

4. Conclusion

It has been shown that the issues of light sensitivity and V_{th} shift can be overcome by blending TiO_2 nanopartilces into the polymer dielectrics. The more stable photocurrent and minimized V_{th} shift can be attributed to the recombination centers induced by the doping of the TiO_2 nanopartilces. The energy levels deep in the energy gap and away from the HOMO and LUMO of the pentacene can serve as the recombination centers, which, in turn, can enhance substantially the recombination process in the OTFTs.

Acknowledgements

The authors would like to acknowledge the financial support from AU Optronics Corp. (AUO). This work is also partially supported by the National Science Council, ROC, and Ministry of Education ATU Program.

References

[1] Y.Y. Lin, D.J. Gundlach, S.F. Nelson, T.N. Jackson, IEEE Trans. Electr. Dev. 44 (1997) 320.
[2] R.A.B. Devine, M.M. Ling, A.B. Mallik, M. Roberts, Z. Bao, Appl. Phys. Lett. 88 (2006) 151907.
[3] M. Shtein, J. Mapel, J.B. Benziger, S.R. Forrest, Appl. Phys. Lett. 81 (2002) 268.
[4] P. Mach, S.J. Rodriguez, R. Nortrup, P. Wiltzius, J.A. Rogers, Appl. Phys. Lett. 78 (2001) 3592.
[5] A. Facchetti, M.H. Yoon, T.J. Marks, Adv. Mater. 17 (2005) 1705.
[6] H. Sirringhaus, Adv. Mater. 17 (2005) 2411.
[7] A. Salleo, F. Endicott, R.A. Street, Appl. Phys. Lett. 86 (2005) 263505.
[8] T. Jung, A. Dodabalapur, R. Wenz, Mohapatra, Appl. Phys. Lett. 87 (2005) 182109.
[9] K.S. Narayan, N. Kumar, Appl. Phys. Lett. 79 (2001) 1891.
[10] T.P. I Saragi, R. Pudzich, T. Fuhrmann, J. Salbeck, Appl. Phys. Lett. 84 (2004) 2334.
[11] M.C. Hamilton, S. Martin, J. Kanicki, IEEE Trans. Electr. Dev. 51 (2004) 877.
[12] S.M. Cho, S.H. Han, J.H. Kim, J. Jang, M.H. Oh, Appl. Phys. Lett. 88 (2006) 071106.
[13] J. Lee, D.K. Hwang, J. –M. Choi, K. Lee, J.H. kim, S. Im, J.H. Park, E. Kim, Appl. Phys. Lett. 87 (2005) 023504.
[14] T. Takenobu, T. Takahashi, T. Kanbara, K. Kanbara, K. Tsukagoshi, Y. Aoyagi, Y. Iwasa, Appl. Phys. Lett. 88 (2006) 033511.

[15] F.C. Chen, C.W. Chu, J. He, Y. Yang, J.L. Lin, Appl. Phys. Lett. 85 (2004) 3295.
[16] F.C. Chen, C.S. Chuang, Y.S. Lin, L.J. Kung, T.S. Chen, H.P.D. Shieh, Org. Electr. 7 (2006) 435.
[17] S. Kobayashi, T. Nishikawa, T. Takenobu, S. Mori, T. Shimoda, T. Mitani, H. Shimotani, N. Yoshimoto, S. Ogawa, Y. Iwasa, Nature Mater. 3 (2004) 317.
[18] K.P. Pernstich, S. Jaas, D. Oberhoff, C. Goldmann, D.J. Gundlach, B. Batlogg, A.N. Rashid, G. Schitter, J. Appl. Phys. 96 (2004).
[19] E.J. Meijer, C. Tanase, P.W.M. Blom, E. Van Veenendaal, B. –H. Huisman, D.M. De Leeuw, T.M. Klapwijk, Appl. Phys. Lett. 80 (2002) 3838.
[20] C.D. Dimitrakopoulos, P.R.L. Malenfant, Adv. Mater. 14 (2002) 99.

Available online at www.sciencedirect.com
ScienceDirect
Organic Electronics 8 (2007) 773–783
Organic Electronics
www.elsevier.com/locate/orgel

Novel cationic water-soluble polyfluorene derivatives with ion-transporting side groups for efficient electron injection in PLEDs

Seung-Hwan Oh, Seok-In Na, Yoon-Chae Nah, Doojin Vak, Seok-Soon Kim, Dong-Yu Kim *

Heeger Center for Advanced Materials (HCAM), Department of Materials Science and Engineering, Gwangju Institute of Science and Technology (GIST), 1 Oryong-Dong, Buk-Gu, Gwangju 500-712, Republic of Korea

Received 9 March 2007; received in revised form 25 June 2007; accepted 26 June 2007
Available online 27 July 2007

Abstract

Synthesis of cationic water-soluble polyfluorene derivatives with various side groups, which are used as electron injecting layers in polymer light emitting diodes, is described. Neutral polyfluorene derivatives containing bromo-alkyl terminal groups were synthesized by a palladium catalyzed Suzuki coupling reaction. The bromo-alkyl terminal groups in the neutral polyfluorenes were quaternized by treatment with a trimethyl amine solution. When a high work-function metal such as Ag is used as a cathode in a light emitting diode with an ITO/PEDOT:PSS/MEH-PPV/water-soluble polyfluorene/Ag configuration, effects of these water-soluble polyfluorenes on the device performance were investigated. In the case of poly[(9,9-bis((6′-(*N*,*N*,*N*-trimethylammonium) hexyl)-2,7-fluorene))-*alt*-(9,9-bis(2-(2-methoxyethoxy)ethyl)-fluorene)] Dibromide (WPF-oxy-F) containing ethylene oxide groups as the electron injecting layer, the electroluminescence efficiency of light emitting devices was significantly enhanced by about two orders of magnitude compared to that of a device without an electron injecting layer because migration of bromide ions *via* the ethylene oxide side groups led to large space charge. As a result, the injection barrier could be reduced between the emitting layer and Ag cathode resulting high electroluminescence efficiency.
© 2007 Elsevier B.V. All rights reserved.

PACS: 71.20.Rv; 73.40.Mr; 73.61.Ph

Keywords: Water-soluble polyfluorene derivative; Electron injection; Ion-transporting side groups; PLED

1. Introduction

Since their introduction, polymer light emitting diodes (PLEDs) [1] based on conjugated polymer [2,3] have attracted continuous attention due to the possibility of fabricating flexible, low cost and high efficiency displays. For over a decade, synthesis and characterization of many types of conjugated polymers have been reported, in attempts to enhance efficiency and stability of PLEDs. In particular, among the various conjugated polymers, water-soluble conjugated polymers have also been

* Corresponding author. Tel.: +82 62 970 2319; fax: +82 62 970 2304.
E-mail address: kimdy@gist.ac.kr (D.-Y. Kim).

1566-1199/$ - see front matter © 2007 Elsevier B.V. All rights reserved.
doi:10.1016/j.orgel.2007.06.011

extensively investigated due to their environment friendly water-soluble nature and multilayer formation capability with organic soluble conjugated polymers. Consequently, many water-soluble conjugated polymers have been reported, including polythiophene [4], poly(*p*-phenylene) [5,6], poly(phenylenevinylene) [7–9], poly(phenylene ethylene) [10] and polyfluorene derivatives [11–13]. They have also been used in a variety of optoelectronic devices such as DNA-sensors [14] using energy transfer [7,8,10] and photovoltaic cells [9] and emitting layers [5,15] or electron injecting layers (EIL) [11–13] in PLEDs.

In PLEDs, high efficiency at low operating voltage and high stability can be achieved through efficient and balanced injection of carriers [16,17]. It is well-known, that the carrier injection is dependent on energy barrier height between the emitting layer and the metal. Thus, low work-function metals such as Ca, Ba, etc. are used to enhance electron injection into organic materials. However, such metals are not stable in air and sometimes may react with and diffuse into organic materials, leading to the deterioration of the device. To complement the weakness of low work-function metals, a stable Al metal cathode together with LiF is used as a bilayer cathode in PLEDs [18,19].

Water-soluble polymers are considered to be potential candidates for the electron injecting layer in PLEDs because a multi-layer structure can be produced without damage to the underlying organic soluble polymer films. Deng et al. [20] reported that the EL efficiency in a PLED with an Al cathode was enhanced by blending water-soluble poly(ethylene glycol) into the MEH-PPV. Guo et al. [21] also reported that inserting water-soluble poly(ethylene oxide) between the emitting layer and the Al cathode improved device efficiency because the built-in potential was increased by interfacial interaction between oxygen atoms in poly(ethylene oxide). Recently, a bilayer cathode consisting of an water-soluble conjugated polymer and Al or Au [11–13] has also been applied to an emitting layer. Due to the enhancement in interfacial dipole between the emitting layer and the metal cathode, it has been reported that this bilayer cathode could improve electron injection.

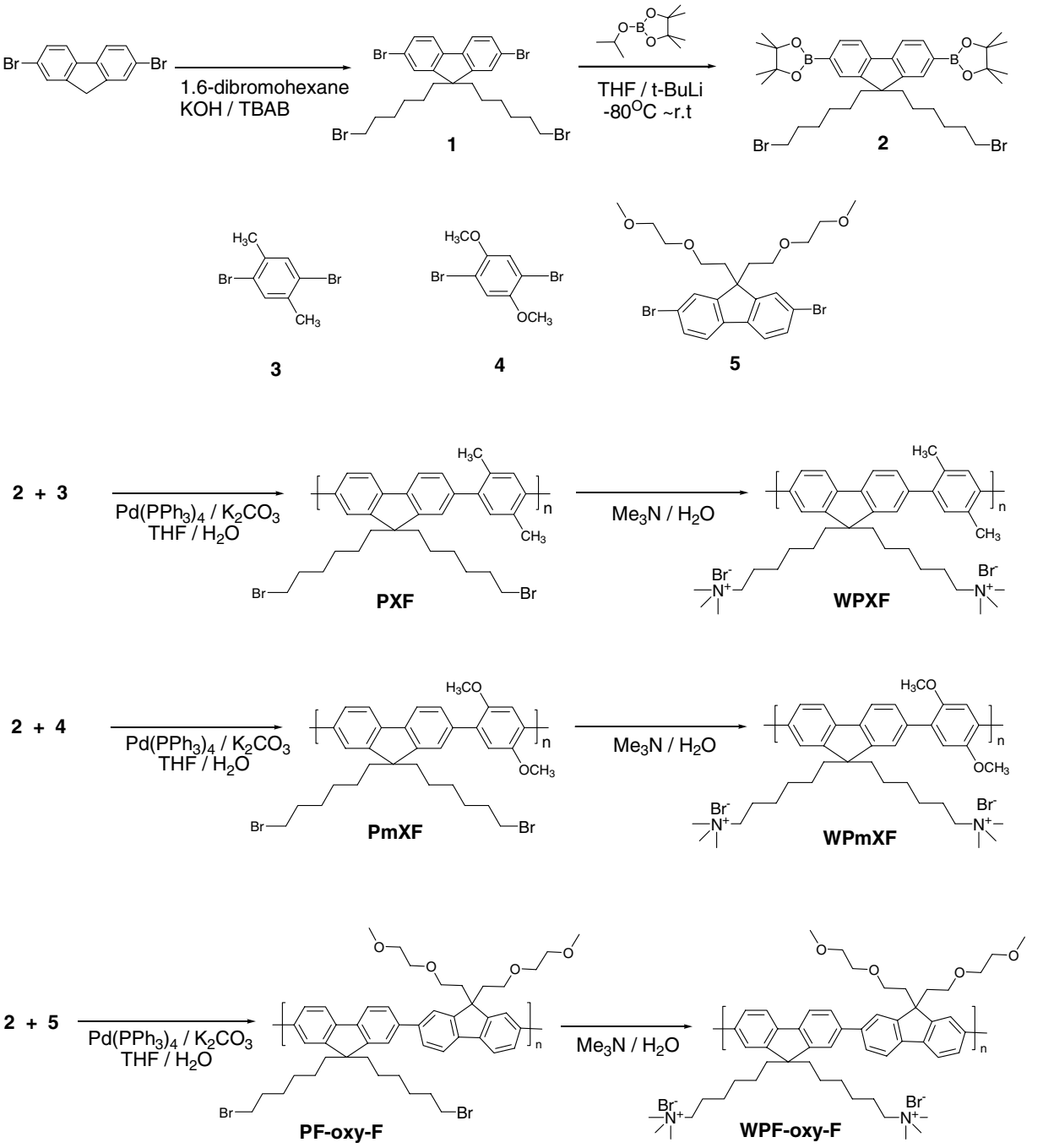
As mentioned above, to improve device performance using an interface dipole effect, the electron injecting layer should contain both ionic and polar groups such as oxygen side groups. In this study, we synthesized new three types of water-soluble polyfluorene derivatives with co-monomers with oxide side groups and without it. PLEDs were fabricated using these polymers as an electron injecting layer. A high work-function metal such Ag was used as a cathode. The findings show that such water-soluble polyfluorene derivatives can be used as an electron injecting layer inserted between the emitting layer and the Ag cathode, leading to a significant enhancement in the device performance. A possible mechanism about enhancement of the device was deduced from this study. Mobile bromide ions could be migrated under the applied bias *via* the ethylene oxide side groups which had an ion-transporting properties. So, the accumulation of mobile Br^- ions and positive ammonium salt near the electrodes induced ion space charge in the electron injecting layer. As a result, the effective injection barrier could be reduced by large space charge between the emitting layer and Ag cathode.

2. Results and discussion

2.1. Synthesis and characterization

The scheme for the preparation of water-soluble polyfluorene is shown in Scheme 1. Compound (**1**) was prepared using a method similar to the literature procedure [22]. Tetrabutylammoniumbromide (TBAB) as a phase transfer catalyst and 2,7-dibromofluorene and were dissolved in 1,6-dibromohexane as the solvent. To eliminate two protons at the 9-position of 2,7-dibromofluorene, a KOH solution was injected into the solution. The solution was stirred at 75 °C for 1 h. The color of the reaction mixture became yellow. The reaction mixture was extracted with dichloromethane, and evaporated. The reaction mixture was distilled under vacuum to remove the excess 1,6-dibromohexane. The product was purified by column chromatography using hexane and dichloromethane as an eluent. Pure (**1**) was obtained as a white solid in a 84% yield.

Compound (**2**) was prepared according to the published procedures [23]. 2,7-Dibromo-9,9-bis(6-bromohexyl)-fluorene (**1**) was dissolved in THF. To eliminate the two bromides at the 2,7-position of 2,7-dibromo-9,9-bis(6-bromohexyl)-fluorene, this solution was cooled to −80 °C and *t*-BuLi was carefully added to the solution. The elimination of the two bromides was confirmed thought GC/MS spectrometry while the solution was stirred for 1 h. 2-Isopropoxy-4,4,5,5-tetramethyl-1,3,2-dioxaborolane was rapidly added to the solution. The reaction



Scheme 1. Synthetic scheme for WPXF, WPmXF and WPF-oxy-F.

mixture was warmed to room temperature and the mixture was extracted with 300 mL ether. The product was purified by column chromatography using hexane and ethylacetate as the eluent. The product (**2**) was a yellowish-white solid, produced in a 70% yield.

Neutral polymers PXF, PmXF and PF-oxy-F were synthesized from monomers *via* Suzuki coupling reaction. Each monomer was dissolved in THF. A 2 M K_2CO_3 solution was added and 1 mol% $Pd(PPh_3)_4$ was added to the solution, followed by refluxing for 3 days. The reaction mixture

was slowly cooled to room temperature. The reaction mixture was poured into a mixture of methanol and water. The precipitate was collected and redissolved in chloroform and slowly poured into stirred methanol. The precipitation process was repeated several times. The molecular weight of the polymer was determined by gel permeation chromatography. The number average molecular weight (Mn) of the neutral polymers PXF and PmXF and PF-oxy-F were determined by gel permeation chromatography. Mn were 12,000, 17,000 and 16,000, respectively.

Water-soluble polyfluorenes, WPXF, WPmXF and WPF-oxy-F were ionized using a trimethylamine solution. Neutral polymers PXF, PmXF and PF-oxy-F were dissolved in THF. A trimethylamine solution was added into the solution which was then stirred at rt for 24 h. The solubility of the ionic polymer was reduced in THF and the polymer precipitated during this period. Water was added to the solution to dissolve the precipitate. The solution was evaporated and the residue was collected and dried under vacuum overnight and then redissolved in methanol. The solution was slowly poured into stirred ether to give the ionic polymer. All the polymers were characterized by ^{1}H NMR. After quaternization, a new peak around 3.00–3.06 ppm appeared in ^{1}H NMR, which shows hydrogens in trimethyl amine groups.

The thermal properties of the neutral polymers PXF, PmXF and PF-oxy-F were characterized. Fig. 1 shows degradation temperature. TGA showed a 5% weight loss of PXF, PmXF and PF-oxy-F at 277, 307 and 271 °C, respectively. The temperature of the 5% weight loss of WPXF, WPmXF and WPF-oxy-F was similarly found at around 206 °C. After quaternization, the quaternized polymers showed a degradation temperature lower than those of the neutral polymers PXF, PmXF and PF-oxy-F, because they have weak parts which are amine salts [15].

2.2. Optical and electrochemical properties

The optical properties of the three types of water-soluble polyfluorenes are shown in Fig. 2. UV–vis-absorption spectra were measured in the solid-state. A film was prepared using a 0.5 wt% solution of WPXF, WPmXF and WPF-oxy-F in methanol and water (methanol:water = 3:7), which was spin coated on the glass and baked at 120 °C for 5 min. The absorption onset and absorption maximum of WPXF appeared at 376 and 340 nm, respectively. In the case of WPmXF, the absorption onset and absorption maximum appeared at 403 and 365 nm. The absorption of WPmXF was shifted to longer wavelength than WPXF due to two electron-donating methoxy groups in WPmXF [24]. The absorption onset and absorption maximum of WPF-oxy-F appeared at 435 and 392 nm, respectively. The optical band gap values of WPXF, WPmXF and WPF-oxy-F were 3.2, 3.0 and 2.8 eV, respectively. In the case of WPXF and WPmXF, the optical band-gap was slightly higher than WPF-oxy-F due to their shorter conjugation length. The bond between the xylene and the fluorene unit in WPXF and WPmXF were tilted by steric hindrance [25].

The HOMO and LUMO of WPXF, WPmXF and WPF-oxy-F were measured by cyclic voltam-

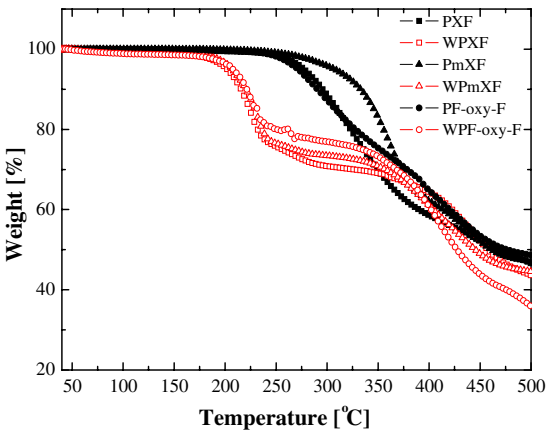


Fig. 1. Thermal gravimetric analysis in nitrogen atmosphere.

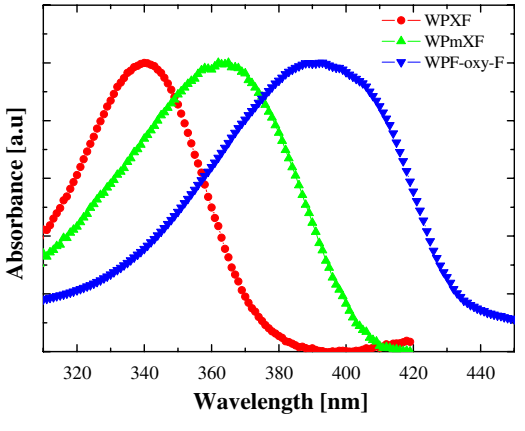


Fig. 2. UV–vis spectra of WPFX, WPmXF and WPF-oxy-F films.

metry. Cyclic voltammetry was performed in 0.1 mol/L of Bu_4NClO_4 in a acetonitrile solution. WPXF, WPmXF and WPF-oxy-F were spin coated on the ITO as a working electrode. A platinum wire was used as a counter electrode and silver wire was used as a reference electrode.

Fig. 3 shows oxidation potentials of WPXF, WPmXF and WPF-oxy-F. The HOMO and LUMO of WPXF, WPmXF and WPF-oxy-F were calculated from the UV–vis absorption on-set and cyclic voltammograms. The HOMO and LUMO of WPXF were 5.4 and 2.2 eV, and those of WPmXF were calculated to be 5.3 and 2.3 eV, respectively. In the case of WPF-oxy-F, the HOMO and LUMO were estimated to be 5.1 and 2.3 eV.

2.3. Device properties

Each WPXF, WPmXF and WPF-oxy-F was used as an electron injection layer in PLEDs with the configuration of ITO/PEDOT:PSS/MEH-PPV/water-soluble polymer/Ag. Fig. 4 shows EL spectra for each device. Due to the location of the recombination zone in the bulk of EL polymer, the EL spectra was almost identical, when an amino-terminated conjugated polymer was used as an electron injecting layer.

All devices were fabricated from the same batch and were measured under air. Device efficiency was determined by measuring the light output only in the front direction. As shown in Fig. 5a and b, the turn-on voltage of a device with a Ag cathode was 6.6 V, and the external quantum efficiency was less than 0.005% with a luminance of 84 cd m^{-2} at

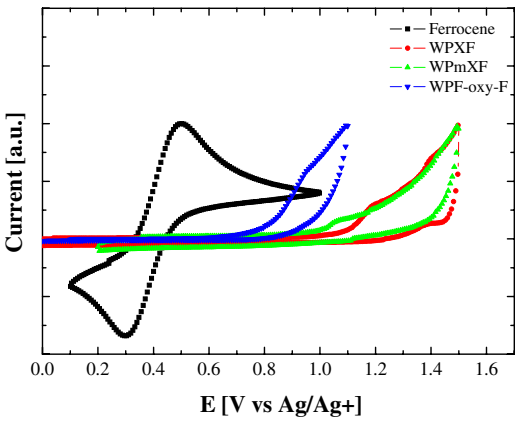


Fig. 3. Cyclic voltammograms of WPXF, WPmXF and WPF-oxy-F coated on ITO glass in 0.1 mol/L Bu_4NClO_4, acetonitrile solution at 50 mV/s scan rate.

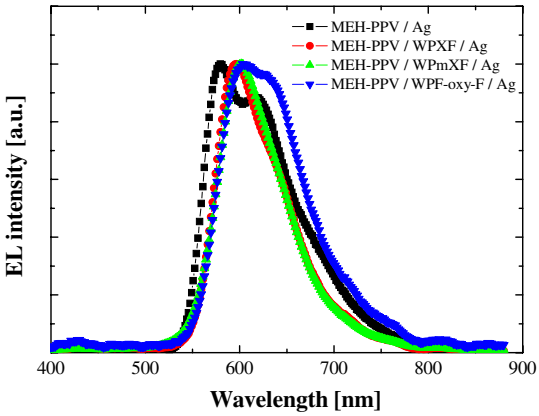


Fig. 4. EL spectra of MEH-PPV devices with WPXF, WPmXF and WPF-oxy-F/Ag cathode.

13.8 V. Because an injection of electron from Ag cathode was not efficient according to high injection barrier between MEH-PPV and Ag cathode.

However, when WPXF, WPmXF and WPF-oxy-F were used as an electron injection layer, the turn-on voltage was reduced to around 3.8, 3.5 and 3.1 V, respectively, and the external quantum efficiency significantly increased by about one to two order of magnitude. This enhancement of efficiency measuring the light output only in the front direction was comparable to reported device [13] measuring that all direction in an integrating sphere. In the case of WPXF used as an electron injection layer, when it was inserted between the emitting polymer (MEH-PPV) and Ag, the operating voltage was reduced and external quantum efficiency and luminance efficiency were 3.8 V, 0.01% and 0.03%, respectively. In the case of WPmXF, the operating voltage, external quantum efficiency and luminance efficiency was 3.5 V, 0.02% and 0.04%, respectively, all of them were slightly enhanced compared to WPXF. As WPmXF has two oxygen side groups that enhance the dipole moment, the performance of the device with WPmXF was slightly enhanced. For a device with a WPF-oxy-F layer inserted between the MEH-PPV and Ag, the operating voltage was reduced to 3.1 V and external quantum efficiency, power efficiency and luminance efficiency were higher than WPXF and WPmXF (Table 1).

In the case of WPF-oxy-F and WPmXF, EL efficiency was higher than that of WPXF. Especially, in the case of WPF-oxy-F, very large enhancement was observed. As two ethylene oxygen side groups in WPF-oxy-F at 9-position led to an interaction between the Ag cathode and the lone-pair electrons

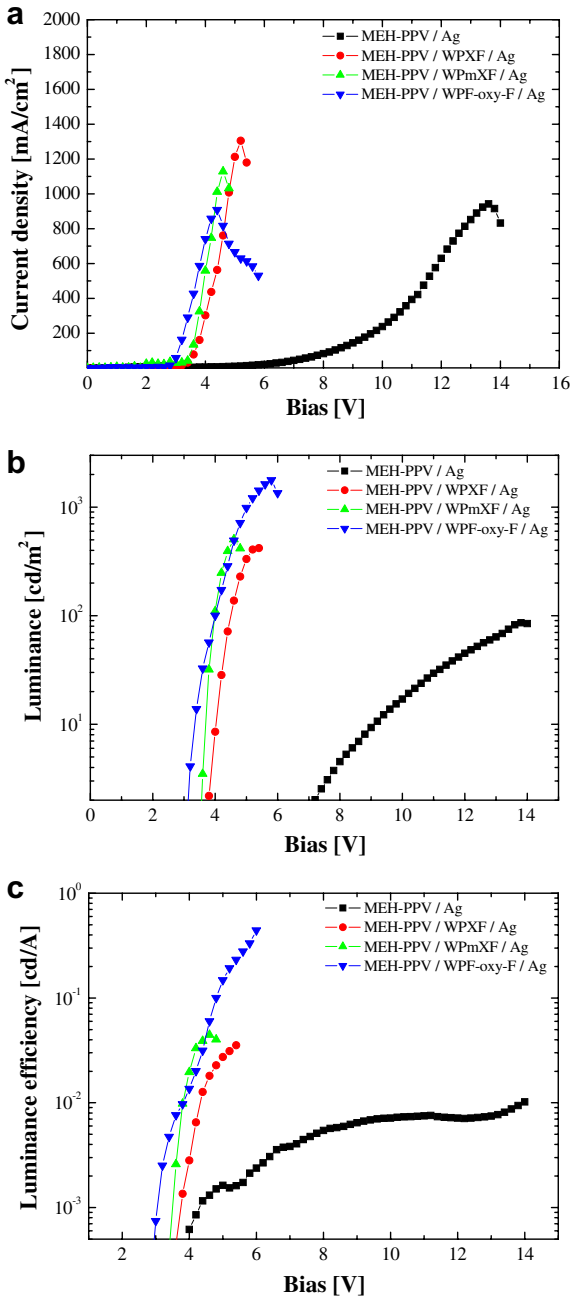


Fig. 5. (a) I–V characteristic of each device. (b) L–V characteristic of each device. (c) LE–V characteristic of each device.

on the oxygen atoms [20,21], the effective charge injection barrier could be reduced between the MEH-PPV and the Ag cathode. As can be seen from Table 1, due to the lowing of the injection barriers to electronic carrier injection by enhancing interface dipole formation according to interaction between oxygen atom and Ag cathode, when WPmXF and WPF-oxy-F containing oxygen atoms were inserted between the MEH-PPV and the Ag cathode, the device efficiencies were significantly more improved compared to that of WPXF without containing oxygen side groups. These results indicate that our water-soluble polymers, when used as electron injecting layer, greatly enhance electron injection. As ammonium bromide salts of water-soluble polyfluorenes in the vicinity of the Ag cathode induce dipole moments [11–13], the effective charge injection barrier could be reduced.

The effective work-function of the cathode could be measured by photovoltaic measurement of the open-circuit voltage (V_{oc}) the across the device [26]. Fig. 6 shows photovoltaic measurement for each device, under AM1.5 irradiation (100 mW cm^{-2}). As the anode of each device was identical, the effective work-function of the cathode influenced the open-circuit voltage. In the case of the MEH-PPV/Ag device, the open-circuit voltage

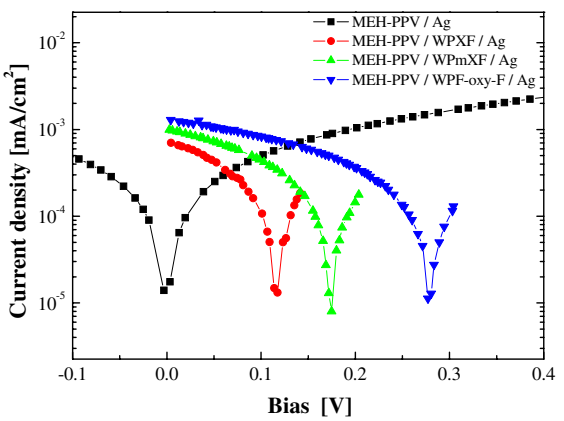


Fig. 6. Photovoltaic characteristics of each device.

Table 1
Device performance with water-soluble electron injection layer (EIL), in a device configuration ITO/PEDOT:PSS/MEH-PPV/EIL/Ag

EIL	Turn-on voltage (V)	^{max}Luminance (cd m^{-2})	Quantum efficiency (%)	Luminance efficiency (%)
–	6.5	86 (at 13.8 V)	0.005 (at 14.0 V)	0.01 (at 14.0 V)
WPXF	3.8	418 (at 5.4 V)	0.01 (at 5.4 V)	0.03 (at 5.4 V)
WPmXF	3.5	502 (at 4.6 V)	0.02 (at 4.6 V)	0.04 (at 4.6 V)
WPF-oxy-F	3.1	1768 (at 5.8 V)	0.2 (at 6.0 V)	0.4 (at 6.0 V)

was close to zero. When WPXF, WPmXF and WPF-oxy-F were used as an electron injecting layer, the V_{oc} was found to be 0.11, 0.17 and 0.27 V, respectively. The V_{oc} of the devices with electron injecting layer was higher than those without it because of improvement of interface dipole formation and consequent lower injection barriers. Therefore, the EL efficiency was increased and turn-on voltage was decreased.

In the case of WPF-oxy-F with two ethylene oxide side groups, EL efficiency was significantly enhanced. It has been reported that because ethylene oxide groups were able to transport mobile ion [27], poly(ethylene oxide) could be used as a solid-state ionic transporting material in light emitting electrochemical cells (LECs) [28,29]. LECs show low turn-on voltage and high efficiency, even thought LEC have a slow response time due to low ionic mobility in the solid-state electrolyte. A mechanism of enhanced EL efficiency, in case of WPF-oxy-F, could be attributed to ethylene oxide side groups. So, luminance of each device was measured as a function of time. As can be seen from Fig. 7, as soon as the bias applied to each device, a slow increase in luminance of WPF-oxy-F was observed compared with other cases, implying Br^- ion migration through the ethylene oxide groups in WPF-oxy-F.

When a bias was applied to PLEDs, mobile bromide ions would move away from the cathode to near the MEH-PPV layer. Because MEH-PPV is hydrophobic and does not include ion stabilizing groups, penetration of bromide ions and damage to the MEH-PPV layer is unlikely. The positive ammonium ion would be accumulated near the cathode. However, these positive ions would not diffuse into the cathode due to the covalent bonding between positive ammonium ions and massive polyelectrolyte. When the operational stability was compared, PLEDs with WPF-oxy-F/Ag cathode were more stable than those with reactive Ca cathode alone under ambient conditions.

For further investigation, current of the device with WPF-oxy-F was measured as a function of time. In Fig. 8, when a forward bias was applied to a device with WPF-oxy-F at +5 V for 20 s, the current of the device gradually increased. After applying a reverse bias to the device at −1 V for 20 s, and applied a forward bias at +5 V again, the pattern of current increasing was identical to the first state. When a forward bias was applied to this device, mobile bromide ion [30] was diffused by the ethylene oxide side group in the direction of anode. A reverse bias was applied to this device again and the diffused bromide ion may have returned to the original state. Therefore, the pattern of increasing current was identical to the first cycle.

These results indicated that the accumulation of mobile Br^- ions and positive ammonium salt near the electrodes induced an increase in ion space charge. As a result, the injection barrier to electronic carrier injection was reduced, due to the ionic space charge near the electrodes [31–33]. Similar as the LEC cases, due to the ion-transporting ethylene oxide groups of WPF-oxy-F, mobile bromide ions could migrate more easily *via* the ethylene oxide side groups compared to WPXF and WPmXF without ethylene oxide side groups, so when WPF-oxy-F

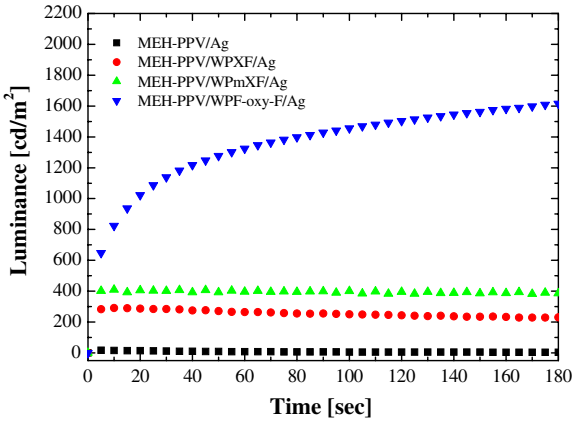


Fig. 7. Luminance as a function of time of each device with EIL biased at 5 V, except MEH-PPV/Ag biased at 10 V.

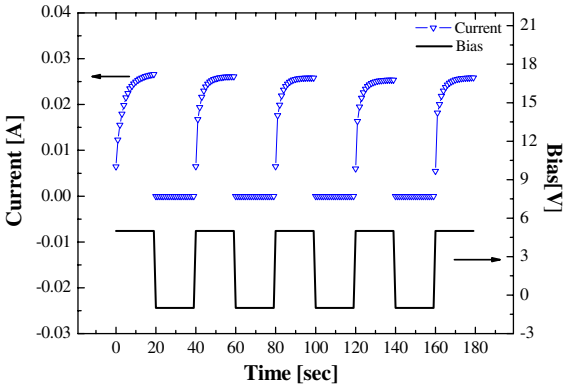


Fig. 8. Current as a function of time for ITO/PEDOT:PSS/MEH-PPV/WPF-oxy-F/Ag device.

was used as an electron injecting layer, EL efficiency was significantly enhanced. The studies of LECs using this polymer as a light emitting layer will be reported in future communications.

3. Conclusions

Cationic water-soluble polyfluorene derivatives with various co-monomers were successfully synthesized. When they were used as an electron injecting layer with a high work-function Ag cathode in a PLED, EL efficiency was improved, due to the reduced electron injection barrier. Especially, in the case where WPF-oxy-F containing ethylene oxide side groups was inserted between MEH-PPV and Ag cathode, the EL efficiency was significantly enhanced by about two orders of magnitude because of ionic transporting properties of the ethylene oxide side groups leading to large space charge. Water-soluble conjugated polymers containing ethylene oxide groups could be promising candidate materials for high efficiency PLED applications.

4. Experimental

4.1. Characterization and measurements

Materials were characterized by ^{1}H, ^{13}C NMR spectroscopy (JEOL JNM-LA300WB 300 MHz). Thermal properties were confirmed by thermogravimetric analysis (TGA; TA-2050) at a heating rate of 10 °C min^{-1} under nitrogen. Elemental analyses were carried out by the Korea Basic Science Institute, Seoul Branch Analytical Laboratory (Elemental analysis; CE Instruments Flash EA 1112 series). Absorption spectra were measured using a UV–vis spectrophotometer (Varian spectrometer, Carry1E). Molecular weight was confirmed by gas chromatography mass spectrometry (GC/MS; Shimadzu, GCMS-QP2010) and by gel permeation chromatography (GPC, Futecs, NS2001). The current–voltage–luminescence characteristics of the devices were measured using a Keithley 237 Source Measurement Unit and an optical power meter (Newport, 1835C) with a calibrated photodiode (Newport, 818 UV). Potocurrent–voltage measurements were performed using an Autolab PGSTAT30 Potentiostat/Galvanostat (Solartron, 1287A) under AM1.5 irradiation (100 mW cm^{-2}) by xenon light source (Müller).

4.2. Materials

All starting materials and 1,4-dibromo-2,5-dimethylbenzene (**3**) and 1,4-dibromo-2,5-dimethoxybenzene (**4**) were obtained from Aldrich Chemical Co. and were used without further purification except THF, which was dried by refluxing over sodium.

4.3. Synthesis

2,7-dibromofluorene and 2,7-dibromo-9,9-bis(2-(2-methoxyethoxy)ethyl)-fluorene (**5**) were prepared according to previously published procedures [34,35].

4.3.1. 2,7-Dibromo-9,9-bis(6-bromohexyl)-fluorene (*1*)

9.72 g of 2,7-dibromofluorene and 0.96 g of tetrabutylammoniumbromide (TBAB) were dissolved in 100 mL of 1,6-dibromohexane and 30 mL of a 45% KOH solution was then injected under nitrogen. The solution was stirred at 75 °C for 1 h. The reaction mixture was extracted with 300 mL dichloromethane and the resulting solution was evaporated. The reaction mixture was distilled under vacuum, to remove the 1,6-dibromohexane. The reaction mixture was purified by column chromatography using hexane and dichloromethane (hexane:dichloromethane = 95:5) as the eluent ($R_f = 0.37$). The final product was a white solid, produced in 84% yield. MP: 68–71 °C. ^{1}H NMR (300 MHz; $CDCl_3$; Me_4Si): δ_H 7.53 (d, 2H, $J = 6.0$, fluorene), 7.46 (dd, 2H, $J = 3.0$ and 6.0, fluorene), 7.44 (d, 2H, $J = 3.0$, fluorene), 3.30 (t, 4H, $J = 9.0$, $–CH_2Br$), 1.92 (t, 4H, $J = 9.0$, $–CH_2–$), 1.67 (t, 4H, $J = 9.0$, $–CH_2–$), 1.20 (m, 4H, $–CH_2–$), 1.08 (m, 4H, $–CH_2–$), 0.58 (m, 4H, $–CH_2–$). ^{13}C NMR (300 MHz; $CDCl_3$; MeSi): δ_C 23.37, 27.66, 28.86, 32.53, 33.75, 39.97, 55.52, 121.29, 121.64, 126.18, 130.42, 139.17, 152.29. Element Anal. Calcd. for $C_{25}H_{30}Br_4$: C, 46.15%; H, 4.61%. Found: C, 46.13; H, 4.59. *m/z* (EI) 649.95 (M^+).

4.3.2. 2,7-bis(4,4,5,5-Tetramethyl-1,3,2-dioxaborolan-2-yl)-9,9-(6-dibromohexyl)-fluorene (*2*)

Three grams of 2,7-dibromo-9,9-bis(6-bromohexyl)-fluorene (**1**) was dissolved in 150 mL of tetrahydrofuran. The solution was cooled to −80 °C and 6 mL of 1.7 M *t*-BuLi was injected under nitrogen followed by stirring for 1 h. 2.1 mL of 2-isopropoxy-4,4,5,5-tetramethyl-1,3,2-dioxa-

borolane was rapidly injected into the solution. The reaction mixture was warmed to room temperature and mixture was extracted with 300 mL of ether. The product was purified by column chromatography using hexane and ethylacetate (hexane:ethylacetate = 20:1) as the eluent ($R_f = 0.14$). The product was a yellowish-white solid, produced in 70% yield. MP: 117–121 °C. ^{1}H NMR (300 MHz, $CDCl_3$, Me_4Si): δ_H 7.82 (d, 2H, $J = 9.0$, fluorene), 7.74 (s, 2H, fluorene), 7.72 (d, 2H, $J = 9.0$, fluorene), 3.25 (t, 4H, $J = 9.0$, –CH_2Br), 1.98 (m, 4H, –CH_2–), 1.62 (m, 4H, –CH_2–), 1.39 (s, 24H, –CH_3), 1.20 (m, 4H, –CH_2–), 1.15 (m, 4H, –CH_2–), 0.55 (m, 4H, –CH_2–). ^{13}C NMR (300 MHz, $CDCl_3$, Me_4Si): δ_C 23.43, 25.01, 27.78, 29.01, 32.73, 33.99, 39.99, 55.15, 83.92, 119.67, 129.00, 134.03, 144.15, 150.34. Element Anal. Calcd. for $C_{37}H_{54}B_2Br_2O_4$: C, 59.71%; H, 7.31%. Found: C, 59.90; H, 7.45. *m/z* (EI) 744.20 (M^+).

4.3.3. Poly[(9,9-bis(6-dibromohexyl)-2,7-fluorene)-alt-1,4-xylene] (PXF)

0.74 g of **2**, 0.26 g of **3** and 60 mL THF were placed in a two-neck flask under a nitrogen atmosphere. Twenty millilitres of 2 M K_2CO_3 solution was injected and 1 mol% of $Pd(PPh_3)_4$ was added to the solution. The solution was refluxed for 3 days. The reaction mixture was slowly cooled to room temperature. The reaction mixture was poured into a mixture of 250 mL of methanol and water (methanol:water = 4:1). The precipitate was collected, redissolved in chloroform and reprecipitated several times by adding methanol. The resulting polymer was a yellowish powder. (Yield 71%). ^{1}H NMR (300 MHz, $CDCl_3$, Me_4Si): δ_H 7.81 (br, 2H, Ph), 7.40 (br, 6H, fluorene), 3.31 (br, 4H, –CH_2Br), 2.38 (br, 6H, –CH_3), 2.03 (br, 4H, –CH_2–), 1.70 (br, 4H, –CH_2–), 1.25 (br, 4H, –CH_2–), 1.12 (br, 4H, –CH_2–), 0.80 (br, 4H, –CH_2–). Element Anal. Calcd. for $C_{33}H_{38}Br_2$: C, 66.67%; H, 6.44%. Found: C, 66.51; H, 6.24.

4.3.4. Poly[(9,9-bis(6-(dibromohexyl)-2,7-fluorene))-alt-1,4-(2,5-dimethoxybenzene)] (PmXF)

0.74 g of **2**, 0.29 g of **4** and 60 mL THF were placed in a two-neck flask under a nitrogen atmosphere. Twenty millilitres of 2 M K_2CO_3 solution was injected and 1 mol% of $Pd(PPh_3)_4$ was added. The solution was refluxed for 3 days. The reaction mixture was slowly cooled to room temperature and then poured into a mixture of 250 mL of methanol and water (methanol:water = 4:1). The precipitate was collected, redissolved in chloroform and reprecipitated several times by adding methanol. The resulting polymer was a gray powder. (Yield 78%). ^{1}H NMR (300 MHz; $CDCl_3$; Me_4Si): δ_H 7.84 (br, 2H, Ph), 7.62 (br, 6H, fluorene), 3.85 (br, 6H, –OCH_3), 3.31 (br, 4H, –CH_2Br), 2.04 (br, 4H, –CH_2–), 1.72 (br, 4H, –CH_2–), 1.29 (br, 4H, –CH_2–), 1.16 (br, 4H, –CH_2–), 0.89 (br, 4H, –CH_2–). Element Anal. Calcd. for $C_{33}H_{38}O_2Br_2$: C, 63.27%; H, 6.11%. Found: C, 63.21; H, 6.12.

4.3.5. Poly[(9,9-bis(6-bromohexyl)-fluorene)-alt-(9,9-bis(2-(2-methoxyethoxy)ethyl)-fluorene)] (PF-oxy-F)

0.74 g of **2**, 0.52 g of **5** and 60 mL THF were placed in a two-neck flask under a nitrogen atmosphere. Twenty millilitres of 2 M K_2CO_3 solution was injected and 1 mol% of $Pd(PPh_3)_4$ was added in the solution. The solution was refluxed for 3 days. The reaction mixture was slowly cooled to room temperature and poured into a mixture of 250 mL of methanol and water (methanol:water = 4:1). The precipitate was collected, redissolved in chloroform and reprecipitated several times by adding methanol. The resulting polymer was a yellowish-white powder. (Yield 70%). ^{1}H NMR (300 MHz; $CDCl_3$; Me_4Si): δ_H 7.85 (br, 6H, fluorene), 7.73 (br,6H, fluorene), 3.35 (br, 4H, –CH_2Br), 3.29 (br, 6H, –OCH_3), 2.95 (br, 4H, –CH_2O–), 2.62 (br, 4H, –OCH_2–), 2.50 (br, 4H, –CH_2O–), 2.19 (br, 8H, –CH_2–), 1.71 (br, 4H, –CH_2–), 1.26 (br, 8H, –CH_2–), 0.81 (br, 4H, –CH_2–). Element Anal. Calcd. for $C_{48}H_{58}Br_2O_4$: C, 67.13%; H, 6.81%. Found: C, 67.27; H, 6.54.

4.3.6. Poly[(9,9-bis(6′-(N,N,N-trimethylammonium) hexyl)-2,7-fluorene)-alt-1,4-xylene] Dibromide (WPXF)

0.25 g of PXF was dissolved in 100 mL of THF. Five millilitres of trimethylamine solution was added to the solution which was then stirred at rt for 24 h. The solubility of the ionic polymer was reduced in THF and precipitated during this period. Twenty millilitres of water was added to the solution in order to dissolve the precipitate. The solution was evaporated and the residue was redissolved in methanol. The ionic polymer was precipitated from ether. The ionic polymer was a yellow powder. (Yield 89%). ^{1}H NMR (300 MHz; CD_3OD; Me_4Si): δ_H 7.88 (br, 2H, Ph), 7.42 (br, 6H, fluorene), 3.23 (br, 4H, –CH_2N–), 3.06 (br, 18H, –NCH_3), 2.36 (br, 6H, –CH_3), 2.16 (br, 4H, –CH_2–), 1.64 (br, 4H, –CH_2–), 1.21 (br, 8H,

–CH_2–), 0.78 (br, 4H, –CH_2–). Element Anal. Calcd. for $C_{39}H_{56}Br_2N_2$: C, 65.73%; H, 7.92; N, 3.93%. Found: C, 65.52; H, 7.85; N, 3.72.

4.3.7. Poly[(9,9-bis(6′-(N,N,N-trimethylammonium) hexyl)-2,7-fluorene)-alt-1,4-(2,5-dimethoxybenzene)] Dibromide (WPmXF)

The same procedure as for poly[(9,9-bis(6′-(*N*,*N*,*N*-trimethylammonium) hexyl)-2,7-fluorene)-*alt*-1,4-xylene] Dibromide was applied to give a dark gray powder. (Yield 91%). ^{1}H NMR (300 MHz; CD_3OD; Me_4Si): δ_H 7.87 (br, 2H, Ph), 7.62 (br, 6H, fluorene), 3.88 (br, 6H, –OCH_3), 3.19 (br, 4H, –CH_2N–), 3.03 (br, 18H, –NCH_3), 2.19 (br, 4H, –CH_2–), 1.60 (br, 4H, –CH_2–), 1.29 (br, 8H, –CH_2–), 0.90 (br, 4H, –CH_2–). Element Anal. Calcd. for $C_{39}H_{56}Br_2N_2O_2$: C, 62.90%; H, 7.58%; N, 3.76%. Found: C, 62.71; H, 7.32; N, 3.61.

4.3.8. Poly[(9,9-bis((6′-(N,N,N-trimethylammonium) hexyl)-2,7-fluorene))-alt-(9,9-bis(2-(2-methoxyethoxy)ethyl)-fluorene)] Dibromide (WPF-oxy-F)

The same procedure as for poly[(9,9-bis(6′-(*N*,*N*,*N*-trimethylammonium) hexyl)-2,7-fluorene)-*alt*-1,4-xylene] Dibromide was applied to give a yellowish-white powder. (Yield 88%). ^{1}H NMR (300 MHz; CD_3OD; Me_4Si): δ_H 7.91 (br, 6H, fluorene), 7.80 (br, 6H, fluorene), 3.26 (br, 4H, –CH_2N–), 3.23 (br, 6H, –OCH_3), 3.00 (br, 18H, –NCH_3), 2.90 (br, 4H, –CH_2O–), 2.61 (br, 4H, –OCH_2–), 2.49 (br, 4H, –CH_2O–), 2.29 (br, 8H, –CH_2–), 1.58 (br, 4H, –CH_2–), 1.19 (br, 8H, –CH_2–), 0.75 (br, 4H, –CH_2–). Element Anal. Calcd. for $C_{54}H_{76}Br_2N_2O_4$: C, 66.38%; H, 7.84%; N, 2.87%. Found: C, 66.49; H, 7.54; N, 2.78.

4.3.9. Device fabrication

These water-soluble polyfluorenes were used as an electron injecting layer in PLEDs. The structure of devices was ITO/PEDOT:PSS (30 nm)/MEH-PPV (70 nm)/water-soluble polyfluorene (10 nm)/Ag (200 nm). The glass substrate, pre-coated with indium-tin-oxide, was cleaned in an ultrasonic bath with acetone, followed by 2-propanol. A surface treatment was carried out by exposing the ITO to an O_2-plasma. The hole injecting poly(3,4-ethylene dioxythiophene):poly(styrene sulfonic acide) (PEDOT:PSS, AI 4083, Bayer AG) layer was spin coated on the ITO at a thickness of 30 nm and baked at 120 °C for 5 min on a hot plate under air. A 0.8 wt% solution of MEH-PPV in chlorobenzene was spin coated on the PEDOT:PSS layer as an emitting layer and baked at 150 °C for 20 min under air. A 0.5 wt% solution of WPXF or WPmXF or WPF-oxy-F in methanol was spin coated on the MEH-PPV layer as an electron injecting layer and baked at 120 °C for 5 min under air. Ag was deposited as the cathode through a shadow mask by thermal evaporation. The area of sample was 4.34 mm^2.

Acknowledgements

This work was supported by the Ministry of Commerce, Industry and Energy of Korea Government, Brain Korea 21 (BK21) and the Korea Science and Engineering Foundation (KOSEF) through the National Research Lab. Program funded by the Ministry of Science and Technology (M10500000077-06J0000-07710).

References

[1] J.H. Burroughes, D.D.C. Bradley, A.R. Brown, R.N. Marks, K. Mackey, R.H. Friend, P.L. Burns, A.B. Holmes, Nature 347 (1990) 539.
[2] J.R. Sheats, H. Antoniadis, M. Hueschen, W. Leonard, J. Miller, R. Moon, D.B. Roitman, A. Stocking, Science 273 (1996) 884.
[3] R.H. Friend, R.W. Gymer, A.B. Holmes, J.H. Burroughes, D.D.C. Bradley, D.A.D. Santos, J.L. Bredas, M. Loglund, W.R. Salaneck, Nature 397 (1999) 121.
[4] A.O. Patil, Y. Ikenoue, F. Wudl, A.J. Heeger, J. Am. Chem. Soc. 109 (1987) 1858.
[5] J.W. Baur, S. Kim, P.B. Balanda, J.R. Renolds, M.F. Rubner, Adv. Mater. 10 (1998) 1452.
[6] B.S. Harrison, M.B. Ramey, J.R. Renolds, K.S. Schanze, J. Am. Chem. Soc. 122 (2000) 8561.
[7] B.S. Gaylord, S. Wang, A.J. Heeger, G.C. Bazan, J. Am. Chem. Soc. 123 (2001) 6417.
[8] Q.-L. Fan, S. Lu, Y.-H. Lai, X.-Y. Hou, W. Huang, Macromolecules 36 (2003) 6976.
[9] H. Li, Y. Li, J. Zhai, G. Cui, H. Liu, S. Xiao, Y. Liu, F. Lu, L. Jiang, D. Zhu, Chem. Eur. J. 9 (2003) 6031.
[10] K.H. Glusac, M.R. Pinto, C. Tan, K.S. Schanze, J. Am. Chem. Soc. 126 (2004) 14964.
[11] H. Wu, F. Huang, Y. Mo, W. Yang, D. Wang, J. Peng, Y. Cao, Adv. Mater. 16 (2004) 1826.
[12] R. Yang, H. Wu, Y. Cao, G.C. Bazan, J. Am. Chem. Soc. 128 (2006) 14422.
[13] H. Wu, F. Huang, J. Peng, Y. Cao, Org. Electron. 6 (2005) 118.
[14] B. Liu, W.-L. Yu, Y.-H. Lai, W. Huang, Macromolecules 35 (2002) 4975.
[15] F. Huang, H. Wu, W. Yang, Y. Cao, Chem. Mater. 16 (2004) 708.
[16] C.W. Tang, S.A. Vanslyke, Appl. Phys. Lett. 51 (1987) 913.
[17] D. Braun, A.J. Heeger, Appl. Phys. Lett. 58 (1991) 1982.
[18] L.S. Hung, C.W. Tang, M.G. Mason, Appl. Phys. Lett. 70 (1997) 152.

[19] G.E. Jabbour, Y. Kawabe, S.E. Shaheen, J.F. Wang, M.M. Morrell, B. Kippelen, N. Peyghambarian, Appl. Phys. Lett. 71 (1997) 1762.
[20] X.Y. Deng, W.M. Lau, K.Y. Wong, K.H. Low, H.F. Chow, Y. Cao, Appl. Phys. Lett. 84 (2004) 3522.
[21] T.-F. Guo, F.-S. Yang, Z.-J. Tsai, T.-C. Wen, S.-N. Hsieh, Y.-S. Fu, C.-T. Chung, Appl. Phys. Lett. 88 (2006) 113501.
[22] S. Wang, B. Liu, B.S. Gaylord, G.C. Bazan, Adv. Funct. Mater. 13 (2003) 463.
[23] M. Ranger, D. Rondeau, M. Leclerc, Macromolecules 30 (1997) 7686.
[24] D.L. Pavia, G.M. Lampman, G.S. Kriz, Introduction to Spectroscopy, Saunders College Publishing, Olando, 1996.
[25] P. Blondin, J. Bouchard, S. Beaupre, M. Belletete, G. Durocher, M. Leclerc, Macromolecules 33 (2000) 5874.
[26] C.J. Brabec, A. Cravino, D. Meissner, N.S. Sariciftci, T. Fromherz, M.T. Rispens, L. Sanchez, J.C. Hummelen, Adv. Funct. Mater. 11 (2001) 374.
[27] F.M. Gray, Polymer Electrolytes, The Royal Society of Chemistry, Cambridge, 1997.
[28] Q. Pei, G. Yu, C. Zhang, Y. Yang, A.J. Heeger, Science 269 (1995) 1086.
[29] Q. Pei, Y. Yang, G. Yu, C. Zhang, A.J. Heeger, J. Am. Chem. Soc. 118 (1996) 3922.
[30] L. Edman, M. Pauchard, B. Liu, G.C. Bazan, D. Moses, A.J. Heeger, Appl. Phys. Lett. 82 (2003) 3961.
[31] J. Morgado, R.H. Friend, F. Cacialli, B.S. Chuah, H. Rost, S.C. Moratti, A.B. Holmes, Synth. Met. 122 (2001) 111.
[32] F. Nuesch, E.W. Forsythe, Q.T. Le, Y. Gao, L.J. Rothberg, J. Appl. Phys. 87 (2000) 7973.
[33] T.-W. Lee, O.O. Park, L.-M. Do, T. Zyung, T. Ahn, H.-K. Shim, J. Appl. Phys. 90 (2001) 2128.
[34] G. Klaerner, R.D. Miller, Macromolecules 31 (1998) 2007.
[35] P. Qibing, Y. Yang, J. Am. Chem. Soc. 118 (1996) 7416.

Available online at www.sciencedirect.com
ScienceDirect
Organic Electronics 8 (2007) 784–790
Organic Electronics
www.elsevier.com/locate/orgel

Electrical properties of dysprosium phthalocyanine films

T. Basova [a,*], A.G. Gürek [b], V. Ahsen [b,c], A.K. Ray [d]

[a] Nikolaev Institute of Inorganic Chemistry, Lavrentiev pr., 3, Novosibirsk 630090, Russia
[b] Gebze Institute of Technology, Department of Chemistry, P.O. Box 141, 41400 Gebze-Kocaeli, Turkey
[c] TÜBITAK-Marmara Research Center, Materials Institute, P.O. Box 21, 41470 Gebze-Kocaeli, Turkey
[d] Department of Materials, Queen Mary, University of London, Mile End Road, London E1 4NS, UK

Received 24 April 2007; received in revised form 14 June 2007; accepted 27 June 2007
Available online 3 July 2007

Abstract

Forty-four nanometers thick films of alkyl-substituted dysprosium phthalocyanine molecules were prepared on carefully cleaned indium tin oxide (ITO) substrates by the spin casting method. UV–vis absorption spectra and dc conduction characteristics were obtained in order to investigate the structure–conduction property relationship. The conduction is Ohmic at low applied voltages but the space charge limited mechanism is prevalent at relatively high voltages. The conductivities of both as-deposited and heat treated films are found to show directionally anisotropic behaviour. The columnar conductivity was found to be significantly large in the liquid crystalline state.
© 2007 Elsevier B.V. All rights reserved.

PACS: 61.30; 61.66; 68.00; 74.25

Keywords: Phthalocyanine; Thin films; Electrical conductivity

1. Introduction

A complex range of electronic states due to intramolecular π–π orbital overlaps has created immense interest in bisphthalocyanines [1,2]. A range of bis[1,2-bis(3,4-dialkoxyphenyl)ethanedione dioximato]palladium(II) complexes showing an enantiotropic hexagonal disordered columnar mesophase were synthesized. The long wavelength (d–p) band and short wavelength band due to the metal-to-ligand charge-transfer transition were found to be sensitive to temperatures [3,4]. Films of discotic liquid crystalline bis[octakis(alkylthio)phthalocyaninato]lutetium(III) were found to be highly conducting with carrier mobility in the order of $0.71\ cm^2\ V^{-1}\ s^{-1}$ and could be promising organic materials for the solar batteries [5]. Long-chain substituted lutetium phthalocyanines show discotic mesomorphism and electrochromism. For example, the special rectangular ordered columnar mesophase of bis(octaalkoxyphthalocyaninato) lutetium(III) complexes $[(C_nO)_8Pc]_2Lu$ ($n = 10$, 12, 14, 16, 18) produced two different stacking distances due to trampoline movement and rotation of the phthalocyanine disks [6]. The influence of intracolumnar order of bis(phthalocyaninato)lutetium in the solid, liquid crystalline, and isotropic phases on ac spectroscopic measurements were observed in the frequency range of 10^{-3}–10^5 Hz [7].

* Corresponding author.
E-mail address: basova@che.nsk.su (T. Basova).

1566-1199/$ - see front matter © 2007 Elsevier B.V. All rights reserved.
doi:10.1016/j.orgel.2007.06.008

The synthesis of hexagonal columnar liquid crystalline alkylthio-substituted bis(2,3-naphthalocyaninato) rare earth complexes were also recently reported. These compounds were found to be stable within the temperature range between 42 and 243 °C and the mesophase domains were dependent on the size of central rare earth ions. The molecular packing of these complexes was, however, independent of the ionic size of the central rare earth [8]. An intermolecular charge transfer band was found to exist at about 2000–2100 nm both for [octakis(3,4-dialkoxyphenoxy)-phthalocyaninato]lutetium complexes $\{[(C_nO)_2PhO]_8Pc\}_2Lu$ ($n = 12$, 13) in the *n*-hexane solution and thin film due to molecular aggregation [9]. Specially synthesized $[(C_{12}S)_8Pc]_2Lu$ and $[(C_{18}S)_8Pc]_2Lu$ showed carrier mobility higher than previously reported values for $[(C_{12}O)_8Pc]_2Lu$ by one order of magnitude [10]. Two substituted bis(phthalocyaninato) rare earth complexes $Y[(OC_8H_{17})_8Pc]_2$ and $Ce[(OC_8H_{17})_8Pc]_2$ were adsorbed onto single crystalline Au(1 1 1) electrodes from benzene saturated with the respective complex at room temperature and it was observed from in situ scanning tunneling microscopic measurements that the molecular planes were parallel to the unreconstructed Au(1 1 1) [11]. Different types of substituted lanthanide bisphthalocyanine compounds were studied with a view to investigating hyperpolarizability and reverse saturable absorption properties for fabricating optical switches [12]. Lanthanide bis-[(4,4′,4″,4‴)-tetrakis-(6-hydroxyhexylthio)phthalocyaninates] were functionalized with hydroxyhexylsulfanyl moieties for potential use as metal ion binding and surface anchors [13]. The physicochemical properties and electrochromic behaviour of lanthanide bishthalocyanines were found to be susceptible to the environment and therefore were extensively exploited as sensing materials for the development of electronic nose and tongue [14,15].

Recent interest was shown in organo-soluble tetrakis(2,9,16,23-*tert*-butyl) dysprosium bisphthalocyanines as photosensitizers [16]. The present article reports the results of electrical studies on spun films of alkyl-substituted dysprosium phthalocyanine $[(C_6S)_8Pc]_2Dy$ derivative. The chemical structure of this molecule is given in Fig. 1. This compound exhibits interesting liquid crystalline properties and forms columnar hexagonal (Col_h) mesophase [17]. The temperature of phase transition to liquid crystalline state is about 55 °C and the mesophase is apparently stable up to decomposition temperature.

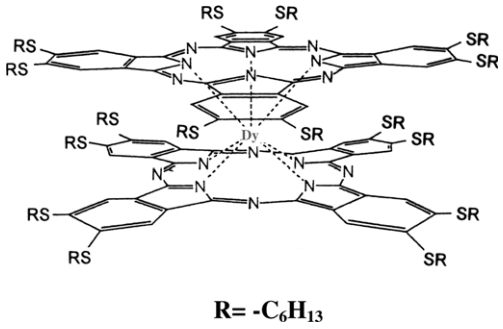


Fig. 1. Chemical structure of an alkyl-substituted dysprosium phthalocyanine.

The Col_h mesophase was transformed into isotropic liquid at 250 °C. This compound is easily soluble in most common organic solvents and therefore suitable for fast deposition of thin film using the spin-coating technique. The resulting as-deposited films were largely amorphous and contained microcrystalline domains. The motivation of this work has originated from our early work on the effect of structural organization of the films of $Lu(PcR_8)_2$ ($R = -SC_6H_{13}$) due to annealing on their dc conductivity [18]. It has already been established that the thermal treatment of films of phthalocyanine exhibiting mesogenic properties at temperatures higher that the temperature of phase transition to liquid crystalline phase for several hours leads to the formation of films with ordered structure [19]. This effect is believed to be due to stacking interaction between neighboring phthalocyanine. In this work, UV–vis absorption spectra and dc conduction characteristics were obtained in order to investigate the structure–conduction property relationship and the columnar conductivity was found to be significantly large in the liquid crystalline state. These studies will provide the physical understanding for potential applications in device engineering such as the fabrication of all organic solar cells using liquid crystalline bisphthalocynine molecules [20].

2. Experimental details

A photoresist spinner (Microsystem model 4000) was employed to deposit $[(C_6S)_8Pc]_2Dy$ films onto ultrasonically cleaned ITO-coated glass substrates by spinning a small volume of the spreading solution at 2000 rpm. The spreading solution was prepared by dissolving $[(C_6S)_8Pc]_2Dy$ compound in chloroform (1 mg/ml). Spinning was continued for 30 s during in order to allow the complete evaporation

of the solvent, producing a uniform phthalocyanine film. Details of the substrate cleaning and the film preparation procedure were described in an earlier publication [21]. Fifty nanometers thick aluminium (Al) films were thermally evaporated as top electrodes on spun $[(C_6S)_8Pc]_2Dy$ layers at the rate of 0.5 nm s^{-1} under vacuum of 10^{-3} Pa to form a sandwich structure for electrical measurements. The active device area (S) was 10 mm^2. The device structures were also made from the $[(C_6S)_8Pc]_2Dy$ films which were heated to the temperature of 270 °C for a period of about 2 h, and then slowly cooled down to room temperature. The cooling rate was approximately 5 °C/min. Current (I) were measured over the temperature range of 150–350 K as a function of voltage (V) for both as-deposited and heat treated samples using a Keithley electrometer and Oxford Instrument constant bath liquid nitrogen cryostat in a microprocessor controlled measuring system. In accordance with the data of DSC measurements the temperature of transition of $[(C_6S)_8Pc]_2Dy$ to liquid crystalline phase is 55 °C (328 K). A selected number of ITO/as-deposited $[(C_6S)_8Pc]_2Dy$/Al structures was, therefore, kept at 350 K for 1 h during the temperature dependence measurements in order to allow the film to obtain the liquid crystalline (LC) phase with good ordering and then the I–V characteristics were recorded for these samples. The LC ordering of the film was found to not be an instant process. This temperature value depends on the heating rate and conditions of measurements and may slightly differ during measurements of I–V characteristics. The bias voltage was taken to be positive when the ITO contact was at higher voltage than the top Al electrode. Values of the thickness d of spun $[(C_6S)_8Pc]_2Dy$ films were determined from spectroscopic ellipsometric measurements. For this purpose, the films were deposited on silicon substrates under similar conditions. The angle of incidence was fixed at the angle of 60°. UV–visible spectra were recorded for $[(C_6S)_8Pc]_2Dy$ molecules under different phases with a UV–vis scanning spectrophotometer (Shimadzu UV-VIS-3101PC) in the range from 300 to 900 nm and absorption data were used to provide an interpretation of structure dependent conduction.

3. Results and discussion

The charge transport mechanisms were investigated by recording current flow through spun films of $[(C_6S)_8Pc]_2Dy$ molecules, sandwiched between the indium tin oxide (ITO) substrates and aluminium (Al) electrodes at different temperatures. Measurements were performed on both as-deposited and heat treated films. Typical current–voltage (I–V) characteristics for ITO/$[(C_6S)_8Pc]_2Dy$/Al sandwich structure are presented in Fig. 2. For low voltages ($V \leqslant 0.4$ V), the conduction is Ohmic irrespective of the condition of the film treatment. It can be seen that $[(C_6S)_8Pc]_2Dy$ films are the most conducting of all while the current through the heat treated samples was lower by about two orders of magnitude than as-deposited samples. In order to determine the directional dependence of current flow, current–voltage characteristics of $[(C_6S)_8Pc]_2Dy$ films on interdigitated platinum systems were obtained and typical results were given in Fig. 3. Through-plane Ohmic ($\sigma_\perp$) conductivity was determined from Fig. 2 from the knowledge that $\sigma_\perp = 10^{-4}\left(\frac{Id}{V}\right)$. In-plane Ohmic ($\sigma_{//}$) dc conductivity was, on the other hand, estimated using the values of the interelectrode distance $L = 60$ μm and width of electrode overlapping $W = 3.125$ mm [22].

Values of through-plane Ohmic ($\sigma_\perp$) and in-plane Ohmic ($\sigma_{//}$) dc conductivities at room temperature for phthalocyanine films are summarised in Table 1. Conductivities of as deposited and heat treated films were of the same order of magnitude but the degree of anisotropy was seen to depend upon the heat treatment. This behaviour may be understood by studying the structural reorganization from

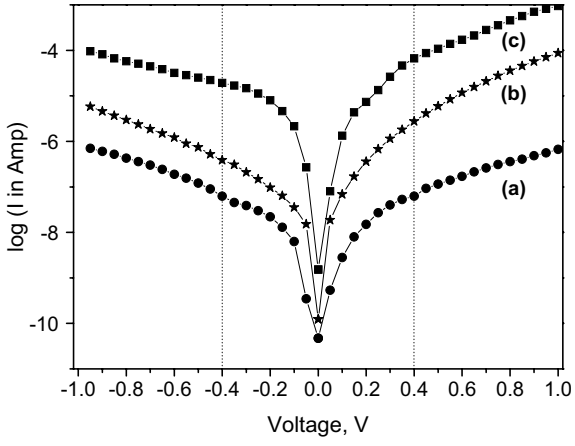


Fig. 2. Current–voltage characteristics for ITO/$[(C_6S)_8Pc]_2Dy$/Al sandwich cell on logarithmic-linear scale: (a) after heat treatment in air measured at room temperature, (b) as-deposited measured at room temperature and (c) the film in liquid crystalline state measured at 350 K.

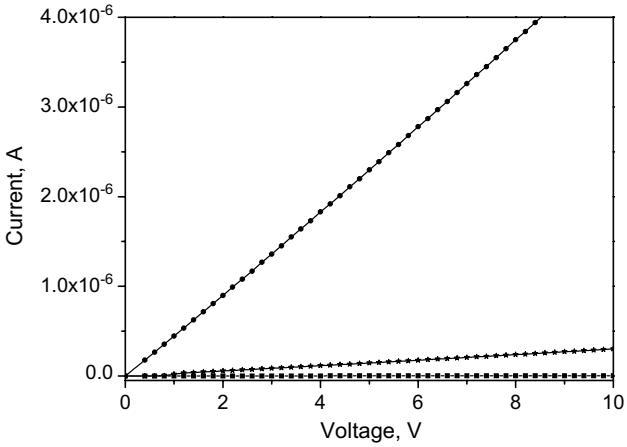


Fig. 3. Current–voltage characteristics for $[(C_6S)_8Pc]_2Dy$ films deposited on interdigitated planar structure: before heat treatment at room temperature (closed stars), after (closed circles) heat treatment in air measured at room temperature and the film in liquid crystalline state measured at 350 K (closed squares).

Table 1
Values of room temperature Ohmic conductivity obtained from experimental $I(V)$ curve

Parameters		As-deposited film	Film after heat treatment	Film in liquid crystalline state
Film thickness (nm)		44	40	40
Room temperature	$\sigma_{//}$	2.91×10^{-8}	2.76×10^{-5}	4.56×10^{-10}
Ohmic conductivity (Ω^{-1} m^{-1})	$\sigma_{\perp}$	6.57×10^{-8}	2.85×10^{-11}	6.42×10^{-6}

UV–vis absorption spectra for $[(C_6S)_8Pc]_2Dy$ molecules under different phases as shown in Fig. 4.

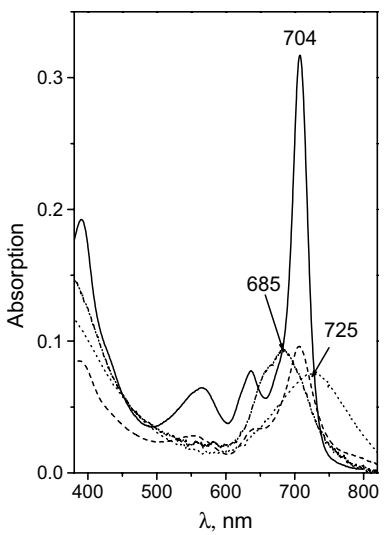


Fig. 4. Absorption spectra of $[(C_6S)_8Pc]_2Dy$ solution in chloroform (solid line) and films on quartz before (dashed line) and after (dotted line) heating recorded at room temperature and the film in liquid crystalline state (broken line) recorded at 350 K.

The absence of any significant Q-band shift for the as-deposited films relative to the one obtained for the solution indicates that the molecules in as-deposited films were disordered [17]. The spectra of $[(C_6S)_8Pc]_2Dy$ films after heating were found to be significantly different from those before heat treatment. Q-bands for the heated $[(C_6S)_8Pc]_2Dy$ films became broadened and the peak was red-shifted to 725 nm. Therefore, the films heated to the isotropic liquid temperature and then slowly cooled to room temperature are believed to become ordered. According to the molecular exciton theory [23], a red-shifted exciton is usually observed when there is a staggered slipped stacking involving inclined alignment of transition dipoles. The molecule arrangement in the films may be described by slipped–stacked columns as in the crystal structure determined in Ref. [17].

The blue shift of the Q-band to 685 nm was observed in the spectra for the $[(C_6S)_8Pc]_2Dy$ films heated at 350 K for 1 h. This effect is believed to be characteristic of the formation of a discotic hexagonal columnar (Col_h) mesophase in which the molecules are oriented parallel to the substrate surface and form columns.

In-plane conductivity ($\sigma_{//}$) was found to be larger than for heat treated films than as-deposited films by three orders of magnitude. On other hand, $\sigma_{\perp}$ decreased significantly on heat treatment of the films. This asymmetrical conduction behaviour may be attributed to the molecular reorganization in the spun dysprosium phthalocyanine films due to thermal treatment. Atomic force microscope images of the film surface showed that $[(C_6S)_8Pc]_2Dy$ molecules were inhomogenously in the as-deposited films with presence of voids having diameters of around 10–20 nm [17]. The surface of $[(C_6S)_8Pc]_2Dy$ film appeared smooth and homogeneous after heating the films. Increased in-plane conductivity is therefore consistent with the observation that heat treatment of the films strongly modified the film surface morphology.

Current–voltage characteristics for the film in liquid crystalline state measured at 350 K are also presented in Figs. 2 and 3. Values of through-plane Ohmic ($\sigma_{\perp}$) and in-plane Ohmic ($\sigma_{//}$) dc conductivities measured at 350 K for this film are summarised in Table 1. The through-plane conductivity is significantly enhanced for the film in liquid crystalline state. In the LC phase, the columnar charge flow was much easier intra-columnar flow.

Further measurements were made on ITO/$[(C_6S)_8Pc]_2Dy$/Al sandwich cells at different temperatures ranging from 150 to 350 K. Linear graphs in Fig. 5 on logarithmic scales for higher voltages ($V > 0.8$ V) may be described by a well known relation of power law dependence of the current on applied voltage in the form

$$I_{SCL} = B\frac{V^{n+1}}{d^{2n+1}}, \tag{1}$$

where the constant B depends upon the carrier mobility, and the density of states at the valence band edge. The index $n = \frac{T_c}{T}$, where T_c is called the characteristic temperature, depending upon the type of distribution of traps within the forbidden gap. The validity of Eq. (1) indicates the dominance of the space charge limited conduction (SCL) mechanism over this voltage range for both films. From the slopes of respective graphs, values of the index n at 300 K were estimated to be 2.3 and 1 for as-deposited and heat treated films, respectively. These values imply that the distribution of trapping states were susceptible to heat treatment. The trapping states are believed to be distributed exponentially within the forbidden gap of the as-deposited film while space charge limited conduction is controlled by trapping energy states predominantly situated at a single energy level within the forbidden gap of the heat treated films [24]. The exponential distribution of energy among traps in the as-deposited films was characterised by the value of $T_c = 690$ K for as-deposited films.

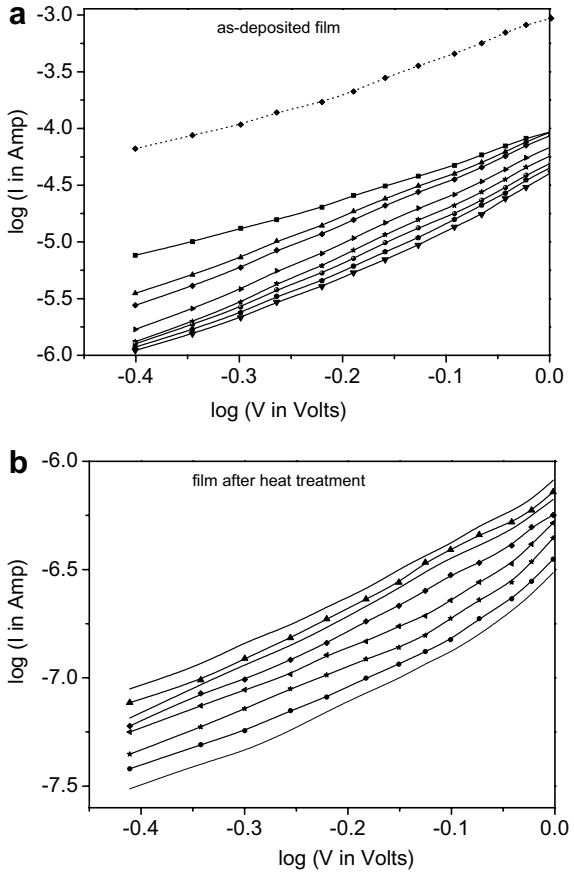


Fig. 5. Forward bias I–V characteristics of ITO/$[(C_6S)_8Pc]_2Dy$/Al sandwich cell on a log I–log V scale over the temperature range 150–350 K for the SCL conduction region ($V > 0.8$ V): (a) as-deposited film and (b) heat treated film. The broken line in (a) corresponds to the forward bias I–V characteristics of ITO/$[(C_6S)_8Pc]_2Dy$/Al sandwich cell kept at 350 K for 1 h.

In order to understand the temperature dependence of conduction, a set of Arrhenius plots of the current through ITO/$[(C_6S)_8Pc]_2Dy$/Al sandwich structures are given in Fig. 6 as a function of inverse temperature in the range of 150–350 K. Two different activation processes were found to exist, depending upon whether the temperature was below or above 270 K. Values of 11 meV and 0.2 eV were obtained for Ohmic activation energies corresponding to temperature regimes of $T \leqslant 270$ K and $T > 270$ K, respectively. This implies that

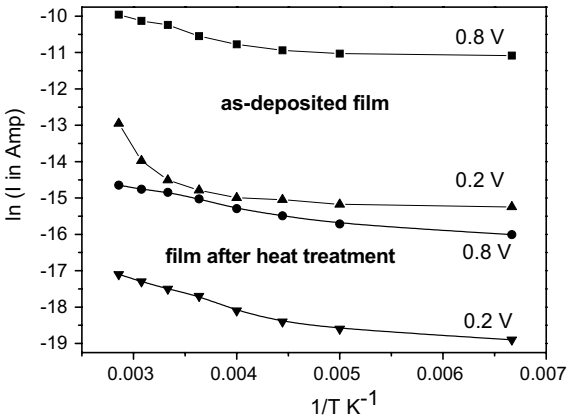


Fig. 6. Current as a function of inverse temperature of ITO/$[(C_6S)_8Pc]_2Dy$/Al film structure for the Ohmic conduction regime ($V = 0.2$ V) and space charge regime ($V = 0.8$ V).

hopping of charge carriers between localised stated within the band gap is responsible for charge transport at low temperatures while the high temperature activation may be associated with the ionisation energy of acceptor type impurities such as oxygen [25]. A value of 60 meV was estimated for activation energy within the SCL regime of conduction through an as-deposited $[(C_6S)_8Pc]_2Dy$ film. The density of defects N_o at the edge of valence band per unit energy is found to be $2.4 \times 10^{46}\ m^{-3}$ for as-deposited phthalocyanine film using the relation [26]

$$N_o = \frac{\varepsilon_o \varepsilon_s}{kT_c e d^2} \exp\left(\frac{E_a}{kT}\right) \quad (2)$$

taking the valence band edge at $E_v = 0$. The permittivity of the free space ε_o and the static relative dielectric constant of phthalocyanine films ε_s are taken to be $8.85 \times 10^{-12}\ Fm^{-1}$ and 3.6, respectively. The density of filled traps N_t was found to be about $7.9 \times 10^{22}\ m^{-3}$ for as-deposited films from the knowledge that

$$N_t = N_0 k T_c \exp\left(-\frac{E_a}{kT_c}\right). \quad (3)$$

One-carrier single set of traps were responsible for charge transport in the heated films. Since the transition from Ohmic to space charge limited case takes place voltage V_Ω, the free carrier density n_0 was estimated to be $3.5 \times 10^{16}\ m^{-3}$ from the modified relation [27]

$$n_0 = \frac{BV_\Omega}{q\mu S d^2}, \quad (4)$$

where a typical value of $10^{-5}\ m^2\ V^{-1}\ s^{-1}$ was assumed for the carrier mobility μ. The value of B was found from the intercept of the graphs in Fig. 5. The ratio of free to trapped charge θ may be written in the form

$$\theta = \frac{N_v}{N_t} \exp\left(-\frac{E_t}{kT}\right), \quad (5)$$

where N_v is the effective density of states assuming the valence band edge at $E_v = 0$. The value of E_t was determined from graph 6 for activation energy within the SCL regime corresponding to heat treated films. This value represents an average value of the location of the single trapping level of density above the valence band, which is close to a value of a single trapping level. Using the expression that

$$\theta = \frac{8}{9} \frac{B}{\mu S \varepsilon_0 \varepsilon_s} \quad (6)$$

the value of N_t was estimated to be $3.5 \times 10^{20}\ m^{-3}$. As expected with improved ordering, this value is smaller than one obtained for the as-deposited films.

4. Concluding remarks

Current–voltage characteristics were obtained for spun films of alkyl-substituted dysprosium phthalocyanine molecules. Spun films were heated to the temperature of 270 °C for a period of about 2 h, and then slowly cooled down at the rate of 5 °C/min to room temperature. Increases in room temperature conductivity for heat treated films are related to thermally induce ordering of the film structure. The liquid crystalline phase was obtained by heating the sample at 350 K for 1 h. Space charge limited conduction is a prevalent mechanism for both as-deposited and heat treated films but the trap distribution was found to be different. Directional anisotropy in conductivity is believed to have arisen from preferential charge flow across the stacks.

Acknowledgement

Two of the authors (T.B. and A.K.R.) are grateful to the Royal Society, London for the award of International Joint Project grant to support this work.

References

[1] M.M. Nicholson, Electrochromism and display devices, in: C.C. Leznoff, A.B.P. Lever (Eds.), Phthalocyanines/

Properties and Applications, vol. 3, VCH Publishers Inc., NY, pp. 75–113.
[2] K. Yoshino, S.B. Lee, T. Sonoda, H. Kawagishi, R. Hidayat, K. Nakayama, M. Ozaki, K. Ban, K. Nishizawa, K. Ohta, H. Shirai, Journal of Applied Physics 88 (2000) 7137.
[3] K. Ohta, M. Moriya, M. Ikejima, H. Hasebe, T. Fujimoto, I. Yamamoto, Bulletin of the Chemical Society of Japan 66 (1993) 3553.
[4] K. Ohta, M. Moriya, M. Ikejima, H. Hasebe, T. Fujimoto, I. Yamamoto, Bulletin of the Chemical Society of Japan 66 (1993) 3559.
[5] K. Ohta, K. Hatsusaka, M. Sugibayashi, M. Ariyoshi, K. Ban, F. Maeda, R. Naito, K. Nishizawa, A.M. van de Craats, J.M. Warman, Molecular Crystals and Liquid Crystals 397 (2003) 325.
[6] F. Maeda, K. Hatsusaka, K. Ohta, M. Kimura, Journal of Materials Chemistry 13 (2003) 243.
[7] Z. Belarbi, C. Sirlin, J. Simon, J.J. Andre, Journal of Physical Chemistry 93 (1989) 8105.
[8] Y. Zhang, N. Pan, Q.B. Xue, M. Bai, J.Z. Jiang, Journal of Porphyrins and Phthalocyanines 10 (2006) 1132.
[9] K. Hatsusaka, K. Ohta, Journal of Porphyrins and Phthalocyanines 7 (2003) 105.
[10] K. Ban, K. Nishizawa, K. Ohta, A.M. de Craats, J.M. Warman, I. Yamamoto, H. Shirai, Journal of Materials Chemistry 11 (2001) 321.
[11] H.Y. Ma, L.Y.O. Yang, N. Pan, S.L. Yau, J.Z. Hang, K. Itaya, Langmuir 22 (2006) 2105.
[12] M.O. Liu, C.H. Tai, A.T. Hu, T.H. Wei, Journal of Organometallic Chemistry 689 (2004) 2138.
[13] M.N. Yarasir, M. Kandaz, A. Koca, B. Salih, Journal of Porphyrins and Phthalocyanines 10 (2006) 1022.
[14] J.A. de Saja, M.L. Rodriguez-Mendez, Advances in Colloid and Interface Science 116 (2005) 1.
[15] A. Arrieta, M.L. Rodriguez-Mendez, J.A. de Saja, Sensors and Actuators B – Chemical 95 (2003) 357.
[16] M.O. Liu, C.H. Tai, M.Z. Sain, A.T. Hu, F.I. Chou, Journal of Photochemistry and Photobiology A – Chemistry 165 (2004) 131.
[17] A.G. Gürek, T. Basova, D. Luneau, C. Lebrun, E. Kol'tsov, A. Hassan, V. Ahsen, Inorganic Chemistry 45 (2006) 1667.
[18] T. Basova, E. Kol'stov, A.K. Hassan, A.K. Ray, A.G. Gurek, V. Ahsen, Materials Chemistry & Physics 96 (2006) 29.
[19] T. Basova, A.G. Gurek, V. Ahsen, Materials Science & Engineering C 22 (2002) 99.
[20] K. Petritsch, R.H. Friend, A. Lux, G. Rozenberg, S.C. Moratti, A.B. Holmes, Synthetic Metals 102 (1–3) (1999) 776.
[21] T. Basova, E. Kol'stov, A.K. Ray, A.K. Hassan, A.G. Gurek, V. Ahsen, Sensors and Actuators B – Chemical 113 (2006) 127.
[22] S.M. Tracey, S.N.B. Hodgson, A.K. Ray, Z. Ghassemlooy, Journal of Materials Processing Technology 77 (1–3) (1998) 86–94.
[23] M. Kasha, Spectroscopy of the Excited State, in: B. DiBartole (Ed.), Plenum Press, New York, 1976.
[24] A.M. Lampert, Volume-controlled current injection in insulators, Reports on Progess in Physics 27 (1964) 329–367.
[25] G. Jarosz, P.D.S.N. Quinn, L. Brehmer, Thin Solid Films 474 (2005) 301.
[26] A.J. Sussmann, Applied Physics 38 (1967) 2748.
[27] M. Arif, M. Yun, S. Gangopadhyay, K. Ghosh, L. Fadiga, F. Galbrecht, U. Scherf, S. Guha, Physical Review B 75 (2007) 195202.

Available online at www.sciencedirect.com
ScienceDirect
Organic Electronics 8 (2007) 791–795
Organic Electronics
www.elsevier.com/locate/orgel

Intrinsic electrochemical doping in blue light emitting polymer devices utilizing a water soluble anionic conjugated polymer

S. Sax [a,b], G. Mauthner [a,b], T. Piok [a,b], S. Pradhan [c], U. Scherf [c], E.J.W. List [a,b,*]

[a] Christian Doppler Laboratory Advanced Functional Materials, Institute of Solid State Physics, Graz University of Technology, A-8010 Graz, Austria
[b] JOANNEUM RESEARCH Institute of Nanostructured Materials and Photonics, A-8160 Weiz, Austria
[c] Bergische Universität Wuppertal, Makromolekulare Chemie, Fachbereich Chemie Gaußstraße 20, D-42119 Wuppertal, Germany

Received 4 December 2006; received in revised form 31 May 2007; accepted 3 July 2007
Available online 20 July 2007

Abstract

We report on light emitting device related properties of the water soluble blue light emitting anionic poly{1,4-phenylene-[9,9-bis(4-phenoxy-butylsulfonate)]fluorene-2,7-diyl} copolymer (PBS-PFP) with alkyl sulfonic acid sodium side chains. Compared to organic solvents water has the advantage of being environmentally friendly, which simplifies the handling during device fabrication by novel preparation techniques such as ink-jet printing. Light emitting devices fabricated from this polymer in thin film configuration show stable blue emission with an emission maximum at approximately 420 nm. Investigations concerning the current–density/voltage and the luminance/voltage device characteristics as well as the current–density over operation time at constant biases allow the identification of intrinsic electrochemical doping effects caused by ionic groups attached on the side chains of the polymer. Due to this fact, firstly the electroluminescence onset voltage for devices using high work-function electrodes for electron injection such as aluminum, which has the advantage of being air stable, can be distinctly reduced, and secondly devices fabricated from this polymer showed luminance in forward bias direction as well as in reverse bias direction.
© 2007 Elsevier B.V. All rights reserved.

PACS: 78.20.Bh; 85.60.Jb; 78.60.Fi; 78.66.Bz

Keywords: Light emitting electrochemical cell; Conjugated polymer; Water soluble polymer; Blue emitter; Polyelectrolyte

1. Introduction

During the last years organic semiconductors – especially in the field of organic light emitting devices – have found their way into commercial applications. Organic light emitting devices developed for flat panel displays or solid state lighting

* Corresponding author. Address: Christian Doppler Laboratory Advanced Functional Materials, Institute of Solid State Physics, Graz University of Technology, A-8010 Graz, Austria. Tel.: +43 316 873 8468; fax: +43 316 873 8478.
E-mail address: e.list@tugraz.at (E.J.W. List).

1566-1199/$ - see front matter © 2007 Elsevier B.V. All rights reserved.
doi:10.1016/j.orgel.2007.07.001

can already be found in consumer electronic products such as car stereo systems or portable music players. Within the scope of industrial applications, environmental friendly solvents, like water, are a matter of particular relevance. Beside polymer light emitting diodes (PLED) [1], light emitting electrochemical cells (LEC) [2–4] are of conceptual interest. By adding a solid state electrolyte to the conjugated polymer the device behavior alters significantly, since electrochemical doping of the polymer near the electrodes takes place; electrochemical p-doping close to the anode and electrochemical n-doping close to the cathode. However, the addition of salt based additives can lead to an unwanted phase separation in the active layer between the in general hydrophobic conjugated polymer and the hydrophilic solid state electrolyte [5–7]. This can be overcome by using conjugated polymers consisting of side chains, which are functionalized with ionic species [8]. The usage of polymers containing ionic components, which lead to electrochemical doping at the polymer–metal interface, is of special importance when utilizing high work-function air stable metals as cathode. Edman et al. investigated a cationic polymer (anions are able to move) finding a very low ion mobility for this class of polymers [9]. In order to obtain a balanced electron injection it will be preferable to use an anionic polymer (cations are able to move), supporting the electron injection, since the energetic injection barrier for electrons is usually larger than for holes.

In this paper we report on the photoluminescence (PL) and electroluminescence (EL) properties of the anionic water soluble blue light emitting poly{1,4-phenylene-[9,9-bis(4-phenoxy-butylsulfonate)]fluorene-2,7-diyl} copolymer (PBS-PFP) with alkyl sulfonic acid sodium salt side chains enabling water solubility (see Fig. 1 for the chemical structure). In particular the influence of the ionic entities on the device performance is analyzed and discussed in detail.

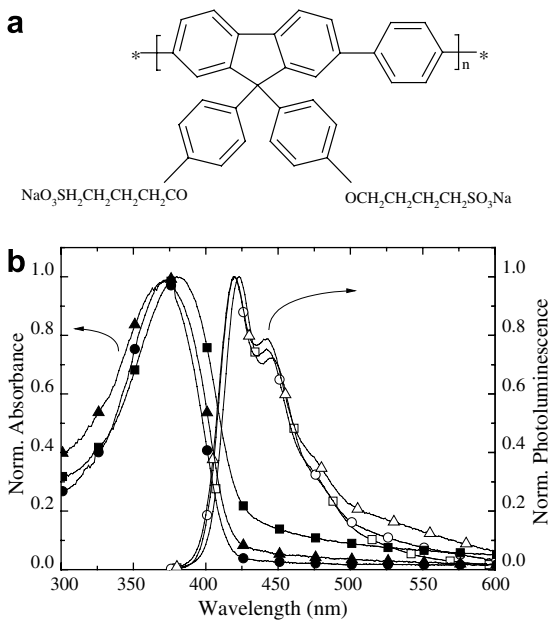


Fig. 1. (a) Chemical structure of the polymer (PBS-PFP). (b) Normalized photoluminescence (right) and absorption spectra (left) of PBS-PFP in solution and film of the pure polymer and the polymer surfactant blend (volume ratio 100:1). Absorption: solution (filled squares), film (filled circles), blended film (filled triangles). Emission: solution (open squares), film (open circles), blend (open triangles).

2. Experimental procedure

The polymer PBS-PFP ($M_n = 6500$ g mol^{-1}) was synthesised by condensation of 2,7-dibromo-9,9-bis(4-sulfonylbutoxyphenyl)fluorene and 1,4-phenylenediboronic acid using $Pd(PPh_3)_4$ as catalyst. Further details concerning the synthesis were published elsewhere [10]. For the basic characterization of the absorption and the PL behavior of the polymer PBS-PFP a two beam PERKIN ELMER LAMBDA 9 spectrophotometer and a SHIMADZU RF-5301PL SPECTROFLUORIMETER were used. The PLEDs consisted of a structured indium tin oxide (ITO) layer (from Balzers, 60 Ω/m^2), which was cleaned in an ultrasonic bath in toluene and isopropanol followed by a completing oxygen plasma cleaning step. The polymer layer was spin cast from an aqueous solution with a concentration of 8 g/l at 900 rpm. This layer was subsequently dried for 6 hours under dynamic vacuum at 80 °C. The evaporation of the aluminum top electrode took place at a base pressure of 1.1×10^{-6} mbar. To achieve better film formation the surfactant triethylene glycol monododecylether (TEGMDE) from Fluka was added in a volume ratio of 100 parts polymer solution to 1 part surfactant. Moreover this surfactant acts as an ionic conductor [11]. The current–density/voltage (jV) characteristics were measured with a computer controlled KEITHLEY 237 SOURCE MEASUREMENT UNIT. The luminescence/voltage (LV) measurements were performed by using an integrating Ulbrich sphere equipped with a silicon-diode. The scan rate at the jV and the LV measurements was 0.2 V/s.

3. Results and discussion

As mentioned above water was used as solvent during the investigation of PBS-PFP. However, the high surface tension of water led to inadequate film forming properties. To improve the wetting behavior, the bi-functional surfactant TEG-MDE was added to the solution which reduces on the one hand the surface tension of the solution, leading to a more homogenous film formation during preperation, and on the other hand supports the ion mobility.

Fig. 1b shows the thin film PL and absorption spectra of the polymer with and without the surfactant TEG-MDE and additionally in diluted solution. The PL spectra of the solution and the film show vibronic features with a maximum at 420 nm for the solution and 423 nm for the pristine and surfactant-blended film. The absorption spectra show no vibronic structure [12], which is typical for this type of polymers, and a maximum at 380 nm in the case of the solution and a maximum at 375 nm for the film in the pristine and surfactant-blended state. From these results it is obvious that the added surfactant does not lead to an alteration of the spectral characteristics of both the PL and the absorption.

Generally, the current passing through a conventional LEC (additionally added salts leading to mobile cations and anions) consists of an ionic and an electronic component. When the device is biased with a sufficiently high voltage the ions will move under the influence of the electric field to their corresponding electrodes. This leads in the course of time to a vanishing ionic component of the current, due to blocking of the ions at the electrodes, and simultaneously ongoing electrochemical doping of the polymer near the polymer/electrode interfaces, lowering the charge carrier injection barrier and supporting the charge transport. As frequently reported, most LECs showed symmetric LV characteristics, which mean that the luminescence onset voltage is independent of the bias direction.

Fig. 2 shows nine LV and jV characteristics of a freshly prepared ITO/PBS-PFP:TEG-MDE/Al device in forward bias direction (FBD; ITO biased as anode). Because of the low ionic conductivity of the active layer a constant voltage of 4 V for 50 s was applied between each cycle in order to support ion transport to the corresponding electrodes. As one can see in the top part of Fig. 2 no electroluminescence was detected during the first sweep. In

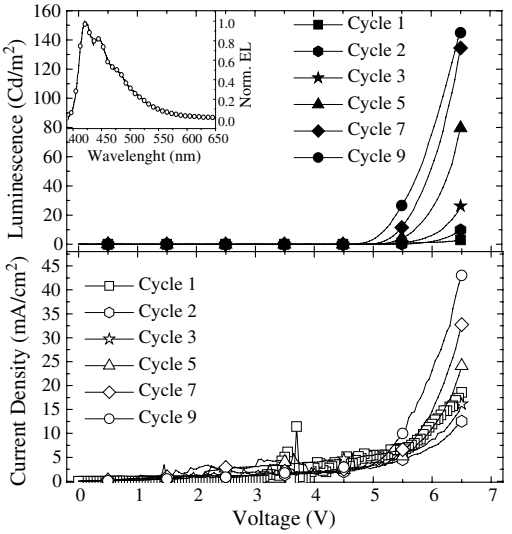


Fig. 2. EL (top) and jV characteristic of a freshly prepared ITO/PBS-PFP:TEG-MDE/Al device biased in forward direction for nine recorded cycles (cycle 1: filled squares, 2: filled hexagons, 3: filled stars, 5: filled triangles, 7: filled diamonds, 9: filled circles). Cycles 4, 6, 8 are not shown. Inset: Electroluminescence emission spectrum of such a device at a bias of 5 V.

the second scan an electroluminescence signal was already measured (9.8 Cd/m^2 at 6.5 V), however, with a lower current–density (see bottom part of Fig. 2) compared to the first scan. The feature of decreased current–density of the second, third, and fourth sweep compared to the first one is a result of the vanishing ionic component, which is a consequence of the movement of the sodium cations to the aluminum cathode, where they are finally blocked. The observation of delayed electroluminescence, however, hints to an ongoing electrochemical n-doping of the polymer near the cathode and electrochemical p-doping near the anode. From cycle five to nine the current–density exceeds the values of cycle 1, which is caused by a better electron injection due to the electrochemical doping. Further jV scans lead on the one hand to larger device currents, and on the other hand to lower EL onsets resulting in luminescence voltages of 4.8 V after 9 cycles. The obtained data, shown in the top part of Fig. 2, point out that the luminescence in forward direction increases with every new cycle reaching 144.8 Cd/m^2 at 6.5 V at the ninth cycle due to electrochemical doping.

Fig. 3 shows nine LV and jV characteristics of a freshly prepared ITO/PBS-PFP:TEG-MDE/Al device in reverse bias direction (RBD; ITO biased

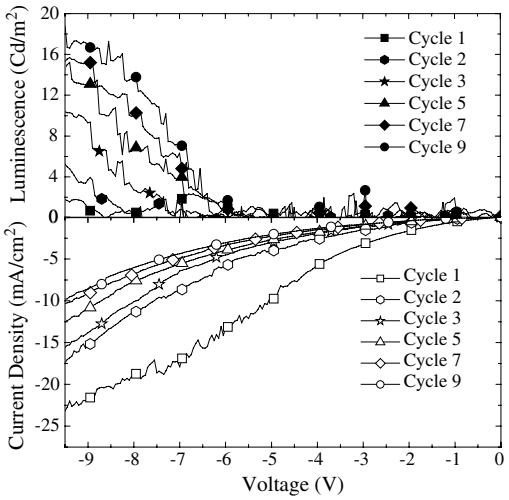


Fig. 3. EL- (top) and jV characteristic of a freshly prepared ITO/PBS-PFP:TEG-MDE/Al device biased in reverse direction for nine recorded cycles (cycle 1: squares, 2: hexagons 3: stars, 5: triangles, 7: diamonds, 9: circles). Cycles 4, 6, 8 are not shown.

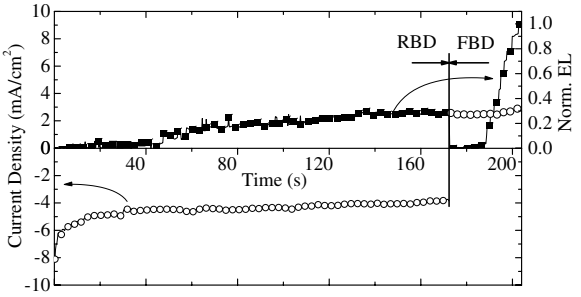


Fig. 4. Normalized EL intensity (right; filled squares) and current–density (left; open circles) over time in reverse and forward bias direction of an ITO/PBS-PFP:TEG-MDE/Al device biased with a constant voltage of 10 V. The measurement was performed on a fresh device staring in RBD followed by FBD on the same device.

as cathode). Like in the case of the FBD, a constant voltage of 4 V for 50 s was applied between each cycle to enhance the ion transport. The EL intensity at a maximum voltage of 9.5 V increases with each cycle and reaching 18.6 Cd/m^2 after the ninth sweep. Furthermore, the luminescence onset voltage after cycle nine in RBD decreases to 6 V, which is still 2.8 V larger compared to the FBD. As depicted in Fig. 3, the current–density as well as the luminance in RBD is distinctly smaller than in FBD due to the larger electron and hole injection barriers (in RBD charge carriers have to overcome the injection barriers between the Fermi level of corresponding electrodes (ITO acting as cathode, Al as anode) and the belonging molecular orbitals (LUMO, HOMO) of the polymer). Since the cations move under the influence of the electric field to the cathode, they leave immobile, uncompensated anionic sites on the polymer. These uncompensated negative ionic charges form during charge carrier injection an electrochemical p-doped region next to the anode, whereas the mobile cations generate an electrochemical n-doped region at the cathode [9,13]. With ongoing accumulation of cations and electrochemical n-doping of the polymer near the cathode interface the electron injection barrier gets conspicuously reduced. However the hole injection barrier at the aluminum anode does not get significantly reduced, since the concentration of immobile, covalently bonded anions in the injection supporting electrochemical p-doped region next to the anode is fixed. The consequences of the immobility of the anions and the bad level alignment in RBD between the Fermi levels of the electrodes and the HOMO/LUMO levels are the observed significantly higher luminescence onset voltages and the smaller electroluminescence intensity and current–density compared to the FBD.

Fig. 4 presents the EL intensity and the current–density characteristics at a constant operation voltage of 10 V in RBD (ITO biased as cathode) and FBD (ITO biased as anode) versus the operation time. When biasing a freshly prepared device first in RBD at 10 V it starts to emit light after approximately 40 s. After 170 s (RBD) switching the bias directly from RBD to FBD the current–density is immediately in the range of 2.5 mA/cm^2, nevertheless it takes 15 s to obtain EL. This correlates with the accumulation of sodium cations near the new anode (ITO), which counteracts the hole injection due to its large positive space charge. For this reason the observed current through the device at this stage of device operation can be solely attributed to electrons. Thus no exciton formation can take place. During further device operation the cations move to the aluminum cathode, hence the positive space charge at the ITO vanishes and holes can be now efficiently injected. Since the electron and hole injection barriers in FBD are distinctly smaller than in RBD, the time to detect luminescence is shorter [14,15] even if the device was biased shortly before in reverse direction. This feature distinctly indicates the presence of mobile sodium ions and an electrochemical doping of the active layer close to the

electrode/polymer interfaces, which is in contrast to common PLEDs, where the RBD is rectifying.

4. Conclusion

We report on the intrinsic photo-physical and electro-optical properties of the water soluble blue light emitting polymer PBS-PFP. The investigated polymer consists of mobile sodium cations whereas the anions are covalently bonded to the polymer. Devices fabricated from the polymer blended with the surfactant TEG-MDE showed a LEC like jV and LV characteristic. Due to the immobile covalently bonded anions and the mobile cations significant electrochemical doping appears only at the corresponding cathode, whereas at the anode the concentration of anions is constant. Since the energetic injection barrier for electrons and holes in FBD is lower than in RBD the onset voltages for the current as well as for the electroluminescence are distinctly smaller in FBD. Additionally, due to a better balanced charge carrier injection in FBD, higher EL yields can be detected compared to the RBD. After switching the bias polarity from RBD directly to FBD, at first no EL can be observed. This is a consequences of the large positive space charge at the new anode (ITO) build up by the cations, which counteracts the hole injection. EL can not be observed until this space charge has vanished by cation migration to the Al cathode.

Acknowledgements

The CDL-AFM gratefully acknowledges the continuous support of AT&S AG. Financial support of the Austrian Nano Initiative RPC ISOTEC - RP 0702 is gratefully acknowledged.

References

[1] (a) J.H. Burroughes, D.D.C. Bradley, A.R. Brown, R.N. Marks, K. Mackay, R.H. Friend, P.L. Burn, A.B. Holmes, Nature 347 (1990) 539;
(b) R.H. Friend, R.W. Gymer, A.B. Holmes, J.H. Burroughes, R.N. Marks, C. Taliani, D.D.C. Bradley, D.A. Dos Santos, J.L. Brédas, M. Lögdlund, W.R. Salaneck, Nature 397 (2000) 121.
[2] Q. Pei, G. Yu, C. Zhang, Y. Yang, A.J. Heeger, Science 269 (1995) 1086.
[3] Q. Pei, Y. Yang, G. Yu, C. Zhang, A.J. Heeger, J. Am. Chem. Soc. 118 (1996) 3922.
[4] L. Edman, Electrochim. Acta 50 (2005) 3878.
[5] F.P. Wenzl, C. Suess, A. Haase, P. Poelt, D. Somitsch, P. Knoll, U. Scherf, G. Leising, Thin Solid Films 433 (2003) 263.
[6] F.P. Wenzl, P. Pachler, C. Suess, A. Haase, E.J.W. List, P. Poelt, D. Somitsch, P. Knoll, U. Scherf, G. Leising, Adv. Funct. Mater. 14 (2004) 441.
[7] F. Habrard, T. Ouisse, O. Stephan, M. Armand, M. Stark, S. Huant, E. Dubard, J. Chevrier, J. Appl. Phys. 96 (2004) 12.
[8] Z. Gu, Q.D. Shen, J. Zhang, C.Z. Yang, Y.J. Bao, J. Appl. Poly. Science 100 (4) (2006) 2930.
[9] L. Edman, M. Pauchard, B. Liu, G. Bazan, D. Moses, A.J. Heeger, Appl. Phys. Lett. 82 (22) (2003).
[10] H.D. Burrows, V.M.M. Lobo, J. Pina, M.L. Ramos, J. Seixas de Melo, A.J.M. Valente, M.J. Tapia, S. Pradhan, U. Scherf, Macromolecules 37 (2004) 7425.
[11] H.D. Burrows, V.M.M. Lobo, J. Pina, M.L. Ramos, J. Seixs de Melo, A.J.M. Valente, M.J. Tapia, S. Pradhan, U. Scherf, S.I. Hintschich, C. Rothe, A.P. Monkman, Colloid: Surf A 270 (2005) 61.
[12] G. Heimel, M. Daghofer, J. Gierschner, E.J.W. List, A.C. Grimsdale, K. Müllen, D. Beljonne, J.L. Bredars, E. Zojer, J. Chem. Phys. 122 (2005) 54501.
[13] L. Edman, B. Liu, M. Vehse, J. Swensen, G.C. Bazan, A.J. Heeger, J. Appl. Phys. 98 (2005) 44502.
[14] Y. Shen, A.R. Hoosseini, M.H. Wong, G. Malliaras, ChemPhysChem 5 (2004) 16.
[15] J.C. deMello, N. Tessler, S.C. Graham, R.H. Friend, Phys. Rev. B 57 (20) (1998) 12951.

Available online at www.sciencedirect.com
ScienceDirect
Organic Electronics 8 (2007) 796–800
Organic Electronics
www.elsevier.com/locate/orgel

High current density and drift velocity in templated conducting polymers

Bjorn Winther-Jensen [a,*], Maria Forsyth [a], Keld West [c], Jens Wenzel Andreasen [c], Gordon Wallace [b], Douglas R. MacFarlane [a]

[a] Australian Centre for Electromaterials Science, Monash University, Clayton, Victoria 3800, Australia
[b] Australian Centre for Electromaterials Science, University of Wollongong, NSW 2522, Australia
[c] The Danish Polymer Centre, Risø National Laboratory, 4000 Roskilde, Denmark

Received 20 March 2007; received in revised form 18 June 2007; accepted 30 July 2007
Available online 19 August 2007

Abstract

Conducting polymers prepared by a templated vapour phase polymerisation process involving solid phase transition metal complexes are found to produce polymers with charge carriers that exhibit maximum drift velocity in the range of 1 m/s. This super-mobility seems to be related to a high degree of ordering in the materials as evidenced by the X-ray diffraction data. This may result from a templated polymerisation process. The high mobility manifests itself as a capacity to sustain very high current densities (>10000 A/cm^2); such high current densities are of importance in thin film conductor applications.
© 2007 Elsevier B.V. All rights reserved.

PACS: 82.35Cd; 72.80Le; 73.61Ph

Keywords: Polypyrrole; PEDOT; Drift velocity; Current density

1. Introduction

The electrical properties of intrinsically conducting polymers (ICPs) such as polypyrrole (PPy) have traditionally been characterised by methods including the temperature and frequency dependency of the conductivity. These results, complemented with optical and X-ray measurements, have helped to develop models for the conductivity in ICPs [1–5]. It is generally recognised that the conductivity of the ICP is very much dependent on the structure of the polymer [6], the distribution and density of highly ordered ''crystalline'' domains playing the most important role. These domains can exhibit almost metallic conductivity. The boundary between such metallic domains, however, represents a major barrier to conduction in the bulk material and hence ways of eliminating, or at least minimizing, such boundaries and creating larger crystalline domains is a significant goal in achieving metal-like conductivities in a polymer.

* Corresponding author. Tel.: +61 3 9905 5343; fax: +61 3 9905 4940.
E-mail address: bjorn.winther-jensen@eng.monash.edu.au (B. Winther-Jensen).

1566-1199/$ - see front matter © 2007 Elsevier B.V. All rights reserved.
doi:10.1016/j.orgel.2007.07.009

Recent developments in vapour phase polymerisation (VPP) [7–9] allow polymerisation of smooth ICP films on a range of iron(III) salts on non-conducting substrates. The VPP technique is unique in the sense that there is no solvent present during the polymerisation and therefore the monomer/Fe(III) salt interaction alone determines the structure of the growing oligomer. Care is taken to avoid the formation of visible salt crystallites on the surface, but even in the micro-crystalline or glassy state there exists a well defined local ordering of the Fe(III) cations acting as oxidants and the corresponding anions that will be incorporated into the ICP as charge compensating dopants. This offers a unique opportunity to template the structure of the polymer and thereby produces structures having a high degree of organization. This paper describes DC conductivity and maximum current density (MCD) measurements on two conducting polymers (poly-3,4-ethylenedioxythiothene (PEDT) and PPy) involving a range of counter-ions. Interpreted in terms of charge carrier drift velocity the VPP films are found to produce very high charge carrier mobilities.

Preparation of various Fe(III) salts was carried out according to previous reports [8,10,11]. The ligands were chosen to cover a range of different molecular sizes and chemical functionality, consistent with the need to drive the oxidation of pyrrole or 3,4-ethylenedioxythiothene (EDT). The ligands used in this study are 2-acrylamido-2-methyl-1-propanesulfonate (AAMPS), camphor-sulfonate (CSA), chloride (Cl) 4-ethylbenzenesulfonate (EBS), tetradecylsulfonate ($C_{14}SO_3$) and *para*-toluenesulfonate (PTS). For the VPP process, polyethylene terephthalate (PET) or glass substrates coated with an Fe(III) salt were exposed to a vapour of the monomer according to procedures earlier reported [7,8]. After the polymerisation the samples were washed twice in distilled water in order to remove iron(II) and excess counter-ion from the ICP films. The thickness of the ICP films (all sub-micron) was determined using a DEKTAK profilometer. For comparison purposes, a free-standing electro-polymerised PPy–PTS films were made at constant potential (0.7–0.8 V) in 0.1 M sodium PTS (50% water, 50% acetonitrile) on a polished stainless steel electrode and lifted off from the electrode in water.

The resistance of the ICP films was measured by a four-point probe method (Jandel MR3) and the current density measurements were made by placing an ICP coated PET sample over a four-line electrode configuration (Fig. 1), where the current was applied

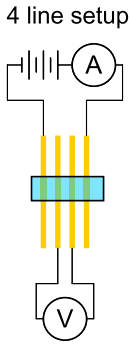


Fig. 1. Setup for measurement of maximum current densities.

to the outer electrodes and the voltage was measured between the inner electrodes. This was done in order to examine any deviation from Ohm's law during the experiment. The sample was pressed onto the electrodes by a system of springs and the measuring cell was air cooled, using a fan to remove the heat developed in the cell during the test. Generally conductivity measurements have been obtained using quite low currents [6,12–15] without "challenging" the maximum current density possible in the sample. In the present work the current was gradually raised until breakdown of the polymer. The last recorded current was used to calculate the maximum current density. The term "breakdown" is used for a rapid and irreversible change in the material properties, where the conducting polymer undergoes a chemical change resulting in dramatically increase in resistance. For PEDT the breakdown results in a visible colour change [9]. The voltage and current required to reach the breakdown is depending on the conductivity and thickness of the given samples. In this study voltage in the range from 3 to 25 V was used. A few reports [16,17] have earlier been published on maximum current density in polyaniline, where values from 100 up to 1200 A/cm^2 have been achieved depending on polymerisation procedure and counter-ion used.

2. Discussion

Fig. 2 shows a typical conductivity and maximum current density plot as a function of the different counter-ions for PPy (a) and PEDT (b). The trends in maximum current density appear to follow the trends in conductivity. In both cases, Fe(III)PTS produces the highest conductivity and maximum current density and there is clearly a significant effect of the chemical structure of the ligand on both properties. The ligand serves two distinct roles in

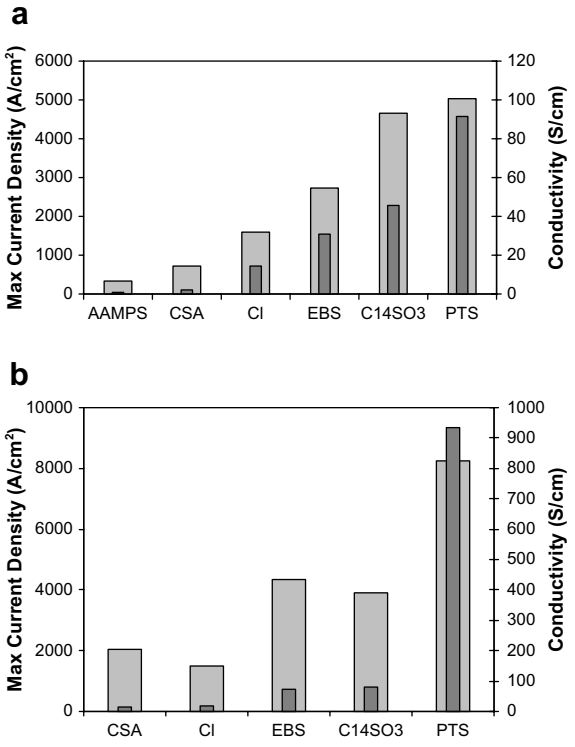


Fig. 2. Conductivity (narrow bars) and maximum current density (wide bars) of (a) polypyrrole and (b) PEDT polymerised by VPP using different Fe(III) salts.

these materials. As a key structural component of the Fe(III) salt it determines geometric aspects of the polymerisation reaction. A fraction of it remains after the polymerisation is complete as the counter-ion for the oxidized polymer. In both roles the ligand thus can directly influence the conduction mechanism as will be discussed further below.

In an in situ Raman measurement on PEDT–PTS, spectra were obtained each time the current was increased. There was no change in the spectra before breakdown of the ICP film at 7500 A/cm^2. The high current density is thus not introducing changes in the conjugated polymeric structure before a sudden and rapid breakdown of the material occurs.

The maximum current density is generally surprisingly high. This bulk material property also has interesting implications for events at the molecular level. Maximum charge carrier drift velocities (ie. the drift velocity at the maximum measured current density for each material) can be calculated from this bulk property via Eq. (1) and are shown in Fig. 3.

$$V_{\mathrm{d}}(\max) = J(\max)/ne \tag{1}$$

where J is the current density and n the charge-carrier density. The drift velocity represents the average rate of movement of a given charge carrier in response to the applied electric field. It reflects Ohm's

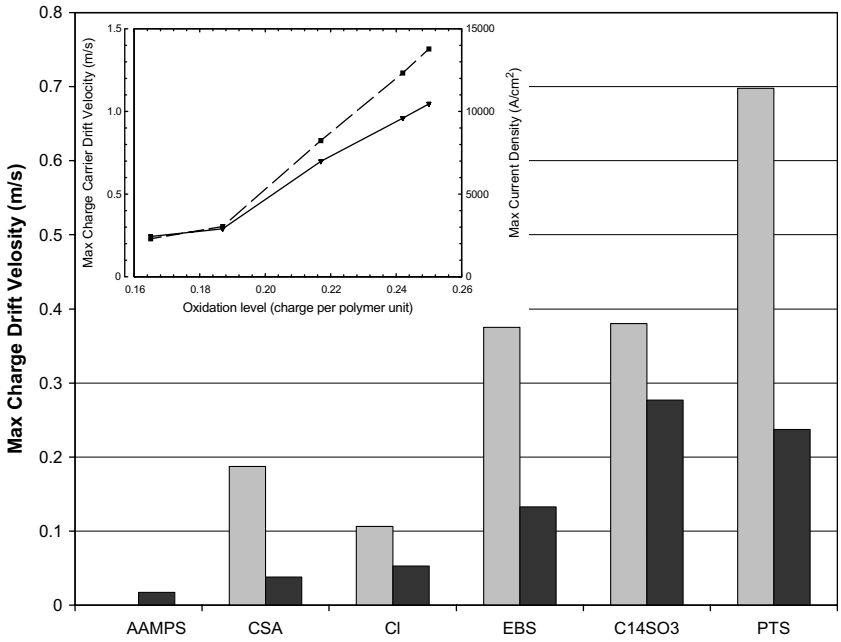


Fig. 3. Maximum charge carrier drift velocities in PPy (black bars) and PEDT (grey bars). Insert: maximum current density (dashed line) and drift velocity dependency of the oxidation level for PEDT–PTS.

law up to the maximum value corresponding to the point of breakdown of a material.

The charge-carrier density in each case is estimated from previous work [8,18,19] in which electrochemical quartz crystal micro-balance and XPS methods were used to determine the state of oxidation of the polymer per unit mass. This is generally found to be between 0.21 and 0.25 charges per monomer unit depending on the polymerisation procedure. For polymers made by VPP and washed in distilled water the number has been reported to 0.23 [8]. This translates into a number of charge carriers per unit volume of ca. $1.3 \times 10^{21}/\mathrm{cm}^{-3}$ for PPY and ca. $7 \times 10^{20}/\mathrm{cm}^{-3}$ for PEDT in both cases depending slightly on the molecular weight of the counter-ion. The values of maximum charge carrier drift velocity thus obtained are plotted in Fig. 3 as a function of the type of polymer and the Fe(III) ligand involved. Prigodin and Epstein [4] suggest that only a fraction of the available charge carriers (~0.1%) are actually involved in DC conduction in ICPs, in which case the drift velocity of these would be even greater. In other words the values plotted in Fig. 3 represent lower bounds on the actual maximum charge carrier mobility.

The values of maximum drift velocity obtained here (Fig. 3) exceed 1 m/s. The Fermi speed in ICPs is thought to be an order of magnitude lower then copper ($\sim 3 \times 10^5$ m/s [5]) hence this difference in maximum drift velocity must relate to structural effects. A perspective on these structural effects can be obtained by investigating the way that these phenomena depend on the charge carrier density, n. The inset to Fig. 3 shows a set of experiments in which the dependence of the maximum current density and maximum drift velocity on oxidation state of the PEDT–PTS polymer has been determined. The higher oxidation levels (higher charge-carrier density) produces a higher conductivity (not shown) and thereby a higher maximum current density. However, $V_d(\max)$ also increases, which is less intuitive since Eq. (1) contains the ratio of $J(\max)$ and n. In fact, the conductivity and maximum current density increase at a higher rate than the number of charge carriers, increasing by a factor of more than five with a change in n of only 50%. Thus the high drift velocity phenomenon is not a simple function of charge carrier number. From the values for conductivity, drift velocity and MCD the carrier mobility can be calculated. For the most conducting polymer (PEDT/PTS) in our study the carrier mobility is 11 $\mathrm{cm}^2/\mathrm{V\,s}$, which is in the high range of what has earlier been reported for conducting polymers [19].

In order to determine whether the nature of the polymer counter-ion is a determining factor in obtaining higher maximum drift velocities, a sample of vapour phase polymerised PEDT–PTS was subsequently ion exchanged with Cl and CSA ions and similarly the PEDT–Cl and PEDT–CSA samples were ion exchanged with PTS. This was achieved by electrochemical cycling in a solution of the corresponding acid. The resultant conductivities and maximum current densities of the ion exchanged materials were little changed from the parent polymer. This indicates that the structural role of the counter-ion is expressed at the moment of polymerisation, by influencing the geometry of the coordination of the monomer and oligomer units on the Fe(III) salt surface, ie by a templating process.

Further evidence for this process, as a reference material for this work, samples of PPy–PTS were made by electropolymerisation and the conductivity and maximum current density were measured. The measured values (0.6 S/cm and 40 $\mathrm{A/cm}^2$) are two orders of magnitude lower than the samples made by VPP. This shows that the presence of the solid Fe(III) salt has a dramatic impact on the properties of the ICP obtained, presumably again by a structural templating effect.

The high drift velocity in an ICP is to an extent predictable from the resonance quantum tunnelling model of Prigodin and Epstein [4] which envisages a tunnelling between metallic domains in the polymer material. The templated polymerisation method used here might be expected to produces a greater degree of order. To investigate the possibility that the super-mobility is related to ordering, X-ray diffraction data were measured for VPP–PEDT films from five different Fe(III) salts. The results are summarised in Table 1.

The π-stacking distance (d_{010}) is essentially constant for all samples and in agreement with earlier

Table 1
X-ray diffraction data for PEDT films polymerised using iron(III) salts with different ligands

Ligand in Fe(III) salt	d_{100}/Å	Normalised I_{100} [a.u/s]	Azimuthal fwhm/° 100	d_{010}/Å
PTS	13.94	0.7e-3	34.7	3.46
$C_{14}SO_3$	13.71	1.2e-3	61.0	3.51
EBS	13.32	0.5e-3	41.1	3.48
CSA	12.87	1.7e-3	42.9	3.46

reports for PEDT–PTS [20–22]. The interchain distance (d_{100}), however, is dependent on the Fe(III) salt used and follows the trend in conductivity and MCD. The increased spacing reflects a larger interchain distance, and it is not obvious why this should lead to materials with higher conductivity. The integrated intensity of the reflection corresponding to the interchain distance (I_{100}) is taken to be an expression of the degree of crystallinity of the materials and indicates that the conductivity and MCD are surprisingly *not* directly linked to this property. On the other hand, the azimuthal half-widths give a representation of the texture of the PEDT films, in other words the alignment along the chain direction; a smaller half-width meaning more alignment. Table 1 indicates that a higher degree of texture is present for PTS correlating with higher conductivity and MCD. The ordering involved could correspond to either larger crystalline domain sizes (producing therefore fewer boundaries per unit volume) and/or improved coherence of the domains at their boundaries (improving the conduction probability at the boundary).

3. Conclusions

Results reported here show that ICPs polymerised on a solid phase Fe(III) oxidant leads to super-mobile charge carriers. This polymerisation process produces a more ordered polymer capable of carrying very high current densities and maximum charge carrier drift velocities. However, these properties are surprisingly not linked to the degree of crystallinity in the materials. A more detailed discussion of the structure of the VPP PEDT films based on the X-ray diffraction pattern, DSC and computer simulations will be reported in a separate communication.

Acknowledgement

The Australian Research Council is acknowledged for the financial support.

References

[1] T. Ishiguro et al., Phys. Rev. Lett. 69 (1992) 660.
[2] R.S. Kohlman et al., Phys. Rev. Lett. 78 (1997) 3915.
[3] R. Menon, Handbook of Conducting Polymers, CRC Press, 1998, ISBN 0824700503, pp. 27–84.
[4] V.N. Prigodin, A.J. Epstein, Physica B 338 (2003) 310–317.
[5] K. Lee, M. Reghu, E.L. Yuh, N.S. Sariciftci, A.J. Heeger, Synthetic Met. 68 (1995) 287.
[6] K. Lee, S. Cho, S.H. Park, A.J. Heeger, C.-W. Lee, S.-H. Lee, Nature 4 (2006) 441.
[7] B. Winther-Jensen, K. West, Macromolecules 37 (2004) 4538–4543.
[8] B. Winther-Jensen, J. Chen, K. West, G. Wallace, Macromolecules 37 (2004) 5930–5935.
[9] B. Winther-Jensen, K. West, React. Funct. Polym. 66 (2006) 479–483.
[10] J.A. Walker, E.F. Witucki, US Patent 4697001, 1987.
[11] D.M. de Leeuw et al., Synthetic Met. 66 (1994) 263–273.
[12] P.A. Lee, T.R. Ramakrishnan, Rev. Mod. Phys. 57 (1985) 287.
[13] H.H.S. Javadi et al., Phys. Rev. B. 43 (1991) 2183.
[14] J. Joo et al., Phys. Rev. B. 49 (1994) 2977.
[15] H.C.F. Martens, J.A. Reedijk, H.B. Brom, D.M. de Leuw, R. Menon, Phys. Rev. B 63 (2001) 073203.
[16] H.S. Xu et al., J. Polym. Sci. Part B 37 (1999) 2845–2850.
[17] J.C. Lacroix, K.K. Kanazawa, A. Diaz, J. Electrochem. Soc. 136 (1989) 1308–1313.
[18] L.A.A. Pettersson, F. Carlsson, O. Inganäs, H. Arwin, Thin Solid Films 313–314 (1998) 356–361.
[19] T.-I. Jeon, D. Grischkowsky, A.K. Mukherjee, R. Menon, Appl. Phys. Lett. 77 (2000) 2452–2454.
[20] K.E. Aasmundtveit et al., Synthetic Met. 101 (1999) 561–564.
[21] K.E. Aasmundtveit et al., Synthetic Met. 113 (2000) 93–97.
[22] T.Y. Kim, C.M. Park, J.E. Kim, K.S. Suh, Synthetic Met. 149 (2005) 169–174.

Available online at www.sciencedirect.com
ScienceDirect
Organic Electronics 8 (2007) 801–812
Organic Electronics
www.elsevier.com/locate/orgel

Electronically asymmetric poly(1,4-phenylenevinylene)s for photovoltaic cells

Bimlesh Lochab [a], Paul L. Burn [a,e,*], Aaron Barkhouse [b], Kiril R. Kirov [b], Hazel E. Assender [b], David J. Keeble [c], Elizabeth A. Thomsen [d], Andrew J. Lewis [d], Ifor D.W. Samuel [d,*]

[a] *Department of Chemistry, University of Oxford, Chemistry Research Laboratory, Mansfield Road, Oxford OX1 3TA, United Kingdom*
[b] *Department of Materials, University of Oxford, Parks Road, Oxford OX1 3PH, United Kingdom*
[c] *Division of Electronic Engineering and Physics, Faculty of Engineering and Physical Sciences, University of Dundee, Dundee DD1 4HN, United Kingdom*
[d] *Organic Semiconductor Centre, SUPA, School of Physics and Astronomy, University of St Andrews, St Andrews, North Haugh, Fife KY16 9SS, United Kingdom*
[e] *Centre for Organic Photonics and Electronics, University of Queensland, Chemistry Building, St Lucia, Queensland 4072, Australia*

Received 19 April 2007; received in revised form 25 June 2007; accepted 4 July 2007
Available online 21 July 2007

Abstract

We report a study on the feasibility of using an intramolecular dipole to enhance charge separation for organic photovoltaic applications. We have developed a poly(1,4-phenylenevinylene) derivative, poly{2-[(9,9-di-*n*-propyl-9*H*-7-nitrofluoren-2-yl)]-5-(2-ethylhexyloxy)-1,4-phenylenevinylene} **12**, which has electronically asymmetric chromophores as a result of the *para* attachment of alkoxy and nitrofluorenyl groups on the phenyl units of the polymer backbone. The luminescence of the polymer with the electronically asymmetric chromophores was found to be smaller by a factor of eight when compared to the equivalent polymer but without the nitro group attached to the fluorenyl unit. Light-induced electron spin resonance experiments showed that the polymer with the electronically asymmetric chromophores had more photo-induced spins, showing that the quenching of the luminescence was due to intramolecular charge separation. Single layer photovoltaic devices containing neat films of **12** showed efficiencies similar to other single layer devices and this was ascribed to poor transport of the separated charges. This was confirmed by a strong improvement in device power efficiency to 0.52% at AM1.5 by blending the polymer with an electron transporting material.
© 2007 Elsevier B.V. All rights reserved.

PACS: 36.20.Kd; 81.20Ka; 81.15.-z; 73.61.Ph; 78.66.Qn; 84.60Jt

Keywords: PPVs; Electronic asymmetry; Exciton dissociation; Solar cells

* Corresponding authors. Address: Centre for Organic Photonics and Electronics, University of Queensland, Chemistry Building, St Lucia, Queensland 4072, Australia. Tel.: +617 33653778; fax: +617 33654299 (P.L. Burn), tel.: +44 0 1334 463114; fax: +44 0 1334 463104 (I.D.W. Samuel).
E-mail addresses: p.burn2@uq.edu.au (P.L. Burn), idws@st-andrews.ac.uk (I.D.W. Samuel).

1566-1199/$ - see front matter © 2007 Elsevier B.V. All rights reserved.
doi:10.1016/j.orgel.2007.07.003

1. Introduction

There is a strong continuing interest in the development of polymer based photovoltaic (PV) devices. Bulk heterojunction polymer PV devices have proved to be the most efficient thus far with efficiencies in excess of 5% now having been reported [1]. The key steps that occur in polymer based PV devices are: light absorption to form an exciton, separation of the exciton into holes and electrons, and movement of the generated holes and electrons to the electrodes. There are clearly many factors that affect each of these steps including the optical density of the polymer and its morphology. To achieve separation of the exciton, the bulk heterojunction approach requires two materials of different electron and hole affinities to be mixed. This has been achieved using polymer blends [2–4] but the most common approach has been to blend the polymer with [6,6]-phenyl-C_{61}-butyric methyl ester (PCBM), a soluble C_{60} derivative [1,5]. Although blended devices can clearly give good efficiencies the problems with using blends include controlling the morphology and phase separation of the films in a reproducible way during processing and long-term device operation. The main strategy explored for controlling phase separation has been to covalently tether the high and low electron affinity materials together [6,7]. However, these tethered materials have tended to give to poorer device performance suggesting that there is an optimal level of phase separation of the donor and acceptor moieties. A second method to achieve charge separation is to have the high and low electron affinity components in conjugation with the polymer backbone. This concept has been explored in the context of copolymers where there are monomer units along the polymer backbone with different electron affinities [8–13]. However, the focus of these latter studies was primarily on the development of low ''band-gap'' polymers. The alternative approach to having the moieties with different electron affinities along the conjugated polymer backbone is to have them attached, in conjugation, as side-groups [14–17]. This latter concept has been less well studied in the context of polymer PV [15] but gives rise to the intriguing possibility that the exciton can be dissociated efficiently intramolecularly.

In this paper we describe the synthesis of a new poly(1,4-phenylenevinylene) (PPV) derivative, poly{2-[(9,9-di-*n*-propyl-9*H*-7-nitrofluoren-2-yl)]-5-(2-ethylhexyloxy)-1,4-phenylenevinylene} **12**, in which each phenyl ring of the polymer backbone is also part of an electronically asymmetric chromophore created by the *para* attachment of alkoxy and 7-nitrofluorenyl groups to the phenyl rings. We compare the photophysical, electronic, and device properties of the polymer with an equivalent polymer that does not contain the electron withdrawing nitro groups and demonstrate that exciton dissociation can occur efficiently in PPVs containing electron-donating and withdrawing groups.

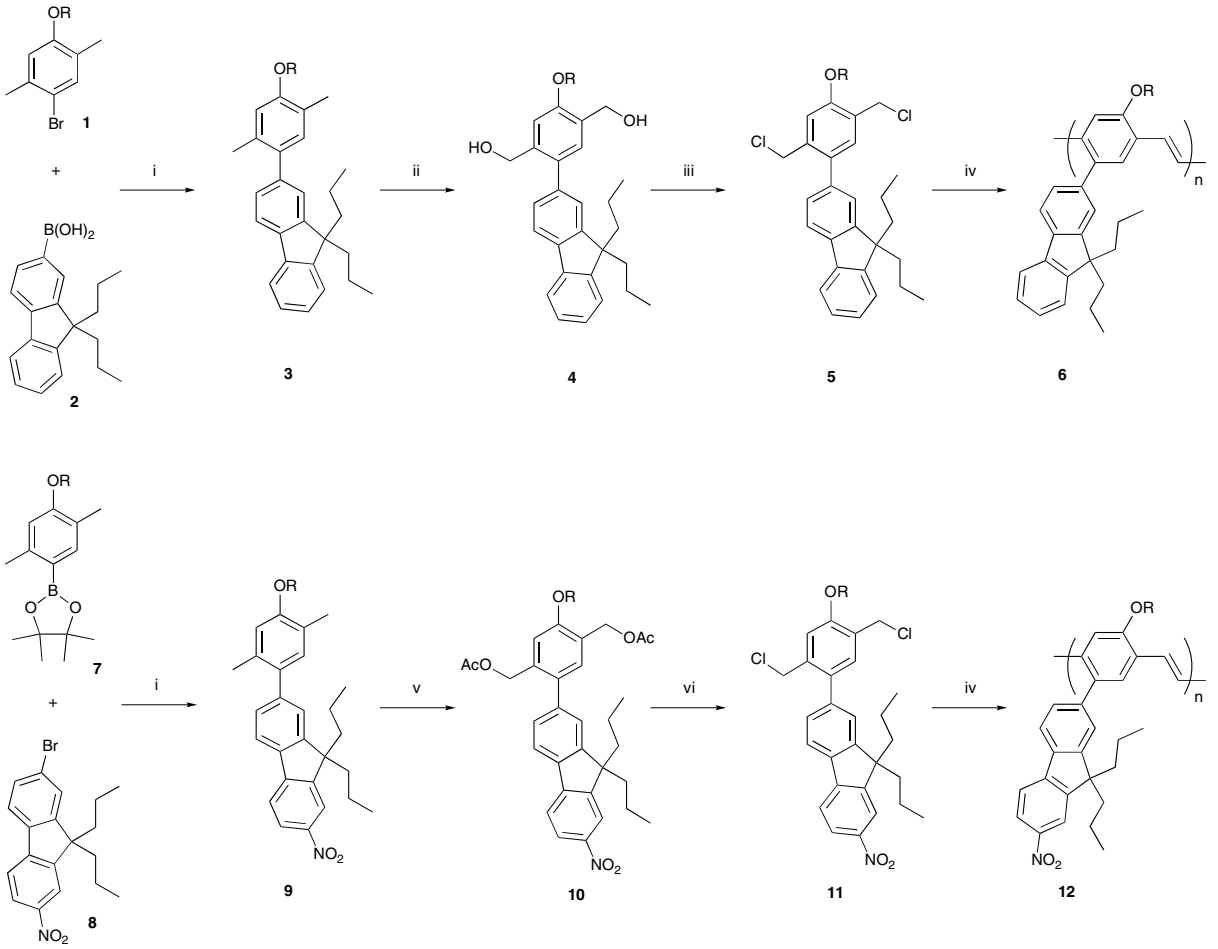
2. Results and discussion

2.1. Polymer syntheses and characterisation

The synthetic routes for the preparation of polymers **6** and **12**, without and with the electron withdrawing nitro groups are shown in Scheme 1. The two routes are similar, with the first step in each case the palladium catalysed coupling of a fluorenyl unit with the phenyl ring that becomes part of the polymer backbone. For the formation of the monomer to polymer **6** the initial reaction involved the coupling of phenylbromide **1** [17] with 2-fluorenylboronic acid **2** [18] to give **3**, and this was achieved in a 54% yield. The next step in the synthesis of **6** required the activation of the methyl groups. Radical bromination of **3** with *N*-bromosuccinimide and azo-bis(*iso*-butyronitrile) as the free radical initiator in carbon tetrachloride heated at reflux yielded an inseparable mixture of mono-, di-, tri-, and tetra-brominated compounds. Previous work using this activation procedure has shown that it is possible to gain pure bis-activated material from the mixture of brominated compounds by acetylation followed by separation of the acetylated products [16]. In the cases where the mixture of acetylated compounds could not be separated, conversion to the hydroxylated derivatives has been reported to enable isolation of the bis-activated material [17,19]. The mixture of brominated material containing **3** was reacted with sodium acetate in glacial acetic acid heated at reflux. However, the bis-acetylated material could not be separated from the other acetylated products and therefore the mixture was reduced with lithium aluminium hydride. The bis-hydroxylated **4** was isolated by column chromatography over silica in a yield of 32% for the three steps from **3**. Finally, monomer **5** was formed by treatment of bis-alcohol **4** with thionyl chloride in dichloromethane in a 96% yield.

The palladium catalysed reaction in the first step to forming the monomer for polymer **12** was carried out with the functionality on the substrates reversed compared to that used in the formation of **3** with bromo group being on the 7-nitrofluorenyl unit and not the phenyl moiety. The reason for this was that the boronic acid or boronate ester derivative could not be easily formed from **8**. The Suzuki coupling of **7** [20] and **8** [21] went smoothly and **9** was formed in a 74% yield. Activation of the methyl groups of **9** was again achieved by radical bromination yielding an inseparable mixture of mono-, di-, tri-, and tetra-brominated compounds. However, in this case after treatment with sodium acetate in glacial acetic acid heated at reflux the bis-acetate **10** could be isolated in a 42% yield for the two steps. The bis-chloro monomer **11** for polymer **12** was then obtained by reaction with concentrated hydrochloric acid in 1,4-dioxane heated at reflux in an 83% yield.

The polymerisation of both **5** and **11** was carried out in tetrahydrofuran with an excess of potassium *tert*-butoxide in tetrahydrofuran. By using an excess of potassium *tert*-butoxide the fully conjugated soluble polymers were formed directly. The reactions were quenched and in each case the polymer isolated and purified by (re-)precipitation from tetrahydrofuran by addition to ice-cold methanol. Under these conditions soluble conjugated polymers **6** and **12** were obtained in 37% and 46% yields, respectively. The weight average molecular weights ($\overline{M}_w$) and polydispersity index (PDI) of the polymers were determined by gel permeation chromatography (GPC) against polystyrene standards.



Scheme 1. *Reagents and conditions*: (i) $Pd(PPh_3)_4$, toluene, $Na_2CO_{3(aq)}$, Δ; (ii) NBS, AIBN, CCl_4, Δ then NaOAc, AcOH, Δ then $LiAlH_4$, THF; (iii) $SOCl_2$, CH_2Cl_2; (iv) KOBu^t, THF; (v) NBS, AIBN, CCl_4, Δ then NaOAc, AcOH, Δ; (vi) $HCl_{(aq)}$, 1,4-dioxane, Δ.

Soluble conjugated polymer **6** had an $\overline{M}_w$ of $>4.3\times10^6$ and PDI of $\approx$2.3 while **12** had an $\overline{M}_w = 3.2\times10^5$ g/mol and a PDI of 7.0.

The thermal stability of the polymers was studied by thermogravimetric analysis (TGA) at a heating rate of 2 °C/min under a nitrogen atmosphere. Polymer **6** showed a weight loss of approximately 5% at 387 °C with **12** showing a similar loss at around 333 °C. The fact that the first significant weight loss occurred at temperatures above 300 °C provides good evidence that the polymers were fully conjugated, that is there are no halo leaving groups present. Thermal elimination of halo leaving groups generally occurs between 160 and 250 °C, depending on the polymer structure [16,17,19,22]. ^{1}H NMR analysis also supported there being no halo leaving groups present on the structure. The methine proton of the CHCl moiety is usually observed at around 5.8 ppm [16,17,19,22] and there were no resonances in this region. While PPV based polymers prepared via the Gilch route [23] are often drawn as in Scheme 1, that is, exclusively head to tail it is important to note that this is not always the case and head-to-head and tail-to-tail arrangements can also sometimes be seen [24]. In simple PPVs head-to-head and tail-to-tail arrangements give rise to ethylene and acetylene linkages respectively with the former being observable, when present at a sufficient level, in the ^{1}H NMR in the region of 2.5–3.0 ppm [25,26]. In the case of **6** and **12** there was not a significant signal in the ^{1}H NMR in the range of 2.5–3.0 ppm, corresponding to $ArCH_2CH_2Ar$ ethylene protons indicating that the polymers were comprised of monomer units predominantly in the head-to-tail arrangement.

2.2. Photophysical properties

We first analysed the UV–visible absorption spectra of polymers **6** and **12** (Fig. 1, the spectra were scaled to take into account of differences in film thickness). The UV–visible spectra show broad absorption across the wavelength range of 200–525 nm. PPV based polymers generally have two main absorption regions. The short wavelength region (at around 210 nm) corresponds to localised π–π* transitions, while the longer wavelength absorptions arise from delocalised π–π* transitions. In general for simple PPVs the better the delocalisation the greater the relative optical density of the delocalised to localised π–π* transitions [22,25]. For polymer **6** four maxima were observed in the

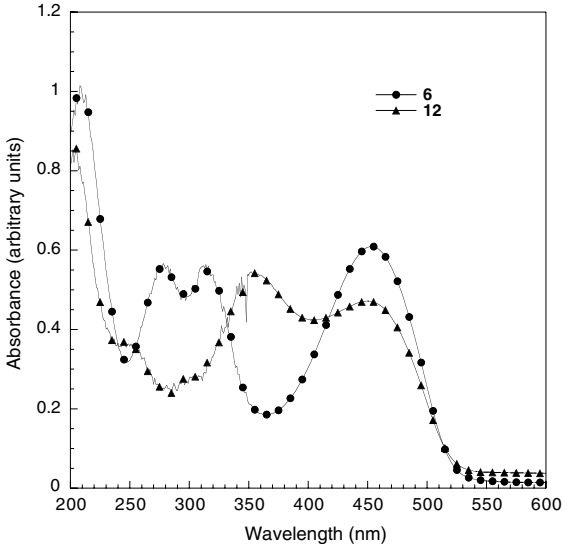


Fig. 1. Film UV–visible absorption spectra of **6** and **12**. The films were spin-coated from chlorobenzene solution. The spectra have been adjusted to take account of differences in film thickness.

UV–visible absorption spectrum. The absorption maximum at the shortest wavelength (211 nm) corresponds to the localised π–π* transitions while those at 283 nm and 312 nm correspond to the chromophore comprised of the phenyl ring of the polymer backbone and the fluorenyl unit. The latter are assigned by analogy to the absorption spectrum of **3**. The broad absorption above 400 nm is due to the delocalised π–π* transitions of the polymer backbone. An interesting feature of the absorption spectrum of **6** is that the ratio of the optical density of the delocalised to localised π–π* transitions is smaller than might be expected for simple PPVs. The smaller ratio of the delocalised to localised transitions could be due to the polymer backbone being twisted out of planarity, the polymer not being fully conjugated, or there being a significant number of *cis* vinyl linkages. Both TGA analysis and the ^{1}H NMR spectrum of **6** indicate that it is fully conjugated, that is, there is no weight loss at the temperatures normally associated with elimination of hydrogen chloride and there are no observable methine protons due to CHCl moieties. In addition, the infrared spectrum of **6** shows a relatively strong absorption at 951 cm^{-1}, which is not present in the monomer, and corresponds to the *trans*-vinyl C–H out-of-plane stretch. *cis*-Vinylene groups have been reported to have infrared absorptions in the region of 865 cm^{-1} [27]. The infrared spectrum of **6** does not show a readily identifiable

absorption in this region indicating that a significant proportion of the vinyl links have the *trans* geometry. Therefore, while the presence of a small number of *cis*-vinylene linkages cannot be discounted the lower level of delocalisation of the polymer backbone is most likely due to the twisting of the polymer backbone caused by the steric interaction of the fluorenyl group with vinyl protons in a similar manner to other sterically encumbered PPVs. The UV–visible absorption spectrum of **12** is similar to that of **6** showing absorption features of the localised π–π* transitions, the ''monomer'' chromophore (the shoulder at 266 nm and peak at 366 nm), and the delocalised π–π* transitions of the polymer backbone.

The next step in the photophysical studies was to determine the effect of the nitro groups on the fluorescence of the materials. We measured the solution and solid-state photoluminescence quantum yields (PLQYs) for **6** and **12**. The solution (chlorobenzene) and solid-state PLQYs for **6** were found to be $19 \pm 3\%$ and $9 \pm 2\%$ respectively while for **12** the corresponding PLQYs were $3 \pm 1\%$ and $1 \pm 0.5\%$. The decrease in PLQY for both polymers in moving from solution to the solid-state is often observed with luminescent materials and is due to increased intermolecular interactions that lead to luminescence quenching. The key point, however, is that the addition of the nitro group causes a substantial reduction in both the solution and solid-state PLQY of **12**. It is interesting to note that when the polymers were deposited onto indium tin oxide the luminescence of the polymer thin films was further quenched with PLQYs of 6% and 0.8% measured for **6** and **12**, respectively. We probed the PL properties of the materials further utilizing time-resolved PL (TRPL) spectroscopy with the solution measurements illustrated in Fig. 2. The excitation wavelength was 480 nm and the sample luminescence was measured at 520 nm, the photoluminescence peak (not shown) for these polymers. Following excitation, the PL from a solution of polymer **6** (without the nitro groups) was found to decay mono-exponentially, with a time constant of 770 ps. The mono-exponential decay indicates that there is only one emissive species. In contrast the TRPL of **12** shows a faster decay component with a lifetime of ~30 ps, with a longer-lived component with a lifetime of 770 ps. This fast decay component indicates that there is another process competing with radiative recombination of excitons within polymer **12**. The fast decay is consistent with the reduced PLQY, and strongly suggests that the nitro groups are quenching the luminescence.

The fact that the PL of **12** is quenched in solution is consistent with intramolecular exciton dissociation caused by the electronically asymmetric chromophore that is in cross-conjugation with the polymer backbone. However, it is conceivable that the nitro group could enhance non-radiative decay without enhancing charge separation. We therefore, performed light-induced electron spin resonance

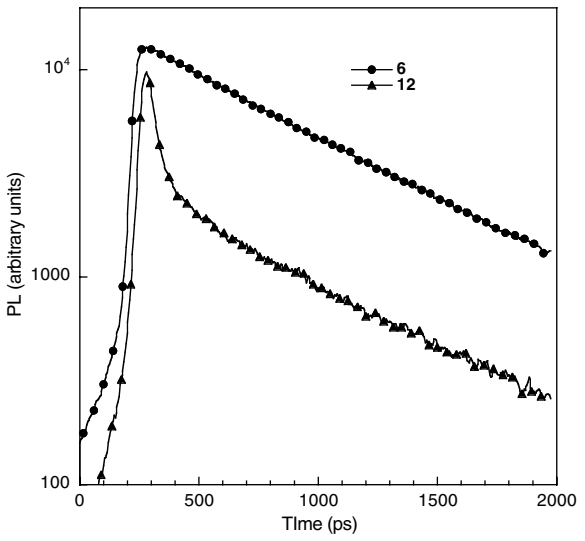


Fig. 2. Solution (chlorobenzene) time-resolved photoluminescence measurements of **6** and **7**.

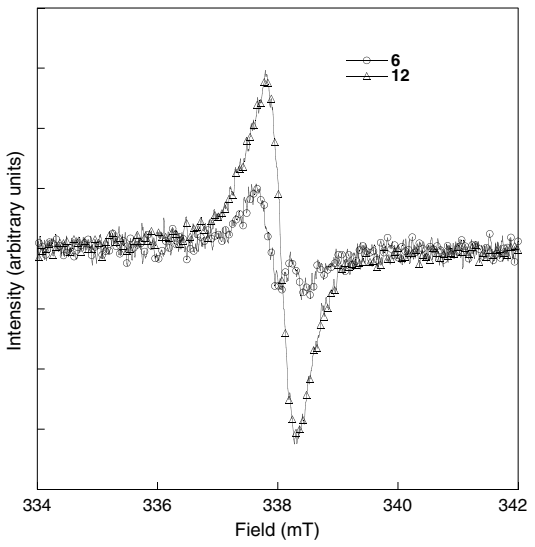


Fig. 3. Light-induced electron spin resonance measurements of **6** and **12**.

(LESR) measurements to address this point. ESR measurements detect unpaired spins and by taking the difference of the ESR signal when the sample is illuminated and when it is dark, light-induced spins can be detected. For example, when an exciton is separated into an electron and hole, an LESR signal will result. Therefore, LESR is a powerful technique for investigating photo-induced charge separation in conjugated polymers [28]. LESR experiments were performed on solutions of **6** and **12** in chlorobenzene at 20 K, using 407 nm excitation light from a gallium nitride laser. The measurement conditions and amount of light absorbed were the same for the two materials, and the results are shown in Fig. 3. We find that the signal (integrated area under the peak) from **12** (with the nitro groups) is a factor of 3 ± 1 larger than for 6 showing that the decrease in PLQY is due to enhanced intramolecular exciton dissociation following photoexcitation.

2.3. Device properties

The first stage in the device study was to determine the effect that the electronically asymmetric chromophore had on the PV response. Single layer devices (ITO/PEDOT:PSS/polymer/Al) containing neat films of the polymers were prepared and the performance results are summarized in Tables 1 and 2. Neat devices containing polymer **12** (with the nitro groups) were found to be slightly more efficient than those containing **6** due to the higher device current (Fig. 4a); for example, there is a six-fold increase in current. However, overall both devices showed performances similar to other neat single layer polymer devices ($\eta_{max} < 0.01\%$), mainly due to low currents ($J_{sc} < 0.01$ mA/cm^2). The increased short-circuit current for devices incorporating **12** could potentially arise from two main sources; first, the polymer film may absorb more of the incident light, or second, there could be a larger number of free charge carriers. To discount the former source as the major reason for the improved short-circuit current for the device containing **12** we determined the percentage of the incident light that was absorbed by each device (both types of device had 50 nm thick polymer layers) by comparing the overlap of the AM1.5 spectrum and the absorption spectra of the two polymers. Polymer **6** had a slightly larger total absorption over the AM1.5 spectrum (13% more than polymer **12** integrated over 420–500 nm, the range of wavelengths of the absorption with the 420 nm UV filter in place) and hence based on light absorption might be expected to have the larger short-circuit current. However, this is not the case and we attribute the higher short circuit current for devices containing polymer **12** primarily to enhanced charge separation. This is consistent with the LESR measurements, which indicate that the excitons are dissociated into charges more effectively in **12** than **6**.

Table 1
Performance of ITO/PEDOT:PSS/[**6**:PCBM]/Al devices

%PCBM	J_{sc} (mA/cm^2)	V_{oc} (V)	FF	Eff (%)
0	$(1.4 \pm 0.1) \times 10^{-3}$	1.21 ± 0.07	0.28 ± 0.01	$(6.3 \pm 0.6) \times 10^{-4}$
25	0.15 ± 0.02	1.07 ± 0.06	0.22 ± 0.01	0.043 ± 0.005
50	0.85 ± 0.05	0.9 ± 0.1	0.27 ± 0.01	0.26 ± 0.02
75	2.4 ± 0.1	0.92 ± 0.01	0.32 ± 0.01	0.95 ± 0.01

The errors indicated are one standard deviation across all the pixels (at least 3) measured. We estimate that there would be a minimum of 10% error in the quoted efficiency associated with uncertainty in the intensity of the light source.

Table 2
Performance of ITO/PEDOT:PSS/[**12**:PCBM]/Al devices

% PCBM	J_{sc} (mA/cm^2)	V_{oc} (V)	FF	Eff (%)
0	$(8.6 \pm 0.9) \times 10^{-3}$	1.20 ± 0.08	0.18 ± 0.02	$(2.1 \pm 0.6) \times 10^{-3}$
25	0.21 ± 0.04	1.10 ± 0.07	0.25 ± 0.02	0.07 ± 0.02
50	0.60 ± 0.08	0.98 ± 0.08	0.21 ± 0.04	0.22 ± 0.06
75	1.20 ± 0.09	1.01 ± 0.08	0.25 ± 0.02	0.52 ± 0.09

The errors indicated are one standard deviation across all the pixels (at least 3) measured. We estimate that there would be a minimum of 10% error in the quoted efficiency associated with uncertainty in the intensity of the light source.

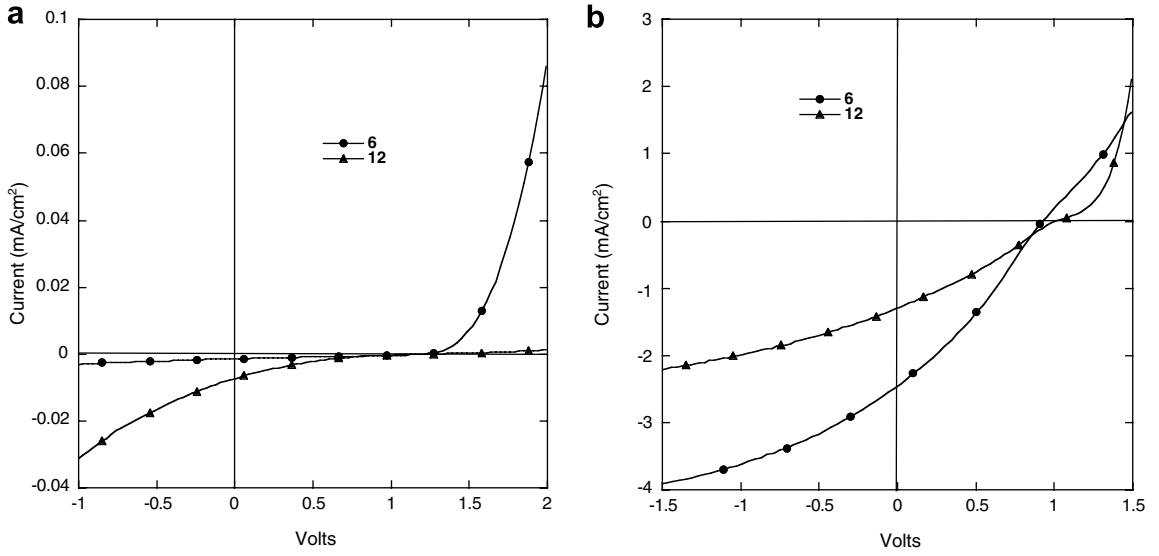


Fig. 4. *IV* characteristics of single layer devices comprised of **6** and **12** both as neat films (a) and a 25:75 blend with PCBM (b).

The question that therefore has to be considered is that given the excitons are dissociated relatively efficiently in **12** why is the device performance and short-circuit current not much higher? Although hole transport on the polymer backbone might be expected to be similar on the two polymers given the similarity of their structures the fact that the performance of devices based on **12** was not much higher than **6** is likely to arise from the fact that once the exciton is separated intramolecularly, the electron is not completely free to hop from one chain to the next. That is, the electron could be strongly bound to the nitro moiety. To test this we blended the polymers with varying amounts of the electron accepting and transporting PCBM. For the devices containing polymer **6** the PCBM plays the normal two roles, that is, separation of the exciton and transport of the electrons, while for devices containing **12** it might be expected to extract the separated electron and provide a path for it to be transported to the electrode. The addition of 25 wt% of PCBM improved the performance of devices based on both polymer types with **12** still giving slightly more efficient devices. When 50 wt% of PCBM was added the performance of devices containing each of the polymers was similar while when the PCBM became the major component (75 wt%) the situation was reversed with devices comprised of **6** being a little more efficient. The improvement in efficiency of the devices incorporating the polymer/PCBM blends is primarily due to an increase in short-circuit current. These results indicate that while intramolecular charge separation can lead to a level of improvement in device efficiency it is not sufficient if the charges are strongly bound to provide the charge transport that leads to high efficiencies. That is, introduction of a high concentration of an electron transporting material, which dominates the device characteristics, improves the efficiency. The fact that at high PCBM concentrations the efficiency of devices containing **6** are higher suggests that they have superior charge transport and extraction when compared with devices comprised of **12** (Fig. 4b). This could arise if, for example, the hole mobility of **12** was in fact lower than that of **6**, or from different film morphologies of the blends (although we note that there was no observable gross phase separation for either polymers when blended with PCBM).

3. Conclusion

A new poly(1,4-phenylenevinylene) derivative incorporating alkoxy and 7-nitrofluorenyl side chains on each phenyl moiety of the polymer backbone was synthesised. The luminescence of the polymer was found to be smaller with respect to the structurally similar polymer that did not have the electron withdrawing nitro group on the fluorenyl units. However, unlike the polymers in which the electron accepting and donating units are in the polymer backbone there was no large decrease in the HOMO–LUMO gap energy of the polymers in this study. Light-induced electron spin resonance

measurements showed that the reduction in fluorescence was due to photo-induced charge generation. However, device efficiencies were modest, indicating that further work on charge extraction is needed to capitalise on the enhanced exciton dissociation.

4. Experimental

4.1. Measurements

NMR spectra were recorded on a Bruker 400 M Hz spectrometer; J values are reported in Hz; FIH = fluorenyl proton. IR spectra were recorded on a Spectrum 1000 IR spectrometer and analysed as either a thin film or a KBr disc. UV–visible absorption spectra were recorded on a Perkin–Elmer UV Lambda 15 spectrometer as either a thin film or as a solution in spectroscopic grade dichloromethane. Spin-coated samples for UV-visible absorption measurements were prepared from chlorobenzene or tetrahydrofuran solutions. Mass spectra were recorded either on a Hewlett Packard 1050 Atmospheric Pressure Chemical Ionisation mass spectrometer (APCI) or VG Bio-Q platform spectrometer. Electronic ionisation was recorded on a VG Bio-Q spectrometer. Microanalysis was carried out at the Inorganic Chemistry Research Laboratory, University of Oxford or at the Metropolitan University, London. Melting points were determined on a Gallenkamp melting point apparatus and are uncorrected. Gel permeation chromatography was carried out with Polymer Laboratories PL gel 20 μm Mixed A columns (600 mm + 300 mm length and 7.5 mm diameter) calibrated with polystyrene narrow standards (M_p 580–6.5×10^6) in tetrahydrofuran with toluene as a flow marker. The UV–visible detector was set at 245 nm and the tetrahydrofuran was degassed with helium and pumped at a flow rate of 1 mL/min at 30 °C. Thermal gravimetric analysis was carried out on a Perkin–Elmer Thermogravimetric Analyser, TGA 7, under a nitrogen atmosphere. LESR measurements were performed with a Bruker EMX X band spectrometer operating at 20 K, and with illumination from a GaN laser at 407 nm. Photoluminescence quantum yield measurements were made by comparison with quinine sulphate in 0.5 M sulphuric acid as standard for the solution measurements, and using an integrating sphere for thin films [29]. Time-resolved photoluminescence measurements were made using a streak camera following excitation of the sample at 400 nm by a frequency doubled Ti:sapphire laser. Devices were fabricated in a low-moisture nitrogen glovebox (<15 ppm O_2, <200 ppm H_2O). Precleaned patterned ITO/glass (20 Ω/sq) was coated with 50 nm PEDOT:PSS and a solution of the polymer mixed with PCBM in chlorobenzene was spin-coated (2000 rpm) to form films, 50 ± 5 nm thick. The thickness of the polymer layers was measured on ITO/glass using atomic force microscopy in contact mode. The back contact of the cells was prepared by thermal evaporation through a shadow mask of a 40 nm thick Al layer to define PV pixels with an active area of 3.75 mm^2. Device measurements were carried out under AM1.5 conditions at 80% sun with a 420 nm filter, under a vacuum of 5×10^{-6} mbar, with I–V curves taken after 5 min illumination.

4.2. 1,4-Dimethyl-2-(9,9-di-n-propyl-9H-fluoren-2-yl)-5-(2-ethylhexyloxy)benzene 3

A mixture of 1-bromo-4-(2-ethylhexyloxy)-2,5-dimethylbenzene **1** [17] (2.6 g, 8.3 mmol), 9,9-di-*n*-propylfluorenyl-2-boronic acid **2** [18] (2 g, 6.8 mmol), aqueous sodium bicarbonate (2 M, 25 mL), and toluene (25 mL) was deoxygenated with nitrogen for 15 min. *Tetrakis*(triphenylphosphine)palladium(0) (0.21 g, 0.18 mmol) was then added and the reaction was heated at reflux under nitrogen for 15 h. After cooling the aqueous layer was removed and the organic layer was washed water (2×50 mL), hydrochloric acid (3 M, 2×30 mL), brine (50 mL), and dried over anhydrous magnesium sulphate. The solution was filtered and then the solvent was removed. The residue was purified by column chromatography over silica using a light petroleum:dichloromethane mixture (6:1) as eluent to give **3** (1.8 g, 54%) as a colourless oil, bp 220 °C, 0.1 mmHg; (Found: C, 87.1; H, 9.6. $C_{35}H_{46}O$ requires C, 87.1; H, 9.6%); λ_{max} (CH_2Cl_2)/nm 288 ($\log_{10}\varepsilon$/$dm^3\,mol^{-1}\,cm^{-1}$ (3.84)) and 312 (3.82); δ_H ($CDCl_3$, 400 MHz) 0.65–0.78 (10H, m, CH_2 and CH_3), 0.91–1.05 (6H, m, $2 \times CH_3$), 1.32–1.66 (8H, m, $4 \times CH_2$), 1.75–1.86 (1H, m, CH), 1.93–2.06 (4H, m, $2 \times CH_2$), 2.28 (3H, s, $ArCH_3$), 2.32 (3H, s, $ArCH_3$), 3.91 (2H, m, $ArOCH_2$), 6.79 (1H, s, PhH), 7.14 (1H, s, PhH), 7.26–7.40 (5H, m, FlH), and 7.74 (2H, m, FlH); δ_C ($CDCl_3$, 100.6 MHz) 11.3, 14.1, 14.5, 15.8, 17.3, 20.6, 23.1, 24.1, 29.1, 30.8, 39.6, 42.8, 55.2, 70.2, 112.7, 119.2, 119.6, 122.8, 124.1, 126.7, 128.0, 132.0, 133.6, 134.0, 139.3, 140.7, 141.0, 150.4, 150.9, and 156.5; m/z (EI^+) 482.4 (M^+,

50%); Exact mass (CI^+) 482.3563. $C_{35}H_{46}O_3$ requires 482.3549.

4.3. 1,4-Bis(hydroxymethyl)-2-(9,9-di-n-propyl-9H-fluoren-2-yl)-5-(2-ethylhexyloxy)benzene **4**

A mixture of **3** (5.7 g, 11.8 mmol), *N*-bromosuccinimide (3.1 g, 26 mmol), carbon tetrachloride (50 mL) was deoxygenated with nitrogen for 10 min. 2,2′-Azo-bis(*iso*-butyronitrile) (0.7 g, 4.1 mmol) was added and reaction mixture was heated at reflux for 2 h. On cooling, the reaction mixture was passed through a silica plug using dichloromethane as eluent. The filtrate was collected and the solvent removed. Sodium acetate (9.7 g, 0.12 mol) and glacial acetic acid (100 mL) were added to the residue and the reaction mixture was heated at reflux for 5 h. After cooling, water (100 mL) was added and the solution was extracted with ether (3×100 mL). The combined ether layers were then washed with aqueous sodium hydroxide (5% w/v, 100 mL), saturated aqueous sodium bicarbonate (2×25 mL), and water (100 mL). The organic layer was then dried over anhydrous magnesium sulphate, filtered, and the solvent removed. The residue was dissolved in anhydrous tetrahydrofuran (125 mL) and cooled to 0 °C under a nitrogen atmosphere before lithium aluminium hydride (0.9 g, 24 mmol) was added in portions. After 15 min the reaction mixture was allowed to warm to room temperature and then stirred for 2 h. Hydrochloric acid (3 M, 10 mL) was carefully added followed by water (100 mL). The mixture was extracted with ether (3×75 mL), and then the combined organic layers were washed with water (2×100 mL), brine (100 mL), dried over anhydrous magnesium sulphate and filtered. The solvent was removed and the residue purified by column chromatography over silica using gradient elution with a dichloromethane:methanol mixture (1:0 to 49:1) as eluent to give **4** (2 g, 32%) as a pale white solid, mp 97–98 °C (Found: C, 81.5; H, 9.2. $C_{35}H_{46}O_3$ requires C, 81.7; H, 9.0%); λ_{max} (CH_2Cl_2)/nm 285 ($\log_{10}\varepsilon$/dm^3 mol^{-1} cm^{-1} (4.91)) and 311 (4.88); ν_{max} (KBr disc)/cm^{-1} 3360 (OH); δ_H ($CDCl_3$, 400 MHz) 0.68–0.82 (10H, m, CH_2 and CH_3), 0.95–1.07 (6H, m, $2 \times CH_3$), 1.36–1.65 (8H, m, $4 \times CH_2$), 1.80–1.91 (1H, m, CH), 1.98–2.09 (4H, m, $2 \times CH_2$), 2.34 (2H, br s, OH), 4.08 (2H, m, ArO*CH*$_2$), 4.72 (2H, s, CH_2O), 4.81 (2H, s, CH_2O), 7.24 (1H, s, PhH), 7.30–7.45 (6H, m, PhH and FlH), and 7.76 (2H, m, FlH); δ_C ($CDCl_3$, 100.6 MHz) 11.3, 14.1, 14.6, 17.3, 23.1, 24.2, 29.1, 30.8, 39.5, 42.8, 55.3, 62.0, 63.1, 70.5, 110.6, 119.4, 119.7, 122.9, 123.9, 126.9, 127.1, 127.9, 128.3, 130.3, 133.7, 138.9, 139.0, 140.0, 140.8, 150.8, 150.9, and 156.6; *m*/*z* (EI^+) 514.4 (M^+, 100); Exact mass (CI^+) 514.3439. $C_{35}H_{46}O_3$ requires 514.3447.

4.4. 1,4-Bis(chloromethyl)-2-(9,9-di-n-propyl-9H-fluoren-2-yl)-5-(2-ethylhexyloxy)benzene **5**

Thionyl chloride (4.4 mL, 59 mmol) was added to a solution of **4** (1.7 g, 3.3 mmol) in anhydrous dichloromethane (50 mL) at 0 °C under nitrogen. After addition the reaction mixture was allowed to warm up to room temperature and stirred for a further 3 h. The dichloromethane and excess thionyl chloride was then removed under vacuum. Water (20 mL) was added and aqueous mixture was extracted with dichloromethane (2×30 mL). The combined organic layers were dried over anhydrous magnesium sulphate, filtered, and the solvent removed. The residue was purified by column chromatography over silica using a light petroleum:dichloromethane mixture (1:1) as eluent to give **5** (1.8 g, 96%) as a pale oil, which solidified on standing, mp 58–59 °C; (Found: C, 76.2; H, 8.1. $C_{35}H_{46}Cl_2O$ requires C, 76.2; H, 8.0%); λ_{max} (CH_2Cl_2)/nm 283 ($\log_{10}\varepsilon$/dm^3 mol^{-1} cm^{-1} (4.30)) and 311 (4.27); δ_H ($CDCl_3$, 400 MHz) 0.75–0.88 (10H, m, $2 \times CH_2$ and CH_3), 1.00–1.14 (6H, m, $2 \times CH_3$), 1.44–1.76 (8H, m, $4 \times CH_2$), 1.88–1.99 (1H, m, CH), 2.04–2.17 (4H, m, $2 \times ArCH_2$), 4.12 (2H, m, ArO*CH*$_2$), 4.63 (2H, s, CH_2Cl), 4.81 (2H, s, CH_2Cl), 7.20 (1H, s, PhH), 7.38–7.53 (5H, m, FlH), 7.60 (1H, s, PhH), and 7.87 (2H, m, FlH); δ_C ($CDCl_3$, 100.6 MHz) 11.4, 14.2, 14.6, 17.4, 22.8, 23.2, 29.2, 30.7, 39.6, 41.3, 42.9, 44.8, 55.4, 70.6, 113.2, 119.6, 119.9, 123.0, 124.0, 126.6, 126.9, 127.3, 128.0, 132.3, 134.9, 136.6, 138.3, 140.4, 140.8, 150.9, 151.0, and 156.6; *m*/*z* (EI^+) 550.3 (M^+, 100); Exact mass (CI^+) 550.2780. $C_{35}H_{44}Cl_2O$ requires 550.2769.

4.5. Poly{2-[(9,9-di-n-propyl-9H-fluoren-2yl)-5-(2-ethylhexyloxy)-1,4-phenylenevinylene]} **6**

To a stirred solution of **5** (0.56 g, 1 mmol) in anhydrous tetrahydrofuran (5.1 mL) at room temperature was added a solution of potassium *tert*-butoxide (0.57 g, 5.1 mmol) in dry tetrahydrofuran (25.5 mL) under nitrogen in the dark. The reaction mixture was stirred for 3 h before being filtered

through a cotton wool plug. The solution was then added to ice-cold methanol (100 mL) and the mixture was centrifuged (4500 rpm, 5 min). The supernatant was removed and the residue was re-dissolved in tetrahydrofuran (65 mL) and then re-precipitated by pouring the solution into ice-cold methanol (120 mL). The mixture was centrifuged (4500 rpm, 5 min), and the supernatant was removed. The residue was collected and dried under vacuum for 18 h to give **6** (180 mg, 37%) as a yellow solid. ν_{max} (film, KBr disc)/cm^{-1} 951 (C=C–H trans); λ_{max} (film)/nm 212, 281, 312, and 441; δ_H ($CDCl_3$, 400 MHz) 0.29–1.00 (br m, alkyl H), 1.07–1.95 (br m, alkyl H), 3.77 (br s, alkyl H), 4.0 (br s, alkyl H), and 6.70–7.80 (br m, vinyl H, PhH, and FlH); $\overline{M}_w > 4.3 \times 10^6$, $\overline{M}_n > 1.9 \times 10^6$ and PDI $\approx$ 2.3 (beyond the high caliberation limit); $TGA_{(5\%)}$ (2 °C/min) 387 °C.

4.6. 1,4-Dimethyl-2-(9,9-di-n-propyl-9H-7-nitrofluoren-2-yl)-5-(2-ethylhexyloxy)benzene **9**

A mixture of 2-[4-(2-ethylhexyloxy)-2,5-dimethylphenyl]-4,4,5,5-tetramethyl-[1,3,2]dioxaborolane **7** [20] (18.3 g, 50.7 mmol), 2-bromo-7-nitro-9,9-di-*n*-propyl-9*H*-fluorene **8** [21] (15.8 g, 42.3 mmol), aqueous sodium carbonate (2 M, 100 mL), and toluene (100 mL) was deoxygenated with nitrogen for 10 min. *Tetrakis*(triphenylphosphine)palladium(0) (1.9 g, 1.7 mmol) was added while maintaining a flow of nitrogen over the reaction mixture. The reaction mixture was heated at reflux in the dark for 48 h. After cooling the organic layer was separated and hydrochloric acid (3 M, 100 mL) was added carefully. The organic layer was washed with water (3×100 mL), brine (100 mL), dried over anhydrous magnesium sulphate, filtered, and solvent removed. The residue was purified by column chromatography over silica using a light petroleum:dichloromethane mixture (3:1) as eluent followed by recrystallisation from a dichloromethane:methanol mixture to give **9** (16.2 g, 74%) as light yellow crystals, mp 115–117 °C; (Found: C, 79.7; H, 8.6; N, 2.7. $C_{35}H_{45}NO_3$ requires C, 79.7; H, 8.6; N, 2.65%); ν_{max} (KBr disc)/cm^{-1} 1330 (NO_2) and 1513 (NO_2); λ_{max} (CH_2Cl_2)/nm 266 ($\log_{10}\varepsilon$/$dm^3\,mol^{-1}\,cm^{-1}$ (4.34)) and 366 (4.48); δ_H ($CDCl_3$, 400.2 MHz) 0.64–0.78 (10H, m, CH_2 and CH_3), 0.92–1.05 (6H, m, $2 \times CH_3$), 1.33–1.67 (8H, m, $4 \times CH_2$), 1.75–1.86 (1H, m, CH), 1.98–2.13 (4H, m, $2 \times ArCH_2$), 2.29 (3H, s, Ar*CH*$_3$), 2.31 (3H, s, Ar*CH*$_3$), 3.94 (2H, m, ArO*CH*$_2$), 6.80 (1H, s, PhH), 7.12 (1H, s, PhH), 7.37 (2H, m, FlH), 7.82 (2H, d, *J* 8, FlH), 8.23 (2H, dd, *J* 2, *J* 8, FlH), and 8.27 (1H, d, *J* 2, FlH); δ_C ($CDCl_3$, 100.6 MHz) 11.3, 14.1, 14.4, 15.8, 17.3, 20.6, 23.1, 24.1, 29.1, 30.7, 39.6, 42.4, 55.8, 70.2, 112.8, 118.3, 119.6, 120.8, 123.4, 124.31, 124.41, 128.8, 131.9, 133.2, 133.5, 136.9, 143.2, 146.9, 147.6, 152.07, 152.12, and 156.9; *m*/*z* (CI^+) 545.4 ($[MNH_4]^+$, 100%) and 527.4 (M^+, 58%); Exact mass (CI^+) 527.3396. $C_{35}H_{45}NO_3$ requires 527.3399.

4.7. 1,4-Bis(acetoxymethyl)-2-(9,9-di-n-propyl-9H-7-nitrofluoren-2-yl)-5-(2-ethylhexyloxy)benzene **10**

A mixture of **9** (16.1 g, 30.5 mmol), *N*-bromosuccinimide (11.2 g, 62.9 mmol), and carbon tetrachloride (70 mL) was deoxygenated with argon for 10 min. 2,2′-Azo-bis(*iso*-butyronitrile) (2.1 g, 12.6 mmol) was added and reaction mixture was heated at reflux for 4 h under argon. The reaction mixture was allowed to cool to room temperature, diluted with dichloromethane (30 mL), and then passed through a silica plug using dichloromethane as eluent. The filtrate was collected and the solvent removed. The residue was dissolved in glacial acetic acid (70 mL) and sodium acetate (27.8 g, 0.32 mol) was added. The reaction mixture was heated at reflux for 5 h and after cooling water (50 mL) was added. The aqueous layer was extracted with ether (3×75 mL) and the combined organic extracts were washed with aqueous sodium hydroxide (5% w/v, 50 mL), water (3×150 mL), and saturated aqueous sodium bicarbonate solution (3×50 mL). The solution was dried over anhydrous magnesium sulphate, filtered, and solvent removed. The residue was purified by column chromatography over silica using a gradient elution with light petroleum:dichloromethane mixtures (1:1 to 0:1) as eluent followed by recrystallisation from a dichloromethane:methanol mixture to give **10** (8.6 g, 42%) as a yellow solid, mp 103.5–104.5 °C; (Found: C, 72.85; H, 7.7; N, 2.2. $C_{39}H_{49}NO_7$ requires C, 72.8; H, 7.7; N, 2.2%); ν_{max} (KBr disc)/cm^{-1} 1331 (NO_2), 1518 (NO_2), and 1730 (C=O); λ_{max} (CH_2Cl_2)/nm 261 ($\log_{10}\varepsilon$/$dm^3\,mol^{-1}\,cm^{-1}$ (4.04)) and 357 (4.20); δ_H ($CDCl_3$, 400.2 MHz) 0.65–0.75 (10H, m, CH_2 and CH_3), 0.90–1.01 (6H, m, $2 \times CH_3$), 1.30–1.58 (8H, m, $4 \times CH_2$), 1.73–1.84 (1H, m, CH), 1.95–2.09 (4H, m, $2 \times ArCH_2$), 2.11 (3H, s, $COCH_3$), 2.12 (3H, s, $COCH_3$), 3.98 (2H, m, ArO*CH*$_2$), 5.04 (2H, s, CH_2O), 5.22 (2H, s, CH_2O), 7.07

(1H, s, PhH), 7.34–7.43 (3H, m, PhH and FlH), 7.83 (2H, m, FlH), 8.23 (1H, d, *J* 2, FlH), and 8.29 (2H, dd, *J* 2, *J* 8, FlH); δ_C ($CDCl_3$, 100.6 MHz) 11.2, 14.1, 14.3, 17.2, 21.0, 21.1, 23.1, 24.0, 29.1, 30.6, 39.4, 42.4, 55.8, 61.7, 64.6, 70.4,112.8, 118.3, 119.8, 121.0, 123.4, 124.3, 124.8, 128.7, 131.4, 134.26, 134.31, 137.7, 141.0, 147.1, 147.2, 152.1, 152.3, 156.8, 170.5, and 170.9; *m/z* (CI^+) 661.5 ($[MNH_4]^+$, 41%), 643.4 (M^+, 55%), and 584.3 ($[M–OCOCH_3]^+$, 100%); Exact mass (CI^+) 643.3516. $C_{39}H_{49}NO_7$ requires 643.3509.

4.8. 1,4-Bis(chloromethyl)-2-(9,9-di-n-propyl-9H-7-nitrofluoren-2-yl)-5-(2-ethylhexyloxy)benzene **11**

A mixture of **10** (7.4 g, 11.5 mmol), hydrochloric acid (35%, 160 mL), and 1,4-dioxane (160 mL) was heated at reflux under nitrogen for 18 h. After cooling the aqueous layer was separated and extracted with ether (3 × 50 mL). The combined organic layers were then washed with aqueous sodium hydroxide (5% w/v, 50 mL), water (3 × 100 mL), saturated aqueous sodium bicarbonate (2 × 50 mL), and brine (50 mL). The organic layer was dried over anhydrous magnesium sulphate, filtered, and the solvent removed. The residue was purified by column chromatography over silica using a light petroleum:dichloromethane mixture (1:1) as eluent and then recrystallised from a dichloromethane:methanol mixture to give **11** (5.6 g, 83%) as a yellow solid, mp 84–85 °C; ν_{max} (KBr disc)/cm^{-1} 1334 (NO_2) and 1520 (NO_2); λ_{max} (CH_2Cl_2)/nm 239sh ($\log_{10}\varepsilon$/$dm^3\,mol^{-1}\,cm^{-1}$ (4.47)), 258 sh (4.34), 316sh (4.20), and 356 (4.52); δ_H ($CDCl_3$, 400.2 MHz) 0.65–0.79 (10H, m, CH_2 and CH_3), 0.92–1.06 (6H, m, 2 × CH_3), 1.34–1.78 (8H, m, 4 × CH_2), 1.80–1.90 (1H, m, CH), 2.03–2.14 (4H, br m, 2 × $ArCH_2$), 4.05 (2H, m, $ArOCH_2$), 4.53 (2H, s, CH_2Cl), 4.72 (2H, s, CH_2Cl), 7.12 (1H, s, PhH), 7.40–7.49 (2H, m, FlH and/or PhH); 7.57 (1H, s, PhH or FlH), 7.87 (2H, m, FlH), and 8.30 (2H, m, FlH); δ_C ($CDCl_3$, 100.6 MHz) 11.3, 14.1, 14.3, 17.3, 23.1, 24.1, 29.1, 30.6, 39.5, 41.2, 42.4, 44.6, 56.0, 70.6, 113.2, 118.3, 119.9, 121.1, 123.4, 124.3, 126.7, 128.6, 132.1, 134.1, 136.5, 137.9, 140.6, 147.2, 152.2, 152.5, and 156.8; *m/z* (CI^+) 595.3 (M^+, 61%) and 560.3 ($[M–Cl]^+$, 100%); Exact mass (CI^+) 595.2602. $C_{35}H_{43}Cl_2NO_3$ requires 595.2620.

4.9. Poly{2-[(9,9-di-n-propyl-9H-7-nitrofluoren-2-yl)]-5-(2-ethylhexyloxy)-1,4-phenylenevinylene} **12**

A solution of potassium *tert*-butoxide (0.66 g, 5.86 mmol) in dry tetrahydrofuran (58.6 mL) was added to a stirred solution of **11** (0.7 g, 1.17 mmol) in dry tetrahydrofuran (23.4 mL) at room temperature under nitrogen. The reaction mixture was stirred in the dark for 3.5 h and then poured into ice-cold methanol (100 mL). The mixture was centrifuged (4500 rpm, 5 min) and then the supernatant was removed. The residue was dissolved in tetrahydrofuran (50 mL), filtered through a cotton wool plug, and then poured into ice-cold methanol (40 mL). The mixture was centrifuged (4500 rpm, 5 min) and then the supernatant was removed. The process of dissolution and precipitation was repeated a third time. The residue was collected and dried under vacuum for 16 h to give **12** (284 mg, 46%) as a yellow solid, ν_{max} (film, KBr disc)/cm^{-1} 969 (C=C–H trans), 1338 (NO_2) and 1523 (NO_2); λ_{max} (film)/nm 206, 260sh, 356, 454sh; δ ($CDCl_3$, 400 MHz) 0.28–2.08 (29H, br m, CH_2 and CH_3), 3.63–4.20 (2H, 2 × br s, $ArOCH_2$), and 6.68–8.40 (10H, br m, PhH, FlH and vinyl H). Note, the number of protons has been assigned in each region by analogy to the monomer but the integrations of the polymer spectrum are not exact. This may be due to different relaxation rates of the protons and/or some level of aggregation in the viscous solution used in the measurement.; $\overline{M}_w = 3.2 \times 10^5$, $\overline{M}_n = 0.5 \times 10^5$ and PDI = 7.0; $TGA_{(5\%)}$ (2 °C/min) 333 °C.

Acknowledgements

We are grateful to A. Ruseckas for assistance with time-resolved photoluminescence measurements. B.L. acknowledges a Felix Scholarship, E.A.T. holds an ORS award, and A.B. is a Rhodes Scholar. We thank the EPSRC (UK), Scottish Funding Council and The Toppan Printing Co., Japan for financial support.

References

[1] C.J. Brabec, Solar Energy Mater. Solar Cells 83 (2004) 273.
[2] J.J.M. Halls, C.A. Walsh, N.C. Greenham, E.A. Marseglia, R.H. Friend, S.C. Morrati, A.B. Holmes, Nature 376 (1995) 498.
[3] S.C. Veenstra, W.J.H. Verhees, J.M. Kroon, M.M. Koetse, J. Sweelsen, J.J.A.M. Bastiaansen, H.F.M. Schoo, X. Yang,

A. Alexeev, J. Loos, U.S. Schubert, M.M. Wienk, Chem. Mater. 16 (2004) 2503.
[4] T. Kietzke, H.-H. Hörhold, D. Neher, Chem. Mater. 17 (2005) 6532.
[5] F. Padinger, R.S. Rittberger, N.S. Sariciftci, Adv. Funct. Mater. 13 (2003) 85.
[6] A. Cravino, N.S. Sariciftci, J. Mater. Chem. 12 (2002) 1931.
[7] J.L. Segura, N. Martin, D.M. Guldi, Chem. Soc. Rev. 34 (2005) 31.
[8] X.S. Luzzati, M. Basso, M. Catellani, C.J. Brabec, D. Gebyehu, N.S. Saricifti, Thin Solid Films 403 (2002) 52.
[9] S.E. Shaheen, D. Vangeneugden, R. Kiebooms, D. Vanderzande, T. Fromherz, F. Padinger, C.J. Brabec, N.S. Saricifti, Synthetic Met. 121 (2001) 1583.
[10] M. Svensson, F. Zhang, S.C. Veenstra, W.J.H. Verhees, J.C. Hummelen, J.M. Kroon, O. Inganäs, M.R. Andersson, Adv. Mater. 15 (2003) 988.
[11] A. Dhanbalan, J.K.J.V. Durren, P.A.V. Hal, J.L.J.V. Dongen, R.A.J. Janssen, Adv. Funct. Mat. 11 (2001) 255.
[12] E. Perzon, X.J. Wang, S. Admassie, O. Inganäs, M.R. Andersson, Polymer 47 (2006) 4261.
[13] L.M. Andersson, F. Zhang, O. Inganäs, Appl. Phys. Lett. 89 (2006) 142111.
[14] S.-J. Chung, K.-Y. Kwon, S.-W. Lee, J.-I. Jin, C.H. Lee, C.E. Lee, Y. Park, Adv. Mater. 10 (1998) 1112.
[15] C.A. Cutler, A.K. Burrell, D.L. Officer, C.O. Too, G.G. Wallace, Synthetic Met. 128 (2002) 35.
[16] J. Gordon, T.J. Sheldon, D.D.C. Bradley, P.L. Burn, J. Mater. Chem. 6 (1996) 1253.
[17] F.H. Boardman, A.W. Grice, M.G. Rüther, T.J. Sheldon, D.D.C. Bradley, P.L. Burn, Macromolecules 32 (1999) 111.
[18] D. Katsis, Y.H. Geng, J.J. Ou, S.W. Culligan, S.H. Chen, L.J. Rothberg, Chem. Mater. 14 (2002) 1332.
[19] S.-C. Lo, A.K. Sheridan, I.D.W. Samuel, P.L. Burn, J. Mater. Chem. 9 (1999) 2165.
[20] S.W. Ko, B.-J. Jung, T. Ahn, H.-K. Shim, Macromolecules 35 (2002) 6217.
[21] S. Ginagunta, P. Zhang, E.P. Nikolaus, L. Juergen, J. Org. Chem. 69 (2004) 987.
[22] P.L. Burn, A.W. Grice, A. Tajbakhash, D.D.C. Bradley, A.C. Thomas, Adv. Mater. 9 (1997) 1171.
[23] H.G. Gilch, W.L. Wheelwright, J. Polym. Sci. Part A: Polym. Chem. 4 (1966) 1337.
[24] H. Becker, H. Spreitzer, W. Kreuder, E. Kluge, H. Schenk, I. Parker, Y. Cao, Adv. Mater. 12 (2000) 42.
[25] G.R. Webster, P.L. Burn, Synthetic Met. 145 (2004) 159.
[26] H. Becker, H. Spreitzer, K. Ibrom, W. Kreuder, Macromolecules 32 (1999) 4925.
[27] H. Huang, W. Huang, J. Guo, C.-Z. Yang, E.-T. Kang, Polymer 42 (2001) 3929.
[28] A.L. Konkin, S. Sensfuss, H.-K. Roth, G. Nazmutdinova, M. Schroedner, M. Al-Ibrahim, D.A.M. Egbe, Synthetic Met. 148 (2005) 199.
[29] N.C. Greenham, I.D.W. Samuel, G.R. Hayes, R.T. Phillips, Y.A.R.R. Kessener, S.C. Moratti, A.B. Holmes, Chem. Phys. Lett. 241 (1995) 89.

ORGANIC ELECTRONICS
materials • physics • chemistry • applications

Editors:

Prof. Chihaya Adachi — Center for Future Chemistry, Kyushu University, 744 Motooka, Nishi, Fukuoka 819-0395, Japan; Fax: +81-92-802-3294, e-mail: adachi@cstf.kyushu-u.ac.jp

Prof. Stephen R. Forrest — EECS, MSE, and Physics, University of Michigan, 4080 Fleming Building, 503 Thompson Street, Ann Arbor, MI 48109-1340, USA; Fax: +1-734-763-0085, e-mail: stevefor@umich.edu

Prof. René Janssen — Molecular Materials and Nanosystems, Eindhoven University of Technology, P.O. Box 513, 5600 MB Eindhoven, The Netherlands; Fax: +31 40 2451036, e-mail: r.a.j.janssen@tue.nl

Prof. Josef Salbeck — Macromolecular Chemistry and Molecular Materials Science Department, University of Kassel, Heinrich Plett Strasse 40, D-34123 Kassel, Germany; E-mail: salbeck@uni-kassel.de

Associate Editorial Board:

V.M. AGRANOVICH (Moscow)
Y. CAO (Guangzhou)
A. DODABALAPUR (Austin)
M. FUJIHIRA (Yokohama)
N. PEYGHAMBARIAN (Tucson)
Z. POPOVIC (Mississauga)
W. RIESS (Rüschlikon)
Y. SHIROTA (Osaka)
C. TALIANI (Bologna)
T. TSUTSUI (Fukuoka)
E. UMBACH (Würzburg)

Founding Editors:

Prof. Donal Bradley, Prof. Stephen Forrest, Prof. Norbert Karl and Prof. Kazuhiko Seki

Aims and scope

An interdisciplinary journal on the physics, chemistry, and engineering of materials with applications to organic electronics and optoelectronics, **Organic Electronics** is a primary journal for physicists, material scientists and chemists who are interested in organic electronic devices such as organic light emitting diodes, thin film transistors, photovoltaic cells, etc. Papers suitable for publication in this journal cover such topics as photoconductive and electronic properties of organic materials, film growth and characterization, organic electronic and optoelectronic devices, and applications.

As an important Journal **Organic Electronics** can ensure that your most significant research receives the recognition that it deserves. As a unique publication outlet, uniting the various research disciplines involved, it provides the only forum for both applied and fundamental contributions spanning the many different disciplines addressing electronic applications of organic materials.

Advertising information

Advertising orders and enquiries can be sent to: James Kenney, Commercial Sales, Elsevier, 84 Theobald's Road, London WC1X 8RR, United Kingdom; phone: (+44) (20) 7611 4494; fax: (+44) (20) 7611 4463; e-mail: j.kenney@elsevier.com.

Abstracted/indexed in:

Current Contents: Engineering, Technology and Applied Sciences; El Compendex Plus; Engineering Index; INSPEC; Physics Briefs; Science Citation Index, expanded; Chemistry Citation Index; Current Contents: Physics, Chemistry and Engineering Science. Also covered in the abstract and citation database SCOPUS®. Full text available on ScienceDirect®.

Publication information: *Organic Electronics* (ISSN 1566-1199). For 2007, Volume 8 is scheduled for publication. Subscription prices are available upon request from the Publisher or from the Regional Sales Office nearest you or from this journal's website: (http://www.elsevier.com/locate/orgel). Further information is available on this journal and other Elsevier products through Elsevier's website: (http://www.elsevier.com). Subscriptions are accepted on a prepaid basis only and are entered on a calendar year basis. Issues are sent by standard mail (surface within Europe, air delivery outside Europe). Priority rates are available upon request. Claims for missing issues should be made within six months of the date of dispatch.

Orders, claims, and journal enquiries: please contact the Customer Service Department at the Regional Sales Office nearest you:

Orlando: Elsevier, Customer Service Department, 6277 Sea Harbor Drive, Orlando, FL 32887-4800, USA; phone: (877) 8397126 or (800) 6542452 [toll free numbers for US customers]; (+1) (407) 3454020 or (+1) (407) 3454000 [customers outside US]; fax: (+1) (407) 3631354 or (+1) (407) 3639661; e-mail: usjcs@elsevier.com or elspcs@elsevier.com

Amsterdam: Elsevier, Customer Service Department, P.O. Box 211, 1000 AE Amsterdam, The Netherlands; phone: (+31) (20) 4853757; fax: (+31) (20) 4853432; e-mail: nlinfo-f@elsevier.com

Tokyo: Elsevier, Customer Service Department, 4F Higashi-Azabu, 1-Chome Bldg, 1-9-15 Higashi-Azabu, Minato-ku, Tokyo 106-0044, Japan; phone: (+81) (3) 5561 5037; fax: (+81) (3) 5561 5047; e-mail: jp.info@elsevier.com

Singapore: Elsevier, Customer Service Department, 3 Killiney Road, #08-01 Winsland House I, Singapore 239519; phone: (+65) 6349 0222; fax: (+65) 6733 1510; e-mail: asiainfo@elsevier.com

Printed by Krips bv, Meppel, The Netherlands

ELSEVIER